

















**TWENTY-FIFTH ANNUAL REPORT**  
**OF THE**  
**NATIONAL ADVISORY COMMITTEE**  
**FOR AERONAUTICS**

---

**1939**

---

**INCLUDING TECHNICAL REPORTS**  
**NOS. 645 TO 680**



**UNITED STATES**  
**GOVERNMENT PRINTING OFFICE**  
**WASHINGTON: 1940**







## TECHNICAL REPORTS

	Page		Page
No. 645. Correction of Temperatures of Air-Cooled Engine Cylinders for Variation in Engine and Cooling Conditions. By Oscar W. Sehey, Benjamin Pinkel, and Herman H. Ellerbrock, Jr., N. A. C. A.-----	49	No. 659. Effect of Service Stresses on Impact Resistance, X-Ray Diffraction Patterns, and Microstructure of 25S Aluminum Alloy. By J. A. Kies and G. W. Quick, National Bureau of Standards-----	343
No. 646. The Compressibility Burble and the Effect of Compressibility on Pressures and Forces Acting on an Airfoil. By John Stack, W. F. Lindsey, and Robert E. Littell, N. A. C. A.-----	73	No. 660. Experimental Investigation of the Momentum Method for Determining Profile Drag. By Harry J. Goett, N. A. C. A.-----	365
No. 647. Tests of N. A. C. A. 0009, 0012, and 0018 Airfoils in the Full-Scale Tunnel. By Harry J. Goett and W. Kenneth Bullivant, N. A. C. A.-----	97	No. 661. Tests in the Variable-Density Wind Tunnel of the N. A. C. A. 23012 Airfoil With Plain and Split Flaps. By Ira H. Abbott and Harry Greenberg, N. A. C. A.-----	373
No. 648. Design Charts for Predicting Downwash Angles and Wake Characteristics Behind Plain and Flapped Wings. By Abe Silverstein and S. Katzoff, N. A. C. A.-----	107	No. 662. Design of N. A. C. A. Cowlings for Radial Air-Cooled Engines. By George W. Stickle, N. A. C. A.-----	383
No. 649. The "Pack" Method for Compressive Tests of Thin Specimens of Materials Used in Thin-Wall Structures. By C. S. Aitchison and L. B. Tuckerman, National Bureau of Standards-----	133	No. 663. The Effect of Continuous Weathering of Light Metal Alloys Used in Aircraft. By Willard Mutchler, National Bureau of Standards--	395
No. 650. The Aerodynamic Characteristics of Six Full-Scale Propellers Having Different Airfoil Sections. By David Biermann and Edwin P. Hartman, N. A. C. A.-----	145	No. 664. Wind-Tunnel Investigation of an N. A. C. A. 23012 Airfoil With Various Arrangements of Slotted Flaps. By Carl J. Wenzinger and Thomas A. Harris, N. A. C. A.-----	423
No. 651. Downwash and Wake Behind Plain and Flapped Airfoils. By Abe Silverstein, S. Katzoff, and W. Kenneth Bullivant, N. A. C. A.-----	179	No. 665. Calculation of the Aerodynamic Characteristics of Tapered Wings with Partial-Span Flaps. By Henry A. Pearson and Raymond F. Anderson, N. A. C. A.-----	455
No. 652. Air Flow in the Boundary Layer of an Elliptic Cylinder. By G. B. Schubauer, National Bureau of Standards-----	207	No. 666. Aircraft Rate-of-Climb Indicators. By Daniel P. Johnson, National Bureau of Standards--	473
No. 653. A Study of Air Flow in an Engine Cylinder. By Dana W. Lee, N. A. C. A.-----	227	No. 667. Determination of the Profile Drag of an Airplane Wing in Flight at High Reynolds Numbers. By Joseph Bicknell, N. A. C. A.-----	483
No. 654. General Airplane Performance. By W. C. Ruckerfeller, California Institute of Technology-----	241	No. 668. Wind-Tunnel Investigation of N. A. C. A. 23012, 23021, and 23030 Airfoils With Various Sizes of Split Flap. By Carl J. Wenzinger and Thomas A. Harris, N. A. C. A.-----	493
No. 655. The Knocking Characteristics of Fuels in Relation to Maximum Permissible Performance of Aircraft Engines. By A. M. Rothrock and Arnold E. Biermann, N. A. C. A.-----	267	No. 669. Airfoil Section Data Obtained in the N. A. C. A. Variable-Density Tunnel as Affected by Support Interference and Other Corrections. By Eastman N. Jacobs and Ira H. Abbott, N. A. C. A.-----	507
No. 656. The Column Strength of Two Extruded Aluminum-Alloy H-Sections. By William R. Osgood and Marshall Holt, National Bureau of Standards and Aluminum Company of America-----	289	No. 670. Tensile Elastic Properties of 18:8 Chromium-Nickel Steel as Affected by Plastic Deformation. By D. J. McAdam, Jr., and R. W. Mebs, National Bureau of Standards-----	539
No. 657. The Influence of Directed Air Flow on Combustion in a Spark-Ignition Engine. By A. M. Rothrock and R. C. Spencer, N. A. C. A.-----	313	No. 671. A Theoretical Study of the Moment on a Body in a Compressible Fluid. By Carl Kaplan, N. A. C. A.-----	581
No. 658. Tests of Two Full-Scale Propellers With Different Pitch Distributions, at Blade Angles Up to 60°. By David Biermann and Edwin P. Hartman, N. A. C. A.-----	327	No. 672. Free-Spinning Wind-Tunnel Tests of a Low-Wing Monoplane With Systematic Changes in Wings and Tails—IV. Effect of Center-of-Gravity Location. By Oscar Seidman and A. I. Neihouse, N. A. C. A.-----	599

	Page		Page
No. 673. Experimental Verification of the Theory of Oscillating Airfoils. By Abe Silverstein and Upshur T. Joyner, N. A. C. A.-----	619	No. 677. Wind-Tunnel Investigation of an N. A. C. A. 23021 Airfoil With Various Arrangements of Slotted Flaps. By Carl J. Wenzinger and Thomas A. Harris, N. A. C. A.-----	665
No. 674. Cooling on the Front of an Air-Cooled Engine Cylinder in a Conventional Engine Cowling. By M. J. Brevoort and U. T. Joyner, N. A. C. A.-----	625	No. 678. Interference of Tail Surfaces and Wing and Fuselage From Tests of 17 Combinations in the N. A. C. A. Variable-Density Tunnel. By Albert Sherman, N. A. C. A.-----	689
No. 675. Effects of Elevator Nose Shape, Gap, Balance, and Tabs, on the Aerodynamic Characteristics of a Horizontal Tail Surface. By Harry J. Goett and J. P. Reeder, N. A. C. A.-----	639	No. 679. Wind-Tunnel Investigation of an N. A. C. A. 23012 Airfoil With a Slotted Flap and Three Types of Auxiliary Flap. By Carl J. Wenzinger and William E. Gauvain, N. A. C. A.-----	699
No. 676. Surface Heat-Transfer Coefficients of Finned Cylinders. By Herman H. Ellerbrock, Jr., and Arnold E. Biermann, N. A. C. A.-----	651	No. 680. The Effect of Nacelle-Propeller Diameter Ratio on Body Interference and on Propeller and Cooling Characteristics. By James G. McHugh and Eldridge H. Derring, N. A. C. A.-----	727



## LETTER OF TRANSMITTAL

---

TO THE CONGRESS OF THE UNITED STATES:

In compliance with the provisions of the act of March 3, 1915, establishing the National Advisory Committee for Aeronautics, I transmit herewith the Twenty-fifth Annual Report of the Committee covering the fiscal year ended June 30, 1939.

FRANKLIN D. ROOSEVELT.

THE WHITE HOUSE,  
*January 8, 1940.*



## LETTER OF SUBMITTAL

---

NATIONAL ADVISORY COMMITTEE FOR AERONAUTICS,  
*Washington, D. C., December 21, 1939.*

MR. PRESIDENT:

In compliance with the provisions of the Act of Congress approved March 3, 1915 (U. S. C., title 50, sec. 153), I have the honor to submit herewith the Twenty-fifth Annual Report of the National Advisory Committee for Aeronautics covering the fiscal year 1939.

The Committee is proceeding with the design and construction at Moffett Field, California, of a second major aeronautical research station authorized by Act approved August 9, 1939. This will materially augment and strengthen the Committee's facilities for research in aerodynamics.

Attention is invited to the report of the Special Survey Committee on Aeronautical Research Facilities which appears on page two. In furtherance of its recommendations, a Special Committee on Engine Research Facilities is now studying costs and preparing detailed plans for an additional engine research laboratory.

Respectfully submitted.

VANNEVAR BUSH, *Chairman.*

THE PRESIDENT,

*The White House, Washington, D. C.*





NATIONAL ADVISORY COMMITTEE FOR AERONAUTICS

HEADQUARTERS, NAVY BUILDING, WASHINGTON, D. C.

LABORATORIES, LANGLEY FIELD, VA.

Created by act of Congress approved March 3, 1915, for the supervision and direction of the scientific study of the problems of flight (U. S. Code, Title 50, Sec. 151). Its membership was increased to 15 by act approved March 2, 1929. The members are appointed by the President, and serve as such without compensation.

- VANNEVAR BUSH, Sc. D., *Chairman*,  
Washington, D. C.

GEORGE J. MEAD, Sc. D., *Vice Chairman*,  
West Hartford, Conn.

CHARLES G. ABBOT, Sc. D.,  
Secretary, Smithsonian Institution.

HENRY H. ARNOLD, Major General, United States Army,  
Chief of Air Corps, War Department.

GEORGE H. BRETT, Brigadier General, United States Army,  
Chief Matériel Division, Air Corps, Wright Field, Dayton,  
Ohio.

LYMAN J. BRIGGS, Ph. D.,  
Director, National Bureau of Standards.

ROBERT E. DOHERTY, M. S.,  
Pittsburgh, Pa.
- CLINTON M. HESTER, A. B., LL. B.,  
Administrator, Civil Aeronautics Authority.

ROBERT H. HINCKLEY, A. B.,  
Chairman, Civil Aeronautics Authority.

JEROME C. HUNSAKER, Sc. D.,  
Cambridge, Mass.

SYDNEY M. KRAUS, Captain, United States Navy,  
Bureau of Aeronautics, Navy Department.

FRANCIS W. REICHELDERFER, Sc. D.,  
Chief, United States Weather Bureau.

JOHN H. TOWERS, Rear Admiral, United States Navy,  
Chief, Bureau of Aeronautics, Navy Department.

EDWARD WARNER, Sc. D.,  
Washington, D. C.

ORVILLE WRIGHT, Sc. D.,  
Dayton, Ohio.

- GEORGE W. LEWIS, *Director of Aeronautical Research*

S. PAUL JOHNSTON, *Coordinator of Research*

JOHN F. VICTORY, *Secretary*

HENRY J. E. REID, *Engineer in Charge, Langley Memorial Aeronautical Laboratory, Langley Field, Va.*

JOHN J. IDE, *Technical Assistant in Europe, Paris, France*

TECHNICAL COMMITTEES

- AERODYNAMICS

POWER PLANTS FOR AIRCRAFT

AIRCRAFT MATERIALS
- AIRCRAFT STRUCTURES

AIRCRAFT ACCIDENTS

INVENTIONS AND DESIGNS

- Coordination of Research Needs of Military and Civil Aviation*

*Preparation of Research Programs*

*Allocation of Problems*

*Prevention of Duplication*

*Consideration of Inventions*

- LANGLEY MEMORIAL AERONAUTICAL LABORATORY

LANGLEY FIELD, VA.
- OFFICE OF AERONAUTICAL INTELLIGENCE

WASHINGTON, D. C.

Unified conduct, for all agencies, of scientific research on the fundamental problems of flight.

Collection, classification, compilation, and dissemination of scientific and technical information on aeronautics.





JOSEPH S. AMES.

PAST CHAIRMAN, NATIONAL ADVISORY COMMITTEE FOR AERONAUTICS.





NATIONAL ADVISORY COMMITTEE FOR AERONAUTICS.

MEETING, OCTOBER 19, 1939.

Left to right: Brig. Gen. George H. Brett, Army Air Corps; Clinton M. Hester, Administrator, Civil Aeronautics Authority; Rear Adm. John H. Towers, Chief, Bureau of Aeronautics, Navy Department; Dr. L. J. Briggs, Director, Bureau of Standards; Col. Charles A. Lindbergh; Dr. Orville Wright; Dr. J. C. Hunsaker; Dr. George W. Lewis, Director of Aeronautical Research; Dr. Vannevar Bush, Chairman; Dr. George J. Mead, Vice Chairman; John F. Victory, Secretary; Dr. Charles G. Abbot, Secretary, Smithsonian Institution; Dr. Edward P. Warner; Maj. Gen. Henry H. Arnold, Chief, Army Air Corps; Robert H. Hinckley, Chairman, Civil Aeronautics Authority; Capt. S. M. Kraus, U. S. N.; Dr. F. W. Reichelderfer, Chief, United States Weather Bureau



# TWENTY-FIFTH ANNUAL REPORT

## OF THE

# NATIONAL ADVISORY COMMITTEE FOR

# AERONAUTICS

WASHINGTON, D. C., *November 16, 1939.*

TO THE CONGRESS OF THE UNITED STATES:

In accordance with the act of Congress approved March 3, 1915 (U. S. C., title 50, sec. 151), which established the National Advisory Committee for Aeronautics, The Committee submits herewith its Twenty-Fifth Annual Report for the fiscal year 1939.

The most significant event of the past year, in its relation to the future of American aeronautics, was the authorization of a second major aeronautical research station for the Committee. This was recommended by the President in February 1939 and was authorized by the Congress in the Third Deficiency Act approved August 9, 1939. The site finally selected by the Committee under authority of that act is Moffett Field, Calif., located about 38 miles south of San Francisco. The details of this important action are set forth in part II of this report. This additional laboratory will serve to relieve the present congestion of work at the Committee's Langley Field laboratory in Virginia and will provide new research facilities necessary to enable the Committee to provide more effectively for an enlarged volume of research work to support and accelerate the technical development of American aircraft.

During the past year important progress was made in many ways in providing, through the Committee's researches at Langley Field, new knowledge which should be the basis of extensive improvements in our aircraft. Discovery during the past year of a new principle in airplane-wing design may prove of great importance. The transition from laminar to turbulent air flow over a wing was so delayed as to reduce the profile drag, or basic air resistance, by approximately two-thirds. It is too early to appraise adequately the significance of this achievement. So far, its application is limited to small airplanes, but there are indications of its ultimate applicability to larger airplanes through continued research. It should increase the range and greatly improve the economy of airplane operation.

**This country's opportunity.**—The advance of commercial aviation during the past few years has been remarkable. The United States is a country of great expanse, with widely separated centers of population and business activity that will require and support a much larger domestic air transportation system than now exists. Increased economy and reduced dependency upon financial aid from the Government, where such aid still exists, depend on technical progress and improvement in the inherent characteristics of the aircraft used.

The United States was the first to establish regular commercial air transport service over the North Atlantic and the Pacific Oceans. Recent progress in the attainment of a high degree of safety in air transportation is most gratifying in this connection. The long distances between the United States and Alaska, and between the United States and the South American Republics, require faster and more efficient air transportation. The development of commercial transport airplanes of ever-increasing efficiency and safety can be accelerated by investigations in our research laboratories.

**Unprecedented expansion of air power.**—From the standpoint of national defense, the United States is most fortunately situated between two great oceans. However, as advances in aeronautical science result in increased range of aircraft the significance of these oceans will gradually diminish and superiority in aircraft design will become more and more essential to our national safety. The year 1939, prior to the outbreak of the European War, was notable as witnessing unprecedented expansion of air power in many nations. Germany has concentrated much of its scientific and industrial resources on the problem of gaining supremacy in the air. England and France are making every effort in the same direction. Research facilities have been greatly expanded in all the major nations.

**Relation of aeronautical research to national defense.**—The effectiveness of an air force is largely dependent on constant activity in research laboratories necessary to



insure continuous improvement in design and performance of aircraft. Orderly prosecution of comprehensive programs of scientific research is indispensable. It is the function of the National Advisory Committee for Aeronautics to "supervise and direct the scientific study of the problems of flight with a view to their practical solution," and to "direct and conduct research and experiment in aeronautics" in such laboratories as may be placed under its direction. The Committee has for many years exercised these functions, by the direct conduct of research in its own laboratories and also by contractual relations with independent laboratories.

To coordinate the research needs of aviation, civil and military, and to prepare programs of research in the various branches of science affecting aeronautics, the Committee has established four major standing technical subcommittees, on aerodynamics, power plants for aircraft, materials for aircraft, and aircraft structures. There are also other special and subordinate subcommittees. The subcommittees are composed in part of specially qualified representatives of the governmental agencies concerned. The main committee, upon recommendations of subcommittees or upon its own initiative, authorizes research programs. The results of researches are either published or kept secret or confidential, as may be advisable in the national interest, but they are always brought promptly to the attention of the proper parties in the Government and in cooperating industry.

**Enlarged plan for coordination.**—The Committee, in order to exercise more fully its functions, has adopted a program of coordination of research as recommended by a special committee appointed to study that subject. The coordination of research entails for the Committee the duty of maintaining close liaison with all organizations, governmental and private, that operate research facilities. This is for the purpose of providing for the utilization, to the maximum advantage of the United States, of available research facilities in the pursuit of a coordinated program.

The Committee is cooperating with the War and Navy Departments, the Civil Aeronautics Authority, and other agencies of the Government to the fullest extent, to the end that the new facilities now being provided by the Committee and by other governmental agencies shall be of the maximum scope that can be provided with the funds available and of proper balance as to character.

**Necessary expansion of research.**—The year 1940 will mark the twenty-fifth anniversary of the Committee's establishment. As the Committee reviews the effects of scientific research on the progress of aeronautics during the last quarter of a century, it is convinced that the systematic conduct of scientific research is the most fundamental activity of the Government in connection with the development of aeronautics. The

Committee is gratified to have had the confidence and support of the President and of the Congress in the past. The years that lie immediately ahead will be critical years in the development of aeronautics. The Committee's work will need to be carried out on an even broader front and on a larger scale in the immediate future.

Because of the increasing relative importance of aeronautics in national defense and in transportation, the Committee believes that the needs of the country justify a further immediate expansion of research activities in two directions, namely, the establishment of an engine research laboratory, and additional stimulation of aeronautical research in educational and scientific institutions.

With Colonel Charles A. Lindbergh as chairman, Major General Henry H. Arnold, Chief of the Army Air Corps, Rear Admiral John H. Towers, Chief of the Bureau of Aeronautics, Navy Department, and Honorable Robert H. Hinckley, Chairman of the Civil Aeronautics Authority, have served as a Special Survey Committee on Aeronautical Research Facilities. That committee, under date of October 19, 1939, submitted a report to the National Advisory Committee for Aeronautics as follows:

#### REPORT OF THE SPECIAL SURVEY COMMITTEE ON AERONAUTICAL RESEARCH FACILITIES

In accordance with the directions to this special committee to "examine into the aeronautical research facilities now available in the country and their best interrelationship, and to prepare a comprehensive plan for the future extension of such facilities, with especial attention to facilities of the N. A. C. A. and the universities," the following report is submitted, supplementing the committee's previous reports.

As a result of its studies, this committee finds that there is a serious lack of engine research facilities in the United States, and that it is of the utmost importance for the development of aviation in general, and for our defense program in particular, to take immediate steps to remedy this deficiency.

This committee, therefore, urgently recommends that an engine research laboratory be constructed at the earliest possible date, in a location easily accessible to the aircraft-engine industry.

In making this recommendation, the committee wishes to call attention to the fact that the reason for foreign leadership in certain important types of military aircraft is due in part to the superiority of foreign liquid-cooled engines. At the present time, American facilities for research on aircraft power plants are inadequate and cannot be compared with the facilities for research in other major fields of aviation.

This committee also recommends that an investigation be made of the engine research facilities which may be available at universities and other scientific organizations, with a view to coordinating these facilities and encouraging their most effective use. The committee is more than ever impressed with the desirability of using to the fullest possible extent the research facilities available in universities and other scientific organizations. The committee believes that the proper use and coordination of these facilities is one of the most



important functions that can be carried on by the National Advisory Committee for Aeronautics.

The foregoing report was unanimously approved at a full meeting of the National Advisory Committee for Aeronautics. To start action on the first recommendation, a Special Committee on Engine Research Facilities was immediately organized under the chairmanship of Dr. George J. Mead, Vice Chairman of the main Committee, and instructed to submit to the main committee a final report with detailed plans.

The Committee had anticipated the second recommendation by including in its regular estimate for the ensuing year an additional amount for research in educational and scientific institutions. This is enlarging the procedure which the Committee has followed since its beginning. In recent years the facilities of educational institutions for conducting research in aeronautics have increased and there is now an opportunity for much greater effectiveness in accelerating progress by substantially enlarging the Committee's employment of these facilities. The Committee cannot too strongly urge the importance of the proposed appropriation, for not only will it yield direct results in the form of new contributions to knowledge along a variety of lines for which the facilities and personnel of such institutions are well adapted, but it will also result in the training of research workers in aeronautics for the benefit alike of the governmental services and of the industry.

Quite as important as liberal appropriations for any aeronautical purpose is the adoption of a farsighted policy to develop trained technical personnel. The Committee believes that the stimulation of aeronautical research in scientific and educational institutions, as proposed, is the most effective and, incidentally, the most economical way to develop in larger numbers and in a democratic manner the talented individuals having the scientific training necessary to engage successfully in what has become an international competition.

**Resignation of Dr. Joseph S. Ames, Chairman.**—On October 7, 1939, Dr. Joseph S. Ames resigned as member and Chairman of the National Advisory Committee for Aeronautics, because his physical condition would not permit him to "take a sufficiently active part in the great work that confronts the Committee."

Dr. Ames was the last of the original members of the Committee appointed by President Wilson in 1915. He had been reappointed in 1938 by President Roosevelt for a 5-year term. For 17 years he was Chairman of the Executive Committee (1919–36), and for 12 years he was Chairman of the main Committee (1927–39). His long service included 8 years as Chairman of the Committee on Aerodynamics (1919–27) and the chairmanship of other important subcommittees, and also of the annual engineering research conferences

with the aircraft industry, and of the special conferences on nomenclature for aeronautics held in 1920, 1922, 1925, and 1933. In 1923, he delivered the Wilbur Wright Memorial lecture before the Royal Aeronautical Society of Great Britain on the subject, "The Relation Between Aeronautical Research and Aircraft Design."

In 1935 Dr. Ames was awarded the Langley Gold Medal by the Board of Regents of the Smithsonian Institution "in recognition of the surpassing improvement of the performance, efficiency, and safety of American aircraft resulting from fundamental scientific researches conducted by the National Advisory Committee for Aeronautics under the leadership of Dr. Ames."

Dr. Ames, while serving as professor of physics and later as president of the Johns Hopkins University at Baltimore, Md., had devoted himself unsparingly to the work of the Committee without compensation or thought of reward. The President of the United States, in accepting his resignation on October 10, 1939, wrote as follows:

THE WHITE HOUSE,  
Washington, October 10, 1939.

Dr. JOSEPH S. AMES,  
*Guilford, Baltimore, Md.*

MY DEAR DR. AMES: It is with sincere regret that I accept your resignation as a member of the National Advisory Committee for Aeronautics, submitted because of your physical inability to take an active part in the Committee's work at this critical time.

Our Republic would not be worthy of the devoted service you have rendered for over 24 years without compensation if it could not on this occasion pause to pay tribute where it is so justly due.

When you were first appointed by President Wilson in 1915, very little was known about the science of aeronautics. To you and to your colleagues were entrusted by law the supervision and direction of the scientific study of the problems of flight. For the past 20 years you have served as Chairman of the National Advisory Committee for Aeronautics, or Chairman of its Executive Committee. The administration and the accomplishments of the Committee under your leadership reflect your great scientific attainments, professional courage, and executive ability.

That the people generally have not known of your brilliant and patriotic service is because it has been overshadowed by your passion for accomplishment without publicity. But the fact remains, and I am happy to give you credit for it, that the remarkable progress for many years in the improvement of the performance, efficiency, and safety of American aircraft, both military and commercial, has been due largely to your own inspiring leadership in the development of new research facilities and in the orderly prosecution of comprehensive research programs.

I wish you many years of peace and contentment in which to enjoy the satisfaction that should be yours as you view the continuing results of your labors.

Very sincerely yours,

FRANKLIN D. ROOSEVELT.

The limitations of a public document preclude the presentation of a full account of Dr. Ames' contribu-



tions to the advancement of the science of aeronautics. In view of his outstanding record of public service, it is deemed appropriate to publish the fact that at a full meeting of the National Advisory Committee for Aeronautics held in Washington, D. C., on October 19, 1939, at which the resignation of Dr. Ames was announced, by unanimous rising vote of the members, the following testimonial to Dr. Ames was adopted:

*Resolved*, That the members of the National Advisory Committee for Aeronautics do adopt and approve the following tribute to their distinguished past Chairman:

For over 20 years Dr. Ames has served as Chairman of the National Advisory Committee for Aeronautics or as chairman of its executive committee. His long service leaves upon the organization the indelible imprint of his character. He is not only a great scientist, he is a great man, and we are proud to have been associated with him.

When aeronautical science was struggling to discover its fundamentals, his was the vision that saw the need for novel research facilities and for organized and sustained prosecution of scientific laboratory research. His was the professional courage that led the Committee along new scientific paths to important discoveries and contributions to progress that have placed the United States in the forefront of progressive nations in the development of aeronautics. His was the executive ability and farsighted policy of public service that, without seeking credit for himself or for the Committee, developed a research organization that holds the confidence of the governmental and industrial agencies concerned and commands the respect of the aeronautical world. Withal, Dr. Ames was an inspiring leader of men and a man beloved by all his colleagues because of his rare personal qualities.

Dr. Ames' retirement from active duty because of his physical inability to carry on is sincerely regretted by all who know of his unparalleled service to American aeronautics.

*Resolved further*, That the Chairman be authorized to appoint a special committee to present this testimonial to Dr. Ames with our heartfelt thanks for all that he has done for the Committee and with our sincere wishes that he may be spared for many years to witness in peace and contentment the continuing fruits of his labors.

The foregoing testimonial to Dr. Ames was engrossed and signed by all the members of the Committee. It

was presented to Dr. Ames at his residence in Baltimore on October 23 by a special committee composed of Dr. Edward Warner, Chairman; Dr. Vannevar Bush, Dr. Lyman J. Briggs, Dr. George W. Lewis, and Mr. John F. Victory. Dr. Warner made the presentation with appropriate expression of the great admiration and esteem in which Dr. Ames is held by all members of the Committee.

**Recommendations.**—The Committee urgently recommends that it be authorized to construct an engine research laboratory at the earliest possible date in a location easily accessible to the aircraft-engine industry. The Special Survey Committee on Aeronautical Research Facilities, as a result of its studies, found "that there is a serious lack of engine research facilities and that it is of the utmost importance for the development of aviation in general, and for our defense program in particular, to take immediate steps to remedy this deficiency." That special committee called attention to the fact that the reason for foreign leadership in certain important types of military aircraft is due in part to the superiority of foreign liquid-cooled engines, and added that "at the present time American facilities for research on aircraft power plants are inadequate and cannot be compared with the facilities for research in other major fields of aviation." Detail studies are being made by the Special Committee on Engine Research Facilities, which will probably develop plans for the construction of an engine research laboratory on a site to be selected by the Committee.

The Committee's regular estimates of appropriations for the fiscal year 1941 include an increased appropriation for the stimulation of aeronautical research in scientific and educational institutions by contracting for research in these institutions supplementing research in Government laboratories. It is strongly recommended that this be approved.



## PART I

### REPORTS OF TECHNICAL COMMITTEES

---

In order to carry out effectively its principal function of the supervision, conduct, and coordination of the scientific study of the problems of aeronautics, the National Advisory Committee for Aeronautics has established a group of technical committees and subcommittees. These technical committees prepare and recommend to the main Committee programs of research to be conducted in their respective fields, and as a result of the nature of their organization, which includes representation of the various governmental agencies concerned with aeronautics, they act as coordinating agencies, providing effectively for the interchange of information and ideas and the prevention of duplication.

In addition to its standing committees and subcommittees, it is the policy of the National Advisory Committee for Aeronautics to establish from time to time special technical subcommittees for the study of particular problems as they arise.

The Committee has four principal technical committees—the Committee on Aerodynamics, the Committee on Power Plants for Aircraft, the Committee on Aircraft Materials, and the Committee on Aircraft Structures. Under these committees there are six standing subcommittees. The membership of these technical committees and subcommittees is listed in part II.

The Committees on Aerodynamics and Power Plants for Aircraft prepare the programs for, and keep in touch with, the aerodynamic and aircraft-engine research, respectively, conducted at the Committee's laboratory at Langley Field, and of special investigations conducted at the National Bureau of Standards. Most of the research under the cognizance of the Committee on Aircraft Materials is conducted by the National Bureau of Standards. A large part of the research under the cognizance of the Committee on Aircraft Structures is carried on by the National Bureau of Standards. In addition, a number of structural investigations, including in particular investigations of a theoretical nature, are conducted at the Committee's laboratory at Langley Field and at educational institutions.

The four technical committees recommend to the main Committee the investigations in their respective fields to be undertaken by educational institutions un-

der contract with the National Advisory Committee for Aeronautics, and keep in touch with the progress of the work and the results obtained. The experimental investigations in aerodynamics, aircraft power plants, aircraft materials, and aircraft structures undertaken by the Army Air Corps, the Bureau of Aeronautics of the Navy, the National Bureau of Standards, and other Government agencies are reported to these four committees.

#### REPORT OF COMMITTEE ON AERODYNAMICS

##### LANGLEY MEMORIAL AERONAUTICAL LABORATORY

###### LANDING SPEED AND SPEED RANGE

The emphasis now being placed on the high-speed performance of military airplanes is resulting in marked increases in wing loadings and is creating a strong demand for improved high-lift devices. To meet this demand, the Committee has been devoting increasing effort to the investigation of the more promising types of partial- and full-span flaps.

The investigation of wings with slotted flaps in the 7- by 10-foot wind tunnel has been extended to include airfoils having thickness ratios of 21 and 30 percent. For the airfoil of 21-percent thickness (Technical Report No. 677), the maximum lift coefficient obtained with the best slotted flap was about the same as for the airfoil of 12-percent thickness (Technical Report No. 664). With the 30-percent-thick airfoil, however, the maximum lift coefficient obtained was about 10 percent less with the best slotted flap than for the thinner airfoils. The drag for a given lift coefficient increased with airfoil thickness; therefore, the best speed-range ratio was obtained with the thinnest airfoil. The investigation has also been extended to cover wide-chord slotted flaps on airfoils of the three thicknesses. Results of tests of the N. A. C. A. 23012 and 23021 airfoils with 40-percent-chord flap (Technical Notes Nos. 715 and 728) showed no appreciable gain in maximum lift coefficient over the 25-percent-chord flap. The thicker airfoil had a considerably higher drag coefficient.

The results of an investigation in the 7- by 10-foot wind tunnel of a multiple-flap arrangement mentioned



in the last annual report have been published as Technical Report No. 679. The investigation of double-slotted flaps has been extended to flaps of wider chord and to airfoils of different thicknesses.

Tests have been made in the 7- by 10-foot wind tunnel on a rectangular and a tapered N. A. C. A. 23012 wing with partial-span slotted flaps. The results of these tests, published in Technical Note No. 719, are similar to the results on the partial-span plain and split flaps previously reported; greater increments of maximum lift were obtained with the slotted flaps.

An investigation has been made (Technical Note No. 699) in the 7- by 10-foot wind tunnel on a slotted deflector-plate flap on an N. A. C. A. 23012 airfoil. This flap gave on this airfoil a somewhat lower maximum lift coefficient than the best slotted flap of the same chord.

Tests have also been made in the 7- by 10-foot wind tunnel of split flaps of 10-, 20-, 30-, and 40-percent chord on N. A. C. A. 23012, 23021, and 23030 airfoils. The results of these tests have been published in Technical Report No. 668. It was found that the final maximum lift coefficients for the three airfoils with 20-percent-chord flaps were equal; for airfoils with 10-percent-chord flaps the maximum lift coefficient decreased with airfoil thickness; and for the flaps of 30- and 40-percent chord, the maximum lift coefficient increased with airfoil thickness.

Data dealing with the air loads on flaps and slats have been collected from various sources, correlated, and published as Technical Note No. 690.

#### CONTROL AND CONTROLLABILITY

**Variation of control effectiveness with airplane size.**—During the past year investigations of the flying qualities of a number of airplanes, ranging in weight from 4,500 to 70,000 pounds, have provided considerable data on the variation of control effectiveness with airplane size. With regard to the aileron control, the reduction in effectiveness with increased wing span, as indicated by the maximum rolling velocity, was found to be greatly in excess of that indicated by the theoretical relationship because of the large aileron hinge moments and the excessive stretch of the control cable. These characteristics prevented the pilot from using what would normally be full aileron and in one instance imposed a severe limit on the aileron control at high speeds. The need for improvement in design to permit full deflection of the ailerons was indicated.

Many of the airplanes investigated displayed strong tendencies to turn in the direction of a low wing following a disturbance from laterally level flight, with resulting difficulty in maintaining a straight course in rough air. In certain instances yawing occurred against full rudder with the wing down less than 5°.

As a result of this characteristic, increased demands were made on the ailerons to maintain the wings level.

The effectiveness of the elevator and the rudder controls was adequate in all the machines tested.

**Lateral controls for use with full-span flaps.**—Because of the inadequacy of partial-span flaps on airplanes with the high wing loadings now contemplated, the development of an acceptable lateral-control device for use on wings employing high-lift devices over the entire span will be necessary.

An investigation has been made in flight (Technical Note No. 714) of retractable ailerons on a wing of 5:1 taper equipped with full-span plain flaps. Although the lateral control obtained with this particular installation was considered inadequate, the deficiency can apparently be ascribed to the fact that the aileron span amounted to only 33 percent of the wing span. With conventional ailerons of approximately the same span, mounted on the same wing, the airplane was equally deficient in lateral control. The lack of an appreciable stick force required to operate the retractable ailerons was considered too small to be desirable for a small airplane, although these ailerons appeared to be satisfactory in other respects.

The investigation in the 7- by 10-foot wind tunnel of lateral-control devices to be used in conjunction with full-span flaps has been continued. The equipment has been modified to make possible a more accurate determination of the time-response characteristics of the various devices than was heretofore possible. Comparative tests have been made on a large variety of devices on plain wings and on wings with full-span split and slotted flaps. The static rolling and yawing moments were determined for all the devices, and the time-response and the hinge moments were determined for most of the devices.

In recent investigations two lateral control systems have been developed for use with full-span flaps, both of which appear to offer promise for successful application.

#### STABILITY

The investigation of flying qualities has contributed much information on the stability of existing airplanes. Several points of general weakness have been noted and are being carefully studied. All the airplanes tested have displayed a tendency to spiral with the controls free. The situation is not considered serious, but complete stability is believed to be a desirable if not an essential characteristic when the requirements do not conflict with those of other essentials. In this connection, it has been noted that irreversible controls or a great amount of control friction are not remedies. When such measures were used, the lack of self-centering action of the controls masked the inherent



stability characteristics of the airplane and always produced a condition of apparent instability.

Many of the airplanes would be improved by increased directional stability. In one case a large diving moment was found to occur when the airplane was yawed. This characteristic, together with nearly neutral directional stability, resulted in frequent changes in longitudinal trim and a general feeling of uncertainty on the part of the pilot. Increased vertical fin area increased the steadiness of this airplane.

Observations of the angles of bank and the accompanying angles of yaw during steady sideslips have indicated a general inability of modern airplanes to develop cross-wind force. As a result of this characteristic, the pilot can judge the severity of a sideslip only by the rudder force and, where the directional stability of the airplane is small, large angles of yaw may be unknowingly attained. In some cases it was found relatively easy to obtain such large angles of yaw that the vertical tail stalled and directional instability was produced. This condition is to be avoided, particularly in large airplanes, in view of the large rudder forces required to regain control.

As a class, the low-wing monoplanes tested have been undesirably weak in longitudinal stability. The midwing and the high-wing monoplanes have exhibited somewhat more satisfactory characteristics, particularly at low speeds, where an increasing degree of stability is desired as a stall warning. None of the airplanes, however, has been completely satisfactory in this respect.

Several studies dealing with the stability of the complete airplane are still in progress. An analysis of the relationship between the longitudinal-control characteristics and the elevator-control effectiveness is practically complete, and a report on the subject will be shortly prepared. The analysis indicates that although the elevator force required for steady flight varied directly with the degree of stability, the force required to produce speed changes decreased only 50 percent when the center of gravity was moved rearward 15 percent of the wing chord to the position that gave zero stability. The investigation of lateral stability with the automatic pilot is also nearing completion. Charts have been drawn to show the correlation of rudder and aileron mechanisms for stability. These data are being prepared for publication.

The function of the rudder and the manner in which this control is influenced by the degree of lateral stability are being investigated. Several tentative criteria have been formulated that when completed may be used directly in design.

A model has been built and tests have started with the gust-tunnel apparatus to determine the effect of

longitudinal stability on the structural loads due to gusts.

Research has been continued on the influence of the design variables on the stability derivatives. The effect of yaw on the lateral-stability characteristics of four N. A. C. A. 23012 wings tested in the 7- by 10-foot wind tunnel is described in Technical Note No. 703. The wing variables investigated were taper, sweep, dihedral, and flap deflection. Technical Note No. 730 describes the effect on the stability characteristics of the position of a rectangular N. A. C. A. 23012 wing when combined with a circular fuselage. The wing was tested in three positions—high, mid, and low. The difference between the high and the low positions was approximately equivalent to 5° dihedral.

Tests have also been made in the 7- by 10-foot wind tunnel to obtain an indication of the difference between single and twin vertical tail surfaces as regards their contribution to the static directional and control forces.

In order to aid in the design of horizontal tail planes for longitudinal stability, a large number of stream-angle and dynamic-pressure surveys have been made in the wake of airfoils and wings of airplane models and airplanes. These data have been correlated with theory. The downwash angles computed from the theoretical span load distribution were found to be in satisfactory agreement with the experimental results. It was also found that by theoretical treatment the wake characteristics can be predicted in terms of distance behind the trailing edge of the wing and the profile-drag coefficient of the wing. The results of this work are presented in Technical Report No. 651.

Technical Report No. 648 presents graphs from which the airplane designer may readily determine the downwash angle in the tail-plane region for elliptical and tapered wings within a practicable range of aspect ratios and with various flap arrangements. Charts and formulas are also included for evaluating the wake width and the velocity distribution in the wake.

The designer has been provided with information on the aerodynamic characteristics of tail planes by an extensive series of tests made on an isolated tail plane in the full-scale tunnel. The effects of various types of elevator nose shape, amount of elevator balance, and gap between the elevator and the stabilizer were investigated. In addition to the usual force-test results, determinations were made of the elevator hinge moment for all conditions, including the use of various sizes of tab. Technical Report No. 675 presents these data.

Further information on the aerodynamic characteristics of the tail surfaces is being furnished by the measurement of section characteristics in the 4- by 6-foot wind tunnel. The test program calls for the systematic variation of elevator or rudder chord and a detailed study of different means of balancing the hinge mo-



ments. The first phase of the work, consisting of pressure distribution tests of an N. A. C. A. 0009 airfoil with three sizes of unbalanced movable surfaces each with three sizes of tabs, is well advanced. One paper on the subject has been prepared for publication.

During the past year, the laboratory facilities for the study of stability have been augmented by the completion of a new 12-foot free-flight wind tunnel. The construction of this tunnel completes the development of the free-flight type of tunnel that has been in progress for several years. In this type of wind tunnel, a model is flown by remote control free from any restraint. Continuous observations may be made by a stationary observer of the inherent and the controlled stability, the motion in gusty air, the stalling characteristics, and many other factors directly related to the free-flight behavior of the airplane. Preliminary investigations on the stability of two service airplanes conducted in the model of the tunnel used for development work have indicated that the 12-foot free-flight tunnel offers a useful, rapid, and relatively inexpensive means for the study and the correction of the stability and the handling characteristics of new airplane designs. The 12-foot tunnel is being calibrated, and testing will shortly be started.

#### SPINNING

The determination, and improvement where needed, of the spinning characteristics of new service airplane designs in the 15-foot free-spinning wind tunnel have been continued. During the past year the characteristics of five specific designs were inspected. As usual, the findings in these investigations were immediately transmitted to the service organizations concerned. The Committee, however, has also compiled and analyzed all such data in the files. As a result of this analysis, an empirical spin criterion has been formulated that can be used in design by laying out the tail surfaces for the most favorable spin-recovery characteristics. The criterion has been presented in Technical Note No. 711.

A further analysis of the data from routine tests has been made in an attempt to obtain a more complete understanding of the action of the ailerons in a spin and during the recovery. The effect of the ailerons was found to be intimately related to the mass distribution of the airplane. With a knowledge of the mass distribution, it is now possible to predict whether the ailerons should be set for or against the spin for most rapid recovery. The possibility of using the ailerons with an abnormal displacement as an antispin device has also been investigated. A paper on the subject is now in preparation.

The reliability of the information on spinning characteristics obtained from the free-spinning tunnel is a matter of some concern. The Committee, with the cooperation of the services, now receives information

on the spinning characteristics of full-scale airplanes the models of which have been previously tested in the tunnel. A comparison of considerable full-scale data with the model data indicated that the wind-tunnel data correctly predicted the full-scale spinning characteristics in 80 percent of the cases. In 10 percent of the cases, the tunnel results were conservative. In only 10 percent of the cases did the model results give an optimistic prediction of the recovery of the corresponding airplanes. Ways of improving the reliability of the tunnel are being considered.

One evident contributing factor to the difference between the model and airplane characteristics is the low scale of the model tests. The influence of scale is being studied in a limited range by comparison of two different-size models of the same airplanes.

The investigation of the relative importance of wing arrangement, tail arrangement, and mass distribution on the spinning characteristics of low-wing monoplanes, started 2 years ago, has been completed. Reports have been published dealing with the effect of changing the relative distribution of mass along the wings and the fuselage and of changing the fore-and-aft position of the center of gravity (Technical Report No. 672). A report dealing with the effect of relative density of the airplane, or its equivalent, the altitude of the spin, is in preparation. Data on the final phase of the work, the effect of a percentage change in the radii of gyration about all three axes, are now being analyzed.

#### STALLING

The investigation of the stall of an airplane and of the means of improving it has been continued. In conjunction with the investigation of flying qualities, inspection is being made of the stalling characteristics of existing airplanes. It has been found that tip stalling is not always entirely responsible for undesirable characteristics. One airplane, for example, that rolled violently when stalled with flaps up was observed to settle with some degree of lateral control when the flaps were extended, even though tuft observation showed that tip stalling was accentuated with the flaps extended. The development of the stall with the flaps extended was sufficiently symmetrical so that no large lateral disturbances occurred.

Of the airplanes tested, those that possessed strong longitudinal stability were rated by the Committee's pilots as having the best stalling characteristics. In these airplanes, where the stall was produced only as a result of a definite forceful use of the elevator control, the stall was robbed of the element of surprise. Under these conditions, the undesirable character of the stall appeared much relieved.

Despite the contributing effects of other factors as shown by the flight tests, the wing characteristics con-



tinued to remain the chief factor in the stalling problem. Several projects are in progress dealing with this phase of the problem. The investigation in the variable-density wind tunnel mentioned in last year's report to determine the relative efficiency of various methods, such as twist, change of section, and change of camber, for the prevention of tip stall is well advanced. Technical Note No. 713 has been published presenting a comparison of several tapered wings in the design of which these methods are employed to avoid tip stalling. It is concluded that for aerodynamic equality and no tip stall, ratios of tip chord to root chord of between one-third and one-half will give the lightest wings. The analysis on which the paper is based is now being extended to obtain general design charts dealing with the stalling of tapered wings. The tests to determine the spanwise progress of the stall of several representative wings with different amounts of taper and sweep have been completed, and the analysis of the results has been started.

If the stalling of the wing tip of a highly tapered wing can be delayed to a higher angle of attack than that of the center section, the lateral stability and the useful maximum lift coefficient of the wing will be greatly improved. One effective method of accomplishing this end is the incorporation of slots in the tip portion of the wing. Tests have been made in the 7- by 10-foot wind tunnel of an N. A. C. A. 23012 airfoil with and without a slotted flap to develop fixed slots that can be employed to increase the useful range of angles of attack. The results of these tests (Technical Note No. 702) show the best position of the slot to be near the leading edge of the airfoil. One arrangement of the fixed slot increased the angle of attack for maximum lift  $11^\circ$  for the plain wing and  $10^\circ$  for the wing with the slotted flap. The chief disadvantage of the fixed slot was the increase in drag at low lift coefficient.

Technical Note No. 670 has been published describing the mechanical stall-warning device discussed in the last annual report.

#### MANEUVERABILITY

The investigation of the maneuverability of Navy airplanes has been continued, and tests on the third and the fourth airplanes of the series have been completed. Originally undertaken to determine the maximum angular accelerations to which an airplane might be subjected, the investigation has now been extended to include studies of the effect of unorthodox manipulation of control stick and tabs.

Flight investigations of the maneuverability of several Army pursuit airplanes have also been completed during the past year. The results have shown that from the pilot's viewpoint maneuverability is greatly affected by the characteristics of the longitudinal control. Airplanes possessing neutral or slight longitudinal stability, and consequently very little control move-

ment to offset large changes of angle of attack, were found to be subject to inadvertent stalling in accelerated maneuvers.

#### TAKE-OFF

The important factors influencing the take-off performance of an airplane are wing loading and power loading. These factors are ordinarily prescribed by the high-speed flight condition and cannot be modified to decrease the take-off run. Consequently, the most practical solution to the problem of improving take-off performance appears to lie either in the development of better high-lift devices for use during take-off or in the improvement of the characteristics of propellers operating under take-off conditions.

During the past year the Committee has conducted two propeller investigations that provide data having a direct bearing on the take-off problem. The results of the first of these investigations, published in Technical Report No. 650, include data from tests of full-scale propellers in the propeller-research tunnel indicating the effect of airfoil section on take-off efficiency. The second investigation, which was made on the special static-thrust apparatus mentioned last year, supplied data on the static thrust of full-scale propellers. These data should prove useful in estimating the distance required for take-off.

#### LANDING

The investigation of the landing characteristics of airplanes to obtain statistical information on the vertical velocities and accelerations in landings has been continued. The evaluation of the data obtained in the tests mentioned in the last annual report has been completed, and the results have been reported to the Army Air Corps and to the Bureau of Aeronautics, Navy Department. Tests of four additional airplanes, including one equipped with a tricycle landing gear, have been made. The results for three of these airplanes have already been reported to the Civil Aeronautics Authority, the Army Air Corps, and the Bureau of Aeronautics, Navy Department. A number of one-wheel landings were included in the tests of one airplane to obtain information concerning the effect of the lateral landing attitude of the airplane with respect to the landing surface upon the maximum loads sustained by the landing gear.

In addition to landing tests involving conventional landings, an investigation has been made of vertical velocities and attitudes and of the resulting landing-gear loads encountered in blind or instrument landings of Army bombers of two different types. The results obtained with one type of bomber have been reported to the Army Air Corps and a report on the results for the other type has been prepared. The maximum vertical velocities in such landings were found to be twice as great as the maximum values for normal landings.



The results of the landing tests made thus far with airplanes equipped with tricycle landing gears have indicated that the maximum nose-wheel loads are likely to be encountered in approximately three-point landings. Nose-wheel loads encountered in two-point landings, wherein the airplane pitches forward after impact on the main wheels, are not likely to be critical.

By use of the apparatus mentioned in the last annual report, tests have been conducted for the purpose of determining the friction required to prevent the shimmy of a castering wheel. Various wheels and tires were tested under varying loads and with varying caster lengths and spindle angles. One interesting feature of the results was that they indicated the desirability of making the inclination of the spindle small. A report presenting the results of these tests is being prepared for publication.

The investigation of ground effect by means of a glider towed by an automobile, which was mentioned in the last annual report, has been completed and the results are being prepared for publication. For most of the conditions tested, which included full-span flaps, the agreement between the experimental results and the ground-effect theory, as regards effects on angle of attack and drag, was reasonably good.

Tests to determine the ground effect on the aerodynamic characteristics of rectangular and tapered wings, both with and without split and slotted flaps, have also been made in the 7- by 10-foot wind tunnel. In these tests the ground was simulated by the use of a plane located various distances from the model. It was found (Technical Note No. 705) that the ground effect on wings with flaps is a marked decrease in drag, a decrease in diving moment, and a substantial reduction in maximum lift.

#### AIRFOILS

**Section characteristics.**—In the last annual report there was considerable discussion of attempts to correlate and reconcile the airfoil data obtained from various sources. Methods of correcting the standard characteristics of airfoil sections determined from tests in the variable-density wind tunnel to allow for turbulence, strut interference, and other features had been evaluated, and the results were published in Technical Report No. 669. In spite of these efforts, however, the situation was unsatisfactory and new methods of making airfoil studies seemed necessary. The presence of turbulence in wind-tunnel air streams had long been a source of trouble and uncertainty and the transition from laminar to turbulent flow was known to be affected by this turbulence in the stream.

At the same time, increasing knowledge of boundary-layer phenomena had given strong indications of the possibility of more extensive laminar boundary

layers and consequent lower drags than have been available with conventional airfoil sections. At least two facts were outstanding: First, airfoils should be designed to take advantage of true low-drag laminar boundary layers over a greater portion of the airfoil; and, second, a nonturbulent air stream as nearly comparable as possible with free-air conditions should be provided to test the new airfoil shapes.

The procurement of such equipment was begun some time ago by the Committee and about a year ago a low-turbulence wind tunnel became available. This tunnel, which is somewhat unusual in design, has a test section 3 by 7½ feet, and is arranged for the testing of large models having chords of several feet and only 3-foot span in essentially two-dimensional flow. The usual methods of measuring the stream turbulence were not considered sufficiently sensitive; direct comparisons of transition on airfoils from measurements in flight, in the new wind tunnel, and in other tunnels, were therefore made. The turbulence level of the new tunnel was found to be well below the level of other wind tunnels of the Committee; nevertheless, it seemed improbable that the desired effective zero turbulence had been attained. It was considered sufficiently low, however, pending more reliable comparisons with flight, to justify some preliminary investigations.

These preliminary investigations were started by the development of new airfoil forms that, when tested in the new equipment, immediately gave drag coefficients of one-third to one-half the values obtained for conventional sections. These studies have been extended to the 8-foot high-speed tunnel and to flight with substantial agreement as to the possibilities of the new airfoils. This work is being continued both in flight and in the low-turbulence tunnel. Extension of this work into the field of compressible flow is being carried on in the 24-inch and 8-foot high-speed wind tunnels.

**Wing characteristics.**—The calculation of wing characteristics has been continued, and the methods and results of comparisons with tests which included wings with partial-span flaps have been presented in Technical Report No. 665. It now seems that the knowledge of the section characteristics is sufficient to make possible the determination, with an accuracy sufficient for many practical purposes, of the important wing characteristics for any particular wing design. Efforts in airfoil work may now be concentrated on the determination of accurate section characteristics.

**Surface roughness.**—The results of tests mentioned in the 1937 annual report showing the effects on wing drag of countersunk and protruding rivet heads, of spot welds, of several types of lapped joints, of surface roughness, and of manufacturing irregularities have been supplemented by data from additional tests and



published in Technical Note No. 695. This note suggests a method of estimating the effects of rivet heads and lapped joints for conditions outside the range of the tests with respect to Reynolds Number or rivet and lap size and arrangement. The method depends on estimating separately the drag increments due to premature transition and to the direct drag of the irregularities. As an example, it is shown that a typical arrangement of rivets and lapped joints on the rear 75 percent of the wing of a large airplane which has a total wing area of 3,600 square feet flying at 250 miles per hour will increase the drag sufficiently to require 180 horsepower more than would be necessary if the wing were smooth.

Additional irregularities investigated have included surface waviness and rib stitching. (See Technical Note No. 724.) The results of the tests of waviness may be simply summarized. Small waves such as occur on wings made according to present standards of workmanship will not seriously increase the drag unless they precipitate premature transition or premature compressibility effects; that is, unless they occur on the forward part of the wing. A single wave only 0.020 inch high and 3 inches wide located 10.5 percent of the chord from the leading edge of an N. A. C. A. 23012 airfoil was sufficient to cause transition to occur at the wave with a consequent drag increase. Rib stitching corresponding to a rib spacing of 6 inches increased the drag 7 percent; the drag increment was proportional to the number of ribs for larger rib spacings. About one-third of the drag increase was due to the premature occurrence of transition at the forward ends of the stitching.

#### AERODYNAMIC INTERFERENCE

For several years the Committee has been conducting in the variable-density wind tunnel a general investigation of fundamental character into the aerodynamic interference between the component parts of airplanes. The initial part of the investigation, described in Technical Report No. 540, comprised tests of 209 combinations of wing and fuselage, in which the variables studied included form of wing, shape of fuselage, position of wing relative to fuselage, and form of wing-fuselage juncture. Subsequent reports dealt with more complete investigations of the same variables and with an extension of the program to study the interference associated with tail surfaces added to wing-fuselage combinations (Technical Report No. 678). The general investigation is now nearing completion with a program of tests of nacelles in combination with a round fuselage, a tapered wing, and conventional arrangement of semielliptical tail surfaces. Two sizes

of streamline nacelles and one of conventionally cowed nacelles are being investigated. Although the program is not yet completed, the results thus far indicate that the adverse interference of streamline nacelles of moderate size on the maximum lift is difficult to control. Further, the drag increase is appreciable and strengthens the conclusion that high-performance airplanes should comprise the minimum number of efficient component parts, efficiently combined. It is therefore desirable that nacelles be eliminated in airplane design.

An extensive investigation of a similar nature but including also the effects of propellers is in progress in the full-scale wind tunnel. An investigation is now under way on a complete airplane model for the purpose of evaluating the effects of air-cooled engine nacelles of the conventional type with N. A. C. A. cowlings over a large range of design conditions. The sizes and numbers of nacelles correspond to arrangements on large four-engine and small high-powered two-engine airplanes. The ratio of nacelle diameter to wing thickness is varied from 0.5 to nearly 4.0 and the position of the nacelles is varied relative to the wing chord line and the leading edge. A study is being made of the nacelle drag, the propulsive efficiency, and the effects of the nacelles on the pitching moment and the maximum lift coefficients of the model.

In the 20-foot wind tunnel, further tests have been made of wing-nacelle-propeller combinations. The first series of tests dealt with the effect of nacelle-propeller diameter ratio on body interference (Technical Report No. 680). This investigation was followed by tests of several model nacelle-propeller arrangements in front of an N. A. C. A. 23018 wing. Data were obtained on the internal air flow, the drag, the interference drag, and the propulsive efficiency. The results, which will be published soon, are in accord with those of earlier investigations.

Supplementing tests of a few years ago, in which the drag of normal landing gears was determined, an investigation has been made in the 20-foot tunnel to determine the drag of the nose-wheel component of tri-cycle landing gears. The variables studied included size of wheel, form of supporting struts, form of fairing, position of nose wheel with respect to the fuselage, and degree of wheel retraction within the fuselage. For the partly retracted condition, no material reduction in drag below that of the completely exposed gear was noted except when the nose wheel was halfway retracted into the very nose of the fuselage. In this condition the gear drag was negligible.

Another extension of the interference research dealing with the effects of compressibility is considered under the subject of compressibility effects.



## COMPRESSIBILITY EFFECTS

Technical Report No. 646 has made available a large amount of information on the nature of compressible-flow phenomena. As a result of this fundamental work, conducted in the 24-inch high-speed wind tunnel, and a study of the information gained as it may affect actual designs of high-speed airplanes, it appears that the propeller will offer the most serious problems. Other parts of the airplanes may be so designed as to avoid serious compressibility losses. The propeller problem is the most serious because the propeller operates at higher relative air speeds than the other parts of the airplane and because its efficiency is decreased by the relatively large section thicknesses commonly used near the blade roots.

At present, therefore, the greatest emphasis is being placed on the development of suitable blade sections for high-speed propellers. Based largely on the data presented in Technical Report No. 646, new sections have been designed and experiments are being conducted in the 24-inch high-speed wind tunnel. Tests already made show that considerable improvement may be obtained. Meanwhile, further fundamental investigations to study the nature of compressible-flow phenomena, particularly at and near the critical speed, are being conducted in the 11-inch high-speed wind tunnel.

It is important to understand, however, that considerable care must be exercised in the design of other components of the high-speed airplane. An investigation in the 8-foot high-speed wind tunnel of a model of a typical transport airplane illustrates two important sources of difficulty: First, misalignment of nacelles having N. A. C. A. radial-engine cowlings with the air flow may result in important decreases of the nacelle critical speed; second, mutual interference between the parts of an airplane may reduce its critical speed below that of any of the individual parts when tested separately. In the case of the transport model investigated, the critical speed of the nacelles was 30 miles per hour lower than the critical speed of the same nacelles isolated from all the other parts of the airplane except the wing. Similar effects must be considered when any two or more basic shapes are combined.

## PROPELLERS AND PROPELLER-BLADE SECTIONS

An extensive program of propeller research conducted in the propeller-research tunnel has been concluded. A large portion of this work has been described in previous reports. Technical Report No. 650, dealing with tests of propellers having different blade sections, and Technical Report No. 658, dealing with tests of propellers having different pitch distribution, have been published during the year. Differ-

ences of 3 percent in maximum efficiency were found for the propellers having different blade sections. Differences in take-off efficiency were much larger. The effects of changes in pitch distribution appeared to be small. It is important to note, however, that at very high blade angles the use of a spinner materially increased the maximum efficiency. The concluding report of this series, yet to be published, deals with an investigation of static thrust conducted on a special outdoor test rig.

Force tests were conducted on three full-scale propellers in conjunction with the more streamlined afterbody mentioned in the discussion of cowling research. Comparisons were made with a streamline nose and an open-nose cowling in front of the better afterbody. The results of these tests are being analyzed on the basis of the preceding propeller data and a report is being prepared presenting this information.

Sufficient data are now available so that a fair approximation to the efficiency and power absorbed can be made in the usual cases. It has been noted, however, that peculiar disturbances occur with some cowlings and it has been impossible to predict these in advance, so that anomalous efficiencies may be expected in some cases. The poor efficiencies often calculated from flight tests as compared with wind-tunnel results have now been quite conclusively proved to be really an effect of reduced horsepower output. The installation of dynamometers on engines in flight has settled this question and more extensive use of this apparatus may be expected.

The present knowledge of propeller art and the increasing speeds and power to be expected with aircraft likely to be developed in the near future indicate that serious propeller problems may be expected. The limitation in tip speed imposed by compressibility phenomena is of increasing importance because actual aircraft speeds will soon be nearly as great as present propeller critical tip speeds. Important design compromises may be necessary to avoid serious compressibility losses. Such compromises may lead to decreased efficiency unless extreme care is used in design. Solidity higher than any values heretofore used is indicated because of tip-speed limitation and increased engine power. Increasing speeds will lead to very high pitch settings so that rotation losses will become important. Considerable study has been given the problem and, as a result, a program of blade-section development is being conducted in the 24-inch high-speed wind tunnel to lead to the development of blade sections that will have higher critical speeds and decreased drag.

As the data become available, the results are being analyzed to study the application to the design of optimum propellers for high-speed aircraft. Work is



now proceeding on the design of a family of propellers having the best blade sections obtainable to reduce the blade drag and compressibility losses and having thrust distribution designed to attain minimum induced loss. The range of solidity has been increased to include the extreme values likely to be encountered. An investigation of counterrotating propellers conducted at Stanford University and financed by the Committee indicates important increases in efficiency likely at high pitch settings. Further study will be made so that good propeller efficiency may be maintained through the elimination of the large rotation loss that occurs at high pitch settings.

An analysis of the operation of the propeller by the use of the distribution of the thrust and torque along the blades combined with theoretical equations has been made. The data for the analysis were obtained in the N. A. C. A. 20-foot wind tunnel on a 2-blade propeller of 4-foot diameter operating in front of four body shapes ranging from a small shaft to support the propeller to a conventional N. A. C. A. cowling. A method of estimating the axial and rotational energy in the wake as a fractional part of the propeller power is given. The average angle of twist in the propeller slipstream is shown to be a function of the torque coefficient  $Q_c$  and charts are given to aid in estimating the angle. Counterrotating propellers are shown to be attractive from considerations of aerodynamic efficiency when the propellers are highly loaded. A report on this work is in the process of publication. Similar work was conducted on two full-scale propellers differing only in pitch distribution along the blades. A report is being prepared on this work.

#### COWLING AND COOLING

**General conditions.**—For several years it has become increasingly apparent that better solutions for the cowlings and cooling problems are required to meet the demands of the military services for increased airplane performances. Work is still in progress dealing with the development and improvement of the N. A. C. A. cowlings, but it now appears that marked advances are at hand through the application of fundamental aerodynamic principles to the problems of cooling.

The present approach to the subject considers the problem divided into two separate ones: The internal-cooling problem; and the residual problem having to do with the scoop, vent, duct, and external-flow conditions. The internal cooling is chiefly a problem of heat transfer from the cylinder or radiator. Considerable progress has been made toward the desired objective of this phase of the problem—to minimize the quantity of air required and to minimize the local internal work of cooling. This internal work, the product of the pres-

sure drop across the cooling unit by the volume per second of air employed, is of fundamental importance because it represents a power-loss increment associated with the heat-transfer mechanism.

The external-flow phase of the problem is approached by considering this power-loss increment and air quantity as specified and then attempting to minimize the resulting power loss associated with the complete system. A certain power-recovery increment may fortunately be associated with the thermodynamic cycle of the cooling system (Meredith effect).

Energy from the propeller slipstream should be readily available. One of the most promising systems of this type, which has been under investigation in the propeller-research and the full-scale tunnels during the year, employs openings in the leading edge of the wing in the propeller slipstream. Other systems, however, may represent a close approach to the ideal, including the wing-duct systems investigated in the 7- by 10-foot tunnel and the full-scale tunnel and also certain applications of the N. A. C. A. cowlings under investigation in the 8-foot high-speed tunnel. The results already obtained with several of these systems suggest that, with careful aerodynamic design of the inlet and outlet openings and the internal-duct systems, a close approach to the ideal performance of these units may be realized. It thus appears that practical systems are within reach for which the power recovery may exceed the power loss and that, for high-performance airplanes, the cooling system may become an asset rather than a liability.

It should be emphasized, however, that high-performance systems must be of fundamentally correct design. Many tests of modern pursuit-type airplanes in the full-scale tunnel have shown large drag losses associated with the cooling and scoop systems commonly employed. Moreover, the difficulties can seldom be adequately corrected because the original design did not include adequate provisions for a fundamentally correct cooling system.

**Cowling research.**—The study of the pressure available for ground cooling in front of the cowlings of an air-cooled engine discussed in the last annual report is described in Technical Note No. 673. The design report on cowlings for radial air-cooled engines is presented in Technical Report No. 662.

The results of flight tests of four designs of nose-slot cowlings with several variations in each design are presented in Technical Note No. 720. The results describe the development of the nose-slot cowlings from flight data. A sample design calculation involving the use of results from flight, wind tunnel, and ground tests is given in an appendix to illustrate the design procedure.



An investigation of full-scale nose-slot cowlings has been conducted in the 20-foot wind tunnel. Engine conductivities from 0 to 0.30 were investigated. Two basic nose shapes were tested to determine the effect of radius of curvature of the nose contour; with the nose shape with the smaller radius of curvature the higher pressure drop across the engine was obtained. The best axial location of the slot for low-speed operation was found to be in the region of maximum negative pressure for the basic shape for the particular operating condition. The effect of the propeller operating condition on the available cooling pressure was determined. The maximum nondimensional pressure drop obtained for the high-speed condition with an engine conductivity equivalent to that of a modern double-row radial engine and a propeller with good blade sections near the hub was 1.45 and for the take-off condition, 3.75. For the propeller with a round blade shank, the values were 1.23 and 1.65, respectively. A report on this work is in the process of publication.

The drag and the power cost associated with the changing of the nose of a nacelle from a streamline shape to a conventional N. A. C. A. cowling shape was investigated in the 20-foot wind tunnel. Full-scale propellers and nacelles were used. The increment of drag associated with the change of nose shape was found to be critically dependent on the afterbody of the nacelle. Two streamline afterbodies were tested. The results of the tests with the more streamlined afterbody showed that the drag approached that of an airship form and that the added drag due to the open-nose cowling was only one-fourth of the drag increase obtained with the other afterbody.

From the experience gained in the investigation of the nose-slot cowling, it was found that the cowling exit would work efficiently if the after part of the body allowed the air to flow smoothly without breakdown of flow in that region. If the shape of the exit allowed breakdown of flow to occur, the slot created high drag and very low available pressure drop across the baffles. From a consideration of the available pressure behind the propeller, it was believed that, if a good exit slot design were used, much higher available pressure drops could be obtained by the use of cowling flaps than is usually supposed. Tests were therefore made to determine the available pressure drop for cowling flaps, care being taken to provide good flow conditions at the exit slot. The pressure drop available for cooling with a conductivity equivalent to that of a double-row radial engine was found to be 4.85 for the take-off condition for a propeller of good blade section and to be 3.17 for the propeller with round blade shank. A report on this work is being prepared.

An investigation in which blowers of various forms were used, in particular in the inlet passage of a modi-

fied N. A. C. A. cowling, has been made both on models in the propeller-research tunnel and in flight. Although the blower absorbs some power, it is evident that there is a definite advantage in reduced drag, in higher propeller efficiency because of the covering of the hub, and in greatly improved cooling. In one case it has been possible to run the engine continuously on the ground with much lower ( $85^{\circ}$  to  $100^{\circ}$  F.) temperatures than were obtained in flight with a normal cowling. Ground cooling is of importance in some types of aircraft and better cooling at higher speeds with large engines is necessary. Several reports have been prepared discussing various phases of the problem, and the investigation is being continued.

**Wing-duct radiators.**—As an extension of the investigation conducted in the 7- by 10-foot wind tunnel on full-span cooling ducts, tests have been made in the full-scale wind tunnel of similar ducts of finite span in a large wing for the purpose of evaluating end effects and investigating the scale effect on the characteristics of the ducts. In the investigation in the full-scale wind tunnel, a special study was made of means for regulating the quantity of air flow for the various flight conditions, particularly in regard to obtaining sufficient cooling air for the climb condition without an excessive amount for the high-speed condition, which would result in a serious penalty in drag.

The ducts of the more efficient types were found to affect inappreciably the maximum lift coefficient of the wing. Tests with operating propellers in front of the ducts indicated that ground cooling would be satisfactory and that in the climb, if the radiator inlet was placed behind the upgoing propeller blades, the cooling-air quantity would be increased about 10 percent. Tests conducted with heat applied to the radiator element indicated that some recovery of the energy lost in cooling is possible.

#### WINDSHIELDS

A systematic series of windshields, of both the transport and the closed-cockpit types, was tested in the 8-foot high-speed wind tunnel to indicate the drag of conventional types and to determine how these conventional types can be improved. It appeared that a typical transport-type windshield might account for about 21 percent of the fuselage drag but that it should be practicable to construct a windshield, with either single-curved or double-curved glass, that would account for only about 2 percent of the fuselage drag. It also appeared that recessed windows should be avoided.

Typical closed-cockpit windshield (including canopy), such as are used on small fighting airplanes, in some cases appeared to account for 15 percent of the drag of the entire airplane, but by improved design the windshield drag should be almost eliminated.



## THEORETICAL AERODYNAMICS

**Normal-force and pressure distribution over airfoils.**—A relatively exact and simple method for the prediction of the chordwise normal-force distribution over an airfoil was developed by the Committee in 1938. As mentioned in the last annual report, this method is applicable to ordinary airfoils and to airfoils equipped with plain, split, or serially hinged trailing-edge flaps. The pressures acting on the upper and the lower surfaces of the airfoils, however, are not separately determined by this method. A method of determining these individual pressures has been described in a report recently published (Technical Note No. 708). This method permits the determination of the pressure distribution over an airfoil section when the normal-force distribution (from Technical Reports Nos. 631 and 634) and the pressure-coefficient distribution over the "base profile" (that is, the profile of the same airfoil if the camber line were straight and the resulting airfoil at zero angle of attack) are known. Distributions of the base-profile pressure coefficients for the usual N. A. C. A. family of airfoils, which are also suitable for several other commonly employed airfoils, are included in Technical Note No. 708.

**Compressibility effects.**—Theoretical investigations of the effect of compressibility on the flow past obstacles have been continued. In particular, the effect of compressibility on the moment of an arbitrary shape has been obtained and the general formulas have been applied both to elliptic cylinders and to symmetrical Joukowski profiles. The results of this investigation have been presented in Technical Report No. 671.

**Span load distribution on wings.**—A simple method of successive approximation for determining the span load distribution on wings has recently been developed by the Committee and the results published in Technical Note No. 732. A straightforward arithmetical procedure is described in which component loads are added to form the distribution sought. The proportions, the magnitudes, and the relative spanwise positions of these component loads are determined from equations derived from the differences between the given chord distribution and the chord distributions associated with the components themselves. The method is comparatively rapid and should prove useful in problems for which the span load distributions cannot otherwise be readily determined.

## WIND-TUNNEL CORRECTIONS

**Profile-drag measurements by momentum method in full-scale wind tunnel and in flight.**—The accurate measurement of the profile drag of a wing by means of surveys of dynamic and static pressure in its wake is of importance because it makes possible the evaluation of the drag of various types of protuberance on the wing and, by comparison with known characteristics of

aerodynamically smooth wings of the same dimensions, the evaluation of the drag caused by surface roughness and manufacturing irregularities. In order to investigate the accuracy of this method and the reduction of the test data by the Jones and the Betz equations, wake surveys and force tests were made in the full-scale wind tunnel on three symmetrical airfoils of different thicknesses. An analysis of the results as presented in Technical Report No. 660 shows that, for zero-lift condition, the profile-drag coefficients reduced by either the Jones or Betz equations agree with the force-test results within 2 percent. For the lifting airfoil, the error resulting from the induced field did not exceed 2.5 percent up to a lift coefficient of 1.0 and outward to a spanwise position of about 0.8 of the semispan.

The effects of turbulence present in the jet of the full-scale wind tunnel were determined by comparative velocity surveys in the boundary layer and wake momentum measurements of a polished section of a wing on an airplane in flight and in the tunnel. The results of the boundary-layer velocity measurements (presented in Technical Note No. 693) show that the end of the transition from laminar to turbulent flow occurs at approximately the same position in flight and in the tunnel but that the transition region as measured in the tunnel is somewhat broader than for flight. This difference in the boundary layer, however, accounts for an increase of only 0.0001 in the profile-drag coefficient as determined by the momentum method over the values obtained in flight.

**The 8-foot high-speed wind tunnel.**—An investigation of N. A. C. A. 0012 airfoil of 5-foot chord has been made in the 8-foot high-speed wind tunnel, which has a circular jet and a closed throat, to establish the spanwise variation of constriction caused by the presence of the airfoil. The results of this investigation will be used to determine the magnitude of the corrections to be applied to the results of later airfoil investigations.

## EFFECTS OF ICE FORMATION AND ITS PREVENTION

**Adhesion of ice to surfaces.**—In the development of methods of preventing ice formation on aircraft parts, it is important to know the force with which ice adheres to various materials. From the magnitude of this force, recommendations can be made as to lines of development that should be followed to perfect a satisfactory de-icing mechanism. An investigation was made on the adhesion of ice to various materials and the results have been published in Technical Note No. 723. The procedure consisted in freezing water onto a block of the material to be tested and then determining the force required to remove the ice. Brass, copper, duralumin, stainless steel, glass, and micarta were tested. With the exception of micarta, the adhesion



force holding the ice to the block was greater than the cohesive force within the ice itself. In each case, the ice failed at a tension of about 140 pounds per square inch leaving ice adhered to the surface. With the mica the ice failed irregularly at a loading of 53 pounds but remained adhered to the mica block in sections of the surface.

The tests indicated that ice will adhere to any solid surface with a force so great as to eliminate the possibility of removing the ice by mechanical means suitable for aircraft. When rubber or a thin sheet of duralumin was used, the ice could be removed with a much lower force because of the "peeling" action that took place.

The tests showed that if a liquid interface were maintained between the ice and the solid surface the ice was easily removed. In this case the force to be overcome was chiefly that exerted by atmospheric pressure. With greases, the force was somewhat greater. The analysis indicated that the commercial de-icing pastes essentially consisted of a freezing-point depressor combined with a substance to form a paste.

**Adhesion of ice to aircraft parts.**—In the ice-research program announced in the last annual report, chemical, heat, and mechanical means of ice prevention have been investigated. Attention has been given to the prevention and removal of ice from the airplane wing, the struts, the propeller, and the windshield. Under the existing program, attempts will be made to determine means for the protection of other parts of the airplane.

Flight tests in simulated icing conditions made with the inflatable-type wing de-icer indicated that only partial ice removal is possible by this method with present equipment. Residual ice accretions were observed on the leading-edge and the cap-strip regions of the de-icer. Tests to determine profile drag and maximum lift in flight have also been made on a wing equipped with a de-icer. Coefficients of profile drag and maximum lift were determined for the plain wing without the de-icer, with the de-icer free from ice accretions, and with several other drag conditions produced by attaching simulated ice formations to the regions of the wing leading edge and the de-icer cap strip. Formations on the de-icer cap strips were shown to have a very undesirable effect on the profile drag and the maximum lift.

An analysis of the results of the preliminary investigations conducted in the ice tunnel on the use of exhaust-gas heat for the prevention of ice on the airplane wings (Technical Note No. 712) indicated that a reasonably small percentage of the exhaust thermal energy will prevent the formation of ice on the wings. This work is being continued in analytical investigations and model tests both in flight and in the ice tunnel. The investigation of the use of steam heat in flight gave

results similar to those from tests made with direct exhaust heat in the ice tunnel and indicated that the quantity of heat required for ice protection was not excessive. Investigations on the use of steam have been temporarily discontinued and emphasis is being placed on tests of direct exhaust heat, which seems to require less mechanical equipment than does steam.

The investigations of chemicals applied prior to flight for the prevention of ice on the airplane wing have been continued, although no satisfactory substance has been found when tested under simulated icing conditions. Alcohols and mixtures of alcohol and glycerin were discharged through perforations along the leading-edge region of a wing. In these tests the perforated surface and the distribution tube were attached to the surface of an inflatable de-icer. Tests conducted with and without the de-icer in operation failed to prevent or remove ice from the wing. A similar investigation with ethylene glycol and a mixture of ethylene glycol and isopropyl alcohol was made on a small strut such as might be used for an antenna mast. The discharged fluid prevented the formation of ice although the quantity required seemed to be excessive.

The distribution pattern of ice-inhibiting fluids over the blades of a propeller of large diameter has been studied in flight. The results indicate (Technical Note No. 727) that ducts or channels along the leading edge of the propeller blade will be required to distribute properly ice-inhibiting fluid on propellers of large diameter. Further studies are planned on the problem of preventing ice formation on the airplane propeller.

An investigation has been made of several methods of preventing ice on the airplane windshield. Models equipped for the application of electric heat and of heated air, and a rotating wiper blade that dispenses alcohol from its center have been tested. Ice was prevented on each of the model test panels when subjected to simulated icing conditions in flight. Air heated by the exhaust to a temperature of about 170° F. and passed through a  $\frac{3}{16}$ -inch gap between two panes of glass with a velocity of 50 feet per second prevented the formation of ice during very severe simulated icing conditions. This method seems to offer the simplest solution to the problem of windshield icing since it prevents ice on both sides of the glass, requires no moving parts, and utilizes what is otherwise waste energy.

#### ROTATING-WING AIRCRAFT

The possibility of improving the lift-drag ratio of rotors of rotating-wing aircraft in forward flight by retarding or preventing the stalling of the inboard elements of the retreating blades is being investigated. A preliminary step in this investigation was to supplement theoretical calculations of the operating condi-



tions of blade elements in various parts of the disk with photographic observations of the behavior of silk tufts mounted on the blades of a YG-1B autogiro. The tuft observations indicated that the portion of the rotor disk in which the elements are stalled is somewhat larger than would be expected from theoretical considerations. A technical note presenting the results of the initial observations is being prepared and additional observations on blades of various airfoil section and plan form are in progress.

An attempt is being made to isolate the factors in the design of rotor hubs and blades that are responsible for the severe vibration present in the control systems of present-day direct-control autogiros. To this end, the varying loads in the control system of a YG-1B autogiro have been recorded in flight at various air speeds. Analysis of the records indicates that mass unbalance or improper matching of the blades is not responsible for the control vibration in this machine and that some modification of hub and blades may be desirable. Similar tests on the same machine equipped with blades of improved design are now in progress.

Data on the blade motion and the control characteristics of nonarticulated feathering rotors have been obtained from flight tests of the Wilford XOZ-1 sea gyroplane and are being evaluated.

#### DETERMINATION OF MOMENTS OF INERTIA

In the determination of the moments of inertia of airplanes by swinging tests, the effect of the ambient air in increasing the apparent mass and moment of inertia must be estimated. Such estimates are chiefly based upon experimental data on the additional mass and moments of inertia of flat plates. During the past year it has been necessary to supplement previously estimated values of the moments of inertia of airplanes by data obtained from experiments with flat plates of tapered plan form. These experiments were conducted in a vacuum chamber and the results are now being prepared for publication.

#### MISCELLANEOUS TESTS OF MODELS AND AIRPLANES

A considerable number of requests have been received from the Army and the Navy during the past year for investigation of complete models of military airplanes and experimental airplanes of the fighter class in the Committee's wind tunnels. Most of the models have been investigated at the request of the military services; some models have been tested for manufacturers at their expense and other models have been built and tested in connection with the Committee's own research programs. The work has been carried out in the full-scale, the 20-foot, the 7- by 10-foot, and the 8-foot high-speed wind tunnels.

The greater portion of the time in the full-scale tunnel has been devoted to tests for the Army and Navy of complete models and single- and two-place airplanes of the combat type. The information obtained in the model tests has resulted in definite improvement of the design of the projected airplanes. The modifications made to airplanes in these tests have indicated substantial increases in the high speed, and these increases have been verified by flight tests.

Investigation of a model of a typical two-engine low-wing transport has been made in the 8-foot high-speed wind tunnel. The investigation has shown the contributions of various components of the airplane model to the total drag. The wing accounted for about 37 percent of the total drag; the fuselage, including interference, 25 percent; the nacelles, 11 percent; and the landing wheels with the main wheels retracted but partly projecting below the nacelles, 14 percent. The landing wheels even in the retracted position contributed a notably large percentage of the total drag. This drag could be eliminated by complete retraction. About 80 percent of the total landing-gear drag was due to the main wheels and the remainder to the tail wheel. The nacelles were the only part of the airplane exhibiting marked compressibility effects at speeds up to 450 miles per hour. The critical speed of the nacelles could have been increased to above 450 miles per hour by proper alinement with the air stream. The results of this investigation are now being prepared for publication.

Aerodynamic tests of five side-float models for seaplanes were made in the 7- by 10-foot wind tunnel and the results have been published in Technical Note No. 680. This investigation indicated that the most promising method of reducing the drag of these floats is to lower the angle at which the floats are rigged.

#### NATIONAL BUREAU OF STANDARDS

##### WIND-TUNNEL INVESTIGATIONS

The aerodynamic activities of the National Bureau of Standards have been conducted in cooperation with the National Advisory Committee for Aeronautics.

**Wind-tunnel turbulence.**—The great progress in the study of the practical effects of turbulence in wind tunnels as related to performance in flight carried out at Langley Field has shifted the interest from the effects of intensities of turbulence of the order of 1 percent to those of intensities of the order of 0.1 percent. As a result, it has been necessary to provide wind-tunnel equipment in which low turbulence levels can be obtained and to increase the sensitivity of the apparatus for measuring turbulence.

The modernization of the 4½-foot wind tunnel provided an air stream of low turbulence. Since this tun-



nel was first placed in operation in October 1938, numerous improvements have been made, each one successively reducing the turbulence of the stream, and further reductions are in prospect as the sources and behavior of wind tunnel turbulence are better understood.

The intensity of the turbulence is so low that its measurement presents some difficulties. However, by the use of a Wollaston wire about 0.00024 inch in diameter and 0.16 inch in length, sufficient sensitivity is obtained to measure intensities as low as 0.05 percent with reasonable precision. It is found necessary to use an antivibration support, and to modify the wire mounting to prevent vibration of the wire itself and to insure vibration of the mounting prongs as a unit when mechanical shock occurs.

The diameter of these small wires cannot be measured with sufficient accuracy to permit a computation of the time constant. Apparatus was constructed for experimental determination of the time constant. The method used is that of vibrating the wire with a fixed velocity amplitude but varying frequency in a stream of low turbulence. The vibrator is an electromagnetic pulsator and the velocity amplitude is measured by an electromagnetic pick-up device. Reproducible and accurate results are obtained.

The great progress in the development of electron tubes, the feed-back amplifier, voltage-stabilizing circuits, etc., has made possible for the first time the design of really portable equipment for measuring turbulence. With suitable hot-wire units, both longitudinal and transverse components of the fluctuations can be measured, as well as the correlation between longitudinal and transverse components. Construction of amplifier and power supply have been completed and their operating characteristics are under study. The design makes possible the use of the condenser-type compensating circuit, permitting a considerable reduction in the weight and size of this component.

A general account of turbulence investigations conducted for the Committee at the National Bureau of Standards was presented at the Fifth International Congress for Applied Mechanics.

**Boundary-layer investigations.**—A report entitled "Air Flow in the Boundary Layer of an Elliptic Cylinder" was published by the Committee as Technical Report No. 652.

The study of transition at low turbulence levels on a thin flat plate parallel to the wind direction has been in progress during the year. In view of the results of previous work, great care has been taken to have all factors which might affect the transition under control. The plate, which is made of aluminum and is  $\frac{1}{4}$  inch thick and 12 feet long, is placed vertically between opposite faces of the octagonal working section of the tunnel. The leading edge was carefully machined to a lenticular form with a very thin edge.

The pressure gradient is adjustable by means of flexible side plates on the two vertical faces of the octagonal test section, making in effect a channel on each side of the plate of adjustable width. The pressure could be adjusted to be constant within 0.05 percent of the velocity pressure.

A number of exploratory measurements of the location of transition as a function of various factors have been made. Contrary to expectation, the transition point is not unduly erratic or sensitive to small changes. Its location still depends markedly on the turbulence and erratic variations in its position obtained in other laboratories are probably due to erratic variations in the turbulence level. A value of the critical Reynolds Number of about 3,000,000 has been obtained for the condition of zero pressure gradient.

The work conducted for the Committee formed the basis of the Second Wright Brothers Lecture of the Institute of the Aeronautical Sciences.

#### AERONAUTIC-INSTRUMENT INVESTIGATIONS

The work on aeronautic instruments has been conducted in cooperation with the National Advisory Committee for Aeronautics and the Bureau of Aeronautics of the Navy Department.

**Investigations.**—A description of, and laboratory performance data on, the gyroscopic turn indicator, the directional gyroscope, the gyro horizon, the gyromagnetic compass, and a description only of the automatic pilot, are included in a report published as Technical Note No. 662.

A report on the theory and performance of modern rate-of-climb indicators has been published as Technical Report No. 666.

The investigation of corrugated diaphragms in progress included measurements of the central deflection against differential pressure of geometrically similar diaphragms of four diameters (1.5, 2, 2.5, and 3 inches) and a number of thicknesses in the range from 0.001 to 0.013 inch. The data were obtained principally on beryllium-copper and phosphor-bronze diaphragms and on a few diaphragms of Z nickel. These data have been analyzed and generalized into a mathematical formula. A report has been completed.

A sensitive diaphragm capsule has been developed which is prevented from deflecting above any desired differential pressure. At the cut-off pressure the diaphragms nest into each other. Two elements, consisting of two evacuated capsules, have been built for measuring air pressure in the range from 140 to 0 millibars. When used on a Diamond-Hinman radio sonde a seven-fold increase in sensitivity was secured in this pressure range.

The theory for the movement of a piston in a cylinder filled with liquid has been formulated in connection with an investigation of dashpots. To check the theory,



eighteen pistons were tested in cylinders of two diameters. Liquids of two viscosities were used. The piston clearance was varied from 0.0005 to 0.005 inch. Theory and experiment checked within  $\pm 10$  percent. A report is being prepared.

#### SUBCOMMITTEE ON METEOROLOGICAL PROBLEMS

The Subcommittee on Meteorological Problems keeps in contact with the progress of investigations being conducted by the various agencies on problems relating to atmospheric conditions which are of particular importance in connection with aircraft design and operation. The Special Committee on Lightning Hazards to Aircraft is organized under the Subcommittee on Meteorological Problems.

**Atmospheric disturbances and their effect on airplane operation.**—The Langley Memorial Aeronautical Laboratory has continued its study of gust intensities and gradients and their effect on airplane accelerations in flight. Additional records have been obtained on both military and commercial airplanes by means of N. A. C. A. V-G recorders, the total number of hours of flying time accumulated on commercial transports having been increased to 82,000. One incident of particular interest was reported in which a military airplane was subjected, without previous warning to the pilot, to an isolated strong gust of an intensity usually associated with that of severe thunderstorm conditions. In this gust the effective gust velocity was more than 30 feet per second.

The accumulation of data by means of V-G recorders has included operation over the principal air lines in the United States, on the routes from the East Coast to Bermuda and to the northern part of South America, over the Andes Mountains, and across the Pacific and the Atlantic.

From statistical data obtained on a number of airplanes it appears that the gust gradient distance is directly proportional to the size of the airplane and is approximately 8.5 times the wing chord length. By means of flights in thermal gusts to altitudes up to 17,000 feet, a correlation has been obtained between the gust velocity and various other factors, including the gradient distance, wind velocity, wind gradient, thermal energy, and altitude.

**Lightning hazards to aircraft.**—Data are being accumulated from air transport operators by means of a questionnaire on incidents of lightning strikes to airplanes, and an analysis of the information so far obtained has been made. It is of interest that, although there have been a number of instances of lightning strikes to airplanes, the resulting damage to the aircraft was slight, and in a large number of cases the passengers, and occasionally even the pilots, were not aware of the incident.

A study is being made at the University of New Mexico, under the cognizance of the Special Subcommittee on Lightning Hazards to Aircraft of the location and intensity of electrical charges in the atmosphere. Evidence obtained in this investigation indicates that discharges from cloud to ground are of a negative polarity. Investigations are being conducted in electrical research laboratories on the effect of electric discharges simulating lightning strikes on sheet metal of various types, particularly those used in aircraft construction. From information so far obtained it appears that it is possible to determine from the size of a hole caused by lightning in any given thickness of metal the amount of current involved. It is planned to accumulate from aircraft operators samples of burned metal removed from airplanes on which lightning strikes had been experienced and determine the amount of the current which caused the burn.

Careful consideration has been given to the specific hazards from lightning to various portions of the airplane such as radio equipment, gasoline tanks, fabric covering, control mechanisms, etc. It is believed that, if suitable precautions are taken in all cases, the danger from lightning to an airplane in flight is slight. The avoidance in all cases of atmospheric conditions which indicate the probability of lightning is considered desirable, however, and instructions to this effect have been issued by one airline operator to its flying personnel, with material reduction in the number of lightning strikes experienced.

#### SUBCOMMITTEE ON SEAPLANES

The relative importance assigned to the various hydrodynamic problems connected with the design and construction of seaplanes, which are under the cognizance of the Subcommittee on Seaplanes, has changed radically during the past year. For several years the major hydrodynamic problem has been that of resistance, and the possibility of successfully getting into the air was considered to be largely determined by that factor. Today the major hydrodynamic problems appear to be (1) dynamic stability while in motion on the water, (2) spray, and (3) seaworthiness. This almost sudden change has come about because of the pressure on the designers of demands for extreme performance in the way of speed, range, and pay load. In the endeavor to produce hulls having minimum air drag and structural weight, the almost universal tendency has been to adopt forms having relatively narrow and deep cross sections.

This form also gives the familiar arrangement of the passenger accommodation in civil craft. But narrow hulls have meant heavily loaded hulls; the high position of wings and engines—and, in many cases, fuel—has caused the center of gravity of the whole



craft to rise to surprisingly high positions; the heavily loaded wings and high air speeds have caused landing speeds to be considerably increased. As a result of these changes, the difficulties associated with obtaining adequate longitudinal stability (freedom from "porpoising"), freedom from excessive spray and from spray thrown into the propellers, and moderate impacts of the bottom on the water while landing and taking off have been greatly increased. At the same time, the use of engines with greatly increased horsepower available for take-off, because of the increased power needed for flight at higher speeds, and the general use of automatic or controllable propellers with greater efficiencies in the range of take-off speeds, have made the water resistance of the hull of much less importance in determining whether a seaplane can get into the air. This situation has made it necessary to broaden the scope of the Committee's work and to undertake the provision of additional facilities to enable adequate consideration of the new problems.

Apparatus and technique to conduct the investigations made necessary by the new problems have been developed and expanded as rapidly as possible. Equipment of a semipermanent type has been constructed, and appropriate methods of operation have been developed for testing dynamically similar models of complete flying boats for the purpose of studying their dynamic stability. Methods of constructing the very special type of models required for this work have been devised. Accurate methods of ballasting the models so that the weight and the moment of inertia about the center of gravity will correspond to those of the full-size craft have been developed. The theory on which a mathematical study and a determination of the stability may be based has been investigated and a revised treatment, based on that of Perring and Glauert, has been begun. A sound theoretical treatment will be very helpful in the understanding of this very complex problem and in the direction of the broad fundamental research that must be carried out if the problem is to be solved.

With the limited equipment already at hand, it has been possible to investigate the dynamic stability of two specific machines for the Bureau of Aeronautics and of one for a private corporation.

Work for the military services of the Government has continued to receive first priority in the work of the tank. Four investigations of specific flying-boat projects and two investigations of novel devices have been completed. Several projects requiring the high towing speeds available only at the N. A. C. A. tank were completed for the Navy.

The fundamental researches completed and under way were of interest because of the use in several cases

of large families of related models to study the influences of form on the hydrodynamic qualities and because the scope of the investigations was extended to include aerodynamic effects as obtained in parallel wind-tunnel tests on the same models.

**Plant and equipment.**—The efficiency of routine tests in smooth water has been increased by the installation in the tank of devices that damp out the surges caused by the operation of the carriage and by the perfecting of more durable wave suppressors. The development of these devices, as well as the design of a wave-making device, has been facilitated by the construction of a small tank one-eighth the cross section of the N. A. C. A. tank and 50 feet long. This tank has large glass panels in the sides and in it large models of the devices can be operated while the motions of the water about the models are observed.

**Hulls for long-range flying boats.**—In a long-range aircraft, small increases in air drag have a large influence on pay load and the best form of hull for such a craft presumably is one that approximates a streamline body and departs from such a form only by the amount required to give satisfactory hydrodynamic qualities. It is anticipated that the trend of design will be toward such forms, and both tank and wind-tunnel data are being accumulated to aid in their further development.

Technical Note No. 668 describes tests in the tank and in the 20-foot wind tunnel of two models of the planing type of hull, the forms of which are derived from a body of revolution and which represent extreme aerodynamic refinement as compared with existing hulls. The tank tests showed that the models were generally satisfactory but under certain conditions developed a tendency to behave unsatisfactorily. Take-off calculations for an assumed giant flying boat indicated that its take-off characteristics would be satisfactory if the trim was properly controlled. These models had lower air drag for the same volume than any models previously tested in the 20-foot wind tunnel. They also possessed the desirable characteristic of having smaller than usual increases in drag with departures from the angle for minimum drag.

It was apparent from the tank tests that there is in general no sharp line between good and poor water performance to determine the practical limits of aerodynamic refinement. A family of models has therefore been devised having systematic variations in the degree of departure from a streamline body. Tests of this family, now in progress, will provide further information on the best compromise between desirable aerodynamic and hydrodynamic qualities.

**Outboard floats.**—The best form of outboard float also represents a compromise between the requirements of low aerodynamic drag and satisfactory characteristics



on the water. As part of a program for the investigation of outboard floats, four models of typical floats were tested in the tank and in the 20-foot wind tunnel (Technical Note No. 678). From the data obtained, the forms were compared on the basis of aerodynamic drag, spray, and yawing moments for given righting moments. Other factors, such as relative angle of heel, possible impact loads, and structural simplicity, were also considered in the analysis. It was concluded that the best form for an outboard float, when all its requirements are considered, is one having a transverse step for good planing characteristics and having its buoyancy distributed horizontally rather than vertically.

**Tests of models of representative flying-boat hulls.**—A one-sixth-size model of the hull of a Navy flying boat was investigated in the tank as part of the general program of tests of typical hull forms. This hull was a more recent adaptation of the NC type and was of special interest because of several features intended to improve take-off performance. These features included pronounced chine flare on both forebody and afterbody, a downward hook in the surface of the bottom at the step, and a tail extension shaped to provide additional hydrodynamic lift at low speeds. The hydrodynamic characteristics were found to be very satisfactory over a wide range of loadings and speeds. The results of the general test have been published in Technical Note No. 681.

In this publication a new type of chart was introduced for use in calculations of take-off performance based on the data from the general test. Since at a given speed, load and resistance are functions of the trim, the data are plotted in the form of resistance coefficient against trim with load coefficient as parameter. A number of such plots are made for a succession of speed coefficients such as would be used in a step-by-step calculation of take-off events. The curves of trimming-moment coefficient are superposed on these plots in the form of contours of constant trimming-moment coefficient. Experience with these charts has shown that they are preferable to the previous charts plotted against speed coefficient because of the greater ease of interpolation and the wider application to problems involving arbitrary conditions of trim or trimming moment.

#### SPECIAL SUBCOMMITTEE ON VIBRATION AND FLUTTER

The problems of flutter and vibration, especially in the case of large fast airplanes, continue to be increasingly important. During the past year, two meetings of the Special Subcommittee on Vibration and Flutter and a special conference on these problems were held. At one of the meetings, the problem of flutter was discussed with representatives of the industry. The calculation of the flutter speed and the parameters

necessary for its determination were considered, particularly with a view to the possible means of reducing the labor involved in making such calculations.

A special conference with manufacturers was held at Langley Field and considered the difficulties being experienced with propeller vibration. At this meeting, equipment for the study of the fundamentals of propeller vibration and damping was discussed. This equipment has now been completed and is ready for operation.

Most of the work on vibration carried out this year by the Committee has been related to the problem of flutter. In addition to the theoretical and experimental work on flutter, several projects on vibration have been undertaken because of their importance in relation to the problem of flutter.

**Ground tests.**—Vibration tests have been made on a number of airplanes on the ground. Equipment and methods have been developed to facilitate these measurements.

**Damping tests.**—The problem of determining values of structural damping for use in flutter calculations has been studied. Methods have been developed for separating the motions associated with different normal modes.

**Model beams.**—Exact solutions have been obtained for the equation of torsional vibration of a very general class of tapered beams (Technical Note No. 697). Tests on a set of tapered beams have been made and compared with theoretical results for both torsion and bending. These results indicate the effect of taper upon frequency for most cases of tapered wings.

**Elastic airplane model.**—A model of convenient size having elastic properties and weights distributed similarly to those of a typical modern airplane has been built. This model has been used in tests conducted to develop a technique of determining the various elastic, mass, and coupling parameters determining the flutter properties of the wing and the tail.

**Flutter problem.**—Flutter calculations have been continued during the past year. Particular attention has been given to the calculations for three degrees of freedom in order to determine more carefully when these can be replaced by the simpler cases for two degrees of freedom. The flutter parameters of several present-day airplane wings have been determined. A number of aircraft companies have cooperated by supplying information concerning the structural parameters.

The theoretical work on flutter has been extended to include the effect of aileron tabs and servorudders.

Further contributions to the flutter problem have been made through the study of unsteady-lift functions for wings of finite aspect ratio (Technical Note No.



682) and the experimental verification of the theory of oscillating airfoils (Technical Report No. 673).

## REPORT OF COMMITTEE ON POWER PLANTS FOR AIRCRAFT

LANGLEY MEMORIAL AERONAUTICAL LABORATORY

### INCREASE IN ENGINE POWER

The prime requisites for aircraft power plants at the present time, either for military or commercial service, are increased power for take-off and altitude operation, as well as greater economy in fuel consumption. Additional power is being striven for, principally through the development of fuels with higher antiknock values and increasing the effectiveness and number of the power strokes. The importance of the fuel work is indicated by the fact that improved fuels have contributed to a large extent in doubling engine power during the past decade. Further improvements in supercharging can be expected to provide materially higher intake manifold pressures and therefore greater power at altitude. Engine operating speeds are also being raised. The power requirements of the larger aircraft, exceeding as they do the capabilities of existing engine types, has led to the development of engines with more cylinders and consequently greater displacement. The thermal and mechanical limitations to achieving increased power centers principally on the cooling of the exposed parts in the combustion chamber and on carrying the loads imposed on the principal bearings. Fuel economy is now of the utmost importance, both because of its effect on the range of military equipment and on the operating expense of commercial aircraft. The greatest improvements in economy are anticipated from the reduction of power-plant and cooling-system drag and the recovery of waste heat. Renewed interest is being taken in in-line liquid-cooled power plants because of their small frontal area, while intensive work is going forward to provide minimum-drag cowlings for the radial air-cooled engine types and more efficient means of dissipating the heat in both air- and water-cooling systems. Savings of as much as 15 to 20 percent of the total airplane drag are possible by these means. The problem of waste heat recovery is particularly important, since only some 30 percent of the heat value of the fuel is utilized in the present-day power plants. The Committee is actively engaged in researches designed to provide practical solutions for many of these problems, as will be seen from the following report.

**High octane number fuels.**—In the development of aircraft engines it is becoming increasingly important that the engine designer know the effect of the different engine operating conditions on the maximum

permissible engine performance. For this reason the Committee is conducting an investigation to determine the relationship between maximum permissible engine performance and the knocking characteristics of aircraft-engine fuels. This investigation is under the cognizance of the Subcommittee on Aircraft Fuels and Lubricants and is described in the report of that subcommittee.

**Flow through engine inlet valves.**—The results of the investigation of flow coefficients with intermittent flow through engine poppet valves have been published in Technical Note No. 701.

A sleeve valve and cylinder have been assembled for determining the flow coefficients of the inlet ports with pressure drops through the valve at values up to 8 pounds per square inch. Over-all flow coefficients have been measured with the valve operating as in an engine. Coefficients with the sleeve valve partly opened have been measured with the sleeve stationary, and the coefficients that apply to these partial openings have been checked against the over-all flow coefficients. A preliminary comparison shows the flow coefficients of sleeve valves to be the same for the partly opened valve as for the fully opened and operating valve. The coefficients derived from the test data are about the same as those obtained previously for the poppet valves.

**Piston temperatures.**—The investigation of the important factors controlling piston cooling and the effect of engine and cooling conditions on piston temperatures has been continued. The temperatures at five locations on a piston of an air-cooled engine have been determined for varying engine speed, load, spark advance, fuel-air ratio, head and barrel temperature, and oil temperature and viscosity. The data are being analyzed and will be prepared for publication.

**Piston rings.**—Piston-ring sticking, loss of tension, and wear are failures that limit the output of high-performance engines. An investigation is in progress to determine the engine-operating characteristics of superior cast-iron and nitrided-steel piston rings when operated in nitrided-steel liners. The use of piston rings of those materials and compounded lubricating oils have greatly reduced ring sticking and loss of tension. The problem of reducing the wear of piston rings in high-output engines is being studied.

**Valve-overlap investigations.**—The use of large valve overlap and increased inlet manifold pressure is an efficient method of removing the residual exhaust gases from an engine cylinder and of cooling the surfaces of the combustion chamber. The work on the single-cylinder test engine has been extended to a nine-cylinder radial spark-ignition engine equipped with an injection system spraying the fuel into the



cylinders. The engine was fitted with a special cam giving approximately  $130^\circ$  overlap between the open periods of the exhaust and the inlet valves. The poor idling of the engine experienced with large amounts of valve overlap was overcome by placing separate throttle valves close to the intake port of each cylinder. With these auxiliary throttles, the idling with large valve overlap was equal to the idling with the standard throttle and standard engine timing.

**The 2-stroke-cycle engine.**—Research has continued on the factors affecting the performance of the 2-stroke-cycle fuel-injection spark-ignition engine. The liquid-cooled engine used in this investigation is a uniflow type having scavenging and charging air admitted to the cylinder through piston-controlled inlet ports and exhaust through four poppet valves in the head. The factors investigated have included the number, the size, and the angle of the inlet ports and the lift and the timing of the exhaust valves. Investigations are in progress to increase performance by more effective breathing capacity and increased engine speed.

**Recovery of energy in exhaust gases.**—The conventional aircraft engines discharge as waste heat 65 percent of the energy of the fuel. Since the weight of fuel constitutes about half of the useful load of a long-range airplane, it is extremely important that methods be developed for utilizing a part of this waste energy. An analysis has been made of the energy recoverable by methods that require no additional prime movers but depend on the forward motion of the airplane. The pressure variation attending the flow of cooling air through the duct of the cooling system provides a convenient thermodynamic cycle for recovering waste heat. Thrust is obtained from the increased velocity of the cooling air as it leaves the duct exit.

The power recoverable by this method has been calculated for three conditions: first, for the normal duct radiator; second, for the duct radiator having the heat in the exhaust gas transferred to the cooling air in the duct; and third, for the duct radiator having the exhaust gas discharge into the duct. The effect of a fan in the duct for increasing the compression ratio of the thermodynamic cycle has been considered. A report is in preparation covering the results of this investigation.

**Jet reaction as take-off aid.**—The possibility of using auxiliary jet propulsion for aid during the take-off has been analyzed and compared with the use of larger engines. The analysis shows that the weight of fuel and liquid oxidant required for an appreciable improvement in take-off performance is sufficiently small to indicate that serious consideration should be given to this method of assisting the take-off when take-off aid becomes necessary. A report based on this analysis is being prepared for publication.

#### COMBUSTION RESEARCH

**Knock investigation.**—The construction of the N. A. C. A. high-speed motion-picture camera was completed during the past year. With this camera motion pictures can be taken at rates up to 40,000 photographs per second, whereas previous pictures had been taken at speeds of 2,400 pictures per second. Projecting these motion pictures at speeds of 16 photographs per second gives the effect of increasing the visual speed of the observer 2,500 times.

The motion pictures of combustion obtained with the new camera and the N. A. C. A. combustion apparatus have made possible a detailed study of the combustion process. Throughout this investigation, schlieren photographs have been taken because past experience has shown them to be superior to the usual flame photographs. When knock occurs in the engine, the photographs show that the phenomenon is completed in from 0.00005 to 0.00010 second. The photographs emphasize the fact that knock appears to be a much different phenomenon from the normal combustion which precedes the knock. The actinic value of the knocking flame is many times that of the flame previous to knock. With severe knock, a preknock reaction in the end gas, which has been previously observed, is clearly shown.

The results of the investigation made to determine the effect on air movement within the engine cylinder of several arrangements of shrouded intake valves have been published in Technical Report No. 653.

An investigation of the effect of air flow within the combustion chamber for spark-ignition engines on the propagation of combustion has been reported in Technical Report No. 657.

**Preignition characteristics of fuels.**—The N. A. C. A. combustion apparatus has been used to investigate the preignition characteristics of aircraft-engine fuels. For the purpose of these tests preignition of the fuel was caused by an electrically heated coil located in the combustion chamber. The temperature of the coil was measured by a thermocouple. Fuels included in the investigation were iso-octane, benzene, toluene, methyl alcohol, and different fuel blends. In general, the results have shown that the preignition temperature is not greatly affected by engine speed or compression ratio. The preignition temperature remains fairly constant as the fuel-air ratio is decreased from a rich mixture until the mixture approaches that for complete combustion of both fuel and air. Any further leaning causes a sharp increase in the preignition temperature. The results have shown that there is no general relation between the knocking characteristics and the preignition characteristics of a variety of fuels. The results of this investigation are being prepared for publication.



**Engine charge temperature.**—An investigation has been undertaken of the heat-transfer process during the intake and compression strokes of an internal-combustion engine in order to facilitate a study of knock in aircraft engines. Indicator diagrams have been obtained on a Wright 1820-G single-cylinder test engine, from which the engine charge temperature at the end of the induction and compression strokes has been computed. The variation of charge temperature with engine speed, throttle setting, air-fuel ratio, inlet-air temperature, and cylinder-wall temperature has been determined.

**Air flow in engine cylinders.**—For fuel injection into the cylinders of an aircraft engine, it is necessary that an air swirl be produced in the cylinder or that a high degree of air turbulence exist to assist in distributing the fuel spray. The investigations to determine the effect of inlet-port and valve design on the air movement within the cylinder of an internal-combustion engine have been continued. Two cylinder heads simulating air-cooled engine practice were constructed and tested on the glass-cylinder engine. In both cases the air movement was partly controlled by the design of the intake port in the cylinder head. With one arrangement the air rotated about the cylinder axis and with the other a vertical swirl was produced. Both designs were effective in giving good engine performance. The results are being prepared for publication.

#### FUEL CONSUMPTION

**Fuel distribution.**—The results of the investigations made to obtain a comparison of the performance of an engine with a carburetor, with fuel injection into the inlet manifold, and with fuel injection into the cylinder have been published in Technical Note No. 688.

**Increase in compression ratio.**—Modern aircraft engines operate at compression ratios of from 6.0 to 7.5. An appreciable reduction in fuel consumption may be obtained by operating at higher compression ratios. An investigation is in progress on a single-cylinder engine to determine the improvement in power output and fuel consumption to be obtained with an air-cooled cylinder having a displacement of 200 cubic inches when operated over a range of compression ratios from 7.4 to 10.2. The fuel is injected into the engine cylinder. At a compression ratio of 9.2 and with atmospheric intake pressure, a brake mean effective pressure of 182 pounds per square inch was obtained at 1,750 r. p. m. The corresponding brake fuel consumption was 0.356 pound per brake horsepower-hour.

**Fuel economy in flight.**—Military operation often requires flight speeds at or near the maximum. As the maximum power condition of an airplane engine is approached, sacrifices in fuel economy must be made to avoid overheating and detonation. It is important that

the fuel consumption be kept as low as possible consistent with safe operation, since the fuel load is a large part of the disposable load of the airplane. An analysis has been made of the methods of increasing power for maximum fuel economy, with detonation and cylinder temperatures as limiting conditions. The results of the analysis showed that the least hourly fuel consumption is obtained at the lowest practicable engine speed and with an approximately correct mixture. Starting from these conditions the methods of increasing power in the order of fuel economy were shown to be:

(a) Increasing manifold pressure at constant minimum practicable engine speed to the point of incipient knock or to full throttle if knock is not encountered.

(b) Increasing engine speed and maintaining constant cylinder temperatures by cooling within knock limits until maximum engine speed is reached.

(c) Retarding the spark or reducing the cylinder temperatures to permit higher manifold pressures.

(d) Increasing the fuel-air ratio to permit higher manifold pressures.

A report has been prepared covering this material.

**Safety fuels.**—Renewed interest has been shown in the use of new safety fuels having the same heating value as gasoline and relatively good antidetonating qualities. The flash point of these fuels is about 115° F., which should result in an appreciable reduction in the fire hazard when used in aircraft. The preliminary tests made with one of these safety fuels having a distillation range from 325° to 425° F. showed that in a single-cylinder engine fitted with a modern air-cooled cylinder the power and fuel consumption are equal to that obtained with gasoline having the same antidetonating qualities.

#### ENGINE COOLING

**Cooling of finned cylinders.**—A report has been published (Technical Report No. 674) covering an investigation of the cooling on the front of an air-cooled engine cylinder. The results show the relative effect of various operating conditions and fin dimensions on the cooling of a finned cylinder in a conventional cowling. An analysis of the cooling problem on an air-cooled engine has been made to show what may be done to improve the cooling and what each improvement requires in increased power expended for cooling. Cooling at altitude was also studied, as well as the relationships between indicated horsepower, cooling requirements, and cooling on the ground.

**Fin dimensions.**—The analysis to determine the proportions of aluminum, copper, magnesium, and steel fins necessary to dissipate maximum quantities of heat for various fin widths, fin weights, and air-flow conditions has been completed. The analysis includes the



determination of the optimum fin proportions when specified limits are placed on the fin dimensions. In addition to the information presented on the design of fins, this investigation shows that optimum fin dimensions are not appreciably affected by the differences in air speed obtained with different air-flow arrangements or by small changes in the length of the air-flow path. For a given fin weight, the highest heat transfer can be obtained with fins of a magnesium alloy; pure copper and aluminum-alloy fins are only slightly inferior to magnesium-alloy fins and will dissipate several times more heat than steel fins. The results of this investigation have been prepared for publication.

**Heat-transfer coefficients.**—The investigation to determine the surface heat-transfer coefficients of finned cylinders has been completed and the results have been published in Technical Report No. 676. The investigation covered the determination of the effect of fin width, fin space, fin thickness, and cylinder diameter on the heat transfer. Wind-tunnel tests were made in a free air stream with and without baffles and also with various devices for creating a turbulent air stream. Tests were also made with blower cooling. Correlation of the surface heat-transfer coefficients measured on 58 finned cylinders was found possible by plotting factors including the air-stream characteristics and the dimensions of the finned cylinders.

**Heat-transfer process.**—A report has been prepared covering the heat-transfer process in a Wright Cyclone engine. Equations for the cylinder head and barrel temperatures as functions of the important engine and cooling conditions are given. A method of correlating and comparing cooling data is presented and is illustrated by curves obtained from data on multicylinder engines in flight and on the test stand, and from single-cylinder test data. The distribution of temperature around the cylinder head and barrel and the correlation of temperatures at individual points on the cylinder are discussed. Calculated curves are presented showing the variation of cylinder temperature with altitude in climb and level flight. Data are also presented showing the variation of cylinder head and barrel temperatures with time when the throttle is suddenly opened and when the cooling air speed is suddenly decreased.

**Heat-transfer coefficients in flight.**—Apparatus has been installed in an airplane and several tests made to determine the surface heat-transfer coefficients of an electrically heated finned cylinder in flight. The object of these tests is to determine heat-transfer coefficients in flight and compare them with those obtained in the laboratory.

**Single-stage axial-flow fan.**—Calculations have been made for a single-stage axial-flow blower to determine its suitability for cooling airplane engines. Pressures

in the neighborhood of 10 inches of water appear to be attainable with efficiencies of more than 80 percent. A fan of this type seems to be suitable for large present-day engines. Although some installation problems have been encountered, they do not seem to be insurmountable, especially for the large radial engines having more than one row of cylinders.

**The N. A. C. A. air-cooled cylinder.**—The method developed by the Committee for bonding preformed aluminum-alloy fins to the cast aluminum-alloy air-cooled cylinder heads has permitted a large increase in the power output that can be obtained from a cylinder having a given displacement. Two air-cooled cylinders have been constructed having the fins attached by this method and the performance of the cylinder has been determined on a single-cylinder engine. The cylinders have the same internal dimensions as a conventional air-cooled engine cylinder but five times the fin surface. For the same power output and same cylinder temperatures, the amount of air required for cooling the N. A. C. A. cylinder is only 35 percent of that required to cool the conventional cylinder. For the same pressure drop across the cylinders, 15 inches of water, and the same cylinder temperatures, it is possible to obtain nearly three times the power from the N. A. C. A. cylinder as from the conventional cylinder.

Preliminary tests showed that satisfactory cooling could be obtained on the N. A. C. A. cylinder with a pressure drop across the cylinder of only 2 inches of water when operating at an engine speed of 2,100 r. p. m. and a boost pressure of 5 pounds per square inch.

#### SUPERCHARGER RESEARCH

**Performance of superchargers.**—The computations on the performance of superchargers having a range of compression exponents from 1 to 2 and operating at altitudes from 0 to 80,000 feet over a wide range of boost pressures are being analyzed. The application of these results to the engine shows that if a geared centrifugal supercharger is used to maintain sea-level pressure to an altitude of 50,000 feet the fuel consumption will be twice that at sea level. This increase is due to the large amount of power required by a gear-driven supercharger. With the turbosupercharger there is no large increase in fuel consumption because the energy to drive the supercharger is taken from the exhaust gases. This analysis will be continued to include the application to engines of high compression ratios.

**Air intercoolers.**—The problem of increasing the anti-knock value of fuels by air intercoolers includes the important consideration of the power necessary to force both cooling air and engine-charge air through the intercooler and also the power required to carry the weight added by the intercooler. A theoretical and experimental investigation is being made of a light-



weight type of intercooler that is expected to reduce charge temperatures materially with relatively low-pressure drop across the intercooler. A test unit of this intercooler is being constructed for laboratory testing.

Programs of investigation have been completed on radiator design and installation and on intercooler design for aircraft. Tests are being continued on tube banks in order to obtain more information on the detached mechanism of heat transfer and friction loss.

**Engine power at altitude.**—The calculation of flight performance at altitude is dependent upon the accurate determination of the variation in engine power with altitude. Several different formulas are available in the literature for correcting engine power at sea level to altitude conditions. A comparison has been made between the calculated engine power and the power as measured on an air-cooled engine in flight by use of the N. A. C. A. torque meter. The range of altitudes covered was from sea level to 20,000 feet. The engine power as measured by the torque meter checked the power as corrected for temperature and pressure by the use of well-established formulas. The results of this investigation and of a study of the variation of engine power with altitude are being prepared for publication.

#### COMPRESSION-IGNITION ENGINES

**Combustion research.**—The performance of high-speed Diesel engines is less than that of the conventional Otto-cycle engine because of the inability of the Diesel engine to burn efficiently the total air charge inducted into the cylinder. As a result, the Diesel engine requires a higher boost to obtain the same take-off mean effective pressure than does the spark-ignition engine. Apparatus has been assembled that will permit an extensive survey to be made of the mixture during combustion in a Diesel engine. Heretofore, such an investigation has been of doubtful value because it required several engine cycles to obtain a large enough sample of the mixture to analyze. The development of an industrial microanalyzer capable of analyzing volumes as small as  $\frac{1}{20}$  milliliter has made it possible to collect an adequate sample from a single cycle. For this purpose a hydraulically operated gas-sampling valve has been developed that, during an opening period of 0.0004 second, will collect a sufficiently large sample from a predetermined section of the combustion apparatus.

A report has been prepared and published as Technical Note No. 707 presenting results of engine performance tests of fuel oils, mixtures of fuel oil and alcohol, and fuel-oil dopes.

The results of the investigation of ignition lag of Diesel oils as determined in a bomb and in an engine have been published in Technical Note No. 710.

**Fuel-injection systems.**—Previous investigations with a simulated unit injection system have demonstrated certain advantages for this type of injection system over the more conventional type in which a length of tubing connects the injection pump to the injection valve. For this reason, a unit injector has been tested to determine the effects of the various operating variables on the rates of fuel discharge. It has been found that, when an outwardly opening injection nozzle is used, the rates of fuel injection closely follow the rate of fuel displacement by the pump plunger. Under very high injection pressures, however, the compression of the fuel in the injection system causes the rate of discharge to be less than the rate of plunger displacement. Secondary discharges are eliminated when a unit injector is used and higher rates of discharge are obtained than are practicable with the injection pump mounted at some distance from the injection valve. The results of this investigation are being prepared for publication.

**The 4-stroke-cycle engine.**—The N. A. C. A. displacer-type combustion chamber has been adapted to an air-cooled cylinder having a 5-inch bore and a  $5\frac{1}{2}$ -inch stroke. From the results of single-cylinder engine performance tests, multicylinder engine performance has been computed. On the basis of the weights of the single-cylinder parts, the weight of a nine-cylinder radial engine has been computed. These computed values indicate a specific weight of 1.6 pounds per horsepower for an output of 500 horsepower. From the results of single-cylinder tests, heat loss, heat-loss distribution, and cooling measurements have been calculated. An investigation has been started to determine the air-charging restrictions peculiar to the displacer-piston type of combustion chamber.

**The 2-stroke-cycle engine.**—The liquid-cooled engine used in this investigation has piston-controlled inlet ports directed at  $56^\circ$  to the radial and exhausts through four poppet valves in the head. Engine-performance tests have been made with various rates of injection and various fuel-spray orifices in two diametrically opposed fuel valves, each valve injecting downstream with the rotating air flow. Tests have been made with reduced inlet and exhaust time areas to determine the amount of power reduction and exhaust characteristics. Preparations have been made to improve the air charging by using four rows of inlet ports and to increase power by increasing the engine speed to 2,400 revolutions per minute.

**The 2-stroke-cycle sleeve-valve engine.**—Analysis has shown that the single sleeve-valve mechanism should give better breathing capacity and higher allowable rotative speeds than the Committee's poppet-valve engine. With the object of determining engine-performance characteristics, a design has been completed



of a single sleeve-valve engine. The necessary parts for the test engine are now under construction by the contractor.

#### NATIONAL BUREAU OF STANDARDS

**Phenomena of combustion.**—A large number of photographs of explosions in a 10-inch spherical bomb were taken through a narrow window which formed a part of the bomb wall. In addition to the flame trace, each record contained a time scale in thousandths of a second and six points on the time-pressure curve. Mixtures of the fuels benzene, normal heptane (zero octane number), and iso-octane (100 octane number) with oxygen and nitrogen were studied. A technical report giving the detailed experimental results and the conclusions which have been drawn for the three hydrocarbons as well as those for previous measurements with carbon monoxide is being prepared for publication.

In all the explosions there is a general increase in the transformation velocity as the temperature and pressure of the unburned charge rise because of the adiabatic compression. Since the range of initial conditions was wider for carbon monoxide, it was possible to analyze these results for the independent effects of temperature and pressure, and both were found to contribute to the increase in transformation velocity. For the hydrocarbons in comparable mixtures, the transformation velocity is highest for benzene and lowest for iso-octane, with heptane intermediate. The addition of tetraethyl lead to the heptane mixture produced no appreciable change in flame speed. Thus, under the conditions of the experiments there appears to be no relation between transformation velocity and the tendency to knock.

Until the late stages of the explosion there is no measurable difference among the hydrocarbon fuels in the pressure rise produced when a given fraction of the charge is inflamed. For all the explosions the rise in pressure for a given mass of charge inflamed is considerably less than would be expected from calculations based on thermal data and the assumption that reaction goes to equilibrium in a very thin flame front. The results therefore indicate that the liberation of energy continues for some time after the flame front has passed. Observations of the gas movements within the sphere of flame, made by following the bright trails left by burning particles of gunpowder suspended in the mixture, also indicate the existence of continued reaction within the inflamed gases.

Since no connection could be found between any of the characteristics of the normal burning of the hydrocarbon fuels and their relative tendency to knock in an engine, a supplementary study of the influence of various factors upon the transition from normal burning to detonation has been undertaken. Construction of ap-

paratus for this purpose was begun, while preparations for a series of measurements in the spherical bomb on triptane (2, 2, 3-trimethylbutane) were being completed.

**Flow characteristics of fuel lines.**—In connection with a cooperative attack on aviation vapor-lock problems, the Bureau has investigated the resistance to fuel flow in fittings and accessories of 1/2-inch tubing and in 5/8-inch tubing as a function of rate of flow and relative amounts of liquid and vapor flowing. The resistance of any fuel-system component to liquid flow is approximately doubled when equal volumes of liquid and vapor are present. It has been demonstrated that the resistance of conventional elbows can be reduced materially by redesign of the fitting, and a simple type of pressure tap has been developed which is suitable for general use, particularly in fuel system mock-ups.

**Engine testing.**—A study of the characteristics of oils and their effect on engine condition was made at the request of the Matériel Division of the Army Air Corps. The tests consisted of a series of 50-hour endurance runs on a 9-cylinder air-cooled engine mounted on a rigid stand.

Altitude tests were made on an aircraft auxiliary power plant for the Bureau of Aeronautics, Navy Department. Altitude tests on stationary power plants for beacon lighting, teletype, and other airway equipment were made at the request of the Civil Aeronautics Authority.

**Temperature surveys.**—Ground and flight temperature surveys have been continued on all new types of Navy aircraft engines. These include cylinder, oil, and intake-mixture temperatures.

**Spark plugs.**—A method of bench testing mica spark plugs has been put into service use with satisfactory results. Further investigation into materials and designs of spark plugs to meet the more exacting requirements of commercial and military services is under way.

**Aircraft-engine cylinder wear.**—An investigation was made to determine the cause of cylinder wear, particularly on the rear wall. From the data obtained for two continuous 50-hour runs on an air-cooled single cylinder engine, it was found that wear on the rear wall was caused chiefly by corrosion. Factors in the acceleration of the corrosion were the antiknock compound used, the lubricant, and the temperature distribution of the cylinder.

#### SUBCOMMITTEE ON AIRCRAFT FUELS AND LUBRICANTS

**Investigation of antiknock characteristics of fuels.**—The investigation of the relationship of engine operating conditions to the antiknock characteristics of fuels has been continued. From the results obtained with a flat-disk combustion chamber and a pent-roof combustion



chamber an analysis has been made in which the maximum permissible engine performance under a variety of engine operating conditions has been derived from an experimental determination of the maximum permissible performance under a few conditions. The analysis shows that, from considerations of knock, the most important independent variables in any one engine are the inlet-mixture density and temperature and the mixture ratio. The data show that preignition must be treated separately from knock if fuels are to be adequately rated in an engine.

The analysis shows that, for any particular fuel, the maximum permissible power increases as the compression ratio is decreased, provided that the inlet air temperature is maintained constant and the performance is limited by knock and not by preignition. For cases in which the inlet air is heated an increasing amount as the boost pressure is increased, an optimum compression ratio exists for the engine from the consideration of maximum permissible power. The data show that a certain amount of correlation is possible between the curves of knock characteristics of several fuels from tests on different engines, but that certain differences are caused by engine design. The results of this investigation have been published in Technical Report No. 655.

A portion of the investigation has been completed on the determination of the knock characteristics of a cylinder with a semispherical combustion chamber. Although in general the results are the same as those obtained from the flat-disk and pent-roof combustion chambers, certain differences in the correlation of the data result from the difference in cooling characteristics of this engine. This investigation is being continued.

Additional tests of fuels are being conducted on a high-speed C. F. R. engine. With several fuels of 100 octane number used in this engine, different values of highest useful compression ratio were obtained as the inlet-air temperature was varied. The results also indicate that the effect of engine speed on maximum permissible performance may be a temperature effect resulting from the transfer of heat from and to the incoming mixture rather than being a time effect as has been previously suggested.

**Investigation to develop nonleaded aircraft fuel of over 100 octane number.**—This investigation, carried on by the National Bureau of Standards for the past two years in cooperation with the National Advisory Committee for Aeronautics, the Army Air Corps, and the Bureau of Aeronautics of the Navy Department, has been in a confidential status until recently. The program calls for the preparation of branched-chain paraffin hydrocarbons in the volatility range of aviation

gasoline, and the investigation of their knocking tendencies and their physical properties.

Two automatically controlled fractionating columns were designed and installed for this work. Both columns have efficiencies of at least 100 theoretical plates and operate, practically without attention, day and night, Sundays and holidays, barring an unexpected failure of the electric power supply. These columns serve to separate and purify synthetic products and to isolate materials from industrial crudes. The project has required the construction of Grignard reactors, hydrogenators, and other necessary equipment for organic synthesis.

One of the first hydrocarbons prepared in this laboratory was 2,2,3-trimethylbutane, also called triptane, preparation of which was begun June 1, 1938. As the fractionating columns had not been completed at the time, this material was not finally purified until early in 1939, shortly after an industrial laboratory had reported that triptane was well over 100 octane number. When the Bureau's final product was blended with an equal volume of 90 octane reference fuel (90 percent iso-octane and 10 percent heptane) the octane number of the blend was over 99, indicating pure 2,2,3-trimethylbutane to be about 108 ASTM octane number. Six liters of this compound were supplied to the Langley Memorial Aeronautical Laboratory for further tests.

All the pentanes, hexanes, heptanes, and octanes of interest are now on hand. Three nonanes have been isolated from a synthetic crude and partially purified. Synthesis of two additional nonanes, one of which has been prepared once before and one never before, is in progress. Between one and two pounds of a solid octane have been recovered as a byproduct of the synthesis of other materials. This melts at  $101^{\circ}\text{C}$ ., boils at  $106^{\circ}\text{C}$ ., and is very soluble in liquid paraffin hydrocarbons.

A study is being made to find a suitable scale for rating pure compounds which have octane number above 100. Various methods of extrapolation by means of an engine characteristic such as compression ratio on manifold pressure have been considered. However, the best proposal appears to be the use for the present of heptane and iso-octane, each containing 0.1 percent tetraethyl lead, as the primary reference fuels. Secondary reference fuels, one of which is technical iso-octane, also containing 0.1 percent tetraethyl lead would be calibrated against the primary scale and used in testing. This choice of a primary scale is dictated by the consideration that such a scale composed of pure compounds, can always be duplicated and hence the ratings can in the future be translated into any other scale subsequently adopted merely by



intercomparison of the two sets of scale constituents. Experimental work on this proposed scale is in progress.

**Stability of aviation oils.**—Last year a laboratory test for oil stability was developed at the National Bureau of Standards and mentioned in the report as in satisfactory accord with changes taking place in the oils during service operation of aircraft engines. This correlation was subsequently extended to include all available information on engine deposits both in service and in test-stand operation. It appears that it is possible by means of a simple laboratory test method to predict not only the extent of the changes which will take place in an oil during service operation in aircraft engines but also to predict the extent of deposits which are formed in these engines.

For the information of the military services, a survey has been started on the stability characteristics of commercial aviation oils and it is planned to keep this survey up to date as new or improved aviation oils are developed.

Through the cooperation of the Research Committee on Aircraft Engine Lubricants of the Society of Automotive Engineers, a set of engine inspection forms has been developed for recording the condition of aviation engine parts at the time of overhaul with particular reference to those parts on which deposits form and to those parts in which differences in lubrication characteristics of the oil are important. This makes it possible for all observers to record data on engine conditions on a uniform and comparable basis.

**Ring sticking with aviation oils.**—Further information has been obtained at the National Bureau of Standards on the thickening of oils at the high temperatures encountered around the upper piston rings, and a simple laboratory test method has been developed which has significance as regards the tendency of oils to cause cold ring sticking. During the course of the extensive engine inspections undertaken in connection with the oil stability program, information was obtained regarding the extent of ring sticking. Comparison of the laboratory and engine data on these oils showed that the laboratory data correlated satisfactorily with the extent of ring sticking in service.

The conclusions reached in the investigation of oil stability and cold ring sticking favor highly solvent refined lubricating oils and work is under way to provide protection against serious difficulties with hot ring sticking and with excessive engine wear which may result if over-refined oils are used. It is expected that suitable test methods of protection against the use of over-refined oils will be available during the coming year.

**Corrosion.**—A new laboratory method of determining the corrosiveness of oils has been developed. It has been determined that corrosion due to oil in engines is critically affected by the preparation of the sliding surfaces during manufacture.

**Bearing corrosion.**—Considerable progress has been made at the National Bureau of Standards in the investigation of the problem of the corrosion of master-rod bearings. The general trend of the investigation has been to evaluate the critical temperatures at which oils form corrosive acids, and marked differences have been found between various oils in this respect. This work is rapidly approaching the stage where a significant laboratory test method can be proposed.

In the course of the corrosion work, it was found that there were appreciable differences between the results obtained by different laboratories in the determination of the neutralization number of used aviation oils. Accordingly, through the cooperation of the Research Committee on Aircraft Engine Lubricants of the Society of Automotive Engineers, a modified method for the determination of neutralization number was developed which was found to give reproducible values in different laboratories. A description of this method has been published by the American Society for Testing Materials in its annual report.

**Lubrication of master-rod bearings.**—A small bearing machine has been developed at the National Bureau of Standards for the investigation of master-rod bearing lubrication under severe operating conditions. This machine uses four small bearings similar metallurgically and in surface composition to full-scale bearings. It is possible to operate the machine over a wide range of speeds, loads, and oil temperatures. Information thus far obtained indicates that the machine is very satisfactory and that the load-carrying capacities of bearing materials can be rapidly and accurately evaluated.

## REPORT OF COMMITTEE ON AIRCRAFT MATERIALS

### SUBCOMMITTEE ON METALS USED IN AIRCRAFT

**Effect of continuous weathering on aircraft metals.**—Aircraft structural parts built up of sheet-metal members are used very extensively. The development of the monocoque or stressed-skin type of airplane structure has served to emphasize strongly the importance of the durability of sheet metal. The effect of continuous exposure to weathering action is a factor which must always be considered.

Technical Report No. 663, "The Weathering of Light Metal Alloys Used in Aircraft," has been published.



This summarizes the results of extensive outdoor exposure tests of 5 years' duration previously carried out on aluminum and magnesium alloys in sheet form, of various commercial compositions and with various types of protective surface treatments and applied coatings.

A report is being published which summarizes the results obtained during the first year in the current series of exposure tests on aircraft metals. This covers aluminum and magnesium alloys and stainless steel, all in sheet form. In one series of tests the materials are exposed continuously in a marine atmosphere, Hampton Roads Naval Air Station, and in a supplementary series the materials are so placed as to be immersed in sea water at high tide. In these exposure tests emphasis has been placed on the determination of the effects on various types of metals when in contact one with another in both riveted and welded joints.

This series of tests, which was planned to extend over a period of several years, is an "open" one in that new materials of promise can be included as they become available. At the request of the manufacturers, an aluminum alloy, the commercial standing of which had been established by usage over a number of years, was included in the test, and arrangements are in progress for the inclusion of a recently developed material of unusual promise, although it is not yet commercially available. Only by prolonged exposure tests of this kind can the merits of such materials for aircraft use be established.

**Elastic properties of high-strength constructional aircraft metals.**—Technical Report No. 670, "Tensile Elastic Properties of 18:8 Chromium Nickel Steel as Affected by Plastic Deformation," has been published. A second report entitled "Tensile Elastic Properties of Typical Stainless Steel and Nonferrous Metals as Affected by Plastic Deformation and by Heat Treatment," is being prepared for publication. This report considers the tensile elastic properties of 18:8 chromium-nickel steel, 13:2 chromium-nickel steel, monel metal, Incomel, and K-monel metal. A general discussion is given of the relationship between stress, strain, and permanent set. Stress-strain relationships are discussed, together with the variation of proof stresses with prior plastic extension; also the influence of work-hardening and internal stress on the form of the proof stress-extension curve. From the stress-strain curves have been derived stress-modulus lines. For all but relatively soft metals, the stress-modulus line is practically straight. Stress deviation, that is, deviation from stress-modulus line, and stress-set curves were determined, and from these were derived various diagrams illustrating the influence of plastic-extension and heat treatment on the elastic strength, on the modulus of elasticity, and on its stress coefficient. Equations have been developed to represent the form of the elastic stress-strain curve.

The next phase of the investigation, the study of the elastic properties at low temperatures ( $-108^{\circ}$  F.) is being started. Steel of the 18:8 chromium-nickel type, the properties of which have already been studied at normal temperature, is the material to be used in this phase of the work.

**Structural changes in aircraft metals occurring as a result of service.**—Service stresses of structural members are, in general, largely of the character known as fatigue stresses. In this investigation, the study of the impact resistance of the metal after it has been subjected to fatigue stressing occupies an important place.

A report entitled "Effect of Service Stresses on Impact Resistance, X-ray Diffraction Patterns, and Microstructure of 25S Aluminum Alloy" has been published, based on a study of the 25S aluminum alloy used extensively for propellers. No outstanding detrimental effects in this material attributable to fatigue stressing were observed.

The second phase of the investigation deals with the impact properties of normalized SAE X4130 steel (0.30 C, 1.00 Cr, 0.20 Mo) after fatigue stressing below the point at which incipient failure can be detected. Tensile impact tests of smooth unnotched specimens after being fatigued-stressed by axial loading have shown: (a) only slight difference in the tensile impact behavior of normalized X4130 steel at  $-32^{\circ}$  C. and at  $+25^{\circ}$  C.; (b) the production of nonductile impact fractures after sufficient numbers of cycles of stress above the fatigue limit; (c) a surface condition of marked significance—microscopic surface ruptures opened by the tensile impact stress, relatively few in number on highly polished fatigue specimens but present in large numbers on specimens for which a slightly coarser polish was used; (d) the fact that removal of a thin surface layer from fatigue-stressed specimens containing these surface ruptures restored their impact resistance to that of similar unstressed (undamaged) specimens, thus indicating that the damage revealed by the check cracks produced by tension-impact is confined to the surface zones. Further work on this subject is in progress.

Transverse impact tests of notched fatigue specimens prestressed in a rotating cantilever-beam fatigue machine showed that the impact resistance of notched specimens at  $-78^{\circ}$  C. was generally one-half to one-fourth of that at normal room temperature, the percentage decrease in low-temperature impact resistance resulting from fatigue being greater than in similar tests at room temperature.

The extent to which a metal structure recovers during periods of rest following intermittent periods of fatigue-stressing is questionable. Definite indication has been obtained of the strengthening of normalized X4130 steel by alternating stressing above the fatigue



limit and resting. A series of rests and runs of rotating-beam fatigue specimens stressed above the fatigue limit resulted in conditioning the specimens so that after a while the specimen could be kept running continuously at the same overstress without further resting. This subject is being studied at greater length.

**Protection of magnesium alloys.**—Marked advance has recently been made in the development of new protective coatings for magnesium alloys. Five are now commercially available which are equal in the corrosion protection which they give to that produced by the anodic treatment in the dichromate-phosphate solution which has hitherto been standard. The improved treatments all involve a final sealing treatment. Only the methods based on anodic treatment, however, are applicable to all types of magnesium alloys. The use of hydrofluoric acid, which is an essential feature of some of the new treatments, is objectionable for several reasons in the practical application of the coatings, and efforts are being continued to eliminate its use.

**Effect of subzero temperatures on aircraft metals.**—The fact is well established that the lowering of the impact resistance of metals at low (subzero) temperatures is the most marked change in the properties of a metal structure which should be guarded against. In cooperation with the Bureau of Aeronautics, Navy Department, the investigation of various heat-treatment methods to improve this condition at low temperature has been continued but so far without complete success. Indications have been obtained that certain heats of steel are consistently superior to other heats of the same nominal composition but the underlying factors are as yet not clearly understood. The impact resistance at normal room temperature is no criterion of this property at subzero temperature. In the case of welds the seriousness of this condition of low impact resistance at low temperatures is augmented by defects incidental to variations in welding technique. The investigation is being continued.

**Commercial aircraft steel tubing.**—In cooperation with the Bureau of Aeronautics, Navy Department, extensive tests have been carried out in seamless steel aircraft tubing (chromium-molybdenum steel, SAE X4130) obtained from all the available domestic sources of supply. Differences of considerable magnitude in the ultimate tensile strength and the yield strength as compared with the requirements set forth in the specifications of the Navy Department for this type of material were found, this being true for practically all of the manufacturers represented. These differences are apparently the results of differences in fabrication and heat-treatment procedures, since they could be practically eliminated by annealing. A change in the specification requirements may be the logical outcome.

## SUBCOMMITTEE ON MISCELLANEOUS MATERIALS AND ACCESSORIES

The work of this subcommittee during the past year has been devoted chiefly to the development of plastic material for aircraft structures. A considerable amount of work has also been done on a continuation of the study of flexible transparent window materials, on the compilation of information about acoustical and thermal insulating materials, and on a study of the properties of the new synthetic fiber and glass with a view toward their utilization in parachute and wing fabrics.

Some consideration has been given to the finding of a substitute for silk for shroud lines, the development of more satisfactory shock-strut guards and fluids, pre-rotation of wheels, and safety tires. Work is under way on the development of fillers for small surface depressions such as rivet heads in wings.

The subcommittee is following with interest the work at Langley Field on the development of de-icers and the cooperative work of the Civil Aeronautics Authority at the National Bureau of Standards on the fire-resistance of aircraft materials. On request, a soap manufacturer is now trying to develop a better soap for cleaning airplanes.

**Development of plastic material for aircraft structures.**—Eighteen synthetic resins have been tested to determine their suitability for impregnating and bonding wood veneers to form a reinforced plastic of the requisite strength and stability for use in aircraft construction. Nine hot-pressed and three cold-pressed phenol-formaldehyde resins, one phenol-furfural resin, four urea-formaldehyde resins and one vinyl acetal resin were investigated. Great differences were observed in the temperatures and pressures required for obtaining satisfactory bonds with these resins and in their degree of resistance to delaminating when alternately wetted and dried. On the basis of these data three of these resins have been selected for use as bonding and impregnating agents in the preparation of laboratory samples of reinforced plastics for strength tests. These are a phenol-formaldehyde resin which requires hot pressing to obtain a good bond and cure, a phenol-formaldehyde resin which cures at room temperature by catalytic action, and a vinyl acetal resin which is permanently thermoplastic and requires heat to make it flow and effect a bond. These are representative of the resins required for investigating three different methods of molding reinforced plastics, namely (1) use of heat and pressure accompanied by thermal curing of the resin, (2) application of pressure at room temperature accompanied by catalytic curing of the resin, and (3) use of heat and pressure with a permanently fusible resin. The preparation of curved and tubular speci-



mens by methods adaptable to the fabrication of large members is now being investigated.

Tensile and compressive strength, modulus of elasticity, and water absorption have also been determined for a number of plastics which have been proposed by various commercial sources for use in building propellers, floats, spars, wings, and fuselages of airplanes. The reinforcing agents in these products included wood veneer, pressed wood, flax, jute, and sisal. The results obtained indicate that maximum strength and stiffness is attained with well-oriented fibers and thermosetting resins.

**Evaluation of new transparent plastics as windshields for aircraft.**—The past year has been a period of particularly active development of new transparent plastics, including such materials as cellulose acetopropionate, cellulose acetobutyrate, vinyl chloride-acetate resin, and polystyrene resin. Further improvement in the methyl methacrylate and cellulose acetate plastics has also been effected. An accelerated aging test developed in the course of experimental work on transparent plastics has proved to be a very useful means of rapidly evaluating these new materials with regard to weathering resistance. It is highly desirable that these new and improved materials, which are found to possess the necessary weathering resistance, should be examined with respect to other properties of importance in connection with their use as aircraft windshields and that a specification should be prepared to permit the procurement of transparent plastics which will most satisfactorily meet aircraft requirements.

It is, therefore, proposed to obtain from the respective manufacturers new samples of the transparent plastics which have been found to be outstanding with respect to weathering resistance and to submit them to tests for the following properties: Light transmission, haze, distortion, scratch resistance, impact strength, tensile strength, flexibility, thermal expansion, dimensional stability including both shrinkage and warping, flame resistance, and resistance to action of water, oil, gasoline, grease, and soap solution. The relative resistance of these plastics to weathering will also be established by exposing them in the accelerated aging apparatus for a longer time than the 500 hours which we now use to evaluate outdoor stability. The effect of weathering, both natural and accelerated, on the strength and optical properties of the plastics will be determined. The variation of the strength properties with temperature will be studied over the range from 140° F. to -40° F. A detailed specification will be prepared on the basis of these experimental procedures and results, to cover those materials which are found to be superior for aircraft use.

## REPORT OF COMMITTEE ON AIRCRAFT STRUCTURES

### LANGLEY MEMORIAL AERONAUTICAL LABORATORY STRUCTURAL RESEARCH

One of the problems that has confronted designers of stressed-skin and monocoque structures for several years has been the proportioning of intermediate frames and ribs. Heretofore very little consideration has been given to this problem in the literature. During the past year, two investigations of this problem were undertaken. The first was concerned with the loads on intermediate frames and the second was concerned with the stiffness required of these members. In practical design problems, it is desirable to check both the strength and the stiffness of the intermediate frames.

**Loads on intermediate frames.**—If the flange members of a beam change direction at an intermediate frame, a force is applied to the intermediate frame. This change of direction can either be built in or result from the deflection of the beam.

The practical design formulas for calculating the load on intermediate frames for each of these cases have been summarized in Technical Note No. 687. In this paper, an analysis of diagonal-tension effects in beams with curved webs is also included and a new semi-empirical formula for the loads on the stiffeners is proposed.

**Stiffness required of ribs.**—In the design of stressed-skin wings, it is common practice to assume that the shear webs and ribs are equivalent to rigid supports which divide the stiffened-skin covering into small panels and that the bending strength of the wing depends upon the compressive strength of these panels. This assumption is sound provided the ribs are sufficiently stiff. A first paper on this subject was presented to the Institute of Aeronautical Sciences during the past year. This paper, entitled "On the Rib Stiffness Required for Box Beams," appears in the *Journal of the Aeronautical Sciences*, May 1939. In this paper the stiffness required of the ribs to divide the compression side of a stressed-skin wing into small panels of length equal to the rib spacing is discussed.

This problem has been further studied and the theory is being extended. This subject is considered one of great importance because, if the ribs of a stressed-skin wing do not have a stiffness equal to or greater than that required to divide the compression surface as assumed, the foundation of the present design procedure crumbles.

**Stress distribution in monocoque structures.**—The stress distribution in monocoque structures is influenced by several factors, one of the most important of which is the shear deformation of the skin. In most practical



cases, the problem of taking shear deformation into account leads to quite laborious methods of analysis. During the past year, a simple numerical method applicable to these problems, as well as to mathematically related problems, has been developed. This method is completely described in Technical Note No. 704, which also includes a practical example.

Continued efforts are being made to find the simplest possible method of solving increasingly complex problems in stress distribution. A continuous check on the validity of the simplifications is being made by strain-gage tests.

**Shell analysis and the shear center.**—There has been some confusion as to how established methods of analysis should be applied to shell structures when the loading consists of combined bending and torsion. The basic principles for this analysis have been established for some time. A summary of the practical design formulas has been made and their use illustrated with a number of problems. The summary and problems have been presented in Technical Note No. 691. In this note it is also pointed out that the use of the shear center offers no advantage over the use of any arbitrary reference point.

**Method of estimating critical loads.**—In most problems of elastic instability the critical buckling load is determined by satisfying certain transcendental equations associated with the condition of neutral stability. In order to solve these equations, it is necessary to assume values of the critical load and to test the equations. By application of methods similar to those proposed by Southwell for the analysis of experimental observations in problems of elastic stability, a method has been developed to estimate quickly the theoretical critical load after the equation for neutral stability has been tested for three assumed critical loads. This method of estimating critical loads, as applied to structural members, has been described in Technical Note No. 717. In this paper a number of examples are given to reveal certain characteristics of the method that should be known by the practical engineer using it.

**Local buckling of compression members.**—During the past year two papers (Technical Notes Nos. 686 and 722) have been published wherein charts are presented for the coefficient in the formula for critical compressive stress at which cross-sectional distortion begins in columns with rectangular-tube, channel, and Z-sections. This work is being extended to include much more comprehensive treatments for buckling problems in general.

**Correlation of structural data.**—During the past year, the Committee has received a large amount of structural-test data from the Army Air Corps, the Bureau of Aeronautics of the Navy, the Civil Aeronautics Au-

thority, and the aircraft industry. These data are being studied with a view to correlating as much of it as possible. Steps are being taken to supplement present information with regard to the geometric dimensions of the test specimens, the material properties, and the types of failure.

A valuable result of the study of these data has been to observe what problems have not been attacked by the industry. This information has been used to revise the structural-research programs of the Committee so as to cover important phases of structural design for which information is needed.

#### STRUCTURAL LOADS ON AIRPLANES

**Statistical measurements of gust loads.**—Coordinated measurements of acceleration and air speed on transport airplanes have been continued. Although several high accelerations have been recorded during the past year, none of them exceed the maximums previously recorded. This subject is more fully presented under the report of the Subcommittee on Meteorological Problems.

**Gust structure.**—An investigation of gust structure under a variety of weather conditions and at various altitudes up to 17,000 feet in the vicinity of Langley Field has been concluded. Analysis of the complete data has led to verification of earlier indications that there is no correlation between gust intensity and gust gradient. In the case of gusts encountered in the lower levels of the atmosphere, a fairly high degree of correlation was found to exist between the wind gradient and a gust-intensity index derived from an elementary analysis based on the concept that gusts arising from mechanical friction or disturbances behave in a manner analogous to the behavior of a simple elastic system. In the case of thermal gusts, the maximum intensities measured during surveys of the gust occurring in different weather situations were found to be dependent on the thermal energy available for convection in these situations.

The indications obtained from gust measurements on a number of airplanes of widely different size, considered in conjunction with tests in the gust tunnel, have led to improved working concepts of the relation between maximum gust intensities and corresponding gradients. Although the subject is too involved to discuss here, for practical design purposes there are strong indications that the gradient distance of the gust may be taken as 8.5 chord lengths. Currently used gust factors derived on a somewhat different basis are not in disagreement with this concept and, in fact, have been more firmly established by the more recent data. Recent advances in the theory of unsteady flow likewise do not upset in any way the practical value of the established gust-load criterions.



**Gust tunnel.**—The results of the first tests in the gust tunnel, reported last year, have been published in Technical Note No. 706.

Tests of a biplane model (Technical Note No. 731) indicate that, when the conventional assumption of the equivalent monoplane is made, calculated accelerations are considerably less than the measured values (20 percent in the case tested). If the wings are assumed to act independently as finite monoplanes, however, agreement between calculated and test results is good, provided the gradient distance does not exceed about 10 to 12 chord lengths. Beyond this distance, a discrepancy appears that is probably due to an increasing approach to steady-flow conditions, with a corresponding increase in induced biplane interference.

Tests on a model of a "canard," or "tail-first," airplane designed to be the equivalent of a particular conventional airplane showed that the "canard" arrangement is unfavorable from considerations of gust loads. In the case studied, the accelerations were about 30 percent higher than those measured on the conventional model throughout the important range of gust gradients.

In order to determine the possibility of reducing gust accelerations by suitable structural design of the wing, a model was provided with a wing flexible in torsion. This wing was tapered, the tip chord being half the root chord, and the construction was such that the tip section twisted  $-1.5^\circ$  per load factor with properly distributed load. Comparative tests on the model alternately equipped with the flexible wing and with a rigid wing indicated that the effect of the flexibility was a reduction in acceleration approximately proportional to the gradient distance and having a value of about 16 percent with a gradient distance of 10 chord lengths.

**Load distribution.**—An analytical study of the variation of the net wing loads under conditions in which combined angular and normal accelerations exist has been completed. This study included the determination of the shear and the moment variation along the wing span during unsymmetrical landings, aileron deflection, and several types of unsymmetrical gusts. The results are being applied in a report, now in preparation, to illustrate the effect of a number of variables such as wing taper, wing weight, and aileron span on the shears and moments.

**Tail loads.**—The possibility of relating tail loads and load factors in maneuvers has been given considerable attention. Within the past year a set of dynamometer springs has been designed and installed in a small airplane for measuring tail loads. Special apparatus for controlling rate and amount of elevator deflection and other equipment has also been installed.

A brief analysis of the loads on horizontal tail surfaces during recovery from spins indicates that for large modern multiengine airplanes there is considerable danger of failure in this condition. The loads become excessive because of high rates of descent resulting from heavy wing loading, clean design, and steep spinning attitude and because the tail operates at maximum lift coefficient while passing from the stalled state of the spin to the unstalled state following recovery. In one case investigated, the upward-acting tail load during recovery was estimated to be several times the normal design load. Wing loads may also be excessive on large modern airplanes in spins.

Measurements of gust loads on the vertical tail surfaces of a twin-engine airplane have been concluded. The results indicate no simple basis for relating the probable gust loads on tail surfaces to the gust loads on the wings, because the tail loads in rough air are a summation of partial loads caused by the direct action of the gust, the angle of the rudder, the yawing velocity of the airplane, and possibly the position of the surface relative to the slipstream determined by yawing of the airplane and irregularities in the slipstream caused by atmospheric turbulence. In order to study these conditions more fully, as well as to obtain further statistical data, more complete instrumentation has been installed in a modern four-engine airplane.

**Loads on seaplane hulls.**—Extensive measurements of hull pressures, stresses, and acceleration on two large flying boats have been completed. The results have given a fairly complete qualitative picture of the nature of the loading conditions. They indicate that forward speed plays a predominant part in determining the magnitude of the maximum pressures and that, at a given speed, the maximum pressures may be of the same value at any point on the bottom, the position in any case depending on the attitude of the hull and the conformation of the water surface. These maximum pressures are usually so localized and shift position so rapidly that they are of little direct structural significance, although under some circumstances in rough water the areas involved may be great enough to give rise to high local loads. In regard to the resultant load on the hull, the vertical momentum is of more importance, inasmuch as it determines the depth of immersion and consequently the wetted area over which the mean pressure acts. For example, on a given hull at constant vertical velocity the acceleration was found to increase with beam loading (vertical momentum) because of the increased wetted area.

**Dynamic overstress.**—Measurements of acceleration and wing stress have been made on a very large airplane in rough air. The results agree with those pre-



viously obtained on an M-130 flying boat in indicating no evidence of dynamic overstress. Measurements of acceleration and wing stress have also been made on a small airplane in maneuvers to demonstrate that the relation between load factor and stress remains the same regardless of the period of application of load under all possible conditions.

#### NATIONAL BUREAU OF STANDARDS

**Tensile and compressive properties of duralumin, magnesium, and alloy steels.**—A paper describing the pack method for compressive tests of thin sheet metal has been published during the past year as Technical Report 649.

The pack method was extended to thinner gages and to higher compressive stresses in order to obtain compressive stress-strain curves for 0.02-inch stainless-steel sheet material for the Bureau of Aeronautics, Navy Department. Additional support was obtained by cementing the leaves of the pack together with shellac and by using external clamps of special design. It was possible with this procedure to apply stresses up to 202 kips per square inch to a pack of about 31 leaves of 0.02-inch stainless-steel sheet before failure occurred by sudden instability of the entire pack.

Column tests and crinkling tests were made on closed sections formed from this material by spot-welding with the load along the direction of rolling in the case of half of the specimens and at right angles to the direction of rolling in the case of the other half. The tests showed differences in strength that agreed with the differences expected from the compressive stress-strain graphs.

A number of tests were made to develop a convenient and rapid method for detecting the presence of aeolotropy in compressive properties of thin sheet. The most promising results were obtained by comparing the buckling loads obtained in fixed-end compressive tests of single strips of suitable length cut from the sheet in a transverse and a longitudinal direction. In the case of stainless-steel strips having a length equal to about 20 times their thickness the transverse buckling load exceeded the longitudinal buckling load by about 50 percent.

**Beryllium.**—Mechanical tests have been made on a number of specimens of beryllium aluminum alloy with a beryllium content from 22.6 to 70 percent (nominal). The Young's modulus for these specimens ranged from 14,300 to 30,000 kips per square inch. Tensile tests resulted in a highly curved stress-strain curve in each case, a tensile yield strength (offset, 0.2 percent) ranging from 15.5 to 20.2 kips per square inch, a tensile strength ranging from 22.8 to 29.1 kips per square inch, and an elongation in 1 inch ranging from 2.0 to 9.0 percent.

**Flat plates under normal pressure.**—The tests of circular plates with clamped edges have been completed and a detailed report has been submitted to the Bureau of Aeronautics, Navy Department. Normal-pressure tests were made on 19 plates 5 inches in diameter ranging in thickness from 0.0149 to 0.0723 inch. Seventeen of the plates consisted of aluminum alloy, one of 18:8 stainless steel and one of magnesium alloy.

The center deflections and stresses at low pressures were found to agree with those calculated for a plate of "medium thickness" from theories by Way and Nadai. At higher pressures the observed center deflections exceeded the calculated values consistently by 4 to 12 percent. With the beginning of permanent set at the center both the total center deflection and the permanent set at the center tended to increase linearly with the pressure for most of the plates.

The pressure required to produce yielding in the plate, as measured by a given permanent set at the center, was between the theoretical pressures for yielding at the edge and for yielding at the center of the plate. Empirical curves are included in the report which relate the pressures for a given permanent set at the center of the plate to the dimensions of the plate and the tensile properties of the material.

**Aircraft tubing.**—The first portion of the program on high-strength chromium-molybdenum-steel tubing of the type used in landing gears was completed by tests in tension, compression, bending and torsion of tubes whose diameter-thickness ratio ranged from 12 to 55.

The tests were complicated by the extreme hardness of the material which caused difficulties in seating strain gages and gripping the specimens for test, and by variations in properties in the individual lengths of tubing. However, these difficulties were overcome and enough tests were made so that the strengths are known sufficiently well in terms of the diameter-thickness ratios and the mechanical properties of the material to proceed with tests under combined loading.

**Wing beams.**—Detailed reports were prepared for the Bureau of Aeronautics, Navy Department, on tests of two series of wing beams under axial loads, transverse loads, and combined axial and transverse loads. The materials were 24ST aluminum alloy in both cases, and the section was an I-section having curved flanges for one series and tilting flanges for the other.

The reports include a stiffness-weight and a strength-weight comparison with the wing beams previously tested for this project (stainless-steel box beams, 17ST and 24ST aluminum-alloy I-beams with straight flanges). For combined axial and transverse loads the strength-weight ratio for all beams tested to date was found to be roughly the same at a slenderness ratio of about 40.



**Sheet-stringer panels.**—A report of end-compression tests of nine aluminum-alloy sheet-stringer panels was submitted to the Bureau of Aeronautics, Navy Department.

The report gives the results of tests on a series of panels reinforced by three Z-stringers that were fastened to the sheet by brazier-head rivets spaced from 0.5 to 6 inches between centers. Four of the panels failed by separation of rivets at a stringer stress of 24.2 to 39.5 kips per square inch. The remaining panels failed by instability of the stringers at a stringer stress from 38 to 42 kips per square inch.

The observed effective widths of the sheet were from -1 to 20 percent greater than the effective widths calculated from Marguerre's formula for simply supported edges up to an edge strain at which buckling occurred between rivets. The sheet load remained approximately constant after buckling of the sheet between rivets.

**Monocoque boxes.**—The monocoque box specimen, the elastic deformation of which under axial load and under various types of transverse loading is to be studied, has been tested in compression. The test data have been analyzed and the results have been described in Technical Note No. 721.

**Strength of riveted joints in aluminum alloy.**—A report on tests of single rivet joints embodying flush rivets

has been prepared for the National Advisory Committee for Aeronautics. The report gives the results of static tests in single shear, in double shear, and in tension of 865 joints prepared by seven different aircraft manufacturers, the Naval Aircraft Factory, and the National Bureau of Standards. A series of graphs is included to show directly the relation between the shearing stress, bearing stress, and diameter-thickness (rivet diameter to sheet thickness) ratio for all the single shearing joints tested.

**Fatigue testing of aluminum-alloy wing beams.**—The third wing beam has been tested to failure in fatigue. The test showed progress toward the solution of certain problems in technique which must be solved whenever structures similar to wing beams are tested by the resonance method under axial loads.

The results for the first two beams tested indicate approximately equal resistance to fatigue throughout the length of each beam, but in the third beam a crack had traversed the web at the edge of the reinforcement near the center of the beam before much more than half the total number of cycles had been completed. This local failure of the web, however, did not lead to final failure of the beam. Cracks later appeared at other points of stress concentration and the final failure was similar to that of the other two beams.



## PART II

### ORGANIZATION AND GENERAL ACTIVITIES

---

#### ORGANIZATION

The National Advisory Committee for Aeronautics was established by act of Congress approved March 3, 1915, and the membership increased from 12 to 15 by act approved March 2, 1929 (U. S. C., title 50, sec. 151). Its membership is appointed by the President and consists of two representatives each of the War and Navy Departments from the offices in charge of military and naval aeronautics, two representatives of the Civil Aeronautics Authority (Civil Aeronautics Act of 1939), one representative each of the Smithsonian Institution, the United States Weather Bureau and the National Bureau of Standards, together with six additional persons who are "acquainted with the needs of aeronautical science, either civil or military, or skilled in aeronautical engineering or its allied sciences." These latter six serve for terms of 5 years. All the members serve as such without compensation. During the past year the following changes occurred in the membership of the main Committee:

Dr. Francis W. Reichelderfer, the new Chief of the United States Weather Bureau, was appointed a member on January 2, 1939, to fill the vacancy occasioned by the death on September 14, 1938, of Dr. Willis Ray Gregg, Chief of the United States Weather Bureau.

Brigadier General George H. Brett, United States Army, Chief of Matériel Division, of the Army Air Corps, Dayton, Ohio, was appointed a member of the Committee on March 11, 1939, to succeed Brigadier General Augustine W. Robins, United States Army, relieved because of transfer to other military duty.

Honorable Robert H. Hinckley, Chairman of the Civil Aeronautics Authority, was appointed a member of the Committee, May 20, 1939, to succeed Honorable Edward J. Noble, who had resigned as Chairman of the Civil Aeronautics Authority.

Rear Admiral John H. Towers, United States Navy, was appointed a member on May 20, 1939, effective June 1, 1939, on which date he succeeded Rear Admiral Arthur B. Cook, United States Navy, as Chief of the Bureau of Aeronautics. Admiral Cook having been transferred to sea duty.

Dr. George J. Mead, of West Hartford, Conn., was appointed from civil life a member of the Committee, on October 11, 1939, to fill out the unexpired term of Dr. Joseph S. Ames, who resigned on October 7 because

of physical inability to take an active part in the work of the Committee. Dr. Ames had served as a member of the Committee since its establishment in 1915. At the time of his resignation, he was Chairman of the Committee and was serving under a 5-year appointment by President Roosevelt, expiring December 1, 1943. Comment on Dr. Ames' service appears in the opening portion of this report.

Under the rules and regulations governing the work of the Committee, as approved by the President, the Chairman and Vice Chairman are elected annually, as are also the Chairman and Vice Chairman of the Executive Committee. On October 19th, 1939, Dr. Vannevar Bush, who had served as Vice Chairman of the main Committee and Chairman of the Executive Committee, was elected Chairman of the main Committee to succeed Dr. Ames. Dr. George J. Mead was elected Vice Chairman of the main Committee. Dr. Bush was also elected Chairman of the Executive Committee and Dr. Charles G. Abbot, Vice Chairman of the Executive Committee.

The executive offices of the Committee, including the office of aeronautical intelligence and the office of aeronautical inventions, are located in the Navy Building, Washington, D. C., in close proximity to the air organizations of the Army and Navy.

The office of aeronautical intelligence was established in the early part of 1918 as an integral branch of the Committee's activities. It serves as the depository and distributing agency for the scientific and technical data on aeronautics comprising the results of fundamental Committee researches and also the scientific and technical information collected by the Committee from governmental and private agencies in this country and abroad. The data collected are classified, cataloged, and disseminated by this office.

The Committee's technical assistant in Europe, Mr. John J. Ide, whose headquarters are at the American Embassy in Paris, visits governmental and private agencies in Europe to collect results of researches and to gain first-hand information as to researches proposed and in progress.

#### RESEARCH FACILITIES

With the consistent support of the President and of the Congress, the Committee has developed at Langley



Field, Va., a large and well-equipped aeronautical research laboratory, known as the Langley Memorial Aeronautical Laboratory. Advances to date in the relatively new engineering science of aeronautics have been made possible largely by the design and construction at Langley Field of novel research equipment.

At the present time, the Langley Field Laboratory comprises the following units: The 8-foot 500-mile-per-hour wind tunnel; the full-scale wind tunnel with a throat 60 by 30 feet; the 20-foot propeller-research-tunnel; the 5-foot variable-density wind tunnel; a 7- by 10-foot wind tunnel; a 4- by 6-foot vertical wind tunnel; a 15-foot free-spinning wind tunnel; two high-velocity jet-type wind tunnels of 11- and 24-inch throat diameters, respectively; the 2,900-foot N. A. C. A. tank; an engine-research laboratory; a flight-research laboratory; an instrument laboratory; and administration and service buildings. The research facilities at Langley Field also include the following recent additions: A 19-foot pressure wind tunnel; a refrigerated wind tunnel with a throat 7½ by 3 feet; a 12-foot free-flight wind tunnel; and an additional shop building.

The Committee is proceeding to construct at Langley Field a structures research laboratory, a two-dimensional flow wind tunnel, a stability wind tunnel, a 16-foot high-speed wind tunnel and a 20-foot free-spinning wind tunnel.

The Committee has in process of construction at Moffett Field, Calif., a second major research station, authorized by act approved August 9, 1939. The facts in connection with this vitally important addition to the Committee's research facilities follow.

#### SECOND RESEARCH STATION

At a meeting of the Executive Committee on August 19, 1938, the late Major General Oscar Westover, then Chief of the Army Air Corps, and Chairman of a Special Committee on the Relation of the N. A. C. A. to National Defense in Time of War, recommended that the Committee plan an additional research center somewhere in the interior of the country or on the West Coast, in order to relieve the situation he described as "the congested bottle neck of Langley Field." As a result of this suggestion General Westover's committee was requested to make a study of long-range planning for the location of additional laboratory activities for the Committee away from the present laboratory at Langley Field.

During the following month, General Westover and Dr. W. R. Gregg, two of the three members of the special committee, met untimely deaths, leaving Admiral Cook as the sole surviving member. At the meeting of the main Committee on October 20, 1938, a Special Committee on Future Research Facilities was formed consisting of Rear Admiral Arthur B.

Cook, chairman, Major General Henry H. Arnold, Honorable Edward J. Noble, Dr. Edward Warner, and Dr. George W. Lewis. This committee studied the need for additional research in aeronautics and the problems involved in a long-range plan for future research facilities as related to national defense and to commercial aviation. The committee also studied the need for more effective coordination of aeronautical research among governmental, industrial, and educational institutions. A subsidiary special committee studied the desirable sites for a second aeronautical research station. As a result of these studies the special committee submitted a report on December 30, 1938, recommending the immediate establishment of a second research station at Sunnyvale, Calif., and the construction of the most advanced research equipment at an estimated cost of \$11,000,000. Additional research facilities were recommended for Langley Field, Va., and a plan for the more effective coordination of applied research in industry was outlined as an immediate need.

On February 3, 1939, the President of the United States transmitted to the Congress supplemental estimates amounting to \$6,723,000. Of this amount \$2,140,000 was for new construction at Langley Field, \$36,000 for the proposed coordination plan, \$250,000 for contracts for research in scientific and educational institutions, \$297,000 for salaries and expenses, and \$4,000,000 for construction of facilities at the proposed new Sunnyvale, Calif., research station. Appropriations for salaries and expenses and the new facilities at Langley Field and for the coordination plan were included in the Second Deficiency Act in the total amount of \$2,363,980. Authorization of the second research station was included in the Third Deficiency Act approved August 9, 1939. The act carried a total appropriation of \$2,000,000. Of this amount \$1,890,980 was provided to begin construction of an additional aeronautical research station at a total cost of not to exceed \$10,000,000 upon such site as may be chosen by the National Advisory Committee for Aeronautics from the sites brought to its attention within 30 days after approval of the act.

In all, 54 sites for the proposed station were brought to the attention of the Committee within the 30-day period fixed by law and were referred to the Special Survey Committee on Aeronautical Research Facilities, consisting of Colonel Charles A. Lindbergh, chairman, Major General Henry H. Arnold, Rear Admiral John H. Towers, and Honorable Robert H. Hinckley. The characteristics of each of the 54 sites, as described in the proposals and as supplemented by additional inquiries, were subjected to an exhaustive analysis. Some of the factors which were considered in rating the sites for their approach to the ideal included: The nature of the flying field on which the station was pro-



posed, the adequacy and cost of electric power, proximity to a suitable industrial center, proximity to the aircraft industry, climatic conditions especially as related to year-round flying, military vulnerability, adequate transportation facilities, and working and living conditions for employees. The subcommittee recommended and the Committee decided by a unanimous vote, after due consideration, that all things considered the best interests of aeronautics would be served by the location of the second research station at Moffett Field near Sunnyvale, and 38 miles south of San Francisco, Calif. The decision was announced on September 22, 1939.

The new site consists of approximately 100 acres, 60 of which have been assigned to the Committee by the War Department and 40 purchased. Moffett Field is a former naval air station of 1,000 acres originally used for lighter-than-air activities but now under the administration of and actively used by the Army Air Corps. The Committee will conduct its research activities there under a status similar to that under which it functions at Langley Field. The planning and construction of research facilities and equipment are progressing as rapidly as possible. The Committee's present plans do not contemplate the conduct of engine research at the Moffett Field laboratory.

#### CONSIDERATION OF AERONAUTICAL INVENTIONS

By act of Congress approved July 2, 1926, an Aeronautical Patents and Design Board was established consisting of Assistant Secretaries of the Departments of War, Navy, and Commerce. In accordance with that act as amended by the act approved March 3, 1927, the National Advisory Committee for Aeronautics passes upon the merits of aeronautical inventions and designs submitted to any aeronautical division of the Government, and submits reports thereon to the Aeronautical Patents and Design Board. That board is authorized, upon the favorable recommendation of the Committee, to "determine whether the use of the design by the Government is desirable or necessary and evaluate the design and fix its worth to the United States in an amount not to exceed \$75,000."

During the past year the inventions section received 1,800 inventions and designs pertaining to the aeronautical art. All of these proposals were given careful consideration and evaluated. The necessary correspondence was conducted to advise the submitters of the evaluations and interviews were granted inventors to discuss new proposals and their merits.

#### AERONAUTICAL RESEARCH IN EDUCATIONAL INSTITUTIONS

The Committee has continued to follow the policy initiated as a result of recommendation of the Federal

Aviation Commission, of making available a special allotment of \$25,000 from each year's funds for aeronautical research in educational institutions. Under this allotment during the fiscal year 1939, contracts were made for 12 special investigations and reports at 10 universities and technical schools, on the basis of the probable usefulness and value of the information to aeronautics.

Several of the papers prepared under contracts have been published by the Committee, and in other cases the results obtained in the investigations have supplied a basis for further research. During the past year nine contract reports have been issued as Technical Notes and one as a confidential report to American manufacturers, and six others are now being revised and edited for publication by the Committee.

The Committee has given much consideration to this policy and is strongly of the opinion that its activities in the encouragement and stimulation of aeronautical research in educational institutions should be greatly extended, and has recommended in its estimates for 1941 that the funds for the purpose be increased from \$25,000 to \$250,000. There is a pressing need to marshal the existing scientific resources of the country on a large variety of scientific problems in aeronautics. Furthermore, with the expansion of the air program and intensification of efforts to improve the performance and efficiency of aircraft, and with increased research facilities being made available to the Committee, there will be great need for additional trained research workers in the United States. The training of these workers should be done by educational institutions. Thus this program will accomplish a twofold purpose in supplying new knowledge and in training research workers.

#### COOPERATION WITH THE AVIATION INDUSTRY

In the formulation of its research programs, the Committee includes provision for the problems of aeronautical research which are of particular importance to the aviation industry, in connection with both the design and operation of aircraft. The representatives of the industry refer their problems of this nature to the Committee as they arise, either by correspondence or through personal contact. The Committee avails itself of every opportunity to obtain suggestions and recommendations from representatives of the aircraft manufacturers and operators as to investigations which are of special importance to them.

For the purpose of familiarizing the industry with the research facilities of the Committee and the programs of research under way, there is held at the Committee's laboratory at Langley Field, Va., once a year, usually in May, an aircraft engineering conference. This conference is attended by the representatives of the aircraft manufacturers and operators. Open dis-



cussions are held wherein suggestions are received which lead to modifications or additions to the programs to obtain the information desired. In some cases these suggestions have initiated new programs of research. It is a long-standing policy of the Committee when the need arises in connection with any particular problem of the industry to call a special conference or to appoint a special subcommittee.

Realizing that frequently the value of information is greatly enhanced by its prompt availability, every effort is made to place in the hands of the industry at the earliest possible date the results of researches that are of particular interest in connection with civil aeronautics. It sometimes appears, in the course of an extensive investigation being conducted by the Committee, that the results so far obtained will be of special interest and value to the aircraft industry if made available immediately. In such cases the Committee issues the information in advance confidential form to American manufacturers and the Government services.

#### COORDINATION OF AERONAUTICAL RESEARCH

In order to provide for the more effective coordination of applied aeronautical research in industry and to utilize more effectively research facilities at scientific and educational institutions, the Committee has set up, with funds provided by the Congress for the purpose, a new section on coordination. It is the expectation of the Committee that this new activity will have the following beneficial results: It will accelerate progress in aeronautics by bringing the results of research more directly to the attention of designers and engineers in the aircraft industry, and by bringing more promptly to the attention of the Committee new problems requiring scientific study and investigation; it will utilize existing facilities in scientific and educational institutions on a larger scale than in the past, to the extent that additional funds may be made available for the purpose; and it will stimulate scientific research in such institutions, coordinate applied research in industry, and at the same time serve to prevent unnecessary overlapping and duplication of effort.

This is not a new function of the Committee but is rather an enlargement of an existing function made necessary by the magnitude of the country's air defense program and the need to accelerate progress in the development of American aeronautics, in order that the performance of American aircraft may equal or excel the performance of the aircraft of any other nation. The new section on coordination will operate under the immediate supervision of a coordinator of research, who will be a member of all the standing technical subcommittees and who will have assistants

in the field keeping in close touch with the progress and needs of aeronautical science by visiting the aircraft industry and scientific and educational institutions.

#### SUBCOMMITTEES

The National Advisory Committee for Aeronautics has organized standing technical committees, with subcommittees, for the purpose of coordinating the research needs of aviation and preparing research programs in their respective fields. The four main technical Committees on Aerodynamics, Power Plant for Aircraft, Aircraft Materials, and Aircraft Structures and their subcommittees prepare the program for the aeronautical research conducted by the Advisory Committee and coordinate the investigations conducted by other agencies.

As previously stated, it is the policy of the Committee to establish from time to time special technical subcommittees for the study of particular problems as they arise, and several such special subcommittees have been organized.

The work of the standing technical committees and subcommittees has been described in part I. Their organization, together with that of the special technical subcommittees, is as follows:

#### COMMITTEE ON AERODYNAMICS

Dr. Edward Warner, Chairman.  
 Dr. George W. Lewis, National Advisory Committee for Aeronautics, Vice Chairman.  
 Dr. L. J. Briggs, National Bureau of Standards.  
 Maj. F. O. Carroll, Air Corps, United States Army, Materiel Division, Wright Field.  
 Comdr. W. S. Diehl, United States Navy.  
 Dr. H. L. Dryden, National Bureau of Standards.  
 John Easton, Civil Aeronautics Authority.  
 Mr. J. T. Gray, Civil Aeronautics Authority.  
 Maj. Carl F. Greene, Air Corps, United States Army, Materiel Division Liaison Officer at N. A. C. A. Laboratories.  
 Delbert M. Little, United States Weather Bureau.  
 Maj. Alfred J. Lyon, Air Corps, United States Army, Materiel Division.  
 Elton W. Miller, National Advisory Committee for Aeronautics.  
 Comdr. F. W. Pennoyer, Jr., United States Navy.  
 H. J. E. Reid, National Advisory Committee for Aeronautics.  
 Comdr. Leslie C. Stevens, United States Navy.  
 Mr. Omer Welling, Civil Aeronautics Authority.  
 Dr. A. F. Zahm, Division of Aeronautics, Library of Congress.

#### SUBCOMMITTEE ON AIRSHIPS

Dr. J. C. Hunsaker, Chairman.  
 Starr Truscott, National Advisory Committee for Aeronautics, Vice Chairman.  
 John Easton, Civil Aeronautics Authority.  
 Captain Garland Fulton, United States Navy.  
 Maj. C. F. Greene, Air Corps, United States Army, Materiel Division Liaison Officer at N. A. C. A. Laboratories.  
 Dr. George W. Lewis, National Advisory Committee for Aeronautics (ex-officio member).



**SUBCOMMITTEE ON METEOROLOGICAL PROBLEMS**

Dr. F. W. Reichelderfer, United States Weather Bureau, Chairman.

Col. E. S. Gorrell, Air Transport Association of America.

Dr. W. J. Humphreys, United States Weather Bureau.

Dr. J. C. Hunsaker, Massachusetts Institute of Technology.

R. W. Knight, Civil Aeronautics Authority.

Dr. George W. Lewis, National Advisory Committee for Aeronautics (ex-officio member).

Delbert M. Little, United States Weather Bureau.

Comdr. Wilber M. Lockhart, United States Navy.

Capt. R. M. Losey, Air Corps, United States Army.

Dr. Charles F. Marvin.

Mr. Richard V. Rhode, National Advisory Committee for Aeronautics.

Dr. C. G. Rossby, United States Weather Bureau.

**SPECIAL SUBCOMMITTEE ON LIGHTNING HAZARDS TO AIRCRAFT**

Delbert M. Little, United States Weather Bureau, Chairman.

J. C. Franklin, Transcontinental & Western Air, Inc.

Dr. O. H. Gish, Carnegie Institution of Washington.

Commander L. M. Grant, United States Navy.

Charles H. Helms, National Advisory Committee for Aeronautics.

Dr. George W. Lewis, National Advisory Committee for Aeronautics (ex officio member).

K. B. McEachron, General Electric Company.

Irving R. Metcalf, Civil Aeronautics Authority.

Capt. C. K. Moore, Air Corps, United States Army, Matériel Division, Wright Field.

Dr. F. B. Silsbee, National Bureau of Standards.

**SUBCOMMITTEE ON SEAPLANES**

Dr. J. C. Hunsaker, Chairman.

Theophile dePort, Matériel Division, Army Air Corps, Wright Field.

Commander W. S. Diehl, United States Navy.

J. T. Gray, Civil Aeronautics Authority.

Dr. George W. Lewis, National Advisory Committee for Aeronautics (ex officio member).

Capt. C. K. Moore, Air Corps, United States Army, Matériel Division, Wright Field.

A. L. Morse, Civil Aeronautics Authority.

Capt. H. C. Richardson, United States Navy.

Starr Truscott, National Advisory Committee for Aeronautics.

**SPECIAL SUBCOMMITTEE ON VIBRATION AND FLUTTER**

H. J. E. Reid, National Advisory Committee for Aeronautics, Chairman.

Capt. Frederick R. Dent, Jr., Air Corps, United States Army, Matériel Division, Wright Field.

Comdr. W. S. Diehl, United States Navy.

Comdr. L. M. Grant, United States Navy.

Charles H. Helms, National Advisory Committee for Aeronautics.

Dr. George W. Lewis, National Advisory Committee for Aeronautics (ex-officio member).

Comdr. R. D. MacCart, United States Navy.

Irving R. Metcalf, Civil Aeronautics Authority.

Ford Prescott, Matériel Division, Army Air Corps, Wright Field.

Dr. Walter Ramberg, National Bureau of Standards.

Edward I. Ryder, Civil Aeronautics Authority.

Benjamin Smilg, Matériel Division, Army Air Corps, Wright Field.

Dr. Theodore Theodorsen, National Advisory Committee for Aeronautics.

**COMMITTEE ON POWER PLANTS FOR AIRCRAFT**

Dr. George J. Mead, Chairman.

Dr. George W. Lewis, National Advisory Committee for Aeronautics, Vice Chairman.

Comdr. Rico Botta, United States Navy.

Dr. H. C. Dickinson, National Bureau of Standards.

John H. Geisse, Civil Aeronautics Authority.

Carlton Kemper, National Advisory Committee for Aeronautics.

Gaylord W. Newton, Civil Aeronautics Authority.

Maj. E. R. Page, Air Corps, United States Army, Matériel Division, Wright Field.

**SUBCOMMITTEE ON AIRCRAFT FUELS AND LUBRICANTS**

Dr. George W. Lewis, National Advisory Committee for Aeronautics, Chairman.

Commander Rico Botta, United States Navy.

Dr. O. C. Bridgeman, National Bureau of Standards.

H. K. Cummings, National Bureau of Standards.

Dr. H. C. Dickinson, National Bureau of Standards.

Lt. Henry R. Dozier, United States Navy.

L. S. Hobbs, The Pratt and Whitney Aircraft Company.

Robert V. Kerley, Matériel Division, Army Air Corps, Wright Field.

Gaylord W. Newton, Civil Aeronautics Authority.

Arthur Nutt, Wright Aeronautical Corporation.

Maj. E. R. Page, Air Corps, United States Army, Matériel Division, Wright Field.

Addison M. Rothrock, National Advisory Committee for Aeronautics.

**COMMITTEE ON AIRCRAFT MATERIALS**

Dr. L. J. Briggs, National Bureau of Standards, Chairman.

Prof. H. L. Whittemore, National Bureau of Standards, Vice Chairman.

S. K. Colby, Aluminum Co. of America.

Lt. Comdr. C. F. Cotton, United States Navy.

Edgar H. Dix, Jr., American Magnesium Corporation.

John Easton, Civil Aeronautics Authority.

Warren E. Emley, National Bureau of Standards.

Capt. Garland Fulton, United States Navy.

J. T. Gray, Civil Aeronautics Authority.

C. H. Helms, National Advisory Committee for Aeronautics.

J. B. Johnson, Matériel Division, Army Air Corps, Wright Field.

Capt. Paul H. Kemmer, Air Corps, United States Army, Matériel Division, Wright Field.

Dr. George W. Lewis, National Advisory Committee for Aeronautics (ex-officio member).

H. S. Rawdon, National Bureau of Standards.

John W. Sands, International Nickel Company.

E. C. Smith, Republic Steel Corporation.

Paul F. Voigt, Jr., Carnegie-Illinois Steel Corporation.

Dr. Edward Warner.

**SUBCOMMITTEE ON METALS USED IN AIRCRAFT**

H. S. Rawdon, National Bureau of Standards, Chairman.

A. W. Dallas, Civil Aeronautics Authority.

E. H. Dix, Jr., American Magnesium Corporation.

Capt. Garland Fulton, United States Navy.

J. B. Johnson, Matériel Division, Army Air Corps, Wright Field.



Dr. George W. Lewis, National Advisory Committee for Aeronautics (ex-officio member).

E. C. Smith, Republic Steel Corporation.

Prof. H. L. Whittemore, National Bureau of Standards.

#### SUBCOMMITTEE ON MISCELLANEOUS MATERIALS AND ACCESSORIES

Warren E. Emley, National Bureau of Standards, Chairman.

C. J. Cleary, Matériel Division, Army Air Corps, Wright Field.

A. W. Dallas, Civil Aeronautics Authority.

C. H. Helms, National Advisory Committee for Aeronautics.

E. F. Hickson, National Bureau of Standards.

Dr. George W. Lewis, National Advisory Committee for Aeronautics (ex-officio member).

J. E. Sullivan, Bureau of Aeronautics, Navy Department.

G. W. Trayer, Forest Service, Department of Agriculture.

#### COMMITTEE ON AIRCRAFT STRUCTURES

Dr. L. J. Briggs, National Bureau of Standards, Chairman.

John Easton, Civil Aeronautics Authority.

Comdr. L. M. Grant, United States Navy.

Capt. Paul H. Kemmer, Air Corps, United States Army, Matériel Division, Wright Field.

Dr. George W. Lewis, National Advisory Committee for Aeronautics (ex-officio member).

Eugene E. Lundquist, National Advisory Committee for Aeronautics.

Comdr. R. D. MacCart, United States Navy.

Capt. C. K. Moore, Air Corps, United States Army, Matériel Division, Wright Field.

Dr. Walter Ramberg, National Bureau of Standards.

Richard V. Rhode, National Advisory Committee for Aeronautics.

Edward I. Ryder, Civil Aeronautics Authority.

Dr. L. B. Tuckerman, National Bureau of Standards.

Dr. Edward Warner.

#### SPECIAL SUBCOMMITTEE TO MAKE SURVEY OF TECHNIQUE AND EQUIPMENT FOR ELASTIC EXAMINATION OF LARGE AIRCRAFT STRUCTURES IN LIEU OF DESTRUCTION TESTS

Richard V. Rhode, National Advisory Committee for Aeronautics, Chairman.

Comdr. L. M. Grant, United States Navy.

Capt. Paul H. Kemmer, Air Corps, United States Army, Matériel Division, Wright Field.

Dr. George W. Lewis, National Advisory Committee for Aeronautics (ex-officio member).

Comdr. R. D. MacCart, United States Navy.

Irving R. Metcalf, Civil Aeronautics Authority.

R. L. Templin, Aluminum Company of America.

Dr. L. B. Tuckerman, National Bureau of Standards.

#### SPECIAL SUBCOMMITTEE TO DIRECT RESEARCH IN APPLIED STRUCTURES

Comdr. L. M. Grant, United States Navy, Chairman.

Capt. Paul H. Kemmer, Air Corps, United States Army, Matériel Division, Wright Field.

Dr. George W. Lewis, National Advisory Committee for Aeronautics (ex-officio member).

Eugene E. Lundquist, National Advisory Committee for Aeronautics.

Edward I. Ryder, Civil Aeronautics Authority.

Dr. L. B. Tuckerman, National Bureau of Standards.

#### COMMITTEE ON AIRCRAFT ACCIDENTS

Dr. Edward Warner, Chairman.

Thomas Hardin, Air Safety Board, Vice Chairman.

Lt. Comdr. W. A. Evans, Jr., United States Navy.

Maj. Barney M. Giles, Air Corps, United States Army.

J. W. Lankford, Civil Aeronautics Authority.

Dr. George W. Lewis, National Advisory Committee for Aeronautics.

Comdr. A. E. Montgomery, United States Navy.

Maj. Lowell H. Smith, Air Corps, United States Army.

Grove Webster, Civil Aeronautics Authority.

#### COMMITTEE ON AERONAUTICAL INVENTIONS AND DESIGNS

Dr. L. J. Briggs, National Bureau of Standards, Chairman.

Brig. Gen. George H. Brett, Air Corps, United States Army, Matériel Division, Wright Field.

Hon. Clinton M. Hester, Civil Aeronautics Authority.

Dr. J. C. Hunsaker.

Capt. S. M. Kraus, United States Navy.

John F. Victory, Secretary.

#### COMMITTEE ON PERSONNEL, BUILDINGS, AND EQUIPMENT

Dr. Vannevar Bush, Chairman.

Dr. Charles G. Abbot.

Dr. George J. Mead.

John F. Victory, Secretary.

During the past year the Committee has organized the following special committees for the study of particular problems:

#### SPECIAL SURVEY COMMITTEE ON AERONAUTICAL RESEARCH FACILITIES

Col. Charles A. Lindbergh, Chairman.

Maj. Gen. Henry H. Arnold, Chief of the Air Corps, United States Army, War Department.

Rear Admiral J. H. Towers, Chief, Bureau of Aeronautics, United States Navy, Navy Department.

Hon. Robert H. Hinckley, Chairman, Civil Aeronautics Authority.

#### SPECIAL COMMITTEE ON COORDINATION

Dr. Jerome C. Hunsaker, Massachusetts Institute of Technology, Chairman.

Capt. Sydney M. Kraus, United States Navy.

Brig. Gen. George H. Brett, United States Army, Chief of the Matériel Division, Air Corps.

Dr. George W. Lewis, Director of Aeronautical Research, National Advisory Committee for Aeronautics.

Dr. Edward Warner, Civil Aeronautics Authority.

#### SPECIAL COMMITTEE ON NEW ENGINE RESEARCH FACILITIES

Dr. George J. Mead, Chairman.

Comdr. Rico Botta, United States Navy.

R. M. Hazen, Allison Engineering Division, General Motors Corporation.

S. D. Heron, Ethyl Gasoline Corporation.

L. S. Hobbs, Pratt and Whitney Aircraft Company.



Carlton Kemper, National Advisory Committee for Aeronautics.

Gaylord W. Newton, Civil Aeronautics Authority.

Arthur Nutt, Wright Aeronautical Corporation.

Maj. E. R. Page, Air Corps, United States Army, Matériel Division, Wright Field.

#### TECHNICAL PUBLICATIONS OF THE COMMITTEE

The Committee has four series of publications, namely, technical reports, technical notes, technical memorandums, and aircraft circulars.

The technical reports present the results of fundamental research in aeronautics. The technical notes are mimeographed and present the results of short research investigations and the results of studies of specific detailed problems which form parts of long investigations. The technical memorandums are mimeographed and contain translations and reproductions of important foreign aeronautical articles. The aircraft circulars are mimeographed and contain descriptions of new types of foreign aircraft. No aircraft circulars were issued during the past year.

The following are lists of the publications issued:

#### LIST OF TECHNICAL REPORTS ISSUED DURING THE PAST YEAR

645. Correction of Temperatures of Air-Cooled Engine Cylinders for Variation in Engine and Cooling Conditions. By Oscar W. Schey, Benjamin Pinkel, and Herman H. Ellerbrock, Jr., N. A. C. A.
646. The Compressibility Burble and the Effect of Compressibility on Pressures and Forces Acting on an Airfoil. By John Stack, W. F. Lindsey, and Robert E. Littell, N. A. C. A.
647. Tests of N. A. C. A. 0009, 0012, and 0018 Airfoils in the Full-Scale Tunnel. By Harry J. Goett and W. Kenneth Bullivant, N. A. C. A.
648. Design Charts for Predicting Downwash Angles and Wake Characteristics behind Plain and Flapped Wings. By Abe Silverstein and S. Katzoff, N. A. C. A.
649. The "Pack" Method for Compressive Tests of Thin Specimens of Materials Used in Thin-Wall Structures. By C. S. Aitchison and L. B. Tuckerman, National Bureau of Standards.
650. The Aerodynamic Characteristics of Six Full-Scale Propellers Having Different Airfoil Sections. By David Biermann and Edwin P. Hartman, N. A. C. A.
651. Downwash and Wake behind Plain and Flapped Airfoils. By Abe Silverstein, S. Katzoff, and W. Kenneth Bullivant, N. A. C. A.
652. Air Flow in the Boundary Layer of an Elliptic Cylinder. By G. B. Schubauer, National Bureau of Standards.
653. A Study of Air Flow in an Engine Cylinder. By Dana W. Lee, N. A. C. A.
654. General Airplane Performance. By W. C. Rockefeller, California Institute of Technology.
655. The Knocking Characteristics of Fuels in Relation to Maximum Permissible Performance of Aircraft Engines. By A. M. Rothrock and Arnold E. Biermann, N. A. C. A.
656. The Column Strength of Two Extruded Aluminum-Alloy H-Sections. By William R. Osgood and Marshall Holt, National Bureau of Standards and Aluminum Company of America.
657. The Influence of Directed Air Flow on Combustion in a Spark-Ignition Engine. By A. M. Rothrock and R. C. Spencer, N. A. C. A.
658. Tests of Two Full-Scale Propellers with Different Pitch Distributions, at Blade Angles up to 60°. By David Biermann and Edwin P. Hartman, N. A. C. A.
659. Effect of Service Stresses on Impact Resistance, X-ray Diffraction Patterns, and Microstructure of 25S Aluminum Alloy. By J. A. Kies and G. W. Quick, National Bureau of Standards.
660. Experimental Investigation of the Momentum Method for Determining Profile Drag. By Harry J. Goett, N. A. C. A.
661. Tests in the Variable-Density Wind Tunnel of the N. A. C. A. 23012 Airfoil with Plain and Split Flaps. By Ira H. Abbott and Harry Greenberg, N. A. C. A.
662. Design of N. A. C. A. Cowlings for Radial Air-Cooled Engines. By George W. Stickle, N. A. C. A.
663. The Effect of Continuous Weathering on Light Metal Alloys Used in Aircraft. By Willard Mutehler, National Bureau of Standards.
664. Wind-Tunnel Investigation of an N. A. C. A. 23012 Airfoil with Various Arrangements of Slotted Flaps. By Carl J. Wenzinger and Thomas A. Harris, N. A. C. A.
665. Calculation of the Aerodynamic Characteristics of Tapered Wings with Partial-Span Flaps. By Henry A. Pearson and Raymond F. Anderson, N. A. C. A.
666. Aircraft Rate-of-Climb Indicators. By Daniel P. Johnson, National Bureau of Standards.
667. Determination of the Profile Drag of an Airplane Wing in Flight at High Reynolds Numbers. By Joseph Bicknell, N. A. C. A.
668. Wind-Tunnel Investigation of N. A. C. A. 23012, 23021, and 23030 Airfoils with Various Sizes of Split Flap. By Carl J. Wenzinger and Thomas A. Harris, N. A. C. A.
669. Airfoil Section Data Obtained in the N. A. C. A. Variable-Density Tunnel as Affected by Support Interference and Other Corrections. By Eastman N. Jacobs and Ira H. Abbott, N. A. C. A.
670. Tensile Elastic Properties of 18:8 Chromium-Nickel Steel as Affected by Plastic Deformation. By D. J. McAdam, Jr., and R. W. Mebs, National Bureau of Standards.
671. A Theoretical Study of the Moment on a Body in a Compressible Fluid. By Carl Kaplan, N. A. C. A.
672. Free-Spinning Wind-Tunnel Tests of a Low-Wing Monoplane with Systematic Changes in Wings and Tails. IV. Effect of Center-of-Gravity Location. By Oscar Seidman and A. I. Neilhouse, N. A. C. A.
673. Experimental Verification of the Theory of Oscillating Airfoils. By Abe Silverstein and Upshur T. Joyner, N. A. C. A.
674. Cooling on the Front of an Air-Cooled Engine Cylinder in a Conventional Engine Cowling. By M. J. Brevoort and U. T. Joyner, N. A. C. A.
675. Effects of Elevator Nose Shape, Gap, Balance and Tabs on the Aerodynamic Characteristics of a Horizontal Tail Surface. By Harry J. Goett and J. P. Reeder, N. A. C. A.
676. Surface Heat-Transfer Coefficients of Finned Cylinders. By Herman H. Ellerbrock, Jr., and Arnold Biermann, N. A. C. A.



677. Wind-Tunnel Investigation of an N. A. C. A. 23021 Airfoil with Various Arrangements of Slotted Flaps. By Carl J. Wenzinger and Thomas A. Harris, N. A. C. A.
678. Interference of Tail Surfaces and Wing and Fuselage from Tests of 17 Combinations in the N. A. C. A. Variable-Density Tunnel. By Albert Sherman, N. A. C. A.
679. Wind-Tunnel Investigation of an N. A. C. A. 23012 Airfoil with a Slotted Flap and Three Types of Auxiliary Flap. By Carl J. Wenzinger and William E. Gauvain, N. A. C. A.
680. The Effect of Nacelle-Propeller Diameter Ratio on Body Interference and on Propeller and Cooling Characteristics. By James G. McHugh and Eldridge H. Derring, N. A. C. A.

#### LIST OF TECHNICAL NOTES ISSUED DURING THE PAST YEAR

No.

667. Operational Treatment of the Nonuniform-Lift Theory in Airplane Dynamics. By Robert T. Jones, N. A. C. A.
668. Hydrodynamic and Aerodynamic Tests of Models of Flying-Boat Hulls Designed for Low Aerodynamic Drag—N. A. C. A. Models 74, 74-A, and 75. By Starr Truscott, J. B. Parkinson, John W. Ebert, Jr., and E. Floyd Valentine, N. A. C. A.
669. The Drag of Inflatable Rubber De-icers. By Russell G. Robinson, N. A. C. A.
670. N. A. C. A. Stall-Warning Indicator. By F. L. Thompson, N. A. C. A.
671. A Method of Rapidly Estimating the Position of the Laminar Separation Point. By Albert E. von Doenhoff, N. A. C. A.
672. Flow Observations with Tufts and Lampblack of the Stalling of Four Typical Airfoil Sections in the N. A. C. A. Variable-Density Tunnel. By Ira H. Abbott and Albert Sherman, N. A. C. A.
673. The Pressure Available for Ground Cooling in Front of the Cowling of Air-Cooled Airplane Engines. By George W. Stickle and Upshur T. Joyner, N. A. C. A.
674. Scavenging a Piston-Ported Two-Stroke Cylinder. By A. R. Rogowski and C. L. Bouchard, Massachusetts Institute of Technology.
675. The Charging Process in a High-Speed, Single-Cylinder, Four-Stroke Engine. By Blake Reynolds, Harry Shecter, and E. S. Taylor, Massachusetts Institute of Technology.
676. Discharge Characteristics of a Simulated Unit Injection System. By Edred T. Marsh, N. A. C. A.
677. Tests of a Contra-Propeller for Aircraft. By William M. Benson, Daniel Guggenheim Aeronautical Laboratory, Stanford University.
678. Hydrodynamic and Aerodynamic Tests of Four Models of Outboard Floats (N. A. C. A. Models 51-A, 51-B, 51-C, 51-D). By John R. Dawson and Edwin P. Hartman, N. A. C. A.
679. Noise from Propellers with Symmetrical Sections at Zero Blade Angle, II. By A. F. Deming, N. A. C. A.
680. The Aerodynamic Drag of Five Models of Side Floats, N. A. C. A. Models 51-E, 51-F, 51-G, 51-H, and 51-J. By R. O. House, N. A. C. A.
681. A General Tank Test of a Model of the Hull of the P3M-1 Flying Boat Including a Special Working Chart for the Determination of Hull Performance. By John R. Dawson, N. A. C. A.
682. The Unsteady Lift of a Finite Wing. By Robert T. Jones, N. A. C. A.

683. Pressure-Distribution Measurements on a Tapered Wing with a Full-Span Split Flap in Curved Flight. By T. T. Troller and F. Rokus, Daniel Guggenheim Airship Institute, Akron, Ohio.
684. Experimental Study of Deformation and of Effective Width in Axially Loaded Sheet-Stringer Panels. By Walter Ramberg, Albert E. McPherson, and Sam Levy, National Bureau of Standards.
685. Circulation Measurements about the Tip of an Airfoil During Flight through a Gust. By Arnold M. Kueth, Daniel Guggenheim Airship Institute, Akron, Ohio.
686. Local Instability of Symmetrical Rectangular Tubes Under Axial Compression. By Eugene E. Lundquist, N. A. C. A.
687. Loads Imposed on Intermediate Frames of Stiffened Shells. By Paul Kuhn, N. A. C. A.
688. Comparative Performance of Engines Using a Carburetor Manifold Injection, and Cylinder Injection. By Oscar W. Schey and J. Denny Clark, N. A. C. A.
689. Tandem Air Propellers. By E. P. Lesley, Daniel Guggenheim Aeronautical Laboratory, Stanford University.
690. Résumé of Air-Load Data on Slats and Flaps. By Carl J. Wenzinger and Francis M. Rogallo, N. A. C. A.
691. Some Elementary Principles of Shell Stress Analysis with Notes on the Use of the Shear Center. By Paul Kuhn, N. A. C. A.
692. Some Fundamental Considerations in Regard to the Use of Power in Landing an Airplane. By Walter S. Diehl, Bureau of Aeronautics, Navy Department.
693. Comparison of Profile-Drag and Boundary-Layer Measurements Obtained in Flight and in the Full-Scale Wind Tunnel. By Harry J. Goett and Joseph Bicknell, N. A. C. A.
694. Physical Properties of Synthetic Resin Materials. By Meyer Fishbein, N. A. C. A.
695. The Effects of Some Common Surface Irregularities on Wing Drag. By Manley J. Hood, N. A. C. A.
696. Torsional Stability of Aluminum Alloy Seamless Tubing. By R. L. Moore and D. A. Paul, Aluminum Research Laboratories, Aluminum Company of America.
697. The Frequency of Torsional Vibration of a Tapered Beam. By Robert P. Coleman, N. A. C. A.
698. Propeller Tests to Determine the Effect of Number of Blades at Two Typical Solidities. By E. P. Lesley, Daniel Guggenheim Aeronautical Laboratory, Stanford University.
699. Tests of an N. A. C. A. 23012 Airfoil with a Slotted Deflector Flap. By R. O. House, N. A. C. A.
700. Theory of Automatic Control of Airplanes. By Herbert K. Weiss, Massachusetts Institute of Technology.
701. Intermittent-Flow Coefficients of a Poppet Valve. By C. D. Waldron, N. A. C. A.
702. Wind-Tunnel Tests of Several Forms of Fixed Wing Slot in Combination with a Slotted Flap on an N. A. C. A. 23012 Airfoil. By M. J. Bamber, N. A. C. A.
703. Wind-Tunnel Investigation of Effect of Yaw on Lateral-Stability Characteristics. I—Four N. A. C. A. 23012 Wings of Various Plan Forms with and without Dihedral. By M. J. Bamber and R. O. House, N. A. C. A.
704. Some Notes on the Numerical Solution of Shear-Lag and Mathematically Related Problems. By Paul Kuhn, N. A. C. A.
705. Wind-Tunnel Investigation of Ground Effect on Wings with Flaps. By Isidore G. Recant.



706. An Experimental Investigation of the Normal Acceleration of an Airplane Model in a Gust. By Philip Donely, N. A. C. A.
707. Compression-Ignition Engine Performance with Undoped and Doped Fuel Oils and Alcohol Mixtures. By Charles S. Moore and Hampton H. Foster, N. A. C. A.
708. A Simplified Method for the Calculation of Airfoil Pressure Distribution. By H. Julien Allen, N. A. C. A.
709. A Semigraphical Method for Analyzing Strains Measured on Three or Four Gage Lines Intersecting at 45°. By H. N. Hill, Aluminum Research Laboratories, Aluminum Company of America.
710. A Comparison of Ignition Characteristics of Diesel Fuels as Determined in Engines and in a Constant-Volume Bomb. By Robert F. Selden, N. A. C. A.
711. An Approximate Spin Design Criterion for Monoplanes. By Oscar Seidman and Charles J. Donlan, N. A. C. A.
712. A Preliminary Study of the Prevention of Ice on Aircraft by the Use of Engine-Exhaust Heat. By Lewis A. Rodert, N. A. C. A.
713. A Comparison of Several Tapered Wings Designed to Avoid Tip Stalling. By Raymond F. Anderson, N. A. C. A.
714. Flight Tests of Retractable Ailerons on a Highly Tapered Wing. By J. W. Wetmore, N. A. C. A.
715. Wind-Tunnel Investigation of an N. A. C. A. 23012 Airfoil with Two Arrangements of a Wide-Chord Slotted Flap. By Thomas A. Harris, N. A. C. A.
716. Hydrodynamic and Aerodynamic Tests of a Family of Models of Seaplane Floats with Varying Angles of Dead Rise N. A. C. A. Models 57-A, 57-B, and 57-C. By John B. Parkinson, Roland E. Olson, and Rufus O. House, N. A. C. A.
717. A Method of Estimating the Critical Buckling Load for Structural Members. By Eugene E. Lundquist, N. A. C. A.
718. Resistance of Transparent Plastics to Impact. By Benjamin M. Axilrod and Gordon M. Kline, National Bureau of Standards.
719. The Effects of Partial-Span Slotted Flaps on the Aerodynamic Characteristics of a Rectangular and a Tapered N. A. C. A. 23012 Wing. By Rufus O. House, N. A. C. A.
720. Flight Tests of N. A. C. A. Nose-Slot Cowlings on the BFC-1 Airplane. By George W. Stickle, N. A. C. A.
721. Compressive Tests of a Monocoque Box. By Walter Ramberg, Albert E. McPherson, and Sam Levy, National Bureau of Standards.
722. Local Instability of Centrally Loaded Columns of Channel Section and Z-Section. By Eugene E. Lundquist, N. A. C. A.
723. Adhesion of Ice in Its Relation to the De-icing of Airplanes. By A. M. Rothrock and R. F. Selden, N. A. C. A.
724. The Effects of Surface Waviness and of Rib Stitching on Wing Drag. By Manley J. Hood, N. A. C. A.
725. Tank Tests to Determine the Effects of the Chine Flare of a Flying-Boat Hull N. A. C. A. Model Series 62 and 69. By Joe W. Bell and Roland E. Olson, N. A. C. A.
726. Combined Beam-Column Stresses of Aluminum-Alloy Channel Sections. By R. Gottlieb, T. M. Thompson, and E. C. Witt, University of Maryland.
727. A Flight Investigation of the Distribution of Ice-Inhibiting Fluids on a Propeller Blade. By Lewis A. Rodert, N. A. C. A.
728. Wind-Tunnel Investigation of an N. A. C. A. 23021 Airfoil with Two Arrangements of a 40-Percent-Chord Slotted Flap. By Frank Duschik, N. A. C. A.

729. An Instrument for Estimating Tautness of Doped Fabrics on Aircraft. By Gordon M. Kline and Herbert F. Schiefer, National Bureau of Standards.
730. Wind-Tunnel Investigation of Effect of Yaw on Lateral-Stability Characteristics. II—Rectangular N. A. C. A. 23012 Wing with a Circular Fuselage and a Fin. By M. J. Bamber and R. O. House, N. A. C. A.

#### LIST OF TECHNICAL MEMORANDUMS ISSUED DURING THE PAST YEAR

878. The Twisting of Thin-Walled Stiffened Circular Cylinders. By E. Schapitz. From Lilienthal-Gesellschaft für Luftfahrtforschung Jahrbuch, 1936.
879. Static Longitudinal Stability and Longitudinal Control of Autogiro Rotors. By M. Schrenk. From Luftfahrtforschung, June 6, 1938.
880. The Effective Width of Curved Sheet after Buckling. By W. A. Wenzek. From Luftfahrtforschung, July 6, 1938.
881. Application and Testing of Transparent Plastics Used in Airplane Construction. By K. Riechers and J. Olms. From Luftwissen, June 1938.
882. Modern Manufacturing Equipment of the Ernst Heinkel Airplane Works. By A. Thormann and H. Jockisch. From Luftfahrtforschung, January 20, 1938.
883. Distribution of Temperatures over an Airplane Wing with Reference to the Phenomena of Ice Formation. By Edmond Brun. From Publications Scientifiques et Techniques du Ministère de l'Air, No. 119, 1938.
884. Calculation of the Induced Efficiency of Heavily Loaded Propellers Having Infinite Number of Blades. By F. Lösch.  
The Induced Efficiency of Optimum Propellers Having a Finite Number of Blades. By K. N. Kramer.  
Prospects of Propeller Drive for High Flying Speeds. By G. Bock and R. Nikodemus.  
From Luftfahrtforschung, July 6, 1938.
885. Meteorological-Physical Limitations of Icing in the Atmosphere. By W. Findeisen. From Hauptversammlung der Lilienthal-Gesellschaft für Luftfahrtforschung, Berlin, October 12-15, 1938.
886. Theory of Two-Dimensional Potential Flow about Arbitrary Wing Sections. By H. Gebelein. From Ingenieur-Archiv, June 1938.
887. Comparison of Theory with Experiment in the Phenomenon of Wing Flutter. By P. Cicala. From L'Aerotecnica, April 1938.
888. Ice Formation on Wings. By L. Ritz. From Hauptversammlung der Lilienthal-Gesellschaft für Luftfahrtforschung, Berlin, October 12-15, 1938.
889. Investigation of the Lift Distribution Over the Separate Wings of a Biplane. By D. Küchemann. From Luftfahrtforschung, October 10, 1938.
890. Experiments on a Slotted Wing. By P. Ruden. From Deutsche Luftfahrtforschung Jahrbuch, 1937.
891. Theoretical and Experimental Study of Ignition Lag and Engine Knock. By Fritz A. F. Schmidt. From VDI—Forschungsheft 392—Supplement to Forschung auf dem Gebiete des Ingenieurwesens, September-October, 1938.
892. Investigations and Tests in the Towing Basin at Guidonia. By C. Cremona. From Hauptversammlung der Lilienthal-Gesellschaft für Luftfahrtforschung, Berlin, October 12-15, 1938.



893. Contribution to the Theory of the Heated Duct Radiator. By H. Winter. From *Luftfahrtforschung*, October 10, 1938.
894. The Way to Increased Airplane Engine Power. By Eugen Vohrer. From *Luftwissen*, October 1938.
895. The Power of Aircraft Engines at Altitude. By Paolo Ragazzi. From *Hauptversammlung der Lilienthal-Gesellschaft für Luftfahrtforschung*, Berlin, October 12-15, 1938.
896. The Drag of Airplane Radiators with Special Reference to Air Heating (Comparison of Theory and Experiment). By B. Göthert. From *Luftfahrtforschung*, September 10, 1938.
897. Airfoil Theory at Supersonic Speed. By H. Schlichting. From *Deutsche Luftfahrtforschung Jahrbuch*, 1937.
898. The Limit of Stability of a Curved Plate Strip Under Shear and Axial Stresses. By A. Kromm. From *Luftfahrtforschung*, October 10, 1938.
899. The Hydrodynamic Theory of Detonation. By Heinz Langweiler. From *Zeitschrift für Technische Physik*, Vol. 19, No. 9, 1938.
900. The Effect of the Masses of the Controls on the Longitudinal Stability with Free Elevator. By Rudolf Schmidt. Part I. From *Luftfahrtforschung*, January 10, 1939.
901. Investigations and Experiments in the Guidonia Supersonic Wind Tunnel. By Antonio Ferri. From *Hauptversammlung der Lilienthal-Gesellschaft für Luftfahrtforschung*, Berlin, October 12-15, 1938.
902. Design of Centrifugal Impeller Blades. By A. Betz and I. Flügge-Lotz. From *Ingenieur-Archiv*, December 1938.
903. Effect of Transition in Cross-Sectional Shape on the Development of the Velocity and Pressure Distribution of Turbulent Flow in Pipes. By Erwin Mayer. From *VDI-Forschungsheft 389—Supplement to Forschung auf dem Gebiete des Ingenieurwesens*, March/April 1938.
904. Stability of Rectangular Plates with Longitudinal or Transverse Stiffeners Under Uniform Compression. By R. Barbre. From *Ingenieur-Archiv*, Vol. VIII, No. 2, 1937.
905. Temperature-Indicating Paints. By F. Penzig. From *Zeitschrift des Vereines deutscher Ingenieure*, January 21, 1939.
906. Forces and Moments on a Yawed Airfoil. By Sigward Hoerner. From *Luftfahrtforschung*, April 20, 1939.
907. Dynamic Stability of a Helicopter with Hinged Rotor Blades. By K. Hohenemser. From *Ingenieur-Archiv*, December 1938.
908. Two-Stroke-Cycle Engines with Unsymmetrical Control Diagram (Supercharged Engines). By J. Zeman. From *Automobiltechnische Zeitschrift*, August 25, 1938.
909. The Theory of Contra-Vanes Applied to the Propeller. By Albert Betz. From *Ingenieur-Archiv*, December 1938.
910. Measurements on a Low-Wing Model in the Rotating Jet and Comparison with Flight Measurements. By W. Bader. From *Luftfahrtforschung*, February 20, 1939.
911. Knocking in the Otto-Cycle Engine. By H. Weinhart. From *Luftfahrtforschung*, February 20, 1939.

#### FINANCIAL REPORT

**Appropriations and expenditures, 1939.**—The general appropriation for the National Advisory Committee for Aeronautics for the fiscal year 1939, as contained in the Independent Offices Appropriation Act approved May 23, 1938, was \$1,679,000. A supplemental appropria-

tion of \$223,980 was made available in the Second Deficiency Appropriation Act, fiscal year 1939, approved May 2, 1939, for the same purposes specified in the Committee's regular appropriation act for 1939, to continue available until June 30, 1940. The total amount available for general purposes during the fiscal year 1939, therefore, was \$1,902,980. The amount expended and obligated under the regular appropriation was \$1,678,996 and under the supplemental appropriation \$29,434, making a total of \$1,708,430, itemized as follows:

Personal services-----	\$1,065,812
Supplies and materials-----	85,146
Communication service-----	3,722
Travel expenses-----	15,136
Transportation of things-----	2,478
Furnishing of electricity-----	43,518
Repairs and alterations-----	5,826
Special and miscellaneous investigations-----	69,384
Contracts for research-----	24,968
Equipment-----	192,440
Structures-----	200,000
<hr/>	
Expended and obligated-----	1,708,430
Unexpended balance-----	4
Balance of supplemental appropriation, available for expenditure during fiscal year 1940-----	194,546
<hr/>	
Total, general appropriation-----	1,902,980

The appropriation for printing and binding for 1939 was \$21,000, of which \$20,996 was expended.

The Second Deficiency Appropriation Act also provided \$2,140,000 for the construction and equipment of additional facilities at Langley Field, Va., including connections to public utilities, and rights-of-way for and installation of power lines, this amount to remain available until expended. No obligations were placed under this fund during the fiscal year 1939.

The amount of \$6,500 was received during the fiscal year 1939 and credited to three special deposit accounts to cover the cost of scientific investigations for manufacturers. Also one remittance of \$1,130 was carried over on account of an uncompleted investigation started in 1938. These four investigations were completed during 1939, resulting in the deposit of \$6,345.52 to Miscellaneous Receipts in the Treasury, as proceeds, and the return of unexpended balances totaling \$1,284.48 to depositors.

An allotment of \$400 was received from the State Department for payments during the fiscal year 1939 to employees stationed abroad, on account of exchange losses due to appreciation of foreign currencies. Of this amount \$71 was paid during the fiscal year 1939 to employees of the Committee stationed in the Paris office, leaving a balance of \$329 which was turned back into the Treasury.



An allotment of \$1,000 was made to the Committee for preparation of models for exhibit at the Golden Gate International Exposition at San Francisco. The total amount was expended for that purpose.

**Appropriations for fiscal year 1940.**—The general appropriation for the fiscal year 1940, as contained in the Independent Offices Appropriation Act approved March 16, 1939, was \$1,717,000, and the amount provided for printing and binding was \$23,000. This act also provided \$340,000 for the completion of the two-dimensional wind tunnel for which the 1939 act had provided an initial amount of \$200,000, and \$100,000 which will be used for the modernization of the free spinning wind tunnel. The total amount provided under the Independent Offices Act for 1940, therefore was \$2,180,000.

The Second Deficiency Appropriation Act, fiscal year 1939, approved May 2, 1939, provided \$2,140,000 for the construction and equipment of additional facilities at Langley Field, Va., including connections to public utilities, and rights-of-way for, and installation of power lines, this amount to remain available until expended. Also provided under the Second Deficiency Act for general purposes for the fiscal years 1939 and 1940 was an additional sum of \$223,980, of which there was at the end of the fiscal year 1939 a balance of \$194,546 available for obligation in the fiscal year 1940, thus making the total amount available under this act for expenditure in 1940, \$2,334,546.

The Third Deficiency Appropriation Act, fiscal year 1939, approved August 9, 1939, provided \$1,890,980 for beginning construction of an additional research laboratory and authorized the Committee to enter into contracts for construction and equipment, including the purchase of land, not to exceed a total of \$10,000,000. Also included in this act was an item of \$109,020 for additional personnel, making the total amount of \$2,000,000 available under this act for expenditure during 1940.

The total amount available for expenditure during 1940 under the three acts mentioned is \$6,514,546.

**Estimates for fiscal year 1941.**—The Committee's estimates for the fiscal year 1941 include the amount of \$3,899,513 for general purposes and \$30,000 for printing and binding. The amount of \$1,177,475 is requested for additional facilities at Langley Field, and \$5,699,020 for construction of new facilities at Moffett Field. The total amount of the regular estimates for 1941 is \$10,806,008.

#### CONCLUSION

The Committee is grateful to the President and to the Congress for the liberal support of its work in the past and especially for the recent approval of a second major research station to be located at Moffett Field, Calif. It strongly urges approval of its recommendations for the construction of a special engine research laboratory and for the stimulation and support of research in scientific and educational institutions.

In the present disturbed condition of world affairs, the importance of accelerating aeronautical progress in the United States cannot be overemphasized. The Committee has been careful and practical in presenting its needs and urges that the appropriations recommended be approved. Nothing will have a more fundamental influence on the progress of American aeronautics than liberal support of a well-rounded and comprehensive program for scientific research. The Army, the Navy, and the Civil Aeronautics Authority depend upon the National Advisory Committee for Aeronautics to meet the research needs of aviation and to provide the constant stream of new knowledge necessary to keep the United States in the forefront of progressive nations in the development of aeronautics for both military and commercial purposes.

Respectfully submitted.

NATIONAL ADVISORY COMMITTEE

FOR AERONAUTICS,

VANNEVAR BUSH, *Chairman*.







## REPORT No. 645

### CORRECTION OF TEMPERATURES OF AIR-COOLED ENGINE CYLINDERS FOR VARIATION IN ENGINE AND COOLING CONDITIONS

By OSCAR W. SCHEY, BENJAMIN PINKEL, and HERMAN H. ELLERBROCK, Jr.

#### SUMMARY

*Factors are obtained from semicempirical equations for correcting engine-cylinder temperatures for variation in important engine and cooling conditions. The variation of engine temperatures with atmospheric temperature is treated in detail, and correction factors are obtained for various flight and test conditions, such as climb at constant indicated air speed, level flight, ground running, take-off, constant speed of cooling air, and constant mass flow of cooling air.*

*Seven conventional air-cooled engine cylinders enclosed in jackets and cooled by a blower were tested to determine the effect of cooling-air temperature and carburetor-air temperature on cylinder temperatures. The cooling-air temperature was varied from approximately 80° F. to 230° F. and the carburetor-air temperature from approximately 40° F. to 160° F. Tests were made over a large range of engine speeds, brake mean effective pressures, and pressure drops across the cylinder. The correction factors obtained experimentally are compared with those obtained from the semicempirical equations and a fair agreement is noted.*

#### INTRODUCTION

In present-day air-cooled engines of high specific output, cooling is very often the factor that limits engine performance. As a result, several problems arise which require that cooling data obtained at one set of test conditions be converted to apply at another. Because of the strict limits set on maximum cylinder temperatures in acceptance tests and because of the difficulty of obtaining a standard set of test conditions both in flight and on the ground, a method is required for correcting the engine-cylinder temperatures to the standard conditions. It is very often necessary to predict cylinder temperatures at altitude from tests made on the ground and cylinder temperatures in the summer from tests made in the winter.

The correction of cylinder temperature for variation in atmospheric temperature is of particular interest to persons concerned with acceptance tests. In the past, several methods have been used for making this correction.

In May 1933 the Chief of the Bureau of Aeronautics, Navy Department, issued to the inspector of naval aircraft the following corrections to be applied to observed cylinder temperatures for change in strut air temperatures: "1.5° F. for every 1° F. strut air for the cylinder-head temperatures and 0.5° F. for every 1° F. strut air for the cylinder-base temperatures."

The Army Air Corps has issued the following instructions for correcting engine-cylinder temperatures: "In determining temperatures for satisfactory operation to be encountered with anticipated summer temperatures, a correction will be added to the actual recorded temperature and the corrected temperature will be the anticipated engine summer temperature. This correction is the difference between the actual air temperature and the anticipated summer air temperature for the particular altitude and it is added directly to all engine temperatures to determine the anticipated summer temperature in each case."

Campbell (reference 1) obtained a correction factor of 1; that is, for every degree rise in air temperature, there is a 1° F. rise in cylinder temperature for a constant-velocity condition. The Army and Navy methods did not specify the conditions for which the corrections applied and it is to be assumed that they were to be applied to all flight conditions.

Besides affecting the temperature of the cooling air, the variation in atmospheric temperature affects other factors that, in turn, influence the engine cooling; for example, the density of the cooling air, the speed of the airplane, the engine power, and the temperature of the mixture at the intake manifold. It is thus evident that the value of the correction factor for variation of cylinder temperature with atmospheric temperature will depend to some extent on the type of test to which it is to be applied.

An expression for the correction factor as a function of the test conditions will be obtained from equations for the rate of transfer of heat from the engine gas to the cylinder wall and from the cylinder wall to the cooling air. Under Application of Results, curves of



this function will be presented and an explanation will be given of the procedure by which the correction factors may be readily determined without reference to the analysis. A table has been prepared covering correction factors for flight and ground conditions of: climb at a designated air speed, level flight at a given pressure altitude, stationary on ground at a given atmospheric pressure, constant airplane velocity, and constant mass flow of cooling air. From this table, a close estimate of the correction factor may be rapidly obtained. A discussion of the table is included later in the report.

In any maneuver of short duration in which there is a sudden increase of power or decrease of cooling-air velocity, the cylinder temperatures, because of the time required for temperatures to stabilize, will depend on the time necessary for the completion of the maneuver. In such cases, the correction factor for the variation of atmospheric temperature will depend on the effect of atmospheric temperature upon the time duration of the maneuver. An equation will be derived for the cylinder temperature as a function of the engine and the cooling conditions and the time. The effect of variation of atmospheric temperature upon cylinder temperature for the take-off and the climb condition will be discussed.

The results of tests made at the request of the Bureau of Aeronautics, Navy Department, by the N. A. C. A. at Langley Field, Va., during 1934, 1935, and 1936 to determine the effect of atmospheric temperature on cylinder temperatures for seven service cylinders at various operating conditions are given in this report.

#### DISCUSSION OF PROBLEM

**Cylinder temperature as a function of engine and cooling conditions.**—As a starting point in the analysis, the equations for the transfer of heat from the combustion gases to the engine cylinder and from the cylinder to the cooling air will be reviewed. It has been shown in reference 2 that the rate of heat transfer (B. t. u. per hr.) from the combustion gases to the cylinder head may be written, as a good first approximation,

$$H = \bar{B}a_1 I^{n'} (T_g - T_h) \quad (1)$$

and the rate of heat transfer from the cylinder head to the cooling air may be written

$$H_1 = Ka_0 (\Delta p \rho / \rho_0)^m (T_h - T_a) \quad (2)$$

where  $H$  is the heat transferred per unit time from combustion gases to cylinder head, B. t. u. per hr.

$\bar{B}$  and  $K$ , constants.

$a_1$ , internal area of head of cylinder, sq. in.

$I$ , indicated horsepower of each cylinder.

$n'$  and  $m$ , exponents.

$T_g$ , effective gas temperature, °F.

$T_h$ , average temperature over the cylinder-head surface when equilibrium is attained,

$H_1$ , heat transferred per unit time from cylinder head to cooling air, B. t. u. per hr.

$a_0$ , outside wall area of head of cylinder, sq. in.

$\Delta p$ , pressure drop across cylinder, in. of water (includes loss out exit of baffle).

$\rho$ , average density of cooling air, lb. ft.<sup>-3</sup> sec.<sup>2</sup>

$\rho_0$ , density of air at 29.92 in. Hg and 70° F., ft.<sup>-3</sup> sec.<sup>2</sup>

$T_a$ , inlet temperature of cooling air, °F. (temperature of atmosphere).

(For convenience, a complete list of the symbols used is given in an appendix.)

For equilibrium the rate of heat transfer to the cylinder head is equal to the rate of heat transfer away from the cylinder head and, solving equations (1) and (2) for  $T_h$ , the following equation is obtained

$$T_h = \frac{T_g - T_a}{\frac{Ka_0 (\Delta p \rho / \rho_0)^m}{\bar{B}a_1 I^{n'}} + 1} + T_a$$

Equation (3) gives the average head temperature as a function of the important engine and cooling variables. A set of equations similar to (1), (2), and (3) may be written for the barrel. In the following discussion wherever an equation is derived for the head, it is to be remembered that a parallel equation applies for the barrel. The values for  $Ka_0$ ,  $\bar{B}a_1$ ,  $m$ , and  $n'$  were obtained from blower-cooling tests on Pratt & Whitney cylinders 1340-H and 1535 (reference 2) and are given in the following table.

Cylinder	$Ka_0$		$\bar{B}a_1$		$m$		$n'$	
	Head	Barrel	Head	Barrel	Head	Barrel	Head	Barrel
1340-H.....	78.1	33.0	5.22	2.77	0.34	0.34	0.64	.....
1535.....	34.5	17.1	2.71	.....	.35	.31	.68	.....

The values for  $\bar{B}a_1$ ,  $m$ , and  $n'$  should be about the same for a cowled engine under flight conditions and  $Ka_0$  should be somewhat higher. The form of equation (3) was checked by flight tests on a Grumman Sea Devil airplane equipped with a Pratt & Whitney 1535 engine (references 2 and 3).

It is also shown in reference 2 that the temperature of the combustion gases  $T_g$  is dependent on the air-fuel ratio, the compression ratio, the carburetor-air temperature, and the spark setting and, as a good first approximation, is independent of the engine speed and the brake mean effective pressure. Curves obtained



from reference 2 showing the variation of  $T_g$  with air-fuel ratio, spark setting, and carburetor-air temperature for a Pratt & Whitney 1340-H cylinder and with air-fuel ratio for a Pratt & Whitney 1535 cylinder are reproduced in figure 1. In the range to the rich side of the theoretically correct mixture,  $T_g$  increases from approximately 1,100° F. at an air-fuel ratio of 10.5 to 1,150° F. at 12.5, and to 1,200° F. at 14.5. The fore-

By a rearrangement of terms, equation (3) may also be written

$$\frac{T_g - T_h}{T_h - T_a} I^{n'} = \frac{K a_0}{B a_1} (\Delta p \rho / \rho_0)^m$$

Thus, for a given engine installed on a given airplane, a straight line is obtained when  $\frac{T_g - T_h}{T_h - T_a} I^{n'}$  is plotted against  $\Delta p \rho / \rho_0$  on logarithmic coordinates. The slope

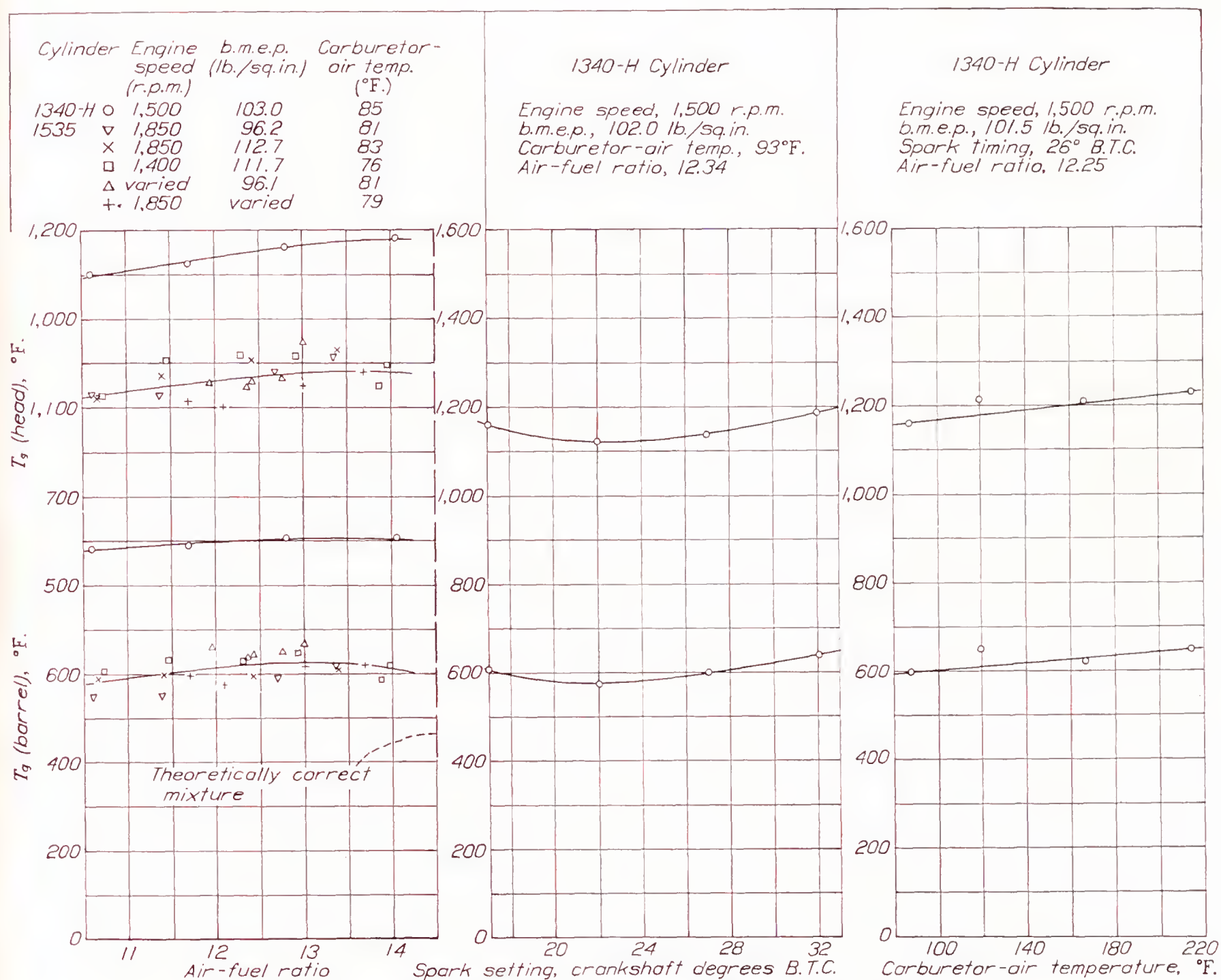


FIGURE 1.—Effect of air-fuel ratio, spark setting, and carburetor-air temperature on  $T_g$  (curves from reference 2).

going values apply for a carburetor-air temperature of about 80° F. A 1° F. variation in the carburetor-air temperature produces approximately a ½° F. variation in  $T_g$ .

For the barrel,  $T_g$  has a value of about 600° F. at an air-fuel ratio of 12.5 and a carburetor-air temperature of 80° F. The effect of carburetor-air temperature on  $T_g$  for the barrel is about the same as for the head.

of the line will be equal to  $m$  and the intercept at  $\Delta p \rho / \rho_0 = 1$  will be equal to  $K a_0 / B a_1$ . All the temperature data for the given installation should fall on this curve provided, in each case, that the equilibrium temperature has been attained. It is evident that the temperature  $T_h$  corresponding to any desired set of test conditions within the useful range can be calculated from this curve. A curve of this type is shown in figure 12 of reference 2.



Change in cylinder temperature with change in engine and cooling conditions.—For a constant mass flow, engine horsepower, and  $T_g$ , the variation of  $T_h$  with  $T_a$  is obtained by differentiating equation (3):

$$\alpha = \frac{\partial T_h}{\partial T_a} = \frac{\frac{Ka_0(\Delta p \rho / \rho_0)^m}{\bar{B}a_1 I^{n'}}}{\frac{Ka_0(\Delta p \rho / \rho_0)^m}{\bar{B}a_1 I^{n'}} + 1} = \frac{T_g - T_h}{T_g - T_a} \quad (4)$$

where  $\alpha$ , which may be called the "basic temperature correction factor" is the change in cylinder-head temperature per degree change in cooling-air temperature. Figure 2 shows  $\alpha$  for the head and the barrel plotted against the average head and barrel temperatures for various values of  $T_a$  and  $T_g$ .

If variations also occur in the density, the pressure drop, the indicated horsepower, and in  $T_g$ , then the increment in cylinder-head temperature for a small change in these factors is given by

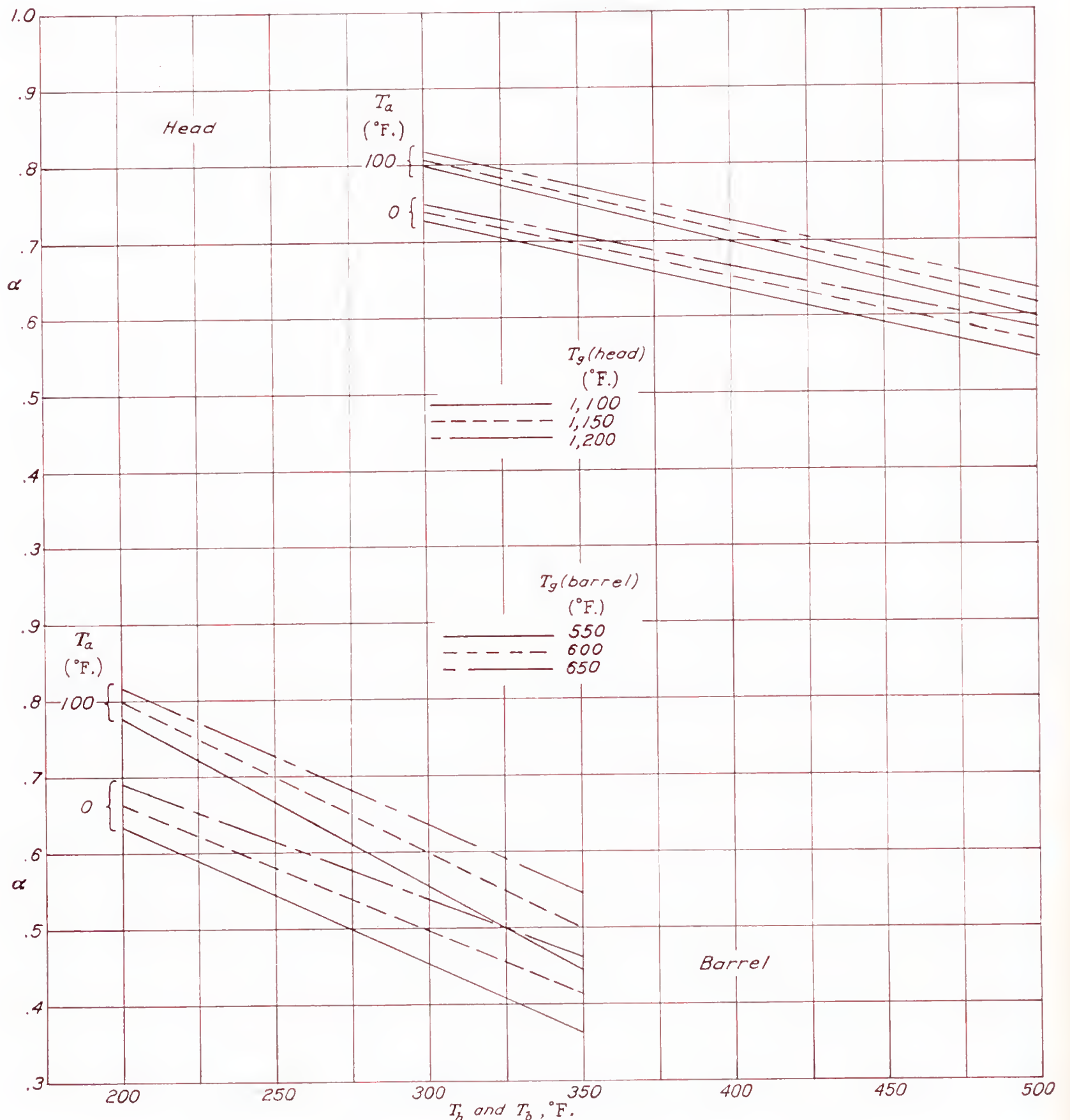


FIGURE 2.—Effect of cylinder temperature  $T_h$  or  $T_b$  on  $\alpha$  at various values of  $T_a$  and  $T_g$ .  
Head,  $\alpha = (T_g - T_h) / (T_g - T_a)$ . Barrel,  $\alpha = (T_g - T_b) / (T_g - T_a)$ .



$$dT_h = \frac{\frac{Ka_0(\Delta p \rho / \rho_0)^m}{Ba_1 I^{n'}}}{\frac{Ka_0(\Delta p \rho / \rho_0)^m}{Ba_1 I^{n'}} + 1} \left[ dT_a - m(T_h - T_a) \frac{d(\Delta p \rho / \rho_0)}{\Delta p \rho / \rho_0} + n'(T_h - T_a) \frac{dI}{I} \right] + \frac{dT_g}{\frac{Ka_0(\Delta p \rho / \rho_0)^m}{Ba_1 I^{n'}} + 1}$$

With  $\alpha$  as previously defined,

$$\frac{dT_h}{T_h - T_a} = \alpha \frac{dT_a}{T_h - T_a} + \frac{(1-\alpha)}{T_h - T_a} dT_g - m\alpha \frac{d(\Delta p \rho / \rho_0)}{\Delta p \rho / \rho_0} + n'\alpha \frac{dI}{I} \quad (5)$$

Thus, for small changes in the variables  $T_a$ ,  $T_g$ ,  $\Delta p \rho / \rho_0$ , and  $I$ ,  $T_h$  is increased by the amounts  $\alpha dT_a$  and  $(1-\alpha)dT_g$  and a percentage change in  $T_h - T_a$  is effected equal to  $-m\alpha$  times the percentage change in  $\Delta p \rho / \rho_0$  and  $n'\alpha$  times the percentage change in  $I$ . For example, with  $\alpha = 0.8$ ,  $m = 0.34$ , and  $n' = 0.64$ , a  $10^\circ$  F. increase in each of  $T_a$  and  $T_g$  causes an  $8^\circ$  F. and a  $2^\circ$  F. increase in  $T_h$ , respectively. A 10-percent change in each of  $\Delta p \rho / \rho_0$  and  $I$  causes a  $-2.7$ -percent and a  $5.2$ -percent change in  $T_h - T_a$ . Similar relations may be obtained for the barrel. The values of  $m$  and  $n'$  are about the same for the barrel as for the head but, as seen from figure 2,  $\alpha$  is slightly lower for the barrel.

From equation (4)

$$T_h - T_a = (1-\alpha)(T_g - T_a) \quad (6)$$

and equation (5) may be written

$$dT_h = \alpha dT_a + (1-\alpha)dT_g - m\alpha(1-\alpha)(T_g - T_a) \frac{d(\Delta p \rho / \rho_0)}{\Delta p \rho / \rho_0} + n'\alpha(1-\alpha)(T_g - T_a) \frac{dI}{I} \quad (7)$$

It is evident from equations (4), (5), and (7) that, when the values of  $T_g$  or  $\alpha$  are known, the variation in cylinder temperature with engine and cooling conditions can be determined for any test condition.

The present tests of seven service cylinders were made to determine the values of  $\alpha$  and  $T_g$  for a range of engine conditions. Tests were also made to obtain the effect of carburetor-air temperature on  $T_g$  and cylinder temperature.

**Effect of variation in atmospheric temperature on cylinder temperature at constant pressure altitude.**—For tests in which atmospheric temperature is changed, in addition to changes in  $T_a$ , there are generally introduced changes in  $T_g$ ,  $\Delta p \rho / \rho_0$ , and  $I$ . These changes depend on the specific tests under consideration.

As the pressure drop across the cylinder in a given flight condition depends on the atmospheric density and the airplane velocity, and the velocity depends on the engine power, the assumption will be made that

$\rho \Delta p$  is proportional to  $\rho^x I^y$ . From this relation between  $\rho \Delta p$  and  $\rho^x I^y$ , there is obtained

$$\frac{d(\Delta p \rho / \rho_0)}{\Delta p \rho / \rho_0} = x \frac{d\rho}{\rho} + y \frac{dI}{I}$$

Since  $\rho$  varies inversely as the absolute atmospheric temperature,

$$\frac{d\rho}{\rho} = -\frac{dT_a}{T_a + 460}$$

With regard to carburetor-air temperature  $T_c$ , two conditions will be considered, one in which the carburetor-air temperature is equal to the atmospheric temperature, and the other in which it is held constant by means of a carburetor-air heater. The relation between the carburetor-air temperature and the atmospheric temperature for these two cases may then be expressed by

$$dT_c = z dT_a$$

where  $z = 1$  for the first case mentioned and  $z = 0$  for the second case. Then, as the indicated horsepower for a constant manifold pressure varies inversely as the square root of the absolute carburetor temperature,

$$\frac{dI}{I} = \frac{d(T_c + 460)^{-1/2}}{(T_c + 460)^{-1/2}} = -z \frac{dT_a}{2(T_a + 460)}$$

Let

$$b = \frac{dT_g}{dT_c}$$

Then

$$dT_g = \frac{dT_g}{dT_c} \frac{dT_c}{dT_a} dT_a = b z dT_a$$

Inserting the foregoing quantities in equation (7) and combining

$$\frac{dT_h}{dT_a} = \alpha_\lambda = \alpha \left[ 1 + 0.34\lambda \frac{(1-\alpha)(T_g - T_a)}{T_a + 460} \right] + zb(1-\alpha) \quad (8)$$

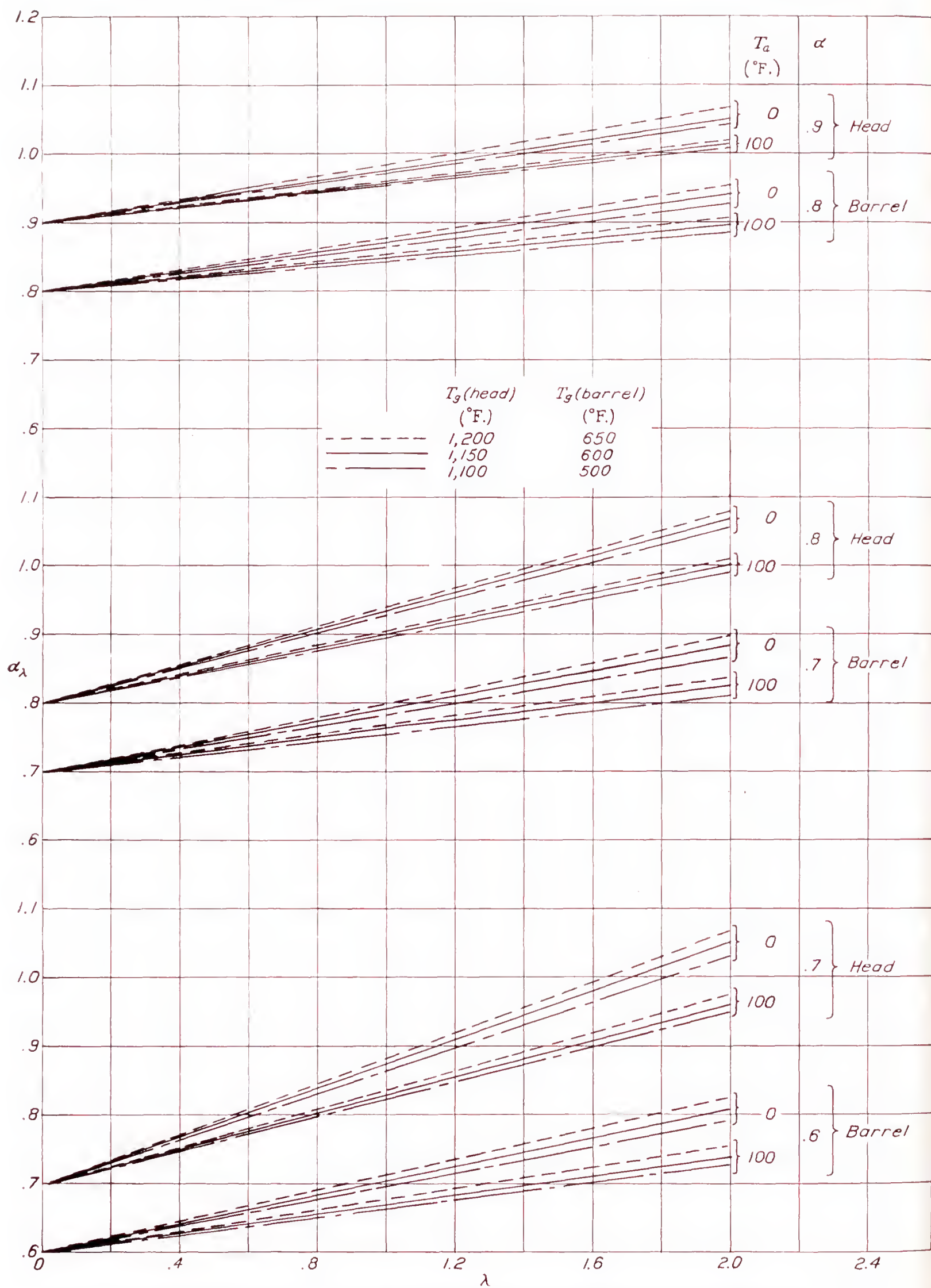
where

$$\lambda = \frac{m}{0.34} \left[ x + \frac{z}{2} \left( y - \frac{n'}{m} \right) \right] \quad (9)$$

The correction factor  $\alpha_\lambda$  is the change in cylinder temperature per degree change in atmospheric temperature at a constant pressure altitude. The effect of both atmospheric pressure and temperature on cylinder temperatures can be obtained from equation (3).

The last term in equation (8) is a small correction for variation in  $T_g$ . When the carburetor-air temperature is held constant,  $z = 0$  and this term is zero. When the carburetor-air temperature is allowed to vary with the atmospheric temperature,  $z = 1$  and this term becomes  $(1-\alpha)b$ . The value of  $b$ , as stated in the results, will be taken equal to 0.50 for both the head and the barrel. In figure 3, the remaining term in  $\alpha_\lambda$  is plotted as  $\alpha_\lambda$  against  $\lambda$  for various values of  $\alpha$ ,  $T_g$ , and  $T_a$ . The curves pass through  $\alpha_\lambda = \alpha$  at  $\lambda = 0$ . It is noticed that, for a given value of  $\alpha$ , the value of  $\alpha_\lambda$  does not depend appreciably on the value of  $T_g$  used.



FIGURE 3.—Variation of correction factor  $\alpha_\lambda$  with  $\lambda$  when carburetor-air temperature is constant, for various values of  $\alpha$ ,  $T_g$ , and  $T_a$ .



From figures 1, 2, and 3, it is apparent that the value of  $\alpha_\lambda$  for any given average cylinder-head temperature and cooling-air temperature may be obtained, provided that the value of  $\lambda$  for the flight or the test condition is known. It will also be noticed that, for large temperature variations, the value of  $\alpha_\lambda$  varies slightly in going from the initial to the final value of  $T_a$  and it is necessary to choose an average value for the range covered. As an added refinement after the first approximation, a corrected value of  $\alpha_\lambda$  may be obtained by averaging the values at the initial and the final conditions. A number of test conditions including those of climb, level flight, ground running, and constant velocity will be considered in a later section on Application of Results.

**Equation for cylinder temperature for varying operating conditions.**—When the power and the cooling conditions of an engine change, time is required for the cylinder temperatures to reach their equilibrium values. For short maneuvers or for maneuvers in which the conditions are varying, the time required to complete the maneuver must be considered in the determination of the effect of atmospheric temperature on cylinder temperature.

The rate  $H$  at which heat is carried from the gas to the cylinder head is equal to the sum of the rate at which the cylinder absorbs heat and the rate  $H_1$  at which heat is transferred to the cooling air:

$$H = cM \frac{dT_h}{dt} + H_1$$

where  $c$  is the specific heat of the head.

$M$ , the weight of the head.

$t$ , the time.

Substituting from equations (1) and (2) for  $H$  and  $H_1$  respectively, there results

$$\bar{B}a_1 I^{n'} (T_g - T_h) = cM \frac{dT_h}{dt} + Ka_0 (\Delta p \rho / \rho_0)^m (T_h - T_a)$$

or

$$cM \frac{dT_h}{dt} + [Ka_0 (\Delta p \rho / \rho_0)^m + \bar{B}a_1 I^{n'}] T_h = \bar{B}a_1 I^{n'} T_g + Ka_0 (\Delta p \rho / \rho_0)^m T_a$$

For any given variation of  $\Delta p$ ,  $\rho$ ,  $I$ ,  $T_g$ , and  $T_a$  with time, the solution for  $T_h$  is

$$T_h = e^{-\frac{1}{cM} \int_0^t A dt} \left[ \int_0^t \frac{B}{cM} e^{\frac{1}{cM} \int_0^t A dt} dt + T_{h_0} \right] \quad (10)$$

where

$$A = Ka_0 (\Delta p \rho / \rho_0)^m + \bar{B}a_1 I^{n'}$$

$$B = \bar{B}a_1 I^{n'} T_g + Ka_0 (\Delta p \rho / \rho_0)^m T_a$$

and  $T_{h_0}$  is the average temperature of the head at  $t=0$ .

For the case where  $A$  and  $B$  change at the time  $t=0$  and thereafter remain substantially constant, equation (10) reduces to

$$T_{h_t} = T_h - (T_h - T_{h_0}) e^{-\frac{At}{cM}} \quad (11)$$

where  $T_h$  is the final average temperature that the head will reach when equilibrium is attained and is given by equation (3), and  $T_{h_t}$  is the average temperature of the head at time  $t$ . Equation (11) may be used for cases in which small variations in  $A$  occur after the initial change at  $t=0$ . In such cases an average of the values of  $A$  should be used.

**Variation of cylinder temperature with atmospheric temperature for a maneuver of short duration.**—With  $t$  now taken as equal to the time of completion of the maneuver,  $T_{h_t}$  is the temperature at the completion of the maneuver. The effect of  $T_a$  on cylinder temperature will be obtained for the case where the carburetor-air temperature and the engine power are assumed to be held constant. From equation (11), for a change in atmospheric temperature of  $dT_a$  for the pressure altitude at which the maneuver is completed and of  $dT_0$  for the pressure altitude at which the maneuver is started, the change in  $T_h$  is given by

$$dT_{h_t} = \alpha_\lambda dT_a + (T_h - T_{h_0}) \frac{tA}{cM} \left( \frac{dA}{A} + \frac{dt}{t} \right) e^{-\frac{At}{cM}} - (\alpha_\lambda dT_a - \alpha_{\lambda_0} dT_0) e^{-\frac{At}{cM}}$$

where  $\alpha_{\lambda_0}$  is the correction factor, and  $T_0$  is the temperature of the atmosphere at time  $t=0$ .

$$\frac{dA}{A} = \frac{mKa_0 (\Delta p \rho / \rho_0)^m}{[Ka_0 (\Delta p \rho / \rho_0)^m + \bar{B}a_1 I^{n'}]} \frac{d(\Delta p \rho / \rho_0)}{\Delta p \rho / \rho_0} = \frac{m\alpha d(\Delta p \rho / \rho_0)}{\Delta p \rho / \rho_0}$$

As  $I$  is held constant,  $\Delta p \rho / \rho_0$  may be assumed to be proportional to  $\rho^x$  and  $t$  proportional to  $\rho^u$  or to  $(T+460)^{-u}$  where  $T$  is the average temperature of the atmosphere during the maneuver; then

$$\frac{dA}{A} + \frac{dt}{t} = (m\alpha x + u) \frac{d\rho}{\rho}$$

Since  $\rho$  is inversely proportional to  $T+460$

$$\frac{d\rho}{\rho} = -\frac{dT}{T+460}$$

and the equation for  $dT_{h_t}$  becomes

$$dT_{h_t} = \alpha_\lambda dT_a - (T_h - T_{h_0}) e^{-\frac{At}{cM}} \frac{tA}{cM} (m\alpha x + u) \frac{dT}{T+460} - (\alpha_\lambda dT_a - \alpha_{\lambda_0} dT_0) e^{-\frac{At}{cM}}$$

From equation (11)

$$e^{-\frac{At}{cM}} = \frac{T_h - T_{h_t}}{T_h - T_{h_0}}$$

and

$$\frac{At}{cM} = \log_e \frac{T_h - T_{h_0}}{T_h - T_{h_t}}$$



FIGURE 4.—Curve showing effect of  $(T_h - T_{h_t}) / (T_h - T_{h_0})$  on  $r$ .

$$r = \frac{T_h - T_{h_t}}{T_h - T_{h_0}} \log_e \frac{T_h - T_{h_0}}{T_h - T_{h_t}}$$

The quantity  $r$  is shown plotted in figure 4 against  $(T_h - T_{h_t}) / (T_h - T_{h_0})$ . When  $T_{h_t}$  is equal to  $T_h$ ,  $r$  is equal to zero and  $dT_{h_t}$  is equal to  $\alpha_\lambda dT_a$ . For  $T_{h_t} = T_{h_0}$ ,  $r$  is again zero and  $dT_{h_t} = \alpha_{\lambda_0} dT_0$ . It is thus evident that, for very short maneuvers, the change in  $T_{h_t}$  depends, as may be expected, more on the change in  $T_a$  than on the change in  $T_h$  with atmospheric temperature. The conditions of climb to critical altitude and take-off will be considered in a later section.

#### APPARATUS

The apparatus consisted of a single-cylinder air-cooled engine, a supercharger for boosting carburetor intake pressures, an electric dynamometer, a cooling system, heaters for varying the temperatures of the cooling and the carburetor air, a refrigerating system for cooling the carburetor air, and the necessary instruments to measure the factors involved. A diagrammatic sketch of the set-up is shown in figure 5 and a photograph of the engine with the cylinder enclosed in the cooling jacket is shown in figure 6.

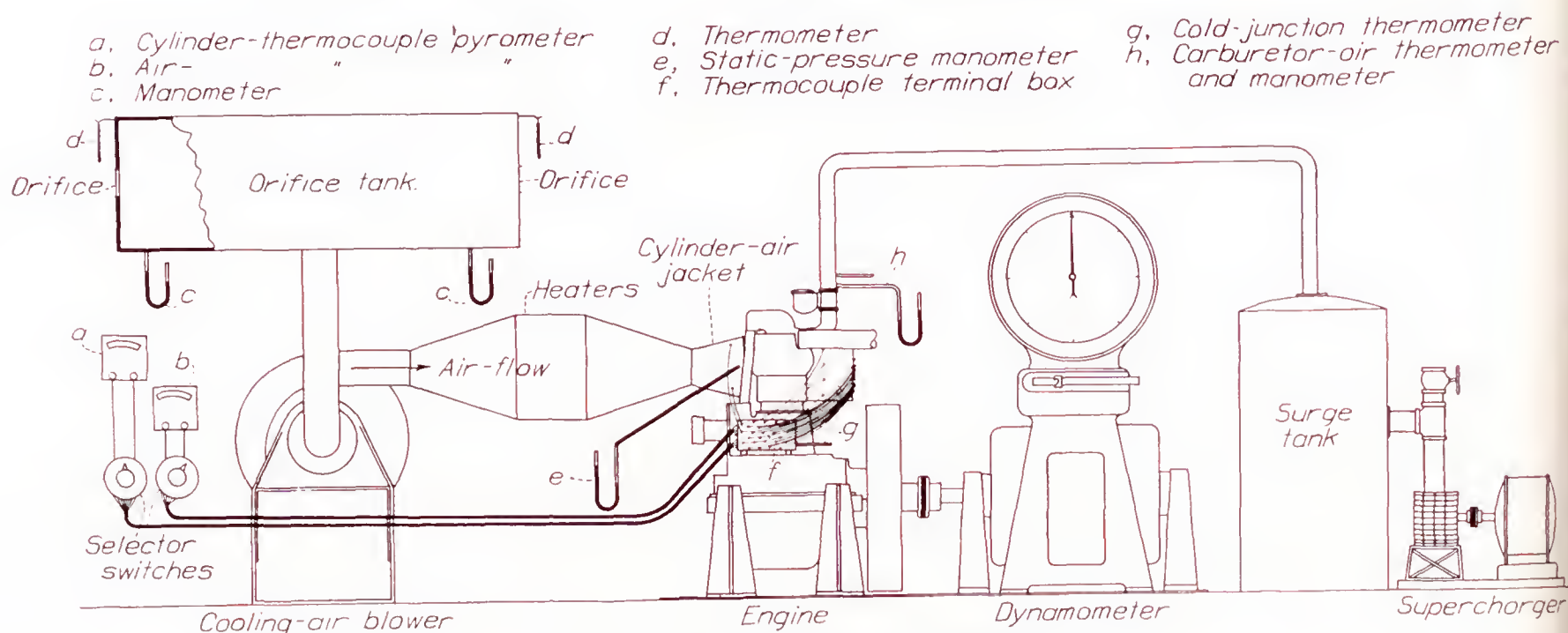


FIGURE 5.—Diagrammatic sketch of equipment.

and the equation for  $dT_{h_t}$  finally becomes

$$dT_{h_t} = \alpha_\lambda dT_a - \frac{T_h - T_{h_0}}{T + 460} (m\alpha_x + u) r dT$$

$$- (\alpha_\lambda dT_a - \alpha_{\lambda_0} dT_0) \frac{T_h - T_{h_t}}{T_h - T_{h_0}} \quad (12)$$

where

$$r = \frac{T_h - T_{h_t}}{T_h - T_{h_0}} \log_e \frac{T_h - T_{h_0}}{T_h - T_{h_t}}$$

#### AIR-COOLED CYLINDERS

The seven air-cooled cylinders (fig. 7) used in the tests were from the following engines: Pratt & Whitney 1340-H, 1535, 1830, and 1690 engines; and Wright 1820-F, 1820-G, and 1510 engines. They were adapted to the base of a universal test engine (reference 4). The valve movements and the timing of the single cylinder engines were approximately the same as of the multicylinder engines. Slight changes in stroke were made on the single-cylinder engines as compared with



the multicylinder engines to permit the use of available crankshafts. The bore, the stroke, and the compression ratio of the cylinders mounted on the single-cylinder test stand are given in the following table.

Cylinder	Bore (in.)	Stroke (in.)	Compression ratio
Pratt & Whitney:			
1340-H	5 $\frac{3}{4}$	6	5.52
1535	5 $\frac{3}{16}$	5 $\frac{1}{2}$	6.73
1830	5 $\frac{1}{2}$	5 $\frac{1}{2}$	6.15
1690	6 $\frac{1}{8}$	6	5.65
Wright:			
1820-F	6 $\frac{1}{8}$	7	6.64
1820-G	6 $\frac{1}{8}$	7	7.40
1510	5	5 $\frac{1}{2}$	6.20

area of the exit of the jackets to the clear area between the fins for the 1340-H, 1820-F, 1690, 1820-G, and 1510 cylinders was approximately 2; for the 1535 and 1830 cylinders, the ratio was approximately 3.

#### TEST EQUIPMENT

An N. A. C. A. Roots supercharger was used to increase the carburetor-intake pressure during tests with manifold pressures greater than atmospheric. A tank was placed in the air duct between the supercharger and the engine to reduce pressure pulsations caused by these units. An electric dynamometer absorbed the power and measured the torque of the engine.

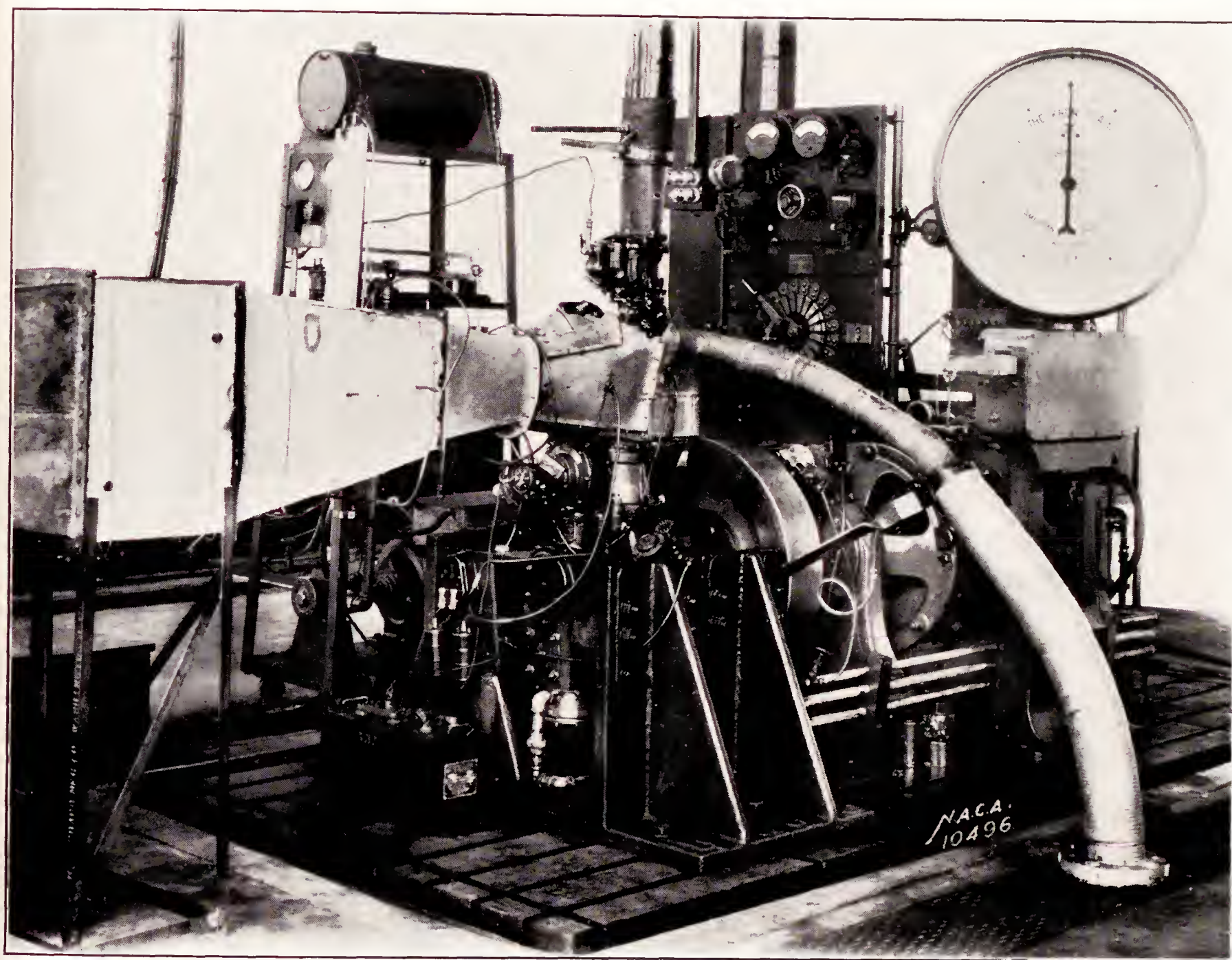


FIGURE 6.—Set-up of single-cylinder air-cooled engine showing jacket and air duct.

#### CYLINDER JACKETS

In each test, the cylinder was enclosed in a sheet-metal jacket open at front and rear. The jacket had a wide entrance section giving a low velocity of approach of the cooling air to the front half of the cylinder and fitted closely against the fins over the rear half, resulting in a high air velocity in this region. The ratio of the

The cooling system consisted of a blower to supply the cooling air, an orifice tank to measure the quantity of air, and an air duct between the blower and the jacket enclosing the cylinder. Baffles and screens were located in the air duct to insure a uniform temperature and velocity distribution.



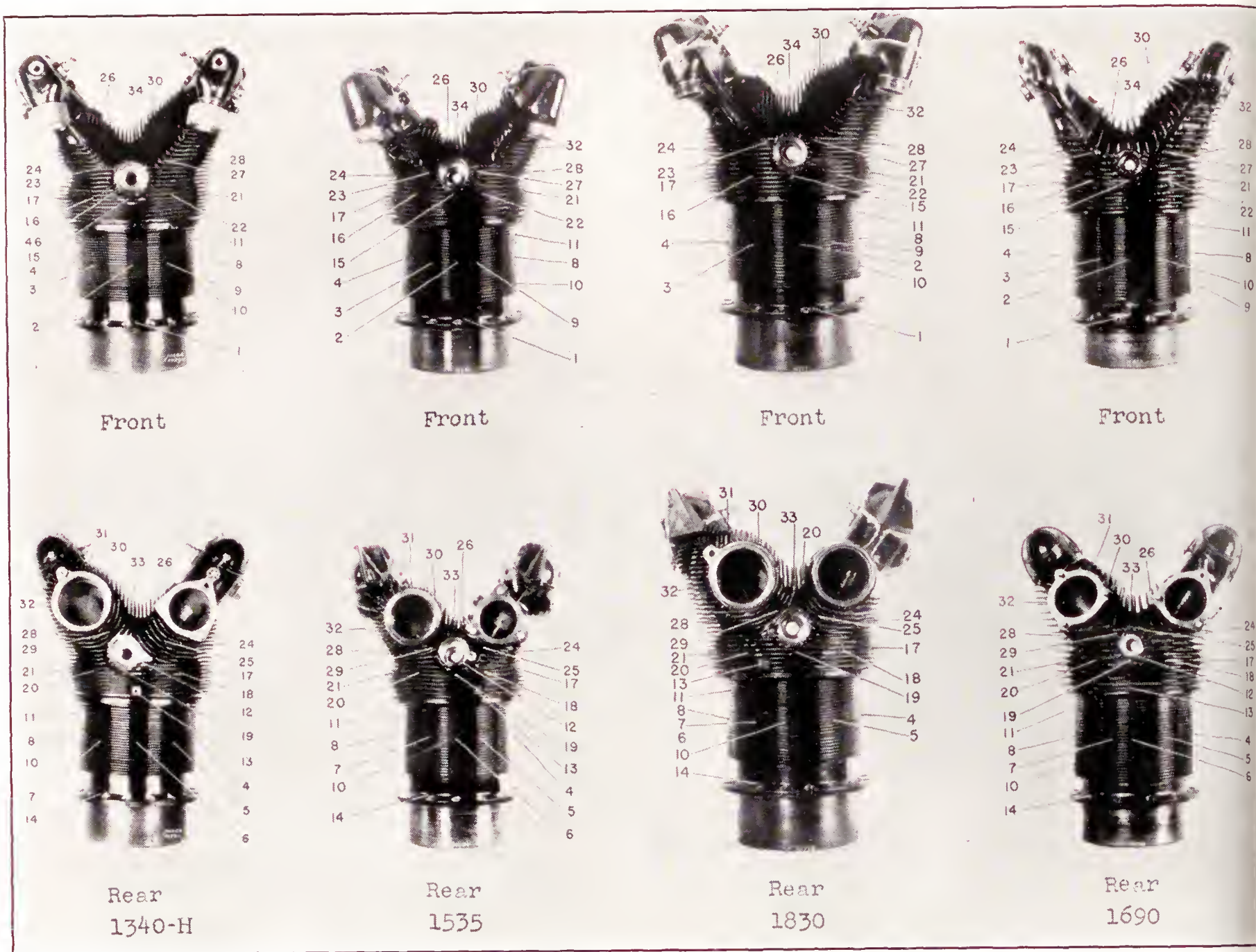


FIGURE 7 (a).—Front and rear views of cylinders from Pratt & Whitney engines showing location of thermocouples.

A 60-kilowatt heater consisting of four groups of separately controlled heating elements located in the air duct between the blower and the jacket was used for varying the temperature of the cooling air. In the tests in which the carburetor-air temperature was varied, temperatures higher than those of the room were obtained by heating the air with electric heaters placed in the intake-air line. For temperatures lower than atmospheric, the air to the carburetor was passed through a radiator submerged in a bath of kerosene into which carbon dioxide was expanded.

The standard test-engine equipment was used for measuring the engine speed and the fuel consumption.

#### INSTRUMENTS

Iron-constantan thermocouples and a direct-reading portable pyrometer were used to measure the cylinder temperatures. The thermocouples were made of 0.016-inch-diameter wire and were peened to the cylinder head and spot-welded to the barrel. The temperatures were measured on all cylinders by 22 thermocouples on the

head, 10 on the barrel, and 2 on the flange, located as shown in figure 7. Thermocouple 12 was a standard Navy gasket-type thermocouple placed under the spark plug. The temperature of the cooling air at the inlet of the jacket was measured near the cylinder by thermocouples connected to a sensitive galvanometer. The temperature of the cooling air at the outlet of the jacket was measured by 10 iron-constantan thermocouples. The cold junctions of all the thermocouples were placed in an insulated box. Liquid thermometers were used to measure the temperature of the air entering the orifice tank, of the cold-junction box, and of the carburetor intake.

The pressure drop across the cylinder was measured by a static tube located in the space ahead of the cylinder where the velocity head was negligible. This static tube was connected to a water manometer. A water manometer was used to measure the pressure in the orifice tank and a mercury manometer was used to measure the carburetor-intake pressure.



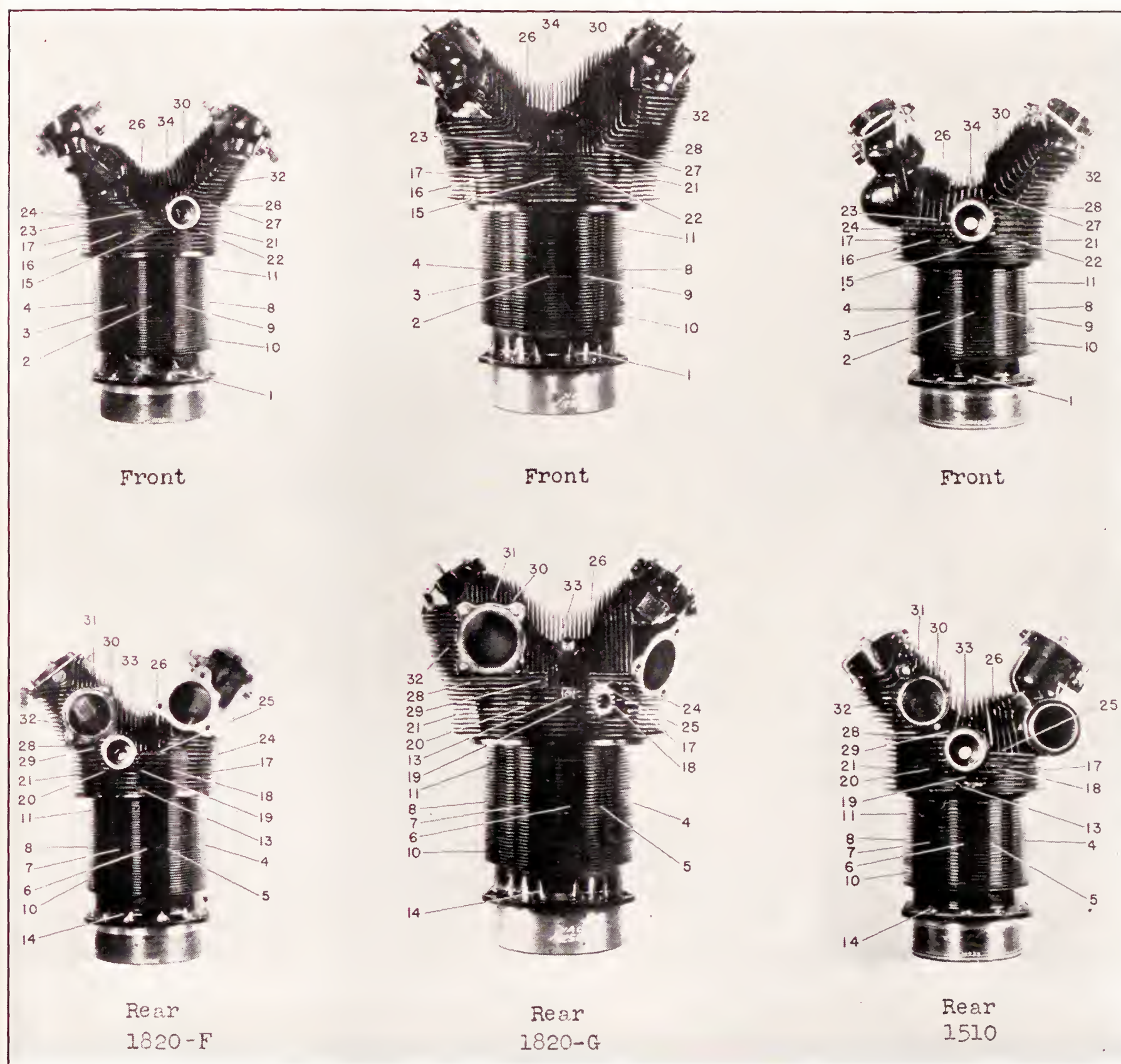


FIGURE 7 (b).—Front and rear views of cylinders from Wright engines showing location of thermocouples.

### TESTS

Tests were made of the seven cylinders to determine the values of  $\alpha$  and  $T_g$  at various engine speeds, indicated horsepowers, and mass flows of the cooling air. A list of the test conditions covered is given in table I. In each test the engine power, the engine speed, the air-fuel ratio, the carburetor-air temperature, the oil temperature, the spark timing, and the mass flow of the cooling air were held constant and the cooling-air temperature was varied. The range of the cooling-air tem-

peratures in most of the tests was from 80° F. to 230° F. The  $\alpha$  in a given test for each of the 34 thermocouples was determined by plotting the temperature measured by the thermocouple against the cooling-air temperature and obtaining the slope of the resulting straight line.

From equation (1) it is evident that, with engine conditions held constant,  $H$  is zero when  $T_h$  is equal to  $T_g$ ; and from equation (2) it is apparent that at equilibrium, for a constant value of the mass flow,  $H$  is proportional to  $T_h - T_a$ .



Thus, in the foregoing tests when the average temperature difference between the cylinder head and the cooling air is plotted against the average head temperature, the value of  $T_h$  at which  $T_h - T_a$  is zero is equal to  $T_g$ . The value of  $T_g$  for the barrel may be obtained in a similar manner. The procedure is illustrated in figure 8. A straight line is drawn through the points

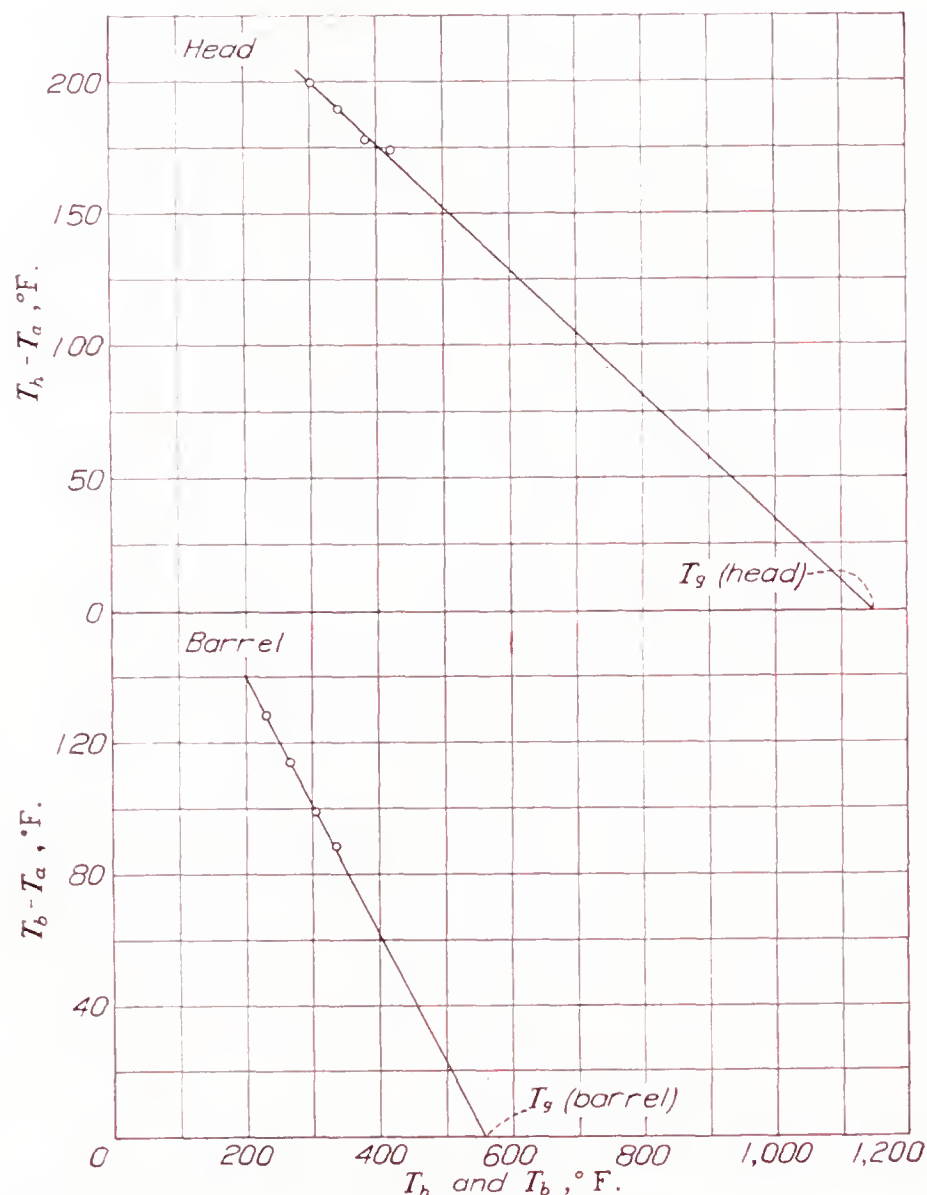


FIGURE 8.—Values of  $T_g$  for head and barrel of 1830 cylinder:

Series.....	4'
Engine speed, r. p. m.....	1,518
Indicated horsepower.....	28.57
Indicated mean effective pressure, lb./sq. in.....	114.1
$\Delta p/p_0$ , in. of water.....	15.27
Carburetor-air temperature, °F.....	94
Fuel consumption, lb./i. hp./hr.....	0.486

and extrapolated to the horizontal axis. Because of the large range through which the extrapolation is made, the value so obtained is approximate.

Additional tests were made of the 1340-H, 1535, 1820-F, 1830, and 1510 cylinders, for which the cooling conditions and the engine power were held constant and the carburetor-air temperature was varied. It was necessary to readjust the throttle setting at each new carburetor-air temperature to maintain constant power.

From equation (7) it is evident that for this case

$$dT_h = (1 - \alpha) dT_g$$

or

$$dT_g = \frac{T_g - T_a}{T_h - T_a} dT_h$$

The quantity  $b$  is then given by the following expression:

$$b = \frac{dT_g}{dT_c} = \frac{T_g - T_a}{T_h - T_a} \frac{dT_h}{dT_c}$$

The value of  $b$  was obtained as indicated by plotting  $T_h$  against  $T_c$ , obtaining the slope, and multiplying by  $(T_g - T_a)/(T_h - T_a)$ , where the values of  $T_g$  and  $T_h$  were taken corresponding to a carburetor-air temperature equal to atmospheric temperature. The value of  $b$  obtained in this manner is approximate but, since the effect of variation of  $T_g$  on  $T_h$  is small, an accurate value is not required.

During each test, observations were made of the engine torque, the engine speed, the fuel consumed, the carburetor-intake pressure and temperature, the spark setting, the temperature of the air entering the orifice tank, the temperature of the cooling air entering and leaving the jacket, the cylinder temperatures, the pressure drop across the orifice tank, the pressure at the entrance of the jacket, and the barometric pressure.

The weight of the cooling air was controlled by varying the speed of the blower. The carburetor-intake pressures were varied either by throttling the intake or by boosting with the supercharger.

Gasoline conforming to Army Specification Y-355 and having an octane number of 87 was used for most tests. For the most severe conditions, ethyl fluid was added to the gasoline in a sufficient amount to suppress audible knock.

#### COMPUTATIONS

The engine horsepowers given in this report are observed values and were calculated from the corrected dynamometer-scale reading and the engine speed. The method of computing the cooling-air weight is given in detail in reference 5.

The cylinder temperatures, the inlet cooling-air temperatures, and the outlet cooling-air temperatures were corrected for instrument calibration and cold-junction temperature.

The specific fuel consumption was calculated from the observed weight of fuel used, the time required to use this fuel, and the indicated horsepower.

The pressure drop obtained from the static tube placed in front of the cylinder included both the drop across the cylinder and the loss out the exit of the jacket. It is denoted by the symbol  $\Delta p$  in this report and is given in inches of water.

#### RESULTS

**Experimental values of  $\alpha$ .**—The experimental values of  $\alpha$  for the various points on the cylinder showed a consistent trend with either the location or the temperature of the points, except that the values on the head grouped about a common value and the values on the barrel grouped about another value. It was also found that thermocouple locations on the cylinder which had higher than average  $\alpha$ 's in some tests had lower than average  $\alpha$ 's in others and, again, no consistent trend could be detected. It was, therefore, considered expedient to average the values of  $\alpha$  for the head and the barrel separately and to present these values in this paper as the correction factors. The values of  $\alpha$  are shown in table II.



**Effective gas temperature  $T_g$ .**—The values of  $T_g$  were obtained in the manner previously described and are listed in table I. An average value of  $T_g$  was obtained as representative of the cylinder for average test conditions and is listed at the bottom of the column in table I. Most of the average values for the head and the barrel were close to 1,150° F. and 600° F., respectively. The largest deviation from these values occurred for the 1690 and 1820-F cylinders and for the barrel of the 1535 cylinder. As shown in figure 1, the values of  $T_g$  vary with the spark timing, the air-fuel ratio, and the carburetor-air temperature. The foregoing values hold for a normal spark timing, a carburetor-air temperature of approximately 80° F., and an air-fuel ratio of approximately 12.5 and agree fairly well with the values given in figure 1.

**Calculated values of  $\alpha$ .**—The values of  $\alpha$  for the various test conditions were calculated, making use of equation (4), and are shown in table II. The values of  $T_g$  used (see table II) were 1,150° F. for the head and 600° F. for the barrel except for the 1690, 1820-F, and 1535 cylinders, for which the average values of  $T_g$  shown in table I were used. The values of  $T_h$ ,  $T_b$ , and  $T_a$  used correspond to the condition in which no heat was added to the cooling air by the electric heaters. The values of  $\alpha$  were calculated for the 1510 cylinder, using the values of  $T_a$ ,  $T_b$ , and  $T_h$  corresponding to maximum cooling-air temperature and are shown in table III. Comparison of these values with the calculated values shown in table II for the 1510 cylinder shows very little difference, as is to be expected.

The experimental values of  $\alpha$  are plotted in figure 9 against the calculated values. A line is drawn in each figure for a 1:1 correspondence between the calculated and the experimental values. The points fall about each line and, although the scatter is wide, the same general trend is indicated.

**Experimental values of  $b$ .**—The values of  $b$ , the ratio of increase of  $T_g$  with increase of carburetor-air temperature, were obtained in the manner already described. The variation of cylinder temperature with carburetor temperature was small, of the order of 15° F. increase in cylinder temperature per 100° F. rise in carburetor-air temperature. It is apparent that small extraneous variations in cylinder temperature due to variation in other conditions would introduce a large percentage error in the value of  $b$ ; however, because of the small effect of variation of  $T_g$  on cylinder temperature, the value of  $b$  need not be very accurately known. The values of  $b$  obtained from several tests of the various cylinders are listed in table IV.

As there is no apparent reason for a large difference between the values of  $b$  for the various cylinders, an average was taken of all the available values. An average value of 0.38 is obtained as compared with the

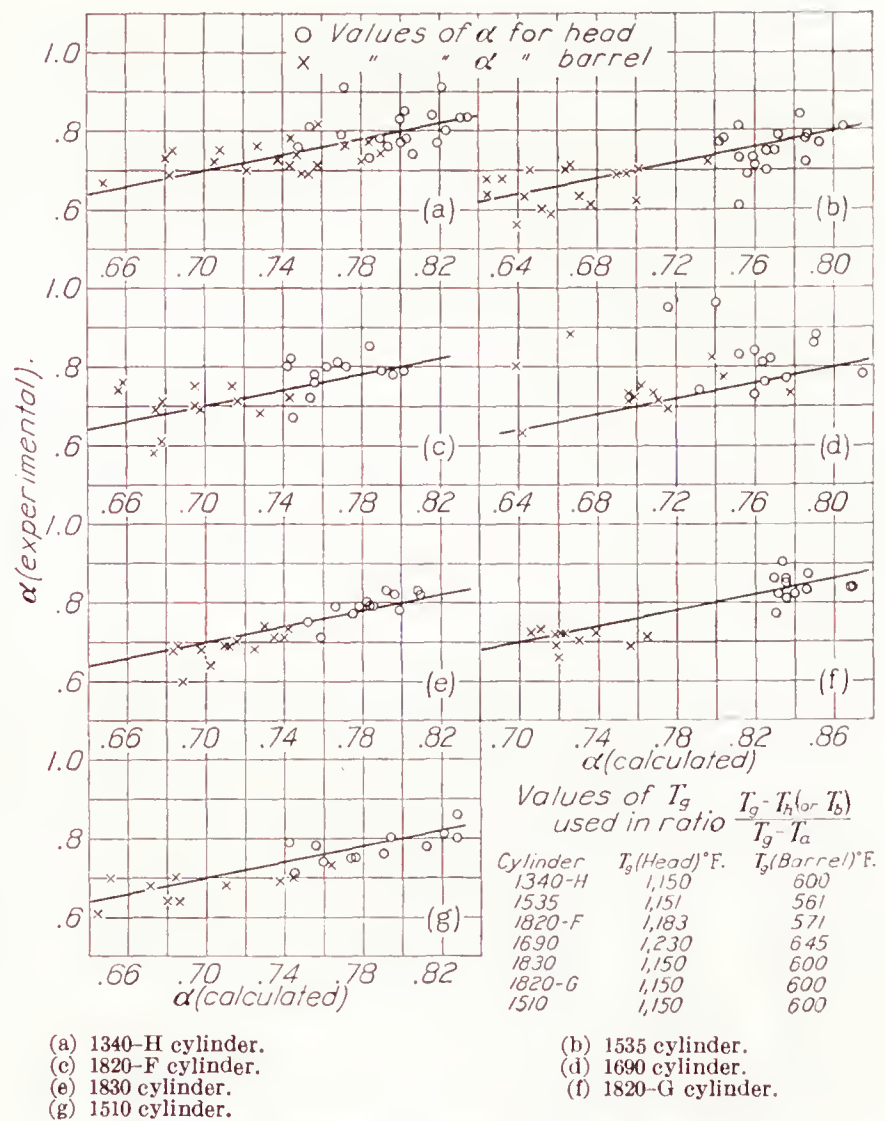


FIGURE 9.—Experimental against calculated values of  $\alpha$ .

value of 0.58 obtained from figure 1. In the present report a value of  $b=0.5$  will be used in making the computations. The term containing  $b$  in equation (8) occurs only in cases where the carburetor-air temperature is allowed to vary with the atmospheric temperature and, for these cases, an uncertainty in the computed value of  $\alpha_\lambda$  equal to 50 percent of  $b(1-\alpha)$  will exist when the foregoing value of  $b$  is used. In most cases, this uncertainty will be a small percentage of  $\alpha_\lambda$ .

#### APPLICATION OF RESULTS

The correction factors for the variation of cylinder temperature with atmospheric temperature will be considered for the following cases:

- A. Constant carburetor-air temperature and engine power.
  1. Climb at constant indicated air speed to a given pressure altitude.
  2. Level flight at a given pressure altitude.
  3. Stationary on ground at a given barometer.
  4. Constant airplane velocity.
  5. Constant mass flow.
- B. Carburetor-air temperature equal to and varying with atmospheric temperature; engine power varying with carburetor-air temperature; constant manifold pressure; and constant engine speed.



1. Climb at constant indicated air speed to a given pressure altitude.
  2. Level flight at a given pressure altitude.
  3. Stationary on ground at a given barometer.
- C. Maneuvers of short time duration. Constant carburetor-air temperature and engine power.
1. Climb to critical altitude.
  2. Take-off.

Cases A and B refer to equilibrium conditions and case C refers to varying conditions.

In the following calculations, the values given for the Pratt & Whitney 1340-H cylinder in the earlier Discussion of the Problem will be used for  $m$  and  $n'$ . The values of  $m$  and  $n'$  for other cylinders differ only by a slight amount from these values and will introduce only a small difference in  $\alpha_\lambda$ .

Throughout the rest of the report, the problem will be simplified by taking the average density of the air flowing around the cylinder as equal to the atmospheric density. This assumption introduces no appreciable error as the two densities are practically proportional and it is only the percentage density change that is of consequence in the analysis.

#### CONSTANT CARBURETOR-AIR TEMPERATURE AND ENGINE POWER

From the relation given earlier, that  $\rho\Delta p$  may be written proportional to  $\rho^x I^y$ , it is evident in the present case (constant engine power) that  $y=0$ . It has also been stated earlier that  $z=0$  when the carburetor-air temperature is held constant. Thus, for the cases noted under A, the values of  $y$  and  $z$  in equations (8) and (9) are zero and  $\lambda=x$ . The value of  $x$  will be found for the various cases.

**Climb at constant indicated air speed (A-1).**—For climb at constant indicated air speed,

$$\rho V^2 = \text{constant}$$

where  $V$  is the true velocity of the airplane.

As  $\Delta p = K_1 \rho V^2$   
 then  $\rho\Delta p = \rho \times \text{constant}$   
 and, thus,  $x=1$ .

The correction factor  $\alpha_\lambda$  may be obtained from figure 3 for  $\lambda=1.0$  for various values of  $T_a$  and  $T_o$ ; it applies for the case of slow climbs in which the final equilibrium temperature is very nearly reached. For fast-climbing airplanes, the cylinder temperature lags behind the equilibrium temperature and the effect of atmospheric temperature on the time of duration of the climb must also be considered in obtaining the correct factor. This case will be discussed later.

**Level flight at a given pressure altitude (A-2).**—At the level-flight condition

$$K_3 C_D \rho V^3 = \text{t.hp.}$$

where  $K_3$  is a constant and  $C_D$  is the drag coefficient. If it is assumed that the thrust horsepower remains

constant for a constant engine power and that the drag coefficient is practically constant at the maximum velocity condition in level flight, then

$$\rho V^3 = \text{constant}$$

and, since  $\Delta p = K_1 \rho V^2$

$$\rho\Delta p = \rho^2 \left(\frac{1}{\rho}\right)^{\frac{2}{3}} \times \text{constant} = \rho^{1.333} \times \text{constant}$$

For this case  $x=\lambda=1.333$ .

**Stationary on ground at a given barometer (A-3).**—From reference 6 a relation may be obtained between the nondimensional quantity  $\sqrt{\Delta p}/\rho^{\frac{1}{2}} n D$  and the nondimensional power coefficient  $P/\rho n^3 D^5$  for a cowling engine stationary on the ground. This relation may be approximated by

$$\frac{\sqrt{\Delta p}}{\rho^{\frac{1}{2}} n D} = K_4 \left( \frac{P}{\rho n^3 D^5} \right)^d$$

where  $n$ , propeller speed.

$P$ , propeller power.

$D$ , propeller diameter.

$K_4$ , a constant.

$d$ , an exponent.

The exponent  $d$  may be taken as a constant for a given propeller and cowling combination and for a short range of variation of  $P/\rho n^3 D^5$ . The values of  $d$  obtained from reference 6 were found to lie between  $\frac{1}{3}$  and  $\frac{1}{2}$ . From the preceding relation for a given engine power, engine speed, and propeller,  $\Delta p$  is proportional to  $\rho^{1-d}$ , and  $\rho\Delta p$  is proportional to  $\rho^{2-d}$ . The value of  $\lambda$  for this case lies between 1.50 and 1.666. As may be seen from figure 3, there is only a small difference between the values of  $\alpha_\lambda$  for these two values of  $\lambda$ .

**Constant airplane velocity (A-4).**—The case of substantially constant airplane velocity with variations in atmospheric temperature occurs in level flight when the carburetor-air temperature and engine power are allowed to vary. This case will be taken up in section E. In some acceptance tests on a dynamometer stand, however, a constant air velocity is maintained irrespective of atmospheric temperature while carburetor-air temperature and engine power are held constant. The following factors apply in correcting the average head and barrel temperatures obtained in these tests to a standard cooling-air temperature.

$$\begin{aligned} V &= \text{constant} \\ \rho\Delta p &= K_1 \rho^2 V^2 = \rho^2 \times \text{constant} \\ \lambda &= 2 \end{aligned}$$

The correction factors for this case are the highest of those obtained. Campbell (reference 1) found that for constant velocity, constant power, and constant carburetor-air temperature,  $\alpha_\lambda$  was approximately 1.0 for the thermocouples on the head of the cylinder tested.



Corresponding to an air temperature of 70° F. (the mean of Campbell's temperatures), a value of  $T_a$  of 1,150° F., and an average of his cylinder temperatures on the head of 358° F., figure 2 gives a value of  $\alpha$  of 0.73. With this  $\alpha$  and a value of  $T_a$  of 70° F., figure 3 shows that, for constant velocity ( $\lambda=2$ ),  $\alpha_\lambda$  is approximately 1.0.

**Constant mass flow (A-5).**—It is advisable in acceptance tests conducted on the dynamometer stand, whenever possible, to maintain a standard mass flow, because then there is no correction necessary for variation of  $\rho\Delta p$  since

$$\rho\Delta p = K_1 \rho^2 V^2 = \text{constant}$$

$$\lambda = 0 \text{ and } \alpha_\lambda = \alpha$$

#### CARBURETOR-AIR TEMPERATURE EQUAL TO AND VARYING WITH ATMOSPHERIC TEMPERATURE

Cases where the carburetor temperature is equal to and varies with the atmospheric temperature will now be considered. For these cases  $z=1$ .

**Climb at constant indicated air speed to a given pressure altitude (B-1).**—The angle of attack for optimum climb for an airplane equipped with a constant-speed propeller depends more on the angle of attack for minimum horsepower required than on the horsepower available. It may therefore be assumed that the slight variation in horsepower available due to temperature change will not appreciably affect the indicated air speed for optimum climb. As in the case of A-1

$$\rho V^2 = \text{constant}$$

$$\rho\Delta p = K_1 \rho^2 V^2 = \rho \times \text{constant} = \rho I^0 \times \text{constant}$$

Thus  $x=1$  and  $y=0$

and from equation (9)

$$\lambda = \left[ 1 + \frac{1}{2} \left( 0 - \frac{0.64}{0.34} \right) \right] = 1 - 0.941 = 0.059$$

**Level flight at a given pressure altitude (B-2).**—In level flight at full open throttle,  $\rho V^3$  is approximately proportional to the thrust horsepower. If the thrust horsepower is assumed proportional to the indicated horsepower of the engine,

$$\rho V^3 = K_5 I$$

$$\rho\Delta p = K_1 \rho^2 V^2 = \rho^{\frac{2}{3}} I^{\frac{2}{3}} \times \text{constant}$$

Thus

$$x = \frac{4}{3} \quad y = \frac{2}{3}$$

and

$$\lambda = \left[ \frac{4}{3} + \frac{1}{2} \left( \frac{2}{3} - 1.882 \right) \right] = 0.725$$

**Stationary on ground at a given barometer (B-3).**—As in case A-3,

$$\frac{\sqrt{\Delta p}}{\rho^{\frac{1}{2}} n D} = K_4 \left( \frac{P}{\rho n^3 D^5} \right)^{\frac{d}{2}}$$

On the assumption that the propeller power is proportional to the indicated horsepower and that the engine speed is held constant,

$$\rho\Delta p = K_6 \frac{\rho^2 I^d}{\rho^d} = K_6 \rho^{2-d} I^d$$

Thus

$$x = 2 - d \quad y = d$$

and

$$\lambda = \left[ 2 - d + \frac{1}{2} (d - 1.882) \right] = 1.059 - \frac{d}{2}$$

When

$$d = \frac{1}{3} \quad \lambda = 0.89$$

$$d = \frac{1}{2} \quad \lambda = 0.81$$

The values of  $x$ ,  $y$ ,  $z$ , and  $\lambda$  for the various conditions considered are listed in table V. Calculated correction factors for the various conditions for several values of atmospheric and average head and barrel temperatures are also given in the table. The value of  $T_a$  in the computations was taken as 1,150° F. for the head and 600° F. for the barrel. The maximum cylinder-head temperature was assumed to be 125° F. higher than the average head temperature and the maximum cylinder-barrel temperature was assumed to be 30° F. higher than the average barrel temperature. Differences between the maximum and the average cylinder-head temperatures as low as 40° F. are being obtained on modern cylinders. For conditions B, in which the carburetor-air temperature was varied, the quantity  $(1-\alpha)b$  was added to the value read from figure 3 to obtain the value of  $\alpha_\lambda$  in the table.

#### MANEUVERS OF SHORT TIME DURATION

**Climb to critical altitude (C-1).**—The ease of climb at constant indicated air speed from a pressure altitude of  $p_0$  to a pressure altitude of  $p$  at constant indicated horsepower, engine speed, carburetor-air temperature, and air-fuel ratio will now be considered. The rate of climb or vertical ascent will be assumed to be practically independent of atmospheric temperature. The height of the climb in feet is given in reference 7 as

$$Z = 122.9 (T + 460) \log_{10} \frac{p_0}{p}$$

Then the time of climb may be obtained by the equation

$$t = 122.9 \frac{T + 460}{v_c \times 60} \log_{10} \frac{p_0}{p}$$

where  $v_c$  is the rate of climb, ft. per min.

From the equation for time of climb, it is evident that the value of  $u$  in equation (12) is  $-1$ . The present climb condition corresponds to the condition A-1, from which the value of  $\lambda = x = 1$  is obtained. If



the last term of equation (12) is omitted as negligible, the increase in cylinder-head temperature with an increase in atmospheric temperature of  $dT_a$  at the pressure altitude  $p$  and an increase in the average atmospheric temperature of  $dT$  is given by

$$dT_{h_t} = \alpha_\lambda dT_a + \alpha_t dT$$

where

$$\alpha_t = \frac{T_h - T_{h_0}}{T + 460} (1 - m\alpha)r$$

The magnitude of the factor  $\alpha_t$ , which was introduced by the variation of the time of climb with the mean atmospheric temperature between the pressure altitude  $p_0$  and  $p$ , will now be investigated. Figure 10

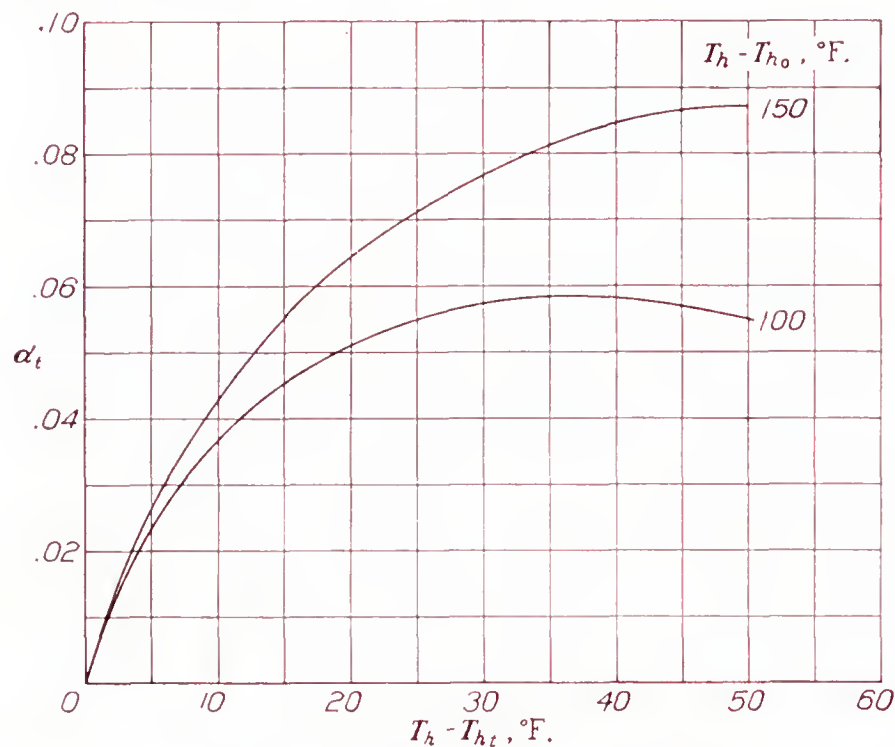


FIGURE 10.—Variation of correction factor  $\alpha_t$  with  $T_h - T_{h_t}$ .

$$\alpha_t = \frac{T_h - T_{h_0}}{T + 460} (1 - m\alpha)r$$

shows  $\alpha_t$  plotted against  $T_h - T_{h_t}$ . The values of  $\alpha$ ,  $m$ , and  $T$  were taken as 0.8, 0.336, and  $0^\circ$  F., respectively. Curves are given for values of  $T_h - T_{h_0}$  of  $100^\circ$  F. and  $150^\circ$  F. It is seen that, when the cylinder temperature lacks only  $10^\circ$  F. of reaching its equilibrium value, the value of  $\alpha_t$  is 0.04. When the equilibrium temperature is reached, as in a slow climb,  $T_h - T_{h_t} = 0$  and  $\alpha_t = 0$ . This case reverts to the case A-1. The maximum value of  $\alpha_t$  for  $T_h - T_{h_0} = 100$  is 0.06 and, for other values of  $T_h - T_{h_0}$ , is in the direct ratio of  $T_h - T_{h_0}$  to 100. Although it is rarely known by what amount the cylinder temperature lags behind the equilibrium temperature in an actual climb test, figure 10 is of interest in showing the magnitude of the error that might be expected in neglecting  $\alpha_t$ . In some cases, where the value of  $T_h - T_{h_t}$  is known roughly, the value of  $\alpha_t$  can be estimated.

A method of estimating  $T_h - T_{h_t}$  in flight for a cowled engine provided with adjustable cowling flaps is to record the cylinder temperatures and the test conditions at the top of the climb and then to fly in level

flight at the final altitude with the flaps adjusted to restrict the pressure drop across the cylinders to the obtained in the climb with the same engine condition and again to record the cylinder temperatures. It should be borne in mind, however, that the two cooling conditions may not be entirely equivalent, as a difference in the turbulent air movement in front of the cylinder may be expected.

It is evident, from the foregoing considerations, that the cylinder temperatures at the end of a climb depend not only on the engine and cooling conditions prevailing at that time but also on their history during the climb. An ideal case was discussed in which the engine conditions were held constant during the climb. In climb tests as they are performed at present, the throttle is set at a definite stop at sea level and is adjusted to new position at a prescribed altitude to bring the manifold pressure up. The mixture control and the carburetor-air temperature are set at sea level and are usually not again adjusted unless the engine functions improperly during the flight. It is known that the mixture becomes richer for a given control setting as the altitude is increased. The manifold pressure drop between the two altitudes at which it is adjusted. Even the maintenance of a constant manifold pressure does not insure constant power, as the charge to the engine depends also on the exhaust back pressure. Therefore, until more complete control of the engine conditions can be maintained during the climb, good correlation of the temperature data for this flight condition cannot be expected. For an engine provided with cowling flaps, more accurate data can be obtained by flying the airplane in level flight at the critical altitude with the flaps adjusted to provide the same pressure drop as obtained in climb. The temperatures obtained in this manner would be close to the equilibrium temperatures corresponding to the engine and cooling conditions in climb at the critical altitude.

The following example is given as an illustration of the variation of cylinder-head temperature in a climb. The airplane is assumed to be provided with a cylinder Pratt & Whitney 1340-H engine operating 550 horsepower. The climb is assumed to take place at a constant indicated air speed that provides a constant pressure drop  $\Delta p$  of 4.7 inches of water across the cylinders. The weight of the cylinder head is 18 pounds and the specific heat is 0.25 B. t. u. per lb.  $^\circ$ F. for aluminum. The average cylinder-head temperature just before entering into the climb is assumed to be  $300^\circ$  F. A climbing speed of 2,700 feet per minute is assumed. The temperatures and densities correspond to the standard altitude (reference 7). The foregoing values were substituted in equation (1). The values used for  $Ka_0$ ,  $\bar{B}a_1$ ,  $m$ , and  $n'$  are those obtained from the single-cylinder-engine tests. The value of  $K$  would probably be somewhat different for the cowled engine in flight. The calculated average



cylinder-head temperature  $T_{h_t}$  at each 1,000 feet of altitude up to 7,000 feet is shown in the following table. The equilibrium temperature  $T_h$  that would be reached at each altitude, if the engine temperature responded instantaneously to a change in conditions, is also listed in the table.

Altitude (ft.)	$T_h$ (°F.)	$T_{h_t}$ (°F.)
0	450	300
1,000	450	337
2,000	450	363
3,000	450	384
4,000	450	400
5,000	450	412
6,000	451	421
7,000	451	428

It will be noticed that, for this case, the equilibrium temperature  $T_h$  is the same at sea level as at 7,000 feet, the effect of the decrease in density being compensated by the effect of the decrease in atmospheric temperature. The actual temperature  $T_{h_t}$  still lacks 23° F. of attaining equilibrium at 7,000 feet.

**Take-off condition (C-2).**—In the take-off, the engine is first warmed up until the oil reaches the desired temperature. The throttle is then opened to the manifold pressure for take-off and the airplane is put into motion. In general, the pressure drop available in take-off is not sufficient to cool the engine at the high power take-off rating. Because of the heat capacity of the cylinder material, however, the temperatures increase at a finite rate with time and the final temperature reached at the instant of take-off depends, other factors remaining constant, on the time of duration of the take-off run. The time duration of the take-off run for landplanes is usually in the neighborhood of 10 to 20 seconds and, in this short time, the cylinder temperatures are considerably less than the equilibrium temperature for the horsepower and the cooling-pressure drop involved.

As an illustration, consider an airplane equipped with a Pratt & Whitney 1340-H cylinder that, in being warmed up preparatory to take-off, has attained an average cylinder-head temperature of 300° F. The throttle is then opened to provide a power of 550 horsepower, or 61.1 horsepower per cylinder, at a propeller speed of 1,500 r. p. m. For a typical cowl and propeller combination, a value of 0.177 was obtained from reference 6 corresponding to the present value of  $\sqrt{\Delta p}/n$  ( $n$  is in revolutions per second, and  $\Delta p$  is in pounds per square foot). Then

$$\Delta p = 3.75 \text{ in. of water.}$$

It is shown in reference 6 that, for low airplane speeds the pressure drop depends mainly on the propeller slipstream and that, as a good approximation,  $\Delta p$  can be assumed to remain constant up to the take-off velocity.

The average cylinder-head temperature for equilibrium at the given power and pressure drop may be

obtained from equation (3). The value of  $T_o$  is taken as 1,150° F. and of  $T_a$  as 59° F.

$$T_h = \frac{T_o - T_a}{\frac{Ka_0(\Delta p \rho / \rho_0)^m}{\bar{B}a_1 I^{n'}} + 1} + T_a = \frac{1,150 - 59}{\frac{78.1(3.75)^{0.34}}{5.22(61.1)^{0.64}} + 1} + 59 = 469^\circ \text{ F.}$$

Inasmuch as the engine and cooling conditions remain constant during the run, equation (11) may be used:

$$A = Ka_0(\Delta p \rho / \rho_0)^m + \bar{B}a_1 I^{n'} = 78.1(3.75)^{0.34} + 5.22(61.1)^{0.64} = 195$$

The weight of the head  $M$  is 18.86 pounds and the specific heat  $c$  for aluminum is 0.25 B. t. u. per lb. per °F. so that

$$\frac{A}{cM} = 41.3 \frac{1}{\text{hr.}}$$

$$T_{h_t} = 469 - (469 - 300)e^{-41.3t} = 469 - 169e^{-41.3t}$$

where  $t$  is in hours.

On the assumption that the take-off run requires 10 seconds, the value of  $T_{h_t}$  over this period is given by

$t$ (sec.)	0	2	4	6	8	10
$T_{h_t}$ (°F.)	300	304	307	311	315	318

It is seen that, for this case, the average head temperature increases only 10.6 percent of the difference between the initial and the final equilibrium temperature.

The time required for take-off varies inversely as the square root of the atmospheric density and it is a simple matter to calculate the effect of variation of atmospheric conditions on the temperature rise of the cylinder during take-off. The cylinder temperature at the time of take-off depends mainly on the initial temperature of the engine and therefore depends on the instructions followed by the pilot in warming up the engine. For example, if the pilot is instructed to warm up the engine to the same temperature at the start of the take-off run irrespective of atmospheric temperature, then variation of atmospheric temperature will have only a small effect on the cylinder temperature at take-off.

As an illustration, refer to the case just considered of take-off at a given engine power, a given carburetor-air temperature, and a given engine speed. The increase in cylinder-head temperature is given by equation (12), where now  $T_o = T_a = T$ . Equation (12) becomes

$$\frac{dT_{h_t}}{dT_a} = \alpha_{\lambda_0} - \frac{T_h - T_{h_0}}{T + 460}(m\alpha x + u)r + \left(\frac{T_{h_t} - T_{h_0}}{T_h - T_{h_0}}\right)(\alpha_\lambda - \alpha_{\lambda_0})$$



where  $\alpha_{\lambda_0}$  is the variation of the initial head temperature  $T_{h_0}$  and  $\alpha_\lambda$  is the variation of the final equilibrium head temperature  $T_h$  with atmospheric temperature. From the values of  $T_g$ ,  $T_h$ , and  $T_a$  previously obtained, a value of  $\alpha=0.63$  is calculated from equation (4). Since the pilot is assumed to warm up the engine to the same temperature prior to take-off independent of atmospheric temperature,  $\alpha_{\lambda_0}$  is equal to zero. If the take-off occurs at a constant indicated air speed, as previously mentioned, the time for take-off is inversely proportional to the square root of the density

$$t \propto \rho^{-\frac{1}{2}}$$

from which there is obtained  $u=-\frac{1}{2}$ . (See development of equation (12).) The value of  $x$  as given by condition A-3 will be used because only a small change in  $\sqrt{\Delta p}/n$  with airplane velocity in the take-off range is indicated in reference 6.

$$x=\lambda=0.5 \text{ to } 0.666$$

Using values of  $x=0.5$ ,  $\alpha=0.63$ ,  $\alpha_{\lambda_0}=0$ ,  $u=-\frac{1}{2}$ , and  $m=0.34$ , the foregoing equation becomes

$$\begin{aligned} \frac{dT_{h_t}}{dT_a} &= \frac{0.4(T_h - T_{h_0})r}{T_a + 460} + \frac{T_{h_t} - T_{h_0}}{T_h - T_{h_0}} \alpha_\lambda \\ &= \frac{0.4 \times 169r}{59 + 460} + 0.106\alpha_\lambda \\ &= 0.13r + 0.106\alpha_\lambda \end{aligned}$$

The maximum value that  $r$  can have is  $1/e$  and the maximum value of  $0.13r$  is

$$\frac{0.13}{2.718} = 0.05$$

For the present case, however,

$$\frac{T_h - T_{h_t}}{T_h - T_{h_0}} = 1 - 0.106 = 0.894$$

and  $r=0.10$  (fig. 4)

$$\frac{dT_{h_t}}{dT_a} = 0.130 \times 0.10 + 0.106\alpha_\lambda = 0.01 + 0.106\alpha_\lambda$$

The value of  $\alpha_\lambda$  ( $\lambda=0.5$ ,  $T_g=1,150$ ,  $T_a=59$ ,  $\alpha=0.63$ ) as obtained from figure 3 is 0.72 and

$$\frac{dT_{h_t}}{dT_a} = 0.08$$

It is evident that the effect of atmospheric temperature on the take-off temperature in the present case is small.

Attention is directed to the fact shown by the calculations that the power in take-off can be increased considerably and still not result in dangerous cylinder head

and barrel temperatures if the temperatures of the cylinders just prior to take-off are low. Piston temperatures, however, will respond more rapidly to a sudden increase in engine power and may be the limiting factor.

#### SUMMARY OF METHOD OF DETERMINING CORRECTION FACTOR FOR VARIATION OF CYLINDER TEMPERATURE WITH ATMOSPHERIC TEMPERATURE

Reference to equation (8) or figure 3 shows that the correction factor  $\alpha_\lambda$  (change in cylinder temperature per degree change in atmospheric temperature) may be determined when the values of  $T_g$ ,  $T_a$ ,  $\alpha$ , and  $\lambda$  are known. As pointed out in the discussion following equation (8) the values given in figure 3 do not include the last term in equation (8),  $zb(1-\alpha)$ . When the carburetor-air temperature is held constant,  $z$  is equal to zero and the term reduces to zero. When the carburetor-air temperature is allowed to vary with the atmospheric temperature,  $z=1$  and this term becomes  $b(1-\alpha)$ , where  $b$  may be taken equal to 0.5. This small correction may be added to the value of  $\alpha_\lambda$  obtained from figure 3 in the case of  $z=1$ . When the exact value of  $T_g$  is not known, it is seen from figure 3 that a value of  $1,150^\circ$  for the head and of  $600^\circ$  F. for the barrel may be chosen without introducing appreciable error. The value of  $b$  corresponding to the condition under consideration may be obtained from table V. It may also be determined from equation (9), as previously shown. The basic correction factor  $\alpha$  (change in cylinder temperature per degree change in cooling-air temperature when mass flow of cooling air, engine power, and carburetor-air temperature are held constant) may be determined from equation (4) or figure 2 when  $T_g$ ,  $T_a$ ,  $T_h$ , and  $T_b$  are known;  $T_a$  is the atmospheric temperature,  $T_h$  the average head temperature, and  $T_b$  the average barrel temperature. As may be seen from figure 2, the assumed values for  $T_g$  may also be used for determining  $b$  without introducing an appreciable error.

In many practical cases only the maximum head and barrel temperatures and the atmospheric temperature are obtained in the tests. The difference between the average head temperature and the maximum cylinder temperature depends on the type of finning and baffling; the better the finning, of course, the smaller the difference. In the following table are given the approximate differences between the average head and maximum cylinder temperatures for the cylinders tested.

Cylinder	Temperature difference ( $^\circ$ F.)
Pratt & Whitney:	
1340-II.....	150
1535.....	50
1535 (flight).....	100
1830.....	60
1690.....	90
Wright:	
1820-F.....	70
1820-G.....	40
1510.....	90



The average barrel temperature is of the order of only 30° F. lower than the maximum and can be quite closely estimated. From figure 2 it may be seen that an error of 25° F. in the estimated value of the average head temperature will cause an error in the value of  $\alpha$  for the head of 0.03; an error of 10° F. in the estimated value of the average barrel temperature will cause an error in the value of  $\alpha$  for the barrel of 0.02.

The preceding method is illustrated with the following example. An engine is tested in level flight and a maximum head temperature of 425° F. and a maximum barrel temperature of 250° F. are obtained at a cooling-air temperature of 20° F. The engine is provided with an air heater adapted to maintain a standard temperature at the carburetor of 70° F. It is desired to determine the value of the maximum cylinder temperatures if the cooling-air temperature were 70° F. at the same altitude and engine condition. If it is assumed that the average head and barrel temperatures are 125° F. and 30° F. lower than the respective maximum temperatures, the values of  $T_h$  and  $T_b$  are 300° F. and 220° F. Corresponding to these values of  $T_h$  and  $T_b$  and to a value of  $T_a$  of 20° F. and  $T_g$  of 1,150° F. and 600° F. for the head and the barrel, respectively, figure 2 shows a value of  $\alpha$  for the head of 0.73 and for the barrel of 0.68. From table V, case A-2, a value of  $\lambda$  of 1.33 is obtained. The required correction factors  $\alpha_\lambda$  corresponding to the values of  $\lambda$ ,  $\alpha$ ,  $T_g$ , and  $T_a$  are read from figure 3. The values obtained are  $\alpha_\lambda=0.93$  for the head and 0.80 for the barrel. The maximum cylinder head and barrel temperatures, corrected to a cooling-air temperature of 70° F., are then 472° F. and 290° F., respectively.

The correction factors for a number of test conditions are included in table V. For each condition, the factors were determined for average head temperatures of 350° F. and 275° F., average barrel temperatures of 300° F. and 225° F., and atmospheric temperatures of 100° F. and 0° F. These values bracket the usual operating range. For most test conditions, the variation of the correction factor over this range is small and an average value may be used. Where a large variation exists, the correction factors corresponding to a desired set of conditions may be obtained by interpolating between the values given in table V. In this connection it should be noted that a probable uncertainty of  $\pm 5$  percent exists in the values of the correction factors. Approximate maximum head and barrel temperatures are also listed in the table and were obtained by adding 125° F. to the average head temperature and 30° F. to the average barrel temperature.

#### GENERAL REMARKS

The dependence of cylinder temperatures on the engine power, the air-fuel ratio, the carburetor-air temperature, the pressure drop of cooling air across the cylinder, and the cooling-air temperature has been shown. It has also been shown that the correction

factor for variation of cylinder temperature with atmospheric temperature depends on the type of flight or test to which it is to be applied. Correction factors have been obtained for several ideal cases. Various airplanes, however, have different refinements of equipment for controlling the engine and cooling factors and therefore present separate problems. These problems can be readily investigated by the methods illustrated.

Obviously, when cooling tests are made for accurate comparisons of cylinder temperatures, the factors that are not intentionally varied should be held as closely as possible to a standard and should be measured in order that corrections may be applied for small variations from the standard.

It is the practice at present to use the temperature of the rear spark-plug gasket as the index of the cooling of a cylinder. The temperature of the rear spark-plug gasket has been found to depend on the condition and construction of the plug, the cleanness of the plug, and the tightness with which it is inserted in the cylinder. For these reasons, the temperature of the rear spark-plug gasket may at times give incorrect indications of the cooling of a cylinder. The comparison of the cooling of a cylinder based on the reading of a single thermocouple may be misleading and it is recommended that the average of a number of thermocouples located at standard positions on the head and the barrel be used to obtain average head and barrel temperatures.

In a multicylinder engine, variations of as much as 50° F. occur between the maximum temperatures of the various cylinders. This fact tends to complicate the problem of correlating the temperature data obtained on such engines. An average of the maximum temperatures for all the cylinders would give the best correlation.

Although the methods in this paper apply for correcting the average head and barrel temperatures, the magnitude of variation of these temperatures indicates closely the magnitude of variation of the maximum cylinder temperatures to be expected.

In the computations, various additional refinements that might have been considered would have introduced small corrections. For example, it was found in the present tests that heating the cooling air tended to reduce the weight of the charge and the engine power even when the carburetor-air temperature and the manifold pressure were held constant.

In the consideration of the supercharged engine, the assumption was made that a 1° F. variation in carburetor-air temperature causes a 1° F. change in inlet manifold temperature. This assumption is only a rough approximation, as compression by the supercharger, cooling of the compressed charge, and evaporation of the gasoline would alter the relationship. The effect of carburetor-air temperature on cylinder temperature for a constant engine power is small, however, and it was not considered worth while to make a more accurate analysis.



Tests of one cylinder were made to determine the effect of oil temperature on cylinder temperature. It was found that a variation in oil-out temperature from 128° F. to 171° F. caused only a very small change in cylinder temperature. Although the majority of the thermocouples indicated a slight increase, some of the thermocouples showed a decrease. The quantity of oil circulated was found to have a greater effect.

The correction factors in the present report apply to the case where the engine is not detonating. When detonation occurs, the engine temperature changes more rapidly with atmospheric temperature because the intensity of detonation is also affected by the change in temperature.

#### CONCLUSIONS

1. The values of the cylinder-temperature correction factors for cooling-air temperature for constant engine conditions and constant mass flow calculated from semiempirical equations agree reasonably well with the experimental values.

2. The cylinder-temperature correction factors are lowest for the constant-mass-flow condition and highest for the constant-velocity condition.

3. The cylinder-temperature correction factors for fast climb are slightly higher than those for a slow climb when the cylinder temperatures do not attain equilibrium in the fast climb.

4. A change in carburetor-air temperature affects the cylinder-temperature correction factors by changing the effective gas temperature, but the effect is small.

5. It is recommended that the average of a number of thermocouples on the cylinder head and barrel be used as a measure of the head and barrel temperature. A single thermocouple, especially one located on the rear spark-plug gasket, may give misleading results.

LANGLEY MEMORIAL AERONAUTICAL LABORATORY,  
NATIONAL ADVISORY COMMITTEE FOR AERONAUTICS  
LANGLEY FIELD, VA., *June 20, 1938.*



## APPENDIX

### SYMBOLS

$a_0$ ,	outside wall area of head of cylinder, sq. in.
$a_1$ ,	internal area of head of cylinder, sq. in.
$A$ ,	$Ka_0(\Delta p\rho/\rho_0)^m + \bar{B}a_1I^{n'}$
$b$ ,	ratio of change of effective gas temperature ( $T_g$ ) to change of carburetor-air temperature ( $T_c$ ).
$\frac{B}{\bar{B}}$ ,	$\bar{B}a_1I^{n'}T_g + Ka_0(\Delta p\rho/\rho_0)^mT_a$ constant.
$c$ ,	specific heat of metal in cylinder head, B. t. u. per lb. per °F.
$C_D$ ,	drag coefficient.
$d$ ,	exponent.
$D$ ,	propeller diameter, ft.
$H$ ,	heat transferred per unit time from combustion gases to cylinder head, B. t. u. per hr.
$H_1$ ,	heat transferred per unit time from cylinder head to cooling air, B. t. u. per hr.
$I$ ,	indicated horsepower of each cylinder.
$K, K_1, K_3, K_4, K_5, K_6$ ,	constants.
$m$ ,	exponent.
$M$ ,	weight of cylinder head, lb.
$n$ ,	propeller speed, r. p. s.
$n'$ ,	exponent.
$p_0$ ,	pressure at initial altitude of climb, in. Hg.
$p$ ,	pressure at final altitude of climb, in. Hg.
$P$ ,	propeller power (brake horsepower), ft.-lb. per sec.
$r$ ,	$\frac{T_h - T_{ht}}{T_h - T_{h0}} \log_e \frac{T_h - T_{h0}}{T_h - T_{ht}}$
$t$ ,	time, hr.
$T_a$ ,	inlet temperature of cooling air, °F. (temperature of atmosphere).
$T_b$ ,	average temperature over the cylinder-barrel surface when equilibrium is attained, °F.
$T_c$ ,	temperature of carburetor air, °F.
$T_g$ ,	effective gas temperature, °F.
$T_h$ ,	average temperature over the cylinder-head surface when equilibrium is attained, °F.
$T$ ,	average temperature of atmosphere during maneuver, °F.
$T_0$ ,	temperature of atmosphere at time $t=0$ , °F.
$T_{h0}$ ,	average temperature of cylinder head at time $t=0$ , °F.
$T_{ht}$ ,	average temperature of cylinder head at time $t$ , °F.
$u$ ,	exponent.

$v_c$ ,	rate of climb, ft. per min.
$V$ ,	true velocity of airplane, m. p. h.
$x, y, z$ ,	exponents.
$Z$ ,	height of climb, ft.
$\alpha$ ,	basic temperature correction factor; change in cylinder temperature per degree change in cooling-air temperature; mass flow of cooling air, engine power, and carburetor-air temperature remaining constant.
$\alpha_\lambda$ ,	correction factor for any test condition when equilibrium is attained; change in cylinder temperature per degree change in atmospheric temperature.
$\alpha_{\lambda_0}$ ,	correction factor for any test condition at time $t=0$ ; change in cylinder temperature ( $T_{h0}$ ) per degree change in cooling-air temperature ( $T_0$ ).
$\alpha_t$ ,	correction factor during a climb; change in cylinder temperature per degree change in atmospheric temperature.
$\lambda$ ,	$\frac{m}{0.34} \left[ x + \frac{z}{2} \left( y - \frac{n'}{m} \right) \right]$
$\rho$ ,	average density of cooling air, lb.-ft. <sup>-4</sup> sec. <sup>2</sup> (average density of the air entering and leaving the fins).
$\rho_0$ ,	density of air at 29.92 in. Hg and 70° F., lb.-ft. <sup>-4</sup> sec. <sup>2</sup>
$\Delta p$ ,	pressure drop across cylinder, in. of water (includes loss out exit of baffle).

### REFERENCES

1. Campbell, Kenneth: Evaluation of Variables Influencing Air Cooling of Engines. S. A. E. Jour., vol. 37, no. 5, Nov. 1935, pp. 401-411.
2. Pinkel, Benjamin: Heat-Transfer Processes in Air-Cooled Engine Cylinders. T. R. No. 612, N. A. C. A., 1938.
3. Schey, Oscar W., and Pinkel, Benjamin: Effect of Several Factors on the Cooling of a Radial Engine in Flight. T. N. No. 584, N. A. C. A., 1936.
4. Ware, Marsden: Description of the N. A. C. A. Universal Test Engine and Some Test Results. T. R. No. 250, N. A. C. A., 1927.
5. Ware, Marsden: Description and Laboratory Tests of a Roots Type Aircraft Engine Supercharger. T. R. No. 230, N. A. C. A., 1926.
6. Theodorsen, Theodore, Brevoort, M. J., and Stickle, George W.: Cooling of Airplane Engines at Low Air Speeds. T. R. No. 593, N. A. C. A., 1937.
7. Diehl, Walter S.: Standard Atmosphere—Tables and Data. T. R. No. 218, N. A. C. A., 1927.



Cylinder	Series	Indicated horse-power	Indicated mean effective pressure (lb./sq. in.)	Engine speed (r. p. m.)	Indicated fuel consumption (lb./i. hp./hr.)	$\Delta p/\rho_0$ (in. of water)	Carburetor-air temperature ( $^{\circ}$ F.)	$T_g$		Cylinder	Series	Indicated horse-power	Indicated mean effective pressure (lb./sq. in.)	Engine speed (r. p. m.)	Indicated fuel consumption (lb./i. hp./hr.)	$\Delta p/\rho_0$ (in. of water)	Carburetor-air temperature ( $^{\circ}$ F.)	$T_g$	
								Head ( $^{\circ}$ F.)	Barrel ( $^{\circ}$ F.)									Head ( $^{\circ}$ F.)	Barrel ( $^{\circ}$ F.)
1340-H	1	37.71	123.2	1,556	0.457	17.37	83	1,155	585	1690	1	35.06	104.6	1,493	0.481	11.15	92	1,320	
	2	41.25	133.6	1,569	.453	17.60	83	990	535		1'	35.16	104.6	1,505	.477	4.51	78	-----	
	3	29.70	97.7	1,545	.438	18.89	74	1,007	557		2	35.02	104.6	1,499	.483	6.45	79	1,430	
	4	56.50	137.6	2,082	.461	17.26	87	1,400	667		2'	34.91	104.5	1,494	.481	8.55	79	1,100	
	4'	50.19	140.8	1,821	.458	17.24	92	1,113	679		3	27.77	82.3	1,508	.453	11.19	87	1,170	
	5	41.64	136.4	1,551	.461	16.35	86	1,373	631		3'	35.03	104.2	1,505	.444	11.13	83	1,345	
	7	32.10	107.6	1,515	.439	18.03	72	1,150	580		4	40.83	121.0	1,510	.448	11.14	88	1,140	
	7'	40.40	134.9	1,521	.472	17.44	77	1,120	584		5	35.13	104.4	1,506	.472	8.42	81	1,035	
	8	33.00	110.4	1,518	.442	12.71	77	1,150	592		6	34.87	104.1	1,499	.479	4.42	76	-----	
	9	28.58	97.3	1,492	.420	9.73	72	1,040	563		7	-----	-----	2,012	-----	11.10	88	1,320	
	9'	27.87	97.2	1,456	.437	13.46	68	1,142	474		8	35.06	104.4	1,503	.471	4.88	80	1,140	
	10	40.00	137.0	1,480	.479	14.53	66	1,134	592		9	-----	-----	1,643	-----	11.23	84	1,080	
	11	44.95	150.6	1,515	.476	16.33	81	1,158	658		9'	-----	-----	1,808	-----	11.30	81	1,445	
	11'	62.69	150.9	2,110	.464	18.01	62	1,273	622		-----	-----	-----	-----	-----	-----	-----	-----	
	14	42.40	146.4	1,470	.471	17.49	64	1,142	599		-----	-----	-----	-----	-----	-----	-----	-----	
	15	42.01	101.4	2,104	.469	17.94	66	1,089	563		-----	-----	-----	-----	-----	-----	-----	-----	
	16	47.97	164.7	1,480	.501	18.18	73	1,139	592		-----	-----	-----	-----	-----	-----	-----	-----	
	17	33.18	111.8	1,508	.508	15.20	93	1,065	635		-----	-----	-----	-----	-----	-----	-----	-----	
	18	41.25	140.4	1,491	.548	13.77	92	905	657		-----	-----	-----	-----	-----	-----	-----	-----	
19	47.98	115.7	2,106	.412	14.49	80	1,180	601	-----	-----	-----	-----	-----	-----	-----	-----			
-----	-----	-----	-----	-----	-----	Average	-----	1,136	598	-----	-----	-----	-----	-----	-----	-----	Average	1,230	
1535	1	26.0	118.1	1,500	0.453	17.92	94	1,105	648	1830	1	32.41	130.6	1,504	0.479	17.88	86	1,125	
	2	26.1	118.0	1,503	.458	12.75	97	1,098	637		1'	32.33	130.8	1,498	.470	11.13	85	1,095	
	3	26.2	118.8	1,501	.449	8.02	91	1,045	485		2	32.34	129.4	1,514	.467	16.86	95	1,125	
	3'	29.3	121.0	1,652	.443	16.47	97	1,100	465		3	32.34	129.5	1,514	.468	12.81			



TABLE II.—CALCULATED AND EXPERIMENTAL VALUES OF  $\alpha$ 

Cylinder	Series	$T_a$ (°F.)	$T_b$ (°F.)	$T_h$ (°F.)	$\alpha$ (calculated)		$\alpha$ (experimental)		$T_o$		Cylinder	Series	$T_a$ (°F.)	$T_b$ (°F.)	$T_h$ (°F.)	$\alpha$ (calculated)		$\alpha$ (experimental)		$T_o$	
					$T_o - T_b$	$T_o - T_h$	Barrel	Head	Barrel (°F.)	Head (°F.)						$T_o - T_b$	$T_o - T_h$	Barrel	Head	Barrel (°F.)	Head (°F.)
					$T_o - T_a$ Barrel	$T_o - T_a$ Head										$T_o - T_a$ Barrel	$T_o - T_a$ Head				
1340-H	1	92	208	271	0.772	0.831	0.76	0.83	600	1,150	1690	1	99	242	335	0.738	0.791	0.82	0.88	645	1,230
	2	106	228	295	.753	.819	.69	.77				1'	81	269	380	.666	.740	.88	.96		
	3	87	195	243	.790	.853	.74	.80				2	84	251	354	.702	.764	.75	.81		
	4	89	251	332	.682	.771	.69	.91				2'	87	245	343	.716	.776	.69	.77		
	4'	88	250	332	.684	.770	.75	.79				3	95	217	306	.778	.815	.73	.78		
	5	91	214	280	.758	.821	.81	.91				3'	93	234	332	.744	.790	.77	.86		
	7	79	192	257	.784	.834	.77	.83				4	98	258	370	.708	.760	.73	.73		
	7'	87	222	296	.737	.803	.72	.78				5	84	246	350	.711	.768	.71	.82		
	8	79	209	276	.750	.816	.69	.84				6	78	283	405	.639	.716	.80	.95		
	9	68	196	259	.758	.823	.71	.80				7	99	274	380	.679	.752	.72	.83		
	9'	70	187	237	.780	.846	.72	.79				8	82	284	390	.642	.732	.63	.74		
	10	67	204	277	.743	.806	.71	.74				9	95	262	362	.696	.765	.73	.76		
	11	90	221	303	.744	.800	.78	.83				9'	92	260	365	.696	.760	.71	.84		
	11'	65	237	332	.680	.754	.73	.81				1	99	229	301	.740	.808	.71	.83	600	1,150
	14	65	214	289	.721	.794	.70	.76				1'	92	252	330	.686	.775	.69	.77		
	15	73	207	285	.747	.802	.74	.85				2	114	247	322	.725	.799	.68	.78		
	16	70	226	297	.705	.790	.72	.78				3	92	239	321	.710	.782	.69	.80		
	17	94	232	305	.727	.800	.76	.77				3'	90	252	337	.683	.766	.68	.79		
	18	86	236	316	.708	.784	.75	.73				4	96	241	315	.712	.792	.69	.83		
19	82	264	351	.648	.748	.67	.76			4'	104	232	304	.742	.809	.73	.82				
1535	1	108	227	311	.736	.805	.72	.81	561	1,151	1830	5	99	232	313	.735	.796	.71	.82		
	2	105	242	329	.700	.786	.62	.72				5'	97	249	358	.698	.752	.68	.75		
	3	90	254	353	.652	.752	.60	.73				5''	102	243	335	.716	.778	.70	.79		
	3'	106	247	329	.690	.786	.69	.78				5'''	104	238	329	.730	.785	.74	.79		
	4	94	245	341	.677	.766	.61	.70				6	105	259	357	.688	.759	.60	.71		
	4'	95	255	348	.657	.760	.58	.71				8	100	249	327	.702	.784	.64	.79		
	5	99	251	340	.671	.770	.63	.75				12	94	236	263	.719	.840	.69	.82	600	1,150
	5'	102	274	361	.632	.752	.68	.81				13	102	246	275	.711	.836	.73	.86		
	6	98	265	354	.639	.756	.56	.69				14	91	224	254	.739	.846	.72	.83		
	6'	104	243	320	.695	.793	.69	.77				15	90	232	268	.721	.832	.72	.82		
	7	104	243	320	.695	.793	.69	.77				16	97	245	277	.706	.830	.72	.86		
	7'	98	253	326	.664	.783	.70	.84				17	98	237	271	.723	.836	.72	.82		
	8	106	288	365	.600	.752	.55	.61				18	93	212	231	.765	.869	.71	.84		
	9	107	268	351	.646	.766	.70	.75				19	99	221	238	.757	.868	.69	.84		
	10	100	273	369	.624	.744	.64	.78				20	93	230	255	.730	.847	.70	.87		
	11	104	257	342	.666	.772	.71	.79				21	97	239	271	.718	.834	.72	.90		
	12	88	266	362	.624	.742	.68	.77				24	104	251	281	.704	.831	.56	.77		
	14	99	264	352	.643	.759	.63	.73				29	103	242	275	.720	.836	.66	.85		
	21	93	233	318	.701	.787	.70	.79				1510	1	99	230	296	.738	.812	.69	.78	600
1	90	254	319	.717	.790	.71	.79	671	1,183	2	91		272	361	.644	.745	.61	.71			
2	84	285	365	.658	.744	.76	.82			3	96		255	334	.684	.774	.70	.75			
3	85	274	346	.678	.762	.71	.80			4	92		252	310	.686	.794	.64	.80			
4	98	262	332	.714	.784	.75	.85			6	108		280	358	.651	.760	.70	.74			
5	95	280	363	.678	.754	.61	.72			7	187		282	351	.764	.828	.73	.80			
6	87	263	337	.698	.772	.69	.80			8	101		265	336	.671	.776	.68	.75			
7	88	237	305	.743	.801	.72	.79			9	100		260	320	.680	.790	.64	.76			
8	93	281	360	.675	.756	.69	.78			10	96		225	277	.744	.828	.70	.86			
9	96	271	346	.695	.768	.75	.81			11	109		290	363	.631	.756	.73	.78			
10	96	252	318	.728	.796	.68	.78			13	91		239	283	.710	.821	.68	.81			
11	91	280	370	.674	.745	.58	.67			14	80		290	356	.597	.742	.70	.79			
13	91	290	372	.656	.742	.74	.80														
14	93	269	359	.695	.756	.70	.76														

TABLE III.—VALUES OF  $\alpha$  CALCULATED AT HIGHEST AIR TEMPERATURE

Cylinder	Series	$T_a$ (°F.)	$T_b$ (°F.)	$T_h$ (°F.)	$\alpha$ (Calculated)		$T_o$	
					$T_o - T_b$	$T_o - T_h$	Barrel (°F.)	Head (°F.)
					$T_o - T_a$ Barrel	$T_o - T_a$ Head		
1510	1	236	325	398	0.756	0.822	600	1,150
	2	237	362	467	.655	.748		
	3	219	340	427	.682	.777		
	4	244	350	431	.702	.793		
	6	205	346	429	.642	.763		
	7	277	350	429	.774	.826		
	8	235	351	436	.682	.780		
	9	249	355	440	.698	.788		
	10	245	334	407	.750	.821		
	11	198	361	434	.595	.752		
	13	227	335	392	.710	.821		
	14	224	393	462	.550	.742		



TABLE IV.—VALUES OF *b* OBTAINED FROM CYLINDER TESTS

Cylinder	Engine speed (r. p. m.)	Indicated mean effective pressure (lb./sq. in.)	Indicated horsepower	$\Delta p/\rho_0$ (in. of water)	Fuel consumption (lb./i. hp./hr.)	Carburetor-air temperature (° F.)	<i>b</i>	
							Head	Barrel
1340-II.....	1, 501	140. 6	41. 53	17. 18	0. 461	45-120. 2	0. 794	0
	1, 502	153. 1	45. 25	18. 50	. 470	47. 3-126	1. 096	. 519
	1, 537	97. 7	29. 54	19. 35	. 448	74-187	. 740	0
1535.....	1, 523	119. 2	26. 7	15. 47	. 444	45-153	. 846	. 364
	1, 787	135. 1	35. 5	15. 97	. 459	34-154	. 607	. 360
1820-F.....	1, 302	94. 25	31. 96	13. 32	. 601	39-148	— . 159	0
	1, 501	117. 12	45. 80	13. 84	. 442	76-128	. 324	. 217
	1, 503	120. 23	47. 07	13. 97	. 477	84-160	. 366	. 279
1830.....	1, 634	117. 9	31. 79	20. 52	. 518	58. 5-150	. 590	. 388
	1, 650	117. 3	31. 93	20. 63	. 467	81-148	. 519	. 634
1510.....	1, 503	118. 0	24. 2	16. 33	. 433	46-157	. 254	. 209
	1, 702	122. 6	28. 5	16. 14	. 442	78-153	. 233	. 117

TABLE V.—EFFECT OF FLIGHT CONDITIONS ON ENGINE TEMPERATURE CORRECTION FACTORS

Flight condition	y	z	x	λ	T <sub>hmax</sub> (° F.)	T <sub>h</sub> (° F.)	T <sub>bmax</sub> (° F.)	T <sub>b</sub> (° F.)	T <sub>a</sub> (° F.)	α <sub>λ</sub>	
										Head	Bar
A. Constant carburetor-air temperature and engine power:											
1. Climb at constant indicated air speed to a given pressure altitude.....	0	0	1	1	475	350	330	300	0	0. 88	0. 88
					475	350	330	300	100	. 87	. 87
					400	275	255	225	0	. 91	. 91
					400	275	255	225	100	. 91	. 91
2. Level flight at a given pressure altitude.....	0	0	1. 33	1. 33	475	350	330	300	0	. 93	. 93
					475	350	330	300	100	. 91	. 91
					400	275	255	225	0	. 96	. 96
					400	275	255	225	100	. 95	. 95
3. Stationary on ground at given barometer.....	0	0	1. 50-1. 66	1. 50-1. 66	475	350	330	300	0	. 98	. 98
					475	350	330	300	100	. 94	. 94
					400	275	255	225	0	1. 00	1. 00
					400	275	255	225	100	. 97	. 97
4. Constant airplane velocity.....	0	0	2	2	475	350	330	300	0	1. 05	1. 05
					475	350	330	300	100	. 98	. 98
					400	275	255	225	0	1. 06	1. 06
					400	275	255	225	100	1. 00	1. 00
5. Constant mass flow.....	0	0	0	0	475	350	330	300	0	. 70	. 70
					475	350	330	300	100	. 76	. 76
					400	275	255	225	0	. 76	. 76
					400	275	255	225	100	. 83	. 83
B. Carburetor-air temperature equal to and varying with atmospheric temperature, engine power varying with carburetor-air temperature, constant manifold pressure, and constant engine speed:											
1. Climb at constant indicated air speed to a given pressure altitude.....	0	1	1	. 032	475	350	330	300	0	. 85	. 85
					475	350	330	300	100	. 88	. 88
					400	275	255	225	0	. 88	. 88
					400	275	255	225	100	. 91	. 91
2. Level flight at a given pressure altitude.....	. 66	1	1. 33	. 70	475	350	330	300	0	. 97	. 97
					475	350	330	300	100	. 96	. 96
					400	275	255	225	0	. 98	. 98
					400	275	255	225	100	. 97	. 97
3. Stationary on ground at a given barometer.....	. 33- . 5	1	1. 50-1. 66	. 81- . 89	475	350	330	300	0	1. 00	1. 00
					475	350	330	300	100	. 97	. 97
					400	275	255	225	0	1. 00	1. 00
					400	275	255	225	100	. 99	. 99

\* The values of  $\alpha_\lambda$  for the head are calculated for  $T_a=1,150^\circ$  F. and for the barrel for  $T_a=600^\circ$  F.



## REPORT No. 646

# THE COMPRESSIBILITY BURBLE AND THE EFFECT OF COMPRESSIBILITY ON PRESSURES AND FORCES ACTING ON AN AIRFOIL

By JOHN STACK, W. F. LINDSEY, and ROBERT E. LITTELL

### SUMMARY

*Simultaneous air-flow photographs and pressure-distribution measurements were made of the N. A. C. A. 4412 airfoil at high speeds to determine the physical nature of the compressibility burble. The tests were conducted in the N. A. C. A. 24-inch high-speed wind tunnel. The flow photographs were obtained by the schlieren method and the pressures were simultaneously measured for 54 stations on the 5-inch-chord airfoil by means of a multiple-tube manometer. Following the general program, a few measurements of total-pressure loss in the wake of the airfoil at high speeds were made to illustrate the magnitude of the losses involved and the extent of the disturbed region; and, finally, in order to relate this work to earlier force-test data, a force test of a 5-inch-chord N. A. C. A. 4412 airfoil was made.*

*The data presented include the results of pressure-distribution measurements and force tests for three low angles of attack for a speed range extending from one-tenth the speed of sound to speeds in excess of the critical values at which a breakdown of the flow, or compressibility burble, occurs.*

*The results show the general nature of the phenomenon known as the compressibility burble. The source of the increased drag is shown to be a compression shock that occurs on the airfoil as its speed approaches the speed of sound. Finally, it is indicated that considerable experimentation is needed in order to understand the phenomenon completely.*

### INTRODUCTION

The development of the knowledge of compressible-flow phenomena, particularly as related to aeronautical applications, has been attended by considerable difficulty. The complicated nature of the phenomena has resulted in little theoretical progress and, in general, recourse to experiment has been necessary. Until recently the most important experimental results have been obtained in connection with the science of ballistics, but this information has been of little value in aeronautical problems because the range of speeds for which most ballistic experiments have been made extends from the speed of sound upward; whereas, the important region in aeronautics at the present time extends from the speed of sound downward. Studies of flow in

nozzles have yielded some valuable results, although the available data do not appear to allow a reliable prediction of the air-flow phenomena associated with airfoils. Previous published aeronautical experiments have generally consisted of measurements of the forces experienced by airfoil sections and propellers at high speeds. These data demonstrate that serious detrimental flow changes may occur as speeds approach the speed of sound but have not shown the character of such flow changes.

The principal result of the propeller tests appears to be the establishment of the critical speeds for many standard blades. The force tests of airfoils have permitted a wider interpretation of the propeller data and have indicated the effects of certain shape changes on the value of the critical speed. The theory of Glauert and Ackeret has been substantiated in fair degree by airfoil tests for speeds below the critical, but their theory gives no clue as to any flow changes that may occur. This deficiency is important because tests of both airfoils and propellers have shown the existence of a critical speed above which resistance to motion becomes impracticably large. Taylor's electric analogy appears to give the best indication of the speed at which these flow changes occur but gives little insight into the phenomena.

It therefore appeared that the nature of the flow changes must be discovered in order to explain the compressibility effects which have been measured in previous experiments. A research program was outlined to obtain this information, to establish the limitations of available theoretical work, and to obtain information upon which developments of practical significance for aeronautical applications could be based. The proposed experiments included pressure-distribution measurements for a typical airfoil and flow-visualization experiments.

Preliminary flow observations by the schlieren method were originally made for a cylinder and an N. A. C. A. 0012 airfoil in the N. A. C. A. 11-inch high-speed wind tunnel. The observations with the airfoil were correlated with previous force tests and the results were first shown at the N. A. C. A. Engineering Research Conference in 1934. A more general program was then formulated that included pressure-distribu-



tion measurements and schlieren photographs. These experiments were made in the N. A. C. A. 24-inch high-speed wind tunnel with an N. A. C. A. 4412 airfoil section of 5-inch chord. After the main program had been completed, some additional tests were made to study the magnitude of the energy losses associated with high-speed flows; these tests comprised measurements of the total-pressure loss that occurred in the compression shock, which was shown to exist in the flow. In order to correlate the data with previous

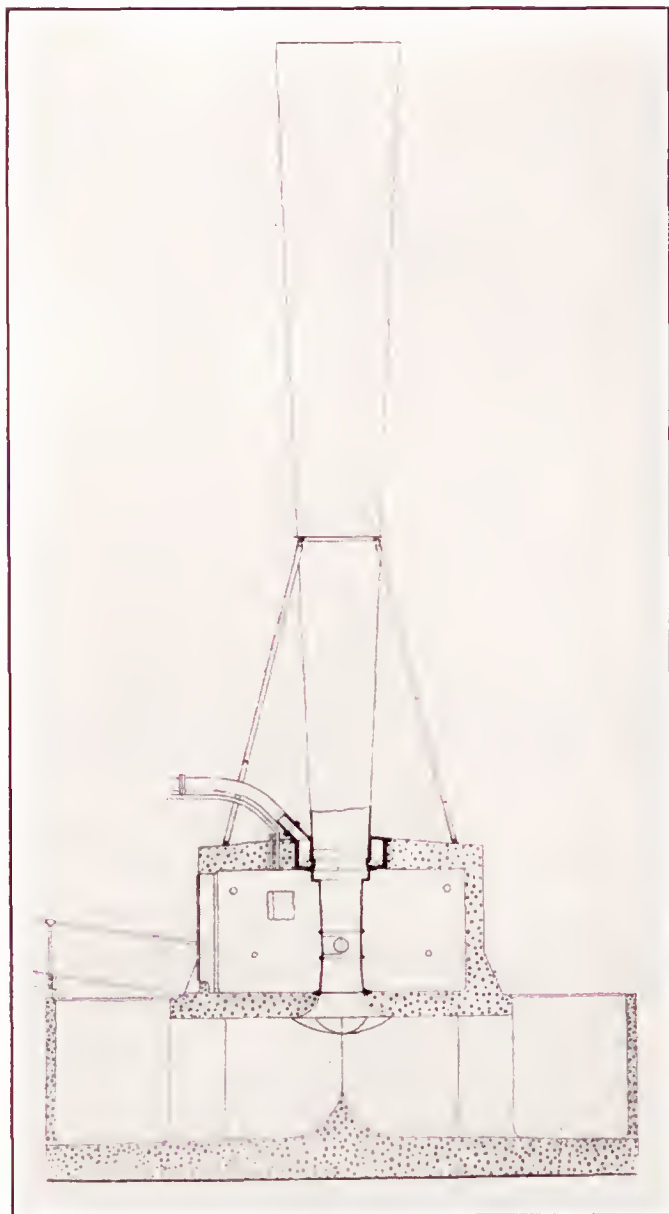


FIGURE 1.—Longitudinal section of the N. A. C. A. 24-inch high-speed wind tunnel.

work, force tests of a 5-inch-chord N. A. C. A. 4412 airfoil were also made.

Most of the experiments were carried out during 1935 and 1936. All the tests were made in the N. A. C. A. 24-inch high-speed wind tunnel. Some of the outstanding results have been published in preliminary form as references 1 and 2.

#### APPARATUS AND METHOD

The N. A. C. A. 24-inch high-speed wind tunnel (fig. 1) in which this investigation was conducted is an induction-type wind tunnel. Compressed air from the variable-density wind tunnel discharged through an

annular nozzle located downstream from the test section induces a flow of air from the atmosphere through the test section. Velocities approaching the speed of sound may be obtained at the test section. The tunnel is located outside the building that houses the variable-density wind tunnel. Except for certain modifications arising from its outside location and its size, the methods of operation are the same as for the 11-inch high-speed wind tunnel (reference 3). The essential air passages are geometrically similar to those of the 11-inch high-speed wind tunnel, and the general air-stream characteristics of the tunnel are equivalent to those of the 11-inch tunnel except for the static-pressure gradient which is zero.

The method for flow observations and photography is the schlieren method devised by Töpler; the fundamental principles are described in reference 4. A simplified diagram of the apparatus used in these experiments is given in figure 2. Light from a source located at C, the principal focus of lens D, emerges from lens D as a parallel beam, passes through the converging lens D', and is brought to focus at E, the

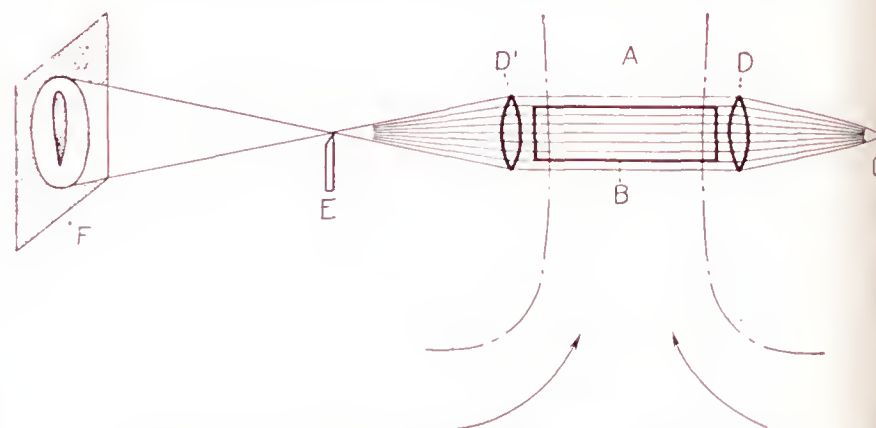


FIGURE 2.—Simplified diagram showing the schlieren method.

principal focus of lens D'. At E a knife edge is located so as to cut off most of the light from the source C. The model B is placed in the parallel beam that crosses the test section A between the lenses so that its cross-section is perpendicular to the light beam and an image is formed on the screen F. When air passes over the model, its density, and therefore its optical index of refraction, change. Thus, portions of the parallel beam of light are bent and some of the rays that were previously interrupted by the knife edge now pass over the knife edge at E to the screen F or, if desired, to a photographic plate. The illumination on the screen then shows regions of varying density.

For these experiments the source light was a high-intensity spark. Lenses D and D' are of 5-inch diameter and 26-inch focal length. The screen F was replaced by a photographic plate mounted in a standard 8- by 10-inch studio-type camera from which the lens had been removed. The camera was mounted so that



the shutter was near the knife edge; photographic operation was then similar to the methods normally used in making photographs. Because of the small diameter of the lenses in relation to the airfoil chord, it was necessary to use the full field of the lenses; and, further, because of the curved transparent wall sections by which the model was supported (described later), the resulting pictures, particularly near the leading and the trailing edges of the model, are not of high quality. The results obtained, however, are satisfactory in that they illustrate clearly the type of phenomenon which occurs.

The pressures acting on the airfoil were measured by means of a multiple-tube photorecording manometer described in detail in reference 5. The manometer contains 60 tubes arranged in a semicircle with a neon light parallel to the tubes located at the center of the semicircle. Photostat paper is drawn from a roll, located at the back of the manometer, around the tubes; and the exposed lengths of paper are drawn up on another roll also located at the back of the manometer. A mechanism for automatic remote control is contained within the manometer. During the tests three manometer liquids were used: mercury for high speeds, tetrabromoethane (specific gravity, approximately 3) for medium speeds, and alcohol for low speeds.

The N. A. C. A. 4412 rectangular airfoil of 5-inch chord and 30-inch span consists of a brass center section of 1-inch span and duralumin end pieces. Fifty-four holes are arranged in two rows, one-fourth inch apart, along the upper and the lower surfaces at the center of the brass section. These holes were connected to the manometer by small brass tubes led out through two large ducts in the lower surface of the duralumin end pieces of the model. The ducts were closed by duralumin covers shaped to the contour of the airfoil. The brass center section and the duralumin end pieces were bolted together and all joints were carefully made to preserve the contour and fairness of the model. A more detailed description of this model is given in reference 5.

Mounted for tests, the airfoil extended through the tunnel walls and was supported in carefully fitted celluloid end plates that preserved the contour of the tunnel wall. The model was originally designed for tests in the variable-density wind tunnel where the supporting system is such that the bending stresses at the center of the model resulting from lift loads are small. For some of the tests in the high-speed wind tunnel, it was necessary to provide auxiliary bracing to support the lift loads because of the inherent structural weakness of the model at the center section. This bracing consisted of cables secured at the quarter-chord point of the airfoil approximately 6 inches out from the center on either side and fastened to the tunnel wall. These cables

appear in some of the schlieren photographs as dark lines extending outward from the airfoil approximately perpendicular to the lower surface; they should not be confused with the compression shock.

The operation of the apparatus was controlled from outside because of the large rate of pressure change within the tunnel chamber as the air speed was rapidly varied. The test procedure consisted in first increasing the speed to the desired value by a motor-driven valve in the compressed-air supply line; the speed was measured by an outside mercury manometer connected to calibrated static plates. The camera shutter, which was operated by an electromagnet, was then opened and, at a signal immediately following, the electric circuit for the manometer light and the source light in the schlieren apparatus were closed. By this procedure the pressure record and the flow photograph were simultaneously obtained.

**Supplementary tests.**—After the completion of the original program, some additional tests consisting of measurements of total-pressure loss behind the airfoil and force tests of a 5-inch-chord duralumin airfoil were made. For the measurements of total-pressure loss, the individual tubes of a rake of impact tubes were connected to a manometer and the pressure distribution and the total-pressure loss were simultaneously measured. Owing to insufficient manometer equipment, these tests were incomplete and the pressure data include, except for one series of tests, the measurements of pressure distribution and total-pressure loss for only the upper surface of the model. Furthermore, the schlieren apparatus had by this time been dismantled so that no flow photographs were made.

The rake of impact tubes was made of 19 tubes and extended from the tunnel wall to a point three-fourths inch past the quarter-chord axis of the model. The forward ends of the tubes were located one-half inch behind the trailing edge of the model. The locations of the tubes are shown by the points on the plots (figs. 18 to 20). Because of the relatively large spacing of the tubes and the insufficient manometer equipment, total-pressure losses for low speeds could not be accurately obtained and the data as presented show only the loss that occurred at high speeds after a compression shock had formed. As previously noted, these measurements were made after the main program had been completed and are exploratory in nature. The results should therefore be considered mainly for qualitative purposes.

The force tests of a 5-inch-chord all-duralumin airfoil were made in the manner described in reference 3. A complete description of this model is given in reference 6. One important difference between the methods employed for the pressure-distribution tests and the force



tests was the manner in which the models were mounted. For the force tests, the model was mounted on the balance and extended across the tunnel, passing through holes, which were of the same shape as but slightly larger than the model, cut in flexible brass end plates that preserved the contour of the tunnel walls. Thus, leakage of air occurred around the model ends. The pressure-distribution model was tested before the installation of the balance and was supported by the end plates; the consequent tight fit permitted no appreciable end leakage.

The balance, except for improvements that permit a more accurate determination of the forces, is similar in principle to the one used in the 11-inch high-speed wind tunnel and the methods of operation are likewise similar to those employed in the operation of the 11-inch tunnel (reference 3).

**Range of tests.**—The speed range over which measurements were made extended, in general, from one-tenth the speed of sound to values in excess of the critical speed. The corresponding Reynolds Number range was from approximately 350,000 to nearly 2,000,000. Tests were made for only small angles of attack because the primary purpose of the experiments, to discover the nature of the flow phenomena at the critical speed, could be accomplished at small angles of attack, and further, the extension of the tests to higher angles of attack would add a considerable amount of work without, it was felt, adding materially to the fundamental significance of the results obtained. In the supplementary tests, the force measurements were made for the speed range and the angle-of-attack range previously noted, but the pressure-loss measurements were made only for speeds in the critical region.

## RESULTS

The following symbols are used in this report:

- $c$ , speed of sound.
- $V$ , speed of the general air stream.
- $u$ , local velocity of the air stream.
- $u_1$ , local velocity in front of the compression shock.
- $u_2$ , local velocity behind the compression shock.
- $\rho_1$ , density in front of the compression shock.
- $\rho_2$ , density behind the compression shock.
- $M$ , compressibility index,  $V/c$ .
- $\gamma$ , specific-heat ratio; value taken, 1.4.
- $p_a$ , atmospheric pressure.
- $p$ , static pressure in the free stream.
- $p_t$ , local static pressure (as at airfoil surface).
- $p_1$ , airfoil surface pressure in front of the compression shock.
- $p_2$ , airfoil surface pressure behind the compression shock.
- $P$ , pressure coefficient,  $(p_t - p)/q$  (the ordinate of the pressure-distribution diagram).

$P_0$ , pressure coefficient for incompressible flow.

$P_c$ , critical-pressure coefficient, that is, the pressure coefficient corresponding to the local velocity of sound  $(0.528 p_a - p)/q$ .

$H$ , total pressure (or impact pressure). Free-stream value of  $H$  equals  $p_a$  for the 24-inch high-speed wind tunnel.

$H_1$ , total pressure in front of the compression shock.

$H_2$ , total pressure behind the compression shock.

$x/c$ , distance from leading edge in percent of chord.

The test data have been reduced to standard nondimensional form. The dynamic pressure  $q$  and the compressibility index  $M$  were determined by measurements of the pressures at calibrated static-pressure orifices in the tunnel wall. These orifices were connected to the photorecording manometer and, like the pressures acting on the surfaces of the airfoil, the orifice pressures were determined by measuring the deflections of the liquid in the manometer tubes shown on the photographic records. A detailed description of the method for computing  $q$  and  $M$  is given in reference 3.

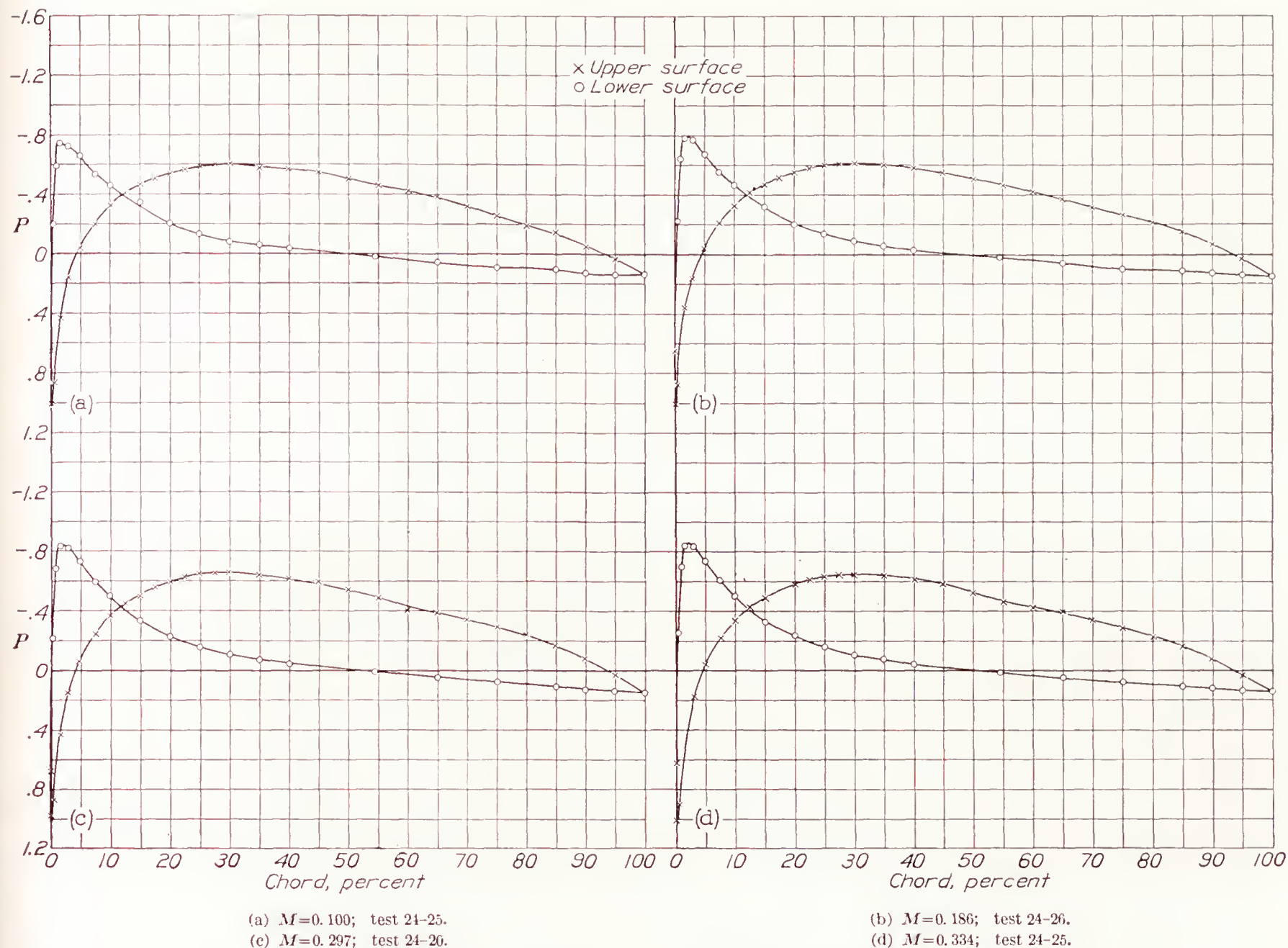
The pressure-distribution data are presented in figures 3 to 5. Figures 6 to 8 are schlieren photographs, each of which corresponds to one of the pressure-distribution diagrams given in figures 3 to 5. Plots of the airfoil characteristics (lift coefficient  $C_L$ , drag coefficient  $C_D$ , and pitching-moment coefficient  $C_{m_{c/4}}$ ) obtained from integrations of the pressure distribution and the force-test data are presented in figures 9 to 11 in a form that illustrates the effect of compressibility. Some of the more significant local effects of compressibility are shown in figures 12 to 14. Figure 15 is included to illustrate the effect that variations in Reynolds Number may have on the local pressures.

The magnitude of the energy losses in the flow that give rise to the large drag increases at high speeds is illustrated by figure 17. Figures 18 to 21 show the loss in total pressure behind the compression shock that occurs at high speeds. In figure 22 a curve from which the critical speed may be estimated is given and comparisons with the test data are included.

## PRECISION

Inaccuracies arising from variations of the dynamic pressure, directional variation of the flow across the test section, and static-pressure gradient are insignificant. The tunnel-wall effect, however, is important particularly as related to the comparison of the results of force and pressure-distribution tests. In the pressure-distribution tests, the tight juncture of the model and the tunnel wall permitted no appreciable end leakage and, furthermore, measurements were made only at the center section of the model; as a result,



FIGURE 3.—Pressure distribution for the N. A. C. A. 4412 airfoil.  $\alpha = -2^\circ$ .

data closely approximate those for two-dimensional flow. For the force tests, however, there was a small clearance where the model passed through the tunnel walls, which appears, from preliminary investigations, to necessitate an important correction for leakage as well as for tunnel-wall effect.

Other errors are indicated by the scatter of the points on the curves. For the pressure-distribution data, figures 3(f), 3(k), 4(c), and 4(f) show that, for low speeds, the accidental error is negligible; but, at speeds approaching and beyond the critical, the error is increased owing to the flow unsteadiness caused by the compression shock. Integrations of the pressure-distribution diagrams are subject to additional errors arising from variations in the fairing of the curves, particularly in the region where compression shock may occur, and the magnitude of these errors is included in the point scatter in figure 9.

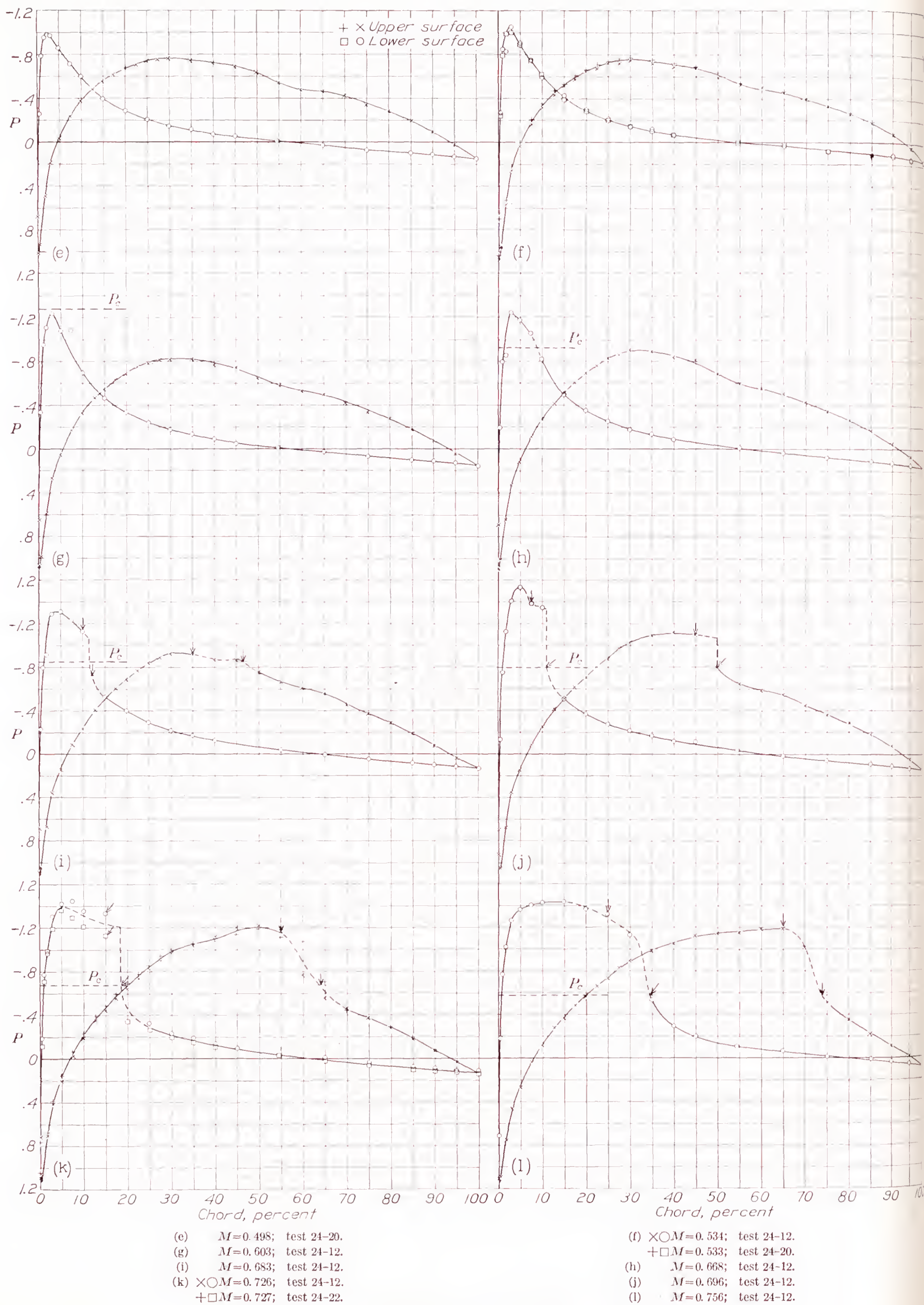
Errors in the integrated values of total-pressure loss may be large owing to the small number of measurements made in the wake of the wing and the corresponding uncertainty in the drawing of the curves. These data, however, are intended to show qualitatively the magnitude of the loss and quantitatively the extent of

the flow disturbance at the compressibility burble. When the data are used for these purposes, the errors are insignificant.

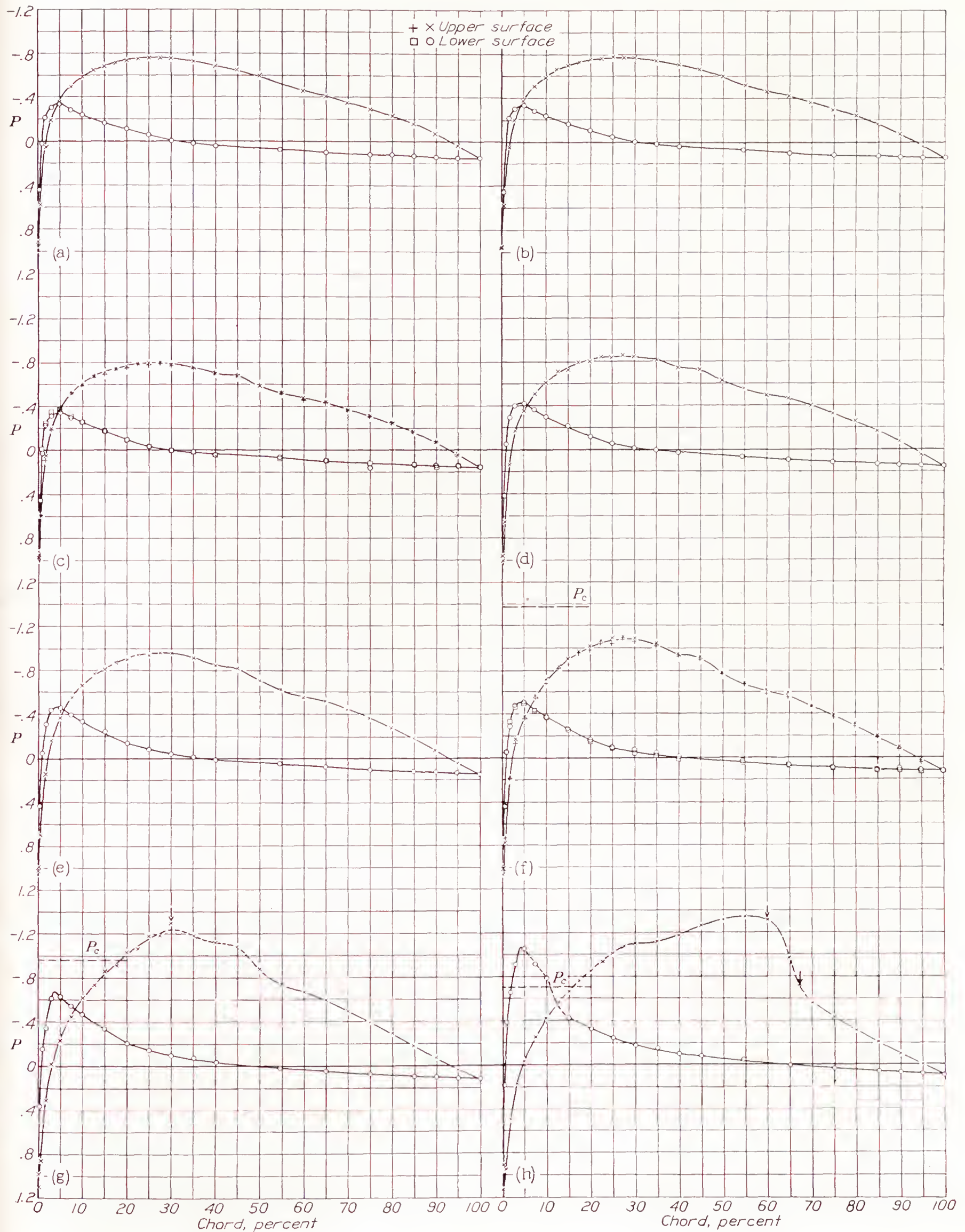
Balance calibrations before and after the force tests agreed very closely. In general, force-test results can be repeated to within 3 percent.

Further errors may arise from variations in the static-plate calibrations and the effect of atmospheric humidity. For these tests, however, there were no measurable changes in the static-plate calibrations, which were repeated several times during the progress of the tests. Humidity effects under certain conditions may be large because of the high expansion and the consequent lowering of temperature that occurs as the air is accelerated to the high speeds attained in the high-speed wind tunnel. Preliminary tests, however, indicated a value of the relative humidity below which no measurable effects occurred and most of the data were therefore taken for humidity conditions corresponding to the region in which no effects could be measured. A small amount of the data was taken at conditions exceeding the indicated limit, but the errors are included in the scatter of the test points.



FIGURE 3.—Pressure distribution for the N. A. C. A. 4412 airfoil.  $\alpha=-2^\circ$ —Continued.



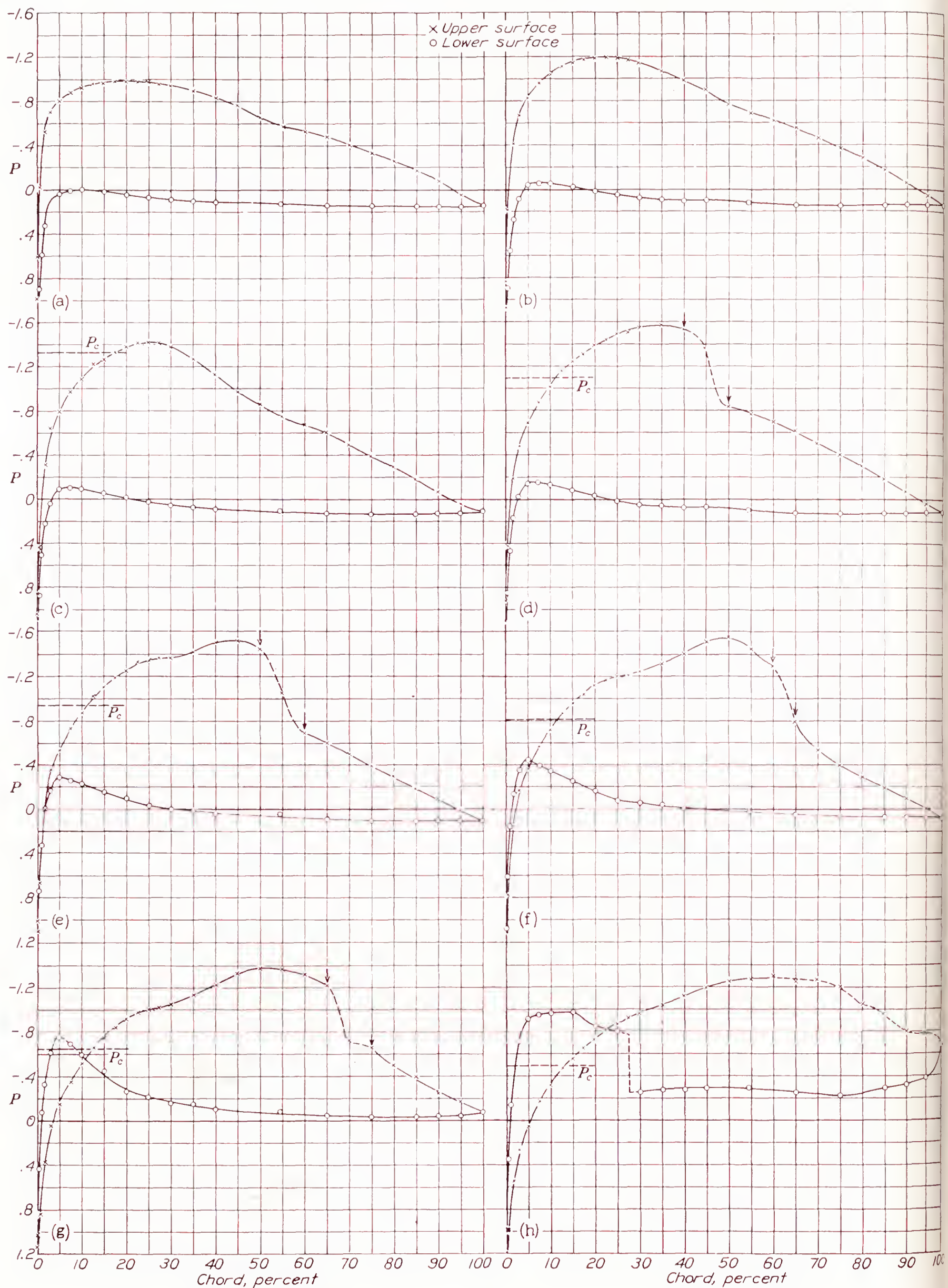


- (a)  $M=0.141$ ; test 24-26.  
 (c)  $\times \circ M=0.299$ ; test 24-25.  
 $+ \square M=0.298$ ; test 24-21.  
 (e)  $M=0.517$ ; test 24-21.  
 (g)  $M=0.659$ ; test 24-12.

- (b)  $M=0.206$ ; test 24-26.  
 (d)  $M=0.427$ ; test 24-21.  
 (f)  $\times \circ M=0.590$ ; test 24-12.  
 $+ \square M=0.589$ ; test 24-21.  
 (h)  $M=0.717$ ; test 24-12.

FIGURE 4.—Pressure distribution for the N. A. C. A. 4412 airfoil.  $\alpha = -0^\circ 15'$ .



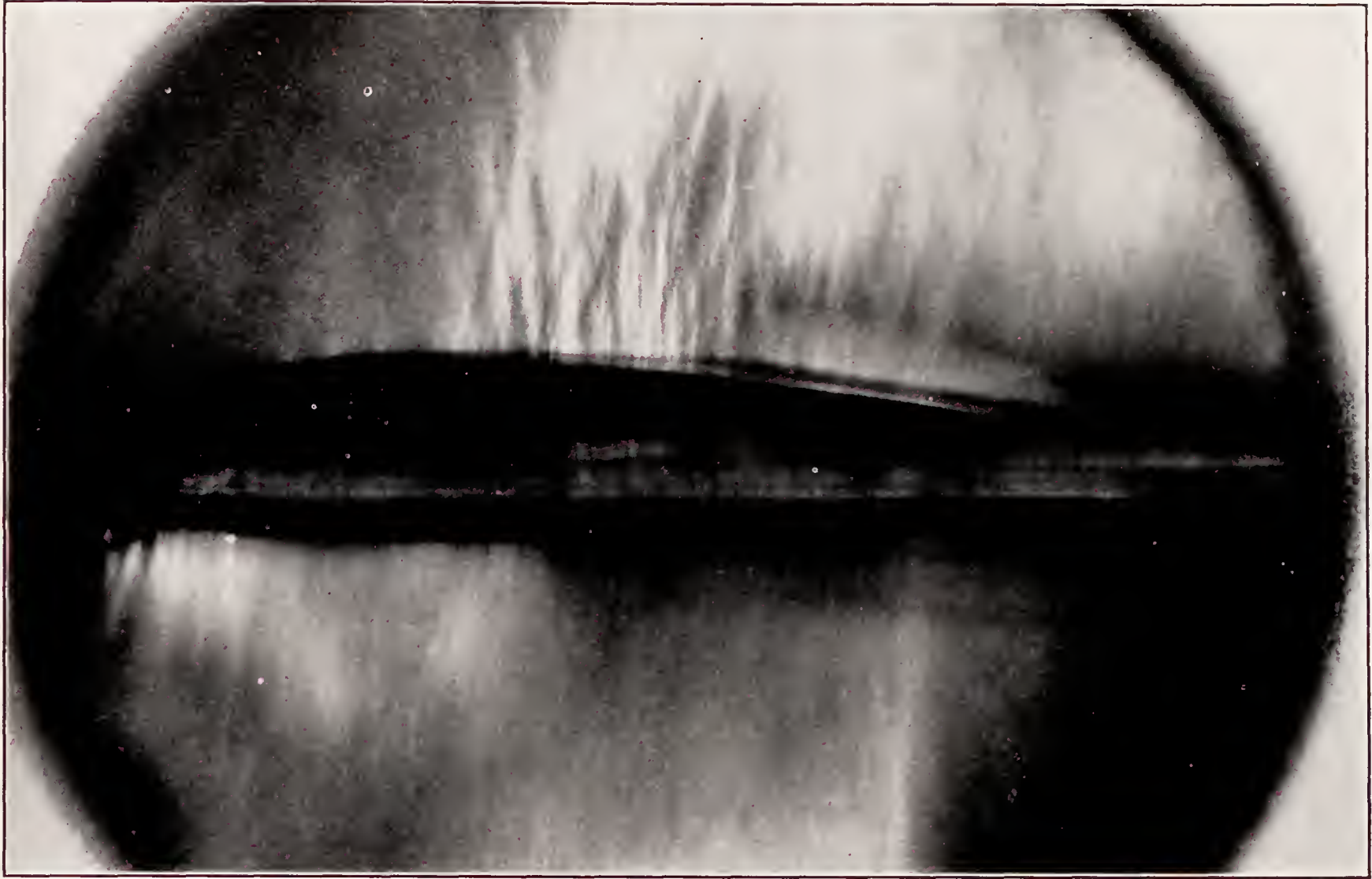
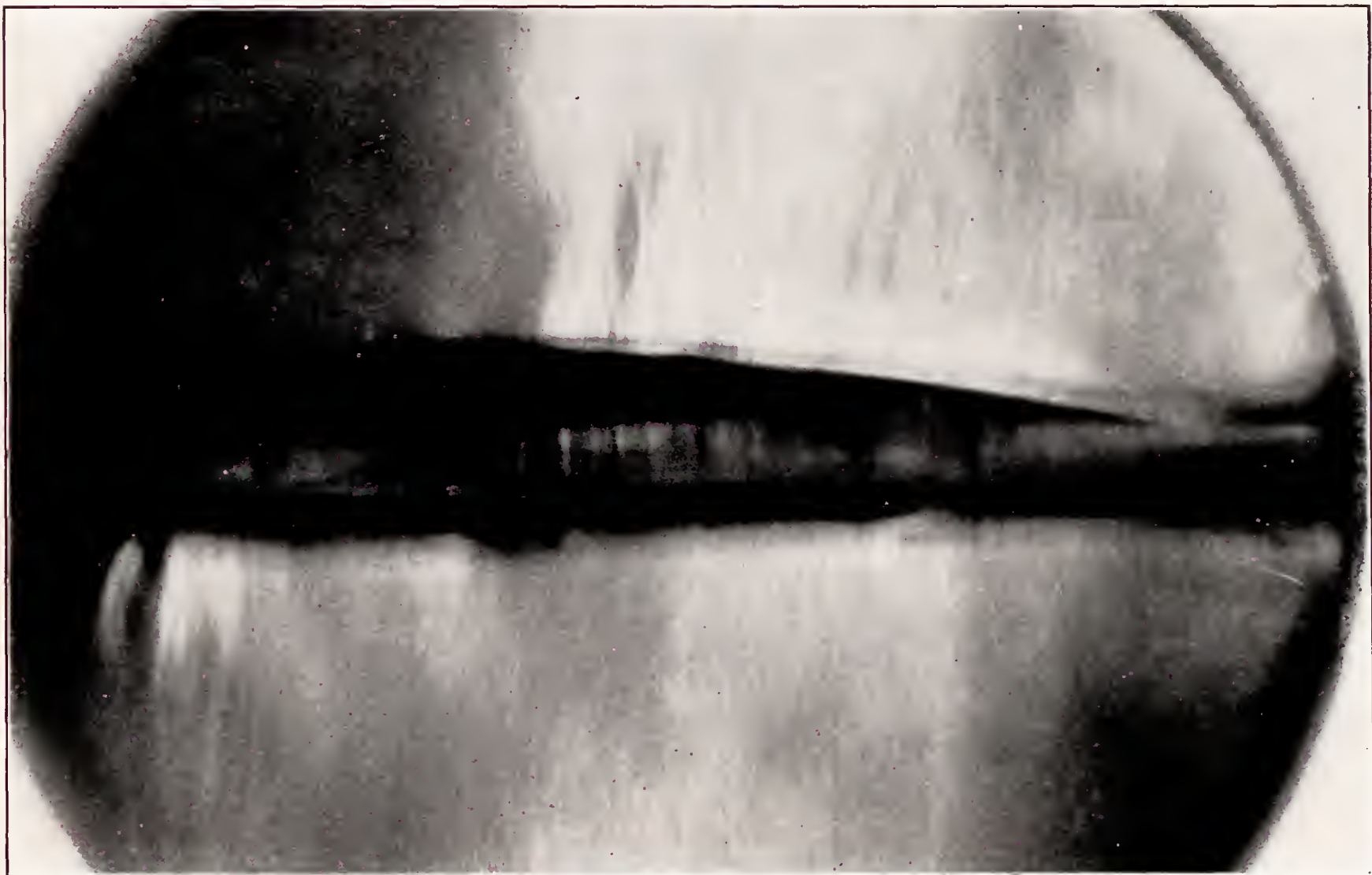


(a)  $M=0.191$ ; test 24-26.  
 (c)  $M=0.596$ ; test 24-12.  
 (e)  $M=0.664$ ; test 24-12.  
 (g)  $M=0.735$ ; test 24-12.

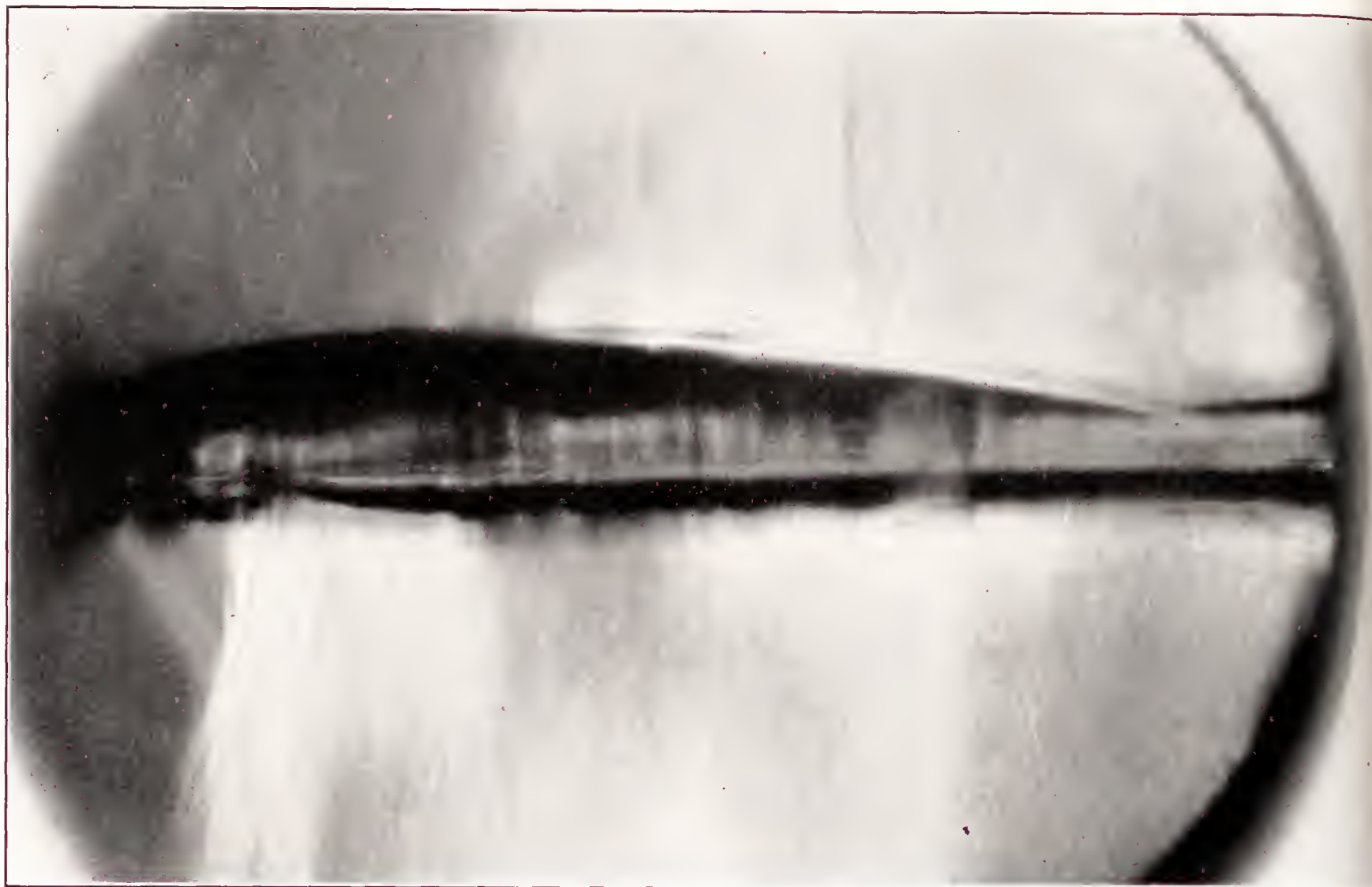
(b)  $M=0.512$ ; test 24-27.  
 (d)  $M=0.640$ ; test 24-27.  
 (f)  $M=0.690$ ; test 24-12.  
 (h)  $M=0.782$ ; test 24-27.

FIGURE 5.—Pressure distribution for the N. A. C. A. 4412 airfoil.  $\alpha=1^{\circ}52.5'$ .



(a)  $M=0.668$ .(b)  $M=0.696$ .FIGURE 6.—Schlieren photographs of flow for the N. A. C. A. 4412 airfoil.  $\alpha=-2^\circ$ .



(c)  $M=0.726$ .(d)  $M=0.756$ .FIGURE 6.—Schlieren photographs of flow for the N. A. C. A. 4412 airfoil.  $\alpha=-2^\circ$ —Continued.



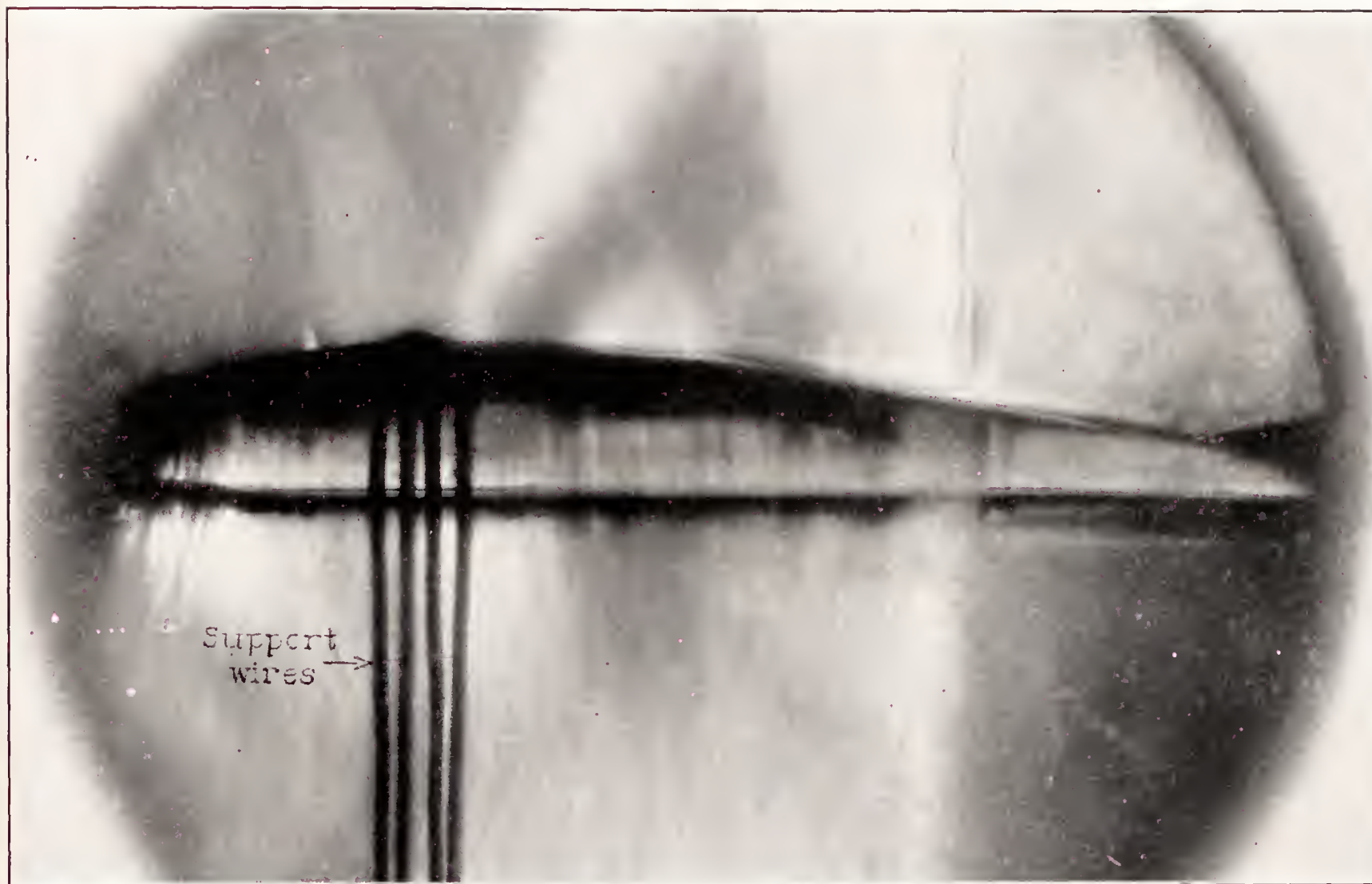


FIGURE 7.—Schlieren photograph of flow for the N. A. C. A. 4412 airfoil.  $\alpha = -0^\circ 15'$ ;  $M = 0.717$ .

## DISCUSSION

Examination of the pressure-distribution diagrams and the flow photographs (figs. 3 to 8) will give a general indication of the effect of compressibility and an illustration of the nature of the flow changes that occur. At low speeds, the shape of the pressure-distribution diagrams is in agreement with the results of previous low-speed tests. As the speeds are increased, however, the area of the diagrams is increased as a result of the increases in the value of the local pressure coefficient. This change continues without appreciable modification of the general flow pattern until speeds in the field of flow equal or exceed the local speed of sound. When this condition occurs, there is a marked change in the type of flow.

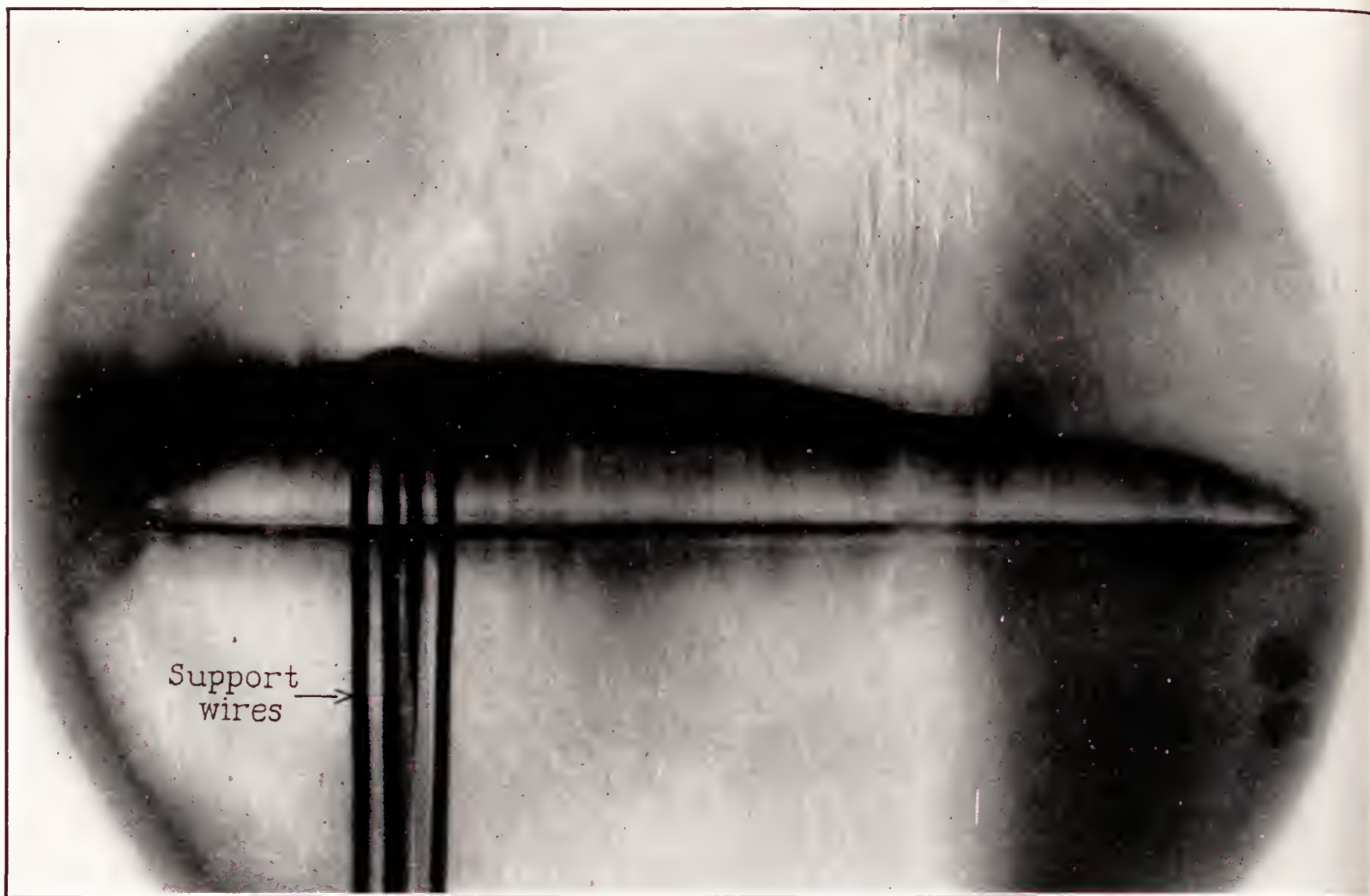
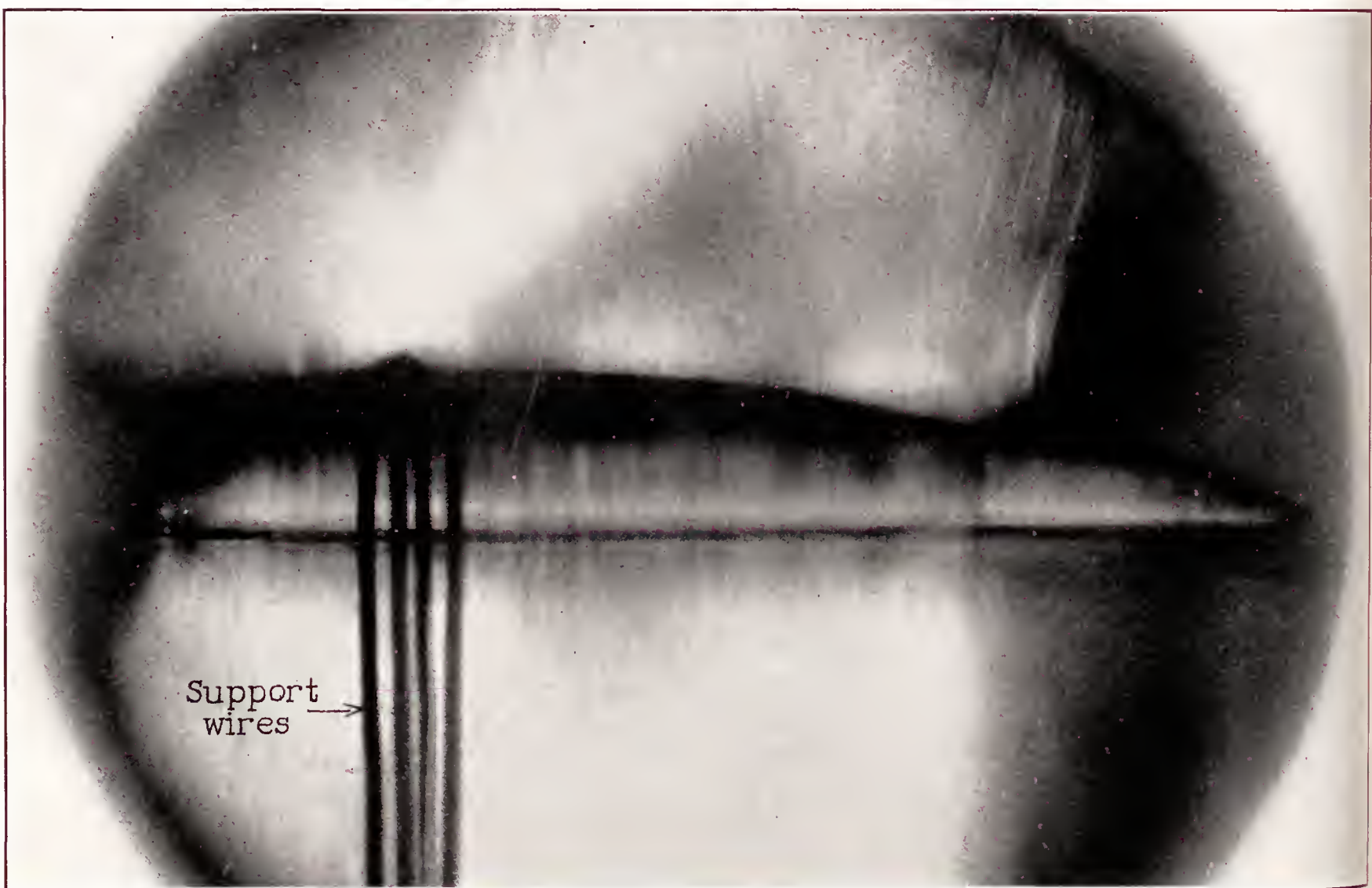
The important characteristic of the flow now established is illustrated by figures 6, 7, and 8. A disturbance is formed as indicated by the sharp lines that project outward from the airfoil approximately perpendicularly to the airfoil surface. Correlation of the photographs and the pressure-distribution diagrams show that the location of the disturbance on the airfoil surface corresponds to the location of the discontinuity in the diagrams.

The dotted line on the diagrams shows the value of the pressure coefficient corresponding to the attainment

of the local speed of sound. When values of the local pressure coefficient rise above the value corresponding to the local speed of sound, examination of the diagrams and the flow photographs indicates that a compression shock is formed which, with a further increase of speed, becomes more intense and moves back along the airfoil, ultimately reaching the trailing edge. Other data (reference 1) show that, when the trailing edge is reached, further increases in speed add considerable downstream slope to the disturbance.

Previous studies of compressibility effects have been based on force-test data; in order to correlate these data with the results of the present investigation, force-test data have been included in figures 9 and 10. A strict comparison is not possible because of previously explained differences in tunnel-wall effects for the force and the pressure-distribution tests. Changes due to compressibility, however, are comparable and it is apparent from examination of the figures that the results of the force tests and the integrated data obtained from the pressure-distribution tests are in excellent agreement regarding the effects of compressibility. As the speed is increased, the lift at first increases, the increase becoming greater until finally a speed is reached at which there is a sudden loss of lift. The rate of increase of lift is approximately the same for both the pressure-distribution and the force-test results, and the critical



(a)  $M=0.690$ (b)  $M=0.735$ .FIGURE 8.—Schlieren photographs of flow for the N. A. C. A. 4412 airfoil.  $\alpha=1^{\circ}52.5'$ .



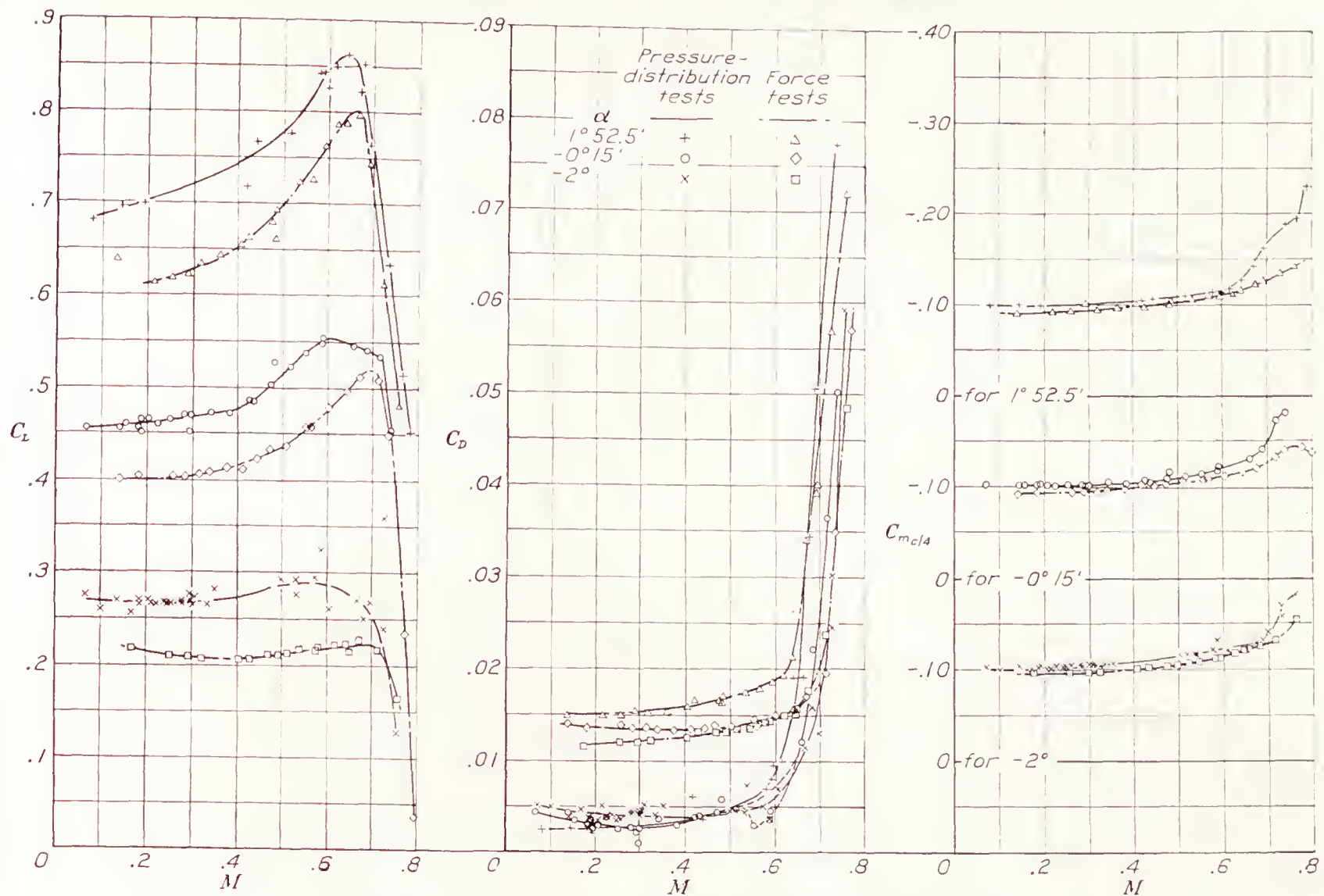
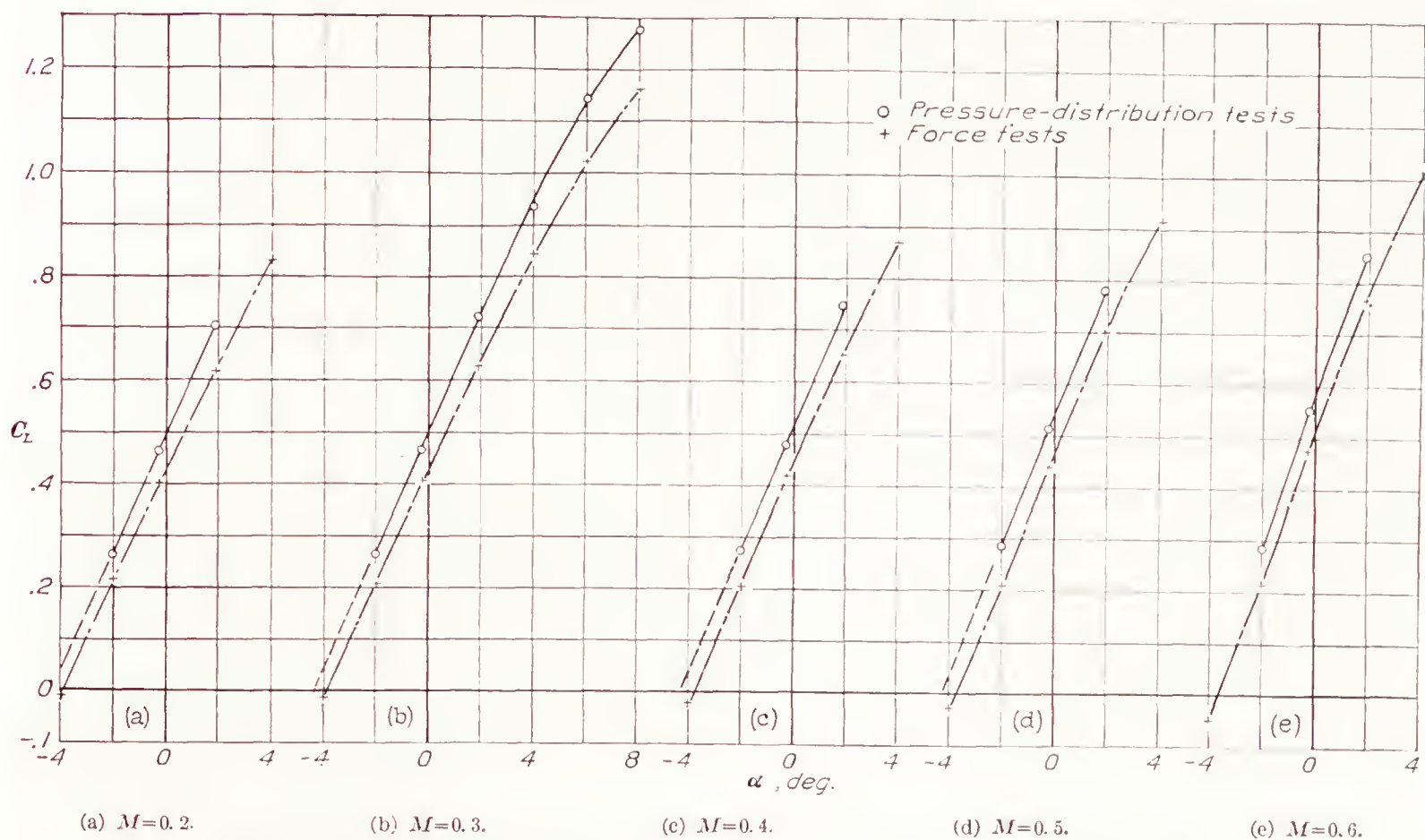


FIGURE 9.—Airfoil characteristics from the integrated pressure measurements and force-test data.

FIGURE 10.—Lift curves for the N. A. C. A. 4412 airfoil at several values of the compressibility index  $M$ .

speed for equal lift coefficients is in approximate agreement. Examination of the drag data illustrates relatively little change in drag until the critical speed is reached, when there is a rapid rise in the drag coefficient. It should be remembered, however, that the pressure-distribution results give only the pressure drag for approximately two-dimensional flow, whereas the

force-test data include the friction drag and some induced drag due to tunnel-wall effects.

The effects of compressibility on the pitching-moment coefficient (fig. 9) are also in good agreement. As the speed is increased, there is first a gradual increase in the diving moment until the critical speed is reached, when the moment undergoes large and rapid increases.



Correlation of these data with the pressure-distribution diagrams and the flow photographs (figs. 3 to 8) shows that the critical speed is approximately the stream

and the loss in lift are therefore associated with the flow change that occurs when the compression shock is formed.

The data, in general, show that two types of flow occur. The first type is a flow similar to the usual low speed type but changing progressively and uniformly in such a way as to give rise to increasing pressure coefficients, which type of flow exists for speeds up to the critical; that is, a flow with speeds nowhere exceeding the local speed of sound. The second type is a flow with compression shock in which speeds both above and below sound speed occur.

#### COMPRESSIBILITY EFFECTS IN THE SUBSONIC REGION

Glauert and Ackeret (references 7 and 8) have studied, theoretically, the effect of compressibility on a potential flow and, although their methods of analysis differed, both arrived at the same result. They found that the lift for a given angle, or the lift-curve slope, was increased by the amount  $1/\sqrt{1-M^2}$ . The theoretical result is in agreement with these experiments, as shown in figure 11. Ordinarily, the agreement is not so good as shown by this particular airfoil but the theoretical variation does, in general, correlate the differences in lift between high and low speeds provide, of course, that the critical speed is not exceeded.

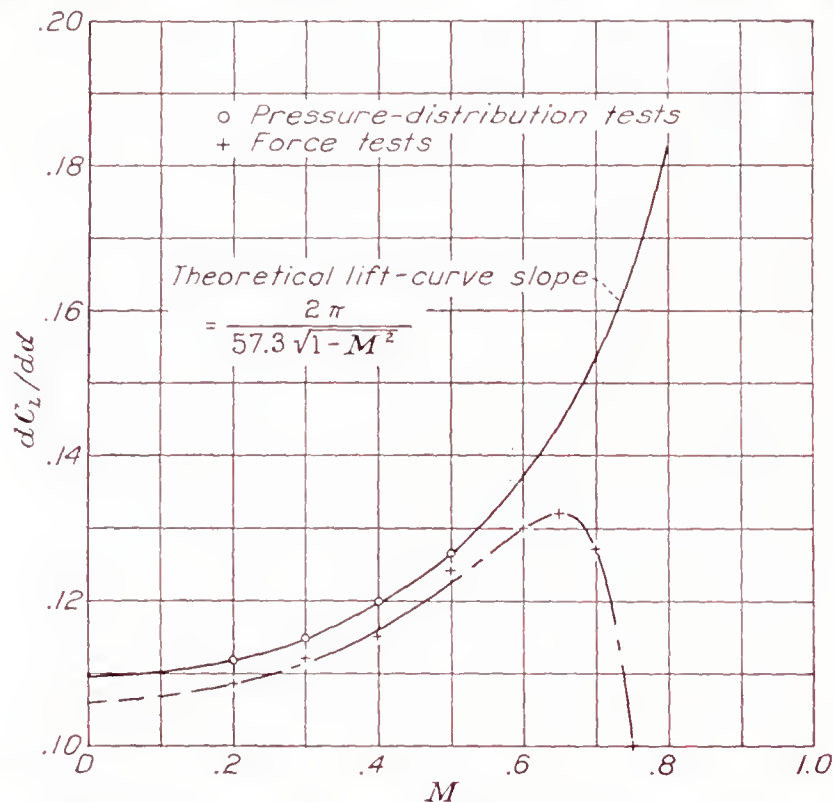


FIGURE 11.—Variation of lift-curve slope for the N. A. C. A. 4412 airfoil with the compressibility index  $M$ .

velocity for which the local speed of sound is attained at some point over the airfoil surface. The rise in drag

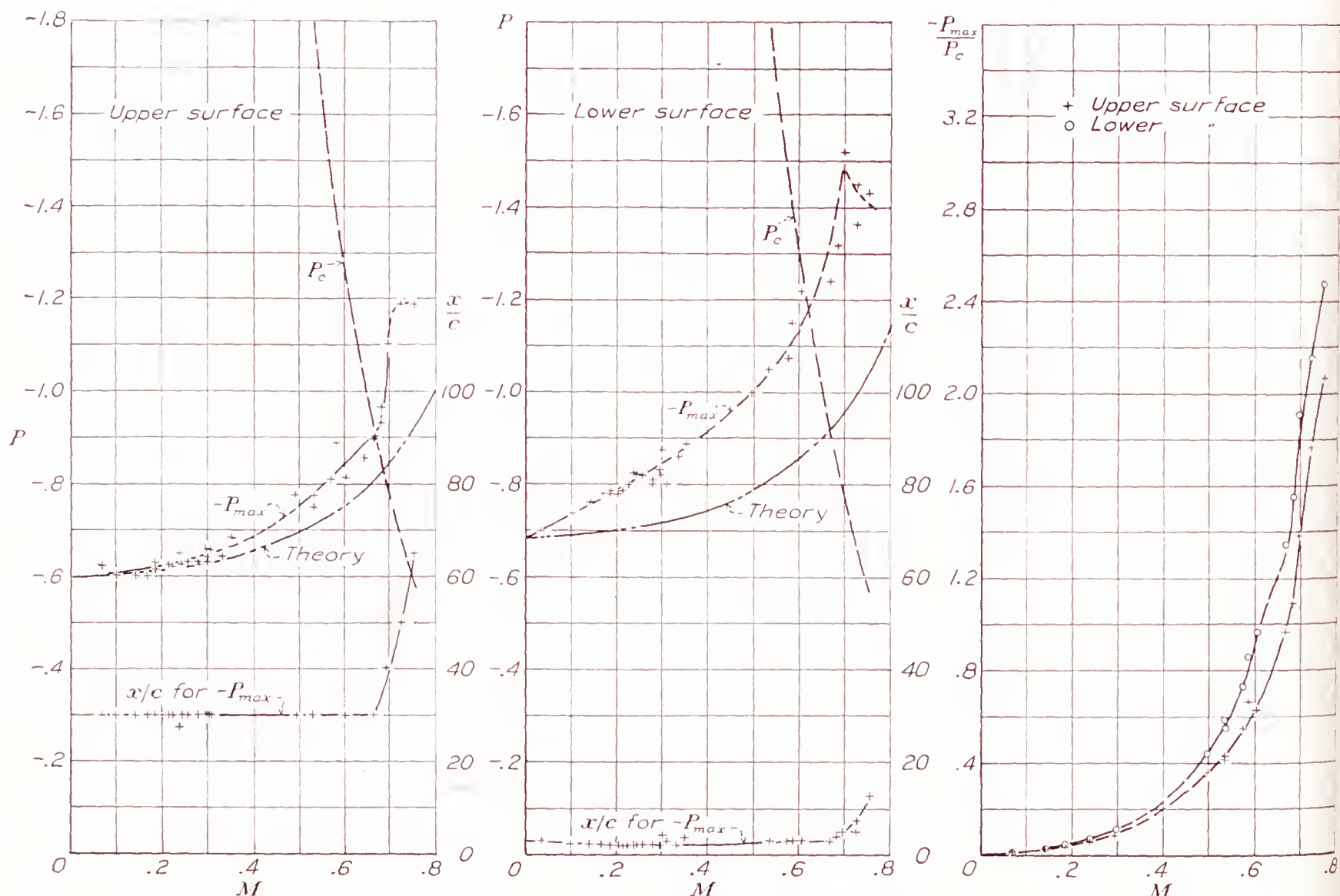
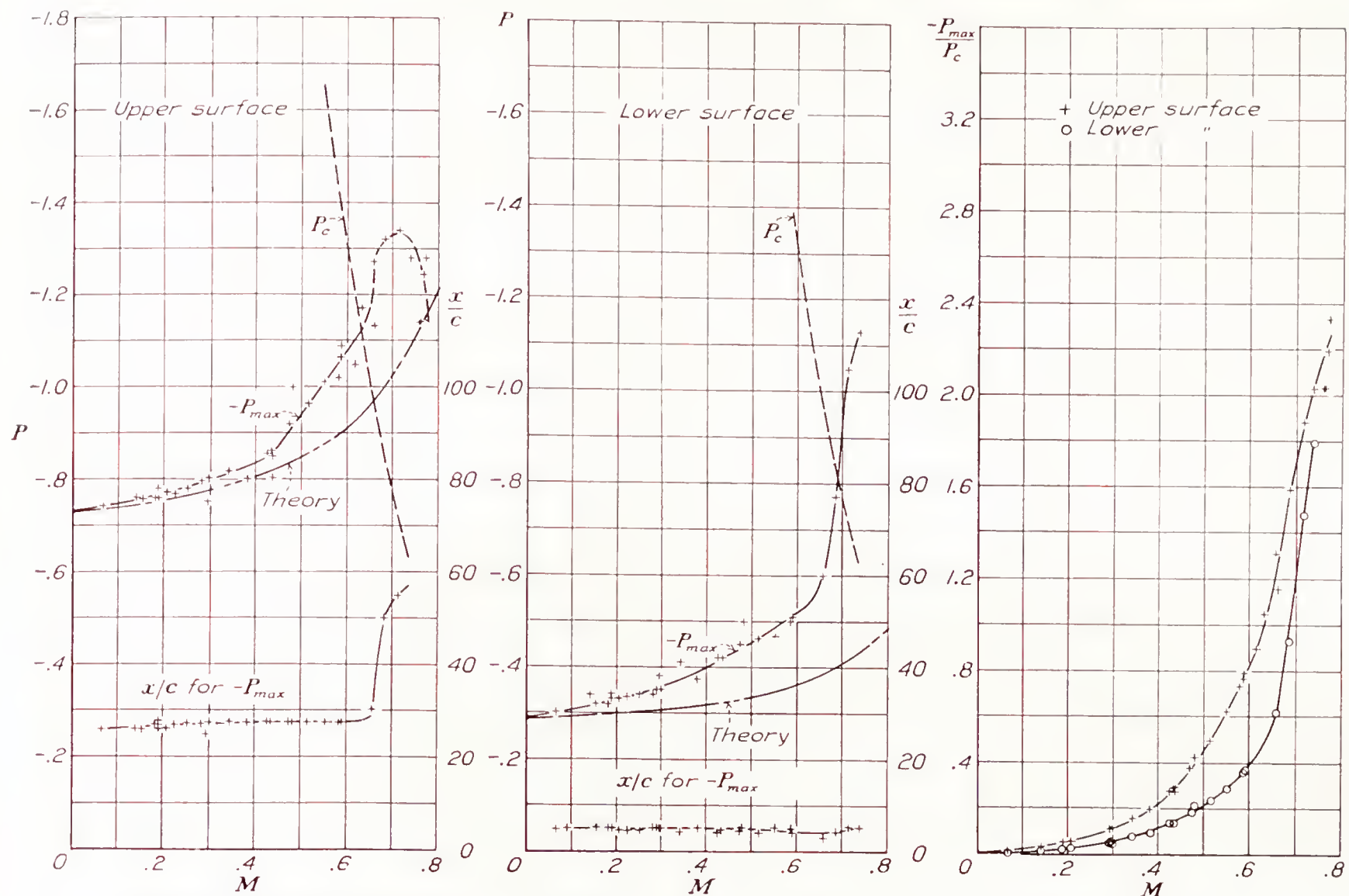
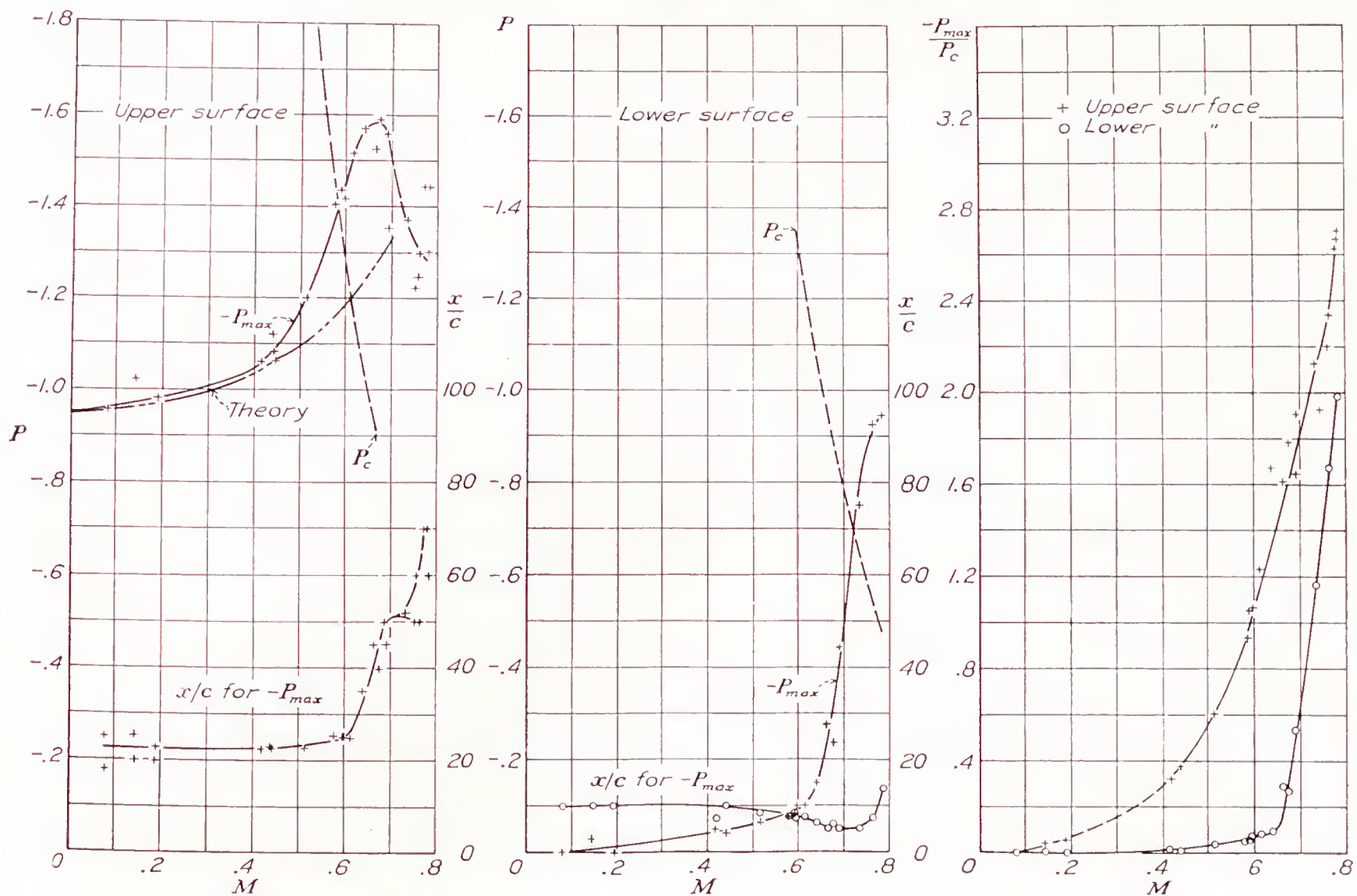


FIGURE 12.—Effect of compressibility on the maximum negative pressure coefficient for the N. A. C. A. 4412 airfoil.  $\alpha = -2^\circ$ .



FIGURE 13.—Effect of compressibility on the maximum negative pressure coefficient for the N. A. C. A. 4412 airfoil.  $\alpha = -0^\circ 15'$ .FIGURE 14.—Effect of compressibility on the maximum negative pressure coefficient for the N. A. C. A. 4412 airfoil.  $\alpha = 1^\circ 52.5'$ .



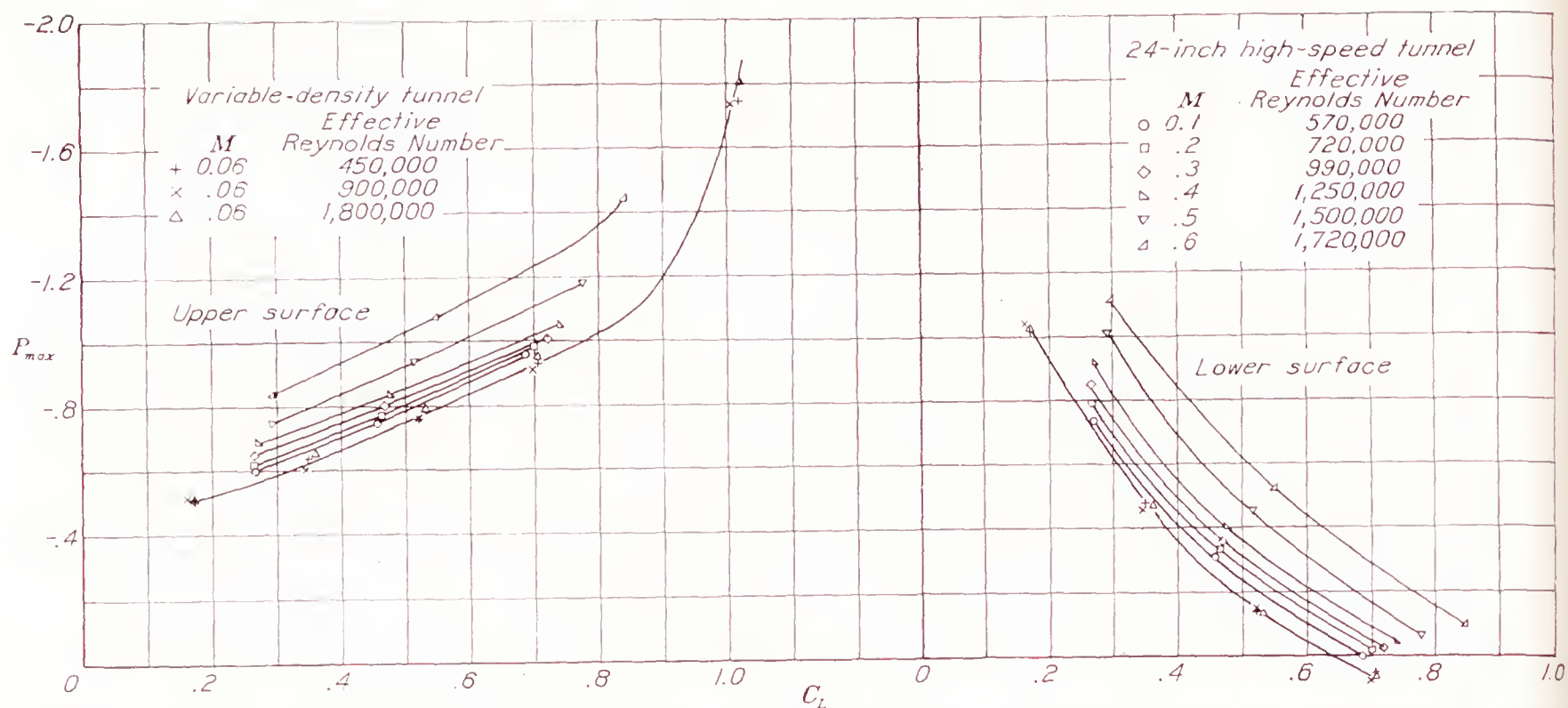


FIGURE 15.—Variation of maximum negative pressure coefficient with lift coefficient as affected by compressibility index  $M$  and effective Reynolds Number for N. A. C. A. 4412 airfoil.

Ackeret concluded from his analysis that the local induced-pressure differences, as well as the lift, would likewise be increased; a comparison of the theoretical result with the maximum negative pressures obtained on the surface of the airfoil is given in figures 12, 13, and 14. The location of the maximum negative-pressure coefficient, the variation of the critical-pressure coefficient, and the ratio of the maximum negative-pressure coefficient to the critical-pressure coefficient are also shown on the figures. The data show that theory underestimates the compressibility effect when the maximum negative pressure occurs near the leading edge and when the speeds exceed four-tenths the speed of sound. At  $-2^\circ$  and  $-0^\circ 15'$  angle of attack (figs. 12 and 13), the disagreement for the lower surface is large. The location of the point of maximum negative pressure for these two conditions is less than 5 percent of the chord from the leading edge, as is shown by the figures. When the maximum negative pressures occur back of approximately 20 percent of the chord, the theoretical variation is in good agreement for speeds up to four-tenths the speed of sound, but above this speed the theoretical and the experimental results diverge. The practical significance of this disagreement is important in that it affects the accuracy of estimates of the critical speed; these estimates will be discussed later.

The probable reasons for the discrepancy lie in the assumptions and the approximations made in the development of the theory. The most important assumption affecting the accuracy of the theory concerns the induced velocities, which are assumed to be negligibly small; and, further, in order to obtain a usable result, the speed of sound is assumed constant throughout the flow field. The approximation for the speed of sound can, in fact, be shown to be equivalent to an assumption of zero as the value of the induced velocity.

Disagreement with the theory may thus be expected when the induced velocities, as is usual, depart considerably from negligibly small values.

The development of a rigorous theory that would enable the computation of the actual pressures appears improbable for practical use, but examination of the theoretical results available (references 5, 9, and 10) appears to indicate that, at least near the leading edge, the approximation  $1/\sqrt{1-M^2}$  is not completely descriptive of the changes that may occur. It may be possible to arrive theoretically at a result that agrees with the experiments. The theoretical treatment is exceedingly complicated and an accurate result, if present methods are used, can be arrived at only by a method of successive approximations. The problem should, nevertheless, be further examined theoretically.

Apart from the discrepancies thus far discussed between the theory and the experiments, theory provides a clue regarding the limits within which the application of the theory may be expected to yield fair results. An effect that Reynolds Number variations may have on the upper limit of speed to which the theory is applicable must of necessity be determined from other sources.

The effect of Reynolds Number on the maximum negative pressures obtained appears to be of no importance within the range of these experiments. Figure 15 shows the results of tests made of the same model at low speeds in the variable-density wind tunnel for a Reynolds Number variation covering the data here presented (reference 11). The measured maximum negative-pressure coefficients for the upper and lower surfaces are plotted against lift coefficient in figure 15. It is apparent from the low-speed results ( $M=0.06$ ) that the Reynolds Number effects are significant. The marked progressive displacement of the curves for the higher speeds then indicates that pressure coefficients are far more seriously affected



compressibility than by Reynolds Number within the range of these tests. It is important to note, therefore, that data taken at high Reynolds Numbers obtained by increasing the speed must be corrected for compressibility if they are to be applied at equal Reynolds Numbers but at lower speeds.

The upper limit of the speed range to which the theoretical allowance for compressibility effects may be applied with fair results can logically be assumed to be the speed at which the potential flow postulated by the theory fails as a result of the formation of a compression shock. In itself, however, the theory indicates no definite limit other than the speed of sound; therefore other means for studying the condition must be used. This problem will be further discussed in connection with the derivation of methods for estimating the critical speed.

#### COMPRESSIBILITY EFFECTS IN THE SUPERCRITICAL REGION

The phenomena in the supercritical region, that is, for speeds above that at which the compressibility burble occurs, are entirely unrelated to those just discussed. The discontinuities in the pressure-distribution diagrams and the corresponding schlieren photographs indicate that compression shock occurs when the maximum velocity over a portion of the airfoil exceeds the local speed of sound. With further increase in stream velocity, the local velocities over the forward portion of the airfoil continue to increase, greatly exceeding the local speed of sound; the discontinuity, or compression shock, moves rearward along the airfoil, ultimately reaching the trailing edge. With further increase of the stream velocity, other tests (reference 1) have shown that the shock remains at or near the trailing edge but with considerable downstream slope, the slope increasing with speed. The significant characteristic of the flow in the supercritical region appears to be the existence of supersonic speeds over a portion of the airfoil and, of course, the compression shock that occurs at the downstream boundary of the supersonic speed region.

The occurrence of the compression shock can be visualized from elementary considerations. It has been shown that the speed of sound is the normal rate of pressure propagation; therefore the high-pressure low-speed field existing at the rear of the airfoil can affect the flow in the supersonic region only at the boundary. Within the supersonic field, the velocity and the pressure at any point are thus uninfluenced by conditions in the low-speed high-pressure region at the rear of the airfoil; but ultimately the low-pressure air must be compressed to return to equilibrium with the air stream back of the model. Compression of the supersonic air in smooth normal fashion requires, as nozzle studies have indicated, a contraction of the stream. The stream boundary formed by the airfoil, however, is the reverse, forming effectively an expan-

sion; and, in supersonic flow, this expansion leads to further increases in speed with still lower pressures. As the low-pressure air cannot pass off into the high-pressure region without setting up the obvious impossibility of tension, some unusual type of flow must occur.

Imagine, momentarily, that the low-pressure air of high kinetic energy meets the high-pressure region and that equilibrium is established through interchange of the kinetic energy of the molecules of the low-pressure and the high-pressure air. If the layer through which equilibrium was brought about were infinitely thin, then the obvious impossibility of regions of tension in the air is circumvented. In the energy interchange, the pressure of the air of supersonic speed would be increased to values that would permit normal compression over the rear part of the airfoil, and these values would generally exceed the pressure corresponding to the local speed of sound. Following the layer or compression shock, subsonic speeds would occur and compression over the remaining portion of the airfoil would take place in the normal manner. Within the compression shock, however, a considerable amount of kinetic energy would be dissipated in the energy interchange because of the internal friction, or viscosity, of the air. The energy dissipated by the internal friction, or viscosity, would be converted into heat, thereby becoming unavailable to the flow, and would appear in the flow as decreased total pressure or increased drag on the model.

The movement of the shock front with increasing speed is not well understood, but it is possible to reason why the shock front should move rearward with increasing speed. If the influence of any local pressure disturbance is considered to be transmitted in all directions at the normal speed of sound, at any and all time intervals a pressure disturbance at the trailing edge will proceed from the trailing edge at the local speed of sound. The forward-moving portion of the disturbance, however, travels at a speed that decreases because of the increasing local velocity of flow at points close to the airfoil surface. Finally, the forward-moving portion of the disturbance is stopped at a point where its local velocity equals the local stream velocity; a sharp front thus results as the continuous disturbance from the trailing edge piles up. In the shock front, however, the local speed of sound is increased over the normal stream value owing to the intensity of the disturbance that has now been formed and because of the increased speed of sound resulting from the temperature or heat increase at the shock. The velocity at the front thus exceeds the normal speed of sound in the stream. Ultimately, however, an equilibrium is reached at some point on the airfoil where the supersonic speed over the forward portion is equal to the local speed of propagation of the disturbance. At this point, then, the transverse compression shock is stationary. Now, with increasing stream velocity,



the local velocities in front of the shock are increased and the shock front therefore tends to be swept farther back to a new equilibrium position. The intensity of the shock tends to become somewhat more severe, as indicated by previous discussion; but it appears from the experimental data that the increase in local speed of sound at the shock front is not so rapid as the increase in the local velocity of flow over the forward portion of the airfoil with increase of stream velocity.

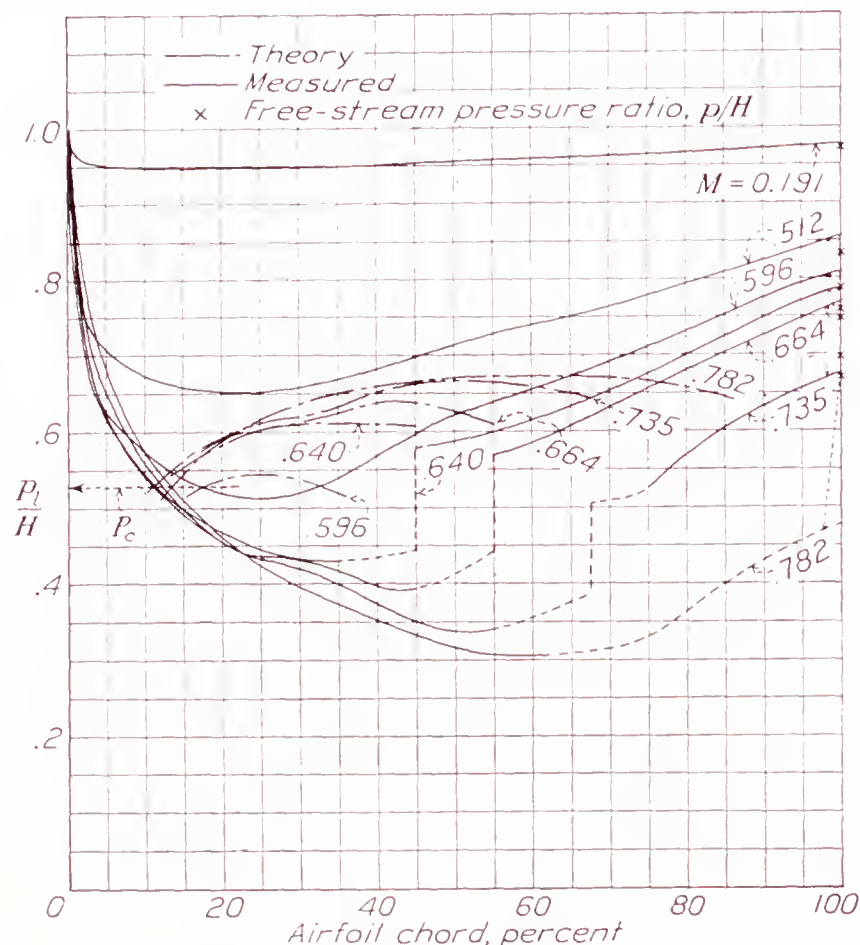


FIGURE 16.—Comparison of theoretical pressure after shock and pressure measurements. N. A. C. A. 4412 airfoil.  $\alpha = 1^\circ 52.5'$ .

If this condition is assumed, then, the shock front must move to the rear with an increase in speed.

Similar phenomena have been observed in nozzles operating with excessive back pressure (reference 12). Prandtl and others have examined the phenomena and find that considerable energy is lost in the compression shock. Briefly, the high-speed air at the compression shock loses a large amount of kinetic energy, only a part of which is recovered as pressure; and the remaining energy, becoming unavailable to the flow, appears as heat. From studies of the phenomena occurring in a nozzle, formulas for calculating the increase in pressure due to the compression shock have been derived. These methods were first applied to an airfoil in reference 2. From the pressure formula of reference 2,

$$\frac{p_2}{p_1} = \frac{2\gamma}{\gamma-1} \left[ \frac{2}{\gamma+1} \left( \frac{p_1}{H} \right)^{\frac{1-\gamma}{\gamma}} - 1 \right] + 1$$

figure 16 has been prepared to compare the results of the calculated and the measured pressures behind the shock. The measured data are for the airfoil upper surface for an angle of attack of  $1^\circ 52.5'$ , and the data are plotted as ratios of the local absolute pressure to

the total pressure or the pressure at the stagnation point of the airfoil.

Because the theory does not give a clear indication of the point at which the compression shock occurs, the theoretical curves of figure 16 were determined by assuming that shock may occur for any pressure in the supersonic-flow region of the airfoil and then computing the corresponding pressure after the shock. The difference between the theoretical and the experimental curves at any point along the chord thus shows the theoretical increment of pressure if shock had occurred at that point on the airfoil. The location of the shock is shown by the experimental results and therefore, at this location, the measured and the theoretical pressure changes in the actual shock can be compared. It is apparent that the calculated pressure increases far exceed the measured values.

There are several reasons for the discrepancy. Fundamentally, however, the theory of simple shock assumes compression in an infinitely thin layer from the pressure corresponding to the maximum flow velocity in front of the shock to the final pressure after the shock. Actually, the compression does not take place in this manner. Some of the diagrams indicate that some small compression occurs smoothly, and probably without material energy loss, just before the shock; likewise, behind the shock, a similar condition appears. Further, the shock does not occur in an infinitely thin layer. These effects would tend to lessen the intensity of the shock by allowing less deceleration of the more rapidly moving molecules in the supersonic region. In the computation of the theoretical pressure increments, the one-dimensional flow equations are used, which are based on the assumption that the flow passes through the shock perpendicular to the wave front; the possibility of separation and its effect that it may have on the direction of the flow is not considered. Separation is extremely likely, because the shock is, in effect, a large adverse-pressure gradient. Considerable further experimentation appears to be necessary.

The magnitude of the kinetic-energy loss in a shock for all the data has been computed from the pressure-distribution data and the results are shown in the plotted points in figure 17. The abscissas have been taken as the ratio of the local pressure in front of the shock to the total pressure in front of the shock rather than the compressibility index of the air stream  $M$ , to permit better correlation of all the data. Had the air stream  $M$  been chosen for the abscissas, the data for each angle of attack would have been displaced and no clear indication of the critical pressure at which the shock forms could have been obtained. The ordinates, the kinetic-energy-loss coefficients, represent the difference between the kinetic-energy change in the shock and the work done by the air in overcoming the pressure difference at the shock divided by the kinetic



energy in front of the shock. When no shock occurs, the value of the kinetic-energy-loss coefficient is zero.

Briefly, the formula is derived as follows:

$$K_{E.L.} = \frac{K.E._{lost}}{K.E._1} = \frac{\Delta K.E. - (\text{work done})}{K.E._1}$$

where  $K_{E.L.}$  is the kinetic-energy-loss coefficient and  $K.E._1$  is the kinetic energy in front of the shock. If it is assumed that

$$\rho_1 u_1 = \rho_2 u_2$$

and

$$p_2 - p_1 = \rho_1 u_1 (u_1 - u_2)$$

where  $u$  is the local velocity of the air stream,

$$K_{E.L.} = \frac{\left(\frac{p_2}{p_1}\right)^2 - 1}{\left(\frac{2\gamma}{\gamma-1}\right)^2 \left[\left(\frac{H}{p_1}\right)^{\frac{\gamma-1}{\gamma}} - 1\right]^2}$$

In the computation of the values of  $K_{E.L.}$  shown in figure 17, the pressures are taken from the pressure-distribution diagrams of figures 3 to 5. In general, the value of  $p_2$  appears to be near the pressure corresponding to the local speed of sound in front of the shock. The values of  $p_1$  and  $p_2$  taken for the calculations are indicated by the arrows on the pressure-distribution diagrams.

The experimental data are consistent in regard to the amount of kinetic energy lost for any given pressure ratio but the actual loss is approximately half the theoretical value. The discrepancy arises for exactly the same reasons that the experimental and the theoretical pressure increments in the shock fail to agree. Theoretically, it is assumed that the shock is an infinitely thin layer and that all the compression occurs within the layer. The pressure diagrams show that the disturbed region is rather wide and indicate that the actual discontinuity is preceded and followed by regions of increasing pressure in which there is probably no loss. Very little is actually known of the flow in the disturbed region but the existence of a region of adiabatic compression immediately ahead of the shock, in particular, should be further investigated to determine the possibility of extending this region and thus of obtaining reduced shock intensity or a delayed compressibility burble.

The loss in total pressure caused by the shock on the upper surface of the airfoil is shown in figures 18 to 21. Figures 18 to 20 show the distribution of the loss and the pressure-distribution diagrams for the upper surface of the airfoil. No loss due to compression shock occurs until the stream velocity exceeds the local speed of sound. For even small speed increments above the critical, however, there are large increases in the total-pressure loss. The extent of the shock in a direction perpendicular to the chord in extreme cases (speeds at the trailing edge in excess of sound speed) is large and is approximately 130 percent of the chord. The shock thus extends about half the tunnel radius from the model. Near the model ends, therefore, there may be

some tunnel-wall effect that may tend to intensify the shock locally. This effect, however, should not be of importance at the center section where these measurements were made.

Integrated values of the total-pressure loss due to the compression shock are a measure of the drag increments experienced by the airfoil. These values for all the angles of attack investigated are shown in figure 21

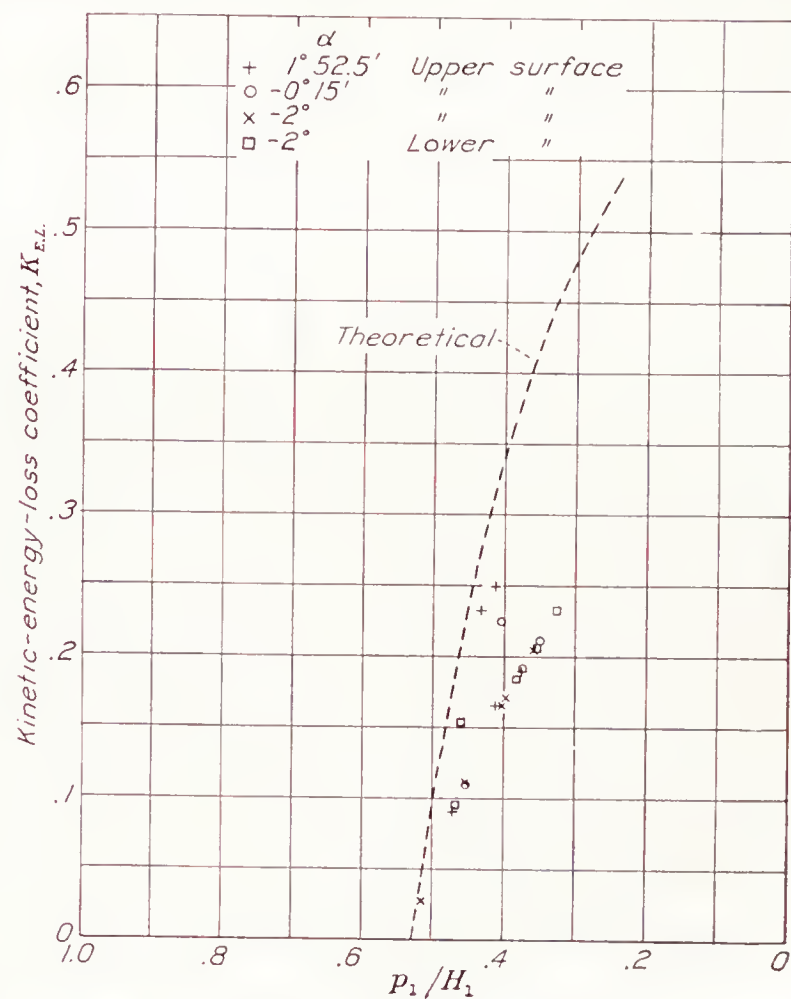
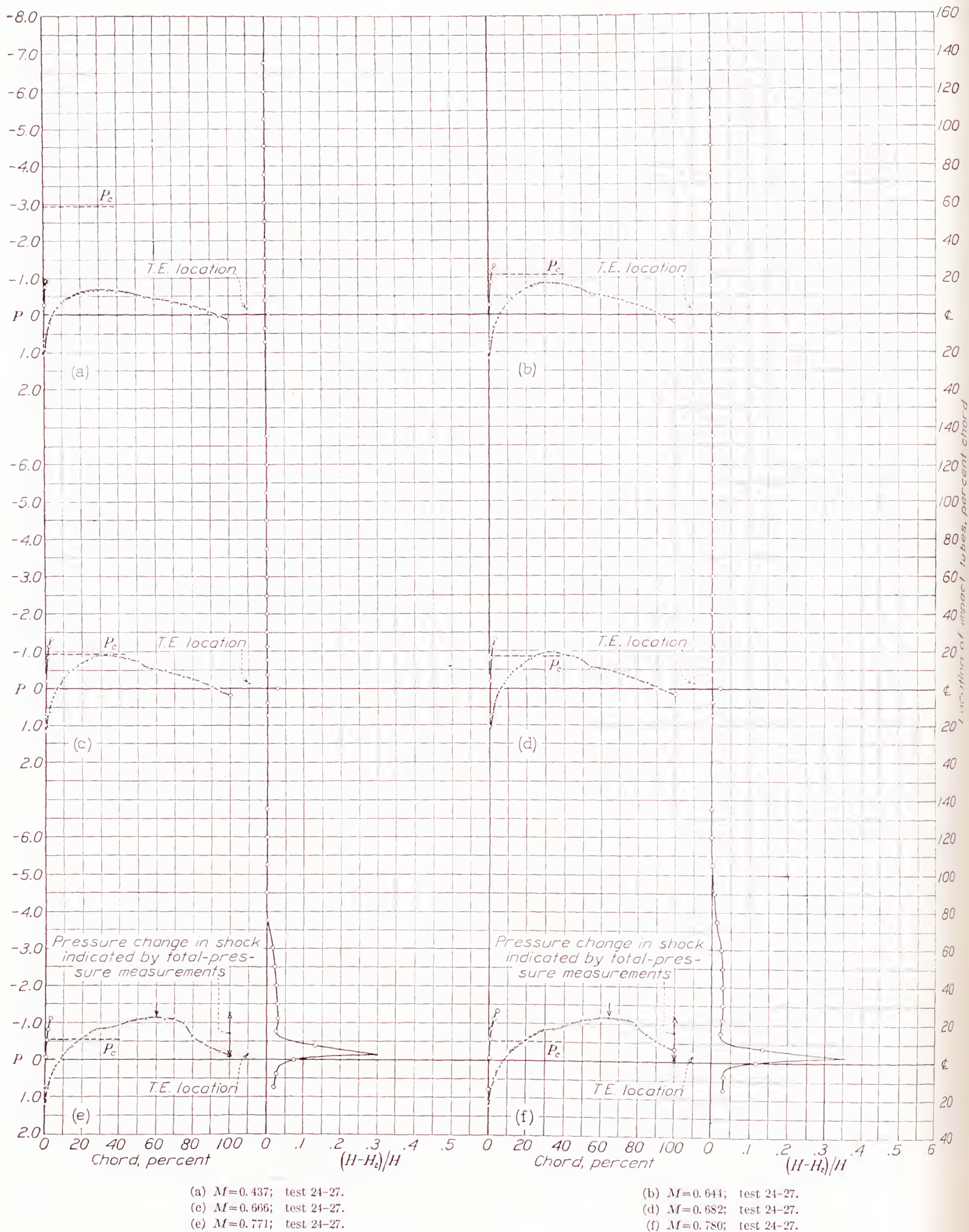


FIGURE 17.—Kinetic-energy-loss coefficient for the compression shock on the N. A. C. A. 4412 airfoil.

against the pressure ratio  $p_1/H$  and, though only qualitative as previously explained, the increase of the loss with decrease of pressure ratio  $p_1/H$  or increase of speed is consistent with the increase that might be expected from pressure-distribution and force-test data.

The theoretical total-pressure loss appears to be somewhat less than the values measured and integrated, which indicates a serious loss other than the direct shock loss. This possibility is further illustrated by the pressure change in the shock, indicated by the total-pressure measurements shown in figures 18 to 21. These pressure differences were obtained by assuming the total-pressure loss in the shock to be represented by the maximum value of the ratio  $(H-H_2)/H$  outside the normal wake region. From the theoretical relation, the corresponding value of the pressure in front of the shock was determined and the corresponding pressure behind the shock was computed. The very large disagreement between the pressure changes thus shown and the measured values indicated by the pressure-distribution diagrams can hardly be accounted for by any of the previously discussed limitations of the theory. The results seem to indicate energy losses in addition to the



FIGURE 18.—Pressure distribution and compression shock total-pressure loss for the N. A. C. A. 4412 airfoil.  $\alpha = -2^\circ$ .



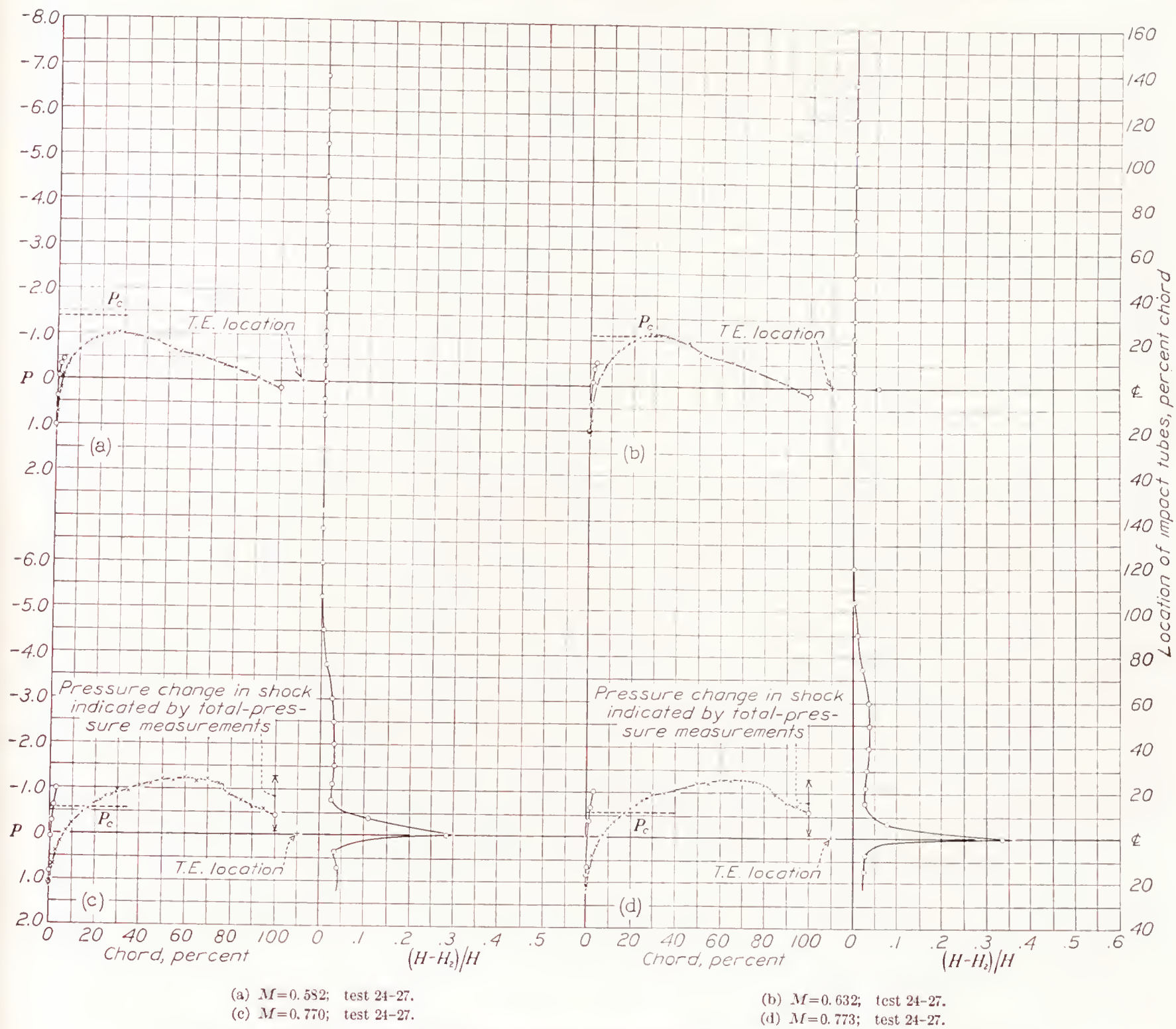


FIGURE 19.—Pressure distribution and compression shock total-pressure loss for the N. A. C. A. 4412 airfoil.  $\alpha = -0^\circ 15'$ .



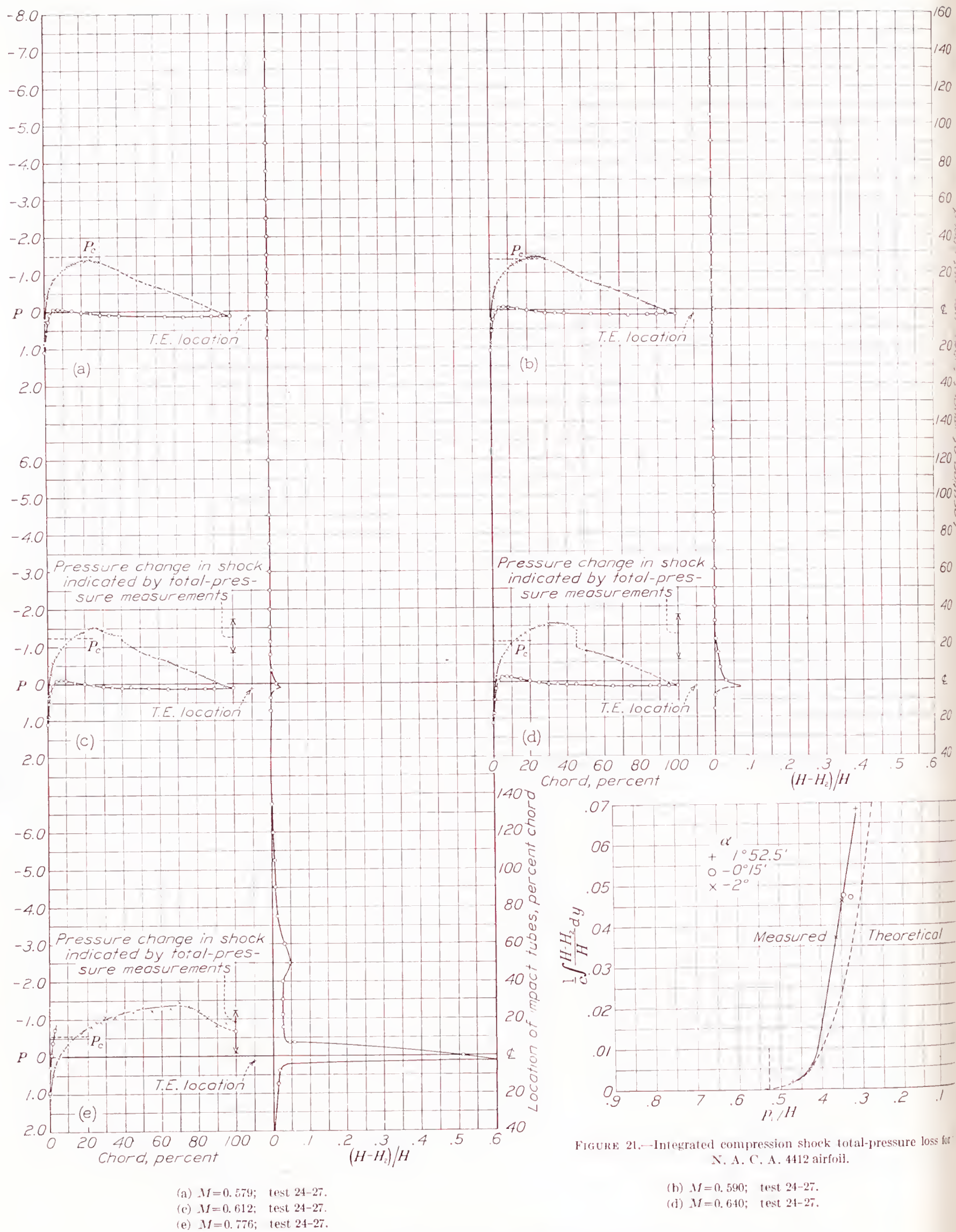


FIGURE 21.—Integrated compression shock total-pressure loss for N. A. C. A. 4412 airfoil.

FIGURE 20.—Pressure distribution and compression shock total-pressure loss for the N. A. C. A. 4412 airfoil.  $\alpha = 1^\circ 52.5'$ .



kinetic energy dissipated in the shock. Considerable further investigation appears necessary before complete understanding of the compressibility-burble phenomenon can be achieved.

### THE CRITICAL SPEED

It is apparent from the preceding discussion that the most important detrimental effects arising from compressibility phenomena do not appear until the critical speed is reached. It is important to know the value of the critical speed for many applications, such as propeller problems and future high-speed aircraft, particularly those designed to operate at altitudes where, owing to the low temperature, the speed of sound is low. The theory thus far developed is not explicit and the first work of consequence was the electric analogy used by G. I. Taylor (references 13 and 14). From this method Taylor found that, when approximately the local speed of sound was attained, the theoretical potential flow failed. Further analytical examination (references 15 and 16) indicated that certain hypothetical flows could exceed the speed of sound without compression shock but by only a few percent. For engineering approximation, this work indicates that the critical speed can be taken as the value of the translational velocity at which the sum of translational and induced velocities equals the local speed of sound.

This assumption is substantiated, in general, by the data reported herein. The kinetic-energy-loss data, nearly all of the pressure-distribution data, and the total-pressure measurements indicate that the compressibility burble occurs when the local speed of sound is reached or only slightly exceeded. Using this assumption and the relation

$$P = \frac{P_0}{\sqrt{1-M^2}}$$

where  $P_0$  is the incompressible or low-speed local-pressure coefficient, Jacobs, by placing  $P$  equal to the value corresponding to the speed of sound, devised a relation for the critical speed. (See reference 2.) The curve derived is given in figure 22. The abscissas are the low-speed or incompressible-flow values of the local-pressure coefficients and the ordinates are the critical-speed indices. A variation of this curve with abscissas equal to the thickness-chord ratios for elliptic cylinders is given in reference 17. For purposes of comparison, however, Jacobs' original curve is given. Results from these and other experiments are shown as the plotted points. The points shown for the circular cylinder are based on Stanton's pressure-distribution experiments (reference 18) and potential-flow theory, and the critical speed is based on low Reynolds Number experiments in the 11-inch high-speed wind tunnel.

All the experimental results indicate lower critical speeds than shown by the curve. The airfoil data for conditions in which the maximum negative pressure occurs near the nose indicate lower critical speeds than the other airfoil data. The reason for the difference

is the underestimation of the compressibility effect by the theoretical term  $1/\sqrt{1-M^2}$ , a detailed discussion of

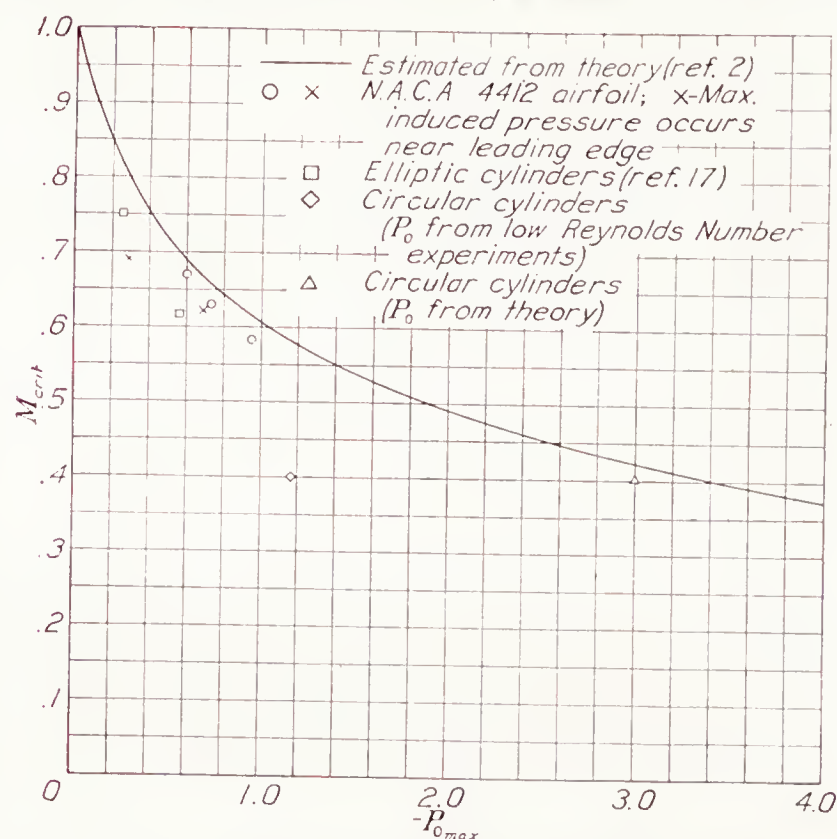


FIGURE 22.—Critical-speed ratio for various values of the maximum induced pressure reduction for compressible flow.

which has previously been given. From the variation shown by the curve and the experimental points, however, reasonably accurate estimates of the critical speed may be obtained for flows approximating two-dimensional conditions.

### CONCLUSIONS

1. The physical nature of the flow change called the compressibility burble is shown. The large drag increments occurring at high speeds are associated with the kinetic-energy losses caused by a compression shock and these losses appear in the flow as decreased total pressure.

2. The theoretical information available is applicable only for speeds below the critical, that is, below the speed at which the compression shock forms; and, even in this range, the theory appears greatly to underestimate the compressibility effect for certain conditions.

3. The data permit a reasonably accurate estimation of the critical speeds for approximately two-dimensional flows.

4. Further theoretical study and experiment are desirable to enable more accurate prediction of the critical speed for two-dimensional flow and an extension of the present knowledge to three-dimensional conditions. The fundamentals of the disturbed flow should be further investigated experimentally to determine completely the nature of the actual flow from which it may be possible to effect a delayed compressibility burble.



## REFERENCES

1. Stack, John: The Compressibility Burble. T. N. No. 543, N. A. C. A., 1935.
2. Jacobs, Eastman N.: Methods Employed in America for the Experimental Investigation of Aerodynamic Phenomena at High Speeds. Misc. Paper No. 42, N. A. C. A., 1936.
3. Stack, John: The N. A. C. A. High-Speed Wind Tunnel and Tests of Six Propeller Sections. T. R. No. 463, N. A. C. A., 1933.
4. Wood, Robert W.: Physical Optics. The Macmillan Co., 1919, pp. 94-98.
5. Pinkerton, Robert M.: Calculated and Measured Pressure Distributions over the Midspan Section of the N. A. C. A. 4412 Airfoil. T. R. No. 563, N. A. C. A., 1936.
6. Jacobs, Eastman N., and Abbott, Ira H.: The N. A. C. A. Variable-Density Wind Tunnel. T. R. No. 416, N. A. C. A., 1932.
7. Glauert, H.: The Effect of Compressibility on the Lift of an Aerofoil. R. & M. No. 1135, British A. R. C., 1928.
8. Ackert, J.: Über Luftkräfte bei sehr grossen Geschwindigkeiten insbesondere bei ebenen Strömungen. *Helvetica Physica Acta*, vol. I, fasci. Quintus, 1928, pp. 301-322.
9. Theodorsen, Theodore: Theory of Wing Sections of Arbitrary Shape. T. R. No. 411, N. A. C. A., 1931.
10. Kaplan, Carl: Two-Dimensional Subsonic Compressible Flow past Elliptic Cylinders. T. R. No. 624, N. A. C. A., 1938.
11. Pinkerton, Robert M.: The Variation with Reynolds Number of Pressure Distribution over an Airfoil Section. T. R. No. 613, N. A. C. A., 1938.
12. Stodola, A.: Steam and Gas Turbines. Vols. I and II. McGraw-Hill Book Co., Inc., 1927.
13. Taylor, G. I., and Sharman, C. F.: A Mechanical Method for Solving Problems of Flow in Compressible Fluids. R. & M. No. 1195, British A. R. C., 1929.
14. Taylor, G. I.: Report on Progress during 1927-28 in Calculation of Flow of Compressible Fluid, and Suggestions for Further Work. R. & M. No. 1196, British A. R. C., 1929.
15. Taylor, G. I.: The Flow of Air at High Speeds past Curved Surfaces. R. & M. No. 1381, British A. R. C., 1930.
16. Taylor, G. I.: Some Cases of Flow of Compressible Fluids. R. & M. No. 1382, British A. R. C., 1931.
17. Lindsey, W. F.: Drag of Cylinders of Simple Shapes. T. R. No. 619, N. A. C. A., 1938.
18. Stanton, T. E.: On the Effect of Air Compression on Drag and Pressure Distribution in Cylinders of Infinite Aspect Ratio. R. & M. No. 1210, British A. R. C., 1929.



## REPORT No. 647

### TESTS OF N. A. C. A. 0009, 0012, AND 0018 AIRFOILS IN THE FULL-SCALE TUNNEL

By HARRY J. GOETT and W. KENNETH BULLIVANT

#### SUMMARY

*An investigation was conducted in the N. A. C. A. full-scale wind tunnel to determine the aerodynamic characteristics of the N. A. C. A. 0009, 0012, and 0018 airfoils, with the ultimate purpose of providing data to be used as a basis for comparison with other wind-tunnel data, mainly in the study of scale and turbulence effects. Three symmetrical 6- by 36-foot rectangular airfoils were used. The Reynolds Number range for minimum drag was from 1,800,000 to 7,000,000 and for maximum lift, from 1,700,000 to 4,500,000. The effect of rounded tips was determined for each of the airfoils. Tests were also made of the N. A. C. A. 0012 airfoil equipped with a 0.20c full-span split flap hinged at 0.80c. Tuft surveys were included to show the progressive breakdown of flow near maximum lift.*

*Momentum surveys were made in conjunction with force measurements at zero lift as an aid in converting force-test data to section coefficients.*

#### INTRODUCTION

Since the inception of wind-tunnel testing, the problem of correcting and applying test results to full-scale flight conditions has existed. Theory indicates that no corrections are necessary when all the conditions of dynamic similitude are satisfied. One of the conditions of similarity, Reynolds Number, was met by the N. A. C. A. variable-density tunnel, in which tests are conducted at Reynolds Numbers in the lower flight range; however, experiments still revealed discrepancies due in part to dissimilarities in turbulence between wind tunnels and free air. Turbulence measurements in the N. A. C. A. wind tunnels resulted in the use of the "effective Reynolds Number" (references 1 and 2) in an attempt to improve the precision of applying data obtained in wind tunnels with high turbulence to flight conditions. The data upon which the effective Reynolds Number correction was based were, however, limited to conventional airfoils of medium thickness and did not include the variation of the effect of turbulence with thickness ratio and other airfoil characteristics. In order to provide data that would afford a broader basis for comparison and assist in improving the turbulence correction, the present investi-

gation was conducted on symmetrical airfoils of N. A. C. A. 0009, 0012, and 0018 sections. The tests were made in the N. A. C. A. full-scale wind tunnel, which is known to have low turbulence and to provide a close approach to free-flight conditions.

In addition to force tests of the plain airfoils, the N. A. C. A. 0012 airfoil was tested with a 0.20c full-span split flap. The Reynolds Number range was from 1,700,000 to 7,000,000. Momentum measurements, made in the wakes of all three airfoils, were used to evaluate the drag caused by the airfoil tips and thus to obtain section drag characteristics. The data obtained in this investigation are presented in order to make them available for comparison and analysis.

#### EQUIPMENT AND AIRFOILS

A description of the full-scale wind tunnel and of its test equipment is given in reference 3. The turbulence



FIGURE 1.—The N. A. C. A. 0012 airfoil mounted in the full-scale wind tunnel.

factor of the tunnel as determined by sphere tests is 1.1 (reference 1).

During the tests, the airfoils were mounted with the main support attached at the quarter-chord point of the airfoils (fig. 1). The angle of attack was changed by a vertical movement of the lower ends of the rear supports.



Three 6- by 36-foot rectangular airfoils having N. A. C. A. 0009, 0012, and 0018 symmetrical sections were constructed for these tests. The airfoils were of



FIGURE 2.—Detachable rounded tip for the N. A. C. A. 0009 airfoil.

steel-spar construction with ribs spaced at 12-inch intervals. The covering was  $\frac{1}{16}$ -inch aluminum sheets, attached with countersunk screws. The seams and



FIGURE 3.—The N. A. C. A. 0012 airfoil with 0.20c full-span split flap.

the screw slots were filled and the entire surface was then sanded, coated with paint primer, and polished to a glossy, wax-like finish. Tolerances on the section ordinates were kept within  $\pm \frac{1}{32}$  inch.

Detachable rounded tips were provided for each airfoil. These tips, shown in figure 2, formed one-half of a solid of revolution, the radius at each chordwise station being equal to one-half of the local airfoil thickness.

A full-span 0.20c split flap constructed of  $\frac{1}{4}$ -inch plywood was provided for the N. A. C. A. 0012 airfoil. Figure 3 shows the flap mounted on the airfoil.

The rack used for the momentum measurements (fig. 4) consisted of a comb of total-head tubes and comb of static tubes. These combs were placed inches apart and the entire assembly was mounted on the survey carriage. The detailed spacing and the



FIGURE 4.—Views of the rack used for momentum measurements.

dimensions of both combs are shown in figure 5. The total-head comb consisted of 39 tubes of 0.065-inch outside diameter by 0.036-inch inside diameter; the static comb consisted of 13 tubes of 0.125-inch outside diameter. Each tube was connected to the multipoint tube, photographic-recording manometer carried in the survey carriage.

#### TESTS

Tare and interference were evaluated by preliminary tests of the airfoils. The tare tests to determine the forces on the supports were made with the airfoil supported independently of the balance by cables. The interference of the supports on the air flow was measured by adding two dummy support struts, shown in figure 6, which were free from contact with the airfoil.



Lift, drag, and pitching moments of the airfoils with square tips were measured at test velocities from 25 to 118 miles per hour over a range of angles of attack from  $-7^\circ$  to  $27^\circ$ . Similar runs were made with the rounded tips on the airfoils at a sufficient number of speeds to afford comparison with the tests of the airfoils with square tips. The N. A. C. A. 0012 airfoil was also tested with a 0.20c full-span split flap deflected  $15^\circ$ ,  $30^\circ$ ,  $45^\circ$ , and  $60^\circ$ . Wool tufts were used to indicate the progression of the stall on the upper surfaces of the airfoils.

By means of the rack previously described, simultaneous measurements were made of the total and the static pressures in the wakes of the airfoils for the zero-

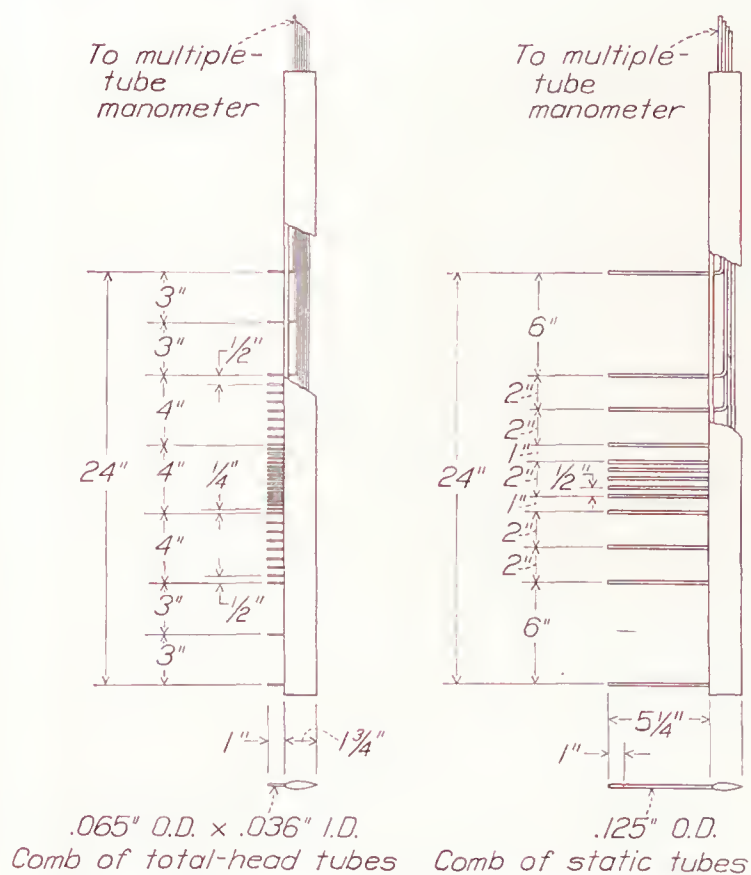


FIGURE 5.—Combs of total-head tubes and static tubes.

lift condition. The measurements were made 15 percent of the chord behind the trailing edge at 27 span-wise locations.

#### REDUCTION OF DATA

The measured wind-tunnel data were corrected in the following manner:

Dynamic pressure was determined from the difference in static pressure between two points in the tunnel. This difference was correlated with the free-stream dynamic pressure at the airfoil location (jet empty); the correlation was then modified for the blocking effect of the airfoil, as outlined in reference 4.

In the computation of the coefficients for the airfoils with rounded tips, the added area of the tips was not included. All coefficients are thus based on the original rectangular area of the square-tip airfoils.

Tare and interference coefficients were deducted from the gross coefficients. Owing to the small portions of the supporting struts exposed to the air stream,

the tare drag is only about 7 percent of the net minimum drag of the airfoils at a test speed of 100 miles per hour. The interference correction was larger; for the thickest airfoil, interference drag was equal to 13 percent of the net drag for the test speed of 100 miles per hour. A small tare and interference correction was required for the pitching moment, but no correction was required for lift.

Pitch-angle surveys in the region of the jet occupied by the airfoils showed an average stream downflow of  $0.6^\circ$ . This value was corroborated by the force tests in that the angle of zero lift was  $0.6^\circ$  with respect to the tunnel axis. Because the scales measured force components perpendicular and parallel to the tunnel axis, these components were corrected to obtain true



FIGURE 6.—Dummy supports added to the N. A. C. A. 0009 airfoil set-up for the interference tests.

lift and drag components with reference to the air stream.

The jet-boundary corrections, as evaluated for the full-scale tunnel in reference 4, were applied.

Coefficients for infinite aspect ratio were derived from the corrected results of the tests of the rounded-tip airfoils of aspect ratio 6 by the formulas:

$$\alpha_0 = \alpha - \frac{C_L}{\pi A} (1 + \tau) 57.3$$

$$C_{D_0} = C_D - \frac{C_L^2}{\pi A} (1 + \sigma)$$

where

$\alpha_0$  is angle of attack for infinite aspect ratio, degrees.

$C_{D_0}$ , profile-drag coefficient.

$A$ , aspect ratio.

$\tau$ , a factor correcting the induced angle of attack to allow for the change from elliptical span loading to a span loading for an airfoil with rectangular plan form.



$\sigma$ , a factor correcting the induced drag to allow for the change from elliptical span loading to a span loading for an airfoil with rectangular plan form.

Values of  $\tau=0.176$  and  $\sigma=0.051$  for aspect ratio 6 were obtained from figure 7 of reference 5.

A deduction for the tip drag obtained from the momentum measurements was also made to obtain the true section drag. (The variation in this correction with thickness ratio for both rounded-tip and square-tip airfoils is shown in fig. 17.) This correction is strictly valid only at the angle of zero lift but is assumed constant throughout the entire angle-of-attack range.

No correction is required for static-pressure gradient in the stream jet because it is so small that the resulting decrement in drag is within the precision of the scales.

No effective Reynolds Number correction is applied because (1) maximum lift coefficients obtained on airplanes in flight and in the full-scale tunnel are in good agreement (references 2, 3, and 6); and (2) there are no known corrections to be applied to profile drag for the small amount of turbulence existing in the jet of the full-scale wind tunnel. An investigation is now being made in which it is planned to compare the section profile-drag coefficients obtained by the momentum method in flight and in the tunnel.

The computation of the section profile-drag coefficients from the momentum data was based on the theory given in the appendix. The formula used was

$$c_{d0} = 2 \int \frac{\sqrt{H-P}}{\sqrt{H_0-P_0}} \left( 1 - \frac{\sqrt{H-P_0}}{\sqrt{H_0-P_0}} \right) d(y/c)$$

where

$H$  is the total pressure in the wake.

$P$ , static pressure in the wake.

$H_0$ , free-stream total pressure.

$P_0$ , free-stream static pressure.

$y$ , vertical displacement from the trailing edge of the airfoil.

$c$ , airfoil chord.

The method of computation was as follows:

1. The values of  $H$  and  $P$  were determined from faired curves of total and static pressures across the wake profile, to which a correction was applied to allow for the vertical gradients existing in the tunnel. The values of  $H_0$  and  $P_0$  were determined from total-head- and static-tube readings taken well outside the wake with a proper calibration applied to obtain the free-stream values of these quantities.

2. The quantity

$$2 \frac{\sqrt{H-P}}{\sqrt{H_0-P_0}} \left( 1 - \frac{\sqrt{H-P_0}}{\sqrt{H_0-P_0}} \right)$$

was then plotted against  $y/c$ . This curve was integrated, the summation being the section profile-drag coefficient at the station of measurement.

#### ACCURACY

An estimate follows of the precision of the final results, based upon a consideration of the accuracy of the measurements of air-stream velocity, balance reading and angle-of-attack setting and the probable errors of the applied corrections.

$$\alpha, \pm 0.1^\circ.$$

$$C_{L_{max}}, \pm 0.03.$$

$$\frac{dC_L}{d\alpha}, \pm 0.0015 \text{ per degree.}$$

$$C_{D_0}, \pm 0.0002 (C_L=0).$$

$$C_{D_0}, \pm 0.0015 (C_L=1.0).$$

$$C_{m_{c/4}}, \pm 0.003.$$

#### RESULTS AND DISCUSSION

The principal aerodynamic characteristics of the N. A. C. A. 0009, 0012, and 0018 square-tip airfoils aspect ratio 6 are given in figures 7, 8, and 9 for an average Reynolds Number of 3,400,000. Lift and drag coefficients for the airfoils with rounded tips are also given. The corresponding section characteristics are presented in figure 10. Table I gives a summary of the results for the square-tip airfoils over a Reynolds Number range from 1,700,000 to 7,000,000.

TABLE I  
IMPORTANT CHARACTERISTICS OF SQUARE-TIP AIRFOILS OF ASPECT RATIO 6

N. A. C. A. airfoil	Reynolds Number (millions)	$C_{L_{max}}$	$\alpha$ at $C_{L_{max}}$ (deg.)	$\frac{dC_L}{d\alpha}$	$C_{D_{min}}$	$\left(\frac{L}{D}\right)_0$
0009-----	1.8	1.09	16.2	0.071	0.0066	-----
	3.0	1.20	17.1	.071	.0062	24
	5.0	1.26	17.7	.071	.0060	-----
	7.0	-----	-----	.072	.0058	-----
0012-----	1.8	1.22	17.6	.072	.0071	-----
	3.0	1.33	18.9	.072	.0069	24
	5.0	-----	-----	.073	.0066	-----
	7.0	-----	-----	.074	.0064	-----
0018-----	1.8	1.15	17.8	.070	.0091	-----
	3.0	1.26	18.4	.071	.0085	21
	5.0	1.36	19.6	.072	.0082	-----
	7.0	-----	-----	.073	.0078	-----
0012; 60°, 0.20c split flap-----	1.7	2.10	17.7	-----	-----	5
	2.2	2.14	18.2	-----	-----	5
	3.0	2.21	19.6	.074	-----	5
	4.0	2.28	20.4	-----	-----	5

Figures 7 to 9 show a marked decrease in the sharpness of the stall of the N. A. C. A. 0018 airfoil as compared with the thinner sections. Figures 11, 12, and 13, which show the history of the flow in the region the stall for the three airfoils, offer an explanation of this phenomenon. It will be noted that, for the N. A. C. A. 0018 airfoil, the initial breakaway of flow precedes the angle of attack at maximum lift to a greater extent than it does for the N. A. C. A. 0009 and 0012 airfoils and that the spread of the stalled region is much more gradual. The lack of a "hysteresis" loop for the N. A. C. A. 0018 airfoil may also be explained by the fact that the unstalled flow is more readily reestablished on an airfoil which stalls "gradually." Comparisons of force tests with and without tufts show negligible differences, justifying the assumption that the tufts cause no important change in the character of the flow.



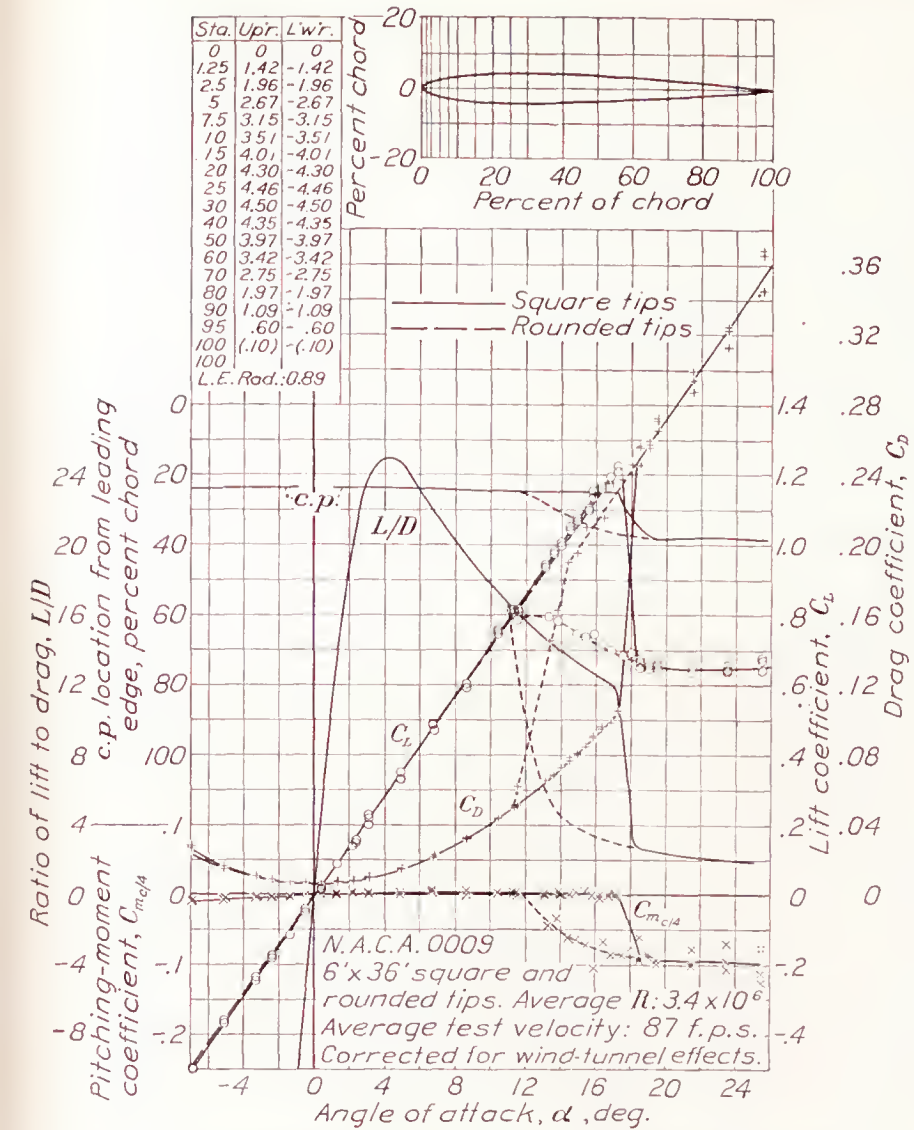


FIGURE 7.—Characteristics of the N. A. C. A. 0009 airfoil of aspect ratio 6.

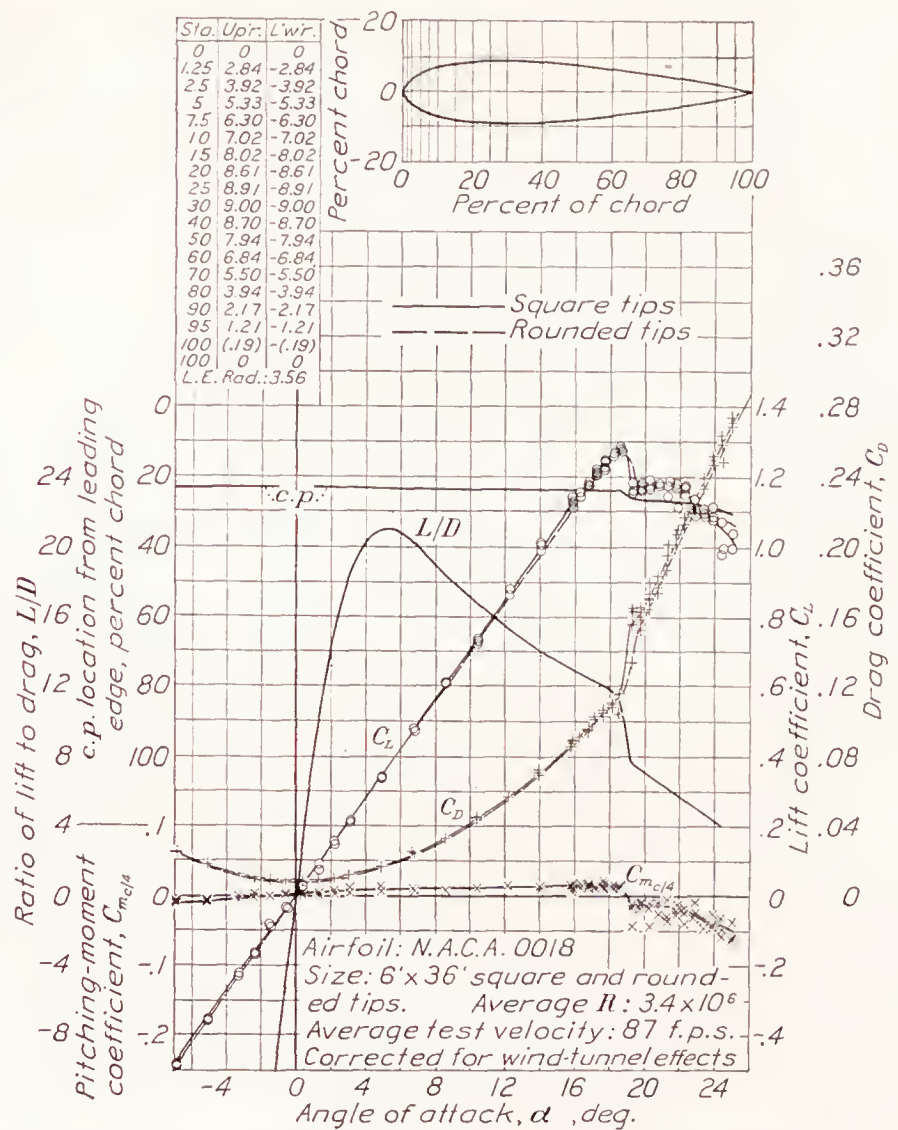


FIGURE 9.—Characteristics of the N. A. C. A. 0018 airfoil of aspect ratio 6.

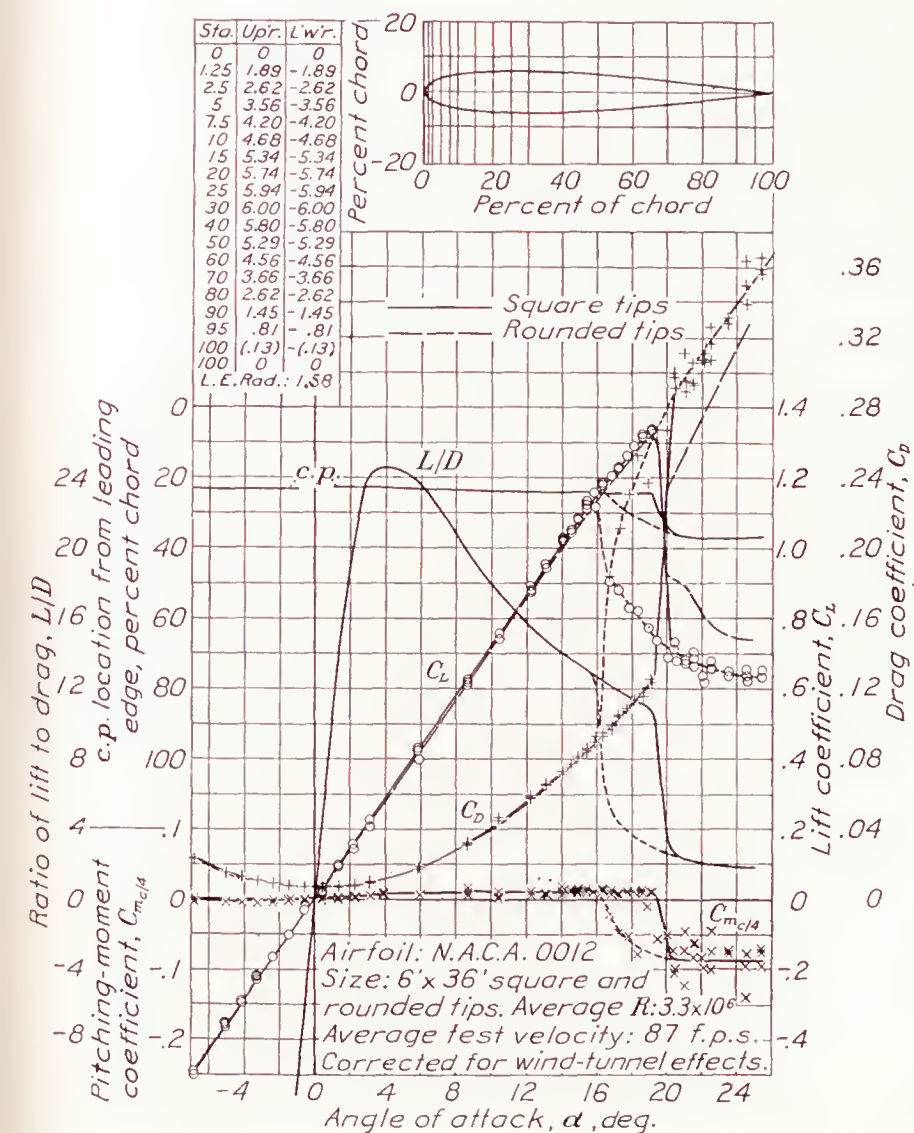


FIGURE 8.—Characteristics of the N. A. C. A. 0012 airfoil of aspect ratio 6.

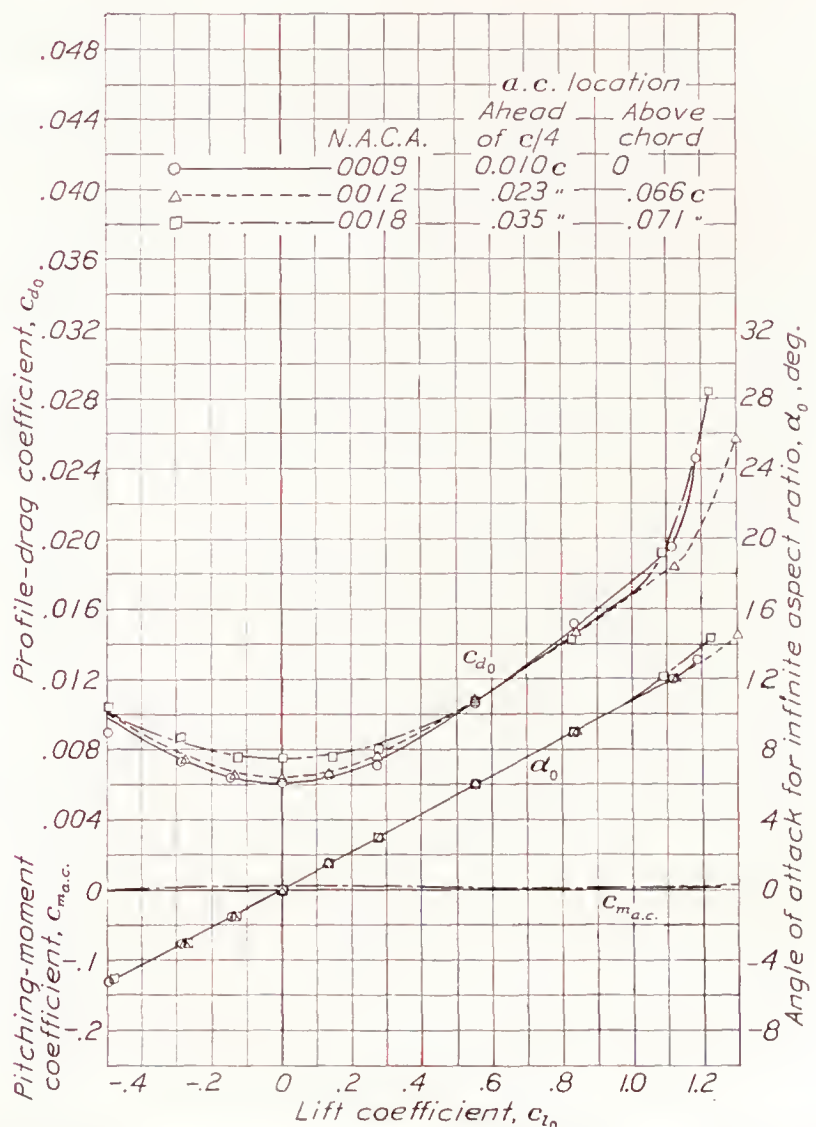


FIGURE 10.—Section characteristics of the N. A. C. A. 0009, 0012, and 0018 airfoils at a Reynolds Number of 3,400,000.



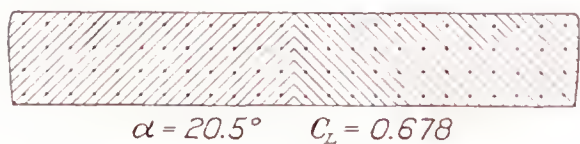
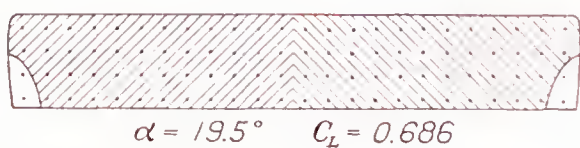
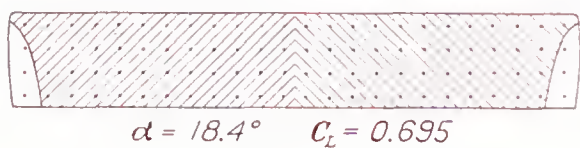
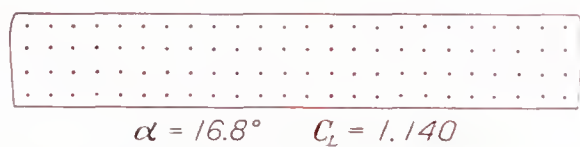
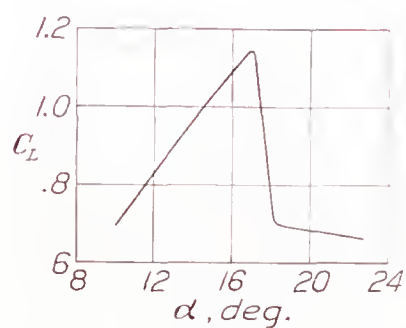


FIGURE 11.—The N. A. C. A. 0009 airfoil.

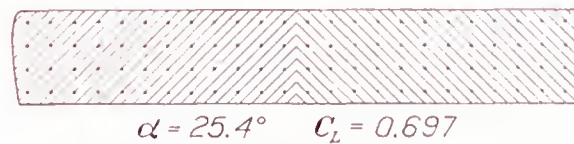
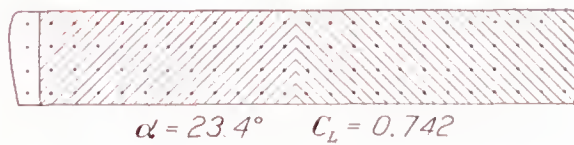
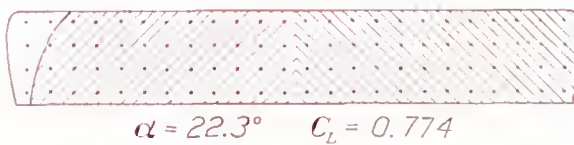
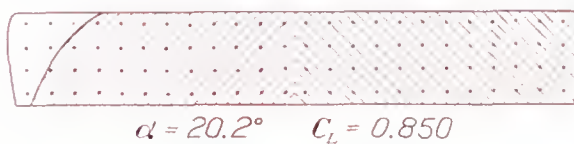
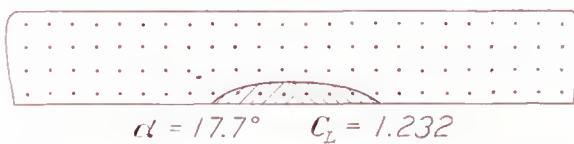
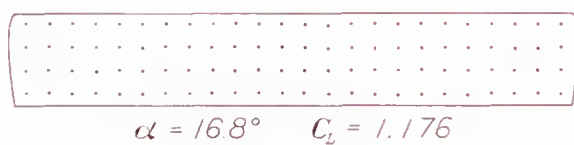
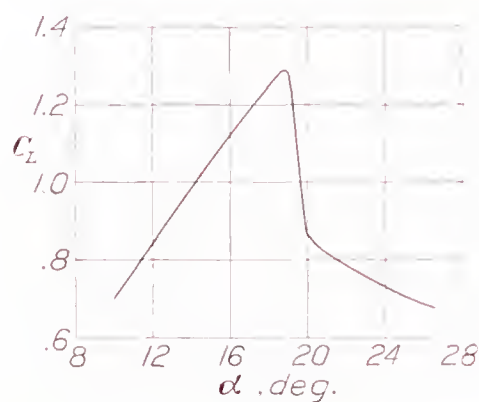


FIGURE 12.—The N. A. C. A. 0012 airfoil.

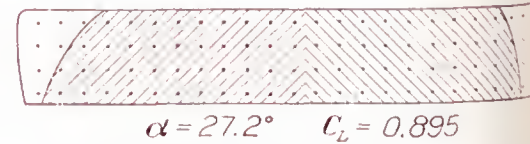
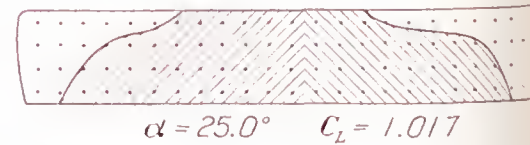
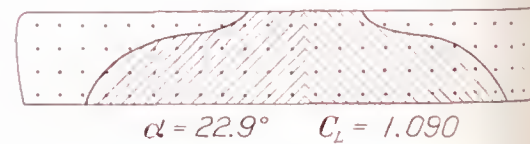
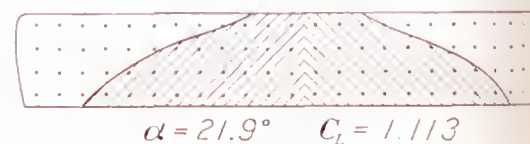
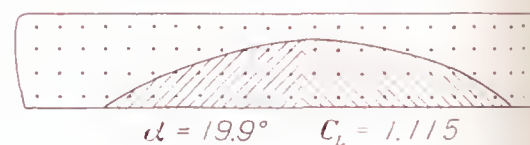
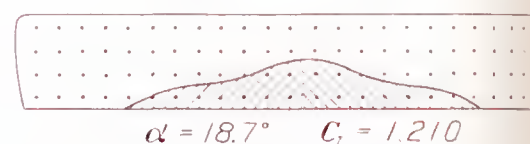
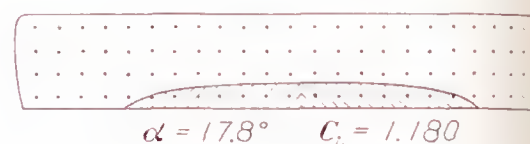
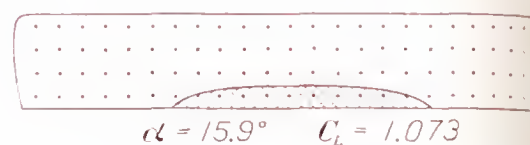
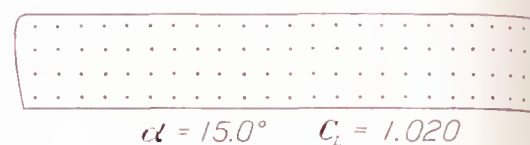
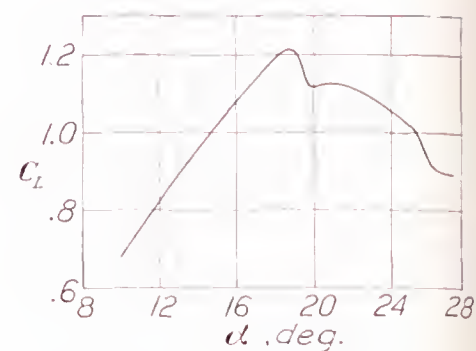


FIGURE 13.—The N. A. C. A. 0018 airfoil.

FIGURES 11 TO 13.—Stalling contours of three N. A. C. A. airfoils with rounded tips. Approximate test velocity, 84 f. p. s. Cross-hatched areas indicate stalled region.



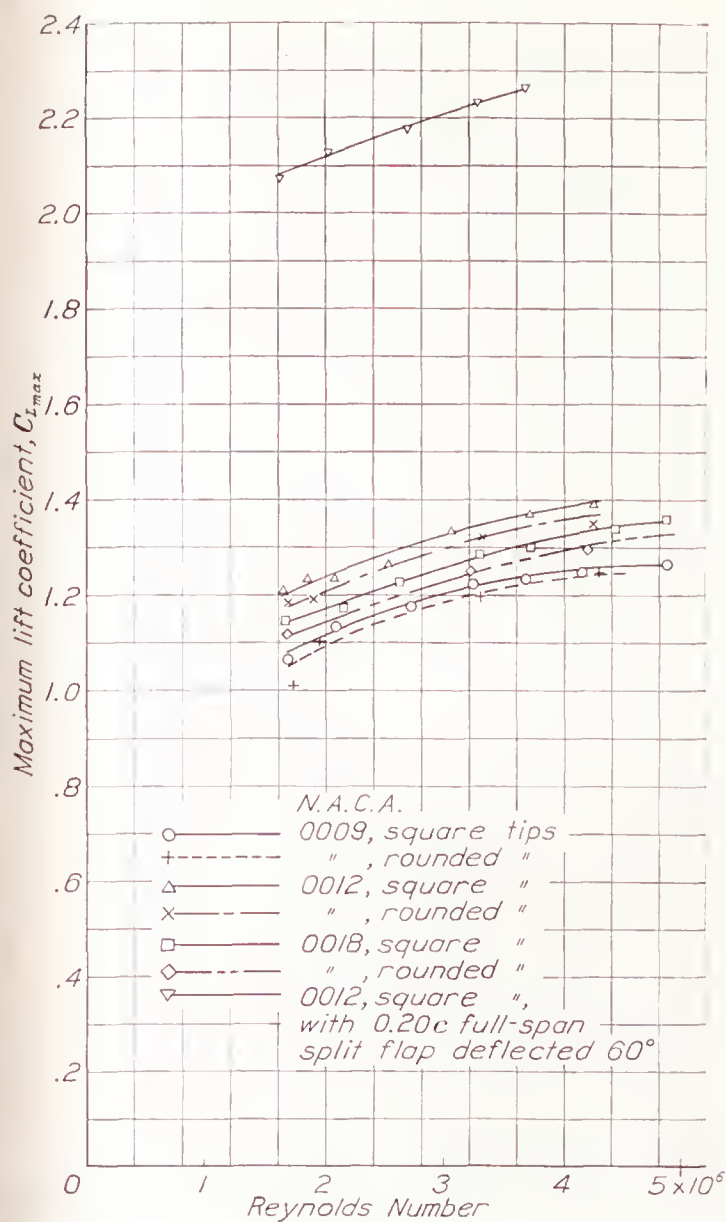


FIGURE 14.—Variation of maximum lift with Reynolds Number for the N. A. C. A. 0009, 0012, and 0018 airfoils of aspect ratio 6.

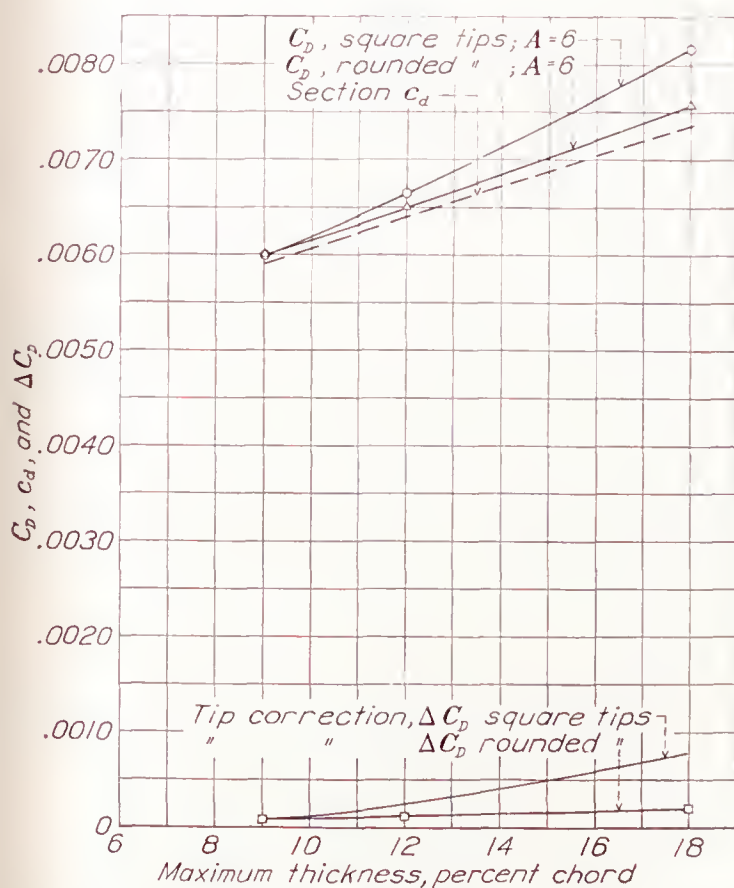


FIGURE 17.—Effect of thickness on profile-drag coefficient and tip correction for airfoils of aspect ratio 6 at zero lift and at a Reynolds Number of 5,000,000.

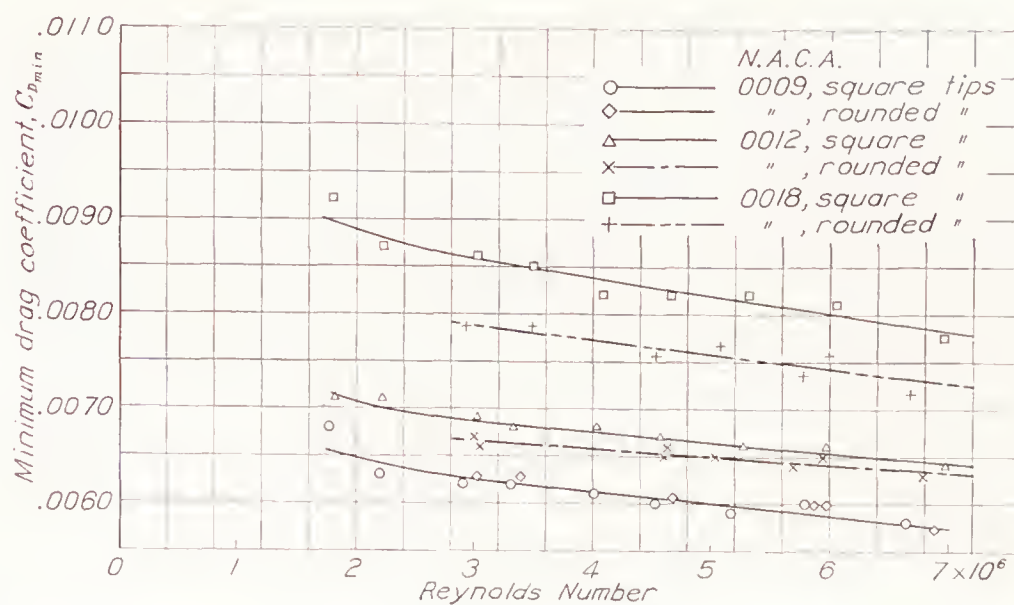


FIGURE 15.—Variation of minimum drag with Reynolds Number for the N. A. C. A. 0009, 0012, and 0018 airfoils of aspect ratio 6.

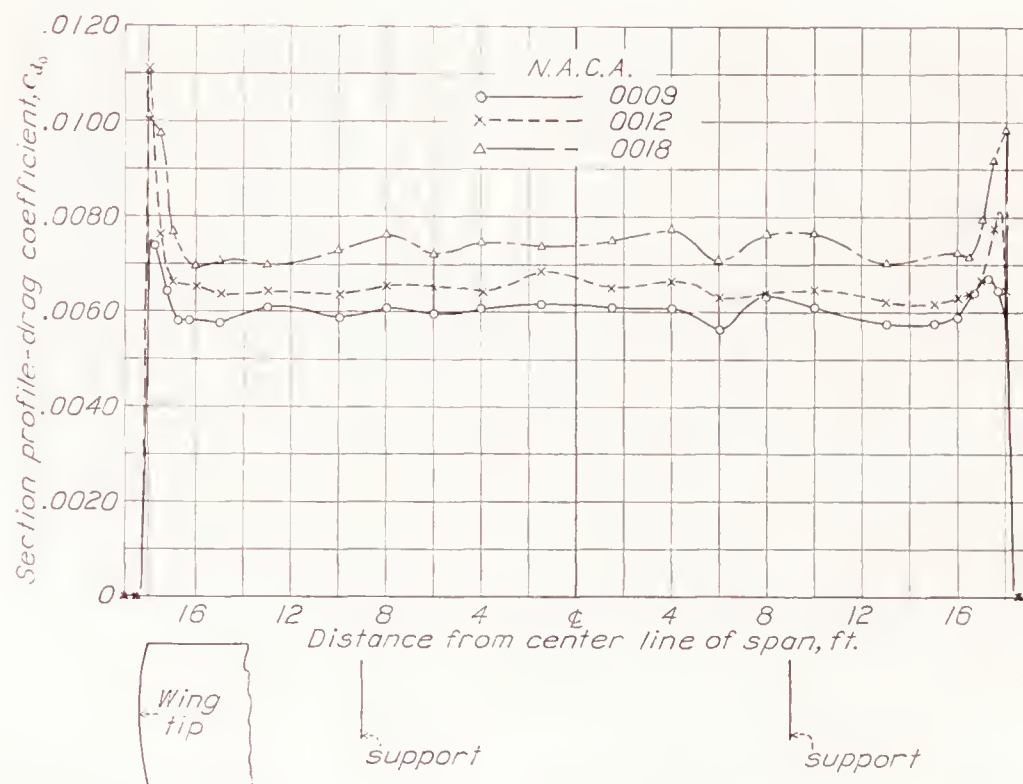


FIGURE 16.—Variation of section profile-drag coefficient across the spans of three rounded-tip airfoils of aspect ratio 6 at zero lift.

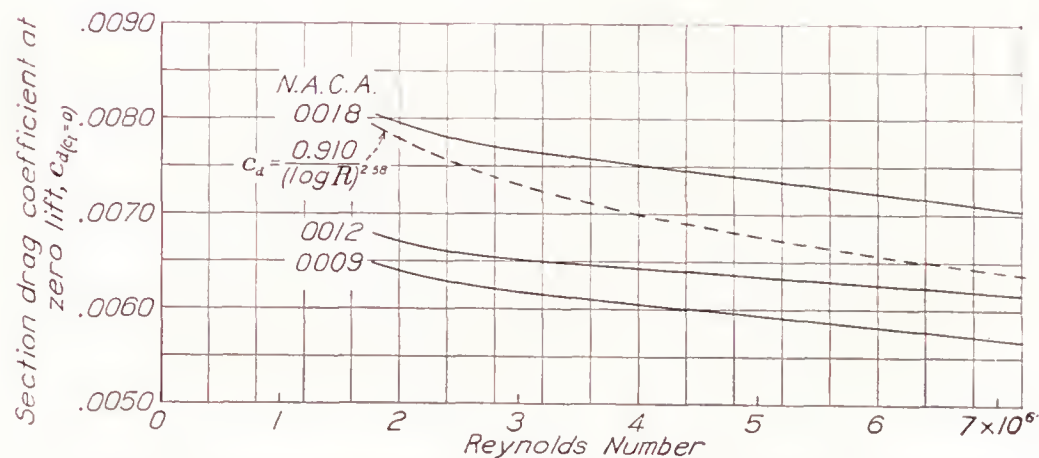


FIGURE 18.—Variation of section drag coefficient with Reynolds Number at zero lift.



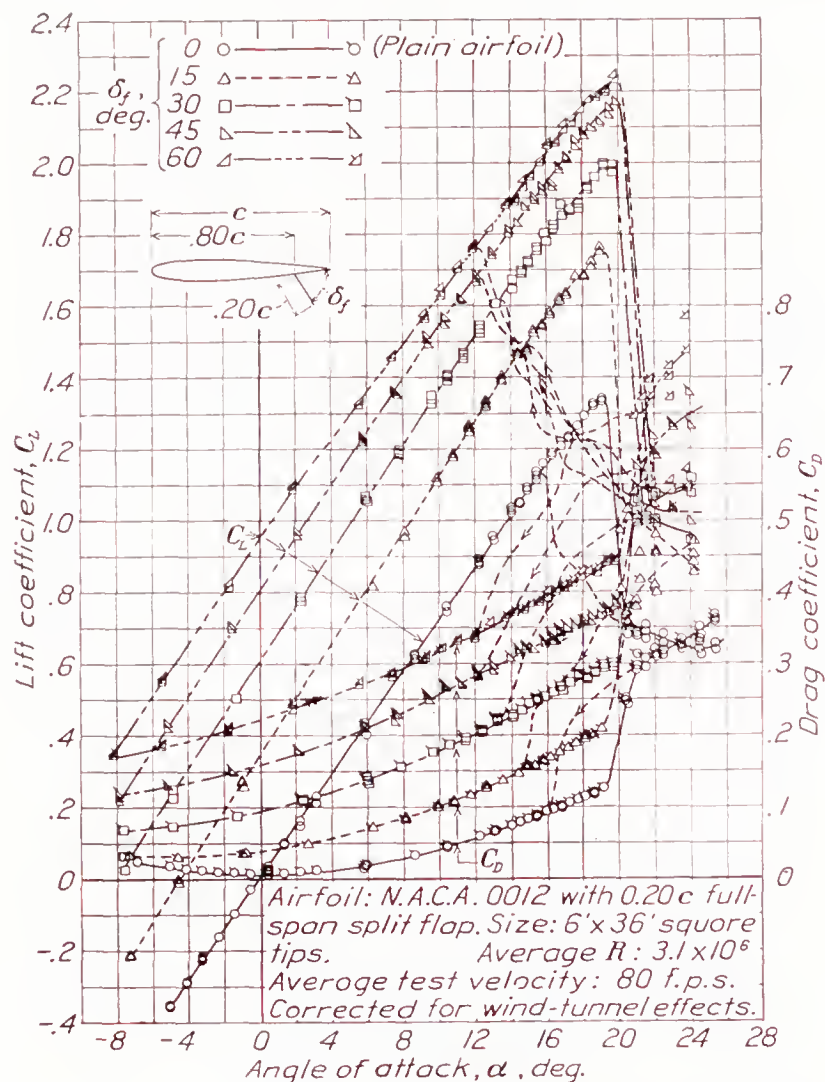


FIGURE 19.—Characteristics of the square-tip N. A. C. A. 0012 airfoil of aspect ratio 6 with a 0.20c full-span split flap.

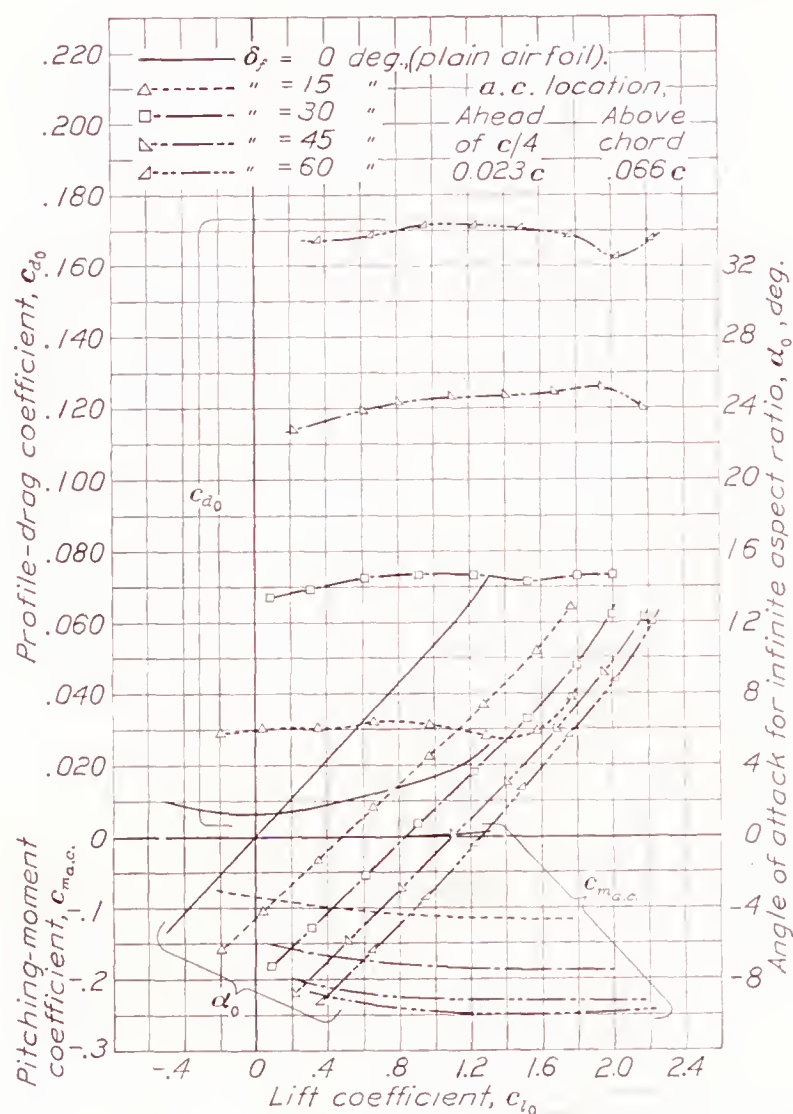
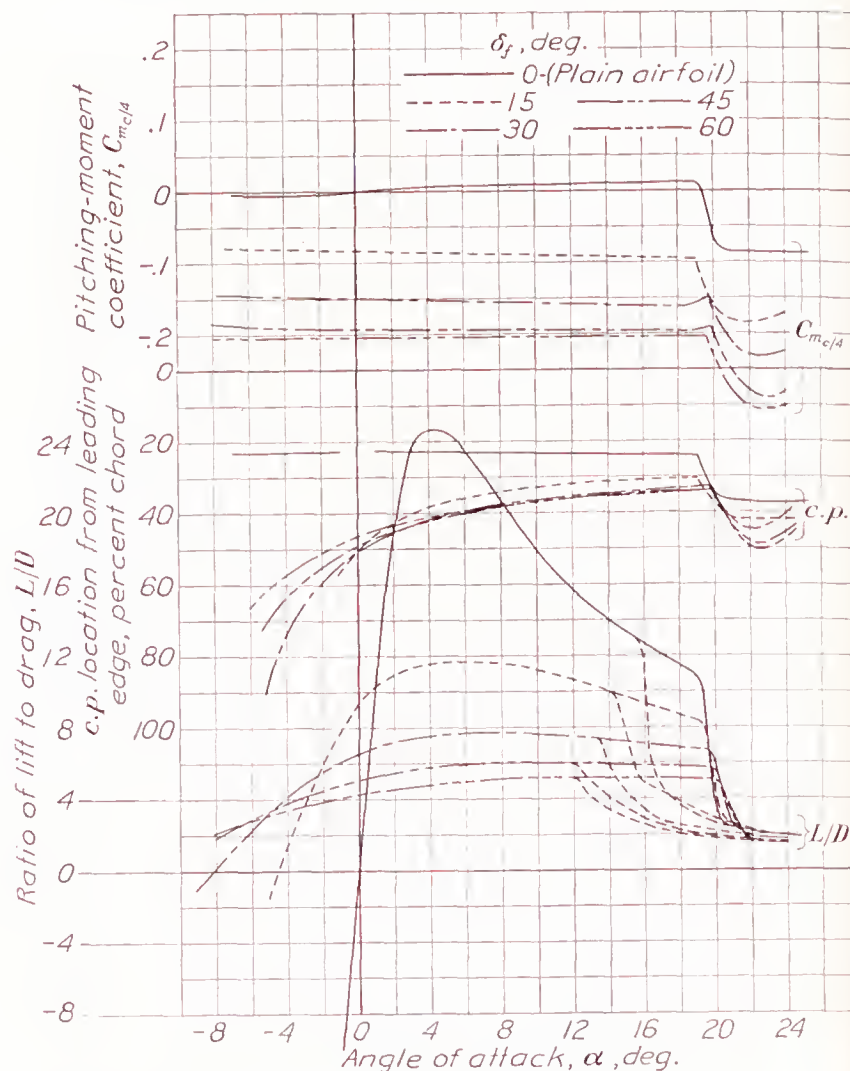


FIGURE 20.—Section characteristics of the N. A. C. A. 0012 airfoil with a 0.20c full-span split flap at a Reynolds Number of 3,100,000.



The effect of Reynolds Number on the maximum lift and the minimum drag coefficients of the three airfoils and of the N. A. C. A. 0012 airfoil with the 0.20c full-span split flap deflected 60° is shown in figures 14 and 15. It will be noted that the addition of the rounded tips to the airfoils causes a decrease in the maximum lift coefficient varying from about 2.5 percent for the N. A. C. A. 0018 airfoil to about 1.5 percent for the N. A. C. A. 0009 airfoil.

The variation in section profile-drag coefficient across the span of the three rounded-tip airfoils, as measured at zero lift by the momentum method, is shown in figure 16. The over-all profile drag obtained by an integration across the span of the airfoils compares with that measured by force tests, as shown in table II

TABLE II

COMPARISON OF PROFILE-DRAG COEFFICIENTS FOR THE ROUNDED-TIP AIRFOILS OF ASPECT RATIO 6 OBTAINED AT ZERO LIFT BY THE FORCE TESTS AND THE MOMENTUM METHOD.  $R=5,000,000$

N. A. C. A. airfoil	$C_{D_0}$	
	Momentum test	Force test
0009	0.0061	0.0060
0012	.0066	.0065
0018	.0075	.0076



This agreement is within the experimental accuracy of the momentum method and is sufficient to warrant the conclusion that this method satisfactorily measures profile drag at zero lift. The maximum variation of  $\pm 0.0002$ , which will be noted in the individual section coefficients across the span of the airfoils (fig. 16), is attributed to a combination of experimental error and unavoidable differences that existed in the surfaces at the various stations. Designers should note that the airfoils used for this investigation, as in all wind-tunnel investigations of airfoil characteristics, were appreciably smoother than wings commonly used in airplane construction.

The increase in drag caused by the rounded tips, shown in figure 16, indicates that something in excess of the section drag is measured by the force test. A comparison between the over-all profile-drag coefficient of the airfoil of aspect ratio 6 and the section profile-drag coefficient is shown in table III. The section profile drag was considered the average across the airfoil inboard of the area affected by the tips. The correction for the tip drag is thus derived from the difference between the section and the over-all profile-drag coefficients. The section drag is obtained by deducting the tip correction shown in figure 17 and given in table III from the force-test results obtained for the rounded-tip airfoil. No appreciable variation in tip drag was noted over a range of Reynolds Numbers between 3,000,000 and 5,000,000.

TABLE III

TIP CORRECTIONS FOR THE ROUNDED-TIP AIRFOILS OF ASPECT RATIO 6 FROM MOMENTUM TEST.  $R=5,000,000$

N. A. C. A. airfoil	$C_{D_0}$	$c_{d_0}$	Rounded-tip drag, $\Delta C_D$
0009	0.0061	0.0060	0.0001
0012	.0066	.0065	.0001
0018	.0075	.0073	.0002

Figure 17 also shows the variation of this tip correction with profile thickness for the square-tip airfoils of aspect ratio 6. The supplementary drag caused by the square tips varies from zero for the airfoil of 9 percent thickness to 13 percent of the minimum drag for the airfoil of 18 percent thickness. Thus the results for square-tip airfoils, when uncorrected for tip drag,

greatly magnify the increase of drag with profile thickness.

Figure 18 gives the variation of section drag at zero lift with Reynolds Number, obtained by applying the proper tip correction to the results given in figure 15.

The aerodynamic characteristics of the N. A. C. A. 0012 airfoil with the full-span  $0.20c$  split flap for flap deflections of  $0^\circ$ ,  $15^\circ$ ,  $30^\circ$ ,  $45^\circ$ , and  $60^\circ$  at a Reynolds Number of 3,100,000 are given in figure 19. Figure

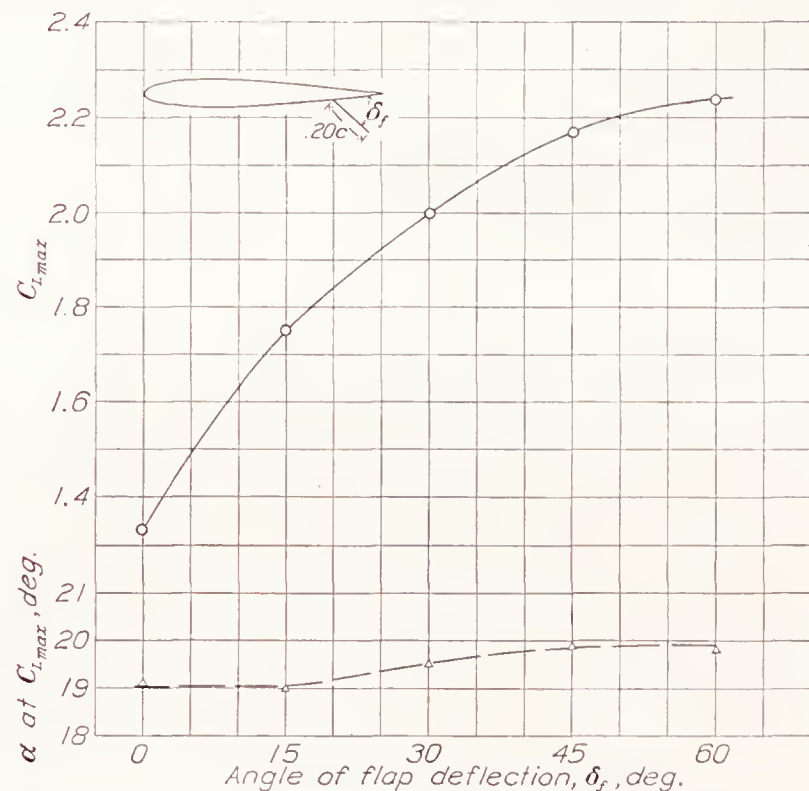


FIGURE 21.—Variation of maximum lift and angle of attack at maximum lift with flap deflection at a Reynolds Number of 3,100,000 for the square-tip N. A. C. A. 0012 airfoil of aspect ratio 6.

20 gives the corresponding section characteristics and figure 21 shows the variation of the maximum lift coefficient and of the angle of attack at maximum lift with flap deflection.

At the present time, the data herein presented and those available from other sources are being compared with a view toward determining the cause and magnitude of existing discrepancies.

LANGLEY MEMORIAL AERONAUTICAL LABORATORY,  
NATIONAL ADVISORY COMMITTEE FOR AERONAUTICS,  
LANGLEY FIELD, VA., July 28, 1938.



## APPENDIX

The computation of drag from the momentum data was made by the method developed by B. Melvill Jones (reference 7). A comparison was made between the drag values given by this method and those given by the method developed by Betz (reference 8). The maximum difference in the profile-drag coefficient was found to be no greater than  $\pm 0.0001$ , when the computations were based on the same data. The Jones method was used because of the greater simplicity of the computations required.

Except for minor changes in notation, the derivation of the Jones momentum equation, as developed in reference 7, is as follows:

Consider an airfoil in a free stream of velocity  $U$ , with a drag  $D$  and no force component perpendicular to  $U$ . The drag experienced by the body will be caused by the change in momentum that the body imposes on the free stream. Thus in a plane AA (fig. 22), far behind the body where the static pressure

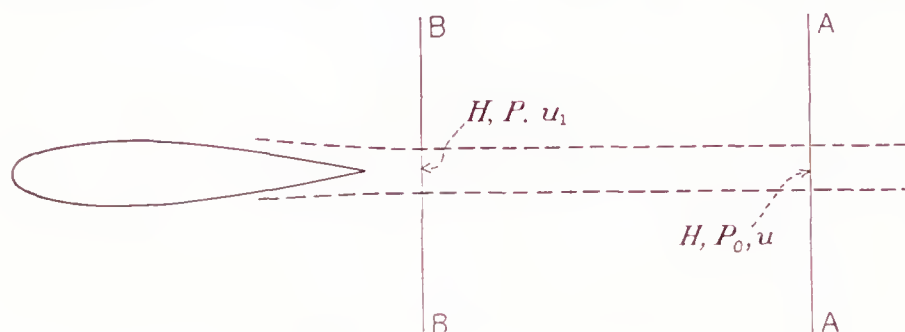


FIGURE 22.—Diagram of airfoil and wake.

is equal to that of the free stream and the velocity is parallel to  $U$ , the magnitude of the velocity is everywhere equal to  $U$  except in a well-defined wake region where it is less than  $U$ . If  $da$  is an element of area in the plane AA in the wake where the air velocity is  $u$ , the drag  $D$  is given by the equation

$$D = \rho \int \int u(U - u) da \quad (1)$$

The actual measurements are to be made in the plane BB, where the static pressure is in excess of that of the free stream. Then the mass flow across an element  $da_1$ , in the plane BB, where the velocity is  $u_1$ , is  $\rho u_1 da_1$  (neglecting the effect of angularity, which will be small). If the symbol  $u$  is retained for the velocity of flow in this tube where it passes through plane AA, the drag, which is equal to the defect of momentum crossing the whole plane AA in unit time, is given by

$$D = \rho \int \int u_1(U - u) da_1 \quad (2)$$

The assumption that *no loss of total pressure occurs in the tubes of flow between BB and AA* permits the final velocity  $u$  to be determined from the total pressure at section BB and the free-stream static pressure. In the actual flow, there is a mixing that causes a widening out of the wake as the distance from the trailing edge increases. The method presumes that this difference

between the real and the imagined flow does not influence the drag.

In order to use equation (2), it must be expressed in terms of the total- and the static-pressure measurements that will actually be made. These measurements will be:

$H$ , total pressure in wake at plane BB.

$P$ , static pressure in wake at plane BB.

$H_0$ , free-stream total pressure.

$P_0$ , free-stream static pressure.

$y$ , vertical displacement from trailing edge of airfoil.

Then

$$H_0 - P_0 = \frac{1}{2} \rho U^2$$

$$H - P = \frac{1}{2} \rho u_1^2$$

$$H - P_0 = \frac{1}{2} \rho u^2$$

Substituting for  $U$ ,  $u_1$ , and  $u$

$$D = 2 \int \int \sqrt{H - P} (\sqrt{H_0 - P_0} - \sqrt{H - P_0}) da_1 \quad (3)$$

Reduced to coefficient form, equation (3) becomes

$$c_{d0} = 2 \int \frac{\sqrt{H - P}}{\sqrt{H_0 - P_0}} \left( 1 - \frac{\sqrt{H - P_0}}{\sqrt{H_0 - P_0}} \right) d(y/c) \quad (4)$$

This equation was used in the computation of drag from the momentum data.

## REFERENCES

1. Platt, Robert C.: Turbulence Factors of N. A. C. A. Wind Tunnels as Determined by Sphere Tests. T. R. No. 558, N. A. C. A., 1936.
2. Jacobs, Eastman N., and Clay, William C.: Characteristics of the N. A. C. A. 23012 Airfoil from Tests in the Full-Scale and Variable-Density Tunnels. T. R. No. 530, N. A. C. A., 1935.
3. DeFrance, Smith J.: The N. A. C. A. Full-Scale Wind Tunnel. T. R. No. 459, N. A. C. A., 1933.
4. Theodorsen, Theodore, and Silverstein, Abe: Experimental Verification of the Theory of Wind-Tunnel Boundary Interference. T. R. No. 478, N. A. C. A., 1934.
5. Silverstein, Abe: Scale Effect on Clark Y Airfoil Characteristics from N. A. C. A. Full-Scale Wind-Tunnel Tests. T. R. No. 502, N. A. C. A., 1934.
6. Silverstein, Abe, Katzoff, S., and Hootman, James A.: Comparative Flight and Full-Scale Wind-Tunnel Measurements of the Maximum Lift of an Airplane. T. R. No. 618, N. A. C. A., 1938.
7. The Cambridge University Aeronautics Laboratory (B. Melvill Jones): Measurement of Profile Drag by the Pitot-Traversal Method. R. & M. No. 1688, British A. R. C., 1936.
8. Betz, A.: A Method for the Direct Determination of Wing-Section Drag. T. M. No. 337, N. A. C. A., 1925.



# REPORT No. 648

## DESIGN CHARTS FOR PREDICTING DOWNWASH ANGLES AND WAKE CHARACTERISTICS BEHIND PLAIN AND FLAPPED WINGS

By ABE SILVERSTEIN and S. KATZOFF

### SUMMARY

*Equations and design charts are given for predicting the downwash angles and the wake characteristics for power-off conditions behind plain and flapped wings of the types used in modern design practice. The downwash charts cover the cases of elliptical wings and wings of taper ratios 1, 2, 3, and 5, with aspect ratios of 6, 9, and 12, having flaps covering 0, 40, 70, and 100 percent of the span. Curves of the span load distributions for all these cases are included. Data on the lift and the drag of flapped airfoil sections and curves for finding the contribution of the flap to the total wing lift for different types of flap and for the entire range of flap spans are also included. The wake width and the distribution of dynamic pressure across the wake are given in terms of the profile-drag coefficient and the distance behind the wing. A method of estimating the wake position is also given.*

*The equations and the charts are based on theory that has been shown in a previous report to be in agreement with experiment.*

### INTRODUCTION

In a recent paper (reference 1) methods are developed for predicting downwash angles and wake characteristics for power-off conditions behind airfoils of known span loading. The calculation of downwash involves several simplifying assumptions that are shown to be justified. Wake characteristics are given by empirical expressions derived from experimental data and are in agreement with available theory.

In order to make the methods of reference 1 readily applicable for design purposes, charts have been prepared covering the range of modern design practice. These charts are given in the present paper. Included are curves of the lift and the drag of flapped airfoil sections and charts for finding the contributions of the different types of flap to the total wing lift. Information is also presented for determining the position of the wake, its width, and the distribution of dynamic pressure across it.

The downwash charts are for elliptical wings and for wings of taper ratios 1, 2, 3, and 5, with aspect ratios of 6, 9, and 12, having flaps covering 0, 40, 70, and 100

percent of the span. The explanatory text accompanying the charts is sufficiently complete to permit their use without study of reference 1.

### SYMBOLS

- $C_L$ , lift coefficient.
- $C_{L_w}$ , lift coefficient at a particular angle of attack, flaps up.
- $C_{L_f}$ , increase of lift coefficient, at the same angle of attack, upon deflecting the flap.
- $c_l$ , section lift coefficient.
- $\Delta c_l$ , increment of section lift coefficient corresponding to a flap deflection (two-dimensional).
- $c_{d_0}$ , section profile-drag coefficient.
- $c$ , wing chord.
- $c_f$ , flap chord.
- $b$ , wing span.
- $b_f$ , flap span.
- $S$ , wing area.
- $x$ , longitudinal distance from quarter-chord point.
- $y$ , lateral distance from symmetry plane.
- $z$ , vertical distance from quarter-chord point.
- $s$ , vortex semispan, in wing semispans.
- $\Gamma$ , vortex strength.
- $w$ , induced vertical velocity.
- $g$ , downwash factor.
- $\epsilon$ , downwash angle.
- $h$ , downward displacement, measured normal to the relative wind, of the center line of the wake and the trailing vortex sheet from its origin at the trailing edge.
- $m$ , vertical distance of the elevator hinge axis from the wake origin, measured perpendicular to the relative wind.
- $\xi$ , distance behind the trailing edge.
- $\zeta$ , wake half-width.
- $\zeta'$ , vertical distance from wake center line.
- $\eta$ , loss in dynamic pressure at wake center, fraction of free-stream dynamic pressure  $q$ .
- $\eta'$ , loss in dynamic pressure, fraction of free-stream dynamic pressure  $q$ .
- $k$ , correction for locating wake origin.
- $\delta_f$ , flap angle.



## RÉSUMÉ OF THEORY

**Downwash, plain wings.**—The downwash behind a wing is mainly a function of the wing loading and is a manifestation of the associated vortex system. This vortex system comprises the bound, or lifting, vortex considered localized at the quarter-chord line and the vortex sheet that is shed from the trailing edge. If the strength of the bound vortex at distance  $s$  from the airfoil center is  $\Gamma$ , the vorticity per unit spanwise length in the sheet as it leaves the trailing edge is  $-d\Gamma/ds$ .

A first approximation to the downwash is obtained by assuming the sheet to originate at the quarter-chord line and to extend unchanged indefinitely downstream, the vortex system thereby consisting of elementary U-vortices (or horseshoe vortices) of semispan  $s$  and strength  $-(d\Gamma/ds)ds$  to which the Biot-Savart equation is applicable. The actual sheet, however, does not extend unaltered from the lifting line to infinity because, as a result of the air motions that the vortex system itself creates, it is rapidly displaced downward and deformed.

For purposes of calculation of the downwash angle at the tail, a satisfactory second approximation is obtained by neglecting the deformation and considering the entire sheet to be uniformly displaced downward by an amount equal to the displacement of the center of the sheet near the tail. This displacement, furthermore, can be readily calculated since the sheet follows the downflow which, with reasonable accuracy, may be taken as that given by the first approximation. Inasmuch as the downwash depends to a predominant extent on the trailing vortex sheet, a vertical displacement of the sheet causes a vertical displacement of the entire downwash pattern by the same amount.

The strength of the vortex system is proportional to  $C_L$ ; hence, the downwash angle  $\epsilon$  and the displacement  $h$  must also be proportional to  $C_L$ . At higher lifts, however, there are three disturbing effects, all of which tend to increase the downwash above the sheet and to decrease it below. These factors are: (1) The effect of the strong tip vortices that, owing to the curvature of the sheet, are above the center; (2) the effect of the bound vortex that, owing to the downward displacement of the sheet relative to it, similarly contributes more to the downwash above than below it; and (3) the flow of air into the wake, which is coincident with the trailing vortex sheet.

**Downwash, flapped wings.**—The effect of a flap on the downwash depends upon its effect on the span load distribution. The change in loading upon lowering a given flap is nearly independent of the angle of attack, and the absolute change in the lift coefficient at any section  $c_l$  is approximately proportional to the total increase in the wing lift coefficient  $C_{L_f}$ . The resultant loading and vortex systems being the sums of those of the plain wing and of the flap, the resultant downwash

is the sum of that due to the plain wing at the given attitude and that due to the flap. The component due to the flap is proportional to  $C_{L_f}$ . The vortex-sheet origin lies between the trailing edges of the plain wing and of the flap. Its vertical displacement is, like the downwash, the sum of that due to the plain wing and that due to the flap.

For wings with flaps, increased importance attaches to the three disturbing effects mentioned for plain wings. The wake, in particular, requires consideration where high-drag flaps are used.

**The wake.**—The wake is characterized by a loss in total pressure, the deficiency being a maximum at its center and decreasing to zero at a fairly well-defined wake edge. Its center line coincides with that of the trailing vortex sheet. On account of turbulent mixing with the surrounding air, the maximum total-pressure loss decreases with distance downstream, whereas the width of the wake increases. The integrated loss in total pressure across the wake remains nearly constant and is proportional to the profile drag of the wing section from which the wake was shed.

## DOWNWASH CHARTS

**Plan forms.**—The downwash charts of figures 1 to 15 contain four groups of diagrams. In the first column of each chart are shown the plan forms of the wings for which the computations were made. Consistent with the assumption made in the calculations that there is no sweepback of the lifting line, the quarter-chord line is drawn perpendicular to the center line in every case. The tips are shown rounded for a spanwise distance equal to the tip chord, as was done in reference 2. Although the flap chord is shown as 20 percent of the wing chord, the actual value of  $c_f/c$  is immaterial as long as it is constant over the entire span of the flap. In actual practice, this condition is not always maintained. As long as the variation of  $c_f/c$  remains within the usual limits, however, this source of error is of secondary importance.

**Span load distributions.**—The span load distributions are shown in the second column of each figure. The distribution for the plain wing was obtained from reference 2. The distributions for the flap conditions were computed by the Lotz method (reference 3). In the computations, the Fourier coefficients for the chord distribution were found by Pearson's system (reference 4) and the Fourier coefficients for the angle distribution were found by the usual method of integration. Ten terms of the series for the loading were derived, which are adequate to give the shape of the loading curve except near the flap tip, where a reasonable number of terms does not suffice to give the shape accurately. The curves are therefore more or less arbitrarily drawn in this region, the main condition being that the slope be infinite at the position of the flap tip.



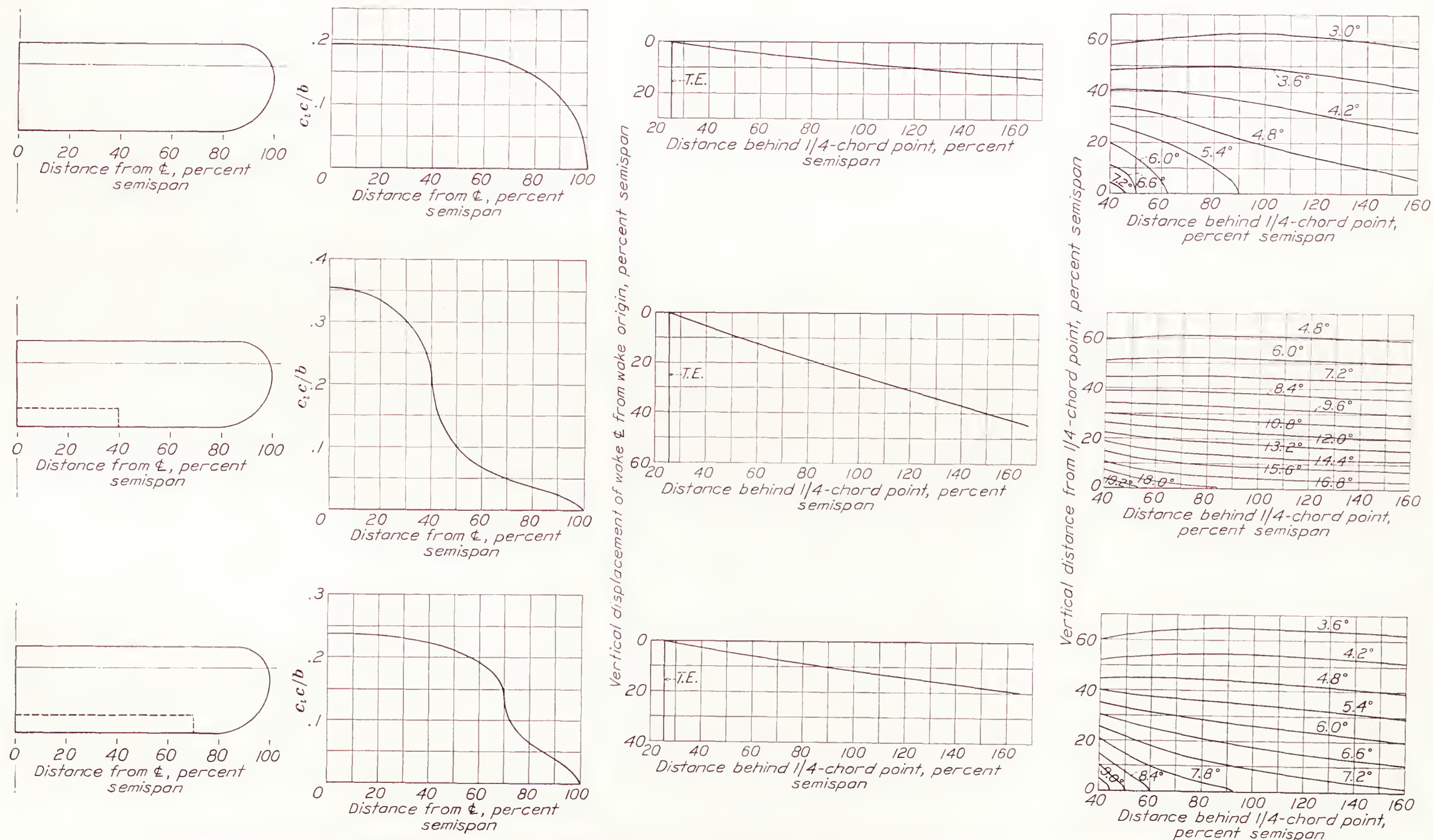


FIGURE 1.—Design charts showing load distribution, downwash displacement, and downwash angles. Plain wing, 0.4b and 0.7b flaps;  $C_L$  and  $C_{L_f}$ , 1.0; taper, 1:1; aspect ratio, 6.



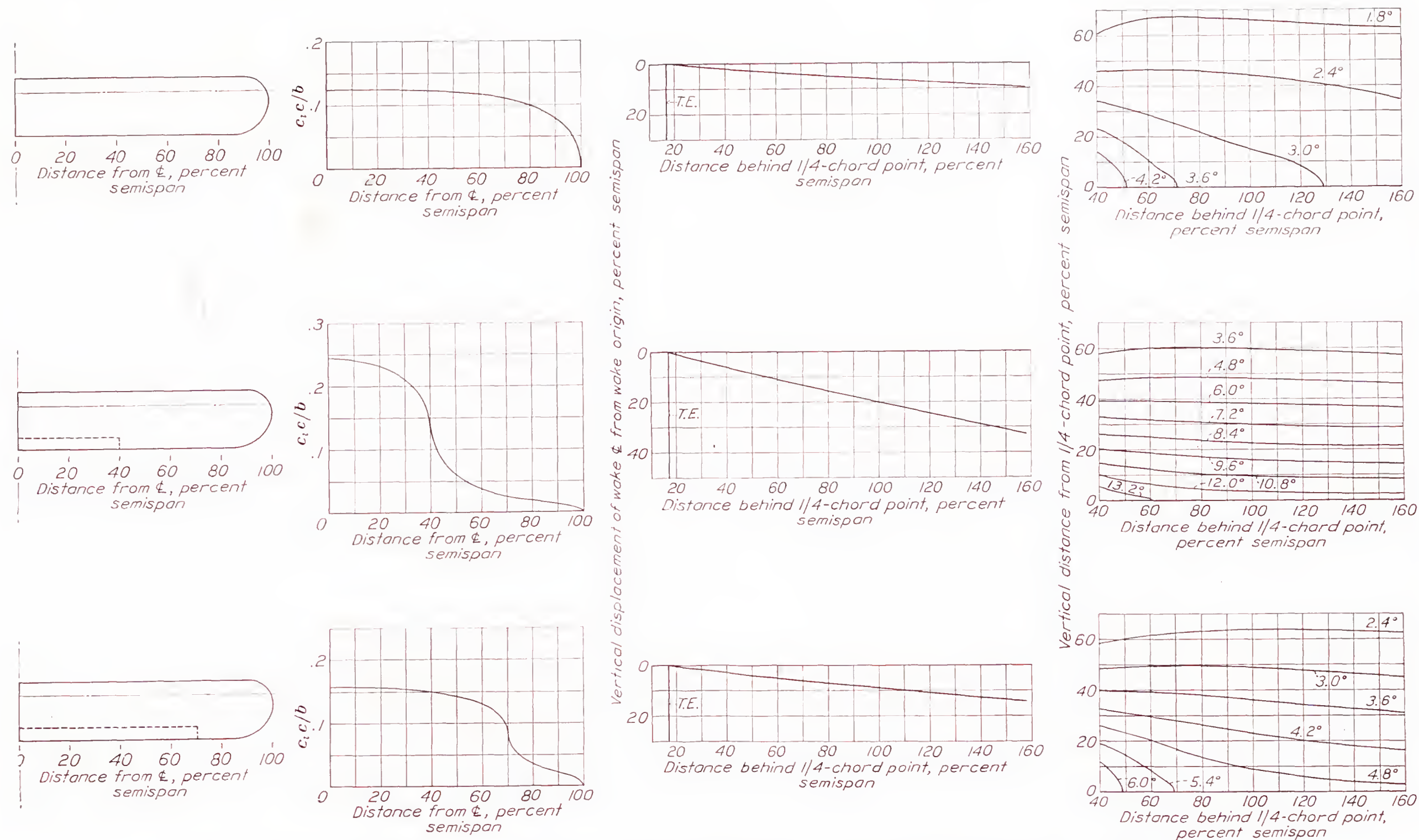


FIGURE 2.—Design charts showing load distribution, downwash displacement, and downwash angles. Plain wing, 0.4b and 0.7b flaps;  $C_L$  and  $C_{L_p}$ , 1.0; taper, 1:1; aspect ratio, 9.



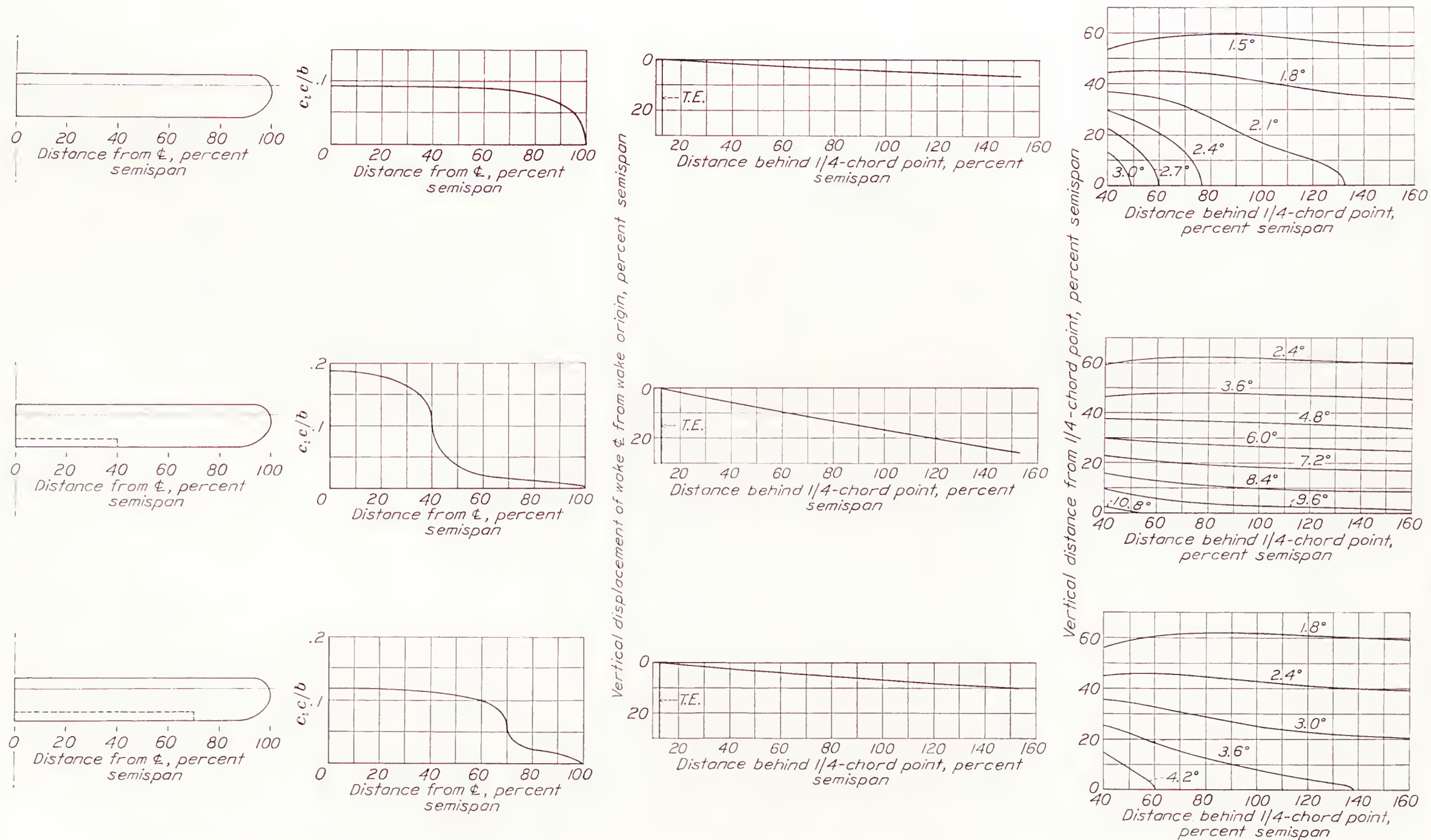


FIGURE 3.—Design charts showing load distribution, downwash displacement, and downwash angles. Plain wing, 0.4b and 0.7b flaps;  $C_L$  and  $C_{Lp}$ , 1.0; taper, 1:1; aspect ratio, 12



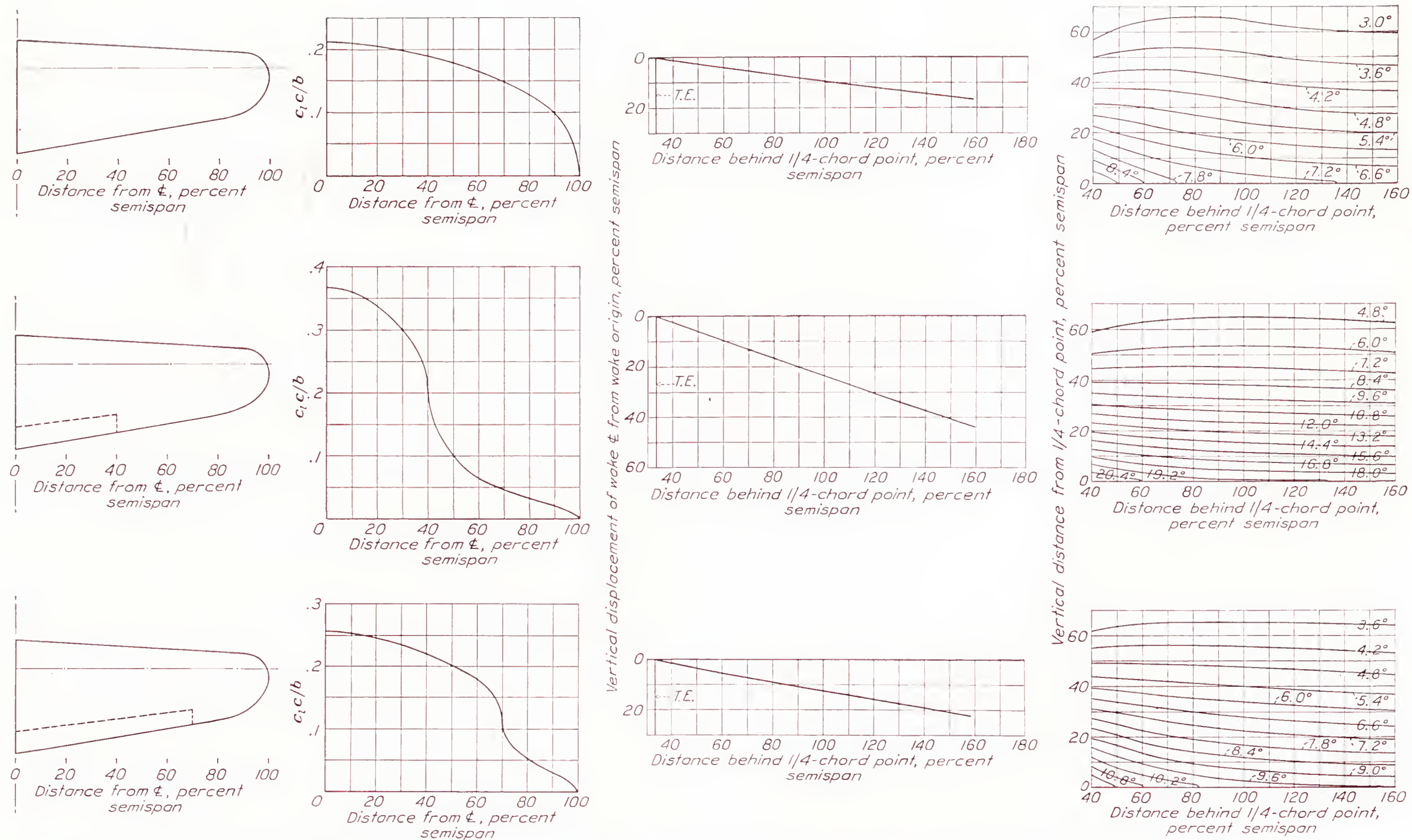


FIGURE 4.—Design charts showing load distribution, downwash displacement, and downwash angles. Plain wing, 0.4b and 0.7b flaps;  $C_L$  and  $C_{L_p}$ , 1.0; taper, 2:1; aspect ratio, 6.



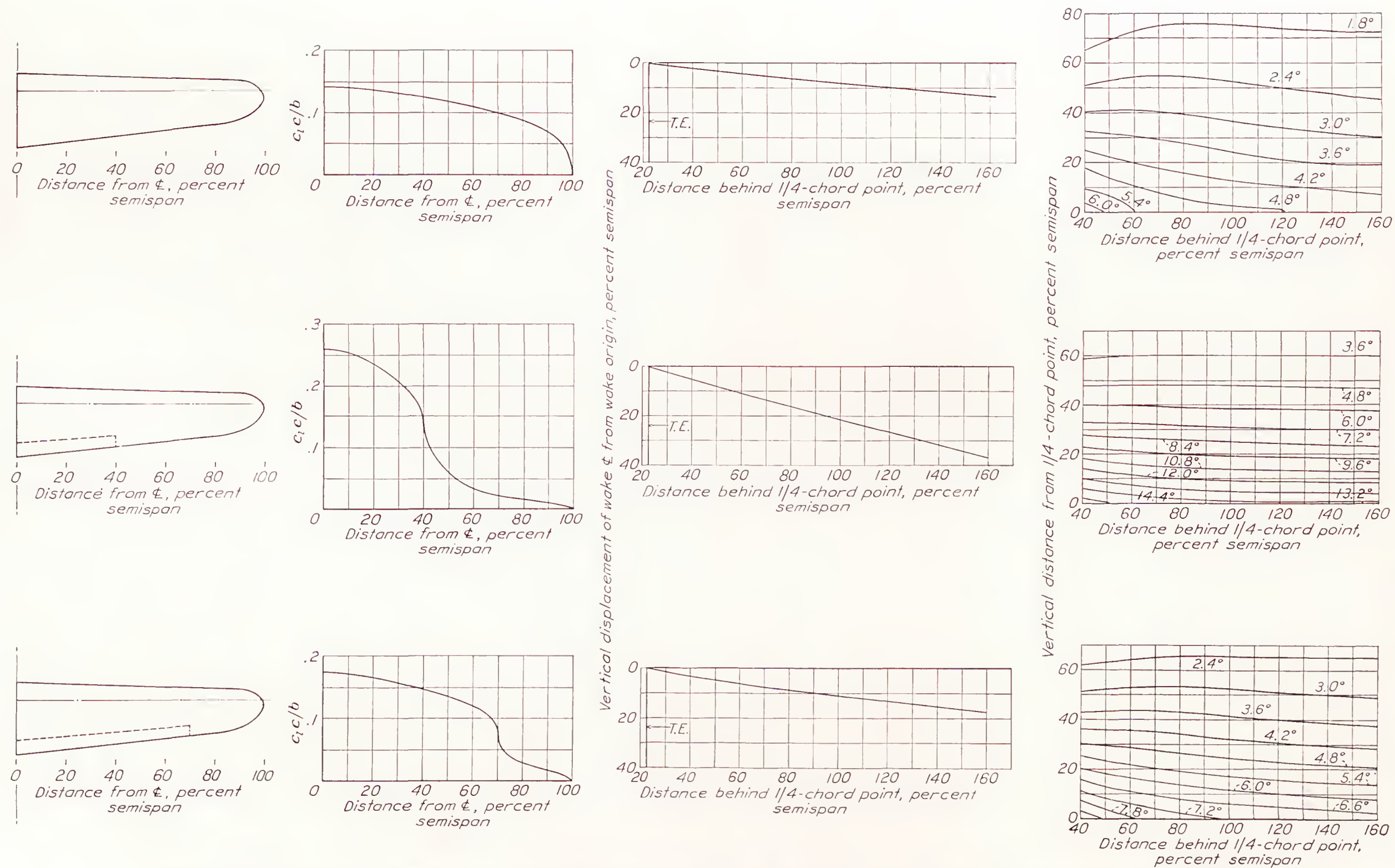


FIGURE 5.—Design charts showing load distribution, downwash displacement, and downwash angles. Plain wing, 0.4b and 0.7b flaps;  $C_L$  and  $C_{L_f}$ , 1.0; taper, 2:1; aspect ratio, 9.



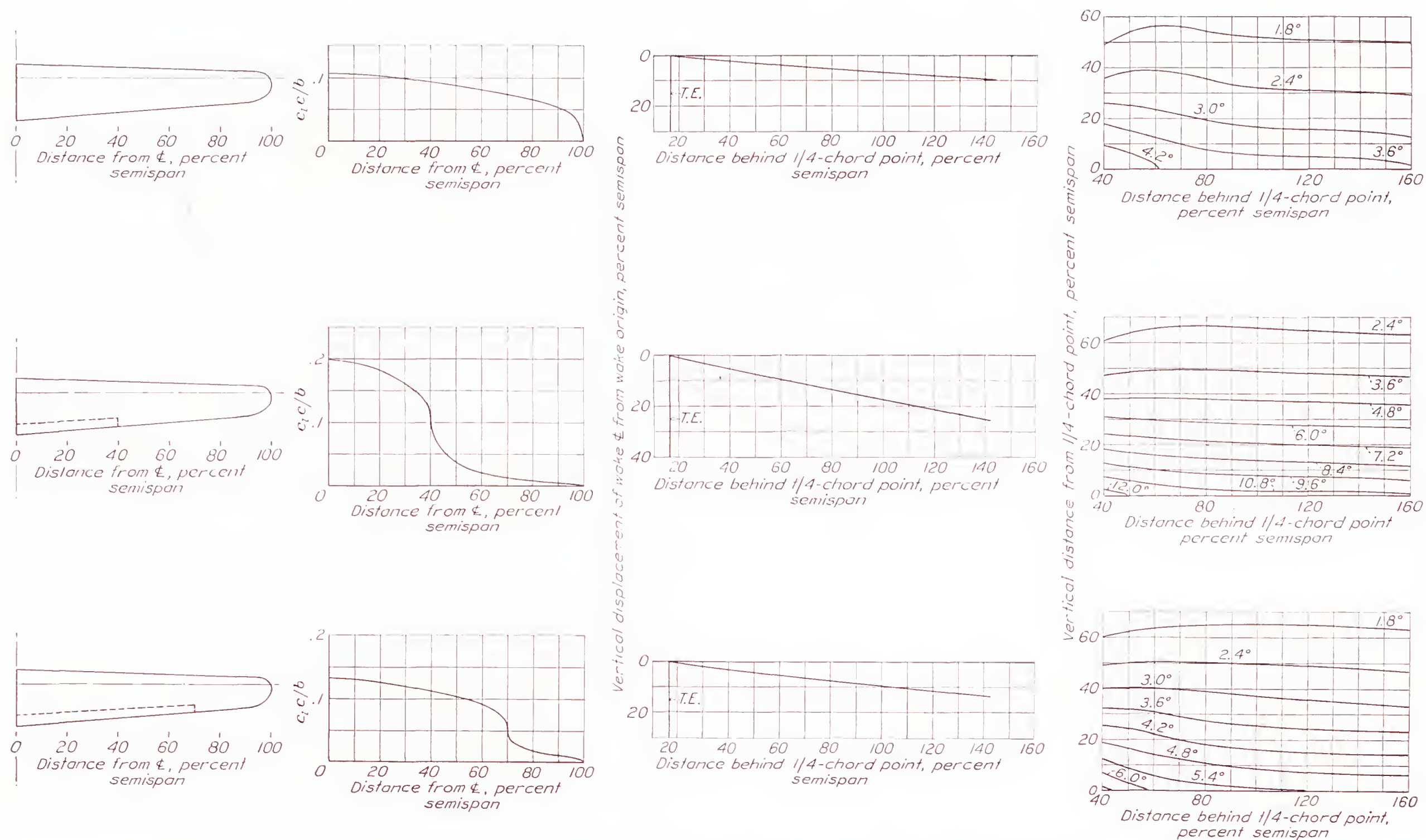


FIGURE 6.—Design charts showing load distribution, downwash displacement, and downwash angles. Plain wing, 0.4b and 0.7b flaps;  $C_L$  and  $C_{Lp}$ , 1.0; taper, 2:1; aspect ratio, 12.



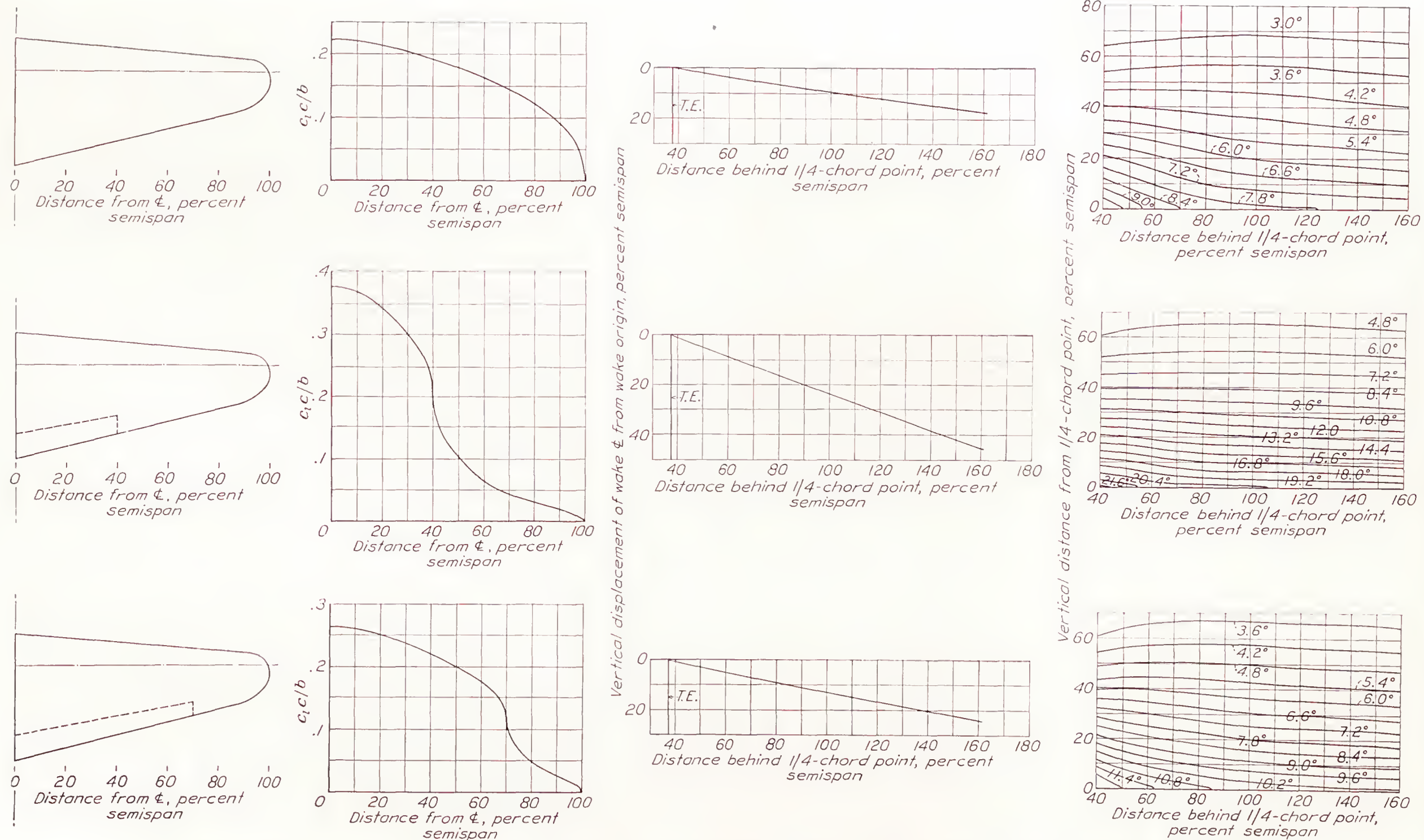


FIGURE 7.—Design charts showing load distribution, downwash displacement, and downwash angles. Plain wing, 0.4b and 0.7b flaps;  $C_L$  and  $C_{L_p}$ , 1.0; taper, 3:1; aspect ratio, 6.



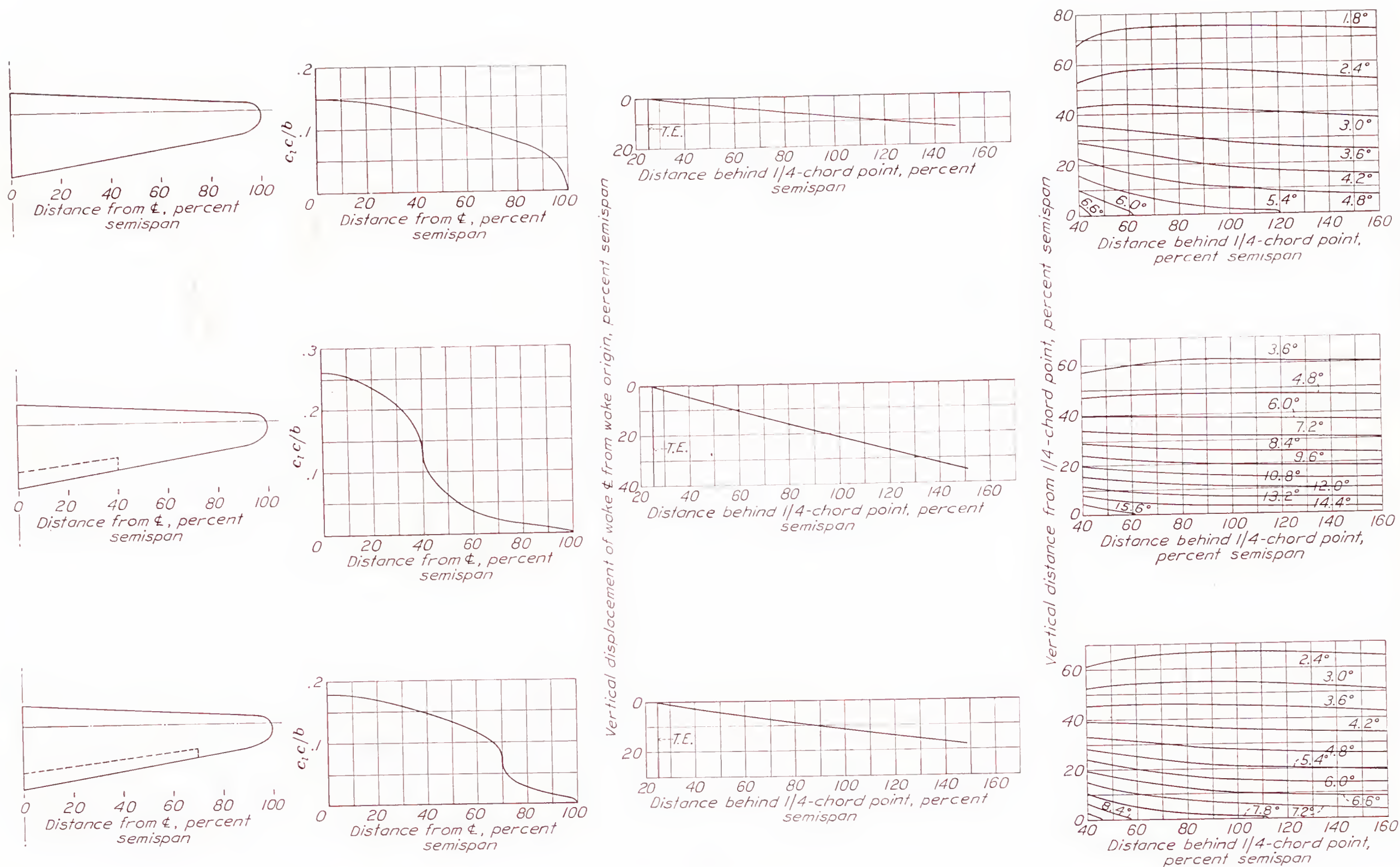


FIGURE 8.—Design charts showing load distribution, downwash displacement, and downwash angles. Plain wing, 0.4b and 0.7b flaps;  $C_L$  and  $C_{Lp}$ , 1.0; taper, 3:1; aspect ratio, 9.



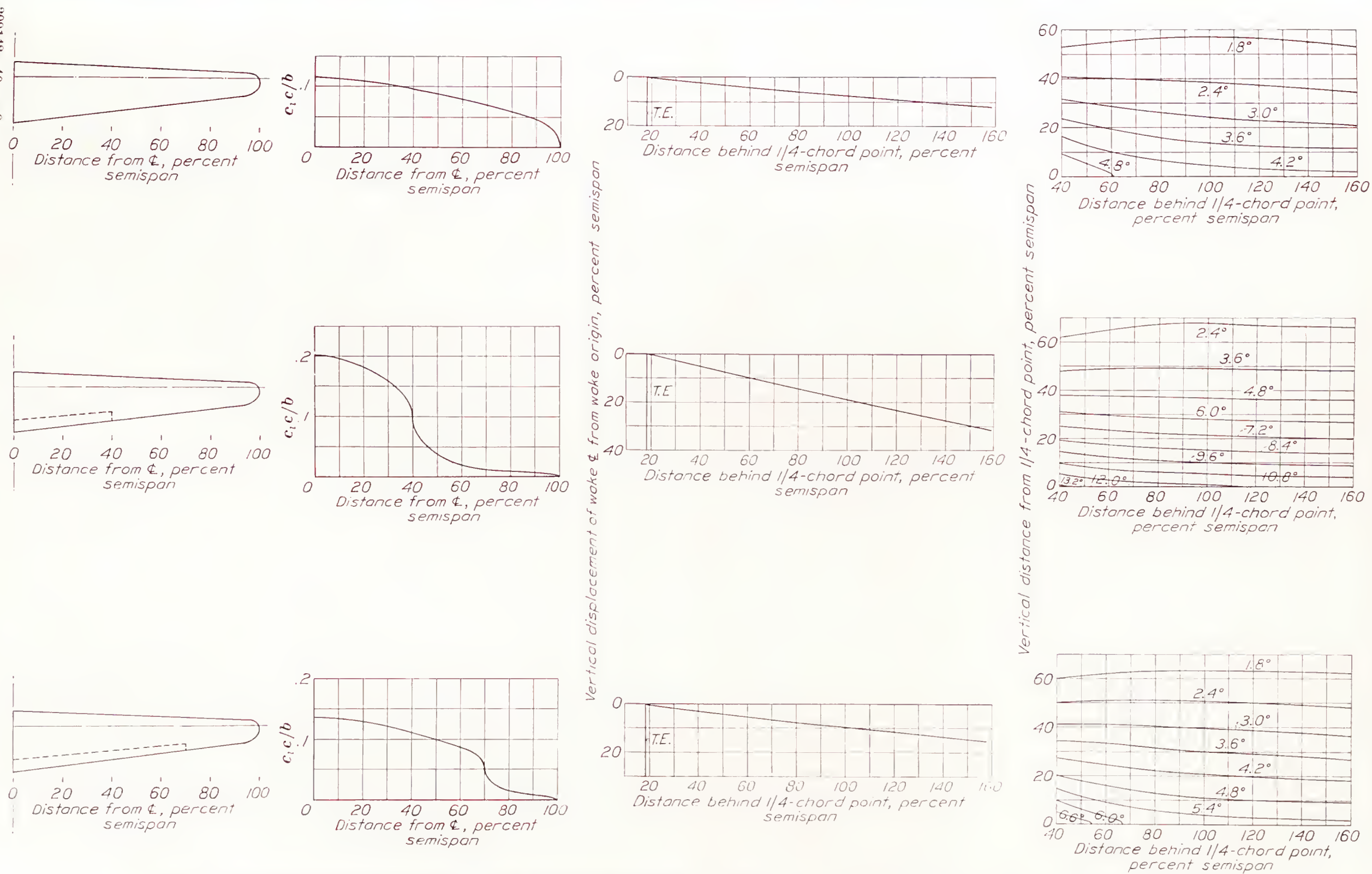


FIGURE 9.—Design charts showing load distribution, downwash displacement, and downwash angles. Plain wing, 0.4b and 0.7b flaps;  $C_l$  and  $C_L$ , 1.0; taper, 3.1; aspect ratio, 12



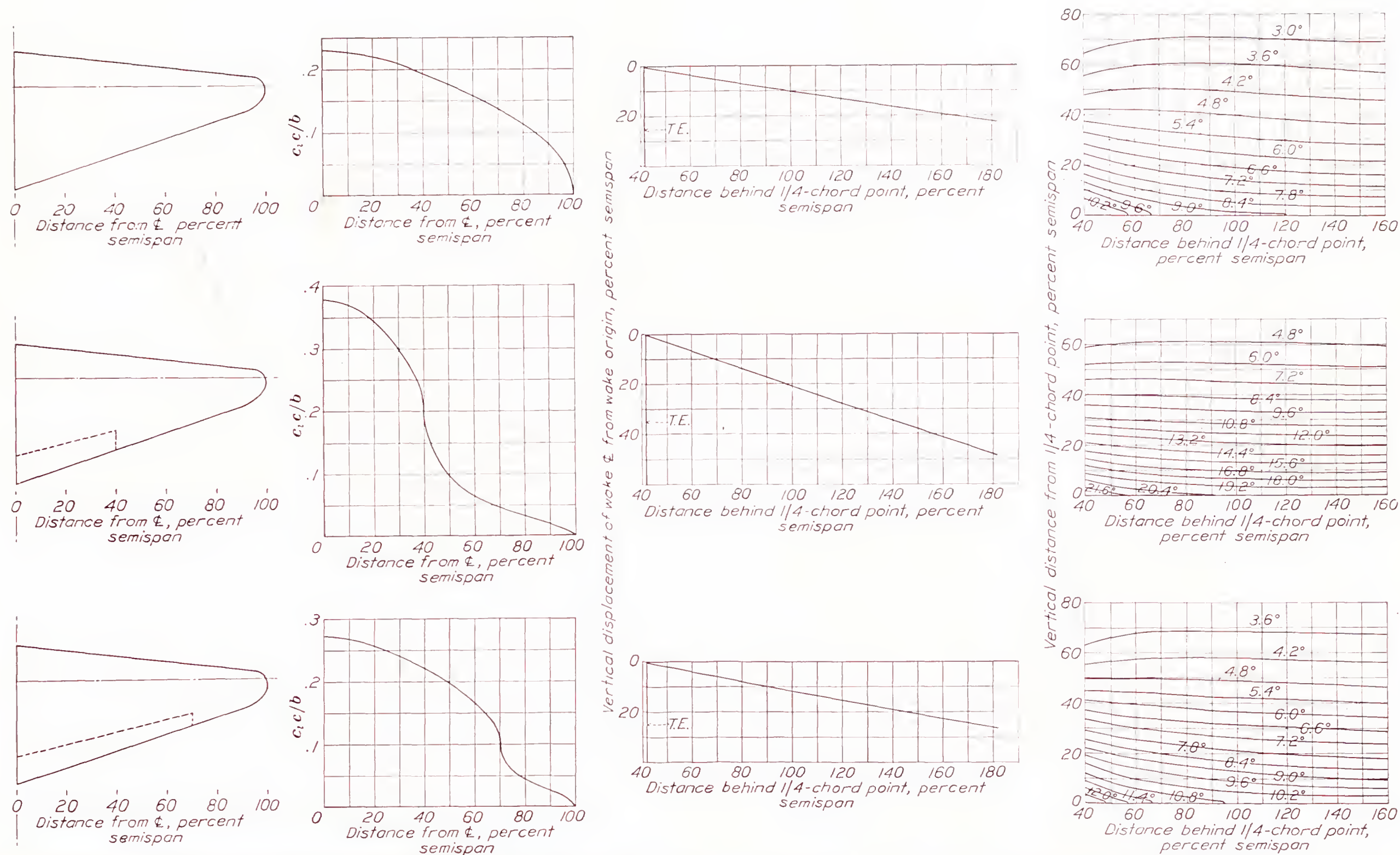


FIGURE 10.—Design charts showing load distribution, downwash displacement, and downwash angles. Plain wing, 0.4b and 0.7b flaps;  $C_L$  and  $C_{Lp}$ , 1.0; taper, 5:1; aspect ratio, 6.



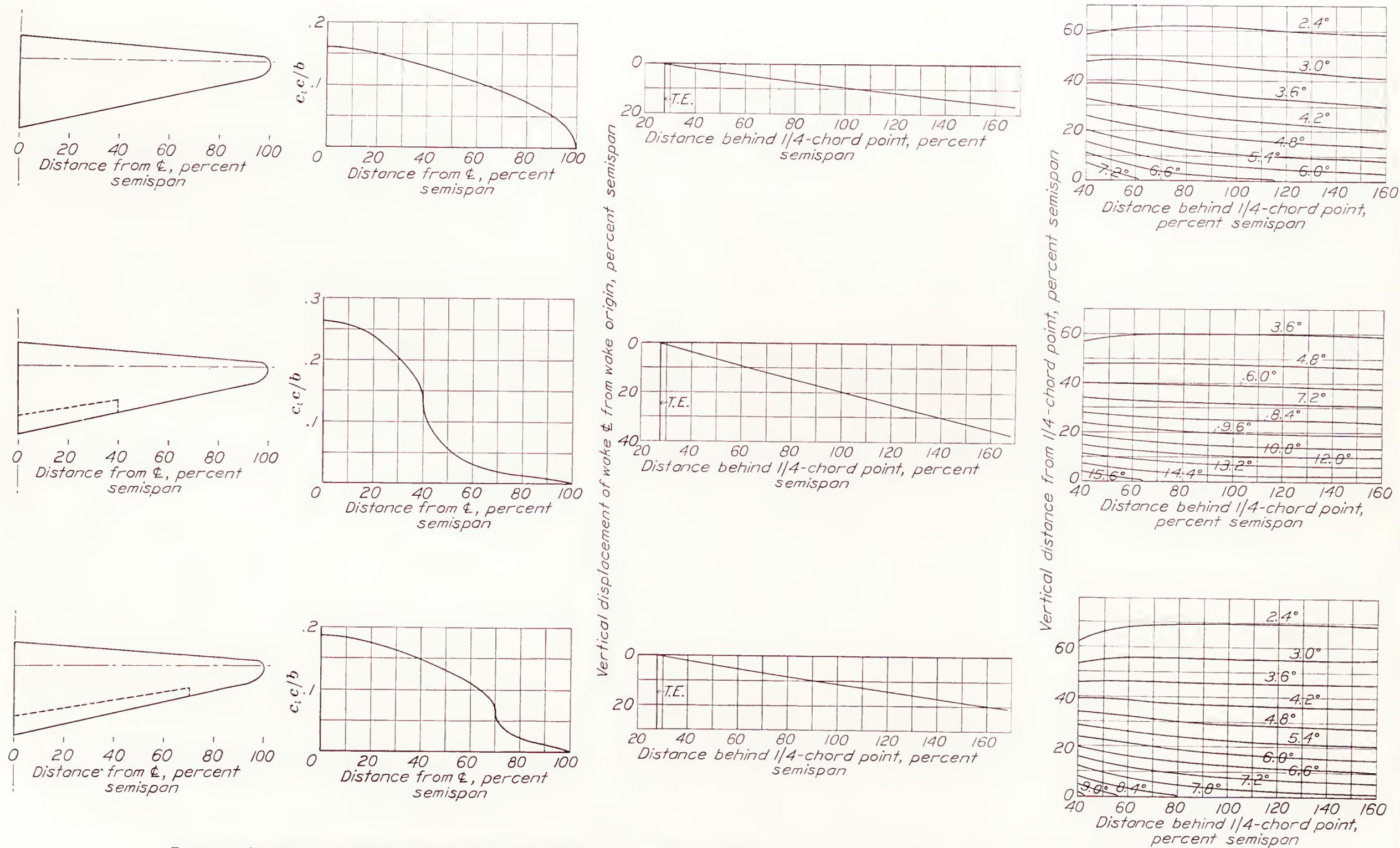


FIGURE 11.—Design charts showing load distribution, downwash displacement, and downwash angles. Plain wing, 0.4b and 0.7b flaps;  $C_L$  and  $C_{Lp}$ , 1.0; taper, 5:1; aspect ratio 9.



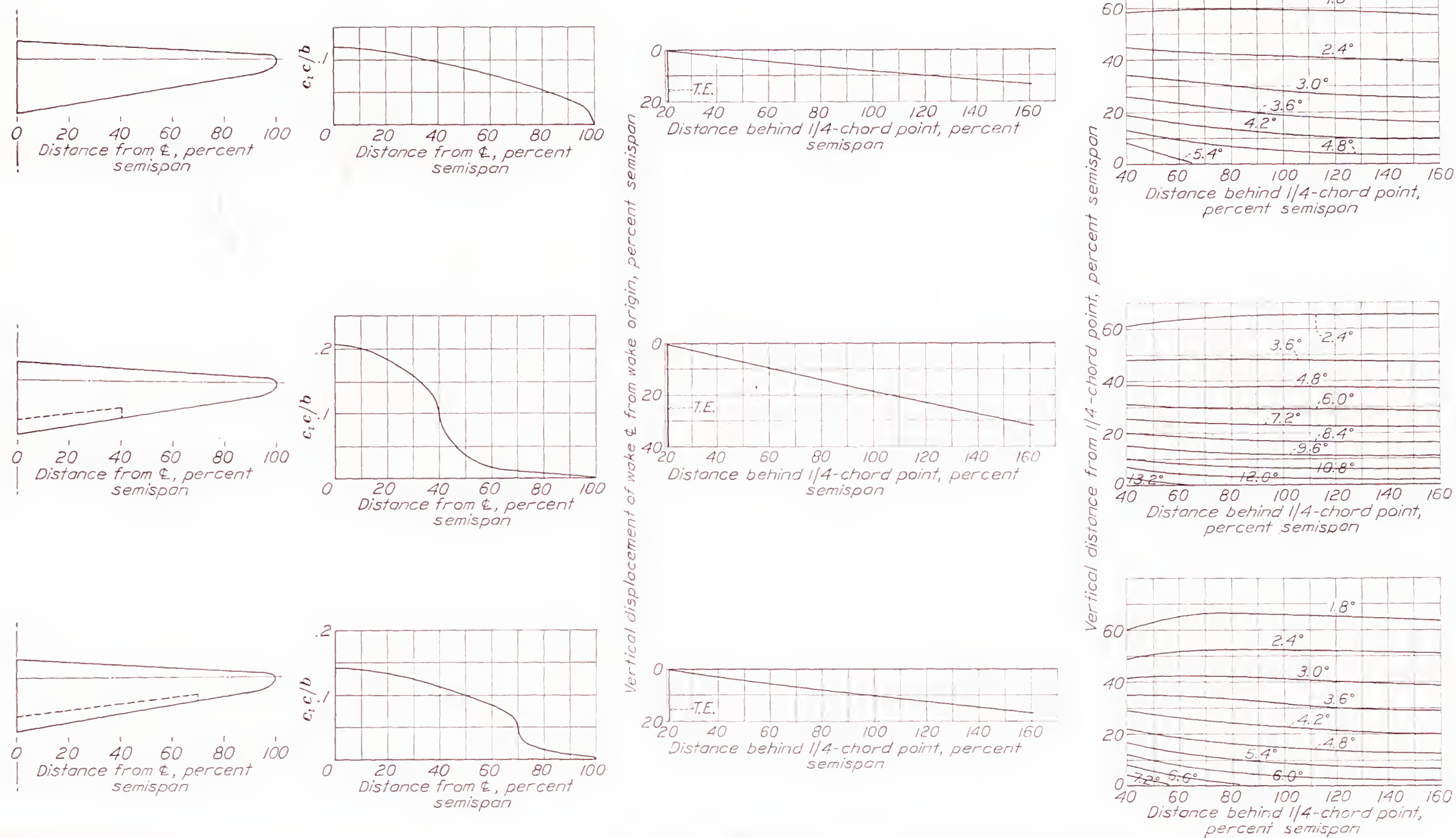


FIGURE 12.—Design charts showing load distribution, downwash displacement, and downwash angles. Plain wing, 0.4b and 0.7b flaps;  $C_L$  and  $C_{L_F}$ , 1.0; taper, 5:1; aspect ratio, 12.



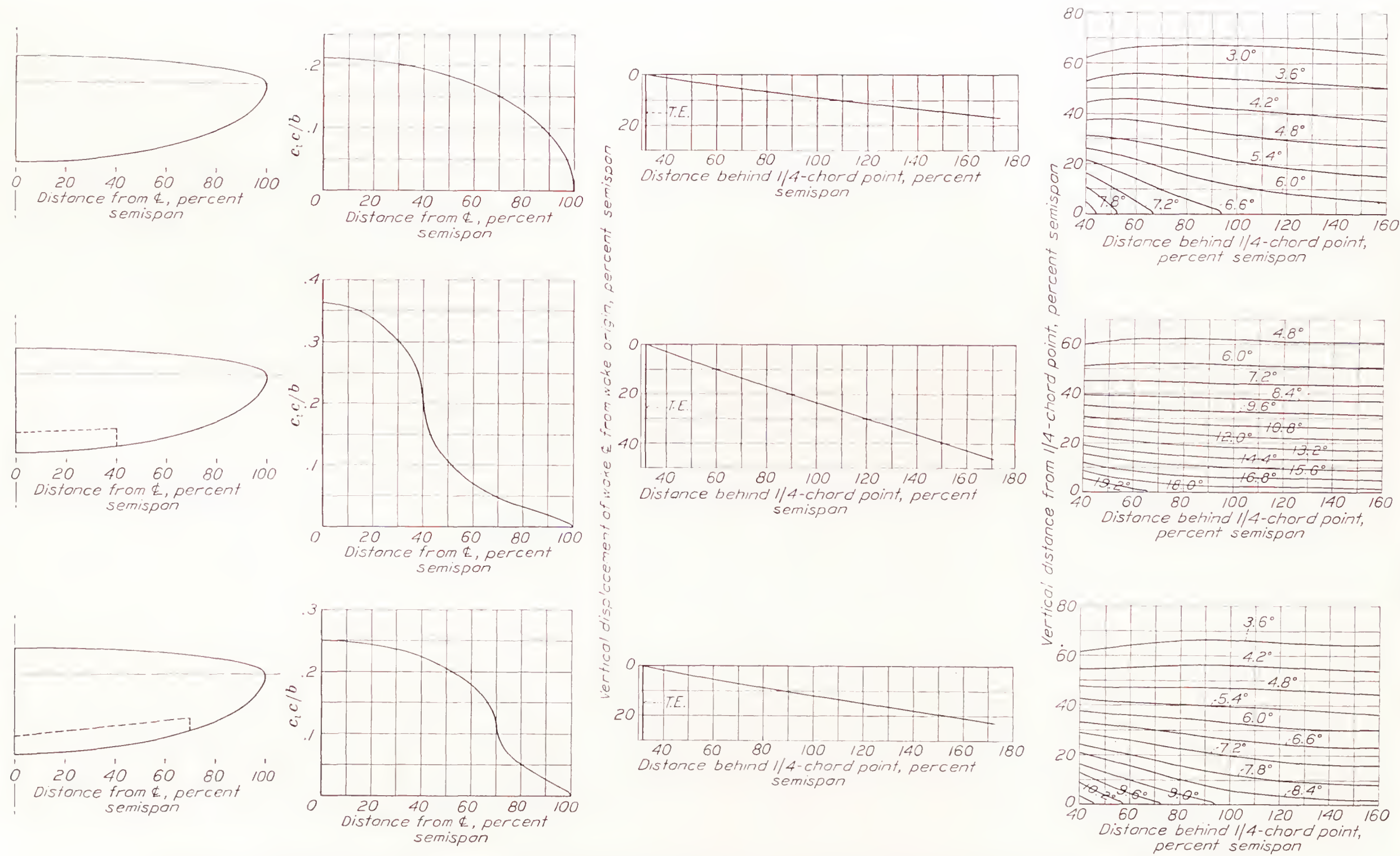


FIGURE 13.—Design charts showing load distribution, downwash displacement, and downwash angles. Plain wing, 0.4b and 0.7b flaps;  $C_L$  and  $C_{l_p}$ , 1.0; elliptical; aspect ratio, 6.



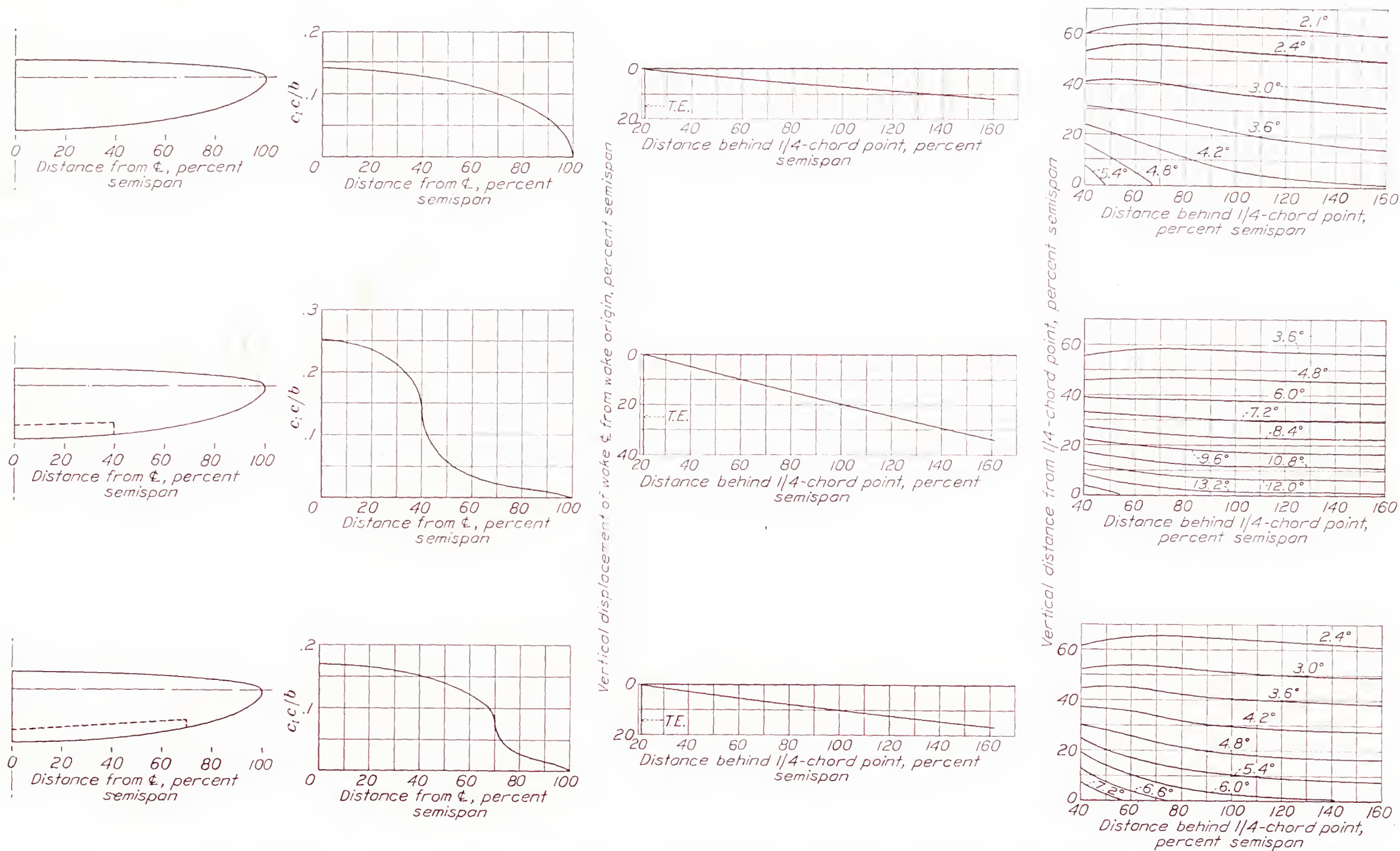


FIGURE 14.—Design charts showing load distribution, downwash displacement, and downwash angles. Plain wing, 0.4b and 0.7b flaps;  $C_L$  and  $C_{Lp}$ , 1.0; elliptical; aspect ratio, 9.



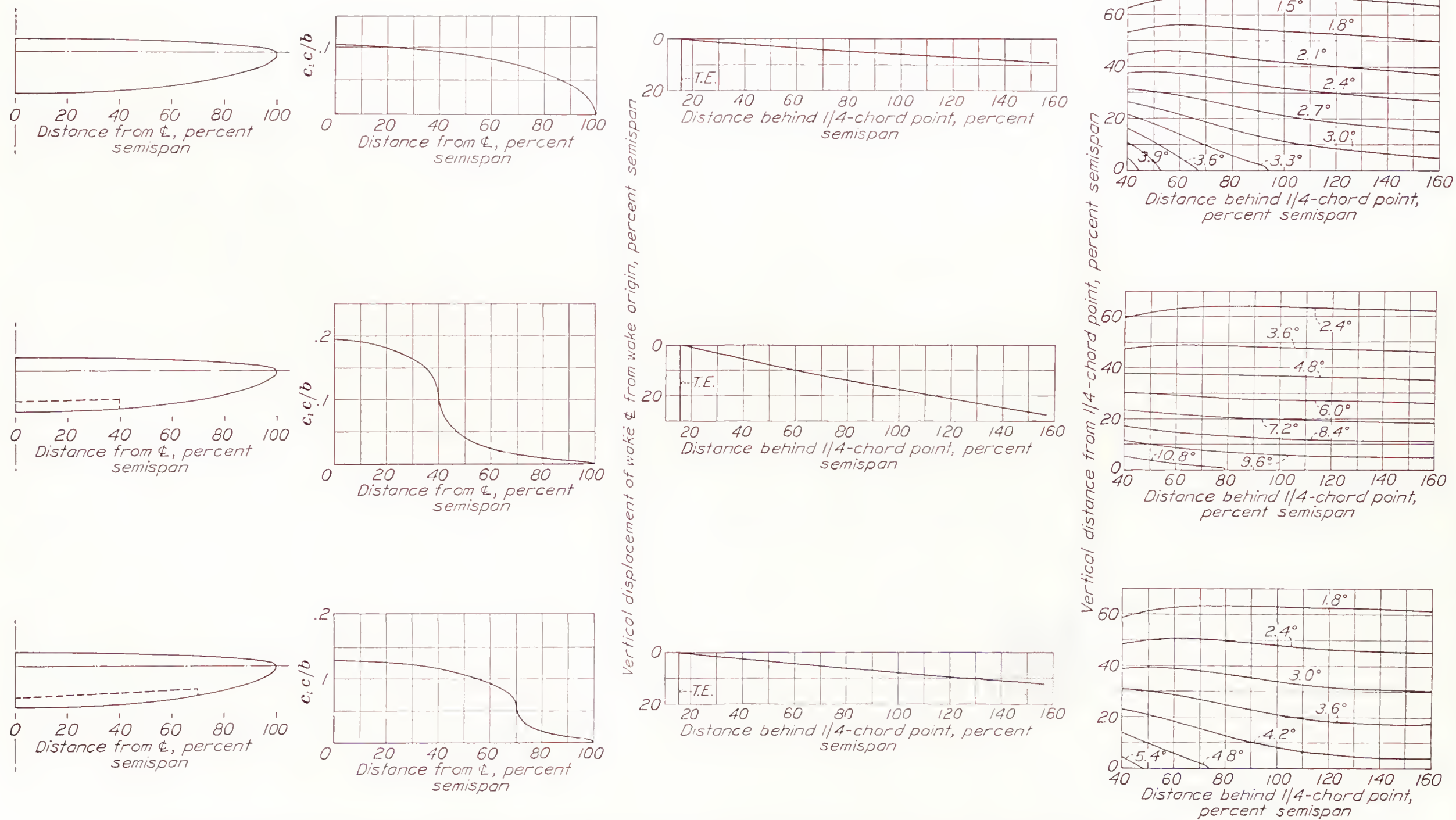


FIGURE 15.—Design charts showing load distribution, downwash displacement, and downwash angles. Plain wing, 0.4b and 0.7b flaps;  $C_L$  and  $C_{Lp}$ , 1.0; elliptical; aspect ratio, 12.



**Undisplaced downwash-contour charts.**—The downwash-contour charts shown in the fourth column are drawn for  $C_{L_w}=1.0$  and  $C_{L_f}=1.0$ . For other lift coefficients, the downwash angles can be obtained by multiplying the angles on the contour charts by the particular values of  $C_{L_w}$  or  $C_{L_f}$ . In the derivation of these charts, the trailing vortex sheet was assumed to start at the quarter-chord line and to extend unchanged indefinitely downstream. As already explained, the vortex system is thereby assumed to be made up of U-vortices of strength  $-(d\Gamma/ds)ds$ , where  $\Gamma$  is the strength of the bound vortex. The downflow velocity at a point  $(x, z)$  in the symmetry plane is given by the equation

$$w = -\frac{1}{\pi b} \int_0^1 s \frac{d\Gamma}{ds} \left[ \frac{x}{\sqrt{s^2 + x^2 + z^2}} \left( \frac{1}{x^2 + z^2} + \frac{1}{s^2 + z^2} \right) + \frac{1}{s^2 + z^2} \right] ds \quad (1)$$

In the actual computation, the indicated integration was replaced by a summation, i. e., the smooth span load distributions were approximated by stepwise distributions of 5 to 7 steps, so that equation (1) was effectively replaced by

$$w = -\frac{1}{\pi b} \sum_{n=1}^n s_n (\Delta\Gamma)_n \left[ \frac{x}{\sqrt{s_n^2 + x^2 + z^2}} \left( \frac{1}{x^2 + z^2} + \frac{1}{s_n^2 + z^2} \right) + \frac{1}{s_n^2 + z^2} \right] \quad (2)$$

where  $(\Delta\Gamma)_n$  is the rise of the  $n$ th step and  $s_n$  is the corresponding semispan. Figure 16 illustrates the substitution of a stepwise distribution for a continuous span load distribution.

Curves of the function

$$g = \frac{s}{2\pi} \left[ \frac{x}{\sqrt{s^2 + x^2 + z^2}} \left( \frac{1}{x^2 + z^2} + \frac{1}{s^2 + z^2} \right) + \frac{1}{s^2 + z^2} \right]$$

were found useful in these computations. They are reproduced in figure 17.

The longitudinal component of the induced flow generally being negligible compared with the free-stream velocity  $V$ , it follows that the tangent of the downwash angle is very nearly  $w/V$ . The downwash-contour charts have been constructed on this basis; only half of each chart is shown, for the axis is a line of symmetry when the longitudinal components of the induced velocities are neglected.

**Displacement of the center line.**—The downwash-contour charts just described require a vertical displacement, as has already been mentioned, because the trailing vortex sheet undergoes downward displacement as it proceeds downstream. The downward displacement is given by the equation

$$h = \int_{T.E.}^x \tan \epsilon \, dx \quad (3)$$

The curves shown in the third column of figures 1 to 15 are plots of this integral as a function of  $x$ , for

$C_{L_w}=1.0$  and  $C_{L_f}=1.0$ . For other lift coefficients, displacements are obtained by multiplying the values on the charts by the particular values of  $C_{L_w}$  or  $C_{L_f}$ .

**Origin of the trailing vortex sheet.**—For a plain wing the sheet is considered to be shed at the trailing edge. For a wing with a flap, the origin is between the trailing edges of the flap and the wing.

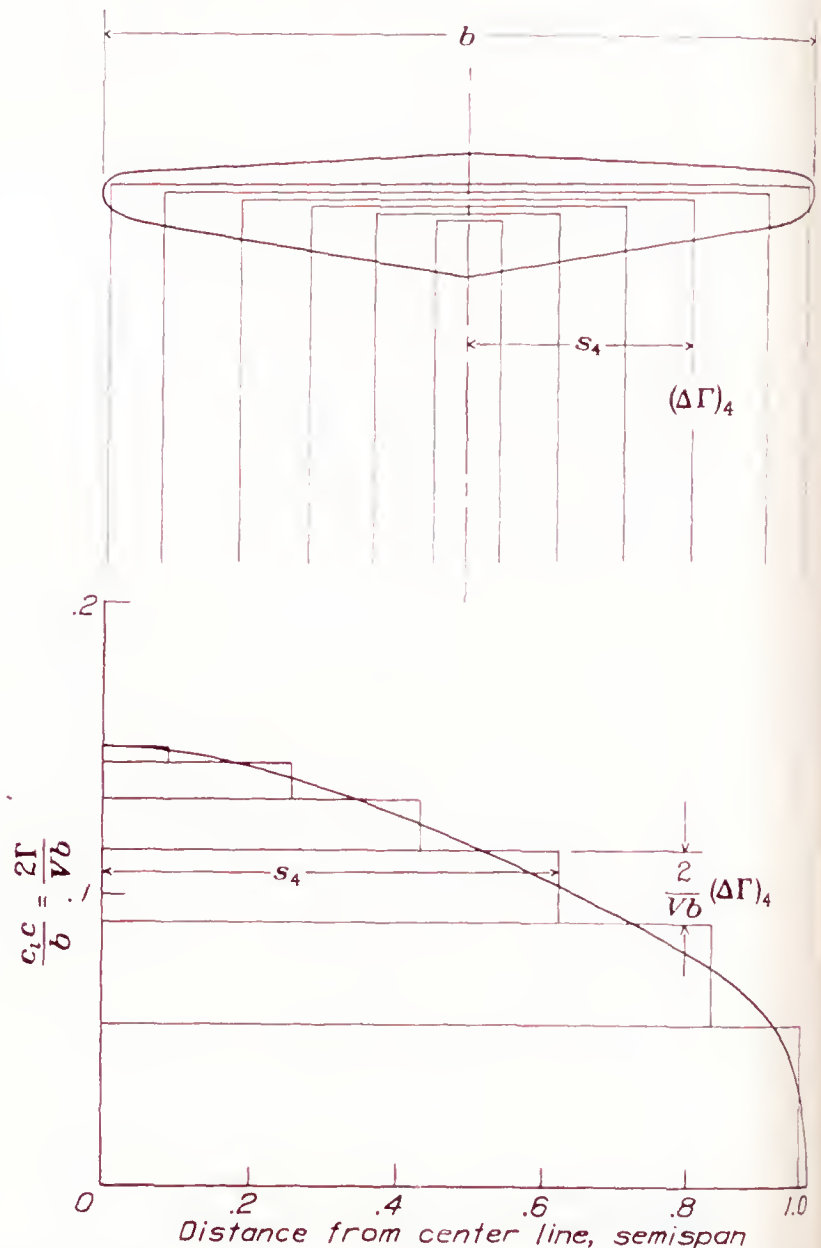


FIGURE 16.—Illustration of the substitution of six U-vortices for the actual vortex system.  $C_L$ , 1.0; taper, 3:1; aspect ratio, 9.

the distance below the trailing edge of the wing, in semispans, being given by the formula

$$h_0 = \frac{(c_f/2) \sin \delta_f + kc}{b/2} \quad (4)$$

which is based on the available experimental data. The factor  $k$  is given in figure 18.

**Contribution of the flap to the total lift.**—Figure 19 shows the theoretical contribution of the flap to the wing lift coefficient. The values of  $C_{L_f}/\Delta c_l$  were derived incidental to the computations of span load distribution, coming directly out of the first term of the Fourier series for the loading. It must be noted that they correspond, as do the span load distributions themselves, to flaps of uniform  $c_f/c$  or, stated differently, to flaps of uniform  $\Delta c_l$ . Where  $\Delta c_l$  is not uniform, an average  $\Delta c_l$  weighted according to chord will usually be satisfactory.



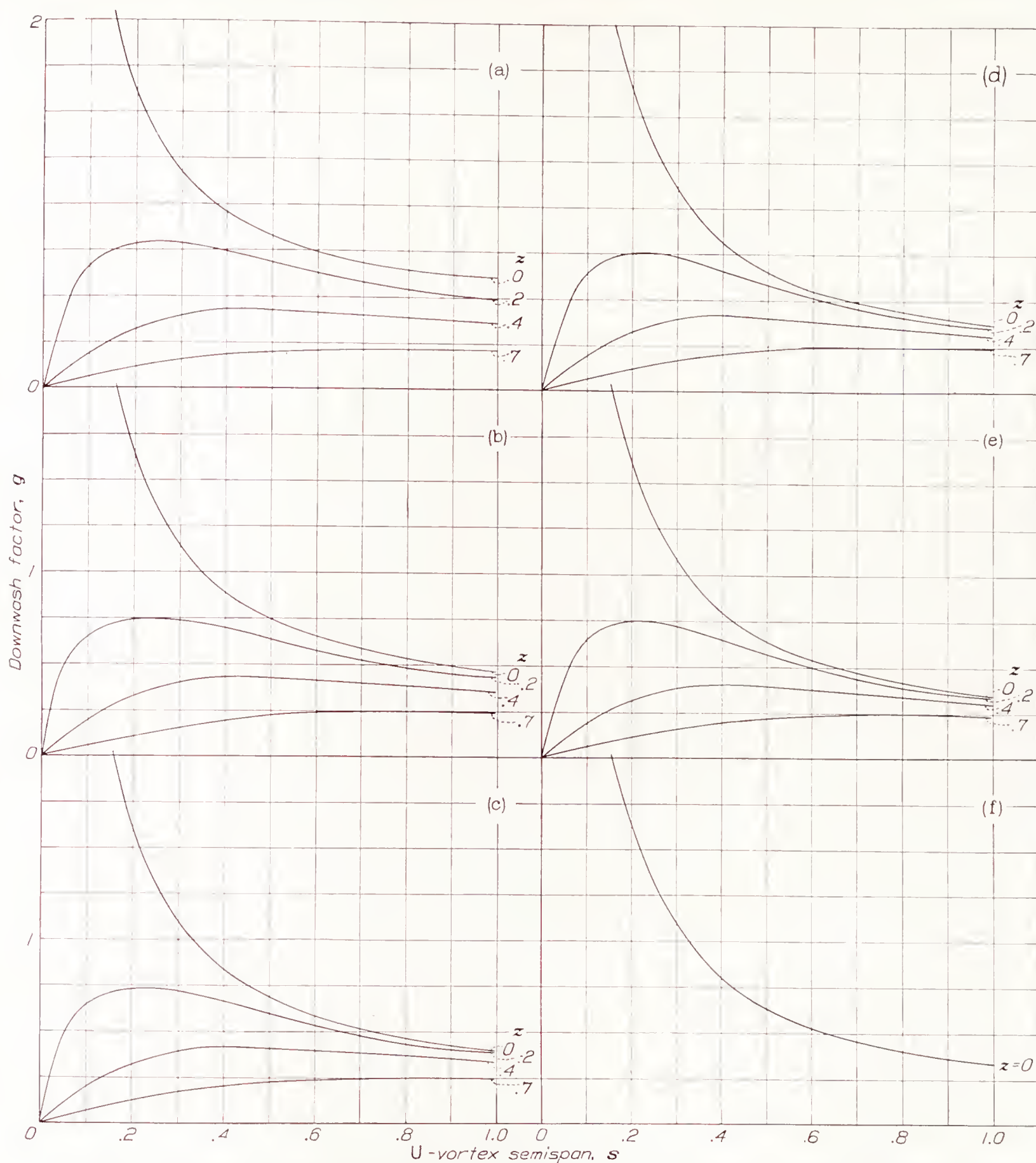


FIGURE 17.—Curves of the  $g$  function for various values of  $x$  and  $z$ . (a)  $x=0.4$ . (b)  $x=0.6$ . (c)  $x=0.9$ . (d)  $x=1.2$ . (e)  $x=1.6$ . (f)  $x=2.5$ .

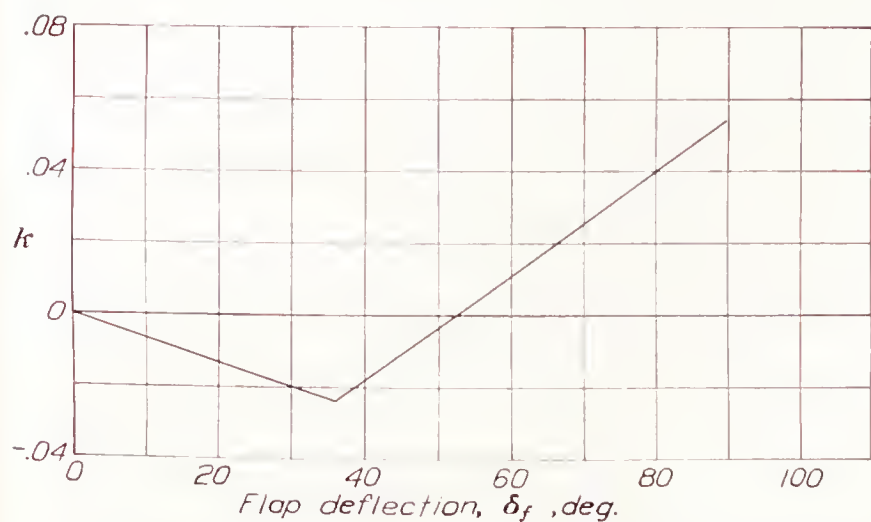


FIGURE 18.—Curve of the  $k$  factor for locating the wake origin for wings with flaps.

209142—40—10

**Curves of  $\Delta c_l$ .**—In order to facilitate the application of the curves of figure 19, data are presented in figure 20 for the increment of section lift coefficient  $\Delta c_l$  obtained by deflecting the various flaps. It must be noted that these increments are *section* characteristics and give the increase in lift coefficient when the flap is lowered in two-dimensional flow. The data were obtained mainly from N. A. C. A. results and from reference 5. No attempt has been made here to give a complete presentation of the lift increments due to flaps. The data given are best applicable at about  $3^\circ$  to  $4^\circ$  below maximum lift; however, they apply with reasonable accuracy at lower angles, for the increments are nearly constant



over the entire useful range. The coefficients for the 0.20c external-airfoil flap are based on the combined chord of the wing and flap; those for the 0.26c Fowler

for the plain wing at the particular angle of attack, plus the further increment given in figure 20 for the particular  $\delta_f$ .

**Variation of downwash across the tail span.**—The discussion thus far has been concerned with the calcula-

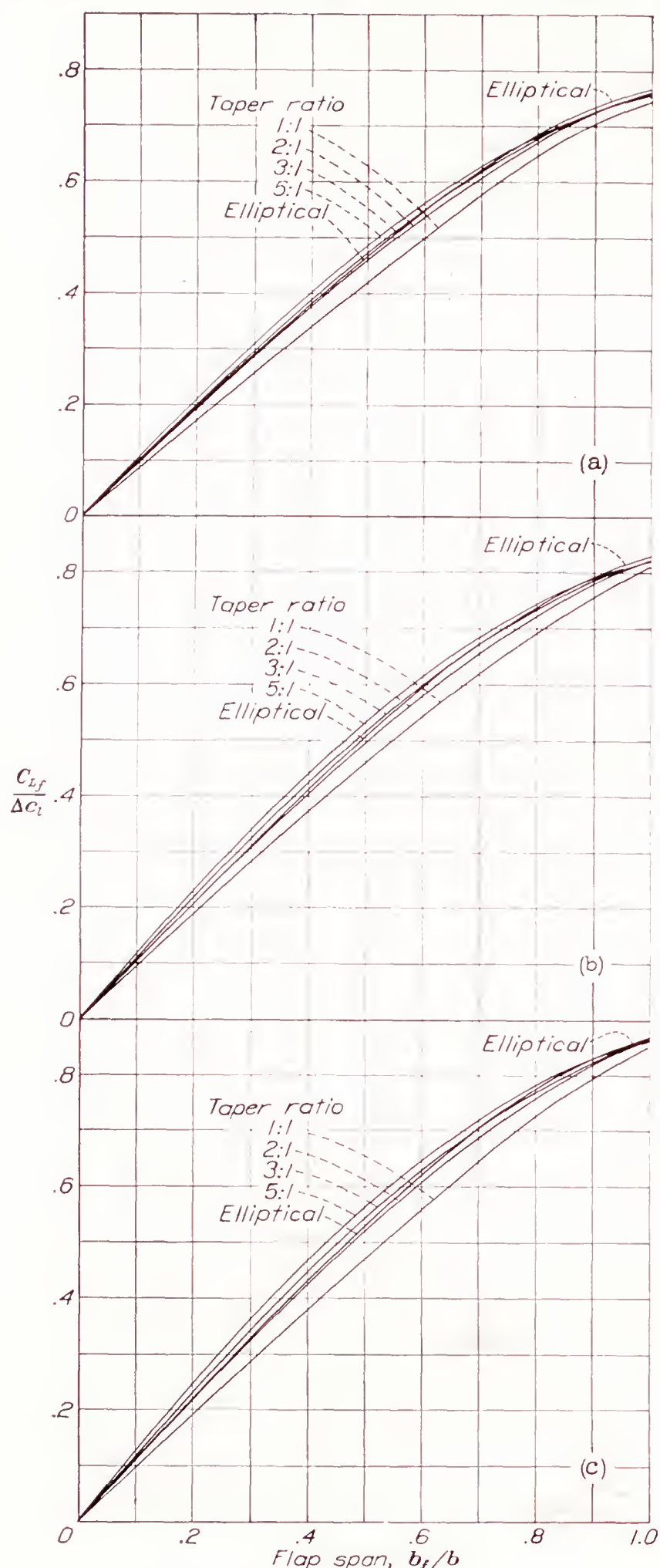
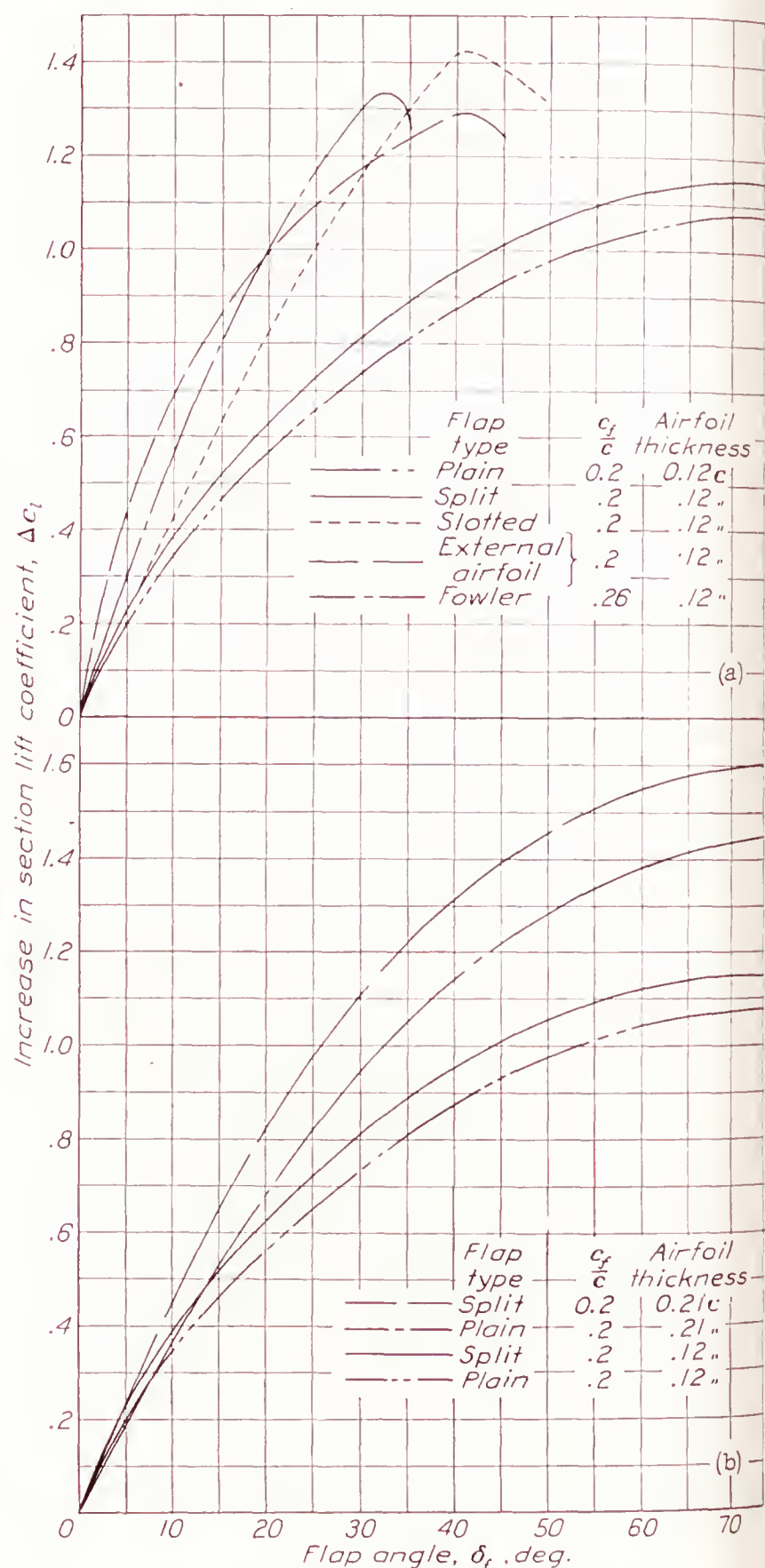


FIGURE 19.—Lift increments for wings with partial-span flaps. (a)  $A=6$ . (b)  $A=9$ . (c)  $A=12$ .

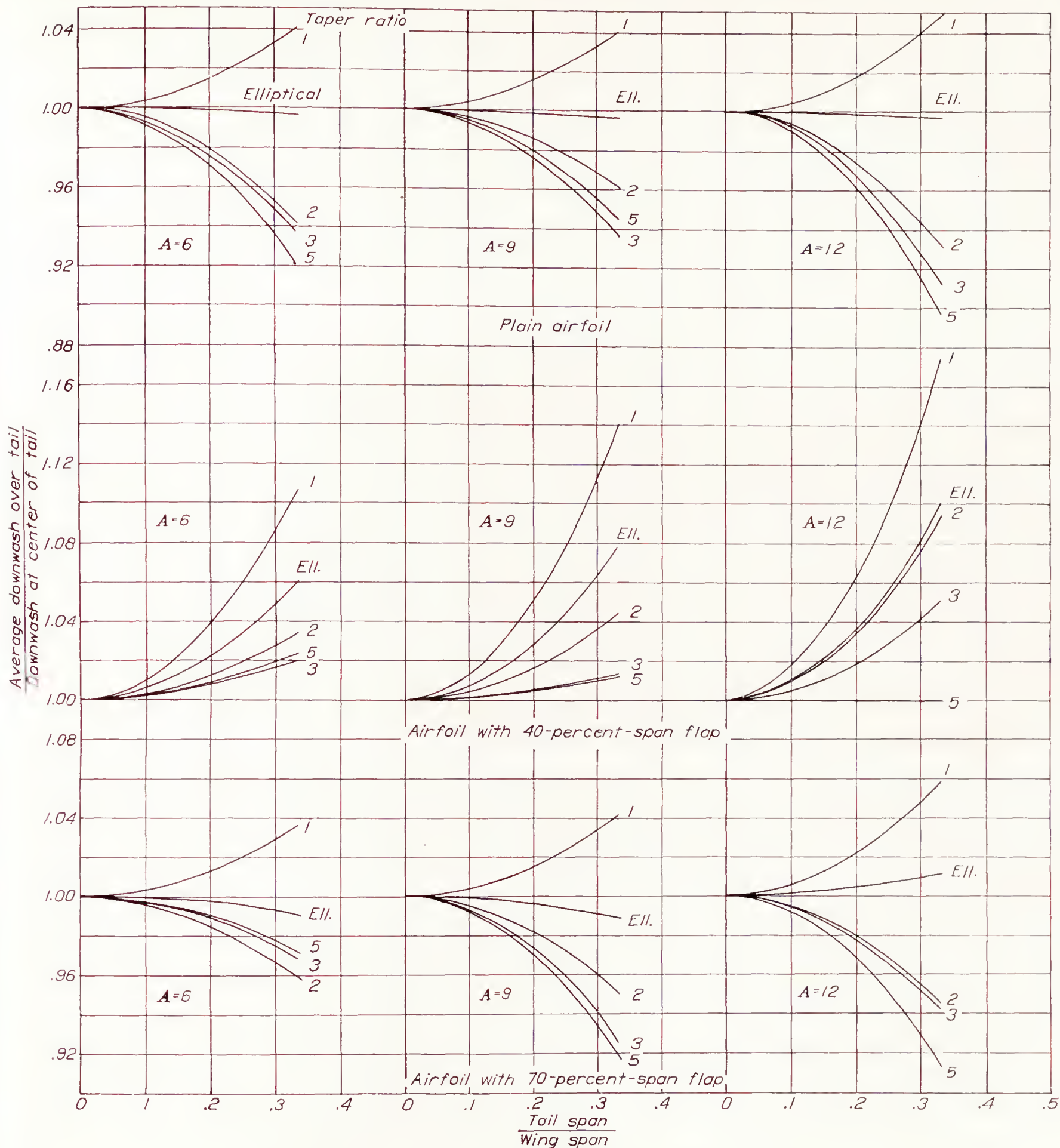
flap are based on the chord of the plain wing. In the case of the Fowler flap, simply extending the flap, with  $\delta_f = 0^\circ$ , increases the lift coefficient by about 26 percent, because the effective chord is increased by this amount. Accordingly, the total increment in lift coefficient on extending the flap is 26 percent of the lift coefficient



(a) Different types of flap on wings 0.12c thick.  
(b) Comparison of flapped wings 0.12c and 0.21c thick.  
FIGURE 20.—Increment in section lift coefficient due to flap.

tion of the downwash in the plane of symmetry and it has been tacitly implied that the downwash so derived applies over the entire tail span. In order to investigate the error thereby involved, calculations of downwash were made for points on the vortex sheet,  $0.75b/2$  back from the quarter-chord line, which is approximately the usual longitudinal position of the tail. The calculations showed that, for some cases, considerable difference exists between the downwash at the center of the tail and the average downwash over the tail.



FIGURE 21.—Correction for the variation of downwash across the tail span for  $x=0.75 b/2$ .

The correction factors have been plotted in figure 21 for all cases.

#### METHODS OF APPLICATION

**Downwash, plain wings.**—The downwash at the tail of an airplane with a wing having neither twist nor a flap is obtained from the charts given in figures 1 to 15 in the following manner:

1. For each angle of attack under consideration, find the longitudinal distance  $x$  of the elevator-hinge axis from the quarter-chord point of the root section and the vertical distance  $m$  of the hinge axis from the trail-

ing edge, or wake origin. Consider  $m$  to be negative if the hinge axis lies below the trailing edge.

2. Find the downward displacement  $h$  of the wake center line at distance  $x$  from the quarter-chord point by multiplying the value at distance  $x$  on the corresponding displacement chart by the lift coefficient  $C_L$ .

3. Locate the point  $(x, |m+h|)$  on the downwash-contour chart<sup>1</sup> and multiply the corresponding down-

<sup>1</sup> The ordinates of the downwash charts are here applied as "vertical distances from the wake" although, corresponding to the method of derivation of the charts, the ordinate scale is labeled "vertical distance from the  $1/4$ -chord point." This interchange is possible because the displacements of the wake center and downwash pattern are equal. (Cf. paragraph 3 of page 2.)



wash angle by the lift coefficient and by the correction factor of figure 21.

**Downwash, flapped wings.**—For an airplane with flaps down, it is first necessary to separate the lift coefficient into two parts. The part  $C_{L_w}$  is the lift coefficient at the particular angle of attack, with flaps up. The part  $C_{L_f}$  is the increase, at the particular angle of attack, on lowering the flap; it may be obtained by the use of figures 19 and 20. Derivation of the downwash proceeds in the following manner:

1. Find the longitudinal distance  $x$  of the hinge axis from the quarter-chord point of the root section, and the vertical distance  $m$  of the hinge axis from the wake origin. The wake origin in this case is not the trailing edge but a point below the trailing edge, as previously explained. (See equation (4).)

2. Find the contribution  $h_1$  of the plain wing to the downward displacement of the wake center line at distance  $x$  from the quarter-chord point by multiplying the value on the corresponding displacement chart (plain wing), at distance  $x$ , by  $C_{L_w}$ .

3. Find the contribution  $h_2$  of the flap to the downward displacement by multiplying the value on the corresponding displacement chart (flap), at distance  $x$ , by  $C_{L_f}$ .

4. Locate the point  $(x, |m+h_1+h_2|)$  on the contour charts for the plain wing and for the flap; multiply the corresponding downwash angles, respectively, by  $C_{L_w}$  and  $C_{L_f}$  and by the correction factors of figure 21 and add in order to get the desired downwash.

This procedure completes the computation of the downwash, except for the wake effect, which increases the downwash above the wake center line and decreases the downwash below it. The amount of this correction will be discussed in the next section. There are two other reasons, previously mentioned, for making still further corrections, seldom exceeding  $0.5^\circ$ , positive above the wake and negative below it. Interference of the fuselage, the nacelles, and the wing-fuselage junctures is only partly predictable; however, for the modern airplane with efficient wing-fuselage junctures and streamline fuselages, it is likely to be of small importance.

For wings or for flap spans other than those covered by the charts, a linear interpolation is usually permissible. For a wing with appreciable aerodynamic twist, the downwash due to the twist will have to be computed from the span load distribution at  $C_L=0$  and applied as an additive correction. Dihedral and sweepback may be neglected.

#### WAKE CHARTS AND FORMULAS

The center line of the wake coincides with the center line of the trailing vortex sheet; hence no new data are

required for locating it. The wake half-width, in chord lengths, is given by the formula

$$\zeta = 0.68c_{d_0}^{1/2}(\xi + 0.15)^{1/2} \quad (5)$$

in which  $\xi$  is in chord lengths. It will be noted that the unit of length in this and the other wake equations is the chord rather than the semispan. Curves of this equation are plotted in figure 22 for different values of the parameter  $c_{d_0}$ .

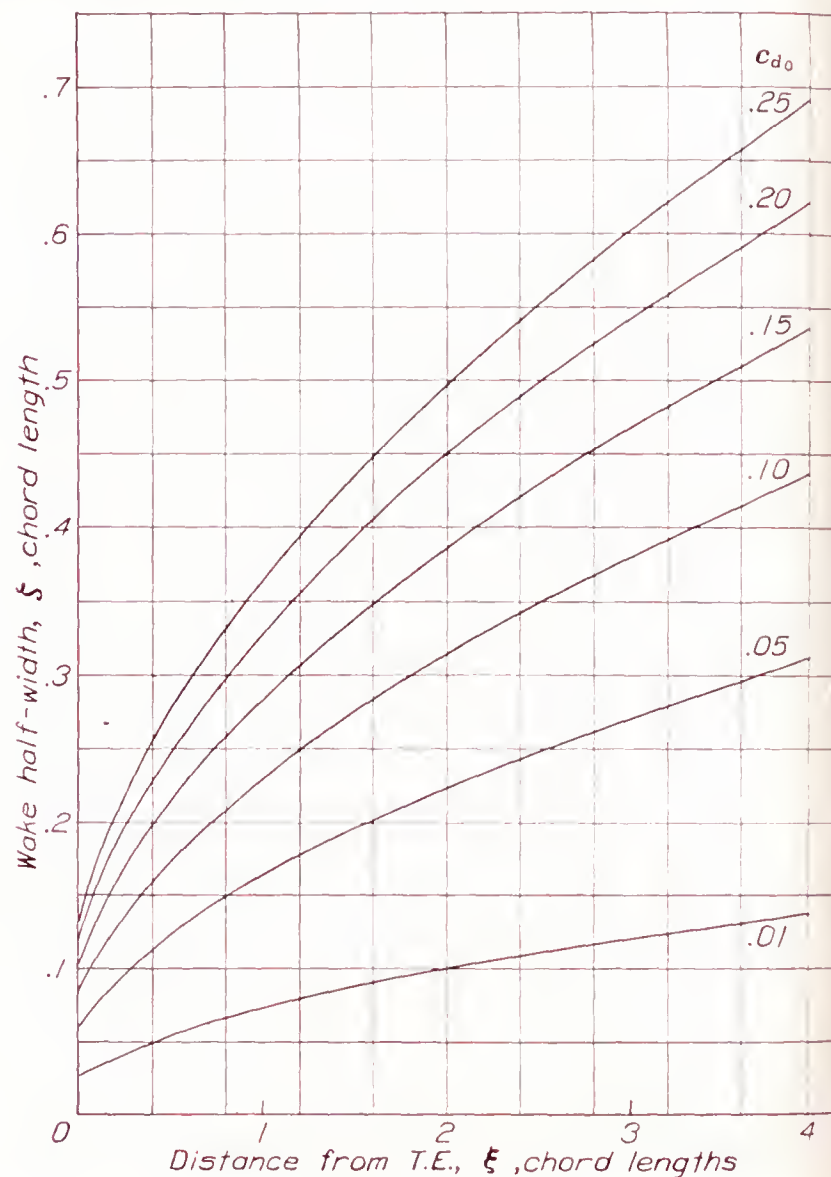


FIGURE 22.—Relation between wake width and distance from trailing edge.  
 $\zeta = 0.68c_{d_0}^{1/2}(\xi + 0.15)^{1/2}$

The maximum loss of dynamic pressure in the wake occurs at the wake center and its value  $\eta$  is given by the formula

$$\eta = \frac{2.42c_{d_0}^{1/2}}{\xi + 0.3} \quad (6)$$

Curves of this equation are plotted in figure 23 for different values of the parameter  $c_{d_0}$ . The distribution of dynamic pressure within the wake is given by the equation

$$\frac{\eta'}{\eta} = \cos^2\left(\frac{\pi \zeta'}{2 \zeta}\right) \quad (7)$$

which is plotted in figure 24.

The effect of the wake on the downwash in and near it is negligible for low profile-drag coefficients as, for example, in the case of plain wings at low angles of attack. It must, however, be taken into account for wings with high-drag flaps and it may be approximately



computed for such cases, as explained in reference 1. Results of some of these computations are shown in

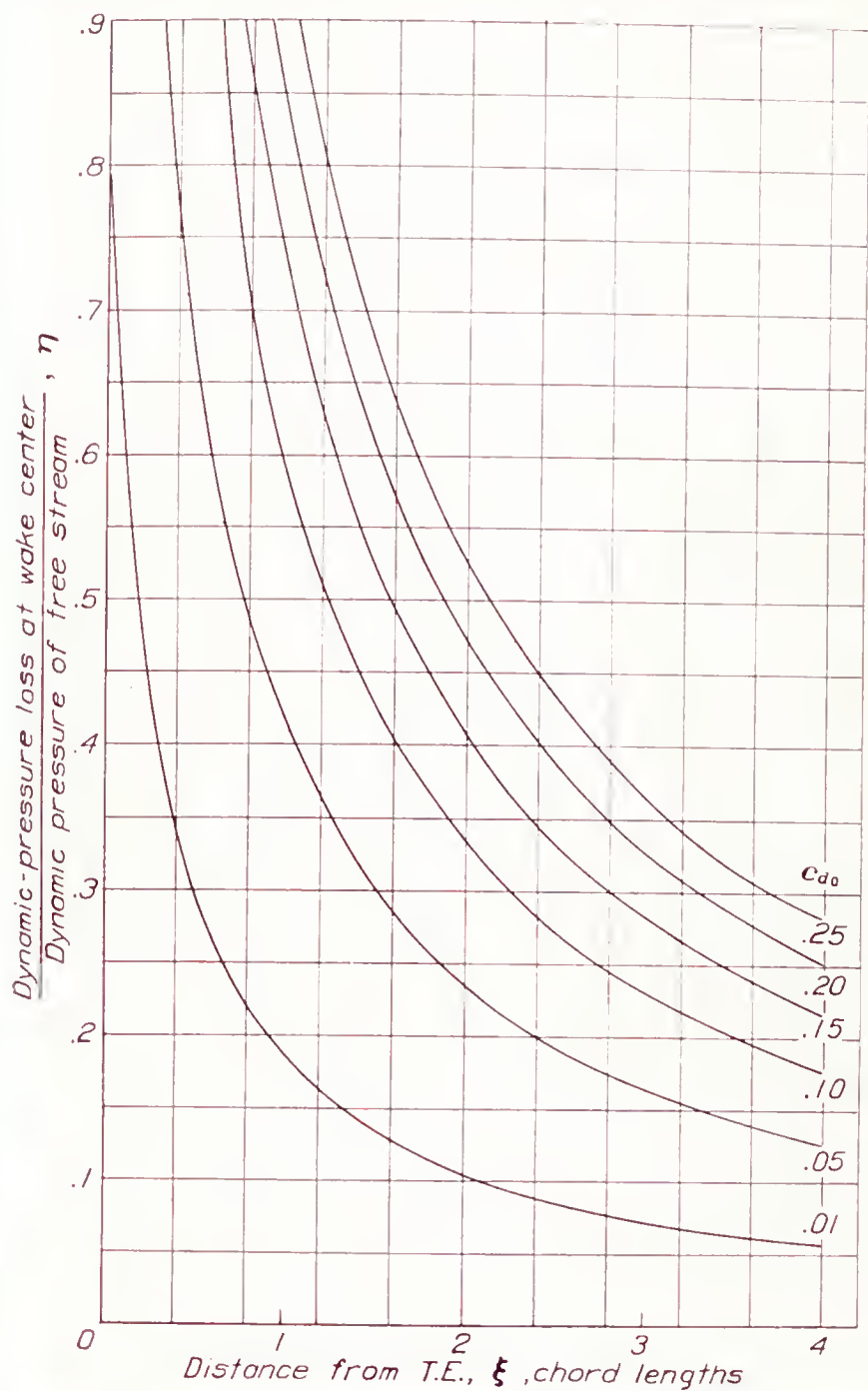


FIGURE 23.—Relation between maximum loss of dynamic pressure in the wake and distance from the trailing edge.

$$\eta = \frac{2.42c_{d0}^{1/2}}{\xi + 0.3}$$

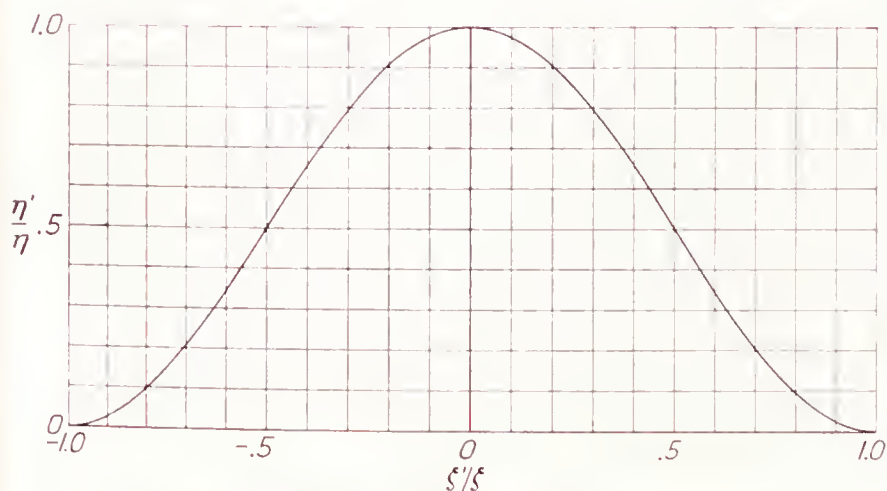
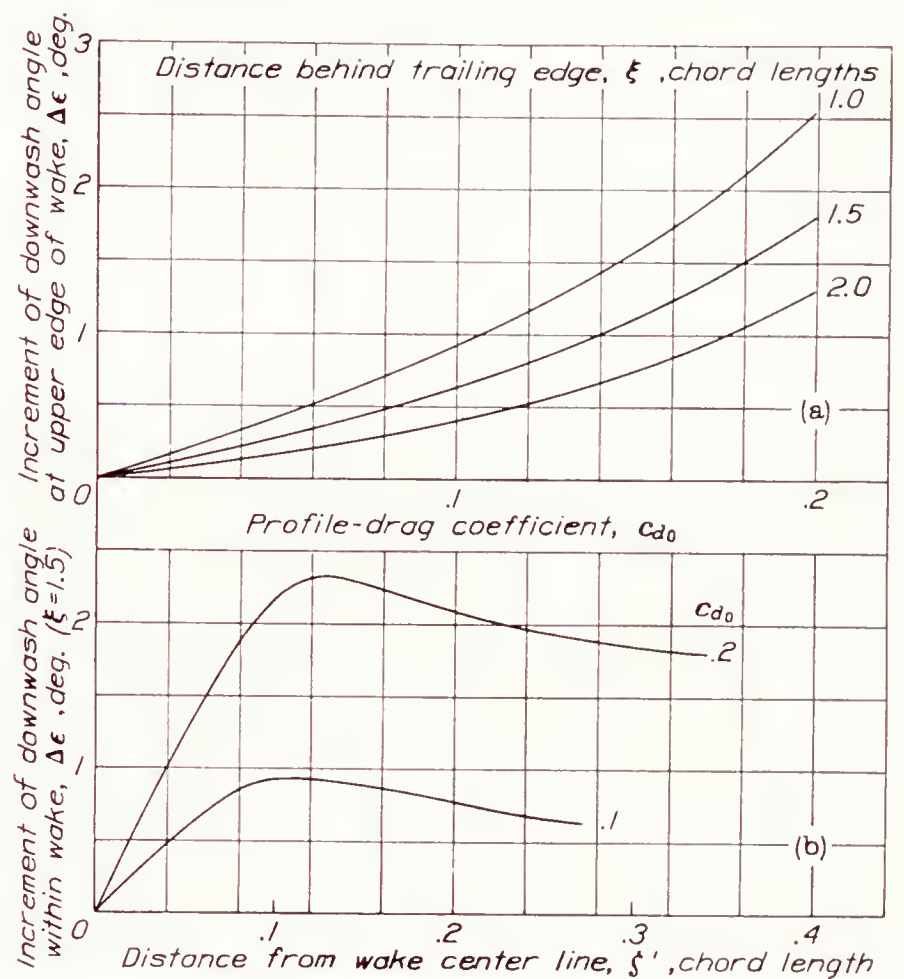


FIGURE 24.—Variation of dynamic-pressure loss across the wake.

$$\frac{\eta'}{\eta} = \cos^2\left(\frac{\pi}{2} \frac{\xi'}{\xi}\right)$$

figure 25. Figure 25 (a) shows the computed effect at the upper edge of the wake for three distances behind the trailing edge; at the lower edge of the wake, it is the same in magnitude but opposite in sign. The effect

diminishes with distance from the wake; for points only a short distance outside the wake (i. e., for the most usual tail positions), however, it is nearly equal to that



(a) At the upper edge of the wake.  
(b) Within the wake.

FIGURE 25.—Wake effect on downwash. The effects are equal, but of opposite sign, below the wake center.

at the wake edge near it. Figure 25 (b) shows some typical variations of the effect within the wake.

In order to facilitate the application of the preceding equations, which involve  $c_{d0}$ , some section profile-drag

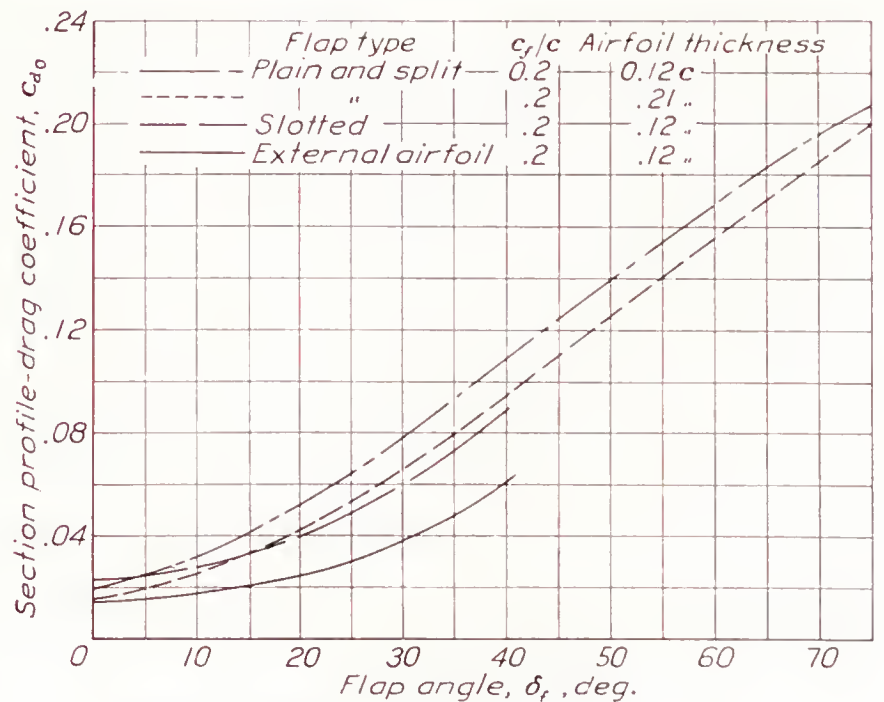


FIGURE 26.—Section profile-drag coefficients for different flaps.

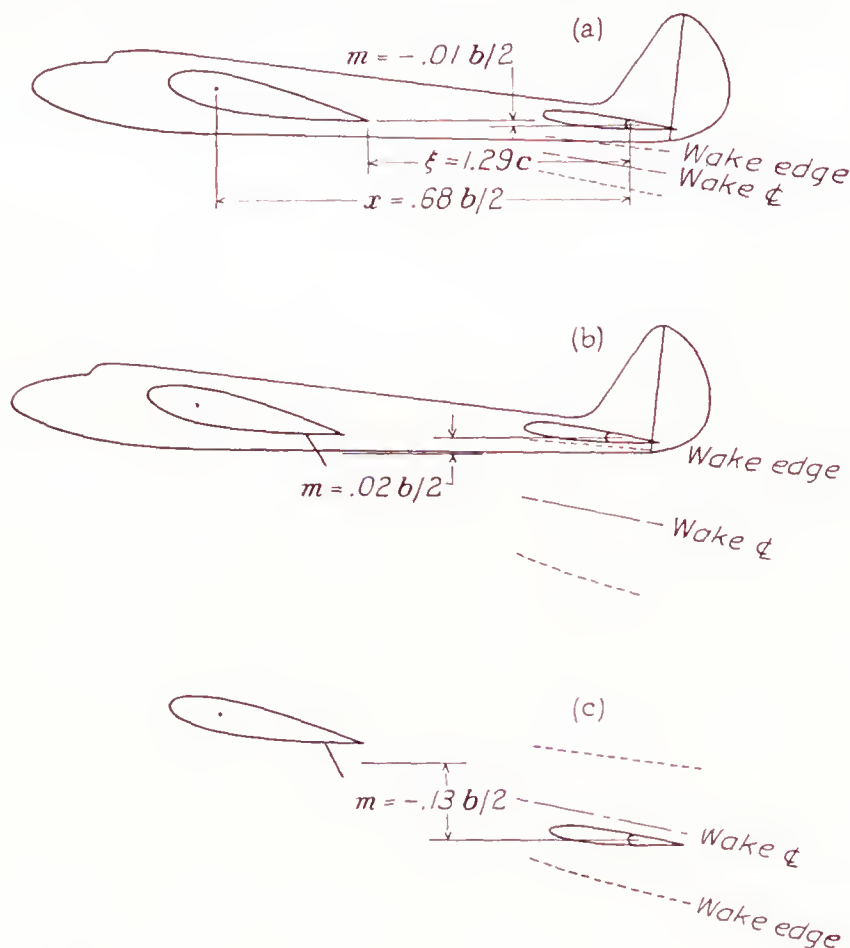
coefficients for the different flaps are presented in figure 26. These data apply particularly in the higher lift range, about  $3^\circ$  to  $4^\circ$  below the stall. They were collected mainly from N. A. C. A. results and from reference 5.



## EXAMPLE OF APPLICATION TO DESIGN

For purposes of illustration, some specimen calculations will be made for a midwing monoplane (fig. 27). The wing is of aspect ratio 9, taper ratio 3:1, and has a split ap of  $0.70b$  span and  $0.20c$  chord. This case is covered by figure 8. The tail span is  $0.3b$ .

The case of the airplane with flaps up will be considered first. It will be assumed that, when the airplane is operating at the attitude shown in figure 27 (a),



(a) Flap up.  
(b) Flap down.  
(c) Flap down, tail in the wake.

FIGURE 27.—Illustration for the specimen calculations of downwash and wake.

the lift coefficient  $C_L$  is 0.9. The steps outlined under Methods of Application are as follows:

1.  $x = 0.68 b/2$ .  $m = -0.01 b/2$ .
2. The downward displacement of the trailing vortex sheet at  $x = 0.68 b/2$  is, for  $C_L = 1.0$ ,  $0.05 b/2$ , so that  $h = 0.9 \times 0.05 = 0.045 b/2$ .
3. Reference to the downwash-contour chart shows that the downwash at point  $(x, |m+h|)$ , or  $(0.68, 0.04)$ , for  $C_L = 1.0$  is  $5.6^\circ$ . Multiplying by  $C_L$  (0.9) and by the correction factor of figure 21 (0.95) gives, for the downwash,

$$\epsilon = 0.9 \times 0.95 \times 5.6 = 4.8^\circ$$

The center of the wake passes  $m+h$  semispans below the hinge axis, as shown, and its half-width  $\zeta$  at this point is obtained from the section profile-drag coefficient (assume  $c_{d_0} = 0.015$ ) and the distance behind the trailing edge ( $\xi = 1.29c$ ), where  $c$  may be taken as the root chord. By equation (5) or figure 22,

$$\zeta = 0.68 \times 0.015^{1/2} \times 1.44^{1/2} = 0.1 \text{ chord}$$

The edges of the wake are shown in the figure. The tail lies outside the wake and, inasmuch as the wake is too slight to affect the downwash, it requires no further consideration.

The airplane at the same attitude, with flap down,  $\delta_f = 60^\circ$ , is shown in figure 27(b). From figure 20,  $\Delta c_i$  is seen to be 1.13 (assuming the wing thickness to be  $0.12c$ ); from figure 19,  $C_{L_f}/\Delta c_i$  is 0.67, so that  $C_{L_f} = 0.76$ . The contribution of the plain wing,  $C_{L_w}$ , is 0.9 as before, since the angle of attack is the same. The steps outlined in Methods of Application are as follows:

1.  $x = 0.68 b/2$ , as before.

$$m = 0.023 b/2.$$

(The wake origin, as indicated by equation (4)

$$\text{and figure 18, is } \frac{(0.1c) \sin 60^\circ + 0.01c}{b/2} \text{ semi-}$$

spans below the wing trailing edge, at the location shown. For this wing,  $b/2 = 3c$ .)

2. The contribution  $h_1$  of the plain wing to the downward displacement is the same as before.  $h_1 = 0.045 b/2$ .

3. For the flap contribution, the chart shows that for  $C_{L_f} = 1.0$  and  $x = 0.68 b/2$ , the displacement is  $0.07 b/2$ .

$$h_2 = 0.76 \times 0.07 = 0.053 b/2.$$

4. The point  $(x, |m+h_1+h_2|)$  is thus  $(0.68, 0.12)$ . Reference to the downwash-contour chart for the plain wing and to figure 21 shows that the plain-wing contribution to the downwash at this point is  $\epsilon_1 = 0.9 \times 0.95 \times 5.0 = 4.3^\circ$ . Similarly, the flap contribution to the downwash at this point is  $\epsilon_2 = 0.76 \times 0.94 \times 6.8 = 4.9^\circ$ . The sum is  $\epsilon_1 + \epsilon_2 = 4.3 + 4.9 = 9.2^\circ$ , to which a wake correction should be applied, as derived in the next paragraph.

The center of the wake in this case passes  $m+h_1+h_2 = 0.12 b/2$  or  $0.36c$  below the hinge axis, as shown. Figure 26 gives  $c_{d_0} = 0.17$  and, with  $\xi = 1.29c$  as before, figure 22 or equation (5) gives the wake half-width:

$$\zeta = 0.68 \times 0.17^{1/2} \times 1.44^{1/2} = 0.34c$$

The edges of the wake are shown in the figure. There is no effect on the dynamic pressure at the tail, for it lies outside the wake. The increase in downwash at the upper edge is found from figure 25 to be  $1.5^\circ$ . The effect at the tail, which is only a small distance from the edge, may be considered to be the same. The downwash is thus  $9.2 + 1.5 = 10.7^\circ$ .

If the relative positions of the wing and tail are such that the tail lies within the wake, as is shown for example in figure 27 (c), the average loss of dynamic pressure at the tail is also required. The loss at the hinge axis may be used for this value although the average over the tail surface may be somewhat different.



The computation of the downwash proceeds as before:

$$x=0.68 \ b/2$$

$$m=-0.13 \ b/2$$

$$h_1=0.045 \ b/2$$

$$h_2=0.053 \ b/2$$

$$|m+h_1+h_2|=0.03 \ b/2=0.09c$$

$$\epsilon_1=0.9 \times 0.95 \times 5.7=4.9^\circ$$

$$\epsilon_2=0.94 \times 0.76 \times 7.8=5.6^\circ$$

$$\epsilon_1+\epsilon_2=10.5^\circ, \text{ which is the downwash uncorrected for wake effect.}$$

The wake effect at the hinge axis is seen, by interpolating between the two curves of figure 25(b), to be about  $1.6^\circ$ , which must now be *subtracted* from the preceding value, for the tail lies below the wake center. The corrected downwash is  $10.5-1.6=8.9^\circ$ .

The computation of the dynamic pressure at this point is as follows:

$$\xi=1.29c$$

$$c_{d_0}=0.17$$

$$\zeta=0.34c$$

$$\zeta'=0.09c, \frac{\zeta'}{\zeta}=0.26$$

$$\eta=\frac{2.42 \times 0.17^{1/2}}{1.29+0.3}=0.63, \text{ from figure 23 or equation (6).}$$

$$\eta'=0.63 \cos^2 \left( 0.26 \frac{\pi}{2} \right)=0.53, \text{ from figure 24 or equation (7).}$$

The dynamic pressure at this point is  $1-\eta'$ , or  $0.47q$ .

LANGLEY MEMORIAL AERONAUTICAL LABORATORY,  
NATIONAL ADVISORY COMMITTEE FOR AERONAUTICS,  
LANGLEY FIELD, VA., *July 14, 1938.*

#### REFERENCES

1. Silverstein, Abe, Katzoff, S., and Bullivant, W. Kenneth: Downwash and Wake Behind Plain and Flapped Airfoils. T. R. No. 651, N. A. C. A., 1939.
2. Anderson, Raymond F.: Determination of the Characteristics of Tapered Wings. T. R. No. 572, N. A. C. A., 1936.
3. Lotz, Irmgard: Berechnung der Auftriebsverteilung beliebig geformter Flügel. Z. F. M., 22. Jahrg., 7. Heft, 14. April 1931, S. 189-195.
4. Pearson, H. A.: Span Load Distribution for Tapered Wings with Partial-Span Flaps. T. R. No. 585, N. A. C. A., 1937.
5. Clark, K. W., and Kirkby, F. W.: Wind Tunnel Tests of the Characteristics of Wing Flaps and Their Wakes. R. & M. No. 1698, British A. R. C., 1936.







## REPORT No. 649

# THE PACK METHOD FOR COMPRESSIVE TESTS OF THIN SPECIMENS OF MATERIALS USED IN THIN-WALL STRUCTURES

By C. S. AITCHISON and L. B. TUCKERMAN

### SUMMARY

*The strength of modern lightweight thin-wall structures is generally limited by the strength of the compression members. An adequate design of these members requires a knowledge of the compressive stress-strain graph of the thin-wall material. The "pack" method was developed at the National Bureau of Standards with the support of the National Advisory Committee for Aeronautics to make possible a determination of compressive stress-strain graphs for such material.*

*In the pack test an odd number of specimens are assembled into a relatively stable pack, like a "pack of cards." Additional lateral stability is obtained from lateral supports between the external sheet faces of the pack and outside reactions. Studies have been made of the reproducibility of the test results by testing packs taken from sheets of aluminum alloy 17ST and steel. The largest spread in yield strength was about 2 percent. Tests were also made to determine whether the results from packs were like those obtained from compact solid specimens. The results indicated that the method of transverse support had no appreciable effect on the yield strength. The largest difference between a pack and a solid specimen was 1.60 percent. Experience gathered in developing the test emphasized the fact that, while the method seemed to furnish results within the same order of accuracy as was usually obtained from other mechanical tests, such as the tensile test, it must be simplified before it can be used economically for inspection testing. The test seems adequate, however, for many problems in structural research.*

### INTRODUCTION

During recent years a remarkable expansion has taken place in the use of thin sheet and thin-wall material in lightweight structures such as airplane wings, and airplane fuselages. The strength of these structures is generally limited by the strength of certain members carrying compressive loads. These members have frequently been designed on the basis of the tensile properties of the material. This is convenient as the tensile test is relatively simple and is widely used. However, it may lead to an unsafe structure, on the

one hand, or an uneconomical structure, on the other hand, if the compressive properties of the material differ from the tensile properties. There is an urgent need for a method which makes possible a direct determination of compressive stress-strain graphs for thin-wall material. In recognition of this need an investigation has been undertaken by the National Bureau of Standards with the financial support of the National Advisory Committee for Aeronautics.

Specimens of thin sheet usually fail through instability before the yield strength is reached. Some methods have been reported for overcoming this difficulty by assembling the material under consideration into a compact unit similar to a compact solid. By these methods failures through instability occur at higher compressive loads.

E. B. Wolff and L. J. G. Van Ewijk (reference) made compressive tests on carefully selected wood and compared the results from "massive" bars with those from bars built up by gluing together lamellae taken from the same wood. They reported that the elastic properties for both kinds of specimens were the same.

A. Robertson (reference 2), in his investigation of the strength of subular struts, gives compressive results on various tubes which were made from strips of wood, about 0.025 inch thick, "\* \* \*" by wrapping the necessary number of strips round a mandril having first spread a fine coating of glue on all the faces that were to come together." He adds that "\* \* \*" the collapsing stress is uniform and practically that of the solid specimen for all values of "\* \* \*" ratios of thickness of the wall to radius of the tube greater than 0.08. In his report Robertson suggests, also, the possibility of combining sheet metal into compact units. He made some experiments on high tensile steel strip, about 0.015 inch thick. He states that "It is very difficult to get a good compression test of the material when in the form of such thin strips. An attempt was made to make a test piece by soldering together a large number of pieces and then machining the resulting block to a square section. The result, however, was not satisfactory."



### PACK TEST

The successful results for tests where pieces of wood are combined into compact units suggest that the compressive properties can be obtained when there is sufficient lateral stability so that the yield strength is reached before the unit buckles.

With this approach a number of methods were tried at this Bureau to develop an adequate technique for compressive tests of thin-wall material. A compressive test (reference 3), which has become known as the pack test, has resulted from this preliminary work. The pack test is described in detail in the following pages. The details are given very fully because minor deviations from these details have, in some cases, produced unsatisfactory results and the necessary time has not been available to investigate just which of these are essential and which are unessential to the success of the test. The method was developed at this Bureau in 1933 and has given satisfactory results in all those cases in which the detail procedure, given below, was closely followed.

The pack test involves the use of external support supplied by a number of transverse members between outside reactions and the external sheet faces of a "pack" of specimens. The test was intended to simulate a block compressive test on a compact solid specimen of the kind described (reference 4), in a tentative specification of the American Society for Testing Materials as a "medium-length" specimen to determine the "general compressive strength properties of metallic materials." It was not intended, however, to determine the modulus of elasticity for which the "long" specimen described in this specification would be preferable.

The pack was composed of an odd number of rectangular specimens taken from the same material. These were assembled with sheet faces in contact to form a compact unit. The strains were measured on the middle specimen of the pack which, therefore, acted as a compression specimen supported on both faces by the remaining specimens of the pack. The specimens were machined using procedures similar to those normally employed for tensile specimens. This avoids other operations, such as forming, riveting, or welding, which are frequently used to stiffen structures and which might change the properties of the specimens.

The lateral supports of the pack were designed to give adequate support against buckling combined with a minimum resistance to displacements parallel to the load. Emphasis was placed on this requirement in order to assure that the method of support would not alter the stress distribution in the compression specimen.

### THE PACK

#### MIDDLE SPECIMEN

The middle specimen *M* of a pack composed of 9 specimens taken from a piece of steel tubing is shown in fig. 1. The middle specimen is also shown in fig. 2

in a pack of 13 specimens taken from aluminum alloy sheet.

The compressive load *P* was applied parallel to the length of the pack and was distributed over the ends of the pack. The lateral edge faces were nominally parallel

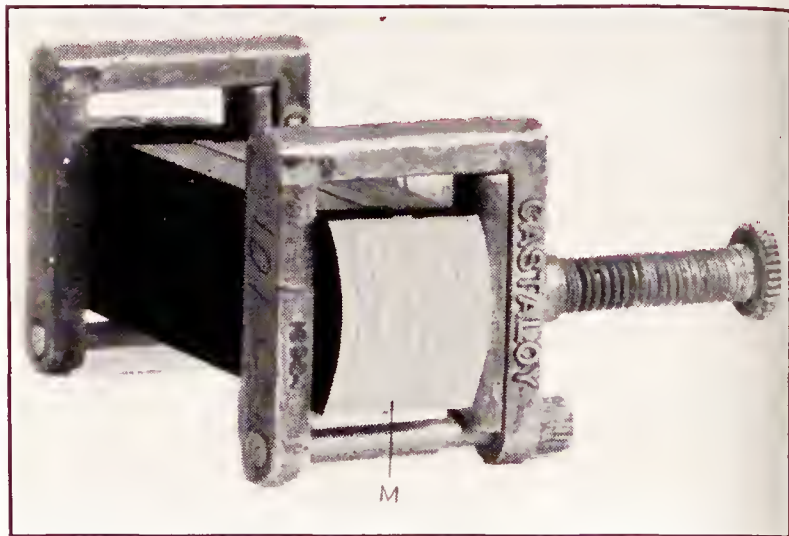


FIGURE 1.—Pack taken from tubing.

allel to the load axis. These faces were left clear so that strain gages to measure the strain could be attached to the specimen. Stability in the direction of the width was obtained by making the specimen sufficiently wide

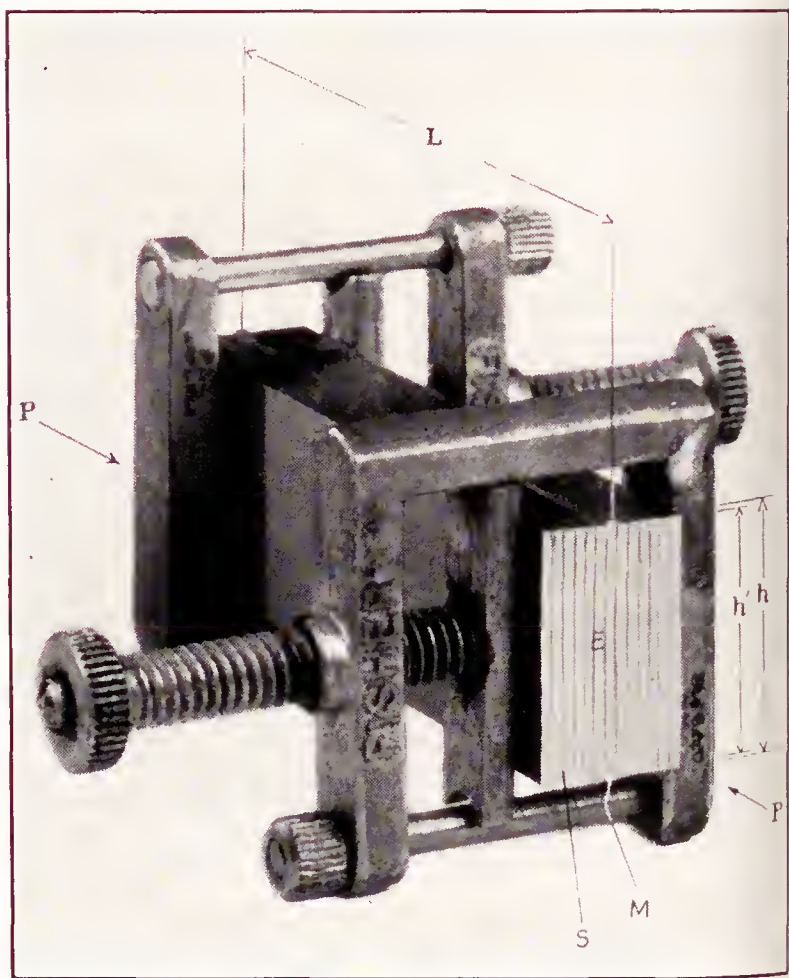


FIGURE 2.—Pack taken from sheet.

comparison to the length. The width *h* was about  $2\frac{3}{32}$  inch. The length *L* was twice the width plus one inch or about  $2\frac{7}{16}$  inches.

#### SUPPORTING SPECIMENS

All of the specimens in the pack were subjected to the axial load. For this reason the supporting specimens *S* (fig. 2) were made the same length as the middle specimen. In order that they would not interfere



with the seating of the strain gages, their width  $h'$  was made 0.02 to 0.05 inch less than the middle specimen.

In practice the specimens were usually slightly warped, bowed, or irregular on the surface. The effect of these deviations from a plane surface was minimized by assembling the supporting specimens, whenever possible, so that they bowed toward the middle specimen. The number of supporting specimens was kept as small as possible consistent with obtaining sufficient stability with the transverse support employed. This was done to limit the sample from the piece, so that specimens would be taken from like material and to obtain packs where only a small amount of material was available. This, also, reduced the cost of machining.

#### MACHINING PROCEDURE

The specimens were finished to width using a series of light cuts in order that the underlying material

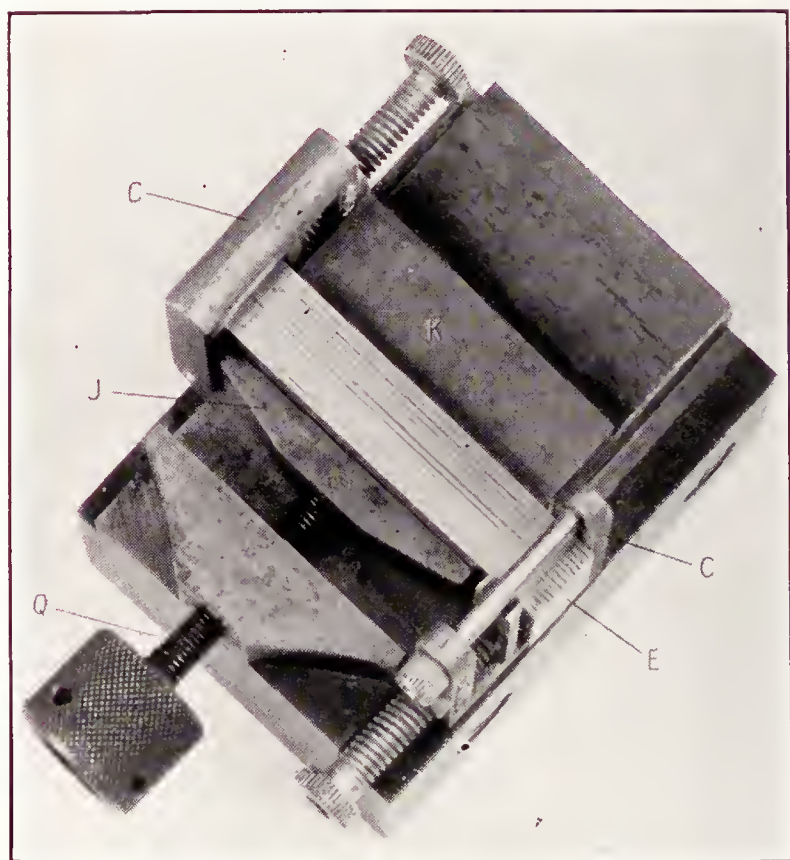


FIGURE 3.—Machining jig.

would be disturbed as little as possible. The lateral edges were finished smooth and the burrs were removed.

The specimens were finished to length after they were assembled in the pack. The machining jig, shown in fig. 3, was used to hold the specimens while they were being machined. This jig was a small vise. The contact surfaces of the jaws were  $1\frac{1}{16}$  inches long and  $\frac{1}{2}$  inch wide. They were plane and smooth. The movable jaw J pivoted at the end of the screw Q. The surfaces of the body of the vise were planes parallel and perpendicular to the stationary jaw K so that the pack could be readily aligned with the machine tool.

A small clamp C was attached at each end of the pack before the ends were machined to hold the specimens in position after the pack was removed from the jig.

The specimens were sawed in a milling machine about  $\frac{1}{32}$  inch longer than the finished length. The ends E were then finished in a surface grinder using a Norton alundum grinding wheel, number 1936:G and kerosene as a lubricant. No attempt was made, however, to make them more than nominally parallel and perpendicular to the axis of the pack. The edges were neither rounded nor marred, appreciably, when the burrs were removed.

#### TRANSVERSE SUPPORT

Transverse support was supplied as shown in fig. 4 by thirty steel pins A on each side of the pack. The pins were in three columns and ten rows. They were  $\frac{1}{8}$  inch in diameter and about two inches long. One end G was hardened and ground to a conical point. The other end H was machined to a hemisphere. The pointed end touched the external sheet face of the pack. The hemispherical end rested in a conical seat in the end of a size 8 machine screw Y, one inch long. The screws were threaded through the webs of two pieces of three inch structural steel channel R and were spaced on  $\frac{1}{4}$ -inch centers.

The channels were bolted at the bottom to the rectangular steel block B and were prevented from spreading at the top by a heavy yoke clamp, not shown in the figure.

#### TEST PROCEDURE

##### TESTING MACHINE

The packs were tested in a vertical, fluid-support, Bourdon-tube hydraulic type of testing machine of 100 kips capacity, using the 10 kip dial and the 50 kip dial to indicate the load. The testing machine is shown in fig. 5.

##### BEARING BLOCKS

The surfaces of bearing blocks which transfer the load from the heads of the testing machine to the pack were flat. They were inspected frequently for dirt or marks. A paper shim D, shown in fig. 4, was used between the  $5\frac{1}{16}$  by 3 by  $1\frac{1}{4}$  inch block B and the surface of the lower head of the testing machine. The bearing block F was a disk of hardened steel  $1\frac{15}{16}$  inches in diameter and  $\frac{1}{16}$  inch thick with top and bottom surfaces smooth-ground.

The bearing block U was attached to the upper head of the testing machine through the  $8\frac{1}{16}$  by  $5\frac{1}{16}$  by  $1\frac{1}{16}$  inch plate I. The upper contact surface of the bearing block was  $3\frac{1}{2}$  inches in diameter and the lower contact surface was  $1\frac{15}{16}$  inches in diameter.

Slight deviations from parallelism of the bearing blocks, the heads of the testing machine, and the ends of the pack which are within the limits of good machine shop practice, may appreciably affect the results of compressive tests. To eliminate these effects and to equalize the load on the specimen a cap-block V and a plaster of paris shim N were used, as shown in fig. 4.



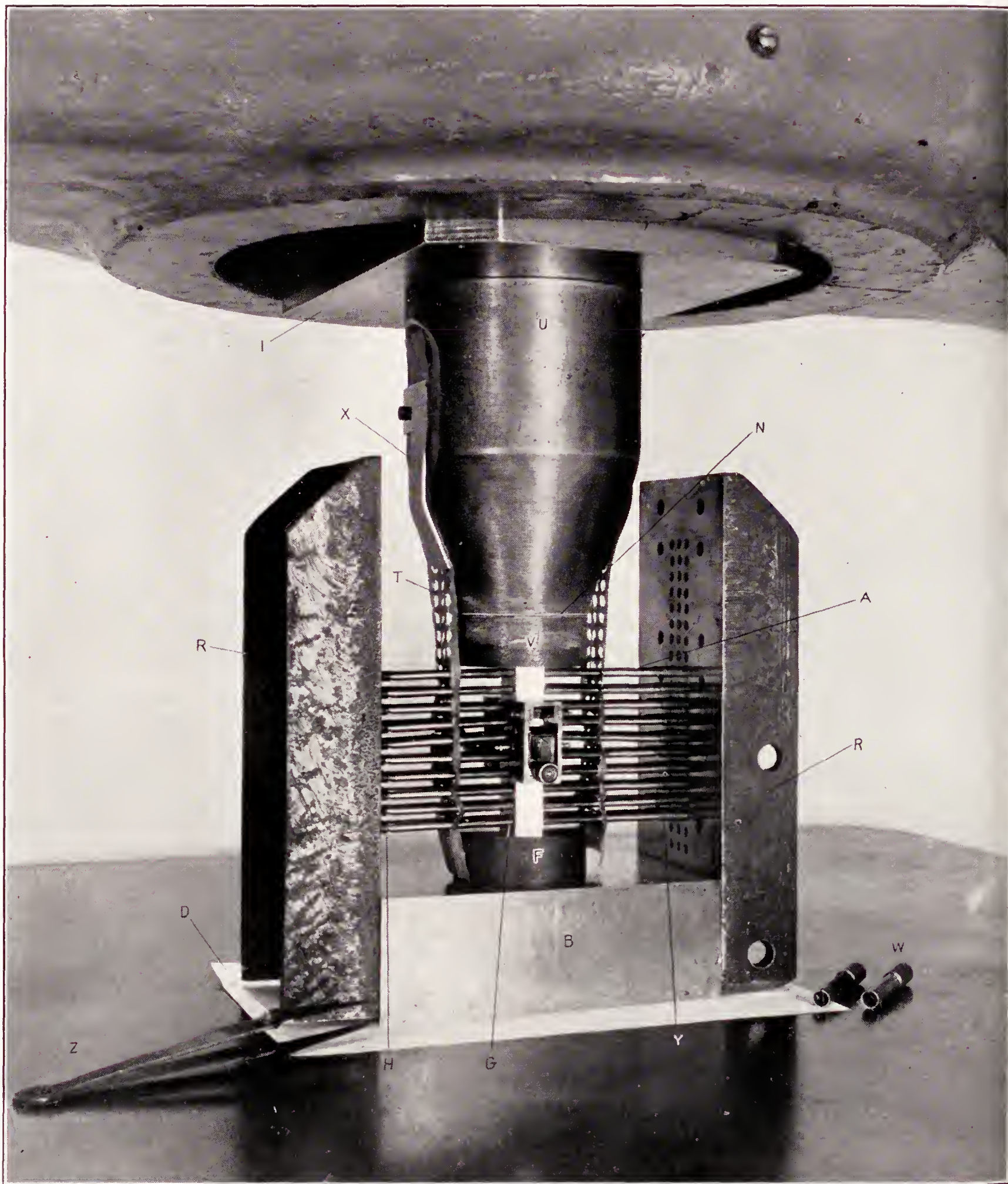


FIGURE 4.—Pack ready for test.



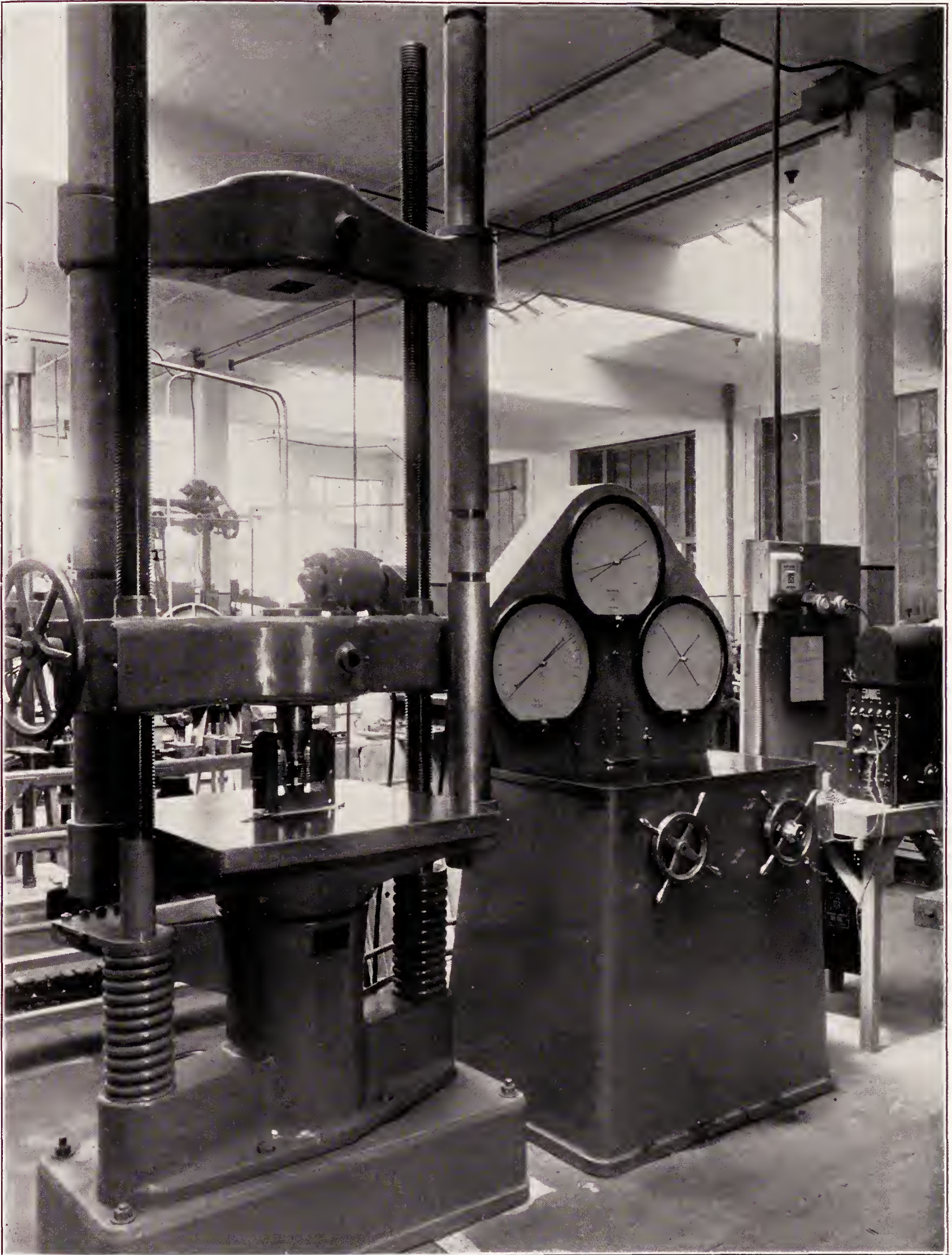


FIGURE 5.—Testing machine.



The cap-block was a disk of hardened steel  $1\frac{5}{16}$  inches in diameter and  $\frac{3}{4}$  inch thick. Its lower surface, which was smooth-ground, made direct contact with the upper end of the pack. The plaster of paris shim did not exceed 0.1 inch in thickness. It was cast, under an initial load of about one kip, between bearing block U and the upper surface of the cap-block V. The plaster was allowed to harden about 10 minutes before the pins were placed in position.

#### ASSEMBLING PINS

The pins providing transverse support were located by a definite procedure. They were first positioned, using the tweezers Z to guide the pins to their proper location and the small wrenches W to turn the screws. The perforated strips of tracing cloth T were used to support the pins in approximately the right position. The screws in the same locations on opposite sides of the pack were then tightened simultaneously and progressively until the points of the pins were slightly embedded in the surface of the pack.

It was considered important to locate the pins in a definite order. Satisfactory results were obtained by using the following sequence. Numbering the pins in rows from 1 to 10 beginning at the top, the pins in rows 5 and 6 of the middle column were located first. Next, those in rows 3, 4, 7, and 8 of the middle column, and then those in rows 3 to 8, inclusive, of the outside columns were located. The clamp at the upper end was then removed and the end of the strip of tracing cloth T placed under the clamp X. The pins in rows 1 and 2 were then located. The clamp at the lower end of the pack was removed and pins in rows 9 and 10 located. All screws were then systematically tried with the wrenches to insure that the ends of all the pins were bearing against the pack.

#### STRAIN GAGES

The strain was measured by a pair of Tuckerman 1-inch optical strain gages (reference 5). These gages were attached on each side of the pack to the edge of the middle specimen.

#### CROSS-SECTIONAL AREA

The cross-sectional area of a pack was computed by dividing the weight of the pack by its length and the density of the material.

#### LIMITATIONS

The limitations of this method of test have not been thoroughly explored. When preliminary results were obtained which apparently furnished satisfactory information for some of the materials generally used in aircraft, tests on a greater number of materials were desired. This has limited the time available for a thorough investigation into the capacity and accuracy of the method under various conditions.

Experience from tests, however, has shown that packs taken from aluminum alloy sheet composed of 13, 7, and 5 specimens of 0.032, 0.064, and 0.081 inch material, respectively, sustained compressive stresses in excess of 60 kips/in.<sup>2</sup> before the packs failed through major instability. Packs composed of five specimens taken from heat-treated chromium-molybdenum steel sheet, 0.05 inch, were subjected to compressive stresses up to 180 kips/in.<sup>2</sup> without failure through major instability. Within these limitations the pack test appears to give the compressive properties of a material within the same order of accuracy as is usually obtained in other mechanical tests, such as the tensile test.

#### TESTS ON BARS

##### PURPOSE

The pack test is based on the assumption that it will give compressive results like those obtained from block compressive tests. A number of comparative tests on packs and on compact solid specimens taken from metal bars were made to see whether or not this assumption was justified.

##### MATERIALS

The following materials were used in making these tests:

- a. Carbon steel bar.  
Condition, cold rolled.  
Shape, round.  
Size, one-inch diameter.
- b. Brass bar.  
Condition, rolled.  
Shape, square.  
Size, one-inch on side.
- c. Aluminum alloy.  
Condition, rolled.  
Shape, round.  
Size, one-inch diameter.

#### SPECIMENS AND PACKS

Compact solid specimens and packs were obtained from alternate locations along each bar. The compact solid specimens were cut with symmetry to the axis of the bar to a size of  $\frac{23}{32}$  by  $\frac{23}{32}$  by  $2\frac{7}{16}$  inch.

The pack specimens were obtained from the same location in the cross section of the bar as the compact solid specimens. The pack was composed of five specimens, 0.1 inch thick. These specimens were prepared by machining with light cuts so that the underlying material was deformed as little as possible. The finished surfaces were smooth and the burrs were removed from the edges.

#### PROCEDURE

The packs were tested using the procedure for pack tests as previously outlined in the section on Test Procedure (p. 3).



One compact solid specimen of each material was tested using pins for transverse support. The remaining compact solid specimens were tested without transverse support. The yield strengths, offset = 0.2 percent, were obtained from the stress-strain graphs in accordance

with American Society for Testing Materials' tentative specification E9-33T (reference 4) method 2 (a).

## RESULTS

The stress-strain graphs for these tests are shown in figs. 6, 7, and 8.

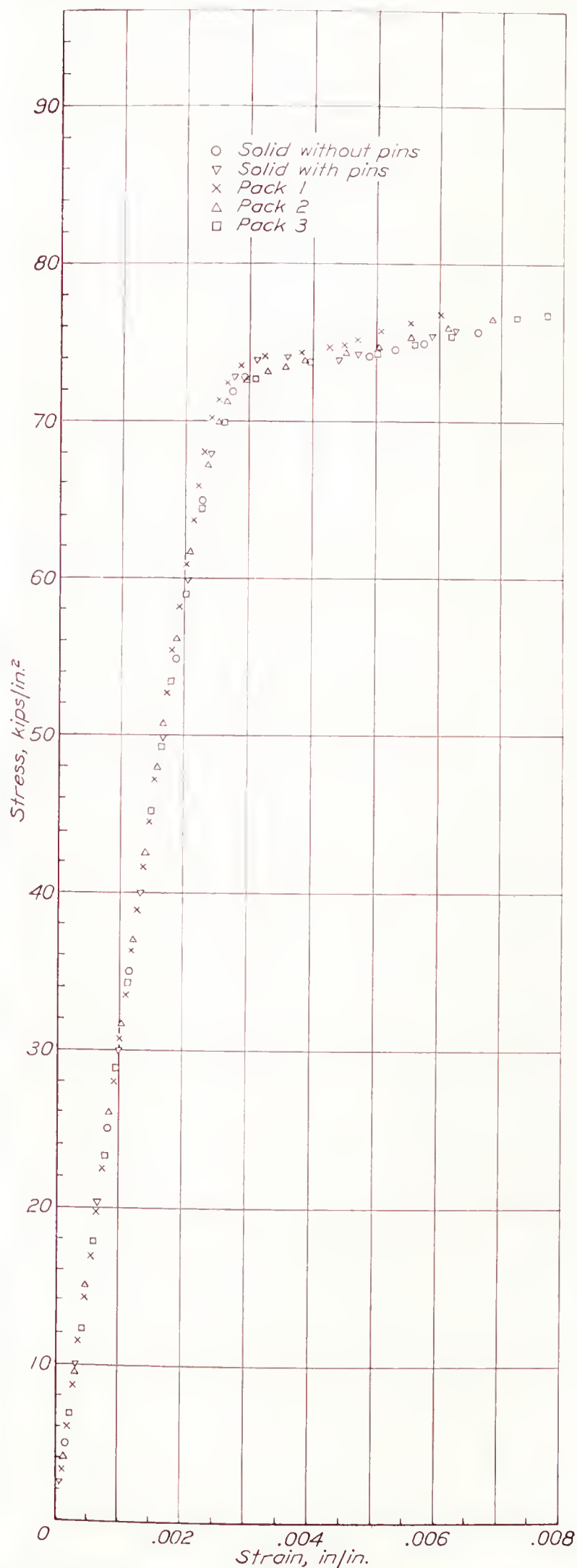


FIGURE 6.—Compressive tests on steel. Packs and compact solid specimens taken from one-inch round bar.

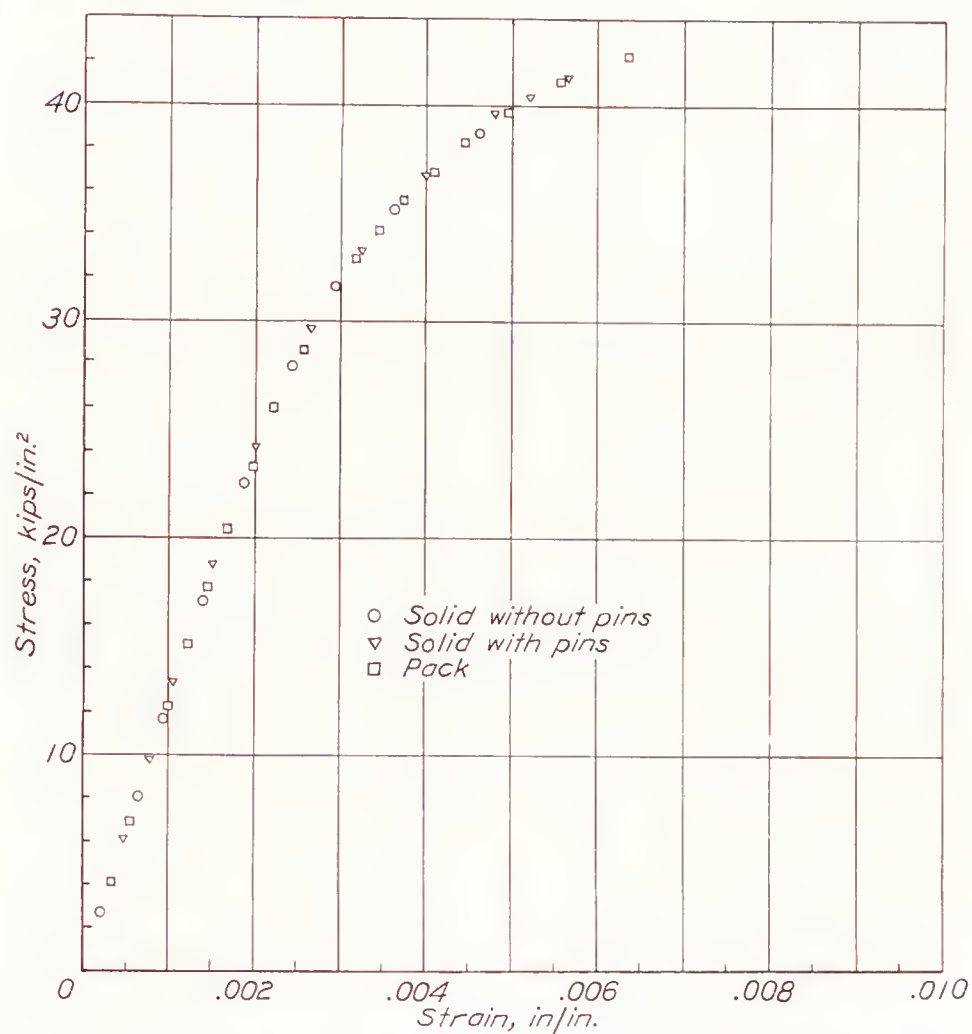


FIGURE 7.—Compressive tests on brass. Pack and compact solid specimens taken from one-inch square bar.

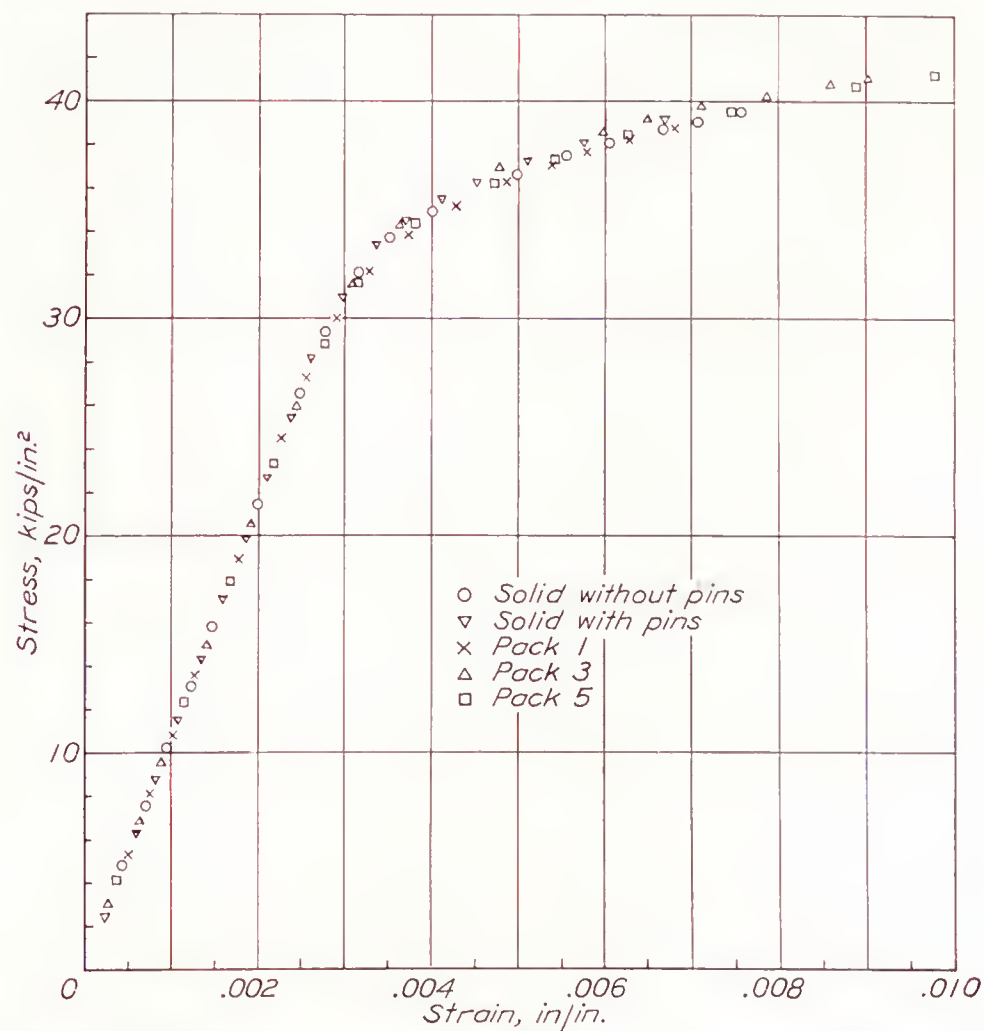


FIGURE 8.—Compressive tests on aluminum alloy. Packs and compact solid specimens taken from one-inch round bar.



The values for yield strength are given in table 1. The last two columns of this table list the difference in yield strength for each specimen from the compact solid specimen, without pins, expressed in kips/in.<sup>2</sup> and in percent.

DISCUSSION

The results of these tests indicate that the pins when used as transverse supports on specimens of steel, brass, and aluminum alloy have no appreciable effect on the value of yield strength. The largest differences between a pack and a solid were 1.22 percent for steel, 0.25 percent for brass, and 1.60 percent for aluminum alloy. These differences are of the same order of magnitude as the spread in yield strengths for successive pack tests on the same material.

TESTS ON SHEET

PURPOSE

Some "pack" compressive tests were made on sheet metal of several materials and several thicknesses. The sheets were from 12 to 18 inches wide and in lengths not less than three feet. The results of these tests were used to obtain information on the effectiveness of the external support and the reproducibility of test results. They were confined to obtaining data for primitive

stress-strain graphs from packs of specimens cut parallel to the long dimension of the sheet, which were called longitudinal packs, and to packs of specimens cut parallel to the short direction of the sheet which were called transverse packs. The tests were not intended to represent a study of present types of sheet metal.

MATERIALS

The following materials were used in making these tests:

- a. Aluminum alloy, 17ST.  
Condition, heat treated.  
Number of sheets, two.  
Thickness, 0.032 and 0.051 inch.  
Width of sheets, 16 inches.  
Received at this laboratory, early in 1932.
- b. Mild-carbon steel (SAE number 1025).  
Condition, cold-finished, quarter-hard.  
Number of sheets, two.  
Thickness, 0.054 and 0.120 inch.  
Width of sheets, 12 inches.  
Received at this laboratory, late in 1930.
- c. Chromium-molybdenum steel.  
Condition, annealed.  
Number of sheets, one.  
Thickness of sheet, 0.053 inch.  
Width of sheet, 18 inches.  
Received at this laboratory, late in 1928.

TABLE 1.—YIELD STRENGTH OF PACKS AND COMPACT SOLID SPECIMENS

Material	Specimen number	Transverse support	Yield strength, offset = 0.2 per cent	Difference from compact solid specimen, without pins	
			kips/in. <sup>2</sup>	kips/in. <sup>2</sup>	Percent
Steel	Compact solid	None	74.0		
	Compact solid	30 pins/side	74.0	0.0	0.00
	Pack #1	30 pins/side	74.9	+0.9	+1.22
	Pack #2	30 pins/side	74.2	+0.2	+0.27
Brass	Compact solid	None	40.5		
	Compact solid	30 pins/side	40.4	-0.1	-0.25
	Pack	30 pins/side	40.5	0.0	0.00
	Compact solid	None	37.5		
Aluminum alloy	Compact solid	30 pins/side	37.9	+0.4	+1.07
	Pack #1	30 pins/side	37.4	-0.1	-0.27
	Pack #3	30 pins/side	38.1	+0.6	+1.60
	Pack #5	30 pins/side	37.6	+0.1	+0.27

SPECIMENS AND PACKS

Longitudinal and transverse specimens were taken from adjacent locations in the sheet. The number of specimens used in each pack is given in table 2, which summarizes the results of the tests. The packs were assembled and machined according to the procedure outlined in the section describing the pack (p. 2).

PROCEDURE

The packs were tested in compression according to the procedure outlined in the section on Test Procedure (p. 3). The initial loads and the cross-sectional areas of each pack are given in table 2.

TABLE 2.—RESULTS OF PACK COMPRESSIVE TESTS ON SHEET

Material	Thick- ness	Direction in sheet	Specimen number	Cross- sectional area	Number of speci- mens in pack	Initial load	Yield strength, offset = 0.2 per- cent	Spread	
	<i>inches</i>			<i>in.<sup>2</sup></i>		<i>kips</i>	<i>kips/in.<sup>2</sup></i>	<i>kips/in.<sup>2</sup></i>	<i>Percent</i>
Aluminum alloy 17ST	0.032	Longitudinal	C-2-L	.295	13	1.1	33.3	0.0	0.00
			C-3-L	.296	13	1.0	33.3		
		Transverse	C-2-T	.297	13	1.1	37.4	0.1	0.27
			C-3-T	.297	13	1.0	37.3		
	0.051	Longitudinal	C-2-L	.189	5	1.1	35.6	0.2	0.53
			C-3-L	.257	7	1.0	35.4		
		Transverse	C-2-T	.187	5	1.1	39.6	0.3	0.76
			C-3-T	.187	5	1.1	39.6		
Chromium-molybdenum steel	0.053	Longitudinal	C-1-L	.195	5	1.0	65.5	1.3	2.00
			C-2-L	.195	5	1.0	61.2		
		Transverse	C-1-T	.197	5	1.1	71.0	0.6	0.84
			C-2-T	.196	5	1.0	71.6		
	0.054	Longitudinal	C-1-L	.196	5	1.1	59.2	0.6	1.01
			C-2-L	.195	5	1.0	59.8		
		Transverse	C-1-T	.194	5	1.1	63.6	0.2	0.31
			C-2-T	.194	5	0.5	63.4		
Mild-carbon steel	0.120	Longitudinal	C-1-L	.429	5	1.1	52.0	0.8	1.53
			C-2-L	.430	5	1.0	52.8		
		Transverse	C-1-T	.425	5	1.1	55.9	0.3	0.53
	C-2-T		.426	5	1.0	56.2			



## RESULTS

The stress-strain graphs for these tests are shown in figs. 9, 10, 11, and 12.

The values for yield strength are given in table 2.

The last two columns of this table list the spread in yield strength, expressed in kips/in.<sup>2</sup> and in percent for specimens of the same kind.

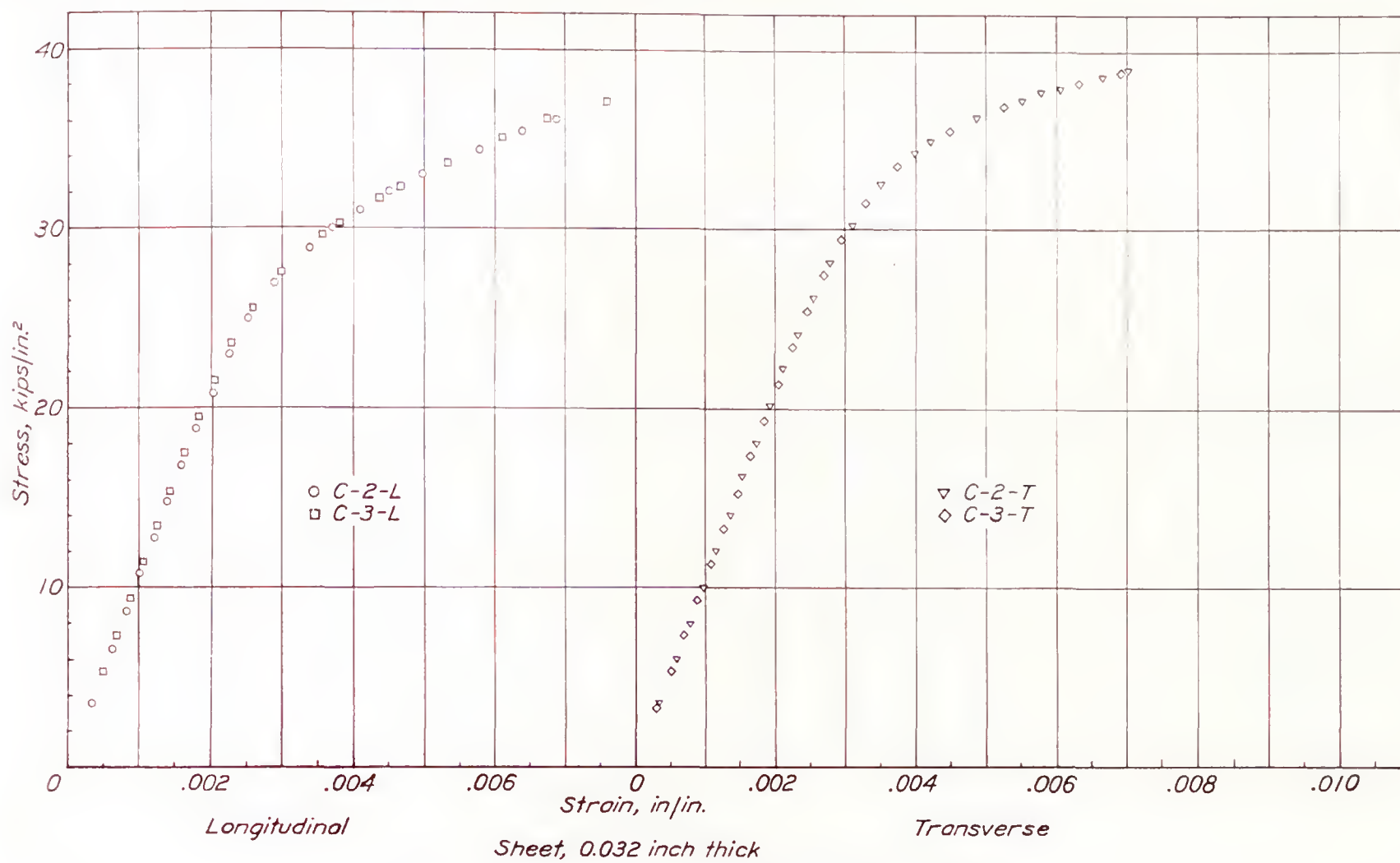


FIGURE 9.—Pack compressive tests on aluminum alloy 17ST sheet.

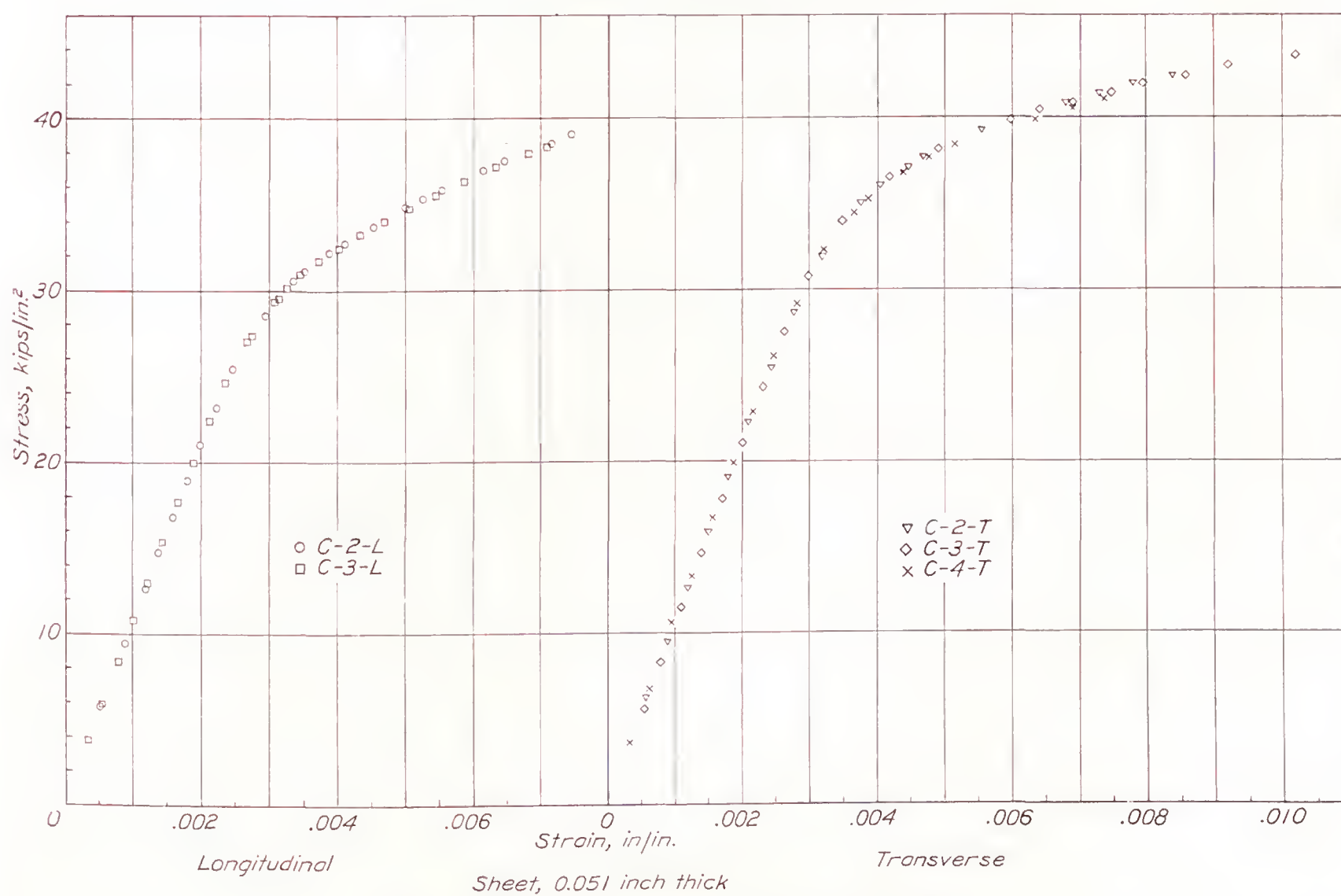


FIGURE 10.—Pack compressive tests on aluminum alloy 17ST sheet.



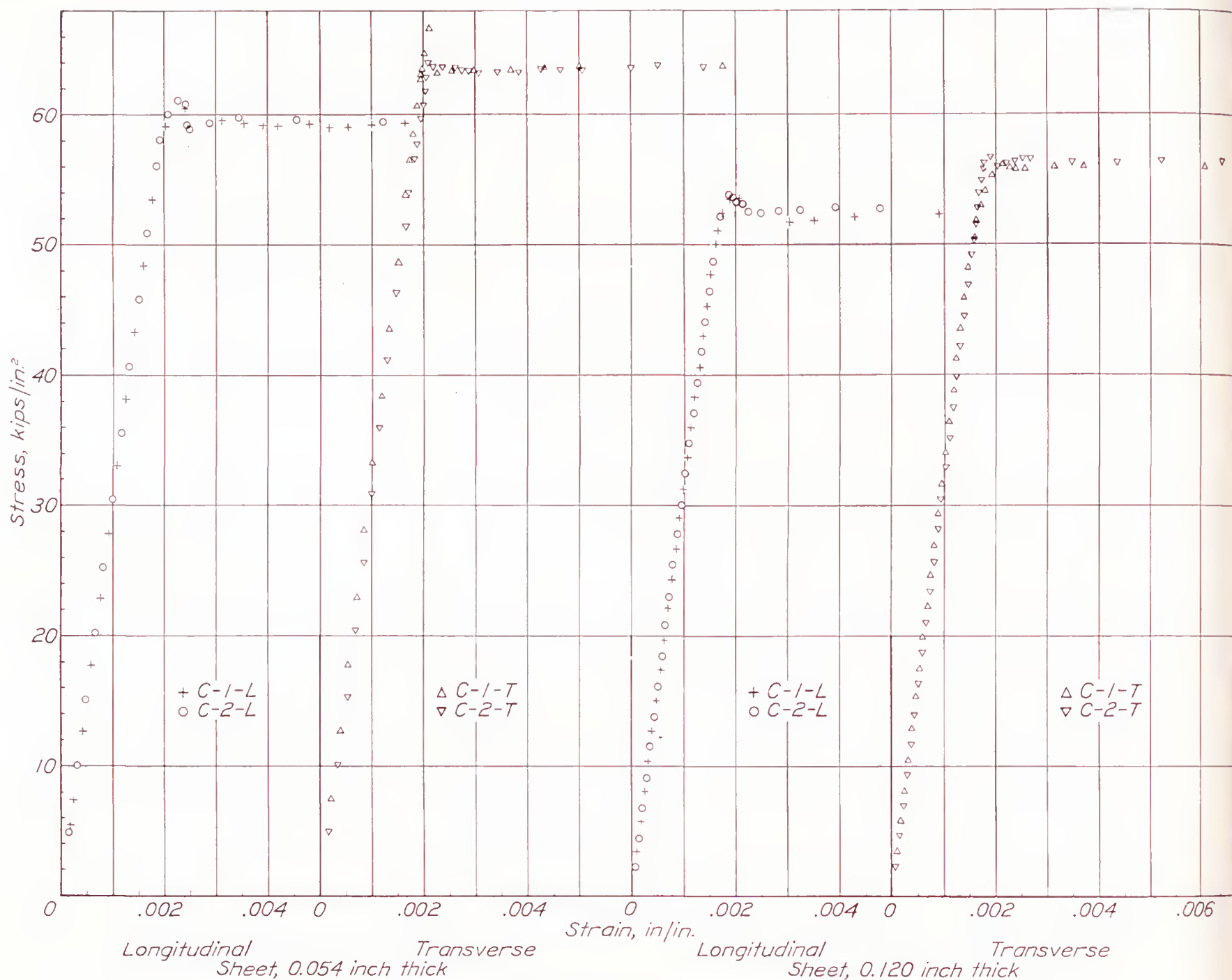


FIGURE 11.—Pack compressive tests on mild-carbon steel sheets (SAE 1025), cold-finished, quarter-hard.

#### DISCUSSION

The pack tests of sheet metal, 0.032 to 0.120 inch thick, include 10 groups of packs with at least 2 packs for each group. With one exception, that of the longitudinal packs for chromium-molybdenum steel 0.053 inch thick, tests in each group were made at different times, a number of months apart. The largest spread in yield strength was about 2 percent. The relatively small spread in yield strengths and the close correspondence of the stress-strain graphs for each group indicate that the test procedure is reproducible within this range of thicknesses of sheet. As metals with markedly different elastic properties were included in the tests the results suggest that the method is suitable for the determination of yield strength for many of the thin materials used in present construction.

#### CONCLUSIONS

Compressive tests on ductile materials with markedly different elastic constants indicate that the compressive stress-strain graphs obtained by the "pack" test agree with those obtained from block compressive tests and

that they can be reproduced within an order of accuracy usually attributed to other mechanical tests, such as the tensile test.

The experience gathered at this laboratory in developing the pack test indicates that the test is adequate for many problems in structural research. It emphasizes, however, the need for simplifying the test procedure before it can be used satisfactorily for inspection testing.

In order to expedite the development of a compressive test of this kind, the details of the apparatus for pack tests have been shown and explained and the test has been demonstrated to representatives of other laboratories. As a result the Aluminum Research Laboratories of the Aluminum Company of America have made pack tests on aluminum alloy sheet using the apparatus and test procedures duplicating as nearly as convenient the apparatus and procedure given in this report. A report entitled "Preliminary Compressive Tests on Thin Sheet using 'Pack' Compression Testing Apparatus" by C. F. Babilon and F. M. Howell was issued by the Aluminum Research Laboratories as "P. T. Report No. 38-17" on April 1, 1938.



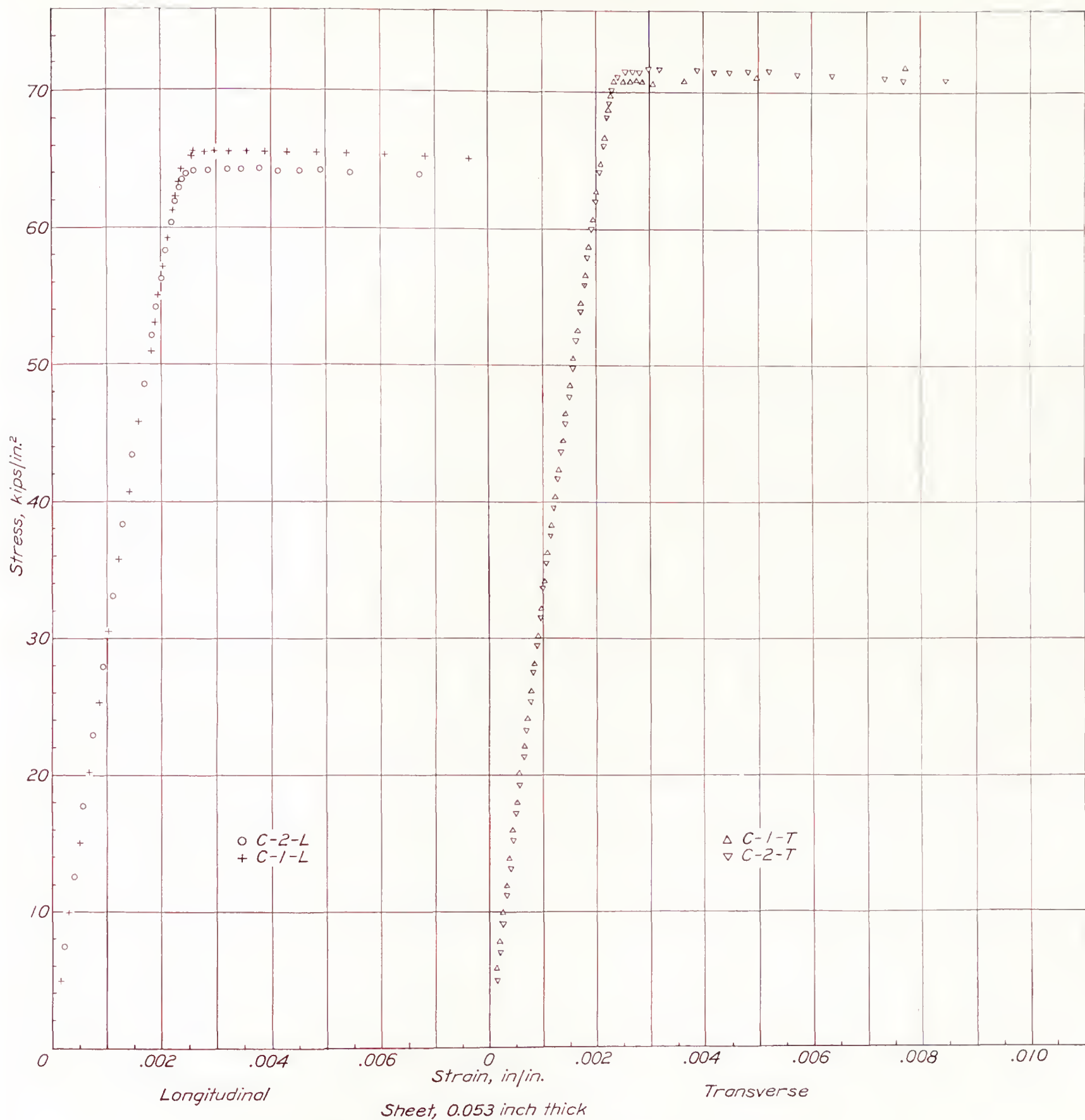


FIGURE 12.—Pack compressive tests on chromium-molybdenum steel sheet, annealed.

## ACKNOWLEDGMENTS

The authors are indebted to their associates in the Engineering Mechanics Section for assistance in the tests and for suggestions concerning test procedures, and to Mr. A. Altman of the machine shop for his suggestions concerning machining procedures. They are indebted to the Bureau of Aeronautics, Navy Department, for sustained interest and cooperation.

## REFERENCES

1. Wolff, E. B., and Van Ewijk, L. J. G.: On Some Elastic Properties of Laminated Wood for Constructional Purposes. International Congress for Testing Materials, Amsterdam, September 12-17, 1927; vol. 2, 1928, pp. 551-566.
2. Robertson, A.: The Strength of Tubular Struts. Proc. Roy. Soc. (London), Series A, vol. 121, 1928, pp. 558-585.
3. National Advisory Committee for Aeronautics Nineteenth Annual Report, 1933, pp. 23-26. Report of Subcommittee on Aircraft Structures.
4. American Society for Testing Materials—Tentative Methods of Compression Testing of Metallic Materials (E9-33T). Tentative Standards, 1936, pp. 1272-1279.
5. Tuckerman, L. B.: Optical Strain Gages and Extensometers. Proc. Am. Soc. for Testing Materials, vol. 23, Part II, 1923, pp. 602-610.







## REPORT No. 650

# THE AERODYNAMIC CHARACTERISTICS OF SIX FULL-SCALE PROPELLERS HAVING DIFFERENT AIRFOIL SECTIONS

By DAVID BIERMANN and EDWIN P. HARTMAN

### SUMMARY

*Wind-tunnel tests are reported of six 3-blade 10-foot propellers operated in front of a liquid-cooled engine nacelle. The propellers were identical except for blade airfoil sections, which were: Clark Y, R. A. F. 6, N. A. C. A. 4400, N. A. C. A. 2400-34, N. A. C. A. 2R<sub>2</sub>00, and N. A. C. A. 6400. The range of blade angles investigated extended from 15° to 40° for all propellers except the Clark Y, for which it extended to 45°.*

*The results showed that the range in maximum efficiency between the highest and the lowest values was about 3 per cent. The highest efficiencies were for the low-camber sections. An analysis of the results indicated that blade sections for controllable propellers which are not limited in diameter should be selected chiefly on a basis of minimum drag (which affects maximum efficiency) inasmuch as the maximum lift coefficients had only a small effect on the take-off characteristics within the range investigated because stalling, in general, did not occur. Sections for fixed-pitch propellers should be selected on a basis of both minimum drag and maximum lift, particularly for blade-angle settings of 20° and over, because the take-off thrust power increased with maximum lift for the higher blade angles.*

### INTRODUCTION

The Clark Y and the R. A. F. 6 airfoil sections have been standard in the design of propellers in this country for many years. The R. A. F. 6 section was favored in early designs but has given way to the Clark Y section more recently, particularly for metal controllable propellers. The relative merits of the two sections for propeller use have been fairly well established by both high-speed airfoil and full-scale propeller tests. The airfoil tests reported in reference 1 showed the Clark Y section to have a lower minimum drag and a lower maximum lift than the R. A. F. 6 section, which indicates that a propeller with the Clark Y section would be

superior for the high-speed or cruising conditions but inferior for take-off with fixed-pitch propellers. The propeller results of reference 2 qualitatively substantiate the airfoil results. The principal physical difference between the two sections is the shape of the mean camber lines; the camber line of the R. A. F. 6 section is higher than that of the Clark Y, particularly for the nose parts of the sections.

The present investigation was made to determine the aerodynamic qualities of six propellers having different sections. The Clark Y and the R. A. F. 6 sections were included for comparative purposes. Two of the other propellers were designed by the Bureau of Aeronautics, Navy Department; the N. A. C. A. 4400 series section was used for one, and the N. A. C. A. 4400 series section was used for the inner half of the other, the N. A. C. A. 2400-34 series section being used for the outer half. It may be noted in reference 3 that the N. A. C. A. 4409 section (used at 0.75 propeller radius) has a high  $C_{L_{max}}$  and a fairly low  $C_{D_{min}}$  and is therefore a good compromise between the Clark Y and the R. A. F. 6 sections. In reference 4 the N. A. C. A. 2409-34 section is recommended for propellers, particularly because of its low  $C_{D_{min}}$  and delayed compressibility stall at high speeds. The section is best suited for only the tip sections of propellers, however, because the  $C_{L_{max}}$  is low at moderate speeds.

In addition to the four propellers described, there were designed at the N. A. C. A. laboratory two additional propellers that incorporated sections of extreme characteristics. One propeller has sections of the low-camber N. A. C. A. 2R<sub>2</sub>00 series, which has a low  $C_{D_{min}}$  and a low  $C_{L_{max}}$ ; the other propeller has the high-camber N. A. C. A. 6400 series section, which has a high  $C_{D_{min}}$  and a high  $C_{L_{max}}$ . (See reference 3.) Tests of these propellers were added to the program to increase the known range of the propeller characteristics that are dependent upon the amount of section camber present.



## APPARATUS AND METHODS

Since the description of reference 5 was written, the propeller-research tunnel has been modified to the extent of installing an electric motor to drive the tunnel propeller and of replacing the balance with a more

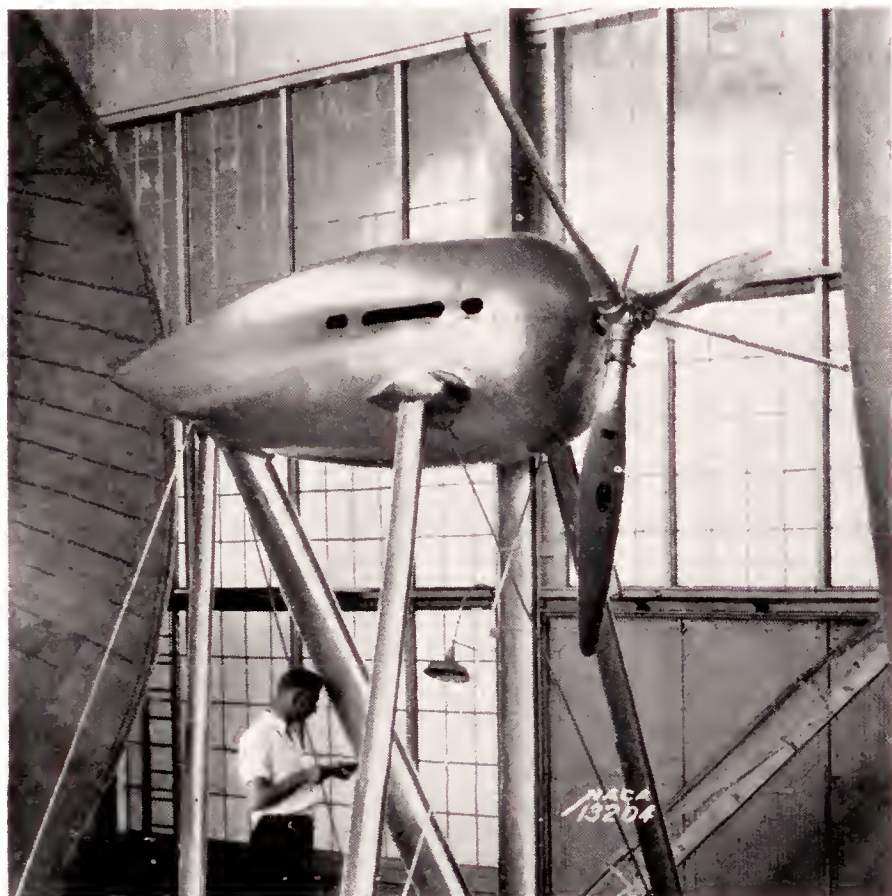


FIGURE 1.—Liquid-cooled engine nacelle.

modern one capable of simultaneously recording all the forces.

A 600-horsepower Curtiss Conqueror engine (GIV-1570) was used to drive the test propellers. The engine was mounted in a cradle dynamometer free to rotate about an axis parallel to the propeller axis and



FIGURE 2.—Photograph showing the plan form of all the propellers tested.

located at one side of the engine. The torque reaction was transmitted from the other side of the engine to recording scales located on the floor of the test chamber. The propeller speed was measured by a calibrated electric tachometer.

The engine was housed in a nacelle representative of the type used for liquid-cooled engines. (See fig. 1.) The nacelle is oval in cross section, 43 inches in

height, 38 inches in width, and 126 inches in length. A scale drawing of the nacelle is given in reference 6.

All six propellers tested have three blades, are 16 feet in diameter, and are identical in shape except for blade sections. Table I gives the principal physical characteristics of the propellers tested.

TABLE I

Propeller (Bureau of Aeronautics, Navy Department drawing No.)	Blade airfoil section	Camber (percent chord)	Position of maximum camber (percent chord)
5868-9	Clark Y	12.6	40
5868-R6	R. A. F. 6	14.0	30
6623-A	N. A. C. A. 4400 series	4.0	40
6623-B	N. A. C. A. 4400 series inner half.	4.0	40
	N. A. C. A. 2400-34 series outer half.	2.0	
6623-C	N. A. C. A. 2R <sub>2</sub> 00	2.0	30
6623-D	N. A. C. A. 6400	6.0	40

<sup>1</sup> For the 0.75 radius station only.

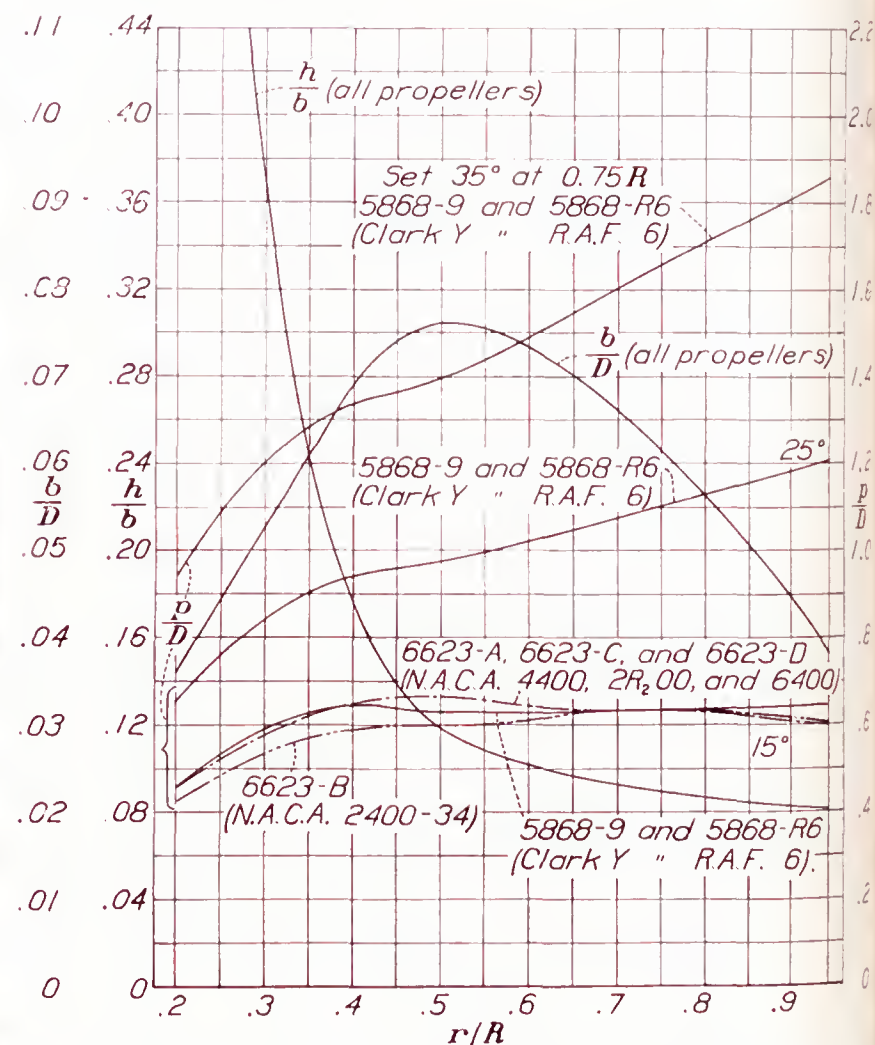


FIGURE 3.—Blade-form curves for all propellers tested.  $D$ , diameter;  $R$ , radius to the tip;  $r$ , station radius;  $b$ , section chord;  $h$ , section thickness;  $p$ , geometric pitch.

Throughout this report, the propellers will be individually referred to according to their sections or grouped according to camber ratio. Propeller 6623-B, for example, will be designated the N. A. C. A. 2400-34 propeller.

Figure 2 shows the plan form of the blades; the blade-form curves are given in figure 3.



It may be noted that the geometric pitch is different for all of the propellers except for the 5868-9 and the 5868-R6. The propellers of N. A. C. A. section were designed with the blade angle of each section, measured from the angle for zero lift, the same as for propeller 5868-9. As a result of this method of design, all the propellers have the same effective pitch distribution along the blade but, of course, the pitches measured with respect to the chord lines are different.

Ordinates for the Clark Y and the R. A. F. 6 propeller sections are given in table II and those for the four propellers with the N. A. C. A. sections are given in table III. The outlines of each blade section for the 0.70 radius are given in figure 4.

The method of testing in the propeller-research tunnel consists in maintaining the propeller speed constant and increasing the tunnel speed in steps up to the maximum value of 115 miles per hour. Higher values of  $V/nD$  are obtained by reducing the engine speed until zero thrust is reached. Complications arising from compressibility were avoided by running the tests at tip speeds of 525 feet per second and less. The standard initial testing propeller speed of 1,000 r. p. m. could not be maintained for the higher blade-angle settings, owing to the limitation of engine power; the following schedule was therefore adhered to:

*Propeller speeds for tunnel speeds below 115 miles per hour*

Blade angle, deg.	Initial propeller speed, r. p. m.
15-----	1, 000
20-----	1, 000
25-----	800
30-----	800
35-----	800
40-----	700
45-----	700

For  $V/nD$  values higher than can be obtained from the foregoing schedule, the approximate test propeller speed may be computed from the relation

$$\text{r. p. m.} = \frac{K}{V/nD}$$

where  $K=1,000$  for  $V=115$  miles per hour and  $D=10$  feet.

## RESULTS AND DISCUSSION

The results are reduced to the usual coefficients of thrust, power, and propulsive efficiency defined as:

$$C_T = \frac{\text{effective thrust}}{\rho n^2 D^4} = \frac{T - \Delta D}{\rho n^2 D^4}$$

$$C_P = \frac{\text{engine power}}{\rho n^3 D^5}$$

$$\eta = \frac{C_T}{C_P} \frac{V}{nD}$$

where

$T$  is tension in propeller shaft, pounds.

$\Delta D$ , increase in body drag due to slipstream, pounds.

$\rho$ , mass density of the air, slugs per cubic foot.

$n$ , propeller rotational speed, revolutions per second.

$D$ , propeller diameter, feet.



Clark Y section, propeller 5868-9.



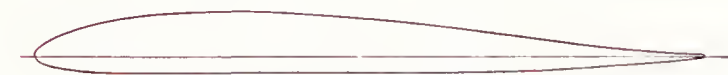
R. A. F. section, propeller 5868-R6.



N.A.C.A. 4400 series, propeller 6623-A; also inner half of propeller 6623-B.



N.A.C.A. 2400-34 series, outer half of propeller 6623-B.



N.A.C.A. 2R200 series, propeller 6623-C.



N.A.C.A. 6400 series, propeller 6623-D.

FIGURE 4.—Blade sections drawn to scale for the 0.70 radius.

Charts for selecting or designing propellers are given in the form of  $C_s$  against  $\eta$  and  $V/nD$ , where  $C_s = \sqrt[5]{\rho V^5 / P n^2}$ .

The procedure of plotting lines of constant thrust with respect to the power is now standardized and facilitates calculating the thrust at all air speeds for controllable and fixed-pitch propellers. The outline of the method is given in reference 6.

The basic results are presented in the form of curves in figures 5 to 28; comparisons and derived data are given in figures 29 to 42. The test results have been tabulated in six tables and are available on request from the National Advisory Committee for Aeronautics.



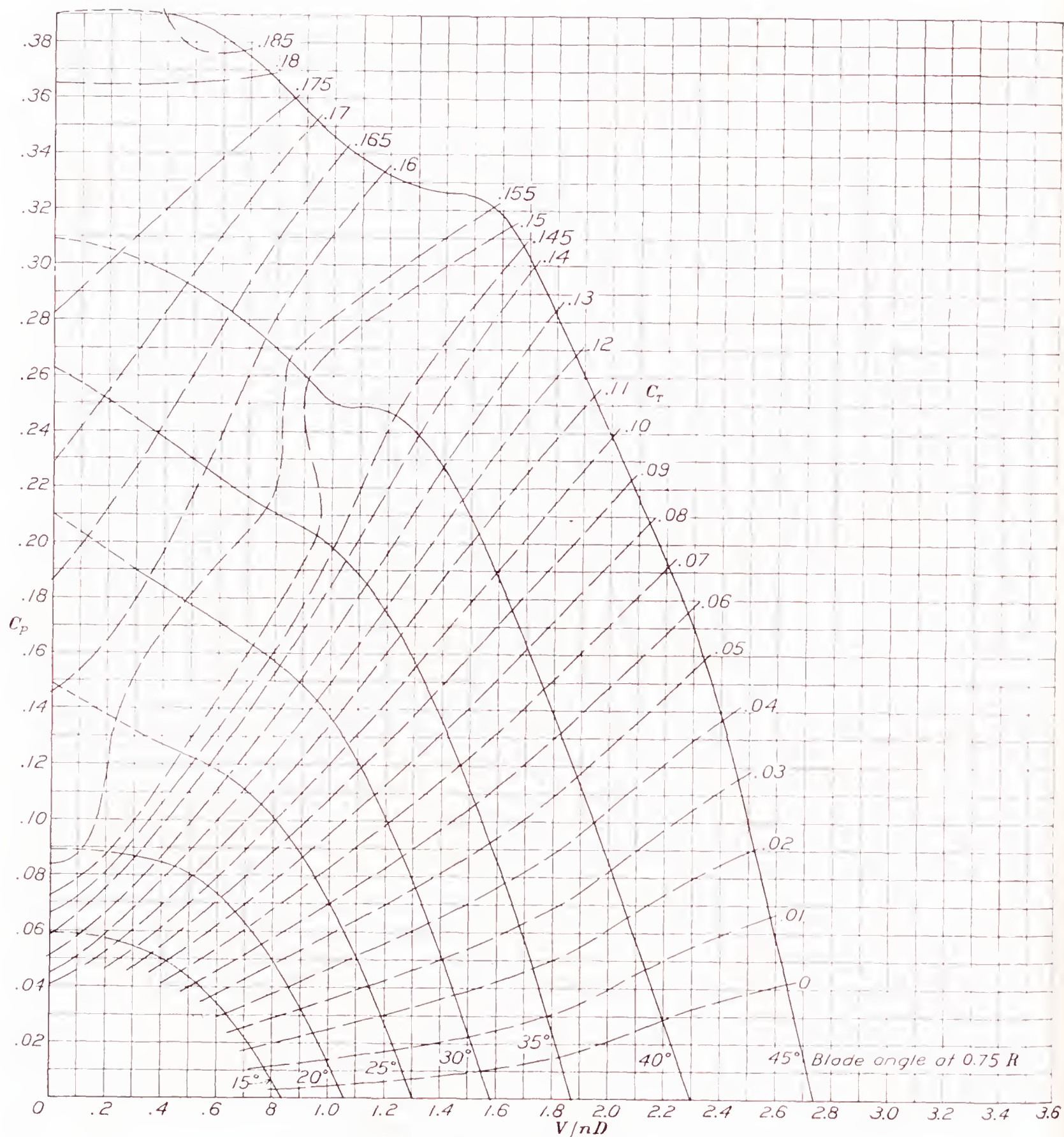


FIGURE 5.—Power-coefficient curves for propeller 5868-9 (Clark Y section).



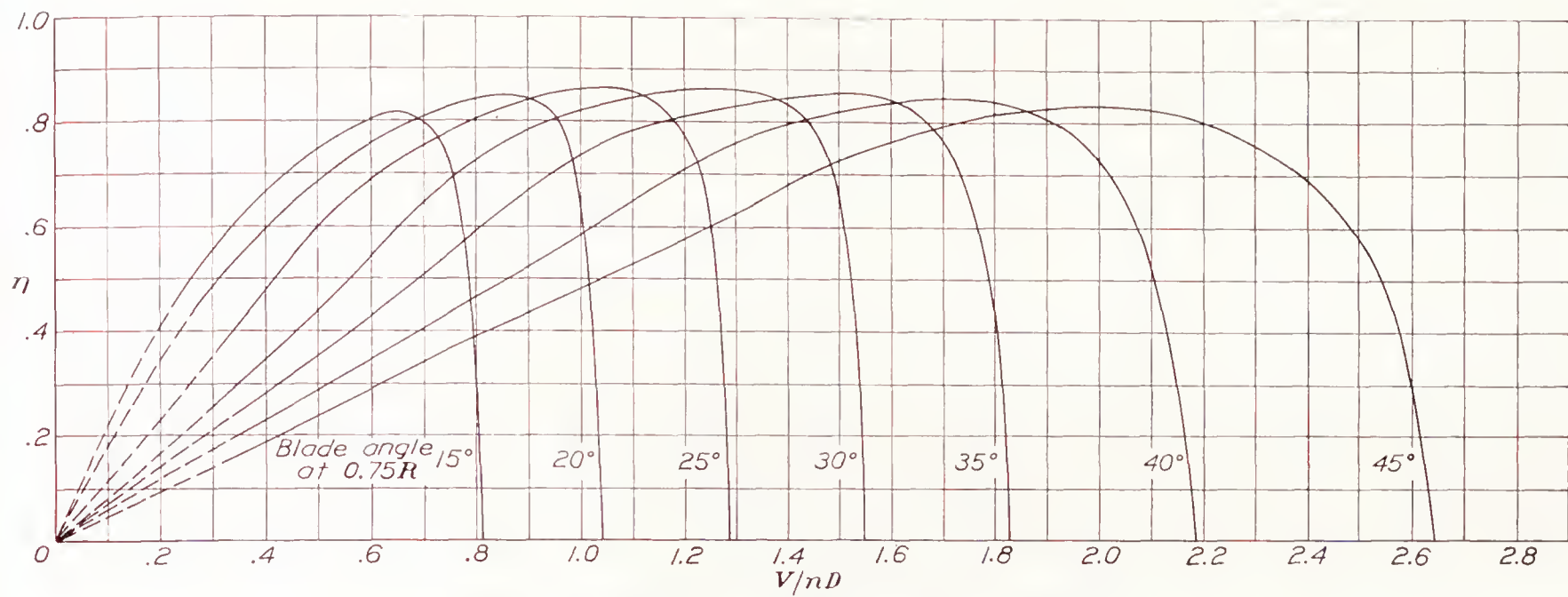


FIGURE 6.—Efficiency curves for propeller 5868-9 (Clark Y section).

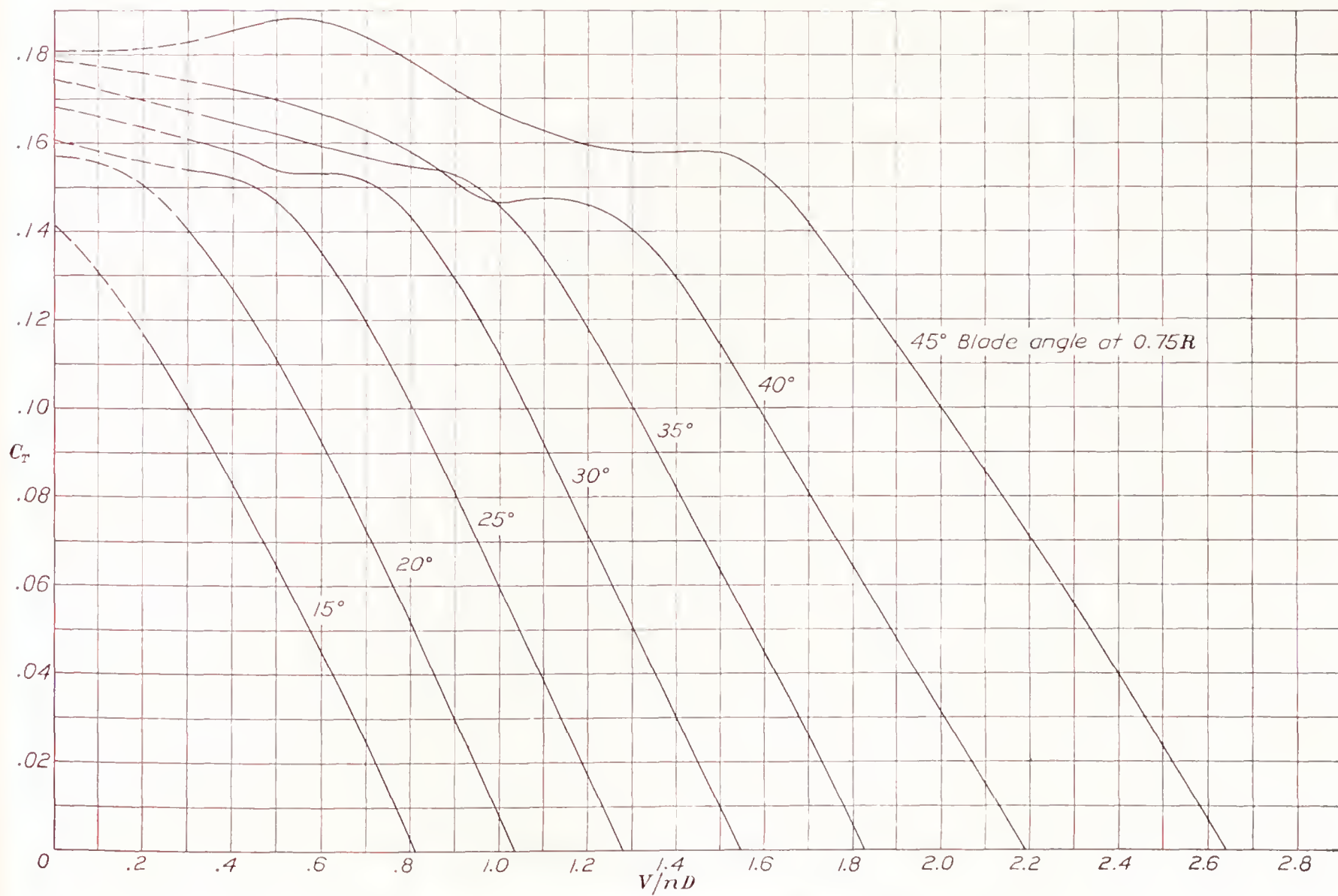


FIGURE 7.—Thrust-coefficient curves for propeller 5868-9 (Clark Y section).



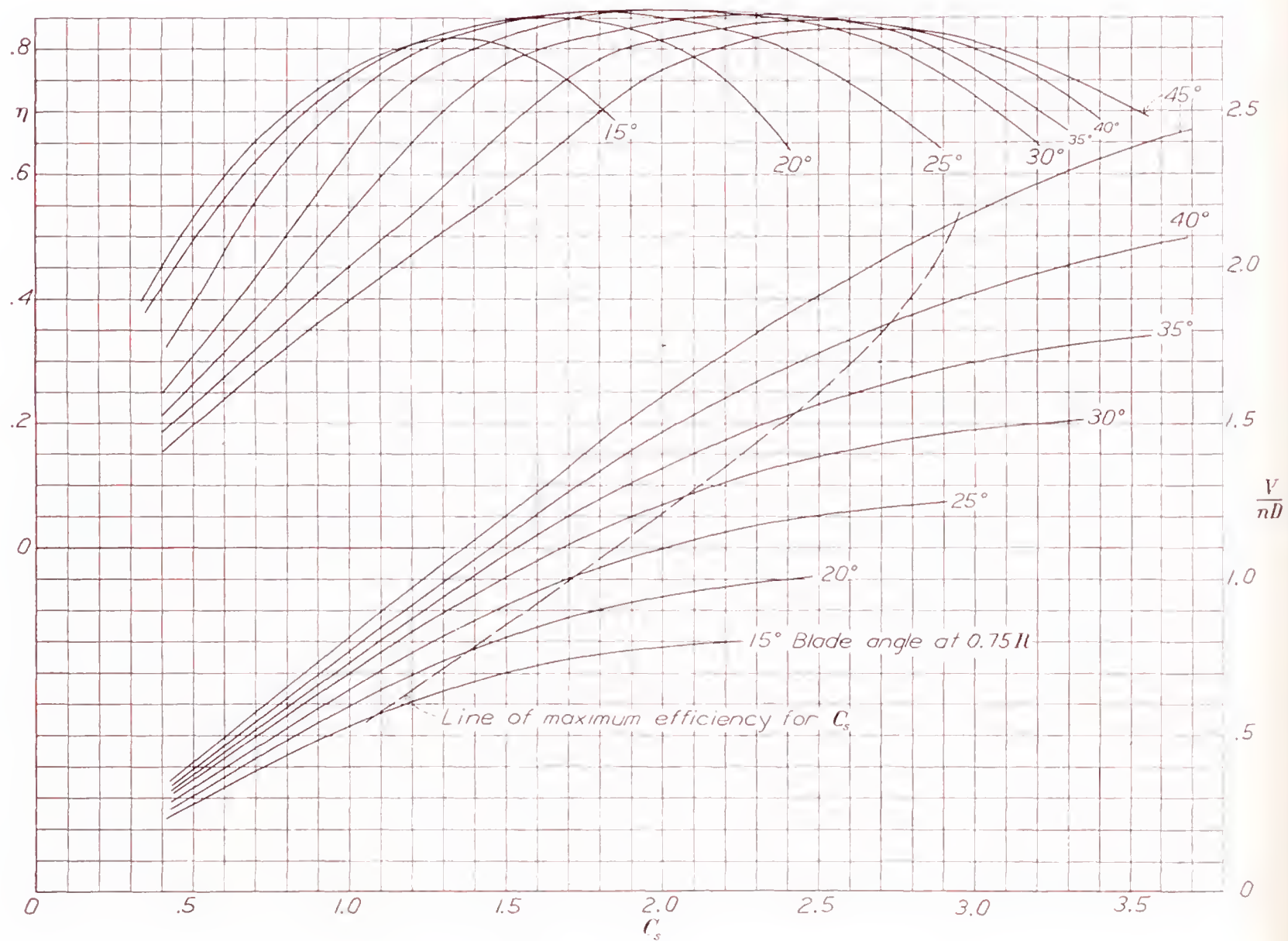


FIGURE 8.—Design chart for propeller 5868-9 (Clark Y section).



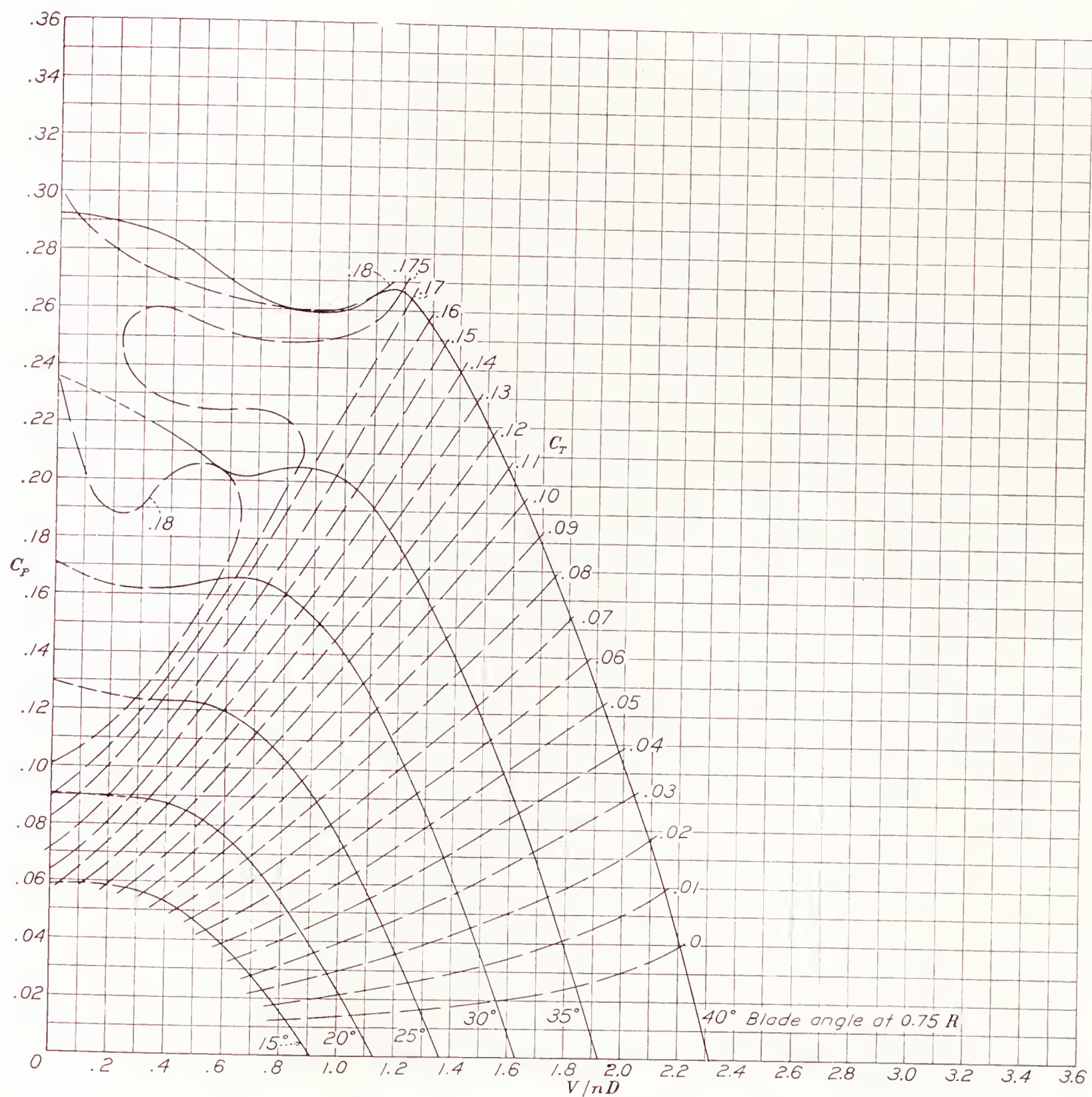


FIGURE 9.—Power-coefficient curves for propeller 586S-R6 (R. A. F. 6 section).



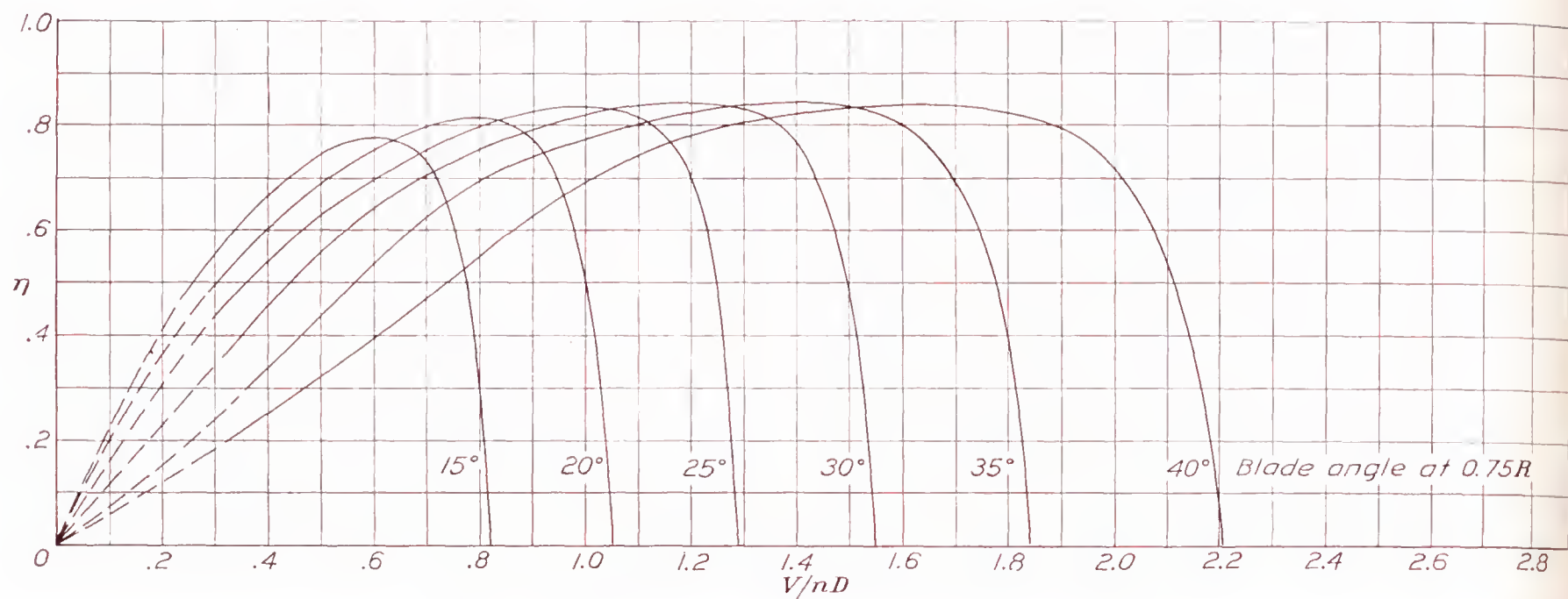


FIGURE 10.—Efficiency curves for propeller 5868-R6 (R. A. F. 6 section).

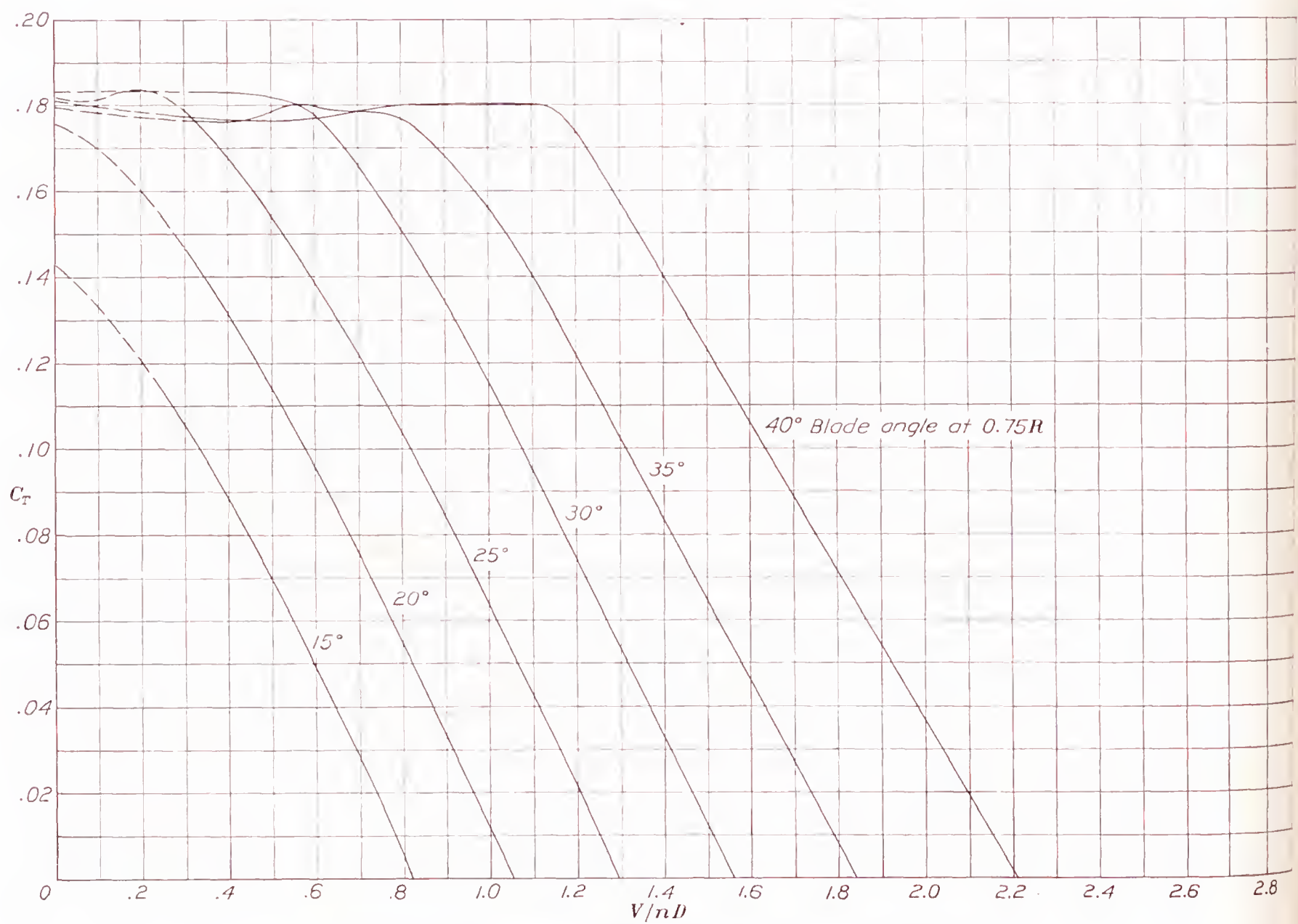


FIGURE 11.—Thrust-coefficient curves for propeller 5868-R6 (R. A. F. 6 section).



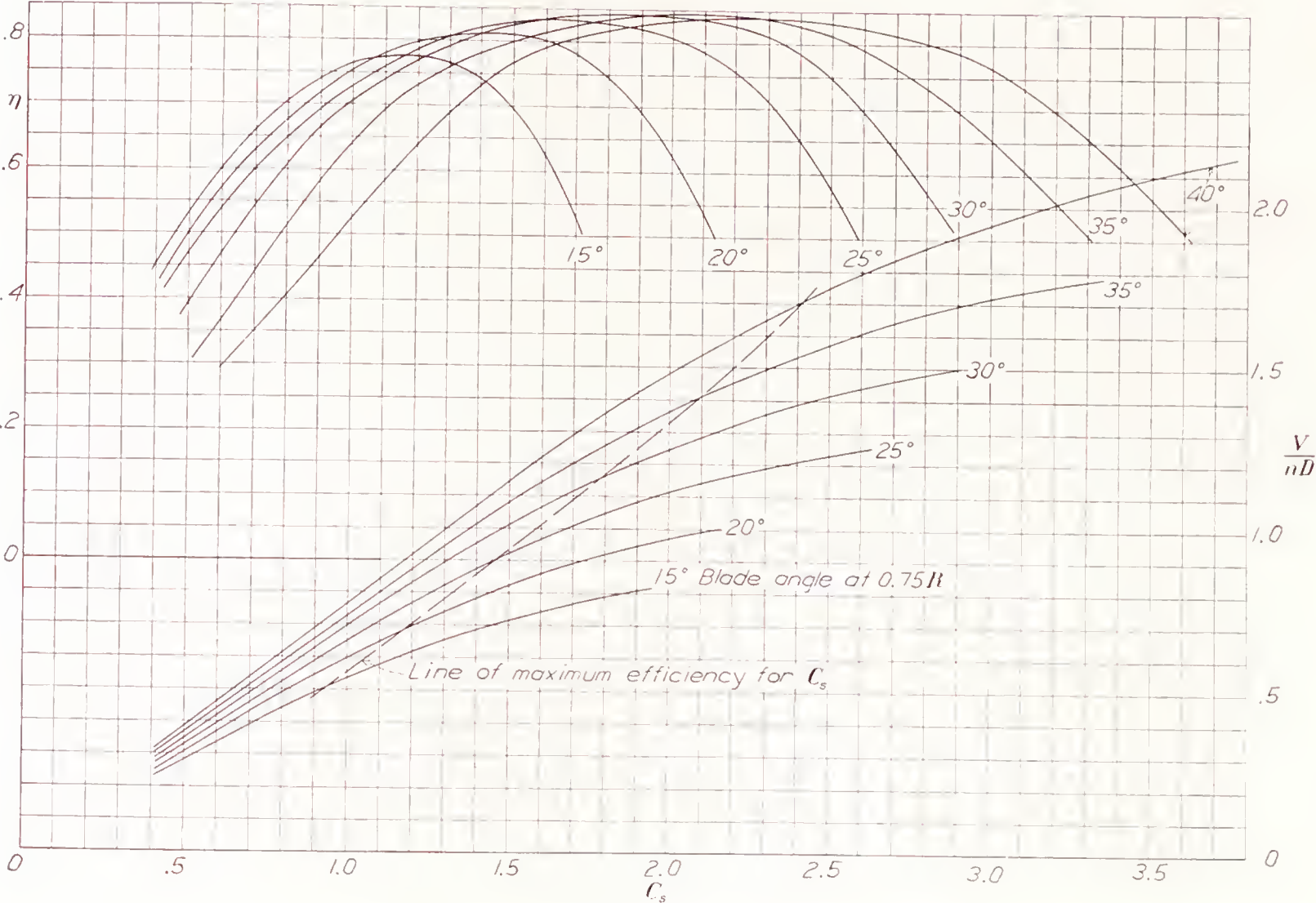


FIGURE 12.—Design chart for propeller 5868-R6 (R. A. F. 6 section).



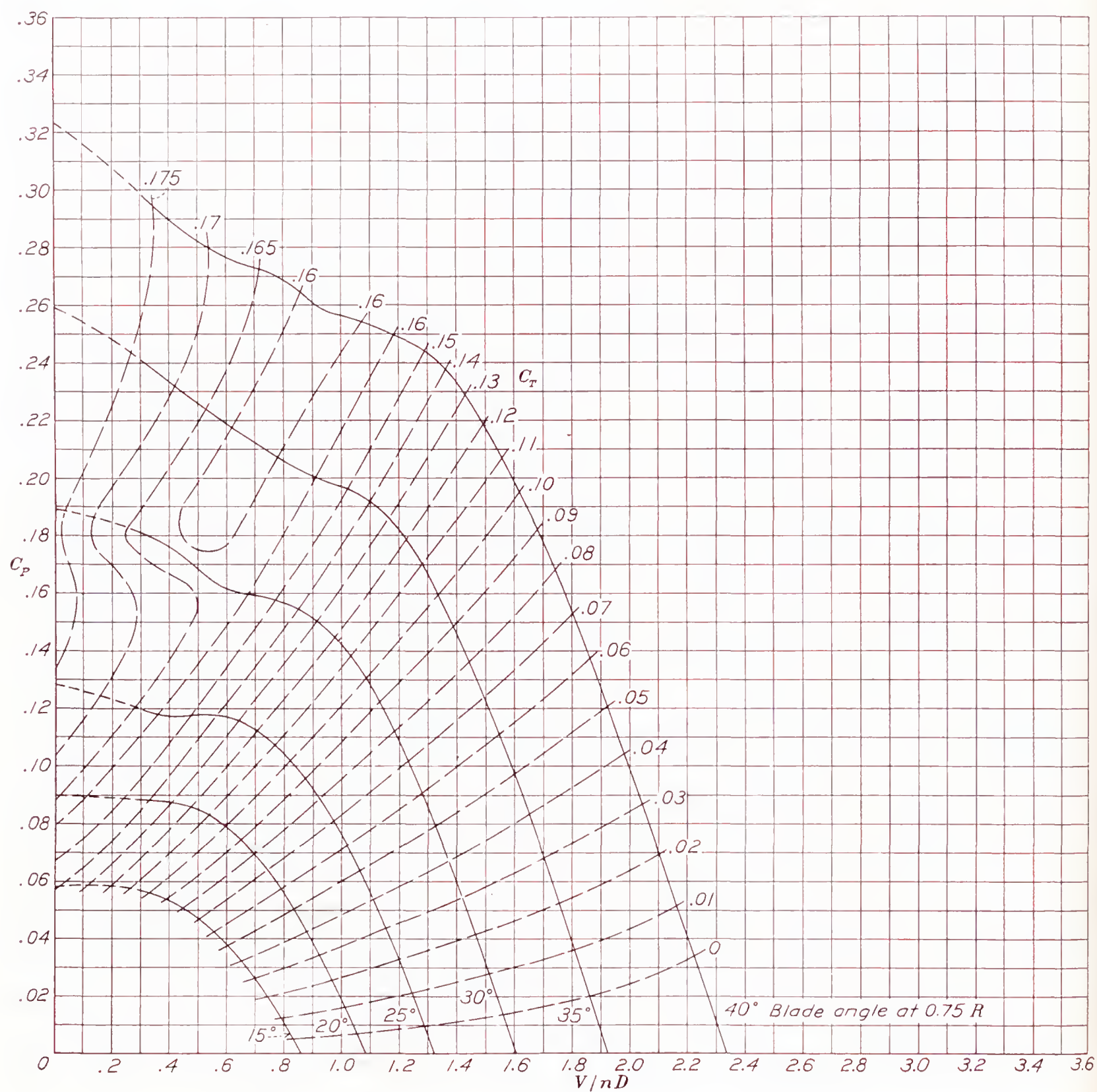


FIGURE 13.—Power-coefficient curves for propeller 6623-A (N. A. C. A. 4400 section).



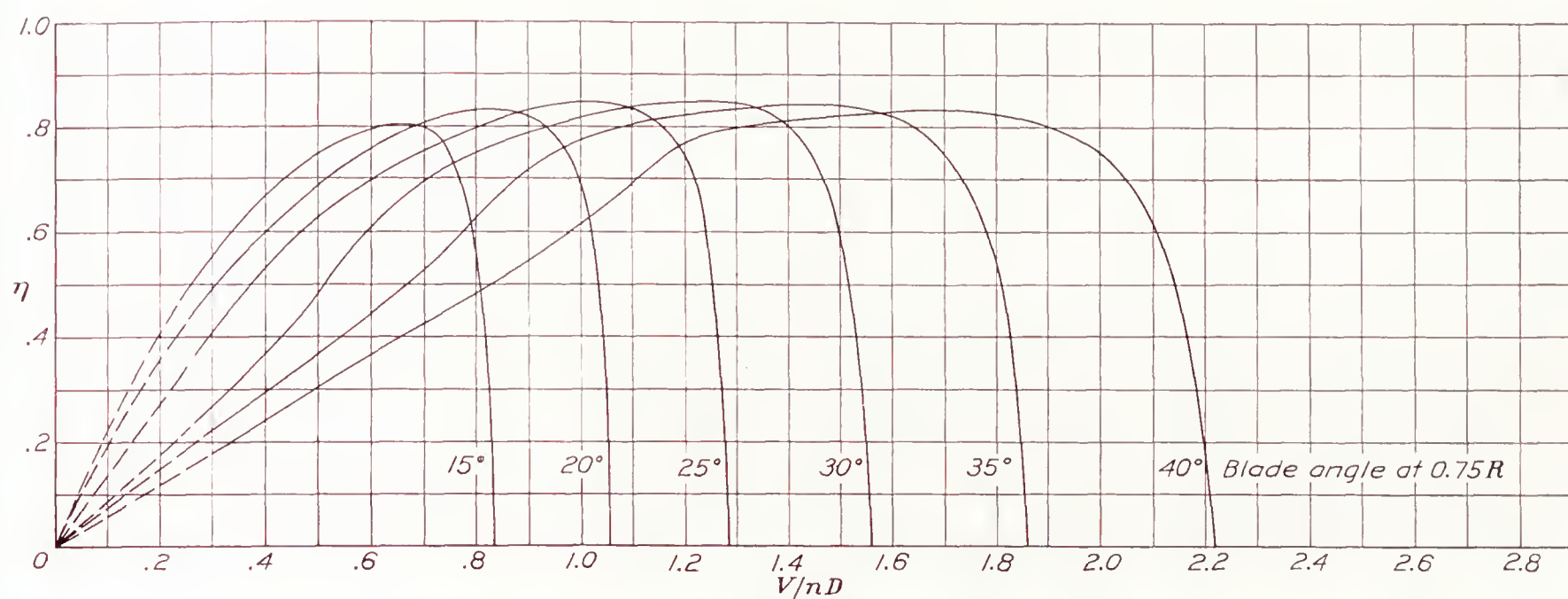


FIGURE 14.—Efficiency curves for propeller 6623-A (N. A. C. A. 4400 section).

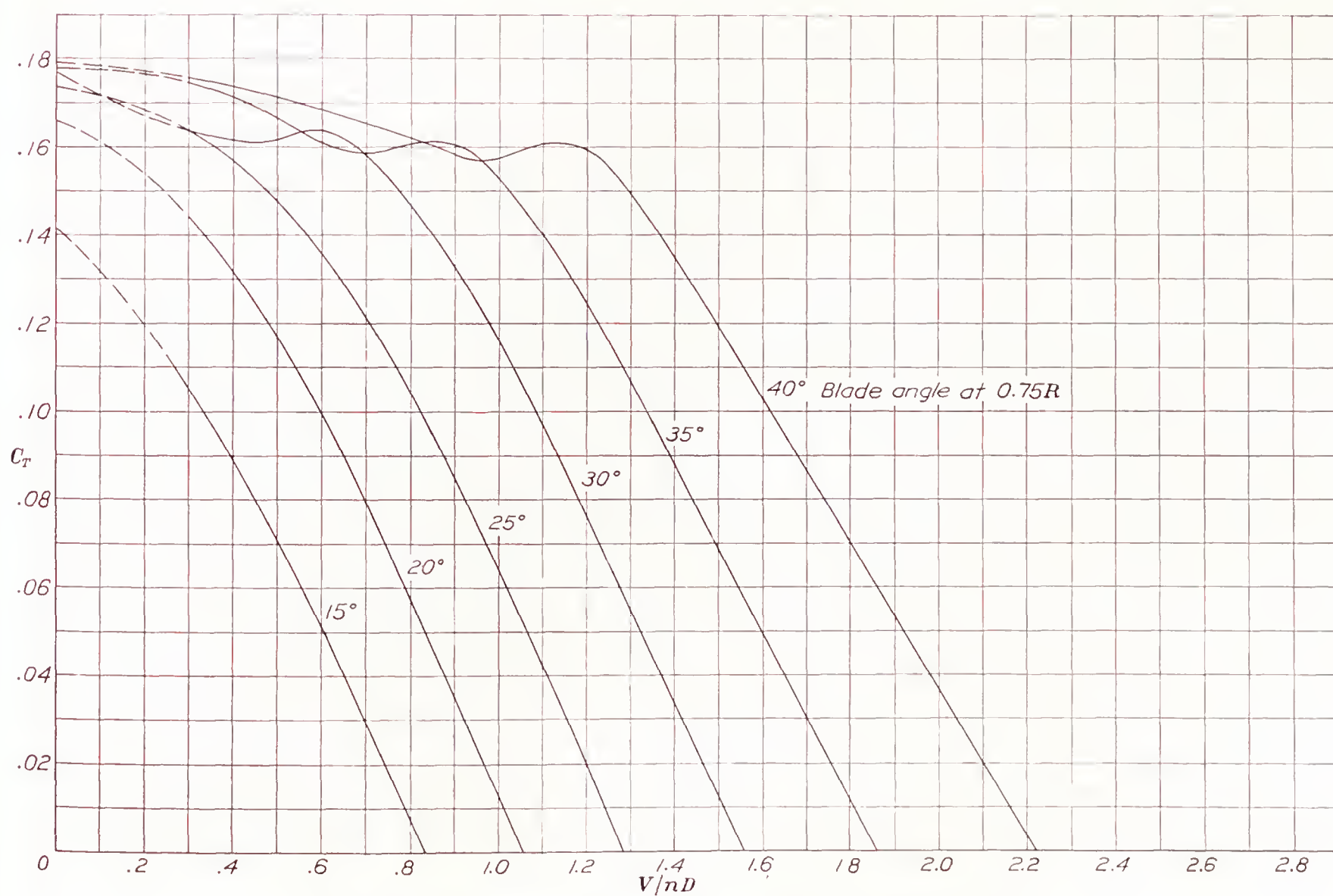


FIGURE 15.—Thrust-coefficient curves for propeller 6623-A (N. A. C. A. 4400 section).



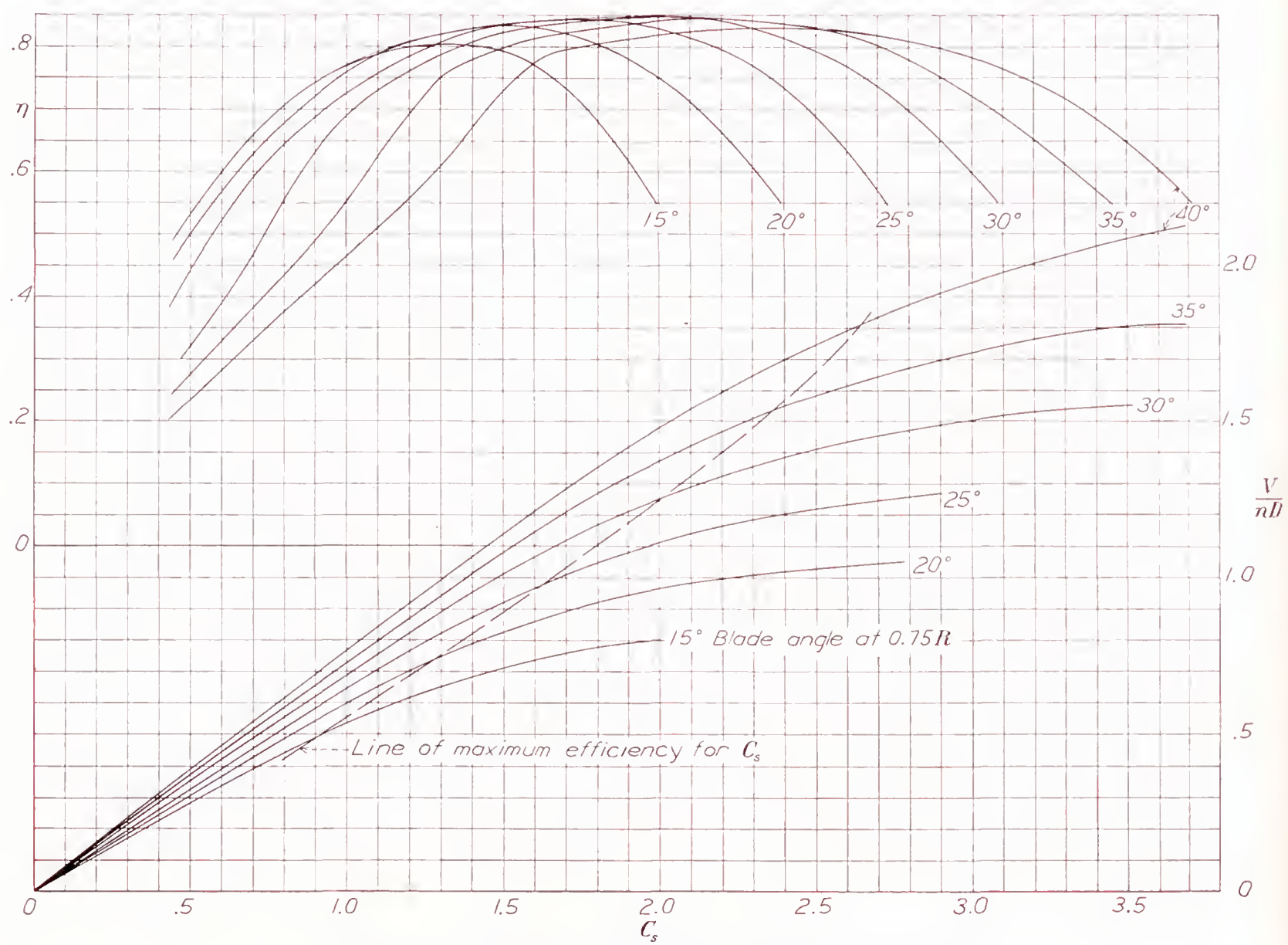


FIGURE 16.—Design chart for propeller 6623-A (N. A. C. A. 4400 section).



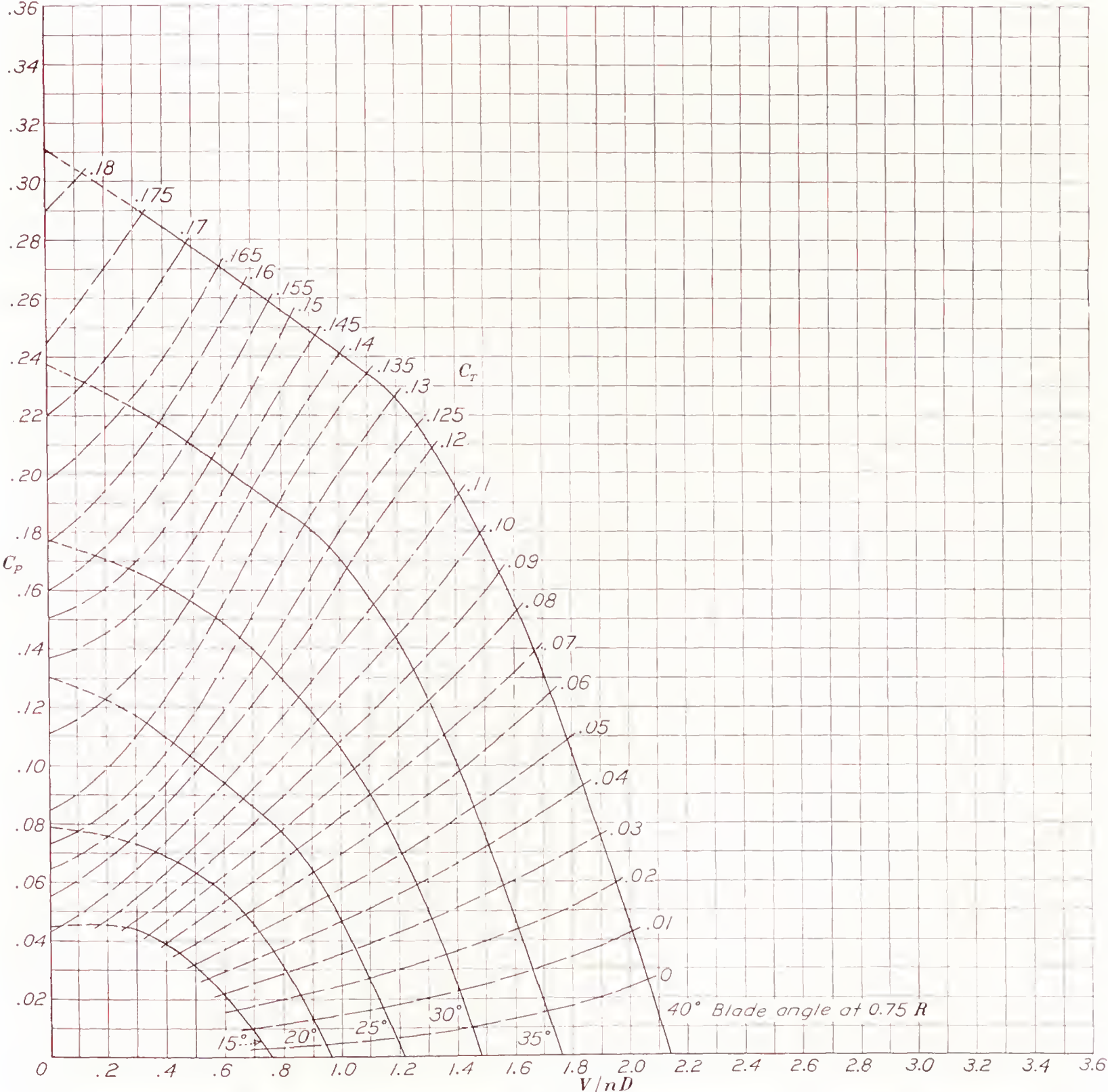


FIGURE 17.—Power-coefficient curves for propeller 6623-B (N. A. C. A. 4400 section inner half; N. A. C. A. 2400-34 section outer half).



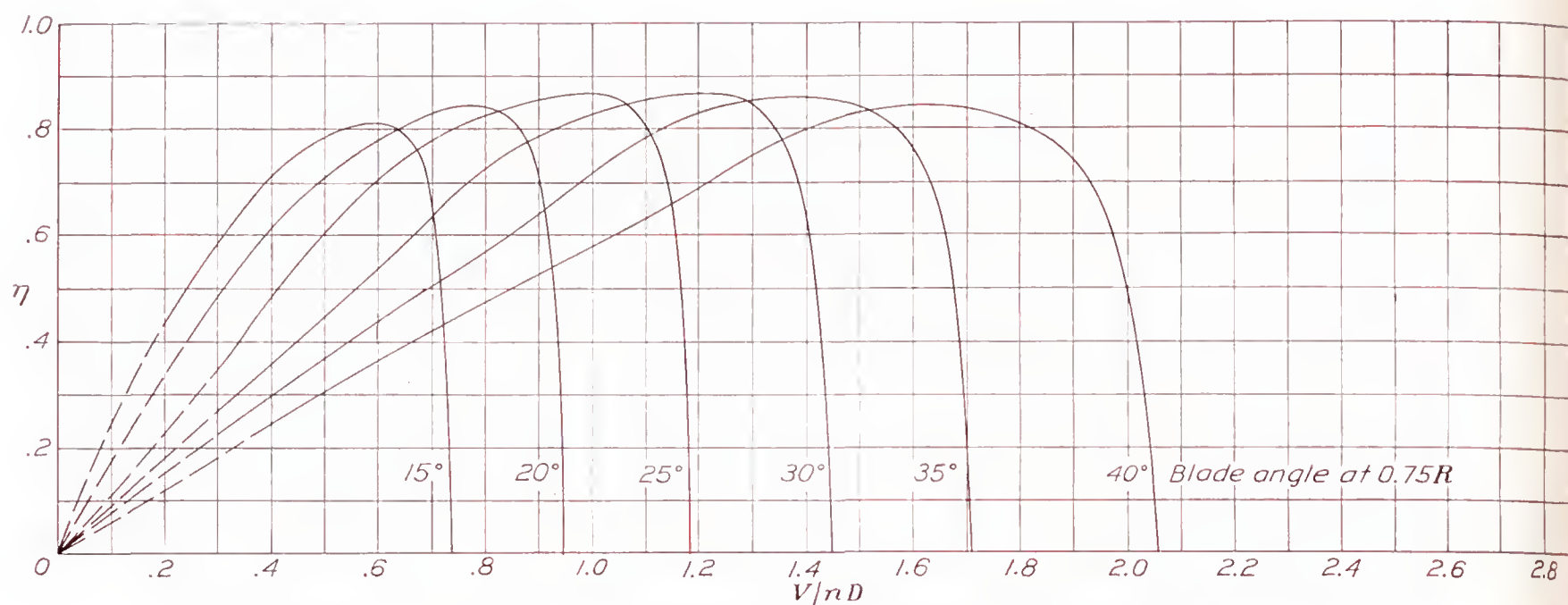


FIGURE 18.—Efficiency curves for propeller 6623-B (N. A. C. A. 4400 section inner half; N. A. C. A. 2400-34 section outer half).

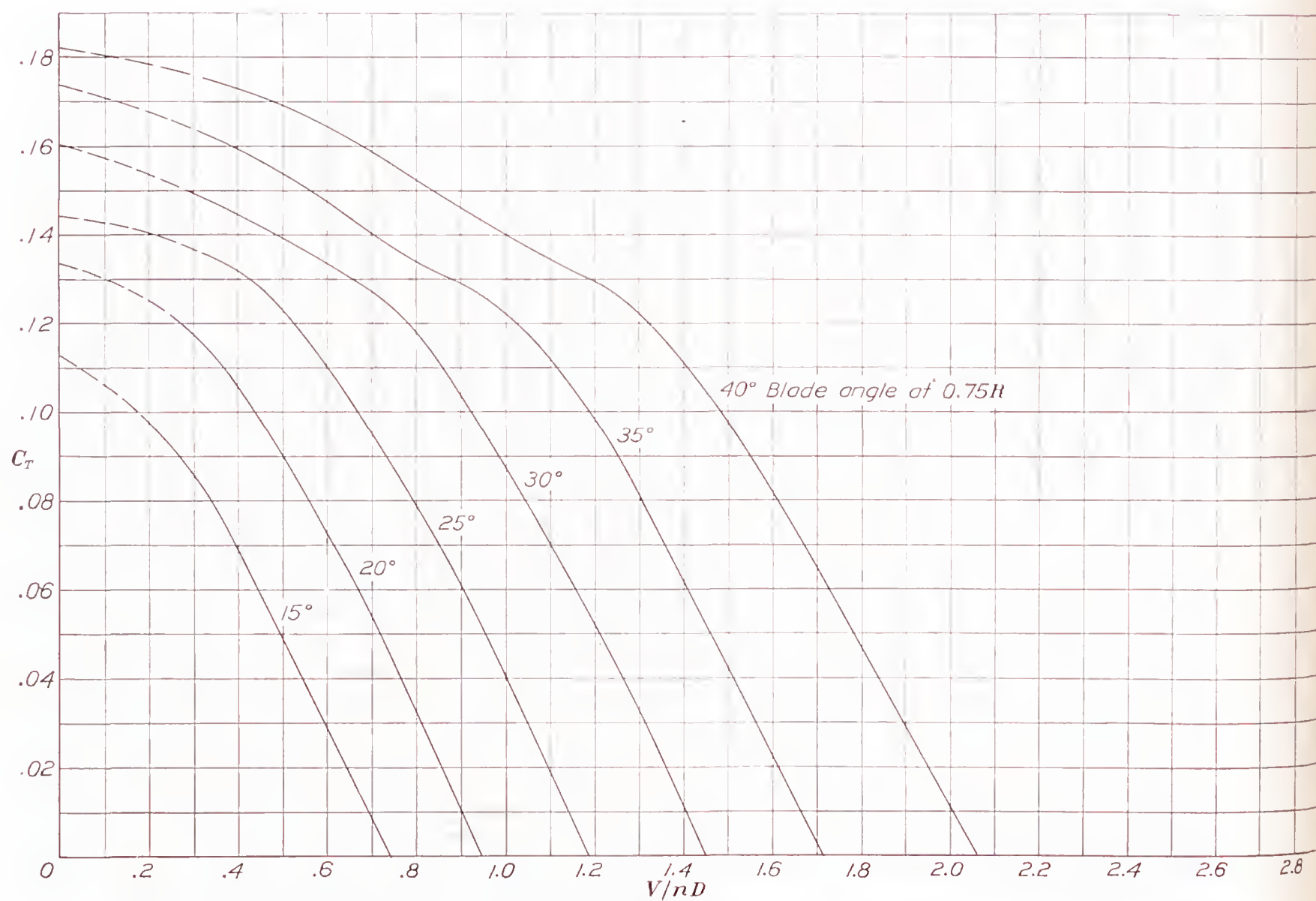


FIGURE 19.—Thrust-coefficient curves for propeller 6623-B (N. A. C. A. 4400 section inner half; N. A. C. A. 2400-34 section outer half).



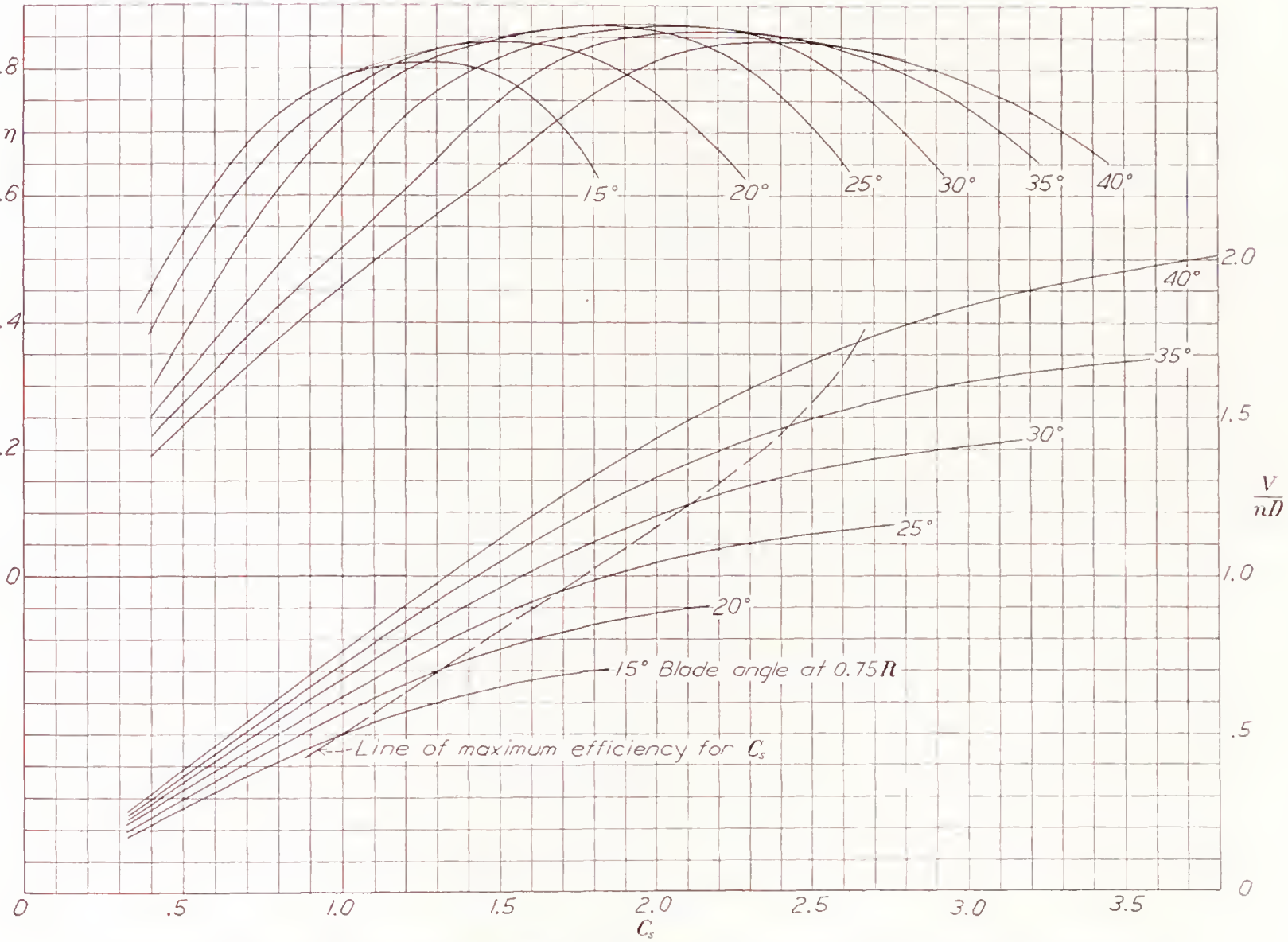


FIGURE 20.—Design chart for propeller 6623-B (N. A. C. A. 4400 section inner half; N. A. C. A. 2400-34 section outer half).



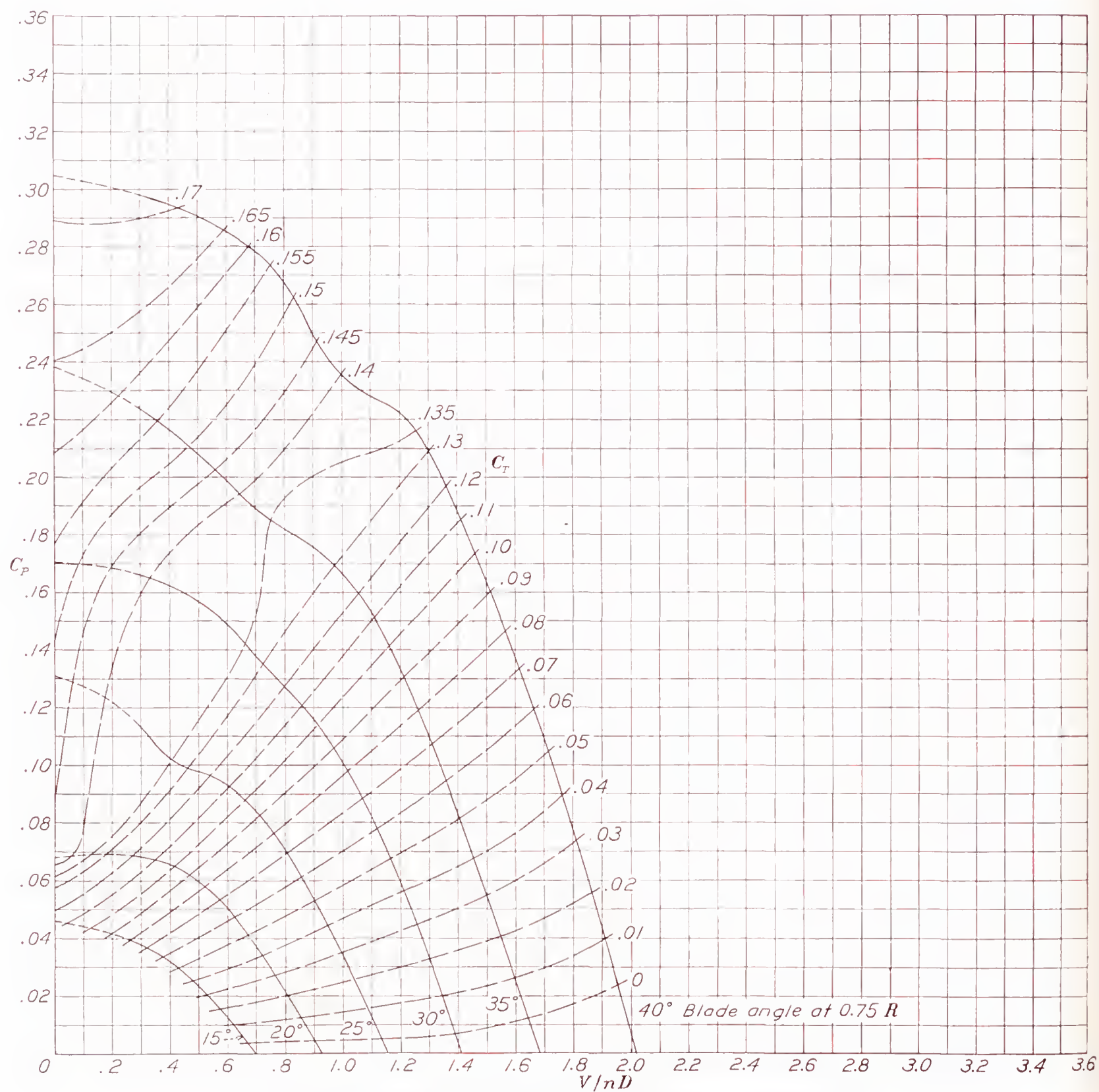


FIGURE 21 — Power-coefficient curves for propeller 6623-C (N. A. C. A. 2R200 section).



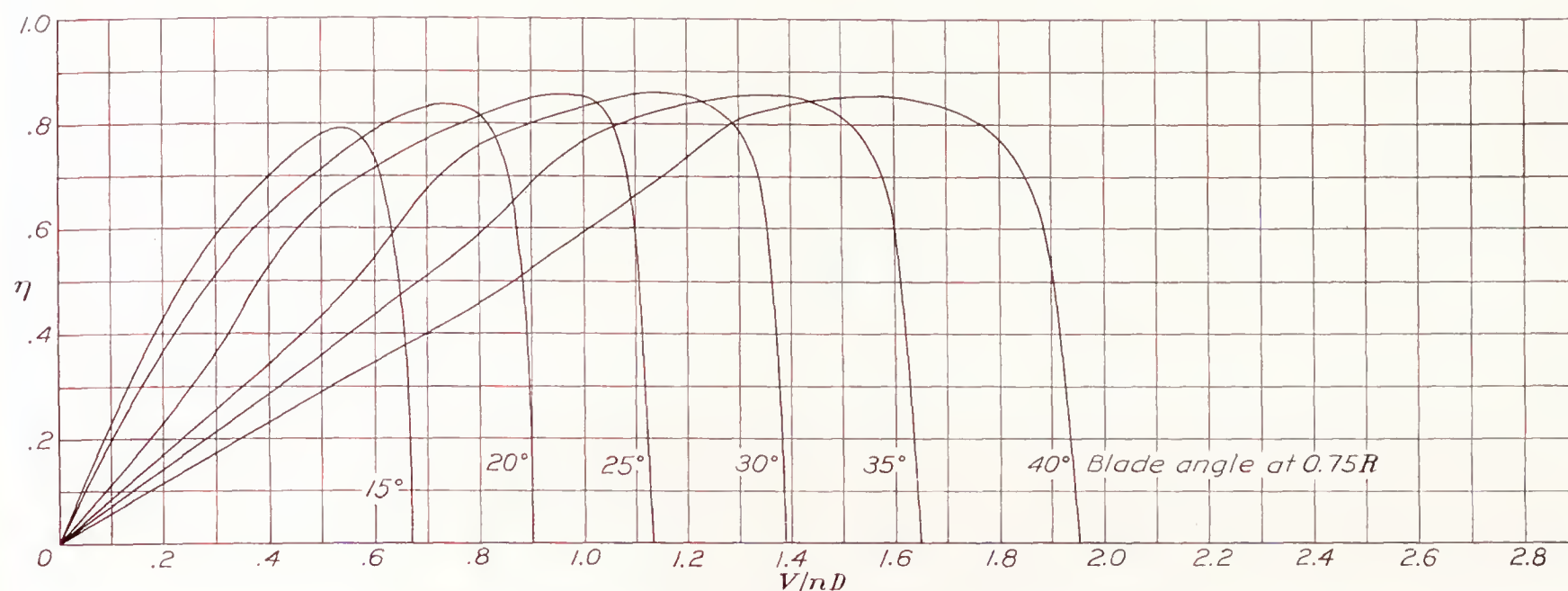


FIGURE 22.—Efficiency curves for propeller 6623-C (N. A. C. A. 2R200 section).

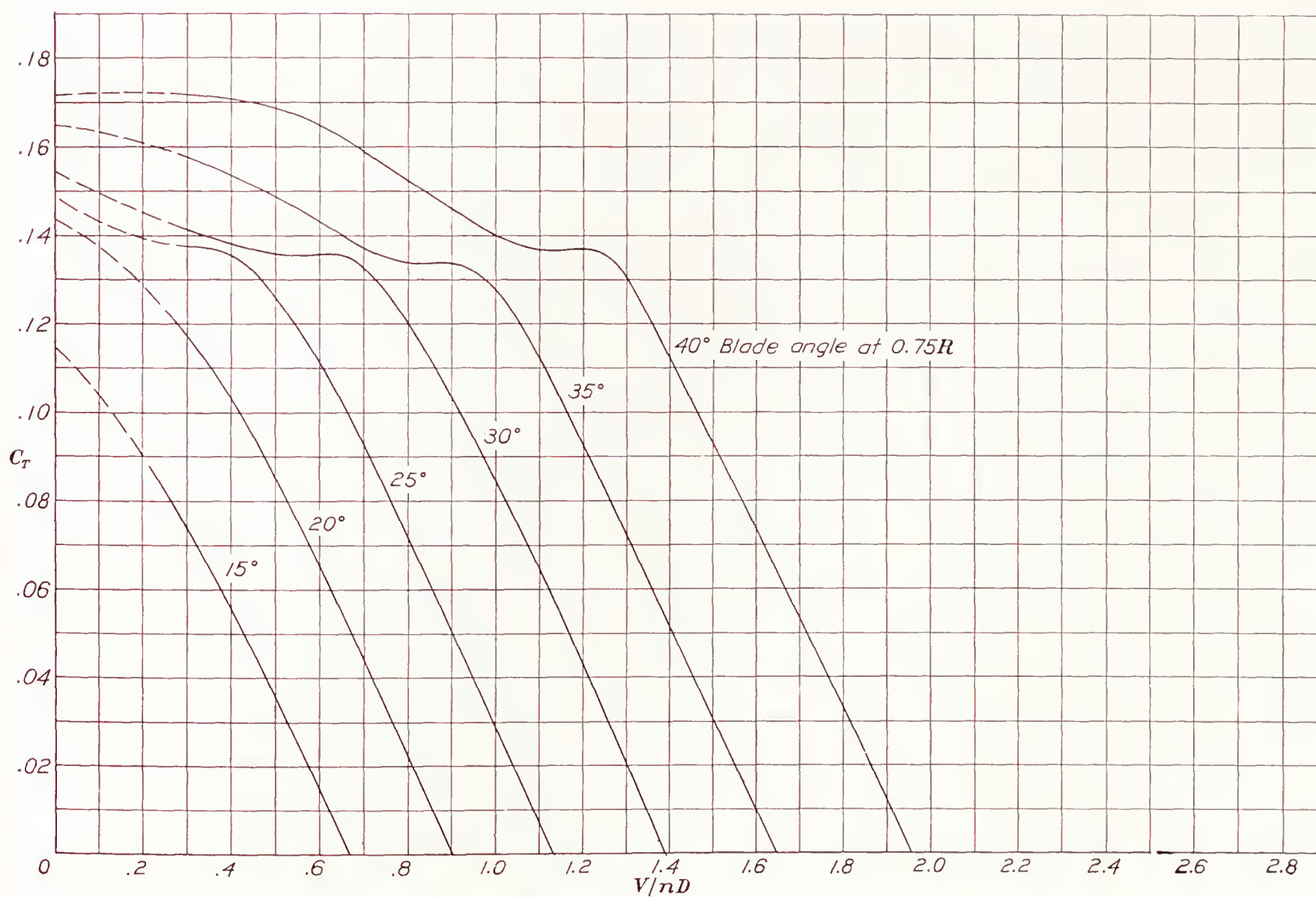


FIGURE 23.—Thrust-coefficient curves for propeller 6623-C (N. A. C. A. 2R200 section)



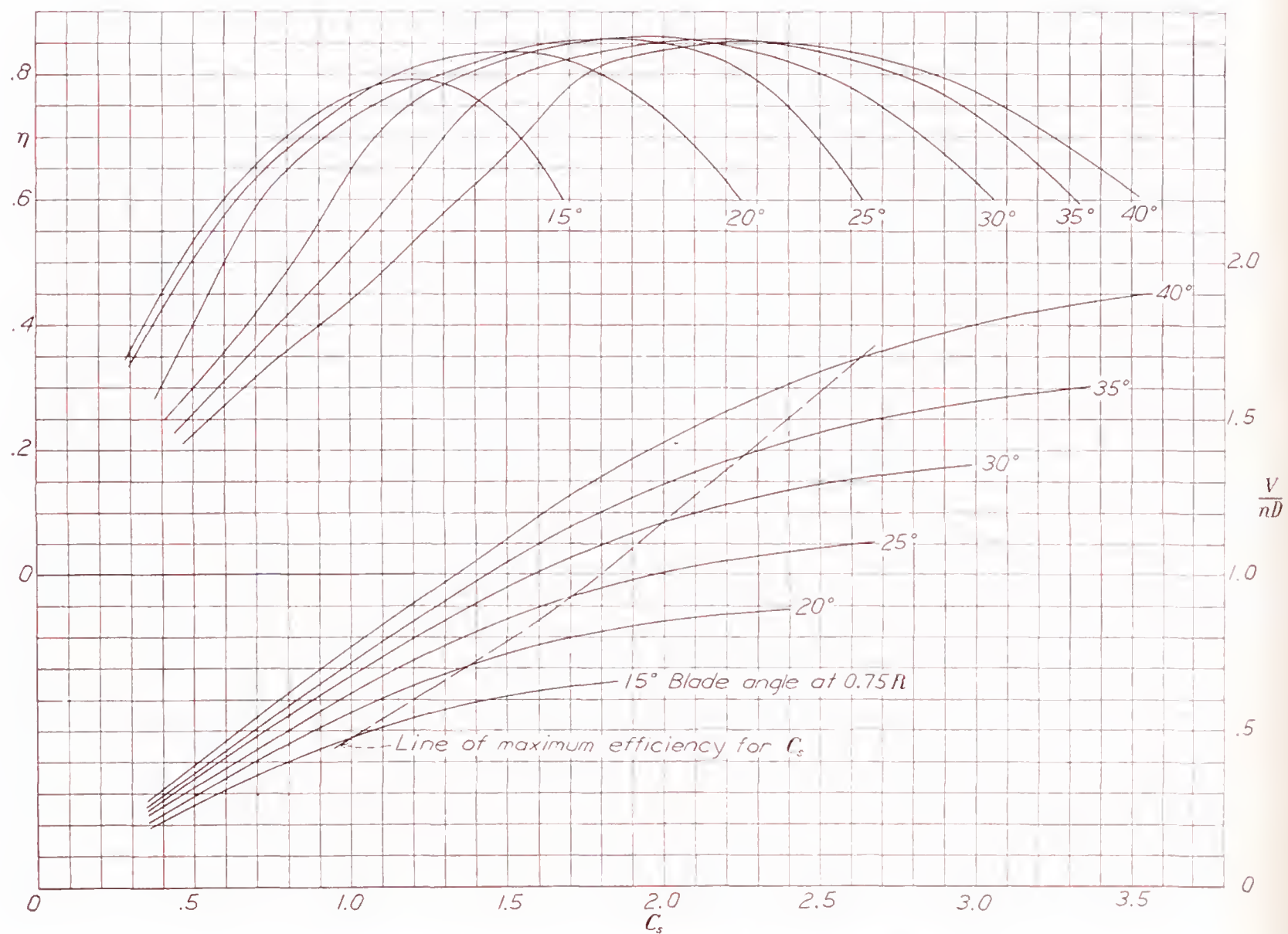


FIGURE 24.—Design chart for propeller 6623-C (N. A. C. A. 2R200 section).



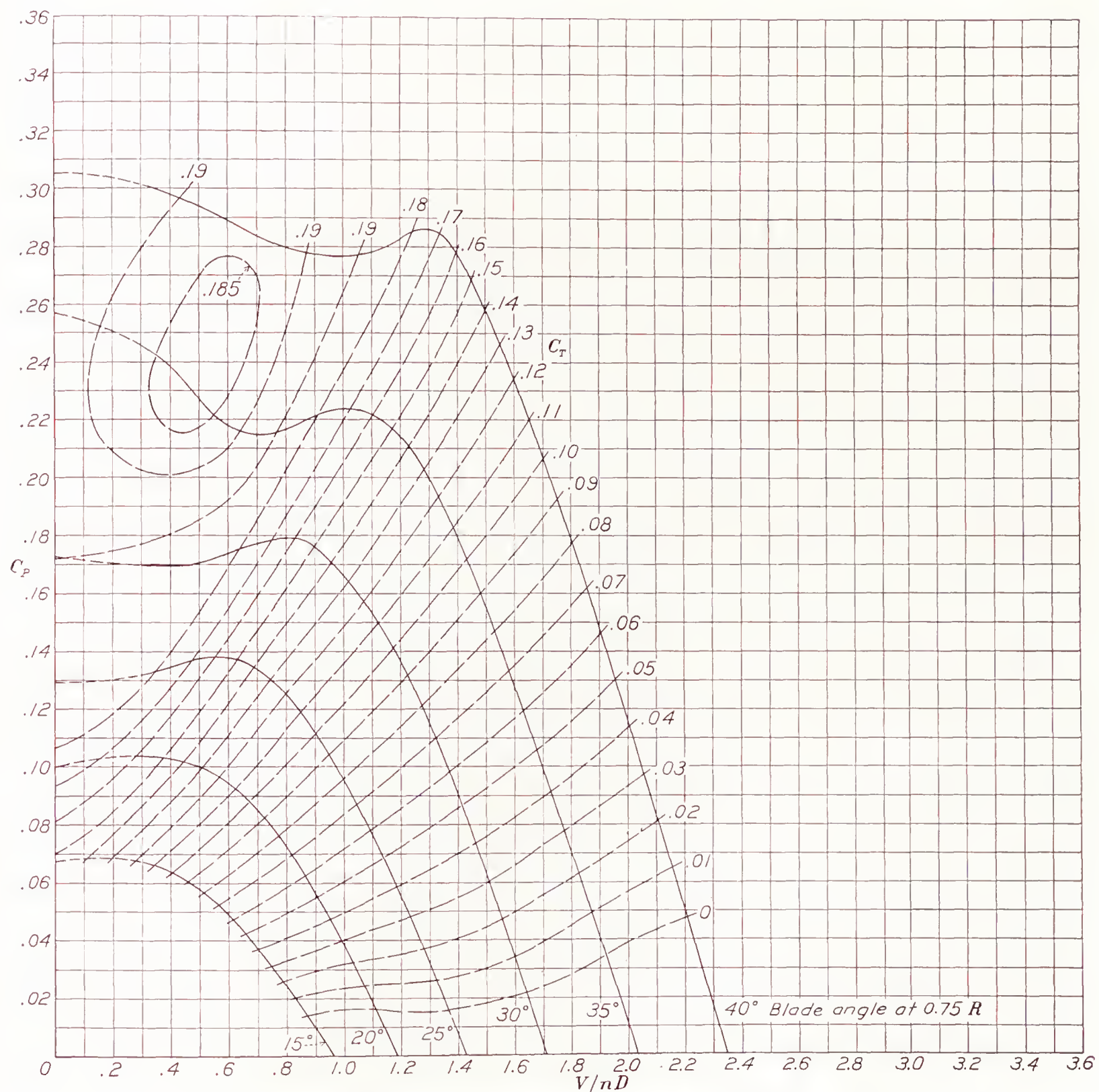


FIGURE 25.—Power-coefficient curves for propeller 6623-D (N. A. C. A. 6400 section).

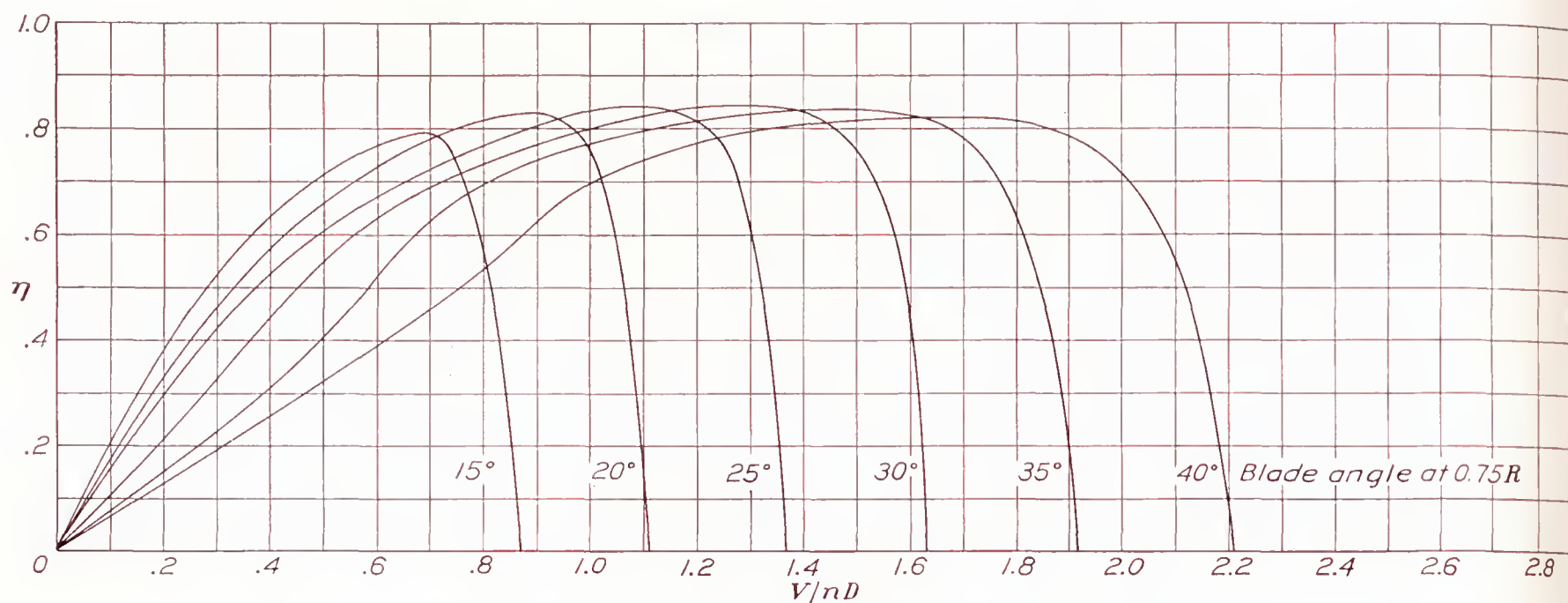


FIGURE 26.—Efficiency curves for propeller 6623-D (N. A. C. A. 6400 section).

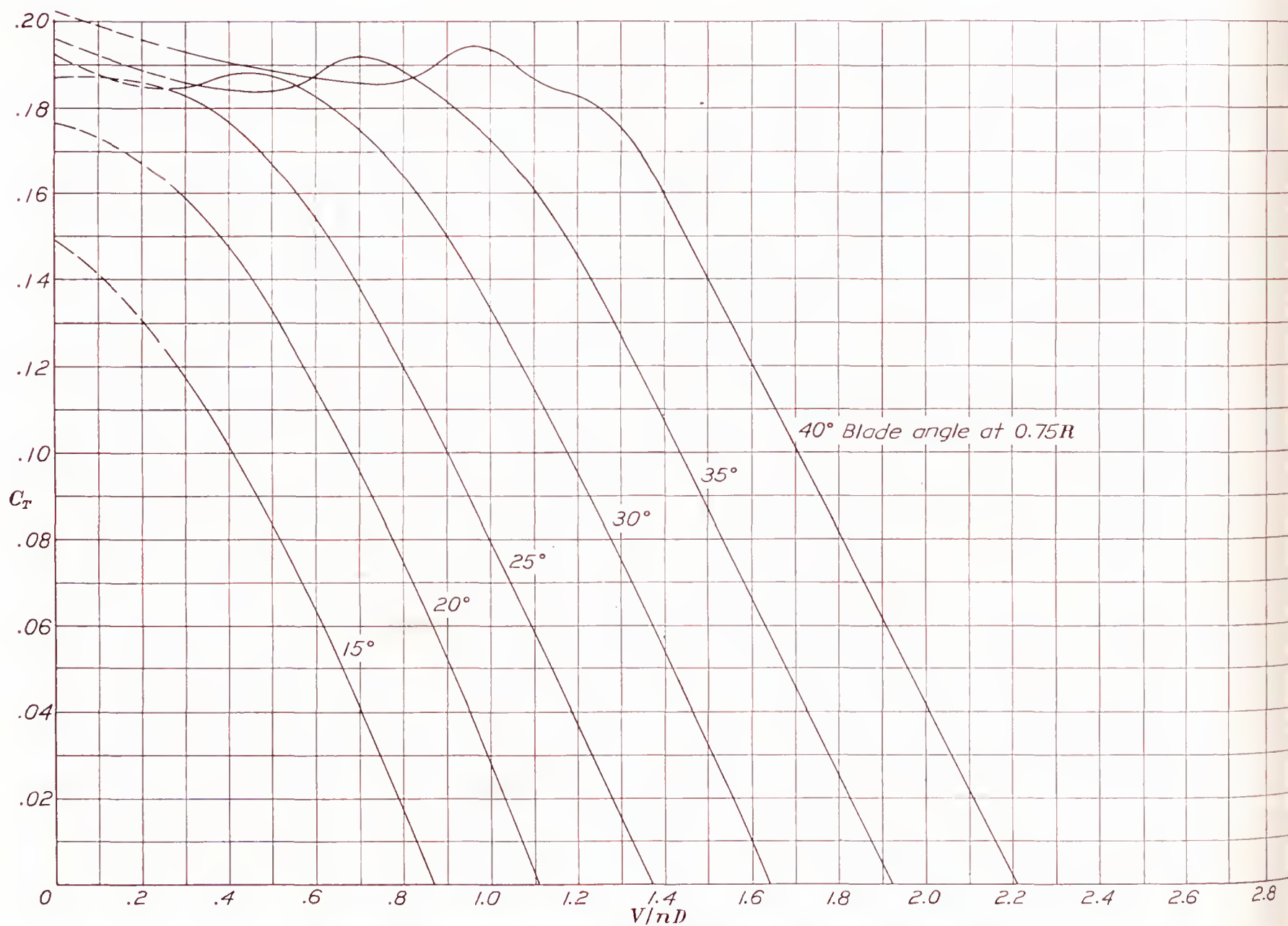


FIGURE 27.—Thrust-coefficient curves for propeller 6623-D (N. A. C. A. 6400 section).



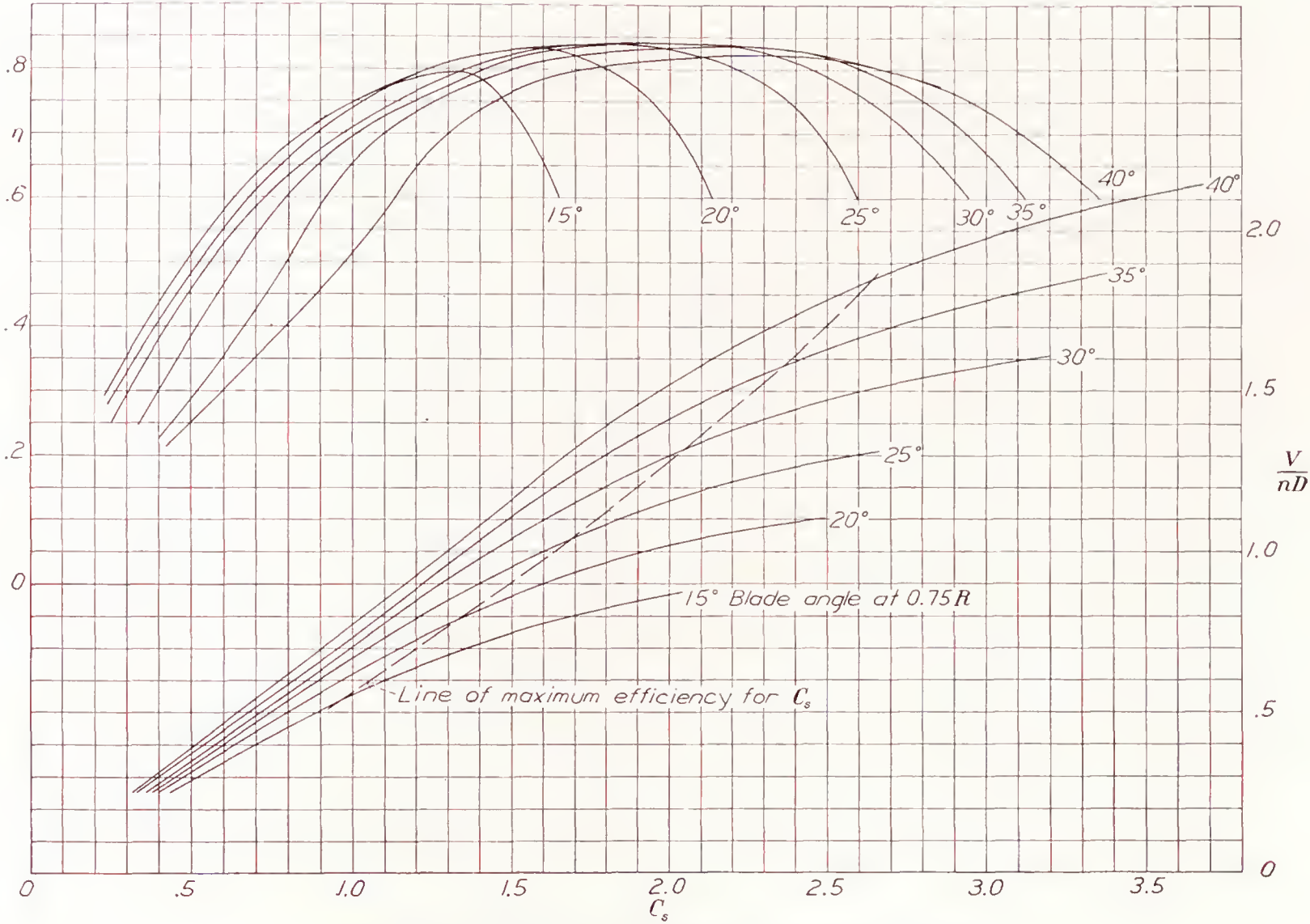


FIGURE 28.—Design chart for propeller 6623-D (N. A. C. A. 6400 section).

## DISCUSSION

**Basic airfoil sections.**—The thickness distribution and the camber lines for the six basic airfoil sections employed in the propeller designs are shown in figure 29. The thickness distribution (fig. 29 (a)) is about the same for all sections with two exceptions. The leading-edge radius of the N. A. C. A. 2400-34 section is shorter and the front portion is thinner than for the other sections; also, the point of maximum thickness occurs at 40-percent chord for the N. A. C. A. 2400-34 section and at 30-percent chord for the other sections. These thickness-distribution differences account for the superior qualities of this section at high speeds; because the radii of curvature of the upper surface are large,

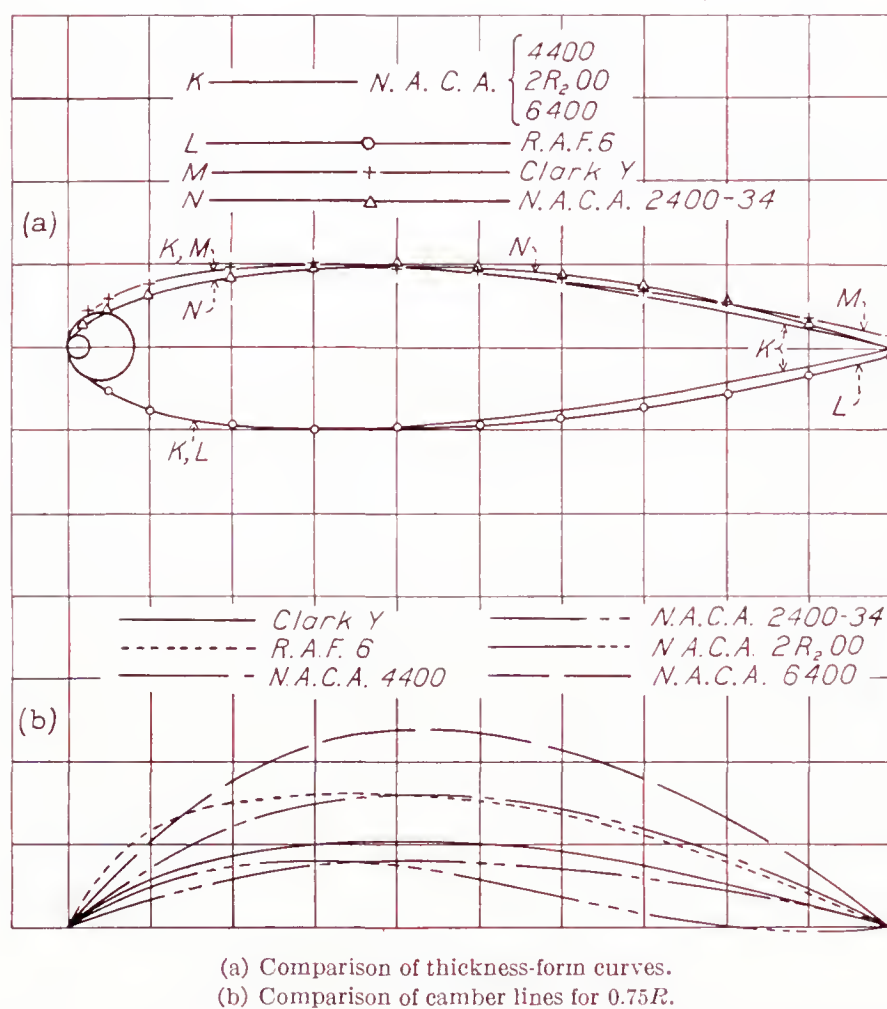


FIGURE 29.—Comparison of thickness-form curves and camber lines. The chord lines for the R. A. F. 6 and the Clark Y sections have been shifted to bring the leading and trailing edges of the camber lines together.

the local induced velocities are kept small. Inasmuch as compressibility losses result from local velocities exceeding the velocity of sound, the critical speed for this section is delayed to higher values. The trailing-edge portions of the R. A. F. 6 and the Clark Y sections are slightly thicker than the others, but this difference in thickness distribution of the sections is probably of small importance.

Except for the thickness distribution of the N. A. C. A. 2400-34 section, the only essential physical differences between the sections are the shapes of the mean camber lines. The camber lines for the N. A. C. A. sections are mathematically derived curves and the camber ratios remain the same for all thickness ratios. In the design of the present propellers of N. A. C. A.

section, the blade sections at different radii are thickened or thinned with respect to the basic section from the mean camber line, which remains constant. In contrast to this method, the Clark Y and the R. A. F. 6 sections are thickened or thinned from the chord line, which is also the lower surface. The mean camber lines are thereby different for each section thickness, the amount of camber being proportional to the thickness. In order to avoid differences in effective pitch distribution for all the propellers, the section blade angles were corrected for differences in the angles for zero lift.

The mean camber lines for the stations at 0.75 radius are plotted in figure 29 (b). Those for the R. A. F. 6 and the Clark Y sections have been plotted with respect to lines passing through the intersections of the camber lines and the leading and trailing edges and not with respect to the chord lines. The general shapes of the mean camber lines are similar for all of the sections except for the R. A. F. 6 and the 2R<sub>2</sub>00 sections. The R. A. F. 6 section is characterized by the rapidly increasing camber at the nose of the section, and the camber line of the N. A. C. A. 2R<sub>2</sub>00 section is reflexed.

The effect of the shape of the mean camber lines and the amount and position of maximum camber on the aerodynamic characteristics are fairly well established. In general, high cambers result in high values of  $C_{L_{max}}$  and  $C_{D_{min}}$  while low cambers result in low values of both  $C_{L_{max}}$  and  $C_{D_{min}}$ . It is to be expected, therefore, that the maximum propeller efficiencies will reflect differences in the profile drag and that the efficiencies at low values of  $V/nD$  will reflect differences in maximum lift and in drag at high values of lift. In the selection of the sections, consideration was given to the minimum drag, the maximum lift, the aerodynamic moment, and the speed at which the compressibility stall occurred. The N. A. C. A. 2R<sub>2</sub>00, the N. A. C. A. 4400, and the N. A. C. A. 6400 sections constitute a series differing essentially in amount of camber and, consequently, display differences in  $C_{D_{min}}$  and  $C_{L_{max}}$ . The N. A. C. A. 2R<sub>2</sub>00 section was chosen in preference to the N. A. C. A. 2400 section for the 2-percent-camber group because it has a lower  $C_{D_{min}}$  and it was thought that there might be some practical advantage in having a zero change in aerodynamic moment for controllable propellers. The N. A. C. A. 2400-34 section was selected because of its delayed compressibility stall.

**Comparison of propeller characteristics.**—In order to study the influence that the different sections exert on the propeller characteristics, superposed sets of curves of the thrust, the power, and the efficiency are given for three pitch-diameter ratios for zero thrust (figs. 30, 31, and 32). The pitch-diameter ratios of 0.82, 1.28, and 1.83 correspond to blade angles of 15°, 25°, and 35°, respectively, for the Clark Y propeller. The blade angles for the other propellers are slightly different, as may be noted.



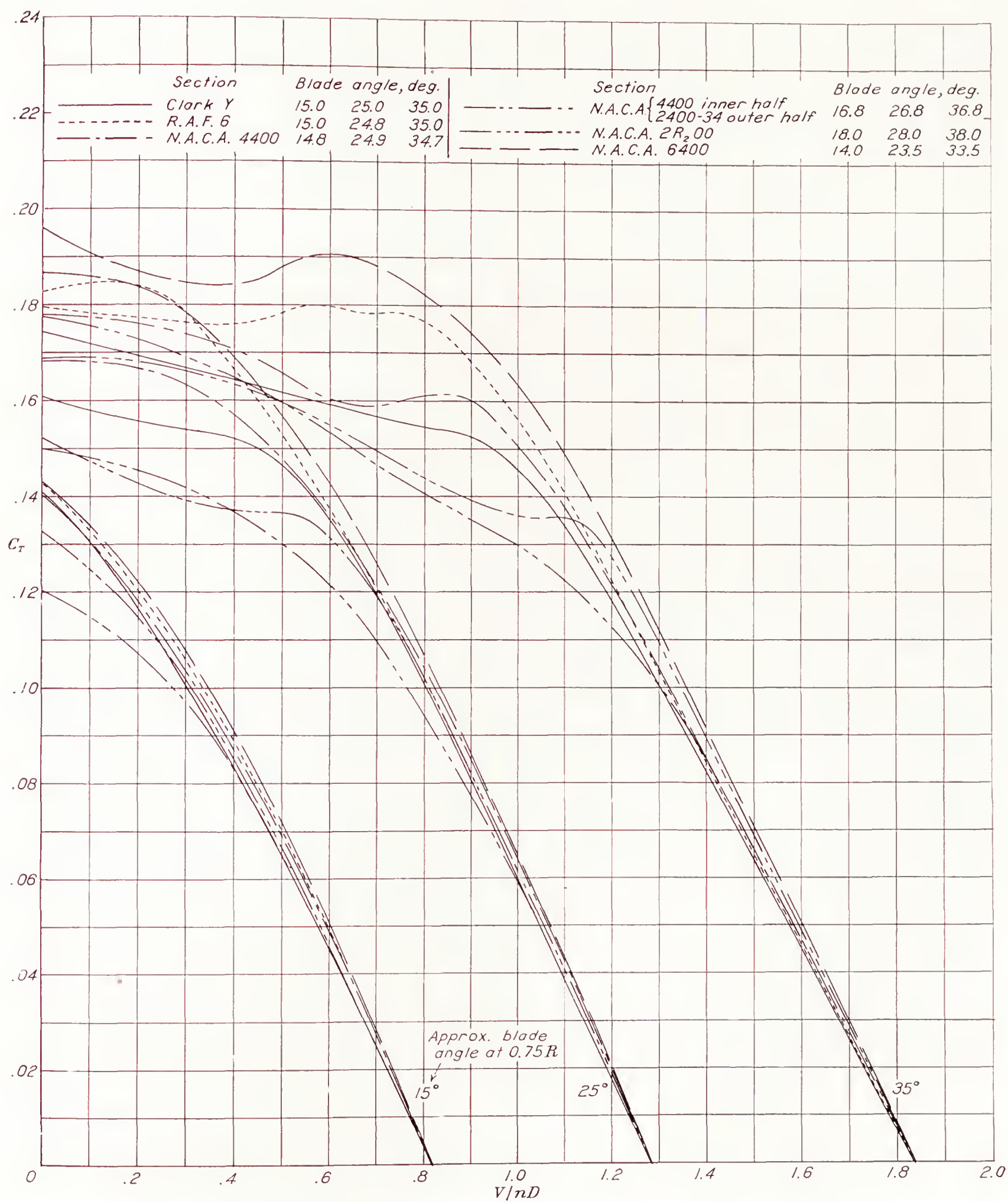


FIGURE 30.—Comparison of typical thrust curves.

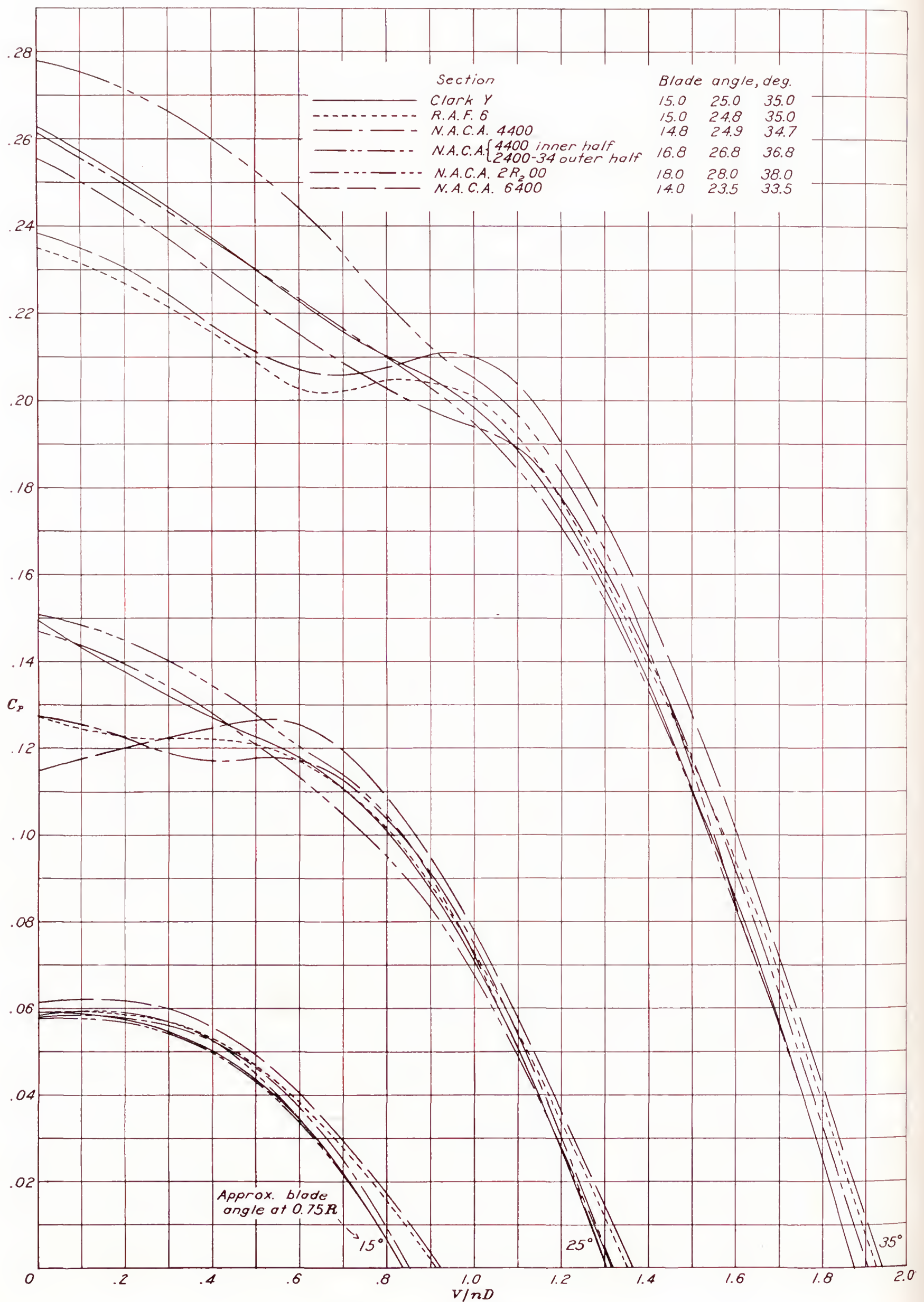


FIGURE 31.—Comparison of typical power curves.



The important difference in the thrust characteristics (fig. 30) attributed to the different sections is the value of  $C_T$  at which the blades stall. The propellers of 2-percent camber, the N. A. C. A. 2400-34 and the N. A. C. A. 2R<sub>2</sub>00 sections, stall at a  $C_T$  value of about 0.13; the propeller of 4-percent camber, the N. A. C. A. 4400 section, stalls at about 0.15; and the propeller of 6-percent camber, the N. A. C. A. 6400 section, at about 0.19. The curves indicate that the propeller of Clark Y section has an average camber ratio of about 0.035 for the entire propeller, inasmuch as the stall is at a  $C_T$  value of about 0.15. The average camber ratio is higher than that for the 0.75 radius station (0.026), probably owing to the fact that the inboard sections are all definitely more highly cambered while the outboard

efficiency approaches the ideal for which the profile drag is zero. Also, the ideal efficiency is highest at zero thrust, which explains why the peak efficiencies occur at higher values of  $V/nD$  for the low-camber propellers. This shifting of the peaks to higher values of  $V/nD$  for propellers of decreasing profile drag is of importance in design work. The closer the  $V/nD$  for peak efficiency approaches the  $V/nD$  for zero thrust, the smaller is the power coefficient and, consequently, the greater the diameter. The extreme condition is for a propeller with the ideal efficiency, i. e., maximum efficiency occurring at zero thrust and zero torque so that the diameter is infinite and the rotational speed zero. The significance of the diameter will be clarified by computations later in the report.

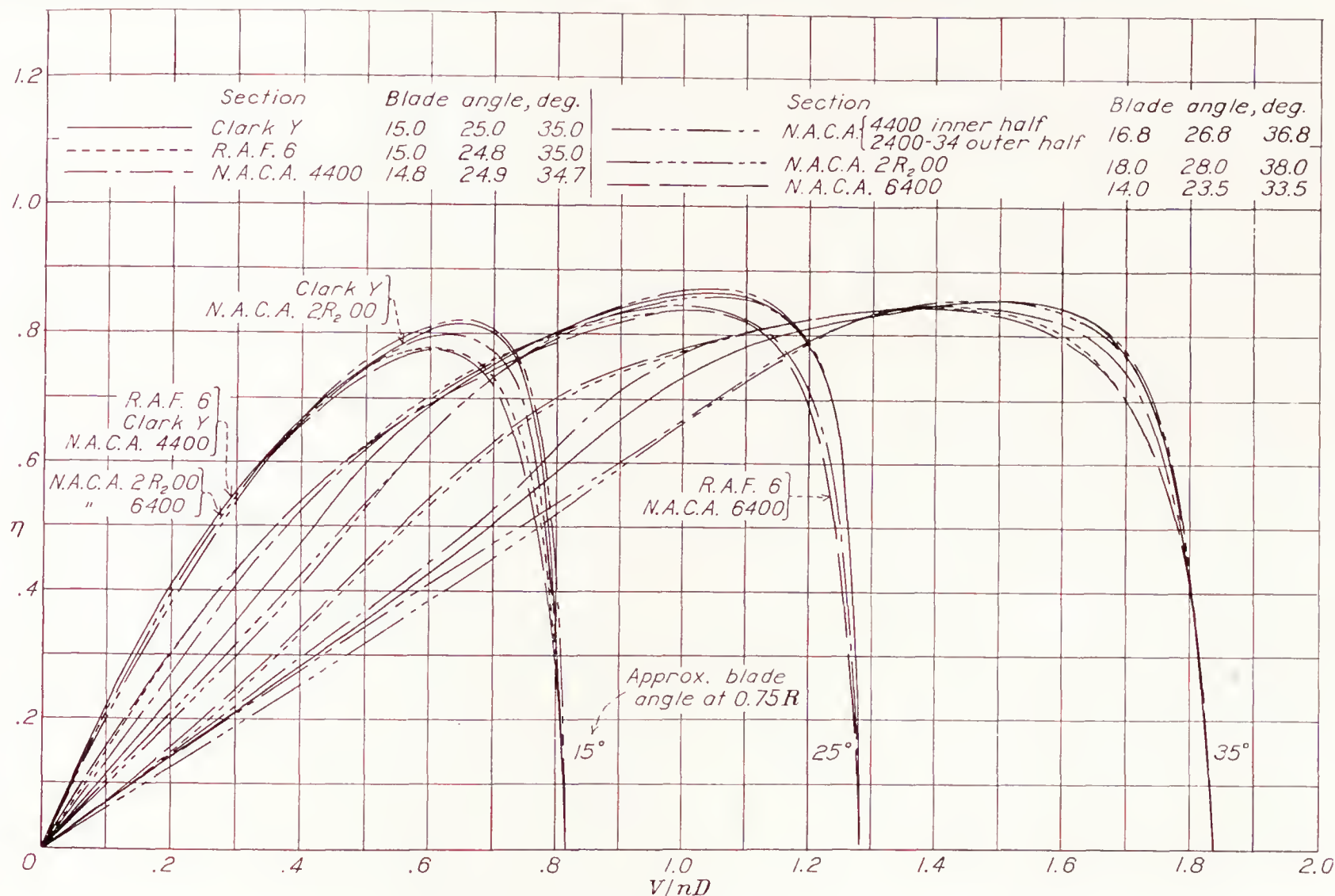


FIGURE 32.—Comparison of typical efficiency curves.

ones are only slightly less cambered. The propeller of R. A. F. 6 section has a higher average effective mean camber ratio than that of its 0.75 radius station for the same reason; it is 0.055 as compared with 0.040.

The corresponding power curves are given in figure 31. In the region where all the propellers are stalled, it may be seen that the high-camber propellers have lower power coefficients than the low-camber ones.

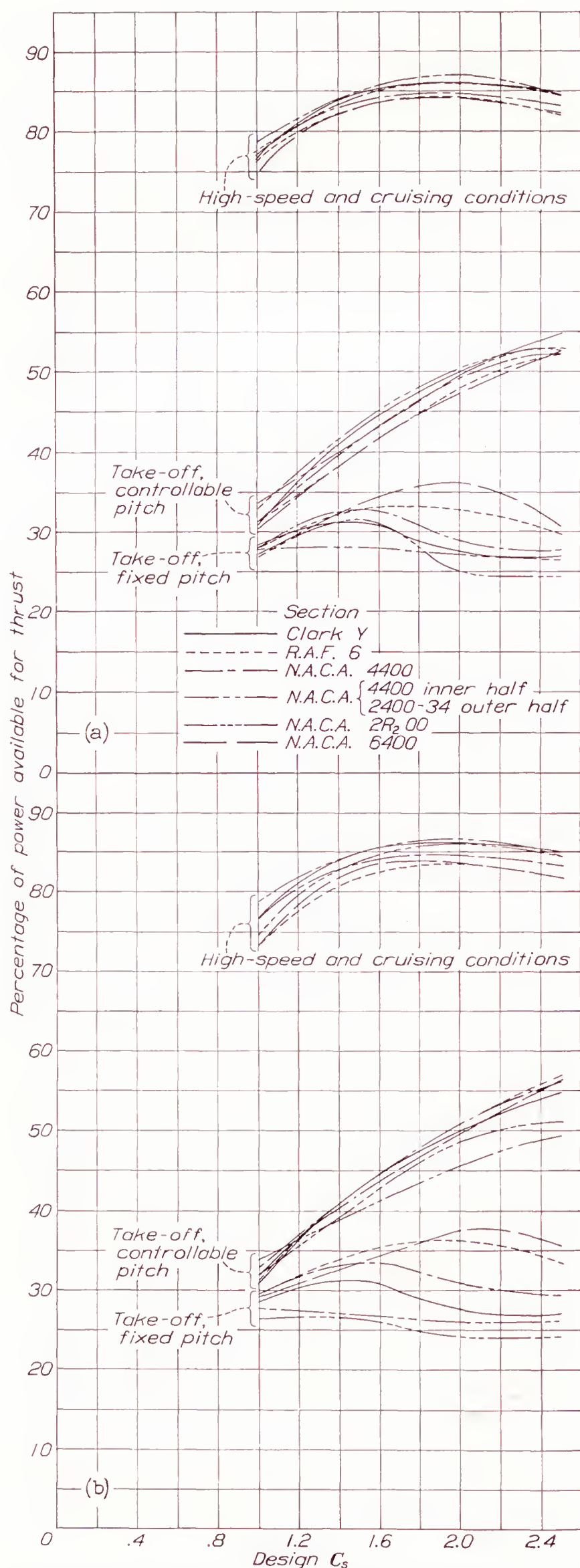
The efficiency curves, given in figure 32, indicate the effect of profile drag on maximum efficiency. The propellers of low camber display efficiencies about 3 percent higher than for the ones of high camber, and the peaks occur at higher values of  $V/nD$ . Both effects are attributed to the lower profile drags of the low-camber propellers. The lower the profile drag, the closer the

The efficiency curves also reflect the high-thrust and the low-drag values observed for the high-camber propellers operating at low values of  $V/nD$ . These differences in efficiency, however, do not necessarily represent true differences in thrust power available for either fixed-pitch or controllable propellers. In the case of a combination of a fixed-pitch propeller and an engine, differences in  $C_{P0}$  (design power coefficient) will determine differences in diameter, so that for a given take-off speed there will be differences in  $V/nD$ ,  $\eta$ , and also engine speed,  $N$ . The thrust horsepower available, if constant torque is assumed, is obtained from

$$\text{t. hp.} = (\text{b. hp.}) \frac{N}{N_0} \eta$$

where  $N_0$  is the engine speed at the high-speed condition





(a) All propellers designed for maximum efficiency at high speed.

(b) All propellers have same diameter for a given  $C_s$  (Clark Y propeller used as standard.).

FIGURE 33.—A comparison of propellers for the high-speed and take-off flight condition. Take-off criterion,  $V=0.25 V_{max}$

of flight. In the case of controllable propellers, the pitch is adjusted to maintain  $C_{P_0}$  and  $N_0$  constant so that different propellers will be set at different blade angles for the same  $V/nD$  or air speed. In order to show the effect of the different blade sections on performance, the thrust power available is computed and will be discussed later for both fixed-pitch and controllable propellers.

**Effect of blade section on the performance of engine-propeller combinations.**—Any conclusion drawn from comparisons of relative engine-propeller performance depends somewhat on the methods employed in the analysis. If each propeller is selected for maximum efficiency at high speed, the diameters of the various propellers will be different, depending upon the design power coefficient,  $C_{P_0}$ , which in turn depends on the  $V/nD$  for peak efficiency. The differences in diameters will have a large effect on the efficiency at the take-off condition; for controllable propellers the larger the diameter, the higher the efficiency. If the  $V/nD$  for peak efficiency could be determined with uniform accuracy for all propellers, the comparison would be a just evaluation of the relative merits, compressibility or tip-speed effects due to the differences in diameters being neglected.

If the propellers are compared on a basis of equal diameters for a given design condition, all the propellers will not operate quite at peak efficiency at high speed. The high-camber propellers will operate beyond the peak and the designs will be, in effect, "compromises" because the take-off efficiencies for controllable propellers, at least, will be increased thereby. The constant-diameter method has the advantage of comparison at equal tip speeds, and the airplane structural limitations on the diameter are often the determining factor.

As neither method is entirely satisfactory and both have their merits, computations have been given for each. In some instances the results appear to be contradictory but, if the methods are well understood, a reasonable interpretation can be made.

In figure 33 (a) the propellers are compared on the basis of maximum efficiency for high speed. Curves are given for high-speed efficiency, for take-off efficiency for controllable propellers of the constant-speed type, and for take-off efficiencies for fixed-pitch propellers, all for a wide range of design conditions (values of design  $C_s$  from 1.0 to 2.5). The take-off criterion is assumed to be the thrust power available at a speed equal to 0.25 of the high speed of landplanes. This value corresponds to 0.7 of the take-off speed for airplanes having a speed ratio of high speed to take-off speed of 2.8. It can be shown that 0.7 of the take-off speed is the best single point for comparing take-off thrust as that point represents the approximate center of the area of the graphically integrated diagram of take-off run of most airplanes represented by  $\int t dv$ , where  $t$  and  $v$  represent time and velocity, respectively.



In the computation of the take-off thrust power, the engine torque is assumed to be equal to the torque at high speed. The engine speeds are assumed to remain constant for the controllable propellers but to decrease for the fixed-pitch propellers in the take-off condition, according to the relation

$$\frac{N}{N_0} = \sqrt{C_{P0}/C_P}$$

Although the percentage of thrust power available also represents propulsive efficiency for the controllable propellers, it represents  $\eta(N/N_0)$  for the fixed-pitch propellers.

The greatest difference in maximum efficiency is about 3 percent; the highest efficiencies are for the low-camber propellers.

It seems strange that the controllable propellers of low and medium camber would also excel for the take-off condition. This paradox is explained by the results presented in table IV. The low-camber propellers are designed with larger diameters than the high-camber ones and, in order to absorb the same power at the take-off, are set to lower blade angles for which the efficiency is higher.

The high-camber propellers are definitely superior for fixed-pitch propellers set at high blade angles. The reason is quite obvious. (See figs. 30, 31, and 32.) The stall is delayed to higher angles of attack, i. e., to lower values of  $V/nD$ , and the gain in efficiency due to the lower drag and the higher lift of the sections is quite pronounced. The decrease in engine speed also plays a prominent part in the available thrust power, as is shown in table IV. The high-camber propellers are designed to operate at higher values of  $C_{P0}$  than the low-camber ones. The higher the  $C_{P0}$ , the less is the increase in  $C_P$  for take-off and, consequently, the less is the drop in rotational speed. The stalling characteristics of the propellers do not enter the problem for low blade angles so that there is less choice of section for low design  $C_s$  conditions.

In figure 33 (b) the propellers are compared on a basis of equal diameters for given values of  $C_s$ . The propeller of Clark Y section is taken as the standard because it is of medium camber. The diameters of the low-camber propellers are slightly decreased from the previous comparison and those for the high-camber ones are increased. The high-speed efficiencies are slightly different from the maximum values but the order of merit is the same.

The order of take-off efficiencies for the controllable propellers is changed. The high-camber propellers are about equal, in general, to the medium-camber ones, and the low-camber ones have the lowest efficiencies. The medium-camber and the high-camber propellers are about equal in this comparison because neither type exceeds the stall for the take-off criterion (see table V); the superior stalling characteristics of the high-camber

propellers are, of course, not utilized. The high-camber propeller is slightly superior at a  $C_s$  value of 2.5, which shows that its stalling characteristics are beginning to be utilized and, for higher  $C_s$  values, they should be definitely superior. The high-camber propellers would have been superior at lower values of  $C_s$  if the diameters had all been smaller. For example, if the propeller of R. A. F. 6 section had been assumed to be the standard of comparison instead of the propeller of Clark Y section, the high-camber propellers would have excelled at  $C_s$  values above 1.5.

Large differences in take-off thrust power are evident for the various fixed-pitch propellers. This comparison is the closest representation given of a pure efficiency comparison because the take-off  $C_P$  has about the same value for all propellers; they therefore all have about the same drop in engine speed. The results given in figure 32 show the same order of merit in the take-off

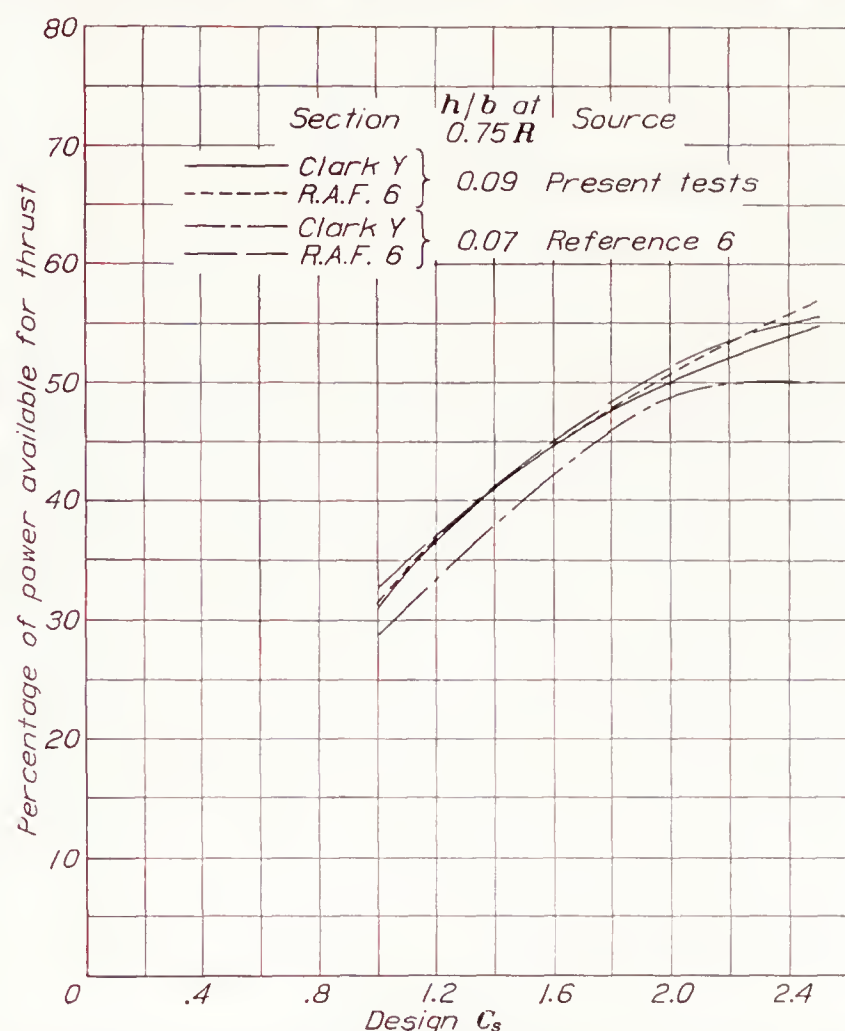


FIGURE 34.—Comparison of propellers of Clark Y and R. A. F. 6 section of two thickness ratios for the take-off condition.  $V=0.25V_{max}$ , controllable operation; all propellers have the same diameter.

range as the comparison in figure 33 (b); both methods indicate the superiority of high-camber propellers for medium and high blade-angle design conditions.

**Effect of thickness.**—In reference 6, comparisons were made between propellers of three different sections: Clark Y, R. A. F. 6, and N. A. C. A. 2400-34. The propellers were thinner than the present ones ( $h/b=0.07$  at  $0.75R$  as compared with  $h/b=0.09$ ). In the former comparison, based on controllable propellers of equal diameter, the propeller of R. A. F. 6 section was best for take-off, while the present tests indicate the propellers of Clark Y and R. A. F. 6 sections to be about



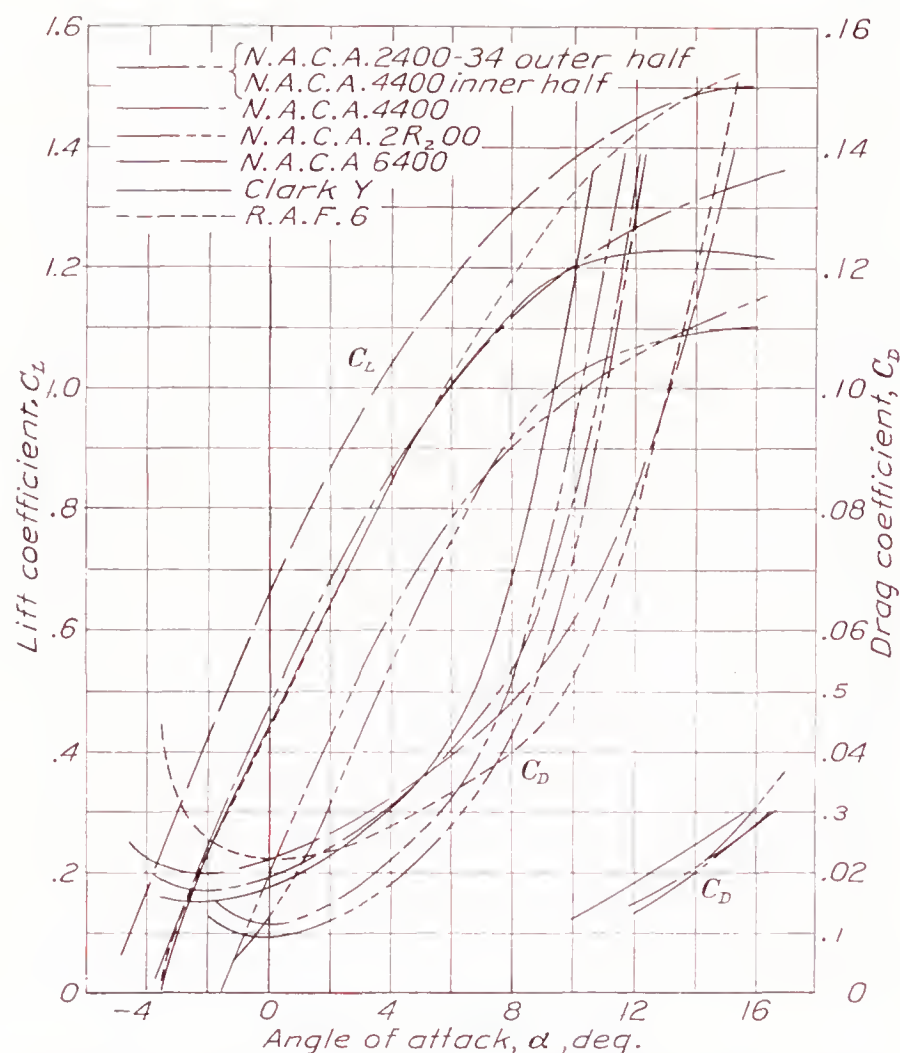


FIGURE 35.—Airfoil characteristics of propeller sections computed from the  $0.70R$  station. Blade angle,  $25^\circ$  at  $0.75R$ .

equal. It is reasonable to assume that the differences in relative efficiency are due to the differences in thickness of the two sets of propellers. Figure 34 shows that the propeller of Clark Y section improves in take-off efficiency with increasing thickness whereas the pro-

PELLER of R. A. F. 6 section does not. It is well known that  $C_{L_{max}}$  increases with airfoil thickness and camber up to a limit. As the R. A. F. 6 section has a higher camber than the Clark Y, it seems logical that it would reach its  $C_{L_{max}}$  limit at lower values of thickness. Reference 2, which is a more general study of the effect of blade thickness, seems to substantiate this contention.

The N. A. C. A. section propellers are not so sensitive to change in thickness because the camber is not a function of thickness.

**Lift and drag coefficients reduced from propeller results.**—In reference 7, Lock presents two methods of reducing propeller characteristics to airfoil results and vice versa. In one method, computations are made for six blade elements and the thrust and the torque grading curves are integrated. The second method is based on only a single radius, the assumption being that the shape of the grading curves remains constant so that a constant integrating factor is used. This method is further simplified by the use of charts so that a propeller may be analyzed within an hour.

Lift and drag curves derived by the single-radius method are plotted against angle of attack in figure 35 for the six propellers with a blade-angle setting of  $25^\circ$  at  $0.75R$ ; polar curves are given in figure 36. The results for only one blade angle are analyzed. The tests from which these curves are derived were made the same day under apparently identical conditions and are therefore considered to be relatively more accurate than for the whole series; the estimated precision is within 0.5 percent for  $\eta_{max}$ .

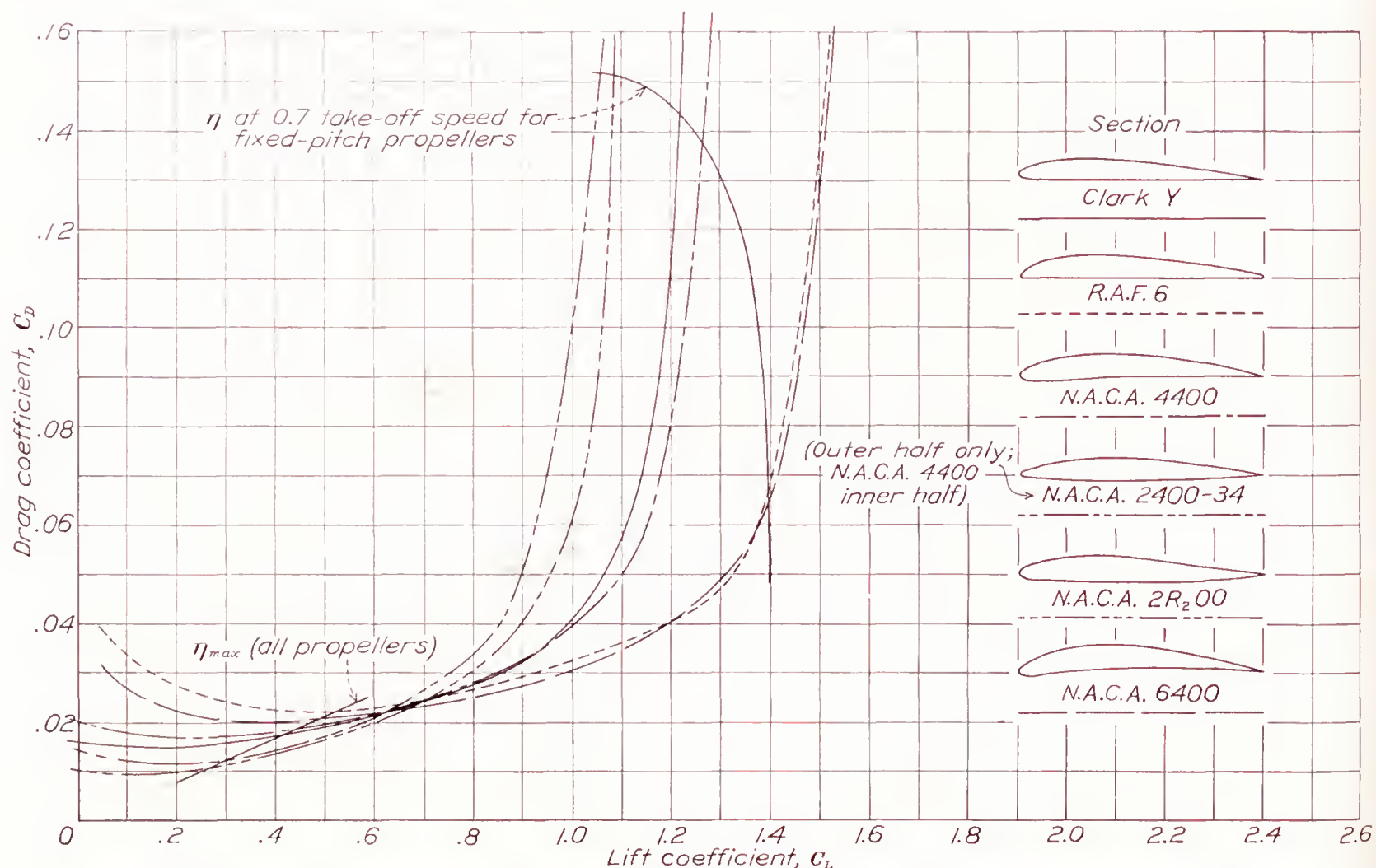


FIGURE 36.—Polar airfoil section characteristics reduced from propeller results.  $V/V_\infty = 0.46$  (approximately); blade angle,  $25^\circ$  at  $0.75R$ .



Of interest are  $C_{D_{min}}$ ,  $C_{L_{max}}$ , and  $C_D$  at high values of  $C_L$ . The sections of 2-percent camber show values of  $C_{D_{min}}$  of about 0.01; the sections of 4-percent camber show values of about 0.017; and the section of 6-percent camber shows a value of about 0.02. The propeller of R. A. F. 6 section, which has a camber line (see fig. 29) different from the other sections, shows the highest  $C_{D_{min}}$ , 0.022. The 2-percent sections show values of  $C_{L_{max}}$  of about 1.1; the 4-percent section, of about 1.3; and the 6-percent section, of about 1.5.

Lift and drag coefficients are of little value in determining the relative merits of the airfoil sections for propellers unless their quantitative importance is determined. The influence of  $C_D$  at  $\eta_{max}$  (approximately  $C_{D_{min}}$ ) on  $\eta_{max}$  is given in figure 37 for the propellers when set at a blade angle of  $25^\circ$  at  $0.75R$ . Large changes in  $C_D$  are seen to affect  $\eta_{max}$  only a small amount. Reducing  $C_D$  from 0.02 to 0.01 increases  $\eta_{max}$  only 3 percent. By extrapolation, if the drag could be reduced to zero, the  $\eta_{max}$  would be increased only to

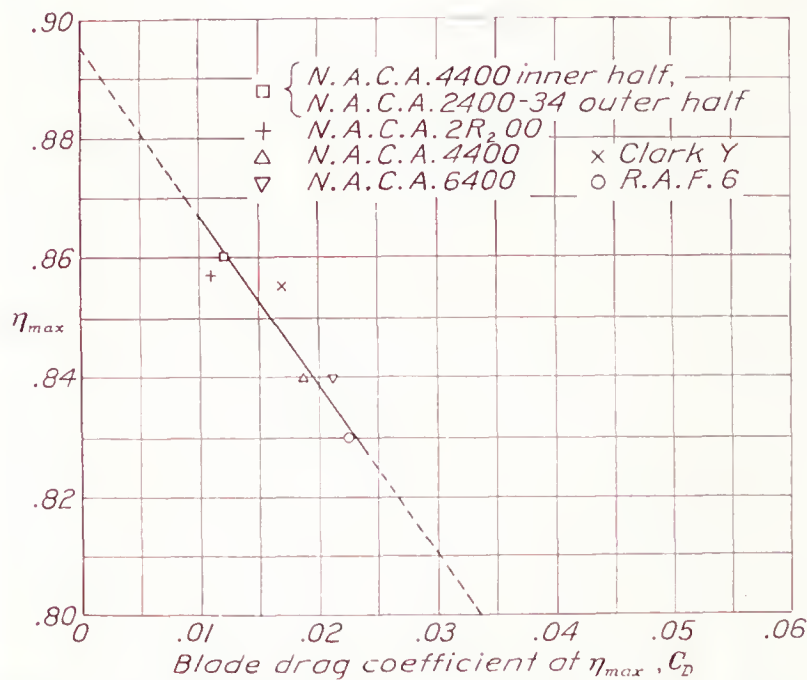


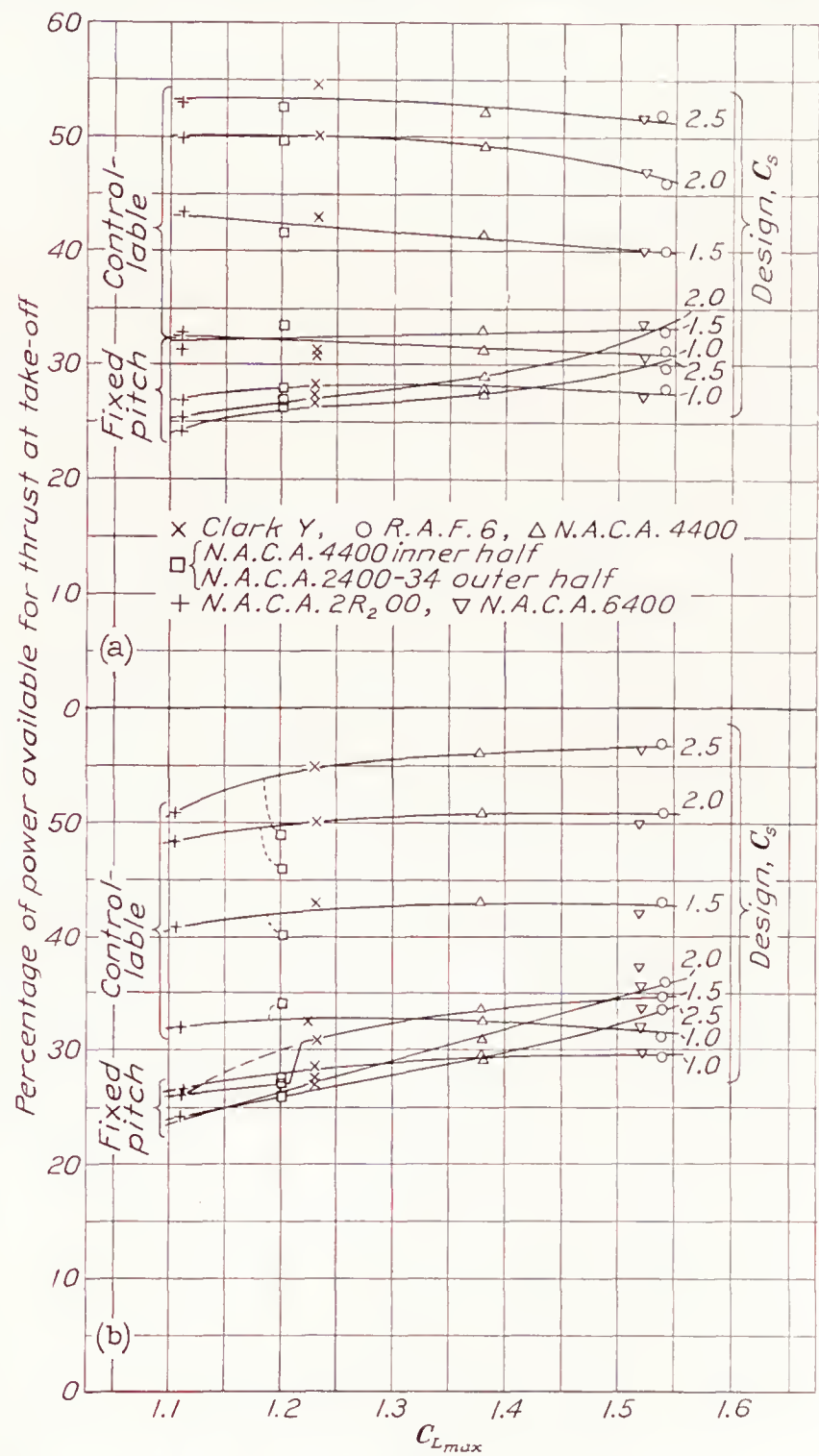
FIGURE 37.—The influence of the blade drag coefficient on the maximum propulsive efficiency. Blade angle,  $25^\circ$  at  $0.75R$ .

0.895, which is only a few percent below the ideal for this condition. (The ideal efficiency neglects profile drag, hub drag, body slipstream drag, rotational losses, tip losses, blade interference, etc.) This result indicates that the possibilities for improving  $\eta_{max}$  by reducing the profile drag of the sections are very limited; the maximum increase is probably not more than 1 or 2 percent above that for the present-day standard sections. It should be emphasized that figure 37 applies only to a blade-angle setting of  $25^\circ$ . For higher angles up to about  $45^\circ$ , according to the simple blade-element theory,  $C_D$  would have a slightly smaller influence on  $\eta_{max}$ .

A direct relationship does not always exist between  $C_{L_{max}}$  and take-off efficiency because in many cases the stall is not reached. Fixed-pitch propellers set at blade angles below about  $20^\circ$  (the approximate blade angle for stalling at zero air speed) and some controllable propellers set at angles as high as  $30^\circ$  do not stall

during the take-off run. Probably some indirect relationship exists, however, between  $C_{L_{max}}$  and the take-off efficiency because of the drag at high angles of attack associated with sections of different camber.

The relationship between the  $C_{L_{max}}$  and the take-off efficiencies of controllable and fixed-pitch engine-propeller combinations is given in figure 38. In figure 38 (a) the analysis is based on propellers designed for  $\eta_{max}$ , the data being taken from figures 33 (a) and 35.



(a) All propellers designed for maximum efficiency at high speed.  
(b) All propellers have same diameter for a given  $C_s$  (Clark Y propeller used as standard).

FIGURE 38.—Relationship between  $C_{L_{max}}$  and the propeller characteristics for the take-off condition. Take-off criterion,  $V=0.25 V_{max}$ .

It may be seen that increasing values of  $C_{L_{max}}$  are associated with a slightly decreasing take-off thrust power of controllable propellers. This trend, as previously explained, is due to the different take-off blade settings necessitated by the differences in diameter.

The trend of take-off thrust power increases with increasing  $C_{L_{max}}$  for the fixed-pitch propellers set at moderately high blade angles but not for the low blade-angle settings because the blades are never stalled.



In figure 38 (b) a similar analysis is presented for propellers having equal diameters, the material being taken from figures 33 (b) and 35. In this example, increasing values of  $C_{Lmax}$  are associated with an increasing take-off thrust power of controllable propellers for only the low  $C_L$  range and the high design  $C_s$  values. The high-pitch low-camber propellers are the only ones exceeding the stall at the take-off, as previously pointed out. Had the diameters of all propellers been smaller, more propellers would have exceeded the stall and the advantage of a high lift coefficient would be more general.

The advantage of high lift coefficients for fixed-pitch propellers is definite over the entire range investigated; it is more definite, however, for the high blade angles than for the low ones. The take-off thrust is increased an average of 1 percent for each 1 percent increase in  $C_{Lmax}$  for  $C_s$  values of 1.5 and over.

**Effect of compressibility.**—In the tests reported in reference 8 it was noted that propellers of R. A. F. 6 section were more affected by compressibility in the take-off and climbing range than those of Clark Y section. It is reasonable to assume that the other propellers would likewise display differences. Of the sections incorporated in the present propellers, the Clark Y, the R. A. F. 6, and the N. A. C. A. 2409-34 have been tested as airfoils in the N. A. C. A. high-

speed wind tunnel and the results are given in figure 39 (from references 1 and 4). The low-speed results  $V/V_c=0.40$ , correspond approximately to the present results. It may be noted that the curves from the tests of low-speed airfoils check in a relative way the airfoil curves derived from the propeller results.

In the airfoil curves for high speed ( $V/V_c=0.80$ , fig. 39), it may be noted that the values of the minimum drag coefficient of the N. A. C. A. 2409-34 section was doubled, the Clark Y tripled, and the R. A. F. 6 nearly tripled by doubling the air speed. If all the elements were traveling at  $0.80V_c$ , the maximum efficiency of the propeller of N. A. C. A. 2409-34 section would be expected to drop about 3 percent, that of Clark Y section about 9 percent, and that of R. A. F. 6 section about 8 percent, judging by the effect of drag on  $\eta_{max}$ , as shown in figure 37 for the 2° blade-angle setting. Fortunately, only the tip elements are affected so the loss is much less.

For the 2-blade propeller of R. A. F. 6 section turning at 1,800 r. p. m. ( $V/V_c=0.83$ ), the loss in peak efficiency is only about 1 percent (within the experimental error) (fig. 40), which means that very little area at the tips is affected. These results have been translated into airfoil results and are shown in figure 41 for the purpose of comparison with the high-speed results shown in figure 39. Some idea of the blade

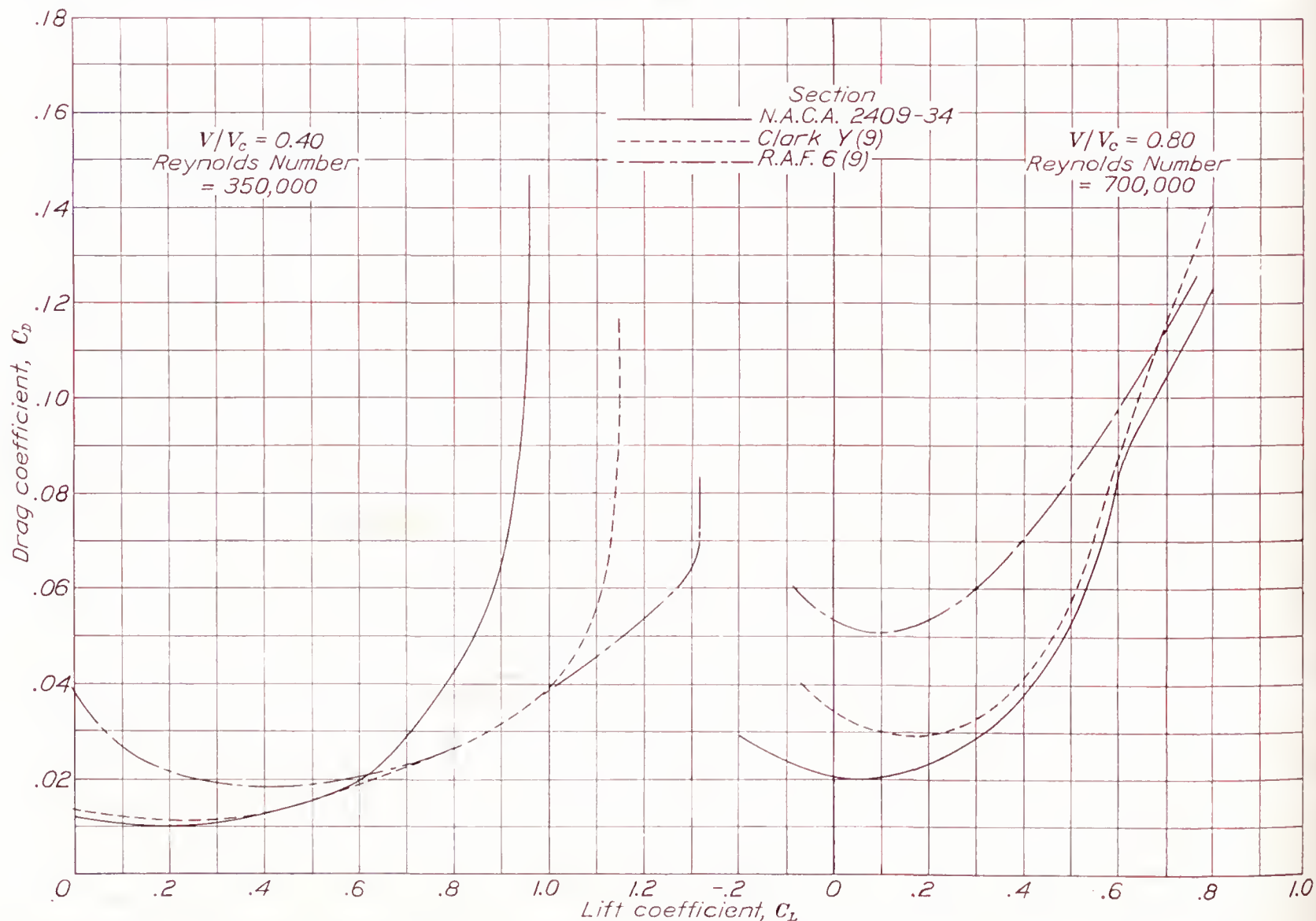


FIGURE 39.—Characteristics of three airfoils at two air speeds as measured in the N. A. C. A. 11-inch high-speed tunnel (from references 1 and 4).



area affected may be obtained by referring to figure 42 wherein  $C_D$  is plotted against  $V/V_c$  (which is also a function of propeller radius, assuming only rotational velocity). If consideration is given to the

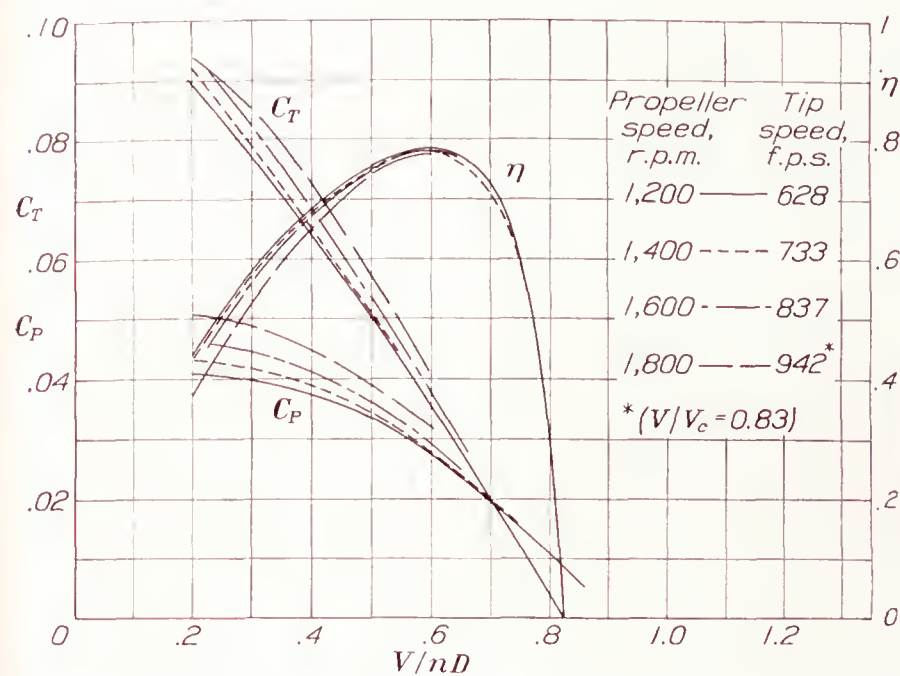


FIGURE 40.—Effect of compressibility on the characteristics of an R. A. F. 6 propeller (from reference 8).

thrust distribution over the blade, which falls off near the tip, it is readily seen why the propeller of the R. A. F. 6 section loses so little in peak efficiency owing to compressibility.

It is pointed out in reference 4 that the N. A. C. A. 2400-34 series section is superior at high speeds to the

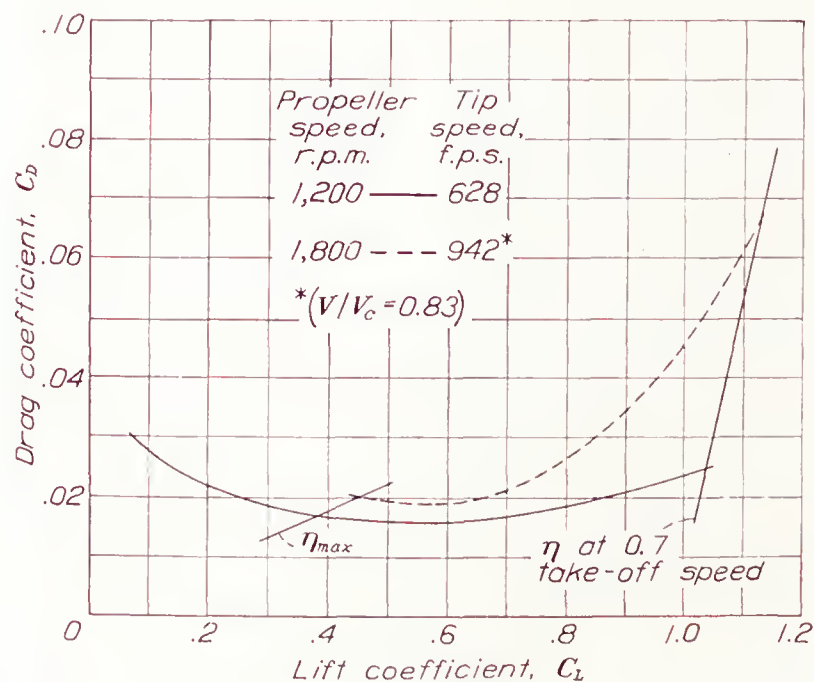


FIGURE 41.—Airfoil section characteristics reduced from propeller results. Two-blade propeller of R. A. F. 6 section; blade angle,  $15^\circ$  at  $0.75R$  (from reference 8).

commonly used propeller sections and the curves that are herein reproduced in figure 39 are given as evidence. As a result of the recommendations of reference 4, propeller 6623-B was designed with the N. A. C. A. 2400-34 series section for the outer half. This propeller was not tested at high tip speeds because the propeller of R. A. F. 6 section showed scarcely any

decrease in peak efficiency; it was concluded that any compressibility effects of the propeller of N. A. C. A. 2400-34 section could not be measured at  $\eta_{max}$  with the present test set-up.

Figure 42 shows the relative blade area affected by compressibility for the propellers of R. A. F. 6 and N. A. C. A. 2400-34 sections. It appears that the tip speed must be at least  $0.90V_c$  before compressibility effects at  $\eta_{max}$  could be measured on the propeller of N. A. C. A. 2400-34 section, and then the loss would probably amount to not more than 1 per cent, judging by the results for the R. A. F. 6 section for a tip speed of  $0.83V_c$ . The results of reference 9 also show that no loss in peak efficiency occurs up to

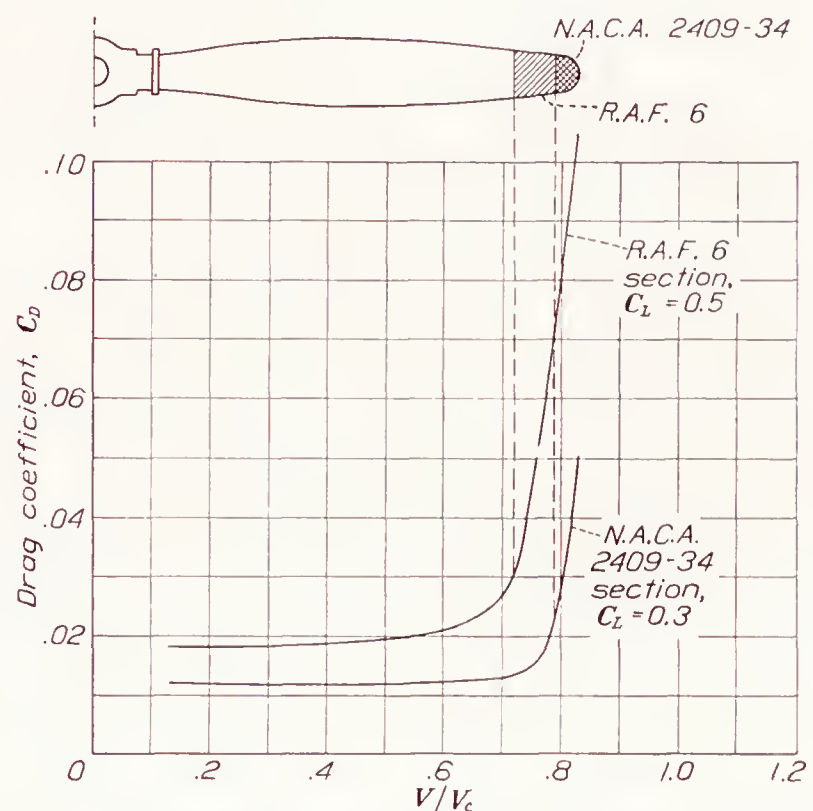


FIGURE 42.—Effect of compressibility on the drag of two sections when working at lift coefficients for maximum propeller efficiency (from reference 4). Blade area appreciably affected by compressibility for a tip speed equal to  $0.83V_c$ .

tip speeds of  $0.85$  or  $0.90V_c$  for the standard propeller sections.

Tests of the propellers with the N. A. C. A. sections at high tip speeds for the take-off and climbing conditions are planned. It is not anticipated, however, that the condition of high tip speed will materially alter the relative merits of the sections for the take-off condition because: First, only the tip sections ordinarily operate at high speeds; and, second, compressibility tends to equalize the characteristics of different airfoils at high angles of attack rather than to accentuate any differences. Figure 39 indicates that all airfoil sections have about the same  $C_{L_{max}}$  at  $0.80V_c$ . This result was also found to be substantially true for propellers. In reference 8 it is pointed out that, although the propellers of R. A. F. 6 section lost more in take-off efficiency owing to compressibility than those of Clark Y section, the efficiency at low tip speeds was higher; consequently, the efficiencies tended to equalize at high tip speeds.



## CONCLUSIONS

1. The difference in maximum propulsive efficiency for propellers of different sections amounted to about 3 percent. The highest efficiencies were for the propeller sections of low mean cambers, as may be noted from the order of merit: N. A. C. A. 2400-34, Clark Y, N. A. C. A. 2R<sub>2</sub>00, N. A. C. A. 4400, R. A. F. 6, and N. A. C. A. 6400.

2. The difference in take-off efficiency for controllable propellers varied from 2 to 8 percent, depending upon the section, the design  $C_s$  value, and the method of comparison. Based on propellers of the same diameter, the order of merit of the sections, in general, was: R. A. F. 6, N. A. C. A. 4400, Clark Y, N. A. C. A. 6400, N. A. C. A. 2R<sub>2</sub>00, and N. A. C. A. 2400-34. Based on propellers of which the diameters were those giving maximum efficiency at high speed, the order of merit of the sections, in general, was: N. A. C. A. 2R<sub>2</sub>00, Clark Y, N. A. C. A. 4400, N. A. C. A. 2400-34, R. A. F. 6, and N. A. C. A. 6400.

3. The difference in take-off efficiency for fixed-pitch propellers varied through wide limits. Based on either method of comparison, the order of merit was: R. A. F. 6 or N. A. C. A. 6400, N. A. C. A. 4400, Clark Y, N. A. C. A. 2R<sub>2</sub>00, and N. A. C. A. 2400-34.

4. The tests indicated that blade sections for controllable propellers not limited in diameter should be selected almost entirely on a basis of minimum drag, as the maximum lift coefficients had only a small effect on the take-off characteristics within the range investigated, because the stall, in general, did not occur.

5. The tests indicated that blade sections for fixed-pitch propellers should be selected on bases of both minimum drag and maximum lift, particularly for blade-angle settings of 20° and over. For propellers of equal diameters, the increase in take-off thrust was proportional, in general, to the maximum lift.

6. A comparison of Clark Y and R. A. F. 6 sections of different thickness ratios for controllable propellers of the same diameter indicated that thin ( $h/b=0.07$ ) propellers of R. A. F. 6 section were superior at take-off to thin propellers of Clark Y section, but that thick

( $h/b=0.09$ ) propellers of Clark Y section were equal to those of R. A. F. 6 section, either thick or thin.

7. Tests already reported on the effect of compressibility indicate that no correction need be applied to the maximum efficiency of the present results for tip-speed values of  $V/V_c$  up to 0.80 or 0.90. Although correction should be applied to the take-off characteristics for somewhat lower tip-speed values, the results show that compressibility tends to decrease any differences between propellers of different section. The present tests probably show the correct order of merit even up to tip speeds of  $0.90V_c$ .

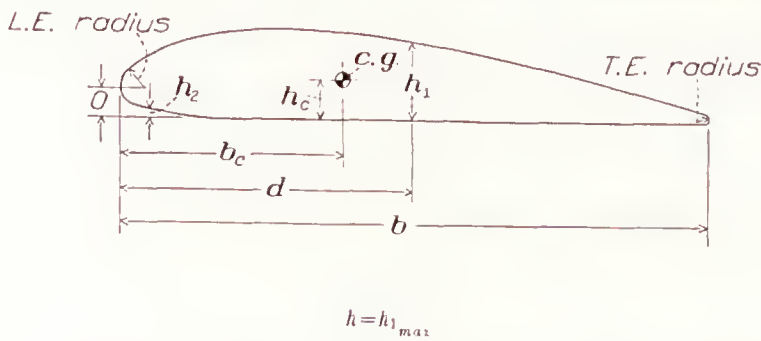
LANGLEY MEMORIAL AERONAUTICAL LABORATORY,  
NATIONAL ADVISORY COMMITTEE FOR AERONAUTICS  
LANGLEY FIELD, VA., *March 23, 1938.*

## REFERENCES

1. Stack, John: The N. A. C. A. High-Speed Wind Tunnel and Tests of Six Propeller Sections. T. R. No. 463, N. A. C. A., 1933.
2. Freeman, Hugh B.: Comparison of Full-Scale Propellers Having R. A. F.-6 and Clark Y Airfoil Sections. T. R. No. 378, N. A. C. A., 1931.
3. Jacobs, Eastman N., Ward, Kenneth E., and Pinkerton, Robert M.: The Characteristics of 78 Related Airfoil Sections from Tests in the Variable-Density Wind Tunnel. T. R. No. 460, N. A. C. A., 1933.
4. Stack, John, and von Doenhoff, Albert E.: Tests of Related Airfoils at High Speeds. T. R. No. 492, N. A. C. A., 1934.
5. Weick, Fred E., and Wood, Donald H.: The Twenty-Foot Propeller Research Tunnel of the National Advisory Committee for Aeronautics. T. R. No. 300, N. A. C. A., 1929.
6. Biermann, David, and Hartman, Edwin P.: Tests of Full-Scale Propellers in the Presence of a Radial and Liquid-Cooled Engine Nacelle, Including Tests of Tip Spinners. T. R. No. 642, N. A. C. A., 1938.
7. Lock, C. N. H.: A Graphical Method of Calculating the Performance of an Airscrew. R. & M. No. 1675, British A. R. C., 1935.
8. Biermann, David, and Hartman, Edwin P.: The Effect of Compressibility on Eight Full-Scale Propellers Operating in the Take-Off and Climbing Range. T. R. No. 650, N. A. C. A., 1938.
9. Wood, Donald H.: Full-Scale Tests of Metal Propellers at High Tip Speeds. T. R. No. 375, N. A. C. A., 1931.



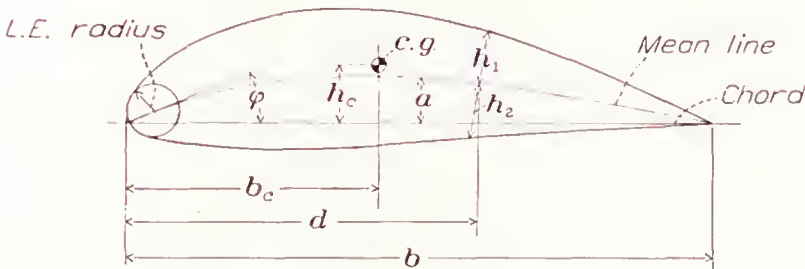
TABLE II  
CLARK Y AND R. A. F. 6 BASIC PROPELLER SECTIONS



$h = h_{1\max}$

Section	Clark Y		R. A. F. 6
$d/b$	$h_1/h$	$h_2/h$	$h_1/h$
0	0.2950	0.2950	
.025	.5490	.1281	0.41
.05	.6625	.0811	.59
.1	.8055	.0384	.79
.2	.9570	.0085	.95
.3	.9950	0	1.00
.4	.9830	0	.99
.5	.9280	0	.95
.6	.8290	0	.87
.7	.6835	0	.74
.8	.5210	0	.56
.9	.3375	0	.35
L. E. radius	0.13		.10
T. E. radius	.08		.07
$h_c$	.416 $h$		.421 $h$
$b_c$	.4405 $b$		.4469 $b$
Area	.7245 $bh$		.738 $bh$
$I_{major}$	.0418 $b^3h$		.0446 $b^3h$
$I_{minor}$	.0454 $bh^3$		.0464 $bh^3$

TABLE III  
N. A. C. A. BASIC PROPELLER SECTIONS



$(h_1 + h_2)_{max} = h$ ;  $h_1$  and  $h_2$  are measured perpendicular to the tangent of the mean line

Section	4400		2400-34		2R200		6400	
$d/b$	$a/b$	$h_1/h = h_2/h$	$a/b$	$h_1/h = h_2/h$	$a/b$	$h_1/h = h_2/h$	$a/b$	$h_1/h = h_2/h$
0.025	0.00184	0.2179	0.00242	0.140	0.00361	0.2179	0.00727	0.2179
.05	.00937	.2962	.00469	.208	.00681	.2962	.01405	.2962
.1	.01750	.3902	.00875	.304	.01204	.3902	.02625	.3902
.2	.03000	.4781	.01500	.425	.01833	.4781	.04500	.4781
.3	.03750	.5001	.01875	.484	.01999	.5001	.05625	.5001
.4	.40000	.4836	.02000	.500	.01821	.4836	.06000	.4836
.5	.03889	.4411	.01944	.486	.01414	.4411	.05834	.4411
.6	.03556	.3803	.01778	.443	.08930	.3803	.05333	.3803
.7	.03000	.3053	.01500	.373	.03710	.3053	.04501	.3053
.8	.02222	.2186	.01111	.277	-.00024	.2186	.03334	.2186
.9	.01222	.1206	.00611	.156	-.00187	.1206	.01834	.1206
1.0	0	.0105	0	.010	0	.0105	0	.0105
L. E. radius/b	1.1 $(h/b)^2$		0.275 $(h/b)^2$		1.1 $(h/b)^2$		1.1 $(h/b)^2$	
$\tan \varphi$	0.200		0.100		0.153		0.300	
$b_c$	.42b		.46b		.42b		.42b	
$h_c$	.0313b		.0172b		.0126b		.0473b	

TABLE IV  
PERFORMANCE OF PROPELLERS HAVING DIAMETER FOR MAXIMUM EFFICIENCY AT HIGH SPEED

Propeller	Section	Design $C_s$	High speed				Take-off, controllable pitch			Take-off, fixed pitch				
			$\frac{V}{nD}$	Diam- eter (ft.)	Blade angle (deg.)	$\eta_{max}$	$\frac{V}{nD}$	Blade angle (deg.)	$\eta$	$\frac{V}{nD}$	Blade angle (deg.)	$\eta$	$\frac{N}{N_0}$	$\eta\left(\frac{N}{N_0}\right)$
5868-9	Clark Y	1.0	0.505	10	13.2	0.766	0.126	10.8	0.307	0.151	13.2	0.340	0.835	0.284
		1.5	.852	10	21.9	.848	.213	15.4	.428	.282	21.9	.411	.757	.311
		2.0	1.213	10	29.1	.861	.304	19.3	.500	.437	29.1	.397	.693	.273
		2.5	1.598	10	36.1	.850	.400	22.7	.548	.595	36.1	.403	.670	.270
5868-R6	R. A. F. 6	1.0	.553	9.14	16.4	.763	.138	13.9	.312	.157	16.4	.320	.877	.284
		1.5	.935	9.12	25.7	.830	.234	20.7	.400	.273	25.7	.384	.855	.313
		2.0	1.282	9.47	31.6	.843	.320	22.8	.480	.410	31.6	.419	.781	.307
		2.5	1.705	9.37	38.8	.828	.426	28.2	.521	.560	38.8	.390	.761	.304
6623-A	N. A. C. A. 4400	1.0	.553	9.14	16.4	.771	.138	13.9	.312	.157	16.4	.320	.878	.284
		1.5	.889	9.59	23.3	.837	.222	17.5	.415	.271	23.3	.401	.820	.313
		2.0	1.244	9.75	29.9	.848	.311	20.9	.492	.422	29.9	.392	.735	.307
		2.5	1.655	9.65	37.2	.832	.414	26.0	.521	.578	37.2	.387	.716	.304
6623-B	N. A. C. A. 4400 inner half, 2400-34 outer half.	1.0	.505	10.00	15.2	.786	.126	12.9	.338	.151	15.2	.334	.835	.273
		1.5	.830	10.27	22.8	.850	.207	16.1	.415	.282	22.8	.383	.734	.284
		2.0	1.154	10.51	28.8	.871	.289	18.4	.496	.438	28.8	.413	.659	.277
		2.5	1.545	10.34	36.4	.846	.386	22.7	.526	.601	36.4	.415	.638	.274
6623-C	N. A. C. A. 2R <sub>200</sub>	1.0	.478	10.57	15.0	.776	.119	11.5	.329	.156	15.0	.349	.764	.274
		1.5	.788	10.81	21.8	.843	.197	14.6	.435	.282	21.8	.452	.698	.284
		2.0	1.168	10.40	30.0	.861	.292	20.0	.503	.448	30.0	.383	.651	.284
		2.5	1.582	10.10	38.3	.845	.396	24.8	.529	.626	38.3	.387	.630	.284
6623-D	N. A. C. A. 6400	1.0	.562	8.98	15.5	.747	.141	13.2	.303	.159	15.5	.307	.885	.274
		1.5	.905	9.41	22.4	.831	.226	16.6	.400	.274	22.4	.406	.826	.284
		2.0	1.282	9.47	29.4	.842	.320	20.7	.474	.396	29.4	.446	.809	.284
		2.5	1.705	9.37	37.4	.823	.426	26.8	.526	.562	37.4	.404	.757	.284

TABLE V  
PERFORMANCE OF PROPELLERS OF EQUAL DIAMETER  
[Clark Y propeller taken as standard]

Propeller	Section	Design $C_s$	High speed				Take-off, controllable pitch			Take-off, fixed pitch				
			$\frac{V}{nD}$	Diam- eter (ft.)	Blade angle (deg.)	$\eta_{max}$	$\frac{V}{nD}$	Blade angle (deg.)	$\eta$	$\frac{V}{nD}$	Blade angle (deg.)	$\eta$	$\frac{N}{N_0}$	$\eta\left(\frac{N}{N_0}\right)$
5868-9	Clark Y	1.0	0.505	10	13.2	0.766	0.126	11.8	0.307	0.151	13.2	0.340	0.835	0.284
		1.5	.852	10	21.9	.848	.213	15.4	.428	.282	21.9	.411	.757	.311
		2.0	1.213	10	29.1	.861	.304	19.3	.500	.437	29.1	.397	.693	.273
		2.5	1.598	10	36.1	.850	.400	22.7	.548	.595	36.1	.403	.670	.270
5868-R6	R. A. F. 6	1.0	.505	10	12.5	.731	.126	10.8	.311	.145	12.5	.338	.869	.284
		1.5	.852	10	21.5	.816	.213	15.3	.428	.276	21.5	.449	.774	.313
		2.0	1.213	10	28.7	.833	.304	18.9	.508	.412	28.7	.491	.734	.307
		2.5	1.598	10	35.8	.817	.400	22.7	.570	.568	35.8	.474	.702	.303
6623-A	N. A. C. A. 4400	1.0	.505	10	13.4	.765	.126	10.8	.327	.154	13.4	.348	.820	.284
		1.5	.852	10	21.5	.835	.213	15.2	.428	.274	21.5	.430	.779	.313
		2.0	1.213	10	28.7	.844	.304	19.0	.508	.420	28.7	.427	.722	.306
		2.5	1.598	10	35.5	.832	.400	23.2	.560	.582	35.5	.420	.695	.294
6623-B	N. A. C. A. 4400 inner half, 2400-34 outer half.	1.0	.505	10	15.3	.786	.126	12.9	.338	.152	15.3	.332	.830	.273
		1.5	.852	10	23.9	.848	.213	17.3	.363	.287	23.9	.361	.743	.284
		2.0	1.213	10	31.0	.866	.304	21.1	.456	.436	31.0	.374	.694	.277
		2.5	1.598	10	37.8	.843	.400	24.6	.492	.600	37.8	.392	.665	.270
6623-C	N. A. C. 2R <sub>200</sub>	1.0	.505	10	16.7	.745	.126	13.0	.319	.159	16.7	.337	.794	.284
		1.5	.852	10	24.7	.837	.213	18.1	.410	.291	24.7	.360	.731	.284
		2.0	1.213	10	31.8	.860	.304	21.9	.486	.445	31.8	.354	.680	.284
		2.5	1.598	10	38.7	.843	.400	25.3	.510	.625	38.7	.377	.637	.284
6623-D	N. A. C. A. 6400	1.0	.505	10	11.3	.731	.126	10.8	.319	.146	11.3	.337	.866	.284
		1.5	.852	10	19.6	.828	.213	13.7	.421	.278	19.6	.435	.766	.313
		2.0	1.213	10	26.9	.835	.304	17.0	.497	.405	26.9	.502	.747	.303
		2.5	1.598	10	33.9	.816	.400	20.6	.563	.557	33.9	.496	.715	.304



## REPORT No. 651

### DOWNWASH AND WAKE BEHIND PLAIN AND FLAPPED AIRFOILS

By ABE SILVERSTEIN, S. KATZOFF and W. KENNETH BULLIVANT

#### SUMMARY

*Extensive experimental measurements have been made of the downwash angles and the wake characteristics behind airfoils with and without flaps and the data have been analyzed and correlated with the theory. A detailed study was made of the errors involved in applying lifting-line theory, such as the effects of a finite wing chord, the rolling-up of the trailing vortex sheet, and the wake.*

*The downwash angles, as computed from the theoretical span load distribution by means of the Biot-Savart equation, were found to be in satisfactory agreement with the experimental results. The rolling-up of the trailing vortex sheet may be neglected, but the vertical displacement of the vortex sheet requires consideration.*

*By the use of a theoretical treatment indicated by Prandtl, it has been possible to generalize the available experimental results so that predictions can be made of the important wake parameters in terms of the distance behind the airfoil trailing edge and the profile-drag coefficient.*

*The method of application of the theory to design and the satisfactory agreement between predicted and experimental results when applied to an airplane are demonstrated.*

#### INTRODUCTION

Rational tail-plane design depends on a knowledge of the direction and the velocity of the air flow in the region behind the wing. Numerous investigations, both experimental and theoretical, have been devoted to the determination of the downwash for wings without flaps. The agreement between theory and experiment has, as a rule, been only partly satisfactory, and the comparisons have been inadequate as bases for generalizations. The existing empirical equations for downwash angles make allowance neither for variations in plan form nor for the use of flaps. Only scant attention has been given to the important problem of the wake behind flapped wings.

As the first part of a comprehensive study of tail-plane design, the air flow in the region behind the wing has been studied for the purpose of developing general

methods for predicting the downwash and the wake. Much of the work on downwash was concerned with the relation of the induced field in the region behind the airfoil to the theoretical span load distribution and to the corresponding vortex system. The basis for the theoretical calculations is the Biot-Savart equation for the induced velocities in a vortex field. Some of the data were particularly useful in investigating the rate of rolling-up of the trailing vortex sheet.

The wake constitutes a not altogether separate problem. Its position and the velocity distribution across it must be known in order to predict the tail efficiency for cases in which the tail is within it. Downwash and wake generally require simultaneous treatment because the downwash determines the position of the wake and the wake has, in turn, an effect on the downwash.

The data used in this analysis were obtained mainly in the N. A. C. A. full-scale wind tunnel with airfoils and airplanes that were usually so small that the jet-boundary corrections either were negligible or could be accurately applied.

An obvious limitation of the present study, insofar as its practical utility is concerned, lies in its neglect of the interference from fuselage, nacelles, etc. Also neglected is the small effect of the tail itself on the air flow ahead of it.

#### EXPERIMENTAL INVESTIGATION

##### SCOPE OF THE TESTS

The airfoils, the airplane model, and the full-scale airplane used in the investigation, together with a synopsis of the downwash and the wake surveys made in each case, are listed as follows:

1. A 5- by 30-inch rectangular Clark Y airfoil. Downwash angles were measured, at three different lift coefficients, in the plane of symmetry. Dynamic-pressure surveys of the wake were made in the same plane.

2. A 10- by 30-inch rectangular Clark Y airfoil. Measurements were the same as for the 5- by 30-inch airfoil.



3. A 2- by 12-foot rectangular Clark Y airfoil tested without a flap, and with the following flaps, each of 20-percent chord:

- (a) 40-percent-span split flap,  $\delta_f=20^\circ$  and  $60^\circ$ .
- (b) 70-percent-span split flap,  $\delta_f=20^\circ$  and  $60^\circ$ .
- (c) Same as (b) except for a 12.5-percent-span cut-away at the center.
- (d) Full-span split flap,  $\delta_f=20^\circ$  and  $60^\circ$ .
- (e) Full-span external-airfoil flap,  $\delta_f=20^\circ$  and  $40^\circ$ .

Downwash measurements were made, at three lift coefficients, in the plane of symmetry of the airfoil and

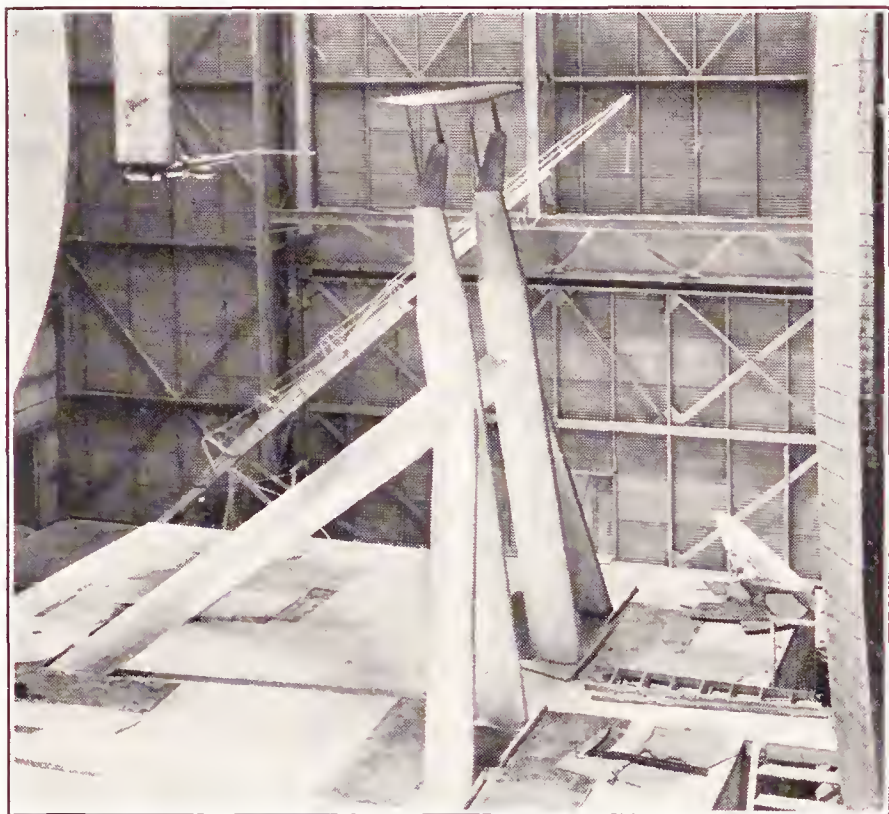


FIGURE 1.—The U. S. A. 45 airfoil mounted in the full-scale wind tunnel and the survey apparatus behind it.

also in a parallel plane one-sixth of the span from the symmetry plane.

4. The 45.75-foot-span, 2:1 tapered U. S. A. 45 airfoil of aspect ratio 6 described in reference 1. Downwash and wake measurements were made at five lift coefficients, in the plane of symmetry, and in planes 3, 8, 18, 21, and 24 feet from the symmetry plane at distances of 10, 18, and 26 feet behind the quarter-chord point.

5. A model of 12-foot span of the 2:1 tapered U. S. A. 45 airfoil. Downwash measurements were similar to those for the 2- by 12-foot rectangular airfoil.

6. The 8- by 48-foot rectangular Clark Y airfoil described in reference 2. Downwash and wake surveys were similar to those for the large U. S. A. 45 tapered airfoil.

7. Three 6- by 36-foot symmetrical airfoils of N. A. C. A. 0009, 0012, and 0018 sections. Detailed measurements of the wake were made at a number of longitudinal stations from the trailing edge to three chord lengths behind the airfoils.

8. A small low-wing monoplane equipped with a 5:1 tapered wing of aspect ratio 10. The wing has a plain sealed flap extending over 65 percent of the span.

Downwash and wake measurements were made with the tail removed, in the region of the tail plane for a number of different lift coefficients with and without the flap deflected.

9. A midwing airplane model equipped with a 4-tapered wing of aspect ratio 8. The wing has a split flap extending over 53 percent of the span. Downwash and wake measurements were made in the region of the tail plane. Pitching-moment measurements were also made with the tail at different settings and with the tail removed.

#### APPARATUS AND METHODS

The experimental work was conducted in the N. A. C. A. full-scale wind tunnel (reference 3) using the survey apparatus that is part of the equipment of the tunnel. Figure 1, showing the survey apparatus behind the 12-foot U. S. A. 45 airfoil, illustrates the experimental arrangement. For the 5- by 30-inch and the 10- by 30-inch airfoils, the measurements were made with a small Y-type yaw head and a Prandtl pitot tube, as described in detail in reference 4. For all other cases the measurements were obtained by means of the combined pitch, yaw, and dynamic-pressure tube shown in detail in figure 2. Force measurements were made by the methods described in references 2, 3, and 4.

Angles of pitch and yaw are accurate to within about  $\pm 0.25^\circ$ . Dynamic-pressure measurements are accurate to within about  $\pm 1$  percent.

Air-stream angles and dynamic pressures were measured without an airfoil in the jet, and these values were applied in correcting all the measurements. Jet boundary corrections were negligible for the two small Clark Y airfoils. Corrections were applied according to reference 4 for the airfoils of 12-foot span and for the two airplanes. For the large airfoils, the corrections

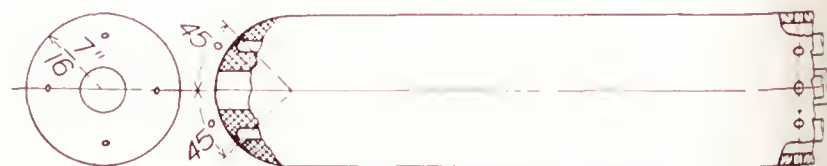


FIGURE 2.—Line drawing showing combined pitch, yaw, and pitot-static tube used for the dynamic-pressure and the downwash surveys.

tions are so large and vary so much from point to point in the region behind the airfoil that a quantitative comparison between the theoretical and the measured downwash angles was not considered advisable.

#### CALCULATION OF DOWNWASH

The induced velocity at a point due to an infinitesimal length of vortex filament is given by the Biot-Savart equation, which may be written in vector notation

$$\vec{w} = \frac{\Gamma}{4\pi} \frac{d\vec{l} \times \vec{a}}{|\vec{a}|^3}$$



in which  $\bar{w}$  is the induced-velocity vector at the point.

$\Gamma$ , the strength of the vortex.

$d\bar{l}$ , a vector having the direction and length of the infinitesimal vortex filament.

$\bar{a}$ , the vector from the vortex filament to the point.

The integration of this expression around a semi-infinite U-vortex of semispan  $s$  and strength  $\Gamma$ , in order to obtain the effect at a point  $x, z$  in the symmetry plane, leads to the following expressions for the separate contributions to the vertical component of the induced velocity at this point.

$$w_1 = \frac{s\Gamma}{2\pi} \frac{x}{(x^2 + z^2) \sqrt{s^2 + x^2 + z^2}}$$

due to the bound vortex.

$$w_2 = \frac{s\Gamma}{2\pi} \frac{1}{s^2 + z^2} \left( 1 + \frac{x}{\sqrt{s^2 + x^2 + z^2}} \right)$$

due to the two trailing vortices.

$$w_1 + w_2 = w = \frac{s\Gamma}{2\pi} \left[ \frac{x}{\sqrt{s^2 + x^2 + z^2}} \left( \frac{1}{x^2 + z^2} + \frac{1}{s^2 + z^2} \right) + \frac{1}{s^2 + z^2} \right] \quad (1)$$

due to the U-vortex.

By means of equation (1) a computation of the downwash angle behind a monoplane airfoil can be made if the load distribution, or circulation distribution, along the airfoil is known. The wing is replaced by its lifting line, where the bound vortex is considered localized, and the vortex sheet that is shed from its trailing edge is considered to originate at the lifting line and extend, unchanged, to infinity. The strength  $\Gamma$  of the bound vortex at any section is related to the section lift coefficient  $c_l$  by the equation

$$\Gamma = \frac{V c c_l}{2}$$

in which  $V$  is the free-stream velocity and  $c$  is the chord length. The intensity of vorticity in the trailing vortex sheet is  $-d\Gamma/dy$ .

In a separate paper (reference 5) are presented, for use in tail-plane design and stability studies, the results of extensive downwash computations based on the foregoing idealized picture. These computations being for wings of various aspect ratios, taper ratios, and flap spans, it is essential to investigate the generality of the method and to justify its application.

The validity of the foregoing concept as a foundation for the computation of downwash angles is, indeed, subject to objection in a number of particulars, which have been separately studied and are discussed in the following sections. The cases of wings without and with flaps are separately treated.

#### WINGS WITHOUT FLAPS

**Flow about an airfoil section.**—An obvious objection to the proposed method of calculation is that a vortex at the lifting line is an inexact substitution for the

actual airfoil. In order to investigate the order of magnitude of the discrepancy, the theoretical two-dimensional flow about a Clark Y airfoil at  $C_L=1.22$  was obtained by a conformal transformation of the

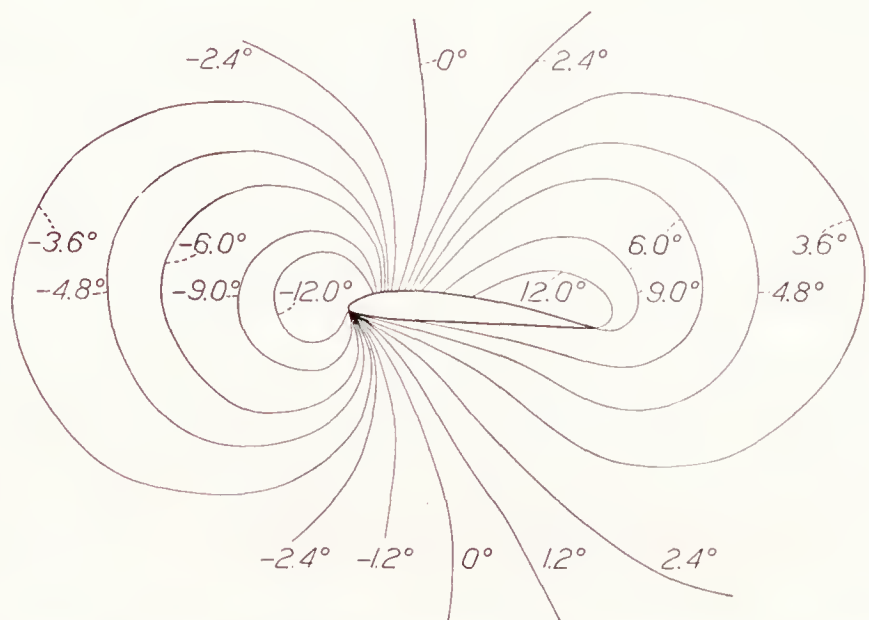


FIGURE 3.—Theoretical downwash-angle contours for two-dimensional flow about a Clark Y airfoil section.  $\alpha, 5.43^\circ$ ;  $C_L, 1.22$ .

flow about a circle. The transformation was effected by the method of Theodorsen (reference 6); the Clark Y airfoil was chosen because much of the experimental work was done with Clark Y airfoils and also because the transformation had already been partly performed

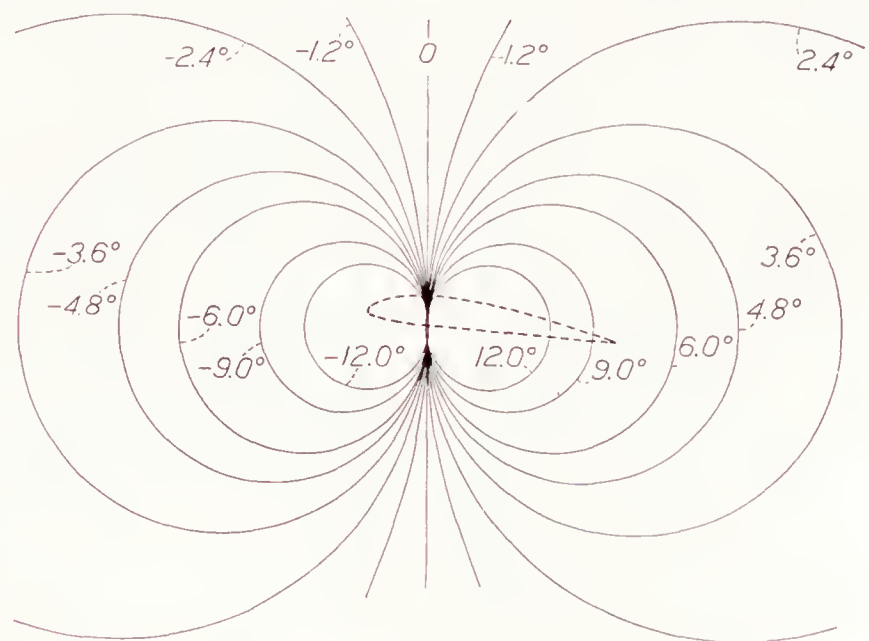


FIGURE 4.—Theoretical downwash-angle contours for a vortex in a uniform stream (two-dimensional flow). Vortex strength corresponds to  $C_L=1.22$ .

in reference 6 for this section. Four complex Fourier coefficients were used, which, inasmuch as they sufficed to transform the circle with good accuracy into the Clark Y section, necessarily sufficed to transform the flow at distances from it.

The results are plotted as downwash-angle contours in figure 3. Comparison with the corresponding map for an equivalent vortex placed at the quarter-chord point (fig. 4) shows that, at a distance of about one chord length behind the trailing edge, the difference is less than  $0.3^\circ$ . It appears reasonable to assume that the difference would be of this order for other airfoils.



The conclusiveness of this result may be open to question inasmuch as the actual flow about an airfoil section only approximates the potential flow, owing to the finite viscosity of air; the difference is probably

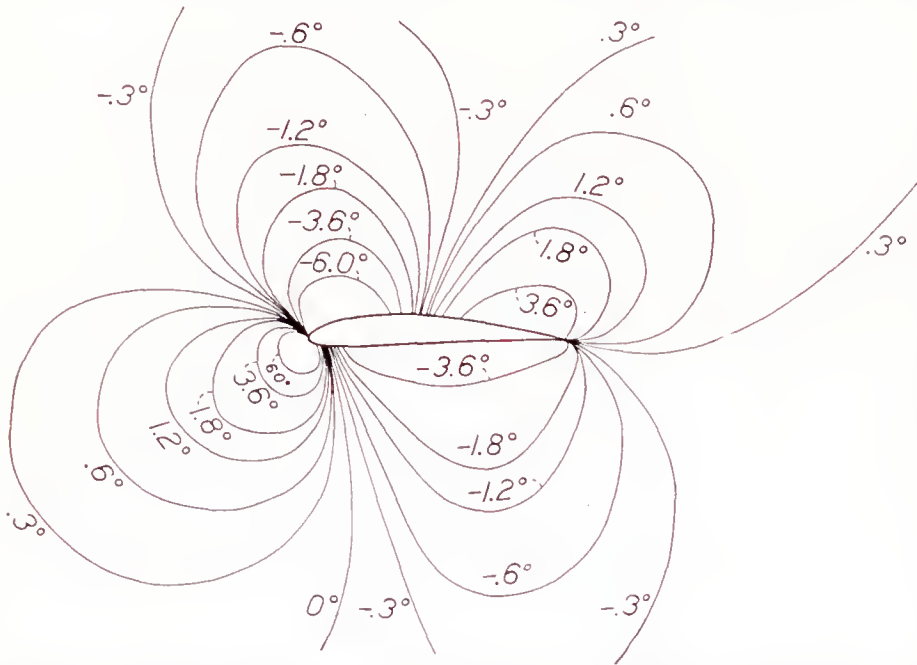


FIGURE 5.—Theoretical downwash-angle contours for two-dimensional flow about a Clark Y airfoil section.  $\alpha$ ,  $-5.57^\circ$ ;  $C_L$ , 0.

slight, however, except in the vicinity of the wake itself.

Figure 5 shows the theoretical stream angles calculated for the Clark Y airfoil at zero lift. The simplified theory for this case predicts zero downwash at every point in the field; and it can be seen that, at one chord length behind the trailing edge, the difference from zero is small.

**Distortion of the trailing vortex sheet.**—The shed vortex sheet does not extend unaltered indefinitely downstream but, as a result of the air motions that the vortex system itself creates, is rapidly displaced down-

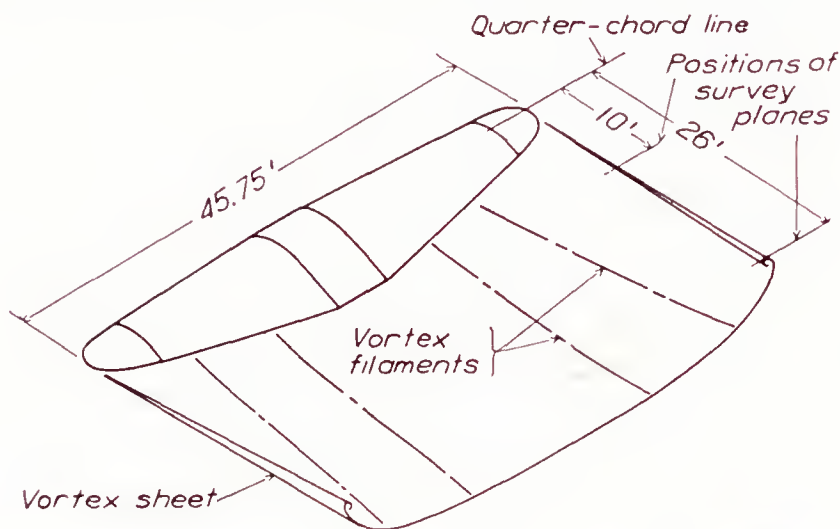


FIGURE 6.—Isometric drawing showing the U. S. A. 45 airfoil and the distorted trailing vortex sheet.  $C_L$ , 1.35.

ward and deformed. It curves into a channel of constantly increasing depth and distends rapidly as it proceeds to roll up like a volute about the tip-vortex cores.

It is essential to know the rate at which this transformation occurs, for the difference in the tail-plane region

between the downwash computed for the unchanged vortex sheet and that for the completely rolled-up sheet is of the order of 20 percent. The surveys behind the large U. S. A. 45 tapered airfoil are of particular interest in this respect, because they were sufficiently extensive to give quantitative information on the rolling-up process. For this purpose, the case of the highest lift coefficient ( $C_L=1.35$ ) will be discussed, not only because the greater magnitude of the measured pitch and yaw angles increases the relative accuracy of the study but also because the distortion of the vortex sheet at the rearmost survey plane (26 feet behind the quarter-chord line) represents the maximum distortion that will have to be considered in practical computations of downwash behind plain wings. The bases for this statement are: (a) the aspect ratio is about the minimum in common use; (b) the lift coefficient is quite high, in fact, nearly the maximum for this airfoil; and (c) the 26-foot survey plane is considerably farther

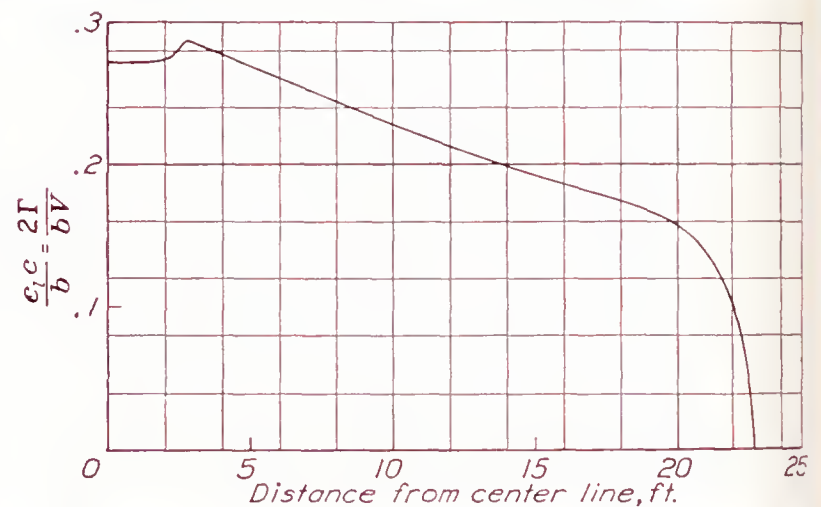


FIGURE 7.—Experimental span load distribution for the U. S. A. 45 airfoil.  $C_L$ , 1.35.

behind the trailing edge than is the usual position of the tail plane.

Figure 6 shows the shape of the airfoil and the positions of the 10-foot and the 26-foot survey planes. Figure 7 shows the span load distribution for  $C_L=1.35$ , experimentally determined by means of pressure orifices in the airfoil surface (reference 1). Figures 8 and 9 show the surveys in the 10-foot and the 26-foot planes, respectively, the vectors representing by magnitude and direction the inclination of the air flow to the tunnel axis. In order to avoid confusion, vectors are not shown for all points where readings were taken.

The line of intersection of the trailing vortex sheet with the plane of the survey has been indicated in the figures; it is the line across which there is an abrupt change in the lateral component of the velocity. It is also the line where the wake intersects the survey plane, as was verified by the dynamic-pressure surveys. The circles indicating the positions of the tip-vortex cores are somewhat more arbitrarily located; they are points that appear to be the approximate centers of rotation of the air flow near them.



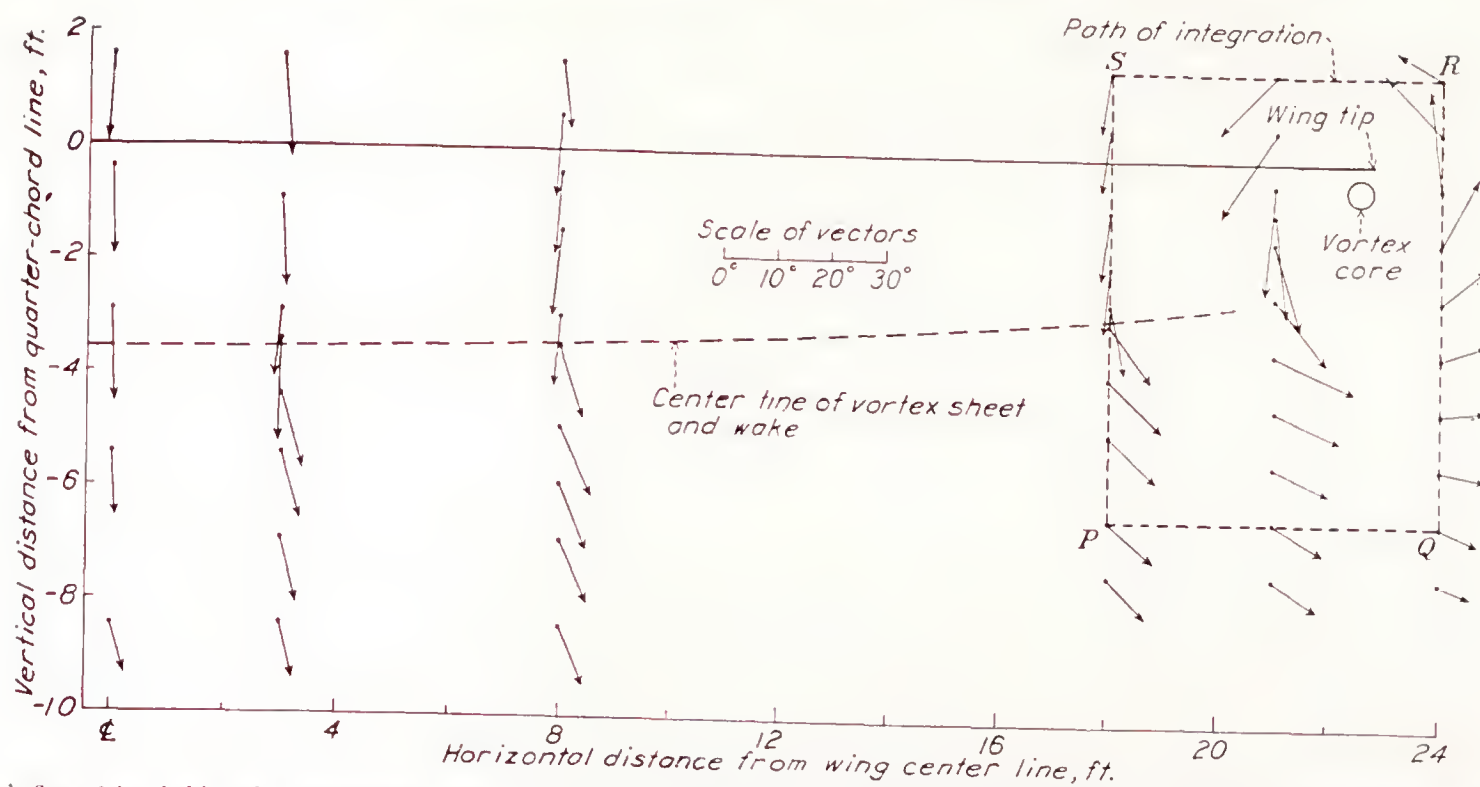


FIGURE 8.—Air flow 10 feet behind the quarter-chord line of the U. S. A. 45 tapered airfoil. Vectors denote deviation of air flow from free-stream direction.  $C_L$ , 1.35.

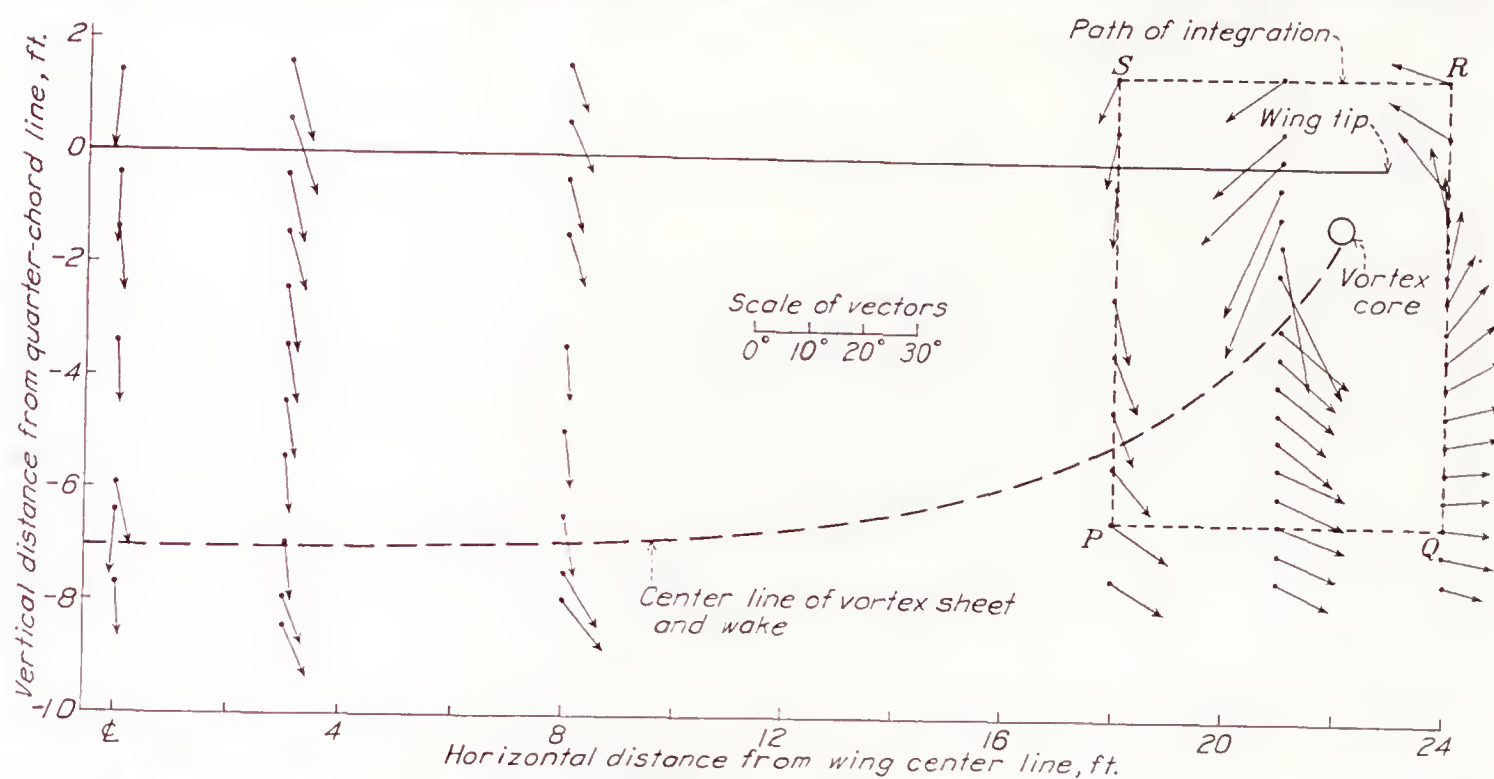


FIGURE 9.—Air flow 26 feet behind the quarter-chord line of the U. S. A. 45 tapered airfoil. Vectors denote deviation of air flow from free-stream direction.  $C_L$ , 1.35.

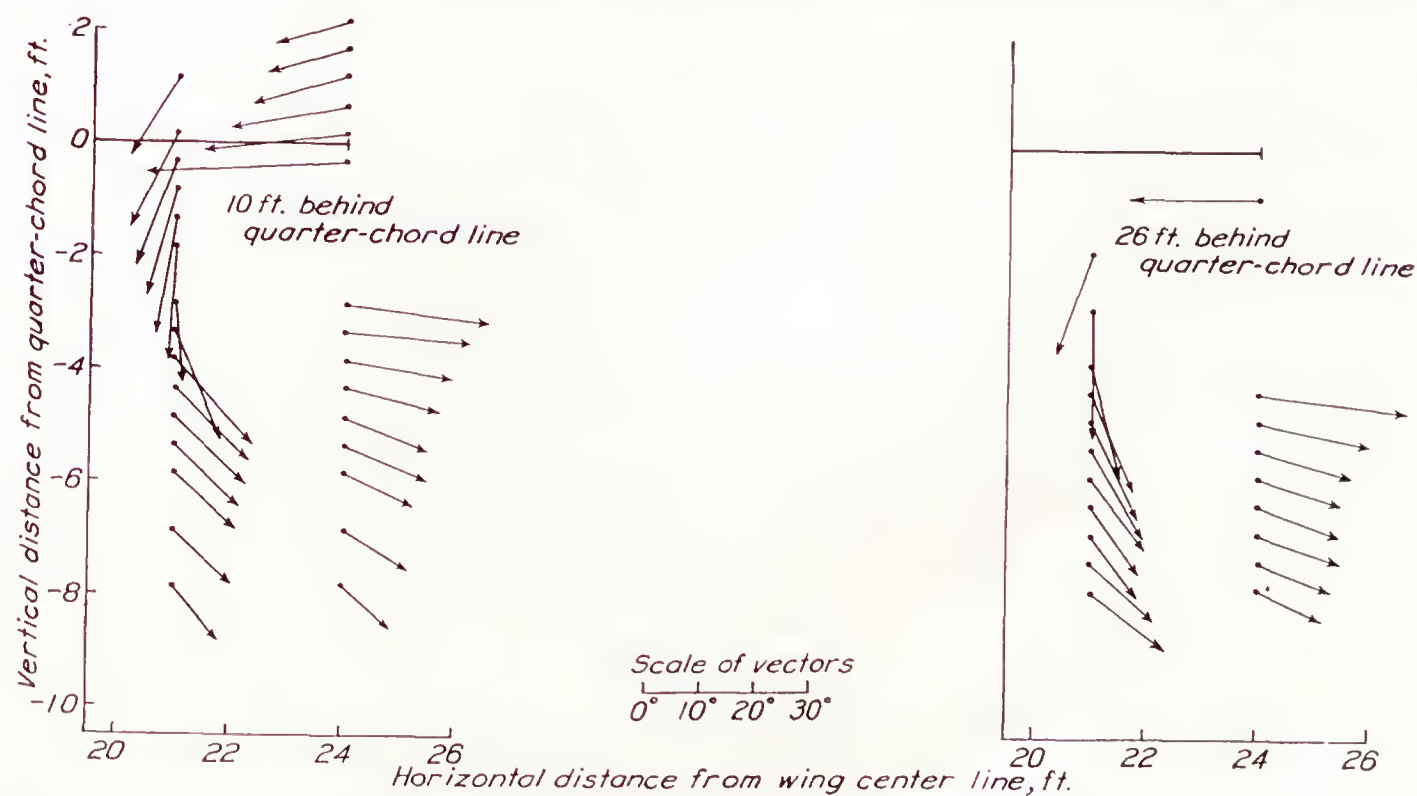


FIGURE 10.—Air flow behind the tip of the 8- by 48-foot Clark Y airfoil. Vectors denote deviation of air flow from free-stream direction.  $C_L$ , 1.44.

**Rolling-up of the trailing vortex sheet.**—It was possible to determine from the surveys the extent of rolling-up of the sheet at each survey plane. From Stokes' theorem, the total strength of the vorticity  $\Gamma$  within an area  $S$  may be determined by integrating the tangential component of the velocity along the boundary  $C$  of the area. Thus, in the usual vector notation,

$$\Gamma = \int_S \text{curl } \bar{V} \cdot d\bar{A} = \oint_C \bar{V} \cdot d\bar{r}$$

where  $d\bar{A}$  and  $d\bar{r}$  are, respectively, vector elements of area and of boundary, and  $\bar{V}$  is the velocity vector.

Now, the circulation around the airfoil at, say, 18 feet from the center is known from the experimental span load distribution and the air speed. This circulation constitutes the amount of vorticity that must be shed from the trailing edge between this point and the airfoil tip. If the trailing vortex sheet extended unchanged indefinitely downstream, the value of  $\oint \bar{V} \cdot d\bar{r}$  along any path that enclosed the edge of the sheet and cut the sheet 18 feet from the center, as, for example, the path  $SPQR$  in figure 9, should equal this circulation. Owing to the rolling-up, however, the amount of vorticity within such a path exceeds this amount, especially when the point at which the path cuts the sheet is well back of the trailing edge. The excess indicates the extent of the rolling-up.

Such integrations were performed along the rectangular paths shown in figures 8 and 9. The integration along these paths is particularly simple, for, along the vertical sides,  $\bar{V} \cdot d\bar{r} = V \sin \theta \, dr$  and, along the horizontal sides,  $\bar{V} \cdot d\bar{r} = V \sin \psi \, dr$ , where  $\theta$  and  $\psi$  are the experimentally determined pitch and yaw angles,  $V$  is the local air speed, and  $dr$  is the length of the path element.

From these integrations it was found that, at 10 feet behind the quarter-chord line, the total vorticity in the area of integration was 1.024 as much as the circulation around the airfoil at the 18-foot station; whereas, at 26 feet behind the quarter-chord line, it was 1.13 as much. These values correspond, respectively, to the circulations that existed on the airfoil at 17.2 feet and 14.3 feet from the center. It follows that the vortex sheet leaving the trailing edge rolls up at such a rate that, in the first survey plane, the vorticity originally between 17.2 feet and the edge has all been concentrated between 18 feet and the tip; and, in the rear survey plane, the part originally outboard of 14.3 feet has been concentrated between 18 feet and the tip. Integrations about the inner parts of the vortex sheet showed, as expected, that the inner part lost as much vorticity as the tip gained.

The rest of the sheet must distend correspondingly. Thus, the portion extending originally between the center and 14.3 feet from the center has, at the 26-foot

survey plane, become so distended that it reaches to 18 feet. Further evidence on this distention is found in the surveys made in the vertical line 8 feet from the center (figs. 8 and 9). The rate of outward displacement of the vortex filaments 8 feet from the center is roughly given by the average of the yaw angles just above and just below the sheet. At the 10-foot and the 26-foot survey planes, these average angles are  $2.5^\circ$  and  $3.5^\circ$ , respectively. The mean along the path being thus about  $3^\circ$  and the length of the path being about 19 feet, it follows that a vortex filament leaving the trailing edge 8 feet from the center has moved out to about  $8 + 19 \tan 3^\circ = 9$  feet from the center by the time it reaches the rearmost survey plane. The paths of this filament, the filament leaving the trailing edge 14.3 feet from the center, and the tip-vortex core have been indicated in figure 6. The surveys in the symmetry plane and in the line 3 feet from it are of uncertain interpretation, because the pressure-orifice measurements showed anomalous lift distribution near the center of the airfoil.

It may be remarked that, although the distortion and distention found are not inconsiderable, the rolling-up process, by which the vorticity is eventually concentrated into a pair of tip vortices, appears to be still far from complete. This result is evident from the position of the tip-vortex core, located at the approximate center of rotation of the air flow near the tip. It has moved in only to 96 percent of the semispan whereas, for complete rolling-up, it would be at 78 percent of the semispan. Figure 10 shows similar surveys behind the tip of the 8- by 48-foot Clark Y airfoil. For complete rolling-up, the tip vortex would be at about 87 percent of the semispan, whereas the survey shows it almost at the tip.

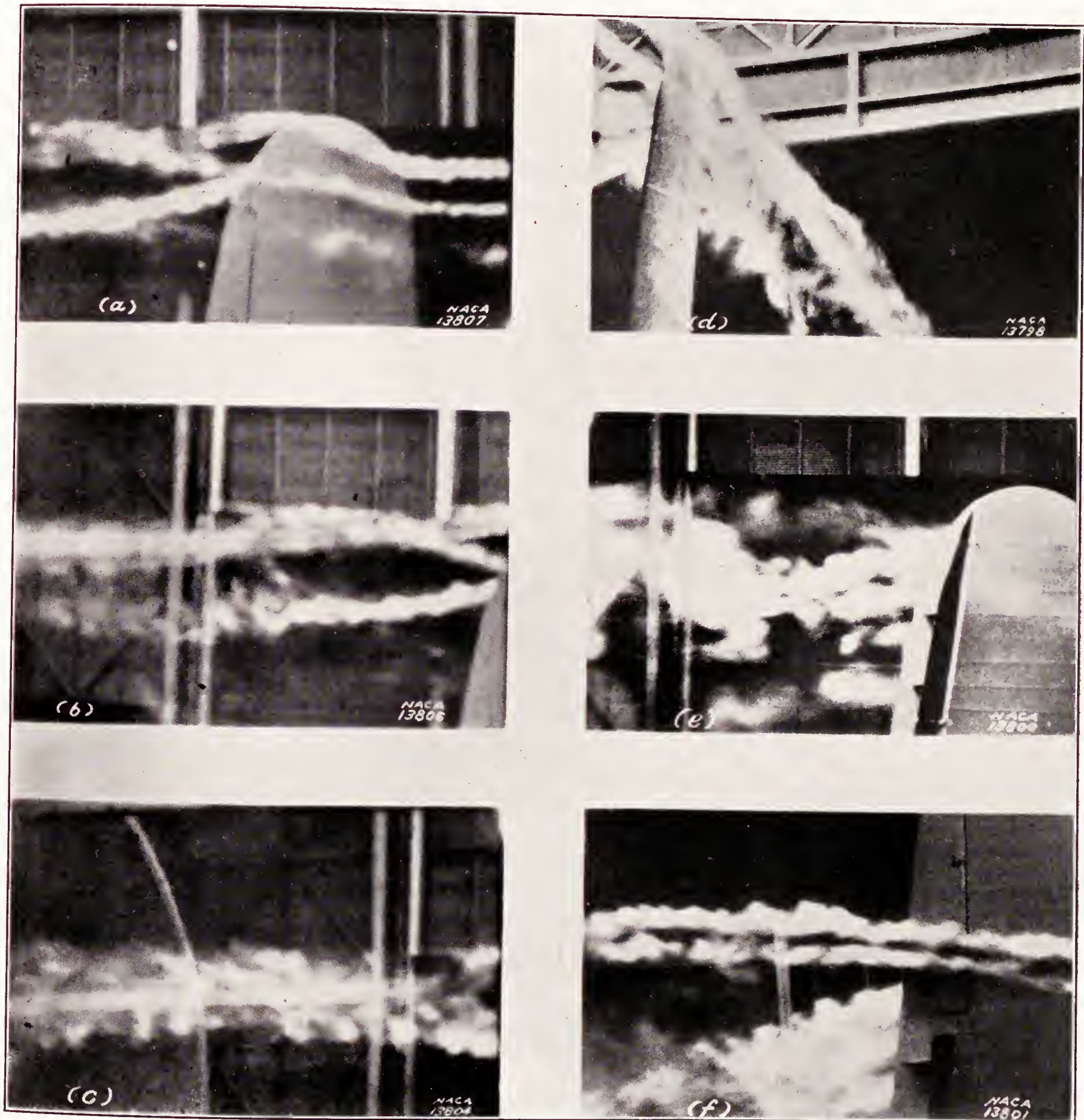
Further evidence of the displacement of the tip-vortex core is found in the photographs obtained in smoke-flow studies and reproduced in figure 11. The visible flows were obtained with kerosene vapor flowing past the tip of the tapered half-wing mounted on a reflecting board. The core of the tip vortex is easily discerned as far back in the mouth of the exit bell as can be seen, a total distance of about 50 feet. This visual method was not capable of yielding quantitative results although, qualitatively, it was clear that the inward displacement of the tip-vortex core was small.

Kaden's theoretical calculations (reference 7) indicate that the rolling-up process is not complete until a distance of  $0.56A/C_L$  semispans behind the trailing edge of the airfoil. For a lift coefficient  $C_L$  of 1.35 and an aspect ratio  $A$  of 6, this value is 2.5 semispans, or about four times as far back as is the usual location of the tail. It may be remarked that, in Muttray's work (reference 8), the rolling-up, as determined by the inward displacement of the tip-vortex core, was found to be slower than is given by the foregoing expression.



The effect of rolling-up on the downwash.—It will be recalled that, in the tentative scheme for calculating downwash angles, the trailing vortex sheet is assumed to originate at the lifting line and to extend unchanged to infinity. The question now arises as to how seriously such rolling-up, distortion, and distention of the trailing vortex sheet as were found in the preceding study affect the accuracy of the results computed on this

basis. For purposes of comparison, calculations were made of the downwash angles in the symmetry plane at a distance of 1.15 semispans behind the quarter-chord line (corresponding to the rearmost survey plane behind the U. S. A. 45 airfoil) using the theoretical span load distribution for a 2:1 tapered airfoil of aspect ratio 6, for the following cases (fig. 12):



(a), (b), (c), (d)—Views showing tip vortex core forming at wing tips and moving downstream. Plain wing without flap. (e)—View of flow at tip of the wing with 0.20c full-span split flap deflected 60°. (f)—View showing flow at the tip of a partial-span split flap.

FIGURE 11.—Smoke-flow pictures for the U. S. A. 45 tapered airfoil in the full-scale wind tunnel. Wing vertical.



(a) The vortex sheet assumed to be distorted and rolled up to the same extent as found at the rearmost survey plane in the foregoing study and to exist in this state from the wing to infinity. The actual vortex sheet, of course, is distorted less than this amount ahead of this position and more than this amount behind this position. It is very difficult to take this variation into account in the calculations, however,

consists of a relative vertical displacement. Thus, curve c, which is the same as b but shifted vertically by an amount equal to the displacement of the center of the curved sheet, does not differ from that for a by more than  $1^\circ$  in the region of interest and differs from it hardly at all at small distances above the wake. For low-wing or midwing monoplanes, the tail will usually be at small distances above the wake

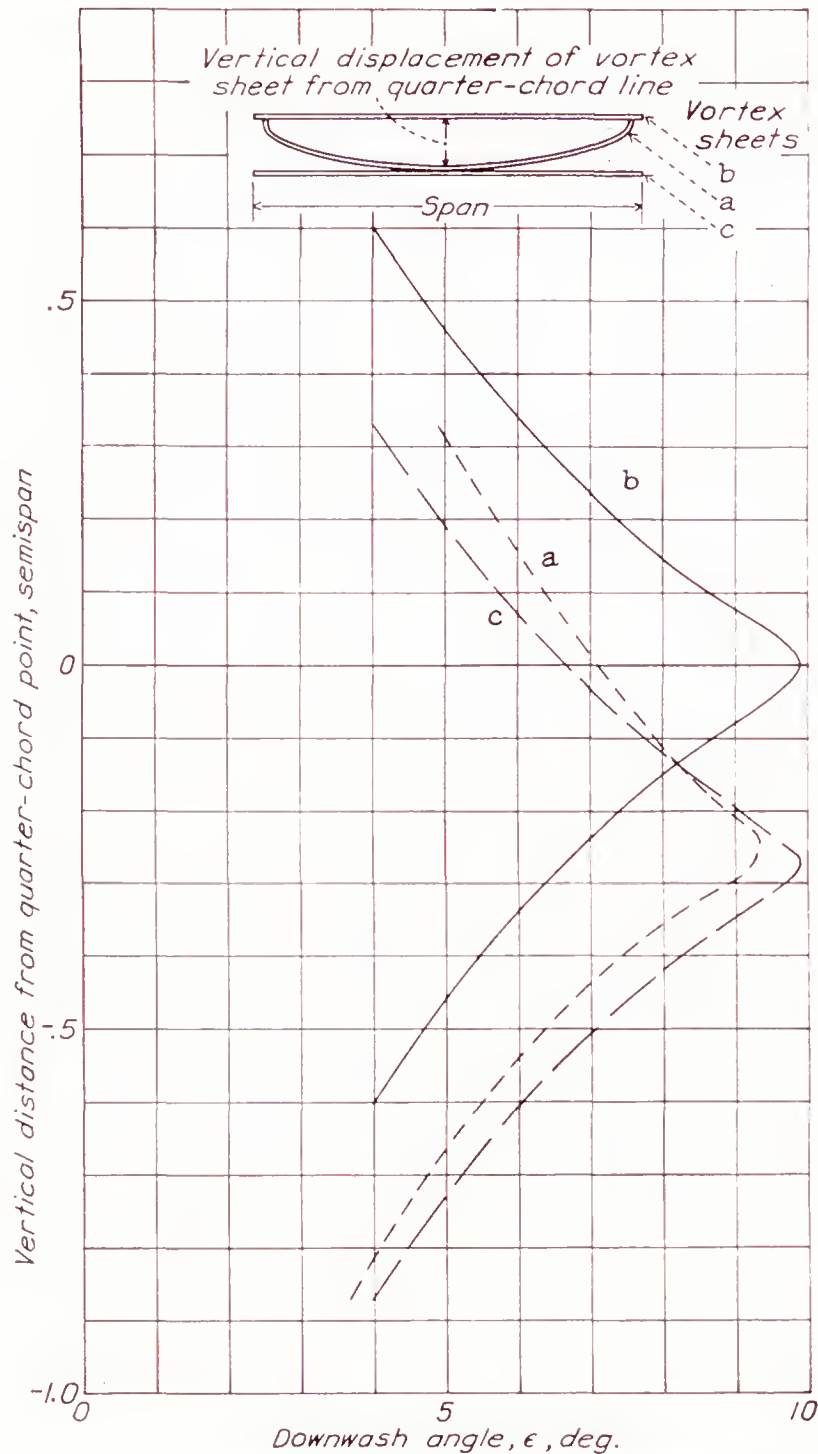


FIGURE 12.—Calculated downwash for the plane of symmetry, 1.15 semi-spans behind the quarter-chord line of a 2:1 tapered airfoil of aspect ratio 6.  $C_L$ , 1.35. a, Vortex sheet distorted as found for the U. S. A. 45 tapered airfoil; b, Vortex sheet assumed to extend unchanged straight behind the quarter-chord line to infinity; c, same as b, but displaced vertically by an amount equal to the displacement at the middle of the distorted sheet.

and the error involved in assuming the distortion to be uniform appears to be negligible.

(b) The vortex sheet assumed to be neither distorted nor rolled up but to extend straight behind the quarter-chord line to infinity.

The curves in figure 12 show the corresponding downwash angles, calculated for  $C_L=1.35$ , plotted against vertical distance from the level of the quarter-chord line. The curve for b is distinctly separate from that for a. Most of the difference, however,

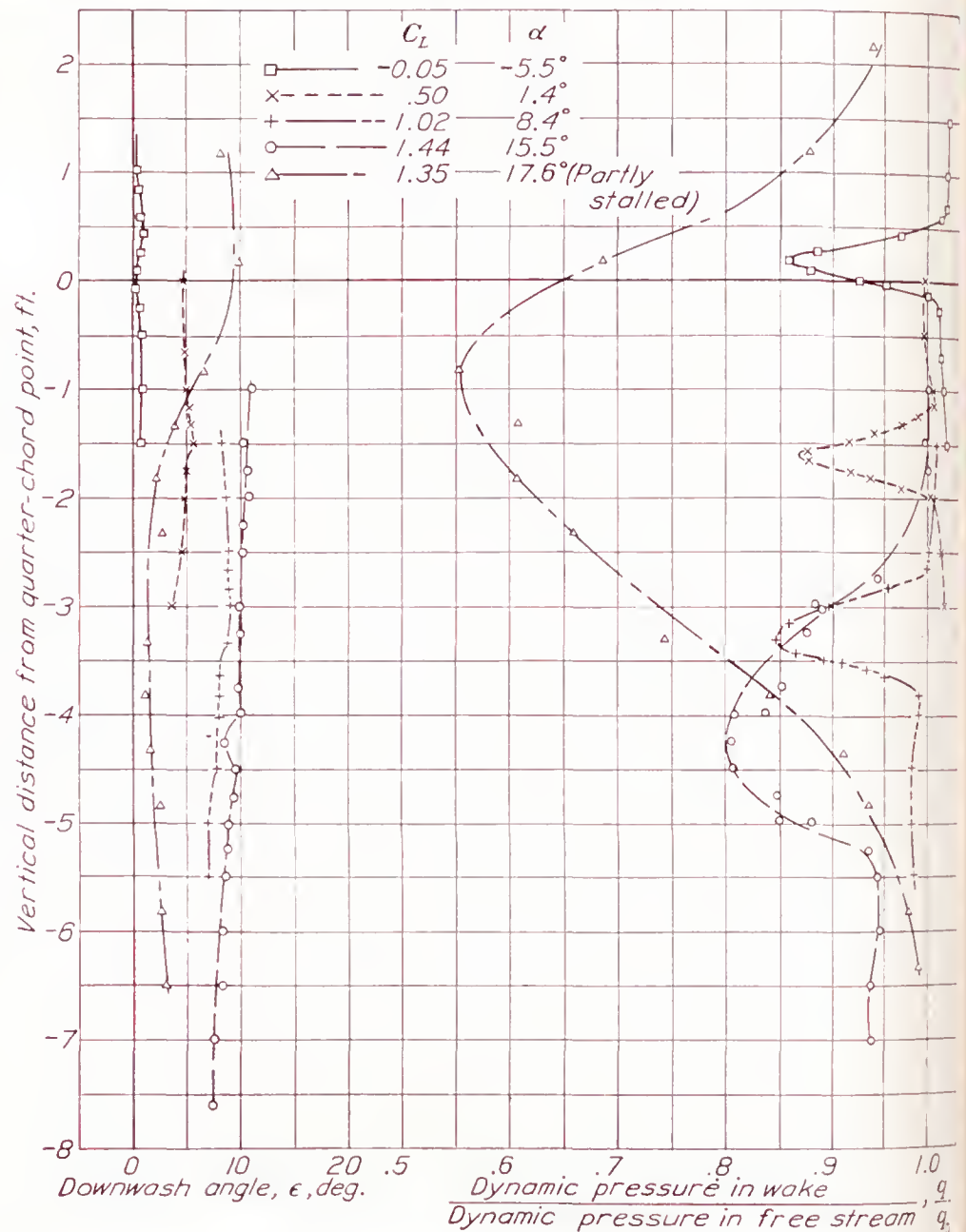


FIGURE 13.—Downwash-angle and dynamic-pressure surveys in the symmetry plane 18 feet behind the quarter-chord line of the 8- by 48-foot Clark Y airfoil.

and the downwash computed as for c will therefore, for these cases, correspond to the actual distorted vortex sheet. Furthermore, it will be recalled that the present example is very nearly a limiting, if not an exaggerated case; for the more usual conditions, the distortion will be much less, and the difference between a and c will be negligible.

The following conclusion is thus reached: In the computation of downwash angles behind plain airfoils, it is usually sufficiently accurate to neglect the distortion of the vortex sheet and to take into account the distortion simply by considering the entire vortex sheet to be displaced vertically by an amount equal to the displacement of the center line of the actual distorted sheet. This displacement, in turn, is readily calculated, for the center line passes through the trailing edge and moves



downward with the downwash itself. Its inclination at every point is the downwash angle  $\epsilon$  at that point; hence the vertical displacement from the trailing edge is given simply by the expression

$$\int_{T.E.}^x \tan \epsilon dx$$

**Influence of the wake.**—The wake, which is the rearward extension of the boundary layer and which

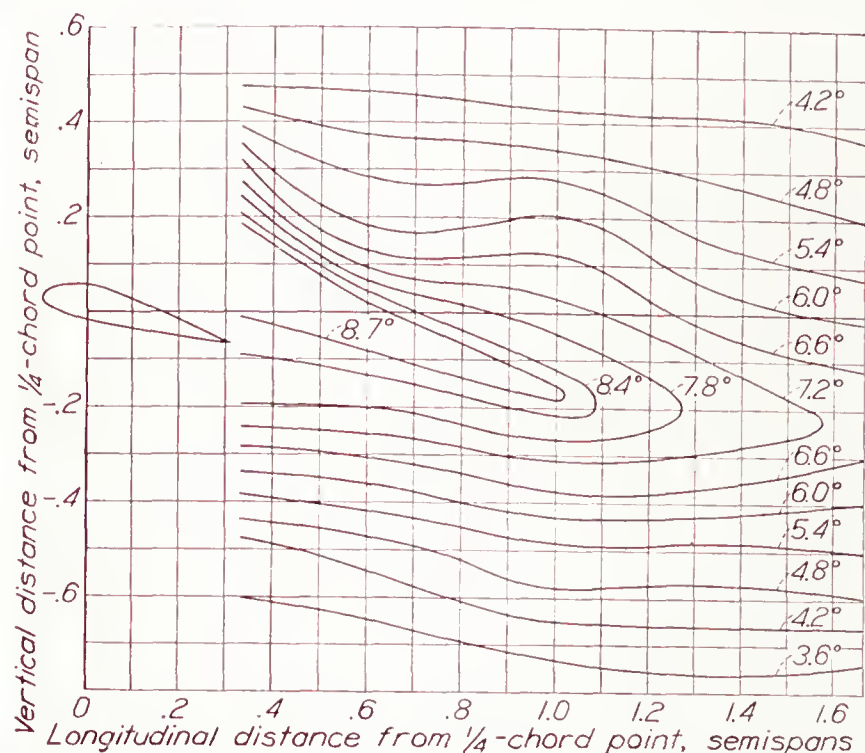


FIGURE 14.—Downwash-angle contours in the symmetry plane behind the 12-foot U. S. A. 45 tapered airfoil.  $\alpha$ , 11.5°;  $C_L$ , 1.175.

coincides with the trailing vortex sheet, affects the motion of the air in its vicinity. There is a flow of air toward the wake center, as will be obvious on considering that the velocity in the wake increases with distance from the trailing edge, requiring that the stream lines converge. The effect therefore consists of an increase in the downwash above the wake and a decrease in the downwash below it.

Some indication as to the magnitude of the effect for airfoils without flaps may be obtained from the surveys made in the symmetry plane behind the 8- by 48-foot Clark Y airfoil. The dynamic pressures and the downwash angles in the wake region are plotted in figure 13 for five different lift coefficients. The effect at the two lowest lift coefficients is too small to be detected. At the next two lift coefficients ( $C_L=1.02$  and 1.44), the downwash above the wake exceeds that below it; but no quantitative information on the wake effect can be obtained from these data, because the distortion of the vortex sheet also contributes a dissymmetry of the same order of magnitude. The curve for the partly stalled wing ( $C_L=1.35$ ) shows an effect amounting to several degrees.

Theoretical calculations of the wake effect on downwash based on the wake description presented in a later section of this report have been made. They indicate, in agreement with these data, that the maximum effect of the wake on the downwash angle at the tail is about 0.2° for unstalled plain wings. For wings with high-

drag flaps or for partly stalled wings, the effect may be ten times as great. Details of these calculations will be given after the discussion of the wake equations.

**Sweepback and dihedral.**—Wings with sweepback introduce some complication into the theory, since the component vortices for such a case do not have the simple rectangular U-shape. Some computations made for a wing with a normal amount of sweepback showed the effect to be much too small to require consideration. The lifting line may therefore be assumed to be perpendicular to the symmetry plane and to pass through the quarter-chord point of the root section.

Dihedral has an indirect effect on the downwash in that it gives the trailing vortex sheet an initial distortion which, however, is usually small. Thus, for the U. S. A. 45 tapered airfoil, the shed vortex sheet leaves the trailing edge with an initial dihedral of about 3.5°, thereby

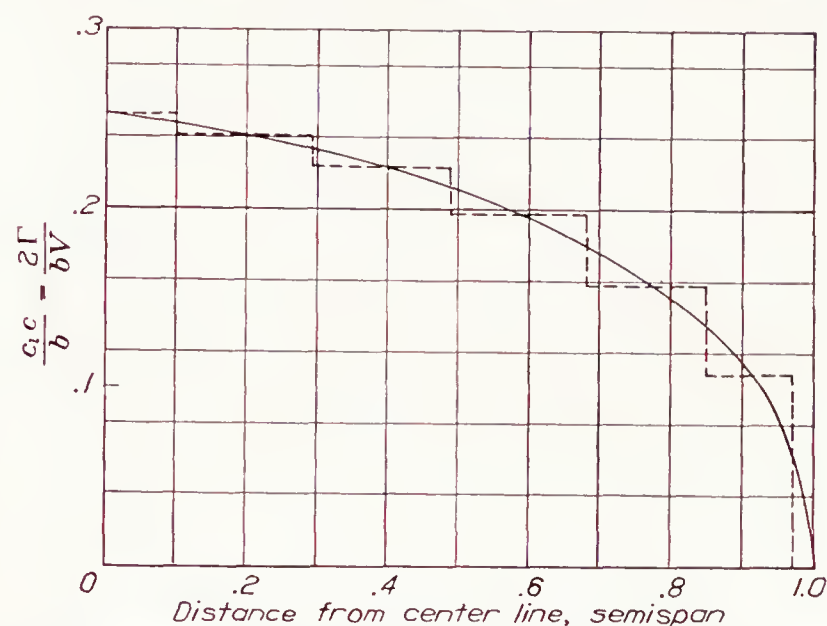


FIGURE 15.—Theoretical span load distribution for the 12-foot U. S. A. 45 tapered airfoil and the equivalent stepwise distribution used in the downwash calculations.  $C_L$ , 1.175.

contributing only about one-fifth of the total distortion found in the rearmost survey plane.

**Span load distribution.**—It may be pointed out that, in order to carry out a computation of the downwash angles, it will usually be necessary to use the theoretical span load distribution as derived, for example, by the method of Glauert (reference 9) or of Lotz (reference 10). The theoretical span load distribution thus derived corresponds closely to the actual distribution, provided that the airfoil has a reasonably high aspect ratio and rounded tips, although its accuracy in the neighborhood of discontinuities in either chord or angle is questionable.

**Sample calculation of downwash and comparison with experiment.**—It may be desirable to illustrate by an example the computation of the downwash angles behind an airfoil and to show, by comparison with experiment, the accuracy of the results. The experimental downwash-angle contour map (fig. 14) for the 12-foot tapered airfoil at  $C_L=1.175$  was chosen for the comparison.

For the theoretical curve of span load distribution (fig. 15), an approximately equivalent, stepwise dis-



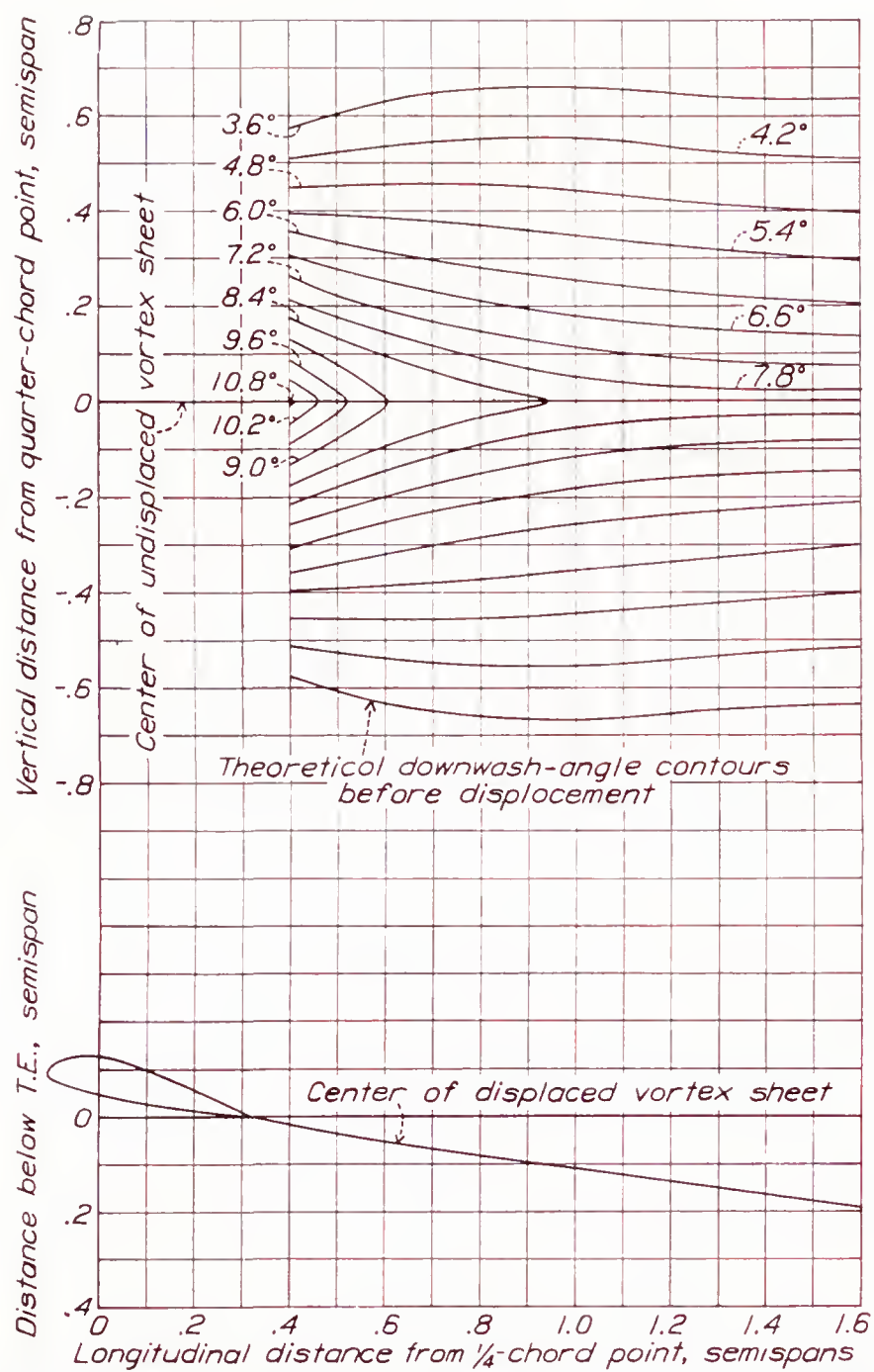


FIGURE 16.—Theoretical undisplaced downwash-angle contours and the center of the displaced vortex sheet. The 12-foot U. S. A. 45 tapered airfoil.  $C_L$ , 1.175.

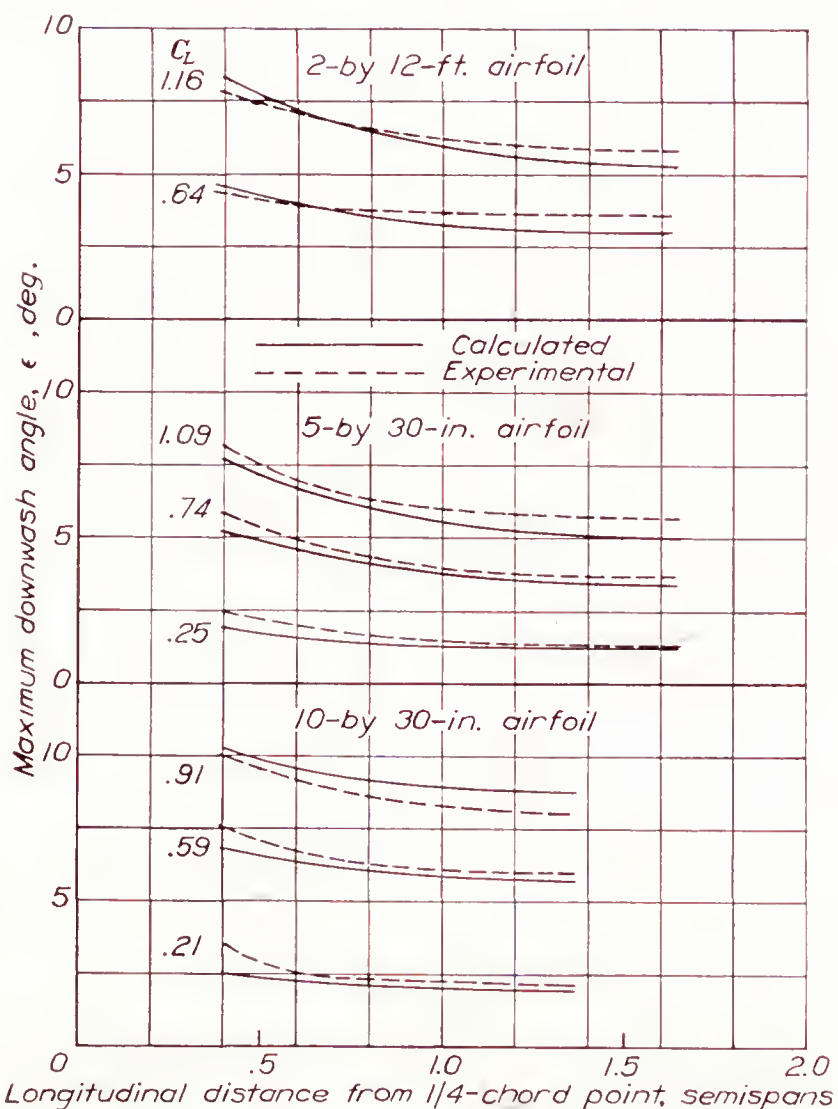


FIGURE 18.—Comparison of calculated and experimental maximum downwash-angles behind rectangular airfoils.

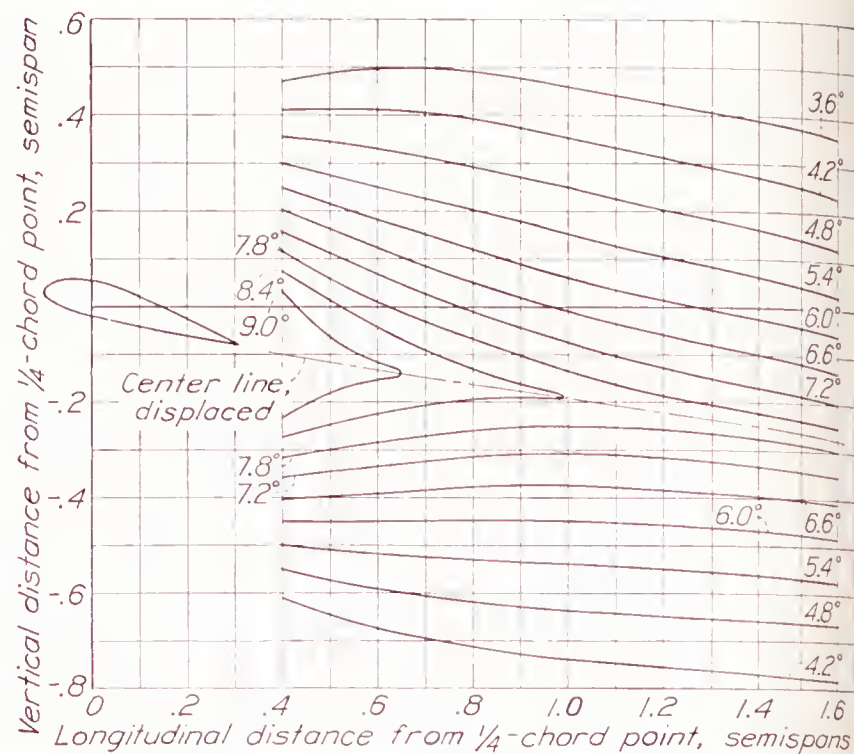


FIGURE 17.—Theoretical displaced downwash-angle contours in the symmetry plane of the 12-foot U. S. A. 45 tapered airfoil.  $C_L$ , 1.175.

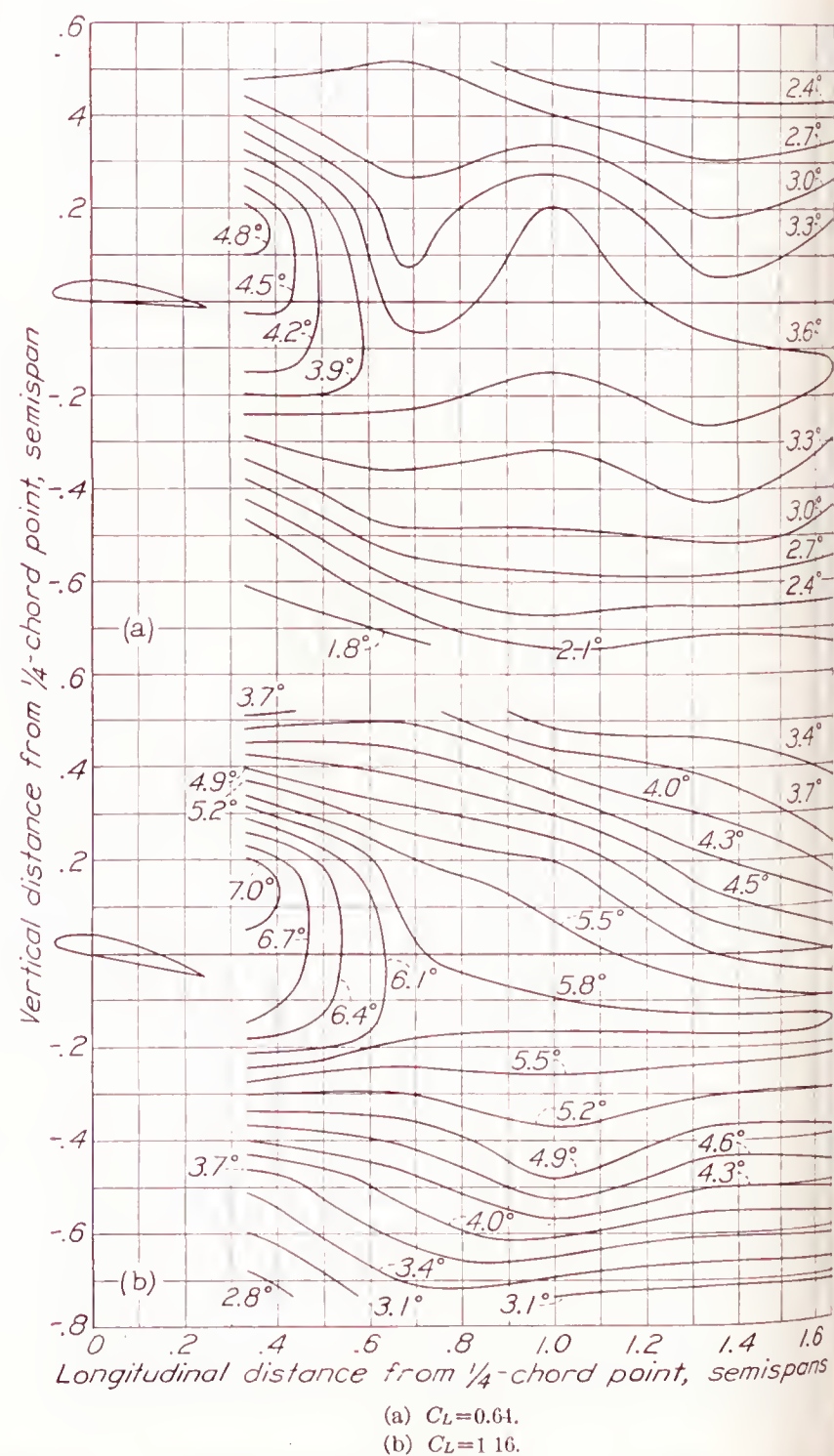


FIGURE 19.—Downwash-angle contours in the symmetry plane of the 2-by 12-ft Clark Y airfoil.  
(a)  $C_L = 0.61$ .  
(b)  $C_L = 1.16$ .



tribution is substituted. A vortex of strength given by the amount of the rise is considered to be shed at each step, and the downwash angles are computed for points in the symmetry plane by means of equation (1).

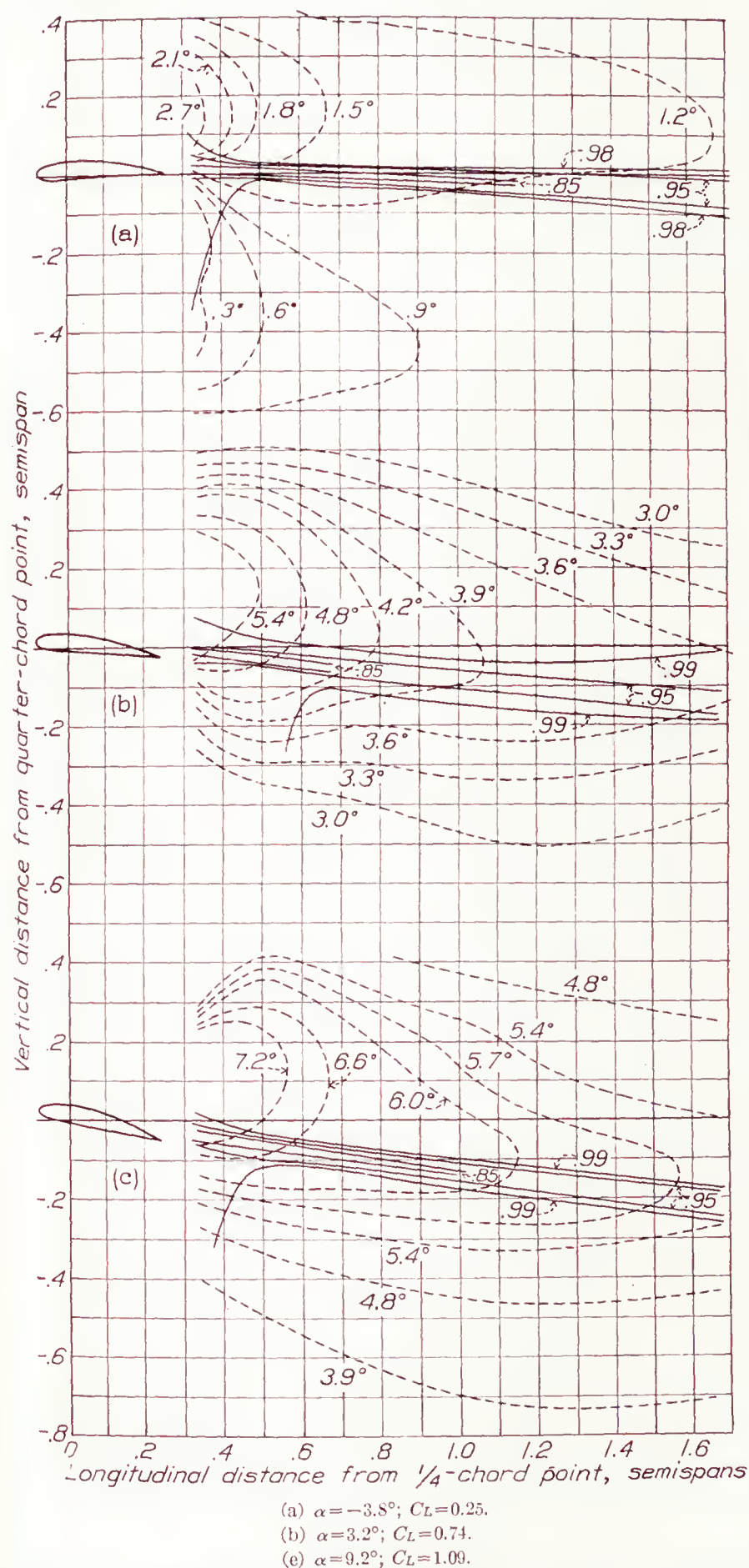


FIGURE 20.—Downwash-angle and dynamic-pressure contours in the symmetry plane of the 5-by 30-inch Clark Y airfoil. Dynamic pressures are shown as fractions of free-stream dynamic pressure.

It is assumed here that the trailing vortices extend unchanged indefinitely downstream. The resulting downwash-angle contour map is shown in figure 16. Distorting this map so that the center line goes through the trailing edge and has, at every point, an inclination equal to the downwash angle at that point, leads to the map of figure 17, which is now to be compared with the experimental map (fig. 14). It will be seen that the

agreement is, on the whole, satisfactory, particularly in the region where the tail plane is usually located, namely, about 0.75 semispan back. The following discrepancies may be noted:

1. The theoretical downwash angle approaches  $7.8^\circ$  on the center line at large distances, whereas the experimental downwash angle has already dropped to  $7^\circ$  at two semispans back and appears to be still decreasing rapidly with distance. This difference, as was shown by computation, is due to the distortion of the vortex sheet into a channel, the depth of which is about 0.4 semispan. It may be remarked that, for complete rolling-up, with the two halves of the trailing vortex sheet concentrated at their centroids, the downwash angle would be  $5.0^\circ$  in this region.

2. There is a dissymmetry in the experimental downwash map at the farther distances behind the airfoil

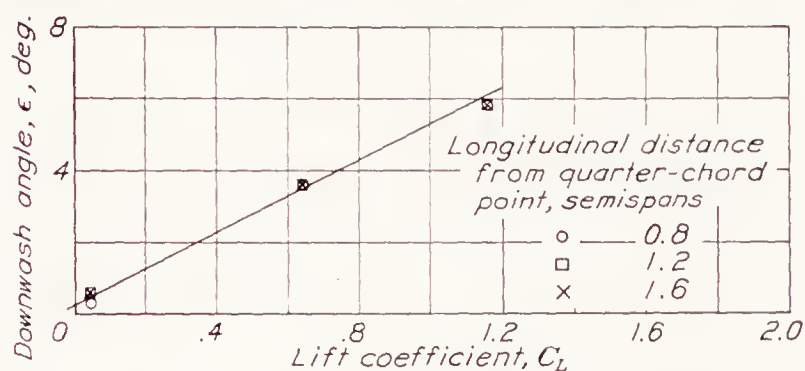


FIGURE 21.—Variation of maximum downwash angle in the symmetry plane with  $C_L$  for the 2-by 12-foot Clark Y airfoil.

in that the angles decrease faster below the maximum than above it. This dissymmetry is also due to the deformation of the sheet, as may be seen by referring to curve a of figure 12.

3. There is a region of large downwash angles above the center line, just behind the airfoil. This characteristic is predicted by airfoil-section theory and may be observed, for example, in the theoretical flow about the Clark Y section (fig. 3).

Other less complete comparisons between theoretical and experimental downwash angles are given in figure 18, where the maximum theoretical and experimental downwash angles are plotted against longitudinal position. The agreement is satisfactory, although the experimental downwash angles are somewhat larger than the theoretical except where the distortion and the rolling-up of the vortex sheet become considerable, as for the 10- by 30-inch airfoil at  $C_L = 0.91$ . Figure 19 shows experimental downwash-angle contour maps for the 2- by 12-foot airfoil at two lift coefficients. Figure 20 shows similar contour maps for the 5- by 30-inch airfoil and also shows the wake. This figure is of particular interest, for it shows clearly that the downwash maxima lie slightly above the wake.

If it is assumed that, for a wing without twist, the span load distributions (or circulation distribution) are similar at all angles of attack, it follows that downwash should be proportional to the lift coefficient. Examples of the proportionality between downwash and lift coefficient are shown in figure 21.



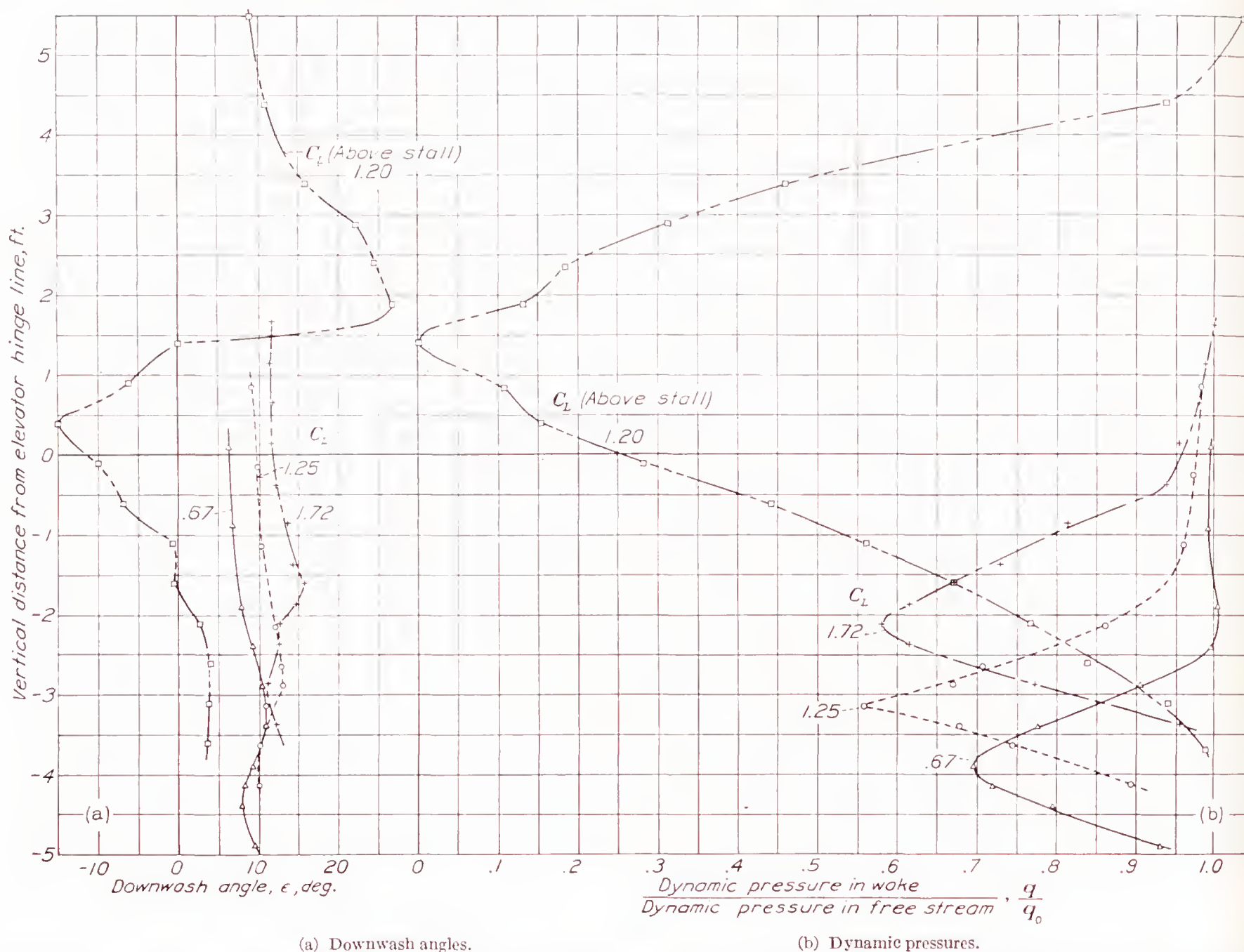


FIGURE 22.—Downwash angles and dynamic pressures in the plane of the elevator hinge, 0.1 span from the symmetry plane. Low-wing monoplane with 65-percent-span plain flap deflected 45°.

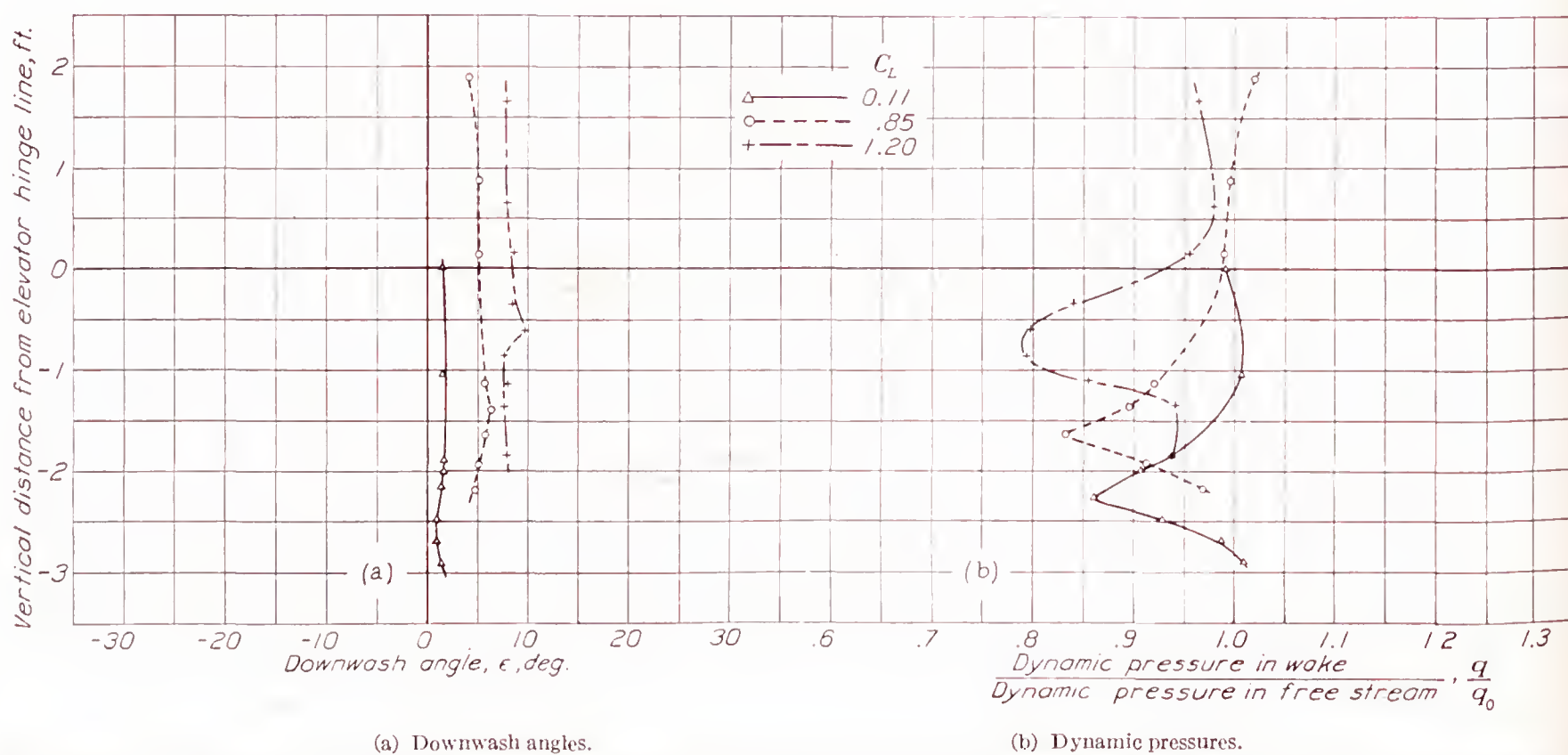


FIGURE 23.—Downwash angles and dynamic pressures in the plane of the elevator hinge, 0.1 span from the symmetry plane. Low-wing monoplane with flap up.



## WINGS WITH FLAPS

Provided that the span load distribution is known, the downwash may be computed for a flapped wing just as for a plain wing. It must be recognized, however, that the inaccuracies discussed in the preceding sections, which were concluded to have relatively small effect for plain wings, here acquire increased importance.

The wake, in particular, is many times stronger than that for a plain wing, and its effect in increasing the downwash angles near its upper border and decreasing them near its lower border is much more pronounced. Figure 22 shows the wake profiles and the corresponding

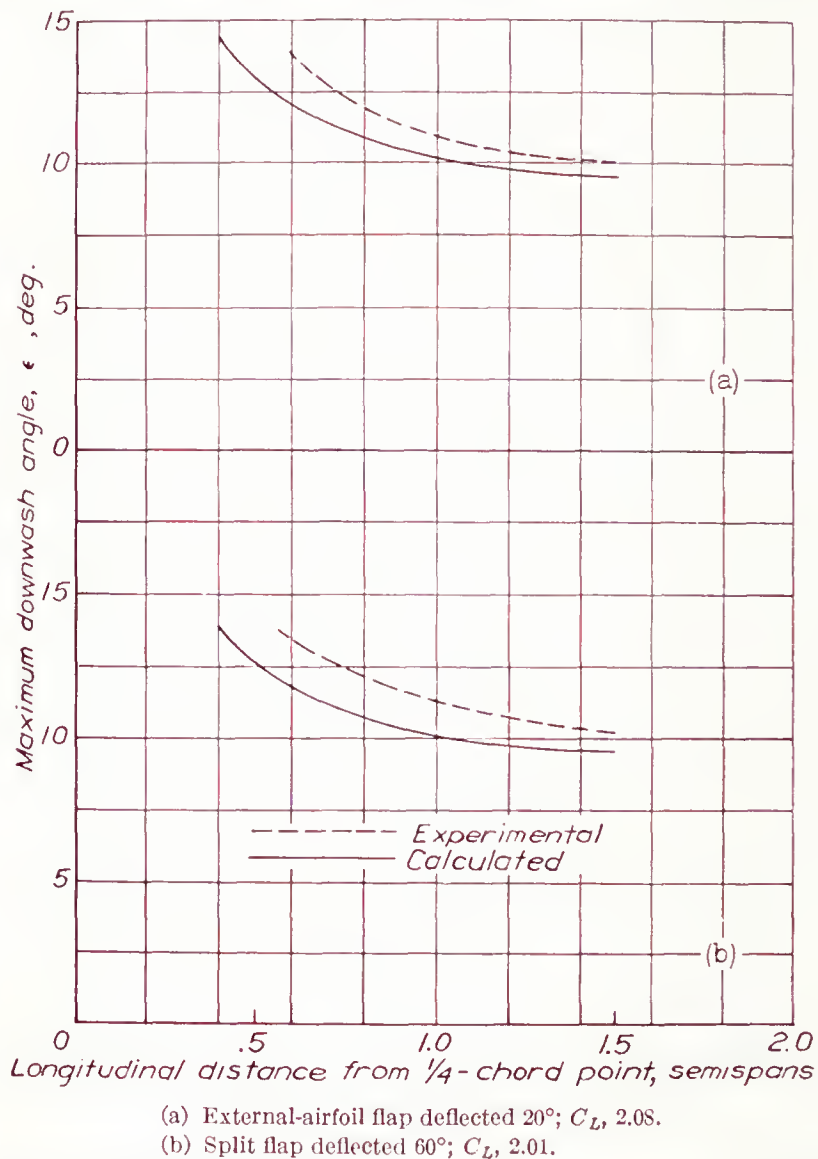


FIGURE 24.—Comparison of experimental with calculated maximum downwash behind the 2- by 12-foot Clark Y airfoil with full-span flaps.

downwash-angle plots in the plane of the elevator hinge line behind the low-wing monoplane with flaps down. The effect mentioned is seen to be considerable near the middle of the wake but is small outside the wake. For comparison, similar plots for the wing with flaps up are shown in figure 23.

In figure 24, the maximum theoretical and experimental downwash angles are plotted against longitudinal position for two cases of the 2- by 12-foot airfoil with full-span flaps. The excess of the experimental over the theoretical maximum downwash is approximately accounted for by the wake effect, as will be shown in a later section of this report. The experimental downwash-angle contour maps for these two cases are given in figures 25 and 26.

The deformation of the trailing vortex sheet for the case of partial-span flaps is also much more extensive than for the plain wing. Such distortion is indicated by the survey shown in figure 27, made in the vertical plane containing the elevator hinge line, behind the low-wing monoplane with flaps down. The trailing vortex sheet has been swept down sharply between the flap tip and the center. The origin of this peculiar deformation will be obvious on considering the direction of rotation of the flap-tip and the wing-tip vortices.

Data with which to study separately the foregoing influences are limited, and an exhaustive discussion of their effects is therefore not warranted. It appears likely, in view of the study for the plain wing, that no large discrepancy need be expected between the actual downwash angles and those computed by the previously described method, unless the flap span is inordinately small.

**Calculation of downwash angles.**—The theoretical downwash angles may be computed by the method that was given for plain wings, using the theoretical span load distribution, which, in these cases, consists of two parts, that for the plain wing and that for the flap. The flap contributions were calculated by the method of reference 10, sufficient data from lift measurements being available in each case to furnish the variables needed for the computation.

It may be desirable to state more explicitly the basis for the computation of the downwash increments due to flaps. The relative change in lift distribution on lowering a flap is nearly independent of the angle of attack, and the absolute change in the section lift coefficient  $c_l$  at any section is approximately proportional to the total increase in the wing lift coefficient  $C_{L_f}$ . The resultant loading and the resultant vortex system are therefore the sums of those of the plain wing at the given angle of attack and those due to the flap, which are proportional to  $C_{L_f}$ . The resulting downwash is, correspondingly, the sum of that of the plain wing at the given attitude and that due to the flap, the flap component again being proportional to  $C_{L_f}$ . The vertical displacement of the center line of the downwash-angle pattern is similarly additive.

In these span-loading calculations, the Fourier coefficients for the chord distribution were found by Pearson's system (reference 11) and the Fourier coefficients for the angle distribution were found by the usual method of integration. Ten terms of the series for the loading were used except in the case of the flap with the center cutaway, for which 20 terms were used. A reasonable number of terms does not suffice to give the shape of the loading curve very close to the edge of a flap; the curve is therefore more or less arbitrarily drawn in this region, the main condition being that it be vertical at the position of the flap tip.



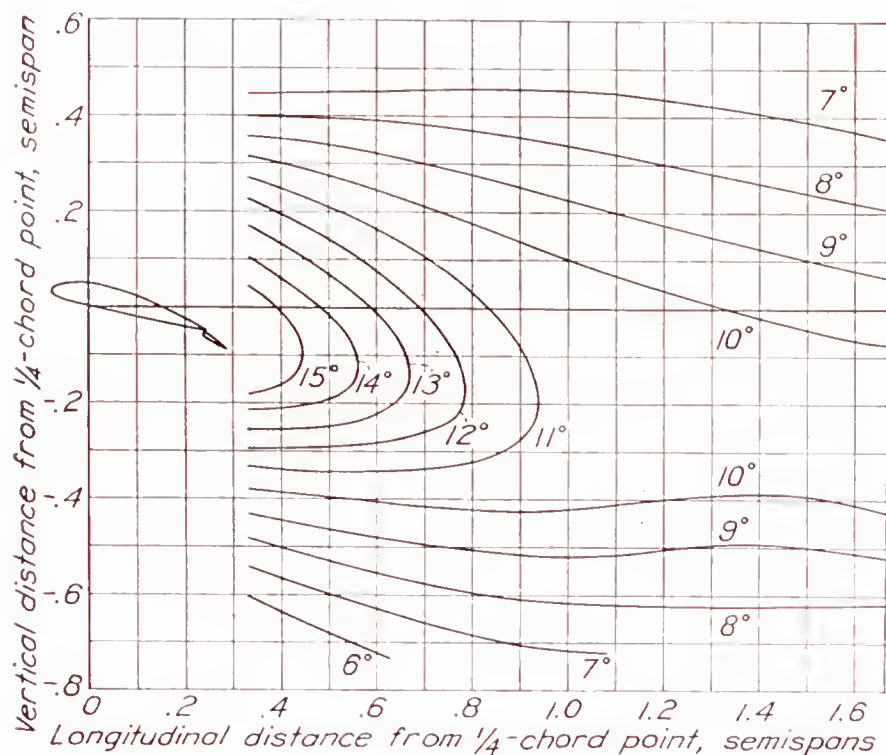


FIGURE 25.—Experimental downwash-angle contours in the symmetry plane behind the 2-by 12-foot Clark Y airfoil with full-span external-airfoil flap.  $\delta_f$ , 20°;  $C_L$ , 2.08.

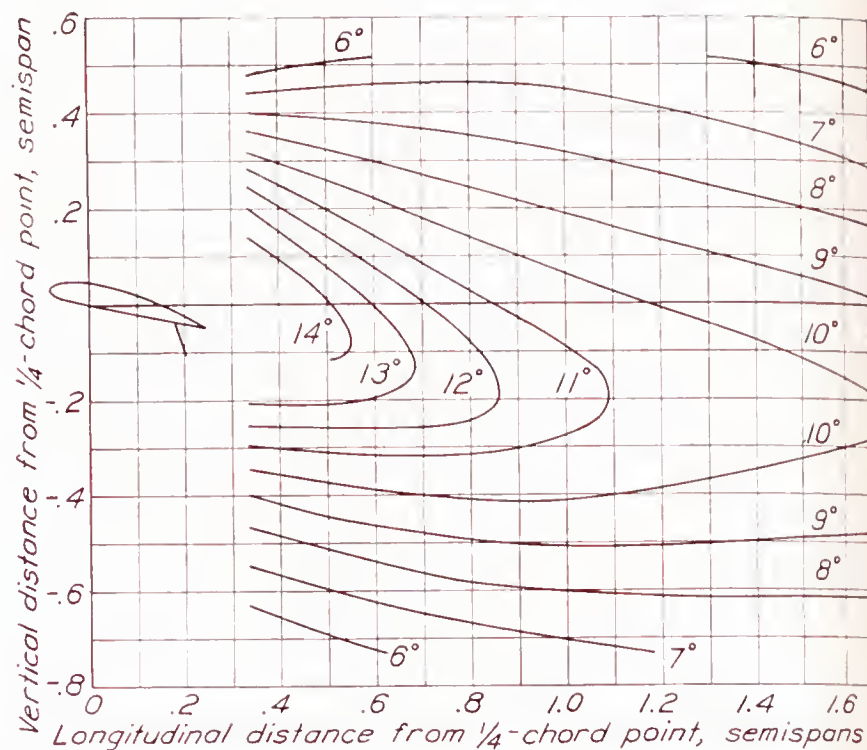


FIGURE 26.—Experimental downwash-angle contours in the symmetry plane behind the 2-by 12-foot Clark Y airfoil with full-span split flap.  $\delta_f$ , 60°;  $C_L$ , 2.01.

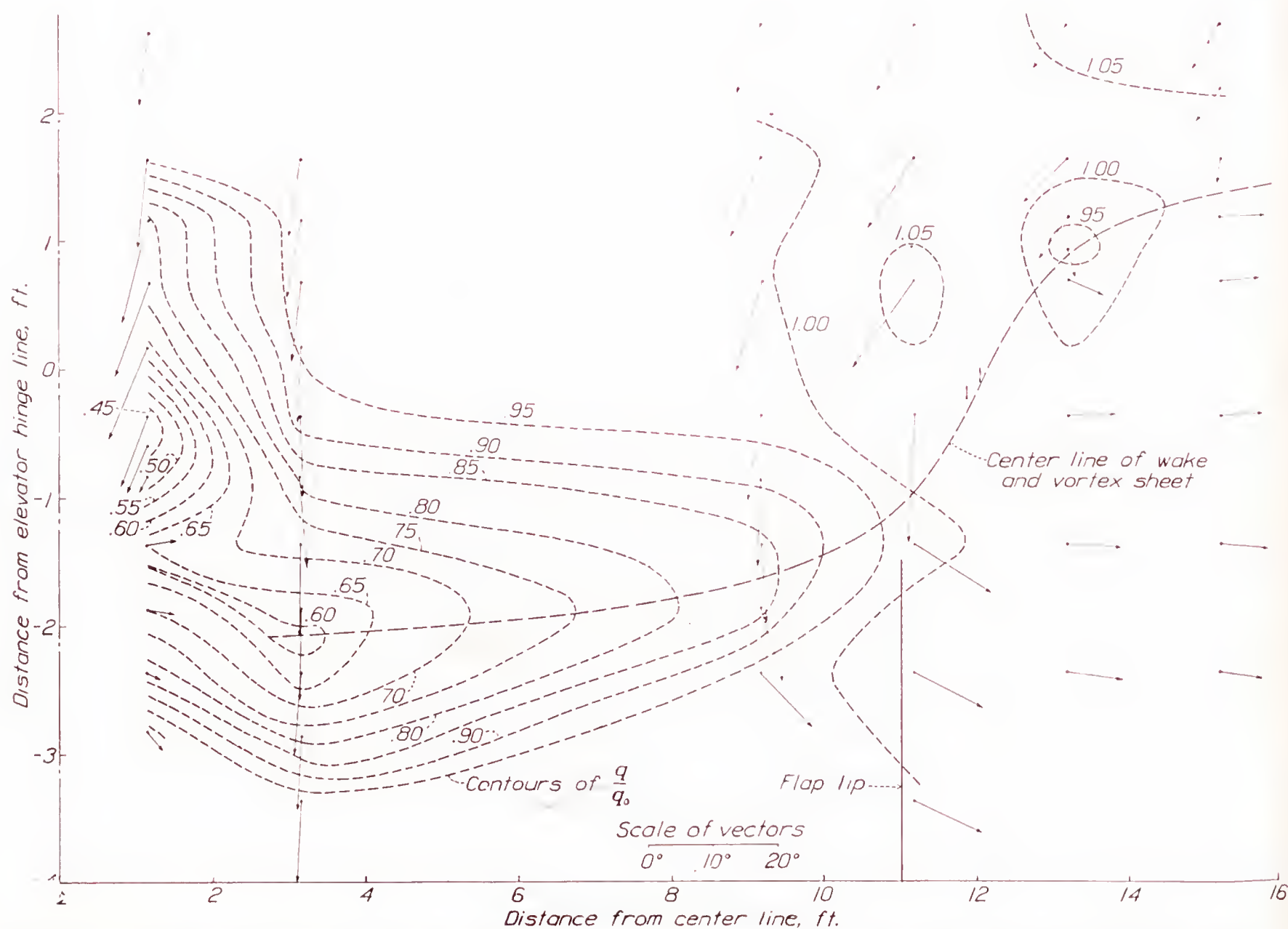


FIGURE 27.—Dynamic pressure and direction of air flow in the vertical plane through the elevator hinge. Vectors denote deviation of air flow from free-stream direction. Dynamic pressures in fractions of the free-stream dynamic pressure. Low-wing monoplane; 65-percent-span plain flap;  $\delta_f$ , 45°;  $C_L$ , 1.725;  $\alpha$ , 11.1°. Note that the vertical scale is twice the horizontal.



Sample calculation for flapped wings and comparison with experiments.—Figures 28 to 30 illustrate steps in the downwash-angle calculation for the case of the 2- by 12-foot airfoil with 70-percent-span split flap at  $C_L=1.85$ . The lift coefficient consists of two parts,  $C_{L_w}=1.16$  and  $C_{L_f}=0.69$ ; the corresponding two contributions to the span load distribution are shown in figure 28. The corresponding downwash-angle patterns, neglecting distortion or displacement of the shed

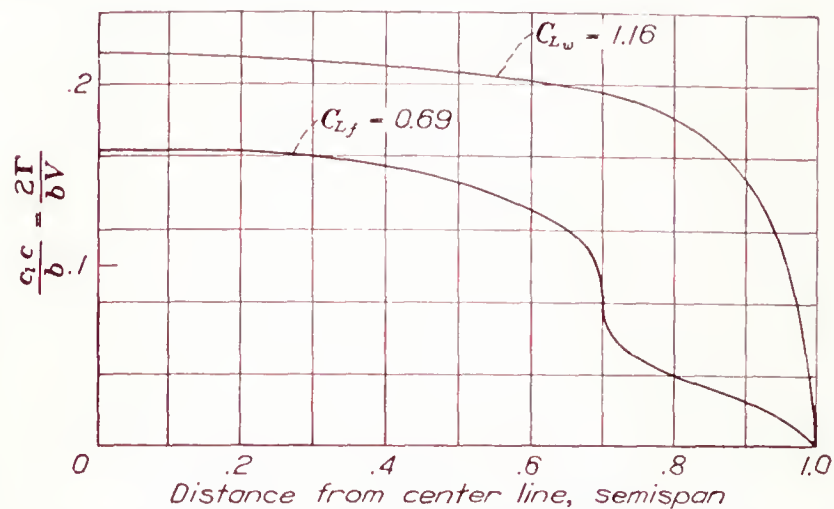


FIGURE 28.—Contributions of plain wing and of flap to span load distribution on the 2- by 12-foot Clark Y airfoil with 70-percent-span split flap.  $\delta_f, 60^\circ$ ;  $C_{L_w}, 1.16$ ;  $C_{L_f}, 0.69$ .

vortex sheet, are shown in figure 29. Adding these two contour maps and shifting the center line so that its inclination equals the downwash angle at every point gives the contour map shown in figure 30, which is now to be compared with the experimental downwash-angle contour map shown in figure 31 (a). The disagreement between the two is not large and is quantitatively attributable to the wake effects, as will appear later.

Figure 31 contains experimental downwash-angle contour maps, in the symmetry planes, for the 2- by 12-foot airfoil with 40-percent-span and 70-percent-span split flaps and with the 70-percent-span split flap having a 12.5-percent-span cutaway at the center. In figure 32, the maximum downwash angle is plotted against the longitudinal position and compared with the computed values. The difference between the experimental and the theoretical values may be ascribed to two effects: that of the wake, which increases the downwash; and that of the rolling-up, which, although insignificant for plain wings, appreciably reduces the downwash for short-span flaps. Thus, for the 70-percent flap, the first effect predominates (fig. 32 (a)); whereas, for the 40-percent flap at the higher lift coefficient, the second effect predominates (fig. 32 (c)).

A discrepancy of the order of  $4^\circ$  exists in the case of the 70-percent flap with the cutaway at the center. Agreement can hardly be expected, however, for there is little justification in using the lifting-line theory to calculate the span load distribution near a cutaway that is smaller than the wing chord or in assuming that the vortex sheet shed from the region of the cut-

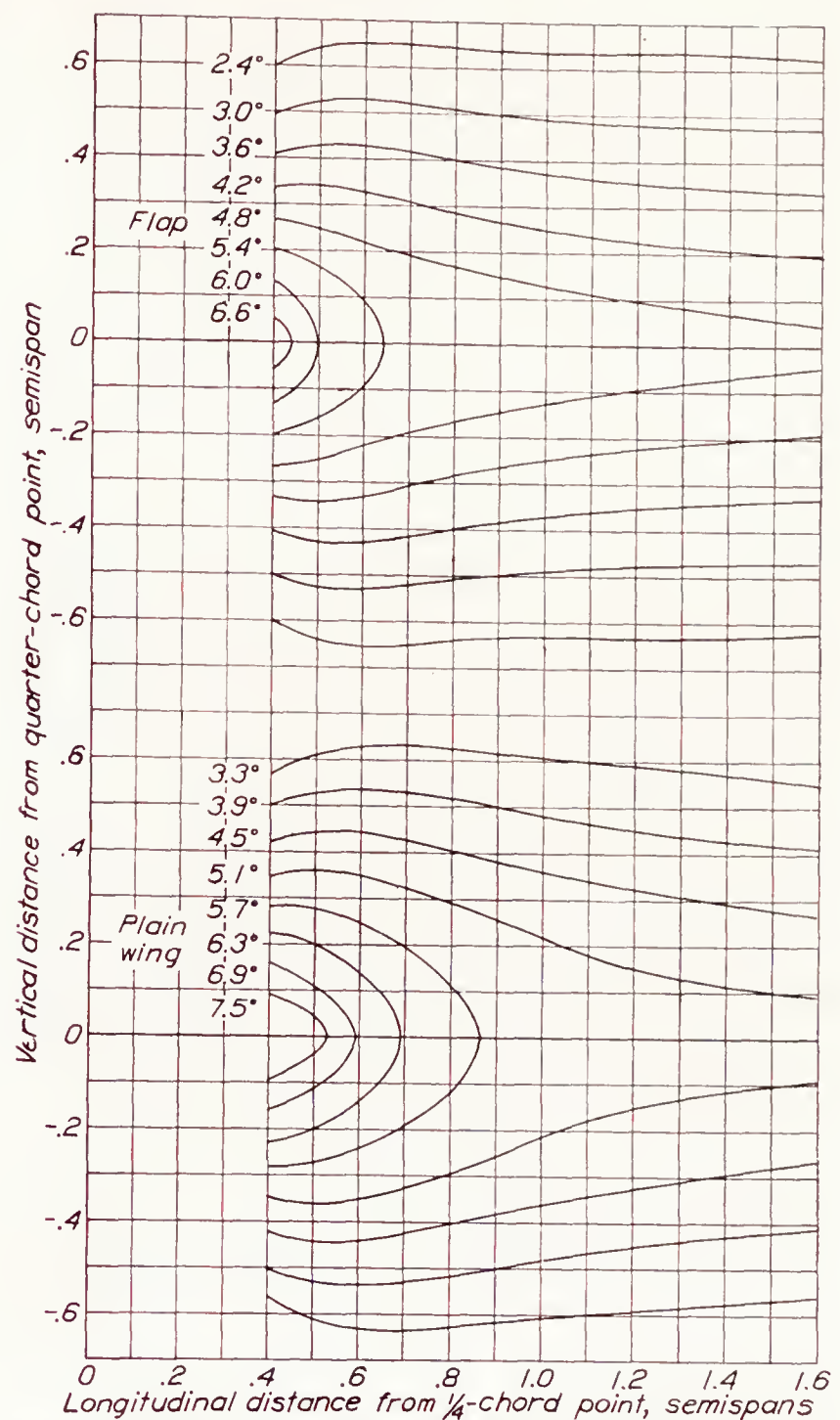


FIGURE 29.—Theoretical undisplaced downwash-angle contours, representing contributions of plain wing and of flap, for the 2- by 12-foot Clark Y airfoil with 70-percent-span split flap.  $\delta_f, 60^\circ$ ;  $C_{L_w}, 1.16$ ;  $C_{L_f}, 0.69$ .

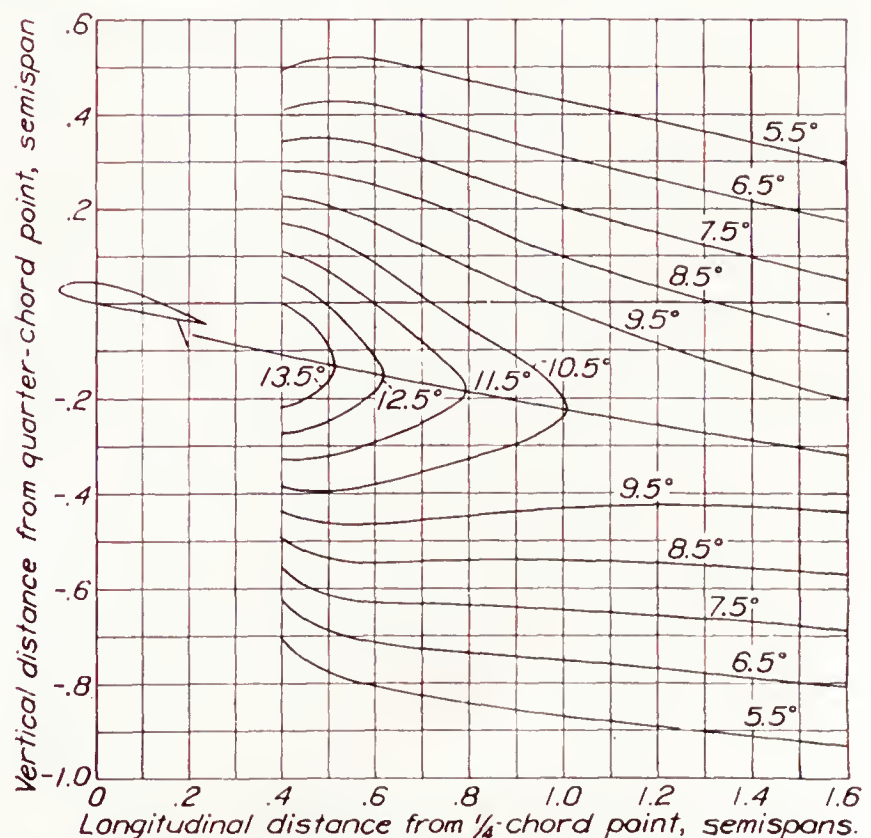
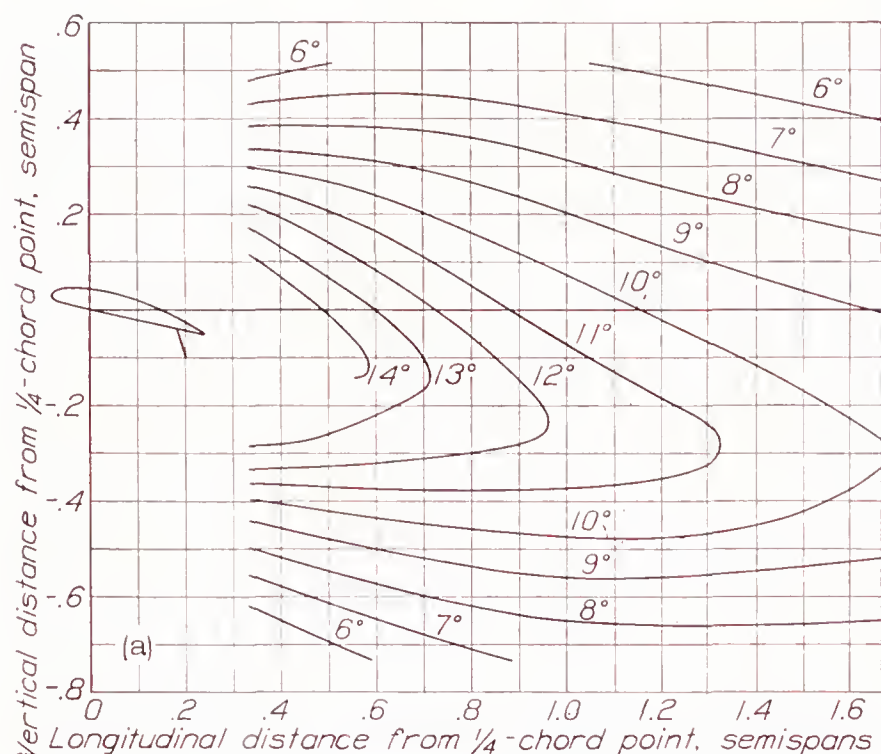
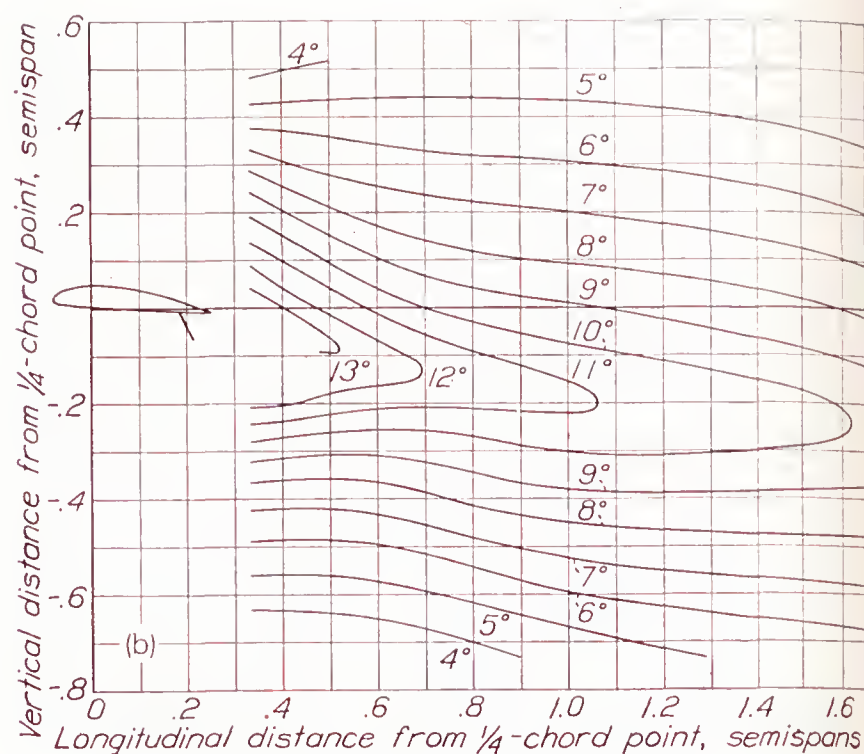
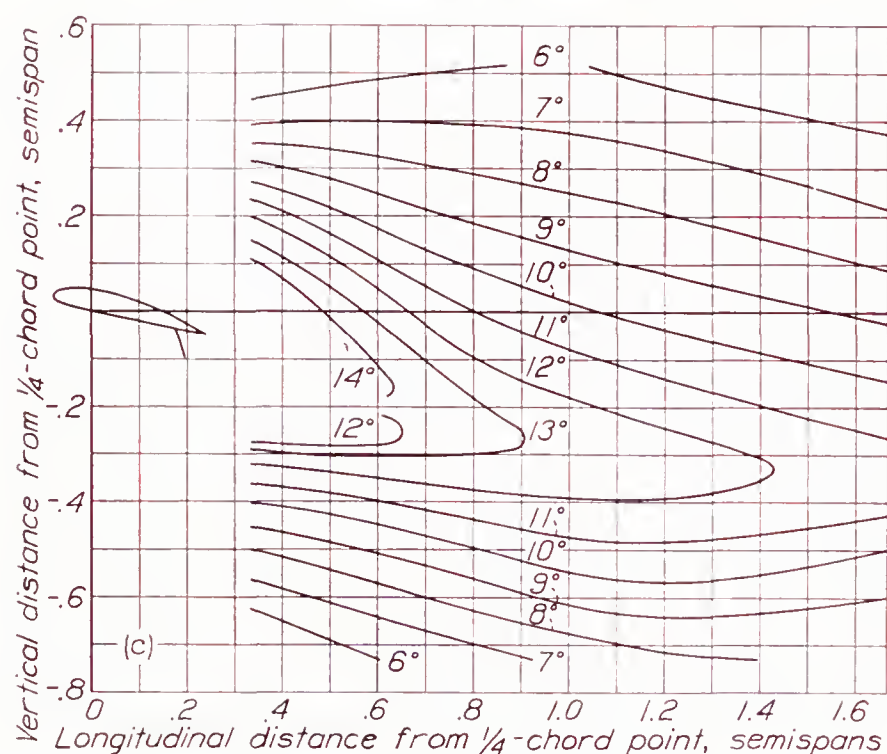
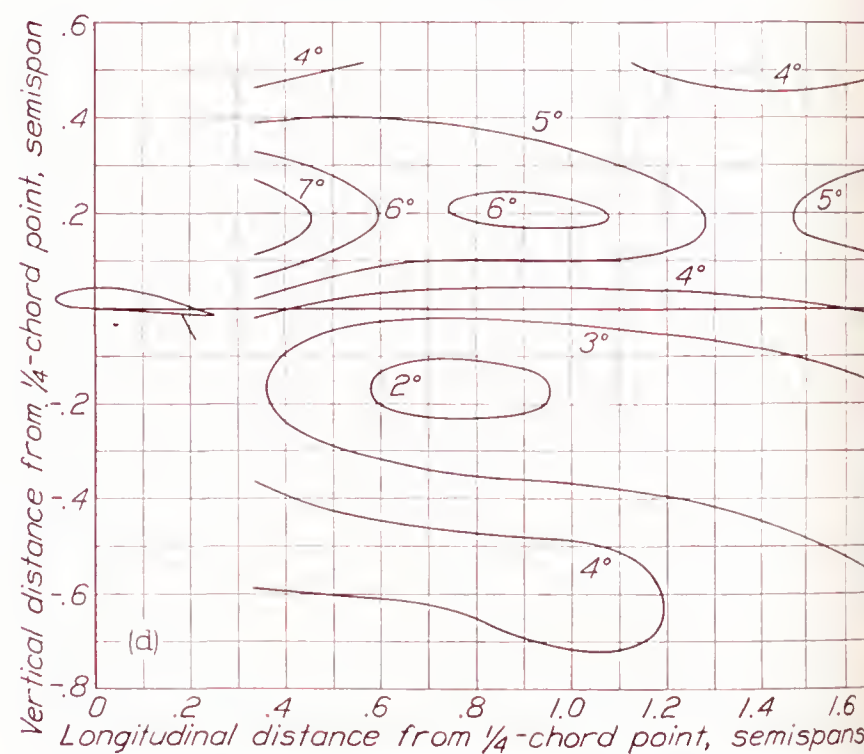


FIGURE 30.—Theoretical displaced downwash-angle contours for the 2- by 12-foot Clark Y airfoil with 70-percent-span split flap.  $\delta_f, 60^\circ$ ;  $C_{L_w}, 1.16$ ;  $C_{L_f}, 0.69$ .



(a) The 70-percent-span split flap;  $C_L$ , 1.85.(b) The 40-percent-span split flap;  $C_L$ , 1.02.(c) The 40-percent-span split flap;  $C_L$ , 1.58.(d) The 70-percent-span split flap with 12.5-percent-span cutaway at center;  $C_L$ , 1.58.FIGURE 31.—Downwash-angle contours in the symmetry plane behind the 2- by 12-foot Clark Y airfoil with partial-span split flaps at various lift coefficients.  $\delta_f$ ,  $60^\circ$ .

away would not be thoroughly distorted after a very short distance. This case is of less practical importance than might be supposed, because the added lift due to a flap appears to be carried across the fuselage even though the flaps themselves may end at the wing-fuselage juncture.

#### DOWNWASH BEHIND STALLED AIRFOILS

The matter of downwash behind stalled airfoils is of importance from considerations of stability and control at the stall. The available data for such cases are limited; hence an extensive treatment of the subject is not possible. A discussion based on that for unstalled airfoils and in agreement with the small amount of data available may, however, be useful.

The subject divides itself naturally into two parts, depending on whether the wing stalls at the tips or at the center. The effects of stalling on downwash fall roughly under two heads: (a) effects of the strong wake, and (b) effects of the change in the span load distribution.

For a wing stalled at the tips, the span load distribution may be compared with that for a wing with a partial-span flap as shown, for example, in figure 28, where the edge of the flap corresponds to the edge of the low-lift stalled region. The downwash in the region of the tail will therefore, for a given lift coefficient, be greater for the stalled wing than for the unstalled wing, because a substantial part of the vorticity that, for the unstalled wing, leaves the wing at the tip, now leaves at the edge of the stalled region.



An example of this effect will be noted when the mid-wing model is discussed. The wing being highly tapered, the stall in this case progresses inward from the tips. After the tips begin to stall, the lift remains nearly constant with increase in angle of attack and, correspondingly, so does the theoretical downwash (as computed for the unstalled wing). The experimental downwash, for the reason just given, continues to increase as the edge of the stalled region moves inward.

Wings with low taper ratio, or with washout, will stall first at the center. In addition to the change in the vortex distribution, corresponding to the change in

$\alpha=1.4^\circ$ , although the lift coefficient is three times as much. The figure also demonstrates the other characteristic of the air flow near a strong wake; namely, that, because of the flow of air into the wake, the downwash above it is increased, while that below it is decreased. The effect in this case amounts to about  $3^\circ$  or  $4^\circ$ .

### WAKE

The wake may be defined as the region behind a wing in which the drag due to skin friction appears as a decreased total pressure. Bernoulli's equation does not apply within it, for there is a gradient in dynamic pressure, whereas the static pressure is almost constant. Owing to turbulent mixing at its boundaries, the wake widens with increasing distance downstream and at the same time becomes less intense. Far behind the wing, the wake becomes so thoroughly diffused with the surrounding stream that its presence can no longer be observed. Typical distributions of dynamic pressure in the wake are shown in figure 33.

Calculations for tail-surface design require a knowledge of the wake location, with reference to the tail, and of the wake dimensions. It will be shown that the wake location is dependent on the airfoil lift and that the wake dimensions are functions of the profile drag and essentially independent of the lift.

### LOCATION OF THE WAKE

The wake behind a wing has been shown (figs. 8, 9, and 27) to coincide with the trailing vortex sheet. This coincidence is due to the common origin of the wake and the vortex sheet at or near the trailing edge of the wing and their equal freedom to move in the induced-velocity field behind the wing. It has previously been shown that the vertical displacement  $h$  of the vortex sheet from an origin at the trailing edge is given with satisfactory accuracy by

$$h = \int_{T.E.}^x \tan \epsilon \, dx$$

for the cases of wings without flaps at low and moderate lift coefficients. The necessity for an accurate knowledge of the vertical location of the wake requires that further consideration be given to the case of flapped wings and wings at lift coefficients at and above the stall.

Difficulties in determining the vertical location of the wake for the aforementioned cases arise, first, in establishing the vertical location of the origin of the wake at the trailing edge and, second, in evaluating the errors introduced by the assumptions made in computing the height of the vortex sheet. The simplified trailing-vortex system that has been shown to give satisfactory accuracy in downwash-angle computations may lead to somewhat larger errors in estimating the wake location.

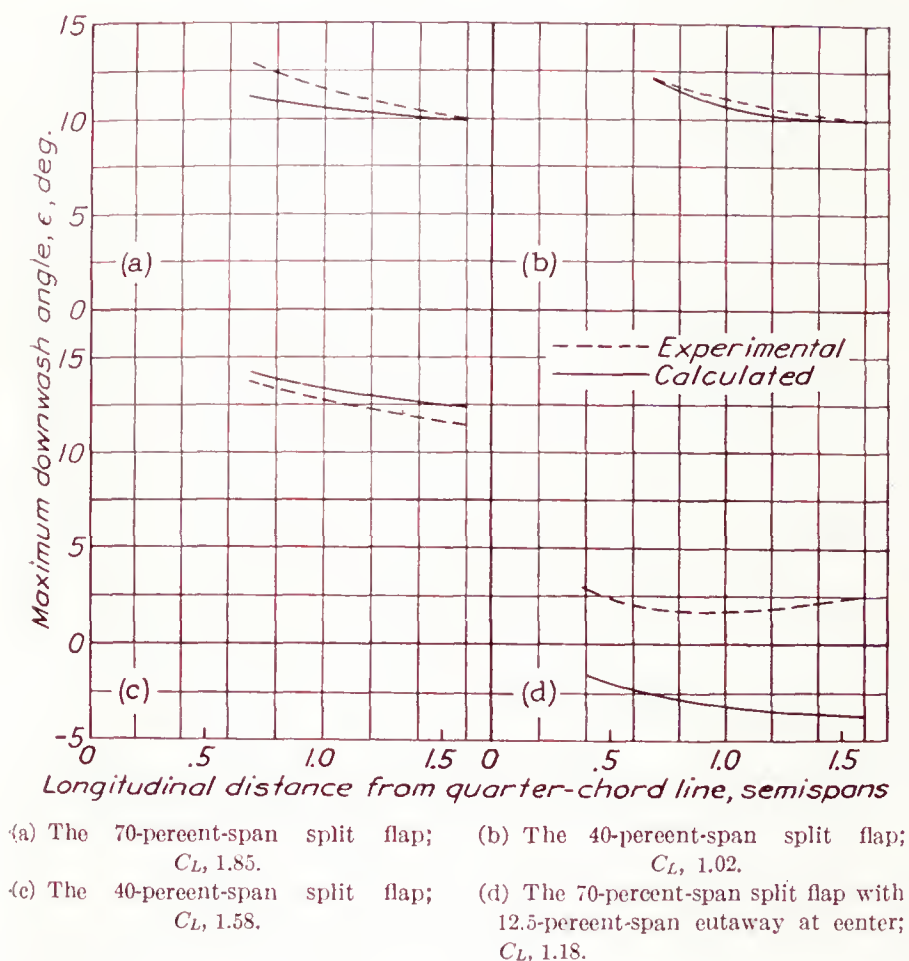


FIGURE 32.—Comparison of calculated and experimental downwash behind the 2-by-12-foot Clark Y airfoil with partial-span split flaps at various lift coefficients.  $\delta_f$ ,  $60^\circ$ .

span load distribution, the presence of the wake close to or passing over the tail is an important factor. The wake is very wide, but the position of its center can probably be predicted with fair accuracy from the span load distribution by the process previously described. As will be explained in a later section, the center of the wake leaves the wing, not at the trailing edge, but at a point about  $(c/2) \sin \alpha$  above the trailing edge. In general, when a wing stalls at the center, the center of the wake moves upward. If the stall is gradual, this displacement will be small; if the lift drops sharply across the center of the wing, the vortices rolling off at the edge of the stalled portion will rotate in such a sense as to contribute an upward motion to the wake. The curve of figure 13 for the Clark Y airfoil at  $\alpha = 17.6^\circ$  illustrates this effect. It will be seen that both the middle position of the wake and the mean downwash angle in the wake are approximately the same as for



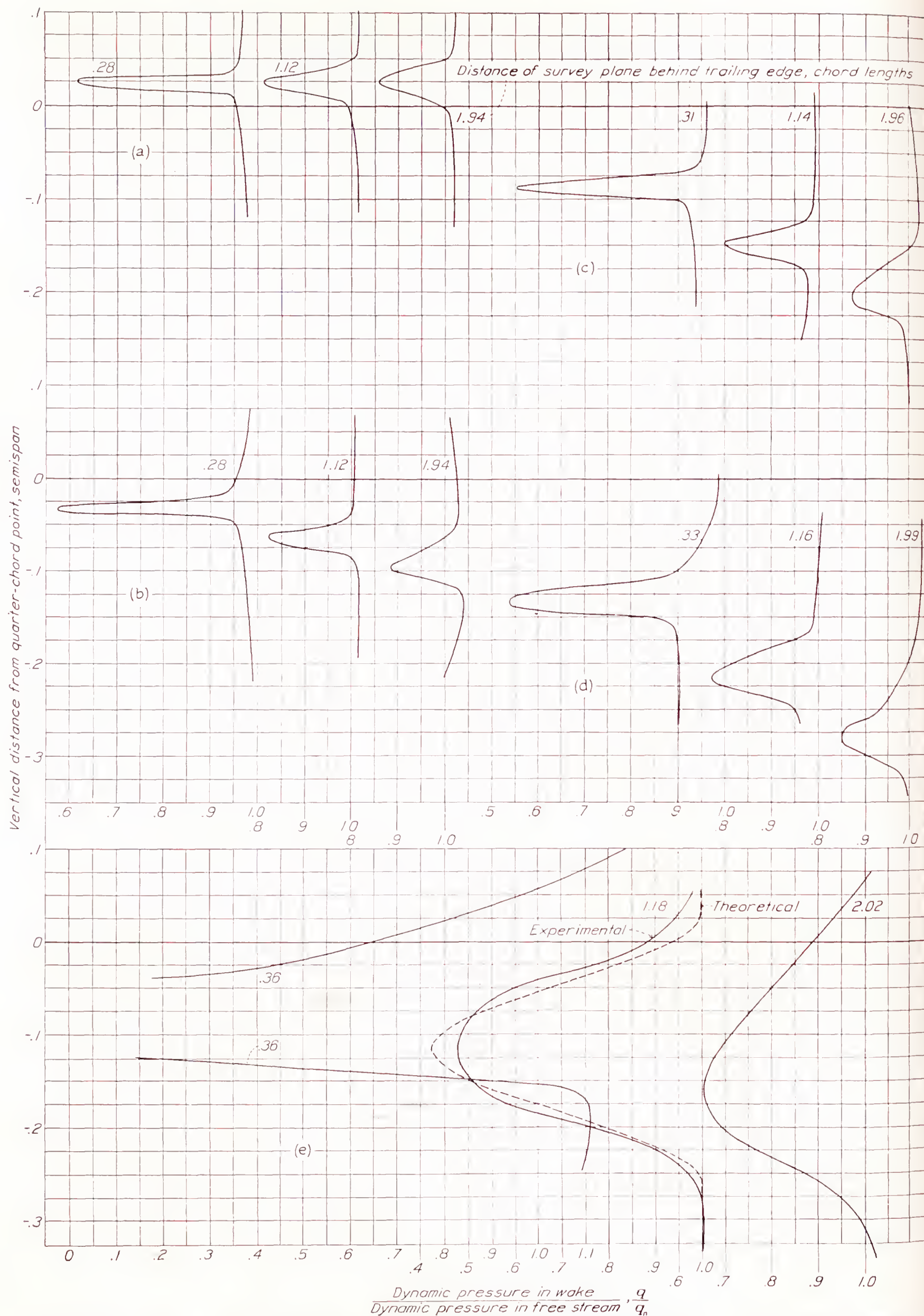


FIGURE 33.—Wake profiles showing dynamic pressure in the symmetry plane at three distances behind the U. S. A. 45 tapered airfoil at different lift coefficients.



From the experimental flap data available, it was not possible to isolate the discrepancies with the theory caused by improper choice of the wake origin from those due to the use of the simplified trailing-vortex system. It was therefore necessary to resort to an empirical method that fits the experimental data for full-span flaps with considerable accuracy. For the cases of partial-span flaps at high lifts, the wake will generally

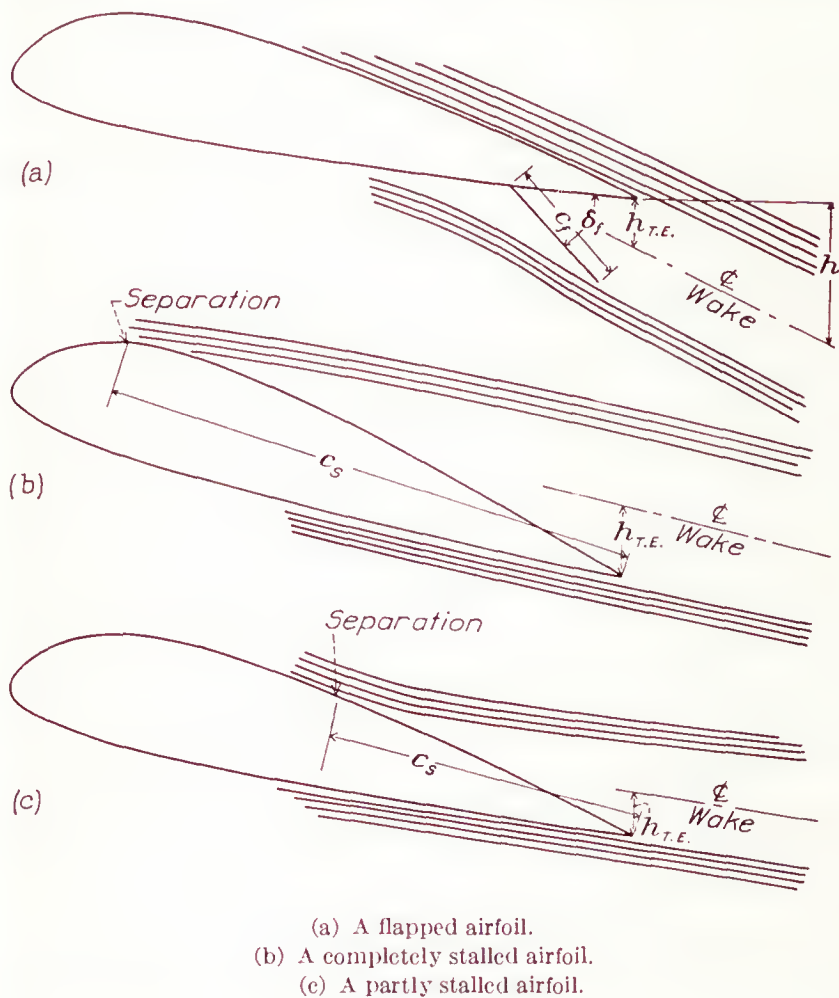


FIGURE 34.—Streamlines illustrating the origin of the wake for flapped and stalled airfoils.

be slightly above the values given by the empirical expression.

For a wing with a deflected flap, it is apparent that the origin of the vortex sheet and the wake is below the original trailing edge of the wing. Inasmuch as the flow over the upper surface and that over the trailing edge of the deflected flap are separated by a distance equal to about  $c_f \sin \delta_f$  (fig. 34), it was assumed as a first approximation that the wake has this thickness at the trailing edge with the center at a distance of  $(c_f/2) \sin \delta_f$  below the original trailing edge. With this assumption of the position of the wake center and the further assumption that the wake was deflected behind

the wing by an amount equal to  $\int_{T.E.}^x \tan \epsilon dx$ , a large

number of comparisons were made with available experimental data on the wake location behind flapped wings. A systematic discrepancy between the theoretical and the experimental values was noted that was primarily a function of the flap deflection. The type of flap (split, plain, or external-airfoil) appeared to be of only secondary importance and has therefore been neglected. Values of  $k$ , which is the correction factor for the loca-

tion of the wake origin at the trailing edge, are given in figure 35. Positive values of  $k$  indicate downward displacements.

The location of the wake origin behind a flapped wing with reference to the original (flap up) trailing edge of the wing is thus given as

$$h = (c_f/2) \sin \delta_f + kc + \int_{T.E.}^x \tan \epsilon dx$$

Owing to the relatively slow change in  $\epsilon$  with distance behind the wing, a graphical integration of  $\tan \epsilon dx$  may readily be performed. The values of  $\epsilon$  are obtained from downwash-angle charts, such as figures 16 and 29.

When the wing stalls, the downwash at the wing center may be either increased or decreased depending on whether the wing stalls first at the tips or at the center. The center of the wake in the region of the trailing edge of a section is always raised, however, when the section either partly or completely stalls.

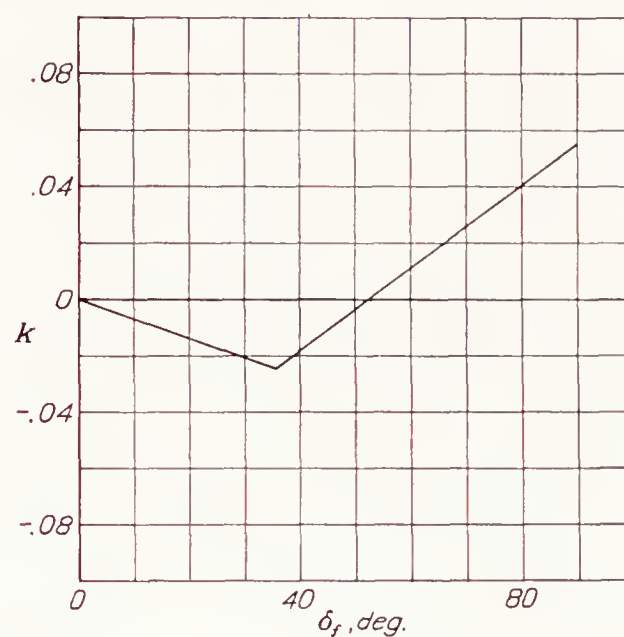


FIGURE 35.—Plot of factor  $k$  for correction to the vertical position of the wake origin at the trailing edge of a wing with a flap.

For cases in which the section is partly stalled (fig. 34 (c)) the wake center may be raised an amount equal to  $(c_s/2) \sin \alpha$ , in which  $c_s$  is the length of the wing chord over which the separation occurs. For a completely stalled wing,  $c_s$  approximately equals  $c$ . The foregoing approximations for location of the center of the wake with reference to the trailing edge of an unflapped wing have shown satisfactory agreement with the experimental data.

For the case of a flapped wing at the stall, the wake center will be raised above the trailing edge by an amount equal to  $(c_s/2) \sin \alpha$  and, owing to the flap, will be lowered by an amount equal to  $(c_f/2) \sin \delta_f$  so that the resultant displacement of the origin may be obtained as the algebraic sum of these two terms.

The wake displacement behind the wing depends directly on the downwash. It is not to be expected, therefore, that the wake location for a stalled wing may be predicted with great accuracy unless the exact nature of the stall is known and the change in the load distribution due to the stall is taken into account.



## WAKE DIMENSIONS

The profile drag of an airfoil section may be approximately equated to the loss of momentum in the wake, as shown by Betz (reference 12) by the equation

$$d_0 = \rho \int_{-\infty}^{\infty} u(U-u) dz$$

in which  $U$  is the velocity in the free stream and  $u$  is the local velocity in the wake. At distances behind the airfoil comparable with the tail-plane location where the static pressure in the wake has reached that of the free stream, the momentum equation may be approximated by the more elementary expression

$$c_{d0} = \frac{1}{c} \int_{-\frac{B}{2}}^{\frac{B}{2}} \left(1 - \frac{q}{q_0}\right) dz \quad (2)$$

in which  $c_{d0}$  is the section profile-drag coefficient,  $q/q_0$  is the ratio of the dynamic pressure in the wake to that in the free stream, and  $B$  is the wake width. Experimental investigations have shown excellent agreement with this expression even for the cases of wings with flaps (reference 13).

The wake may be completely described by the width  $B$ , the loss of dynamic pressure at the wake center  $\Delta q$ , and the shape of the wake profile.

As an aid in generalizing the results, the following nondimensional ratios have been adopted:

$$\eta = \frac{\text{dynamic-pressure loss at center line of wake}}{\text{dynamic pressure in free stream}}, \frac{\Delta q}{q_0}$$

$$= 1 - \frac{q}{q_0}$$

$$\zeta = \frac{1}{2} \frac{\text{wake width}}{\text{wing chord}}, \frac{B}{2c}$$

$$\xi = \frac{\text{distance behind trailing edge of wing}}{\text{wing chord}}, \frac{l}{c}$$

In a theoretical analysis of the wake behind a two-dimensional body, assuming the turbulent mixing length to be proportional to the wake width, Prandtl (reference 14) has indicated the following relations:

$$\zeta \propto \xi^{\frac{1}{2}} c_{d0}^{\frac{1}{2}}$$

$$\eta \propto \frac{c_{d0}^{\frac{1}{2}}}{\xi^{\frac{1}{2}}}$$

These proportionalities have been investigated by means of the experimental data. The wake widths for the three symmetrical airfoils at zero lift are plotted against distance from the wing trailing edge in figure 36. The curves are all parabolic, as indicated by the Prandtl expression. The origin is shifted to  $\xi = -0.15$ , which is to be expected, owing to the already finite boundary-layer width at the wing trailing edge. In figure 37 is shown the variation of the wake width  $2\zeta$  with  $c_{d0}$  for

a fixed value of  $\xi$  ( $\xi \approx 1.5$ ). The predicted proportionality with  $c_{d0}^{\frac{1}{2}}$  is verified, for the test points may be fitted to a parabola, the equation of which is  $\zeta = 0.89 c_{d0}^{\frac{1}{2}}$ .

From the same test data, corresponding values of the relative losses in dynamic pressure at the wake center

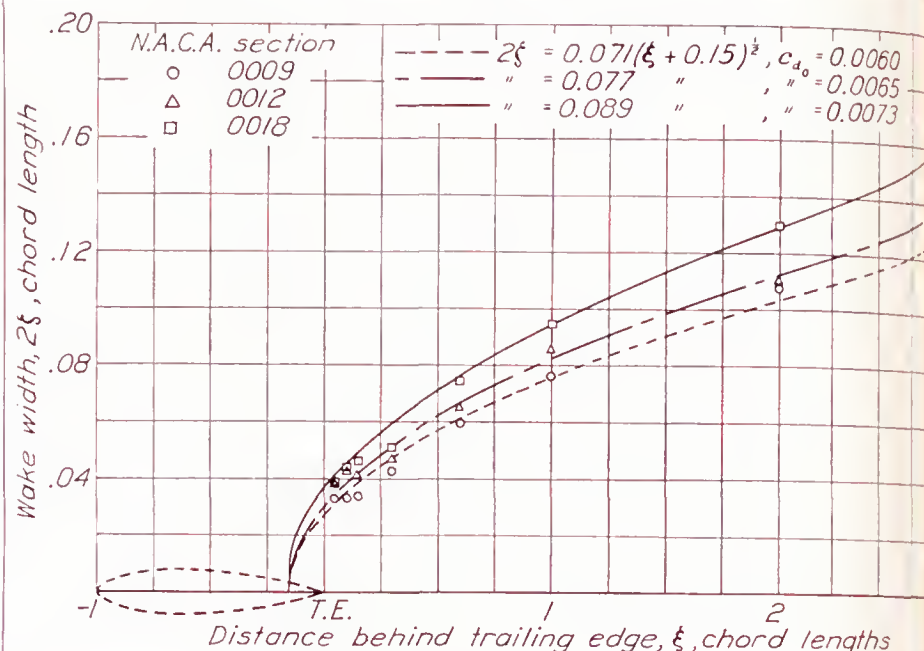


FIGURE 36.—Illustrations of parabolic relation between wake width and distance behind the trailing edge.

$\eta$  are plotted against  $c_{d0}$  (fig. 38); the predicted proportionality of  $\eta$  with  $c_{d0}^{\frac{1}{2}}$  is again substantiated. The variation in  $\eta$  with distance from the trailing edge is shown in figure 39 for the N. A. C. A. 0018 airfoil. In contrast to the Prandtl relation, the variation in this case appears to be with the inverse first power of  $\xi$ .

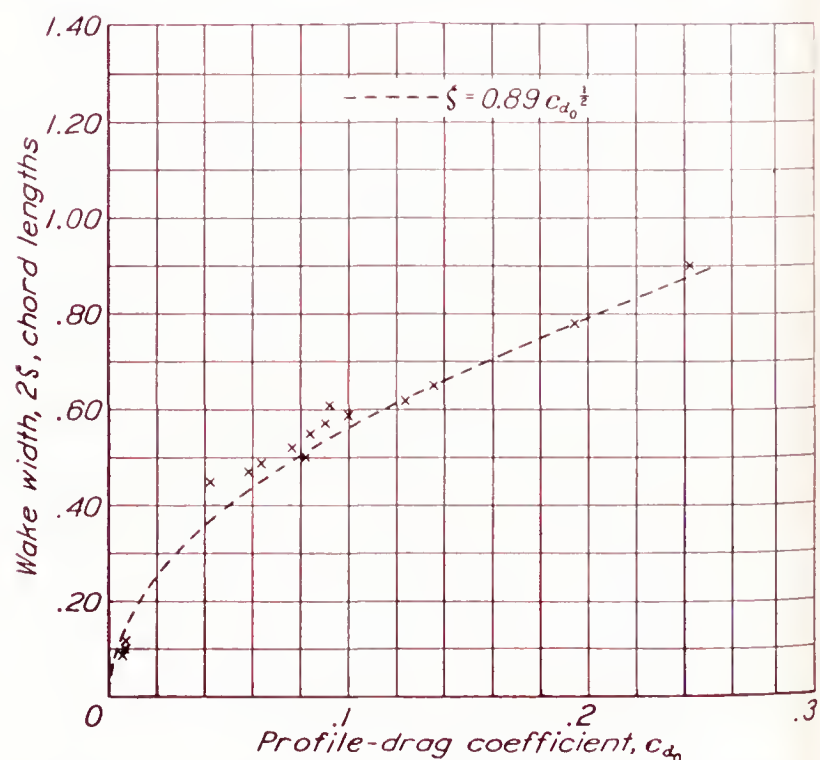


FIGURE 37.—Illustration of parabolic relation between wake width and profile drag. Distance behind trailing edge,  $\xi$ , 1.5 chord lengths. (Data from reference 13.)

rather than with the inverse  $\frac{1}{2}$  power. The discrepancy is doubtless associated with the high values of  $\eta$  near the trailing edge, for in Prandtl's discussion it was assumed that  $\eta$  is small. The inverse first power will be tentatively retained, although it is recognized that an obvious inconsistency exists for large values of  $\xi$ .



Applying the proportionality constants derived from the data leads to the equations

$$\eta = \frac{2.42 c_{d0}^{\frac{1}{2}}}{\xi + 0.3} \quad (3)$$

$$\zeta = 0.68 c_{d0}^{\frac{1}{2}} (\xi + 0.15)^{\frac{1}{2}} \quad (4)$$

Curves representing these equations are plotted in figures 40 and 41. Combining (3) and (4) leads to the equation

$$\zeta/\eta = 0.28(\xi + 0.15)^{\frac{1}{2}} (\xi + 0.3)$$

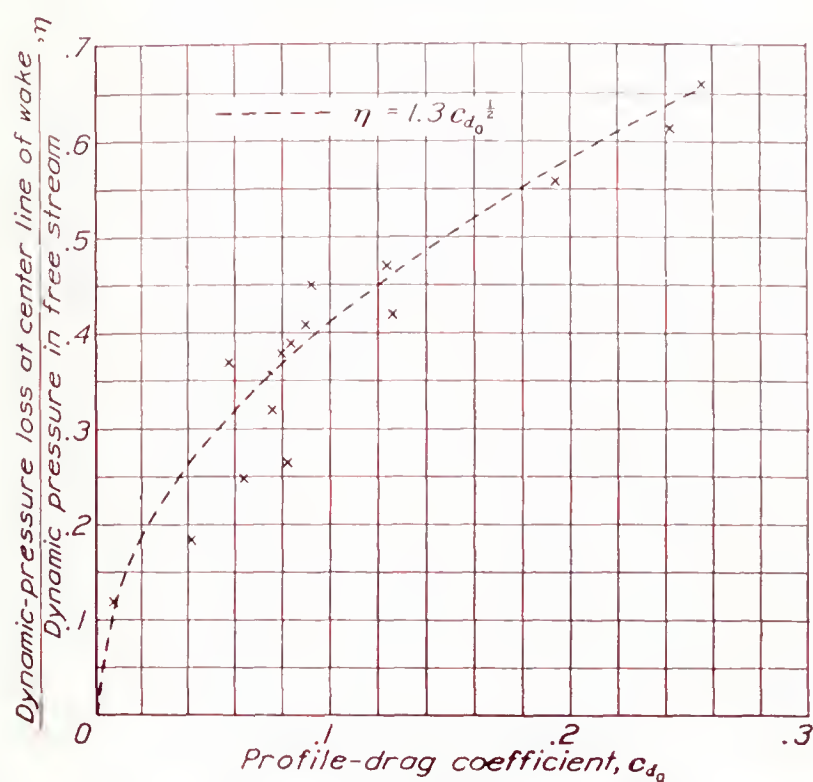


FIGURE 38.—Illustration of parabolic relation between maximum dynamic-pressure loss in wake and profile-drag coefficient. Distance behind trailing edge,  $\xi$ , 1.5 chord lengths. (Data from reference 13.)

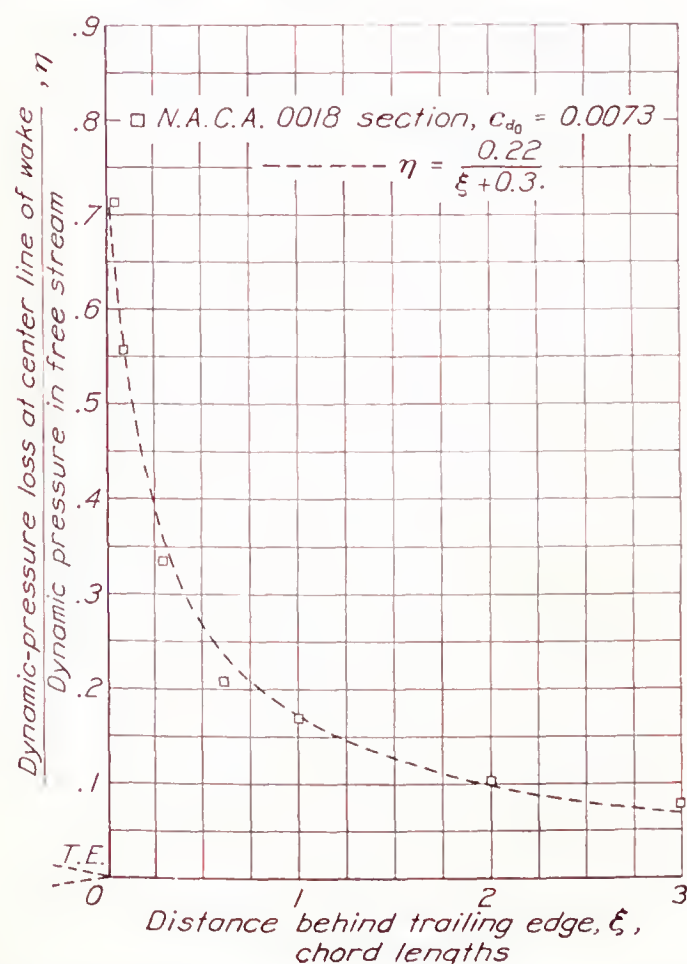


FIGURE 39.—Illustration of inverse relation between dynamic-pressure loss and distance behind the trailing edge for the N. A. C. A. 0018 airfoil.

The ratio of the wake width to the deficiency of dynamic pressure at the wake center is thus shown to be independent of the value of  $c_{d0}$ .

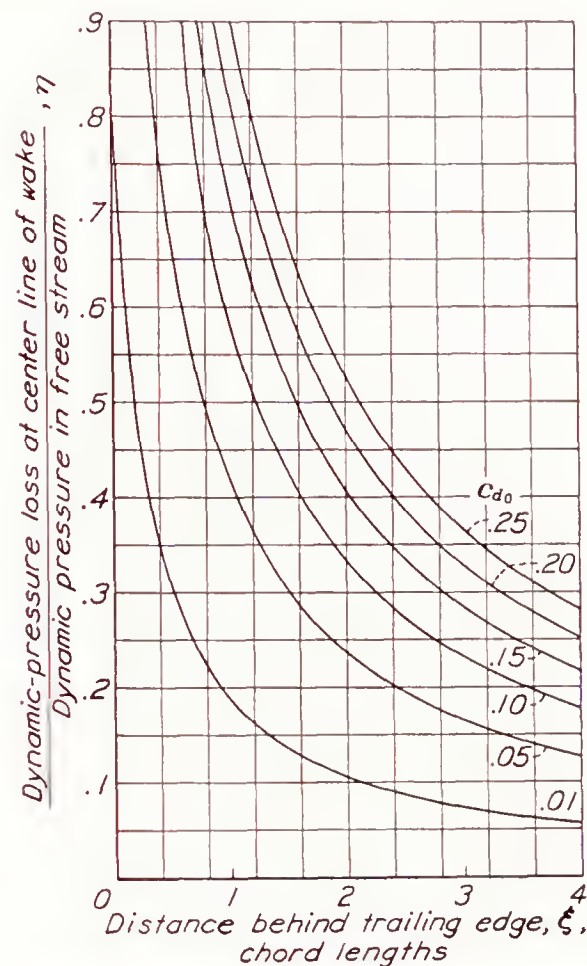


FIGURE 40.—Variation of maximum dynamic-pressure loss in the wake with distance behind the trailing edge.

$$\eta = \frac{2.42 c_{d0}^{\frac{1}{2}}}{\xi + 0.3}$$

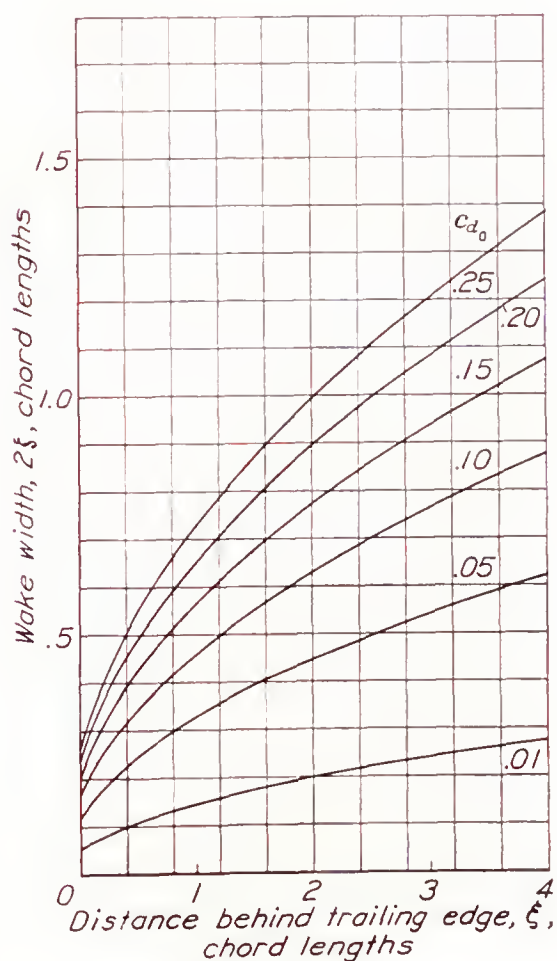


FIGURE 41.—Variation of wake width with distance behind the trailing edge.

$$\zeta = 0.68 c_{d0}^{\frac{1}{2}} (\xi + 0.15)^{\frac{1}{2}}$$

A complete description of the wake requires, in addition to  $\zeta$  and  $\eta$ , the variation of the relative loss in dynamic pressure  $\eta'$  with the distance  $\zeta'$  from the wake center line. The nondimensional wake profiles measured on the three symmetrical airfoils at different distances behind the trailing edge are shown in figure 42. Although the profiles vary somewhat, in the range of distances corresponding to the usual tail loca-

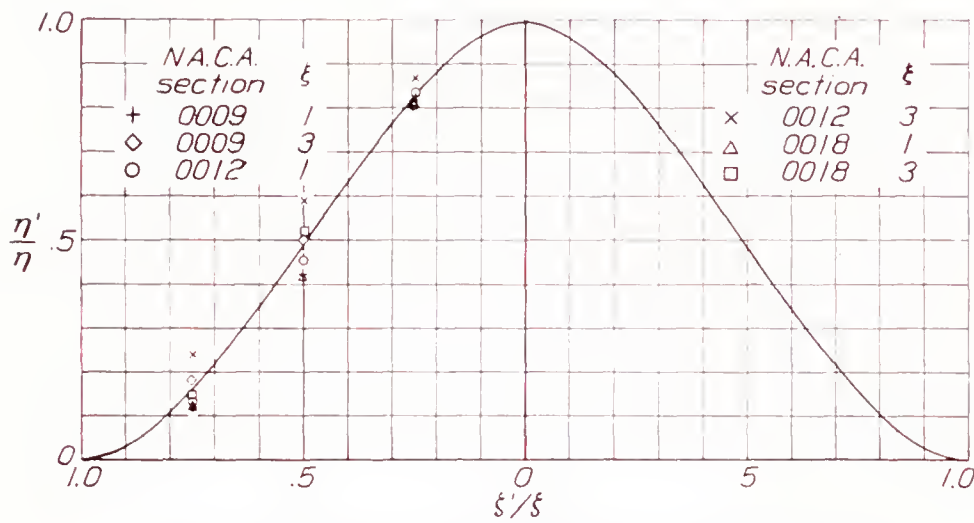


FIGURE 42.—Variation of dynamic-pressure loss across the wake.

$$\frac{\eta'}{\eta} = \left[ 1 - \left( \frac{\zeta'}{\zeta} \right)^{1.75} \right]^2$$

tion the profile shape may be closely approximated by either of the following empirical equations:

$$\left. \begin{aligned} \frac{\eta'}{\eta} &= \left[ 1 - \left( \frac{\zeta'}{\zeta} \right)^{1.75} \right]^2 \\ \frac{\eta'}{\eta} &= \cos^2 \frac{\pi \zeta'}{2\zeta} \end{aligned} \right\} (5)$$

Equation (2) can be rewritten as

$$c_{d0} = \int_{-\zeta}^{\zeta} \eta' d\zeta'$$

Substitution of values of  $\eta'$  from equation (5) and integration of the area under the wake profile provide the interesting result that

$$c_{d0} \cong \eta \zeta \quad (6)$$

An expression for  $c_{d0}$  in terms of  $\eta$  and  $\zeta$  may also be obtained from equations (3) and (4):

$$c_{d0} = \frac{\eta \zeta (\zeta + 0.3)}{1.65 (\zeta + 0.15)^{\frac{1}{2}}} = K_3 \eta \zeta \quad (7)$$

Values of  $K_3$  from equation (7) are plotted against  $\xi$  in figure 43. The value of  $K_3$  is unity at two chord lengths behind the airfoil; accordingly, only in this region are equations (6) and (7) in good agreement. The differences at the other values of  $\xi$  are attributed to the changing shape of the wake profiles with distance behind the airfoil and to the relative inaccuracy of equation (2) at small distances behind the wing.

**Wake of stalled airfoils.**—Although the empirical equations (3) and (4) for the wake dimensions were developed from results obtained at lifts below the stall, they apply with reasonable accuracy above the stall provided that the profile-drag coefficient of the stalled wing ahead of the particular region is known.

The rapid variation of  $c_{d0}$  with  $C_L$  at the stall and the inexact knowledge of the profile-drag coefficients of stalled or partly stalled sections usually make an exact calculation difficult. When these data are available, satisfactory agreement is obtained, as shown by the comparison of the experimental and the predicted wake dimensions for the case of the stalled U. S. A. 45 airfoil in figure 33.

Interesting comparisons of the wake of the U. S. A. 45 airfoil at lift coefficients slightly above and below the stall can be obtained from a study of figures 44 to 47. The wake contours are marked in fractions of the free-stream dynamic pressure ( $1 - \eta'$ ) and results are given for surveys in planes at three longitudinal distances behind the airfoil and in the plane of symmetry of the airfoil.

It may be noted for the surveys at a longitudinal distance of 1.18 chord lengths (figs. 44 (b) and 45 (b)) behind the trailing edge of the wing, which most nearly

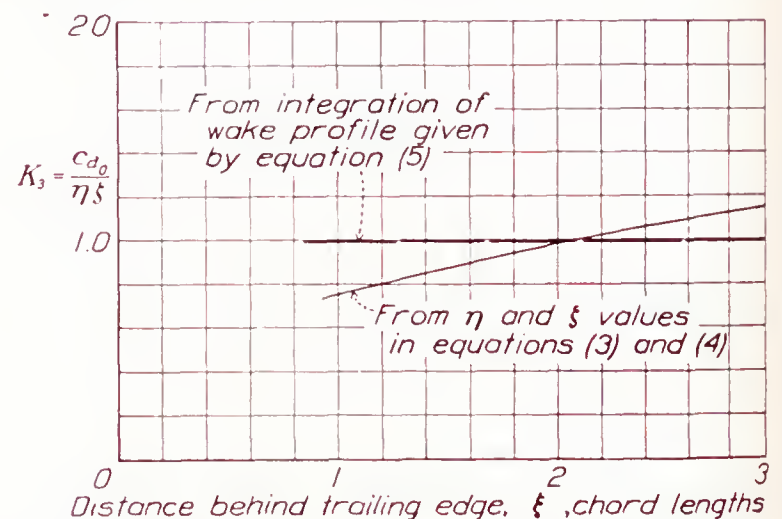


FIGURE 43.—Relation between profile-drag coefficient and the product of wake half width by maximum dynamic-pressure loss.

corresponds to the usual tail location, that the dynamic pressure in the plane of symmetry of the wing and at the wake center line changes from  $0.8 q_0$  for the unstalled condition to  $0.5 q_0$  at several degrees above the stall. The value of  $\eta$  is therefore increased from 0.2 to 0.5. The corresponding profile-drag coefficients for the unstalled and the stalled conditions are 0.018 and 0.130, respectively (reference 1).

Since  $\eta \propto c_{d0}^{\frac{1}{2}}$ , it may be expected that

$$\frac{\eta_{\text{stalled}}}{\eta_{\text{unstalled}}} \text{ and } \frac{c_{d0}^{\frac{1}{2}} \text{ stalled}}{c_{d0}^{\frac{1}{2}} \text{ unstalled}} \text{ should be equal.}$$

A fairly satisfactory agreement is found; thus, upon substitution of the numerical values, the first ratio gives 2.5 and the second gives 2.7.



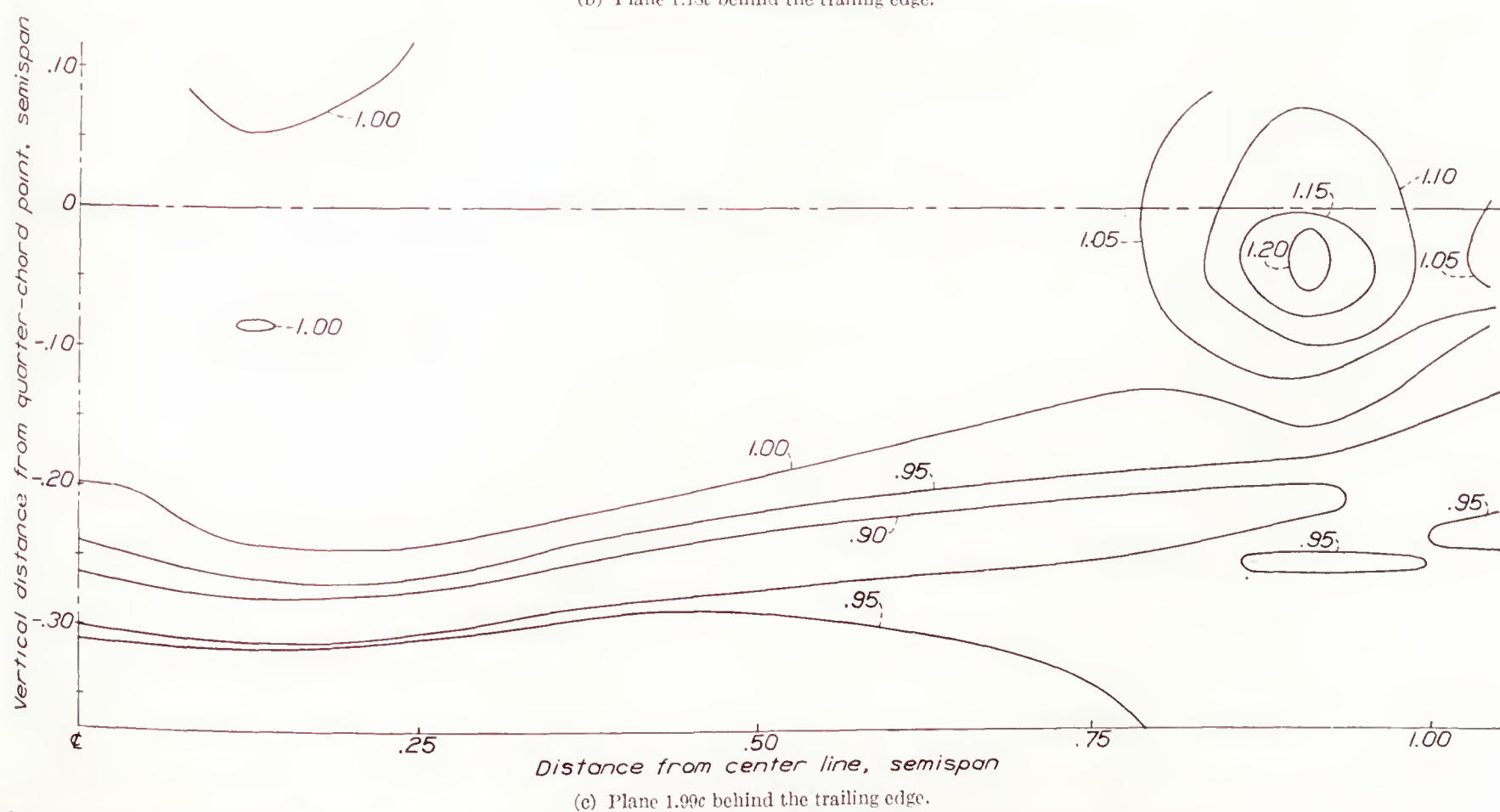
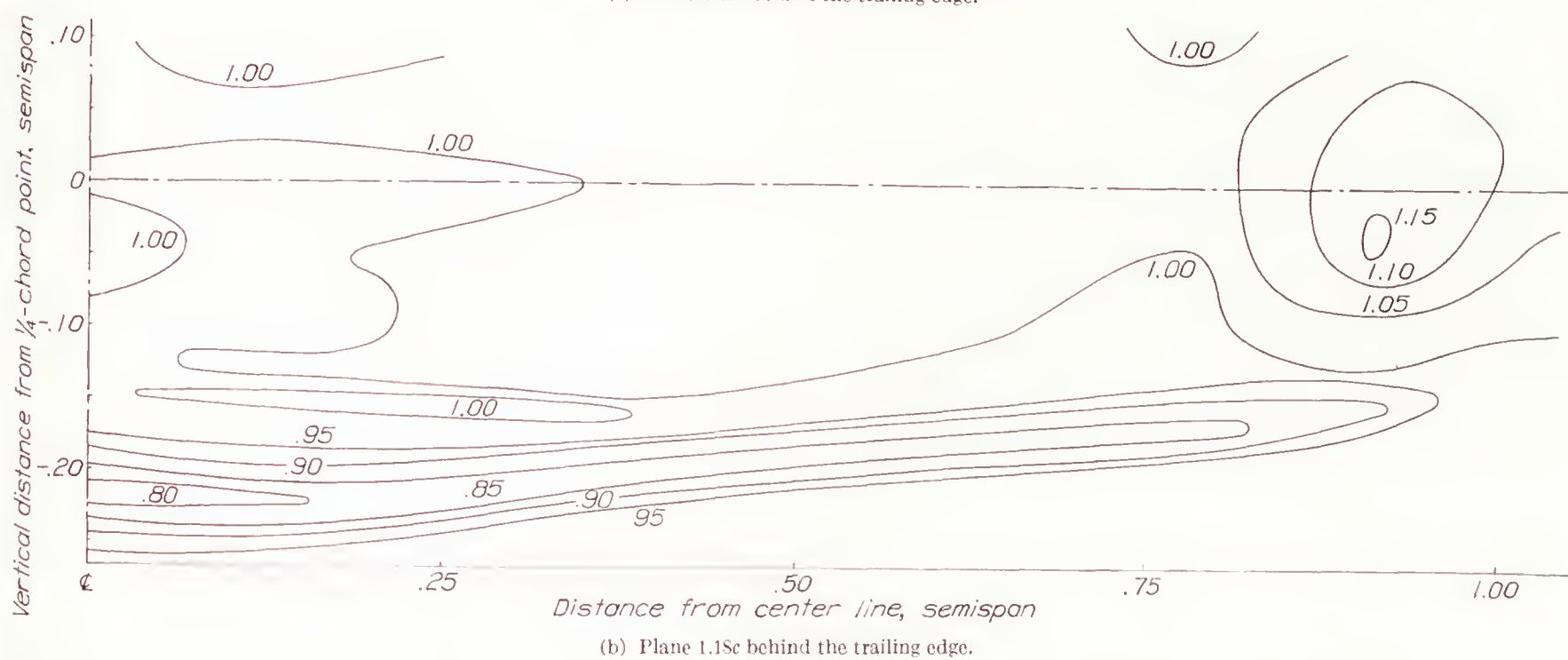
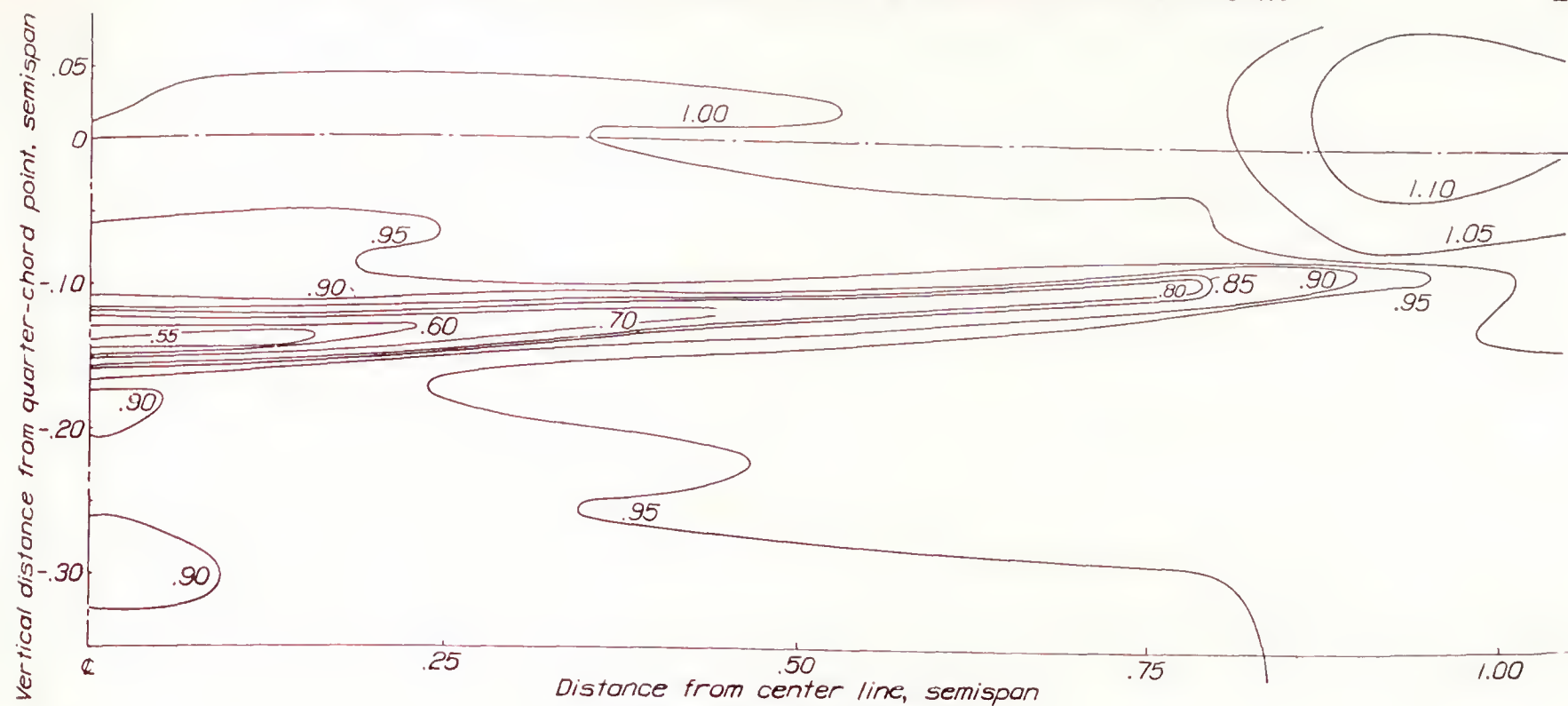


FIGURE 44.—Contour lines of dynamic pressure in planes parallel to the span and various distances behind the trailing edge of the center section of the U. S. A. 45 tapered airfoil. Dynamic pressures in fractions of free-stream dynamic pressure;  $\alpha$ ,  $15.2^\circ$ ;  $C_L$ , 1.35.

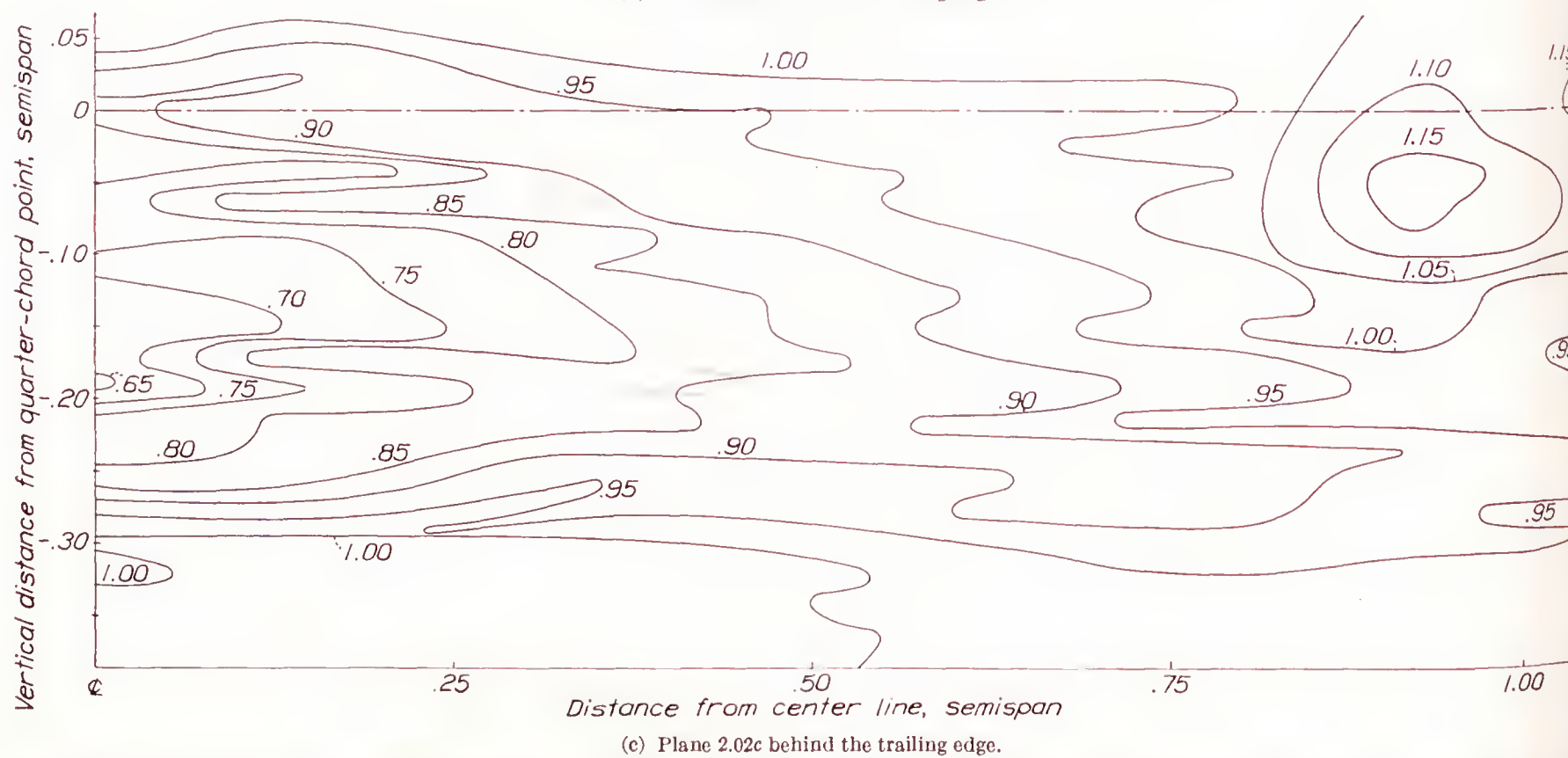
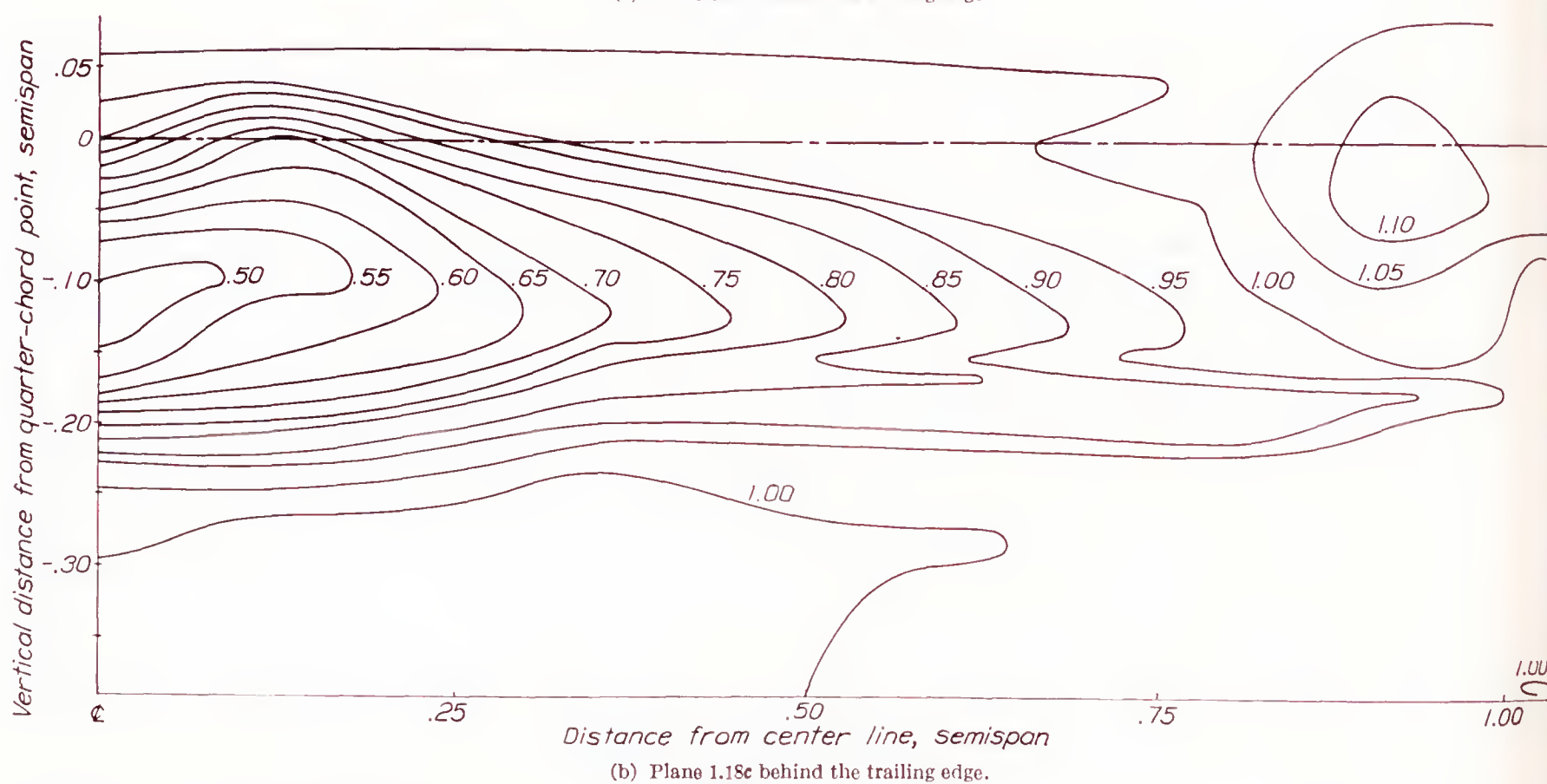
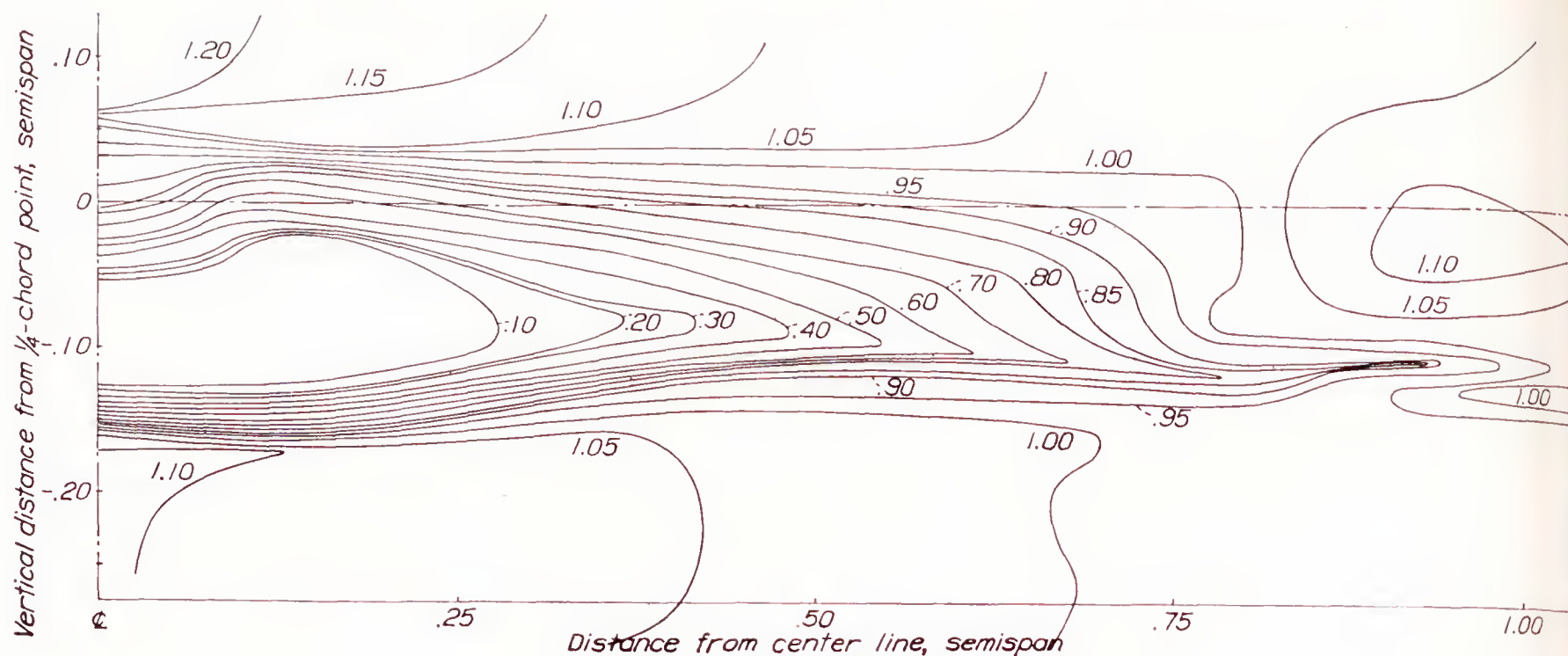


FIGURE 45.—Contour lines of dynamic pressure in planes parallel to the span and various distances behind the trailing edge of the center section of the U. S. A. 45 tapered airfoil. Dynamic pressures in fractions of free-stream dynamic pressure; airfoil stalled;  $\alpha$ ,  $18.5^\circ$ ;  $C_L$ , 1.00.



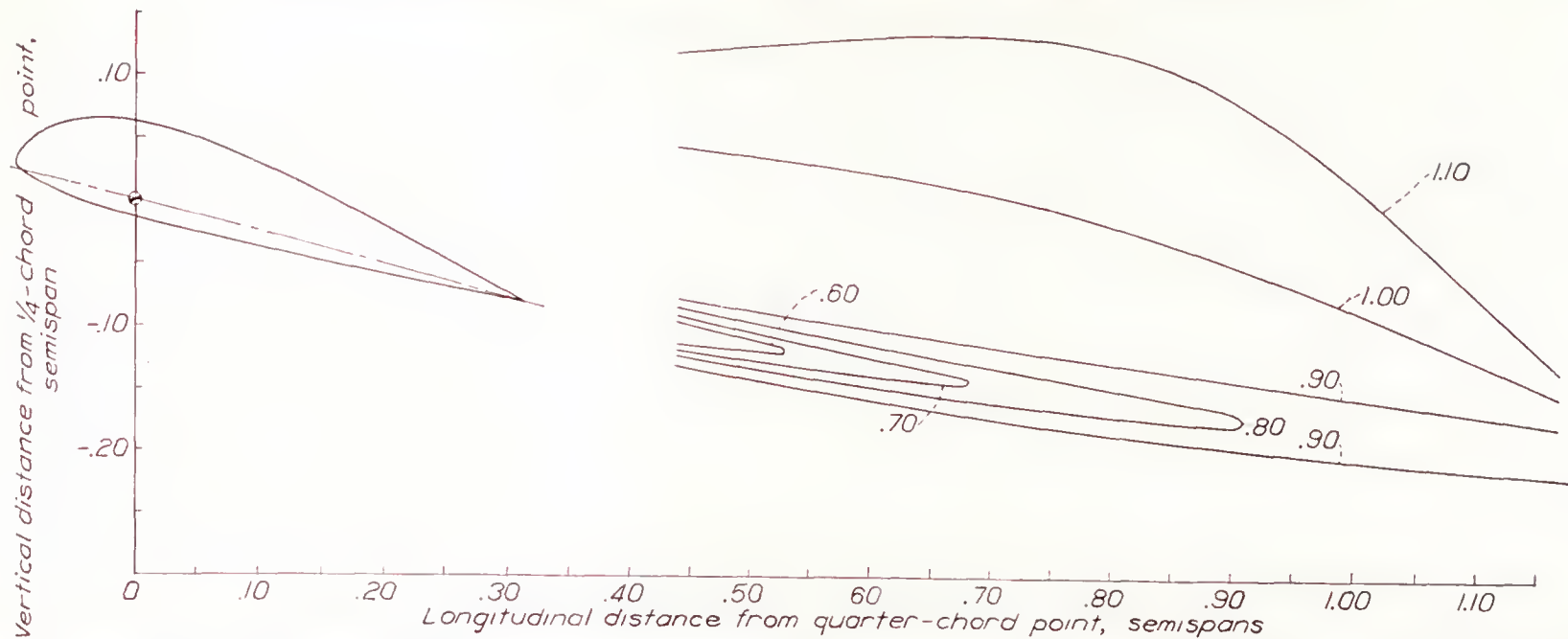


FIGURE 46.—Contour lines of dynamic pressure in the symmetry plane behind the U. S. A. 45 tapered airfoil. Dynamic pressures in fractions of free-stream dynamic pressure;  $\alpha$ ,  $15.2^\circ$ ;  $C_L$ , 1.35.

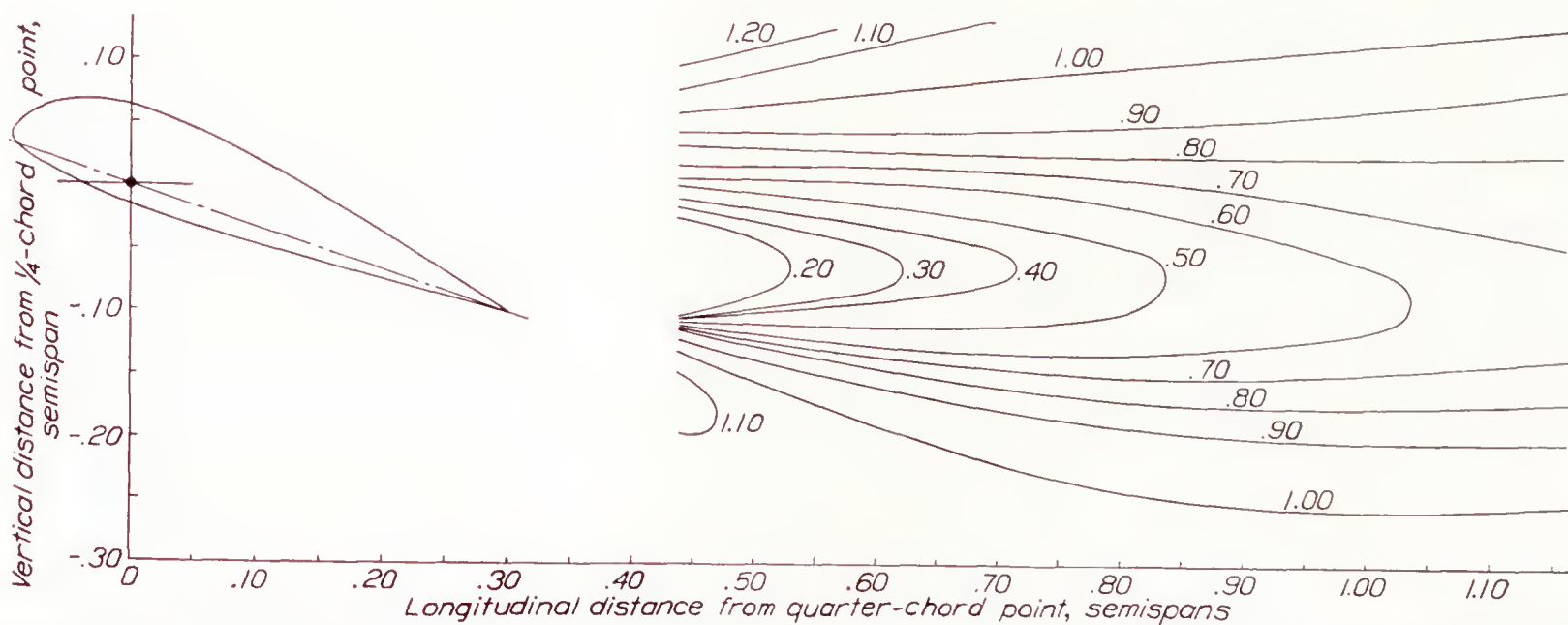


FIGURE 47.—Contour lines of dynamic pressure in the symmetry plane behind the U. S. A. 45 tapered airfoil. Dynamic pressures in fractions of free-stream dynamic pressure; airfoil stalled;  $\alpha$ ,  $18.5^\circ$ ;  $C_L$ , 1.00.

#### Calculation of the wake effect on downwash angle.—

From the equation  $\eta' = \eta \cos^2 \frac{\pi \zeta'}{2\zeta}$  and the definition of  $\eta'$ ,

$$\eta' = 1 - \frac{V^2}{V_0^2}$$

it follows that the velocity  $V$  at a point  $(\xi, \zeta)$  in the wake is given by

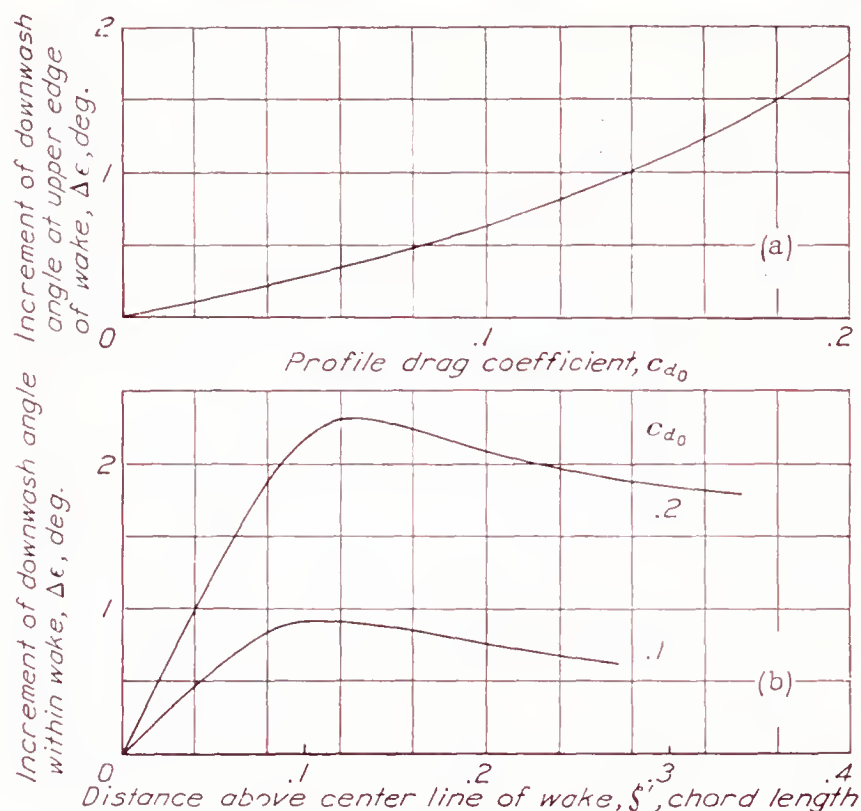
$$\frac{V}{V_0} = \sqrt{1 - \eta \cos^2 \frac{\pi \zeta'}{2\zeta}}$$

The flow (in two dimensions) passing between a point  $(\xi, 0)$  on the wake center and the point distant  $\zeta'$  above it  $(\xi, \zeta')$ , is

$$\psi = c \int_0^{\zeta'} V d\zeta' = c V_0 \int_0^{\zeta'} \sqrt{1 - \eta \cos^2 \frac{\pi \zeta'}{2\zeta}} d\zeta'$$

in which  $\eta$  and  $\zeta'$  are functions of  $c_{d0}$  and  $\xi$ . The stream function  $\psi$  can be evaluated from tables of elliptic integrals; for a particular pair of values of  $c_{d0}$  and  $\xi$ , it is a function of  $\zeta'$ . After this function has been computed for different values of  $\xi$ , streamlines may be drawn, for they are loci of points for which the values of  $\psi$  are constant. The inclination of the streamline passing through any point is the wake effect on the downwash angle at that point.

The calculation, as here described, applies for points lying within the wake ( $\xi'/\xi \leq 1$ ). The effect diminishes with distance from the edge of the wake. Inasmuch as the tail plane is not usually very far from the wake, the effect at the tail may be considered equal to that at the wake edge near it. Figure 48 shows the results of the calculations for  $c_{d0}=0.1$  and  $0.2$ , for  $\xi=1.5$ , which corresponds approximately to the usual longi-



(a) Variation with profile-drag coefficient.  
(b) Variation with distance above wake center line.

FIGURE 48.—Effect of wake on downwash at 1.5 chord lengths behind the trailing edge.

tudinal location of the tail plane. At much higher drag coefficients, the effect becomes so large that it is not possible to predict, with any accuracy, the downwash in the wake behind completely stalled airfoils. An example may be seen in the surveys behind the stalled low-wing monoplane with flaps down (fig. 22(a)); the profile-drag coefficient of the stalled section is about 0.5, and the maximum effect on the downwash angle is about  $15^\circ$ .

#### APPLICATION TO AN AIRPLANE

In order to show the application of the method, it will be applied to the case of the typical midwing-monoplane model, for which experimental data are available for comparison.

The calculations are based on the theoretical span load distributions of figure 49. For convenience, the curve for the plain wing is shown for  $C_{Lw}=1.00$  and that for the flap is for  $C_{Lf}=0.64$ . Figure 50 indicates the progress of the calculation for the case of flaps up, at  $C_L=1.1$ . The downwash-angle contours are shown first undisplaced and then displaced in the manner previously discussed, so that the center line passes through

the trailing edge and follows the downflow. For purposes of comparison with pitching-moment results, a correction factor of 0.95 should be applied in order to obtain the average value along the span of the tail. Incidentally, it may be noted that this center line and the wake center line which coincides with it fall below

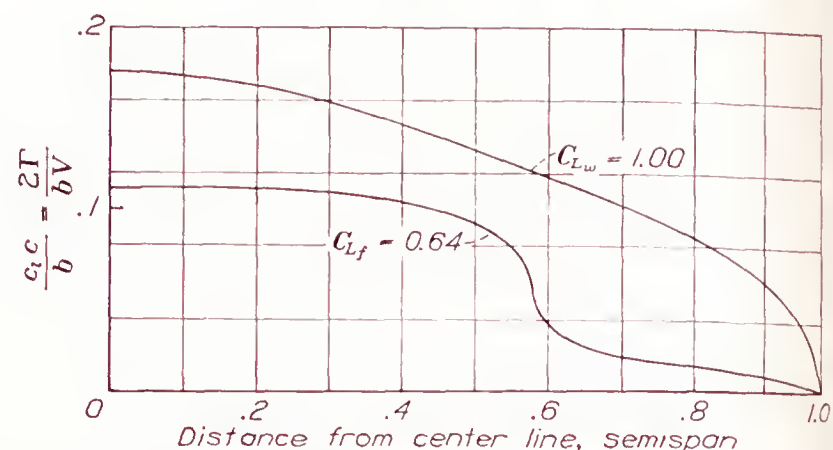
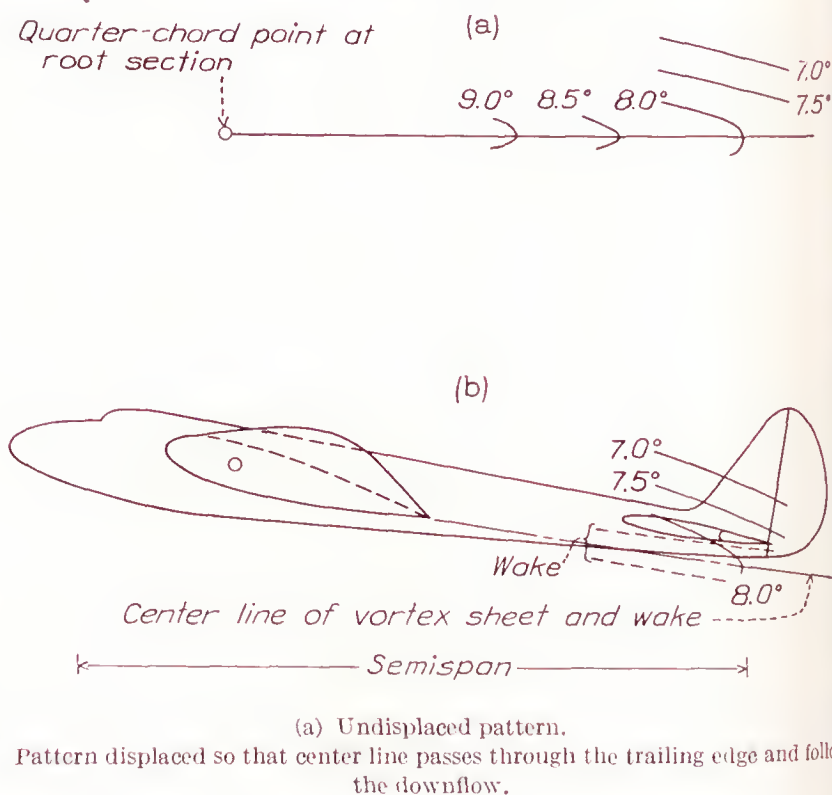


FIGURE 49.—Contributions of plain wing and of flap to the span load distribution for the midwing-monoplane model.

the tail and that the wake as computed by equation (4) does not flow over the tail.

Steps in the calculation for a case of the airplane with flaps down appear in figure 51. The undisplaced downwash-angle contours corresponding to the plain wing ( $C_{Lw}=0.96$ ) are shown as well as the contribution of the

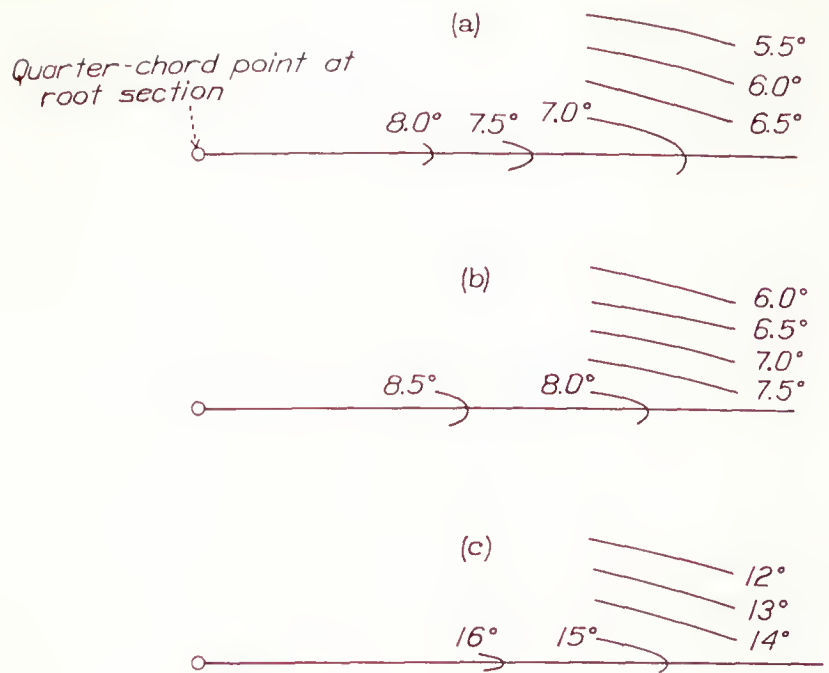


(a) Undisplaced pattern.  
(b) Pattern displaced so that center line passes through the trailing edge and follows the downflow.

FIGURE 50.—Theoretical downwash-angle contours and wake location for the midwing-monoplane model. Flaps up;  $C_L$ , 1.1.

flap ( $C_{Lf}=0.64$ ). Addition of these two contour maps leads to the contours shown in figure 51 (c). When the center line is so displaced that it passes through the wake origin, which in this case is just below the middle of the flap opening (see fig. 35), and follows the downflow, the contours of figure 51 (d) are obtained. The edge of the wake, as found by equation (4), again falls below the tail.





Center line of vortex sheet and wake

(a) Contribution of plain wing.

(b) Contribution of flap.

(c) Total calculated downwash, (a)+(b), undisplaced.

(d) Pattern displaced so that center line passes through the wake origin and follows the downflow.

FIGURE 51.—Theoretical downwash-angle contours and wake location for the midwing-monoplane model. Flaps down;  $C_{L_w}$ , 0.96;  $C_{L_f}$ , 0.64

The downwash angles so obtained should, for purposes of comparison with pitching-moment measurements, be corrected by a factor of 0.9 in order to get the average value along the span of the tail and by an increment of  $0.5^\circ$ , which is the estimated effect of the wake.

Experimental values of the downwash angles were obtained by comparing tail-off pitching moments with tail-on pitching moments obtained at different stabilizer settings. The stabilizer settings corresponding to zero load on the tail are found by interpolation or extrapolation. From these values, the corresponding angles of attack of the airplane, and the jet-boundary corrections (reference 4), the downwash angles are derived. The agreement between theory and experiment is shown in figure 52 to be satisfactory, except at the higher angles of attack, where the tips are stalled.

This case may be considered a particularly favorable one, for the model was well streamlined and had a relatively small fuselage. It is likely, however, that, as in the present example, interference will be small in modern carefully streamlined airplanes.

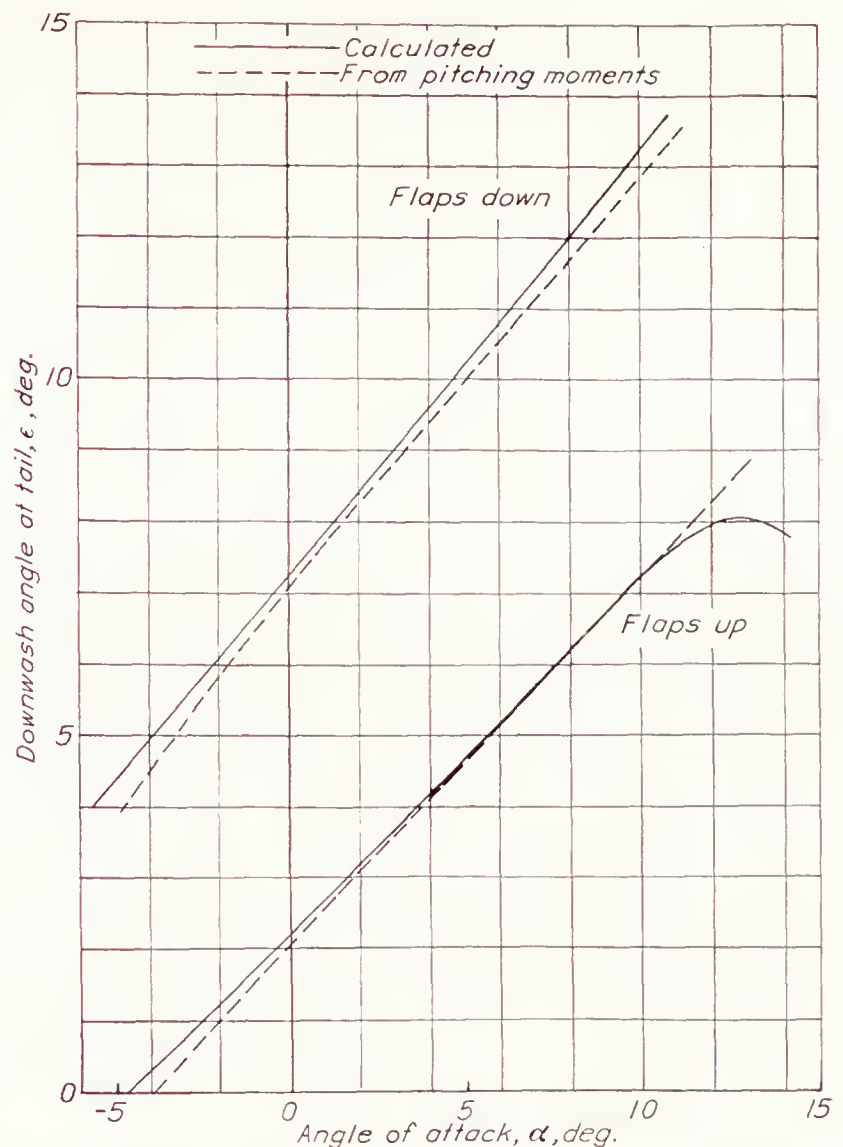


FIGURE 52.—Comparison of calculated and experimental downwash at the tail of the midwing-monoplane model.

## CONCLUSIONS

1. The Biot-Savart equation, the theoretical span load distribution, and the lifting-line concept provide a sufficient basis for computation of the downwash angle behind airfoils with and without flaps.

2. The concentration of the trailing vortex sheet into a single pair of trailing vortices may be neglected for purposes of downwash computations.

3. The potential flow about an airfoil section is closely approximated by that about a vortex at its lifting line for distances greater than one chord from the airfoil trailing edge.

4. The vertical displacement of the trailing vortex sheet due to the downflow must be taken into account in the calculations.

5. The loss in dynamic pressure at the wake center is directly proportional to the square root of the profile-drag coefficient and inversely proportional to the distance behind the airfoil trailing edge.

6. The wake width is directly proportional to the square root of the product of the profile-drag coefficient and the distance behind the airfoil.

7. The wake profile may be accurately given by an empirical expression involving as parameters only the wake width and the loss in dynamic pressure at the wake center.

8. The wake parameters are relatively independent of the airfoil lift, and the relations for the unstalled airfoil apply with almost equal accuracy above the stall.

LANGLEY MEMORIAL AERONAUTICAL LABORATORY,  
NATIONAL ADVISORY COMMITTEE FOR AERONAUTICS,  
LANGLEY FIELD, VA., *June 23, 1938.*

#### REFERENCES

1. Parsons, John F.: Full-Scale Force and Pressure-Distribution Tests on a Tapered U. S. A. 45 Airfoil. T. N. No. 521, N. A. C. A., 1935.
2. Silverstein, Abe: Scale Effect on Clark Y Airfoil Characteristics from N. A. C. A. Full-Scale Wind-Tunnel Tests. T. R. No. 502, N. A. C. A., 1934.
3. DeFrance, Smith J.: The N. A. C. A. Full-Scale Wind Tunnel. T. R. No. 459, N. A. C. A., 1933.
4. Silverstein, Abe, and Katzoff, S.: Experimental Investigation of Wind-Tunnel Interference on the Downwash behind an Airfoil. T. R. No. 609, N. A. C. A., 1937.
5. Silverstein, Abe, and Katzoff, S.: Design Charts for Predicting Downwash Angles and Wake Characteristics behind Plain and Flapped Wings. T. R. No. 648, N. A. C. A., 1939.
6. Theodorsen, Theodore: Theory of Wing Sections of Arbitrary Shape. T. R. No. 411, N. A. C. A., 1931.
7. Kaden, H.: Aufwicklung einer unstablen Unstetigkeitsfläche. Ingenieur-Archiv, II Band, no. 2, May 1931, S. 140-168.
8. Muttray H.: Investigations on the Amount of Downwash behind Rectangular and Elliptical Wings. T. M. No. 787, N. A. C. A., 1936.
9. Glauert, H.: The Elements of Aerofoil and Airscrew Theory. Cambridge University Press, 1926, p. 138.
10. Lotz, Irmgard: Berechnung der Auftriebsverteilung beliebig geformter Flügel. Z. F. M., 22. Jahrg., 7. Heft, 14. April 1931, S. 189-195.
11. Pearson, H. A.: Span Load Distribution for Tapered Wings with Partial-Span Flaps. T. R. No. 585, N. A. C. A., 1937.
12. Betz, A.: A Method for the Direct Determination of Wing-Section Drag. T. M. No. 337, N. A. C. A., 1925.
13. Clark, K. W., and Kirkby, F. W.: Wind Tunnel Tests of the Characteristics of Wing Flaps and Their Wakes. R. & M. No. 1698, British A. R. C., 1936.
14. Prandtl, L.: The Mechanics of Viscous Fluids. Spread of Turbulence. Vol. III, div. G, sec. 25 of Aerodynamic Theory, W. F. Durand, ed., Julius Springer (Berlin), 1935, p. 165.



# REPORT No. 652

## AIR FLOW IN THE BOUNDARY LAYER OF AN ELLIPTIC CYLINDER

By G. B. SCHUBAUER

### SUMMARY

*The boundary layer of an elliptic cylinder of major and minor axes 11.78 and 3.98 inches, respectively, was investigated in an air stream in which the turbulence could be varied. Conditions were arranged so that the flow was two-dimensional with the major axis of the ellipse parallel to the undisturbed stream. Speed distributions across the boundary layer were determined with a hot-wire anemometer at a number of positions about the surface for the lowest and highest intensities of turbulence, with the air speed in both cases sufficiently high to produce a turbulent boundary layer over the downstream part of the surface. The magnitude and the frequency of the speed fluctuations in the boundary layer were also measured by the use of the conventional type of hot-wire turbulence apparatus. Stream turbulence was found to affect both the nature of transition from laminar to turbulent flow in the layer and the position on the surface at which transition occurred.*

*Transition was then investigated in detail with stream turbulence of several different scales and intensities. It was found that the position of transition could be expressed as a function of the intensity divided by the fifth root of the scale.*

### INTRODUCTION

The present boundary-layer investigation was conducted on an elliptic cylinder of major and minor axes 11.78 and 3.98 inches, respectively, placed in the 4½-foot wind tunnel of the National Bureau of Standards with the major axis of the ellipse parallel to the wind. This same cylinder, similarly placed in the same tunnel, was used in earlier work (reference 1), in which the laminar boundary layer and the laminar separation were investigated at a low air speed. The present investigation was carried out for the purpose of supplementing the earlier work with information on the boundary layer under such conditions of air speed and turbulence that transition occurs and the layer is partly laminar and partly turbulent. The investigation comprised the measurement of mean speeds and speed fluctuations in various sections of the boundary layer and the location of the transition and the separation points. Special attention was given to the nature and the position of the transition and the manner in which they are affected by stream turbulence and Reynolds Number.

In the work reported in reference 1, the air speed was about 12 feet per second, and it was assumed that the

boundary layer remained in the laminar condition until after separation because the separation point remained fixed and the pressure distribution about the cylinder was unaffected until an air speed of about 15 feet per second was reached. Above 15 feet per second the separation point began to shift toward the trailing edge and the pressure distribution began to change, indicating that transition was beginning either in the attached part of the layer or in the separated layer near enough to the cylinder to affect the flow. It was therefore assumed that a turbulent layer could be obtained over the rear part of the cylinder simply by increasing the speed. Accordingly, at the outset of the present work, the pressure distribution was determined at successively increasing speeds until a critical speed region, similar to that found with spheres, had been passed and the pressure distribution again attained a stationary value. The critical region ended in the neighborhood of 55 feet per second. Since the downstream part of the boundary layer was assumed to be turbulent above the critical region, a speed of 70 feet per second was chosen as a suitable working speed for the boundary-layer investigation.

Not until the speed profiles in the boundary layer had been determined at numerous points about the surface and studies of separation had been made, was it discovered that the actual flow conditions were more complicated than those originally assumed. There first occurred the separation of a layer having the general characteristics of a laminar layer; this separation was followed by a reattachment of the layer to the surface as a turbulent layer; and finally the separation of the turbulent layer occurred. In this part of the work, the stream turbulence was as low as could be attained in the tunnel.

Under such conditions the turbulent layer was too limited in extent for the type of investigation originally planned, and an effort was made to obtain a greater length of turbulent layer by increasing the turbulence of the air stream with a 1-inch square mesh screen placed 18 inches upstream from the leading edge of the cylinder. This increased turbulence was found to have a marked effect on the layer, in that a turbulent layer developed without the intervening separation. Since the layer was now more like that originally sought, the measurements were repeated.



When it was found from the measurements that the amount of stream turbulence had an important effect on transition from laminar to turbulent flow in the layer, the investigation was extended to include a detailed study of transition as a function of both the scale and the intensity of the turbulence.

The present investigation therefore covers:

1. Boundary-layer phenomena at low stream turbulence.
2. Boundary-layer phenomena at high stream turbulence.

a smooth surface obtained by alternate varnishing and sandpapering and finally polishing with crocus paper. Twenty-one pressure orifices were inserted in the cylinder  $2\frac{1}{2}$  inches below the center for obtaining the pressure distribution over the surface. Eighteen of the orifices were distributed around the side on which boundary-layer measurements were to be made, one was at the leading edge and two were placed on the opposite side near the leading edge to aid in aligning the cylinder with its major axis parallel to the wind direction. Only this position was used in the investigation.

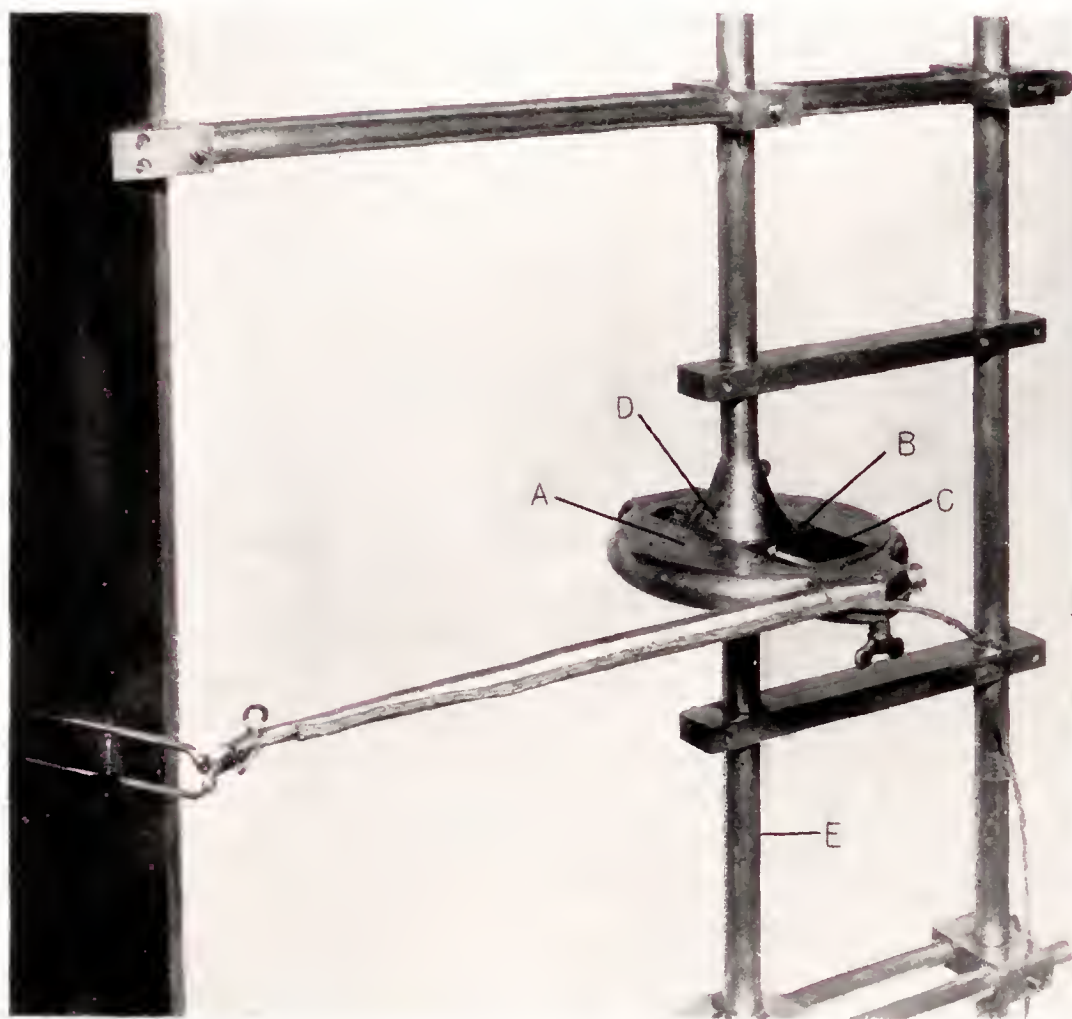


FIGURE 1.—Photograph showing details of hot-wire anemometer and traversing equipment. A, micrometer carriage; B, fixed way; C, micrometer screw; D, housing; E, tubular member.

3. The effect of intensity and scale of stream turbulence on transition at a fixed Reynolds Number.

The work was conducted at the National Bureau of Standards with the cooperation and financial assistance of the National Advisory Committee for Aeronautics.

The author wishes to acknowledge his indebtedness to Dr. Hugh L. Dryden for many valuable suggestions, to W. H. Boyd for the design and construction of traversing equipment, and to W. C. Mock, Jr., for his assistance with the experimental program.

#### DESCRIPTION OF ELLIPTIC CYLINDER, HOT-WIRE ANEMOMETER, AND TRAVERSING EQUIPMENT

##### THE ELLIPTIC CYLINDER

As stated in the introduction, the elliptic cylinder had major and minor axes of 11.78 and 3.98 inches, respectively, and was  $4\frac{1}{2}$  feet long. When mounted vertically in the wind tunnel, it extended completely from the upper to the lower face of the octagonal working section. The cylinder was made of wood, and had



FIGURE 2.—Photograph showing over-all view of elliptic cylinder and traversing equipment.

##### HOT-WIRE ANEMOMETER AND TRAVERSING EQUIPMENT

Speed measurements in the boundary layer were made with a hot-wire anemometer consisting of a fine platinum wire mounted on the end of a pair of prongs through which an electric current could be passed to heat the wire. The particular arrangement of the anemometer used for the measurement of mean speeds is shown with the traversing mechanism in figure 1. The requirement that the prongs and the mounting be rigid enough to withstand deflection in the wind and still cause no measurable interference led to the arrangement shown, in which the traversing assembly was placed downstream from the cylinder. The distance from the trailing edge of the cylinder to the nearest point of the micrometer carriage A was 14 inches. In order to



prevent accidental movement between the cylinder and the wire, the cylinder and the traversing equipment were rigidly attached to two end boards, the entire assembly forming the unit shown in figure 2. When the unit was placed in the tunnel, the end boards were fitted into two rectangular openings in the tunnel walls.

Interference from the prongs themselves was made negligibly small by tapering and by using fine steel needles about 1 inch long to form the ends. There still remained a troublesome flow disturbance caused by the wire itself, when an attempt was made to use the customary 0.002-inch-diameter wire. It turned out to be necessary to use a wire 0.00063 inch in diameter and to limit its length as much as possible. Even with the smaller size of wire some interference persisted, as evidenced by a slight shift in the position of separation back of the wire when the wire was in some upstream part of the boundary layer.

Traversing of the wire through the boundary layer was accomplished by movement of carriage A with respect to the fixed ways B shown in figure 1. In this arrangement the micrometer screw C was fixed to the carriage and the two were propelled together by a nut inside housing D. The nut was rotated by bevel gears from which a shaft extended to the outside of the tunnel through the tubular member E. Carriage A could be rotated about E as an axis to permit traversing along any normal to the surface of the cylinder.

#### DETERMINATION OF MEAN SPEED

In the measurement of mean speed with the hot-wire anemometer, the method known as the "constant temperature method" was used; that is, the current through the wire was varied with the speed so as to maintain the wire at some fixed temperature above that of the surrounding air. The electric circuit was arranged so that the wire formed one arm of a Wheatstone bridge. With a very small bridge current, the cold resistance of the wire was measured. Then the resistance of the opposite arm of the bridge was increased by a definite amount and a balance of the bridge was again obtained by increasing the bridge current until the wire resistance increased through heating by the amount of the added resistance. In this way a definite temperature rise was maintained by the bridge. If  $E$  is the voltage drop across the wire and  $R$  is its resistance, then by the well-known hot-wire equation due to King (reference 2), the heat loss  $E^2/R$  may be expressed as a function of the air speed, the dimensions of the wire, the temperature rise, and the properties of the air. King's equation is useful to show the quantities upon which the heat loss depends but cannot be relied upon to determine the absolute value of the speed. Hence calibration of the instrument at known speeds is necessary. Using the present procedure, readings of  $E$  on a potentiometer and of  $R$  on the Wheatstone bridge served, with a calibration curve, to determine the speed.

Frequent calibrations were made necessary by a steady change with use in the cooling properties of the wire. The cause of this change was found to be the gradual accumulation of very fine dust from the air on the upstream side of the wire. When the cause was discovered, precautions were taken to suppress dust as much as possible. This precaution improved the conditions somewhat but frequent calibration was continued. Changes in the density and the thermal conductivity of the air, upon which the heat loss also depends, were never large enough to cause any detectable change from one calibration to another.

#### HEAT LOSS TO THE SURFACE

A disadvantage of the hot-wire anemometer, when applied to the measurement of speed very near to a surface, is the error caused by heat loss from the wire to the surface. The error, causing the speed to appear too high, becomes greater the nearer the surface the measurement is made. Several investigators have endeavored to determine the heat loss to the surface by conducting an experiment in still air at several wire temperatures to find the difference between the rate of heat loss near the surface and that far from the surface. In this manner the heat loss is found as a function of the wire temperature and the distance from the surface. Dryden (reference 3) found the heat loss to an aluminum plate to be given empirically by

$$H_p = 1.27 \times 10^{-8} \frac{l}{y} \theta^2 \quad (1)$$

where  $H_p$ , is the heat loss to the plate, watts.

$l$ , the length of the wire, inches.

$y$ , the distance from the plate, inches.

$\theta$ , the temperature difference between the wire and the plate, degrees C.

A similar relation with the constant roughly  $1.0 \times 10^{-8}$  was found for a varnished wooden surface in the earlier work on the elliptic cylinder.

From the obvious error often introduced by applying the correction, corrections based on such determinations made in still air are known to be much too large for moving air. Needless to say, it would be very difficult to determine a heat-loss correction for moving air that would apply under all conditions.

In view of these difficulties, a procedure that obviated the need for heat-loss corrections was adopted in the present work. By equation (1), the heat loss to the surface is proportional to  $\theta^2$  and, by King's hot-wire equation, the heat loss to the air is proportional to  $\theta$ . Obviously, the smaller  $\theta$  is made, the less is the amount of the heat lost to the surface relative to that lost to the air. The procedure adopted was to make  $\theta$  small enough so that the heat lost to the surface was insignificant compared with that lost to the air. Using several values of  $\theta$ , measurements of the speed were made in that part of the boundary layer where the speed near the surface was low, and it was found that values of  $\theta$



as high as  $150^{\circ}\text{C}$ . caused no measurable error. How much higher the allowable value of  $\theta$  might have been was not determined, since  $150^{\circ}\text{C}$ . was sufficient to give the desired sensitivity at the highest speed.

#### DETERMINATION OF SPEED FLUCTUATIONS

The measurement of speed fluctuations with the hot-wire anemometer required a technique considerably different from that described. The problem here is one of measuring variations in speed from the mean, when such variations occur with frequencies ranging from a few cycles per second to over 1,000. Only variations in magnitude of the velocity are considered here because the cooling of a simple hot wire does not respond to changes in direction. Hence the term "fluctuation" refers to an increase or a decrease in the instantaneous speed only. The fluctuations vary the wire temperature and hence the voltage drop across the wire; and, when the relation between speed change and voltage change is known, the voltage fluctuations serve as a measure of the speed fluctuations. The important features of the wire are fineness, to reduce lag arising from thermal capacity, and shortness, to reduce the error caused by variations in the instantaneous value of the fluctuations from point to point. The shortness requirement limits the magnitude of the

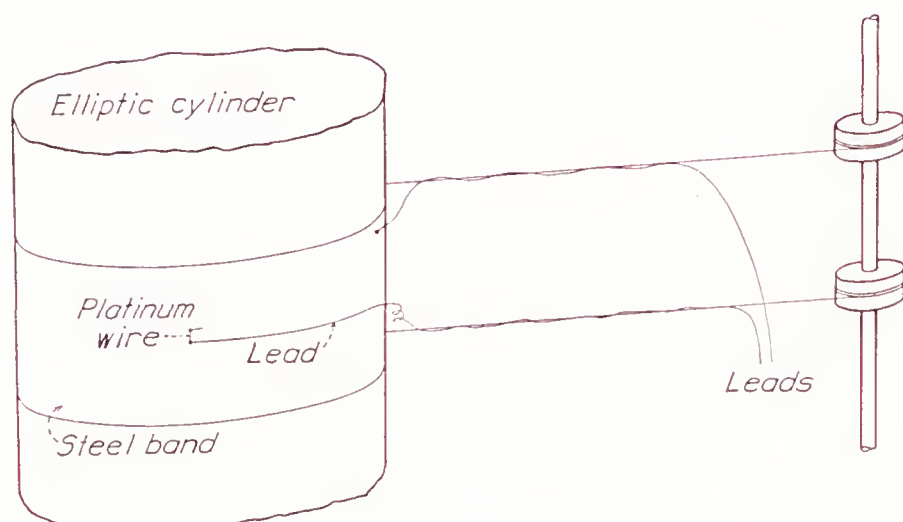


FIGURE 3.—Diagram of sliding band carrying hot wire.

voltage fluctuations and makes it necessary to amplify the voltages before they can be measured.

The amplifier used was the one described in reference 4. A compensating circuit is incorporated in the amplifier by which it is possible to compensate for the lag of the hot wire, if the diameter of the wire is not too large. The range of compensation was such that a wire 0.00063 inch in diameter could be used and the over-all gain of the amplifier was sufficient to allow the length of the wire to be reduced to about 0.15 inch. The wire was then of the same diameter as that used for measuring mean speeds but was only about one-seventh as long.

In this case, the mean value of the heating current rather than the mean temperature, was kept constant at all speeds and the voltage fluctuations were read on

a thermal-type milliammeter connected to the output of the amplifier. The calibration consisted in measuring the mean voltage at different speeds with the same constant value of the current. The method of using the calibration to calculate the root-mean-square of the speed fluctuations is described in reference 5. The lag characteristics of the wire and the adjustment of the compensation were calculated by the method described in reference 6. With the correct compensation, the over-all response of wire and amplifier was uniform from 3 to 1,000 cycles per second. Most of the fluctuations fall within this range.

When details of the fluctuations such as wave form and frequency were to be studied, a cathode-ray oscillograph was connected to the output of the amplifier and the screen photographed with a moving-film camera.

#### HOT WIRE MOUNTED ON SLIDING BAND

In the course of the experiment the advantage of being able to move the hot wire around the contour of the ellipse at a small fixed distance from the surface became apparent. The need for doing so first arose when it became necessary to follow the changes in mean speed from point to point about the surface in order to detect transition. After several attempts to use a modification of the traversing equipment and the hot-wire anemometer shown in figure 1 had proved unsuccessful owing to the difficulty of keeping the distance between the wire and the surface constant, the scheme of placing a hot wire on a sliding band attached to the cylinder was tried. A strip of sheet steel 0.002 inch thick and 6 inches wide was fitted about the elliptic cylinder in such manner as to make a snugly fitting band capable of being slipped around the cylinder and remaining in any desired position. The arrangement is shown in figure 3. At the center of the band a short length of platinum wire of the usual 0.00063-inch diameter was mounted parallel to the surface and normal to the direction of flow. One end of the wire was soldered to a fine copper lead cemented to the surface and suitably insulated and the other was soldered to a short lead of the same diameter grounded to the band. The spacing between the platinum wire and the surface was usually 0.008 inch. In order to slip the band about the surface from the outside of the tunnel, two steel wires were attached to the band on the side opposite the platinum wire and were run to pulleys and shaft, as shown in figure 3.

The disturbance caused by the band was investigated by coating the surface with a mixture of kerosene and lampblack and noting the pattern produced in a wind of about 60 feet per second. While using the kerosene and lampblack-method to investigate separation, it was found that the lampblack not only showed the position of separation but also afforded a very sensitive indication of the presence of small particles of dirt on the



surface by the distortion produced in the line of accumulated lampblack at separation. With the band in place, the line showed small kinks at the edges of the band and a third kink at the center caused by the wire. Since the general course of the line was the same as for the bare cylinder, it was concluded that the disturbance was of no consequence.

The present arrangement turned out to be useful in the study of speed fluctuations as well as of mean speeds. The only modification required in the general scheme was the replacement of the grounded lead with an insulated lead to avoid troubles from a double ground.

#### METHOD OF PRESENTING OBSERVATIONS

Before the elliptic cylinder was installed in the tunnel, a standard pitot-static tube was placed at the position to be occupied by the leading edge of the cylinder and the speed was determined for this position in terms of the pressure at a tunnel-wall orifice about 8 feet upstream. The pressure at this orifice was then used to calculate the speed when the cylinder was in the tunnel. This speed, denoted by  $U_0$ , is therefore the speed which would prevail in the tunnel with the cylinder absent and, consequently, may be regarded as the speed of the undisturbed stream.

The actual speed near the cylinder (in the potential region just outside the boundary layer) may be computed from the pressure distribution over the cylinder as follows:

The dynamic pressure  $q$  for the undisturbed stream is defined by  $q = \frac{1}{2} \rho U_0^2$ , where  $\rho$  is the air density. If  $p_s$  is the static pressure of the undisturbed stream and  $p_t$  is the total pressure (a constant everywhere in the potential region),  $q$  may be expressed also as  $q = p_t - p_s$ . The pressure on the surface, which was determined by pressure orifices in the cylinder, is denoted by  $p$ . Since the pressure is assumed to remain constant across the boundary layer,  $p$  may be regarded as the static pressure in the potential region just outside the boundary layer and is therefore related to  $U$ , the speed just outside the boundary layer by

$$p_t - p = \frac{1}{2} \rho U^2$$

The pressure distribution about the cylinder is given in terms of  $p - p_s$  and is expressed nondimensionally by  $(p - p_s)/q$ . Likewise the speed at the outside of the boundary layer is expressed nondimensionally by  $U/U_0$  and is obtained from the pressure distribution by

$$\left(\frac{U}{U_0}\right)^2 = \frac{p_t - p}{q} = \frac{p_t - p_s - (p - p_s)}{q} = 1 - \frac{p - p_s}{q}$$

Lengths, specifying position on the surface or in the

boundary layer, will generally be expressed nondimensionally in terms of  $D$ , the minor axis of the ellipse. The Reynolds Number of the cylinder is defined by

$$R = \frac{U_0 D}{\nu}$$

where  $\nu$  is the kinematic viscosity.

The speed fluctuations both in the boundary layer and in the free stream will be termed " $u$ -fluctuations" in order to denote the component of the fluctuation in the direction of mean flow. The root-mean-square value of  $u$ -fluctuations will be denoted by  $u'$  and will always be expressed nondimensionally as  $u'/U_0$ . In the free stream and in the turbulent part of the boundary layer,  $u'/U_0$  will be termed the "intensity" of the turbulence. The term "percentage turbulence," to express  $100 u'/U_0$ , is in common usage in the literature and will be used in the same sense here.

The scale of the turbulence will be denoted by  $L$  and is defined by

$$L = \int_0^\infty R(z) dz$$

where  $R(z)$  is the coefficient of correlation between instantaneous values of two  $u$ -fluctuations separated by the cross-stream distance  $z$ . For a more complete discussion of  $L$  and of the relation between  $R(z)$  and  $z$ , the reader is referred to reference 7.

#### SYMBOLS

$D$ , minor axis of ellipse (3.98 inches), used as the reference length.

$U_0$ , speed of the undisturbed stream, feet per second.

$R$ , Reynolds Number  $U_0 D/\nu$ .

$q$ , dynamic pressure of the undisturbed stream

$$\left(\frac{1}{2} \rho U_0^2\right).$$

$p/q$ , dimensionless pressure on surface of cylinder.

$p_s/q$ , dimensionless static pressure in undisturbed stream.

$x/D$ , dimensionless distance from the leading edge to any point on the surface.

$y/D$ , dimensionless distance from the surface measured along the normal.

$\delta$ , boundary-layer thickness.

$\delta/D$ , dimensionless boundary-layer thickness.

$U/U_0$ , dimensionless speed in the potential region just outside the boundary layer.

$u/U_0$ , dimensionless speed in the boundary layer.

$u'$ , root-mean-square value of the  $u$ -fluctuations.

$u'/U_0$ , fluctuation intensity or intensity of turbulence.

$L$ , scale of turbulence.

$t$ , turbulent boundary layer.

$S, S_t$ , separation points.

$\tau$ , shearing stress.

$l$ , mixing length.



# BOUNDARY-LAYER PHENOMENA AT LOW STREAM TURBULENCE

## PRESSURE DISTRIBUTIONS

As pointed out in the introduction, pressure distributions were determined about the elliptic cylinder in order to find an air speed for which the boundary layer over the rear part of the cylinder would be turbulent. Since the turbulence normally prevailing in the wind-tunnel stream was 0.85 percent and the critical Reynolds Number of a 5-inch sphere was 268,000, it seemed that such a condition would be found well below the maximum speed attainable in the tunnel. By a determination of the pressure distribution at different speeds, a critical region like that of spheres was found for the elliptic cylinder extending from about 15 to 55 feet per second. The change in the pressure distribution occurring through this region is shown by the several curves of figure 4. The curves for 11.2 and 70.0 feet per

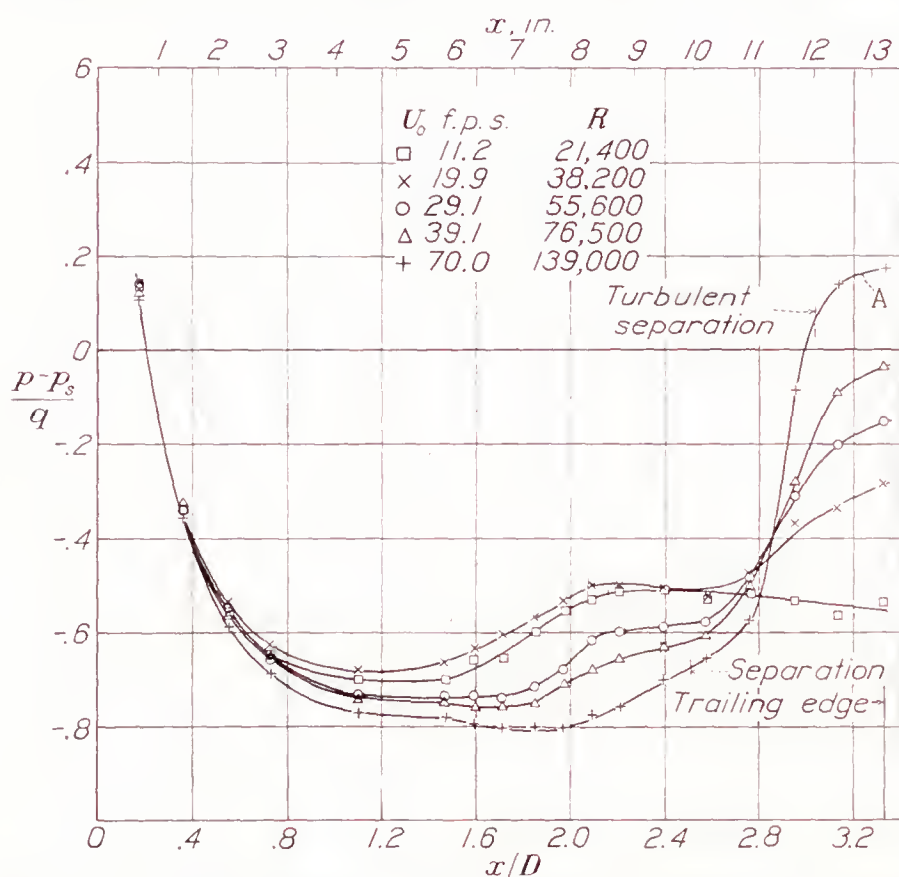


FIGURE 4.—Pressure distribution around one side of elliptic cylinder. Stream turbulence, 0.85 percent.

second represent the two invariable forms occurring below and above the critical region. The term "invariable" is used here in a restricted sense to mean fixed or showing very little change over a certain speed interval. The lower-speed type would certainly change for extremely low speeds and the same is true of the higher-speed type, if the speed were made sufficiently high. The speed was not carried high enough to determine where a change would occur in the distribution above the critical region. No observable change could be found in the distribution shown for 70.0 feet per second from 60 to 80 feet per second.

## SEPARATION STUDIES

As indicated in figure 4, the change in the pressure distribution was accompanied by a change in the point at which the boundary layer separated from the surface.

The method of detecting separation was the well-known one of applying a mixture of kerosene and lampblack to the surface and then running the tunnel at the desired speed for a sufficient length of time for the surface drag to establish a flow pattern. The vertical position of the cylinder was well adapted to this method because only the frictional drag of the air tended to carry the mixture horizontally. Downward drainage along the surface occurred, of course, but was a distinct advantage in that it reduced the film thickness, thus preventing flow under pressure gradient and, in addition, indicated the direction of the surface friction by the inclination of the drainage lines.

After the flow pattern was established and the kerosene had partly evaporated, a record of the pattern was easily made by pressing a piece of white paper against the surface. Figure 5 shows three such records made at 25, 43, and 70 feet per second. It will be noted that the patterns on the upstream part of the surface show a surface drag in the direction of the stream, indicated by the inclination of the streaks, which is followed by a region of stagnant air where the streaks are vertical. Although not clearly shown in the figure, it was usually possible to find a third region of short length just back of the stagnation region in which the streaks were inclined forward, giving evidence of reverse flow. Separation was assumed to occur in the stagnation region.

Because of the rearward movement of separation with increasing speed, it was at first assumed that the boundary layer became turbulent ahead of separation and that separation of a turbulent layer was being observed. This interpretation sufficed for patterns A and B, but not for C, where a second line of separation was found at the point marked  $S_1$ . This double separation, illustrated by C, was a characteristic of the flow above the critical region and always occurred at the same points on the surface. It was not until speed distributions had been determined throughout the layer with both high and low stream turbulence and studies of transition had been made with different amounts of turbulence that a satisfactory explanation of this phenomenon was afforded. The boundary layer was found to maintain the general aspects of a laminar boundary layer up to separation, but in no case was it purely laminar at the separation point above 15 or 20 feet per second because of a faint beginning of transition near the 6-inch position. Patterns A and B of figure 5 therefore show the separation of a "nearly laminar" layer. In pattern C the first separation at  $S$  is also the separation of a nearly laminar layer and the second at  $S_1$  is that of a turbulent layer, a complete transition having occurred in the free layer between  $S$  and  $S_1$  and the resulting turbulent layer having reattached itself to the surface. As indicated in the figure, the first separation began at 10 inches, and the final turbulent separation occurred at 12.05 inches.



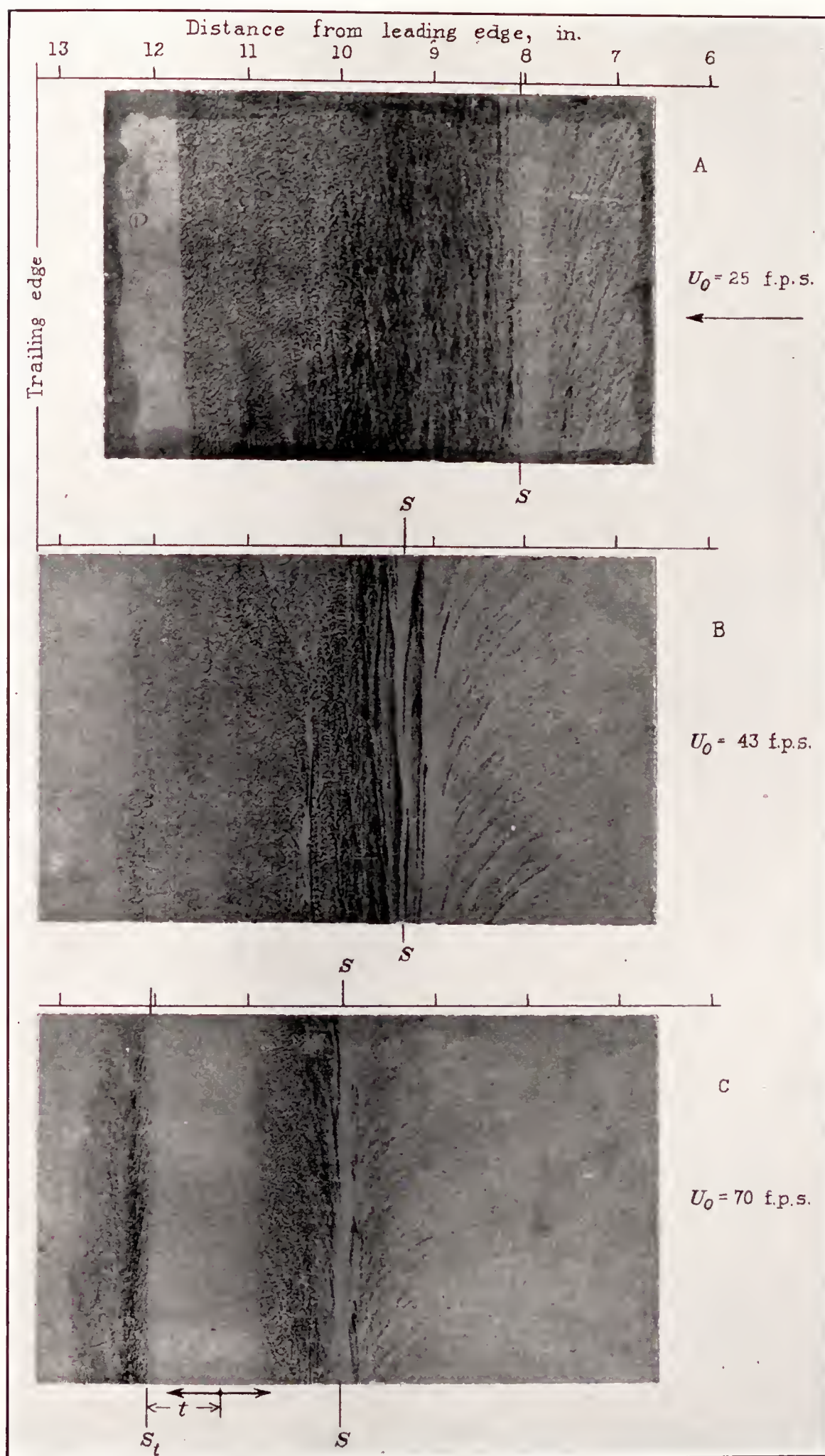


FIGURE 5.—Kerosene- and lampblack patterns showing movement of separation with speed and development of reattached turbulent layer. Stream turbulence, 0.85 percent. Distances were measured along surface.  $S$ ,  $S_t$ =separation points.  $t$ =Turbulent boundary layer. Arrows indicate direction of flow.



The direction of flow in the separation region of pattern C and the extent of the region were obtained by a second method of detecting separation that proved to possess certain advantages over the kerosene-and-lampblack method. The procedure was to apply to the surface a concentrated water solution of litmus, which was then reddened by fumes of hydrochloric acid and allowed to dry. Then, with a wind of the desired speed, a small amount of ammonia gas was released at the surface through a hypodermic needle in the neighborhood of the point to be investigated. The direction of the flow was clearly indicated by the blue color of the litmus. This method gave a definite indication of the direction of flow in the low-speed regions about separation points and showed details of the air motion impossible to obtain with the kerosene- and lampblack-method. In this way the first separation region was found to extend from 10 inches to 11.2 inches, as indicated in figure 5.

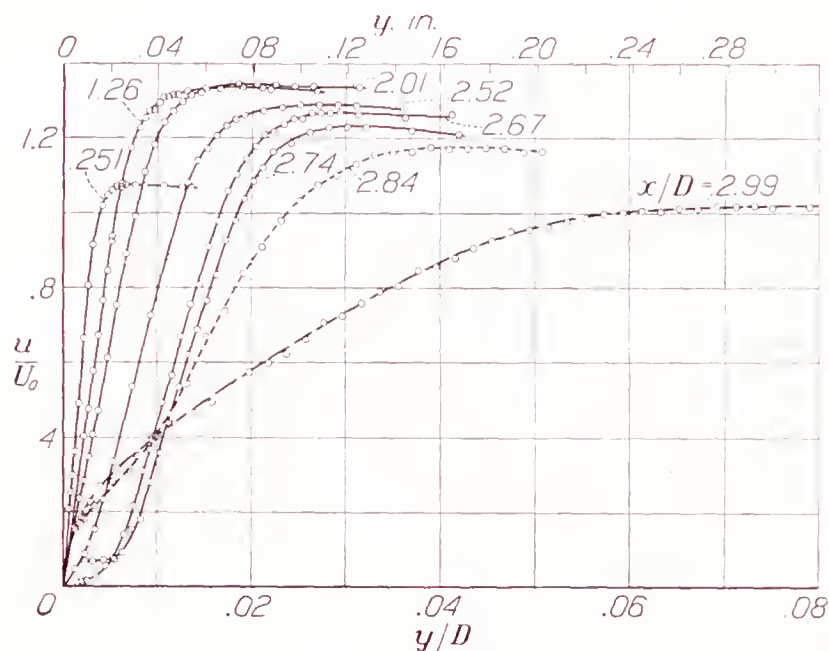


FIGURE 6.—Speed distribution in boundary layer of elliptic cylinder. Air speed ( $U_0$ ), 70 feet per second;  $R$ , 139,000; stream turbulence, 0.85 percent.

#### MEAN-SPEED DISTRIBUTION IN THE BOUNDARY LAYER

Traverses normal to the surface of the elliptic cylinder were made with the hot-wire anemometer to determine the speed distribution in the boundary layer at 15 positions about the surface, beginning 1 inch from the leading edge and ending at 12.6 inches. In terms of  $x/D$ , in which positions on the surface will generally be expressed, the traverses were begun at 0.251 and ended at 2.99. In all cases the speed of the stream  $U_0$  was 70 feet per second, corresponding to a Reynolds Number of the cylinder of 139,000.

Several of the speed distributions are shown in figure 6. It will be observed that the profiles from  $x/D=0.251$  to 2.01 show little change other than that caused by a thickening of the boundary layer and all have the shape generally found in a laminar boundary layer. At 2.52 the profiles show the beginning of separation. From 2.67 to 2.74 the very small initial slope of the curves shows that separation has occurred. Between 2.74 and 2.84 a marked change has occurred, since all evidence of separation has disappeared at 2.84. The

profile at 2.99 is certainly not that ordinarily ascribed to a laminar boundary layer, neither does it have the characteristics found in a turbulent boundary layer of a flat plate where the customary  $1/7$ -power law represents the speed distribution. As pointed out by Fediaevsky in reference 8, however, an adverse pressure gradient has a marked effect on the turbulent-speed profile. If the nature of this effect is considered and the strong adverse gradient existing at 2.99 is noted, it can be said that the profile is characteristic of a turbulent boundary layer.

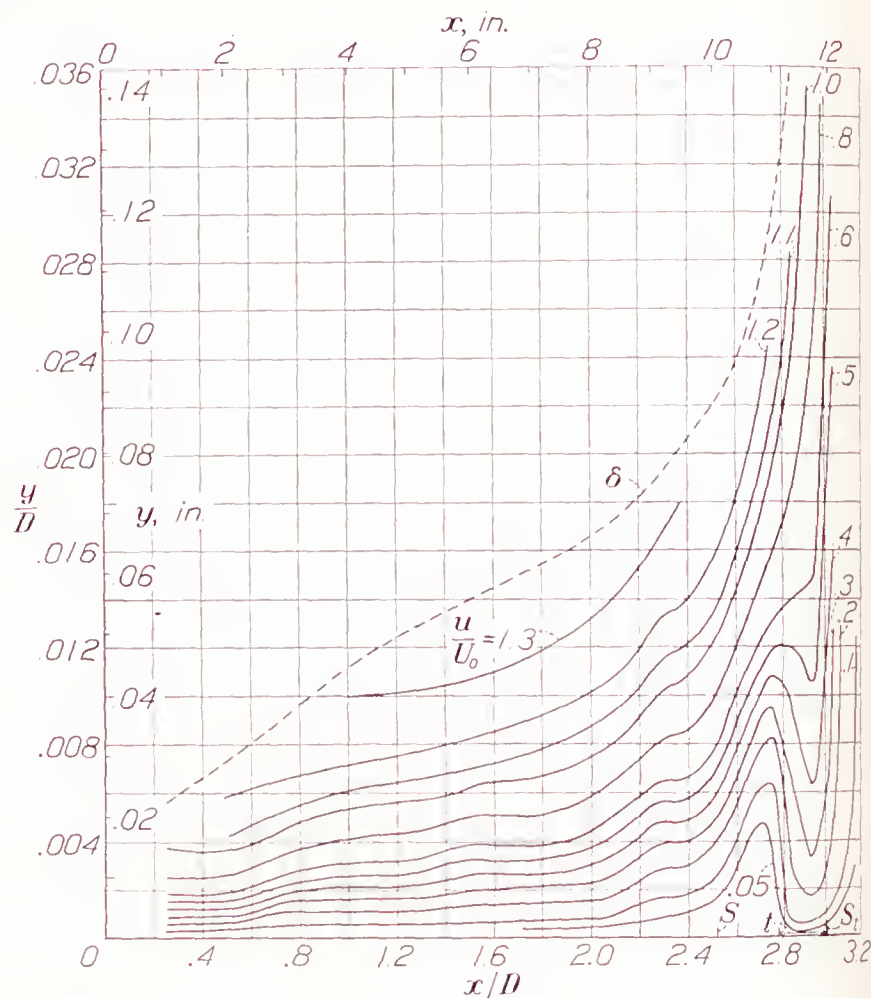


FIGURE 7.—Contours of equal speeds in boundary layer of elliptic cylinder. Air speed ( $U_0$ ), 70 feet per second;  $R$ , 139,000; stream turbulence, 0.85 percent.

A picture of the boundary layer as a whole may best be obtained from the contour diagram of figure 7, where each curve represents a particular value of  $u/U_0$ . The dotted curve shows the boundary-layer thickness  $\delta$ , which is here defined as the value of  $y$  where  $u/U_0=0.995 U/U_0$ . The occurrence of a separation followed by a reattachment of the layer to the surface is evidenced by the hump in the contours from  $x/D=2.5$  to 2.9. The approach to separation of the turbulent layer is shown by the very rapid increase in slope of the curves beyond the hump. Owing to the fact that the hot wire is insensitive to direction of flow, the measurements are not exact in the immediate vicinity of separation and hence neither figure 6 nor figure 7 serves to locate accurately the separation. The separation points and the extent of the turbulent layer were therefore obtained from figure 5. The values of  $x/D$  at  $S$  and  $S_t$  are, respectively, 2.51 and 3.03. The attached turbulent layer extends from 2.81 to 3.03.

The chief function of figures 6 and 7 is to show the



condition of the boundary layer upon separation—whether laminar or turbulent. By inspection it would be concluded from figure 6 that the boundary layer was laminar at the first separation point and turbulent at the second. Mere inspection is, however, rather inadequate because the conclusion depends on the judgment of the observer. A far better criterion of the state of the boundary layer would be provided by a comparison of observed speed distributions and positions of separation with these same quantities computed by boundary-layer theory. At present, existing solutions involve approximations whose validity is usually tested by comparison with experiment. Hence such solutions may not be relied upon for accurately defining the type of boundary layer found by experiment. With full recognition of the weakness of the procedure, certain simple comparisons with theory will be made in an effort to throw a little additional light on the problem.

In the von Kármán-Pohlhausen theory of the laminar boundary layer (reference 9) the criterion for separation is that the parameter  $\frac{dU}{dx} \frac{\delta^2}{\nu}$ , usually denoted by  $\lambda$ , shall have the value  $-12$  at the separation point. Using the pressure gradient and the boundary-layer thickness observed at the first separation point,  $\lambda$  was computed to be  $-11.8$ . This value is in excellent agreement with theory and strongly supports the view that the separation at 2.51 is of the laminar type.

The von Kármán-Millikan theory (reference 10) has shown considerable promise in the solution of the laminar boundary-layer problem and has been used by von Doenhoff (reference 11) to calculate the separation point on the elliptic cylinder used in the present work for the perfect-fluid pressure distribution. In order to obtain a result applicable to actual conditions, the observed pressure distribution must be used. It so happens that the curve for the perfect-fluid pressure distribution fits the observed pressures (curve A, fig. 4) so closely up to  $x/D=2.8$  that no better smoothed curve could be drawn. Since the method of solution requires, in effect, that the pressure distribution be fitted by a smoothed curve, von Doenhoff's solution may be regarded as the best possible. The computed separation point is 2.38. In view of the approximations involved in the theory and its application, the agreement with the observed separation at 2.51 must be considered good. Theory therefore supports the general impression given by figures 6 and 7 that the first separation is of the laminar type.

In order to test the second separation, turbulent boundary-layer theory might be applied to the reattached layer. This method was not believed to be worth while, however, in view of the limited length of the boundary layer and the unusual conditions under which it was formed. As has been pointed out, theory offers no completely satisfactory criterion even under the best circumstances.

It is well, therefore, to examine further experimental evidence that may contribute information as to the nature of the layer.

#### SPEED FLUCTUATIONS IN THE BOUNDARY LAYER

In the investigation of the boundary layer near a flat plate (reference 3), Dryden found speed fluctuations ( $u$ -fluctuations) in the laminar boundary layer having amplitudes as great as those in the turbulent part of the layer. On the mere existence of fluctuations alone it was therefore impossible to distinguish between the turbulent and the laminar parts of the boundary layer.

It is generally recognized that the fundamental difference between the fluctuations in turbulent and laminar parts of the boundary layer is one of correlation between the  $u$ -fluctuations and the  $v$ -fluctuations, the  $v$ -fluctuations being those occurring normal to the surface. If the instantaneous values of  $u$ - and  $v$ -fluctuations are denoted by  $u_i$  and  $v_i$ , respectively, the essential difference may be expressed in terms of the value of  $\overline{u_i v_i}$ , where the bar denotes average value. The turbulent shearing stress is given by  $\rho \overline{u_i v_i}$ . A turbulent shearing stress must be absent in a laminar boundary layer and  $\overline{u_i v_i}$  must be zero. By definition, a turbulent or partly turbulent layer is one in which a turbulent shearing stress exists, that is, where  $\overline{u_i v_i}$  has a value other than zero. The value of  $\overline{u_i v_i}$  therefore furnishes the best criterion as to the turbulent or the laminar condition of the layer.

With the simple hot-wire anemometer used by Dryden, it was impossible to determine  $\overline{u_i v_i}$ . The experimental difficulties attending such a measurement appear to be very great, especially in a thin boundary layer, and no means of doing so was found in the present investigation. Dryden has shown, however, in reference 3, that the simple hot wire does reveal an important difference between the fluctuations in the two parts of the boundary layer, namely, that the average frequency of the fluctuations is much greater in the turbulent than in the laminar boundary layer. On the flat plate, transition occurred quite abruptly and the position of transition was clearly defined by the marked difference in frequency on its two sides.

An effort was made in the present investigation to see whether a similar condition existed on the elliptic cylinder and, in particular, to determine whether the frequency of the fluctuations would serve to distinguish between the turbulent and the laminar parts of the layer. Accordingly, with a hot wire attached to the sliding band as previously described, records of the fluctuations were made by photographing the screen of a cathode-ray oscillograph connected to the output of the compensated amplifier. The wire was 0.00063 inch in diameter and 0.18 inch long and was attached to the band at a fixed distance of 0.0158 inch from the surface.

Figure 8 shows several of the records obtained at



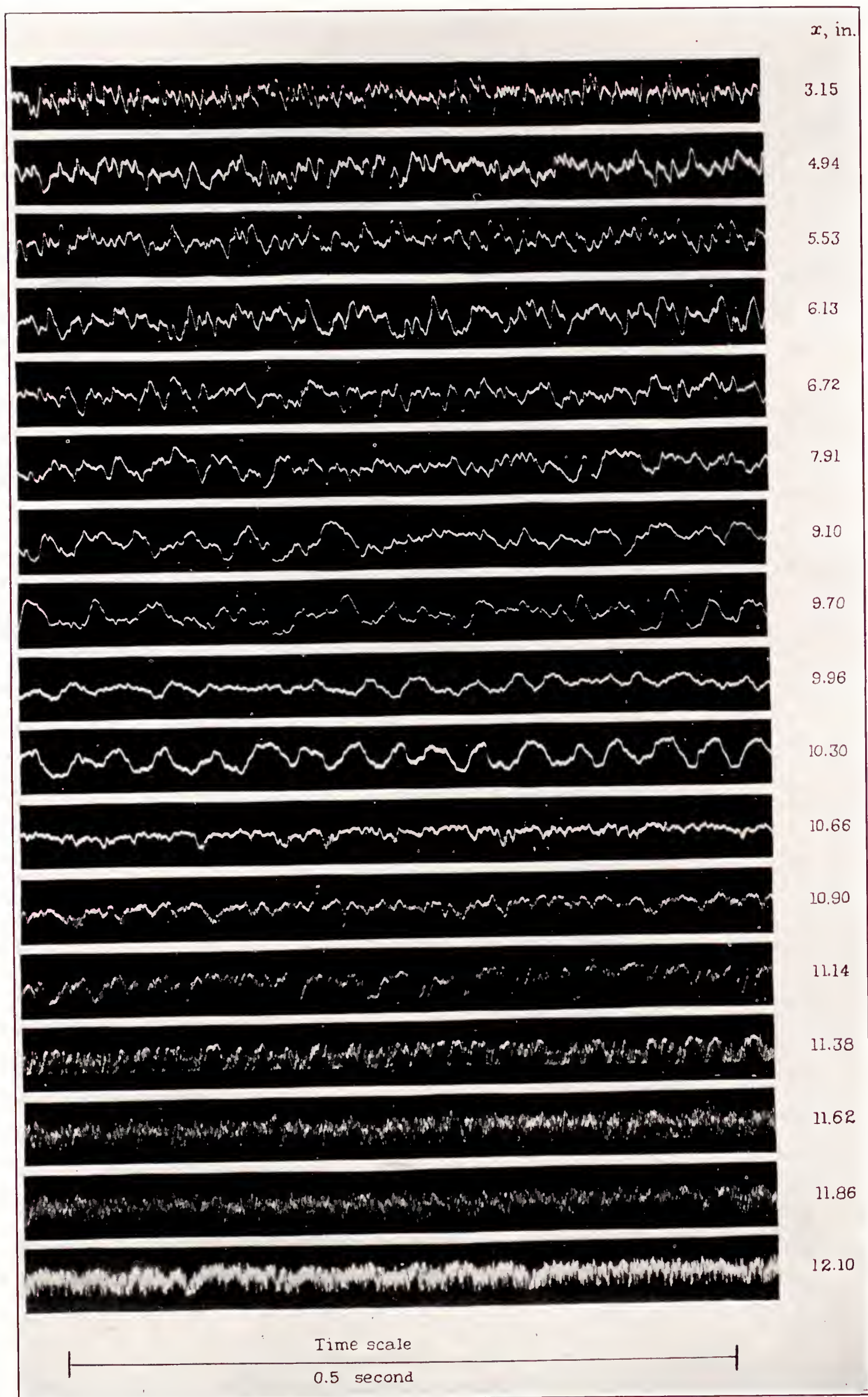


FIGURE 8.—Oscillograph records of  $u$ -fluctuations in boundary layer at 0.0158 inch from surface. Obtained with hot wire on sliding band. Air speed ( $U_0$ ), 70 feet per second; stream turbulence, 0.85 percent.



different positions about the surface. It is immediately evident that the frequency is much higher throughout the reattached layer, beginning near 11.14 inches, than in any other parts of the layer. No noticeable change has occurred in either the general character of the wave or the frequency up to  $x=9.10$  inches. Beyond this point, a regularity in the wave has begun to develop, which persists through the first separation region. In the record at 10.30 inches, situated near the center of the separation region, the regularity is quite marked, having a frequency of about 32 cycles per second. It is interesting to note that the fluctuations are everywhere quite random except through the separation region. The regular fluctuations are believed to be due to a slight fore-and-aft oscillation of the separation point, caused perhaps by pressure pulsations from the vortex street in the rear of the cylinder.

Owing to the absence of any perceptible increase in frequency with distance from the leading edge until the

the surface affords a more sensitive means of detecting transition than any yet employed. Using this device to examine the boundary layer, it was found that a weak and very incomplete transition began at  $x/D=1.53$ , or very near the 6.1-inch position. The boundary layer has therefore separated at 2.51, not as a purely laminar layer but as a transition type with transition so incomplete that the layer continues to exhibit most of the properties of a laminar layer.

#### BOUNDARY-LAYER PHENOMENA AT HIGH STREAM TURBULENCE

When it was thus found impossible to obtain a complete transition without an intervening separation with the low turbulence normally prevailing in the tunnel, the stream turbulence was increased by placing a 1-inch-square-mesh wire screen 18 inches ahead of the leading edge of the cylinder. (See table I.) The intensity and the scale of the turbulence produced by this screen had been measured previously and reported

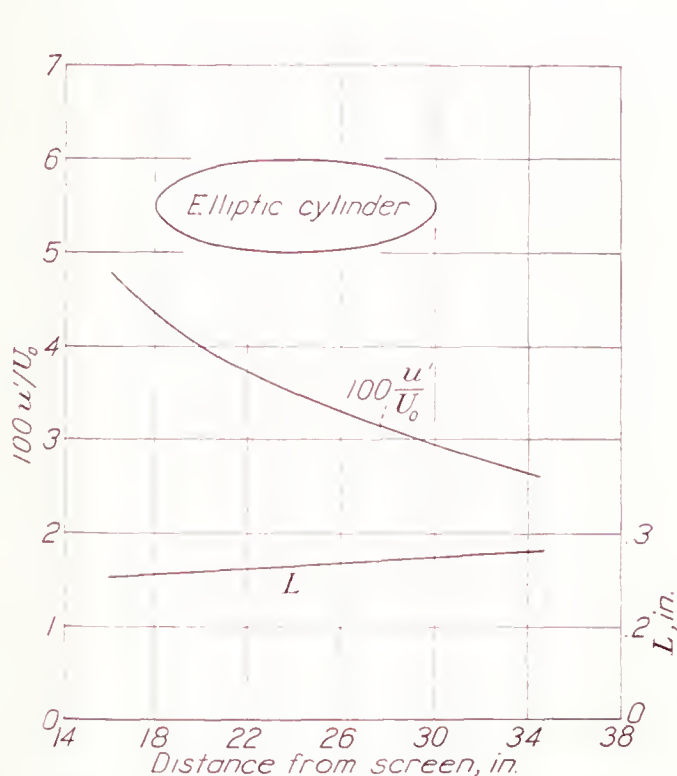


FIGURE 9.—Intensity and scale of stream turbulence produced by 1-inch mesh screen (from reference 7).

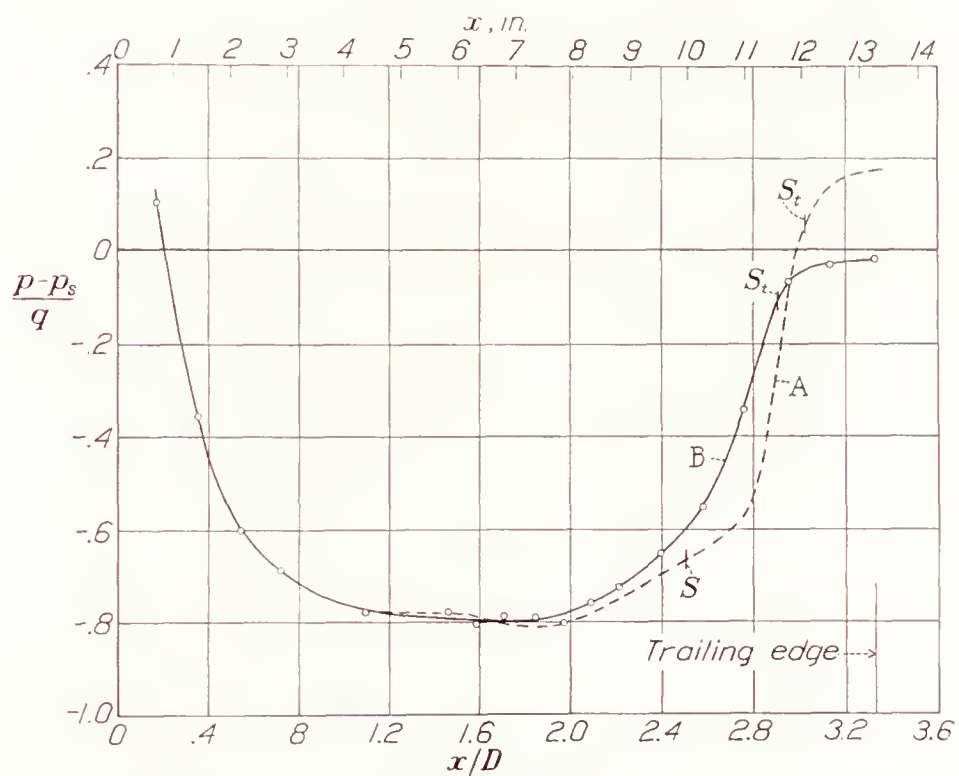


FIGURE 10.—Pressure distribution around one side of elliptic cylinder. Curve A—stream turbulence, 0.85 percent; air speed ( $U_0$ ), 70 feet per second. Curve B—stream turbulence as shown by figure 9.

reattached layer is reached, it would be concluded by analogy with Dryden's results on the flat plate that transition to a definitely turbulent layer occurred in the separation region. With no evidence of transition ahead of the first separation point, it appears from all the tests applied thus far that laminar separation occurred at  $x/D=2.51$ . This was the general conclusion drawn by the author before a more detailed study of transition had been made with different amounts of stream turbulence. In anticipation of some of the results to be given later, it may be stated that a gradual and incomplete transition may occur without any noticeable change in the frequency of the fluctuations and that conclusions drawn from the nature of the fluctuations may be in error in such cases. In the following sections it will be shown that the sliding band and the hot wire arranged to detect changes in the average speed near

in reference 7. Figure 9 gives results taken from this reference and shows the turbulent conditions prevailing at the position of the cylinder.

Kerosene-and-lampblack patterns made at various wind speeds showed a rearward movement of the separation point with increasing speeds up to 40 feet per second and no detectable movement for further speed increases. The final position of separation fell at  $x/D=2.91$ . Since the separation found at the lower turbulence was absent at all speeds with the higher turbulence, it was assumed that the transition occurred at a small value of  $x/D$  and that conditions were favorable for a study of a turbulent boundary layer of considerable length. A working speed of 60 feet per second, corresponding to a Reynolds Number of the cylinder of 118,000, was chosen for carrying out boundary-layer measurements.



Curve B of figure 10 shows the pressure distribution about the elliptic cylinder at 60 feet per second with the higher stream turbulence compared with curve A taken from figure 4. It will be observed that, even though each curve represents an invariable condition of the flow above the critical region, the two curves are different and the two turbulent separation points fall at slightly different positions.

#### MEAN-SPEED DISTRIBUTION IN THE BOUNDARY LAYER

At  $U_0=60$  feet per second, traverses across the boundary layer were made with the hot-wire anemometer at 12 positions about the surface, beginning 1 inch from the leading edge and ending at 11.46 inches, 0.12 inch ahead of the separation point. The traverses at these extreme positions together with six traverses at intermediate positions are shown in figure 11. It is obvious that the distributions near the leading edge resemble those of a laminar boundary layer while those near the separation point resemble those of a turbulent layer but, because of the gradual change, it is impossible to tell just where transition has begun.

The corresponding contour diagram, giving curves of equal  $u/U_0$ , is shown in figure 12. This figure was prepared by making use of all the traverses and reading values of  $y$  from faired curves, like those shown in figure 11, for chosen values of  $u/U_0$ . Figure 12 shows

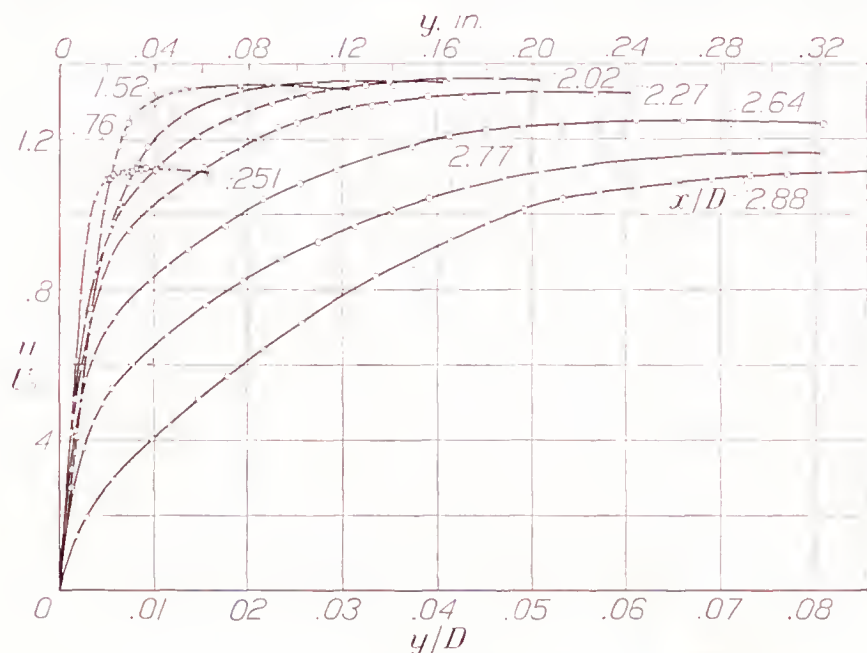


FIGURE 11.—Speed distributions in boundary layer of elliptic cylinder. Air speed ( $U_0$ ), 60 feet per second;  $R$ , 118,000; stream turbulence as shown by figure 9.

the result of the change in type of distribution in such a manner that transition may be more easily recognized than in figure 11. The phenomenon usually associated with transition is found after  $x/D=1.25$ ; that is, the bending of the contours toward the surface followed by an abrupt bending of the outer contours away from the surface. The bending away is due partly to the development of the turbulent boundary layer and partly to the approach to separation. It will be recalled by reference to figure 7 that a similar bending toward the surface, although considerably more abrupt, is caused by transition after separation and a reattachment of the layer to the surface. Al-

though figure 12 shows that transition does take place, it fails to show where transition begins and ends. To bound the transition zone definitely requires a different treatment of the data or measurements of a different nature.

Again, testing by comparison with laminar or turbulent boundary-layer theory might be called into play; but the detection of small departures from the purely laminar or purely turbulent condition is made impossible by the approximate nature of the theories. For this reason it was believed useless to attempt to locate the beginning of transition by this procedure. It

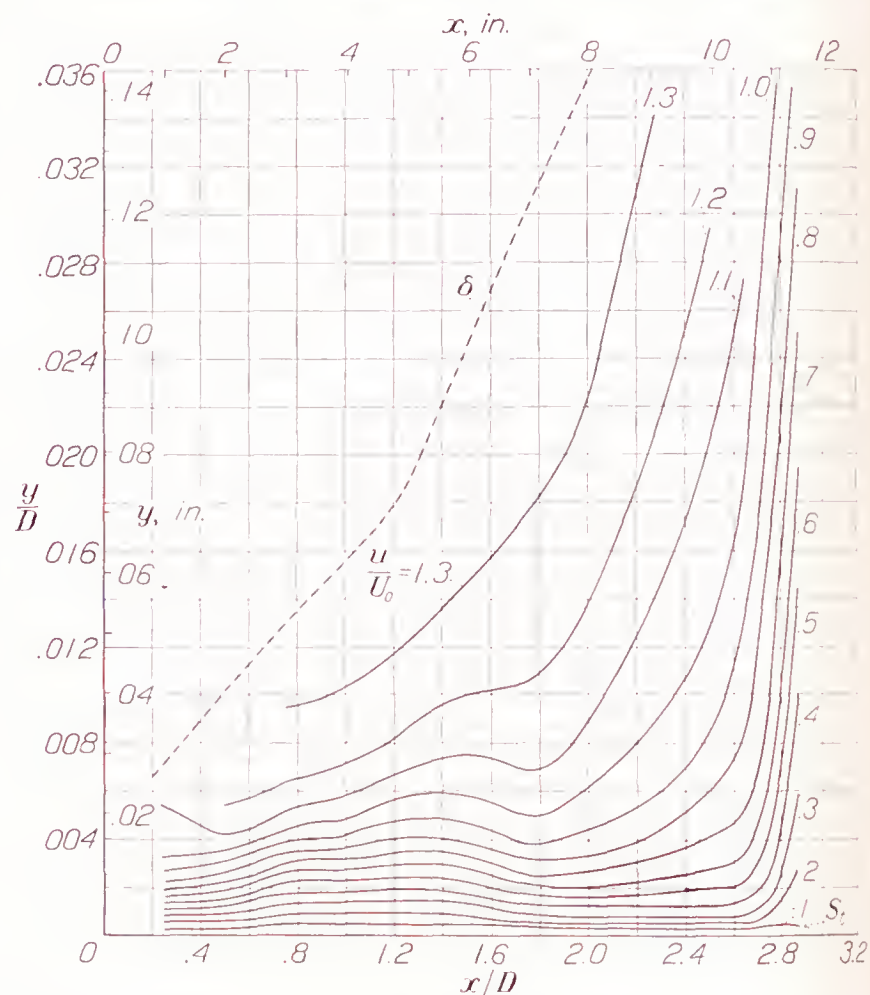


FIGURE 12.—Contours of equal speed in boundary layer of elliptic cylinder. Air speed ( $U_0$ ), 60 feet per second;  $R$ , 118,000; stream turbulence as shown by figure 9.

appeared worth while, however, to compare the profiles back of  $x/D=2$  with the usual  $1/7$ -power law and with the type of curve computed by the theory of Fediaevsky (reference 8) to aid in deciding whether the turbulent layer became fully developed before separation or whether the layer was still of the transition type when it separated.

Figure 13 shows speed distributions for  $x/D=2.02$ , 2.27, 2.64, 2.77, and 2.88 compared with that given by the  $1/7$ -power law. In the preparation of this figure,  $\delta$  and  $U/U_0$  were taken from figure 11 at the point where the slope of the curves is zero. Departures from the  $1/7$ -power law are to be expected, whether the layer is fully turbulent or not, where the adverse pressure gradient is great as at 2.64, 2.77, and 2.88. At 2.02 and 2.27, where the adverse pressure gradient is small, the departure can reasonably be attributed to incomplete transition, especially since the departure is in the direction to be expected if the layer here were partly laminar. It remains then to examine the effect



of pressure gradient on the distributions near the separation point.

The theory advanced by Fediaevsky in reference 8 is based on the fundamental relation

$$\tau = \rho l^2 \frac{du}{dy} \frac{du}{dy} \quad (2)$$

in which  $\tau$  is the shearing stress and  $l$  is the mixing length. The development by Fediaevsky differs from those by Prandtl and von Kármán, who have developed theories based on equation (2), in that the variation of  $l$  across the boundary layer is expressed by

$$\frac{l}{\delta} = 0.14 - 0.08 \left(1 - \frac{y}{\delta}\right)^2 - 0.06 \left(1 - \frac{y}{\delta}\right)^4$$

and the variation of  $\tau$  across the boundary layer is expressed by a power series of the form

$$\frac{\tau}{\tau_0} = A_0 + A_1 \left(\frac{y}{\delta}\right) + A_2 \left(\frac{y}{\delta}\right)^2 + A_3 \left(\frac{y}{\delta}\right)^3 + A_4 \left(\frac{y}{\delta}\right)^4 + \dots$$

where  $\tau_0$  is the shearing stress at the surface. Sufficient boundary conditions exist for the determination of  $A_0$ ,  $A_1$ ,  $A_2$ ,  $A_3$ , and  $A_4$ , and their values are given as

$$A_0 = 1, A_1 = \frac{\delta}{\tau_0} \left(\frac{\partial p}{\partial x}\right), A_2 = 0$$

$$A_3 = -4 - 3 \frac{\delta}{\tau_0} \left(\frac{\partial p}{\partial x}\right), A_4 = 3 + 2 \frac{\delta}{\tau_0} \left(\frac{\partial p}{\partial x}\right)$$

When the substitutions for  $\tau$  and  $l$  are made in equation (2), the differential equation for the speed distribution across the layer becomes

$$\frac{d\left(\frac{u}{U}\right)}{d\left(\frac{y}{\delta}\right)} = \frac{\sqrt{\frac{\tau_0}{\rho U^2}} \sqrt{1 + A_1 \left(\frac{y}{\delta}\right) + A_3 \left(\frac{y}{\delta}\right)^3 + A_4 \left(\frac{y}{\delta}\right)^4}}{0.14 - 0.08 \left(1 - \frac{y}{\delta}\right)^2 - 0.06 \left(1 - \frac{y}{\delta}\right)^4} \quad (3)$$

It is shown in reference 8 that the expression for  $l/\delta$ , although not universally true, is a fair approximation

for a wide variety of pressure gradients. It is seen from the foregoing expressions for  $A_1$ ,  $A_3$ , and  $A_4$  that the effect of pressure gradient in the present theory is to influence the distribution of shearing stress. For a critical examination of the underlying concepts the original reference should be consulted.

By the use of values of  $\delta$  obtained from figure 11, where the slope of the curves is zero, values of  $\tau_0$  obtained from the initial slope of the curves of figure 11, and values of  $\frac{\partial p}{\partial x}$  from the slope of curve B in figure 10,  $A_1$ ,  $A_3$ , and  $A_4$

were evaluated for  $x/D = 2.77$  and  $2.88$ . The integration of equation (3) was then carried out graphically to give the curves shown in figure 14. The differences between theory and experiment are greater than those found by Fediaevsky in his comparisons with the experimental curves obtained by Gruschwitz in the turbulent boundary layer of an airfoil. In one case, where the comparison was made near the beginning of the turbulent layer, a difference like that shown in figure 14 was found and the discrepancy was attributed to incomplete transition. Since neither  $\tau_0$  nor  $\delta$  could be accurately determined in the present work, the effect of possible errors in these quantities was investigated. In no case could such errors account for more than a small part of the difference between the computed and the observed curves. It is probable, therefore, that separation occurred before the turbulent layer was fully developed.

Some investigators have associated the beginning of transition with the point of minimum skin friction (reference 12). This view seems reasonable when it is considered that the skin friction normally decreases as the boundary-layer thickness increases and only the introduction of turbulent shearing stresses can arrest the decrease or cause an increase in the skin friction. In an effort to locate the point of minimum skin friction, the local skin friction  $\tau_0$  was calculated from the initial slope of the speed-distribution curves of figure 11 and plotted as a friction coefficient against  $x/D$  in figure 15.

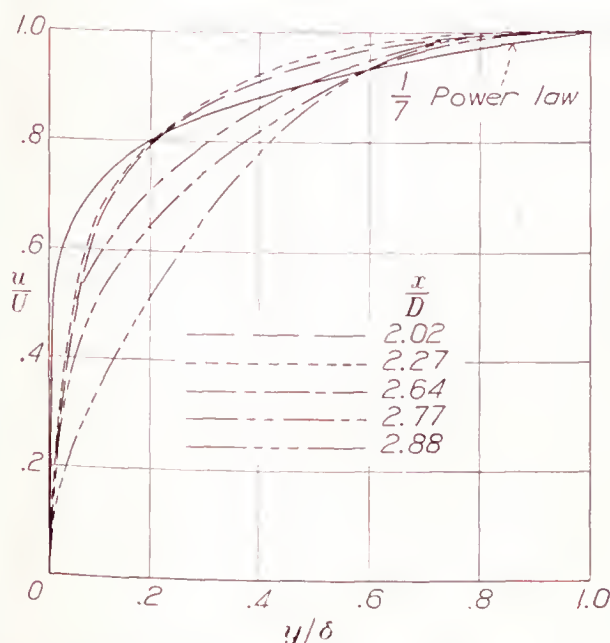


FIGURE 13.—Comparison of observed profiles with  $1/7$ -power law.

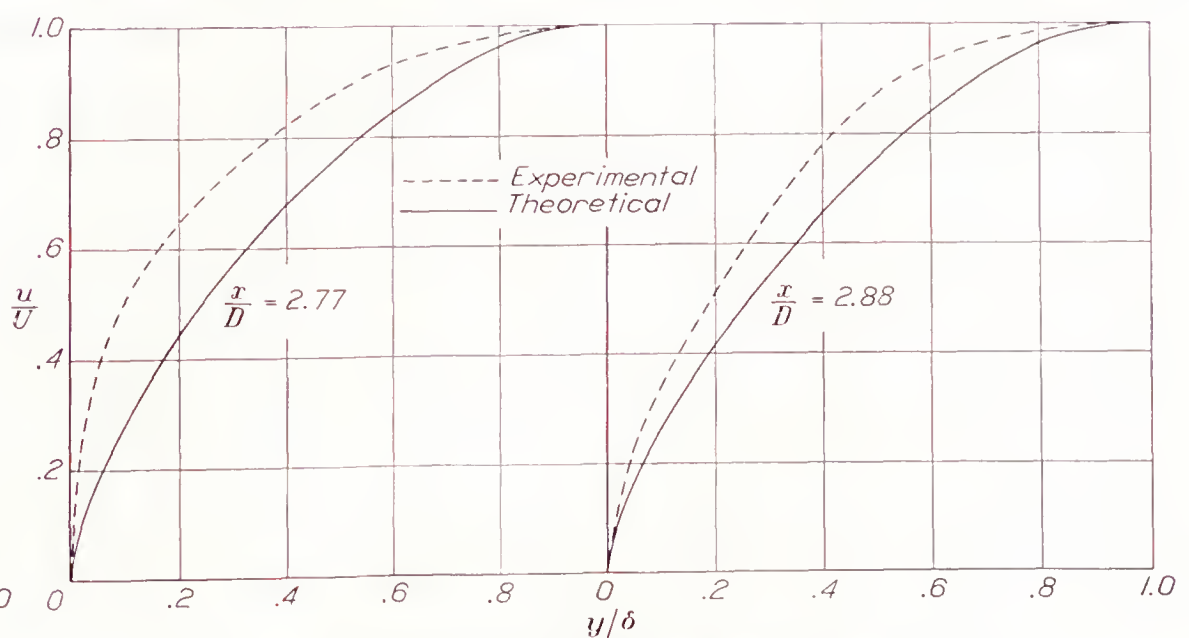


FIGURE 14.—Comparison of observed profiles with Fediaevsky theory.



A definite minimum exists, although the scatter of the points and the limited number of observations leave the position of the minimum rather indefinite. The final drop in the curve beginning at  $x/D=2.2$  shows the effect of nearing the separation point.

To have obtained more values of  $\tau_0$  would have required more speed traverses at the expense of considerable time and effort. It proved to be quite easy, however, to follow the course of  $\tau_0$  by following the changes in speed from point to point at a small fixed distance from the surface with the sliding-band apparatus previously described. The essential conditions were that the distance from the surface remain fixed and small enough for the velocity gradient over that distance to be regarded as linear. A platinum wire 0.00063 inch in diameter and 0.5 inch long was fixed at the center of the band 0.008 inch from the surface, the arrange-

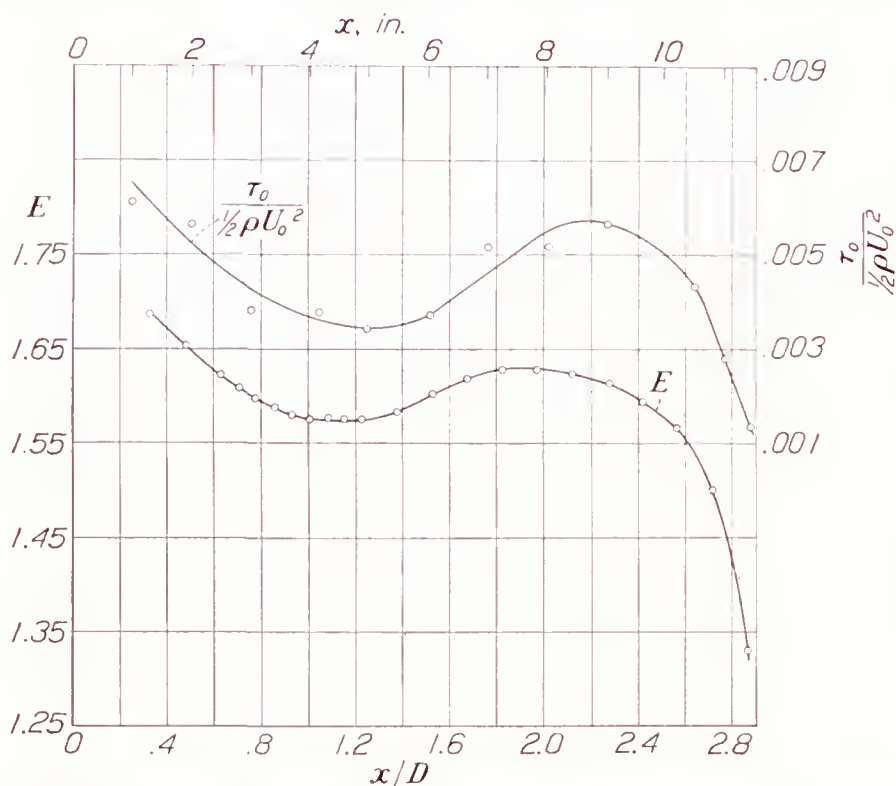


FIGURE 15.—Variation of shearing stress along surface of elliptic cylinder.  $\tau_0$ , shearing stress at surface, computed from data of figures 11 and 12.  $E$ -curve obtained from not wire on sliding band 0.008 inch from surface.  $E$ =voltage drop across wire

ment being shown diagrammatically in figure 3. Since the wire could not be calibrated, the actual value of the speed could not be obtained; but, with the wire carried at a constant temperature of about 110° C. above room temperature, the change in the voltage drop, as the wire was moved from one position to another, served to indicate changes in speed and hence in  $\tau_0$ . The lower curve of figure 15 was obtained in this way. Although the minimum in the voltage curve is not sharp, it is possible to locate its position to within  $\pm 0.05$  in  $x/D$ . The position was estimated to be 1.13, or 4.5 inches from the leading edge.

The speed changes may be deduced roughly from the crossing of the contours by referring again to figure 12 and remembering that moving the wire by the sliding band at a height of 0.008 inch from the surface would correspond to passing along the abscissas of figure 12 at a height of  $y/D=0.002$ . It will be noted that the speed decreases to about  $x/D=1.25$  and increases

again beyond this point. Considering the coarseness of the diagram, this result is in satisfactory agreement with figure 15, which places the minimum at  $x/D=1.13$ . The presence of transition is not greatly in evidence in figure 12 before 1.4, hence the minimum in the voltage curve of figure 15 possibly coincides with the very beginning of transition.

A somewhat different method of locating transition, involving the use of small pitot tubes, was employed by Jones (reference 13) in his study of transition on a wing in flight. The method depended on the change occurring in the mean speed distribution in the layer through the transition region. In order to detect the change, several small pitot tubes, arranged in a compact group, were placed within the layer at different distances from the surface and moved from one position to another. Jones points out that one pitot tube placed in contact with the surface is sufficient and may be used in wind-tunnel experiments but that in flight the bank of several tubes had certain advantages. A single pitot tube at the surface is nearly equivalent to the hot wire as used in the present experiment.

#### SPEED FLUCTUATIONS IN THE BOUNDARY LAYER

The point at  $x/D=1.13$  ( $x=4.5$  inches) having been identified as the point at which transition probably began, oscillograph records of the  $u$ -fluctuations in the layer were taken in the neighborhood of the 4.5-inch position, to detect a change in frequency. The records are shown in figure 16, the apparatus being the same as that used to obtain figure 8. It is not evident from mere inspection that any change in the average frequency has occurred in crossing the 4.5-inch position.

In view of the importance of finding additional evidence of transition, it seemed worth while to measure the distribution of the root-mean-square value of the  $u$ -fluctuations across the layer at a number of positions about the surface. Eleven distributions were determined at the same positions in which the mean-speed measurements with the higher turbulences were made. The hot-wire anemometer and the amplifier have been described in an earlier section. The length of the hot wire in the present case was 0.152 inch. Seven of the distributions are shown in figure 17. By comparison with the measurements given by Dryden in reference 3, the curves up to and including the one at 1.26 show a marked similarity to the laminar type, while those at 1.52, 1.76, and particularly the one at 2.88 show similarity to the turbulent type. It will be observed that the peaks of successive curves increase to a maximum and then decrease as the distribution changes over into the turbulent type. The decrease in the peak appears to begin between 1.00 and 1.26.

The contour diagram of figure 18 was prepared by taking values of  $y/D$  for particular values of  $u'/U_0$  from faired curves, of which those shown in figure 17 are examples. On each curve of equal  $u'/U_0$  the value is given, expressed as a percentage ( $100 u'/U_0$ ). This



diagram presents a picture of the fluctuations in the layer as a whole and again shows the region of large fluctuations near the surface in the neighborhood of  $x/D=1.00$ .

It will be recalled that the minimum in the skin friction, as indicated by the voltage curve of figure 15, fell at  $x/D=1.13$ , just midway between the curves at 1.00 and 1.26 in figure 17 where the peak in  $u'/U_0$  began to decrease. It is also quite evident from figure 18 that the fluctuations possess certain singularities in this

to a sliding band was a reliable device for indicating the beginning of transition. Since the simplicity of the procedure made it possible to detect transition very quickly, a somewhat extended investigation was undertaken to determine how the beginning point of transition shifted when the stream turbulence was changed. Several screens for producing turbulence were available, as part of the standard wind-tunnel equipment, for which the intensity and the scale of the turbulence were known as a function of distance downstream from the

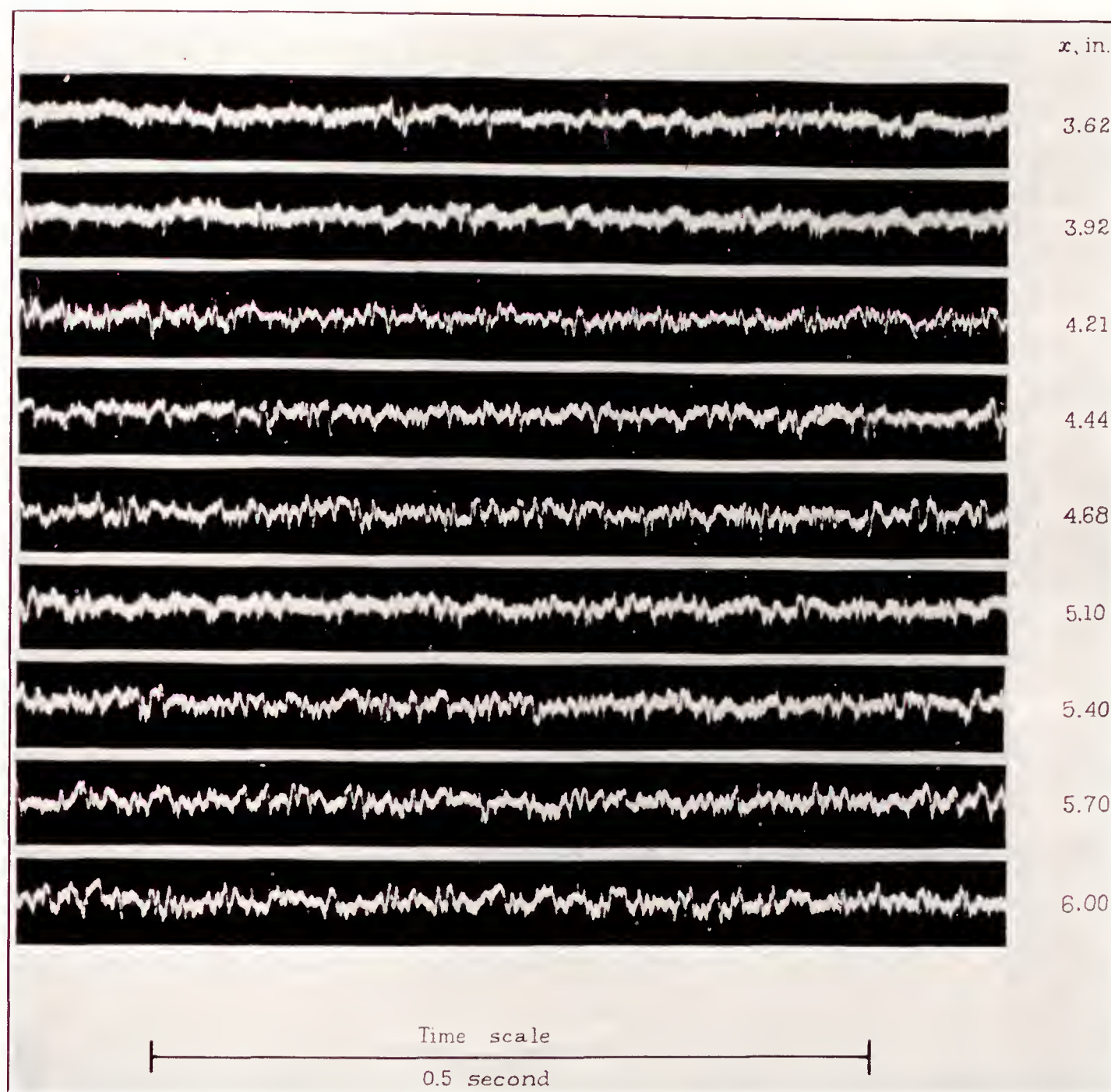


FIGURE 16.—Oscillograph records of  $u$ -fluctuations in boundary layer at 0.0158 inch from surface obtained with hot wire on sliding band. Air speed ( $U_0$ ), 60 feet per second; stream turbulence as shown in figure 9.

region. The evidence from the magnitude and the distribution of the fluctuations supports the assumption that the minimum in the skin friction denotes the beginning of transition. The fact that no frequency change was apparent in this region may be construed to mean that frequency change is an insensitive test of the beginning of a very gradual transition.

#### EFFECT OF INTENSITY AND SCALE OF STREAM TURBULENCE ON TRANSITION

By the time the work already described had been done, it seemed fairly certain that a hot wire attached

screen. The procedure was to vary the intensity of the turbulence, and to a limited extent the scale, by placing one of the screens at different distances upstream from the cylinder. The chief changes in scale were accomplished by using screens of different mesh size. The screens are described in table I. Measured values of intensity,  $u'/U_0$ , and scale,  $L$ , of the turbulence produced by these screens are given in reference 7. The values of  $u'/U_0$  and  $L$  used in the present work were taken from the least-square lines of figures 10 and 7, respectively, of reference 7.



The variation of  $u'/U_0$  and  $L$  with distance from the 1-inch screen is shown in figure 9. The figure illustrates one source of uncertainty in this procedure, namely, that  $u'/U_0$  decreases from the leading to the trailing edge of the cylinder and  $L$  increases slightly, leaving the choice of values for  $u'/U_0$  and  $L$  somewhat arbitrary. The change was the greater the smaller the mesh of the screens, hence screens of smaller mesh than the 1-inch were not used. There were available, besides the 1-inch mesh, a  $3\frac{1}{4}$ -inch and a 5-inch mesh, all screens being approximately geometrically similar.

appeared at distances of about 12 mesh lengths for all the screens. The uniformity of speed back of the screens is treated in detail in reference 7.

The sliding band and the mechanism for moving it have already been described in connection with figure 3. A wire 0.00063 inch in diameter and 0.5 inch long was attached to the band at a distance of 0.008 inch from the surface, the set-up being the same as that used to obtain the voltage curve of figure 15. The wire was connected as one arm of a Wheatstone bridge, which was used in the preliminary part of the work to hold

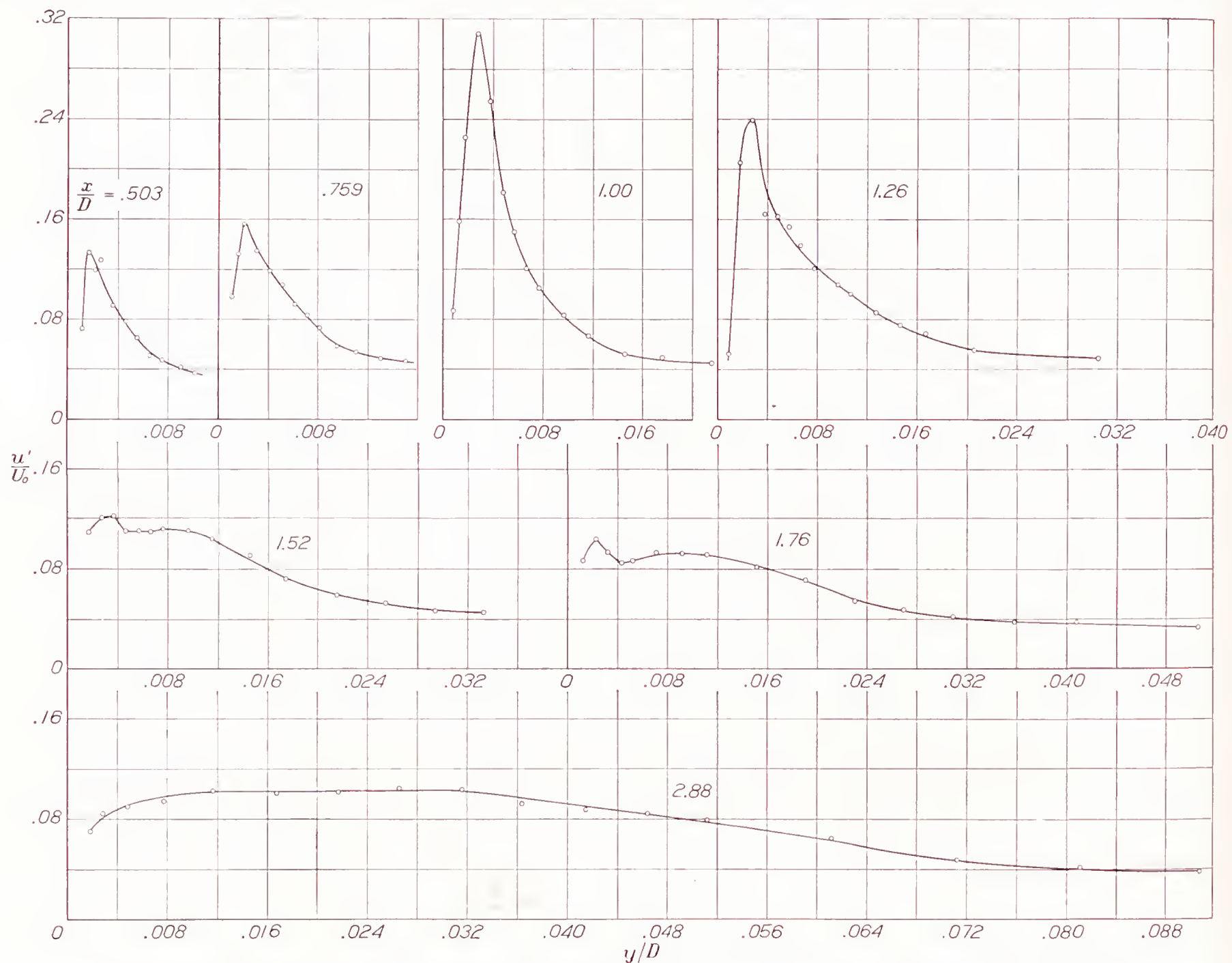


FIGURE 17.—Distribution of  $u$ -fluctuations in boundary layer. Air speed ( $U_0$ ), 60 feet per second; stream turbulence as shown in figure 9.

In order to specify a definite value of intensity and scale, the values of  $u'/U_0$  and  $L$  selected were those found in the undisturbed stream at the section of the tunnel midway between the leading edge of the cylinder and the beginning of transition.

In order to avoid irregularities in the average speed over the cross section of the stream and to insure isotropic turbulence, the screens were not placed nearer to the leading edge than 16 mesh lengths. In the investigation reported in reference 7, it was found that the regular pattern of maxima and minima in mean speed caused by the wake of the individual wires dis-

the wire at a fixed temperature of about  $100^\circ\text{C}$ . above room temperature while the voltage across the wire was read on a potentiometer. Later the procedure was changed simply to reading the unbalance of the bridge on a galvanometer for each position of the band. Since the two methods gave curves with minima in identical positions, the latter method was adopted because of the rapidity with which readings could be taken.

Figure 19 gives three examples of the type of curve obtained when the galvanometer reading was plotted against position of the wire. The wind speed was set



at 60 feet per second in each case, giving a fixed Reynolds Number of 118,000, and the turbulence was varied by shifting the position of the 1-inch screen. Curve A was obtained with the screen 18 inches ahead of the leading edge of the cylinder, curve B with the screen 24 inches ahead, and curve C with the screen 33 inches ahead. Since the same screen was used, the shift in the position of the minimum along the abscissa is due mainly to the change in the intensity of the turbulence.

The minimum was usually found from a more complete curve like those shown in figure 15; then, with the galvanometer sensitivity greatly increased, the region of the minimum was explored in detail, as in figure 19. An unaccounted-for irregularity in the curves was always found near the 4-inch position. The irregularity was small compared with the minimum denoting transition and was never confused with it but, when the two fell close together, the irregularity in the curve tended to obscure the position of the minimum.

A somewhat puzzling situation was encountered when curves were obtained with no screen in the tunnel and the lowest condition of turbulence prevailed. It will be recalled that all available evidence pointed to a laminar separation under this condition with the turbulent layer developing only after separation. It was surprising, therefore, to find the curves shown in figure 20 with an

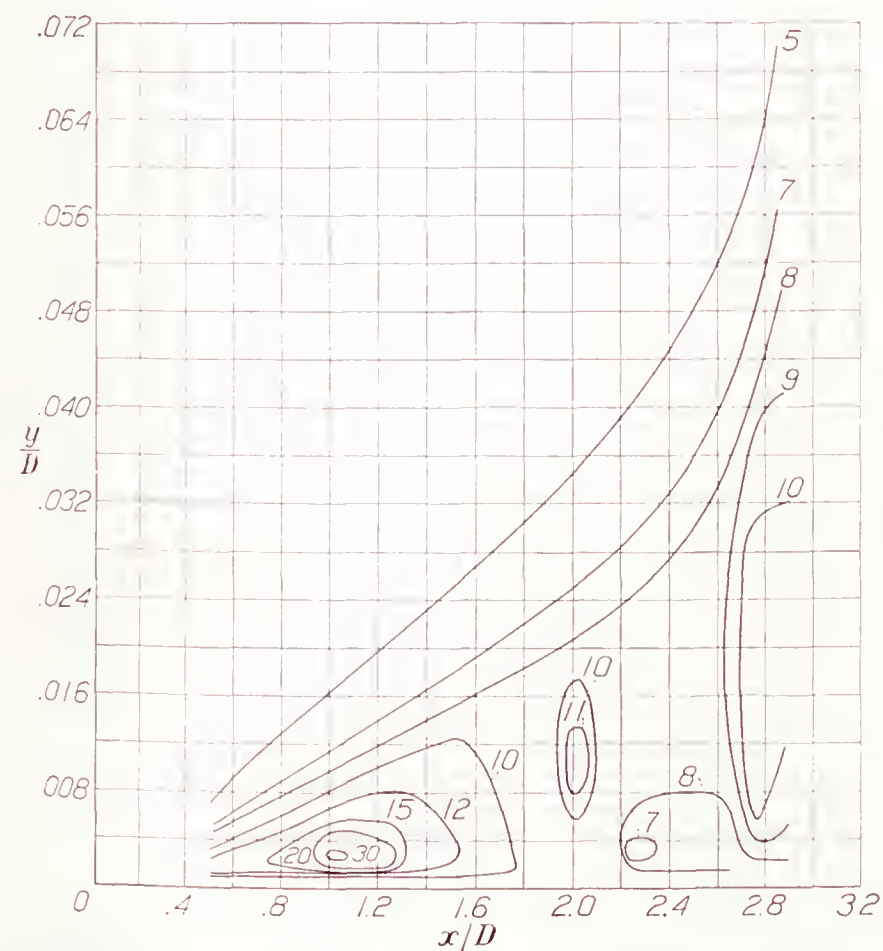


FIGURE 18.—Contours of equal  $u'/U_0$  in boundary layer. Numbers on curves give values of  $100 u'/U_0$ . Air speed, 60 feet per second; stream turbulence as shown in figure 9.

unmistakable minimum near the 6.1-inch position, much ahead of separation at the 10-inch position. Curves taken at successively decreasing speeds showed minima gradually fading into an inflection and then disappearing. The minima in figure 20 back of the 8-inch position are

the result of separation, the ensuing rise following the minima being caused either by a reattachment of the layer or reverse flow. It should be pointed out that, even though a minimum is found in the separation region, the hot wire and the sliding band is not an appro-

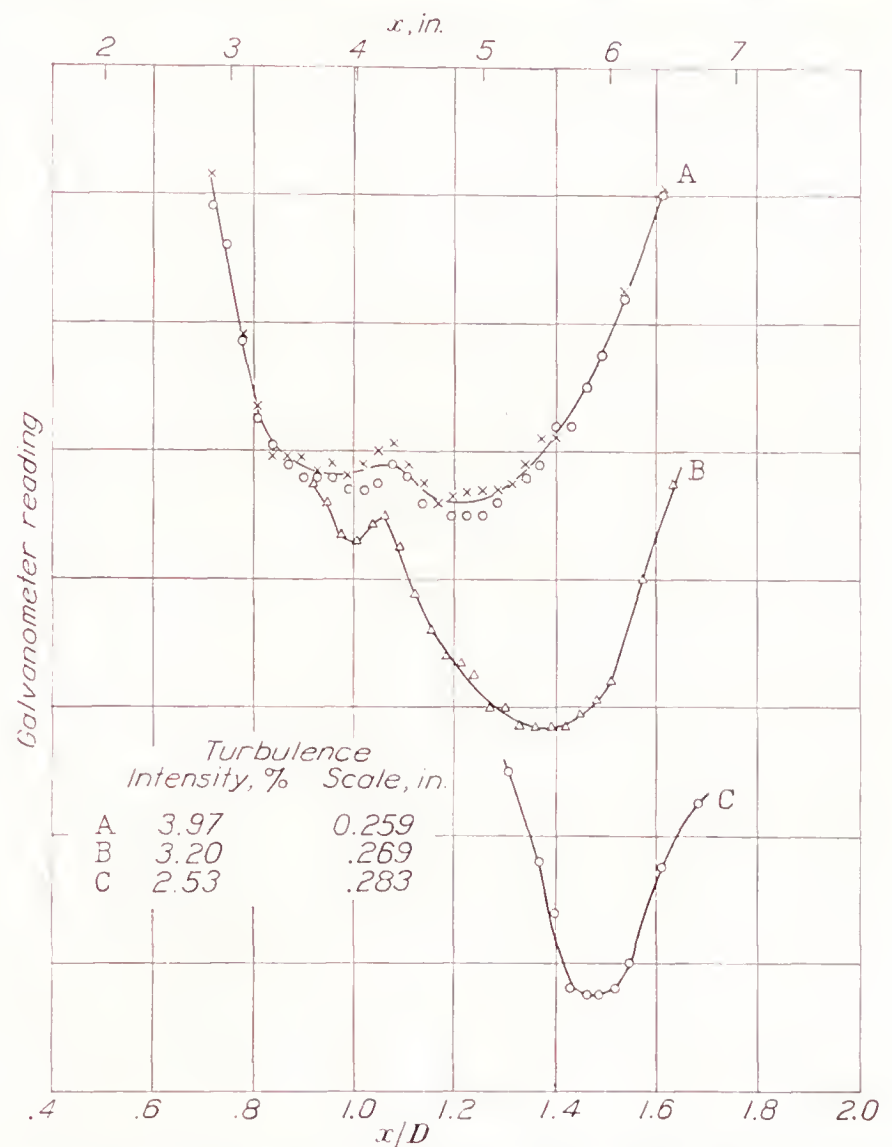


FIGURE 19.—Effect of stream turbulence on position of skin friction minima. Turbulence produced by 1-inch screen. Air speed ( $U_0$ ), 60 feet per second; hot wire on sliding band 0.008 inch from surface.

prate device for accurately locating separation because of the insensitivity of the wire to direction of flow. In general, the minima do not coincide exactly with the position of separation as indicated by kerosene and lamp-black.

Another feature of the minima shown in figure 20 is that they do not shift appreciably from the 6.1-inch position as the speed of the stream is changed. It was noted also, when the speed was kept constant at 60 feet per second and the turbulence was varied by screens, that the intensity could be raised to about 2 percent with the 1-inch screen and still higher with the larger screens before the minimum moved perceptibly from the 6.1-inch position. These facts made the connection between the minima at this point and transition look somewhat doubtful. If the minima were really due to the beginning of transition, the boundary layer just back of the 6.1-inch position was evidently unstable enough to permit transition at all but very low speeds and was so stable just ahead of this position that only high speed and high intensity of turbulence could cause transition to progress forward. To account for such a



condition one is led to look for some natural cause of instability at this point.

It is known that pressure gradient has a marked influence on transition, an accelerating pressure gradient tending to prevent transition and an opposing pressure gradient tending to promote transition. Figures 4 and

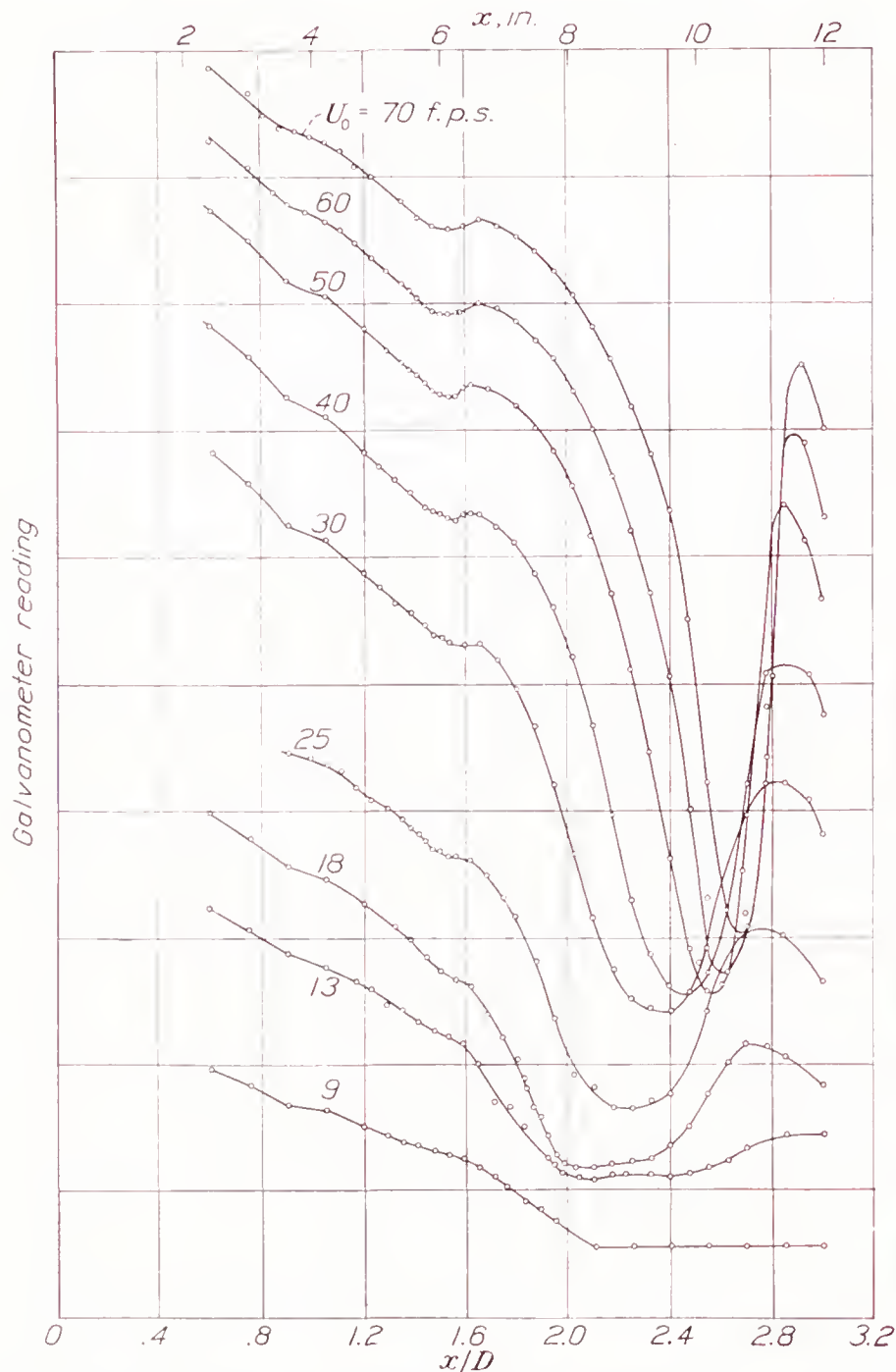


FIGURE 20.—Skin friction minima in boundary layer of elliptic cylinder for free tunnel condition; stream turbulence, 0.85 percent.

10 show that the 6.1-inch position roughly divides the accelerating from the opposing pressure gradient at the lower speeds and, at the higher speeds, marks the end of the accelerating pressure gradient. The 6.1-inch position appears therefore to be the first favorable one for transition.

The possibility that transition might remain relatively fixed in this position until the speed and the turbulence became sufficiently high may be seen in the following way. At the lower speeds, the presence of an opposing pressure gradient makes transition easy. As the speed is raised, the increasing boundary-layer Reynolds Number tends to move transition forward, but this effect is counteracted at first by a decrease in the opposing pressure gradient accompanying the increased speed and later by a slight increase in the accelerating

pressure gradient. It is well known that transition rarely occurs in a region of accelerating pressure gradient, hence the necessity for high turbulence to force transition ahead of 6.1 inches. The beginning of transition coinciding with a minimum in the 6.1-inch position is therefore not contradictory to reason. When such behavior of the minimum as movement forward with sufficiently increased turbulence and disappearance with sufficiently increased speed was considered in addition, it was impossible to escape the conclusion that this minimum was not like the fixed irregularity at the 4-inch position but was associated with the beginning of transition just as definitely as the minima in figure 15.

Curves similar to those of figure 19 were next obtained with the 3/4- and 5-inch screens, the speed in all cases being 60 feet per second. The positions of the minima, found from the several curves, were then plotted against the intensity of the turbulence from the different screens to give the three curves shown in figure 21. The effect of the scale is quite evident from the separation of the curves. Figure 21 shows that a greater intensity of large-scale turbulence is required to move transition forward than is required of a turbulence of

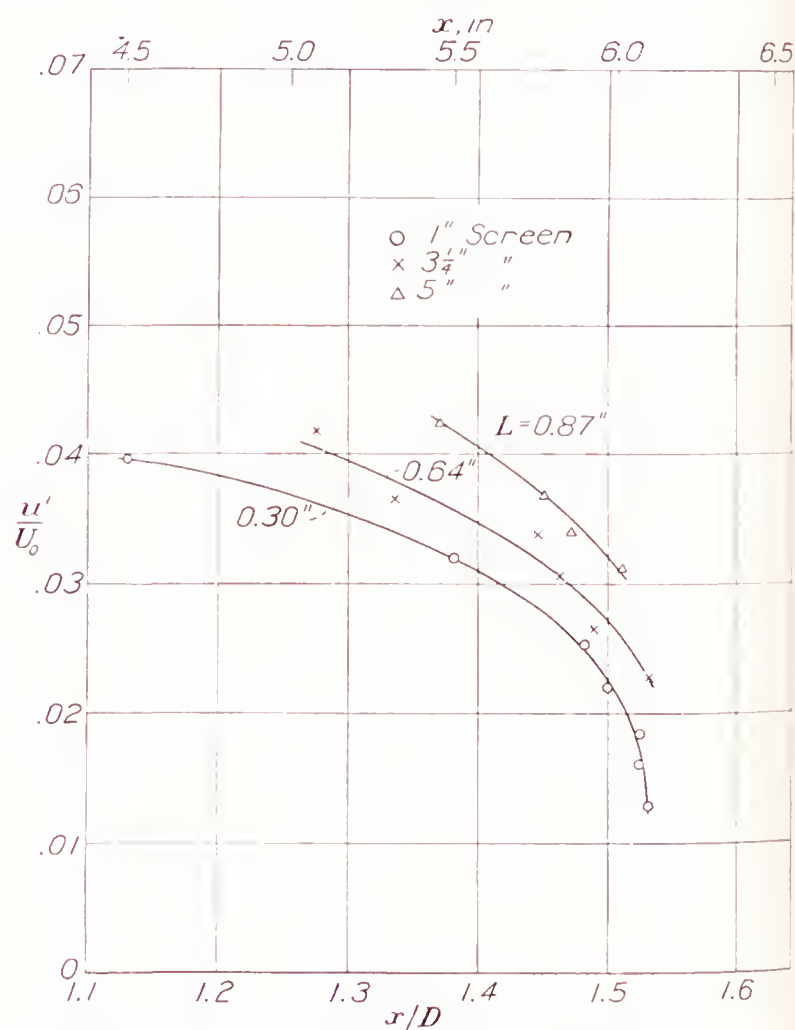


FIGURE 21.—Effect of stream turbulence on position of transition, showing effect of intensity and scale. Air speed, 60 feet per second;  $R$ , 118,000.

small scale. The turbulence is therefore the more effective the smaller the scale.

In reference 7 a similar effect is shown for spheres, where, for a given intensity, a small-scale turbulence lowered the critical Reynolds Number of spheres more than did a large-scale turbulence. In reference 14, G. I. Taylor has suggested a functional relation between



the critical Reynolds Number of spheres and the scale and intensity of the turbulence. His relation is

$$R_c = f \left[ \frac{u'}{U_0} \left( \frac{D}{L} \right)^{1/5} \right]$$

where  $R_c$  is the critical Reynolds Number,  $D$  is the diameter of the sphere, and  $f$  is a function to be determined by experiment. In figure 18 of reference 7, this relation was tested by plotting  $\frac{u'}{U_0} \left( \frac{D}{L} \right)^{1/5}$  against  $R_c$ .

The results for a 5-inch and an 8.55-inch sphere and for turbulence ranging in scale from 1.25 inches to 0.055 inch approximate a single curve to within the observational error.

The details of the development of Taylor's relation are discussed in reference 14. It may be stated in general terms that the foregoing combination of intensity and scale occurs in the expression for the root-mean-square pressure gradient in the turbulent flow and that the effect of turbulence is assumed to be that of the pressure gradient on transition. The critical Reynolds Number was brought into the relation by assuming that the critical Reynolds Number corresponded to a definite position of transition on the sphere for all conditions of turbulence. With the position of transition fixed, the critical Reynolds Number became the variable.

In the case of the elliptic cylinder the procedure was arranged so that the Reynolds Number remained fixed and the position of transition was allowed to vary. There should therefore exist a functional relation between position of transition and the same combination of scale and intensity of the turbulence.

In figure 22,  $\frac{u'}{U_0} \left( \frac{D}{L} \right)^{1/5}$  has been plotted against the observed position of the minima. For each point the value of  $u'/U_0$  and  $L$  was taken as that corresponding to the undisturbed stream at the section of the tunnel midway between the leading edge of the cylinder and the position of the point on the surface. This procedure for selecting  $u'/U_0$  and  $L$  was adopted on the assumption that no one part of the laminar layer was more sensitive to outside disturbances than another. It will be observed that the points fall nearer to a single curve in this figure than they do in figure 21, where the scale was not taken into account. Although there are systematic departures from the curve of figure 22, these departures do not follow in the order of the changes in scale, i. e., the points for the 3/4-inch screen tend to lie below the curve, whereas those for the 5-inch screen tend to lie above the curve. In this connection, it should be pointed out that the sliding-band method was not entirely free from systematic errors, for it was found that the position of the minimum became displaced slightly if at any time the band did not fit the cylinder snugly. The magnitude of the shift was large enough to cause the systematic differences in figure 22.

This part of the investigation has dealt with only the beginning of transition. It seems entirely possible that turbulence may affect the extent of transition as well as the beginning, in which case the full effect of turbulence is not taken into account. In consideration of this fact, together with the uncertainties inherent in the procedure and the arbitrariness in the choice of  $u'/U_0$  and  $L$ , the approximation to a single curve in figure 22 is as good as may be expected. Taylor's theory therefore appears to account for the relative effects of the scale and the intensity of stream turbu-

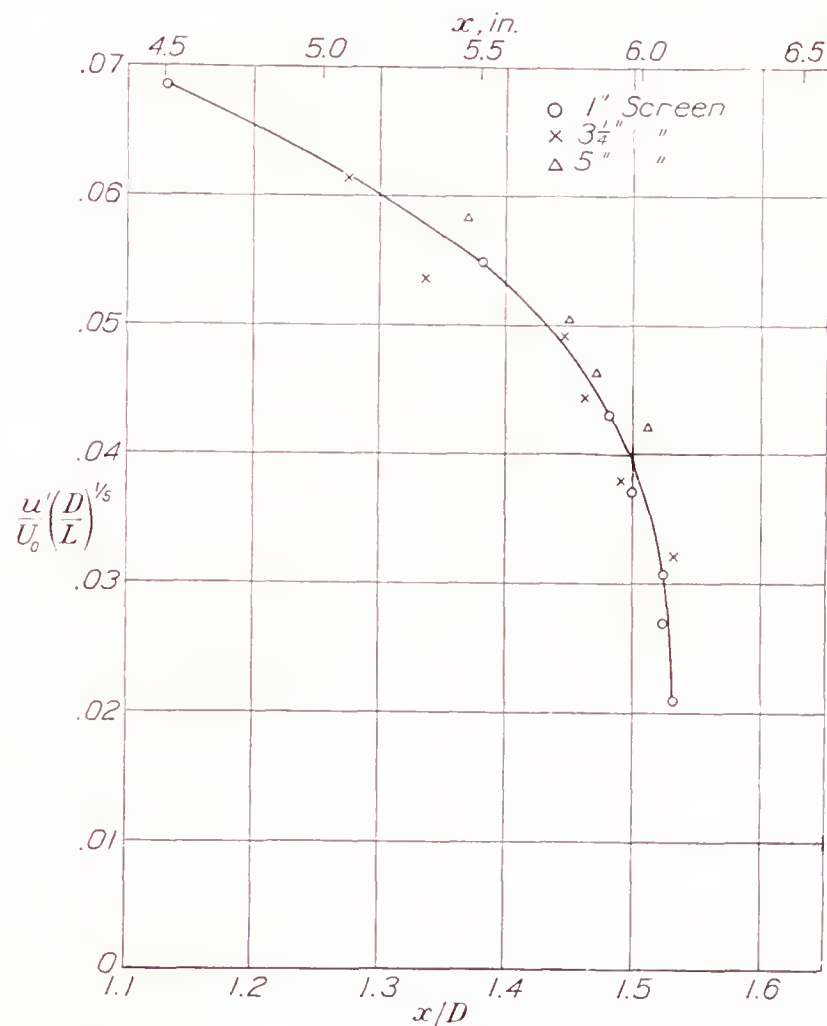


FIGURE 22.—Position of transition as function of  $\frac{u'}{U_0} \left( \frac{D}{L} \right)^{1/5}$ . Air speed, 60 feet per second;  $R_c$ , 118,000.

lence on transition to as close a degree of approximation as the present experiment can detect.

### CONCLUSION

A case has been presented in which boundary-layer separation was followed by a reattachment of the layer to the surface. Transition occurred in the separation zone and the reattached layer was turbulent. The separation was of a nearly laminar type but not purely laminar because of a very incomplete transition beginning ahead of the separation point near the pressure minimum. This case might be called "transition by separation," although such a designation would not mark the phenomenon as unique, since transition probably always occurs somewhere in the detached layer after a laminar or nearly laminar separation. It was probably the occurrence of this transition near the separation point, brought about by a particular set of conditions, that made a reattachment of the layer



possible. The conditions were a low stream turbulence and a Reynolds Number in the neighborhood of 139,000.

When the stream turbulence was raised to about 4 percent, it was impossible to obtain separation before transition at any Reynolds Number. In this case, transition took place gradually, beginning at  $4\frac{1}{2}$  inches from the leading edge of the elliptic cylinder.

It was shown that the minimum in the distribution of skin friction along the surface of the cylinder marked the beginning of transition and that a hot wire mounted on a sliding band served as a satisfactory device for finding the minimum.

At a fixed Reynolds Number, the position of the beginning of transition on the cylinder was found to depend on the scale of the turbulence as well as on the intensity. A functional relation was found to exist between the position  $x/D$  of the beginning of transition and  $\frac{u'}{U_0} \left( \frac{D}{L} \right)^{1/5}$ .

NATIONAL BUREAU OF STANDARDS,  
Washington, D. C., August 6, 1938.

TABLE I.—DIMENSIONS OF SQUARE-MESH SCREENS  
FOR PRODUCING TURBULENCE

Nominal mesh, in.	Average measured mesh, in.	Average measured wire or rod diameter, in.	Material
1	1.007	0.196	Iron wire.
$3\frac{1}{4}$	3.285	.626	Cylindrical wooden rods.
5	5.016	.976	Cylindrical wooden rods.

#### REFERENCES

- Schubauer, G. B.: Air Flow in a Separating Laminar Boundary Layer. T. R. No. 527, N. A. C. A., 1935.

- King, L. V.: On the Convection of Heat from Small Cylinders in a Stream of Fluid: Determination of the Convection Constants of Small Platinum Wires with Applications to Hot-Wire Anemometry. Phil. Trans. Roy. Soc., ser. A, vol. 214, 1914, pp. 373-432.
- Dryden, Hugh L.: Air Flow in the Boundary Layer Near a Plate. T. R. No. 562, N. A. C. A., 1936.
- Mock, W. C., Jr.: Alternating-Current Equipment for the Measurement of Fluctuations of Air Speed in Turbulent Flow. T. R. No. 598, N. A. C. A., 1937.
- Dryden, H. L., and Kuethe, A. M.: Effect of Turbulence in Wind Tunnel Measurements. T. R. No. 342, N. A. C. A., 1930.
- Dryden, H. L., and Kuethe, A. M.: The Measurement of Fluctuations of Air Speed by the Hot-Wire Anemometer. T. R. No. 320, N. A. C. A., 1929.
- Dryden, Hugh L., Schubauer, G. B., Mock, W. C., Jr., and Skramstad, H. K.: Measurements of Intensity and Scale of Wind-Tunnel Turbulence and Their Relation to the Critical Reynolds Number of Spheres. T. R. No. 581, N. A. C. A., 1937.
- Fedisevsky, K.: Turbulent Boundary Layer of an Airfoil. T. M. No. 822, N. A. C. A., 1937.
- Pohlhausen, K.: Zur näherungsweise Integration der Differentialgleichung der laminaren Grenzschicht. Z. f. a. M. M., Bd. 1, 1921, S. 252-268.
- von Kármán, Th., and Millikan, C. B.: On the Theory of Laminar Boundary Layers Involving Separation. T. R. No. 504, N. A. C. A., 1934.
- von Doenhoff, Albert E.: An Application of the von Kármán-Millikan Laminar Boundary-Layer Theory and Comparison with Experiment. T. N. No. 544, N. A. C. A., 1935.
- Fage, A.: Experiments on a Sphere at Critical Reynolds Numbers. R. & M. No. 1766, British A. R. C., 1937.
- Jones, B. Melvill: Flight Experiments on the Boundary Layer. Jour. Aero. Sci., vol. 5, no. 3, Jan. 1938, pp. 81-94.
- Taylor, G. I.: Statistical Theory of Turbulence. V. Effect of Turbulence on Boundary Layer. Theoretical Discussion of Relationship between Scale of Turbulence and Critical Resistance of Spheres. Proc. Roy. Soc. (London), ser. A, vol. 156, no. 888, Aug. 1936, pp. 307-317.



# REPORT No. 653

## A STUDY OF AIR FLOW IN AN ENGINE CYLINDER

By DANA W. LEE

### SUMMARY

*A 4-stroke-cycle test engine was equipped with a glass cylinder and the air movements within it were studied while the engine was being motored. Different types of air flow were produced by using shrouded intake valves in various arrangements and by altering the shape of the intake-air passage in the cylinder head. The air movements were made visible by mixing feathers with the entering air, and high-speed motion pictures were taken of them so that the air currents might be studied in detail and their velocities measured. Motion pictures were also taken of gasoline sprays injected into the cylinder on the intake stroke.*

*The photographs showed that: A wide variety of induced air movements could be created in the cylinder; the movements always persisted throughout the compression stroke; and the only type of movement that persisted until the end of the cycle was rotation about the cylinder axis. The velocities of the air currents were approximately proportional to the engine speed and had about the same value whether the flow was orderly or turbulent. Orderly air movements greatly aided the distribution of the sprays about the cylinder.*

### INTRODUCTION

The performance of spark-ignition engines that spray fuel into the cylinders during the intake stroke is improved when air flow is used to assist the mixing of the fuel and the air. Tests have been made with the N. A. C. A. combustion apparatus (reference 1) to determine the effect of directed air flow on the combustion characteristics of such an engine. The present paper describes apparatus constructed and tests made to study the air movements in an engine cylinder and reports the effects of such movements on the fuel sprays with no combustion taking place. The size and the shape of the cylinder head were the same as those used for the tests of reference 1 and, in both cases, the direction of the air flow was principally controlled by the use of shrouds on the intake valves.

### APPARATUS AND TEST METHODS

#### TEST ENGINE

A steel casting that surrounded and supported a glass cylinder was inserted between the barrel and the head of a single-cylinder test engine. (See figs. 1 and 2.)

Four large openings in the steel casting afforded an unobstructed view through the center of the cylinder. The inside surface of the glass cylinder was accurately ground and polished to the same diameter as the engine bore, and its length was equal to the engine stroke. The wall thickness was 0.5 inch. The lower side of the cylinder head was modified to fit the steel casting and,

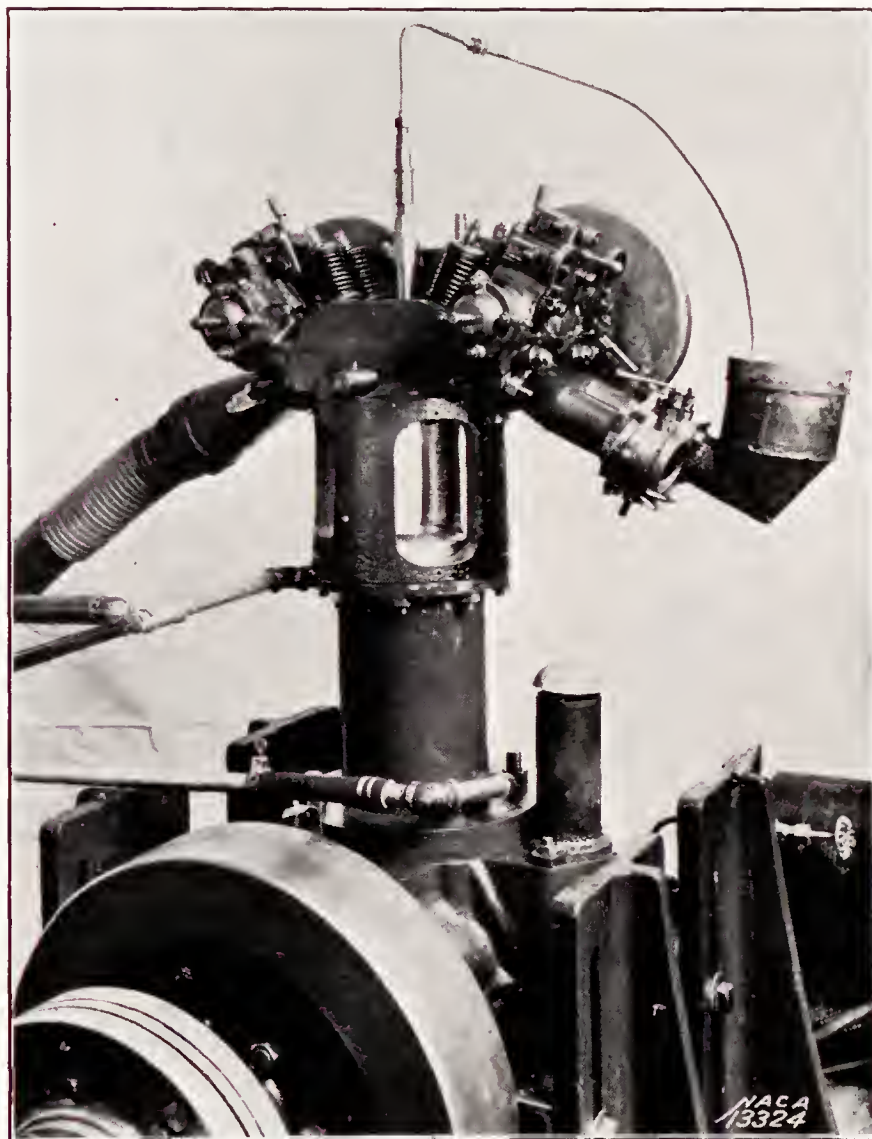


FIGURE 1.—Test engine with glass cylinder.

when bolted down on the casting, it clamped the glass cylinder firmly in place.

A hollow aluminum extension was fastened on top of the piston, its diameter being 0.032 inch less than the inside diameter of the glass cylinder. This clearance was determined from the height of the extension above the piston pin and the maximum angle of oscillation allowed by the clearance of the main piston in the cylinder bore.



There are two inlet and two exhaust valves in the head, each 2 inches in diameter. Other engine constants are as follows:

Engine bore.....	5 inches.
Engine stroke.....	7 inches.
Connecting-rod length.....	12 inches.
Compression ratio.....	6.0.
Ridge angle of pent-roof head.....	130°.
Valve lift.....	$\frac{3}{8}$ inch.
Valve timing:	
Inlet opens.....	15° B. T. C.
Inlet closes.....	45° A. B. C.
Exhaust opens.....	50° B. B. C.
Exhaust closes.....	10° A. T. C.

#### MEANS OF CONTROLLING DIRECTION OF AIR ENTERING CYLINDER

A set of intake valves was equipped with shrouds that forced the air to flow past one side of the valves and thus imparted definite directions to the incoming

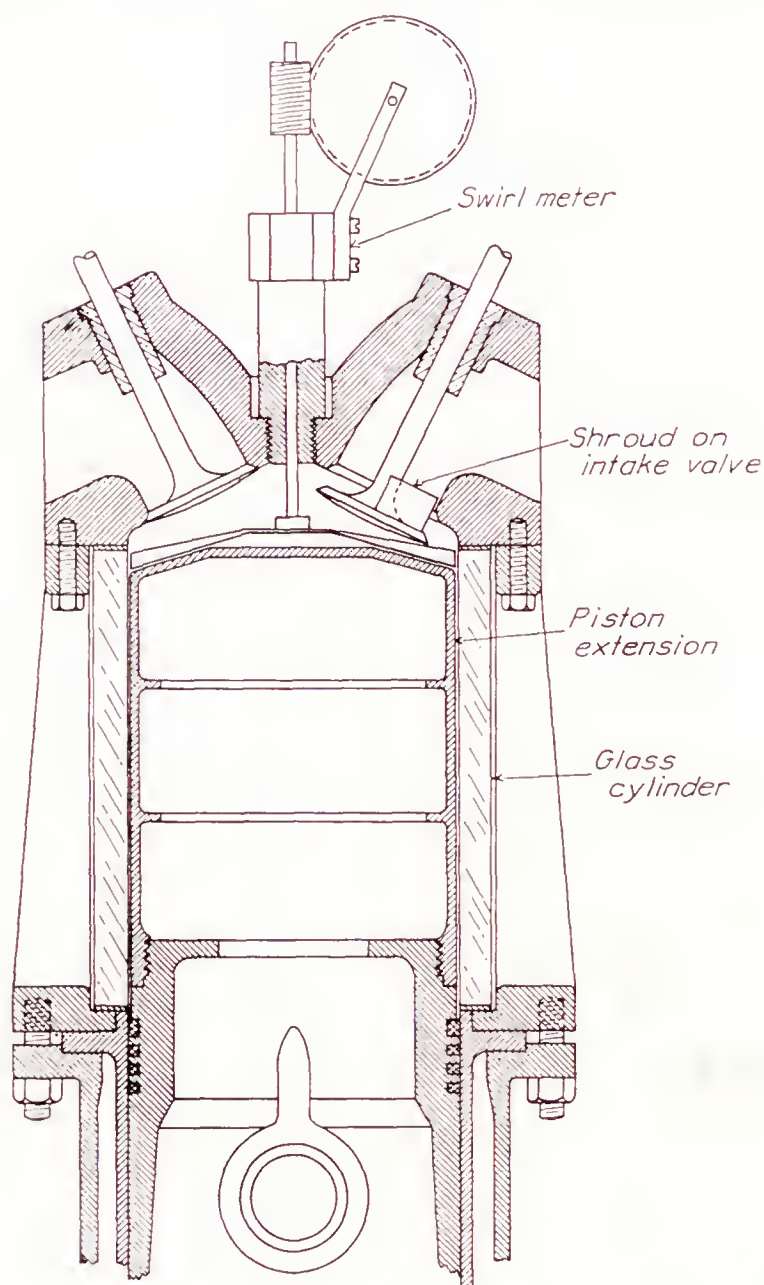


FIGURE 2.—Sketch showing glass cylinder and cylinder head.

air streams. The shrouds were thin brass strips soldered to the valve heads. They normally extended 180° around the head but, for one test, the shroud angle was reduced to 135° and then to 90°. (See figs. 2 and 3.) No means were provided for preventing rotation of the valves, for it was observed that they did not change their positions during the brief test periods.

Another method of controlling the direction of the air as it entered the cylinder was to alter with modeling clay the shape of the intake-air passage in the cylinder head. Figure 4 shows how the passage to one of the intake valves was blocked off and the roof of the passage

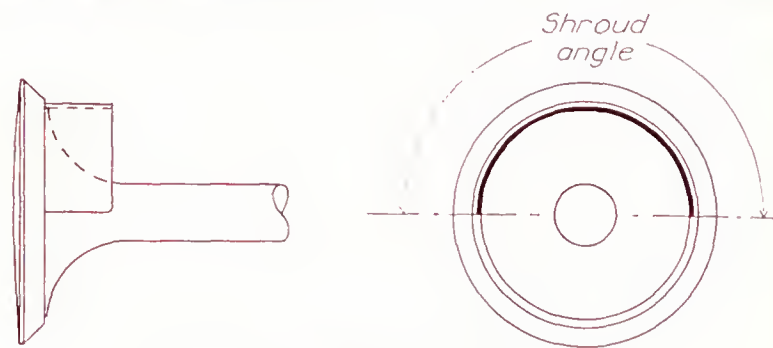


FIGURE 3.—Sketch of shrouded intake valve.

to the other valve was filled in. These changes resulted in the creation of an air swirl in the engine cylinder.

#### MEANS OF MAKING AIR FLOW VISIBLE IN CYLINDER

Smoke was tried as an indicator of the air movements, but the turbulent flow caused it to become intimately mixed with the air shortly after it entered the cylinder.

Metaldehyde crystals, formed by sublimation and recrystallization in air, were used in some of the pre-

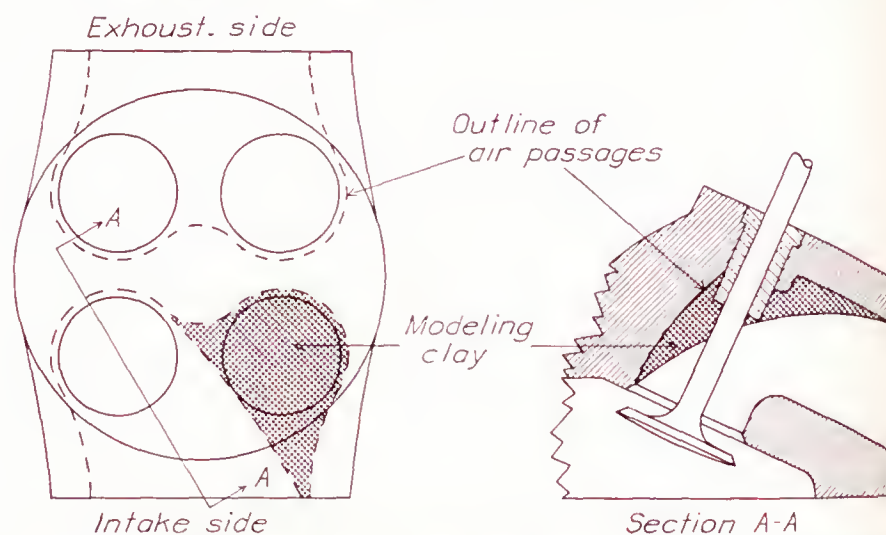


FIGURE 4.—Sketch showing parts of intake-air passage in cylinder head filled with modeling clay.

liminary tests. Although they followed the air better than any other substance tried, they could not be satisfactorily photographed inside the engine nor could individual groups of crystals be identified in successive pictures for the purpose of air-velocity measurements.

The material that proved to be the most satisfactory indicator of air movement was white goose down, cut into short pieces after the heavier pieces had been removed. Its sinking speed in still air averaged about 6 inches per second. It was introduced into the engine at the desired time by a double-barrel intake pipe. One side of this pipe admitted air from the room and the other side was attached to the bottom of a chamber containing the feathers. Butterfly valves in the two barrels were interconnected, one opening as the other closed, so that either air or air mixed with feathers could be admitted to the engine.



## PHOTOGRAPHIC EQUIPMENT

The camera used to photograph the feathers was developed in the laboratories of the Eastman Kodak Company (reference 2). The film moves continuously behind the lens; a rotating parallel-sided prism between the film and the lens moves the image in the same direc-

was painted black so that the feathers appeared white against a black background. (See fig. 5.)

## SWIRL METER

A swirl meter was used to indicate the rate of rotation of the air about the cylinder axis. It consisted of four vanes attached to a spindle extending through the

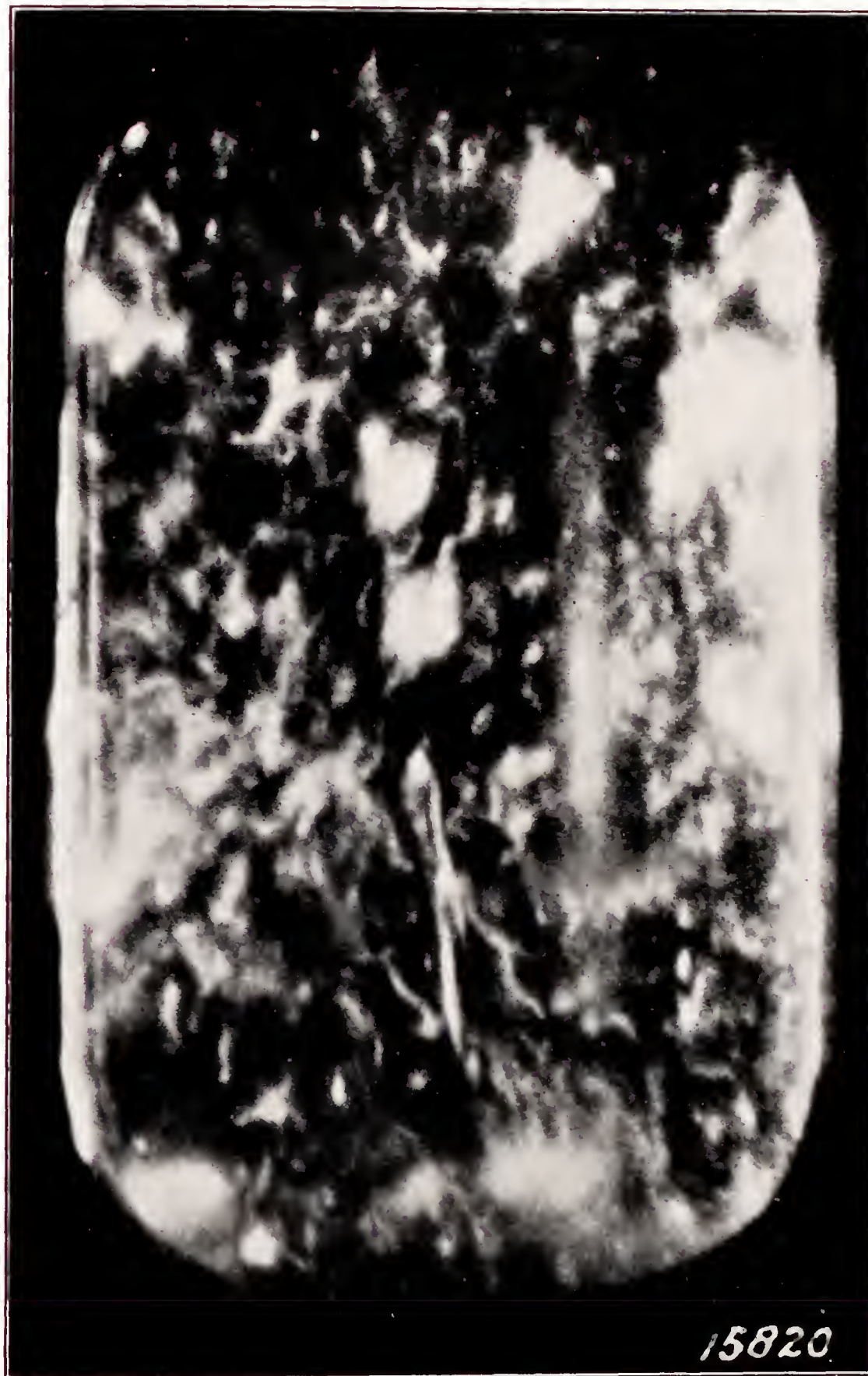


FIGURE 5.—One frame from high-speed motion-picture film showing feathers inside the glass cylinder

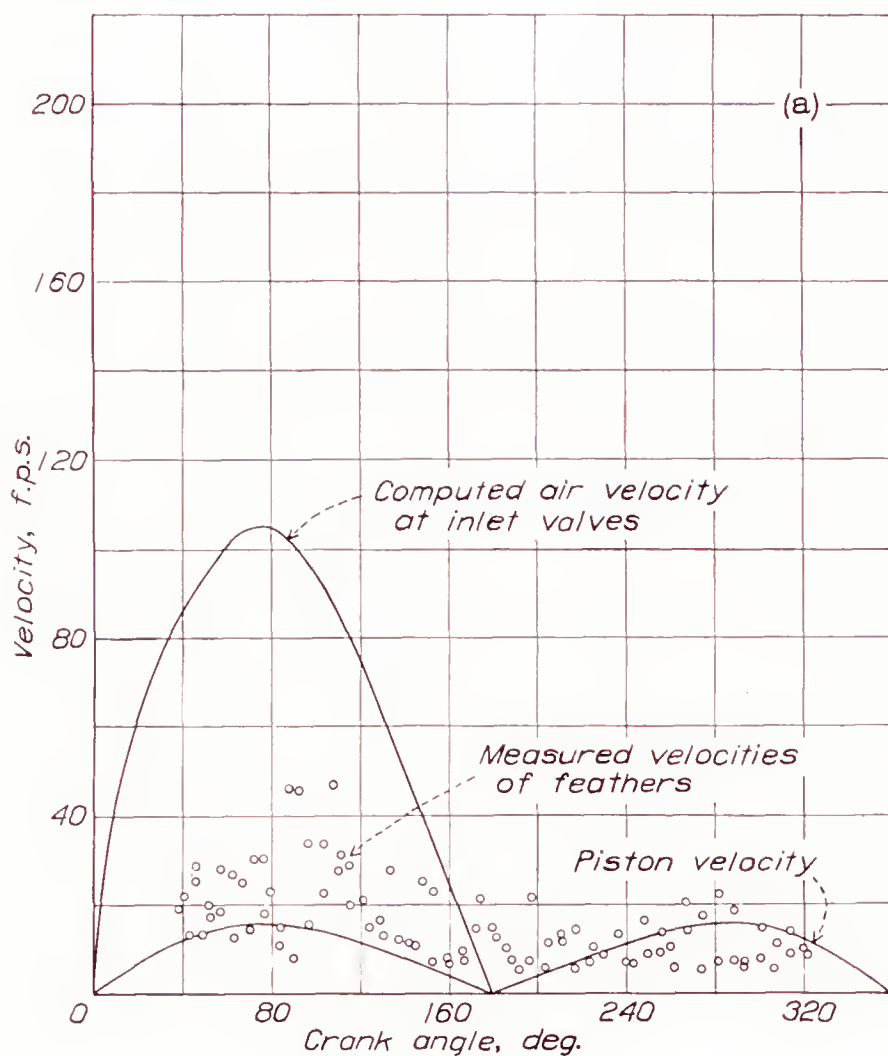
tion and at the same rate as the film during the exposure time. The pictures taken for this investigation were made at rates from 1,700 to 2,400 frames per second. The light from a large electric arc was directed through the glass cylinder at right angles to the camera axis, and the side of the glass cylinder farthest from the camera

center of the cylinder head. (See fig. 2.) The vanes were driven by the rotating air and the number of turns was indicated by a gear driven by a worm on the spindle. Each vane had an area of about 0.42 square inch. End thrust was taken by a ball bearing, and a lap fit around the spindle practically eliminated air leakage.

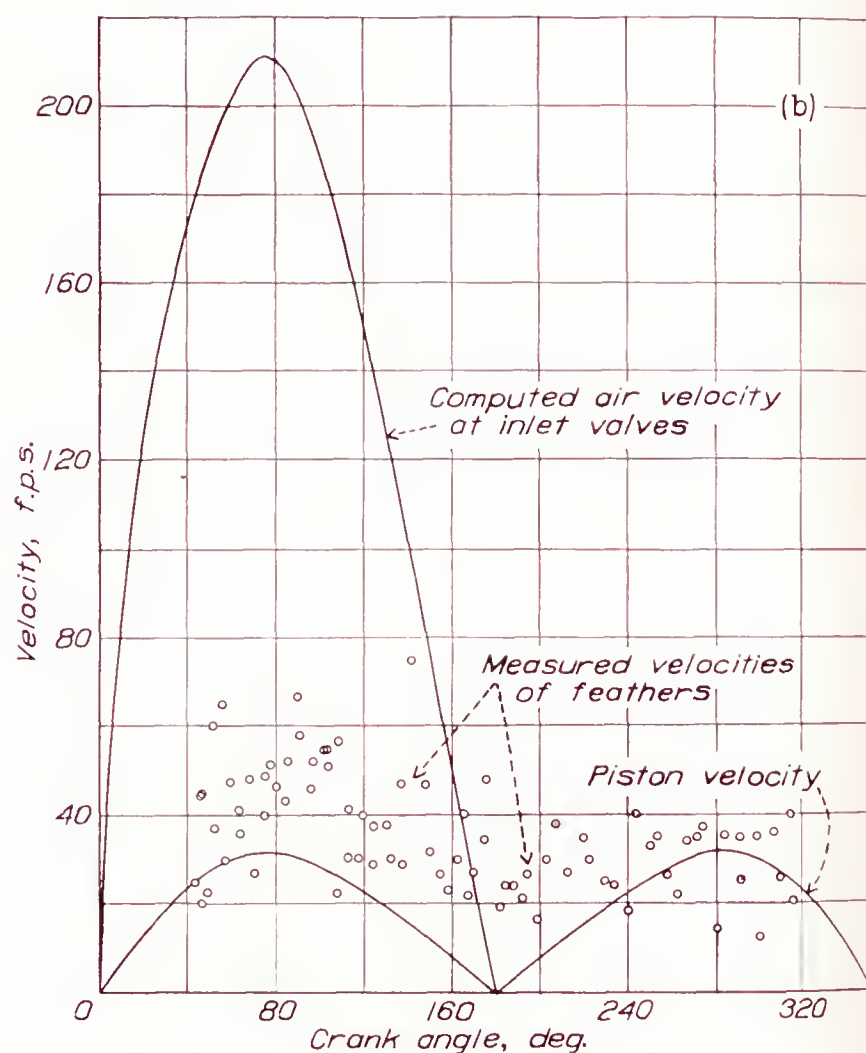


## FUEL-INJECTION EQUIPMENT

The fuel-injection system of the N. A. C. A. spray photographic apparatus (reference 3) was mounted on the engine, and a differential-pressure injection valve was screwed into the spark-plug hole at the center of the cylinder head. (In fig. 2, the swirl meter is shown installed in this hole.) Nozzles of two different types were used. One had four round orifices in a single plane, with diverging axes. The diameter of the two central orifices was 0.018 inch, that of the outer two was 0.010 inch, and the angle between the spray axes was  $20^\circ$ . The other nozzle was of the annular-orifice type, forming a hollow conical spray with an apex angle of  $30^\circ$ .



(a) Engine speed, 500 r. p. m.



(b) Engine speed, 1,000 r. p. m.

FIGURE 6.—Velocities of feathers during the intake and the compression strokes when plain intake valves were used.

## TEST METHODS

Separate series of high-speed motion pictures were made to study the air flow as indicated by the movements of the feathers and to study the effect of the air flow on the fuel sprays. Some motion pictures were made of feathers and fuel sprays together, but they were unsatisfactory because the feathers hid the sprays. The swirl meter was not installed on the engine while any of the motion pictures were being made, but separate motoring tests were later made with it. Engine speed was limited to 1,000 r. p. m. because the motion pictures of the feathers became blurred at higher speeds.

When the high-speed motion pictures were projected on a screen at the normal rate of 16 per second, the velocities of the piston and the feathers were reduced

to less than 1 percent of their actual velocities. The pictures taken at the various conditions were repeatedly projected and studied.

The velocities of the feathers used to indicate the movements of the air were measured by projecting the motion pictures one at a time onto a piece of paper and marking the successive positions of individual feathers. Velocities were then computed from the movement of the feathers and the time interval between pictures. Although it was impossible under the test conditions to obtain sharply defined photographs of the feathers, there never was any uncertainty in identifying them in successive frames from their relative size and shape. The velocities obtained in this manner are not the true

air velocities for two reasons: Motion parallel to the camera axis was neglected; and, in all accelerated movements, the feathers lagged behind the air because of their greater density. The first factor was partly compensated by selecting only the more rapidly moving feathers for measurement or, in the case of orderly air flow, by selecting those moving approximately perpendicular to the camera axis. The inertia of the feathers was probably not a serious factor except in the entering air streams.

## MOTION PICTURES SHOWING AIR MOVEMENTS

## AIR MOVEMENTS WITH PLAIN INTAKE VALVES

When plain intake valves were used in the engine, the air in the cylinder was in a very agitated and turbulent



state during the intake stroke. Some air movement across the top of the chamber from the intake to the exhaust valves and thence down the cylinder wall was caused by the masking effect of the cylinder wall close to the intake valves, but this flow was very slight compared with the indiscriminate movements. The air movements created during the intake stroke continued throughout the compression stroke, at slowly reducing velocities. By the time the piston had descended far enough on the expansion stroke to reveal the inside of the cylinder (about  $40^\circ$  A. T. C.), most of the turbulence had died out and, during the last two strokes of the cycle, the air movements were mostly due to expansion and expulsion of the air by the piston.

The air in the cylinder always became densely fogged with water vapor early on the expansion stroke. This phenomenon was observed at all engine speeds and on dry days as well as on days of high humidity. It was probably caused by the transfer of heat from the compressed air to the cylinder head and walls during the compression stroke, so that on the expansion stroke the temperature of the air fell below the dew point.

Figure 6 shows the measured velocities of feathers obtained during the intake and the compression strokes of the engine while using plain intake valves. The corresponding crank angles were determined from the positions of the piston extension in each picture. The velocities of the entering air streams at the valve seats were computed, the air being assumed inelastic, and they are also shown in the figure. The great range of velocities during the intake stroke shows how varied the air speed was in different parts of the cylinder at the same time. The higher values were obtained from feathers in the air streams from the intake valves, and the lower values were obtained from feathers in the lower parts of the cylinder where the air had lost much of its entering velocity. The highest feather velocities were less than the computed inlet-air velocities because they were measured 1.5 inches or more from the valve seats. The range of velocities was greatly reduced after the end of the intake stroke, and most of the air motion caused by the entering air streams died out during the expansion and the exhaust strokes.

#### AIR MOVEMENTS WITH SHROUDED INTAKE VALVES

Tests were made with the shrouded intake valves arranged in the nine different positions shown in figure 7, the shrouds extending  $180^\circ$  around the valves in each case. Arrangements A, B, C, D, and E produced a rotation of all the air in the cylinder about the vertical axis. Arrangement A produced the highest rate of rotation with the least turbulence. Measured velocities of feathers obtained with this valve arrangement are shown in figure 8. The velocities are about twice those obtained with plain intake valves, probably because of the doubled air velocity through the intake valves with  $180^\circ$  shrouds. The range of ve-

locities during the intake stroke was as great as when plain valves were used, although the direction of the air flow was very consistently a rotation about the cylinder axis. The scatter of the test points on the figures showing feather velocities cannot, therefore, be taken as an indication of turbulence. The best method of evaluating turbulence was found to be a careful observation of the motion pictures.

Arrangement C produced almost as high a rate of rotation as A but with slightly greater turbulence.

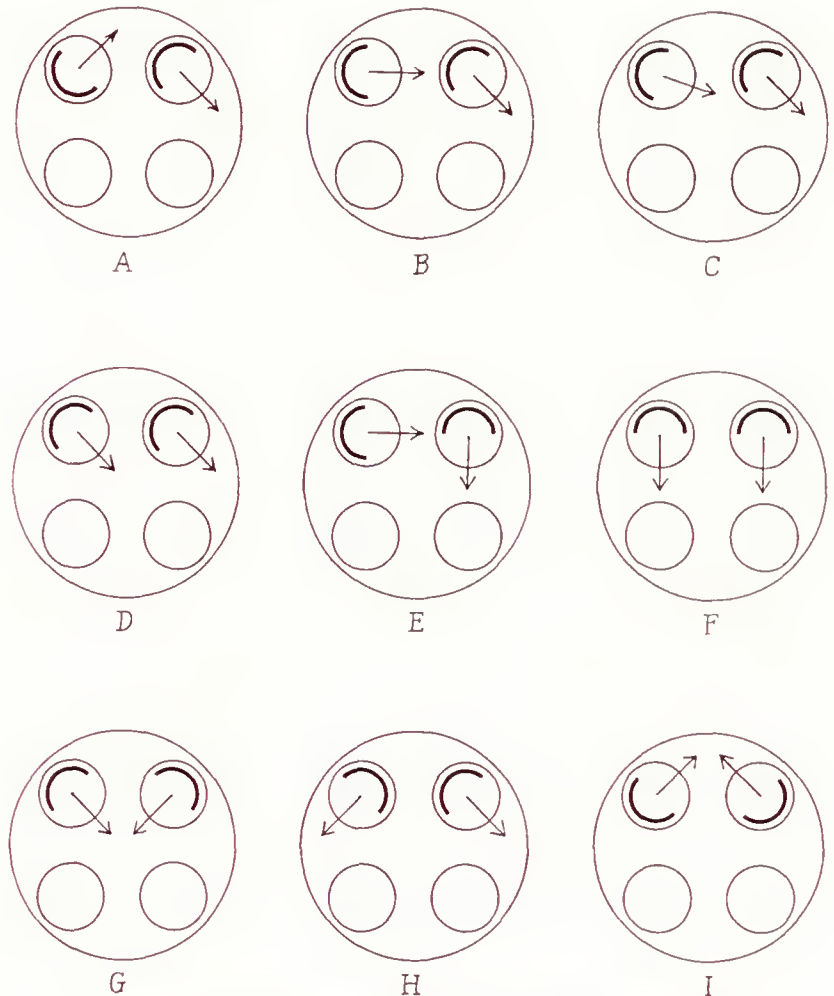


FIGURE 7.—Arrangements of the shrouded intake valves.

The rates of rotation produced by arrangements B and E were about equal and both were decidedly less than those produced by A and C. The amounts of turbulence were greater, probably because in each case one of the valves discharged air directly toward the other.

With arrangement D, the air movements in the cylinder during the first  $140^\circ$  of the cycle were dominated by the flow from the valve directing air radially inward. After crossing the top of the chamber, this air flowed down along the cylinder wall, back across the top of the piston extension, and then up along the opposite side of the cylinder, thus completing a vertical loop. At the same time, air from the other valve was being directed tangentially, so that a rotary motion was also being built up. During the compression stroke the vertical movement died out, leaving a relatively slow rotation of the entire air charge about the cylinder axis. Turbulence was greater with arrangement D than with any other arrangement producing air rotation about the cylinder axis.

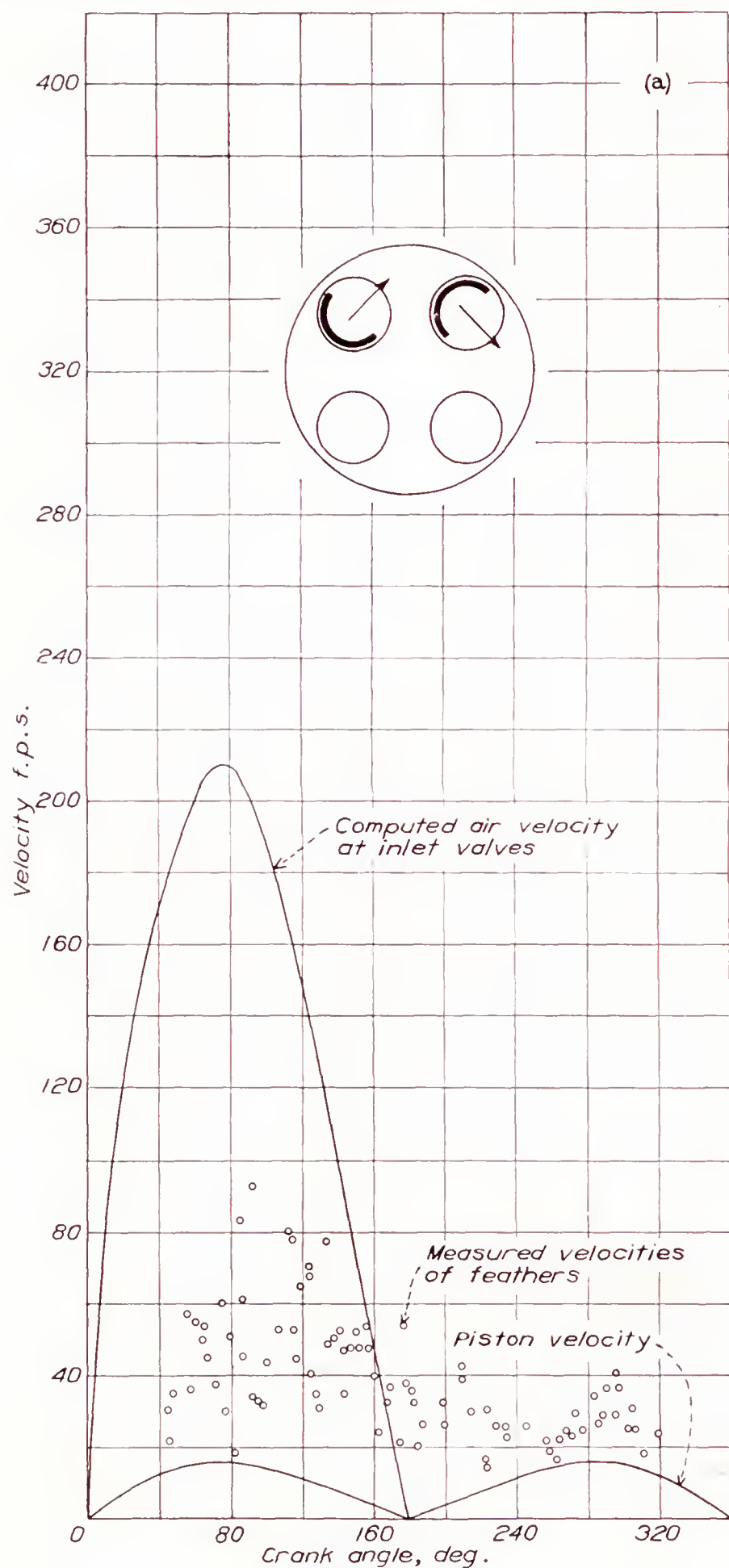


In general, it may be stated that shroud arrangements which result in the greatest rate of air rotation produce the least turbulence and vice versa.

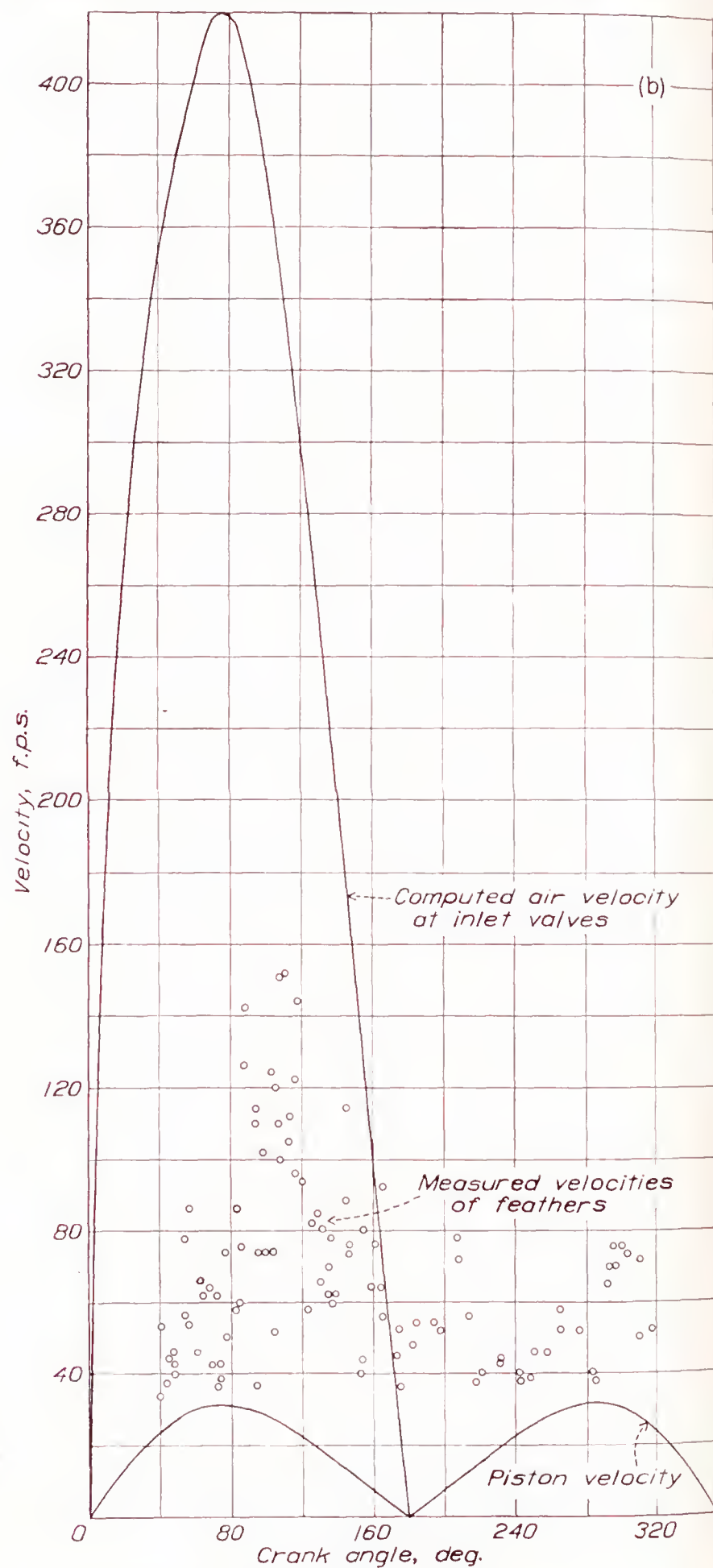
The motion pictures indicated that the air rotated with uniform angular velocity rather than with uniform

intake stroke always persisted, at a decreasing rate, throughout the compression, the expansion, and the exhaust strokes.

When both of the shrouded intake valves were set to direct the incoming air across the top of the chamber,



(a) Engine speed, 500 r. p. m.



(b) Engine speed, 1,000 r. p. m.

FIGURE 8.—Velocities of feathers when shroud arrangement A was used.

linear velocity. Of course, the air in the entering streams was at a much higher velocity than the rest, but it soon expended its energy in turbulence or in accelerating the rotation of the air already in the cylinder. Any horizontal rotation set up during the

as in arrangements F, G, and H, the air moved in a vertical loop as previously described. With arrangement F, the loop movement started early on the intake stroke. It was faster and contained less turbulence than the movements with arrangements G or H. Ve-



locities of feathers measured while arrangement F was used are shown in figure 9. The range of velocities is about the same as that obtained when other valve arrangements were used or when plain intake valves were used at twice the engine speed. With arrangement G, a marked turbulence preceded the loop motion, which did not begin until about the middle of the intake stroke. With arrangement H, there was

in the cylinder was complicated. During the intake stroke, the air moved in a loop similar to that described except that, instead of being in a vertical plane, it was slanted across the cylinder. This air movement set up a general rotation of the air charge, which continued to the end of the cycle. Turbulence was general throughout the cylinder during the intake stroke but died out during the compression stroke.

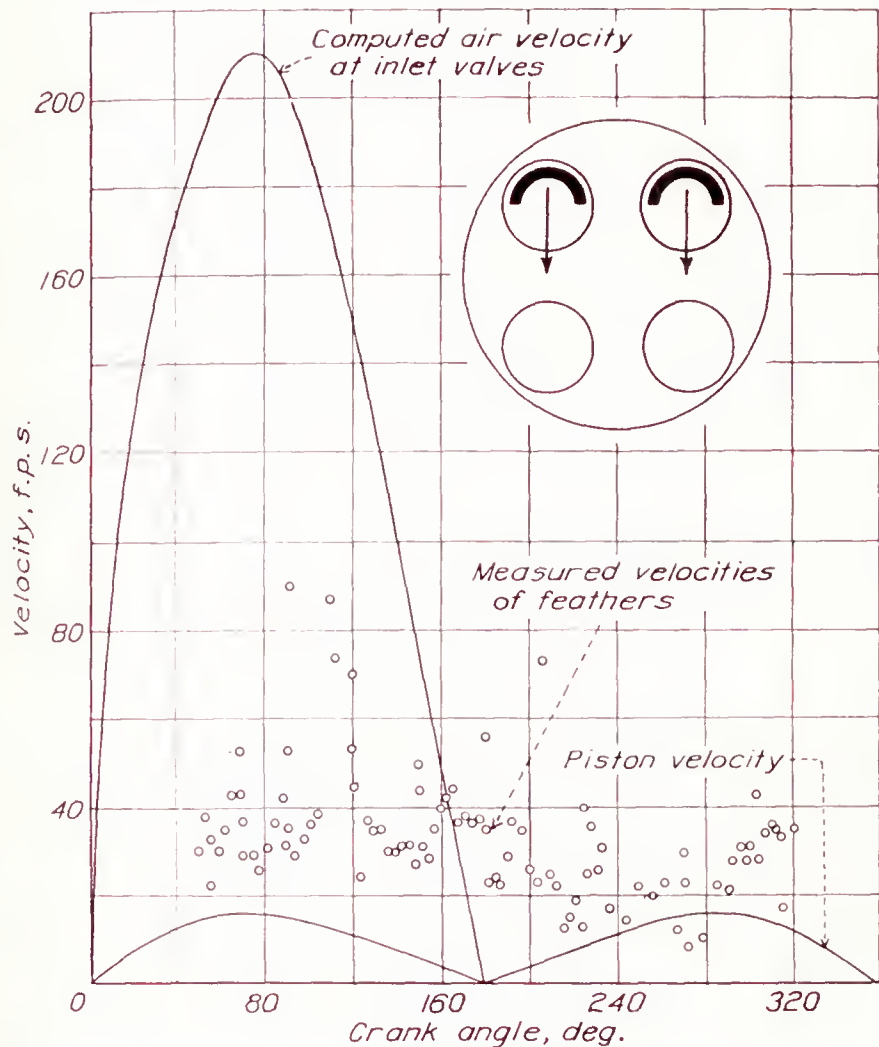


FIGURE 9.—Velocities of feathers when shroud arrangement F was used. Engine speed, 500 r. p. m.

turbulent motion with some parts of the air charge rotating in either direction about the cylinder axis during most of the intake stroke. A slow vertical-loop motion appeared near the end of the intake stroke. Arrangement I also resulted in a slow vertical-loop movement but the direction was the reverse of that with arrangements F, G, and H; that is, the air first descended along the cylinder wall nearest the intake valves, then crossed the top of the piston, and ascended the other side of the cylinder. The loop motion began early on the intake stroke and was accompanied by marked turbulence. With each of the last four arrangements discussed, the vertical-loop movement continued during the compression stroke but was never observed on the expansion and the exhaust strokes.

#### AIR MOVEMENTS WITH ALTERED INTAKE PASSAGE

When the intake-air passage in the cylinder head was altered as shown in figure 4, all the air entered the cylinder through a single plain valve. The shape of the intake passage caused the entering air stream to pass to one side of the cylinder axis and be slanted downward about 45°. The resulting air movement

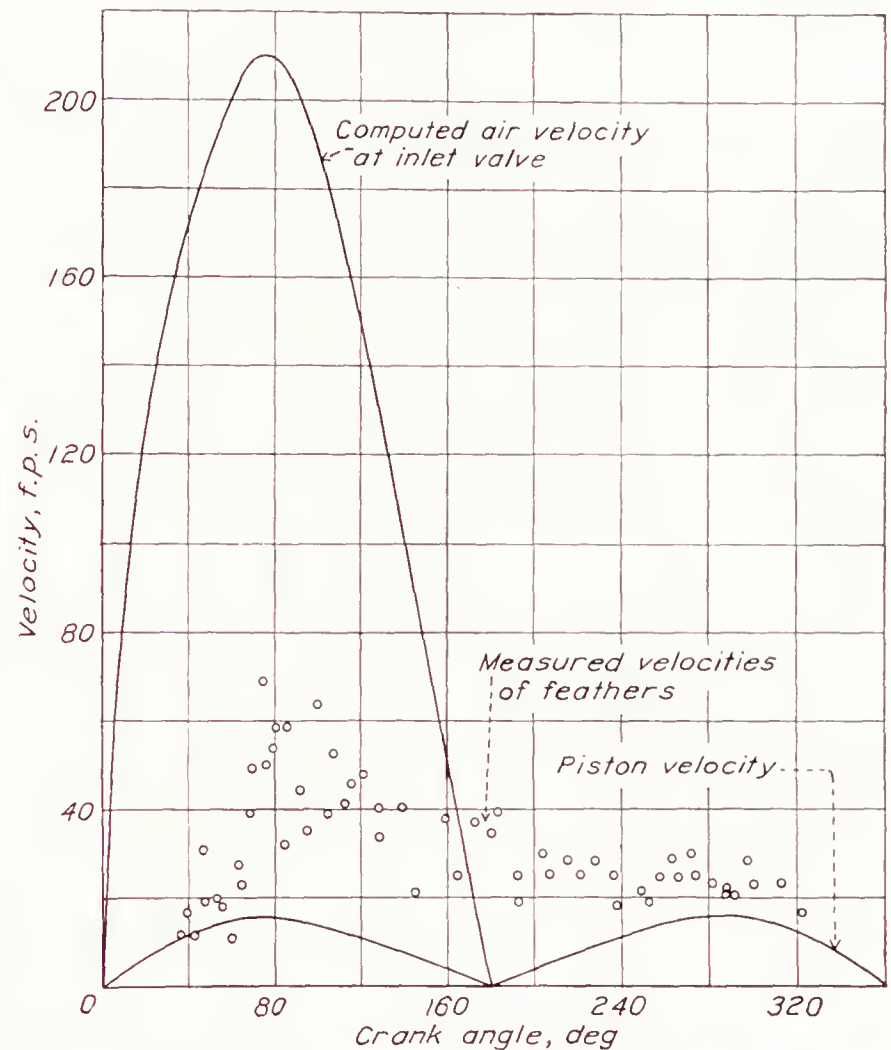


FIGURE 10.—Velocities of feathers after the intake-air passage had been altered. Engine speed, 500 r. p. m.

Velocities of feathers obtained when the altered intake passage was used are shown in figure 10. They are slightly lower than those obtained with shrouded valves in arrangement A.

#### MEASUREMENT OF THE RATES OF AIR SWIRL

Two methods were used to measure the rates at which the air rotated about the cylinder axis. In one, the high-speed motion pictures were projected onto a screen one at a time and the angular velocities of the feathers were obtained from the time it took them to pass between two vertical lines on the screen, spaced to represent 30° of rotation. A distance of 2 inches was chosen as the mean radius of the rotating feathers because some stereoscopic high-speed motion pictures made with a special attachment on the camera showed that the paths of most of the feathers lay within 1 inch of the cylinder wall. The results of measuring the rates of air swirl in the foregoing manner are shown in figures 11 to 14. The test points were scattered as widely as those in the figures showing velocities of feathers, but they are shown only in figure 14, which contains a single test condition. The entire 4-stroke cycles are represented, the dashed portions of the



curves being the regions near top center where the inside of the cylinder was not visible.

The second method used to measure rates of air rotation was to obtain with a stop watch the time required for several hundred turns of the swirl meter. This method is considered less reliable than the photo-

graphic method because of the inertia and the friction of the rotating parts and because it measures the swirl in only a small part of the chamber. It was used, however, mostly as a check on the other tests, and the conclusions given at the end of this report are based mostly on the results of the photographic method.

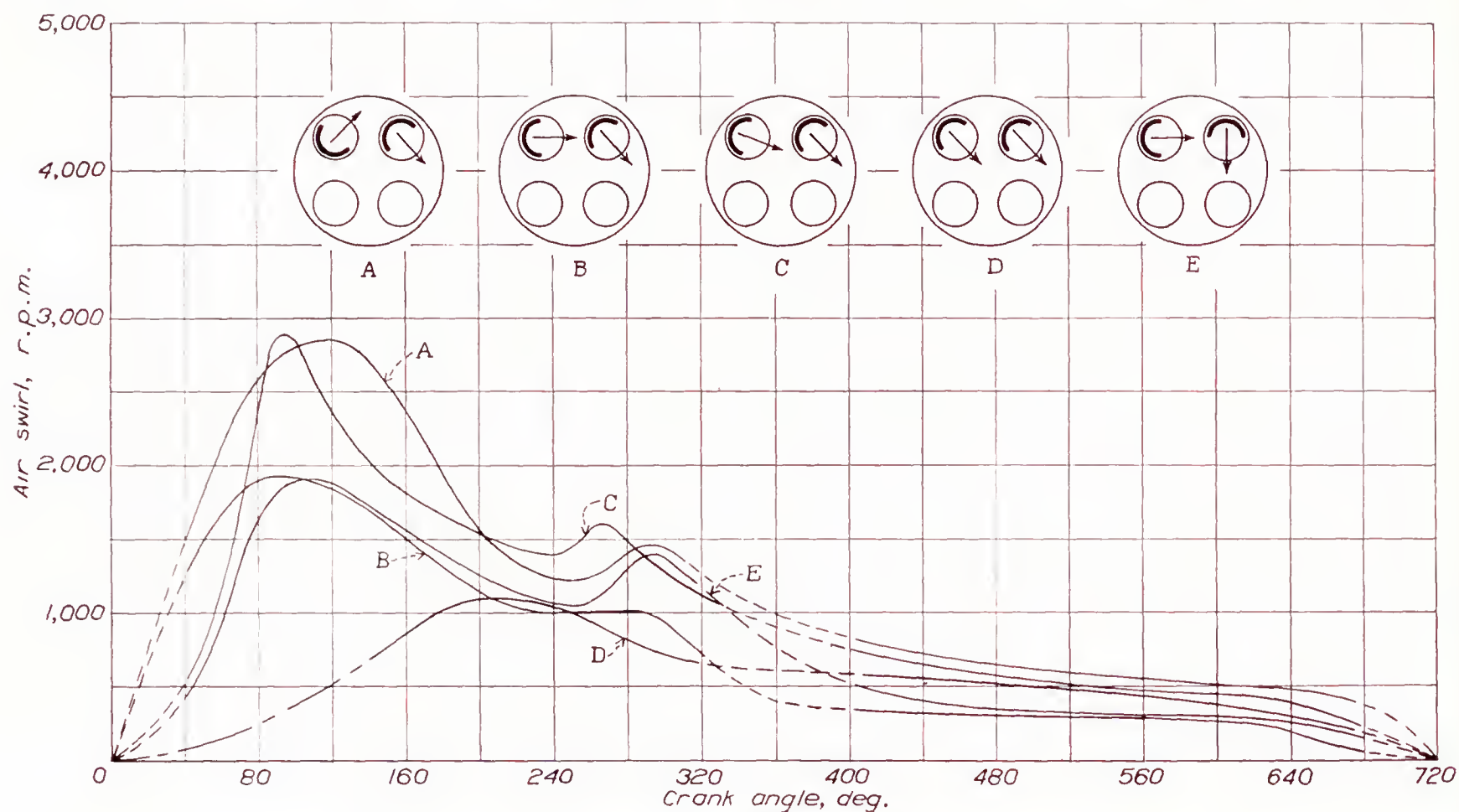


FIGURE 11.—Effect of shrouded intake-valve arrangement on rate of air swirl. Engine speed, 500 r. p. m.

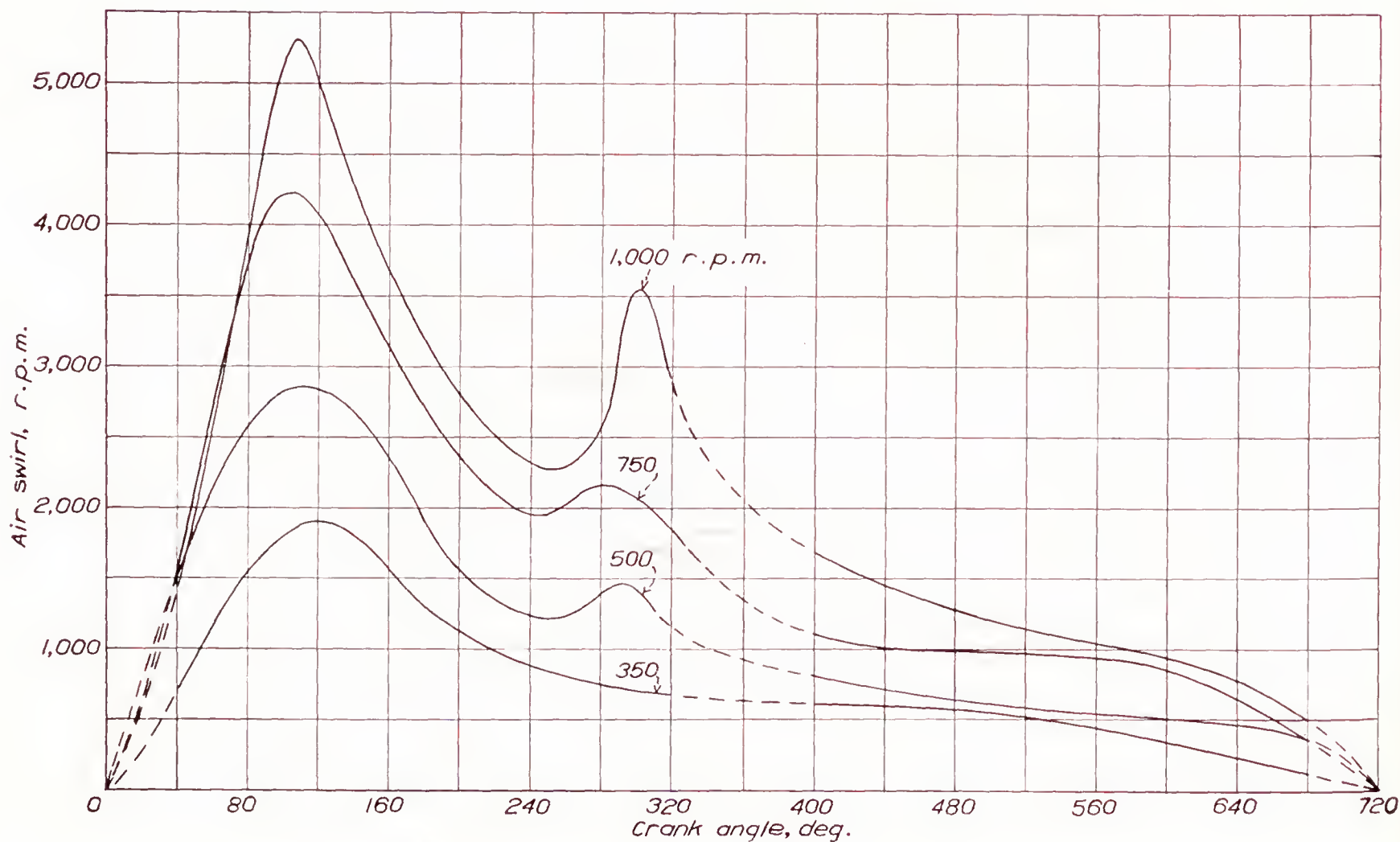


FIGURE 12.—Effect of engine speed on rate of air swirl when shroud arrangement A was used.



Table I gives the mean swirl rates obtained by integrating the curves in figures 11 to 14 and also gives the results of the swirl-meter tests. The meter usually gave a higher mean rate than the photographic method, probably because the rotating vane of the meter was close to the intake valves where the air velocity was high.

TABLE I  
MEAN SWIRL RATES

Condition causing swirl	Shroud angle (deg.)	Engine speed (r. p. m.)	Mean swirl rate (r. p. m.)		
			Photo-graphic method	Swirl meter	
Shrouds	Arrangement: A..... B..... C..... D..... E.....	180	500	1, 100	1, 340
				700	1, 260
				950	720
				-----	380
				750	1, 090
	A.....	180	1, 000	350	700
				500	1, 100
				750	1, 600
				2, 000	2, 140
				-----	2, 960
Altered intake passage.....	-----	500	1, 100	-----	
			950	-----	
			650	-----	
			850	1, 060	

Variations in swirl rate with crank angle, when the shrouded intake valves were used in arrangements A to E, are shown in figure 11. With each arrangement except D, the swirl rate was greatest at about 110 crank degrees after the beginning of the intake stroke, dropped to about half the maximum value at 250 crank degrees, then slightly increased while the piston was moving most rapidly on its compression stroke, and finally decreased slowly for the rest of the cycle. Valve arrangement A gave the highest mean swirl rate, and arrangement D gave the lowest. As explained earlier, the air movements with arrangement D were dominated during the first 140 crank degrees by air from the radially set valve. Although rotation was slowly building up during this period, it could not be measured from the movements of the feathers; this part of the curve in figure 11 is therefore given as a broken line.

The effect of engine speed on the rate of air swirl, when shroud arrangement A was used, is shown in figure 12. Swirl rates were approximately proportional to the engine speed, the maximum rate being about 5.5 times the engine speed and the mean rate being about twice the engine speed.

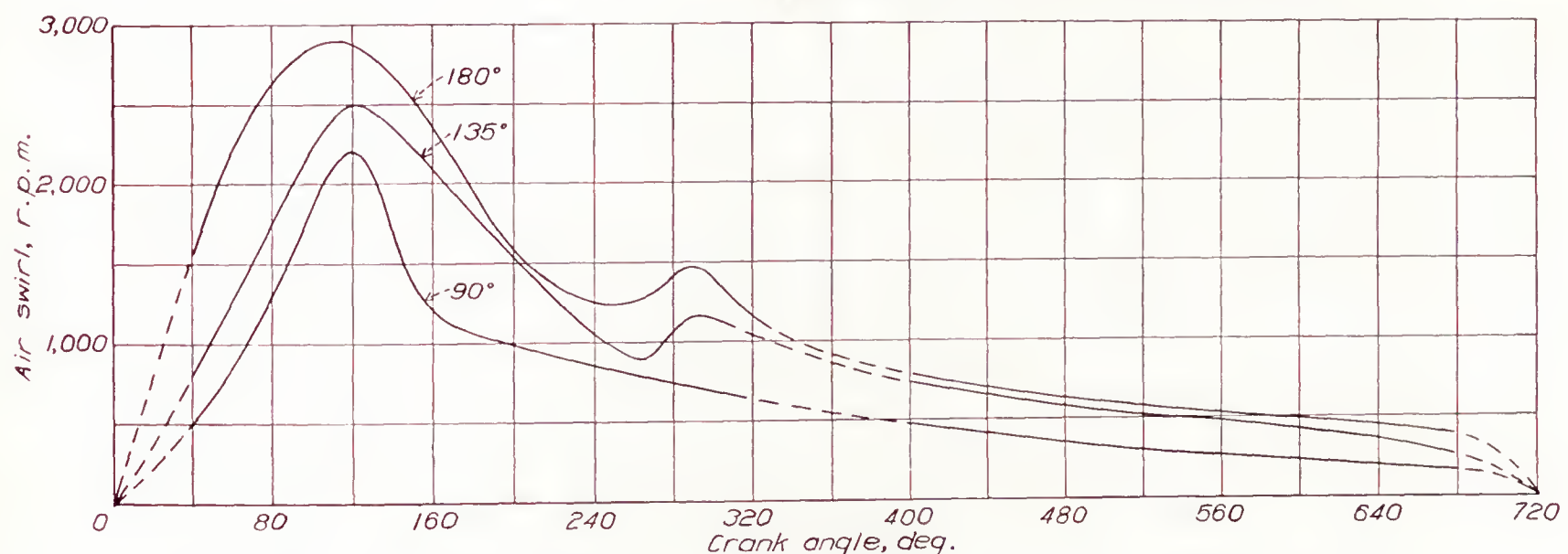


FIGURE 13.—Effect of shroud angle on rate of air swirl when shroud arrangement A was used. Engine speed, 500 r. p. m.

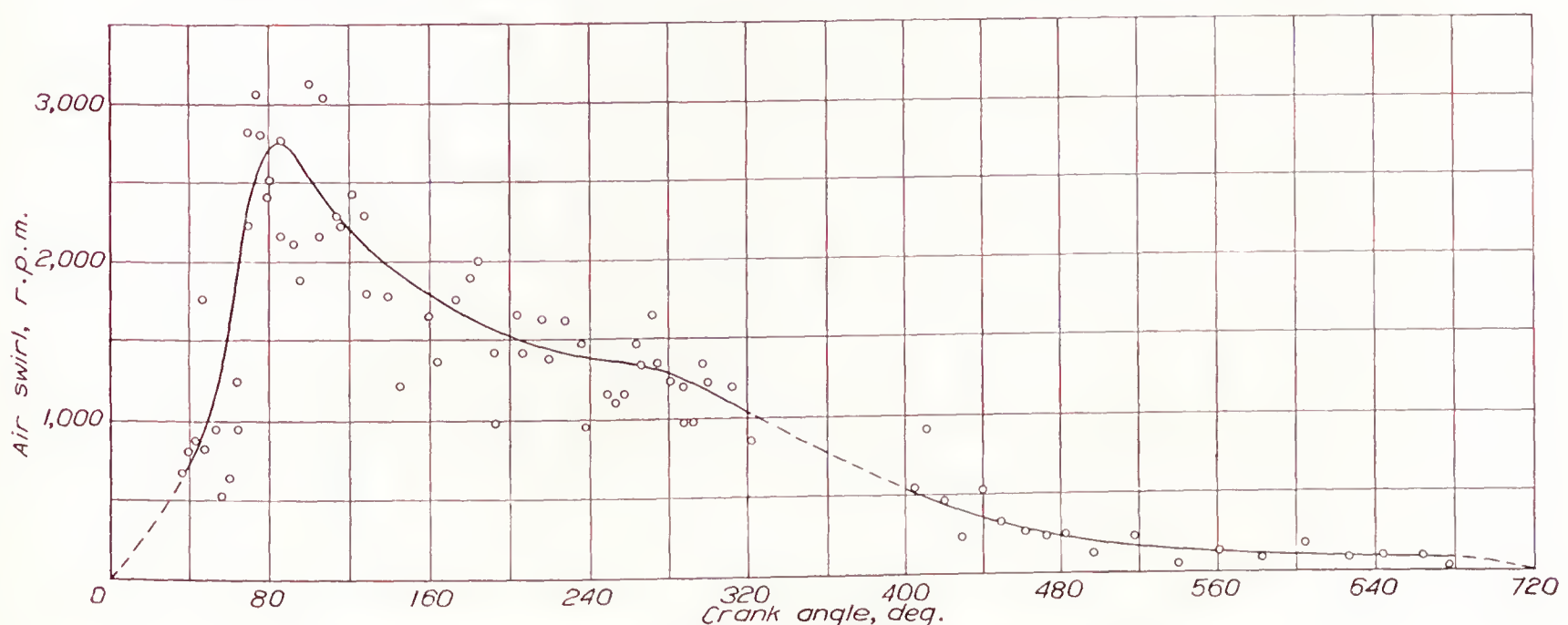


FIGURE 14.—Air swirl created by altering shape of intake-air passage. Engine speed, 500 r. p. m.



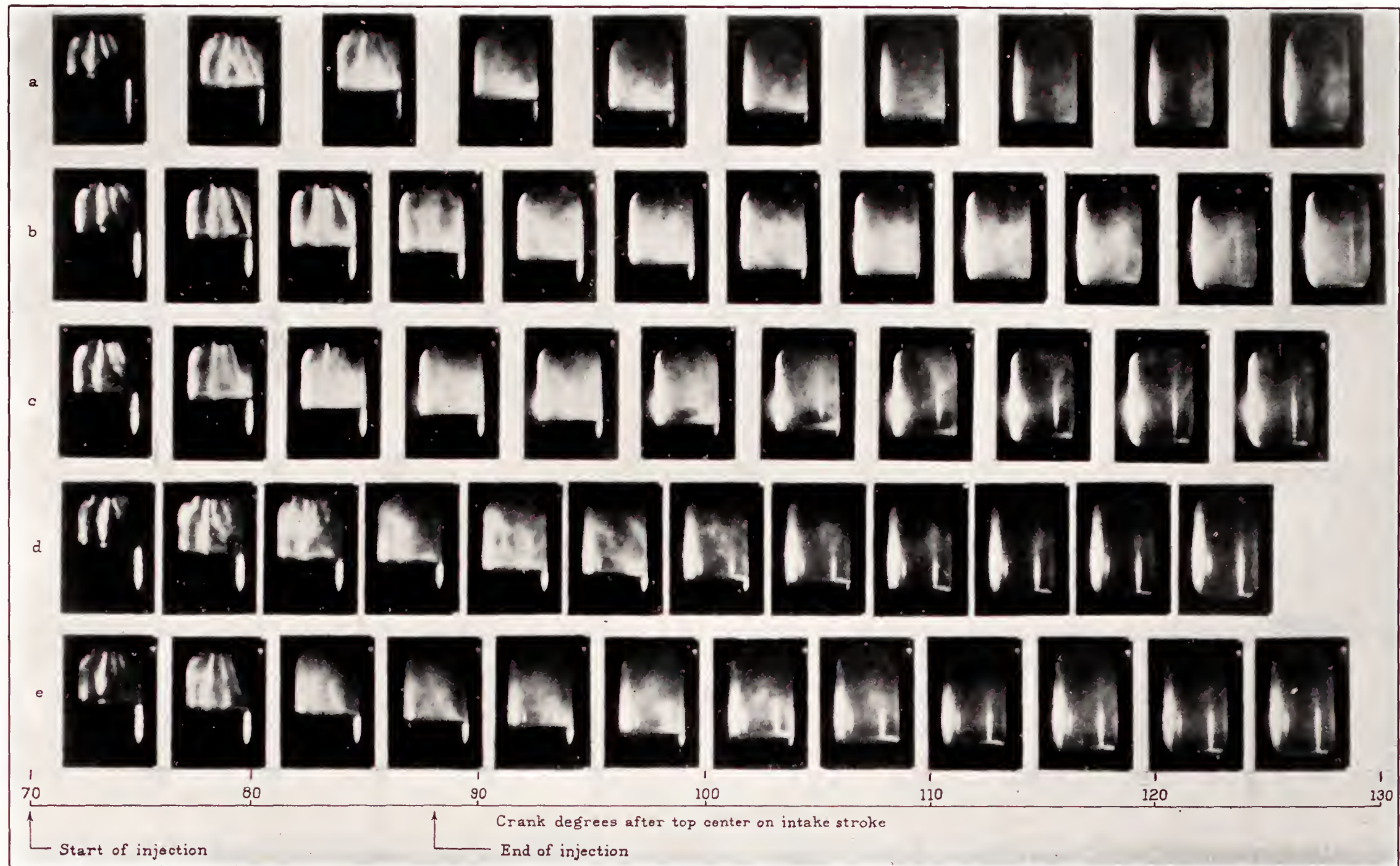


FIGURE 15.—High-speed motion pictures of sprays from the 4-orifice nozzle using different intake conditions and fuels. (a) Plain valves, gasoline spray; (b) shrouded valves in arrangement A, gasoline spray; (c) shrouded valves in arrangement F, gasoline spray; (d) altered intake passage, gasoline spray; (e) altered intake passage, Diesel-fuel spray.



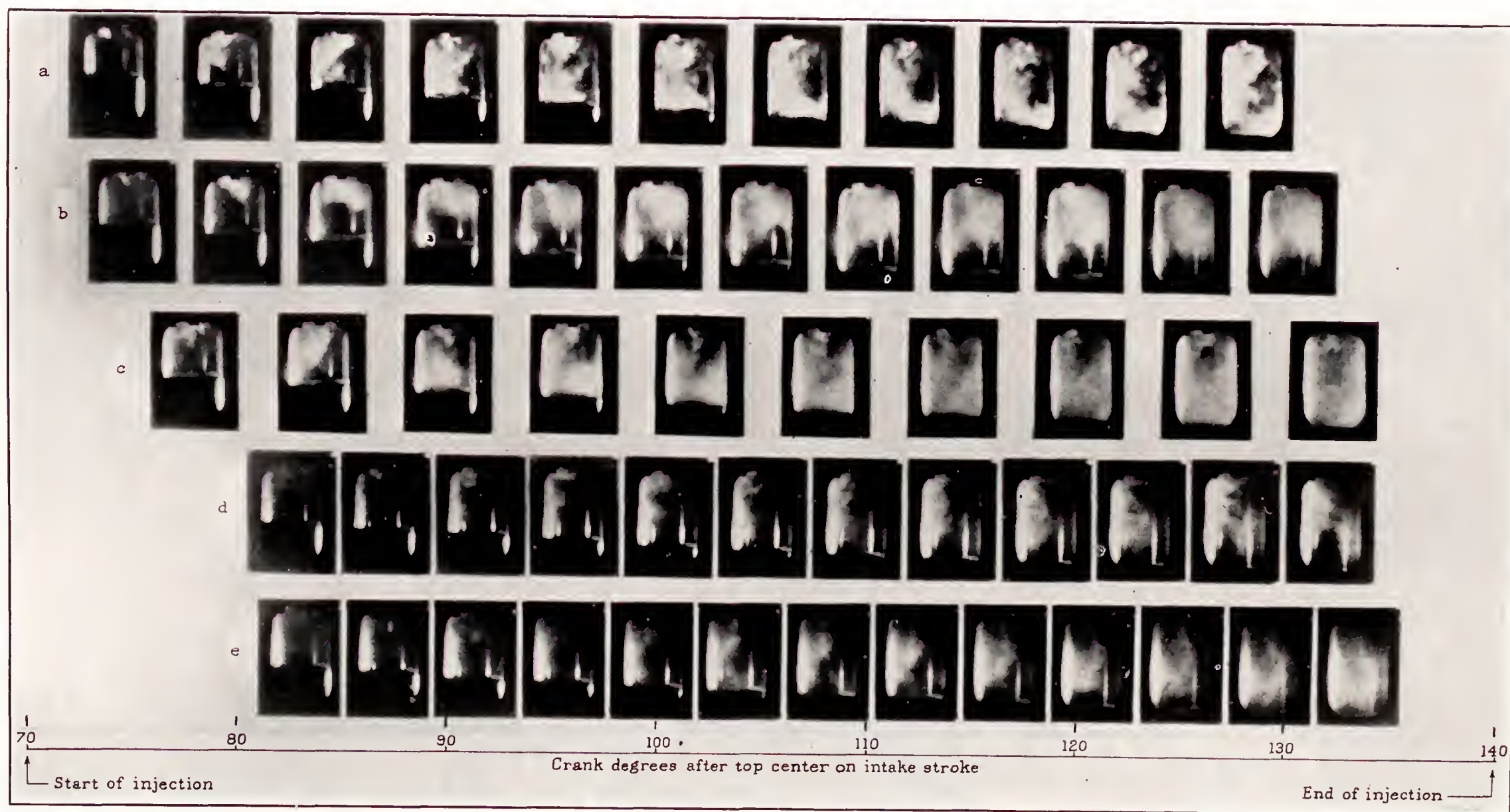


FIGURE 16.—High-speed motion pictures of sprays from the annular-orifice nozzle using different intake conditions and fuels. (a) Plain valves, gasoline spray; (b) shrouded valves in arrangement A, gasoline spray; (c) shrouded valves in arrangement F, gasoline spray; (d) altered intake passage, gasoline spray; (e) altered intake passage, Diesel-fuel spray.



The effect of decreasing the angular extent of the intake-valve shrouds from  $180^\circ$  to  $135^\circ$  and then to  $90^\circ$ , while shroud arrangement A was used, is shown in figure 13. Table I indicates that the mean swirl rates were roughly proportional to the shroud angle. Figure 14 shows how the swirl rate changed when the intake-air passage was altered. The maximum rate of swirl came at about 85 crank degrees after the beginning of the intake stroke, earlier than when shrouded intake valves were used; and the swirl rate during the last half of the cycle was very low.

### EFFECT OF AIR MOVEMENT ON FUEL SPRAYS

#### TEST CONDITIONS

High-speed motion pictures were taken of sprays from the 4-orifice nozzle and from the annular-orifice nozzle injected into the cylinder on the intake stroke. Injection began at  $70^\circ$  A. T. C. in each case and lasted 18 crank degrees with the 4-orifice nozzle and 70 crank degrees with the annular-orifice nozzle. An injection pressure of 2,000 pounds per square inch was used with both nozzles, and the amount of fuel injected was approximately equivalent to full-load fuel quantity. Two fuels were used, aviation gasoline and a high-grade automotive Diesel fuel. The Diesel fuel was used at only one condition, so the following description of results refers to gasoline sprays unless it is otherwise stated. Neither fuel was ignited, but the penetration, the distribution, and the rate of vaporization of the sprays were studied from the motion pictures. Four air-intake conditions were used at an engine speed of 500 r. p. m., as follows: with plain intake valves, with shrouded intake valves in arrangements A and F, and with the intake passage altered.

#### SPRAYS FROM THE 4-ORIFICE NOZZLE

Some of the motion pictures of the 4-orifice sprays are reproduced in figure 15. Only every third picture taken is shown, and they have been spaced to fit a uniform scale of crank degrees. The penetration of the sprays was unaffected by the air movements in the cylinder, the tips of the two inner sprays reaching the piston about 5 crank degrees after the start of injection in each case. Most of the fuel impinged on the piston or the cylinder walls, showing that the orifices were too large or the injection pressure too great. The central parts of the four jets were not deflected by even the most rapid air movements; but the fine mist in the spray envelopes, and also the mist formed by impingement on the piston, was picked up and distributed by the air currents. When shroud arrangement A was used, the mist was well distributed in the lower part of the cylinder where most of the fuel went, but it failed to mix with the air in the upper part of the cylinder. When shroud arrangement F was used, the mist was carried to the upper part of the cylinder, leaving the

center of the cylinder relatively "lean." Altering the intake-air passage in the engine head seemed to be the most effective way to secure rapid and complete mixing of the fuel and the air in the cylinder, probably because this change resulted in air movements having both horizontal and vertical components and also containing much small-scale turbulence.

#### SPRAYS FROM THE ANNULAR-ORIFICE NOZZLE

The penetration of sprays from the annular-orifice nozzle was markedly affected by air movements in the cylinder. (See fig. 16.) With plain intake valves, the sprays reached the piston about  $20^\circ$  after the start of injection. With shrouded intake valves in arrangement A, the spray never quite reached the piston; but, with shroud arrangement F, it reached the piston in 25 crank degrees. When the intake passage in the head was altered, it took the spray 110 crank degrees to reach the piston, and by then it had been well broken up by the air currents. The lack of penetrating power in this type of spray is well illustrated by the fact that the sprays were deflected by even the slow vertical-loop movement obtained with plain intake valves, caused by the partial masking effect of the nearby cylinder wall. The air movements obtained with shrouded valves and with the altered intake passage distributed all the fuel in the conical sprays about the cylinder in much the same way that they distributed the mist surrounding the sprays from the 4-orifice nozzle.

#### COMPARISON OF GASOLINE AND DIESEL-FUEL SPRAYS

Diesel-fuel sprays were used only with the altered intake passage. In this case their appearance and behavior were about the same as gasoline sprays. A failure of part of the apparatus terminated the test program before additional pictures of Diesel-fuel sprays could be taken.

### CONCLUSIONS

The results of the experiments described in this report may be summed up as follows:

1. Air movements created in the engine cylinder during the intake stroke continued throughout the compression stroke and were a distinct aid to the distribution of gasoline sprays injected into the cylinder.
2. The velocities of induced air movements were approximately proportional to the engine speed and about inversely proportional to the flow area at the intake valves. They were about the same whether the air flow was orderly or turbulent.
3. The use of shrouded intake valves set to direct the incoming air tangentially caused the air to rotate rapidly about the cylinder axis. The maximum rate of rotation was reached at about 110 crank degrees after the beginning of the intake stroke, and the rotation continued until the end of the exhaust stroke.



4. When shrouded intake valves were set to direct the incoming air across the tops of the cylinders, the air moved in vertical loops and the movement died out at the end of the compression stroke.

5. The use of a single plain intake valve with its manifold shaped to direct the incoming air tangentially resulted in a rotation of the air accompanied by considerable turbulence and some vertical air movements.

LANGLEY MEMORIAL AERONAUTICAL LABORATORY,  
NATIONAL ADVISORY COMMITTEE FOR AERONAUTICS,  
LANGLEY FIELD, VA., *September 15, 1938.*

## REFERENCES

1. Rothrock, A. M., and Spencer, R. C.: The Influence of Directed Air Flow on Combustion in a Spark-Ignition Engine. T. R. No. 657, N. A. C. A., 1939.
2. Tuttle, F. E.: A Non-Intermittent High-Speed 16 mm Camera. Soc. Motion Picture Eng. Jour., vol. XXI, no. 6, Dec. 1933, pp. 474-477.
3. Rothrock, A. M.: Pressure Fluctuations in a Common-Rail Fuel Injection System. T. R. No. 363, N. A. C. A., 1930.







# REPORT No. 654

## GENERAL AIRPLANE PERFORMANCE

By W. C. ROCKEFELLER

### SUMMARY

*Equations have been developed for the analysis of the performance of the ideal airplane, leading to an approximate physical interpretation of the performance problem. The basic sea-level airplane parameters have been generalized to altitude parameters and a new parameter  $\Omega_\sigma$  has been introduced and physically interpreted.*

*The performance analysis for actual airplanes has been obtained in terms of the equivalent ideal airplane in order that the charts developed for use in practical calculations will for the most part apply to any type of engine-propeller combination and system of control, the only additional material required consisting of the actual engine and propeller curves for the propulsion unit.*

*Finally, a more exact method for the calculation of the climb characteristics for the constant-speed controllable propeller is presented in the appendix. This method replaces the approximate method, contained in the main body of the paper, in cases where the approximate method is not sufficiently accurate.*

### INTRODUCTION

Considerable interest has been evidenced in the past few years in the field of aircraft-performance analysis. With the increased use of the new types of engine and propeller equipment, many modifications of the existing performance-analysis methods have been introduced, which are designed for use in calculating the effect of these new developments on performance.

Oswald has investigated the problem and drawn up charts (reference 1) that can be used to calculate the performance of aircraft using unsupercharged engines and fixed-pitch propellers. Later he extended this analysis to include the case of supercharged engines (reference 2). White and Martin (reference 3) made a similar analysis for the case of constant-speed propellers with no supercharging, which can be extended to include supercharging.

In each of the foregoing analyses, special assumptions were made with regard to the variation of engine power with altitude and engine speed and the variation of propulsive efficiency with altitude and air speed. New engine and propeller developments that will cause changes in the characteristics of these units can, however, be expected to take place in the future, thus

necessitating a complete recalculation and revision of the charts to correspond to these changes. For this reason it was considered desirable to attack the problem in a more general manner, in order to obtain a method of performance calculation basically independent of the particular engine-propeller combination but readily adaptable to any type. In the following analysis, the attempt was made to eliminate from the basic relations any assumptions that were likely to require adjustment as a result of future design or experiment.

The author wishes to thank the men who have aided greatly in the development and preparation of the paper by contributing many excellent suggestions and criticisms.

The  $\frac{d\eta}{dJ}$  against  $J$  charts presented in the appendix are due to Mr. Richard W. Palmer of the Vultee Aircraft Co., and the rest of the charts in this section were designed to conform to this suggestion. As mentioned in the body of the paper, Dr. Th. von Kármán and Dr. Clark B. Millikan are primarily responsible for the accurate physical interpretation of the three major parameters,  $\Lambda_\sigma$ ,  $\Gamma_\sigma$ , and  $\Omega_\sigma$ . The author particularly wishes to thank Dr. Millikan for the considerable time and effort spent in the form of suggestions and criticisms throughout the preparation of the paper. Dr. Norton B. Moore and Dr. W. Bailey Oswald of the Douglas Aircraft Co. have also aided considerably in this regard. Various members of the wind-tunnel staff of the Daniel Guggenheim Aeronautics Laboratory contributed greatly in the technical preparation of the paper. In particular, Messrs. Frank J. Malina and W. T. Butterworth aided in the preparation of the numerous charts.

### SUMMARY OF NOTATION

Subscripts:

$\sigma$ , at altitude.

0, at sea level.

$m$ , maximum.

$c$ , at maximum rate of climb.

$MP$ , at theoretical minimum power required.

$V$ , velocity  $\left\{ \begin{array}{l} \text{miles per hour in engineering equations} \\ \text{and charts.} \\ \text{feet per second in physical equations} \\ \text{and charts.} \end{array} \right.$



$V_0$ , maximum velocity in level flight at sea level.

$V_\sigma$ , maximum velocity in level flight at altitude corresponding to  $\sigma$ .

$V_{MP}$ , velocity at minimum power required for the ideal airplane.

$V_c$ , velocity at maximum rate of climb.

$V_{max}$ , maximum possible velocity at all altitudes.

$V_t$ , minimum velocity in level flight for an ideal airplane with no parasite drag.

$V_p$ , maximum velocity in level flight for an ideal airplane with no induced drag.

$$R_v = \frac{V \text{ at altitude corresponding to } \sigma}{V_\sigma}$$

$$R_{v_0} = \frac{V}{V_0}$$

$$R_{vMP} = \frac{V_{MP}}{V_0} \text{ in section IV C.}$$

$$= \frac{V_{MP}}{V_\sigma} \text{ in all other sections.}$$

$$= \frac{V_c}{V_0} \text{ in section IV C.}$$

$$= \frac{V_c}{V_\sigma} \text{ in all other sections.}$$

$$R_R = \frac{V_c}{V_{MP}} \text{ both at same altitude.}$$

$$R_P = \frac{P}{P_0} = \frac{\text{t.hp.}}{\text{t.hp. (design)}}$$

$$R_{vM} = \frac{V}{V_{MP}} \text{ both at same altitude.}$$

$C$ , maximum rate of climb  $\left\{ \begin{array}{l} \text{feet per minute in engi-} \\ \text{neering equations and} \\ \text{charts.} \\ \text{feet per second in physical} \\ \text{equations.} \end{array} \right.$

$C_0$ , maximum rate of climb of the ideal airplane with no drag.

$h$ , altitude (feet).

$H$ , absolute ceiling (feet).

$h_m$ , altitude for  $V_{max}$ .

$C_L$ , lift coefficient.

$C_D$ , drag coefficient.

$$C_P = 5 \times 10^{10} \frac{\text{b. hp.}}{\sigma N^3 D^5}$$

$P$ , thrust horsepower available.

$P_c$ , thrust horsepower available at maximum rate of climb.

$P_0$ , thrust horsepower available at  $V_0$  ( $\sigma=1$ ).

b. hp., brake horsepower.

(t. hp.)<sub>a</sub>, thrust horsepower available.

(t. hp.)<sub>r</sub>, thrust horsepower required.

$N$ , propeller revolutions per minute.

$D$ , propeller diameter (feet).

$$J = \frac{88V}{ND}$$

$$J_c = J \text{ at } V_c.$$

$$J_{MP} = J \text{ at } V_{MP}.$$

$\rho$ , mass density of air.

$\rho_0 = 0.002378$  (slugs per cu. ft.) = mass density of standard air at sea level.

$\sigma = \rho/\rho_0$ , density ratio.

$\sigma_m = \sigma$  at altitude for  $V_{max}$ .

$W$ , weight (lb.).

$f$ , equivalent parasite area (sq. ft.).

$e$ , airplane efficiency factor (reference 1).

$k$ , Munk's span factor.

$b_1$ , largest individual span of wing cellule.

$b$ , equivalent monoplane span  $= kb_1$ .

$b_e = \sqrt{e(kb_1)^2}$ , effective span.

$\eta$ , propulsive efficiency.

Engineering parameters:

$$l_{s\sigma} = \frac{W}{\sigma e(kb_1)^2} = \frac{1}{\sigma} l_s, \text{ effective span loading (lb./sq. ft.).}$$

$$l_{p\sigma} = \frac{W}{\sigma f} = \frac{1}{\sigma} l_p, \text{ parasite loading (lb./sq. ft.).}$$

$$l_{t\sigma} = \frac{W}{\text{t. hp.}} = l_t, \text{ thrust horsepower loading (lb./hp.).}$$

$$\Lambda_\sigma = \left(\frac{1}{\sigma}\right)^{2/3} \Lambda = \left(\frac{1}{\sigma}\right)^{2/3} \frac{l_s l_t^{4/3}}{l_p^{1/3}}, \text{ major performance parameter.}$$

Physical parameters:

$A$ , horsepower conversion factor (550 in American system).

$$\lambda_{s\sigma} = \frac{2}{\pi \rho_0} \frac{W}{\sigma e(kb_1)^2} = 267.7 l_{s\sigma}$$

$$\lambda_{p\sigma} = \frac{2}{\rho_0} \frac{W}{\sigma f} = 841.0 l_{p\sigma}$$

$$\lambda_{t\sigma} = \frac{1}{A} \frac{W}{\eta \text{ b. hp.}} = 0.001818 l_{t\sigma}$$

$$\Lambda_\sigma = \frac{\lambda_{s\sigma} \lambda_{t\sigma}^{4/3}}{\lambda_{p\sigma}^{1/3}} = \left(\frac{1}{\sigma}\right)^{2/3} \frac{\lambda_s \lambda_t^{4/3}}{\lambda_p^{1/3}} = \left(\frac{1}{\sigma}\right)^{2/3} \Lambda' = 0.006293 \Lambda_\sigma$$

$$\Omega_\sigma = \left(\frac{\lambda_{t\sigma}}{\lambda_{p\sigma}}\right)^{1/3} V_\sigma = \sigma^{1/3} \left(\frac{\lambda_t}{\lambda_p}\right)^{1/3} V_\sigma \text{ (} V_\sigma \text{ in ft./sec.)}$$

$$\Gamma_\sigma = \frac{\lambda_{s\sigma} \lambda_{t\sigma}}{V_\sigma} = \frac{1}{\sigma} \frac{\lambda_s \lambda_t}{V_\sigma} \text{ (} V_\sigma \text{ in ft./sec.)}$$

$$\Gamma_{\sigma MP} = \frac{\lambda_{s\sigma} \lambda_{t\sigma}}{V_{MP}} = \frac{1}{\sigma} \frac{\lambda_s \lambda_t}{V_{MP}} \text{ (} V_\sigma \text{ in ft./sec.)}$$

## I. FUNDAMENTAL PERFORMANCE EQUATION

The fundamental performance equation may be written

$$W \frac{dh}{dt} = A \eta \text{ b. hp.} - \frac{\rho}{2} f V^3 - \frac{W^2}{\pi \frac{\rho}{2} e (kb_1)^2} \frac{1}{V} \quad (1)$$

where  $dh/dt$  is the rate of climb.



Writing this equation in terms of the  $\lambda$  parameters (reference 1), there results

$$\frac{dh}{dt} = \frac{1}{\lambda_t} \left[ \frac{P}{P_0} - \sigma R_{v_0}^3 \frac{\lambda_t}{\lambda_p} V_0^3 - \frac{1}{\sigma R_{v_0}} \frac{\lambda_s \lambda_t}{V_0} \right] \quad (2)$$

where the parameters are defined as

$$\lambda_p = \frac{2W}{\rho_0 f} = \frac{2}{\rho_0} l_p$$

$$\lambda_s = \frac{2}{\pi \rho_0} \frac{W}{e(kb_1)^2} = \frac{2}{\pi \rho_0} l_s$$

$$\lambda_t = \frac{1}{A} \frac{W}{(\text{b. hp.})_0 \eta_0} = \frac{1}{A} l_t$$

and where

$$R_{v_0} = V/V_0$$

$V$ , velocity under arbitrary conditions.

$\eta_0$ , propulsive efficiency at  $V_0$  ( $\sigma=1$ ).

In equation (2) the ratio  $P/P_0$  represents the combined variation in engine output and propulsive efficiency from the design value  $P_0$ .

## II. METHODS OF PERFORMANCE ANALYSIS

There are two general methods of attack that may be employed in the calculation of airplane performance:

1. As suggested by Oswald, the sea-level performance may first be calculated and the performance at altitude may then be compared with that at sea level. In this case all the parameters used in the analysis will be "sea-level parameters" such as  $\lambda_p$ ,  $\lambda_s$ ,  $\Gamma$ , and  $\Lambda'$ . These parameters are used in Oswald's analysis.

2. The performance at altitude may be calculated directly without reference to the sea-level, or "reference-level," performance. In this case the parameters involved are somewhat altered and become what may be termed "altitude parameters."

Both methods are basically similar but take somewhat different forms insofar as the final formulas and charts are concerned. Each method has its own advantages, particularly as regards physical significance and facility for practical calculation, but the relative advantages vary with the particular problems to be solved. For this reason both methods will be herein presented, together with recommendations concerning the adaptability of each to specific types of problems that are encountered in practical performance calculation.

## III. ANALYSIS INDEPENDENT OF THE SEA-LEVEL PERFORMANCE—ALTITUDE PARAMETERS

The second of the preceding methods will first be considered. As previously mentioned, Oswald's analysis has been developed on a sea-level basis; that is, the velocity and power ratios have been referred to the maximum speed and maximum power available in level flight at sea level, and all the parameters,  $\lambda_p$ ,  $\lambda_s$ ,  $\Gamma$ , and  $\Lambda'$ , with their corresponding engineering equiva-

lents,  $l_p$ ,  $l_s$ ,  $\frac{l_s l_t}{V_0}$ , and  $\Lambda$ , are based on sea-level density and sea-level performance. This reference level is purely arbitrary and was chosen because of its convenience and because sea-level performance constitutes an important practical case in performance calculation. In many cases, however, it is desirable to determine the performance at some altitude other than sea level and, if no particular interest is attached to sea-level performance, it would be more convenient to calculate this performance directly without going through the intermediate step of the sea-level calculation. It is the object of this section to develop formulas and charts that will be useful for such calculations.

Since the analysis is to be based on altitude instead of on sea-level characteristics, it is only logical that altitude parameters should be introduced which will take the place of the sea-level parameters. The new parameters are, accordingly, defined as follows:

Physical parameters:

$$\left. \begin{aligned} \lambda_{p_\sigma} &= \frac{2W}{\rho f} = \frac{1}{\sigma} \frac{2W}{\rho_0 f} = \frac{1}{\sigma} \lambda_p \\ \lambda_{s_\sigma} &= \frac{2W}{\pi \rho e (kb_1)^2} = \frac{1}{\sigma} \frac{2W}{\pi \rho_0 e (kb_1)^2} = \frac{1}{\sigma} \lambda_s \\ \lambda_{t_\sigma} &= \frac{W}{A \eta_0 (\text{b. hp.})_0} = \lambda_t \end{aligned} \right\} \quad (3)$$

Engineering parameters:

$$\left. \begin{aligned} l_{p_\sigma} &= \frac{1}{\sigma} l_p \\ l_{s_\sigma} &= \frac{1}{\sigma} l_s \\ l_{t_\sigma} &= l_t \end{aligned} \right\} \quad (4)$$

It will be noted that the new parameters are obtained by merely replacing  $\rho_0$ , the density at sea level, by  $\rho$ , the density at the altitude in question, wherever it occurs in the sea-level parameters.

In accordance with the previous analysis, it would be desirable to develop parameters similar in form to the sea-level parameters,  $\Gamma$  and  $\Lambda'$ , together with their associated engineering equivalents. Rewriting the general performance equation (2) in terms of the new altitude parameters

$$\frac{dh}{dt} = \frac{1}{\lambda_t} \left[ \frac{P}{P_0} - \frac{\lambda_t}{\lambda_p} R_v^3 V_\sigma^3 - \frac{1}{R_v} \frac{\lambda_s \lambda_t}{V_\sigma} \right] \quad (5)$$

where  $V_\sigma$  has been defined as the maximum velocity in level flight at the altitude corresponding to  $\sigma$  and the new velocity ratio  $R_v$  has been defined as

$$R_v = V/V_\sigma$$

Now, considering level flight with the thrust power equal to the design thrust power  $P_0$ , i. e.,

$$\frac{dh}{dt} = 0, R_v = 1, \text{ and } \frac{P}{P_0} = 1$$



equation (5) becomes

$$1 = \frac{\lambda_t}{\lambda_{p\sigma}} V_\sigma^3 - \frac{\lambda_{s\sigma} \lambda_t}{V_\sigma} = 0 \quad (6)$$

Rearranging and multiplying by  $\frac{\lambda_{s\sigma}^3 \lambda_t^5}{V_\sigma^3}$ , equation (6) becomes

$$\frac{\lambda_{s\sigma}^3 \lambda_t^4}{\lambda_{p\sigma}} = \frac{\lambda_{s\sigma}^3 \lambda_t^3}{V_\sigma^3} \left[ 1 - \frac{\lambda_{s\sigma} \lambda_t}{V_\sigma} \right] \quad (7)$$

and finally, defining

$$\left. \begin{aligned} \Gamma_\sigma &= \frac{\lambda_{s\sigma} \lambda_t}{V_\sigma} = \frac{1}{\sigma} \frac{V_0}{V_\sigma} \frac{\lambda_s \lambda_t}{V_0} = \frac{1}{\sigma} \left( \frac{V_0}{V_\sigma} \right) \Gamma \\ \Lambda'_\sigma &= \frac{\lambda_{s\sigma} \lambda_t^{4/3}}{\lambda_{p\sigma}^{1/3}} = \left( \frac{1}{\sigma} \right)^{2/3} \frac{\lambda_s \lambda_t^{4/3}}{\lambda_p^{1/3}} = \left( \frac{1}{\sigma} \right)^{2/3} \Lambda' \end{aligned} \right\} \quad (8)$$

equation (6) becomes

$$\Lambda'_\sigma = \Gamma_\sigma (1 - \Gamma_\sigma)^{1/3} \quad (9)$$

which is identical in form with the equation obtained by Oswald (reference 1). In fact, substituting for sea-level conditions, equation (9) reduces identically to Oswald's equation. Thus, equation (9) is a generalization of Oswald's equation to include the level-flight-velocity performance at any altitude, and the same restrictions and physical interpretation apply to this equation at altitude as apply to the sea-level equation. It may be anticipated from this comparison that, if the altitude parameters and variables,  $\lambda_{s\sigma}$ ,  $\lambda_{p\sigma}$ ,  $\Gamma_\sigma$ ,  $\Lambda'_\sigma$ ,  $R_v$ , and  $V_\sigma$ , are substituted for the sea-level parameters and variables,  $\lambda_s$ ,  $\lambda_p$ ,  $\Gamma$ ,  $\Lambda'$ ,  $R_{v_0}$ , and  $V_0$ , in the equations for the various performance characteristics for sea level, the result will be the generalized equations for the performance at any altitude corresponding to the density ratio  $\sigma$ . This supposition will be verified in the subsequent analysis.

It will be found desirable for later analysis to develop another parameter that will aid both in the physical interpretation and in practical calculation. Accordingly, again rearranging equation (6) and multiplying by

$$\left( \frac{\lambda_t}{\lambda_{p\sigma}} \right)^{1/3} V_\sigma^3$$

$$\frac{\lambda_{s\sigma} \lambda_t^{4/3}}{\lambda_{p\sigma}^{1/3}} = \left( \frac{\lambda_t}{\lambda_{p\sigma}} \right)^{1/3} V_\sigma^3 \left[ 1 - \frac{\lambda_t}{\lambda_{p\sigma}} V_\sigma^3 \right] \quad (10)$$

Finally defining

$$\Omega_\sigma = \left( \frac{\lambda_t}{\lambda_{p\sigma}} \right)^{1/3} V_\sigma = \sigma^{1/3} \left( \frac{V_\sigma}{V_0} \right) \left( \frac{\lambda_t}{\lambda_p} \right)^{1/3} V_0 = \sigma^{1/3} \left( \frac{V_\sigma}{V_0} \right) \Omega \quad (11)$$

equation (10) becomes

$$\Lambda'_\sigma = \Omega_\sigma (1 - \Omega_\sigma^3) \quad (12)$$

which is similar in form to equation (9).

Now returning to the general performance equation (5) and substituting for  $\frac{\lambda_t}{\lambda_{p\sigma}} V_\sigma^3$  from equation (6)

$$\frac{dh}{dt} = \frac{1}{\lambda_t} \left[ \frac{P}{P_0} - R_v^3 + \left( R_v^3 - \frac{1}{R_v} \right) \Gamma_\sigma \right] \quad (13)$$

A second form of the equation may be obtained by substituting for  $\frac{\lambda_{s\sigma} \lambda_t}{V_\sigma}$  instead of for  $\frac{\lambda_t}{\lambda_{p\sigma}} V_\sigma^3$  from the same equation. This substitution will give

$$\frac{dh}{dt} = \frac{1}{\lambda_t} \left[ \frac{P}{P_0} - \frac{1}{R_v} + \left( \frac{1}{R_v} - R_v^3 \right) \Omega_\sigma^3 \right] \quad (14)$$

Both these equations materially simplify the calculation of airplane performance by reducing the number of airplane parameters to two,  $\lambda_t$  and  $\Gamma_\sigma$  in the case of equation (13) or  $\lambda_t$  and  $\Omega_\sigma$  in the case of equation (14).

#### A. PHYSICAL SIGNIFICANCE OF THE PARAMETERS<sup>1</sup>

$\Lambda'_\sigma$ ,  $\Gamma_\sigma$ , and  $\Omega_\sigma$

The physical significance of the dimensionless parameter  $\Lambda'$  introduced in Oswald's analysis has been discussed by Millikan (reference 1), and it has been found that the parameter is approximately proportional to the ratio of the minimum to the maximum speed at sea level for an ideal airplane. It will be desirable, however, to discuss these parameters more fully, particularly in view of their generalization to all altitudes and of the introduction of the new parameter  $\Omega_\sigma$ .

For this purpose the ideal airplane, defined by Millikan (reference 1), will again be considered. This airplane, it will be noted, is one for which the thrust power is independent of speed and for which the phenomenon of burbling does not occur. Such an airplane would obey the performance equation for all values of the velocity and is one for which the thrust power is always equal to the design thrust power  $P_0$ . These stipulations will be assumed to hold for all altitudes as well as for all velocities.

Three conditions of flight will be considered for this airplane:

1. Level flight with no induced drag (infinite span).

$$\frac{P}{P_0} = 1, V = V_p, \frac{dh}{dt} = 0, \lambda_{s\sigma} = 0$$

2. Level flight with no parasite drag ( $f=0$ ).

$$\frac{P}{P_0} = 1, V = V_i, \frac{dh}{dt} = 0, \lambda_{p\sigma} = \infty$$

3. Maximum rate of climb with no parasite or induced drag,

$$\frac{P}{P_0} = 1, \lambda_{s\sigma} = 0, \lambda_{p\sigma} = \infty, \frac{dh}{dt} = C_0$$

<sup>1</sup> The physical significance of these parameters was developed by Dr. C. B. Millikan after several discussions of the problem with Dr. Th. von Kármán and the author. The conclusions were first presented in Millikan's lectures in the fall of 1935.



Consider the first condition. Substituting the flight conditions in equation (5), equation (6) results. Solving for  $V_\sigma$

$$V_\sigma = \left( \frac{\lambda_{p\sigma}}{\lambda_t} \right)^{1/3} \left( 1 - \frac{\lambda_{s\sigma} \lambda_t}{V_\sigma^3} \right)^{1/3} \quad (15)$$

Substituting the conditions for zero induced drag, i. e.,  $\lambda_{s\sigma} = 0$  and  $V_\sigma = V_p$ , equation (15) becomes

$$V_p = \left( \frac{\lambda_{p\sigma}}{\lambda_t} \right)^{1/3} \quad (16)$$

and dividing into  $V_\sigma$

$$\frac{V_\sigma}{V_p} = \left( \frac{\lambda_t}{\lambda_{p\sigma}} \right)^{1/3} V_\sigma = \Omega_\sigma \quad (17)$$

Now consider the second condition. Again substituting the flight conditions in equation (5), equation (6) results and, solving for  $V_\sigma$ , this time using the other term in equation (6),

$$V_\sigma = \frac{\lambda_{s\sigma} \lambda_t}{1 - \frac{\lambda_t}{\lambda_{p\sigma}} V_\sigma^3} \quad (18)$$

Substituting the conditions for zero parasite drag, i. e.,  $\lambda_{p\sigma} = \infty$  and  $V_\sigma = V_i$ , equation (18) becomes

$$V_i = \lambda_{s\sigma} \lambda_t \quad (19)$$

Dividing by  $V_\sigma$

$$\frac{V_i}{V_\sigma} = \frac{\lambda_{s\sigma} \lambda_t}{V_\sigma} = \Gamma_\sigma \quad (20)$$

Finally, from equation (8),

$$\Lambda'_\sigma = \frac{\lambda_{s\sigma} \lambda_t^{4/3}}{\lambda_{p\sigma}^{1/3}} = \frac{\lambda_{s\sigma} \lambda_t}{\left( \frac{\lambda_{p\sigma}}{\lambda_t} \right)^{1/3}} \quad (21)$$

so that, using equations (16) and (19),

$$\Lambda'_\sigma = \frac{V_i}{V_p} \quad (22)$$

and also

$$\Lambda'_\sigma = \Gamma_\sigma \Omega_\sigma \quad (23)$$

Finally, considering the third condition, equation (5) becomes

$$C_0 = \frac{1}{\lambda_t} \quad (24)$$

The three velocities,  $V_p$ ,  $V_i$ , and  $C_0$ , may be called the "design speeds" of the ideal airplane considered. The term  $V_\sigma$  represents the maximum speed of the airplane,  $V_p$  the maximum speed with no induced drag,  $V_i$  the minimum speed with no parasite drag, and  $C_0$  the maximum rising speed with no induced or parasite drag, all at the design thrust power  $P_0$ . The power curves and velocity relationships for a normal airplane with its associated ideal airplane are represented in figure 1. In the preceding analysis, all the dimensionless parameters have been obtained in terms of the design speeds. In particular,  $\Lambda'_\sigma$  is the ratio of the minimum

speed with no parasite drag to the maximum speed with no induced drag at the altitude corresponding to  $\sigma$ . In the analysis of reference 1, it was found that the parameter  $\Lambda'$ , to which  $\Lambda'_\sigma$  reduces at sea level, was

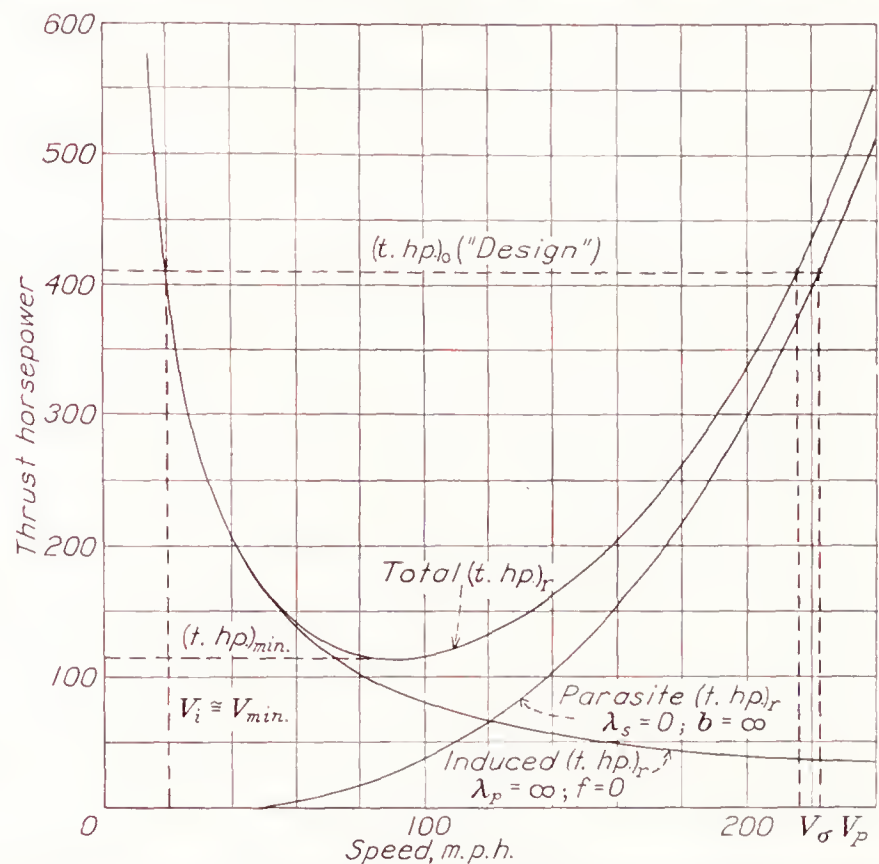


FIGURE 1.—Power characteristics for an ideal airplane with the following characteristics:  $\lambda_{p_0} = 841,000$ ;  $\lambda_{s_0} = 1,203$ ;  $\lambda_t = 0.0844$ ;  $\Lambda'_\sigma = 0.0823$ ;  $W = 5,500$  lb.

approximately equal to the ratio of the minimum speed to the maximum speed of the ideal airplane, including both parasite and induced drag. Examination of figure 1 will show the extent of this approximation.

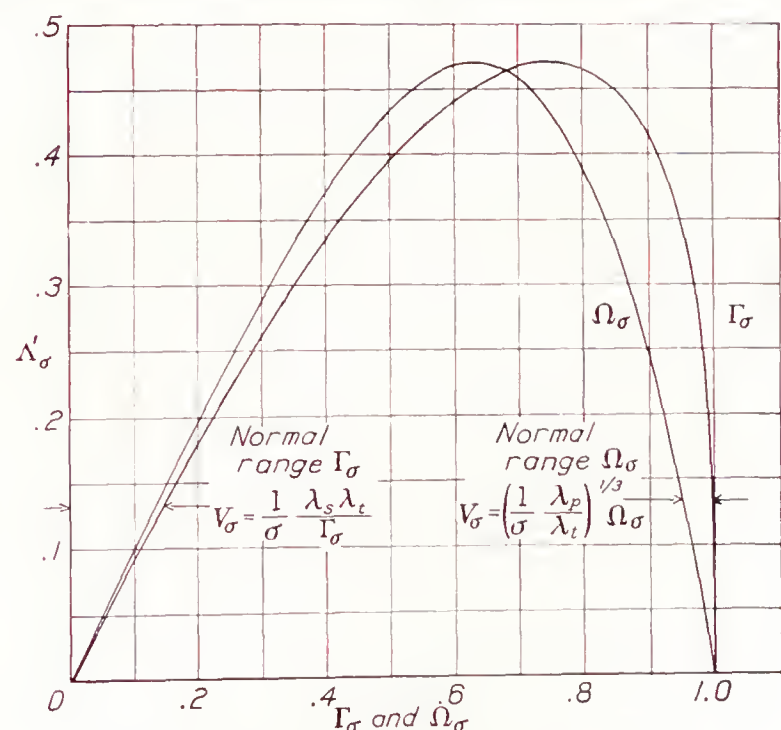


FIGURE 2.—The parameters  $\Gamma_\sigma$  and  $\Omega_\sigma$  as functions of  $\Lambda'_\sigma$ .

Since all the parameters that appear in the general performance equation can now be represented by speed ratios, it is only logical that the entire equation may be represented by these same ratios. Thus, substitution in equation (5) from equations (16), (19), and (24) gives, since  $V = R_\sigma V_\sigma$ ,

$$\frac{C}{C_0} = \frac{P}{P_0} - \left( \frac{V}{V_0} \right)^3 - \left( \frac{V_i}{V} \right) \quad (25)$$



which is an equation of speed and power ratios and is valid for any altitude. This is the most general form of the performance equation for an ideal airplane.

The relationships between the three parameters  $\Lambda'_\sigma$ ,  $\Gamma_\sigma$ , and  $\Omega_\sigma$  given by equations (9), (12), and (23), are plotted in figure 2 and show the maximum possible value of  $\Lambda'_\sigma$ , the significance of which will be explained later.

#### B. MAXIMUM VELOCITY AT ALTITUDE

Equations (9) and (12) give the relationship between the parameters and the maximum speed in level flight at the altitude corresponding to the density ratio  $\sigma$ . These

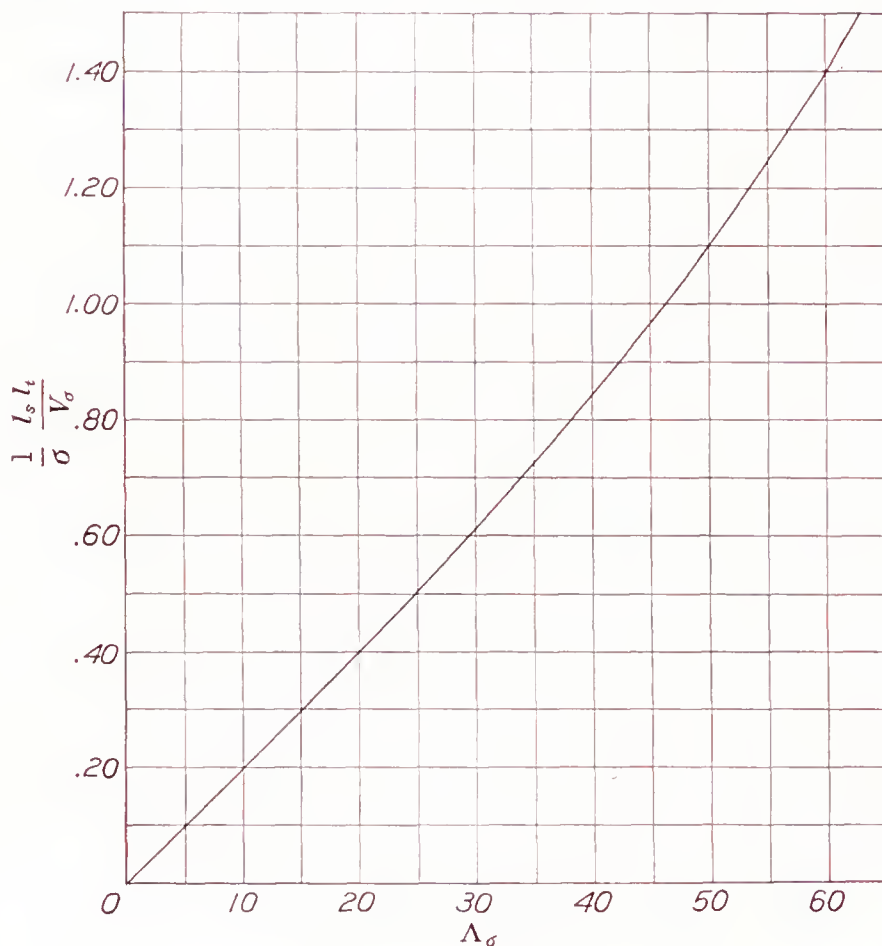


FIGURE 3.—The quantity  $\frac{1}{\sigma} \frac{l_s l_t}{V_\sigma}$  as a function of  $\Lambda_\sigma$ .

The maximum velocity in level flight at an altitude corresponding to  $\sigma$  is  $V_\sigma$ , where  $V_\sigma = \frac{1}{\sigma} \frac{l_s l_t}{\left(\frac{1}{\sigma} \frac{l_s l_t}{V_\sigma}\right)}$

equations have been plotted in figures 3 and 4 in terms of the engineering parameters, where

$$\left. \begin{aligned} \lambda_{s\sigma} &= 267.7 \frac{W}{\sigma \epsilon (k b_1)^2} = 267.7 l_{s\sigma} \\ \lambda_{p\sigma} &= 841.0 \frac{W}{\sigma f} = 841.0 l_{p\sigma} \\ \lambda_t &= 0.001818 \frac{W}{\eta_0 \text{ b. hp.}_0} = 0.001818 l_t \\ \Lambda'_\sigma &= 0.006293 \frac{l_{s\sigma} l_t^{4/3}}{l_{p\sigma}^{1/3}} = 0.006293 \Lambda_\sigma \end{aligned} \right\} \quad (26)$$

as defined in equation (4). Although the two charts are basically the same, each has certain advantages in many problems that arise in performance calculation and flight-test reduction. In general, the type of performance chart presented later (see examples) is more useful because of the greater ease with which accuracy may be attained in normal calculations.

#### C. MAXIMUM RATE OF CLIMB

The maximum rate of climb is realized at the speed at which the excess of thrust power available over thrust power required for level flight is a maximum. Examination of figure 1 shows that, for constant thrust power available, this maximum occurs at the speed for minimum power required. Thus, by differentiating  $dh/dt$  with respect to  $R_p$  and equating to zero, the speed for minimum power required may be obtained, assuming that the characteristics of the actual airplane follow those for the ideal airplane. This latter assumption is not correct in general, nor do normal propeller

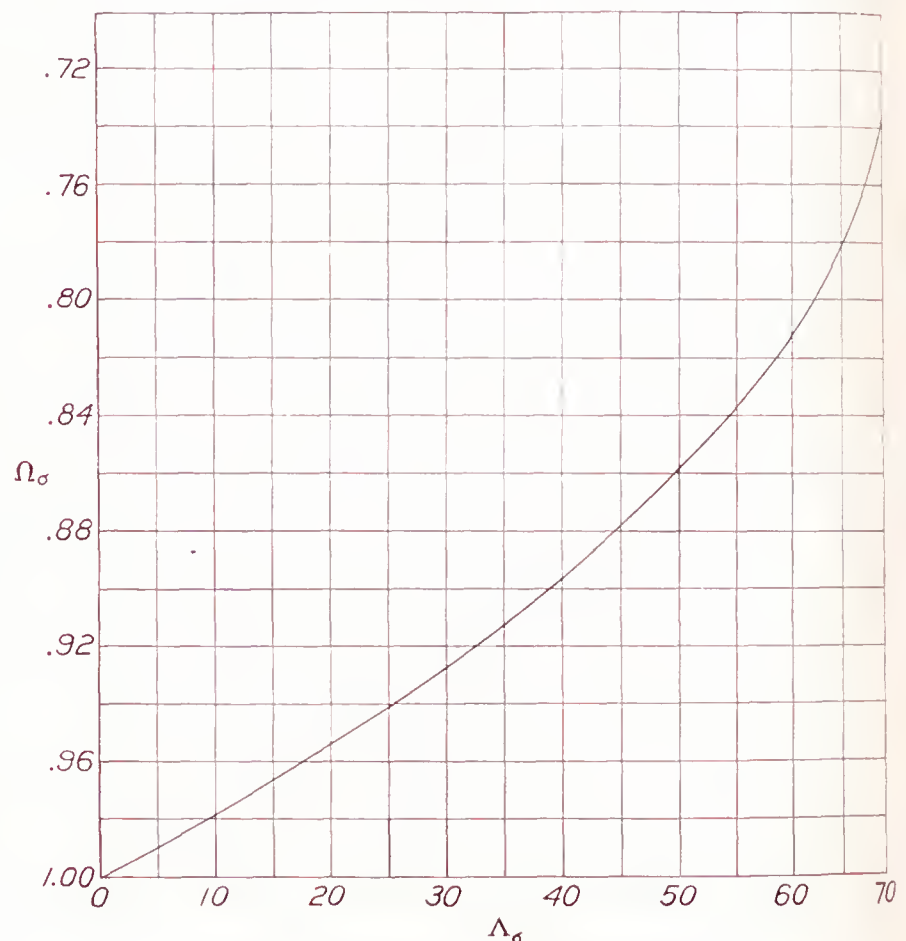


FIGURE 4.—The parameter  $\Omega_\sigma$  as a function of  $\Lambda_\sigma$ .

The maximum velocity in level flight at an altitude corresponding to  $\sigma$  is  $V_\sigma$ , where  $V_\sigma = 52.73 \left( \frac{1}{\sigma} \frac{l_p}{l_t} \right)^{1/3} \Omega_\sigma$ .

characteristics allow constant thrust power available independent of speed. It will be assumed for the moment, however, that the ideal characteristics hold, and a correction will later be made to allow for the effect that the actual airplane and propeller characteristics will have on the speed for the maximum rate of climb and on the rate itself.

Following the procedure outlined in the last paragraph, i. e., differentiating  $dh/dt$  with respect to  $R_\sigma$  in equation (13) and equating to zero, assuming  $P=P_0$ , obtain the resulting expression for the speed ratio for minimum power required,  $R_{v_{MP}} = V_{MP}/V_\sigma$

$$R_{v_{MP}} = \left[ \frac{\Gamma_\sigma}{3(1-\Gamma_\sigma)} \right]^{1/4} \quad (27)$$

By substituting this expression back into equation (13) and again assuming  $P=P_0$ , obtain the equation for the maximum rate of climb of the ideal airplane:

$$C \lambda_t = 1 - \frac{4}{(27)^{1/4}} \Lambda'_\sigma{}^{3/4} \quad (28)$$



or, in terms of engineering parameters and units,

$$Cl_i = 33,000 - 1,294 \Lambda_\sigma^{3/4} \quad (29)$$

Equations (27) and (29) are plotted in figures 5 and 6, respectively. In these figures the curves labeled  $\Lambda_\sigma$  should be used. The other curves correspond to engineering equivalents of equations (53) and (54) developed in section IV C.

fore  $P/P_0$ , for actual propeller-engine combinations does vary with speed in such a way that the speed for maximum rate of climb falls considerably above the speed for minimum power required for the corresponding ideal airplane, the theoretical power-required variations are still followed by the actual airplane at the speed for maximum rate of climb. This result is illustrated in figure 7. A large number of cases of

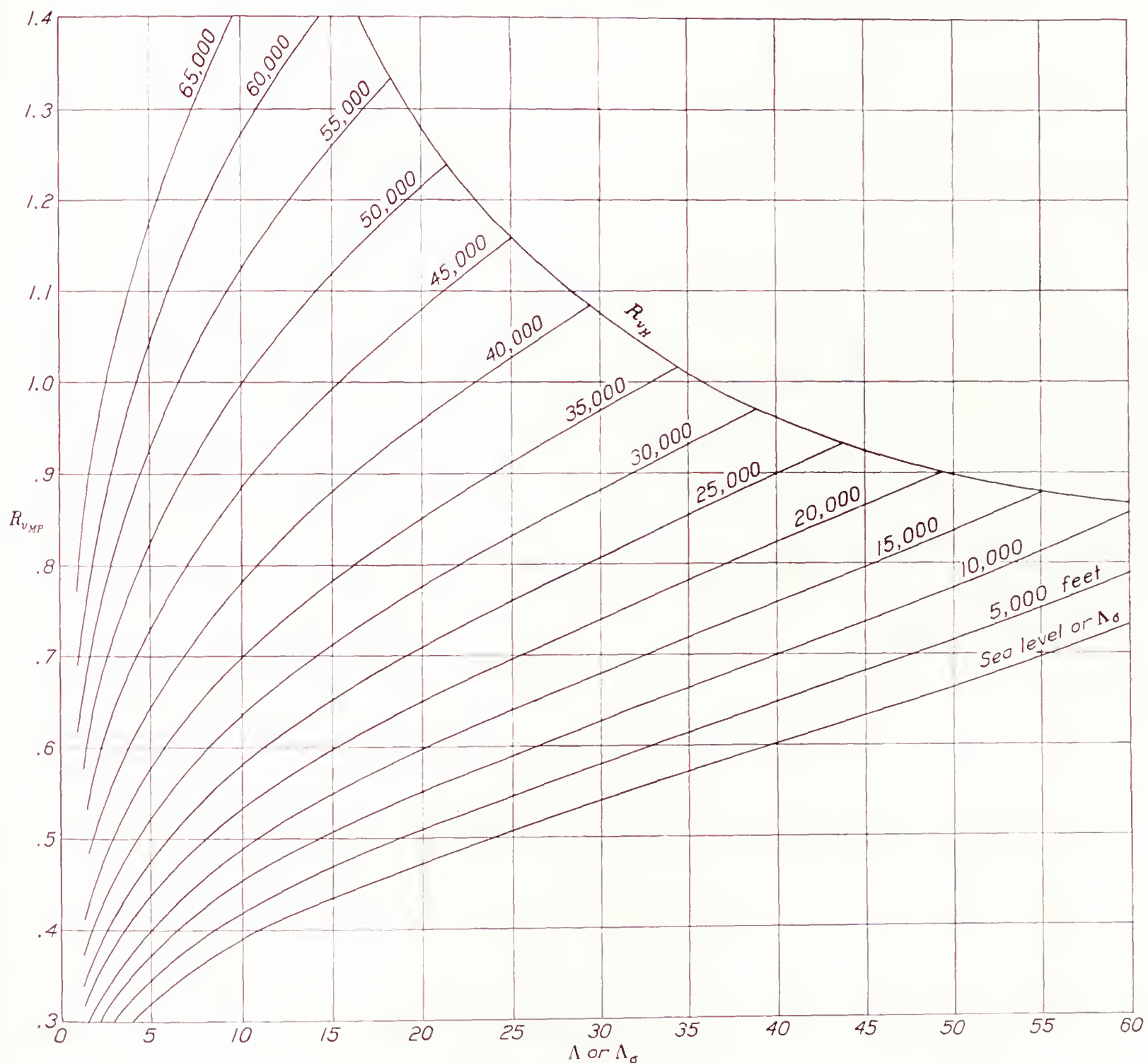


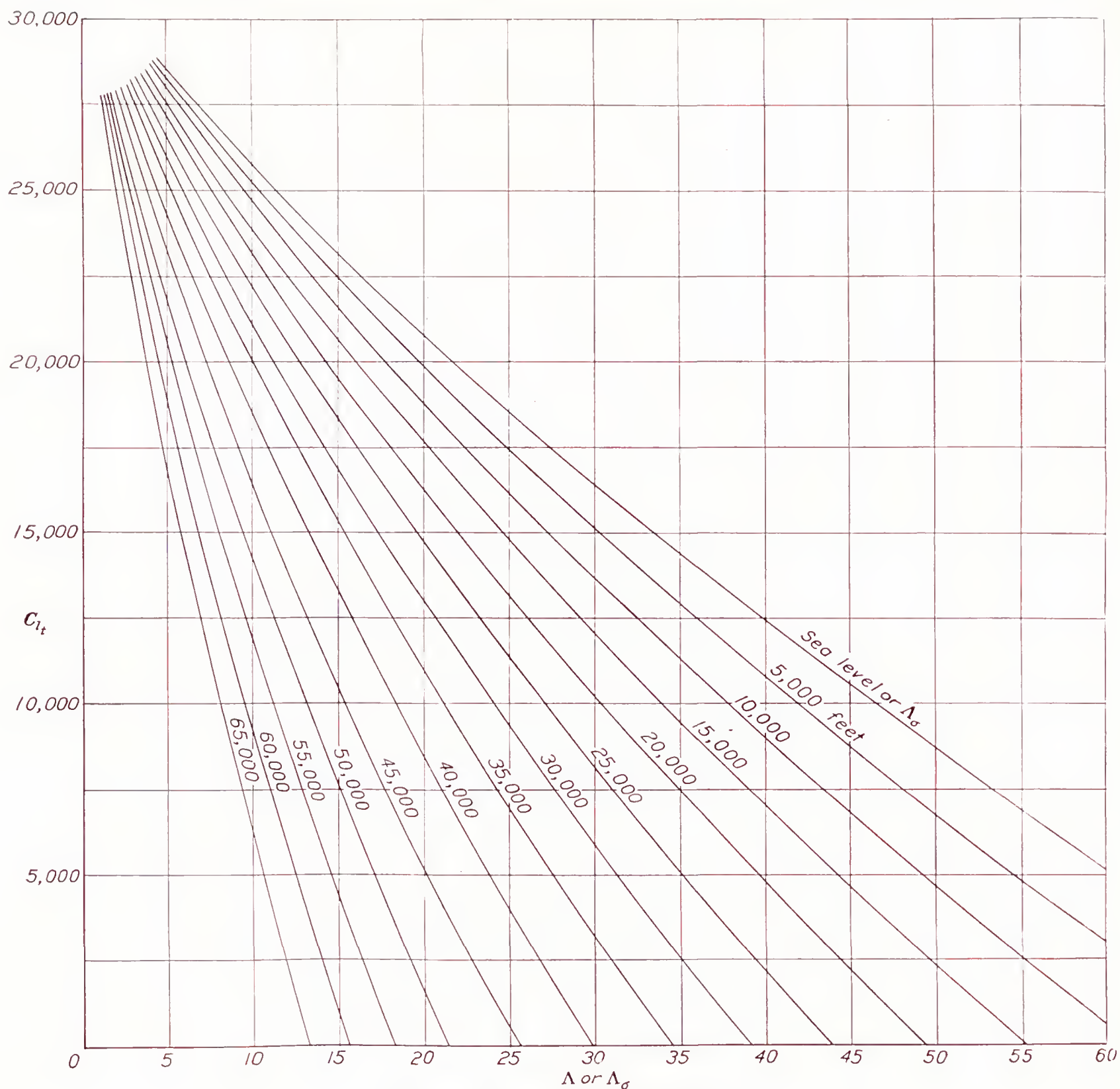
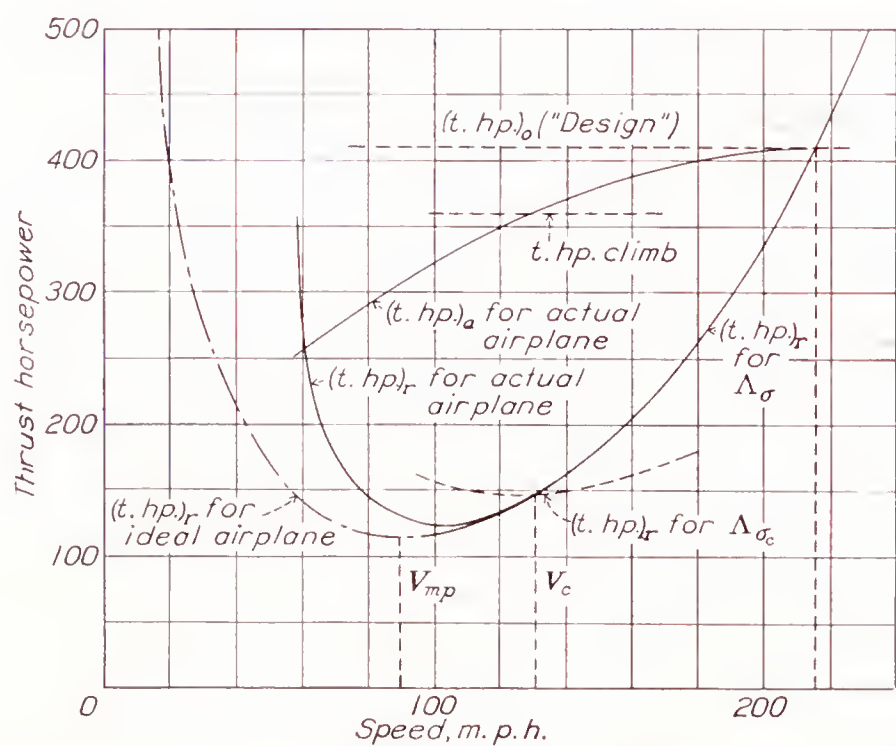
FIGURE 5.—The ratio  $R_{VMP} = V_{MP}/V_0$  as a function of  $\Lambda$ .

Now consider the case of the actual airplane with normal airplane characteristics. The solid curves in figure 7 present the thrust power required and available for a representative airplane. Equations (27), (28), and (29) would not, in general, be true for the actual airplane since the actual airplane does not, in general, follow the ideal airplane characteristics at the speed for minimum power of the ideal airplane. Therefore, even if the power ratio  $P/P_0$  were independent of speed, the maximum rate of climb and the speed for maximum rate of climb would not be those given by the equations. However, since the thrust power available, and there-

actual modern airplanes has been investigated for which complete wind-tunnel data were available, and in every case the speed for maximum rate of climb lay well within the region where the theoretical power-required variations hold true.

It is convenient in the analysis of an actual airplane to consider the speed for minimum power of the corresponding ideal airplane. Then the speed for maximum rate of climb of the actual airplane will be determined in the form of a ratio between best climbing speed and the speed for minimum power of the ideal airplane. The speed for maximum rate of climb for the actual



FIGURE 6.—The quantity  $C_{lt}$  as a function of  $\Lambda$ .FIGURE 7.—Power characteristics for an actual airplane corresponding to  $\Lambda_{\sigma}$  and its associated ideal climbing airplane corresponding to  $\Lambda_{\sigma_c}$ .

airplane is indicated as  $V_c$ . The value of this speed will depend, for given thrust power-required characteristics, on the slope of the power-available curve, which in turn will depend upon the particular engine-propeller combination and the method of control.

The first problem is to determine  $V_c$  for the actual airplane. This value has been obtained for constant-pitch propellers from Oswald's analysis (reference 1) and for constant-speed propellers from reference 3, assuming best performance propellers selected for high-power cruising or high speed. The results are presented in the form of ratios of  $V_c/V_{MP}$ , called  $R_R$ , and are plotted in figure 8 as functions of  $\Lambda_{\sigma}$ .

In most practical cases of modern airplanes, the propellers are selected as a compromise between many factors including high speed and cruising speed at altitude, climb, partial-engine performance, and take-off. For this reason the results presented in figure 8 are not sufficiently general for calculating speed for



maximum rate of climb for many actual airplanes. In the appendix to the present paper is presented an analysis by which the speed for maximum climb can be determined for an arbitrary propulsive unit.

Now, in order to determine the maximum rate of climb from figure 6, it is necessary to find a value of  $\Lambda_\sigma$ , say  $\Lambda_{\sigma_c}$ , which has the same values of thrust power required and available at its  $V_{MP}$  as the actual airplane has at its  $V_c$ . The sinking speed for the actual air-

the second part of equation (32), and transferring to engineering parameters,

$$\frac{\Lambda_{\sigma_c}}{\Lambda_\sigma} = \left( \frac{R_R^4 + 3}{4R_R} \right)^{4/3} \left( \frac{l_{tc}}{l_t} \right)^{4/3} \quad (34)$$

Now, if  $l_{tc}$  is designated to be the thrust power loading of the ideal airplane with its thrust power equal to that of the actual airplane at maximum rate of climb, then  $\Lambda_{\sigma_c}$  and  $l_{tc}$  designate an ideal airplane which, at its

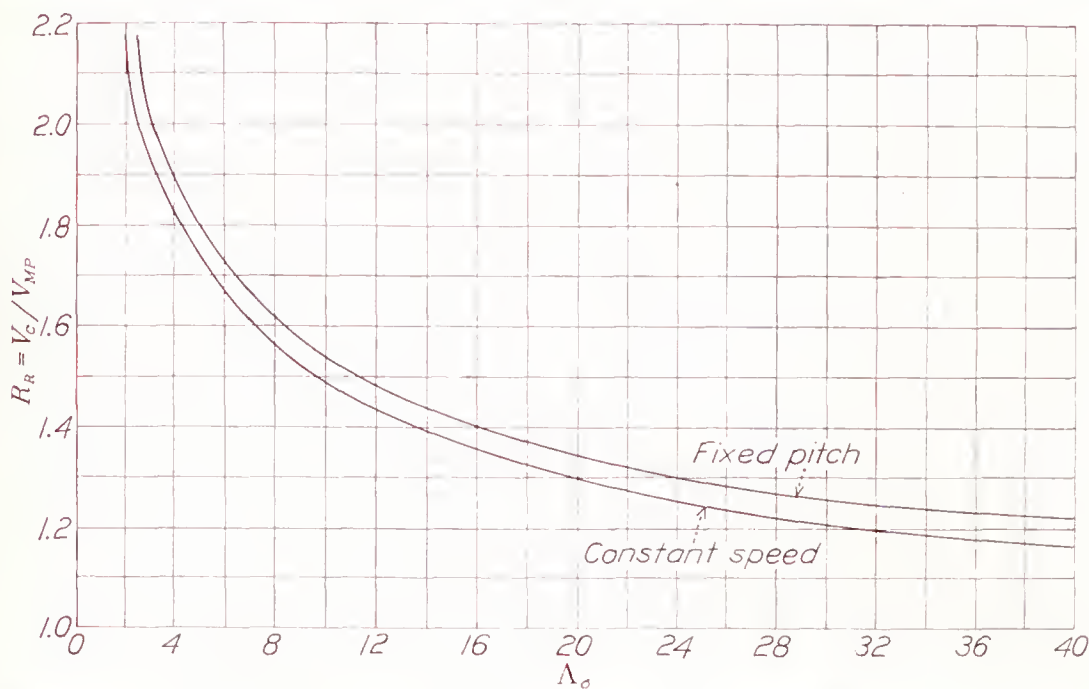


FIGURE 8.—The ratio  $R_R = \frac{V_c}{V_{MP}}$  as a function of  $\Lambda_\sigma$  for fixed-pitch and constant-speed propellers. (For approximate method, see section 111 C.)

plane, i. e.  $(t. \text{ hp.})_r/W$ , may be written, from equation (13)

$$\left( \frac{(t. \text{ hp.})_r}{W} \right) = \frac{1}{\lambda_t} \left[ R_v^3 - \left( R_v^3 - \frac{1}{R_v} \right) \Gamma_\sigma \right] \quad (30)$$

Thus, for the speed for maximum rate of climb,

$$\left( \frac{(t. \text{ hp.})_r}{W} \right)_c = \frac{1}{\lambda_t} \left[ R_R^3 R_{v_{MP}}^3 - \left( R_R^3 R_{v_{MP}}^3 - \frac{1}{R_R R_{v_{MP}}} \right) \Gamma_\sigma \right] \quad (31)$$

Substituting for  $R_{v_{MP}}$  from equation (27)

$$\begin{aligned} \left( \frac{(t. \text{ hp.})_r}{W} \right)_c &= \frac{1}{\lambda_t} \frac{R_R^4 + 3}{3R_R} \Gamma_\sigma \left[ \frac{3(1 - \Gamma_\sigma)}{\Gamma_\sigma} \right]^{1/4} \\ &= (3)^{1/4} \frac{R_R^4 + 3}{3R_R} \frac{\Lambda_{\sigma_c}^{3/4}}{\lambda_t} \end{aligned} \quad (32)$$

The sinking speed for a hypothetical ideal airplane, designated by  $\Lambda'_{\sigma_c}$ ,  $\Gamma_{\sigma_c}$ , and  $\lambda_{tc}$ , flying at its  $V_{MP}$ , will be given by setting  $R_R = 1$  in equation (32). Thus

$$\left[ \frac{(t. \text{ hp.})_r}{W} \right]_{MP} = \frac{4}{(27)^{1/4}} \frac{\Lambda'_{\sigma_c}^{3/4}}{\lambda_{tc}} \quad (33)$$

But it is desired to find a value of  $\Lambda'_{\sigma_c}$ , corresponding to an ideal airplane with  $\lambda_{tc}$ , for which the thrust power required at minimum power is the same as that for the actual airplane, corresponding to  $\Lambda'_\sigma$  and  $\lambda_t$ , at maximum rate of climb. Thus, equating equation (33) and

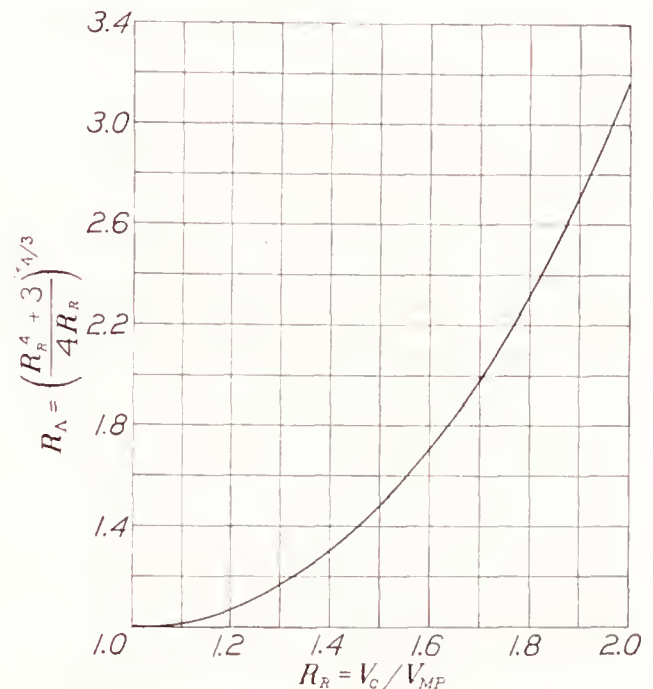


FIGURE 9.—The ratio  $R_A$  as a function of  $R_R$ .

speed for minimum power, will have the same rate of climb as the actual airplane at its speed for best climb. It is clear from the foregoing definition of  $l_{tc}$  that

$$l_{tc} = \left( \frac{P_0}{P_c} \right) l_t \quad (35)$$

and therefore that

$$\Lambda_{\sigma_c} = \left( \frac{R_R^4 + 3}{4R_R} \right)^{4/3} \left( \frac{P_0}{P_c} \right)^{4/3} \Lambda_\sigma \quad (36)$$

where  $P_c$  is the thrust horsepower available at the speed for maximum rate of climb of the actual airplane. Knowing  $R_R$  and  $P_c$  from previous calculation and substituting  $\Lambda_{\sigma_c}$  and  $l_{tc}$ , determined by equations (35) and (36), into equation (29), the maximum rate of climb of the actual airplane may be determined. For the important case of constant-speed propellers,  $P_0/P_c$  reduces to the ratio  $\eta_0/\eta_c$ , which may be found for each individual case from charts giving the propeller characteristics. This method will be illustrated by an example at the end of the present paper. The expression  $\left( \frac{R_R^4 + 3}{4R_R} \right)^{4/3}$ , called  $R_A$ , is represented in figure 9 for convenience in calculation.

It is important to note that throughout the foregoing analysis none of the equations or charts, with the exception of figure 8, are dependent upon any empirical data. Thus the only modification that would be required to extend the analysis and charts to cover new types of propulsive systems or new propeller-blade designs



would be to construct new  $R_R$  against  $\Lambda_\sigma$  curves in figure 8 to correspond to the new systems.

#### D. ABSOLUTE CEILING

The absolute ceiling occurs where the maximum rate of climb is zero. Thus, setting  $C=0$  in equation (28), the value of  $\Lambda'_\sigma$  for any airplane at its absolute ceiling will be

$$\Lambda'_\sigma \sigma_H = \frac{3\sqrt{2}}{8} \quad (37)$$

and, in engineering units according to (26),

$$\Lambda \sigma_H = 75.075 \quad (38)$$

Solving for  $\sigma_H$  in equation (38),

$$\sigma_H = 0.001539 \Lambda^{3/2} \quad (39)$$

This equation is plotted in figure 10,  $\sigma_H$  being replaced by its corresponding altitude  $H$ .

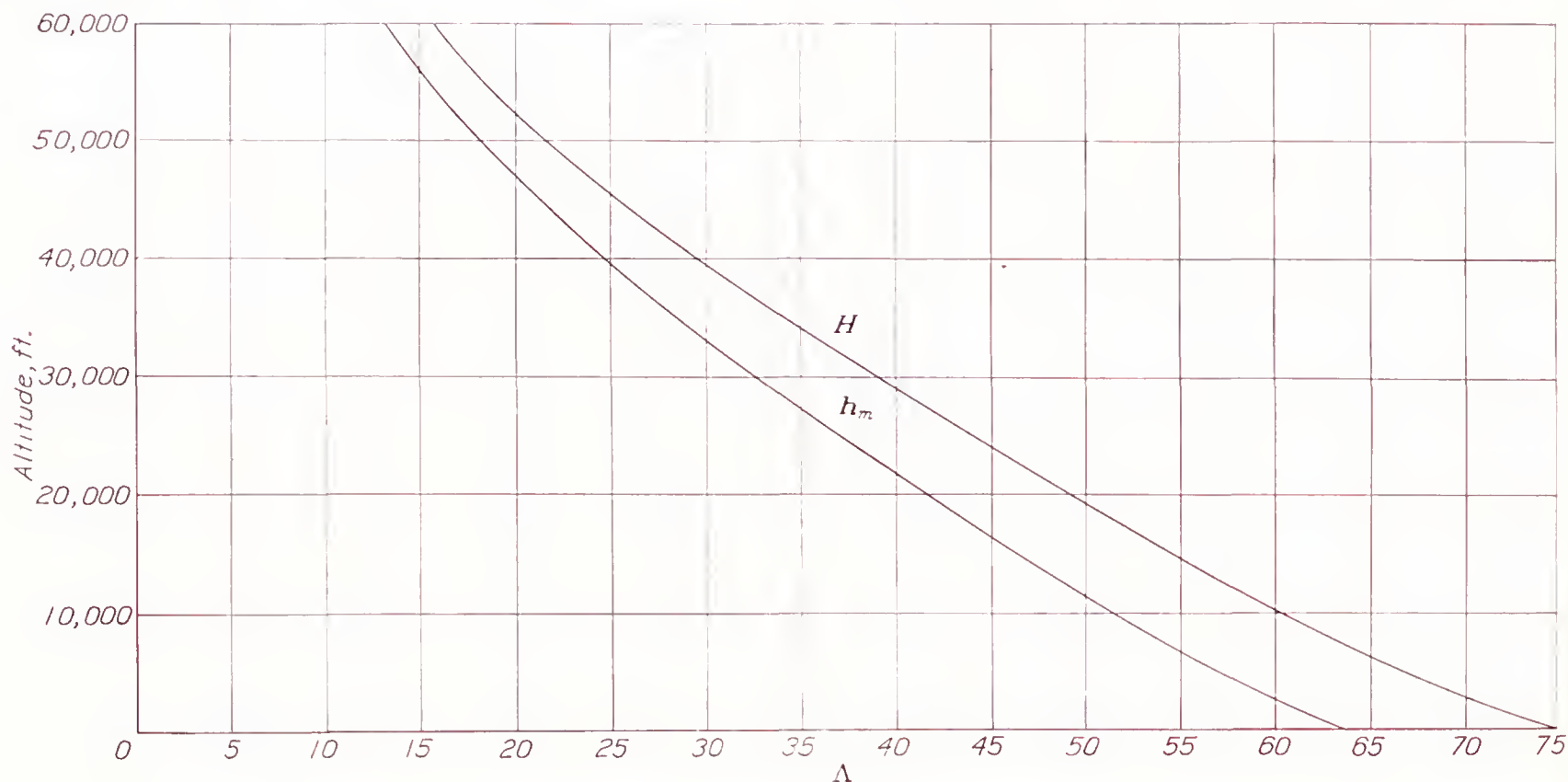


FIGURE 10.—The absolute ceiling  $H$ , and the altitude  $h_m$  corresponding to  $\sigma_m$  as functions of  $\Lambda$ .

The analysis in this particular section has little practical value but has rather interesting physical significance. It is shown that an airplane having a value of  $\Lambda_\sigma$  greater than that given will be unable to maintain level flight at the altitude on which the particular value of  $\Lambda_\sigma$  is based. This result is in agreement with the value obtained by Millikan for sea level (reference 1). The foregoing equations will be useful in the next section in developing the variation in performance due to variations in the parameters.

The only method that is satisfactory in general for the practical calculation of the absolute ceiling of an airplane is the method normally used for determining the ceiling from flight-test data; namely, calculating the maximum rates of climb at various altitudes at and above the critical altitude of the engine, plotting these rates of climb against density altitude, and extrapolating the curve so determined to zero rate of climb.

The altitude at which the rate of climb becomes zero is the absolute ceiling and at this altitude the relation between the parameters expressed by equation (39) is obeyed.

#### E. VARIATIONS IN PERFORMANCE DUE TO VARIATIONS IN THE PARAMETERS

It must be remembered that in all of the previous analysis, with the exception of the latter part of section III C, the basic assumption was that the power ratio  $P/P_0$  remained constant and equal to 1.00. This assumption is obviously not correct, in general, and some provision must be made for taking into account the variation in  $P/P_0$ . For this reason the variations of all the performance characteristics with thrust-power variations are investigated. At the same time the variations with respect to the other parameters are considered. Oswald (reference 1) makes a similar analysis, but the approximations that he makes would

introduce comparatively large errors in calculations for which the present analysis is to be extended. His approximations are sufficiently accurate for small values of  $\Lambda$  but introduce appreciable errors for large values of  $\Lambda_\sigma$  such as are encountered in low-power cruising conditions and at high altitudes. Furthermore, in the present analysis, analytic expressions are obtained for all the variations extended to include all altitudes.

Taking the logarithmic derivatives of  $V$ ,  $C$ , and  $\sigma_H$  in equations (9), (29), and (39), respectively, obtain the following equations, which are true for small variations in the parameters:

$$\frac{dV}{V} = -\left(\frac{1-\Gamma_\sigma}{3-4\Gamma_\sigma}\right) \frac{df}{f} \quad (40a)$$

$$\frac{dV}{V} = \left(\frac{1}{3-4\Gamma_\sigma}\right) \frac{d(\text{t. hp.})_a}{(\text{t. hp.})_a} \quad (40b)$$

$$\frac{dV}{V} = -\left(\frac{2\Gamma_\sigma}{3-4\Gamma_\sigma}\right) \frac{dW}{W} \quad (40c)$$



$$\frac{dV}{V} = \left( \frac{2\Gamma_\sigma}{3-4\Gamma_\sigma} \right) \frac{db}{b} \quad (40d)$$

$$\frac{dV}{V} = \left( \frac{\Gamma_\sigma}{3-4\Gamma_\sigma} \right) \frac{de}{e} \quad (40e)$$

$$\frac{dV}{V} = - \left( \frac{1-2\Gamma_\sigma}{3-4\Gamma_\sigma} \right) \frac{d\sigma}{\sigma} \quad (40f)$$

$$\frac{dV}{V} = \left( \frac{1-2\Gamma_\sigma}{3-4\Gamma_\sigma} \right) \frac{dT}{T} \quad (40g)$$

$$\frac{dC}{C} = - \left( \frac{1}{4} \frac{m\Lambda_\sigma^{3/4}}{1-m\Lambda_\sigma^{3/4}} \right) \frac{df}{f} \quad (41a)$$

$$\frac{dC}{C} = \left( 1 + \frac{m\Lambda_\sigma^{3/4}}{1-m\Lambda_\sigma^{3/4}} \right) \frac{d(\text{t. hp.})_a}{(\text{t. hp.})_a} \quad (41b)$$

$$\frac{dC}{C} = - \left( 1 + \frac{3}{2} \frac{m\Lambda_\sigma^{3/4}}{1-m\Lambda_\sigma^{3/4}} \right) \frac{dW}{W} \quad (41c)$$

$$\frac{dC}{C} = \left( \frac{3}{2} \frac{m\Lambda_\sigma^{3/4}}{1-m\Lambda_\sigma^{3/4}} \right) \frac{db}{b} \quad (41d)$$

$$\frac{dC}{C} = \left( \frac{3}{4} \frac{m\Lambda_\sigma^{3/4}}{1-m\Lambda_\sigma^{3/4}} \right) \frac{de}{e} \quad (41e)$$

$$\frac{dC}{C} = \left( \frac{1}{2} \frac{m\Lambda_\sigma^{3/4}}{1-m\Lambda_\sigma^{3/4}} \right) \frac{d\sigma}{\sigma} \quad (41f)$$

$$\frac{dC}{C} = - \left( \frac{1}{2} \frac{m\Lambda_\sigma^{3/4}}{1-m\Lambda_\sigma^{3/4}} \right) \frac{dT}{T} \quad (41g)$$

where  $m=0.03923$  (a dimensionless constant) and  $T$  is the absolute temperature, and

$$\frac{d\sigma_H}{\sigma_H} = \frac{1}{2} \frac{df}{f} \quad (42a)$$

$$\frac{d\sigma_H}{\sigma_H} = -2 \frac{d(\text{t. hp.})_a}{(\text{t. hp.})_a} \quad (42b)$$

$$\frac{d\sigma_H}{\sigma_H} = 3 \frac{dW}{W} \quad (42c)$$

$$\frac{d\sigma_H}{\sigma_H} = -3 \frac{db}{b} \quad (42d)$$

$$\frac{d\sigma_H}{\sigma_H} = -\frac{3}{2} \frac{de}{e} \quad (42e)$$

where  $\frac{d\sigma_H}{\sigma_H}$  may be replaced by

$$\frac{dH}{H} = \left( \frac{\sigma_H}{H} \frac{dH}{d\sigma_H} \right) \frac{d\sigma_H}{\sigma_H} \quad (42f)$$

Values of  $\frac{\sigma_H}{H} \frac{dH}{d\sigma_H}$  may be calculated from the equations of the standard atmosphere (reference 4), which may be obtained in the following form (for altitudes below the isothermal stratosphere):

$$\frac{\sigma_H}{H} \frac{dH}{d\sigma_H} = -0.235 \left( \frac{T_0}{a} \frac{1}{H} - 1 \right) = -0.235 \left( \frac{145373}{H} - 1 \right) \quad (42g)$$

and (for altitudes within the stratosphere)

$$\frac{\sigma_H}{H} \frac{dH}{d\sigma_H} = - \left( \frac{T_i}{T_0} \right) \frac{p_0}{g\rho_0} \frac{1}{H} = - \frac{20937}{H} \quad (42h)$$

The additional symbols in equations (42g) and (42h) are defined as:

$g$ , the gravitational constant = 32.17 ft./sec.

$p_0$ , the standard pressure at sea level = 2,116 lb./sq. ft.

$a$ , the standard lapse rate of temperature in the troposphere = 0.003566° F./ft.

$T_0$ , the standard absolute temperature at sea level = 518.4° F.

$T_i$ , the standard absolute temperature in the stratosphere = 392.4° F.

It will be noticed in equations (40a-g) and (41a-g) that the variations of the velocity and maximum rate of climb here considered are not limited to the velocity and rate of climb at sea level, but apply as well at any altitude corresponding to  $\sigma$ . The variations depend only on the single parameter  $\Lambda_\sigma$  defined earlier.

Variations in velocity and maximum rate of climb are considered with respect to variations in density ratio and absolute temperature in addition to the usual parametric variations because of their usefulness in flight-test reduction. The variation equations are represented in chart form by figure 11.

All the foregoing variation formulas apply for small variations in the parameters. Many cases arise in performance problems in which it is necessary to calculate the effect of large changes of power on speed. For this purpose figure 12 has been constructed and gives the percentage change in  $V$  for 1 percent change in power for large changes in power. (See example C1.) This chart was calculated directly from equation (9).

#### F. MAXIMUM POSSIBLE VELOCITY FOR A GIVEN AIRPLANE

One of the interesting questions that arises in the field of aircraft performance is the problem as to what is the maximum possible velocity available at all altitudes for a given airplane with a given power. This maximum possible velocity can be obtained directly from equation (40f). The condition is that for a change in  $\sigma$ ,  $dV/V$  must be zero. In other words,

$$\Gamma_\sigma = \frac{1}{2} \text{ or } \sigma_m = 2 \frac{\lambda_s \lambda_t}{V_{max}} \quad (43)$$

where  $\sigma_m$  is the density ratio at the altitude where the maximum velocity occurs. Substituting the value of  $\Gamma_\sigma$  from (43) into equation (9) and using (8) and (26), the equation for this density ratio becomes

$$\sigma_m = 4\Lambda'^{3/2} = 0.001998 \Lambda'^{3/2} \quad (44)$$

This equation has been plotted in figure 10. Using (8) in equation (9) and substituting the value of  $\sigma_m$  obtained in (43), the expression for the maximum velocity becomes

$$V_{max} = \frac{1}{2} \frac{\lambda_s \lambda_t}{\Lambda'^{3/2}} \quad (45)$$

and, changing to engineering units,

$$V_{max} = 332.3 \frac{l\lambda_t}{\Lambda'^{3/2}} = 332.3 \frac{l\lambda_t}{W} \sqrt{\frac{b_e^2}{f}} \quad (46)$$

where  $b_e = kb_1\sqrt{e}$ , the effective span.



The physical significance of this maximum possible velocity is apparent when the two factors that contribute to the total drag of the airplane are considered. The thrust power available has been assumed constant, independent of altitude. Thus the only variation in velocity with altitude must occur as a result of a variation in the drag. The drag coefficient has been

largely with regard to the importance of power and more especially of weight in the limit of the maximum velocity. The quantity  $\sqrt{\frac{b_e^2}{f}}$  might be termed the "frontal" or "parasite" aspect ratio. The values of  $V_{max}$  and  $\sigma_m$ , of course, correspond to the condition for maximum lift/drag ratio of the airplane.

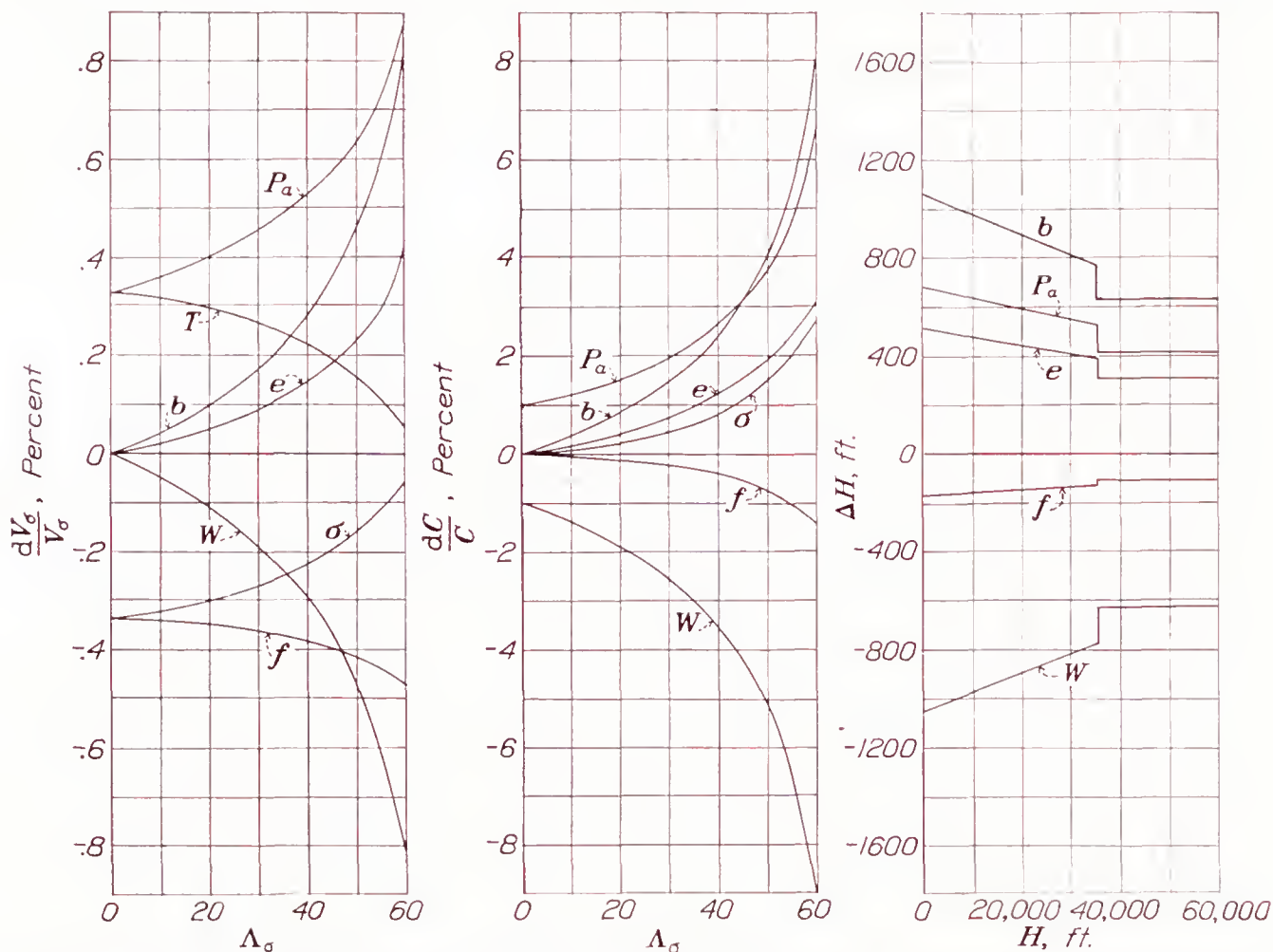


FIGURE 11.—Variation of performance with change of parameters. Charts show percentage change in performance due to a 1 percent change in parameter.  $V_s$  maximum velocity at altitude;  $C$ , maximum rate of climb at altitude;  $H$ , absolute ceiling.

divided into two portions, that portion which is independent of  $C_L$  and that portion which varies with  $C_L$ . The drag forces corresponding to these coefficients can be written as follows:

$$D_1 = \frac{\rho_0 f}{2W} W V^2 \sigma = \frac{W}{\lambda_p} V^2 \sigma$$

and

$$D_2 = \frac{2W}{\pi \rho_0 e (kb_1)^2} \frac{W}{V^2 \sigma} = \lambda_s \frac{W}{V^2 \sigma}$$

where  $\lambda_p$ ,  $\lambda_s$ , and  $W$  are constant for a given airplane. Now the altitude at which the maximum velocity is reached is that at which the total drag is a minimum for a given velocity; in other words, the altitude at which  $D_2$  increases (with altitude) at the same rate as  $D_1$  decreases, all for constant velocity. Thus for an ideal airplane, i. e., one for which  $e=1.00$ , this value is the altitude at which the rate of increase of induced drag is equal to the rate of decrease of parasite drag. Considered from this standpoint it is at once apparent that, as the span is increased other factors remaining constant, the altitude for maximum velocity is raised.

The form of the equation for the maximum possible velocity given in equation (46) is interesting, particu-

#### IV. PERFORMANCE ANALYSIS WITH SEA-LEVEL BASIS

In the previous sections an analysis has been presented that is independent of the sea-level performance of the airplane. There are many cases in practical performance calculation when it is desirable to obtain values of some performance characteristic, such as maximum speed, at a series of altitudes. For this purpose it is more convenient to calculate the performance at some reference level and then to find the performance at the other levels in terms of this reference-level performance. The choice of the reference level is purely arbitrary but, since sea-level characteristics constitute an important practical case, that altitude is chosen as the reference altitude.

After the reference altitude is chosen, the parameters are automatically determined. These parameters will be the sea-level parameters  $\lambda_s$ ,  $\lambda_p$ ,  $\Lambda'$ ,  $\Gamma$ , and  $\Omega$ . The maximum speed at sea level  $V_0$ , can be calculated as a special case of section III B. The maximum speeds at all other altitudes may then be referred to that at sea level by the ratio  $R_{v_0} = V/V_0$ .

From section III B the relations between the sea-level parameters can be obtained. These will, of



course, be similar to the altitude relations. Thus, letting  $\sigma=1.00$  in equations (6), (9), and (12),

$$\left. \begin{aligned} 1 - \frac{\lambda_t}{\lambda_p} V_0^3 - \frac{\lambda_s \lambda_t}{V_0} &= 0 \\ \Lambda' = \Gamma(1 - \Gamma)^{1/3} &= \Omega(1 - \Omega^3) \end{aligned} \right\} \quad (47)$$

based on the assumption of constant thrust power. This last equation has been represented graphically in the upper left-hand corner of figure 13, plotting against the engineering parameter  $\Lambda$  instead of the physical parameter  $\Lambda'$ . For rapid calculation of new values of  $\Lambda$  based on thrust horsepower available less than  $P_0$ ,

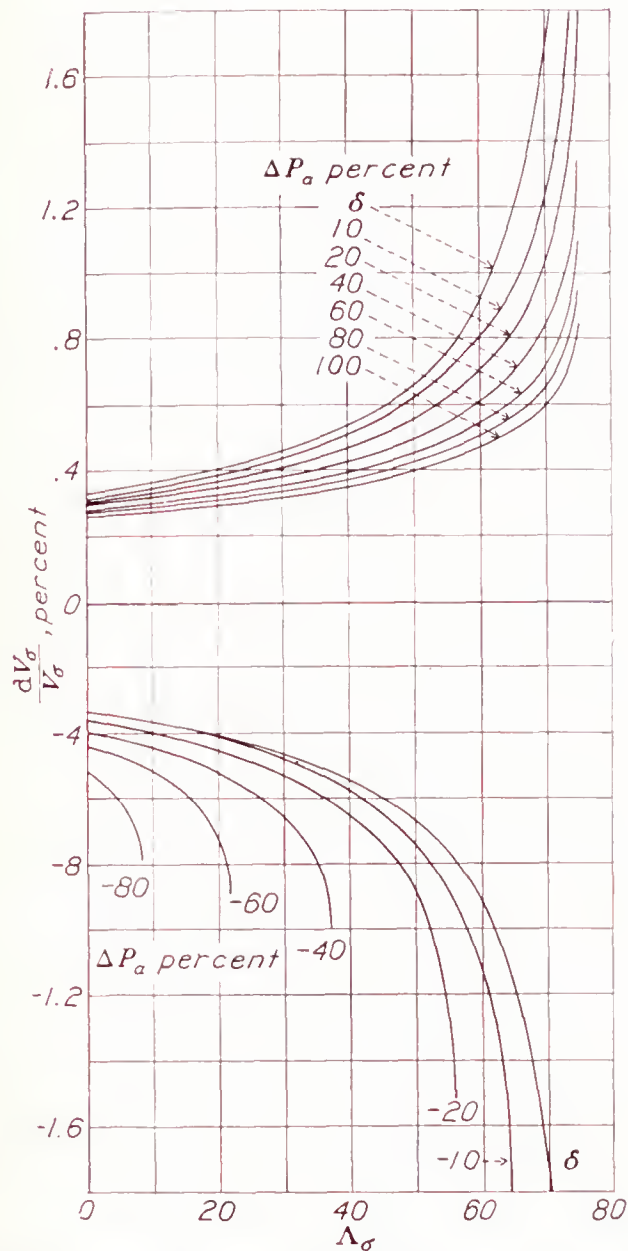


FIGURE 12.—Variation of maximum velocity at altitude with variation of thrust power available. Chart shows percentage change in velocity due to a 1-percent change in power for various percentage changes in power.

#### A. VELOCITY RATIO AT ALTITUDE

Using the sea-level parameters and the first equation in (47), equation (2) may be written

$$\frac{dh}{dt} = \frac{1}{\lambda_t} \left[ \frac{P}{P_0} - \sigma R_{v_0}^3 + \left( \sigma R_{v_0}^3 - \frac{1}{\sigma R_{v_0}} \right) \Gamma \right] \quad (48)$$

Now, considering the condition of level flight at altitude with the design power  $P_0$ , equation (48) becomes, omitting the subscript 0,

$$\Gamma = \sigma R_v \frac{1 - \sigma R_v^3}{1 - \sigma^2 R_v^4} \quad (49)$$

This equation gives the relationship

$$R_v = F(\sigma, \Gamma)$$

or, using equation (47),

$$R_v = F(\sigma, \Lambda')$$

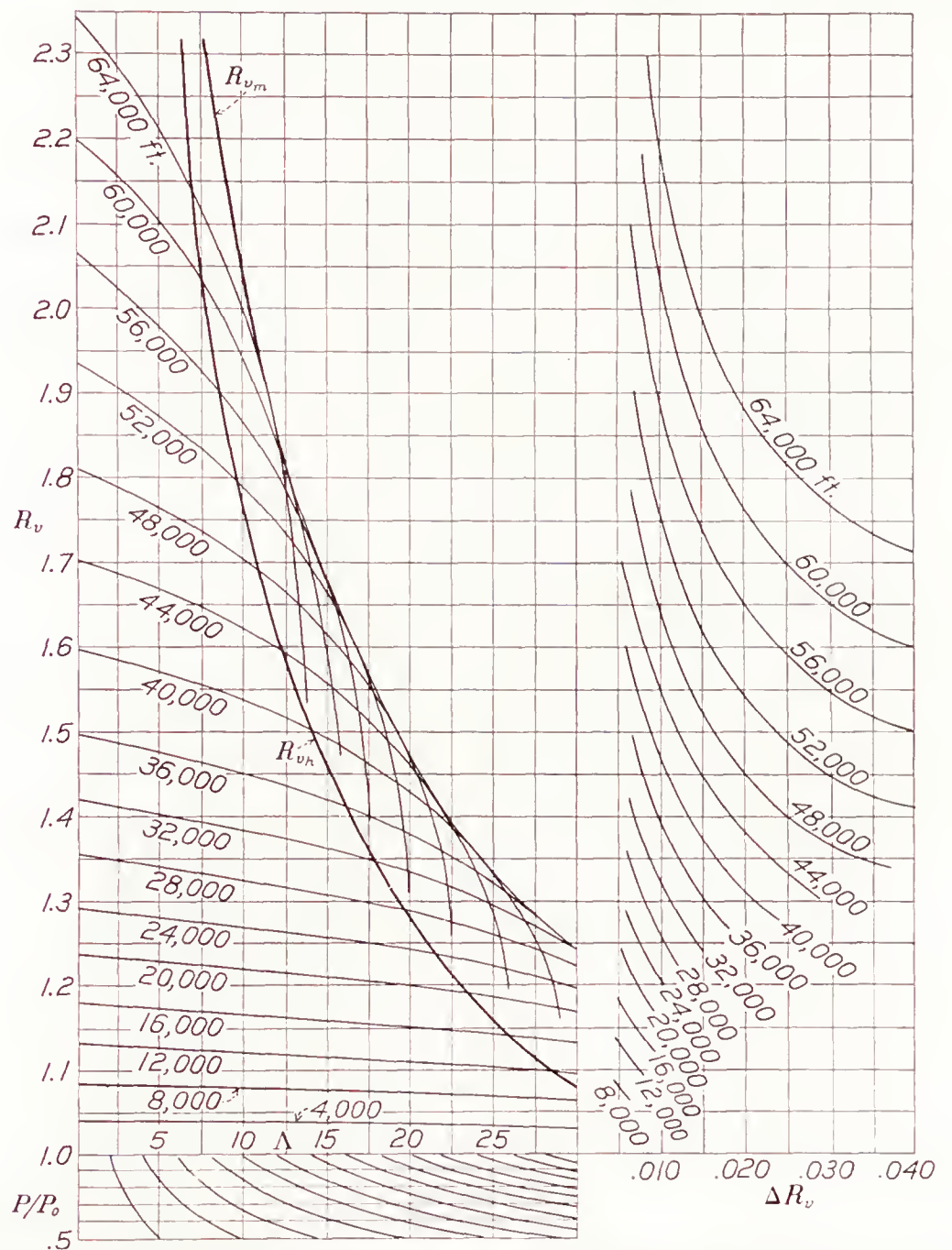


FIGURE 13.—The ratio  $R_v = V_v/V_0$  as a function of  $\Lambda$  and altitude and  $\Delta R_v$  as a function of  $R_v$  and altitude.

the chart at the lower left-hand corner of figure 13 is included. Entering the chart at  $P/P_0=1.00$  with the value of  $\Lambda$  corresponding to  $P_0$  and following down the curved lines to the desired value of  $P/P_0$ , the value of  $\Lambda_1$ , defined by  $\Lambda_1 = \left( \frac{P_0}{P} \right)^{1/3} \Lambda$  may be obtained.

#### B. VARIATION OF MAXIMUM VELOCITY AT ALTITUDE WITH SMALL CHANGES IN PROPULSIVE EFFICIENCY

In section III E charts were developed from which the variations in maximum speed due to variations in power could be computed. These charts were based upon the altitude parameter  $\Lambda_\sigma$ . When calculations are being made, using the sea-level parameters and charts, however, it is desirable to have more rapid and convenient methods available.



The effect of variations in power can be handled in either of two ways. A modified value of the thrust power loading based on the changed power can be calculated and used in the charts representing equation (9). If the changes in power are relatively large, this method is recommended. Figure 12 gives a chart for use in such cases since this method was exactly the one by which figure 12 was constructed. If the variations in power are small, as is generally the case when variations in propulsive efficiency are considered, a second method, the analysis of which follows, is more convenient.

The variation in propulsive efficiency may be represented by the ratio  $\eta/\eta_0$ . If the brake horsepower is constant, then the variation in thrust horsepower is given by the ratio  $\eta/\eta_0$ . The ratio  $P/P_0$  then becomes  $\eta/\eta_0$ . Introducing this ratio into equation (48) and considering the level-flight condition (again omitting the subscript  $0$ ), the following equation is obtained:

$$\eta = \eta_0 \left[ \sigma R_v^3 - \left( \sigma R_v^3 - \frac{1}{\sigma R_v} \right) \Gamma \right] \quad (50)$$

Differentiating both sides with respect to  $\eta$ , solving for  $dR_v/d\eta$ , and substituting for  $\Gamma$  from equation (49),

$$\frac{dR_v}{d\eta} = \frac{R_v(1 - \sigma^2 R_v^4)}{\eta_0(4\sigma R_v^3 - 3\sigma^2 R_v^4 - 1)} \quad (51)$$

Thus, the change in  $R_v$  for a change in  $\eta$  of 0.01 is given by

$$\Delta R_v = \frac{R_v(1 - \sigma^2 R_v^4)}{\eta_0(4\sigma R_v^3 - 3\sigma^2 R_v^4 - 1)} \frac{1}{100} \quad (52)$$

Since the values of  $\Delta R_v$  will always be small compared with  $R_v$  for most practical variations in  $\eta$ , an average value for  $\eta_0$  can be used in equation (52) with a negligible error, and  $\Delta R_v$  can be plotted in chart form as a function of  $R_v$  and  $\sigma$ . Such a plot is shown in the upper right-hand corner of figure 13, assuming  $\eta_0$  to be 0.75.

#### C. MAXIMUM RATE OF CLIMB—SPEED FOR MAXIMUM RATE OF CLIMB

The speed ratio for minimum power required (maximum rate of climb for constant thrust power) is obtained by differentiating  $dh/dt$  with respect to  $R_v$  in equation (48) and equating to zero. When this operation is done, assuming  $P=P_0$ , the resulting expression for  $R_{vMP}$  is

$$R_{vMP} = \left[ \frac{1}{3\sigma^2} \frac{\Gamma}{1-\Gamma} \right]^{1/4} \quad (53)$$

By substituting this expression back into equation (48) and again setting  $P=P_0$ , obtain the equation for maximum rate of climb for constant thrust power:

$$C\lambda_t = 1 - 4 \left[ \frac{\Lambda'^3}{27\sigma^2} \right]^{1/4} \quad (54)$$

Equations (53) and (54) in the sea-level analysis are directly parallel to equations (27) and (28) in the altitude analysis. In the sea-level analysis,  $R_{vMP}$  is referred to the maximum speed at sea level and the parameters are sea-level parameters; whereas, in the altitude analysis,  $R_{vMP}$  is referred to the maximum speed at altitude and the parameters are altitude parameters. Equations (53) and (54) are plotted in figures 5 and 6 along with equations (27) and (29) and, as will be seen

from the equations, these reduce to the same curve for the special case of sea level. In these figures the curves for the sea-level analysis are plotted against  $\Lambda$  while the curve in each figure for the altitude analysis is plotted against  $\Lambda_\sigma$ . The additional analysis in section III C (given by figs. 8 and 9) for correcting the speed for climb and rate of climb for actual thrust power variation applies to both analyses except that it must be remembered that  $\left(\frac{1}{\sigma}\right)^{2/3} \Lambda$  must be used to enter figure 8 in both cases.

#### D. ABSOLUTE CEILING—SPEED AT ABSOLUTE CEILING

Setting  $C=0$  in equation (54), the same equation (39) that was found before for absolute ceiling is obtained. Substituting this value of  $\sigma_H$  into equation (53), the equation for speed ratio at absolute ceiling (assuming constant thrust horsepower) becomes

$$R_{vH} = \frac{\sqrt{3}}{4\sqrt{\Gamma(1-\Gamma)}} \quad (55)$$

This equation is of academic rather than practical interest, since it assumes that the airplane is flying at theoretical minimum power, which will usually be below the actual speed for best climb for the airplane.

#### E. MAXIMUM POSSIBLE VELOCITY FOR A GIVEN AIRPLANE

Examination of the curves in figure 13, which represent equation (49), will show that for a given airplane, i. e., for a given value of  $\Lambda$ , there is a maximum possible value of  $R_v$  that lies on the envelope of the constant-altitude curves. This value corresponds to the maximum possible velocity obtained in the altitude analysis, as given by equation (46).

It is of interest to obtain an analytical expression for the maximum speed ratio  $R_{vmax}$ . This expression is obtained by taking the partial derivative of equation (49) with respect to  $\sigma$  and setting this expression equal to zero. Then the resulting equation is solved simultaneously with equation (49), eliminating  $\sigma$ . This operation gives an equation for the maximum speed ratio:

$$R_{vmax} = \frac{1}{2\sqrt{\Gamma(1-\Gamma)}} = \frac{1}{\sqrt{\sigma_m(2-\sigma_m)}} \quad (56)$$

Calculating the ratio  $R_{vH}/R_{vmax}$ , the following interesting result is obtained:

$$\frac{R_{vH}}{R_{vmax}} = \frac{\sqrt{3}}{2} = 0.866 \quad (57)$$

Equations (55) and (56) are represented graphically in figure 13 along with the family of constant-altitude curves, using equation (47) to obtain the relation between  $\Gamma$  and  $\Lambda'$  and plotting against the engineering parameter  $\Lambda$ . Equations (39) and (44) are plotted in figure 10 in terms of altitude and  $\Lambda$ .

DANIEL GUGGENHEIM GRADUATE SCHOOL OF AERONAUTICS, CALIFORNIA INSTITUTE OF TECHNOLOGY, PASADENA, CALIF., June 1, 1937.



## APPENDIX

### SPEED FOR MAXIMUM RATE OF CLIMB FOR ARBITRARY PROPELLER

In section III C of the main paper there has been presented a means for obtaining the speed for maximum rate of climb at any altitude provided the propeller is selected for high speed at the same altitude. These values of the speed for maximum climb are then strictly true only at the critical altitude for high speed and are given in terms of the speed for minimum power at that altitude. Since the maximum excess power available for climb varies only slightly with speed near the best theoretical speed, the values of the speed for maximum climb will be approximately correct for propellers selected for cruising speed and for altitudes reasonably near the critical altitude.

One of the chief difficulties, however, with the method of section III is that the propellers are often selected as a compromise governed by best take-off, maximum rate of climb, best cruising speed at some relatively high altitude, propeller tip speed, and finally propeller clearance. Thus, for many cases, and particularly for high supercharging, such a determination of the speed for maximum climb will give a speed considerably below the true speed for best climb of the actual airplane so that an underestimate of the excess power will result with a consequent conservative estimate of the maximum rate of climb. For this reason it is desirable to develop a method for calculating this speed for any arbitrary propeller. It is the object of the following analysis to develop such a method.

The general performance equation has been written as in equation (5), letting  $R_p = P/P_0$ ,

$$\frac{dh}{dt} = \frac{1}{\lambda_t} \left[ R_p - \frac{\lambda_t}{\lambda_{p\sigma}} V^3 - \frac{\lambda_{s\sigma} \lambda_t}{V} \right] \quad (A1)$$

To find the conditions for maximum rate of climb, differentiate with respect to  $V$  and equate to zero as before. Thus,

$$\frac{dR_p}{dV} - 3 \frac{\lambda_t}{\lambda_{p\sigma}} V^2 + \frac{\lambda_{s\sigma} \lambda_t}{V^2} = 0 \quad (A2)$$

where  $V_c$  is the speed for maximum rate of climb. Now consider the case in which  $dR_p/dV = 0$ , which will correspond to the theoretical speed for minimum power as shown in the analysis in section III. Thus,

$$3 \frac{\lambda_t}{\lambda_{p\sigma}} V_{MP}^2 = \frac{\lambda_{s\sigma} \lambda_t}{V_{MP}^2} \quad (A3)$$

Multiplying both sides by  $\frac{\lambda_{s\sigma} \lambda_t}{V_{MP}^2}$  and defining

$$\Gamma_{\sigma MP} = \frac{\lambda_{s\sigma} \lambda_t}{V_{MP}} = \Gamma_{\sigma} \frac{V_{\sigma}}{V_{MP}} \quad (A4)$$

gives

$$\Gamma_{\sigma MP} = (3)^{1/4} \Lambda_{\sigma}'^{3/4} \quad (A5)$$

Replacing the physical by the engineering parameters, this equation is plotted in figure 14. Now defining  $R_{\sigma M} = \frac{V}{V_{MP}}$  and substituting for  $\frac{\lambda_t}{\lambda_{p\sigma}} V^3$  in equation (A1)

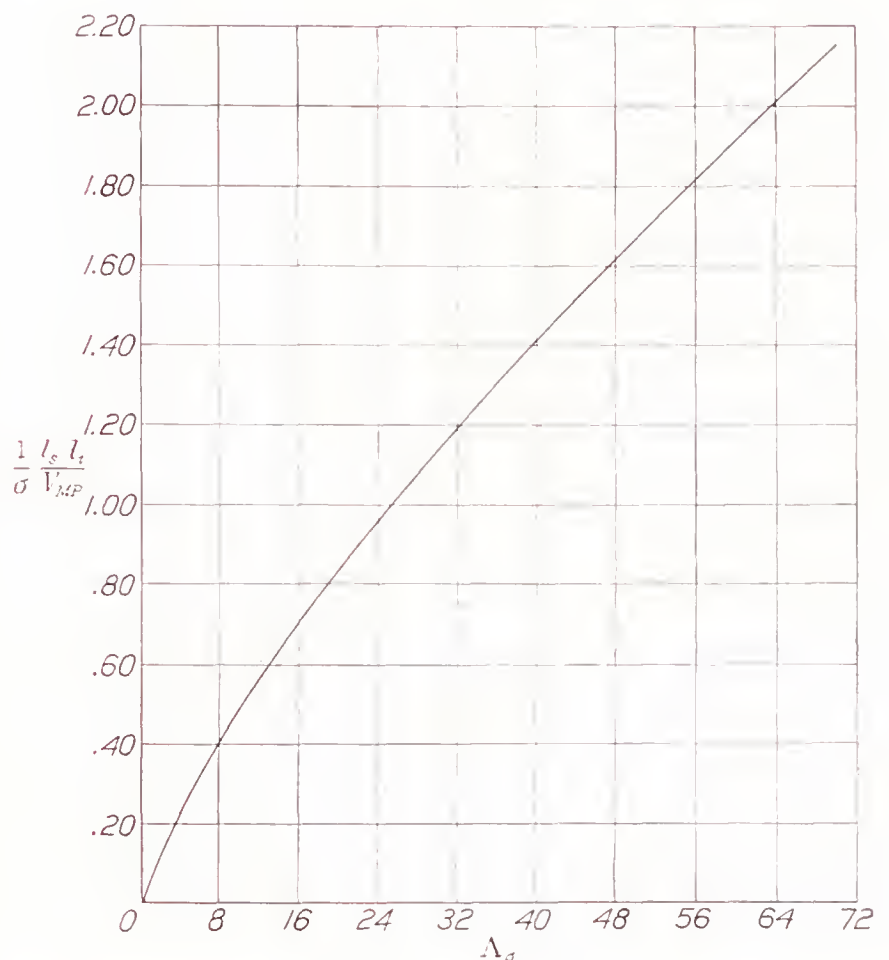


FIGURE 14.—The quantity  $\frac{1}{\sigma} \frac{l_s l_t}{V_{MP}}$  as a function of  $\Lambda_{\sigma}$ . The velocity for minimum power required of the ideal airplane is  $V_{MP}$ , where  $V_{MP} = \frac{1}{\sigma} \frac{l_s l_t}{\left( \frac{1}{\sigma} \frac{l_s l_t}{V_{MP}} \right)}$

according to (A3) and (A4), obtain

$$\frac{dh}{dt} = \frac{1}{\lambda_t} \left[ R_p - \left( \frac{R_{\sigma M}^3}{3} + \frac{1}{R_{\sigma M}} \right) \Gamma_{\sigma MP} \right] \quad (A6)$$

Also, making a similar substitution and defining  $R_R = \frac{V_c}{V_{MP}}$ , as in section III C of the main paper, equation (A2) becomes

$$\frac{dR_p}{dR_R} = \left( R_R^2 - \frac{1}{R_R^2} \right) \Gamma_{\sigma MP} \quad (A7)$$

Substituting for  $\Gamma_{\sigma MP}$  in equation (A7) according to (A5) and converting to the engineering parameter  $\Lambda$  according to (26), obtain

$$\frac{dR_p}{dR_R} = 0.02935 \left( R_R^2 - \frac{1}{R_R^2} \right) \Lambda_{\sigma}^{3/4} \quad (A8)$$



## CASE FOR CONSTANT SPEED PROPELLER

The foregoing analysis has been concerned with the power-required phase of the problem. The power available will now be considered. Propeller characteristics are normally available in terms of the dimensionless coefficients,  $C_P$  the power coefficient, and  $J$  the advance-diameter ratio, where

$$\left. \begin{aligned} C_P &= 5 \times 10^{10} \frac{\text{b. hp.}}{\sigma N^3 D^5} \\ J &= \frac{88 V}{ND} \end{aligned} \right\} \quad (\text{A9})$$

$\sigma$ , relative air density.

$V$ , true speed of the airplane (m. p. h.).

b. hp., engine brake horsepower.

$N$ , angular velocity of the propeller (r. p. m.).

$D$ , diameter of the propeller (ft.).

since both  $N$  and  $D$  are constant. Differentiating

$$dR_R = \frac{1}{J_{MP}} dJ \quad (\text{A13})$$

Thus, from (A11) and (A13)

$$\frac{dR_P}{dR_R} = \frac{J_{MP}}{\eta_0} \frac{d\eta}{dJ} \quad (\text{A14})$$

At the maximum rate of climb  $dR_P/dR_R$ , which is proportional to  $dP/dV$ , must be the same for the power-required as for the power-available characteristics. Thus, equating (A8) and (A14) and solving for  $d\eta/dJ$ ,

$$\frac{d\eta}{dJ} = 0.02935 \frac{\eta_0}{J_{MP}} \left( R_R^2 - \frac{1}{R_R^2} \right) \Lambda_\sigma^{3/4} \quad (\text{A15})$$

which is the condition that must be satisfied for maximum rate of climb. It should be noted in (A15) that

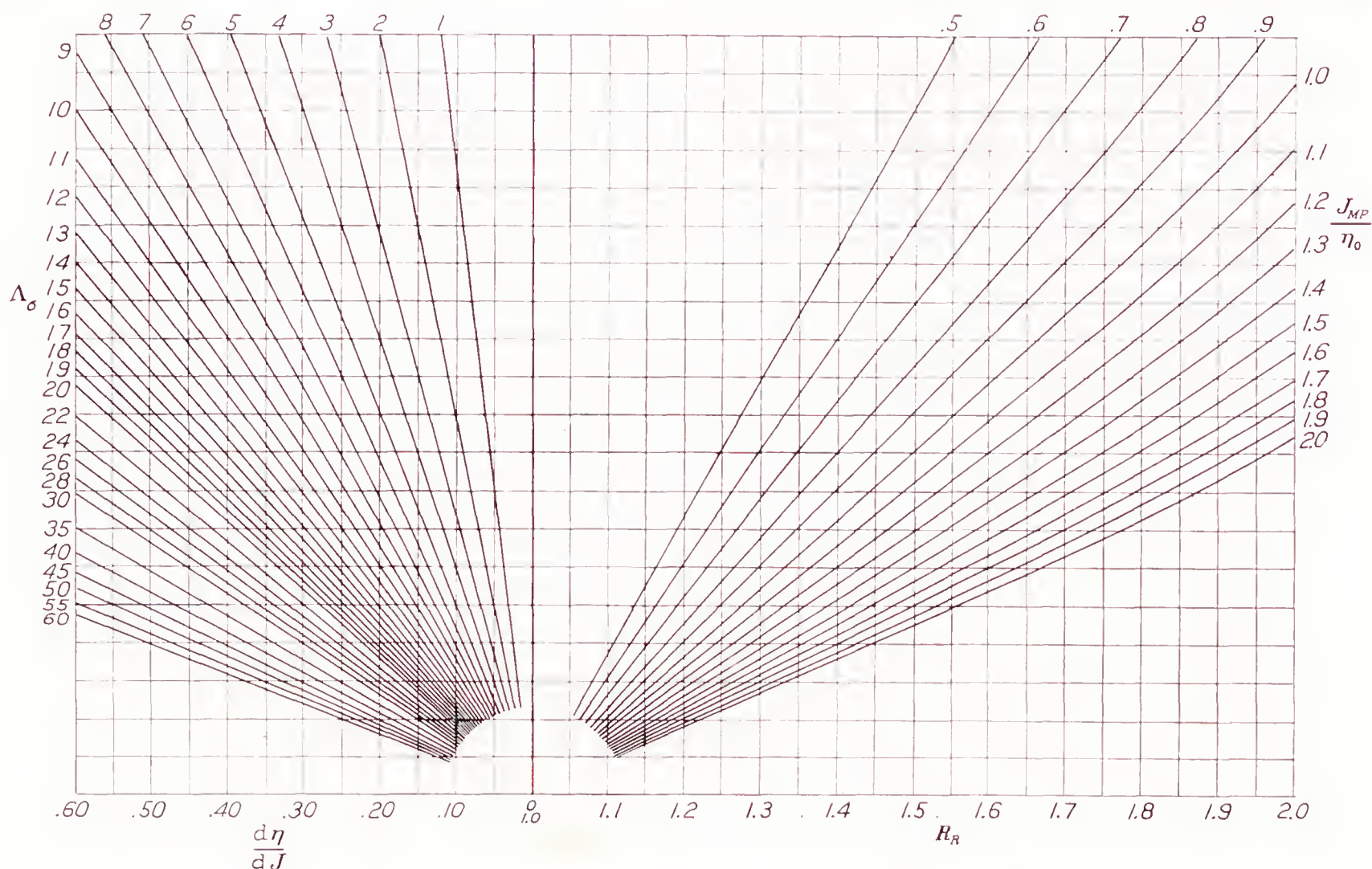


FIGURE 15.—Chart for calculating  $d\eta/dJ$  as a function of  $J_{MP}/\eta_0$ ,  $\Lambda_\sigma$ , and  $R_R$ .

An equivalent expression for  $dR_P/dR_R$  for the propulsive unit must now be obtained.

For constant-speed-propeller control, the brake horsepower is constant and therefore

$$R_P = \frac{P}{P_0} = \frac{\eta}{\eta_0} \quad (\text{A10})$$

Differentiating

$$dR_P = \frac{1}{\eta_0} d\eta \quad (\text{A11})$$

Also, as previously defined

$$R_R = \frac{V}{V_{MP}} = \frac{J}{J_{MP}} \quad (\text{A12})$$

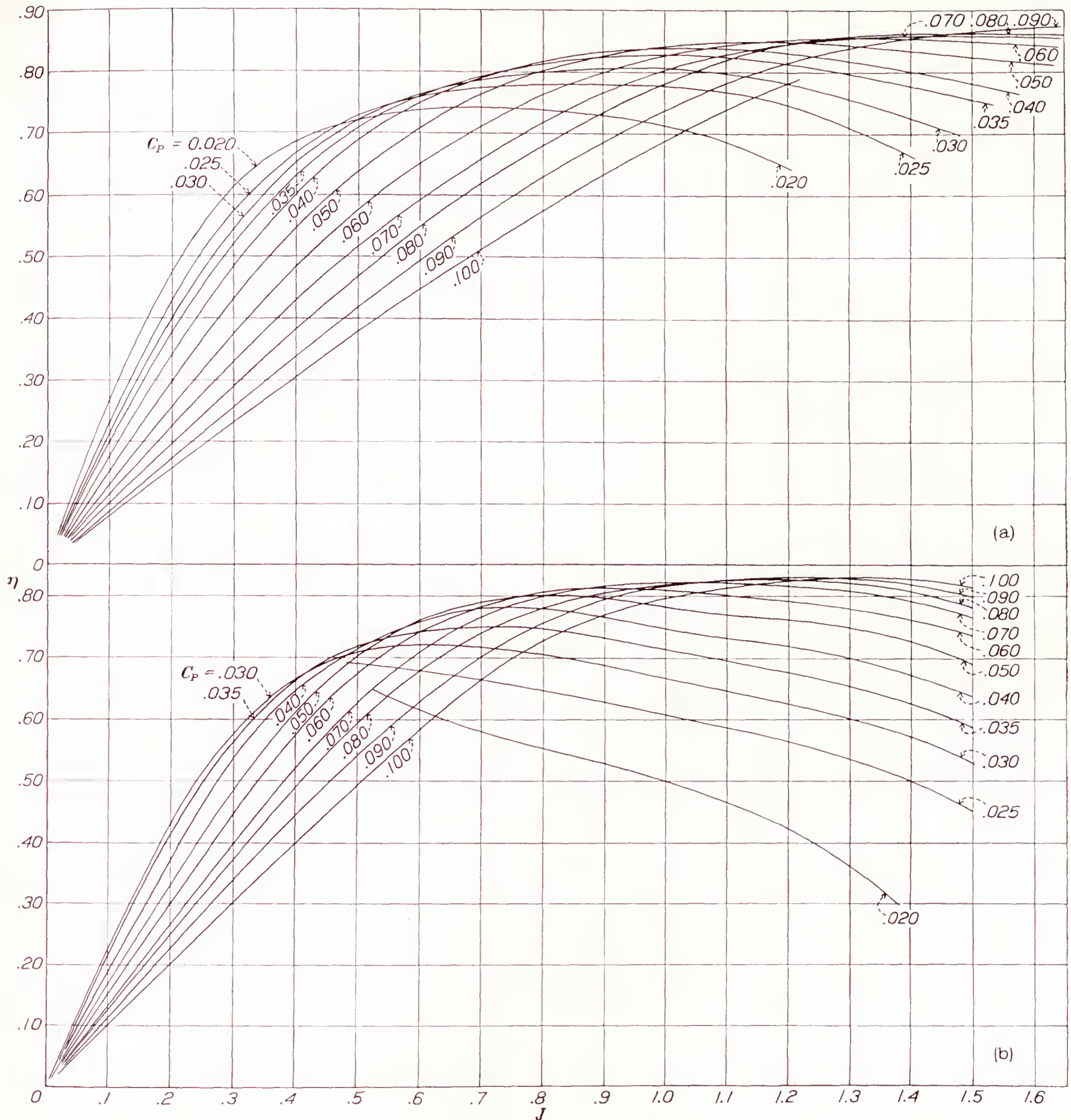
$\eta_0$  is multiplied by  $\Lambda_\sigma^{3/4}$ . By the definition of  $\Lambda_\sigma$  as given by (26)

$$\Lambda_\sigma^{3/4} = \frac{l_{s\sigma}^{3/4} l_t}{l_{p\sigma}^{1/4}} = \left( \frac{l_{s\sigma}^3}{l_{p\sigma}} \right)^{1/4} \frac{W}{\eta_0 \text{ b. hp.}}$$

Thus the product  $\eta_0 \Lambda_\sigma^{3/4}$  is independent of the assumed value of  $\eta_0$  as long as the same value is used in calculating  $\Lambda_\sigma$ . It is usually convenient to use a value of  $\eta_0$  that has been used before in calculating  $\Lambda_\sigma$ , thus saving an additional calculation for  $\Lambda_\sigma$ .

For a given set of conditions defined for a given airplane, i. e.,  $N$ , b. hp.,  $\eta_0$ , and  $\Lambda_\sigma$ , the entire right-hand





(a) Two-blade propeller characteristics.  
 (b) Three-blade propeller characteristics.

FIGURE 16.—Plot of  $\eta$  against  $J$  for different values of  $C_P$ . (See reference 5.)

$$C_P = 5 \times 10^{10} \frac{\text{b. hp.}}{\sigma N^3 D^5}; \quad J = \frac{V}{nD}$$

side of (A15) is determined except for the variable  $R_R = V_c/V_{MP}$ , since  $J_{MP}$  depends only upon the power-required characteristics of the airplane.

For rapid calculation figure 15 has been constructed from which  $d\eta/dJ$  may be determined in terms of the constant parameters,  $J_{MP}/\eta_0$  and  $\Lambda_\sigma$ , and the variable  $R_R$ . The left-hand side of the equation must now be defined from the propeller characteristics in terms of the same variable  $R_R$ .

For this purpose, the dimensionless parameters  $C_P$

and  $J$ , defined by (A9), are chosen, and the propeller characteristics in terms of these parameters and the efficiency  $\eta$  are plotted. Such a plot is shown in figure 16, the data for which were taken from reference 5. As shown by the definition of  $C_P$  and  $J$ ,  $C_P$  depends only upon the assumed characteristics of the airplane and is independent of the velocity  $V$  while

$$J = J_{MP} \frac{V}{V_{MP}}$$



which, at the speed for climb, becomes

$$J_c = J_{MP} \frac{V_c}{V_{MP}} = J_{MP} R_R \quad (A16)$$

Figure 17 has been constructed by graphical differentiation, plotting  $d\eta/dJ$  against  $J$  for constant  $C_P$ . Thus, the propeller characteristics have been obtained in the form  $\frac{d\eta}{dJ} = f_1(J, C_P)$  which, upon defining  $J_{MP}$ , becomes

$$\frac{d\eta}{dJ} = f_2(R_R, C_P)$$

Equation (A15) then becomes

$$f_2(R_R, C_P) = \frac{d\eta}{dJ} = 0.02935 \frac{\eta_0}{J_{MP}} \left( R_R^2 - \frac{1}{R_R^2} \right) \Lambda_\sigma^{3/4} \quad (A17)$$

Knowing  $\Lambda_\sigma$ ,  $\left( \frac{J_{MP}}{\eta_0} \right)$ , and  $C_P$ ,  $R_R$  may be calculated by iteration using figures 15 and 17(a) or 17(b). This method is shown clearly in the examples.

### EXAMPLES

Two major examples have been illustrated. Example A is of a normal type and the calculations are standard. Example B was chosen for the specific purpose of illustrating a condition under which the approximate method of selecting  $R_R$  (figure 8) fails. As may be found, consulting figure 8, the approximate method would have given satisfactory results in example A. However, in example B, the approximate method is good at the altitude for which the propeller was chosen (30,000 feet) but becomes increasingly bad for the constant brake-horsepower case at other altitudes. It is a satisfactory approximation above the altitude mentioned, provided that the brake horsepower decreases in a normal manner above this altitude.

#### EXAMPLE A (SEE FIG. 18)

Given: A two-engine monoplane with constant-speed and three-blade propellers:

$$W = 24,000 \text{ lb.}$$

$$b = 95 \text{ ft.}$$

$$e = 0.88.$$

$$f = 21 \text{ sq. ft.}$$

$$(b. \text{ hp.})_m = 850 \text{ hp. per engine at 2,100 r. p. m. at 8,000 ft. (assume constant (b. hp.)}_m \text{ from sea level to 8,000 ft.).}$$

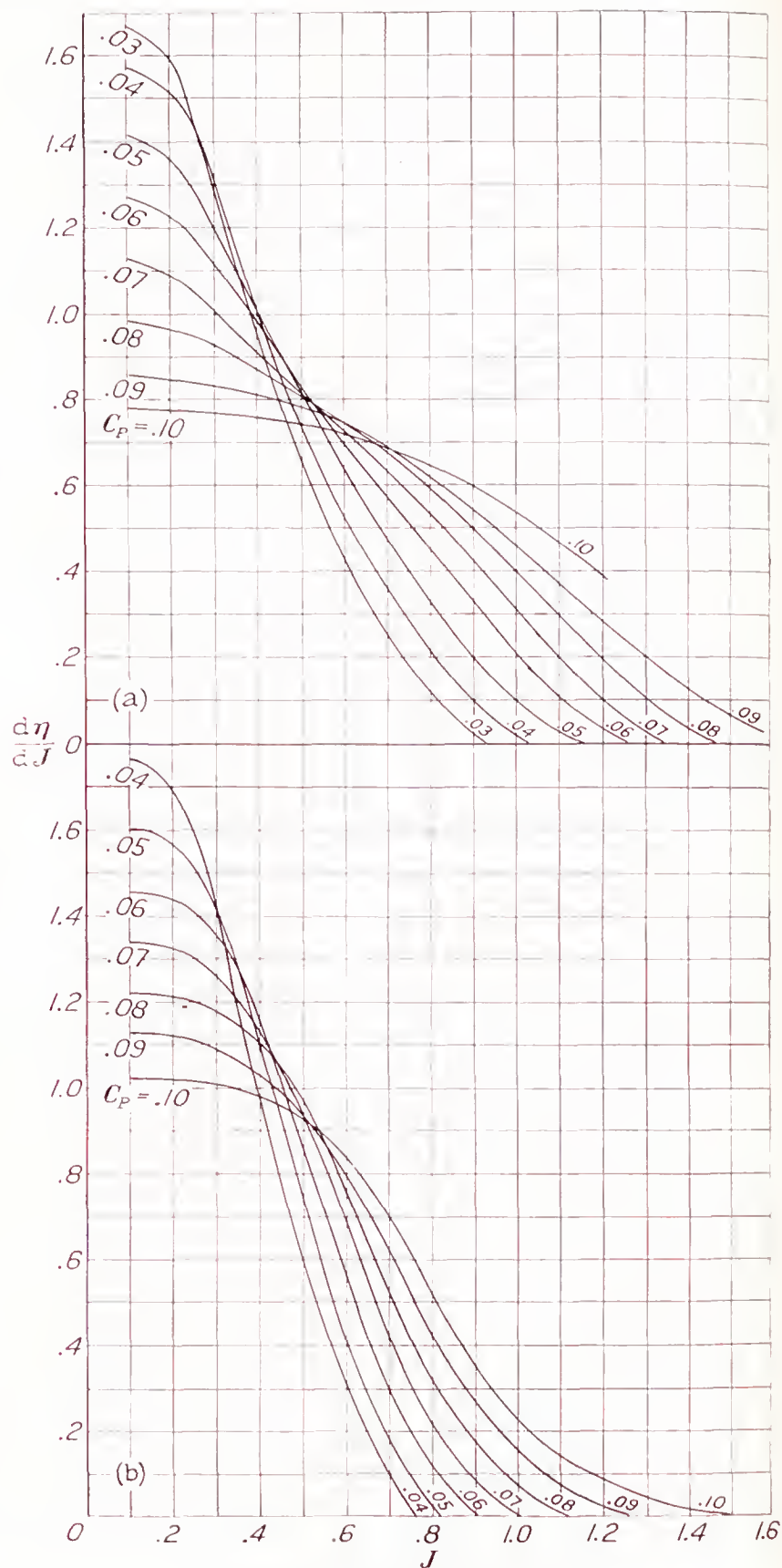
$$k = 1.00.$$

Select propeller for best performance at  $V_m$  with full throttle at 2,100 r. p. m. (geared 16:11) at 15,000 ft.

1. Calculate  $V_m$  at 15,000 feet.

$$\eta_0 = 0.84 \text{ assumed.}$$

$$\frac{1}{\sigma} = 1.590 \text{ (fig. 19).}$$



(a) Two-blade propeller (see fig. 16(a)).

(b) Three-blade propeller (see fig. 16(b)).

FIGURE 17.—Plot of  $d\eta/dJ$  against  $J$  for different values of  $C_P$ .

$$\left. \begin{aligned} l_s &= 3.02 \\ l_p &= 1,142 \end{aligned} \right\} \text{equation (26).}$$

$$(b. \text{ hp.})_m \text{ (at 15,000 ft.)} = [(b. \text{ hp.})_m \text{ (at 8,000 ft.)}] \times \left[ \frac{(b. \text{ hp.})_m \text{ (at 15,000 ft.)}}{(b. \text{ hp.})_m \text{ (at sea level)}} \right] \left[ \frac{(b. \text{ hp.})_m \text{ (at sea level)}}{(b. \text{ hp.})_m \text{ (at 8,000 ft.)}} \right] = 649 \text{ hp. (fig. 20)}$$

$$\left. \begin{aligned} l_{t0} &= 22.0 \\ \Lambda_\sigma &= 24.25 \end{aligned} \right\} \text{equation (26).}$$

$$\Omega_\sigma = 0.942 \text{ (fig. 4).}$$

$$V_\sigma = 52.73 \left( \frac{1}{\sigma} \frac{l_p}{l_t} \right)^{1/3} \Omega_\sigma = 216 \text{ m. p. h.}$$

$$\text{r. p. m.} = 2,100 \frac{11}{16} = 1,442.$$



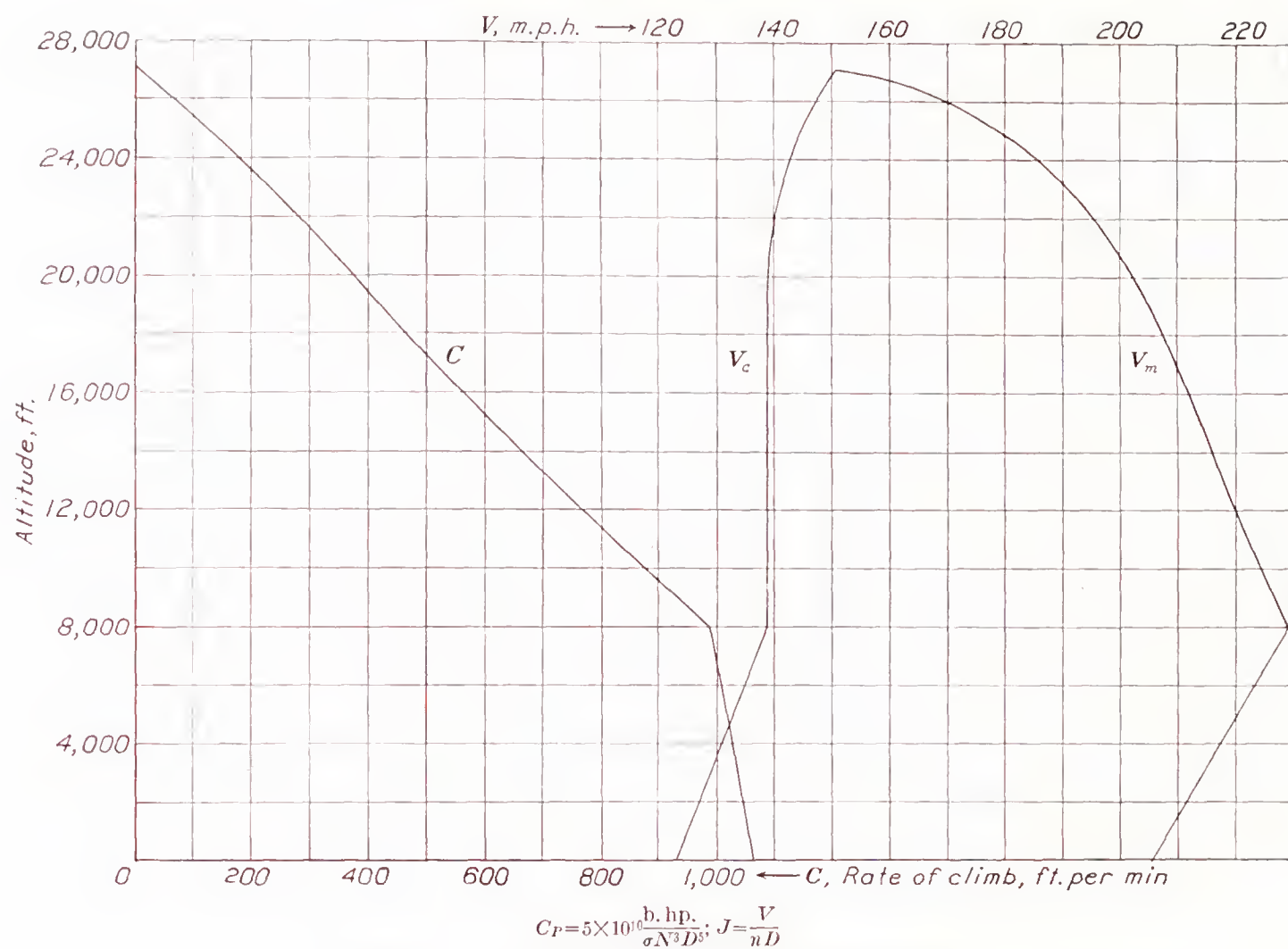


FIGURE 18.—Airplane performance summary chart for Example A.

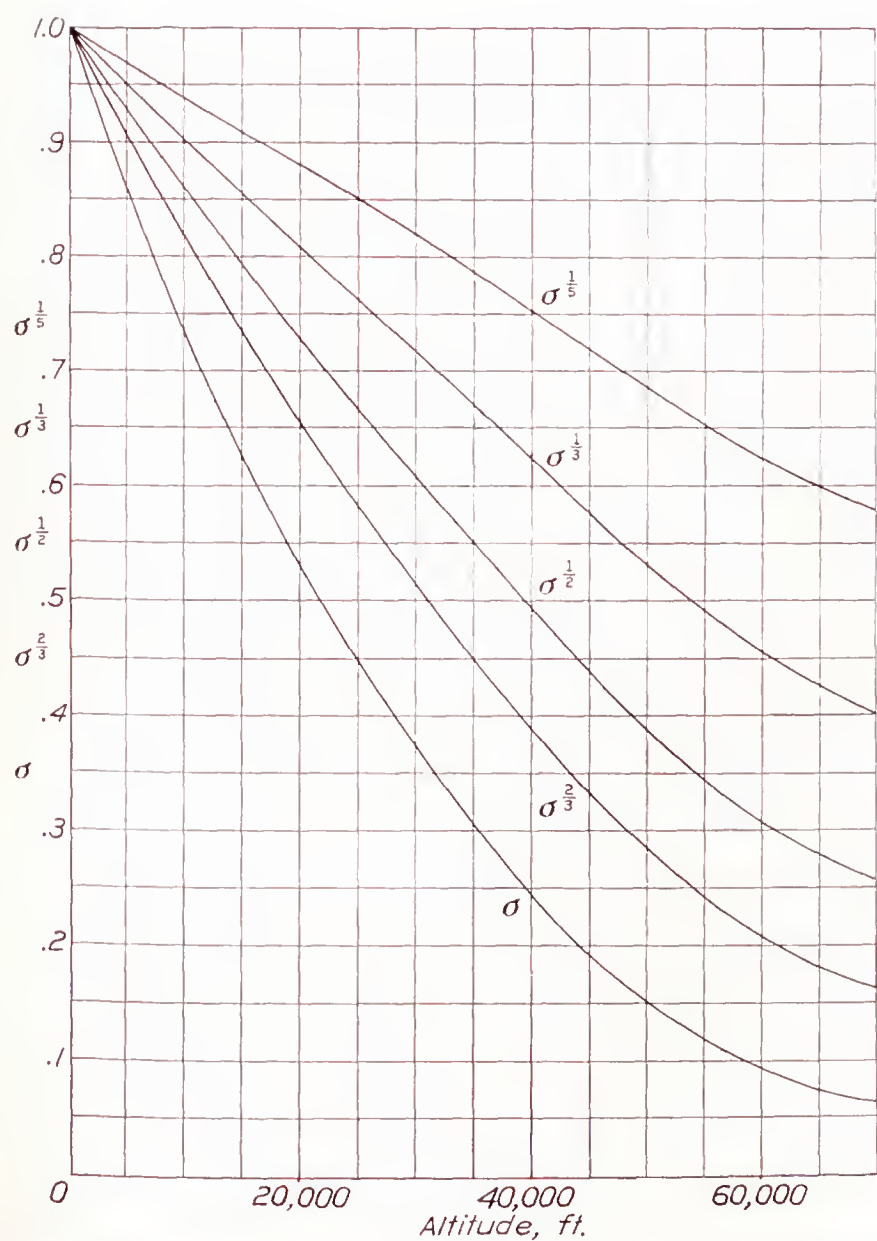
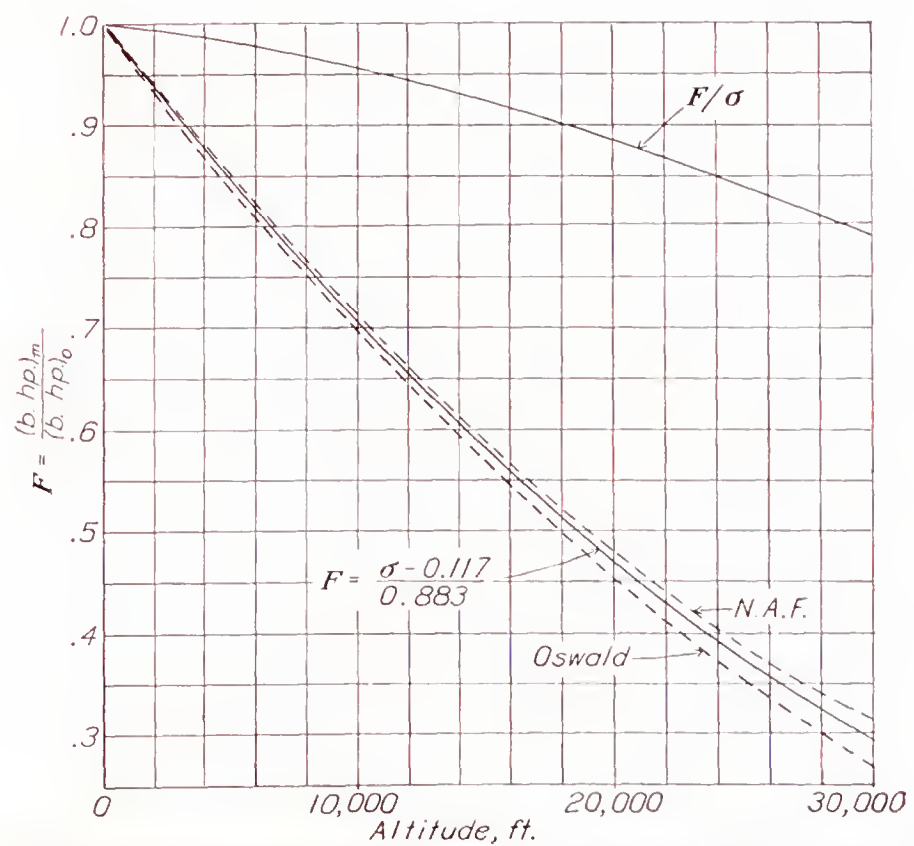
FIGURE 19.—Relative density as a function of altitude.  $\sigma = \rho/\rho_0$ ;  $\rho$ , mass density of air;  $\rho_0 = 0.002378$  slug/cu. ft. at sea level.

FIGURE 20.—Variation of full-throttle brake horsepower with altitude at constant r. p. m.



$C_s=0.638\frac{\sigma^{1/5}V}{(b. \text{ hp.})^{1/5}N^{2/5}}=1.87.$

$J=1.13$  (fig. 7 of reference 5).

$D=\frac{88V}{NJ}=11.65.$

$\eta=0.825$  (fig. 7 of reference 5).

$\frac{\Delta\eta}{\eta}=-1.8$  percent.

$\frac{dV}{V}=0.42$  percent per percent change in power (fig. 11).

$V_{corr}=216(1-0.0042\times1.8)=214$  m. p. h.

2. Calculate  $V_m$  at sea level, 8,000, 20,000, and 25,000 feet.

$\eta_0=0.84$  assumed.

$h$ (ft.)	$(b. \text{ hp.})_m$	$l_t$	$\Lambda_\sigma$	$\Omega_\sigma$	$V_\sigma$ (m. p. h.)	$C_P$	$J$	$\eta$	$\frac{\Delta\eta}{\eta_0}$ (percent)	$\frac{dV}{V}$ (percent)	$V_{corr}$ (m. p. h.)
0	850	16.82	12.43	0.973	209	0.0659	1.09	0.81	-3.6	0.37	206
8,000	850	16.82	15.60	.965	230	.0842	1.20	.83	-1.2	.38	229
20,000	524	27.25	36.1	.909	205	.0762	1.07	.825	-1.8	.50	203
25,000	418	34.20	54.7	.839	186	.0724	.973	.805	-4.2	.74	178

Fig. 20 (constant to 8,000 ft.).

$l_t=\frac{W}{\eta_0 b. \text{ hp.}}$

$\Lambda_\sigma=\left(\frac{1}{\sigma}\right)^{2/3}\frac{l_d l_t^{1/3}}{l_p^{1/3}}$

Fig. 4.

$V_\sigma=52.73\left(\frac{1}{\sigma}\frac{l_p}{l_t}\right)^{1/3}\Omega_\sigma$

$C_P=5\times10^{10}\frac{b. \text{ hp.}}{\sigma N^3 D^5}$

$J=\frac{88V}{ND}$

Fig. 16(b).

$\frac{\Delta\eta}{\eta_0}=\frac{\eta_{actual}-\eta_0}{\eta_0}$

Fig. 11.

$V_{corr}=V_\sigma\left[1+\left(\frac{dV}{V}\right)\left(\frac{\Delta\eta}{\eta_0}\right)\right]$

3. Calculate the maximum rate of climb at sea level, 8,000, 15,000, 20,000, and 25,000 feet.

$\left. \begin{matrix} l_t=16.82 \\ \eta_0=0.84 \end{matrix} \right\} \text{at sea level. Example A1}$   
(b. hp.)<sub>m</sub> = 850

$h$ (ft.)	$(b. \text{ hp.})_m$	$\Lambda_\sigma$	$V_\sigma$ (m. p. h.)	$R_{MP}$	$V_{MP}$ (m. p. h.)	$J_{MP}$	$\frac{J_{MP}}{\eta_0}$	$C_P$	$R_R$	$J_C$	$\frac{d\eta}{dJ}$	$R_R$	$V_C$ (m. p. h.)	$R_A$	$\eta_c$	$\Lambda_{\sigma_c}$	$l_{t_c}$	$Cl_{t_c}$	$C$ (ft./min.)
0	850	12.43	209	0.414	86.5	0.453	0.539	0.0659	1.42	0.638	0.54	1.42	123	1.33	0.725	20.2	19.49	20,700	1,062
8,000	850	15.60	230	.442	101.5	.531	.634	.0842	1.37	.728	.49	1.37	139	1.26	.735	24.0	19.23	19,000	988
15,000	649	24.25	216	.503	108.5	.568	.675	.0802	1.28	.727	.50	1.28	139	1.14	.745	32.9	24.8	15,200	613
20,000	524	36.1	205	.578	118.0	.620	.738	.0762	1.18	.732	.39	1.18	139	1.06	.760	43.6	30.1	11,100	369
25,000	418	54.7	186	.693	129	.674	.802	.0724	1.12	.755	.33	1.12	145	1.02	.780	61.5	36.8	4,500	122

Example A2.

Examples A1 and A2.

Examples A1 and A2.

Fig. 5.

$V_{MP}=V_\sigma R_{MP}$

$J_{MP}=\frac{88V_{MP}}{ND}$

$C_P=5\times10^{10}\frac{b. \text{ hp.}}{\sigma N^3 D^5}$

Assumed.

$J_C=J_{MP}R_R$

Fig. 17(b).

Fig. 15. Checks assumed value.

$V_C=V_{MP}R_R$

Fig. 9.

Fig. 16(b).

$\Lambda_{\sigma_c}=\Lambda_\sigma R_A\left(\frac{\eta_0}{\eta_c}\right)^{4/3}$

$l_{t_c}=l_t\left(\frac{\eta_c}{\eta_0}\right)\left(\frac{(b. \text{ hp.})_m \text{ at sea level}}{(b. \text{ hp.})_m}\right)$

Fig. 6.

$C=\frac{Cl_{t_c}}{l_{t_c}}$

EXAMPLE B (SEE FIG. 21)

Given: A single-engine monoplane with a constant-speed and three-blade propeller:

$W=6,000$  lb.

$b=45$  ft.

$e=0.85$  ft.

$f=6$  sq. ft.

(b. hp.)<sub>m</sub>=700 hp. at 2,000 r. p. m. geared 4:3 at 30,000 ft. (assume constant (b. hp.)<sub>m</sub> from sea level to 30,000 ft.)

$k=1.00$

Select propeller for best performance at  $V_m$  at 30,000 ft.

1. Calculate  $V_m$  at 30,000 feet.

Assume  $\eta_1=0.83$

$\left(\frac{1}{\sigma}\right)^{2/3}=1.93$  (fig. 19)

$l_s=\frac{W}{e(kb_1)^2}=3.49$

$l_p=\frac{W}{f}=1,000$

Equation (26)

$l_{t_1}=\frac{W}{\eta_1 b. \text{ hp.}_m}=10.33$

$\Lambda=\frac{l_s l_t^{4/3}}{l_p^{1/3}}=7.85$



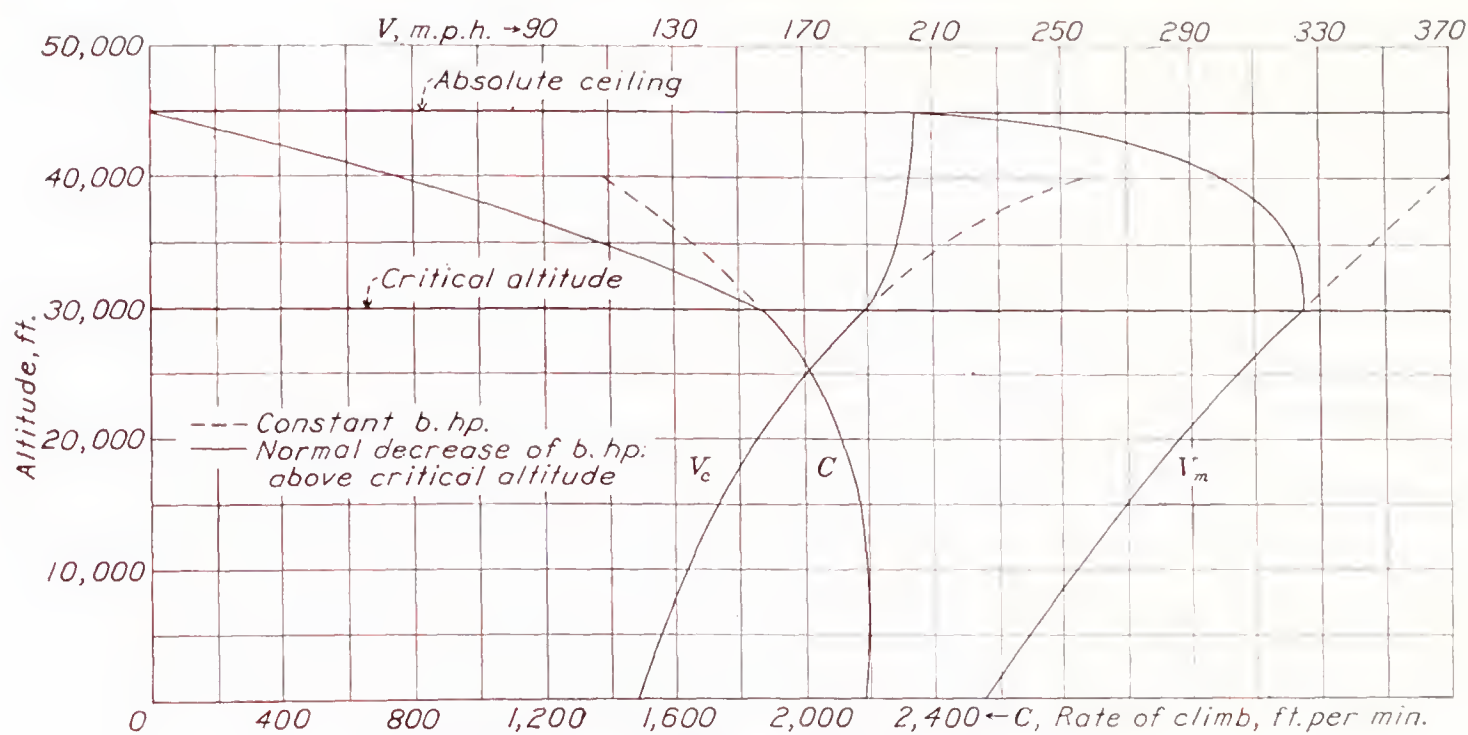


FIGURE 21.—Airplane performance summary chart for Example B.

$\Lambda_{\sigma} = \left(\frac{1}{\sigma}\right)^{2/3} \Lambda = 15.15$

Method (a)

$\Omega_{\sigma} = 0.966$  (fig. 4)

$V_{\sigma} = 52.73 \left(\frac{1}{\sigma} \frac{l_p}{l_t}\right)^{1/3} \Omega_{\sigma} = 325 \text{ m. p. h.}$

Method (b)

$\frac{1}{\sigma} \frac{l_p l_t}{V_{\sigma}} = 0.2977$

$V_{\sigma} = \frac{1}{\sigma} \frac{l_s l_t}{\left(\frac{1}{\sigma} \frac{l_s l_t}{V_{\sigma}}\right)} = 325 \text{ m. p. h.}$

$C_s = 0.638 \frac{\sigma^{1/5} V}{(\text{b. hp.})^{1/5} \Lambda^{2/5}} = 2.47$

$\eta_1 = 0.83$  Checks assumed value (fig. 7 of reference 5)

$J = \frac{88V}{ND} = 1.55$  (fig. 7 of reference 5)

$D = \frac{88V}{NJ} = 12.3 \text{ ft.}$

2. Calculate  $V_m$  at sea level, 10,000, 20,000, and 40,000 feet, assuming constant brake horsepower.  
Method (a):

$\Lambda = 7.85$   
 $\eta_1 = 0.83$  } Example B1

$h$ (ft.)	$\left(\frac{1}{\sigma}\right)^{2/3}$	$\Lambda_{\sigma}$	$\Omega_{\sigma}$	$\frac{1}{\sigma} \frac{l_p l_t}{V_{\sigma}}$	$V_{\sigma}$ (m. p. h.)	$C_P$	$J$	$\eta$	$\frac{\Delta P}{P}$ (percent)	$\frac{dV}{V}$ (percent)	$V$ (m. p. h.)
0	1.000	7.85	0.983	0.1515	238	0.0369	1.13	0.705	-15.1	0.36	225
10000	1.223	9.60	.979	.1861	262	.0502	1.25	.755	-9.0	.36	254
20000	1.522	11.95	.974	.2327	291	.0693	1.35	.795	-4.2	.37	286
30000	1.930	15.15	.966	.2977	325	.0983	1.55	.830	0	-----	325
40000	2.558	20.33	.953	.405	369	.1500	1.75	*.830	0	-----	369

$V_{\sigma} = 52.73 \left(\frac{l_p}{\sigma l_t}\right)^{1/3} \Omega_{\sigma}$  or  $\frac{1}{\sigma} \left(\frac{l_p l_t}{V_{\sigma}}\right)$

$C_P = 5 \times 10^{10} \frac{\text{b. hp.}}{\sigma N^3 D^3}$

$J = \frac{88V}{ND}$

$\frac{\Delta P}{P} = \frac{\eta_{\sigma} \eta_{\text{fuel}} - \eta_1}{\eta_1}$

$V = V_{\sigma} \left[ 1 + \frac{\Delta P}{P} \right] \text{ (in percent) } \frac{dV}{V}$

\* By extrapolation.



Method (b):

$$\left. \begin{aligned} \Lambda &= 7.85 \\ \eta_1 &= 0.83 \end{aligned} \right\} \text{Example B1}$$
$$^aV_0=238 \text{ at sea level for } \eta_0=0.83$$

$h$ (ft.)	$R_v$	$C_P$	$J$	$\eta$	$\Delta\eta$ (percent)	$\Delta R_v$	$R_{v_{corr}}$	$V$ (m. p. h.)
0	1.000	0.0369	1.13	0.705	-12.5			<sup>b</sup> 225
10,000	1.102	.0502	1.25	.755	-7.5	0.0045	1.068	254
20,000	1.223	.0693	1.35	.795	-3.5	.0061	1.202	286
30,000	1.364	.0983	1.55	.830	0		1.364	325
40,000	1.551	.1500	1.75	.830	0		1.551	369
	Fig. 13.	$C_P=C_P \text{ (at sea level)} \frac{1}{\sigma}$	$J=J \text{ (at sea level)} R_v$	Fig. 16 (b).	$\Delta\eta=\eta_{actual}-\eta_0$	Fig. 13.	$R_{v_{corr}}=R_v(1+\Delta\eta\times\Delta R_v)$	$V=V_0R_{v_{corr}}$

$$^aV_0=\frac{V \text{ (at 30,000 ft.)}}{R_v \text{ (at 30,000 ft.)}}=\frac{325}{1.364}=238 \text{ m. p. h.}$$
$$^bV=V_0\left[1+\left(\frac{\Delta P}{P}\right) \text{ (in percent)} \frac{dV}{V}\right]=225 \text{ m. p. h.}$$
$$\frac{dV}{V} \text{ from fig. 12.}$$

3. Calculate  $V_m$  at 35,000, 40,000, and 42,000 feet, assuming an engine critical altitude of 30,000 feet

$$\left. \begin{aligned} \Lambda &= 7.85 \\ \eta_1 &= 0.83 \end{aligned} \right\} \text{Example B1}$$
$$(\text{b. hp.})_0=700$$

$h$ (ft.)	$\left(\frac{1}{\sigma}\right)^{2/3}$	(b. hp.) <sub>m</sub>	$\Lambda_\sigma$	$\Omega_\sigma$	$V_\sigma$ (m. p. h.)	$C_P$	$J$	$\eta$	$\frac{\Delta P}{P}$ (percent)	$\frac{dV}{V}$ (percent)	$V$ (m. p. h.)
35,000	2.195	605	20.9	0.951	325	0.1034	1.55	0.810	-2.4	0.41	322
40,000	2.558	446	36.6	.908	302	.0960	1.44	.820	-1.2	.51	300
42,000	2.726	387	47.2	.871	284	.0913	1.35	.825	-.6	.62	283
	Fig. 19.	Assumed.	$\Lambda_\sigma=\left(\frac{1}{\sigma}\right)^{2/3}\left(\frac{(\text{b. hp.})_0}{(\text{b. hp.})_m}\right)^{4/3}\Lambda$	Fig. 4.	$V_\sigma=52.73\left(\frac{1}{\sigma}\frac{t_p}{t_t}\right)^{1/3}\Omega_\sigma$	$C_P=5\times 10^{10}\frac{\text{b. hp.}}{\sigma N^3 D^5}$	$J=\frac{88V}{ND}$	Fig. 16 (b).	$\frac{\Delta P}{P}=\frac{\eta_{actual}-\eta_1}{\eta_1}$	Fig. 12.	$V=V_\sigma\left[1+\left(\frac{\Delta P}{P} \text{ (percent)}\times\frac{dV}{V}\right)\right]$



4. Calculate the maximum rate of climb from sea level to 40,000 feet assuming constant brake horsepower.

(a) Calculate  $V_{MP}$

Method (1):

$$\left. \begin{matrix} l_s = 3.49 \\ l_{t1} = 10.33 \end{matrix} \right\} \text{Example B1}$$

$h$ (ft.)	$\frac{1}{\sigma}$	$\Lambda_\sigma$	$\frac{1}{\sigma} \frac{l_s l_t}{V_{MP}}$	$V_{MP}$ (m.p.h.)
0	1.000	7.85	0.415	87
10,000	1.353	9.60	.482	101
20,000	1.877	11.95	.569	119
30,000	2.675	15.15	.682	140
40,000	4.085	20.33	.847	174

Fig. 19.

Examples B1 and B2.

Fig. 14.

$$V_{MP} = \frac{\frac{1}{\sigma} \frac{l_s l_t}{V_{MP}}}{\frac{1}{\sigma} \frac{l_s l_t}{V_{MP}}}$$

Method (2):

$\Lambda = 7.85$

$V_0 = 258 \text{ m. p. h. (corresponds to } \eta_0 = 0.83 \text{). Example B2.}$

$h$ (ft.)	$R_{MP}$	$V_{MP}$ (m. p. h.)
0	0.364	87
10,000	.423	101
20,000	.498	119
30,000	.590	140
35,000	.650	155
40,000	.750	174
42,000	.767	183

Fig. 5.

$$V_{MP} = R_{MP} V_0$$

(b) Calculate the maximum rate of climb.

Method (1) (approximate method):

$$\left. \begin{matrix} l_{t1} = 10.33 \\ \eta_1 = 0.83 \end{matrix} \right\} \text{Example B1}$$

$h$ (ft.)	$\Lambda_\sigma$	$R_R$	$V_{MP}$ (m. p. h.)	$V_c$ (m. p. h.)	$R_\Lambda$	$J_c$	$C_P$	$\eta_c$	$\Lambda_{\sigma_c}$	$l_{t_c}$	$Cl_{t_c}$	$C$ (ft./min.)
0	7.85	1.57	87	137	1.64	0.653	0.0369	0.760	14.5	11.30	23,400	2,070
10,000	9.60	1.50	101	152	1.48	.725	.0502	.790	15.2	10.85	23,000	2,120
20,000	11.95	1.43	119	170	1.35	.811	.0693	.800	16.9	10.72	22,000	2,070
30,000	15.15	1.37	140	192	1.25	.915	.0983	.780	20.6	11.00	20,500	1,860
40,000	20.33	1.29	174	225	1.15	1.072	.1500	.660	31.8	13.00	15,600	1,200

Examples B1 and B2.

Fig. 8.

Example B4.

$$V_c = V_{MP} R_R$$

Fig. 9.

$$J_c = \frac{88 V_c}{ND}$$

Example B2.

Fig. 16 (b).

$$\Lambda_{\sigma_c} = \Lambda_\sigma R_\Lambda \left( \frac{\eta_1}{\eta_c} \right)^{4/3}$$

$$l_{t_c} = l_{t1} \left( \frac{\eta_1}{\eta_c} \right)$$

Fig. 6.

$$C = \frac{Cl_{t_c}}{l_{t_c}}$$

<sup>a</sup> By extrapolation.

Method (2) (exact method):

$$\left. \begin{matrix} l_{t1} = 10.33 \\ \eta_1 = 0.83 \end{matrix} \right\} \text{Example B1}$$

$h$ (ft.)	$\Lambda_\sigma$	$V_{MP}$ (m.p.h.)	$J_{MP}$	$\frac{J_{MP}}{\eta_1}$	$C_P$	$R_R$	$J_c$	$\frac{d\eta}{dJ}$	$R_R$	$V_c$ (m.p.h.)	$R_\Lambda$	$\eta_c$	$\Lambda_{\sigma_c}$	$l_{t_c}$	$Cl_{t_c}$	$C$ (ft./min.)
0	7.85	87	0.415	0.500	0.0369	1.36	0.565	0.360	1.36	118	1.24	0.745	11.2	11.50	25,100	2,180
10,000	9.60	101	.481	.580	.0502	1.32	.635	.320	1.32	133	1.19	.775	12.5	11.05	24,400	2,200
20,000	11.95	119	.567	.684	.0693	1.31	.742	.315	1.31	156	1.17	.785	15.1	10.90	23,100	2,120
30,000	15.15	140	.667	.804	.0983	1.34	.893	.340	1.34	188	1.21	.770	20.2	11.14	20,700	1,860
40,000	20.33	174	.830	1.000	.1500	1.46	1.210	.460	1.46	254	1.40	.760	31.9	11.28	15,600	1,380

Examples B1 and B2.

Example B4.

$$J_{MP} = \frac{88 V_{MP}}{ND}$$

Example B2.

Assumed.

$$J_c = J_{MP} R_R$$

Fig. 17 (b).

Fig. 15. Checks assumed value.

$$V_c = V_{MP} R_R$$

Fig. 9.

Fig. 16 (b).

$$\Lambda_{\sigma_c} = \Lambda_\sigma R_\Lambda \left( \frac{\eta_1}{\eta_c} \right)^{4/3}$$

$$l_{t_c} = l_{t1} \left( \frac{\eta_1}{\eta_c} \right)$$

Fig. 6.

$$C = \frac{Cl_{t_c}}{l_{t_c}}$$



5. Calculate the maximum rate of climb at 35,000, 40,000 and 42,000 ft. assuming an engine critical altitude of 30,000 ft. as in Example B3.

Approximate method:

$$\left. \begin{aligned} l_{t_1} &= 10.33 \\ \eta_1 &= 0.83 \\ (b.\text{ hp.})_0 &= 700 \end{aligned} \right\} \text{Example B1}$$

$h$ (ft.)	$(b.\text{ hp.})_m$	$\Lambda_\sigma$	$R_R$	$V_{MP}$ (m. p. h.)	$V_c$ (m. p. h.)	$R_\Lambda$	$J_c$	$C_P$	$\eta_c$	$\Lambda_{\sigma_c}$	$l_{t_c}$	$Cl_{t_c}$	$C$ (ft./min.)
35,000 40,000 42,000	605 446 387	20.9 36.6 47.2	1.29 1.18 1.16	155 174 183	200 205 212	1.15 1.05 1.04	0.953 .977 1.010	0.1034 .0960 .0913	0.770 .800 .810	26.6 40.3 50.6	12.90 16.82 19.12	17,800 12,300 8,400	1,380 732 440
<div>Example B3.</div> <div>Example B3.</div> <div>Fig. 8.</div> <div>Example B4 (a) (2).</div> <div><math>V_c = V_{MP} R_R</math></div> <div>Fig. 9.</div> <div><math>J_c = \frac{88 V_c^2}{N D}</math></div> <div>Example B3.</div> <div>Fig. 16 (b).</div> <div><math>\Lambda_{\sigma_c} = \Lambda_\sigma R_\Lambda \left( \frac{\eta_1}{\eta_c} \right)^{4/3}</math></div> <div><math>l_{t_c} = l_{t_1} \left( \frac{(b.\text{ hp.})_m \eta_1}{(b.\text{ hp.})_m \eta_c} \right)</math></div> <div>Fig. 6.</div> <div><math>C = Cl_{t_c} / l_{t_c}</math></div>													

Exact method:

$$\left. \begin{aligned} l_{t_1} &= 10.33 \\ \eta_1 &= 0.83 \\ (b.\text{ hp.})_0 &= 700 \end{aligned} \right\} \text{Example B1}$$

$h$ (ft.)	$(b.\text{ hp.})_m$	$\Lambda_\sigma$	$V_{MP}$ (m.p.h.)	$J_{MP}$	$\frac{J_{MP}}{\eta_1}$	$C_P$	$R_R$	$J_c$	$\frac{d\eta}{dJ}$	$R_R$	$V_c$ (m.p.h.)	$R_\Lambda$	$\eta_c$	$\Lambda_{\sigma_c}$	$l_{t_c}$	$Cl_{t_c}$	$C$ (ft./min.)
35,000 40,000 42,000	605 446 387	20.9 36.6 47.2	155 174 183	0.738 .829 .872	0.889 .999 1.051	0.1034 .0960 .0913	1.28 1.16 1.11	0.943 .945 .967	0.325 .260 .200	1.28 1.16 1.11	199 202 203	1.14 1.04 1.02	0.770 .795 .805	26.3 40.2 50.2	12.90 16.90 19.30	18,000 12,400 8,600	1,395 734 445
<div>Example B3.</div> <div>Example B3.</div> <div>Example B4 (a) (2).</div> <div><math>J_{MP} = \frac{88 V_{MP}}{N D}</math></div> <div>Example B3.</div> <div>Assumed.</div> <div><math>J_c = J_{MP} R_R</math></div> <div>Fig. 17 (b).</div> <div>Fig. 15 (checks).</div> <div><math>V_c = V_{MP} R_R</math></div> <div>Fig. 9.</div> <div>Fig. 16 (b).</div> <div><math>\Lambda_{\sigma_c} = \Lambda_\sigma R_\Lambda \left( \frac{\eta_1}{\eta_c} \right)^{4/3}</math></div> <div><math>l_{t_c} = l_{t_1} \left( \frac{(b.\text{ hp.})_m \eta_1}{(b.\text{ hp.})_m \eta_c} \right)</math></div> <div>Fig. 6.</div> <div><math>C = Cl_{t_c} / l_{t_c}</math></div>																	

EXAMPLE C

Given: An airplane for which, for full power at 10,000 feet altitude:

$$\Lambda_\sigma = 15.0$$
$$V_\sigma = 250 \text{ m. p. h.}$$
$$W = 15,000 \text{ lb.}$$

1. Calculate the speed at the same altitude for 60 percent full power, assuming no change in propulsive efficiency.

$$\frac{\Delta P}{P} = -40 \text{ percent}$$
$$\frac{dV}{V} = 0.47 \text{ percent per percent of } \frac{\Delta P}{P} \text{ (fig. 12)}$$
$$V_{corr} = 250 (1 - 0.0047 \times 40) = 203 \text{ m. p. h.}$$

2. Calculate the speed for a 1,000-pound increase in  $W$ .

$$\frac{\Delta W}{W} = \frac{1000}{15000} = 6.7 \text{ percent}$$
$$\frac{dV}{V} = 0.075 \text{ percent (fig. 11)}$$
$$V = 250 (1 - 0.00075 \times 6.7) = 248 \text{ m. p. h.}$$

3. Calculate the speed for an overload of 7,500 pounds.

$$W = 15,000 \text{ lb., } \Lambda_\sigma = 15.0, \Omega_\sigma = 0.966 \text{ (fig. 4).}$$
$$W = 22,500 \text{ lb., } \Lambda_\sigma = 15.0 \left( \frac{22500}{15000} \right)^2 = 33.8,$$
$$\Omega_\sigma = 0.916 \text{ (fig. 4).}$$
$$V \text{ (for 22,500 lb.)} = 250 \times \frac{0.916}{0.966} = 237 \text{ m. p. h.}$$



## COMPOSITE CHART

The introduction of the altitude parameters into the performance analysis of the previous pages makes it possible to construct charts composed of single curves, in place of families of curves necessary in the case of the sea-level parameters, to represent the performance at all altitudes. This method results in a more compact form for all charts using the altitude parameters.

Accordingly, Mr. W. R. Sears of the California Institute of Technology has devised an arrangement of all of the curves, except for the propeller curves, in one compact, composite chart. This method avoids the necessity of cross reference from one chart to another in most performance calculations. Figure 22 shows the arrangement of the curves on this chart.

## REFERENCES

1. Oswald, W. Bailey: General Formulas and Charts for the Calculation of Airplane Performance. T. R. No. 408, N. A. C. A., 1932.
2. Ashley, R. B.: Methods of Performance Calculation for Airplanes with Supercharged Engines Developed by W. Bailey Oswald. A. C. I. C. No. 679, Matériel Division, Army Air Corps, 1933.
3. White, Roland J., and Martin, Victor J.: Charts for Calculating the Performance of Airplanes Having Constant-Speed Propellers. T. N. No. 579, N. A. C. A., 1936.
4. Diehl, Walter S.: Standard Atmosphere—Tables and Data. T. R. No. 218, N. A. C. A., 1925.
5. Russell, J. S., and McCoy, H. M.: Wind Tunnel Tests on a High Wing Monoplane with Running Propeller. Part I—Propulsive Characteristics of Two and Three Bladed Adjustable Pitch Propellers Extended to Fairly Large Blade Angles. Jour. Aero. Sci., vol. 3, no. 3, January 1936, pp. 73-78.

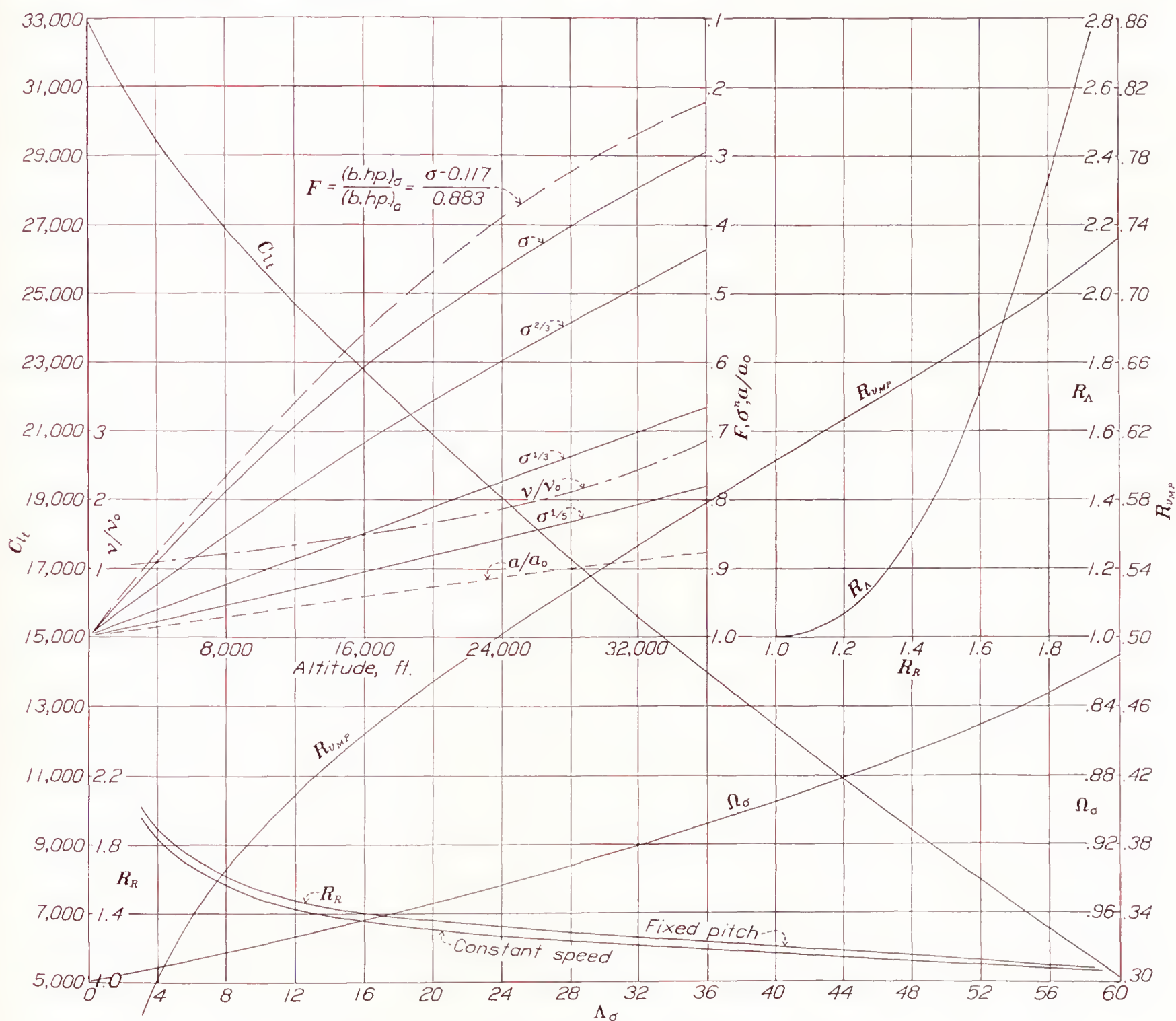


FIGURE 22.—Composite chart for the calculation of airplane performance.

$$\frac{\nu}{\nu_0} = \frac{\text{kinematic viscosity at altitude}}{\text{kinematic viscosity at sea level}}$$

$$\frac{a}{a_0} = \frac{\text{speed of sound at altitude}}{\text{speed of sound at sea level}}$$







## REPORT No. 655

# THE KNOCKING CHARACTERISTICS OF FUELS IN RELATION TO MAXIMUM PERMISSIBLE PERFORMANCE OF AIRCRAFT ENGINES

By A. M. ROTHROCK and ARNOLD E. BIERMANN

### SUMMARY

*An analysis is presented of the relationship of various engine factors to knock or preignition in an aircraft engine. From this analysis and from the available experimental data, a method of evaluating the knocking characteristics of the fuel in an aircraft-engine cylinder is suggested. Because the method is based on the physical factors controlling knock, the knocking-characteristic curve for each fuel expresses the relative maximum permissible engine performance obtainable from the fuel. Curves are presented showing the manner in which the knocking-characteristic curve can be used to predict the relationship between compression ratio and maximum permissible indicated mean effective pressure, minimum permissible specific fuel consumption, and maximum permissible peak pressure for any one fuel. Additional curves show that the knocking-characteristic curves permit a rational choice to be made between two or more fuels or permit the fuel to be selected that most satisfactorily meets the given engine requirements. The suggested method of determining the knocking characteristics is compared with the octane-number scale. Throughout the discussion, the susceptibility of the fuels to the temperature conditions within the engine is emphasized.*

### INTRODUCTION

The knocking characteristic of a fuel is the most important factor in determining the maximum permissible performance obtainable from that fuel in a spark-ignition engine. For this reason, extensive researches have been conducted in an effort to rate fuels according to their knocking characteristics in aircraft engines. Most of these investigations have been conducted with the idea of determining a simple method by which the knocking characteristics of various fuels can be compared on an empirical basis. In order to determine the maximum permissible engine performance obtainable from any one fuel, the problem must be attacked from a somewhat different angle. The question becomes one of defining basic relationships between the different engine variables and the limiting engine performance. The characteristics of the individual engine

become important as well as the characteristics of the fuel. If the basic relationships can be determined, it should be possible to predict the maximum permissible engine performance under numerous engine operating conditions from tests conducted under a few operating conditions.

The problem resolves itself, therefore, into two parts: First, a correlation of the effect of the various engine factors on the knocking characteristics of the fuel or, since the knocking characteristic of the fuel is the primary independent variable, the correlation between the knocking characteristics of the fuel and the permissible combinations of the different engine variables; and, second, a determination of the maximum permissible engine performance based upon this correlation.

A correlation between the different variables having once been obtained, the results can be expressed in the form of one or more curves depending on the number of independent variables. Such curves have already been presented in reference 1 and have been suggested as a method of rating fuels. Serruys (reference 2) has shown data that correlate maximum permissible peak pressure, compression ratio, and power output.

In the present report, the data presented in reference 1 are extended and analyses are made of these data and of the results of other investigators so that a correlation of the various engine factors can be obtained. From this analysis it is shown that a single curve obtained from the variation of a few conditions represents the knocking characteristics of the fuel in an engine over a wide variety of conditions.

In the second part of the report it is shown that, from the knocking characteristics of the fuels obtained on various engines, estimates can be made of the effect of compression ratio, inlet-air temperature, and inlet-air pressure on the maximum permissible indicated mean effective pressure, minimum permissible specific fuel consumption, and maximum permissible peak pressure.

A third section is included in which the knocking characteristics are compared with the octane numbers of the fuels investigated.



## I—DETERMINATION OF KNOCKING CHARACTERISTICS

The phenomena that limit the severity of engine conditions to which a fuel can be subjected are knock and preignition. Knock, or detonation, is defined as a combustion phenomenon that results in an abnormal and uncontrollable rate of pressure rise near the end of combustion, which takes place with sufficient rapidity to set up waves within the gas that travel at velocities equal to or greater than that of sound in the gaseous medium. Preignition is defined as ignition of the charge by some source other than the ignition spark and prior to the ignition spark.

### KNOCK

Knock in spark-ignition engines, according to the most generally accepted concept, is the result of the almost simultaneous burning of the end gases in the combustion chamber. This burning is of sufficient rapidity to cause a sudden increase in the pressure in part of the combustion chamber. The pressure increase takes place at a rate more rapid than the rate at which the pressure is transmitted through the gas. Therefore a system of pressure waves is set up within the chamber. These gas vibrations strike the combustion-chamber wall and induce vibrations in the engine structure, which give rise to the metallic knock.

More recent data obtained at this laboratory (reference 3) have led to the conclusion that knock may not necessarily be the auto-ignition of the end gas, because knock has been observed after the combustion front has apparently traversed the end gas. Regardless of the nature of knock, the effect on the pressures within the cylinder is the same—a sudden increase in the local pressures, and, with heavy knock, a sudden increase also in the mean pressure throughout the chamber. Knock, if sufficiently severe, is accompanied by an eventual loss in power, possible preignition, and, if continued, results in overheating of the engine and consequent engine failure.

### PREIGNITION

Preignition is generally surface ignition at some hot spot in the combustion chamber. The effect of preignition is the same as that obtained by advancing the spark timing, that is, combustion starts too early in the cycle. As a result, there is loss of power and overheating of the engine (unless the spark has been retarded to a value less than that for optimum power). The early start of combustion may also be accompanied by knock although this is not necessarily the case. Some fuels, such as benzene, are prone to preignite although in the pure state they do not knock. The combustion started by preignition is not essentially different from that started by the electric spark at the spark plug. The difficulties caused by preignition result from a lack of control of the time at which ignition starts.

In the present report, most of the data discussed relate to knock and not to preignition. The analysis of the method of estimating maximum permissible engine

performance will be based on knocking fuels and not on preigniting fuels.

### ENGINE FACTORS INVOLVED

Knock and preignition are phenomena of combustion; they must therefore be controlled by the physical state of the gases within the combustion chamber as well as by the chemical composition of the gases. The conditions that control the state and the composition of the gases within the combustion chamber are:

- (a) Chemical composition of the fuel.
- (b) Fuel-air ratio.
- (c) Exhaust-gas dilution.
- (d) Humidity.
- (e) Compression ratio.
- (f) Inlet-air temperature.
- (g) Inlet-air pressure or density.
- (h) Wall temperature of combustion chamber and cylinder.
- (i) Spark advance.
- (j) Engine speed.
- (k) Engine dimensions.
- (l) Combustion-chamber form.

All these factors affect, either directly or indirectly, the chemical and the physical properties of the gases within the combustion chamber at the time knock or preignition takes place. In the determination of knocking or preigniting characteristics of fuels, the relationship that is to be derived is the effect of the chemical composition of the fuel or the effect of different fuels on the values of the other 11 factors that result in knock or preignition.

### TEMPERATURE-DENSITY RELATIONSHIP

It seems reasonable to assume that the temperature and the density of the combustion gas just prior to knock are the physical properties of the combustion gas which determine whether or not the fuel knocks. If the assumption is accepted that the two physical properties controlling knock are the gas temperature and the gas density, it can be said that, for each gas density, there is a corresponding gas temperature at which knock will occur. It follows that, if this contention is true, the knocking characteristics of a fuel in any engine can be determined from the relationship between the gas temperature and density which results in knock. A second and equally important contention that must necessarily follow is the impossibility of adequately expressing the knocking characteristics of a fuel by determining one and only one combination of temperature and density at which knock occurs.

Since preignition is generally the result of a hot spot in the combustion chamber, it is reasonable to assume that the secondary ignition characteristics of fuel can best be obtained by determining the relationship between the hot-spot temperature and the temperature and the density of the combustion gases which result in this secondary ignition. It is probable that the temperature of the hot spot in this case is more important



than the temperature of the gases. But, again, the fuels must not be evaluated at any one set of engine conditions but over a sufficient variety of engine conditions to permit a temperature-density relationship for preignition to be determined.

**Determination of temperature-density relationship.**—The immediate cause of knock is the gas density and temperature in the knocking region of the combustion chamber the instant before knock occurs. If the explosion pressure just previous to knock can be measured, the temperature-density relationship can be obtained from a method similar to that presented by Serruys in reference 2. Inasmuch as the knock apparently occurs in the last part of the charge to burn (whether it is previous to or after the propagation of the normal flame through this region does not affect the analysis), the temperature and the density of this gas can be used as the criterion for determining the conditions that cause knock. This portion of the charge is compressed by the previously burning mixture as well as by the piston during the compression stroke. The actual value of these ratios need not be known to estimate the temperature and the density, provided that the peak combustion pressure preceding knock is known.

From the conventional thermodynamic equations, the density of this end gas previous to its combustion, as the intensity of the knock approaches zero, can be expressed as:

$$K\rho_3 = \frac{P_1}{T_1} \left( \frac{P_3}{P_1} \right)^{\frac{1}{\gamma}} \quad (1)$$

and the temperature in the knocking zone as:

$$T_3 = T_1 \left( \frac{P_3}{P_1} \right)^{\frac{\gamma-1}{\gamma}} \quad (2)$$

in which  $\rho_3$  is the gas density in the knocking zone immediately preceding knock.

$P_1$ , the inlet-air pressure.

$T_1$ , the inlet-air temperature.

$P_3$ , the pressure immediately preceding knock.

$\gamma$ , the adiabatic coefficient.

$T_3$ , the temperature in the knocking zone immediately preceding knock.

$K$ , a constant.

It will be noticed that these expressions are the same as those given in reference 2 except that the density is used in place of the pressure.

In accordance with expressions (1) and (2), tests can be run with an engine at combinations of compression ratio, spark advance, inlet-air temperature, and inlet-air pressure that cause knock. From these results, equations (1) and (2) can be evaluated and a curve constructed from the resulting data. The equations involve neither the compression ratio of the engine nor the spark advance.

In general, it is not easy to make an accurate measurement of the peak pressures in an engine; therefore, the problem of correlating the effects of the different engine

variables will be simplified if some other temperature and density in the cycle can be used. When the other factors are maintained constant, for optimum spark advance, the gas temperature and density in the knocking zone can be expressed in terms of the inlet-air pressure, the inlet-air temperature, and the compression ratio in the following manner: Equation (1) can be expressed as

$$K\rho_3 = \frac{P_1}{T_1} \left( \frac{P_3}{P_2} \times \frac{P_2}{P_1} \right)^{\frac{1}{\gamma}}$$

If  $P_2$  is the compression pressure,  $T_2$  the absolute compression temperature, and  $T_3'$  the mean absolute temperature throughout the combustion chamber immediately preceding knock, the density  $\rho_3$  can be expressed by:

$$K\rho_3 = \frac{P_1}{T_1} \left( \frac{T_3'}{T_2} \right)^{\frac{1}{\gamma}} \left( \frac{P_2}{P_1} \right)^{\frac{1}{\gamma}}$$

But

$$T_3' = T_2 + \frac{H}{c_v} = T_1 R^{\gamma-1} + \frac{H}{c_v}$$

and

$$\left( \frac{P_2}{P_1} \right)^{\frac{1}{\gamma}} = R$$

in which  $H$  is the heat content per pound of mixture;  $c_v$ , the specific heat of the mixture at constant volume; and  $R$ , the compression ratio of the engine. Therefore

$$K\rho_3 = \frac{RP_1}{T_1} \left( 1 + \frac{H}{c_v T_1 R^{\gamma-1}} \right)^{\frac{1}{\gamma}} \quad (1a)$$

In expression (1a),  $RP_1/T_1$  represents the density of the gases at top center, and the expression  $(1 + H/c_v T_1 R^{\gamma-1})^{\frac{1}{\gamma}}$  represents the further compression of the gases in the end zone during the combustion period. By a similar analogy, it can be shown that

$$T_3 = T_1 R^{\gamma-1} \left( 1 + \frac{H}{c_v T_1 R^{\gamma-1}} \right)^{\frac{\gamma-1}{\gamma}} \quad (2a)$$

In expression (2a),  $T_1 R^{\gamma-1}$  represents the compression temperature, and the expression  $(1 + H/c_v T_1 R^{\gamma-1})^{\frac{\gamma-1}{\gamma}}$  represents the temperature increase in the end gas caused by the compression in this zone during the combustion.

In the evaluation of expressions (1a) and (2a),  $c_v$  is estimated to be 0.25 B. t. u. per pound per °F.,  $\gamma$  to be 1.29, and  $H$  to be 1,160 B. t. u. per pound of mixture.

TABLE I  
ESTIMATED TEMPERATURES OF END GAS  $T_3$  FOR VARIOUS COMPRESSION RATIOS AND INLET-AIR TEMPERATURES

Compression ratio	Inlet-air temperature (° F.)			
	120	160	200	240
	$T_3$ (° F.)			
6	1,440	1,520	1,600	1,680
8	1,540	1,620	1,700	1,780
10	1,630	1,720	1,810	1,900
12	1,700	1,790	1,880	1,970



The values of  $T_3$  for a series of compression ratios and inlet-air temperatures are given in table I. The table shows that, whereas an increase in compression ratio of from 6 to 8 increases the end-gas temperature 100° F., an increase in inlet temperature of from 120° F. to 240° F. at the lower ratio increases the end-gas temperature 240° F. It can be concluded that, if temperature alone is considered, an increase in compression ratio in the normal operating range should not have any great effect on the fuel requirements of the engine. Any effect of increasing the compression ratio must therefore lie mainly in the increase of the gas density at top center.

In the determination of the knocking characteristics of fuels in an engine, it will be necessary to determine the temperature-density relationship for knocking combustion over a sufficient range of engine conditions to establish a definite curve. If the assumption is made for the moment that this curve (over the operating range) is a straight line, the results for two fuels of different chemical properties may appear as shown in figure 1. In this case, fuel A is superior to fuel B at low gas temperatures but fuel B is the better at high temperatures; fuel A is more susceptible to temperature variations than fuel B.

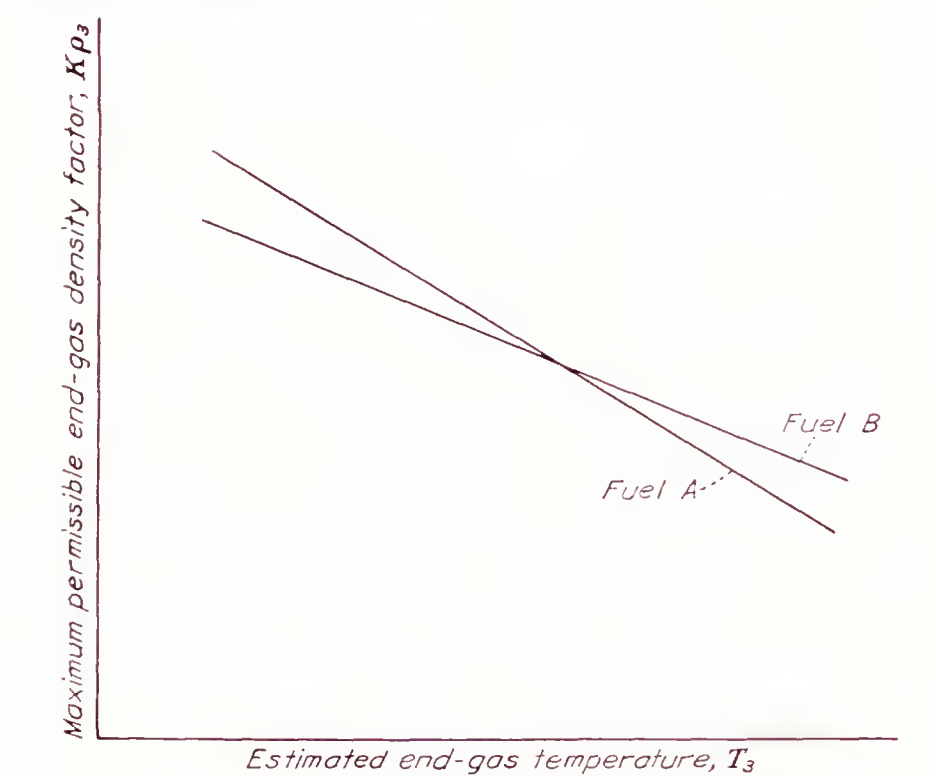


FIGURE 1.

The foregoing relationship can be established by keeping the compression ratio constant and varying the inlet-air temperature and pressure; by keeping the inlet-air pressure constant and varying the compression ratio and the inlet-air temperature; or, as will later be shown, by varying the engine-coolant or the jacket temperature instead of the air temperature.

**Experimental check of temperature-density relationship.**—Recent tests completed by the N. A. C. A. (reference 1) show the maximum permissible inlet-air pressure without knock for a series of compression ratios and inlet-air temperatures, using fuels made by blending commercial iso-octane (2, 2, 4—trimethylpentane) with a reference fuel of low knock rating. The commer-

cial iso-octane was similar to the C. F. R. S-1 reference fuel and the fuel with low knock rating was similar to the C. F. R. M-1 reference fuel. The blends tested consisted of 85, 90, 95, and 100 percent of the iso-octane fuel and are so designated. In addition, the iso-octane was tested with 1.0 ml per gallon of tetraethyl lead.

TABLE II  
EFFECT OF INLET-AIR TEMPERATURE ON MAXIMUM PERMISSIBLE INLET-AIR PRESSURE AT DIFFERENT COMPRESSION RATIOS

[Engine speed, 2,500 r. p. m.; coolant temperature, 250° F.; fuel-air ratio, 0.081; flat-disk combustion chamber]

Knock	Fuel	Inlet-air temperature, (° F.)	Compression ratio			
			6.50	7.25	8.00	8.75
			Inlet-air pressure (in. Hg abs.)			
Audible	85 percent iso-octane	120	32.5	-----	-----	-----
		160	32.5	-----	-----	-----
		200	32.5	-----	-----	-----
		240	32.5	-----	-----	-----
		280	-----	-----	-----	-----
Do	90 percent iso-octane	120	35.0	32.5	-----	-----
		160	35.0	32.5	-----	-----
		200	32.5	-----	-----	-----
		240	32.5	-----	-----	-----
		280	32.0	-----	-----	-----
Do	95 percent iso-octane	120	37.5	35.0	30.0	-----
		160	37.5	35.0	-----	-----
		200	35.0	32.5	-----	-----
		240	32.5	-----	-----	-----
		280	30.0	-----	-----	-----
Do	Iso-octane	120	40.0	37.5	32.5	30.0
		160	40.0	32.5	32.5	30.0
		200	35.0	32.5	30.0	-----
		240	35.0	32.5	-----	-----
		280	30.0	30.0	-----	-----
Do	Iso-octane + 1.0 ml tetraethyl lead	120	(1)	(1)	37.5	32.5
		160	(1)	(1)	35.0	32.5
		200	(1)	(1)	32.5	30.0
		240	(1)	(1)	30.0	-----
		-----	-----	-----	-----	-----

Improved cooling in center of cylinder head

Audible	85 percent iso-octane	120	34.4	29.5	-----	-----
		160	33.1	-----	-----	-----
		200	32.1	-----	-----	-----
		240	29.9	-----	-----	-----
		280	29.7	-----	-----	-----
Do	Iso-octane	120	40.7	35.8	34.2	31.4
		160	41.6	35.6	32.4	-----
		200	39.8	33.2	29.4	-----
		240	36.6	30.9	-----	-----
		280	33.0	-----	-----	-----
Incipient	do	120	37.6	30.7	29.2	27.1
		160	36.7	30.9	27.9	-----
		200	35.6	29.4	-----	-----
		240	33.7	29.5	-----	-----
		280	30.2	-----	-----	-----
Do	Iso-octane + 1.0 ml tetraethyl lead	120	-----	48.5	43.9	41.8
		160	-----	48.2	45.6	41.2
		200	-----	46.2	39.3	33.1
		240	-----	42.9	34.7	32.5
		280	-----	40.6	32.7	30.3

(1) Maximum inlet-air pressure limited by preignition or afterignition.

Tables II, III, and IV show a summary of the results presented in reference 1 and of results subsequently obtained with the test engine. The test engine was operated at 2,500 and 2,200 r. p. m. and was cooled with ethylene glycol maintained at a temperature of 250° F. The engine dimensions are 5 by 5¾ inches. One flat-disk and one pent-roof combustion chamber were tested. The piston used with the pent-roof chamber had recesses cut in the top to prevent its contacting the valves at the high compression ratios. In the first series of



TABLE III

EFFECT OF INLET-AIR TEMPERATURE ON MAXIMUM PERMISSIBLE INLET-AIR PRESSURE AT DIFFERENT COMPRESSION RATIOS

Engine speed, 2,200 r. p. m.; coolant temperature, 250° F.; fuel-air ratio for best power; knock, incipient; pent-roof combustion chamber; fuel, iso-octane]

Inlet-air temperature (° F.)	Compression ratio		
	6.50	7.25	8.00
	Inlet-air pressure (in. Hg absolute)		
120	40.2	36.1	33.3
160	40.0	36.6	32.1
200	37.2	---	32.6
240	35.2	33.5	30.0
280	34.2	31.2	---

TABLE IV

EFFECT OF INLET-AIR TEMPERATURE ON MAXIMUM PERMISSIBLE INLET-AIR PRESSURE AT DIFFERENT COMPRESSION RATIOS

[Engine speed, 2,500 r. p. m.; coolant temperature, 250° F.; fuel-air ratio, 0.078; knock, incipient; pent-roof combustion chamber]

Fuel	Inlet-air temperature (°F.)	Compression ratio		
		6.50	7.25	8.00
		Inlet-air pressure (in. Hg absolute)		
85 percent iso-octane...	120	32.7	29.2	---
	160	32.0	---	---
	220	31.1	---	---
	240	30.7	---	---
	290	30.3	---	---
90 percent iso-octane...	120	34.6	31.6	---
	160	34.1	31.1	---
	210	33.3	30.2	---
	250	32.5	---	---
	300	31.5	---	---
95 percent iso-octane...	120	37.9	34.2	32.2
	160	37.8	33.8	31.0
	210	36.4	33.1	31.1
	260	35.6	31.2	---
	300	33.2	30.8	---
Iso-octane.....	120	43.1	38.3	34.7
	170	42.7	37.7	35.1
	210	41.2	37.1	34.8
	250	39.8	34.9	32.9
	300	37.4	33.7	31.6
Iso-octane+1.0 ml tetraethyl lead.....	210	55.1	49.5	44.3
	250	53.5	47.0	40.7
	300	48.9	44.3	39.1

tests with the flat-disk chamber and the leaded fuel, preignition or afterignition was observed at the two lower compression ratios. Afterignition consisted of firing after the ignition switch had been turned off. These data are not listed because in these tests the limit imposed by knock was desired. Improved cooling to the center of the cylinder head removed the hot spot that caused this secondary ignition, and the second set of data so indicated was recorded. It will be noticed that, for the 85- and 100-percent iso-octane, there was no appreciable change in the maximum permissible inlet-air pressure when the cooling of the cylinder head was improved. This fact will later be discussed in more detail.

In figure 2 is plotted the maximum permissible density factor as a function of the estimated end-gas temperature

obtained by substituting in equations (1a) and (1b) data from table II for the iso-octane and the iso-octane plus 1.0 ml of tetraethyl lead with the improved cooling. The important fact to be noted from the curves is that, although the data for each fuel were obtained for a variety of compression ratios, inlet-air pressures, and inlet-air temperatures, the data for each fuel can be expressed as a single curve and from this curve various combinations of the three aforementioned variables can be chosen which will represent the maximum conditions at which the engine can be operated without knock.

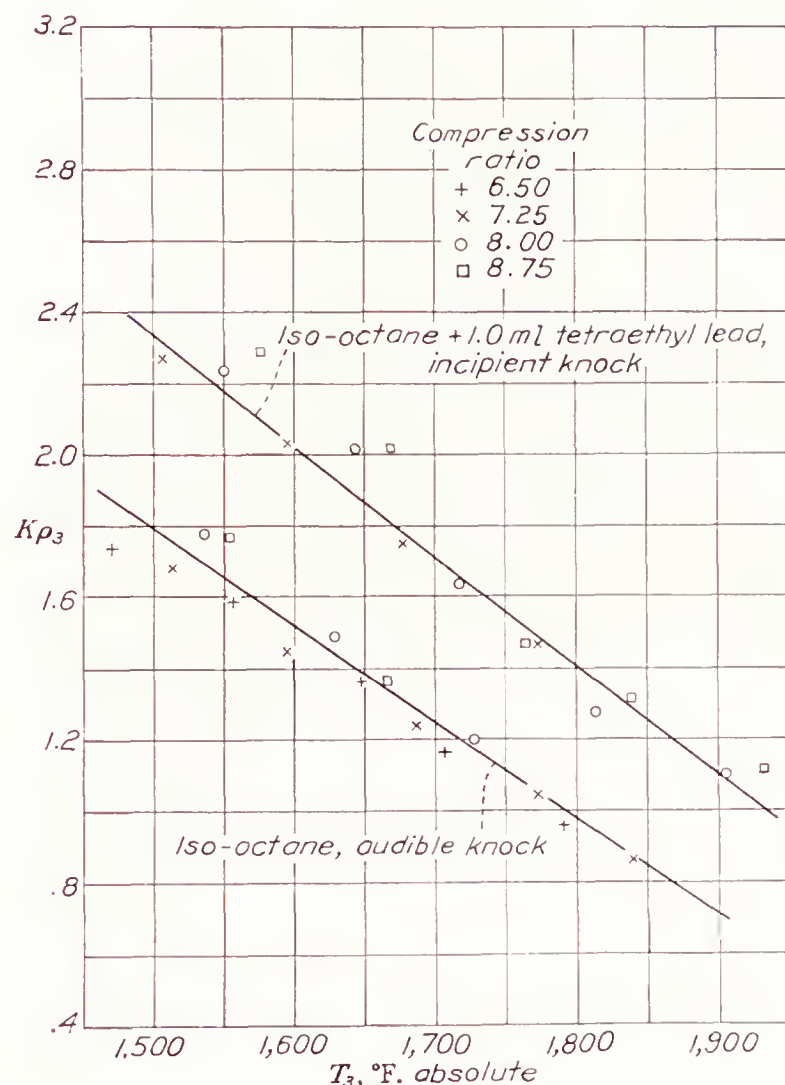


FIGURE 2.—Effect of estimated temperature  $T_3$  of end gas on maximum permissible density factor. Flat-disk combustion chamber; engine speed, 2,500 r. p. m.; improved cooling in cylinder head; fuel-air ratio, 0.081.

The problem of determining the knocking characteristics of the fuel within the engine is simplified if recorded test temperatures and pressures can be used in place of the estimated values shown in figure 2. For the range of values shown in table II, the value of  $(1 + H/c_e T_1 R^{\gamma-1})^{1/\gamma}$  at an inlet-air temperature of 120° F. varied from a value of 3.82 at a compression ratio of 6.5 to a value of 3.62 at a compression ratio of 8.75. Consequently, it is reasonable to assume that, for any given inlet-air temperature, the density factor can be expressed by  $RP_1/T_1$ . The value of the expression in the parentheses raised to  $(\gamma-1)/\gamma$  shows even less variation, the range being from 1.48 to 1.39 for all the values listed in table II. For practical purposes, the expression in the parentheses can be eliminated from equations (1a) and (2a). The density factor is then expressed by  $RP_1/T_1$



and the temperature factor by  $T_1 R^{\gamma-1}$ . As a further simplification,  $R^{\gamma-1}$  will also be eliminated. The deletion of this factor from the temperature expression is justified, not from an analysis of the equation, but from the experimental results as shown in figure 3. In this figure the inlet-air temperature is plotted against the maximum permissible density factor,  $RP_1/T_1$ , for the conditions shown in figure 2 together with some check runs. The results show that the data can be expressed in this manner by a straight line for each fuel. Similar curves for all the fuels listed in table II are shown in figure 4.

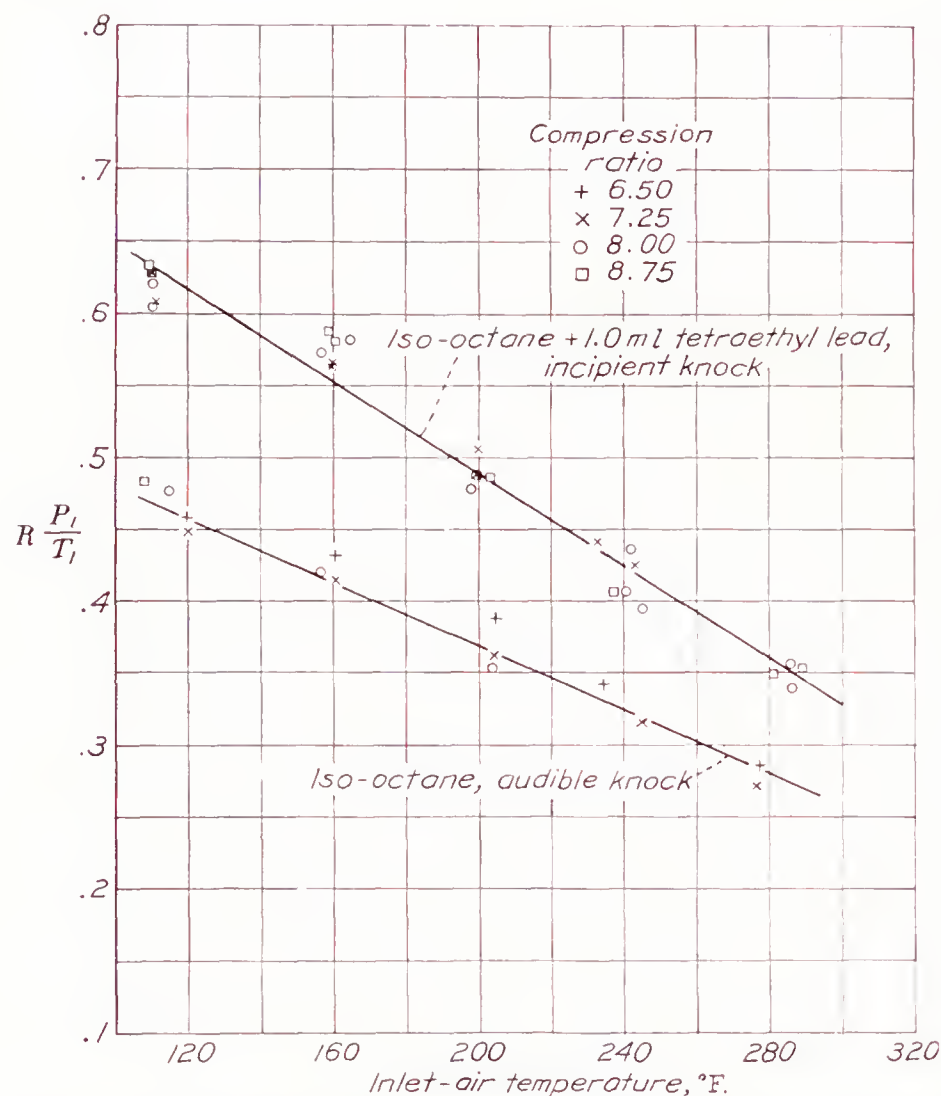


FIGURE 3.—Effect of inlet-air temperature on maximum permissible density factor. Flat-disk combustion chamber; engine speed, 2,500 r. p. m.; improved cooling in center of cylinder head; fuel-air ratio, 0.081.

The improved cooling of the flat-disk cylinder head increased the maximum permissible density factor for the fuel that showed preignition or afterignition but not for the other fuels. This fact indicates that fuels subject to this secondary ignition because of a hot spot in the combustion chamber can be used at more severe engine conditions if this hot spot is removed, whereas fuels that knock without first preigniting or afterigniting are not necessarily improved. A still more important conclusion is that preignition and afterignition are separate phenomena from knock and must be treated as such. It is quite probable that the hot spot in this case appeared only after the heat flow through the

cylinder wall had exceeded a certain value and consequently was not present with the fuels of lower knock rating.

The data from table IV for the pent-roof combustion chamber are plotted in figure 5. The deviation of the experimental data from the curves in figure 5 is much less than that in figure 3. Extreme care was taken to decrease the cyclic variation of the spark timing in obtaining the data presented in figure 5. This variation was decreased to  $\pm 3/4$  crankshaft degree by mounting the breaker on an extension to the crankshaft.

Plotting the values of  $RP_1/T_1$  against inlet-air temperature instead of compression temperature and using a single curve to represent all compression ratios assumes that, for a given inlet-air temperature, the value of the factor  $RP_1/T_1$  is a constant regardless of compression ratio. The data in figures 3 and 5 indicate that this factor is approximately constant for the engine tested over a range of compression ratios from 6.50 to 8.75. Data obtained by Muecklow (reference 4) on two engines and by Taylor (reference 5) on one engine (table V) over a similar range of compression ratios and for engines of a similar size also show this factor to be approximately constant for a constant inlet-air temperature. These data also indicate that the approximation is justified.

TABLE V  
EFFECT OF COMPRESSION RATIO ON ALLOWABLE BOOST PRESSURE. INLET-AIR TEMPERATURE CONSTANT FOR EACH SERIES OF TESTS

Engine	Fuel	Compression ratio	Maximum induction pressure (in. Hg abs.)	$RP_1/10$
Single-cylinder Napier (reference 4).	Petrol.....	4.5	42.3	19.0
		4.0	54.3	21.7
		3.5	60.8	21.3
Single-cylinder Rolls-Royce (reference 4).	Benzole.....	4.0	65.4	26.1
		5.0	56.8	28.4
		5.5	51.4	28.3
		6.0	50.9	30.6
		6.5	45.3	29.4
		7.0	41.1	28.8
N. A. C. A. universal test engine (reference 5, fig. 11).	Domestic aviation gasoline.	3.5	44.0	15.4
		4.0	37.5	15.5
		4.5	32.5	15.3
		5.0	30.0	15.5

Boerlage (reference 6) has reported a series of tests on a C. F. R. engine in which the compression ratio and boost pressure were varied to determine the maximum permissible values for a series of fuels from 50 to 100 octane number. The inlet-air temperature was maintained constant at 68° F. Table VI lists the products of the compression ratio by the maximum permissible inlet-air pressure for two of the fuels reported.

For the C. F. R. engine, there is a definite decrease in the maximum permissible density factor for an increasing compression ratio. It seems that, with the



TABLE VI

EFFECT OF COMPRESSION RATIO ON ALLOWABLE BOOST PRESSURE ON C. F. R. ENGINE (REFERENCE 6)

Fuel	Compression ratio	Pressure $P_1$ (in. Hg abs.)	$\frac{RP_1}{10}$
100 octane number fuel-----	6.5	45.7	29.7
	7.0	41.0	28.7
	7.5	37.7	28.4
	8.0	34.6	27.7
90 octane number fuel-----	6.0	41.8	27.1
	6.5	37.0	24.1
	7.0	32.3	22.9
	7.5	29.9	22.5

engines of larger bore, the data for which are given in tables II to V, the effect of the increased temperature caused by increasing the compression ratio is small or is offset by some other factor; whereas, in the smaller engine, the effect of the increased temperature caused by increasing the compression ratio is appreciable. Since the present report is limited to cylinder sizes

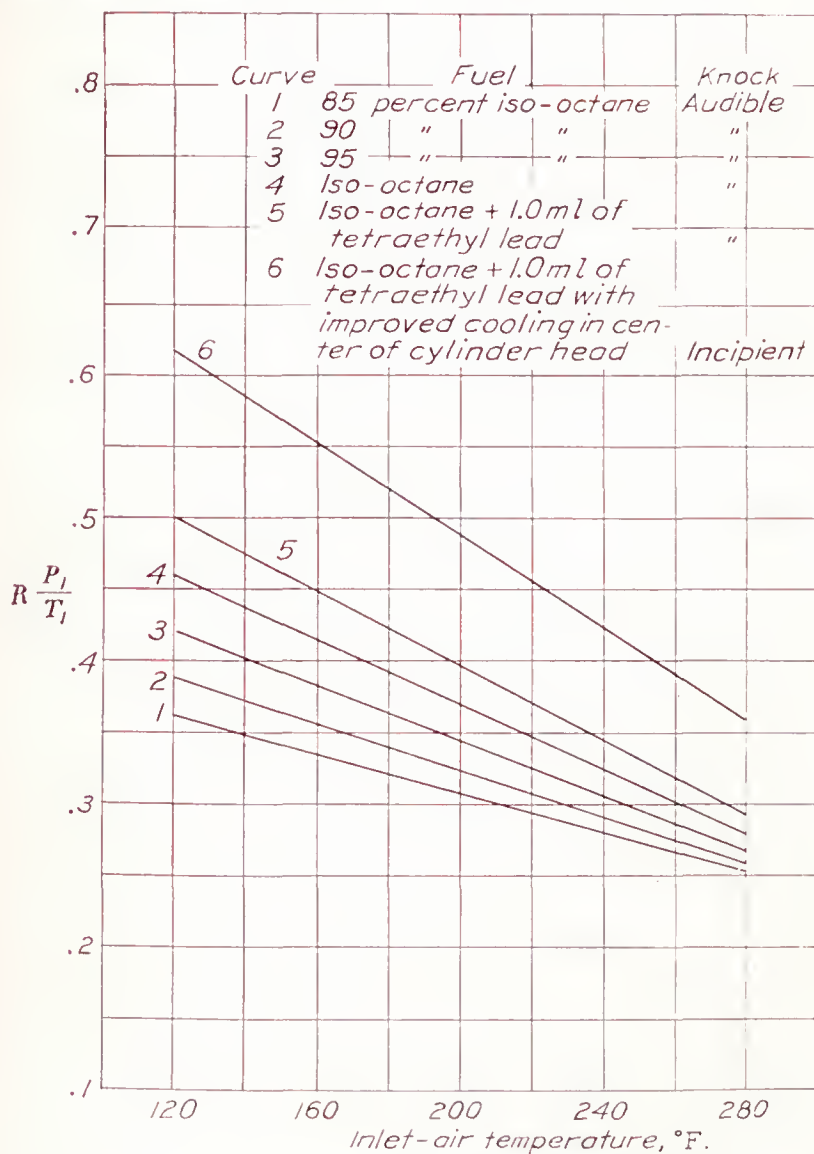


FIGURE 4.—Effect of inlet-air temperature on maximum permissible density factor for a series of fuel blends. Flat-disk combustion chamber; engine-speed, 2,500 r. p. m.; fuel-air ratio, 0.081.

suitable for aircraft engines of high power output, the assumption will be made that the maximum permissible value of  $RP_1/T_1$  is a constant regardless of compression ratio. It is emphasized, however, that more experimental data are necessary fully to justify this assumption. In either case, the principles upon which the analysis is based are equally applicable, the point at

issue being whether the inlet-air temperature can be taken as the abscissa of the rating curve or whether some other temperature in the cycle, such as the estimated end-gas temperature, must be used.

As is to be expected, the curves in figures 3 and 5 are similar on account of the similarity of the fuels. The curves bring out clearly the limits at which each fuel can be operated and the temperature susceptibility of the fuels. The curves present the knocking characteristics of the fuels in a more satisfactory manner than could be done by any single value. For instance, the data indicate that the leaded fuel should be capable of operation at a compression ratio of about 12, provided that the inlet-air temperature does not exceed 120° F. and the inlet-air pressure does not exceed 30 inches of mercury absolute.

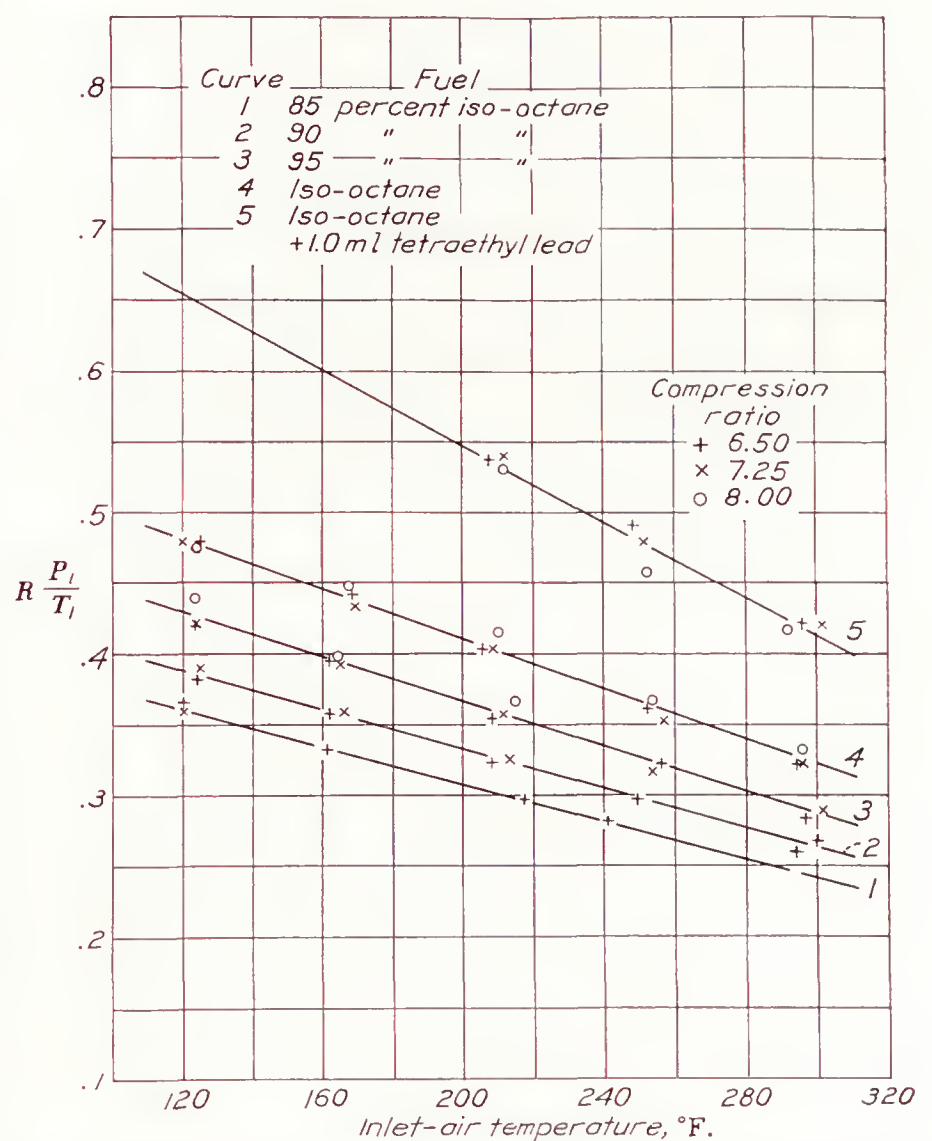


FIGURE 5.—Effect of inlet-air temperature on maximum permissible density factor for a series of fuel blends. Pent-roof combustion chamber; engine speed, 2,500 r. p. m.; fuel-air ratio, 0.078; incipient knock.

As has been previously stated, the rating curve could have been obtained from the peak combustion pressures rather than the compression ratio. In table VII the values for the 95 percent iso-octane used under the conditions listed in table IV are given. From these data, the values of  $Kp_3$  and  $T_3$  are computed from equations (1) and (2). The value of  $\gamma$  is estimated to be 1.29 for the compression of the unburned mixture. This value is based on experimental investiga-



tions of cycle efficiencies. The results are shown in figure 6. Because of the difficulty of accurately measuring the peak pressures, it is not to be expected that the results will show the same uniformity as is the case with the data in figure 5. The data, nevertheless, show a definite relation between the estimated peak temperature and the estimated peak density for the condition of incipient knock regardless of the engine conditions used to obtain the knock.

The values in the last column of table VII are the values of peak pressures estimated from the curve in figure 6; that is, they are the peak pressures that give values of  $\rho_3$  and  $T_3$  which will lie on the curve of figure 6.

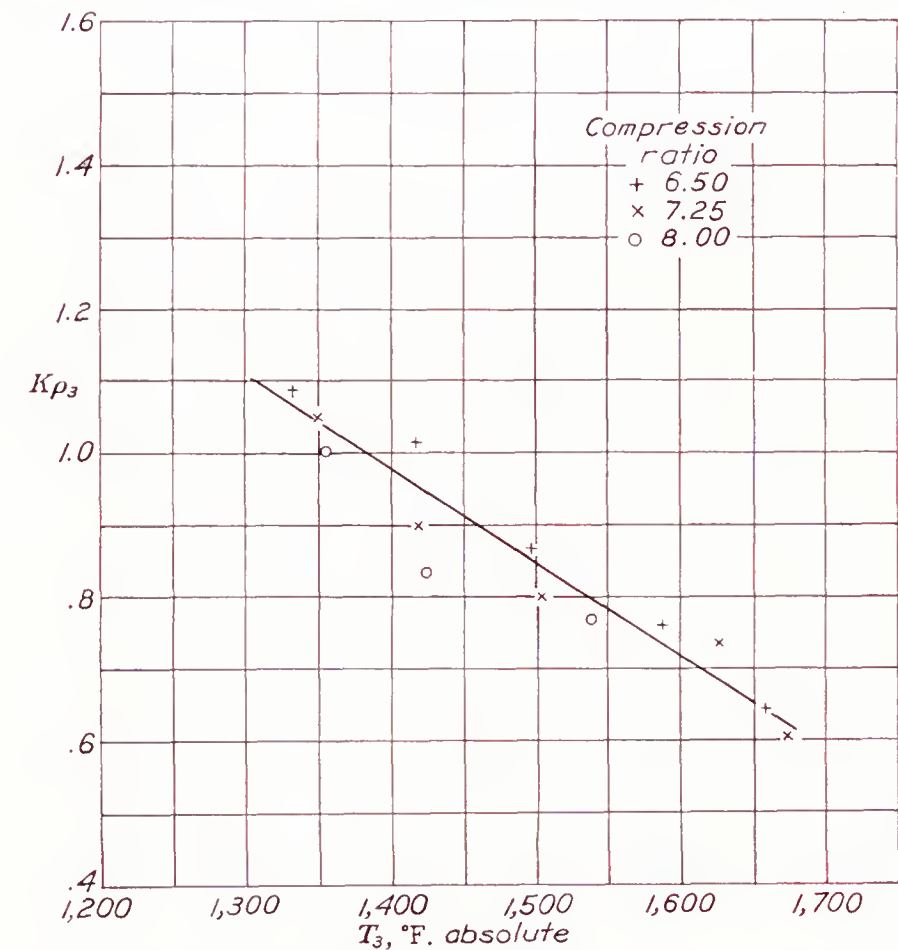


FIGURE 6.—Rating curve determined from peak pressure, inlet-air pressure, and inlet-air temperature. Fuel, 95 percent iso-octane;  $\gamma$ , 1.29. (See table VII.)

TABLE VII  
EFFECT OF INLET-AIR TEMPERATURE AND INLET-AIR PRESSURE ON MAXIMUM PERMISSIBLE PEAK PRESSURE  
[Engine speed, 2,500 r. p. m.; fuel, 95 percent iso-octane; knock, incipient; pent-roof combustion chamber]

Compression ratio	$T_1$ (°F. abs.)	$P_1$ (in Hg abs.)	$P_3$ (lb. per sq. in.)	
			Recorded	Estimated from fig. 6
6.50	584	37.9	720	710
	622	37.8	720	680
	669	36.4	650	640
	717	35.6	600	590
	757	23.2	530	530
7.25	584	34.2	700	700
	625	33.8	630	670
	671	33.1	600	620
	714	31.2	590	570
	761	30.8	500	510
8.00	583	32.2	675	700
	624	31.0	590	660
	675	31.1	590	610

EFFECT OF JACKET OR COOLANT TEMPERATURE

Tests of fuels in which the coolant temperature ( $T_c$ ) is varied should be capable of similar analysis

provided that the coolant temperature is used in place of the inlet-air temperature. It is probable that cylinder-wall temperature is of more significance than coolant temperature. Figure 7 shows results computed from data obtained by Edgar with different benzene blends (reference 7), using the coolant temperature. In these tests, the inlet-air temperature and pressure were maintained constant, and the coolant temperature and the compression ratio were varied. The data indicate that the effect on the maximum permissible density factor of the coolant temperature is of the same order of magnitude as the effect of inlet-air temperature.

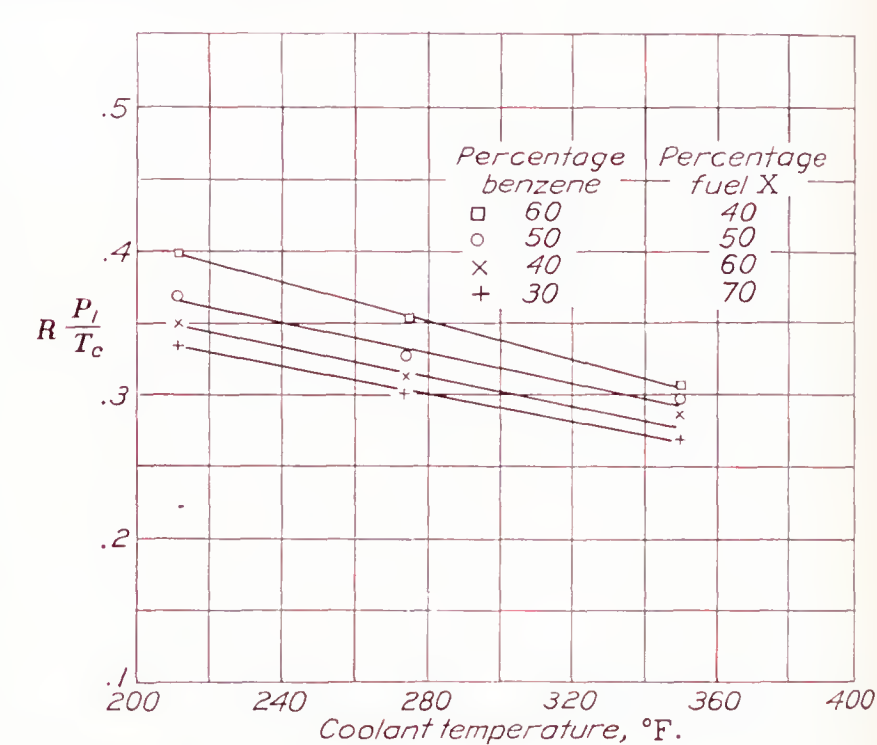


FIGURE 7.—Effect of coolant temperature on maximum permissible density factor (data from reference 7). C. F. R. engine at 600 r. p. m.; inlet-air pressure, atmospheric; 30 inches Hg assumed. Inlet-air temperature varied from 68° to 78° F.

VARIATION OF KNOCKING CHARACTERISTICS OF DIFFERENT FUELS

Kurtz (reference 8) has presented data on the maximum permissible inlet pressure as a function of charge temperature on a single-cylinder test engine at a compression ratio of 6. His results for three fuels have been replotted in figure 8. The data can be satisfactorily represented by straight lines. The curves show that, at a temperature of 100° F., xylol and the blended fuel have the same rating; whereas, at 300° F., the blended fuel and "iso-octane 95" have the same rating. The curves illustrate the different slopes that may occur with different fuels, as suggested in figure 1.

A rather extensive series of tests has recently been completed by Heron and Gillig (reference 9) in which the maximum permissible inlet-air pressure was determined for different fuel blends and chemical compounds at two engine coolant temperatures and two engine speeds. These data are made particularly significant by the fact that Heron and Gillig carefully distinguish between knock and preignition or afterignition. Figure 9 shows their results for mixtures of C. F. R. S-1 reference fuel and C. F. R. M-1 reference fuel. The octane numbers of these blends (C. F. R. method)



are within one octane number of the corresponding blends presented in tables II to IV. Because only two points are given, the curves are drawn as straight lines. In each case the maximum permissible inlet-air pressure was limited by knock.

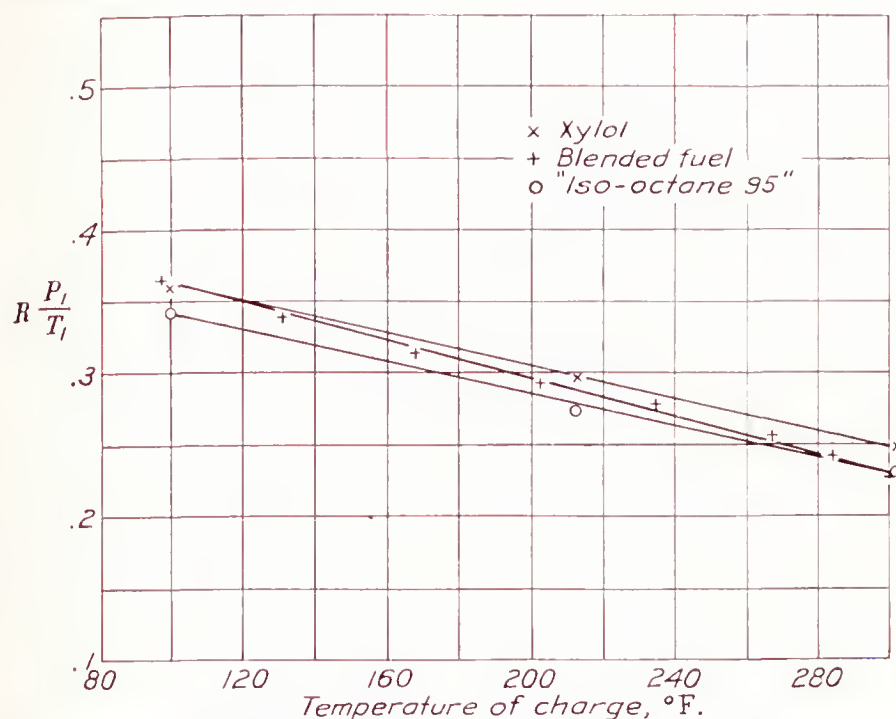


FIGURE 8.—Effect of temperature of charge on maximum permissible density factor for three different fuels (data from reference 8).

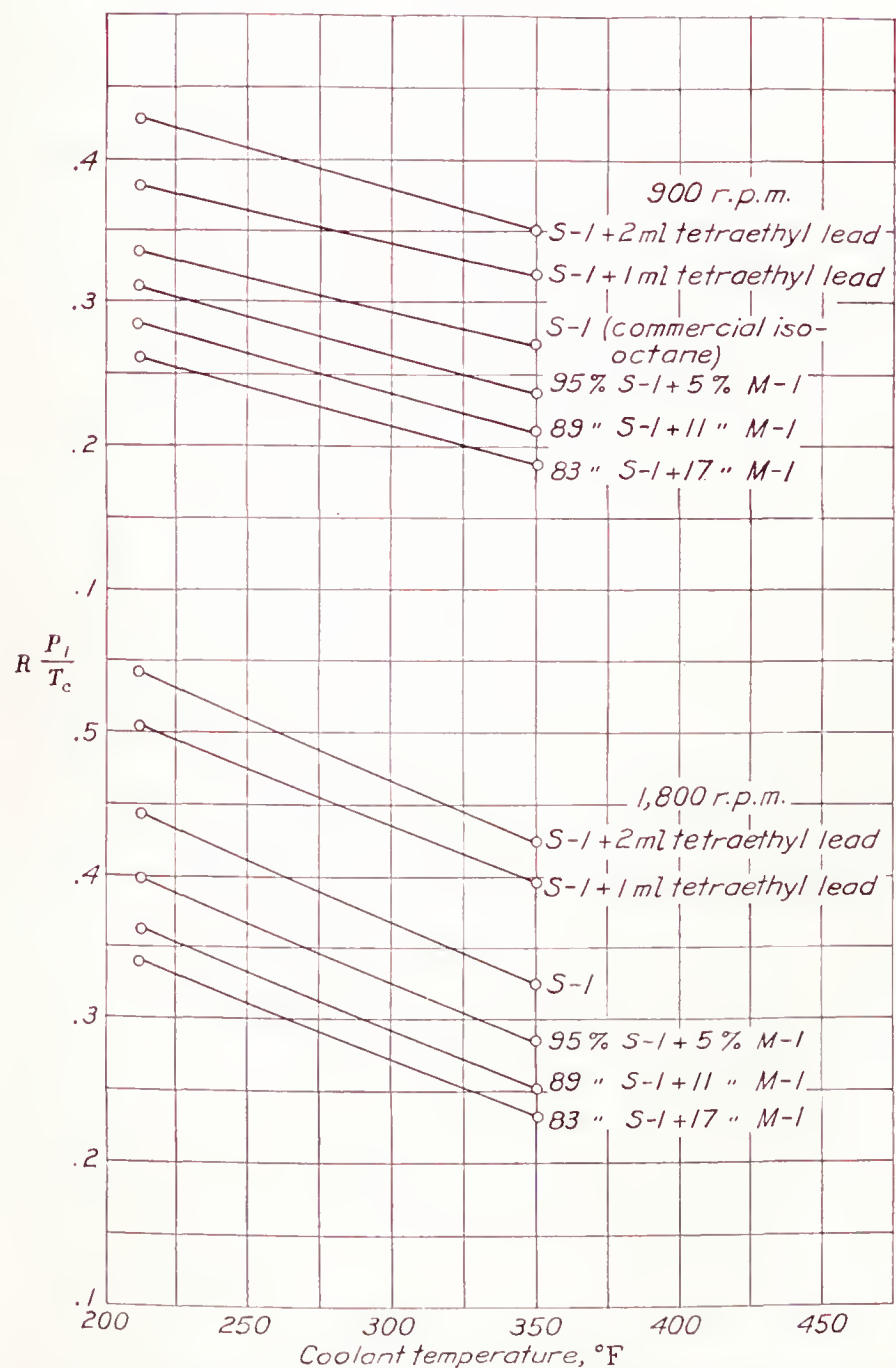


FIGURE 9.—Effect of coolant temperature on maximum permissible density factor (data from reference 9). C. F. R. engine; compression ratio, 5.5; inlet-air temperature, 80°–95° F.

Figure 10 shows the wide divergence that may be expected for performance of different fuels under a variety of engine conditions. The factor that was the cause of limiting the maximum permissible inlet-air pressure is indicated for each fuel. Toluene and benzene have curves that are somewhat similar, as might be expected. Iso-octane and di-isopropyl ether have curves which are even more similar but which bear no

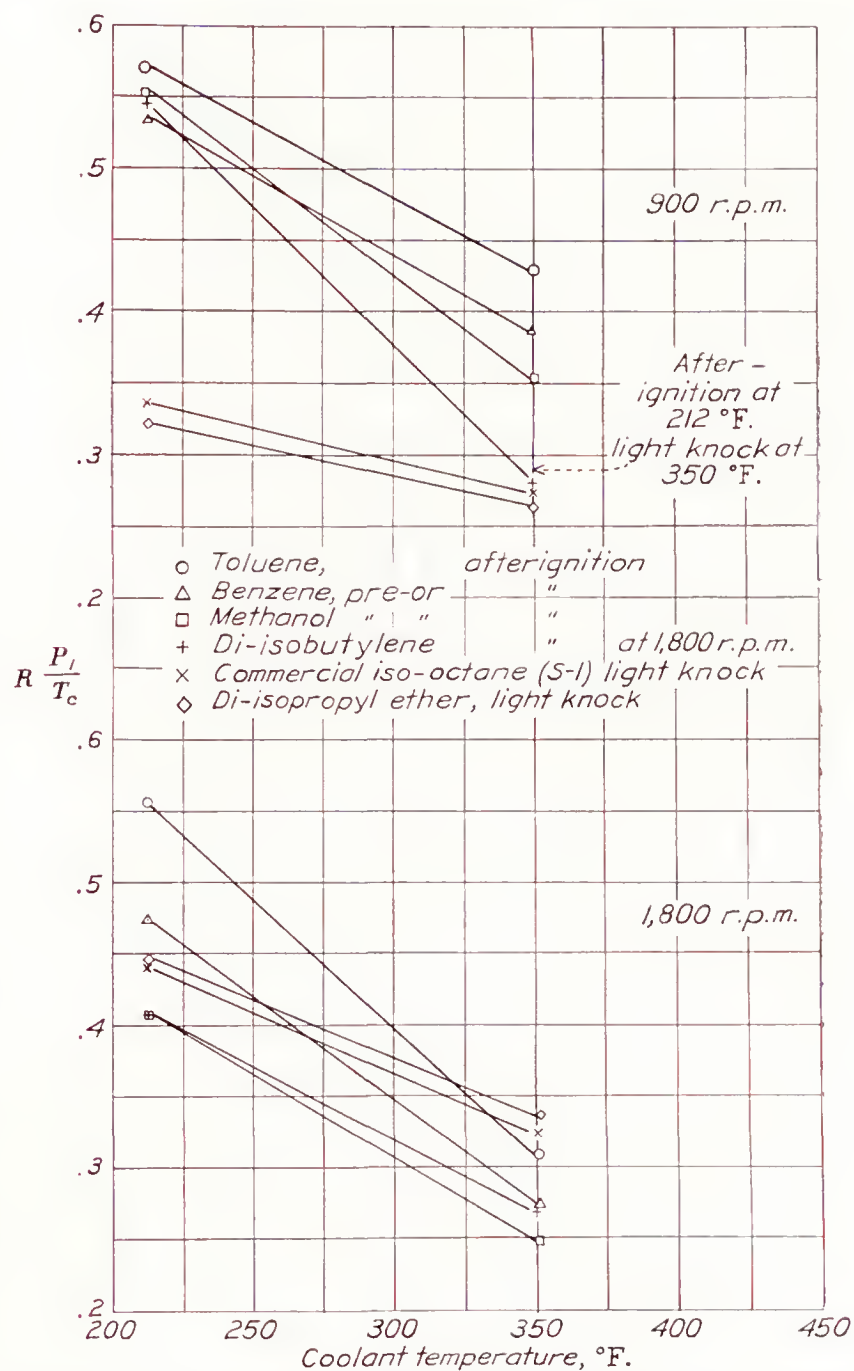


FIGURE 10.—Effect of coolant temperature on maximum permissible density factor for various chemical compounds (data from reference 9). C. F. R. engine; compression ratio, 5.5; inlet-air temperature, 80°–95° F.

relation to those for benzene and toluene, benzene and toluene showing a much greater degree of temperature variation. At 1,800 r. p. m. and at the lower coolant temperature, benzene and toluene are superior to any of the others listed, but they are inferior to either iso-octane or di-isopropyl ether at the higher temperature. The fuels that were subject to preignition or afterignition showed much more dependency on the coolant temperature than did those that knocked. This fact is in agreement with the analysis presented in the first part of this discussion. The differences between the curves for the two speeds will be discussed later.



## EFFECT OF FUEL-AIR RATIO

The effect of fuel-air ratio on the knocking characteristics of a fuel depends both on the changes in the chemical mixture and the changes in the temperature of the charge just before knock or secondary ignition. Boerlage (reference 6) has shown the maximum permissible inlet-air pressure as a function of fuel-air ratio (fig. 11). In these tests, the maximum permissible inlet-air pressure was a minimum at the mixture ratio corresponding to the maximum cylinder temperature and exhaust-gas temperature. These maximum temperatures occurred at a mixture ratio near the chemically correct value.

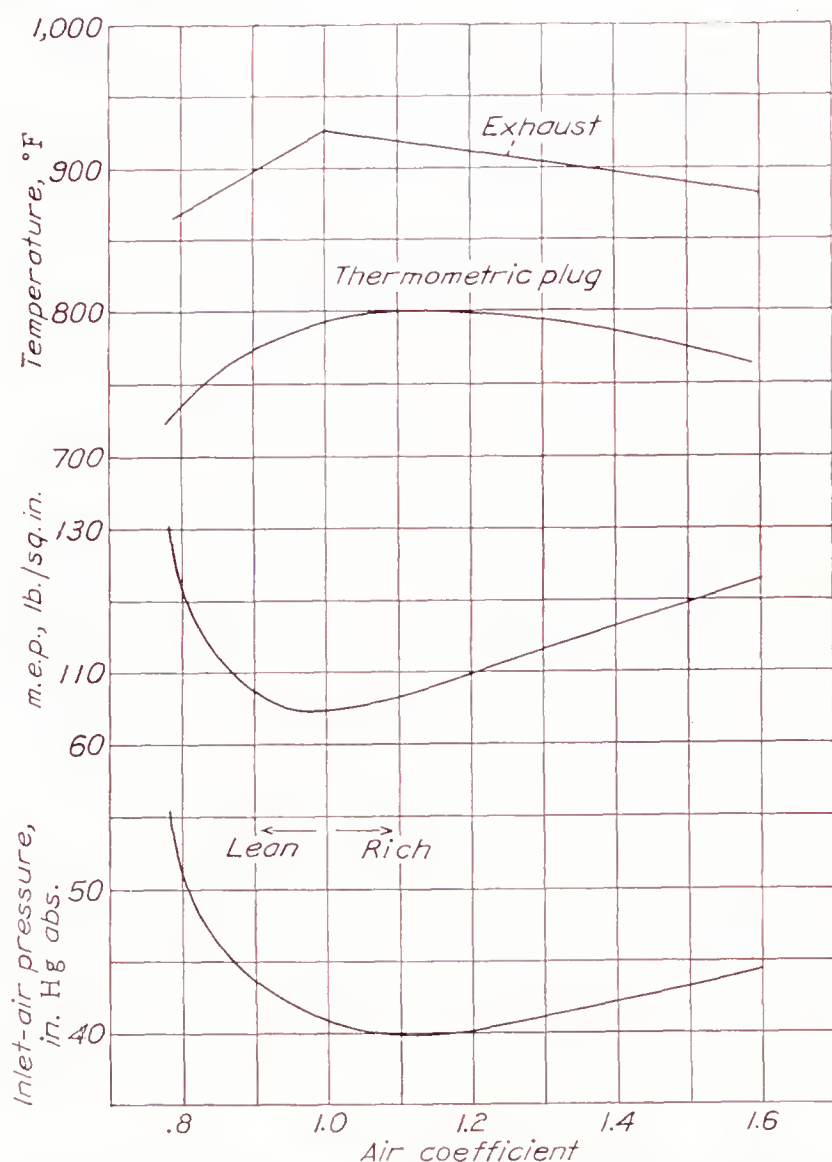


FIGURE 11.—Relation between mixture ratio and maximum permissible inlet-air pressure and m. e. p. and between mixture ratio and cylinder- and exhaust-gas temperature (curves from reference 6).

MacClain and Buck (reference 10) have shown that, for constant power, the cylinder temperatures reach a maximum and then decrease as the mixture is leaned and the manifold pressure is increased to maintain the specified power. This fact, in conjunction with Boerlage's data (fig. 11), which show that for a constant degree of knock the increase in maximum permissible inlet-air pressure permits an appreciable increase in power with the lean mixtures, indicates that an increasing amount of interest should be shown in the operation of aircraft engines at mixtures leaner than the chemically correct mixture.

Figure 12 shows the effect of fuel-air ratio on the maximum permissible density factor and on the specific fuel consumption for the pent-roof combustion cham-

ber, for which other data have already been given in table IV. The fuel-air ratio for the data in table IV (0.078) was the ratio giving maximum knock. The curves in figure 12 show that this ratio has the lowest permissible maximum density factor. When the curves are cross-plotted, as in figure 13, it is seen that, from a fuel-air ratio of 0.080 to one of 0.140, each increase of 0.02 in the ratio permits the same increase in the density factor as a decrease of 40° F. in the inlet-air

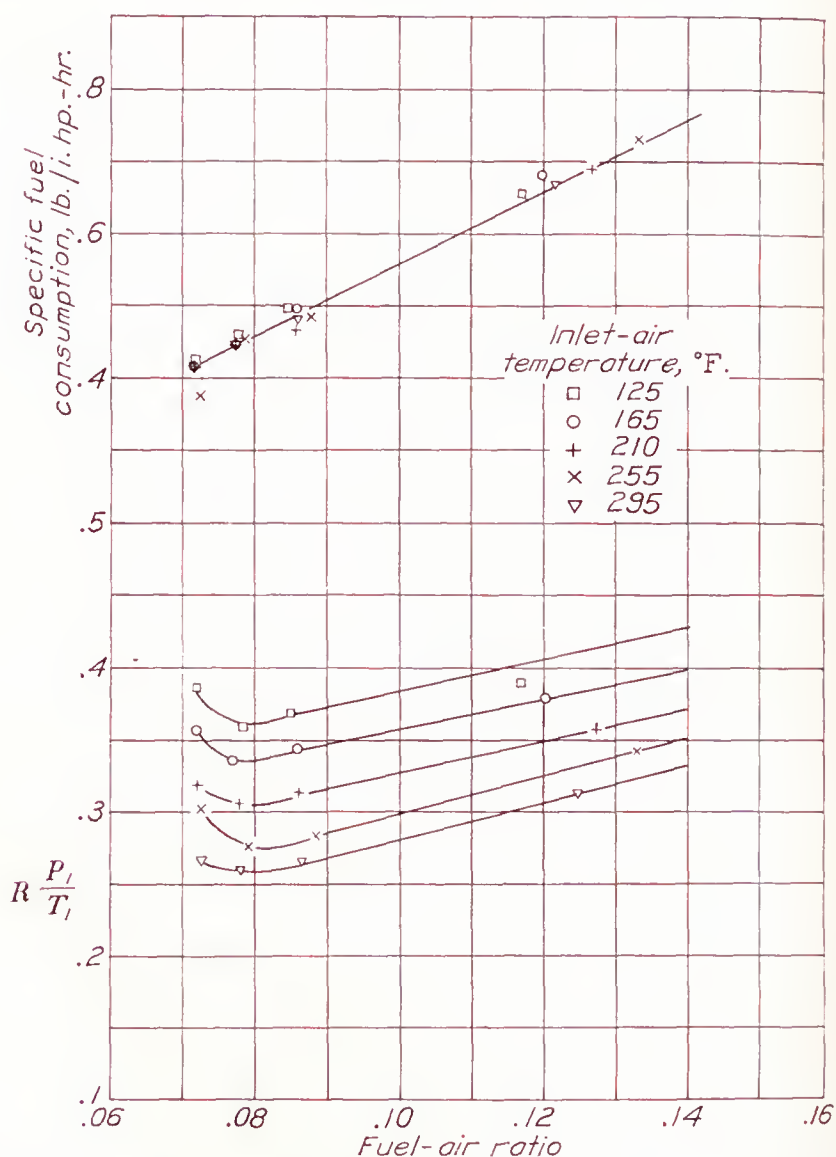


FIGURE 12.—Effect of fuel-air ratio on maximum permissible density factor and specific fuel consumption. Pent-roof combustion chamber; engine speed, 2,500 r. p. m.; 85 percent iso-octane; compression ratio, 6.5; incipient knock.

temperature. Tests of additional fuels are necessary to obtain a general conclusion relative to the numerical effects of fuel-air ratio. Within the range of fuels used in aircraft, this effect may be independent of the fuel.

In figure 11 it is shown that, even though the maximum permissible power increases at fuel-air ratios richer or leaner than the correct, the measured engine temperatures decreased. This fact indicates that the cooling effects of the excess fuel or the excess air more than compensated for the increased rate of heat transfer resulting from the increased density of charge accompanying the higher inlet-air pressures. Further information on the actual end-gas temperatures and densities for the condition of incipient knock is given in figure 14, in which values of  $K\rho_3$  and of  $T_3$  obtained from figure 12 and equations (1a) and (2a) are given. Figure 14 shows that the maximum permissible end-gas density at any given end-gas temperature decreases



as the fuel-air ratio is increased. This effect is to be expected from researches on combustion. Peletier, for example, has shown in reference 11 that the highest permissible compression ratio without auto-ignition decreased from 9 at a fuel-air ratio of about 0.020 to a

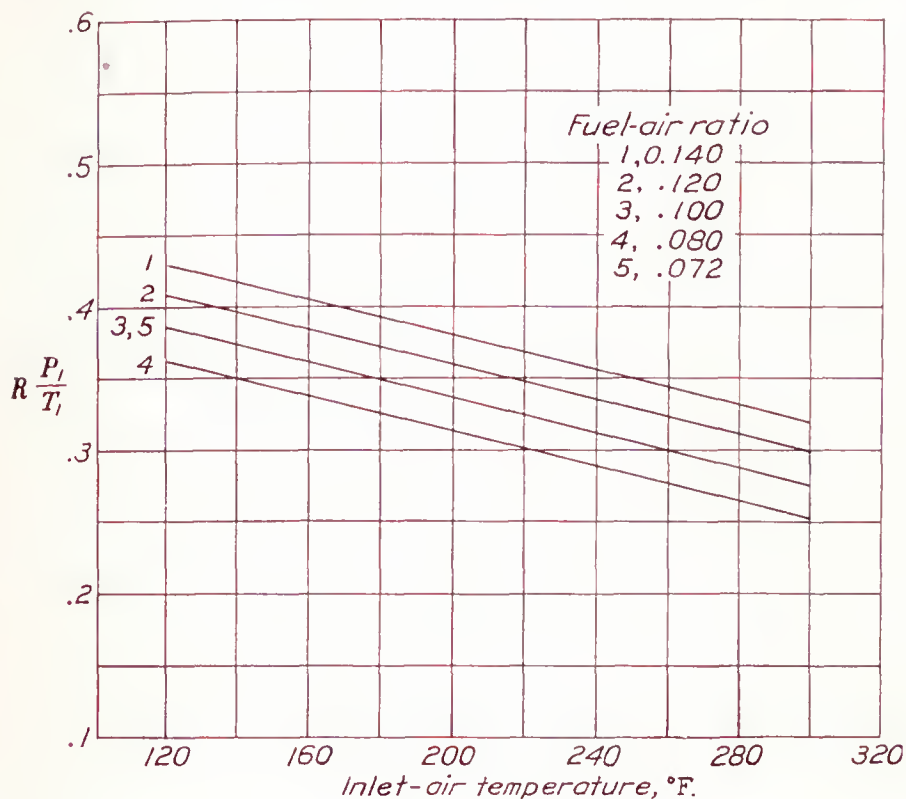


FIGURE 13.—Effect of inlet-air temperature on maximum permissible inlet density factor at a series of fuel-air ratios. Pent-roof combustion chamber; engine speed, 2,500 r. p. m.; 85 percent iso-octane; compression ratio, 6.5; incipient knock.

minimum of 6 at a fuel-air ratio of about 0.11. The data in figures 13 and 14 show that, for equal end-gas temperatures and densities, knock increases as the mixture becomes richer but that, in the engine, the cooling effects of excess air or of excess fuel are sufficiently great so that higher inlet-air densities can be used as the mixture ratio is either increased or decreased from the approximately chemically correct mixture.

In the determination of the curves in figure 14, it was necessary to express the variation of  $H$  as a function of fuel-air ratio since  $H$  appears both in equation (1a) and in equation (2a). It was assumed that the value of  $H$  was expressed by

$$H = \frac{E_{com} \times 18000 \times \text{mass of fuel}}{\text{mass of fuel} + \text{mass of air}} = \frac{E_{com} \times 18000 \times F}{1 + F} \quad (3)$$

in which  $F$  is the fuel-air ratio. Values of  $E_{com}$ , the combustion efficiency, were obtained from the test data given by Gerrish and Voss in reference 12.

#### EFFECT OF HUMIDITY

Humidity of the inlet air has two effects on the combustion: It changes the chemical constituents of the mixture, and it introduces a heat absorbent in the form of water vapor. In the N. A. C. A. tests already presented, although no attempt was made to keep the humidity constant, the indications are that the effect of humidity is small. There is a great deal of data available on the effect of humidity on knock rating of

fuels by octane number, but most of these data are difficult to place on an absolute basis such as described in this report.

Stansfield and Thole (reference 13) have presented the results of tests in which they determined the effect of humidity on the highest useful compression ratio for a series of fuels. They state that the effect of humidity up to saturation at 65° F. is unimportant and that, if the proportion of water vapor is greater, a correction is

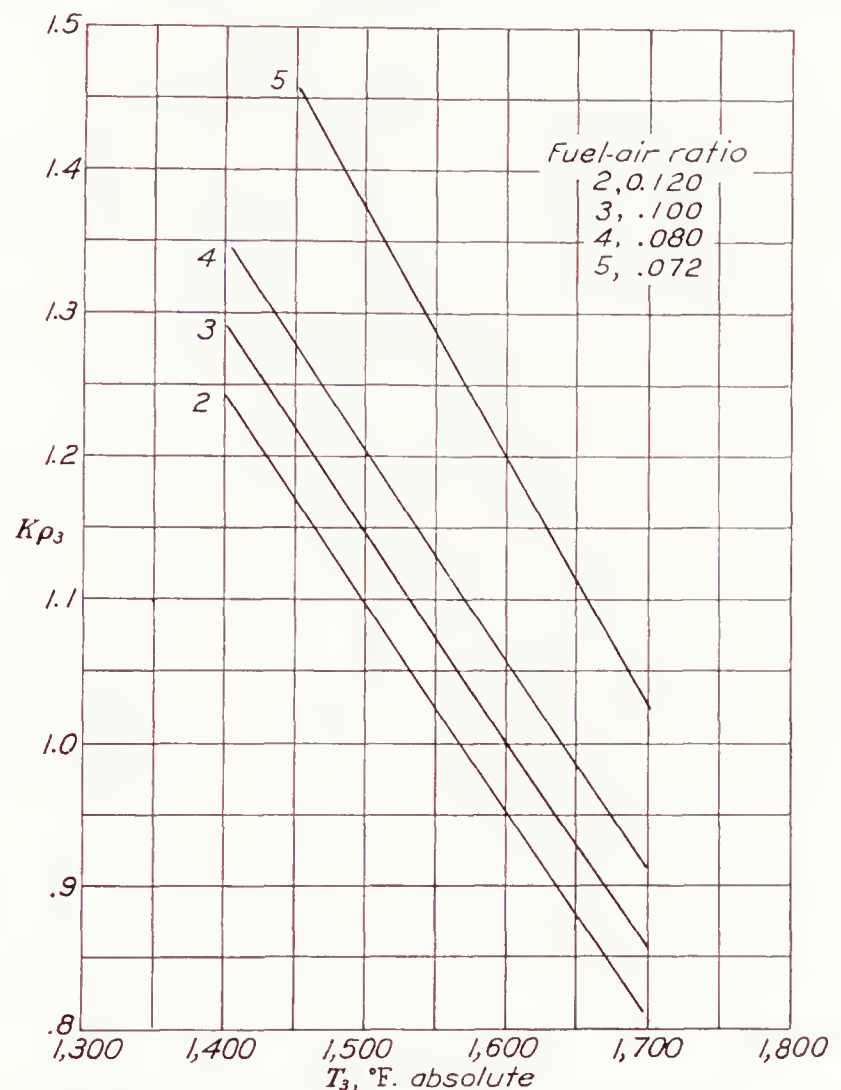


FIGURE 14.—Effect of end-gas temperature on maximum permissible end-gas density for incipient knock for a series of fuel-air ratios. Pent-roof combustion chamber; engine speed, 2,500 r. p. m.; 85 percent iso-octane; compression ratio, 6.5.

necessary for certain fuels when results of a high order of accuracy are required. They also found that water vapor up to 50 percent of the fuel weight raised the highest useful compression ratio by 0.55. Computations indicate that this quantity of water vapor decreases the compression temperature 40° F. This decrease in compression temperature corresponds to a decrease of about 15° F. in the temperature at the start of compression. At 100° F. and 29.92 inches of mercury absolute pressure, the water-air ratio for saturation is 0.048. Since water vapor absorbs heat, it is to be expected that the knocking fuels which show the greatest temperature variation will show the greatest increase in maximum permissible density factor for a given amount of water vapor or for a given amount of water introduced into the fuel-air mixture. If the presence of the water vapor has any chemical effect on the combustion, it must be determined by test. There are at present, however, no indications that such chemical effects exist within the range of fuels or engine conditions used in operation.



## EFFECT OF EXHAUST-GAS DILUTION

Exhaust-gas dilution generally increases the temperature of the mixture to a degree depending on the percentage of exhaust gases remaining in the cylinder following the scavenging stroke. Computations indicate that doubling the percentage of exhaust gas remaining in the cylinder over that normally experienced at full throttle increases the temperature at the beginning of compression 60° F. and at the end of compression 100° F. In a throttled engine, the exhaust-gas dilution may be increased to a sufficient amount to affect also the maximum permissible density factor on the basis of decreasing the fuel-gas ratio.

Some interesting data on the effect of exhaust-gas dilution are presented by Tizard in reference 14. These data show that, when a test engine was throttled, the maximum permissible density factor based on the fresh charge inducted was decreased from 0.49 to 0.26 for a decrease in initial charge from 1.00 to 0.54. Introducing the exhaust gas with the incoming air and at the same temperature as the air permitted the maximum permissible density factor, based on the fuel-air mixture inducted, to be increased from 0.49 to 0.62 for an addition of from 0 to 15 percent exhaust gas in the mixture. The data show that the effect of the exhaust gas itself is to increase the maximum permissible density factor probably in the same manner that the water vapor increases this factor by acting as a heat absorbent. In throttling, however, this density effect is more than offset by the increased resultant temperature of the gases. In actual service engines, it is doubtful if the effect of exhaust gas need be considered unless comparison is being made with an engine that is completely scavenged or one using a turbosupercharger for boosting at sea level. The results of the N. A. C. A. tests presented in this report gave satisfactory knock-rating curves even though the percentage of exhaust-gas content varied by about 2:1.

## EFFECT OF ENGINE SPEED

The effect of engine speed is twofold. Increasing the speed decreases the time interval for heat exchange between the inducted charge and the walls of the cylinder and the combustion chamber and decreases the induction time preceding ignition by the electric spark during which precombustion reactions may take place within the fuel-air charge. The difference in time interval for heat transfer to the charge changes not only the temperature of the charge but also the density at any given inlet-air temperature and density.

Data obtained by Heron and Gillig (reference 9) show that, with the C. F. R. engine used by them at any given inlet-air pressure, the indicated mean effective pressure at a coolant temperature of 212° F. did not change for an increase of speed from 900 to 1,800 r. p. m. When the coolant temperature was increased to 350° F., the indicated mean effective pressure at 900 r. p. m.

decreased 15 percent and, at 1,800 r. p. m., decreased only 6 percent. In these tests the spark advance was 30° B. T. C.

Figure 15 shows the data from reference 9 for the two engine speeds; again straight lines have been drawn connecting the two points for each fuel. The most interesting fact obtained from figure 15 is that, with the exception of S-1 plus tetraethyl lead (which after-ignited), the fuels which knocked appreciated with engine speed and the fuels which preignited or after-ignited depreciated with engine speed. This fact again indicates that secondary ignition is a different phenomenon from knock and must be so recognized.

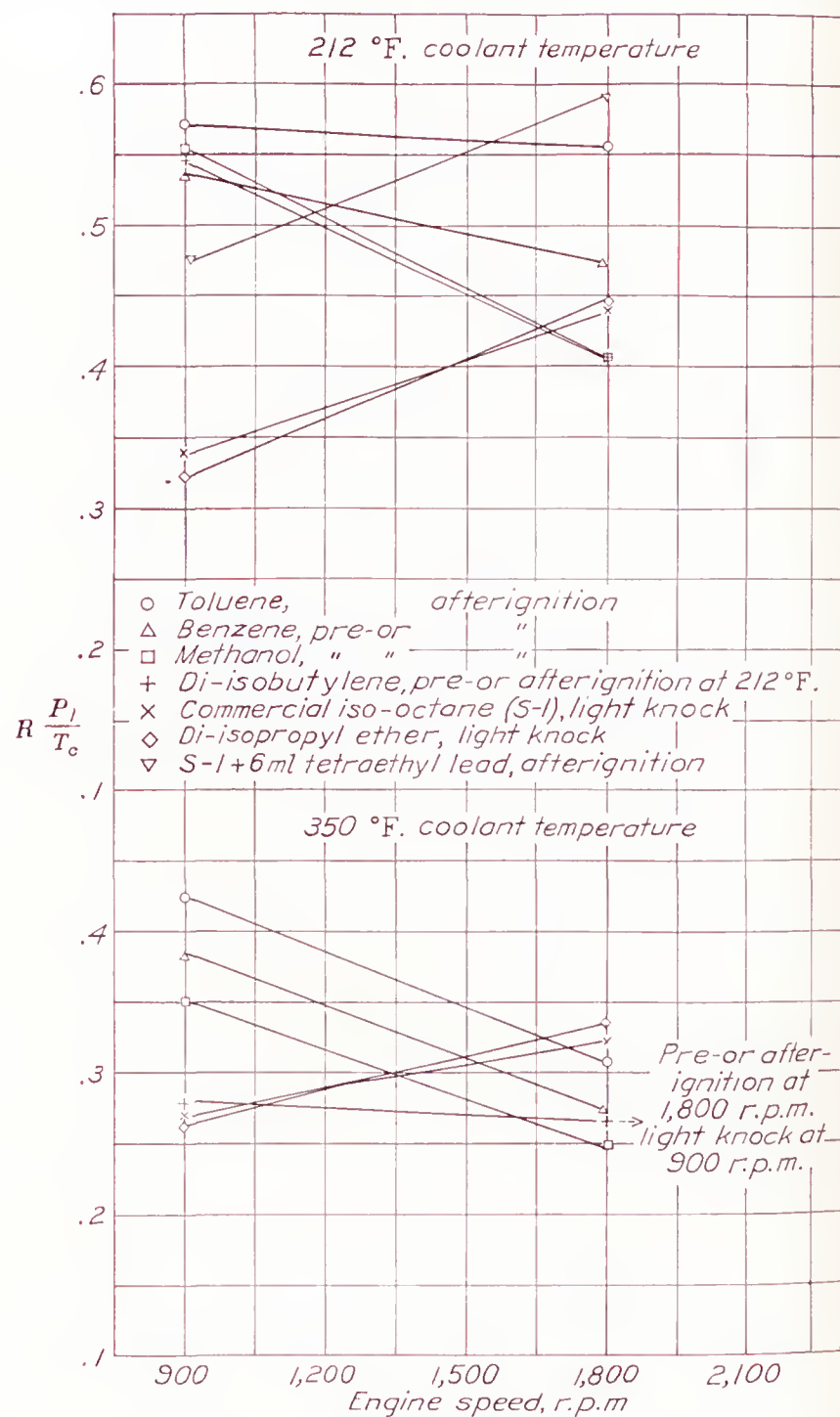


FIGURE 15.—Effect of engine speed on maximum permissible density factor for various chemical compounds (data from reference 9). C. F. R. engine; compression ratio, 5.5; inlet-air temperature, 80°–95° F.

The cause of the depreciation with speed of the secondary igniting fuels may be chemical, and the explanation may be that decreasing the induction period for precombustion reactions favors the formation of certain compounds which lead to secondary ignition. A more likely explanation is that, since increasing the speed increases the total heat flow through the cylinder walls, it increases the tempera-



ture of any hot spot to a greater extent than it increases the temperature of the rest of the walls.

The fact that the knocking fuels appreciated with engine speed may be the result of the increased rate of burning at the higher speed or it may be a temperature spark effect. The true effect of speed on knock should be determined by the use of the optimum spark advance at each speed tested. In this manner, the effect of engine speed together with the effect of heat transfer during the induction and the compression strokes will be determined. The speed and the heat-transfer effects should be partly separated by maintaining the cylinder-wall temperature constant and by measuring the mass of air inducted at each inlet-air temperature rather than the inlet-air pressure.

Heron and Gillig in subsequent tests (unpublished) found that using a sodium-cooled piston permitted the boost pressure to be increased 32 percent with benzene but only 3 percent with S-1 fuel. They also found that, with this piston and a coolant temperature of 350° F. at an engine speed of 1,800 r. p. m. and inlet-air temperatures of 100° and 212° F., benzene permitted a boost 6 percent higher than that permitted by S-1, and that benzene (which was limited by preignition or after-ignition) was very sensitive to spark-plug condition whereas S-1 was not. These data indicate that knocking fuels are inherently less sensitive than preigniting fuels to the uniformity of engine temperature.

#### EFFECT OF SPARK ADVANCE

Varying the spark advance has the effect of varying the temperature and the density at the time of knock. Therefore varying the spark advance has much the same effect as varying the compression ratio. It is to be expected that all fuels will not react the same to changes in spark advance because of the variation in the temperature-density relationship of the different fuels.

The effect of varying the compression ratio on the knock rating of the fuel in an engine has been shown to be an effect chiefly of changing the gas density. As the compression ratio is increased above the maximum permissible value for any inlet-air condition, retarding the spark to prevent knock should decrease the effective compression ratio to the value that was found to be permissible. The same idea can be expressed in a different manner by saying that, for any given condition of inlet-air temperature and pressure, the maximum permissible power output should be independent of compression ratio provided that the ignition spark is sufficiently retarded to prevent knock and the spark advance is equal to or less than the value required for optimum advance. That this fact is approximately true is shown in figure 16 from tests reported by Gardiner and Whedon (reference 15). In this figure the broken curve shows the effect of compression ratio on the indicated mean effective pressure of the engine

tested for a nonknocking fuel and a constant spark advance. The solid curves are for the same engine operating on a gasoline that knocked at a compression ratio of 4.7. As the compression ratio was increased above this value and the spark retarded so that the knock was maintained at a constant level, the indicated mean effective pressure remained practically constant.

Data showing the permissible increase in inlet-air pressure with a retarded spark (reference 16) are shown in figure 17. The optimum spark advance in this case was 29°. The data represent an effective decrease in the compression ratio caused by the retarded spark

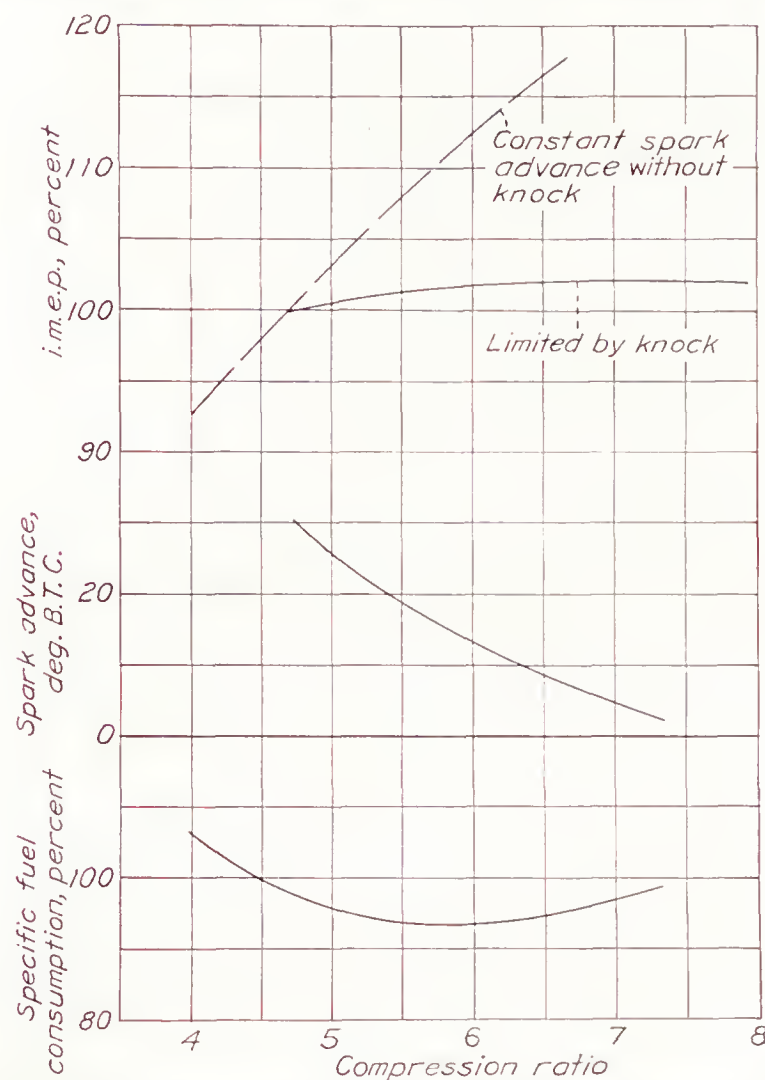


FIGURE 16.—Relationship between compression ratio and engine performance with spark advance adjusted for a constant degree of knock (curves from reference 15).

with the accompanying increase in the permissible boost pressure.

#### EFFECT OF ENGINE DESIGN

The effect of engine design (such as combustion-chamber shape, turbulence, spark-plug position, bore-stroke ratio, cooling medium, effectiveness of the cooling, and size) has many ramifications. Probably the more important effects to be considered are the time required for completion of combustion, the surface-volume ratio of the combustion chamber, and the uniformity of the cooling of the walls of the cylinder and the combustion chamber.

The surface-volume ratio is important from considerations of the cooling of the gases during the induction and combustion periods. This ratio will probably not in itself affect fuels that preignite, uniform cooling of the combustion chamber being assumed, and will probably affect knocking fuels. As the ratio is increased, the



heat flow between the gases and the metal walls is increased, which, in turn, affects the end-gas temperatures and consequently the maximum permissible density factor.

Decreasing the engine size will tend to increase the charge temperature if the wall is at a higher temperature than the incoming charge and to decrease the charge temperature if the wall is at a lower temperature

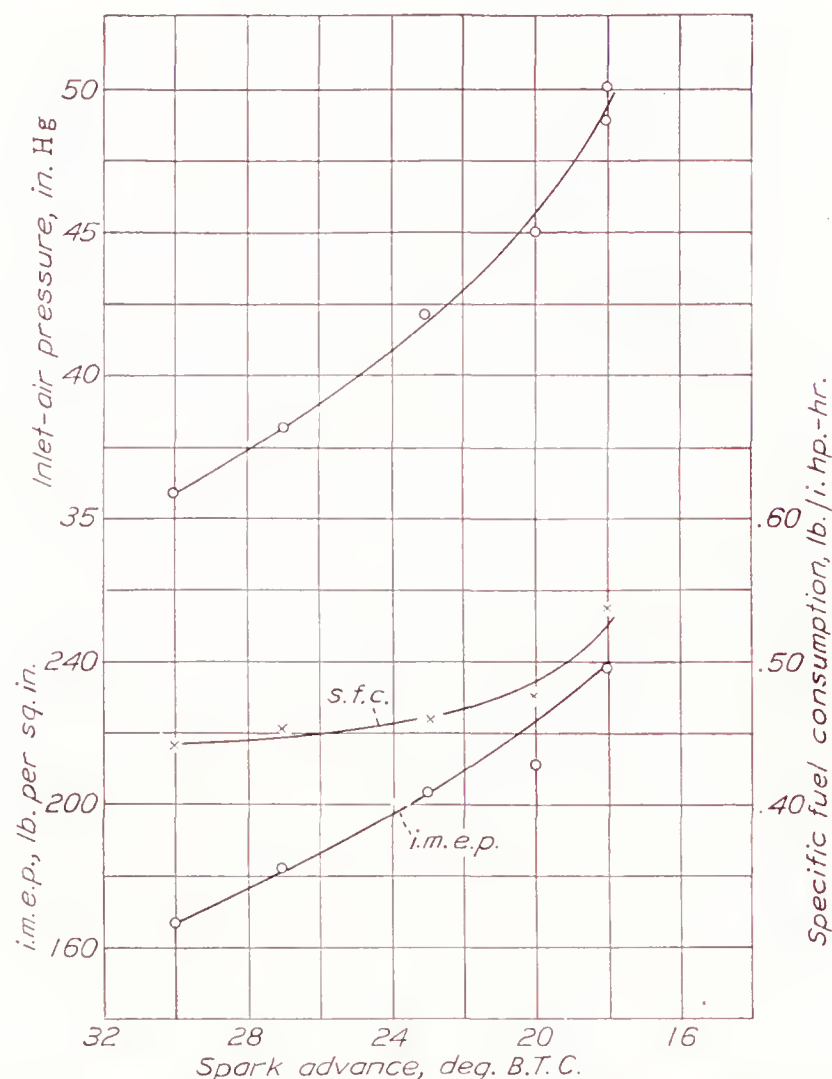


FIGURE 17.—Effect of spark advance on maximum permissible inlet-air pressure and on maximum permissible i. m. e. p. (data from reference 16). Engine speed 2,500 r. p. m.; iso-octane+ml tetraethyl lead; compression ratio, 8.0; inlet-air temperature, 200° F.

than that of the incoming charge. With preigniting or afterigniting fuels, it is probable that changing the engine dimensions will not have much effect other than that produced by the temperature change. Additional experimental evidence is necessary on this point.

Hawley and Bartholomew have presented data on the effect of bore and stroke on highest useful compression ratio (reference 17). Their data show this ratio to decrease as either the bore or the stroke is increased but the rate of decrease to become less at the larger bores.

The uniformity of the cooling of the combustion-chamber walls and the occurrence of hot spots within the combustion chamber are particularly important in that hot spots may cause a fuel to preignite at a lower value of the charge density factor than would have been the case had the fuel been limited by knock.

This action occurred in the N. A. C. A. tests, the results of which have already been presented in table II. Aircraft engines probably show considerable variation from any single standard because of variations in method and uniformity of cooling. Hot spots produced by exhaust valves and by spark plugs vary considerably between engines. The uniformity of the cooling of the cylinder head depends on both the cooling medium and the efficiency with which the medium is brought into contact with the metal of the cylinder and the cylinder head. A comparison of the rating curves in figures 4 and 5 gives additional information on the effects of engine design. The relationship of these two sets of data will be discussed in more detail in the section on correlation of data.

Turbulence or air flow in the combustion chamber is known to affect knock, but the manner in which its effect is produced is not known and must be the subject of further investigation.

From the foregoing analyses, it is evident that a single curve expresses the knocking characteristics of a fuel in any one engine for a large range of engine operating conditions. For a given engine, this curve can be obtained from a series of runs at one compression ratio and various inlet-air pressures and temperatures or from a series of runs at one inlet-air pressure and a series of compression ratios and inlet-air temperatures. In either case, the results represent a wide range of the three variables. Once the rating curve of the fuel has been determined, the next problem is to estimate the maximum permissible performance of the engine with this fuel under different operating conditions.

## II—DETERMINATION OF MAXIMUM PERMISSIBLE ENGINE PERFORMANCE

The maximum permissible performance obtainable from any engine using a given fuel depends on the service in which the engine is to be used. The requirements for a long-range flying boat are different from those of a transport airplane flying comparatively short distances. The two factors that are probably of most interest in this respect are maximum permissible indicated mean effective pressure and minimum permissible fuel consumption. Peak pressures are of interest from considerations of engine reliability. These three factors are all dependent on the compression ratio of the engine once the maximum permissible density factor is obtained.

In the succeeding analysis, the dependency of the factors will be presented as a function of compression ratio for conditions of intercooling (constant inlet-air temperature) and of no or partial intercooling between the supercharger and the engine cylinders (variable inlet-air temperature).



## CONSTANT INLET-AIR TEMPERATURE

The indicated mean effective pressure for a constant fuel-air ratio varies directly as the inlet-air density and the cycle efficiency:

$$i. m. e. p. \propto \rho_1 \times E_c \quad (4)$$

in which  $\rho_1$  is the inlet-air density and  $E_c$  is the cycle efficiency. The inlet-air density is proportional to  $P_1/T_1$ . The relationship between  $RP_1/T_1$  at a constant compression ratio and the indicated mean effective pressure is given in figure 18. These data are for the conditions listed in table IV at a compression ratio of 6.50. It is seen that assuming  $i. m. e. p. \propto \rho_1 \propto P_1/T_1$  introduces a deviation of about  $\pm 3$  percent. The data presented in the previous section indicate that, for any given fuel and for a constant inlet-air temperature, the product of the inlet-air density times the compression ratio must not exceed a certain constant in order to prevent knock, the value of the constant being dependent on the particular engine. The maximum permissible inlet-air density for any given compression ratio is therefore expressed by:

$$R\rho_1 = K \quad (5)$$

The value of the constant  $K$  at any specified inlet-air temperature is determined by the rating curve of the fuel under consideration. Multiplying the right-hand side of proportionality (4) by  $R/R$  and eliminating the constant  $R\rho_1$ , it is seen that

$$i. m. e. p. \propto \frac{E_c}{R} \quad (6)$$

Therefore, for a given fuel at a given inlet-air temperature, the maximum permissible indicated mean effective pressure varies directly as the cycle efficiency and inversely as the compression ratio. Values of  $E_c$  can be determined by computation, taking into account the variation of the specific heats of the gases with temperature and considering the effect of the residual gases. Such computations give the values listed in table VIII for the cycle efficiencies and for the indicated specific fuel consumption in pounds of fuel per indicated horsepower-hour.

TABLE VIII  
ESTIMATED CYCLE EFFICIENCIES AND SPECIFIC FUEL CONSUMPTION

Compression ratio	Cycle efficiency	Specific fuel consumption (lb./i. hp.-hr.)
4	0.341	0.408
6	.415	.335
8	.467	.298
10	.500	.278
12	.528	.263

It must be remembered that the values of the cycle efficiencies and the fuel consumptions listed in table VIII do not consider the heat losses during the com-

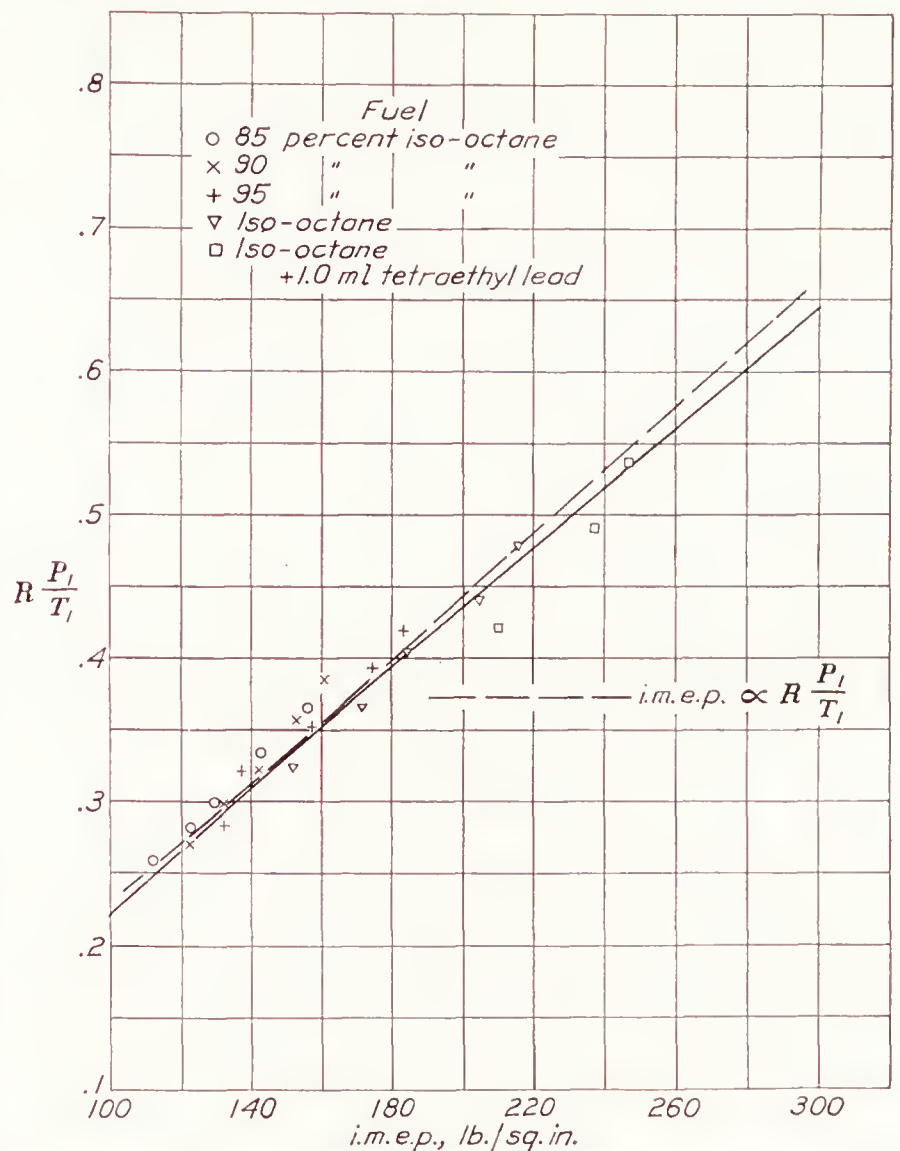


FIGURE 18.—Relationship between indicated mean effective pressure and density factor. Pent-roof combustion chamber; engine speed, 2,500 r. p. m.; fuel-air ratio, 0.078; compression ratio, 6.5; incipient knock; coolant temperature, 250° F.

bustion cycle; consequently, the indicated fuel consumptions obtained on an engine are in excess of the values listed. The values are satisfactory for a comparison. From table VIII and expressions (6) and (5), factors proportional to the maximum permissible indicated mean effective pressure and the maximum permissible boost pressure can be obtained for any inlet-air temperature.

The maximum permissible peak pressure at any given inlet-air temperature can be estimated from the thermodynamic equation:

$$P_3 = P_1 \left( R^\gamma + \frac{R}{T_1} \times \frac{H}{c_v} \right) \quad (7)$$

As has already been shown, for any constant inlet-air temperature,  $P_1 R$  must be a constant. Equation (7) can then be written as the following proportionality:

$$P_3 \propto \left( R^{\gamma-1} + \frac{H}{T_1 c_v} \right) \quad (8)$$

Assuming a value of 18,000 B. t. u. per pound of fuel, 580° F. absolute for  $T_1$ , 0.25 B. t. u. per pound per degree Fahrenheit for  $c_v$ , and a fuel-air ratio of 0.069, the proportionality becomes:

$$P_3 \propto R^{\gamma-1} + 8.0 \quad (9)$$



These relationships, assuming a value of 1.29 for  $\gamma$  in expression (9), are shown graphically in figure 19. The values for the indicated mean effective pressure

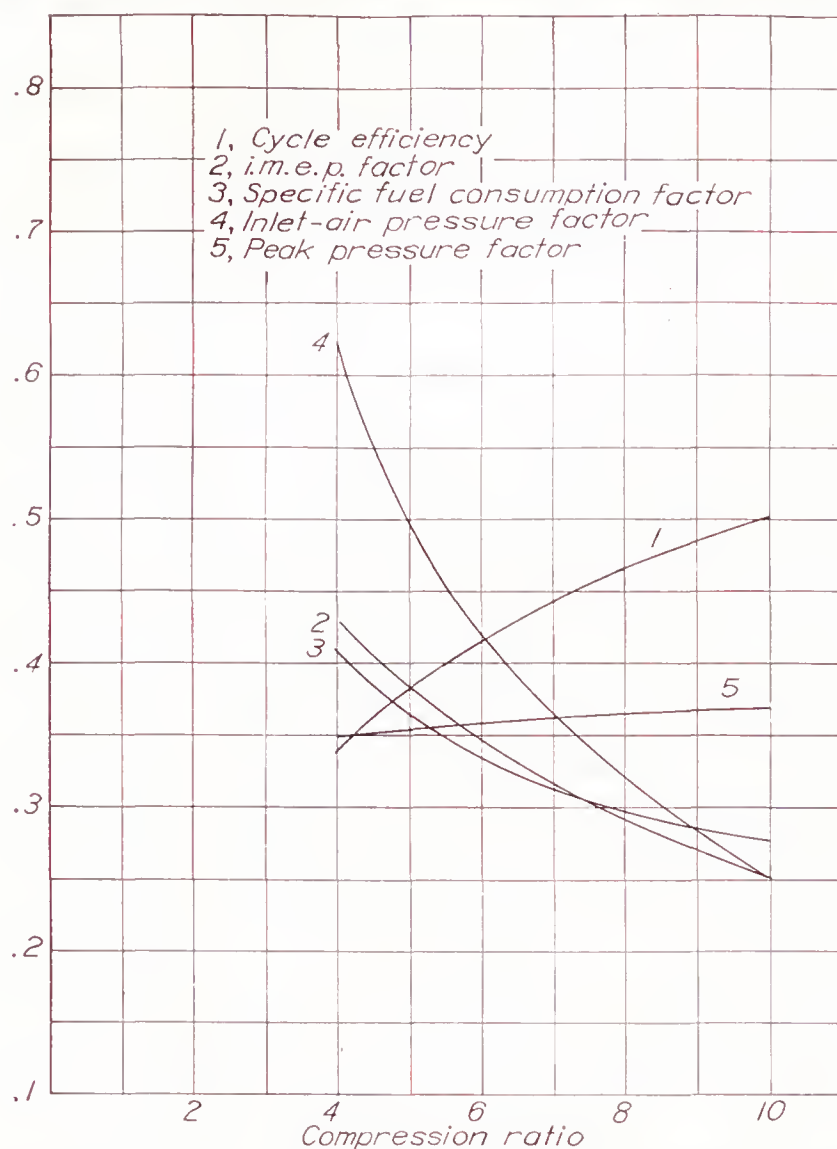


FIGURE 19.—Effect of compression ratio on maximum permissible performance factors.

factor and the peak pressure factor have been multiplied by suitable constants so that the same ordinate scale can be used for all the curves. These curves express the relationship between the maximum permissible indicated mean effective pressure, the lowest permissible indicated specific fuel consumption, and the peak pressure for any one fuel at any one inlet-air temperature for a series of compression ratios. The curve for the necessary inlet-air pressure for the maximum permissible indicated mean effective pressure factor is also given and is proportional to the reciprocal of the compression ratio. It is emphasized again that these curves represent any fuel at any given inlet-air temperature. The results for any two fuels have the same relation as the respective values of  $RP_1/T_1$  for the assumed inlet-air temperature. Curve 5 shows that the estimated maximum permissible peak pressure increases slightly with compression ratio, whereas the data in table VII show that the peak pressures decrease slightly.

#### VARIABLE INLET-AIR TEMPERATURE

For an engine in which the mixture is not cooled to atmospheric temperature after passing through the supercharger, the effects of the heating of the air during the compression in the supercharger must be taken into account. In the discussion of the previous section in which a constant inlet-air temperature was assumed, it

was also assumed that the variation in compression temperature because of the change in compression ratio was negligible. Although this assumption is justified by the data already presented, it is doubtful that it can also be applied to the compression in the supercharger.

An exponent of 1.4 for the compression of the air in the supercharger and an initial air temperature of 120° F. being assumed, the values listed in table IX are obtained for the supercharger compression ratio  $R_s$  and for  $T_1$ , over a range of  $P_1$  from 30 to 58 inches of mercury absolute. In the fourth column are tabulated the values of  $RP_1/T_1$  for iso-octane, these values having been obtained from column 3 in table IX and figure 4. The fifth column lists the maximum permissible compression ratio for the tabulated inlet-air pressures. It is emphasized that whereas, for a constant inlet-air temperature, curves varying only in the proportionality constant can be drawn which are applicable to any fuel, for a variable inlet-air temperature each set of data applies to only one fuel.

Without the intercooler between the supercharger and the cylinders, the indicated mean effective pressure is no longer proportional to the inlet-air pressure  $P_1$  because of the heating that has taken place within the supercharger. Instead, the indicated mean effective pressure for a constant inlet-air temperature and pressure to the supercharger is proportional to the supercharger compression ratio  $R_s$  and, as before, to the cycle efficiency as expressed by the relationship:

$$i. m. e. p. \propto R_s \times E_c \quad (10)$$

The values of  $R_s$  are obtained from the second column in table IX, and the values of  $E_c$  from the compression ratios listed in column 5 and the corresponding values of  $E_c$  obtained from the tabulated cycle efficiencies already given. The indicated mean effective pressure factors are given in column 7 and are again a proportionality factor.

TABLE IX

ESTIMATION OF MAXIMUM PERMISSIBLE I. M. E. P. FACTOR FOR ISO-OCTANE FROM FUEL-RATING CURVE IN FIGURE 4  
[Inlet-air temperature, 120° F.; audible knock; flat-disk combustion chamber; no intercooler]

1	2	3	4	5	6	7	8
Inlet-air pressure, $P_1$ (in. Hg abs.)	Supercharger compression ratio, $R_s$	$T_1$ (°F. abs.)	$RP_1/T_1$ (fig. 4)	Engine compression ratio, $R$	$E_c$	$R_s \times E_c$	(7) $\times$ 0.273/0.480
30	1.00	580	0.455	8.80	0.480	0.480	0.273
34	1.09	601	.435	7.70	.466	.504	.287
38	1.18	619	.415	6.77	.436	.514	.292
42	1.27	640	.392	5.97	.413	.524	.298
46	1.35	658	.370	5.29	.392	.530	.301
50	1.44	672	.355	4.78	.372	.536	.305
54	1.52	687	.340	4.33	.355	.540	.307
58	1.60	700	.325	3.92	.338	.540	.307

These values can be compared with those presented in figure 19 for the condition of constant inlet-air temperature by using a corresponding set of conditions, that is, the condition of no boost. In the second series of data, the compression ratio for no boost is 8.80, and the indicated mean effective pressure factor is 0.480.



For the condition of constant inlet-air temperature, the indicated mean effective pressure factor at a compression ratio of 8.80 is 0.273. Consequently, in order to compare the values from the foregoing proportionality factor with the indicated mean effective pressure factors for constant inlet-air temperature, the term  $R_s \times E_c$  must be multiplied by 0.273/0.480 as given in column 8.

In figure 20 is shown the effect of compression ratio on the maximum permissible indicated mean effective

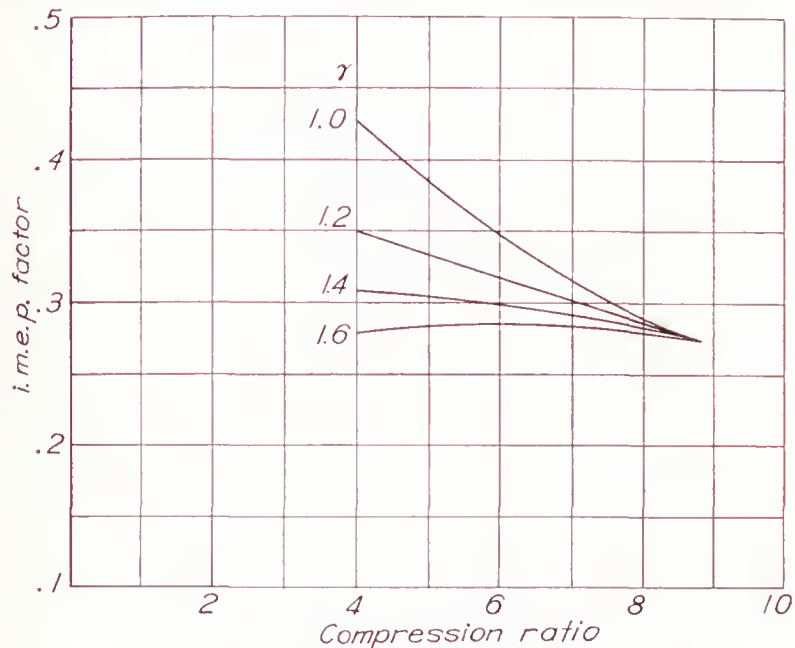


FIGURE 20.—Effect of various degrees of intercooling between supercharger and engine cylinders on maximum permissible i. m. e. p. factor. Iso-octane; audible knock.

pressure factor for various degrees of intercooling between the supercharger and the engine cylinders. The compression exponent indicated for each curve expresses the degree of intercooling. For an exponent of  $\gamma=1.0$ , the curve is the same as that shown in figure 19, in which it was assumed that the air entered the engine at a constant temperature, 120° F. The curves for the exponents of 1.2 and 1.6 were obtained in the manner illustrated for the value of 1.4. The curves emphasize the gain in maximum power that can be obtained by installing an intercooler so that the air or charge enters the cylinders at a temperature close to or equal to that at which it enters the supercharger. With an exponent of 1.6, the maximum permissible indicated mean effective pressure factor reaches a maximum at a compression ratio of 6.3. Dicksee (reference 18) pointed out in 1927 that, for any one fuel, one certain compression ratio would give the maximum permissible power provided that the air or charge not be cooled after it left the supercharger.

In the subsequent calculations presented in this report, it will be assumed that the value of  $\gamma$  is 1.4 for the condition of no intercooling or partial intercooling between the supercharger and the engine cylinders.

#### MAXIMUM PERMISSIBLE ENGINE PERFORMANCE WITH DIFFERENT FUELS

In figure 21 are compared the maximum permissible indicated mean effective pressure factors for three fuels with no intercooler between the supercharger and the cylinders. The corresponding inlet-air pressures are given in figure 22. The right-hand end of the indicated

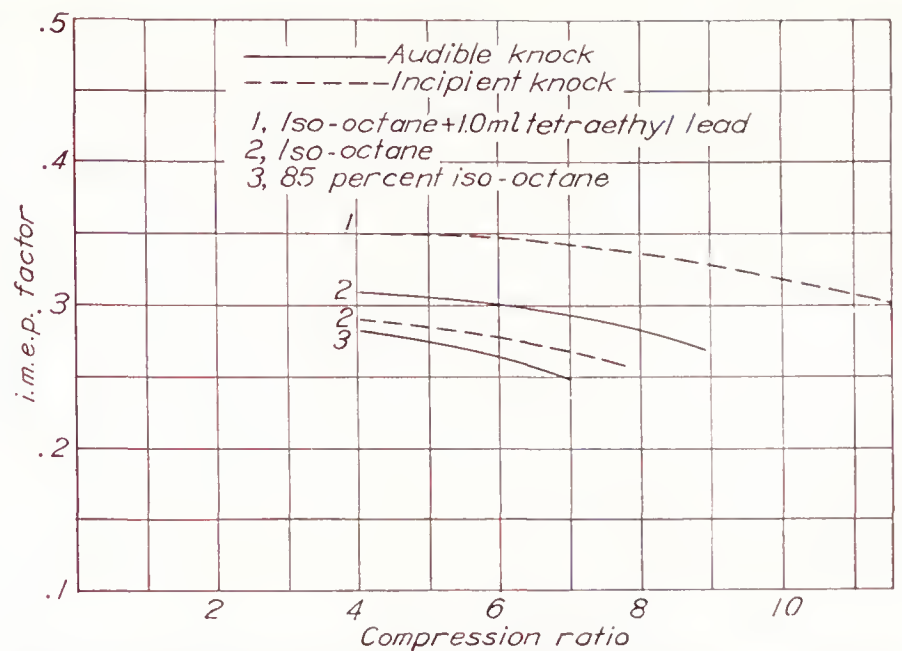


FIGURE 21.—Comparison of maximum permissible i. m. e. p. factors at different compression ratios for three different fuels. No intercooler ( $\gamma$ , 1.4) between supercharger and engine cylinders.

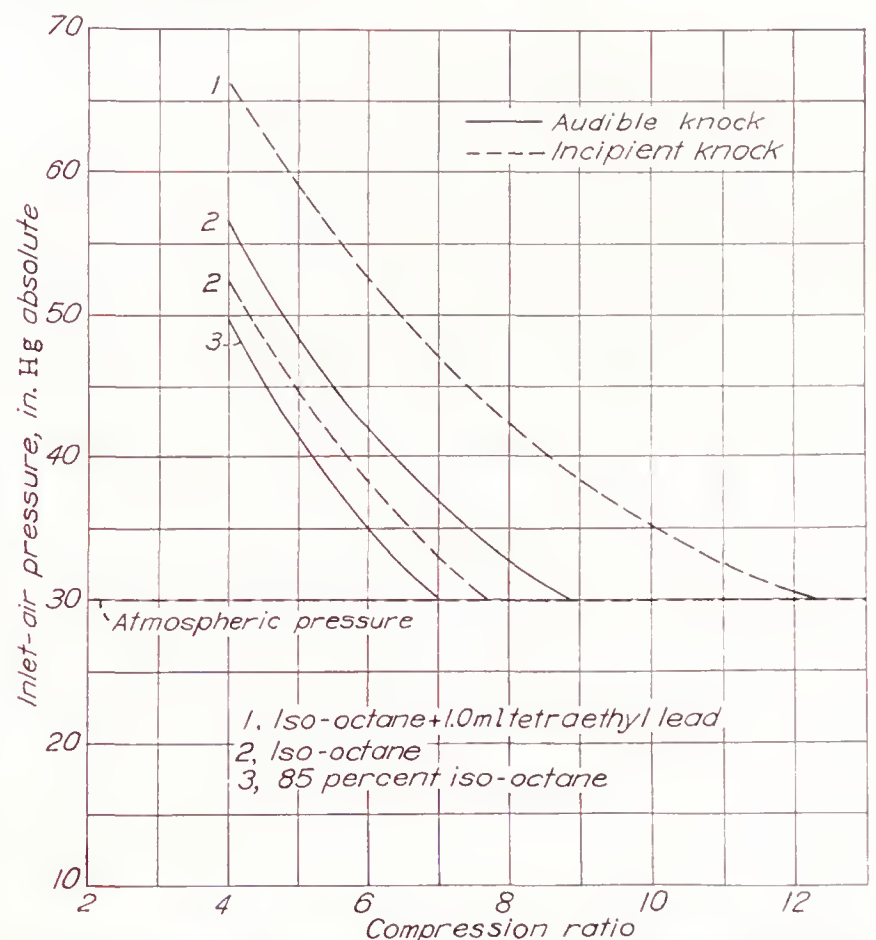


FIGURE 22.—Comparison of maximum permissible inlet-air pressures at different compression ratios for three different fuels. No intercooler ( $\gamma$ , 1.4) between supercharger and engine cylinders.

mean effective pressure curves represents in each case the condition of 120° F. inlet-air temperature and 30 inches of mercury inlet-air pressure. As the compression ratio is decreased, the curves tend to approach each other in the same manner that the rating curves of the fuels approached each other as the temperature of the inlet air was increased (fig. 4).

If it is assumed that a maximum boost pressure of 10 inches of mercury can be obtained, the maximum performances possible with the three fuels are shown in the following table:

Fuel	Compression ratio	i. m. e. p. factor	Specific fuel consumption factor	Knock
1	8.5	0.34	0.29	Incipient.
2	6.3	.30	.33	Audible.
3	5.2	.27	.36	Do.



Fuel 1 therefore represents a gain of 25 percent in maximum indicated mean effective pressure over fuel 3 and a decrease of 22 percent in the specific fuel consumption. With fuel 1, the peak pressures for this performance would be 1.5 to 2 times those with fuel 3.

CORRELATION OF RATING CURVES OBTAINED ON DIFFERENT ENGINES

As was shown in table II, it is possible to get two different rating curves for one fuel on the same engine by eliminating hot spots. This variation should be attributed to the engine. The data in reference 6 showed a greater temperature effect from variations in compression ratio than is shown by the N. A. C. A. data presented herein and by the data presented in references 3 and 5. The general trends shown in the previous figures should nevertheless be applicable to different engines.

The data obtained at the N. A. C. A. laboratories on the flat-disk and the pent-roof combustion chambers installed on the 5- by 5¼-inch engine permit a correlation to be made between the data for the two forms of combustion chamber.

The rating curve for iso-octane at incipient knock in the pent-roof combustion chamber determined from the data in table III is shown in figure 23, together

curves from the two rating curves for the conditions listed.

Column 7 of table X contains the indicated mean effective pressure factors for the two combustion chambers using the same fuel. In column 8 the indicated mean effective pressure factors for the flat-disk combustion chamber have been multiplied by 0.273÷0.480 so that the factors can be directly compared with those previously given. These values have already been plotted in figure 21. The performance factors for the fuels, and not for the engines, can be compared by finding a factor by which to multiply the values in column 7 to correlate the values with those for the flat-disk combustion chamber. At any one compression ratio, the two heads should show the same factor for the one fuel. The disk combustion chamber has a factor of 0.262 at a compression ratio of 7.70. The compression-ratio column for the pent-roof combustion chamber shows a compression ratio of 7.69 with a factor of 0.502. Because these two values of compression ratio are practically the same, the values in column 7 for the pent-roof combustion chamber are multiplied by 0.262/0.502. The resulting indicated mean effective pressure factors are given in column 8. The factors for the two combustion chambers are plotted in figure 24. The data show that a single curve represents both combustion chambers (curve 2).

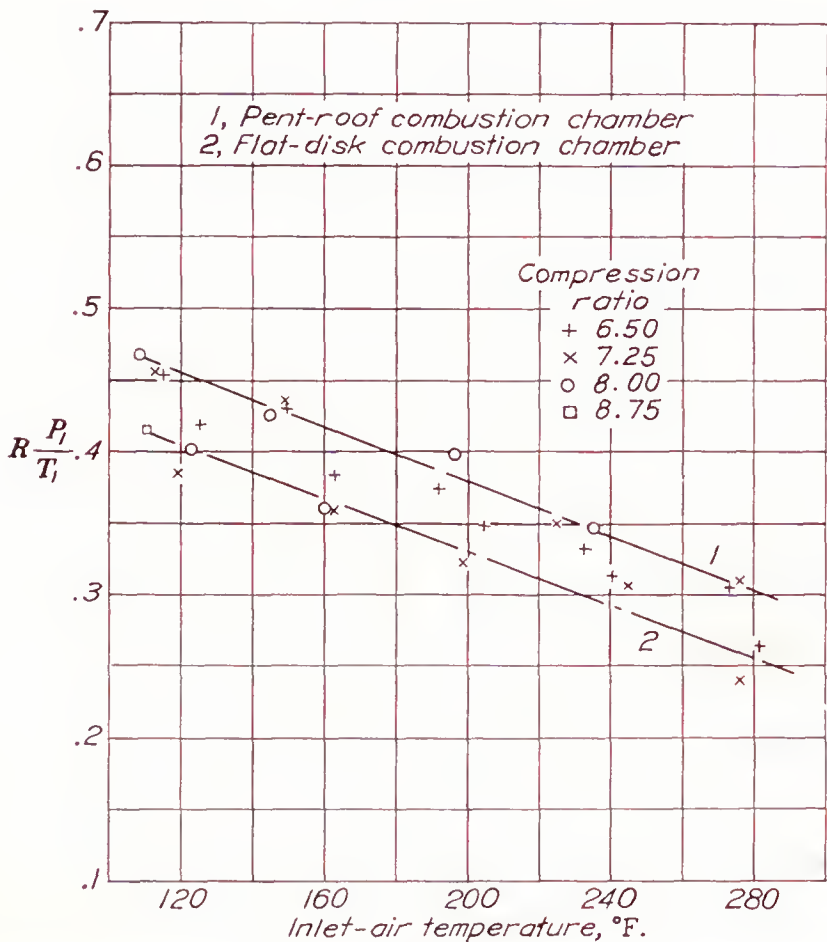


TABLE X  
ESTIMATION OF MAXIMUM PERMISSIBLE I. M. E. P. FACTOR FOR TWO DIFFERENT COMBUSTION CHAMBERS USING THE SAME FUEL

[Fuel, iso-octane; knock, incipient; inlet-air temperature to supercharger, 120° F.; no intercooler]

1	2	3	4	5	6	7	8
$P_1$ (in. Hg abs.)	$R_s$	$T_1$ (°F. abs.)	$RP_1/T_1$	$R$	$E_c$	$E_c R_s$	(7) $F$
Flat-disk combustion chamber, 2,500 r. p. m.							
							$F=0.273/0.480$
30	1.00	580	0.405	7.70	0.460	0.460	0.262
34	1.09	601	.386	6.82	.478	.478	.272
38	1.18	619	.370	6.03	.489	.489	.278
42	1.27	640	.350	5.34	.499	.499	.284
46	1.36	658	.332	4.75	.502	.502	.286
50	1.44	672	.320	4.38	.507	.507	.288
54	1.52	687	.305	3.88	.509	.509	.289
Pent-roof combustion chamber, 2,200 r. p. m.							
							$F=0.262/0.502$
30	1.00	580	0.455	8.80	0.480	0.480	0.253
34	1.09	601	.435	7.69	.461	.502	.262
38	1.18	619	.418	6.81	.438	.517	.270
42	1.27	640	.398	6.07	.416	.528	.276
46	1.36	658	.381	5.45	.396	.538	.281
50	1.44	672	.367	4.93	.378	.544	.284
54	1.52	687	.353	4.49	.362	.550	.287
58	1.60	700	.340	4.11	.348	.557	.289

FIGURE 23.—Comparison of rating curve for iso-octane with two different combustion chambers. Incipient knock.

with the curve for the flat-disk combustion chamber. The curves are approximately parallel, but that for the flat-disk combustion chamber is 0.050  $RP_1/T_1$  lower than that for the pent-roof combustion chamber. In table X are given the necessary computations to determine the estimated indicated mean effective pressure

The curves presented in figure 24 do not indicate which form of combustion chamber permits the highest indicated mean effective pressure. Small changes in design, such as the elimination of the recesses in the



piston used with the pent-roof chamber, might change the relationship of the curves in figure 23. The figures indicate that this method of estimating maximum permissible performance permits a certain degree of correlation between different combustion-chamber forms, but that certain differences are dependent on the design.

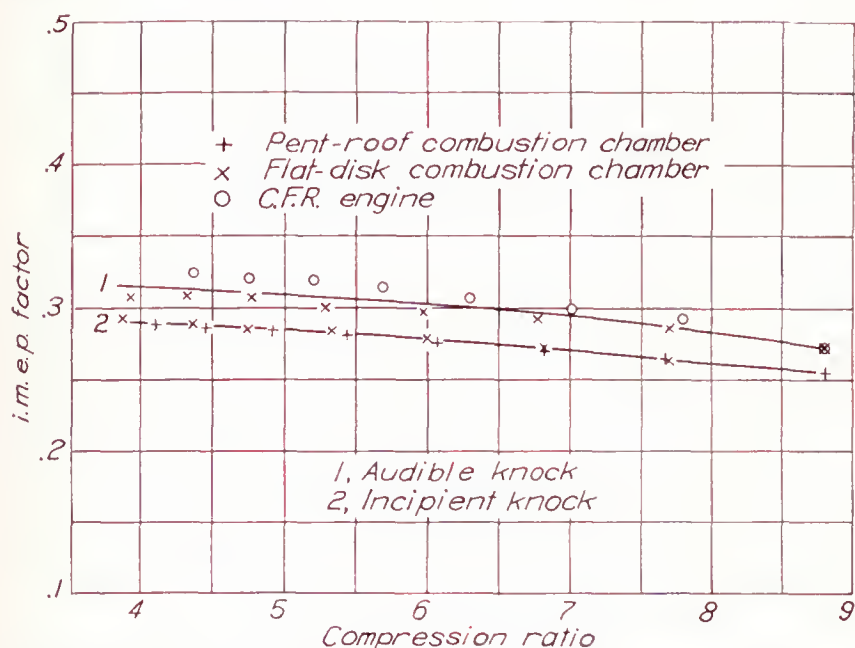


FIGURE 24.—Effect of compression ratio on maximum permissible i. m. e. p. factor for iso-octane for two different combustion chambers. No intercooler between supercharger and engine cylinders.

Curve 1 in figure 24 shows the correlated data for the flat-disk combustion chamber with iso-octane and the data obtained by Heron and Gillig from a C. F. R. engine using C. F. R. S-1 fuel (unpublished data). The S-1 fuel is practically identical with the fuel listed as iso-octane in the N. A. C. A. tests. Heron and Gillig found that, at a speed of 1,800 r. p. m. and a coolant temperature of 350° F., the C. F. R. S-1 reference fuel permitted an inlet-air pressure of 49.7 inches of mercury at an inlet-mixture temperature of 110° F. and an inlet-air pressure of 48.2 inches of mercury at an inlet-

mixture temperature of 212° F. The correlation between the C. F. R. engine and the N. A. C. A. 5- by 5¾-inch engine shows more variation than that for the two combustion chambers on the N. A. C. A. engine. Even so, the variation is only  $\pm 3$  percent. Although more test data are needed, the curves indicate that satisfactory correlation between different engines can be obtained provided that the performance is limited by knock.

Correlation between two fuels used in two different types of combustion chamber can be obtained from tables II and IV. By the method used to obtain the previous figures, it can be shown that, for the pent-roof combustion chamber, the indicated mean effective pressure factors for the iso-octane, when multiplied by 0.500, lie on the same curve as the data for the flat-disk combustion chamber (fig. 25). In the correlation of data for more than one fuel, the same factor should be used for all fuels. The use of this same factor gives the curve indicated for the pent-roof combustion chamber with the iso-octane plus 1.0 ml of tetraethyl lead. The curve lies below the corresponding curve for the flat-disk combustion chamber. The data show that the flat-disk combustion chamber permitted a greater percentage increase in performance than did the pent-roof chamber when 1.0 ml of tetraethyl lead was added to the iso-octane. It is concluded from the curves that no method of fuel rating on a single engine will give results which are accurately applicable to all engines but that it is possible to make an estimation of the approximate gain permitted by the use of improved fuels which will indicate basic differences in the behavior of different engines with these fuels. It is emphasized that these curves do not show which combustion chamber gave the highest engine output but indicate only the proportional increases permitted by the two fuels.

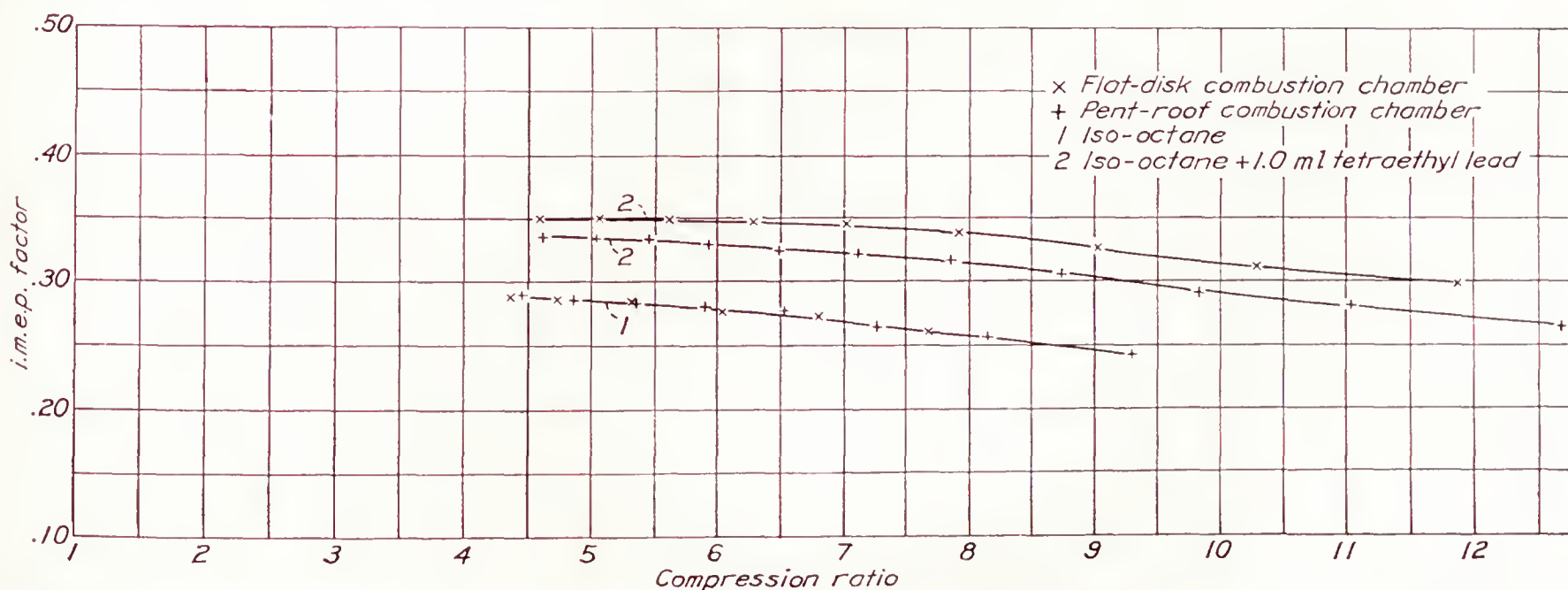


FIGURE 25.—Correlation of maximum permissible i. m. e. p. factors for two fuels in two combustion chambers of different design. No intercooler between supercharger ( $\gamma$ , 1.4) and engine cylinders; incipient knock; engine speed, 2,500 r. p. m.



## MAXIMUM PERMISSIBLE ENGINE PERFORMANCE

In the figures presented, it has been assumed that the engine is operated at a constant compression ratio. The data show that, in order to obtain maximum power for take-off and minimum fuel consumption for cruising, the engine should be operated at a variable compression ratio. The variation of the actual compression ratio of an engine leads to considerable mechanical complication. The effective compression ratio can be varied, as shown in figures 16 and 17, by changing the spark advance.

The most important fact to be learned from figures 16 and 17 is that, by retarding the spark, the maximum permissible boost pressure can be considerably increased. Consequently, for the most efficient use of any fuel, the compression ratio should be the highest value permissible for the desired power output, and the inlet-air temperature should be the lowest compatible with the volatility and freezing characteristics of the fuel. This condition represents the lowest specific fuel consumption, and it has been shown that, with iso-octane plus 1.0 ml of tetraethyl lead, the compression ratio at atmospheric inlet pressure is about 12. For maximum power in take-off, the spark can be retarded and the inlet-air pressure can be increased. If no or partial intercooling is provided, the optimum performance of the engine is represented by the data given in figures 20 and 21. With a degree of intercooling represented by  $\gamma=1.4$  and with iso-octane plus 1.0 ml of tetraethyl lead, the permissible power can be increased 19 percent by retarding the spark until the effective compression ratio is reduced from 10 to 6.

Figure 19 shows that, with intercooling, the same decrease in effective compression ratio permits the maximum permissible power to be increased 38 percent. In neither of these cases has any change in speed been considered. The compression ratio of 10 results in a decrease of 17 percent in the specific fuel consumption factor from the consumption at a compression ratio of 6.

The amount the spark can be retarded at high compression ratios will probably be limited by preignition because, although the end-gas temperature and density can be maintained constant, the density and the temperature preceding ignition is increased at the late spark advances.

Although these values may be overoptimistic, it is probable that, by the use of a high-compression-ratio engine and a retarded spark for take-off conditions, compression ratios higher than those used at present can be employed for cruising conditions and that the use of these compression ratios will result in a saving in fuel consumption. There seems to be no reason to believe that fuel consumptions of 0.35 pound per brake horsepower-hour should not be obtained with iso-octane fuel plus 1.0 ml or more of tetraethyl lead per gallon by operating the engine at a compression ratio

of about 10 for cruising, by retarding the spark to a lower compression ratio, and by boosting to provide sufficient power for take-off, provided that an intercooler for the incoming mixture can be provided.

Taylor, Ku, and Kennedy (reference 19) ran similar tests simulating altitude conditions and suggested varying the spark advance as an effective method of maintaining critical altitude power down to sea level.

Additional data on the foregoing method of engine operation are shown in table XI. In this test the engine was operated at the optimum spark advance at a compression ratio of 6.5 and the maximum permissible inlet-air pressure was determined for an inlet temperature of 200° F. The compression ratio was then increased to 8.0 and the spark retarded until the engine could be operated at this same inlet-air pressure and temperature. The results show that engine data were nearly the same for both conditions of operation except that the exhaust temperatures were slightly lower at the higher compression ratio. When the spark advance was set for the optimum value at the higher compression ratio, the maximum permissible indicated mean effective pressure was decreased to 173 pounds per square inch but the specific fuel consumption was decreased to 0.445 pound per indicated horsepower hour.

TABLE XI

EFFECT OF SPARK ADVANCE ON MAXIMUM PERMISSIBLE INLET-AIR PRESSURE AT TWO COMPRESSION RATIOS

[Engine speed, 2,500 r. p. m.; fuel, iso-octane+1.0 ml of tetraethyl lead per gallon; inlet-air pressure, maximum without knocking; air-fuel ratio, 12.5 (maximum power); inlet-air temperature, 200° F.]

	Compression ratio		
	6.50	8.00	8.00
Optimum spark advance, deg.....	31	29	29
Inlet-air pressure, in. Hg.....	45	45	37
Spark advance, deg.....	31	20	29
I. m. e. p., lb. per sq. in.....	210	214	173
I. f. c., lb. per i. hp.-hr.....	0.513	0.498	0.445
Exhaust temperature, °F.....	1,430	1,400	-----
Temperature rise, °F.....	11	10	-----
Maximum cylinder pressure, lb. per sq. in.....	925-750	825-750	-----

### III—COMPARISON OF KNOCKING-CHARACTERISTIC CURVES WITH OCTANE NUMBER

The most generally accepted index of fuel rating is octane number. This index depends on a comparison of the knocking characteristics of a given fuel with a blend of heptane and iso-octane. Since the knocking characteristics of different fuels do not necessarily have the same relative values for different engine operating conditions, the octane number of a fuel will vary with engine operating conditions unless the characteristics of the fuel are similar to heptane and iso-octane blends, as has been pointed out by Heron and Beatty (reference 20). The purpose of octane number is not to indicate the maximum permissible performance that can be obtained from a fuel under any operating conditions but



to indicate whether the fuel will knock under the most severe conditions to which it will be subjected. In general, this most severe condition will be either at take-off when the power output of the engine is high but knock is suppressed by enriching the mixture or at cruising when the power output is low but the mixture has been leaned to the minimum permissible value. If the fuels to be rated have similar characteristics, a single value of octane number representing one of these two conditions will probably be satisfactory. If fuels of different characteristics are to be rated, it may be necessary to determine octane numbers at these two most severe conditions.

The method of considering the fuels and the engines presented in the present report is suggested as a means of determining the relative maximum permissible engine performance that can be obtained under any operating conditions. It presents a method of determining the manner in which the combination of engine and fuel can be used most efficiently. Although these two methods of fuel rating serve different purposes, they should be compared.

In figures 26 and 27, the maximum permissible density factors are plotted against ASTM octane numbers for the blends used in the N. A. C. A. tests and for the blends used by Heron and Gillig in the tests reported in reference 9. In each case for the

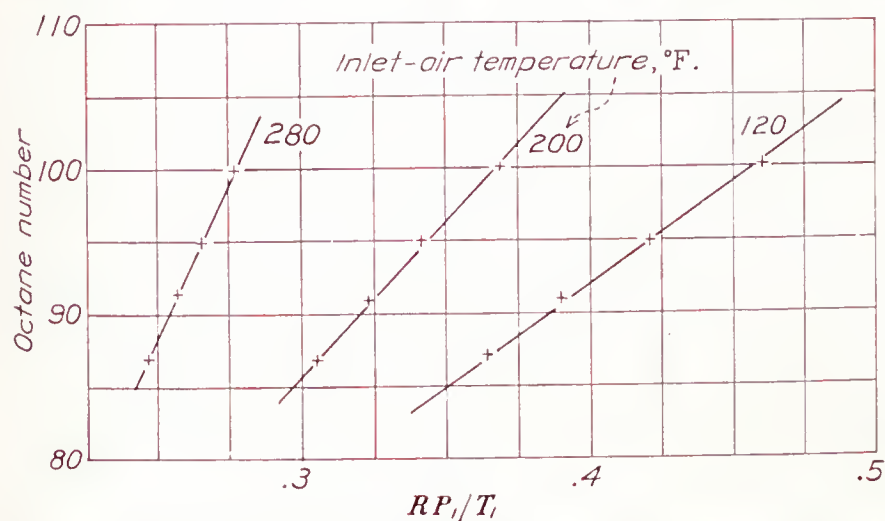


FIGURE 26.—Relationship between maximum permissible density factor and octane number for fuel blends used in N. A. C. A. tests.

N. A. C. A. data, the curves are straight lines (fig. 26). The slopes of the lines vary and, as a result, the actual variation in engine performance is not a constant with respect to octane number. At the lowest inlet-air temperature tested, 10 octane numbers represent a change in the maximum permissible density factor of 0.070; and, at the highest inlet-air temperature, the same range represents a change of 0.023. If a constant compression ratio is assumed, the increase in the maximum permissible density factor represents a proportional increase in maximum permissible indicated mean effective pressure.

The data of reference 9 (fig. 27) extend over a greater range of octane number than those of the N. A. C. A. tests and show that the curves at different engine speeds

have different slopes and also that, for a series of blends at constant engine speed and jacket temperature, the slope of the curve changes. With the data presented in figure 27, each curve apparently consists of two straight lines. These curves emphasize the fact brought out in various other papers that, as the octane number is increased, the corresponding improvement in maximum permissible engine output becomes greater for a constant increment of octane number.

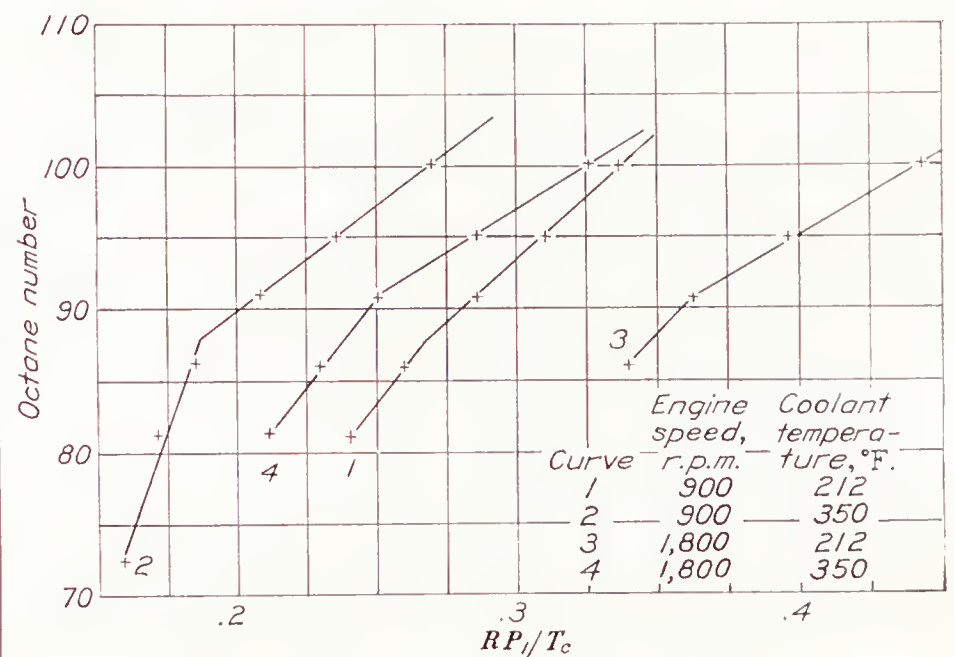


FIGURE 27.—Relationship between maximum permissible density factor and octane number for blends of S-1 and M-1 reference fuels (data from reference 9).

## CONCLUSIONS

The results presented in this report show that, by a determination of the knocking characteristics of a fuel in an engine as a function of the highest permissible inlet-air density at any inlet-air temperature, data obtained at one compression ratio or at one inlet-air pressure are applicable to a series of inlet-air pressures and compression ratios at the different inlet-air temperatures tested.

Analysis of the more important engine factors affecting knock leads to the conclusion that the most important independent variables in any one engine are the inlet-mixture density and temperature and the mixture ratio.

The data show that preignition must be treated separately from knock if the fuels are to be adequately rated in the engine. In the case of knock, the maximum permissible performance increases with speed for a constant spark advance; whereas, with preignition, the indication is that the maximum permissible performance decreases with engine speed.

The analysis shows that for any particular fuel the maximum permissible power increases as the compression ratio is decreased provided that the inlet-air temperature is kept constant and the performance is limited by knock and not by preignition. For the cases in which the inlet air is heated an increasing amount as the boost pressure is increased, the rate of maximum permissible power increase with decreasing



compression ratio decreases and finally passes through a value of zero as the exponent of adiabatic compression within the supercharger is increased. For the particular example cited in this report, an exponent of 1.6 resulted in an increase in the maximum permissible power as the compression ratio of the engine was decreased until the ratio reached a value of 6.3. Further decrease in the compression ratio caused a decrease in the maximum permissible power output.

The data show that a certain amount of correlation can be obtained between the knocking-characteristic curves of several fuels obtained on different engines but that there are certain differences which are caused by the variation in engine designs.

Presentation of the data on the basis of maximum permissible inlet-air density shows that the octane scale has a value in relation to engine output that varies with both octane number and the conditions of engine operation.

LANGLEY MEMORIAL AERONAUTICAL LABORATORY,  
NATIONAL ADVISORY COMMITTEE FOR AERONAUTICS,  
LANGLEY FIELD, VA., *September 14, 1938.*

#### REFERENCES

1. Rothrock, A. M., and Biermann, Arnold E.: Engine Performance and Knock Rating of Fuels for High-Output Aircraft Engines. T. N. No. 647, N. A. C. A., 1938.
2. Serruys, Max: La Combustion détonante dans les moteurs à explosion. Publications Scientifiques et Techniques du Ministère de l'Air, No. 103, 1937.
3. Rothrock, A. M., and Spencer, R. C.: A Photographic Study of Combustion and Knock in a Spark-Ignition Engine. T. R. No. 622, N. A. C. A., 1938.
4. Mucklow, G. F.: Experiments with a Supercharged Single-Cylinder Unit. R. & M. No. 1460, British A. R. C., 1932.
5. Taylor, Philip B.: Increasing the Thrust Horsepower from Radial Air-Cooled Engines. S. A. E. Jour., vol. XXVIII, no. 4, April 1931, pp. 417-428.
6. Boerlage, G. D.: Detonation and Autoignition. Some Considerations on Methods of Determination. T. M. No. 843, N. A. C. A., 1937.
7. Edgar, Graham: Jacket and Cylinder-Head Temperature Effects upon Relative Knock-Ratings. S. A. E. Jour., vol. XXIX, no. 1, July 1931, pp. 52-56.
8. Kurtz, Oskar: Research and Design Problems Introduced by Increased Power Output. T. M. No. 840, N. A. C. A., 1937.
9. Heron, S. D., and Gillig, F.: Essais de détonation avec suralimentation. World Petroleum Congress, Paris, June 14-19, 1937. Shell Aviation News, Dec. 1937.
10. MacClain, A. Lewis, and Buck, Richard S.: Flight-Testing with an Engine Torque Indicator. S. A. E. Jour., vol. 42, no. 2, Feb. 1938, pp. 49-62.
11. Peletier, L. A.: Effect of Air-Fuel Ratio on Detonation in Gasoline Engines. T. M. No. 853, N. A. C. A., 1938.
12. Gerrish, Harold C., and Voss, Fred: Mixture Distribution in a Single-Row Radial Engine. T. N. No. 583, N. A. C. A., 1936.
13. Stansfield, R., and Thole, F. B.: The Influence of Engine Conditions on the Anti-Knock Rating of Motor Fuels. Engineering, vol. CXXX, no. 3380, Oct. 24, 1930, pp. 512-514.
14. Tizard, H. T.: The Causes of Detonation in Internal-Combustion Engines. Trans. N. E. Coast Inst. Eng. and Shipbuilders, vol. XXXVII, published by the Inst., 1921, pp. 381-440.
15. Gardiner, Arthur W., and Whedon, William E.: The Relative Performance Obtained with Several Methods of Control of an Overcompressed Engine Using Gasoline. T. R. No. 272, N. A. C. A., 1927.
16. Biermann, Arnold E.: Effect of Spark-Timing Regularity on the Knock Limitations of Engine Performance. T. N. No. 651, N. A. C. A., 1938.
17. Hawley, C. D., and Bartholomew, Earl: The Relation of Fuel Octane Number to Engine Compression Ratio. Paper presented before the Amer. Petroleum Inst., Pittsburgh, 1934.
18. Dicksee, C. B.: Discussion of paper by A. H. R. Fedden entitled "The Supercharging of Aircraft and Motor-Vehicle Engines." R. A. S. Jour., vol. XXXI, no. 202, Oct. 1927, pp. 964-965.
19. Taylor E. S., Ku, K. F., and Kennedy, W. P.: Spark Control of Supercharged Aircraft Engines. Jour. Aero. Sci., vol. 3, no. 9, July 1936, pp. 326-328.
20. Heron, S. D., and Beatty, Harold A.: Aircraft Fuels. Jour. Aero. Sci., vol. 5, no. 12, Oct. 1938, pp. 463-479.



## REPORT No. 656

### THE COLUMN STRENGTH OF TWO EXTRUDED ALUMINUM-ALLOY H-SECTIONS

By WILLIAM R. OSGOOD and MARSHALL HOLT

#### SUMMARY

*Extruded aluminum-alloy members of various cross sections are used in aircraft as compression members either singly or as stiffeners for aluminum-alloy sheet. In order to design such members, it is necessary to know their column strength or, in the case of stiffeners, the value of the double modulus, which is best obtained for practical purposes from column tests.*

*Column tests made on two extruded H-sections are described, and column formulas and formulas for the ratio of the double modulus to Young's modulus, based on the tests, are given.*

#### INTRODUCTION

Extruded aluminum-alloy members of various cross sections are used in aircraft as compression members either singly or as stiffeners for aluminum-alloy sheet. In order to design such members, it is necessary to know their column strength, or in the case of stiffeners, the value of the double modulus (references 1 and 2), which is best obtained for practical purposes from column tests.

The interest of the National Advisory Committee for Aeronautics in stiffened-sheet construction as applied to monocoque design led to the allotment of funds to the National Bureau of Standards for research in this field, and a part of these funds was used to investigate the column strength of an extruded aluminum-alloy shape comparable with those used in stiffened-sheet construction. The data obtained in the tests made at the National Bureau of Standards are presented and discussed in part I of this report. The material for this investigation was supplied by the Aluminum Company of America.

Column tests were conducted at the Aluminum Research Laboratories on pieces of extruded aluminum alloy taken from the same lot of material supplied to the National Bureau of Standards. Column tests were also made at the Aluminum Research Laboratories on another extruded aluminum-alloy shape, the data on which had been requested by the National Advisory Committee for Aeronautics. The results of these tests are presented and discussed in part II of this report.

A correlation of the test data from the National Bureau of Standards and those from the Aluminum Research Laboratories is made in part III of this report.

#### MATERIAL

The material used in these investigations of column strength is designated Alcoa 24S-T by the Aluminum Company of America and complies with Navy Department Specifications 46A9a, June 1, 1938: Aluminum-alloy (aluminum-copper-magnesium (1.5 percent)-manganese): Bars, Rods, Shapes, and Wire. The material was furnished in the form of extruded H-beams. The nominal dimensions of the cross sections are shown in

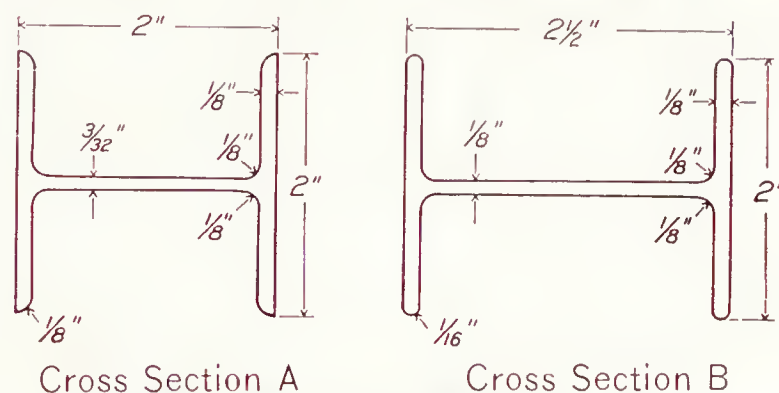


FIGURE 1.—Dimensions of extruded 24S-T H-sections.

figure 1. The National Bureau of Standards tests were made only on cross section A and the Aluminum Company tests included both cross sections.

The mechanical tests to determine properties and the results of these tests are discussed in the following three parts of this report.

#### I. TESTS MADE AT THE NATIONAL BUREAU OF STANDARDS

##### PREPARATION OF SPECIMENS

The tensile specimens were three standard type-5 tensile-test specimens, as defined in Navy Department General Specifications for Inspection of Material, Appendix II (Metals). They were cut from the same length of extruded shape, one specimen from the middle of the web and the other two from diagonally opposite positions in the two flanges. The cross-sectional areas of the reduced portions of these specimens were determined by calipering them.



The lengths of all the compressive and the column specimens were measured. In order to determine the required cross-sectional properties of the compressive and the column specimens, more than half of them were weighed and, for each of these specimens, measurements were made of the thickness and the width of each flange and the depth of the section at the middle and of the thickness of the web at each end. The density of a sample of the material was determined by the Division of Weights and Measures of the National Bureau of Standards. The cross-sectional areas were computed

The most suitable machine available for making the compressive tests was considered to be a fluid-support, Bourdon-tube, hydraulic machine. Auxiliary nuts on the screws of this machine were tightened against the lower surface of the adjustable head to bring it into contact with the lower surface of the threads on the screws, so that rotation of the head relative to the platen of the machine due to clearance between the nuts of the head and the screws was obviated. The unsymmetrical position of the motor, the handwheel, and the other mechanism for raising and lowering the adjustable

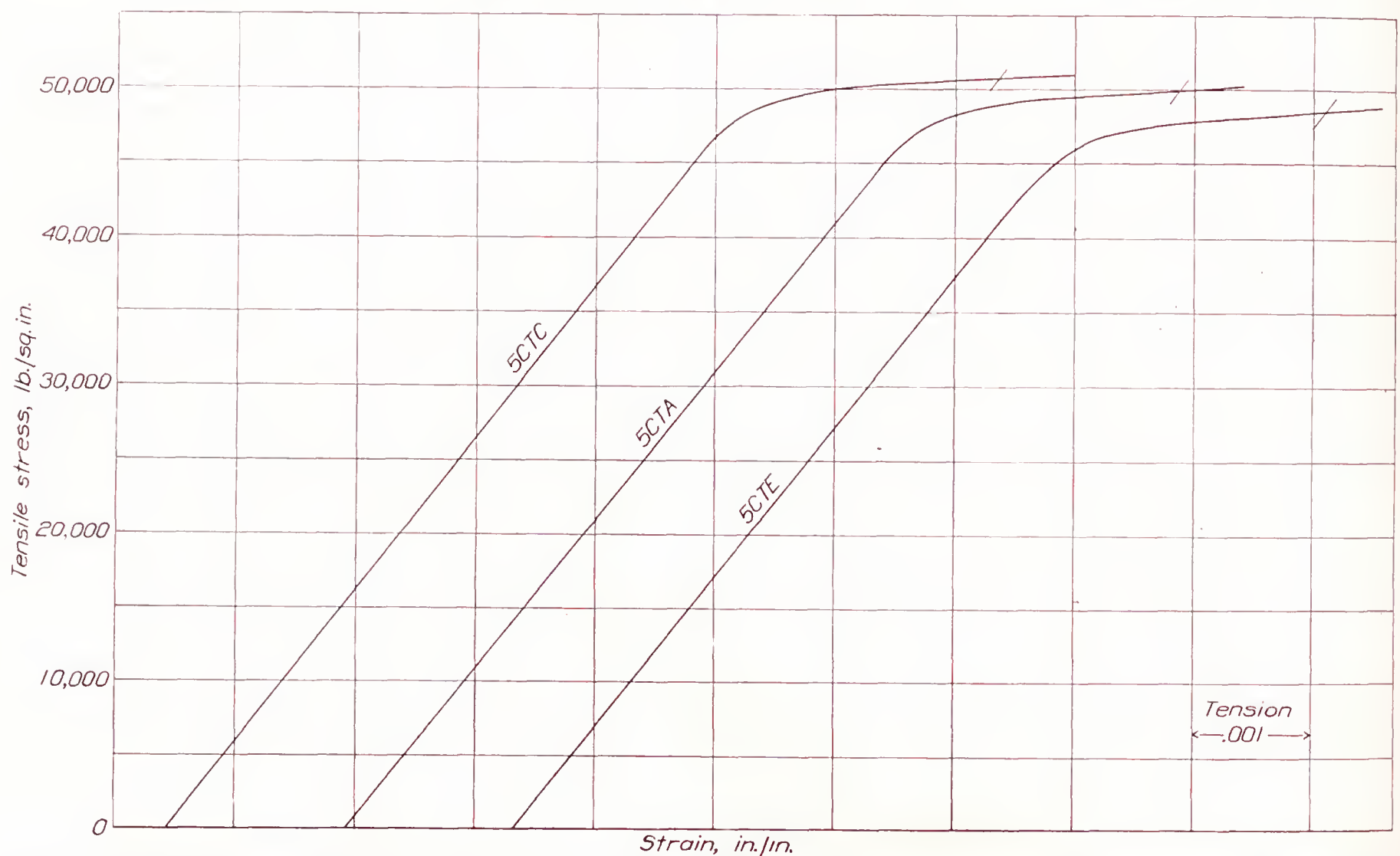


FIGURE 2.—Typical tensile stress-strain diagrams for 24S-T of cross section A. Strains measured on 2-inch gage length with Ewing extensometer. National Bureau of Standards.

from the weights, the lengths, and the densities; and the least radii of gyration were computed from the measured cross-sectional dimensions and the nominal radii of the roundings and fillets.

#### TENSILE AND COMPRESSIVE TESTS

Tensile tests were made in screw-driven, beam-and-poise testing machines. The specimens were held in Templin grips supported by spherical bearings. Strains were measured in 2-inch gage lengths by means of Ewing extensometers. Three typical tensile stress-strain diagrams are shown in figure 2. Specimens 5CTC and 5CTA were taken from the flanges and specimen 5CTE from the web. The tensile yield strength was obtained from the stress-strain diagram as the stress at a strain 0.002 in excess of the elastic strain corresponding to this stress.

head causes it to exert on the portion of the two screws below it a constant moment of roughly 1,000 pound-inches in a plane normal to that of the screws. Consequently the screws are slightly bent elastically and, as they tend to straighten under load, produce rotation of the head. This condition causes a slight eccentricity of loading, which is especially undesirable in compression testing; but, with the short specimens and comparatively low loads (maximum, one-third the capacity of the machine) of the present investigation, the effect was not considered serious. Another possible source of error in making compressive tests in this type of machine arises from the possibility of rotation of the platen about a horizontal axis. The platen is rigidly connected to the piston of the hydraulic jack, which is packed, and the clearance between the cylinder and the piston permits rotation of the platen under eccentric



load. This effect can be minimized by keeping as much of the piston in the cylinder as possible.

The compressive specimens were 8-inch lengths of the extruded shape, with ends machined plane and normal to the axis. A specimen to be tested was placed centrally on a ground hardened-steel bearing block located centrally in the testing machine, and a similar, smaller block was placed centrally on the upper end of the specimen. In order to secure as nearly uniform bearing as possible, the upper bearing block was capped with plaster of paris. The capping was done by placing a stiff mix of plaster between two sheets of relatively

## COLUMN TESTS

Fifteen column specimens were tested with freely supported ends and, upon recommendation of the Committee on Aircraft Structures of the National Advisory Committee for Aeronautics, six specimens were tested with elastically restrained ends. The apparatus and the procedure used for making the tests were identical with those described in reference 3. It will be sufficient to explain here that the specimens were supported on knife-edge carriers and centered under load. That is, a load was applied which would not produce anywhere in the specimen stresses greater

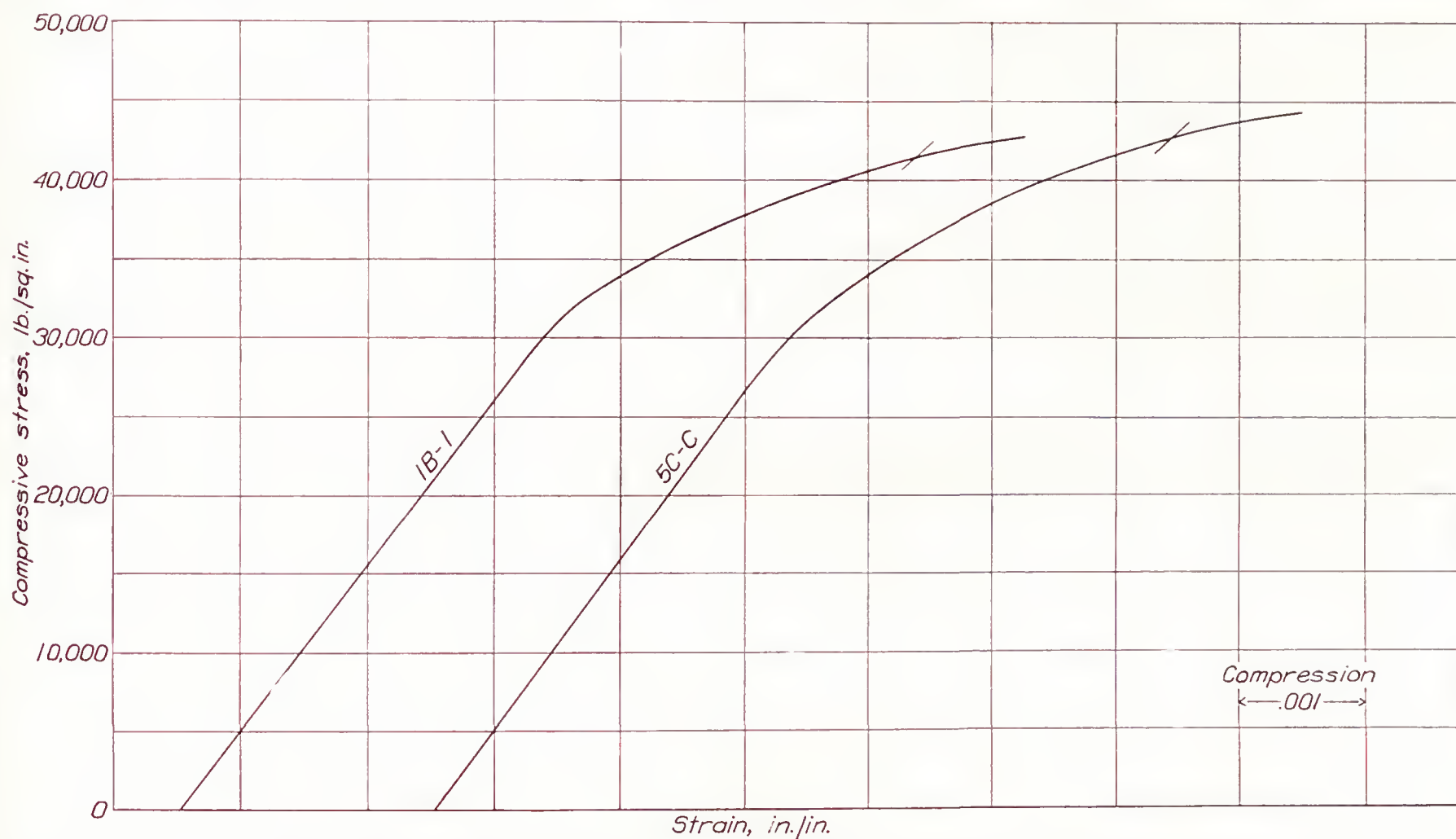


FIGURE 3.—Compressive stress-strain diagrams for 24S-T of cross section A. Strains measured with Tuckerman optical strain gages (up to 0.002) and with Huggenberger strain gages on 2-inch gage length. Length of specimen, 8 inches. National Bureau of Standards.

nonabsorbent oiled tracing paper and transferring it to the bearing block. A load of 1,000 pounds was then applied immediately and held for about 15 minutes to allow the plaster to set.

Strains were measured on 2-inch gage lengths along the middle of each flange. Tuckerman optical strain gages were used to measure strains up to about 0.002 to determine the modulus of elasticity, and Huggenberger Tensometers were used to measure the larger strains. Compressive stress-strain diagrams were obtained for two specimens and are shown in figure 3. The compressive specimens ultimately failed by local buckling, as shown by 1B-1 in figure 4. The compressive yield strength was obtained as the stress corresponding to the intersection with the stress-strain curve of a line drawn through the origin with a slope  $2/3 E$ , where  $E$  is the modulus of elasticity (reference 3).

than the expected maximum average column stress, the deflection of the middle of the specimen and the rotations of the ends were noted, the load was reduced to a low value (150 pounds), one or both ends of the specimen were shifted on the carriers to reduce the deflection under load and equalize the rotations, and the process was repeated with increasing loads until at 90 percent or more of the expected maximum column load the deflection was only a few ten-thousandths of an inch (not over 0.0005 inch).<sup>1</sup> When this condition was reached, the load was reduced to 150 pounds and then gradually increased to the maximum value that could be supported by the specimen. Readings of deflection were taken while applying the load.

Curves of load divided by maximum load plotted against deflection within the free length divided by the

<sup>1</sup> Lest anyone be alarmed by such high centering loads, let him read the appendix.



free length serve as a check on the centering operation. Figure 5 shows typical curves of this kind. If the knee of any such curve is blunt relative to the knees of the curves for the other specimens, as occasionally happens, it indicates that the specimen represented by that curve was not so well centered as the others. In the present investigation all specimens tested with freely supported ends appeared to be well centered.

RESULTS

The results of the column tests are given in table I and in figures 6 and 7. The free lengths,  $l_0$ , of the test columns were determined from the equation (reference 3)

$$\cot \frac{\phi}{2} + \nu \phi = 0 \tag{1}$$

where

$$\phi = \frac{\pi l}{l_0}, \quad \nu = \frac{m}{Pl} - \frac{s}{l} \tag{2}$$

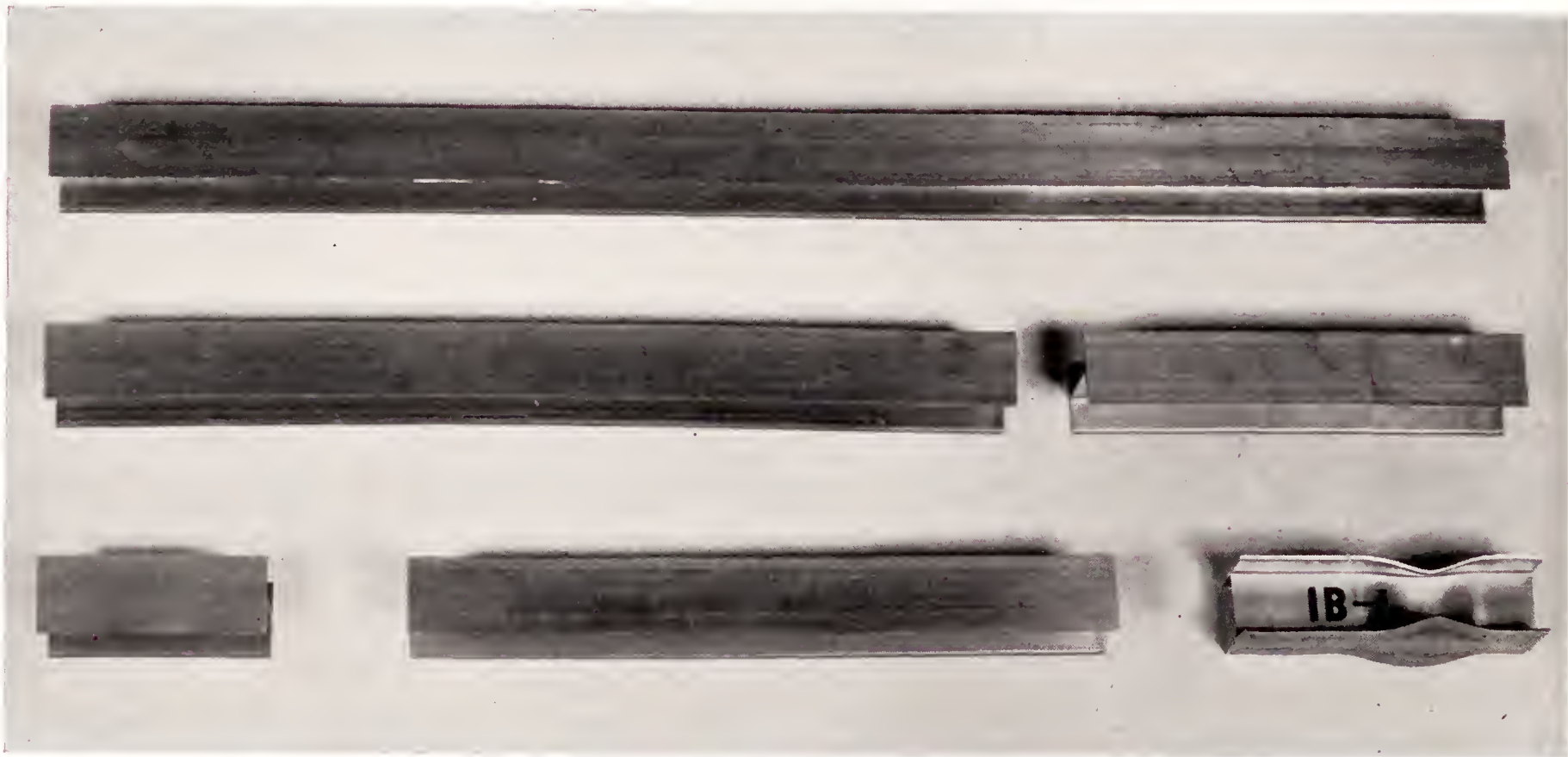


FIGURE 4.—Some column specimens and one compressive specimen (1B-1) of cross section A after test.

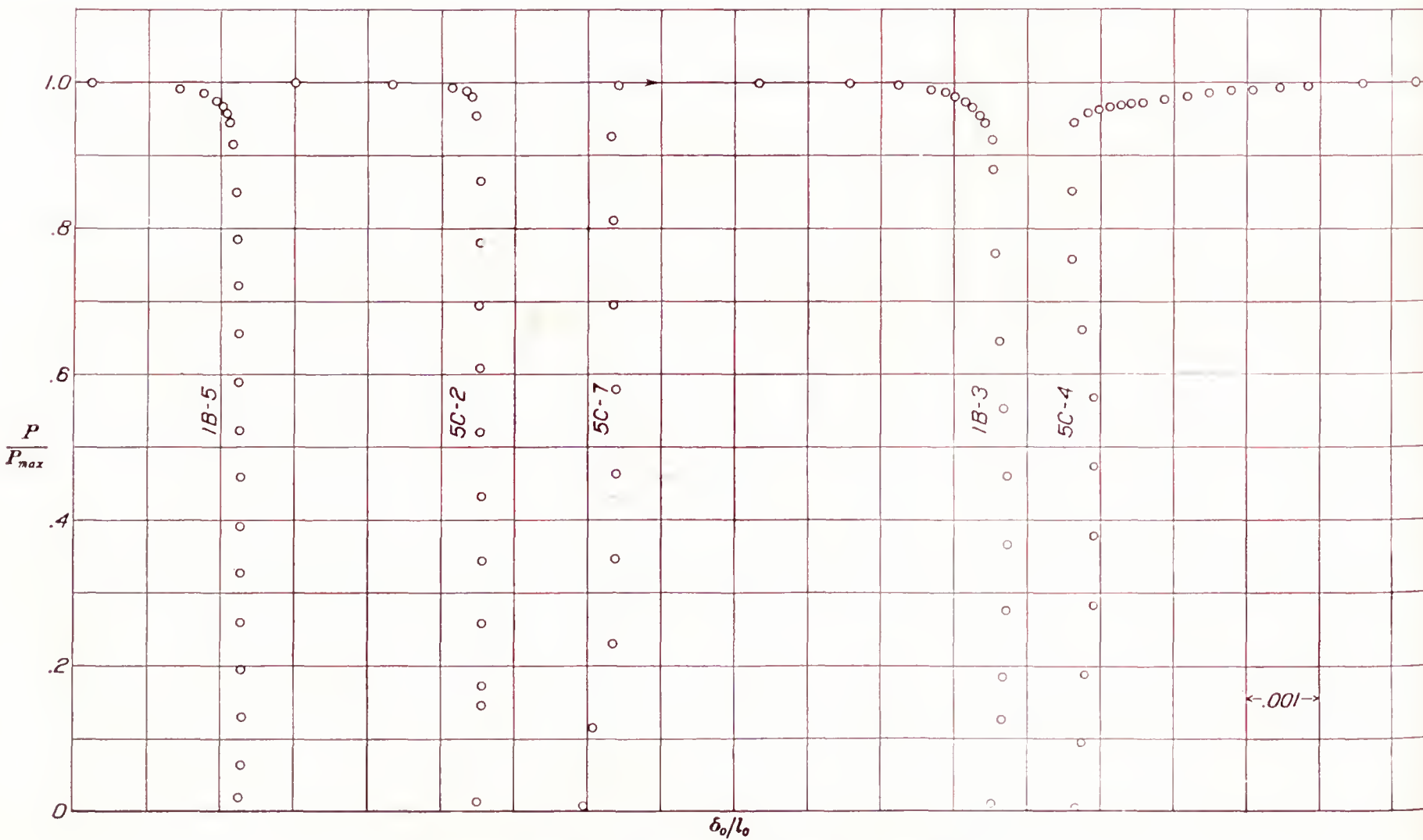


FIGURE 5.—Typical  $P/P_{max}$ ,  $\delta_0/l_0$ -diagrams for 24S-T of cross section A.



$l$  is the length of the test specimen,  $s$  is the length of the carrier (distance from a supporting knife edge to the adjacent end of the specimen),  $m$  is the elastic restraint at each end of the column ( $m=0$  for freely supported ends), and  $P$  is the maximum load carried by the column. The least radius of inertia, or radius of gyration, of the cross section has been denoted by  $i$ , the cross-sectional area by  $A$ , and the compressive yield strength by  $S$ . The significance of plotting

$$\sigma = \frac{P}{AS} \text{ against } \lambda_0 = \frac{1}{\pi} \frac{l_0}{i} \sqrt{\frac{S}{E}} \quad (3)$$

has been discussed in reference 3. The use of these non-dimensional variables makes it possible to reduce in a rational way data representing column tests made with material exceeding specified values in yield strength to a representation that would be expected from material just complying with the specified values.

In figure 6 values of  $\sigma$  have been plotted against  $\lambda_0$ . The three specimens having the lowest values of  $\lambda_0$  showed evidence of local buckling due to bending before their maximum loads were reached, so that the corresponding values of  $\sigma$  may be slightly low (on the safe side). It is much more difficult to center a short specimen under load than a long one, because the deflection at the middle becomes so small for a short specimen. The results obtained from the tests with elastically restrained ends agree with those obtained from the other tests as well as could be expected.

If the load-deflection curve (fig. 5) for any specimen has a blunt knee relative to the knees of the other curves, and if also the value of  $\sigma$  for this specimen in the  $\sigma, \lambda_0$ -plot is low, justification exists for throwing it out. No such cases arose in this investigation, however, and low points in figure 6 are to be explained largely by unavoidable variations in the material.

Figure 6 shows the reduced Euler curve and a straight line fitted to the observed  $\sigma, \lambda_0$ -values for the condition of freely supported ends. The straight line has been cut off at the top at the average value of  $\sigma$  found for the two compressive specimens, which failed by local buckling (specimen 1B-1 in fig. 4). The column strength of the aluminum-alloy shape tested can be given in non-dimensional form by

$$\sigma_{max} = 1.153 \quad (4)$$

$$\left. \begin{aligned} \sigma &= 0.55 + \frac{0.5}{\sqrt{0.55}} - 0.5\lambda_0 \\ \sigma &= 1.224 - 0.5\lambda_0 \end{aligned} \right\} 1.153 > \sigma > 0.55 \quad (5)$$

$$\sigma = \frac{1}{\lambda_0^2}, \sigma < 0.55 \quad (6)$$

It is to be expected that equations (5) and (6) would hold closely for any heat-treated bar, rod, or shape complying with Navy Department Specification 46A9a so long as failure occurred by primary buckling. Equa-

tion (4) expresses the condition of failure by local buckling, or wrinkling, or erinkling, and this equation would have to be modified depending on the shape of cross section.

In figure 7 the observed values of the maximum average stress,  $P/A$ , have been plotted against the ratio of slenderness,  $l_0/i$ . By introducing in equations (4), (5), and (6) the values of  $\lambda_0$  and  $\sigma$  from equations (3), relations can be obtained between  $P/A$  and  $l_0/i$  in terms of  $S$  and  $E$ . For use in design, these relations should contain numerical values of  $S$  and  $E$  related as far as possible to specified minimum properties of the material. The specified property most closely related to the compressive yield strength is the tensile yield strength. The average ratio of the compressive yield strength to the tensile yield strength<sup>2</sup> of the material of this investigation was 0.85. Navy Department Specification 46A9a for aluminum-alloy shapes such as those tested requires a minimum tensile yield strength of 42,000 pounds per square inch. Material just complying with this specification may therefore be expected to have a compressive yield strength  $S = 0.85 \times 42,000 = 35,700$  pounds per square inch. If then, this value is taken for  $S$  and for  $E$  the average value found, 10,660,000 pounds per square inch, there is obtained for design,  $P/A$  in pounds per square inch:

$$\left(\frac{P}{A}\right)_{max} = 41,200 \quad (7)$$

$$\frac{P}{A} = 43,700 \left(1 - 0.00752 \frac{l_0}{i}\right), \quad 41,200 > \frac{P}{A} > 19,600 \quad (8)$$

$$\frac{P}{A} = \frac{105,200,000}{\left(\frac{l_0}{i}\right)^2}, \quad \frac{P}{A} < 19,600 \quad (9)$$

The curves represented by these equations are shown in figure 7.

In analyzing stiffened-sheet construction it may be necessary to know the quantity  $\tau = \frac{\bar{E}}{E}$  as a function of the average stress  $P/A$  in the stiffener (reference 1), where  $\bar{E}$  is the double modulus (reference 2). The desired relation between  $\tau$  and  $P/A$  may be obtained by eliminating  $\lambda_0$  between the "universal" column formula (reference 3)

$$\sigma = \frac{\tau}{\lambda_0^2} \quad (10)$$

and each of equations (4), (5), and (6), and then substituting  $\sigma$  from equation (3). Elimination of  $\lambda_0$  between equation (10) and equations (4), (5), and (6) gives for  $\tau$  in terms of  $\sigma$

$$\tau_{min} = 0.0231 \quad (11)$$

$$\tau = 4\sigma \left(0.55 + \frac{0.5}{\sqrt{0.55}} - \sigma\right)^2 \left\{ 1.153 > \sigma > 0.55 \right. \quad (12)$$

$$\left. \begin{aligned} \tau &= 4\sigma(1.224 - \sigma)^2 \\ \tau &= 1 \end{aligned} \right\} \sigma < 0.55 \quad (13)$$

<sup>2</sup> The values of tensile yield strength were weighted averages from tests of two specimens of flange material and one specimen of web material.



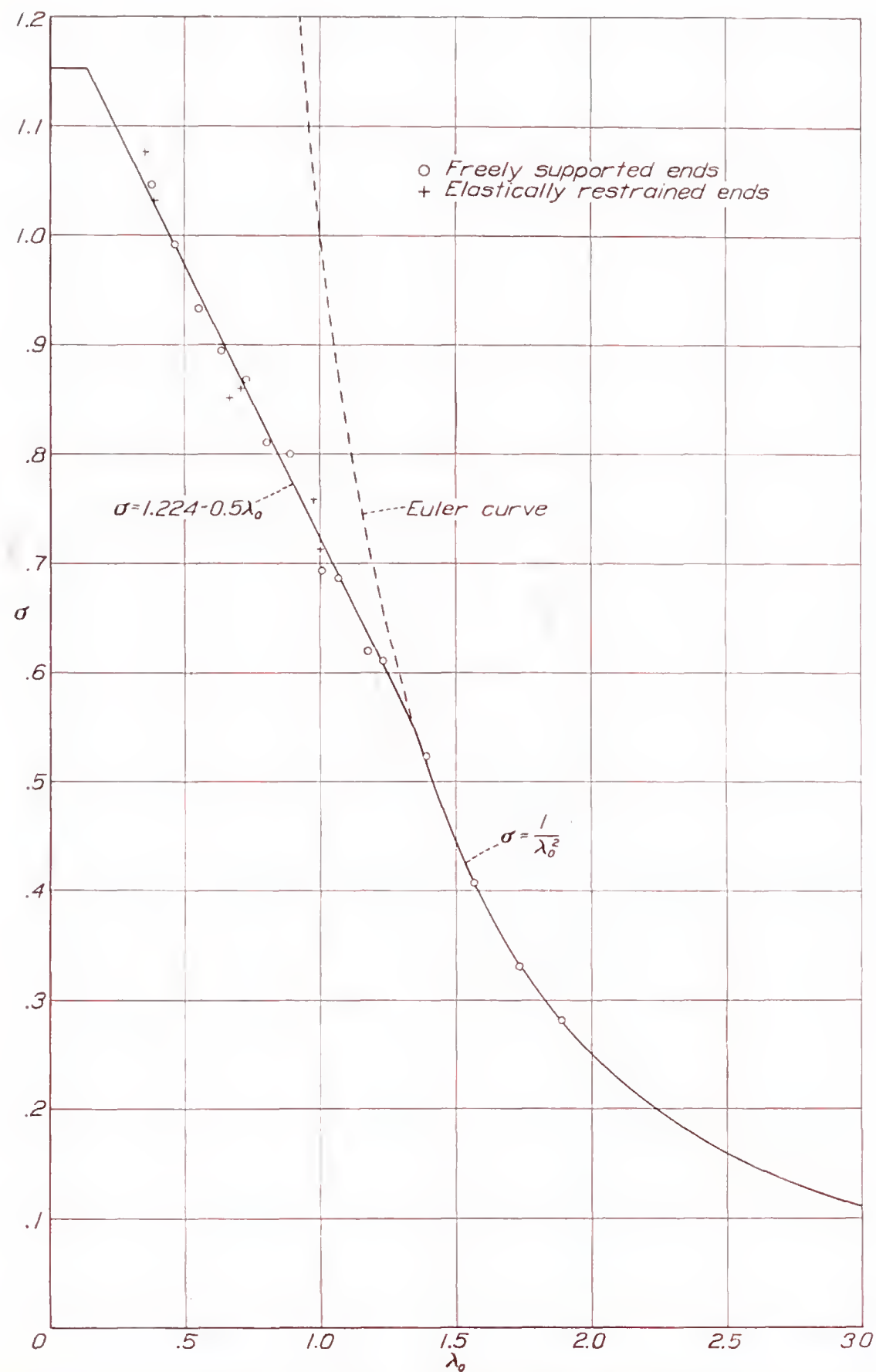
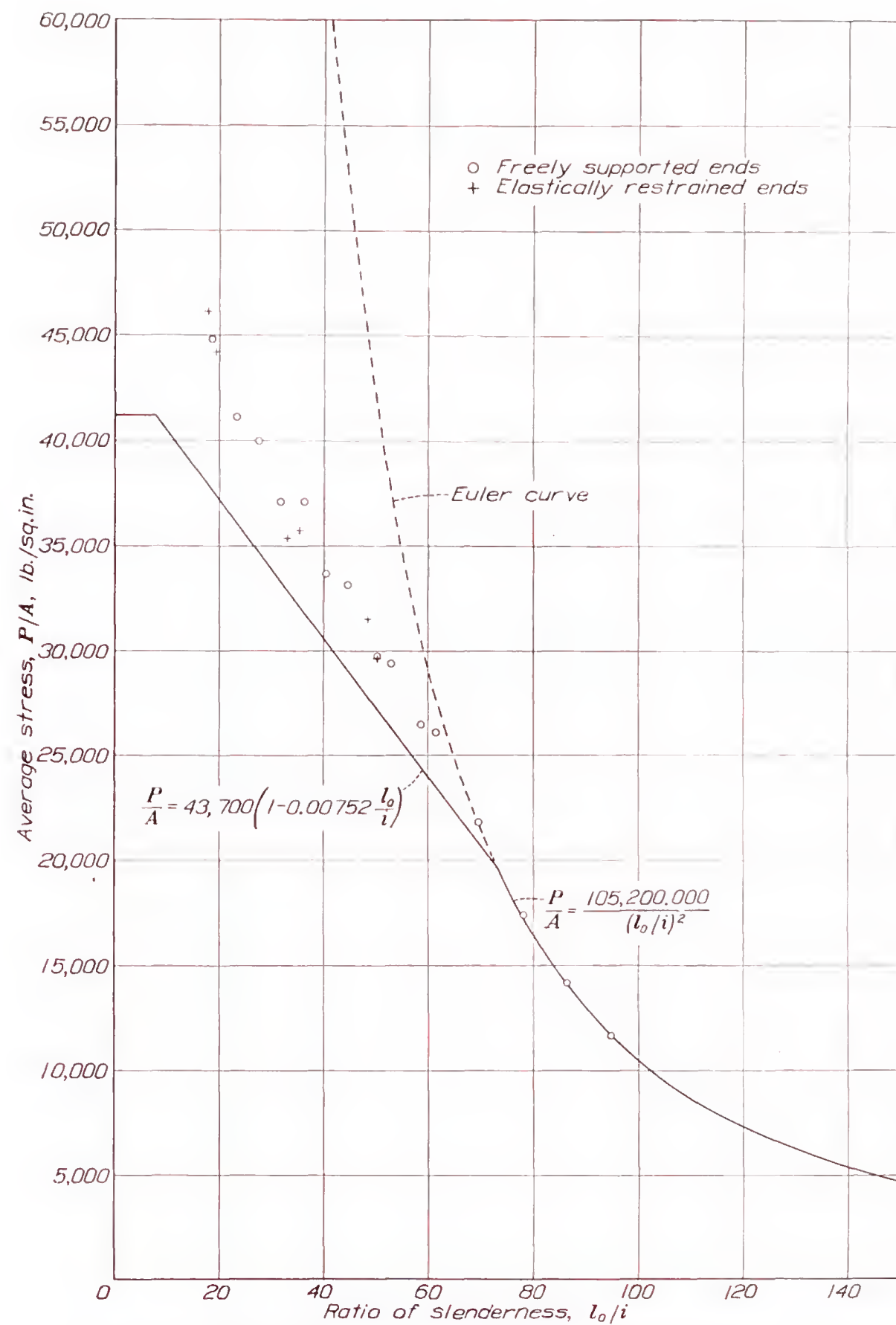
FIGURE 6.—The  $\sigma$ ,  $\lambda_0$ -diagram for 24S-T of cross section A.FIGURE 7.—The  $P/A$ ,  $l_0/i$ -diagram for 24S-T of cross section A.



Figure 8 shows the curves represented by these equations. Substitution of  $\sigma$  from equation (3), with  $S$  taken as 35,700 pounds per square inch gives,  $P/A$  in pounds per square inch,

$$\tau_{min}=0.0231 \quad (14)$$

$$\tau=\frac{P}{8925A}\left(1.224-\frac{P}{35700A}\right)^2, \quad 41,200>\frac{P}{A}>19,600 \quad (15)$$

$$\tau=1, \quad \frac{P}{A}<19,600 \quad (16)$$

Figure 9 shows the curves represented by these equations.

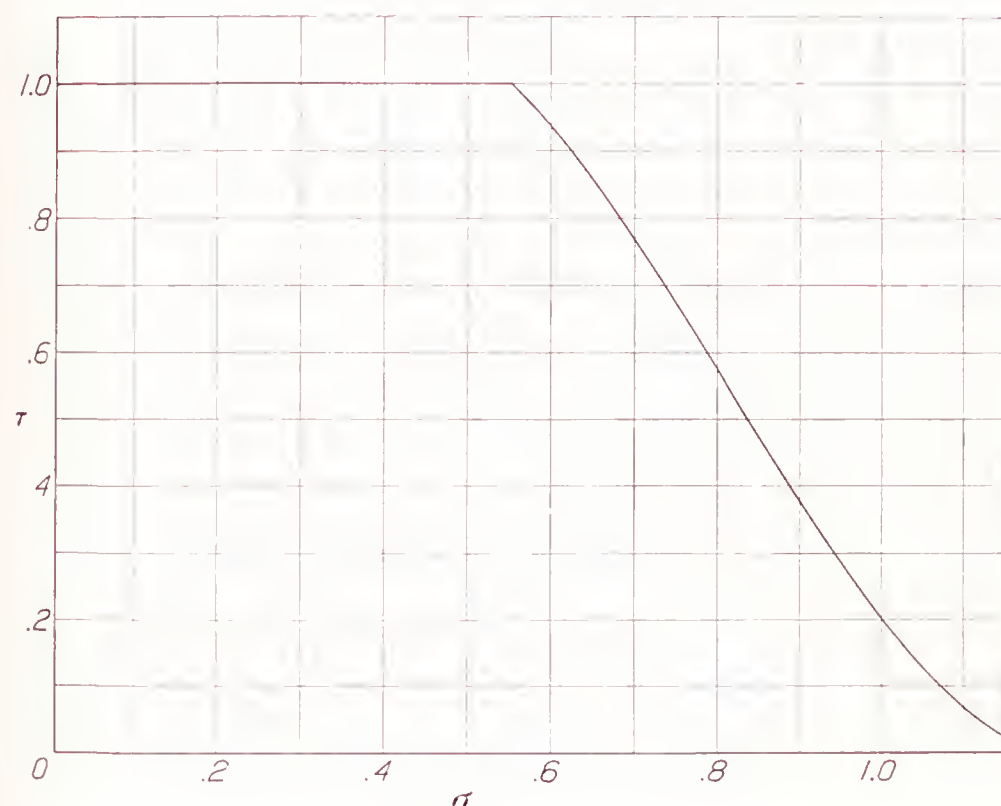


FIGURE 8.—The  $\tau$ ,  $\sigma$ -curve for 24S-T of cross section A.

	<i>Lb. per sq. in.</i>
Cross section A.....	44,700
Cross section B.....	40,000

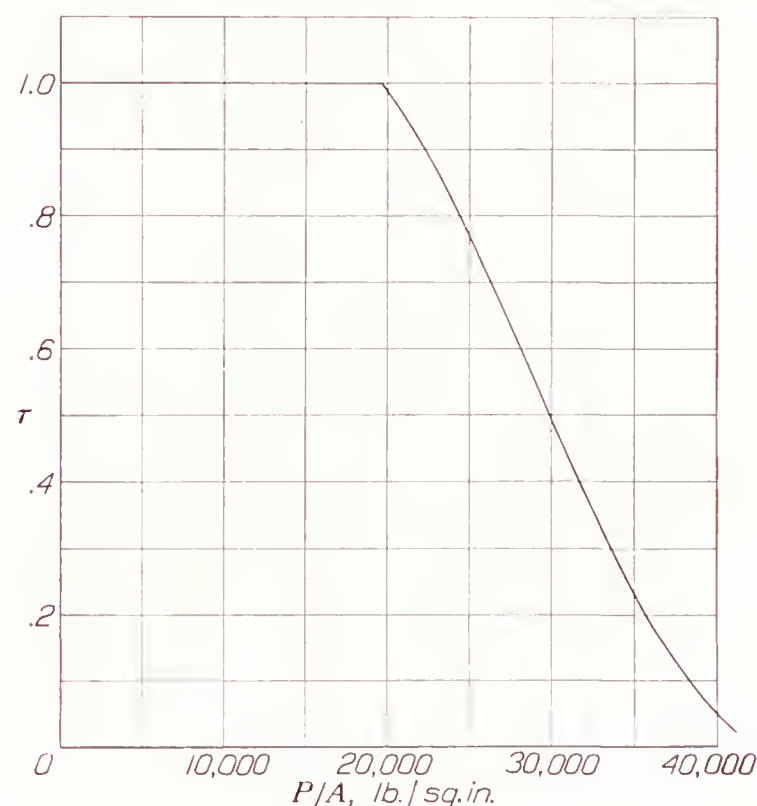


FIGURE 9.—The  $\tau$ ,  $P/A$ -curve for 24S-T of cross section A.

## II. TESTS MADE AT THE ALUMINUM RESEARCH LABORATORIES

### MECHANICAL PROPERTIES TESTS

The test specimens for the mechanical properties tests were identified by the same numbers assigned the extruded pieces: 1 to 4, inclusive, for cross section A and 5 to 8, inclusive, for cross section B. In the case of cross section A, pieces 1 and 2 were from one 46-foot extruded piece, likewise pieces 3 and 4.

The tensile properties of the material were obtained on standard 1/2-inch wide flat tensile specimens and the results of the tests are summarized in table II. The average tensile properties are as follows:

	Cross section A	Cross section B
Tensile strength.....lb. per sq. in..	63,440	62,200
Yield strength, <sup>3</sup> .....lb. per sq. in..	48,200	49,900
Elongation in 2 inches.....percent..	18.4	19.2

These tensile properties compare favorably with typical values for 24S-T extruded shapes. Figures 10 and 11 show typical tensile stress-strain curves. The

<sup>3</sup> Yield strength is the stress that produces a permanent set of 0.2 percent of the initial gage length (Navy Department Specification 46A9a, also American Society for Testing Materials Standard Definitions of terms Relating to Methods of Testing, E6-36).

stress-strain relations were determined with the use of Huggenberger tensometers using a gage length of 0.5 inch. Specimens were taken from both the flange and the web.

The compressive properties of the material were obtained on short lengths of the full cross section ( $l/i=10$ ). The average values of the compressive yield strength of the several pieces of material are given in table II as:

The stress-strain relations shown in figures 12 and 13 were obtained by use of Huggenberger tensometers using a gage length of 1 inch.

Additional compressive tests were made on specimens consisting of a pack of three or five pieces, each five-eighths inch wide, cut from either the web or the flange of the section. Specimens were taken both longitudinally and transversely from both the flange and the web. The jig for holding the pack specimen during testing is shown in figure 14. Typical stress-strain curves determined with the pack specimens are shown in figures 15 and 16. The values of yield strength are summarized in table II.

All these values of mechanical properties indicate that each lot of extruded material was uniform.

### COLUMN SPECIMENS AND METHODS OF TEST

The specimens used in the column tests are described in table III. The specimen number, which is a combination of two numbers, designates the piece of material from which the specimen was cut and the approximate length in inches. The actual average area of each specimen was computed from the length and the



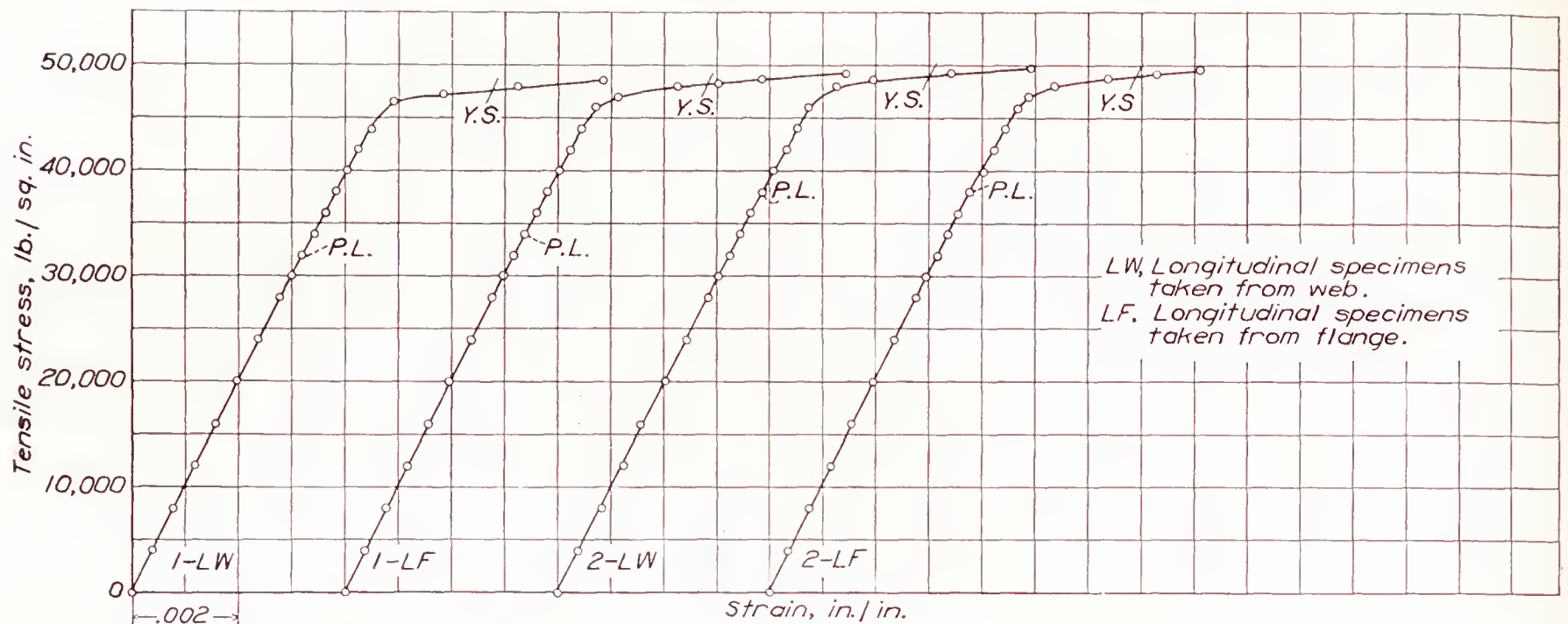


FIGURE 10.—Tensile stress-strain diagrams for 24S-T of cross section A. Strains measured on 0.5-inch gage length with Huggenberger Tensometers.

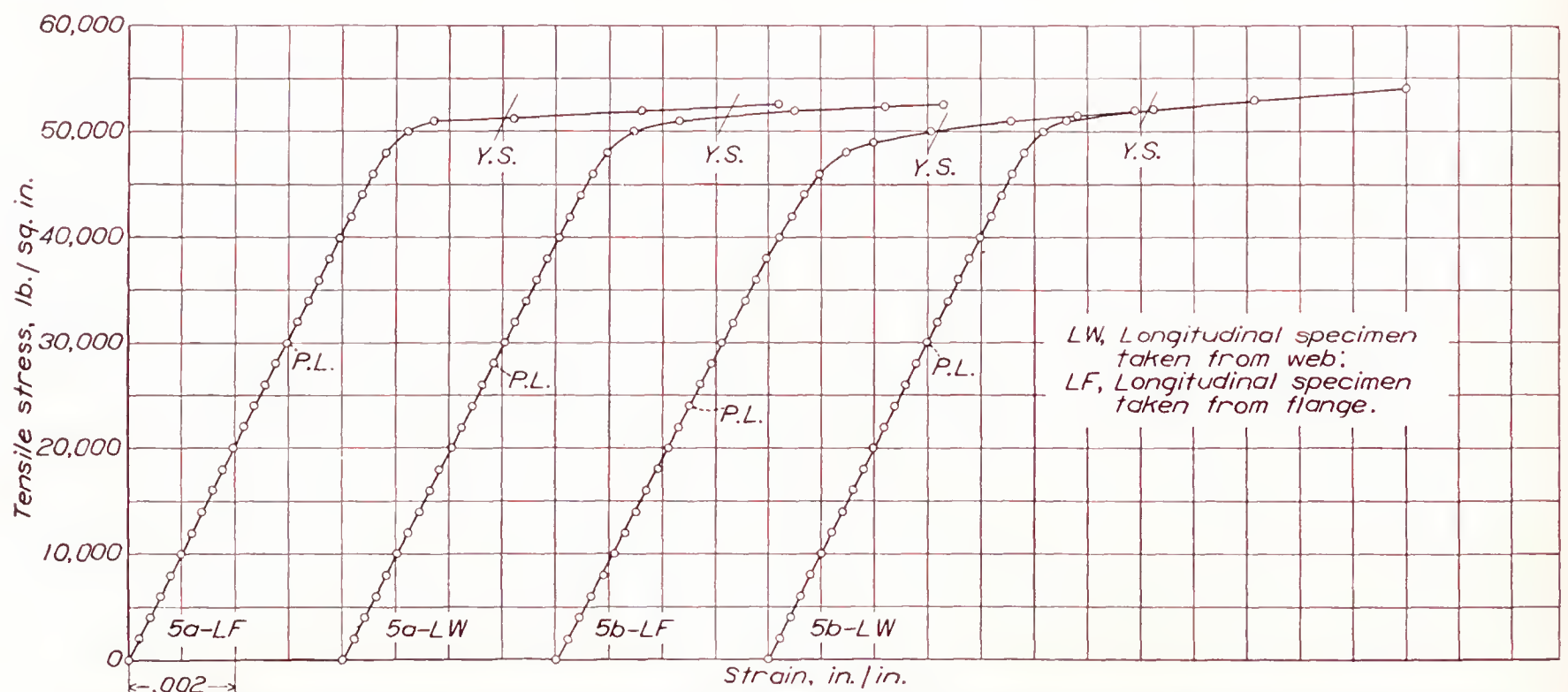


FIGURE 11.—Tensile stress-strain diagrams for 24S-T of cross section B. Strains measured on 0.5-inch gage length with Huggenberger Tensometers.

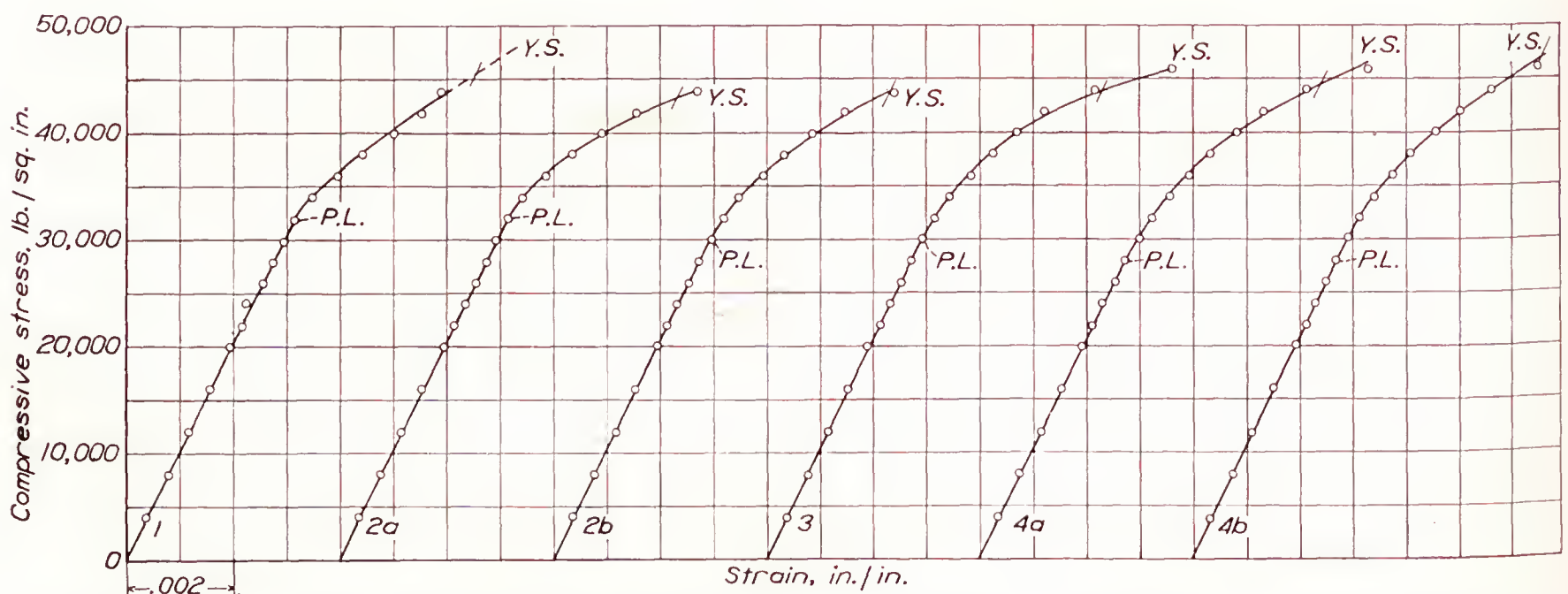


FIGURE 12.—Compressive stress-strain diagrams for 24S-T of cross section A. Strains measured with two Huggenberger Tensometers mounted at the middle of the flanges on 1-inch gage length. Slenderness ratio of specimens, 10; length of specimens, 4.9 inches; ultimate strength, about 50,900 pounds per square inch.



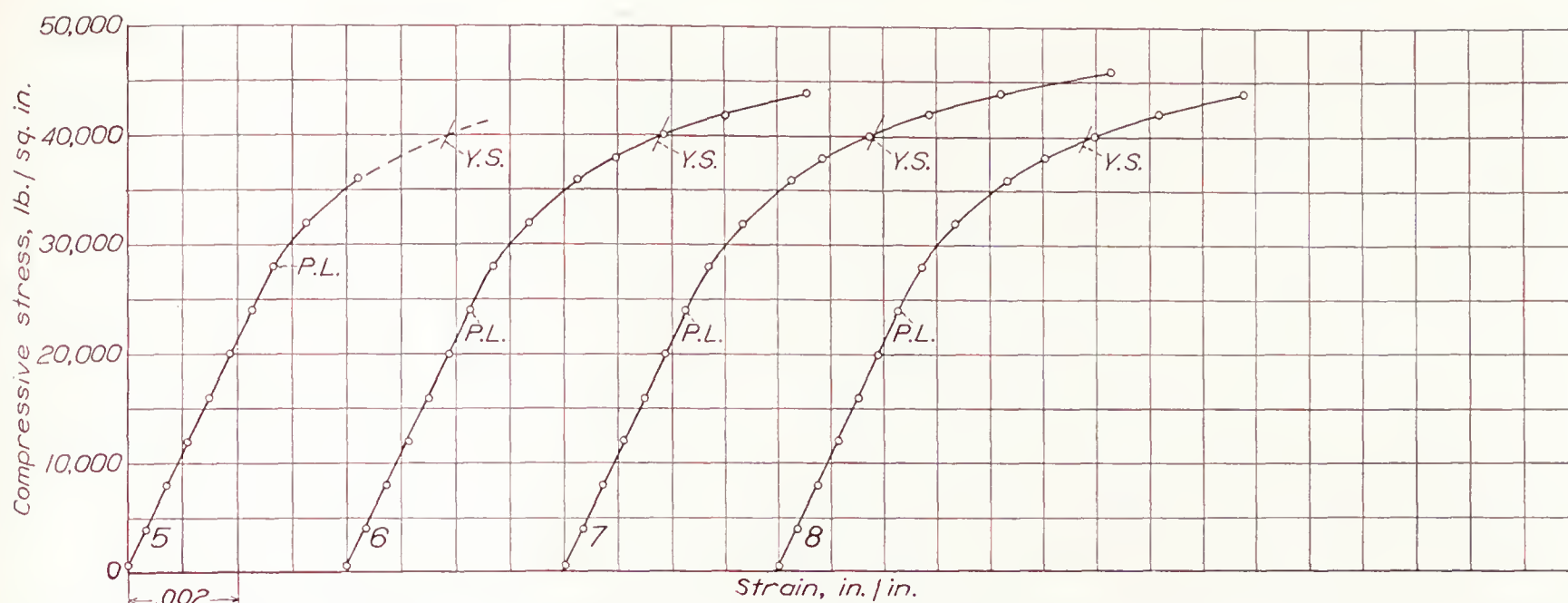


FIGURE 13.—Compressive stress-strain diagrams for 24S-T of cross section B. Strains measured with two Huggenberger Tensometers mounted at the middle of the flanges on 1-inch gage length. Slenderness ratio of specimen, 10; length of specimen, 4.6 inches; ultimate strength, about 50,000 pounds per square inch.

weight of the specimen and the nominal density of the material (0.100 lb. per cu. in.). The crookedness was measured by placing thickness gages between the specimen and a plane surface on which it rested. The maximum crookedness of 1 part in 1,500 was found in specimen 4-19 with a length of 19.44 inches and a measured crookedness of 0.013 inch. The ends of the specimens were carefully finished flat, mutually parallel, and perpendicular to the axis.

Column tests were made using the conditions of flat ends and round ends.

The condition of flat ends was obtained by centering the specimens on the fixed heads of the testing machine as shown in figure 17. The ends of the specimens were restrained to the extent that the bearings did not tip. Under a large sidewise deflection, usually greater than that corresponding to the maximum column load, the ends of the specimen could lift free of the bearing plate on one side.

The condition of round ends was produced by two methods. In the tests of cross section A the bearing plates permitted the specimen to deflect in any direction and twist with practically no restraint. The bearing plates were provided with a spherical seat resting in a nest of 25 hardened-steel balls. The center of rotation of the plates coincided with the ends of the specimen. A specimen was centered on the plates by shifting it on the bearing surfaces until comparable dial readings, representing shortening of the specimen, were obtained at the four corners of the bearing plates for several increments of load. The test set-up is shown in figure 18.

In the tests of cross section B the condition of round ends was obtained by centering the specimens on bearing plates equipped with ball-bearing supports that allow free tipping about only one axis. The specimens were placed on the bearing plates with the axis of least stiffness parallel to the axis of tipping of the plates. The center of rotation of the plates coincided with the end of the specimen. Figure 19 shows a specimen in

the testing machine. Because of the relatively low capacity of these bearings (10,000 pounds) only relatively long specimens ( $l/i > 90$ ) could be tested. In each test the specimen was placed as nearly centrally on the heads as possible and loaded until a maximum load was reached, after which the loading was quickly stopped to prevent permanent set. The specimen was then moved on the bearing plates a very small distance in the direction opposite to that in which the specimen bent in the first loading. The loading was then repeated. This procedure was continued until failure occurred by bending in the direction opposite to the first failure. From the several loads thus obtained the greatest was taken as the column strength of the specimen. It should be recognized that this method of centering could be used only in cases where the failure was entirely elastic, as in these tests.

Both sets of the column tests of cross section A and the flat-end tests of cross section B were made in an Amsler hydraulic testing machine having a maximum capacity of 300,000 pounds. The round-end tests of cross section B were made in a similar machine with a maximum capacity of 40,000 pounds. In all cases, an intermediate load range was used.

#### RESULTS AND DISCUSSION

The results of the column tests are given in table III and are shown with column-strength curves in figures 20 and 21. The results from cross sections A and B are shown in different figures, not because the column action of the two sections is different but because of the difference in the values of compressive yield strength, 44,700 pounds per square inch and 40,000 pounds per square inch. It will be noted that the results from the round-end tests and flat-end tests are both plotted in the same figure, using values of effective slenderness ratio,  $l_0/i$ , for the abscissas in which  $l_0/l = 1.0$  for the round-end tests and 0.5 for the flat-end tests.

This method of plotting is used because it yields a more direct comparison of the two types of test than



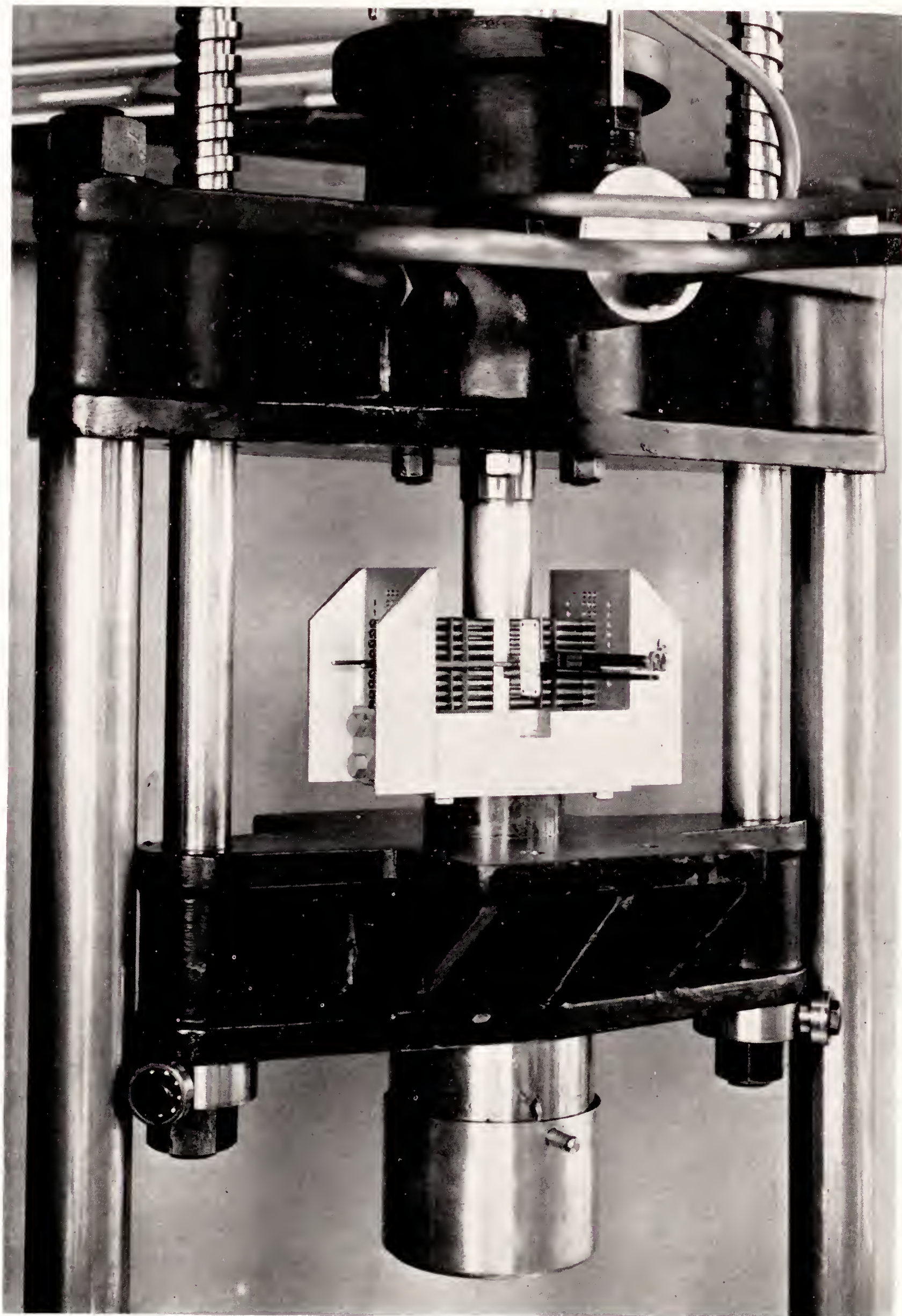


FIGURE 14.—Test of thin sheet-metal specimen in compression.



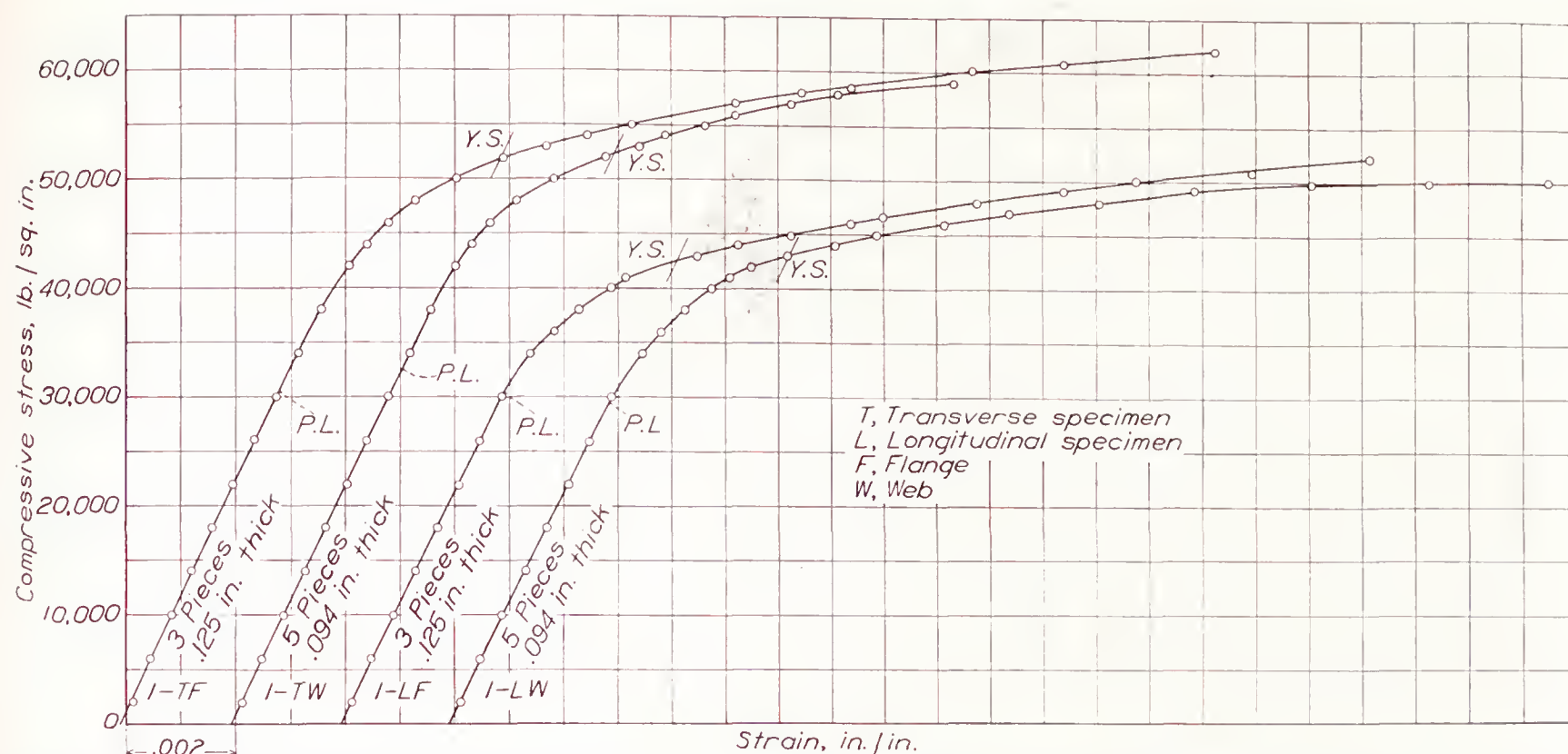


FIGURE 15.—Compressive stress-strain diagrams for 24S-T of cross section A. Strains measured with Huggenberger Tensometers. Pack compression specimen used.

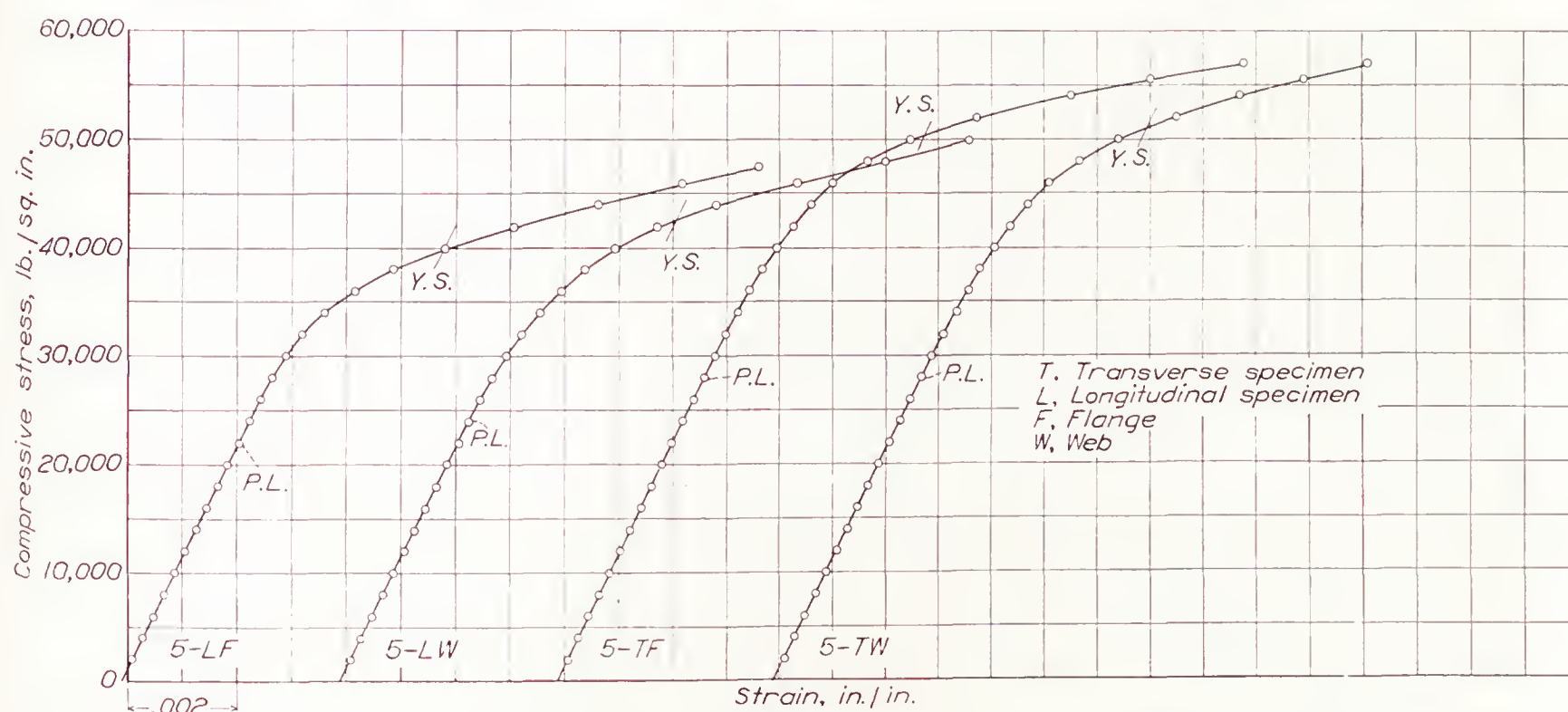


FIGURE 16.—Compressive stress-strain diagrams for 24S-T of cross section B. Strains measured with Huggenberger Tensometers. Pack compression specimen used, three pieces in pack.

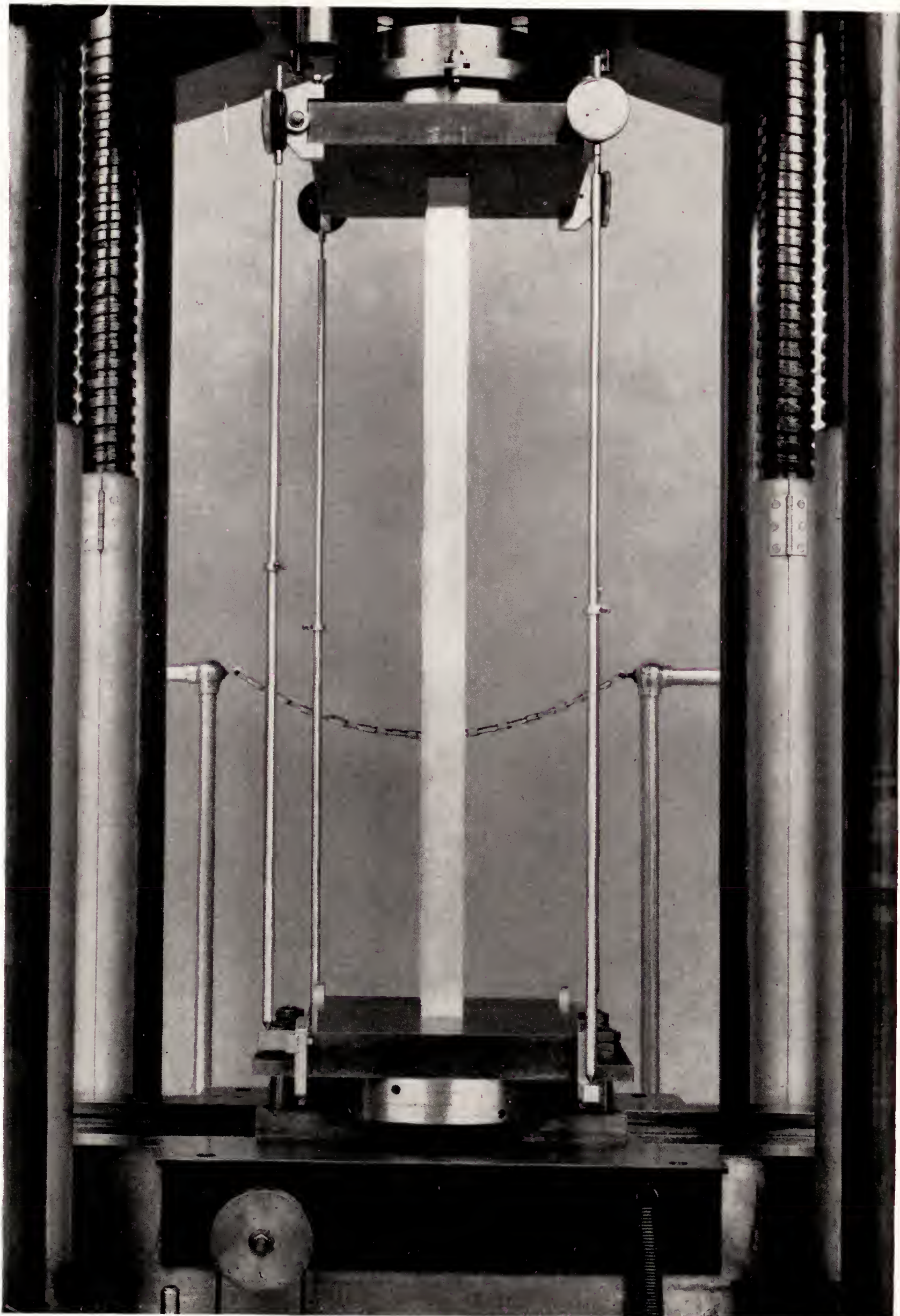
would be possible if the data were plotted separately. The value of 0.5 for  $l_0/l$  in the flat-end tests has been found to be justified by the results of previous investigations, and the good agreement between these results from the two methods of test gives additional evidence that this value of  $l_0/l$  is satisfactory.

In addition to the test results, figures 20 and 21 show four curves of column strength. One of these is the ordinary Euler column curve. The equations of two of the other curves are of the same form as the Euler curve. These two equations take into account the inelastic behavior of the material at stresses greater than the proportional limit by using reduced values of the modulus instead of the initial modulus in the range of plastic action. In one, the initial modulus has been

replaced by the tangent modulus and in the other by the effective modulus based on the double-modulus theory. (See reference 2.) These curves and the Euler curve are exactly the same, of course, for stresses below the proportional limit. In these curves the values of tangent modulus and the values of effective modulus based on the double-modulus theory were obtained from the compressive stress-strain data plotted in figures 12 and 13. The stress-modulus relations are shown in figures 22 and 23.

The fourth curve in figures 20 and 21 is simply a straight line drawn tangent to the Euler curve. The equations of these lines are the ones that would be predicted for this material on a basis of previous investigations of the column strength of various aluminum

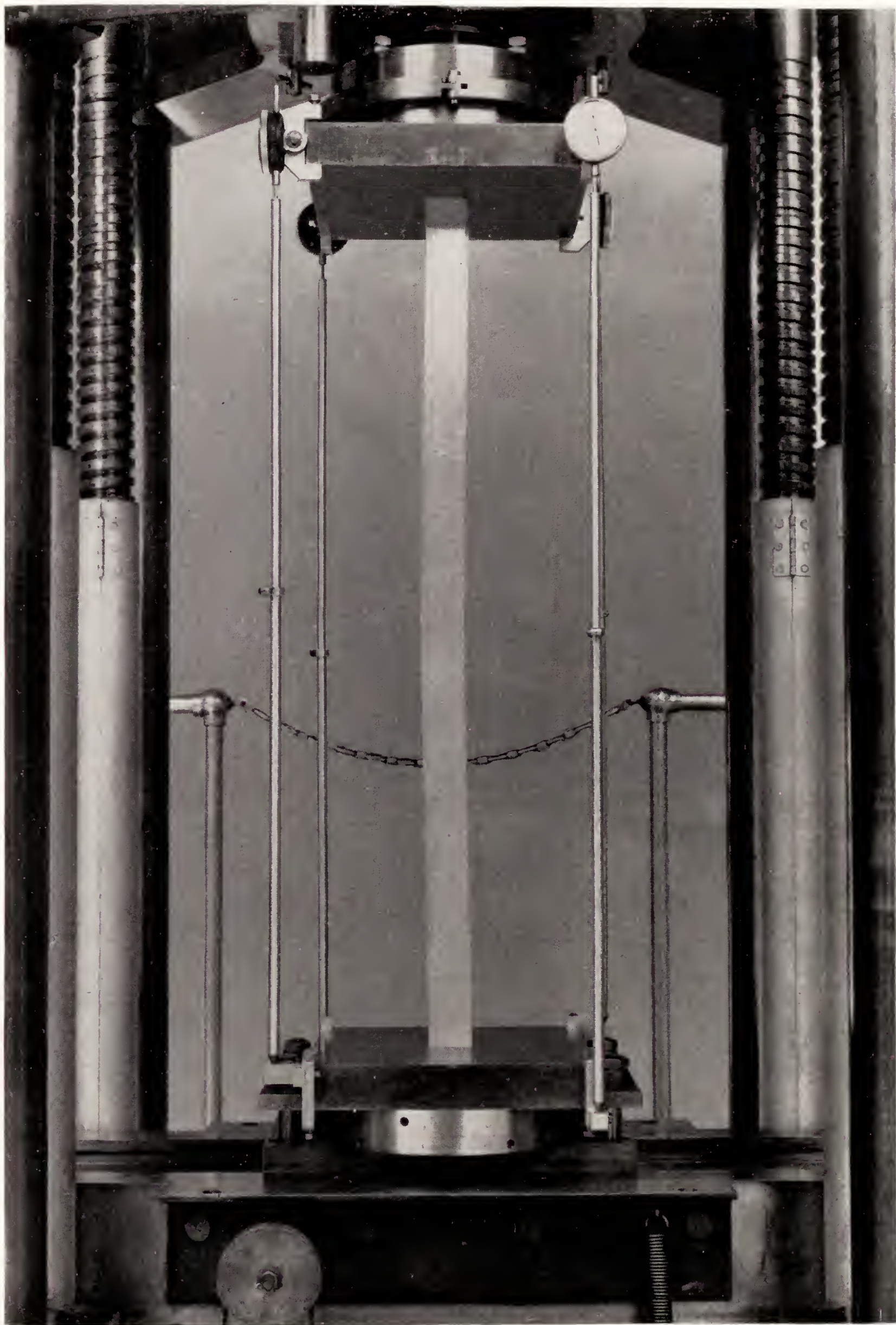




(a) Set-up for test.

FIGURE 17a.—Test of a column with flat ends.





(b) Specimen after failure.

FIGURE 17b.—Test of column with flat ends.

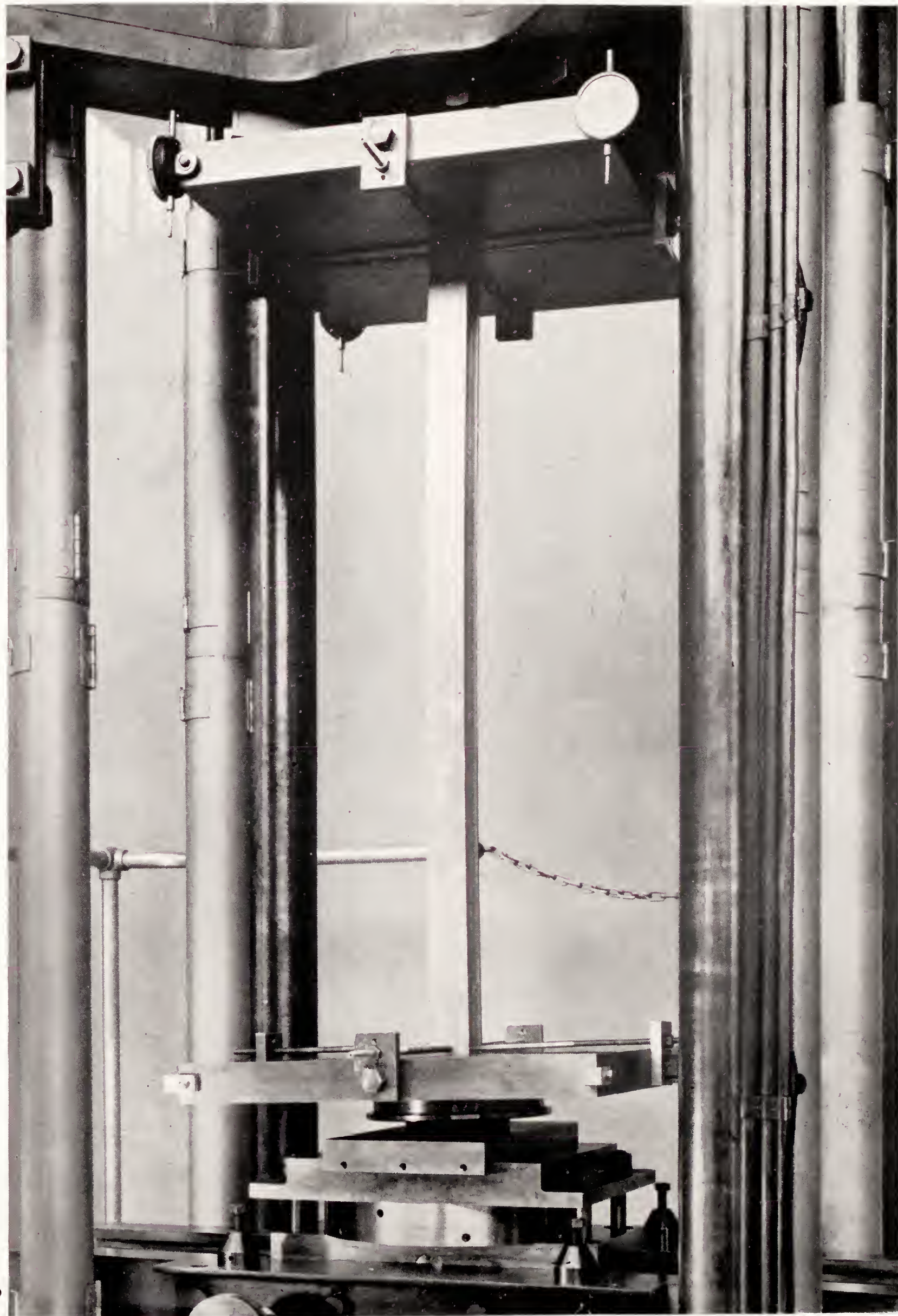




(a) Set-up for test.

FIGURE 18a —Test of a column with round ends. Cross section A.

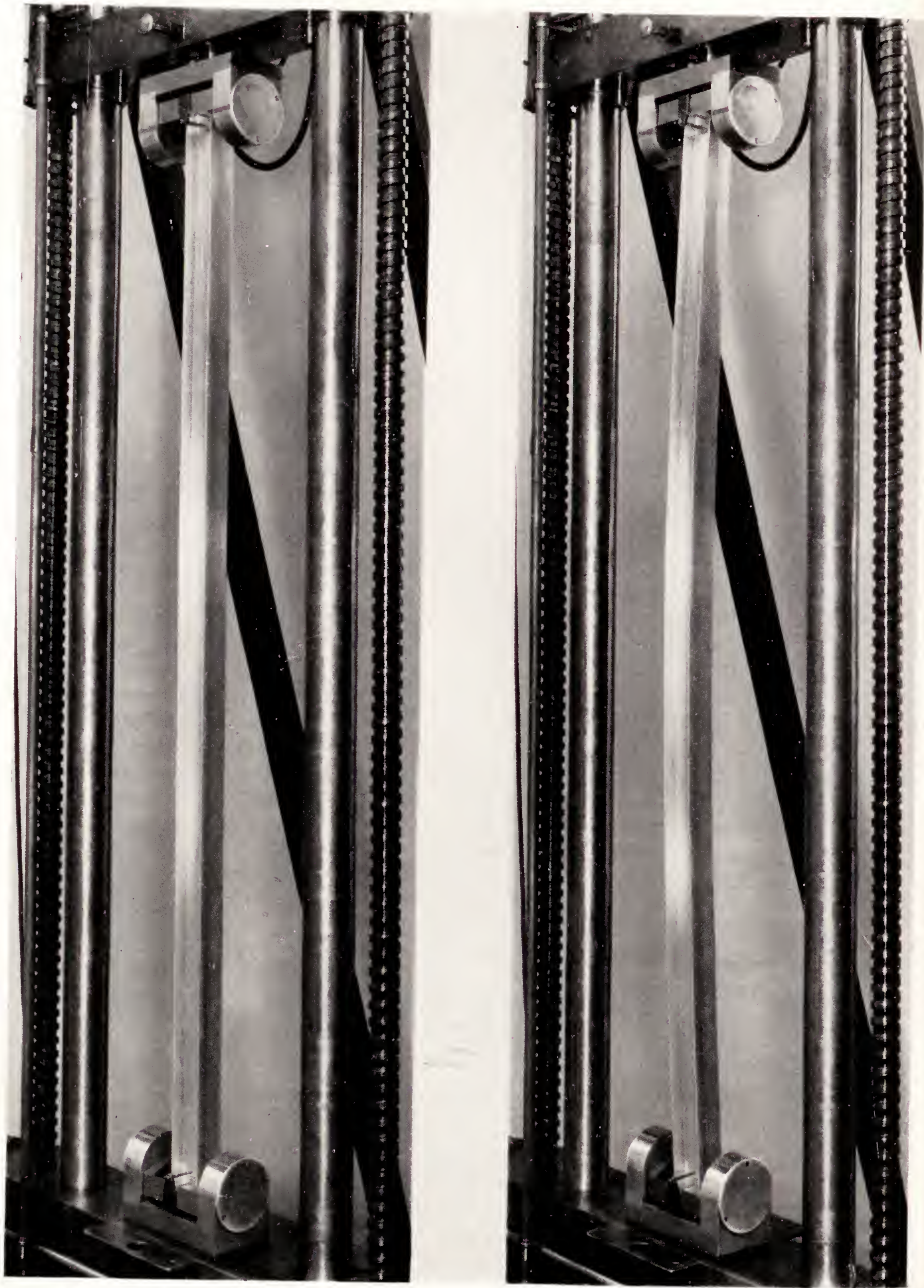




(b) Specimen after failure.

FIGURE 18b.—Test of a column with round ends. Cross section A





(a) Set-up for test.

(b) Specimen after failure.

FIGURE 19.—Test of a column with round ends. Cross section B.



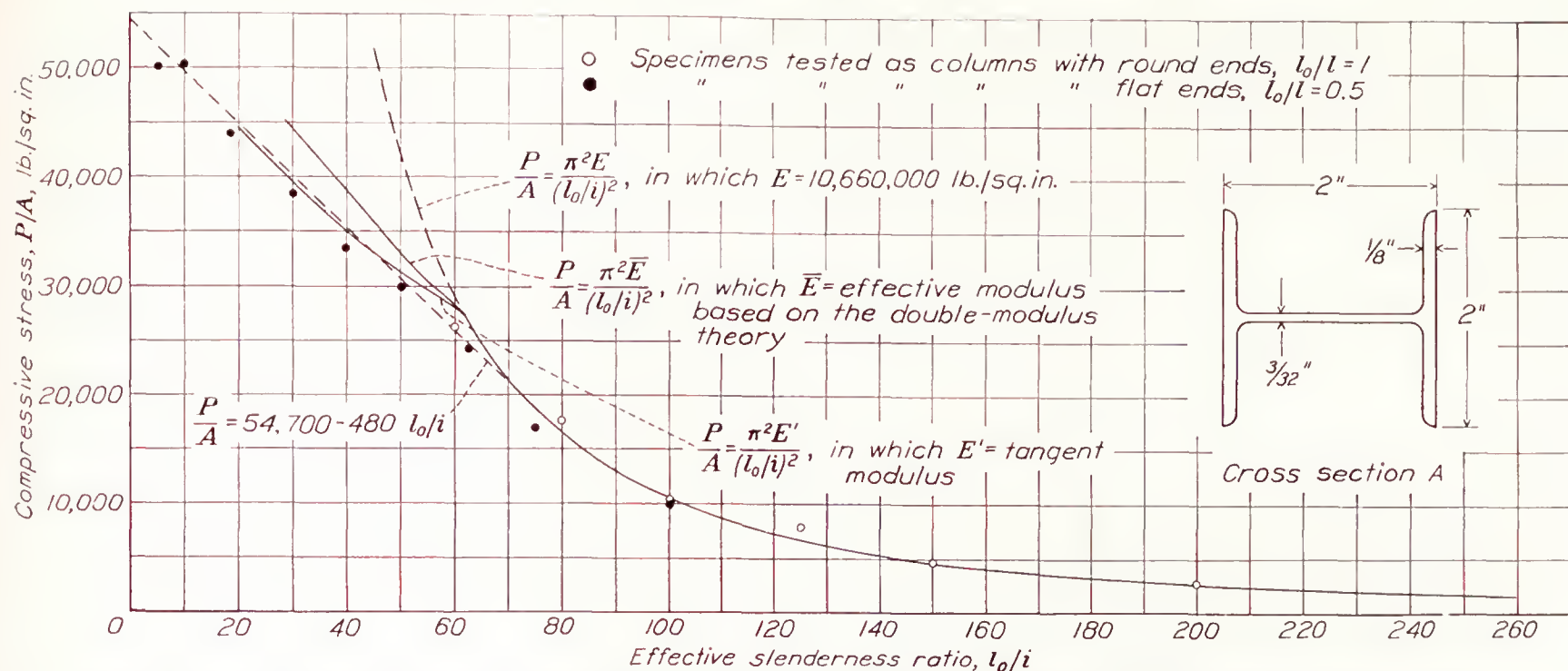


FIGURE 20.—Column strength of 24S-T of cross section A. Average compressive yield strength (offset=0.2 percent), 44,700 pounds per square inch.

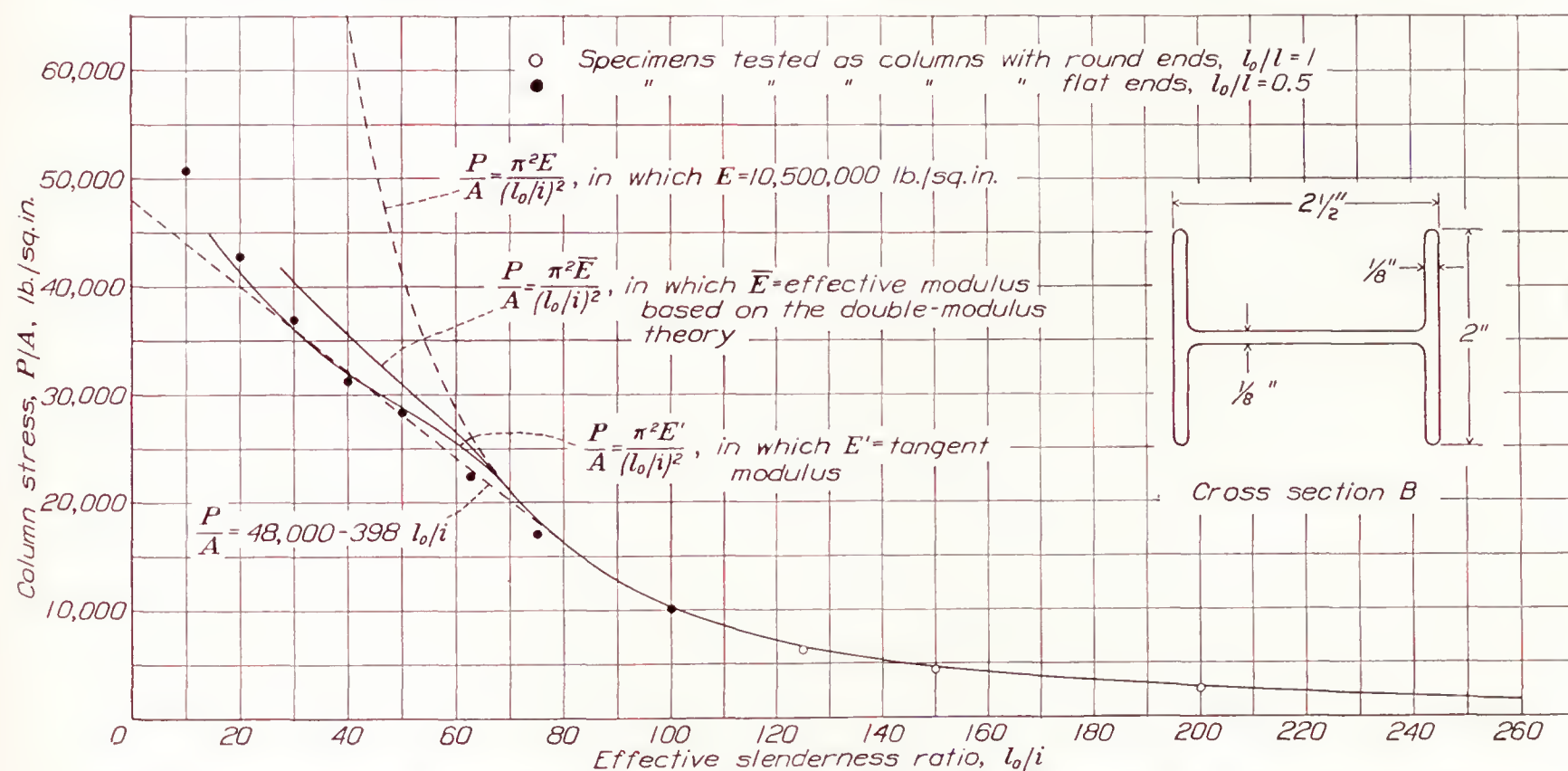


FIGURE 21.—Column strength of 24S-T of cross section B. Average compressive yield strength (offset=0.2 percent), 40,000 pounds per square inch.

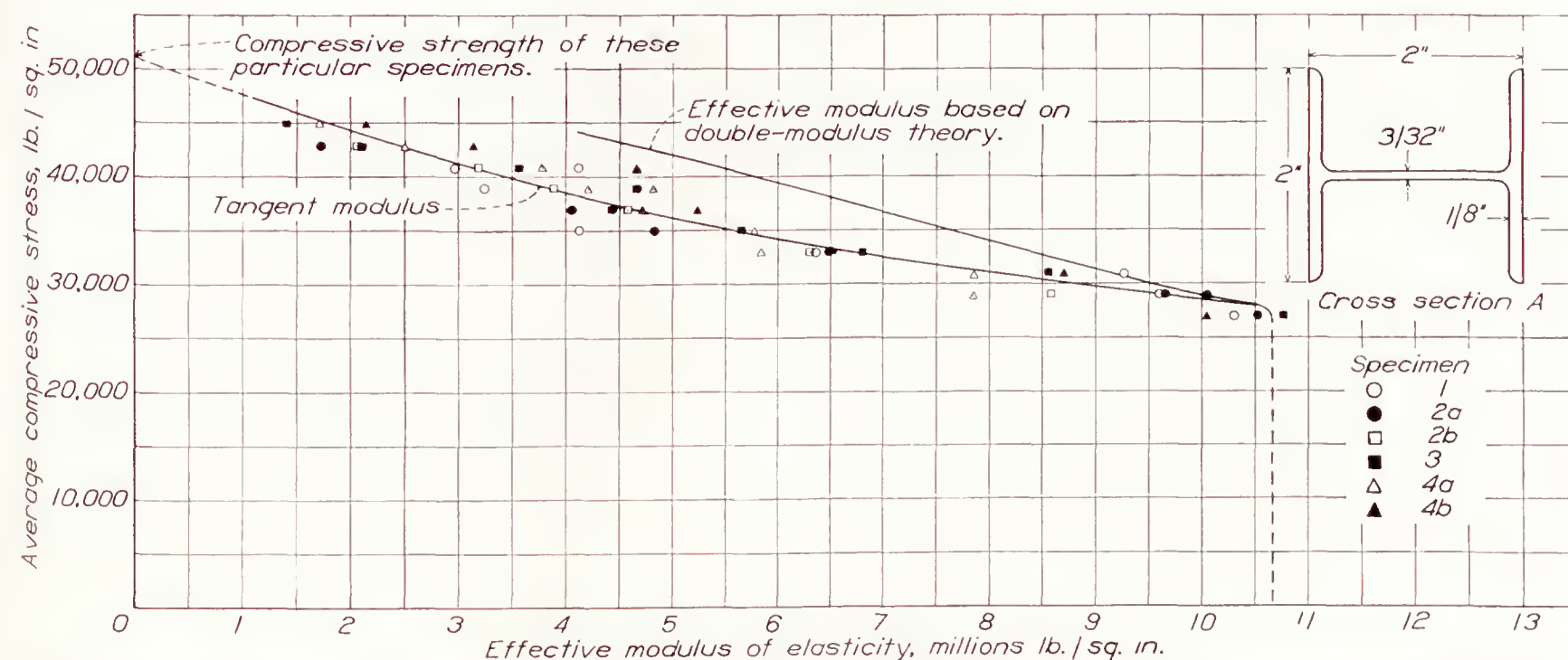


FIGURE 22.—Stress-tangent modulus curve for 24S-T of cross section A. Values of tangent modulus taken from compressive stress-strain relations obtained with Huggenberger Tensometers mounted at the middle of the flanges. Slenderness ratio of specimen, 10.



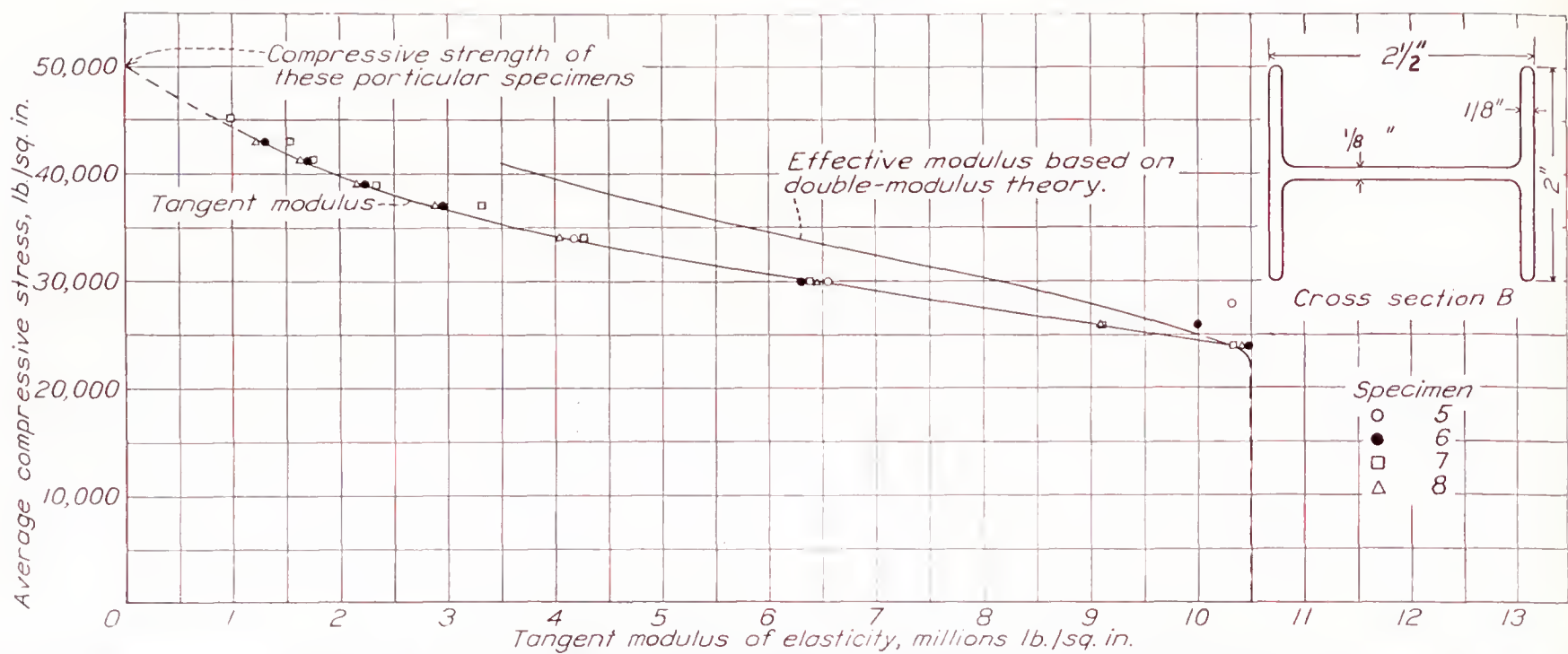


FIGURE 23.—Stress-tangent modulus curve for 24S-T of cross section B. Values of tangent modulus taken from compressive stress-strain relations obtained with Huggenberger Tensometers mounted at the middle of the flanges. Slenderness ratio of specimen, 10

alloys (reference 4). The equation of the straight lines is of the form

$$\frac{P}{A}=B-D\left(\frac{l_0}{i}\right)$$

in which

- $P$  is the ultimate column load, pound.
- $A$ , cross-sectional area of member, square inch.
- $\frac{l_0}{i}$ , effective slenderness ratio.
- $B$ , constant depending on the compressive yield strength of the material.
- $D$ , constant depending on the compressive yield strength and on the modulus of elasticity of the material.

The intercept on the axis of zero slenderness,  $B$ , is arrived at by the following simple calculation involving the compressive yield strength of the material:

$$\text{Intercept } B=\text{yield strength}\left(1+\frac{\text{yield strength}}{200,000}\right).$$

None of the curves shown agree with the data exactly but both the straight line and the curve based on the tangent modulus of elasticity show good agreement with the data. The curve based on the double-modulus theory lies somewhat above the test results in the region of plastic action of the material.

The specimens after failure are shown in figures 24 and 25. Although the shorter specimens show considerable local distortion, it should be pointed out that this action was not apparent until the average stress

exceeded the yield strength or until the maximum column strength had been attained.

III. CORRELATION OF TEST RESULTS

The average mechanical properties of the material of cross section A may be summarized as follows:

Tensile yield strength (offset=0.2 percent):	<i>Lb. per sq. in.</i>
National Bureau of Standards.....	49, 800
Aluminum Research Laboratories.....	48, 200
Compressive yield strength:	
National Bureau of Standards (2/3 E method)....	42, 050
National Bureau of Standards (offset=0.2 percent) _	42, 200
Aluminum Research Laboratories (offset=0.2 per-	
cent).....	44, 700

The difference in the values of the tensile yield strength is 1,600 pounds per square inch or about 3 percent, and the difference in the values of the compressive yield strength is 2,500 pounds per square inch or about 6 percent. The National Bureau of Standards tests indicate the higher tensile yield strength and the lower compressive yield strength. The ratios of the average compressive yield strength to the average tensile yield strength are:

National Bureau of Standards,

$$\frac{\text{compressive yield strength}}{\text{tensile yield strength}}=0.85$$

Aluminum Research Laboratories,

$$\frac{\text{compressive yield strength}}{\text{tensile yield strength}}=0.93$$

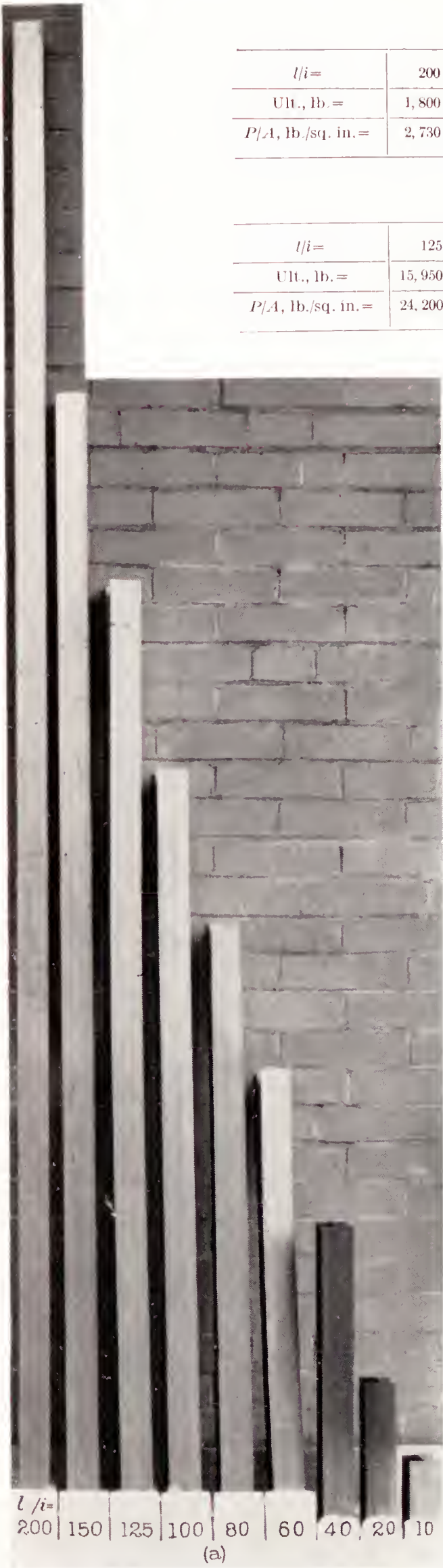


Table for (a)

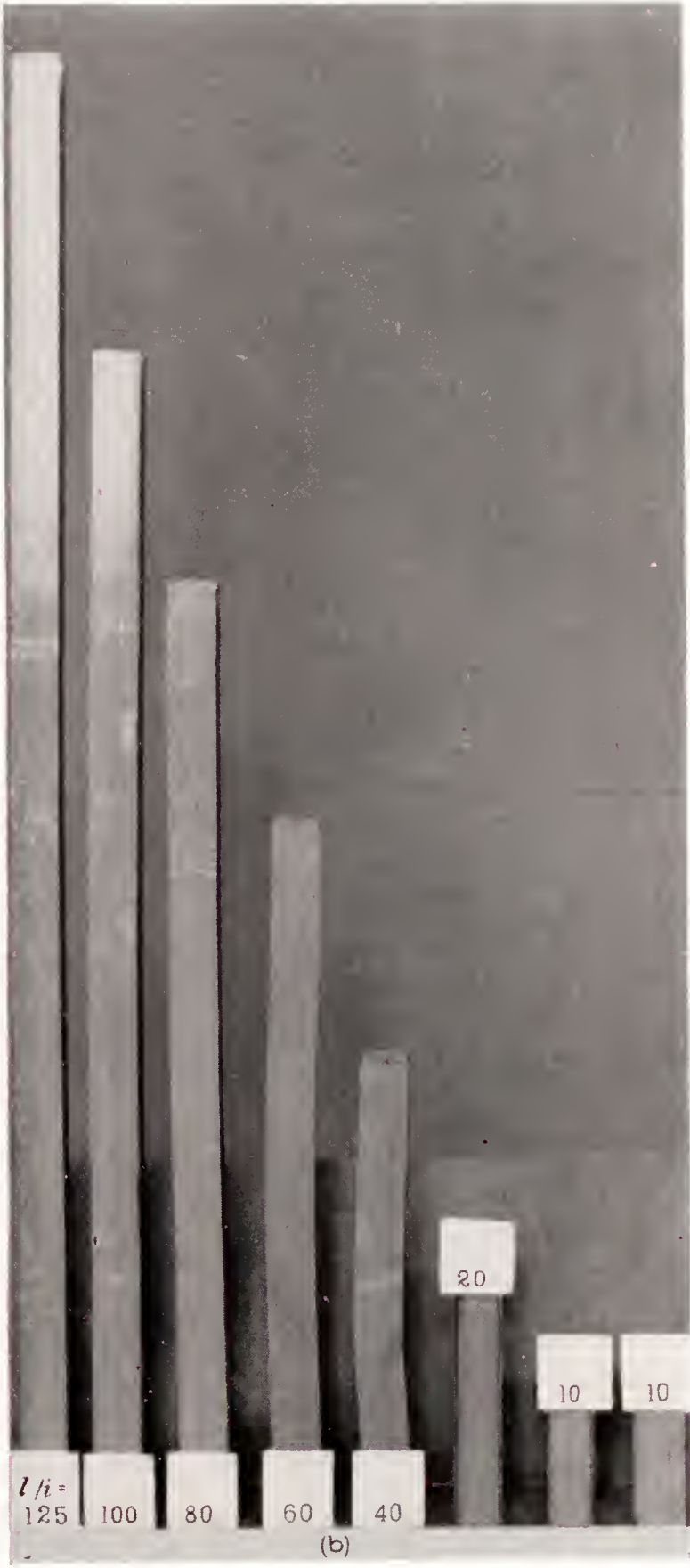
$l/i=$	200	150	125	100	80	60	40	20	10
Ult., lb. =	1,800	3,050	5,200	6,850	11,600	17,330	-----	-----	-----
$P/A$ , lb./sq. in. =	2,730	4,640	7,840	10,420	17,550	26,300	-----	-----	-----

Table for (b)

$l/i=$	125	100	80	60	37	20	10	10	-----
Ult., lb. =	15,950	19,600	22,030	25,600	29,300	33,180	32,200	31,440	-----
$P/A$ , lb./sq. in. =	24,200	29,790	33,450	38,440	43,990	50,425	49,850	48,700	-----



(a) Tested with round ends.



(b) Tested with flat ends.

FIGURE 24.—Specimens of 24S-T of cross section A after testing.



Table for (a)

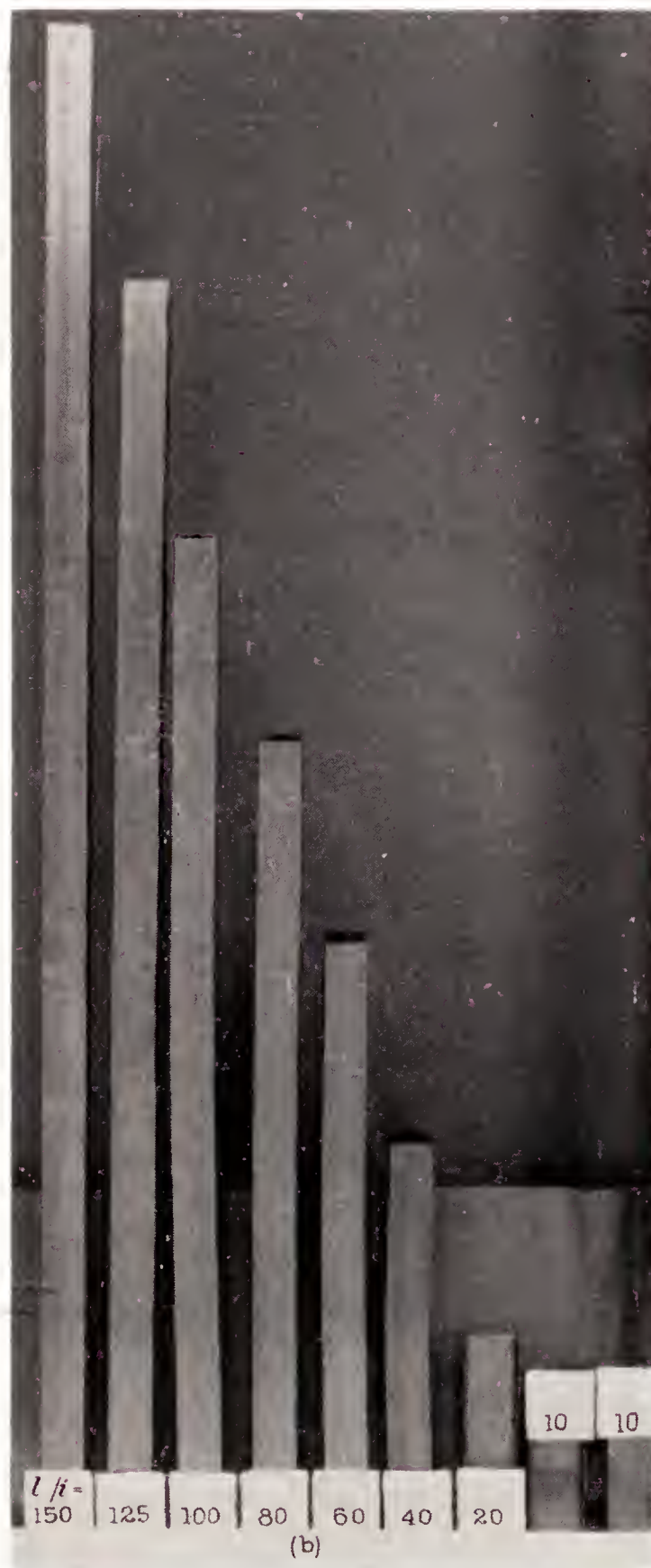
$l/i =$	200	150	125	100	-----	-----	-----	-----	-----
Ult., lb. =	1,995	3,510	5,000	8,000	-----	-----	-----	-----	-----
$P/A$ , lb./sq. in. =	2,550	4,480	6,390	10,190	-----	-----	-----	-----	-----

Table for (b)

$l/i =$	150	125	100	80	60	40	20	10	10
Ult., lb. =	13,375	17,600	22,260	24,500	28,930	33,700	39,900	39,100	38,500
$P/A$ , lb./sq. in. =	17,038	22,478	28,357	31,370	36,995	42,875	50,763	49,810	49,110



(a) Tested with round ends.



(b) Tested with flat ends.

FIGURE 25.—Specimens of 24S-T of cross section B after testing.



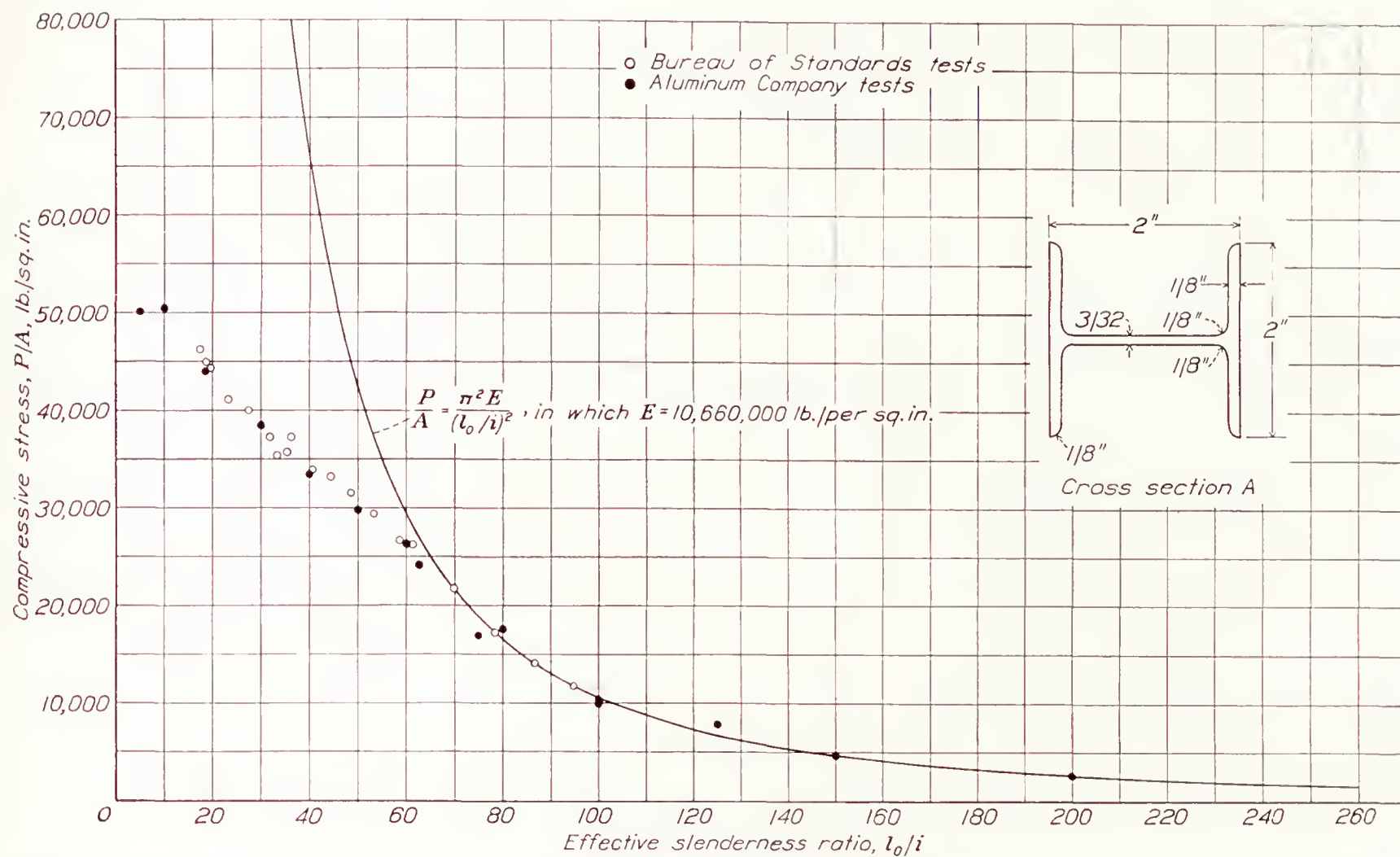
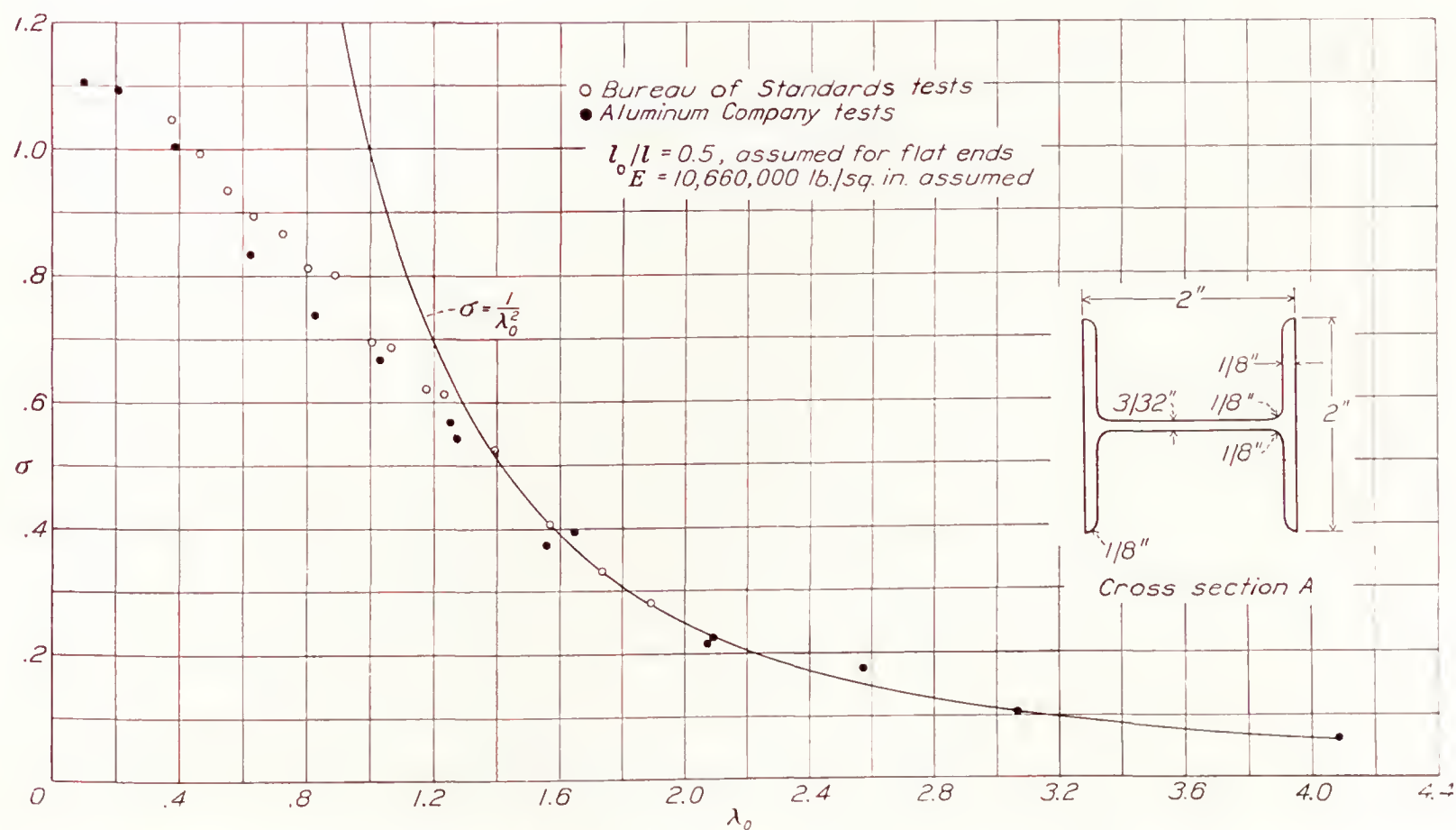

 FIGURE 26.—Comparison of results from National Bureau of Standards and Aluminum Company tests for 24S-T of cross section A.  $l_0/l = 0.5$ , assumed for flat ends.

 FIGURE 27.—Comparison of results from National Bureau of Standards and Aluminum Company tests for 24S-T of cross section A. The nondimensional method of part I in which  $\sigma$  is plotted against  $\lambda_0$ .



Figure 26 shows the column test results of cross section A and the Euler column curve, plotted as  $P/A$  against  $l_0/i$  ( $l_0/l=0.5$ , assumed for flat-end specimens, and  $E=10,660,000$  pounds per square inch assumed for Euler curve).

Figure 27 shows the column test results of cross section A and the nondimensional Euler column curve,

plotted as  $\sigma=P/(AS)$  against  $\lambda_0=\frac{1}{\pi} \frac{l_0}{i} \sqrt{\frac{S}{E}}$  (the free length

of the Aluminum Company's flat-end specimens has been assumed one-half of the length of the specimen,

and the modulus of elasticity for their specimens has been assumed as 10,660,000 pounds per square inch).

NATIONAL BUREAU OF STANDARDS,

WASHINGTON, D. C.,

and

ALUMINUM RESEARCH LABORATORIES,

ALUMINUM COMPANY OF AMERICA,

NEW KENSINGTON, PA.,

*September 30, 1938.*



## APPENDIX

### CENTERING LOADS

When centering is done under load in the plastic range, it is necessary to limit the maximum deflections to values which insure that the maximum stress at no point of the middle cross section exceeds the expected maximum average column stress. An estimate of the maximum allowable deflection may be obtained by considering that the center line of the specimen goes into a sine curve. Then for the middle cross section

$$\frac{\epsilon}{c} = \frac{1}{\rho} = \delta_0 \frac{\pi^2}{l_0^2}$$

where  $\epsilon$  is the bending strain at the extreme fiber distance  $c$ ,  $\rho$  is the radius of curvature,  $\delta_0$  is the maximum deflection, and  $l_0$  is the free length of the specimen. Solved for  $\epsilon$ , this equation gives

$$\epsilon = \frac{\pi^2 c \delta_0}{l_0^2}$$

In the present investigation, corresponding to a maximum value of  $\delta_0 = 0.0005$  inch,

$$\epsilon = \frac{0.005}{l_0^2}$$

when  $l_0$  is measured in inches. If  $l_0 = 10$  inches, a low value,  $\epsilon = 0.00005$ ; and if  $l_0 = 25$  inches, a medium value,  $\epsilon = 0.000008$ .

The column stresses corresponding to these values of  $l_0$  ( $\frac{l_0}{i} = 21$  and 52, respectively) may be obtained roughly from figure 7 as 42,000 and 30,000 pounds per square inch. The stress-strain diagrams (fig. 3) show that at a stress of 42,000 pounds per square inch an increase of strain of 0.00005 results in an increase of stress of only about 100 pounds per square inch, or 0.24 percent; and at 30,000 pounds per square inch an increase of strain of 0.000008 results in an increase of stress of about 80 pounds per square inch, or 0.27 percent. These small increases of stress due to a deflection of 0.0005 inch at the maximum column load indicate that the final centering load may be close to the column load without danger of overstressing any part of the cross section.

### REFERENCES

1. Lundquist, Eugene E., and Fligg, Claude M.: A Theory for Primary Failure of Straight Centrally Loaded Columns. T. R. No. 582, N. A. C. A., 1937.
2. Osgood, William R.: The Double-Modulus Theory of Column Action. Civil Engineering, vol. 5, no. 3, March 1935, pp. 173-175.
3. Osgood, William R.: Column Strength of Tubes Elastically Restrained against Rotation at the Ends. T. R. No. 615, N. A. C. A., 1938.
4. Templin, R. L., Sturm, R. G., Hartmann, E. C., and Holt, M.: Column Strength of Various Aluminum Alloys. Tech. Paper No. 1, Aluminum Res. Lab., Aluminum Co. of America, 1938.

TABLE I.—RESULTS OF COLUMN TESTS AND COMPRESSIVE TESTS MADE AT THE NATIONAL BUREAU OF STANDARDS ON 24S-T EXTRUDED H-BEAM SPECIMENS OF CROSS SECTION A

Specimen	Slenderness ratio $l_0/i$	Average stress $P/A$ (lb./sq. in.)	$\lambda_0 = \frac{1}{\pi} \frac{l_0}{i} \sqrt{\frac{S}{E}}$	$\sigma = \frac{P}{AS}$	Specimen	Slenderness ratio $l_0/i$	Average stress $P/A$ (lb./sq. in.)	$\lambda_0 = \frac{1}{\pi} \frac{l_0}{i} \sqrt{\frac{S}{E}}$	$\sigma = \frac{P}{AS}$
Freely supported ends, $m=0$									
5C-5.....	18.82	44,820	0.378	1.047	5C-3.....	53.01	29,400	1.064	0.687
1B-5c.....	23.24	41,140	.464	.991	5D-1.....	58.62	26,520	1.177	.620
5C-4.....	27.62	39,990	.554	.934	5C-7.....	61.40	26,140	1.233	.611
1B-5b.....	31.92	37,130	.637	.895	1B-4.....	69.81	21,750	1.392	.524
5C-6.....	36.12	37,160	.725	.868	5C-2.....	78.08	17,410	1.567	.407
1B-5a.....	40.42	33,650	.806	.811	5C-8.....	86.44	14,170	1.735	.331
1B-3.....	44.60	33,180	.890	.800	1B-5.....	94.79	11,680	1.891	.281
5D-2.....	50.17	29,720	1.007	.694					
Elastically restrained ends, $m=192,000$ lb.-in. per radian									
5C-9.....	17.79	46,110	0.357	1.077	1A-2.....	48.87	31,460	0.975	0.758
1A-4.....	33.22	35,310	.663	.851					
Elastically restrained ends, $m=385,000$ lb.-in. per radian									
5C-1.....	19.32	44,180	0.388	1.032	1A-1.....	50.34	29,610	1.004	0.713
1A-3.....	35.28	35,670	.704	.860					
Flat ends (compressive specimens)									
1B-1.....	-----	48,390	-----	1.166	5C-C.....	-----	48,850	-----	1.141



TABLE II.—SUMMARY OF MECHANICAL PROPERTIES OF MATERIAL

[24S-T Extruded H-Beam

	Specimen	Cross section A			Cross section B		
		Mini- mum	Maxi- mum	Average	Mini- mum	Maxi- mum	Average
Tensile strength.....lb. per sq. in.	Web.....	62,770	62,960	62,890	60,450	63,670	62,070
	Flange.....	62,930	64,980	63,990	60,560	64,150	62,370
Tensile yield strength (offset=0.2 percent) lb. per sq. in.	Web.....	47,700	49,100	48,470	48,100	51,900	50,075
	Flange.....	48,100	49,000	47,940	49,000	51,300	49,750
Elongation in 2 in.....percent	Web.....	16.5	18.5	17.3	16.5	22.5	18.8
	Flange.....	17.0	21.5	19.5	15.0	22.0	19.6
	Full section.....	43,400	46,700	44,700	39,700	40,300	40,000
Compressive yield strength (offset=0.2 percent).....lb. per sq. in.	Longitudinal pack, web.....	42,600	43,800	43,100	39,600	43,000	41,925
	Longitudinal pack, flange.....	42,600	43,800	43,000	38,400	40,000	39,150
	Transverse pack, web.....	52,200	52,600	52,400	47,600	54,700	51,725
	Transverse pack, flange.....	51,800	53,400	52,800	48,000	51,200	49,975

TABLE III.—DESCRIPTION OF SPECIMENS AND RESULTS OF COLUMN TESTS MADE AT ALUMINUM RESEARCH LABORATORIES

24S-T Extruded H-Beam

Specimen	Length (in.)	Weight (lb.)	Slender- ness ratio	Measured crooked- ness <sup>1</sup> (in.)	Actual average area <sup>2</sup> (sq. in.)	Maxi- mum column load (lb.)	Column strength (lb./sq. in.)
Cross section A, specimens tested as columns with flat ends							
1-96.....	96.46	6.357	200	0.025	0.659	6,530	9,910
1-72.....	72.42	4.765	150	.013	.658	11,150	16,950
3-60a.....	60.31	3.976	125	.030	.659	15,950	24,200
3-48.....	48.27	3.176	100	.006	.658	19,600	29,790
1-39.....	38.96	2.564	80	-----	.658	22,030	33,480
4-29a.....	28.96	1.929	60	.011	.666	25,600	38,440
2-19.....	18.04	1.201	37	-----	.666	29,300	43,990
4-10.....	9.73	.640	20	-----	.658	33,180	50,430
1-5.....	4.94	.319	10	-----	.646	32,330	50,050
Cross section A, specimens tested as columns with round ends. <sup>3</sup>							
2-96.....	96.48	6.358	200	0.040	0.659	1,800	2,730
2-72.....	72.44	4.770	150	.014	.658	3,050	4,640
3-60b.....	60.35	4.000	125	.024	.663	5,200	7,840
4-48.....	48.30	3.173	100	.021	.657	6,850	10,420
3-39.....	38.68	2.557	80	.014	.661	11,600	17,550
4-29b.....	29.01	1.909	60	.015	.658	17,330	26,300
4-19.....	19.44	1.276	40	.013	.656	( <sup>4</sup> )	( <sup>4</sup> )

<sup>1</sup> Crookedness measured by placing thickness gages between the specimen and a plane surface on which it rested.

TABLE III.—DESCRIPTION OF SPECIMENS AND RESULTS OF COLUMN TESTS MADE AT ALUMINUM RESEARCH LABORATORIES—Continued

24S-T Extruded H-Beam

Specimen	Length (in.)	Weight (lb.)	Slender- ness ratio	Measured crooked- ness (in.)	Actual average area (sq. in.)	Maxi- mum column load (lb.)	Column strength (lb./sq. in.)
Cross section B, specimens tested as columns with flat ends							
5-90a.....	90.28	7.096	200	0.008	0.786	8,000	10,180
6-68a.....	67.80	5.320	150	.011	.785	13,375	17,040
7-56a.....	56.60	4.430	125	.008	.783	17,600	22,480
8-45a.....	45.25	3.550	100	.006	.785	22,260	28,360
7-36.....	36.10	2.820	80	.005	.781	24,500	31,370
7-27.....	27.15	2.122	60	-----	.782	28,930	37,000
8-18.....	18.10	1.422	40	-----	.786	33,700	42,880
5-9.....	8.97	.705	20	-----	.786	39,900	50,760
Cross section B, specimens tested as columns with round ends <sup>5</sup>							
5-90b.....	90.15	7.053	200	0.014	0.782	1,995	2,550
6-68b.....	67.81	5.310	150	.010	.783	3,510	4,480
7-56b.....	56.60	4.429	125	.011	.783	5,000	6,390
4-45b.....	45.25	3.551	100	.007	.785	8,000	10,190

<sup>2</sup> Area computed from the weight and length of the specimen and the nominal specific gravity of the material.

<sup>3</sup> Ball-bearing spherical heads used, specimen free to deflect in any direction and twist.

<sup>4</sup> Strength greater than the capacity of the ball-bearing spherical seats.

<sup>5</sup> Roller-bearing heads used, specimen free to deflect in only one direction.



## REPORT No. 657

# THE INFLUENCE OF DIRECTED AIR FLOW ON COMBUSTION IN A SPARK-IGNITION ENGINE

By A. M. ROTHROCK and R. C. SPENCER

### SUMMARY

*The air movement within the cylinder of the N. A. C. A. combustion apparatus was regulated by using shrouded inlet valves and by fairing the inlet passage. Rates of combustion were determined at different inlet-air velocities with the engine speed maintained constant and at different engine speeds with the inlet-air velocity maintained approximately constant.*

*The rate of combustion increased when the engine speed was doubled without changing the inlet-air velocity; the observed increase was about the same as the increase in the rate of combustion obtained by doubling the inlet-air velocity without changing the engine speed.*

*Certain types of directed air movement gave great improvement in the reproducibility of the explosions from cycle to cycle, provided that other variables were controlled.*

*Directing the inlet air past the injection valve during injection increased the rate of burning.*

### INTRODUCTION

The efficient utilization of fuel in an internal-combustion engine embodies two main operations: The introduction and the mixing of the fuel with the air charge, and the combustion of the charge after it is mixed. During the course of the general program of research on combustion at the laboratories of the N. A. C. A., detailed investigations have been carried out and a large amount of fundamental information has been obtained concerning mixture formation, distribution, and the combustion in the engine. It has long been recognized that air movement is of value in attaining higher engine efficiencies, and the program of research has included investigations of the effects of air flow on the fuel spray and on the combustion in a compression-ignition engine (references 1, 2, and 3).

Interest in the use of air flow in spark-ignition engines has greatly increased in recent years and, in recognition of the need for additional information concerning air flow and its effects on combustion, this program of research has been extended. Various types of air

movement (without combustion) have been investigated in detail using the N. A. C. A. glass-cylinder engine (reference 4). Concurrently the investigation reported herein was conducted during the summer of 1937 to determine the effects of directed air flow on combustion; the N. A. C. A. combustion apparatus was used.

### APPARATUS AND METHOD

The N. A. C. A. combustion apparatus has been described in references 5 and 6. Briefly, it is a 5- by 7-inch single-cylinder test engine with a large glass window in the cylinder head to permit the combustion to be studied photographically. The engine is driven at the test speed by an electric motor and is then fired once by injecting and igniting a single charge of fuel. The cylinder-wall temperature is maintained by circulating heated glycerin through the jacket. A diagrammatic sketch of the apparatus is shown in figure 1. The cylinder head is of the pent-roof type normally having two exhaust and two inlet valves. In the present design, the space occupied by the two exhaust valves is used for the glass window. As the engine fires only once, the two inlet valves operate simultaneously and serve both for inlet and exhaust.

The directed air movement was obtained by shrouding the valves as shown in figure 2. The valve arrangements are shown in figure 3 and are designated by the letters used by Lee in reference 4. Conditions B and C (intermediate between A and D, in the setting of the rear valve) were omitted in the combustion tests. In one set of experiments, only one valve was used and the inlet passage was faired so as to direct the incoming air tangentially.

The ignition system has been described in reference 5. It is especially designed to provide accurate spark timing, and the maximum variation in timing is not greater than  $\pm 1$  crankshaft degree.

The N. A. C. A. spark-photography apparatus (reference 7) and the N. A. C. A. optical-type pressure indicator (reference 8) were used in conjunction with the combustion apparatus in this study



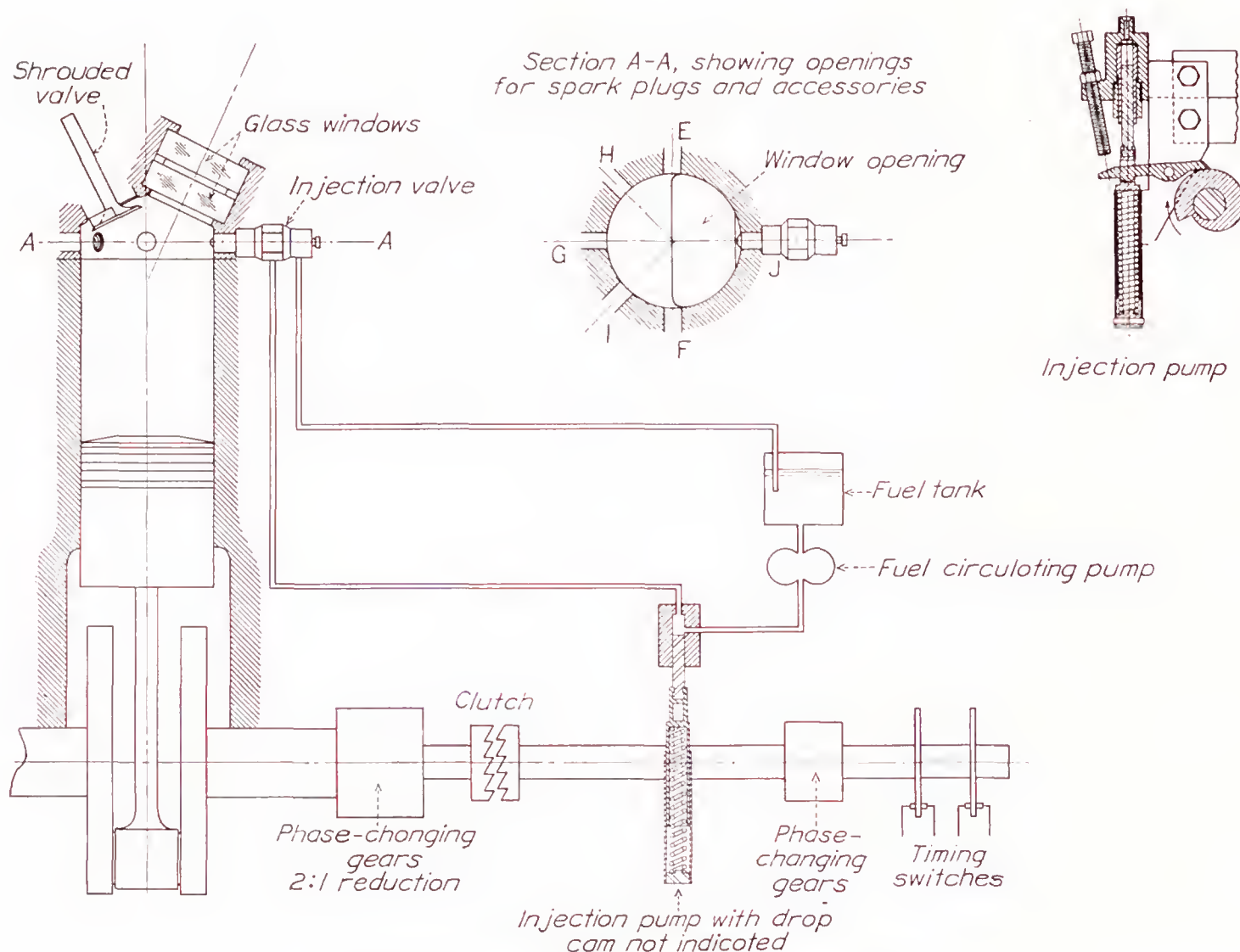


FIGURE 1.—Diagrammatic sketch of combustion apparatus.

The spark-photography apparatus consists of a battery of high-voltage condensers and a rotary distributor so arranged that the condensers are discharged consecutively, furnishing a series of spark discharges. For

detailed description of the set-up and the method of interpreting the pictures is given in reference 5.

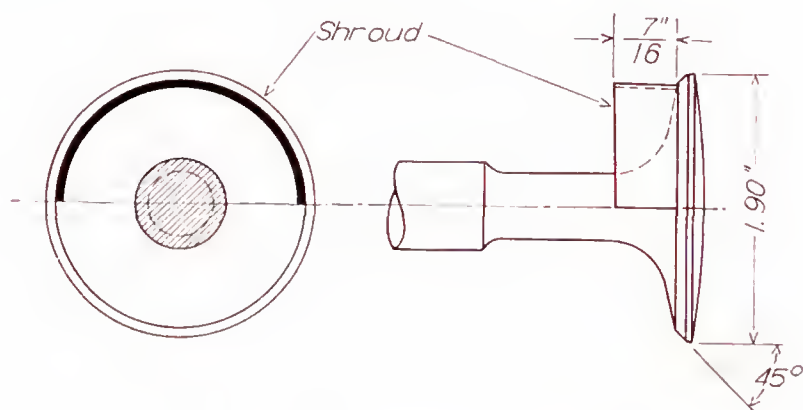


FIGURE 2.—Sketch of shrouded valve.

these tests, the apparatus was used in conjunction with a schlieren optical arrangement (reference 9), by which slight differences in index of refraction can be made visible or photographed. The spark arrangement used gave 13 sparks at a rate of about 1,000 per second.

The optical arrangement for taking the schlieren pictures is shown diagrammatically in figure 4, and a

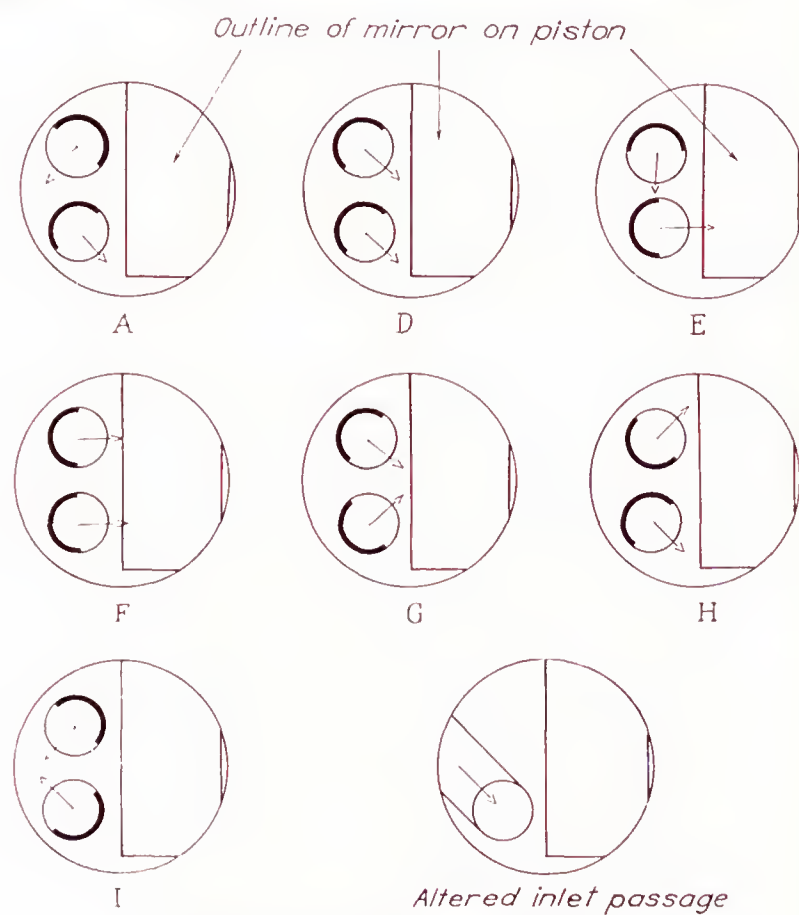


FIGURE 3.—Valve arrangements used.



The variation of pressure in the engine cylinder during intake was determined by means of a Farnboro indicator.

The air quantity was estimated, assuming that, at the time the valves closed, the air temperature in the cylinder had reached a value midway between the inlet temperature and the engine-coolant temperature. The air pressure in the cylinder at that time was atmospheric. The fuel quantity was determined by catching single injections in a vial filled with cotton and weighing the container on a chemical balance.

The fuel used throughout the tests was C. F. R. S-1 reference fuel, having an octane rating of 100 without the addition of tetraethyl lead and containing between

The more important effects noticeable in the results are the differences in burning speeds and the differences in cycle reproducibility with different valve-shroud settings. When the shrouds were set to cause tangential swirl, the burning area was noticeably displaced in the direction of the swirl.

As an aid in the interpretation of the schlieren photographs, a brief description will be given of a typical example taken at 500 r. p. m. (See record 152, fig. 5 (a).) With the type of schlieren arrangement used, the combustion appears darker than the field. The front edge of the combustion region is very sharply defined, and the line of demarcation between the burning region and the burned region is also definite but irregular.

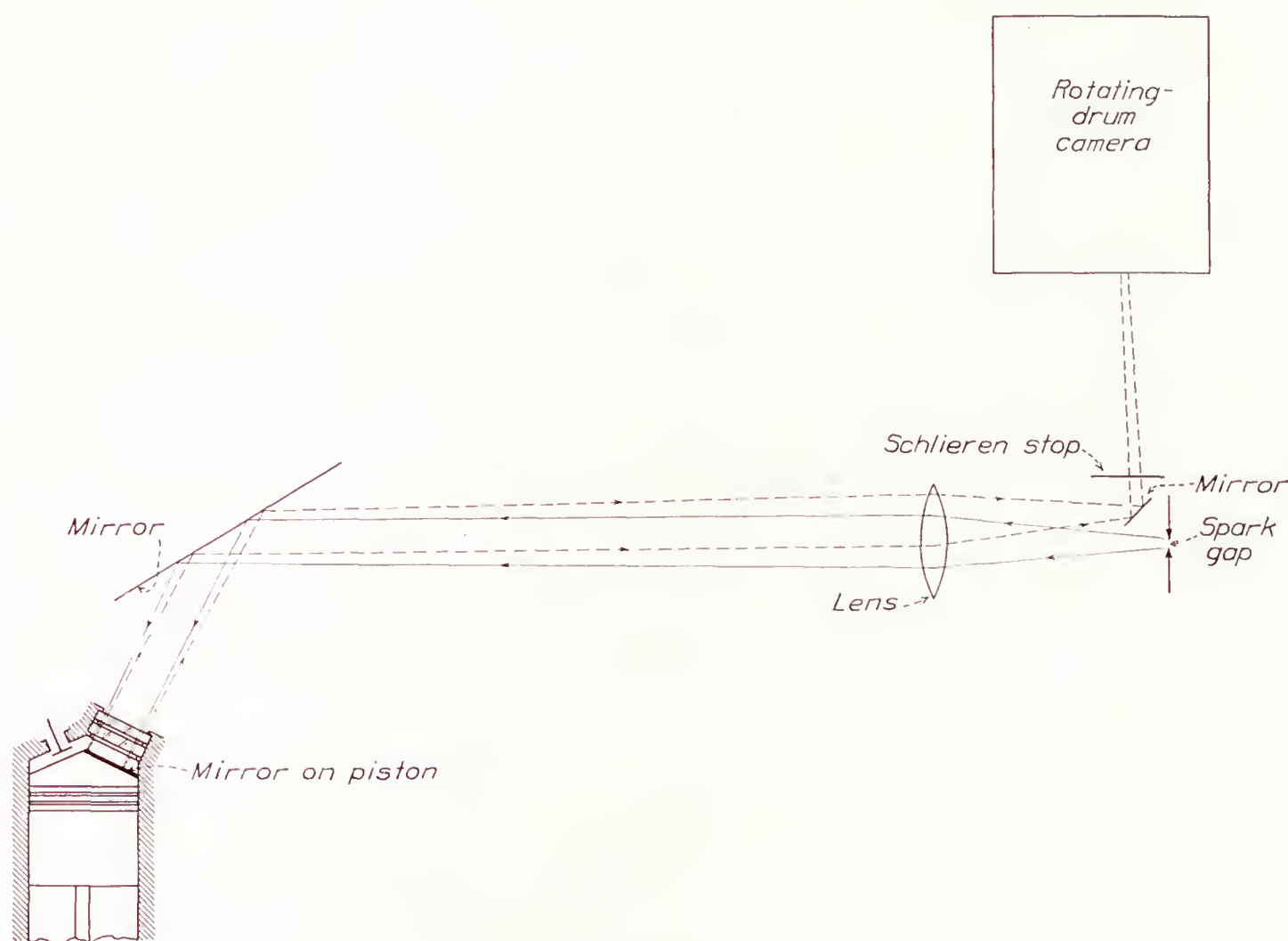


FIGURE 4.—Diagram of schlieren set-up.

90 and 100 percent iso-octane (2, 2, 4 trimethyl pentane).

Constant engine conditions for the tests were as follows:

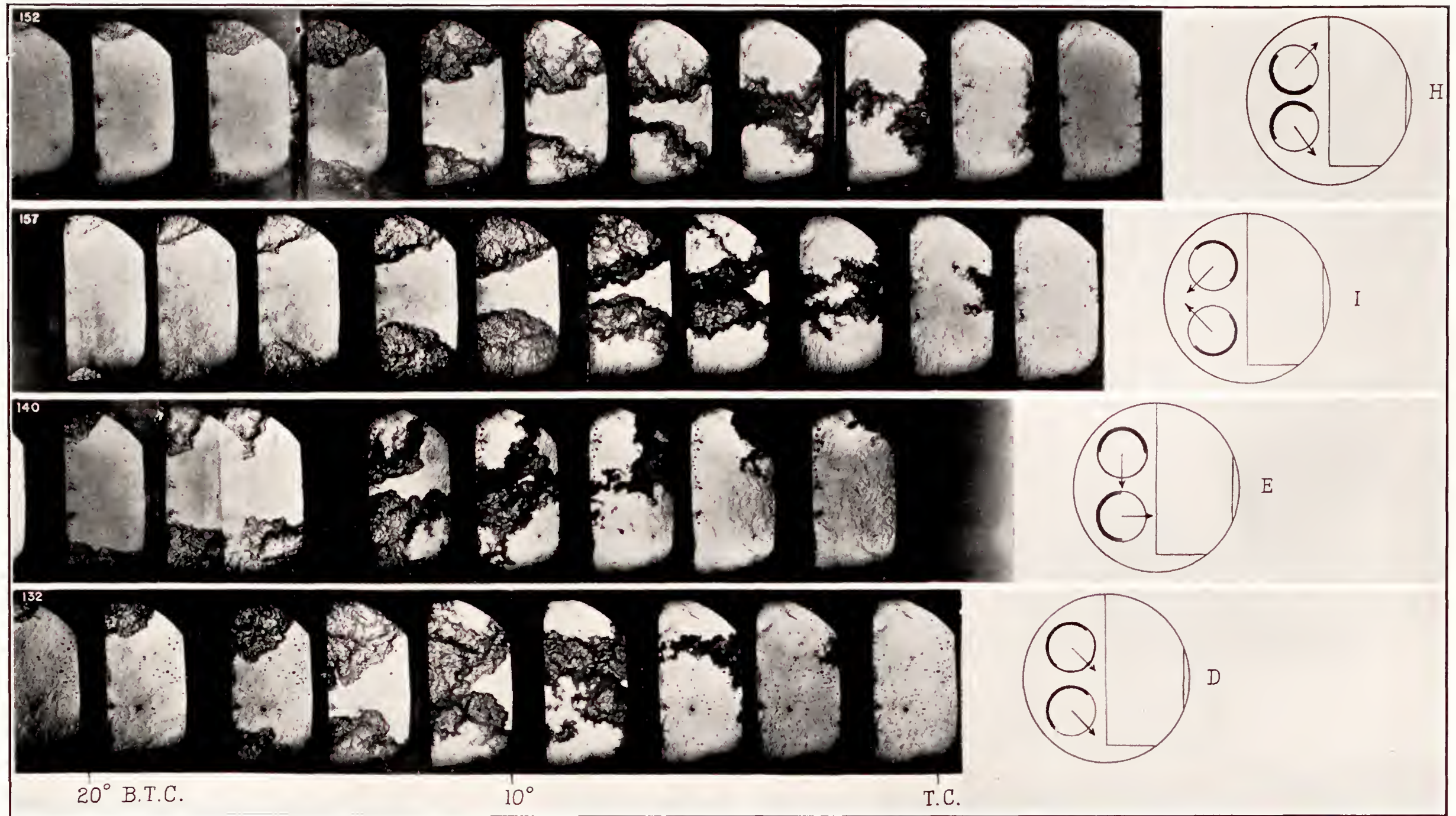
Compression ratio	7.0.
Engine-coolant temperature	250° F.
Air-fuel ratio	14.
Spark advance	30° B. T. C.
Spark-plug location	E and F (fig. 1).
Fuel-injection start	20° A. T. C. on intake stroke.

## RESULTS

Throughout this report, whenever reference is made to the type of air flow induced by a particular shroud arrangement, the description of the air movement was obtained from reference 4, where the air movements generated by each valve arrangement are described in detail.

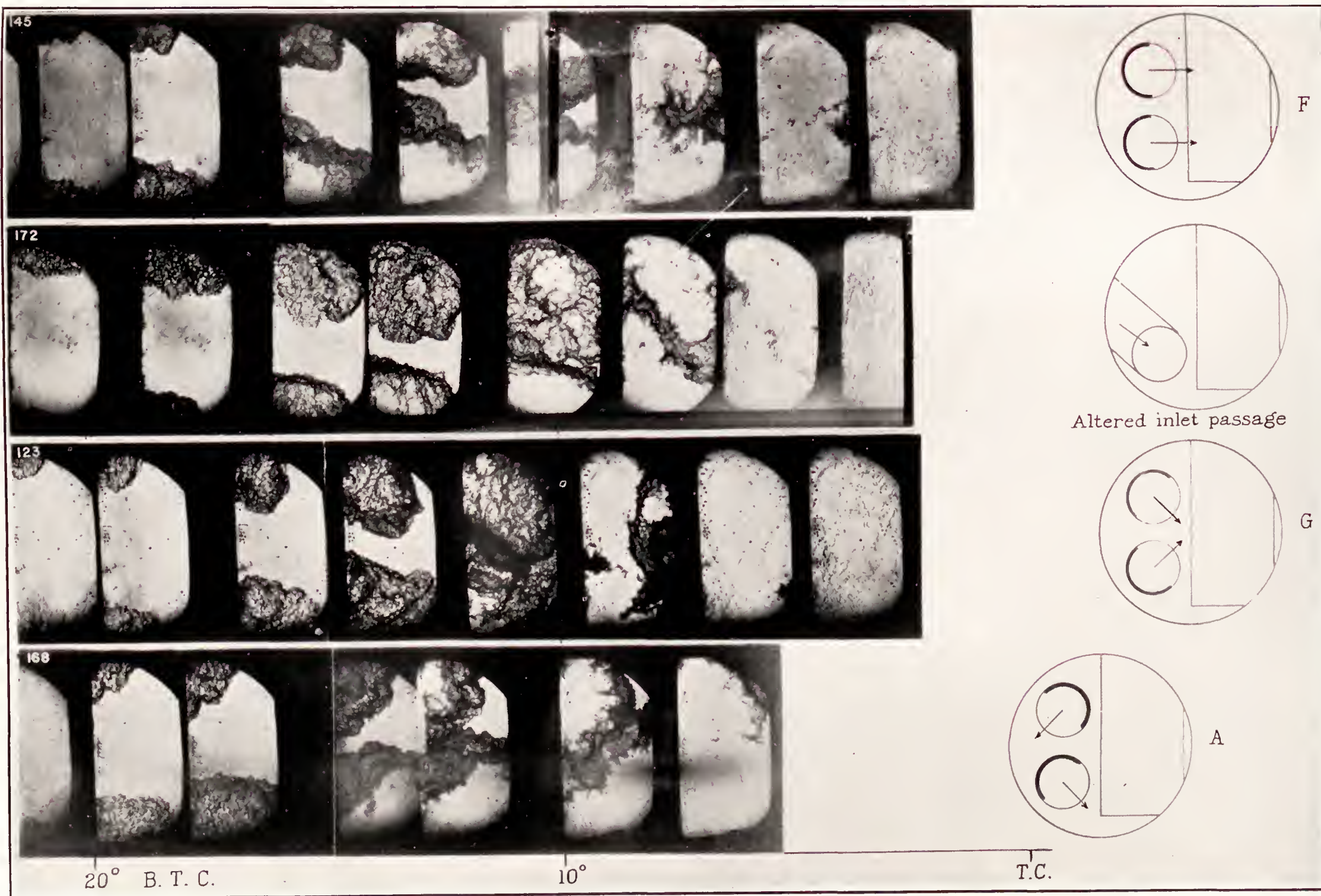
In the first frame on the left, the start of combustion can be seen just below the record number. In the third frame from the left, the burning from the other spark plug is visible at the lower edge of the picture. (The burning appears at the lower edge later than at the upper edge because it is not visible until it reaches the edge of the mirror which, because of structural requirements, does not cover a half-inch space at that side of the piston.) The burning regions grow until the two fronts meet in the eighth frame, where the clear spaces indicating the burned portion of the charge (first visible in the sixth frame) are plainly visible behind the burning regions. The area of burning then decreases until the last frame shows the burning apparently completed except for traces at the right-hand edge.





(a) Arrangements H, I, E, and D.





(b) Arrangements F, altered inlet passage, G, and A.

FIGURE 5.—Effect of gas movement on combustion. Engine speed, 500 r. p. m.; two spark plugs.



In figure 5, spark schlieren photographs of the combustion are shown for the eight different air-flow conditions shown in figure 3. The photographs are arranged in order of burning speeds with the setting giving the slowest burning at the top of figure 5 (a). In each case, at least three records were taken for each condition and the record reproduced was chosen as representative.

The approximate burning times as determined by inspection of the photographs are given in the following table. For comparison, the burning time for plain valves has been included.

TABLE I  
BURNING TIMES OF RECORDS SHOWN IN FIGURE 5

Valve arrangement	Record	Burning time (crank-shaft deg.)	Burning time (sec.)
Plain <sup>1</sup> .....	272	35.0	0.0117
H.....	152	32.0	.01067
I.....	157	31.5	.0105
E.....	140	29.5	.00983
D.....	132	29.0	.00967
F.....	145	28.5	.0095
Altered inlet passage.....	172	28.0	.00933
G.....	123	27.5	.00917
A.....	168	27.5	.00917

<sup>1</sup> See fig. 8.

In figure 5 (a), record 152 shows the burning with the valves set at arrangement H. The burning in this case was slow although the induced indiscriminate turbulence was high. The general air movement was a vertical-loop motion and could not be detected in the plane of the photographs.

Record 157, for arrangement I, also shows slow burning. The general air movement was a vertical loop, moving in the opposite direction from that given by arrangement H, and the indiscriminate turbulence was very high.

Record 140, for arrangement E, shows clearly the displacement of the burning region caused by the rotary air movement. Although the rotary movement during intake was not so rapid as for some of the other arrangements, the rate at the end of the compression stroke was nearly the same as that of all the other arrangements giving tangential swirls. This result is true also of arrangement D, record 132, which also shows the effect of the swirl. The swirl given by arrangement D had a predominantly vertical component during intake but, on the compression stroke, the vertical component was damped out and only the tangential component persisted.

All the four arrangements in figure 5 (b) show burning rates of somewhere near the same values. The rate appears slightly slower for record 145, arrangement F, although the air motion, a vertical loop at fairly high velocity, would be expected to give good mixing, particularly as the air is directed at the injection valve (fig. 1).

Record 172 shows the burning when one valve was blocked and the inlet passage was faired to give the air

a tangential entry. In his air-swirl tests, Lee found that this arrangement gave a swirl with the axis inclined at about 45°. In these combustion tests, however, the fairing could not be done in the same manner as in Lee's tests, and it is probable that the vertical component of the motion predominated. The photographs show no evidence of a tangential swirl from the single inlet valve.

Record 123, for arrangement G, shows very rapid burning. The burning in this case, however, was rather erratic. Lee found that the vertical-loop motions were damped by 40° A. T. C. on the expansion stroke, but apparently there was some tendency in this case for the burning region to be carried to the side of the chamber nearest the injection valve.

Record 168, for arrangement A, again shows the influence of the axial swirl. In this case, the high swirl rate during intake undoubtedly aided the mixing, and the swirl persisted through the compression stroke and carried the burning region with it. The burning was very rapid and uniformly reproducible.

Figure 6 shows records taken with one spark plug for four of the arrangements included in figure 5, the photographs being arranged in the same order. The slow burning given by arrangement H is again evident in record 150, where all 13 of the available spark discharges were required to record the complete history of the burning.

Record 138 appears to be somewhat out of step with respect to burning speed, although this apparent discrepancy may be due to the fact that the rotary air movement swept the burning region out of sight. Records 143 and 161 show very nearly the same burning speeds.

When only one spark plug is used, the displacement of the burning region by the air movement cannot be separated from increase or decrease in the speed of combustion travel. The actual rate of combustion travel may possibly have been greater in record 143 than it was in record 161; the burning region in record 161 may have been carried around by the rotary air movement and the burning completed in the rear part of the chamber outside the field of view.

Figure 7 shows two records with shrouded valves and a record of the burning with the altered inlet passage; the records were made at an engine speed of 1,000 r. p. m. and with two spark plugs. Record 185, arrangement H, again shows the slowest burning speed, with no indication of displacement by air movement. Record 178, with the altered inlet passage, shows the highest rate of burning of the three arrangements. The rate of air flow through the single valve must necessarily have been high at 1,000 r. p. m. and some residual vertical-loop motion probably remained at the end of the compression stroke. In record 179, the rotary air movement is again made apparent by the displacement of the burning region.



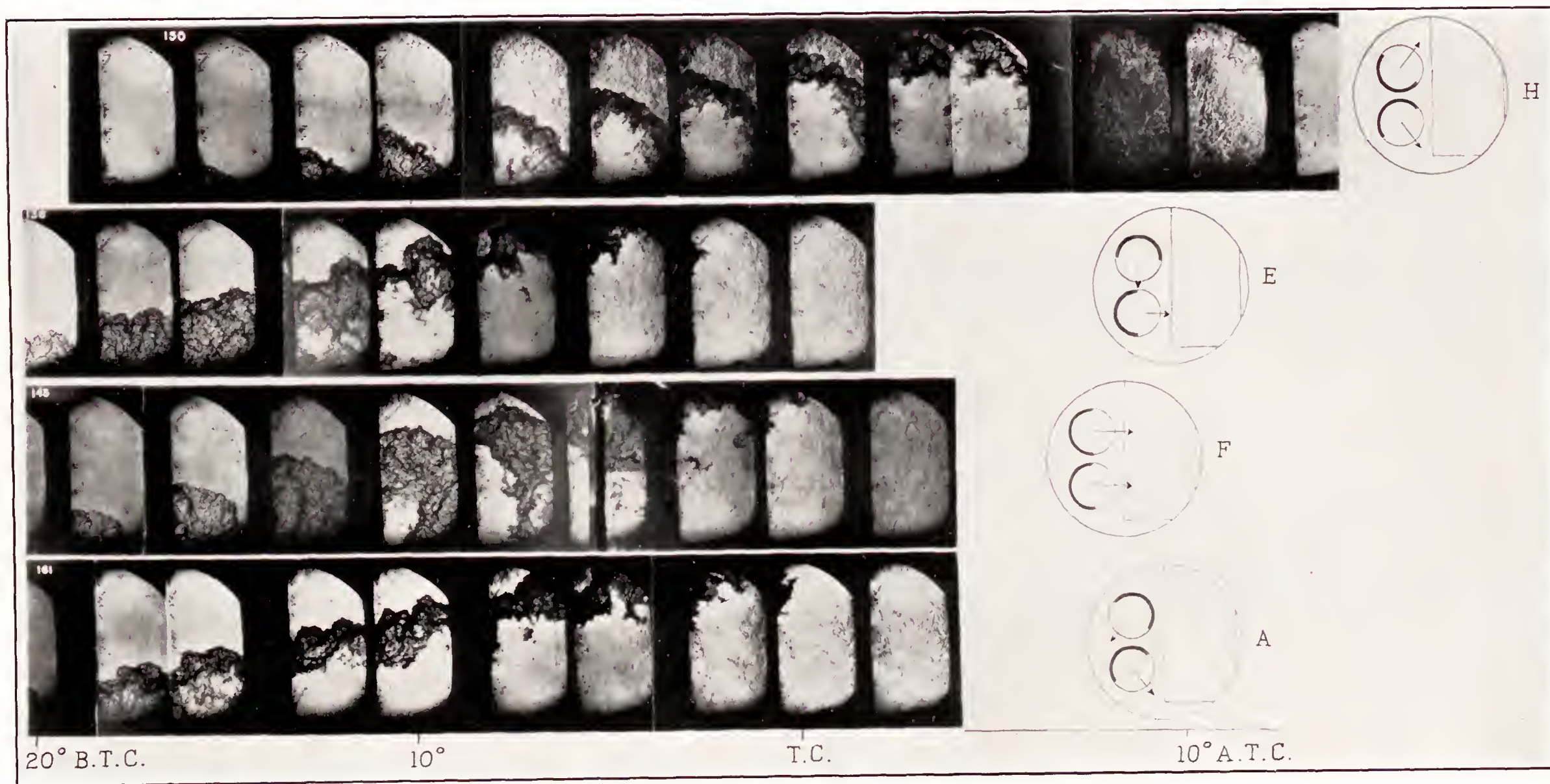


FIGURE 6.—Effect of gas movement on combustion. Engine speed, 500 r. p. m.; one spark plug.



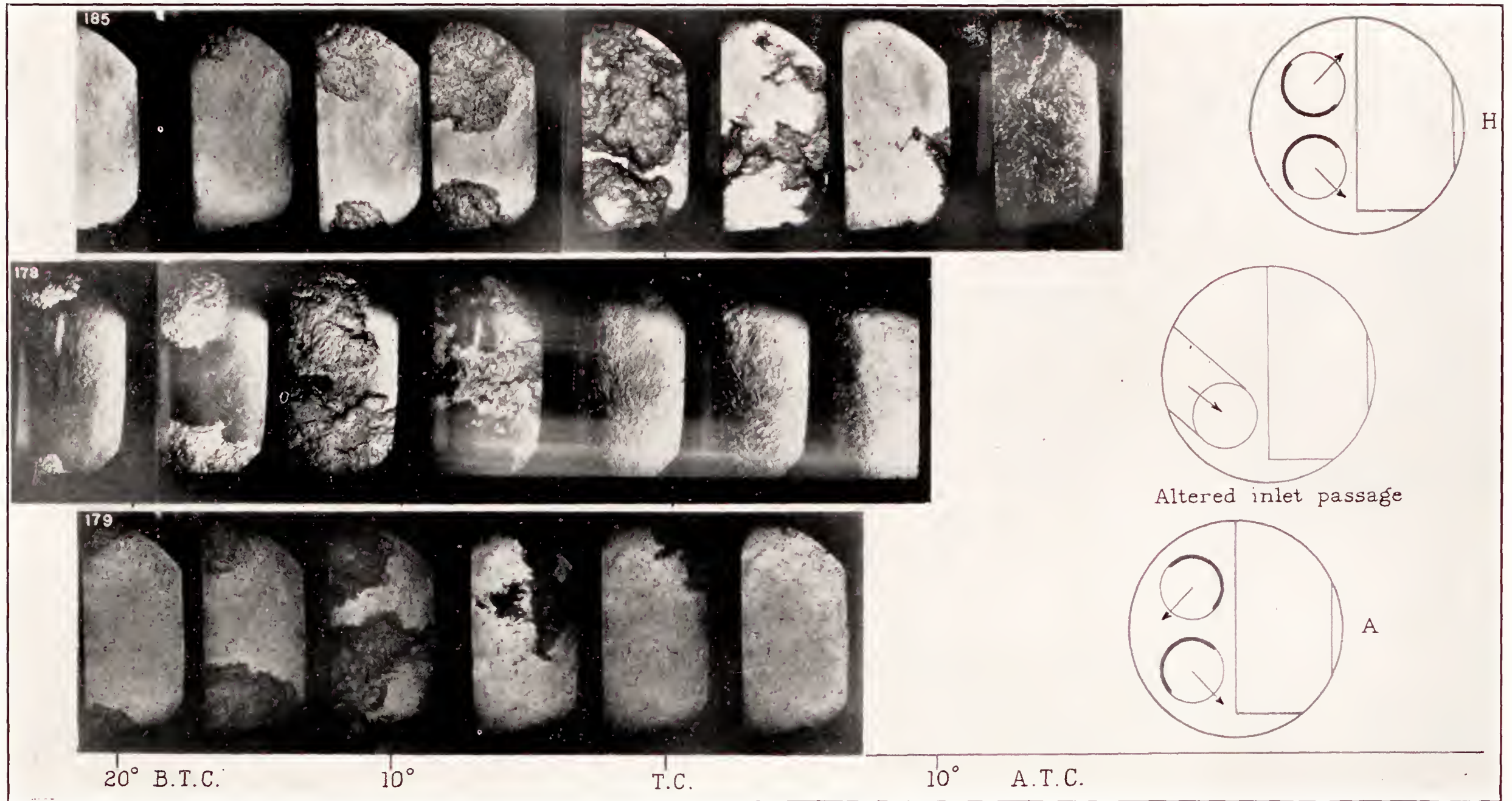


FIGURE 7.—Effect of gas movement on combustion. Engine speed, 1,000 r. p. m.; two spark plugs.



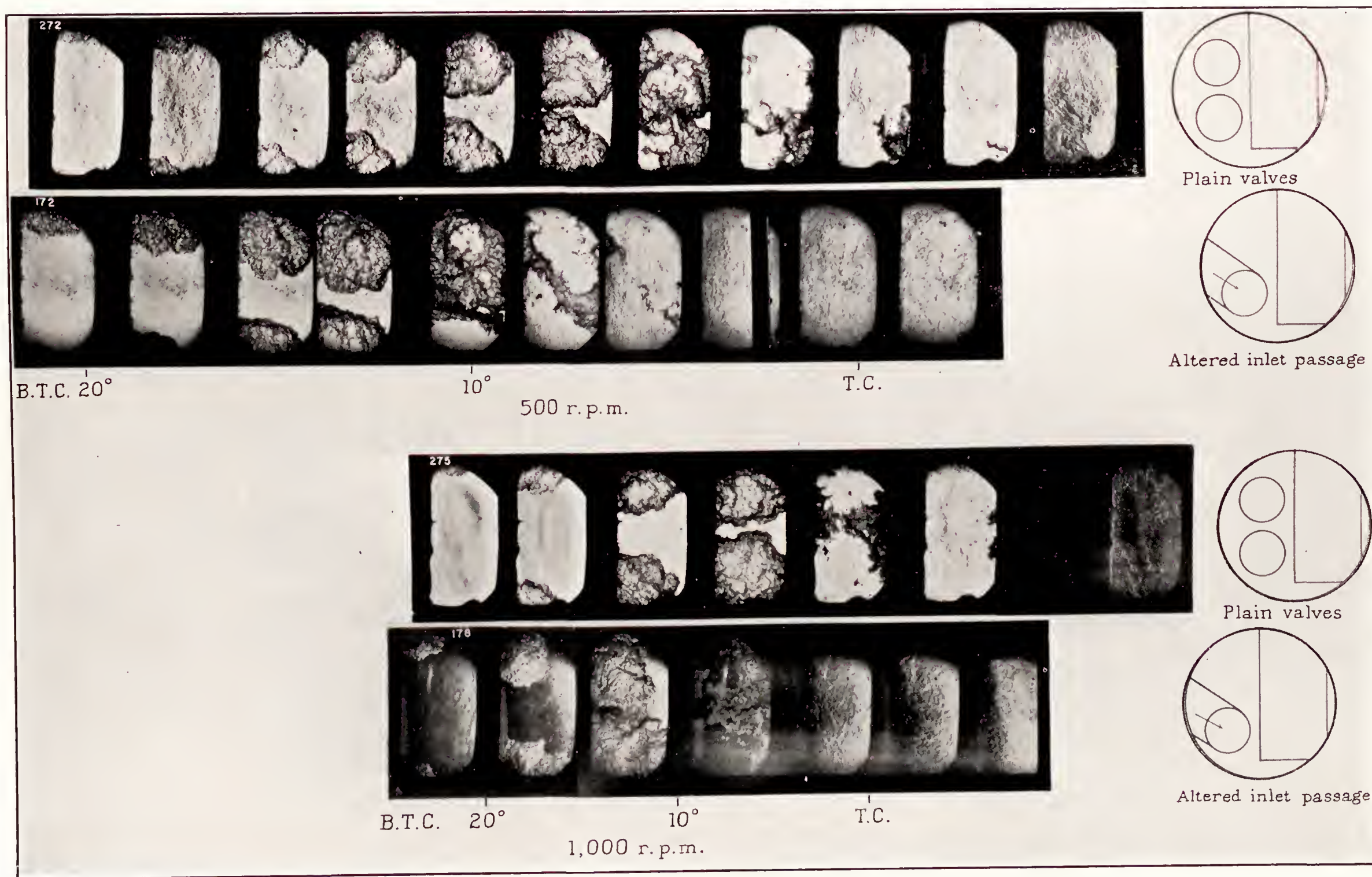


FIGURE 8.—Effects of engine speed and inlet-air velocity on combustion. Two spark plugs; spark advance, 30°.



Photographs of the burning at 500 and 1,000 r. p. m., when two plain valves were used and when one valve was blocked and the intake passage was faired, are shown in figure 8. The Farnboro indicator records for an engine speed of 500 r. p. m. with one and with two valves and for a speed of 1,000 r. p. m. with two valves show that the pressure remained very nearly atmospheric throughout the intake stroke. At 1,000 r. p. m. with one valve, a pressure difference of about 2.4 inches of mercury existed through part of the inlet stroke. On the basis of this evidence, it is assumed that the inlet-air velocity at 500 r. p. m., and at 1,000 r. p. m. with two valves, varies directly as the piston speed and inversely as the flow area. At 1,000 r. p. m. with one valve, the velocity probably reached a value from 10 to 25 percent greater (depending on the coefficient of discharge of the valve) than it would have reached if the velocity had remained a linear function of piston speed and flow area. The two groups of photographs, if taken separately, show the burning when the engine speed was kept constant and the inlet-air velocity was approximately doubled. A comparison between record 172 for one valve at 500 r. p. m. and record 275 for two valves at 1,000 r. p. m. represents the condition in which the linear velocity of the inlet air remains approximately constant (although the rates of mass flow differed) while the engine speed is doubled.

Inspection of figure 8 shows that increasing the engine speed without changing the linear air speed caused a large increase in burning speed. Increasing the inlet-air velocity without changing the engine speed also caused a definite increase in the burning speed, as shown by the comparison of the records given in figure 8 and in the following table.

TABLE II

VARIAION OF BURNING TIMES WITH INLET-AIR VELOCITY AND ENGINE SPEED

Record	Engine speed (r. p. m.)	Number of valves	Burning time (crankshaft deg.)	Burning time (sec.)
272	500	2	35	0.0117
172	500	1	25	.0083
275	1,000	2	35	.0058
178	1,000	1	25	.0042

A comparison of records 272, 172, and 275 shows that the proportional increase in burning speed obtained by increasing the engine speed and maintaining the inlet-air velocity approximately constant is about the same as that obtained by increasing the inlet-air velocity. Record 172 shows a burning time 0.71 that of record 272; and record 275, a burning time 0.70 that of record 172. Comparison of the records of figure 8 on the basis of engine speed shows that the burning speed increased

linearly with engine speed when either one or two valves were used. (Compare records 272 and 275 and records 172 and 178.)

The indicator-card records in figures 9, 10, and 11 show the cylinder pressures under the various air-flow conditions tested at different speeds and with one and two spark plugs. Each record shown is a composite of 10 or more indicator cards. The composites were obtained by superimposing the negatives for the indicator cards and printing them simultaneously. In cases where the individual lines were too faint to reproduce readily when the composites were rephotographed, they were retouched. Usually some of the lines were exactly superimposed, so that one line showing in the print may correspond to several records. Some striking differences in reproducibility are at once apparent.

Arrangement I is omitted because of the general similarity of its results to those obtained with arrangement H, and a composite of cards taken with plain valves is substituted. Considerable spread is shown in records 316-325, for plain valves. Peak pressure was attained at or slightly before top center. The occasional light knock does not show in the composite print because of the overlapping of the lines. Records 240-250 for arrangement H also show considerable spread, and about half of the records show knock. Peak pressure was reached at approximately top center. The remaining six groups of records were nonknocking. A striking improvement in reproducibility is noted in the group of records 222-231, for arrangement E. Records 262-271, for arrangement D, again show some spread, as do the groups 149-158 and 242-251, for the faired inlet passage and for arrangement F, respectively. Records 212-221, for arrangement G, show the highest rates of pressure rise of any of the records, but successive cycles were erratic. The best reproducibility of all was shown by records 252-261, for arrangement A. Although there is little difference in the composite of records 222-231 and that of records 252-261, records 222-231 showed slight individual differences not apparent in records 252-261.

Figure 10 is a comparison of the reproducibility at the two extreme conditions of valve-shroud settings (arrangements H and A) with only one spark plug. The change in reproducibility is very evident although perfect reproducibility was not attained with one plug, even with the most favorable air-flow conditions. Records 214-224 do not show any knock, whereas records 228-237 do.

Figure 11 compares the reproducibility of the indicator cards taken at 1,000 r. p. m. with plain valves and with shrouded valves set for full tangential swirl (arrangement A.) The reproducibility shown by records 119-128 is very striking. Any two individual cards can be superimposed as though they were stamped by a single die.



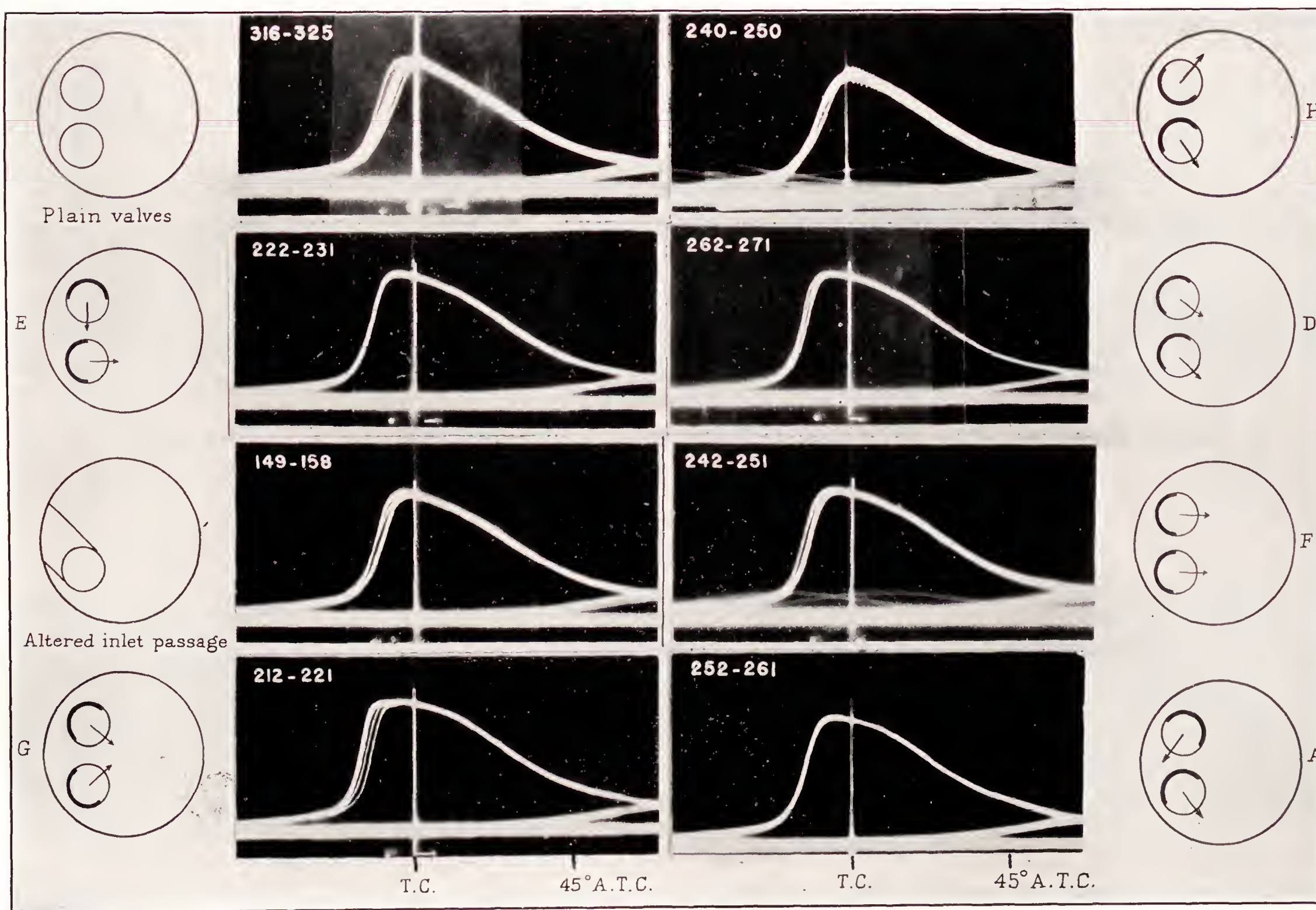


FIGURE 9.—Effect of gas movement on cycle reproducibility. Engine speed, 500 r. p. m.; two spark plugs.



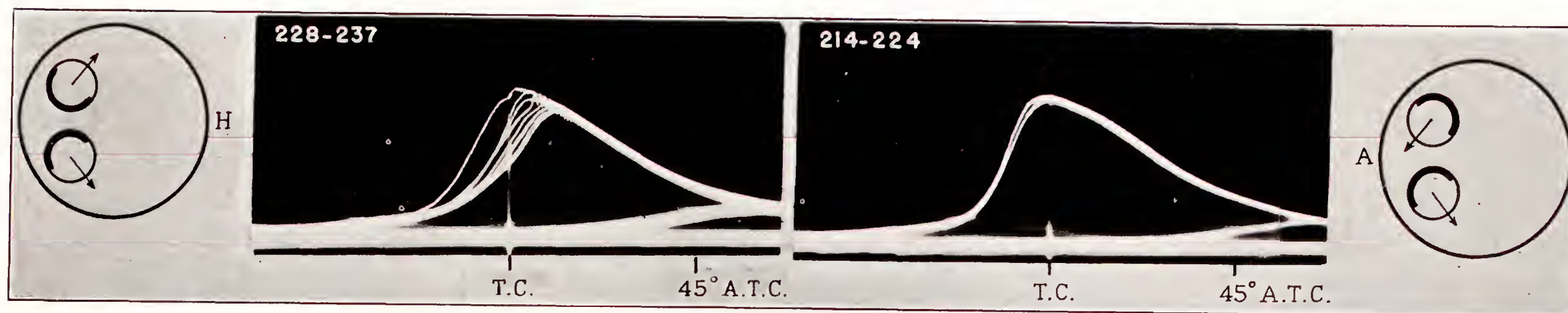


FIGURE 10.—Effect of gas movement on cycle reproducibility. Engine speed, 500 r. p. m.; one spark plug.

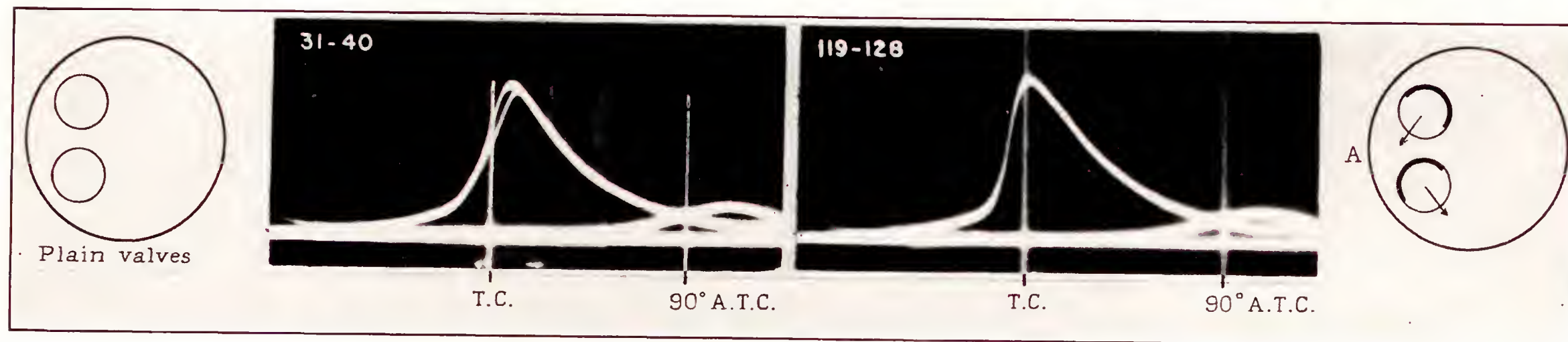


FIGURE 11.—Comparison of effects on cycle reproducibility of plain valves and of shrouded valves set for full axial swirl. Engine speed, 1,000 r. p. m.; two spark plugs.



## DISCUSSION

In the analysis of the data presented in this report, no attempt has been made to determine the actual mechanism by which the final effects of air flow on combustion were attained. It is difficult to determine whether some of the effects are caused by improved mixing of the charge, by increase in turbulence during combustion, or by other factors.

The most evident effects in this series of tests were the changes in burning speed and the differences in the reproducibility of the indicator cards from cycle to cycle.

## BURNING SPEEDS

It is well known that the flame speed increases almost linearly with engine speed. This increase in flame speed is usually attributed to the increased turbulence of the charge, caused by the higher inlet-air velocities accompanying the higher engine speed. Marvin and Best, using gaseous fuel well mixed before entering the cylinder, attributed the increase in flame speed with engine speed to increased turbulence (reference 10). David (reference 11) found that turbulence induced by a fan in a bomb increased the flame speed. Schnauffer (reference 12) attributed variations in measured flame speeds to variations in turbulence and investigated the effects of turbulence by varying the engine speed. Bouchard and his co-workers (reference 13) report an investigation of different variables affecting flame speed in which it was found that the speed varied almost linearly with engine speed. They attribute the increase in maximum rate of combustion with increased engine speed to an increase in small-scale turbulence resulting from higher gas velocities through the inlet system.

In all the available literature relating to the variation of combustion speed with engine speed, the changes have been attributed to changes in turbulence because of the known effects of turbulence on combustion in bombs and probably because no other logical explanation has been readily available. So far as is known, no attempt has been made by investigators to separate the effects of the gas velocities in the inlet system from the effects of the time interval elapsing between mixing and ignition. Such a separation of the two effects has been partly done in the data shown in figure 8, and the indicator cards in figures 9 and 11 can be used for similar comparisons.

The results shown in table II may indicate that the increased burning rate accompanying an increase in engine speed is caused equally by the increased turbulence and by the decreased time interval. Previous work at this laboratory has given evidence that the time interval between the mixing of the fuel and the air and the occurrence of ignition may influence the rate of combustion. In tests of fuel injection and spark ignition of various fuels in the N. A. C. A. combustion apparatus, Rothrock and Cohn (reference 14)

found that, as the injection advance angle was increased (above a certain minimum), the rate of combustion decreased. In compression-ignition tests, Rothrock and Waldron (reference 6) found that, as the injection advance angle was increased, the rate of combustion first increased until a limiting value of advance angle was reached and then decreased with further increase in advance angle. Cohn and Spencer (reference 15), studying the combustion of fuels injected into a bomb and ignited by a spark, found the rate of combustion to decrease as the time interval between injection and ignition increased. The intervals between injection and ignition were comparable with those occurring in an engine.

It may be suggested that the turbulence induced by the inlet air might have been damped out by the end of compression at 500 r. p. m., whereas the damping was not so great at 1,000 r. p. m. Direct examination of Lee's photographs (reference 4) for these conditions shows, however, that the turbulence was about the same for 500 r. p. m. and one valve as it was for 1,000 r. p. m. and two valves. The measured swirl velocities for the two conditions show about the same velocities persisting during the compression stroke.

A comparison of record 272 (fig. 8) with records 152 and 157 (fig. 5 (a)) indicates that doubling the inlet-air velocity by shrouding half of each inlet valve does not necessarily increase the burning speed to any great extent.

## MIXING EFFECTS

One definite effect of the directed air flow may be observed by a study of the photographs of figures 5, 6, and 7. It will be seen that the rate of combustion was increased whenever the inlet air was directed in such a manner as to be carried past the injection valve in an orderly fashion during injection, as in arrangements A, F, and G; in the altered inlet passage with one valve; and, to a lesser extent, in arrangements D and E. According to the tests reported in reference 4, the swirl velocity during inlet was lower for arrangements D and E than it was for the other four arrangements. It is believed that the effect of the orderly swirl in increasing the combustion rate is attributable to the improvement in mixing.

## REPRODUCIBILITY

It is generally known that successive cycles of a spark-ignition engine vary widely in rates of pressure rise and in total pressures. Different causes have been suggested, among them being: Variations in spark timing, in amount of charge per cycle, in mixture strength, and in quantity of oil that gets past the piston rings. It has been suggested that the distillation range of the fuel might influence the reproducibility. Attempts toward improvement have included the use of several spark plugs. Both fuel-injection spark-



ignition engines and carburetor engines have been found to be affected to the same extent.

In all probability, several factors enter into the problem. Obviously the spark timing must be uniform and the mixture strength and the amount of charge must be constant, or there will be variation.

Even though the foregoing conditions are controlled, variations in successive cycles will occur, as has been determined by engine tests. The indicator cards of figures 9, 10, and 11 show that the variation can be controlled by properly directing the air movement, provided that the other factors (spark timing, mixture strength, and amount of charge per cycle) are properly controlled. The tests with valve arrangement A, in particular, have been repeated several times. On one occasion, because of failure of the glass mirror on the piston, the engine was torn down, new valves and shrouds were installed, and the engine was reassembled. Results after the overhaul were fully as consistent as before. After those tests, a new piston was installed in the engine, having a crown such as that shown in figure 1 instead of the V-shaped crown used when the schlieren photographs were taken. The engine was then somewhat more sensitive to slight changes in the valve-shroud settings, and some experimentation was usually necessary to attain as good results as before. When the proper valve-shroud settings were used, however, the results were quite reproducible. Out of 50 or 60 records taken with valve arrangement A (or approximately that setting) and two spark plugs, only two or three records have shown any appreciable variation and those variations were traced to such causes as variations in mixture strength.

It will be noted, in an examination of figure 9, that arrangements A, D, and E, which gave an axial type of swirl, also showed the best reproducibility. For arrangement D, the improvement was only slightly greater than that shown by some of the other settings. Arrangement D tended to give a vertical-loop motion during the early part of the inlet stroke, which may or may not have influenced the reproducibility. Apparently a swirl that moved the charge past the spark plugs while the spark was occurring was of most value in improving the reproducibility.

In application to actual engine use, it is probable that experimental results are necessary to determine the type of air swirl best suited to the particular design of combustion chamber and location of spark plugs.

### CONCLUSIONS

1. Excellent cyclic reproducibility was obtained by directing the air so that the swirl moved past the spark plug and was in a plane normal to the axis of the cylinder.

2. Doubling the engine speed without increasing the linear velocity of the inlet air caused an increase in the

rate of combustion of the same magnitude as that caused by doubling the inlet-air velocity without increasing the engine speed.

3. When the valves were shrouded so that the inlet-air velocity was doubled and were set to cause a directed air swirl, the rate of burning was increased.

4. When the valves were shrouded so that the inlet-air velocity was doubled but were set so that there was no directed swirl, the rate of burning was not necessarily increased.

LANGLEY MEMORIAL AERONAUTICAL LABORATORY,  
NATIONAL ADVISORY COMMITTEE FOR AERONAUTICS,  
LANGLEY FIELD, VA., *October 10, 1938.*

### REFERENCES

1. Rothrock, A. M.: Effect of High Air Velocities on the Distribution and Penetration of a Fuel Spray. T. N. No. 376, N. A. C. A., 1931.
2. Rothrock, A. M., and Spencer, R. C.: Effect of Moderate Air Flow on the Distribution of Fuel Sprays after Injection Cut-Off. T. R. No. 483, N. A. C. A., 1934.
3. Rothrock, A. M., and Waldron, C. D.: Fuel Spray and Flame Formation in a Compression-Ignition Engine Employing Air Flow. T. R. No. 588, N. A. C. A., 1937.
4. Lee, Dana W.: A Study of Air Flow in an Engine Cylinder. T. R. No. 653, N. A. C. A., 1939.
5. Rothrock, A. M., and Spencer, R. C.: A Photographic Study of Combustion and Knock in a Spark-Ignition Engine. T. R. No. 622, N. A. C. A., 1938.
6. Rothrock, A. M., and Waldron, C. D.: Some Effects of Injection Advance Angle, Engine-Jacket Temperature, and Speed on Combustion in a Compression-Ignition Engine. T. R. No. 525, N. A. C. A., 1935.
7. Beardsley, Edward G.: The N. A. C. A. Photographic Apparatus for Studying Fuel Sprays from Oil Engine Injection Valves and Test Results from Several Researches. T. R. No. 274, N. A. C. A., 1927.
8. Tozier, Robert E.: The N. A. C. A. Optical Engine Indicator. T. N. No. 634, N. A. C. A., 1938.
9. Taylor, H. G., and Waldram, J. M.: Improvements in the Schlieren Method. Jour. Sci. Inst., vol. 10, no. 12, Dec. 1933, pp. 378-389.
10. Marvin, Charles F., Jr., and Best, Robert D.: Flame Movement and Pressure Development in an Engine Cylinder. T. R. No. 399, N. A. C. A., 1931.
11. David, W. T.: Turbulence in Internal Combustion Engines. The Engineer, vol. CXLIV, no. 3755, Dec. 31, 1937, pp. 733-734.
12. Schnauffer, Kurt: Combustion Velocity of Benzine-Benzol-Air Mixtures in High-Speed Internal-Combustion Engines. T. M. No. 668, N. A. C. A., 1932.
13. Bouchard, C. L., Taylor, C. Fayette, and Taylor, E. S.: Variables Affecting Flame Speed in the Otto-Cycle Engine. S. A. E. Jour., vol. 41, no. 5, Nov. 1937, pp. 514-520.
14. Rothrock, A. M., and Cohn, Mildred: Some Factors Affecting Combustion in an Internal-Combustion Engine. T. R. No. 512, N. A. C. A., 1934.
15. Cohn, Mildred, and Spencer, Robert C.: Combustion in a Bomb with a Fuel-Injection System. T. R. No. 544, N. A. C. A., 1935.



## REPORT No. 658

### TESTS OF TWO FULL-SCALE PROPELLERS WITH DIFFERENT PITCH DISTRIBUTIONS, AT BLADE ANGLES UP TO $60^\circ$

By DAVID BIERMANN and EDWIN P. HARTMAN

#### SUMMARY

Two 3-blade 10-foot propellers were operated in front of a liquid-cooled engine nacelle. The propellers differed only in pitch distribution; one had normal distribution (nearly constant pitch for a blade angle of  $15^\circ$  at 0.75 radius), and the other had the pitch of the tip sections decreased with respect to that for the shank sections (blade angle of  $35^\circ$  for nearly constant pitch distribution). Propeller blade angles at 0.75R from  $15^\circ$  to  $60^\circ$ , corresponding to design speeds up to 500 miles per hour, were investigated.

The results indicated that the propulsive efficiency at a blade angle of  $60^\circ$  was about 9 percent less than the maximum value of 86 percent, which occurred at a blade angle of about  $30^\circ$ . The efficiency at a blade angle of  $60^\circ$  was increased about 7 percent by correcting for the effect of a spinner and, at a blade angle of  $30^\circ$ , about 3 percent. The peak efficiencies for the propeller having the washed-out pitch distribution were slightly less than for the normal propeller but the take-off efficiency was generally higher.

#### INTRODUCTION

Tests of full-scale propellers made at the N. A. C. A. have previously been confined to blade angles at 0.75R of  $45^\circ$  and less, which correspond to airplane speeds below 400 miles per hour for tip speeds of 1,000 feet per second. If lower tip speeds were employed to reduce compressibility losses for the take-off, the corresponding air speeds would be even lower. In view of the trend toward greater airplane speed, it is obviously desirable to have available propeller data covering all contemplated design conditions for a period of several years. The present investigation extends the blade-angle range to  $60^\circ$ , which corresponds to a design air speed of about 500 miles per hour for a tip speed of 1,000 feet per second or to 400 miles per hour for a tip speed of 800 feet per second. (See fig. 1.)

One of the propellers investigated was designed with a nearly uniform pitch distribution for a blade-angle setting of about  $15^\circ$  at the 0.75 radius. When the blades are set at higher angles, the pitch increases with the radius. Tests of model propellers (reference 1) have shown that, for a tractor propeller, a radial increase in pitch near the hub is beneficial but that a further radial increase in pitch near the tips is harmful.

As the present investigation was to cover a wide range of blade angles, it was believed that the pitch distribution of the test blades would not be entirely satisfactory for all blade angles. The program was therefore laid out to include tests with the pitch maintained constant over the outer halves of the blades for blade angles of  $15^\circ$ ,  $25^\circ$ , and  $35^\circ$  and also to include tests showing

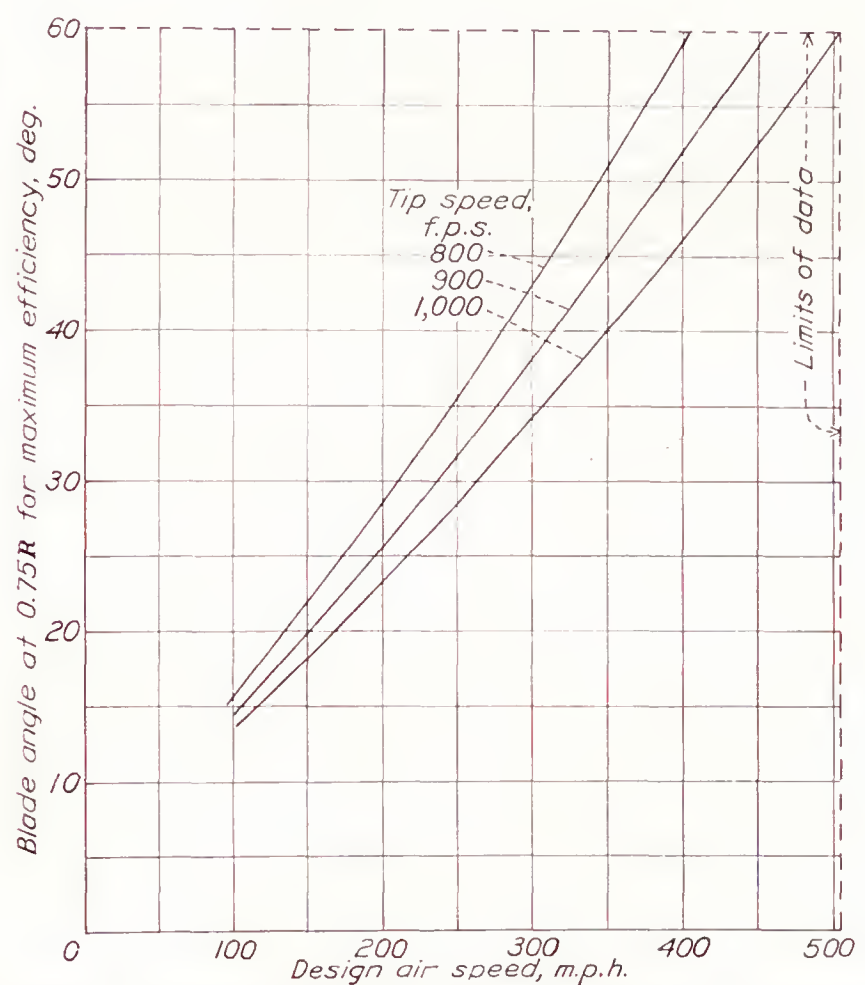


FIGURE 1.—Design conditions for maximum efficiency. Propeller 5868-9 with spinner.

the effects of a radial engine nacelle and of a liquid-cooled engine nacelle. Unfortunately, some of the results were in error owing to breakage in the balance system; only the results for the two extreme pitch distributions with the liquid-cooled engine nacelle are therefore reported.

In view of the fact that propeller spinners are very beneficial for high-speed airplanes equipped with liquid-cooled engine nacelles, the results of the tests of the propeller with the standard pitch distribution at a blade angle of  $15^\circ$  are also given for the spinner condition.



## APPARATUS AND METHODS

The propeller-research tunnel has been modified since the description of reference 2 was written to the extent of installing an electric motor to drive the tunnel propeller and of replacing the balance with a more modern one capable of simultaneously recording all the forces.

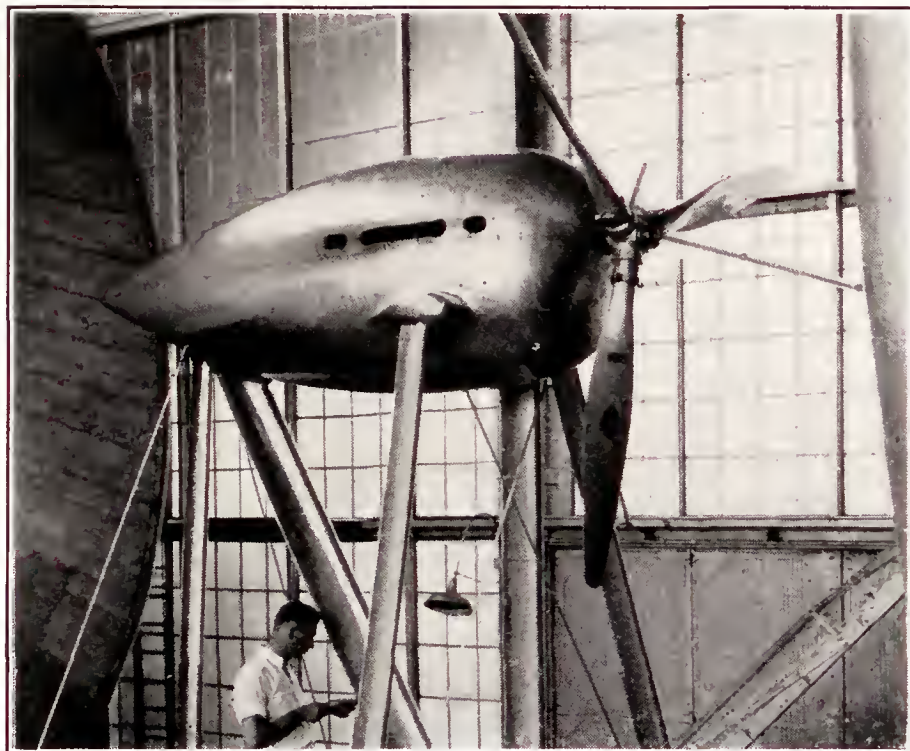


FIGURE 2.—The propeller test set-up with liquid-cooled engine nacelle.

A 600-horsepower Curtiss Conqueror engine (GIV-1570) was used to drive the test propellers. The engine was mounted in a cradle dynamometer free to rotate about an axis parallel to the propeller axis and located at one side of the engine. The torque reaction was transmitted from the other side of the engine to record-

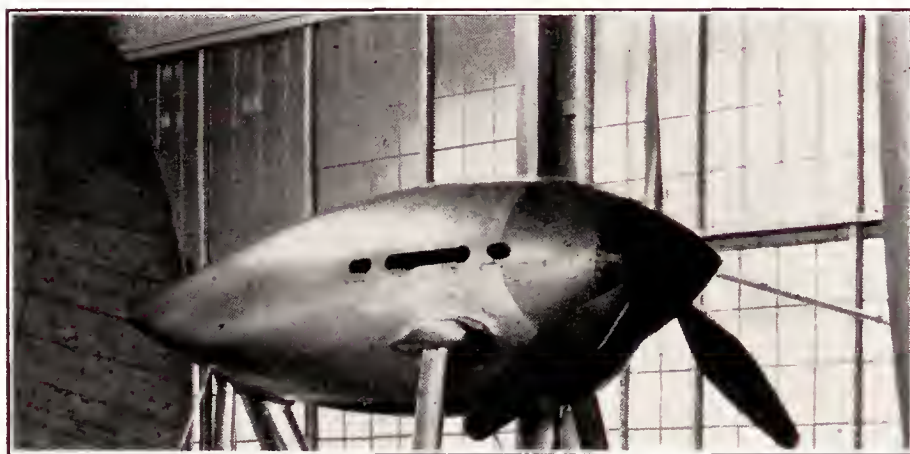


FIGURE 3.—Liquid-cooled engine nacelle with spinner.

ing scales located on the floor of the test chamber. The propeller speed was measured by a calibrated electric tachometer.

The liquid-cooled engine nacelle, shown in figure 2, is oval in cross section, 43 inches in height, 38 inches in width, and 126 inches in length. A detailed drawing of the liquid-cooled and the radial engine nacelle is

given in figure 1 of reference 3. Figure 3 shows the liquid-cooled engine nacelle and the propeller fitted with the spinner.

The two propellers tested in this investigation are 3-blade 10-foot-diameter propellers of Clark Y section and are identical except for pitch distribution. Propeller 5868-9 is a Navy Bureau of Aeronautics design having a fairly uniform pitch distribution over the outer half of the blades when set  $15^\circ$  at  $0.75R$ . The 5868- $X_2$  propeller has a uniform pitch distribution over the outer half of the blades when set  $35^\circ$ . The plan form and the blade-form curves are given in figure 4

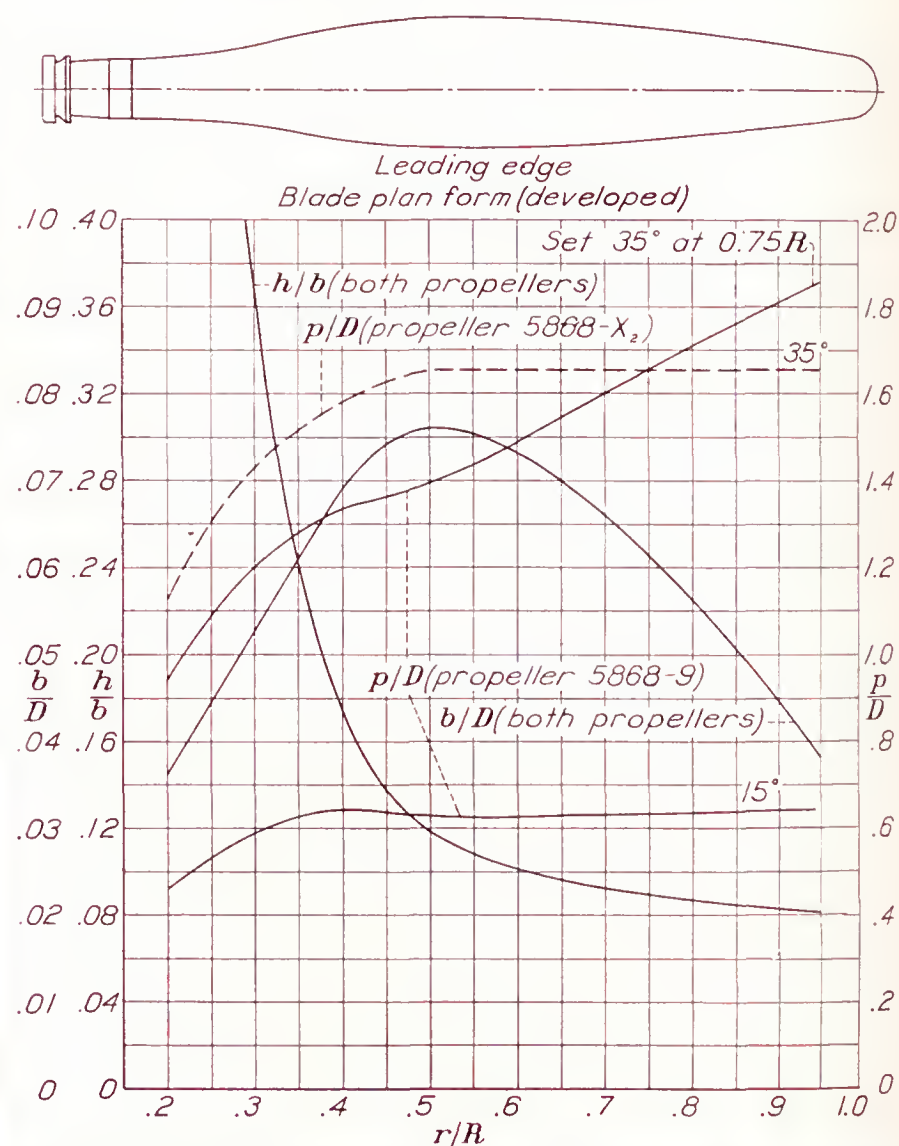


FIGURE 4.—Plan form and blade-form curves for propellers 5868-9 and 5868- $X_2$ .  $D$ , diameter;  $R$ , radius to the tip;  $r$ , station radius;  $b$ , section chord;  $h$ , section thickness;  $p$ , geometric pitch.

and a comparison of the pitch distributions is given in figure 5.

The method of testing in the propeller-research tunnel consists in maintaining the propeller speed constant and increasing the tunnel speed in steps up to the maximum value of 115 miles per hour. Higher values of  $V/nD$  are obtained by reducing the engine speed until zero thrust is reached. The tests were run at tip speeds of 525 feet per second and less to avoid complications arising from compressibility. The standard initial testing propeller speed of 1,000 r. p. m. could not be maintained for the higher blade-angle settings



owing to the limitation of engine power. The following schedule was adhered to:

*Propeller speeds for tunnel speeds below 115 miles per hour*

Blade angle (deg.)	Initial propeller speed (r. p. m.)	Blade angle (deg.)	Initial propeller speed (r. p. m.)
15	1,000	40	700
20	1,000	45	700
25	800	50	650
30	800	55	600
35	800	60	560

For  $V/nD$  values higher than can be obtained from the foregoing schedule, the approximate test propeller speed may be computed from the relation  $r.p.m. = \frac{K}{V/nD}$  where  $K=1,000$  for  $V=115$  miles per hour and  $D=10$  feet.

An analysis of results from tests with the spinner for propeller blade angles of  $15^\circ$ ,  $25^\circ$ , and  $35^\circ$  indicated that the effect of the spinner could be translated into a drag value independent of the blade angle (5.5 pounds at 100 miles per hour). The results without the spinner were consequently corrected for the effect of the spinner by the formula

$$\Delta C_T = 0.001075 (V/nD)^2$$

instead of making additional tests with the spinner. Any errors incidental to this process are considered to be within the experimental error. This formula applies only to the conditions of the present tests.

The spinner was regarded as a part of the body; the reduction in drag of 5.5 pounds at 100 miles per hour was therefore primarily due to enclosing the hub portions of the propeller.

## RESULTS AND DISCUSSION

The results are reduced to the usual coefficients of thrust, power, and propulsive efficiency defined as

$$C_T = \frac{\text{effective thrust}}{\rho n^2 D^4} = \frac{T - \Delta D}{\rho n^2 D^4}$$

$$C_P = \frac{\text{engine power}}{\rho n^3 D^5}$$

$$\eta = \frac{C_T}{C_P} \frac{V}{nD}$$

where

$T$ , tension in propeller shaft, pounds.

$\Delta D$ , change in body drag due to slipstream, pounds.

$\rho$ , mass density of the air, slugs per cubic foot.

$n$ , propeller speed, r. p. s.

$D$ , propeller diameter, feet.

$V$ , air speed, feet per second.

Charts for selecting or designing propellers are given in the form of  $C_s$  against  $\eta$  and  $V/nD$ ,

$$C_s = \sqrt[5]{\frac{\rho V^5}{P n^2}}$$

Lines of constant thrust coefficient have been superposed on the power-coefficient curves to facilitate thrust computations at all air speeds for fixed-pitch and controllable propellers. For an outline of the methods, see reference 3.

The test results are given in the form of charts in figures 6 to 17. These results have also been tabulated

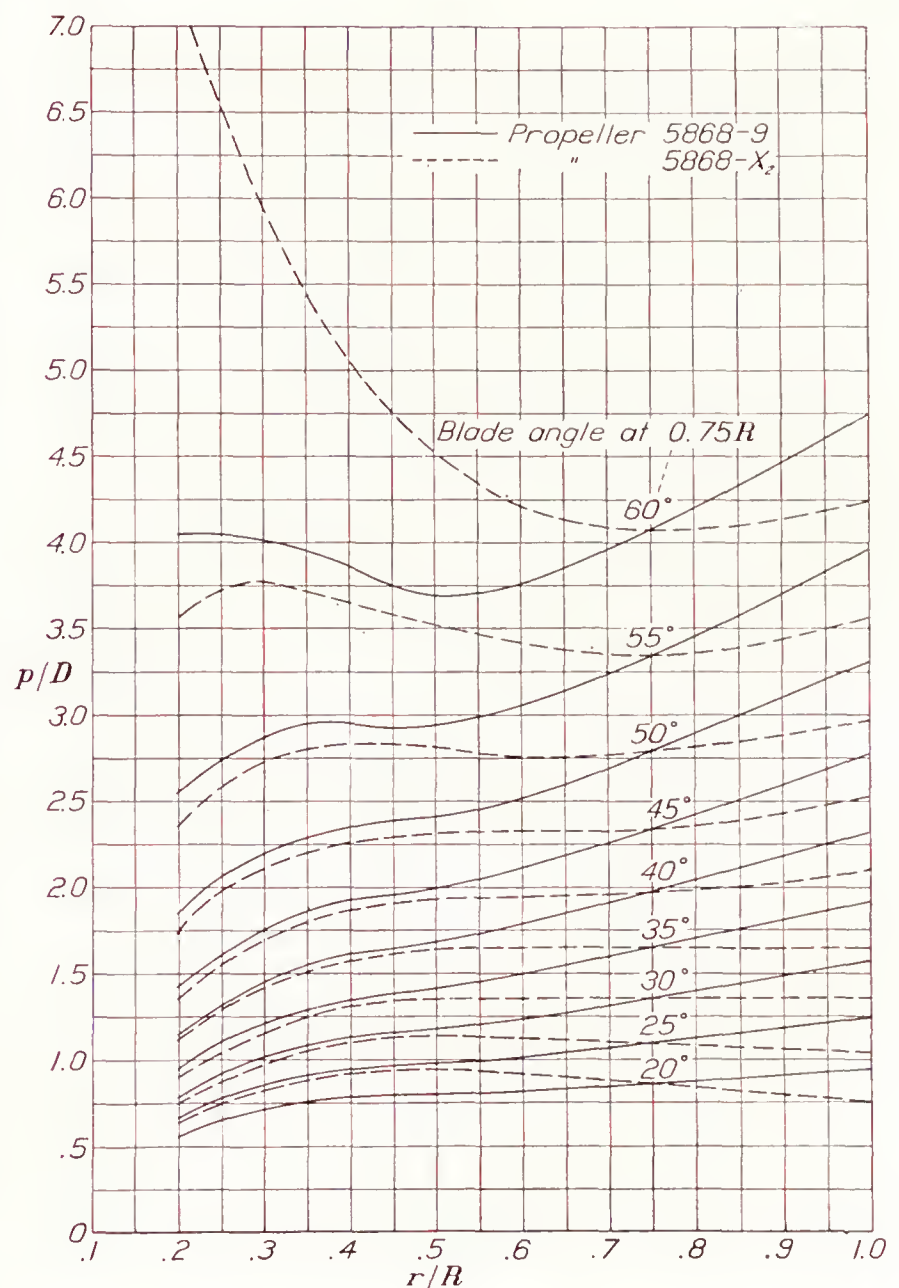


FIGURE 5.—Comparison of pitch distribution of propellers 5868-9 and 5868-X<sub>2</sub>.

in three tables that are issued as a supplement to this report.

**Propeller 5868-9.**—There is nothing unusual about the characteristics of propeller 5868-9 without the spinner for the blade angles above  $45^\circ$ , that is, for the extended range of the tests. The efficiency envelope reaches a maximum efficiency value of about 86 percent at a blade-angle setting of about  $30^\circ$ . (See fig. 18.) For higher angles, the efficiency drops progressively to 77 percent for the  $60^\circ$  setting.

The take-off criterion for a controllable propeller, taken as the efficiency at 25 percent of the design speed, reaches a maximum value at a design  $C_s$  of 2.4, which



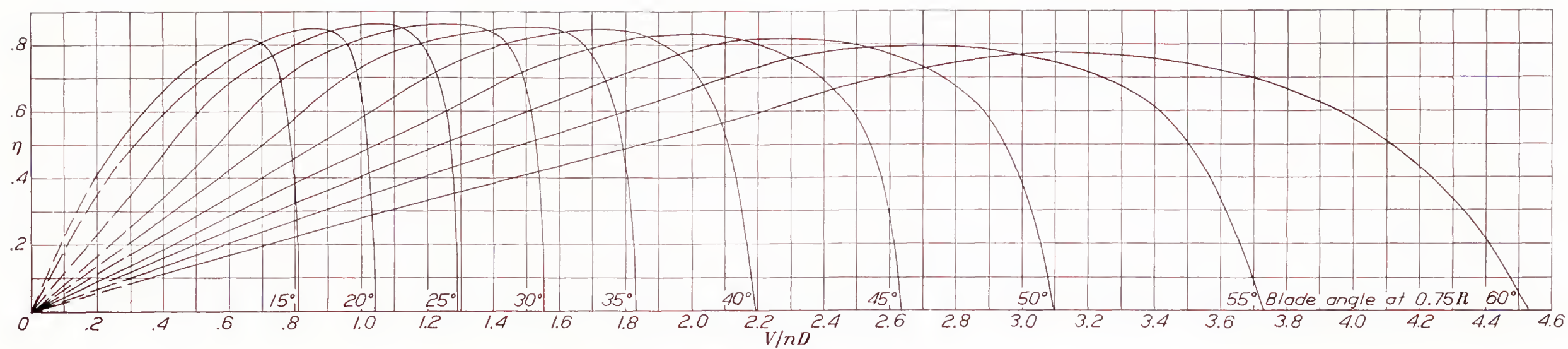


FIGURE 6.—Efficiency curves for propeller 5868-9.

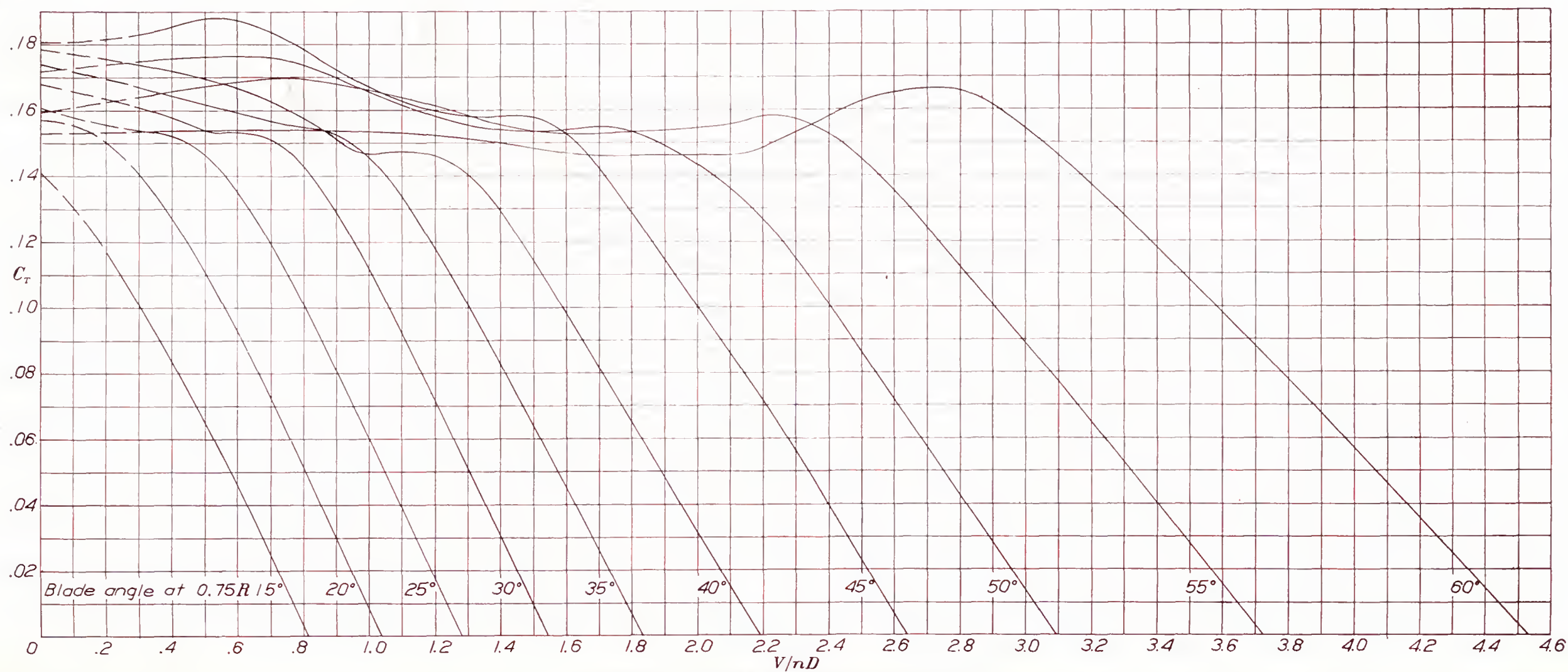


FIGURE 7.—Thrust-coefficient curves for propeller 5868-9.



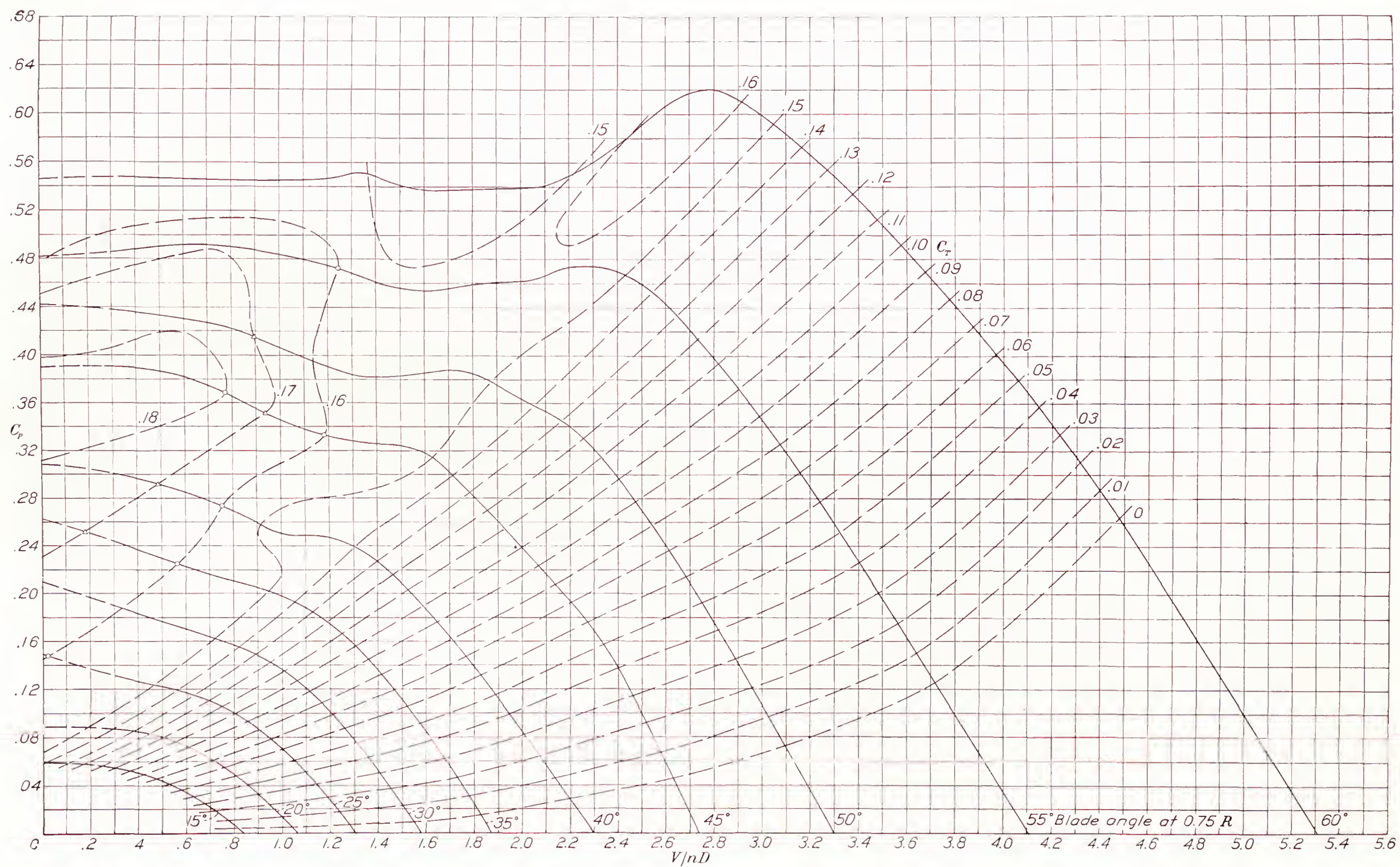


FIGURE 8.—Power-coefficient curves for propeller 5868-9.



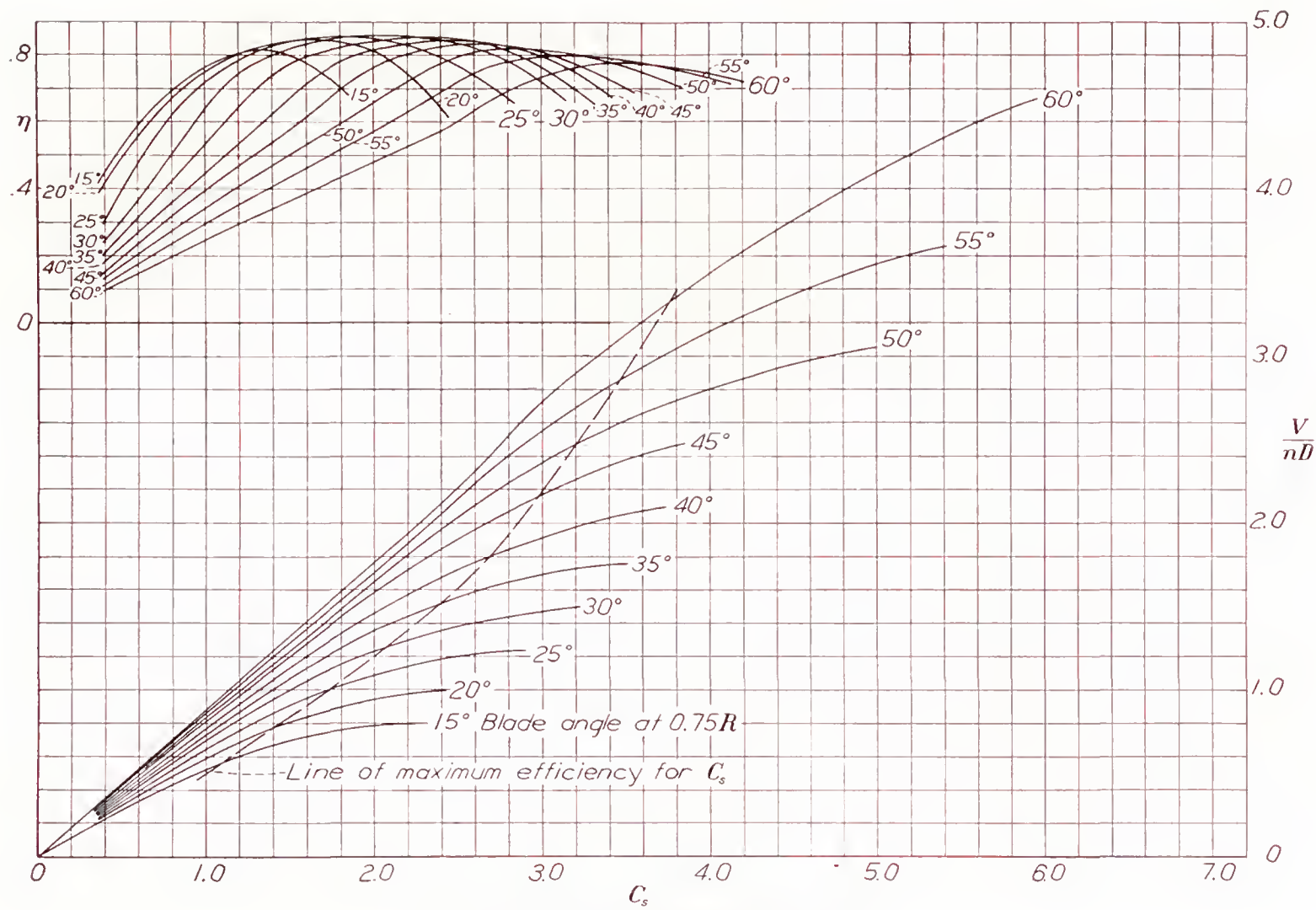


FIGURE 9.—Design chart for propeller 5868-9.

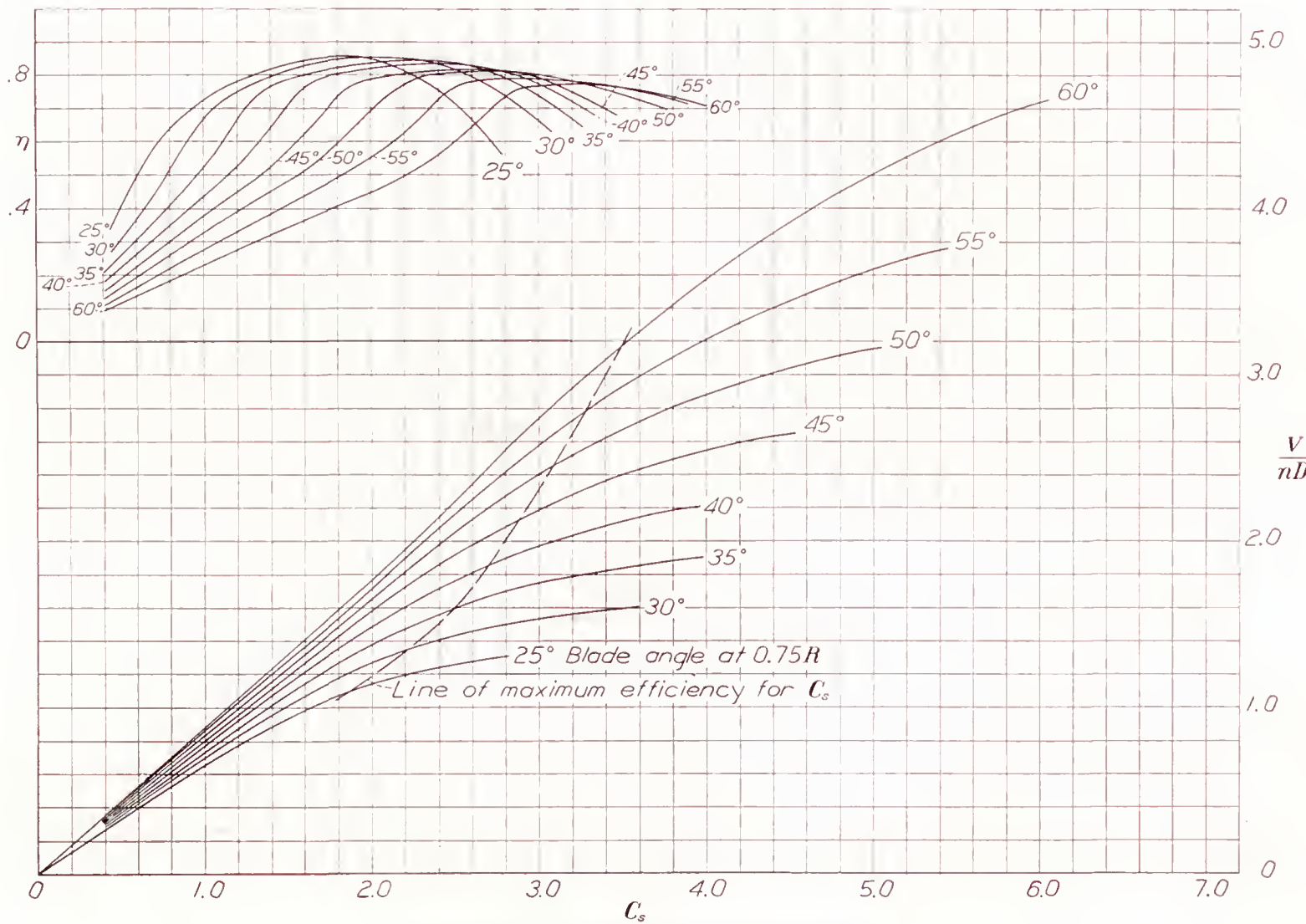
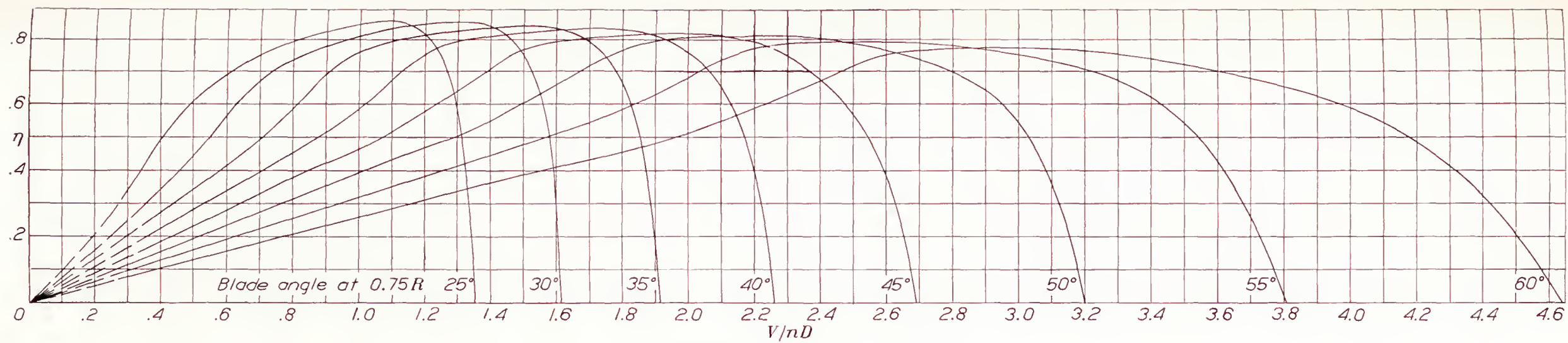
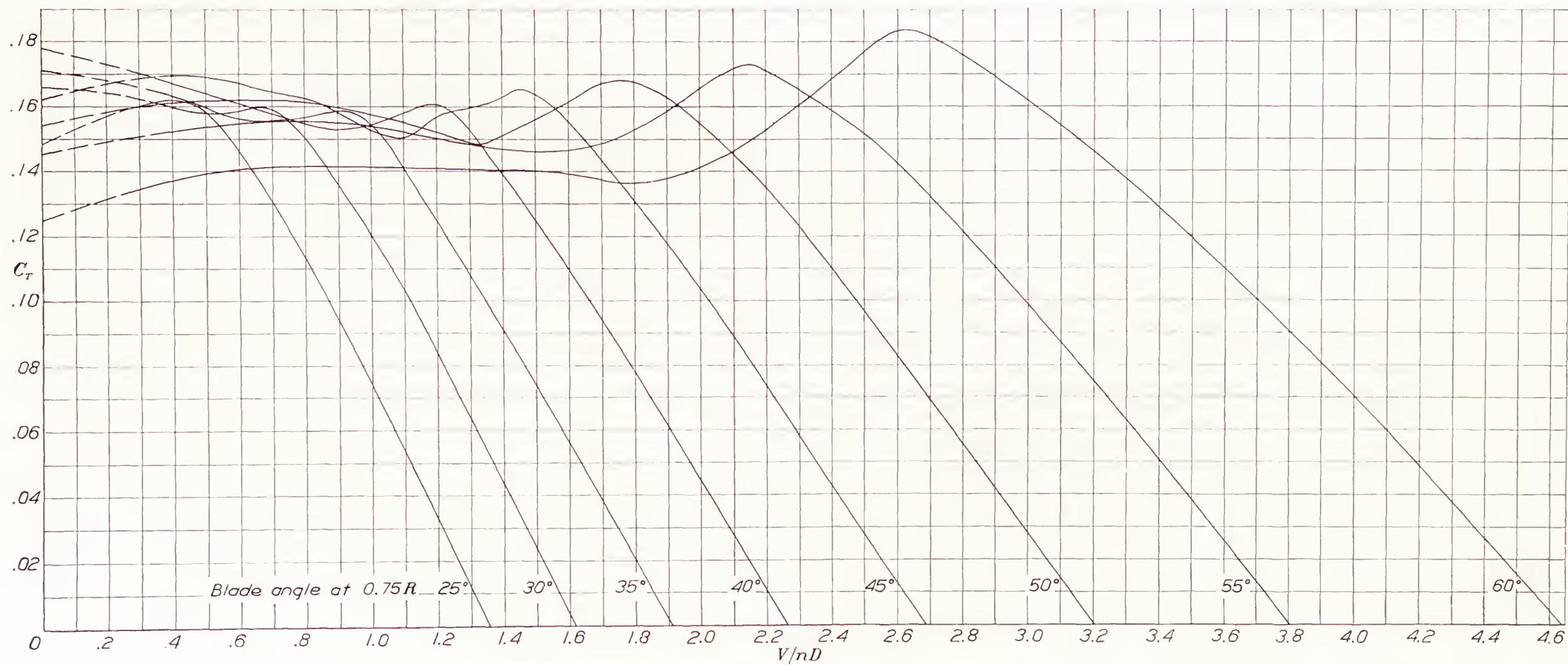


FIGURE 10.—Design chart for propeller 5868-X2.



FIGURE 11.—Efficiency curves for propeller 5868-X<sub>2</sub>.FIGURE 12.—Thrust-coefficient curves for propeller 5868-X<sub>1</sub>.



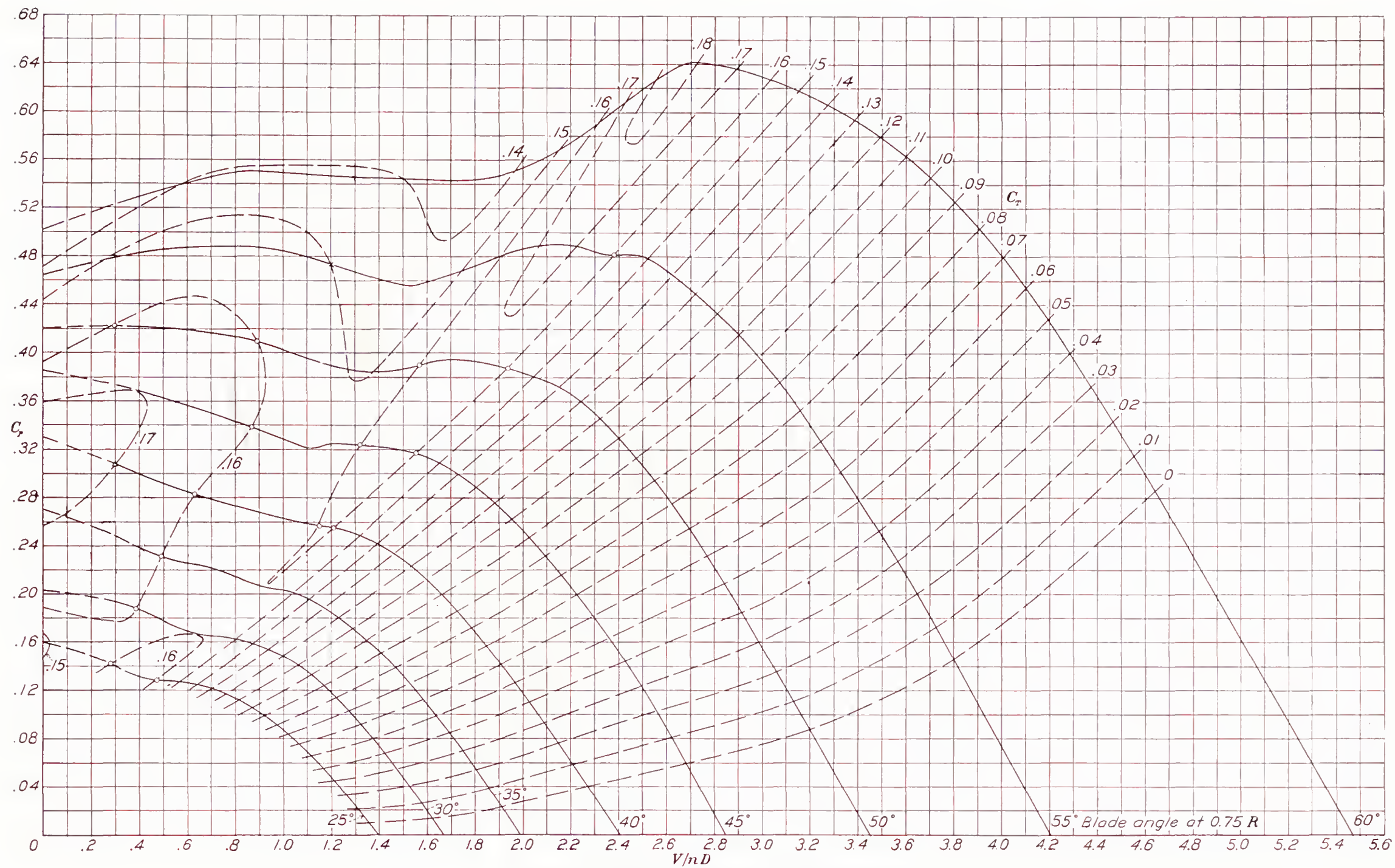


FIGURE 13.—Power-coefficient curves for propeller 5868-X2.



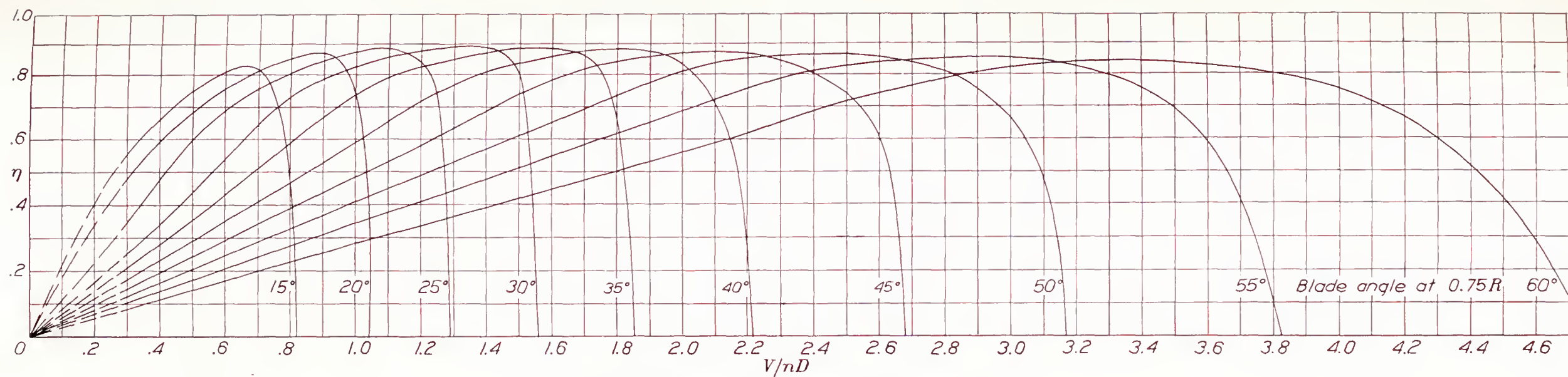


FIGURE 14.—Efficiency curves for propeller 5868-9 with spinner.

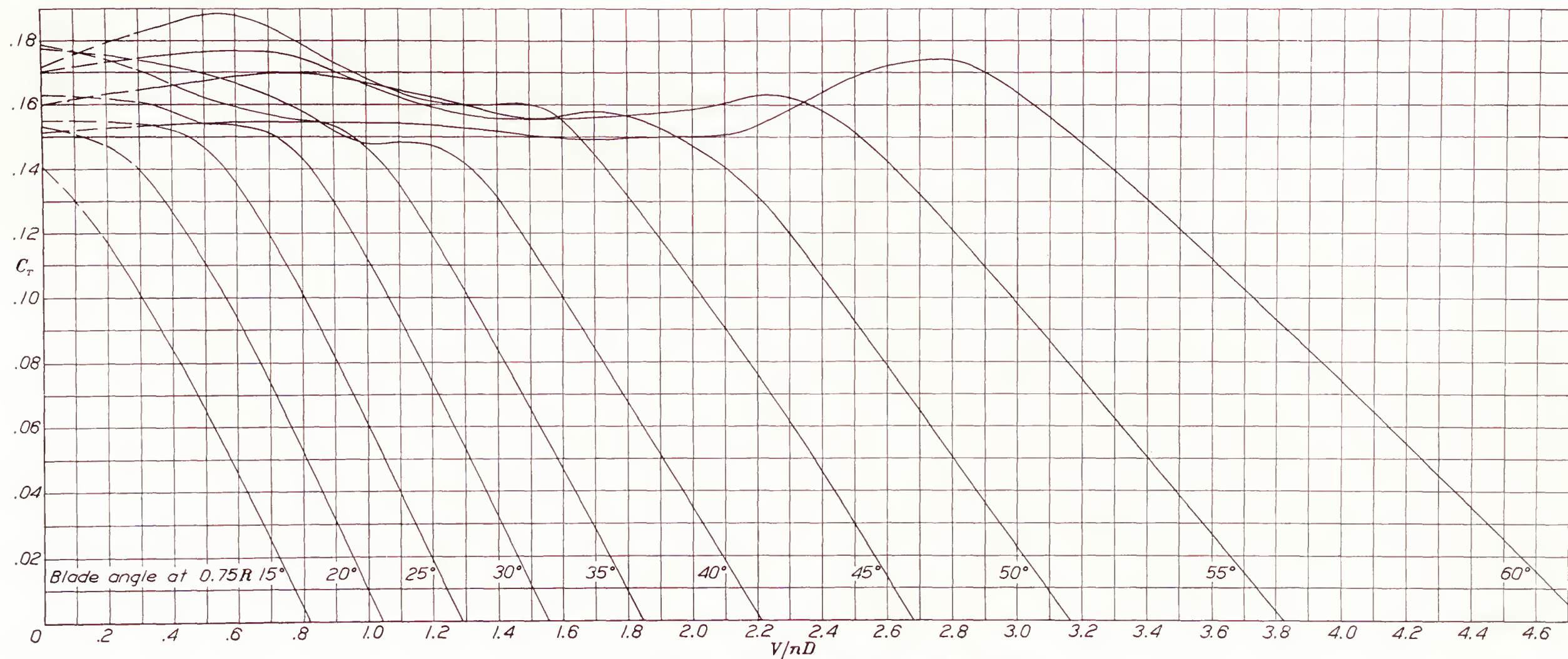


FIGURE 15.—Thrust-coefficient curves for propeller 5868-9 with spinner.



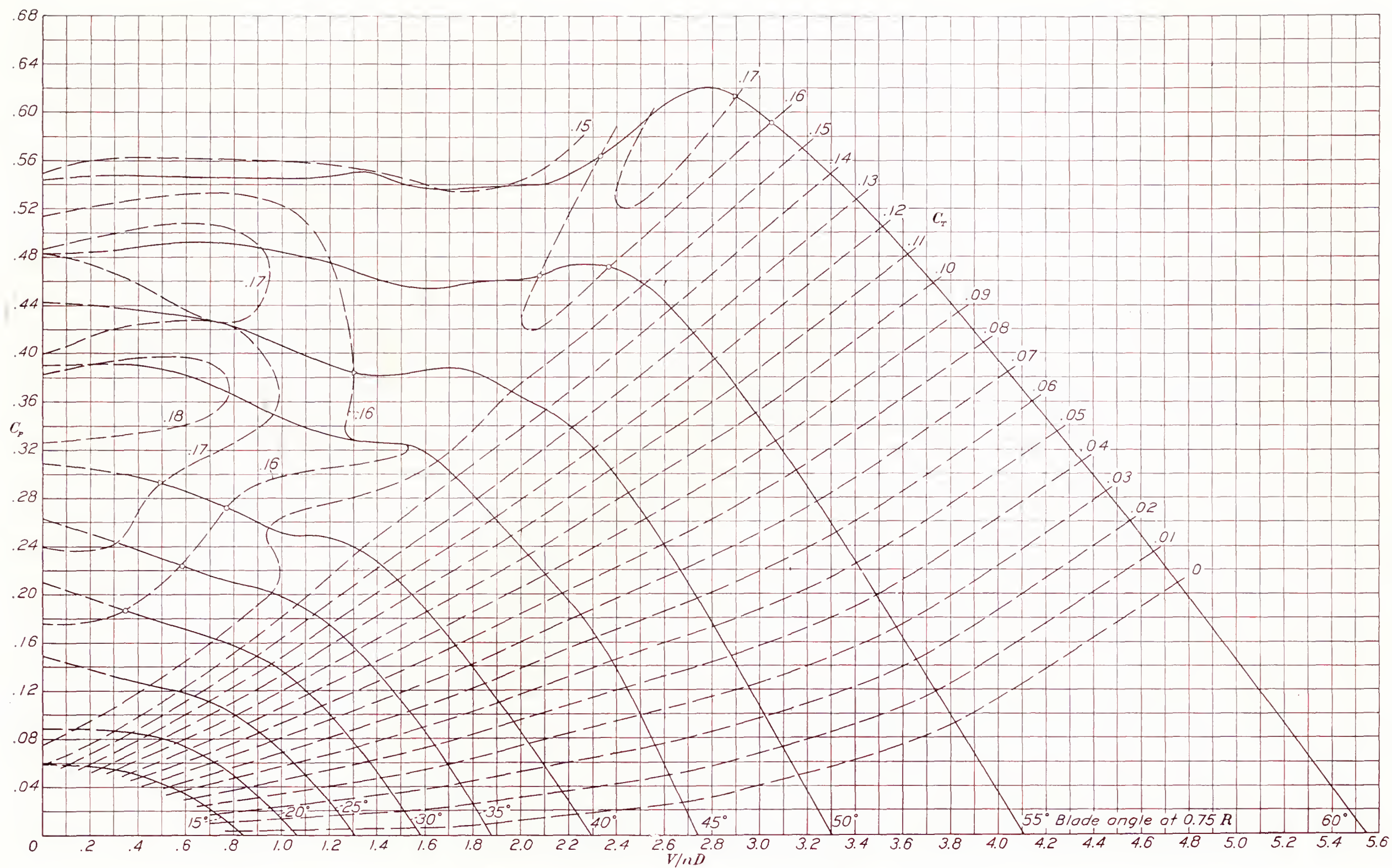


FIGURE 16.—Power-coefficient curves for propeller 5868-9 with spinner.



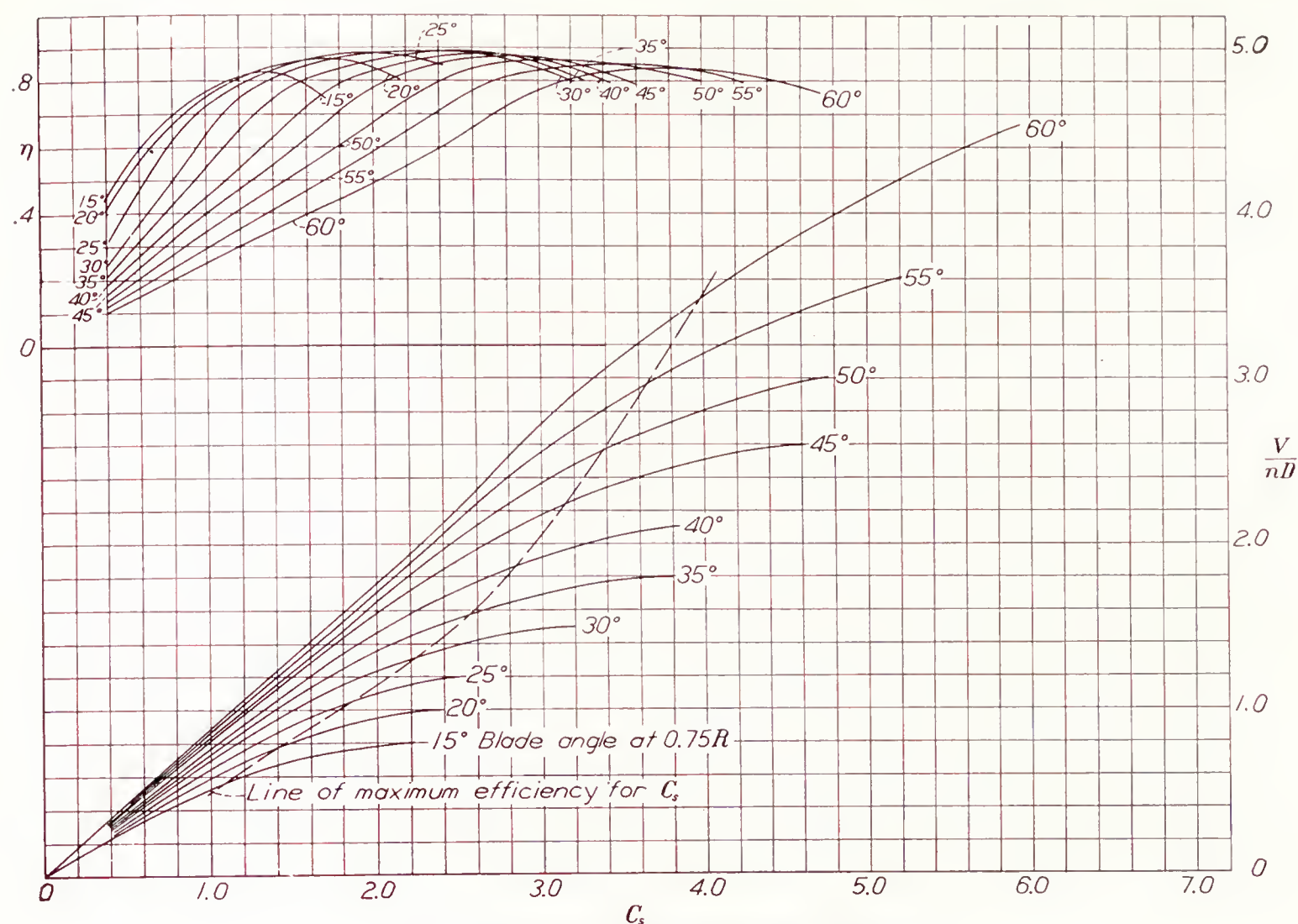


FIGURE 17.—Design chart for propeller 5868-9 with spinner.

corresponds to a blade-angle setting of  $35^\circ$  for the high-speed condition. It may be noted that the take-off setting is about  $23^\circ$ , a condition at which the blades are on the verge of stalling. The take-off efficiency drops with increasing design  $C_s$  chiefly because of the higher drag coefficients of the blade sections associated with angles of attack beyond the stall. An obvious method of reducing the take-off blade angle and yet absorbing the power is to increase the diameter, termed a "compromise" design because the high-speed efficiency suffers slightly.

A spinner is very beneficial for propeller-body combinations with liquid-cooled engine nacelles, particularly for conditions of high speed or high blade angle. A gain of about 8 percent in propulsive efficiency for a  $C_s$  value of 3.8 (approximately  $60^\circ$  blade angle) is obtained with the spinner and a lesser amount for lower blade angles (fig. 18). The use of the spinner raises the optimum design blade angle slightly and flattens the envelope of the efficiency curves to the extent that the efficiency remains relatively high for all angles up to  $60^\circ$ . Spinners are more advantageous for high speeds because the drag of the hub portions of the blades (5.5 pounds at 100 miles per hour) is a higher percentage of the thrust than for low speeds.

**Propeller 5868-X<sub>2</sub>.**—When the blades of adjustable or controllable propellers are set at angles above that for nearly constant pitch distribution ( $15^\circ$  for propeller 5868-9), the geometric pitch of the tip sections increases at a more rapid rate than for the shank sections up to

some blade angle, depending upon the amount of twist in the blades. Beyond this angle the pitch of the shank sections increases at a more rapid rate, as may be seen from the relation

$$p = D\pi \frac{r}{R} \tan \beta$$

where  $\beta$  is the blade angle for any section. As the value of  $\beta$  for the tip section is always smaller than that for a shank section by the amount of blade twist present, the difference in the tangents of the two angles becomes greater in proportion to the differences in radii as the blade angle at  $0.75R$  is increased. For propeller 5868-9, the rate of increase in pitch of the 0.2-radius section exceeds the rate for the tip section at blade angles, at  $0.75R$ , greater than  $50^\circ$ . (See fig. 5.)

Although pitch distribution has only a small effect on propeller characteristics, it would appear that some improvement is possible, particularly for high blade angles. The present attempt to improve the propulsive efficiency through different pitch distributions has thus far been unsuccessful, chiefly because the results for only one propeller (5868-X<sub>2</sub>) are available.

The envelopes of the efficiency curves for propellers 5868-9 and 5868-X<sub>2</sub> are shown in figure 18. The small loss in efficiency of propeller 5868-X<sub>2</sub> as compared with that for propeller 5868-9 throughout the range investigated is attributed to the difference in pitch distribution. The optimum blade angle for nearly constant



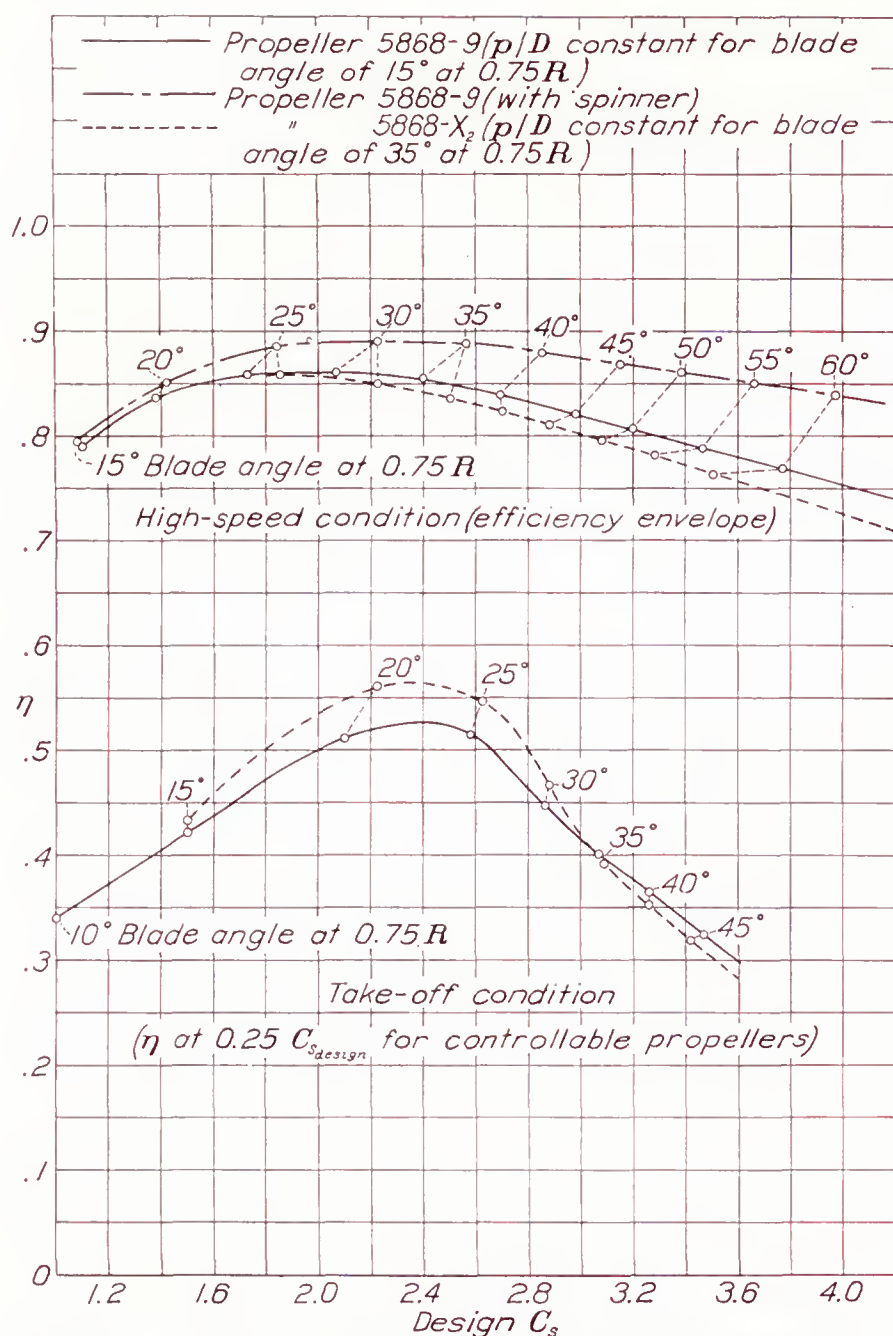


FIGURE 18.—Comparison of propellers having different pitch distributions and the effect of a spinner on the high-speed efficiency of the propeller.

pitch is evidently less than  $35^\circ$  for the conditions investigated. Some model tests made at Wright Field (reference 4) in which no body was mentioned indicated that the blade angle for constant pitch should lie between  $22^\circ$  and  $34^\circ$ .

The efficiency for the take-off conditions shows a gain for propeller 5868- $X_2$  over that for propeller 5868-9 for design  $C_s$  values up to about 3.0; beyond this value there is a small loss. The reasons for this condition are apparent in figures 19 and 20, wherein a comparison is made of the propeller characteristics for three effective pitch-diameter ratios for zero thrust. It may be noted that propeller 5868- $X_2$  does not stall so soon with increasing angle of attack (decreasing  $V/nD$ ) as does propeller 5868-9, which accounts for the gain in efficiency. The efficiency computed for the take-off criterion is taken at a value of  $V/nD$  of one-fourth that for high speed. Propeller 5868- $X_2$  consequently has a higher take-off efficiency for conditions where the  $V/nD$  for stall coincides with the take-off criterion  $V/nD$  and has a lower efficiency when the values do not coincide. The delayed and abrupt stalling character-

istic noted for propeller 5868- $X_2$  is evidently due to the fact that more of the blade elements stall at the same time than for propeller 5868-9.

**Limitations and application of the test data.**—In view of the fact that the present tests were run at relatively low tip and tunnel speeds, the effect of compressibility, which enters the problem at higher speeds, should not be forgotten. It is pointed out in reference 5 that corrections to the propeller characteristics for the take-off condition should be made for tip speeds above about 0.5 the speed of sound.

Earlier tests (reference 6) had indicated that no appreciable loss in efficiency was evident at tip speeds below about 0.9 the speed of sound for the high-speed condition. Later evidence shows that this value applies only to forward speeds up to 200 or 300 miles per hour. Figure 21 is a plot of the true speeds of each propeller section for a true tip speed of 1,000 feet per second (approximately 0.9 the speed of sound at sea level) and for different flight speeds. The curve of the section speeds corresponding to the compressibility stall was computed from airfoil data given in references 7 and 8 and from other high-speed airfoil data not published. An arbitrary correction for three-dimensional flow was made for the tip sections to bring the airfoil and the propeller data into agreement at the tip. Such a correction is justifiable on the grounds that induced velocities are reduced for three-dimensional flow.

Figure 21 indicates that, for air speeds above 300 miles per hour, sections at both the hub and the tips will be operating beyond the compressibility stall, assuming that the airfoil data as plotted apply to propellers, and that, at 500 miles per hour, all but a small part of the propeller will be operating beyond the critical speed. Losses at the tips may be avoided by reducing the tip speed, and losses at the hub sections may be avoided either by using a large spinner or by enclosing the blade shanks in cuffs of greater fineness ratio than the shanks themselves. The hub sections of a propeller operating in front of a radial engine are shielded by the cowling, an arrangement that produces about the same effect as a spinner. For very high-speed airplanes, it probably would be advisable to design the blade shanks to meet the conditions imposed by compressibility and to use airfoil sections having a higher critical speed than the Clark Y section, such as the N. A. C. A. 2400-34 series.

Another factor limiting the tip speed is the diminishing speed of sound with temperature at increased altitude. From figure 22, the probable upper limits in the application of the present data may be estimated for different altitudes. Although 500 miles per hour seems to be about the upper limit at sea level, neglecting tip and shank effects, that limit is reduced to about 425 miles per hour at 35,000 feet.



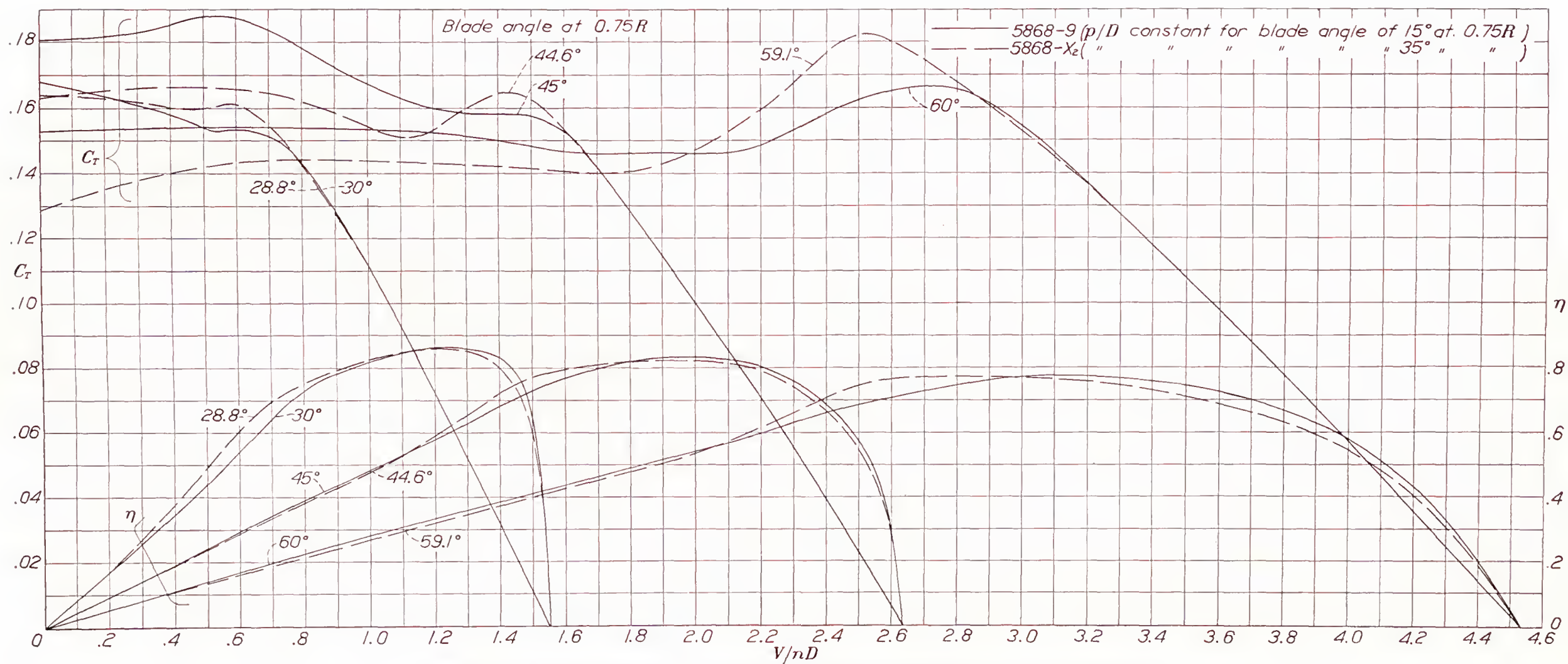


FIGURE 19.—Comparison of thrust and efficiency curves for propellers having two pitch distributions.







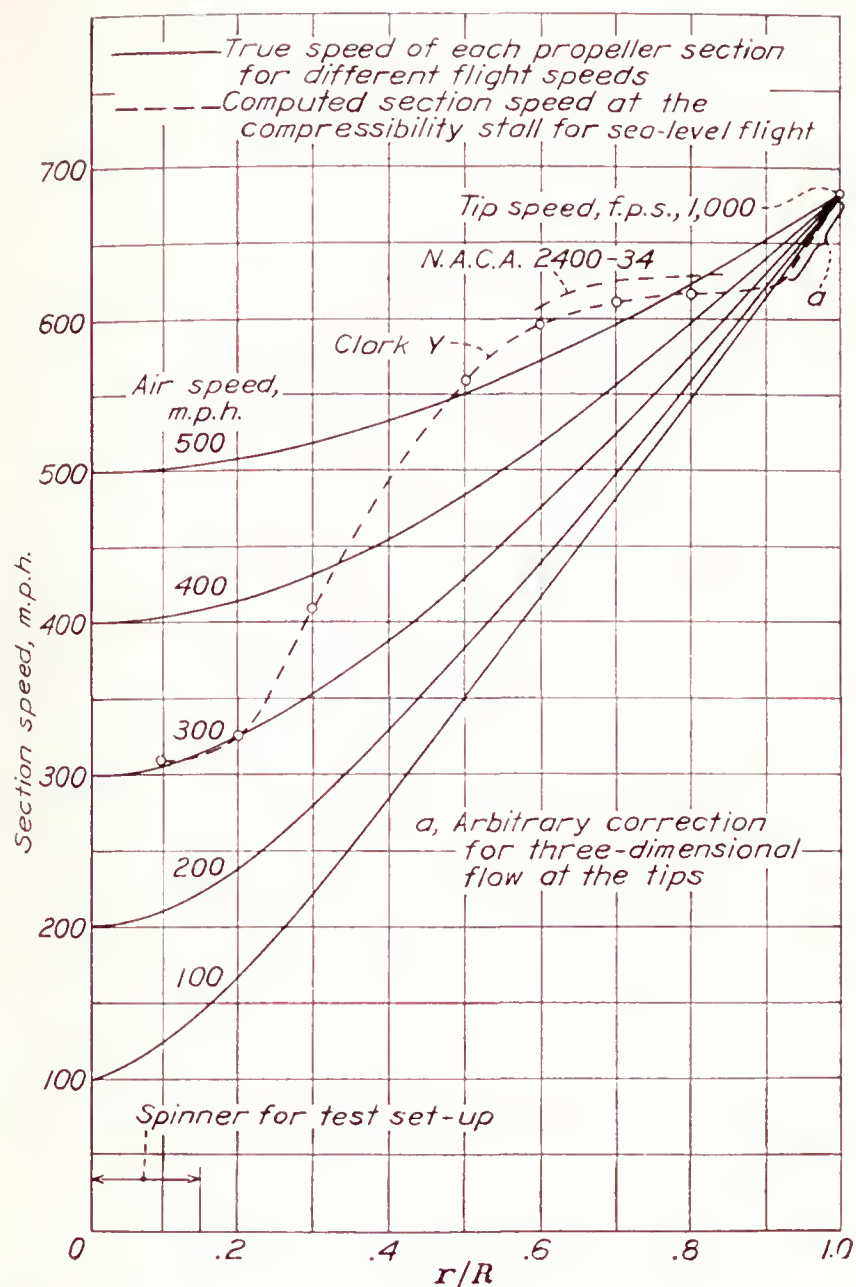


FIGURE 21.—Curves showing true speeds of propeller sections for a tip speed of 1,000 f. p. s. and different flight speeds; also computed section speeds at the compressibility stall.

### CONCLUSIONS

The propulsive efficiency at a blade angle of  $60^\circ$  was about 9 percent less than the maximum value of 86 percent, which occurred at a blade angle of about  $30^\circ$ . The efficiency at a blade angle of  $60^\circ$  was increased about 7 percent by correcting for the effect of a spinner and at a blade angle of  $30^\circ$ , about 3 percent.

An attempt to improve the propulsive efficiency of propellers set at high blade angles by reducing the geometric pitch of the tip sections with respect to the shank sections (namely, increasing the blade angle for nearly constant pitch distribution from  $15^\circ$  to  $35^\circ$ ) resulted in a small loss in the high-speed efficiency and a gain in the take-off efficiency for low blade angles.

The blade-angle range covered in this report is applicable to flight conditions up to about 500 miles per hour at sea level and about 425 miles per hour at 35,000 feet, provided that compressibility effects at the blade tips and shanks do not become critical.

LANGLEY MEMORIAL AERONAUTICAL LABORATORY,  
NATIONAL ADVISORY COMMITTEE FOR AERONAUTICS,  
LANGLEY FIELD, VA., April 14, 1938.

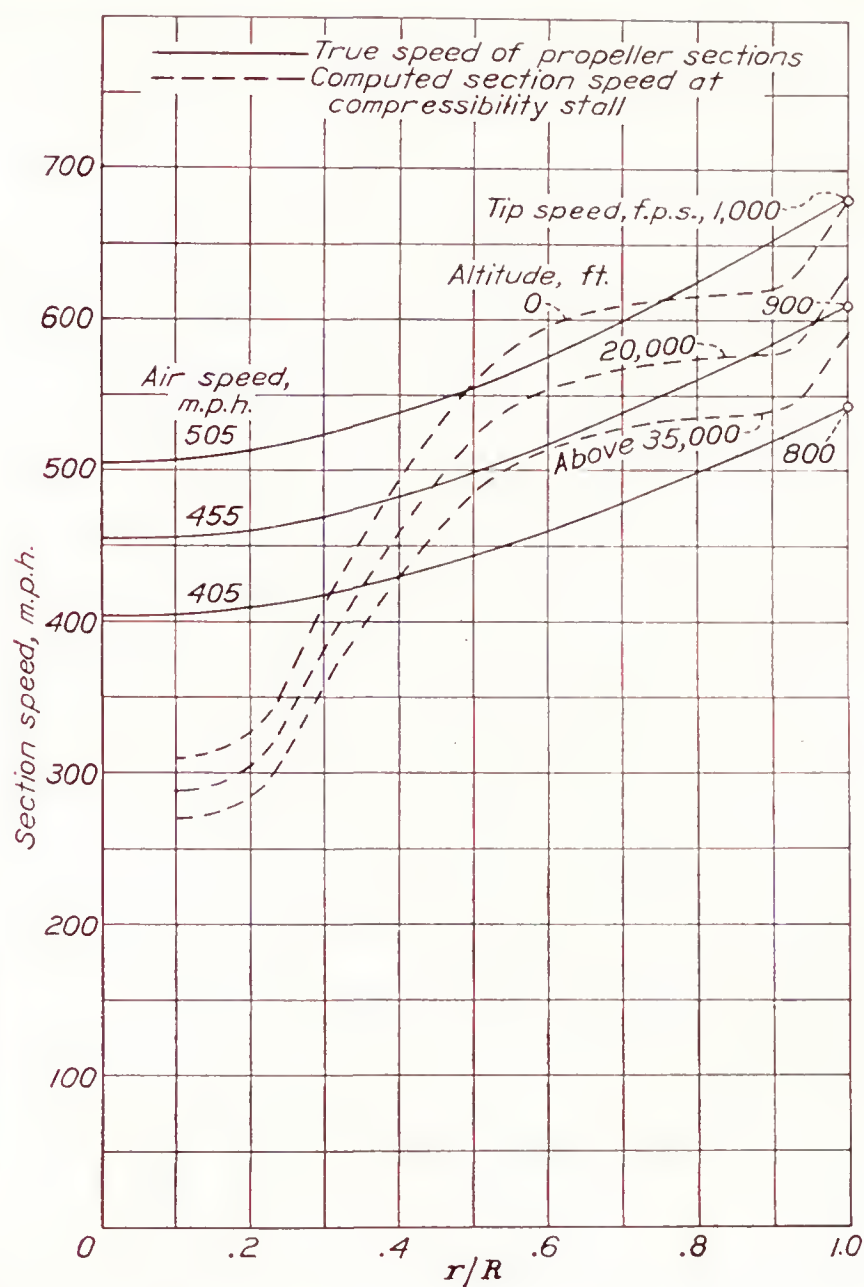


FIGURE 22.—Blade-section speeds corresponding to high-speed operation at  $60^\circ$  blade angle, and computed section critical speeds for different altitudes. Propeller 5868-9 with spinner.

### REFERENCES

1. Lesley, E. P., and Reid, Elliott G.: Tests of Five Metal Model Propellers with Various Pitch Distributions in a Free Wind Stream and in Combination with a Model VE-7 Fuselage. T. R. No. 326, N. A. C. A., 1929.
2. Weick, Fred E., and Wood, Donald H.: The Twenty-Foot Propeller Research Tunnel of the National Advisory Committee for Aeronautics. T. R. No. 300, N. A. C. A., 1928.
3. Biermann, David, and Hartman, Edwin P.: Tests of Five Full-Scale Propellers in the Presence of a Radial and a Liquid-Cooled Engine Nacelle, Including Tests of Two Spinners. T. R. No. 642, N. A. C. A., 1938.
4. Anon.: Comparison of Wind Tunnel Tests with Flight Tests on a Number of Detachable Blade Propellers Made from the Same Plan Form. A. C. I. C., vol. VII, No. 632 (A. C. T. R. No. 2943), 1929.
5. Biermann, David, and Hartman, Edwin P.: The Effect of Compressibility on Eight Full-Scale Propellers Operating in the Take-Off and Climbing Range. T. R. No. 639, N. A. C. A., 1938.
6. Wood, Donald H.: Full-Scale Tests of Metal Propellers at High Tip Speeds. T. R. No. 375, N. A. C. A., 1931.
7. Stack, John: The N. A. C. A. High-Speed Wind Tunnel and Tests of Six Propeller Sections. T. R. No. 463, N. A. C. A., 1933.
8. Lindsey, W. F.: Drag of Cylinders of Simple Shapes. T. R. No. 619, N. A. C. A., 1938.







## REPORT No. 659

# EFFECT OF SERVICE STRESSES ON IMPACT RESISTANCE, X-RAY DIFFRACTION PATTERNS, AND MICROSTRUCTURE OF 25S ALUMINUM ALLOY

By J. A. KIES and G. W. QUICK

### SUMMARY

*A great number of tests were made to determine the effect of service stresses on the impact resistance, the X-ray diffraction patterns, and the microstructure of 25S aluminum alloy. Many of the specimens were taken from actual propeller blades and others were cut from  $\frac{1}{16}$ -inch rod furnished by the Aluminum Company of America.*

*The average impact resistances were found to be unchanged even after 288,000 cycles in a 33,400 pound-per-square inch range that exceeded the fatigue limit and the original proof stress of the material. The X-ray diffraction patterns were unchanged as regards any indication of structural change resulting from the fatigue stressing of the alloy. Two structural conditions known as slip-plane precipitation and veining were observed. The service stresses were not responsible for the slip-plane precipitation and the endurance limit was not reduced by it. Veining could be made to disappear and reappear by alternate solution heat treatment and age hardening.*

### INTRODUCTION

During the course of its useful service life, any assembled structure, such as an airplane, is subjected to stresses varying greatly in their magnitude and nature. Although no single type of stress or simple combination of stresses can be considered most important in determining the duration of the service life, fatigue overshadows any other single factor under ordinary service conditions.

Recently Ravilly (reference 1) and Cazaud and Persoz (reference 2) have reviewed the various theories concerning the mechanism of the fatigue process. Study of the possible detrimental effect on the properties of a metal of continued fatigue stressing short of failure has, however, received scant attention. Attention has rather been directed to the determination of the number of applications of stress of known magnitude required to produce failure and the conditions that favor local overstressing, and therefore premature failure.

The possibility of detrimental changes occurring in the structure of the aluminum alloys used for aircraft propellers was made the subject of a group of tests

conducted at the National Bureau of Standards laboratories in 1938. If damage did result, some short-time test to detect it was sought. In order to decide on a suitable testing procedure, two general assumptions regarding the nature of fatigue damage were made:

(a) The important changes occur throughout a large portion of the stressed body and are essentially dependent on the stress history of the body as a whole.

(b) The regions of extreme damage by repeated stresses are highly localized; hence, unless the effective cross section is reduced by the presence of cracks already formed, the use of any physical test whose results represent an averaging process throughout a large column of metal must necessarily show little if any correlation with fatigue damage.

Inasmuch as the main body of the work was devoted to (a), notch and corrosion effects were excluded as far as possible.

The subject was considered in three phases, each constituting a part of the paper. Part I, by J. A. Kies, deals with a possible lowering of the impact resistance of the metal after prolonged fatigue testing. Part II, by the same author, considered the use of X-ray diffraction patterns as a method of detecting fatigue damage prior to the actual failure of the member. Part III, by Kies and G. W. Quick, reports on slip-plane precipitation and veining.

Although no positive evidence of detrimental changes was obtained, the results are presented for the light they throw on the problem and the use of short-time methods to detect damage done to a metal by fatigue.

### I. IMPACT RESISTANCE OF 25S ALUMINUM ALLOY BEFORE AND AFTER FATIGUE STRESSING

Apparently little has been done on the subject of the possible lowering of impact resistance of aluminum alloys. K. Honda (reference 3) used the percentage decrease in impact resistance of plain carbon steels under repeated impact as an indication of the degree of fatigue damage. F. Oshiba (reference 4) showed a close correlation between the growth of fatigue cracks and the degree of fatigue in the case of plain carbon steels sub-



jected to repeated impacts and later (reference 5) reported a similar relation in the case of annealed plain carbon steel specimens of the rotating-beam type. In all cases, a small decrease in impact resistance was believed to precede the beginning of visible fatigue cracks.

In 1933 Moore and Wishart (reference 6) reported that lowering of the tensile strength resulted from stresses in excess of the fatigue limit provided that the number of cycles was sufficiently great. A value of 1,400,000 cycles was sufficient to establish fatigue limits in this manner for five steels, one brass, and monel metal. Although the number of reversals necessary for duralumin was not determined, it was thought to exceed the foregoing value. Earlier work by Davidenkow and Schewandin (reference 7) on annealed 0.15 to 0.20 percent carbon steel showed immediate lowering of the static breaking strength of notched specimens stressed above the fatigue limit in a rotating-beam machine and then broken by bending while immersed in liquid air. Brittle fractures permitted the course of the fatigue crack to be followed. It was found that, in specimens normally expected to fail after 700,000 cycles of the stress employed, the first visible evidence of damage appeared after 300,000 cycles. This result was considered to indicate that a general weakening in the material preceded the beginning of the crack. Neither the method of Davidenkow and Schewandin nor that of Moore and Wishart has led to any important application. It would appear, however, that sufficient evidence of important general changes exists to justify serious consideration of a program of impact testing of fatigued material. Presumably lowered impact resistance in such material might be due to one of two causes, the presence of incipient cracks or to a cold-worked condition of the metal.

One of the most highly stressed members of any air-craft structure is the propeller. Despite the fact that no evidence of impending failure may be observed in the frequent inspections made of the structure, it is customary to place an arbitrary limit on the number of hours of service permitted for any propeller. Because of such important considerations, an aluminum alloy in wide use for propeller blades was selected as the first material for study. Many of the specimens were taken from propeller blades in the possession of the National Bureau of Standards. Others were cut from  $\frac{13}{16}$ -inch rod of 25S alloy furnished especially for the purpose by the Aluminum Company of America. The composition of the rod according to information furnished by the manufacturer, was:

Copper.....	4. 4 percent.
Manganese.....	0. 76 percent.
Silicon.....	0. 82 percent.
Iron.....	0. 43 percent.
Aluminum.....	Remainder.

The heat treatment of aluminum alloy 25S recommended by the Aluminum Company of America (reference 8) consists in three steps:

- (a) Soaking at 960° to 980° F. The time required for this treatment depends on the load and on the nature of the heating bath.
- (b) Quenching in cold water, the temper designation then being 25SW.
- (c) Aging for 12 hours at 285° to 295° F., the temper designation being 25ST.

The tensile properties of the alloy 25ST rod as determined at the National Bureau of Standards were as follows:

TABLE I.—TENSILE PROPERTIES OF HEAT-TREATED ALUMINUM ALLOY, 25ST

[Values in lb./sq. in.]

Ultimate tensile strength.....	60, 600
True ultimate stress <sup>1</sup> .....	77, 000
Nominal stress at fracture <sup>2</sup> .....	52, 100
True stress at fracture <sup>3</sup> .....	89, 300
Proportional limit <sup>4</sup> .....	22, 300
Proof stress at 0.2 percent set.....	32, 300

<sup>1</sup> Maximum load divided by the actual cross-sectional area.  
<sup>2</sup> Load at fracture divided by the initial cross-sectional area.  
<sup>3</sup> Load at fracture divided by the actual cross-sectional area.  
<sup>4</sup> Estimated stress when stress-strain curves departed from the slope of the modulus line.

The fatigue limit of 25ST as determined on the rotating-beam machine (R. R. Moore type) and based on 500,000,000 cycles of stress without failure, is given as ±15,000 pounds per square inch (reference 8).

TEST SPECIMENS AND MACHINES

The Haigh axial-loading fatigue-testing machine was used to stress in fatigue the material to be tested later for impact resistance. Figure 1 shows the fatigue

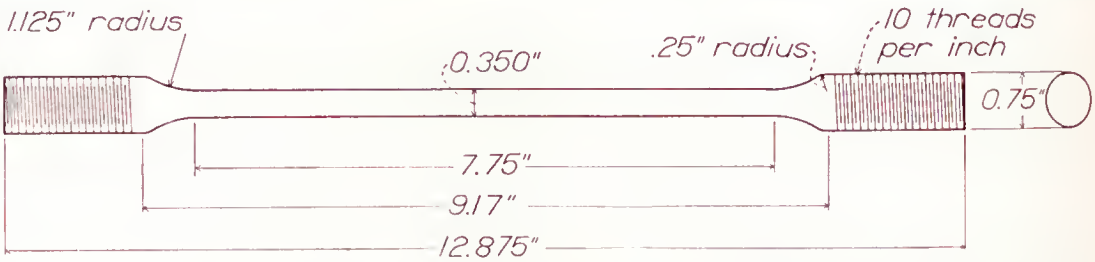


FIGURE 1.—Dimensions of the Haigh fatigue specimens used for the 13,000 pounds per-square-inch stress amplitude.

specimen used for the 13,000 pounds per square inch range, and figure 2 shows the specimens for the ranges higher than 13,000 pounds per square inch. Specimens machined from the fatigue bars were tested for impact resistance by the Charpy method and by the Luerssen-Greene torsion-impact method (reference 9).

Figure 3 (a, b, c,) gives the dimensions and form of the Charpy specimens, two different notch depths being used (0.005 and 0.039 inch). Figure 4 shows the torsion-impact specimens. The reproducibility of results obtained with the Charpy machine exceeded that obtained with the torsion-impact machine for the purpose of this work.

If  $W$  is the average impact energy indicated and  $\Delta W$  is the smallest difference of energy that can be



read directly or estimated from the indicating mechanism, then

$$\frac{\Delta W}{W} = 0.007 \text{ for } 0.005\text{-inch-notch depth (Charpy test)}$$

$$\frac{\Delta W}{W} = 0.017 \text{ for } 0.039\text{-inch-notch depth (Charpy test),}$$

and

$$\frac{\Delta W}{W} = 0.04 \text{ (torsion impact).}$$

These results are without regard to natural errors caused by faulty manipulation or to energy losses in the machines. In the case of the torsion tests, the impact value was meaningless when premature striking of the horns on the specimen holder occurred. In obvious cases of this kind, the test results were discarded.

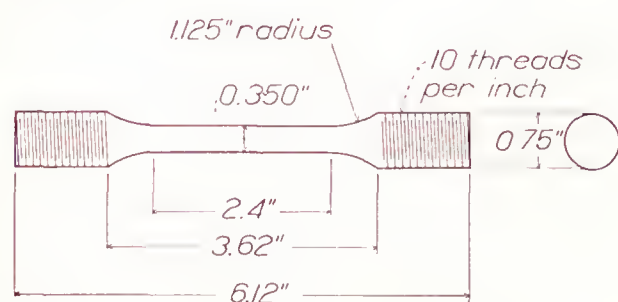
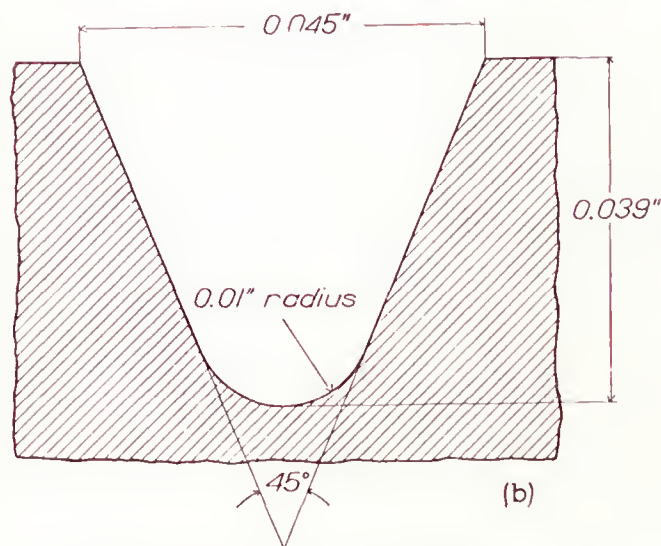


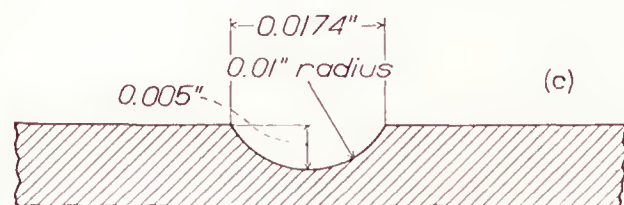
FIGURE 2.—Dimensions of the Haigh fatigue specimens used for stress amplitudes greater than 12,000 pounds per square inch.



(a) Machined from the Haigh fatigue specimens.



(b) Contour of the Charpy notch 0.039 inch deep.



(c) Contour of the special Charpy notch.

FIGURE 3.—Dimensions and form of Charpy type impact specimens.

The preliminary results showed that the percentage deviation from the mean for torsion impact tests was less than that for Charpy specimens with the 0.039-inch

notch depth but more than for Charpy specimens having notches 0.005 inch deep.

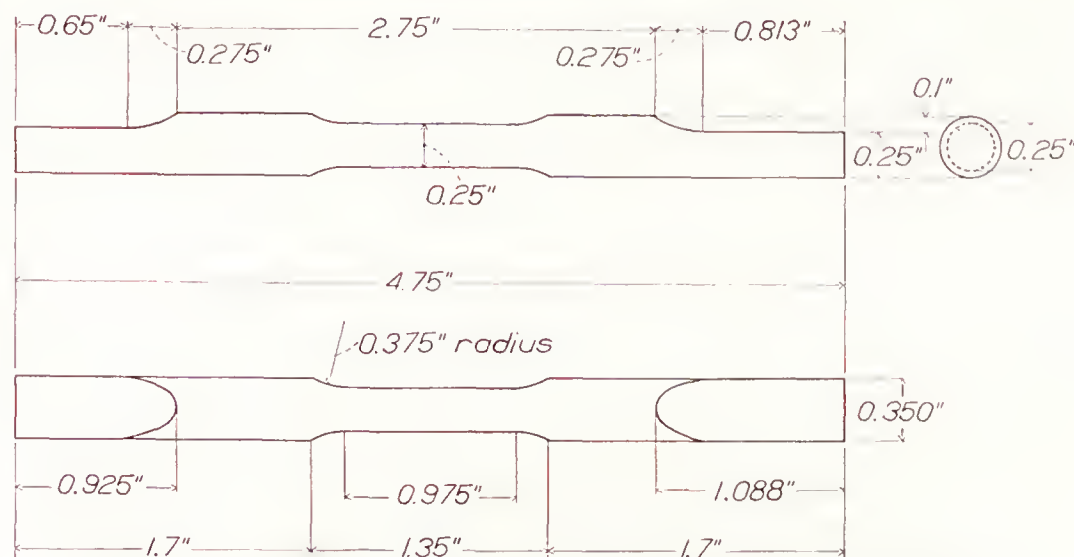


FIGURE 4.—Torsion impact test specimen machined from Haigh fatigue specimens.

#### TEMPERATURES FOR IMPACT TESTS

In the attempt to find test conditions that would yield the least ambiguous results, Charpy specimens comparable with those to be cut from Haigh fatigue specimens, were broken at various temperatures ranging from  $-190^{\circ}\text{C}$ . to  $99^{\circ}\text{C}$ . As is shown in figure 5, the smallest average percentage deviation from the mean was obtained at room temperature. Ample time for carefully centering the specimens may be the reason for the better uniformity at this temperature. The best obtainable agreement among check specimens was thought to be least obscuring to a possible change in impact resistance either with regard to scatter or to average value. On the other hand, low temperatures representing extremes encountered

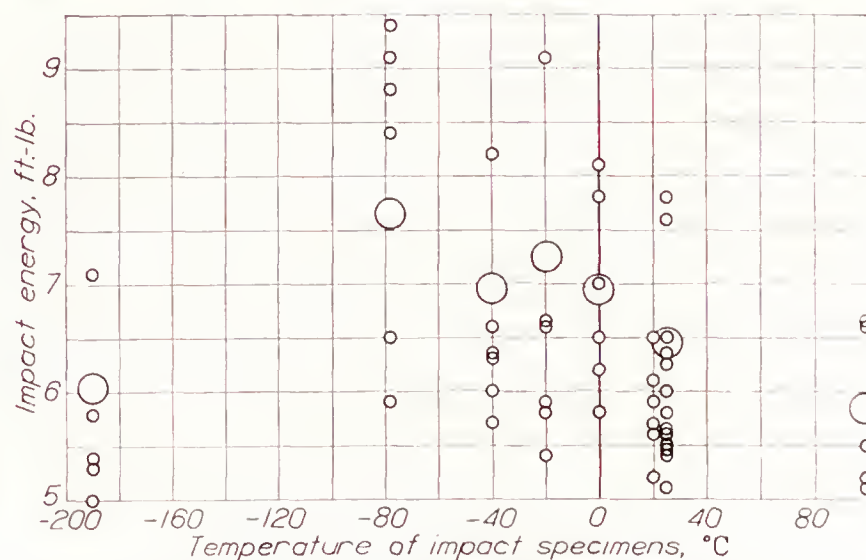


FIGURE 5.—Results of impact tests on Charpy type specimens of 25ST bar stock at various temperatures. The specimens are shown in figures 3(a) and 3(b). Each large circle indicates the midpoint of the scatter for one temperature.

in service could not be neglected and, accordingly, it was decided to make impact tests on fatigued material both at room temperature and at  $-78^{\circ}\text{C}$ .

#### SIGNIFICANCE OF THE FIBERED APPEARANCE OF LONGITUDINAL SECTIONS OF 25ST ROD

A photograph (fig. 6) shows grains elongated in a direction parallel with the rod axis, but cross sections (fig. 7) show no preferential grain alignment. The



elongated grain structure is also quite prominent in 25ST rolled plate, and a definite difference in impact resistance is known to exist for specimens cut in the parallel and the transverse directions.

Preferred crystal orientation in varying degrees generally accompanies fibering. X-ray diffraction patterns can sometimes show the presence of preferred orientation. A diffraction pattern that showed definite preferred crystal orientation might therefore indicate indirectly the presence of a possible directional weakness in impact resistance.

X-ray diffraction patterns of the reflection type were obtained with a view toward devising a nondestructive

impact specimens cut longitudinally from the center of the 25ST rod need not have their notches oriented uniformly with respect to any certain rod diameter.

#### THE EFFECT OF SMALL VARIATIONS IN NOTCH DEPTH

Before the specimens were tested, the notch depths of the impact specimens were measured by a Hilger measuring microscope. Measurements were made at both ends of each notch. The average values plotted against the impact resistance showed no consistent relation between impact values and notch depth for the variations measured, that is, from  $-0.0015$  to  $0.0015$  inch deviation from the nominal value. Larger

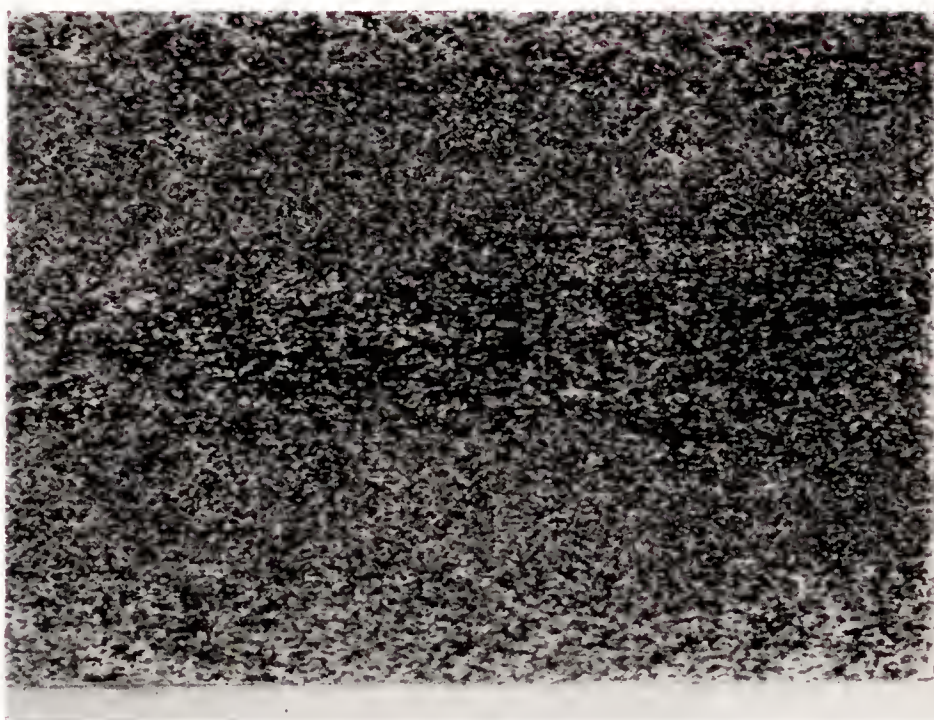


FIGURE 6.—Longitudinal section through 25ST rod showing elongation of the grains in direction of the rod axis,  $\times 3$ .

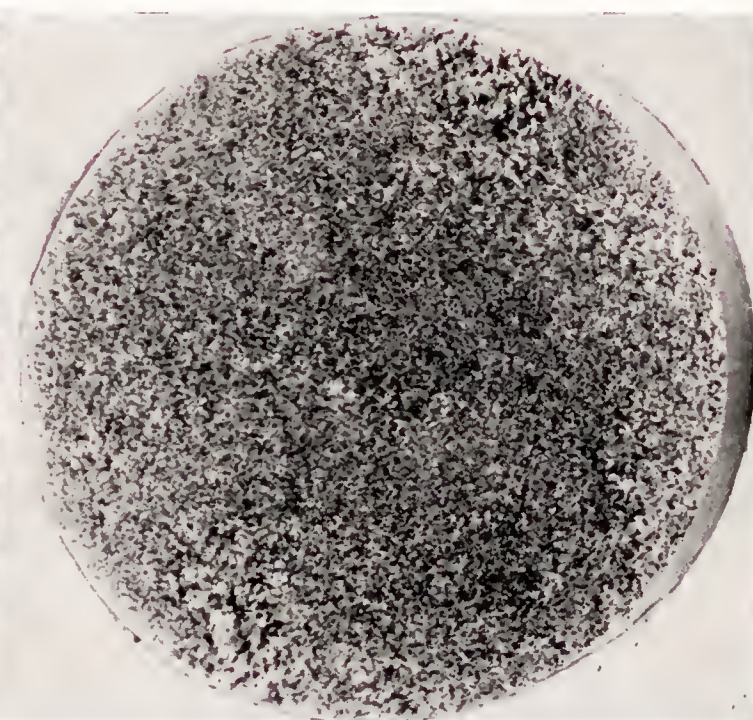


FIGURE 7.—Transverse section through 25ST rod showing no preferential elongation of the grains in any direction, such as shown in figure 6,  $\times 3$ .

method of inspection for propeller blades. The X-ray beam was allowed to fall on the etched specimen at grazing incidence and at right angles to the fibered direction. The specimen was moved in such a manner that the orientation of the fibered axis was constant with respect to the beam and to the film. In this way a large number of crystals was made to contribute to the pattern. No evidence of preferred orientation was found in the 25ST rod, in rolled 25ST plate known to have directional variation in impact resistance, or in a commercial duralumin rod, all of which showed a fibered appearance when polished and etched.

X-ray transmission patterns were obtained using thin etched slices of the 25ST rod. Transverse and longitudinal sections were studied, both stationary and moving. The section surface was kept in the same plane and no rotation about the direction of the beam was permitted. No preferred orientation was found.

It was concluded that X-rays are not suitable for the detection of directional variations in impact resistance in thick structural members such as aluminum-alloy propeller blades. Figure 7 shows no fibering transverse to the rod axis; consequently, it was decided that

variations, such as from 0.005 inch to 0.039 inch, do show marked effect on impact resistance.

#### TEST PROCEDURE AND RESULTS

Table II lists the various repeated stress treatments given the Haigh specimens.

TABLE II.—FATIGUE STRESSING OF SPECIMENS IN HAIGH AXIAL LOADING MACHINE AT ROOM TEMPERATURE PRIOR TO IMPACT

[The frequency was 2,400 cycles per minute in all cases]

Mode of repeated stressing	Mean stress (lb./sq. in.)	Stress limits		Stress range (lb./sq. in.)	Cycles of stress	Remarks
		Maximum (lb./sq. in.)	Minimum (lb./sq. in.)			
a-----	3,650	10,150	-2,850	13,000	25,000,000	Unbroken.
b-----	20,900	37,600	4,200	33,400	288,000	Do.
e-----	20,900	37,600	4,200	33,400	153,000 to 480,000	Broken.
d-----	20,900	38,200	3,600	34,600	144,000	Unbroken.
e-----	20,900	38,200	3,600	34,600	288,000	Do.
f-----	20,900	38,200	3,600	34,600	192,000 to 276,000	Broken.
a. r.-----	0	0	0	0	0	As received.

Specimens, machined from the reduced portions of the Haigh bars after stressing, were tested in impact.



with the results shown in table III. It is evident that no significant embrittlement was induced by any of the repeated stress treatment, however damaging it may have been insofar as fatigue was concerned.

TABLE III.—IMPACT RESISTANCE OF 25ST ALUMINUM ALLOY PREVIOUSLY SUBJECTED TO FATIGUE STRESS

Impact test method	Number of impact specimens broken	Temperature of test (° C.)	Mode of previous fatigue stress <sup>1</sup>	Notch depth (in.)	Average impact energy (ft.-lb.)	Average deviation from mean (percent)	Total width of scatter (ft.-lb.)
Charpy-----	18	25	a. r.	0.039	6.0	8.3	2.6
	20	25	(a)	.039	5.7	9.3	2.0
	20	25	a. r.	.005	14.6	5.1	3.4
	14	25	(b)	.005	14.7	7.5	4.0
	5	25	(c)	.005	15.1	7.3	2.7
Torsion-----	18	25	a. r.	None	54.0	7.2	28.0
	2	25	(a)	None	57.0	7.0	8.0
	15	-78	a. r.	0.005	16.7	6.0	5.2
Charpy-----	8	-78	(d)	.005	16.9	10.0	5.4
	4	-78	(e)	.005	15.7	7.6	2.5
	3	-78	(f)	.005	18.8	3.2	1.8
	6	-78	a. r.	.039	8.0	15.0	3.5
	6	-78	(d)	.039	6.5	21.5	4.3

<sup>1</sup> See table II for mode of previous fatigue stress.

The distribution in impact energy of the individual specimens previously subjected to repeated stress was closely similar to that for the specimens machined from

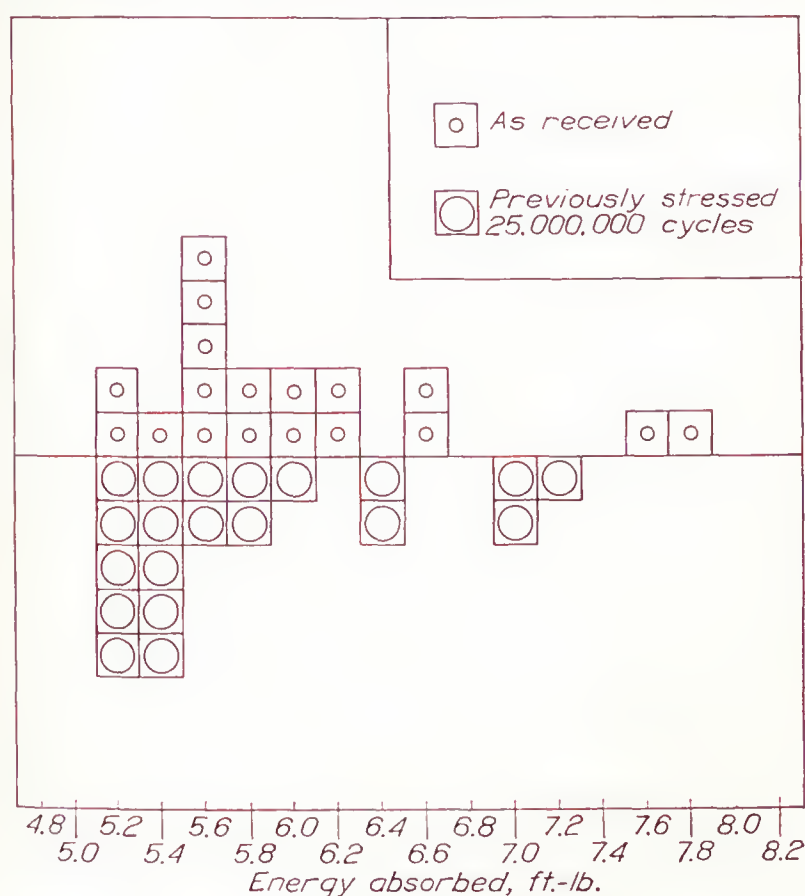


FIGURE 8.—Distribution of Charpy specimens according to energy absorbed in impact fracture. No significant change is found to result from prestressing 25,000,000 cycles in the range from 2,850 pounds per square inch compression to 10,150 pounds per square inch tension. Cyclic rate, 2,400 per minute; Charpy specimens were as shown in figures 3(a) and 3(b); each square represents one impact test at room temperature.

material in the "as received" condition. Figures 8, 9, 10, and 11 compare the distributions with the corresponding ones for unstressed material.

## DISCUSSION OF RESULTS

In mode a (table II) of repeated stress treatment, it is reasonably certain that the specimens were stressed in a safe range. Assuming a sine wave for the stress-time relation, one can show that the original proof stress (at 0.2 percent set) was exceeded during approximately 24 percent of the cycle in modes b and c and during approximately 27 percent of the cycle in modes d, e, and f.

The decrease in specimen diameter during the repeated stress (modes b, c, d, e, and f) averaged  $0.43 \pm$

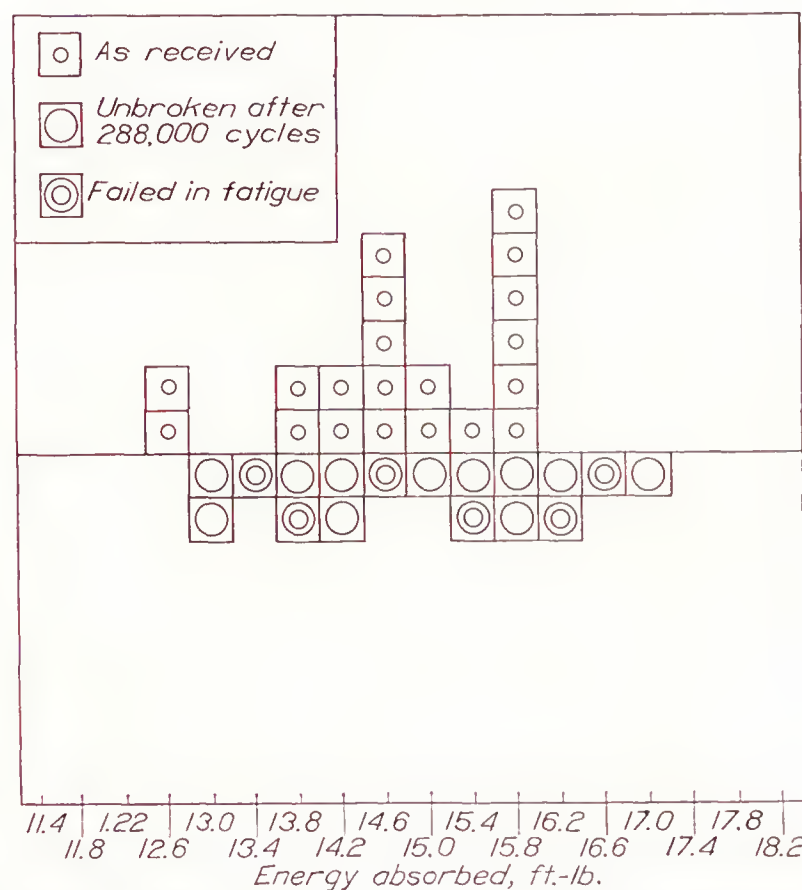


FIGURE 9.—Distribution of Charpy specimens according to energy absorbed. No significant change in impact resistance is found to result from repeated stresses in the unsafe range. The maximum tension exceeded the original proof stress of the alloy (25ST). Stress range, 4,200 to 37,600 pounds per square inch in tension; cyclic rate, 2,400 per minute; Charpy specimens were as shown in figures 3(a) and 3(c); impact testing temperature, 25° C.; each square represents one impact test.

0.03 percent with a corresponding increase in stress of  $0.86 \pm 0.06$  percent. This change is smaller than the uncertainty in adjusting the load in the Haigh machine. It also illustrates the fact that the amount of *general* cold work was very slight.

## CONCLUSIONS

The average impact resistances, as measured by Charpy tests at 25° C. and at -78° C. and by torsion-impact tests at 25° C., were unchanged by any of the following conditions of prior fatigue stressing at 25° C.:

25,000,000 cycles of safe stress, the total range being 13,000 pounds per square inch, part of which was in compression. Torsion and Charpy impact tests were made at room temperatures.



288,000 cycles in a 33,400 pounds per square inch range that exceeded the fatigue limit and the original proof stress of the material. All the stress was in tension, and the number of cycles exceeded half the greatest number required to cause failure in five similar specimens. Charpy impact tests were made at room temperature.

Various numbers of cycles (153,000 to 480,000) causing fatigue failure in a stress range of 33,400 pounds

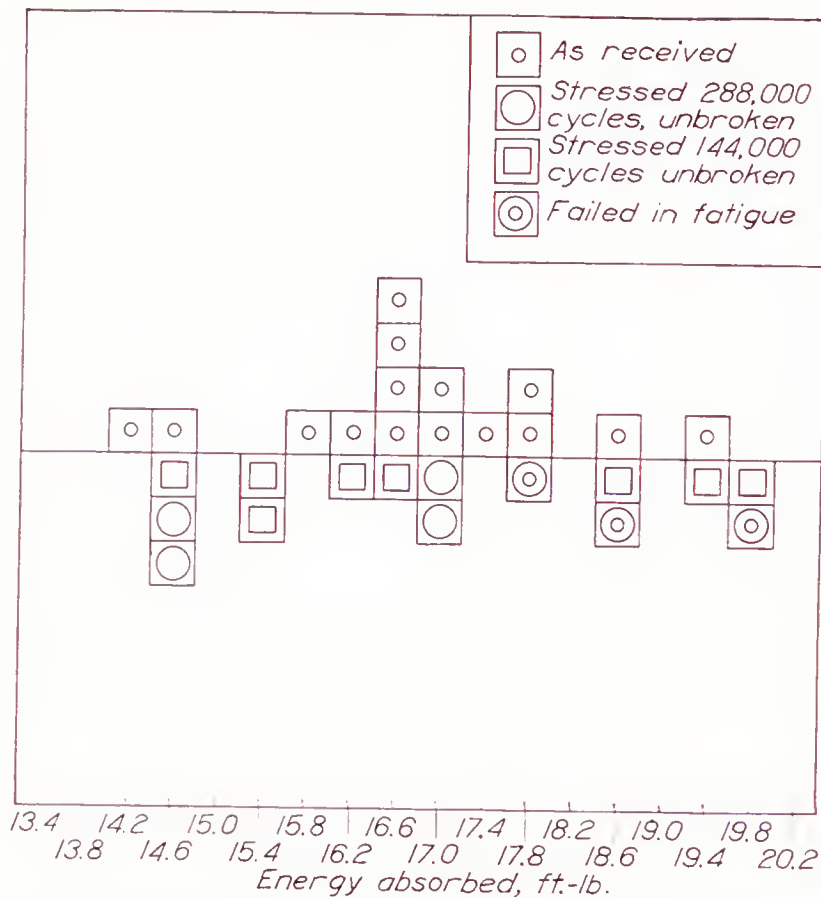


FIGURE 10.—Distribution of Charpy specimens according to energy absorbed at  $-78^{\circ}\text{C}$ . Special notch; no embrittlement was found to occur as a result of stressing alloy 25ST for various numbers of cycles in the stress range 3,600 to 38,200 pounds per square inch in tension; impact specimens of the type shown in figures 3(a) and 3(c) were used; each square represents one test.

per square inch, all of which was in tension. Charpy impact tests were made at room temperature.

288,000 cycles in a 34,600 pounds per square inch range. The Charpy tests were made at  $-78^{\circ}\text{C}$ .

Various numbers of cycles (192,000 to 276,000) causing fatigue failure in a stress range of 34,600 pounds per square inch. Charpy impact tests were made at  $-78^{\circ}\text{C}$ .

## II. X-RAY DIFFRACTION PATTERNS OF 25S ALUMINUM ALLOY BEFORE AND AFTER FATIGUE STRESSING

The great advantage of a nondestructive test for determining the extent to which metals may have been damaged by fatigue scarcely needs explanation. In addition to possessing the advantage of not injuring the metal tested, the X-ray method can be applied to small areas on the surface of fatigue specimens or structures under investigation. It is well known that severe fatigue damage is usually highly localized and that the geometric forms of the specimens and the method of stress application frequently induce the beginning of

the fatigue cracks in or near the surface at locations of relatively high stress concentration.

The successful application of X-ray diffraction to the study of metals that may have been damaged by fatigue stressing depends on whether or not the changes detectable by X-ray diffraction are the significant ones in fatigue. The question of whether or not the X-ray diffraction method may be of use for the purpose is still controversial, and the correct testing procedure is by no means standardized. The aim in such studies, of course, has not been to detect actual cracks, for which other methods of inspection are in common use, but to tell whether or not the formation of a crack is imminent.

The essential details of what happens in the early stages of a fatigue failure, before a crack has been started, are obscure; hence, X-ray diffraction studies are as yet empirical as far as correlation with fatigue is concerned. It is important to interpret correctly the

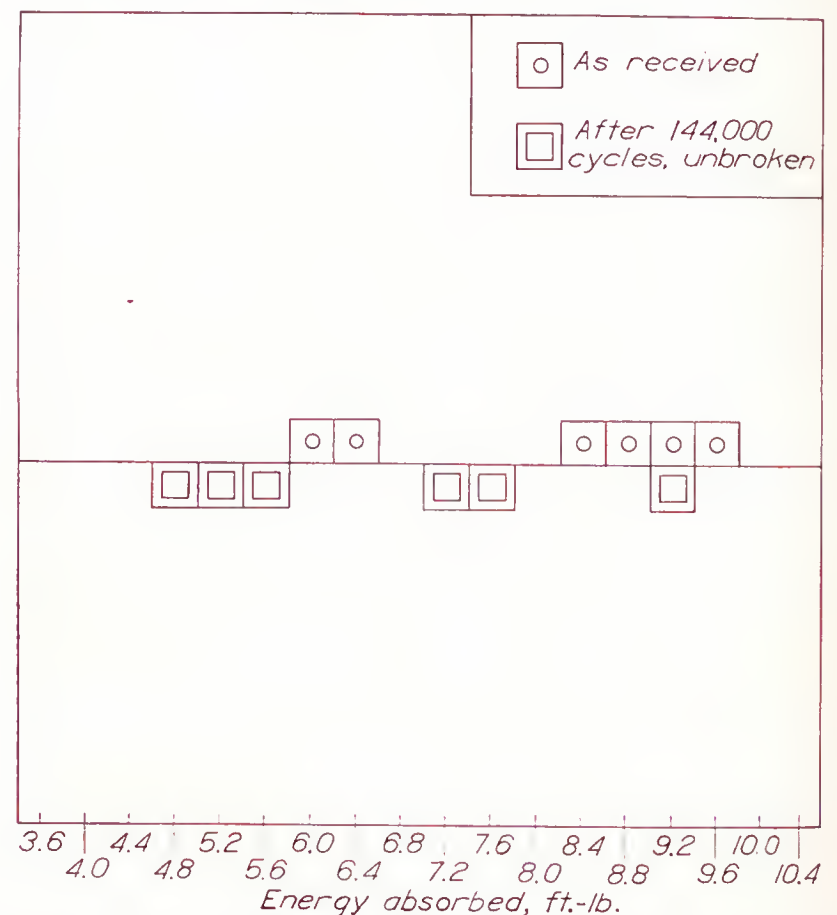


FIGURE 11.—Distribution of Charpy type specimens according to energy absorbed at  $-78^{\circ}\text{C}$ . Standard notch; no embrittlement was found to occur as a result of stressing alloy 25ST for 144,000 cycles of stress in the range 3,600 to 38,200 pounds per square inch in tension.

changes in diffraction pattern in terms of crystal structure in order to learn the limitations and the possibilities of the method.

According to published results, changes in an X-ray diffraction pattern occurring as a result of fatigue stressing may all be attributed to a condition of cold working in the metal. The various effects of cold working on metallic crystals have been classified (references 10 and 11), together with the changes in X-ray pattern associated with them, as follows: Block dislocation with negligible lattice distortion, extended block dislocation, lattice distortion, and preferred orientation. It should be understood that all these effects accompany the breakdown of metallic crystals by cold work and



are expected to occur simultaneously to varying degrees.

Block dislocation with negligible lattice distortion connotes the fragmentation of crystals into smaller units or blocks that tilt slightly with respect to the orientation of the parent grain. The diffraction pattern obtained with monochromatic radiation shows the diffraction spots of the original grains smeared along the circumference of the diffraction (Debye) rings to which they belong. No radial widening of the rings occurs. Continuous radiation gives a diffraction pattern characterized by radial asterism that varies with the X-ray method used.

Extreme amounts of cold work may result in continued fragmentation and extended dislocation of the crystal. The diffraction spots of the parent structure are then indistinguishable. With monochromatic radiation a continuous diffraction (Debye) ring is formed and the smaller the crystallites are, the wider and more diffuse is the diffraction ring up to a certain limit. Continuous radiation produces a general fogging of the diffraction pattern.

Elastic deformation produces changes in the lattice constants. The changes vary from grain to grain in a polycrystalline material, and even in a single crystal a given lattice spacing may vary from point to point. Elastic bending cannot occur without producing some lattice distortion (reference 11); the resulting curved reflecting crystal planes yield qualitatively the same diffraction effects as the small dislocations described.

Preferred orientation results from a relatively high degree of cold working and occurs by readjustment of crystalline fragments in certain preferred directions that depend on the crystalline habit of the parent crystal and the mode of stress application causing fragmentation. The preferred orientation encountered in cold-rolled sheet ordinarily requires a fairly high degree of general plastic deformation of the metal before its presence can be shown by X-ray diffraction patterns.

Some of the recent studies by X-ray methods (references 12, 13, and 14) of fatigue damage have been accomplished by locking the test specimen in the same position for each exposure to X-rays and observing the changes in individual diffraction spots from time to time after increasing numbers of stress cycles. Very considerable difficulty of reproducing exactly the same system of spots is encountered.

A number of the earlier attempts at correlating changes in X-ray diffraction patterns with the progress of fatigue have been reviewed and summarized by Barrett (reference 15). Recently Gough and Wood (reference 16) associated changes in X-ray patterns with (a) dislocation of the grain into components that vary in tilt up to  $2^\circ$  from the orientation of the parent grain; (b) the formation of crystallites or fragments approximately  $10^{-4}$  to  $10^{-5}$  centimeters in diameter; and (c) the presence of lattice distortion.

Gough and Wood found progressive changes in the diffraction patterns obtained from specimens of normalized 0.12 percent carbon steel subjected to repeated stresses in the unsafe range. Some of the specimens were subjected to alternating torsion and others to alternating axial tensile stress.

Erich Martin (reference 17) found that changes in X-ray pattern during repeated stress depend on the previous condition of the metal. For instance, a cold-worked steel containing 0.17 percent C, 0.71 percent Si, and 0.90 percent Mn gave a back reflection Debye diffraction ring in which the  $K\alpha_1$  and  $K\alpha_2$  doublet was not resolved. After 1,000 repeated impacts in an unsafe range, the specimen showed the doublet nicely resolved, whereas the initially blurred doublet from a heat-treated rimming steel remained blurred after similar repeated impact. Tests by Gough (reference 18), however, indicated that resolution of the  $K\alpha$  doublet does not always occur as a result of fatigue stressing cold-worked steel. For instance, in the case of a cold-rolled low-carbon steel, the diffraction patterns showed a uniform diffuse diffraction ring before and after repeated stressing.

Wever and Möller (reference 13) decided that there is too much variation from place to place on a fatigue specimen to make X-ray patterns taken at random positions dependable criteria of damage. Accordingly, they followed the practice of etching a small spot to localize the fatigue failure. In addition, the specimen was always locked in the same position with respect to the beam and the film so that the etched spot was always irradiated. The same diffraction spots could then be studied on each of a series of films. Wever and Möller believed that safe and unsafe stress could be differentiated in this way, although the question of whether the dividing line was indicated with high accuracy was still unsettled. They emphasized again the need for a progressive study of each specimen. Barrett (reference 19) disagreed, however, with Wever and Möller on their ability to foretell fatigue failure from X-ray data.

Later Wever, Hempel, and Möller (reference 14) confirmed the previous work of Wever and Möller on annealed steel and concluded that fatigue damage could also be detected in the case of cold-worked steel. They depended on the progressive study of diffraction spots for stresses above the fatigue limit. Möller and Hempel (reference 12) published a detailed account of their examination of annealed low-carbon steel fatigue specimens and, although the test seems to indicate that plastic deformation is the condition to which X-ray patterns are sensitive, Möller and Hempel believed that the observed changes could differentiate between safe and unsafe stresses.

All the published work to date indicates that no single X-ray examination is sufficient to show whether or not a specimen or a service member has been dam-



aged by prior fatigue stressing. In fact, it would appear that more than two such examinations are necessary. A comparison must be made from time to time with previous photograms; even then the possibility of showing fatigue damage has not been demonstrated except for a very few metals and no demonstration in the case of a service member was found in the literature.

#### MATERIALS, TESTS, AND RESULTS

In view of the incompleteness of Barrett's work on the aluminum alloy 25ST, attempts were made to find evidence of damage to this material after it had been subjected to fatigue stress for various periods. The first specimens were cut from an airplane propeller of 25ST alloy, which was re-heat-treated to the 25SW condition. A composition typical of this alloy has been given in Part I of this report. Material in the W, or quenched, condition was first selected because of the lower stress necessary to produce plastic deformation in such material. The surface of the reduced section of a Krouse fatigue specimen, which is of the cantilever type, 2 inches long and 0.25 inch in diameter with a central section reduced to 0.185 inch in diameter, was etched to a depth of about 0.002 inch. The specimen was keyed in such a position that the same spot could be used for each successive photogram. An X-ray beam, iron  $K\alpha$  radiation, was directed at the specimen at grazing incidence and the diffraction patterns shown in figure 12 (a) to 12 (e) were obtained. The diffraction patterns obtained are therefore representative of the same specimen in the course of a series of fatigue-stress applications. Figure 12 shows the photograms after each treatment as follows:

- (a) Before being fatigue-stressed.
- (b)  $\pm 12,000$  lb./sq. in. for  $11.9 \times 10^6$  cycles.
- (c)  $\pm 14,500$  lb./sq. in. for  $1.8 \times 10^6$  cycles.
- (d)  $\pm 16,000$  lb./sq. in. for  $1.5 \times 10^6$  cycles.
- (e)  $\pm 17,000$  lb./sq. in. for  $1.4 \times 10^6$  cycles, plus  $8.7 \times 10^6$  cycles at  $\pm 18,000$  lb./sq. in.

No changes of known significance in the diffraction pattern after stressing at successively increasing amplitudes are apparent. After additional stressing at  $\pm 18,000$  pounds per square inch nominal stress amplitude, the specimen was broken.

Further studies were made with the Haigh axial-loading fatigue machine on specimens cut from  $1\frac{3}{16}$ -inch rod of the fully heat-treated aluminum alloy 25 ST, but no progressive changes in the X-ray diffraction patterns that can be considered as significant for foretelling failure in a fatigued member have been found. The grain size of the material was small enough to produce a large number of spots on the diffraction patterns so that one difficulty encountered by Barrett (reference 16)

while studying this alloy, namely, that of too few spots, was not a consideration.

The specimens were carefully machined with a narrow-nosed sharp tool, finishing with four or five cuts 0.0025 inch deep, followed by two cuts 0.001 inch deep. The reduced sections and fillets were then polished longitudinally with 1G emery paper and aloxite. Four trial specimens were etched to various depths and examined to determine if the X-ray patterns were influenced by the polishing process. Molybdenum radiation and a collimating system consisting of two holes in lead, one millimeter in diameter and 5.8 centimeters apart, were used throughout. The group of diffraction patterns in figure 13 (a) to 13 (d) are in order of the depth to which the surfaces of four specimens were etched: 0, 0.0005, 0.0025, and 0.0075 inch, respectively. It will be noted that the spots are equally sharp in all cases. It was concluded that etching was unnecessary.

The next step was a progressive study of a Haigh bar fatigue-stressed in a tensile range sufficient to cause failure, as follows:

Specimen 4H4A	Stress range 4,200 to 37,600 lb./sq. in. tension		
	Date stressed	Cycles	Date of X-ray Figure
	2/23/38	288,000.....	4/27/38 14 (a)
	4/29/38	36,000 additional.....	4/28/38 14 (b)
	5/26/38	79,200 additional (failed).....	4/29/38 14 (c)
			6/2/38 14 (d)

Figure 14 (b), (c), and (d) were all obtained on the specimen after locking it in a position so that approximately the same area was repeatedly exposed to the beam, although the settings were not accurate enough to give exactly the same diffraction spot pattern each time. It was concluded, however, that the general nature of the diffraction pattern remained unchanged during the period in which the specimen was subjected to fatigue stressing. The fact that crystal fragmentation or dislocation occurred close to the crack may be seen by the drop in intensity of the higher-order reflections in figure 14 (e). A slight diminution in relative intensity of the outer rings with respect to the inner ones seems to have occurred in figure 14 (d). Figure 14 (e) shows a somewhat greater loss in intensity in the outer rings. The significance of this result is somewhat doubtful in the absence of confirmatory evidence.

A similar result was obtained on Haigh specimen (3H5B) stressed in tension from 0 to 33,400 lb./sq. in. The record follows:

Date stressed	Cycles	Date of X-ray	Remarks
Not stressed.....		5/2/38	No change. Do.
5/6/38.....	1	5/6/38	
5/26/38.....	36,000	6/9/38	





(a) Before being fatigue-stressed, etched to 0.002 in



(b) After  $11.9 \times 10^6$  cycles at  $\pm 12,000$  lb./sq. in.



(c) After  $1.8 \times 10^6$  additional cycles at  $\pm 14,500$  lb./sq. in.



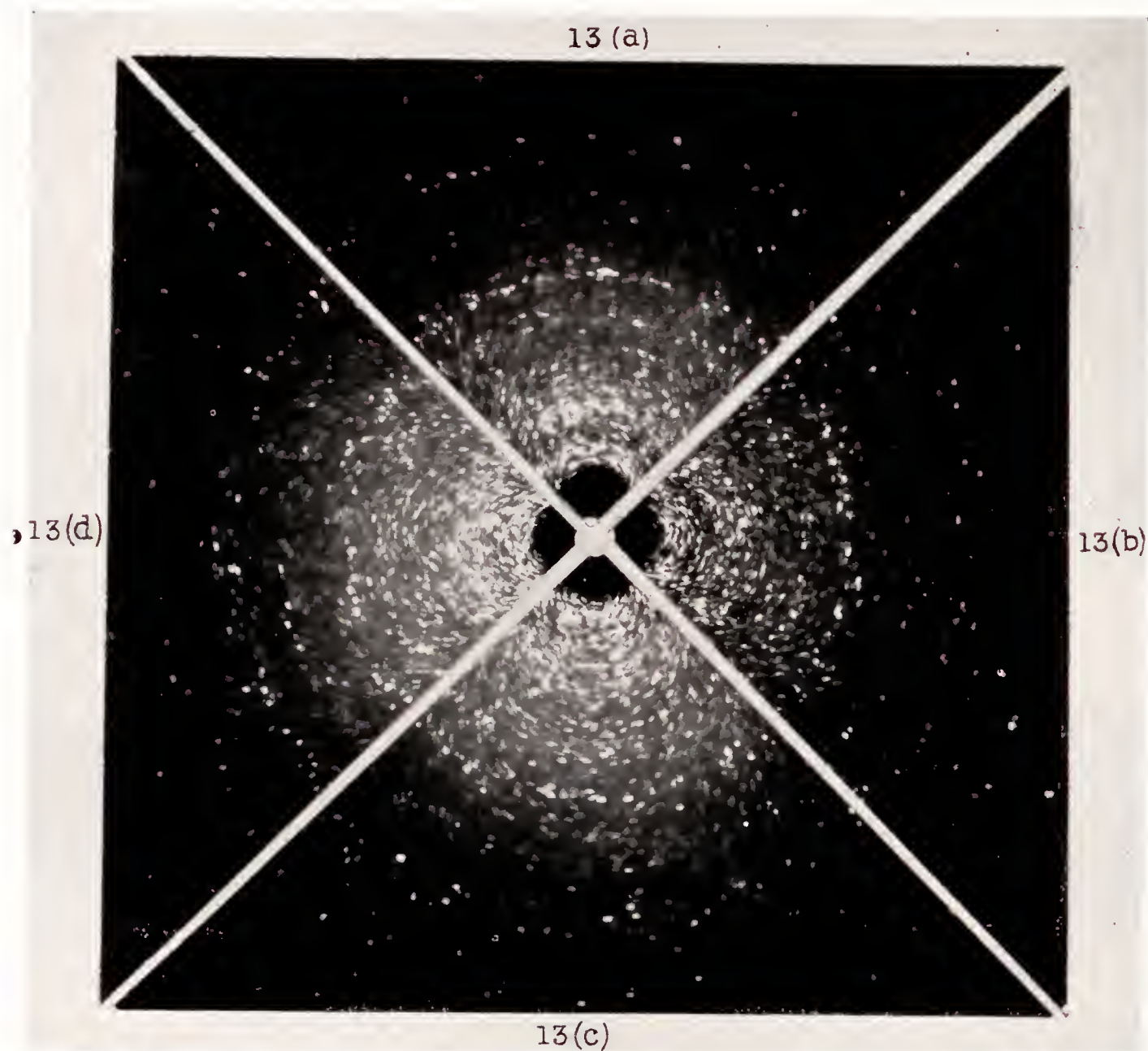
(d) After  $1.5 \times 10^6$  additional cycles at  $\pm 16,000$  lb./sq. in.



(e) After  $1.4 \times 10^6$  additional cycles at  $\pm 17,000$  lb./sq. in. plus  $8.7 \times 10^6$  cycles at  $\pm 18,000$  lb./sq. in.

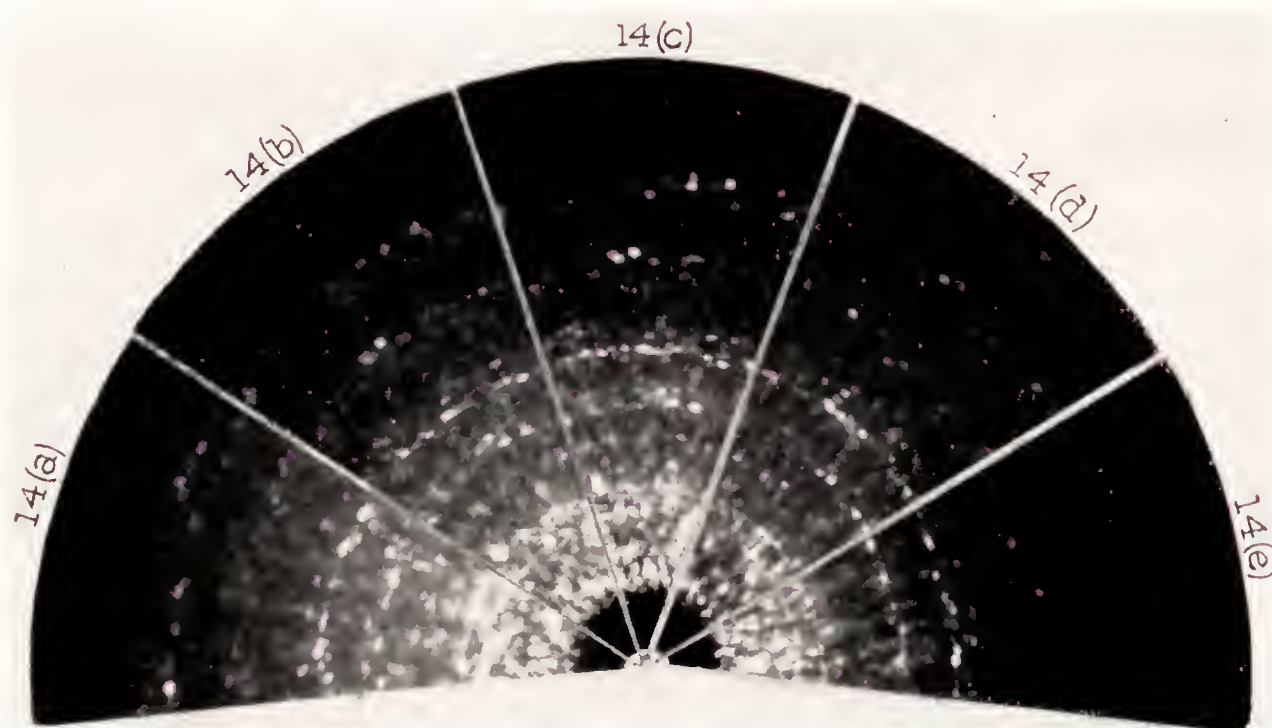
FIGURE 12.—grazing incidence patterns made by reflections of iron radiation from the same spot on an etched fatigue specimen of 25SW after successive treatments. No extended crystal fragmentation is indicated although the continuous portion of some of the rings in (e) show a suggestion of a slight increase in intensity.





(a) 0 inch. (b) 0.0005 inch. (c) 0.0025 inch. (d) 0.0075 inch.

FIGURE 13.—Diffraction patterns showing equal sharpness of spots after polishing on aloxite paper and etching to various depths.



(a) and (b) Taken at the end of 288,000 cycles, different areas being exposed to the X-ray beam.  
 (c) After 36,000 additional cycles on the same spot as (b).  
 (d) The same spot after 79,200 additional cycles, resulting in fatigue failure. The crack formed several centimeters from the X-rayed spot.  
 (e) Diffraction pattern at the fatigue crack after failure. The spot exposed to the X-ray beam was near the origin of the crack.

FIGURE 14.—Progressive X-ray study during the last stages of fatigue of alloy 25ST stressed in the range 4,200 to 37,600 pounds per square inch in tension by the Haigh method.



Likewise, another Haigh specimen (3H2A) stressed repeatedly in tension from 3,600 to 38,200 pounds per square inch showed no general changes to have occurred between the 144,000 cycle and the 180,000 cycle. All three of these specimens were stressed in the unsafe range.

Since considerable time had elapsed in some cases between the end of the period of stressing and the exposure to the X-rays, a check was made on the possibility of an obscuring effect by recovery at room temperature. No effect suggestive of a recovery in the previous tests was found, however, in material stressed 1 cycle between 0 and 30,000 pounds per square inch or between 0 and 26,000 pounds per square inch in tension.

These conditions were first noticed during the examination of an airplane propeller blade made of the aluminum alloy 25ST that had failed in service. The same structural features were subsequently detected in other propeller blades. Although there was no a priori reason for regarding the material with suspicion because of the presence of these features, their discovery in a structural member that had failed in service prompted a study of their origin and probable significance.

#### SLIP-PLANE PRECIPITATION

The usual appearance of the condition of slip-plane precipitation, as found in specimens cut from a propeller blade of the 25ST aluminum alloy, is shown by figures



FIGURE 15.—Slip-plane precipitation in a propeller blade of the aluminum alloy 25ST. The fact that the criss-cross lines change direction at grain boundaries proves that the markings are not scratches.  $\times 100$ .

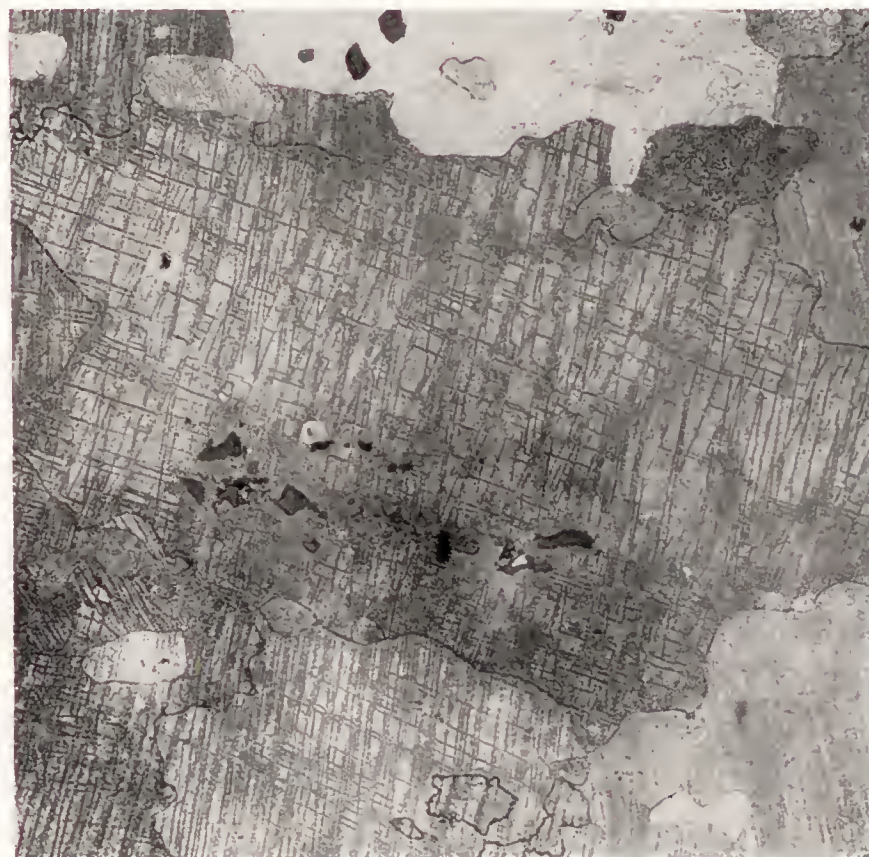


FIGURE 16.—Slip-plane precipitation in a propeller blade of the aluminum alloy 25ST. The offsetting of the lines in some localities suggests shearing in the direction of lines crossing the offset ones.

Exposures of 9 hours were used and about 1 hour elapsed between stressing and the beginning of the first exposure.

#### CONCLUSIONS

The results of the foregoing studies on the aluminum alloy 25S failed to show any difference in the X-ray diffraction patterns that could be considered significant of structural changes resulting from prior fatigue stressing of the alloy.

#### III. SLIP-PLANE PRECIPITATION AND VEINING IN 25S ALUMINUM ALLOY BEFORE AND AFTER FATIGUE STRESSING

The terms "slip-plane precipitation" and "veining" apply to quite unrelated structural conditions. The appropriateness of these designations, especially the first one, will appear as the results of the work are described.

15 and 16. Many of the individual grains are criss-crossed by intersecting groups or families of parallel lines. Any doubt as to the confusion of these lines with scratches produced in polishing the metallographic specimen is removed by noting the abrupt change in direction of the lines from one grain to another. The fact that the individual lines are not continuous but that each one consists of a series of discrete particles is revealed by the series of micrographs at successively increasing magnification shown in figure 17 (a) to 17 (d).

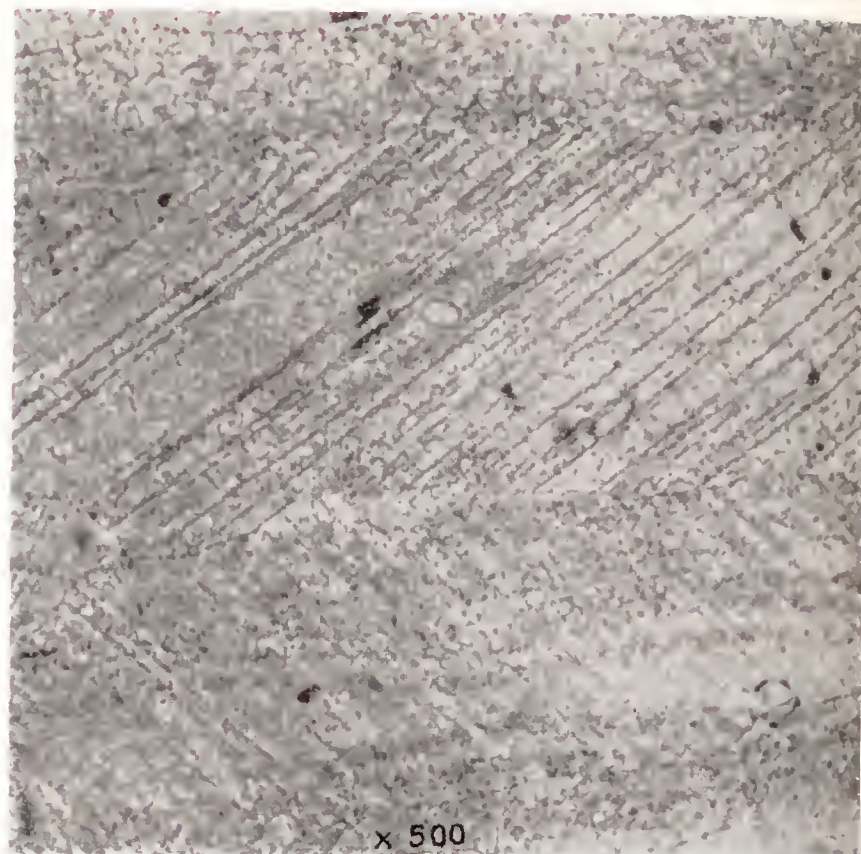
The hardening, by heat treatment, of the aluminum copper alloys, of which the 25S alloy is representative, consists of three steps. The first is a solution treatment during which the alloy is heated to a temperature sufficiently high to permit the diffusion into solid solution of the various structural constituents of the alloy; this treatment is immediately followed by quenching in water to retain this structural condition at ordi-





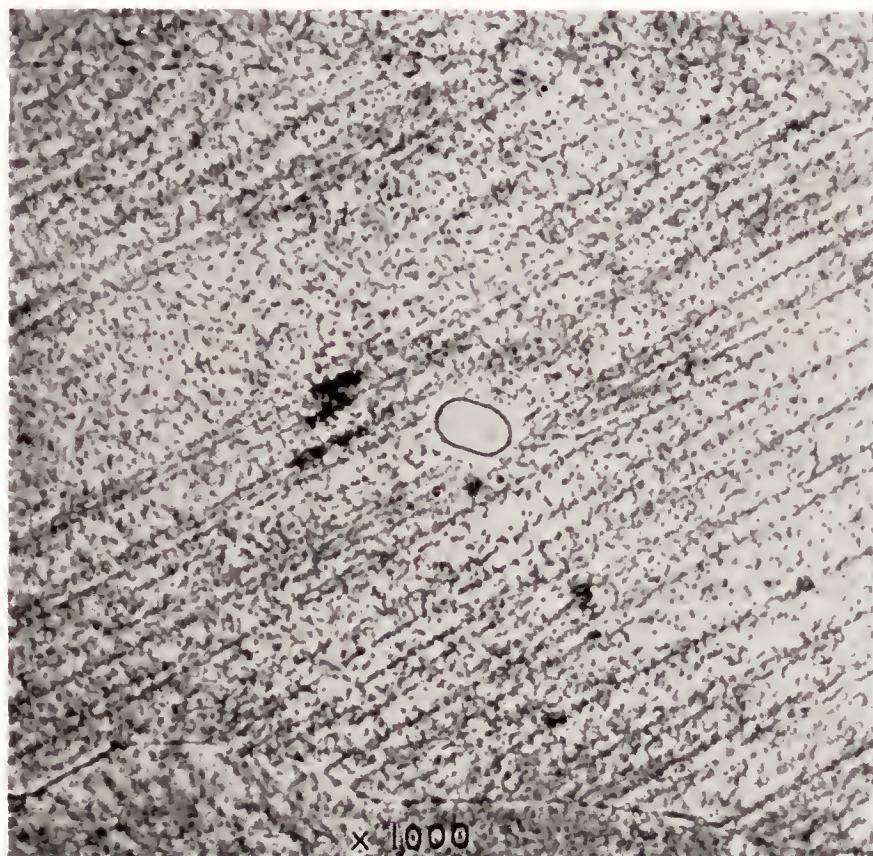
x 100

(a)  $\times 100$ .



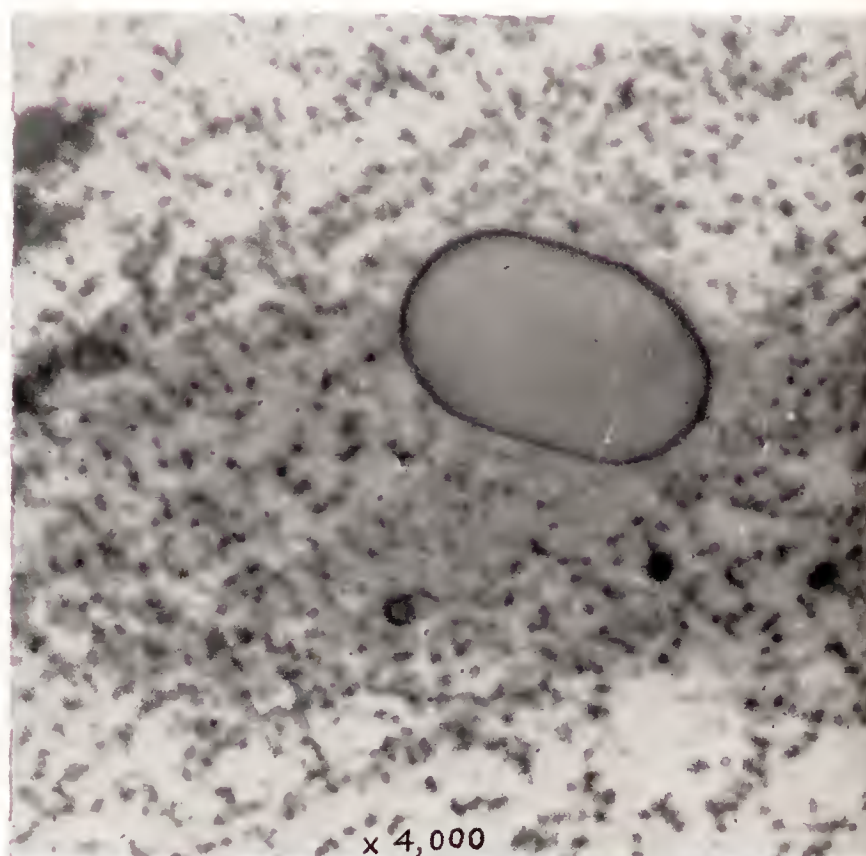
x 500

(b)  $\times 500$ .



x 1,000

(c)  $\times 1,000$ .



x 4,000

(d)  $\times 4,000$ .

FIGURE 17.—Slip-plane precipitation at the same location on a polished and etched surface of aluminum alloy 25ST at different magnifications. The lines of (a) are resolved at higher magnifications into rows of particles. Etchant,  $\frac{1}{2}$  percent HF.



nary temperature. The third step in treatment, aging or reheating at a slightly elevated temperature or simple aging at room temperature in case of a few alloys, permits the precipitation of the excess of the constituents held in solid solution in the matrix of the unstable or quenched alloy in the form of tiny particles dispersed throughout the matrix of the alloy (reference 20). (Details of the heat treatment of the 25S alloy are given in Part I of this report.) Fink and Smith (reference 21) have shown that indications of the precipitation in the aluminum-copper alloys may be detected after as little as one-half hour of aging time following the solution treatment and that the particle size increases as the time of aging is extended. The 25S alloy is essentially an aluminum-copper alloy, as is shown by the table on page 2.

The crystal lattice of the 25S alloy behaves during plastic deformation in the same manner as any other face-centered cubic lattice, that is, deformation occurs by slippage on octahedral planes. The micrographs given in figure 17 indicate that the term "slip-plane precipitation" correctly describes the phenomenon. Observations by Wassermann (reference 22) on a similar condition in the structure of an aluminum-copper alloy are in confirmation of those reported here.

A further step in the study of slip-plane precipitation consisted in the identification of the crystal planes on which the precipitated phase was localized.<sup>1</sup> This identification was done on some of the large crystals found in a section of a propeller blade. Figure 18, a micrograph of one of these crystals, shows the directions of the slip-plane precipitation. The directions were measured with respect to reference scratches drawn on the polished surface. The crystal orientation was determined in the usual way from the X-ray diffraction pattern obtained by the back-reflection method. Stereographic projections (reference 23) of the octahedral planes are represented by small circles called poles in figure 19. The loci of normals to the rows of precipitated particles of figure 18 are projected as straight lines in figure 19. These lines were prepared in their proper relation to the reference scratches and the polished plane of the specimen. In all the cases examined the octahedral poles fell on the normals to the slip lines. This result means that the octahedral planes were in such a position that their traces in the plane of polish coincided with all the directions taken by the rows of precipitated particles. No other single family of poles of simple indices would account for all the slip-line directions. Confirmatory evidence that only the



FIGURE 18.—Slip-plane precipitation in a large grain of the heat-treated aluminum alloy 25S<sup>1</sup>,  $\times 100$ . The orientation of this crystal is shown in figure 19.

<sup>1</sup> The valuable assistance of H. C. Vacher, Metallurgist, National Bureau of Standards, is acknowledged in this phase of the work.



octahedral planes of the crystals are concerned in this structural change is obtained by counting the number of directions of the observed slip lines. If these lines

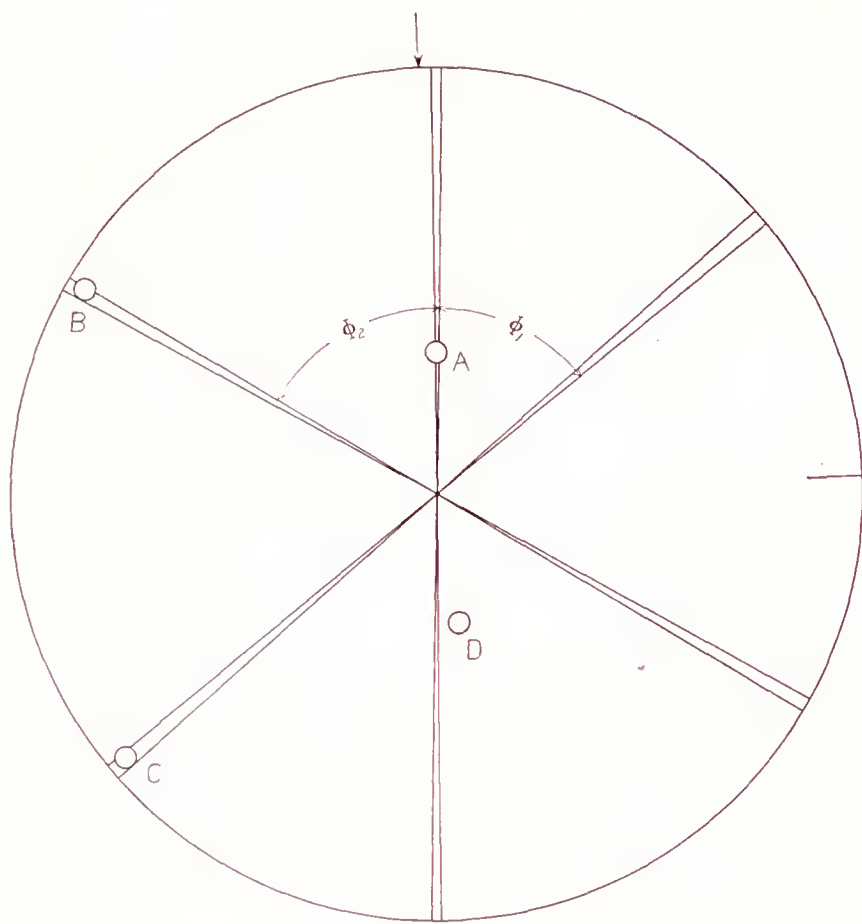


FIGURE 19.—A stereographic projection of octahedral poles, A, B, C, and D, as determined from a back-reflection diffraction pattern of the 25ST crystal shown in figure 18. The straight lines are projections of the loci of normals to the observed slip lines. All the observed slip lines can thus be accounted for by glide on three of the four octahedral planes,  $\Phi_1=48^\circ$  to  $51\frac{1}{2}^\circ$ ;  $\Phi_2=58\frac{1}{2}^\circ$  to  $62^\circ$ . The angles between the normals to the various octahedral planes and the normal to the surface of polish are:  $\Theta_A=37^\circ$ ;  $\Theta_B=87\frac{1}{2}^\circ$ ;  $\Theta_C=87\frac{1}{2}^\circ$ ;  $\Theta_D=34^\circ$ .

are the traces of only octahedral planes, then four is the maximum possible number of directions that may be marked out by the precipitated particles in any plane

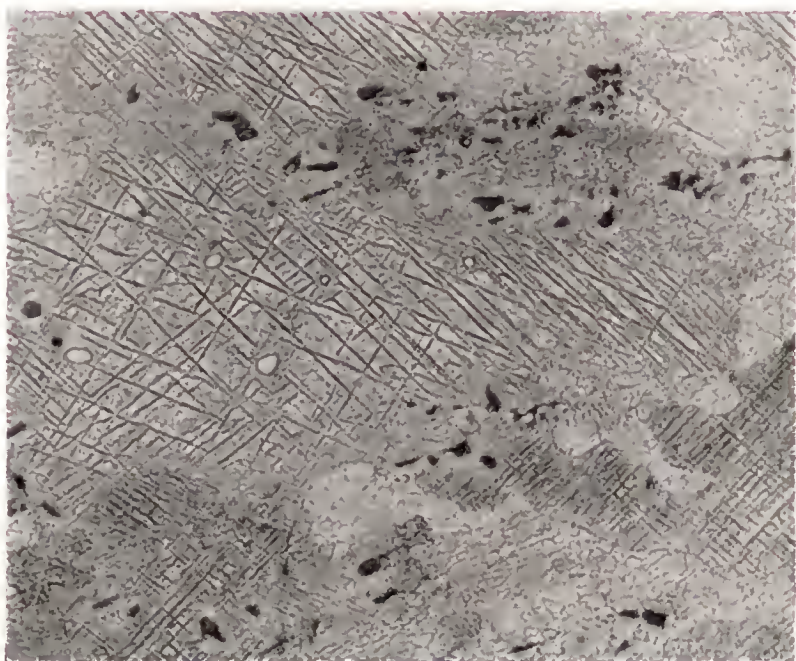


FIGURE 20.—Slip-plane precipitation in the heat-treated aluminum alloy 25ST.  $\times 200$ . Note four families of lines in one grain; the maximum possible number if slip-plane precipitation is confined to octahedral planes.

of polish. The observations are in agreement with this rule. Figure 20 depicts a grain showing four families of slip planes and figure 21 is its stereographic repre-

sentation. Fewer directions than four are usually observed but no more than four were found in this investigation.

#### PRODUCTION AND ELIMINATION OF SLIP-PLANE PRECIPITATION

A question that immediately arises concerning the structural condition is whether this change from the normal structure occurred during service, presumably as a result of service stresses, and whether the condition is detrimental to the material, particularly its resistance to fatigue stresses. In a study of the fatigue characteristics of telephone-cable sheath, Townsend (reference 24) concluded that structural changes occurred in antimony-lead alloy *as a result of the service conditions*, primarily of the stresses and that these changes had an important bearing on the subsequent behavior of the material as a whole. In that case, the change, which consisted essentially of the precipitation from solid solution of the antimony, was confined principally

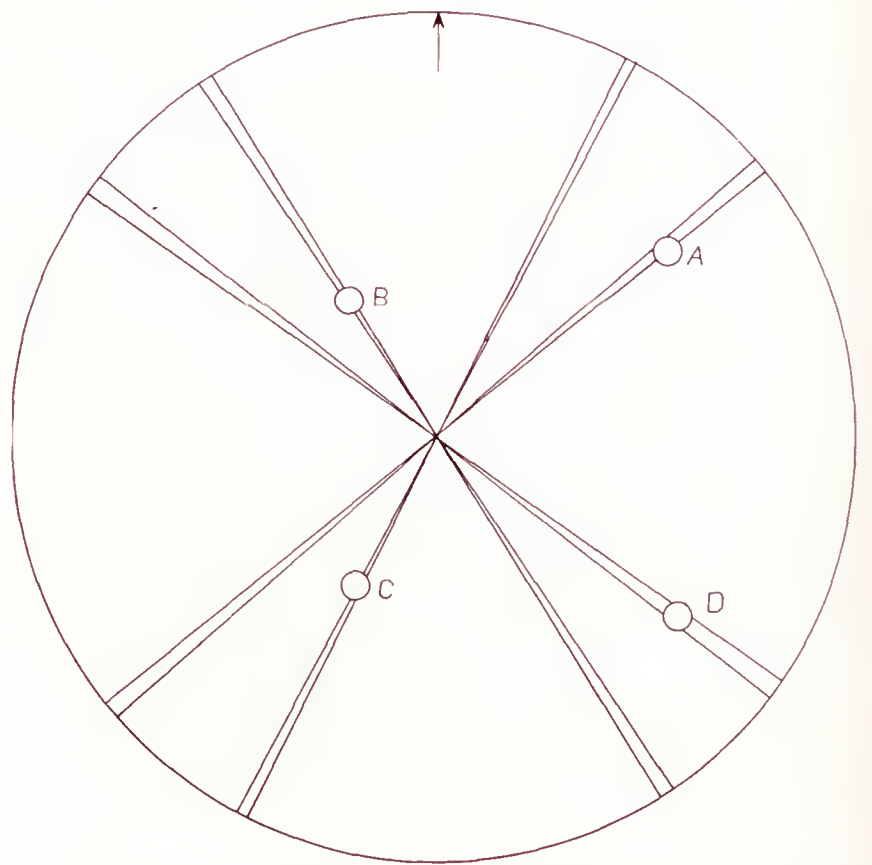


FIGURE 21.—A stereographic projection of octahedral poles, A, B, C, and D, of the aluminum lattice in a possible position such that each slip line of figure 20 is accounted for by glide on octahedral planes. The straight lines are projections of the loci of normals to the observed traces of slip planes and, as in figure 19, the maximum variation in direction among members of each set of slip lines is indicated on the drawing. The angles between the normals to the various octahedral planes and the normal to the surface of polish are:  $\Theta_A=70^\circ$ ;  $\Theta_B=42^\circ$ ;  $\Theta_C=43^\circ$ ;  $\Theta_D=70^\circ$ .

to the regions of the grain boundaries. The possibility of a similar occurrence in other cases, such as the present one, with the precipitated phase located on certain favored crystallographic planes, should not be overlooked.

In addition to an estimation of the probability of a damaging condition arising from the presence of slip-plane precipitation in the 25ST alloy, it is also desirable to know the circumstances under which this condition may and may not be produced.

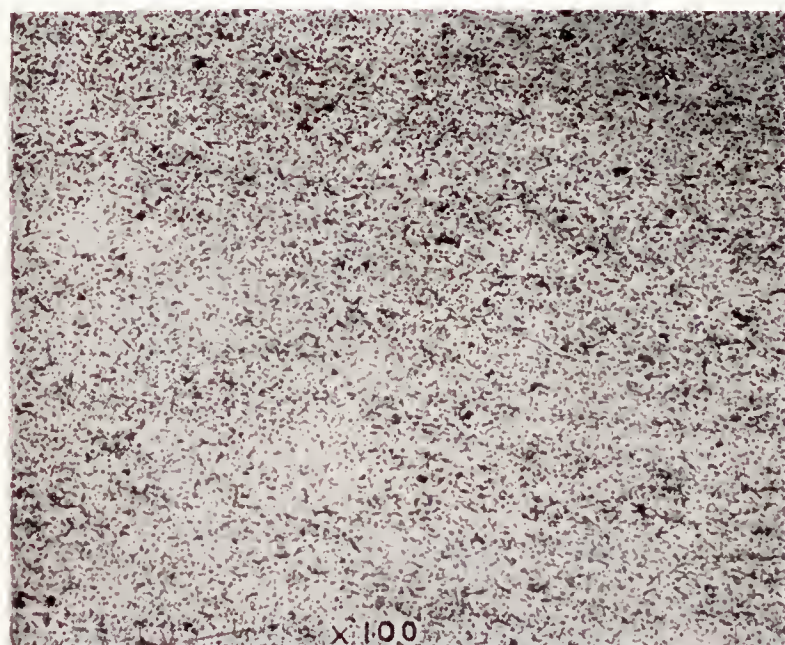


In the numerous attempts made, it was found impossible to produce slip-plane precipitation in either 25SW or 25ST alloy in quantities visible in the microscope, by merely deforming the material, either elastically or plastically. Fatigue stresses of various kinds have also been tried and negative results obtained. Also all attempts to produce slip-plane precipitation in fully

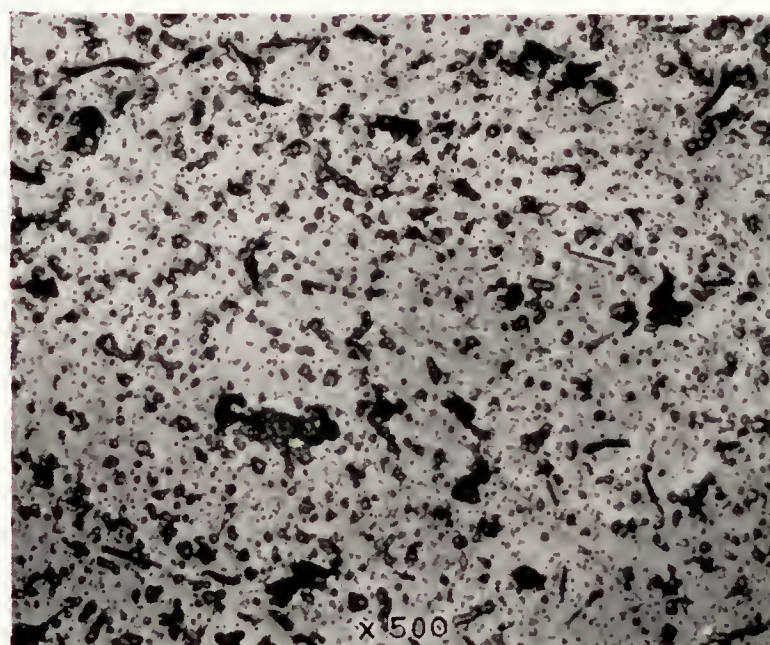
and then aging it at elevated temperatures, some of the modes of deformation being:

(a) Compressive deformation under a Brinell ball, under a forging press, and under a forging hammer.

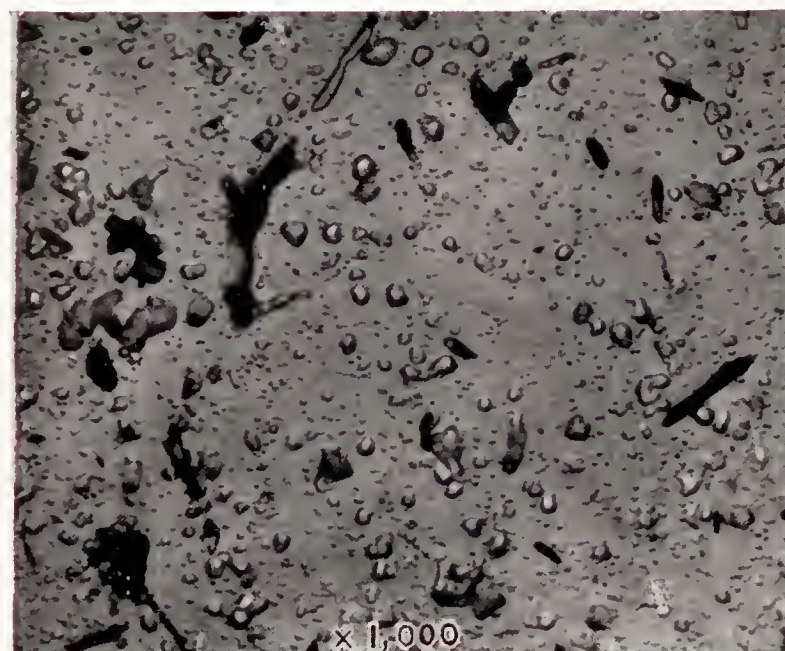
(b) Slow tensile deformation. Figure 23 shows a photograph of slip-plane precipitation on a longitudinal section developed by stretching a tensile specimen of



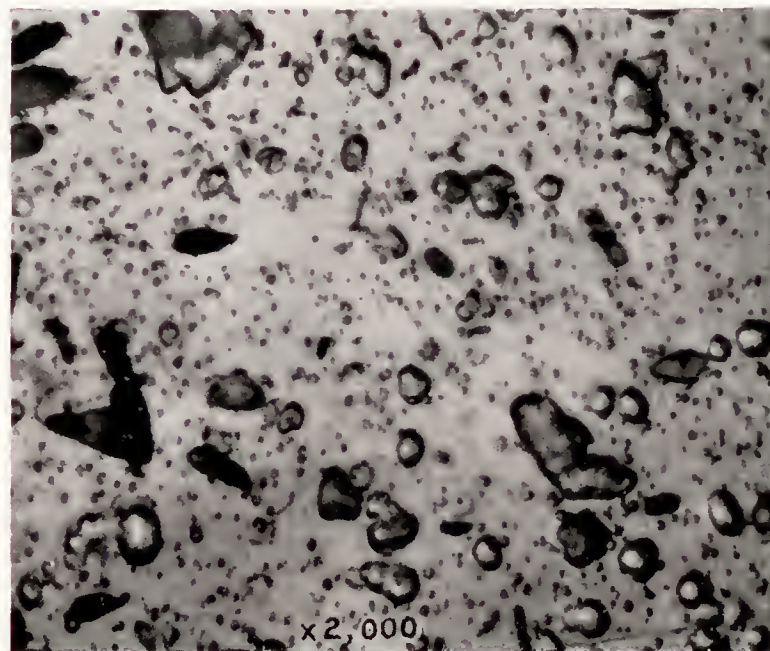
(a)  $\times 100$ .



(b)  $\times 500$ .



(c)  $\times 1,000$ .



(d)  $\times 2,000$ .

FIGURE 22.—The same location of a polished and etched surface of aluminum alloy 25S at different magnifications. All the micrographs were taken at the end of a sequence of treatments consisting in a slow cooling from 525° C. to room temperature, plastic bending, and heating for 18 hours at 143° C. in air. Note that the precipitated particles are not arranged in rows as in figure 17. Presumably the failure to produce the familiar slip-plane precipitation is explained by the fact that insufficient quantities of material remained in solid solution after the annealing process to permit further precipitation on slip planes.

annealed 25S alloy by deforming it in various ways and by subsequent aging for various periods at 143° C. failed to develop this structural condition. Figure 22 shows the appearance of 25S alloy annealed, bent, and aged 18 hours at 143° C. It is evident that, although precipitation from the matrix of microstructural particles occurred presumably during the annealing process, no tendency toward localized precipitation on slip planes of the crystals was observed.

No slip-plane precipitation was found in any specimen of 25S alloy in the quenched condition. This structural feature was produced in the alloy, however, by deforming the quenched material in various ways

quenched 25S alloy then aging at 143° C. for 17 hours. The slip lines are fairly straight.

(c) Impact by the Charpy and the tensile impact methods. Figure 24 is a photograph of a longitudinal section of a broken tensile impact specimen subsequently aged at 143° C. for 17 hours. The slip lines are crooked in this case.

(d) Plastic bending, one side of the specimen being in compression and the opposite in tension. A curious property of this type of deformation is the great difference of abundance of slip-plane precipitation found in various parts of specimens. Figure 25 shows a macrograph of two bars of 25S alloy, both of which were bent





FIGURE 23.—Slip-plane precipitation developed by slow tensile deformation of a specimen of the quenched aluminum alloy 25SW followed by aging at 143° C. for 17 hours.  $\times 100$ .



FIGURE 24.—Slip-plane precipitation resulting from deformation of a specimen of the quenched aluminum alloy 23SW in tensile impact followed by aging at 143° C. for 17 hours.  $\times 100$ .

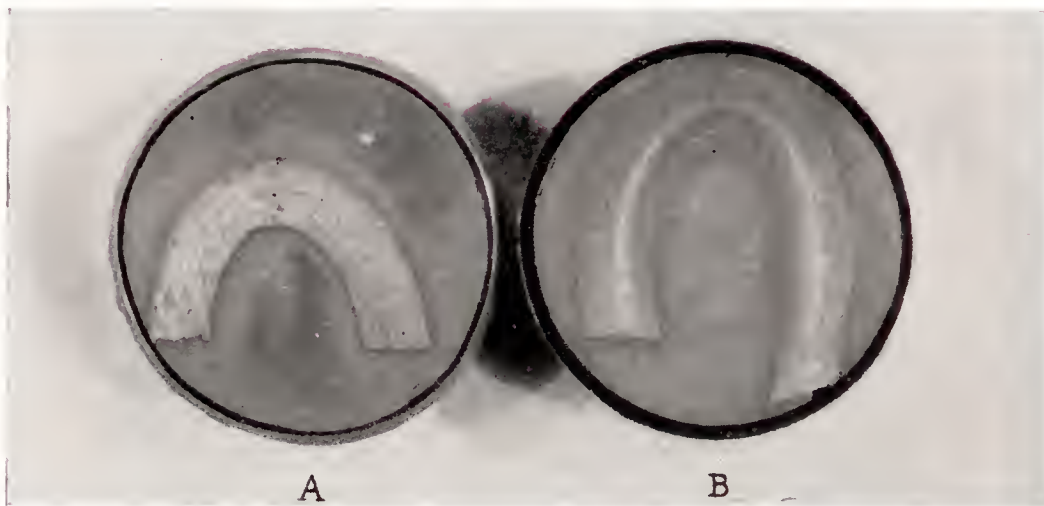


FIGURE 25.—Macrograph of sections of specimens of the aluminum alloy 25S bent while in the quenched condition. A, as quenched; B, aged after quenching.  $\times 1$ . Note the curved light streak in the center of B marking the region of greatest density of slip-plane precipitation. A showed no slip-plane precipitation and etched more uniformly.

cold while in the quenched condition. Bar B was subsequently age-hardened whereas A was not. The white streak along the neutral axis of B marks the region of greatest abundance of slip-plane precipitation and the zone widens in the portions of the specimen least deformed. No slip-plane precipitation was found in A. The uniform etching of the specimen in this case is noteworthy.

(e) Fatigue failure. One end of a failed fatigue specimen, after fracture, was split longitudinally perpendicular to the fatigue fracture. Figures 26 and 27 show the pair of "imaged" surfaces thus obtained. The portion aged at elevated temperature, after being fractured by fatigue stressing, shows slip-plane precipitation whereas the imaged portion was practically free from it.

It is not always necessary to deform plastically the quenched 25S alloy by mechanical means in order to produce slip-plane precipitation. Quenching and age-hardening, in themselves, are sometimes sufficient, although the amount of slip-plane precipitation obtained is ordinarily much less than if the quenched alloy has

been mechanically deformed. Figure 20 illustrates the condition found near one corner of a rectangular block quenched and age-hardened without any mechanical working. It is not to be concluded, however, that absolutely no plastic deformation occurred because it has been shown by Kempf, Hopkins, and Ivanso (reference 25) that the quenching process leaves residual stresses. These stresses may approach the yield point of the material for extreme quenching conditions.

Perhaps the most important of all the observations on the production of slip-plane precipitation are those made on fatigue specimens of the quenched alloy 25SW and of the quenched-and-aged alloy 25ST. The results of the observations, stated briefly, are:

No slip-plane precipitation was found in any fatigued specimen of quenched 25S alloy, stressed or not stressed, until after an aging treatment at elevated temperatures.

Fatigue stressing followed by aging, however, did not invariably result in slip-plane precipitation in the quenched alloy 25SW. Rotating-beam specimens of quenched 25S alloy stressed in fatigue, but not to complete failure, at various amplitudes from  $\pm 14,000$  to  $\pm 20,000$  pounds per square inch showed no slip-plane precipitation even after aging at 143° C. to 146° C. for 18 hours. Aging, at 165° C. to 171° C. for 16 hours, of specimens stressed above and below the fatigue limit, did produce some slip-plane precipitation, but no special importance could be attached to this result since unstressed control specimens cut from the material adjacent to the fatigue specimens also developed slip-plane precipitation when aged under similar conditions.

Specimens of quenched-and-aged alloy 25ST, stressed in the Haigh axial-loading fatigue machine for 25,000,-



000 cycles in the range from 2,850 pounds per square inch in compression to 10,150 pounds per square inch in tension were not visibly different in structure from companion, unstressed material in respect to the amounts of slip-plane precipitation developed by equal aging treatments. Figure 28 (a) to 28 (f) show the close parallelism between the unstressed and stressed material as aging proceeds.

tests having been made on the same Krouse cantilever rotating-beam machine. The fatigue limits based on  $10^8$  cycles of stress without failure, were  $\pm 18,500$  and  $\pm 19,000$  pounds per square inch for the requeenched-and-aged alloy and for the as-received material, respectively. It is therefore evident that, although slip-plane precipitation occurs in the quenched alloy 25SW, only as a result of deformation followed by aging, the



FIGURE 26.—Slip-plane precipitation in the plastically deformed portion of a Moore rotating-beam fatigue specimen. The 25S specimen was broken by repeated stress while in the quenched condition. The portion adjacent to the fracture was split longitudinally; one portion was aged 6 hours at  $145^\circ$  C. and used for this figure; the other portion was used for figure 27.  $\times 100$ .



FIGURE 27.—This surface has been separated from the one shown in figure 26 by a longitudinal cut. The portion shown here was not aged at an elevated temperature. No slip-plane precipitation is in evidence although plastic deformation was present to about the same degree as in the portion shown in figure 26.  $\times 100$ .

#### PRACTICAL SIGNIFICANCE OF SLIP-PLANE PRECIPITATION

Of most importance in connection with determining the practical significance of slip-plane precipitation is its relation to fatigue resistance, especially as to whether it is an indication of weakness in fatigue.

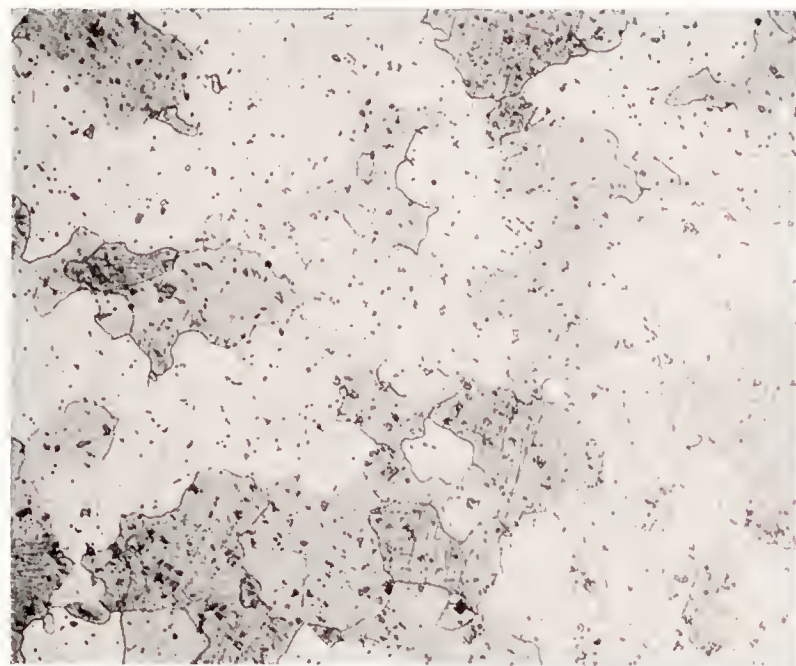
It was found that 25ST propeller-blade material could be requeenched and aged according to standard commercial practice with only a slight decrease in Vickers hardness number. After this reheat treatment, the material contained only comparatively small amounts of slip-plane precipitation, as is shown by figures 29 and 30. The results of determinations of the fatigue strength of the alloy as received and of the requeenched-and-aged material revealed no marked difference between the two but rather a slight superiority, if anything, in favor of the material containing much slip-plane precipitation. Figure 31 shows the results obtained for these two materials, all the fatigue

existence of this structural condition in the material does not constitute a dependable criterion of prior fatigue stressing. Material that had been intentionally subjected to fatigue stressing often did not exhibit this structural condition on being aged after being stressed.

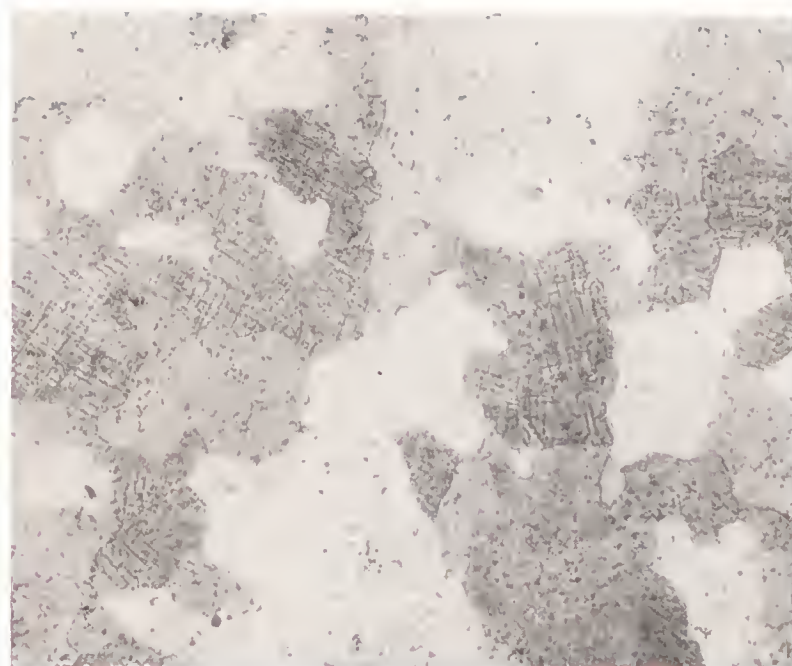
#### VEINING

A network structure termed "veining" that occurs within crystals is prevalent in service structures of the quenched-and-aged alloy 25ST and, although there is no a priori reason to be suspicious of it, a study was made to show whether or not this phenomenon can be used as an indication of damage by fatigue stressing. Experiments showed that quenching and aging are the important factors necessary in causing its extinction and recurrence, respectively. The following characteristics of veining were those to which attention was directed in making the observations and experiments.

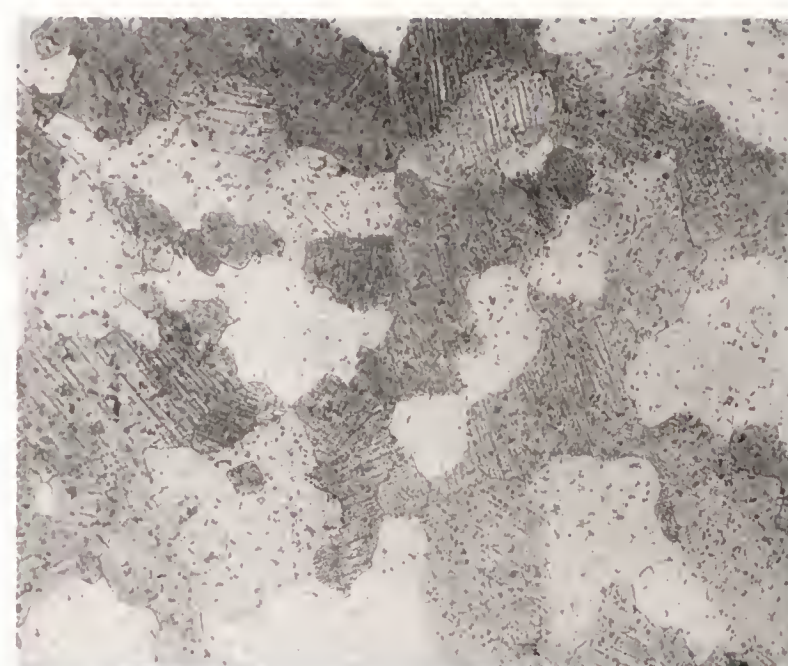




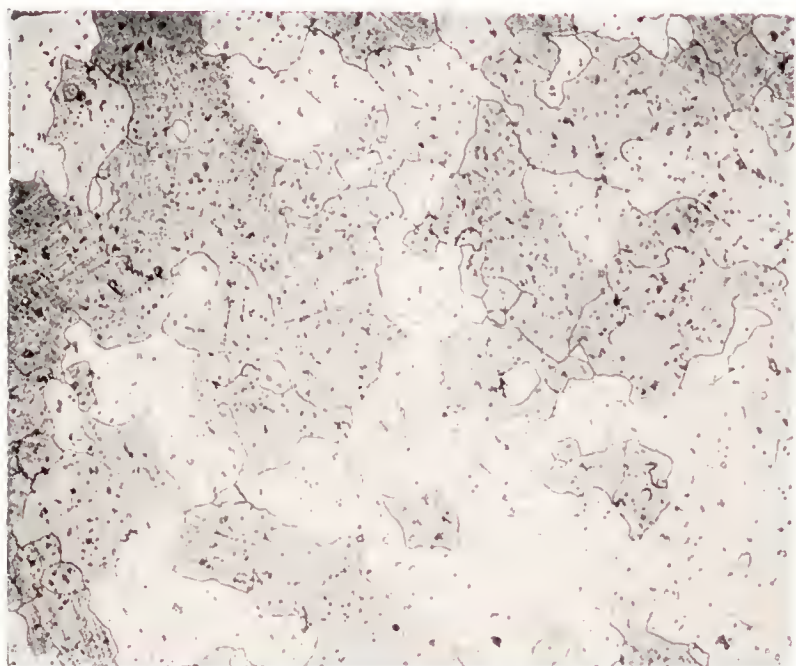
(a) Not stressed in fatigue, aged 10 hours at 159° C



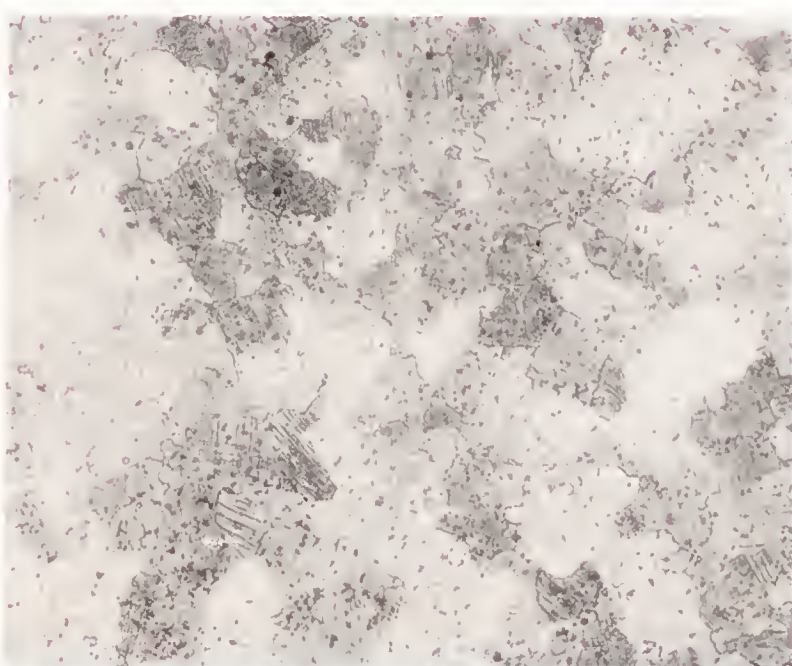
(c) Not stressed in fatigue, aged 18 hours at 159° C.



(e) Not stressed in fatigue, aged 4 hours at 145° C. and 30½ hours at 159° C.



(b) Fatigued, 25,000,000 stress cycles, and aged as in (a).



(d) Fatigued, 25,000,000 stress cycles and aged as in (c).



(f) Fatigued, 25,000,000 stress cycles and aged as in (e).

FIGURE 28.—The close parallelism in the development of slip-plane precipitation in specimens of the fully heat-treated aluminum alloy 25ST as received from the maker and after fatigue stressing, 25,000,000 cycles of axial loading in the range from -2,850 to 10,150 pounds per square inch.  $\times 100$ .





FIGURE 29.—A section through a 25ST aluminum alloy propeller blade after quenching and aging to produce nominal full hardness. Note the absence of slip-plane precipitation.  $\times 100$ .

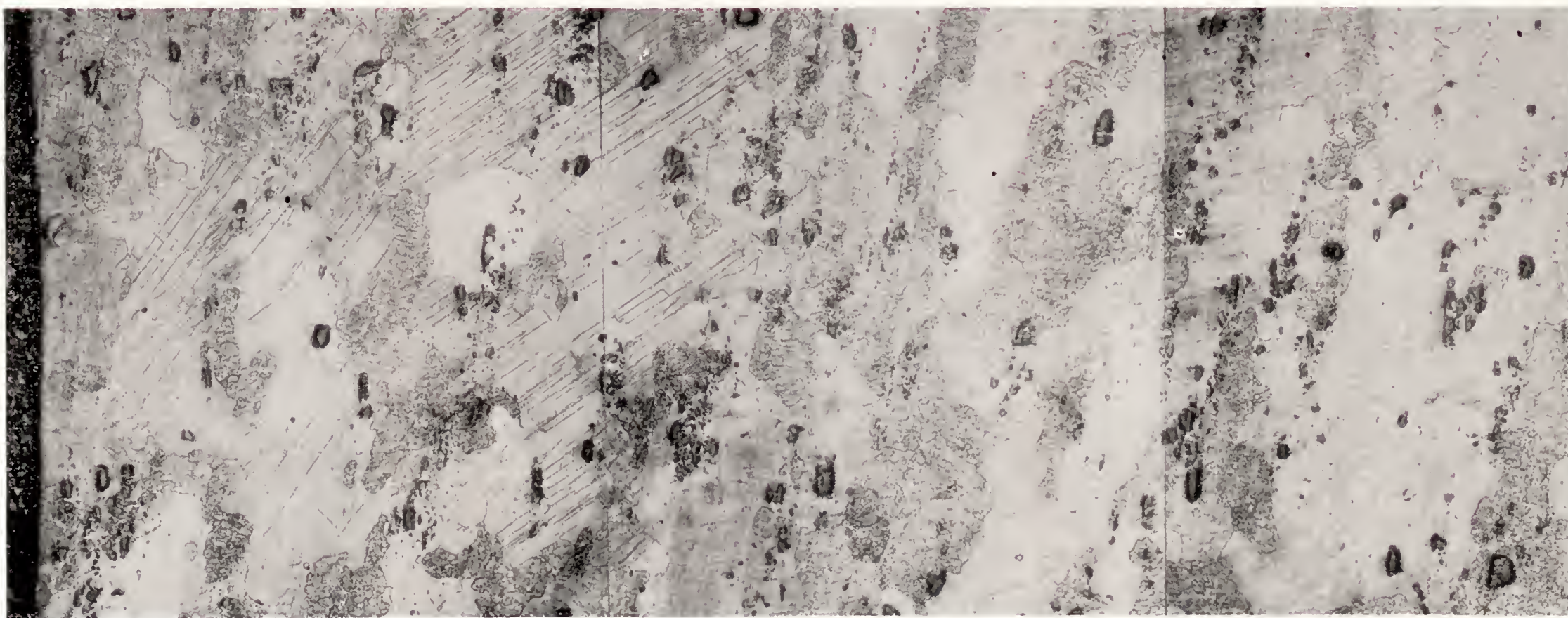


FIGURE 30.—A section through the same propeller blade shown in figure 29, as received. Much more slip-plane precipitation is in evidence than in the quenched and age-hardened sample shown in figure 29.  $\times 100$ .



The veins are continuous and give the impression of being cell walls. Figure 32 (a) and (d) show typical examples.

If the veining is an indication of subdivision into sub grains, it is evident that the orientation is essentially the same throughout the limits of the mother grain. Figure 32 (c) shows slip planes crossing the veins and apparently not deviated by them.

Veining is eliminated, insofar as its visibility is concerned, by the solution heat treatment. Figure 32 (b) shows approximately the same region as figure 32 (a) after heating at 521° C. and quenching in cold water.

Veining can be suppressed and restored repeatedly by alternately quenching and aging, which is in general

Cold plastic deformation of 25S aluminum alloy in the quenched condition in appropriate amounts followed by aging at the temperature usually employed, namely, about 143° C. for 15 to 18 hours, produces copious amounts of slip-plane precipitation, but if the material is initially in the age-hardened condition, very little slip-plane precipitation is obtained under like aging conditions. Deformation without subsequent aging at elevated temperatures produces no slip-plane precipitation.

Small amounts of slip-plane precipitation normally result from the sequence of solution treatment and age-hardening. Regions near the periphery, and especially the corners of angular specimens where quench-

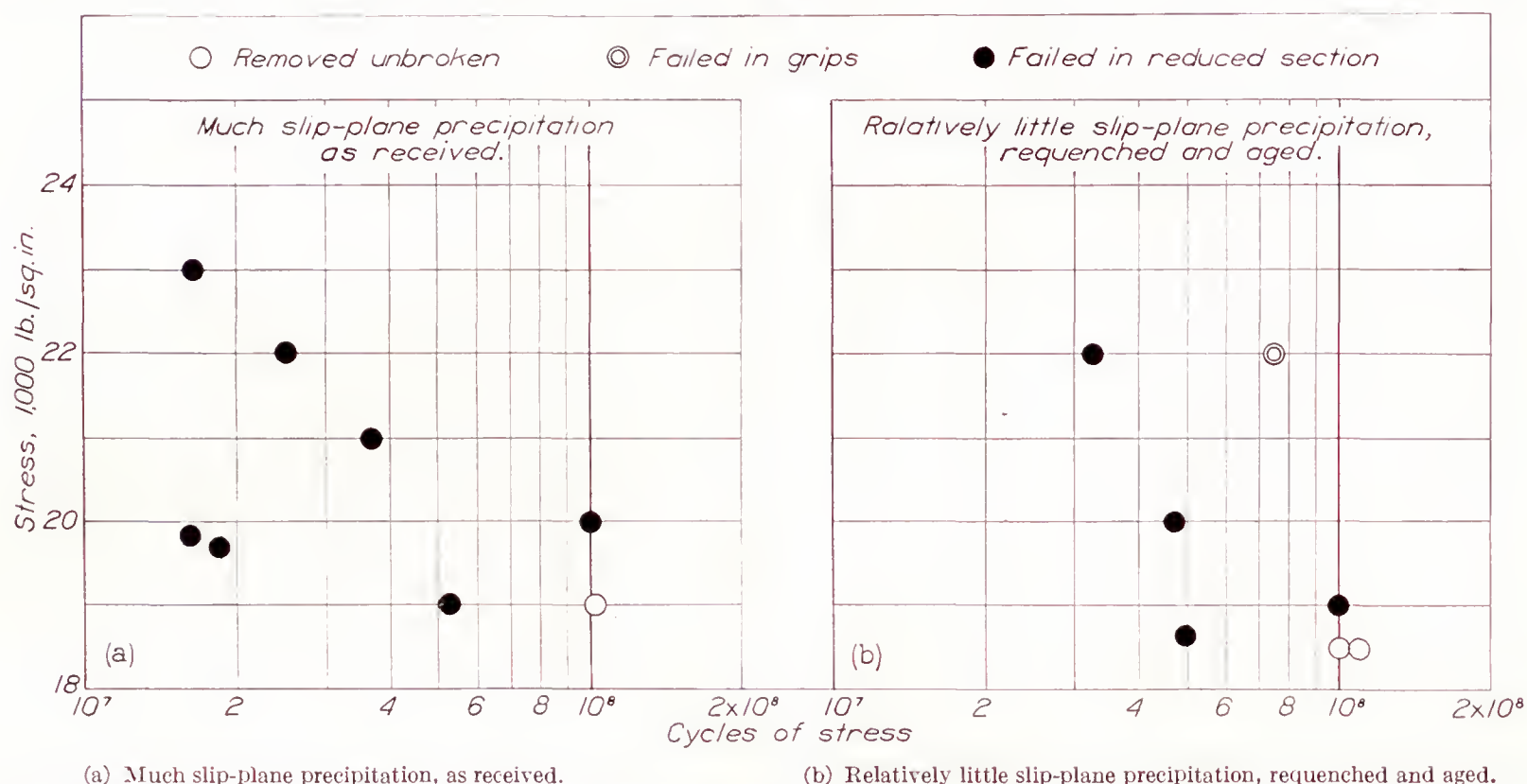


FIGURE 31.—Results of Krouse rotating-beam cantilever fatigue tests on two samples of aluminum alloy 25ST, one containing much more slip-plane precipitation than the other, as shown in figures 29 and 30.

agreement with the findings of Northcott (reference 26) in the case of other metals. A specimen cut from an airplane propeller blade was alternately quenched and aged. The treatments and results of the subsequent metallographic examinations are tabulated in table IV, the observations being carried out in each case on the same grain.

TABLE IV.—EFFECT OF HEAT TREATMENT ON VEINING IN THE ALUMINUM ALLOY, 25S

Treatment	Structure
Solution heat treatment, quenched in water from 521° C. (970° F.).	No veining.
Aged 6 hours at 145° C.-----	Veining present, figure 32 (d).
Solution heat treatment-----	No veining, figure 32 (e).
Aged 6 hours at 145° C.-----	Veining present, figure 32 (f).

### CONCLUSIONS

The general conclusions of this study of two structural conditions observed in the 25S aluminum alloy are summarized as follows:

The correctness of the term “slip-plane precipitation” has been established.

Service stresses are not responsible for slip-plane precipitation in 25ST propeller blades.

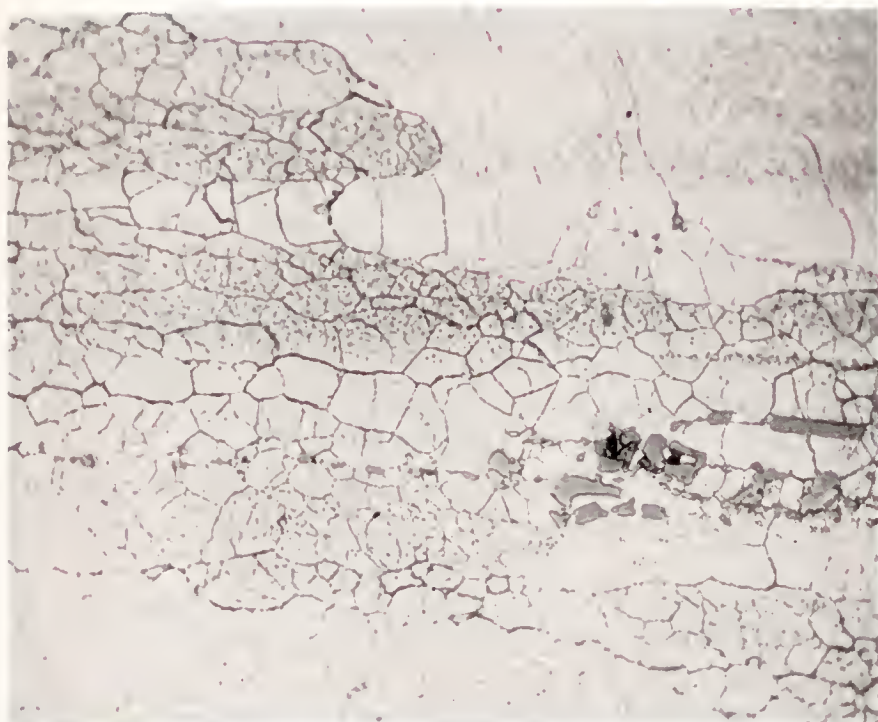
ing strains are supposedly greatest, are the regions of greatest density of slip-plane precipitation.

The use of slip-plane precipitation as a reliable indication of damage by fatigue stress is not promising because of the frequent presence of this structural feature in 25ST stock whose fatigue resistance is known to be unimpaired.

The endurance limit of the quenched-and-aged aluminum alloy 25ST is not reduced by the presence of slip-plane precipitation in the amounts ordinarily found in the material.

The structural condition termed “veining” can be made to disappear and reappear repeatedly by alternately subjecting the material to the solution heat treatment and to age-hardening, without any further stress treatment; hence, it is improbable that veining can be used to betray damage in this alloy by fatigue stresses.





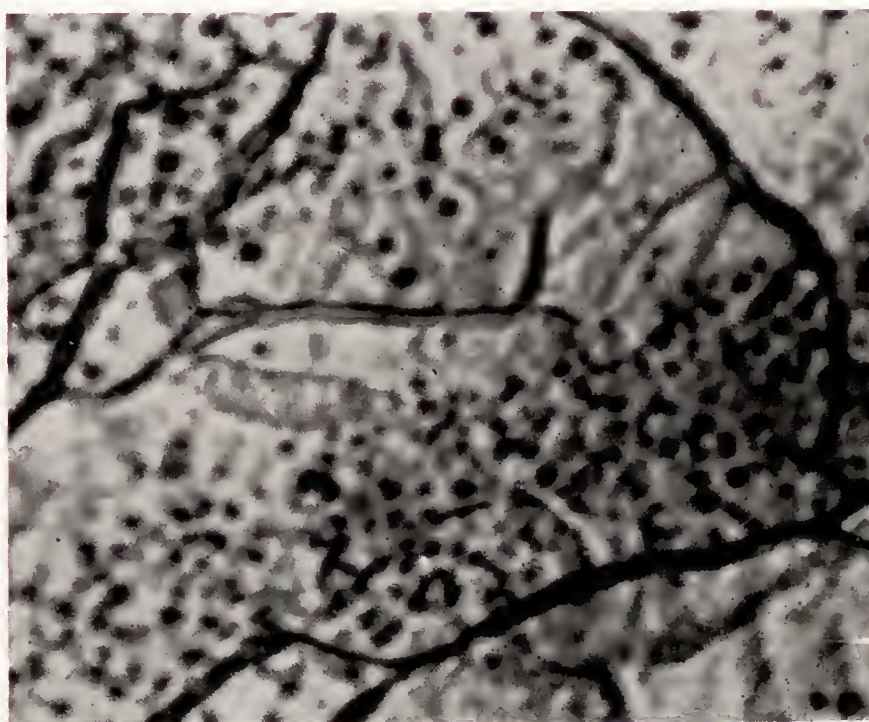
(a) Veining in a specimen, as received.  $\times 500$ .



(b) Approximately the same region as in (a), after solution heat treatment.  $\times 500$ .



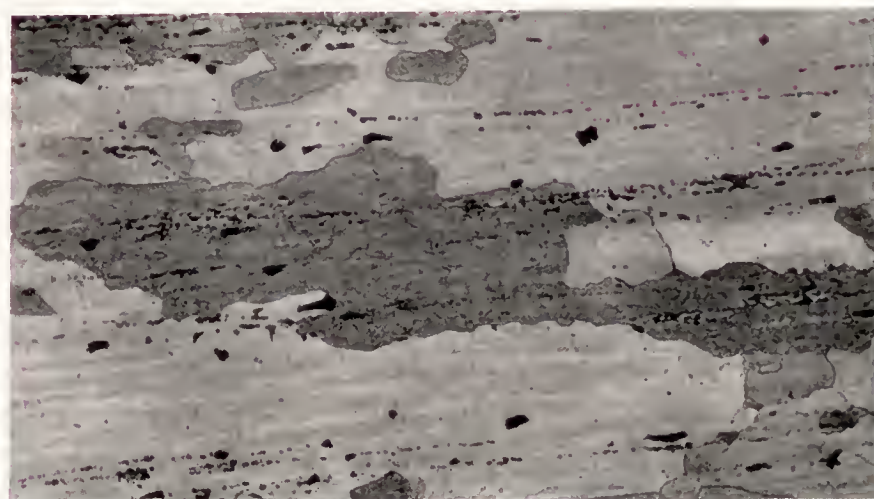
(c) Showing both slip-plane precipitation and veining. No apparent deviation in the direction of the slip lines occurs on crossing the veins and indicates that the various subdivisions are in approximately the same orientation throughout.  $\times 200$ .



(d) Veining in quenched and aged alloy. Note the continuity of the veins in contrast to the particle nature of slip-plane precipitation. No veining was found in this specimen in the previous, or quenched, condition. Aging treatment, 6 hours at  $145^{\circ}\text{C}$ .  $\times 3,600$ .



(e) Large dark grain free from veining. Same grain shown in (d) after a quench from  $525^{\circ}\text{C}$ , followed by a light polish and etch.  $\times 100$ .



(f) Same grain as in (d) and (e) after having been aged at  $146^{\circ}\text{C}$  for 6 hours, repolished, and etched. A very thin layer was removed by polish so as to make identification of the grain certain. The veining is restored although it is not so distinct as before. Even if the same system of veins had been restored, the fact could not have been ascertained owing to the removal of the surface layers in polishing.  $\times 100$ .

FIGURE 32.—Veining and slip-plane precipitation in the heat-treated aluminum alloy 25ST as received and after different treatments.



## REFERENCES

1. Ravilly, E.: Contribution à l'Étude de la Rupture des Fils Métalliques Soumis à des Torsions Alternées. Publications Scientifiques et Techniques du Ministère de l'Air. Publication No. 120, Travaux de l'Institut Polytechnique de l'Ouest, 1938.
2. Cazaud, R., and Persoz, L.: La Fatigue des Métaux. Dunod, (Paris) 1937.
3. Honda, K.: Theoretical Considerations on Static and Dynamic Tensile and Notched Bar Tests. The Science Reports of the Tohoku Imperial Univ., first series, Sendai, Japan, vol. 16, 1927, pp. 265-277.
4. Oshiba, F.: The degree of Fatigue and Recovery therefrom of Carbon Steels under Repeated Impacts. The Science Reports of the Tohoku Imperial Univ., first series, Sendai, Japan, vol. 23, 1934-35, pp. 589-611.
5. Oshiba, F.: The Degree of Fatigue of Carbon Steels under Reversed Bendings. The Science Reports of the Tohoku Imperial Univ., first series, Sendai, Japan, vol. 26, 1937-38, pp. 323-340.
6. Moore, H. F., and Wishart, H. B.: An "Overnight" Test for Determining Endurance Limit. Proc. A. S. T. M., vol. 33, pt. II, 1933, pp. 334-340.
7. Davidenkow, N., and Schewandin, E.: Über den Ermüdungs-riss. Metallwirtschaft, vol. 10, pt. II, 1931, pp. 710-714.
8. Aluminum Company of America: Alcoa Aluminum. Aluminum Company of America, 1931.
9. Luerssen, G. V., and Greene, O. V.: The Torsion Impact Test. Proc., A. S. T. M., vol. 33, pt. II, 1933, pp. 315-333.
10. Gough, H. J., and Wood, W. A.: Strength of Metals in the Light of Modern Physics. Jour., R. A. S., vol. 40, 1936, pp. 586-616.
11. Barrett, Charles S.: Internal Stresses. Metals and Alloys, vol. 5, 1934, pp. 154-158, 170-175.
12. Möller, H., and Hempel, Max: Wechselbeanspruchung und Kristallzustand. Mitteilungen aus dem Kaiser-Wilhelm Institut für Eisenforschung, zu Düsseldorf, no. 2, vol. 20, 1938, pp. 15-33.
13. Wever, F., and Möller, H.: Über den Einfluss der Wechselbeanspruchung auf den Kristallzustand metallischer Werkstoffe. Die Naturwissenschaften, vol. 25, 1937, pp. 449-453.
14. Wever, F., Hempel, M., and Möller, H.: Die Änderungen des Kristallzustandes wechselbeanspruchter Metalle im Röntgenbild. Archiv für das Eisenhüttenwesen, vol. 11, 1937-38, pp. 315-318.
15. Barrett, C. S.: The Application of X-Ray Diffraction to the Study of Fatigue in Metals. Trans., A. S. M., vol. 25, 1937, pp. 1115-1143.
16. Gough, H. J., and Wood, W. A.: A New Attack upon the Problem of Fatigue of Metals Using X-Ray Methods of Precision. Proc., Roy. Soc., series A, vol. 154, 1936, pp. 510-539; Incipient Fracture Revealed by X-Rays. Metal Progress, vol. 32, 1937, pp. 276-282.
17. Martin, Erich: Auswirkung kleiner Verformungen auf das Röntgen-Feingefügebild. Archiv für das Eisenhüttenwesen, vol. 10, 1936-37, pp. 415-418.
18. Gough, H. J.: Mechanism of Fatigue Failure. Metal Progress, vol. 33, 1938, pp. 620, 622.
19. Barrett, C. S.: Predicting a Fatigue Failure; Are X-Rays Competent? Metal Progress, vol. 32, 1937, pp. 677-678.
20. Merica, Paul D.: The Age-Hardening of Metals. Trans., A. I. M. M. E., Inst. of Metals Div., vol. 99, 1932, pp. 13-54.
21. Fink, W. L., and Smith, D. W.: Age-Hardening of Aluminum Alloys. I. Aluminum-Copper Alloy. Trans., A. I. M. M. E., Inst. of Metals Div., vol. 122, 1936, pp. 284-293.
22. Wassermann, G.: Untersuchung über die Aushärtungsvorgänge in binären Aluminum Kupfer-Legierungen. Zeitschrift für Metallkunde, vol. 30, 1938, pp. 62-67.
23. Barrett, C. S.: The Stereographic Projection. Trans., A. I. M. M. E., Inst. of Metals Div., vol. 124, 1937, pp. 29-58.
24. Townsend, J. R.: Fatigue Studies on Telephone Cable Sheath Alloys, Proc., A. S. T. M., vol. 37, pt. II, 1927, pp. 153-172.
25. Kempf, L. W., Hopkins, H. L., and Ivanso, E. V.: Internal Stresses in Quenched Aluminum and Some Aluminum Alloys. Trans., A. I. M. M. E., Inst. of Metals Div., vol. 111, 1934, pp. 158-180.
26. Northcott, L.: Veining and Sub-boundary Structures in Metals. Jour., Inst. of Metals, vol. 59, 1936, pp. 225-253.



## REPORT No. 660

### EXPERIMENTAL INVESTIGATION OF THE MOMENTUM METHOD FOR DETERMINING PROFILE DRAG

By HARRY J. GOETT

#### SUMMARY

*An experimental investigation has been conducted in the full-scale tunnel to determine the accuracy of the Jones and the Betz equations for computing profile drag from total- and static-pressure surveys in the wake of wings. Surveys were made behind 6- by 36-foot airfoils of the N. A. C. A. 0009, 0012, and 0018 sections at zero lift and behind the N. A. C. A. 0012 airfoil at positive lifts. The surveys were made at various spanwise positions and at distances behind the airfoil ranging from 0.05c to 3.00c.*

*The reduction of the test data by either the Jones or the Betz equation gave profile-drag coefficients agreeing within 2 percent with those obtained by force tests at zero lift. The variation of the profile drag determined at stations from 0.05c to 3.00c behind the trailing edge was small and the error resulting from the induced field of a lifting airfoil did not exceed 2.5 percent at a  $C_L$  of 1.0 and a spanwise station of 0.78 b/2.*

#### INTRODUCTION

The use of the momentum method for the determination of profile drag has recently increased, owing mainly to the equations developed by Betz (reference 1) and by Jones (reference 2) by which the method has been made applicable in the region of increased static pressure close behind a body. The derivation of these equations, which are based on the original principle stated by Froude in 1874, requires certain assumptions. The errors introduced by these assumptions have been the subject of theoretical analyses (references 2 and 3), which have set an upper limit for the errors involved but fail to define their actual value.

The investigation reported herein was conducted to determine experimentally the magnitude of these errors by determining the effect of a number of variables upon the measured drag. (See reference 4.) The necessary wake surveys were made in the N. A. C. A. full-scale wind tunnel behind symmetrical airfoils of three thickness ratios. The effect of distance behind the airfoils was first investigated by a comparison of drag determinations made at locations ranging from 0.05c to 3.00c behind the trailing edge. A check was then obtained on the accuracy of the method by a comparison

with force-test drag measurements at zero lift. Finally, the effect of the induced-flow system of a lifting wing was investigated.

#### SYMBOLS

The symbols used in the report are defined as follows:

- $H_0$ , free-stream total pressure.
- $H_1, H_2, H_3$ , total pressures in field of airfoil. (See fig. 4.)
- $p_0$ , free-stream static pressure.
- $p_1, p_2, p_3$ , static pressures in field of airfoil.
- $q_0$ , free-stream dynamic pressure,  $1/2\rho U_0^2$ .
- $U_0$ , free-stream velocity.
- $U_1, U_2, U_3$ , local velocity in field of airfoil.
- $U_2'$ , hypothetical velocity in wake (Betz equation).
- $y$ , vertical coordinate of point.
- $c$ , airfoil chord.
- $dS, dS_1, dS_2, dS_3$ , elemental areas.
- $\rho$ , density.
- $b$ , airfoil span.
- $v$ , velocity along the  $Y$  axis.
- $w$ , velocity along the  $Z$  axis.
- $D_0$ , airfoil profile drag.
- $C_{D_0}$ , airfoil profile-drag coefficient.
- $c_{d_0}$ , section profile-drag coefficient.
- $C_L$ , airfoil lift coefficient.
- $c_l$ , section lift coefficient.

#### EXPERIMENTAL INVESTIGATION

##### APPARATUS

The experimental work was conducted in the N. A. C. A. full-scale wind tunnel (reference 5). This tunnel has a turbulence factor of 1.1 as determined by sphere tests (reference 6). A typical static-pressure gradient along the axis of the tunnel (jet empty) is shown in figure 1. This gradient was allowed for in determining the free-stream reference pressure for the momentum measurements. The buoyancy effect of the gradient is small.

Three 6- by 36-foot rectangular airfoils having N. A. C. A. 0009, 0012, and 0018 sections were used in these tests. The airfoils, which were covered with



$\frac{1}{16}$ -inch aluminum sheets, had all the screw heads filled and the surface painted, sanded, and polished to a glossy waxlike finish to insure aerodynamic smoothness. The airfoil tips were rounded, each tip forming one-half of a solid of revolution with the radius at each chordwise station equal to one-half the local airfoil thickness. Figure 2 shows one of the airfoils mounted in the tunnel jet.

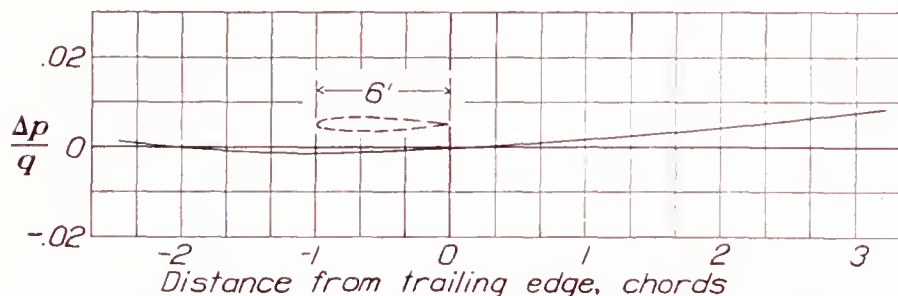


FIGURE 1.—Typical static-pressure gradient along test section of full-scale wind tunnel (jet empty).

The rack used for the total- and the static-pressure surveys consisted of a comb of 39 total-pressure tubes and one of 13 static-pressure tubes. These combs were spaced 6 inches laterally and the entire assembly was mounted on the survey carriage. The detailed spacing and the dimensions of the tubes on both combs are shown in figure 3. Each tube was connected to a multiple-tube, photographic-recording manometer carried in the survey carriage.



FIGURE 2.—The 6- by 36-foot N. A. C. A. 0012 airfoil mounted in the full-scale wind tunnel.

#### METHOD

A survey was first made with the total- and the static-pressure combs at each station of measurement with the jet empty. This survey established the total-pressure and the static-pressure gradients in the tunnel at the points of measurement. Pitch-angle surveys were next made behind the airfoils to establish the average downwash angle across the field of measurement. Total-pressure and static-pressure readings were then taken in the wake region with the rack perpendicular to the average downwash direction at each station.

This procedure kept the effect of flow angularity on the measurements at a minimum, since the local angle across the rack varied no more than  $\pm 3^\circ$  from the average. The effect of periodic pressure fluctuations in the tunnel jet was eliminated by the instantaneous readings taken on the photographic manometer.

#### SCOPE OF TESTS

Pressure and drag measurements were made at locations and under conditions as follows:

1. Total- and static-pressure surveys were made at zero lift behind the three airfoils at 27 spanwise loca-

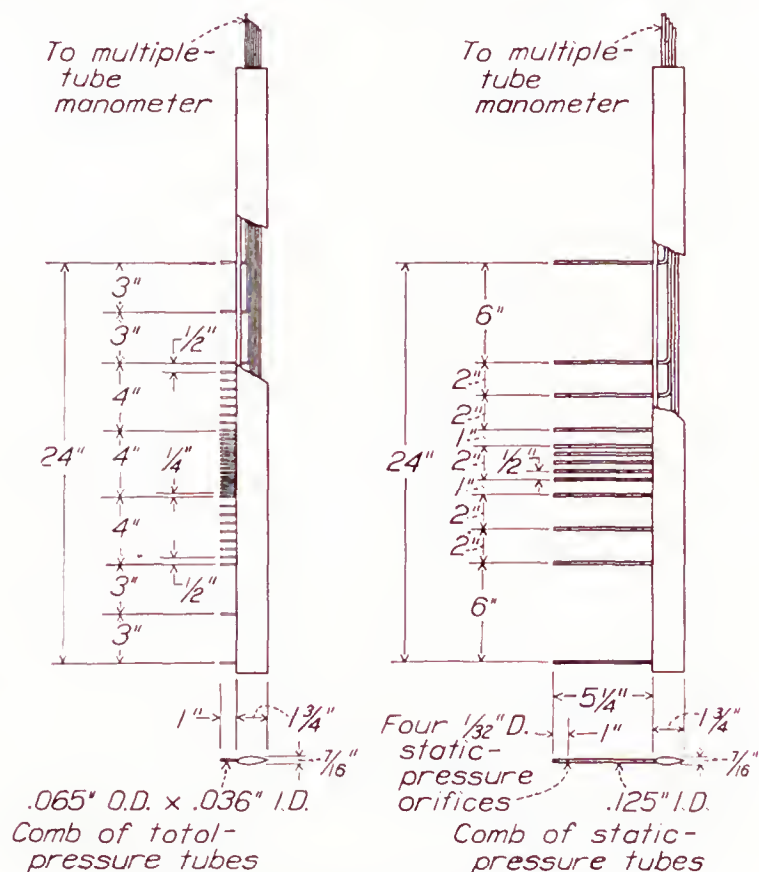


FIGURE 3.—Combs of total- and static-pressure tubes.

tions,  $0.15c$  behind the trailing edge. At the  $0.06 b/2$  station, surveys were obtained at longitudinal stations varying from  $0.05c$  to  $3.00c$  behind the trailing edge. Force tests were made to furnish comparative drag data.

2. Total- and static-pressure surveys were obtained behind the N. A. C. A. 0012 airfoil at lift coefficients of 0, 0.28, 0.47, 0.65, 0.83, and 1.13 at six spanwise locations,  $0.15c$  and  $0.30c$  behind the trailing edge. Force tests were made to furnish comparative drag data.

All tests were run at an air speed of 90 miles per hour, giving a test Reynolds Number of 5,000,000.

#### THEORY

The profile drag of a body can be determined from the loss of momentum per unit time that it imposes upon the free stream. If a region exists behind the body where the static pressure has returned to that of the free stream (fig. 4 (c)), the profile drag of a nonlifting body will be given by the expression

$$D_0 = \rho \int^W \int U_3 (U_0 - U_3) dS \quad (1)$$

where  $W$  indicates that the integration is confined to the wake region. For practical reasons, it is desirable



in most cases to make the survey in the region close behind the airfoil where  $p$  is in excess of  $p_0$  (fig. 4 (b)). In this region the drag will be equal to

$$D_0 = \iint (p_1 + \rho U_1^2) dS_1 - \iint (p_2 + \rho U_2^2) dS_2 \quad (2)$$

where both integrations are carried to infinity.

Since it is impossible to survey to infinity as required by equation (2), this equation must be transformed into one involving only quantities in the wake region. This transformation has been made by Betz (reference 1) and by Jones (reference 2).

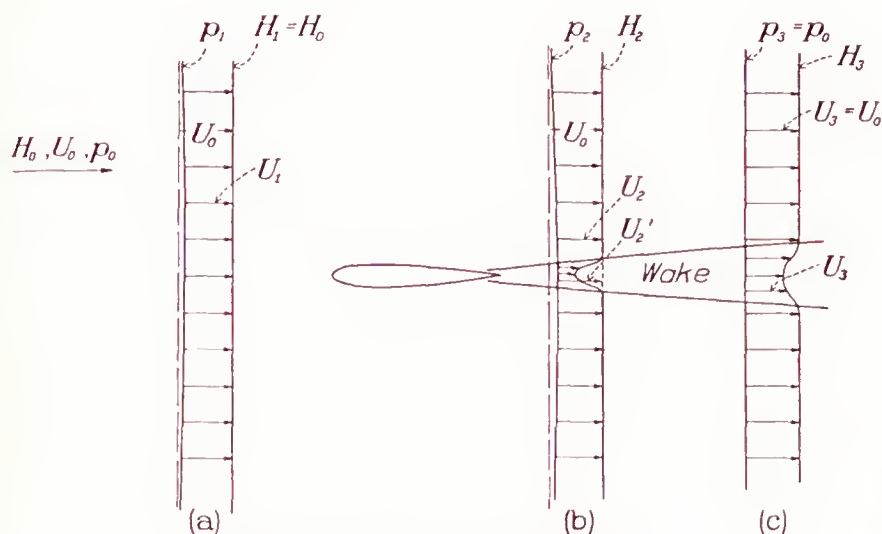


FIGURE 4.—Diagram of airfoil and wake.

Betz builds up a hypothetical flow by means of a system of sources of such strength that the total pressure in the wake of the body is restored to the value it would have in potential flow. (See fig. 4,  $H_2=H_0$ ,  $U_2=U_2'$ .) This system has a resultant thrust equal to the thrust of the sources. It differs from the real system only in the region of the wake so that the difference in thrust between the two systems is equal to the difference in momentum per unit time passing through the wake region of each. It then follows that

Drag of real system = (Difference in thrust between hypothetical and real systems) — (Thrust of hypothetical system)

Thus, the integration over the region external to the wake is eliminated and the expression for profile drag reduces to

$$D_0 = \int^w \int (H_0 - H_2) dS + \frac{\rho}{2} \int^w \int (U_2' - U_2)(U_2' + U_2 - 2U_0) dS \quad (3)$$

In terms of total and static pressures to be measured, the section profile-drag coefficient becomes

$$c_{d0} = \frac{1}{c} \int^w \left\{ \left[ \frac{H_0 - H_2}{H_0 - p_0} \right] + \left[ \frac{(\sqrt{H_0 - p_2} - \sqrt{H_2 - p_2})(\sqrt{H_0 - p_2} + \sqrt{H_2 - p_2} - 2\sqrt{H_0 - p_0})}{H_0 - p_0} \right] \right\} dy \quad (4)$$

The last step involves the assumption that, for a lifting airfoil,

$$H_2 = \frac{1}{2} \rho U_2^2 + p_2 \quad (5)$$

instead of

$$H_2 = \frac{1}{2} \rho (U_2^2 + v_2^2 + w_2^2) + p_2 \quad (6)$$

Jones (reference 2) assumes a hypothetical flow in the wake in which there is no energy interchange between tubes of flow in the wake behind the point of measurement and consequently that Bernoulli's equation may be applied to these tubes of flow. On the basis of such an assumption, the total and the static pressures measured close behind a body in a region of increased static pressure give sufficient data to obtain the corresponding velocity loss (and therefore momentum defect) at a point where the static pressure has reached the free-stream value. Thus on a non-lifting airfoil,

$$D_0 = \rho \int^w \int U_2 (U_0 - U_3) dS \quad (7)$$

and (on the foregoing assumption)

$$H_2 - p_0 = \frac{1}{2} \rho U_3^2 \quad (8)$$

Then

$$D_0 = 2 \int^w \int \sqrt{H_2 - p_2} (\sqrt{H_0 - p_0} - \sqrt{H_2 - p_0}) dS \quad (9)$$

Reduced to coefficient form, equation (9) becomes

$$c_{d0} = \frac{2}{c} \int^w \frac{\sqrt{H_2 - p_2}}{\sqrt{H_0 - p_0}} \left( 1 - \frac{\sqrt{H_2 - p_0}}{\sqrt{H_0 - p_0}} \right) dy \quad (10)$$

which Jones also applies to a lifting airfoil.

The effect of the assumptions made in the derivation of the Betz and the Jones equations has received considerable study. The errors involved in the method of Betz are difficult to estimate and the validity of the derivation is difficult to establish.

Taylor (reference 3) has shown that the neglect in the Jones method of the internal tangential stresses ("mixing") which occur in the wake downstream of the measured section is theoretically unsound. From the examination of a number of typical profiles, Taylor has shown that the error does not exceed 1.5 percent but he also shows that much larger errors are possible.

The induced field of a finite lifting wing may cause errors in the methods. First, the assumption made in equation (5), that the  $v$  and the  $w$  components may be neglected, will be a source of error. Second, there is the possibility that the vortices in the wake region may damp out causing a loss of total pressure, which appears erroneously as profile drag. An analysis of this possibility, based on certain typical wake profiles, has been made by Jones in reference 2 and the maximum value of the error due to this possible pressure loss has been estimated.



In addition to the foregoing errors, inaccuracies will possibly arise from incorrect readings of static and total pressures caused by turbulence and stream angularities behind the airfoil.

## RESULTS AND DISCUSSION

### COMPUTATION OF RESULTS

In the computation of results, the values of  $H_2$  and  $p_2$  across the wake profile were determined from faired curves of total and static pressures, to which a correction was applied to allow for the vertical gradients existing in the tunnel. The values of  $H_0$  and  $p_0$  were determined from readings taken well outside the wake with a correction applied to obtain the values of these quantities at the position of the airfoil. These values were then substituted in equations (4) and (10) and the results were plotted against the vertical position in the wake. The resulting curve was integrated, the summation being the section profile-drag coefficient at the station of measurement. An additional correction was applied for displacement of the effective center of the total-pressure tubes in a velocity gradient.

### EFFECT OF DISTANCE BEHIND THE AIRFOIL

The variation in measured drag with distance behind the airfoil is shown in figure 5 for the three airfoils at a  $c_l$  of 0.05 and for the N. A. C. A. 0012 at values of  $c_l$  of 0.78 and 1.32. Each point is the average of results

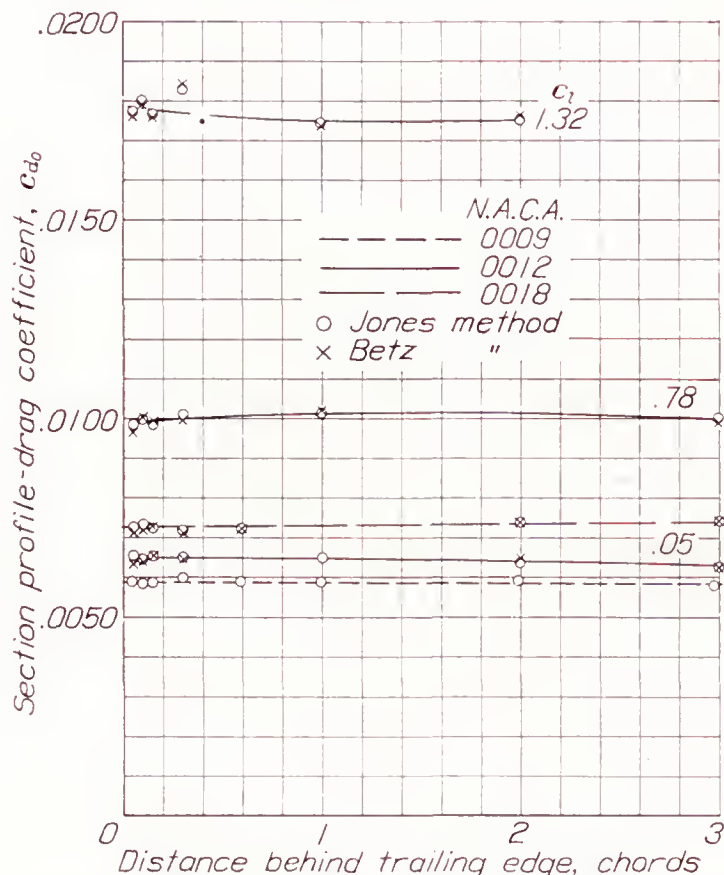


FIGURE 5.—Variation of measured drag with distance behind the airfoil.

from two or more surveys. The curves show that the greatest difference in drag, as measured at the foremost and the rearmost positions, is approximately 3 percent. This difference is within the experimental scatter of the measurements, estimated to vary from  $\pm 1$  percent at the  $0.15c$  station to  $\pm 3$  percent at the  $3.00c$  station (where the wake profiles are shallow and

wide). It is therefore concluded that the measured drag, as evaluated by either the Jones or the Betz method, is unaffected by distance behind the airfoil within the accuracy of the measurements.

Figure 5 also indicates that there is no significant difference between the drag as determined by the Betz and the Jones equations. The maximum spread between the two methods is less than 1 percent. All

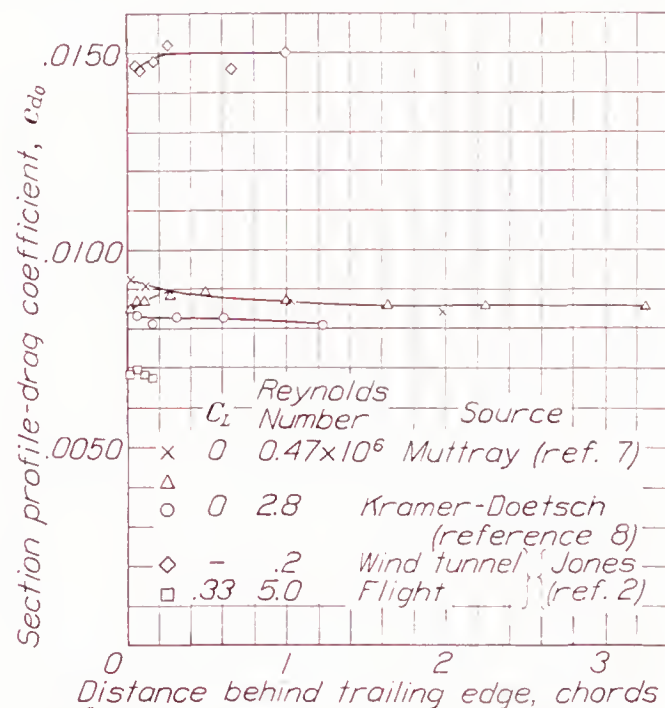


FIGURE 6.—Results of drag determinations obtained by the momentum method by Muttray, Kramer and Doetsch, and Jones.

further drag determinations were therefore made by the Jones equation because of the greater simplicity of the necessary computations.

The results of other similar investigations (references 2, 7, and 8) are shown in figure 6. From these results, Muttray concluded (reference 7) that sufficient data had not yet been obtained to warrant the conclusion that the measured drag was independent of the distance behind the airfoil. The present investigation is considered, however, to have furnished sufficient data to support this conclusion.

### EFFECT OF TURBULENCE ON STATIC-PRESSURE MEASUREMENTS

In relation to the possible effect of turbulence on the measurement of static pressure in the wake, a comparison of measured static pressures with computed static pressures behind the N. A. C. A. 0012 and 0018 airfoils at zero lift is shown in figure 7. The pressures behind the airfoils at zero lift were computed for the case of ideal flow about the airfoils and for flow with a boundary layer and a wake by means of a source-sink distribution to represent the airfoil and the wake.

### COMPARISON OF MOMENTUM- AND FORCE-TEST RESULTS

The accuracy of the momentum method is indicated from a direct comparison with force-test results. The drag coefficients obtained from momentum surveys at 27 spanwise locations at  $0.15c$  behind the three airfoils at zero lift are plotted in figure 8. These curves, when integrated across the span, give an over-all  $C_{D0}$  for each airfoil. The drag coefficients obtained in this



TABLE I

COMPARISON OF PROFILE-DRAG COEFFICIENTS AT ZERO LIFT OBTAINED FROM MOMENTUM AND FORCE TESTS

N. A. C. A. airfoil	$C_{D_0}$		Difference (percent)
	Momen- tum test	Force test	
0009	0.0061	0.0060	1.7
0012	.0066	.0065	1.6
0018	.0075	.0076	1.3

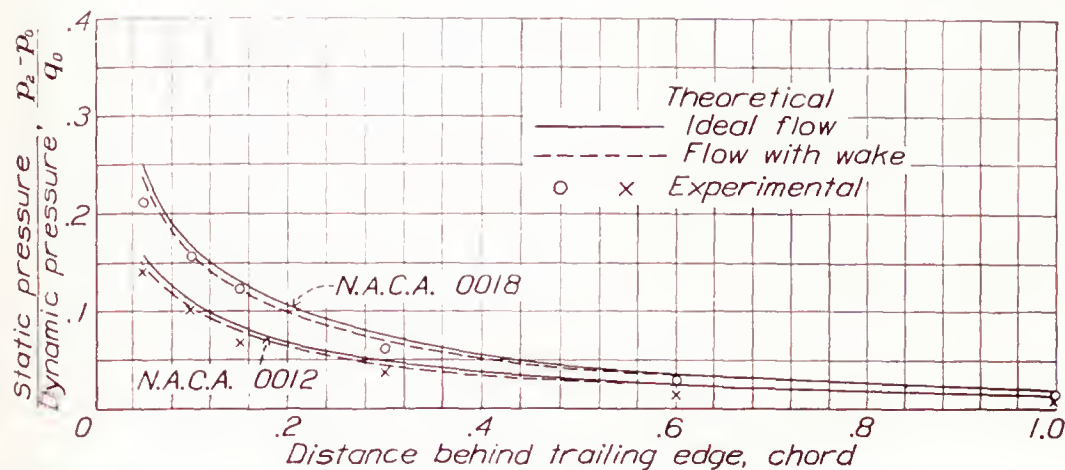


FIGURE 7.—Experimental and theoretical static-pressure variation behind the N. A. C. A. 0012 and 0018 airfoils at zero lift.

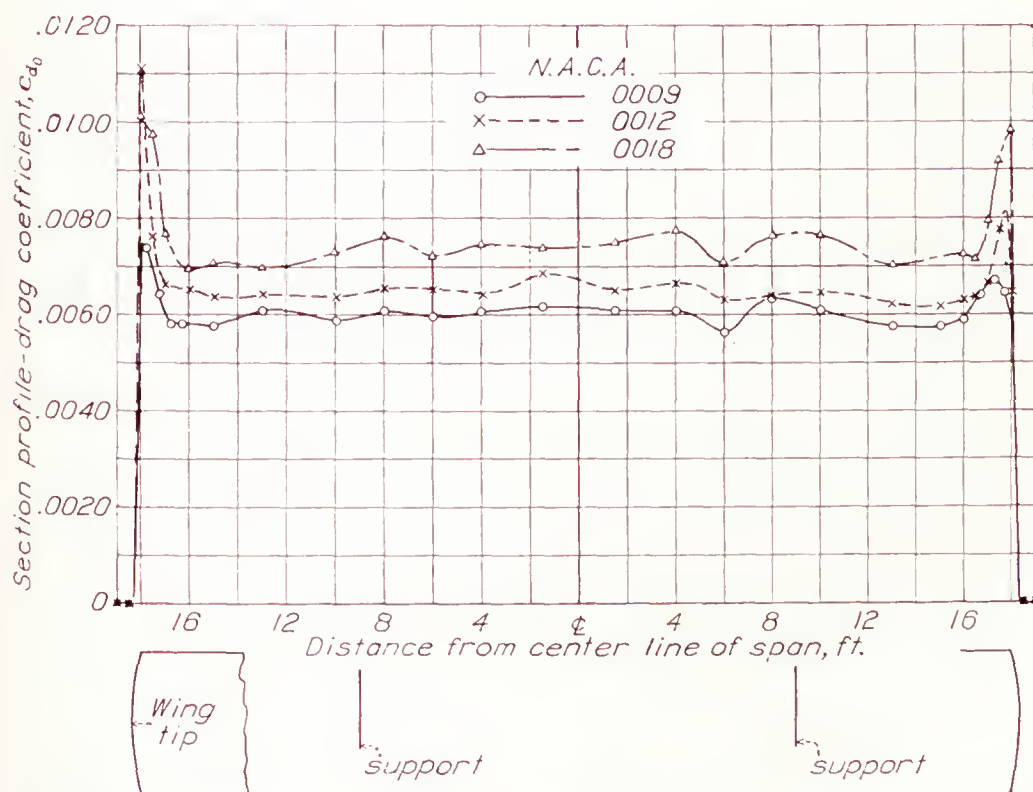


FIGURE 8.—Variation of section profile drag coefficient across the span of the rounded-tip airfoils at zero lift.

manner are compared with those measured by force tests in table I. The maximum difference is less than 2 percent, indicating the order of accuracy of the momentum method. A similar comparison cannot be made at positive lifts because it is impossible to obtain results from the momentum method in the region of the airfoil tips owing to the intensity of the vortices.

#### EFFECT OF INDUCED FLOW

The total effect of the errors caused by the induced-flow field of a lifting airfoil may be determined from a comparison of the curves of section profile-drag coeffi-

cient against section lift coefficient obtained under the various conditions of induced flow that exist between the center line and the tip of a finite airfoil at positive lifts. Such curves are given in figure 9 for six spanwise locations from 0.06 to 0.90  $b/2$ . The section lift coefficients were computed on the basis of a lift distribution given by Glauert (reference 9), which was found to check well with pressure-distribution tests. These curves, having been slightly shifted in order to make them agree at zero lift, are superimposed in figure 10. It will be noted that, out to 0.78  $b/2$  and up to a  $c_l$  of 1.0, the maximum dispersion is  $\pm 2.5$  percent from the 0.06  $b/2$  curve. This variation compares with a difference of approximately 7 percent that is indicated by Jones' analysis, which is based on the assumption of complete damping out of the vortices (reference 2). Inasmuch as part of the dispersion in figure 10 is due to experimental scatter, the  $\pm 2.5$  percent is considered a conservative estimate of the effect of the induced field upon the measurements. At the 0.90  $b/2$  station, the distorted curve indicates that, above a section lift coefficient of zero, the air-stream angularities become such as to make the measurements unreliable.

#### COMPARISON OF MOMENTUM- AND FORCE-TEST RESULTS AT POSITIVE LIFTS

A direct comparison between drag results obtained from momentum and force tests of a lifting airfoil is impossible because of the failure of the momentum method near the tip as well as the inclusion of induced drag in the force-test measurements. If the induced drag is deducted from the force-test drag, however, the two methods should give results differing only by the drag contributed by the tips. Such a comparison has been made in figures 11 and 12. A plot of profile drag (determined by the momentum method) against span-wise position is given in figure 11; the curves were extrapolated in the tip region and no allowance was made for an increase in drag at the tips. Integration of these curves across the span gives the average pro-

file-drag coefficient  $C_{D_0}$ , which has been plotted against  $C_L$  in figure 12. The result is compared with the profile-drag coefficient determined from force tests in the usual manner (i. e., by deducting the computed induced drag). A curve of section characteristics obtained by the momentum method (0.06  $b/2$  curve from fig. 10) is also given to show the comparison with the average profile drag across the span.

An appreciable spread will be noted between the momentum- and the force-test results; the difference varies from 1 percent at zero lift to 22 percent at a  $C_L$  of 1.0. A number of causes other than tip effects



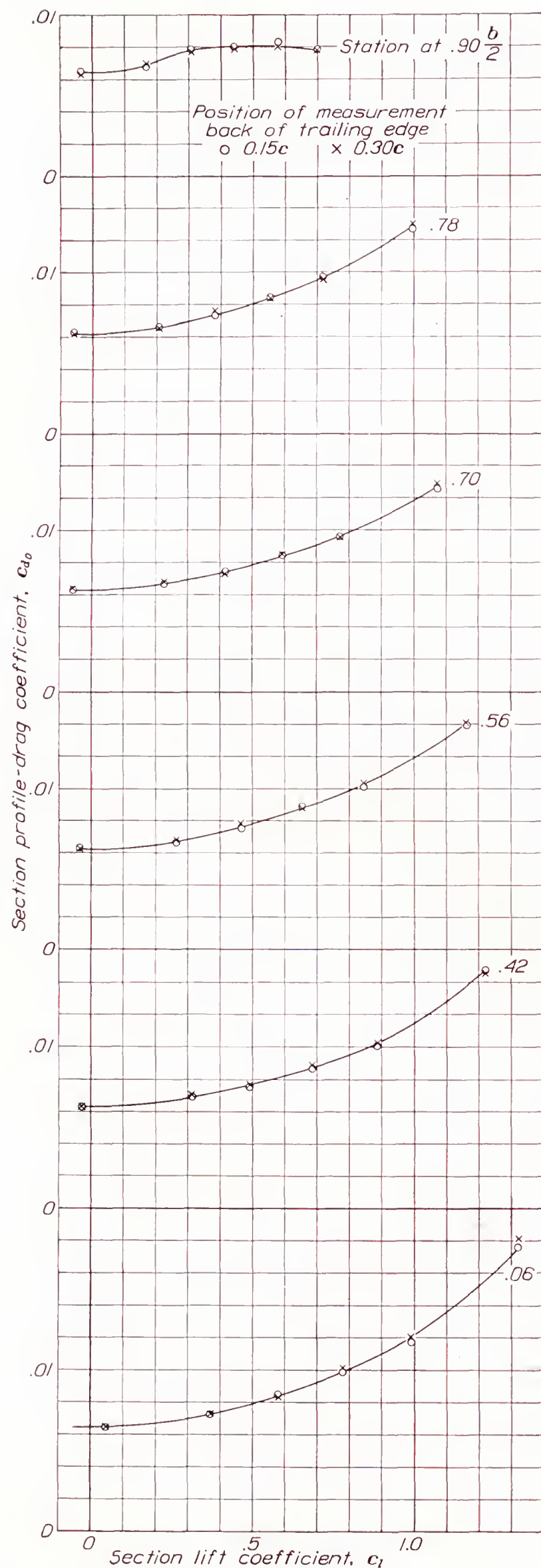


FIGURE 9.—Variation of  $c_{d0}$  with  $c_l$  from wake surveys at several spanwise stations. N. A. C. A. 0012 airfoil.

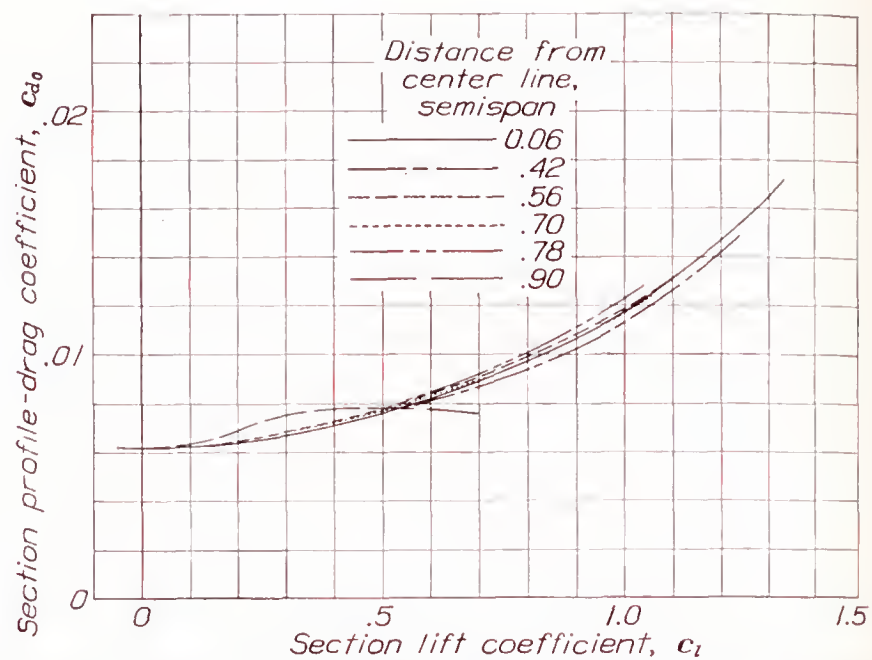


FIGURE 10.—Comparison of curves of  $c_{d0}$  against  $c_l$  obtained from wake surveys at several spanwise stations. N. A. C. A. 0012 airfoil.

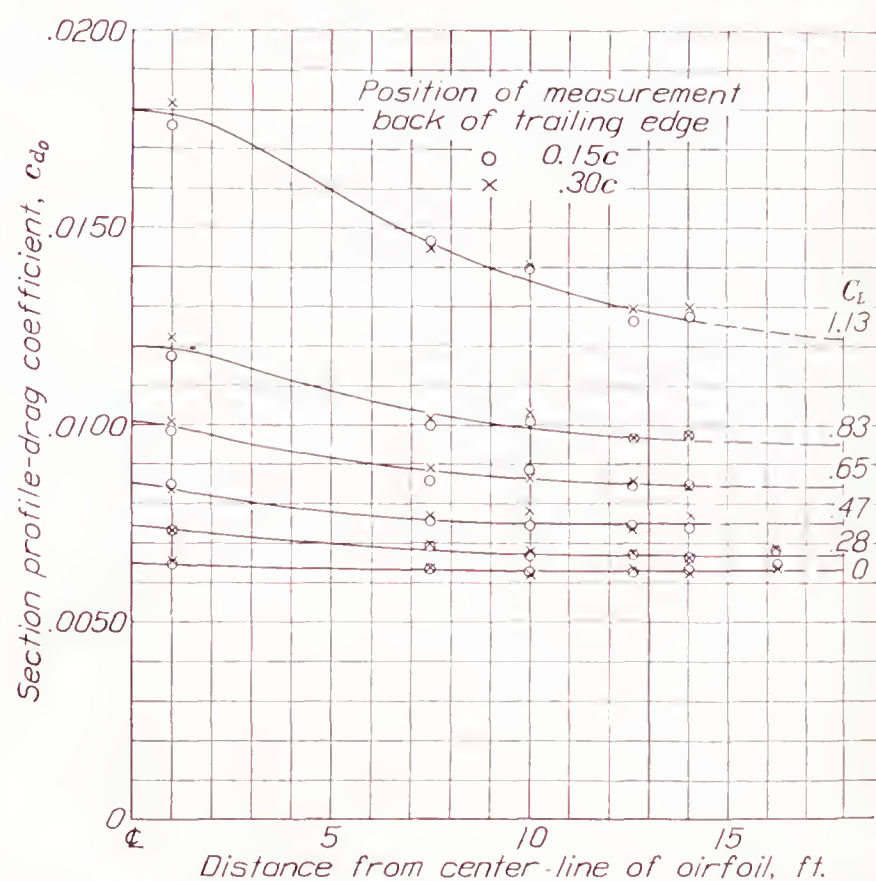


FIGURE 11.—Variation of  $c_{d0}$  across the span of the N. A. C. A. 0012 airfoil at various lift coefficients.

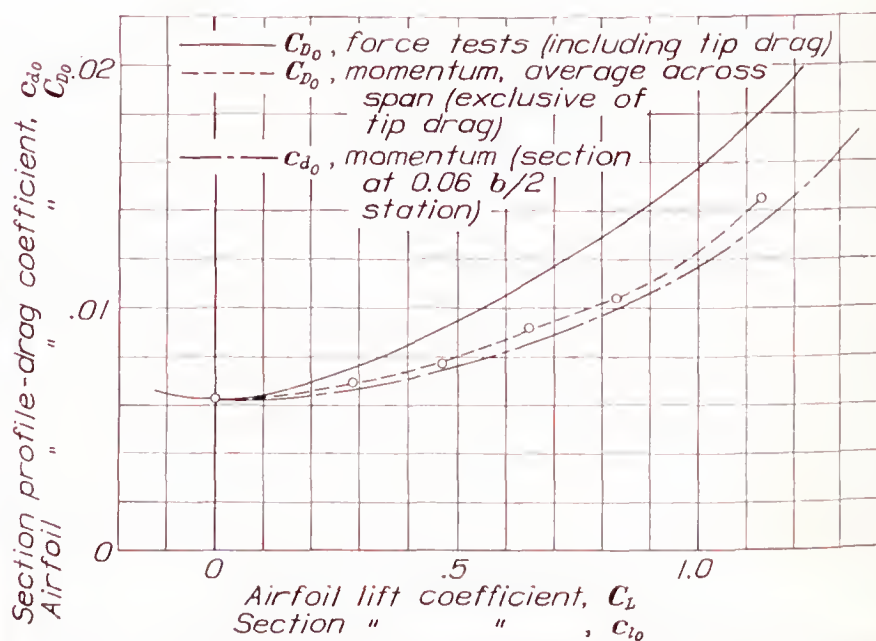


FIGURE 12.—Profile drag against lift curves obtained from momentum and force tests.



may contribute to this difference, including possible errors in the momentum method and uncertainties in computed induced drag and in the several corrections applied to the force-test results.

### CONCLUSIONS

The results presented herein lead to the following conclusions with regard to the determination of profile drag by the momentum method and the application of the Betz and the Jones equations under the conditions of the present investigation:

1. The drag determined by the momentum method did not vary appreciably with distance behind the airfoil between stations ranging from  $0.05c$  to  $3.00c$  behind the trailing edge.

2. At zero lift, the drag determined by the momentum method agreed with that measured by force tests within 2 percent.

3. Inboard of 78 percent of the semispan, the effects of the induced-flow system of a lifting wing did not cause errors exceeding 2.5 percent at a  $c_l$  of 1.0.

4. The Betz and the Jones equations gave results that agree within 0.5 percent at stations ranging from  $0.05c$  to  $3.00c$  back of the trailing edge.

5. For measurements made no farther than  $3.00c$  behind the trailing edge, the experimental scatter varied from 1 percent at zero lift to 3 percent at a  $c_l$  of 1.0.

LANGLEY MEMORIAL AERONAUTICAL LABORATORY,  
NATIONAL ADVISORY COMMITTEE FOR AERONAUTICS,  
LANGLEY FIELD, VA., *December 20, 1938.*

### REFERENCES

1. Betz, A.: A Method for the Direct Determination of Wing-Section Drag. T. M. No. 337, N. A. C. A., 1925.
2. The Cambridge University Aeronautics Laboratory: The Measurement of Profile Drag by the Pitot-Traverse Method. R. & M. No. 1688, British A. R. C., 1936.
3. Taylor, G. I.: The Determination of Drag by the Pitot-Traverse Method. R. & M. No. 1808, British A. R. C., 1937.
4. Silverstein, Abe: Wake Characteristics and Determination of Profile Drag by the Momentum Method. Paper presented at the Fifth International Congress for Applied Mechanics, Cambridge, Mass., Sept. 12-16, 1938. (Abstract in Jour. Applied Mech., vol. 5, no. 3, Sept. 1938, p. A-129.)
5. DeFrance, Smith J.: The N. A. C. A. Full-Scale Wind Tunnel. T. R. No. 459, N. A. C. A., 1933.
6. Platt, Robert C.: Turbulence Factors of N. A. C. A. Wind Tunnels as Determined by Sphere Tests. T. R. No. 558, N. A. C. A., 1936.
7. Muttray, H.: Zusehrift zu dem Bericht von H. Doetsch, Profilwiderstandsmessungen im grossen Windkanal der DVL. Luftfahrtforschung, Bd. 14, Lfg. 7, 20. July 1937, S. 371-372.
8. Doetsch, H.: Profilwiderstandsmessungen im grossen Windkanal der DVL. Luftfahrtforschung, Bd. 14, Lfg. 4/5, 20. April 1937, S. 173-178.
9. Glauert, H.: The Elements of Aerofoil and Airscrew Theory. Cambridge University Press, 1930, p. 149.







## REPORT No. 661

### TESTS IN THE VARIABLE-DENSITY WIND TUNNEL OF THE N. A. C. A. 23012 AIRFOIL WITH PLAIN AND SPLIT FLAPS

By IRA H. ABBOTT and HARRY GREENBERG

#### SUMMARY

*Section characteristics for use in wing design are presented for the N. A. C. A. 23012 airfoil with plain and split flaps of 20 percent wing chord at a value of the effective Reynolds Number of about 8,000,000. The flap deflections covered a range from 60° upward to 75° downward for the plain flap and from neutral to 90° downward for the split flap. The split flap was aerodynamically superior to the plain flap in producing high maximum lift coefficients and in having lower profile-drag coefficients at high lift coefficients.*

#### INTRODUCTION

The prevailing method of modifying the aerodynamic characteristics of airplane wings so that higher lift coefficients can be obtained is to equip the wings with trailing-edge flaps. For the design of such wings, airfoil section data at the proper values of the Reynolds Number are needed for the various sections used along the span with and without flap deflection. The purpose of this report is to present some additional section characteristics for such use.

The investigation comprised tests of the N. A. C. A. 23012 airfoil equipped with plain and split flaps of 20 percent chord. The ranges of flap settings were very comprehensive. The angle-of-attack range extended from below zero lift to beyond maximum lift for all conditions and was extended through negative maximum lift for most of the settings of the plain flap. All tests were made in the N. A. C. A. variable-density tunnel at a high value of the Reynolds Number. Maximum lift coefficients were also obtained for all combinations at a lower value of the Reynolds Number.

#### APPARATUS AND TESTS

The N. A. C. A. variable-density tunnel, in which these tests were made, is described in reference 1, and the N. A. C. A. 23012 airfoil section is described in reference 2. The two aluminum-alloy models were made as described in reference 1, except that they were anodically treated to provide hard smooth surfaces that could be more easily maintained during the course of the tests than the usual polished metallic surfaces.

The model that was used for the tests of the plain flap was provided with a brass flap hinged at five

points along the span at the station 80 percent of the chord midway between the upper and the lower surfaces. After the flap had been set at the required deflection for each test, the gap between the flap and the wing was filled with plaster of paris, which was then painted and rubbed to produce a smooth, fair surface of the proper contour.

The other model was used for the tests of the split flap. A 0.20c split flap was made of brass for each flap deflection tested and was fastened to the lower surface of the model with screws. For flap deflections up to 20°, the flap was made as a solid triangular prism. For flap deflections of 30° and more, the flap was made of two brass strips, each 1 inch by 30 inches, joined at one pair of long edges and kept apart at the proper angle by eight triangular stiffeners equally spaced along the span. In either case, the flap trailing edge was a sharp acute angle.

Standard force tests were made of each combination at a value of the effective Reynolds Number of approximately 8,000,000; the maximum lift coefficient was also determined at an effective Reynolds Number of about 3,800,000. The flap settings covered a range from 60° upward to 75° downward for the plain flap and from 0° to 90° downward for the split flap. The range of angle of attack for all combinations extended from below zero lift to above maximum lift and, for the plain-flap combinations, extended through negative maximum lift except for flap deflections between 20° upward and the neutral position.

#### PRECISION

The precision of the data obtained from force tests in the N. A. C. A. variable-density tunnel is discussed in considerable detail in references 3 and 4. It is believed that the results may be applied with normal engineering accuracy to free-flight conditions at the stated values of the effective Reynolds Number. It should be noted, however, that the data presented herein for the increments of maximum lift due to the flap are somewhat lower than those obtained in some other wind tunnels (references 5 and 6). The values of maximum lift coefficient contained in this report may be somewhat conservative.



## RESULTS AND DISCUSSION

**Presentation of results.**—The results are presented in figures 1 to 9. Figures 1, 4, and 5 show lift curves for the rectangular wing of aspect ratio 6 at both values of the Reynolds Number. The other six figures show the section characteristics usually presented, which were derived as explained in reference 4 and which may be distinguished from the wing characteristics usually presented and from previously used profile characteristics by the lower-case symbols. Thus  $c_{d0}$  represents the profile-drag coefficient for the airfoil section corrected from the older profile-drag coefficient  $C_{D0}$  by applying corrections for tip effects, for variation of lift along the wing span, and for turbulence to correct to

derived wing characteristics. The characteristics of the wing with flap neutral are obtained from tests of a plain airfoil.

**Maximum-lift coefficients.**—The increment of maximum-lift coefficient due to the flap is plotted against flap deflection for both the plain and the split flaps in figure 10. This maximum-lift increment has been plotted instead of the more usual maximum lift coefficient because it has been shown (references 4 and 5) to be nearly independent of Reynolds Number. The maximum-lift increment for the split flap increases more rapidly with flap deflection and reaches an appreciably higher value than that for the plain flap.

The maximum-lift increments obtained from these tests are appreciably lower than those obtained from

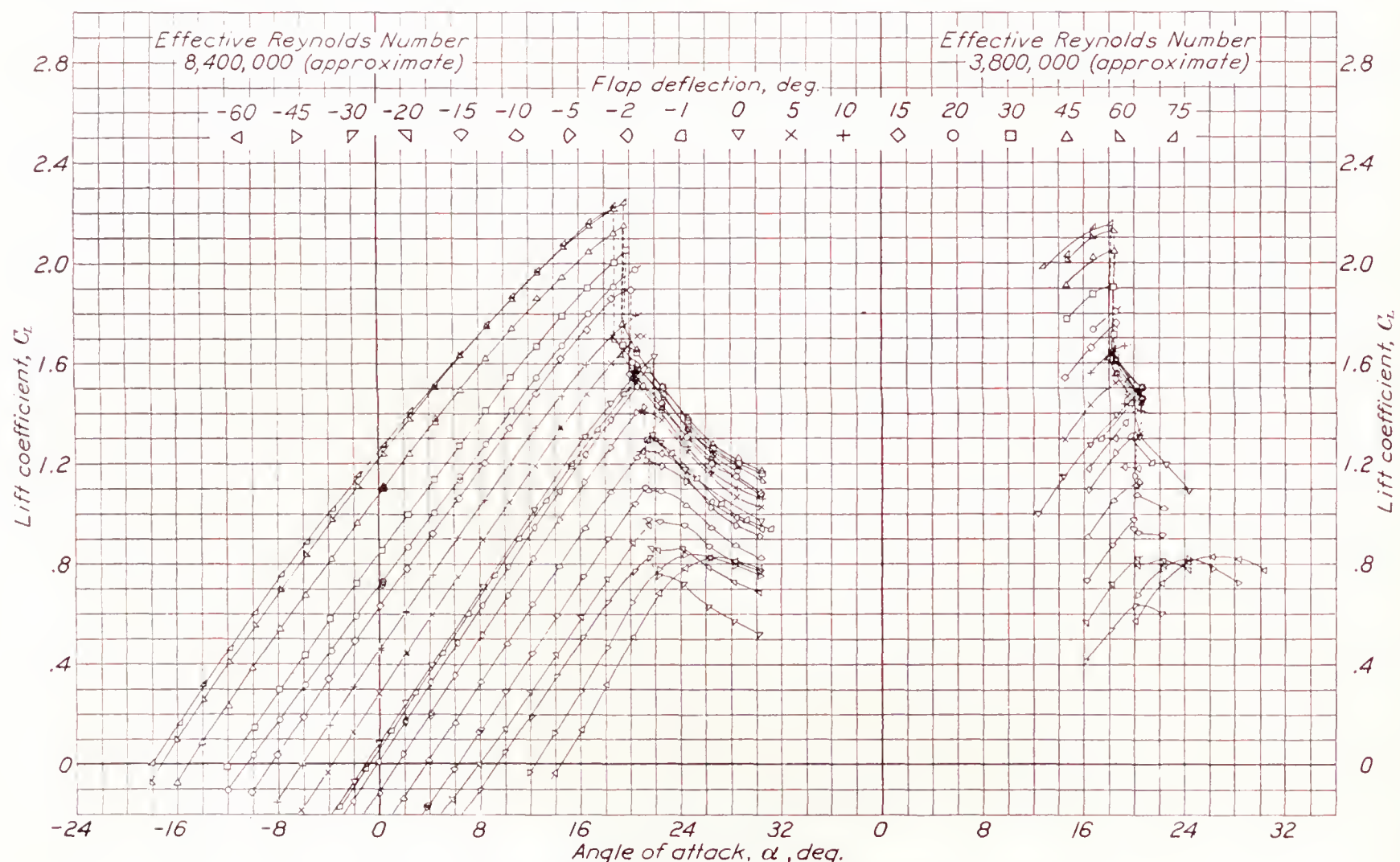


FIGURE 1.—Lift for the N. A. C. A. 23012 rectangular wing of aspect ratio 6 with 0.20c full-span plain flap.

the effective Reynolds Number. The methods of correction are explained in reference 4 and the results so corrected are intended to represent the section data in the form required for application to wing-design problems.

Standard airfoil plots, of the form presented in reference 7, for each flap deflection tested are available upon request from the National Advisory Committee for Aeronautics.

The pitching-moment coefficients  $c_{m(a.c.)_0}$  for the flapped airfoils are computed about the aerodynamic center of the unflapped airfoil. Table I presents important section characteristics and also certain

tests in the N. A. C. A. 7- by 10-foot tunnel (reference 5). German tests (reference 6) of the N. A. C. A. 23012 airfoil with and without a 0.20c split flap deflected 60° were made over a range of Reynolds Numbers. At the lower end of the scale range, the results agree with those obtained in the N. A. C. A. 7- by 10-foot tunnel but, at the higher end, the increment of maximum lift lies about midway between that obtained in the N. A. C. A. variable-density tunnel and in the 7- by 10-foot tunnel. Results obtained in the N. A. C. A. variable-density tunnel for the N. A. C. A. 23021 airfoil with a 0.20c split flap deflected 75° agree, however, with results obtained for a similar model in the N. A. C. A. 7- by 10-foot tunnel (reference 5).



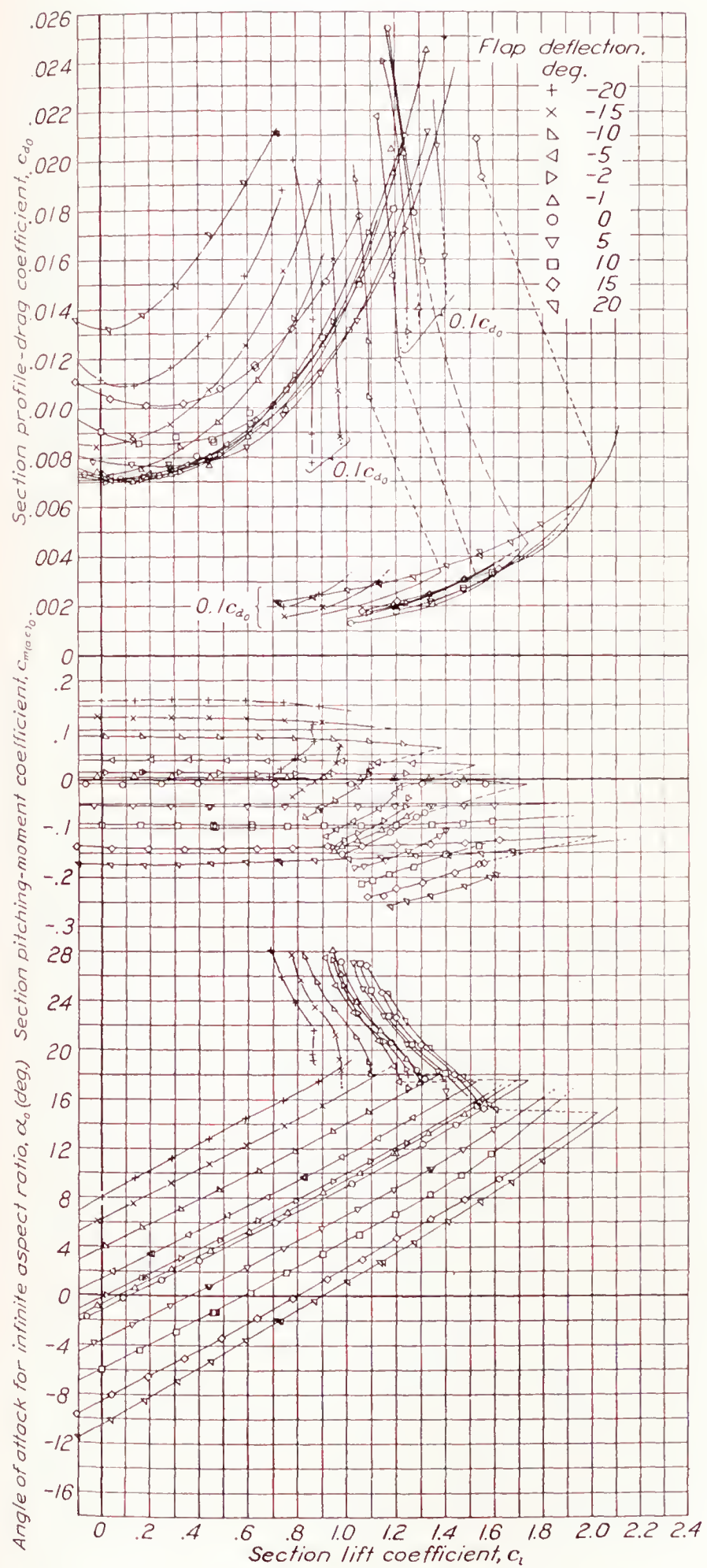


FIGURE 2.—Section characteristics for the N. A. C. A. 23012 airfoil with 0.20c plain flap. Small flap deflections.

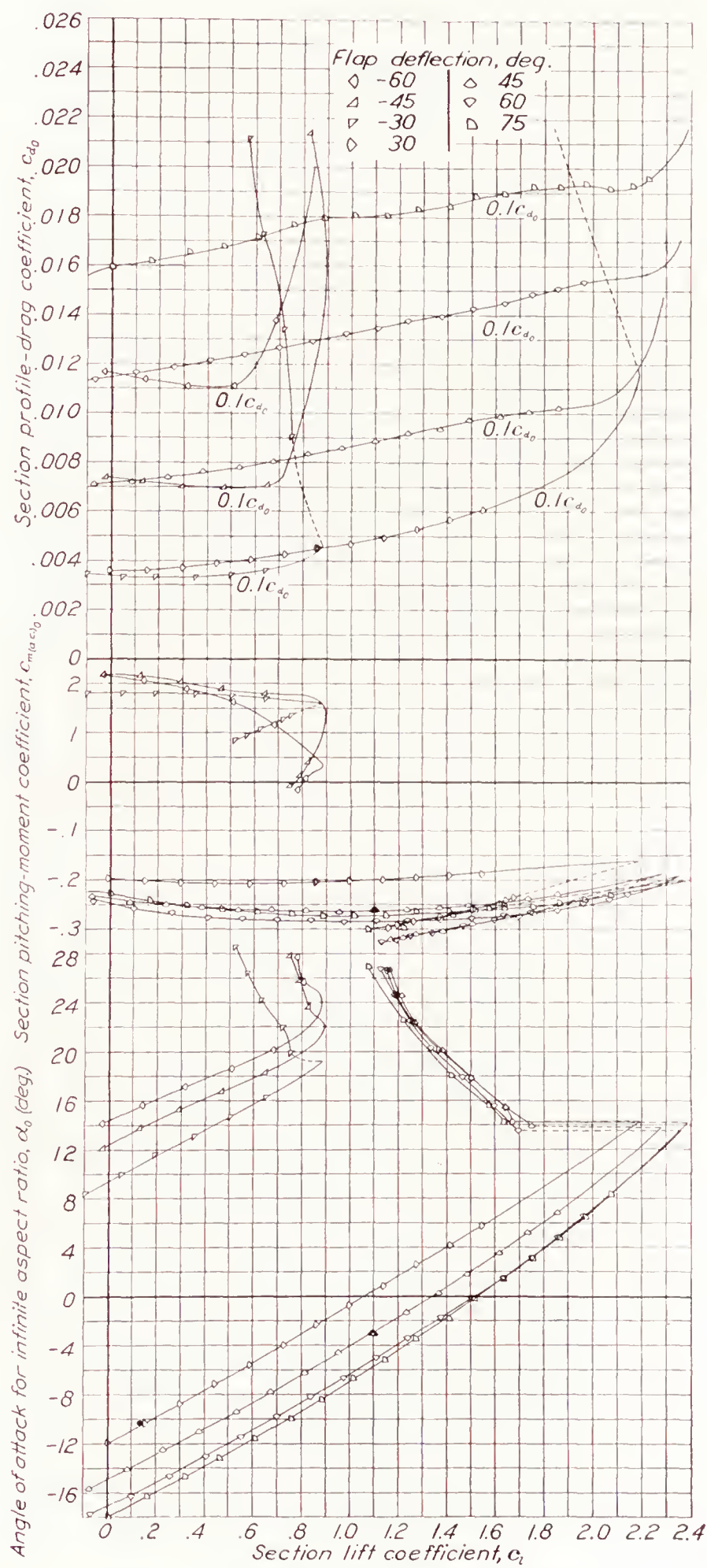


FIGURE 3.—Section characteristics for the N. A. C. A. 23012 airfoil with 0.20c plain flap. Large flap deflections.



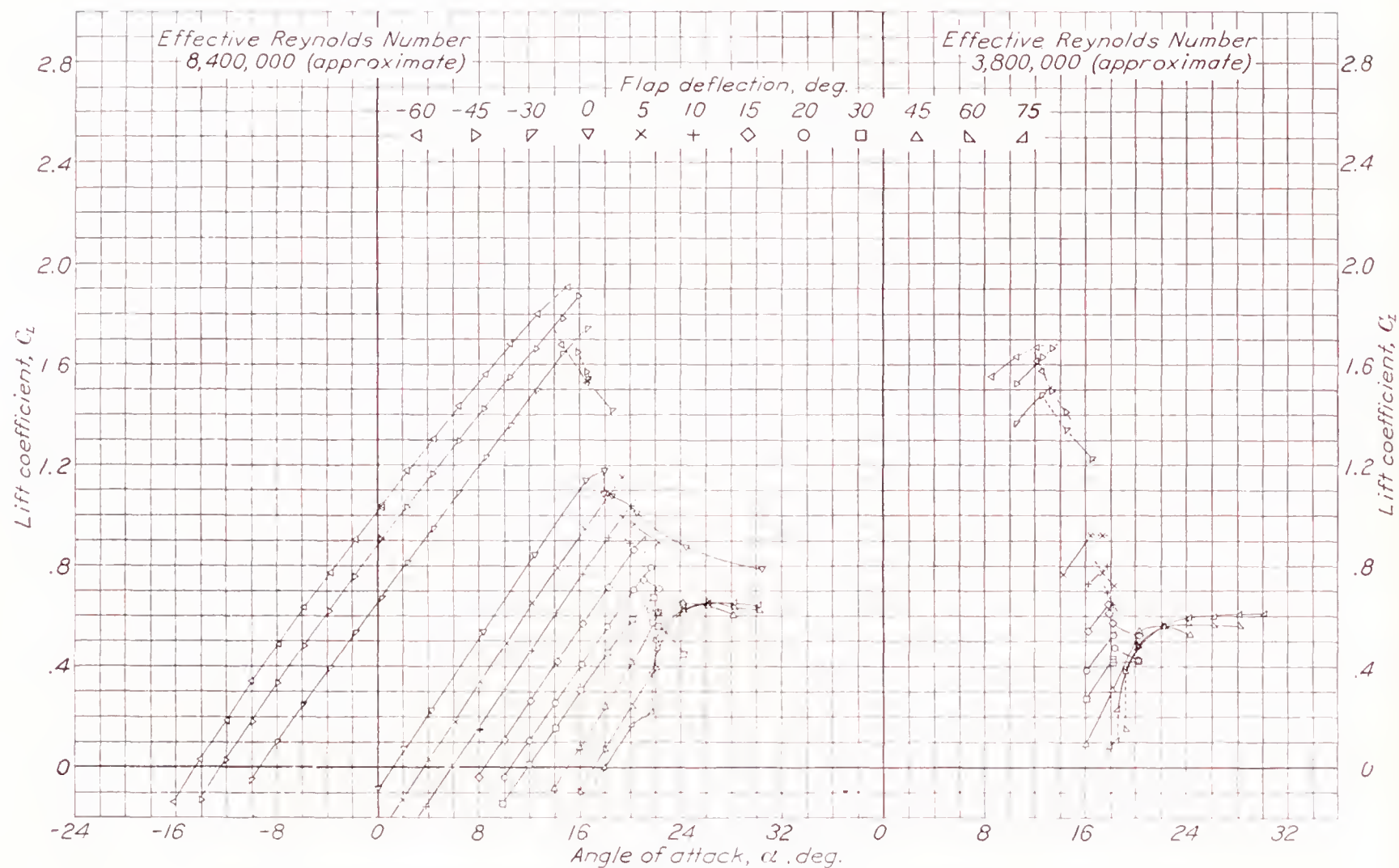


FIGURE 4.—Lift for the N. A. C. A. 23012 rectangular wing of aspect ratio 6 (inverted) with 0.20c full-span plain flap.

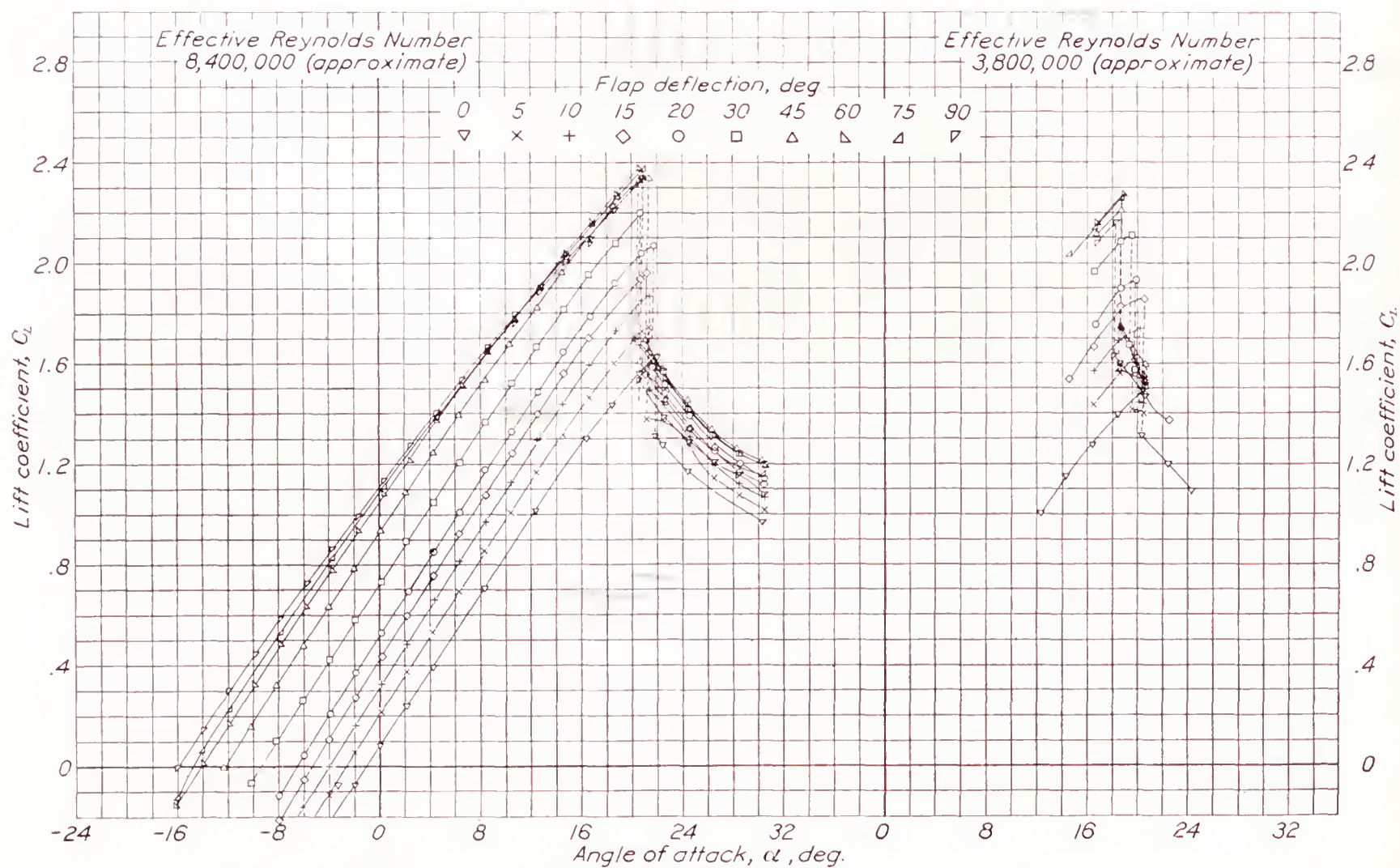


FIGURE 5.—Lift for the N. A. C. A. 23012 rectangular wing of aspect ratio 6 with 0.20c full-span split flap.



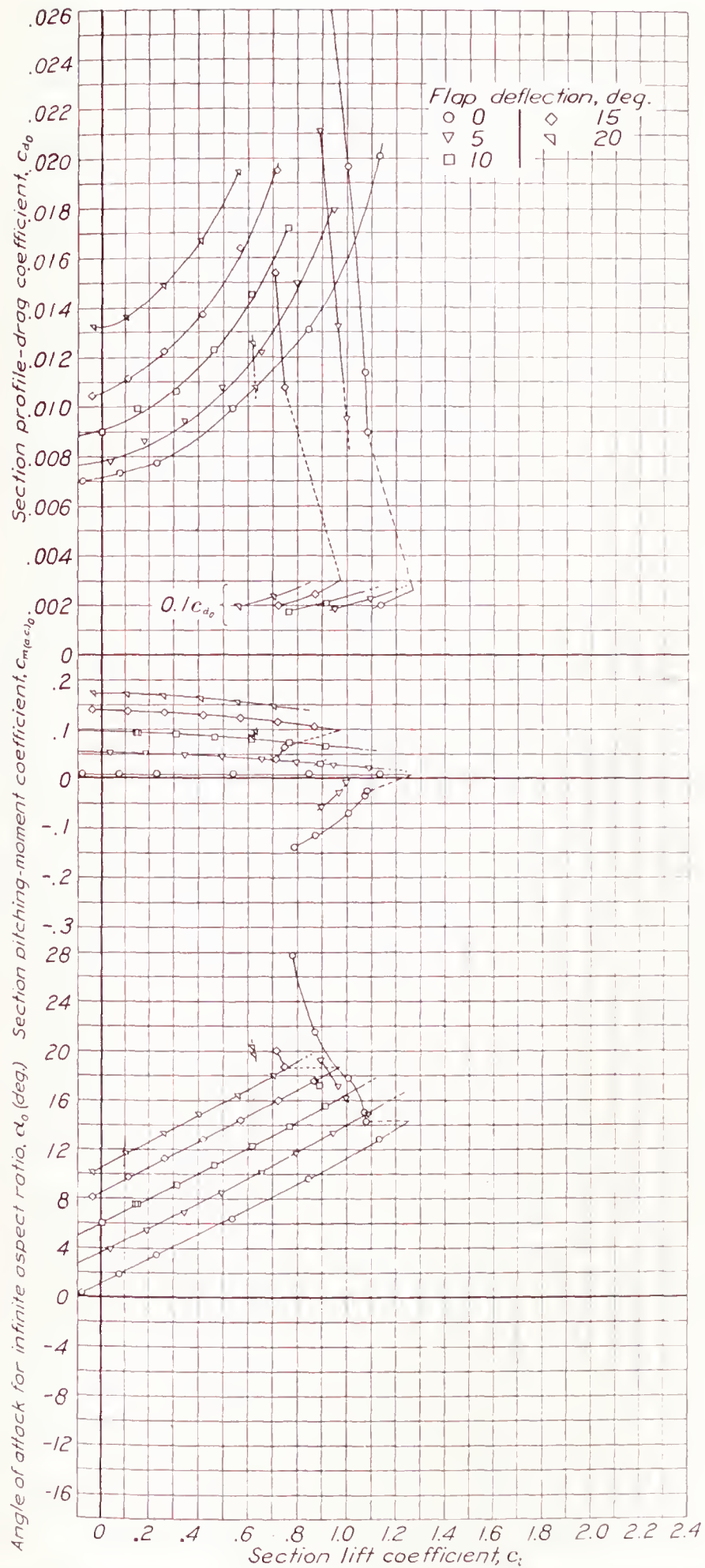


FIGURE 6.—Section characteristics for the N. A. C. A. 23012 airfoil (inverted) with 0.20c plain flap. Small flap deflections.

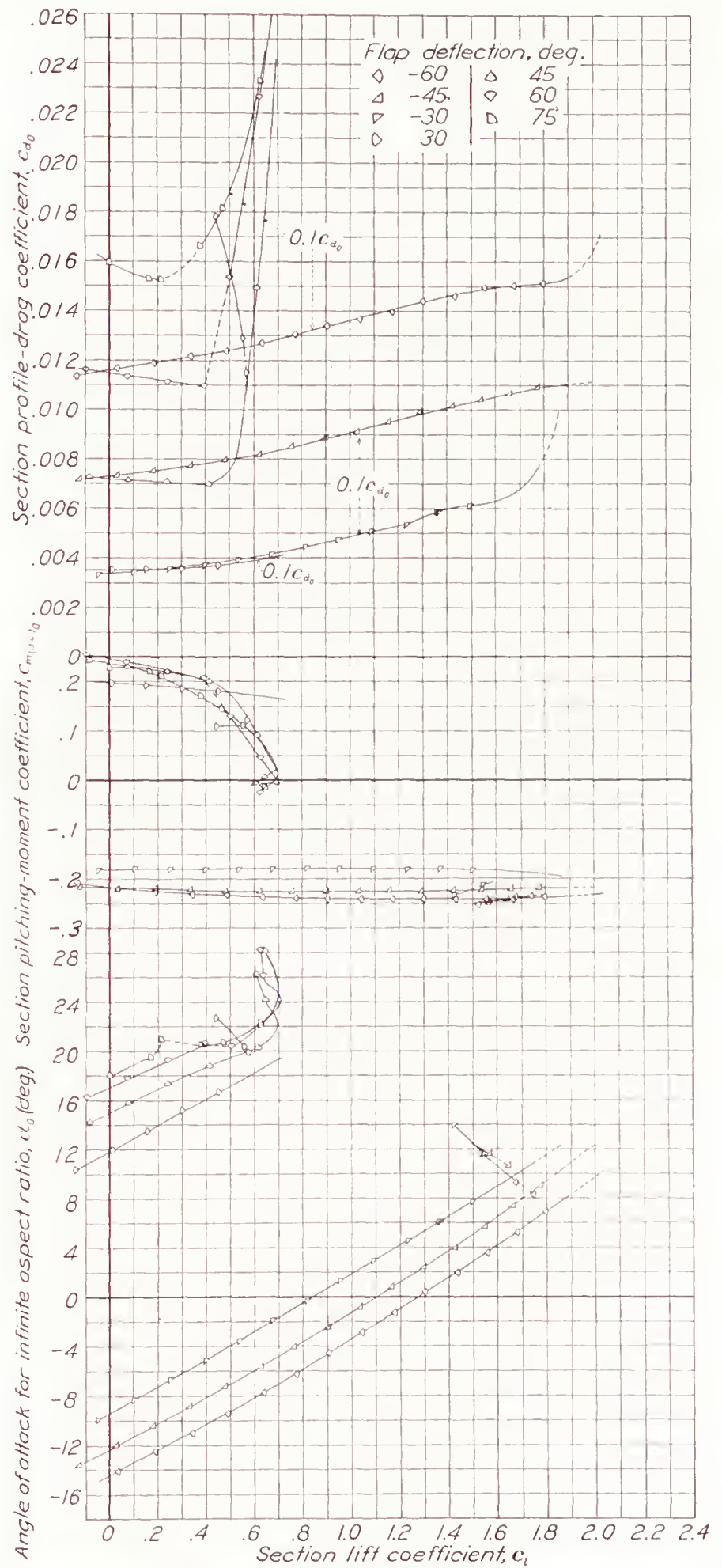


FIGURE 7.—Section characteristics for the N. A. C. A. 23012 airfoil (inverted) with 0.20c plain flap. Large flap deflections.



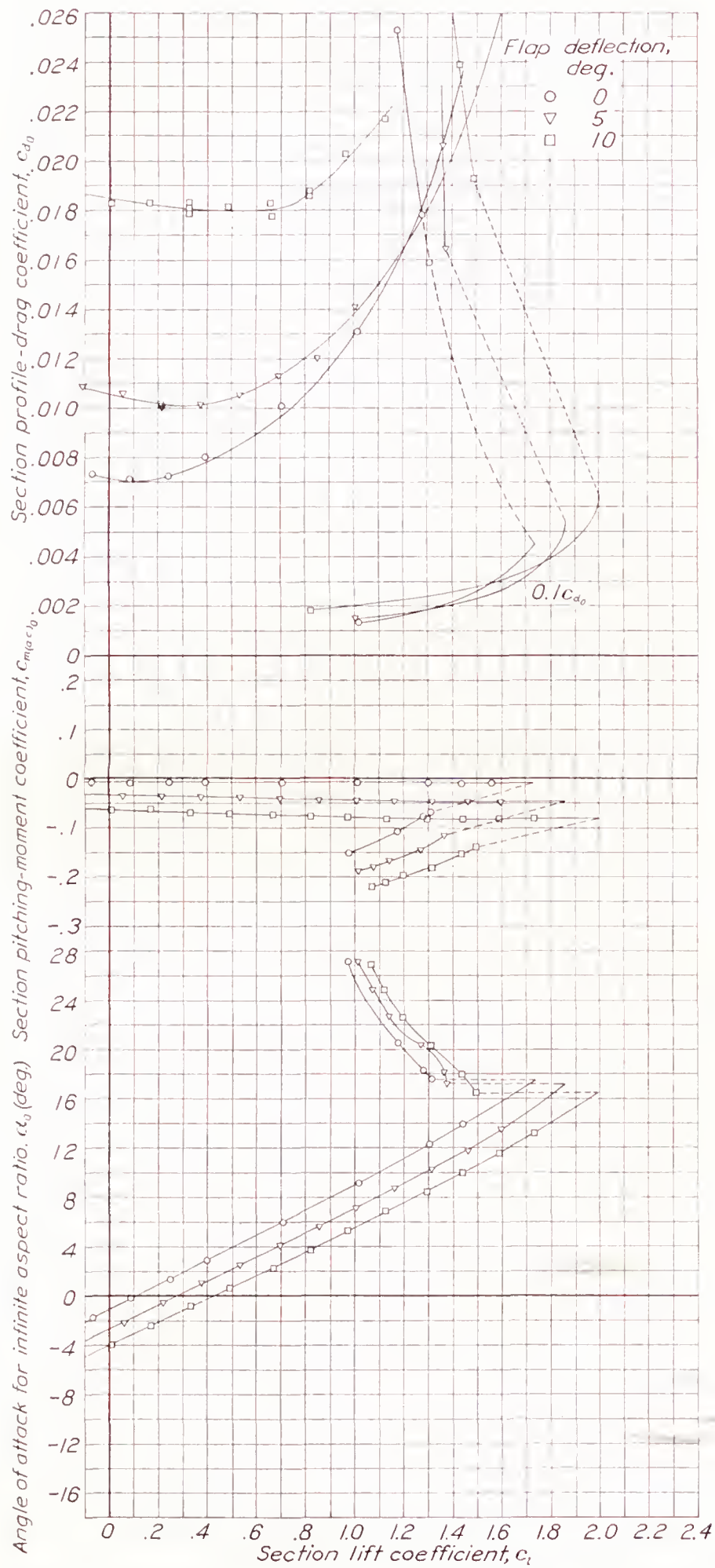


FIGURE 8.—Section characteristics for the N. A. C. A. 23012 airfoil with 0.20c split flap. Small flap deflections.

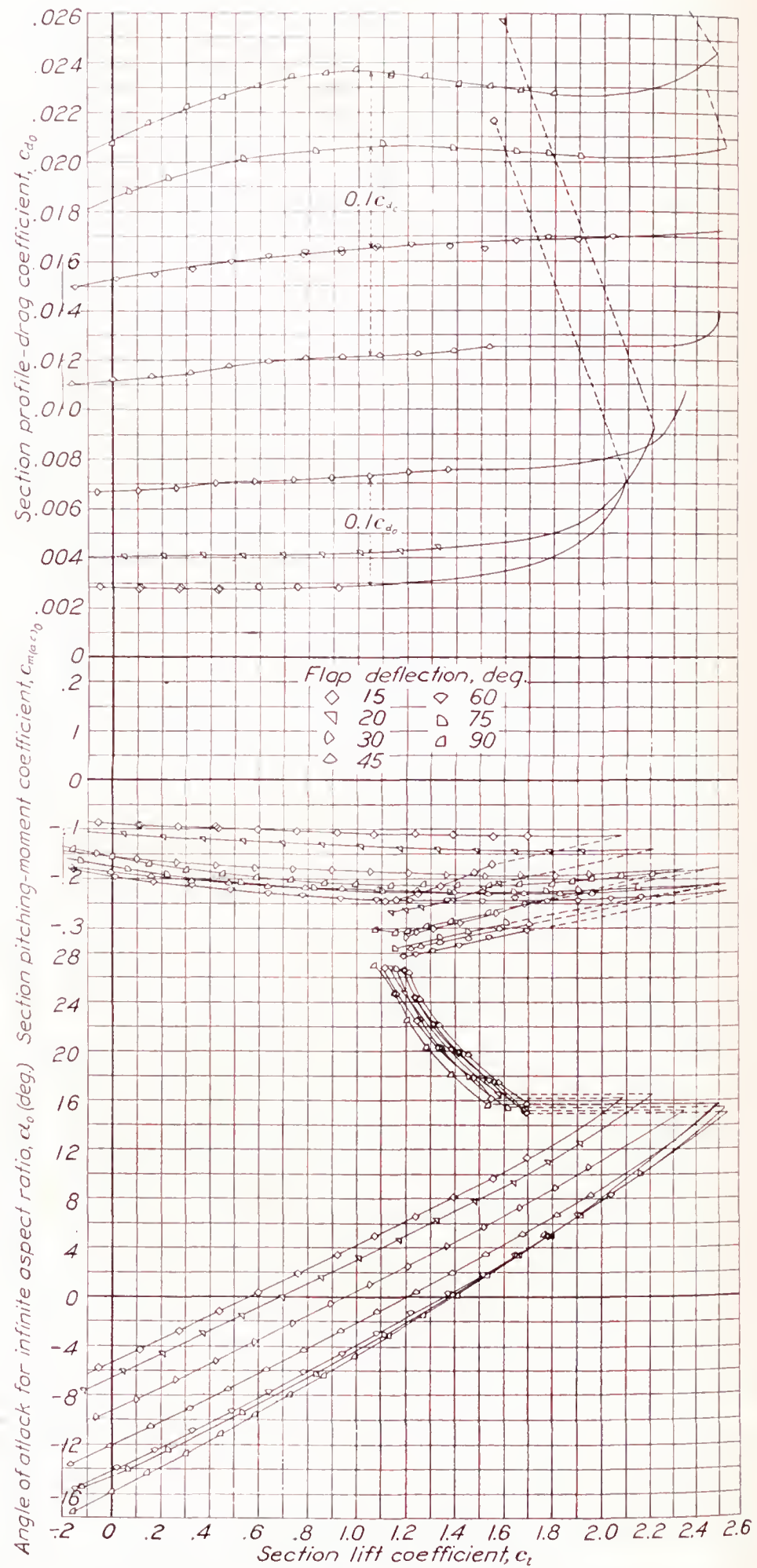


FIGURE 9.—Section characteristics for the N. A. C. A. 23012 airfoil with 0.20c split flap. Large flap deflections.



Similarly, results obtained in the N. A. C. A. variable-density tunnel for the N. A. C. A. 23009 airfoil with a  $0.20c$  split flap deflected  $60^\circ$  (reference 7) agree with

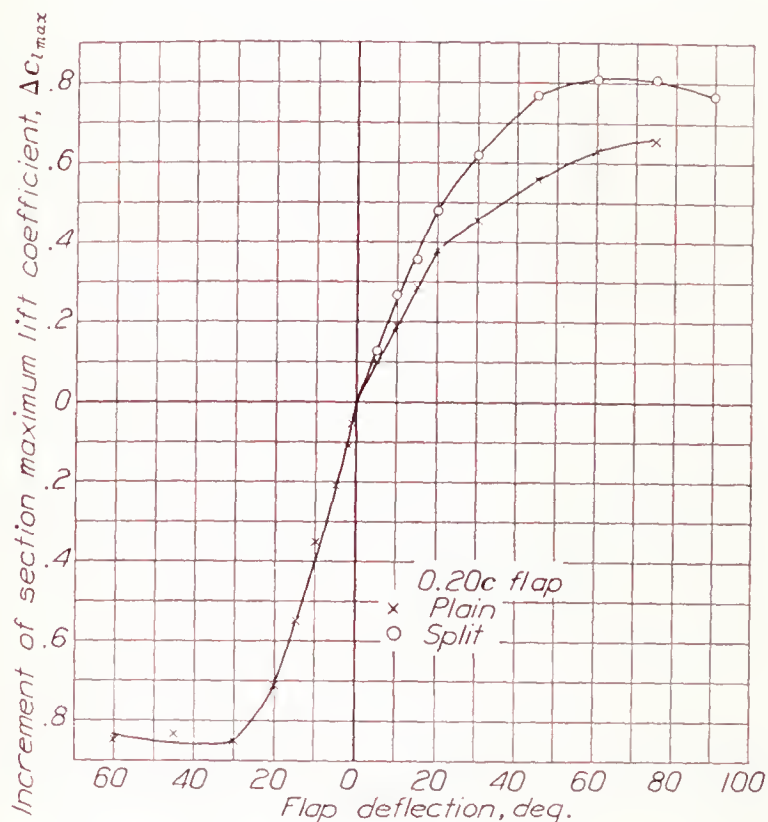


FIGURE 10.—Variation with flap deflection of the increment of section maximum lift coefficient caused by  $0.20c$  plain and split flaps on the N. A. C. A. 23012 airfoil.

those obtained in Germany for a similar model (reference 6). Until more data have been obtained, the reason for the inconsistency in the results from tests of different airfoils in various wind tunnels must remain unexplained.

The N. A. C. A. 23012 airfoil with and without the flap shows a sudden large loss of lift as the angle of attack for maximum lift is exceeded, except for the cases where the plain flap is deflected in such a manner as greatly to reduce the value of the maximum lift. In general, the amount of lift lost at the peak increases as the maximum-lift increment due to the flap increases. Thus, the type of lift-curve peak is usually either type A or type C (table I), where the fluctuations of the type C peaks extend over a very narrow range of angle of attack and thus the lift-curve peak approximates type A.

**Drag coefficients.**—Profile-drag coefficients for the two combinations tested are plotted against lift coefficient in figure 11. These polar curves for the flap combinations are envelope curves of the series of polars obtained at the various flap-angle settings, thus giving at each lift coefficient the minimum profile-drag coefficient obtainable from the airfoil-flap combination. The profile-drag coefficient increases much more rapidly with lift coefficient for both the plain and the split flap than for a good slotted flap, such as slotted flap 2-h reported in reference 9. Neither flap can therefore be considered as suitable for improving take-off as the slotted flap.

Although the plain flap has comparatively low profile drag at small deflections and low lift coefficients, the drag even with low deflections increases more rapidly with lift coefficient than for the split flap; the split flap is slightly superior to the plain flap in producing high lift coefficients with lower profile-drag coefficients.

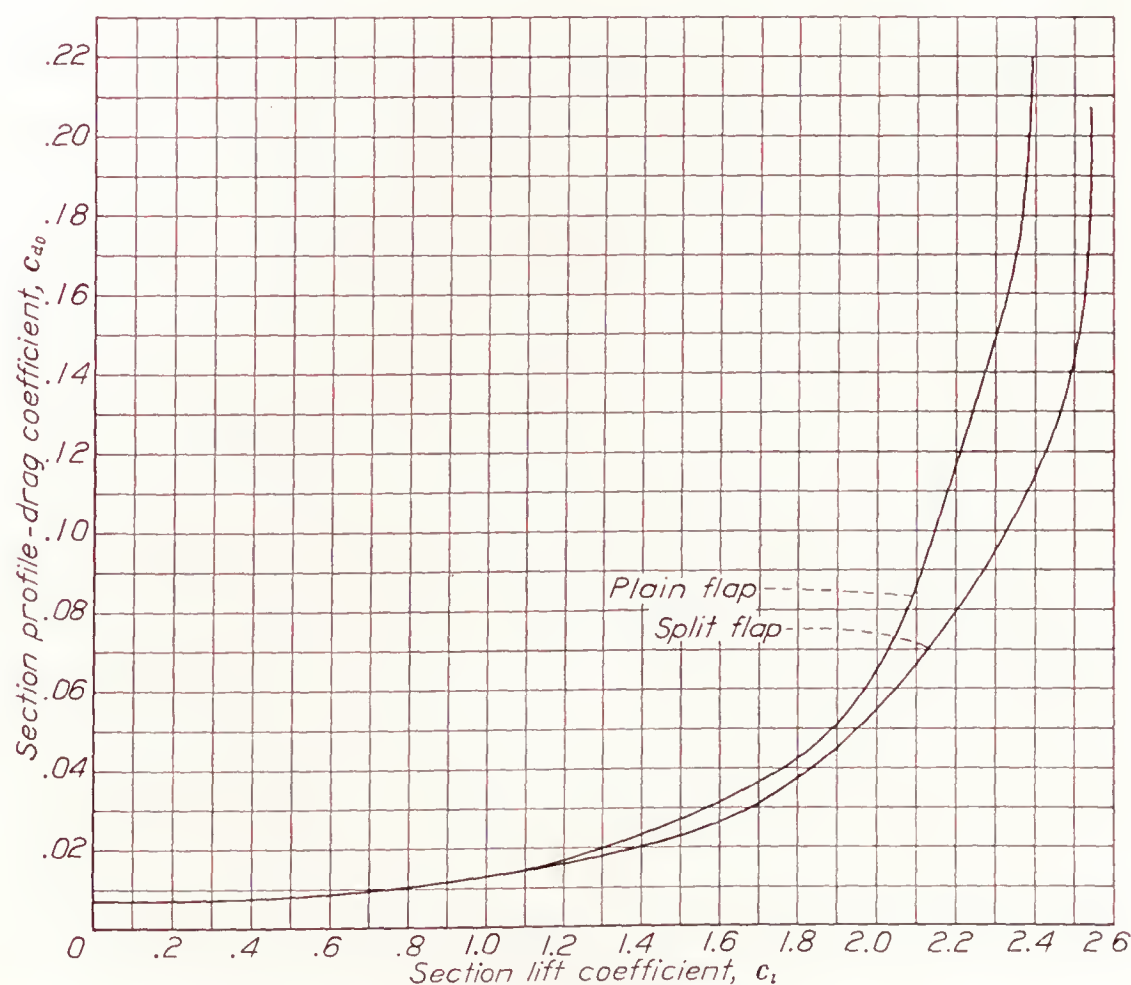


FIGURE 11.—Comparison of profile-drag envelope polars for the N. A. C. A. 23012 airfoil with  $0.20c$  plain and split flaps.



**Pitching-moment coefficients.**—The pitching-moment coefficients for either flap are about equal for equal flap deflection but are lower for the split flap for flap deflections producing equal maximum lift coefficients. It should be pointed out that the values given in table I are average values of the pitching moment and that, in certain cases, the actual pitching moment at any lift coefficient varies considerably from the average.

### CONCLUSIONS

As applied to the N. A. C. A. 23012 airfoil section, the split flap was superior to the plain flap in producing high maximum lift coefficients, in having slightly lower profile-drag coefficients at lift coefficients useful in take-off, and in having smaller pitching-moment coefficients for equal maximum lift coefficients. Both types were unsatisfactory in producing low profile-drag coefficients at lift coefficients useful in take-off as compared with low-drag slotted flaps.

LANGLEY MEMORIAL AERONAUTICAL LABORATORY,  
NATIONAL ADVISORY COMMITTEE FOR AERONAUTICS,  
LANGLEY FIELD, VA., *January 21, 1938.*

### REFERENCES

1. Jacobs, Eastman N., and Abbott, Ira H.: The N. A. C. A. Variable-Density Wind Tunnel. T. R. No. 416, N. A. C. A., 1932.
2. Jacobs, Eastman N., and Pinkerton, Robert M.: Tests in the Variable-Density Wind Tunnel of Related Airfoils Having the Maximum Camber Unusually Far Forward. T. R. No. 537, N. A. C. A., 1935.
3. Jacobs, Eastman N., Ward, Kenneth E., and Pinkerton, Robert M.: The Characteristics of 78 Related Airfoil Sections from Tests in the Variable-Density Wind Tunnel. T. R. No. 460, N. A. C. A., 1933.
4. Jacobs, Eastman N., and Sherman, Albert: Airfoil Section Characteristics as Affected by Variations of the Reynolds Number. T. R. No. 586, N. A. C. A., 1937.
5. Wenzinger, Carl J.: Wind-Tunnel Investigation of Ordinary and Split Flaps on Airfoils of Different Profile. T. R. No. 554, N. A. C. A., 1936.
6. Doetsch, H., and Kramer, M.: Systematic Airfoil Tests in the Large Wind Tunnel of the DVL. T. M. No. 852, N. A. C. A., 1938.
7. Jacobs, Eastman N., Pinkerton, Robert M., and Greenberg, Harry: Tests of Related Forward-Camber Airfoils in the Variable-Density Wind Tunnel. T. R. No. 610, N. A. C. A., 1937.
8. Jacobs, Eastman N., and Rhode, R. V.: Airfoil Section Characteristics as Applied to the Prediction of Air Forces and Their Distribution on Wings. T. R. No. 631, N. A. C. A., 1938.
9. Wenzinger, Carl J., and Harris, Thomas A.: Wind-Tunnel Investigation of an N. A. C. A. 23012 Airfoil with Various Arrangements of Slotted Flaps. T. R. No. 664, N. A. C. A., 1939.



TABLE I.—CHARACTERISTICS OF N. A. C. A. 23012 AIRFOIL WITH 20-PERCENT-CHORD PLAIN AND SPLIT FLAPS

Airfoil	0.20c flap		Classification				Fundamental section characteristics										Derived and additional characteristics that may be used for structural design			
	Type	Deflection (deg.)	Chord	PD	SE	$C_{L_{max}}$	Effective Reynolds Number (millions) <sup>(6)</sup>	$C_{l_{max}}$	$\alpha_{l_0}$ (deg.)	$a_0$ (per deg.)	$C_{l_{opt}}$	$Cd_{0_{min}}$	$C_m(a.c.)_0$	$a.c.$ (percent $c$ from $c/4$ )		$\frac{C_{l_{max}}}{Cd_{0_{min}}}$	$c.p.$ at $C_{l_{max}}$ (percent $c$ )	Wing characteristics $A=6$ ; round tips		
														Ahead	Above			$m_6$ (per radian)	$C_{D_{min}}$	
		(1)	(2)	(3)	(4)	(5)	(6)	(7)	(8)	(7, 9)	(7)	(7)	(11)			(12)				
N. A.	Plain	-60	A			D	8.3	0.88	14.4	0.119	0.4	0.110				126	23	4.95	0.114	
C. A.	do	-60	A			C	8.4	2.04	-15.6	.081						291	36	3.68		
23012	inv.	-45	A			D	8.4	.90	12.4	.109	.5	.069				128	18	4.63	.073	
23012	do	-45	A			C	8.5	2.00	-13.8	.078						286	35	3.57		
23012	do	-30	A			B	8.3	.88	9.4	.095	.2	.033	0.18			126	6	4.17	.034	
23012	do	-30	A			C	8.4	1.87	-9.6	.086			-.18			267	34	3.86		
23012	inv.	-20	A		D2	C	8.4	1.02	8.0	.092	.1	.0109	.16			146	10	4.07	.0110	
23012	do	-15	A		D2	C	8.2	1.18	6.1	.095	0	.0085	.12			169	16	4.17	.0085	
23012	do	-10	A		D2	A	8.5	1.38	3.8	.099	0	.0073	.08			197	20	4.31	.0073	
23012	do	-5	A		D2	B	8.4	1.52	1.4	.100	0	.0071	.04			217	24	4.34	.0071	
23012	do	-2	A		D2	C	8.3	1.62	-.2	.099	.05	.0071	.01			231	25	4.31	.0071	
23012	do	-1	A		D2	C	8.4	1.68	-.7	.098	.15	.0070	0			240	26	4.28	.0072	
23012	do	0	A	C12	D2	A	8.4	1.74	-1.2	.100	.08	.0070	-.008	1.2	7	249	25	4.34	.0071	
23012	do	0	A	C12		A	8.0	1.26	1.1	.099			.008	1.3	4	180	24	4.31		
23012	inv.	5	A		D2	C	8.4	1.83	-3.6	.097	.25	.0076	-.05			261	29	4.24	.0079	
23012	do	5	A			C	8.5	1.23	3.6	.097			.04			176	20	4.24		
23012	inv.	10	A		D2	C	8.3	1.92	-6.0	.094	.25	.0085	-.09			274	30	4.14	.0089	
23012	do	10	A			C	8.4	1.11	6.0	.098			.09			159	16	4.28		
23012	inv.	15	A		D2	A	8.3	2.02	-9.1	.087	.25	.0101	-.13			289	31	3.89	.0105	
23012	do	15	A			A	8.4	.98	8.6	.096			.13			140	11	4.20		
23012	inv.	20	A		D2	C	8.5	2.11	-10.5	.086	0	.0132	-.15			301	32	3.86	.0132	
23012	do	20	A			C	8.6	.85	10.5	.094			.16			121	3	4.14		
23012	inv.	30	A		D2	A	8.5	2.19	-12.3	.086	0	.035	-.19			313	34	3.86	.035	
23012	do	30	A			C	8.6	.72	11.9	.094						103	-4	4.14		
23012	inv.	45	A		D2	A	8.2	2.29	-15.6	.085			-.25			327	34	3.82		
23012	do	45	A			D	8.3	.70	15.0	.111	.4	.070				100	18	4.70	.072	
23012	inv.	60	A		D2	A	8.3	2.36	-17.9	.082			-.28			337	34	3.72		
23012	do	60	A			D	8.4	.71	17.1		.4	.109				101	23		.114	
23012	inv.	75	A		D2	A	8.4	2.39	-19.0	.078			-.26			341	34	3.57		
23012	do	75	A			D	8.5	.70	18.0		.2	.152				100	27		.153	
23012	inv.	5	A		D2	A	8.4	1.86	-2.7	.102	.3	.0101	-.04			266	28	4.41	.0105	
23012	Split	10	A		D2	A	8.4	2.00	-4.0	.106	.5	.0180	-.08			286	30	4.54	.0185	
23012	do	15	A		D2	A	8.3	2.09	-5.4	.104	.5	.028	-.10			299	31	4.47	.028	
23012	do	20	A		D2	A	8.4	2.21	-6.6	.105		<sup>10</sup> .042	-.13			316	32	4.51		
23012	do	30	A		D2	A	8.4	2.35	-9.5	.090		<sup>10</sup> .072	-.18			336	34	4.00		
23012	do	45	A		D2	A	8.5	2.50	-12.5	.095		<sup>10</sup> .12	-.22			357	34	4.18		
23012	do	60	A		D2	A	8.4	2.54	-14.6	.091		<sup>10</sup> .16	-.23			363	35	4.04		
23012	do	75	A		D2	A	8.1	2.54	-15.6	.087		<sup>10</sup> .20	-.27			363	34	3.89		
23012	do	90	A		D2	A	8.4	2.50	-16.7	.082		<sup>10</sup> .23	-.20			357	33	3.72		

<sup>1</sup> When the airfoil is inverted, a minus deflection of the flap indicates that the flap is deflected downward.<sup>2</sup> Type of chord of the airfoil with flap neutral. A refers to a chord defined as a line joining the extremities of the mean line.<sup>3</sup> Type of pressure distribution. See reference 8.<sup>4</sup> Type of scale effect on maximum lift. See reference 4.<sup>5</sup> Type of lift-curve peak as shown in the sketches.<sup>6</sup> Turbulence factor is 2.64.<sup>7</sup> These data have been corrected for tip effect.<sup>8</sup> Angle of zero lift obtained from linear lift curve approximating experimental lift curve.<sup>9</sup> Slope obtained from linear lift curve approximating experimental lift curve.<sup>10</sup>  $C_{d_{0_{min}}}$  lay outside range of lift coefficients covered in these tests. Value of  $C_{d_{0_{min}}}$  given applies approximately over entire useful range of lift coefficients.<sup>11</sup>  $C_{m(a.c.)_0}$  is taken about the aerodynamic center of the airfoil without the flap and is the average value.<sup>12</sup> Values of  $C_{d_{0_{min}}}$  used in computing this ratio are taken from tests of the plain airfoil.







# REPORT No. 662

## DESIGN OF N. A. C. A. COWLINGS FOR RADIAL AIR-COOLED ENGINES

By GEORGE W. STICKLE

### SUMMARY

*The information on the propeller-cowling-nacelle combinations, presented in Technical Reports Nos. 592, 593, and 596 and in Technical Note No. 620, is applied to the practical design of N. A. C. A. cowlings. The main emphasis is placed on the method of obtaining the dimensions of the cowling; consequently, the physical functioning of each part of the cowling is treated very briefly. A practical method of designing cowlings and some examples are presented.*

### INTRODUCTION

When the radial air-cooled engine was first introduced, the engine cylinders were cooled by exposing them to the air stream. In 1929 the N. A. C. A. reported the results of some tests (references 1 and 2) in which the cylinders were enclosed by a sheet-metal ring or cowling, which became known as the "N. A. C. A. cowling." This cowling reduced the drag of the radial engine to less than one-fifth its original value and gave sufficient cooling for flight operation. In order to improve the cooling obtainable with this cowling, deflectors or baffles were used to guide the air close to the cylinders. With the combination of baffles and cowling, a large gain over the exposed engine in both cooling and drag was realized. At this stage of the development, cut-and-try methods were largely used in cowling design. Often a supposed improvement in design resulted in a decrease in performance and cooling.

A very comprehensive investigation of the cowling and cooling problem was made by the N. A. C. A. in 1935. The general purpose of this investigation was to furnish information on the physical functioning of the propeller-nacelle-cowling unit under various conditions of flight operation. The information obtained (references 3, 4, 5, and 6) embodies the detailed principles of operation. If a complete understanding of the cowling and cooling problem is obtained, the problem of the dimensions of the installation is a very simple one. Such an understanding may be obtained from the fundamental principles of cowling operation presented in references 3 to 6. Inasmuch as the designer of an airplane has neither the time nor the opportunity to acquire a

detailed knowledge of every part of the airplane, he wants a simple method of obtaining the optimum cowling dimensions and, perhaps, some of the more important reasons for selecting these dimensions. It is the purpose of this report to present such a method and to illustrate the method with a discussion of practical examples.

The design of a cowling may be divided into two parts: (1) The nose section, and (2) the exit slot. Each part may be considered separately because the functions of each part are separate and distinct. The nose section, or leading edge of the cowling, must have an opening in the center to allow cooling air to enter the engine compartment and be of such shape that it will smoothly divide the air entering the cowling from the air going around the outside. The exit slot returns the cooling air to the main air stream and its area controls the amount of air flowing around the engine.

The complement of a good cowling design is a good baffle design. A brief discussion of baffle design and dimensions will therefore be given to complete the analysis of the design problem.

### DESIGN DISCUSSION

#### THE NOSE SECTION

Figure 1 (from reference 3) is a portion of a motion-picture film of smoke flowing over the nose of an N. A. C. A. cowling. Three significant facts can be discerned from this figure: (1) The direction of the air stream immediately in front of the cowling is almost radial; (2) the percentage of the main air stream that enters the cowling is very small, as can be observed by noting the distance between the nozzle producing the smoke and a straight line drawn through the engine propeller-shaft axis; and (3) the velocity inside the nose of the cowling is low, shown by the way the smoke accumulates in this region. These photographs are for the condition of propeller off. It has been shown (reference 3), however, that the same conditions exist with propeller on.

In terms of design conditions, these conditions indicate that: (1) The contour of the nose shape must meet the local radial air flow and have a large enough radius



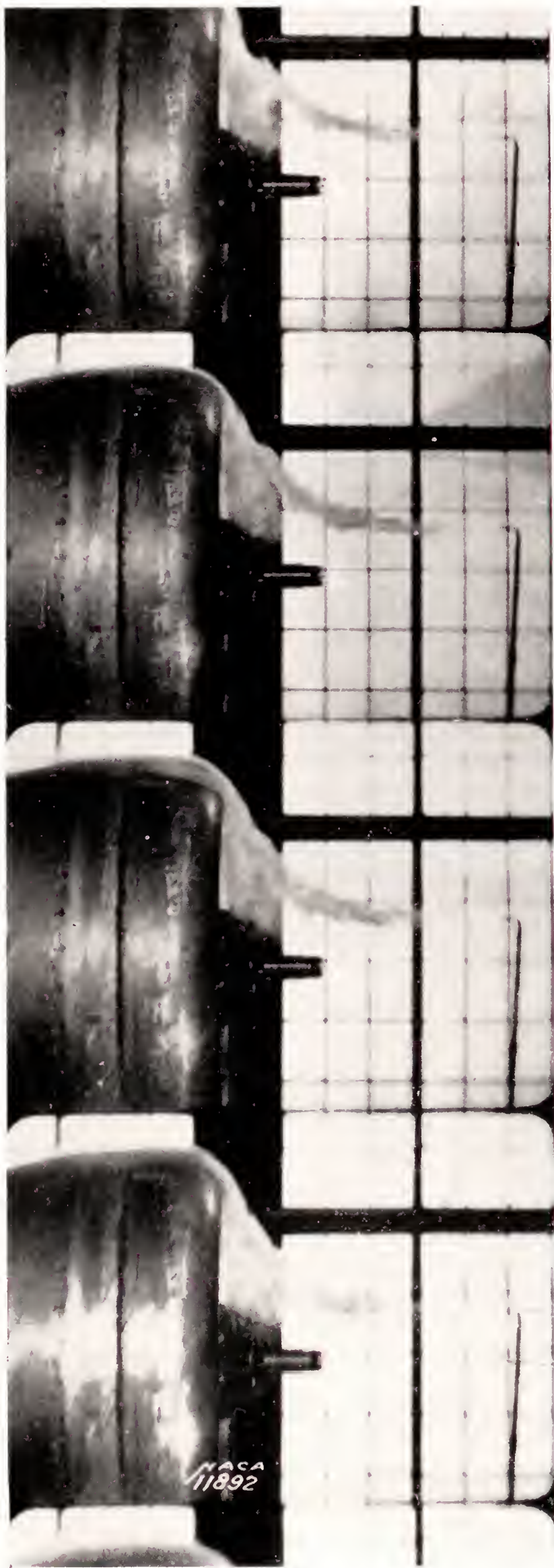


FIGURE 1.—Smoke flow over the nose of an N. A. C. A. cowling.

of curvature to allow the flow to follow the shape smoothly and efficiently until it is flowing parallel to the main air stream; and (2) the shape of the inside of the cowling or of anything located inside the nose of the cowling is unimportant, for the velocity is low in this region. The shape of the inside of the nose being unimportant, the only necessary dimensions for the design of the nose section are those of the outside contour. Well-designed nose sections must therefore have a change in angular direction of approximately  $90^\circ$ . The curvature is determined by the length in which this angular change takes place and is governed by the distance between the engine rocker boxes and the trailing edge of the propeller. The two designs given in figure 2 are the best contours for their particular dimensions and cover the normal variation of length as encountered in practice. Either design may be used with almost identical results at speeds below 350 miles per hour. Above that speed, nose 1 is recommended, as the maximum local velocity produced by this cowling is less than that for nose 2 and, if the local velocities exceed the velocity of sound, the drag of the cowling will be multiplied many times.

#### THE EXIT SLOT

The important factors in the design of an efficient exit slot are the shape and the area of the exit passage. The shape determines the efficiency of the slot; and the area, the pressure available for cooling the engine. The exit passage should be smooth, with a gradually diminishing area so that the cooling air will have a maximum speed at the exit, and should be of such shape as to give this air a direction parallel to the direction of the outside flow. For maximum efficiency in mixing the two air streams, the streamlines of the outside flow should be straight as they pass the exit passage. An example of a good exit passage is given in figure 2.

The conductivity of the exit slot may be represented by the ratio of its area to the frontal area of the engine.

$$K_2 = \frac{\text{area of exit slot}}{F}$$

In like manner the conductivity of the engine may be defined as the ratio of the "equivalent leak area" and the frontal area of the engine.

$$K = \frac{Q}{FV\sqrt{\frac{\Delta p}{\rho}}} = \frac{\text{equivalent leak area}}{F}$$

where

$$\frac{Q}{V\sqrt{\frac{\Delta p}{\rho}}} = \frac{Q}{\sqrt{\frac{2\Delta p}{\rho}}} = \text{equivalent leak area}$$

$Q$ , quantity of air flowing through the engine.



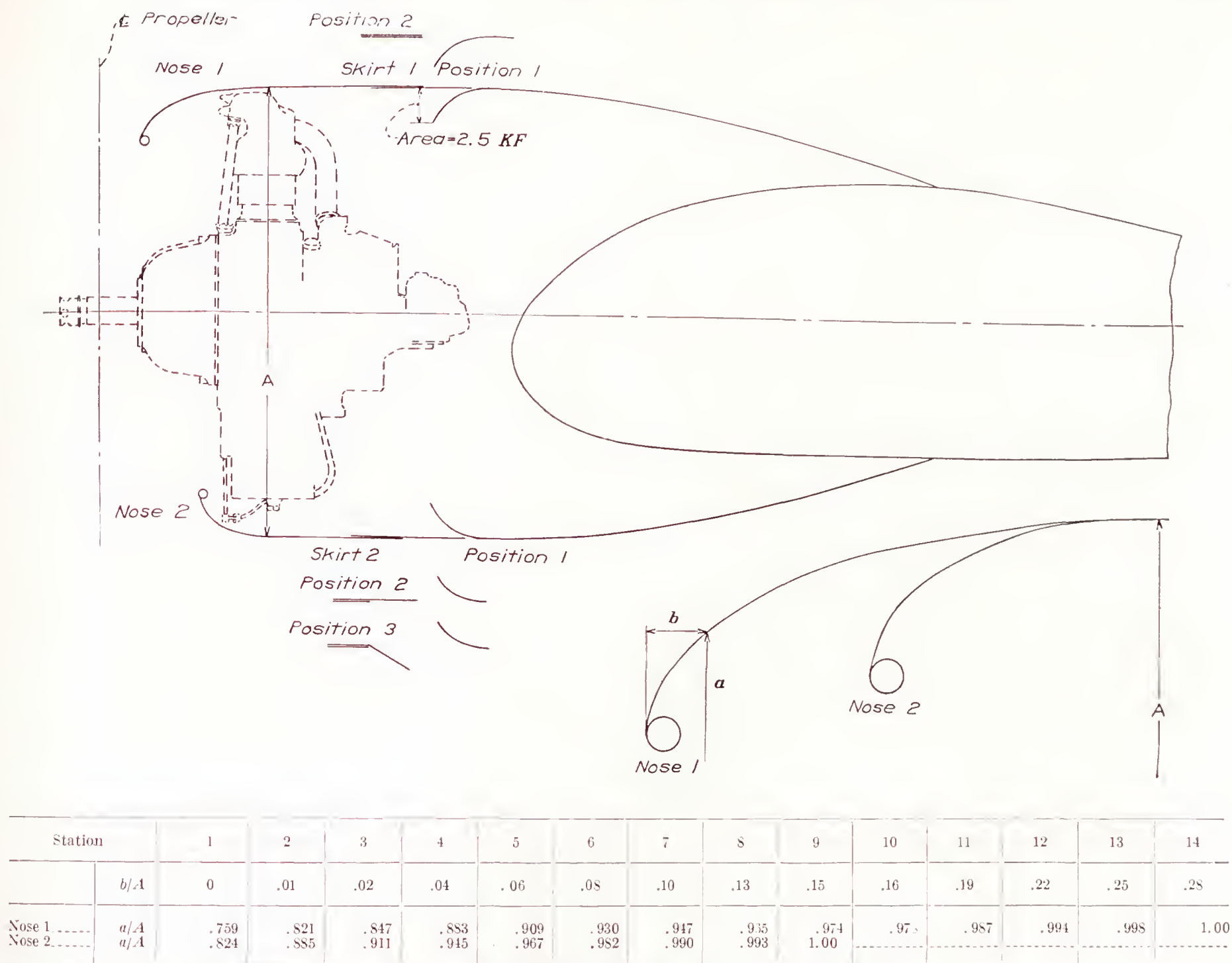


FIGURE 2.—Diagrammatic sketch of N. A. C. A. cowlings.

$V$ , velocity of the air stream.

$q$ , dynamic pressure of the air stream.

$\Delta p$ , the pressure drop across the engine baffles.

$F$ , the frontal area of the engine.

$\rho$ , density of the air.

The equivalent leak area may be experimentally determined by measurement of the volume of air flowing through the engine and the pressure drop across the baffles. If these measurements cannot be made, an approximate determination of the equivalent leak area can be substituted. The equivalent leak area is equal to the geometric leak area multiplied by an orifice coefficient ranging from 0.65 for a poorly designed baffle exit to 0.85 for a good exit. (See reference 5.)

From reference 3 the use of the total available pressure across the cowl is governed by these two quantities in accordance with the following formula:

$$\frac{\Delta P}{q} = \left( \frac{Q}{FV} \right)^2 \left[ \frac{1}{K^2} + \frac{1}{K_2^2} \right]$$

where  $\Delta P$  is the total available pressure across the cowl.

From reference 3

$$\frac{\Delta p}{q} = \left( \frac{Q}{KFV} \right)^2 = \frac{1}{K^2} \left( \frac{Q}{FV} \right)^2$$

By substitution

$$\frac{\Delta P}{q} = K^2 \frac{\Delta p}{q} \left[ \frac{1}{K^2} + \frac{1}{K_2^2} \right] = \frac{\Delta p}{q} \left[ 1 + \left( \frac{K}{K_2} \right)^2 \right]$$

For the usual type of cowl,  $\Delta P/q$  is nearly equal to unity. It is therefore possible to determine the  $\Delta p/q$  available across the engine from a knowledge of the ratio  $K/K_2$ .



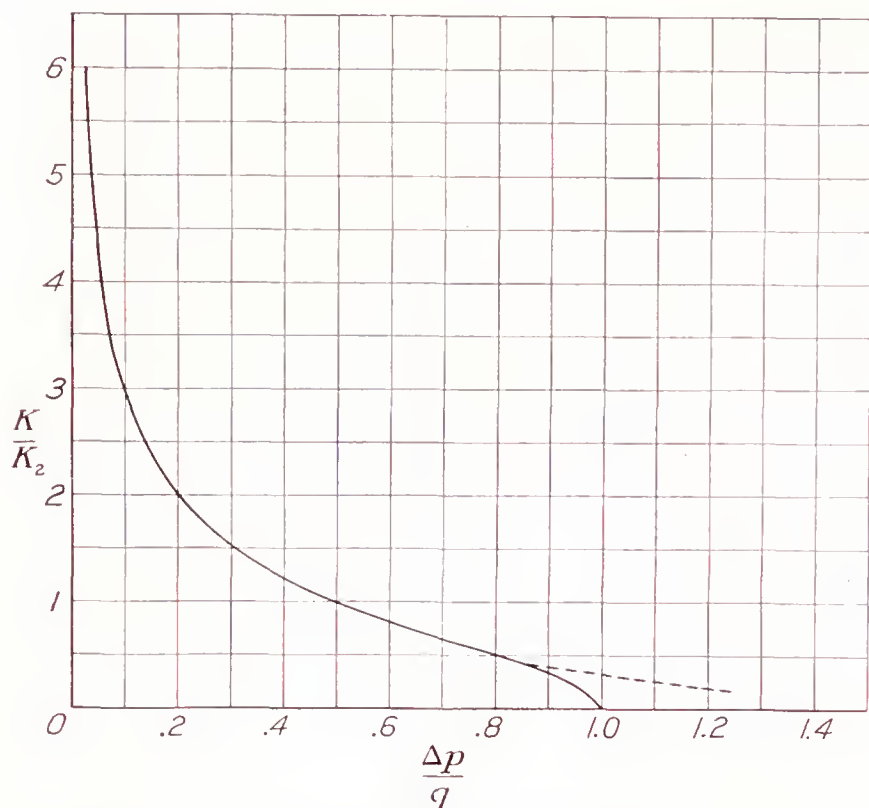


FIGURE 3.—Relationship of  $\Delta p/q$  and  $K/K_2$  for a slot design as shown in figure 2.

A plot showing the relationship of these quantities is given in figure 3. The solid line is for normal cowlings that have an available  $\Delta P/q$  of unity, and the dotted part is an extrapolation to an experimental point obtained with cowling flaps.

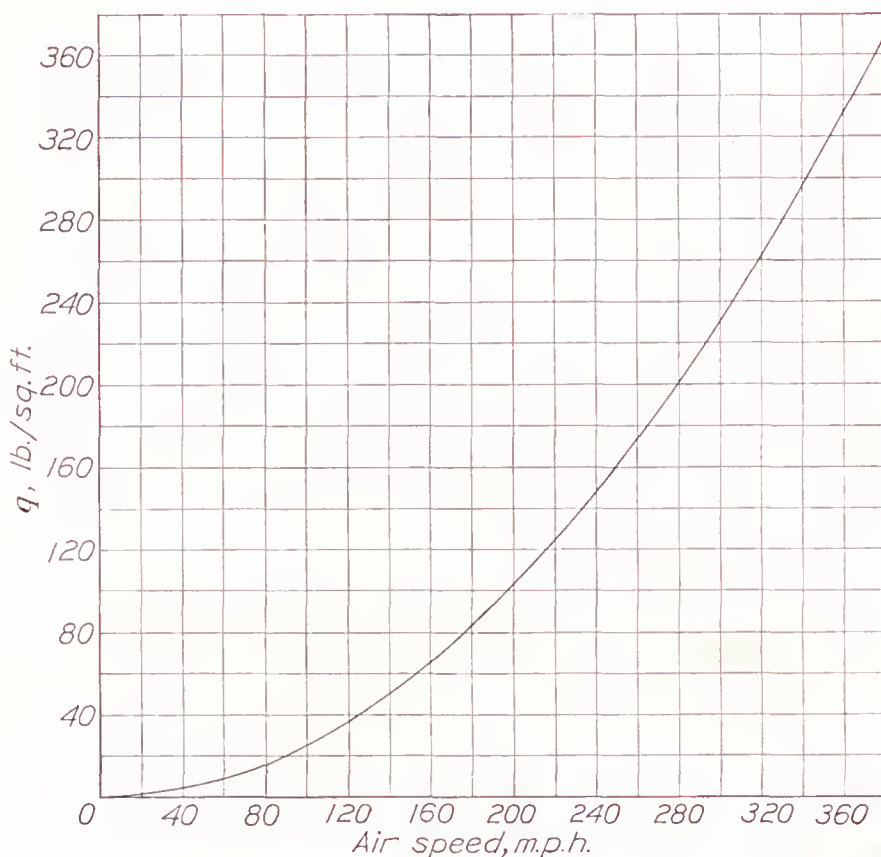


FIGURE 4.—Relationship of air speed and  $q$  for standard conditions.

Figure 4 is a plot of dynamic pressure  $q$  against air speed. It has been shown from tests that a fixed exit slot will give a constant  $\Delta p/q$  regardless of air speed.

Figure 5 is a plot of the power required for standard air conditions for cooling an engine of 52-inch diameter for which  $K=0.05$ . The plot represents two types of exit slot that will furnish a  $\Delta p$  equal to 20 pounds per

square foot at a climbing speed of 100 miles per hour. The fixed-slot design will give this same  $\Delta p/q$ , which is equal to 0.78, at the higher speeds and consequently will overcool the engine at a large expenditure of unnecessary power. The controllable-slot design will furnish the same  $\Delta p$  regardless of speed and the enormous saving in power can be noted from the curves.

In order to maintain a fixed pressure drop across the baffles, it is necessary to have an exit slot of variable area. Two methods of varying this area are: (1) By moving the skirt forward and backward, as skirt 1 (fig. 2); and (2) by the use of cowl flaps that open outward, as skirt 2, position 3. Method (1) has the distinct advantage of maintaining a good slot design by a variation of area. A maximum  $\Delta p/q=1.0$  is available, which will furnish sufficient cooling for most commercial designs and also for many military designs. If cowl flaps

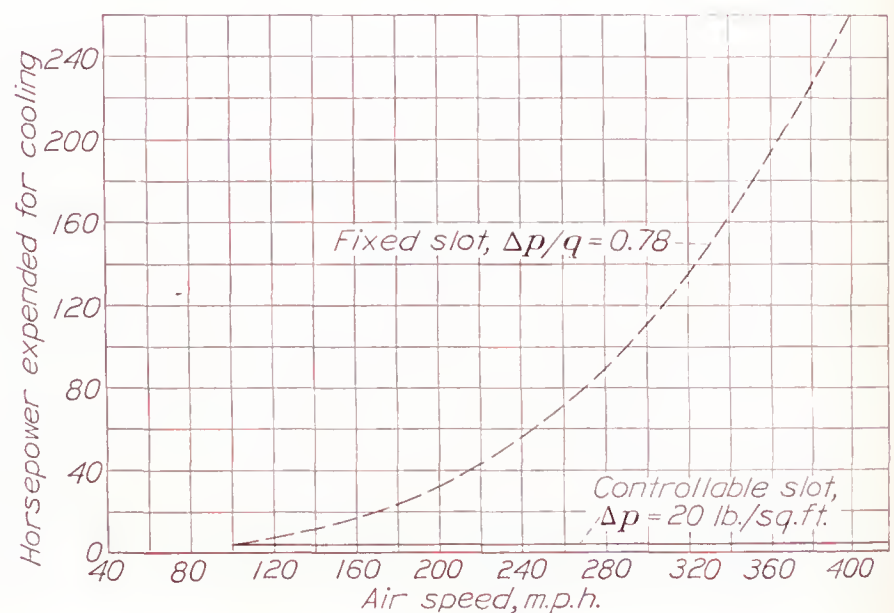


FIGURE 5.—Comparison of power expended for cooling with fixed-slot and controllable-slot designs.

are used, as shown in figure 2, the slot efficiency is not so high for large areas but there is about a 30-percent increase in the available pressure drop for cooling for the low-speed climbing condition. If cooling on the ground, or on the water, is a difficult problem, a combination of the two methods (skirt 2) will give the best results.

#### COWLING DRAG

The cost of cooling an engine was evaluated by plotting test data, taken from reference 3, to show the cooling drag associated with the flow of air through the cowling,  $\Delta C_D = C_D - C_{D_0}$ , where  $C_{D_0}$  is the drag coefficient of a cowling that has a closed skirt smoothly faired into the nacelle, or the  $C_D$  obtained with zero cooling air.

Figure 6 is a plot of  $\Delta p/q$  against  $\Delta C_D$  taken from a cross plot of the results presented in reference 3. It covers all the normal conductivities encountered with baffled engines and shows the increase in drag due to pumping the air through the engine. This value of



$\Delta C_D$  should remain nearly constant for any well-designed exit slot, regardless of the interference drag of wing or fuselage near the nacelle. The power required for cooling may be determined by the use of figures 4 and 6 and the equation

$$\begin{aligned}\text{Power} &= \Delta C_D q F V \\ &= \Delta C_D \frac{\rho}{2} F V^3\end{aligned}$$

or

$$\text{hp.} = \Delta C_D \frac{\rho F V^3}{2 \cdot 550}$$

The total drag of a nacelle alone is subject to interference corrections, determined by the location of the engine on the airplane. If the cowl is mounted on the wing of an airplane, the interference drag can be computed from references 7 and 8, which give data for a ratio of wing thickness to nacelle diameter of 60 percent. As the wing thickness becomes more nearly equal to the nacelle diameter, as is the case for many modern airplanes, the interference correction will become larger, reducing the nacelle drag even more than is indicated in references 7 and 8.

Mounting an N. A. C. A. cowl on the front of a fuselage is similar to mounting it on the front of a nacelle. If the drag of the nacelle or fuselage with a streamline nose shape is known, the additional drag caused by adding a cowl can be computed from test data. Reference 3 gives  $C_D = 0.0861$  for the nacelle with a streamline nose and 0.1193 for the same nacelle with an N. A. C. A. cowl and zero cooling air. The difference between these two values,  $C_D = 0.0332$ , is the  $C_D$  added by the cowl. As the only change is that of the nose shape, the same increment of drag can be expected when a cowl is placed on the front of a fuselage. It should be noted that the value is

$$C_D = \frac{D}{qF}$$

where  $F$  is the frontal area of the engine.

The performance for the condition without the propeller has thus far been discussed. The tests of references 3 to 6 were made with propellers and the net efficiencies of the combinations were determined. It has been shown (reference 3) that the best cowl without a propeller is also best with a propeller.

Mounting the nacelle in front of a wing introduces interference effects that are of the order of half the drag of the well-designed nacelle alone. Tests have been made of many combinations of cowlings, propellers, nacelles, and wings (references 7 and 8) to determine the best location of the nacelle with reference to the wing. Although the best location determined in those tests probably remains the same, the magnitude

of the interference is changed by the relative sizes of the nacelle and the wing and by the drag of the nacelle. Interference tests are necessary for wings of a thickness equal to or greater than the nacelle diameter. The basic nacelle without cooling air should be tested so that a change in the amount of cooling air, due to changing the location of the nacelle, would not affect the results. Such tests are being planned; they should help evaluate the performance of the units of cowlings, propellers, nacelles, and wings that are encountered in modern airplanes.

It should be pointed out that the interference does not affect the design of the best cowl for a given engine. The cooling drag can easily be computed and will not seriously affect the interference drag.

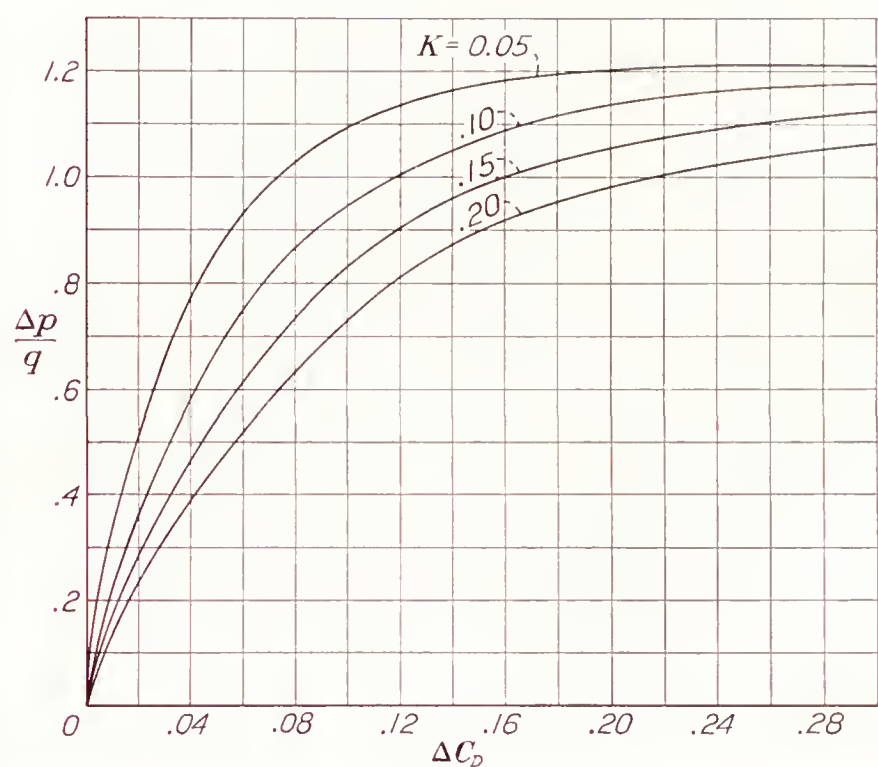


FIGURE 6.—Curves of  $\Delta p/q$  against  $\Delta C_D$  for the most useful conductivities of baffled engines.

#### COMMON MISCONCEPTIONS REGARDING EXIT SLOTS

Thus far, the discussion has dealt with the "ideal" exit slot. Poorly designed exit slots will now be discussed and some suggestions for improvement will be given.

The practice of placing the exhaust collector ring at the exit of the slot (fig. 7 (a)) greatly increases the drag and has little to recommend it as a means of keeping the exhaust heat from the accessory compartment. The two exit slots illustrated would provide equal cooling pressure for the engine but the drag of the poor shape would be much higher than that of the improved design. The amount of exhaust heat reaching the accessory compartment would be almost equal in the two cases, because the radiated heat from the exhaust ring is constant and the induced flow past the ring is sufficient in both cases to keep any heat from entering the accessory compartment by conduction.



The practice of keeping the frontal area of the engine cowl small when the cowl is placed on the front of a large fuselage (fig. 7 (b)) is very detrimental to the available cooling pressure and does not decrease the drag. If the slot is located in front of a large obstruction, the static pressure at the slot will be high and very poor cooling will result. This fact is especially true at low air speeds and at large propeller thrust.

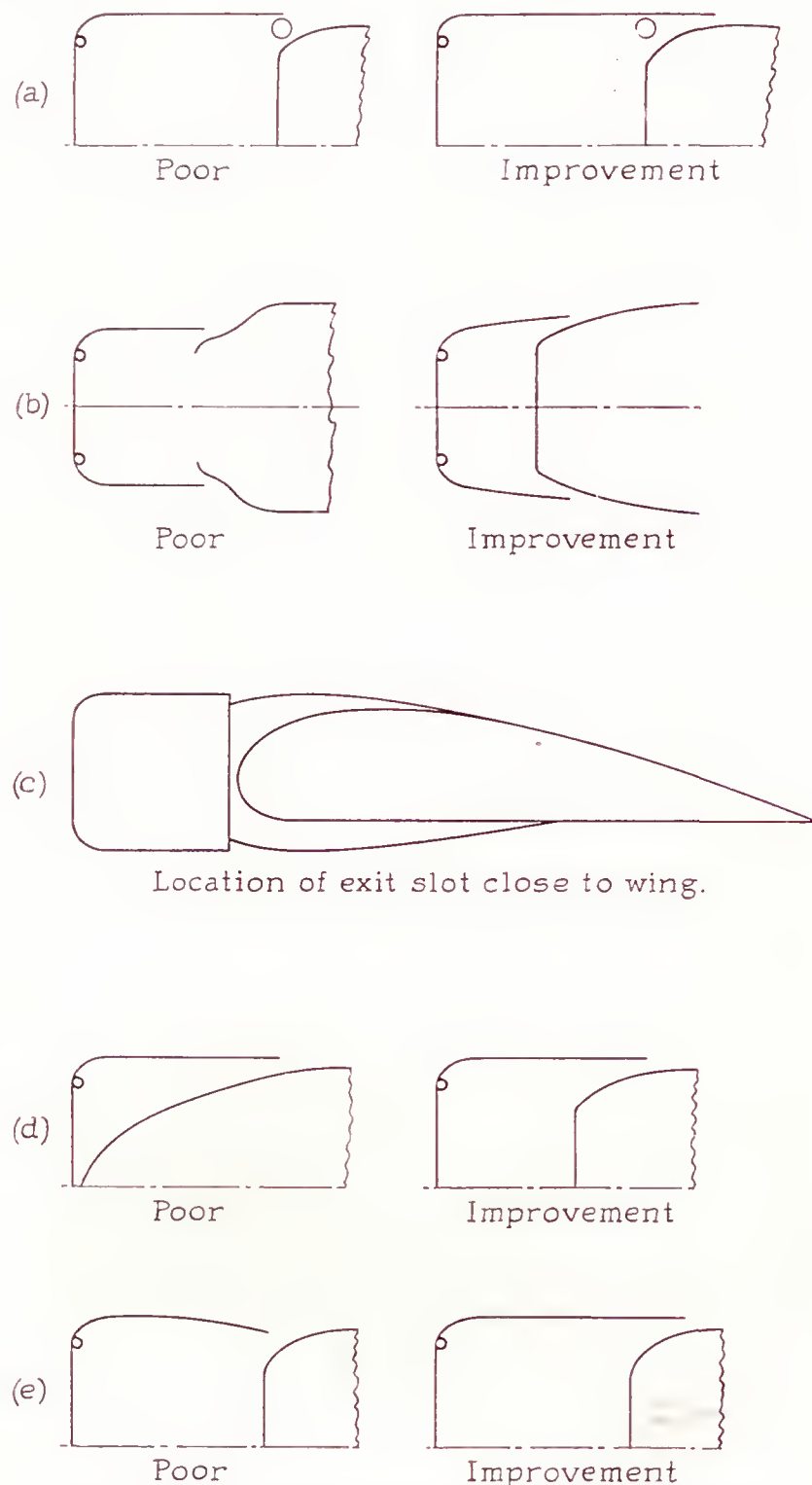


FIGURE 7.—Examples of exit-slot designs sometimes seen in practice.

For one airplane, the ground cooling pressure was zero with the slot located in a much smaller depression than that shown. In many installations, only part of the slot is located in front of an obstruction. This condition may give rise to a reversal of flow in the slot and produce a circulation within the slot itself. The remedy in this case would be to close the slot in the high-pressure region and to provide the required area in the unobstructed region. Flaps are sometimes put

on the cowl skirt to improve the cooling for this condition. Their effectiveness is greatly reduced if not eliminated, however, owing to the low velocity caused by the obstruction.

If the nacelle is mounted in front of a wing (fig. 7 (c)), the flow over the wing will affect the static pressure of the main air stream at the exit slot. If it is located close to the leading edge of the wing, the pressure distribution over the wing will largely determine the static pressure. For example, on the top of the nacelle and wing the static pressure will be negative, immediately in front of the leading edge the static pressure will be nearly equal to  $q$ , and below the wing the static pressure will be positive. As the nacelle is moved farther forward, this effect will be diminished. In the design of the exit slot, these factors should be considered. If a part of the slot is opened in a region of high positive pressure and part in a region of low pressures, a circulation of air occurs within the slot itself. The air enters the slot in the high-pressure region and is expelled in the low-pressure region, causing a needless loss of energy and a reduction in the ability of the slot to induce flow through the cowl.

The long inner cowl that extends through the cylinders to the front of the cowl (fig. 7 (d)) is a needless weight and complication and has a detrimental effect on the cooling of the crankcase. The improved shape shown in figure 7 (d) is equally effective and is much simpler to construct. There is no advantage in extending the inner cowl beyond the plane in which the cross-sectional area of the exit passage is three times the area of the exit slot.

Certain designers believe that the most efficient skirt design is one having a smaller diameter at the exit than the maximum cowl diameter (fig. 7 (e)). This idea arose from the practice of comparing the performance of exit slots without considering the available cooling pressure. Test results (reference 3) show that this conception is wrong and that the best skirt design is one for which the streamlines of the main air flow are straight.

Many misconceptions with regard to skirt and slot design prevail because tests have not been compared on the basis of equal cooling. The exit passage having a smooth contour that speeds up the air to a maximum at the exit and gives it a direction parallel to the main air stream is the most efficient. Skirt 1 (fig. 2) will give maximum efficiency at any cooling with a sufficient range of cooling for most airplane designs. Skirt 2 provides maximum efficiency for conditions where efficiency is the controlling design factor and maximum cooling for the condition of low-speed operation where maximum cooling is the controlling design factor.



## BAFFLE DESIGN

In the design of a cowl, a certain pressure drop across the cylinders is made available. Baffles should be designed to make the best use of this available pressure drop for cooling. The best baffles cause the greatest amount of heat to be carried away from the cylinder fins and maintain an even temperature distribution.

The correct baffles and the  $\Delta p$  required for adequate cooling at any power may be determined for any engine. All other engines of the same specifications will require the same pressure drop and baffles. Thus the designing of baffles is a problem for the engine manufacturer and the solution should be furnished as part of the standard engine data. The front of the engine cylinder is cooled in flight by large-scale turbulence; therefore it is important that the determination of the required  $\Delta p$  be made either in flight tests or in tests simulating flight conditions. If this turbulence is not present in the test determination of  $\Delta p$ , the pressure drop required for adequate cooling will be too large.

The front part of the engine cylinder should be left entirely free of baffles to allow this turbulent air to come in contact with the cylinder fins. The amount of the cylinder that can be satisfactorily cooled by this low-velocity, highly turbulent air is a little uncertain. It is known that at least the front half of the cylinder should be left open to this turbulent cooling air; perhaps even more of the cylinder can be so cooled.

In the design of the best baffle to cool the rear half of the cylinder, the work reported in reference 5 is very helpful. The preliminary baffles designed for a new engine should be tightly fitting; they should have a rear opening approximately 1.4 times the free area between the fins, a bend at the exit having a radius equal to the fin depth, and as long an expanding duct as is practicable for the given installation. The included angle between the sides of the expansion duct should not be more than  $20^\circ$ . (See fig. 8.) The temperature distribution around the cylinder or over the head should be determined for this baffle. If this distribution is not satisfactory, it may be improved by a suitable alteration in the baffle. For example, if the tightly fitting baffle gives a temperature too low at the baffle entrance and too high at the rear of the cylinder, the baffle may be moved away from the fins at the front and a higher velocity to cool the rear of the cylinder will result. (See reference 5.)

The same principles apply to the baffling of a double-row radial engine. The rear bank of cylinders is cooled in the same manner as the front bank. The front of the cylinders should be left as open as possible to allow the turbulent cooling on the front to have free access to the cylinder fins. An example of a good baffle design for a

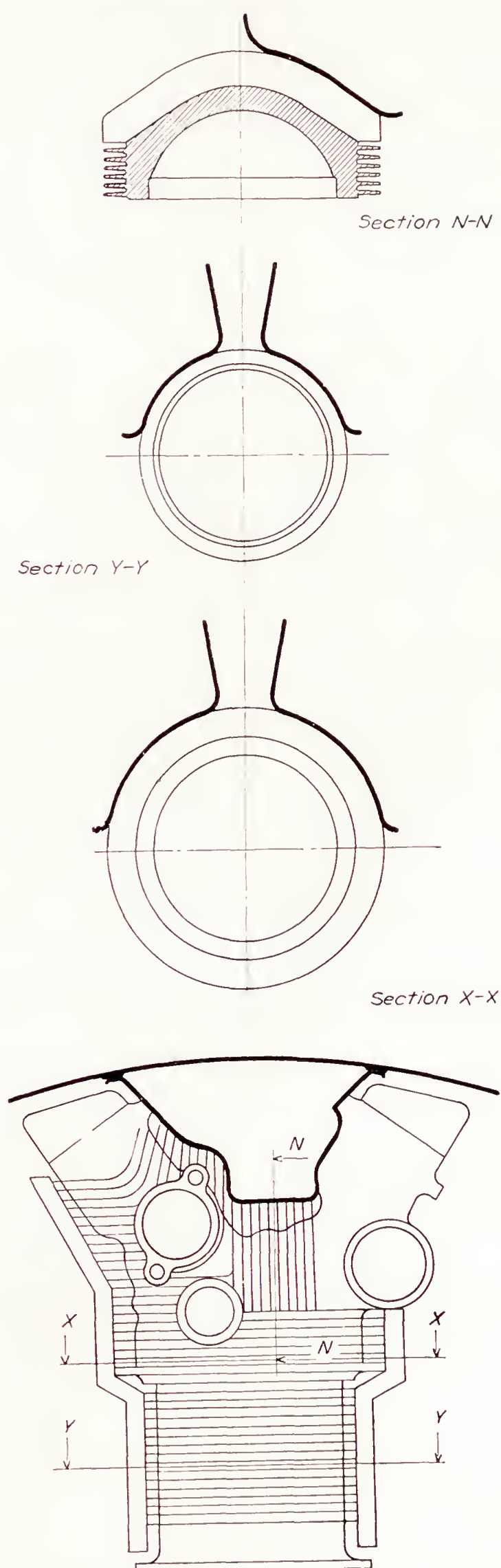


FIGURE 8.—Typical baffle design for a cylinder of a radial engine.



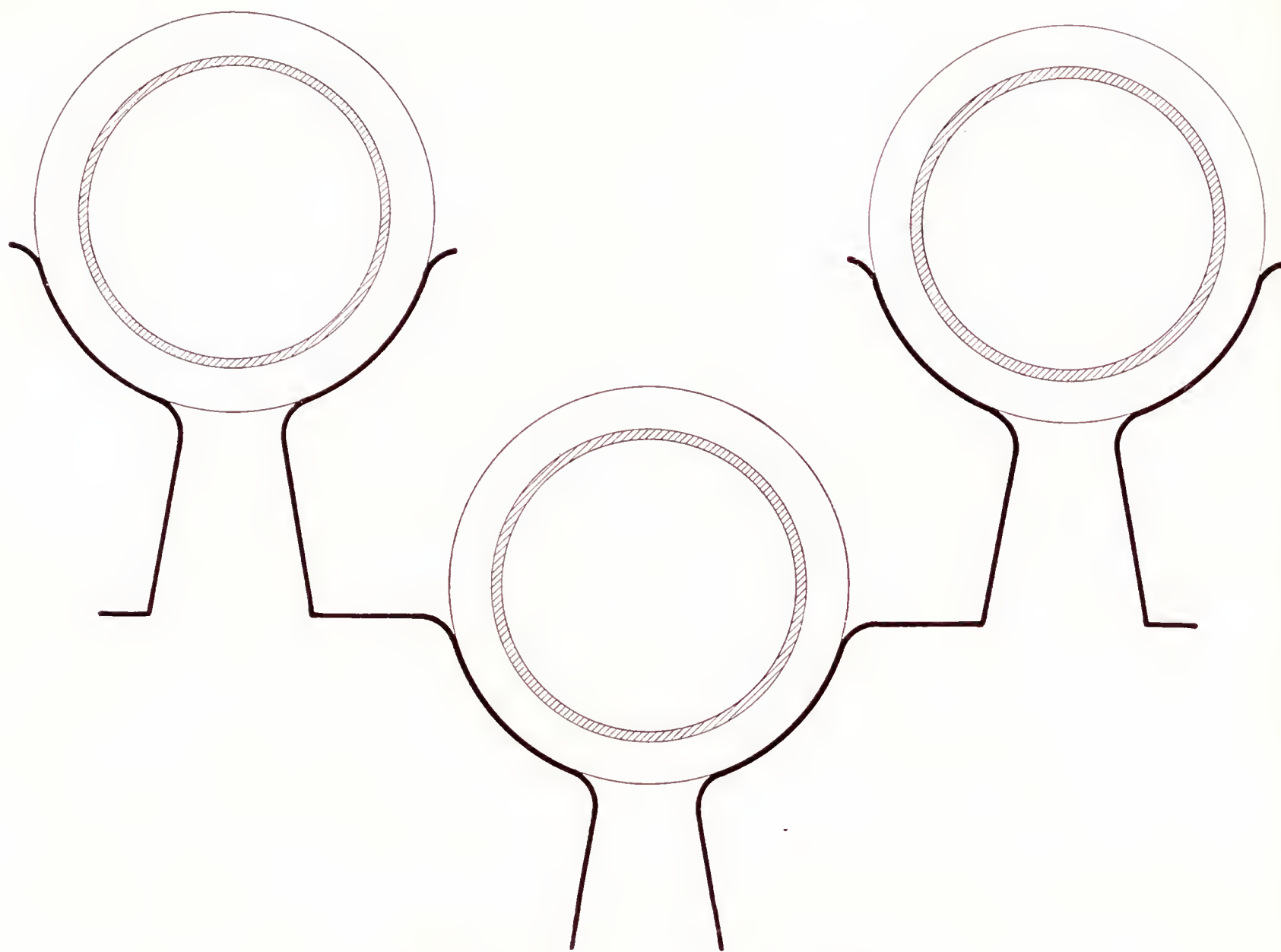


FIGURE 9.—Baffle design for a double-row radial engine.

double-row radial engine is given in figure 9. The straight portion between the exit of the front baffle and the entrance to the rear baffle can be varied in length to accommodate the change in distance between the cylinders as the radius is varied.

The application of the design discussion will be illustrated by two examples.

#### EXAMPLE I

##### DESIGN COMPUTATIONS

Airplane type: Commercial land monoplane.

Number of engines: 2.

Cruising speed of airplane: 200 m. p. h.

Climbing speed of airplane: 170 m. p. h.

Engine diameter:  $51\frac{1}{16}$  in.

Engine power: 550 hp. at 2,200 r. p. m.

Number of cylinders: 9.

Type of baffle: Commercial.

Propeller drive: Geared.

Maximum wing thickness at engine location: 30 in.

The engine specifications of this design were purposely made the same as those of the engine reported in reference 6 in order to illustrate the knowledge of the engine necessary for an intelligent design. From reference 6, the engine has a conductivity of 0.06 and requires a  $\Delta p$  of 25 pounds per square foot for ade-

quate cooling at full power. These values complete the information necessary for design.

Inasmuch as the engine is geared, the clearance between the cylinders and the propeller is sufficient to allow nose 1 to be used. The minimum cowling diameter (A, fig. 2) that can be used for this engine is 52 inches. The ordinates of the nose section calculated from figure 2 are as follows:

Station	<i>b</i> (in.)	<i>a</i> (in.)	Station	<i>b</i> (in.)	<i>a</i> (in.)	Station	<i>b</i> (in.)	<i>a</i> (in.)
1.....	0	39.5	6.....	4.16	48.4	11.....	9.88	51.3
2.....	.52	42.7	7.....	5.20	49.2	12.....	11.44	51.7
3.....	1.04	44.0	8.....	6.76	50.2	13.....	13.00	51.9
4.....	2.08	45.9	9.....	7.80	50.6	14.....	14.56	52.0
5.....	3.12	47.3	10.....	8.32	50.9			

It is desirable to locate the exit slot in a nonexpanding flow; the maximum cowling diameter should therefore not be decreased before the end of the exit passage. From that point the nacelle should fair smoothly into the wing surface, care being taken to keep the angle of convergence small to prevent any breakaway of flow.

Next compute the dimensions of the slot.

From figure 4

$$q \text{ at } 200 \text{ m. p. h.} = 102.5 \text{ lb./sq. ft.}$$

$$q \text{ at } 170 \text{ m. p. h.} = 74 \text{ lb./sq. ft.}$$



Then

$$\frac{\Delta p}{q} = 0.24 \text{ and } 0.34, \text{ respectively.}$$

From figure 3

$$\frac{K}{K_2} = 1.78 \text{ and } 1.40, \text{ respectively.}$$

Given

$$K = 0.06.$$

Then

$$K_2 = \frac{K}{K/K_2} = \frac{0.06}{1.78} = 0.034 \text{ at } 200 \text{ m. p. h.}$$

and

$$= \frac{0.06}{1.40} = 0.043 \text{ at } 170 \text{ m. p. h.}$$

The area of the slot is

$$K_2 F = 0.034 \times 14.75 = 0.50 \text{ sq. ft.}$$

and

$$= 0.043 \times 14.75 = 0.63 \text{ sq. ft.}$$

The distance around the nacelle is  $52\pi = 163$  in.

If the slot extended completely around the nacelle, the openings would be approximately  $0.50 \times 144/163 = 0.44$  inch for cruising and  $0.63 \times 144/163 = 0.56$  inch for climbing.

As such a small area is required for cooling, it may be desirable to exhaust all the air over the upper surface of the wing. If the slot is extended halfway around the nacelle, the opening will be doubled. For ground operation, the skirt can be moved forward approximately 6 inches, giving an effective opening of approximately 3 inches. The slot area would then be

$$\frac{3}{144} \times \frac{163}{2} = 1.7 \text{ sq. ft.}$$

or

$$K_2 = \frac{1.7}{14.75} = 0.115$$

and

$$\frac{K}{K_2} = \frac{0.06}{0.115} = 0.52$$

From figure 3, the available  $\Delta p/q = 0.78$ , or sufficient cooling would be available at

$$q = \frac{25 \text{ lb./sq. ft.}}{0.78} = 32 \text{ lb./sq. ft.}$$

which corresponds to an air speed of 113 miles per hour.

It is probable that more cooling will be obtained than is shown by this computation for low speeds, which assumes an available pressure drop across the entire cowl equal to the dynamic pressure of the air stream. With the slot located above the wing and in the propeller slipstream, the pressure available for cooling at low air speeds will probably be increased in the order of 10 percent.

#### DRAG COMPUTATIONS

The drag associated with the design must now be computed. The drag may be divided into two parts: (1) the cooling drag defined in the discussion as  $\Delta C_D$ ,

and (2) the basic drag or the drag of the basic shape of the cowl without cooling air flowing through it.

**Cooling drag.**—From figure 6, where

$$\frac{\Delta p}{q} = 0.24 \text{ and } K = 0.06$$

$$\Delta C_D = 0.006$$

$$\Delta D = 0.006 \times 102.5 \times 14.75 = 9 \text{ lb.}$$

and where

$$\frac{\Delta p}{q} = 0.34 \text{ and } K = 0.06$$

$$\Delta C_D = 0.012$$

$$\Delta D = 0.012 \times 74 \times 14.75 = 13 \text{ lb.}$$

The cooling horsepower for 200 miles per hour

$$\begin{aligned} &= \frac{\Delta C_D q F V}{375} \\ &= \frac{0.006 \times 102.5 \times 14.75 \times 200}{375} = 5 \text{ hp.} \end{aligned}$$

and for 170 miles per hour

$$= \frac{0.012 \times 74 \times 14.75 \times 170}{375} = 6 \text{ hp.}$$

**Drag of the basic shape.** The computation of the drag of the basic cowl shape is a little more difficult and indirect; it depends on the interrelation of the nacelle, the propeller, and the wing. A rough estimation of this drag will be made in order to illustrate the example, but any particular case will require more detailed analysis of all the component parts.

The position as indicated in figure 2 was chosen from reference 7 as the most efficient location of the nacelle on the wing. The drag coefficient of the basic shape of the nacelle alone is given as  $C_{D_0} = 0.1193$ . From reference 7, table XI, the effective nacelle drag divided by the drag of the nacelle alone equals 38 percent, or

$$\text{effective } C_{D_0} = 0.38 (0.1193) = 0.045$$

which gives a basic drag at 200 miles per hour of

$$D_0 = 0.045 \times 102.5 \times 14.75 = 68 \text{ lb.}$$

or total drag  $D = D_0 + \Delta D = 68 + 9 = 77 \text{ lb.}$

The power required to overcome this drag is:

$$\text{hp.} = \frac{DV}{375} = \frac{77 \times 200}{375} = 41 \text{ hp.}$$

The primary purpose of this report is to present a method of obtaining the best cowl and not to present a method of performance calculation; the intricate performance problem of propeller, nacelle, and wing will therefore not be discussed further.

#### EXAMPLE II

##### DESIGN COMPUTATIONS

Airplane type: Military pursuit landplane.

Number of engines: 1.

Top speed of airplane: 300 m. p. h.

Climbing speed: 150 m. p. h.



Engine diameter:  $54\frac{1}{2}$  in.

Engine power:

Take-off: 1,000 hp. at 2,100 r. p. m.

Continuous: 850 hp. at 2,100 r. p. m.

Cruising: 600 hp. at 1,900 r. p. m.

Number of cylinders: 9.

Type of baffle: Commercial.

Propeller drive: Geared.

Maximum diameter of fuselage: 5 ft.

$K=0.10$ .

Required  $\Delta p=40$  lb./sq. ft.

The design of the nose section will be similar to example I; the ordinates are given in the following table. The minimum cowling diameter that will enclose the engine is 55 inches.

Station	$b$ (in.)	$a$ (in.)	Station	$b$ (in.)	$a$ (in.)	Station	$b$ (in.)	$a$ (in.)
1-----	0	41.7	6-----	4.40	51.2	11-----	10.45	54.3
2-----	.55	45.2	7-----	5.50	52.1	12-----	12.10	54.7
3-----	1.10	46.6	8-----	7.15	53.1	13-----	13.75	54.9
4-----	2.20	48.6	9-----	8.25	53.6	14-----	15.40	55.0
5-----	3.30	50.0	10-----	8.80	53.8			

The computations for the slot dimensions are:  
From figure 4

$$q \text{ at } 300 \text{ m. p. h.} = 230 \text{ lb./sq. ft.}$$

$$q \text{ at } 150 \text{ m. p. h.} = 58 \text{ lb./sq. ft.}$$

Given

$$\Delta p = 40 \text{ lb./sq. ft.}$$

Then

$$\frac{\Delta p}{q} \text{ at } 300 \text{ m. p. h.} = \frac{40}{230} = 0.17.$$

$$\frac{\Delta p}{q} \text{ at } 150 \text{ m. p. h.} = \frac{40}{58} = 0.69.$$

From figure 3

$$\frac{K}{K_2} = 2.23 \text{ and } 0.66, \text{ respectively.}$$

Given

$$K = 0.10.$$

Then

$$K_2 = \frac{0.10}{2.23} = 0.045 \text{ at } 300 \text{ m. p. h.}$$

and

$$= \frac{0.10}{0.66} = 0.15 \text{ at } 150 \text{ m. p. h.}$$

Area of slot

$$K_2 F = 0.045 \times \frac{55^2 \pi}{144 \cdot 4} = 0.045 \times 16.5 \\ = 0.74 \text{ sq. ft. at } 300 \text{ m. p. h.}$$

and

$$0.15 \times 16.5 = 2.48 \text{ sq. ft. at } 150 \text{ m. p. h.}$$

$$\text{Slot opening} = \frac{\text{slot area}}{\text{circumference}} = \frac{144 \times 0.74}{55 \pi} \\ = 0.62 \text{ in. at } 300 \text{ m. p. h.}$$

and

$$\frac{144 \times 2.48}{55 \pi} = 2.07 \text{ in. at } 150 \text{ m. p. h.}$$

#### DRAG COMPUTATION

Cooling drag.—From figure 6

$$\text{at } \Delta p/q = 0.17 \text{ and } K = 0.10$$

$$\Delta C_D = 0.0067$$

$$\text{at } \Delta p/q = 0.69 \text{ and } K = 0.10$$

$$\Delta C_D = 0.052$$

$$\Delta D = \Delta C_D q F = 0.0067 \times 230 \times 16.5 = 25 \text{ lb.}$$

and

$$\Delta D = 0.052 \times 58 \times 16.5 = 50 \text{ lb.}$$

$$\text{The cooling power} = \frac{25 \times 300}{375} = 20 \text{ hp.}$$

and

$$= \frac{50 \times 150}{375} = 20 \text{ hp.}$$

**Drag of the basic shape.**—The basic drag of the engine cowling can be computed quite accurately if the value of the drag of the airplane with a streamline nose shape is known.

In reference 3, the drag coefficient for the nacelle with streamline nose shape is given as  $C_D = 0.0861$  and the drag coefficient for the same nacelle with an engine cowling on the front and zero cooling air is  $C_D = 0.1193$ . The difference between these two coefficients,  $0.1193 - 0.0861 = 0.0332$ , is the drag coefficient corresponding to the increase in drag due to the cowling.

This same increase in drag could be expected when an engine cowling replaces the streamline nose of the fuselage. The additional drag of the airplane due to the cowling is then

$$0.0332 q F = 0.0332 \times 230 \times 16.5 = 126 \text{ lb.}$$

and

$$0.0332 \times 58 \times 16.5 = 32 \text{ lb.}$$

The total cowling drag at 300 m. p. h. is

$$\text{Basic drag} + \text{cooling drag} = 126 + 25 = 151 \text{ lb.}$$

and at 150 m. p. h.  $= 32 + 50 = 82 \text{ lb.}$

Some additional examples are presented in table I. Only the cooling drag and horsepower are given in the table because the computation of the basic drag depends on many factors not easily computed.



CONCLUDING REMARKS

- 1. The ordinates for two nose shapes that can be applied to most cowlings are given.
- 2. A method of obtaining the dimensions of the exit of a cowlings is presented.
- 3. An evaluation of the increment of drag associated with the flow of cooling air through the engine is given.
- 4. An evaluation of the increment of drag associated with the addition of an engine cowlings to the nose of a streamline fuselage is given.

LANGLEY MEMORIAL AERONAUTICAL LABORATORY,  
NATIONAL ADVISORY COMMITTEE FOR AERONAUTICS,  
LANGLEY FIELD, VA., *March 5, 1938.*

REFERENCES

1. Weick, Fred E.: Drag and Cooling with Various Forms of Cowling for a "Whirlwind" Radial Air-Cooled Engine—I. T. R. No. 313, N. A. C. A., 1929.

2. Weick, Fred E.: Drag and Cooling with Various Forms of Cowling for a "Whirlwind" Radial Air-Cooled Engine—II. T. R. No. 314, N. A. C. A., 1929.

3. Theodorsen, Theodore; Brevoort, M. J., and Stickle, George W.: Full-Scale Tests of N. A. C. A. Cowlings. T. R. No. 592, N. A. C. A., 1937.

4. Theodorsen, Theodore; Brevoort, M. J., and Stickle, George W.: Cooling of Airplane Engines at Low Air Speeds. T. R. No. 593, N. A. C. A., 1937.

5. Brevoort, Maurice J.: Energy Loss, Velocity Distribution, and Temperature Distribution for a Baffled Cylinder Model. T. N. No. 620, N. A. C. A., 1937.

6. Brevoort, M. J.; Stickle George W., and Ellerbrock, Herman H., Jr.: Cooling Tests of a Single-Row Radial Engine with Several N. A. C. A. Cowlings. T. R. No. 596, N. A. C. A., 1937.

7. Wood, Donald H.: Tests of Nacelle-Propeller Combinations in Various Positions with Reference to Wings. Part I. Thick Wing—N. A. C. A. Cowled Nacelle—Tractor Propeller. T. R. No. 415, N. A. C. A., 1932.

8. Wood, Donald H.: Tests of Nacelle-Propeller Combinations in Various Positions with Reference to Wings. II.—Thick Wing—Various Radial-Engine Cowlings—Tractor Propeller. T. R. No. 436, N. A. C. A., 1932.

TABLE I.—EXAMPLES OF COWLING DESIGN

	Given				Level flight					
	Top speed (m. p. h.)	$\Delta p$ (lb. per sq. ft.)	$K$	Climb- ing speed (m. p. h.)	$q$ (lb. per sq. ft.)	$\frac{\Delta p}{q}$	$\Delta C_D$	hp. to cool for $F=14.75$ sq. ft.	$\frac{K}{K_1}$	Area of slot (sq. ft.)
1	150	20	0.05	110	58	0.35	0.010	3	1.37	0.54
2	150	40	.10	110	58	.70	.054	19	.65	2.27
3	230	20	.05	120	135	.15	.002	2	2.42	.30
4	230	40	.10	120	135	.30	.015	18	1.53	.96
5	230	60	.10	120	135	.44	.026	32	1.12	1.32
6	300	20	.05	150	230	.09	.001	3	3.15	.23
7	300	40	.10	150	230	.17	.007	19	2.33	.66
8	300	60	.10	150	230	.26	.012	33	1.69	.87
9	300	80	.10	150	230	.35	.019	52	1.37	1.08

	Climb					
	$q$ (lb. per sq. ft.)	$\frac{\Delta p}{q}$	$\Delta C_D$	hp. to cool for $F=14.75$ sq. ft.	$\frac{K}{K_1}$	Area of slot (sq. ft.)
1	31	0.65	0.030	4	0.73	1.01
2	31	1.29				
3	37	.54	.022	4	.92	.80
4	37	1.15	.217	37	.22	6.71
5	37					
6	58	.35	.010	3	1.37	.54
7	58	.70	.054	19	.65	2.27
8	58	1.04	.134	46	.31	4.76
9	58	1.39				

<sup>1</sup> Flaps.







## REPORT No. 663

# THE EFFECT OF CONTINUOUS WEATHERING ON LIGHT METAL ALLOYS USED IN AIRCRAFT

By WILLARD MUTCHLER

### SUMMARY

*An investigation of the corrosion of light metal alloys used in aircraft was begun at the National Bureau of Standards in 1925 and has for its purpose the study of the causes of corrosion in aluminum-rich and magnesium-rich alloys together with the development of methods for its prevention.*

*The results, obtained in an extensive series of laboratory and weather-exposure tests, reveal the relative durability of a number of commercially available materials and the extent to which the application of various surface coatings of oxide alone and with paint coatings afforded additional protection. The paper may be considered as a supplement to N. A. C. A. Report No. 490.*

### INTRODUCTION

The results of earlier laboratory corrosion and weather-exposure tests, which yielded information of considerable value, have previously been published (references 1 to 9). The present report is, in effect, a résumé of the most important features and findings from additional weather-exposure and laboratory tests, started in 1932 and covering a period of 5 years, in which more than 7,000 specimens of aluminum and magnesium alloys were tested.

In the previously published papers, emphasis was placed primarily upon the causes and elimination of deterioration by embrittlement of high-strength aluminum alloys of the so-called "duralumin" type. It was learned that, although the seriously objectionable intercrystalline type of corrosion could be eliminated by correct procedures in heat treatment, the copper-containing duralumin alloys were more prone to attack than lower-strength alloys in which this constituent was absent. It was learned further that duralumin could be adequately protected against severe saline conditions when covered with outer layers of aluminum of high purity and that certain combinations of surface oxidation treatments and pigmented varnishes afforded the next best degree of protection.

In line with these findings, manufacturers developed noncopper-containing alloys of higher strengths than

were previously available. The more important of these alloys were included in the present investigation for the purpose of securing comparative data. Also, emphasis was placed upon a rather systematic study of the most promising methods of surface treatment as a means of protecting duralumin-type alloys from corrosion. The entire program embraced in the present series of tests had for its objectives the accumulation of data regarding the relative corrosion resistance of commercially available aluminum and magnesium alloys uncoated and coated with different protective surfaces.

The author acknowledges his great indebtedness to H. O. Willier, who assisted in examining and testing all the samples. He also thanks H. C. Dudley, who assisted in their preparation and heat treatment. The cooperation furnished by the sponsors, the National Advisory Committee for Aeronautics, the Army Air Corps, and the Bureau of Aeronautics, Navy Department, as well as by officials and inspectors at the Naval Air Station, Hampton Roads, Va., and the Fleet Air Base, Coco Solo, C. Z., is also appreciated.

### WEATHERING OF ALUMINUM ALLOYS

#### EXPERIMENTAL PROCEDURE

All the aluminum alloys consisted of 0.064 inch (14 gage) sheet of which by far the greater number were in the form of 9- by ¾-inch strips. These strips were machined, after corrosion, into standard A. S. T. M. tensile bars with ½-inch reduced section (fig. 1a). Some samples were initially exposed in the form of tensile bars of the dimensions given in figure 1b. All spot-welded and riveted assemblies had a width of 1 inch and an over-all length of 9 inches, of which 1¾ inches represented the faying surfaces. All machining operations prior to exposure were done by the cooperating manufacturers, and all after exposure at the National Bureau of Standards.

All specimens, before corrosion tests and prior to the application of protective coatings, were cleaned free from grease by washing twice with clean benzol and once with alcohol. Specimens having identical chemi-



cal compositions and/or surface treatments were designated as "sets." Each set usually consisted of 52 specimens that were distributed thus: 6 tested for initial tensile properties; 10 kept in sealed containers (dry atmosphere); 10 each exposed to the weather at Washington, D. C., at Hampton Roads, Va., and at Coco Solo, C. Z.; and 6 exposed to laboratory salt-spray test. In those instances where a set consisted of both strips and tensile bars, the number of specimens at each locality was, of course, doubled.

The racks for the weather-exposure tests were installed at the same three locations used in the previous series (reference 9), namely:

(1) National Bureau of Standards, Washington, D. C., representative of a temperate inland atmosphere,

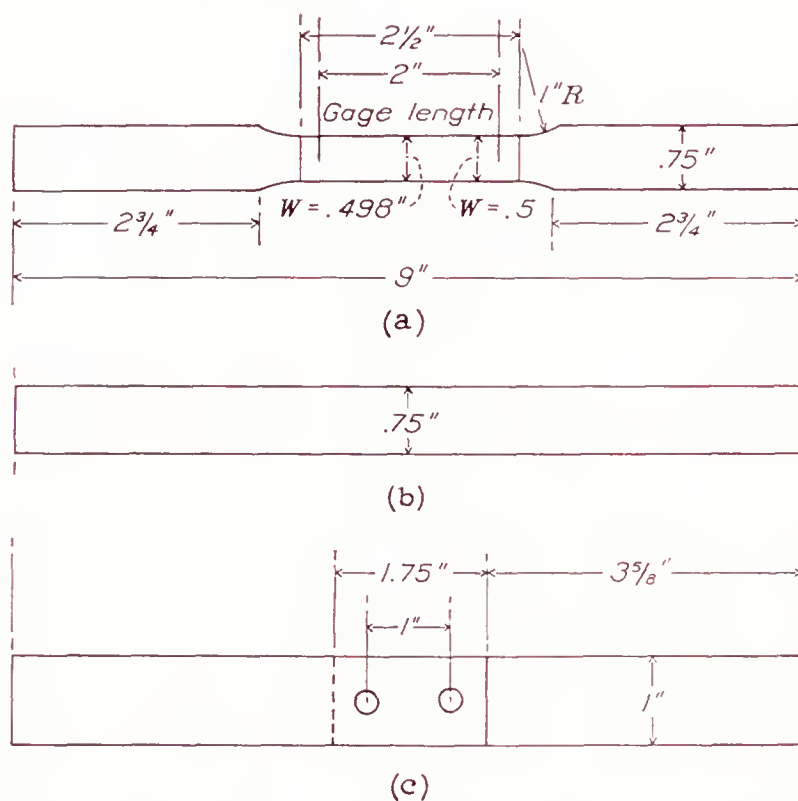


FIGURE 1.—Dimensions of 0.064-inch thick aluminum-alloy materials used in the weathering tests. (a), tensile bar; (b), strip sample; (c), spot-welded or riveted panel. The welds and rivet heads were approximately  $\frac{1}{4}$  inch in diameter; the rivet shanks were  $\frac{1}{8}$  inch in diameter.

free from industrial contamination and from marine conditions.

(2) Naval Air Station, Hampton Roads, Va., representative of temperate seacoast conditions, with occasional contact with salt water (fig. 2).

(3) Fleet Air Base, Coco Solo, C. Z., representative of tropical seacoast conditions (fig. 2).

In the preceding series of tests, the racks at Coco Solo were so situated as to assure frequent contact of the specimens with spray from the Caribbean Sea. In the present series they were located approximately 15 feet back from the shore line, and thus received spray much less frequently. This change resulted in making corrosive conditions at Coco Solo less severe than at Hampton Roads, the reverse of which was true in the previous investigation.

Withdrawals of samples at all three weather-exposure sites, and from the sealed containers, were made after periods of 12, 24, 36, and 48 months. Other with-

drawals were made as follows: At Washington, Coco Solo, and from the sealed containers after 18, 30, and 60 months; at Hampton Roads and Coco Solo after 3 months; and at Coco Solo after 42 months. A few racks still remain at Washington and Hampton Roads, and it is planned to remove these after more prolonged periods, probably 10 or more years. Withdrawals of samples from the laboratory salt-spray tests were governed by the susceptibility to corrosion of the various sets, the better ones being left for longer periods, the intervals being as follows:  $\frac{1}{4}$ ,  $\frac{1}{2}$ , 1, 2, 4, 6, 8, 9, 12, and 18 months. The salt-spray tests were conducted in an apparatus conforming strictly to Navy Department Specifications (references 10 and 11). A 20-percent solution of chemically pure sodium chloride was atomized to serve as the corroding medium and the temperature of the chamber was maintained at  $95^{\circ}\text{F.} \pm 2^{\circ}$ .

The progress of corrosion on all the samples was followed in three ways:

(1) By direct visual examination, supplemented by macrophotographs at natural size of both sides of each specimen.

(2) By a comparison of the tensile properties of the corroded bars, with those of uncorroded bars, which served as an indirect measure of corrosion. Elongation values were measured over a 2-inch gage length.

(3) By direct measurement of the depth and the area of corroded portions. Two random cross sections, each having an area of 0.5 by 0.064 inch, were photographed in their entirety at 50 magnification, thus yielding a permanent record of the micrographic features of the corrosive attack. The photomicrographs were made by a rapid method, developed at the National Bureau of Standards, on photostat paper negatives (reference 12).

#### UNCOATED MATERIALS COMMERCIALY AVAILABLE

The chemical compositions of these materials, which were exposed in the condition "as received" from their manufacturers, are given in table I. Alloys 25SW, 51SW, and 51ST were exposed only in strip form and represented materials from the same lots as were used in the previous series of exposure tests. All of the remaining materials were exposed both as strips and as tensile bars.

It will be seen from the table that the alloys fall naturally into two groups: (1) those in which copper is present as an alloying constituent, and (2) those in which it is absent. The alloys of the first group are commonly considered as being of the duralumin type. Alloy 17S is considered representative and nominally contains 4 percent of copper, 0.5 magnesium, and 0.5 manganese, with minor quantities of silicon and iron. Alloy 24S differs only in having an additional 1 percent of magnesium, while the Aeral alloy contains 2 percent of cadmium. In alloy 25S the magnesium is omitted,



while in Nicalumin most of the copper is replaced by heavy metal substitutes, supposedly less conducive to intercrystalline attack, such as nickel, chromium, tungsten, and molybdenum. The aluminum-coated (Alclad) material might be regarded as duralumin with a protective metallic coating but, for practical

contain, respectively, 1.25, 3.5, and 6 percent of magnesium. In the second group are: alloys 4S, with 1 percent of magnesium and 1.25 manganese; 51S, with 0.6 magnesium and 1 silicon; and Inalium, with 0.8 magnesium and 2 cadmium.

The Aeral and Inalium materials were prepared by

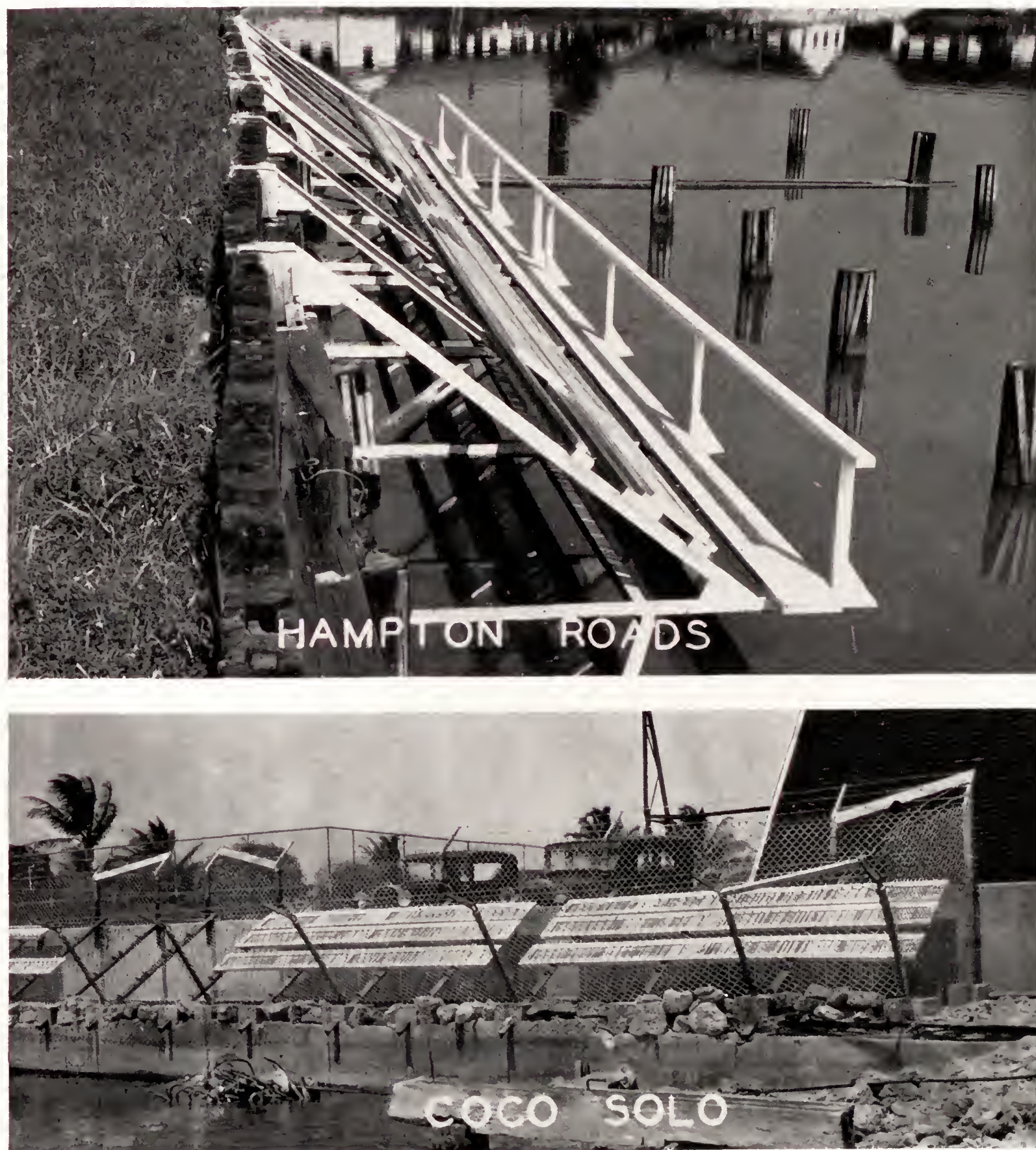


FIGURE 2.—Views of the weather-exposure racks and specimens situated at the two marine locations.

purposes, it is considered as a distinct commercial product.

The copper-free alloys may be further subdivided into (1) the essentially binary alloys of aluminum and magnesium, and (2) the essentially ternary alloys of aluminum, magnesium, and a third element. In the first group are X52S, XB52S, and 56S which nominally

the Société des Brevets Berthelemy de Monthy of Paris, France. These alloys apparently offer difficulties in fabrication because the surface finishes were much rougher than usual and approximately 5 percent of the individual strips and tensile bars contained internal cracks and flaws. The Nicalumin samples were furnished by the Nicalumin Co. and the remaining



alloys were supplied by the Aluminum Co. of America. All materials were representative of commercial products prepared in accordance with the manufacturer's recommended procedure.

The average tensile properties of the materials are given in table II where also appear the ultimate tensile strength, elongation, and maximum depth of penetration of corrosive attack after 5 years' exposure at Washington and Coco Solo, 4 years at Hampton Roads, and the maximum period in the salt-spray test. For purposes of convenience in comparison, the data are repeated in table III, expressed in terms of percentage loss from the initial properties.

These data indicate that the binary aluminum-magnesium alloys (X52S- $\frac{1}{2}$ H and XB52S) proved exceptionally corrosion resistant. No loss in tensile properties occurred and the maximum depth of penetration of attack was approximately 0.002 inch. The higher strength Alclad materials were likewise very resistant. Losses in tensile properties were small and the attack did not penetrate beyond the protective aluminum layers.

Somewhat less corrosion resistant, but definitely superior to the remaining materials, were the copper-free alloys (4S- $\frac{1}{2}$ H, 56S- $\frac{1}{2}$ H, and Inalium). As previously pointed out, however, the Inalium material was inferior from considerations of original surface finish. The 6 percent magnesium alloy (56S- $\frac{1}{2}$ H) was peculiar in that it exhibited no pronounced corrosion or loss in tensile properties until after the third year at Hampton Roads and at Coco Solo, and after the ninth month in the salt spray. Then intercrystalline attack developed and the tensile properties dropped rapidly.

Increasingly inferior, in the order named, were the magnesium-silicon alloys (51SW, XA51ST, 51ST), and the complex "heavy-metal" alloy Nicralumin, on which marked loss in tensile properties occurred and corrosive attack penetrated approximately 0.01 inch at the severe localities. Except on the Nicralumin material, the attack tended to be intercrystalline in nature.

Under severe conditions of exposure, as exemplified in the salt spray, the copper-containing materials (17ST, 17SRT, 24SRT, and Aeral) proved much more susceptible to attack, which was confined to the pitting type. For all practical purposes, little difference was to be noted in their behavior when compared with each other.

Worst from considerations of corrosion resistance was the copper-aluminum alloy, 25SW, in which a very pronounced loss in tensile properties occurred, and in which a severe intercrystalline attack took place.

The changes in surface appearance of representative materials are shown in figure 3, where it may be seen that the amount of corrosion products was much greater on the more susceptible alloys and that they tended to

accumulate more on the earthward surfaces of the weather-exposure samples than on the skyward.

The character of the attack on the various alloys, when viewed at 50 diameters, is shown in figures 4 and 5. Differences in the area and the depth of attack between the different alloys are plainly shown, as well as differences dependent upon the severity of the locality.

Thus far, attention has been confined to the appearances and properties of the alloys at the expiration of the maximum periods of exposure. Marked differences in the rates of attack were, of course, found also in the earlier stages of the tests. The more important of these are illustrated in figure 6, where the relation is shown between time of exposure and percentage loss in elongation and maximum depth of attack.

**Effect of corrosion on the cut edges.**—Specimens of all the more corrosion-resistant alloys, exposed as tensile bars and those from which such bars were cut after exposure, possessed practically identical tensile properties. The properties of some of the copper-containing alloys, such as 17ST, 17SRT, and 24SRT, when exposed as tensile bars, were appreciably lower, especially in the laboratory salt-spray tests. Table IV illustrates the magnitude of the differences. The microscopic examinations disclosed a pronounced tendency for the attack to penetrate very much more rapidly from the cut edges than from the sides of the sheet. The attack frequently presented a characteristically elongated course suggesting that relatively thin layers were much more prone to attack than adjacent metal. This suggestion is confirmed by the appearance of corroded areas, other than those originating on the cut edges, indicated by the arrow in figure 7. The typical elongated shape of the areas indicates strongly that fabrication processes play an important part in originating the "layers" susceptible to attack.

**Corrosion of spot-welded and riveted joints.**—The chemical compositions of the alloys used for the spot-welded and riveted panels are given in table I, and the breaking loads before and after corrosion for the maximum periods are given in table V. The locations of the rivets and welds and the dimensions of the exposure panels are shown in figure 1c. Owing to the rather wide range of the breaking loads on uncorroded samples, 30 of these panels were exposed at each locality instead of 10, and 3 were removed at each test period.

It is evident from table V that the strength of the spot-welded joints was considerably higher than that of the riveted joints but that the former varied over a much wider range. Marked loss in breaking load occurred only on the Alclad 17ST sheets joined by rivets of the alloy containing magnesium (X56S- $\frac{1}{4}$ H). These specimens developed severe intercrystalline at-



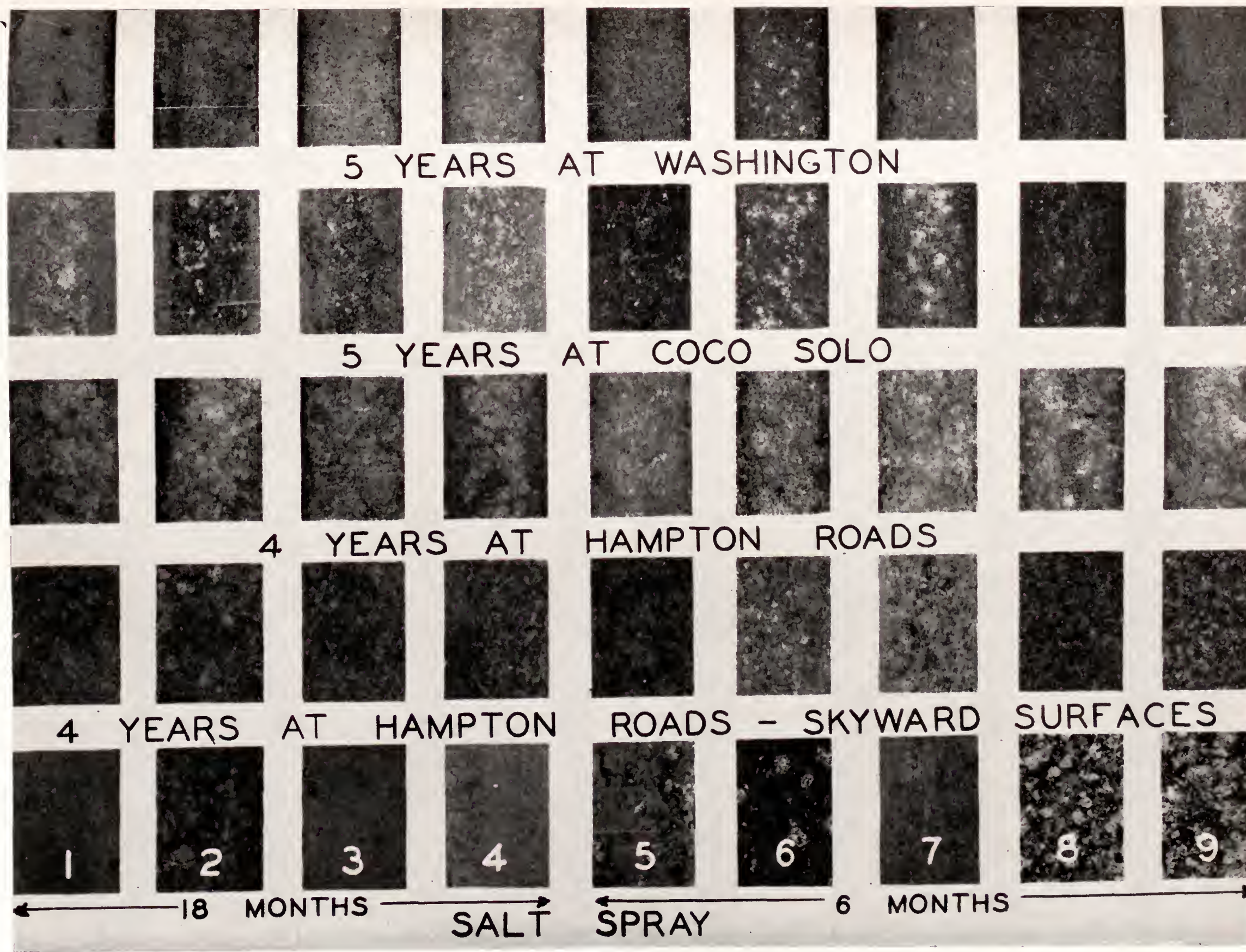


FIGURE 3.—Surface appearance of the various unprotected sheet materials after the maximum exposure at each locality. Earthward surfaces are shown in all except the fourth row. The materials are: (1) X52S- $\frac{1}{2}$ H; (2) Alclad 17ST; (3) 4S- $\frac{1}{2}$ H; (4) 56S- $\frac{1}{2}$ H; (5) XA51ST; (6) Niralumin; (7) Inalium; (8) 17SRT; (9) 25SW.  $\times 1$ .



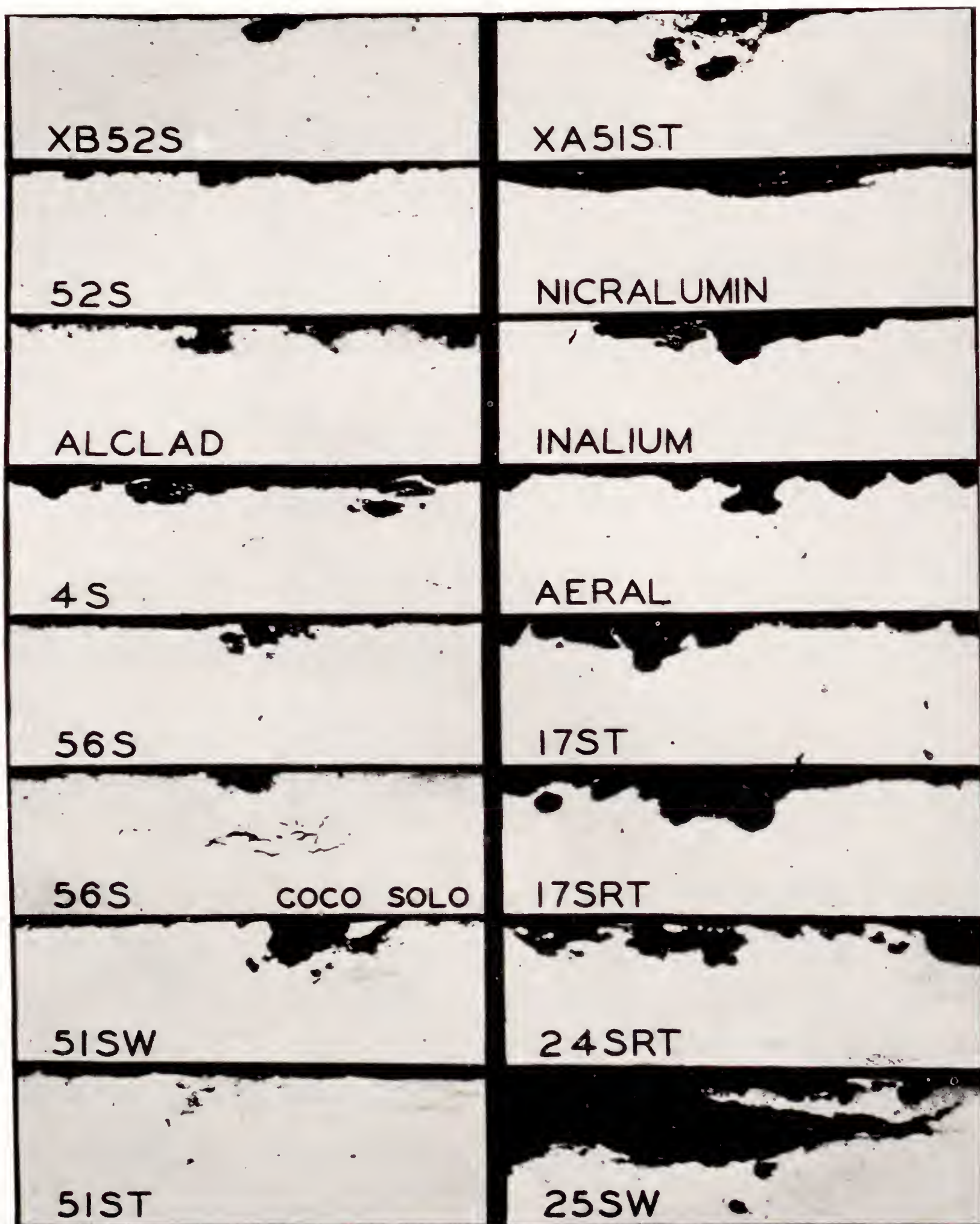


FIGURE 4.—Representative cross sections showing the maximum penetration of corrosive attack on sheets exposed 4 years at Hampton Roads.  $\times 50$ .



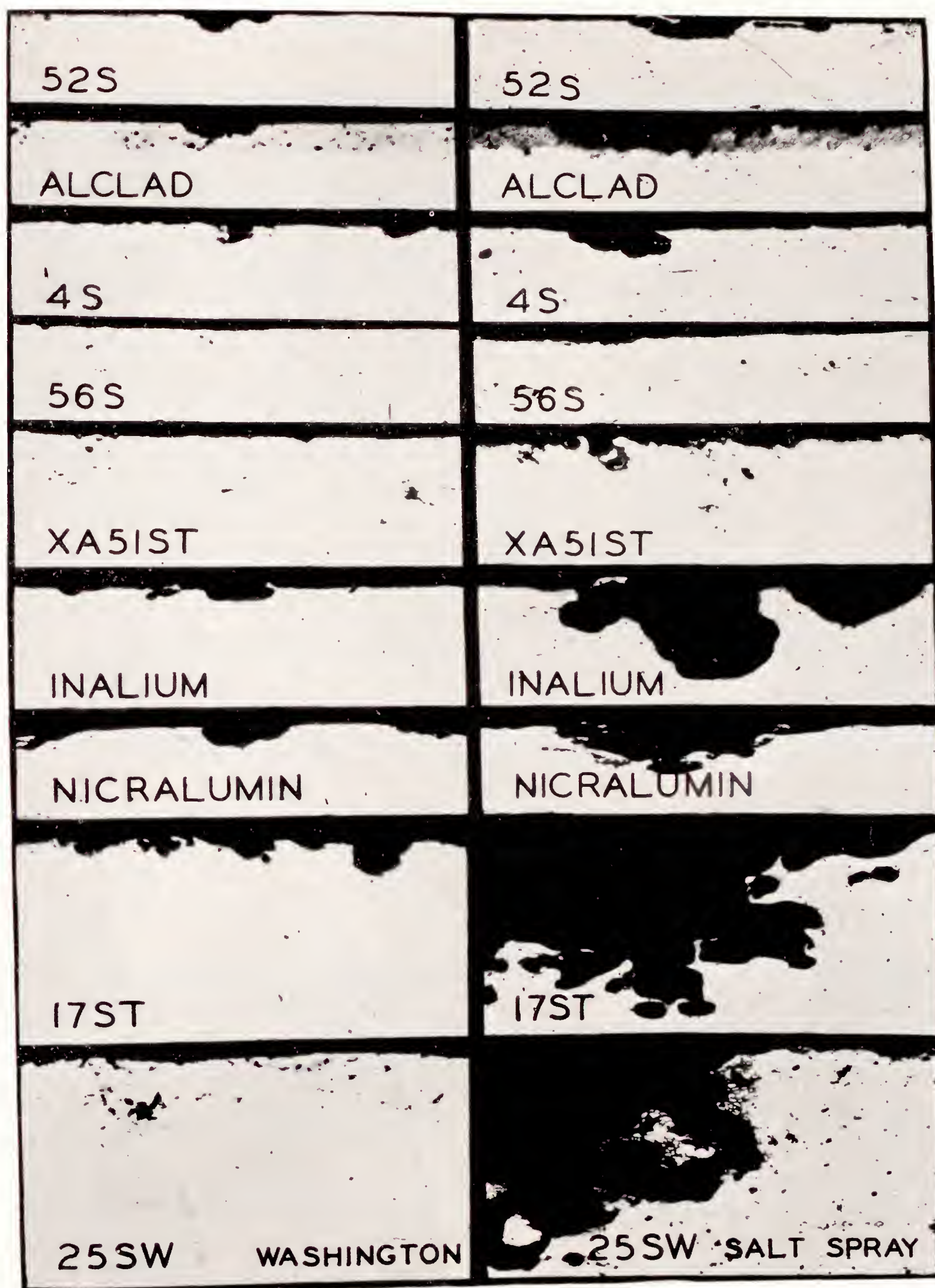


FIGURE 5.—Representative cross sections showing the maximum penetration of corrosive attack on sheets exposed 5 years at Washington (left column) and in the laboratory salt-spray tests (right column). The Nicalumin, XA51ST, 17ST, and 25SW materials were exposed 6 months to the spray; the others were exposed 18 months. Note the intercrystalline attack on alloys 56S, XA51ST, and 25SW.  $\times 50$ .



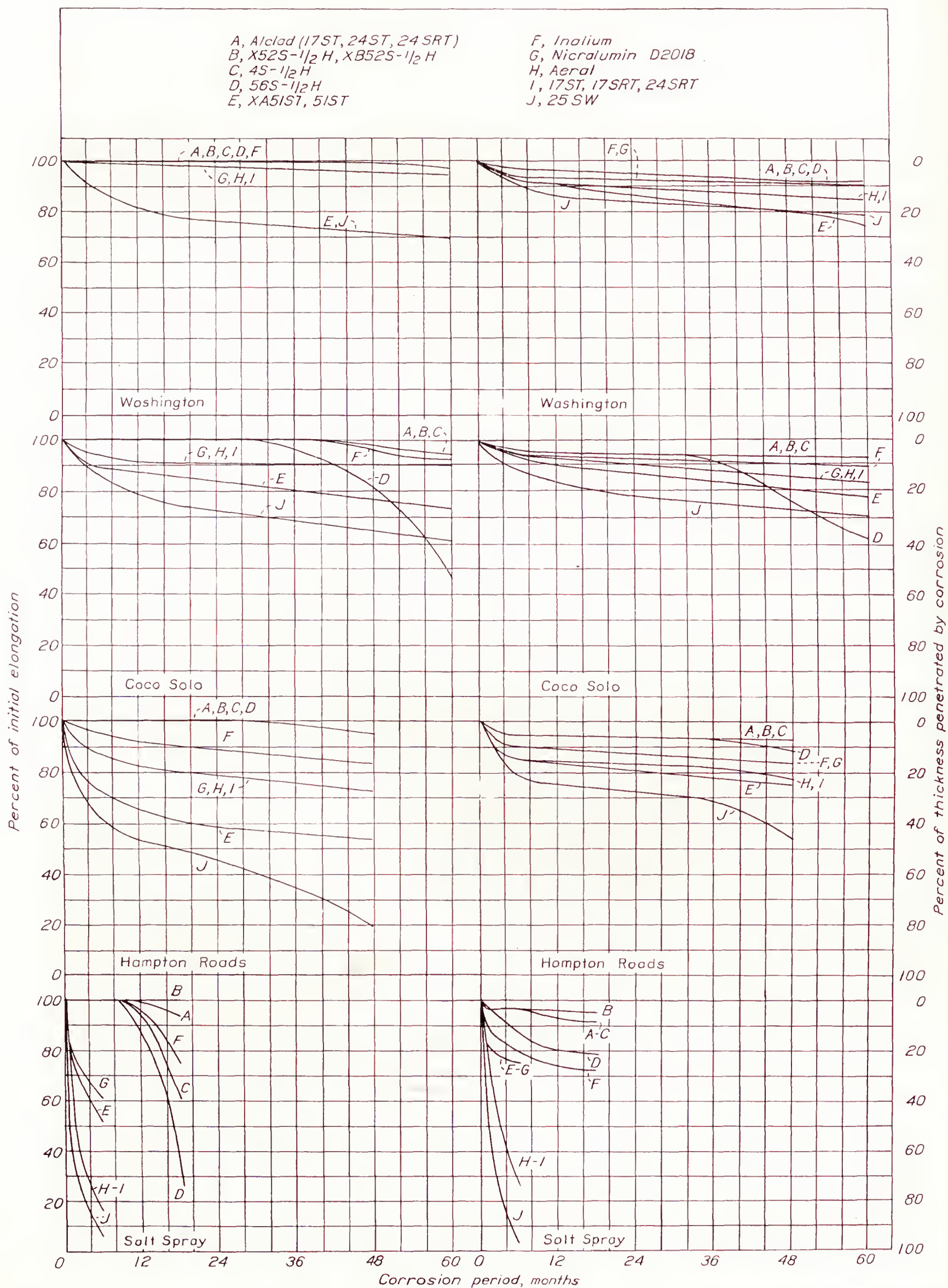


FIGURE 6.—The rates of penetration of corrosive attack and of loss in ductility for the various materials at each exposure locality. Note the marked superiority of the Alclad and X52S materials.



tack (fig. 8). In general, less corrosion was present at the faying surfaces of the spot-welded specimens than of the riveted ones. This result may be attributed, in part, to the fact that it was impossible to remove all the oil from the faying surfaces of the spot-

Effect of heat treatment on the corrosion of duralumin.—The corrosion of the duralumin-type alloy (17S as influenced by various heat treatments has already been reported in considerable detail (reference 9). A relatively few additional treatments were included

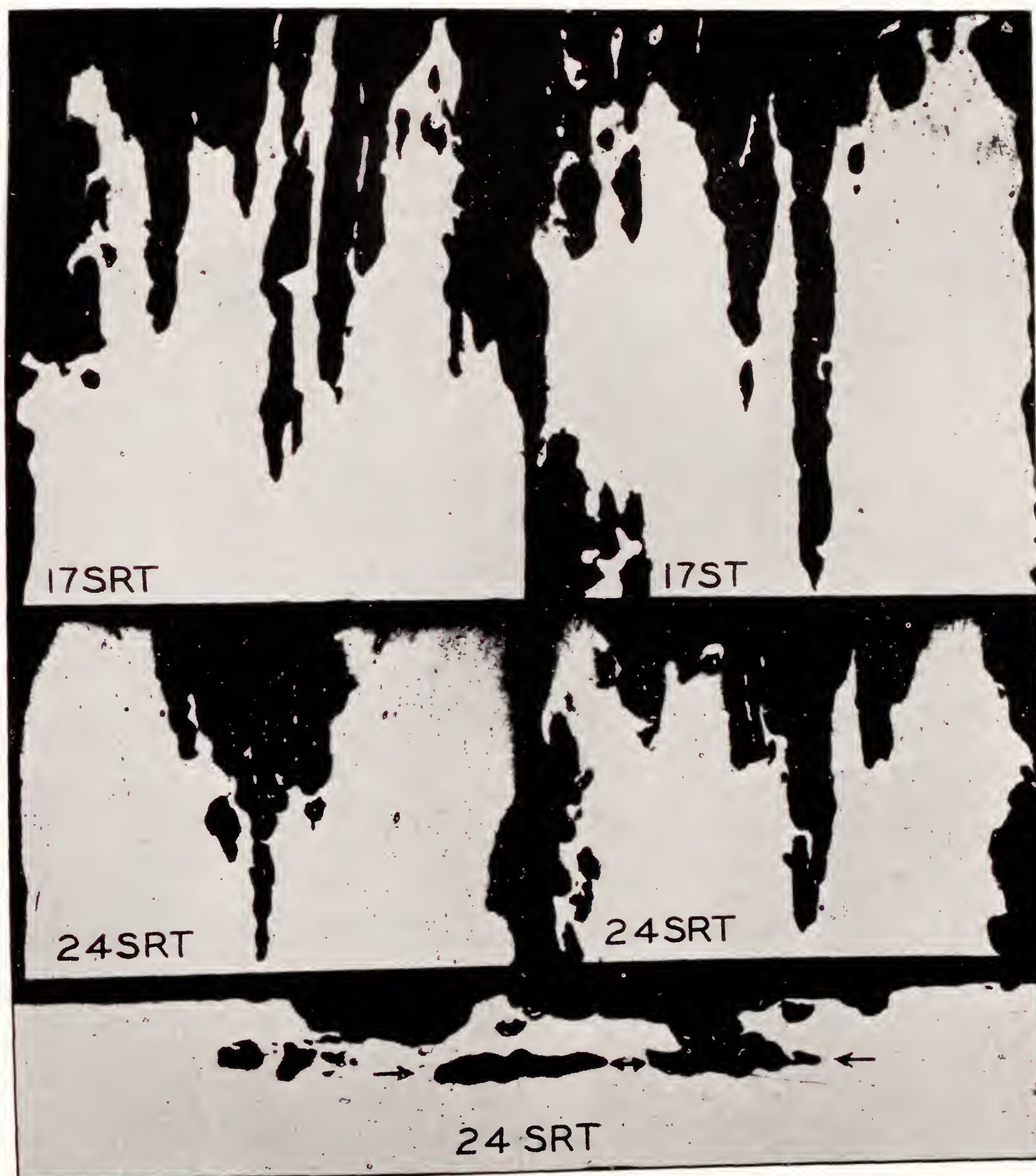


FIGURE 7.—Representative cross sections from specimens exposed 6 months to the laboratory salt-spray test, showing much greater penetration of attack from the cut edges, along "susceptible layers," than from the side surfaces. The cut edges are those at the top of the four upper specimens. The bottom specimen shows a side surface upon which the base of the corrosive attack spread laterally along a susceptible layer.  $\times 50$ .

welded panels prior to exposure. There was a definite tendency for localization of attack on the spot welds of all four materials, the attack being least on the copper-free alloys (X52S-1/2H and 4S-1/2H). In no instance, as far as could be determined, was the penetration sufficient to influence greatly the breaking load.

in the investigation, in which "as received" 17S-H material (table I) was treated as follows:

(1) "Solution heat-treated" at  $505^{\circ}\text{C}$ ., removed from the furnace and held in air for 5 seconds before quenching in ice water. Measurements indicated that the temperature of the samples was approximately



470° C. on entering the quenchant.

(2) Same as (1), but held 30 seconds in air, at the end of which the temperature of the samples was approximately 375° C.

(3) Solution heat-treated at 475° C. ("underheated") and quenched in ice water.

(4) Solution heat-treated at 550° C. ("overheated") and quenched in ice water.

(5) Solution heat-treated at 505° C. and quenched in ice water.

(6) Solution heat-treated at 505° C. and quenched in boiling water.

(7) Solution heat-treated at 505° C., quenched in

corrosion (reference 9) and were the most susceptible to attack of all the materials tested. Reference to table III will show that samples heat-treated by the other methods closely resembled the 17ST and related alloys in their corrosion behavior.

#### PROTECTIVE COATINGS APPLIED TO DURALUMIN

**Oxide surface coatings.**—A brief description will be given of the methods of application of the various oxide surface treatments used in the present investigation. The treatments were made at the National Bureau of Standards on a duralumin alloy (17S) quenched in boiling water after solution heat treatment at 505° C.

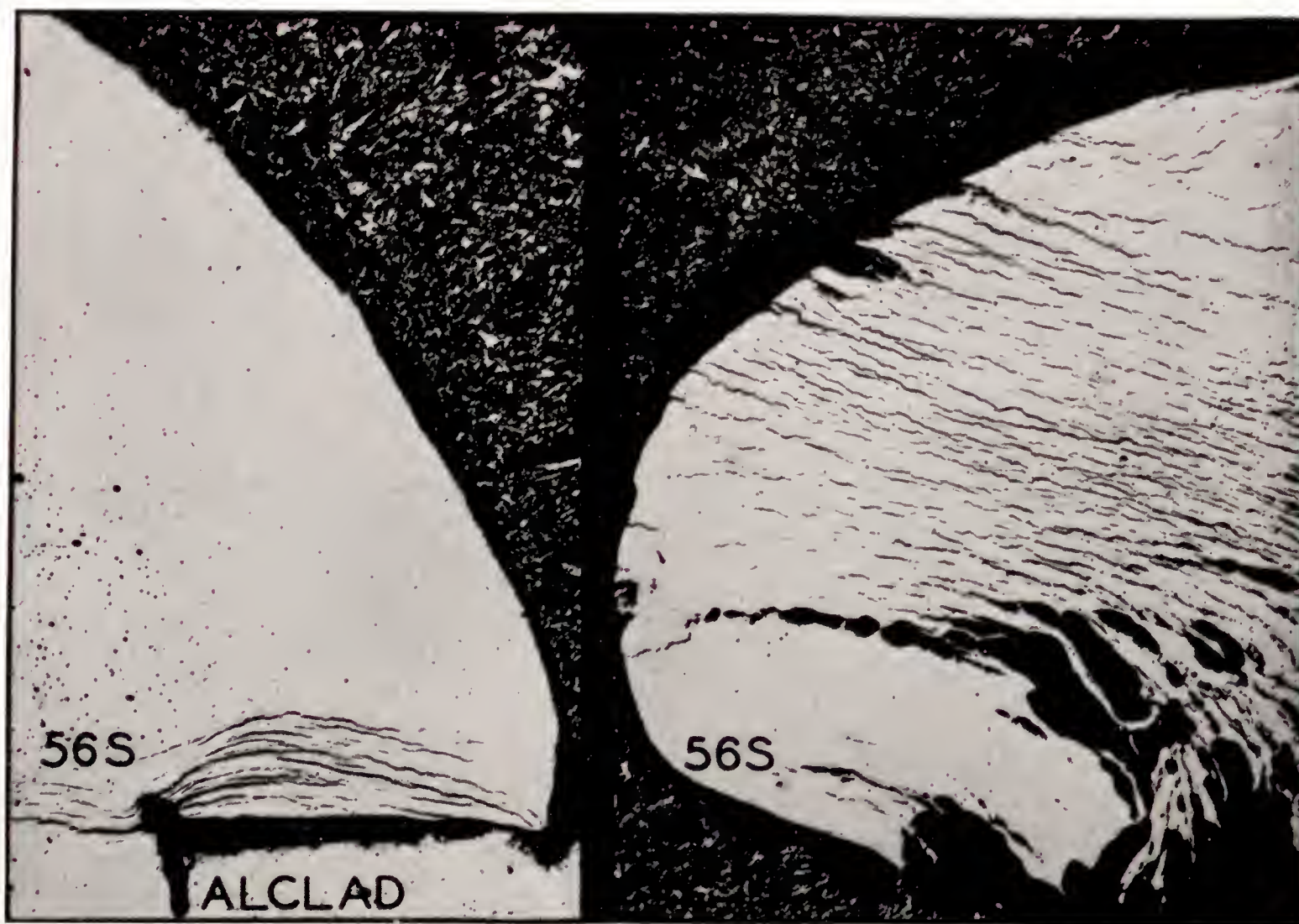


FIGURE 8.—Severe intercrystalline corrosive attack on X56S-1/4H rivet heads exposed 2½ years at Coco Solo.  $\times 50$ .

ice water, and "baked" 3 hours, some at (a) 100° F. (38° C.), some at (b) 200° F. (93° C.), and others at (c) 300° F. (149° C.).

A 30-minute solution heat-treatment was employed throughout, and all samples were allowed to age-harden for 3 months at room temperature prior to exposure. The treatments listed as (5) and (6) were the ones used on 17S samples subsequently given protective surface coatings, most of which were heat-treated at the National Bureau of Standards.

The properties of the uncorroded specimens and those exposed for the maximum periods are given in table VI. Those quenched in boiling water or baked at 300° F. were very susceptible to intercrystalline attack and exhibited great loss in tensile properties. Specimens baked at 300° F. were characterized by "pock-form"

Since underlying metal was thus purposely rendered susceptible to corrosion, failure of the coatings to afford protection was immediately reflected in a loss of tensile properties and the presence of intercrystalline attack. A number of the treatments, however, were also applied to cold-water-quenched 17S material, so as to obtain a more reliable criterion of their probable behavior in service. The coatings designated as Alcoa were applied solely to cold-water-quenched 17S material and to commercially heat-treated Alclad 17ST material. These treatments were applied at the Aluminum Co. of America Research Laboratories.

The objectives were (1) to determine the relative efficiencies of the various surface treatments as evidenced by the time required for their failure, and (2) to determine their behavior when painted with three coats



of a "standard" aluminum-pigmented spar varnish. The varnish selected for the latter purpose was one of the "long-oil" type which conformed to Federal Specification TTV81. (See table IX, schedule 11.)

The surface oxide coatings applied may be grouped into three categories, namely, those in which the protective film was formed by (1) simple immersion methods such as the Deoxidine, Jirotko, McCulloch, and Alcoa Dip processes; (2) anodic treatments in chromic or sulphuric acid electrolytes such as the Bengough, 10-percent chromic acid, chromic acid-dichromate, and Alcoa Electrolytic processes, and (3) impregnating anodically treated samples with inhibitive chromates, or "sealing."

(1) *Deoxidine process*.—Samples were immersed for 15 minutes in a 15-percent aqueous solution of phosphoric acid maintained at 55° C.

(2) *Jirotko "American" process*.—Specimens were immersed 1 hour at 96° C. in a bath consisting of 3½ liters of water, 4 grams of chromium sulphate, 50 grams of anhydrous sodium carbonate, and 12 grams of potassium dichromate.

(3) *McCulloch process*.—Samples were immersed 1 hour at 96° C. in a bath containing 10 grams of anhydrous calcium sulphate and 10 grams of calcium oxide per liter of water.

(4) *Alcoa Dip process (sealed)*.—Specimens were immersed 15 minutes at 98° C. in a solution containing 20 grams of sodium carbonate and 5 grams of potassium dichromate per liter of water. Samples were sealed by impregnation with lead chromate formed by successive immersions in solutions of potassium dichromate and lead acetate.

(5) *Bengough process*.—Samples were given an anodic treatment in an electrolyte of 3 percent chromium trioxide at 40° C. The voltage across the bath was raised gradually from zero to 40 volts in 15 minutes, maintained at 40 volts for 35 minutes, raised to 50 volts in 5 minutes, and maintained at 50 volts for 5 minutes. The electrolyte was changed frequently to preclude loss in its efficiency. Current densities were maintained between 3.8 and 4.8 amperes per square foot. The treatment was applied to 17S and Alclad 17S materials quenched (1) in ice water and (2) in boiling water.

(6) *Bengough process ("spent" bath)*.—The procedure used was the same as in (5) except that the bath had been used until its efficiency was very definitely impaired. The current density was approximately 1 ampere per square foot.

(7) *Ten-percent Chromic-Acid process*.—The specimens were anodically treated in accordance with Navy Department Specifications (reference 13). The electrolyte was a 10-percent solution of chromium trioxide maintained at 35° C. The voltage was raised as rapidly as possible to 30 volts and maintained there 1 hour. The average current density was approximately 5 amperes per square foot.

(8) *Chromic Acid-Dichromate Process*.—Samples were given an anodic treatment in a bath at 40° C. containing 4.6 percent by weight each of chromium trioxide and potassium dichromate. Anodization was effected by raising the voltage as rapidly as possible to 40 volts and maintaining it for 1 hour.

(9) *Alcoa Electrolytic No. 1 Process (sealed)*.—Specimens were anodically oxidized in 15-percent sulphuric acid electrolyte at 25° C., with a current density of 12 amperes per square foot for 30 minutes, and sealed in boiling water for 30 minutes.

(10) *Alcoa Electrolytic No. 2 process (sealed)*.—Specimens were anodized as in (9), but were sealed by impregnation with lead chromate formed by immersion in lead acetate solution, washing, and immersing in potassium dichromate solution.

(11) *Bengough process (sealed)*.—Samples were treated as in (5) but the electrolyte was permitted to impregnate the oxide film and dry thereon.

(12) *Ten-percent Chromic-Acid process (sealed)*.—Samples were treated as in (7) but the electrolyte was permitted to impregnate the oxide film and dry thereon.

The unpainted specimens receiving the oxide treatments designated as McCulloch, Deoxidine, Jirotko American, Alcoa Dip, Bengough ("spent" bath), and Chromic Acid-Dichromate all, on visual examination, exhibited more or less advanced stages of failure after an exposure of 6 months at Washington, 3 months at Coco Solo and Hampton Roads, and 1 month in the laboratory salt-spray tests. These oxide treatments were definitely inferior to the others tested and, for all practical purposes, may be considered as similar to each other in their failure to protect against corrosion. Their failure to afford protection was reflected in loss of tensile properties (table VII). The cold-water-quenched material coated by the Alcoa Dip process exhibited no loss in tensile properties after 5 years' exposure at Washington. This result, however, is to be attributed to the inherent corrosion resistance resulting from the heat treatment. Small, localized areas of corrosion product were visible on the samples after 6 months at Washington, which indicated that the coating had failed to protect completely.

The coatings produced by anodic treatment (10-percent Chromic Acid, Bengough, and Alcoa) were definitely much superior and retarded corrosive attack on the hot-water-quenched 17S material for an appreciable period. The first two were especially effective, on cold-water-quenched samples, at all the weather-exposure locations.

By far the best protection was afforded, however, by the oxide films sealed with an inhibitive chromate. Sheets anodized in chromic acid, and from which the electrolyte has not been thoroughly removed, present a somewhat undesirable mottled appearance. Since such sheets are ordinarily painted, this feature becomes relatively unimportant.



An excellent idea of the relative efficiencies of the various oxide coatings may be gleaned from figure 9, which shows their surface appearance at various stages of the laboratory salt-spray tests.

**Painted with a standard aluminum-pigmented spar varnish.**—Past experiments and experience have proved

Specimens initially treated by the McCulloch, Deoxidine, Jirotko, and Alcoa Dip processes and then painted, showed no loss in tensile properties after 5 years' exposure at Washington. Small localized areas, indicative of the commencement of paint failure, began to appear on the edges of the specimens during the fifth

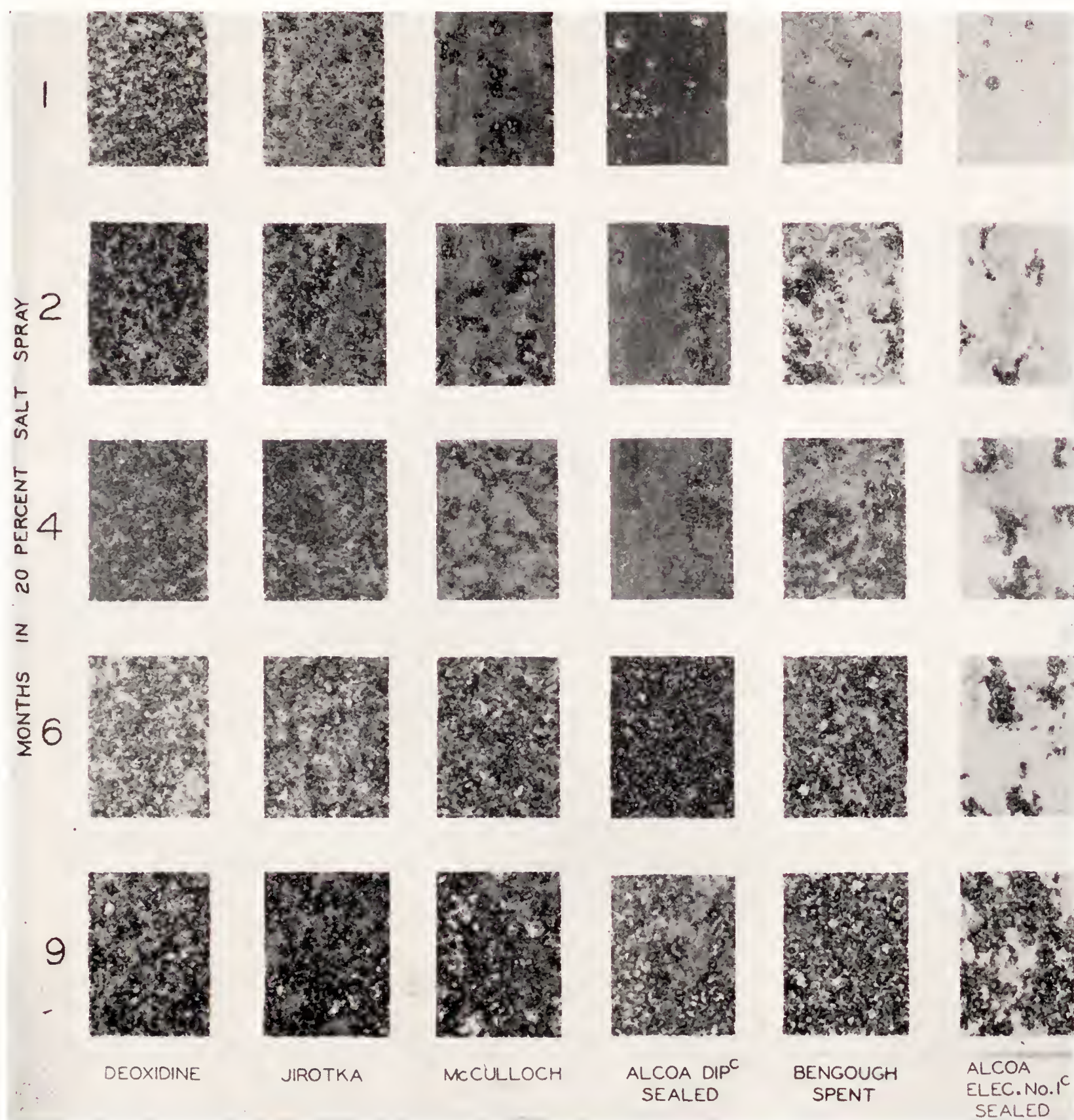


FIGURE 9.—Surface appearance, showing relative efficiencies of various surface oxide coatings applied to 17S specimens that were exposed to the laboratory salt-spray applied anodically and subsequently

that, under severe corrosive conditions, the greatest value of the oxide coatings lies in their ability to improve the adherence of additional protective coatings of the organic types. This fact was confirmed in the present investigation when a good grade of aluminum-pigmented spar varnish was applied in conjunction with the oxide surface treatment.

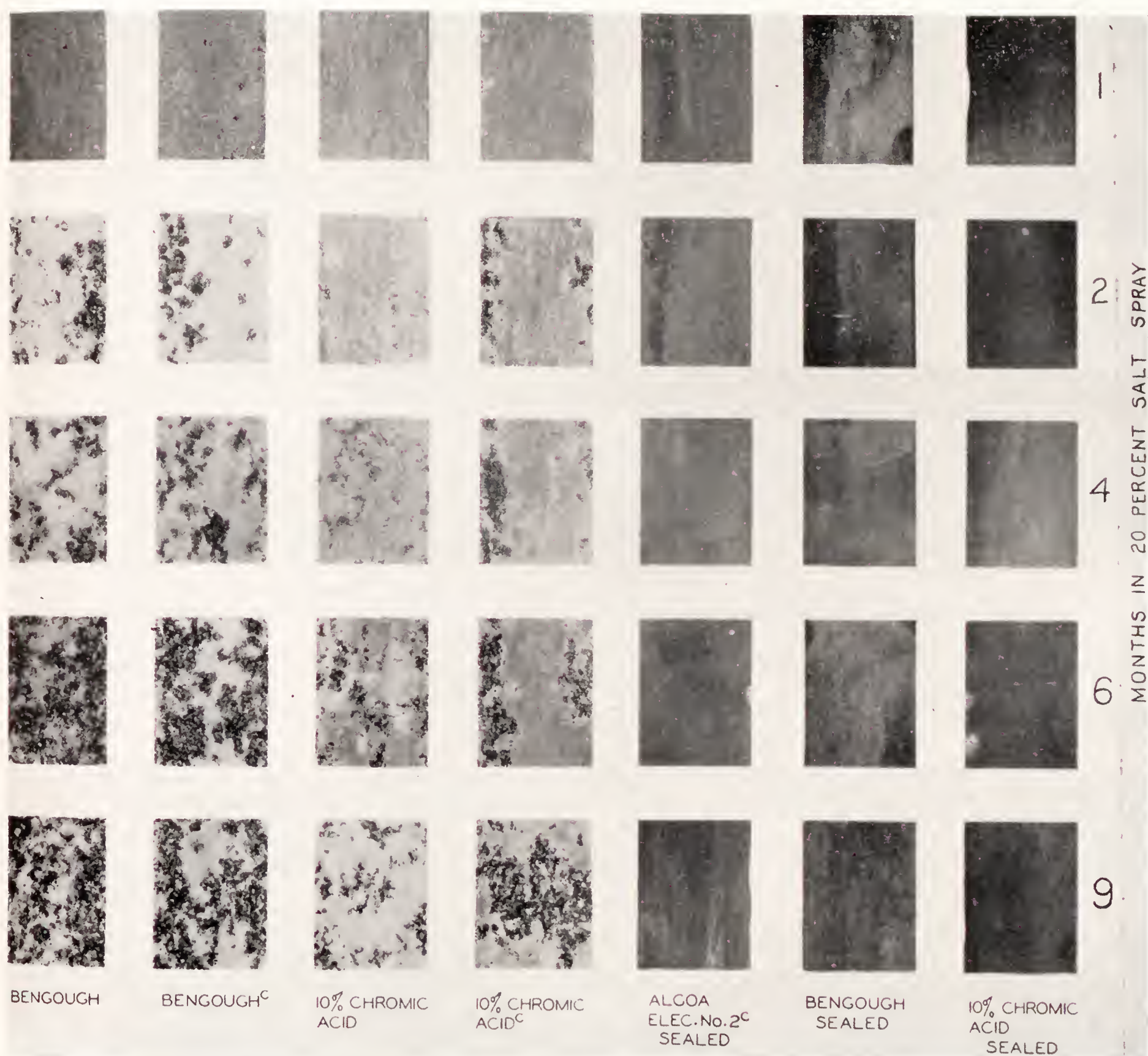
year. In the absence of saline conditions, however, these combination coatings afforded practically complete protection over this period despite the fact that the metal had purposely been made susceptible to intercrystalline attack. At Coco Solo and Hampton Roads, paint failures became more or less complete during the second year and, in the salt-spray tests, in 2 months.



Evidences of the beginning of paint failure on the improperly heat-treated, anodically treated duralumin made their appearance during the third year at Hampton Roads and Coco Solo, but failure was still in the initial stage at the conclusion of the

appearance at the end of the 1½-year test period.

**Paint and varnish coatings.**—The vehicles used were all marine spar varnishes designed primarily to withstand exposures to saline conditions. Details relative to the nature of the vehicles, the trade names, and the



test for the periods indicated. Coatings were applied to hot-water-quenched and cold-water-quenched (c) specimens. Note the marked superiority of the coatings given sealing treatments.  $\times 1$ .

tests. Loss in tensile properties (table VIII) was not appreciable. No loss occurred on the correctly heat-treated material or on the aluminum-coated (Alclad) specimens similarly protected, but traces of failure occurred during the fourth year and were confined usually to the edges of the samples. In the laboratory salt-spray tests the specimens presented a comparable

specifications to which the varnishes conformed are listed in table IX. All the varnishes were applied by spraying. Schedules 2, 3, and 10 were applied at Hampton Roads Naval Air Station. Schedule 5 was applied by Stoner-Mudge, Inc., of Pittsburgh, Pa., and the remaining specimens were painted at the National Bureau of Standards.



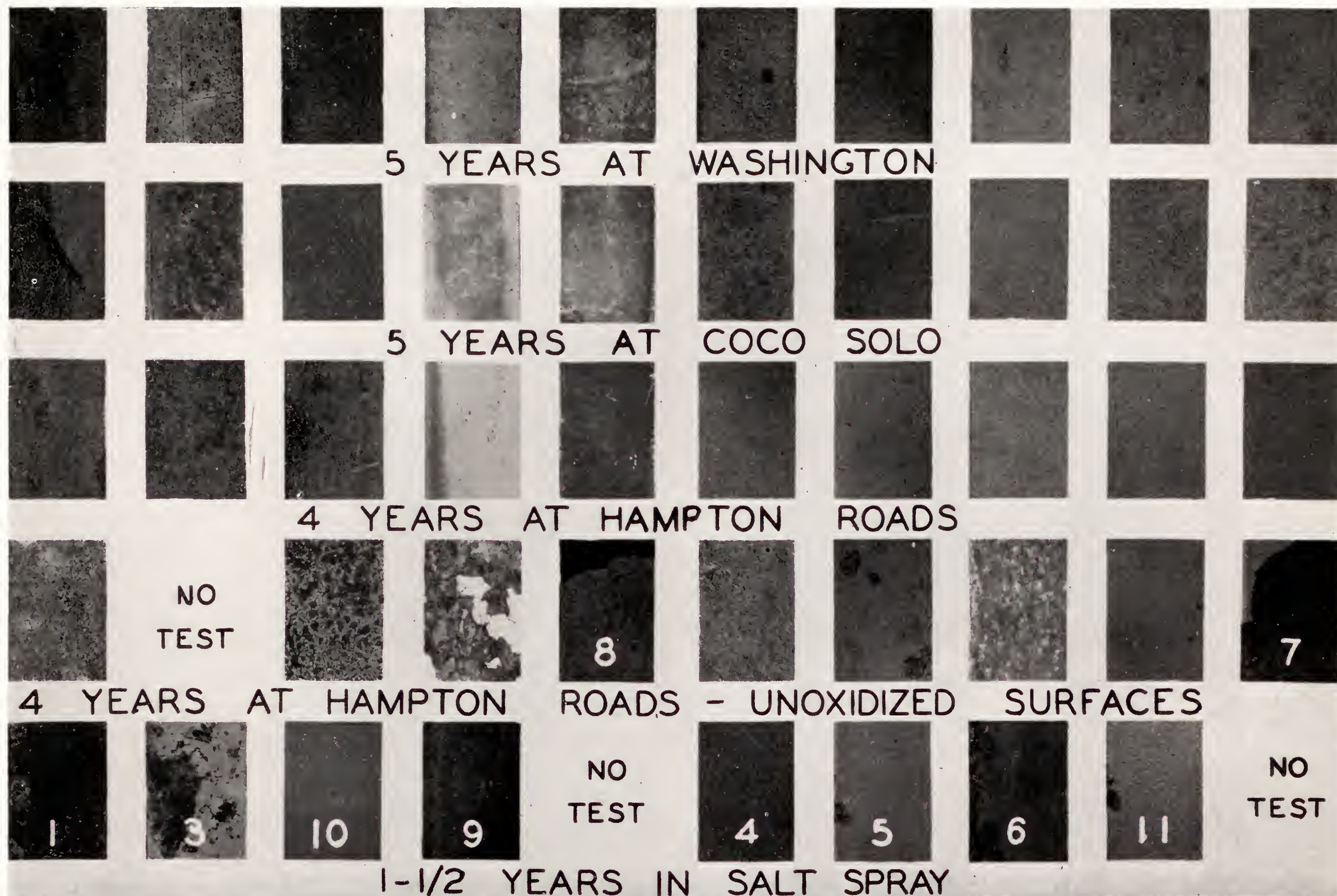


FIGURE 10.—Surface appearance of paint coatings applied to anodically treated 17S material and exposed for the maximum period at each locality. The superiority of the aluminum-pigmented varnishes is quite evident. The coatings were (1) clear Dulux, (3) aluminum foil over Thresher varnish, (10) Navy gray on red oxide primer, (9) zinc-pigmented Bakelite Marine Spar varnish, (8) zinc chromate-zinc oxide pigmented Bakelite Marine Spar varnish, (4) aluminum-pigmented Dulux, (5) aluminum-pigmented Vinylite, (6) aluminum-pigmented Thresher varnish, (11) aluminum-pigmented long-oil varnish, (7) aluminum-pigmented long-oil varnish on zinc chromate-zinc oxide pigmented primer.  $\times 1$ .



The tensile properties of the painted specimens at the conclusion of the exposure periods are given in table X, and the approximate times at which paint failure was noted are shown in table XI. The surface appearance of specimens after weather exposure for prolonged periods at each location is shown in figure 10.

The marked improvement of the durability of paints applied to an anodically treated surface makes it strongly advisable to use such a treatment if optimum service is to be attained under severe weathering conditions. The data show that the aluminum-pigmented varnishes on anodized panels all afforded relatively excellent protection irrespective of whether the vehicle was of the long oil, glyceryl phthalate, vinyl resin, or phenol formaldehyde varieties. Failure was confined almost entirely to small areas on the edges of the samples and commenced during the third year, although faint yellow discolorations were present during the first year. At the end of the tests all the aluminum-pigmented coatings on anodically treated surfaces were in relatively good condition. Even when this paint was applied to unanodized specimens the protection was greater than that obtained on the unpainted anodically treated specimens.

The zinc chromate-zinc oxide primer (coating 8) exhibited very poor adherence qualities on the unanodized samples but afforded good protection on the anodized samples, especially when finish coats of aluminum-pigmented varnish were employed. Owing to the lower flexibility of varnishes thus pigmented, it is to be questioned whether they would prove as satisfactory as aluminum-pigmented primers on aircraft parts subjected to vibratory or flexural stresses.

The tests with zinc dust-zinc oxide pigment indicated that it was not protective to the vehicle, as was the case with aluminum, and under marine conditions the zinc pigment was attacked more or less rapidly, giving rise to a uniform whitish-gray discoloration. The Navy gray enamel pigment also proved inferior in the exposure tests, as chalking, cracking, and alligatoring occurred within 6 months at all the outdoor locations. On the unanodized specimens failure was complete within a year and large areas of metal were visible. On the anodized samples, the red oxide primer became visible but it adhered well to the end of the tests. The unpigmented varnishes likewise proved unsatisfactory, as practically complete failure occurred during the first year on unanodized material and from the second to the fourth year on anodized samples. Although no loss in tensile properties appeared on anodized samples upon which aluminum foil had been applied over a tacky varnish, the use of this coating under saline conditions does not appear promising for the reason that the foil was attacked when subjected to salt-water conditions.

## WEATHERING OF MAGNESIUM ALLOYS

The weathering tests on the magnesium-alloy panels furnished by the American Magnesium Corporation were conducted only at Washington and Coco Solo. The purpose of the tests was threefold: (1) to obtain information relative to the probable behavior in service of alloys exposed after surface treatment and painting; (2) to determine which of two surface treatments yielded better adherence of paint; and (3) to determine the relative inherent corrosion resistance of the various alloys as manifested by the rapidity of their attack when the coatings failed to protect them completely.

The eight alloys tested are listed in table XII. The exposure panels were approximately 9 by 6 by  $\frac{1}{4}$  inches and, after surface treatment, all were protected with 4 coats of paint applied at the manufacturer's research laboratories. The paint consisted of Bakelite XV952 Aluminum Vehicle containing 2 pounds per gallon of Albron Standard Varnish Powder. The first coat was brushed on, and the rest were sprayed. Two surface treatments were used:

(1) *Chrome-pickle treatment*.—The panels were immersed for approximately 2 minutes at room temperature in a bath containing 1.5 pounds of sodium dichromate and 1.8 pints of concentrated nitric acid (specific gravity 1.42) per gallon of water. This treatment has been used commercially to a considerable extent.

(2) *Phosphoric-acid treatment*.—The panels were immersed for approximately 30 minutes at 125° F. in a solution consisting of 1 pound of 85-percent phosphoric acid and 3 ounces of magnesium oxide per gallon of water.

A single panel representative of each treatment and material was exposed for 5 years at each location. The progress of attack was followed closely by means of monthly inspections. At the end of the exposure tests the panels were photographed, the number of corroded spots or blisters was counted, and their areas were determined. The paint coatings were stripped off to determine to what extent corrosion appeared underneath.

Representative sections from the panels, showing the worst areas of attack, appear in figure 11; figure 12 illustrates that corrosion beneath the paint coating was quite superficial. Data on the number and area of blisters and corroded portions are given in table XIII.

The superiority of the phosphoric-acid surface treatment as a basis for paints is apparent from the table but, from practical considerations, there appears to be little evidence to support a choice of either of the methods investigated. Under mild exposure conditions, as at Washington, the paint coatings, although somewhat discolored, remained intact for 5 years. No appreciable corrosion of the panels took place but small blisters were fairly numerous on the paints applied to two of the chrome-pickled alloys (AM240 and AZM).



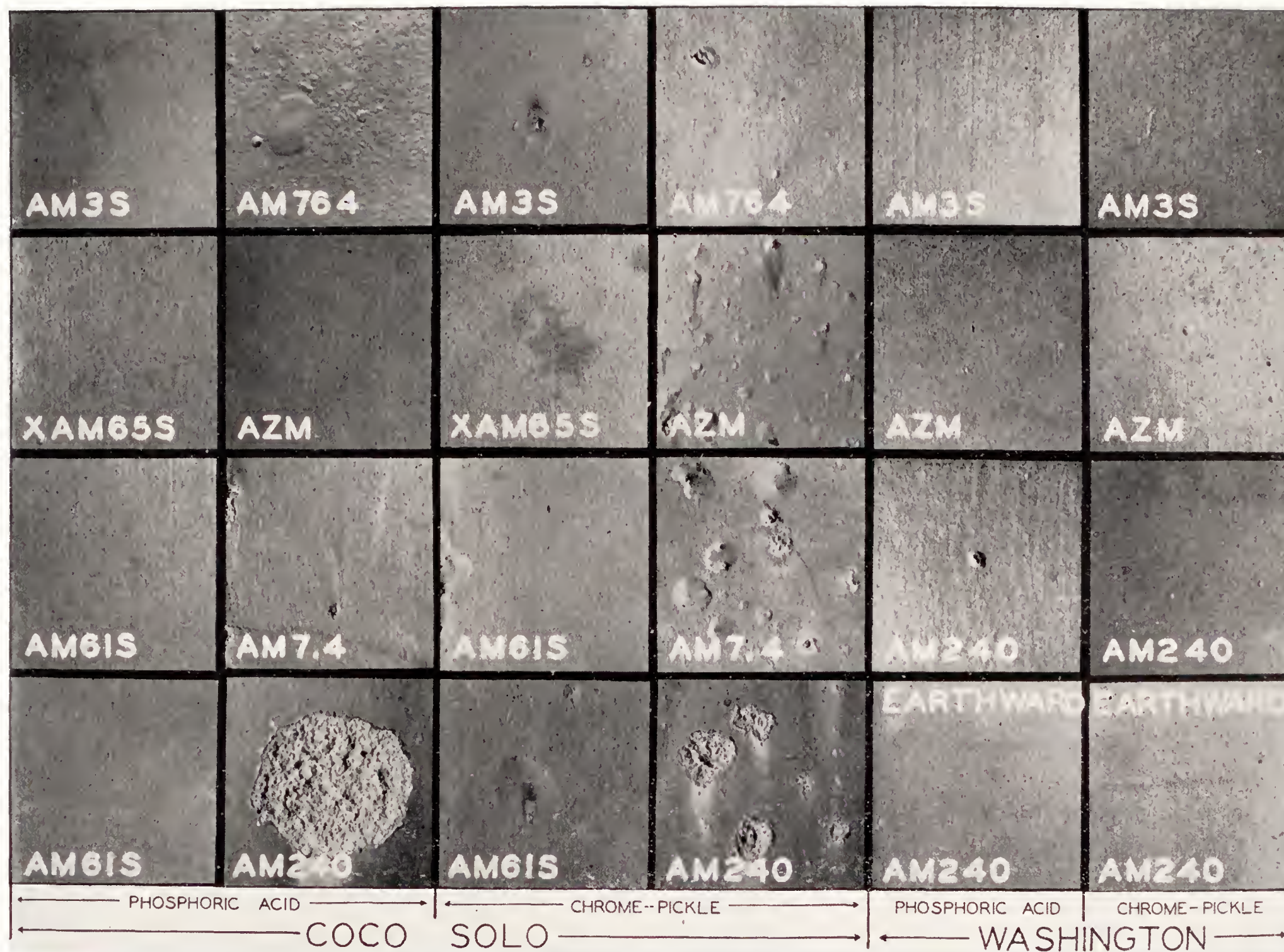


FIGURE 11.—Surface appearance of magnesium alloy panels given the surface treatments indicated, painted with aluminum-pigmented spar varnish, and exposed 5 years at each locality. Note the superiority of the phosphoric-acid surface treatment in improving paint adherence, and the excellence of the AM3S, XAM65S, and AM61S panels.  $\times \frac{1}{2}$ .



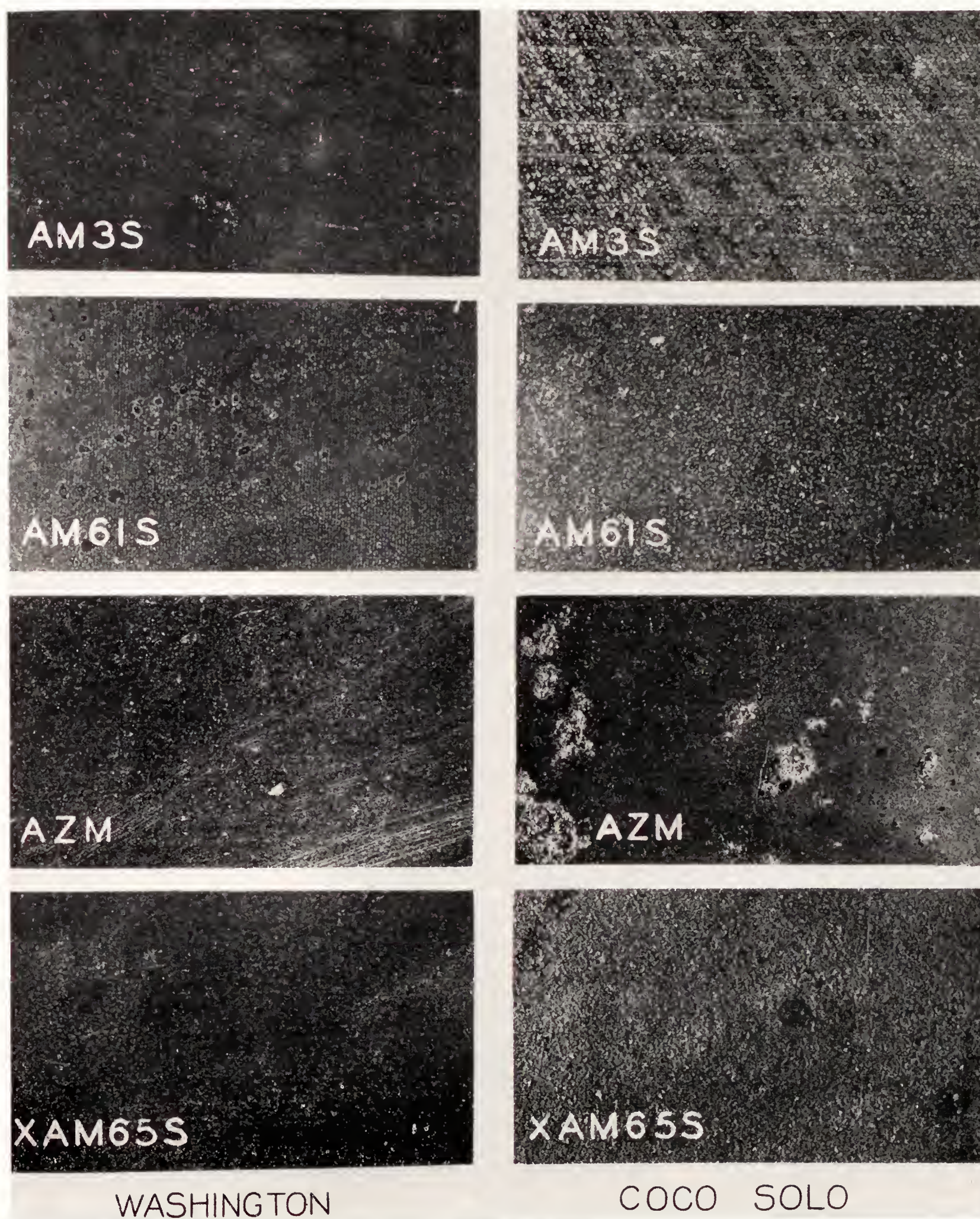


FIGURE 12.—Surface appearance of chrome-pickle treated magnesium alloys, exposed 5 years at Washington (left column) and Coeo Solo, from which the protective paint was removed after exposure. The small amount of corrosion product indicates the comparative absence of attack on all except the AZM panel at Coeo Solo.  $\times 1$ .



At Coco Solo, corrosion of serious proportions occurred on only one of the alloys (AM240), upon which approximately 35 percent of the total surface area was affected. On none of the others was more than 3

percent (AM7.4 and AM240) were comparatively susceptible to attack, the more so with the higher aluminum contents. Much more resistant to attack were the tin-containing alloys (AM764, AM61S, and XAM65S),

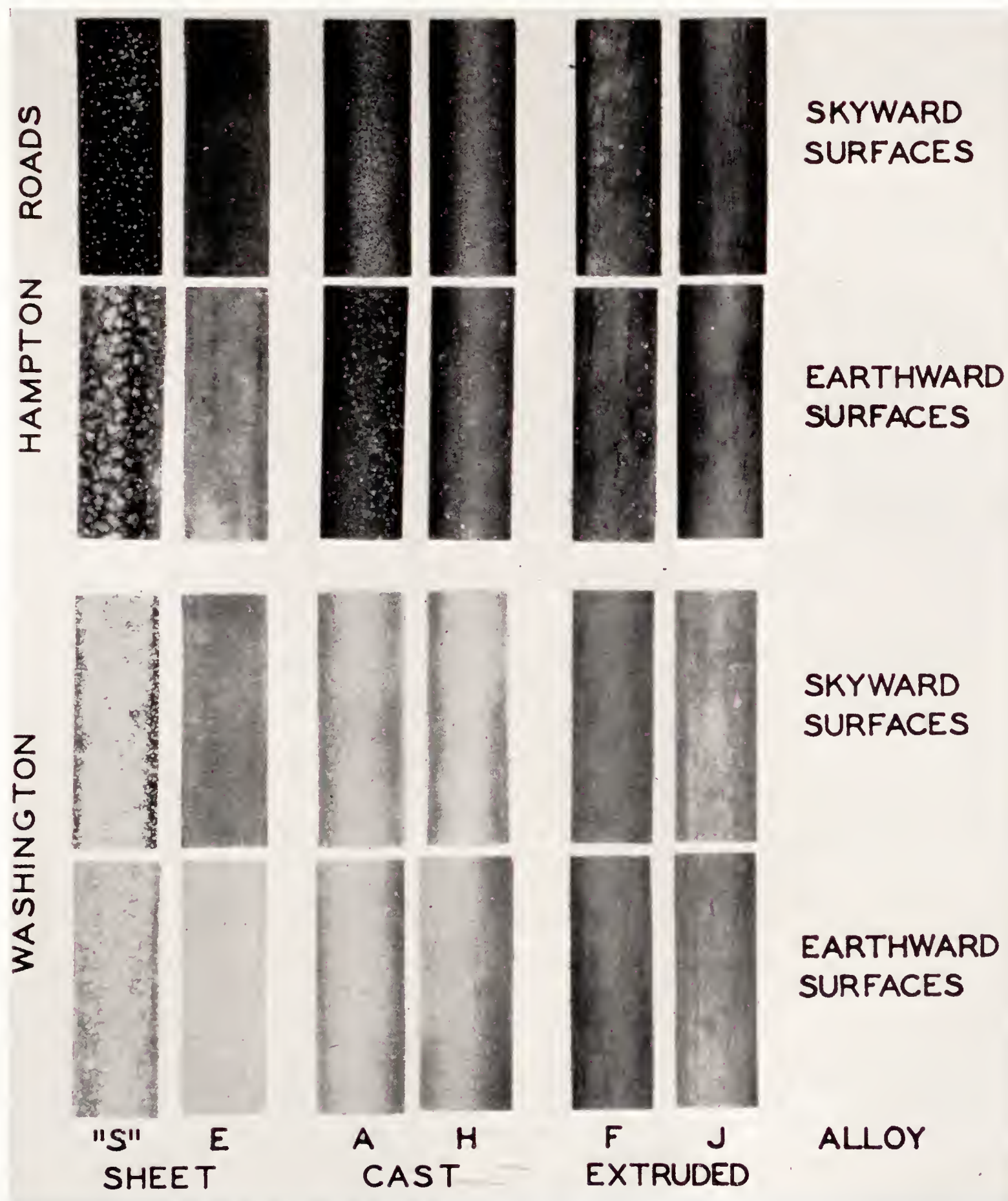


FIGURE 13.—Typical surface appearance of chrome-pickle treated Dowmetal materials after 1 year's exposure at Washington and Hampton Roads. Note the uniformly heavy deposition of corrosion products on S and the absence of the same on alloys H and J.  $\times 1$ .

percent of the surface affected. The severity of the attack was approximately as follows: Alloys AM7.4 and AZM, 3 percent; alloys AM764 and AM61S, less than 2 percent; and alloys XAM65S and AM3S, about 0.2 percent. It is apparent from the data that alloys of magnesium containing between 6 and 10 percent alumi-

num (AM7.4 and AM240) were comparatively susceptible to attack, the more so with the higher aluminum contents. Much more resistant to attack were the tin-containing alloys (AM764, AM61S, and XAM65S),

while the aluminum-manganese alloy AM3S was the most resistant. Another series of exposure tests was begun on a group of selected Dowmetal materials at both Washington and Hampton Roads. At Washington one rack, containing three specimens of each material, remains



to be removed, pending the completion of a 5-year exposure period. At Hampton Roads an identical rack was removed after a year's exposure and shortly thereafter the remaining specimens were lost in a hurricane. Information of some value was obtained, however, and its inclusion here is warranted. The materials used are listed in table XII. Alloys S and E were exposed in the form of sheet, cut into tensile bars having a half-inch reduced section, while alloys H, F, J, and A were exposed as standard A. S. T. M. half-inch round tensile bars.

The samples were prepared by the Dow Chemical Co. Specimens were given the chrome-pickle treatment previously described, and were exposed (1) with no additional coating, (2) coated according to paint schedule A, and (3) coated according to paint schedule B. Paint schedule A consisted of one coat of Brooklyn Varnish Co. P-15 primer, one coat Dux Surfacers No. 2304, and two coats of Brooklyn Varnish Co. Bakelite Varnish 74 plus 2 pounds of aluminum pigment per gallon. Schedule B included coats of the aforementioned primer and surfacer, each baked one hour at 225° F., and two coats of Dulux Black Baking Enamel No. 94005, each baked one hour at 200° F.

Specimens so protected showed no evidence of paint failure at the expiration of the 1-year exposure period at Hampton Roads and, except for a slight yellowish discoloration on the aluminum-pigmented finish and a pronounced dulling of the black enamel, are still in fairly good condition as they near the end of their fourth year at Washington.

Figure 13 shows selected portions of the surface of unpainted samples after 1 year's exposure at each locality. Representative cross sections picturing the extent of corrosion on the materials exposed at Hampton Roads are shown in figures 14 and 15; the results of the tensile tests and microscopic examination are given in table XIV.

The results confirm those obtained in the other series of tests on magnesium-alloy panels, in that the magnesium-aluminum alloys, namely, F, E, and A, were definitely inferior in corrosion resistance to alloys H and J, which were essentially magnesium-aluminum-zinc alloys. The corrosion resistance decreased as the aluminum content of the materials increased. The magnesium-cadmium-zinc alloy S was decidedly the most corrosion-susceptible of the lot, which indicates that the substitution of cadmium for aluminum is not to be recommended in alloys of this type.

### CONCLUSIONS

Weather-exposure tests of the kind undertaken in the present investigation require a period of years for the accumulation of data. Inasmuch as they simulate actual service conditions more closely than is practicable by any other means, however, the results of such tests should be especially useful in the selection

of corrosion resistant materials and coatings for use in aircraft, particularly the ones likely to be used at or near marine localities. The correlation of results of the weathering tests with those obtained in laboratory tests, such as by the salt-spray method used in this investigation, yields valuable data concerning the extent to which laboratory corrosion tests are indicative of the probable behavior of materials in service. From the results of the systematic program of the present investigation, which embraced tensile, macrographic, and microscopic tests on approximately 7,000 samples, the following outstanding conclusions may be drawn regarding the corrosion behavior of light alloy sheet materials for use in aircraft.

#### DURABILITY OF VARIOUS ALUMINUM ALLOYS

1. Aluminum-rich alloys containing 1.25 or 3.5 percent magnesium and 0.25 percent chromium were exceedingly resistant to corrosive attack in saline atmospheres. Where their somewhat lower tensile strength is of relatively minor importance, the use of these alloys, commercially designated as X52S and XB52S, can be strongly recommended. No loss in tensile properties had occurred on these materials at the end of the maximum exposure periods, and corrosion was confined to very small isolated pitted areas less than 0.002 inch in depth.

2. The aluminum-rich sheet alloy containing 6 percent magnesium (56S) proved very resistant to attack for periods approximating three years at the marine localities. Thereafter, severe intercrystalline attack developed, accompanied by rapid loss in tensile properties. Rivets made from this material exhibited very severe intercrystalline attack after the second year.

3. Aluminum-rich alloys with no copper, but containing small amounts of magnesium and added manganese, silicon, or cadmium (4S, 51S, XA51S, and Inalium alloys) were definitely much superior in corrosion resistance, under saline conditions, to materials that contained copper as a chief alloying constituent. The 4S and Inalium materials showed an absence of the intercrystalline attack present in the 51S alloys.

4. The corrosion resistance of the aluminum-magnesium-silicon alloy (51SW) when aged at room temperature was somewhat better than it was when aged at elevated temperature (51ST or XA51ST); whereas XA51ST, in turn, proved better than 51ST. Additional protective coatings are advisable, however, if these alloys are to be exposed to severe conditions.

5. The high-strength copper-bearing alloys of the duralumin type (Nicalumin, Aeral, 17ST, 17SRT, 24ST, and 24SRT) were shown to be appreciably inferior in corrosion resistance to the non-copper-containing materials. Even though these alloys are properly heat treated, the application of additional surface protective coatings is strongly recommended. For all practical purposes, the corrosion behavior of these materials



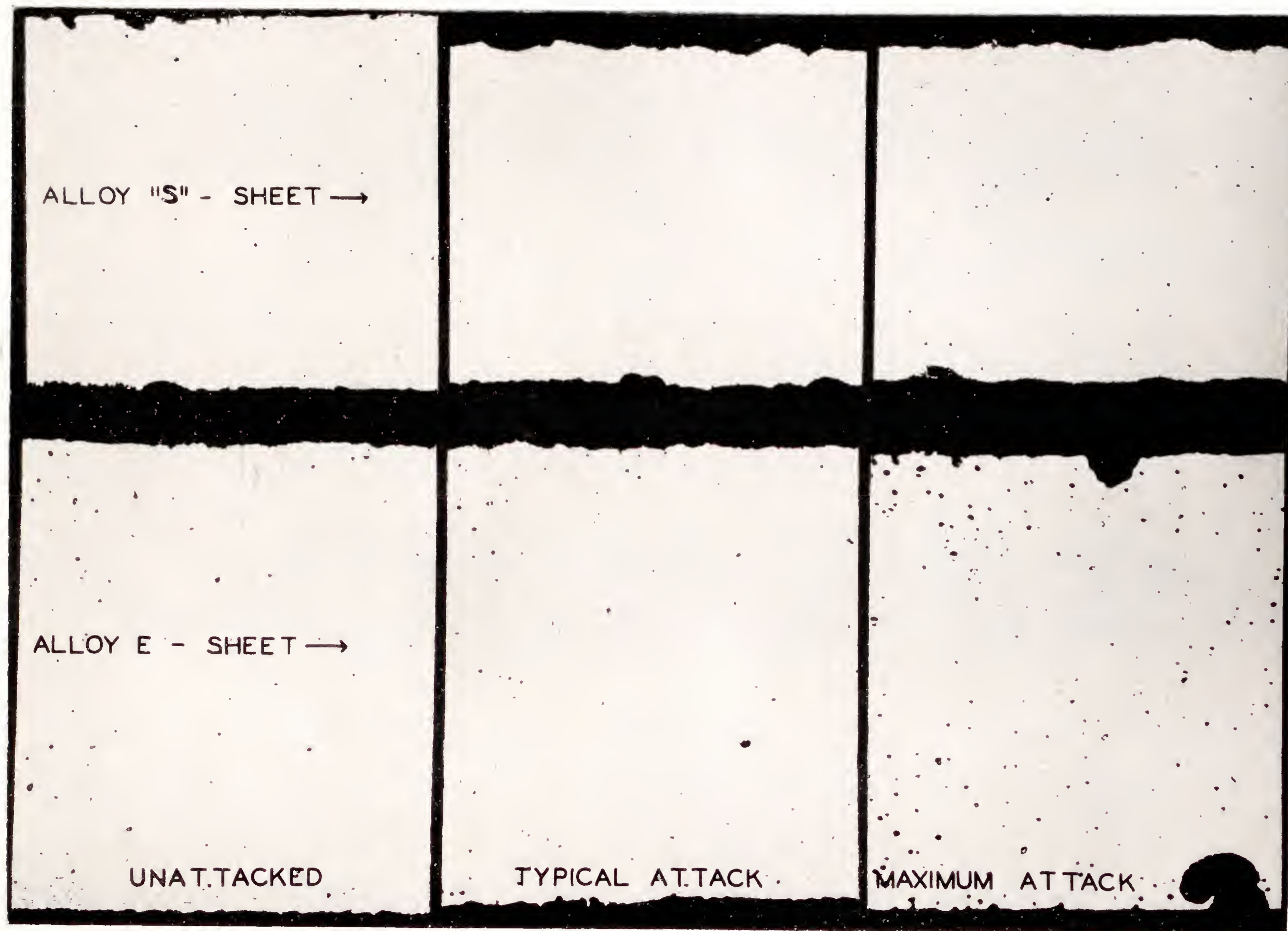


FIGURE 14.—Representative cross sections showing corrosion on Duralumin sheet materials given the chrome-pickle surface treatment. The unattacked specimens were stored 1 year in sealed containers, and the others were exposed 1 year at Hampton Roads. The upper edges are the skyward surfaces. Note the absence of localized attack on alloy S, on which the uniform attack resulted in reducing the thickness.  $\times 50$ .



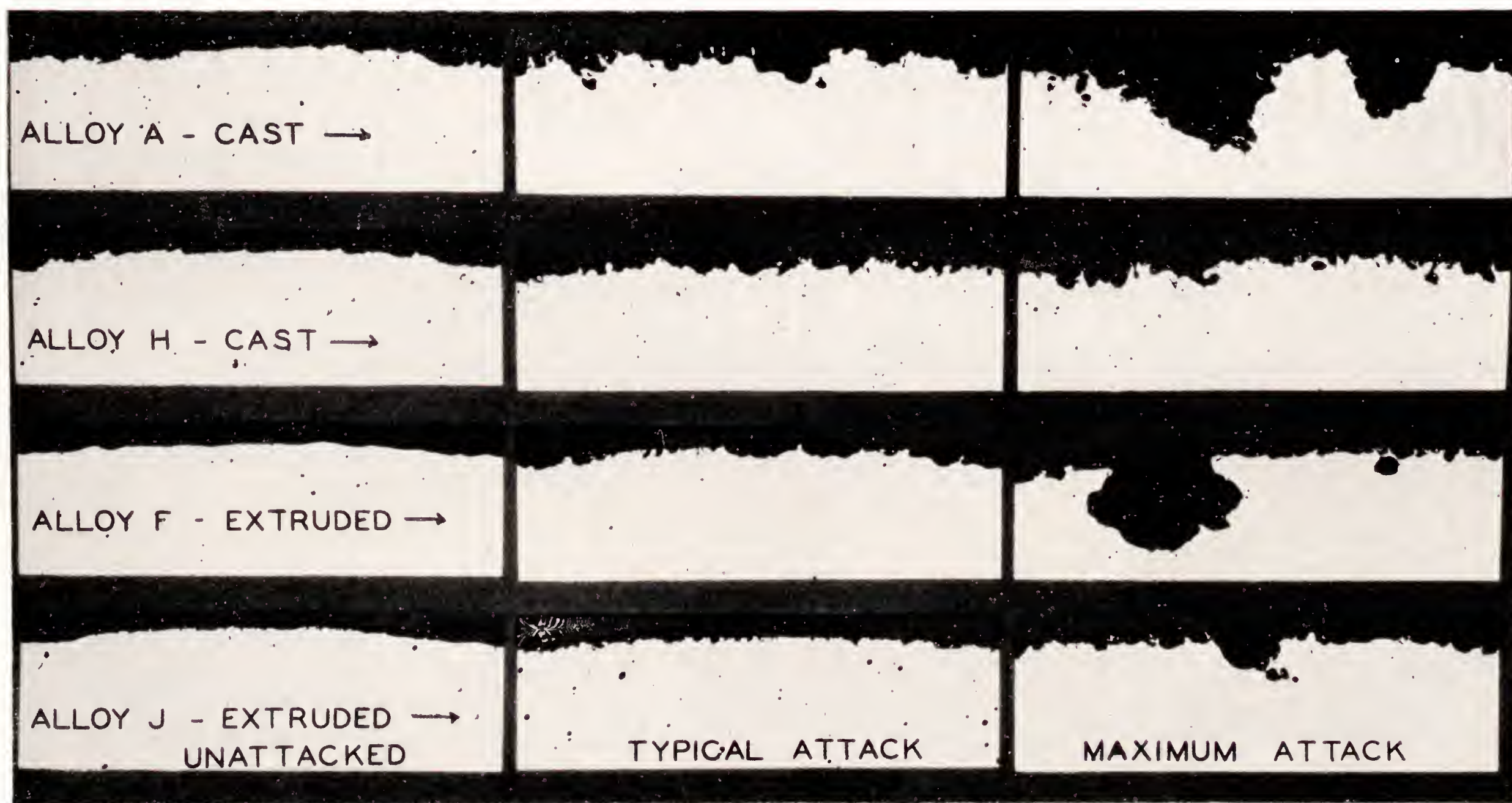


FIGURE 15.—Representative cross sections showing corrosion on Dowmetal tensile bars 0.5 inch diameter exposed at Hampton Roads for 1 year. The specimens were all given the chrome-pickle surface treatment. Those designated "unattacked" were given additional paint protection. Note the superiority of alloys H and J, and the areas of localized attack on alloys A and F.  $\times 50$ .



may be regarded as similar. Under inland conditions of exposure, no appreciable loss in tensile properties occurred in 5 years and pitting attack penetrated less than 0.005 inch.

6. The Aeral and Inalium alloys, containing 2 percent of cadmium, appeared relatively unsatisfactory from considerations of surface finish. Approximately 5 percent of the samples contained internal flaws, which in some instances markedly lowered the tensile properties.

7. Alloy 25SW was the most susceptible to corrosion of the commercially available sheet materials investigated. Its behavior was quite similar to that of duralumin (17S) improperly heat treated by quenching in boiling water.

8. In general, corrosion at the cut edges, on the various materials exposed as tensile bars, was similar in depth and extent to that present on the sides of the sheet and the tensile properties were not lowered appreciably. The copper-bearing alloys (17ST, 17SRT, and 24SRT) were characterized by the presence of relatively thin longitudinal layers more prone to attack than adjacent metal. Along these layers, corrosion penetrated very much more rapidly and deeply than on the sides. This preferential attack occurred only under saline exposures and caused an appreciable lowering of the tensile properties. It was not noted with the Alclad materials.

9. Aluminum-coated (Alclad) products, containing high-strength cores of 17S or 24S alloys, proved exceptionally resistant to attack. No consistent loss in tensile properties was found at the end of the tests at any of the locations and corrosion had not penetrated the alloying zone.

#### HEAT TREATMENT OF ALUMINUM ALLOYS

1. The recommended heat-treatment procedure for sheet duralumin (17S alloy) entails solution-heat-treatment from 15 to 30 minutes at 505° C., followed by quenching quickly in cold water and aging at room temperature. Minor delays in the quenching operation, for intervals of from 5 to 30 seconds between the withdrawal of specimens from the furnace and their immersion in the quenchant, resulted in no appreciable differences in corrosion behavior, and neither did variations in the solution-heat-treatment temperature, between 475° and 545° C. Samples treated at the lower temperature, however, possessed somewhat lower initial properties. It is therefore advisable to follow strictly the recommended procedure in heat treatment.

2. Baking of properly quenched-and-aged duralumin at temperatures in excess of 100° C. rendered the material exceptionally susceptible to intercrystalline attack.

#### JOINING OF ALUMINUM ALLOYS

Spot welding appears to offer considerable promise as a method of joining Alclad, X52S, and 4S materials. The strengths of such joints were consistently much

higher than those formed with similarly spaced aluminum-alloy rivets; but the range in breaking loads was appreciably greater, indicating a need for more precise control of welding operations. Although localized corrosive attack occurred on the welds, penetration was insufficient to result in pronounced lowering of the breaking loads at the end of the exposure tests.

#### SURFACE TREATMENT OF ALUMINUM ALLOYS

1. Surface oxide coatings, when used alone, proved inadequate to protect duralumin over prolonged exposure to saline conditions. Coatings formed by various immersion methods, such as the McCulloch, Deoxidine, Jirotko, and Alcoa Dip processes, were decidedly inferior from protective considerations to coatings formed by anodic treatment in chromic-acid or sulphuric-acid electrolytes.

2. Although unsealed anodic coatings applied by the Bengough or by the 10-percent chromic-acid processes afforded somewhat better protection than the Alcoa electrolytic No. 1 process, these coatings may, for all practical purposes, be considered essentially similar in behavior.

3. Anodized coatings sealed with chromic-acid electrolytes or with chromates rendered properly heat-treated duralumin very resistant to corrosive attack under severe saline conditions.

4. Good grades of aluminum-pigmented spar varnish coatings, applied to duralumin surfaces given no previous oxide treatment, afforded better protection than unpainted and unsealed oxide surface coatings.

5. Similar paints, applied to surfaces oxidized by immersion methods, afforded good protection for 5 years at Washington but failed during the second year at the marine localities. When the paints were applied to anodically treated surfaces, no loss in tensile properties occurred at the marine localities until after the third year.

6. Optimum protection of duralumin may be expected when good grades of aluminum-pigmented marine spar varnishes are applied to anodically treated surfaces that have been sealed with chromium trioxide or chromates.

7. The tests indicated that increased protection with the paint coatings was due to the aluminum pigment. The results obtained with pigments consisting of zinc dust, zinc oxide, zinc chromate, iron oxide, titanium oxide, or mixtures thereof were very much inferior. The results with unpigmented varnishes were, in general, unsatisfactory.

8. Zinc chromate-zinc oxide primers, generally highly regarded because of the inhibitive effect of the chromate ions, afforded no better protection on anodized material than aluminum-pigmented primers and, owing to their lower flexibility, may be disadvantageous on flexed or vibrated aircraft parts.

9. Aluminum-pigmented varnishes, irrespective of whether the vehicle was of the long oil, glyceryl phthalate, vinyl resin, or phenol formaldehyde type, all



afforded adequate protection when applied to anodized surfaces. The occasional variations in quality between different lots of any one of these varnishes are greater than can be attributed to the different vehicles. It is therefore desirable to develop specifications that will assure the required properties.

#### DURABILITY OF VARIOUS MAGNESIUM ALLOYS

1. Magnesium-alloy sheets containing 1 percent of zinc and 3 percent of cadmium proved very susceptible to attack.

2. Magnesium alloys of essentially the binary type, containing from 4 to 10 percent of aluminum (Dowmetals F, E, A, and G, AM7.4 and AM240) were increasingly susceptible to corrosive attack in the order of their higher aluminum contents. Binary alloys containing more than 7 percent of aluminum are not suited for exposed structures under severe saline conditions, even though protected by surface treatment and painting.

3. The addition of zinc to magnesium-aluminum alloys tends to render them definitely more resistant to attack. Cast alloys containing approximately 3 percent of zinc and 6.5 percent of aluminum (Dowmetal H), if given adequate protection, should prove satisfactory for use in nonsaline atmospheres. Somewhat less resistant were alloys AZM and Dowmetal J, which contained approximately 6 to 7 percent of aluminum and 1 percent of zinc.

4. Magnesium alloys containing additions of tin, such as AM764, AM61S, and XAM65S, and especially the last two, exhibited better corrosion resistance than the binary magnesium-aluminum alloys. These alloys and the magnesium-manganese alloy AM3S, proved definitely superior to the others in the weathering tests.

#### SURFACE TREATMENT OF MAGNESIUM ALLOYS

1. Surface treatment by the phosphoric-acid process yielded somewhat better adherence of paint on the magnesium alloys than did the chrome-pickle process but, for all practical purposes, either method is suitable.

2. Aluminum-pigmented paint, used in conjunction with the foregoing surface treatments, adequately protected the more corrosion-resistant magnesium alloys for a period of 5 years at Coco Solo. These alloys, so protected, may therefore be expected to prove satisfactory for use in saline atmospheres provided that they are not subjected to frequent thorough wettings.

NATIONAL BUREAU OF STANDARDS,  
WASHINGTON, D. C., December 2, 1938.

#### REFERENCES

1. Rawdon, Henry S.: Corrosion Embrittlement of Duralumin. I—Practical Aspects of the Problem. T. N. No. 282, N. A. C. A., 1928.

2. Rawdon, Henry S.: Corrosion Embrittlement of Duralumin. II—Accelerated Corrosion Tests and the Behavior of High-Strength Aluminum Alloys of Different Compositions. T. N. No. 283, N. A. C. A., 1928.
3. Rawdon, Henry S.: Corrosion Embrittlement of Duralumin. III—Effect of the Previous Treatment of Sheet Material on the Susceptibility to This Type of Corrosion. T. N. No. 284, N. A. C. A., 1928.
4. Rawdon, Henry S.: Corrosion Embrittlement of Duralumin. IV—The Use of Protective Coatings. T. N. No. 285, N. A. C. A., 1928.
5. Rawdon, Henry S.: Corrosion Embrittlement of Duralumin. V—Results of Weather-Exposure Tests. T. N. No. 304, N. A. C. A., 1929.
6. Rawdon, Henry S.: Corrosion Embrittlement of Duralumin. VI—The Effect of Corrosion, Accompanied by Stress, on the Tensile Properties of Sheet Duralumin. T. N. No. 305, N. A. C. A., 1929.
7. Buzzard, R. W., and Mutchler, W. H.: Advantages of Oxide Films as Bases for Aluminum Pigmented Surface Coatings for Aluminum Alloys. T. N. No. 400, N. A. C. A., 1931.
8. Mutchler, W. H.: Surface Coatings for Aluminum Alloys. Metals and Alloys, vol. 2, No. 6, December 1931, pp. 324-330.
9. Mutchler, Willard: The Weathering of Aluminum Alloy Sheet Materials Used in Aircraft. T. R. No. 490, N. A. C. A., 1934.
10. Naval Aircraft Factory: Process Specifications for Salt Spray Corrosion Test (Aircraft). No. PS-1, April 25, 1933.
11. Mutchler, W. H., Buzzard, R. W., and Strausser, P. W. C.: Salt Spray Test. National Bureau of Standards Letter Circular No. 530, July 1, 1938.
12. Mutchler, W. H., and Willier, H. O.: A Note on Rapid Photomicrography. Trans. American Soc. for Metals, vol. 26, No. 1, March 1938, pp. 279-288.
13. Bureau of Aeronautics, Navy Department: General Instructions for Protective Treatment of Aluminum and Aluminum Alloy by Anodic Oxidation Process. Specification SR-19a, Aug. 16, 1932.
14. Edwards, J. D.: Aluminum Paint and Powder. Second Edition, Reinhold Publishing Corporation, 1936.

TABLE I.—CHEMICAL COMPOSITION OF ALUMINUM-ALLOY SHEET MATERIALS

Designation of material <sup>a</sup>	Chemical composition (percent)							Other elements
	Al <sup>b</sup>	Cu	Mg	Mn	Fe	Si	Cr	
X52S -1/2H	97.98	0.02	1.24	0.00	0.37	0.20	0.19	
XB52S-50 percent red.	95.79	.02	3.57	0.00	.23	.14	.25	
Alclad 17ST <sup>c</sup>	93.75	4.10	.59	.58	.48	.50	—	
Alclad 24ST <sup>c</sup>	93.44	4.17	1.59	.57	.14	.09	—	
Alclad 24SRT <sup>c</sup>	93.44	4.17	1.59	.57	.14	.09	—	
4S-1/2H	97.32	.10	.89	1.04	.43	.22	—	
56S-1/2H	93.73	.05	6.01	0.00	.13	.08	—	
Inalium <sup>d</sup>	96.50	—	.80	—	.25	.45	—	Cd 2.0.
51SW <sup>e</sup>	97.95	.05	.61	.01	.38	1.00	—	
51ST <sup>e</sup>	97.95	.05	.61	.01	.38	1.00	—	
XA51ST	97.61	.05	.51	.01	.52	1.08	.22	
Nieralumin D4018	96.52	.45	.48	.19	.42	.30	.20	Ni 1.01; Mo 0.17; Zn 0.18; W 0.08.
Aeral <sup>d</sup>	92.55	3.75	.80	.25	.25	.40	—	Cd 2.0.
17ST	94.02	3.94	.56	.57	.47	.44	—	
17SH <sup>f</sup>	93.73	4.20	.58	.62	.40	.47	—	
17SH <sup>f</sup>	94.17	3.76	.55	.53	.48	.51	—	
17SRT	94.45	4.17	.53	.58	.16	.11	—	
24SRT	93.44	4.17	1.59	.57	.14	.09	—	
25SW <sup>f</sup>	93.67	4.20	—	.68	.45	.90	—	
4S rivets	97.21	.08	1.05	1.11	.41	.14	—	
X56S rivets	93.72	0.00	6.12	0.00	.11	.05	—	

<sup>a</sup> Analyses by the cooperating manufacturer, the Aluminum Co. of America unless otherwise indicated. The letter symbols indicate: S, sheet; W, heated and quenched; T, heated, quenched, and aged; R, heated, quenched, aged, and cold-rolled; H, hard worked.

<sup>b</sup> By difference.

<sup>c</sup> Analysis of the core. Material coated with 99.75 percent aluminum.

<sup>d</sup> Nominal composition furnished by manufacturer, the Société des Brevets Berthelmy de Montby.

<sup>e</sup> Analyzed at National Bureau of Standards. Material was also used in previous series of exposure tests.

<sup>f</sup> Material subsequently heat treated at the National Bureau of Standards and used for the application of protective surface coatings, etc.



TABLE II.—PHYSICAL PROPERTIES AND DEPTH OF PENETRATION OF CORROSIVE ATTACK ON UNCOATED ALUMINUM-ALLOY SHEET MATERIALS BEFORE AND AFTER THEIR MAXIMUM PERIOD OF EXPOSURE AT EACH LOCALITY

Material	Tensile properties										Maximum depth of penetration <sup>a</sup>			
	Ultimate tensile strength					Elongation in 2 inches					Wash- ington <sup>c</sup>	Coco Solo <sup>c</sup>	Hamp- ton Roads <sup>d</sup>	Salt spray <sup>e</sup>
	Uncor- roded <sup>b</sup>	Wash- ington <sup>c</sup>	Coco Solo <sup>c</sup>	Hamp- ton Roads <sup>d</sup>	Salt spray <sup>e</sup>	Uncor- roded <sup>b</sup>	Wash- ington <sup>c</sup>	Coco Solo <sup>c</sup>	Hamp- ton Roads <sup>d</sup>	Salt spray <sup>e</sup>				
	<i>Lb./sq. in.</i>	<i>Lb./sq. in.</i>	<i>Lb./sq. in.</i>	<i>Lb./sq. in.</i>	<i>Lb./sq. in.</i>	<i>Percent</i>	<i>Percent</i>	<i>Percent</i>	<i>Percent</i>	<i>Percent</i>	<i>Thou- sandths inch</i>	<i>Thou- sandths inch</i>	<i>Thou- sandths inch</i>	<i>Thou- sandths inch</i>
X52S-1/2H.....	26,100	26,000	26,000	26,200	26,500	8.1	7.8	8.5	8.2	8.3	2	1	2	2
XB52S-50 percent red.....	48,500	47,850	47,200	48,200	48,100	7.5	8.5	8.0	6.9	7.5	2	2	3	2
Alclad 17ST.....	58,300	59,300	59,000	59,000	59,300	20.3	20.0	20.0	19.5	18.9	2	3	3	3
Alclad 24ST.....	64,900	65,000	65,100	64,600	64,750	19.6	19.3	19.3	17.8	16.2	2	3	3	3
Alclad 24SRT.....	65,400	66,200	66,200	65,850	65,600	14.5	15.5	14.3	13.5	13.0	3	3	3	3
4S-1/2H.....	33,700	34,000	34,450	33,550	33,200	5.6	5.5	6.0	5.0	4.0	2	2	4	2
56S-1/2H.....	54,900	53,500	44,650	54,900	44,150	12.0	12.3	5.5	11.4	3.0	4	12	4	7
Inalium CR.....	31,400	31,900	32,600	31,300	32,500	5.4	6.5	7.0	5.5	5.3	4	5	6	8
Inalium HT.....	41,400	42,300	41,600	41,900	41,800	15.5	16.5	15.0	15.2	11.1	3	4	7	14
51SW.....	40,700	40,500	41,700	40,300	39,000	24.9	20.5	25.0	18.5	12.0	4	4	9	7
XA51ST.....	47,100	48,100	45,850	45,850	45,850	13.6	11.3	12.5	8.2	6.8	10	8	9	7
51ST.....	49,300	49,100	48,700	45,500	45,300	12.6	8.2	7.5	4.3	3.2	5	9	10	10
Nicalumin D 4018.....	45,800	45,700	45,350	43,900	44,500	8.4	8.3	8.0	5.8	5.0	6	7	7	8
Aeral HT.....	56,800	56,000	54,500	54,500	34,400	21.4	22.0	22.0	16.2	4.1	4	5	7	20
Aeral CR.....	57,850	57,900	58,200	55,750	38,600	22.0	22.0	19.5	14.5	4.8	4	5	8	24
17ST.....	64,100	64,400	65,100	63,300	38,600	20.5	19.5	19.3	14.3	3.0	4	6	7	28
17SRT.....	64,000	64,000	63,750	62,600	38,400	16.3	15.8	16.3	13.1	2.0	5	7	8	27
24SRT.....	70,100	70,000	68,400	67,500	47,200	15.4	14.0	12.0	9.1	1.5	6	7	7	22
25SW.....	54,900	53,200	52,050	40,000	28,700	18.7	14.2	12.0	3.0	1.0	5	10	15	31

<sup>a</sup> Measured from the earthward surface of weather-exposure specimens, on which the depth was usually greater than on the skyward surface.  
<sup>b</sup> Average of 6 initial specimens, and 10 from sealed containers.  
<sup>c</sup> Exposed 5 years.  
<sup>d</sup> Exposed 4 years.  
<sup>e</sup> The Alclad, 52S, 4S, Inalium, and 56S materials were exposed 18 months in the salt spray. All of the other alloys were exposed 6 months.

TABLE III.—PERCENTAGE LOSS IN TENSILE PROPERTIES AND PERCENTAGE PENETRATION OF CORROSIVE ATTACK ON UNCOATED ALUMINUM-ALLOY SHEET MATERIALS EXPOSED AS INDICATED

Material	Percentage loss in tensile properties										Percentage of thickness penetrated <sup>a</sup>			
	Ultimate tensile strength					Percentage loss in elongation					Wash- ington <sup>c</sup>	Coco Solo <sup>c</sup>	Hamp- ton Roads <sup>d</sup>	Salt spray <sup>e</sup>
	Uncor- roded <sup>b</sup>	Wash- ington <sup>c</sup>	Coco Solo <sup>c</sup>	Hamp- ton Roads <sup>d</sup>	Salt spray <sup>e</sup>	Uncor- roded <sup>b</sup>	Wash- ington <sup>c</sup>	Coco Solo <sup>c</sup>	Hamp- ton Roads <sup>d</sup>	Salt spray <sup>e</sup>				
	<i>Lb./sq. in.</i>					<i>Percent</i>								
X52S-1/2H.....	26,100	0	0	0	0	8.1	0	0	0	0	6	3	6	6
XB52S-50 percent red.....	48,500	0	0	0	0	7.5	0	0	0	0	6	6	9	6
Alclad 17ST.....	58,300	0	0	0	0	20.3	0	0	0	3	6	9	9	9
Alclad 24ST.....	64,900	0	0	0	0	19.6	0	0	6	12	6	9	9	9
Alclad 24SRT.....	65,400	0	0	0	0	14.5	0	0	4	7	9	9	9	9
4S-1/2H.....	33,700	0	0	0	2	5.6	0	0	9	20	6	6	12	6
56S-1/2H.....	54,900	2	19	0	19	12.0	0	54	5	75	12	37	12	22
Inalium CR.....	31,400	0	0	0	0	5.4	0	0	0	0	12	16	19	25
Inalium HT.....	41,400	0	0	0	0	15.5	0	5	0	17	9	12	22	44
51SW.....	40,700	0	0	0	3	24.9	13	10	23	49	12	12	28	22
XA51ST.....	47,100	0	1	1	1	13.6	13	18	33	44	31	25	28	22
51ST.....	49,300	1	1	7	8	12.6	34	48	66	74	16	28	31	31
Nicalumin D 4018.....	45,800	0	0	3	3	8.4	0	15	33	40	19	22	22	25
Aeral HT.....	56,800	0	4	2	49	21.4	0	0	23	81	12	16	22	62
Aeral CR.....	57,850	0	0	2	33	22.0	0	10	28	77	12	16	25	75
17ST.....	64,100	0	0	0	39	20.5	3	7	28	85	12	19	22	87
17SRT.....	64,000	0	1	1	39	16.3	0	7	20	88	16	21	25	84
24SRT.....	70,100	0	2	3	30	15.4	2	18	37	90	19	21	22	69
25SW.....	54,900	3	5	30	48	18.7	24	50	84	95	16	31	47	97

<sup>a</sup> Computed on the basis of the thickness of half a sheet, namely, 0.032 inch.  
<sup>b</sup> Average values of 6 initial specimens, and 10 from sealed containers.  
<sup>c</sup> Exposed 5 years.  
<sup>d</sup> Exposed 4 years.  
<sup>e</sup> The Alclad, 52S, 4S, Inalium, and 56S materials were exposed 18 months in the salt spray. All of the other alloys were exposed 6 months.



TABLE IV.—DIFFERENCES IN TENSILE PROPERTIES ON ALUMINUM-ALLOY SHEET MATERIALS EXPOSED TO THE 20 PERCENT SALT-SPRAY TEST AS STRIPS (TENSILE BARS MACHINED AFTER CORROSION) AND AS TENSILE BARS

Material	Exposure period	Ultimate tensile strength		Elongation in 2 inches	
		Strip	Tensile bar	Strip	Tensile bar
		Lb./sq. in.	Lb./sq. in.	Percent	Percent
17ST	Months				
	1/4	62,500	61,800	20.0	19.0
	1/2	62,500	62,200	17.5	16.0
	1	63,500	60,900	16.5	14.5
	2	59,600	53,200	10.5	6.5
	4	49,300	46,700	6.0	5.0
17SRT	6	40,200	37,100	3.0	3.0
	1/4	62,200	64,300	16.5	18.0
	1/2	61,200	63,400	15.0	15.0
	1	61,200	57,800	12.0	7.5
	2	53,100	51,600	5.5	4.0
	4	45,300	46,600	2.5	3.5
24SRT	6	40,600	36,200	2.0	2.0
	1/4	67,800	68,800	16.0	15.5
	1/2	67,200	67,500	12.0	13.0
	1	66,000	66,600	8.0	10.0
	2	64,000	60,300	7.5	4.0
	4	60,900	52,500	4.0	2.0
	6	48,800	45,600	1.6	1.5

TABLE V.—BREAKING LOADS OF SPOT-WELDED AND RIVETED SAMPLES BEFORE AND AFTER WEATHER-EXPOSURE TESTS. THE PANELS WERE 1 INCH WIDE. (Cf. fig. 1c)

Material	Joined by—	Breaking load					
		Uneorroded			Washing-ton 5 years <sup>b</sup>	Coco Solo 5 years <sup>b</sup>	Ham-ton Roads 4 years <sup>b</sup>
		Maxi-mum	Aver-age <sup>a</sup>	Mini-mum			
		Lb.	Lb.	Lb.	Lb.	Lb.	Lb.
Alclad 24SRT	Spot-welds <sup>c</sup>	2,550	2,190	1,800	2,270	2,040	2,150
Alclad 17ST	Spot-welds <sup>c</sup>	2,460	2,090	1,650	1,970	2,010	1,880
4S-1/2H	Spot-welds <sup>d</sup>	2,110	1,990	1,900	2,000	2,020	2,000
X52S-1/2H	Spot-welds <sup>d</sup>	1,640	1,570	1,500	1,590	1,570	1,570
Alclad 17ST	17S rivets <sup>c</sup>	1,160	1,070	1,040	1,150	1,200	1,150
Alclad 17ST	X56S-1/4H rivets <sup>c</sup>	1,010	985	960	825	600	760
X52S-1/2H	4S-1/4H rivets <sup>c</sup>	565	540	510	570	550	575

<sup>a</sup> Average of 13 specimens tested initially or after being kept in sealed containers.  
<sup>b</sup> Average of 3 specimens.  
<sup>c</sup> The majority of specimens broke longitudinally, through the welds or rivets.  
<sup>d</sup> The majority of specimens broke in areas immediately adjacent to the welds.

TABLE VI.—PERCENTAGE LOSS IN TENSILE PROPERTIES AND PERCENTAGE PENETRATION OF CORROSIVE ATTACK ON UNCOATED 17S MATERIALS, HEAT TREATED AS INDICATED

Solution heat-treated for 30 minutes	Quenchant	Aged at room temperature before test	“Bak-ing” temperature	Percentage loss in tensile properties								Percentage of thickness penetrated <sup>a</sup>		
				Ultimate tensile strength				Elongation in 2 inches				Washing-ton 5 years	Hampton Roads 4 years	Salt spray 1/2 year
				Uneor-roded <sup>b</sup>	Washing-ton 5 years	Ham-pton Roads 4 years	Salt spray 1/2 year	Uneor-roded <sup>b</sup>	Washing-ton 5 years	Ham-pton Roads 4 years	Salt spray 1/2 year			
				Lb./sq. in.				Percent						
Temp. ° C.		Months	° C.											
505	Ice water	3		61,800	0	0	41	21.0	0	29	85	16	22	75
505	do. <sup>c</sup>	3		63,100	0	0	31	21.0	0	21	71	12	19	69
505	do. <sup>d</sup>	3		62,700	2	2	47	20.6	9	20	91	12	22	75
545+	do.	3		60,100	0	0	43	16.0	0	24	90	12	31	75
475	do.	3		57,300	0	2	36	18.9	11	17	73	16	25	72
505	do. <sup>e</sup>	1 1/2	38	61,600	0	2	52	20.3	7	27	90	12	22	69
505	do. <sup>e</sup>	1 1/2	93	62,500	0	4	41	20.3	4	26	83	31	19	69
505	do. <sup>e</sup>	1 1/2	149	62,100	8	100	97	20.5	48	100	100	44	100	100
505	Boiling water	3		61,900	3	58	63	21.2	49	86	96	25	100	87

<sup>a</sup> Computed on the basis of the thickness of half a sheet, namely, 0.032 inch.  
<sup>b</sup> Average value of 6 initial, and 10 sealed-container specimens.  
<sup>c</sup> Quench delayed 5 seconds after removal from furnace.  
<sup>d</sup> Quench delayed 30 seconds after removal from furnace.  
<sup>e</sup> Prior to baking. Aged 3 months after baking.



TABLE VII.—EFFECT OF WEATHERING ON THE ELONGATION OF 17S ALLOY GIVEN VARIOUS SURFACE OXIDE TREATMENTS. SPECIMENS WERE QUENCHED IN BOILING WATER, UNLESS OTHERWISE INDICATED

Surface oxide treatment	Exposure time and elongation in 2 inches <sup>a</sup>					
	Washington		Hampton Roads		Salt spray	
	Months	Percent	Months	Percent	Months	Percent
None	6	14.0	3	8.0	1	10.0
	60	10.5	48	3.0	2	9.0
					6	.8
None <sup>b</sup>	6	20.5	3	18.0	1	19.0
	60	19.5	48	14.5	2	17.5
					6	3.0
Deoxidine	6	14.5	3	10.5	1	8.5
Jirotka	6	14.5	3	10.5	1	7.5
McCulloch	6	13.5	3	10.5	1	9.0
Alcoa Dip <sup>b</sup>	60	20.0	48	17.5	2	13.0
Bengough "spout"	6	16.0	3	15.5	1	13.0
Chromic acid-dichromate	6	17.5	3	12.5		
Alcoa Electrolytic No. 1 <sup>b</sup>	60	20.0	48	15.0	2	13.0
Bengough	6	17.5	3	17.0	1	13.5
Bengough <sup>b</sup>	60	20.5	48	19.0	2	13.0
10 percent Chromic acid	6	17.5	3	17.0	1	19.0
10 percent Chromic acid <sup>b</sup>	60	20.5	48	19.0	2	15.0
Alcoa Electrolytic No. 2 (sealed) <sup>b</sup>	60	20.0	48	19.5	18	20.0
Bengough (sealed)	18	20.0	3	19.0	9	20.5
10 percent Chromic acid (sealed)	18	20.0	3	18.0	9	18.5
Alcoa Dip <sup>c</sup>	60	20.5	48	17.5	18	18.8
Alcoa Electrolytic No. 1 <sup>c</sup>	60	20.0	48	20.5	18	20.0
Alcoa Electrolytic No. 2 <sup>c</sup>	60	20.0	48	20.0	18	19.8
Bengough <sup>c</sup>	60	20.0				
Bengough <sup>d</sup>	60	20.0	24	20.0		

<sup>a</sup> Values on uncorroded specimens ranged between 19.0 and 22.0, and averaged 20.5 percent.

<sup>b</sup> Quenched in ice water after solution heat treatment.

<sup>c</sup> Coatings on Alclad 17ST material.

<sup>d</sup> Coatings on Alclad 17S material quenched in boiling water after solution heat treatment.

TABLE IX.—THE PAINT SCHEDULES USED AND THE SPECIFICATIONS TO WHICH THE PRODUCTS CONFORMED

Schedule	Number of coats	Vehicle		Pigment	
		Type and trade name	Navy specification	Type	Navy specification
1	3	Glyceryl phthalate, Dulux RC-147.	V11	None	
2	3	Phenol formaldehyde, Thresher No. 440.	V10	None	
3	1	Phenol formaldehyde, Thresher No. 440.	V10	None. Covered with aluminum foil before varnish became dry.	47A5
4	3	Glyceryl phthalate, Dulux RC-165.	V11	Standard, Type A, aluminum powder. <sup>a</sup>	52A1
5	3	Vinyl resin, Vinylite N. <sup>b</sup>		Fine, Type B, aluminum powder. <sup>a</sup>	52A1
6	3	Phenol formaldehyde, Thresher No. 440.	V10	Fine, Type B, aluminum powder. <sup>a</sup>	52A1
7	1, 2	Primer as in 8. Finish coats as in 11.		Primer as in 8. Finish coats as in 11.	
8	3	Phenol formaldehyde <sup>c</sup>	V10	85 percent zinc chromate, 15 percent XX Process zinc oxide.	
9	3	Same as 8 <sup>d</sup>	V10	85 percent zinc dust, 15 percent XX Process zinc oxide.	52Z3
10	1	33-gallon varnish. Philadelphia Navy Yard Red oxide Primer No. 64.	P23	33 percent zinc chromate, 67 percent iron oxide.	P23
	2	Navy gray enamel, Dupont, Finish coats. <sup>e</sup>	M-67-B	48 percent titanium dioxide, 48 percent zinc oxide, 2 percent lamp-black.	M-67-B
11	3	Long oil, ester gum, Pratt & Lambert No. 10. <sup>f</sup>	52V15	Standard, type A, aluminum pigment. <sup>a</sup>	52A1

<sup>a</sup> Two pounds of pigment per gallon of vehicle.

<sup>b</sup> The vehicle contained (parts by weight): 500, 20 percent 1/2 sec. R. S. Nitrocellulose in solvent S-7; 189, 53 percent Vinylite N in toluol; 20, dibutyl phthalate; 40, ethyl acetate; 500, solvent S-7. Solvent S-7 contained (parts by volume): 60, toluol; 10, butanol; 10, ethyl acetate; 10, cellosolve; 10, cellosolve acetate.

<sup>c</sup> The varnish contained 100 pounds phenol formaldehyde XR-821 resin, 50 gallons tung oil, 6.4 pounds lead resinate, 1.75 pounds cobalt resinate, 48.5 gallons mineral spirits, and 18.5 gallons xylol. The product contained approximately 55 percent vehicle and 45 percent pigment.

<sup>d</sup> Same varnish as in (c), but the final product contained approximately 27.5 percent vehicle and 72.5 percent pigment.

<sup>e</sup> The varnish contained approximately 50 percent pigment.

<sup>f</sup> A 66-gallon varnish with tung and linseed oils, the former predominating. The resin was a mixture of rosin ester and rosin. It contained a nonvolatile of approximately 52 percent and passed a kauri reduction of approximately 70 percent.

TABLE VIII.—EFFECT OF WEATHERING ON THE ELONGATION AND MAXIMUM DEPTH OF PENETRATION OF CORROSIVE ATTACK ON 17S MATERIAL GIVEN VARIOUS SURFACE OXIDE TREATMENTS AND PAINTED WITH THREE COATS OF ALUMINUM PIGMENTED VARNISH <sup>a</sup>

Oxide surface treatment	Percentage elongation in 2 inches <sup>b</sup>				Percentage maximum depth of penetration			
	Washington 5 years	Coco Solo 5 years	Hampton Roads 4 years	Salt spray 1 1/2 years	Washington 5 years	Coco Solo 5 years	Hampton Roads 4 years	Salt spray 1 1/2 years
Deoxidine	19.8	13.0	16.0	5.2	2	2	2	62
Jirotka	21.0	12.0	16.0	7.9	2	3	3	47
McCulloch	19.8	16.0	17.5	14.1	2	2	2	32
Alcoa Dip <sup>c</sup>	20.2	20.5	19.5	18.5	2	3	2	2
Bengough "spout"	19.0	13.0	18.5	18.5	2	2	2	2
Chromic acid-dichromate	21.0	16.5	15.0		2	2	2	x
Alcoa Electrolytic No. 1 <sup>c</sup>	20.8	20.5	20.5	20.0	2	2	2	2
Bengough	20.0	20.0	20.2	17.7	2	12	2	2
Bengough <sup>c</sup>	20.2	20.5	19.2	20.6	2	2	2	2
10 percent chromic acid	19.0	20.5	17.5	20.4	2	2	2	2
Alcoa Electrolytic No. 2 <sup>c</sup>	20.5	20.5	21.5	18.2	2	2	2	2
Bengough (sealed)	19.2	19.5	15.5	18.0	2	2	2	2
10 percent chromic acid (sealed)	21.0	20.0	20.0	18.5	2	2	2	2
Alcoa Dip <sup>d</sup>	20.2	19.5	19.5	19.8	2	2	2	2
Alcoa Electrolytic No. 1 <sup>d</sup>	19.5	20.0	19.5	17.6	2	2	2	2
Alcoa Electrolytic No. 2 <sup>d</sup>	19.0	19.0	19.5	18.4	2	2	2	2
Bengough <sup>d</sup>	20.2	21.0	19.5		2	2	2	2
Bengough <sup>e</sup>	21.2	21.0	20.0		2	2	2	2

<sup>a</sup> The only marked losses in tensile strength occurred on Jirotka and McCulloch coated specimens exposed 1 1/2 years to the salt spray. The values dropped to 57,900 and 50,500 pounds per square inch, respectively.

<sup>b</sup> Values on uncorroded specimens ranged between 19.0 and 22.0, and averaged 20.5 percent.

<sup>c</sup> Quenched in ice water after solution heat treatment.

<sup>d</sup> Coatings on Alclad 17ST material.

<sup>e</sup> Coatings on Alclad 17S material, quenched in boiling water after solution heat treatment.

TABLE X.—EFFECT OF WEATHERING ON THE ELONGATION VALUES OF 17S MATERIAL, QUENCHED IN BOILING WATER, ON WHICH VARIOUS VARNISHES WERE APPLIED TO UNTREATED AND ANODICALLY TREATED SURFACES

Coating	Paint schedule	Percentage elongation in 2 inches <sup>a</sup>							
		Washington 5 years		Coco Solo 5 years		Hampton Roads 4 years		Salt spray	
		Untreated	Anodized	Untreated	Anodized	Untreated	Anodized	Untreated	Anodized
1	Clear Dulux RC-147	14.2	19.8	1.5	8.5	3.3	15.5	1.0	13.5
2 <sup>b</sup>	Clear Thresher Bakelite No. 440.		21.5		17.5		18.3		20.3
3 <sup>b</sup>	Clear Thresher Bakelite No. 440 with aluminum foil.		20.5		20.5		18.0		20.3
4	Dulux RC-165, aluminum pigment.	18.2	17.5	17.5	20.5	12.0	19.1	2.5	17.7
5	Vinylite N, aluminum pigment.	18.0	18.0	12.0	16.0	9.5	17.1	4.0	14.5
6	Thresher Bakelite No. 440, aluminum pigment.	14.2	20.0	12.5	19.0	15.5	20.0	4.0	17.3
7	Bakelite Varnish, aluminum pigment, on zinc chromate primer.	20.5	21.0	20.5	20.5	16.8	20.0		
8	Bakelite Varnish, zinc chromate pigment.	17.8	18.8	19.5	20.5	18.5	19.3		
11	Pratt & Lambert No. 10, aluminum pigment.	21.0	20.0	20.5	20.0	19.8	20.2	2.0	17.7
11 <sup>b</sup>	do	20.4	20.2	20.5	20.5	20.8	20.5	20.3	20.5
9	Bakelite Varnish, zinc dust pigment.	18.8	18.5	9.0	20.5	4.8	17.5	7.0	19.4
10	Navy Gray enamel on red oxide primer.	11.2	16.1	13.5	17.5	11.8	15.8	10.8	17.9
10 <sup>b</sup>	do	19.5	20.5	18.8	20.0	17.0	18.8	14.5	18.1

<sup>a</sup> Values of initial or uncorroded specimens ranged from 19.0 to 22.0, and averaged 20.5 percent.

<sup>b</sup> Applied to material quenched in ice water after solution heat treatment.



TABLE XI.—APPROXIMATE MONTH OF THE EXPOSURE PERIOD AT WHICH VISIBLE EVIDENCE OF PAINT FAILURES OCCURRED ON 17S MATERIAL, QUENCHED IN BOILING WATER

Coating	Paint schedule	Month failure was noted							
		Washington		Coco Solo		Hampton Roads		Salt spray	
		Untreated	Anodized	Untreated	Anodized	Untreated	Anodized	Untreated	Anodized
1	Clear Dulux RC-147	6	18	3	24	3	36	1	4
2 <sup>a</sup>	Clear Thresher Bakelite No. 440		48		24		36		18
3 <sup>a</sup>	Clear Thresher Bakelite No. 440 with aluminum foil.		<sup>b</sup> 18		<sup>b</sup> 3		<sup>b</sup> 3		<sup>b</sup> 1
4	Dulux RC-165, aluminum pigment.	48	60	<sup>c</sup> 24	48	12	36	4	18
5	Vinylite N, aluminum pigment.	<sup>c</sup> 48	( <sup>d</sup> )	<sup>c</sup> 48	48	<sup>c</sup> 24	48	2	8
6	Thresher Bakelite No. 440, aluminum pigment.	60	( <sup>d</sup> )	60	48	36	48	2	18
7	Bakelite Varnish, aluminum pigment on zinc chromate primer.	<sup>c</sup> 36	60	<sup>e</sup> 18	48	<sup>c</sup> 12	36		
8	Bakelite Varnish, zinc chromate pigment.	<sup>c</sup> 36	( <sup>d</sup> )	<sup>c</sup> 30	60	<sup>c</sup> 24	48		
9	Bakelite Varnish, zinc dust pigment.	6	<sup>e</sup> 12	3	<sup>e</sup> 3	3	<sup>e</sup> 3	1	18
10	Navy gray enamel on red oxide primer.	<sup>c</sup> 3	<sup>f</sup> 12	<sup>c</sup> 3	<sup>f</sup> 12	<sup>c</sup> 3	<sup>f</sup> 12	12	18
11	Pratt & Lambert No. 10, aluminum pigment.	( <sup>d</sup> )	( <sup>d</sup> )	48	48	36	48	4	18

<sup>a</sup> Applied only to material quenched in ice water after solution heat treatment.  
<sup>b</sup> Pinholes present on the aluminum foil.  
<sup>c</sup> Metal exposed to view.  
<sup>d</sup> Failure confined to faint yellow discoloration at end of test period.  
<sup>e</sup> Became white. No further evidence of failure occurred until after the 36th month.  
<sup>f</sup> Chalked, cracked, and alligatored.

TABLE XII.—THE MAGNESIUM ALLOYS AND THEIR CHEMICAL COMPOSITIONS

Material	Fabrication	Panel thickness	Chemical composition, percent <sup>a</sup>					
			Mg <sup>b</sup>	Al	Zn	Sn	Mn	Cd
AM240-T61	Cast	<i>In.</i> 0.28	90.71	9.16			0.13	
AM7.4-T4 <sup>c</sup>	Cast	.28	92.39	7.3			.31	
Dowmetal A	Sand cast, sand blasted	<sup>d</sup> .505	92.28	7.5			.22	
Dowmetal E	Sheet, wire brushed	<sup>d</sup> .067	93.76	5.9			.34	
Dowmetal F	Extruded, machined	<sup>d</sup> .505	95.37	4.37			.26	
AZM <sup>e</sup>	Hot pressed	.22	91.80	7.04	0.85		.31	
Dowmetal J	Extruded, machined	<sup>d</sup> .505	92.40	6.15	1.14		.31	
Dowmetal H	Sand cast, sand blasted	<sup>d</sup> .505	90.04	6.44	3.21		.31	
Dowmetal S	Sheet, wire brushed	.053	96.01		.97			3.02
AM764-T6 <sup>c</sup>	Cast	.29	91.66		3.44	4.63	.27	
XAM65S <sup>f</sup>	Forged	.26	89.57	4.28		5.18	.97	
AM61S	Forged	.32	92.49		6.42	1.09		
	Rolled	.18						
AM3S <sup>g</sup>	Rolled	.20	98.5				1.5	

<sup>a</sup> Analyses by the cooperating manufacturers, the American Magnesium Corporation and the Dow Chemical Co.  
<sup>b</sup> By difference.  
<sup>c</sup> Alloys no longer manufactured.  
<sup>d</sup> Value of diameter.  
<sup>e</sup> Now designated AM57S.  
<sup>f</sup> Now designated AM65S.  
<sup>g</sup> Nominal composition.

TABLE XIII.—APPROXIMATE NUMBER AND AREAS OF CORROSION OR BLISTERING RESULTING FROM EXPOSURE ON MAGNESIUM ALLOYS GIVEN THE SURFACE TREATMENTS INDICATED AND PAINTED WITH FOUR COATS OF ALUMINUM PIGMENTED VARNISH

Material	Surface treatment	Exposed 5 years at Coco Solo				Exposed 5 years at Washington <sup>a</sup>	
		Corroded areas <sup>b</sup>		Blisters on paint		Blisters on paint	
		Number	Total area	Number	Total area	Number	Total area
			<i>Sq. in.</i>		<i>Sq. in.</i>		<i>Sq. in.</i>
AM3S, rolled	Phosphoric acid	0	0	8	0.06	1	0.01
	Chrome-pickle	9	0.08	8	<sup>c</sup> 2.6	0	0
XAM65S, forged	Phosphoric acid	1	.01	0	0	0	0
	Chrome-pickle	13	.17	0	0	0	0
AM764, cast	Phosphoric acid	4	.03	22	1.3	0	0
	Chrome-pickle	9	.10	30	.59	0	0
AM61S, rolled	Phosphoric acid	8	.03	0	0	0	0
	Chrome-pickle	12	.53	5	.45	1	.01
AM61S, forged	Phosphoric acid	5	.01	3	.05	1	.01
	Chrome-pickle	10	.21	28	1.91	4	.02
AM7.4, cast	Phosphoric acid	9	.20	<sup>d</sup> 5	.06	0	0
	Chrome-pickle	26	1.34	<sup>d</sup> 94	1.57	6	.22
AZM, hot pressed	Phosphoric acid	3	.02	0	0	0	0
	Chrome-pickle	66	.85	393	3.0	51	.26
AM240, cast	Phosphoric acid	10	15.9	<sup>d</sup> 2	.39	0	0
	Chrome-pickle	49	18.8	<sup>d</sup> 300	1.5	41	.33

<sup>a</sup> No corroded areas were visible on material exposed at Washington, D. C., the paint being intact on all samples.  
<sup>b</sup> The entire surface area of each panel exposed to the weather was approximately 85 square inches.  
<sup>c</sup> One blister had an area of 2.5 square inches, but no corrosion was visible beneath it.  
<sup>d</sup> Corrosion product was present in appreciable amounts under these blisters.

TABLE XIV.—TENSILE PROPERTIES AND DEPTH OF PENETRATION OF CORROSIVE ATTACK ON MAGNESIUM ALLOYS EXPOSED 1 YEAR AT HAMPTON ROADS, VA.

Dowmetal materials	Surface finish	Average tensile properties <sup>a</sup>				Maximum depth of penetration
		Ultimate tensile strength	Elongation in 2 inches	Yield strength <sup>b</sup>	Reduction of area	
		<i>Lb./sq. in.</i>	<i>Percent</i>	<i>Lb./sq. in.</i>	<i>Percent</i>	<i>Thousandths inch</i>
E, Sheet	Paint	43,600	13.0	34,300	18.6	0
	Chrome-pickle	39,600	3.0	33,200	5.8	10
S, Sheet	Paint	33,000	15.0	25,100	17.9	0
	Chrome-pickle	30,700	11.0	23,600	13.1	6
A, Cast	Paint	26,600	6.0	11,600	8.6	0
	Chrome-pickle	26,200	6.0	11,500	9.4	12
H, Cast	Paint	28,000	5.5	13,100	8.3	0
	Chrome-pickle	27,200	5.0	12,500	8.2	3
F, Extruded	Paint	40,700	17.5	30,100	35.9	0
	Chrome-pickle	40,600	14.0	30,200	14.0	12
J, Extruded	Paint	46,200	17.0	32,700	20.8	0
	Chrome-pickle	45,800	15.0	32,700	17.8	<sup>c</sup> 6

<sup>a</sup> Values for the painted specimens are average obtained on 9 samples, 3 of which were kept in sealed containers (dry atmosphere). Since there was no loss on the painted specimens, these are typical of uncorroded material. Values for the chrome-pickled are the average on 3 specimens, all exposed.  
<sup>b</sup> Stress at which stress-strain curve showed a departure of 0.2 percent from the initial modulus line.  
<sup>c</sup> The attack, which was more or less uniform, resulted in a reduction in thickness of the sheet of between 0.003 and 0.004 inch.







# REPORT NO. 664

## WIND-TUNNEL INVESTIGATION OF AN N. A. C. A. 23012 AIRFOIL WITH VARIOUS ARRANGEMENTS OF SLOTTED FLAPS

By CARL J. WENZINGER and THOMAS A. HARRIS

### SUMMARY

*An investigation was made in the 7- by 10-foot wind tunnel and in the variable-density wind tunnel of the N. A. C. A. 23012 airfoil with various slotted-flap arrangements. The purpose of the investigation in the 7- by 10-foot wind tunnel was to determine the airfoil section aerodynamic characteristics as affected by flap shape, slot shape, and flap location. The flap position for maximum lift; polars for arrangements considered favorable for take-off and climb; and complete lift, drag, and pitching-moment characteristics for selected optimum arrangements were determined. The best arrangement was tested in the variable-density tunnel at an effective Reynolds Number of 8,000,000. In addition, data from both wind tunnels are included for plain, split, external-airfoil, and Fowler flaps for purposes of comparison.*

*The optimum arrangement of the slotted flap was superior to the plain, the split, and the external-airfoil types of flap on the basis of maximum lift coefficient, low drag at moderate and high lift coefficients, and high drag at high lift coefficients. The increment of maximum lift due to the slotted flap was found to be practically independent of the Reynolds Number over the range investigated. The slotted flap, however, gave slightly lower maximum lift coefficients than the Fowler flap. It was found that slot openings in the airfoil surface at the flap caused a measurable increase in drag of the airfoil for the condition of high-speed flight even if the slot was smoothly sealed on the upper surface and there was no flow through the slot. It was also found that, in order to obtain the highest lift coefficients, the nose of the flap should be located slightly ahead of and below a slot lip that directs the air downward over the flap. The nose of the flap should have a good aerodynamic form and the slot entry should have an easy shape to obtain low drags at moderate lift coefficients.*

### INTRODUCTION

Most present-day airplanes, because of their high wing loadings and cleanness of aerodynamic design, employ some form of lift-increasing and drag-increasing device to assist in landing them in a field of restricted size. Also, increases in lift without increases in drag appear desirable in the take-off and in the climbing conditions of flight.

The foregoing considerations indicate that the most desirable form of high-lift device is one capable of providing high lift with relatively low drag, and also probably high lift with high drag. Some other desirable aerodynamic features are: no increase in drag with the flap neutral; small changes in wing pitching moment with flap deflection; low forces required to operate the flap; and freedom from possible hazard due to icing.

Some form of slotted flap was believed to be the most promising for the conditions noted. Various forms of slotted flap include the external-airfoil (references 1 and 2), the Fowler (references 3 and 4), and the Handley Page types (references 5, 6, 7, 8, and 9).

The present investigation was made in two main parts. The tests reported in part I were made in the 7- by 10-foot tunnel of slotted flaps somewhat similar to the Handley Page type. Flaps of three different sections and with several different slot shapes were tested. Surveys were made of flap location to obtain the best aerodynamic characteristics for each arrangement. In addition, a plain flap, a split flap, an external-airfoil flap, and a Fowler flap were included for purposes of comparison.

Part II reports tests made in the variable-density tunnel of the best slotted flap arrangement (2-h) developed in part I, to determine the effects at high Reynolds Numbers. In addition, slotted flap 2-h was tested in combination with a 60-percent-chord plain flap to see whether, as in previous unpublished tests of the plain flap alone, rounded lift-curve peaks could be obtained.

The tests reported in part II were made by the variable-density-tunnel staff and the material presented as part II was prepared for publication by Harry Greenberg and Neal Tetervin.

### I. TESTS IN 7- BY 10-FOOT WIND TUNNEL

#### APPARATUS AND TESTS

##### THE MODIFIED 7- BY 10-FOOT WIND TUNNEL

Before the present investigation was started, the 7- by 10-foot open-jet wind tunnel (reference 10) had been modified, mainly by the addition of a closed test



section and a new entrance cone. (See fig. 1.) With these changes, the static pressure is practically constant along the axis of the test section and the noise during tunnel operation is fairly low. In addition, by making the top and the bottom of the test section parallel, an arrangement is obtained whereby two-dimensional-flow tests can conveniently be made of large-chord models completely spanning the jet in a vertical plane. The use of such an installation permits a large ratio of chord of model to height of jet together with small wind-tunnel corrections (references 11 and 12) so that the range of Reynolds Numbers of the tests for obtaining airfoil

tween the model and the tunnel walls is indicated by the flashing of neon lamps connected in an electrical circuit including the walls of the test section and thin metal plates fastened to each end of the model.

The standard force-test tripod used with the previous open-jet wind tunnel (reference 10) to support horizontally the smaller finite-aspect-ratio models has been replaced by a single cantilever streamline strut. The opening in the floor of the closed test section through which the strut passes is made airtight by a mercury seal. The existing scales are used with both types of test; however, in the case of the two-dimen-

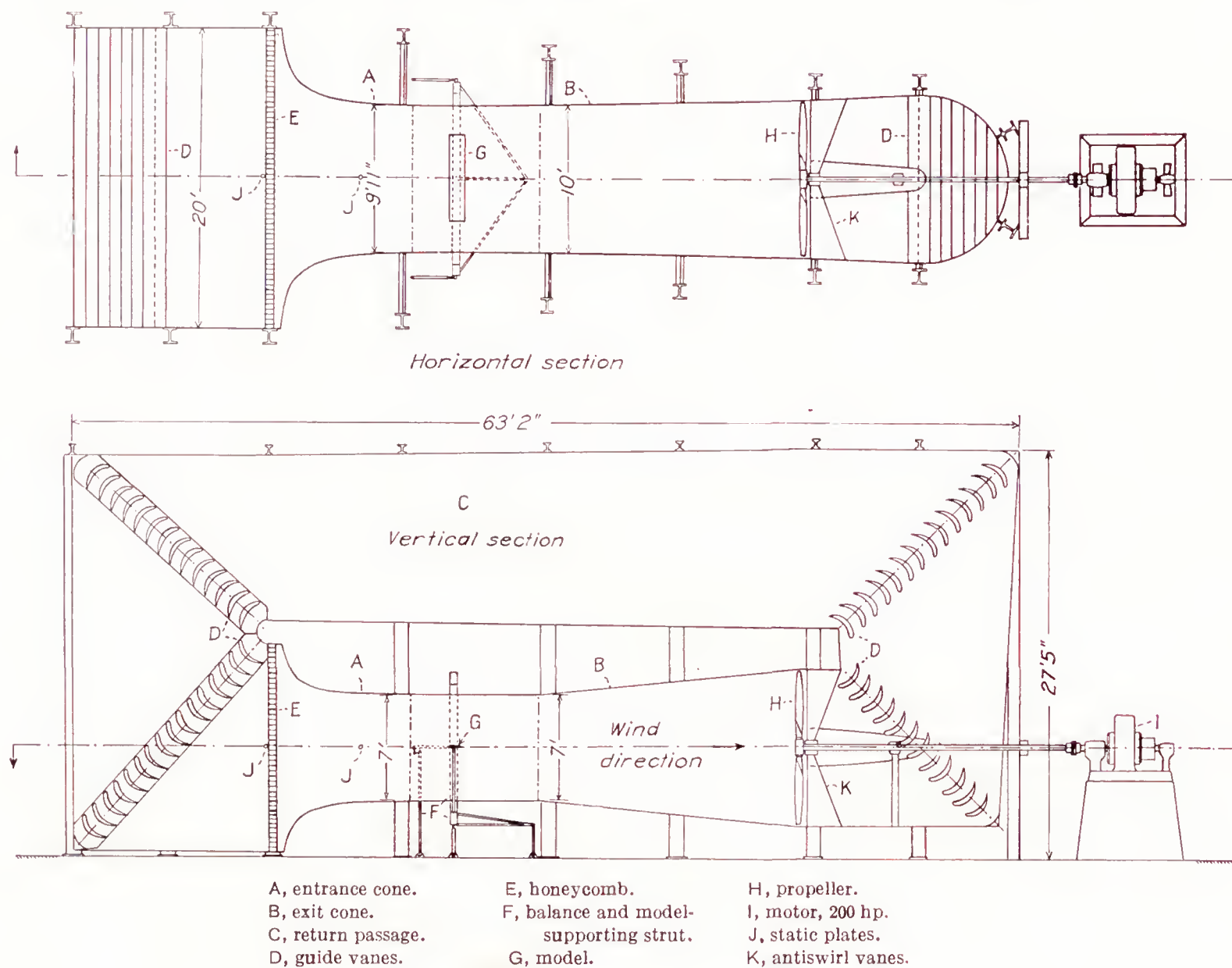


FIGURE 1.—Diagram of the 7 by 10-foot wind tunnel with closed test section

section data in a given wind tunnel can be considerably increased.

The wind-tunnel balance has been slightly modified by installing tubular supports on the top and the bottom of the balance frame surrounding the test section so that the model can be held vertical. The tubular supports extend through circular holes in the closed test section to sockets with clamps in the ends of the model; they can be rotated with a motor drive by gears and shafting to change the angle of attack from outside the wind tunnel. A clearance of about  $\frac{1}{32}$  inch is allowed between the ends of the model and the top and the bottom of the test section (fig. 2). Any contact be-

sional-flow tests, lift is measured on the cross-wind scale and pitching moment on the yawing-moment scale. (See reference 10 for arrangement of scales.)

Sphere tests have been made to obtain an indication of the turbulence present in the air stream of the closed test section. The turbulence was found to have changed slightly from that of the open-jet wind tunnel, so that the turbulence factor (reference 13) has been increased from a value of 1.4 to 1.6. The dynamic pressure of the air stream at the working section in either horizontal or vertical planes is constant within  $\pm 0.5$  percent, and the air stream is parallel to the axes of the test section within  $\pm 0.5^\circ$ .



## MODELS

**Plain airfoil.**—The basic model, or plain airfoil, (fig. 3) was built of laminated pine to the N. A. C. A. 23012 section (table I) and has a chord of 3 feet and a span of 7 feet. The trailing-edge portion of this airfoil was made easily removable so that the model can be quickly altered for testing different flap arrangements.

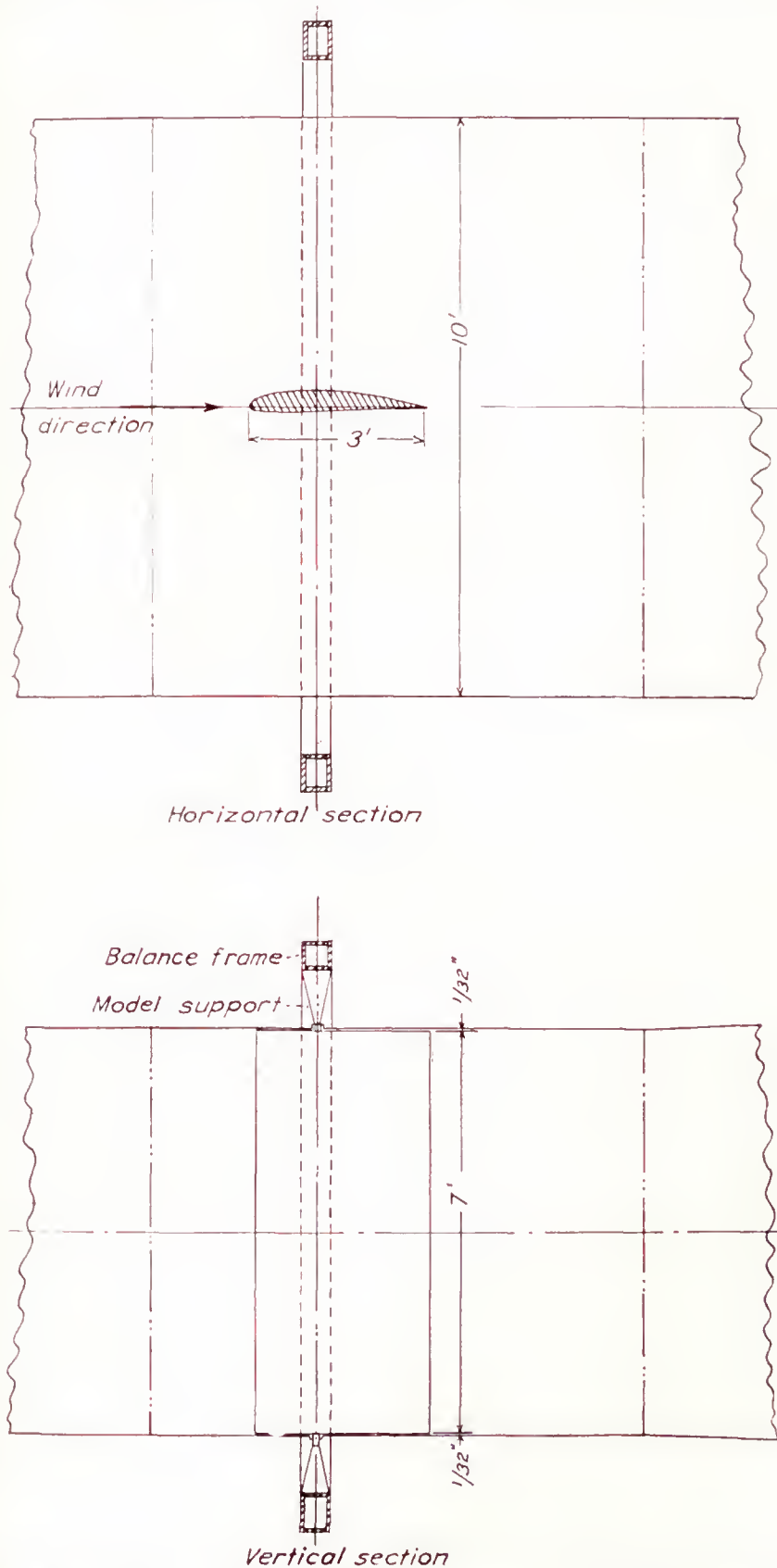


FIGURE 2.—Model installation for two-dimensional-flow tests in the 7- by 10-foot wind tunnel.

**Split flap.**—A simple split flap with a chord 20 percent of the airfoil chord (fig. 3) was used in conjunction with the plain airfoil. This flap is of plywood,  $\frac{1}{4}$  inch thick, and is fastened to the model by screws. The flap angles ( $0^\circ$  to  $75^\circ$ ) are set by wooden blocks cut to the desired angles and placed between the flap and the airfoil.

**Plain flap.**—The plain flap (fig. 3) also has a chord 20 percent of the airfoil chord and is mounted on a removable section, which replaces that of the plain airfoil. Fittings supporting the wooden flap are of thin steel and are equipped with ball-bearing hinges so that the hinge moments of the flap can be measured. The flap angles ( $38^\circ$  up to  $75^\circ$  down) are set by a push rod and bell cranks, so arranged that the settings can be changed from outside the wind tunnel. The gap between the flap and the airfoil is sealed top and bottom by thin metal plates.

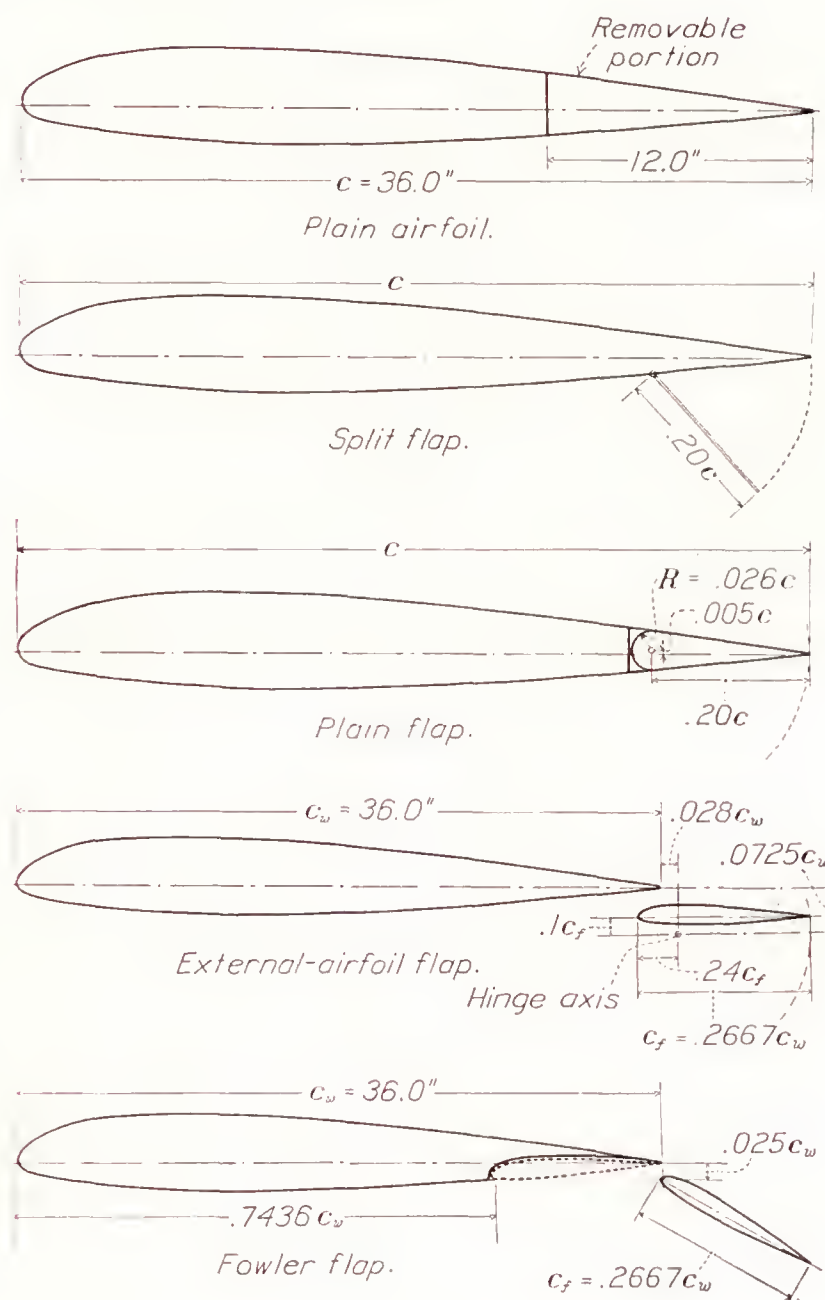


FIGURE 3.—Sections of the plain N. A. C. A. 23012 airfoil and of the airfoil with different types of flap.

**External-airfoil flap.**—The external-airfoil flap, available from another investigation, was used without alteration although it was somewhat larger than desired, having a chord 26.67 percent of the airfoil chord (fig. 3). The flap has the N. A. C. A. 23012 section and was located with respect to the main airfoil in accordance with the results of reference 2. The flap is supported on the main airfoil by thin metal fittings arranged so that the flap angle can be set  $3^\circ$  up to  $50^\circ$  down.



**Fowler flap.**—The external-airfoil flap was also used as a Fowler flap (26.67 percent of the main airfoil chord) after modification of the main airfoil (fig. 3). No actual data were available showing the best location of a Fowler flap of N. A. C. A. 23012 profile with a main airfoil of the same profile; however, the flap was located on the basis of tests of external-airfoil flaps of N. A. C. A. 23012 profile (reference 2) and of tests of Fowler flaps of Clark Y profile (reference 4). The flap is supported on the main airfoil by thin metal fittings so that the flap can be set from  $0^\circ$  to  $60^\circ$  down when completely extended. The main airfoil is ar-

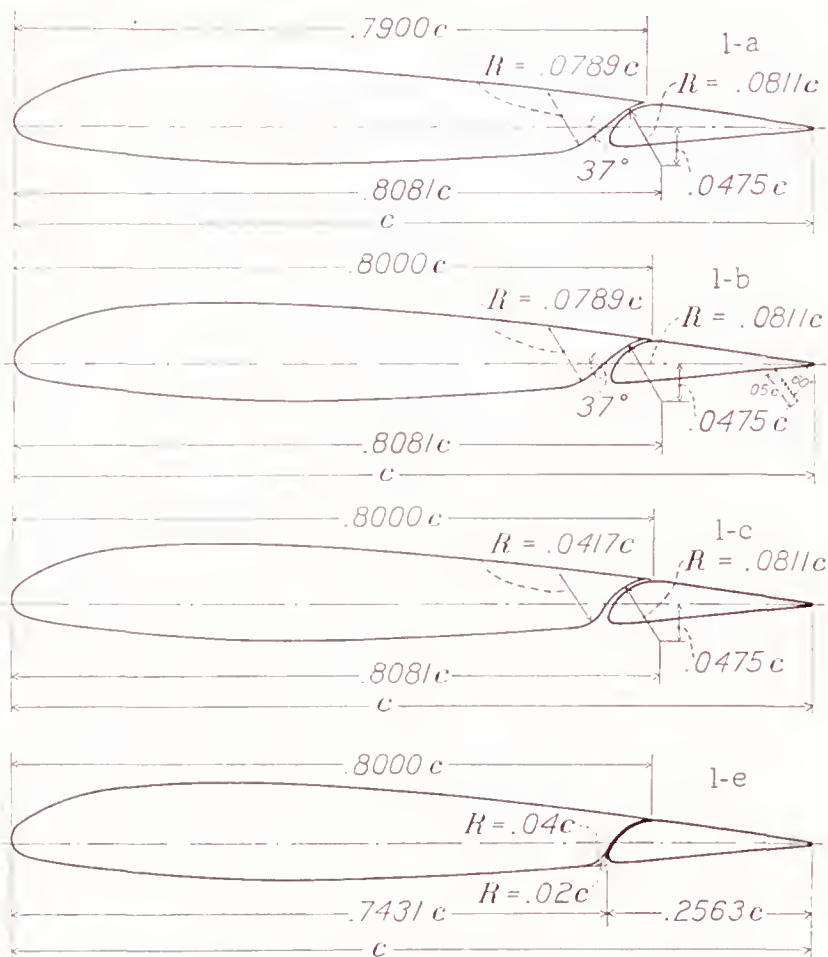


FIGURE 4.—Sections of airfoil with arrangements of slotted flap 1.

ranged so that the N. A. C. A. 23012 Fowler flap may be almost completely retracted for the flap-neutral condition. (See fig. 3.)

**Slotted flap 1.**—The three slotted flaps tested are designated by numbers and the slot shapes by appended letters. Slotted flap 1 (fig. 4), which is representative of recent Handley Page practice, was built according to dimensions taken from reference 8. The ordinates for this flap are given in table II. The slot variations used with flap 1 are shown in figure 4 and in table I. Shape a is also representative of recent Handley Page practice and was built according to dimensions taken from reference 8. Shape b is the same as shape a except for an increase in the length of the slot lip to close the slot on the upper surface of the airfoil with the flap neutral. Shape c is an intermediate step toward closing the slot on the lower surface, and shape e has the slot sealed all the way through the airfoil

when the flap is neutral. Shape e was further modified by different roundings of the slot entry. The slot entry with the  $0.02c$  radius is designated  $e_2$  and the one with the  $0.04c$  radius,  $e_4$ .

Two methods of hinging flap 1 were employed. The first method was to hinge it about a single predetermined axis location obtained from reference 8 for com-

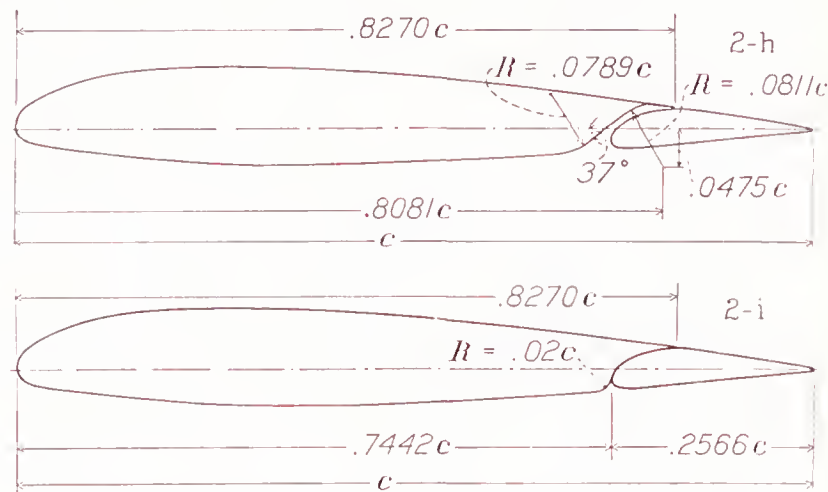


FIGURE 5.—Sections of airfoil with arrangements of slotted flap 2.

parison with recent Handley Page practice. The second method was to mount the flap on the main airfoil by special fittings that allowed the flap to be located at any point over a considerable area with respect to the main airfoil.

**Slotted flap 2.**—It was believed that a good airfoil section would probably make the best flap shape, especially from considerations of drag at low flap deflections. The front portion of slotted flap 2 was therefore made to the N. A. C. A. 6318 airfoil section back to the maxi-

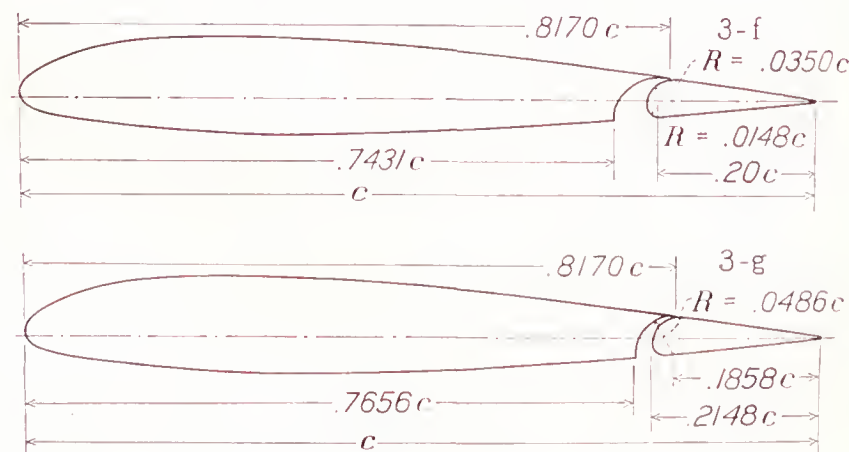


FIGURE 6.—Sections of airfoil with arrangements of slotted flap 3.

imum thickness and was faired into the contour of the main airfoil over the rest of its length. The arrangements of slotted flap 2 and the slot variations used in conjunction with it are shown in figure 5 and in tables I and II. Slot shape h is the same as shape a except that the lip is made long enough to seal the slot on the upper surface of the airfoil with the flap neutral. Slot shape i (table I) is sealed all the way through the wing with the flap neutral except for the radius at the slot entry. Flap 2 was hinged in a manner similar to the second method for flap 1.



**Slotted flap 3.**—Slotted flap 3 has an arbitrary shape with a very blunt nose (fig. 6). Slot shape f is the same as slot shape e except for the longer lip to seal the slot on the upper surfaces of the airfoil when the flap is neutral. The ordinates for this slot shape are given in table I. Slot shape g (fig. 6) is designed to give a good expanding slot shape for flap deflections up to  $50^\circ$  with the flap hinged at a point on the lower surface of the flap 20 percent of the airfoil chord from the trailing edge. The same main fittings were used on the airfoil to support this flap as for flaps 1 and 2; they allow the flap to be located at any point over a considerable area with respect to the main airfoil.

#### GENERAL TEST CONDITIONS

The two-dimensional-flow installation in the 7- by 10-foot closed-throat wind tunnel was used for the tests. (See fig. 2.) The regular six-component balance (reference 10) was used to measure the lift, the drag, and the pitching moment of the model. The hinge moments were measured with a special torque-rod balance.

A dynamic pressure of 16.37 pounds per square foot was maintained for all of the tests except those of the external-airfoil and the Fowler flaps. This dynamic pressure corresponds to a velocity of about 80 miles per hour under standard atmospheric conditions and to an average test Reynolds Number of 2,190,000. Because of the turbulence in the tunnel, the effective Reynolds Number  $R_e$  of the tests was approximately 3,500,000. The models with the external-airfoil and the Fowler flaps were tested at a dynamic pressure corresponding to a velocity of 63.2 miles per hour under standard atmospheric conditions. With this velocity, the test Reynolds Numbers were also 2,190,000 for the tests with the external-airfoil flap and with the Fowler flap fully extended, based on the sum of the chords of the main wing and the flap. In addition, tests were made of the wing with the Fowler flap fully retracted at both 80 and 63.2 miles per hour.

Tests were first made of the plain airfoil and of the airfoil with split, plain, external-airfoil, and Fowler flaps through a complete range of flap deflections and angles of attack for comparison with other tests and also for comparison with the slotted flaps of the present investigation. As an example of one of the recently used Handley Page slotted flaps (reference 8), a few tests were made of one slotted flap hinged about a pre-determined axis location. The greater part of the investigation, however, consisted of surveys to determine the optimum flap positions and deflections for maximum lift and climb. Sufficient angles of attack at each flap deflection were taken to determine envelope polars over the complete lift range from zero to maximum lift. Data were obtained at  $2^\circ$  increments of angle of attack and at  $10^\circ$  increments of flap deflection for each flap location. Lift, drag, and pitching moments were measured for all positions of the flaps over the

angle-of-attack range tested. Hinge moments of the plain flap and of one slotted-flap arrangement were also measured.

#### RESULTS AND DISCUSSION

##### COEFFICIENTS

All test results are given in standard section nondimensional coefficient form as follows:

- $c_l$ , section lift coefficient ( $l/qc$ ).
- $c_{d_0}$ , section profile-drag coefficient ( $d_0/qc$ ).
- $c_{m(a.c.)_0}$ , section pitching-moment coefficient about aerodynamic center of section with flap in neutral position ( $m_{(a.c.)_0}/qc^2$ ).
- $c_{h_f}$ , section hinge-moment coefficient of flap ( $h/qc_f^2$ ).

where

- $l$  is section lift.
- $d_0$ , section profile drag.
- $m_{(a.c.)_0}$ , section pitching moment.
- $h$ , section hinge moment of flap about a specified axis.
- $q$ , dynamic pressure ( $\frac{1}{2}\rho V^2$ ).
- $c$ , airfoil chord including flap; for models with external-airfoil and Fowler flaps,  $c$  is the sum of the chords of the main airfoil and the flap ( $c_w + c_f$ ).
- $c_f$ , flap chord.

and

- $\alpha_0$  is the angle of attack for infinite aspect ratio.
- $\delta_f$ , flap deflection.

##### PRECISION

**Accuracy of tests.**—From repeat tests the accidental experimental errors in the results presented in this report are believed to lie within the limits indicated in the following table:

$\alpha_0$ -----	$\pm 0.5^\circ$	$c_{d_0(c_l=1.0)}$ -----	$\pm 0.0006$
$c_{l_{max}}$ -----	$\pm 0.03$	$c_{d_0(c_l=2.5)}$ -----	$\pm 0.002$
$c_{m(a.c.)_0}$ -----	$\pm 0.003$	$\delta_f$ -----	$\pm 0.2^\circ$
$c_{d_0(c_l=0)}$ -----	$\pm 0.0003$	Flap position---	$\pm 0.001c$

The profile-drag coefficient  $c_{d_0}$  of the airfoil-flap combinations has not been corrected for the effect of the flap-hinge fittings. From tests of the airfoil with various flaps neutral and hinge fittings in place, but with all openings in the airfoil surface sealed, it was found that the drag increment was consistently about 0.001. No tests were made to determine the hinge-fitting drag with the flaps deflected because of the large number of additional tests required. The relative merits of the various flap arrangements should not be appreciably affected by hinge-fitting drag since the same hinge fittings were used for all the tests.

With a few of the slotted-flap arrangements, two sets of data could be obtained, an indication of two types of air flow. For these cases, the data for the more stable of the two flow conditions were used.



**Wind-tunnel corrections.**—Certain theoretical corrections have been derived for the effect of tunnel walls on the lift of a flat plate completely spanning the jet at an angle of attack (references 11 and 12). An attempt was made to check these corrections experimentally for an airfoil in the two-dimensional-flow installation and, at the same time, to examine the effect of tunnel walls on the drag and the pitching moment. This experimental investigation showed the correction for lift to be about 1 percent greater than the theoretically derived correction for ratios of model chord to jet height up to 0.4. The experimentally determined correction has been used to correct all the lift data presented in this report. The maximum lift coefficients

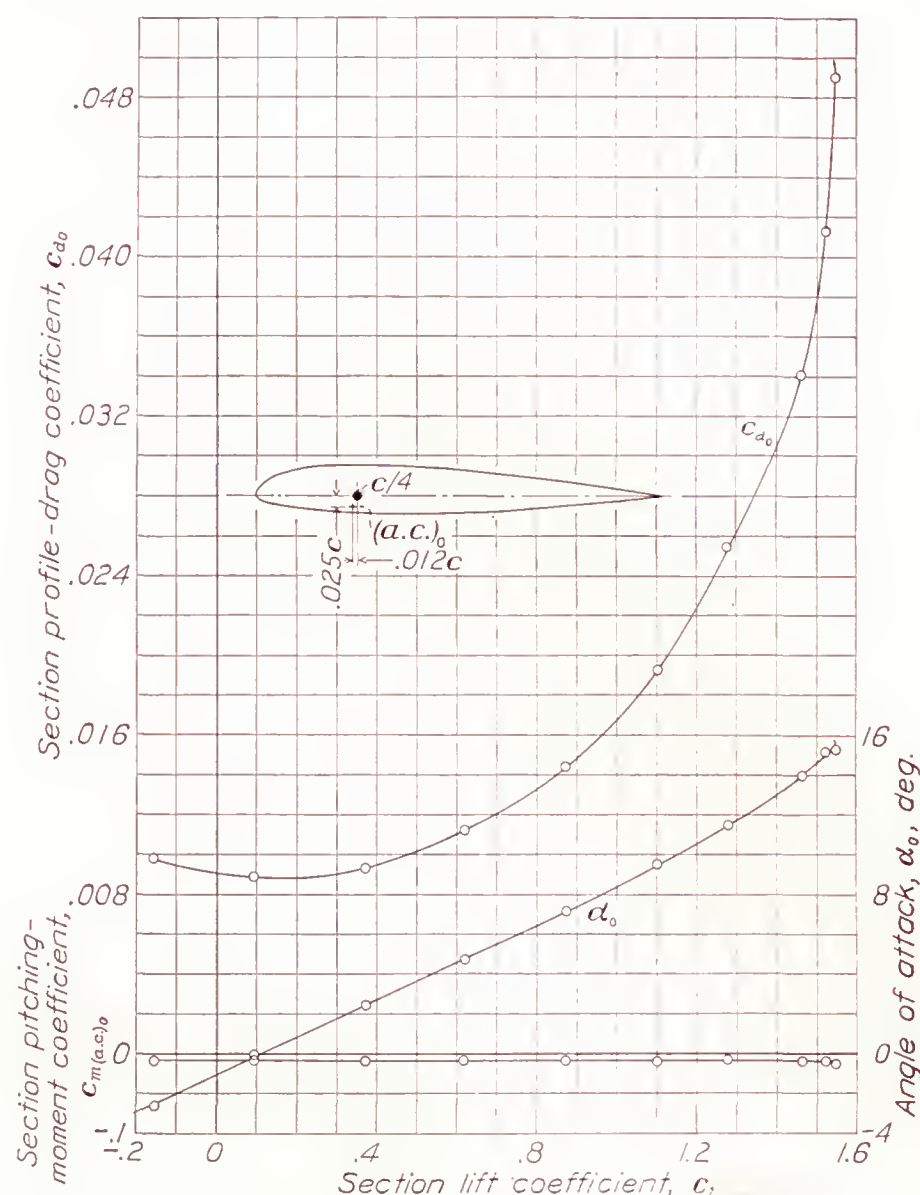


FIGURE 7.—Section aerodynamic characteristics of N. A. C. A. 23012 plain airfoil.

given are about 10 percent higher than those given by a rectangular airfoil of aspect ratio 7 but are probably the same as would be obtained with an airfoil designed to give elliptical lift distribution. This excess of lift was checked by testing the same model (12 inches chord by 84 inches span) in the two-dimensional-flow installation and on the regular three-dimensional-flow set-up. The results agree very closely with the results of pressure-distribution tests and with theoretical considerations of the span loading on rectangular wings. (See reference 14.)

The investigation to determine a correction for drag has not been conclusive. The tests completed up to

the present time, however, indicate that the drag results are about 10 percent higher than expected. There are no theoretical corrections for the drag (reference 11) except for a symmetrical body at zero lift. No corrections for the apparent tunnel effect were applied to the drag data. Since any correction would presumably be about the same for any of the airfoil-flap arrangements at given lift coefficients, the relative merits of the various combinations should not be markedly affected by a drag correction. All the drag data have been corrected in accordance with reference 14 by a constant  $\Delta c_{d_0}$  of  $-0.0008$  so as to apply at an effective Reynolds Number of 3,500,000.

Tests to determine tunnel corrections showed that the pitching-moment coefficients required no correction within the experimental accuracy of the tests.

#### PLAIN N. A. C. A. 23012 AIRFOIL

The section aerodynamic characteristics of the plain N. A. C. A. 23012 airfoil, as determined in the two-dimensional-flow installation, are shown in figure 7. The polar is in good agreement with a generalized polar for the N. A. C. A. airfoils given in reference 14. The minimum profile drag is, however, about 10 percent higher than the minimum profile drag of the same airfoil section for the same effective Reynolds Number. This difference is not considered serious, and some contemplated additional tunnel-effect tests will probably furnish information as to the indicated differences. The pitching-moment coefficient about the aerodynamic center checks the pitching-moment coefficient given in reference 14 for the same effective Reynolds Number. The slope of the lift curve  $dc_l/d\alpha$  is 0.107 from the present tests, as compared with 0.098 from the results for infinite aspect ratio of tests of models of finite aspect ratio given in reference 14. This difference in lift-curve slope, although not yet adequately explained, should not affect the relative merits of the test results of the flap combinations presented in this report. The angle of zero lift, within the experimental accuracy of the tests, agrees with the angle of zero lift as determined by other tests (reference 14).

#### FLAPS FOR COMPARISON WITH SLOTTED ARRANGEMENT

**Split flap.**—The section aerodynamic characteristics of the N. A. C. A. 23012 airfoil with a  $0.20c$  split flap are shown in figure 8. The lift curves have about the same slope as that of the plain airfoil. The angle of attack for maximum lift decreases from about  $15^\circ$  with the flap neutral to  $14^\circ$  with the flap down  $45^\circ$ . With the flap down  $60^\circ$  or  $75^\circ$ , however, the angle of maximum lift is only about  $12^\circ$ , a change of  $3^\circ$  from the plain airfoil. A change of this magnitude in the angle of attack for maximum lift may have considerable effect on the manner in which a wing stalls for combinations with partial-span split flaps.



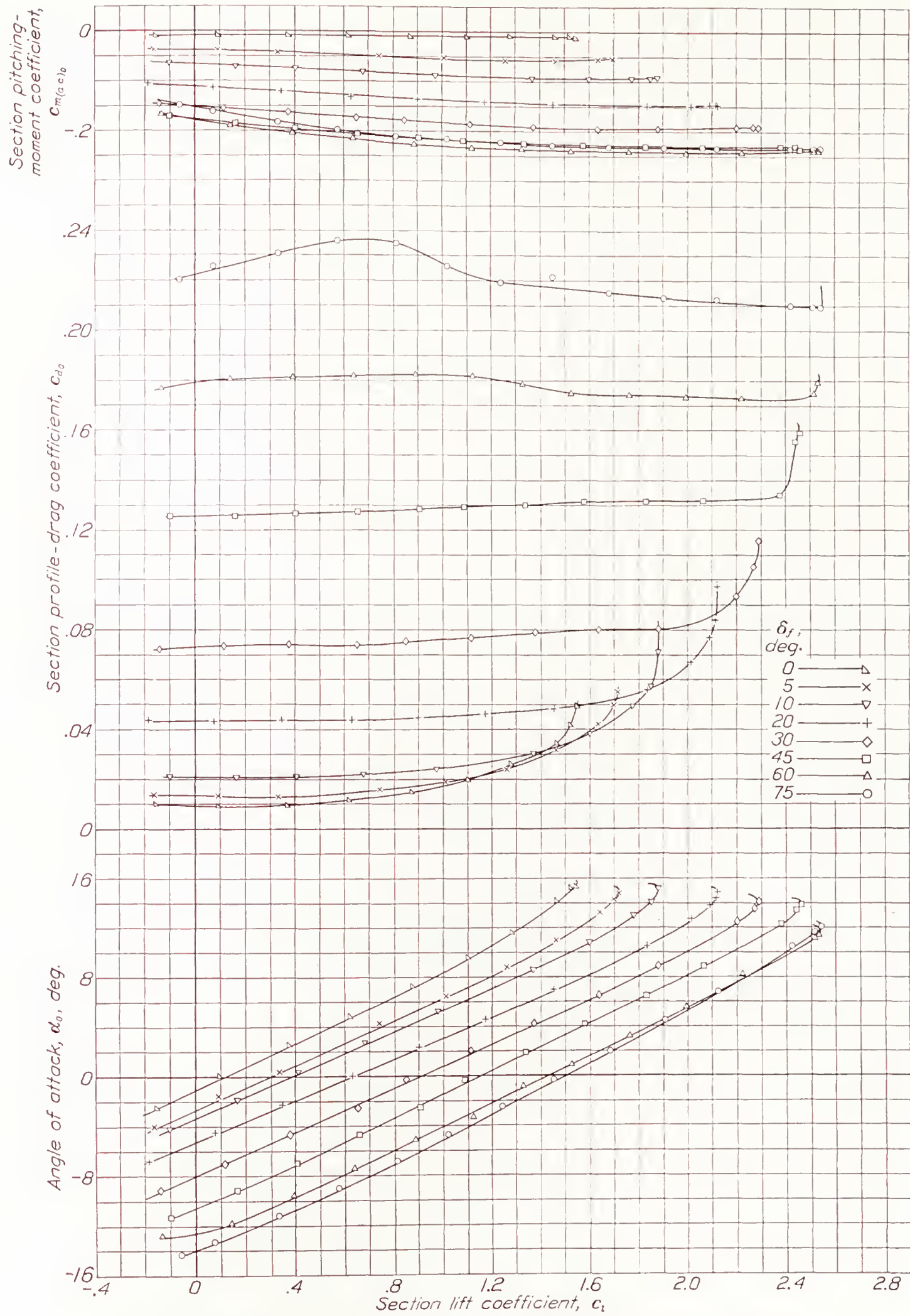


FIGURE 8.—Section aerodynamic characteristics of N. A. C. A. 23012 airfoil with a 0.20c split flap.



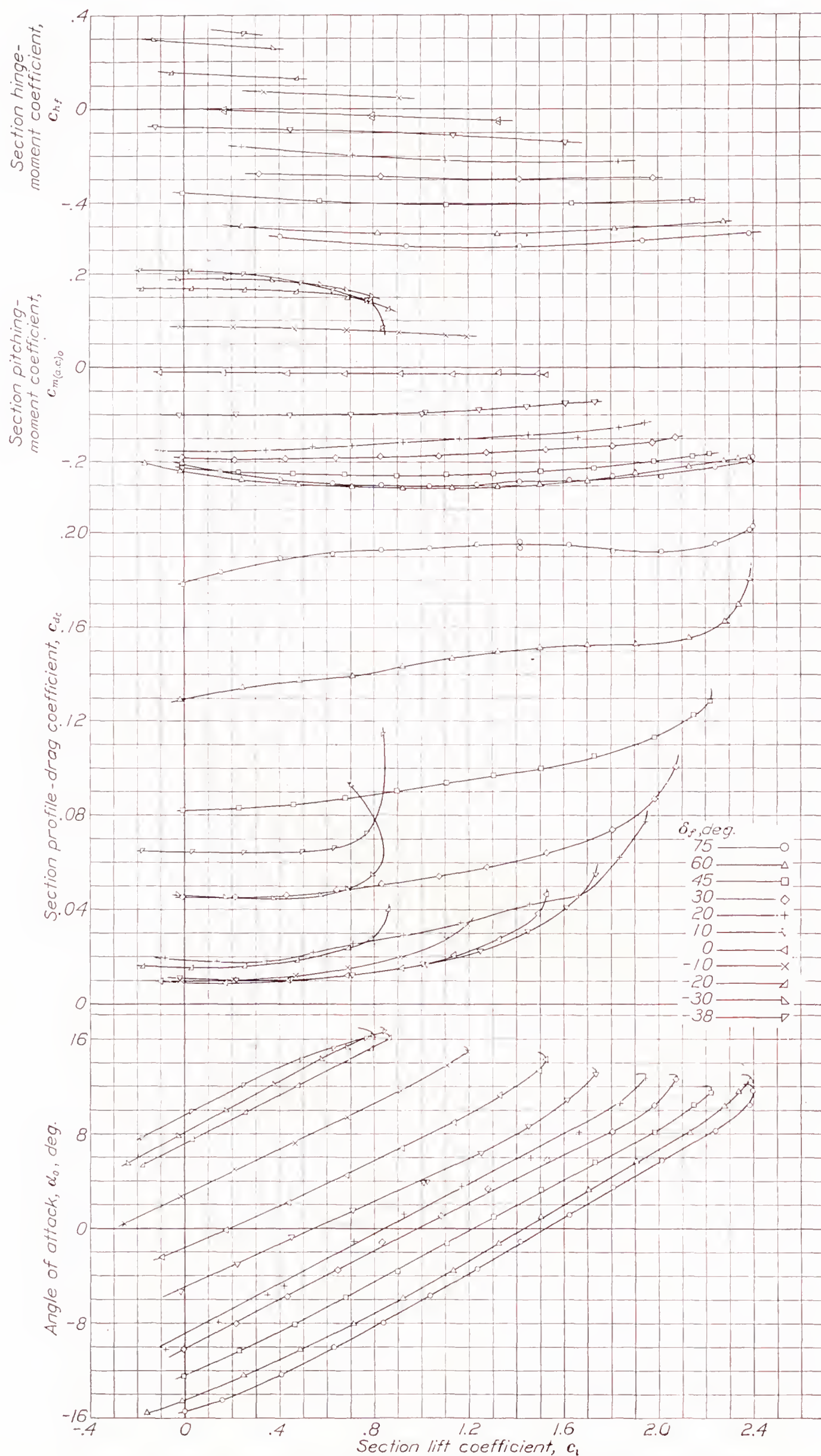
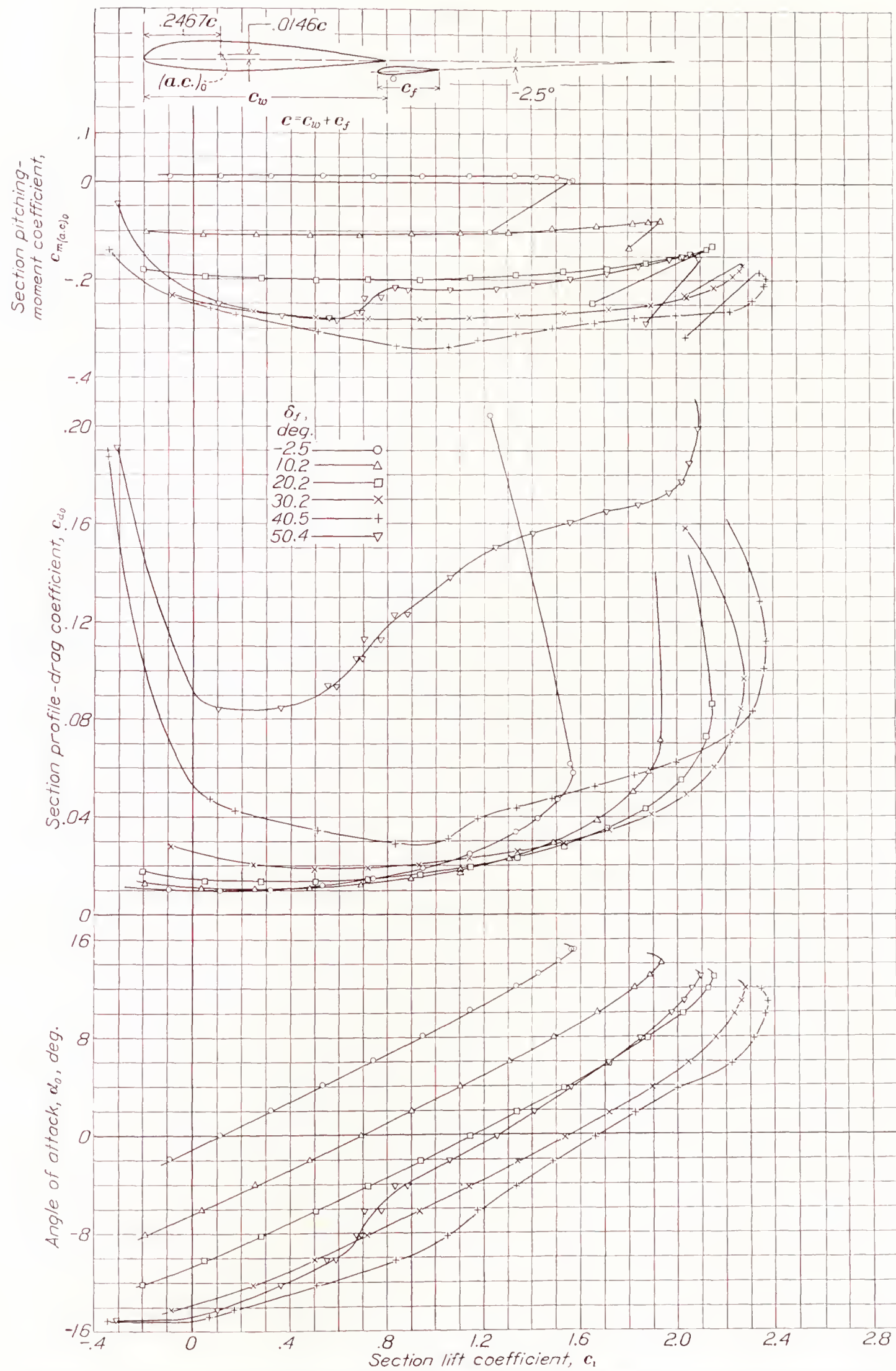
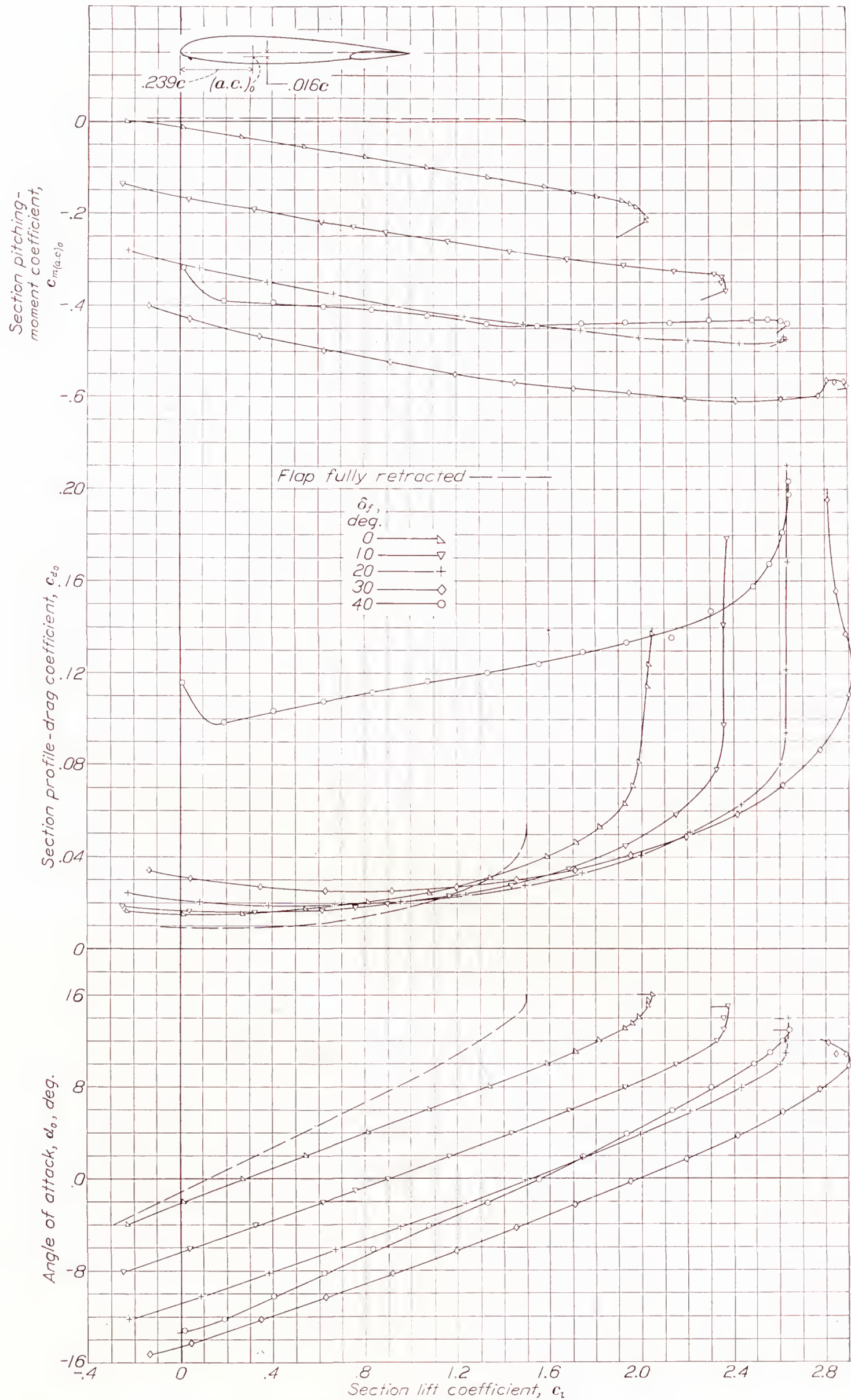


FIGURE 9.—Section aerodynamic characteristics of N. A. C. A. 23012 airfoil with a 0.20c plain flap.



FIGURE 10.—Section aerodynamic characteristics of N. A. C. A. 23012 airfoil with a 0.2667 $c_e$  N. A. C. A. 23012 external-airfoil flap.



FIGURE 11.—Section aerodynamic characteristics of N. A. C. A. 23012 airfoil with a  $0.2667c_w$  N. A. C. A. 23012 Fowler flap.



The increment of maximum lift coefficient for a given flap deflection is from 4 to 10 percent larger than the increment obtained in previous tests of a model of finite span at a much lower Reynolds Number (reference 15). The increases may be almost entirely accounted for by the difference in span loadings because the reference tests were made with a rectangular airfoil in three-dimensional flow. Increments of maximum lift coefficient of an airfoil with a split flap may be considered to be practically independent of Reynolds Number. The increment of minimum profile-drag coefficient for a given flap deflection for these tests is about 10 percent greater than for the tests of reference 15. The pitching-moment coefficients from the two-dimensional-flow tests are in good agreement with the pitching-moment coefficients given in reference 15 for the same flap deflections.

**Plain flap.**—The section aerodynamic characteristics of the N. A. C. A. 23012 airfoil with a  $0.20c$  plain flap are shown in figure 9. Comparison of these results with the plain-flap results of reference 15 shows about the same differences that were observed for the split flap. The section hinge-moment coefficients given in figure 9 are of about the same magnitude as hinge-moment coefficients of a  $0.20c$  plain flap on a Clark Y airfoil (reference 15). It should be noted that the characteristics for the plain flap with both up and down deflections are useful for the estimation of aileron as well as flap effects.

**External-airfoil flap.**—The section aerodynamic characteristics of the N. A. C. A. 23012 airfoil with an N. A. C. A. 23012 external-airfoil flap are given in figure 10. The relative merits of this flap arrangement are about the same as a similar arrangement tested in three-dimensional flow (reference 2) at the same effective Reynolds Number. Peculiarities in the curves of lift, profile drag, and pitching moment at the high flap deflections seem to be characteristic of this type of flap and probably indicate a marked change in flow pattern around the combination. As pointed out in reference 2, the pitching-moment coefficients with this type of flap are higher than with the split or plain flaps.

**Fowler flap.**—The section aerodynamic characteristics of the N. A. C. A. 23012 airfoil with an N. A. C. A. 23012 Fowler flap are given in figure 11. The data for the model with the Fowler flap fully retracted included on this figure are taken from the tests at 80 miles per hour. These results are in good agreement with previous results of tests of Fowler flaps. (See references 4 and 16.) The large pitching-moment coefficients obtained with this flap may, in a large measure, affect its use for a particular design. It is of interest to note that, with the flap fully retracted, there is no measurable increase in profile drag over that of the plain wing (fig. 7) for lift coefficients ( $c_l$ ) below 0.8 but there is a loss of

about 0.05 in maximum lift coefficient. The angle of attack for maximum lift with the flap set at  $30^\circ$  is only  $10^\circ$ , which is a decrease of  $5^\circ$  when compared with that for the plain wing. This decrease is greater than that for any of the other flap arrangements.

#### PRELIMINARY TESTS OF SLOTTED FLAPS

A preliminary investigation was conducted of the Handley Page slotted flap, designated flap 1, and of four slot shapes, the combinations being designated

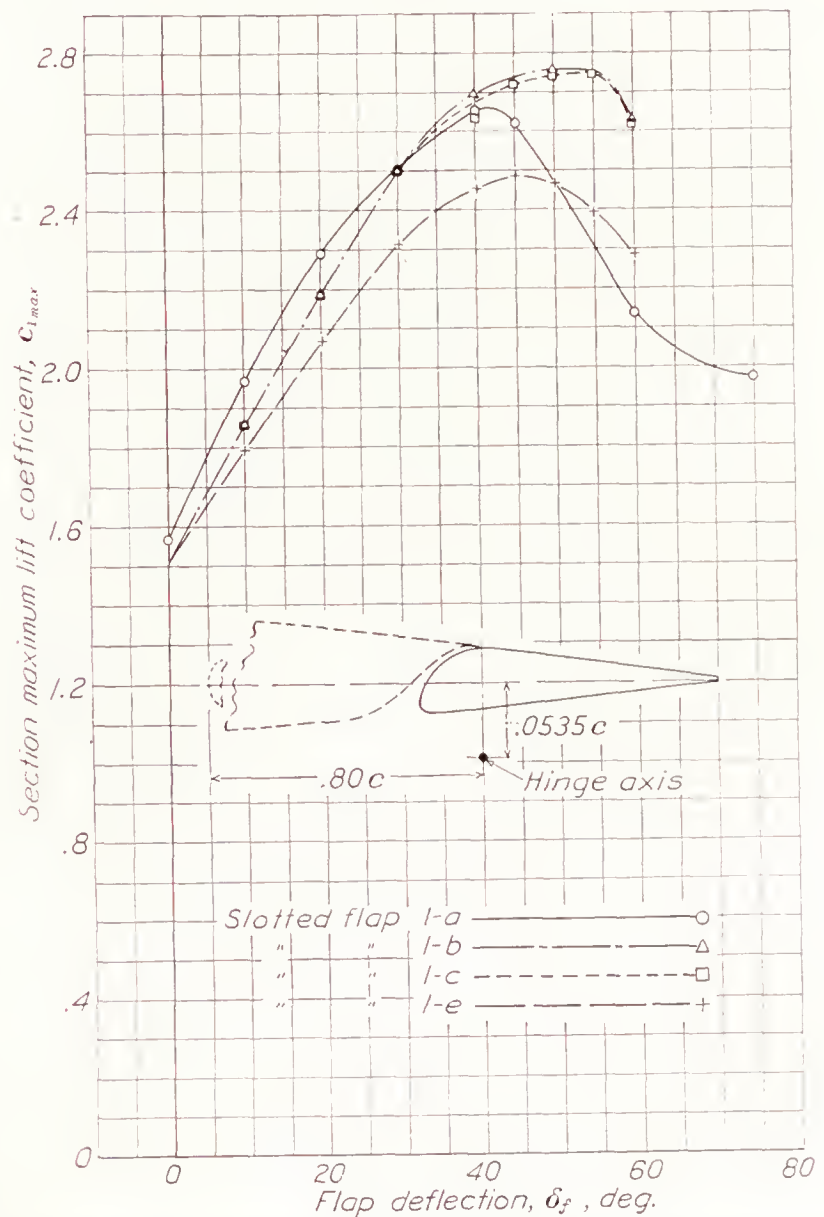


FIGURE 12.—Effect of slot shape on  $c_{l_{max}}$ . Flap 1 at predetermined axis location

1-a, 1-b, 1-c, and 1-e (fig. 4). For this part of the investigation, the axis about which the flap was deflected was determined from the data of reference 8.

**Effect of slot shape on maximum lift.**—The maximum lift coefficients  $c_{l_{max}}$  are plotted against flap deflection  $\delta_f$  in figure 12 for the several slot shapes. These data show that extending the lip of the slot so that the slot is sealed at the exit when the flap is neutral (shape 1-b) gave an increase of 4 percent in maximum lift coefficient over shape 1-a. Increasing the slot-entry angle (shape 1-c) caused a very slight decrease in maximum lift coefficient. A further change in slot shape to close the gap through the airfoil with the flap neutral (shape 1-e) decreased the maximum lift coefficient 11 percent from the value obtained with slotted flap 1-b.



**Effect of slot shape on profile drag.**—A comparison of the envelope polars for slotted flaps 1-a and 1-b (fig. 13) shows that, for both high lift and low drag, slotted flap 1-b is superior. The higher drag of arrange-

coefficient for take-off with a good slotted flap seems to be around 2.5; therefore, it is important to have as low a profile drag as possible at these high lift coefficients. It is probable that the lower drag of slotted flap 1-b at

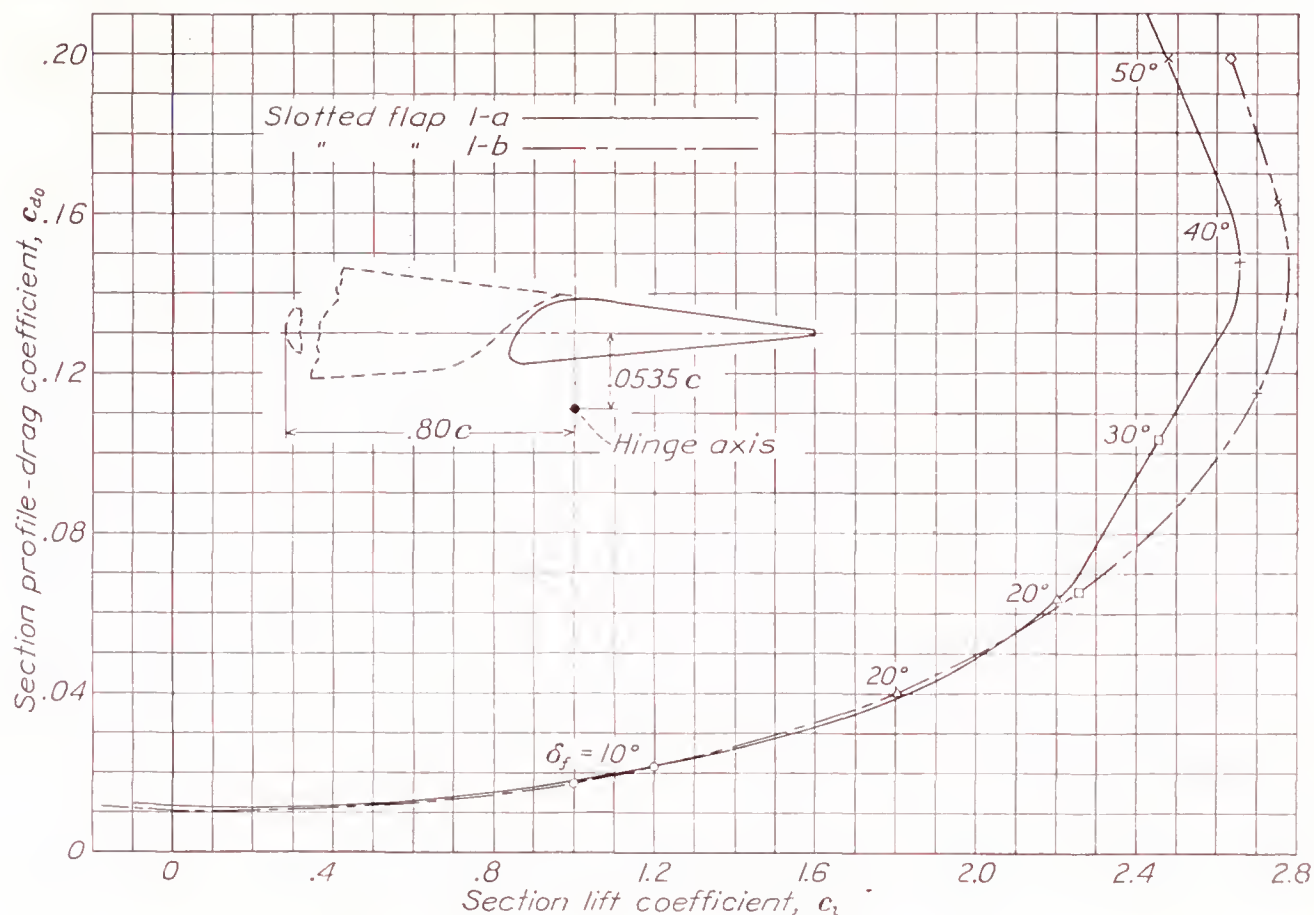


FIGURE 13.—Comparison of slotted flaps 1-a and 1-b.

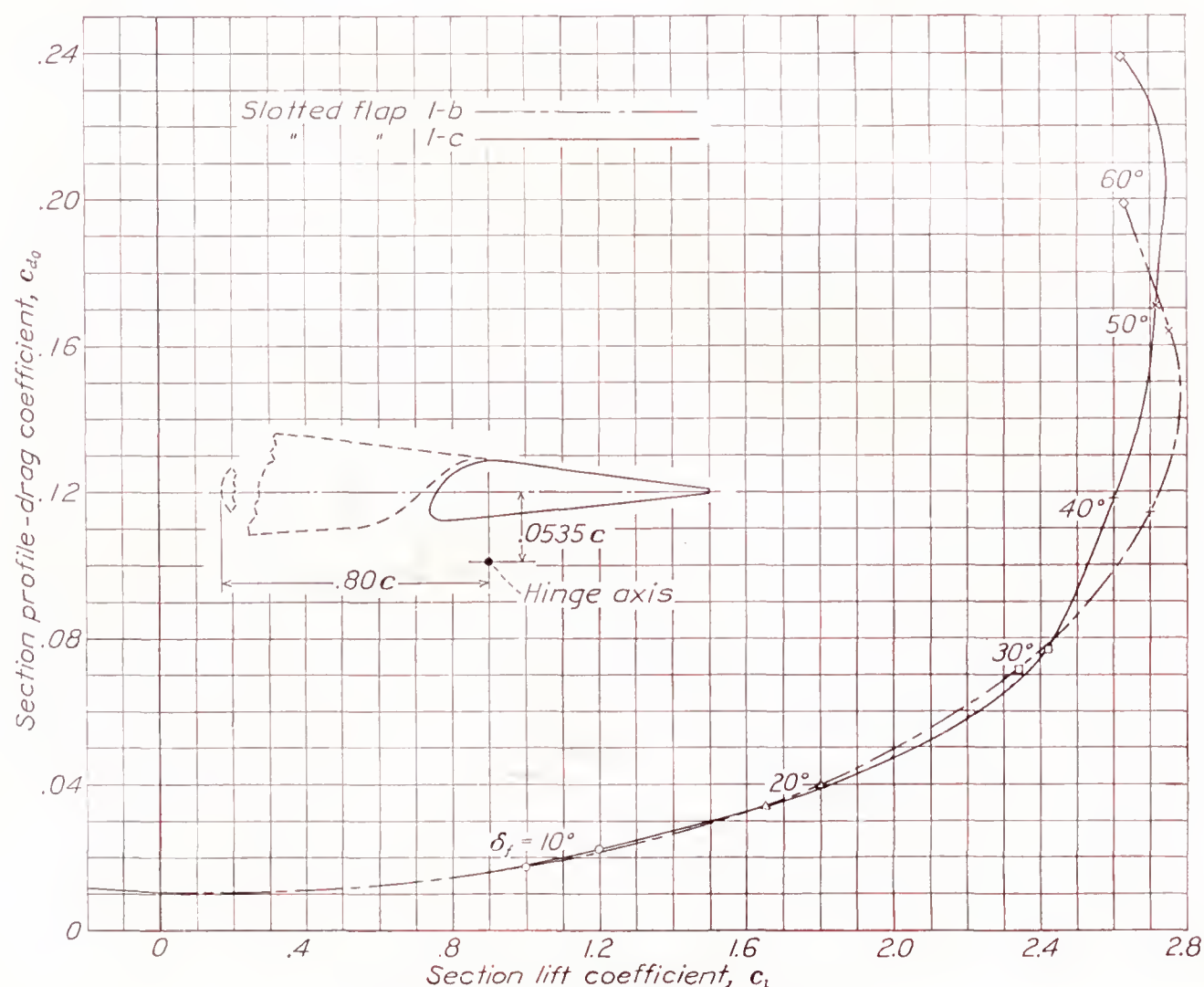


FIGURE 14.—Comparison of slotted flaps 1-b and 1-c.

ment 1-a in the low-lift (high-speed) range can be accounted for by the open slot through the airfoil with the flap neutral. With the wing and the power loadings of present-day large transport airplanes, the best lift

the higher lift coefficients may be accounted for by the better shape of this slot lip, which directs the air downward over the flap and prevents it from stalling at the higher flap deflections. There is no appreciable dif-



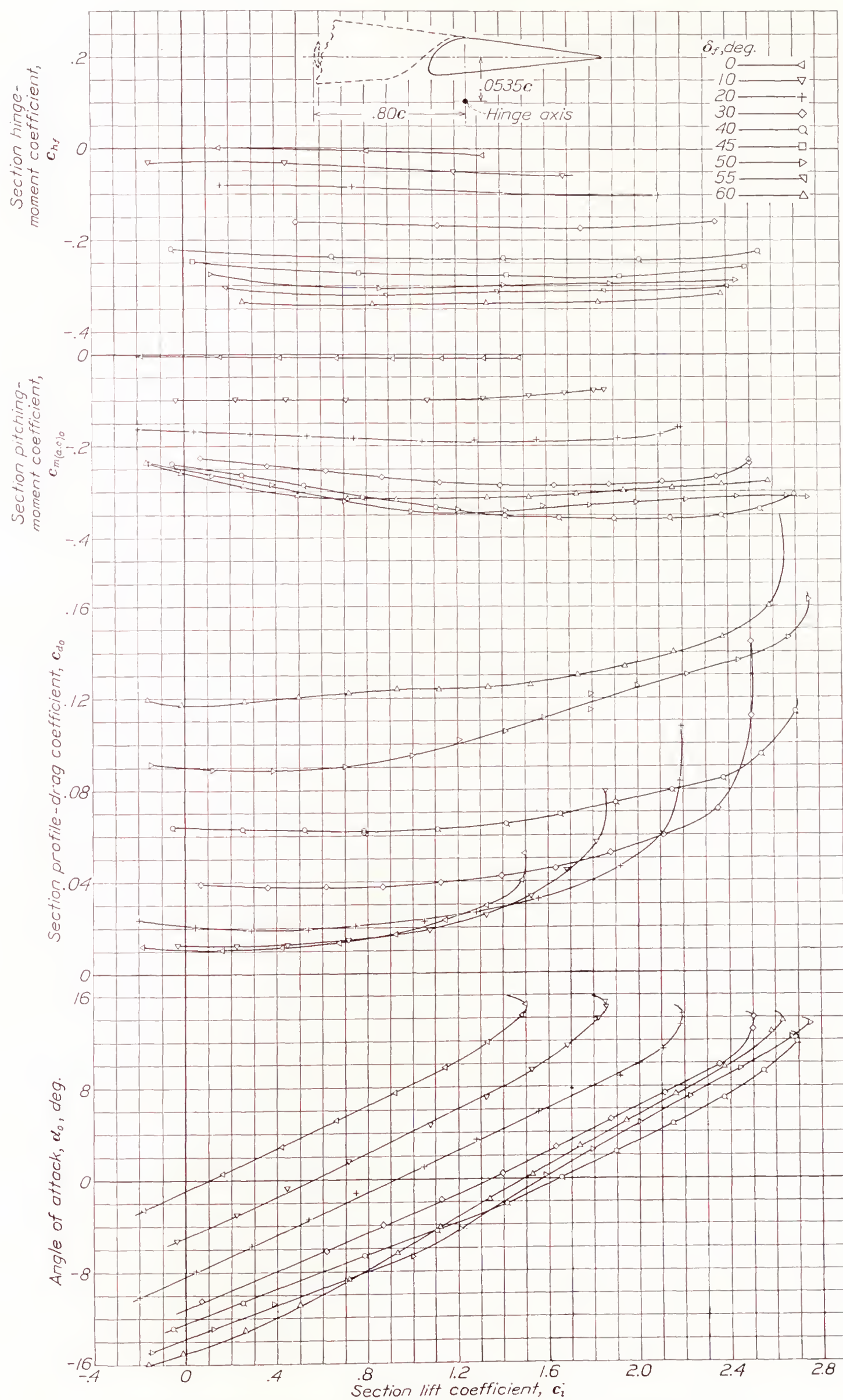


FIGURE 15.—Section aerodynamic characteristics of N. A. C. A. 23012 airfoil with slotted flap 1-b.



ference in drag between slotted flaps 1-b and 1-c up to lift coefficients of about 2.5 (fig. 14). Because of the lower maximum lift of slotted flap 1-e, the drag data for it were not obtained. Other tests of slotted flap 1-e will be discussed later.

axis location was used. The profile drag was also among the lowest. An inspection of the curves of  $\alpha_0$  against  $c_l$  in figure 15 shows that the slope of the lift curves is practically unaffected by flap deflection except for the very large values. As previously mentioned, compari-

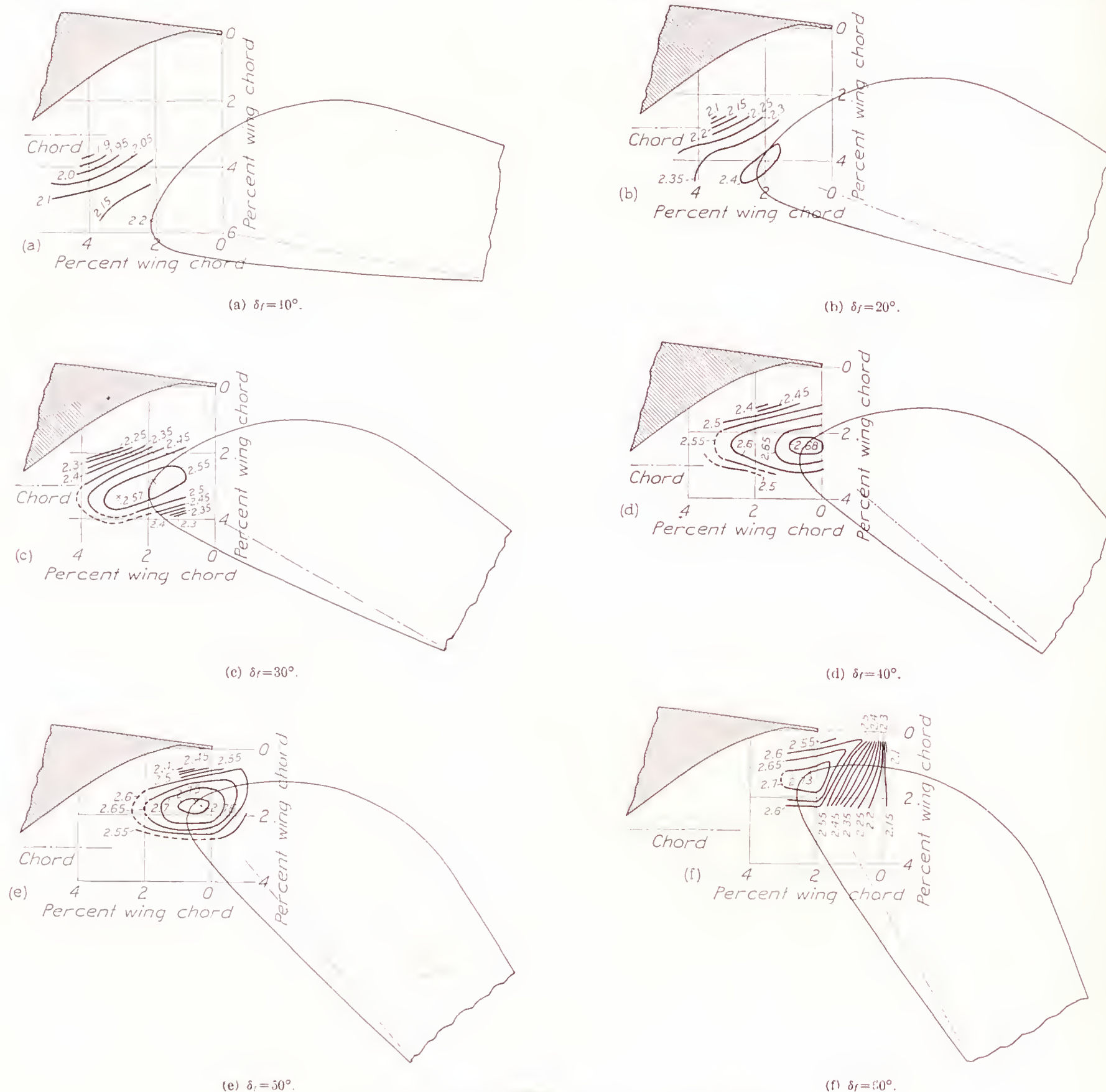


FIGURE 16.—Contours of flap location for  $c_{l_{max}}$ . Slotted flap 1-b.

Complete data on slotted flap 1-b.—The complete section aerodynamic characteristics of the N. A. C. A. 23012 airfoil with slotted flap 1-b deflected downward various amounts are given in figure 15. This flap arrangement gave the highest lift coefficient of any of the four arrangements for which the Handley Page fixed-

son of the  $c_{d0_{min}}$  with the flap neutral with the  $c_{d0_{min}}$  of the plain wing (fig. 7) shows that there is a difference of about 0.001. The greater part of this increase in drag is caused by the flap hinge fittings; the remaining  $\Delta c_{d0}$  is due to the break in the lower surface of the airfoil caused by the slot and will be discussed later.



The pitching-moment coefficients for this flap arrangement are about the same as for the external-airfoil flap. A small change between the pitching-moment coefficients for the flap undeflected ( $\delta_f = 0^\circ$ ) and for the plain airfoil (fig. 7) may be attributed to a slight downward deflection of the slotted flap. The hinge-moment coefficients are about one-half as great as those for the plain flap (fig. 9) because the hinge-axis location for the slotted flap was designed to give partial balance.

#### DETERMINATION OF OPTIMUM SLOTTED-FLAP ARRANGEMENT FOR MAXIMUM LIFT

The data presented in this section are the results of the maximum-lift investigation of the various flap-and-slot combinations in which the flap, at a given deflection, was located at points over a considerable area with respect to the main airfoil. The data are presented as contours of the position of the nose point of the flap for a given lift coefficient. The nose point of the flap is defined as the point of tangency of a line drawn perpendicular to the airfoil chord and tangent to the leading-edge arc of the flap when neutral.

**Slotted flap 1.**—Contours of flap location for maximum lift coefficient for a given flap angle are given in figure 16 for flap 1-b. At  $10^\circ$  flap deflection (fig. 16 (a)), the area of flap positions covered was not sufficient to define the optimum position. The highest  $c_{l_{max}}$  is, however, 19 percent higher than it was for flap 1-b at  $10^\circ$  deflection about the predetermined axis location (fig. 15). It appears that a large gap between wing and flap is desirable for low flap deflections from considerations of maximum lift. At  $20^\circ$  flap deflection (fig. 16 (b)), the optimum position of the nose of the flap is 4 percent below and 2 percent ahead of the slot lip. In this position, the maximum lift is 10 percent higher than it was for the combination given in figure 15. At  $30^\circ$  deflection (fig. 16 (c)), the optimum position of the flap for maximum lift is slightly above the position for the  $20^\circ$  deflection. The maximum lift is 3 percent higher with the flap in the optimum position at this deflection than it was for the same deflection about the predetermined axis location (fig. 15). The optimum position of the flap for deflections up to  $30^\circ$  probably should be chosen from a consideration of the drag coefficients rather than the maximum lift coefficient because the take-off distance of an airplane may be decreased by depressing the flap. It is therefore desirable that the drag coefficient be a minimum for a given lift coefficient corresponding to the lift coefficient for best climb. With the flap deflected  $40^\circ$  and  $50^\circ$  (figs. 16 (d) and (e)), the maximum lift coefficient is about the same as for the same deflections about the predetermined axis location (fig. 15). The optimum positions of the nose point of the flap for these deflections are, respectively, about 2.5 percent below and 0.5 percent ahead of the slot lip and 1.75 percent below and 0.5 percent ahead of the slot lip. For the  $60^\circ$  flap deflection (fig. 16 (f)), the maximum lift coefficient is about 4 percent higher

than for the same deflection about the predetermined axis location (fig. 15). The optimum position of the nose point of the flap for this deflection is about 1 percent below the slot lip.

The contours of figure 16 show that, for small flap deflections, the optimum position of the flap for maximum lift coefficient is much less critical than it is for the larger flap deflections. It is also evident that there is a considerable loss in lift coefficient if the nose of the flap is moved back of the slot lip. These results are in agreement with previous tests of external-airfoil and Fowler flaps. The highest maximum lift coefficient

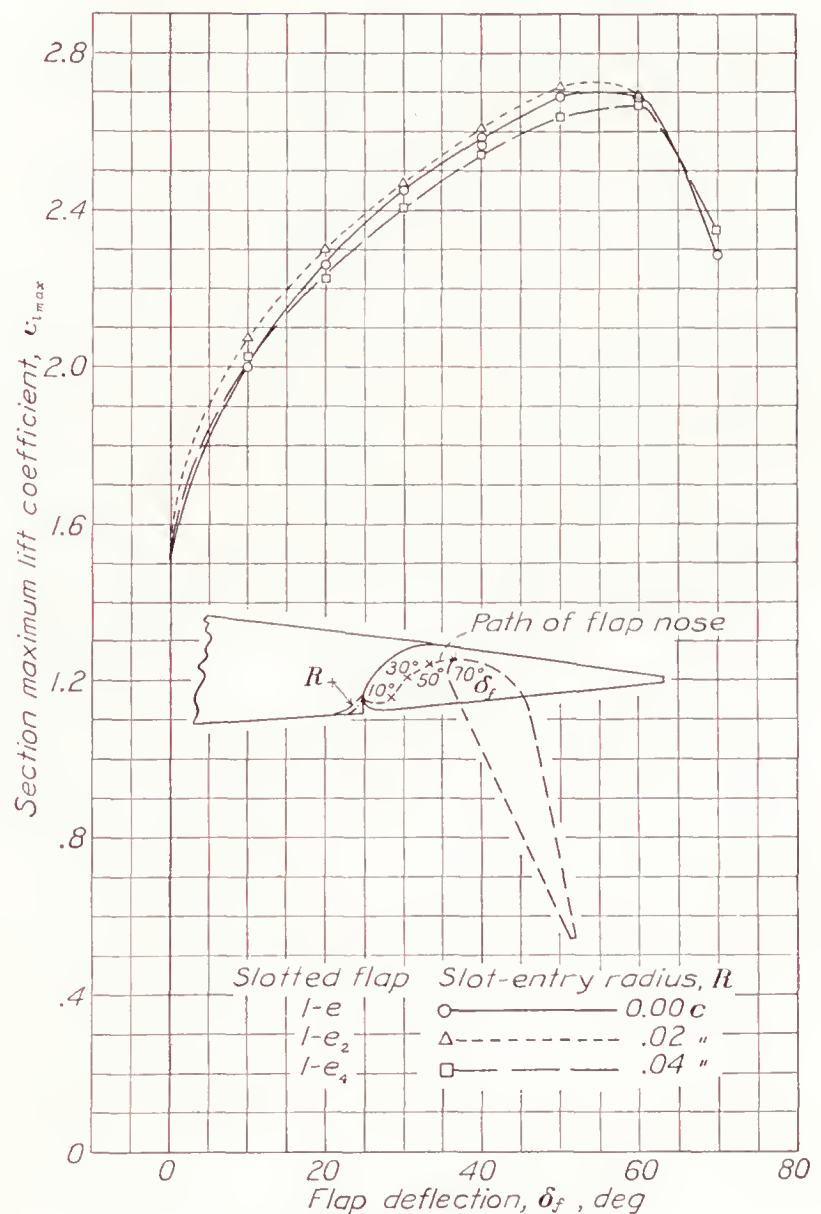


FIGURE 17.—Effect of slot-entry radius on  $c_{l_{max}}$ .

was obtained with the nose of the flap directly under the slot lip and with a gap between the flap nose and the slot lip of about  $1\frac{3}{4}$  percent of the wing chord.

Because of a possible hazard from icing of large openings in the surface of a wing, flap 1 was also tested using slot shape e, with the flap in the best position for maximum lift coefficient from the tests of shape b. The results of these tests are given in figure 17 as plots of maximum lift coefficient against flap deflection. The effect of rounding the slot entry on maximum lift coefficient is also shown in this figure. The maximum lift coefficient of slotted flap 1-e from these tests is about 8 percent higher than it was for this combination with the flap deflected about the predetermined



axis location (fig. 12). With the slot entry rounded to a radius 2 percent of the wing chord (slotted flap 1-e<sub>2</sub>), the maximum lift coefficient is about the same as it was for slotted flap 1-b (fig. 16 (f)). A further rounding of the slot entry to a 4-percent-chord radius had a detrimental effect on the maximum lift. It appears from these results that the shape of the slot is not

combination with flap 1-b, which accounts for the increases in lift. The best positions for the nose of flap 2-h relative to the slot lip are practically the same as for flap 1-b.

The contours showing the maximum lift coefficients for the various deflections of slotted flap 2-i are given in figure 19. This arrangement is inferior to both 1-b

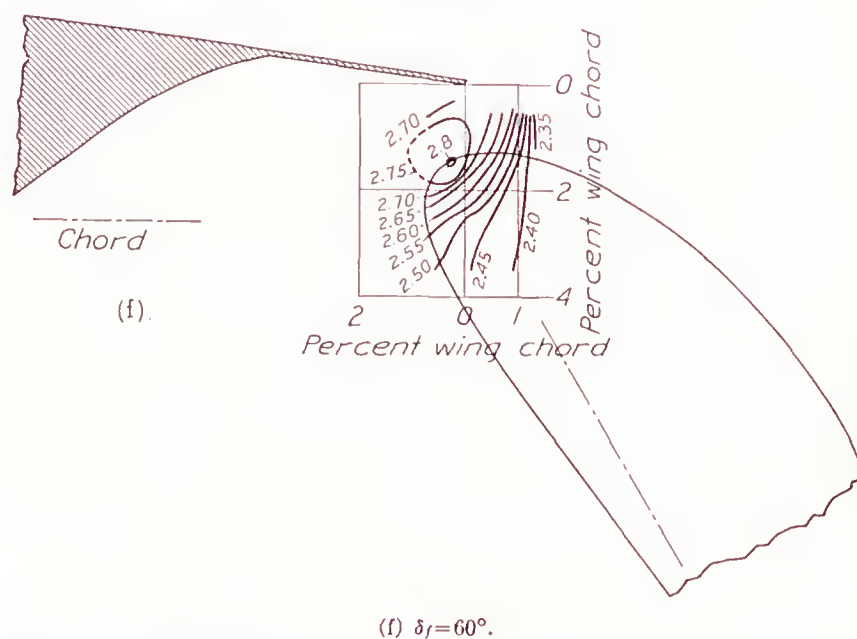
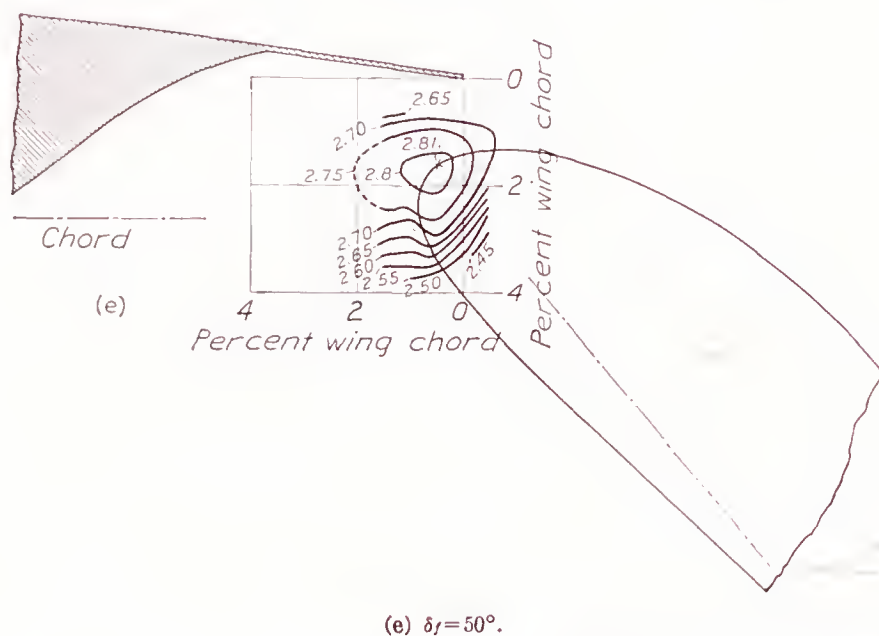
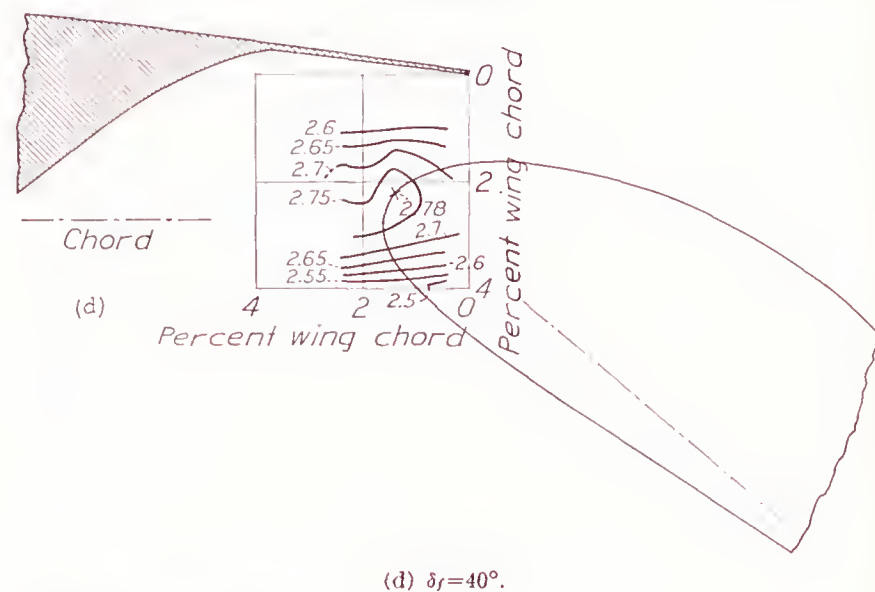
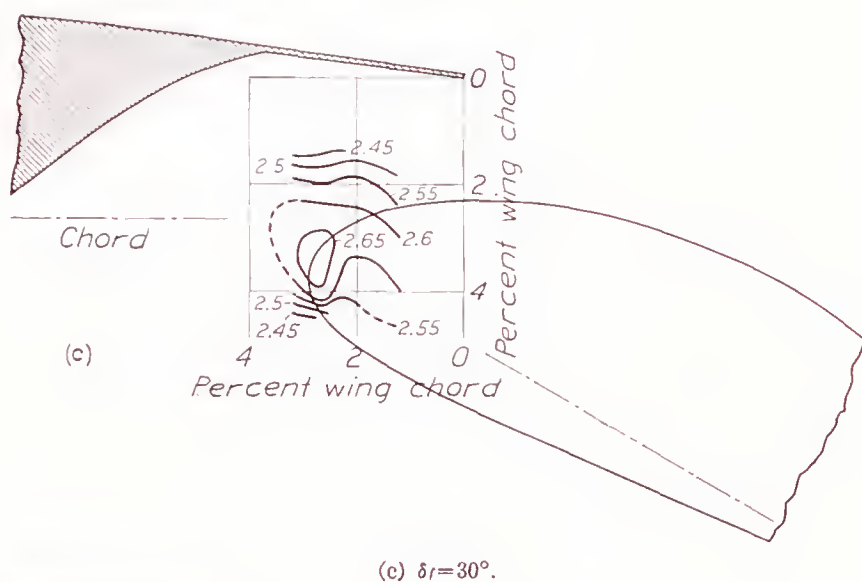
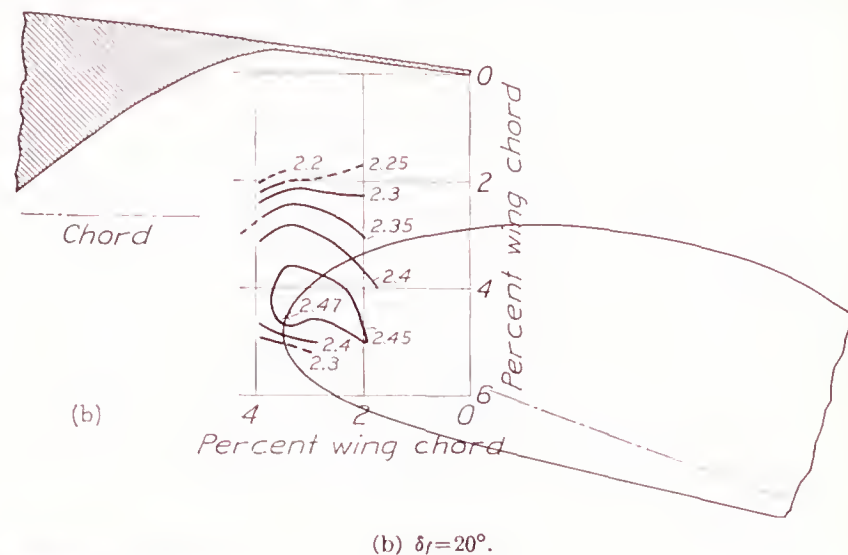
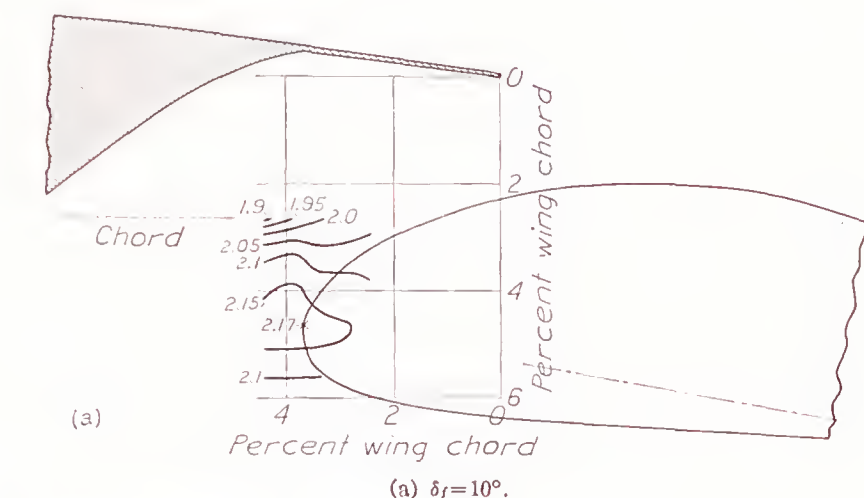


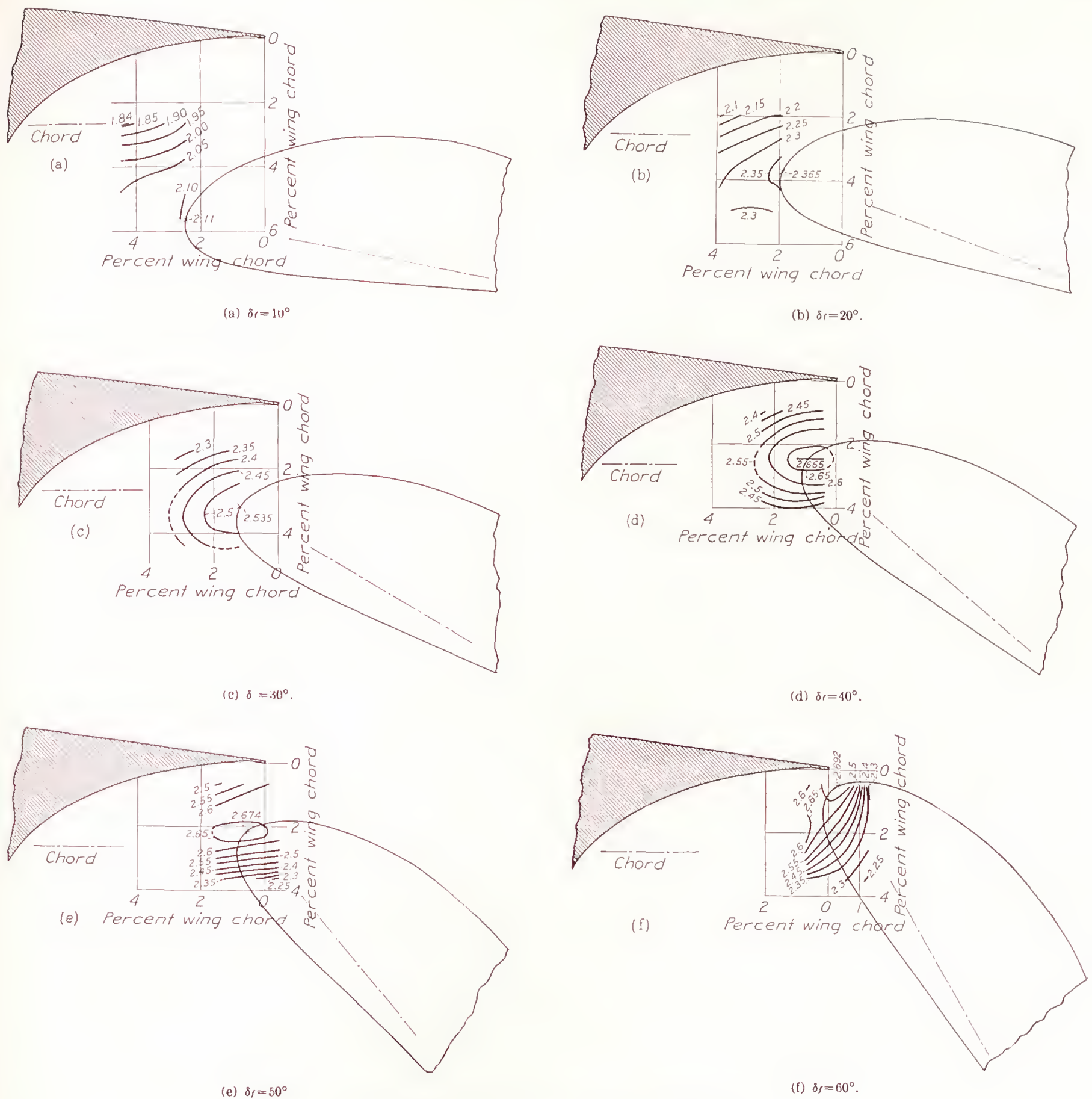
FIGURE 18.—Contours of flap location for  $c_{l_{max}}$ . Slotted flap 2-h.

critical for maximum lift provided that the flap is located properly with respect to the slot lip.

**Slotted flap 2.**—The contours showing maximum lift coefficients for the various deflections of slotted flap 2-h are given in figure 18. This combination gives a higher lift coefficient at each deflection than was obtained at the corresponding flap deflections with flap 1-b (fig. 16). The total projected area of flap 2-h and the main airfoil is greater than the area of the com-

and 2-h throughout the complete range of flap deflections. The maximum lift coefficient was obtained with the flap deflected  $60^\circ$ , which is  $10^\circ$  greater than for either flap 1-b or flap 2-h. The maximum lift coefficient with flap 2-i is about the same as it was for flap 1-e<sub>2</sub> (fig. 17), a comparable arrangement. The position of the flap nose for maximum lift coefficient for this arrangement is only about 0.5 percent of the chord below and about 0.25 percent back of the slot lip.



FIGURE 19.—Contours of flap location for  $c_{l_{max}}$ . Slotted flap 2-i.

**Slotted flap 3.**—Contours of the flap-nose position for the maximum lift coefficients of slotted flaps 3-f and 3-g are given in figures 20 and 21, respectively. Both of these flaps are inferior to all the other slotted-flap combinations tested, and both have about the same maximum lift coefficient. No tests were made at the small flap deflections because of the inferiority of the flaps at the large flap deflections. The nose shape of this flap is probably too blunt to obtain a satisfactory flow of the air over the upper surface of the flap.

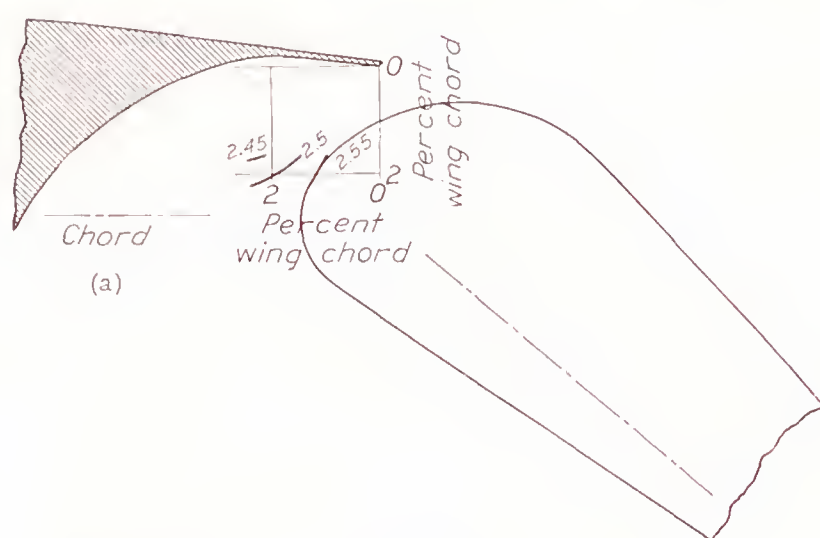
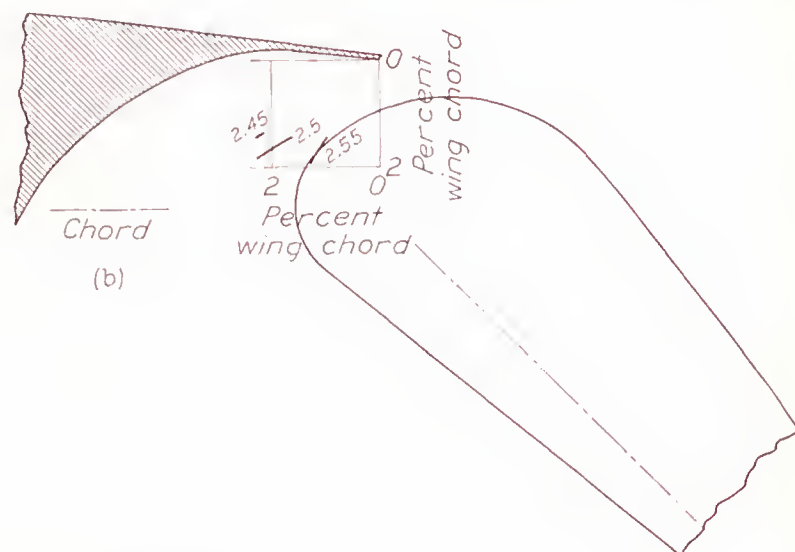
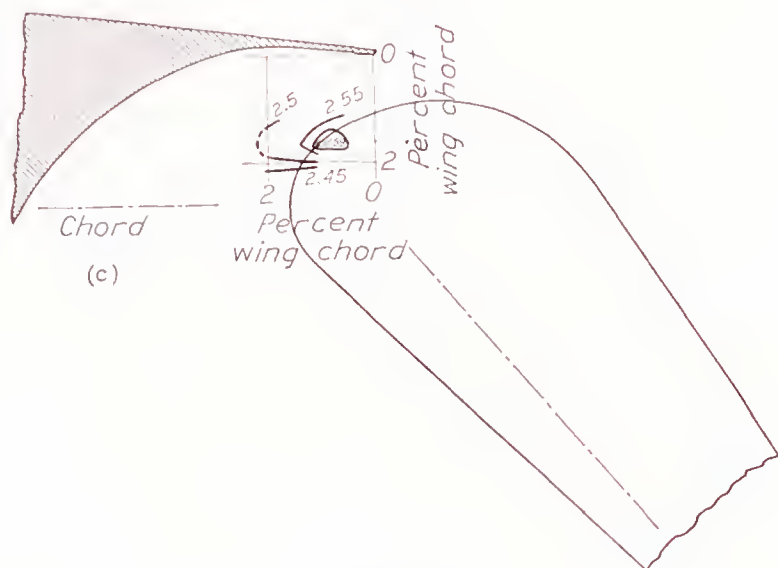
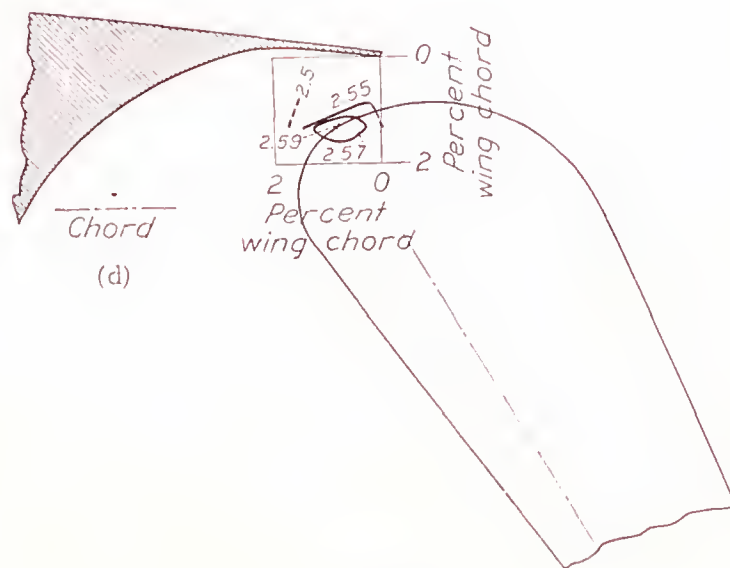
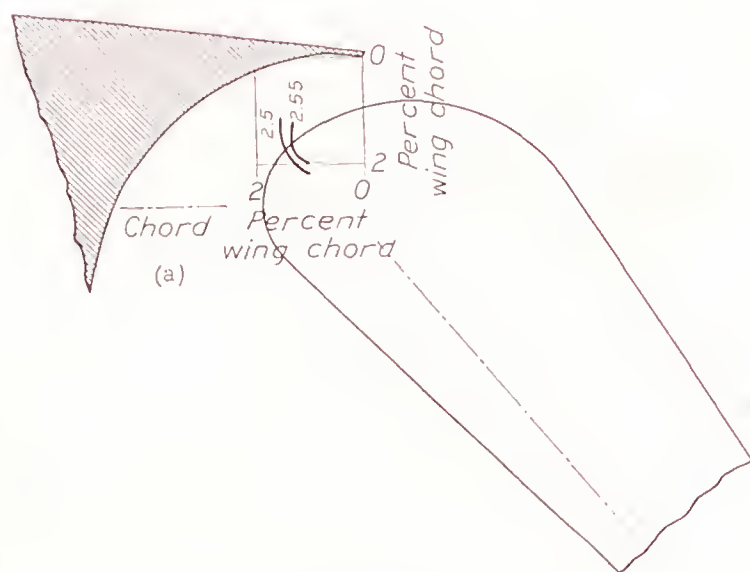
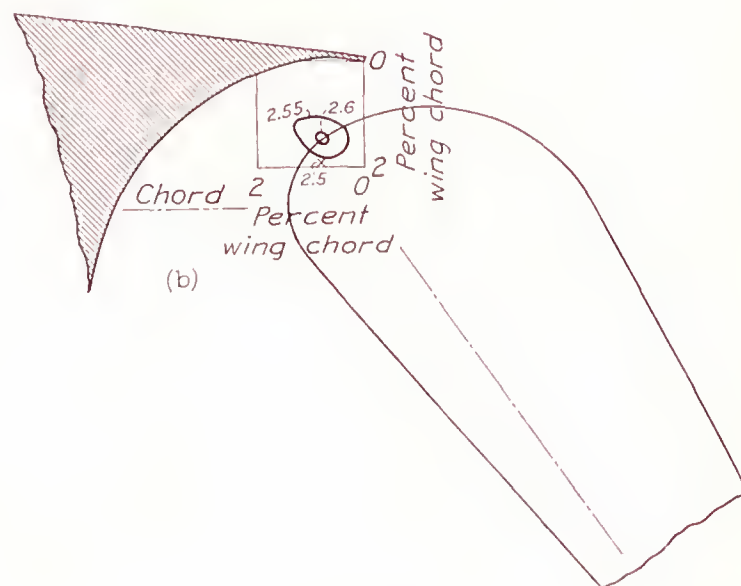
#### EFFECT ON PROFILE DRAG OF BREAK IN AIRFOIL SURFACE DUE TO SLOT

The increments of profile drag  $\Delta c_{d_0}$  caused by the breaks in the airfoil surface at the flap are plotted in figure 22. These data were obtained by making tests with the flap undeflected both with and without the breaks in the surface. (The breaks in the surface were sealed with plasticine for the tests without the breaks.) The curves given in figure 22 are differences between faired curves through the test points for the individual



tests. Slotted flap 1-a, which has an open slot through the airfoil with the flap undeflected, gave the largest increment of profile-drag coefficient for all lift coefficients up to 0.60. At the higher lift coefficients, the  $\Delta c_{d_0}$  decreases probably because of some boundary-layer con-

gave a  $\Delta c_{d_0}$  of 0.0004, which increased to 0.0009 at the higher lift coefficients. Slotted flaps 1-e<sub>2</sub> and 2-i are the next in order giving, at zero lift, a  $\Delta c_{d_0}$  of 0.0003 increasing nearly to 0.0008 at the higher lift coefficients. Slotted flap 1-e gave a  $\Delta c_{d_0}$  of about 0.0001 for the low-

(a)  $\delta_f = 40^\circ$ .(b)  $\delta_f = 45^\circ$ .(c)  $\delta_f = 50^\circ$ .(d)  $\delta_f = 60^\circ$ .FIGURE 20.—Contours of flap location for  $c_{l_{max}}$ . Slotted flap 3-f.(a)  $\delta_f = 50^\circ$ .(b)  $\delta_f = 55^\circ$ .FIGURE 21.—Contours of flap location for  $c_{l_{max}}$ . Slotted flap 3-g.

trol from the air ejected on the upper surface of the airfoil. The  $\Delta c_{d_0}$  for slotted flaps 1-b and 2-h increased from about 0.0008 at zero lift to about 0.0013 at a lift coefficient of 1.0. At zero lift, slotted flap 1-e<sub>4</sub>

lift condition, which increased nearly to 0.0003 at a lift coefficient of about 0.50 and then decreased to zero at higher lift coefficients. Slotted flap 1-e showed no increase in profile drag. It should be pointed out



that a  $\Delta c_{d0}$  less than 0.0003 is too small to measure definitely because such a small value is within the experimental accuracy of the tests.

#### DETERMINATION OF THE OPTIMUM SLOTTED-FLAP ARRANGEMENT FOR PROFILE DRAG

The results presented in this section are intended to aid in the determination of the optimum positions of the several slotted flaps for take-off and climb from considerations of low drag. The best take-off and climb to clear a specified height in the shortest horizontal distance will be the lowest drag coefficient at the lift coefficients corresponding to take-off and climb. The data are therefore given as contours of the nose position of the flap for constant drag coefficients at certain selected lift coefficients that cover the range for which the drag coefficient is decreased by deflecting the flap. The data previously presented show that, for

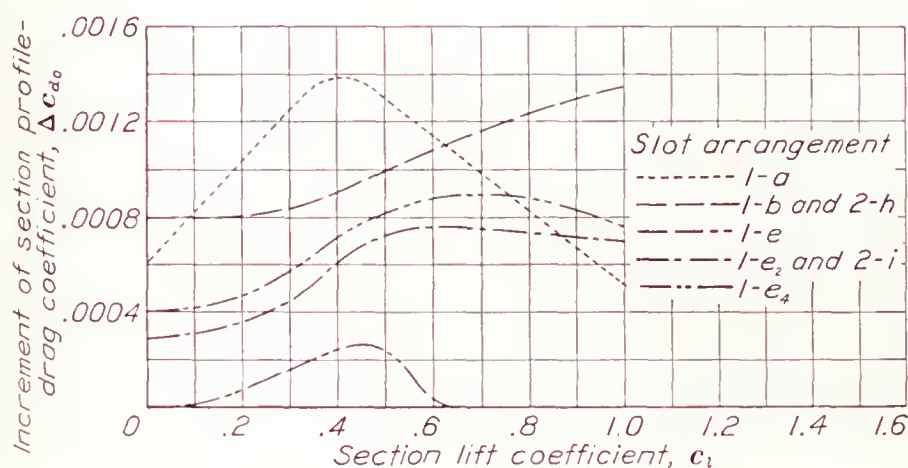


FIGURE 22.—Effect of slot openings in surface of airfoil on increments of profile drag  $\delta_f$ ,  $0^\circ$ ; effective Reynolds Number, 3,500,000.

lift coefficients of 1.0 or less, the drag is lowest with the flap undeflected.

**Slotted flap 1.**—The contours of the position of the nose point of slotted flap 1-b for constant  $c_{d0}$  are given in figure 23. The best position for this flap at a lift coefficient of 1.5 (fig. 23 (a)) is with the nose point of the flap 5 percent of the chord below and 4 percent of the chord ahead of the slot lip. The minimum profile-drag coefficient is 0.027, and the position for drag coefficients up to 0.028 is not very critical. At a lift coefficient of 2.0 (fig. 23 (b)), the best position is about 1 percent above and much more critical than the best position for a lift coefficient of 1.5. The minimum profile-drag coefficient is 0.046 with the flap in the best position at a lift coefficient of 2.0. The optimum position of the nose of the flap, for minimum drag at a lift coefficient of 2.5 (fig. 23 (c)), is 2.5 percent below and 2.5 percent of the chord ahead of the slot lip. The minimum profile-drag coefficient, when the flap is in this position, is 0.096 and the position for the low drag is very much more critical than at the lower lift coefficients. The flap angles for minimum profile

drag at  $c_l=1.5$ , 2.0, and 2.5 are, respectively, about  $15^\circ$ ,  $22^\circ$ , and  $30^\circ$ .

No detailed surveys were made with slotted flap 1-e, but the effect on  $c_{d0}$  of rounding the slot entry is shown in figure 24 as envelope polars. Rounding the slot entry with a radius 2 percent of the wing chord gives

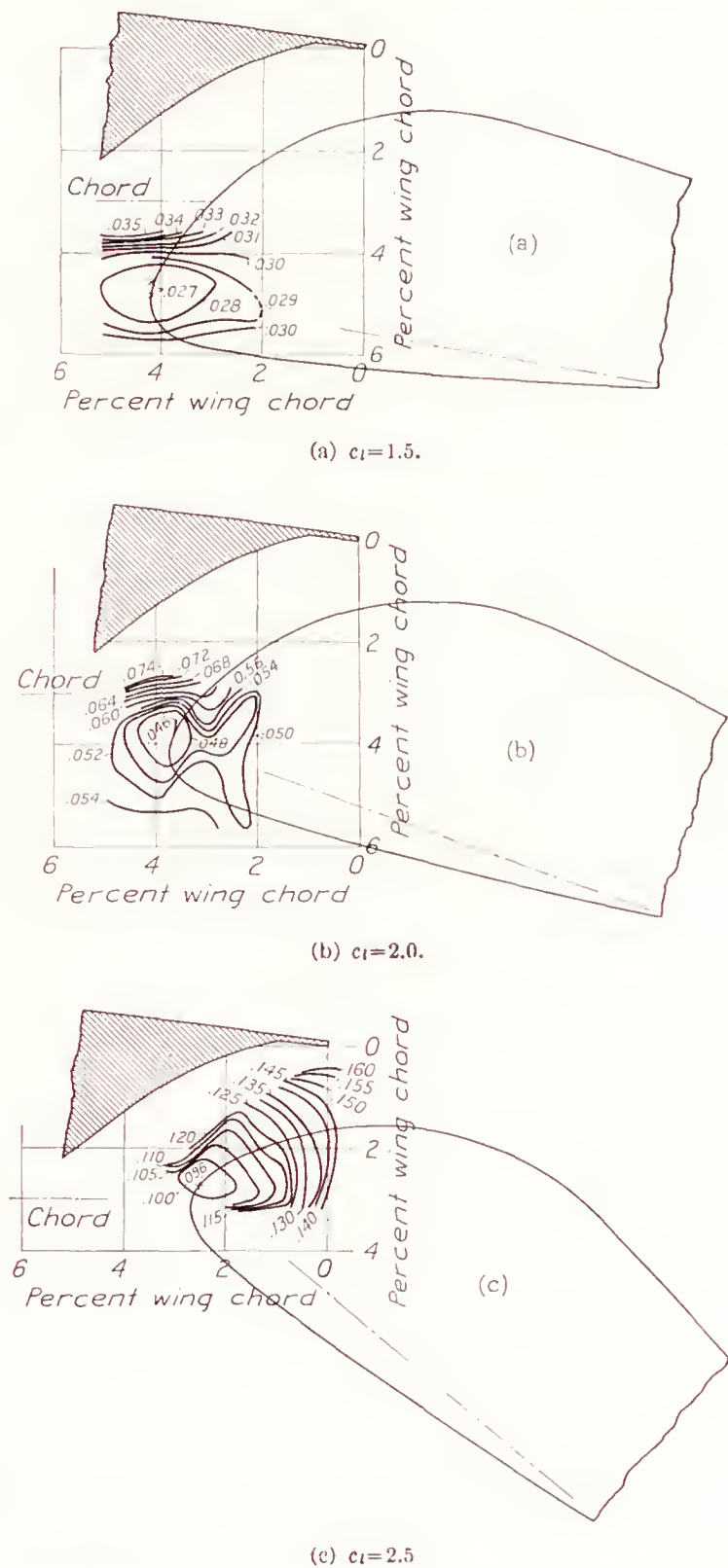


FIGURE 23.—Contours of flap location for  $c_{d0}$ . Slotted flap 1-b.

a considerable decrease in  $c_{d0}$  at all values of the lift coefficient. When the entry radius is increased to 4 percent of the wing chord, however, there is no further decrease in  $c_{d0}$  but a considerable increase at the high lift coefficients. The best arrangement of slot shape e, slotted flap 1-e<sub>2</sub>, is inferior to slotted flap 1-b throughout the complete range of flap deflections.



**Slotted flap 2.**—The contours of the position of the nose point of slotted flap 2-h for constant  $c_{d0}$  are given in figure 25. At  $c_l=1.5$  (fig. 25 (a)), the minimum profile-drag coefficient is about 4 percent less than it was for slotted flap 1-b. The position of the flap nose for the minimum profile-drag coefficient is not very critical and the tests did not cover a sufficient area to close any of the contours. For  $c_l=2.0$  (fig. 25 (b)), the minimum profile-drag coefficient is about 8 percent

ceding comparison of slotted flap 1-b and 2-h shows arrangement 2-h to be superior throughout, probably because of the better nose shape of the flap.

The contours of the position of the nose point of slotted flap 2-i for given profile-drag coefficients are shown in figure 26. A comparison of these contours with those for slotted flap 1-b (fig. 23) and 2-h (fig. 25) shows flap 2-i to be inferior to both of the others throughout the lift range. It is therefore apparently necessary

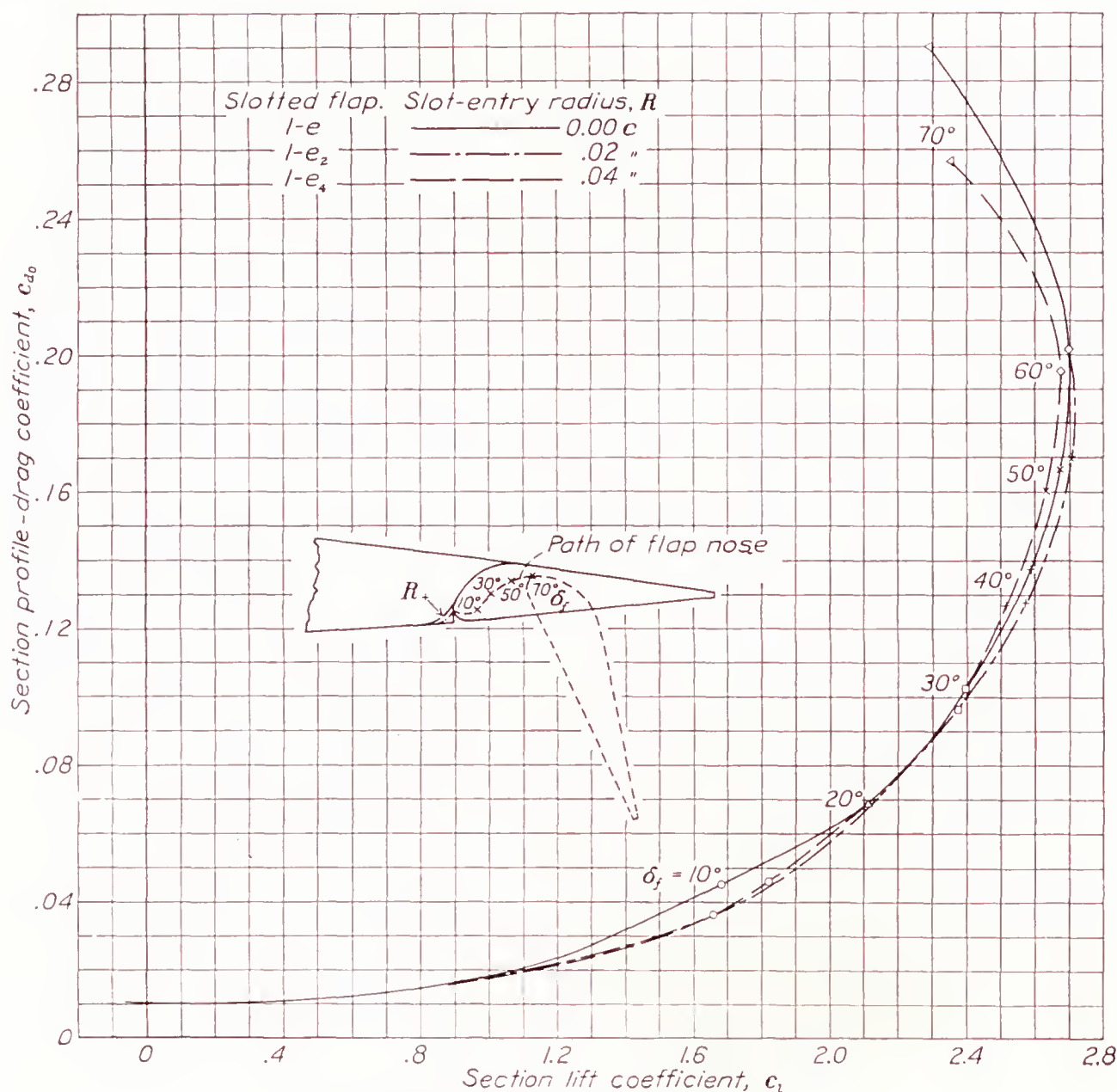


FIGURE 24.—Effect of slot-entry radius on  $c_{d0}$ .

lower than for slotted flap 1-b. The contours are not closed for this lift coefficient and the position for minimum profile drag is again not very critical. The contours of profile-drag coefficient at  $c_l=2.5$  (fig. 25 (c)) show the minimum to be 25 percent less than it was for slotted flap 1-b. The position of the flap nose for minimum profile drag is critical at about 3.5 percent below and 3.0 percent of the wing chord ahead of the slot lip. There is, however, a second region of low drag farther ahead and closer to the slot upper boundary for which the contours are not closed. The pre-

that the slot have an easy entry in order to have low drag together with high lift.

#### EFFECTS OF SLOTTED FLAP WITH SPLIT FLAP

**Effect on maximum lift.**—The effect on  $c_{l_{max}}$  of the addition of a  $0.05c$  split flap, deflected downward  $60^\circ$ , to slotted flap 1-b is shown in figure 27. This comparison was made with the slotted flap hinged in such a way that it was in the optimum position for the maximum lift coefficient when deflected downward  $60^\circ$  without the split flap. The increase in maximum lift



coefficient for small deflections of the combination is quite large. The maximum lift coefficient with the combination down  $25^\circ$  is the same as it is with slotted flap 1-b alone down  $50^\circ$ . The maximum lift coefficient with the combination down  $50^\circ$  is, however, only 2 percent higher than for the slotted flap alone in its opti-

higher drag than the slotted flap alone for lift coefficients less than 2.2. It is possible, however, that lower drags could be obtained by using smaller deflections of the split flap at the smaller deflections of the slotted flap. The combination has a lower drag than the slotted flap alone at lift coefficients above 2.2. These results indi-

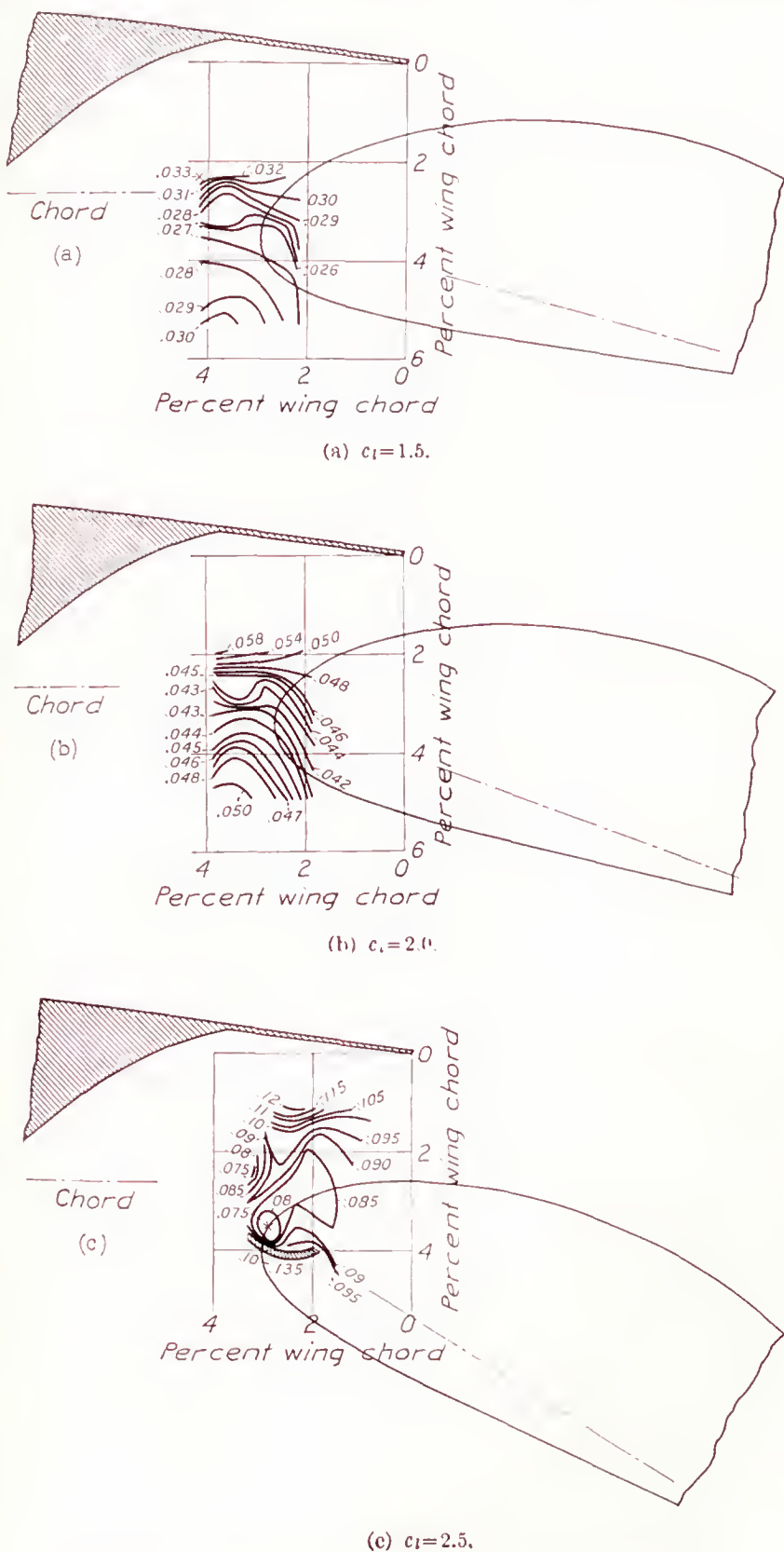


FIGURE 25.—Contours of flap location for  $c_{d0}$ . Slotted flap 2-h.

imum position. It is possible, however, that higher maximum lift coefficients may be obtained by a more comprehensive investigation.

**Effect on profile drag.**—The effect on  $c_{d0}$  of the addition of the split flap to slotted flap 1-b is shown in figure 28 by envelope polars. The combination has

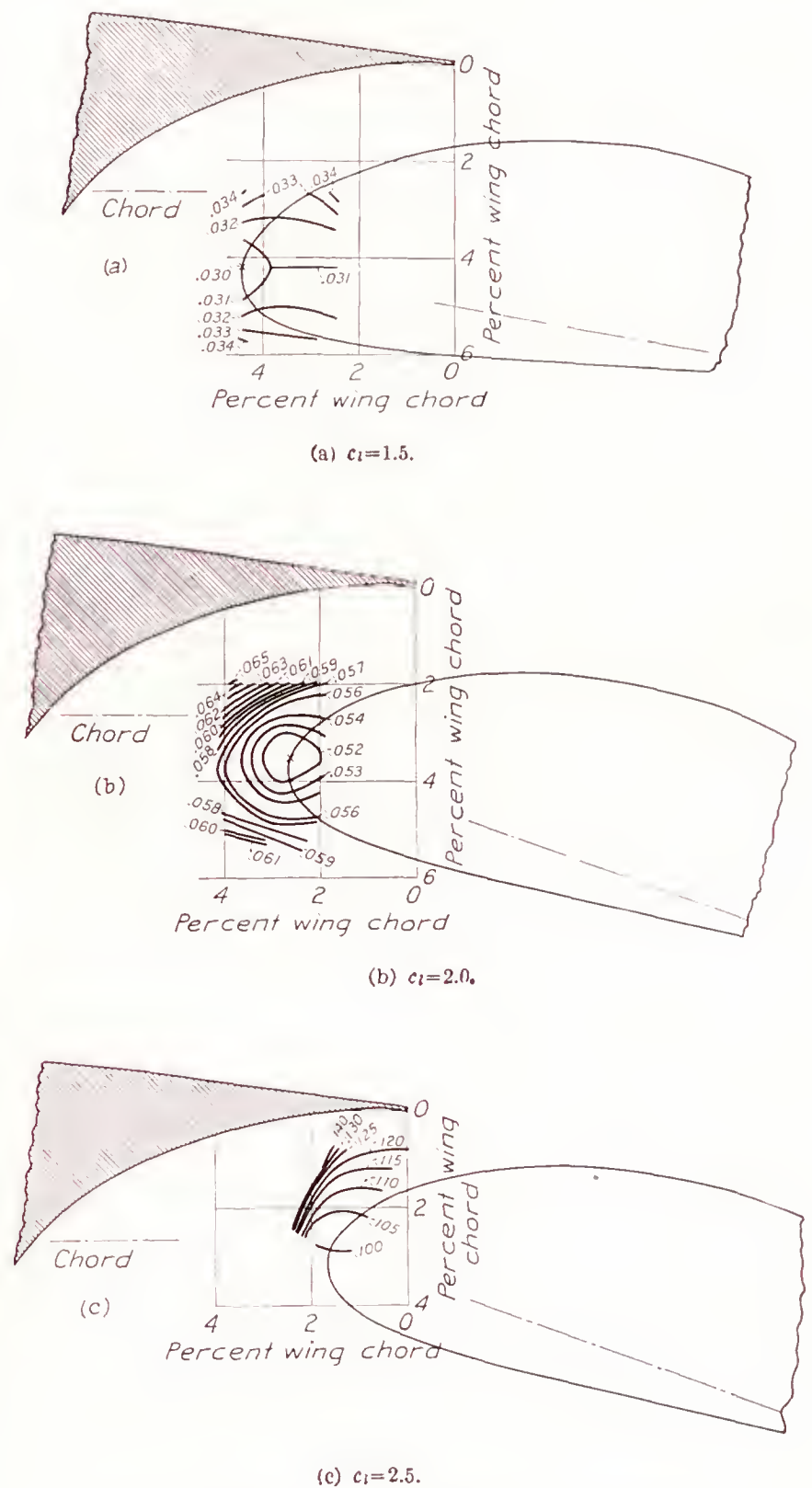


FIGURE 26.—Contours of flap location for  $c_{d0}$ . Slotted flap 2-i.

cate that multiple-slot flaps might be developed which would be superior, from considerations of low drag for take-off and high lift for landing, to any of the slotted flaps investigated. Further investigation is recommended of multiple-slot flaps and of slotted flaps in combination with plain and with split flaps.



## OPTIMUM ARRANGEMENT OF SLOTTED FLAP

The optimum flap arrangement was chosen on the basis of minimum profile-drag coefficient at a given lift coefficient for lift coefficients less than 2.5 and of maximum lift coefficient for the larger flap deflections. On this basis, slotted flap 2-h was superior to any of the other flap combinations tested. The data for slotted flap 2-h, when moved along the optimum path shown, are given in figure 29. Flap-load and moment data from pressure-distribution tests will be available for this combination at a later date.

## COMPARISON OF FIVE TYPES OF FLAP

**Effect on maximum lift.**—Increments of maximum lift coefficient  $\Delta c_{l_{max}}$  are plotted in figure 30 against flap deflection to show how the effect of flap deflection upon maximum lift varies with the five types of flap tested; namely, split, plain, external-airfoil, Fowler, and slotted flap 2-h. All coefficients are, of course, based on area with the flap neutral and the increments, except for the external-airfoil flap, are taken from the  $c_{l_{max}}$  of the plain wing.

It is evident that the two slotted types which give increased area in the deflected positions give the highest maximum-lift increments. The values for slotted flap 2-h are somewhat lower than for the Fowler flap. The Fowler flap, however, may be considered as a special case of the slotted flap in which the

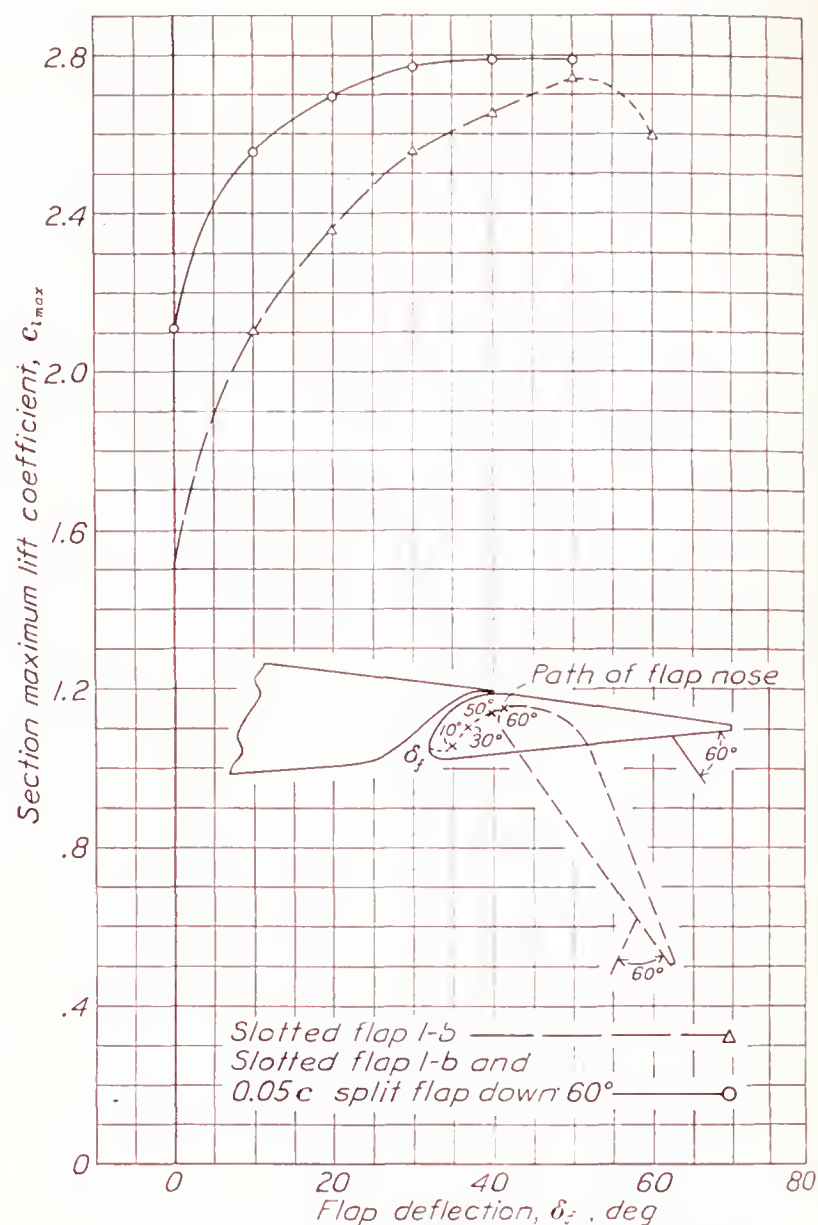


FIGURE 27.—Effect on  $c_{l_{max}}$  of combining split flap with slotted flap. Slotted flap 1-b.

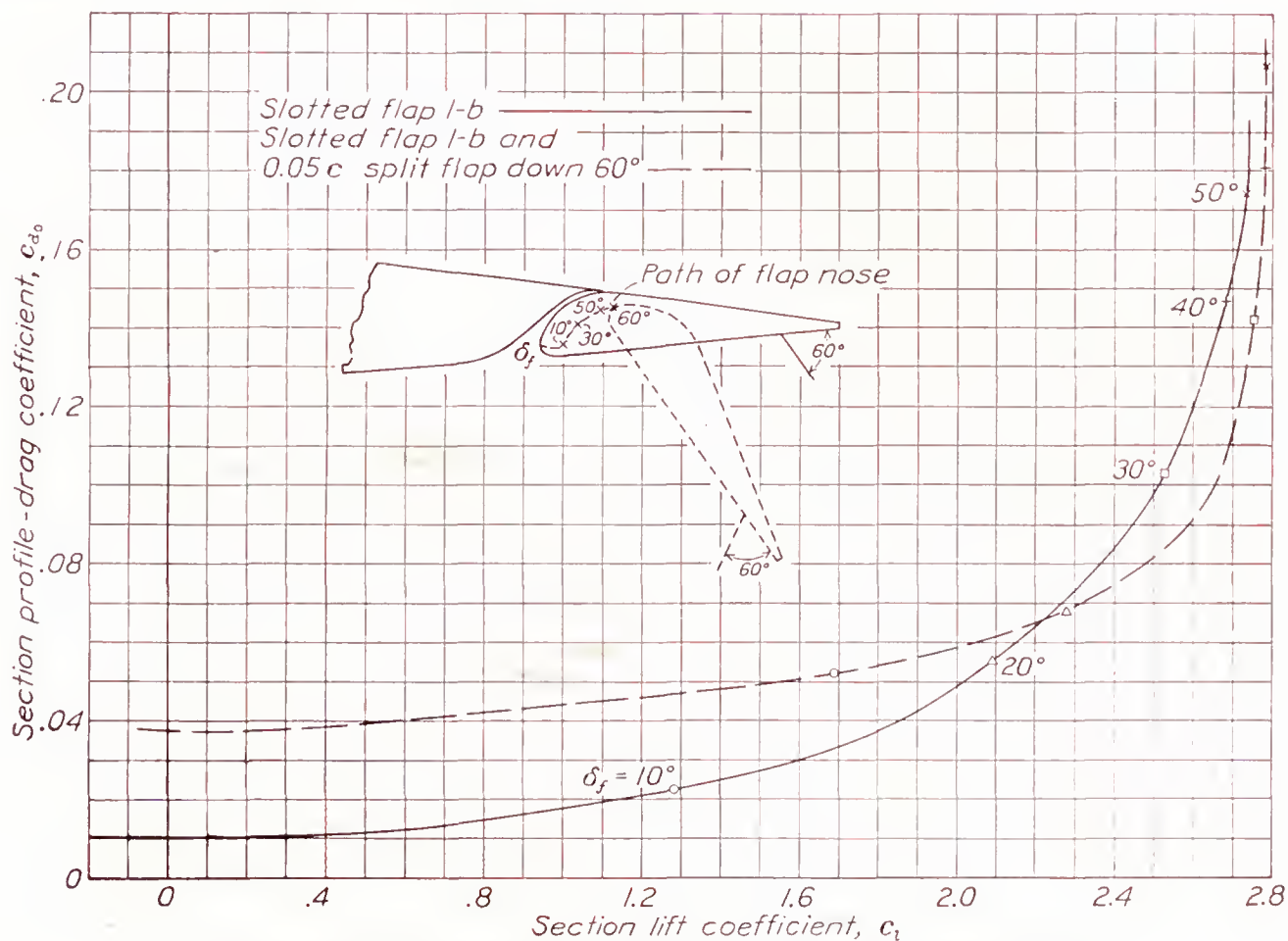
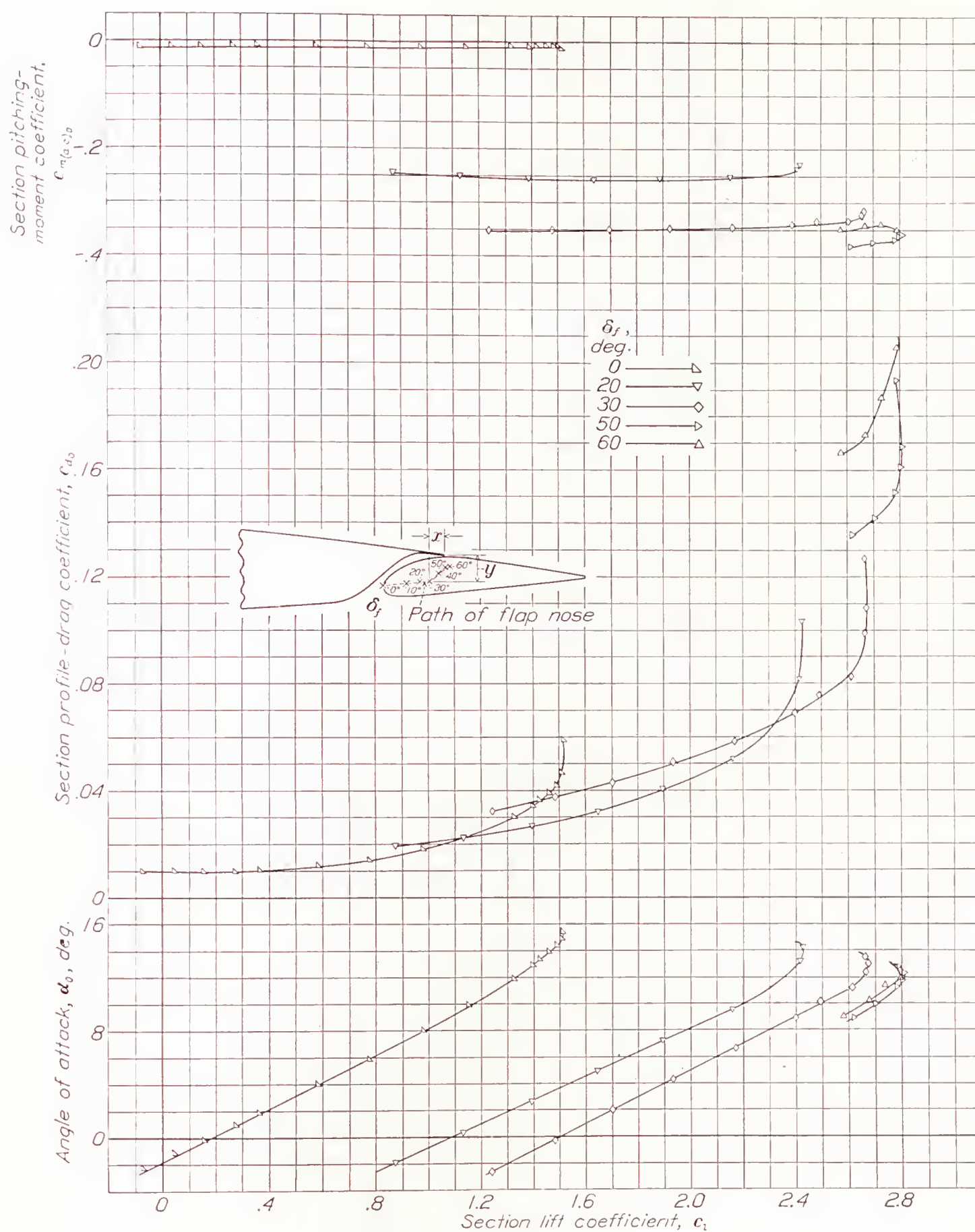


FIGURE 28.—Effect on  $c_{d_0}$  of combining split flap with slotted flap. Slotted flap 1-b.





Path of flap nose for various flap deflections. Distances measured from lower edge of lip in percent airfoil chord  $c$

$\delta_f$ (deg.)	$x$	$y$
0	8.36	3.91
10	5.41	3.63
20	3.83	3.45
30	2.63	3.37
40	1.35	2.43
50	.50	1.63
60	.12	1.48

FIGURE 29.—Section aerodynamic characteristics of N. A. C. A. 23012 airfoil with slotted flap 2-h.



lip of the slot is extended to the trailing edge of the basic airfoil. The flap is therefore moved through a greater distance when extended and deflected and, consequently, gives more lift because of the greater lifting surface exposed to the air. Slotted flaps could be developed with the slot lip terminated at any point between the location for slotted flap 2-h, or farther forward, and the trailing edge of the airfoil. These slotted flaps would be expected to give  $c_{l_{max}}$  increases corresponding to the increased airfoil area.

**Effect on profile drag.**—The effect on  $c_{d_0}$  of the five types of flap is shown in figure 31 by envelope polars. The five types of flap have about the same profile-drag coefficients for lift coefficients less than 0.90. The airfoil with slotted flap 2-h has the lowest profile drag for lift coefficients from about 1.0 to 1.7. The airfoil with the Fowler flap is somewhat better than slotted flap 2-h as regards low profile drag at lift coefficients greater than 1.7. Here again it is probable that a slotted flap with a greater lip extension could be developed to give an even lower drag at high lift coefficients.

When the horizontal distance to land over a given obstacle is restricted, if a high drag together with a high lift is desirable, slotted flap 2-h is superior to the four other types of flap tested.

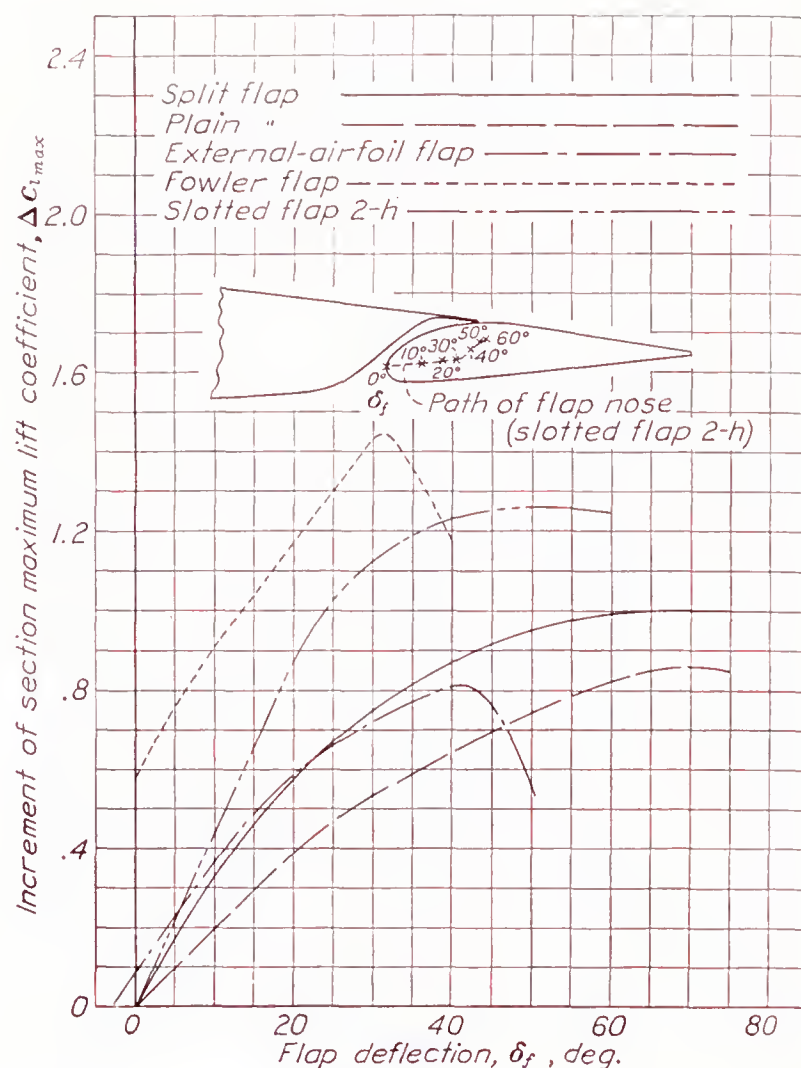


FIGURE 30.—Comparison of increments of maximum lift coefficients for five types of flap.

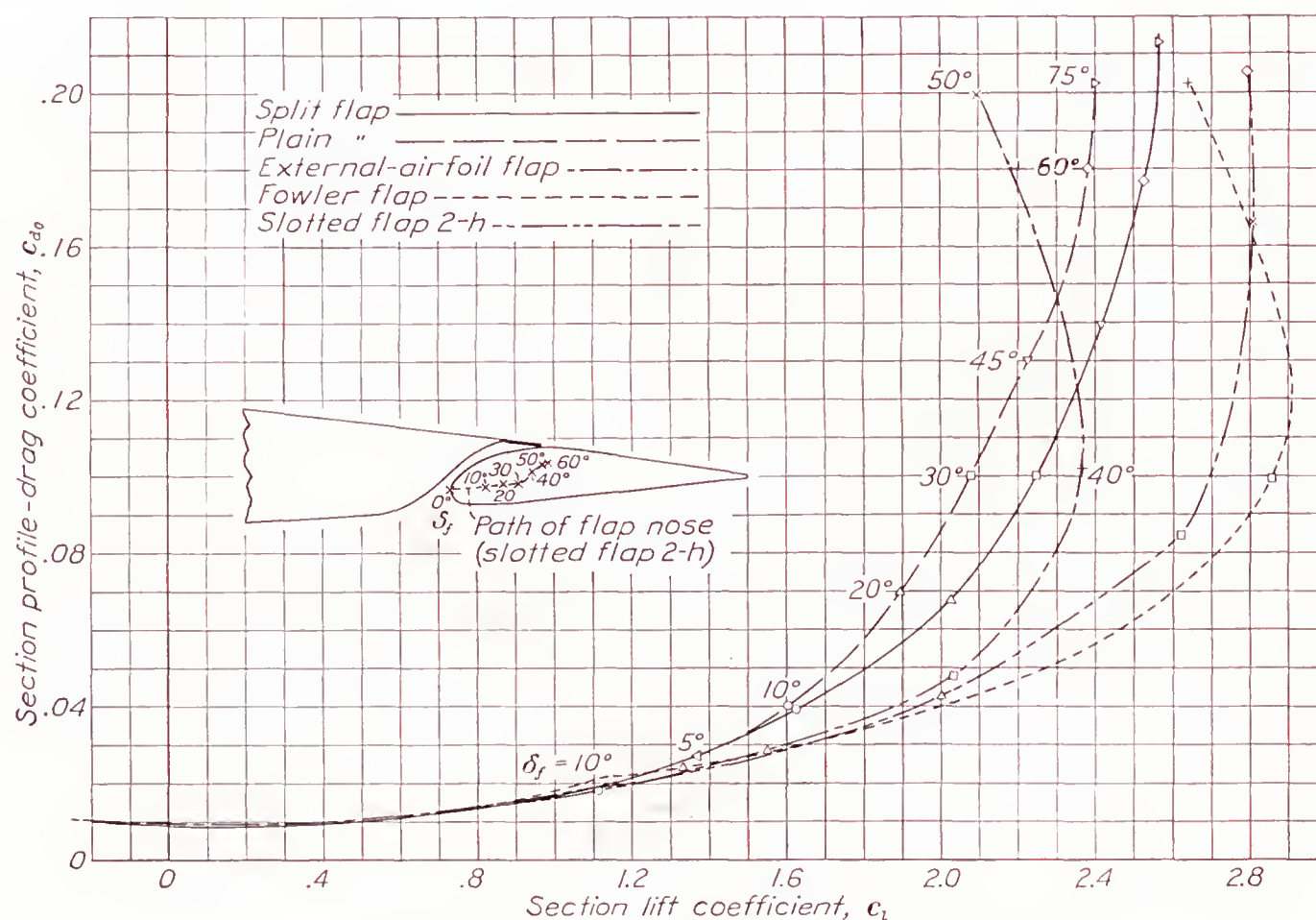


FIGURE 31.—Comparison of profile-drag coefficients for five types of flap.



## II. TESTS IN VARIABLE-DENSITY WIND TUNNEL

### APPARATUS AND TESTS

The variable-density wind tunnel is described in reference 17, except that an automatic electric balance has been installed to measure force coefficients. The precision is discussed in references 14 and 18.

The basic airfoil was made of duralumin to the N. A. C. A. 23012 profile. The 25.66-percent-chord slotted flap was built of brass to the ordinates given for flap 2 in table II. The shape of the slot and the posi-

lower surface. When the flap was deflected, the V-shape groove formed on the upper surface at the 40-percent point was filled with plaster of paris, forming a fair and rounded juncture.

The lift, the drag, and the pitching moment were measured from below zero lift to beyond maximum lift at an effective Reynolds Number of about 8,000,000. The lift in the region of maximum lift was also measured at an effective Reynolds Number of about 3,800,000. The measurements were made at flap settings of 0°,

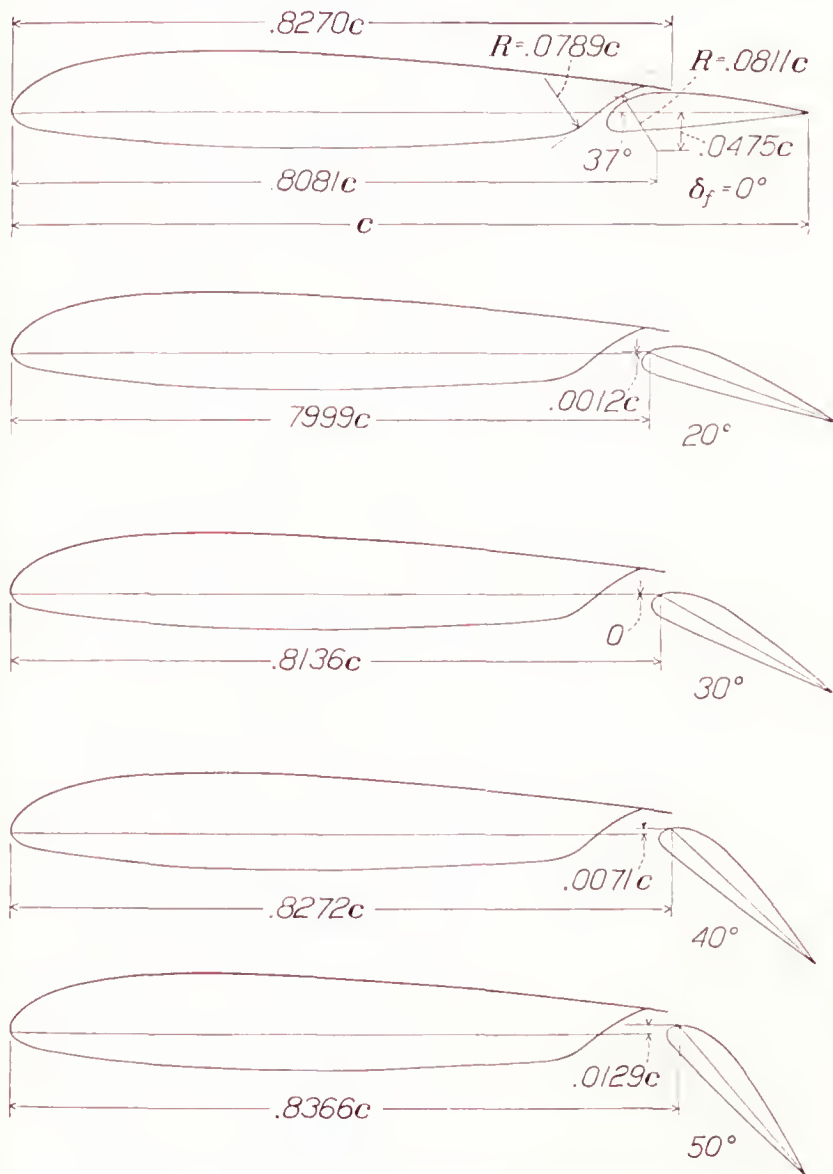


FIGURE 32.—Sections of airfoil with 0.2566c slotted flap 2-h.

tions of the flap for the various flap deflections ( $\delta_f$ ) are shown in figure 32. In the investigation made in the 7- by 10-foot tunnel, these positions were selected as the optimum, the criterion being low drag in the lift range below a value of 2.5 and high maximum lift above this range.

The flap was attached to the wing by five small steel brackets; a different set of brackets was made for each flap position because the position was determined by the size and the shape of the brackets.

The 60-percent-chord plain flap (fig. 33) was built by cutting the wing at the 40-percent station and connecting the two parts by a narrow flexible plate flush with the

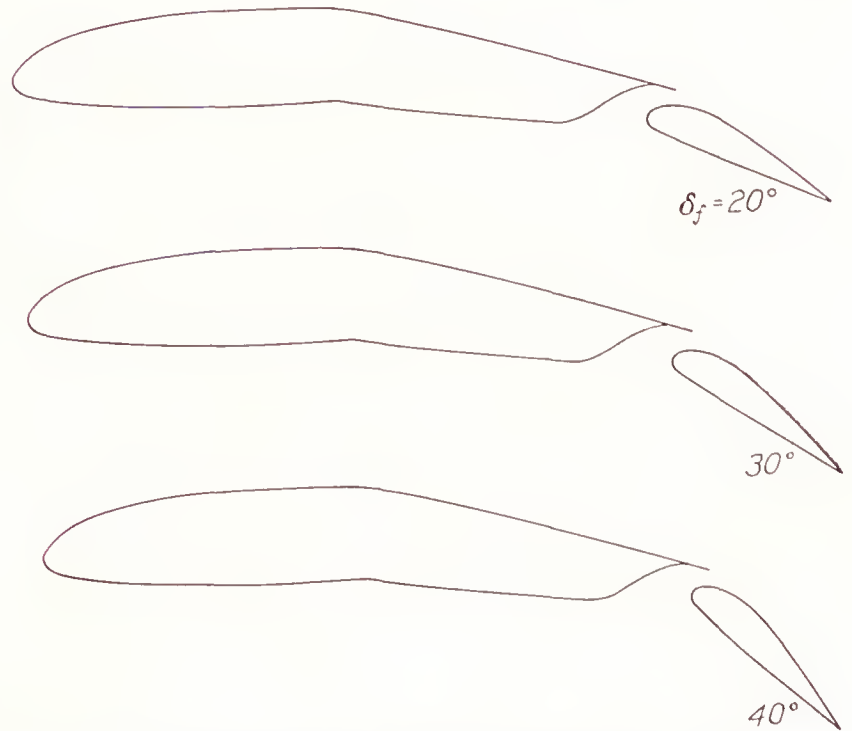


FIGURE 33.—Sections of airfoil with 0.60c plain flap deflected 12° and 0.2566c slotted flap 2-h.

20°, 30°, 40°, and 50°. In addition, at flap settings of 30° and 40°, the Reynolds Number range from 900,000 to 8,000,000 was covered.

The slotted flap was also tested at deflections of 20°, 30°, and 40° in combination with the 60-percent-chord plain flap deflected 12°.

## RESULTS AND DISCUSSION

### PRESENTATION

The results are presented as a series of lift curves for a rectangular wing of aspect ratio 6 in figure 34; the two groups of curves in the figure correspond to the two Reynolds Numbers at which all the tests were run.

The section characteristics, indicated by lower-case letters and presented in figures 35 and 36, were worked up as explained in reference 18.

### MAXIMUM LIFT

The lift reaches a maximum at a flap deflection of 40° (fig. 34). The variation with Reynolds Number is shown in figure 37. The maximum lift increases with Reynolds Number but appears to be leveling off at the end of the Reynolds Number range tested (about 8,000,000). The results of tests in the 7- by 10-foot



wind tunnel are also shown on the figure and the agreement with the variable-density-tunnel results, for the two points shown, is good. It will be noted that the increment of maximum lift is nearly constant over the range tested. A comparison of these results with those of references 2 and 19 shows that, at a Reynolds Number of 8,000,000, the slotted flap can reach a maximum lift coefficient of 2.86 as compared with 2.54 for

had practically no effect on the drag. If the slot is perfectly sealed when the flap is neutral, a decrease of the minimum drag of the order of 15 percent may accordingly be expected.

The drag of the wing at high lifts, with slotted flap 2-h deflected to its most favorable position at each lift coefficient, is included in figure 39. This curve, which may be called a profile-drag envelope polar, is

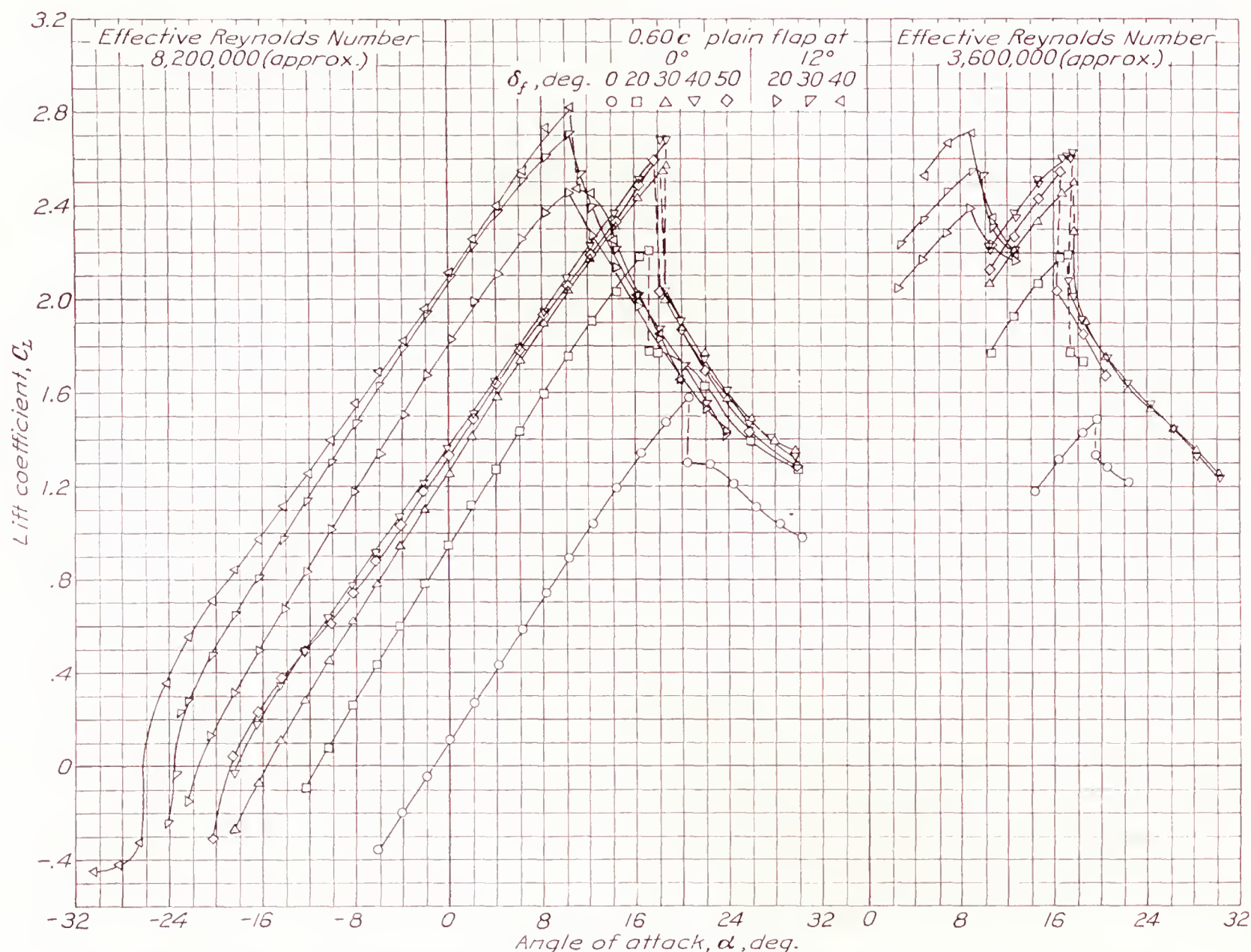


FIGURE 34.—Lift against angle of attack for N. A. C. A. 23012 airfoil with 0.2566c slotted flap 2-h, rectangular wing, aspect ratio 6.

the split flap, 2.39 for the plain flap, and 2.37 for the external-airfoil flap.

The deflection of the 0.60c plain flap had only a minor effect on either the maximum lift or the shape of the lift curve near the maximum (fig. 34).

#### PROFILE DRAG

The wing with the slotted flap in the neutral position had 15 percent higher minimum drag than the plain airfoil, as shown in figure 38. In order to find out to what extent this drag increment could be reduced by preventing flow through the slot, tests were made with the upper slot closed. The closing of the slot exit

the envelope of all the polars for the wing with all flap settings. A series of such curves for various flap types and arrangements shows the relative merit of each type for such an item of performance as take-off where, other things being equal, lower drag at high lift coefficients is advantageous. Such a series of curves (fig. 39) shows the 0.2566c slotted flap 2-h to be definitely superior to the 0.20c plain and split flaps, as was also shown by the 7- by 10-foot tunnel tests. Slotted flap 2-h is also slightly superior to the external-airfoil flap on the basis of low drag and is greatly superior to it on the basis of maximum lift. The data for these other flap arrangements are taken from references 2 and 19.



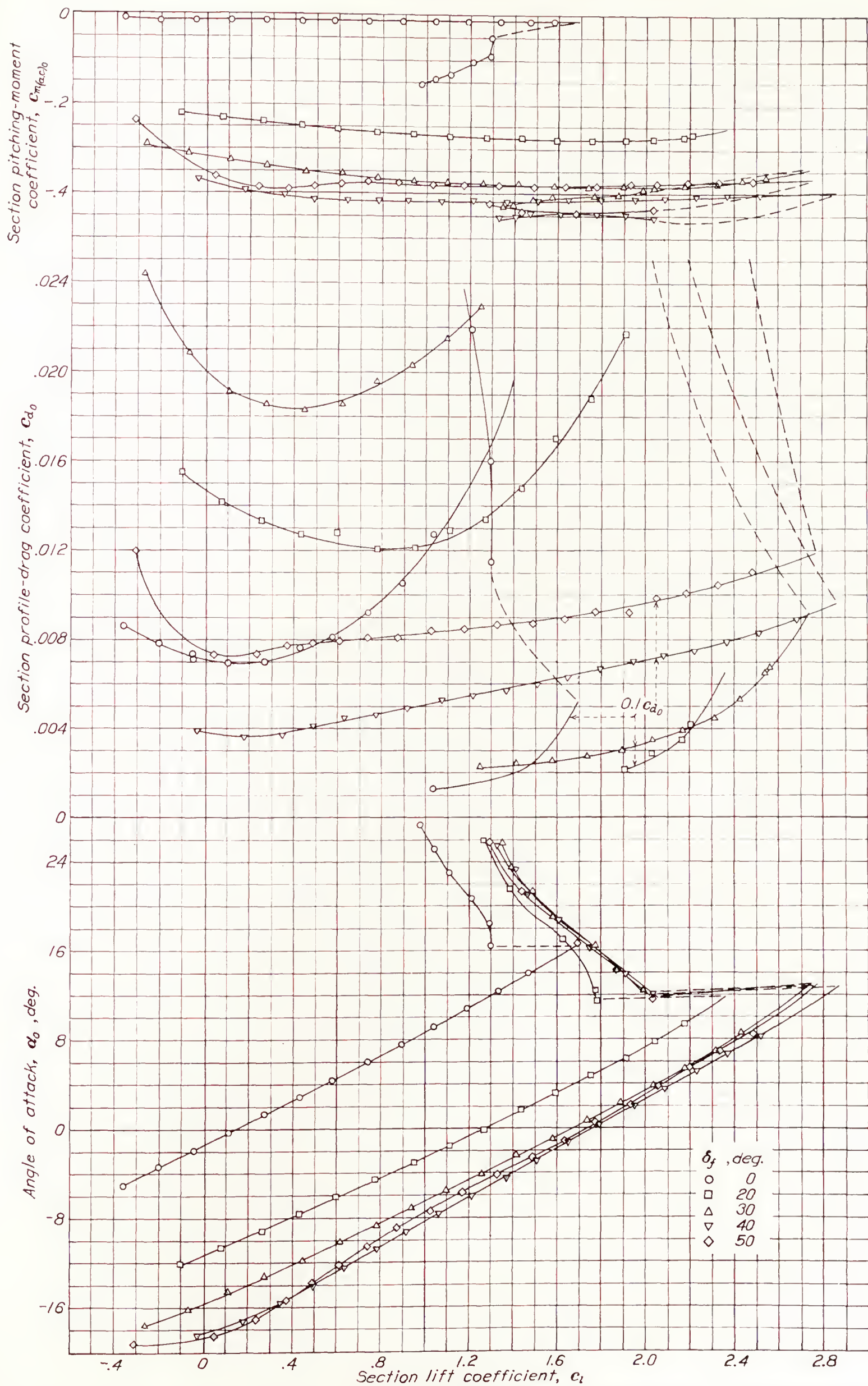


FIGURE 35.—Section aerodynamic characteristics of N. A. C. A. 23012 airfoil with 0.256c slotted flap 2-h and the 0.60c plain flap neutral. Effective Reynolds Number, approximately 8,200,000.



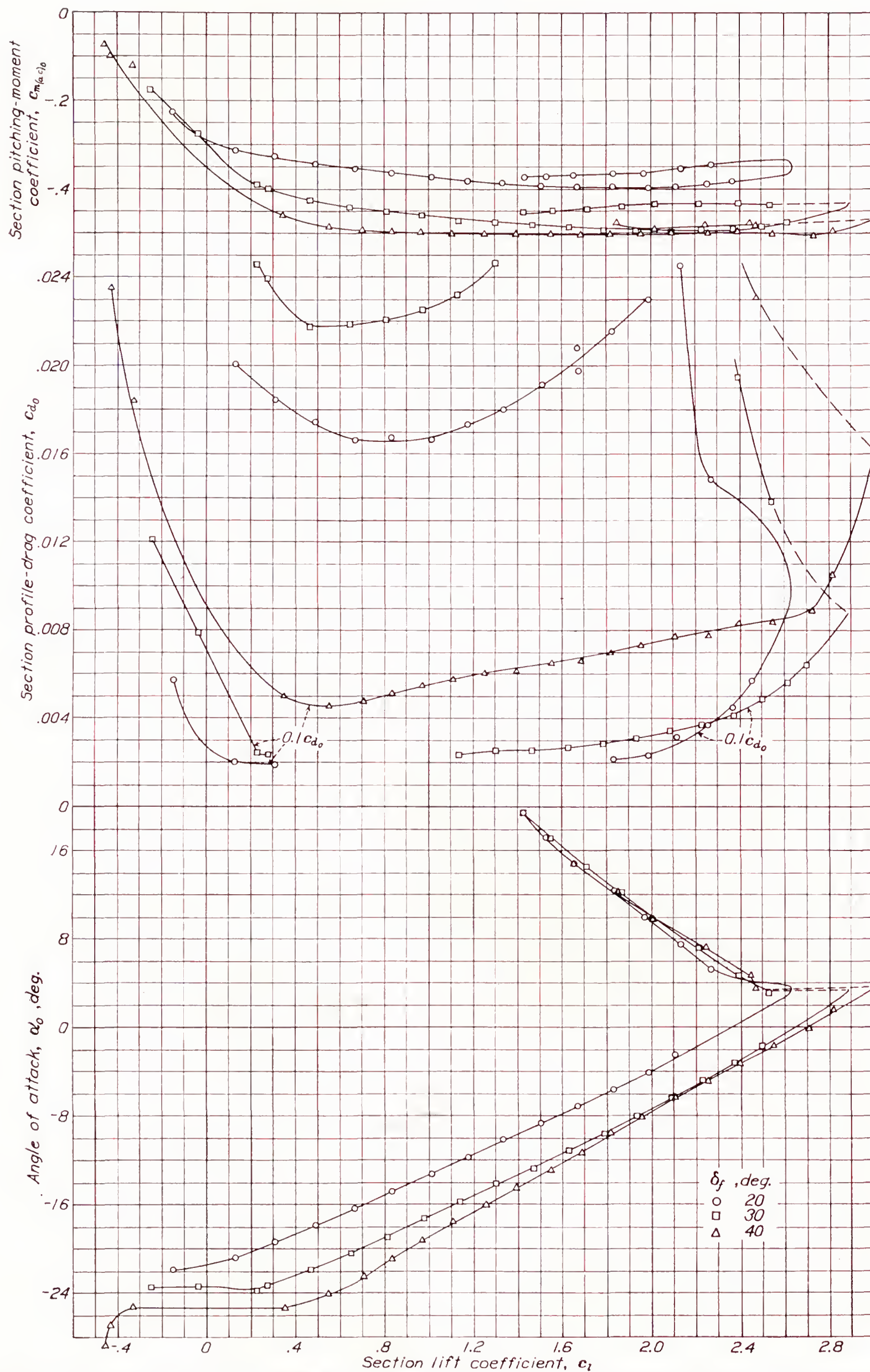


FIGURE 36.—Section aerodynamic characteristics of N. A. C. A. 23012 airfoil with 0.256c slotted flap 2-h and the 0.60c plain flap deflected 12°. Effective Reynolds Number approximately 8,200,000.



## PITCHING-MOMENT COEFFICIENT

The pitching-moment coefficient increased with flap deflection up to  $40^\circ$ . The pitching moment for the same deflection is greater than that of the plain and the split flaps but, when the comparison is made on the basis of deflections giving the same lift at the same angle

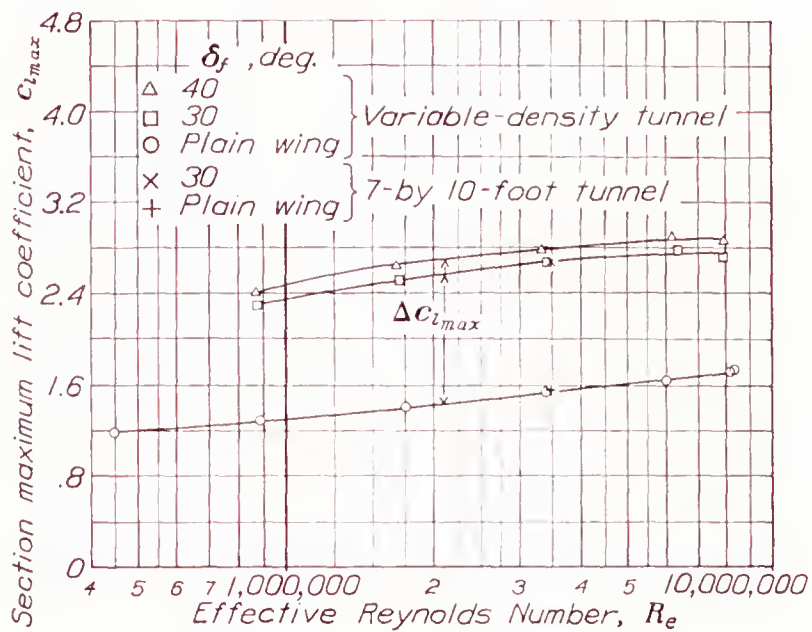


FIGURE 37.—Scale effect on  $c_{l_{max}}$  for N. A. C. A. 23012 airfoil with and without 0.2566c slotted flap 2-h.

of attack, the pitching moments are the same for all three flaps.

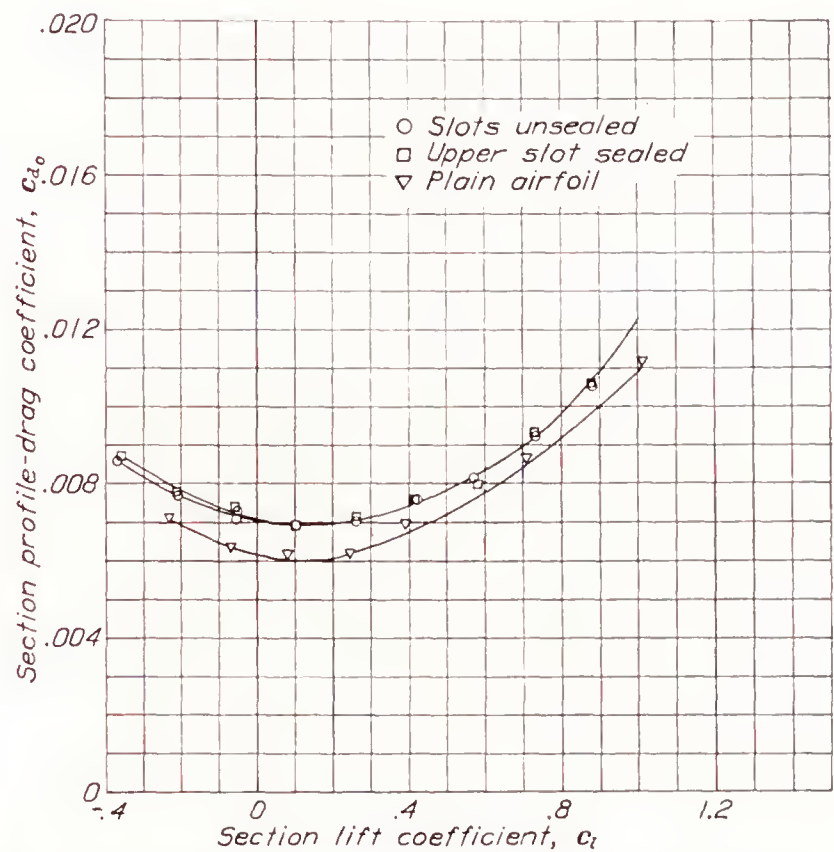


FIGURE 38.—Effect of slot opening on profile drag of N. A. C. A. 23012 airfoil with slotted flap 2-h neutral. Effective Reynolds Number, approximately 8,200,000.

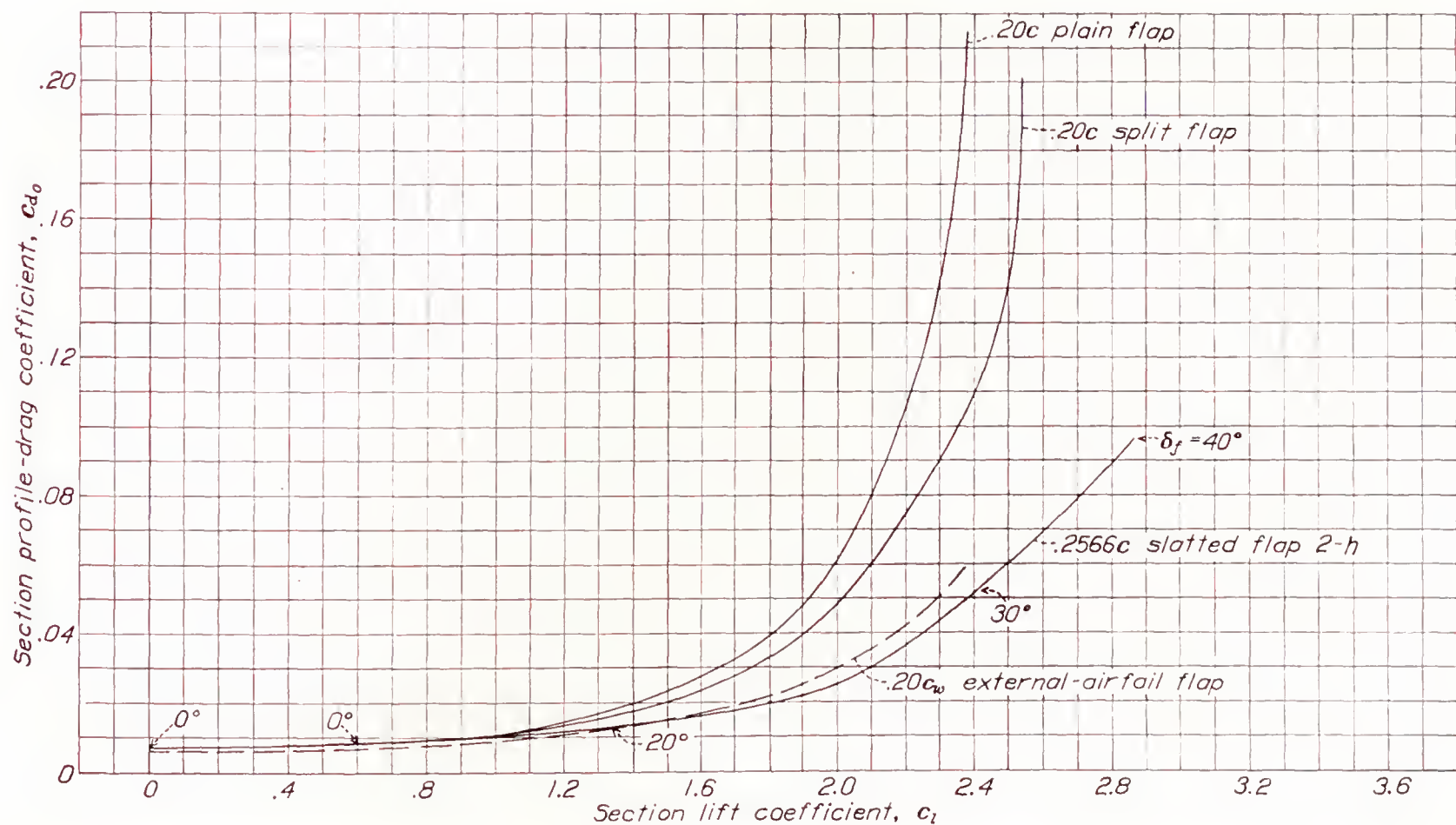


FIGURE 39.—Profile-drag envelope polars, N. A. C. A. 23012 airfoil with various flaps. Effective Reynolds Number, approximately 8,200,000.



CONCLUSIONS

- 1. The optimum arrangement of the slotted flap tested was superior to the split, the plain, and the external-airfoil types of flap compared on the basis of maximum lift coefficient, low drag at moderate and at high lift coefficients, and high drag at high lift coefficients. The slotted flap, however, gave slightly lower maximum lift coefficients than the Fowler flap.
- 2. The increment of maximum lift due to the slotted flap was found to be practically independent of the Reynolds Number over the range investigated.
- 3. Openings in the lower surface of the airfoil for the slotted flaps tested had a measurable effect on the drag for high-speed flight conditions even when the slot was smoothly faired to maintain the contour of the upper surface and there was no air flow through the slot.
- 4. The slotted flap gave the highest maximum lift coefficients when the nose of the flap was located slightly ahead of and below the slot lip and with a slot lip that directed the air down over the flap.
- 5. The lowest profile drags at moderate lift coefficients were obtained by using a slotted flap with an airfoil nose shape and with an easy entrance to the slot.
- 6. It appears that still further improvement may be obtained in low drag characteristics at moderate and high lift coefficients by the use of multiple flaps or by slotted flaps with greater lip extensions.

LANGLEY MEMORIAL AERONAUTICAL LABORATORY,  
NATIONAL ADVISORY COMMITTEE FOR AERONAUTICS,  
LANGLEY FIELD, VA., *February 12, 1938.*

TABLE I  
ORDINATES FOR AIRFOIL AND SLOT SHAPES  
[Stations and ordinates in percent of wing chord]

N. A. C. A. 23012 Airfoil		
Station	Upper surface	Lower surface
0		0
1.25	2.67	-1.23
2.5	3.61	-1.71
5	4.91	-2.26
7.5	5.80	-2.61
10	6.43	-2.92
15	7.19	-3.50
20	7.50	-3.97
25	7.60	-4.28
30	7.55	-4.46
40	7.14	-4.48
50	6.41	-4.17
60	5.47	-3.67
70	4.36	-3.00
80	3.08	-2.16
90	1.68	-1.23
95	.92	-.70
100	.13	-.13
L. E. radius: 1.58. Slope of radius through end of chord 0.305.		

TABLE I—Continued  
ORDINATES FOR AIRFOIL AND SLOT SHAPES—Cont.

Slot shape e	
Station	Ordinate
74.89	-0.18
75.41	.59
75.93	1.18
76.46	1.64
77.50	2.32
78.98	2.87
80.00	2.97

Slot shape f	
Station	Ordinate
74.89	-0.18
75.41	.59
75.93	1.18
76.46	1.64
77.50	2.32
78.98	2.87
80.00	2.97
81.70	2.72

Slot shape i	
Station	Ordinate
74.42	
74.74	-0.22
75.06	.13
75.69	.68
76.33	1.11
76.97	1.46
78.25	2.00
79.53	2.36
80.81	2.59
82.08	2.68
82.50	2.60

TABLE II  
ORDINATES FOR FLAP SHAPES  
[Stations and ordinates in percent of wing chord]

Flap 1		
Station	Upper surface	Lower surface
0	-1.61	-1.61
.52	-.18	-----
1.04	.58	-2.41
1.56	1.16	-2.43
2.09	1.63	-2.42
3.13	2.30	-2.37
4.61	2.84	-----
5.63	2.97	-2.16
6.82	2.88	-----
15.63	1.68	-1.23
20.63	.92	-.70
25.63	.13	-.13
Center of L. E. arc		
0.72	-1.61	
L. E. radius: 0.72		



TABLES II—Continued  
ORDINATES FOR FLAP SHAPES—Continued

Flap 2		
Station	Upper surface	Lower surface
0	-1.29	-1.29
.40	-.32	-2.05
.72	.04	-2.21
1.36	.61	-2.36
2.00	1.04	-2.41
2.64	1.40	-2.41
3.92	1.94	-----
5.20	2.30	-----
5.66	-----	-2.16
6.48	2.53	-----
7.76	2.63	-----
9.03	2.58	-----
10.31	2.46	-----
15.66	1.68	-1.23
20.66	.92	-.70
25.66	.13	-.13
Center of L. E. arc		
0.91	-1.29	
L. E. radius: 0.91		

## REFERENCES

1. Platt, Robert C.: Aerodynamic Characteristics of Wings with Cambered External-Airfoil Flaps, Including Lateral Control with a Full-Span Flap. T. R. No. 541, N. A. C. A., 1935.
2. Platt, Robert C., and Abbott, Ira H.: Aerodynamic Characteristics of N. A. C. A. 23012 and 23021 Airfoils with 20-Percent-Chord External-Airfoil Flaps of N. A. C. A. 23012 Section. T. R. No. 573, N. A. C. A., 1936.
3. Weick, Fred E., and Platt, Robert C.: Wind-Tunnel Tests of the Fowler Variable-Area Wing. T. N. No. 419, N. A. C. A., 1932.
4. Platt, Robert C.: Aerodynamic Characteristics of a Wing with Fowler Flaps Including Flap Loads, Downwash, and Calculated Effect on Take-Off. T. R. No. 534, N. A. C. A., 1935.
5. Glauert, H.: The Handley Page Slotted Wing. R. & M. No. 834, British A. R. C., 1923.
6. Irving, H. B., and Batson, A. S.: Summary of Data on Slotted Wings Obtained in the Wind Tunnel of Messrs. Handley Page, Ltd. R. & M. No. 930, British A. R. C., 1925.
7. Anon.: Résumé of Investigations Made on Handley Page Slots and Flaps. A. C. I. C., vol. VII, no. 639, Matériel Div., Army Air Corps, 1929.
8. Clark, K. W., and Kirkby, F. W.: Wind Tunnel Tests of the Characteristics of Wing Flaps and Their Wakes. R. & M. No. 1698, British A. R. C., 1936.
9. Higgins, George J.: An Airfoil Fitted with a Slotted Flap. Jour. Aero. Sci., vol. 3, no. 12, Oct. 1936, pp. 431-433.
10. Harris, Thomas A.: The 7 by 10 Foot Wind Tunnel of the National Advisory Committee for Aeronautics. T. R. No. 412, N. A. C. A., 1931.
11. Glauert, H.: Wind Tunnel Interference on Wings, Bodies, and Airscrews. R. & M. No. 1566, British A. R. C., 1933.
12. Tomotika, Susumu: The Lift on a Flat Plate Placed in a Stream between Two Parallel Walls and Some Allied Problems. Report No. 101 (vol. VIII, 5), Aero. Res. Inst., Tokyo Imperial Univ., Jan. 1934.
13. Platt, Robert C.: Turbulence Factors of N. A. C. A. Wind Tunnels as Determined by Sphere Tests. T. R. No. 558, N. A. C. A., 1936.
14. Jacobs, Eastman N., and Sherman Albert: Airfoil Section Characteristics as Affected by Variations of the Reynolds Number. T. R. No. 586, N. A. C. A., 1937.
15. Wenzinger, Carl J.: Wind-Tunnel Investigation of Ordinary and Split Flaps on Airfoils of Different Profile. T. R. No. 554, N. A. C. A., 1936.
16. Wenzinger, Carl J., and Anderson, Walter B.: Pressure Distribution over Airfoils with Fowler Flaps. T. R. No. 620, N. A. C. A., 1938.
17. Jacobs, Eastman N., and Abbott, Ira H.: The N. A. C. A. Variable-Density Wind Tunnel. T. R. No. 416, N. A. C. A., 1932.
18. Jacobs, Eastman N., and Abbott, Ira H.: Airfoil Section Data Obtained in the N. A. C. A. Variable-Density Tunnel as Affected by Support Interference and Other Corrections. T. R. No. 669, N. A. C. A., 1939.
19. Abbott, Ira H., and Greenberg, Harry: Tests in the Variable-Density Tunnel of the N. A. C. A. 23012 Airfoil with Plain and Split Flaps. T. R. No. 661, N. A. C. A., 1939.







## REPORT No. 665

### CALCULATION OF THE AERODYNAMIC CHARACTERISTICS OF TAPERED WINGS WITH PARTIAL-SPAN FLAPS

By HENRY A. PEARSON and RAYMOND F. ANDERSON

#### SUMMARY

Factors derived from wing theory are presented. By means of these factors, the angle of zero lift, the lift-curve slope, the pitching moment, the aerodynamic-center position, and the induced drag of tapered wings with partial-span flaps may be calculated. The factors are given for wings of aspect ratios 6 and 10, of taper ratios from 0.25 to 1.00, and with flaps of various lengths.

An example is presented of the method of application of the factors. Fair agreement with experimental results is shown for two wings of different taper ratio having plain flaps of various spans.

#### INTRODUCTION

Because of the widespread use of tapered wings equipped with partial-span flaps, it is desirable to have means for computing their aerodynamic characteristics. Previous reports (references 1, 2, and 3) have presented theoretical factors for use in computing the aerodynamic characteristics of wings with linear and with arbitrary twist and for use in finding the load distribution of wings with partial-span flaps.

This report presents factors, based on airfoil theory, for use in calculating the induced drag, the angle of zero lift, the pitching moment, and the aerodynamic center of tapered wings with partial-span flaps of constant flap-chord ratio. The factors, when used with adequate section data, should apply to various types of flap and various amounts of flap deflection.

#### THEORETICAL RESULTS

The particular wing chord distributions for which the theoretical computations were specifically made are given in figure 1 where the wing quarter-chord line is shown as straight. Two aspect ratios ( $A=6$  and 10) and four taper ratios ( $\lambda=1.00$ , 0.75, 0.50, and 0.25) were used. A list of the symbols used herein is given in appendix A. Inasmuch as the various characteristics for elliptical wings with partial-span flaps could be obtained relatively easily, they were sometimes computed in order to aid in determining the shape of the various computed curves for the tapered wings.

The span load distributions from which the aerodynamic characteristics were obtained are given in ref-

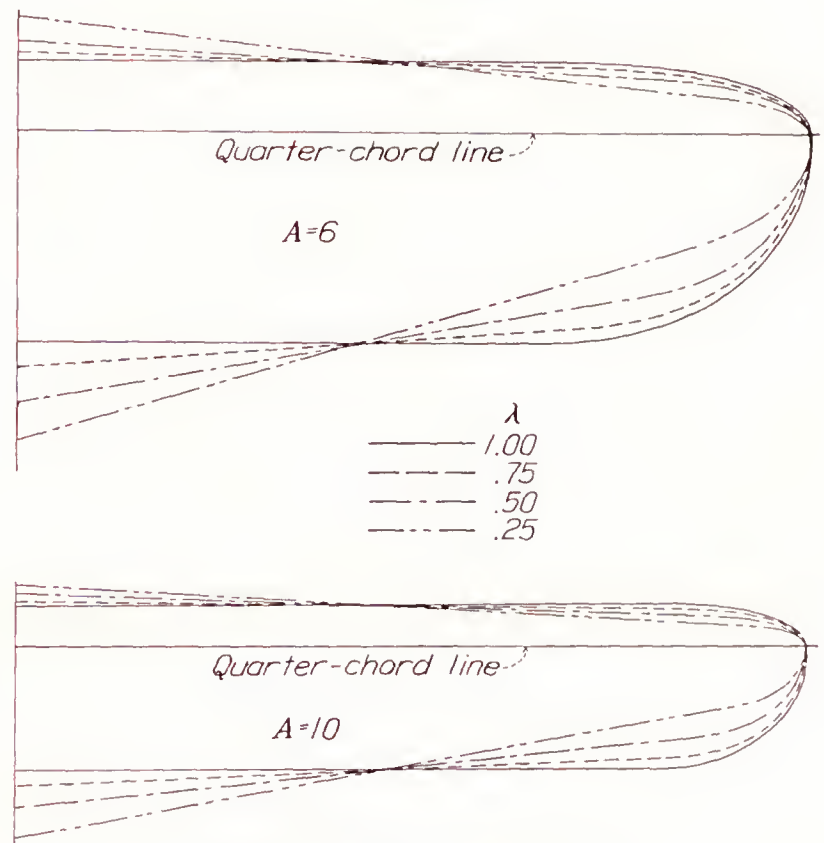


FIGURE 1.—Wing chord distributions.

erence 2 where a slope of the section lift curve equal to 5.67 per radian was used. The computations apply only to those cases in which no aerodynamic twist is present before the flaps are deflected.

Although the ordinary lifting-line theory is applicable only to wings without sweepback, experimental evidence indicates that small amounts of sweepback have no appreciable effect on the span loading. The computations may thus be applied to wings with moderate sweepback as long as the chord distributions are similar to those indicated in figure 1.

The computed aerodynamic characteristics are given in terms of factors such as  $J$ ,  $H$ , and  $G$ . The method of calculating the factors is omitted because of its length, but the formulas for the factors are presented in appendix B. The physical significance of the factors and of the aerodynamic characteristics they represent, however, is explained in the following sections.

**Angle of zero lift.**—The change in the angle of zero lift of a finite wing accompanying a flap deflection depends upon several variables, such as flap span, flap deflection, flap chord, and flap type. The effect of the last three variables can be conveniently represented



by the section characteristic  $\Delta c_l$ , the increment of section lift coefficient obtained by deflecting the flap.

By this grouping of variables, the change in the angle of zero lift (in degrees) for a wing with partial-span flaps can be expressed by the equation

$$\Delta\alpha_{s(L=0)} = -J\Delta c_l \quad (1)$$

In order to obtain the angle of zero lift for the wing, this increment must be added to the initial angle of zero lift, i. e., the angle before the flap is deflected. If this initial angle is measured from the chord of the root section, as is usually the case, the angle of zero lift for the wing is given by

$$\alpha_{s(L=0)} = \alpha_{l_0_s} - J\Delta c_l \quad (2)$$

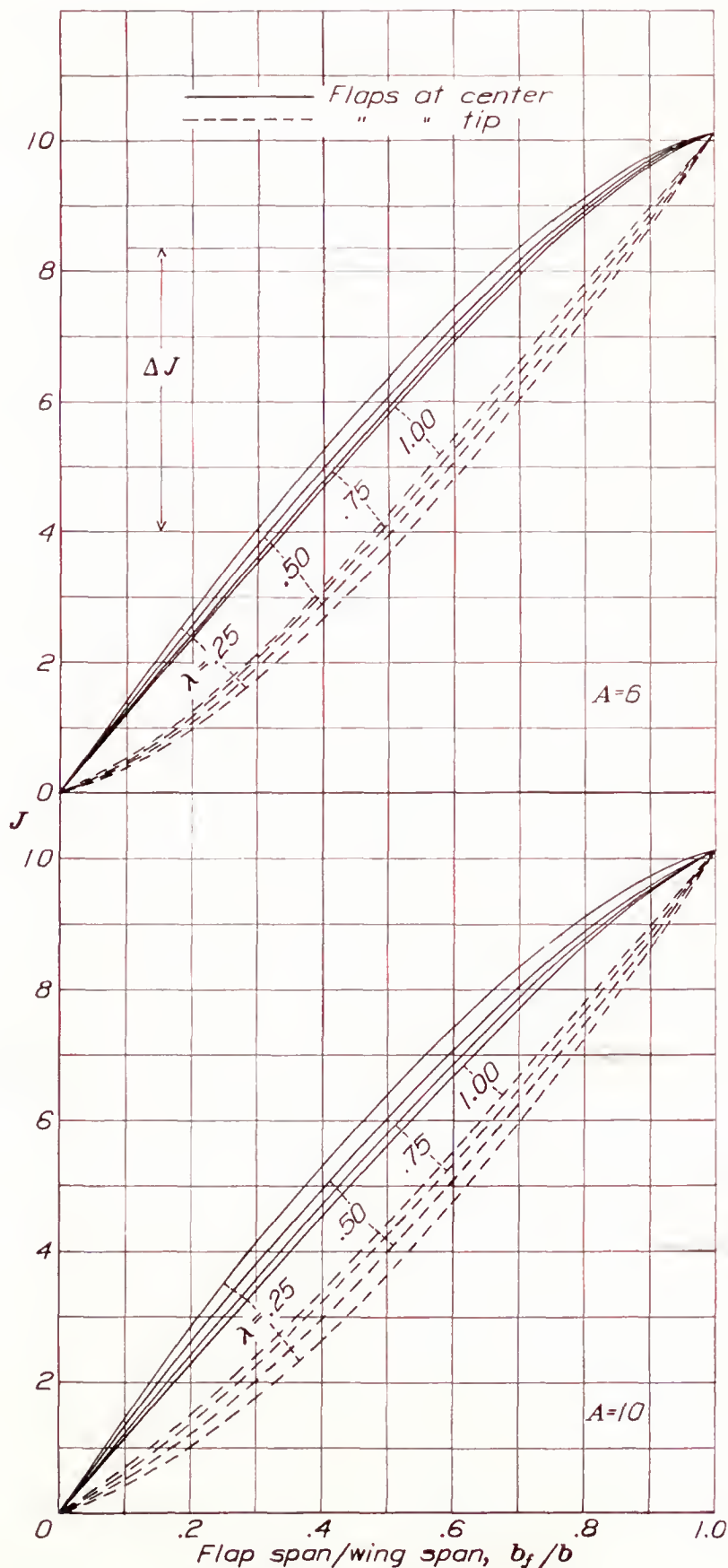


FIGURE 2.—Factor of angle of zero lift,  $J$ .  
 $\alpha_{s(L=0)} = \alpha_{l_0_s} - J\Delta c_l$

The computed variation of the factor  $J$  with flap span is shown in figure 2 for various aspect ratios and taper ratios.

Although the values of  $J$  given in figure 2 apply specifically to wings in which the flap-chord ratio, or  $\Delta c_l$ , is constant along the portion with flaps and in which the flaps begin either at the center or at the tips, the results may be used to predict the angle of zero lift for any starting point of the flaps and for any  $\Delta c_l$  distribution as long as they are symmetrical about the wing center. For example, if flaps of uniform flap-chord ratio extend from  $0.3b$  to  $0.7b$ , the proper value of the factor  $J$  is the difference between the values for  $0.3b$  and  $0.7b$  as shown by  $\Delta J$  in figure 2. The extension to the case of a nonuniform symmetrical distribution of  $\Delta c_l$  consists simply in considering the resulting  $\Delta c_l$  distribution to be caused by a series of elemental flaps of various lengths and performing either a numerical or a graphical integration for the value of  $J$ . (See procedure given in reference 3.) In cases where the variation of  $\Delta c_l$  along the span is slight, however, the use of an average value of  $\Delta c_l$  is justified.

**Lift-curve slope.**—The wing lift-curve slope,  $a$ , per degree may be found from the equation

$$a = f \frac{\bar{a}_0}{1 + \frac{57.3 \bar{a}_0}{\pi A}} \quad (3)$$

where

$A$  is wing aspect ratio,  $b^2/S$ .

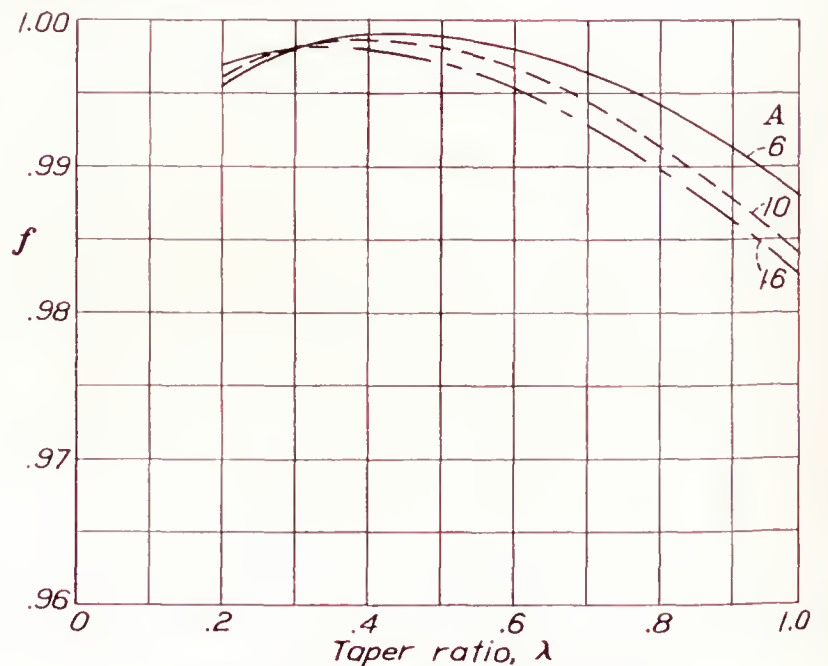


FIGURE 3.—Factor of wing lift-curve slope,  $f$ .

$$a = f \frac{\bar{a}_0}{1 + \frac{57.3 \bar{a}_0}{\pi A}}$$

$f$ , a theoretical factor given in figure 3. This factor has been plotted from results given in reference 1.

$\bar{a}_0$ , the weighted average of the section lift-curve slopes.

An average slope, weighted according to chord length, must be used because the slope of the sections with flaps may be considerably different from the slope of the



sections without flaps. If the section lift-curve slopes are constant across the spans of the flapped and the unflapped parts of the wing, then  $\bar{a}_0$  may be found in terms of the fraction of the area of the wing equipped with flaps:

$$\bar{a}_0 = \frac{S_f}{S} a_{0f} + \left(1 - \frac{S_f}{S}\right) a_0 \quad (4)$$

where

$a_0$  is the lift-curve slope of section without flaps, per degree.

$a_{0f}$  lift-curve slope of section with flaps, per degree.

$S$ , area of wing.

$S_f$ , area of part of wing equipped with flaps.

If  $a_0$  and  $a_{0f}$  are not constant across the two parts of the wing, then  $\bar{a}_0$  may be found by integration.

dynamic centers is unaltered by deflecting the flaps, the  $x$  position of the wing aerodynamic center would be the same with the flaps either deflected or neutral.

If the aerodynamic center of the root section is taken as a reference point and the aerodynamic centers of all the wing sections are assumed to lie on a straight line making an angle  $\Lambda$  with the lateral axis (see fig. 4), then the  $x$  location of the load center is given by

$$x_{a.c.} = Hb \tan \Lambda \quad (5)$$

From equation (5), the aerodynamic-center position may also be related to the mean chord  $S/b$  and to the aspect ratio  $A$  by the equation

$$\frac{x_{a.c.}}{S/b} = HA \tan \Lambda \quad (6)$$

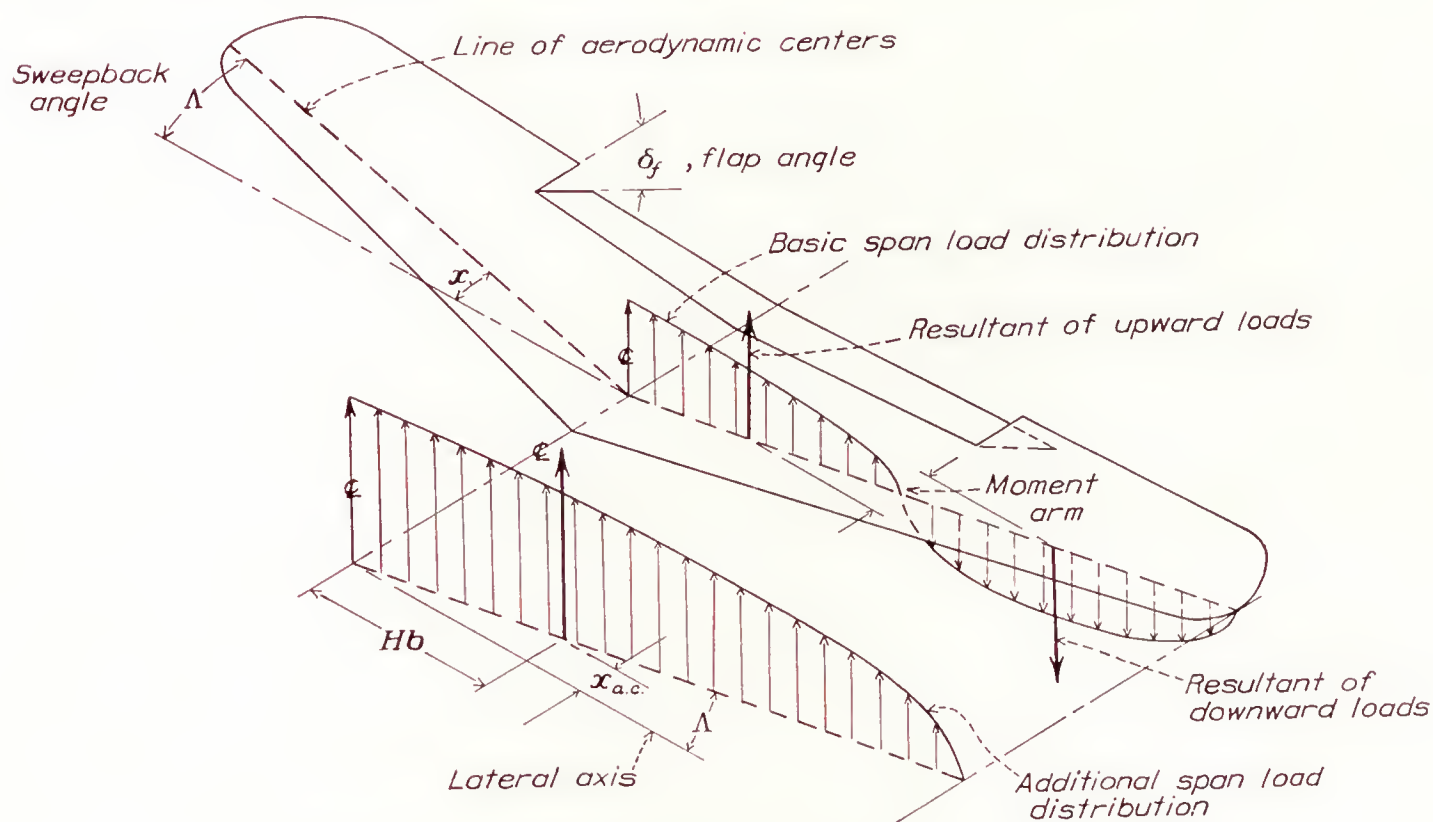


FIGURE 4.—Typical wing-flap combination showing basic and additional distributions.

**Aerodynamic-center location.**—The aerodynamic center of a wing is defined as the point about which the pitching moment is constant up to high lift coefficients; and, since the resultant lift must act through this point, the  $x$  position of the wing aerodynamic center is, in effect, nothing more than the fore-and-aft location of the centroid of the load distribution.

The load distribution of a wing with flaps is considered in this report to consist of the two components that are shown in figure 4. The basic load distribution is the span loading for zero lift with the flaps deflected; its ordinates are proportional to the value of  $\Delta c_l$ . The additional load distribution is that for the wing with flaps neutral; the total lift, however, is the same as that for the wing with flaps deflected. Since the basic load distribution contributes no lift, it does not enter into the determination of the aerodynamic center. Thus, if the chordwise position of the section acro-

dynamic center of the wing is ahead of the aerodynamic center of the root section.

Values of  $H$  are shown in figure 5.

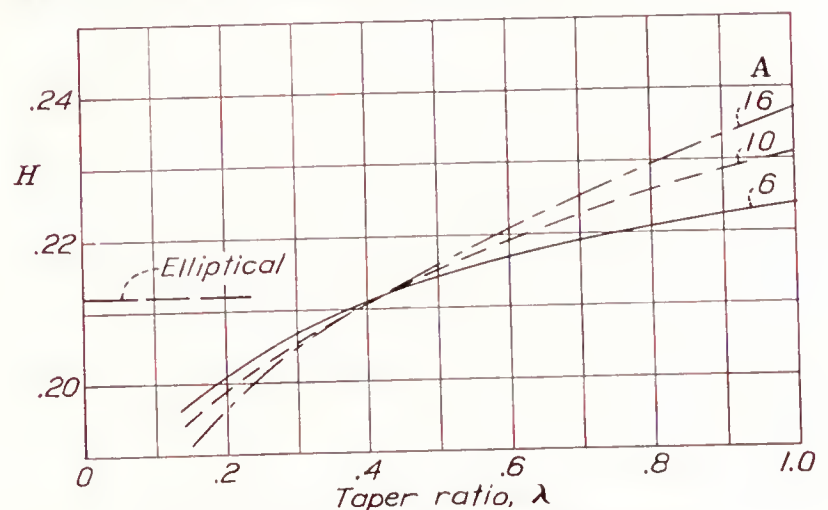


FIGURE 5.—Factor of wing aerodynamic center,  $H$ .

$$\frac{x_{a.c.}}{S/b} = HA \tan \Lambda$$



**Pitching moment.**—As shown in figure 4, the upward and the downward parts of the basic load form a couple having a magnitude that increases directly with the semispan length, the angle of sweepback, and the flap deflection, i. e.,  $\Delta c_l$ . An equation for the pitching moment due to the basic load distribution can thus be written:

$$M_{lb} = k \frac{b}{2} \Delta c_l \tan \Lambda q S$$

where  $k$  accounts for variations with wing taper, aspect ratio, and flap span. Because the basic load distribution is zero with no flap and is also zero with a full-span flap, the factor  $k$  would have a maximum value at an intermediate flap span.

Transforming the preceding equation into the coefficient form gives

$$C_{m_{lb}} = G \Delta c_l A \tan \Lambda \quad (7)$$

where values of  $G$  are given in figure 6. For a wing with sweepback ( $\Lambda$  positive), the sign of the pitching-moment coefficient due to the basic lift is positive if the flap deflection introduces an effective washout toward the tip (e. g., flaps at the center deflected downward or flaps at the tip deflected upward). For a wing with sweepforward, the sign of  $C_{m_{lb}}$  is negative for the same flap deflections.

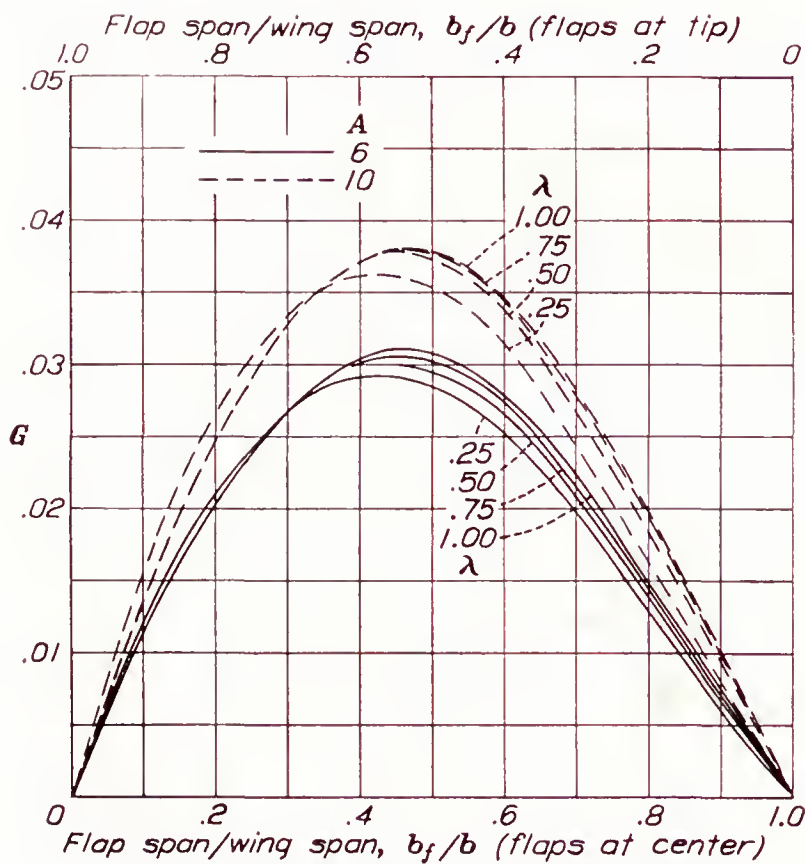


FIGURE 6.—Factor of basic lift pitching moment,  $G$ .  
 $C_{m_{lb}} = G \Delta c_l A \tan \Lambda$

In case the aerodynamic centers do not lie on a straight line so that the angle of sweepback is not constant along the span,  $C_{m_{lb}}$  may be graphically obtained from the equation

$$C_{m_{lb}} = \frac{2b}{S^2} \int_0^{b/2} x c_{lb} c dy \quad (8)$$

where, at any point along the span,

$x$  is the moment arm measured from the aerodynamic center of the root section and parallel to the root chord (positive, rearward; negative, forward).

$c_{lb}$ , the section lift coefficient for the basic loading.  
 $c$ , the chord.

In order to obtain the total pitching-moment coefficient, that due to the sections must also be added. This pitching-moment coefficient is given by

$$C_{m_s} = \frac{2b}{S^2} \int_0^{b/2} c_{m_{a.c.}} c^2 dy \quad (9)$$

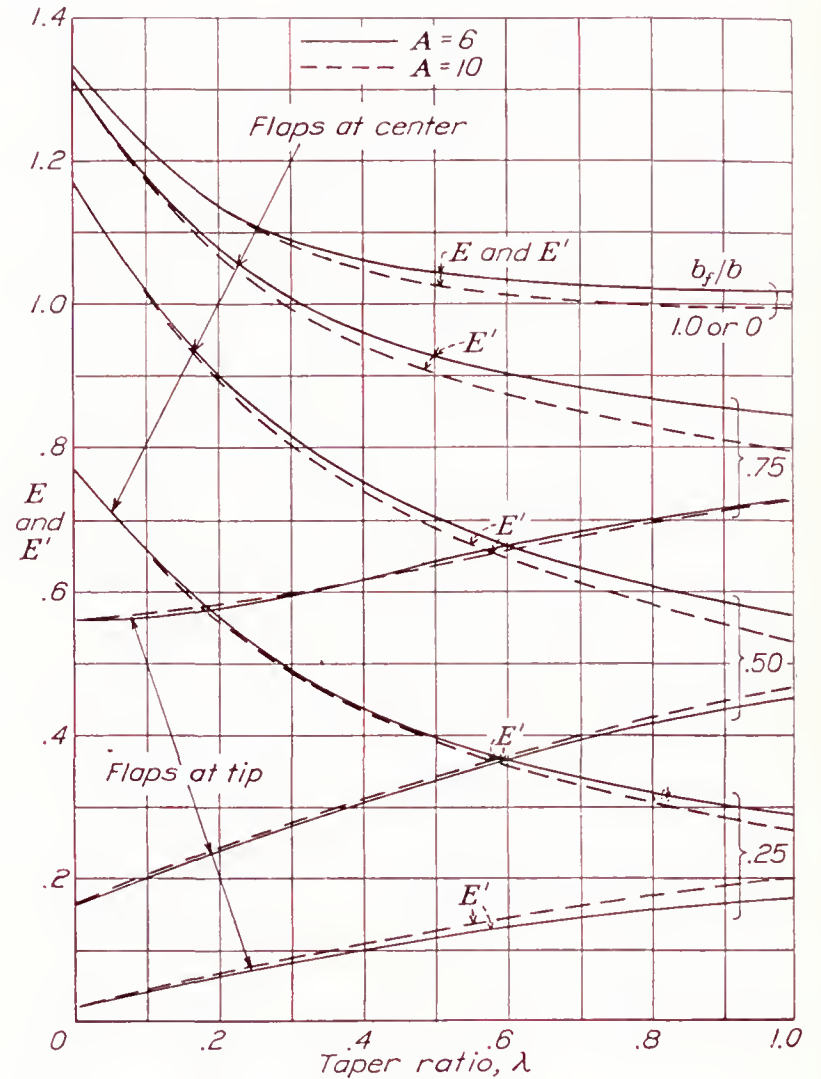


FIGURE 7.—Factors of section pitching moment,  $E$  and  $E'$ .  
 $C_{m_s} = E c_{m_0} + E' \Delta c_m$

For wings with flaps, however, the value of the section pitching-moment coefficient  $c_{m_{a.c.}}$  may be assumed to consist of two parts: One denoted by  $c_{m_0}$ , the section coefficient with flaps neutral; and the other denoted by  $\Delta c_m$ , the increase in the section coefficient above  $c_{m_0}$  due to the flaps. If  $c_{m_0}$  is constant across the span and  $\Delta c_m$  is constant across the flap span (i. e., the flap-chord ratio is constant), then the pitching-moment coefficient due to the sections can be given by

$$C_{m_s} = E c_{m_0} + E' \Delta c_m \quad (10)$$

Values of  $E$  and  $E'$  for these conditions are given in figure 7 for the tapered wings. These values have been determined from the relations

$$E = \frac{2b}{S^2} \int_0^{b/2} c^2 dy$$

$$E' = \frac{2b}{S^2} \int_{y_f}^{b/2} c^2 dy$$

If neither  $c_{m_0}$  nor  $\Delta c_m$  were constant across the span, then it would be necessary to use equation (9) and to evaluate  $C_{m_s}$  by an integration, as will be illustrated



later. The total wing pitching-moment coefficient is given by

$$C_{m_{a,c}} = C_{m_s} + C_{m_{l_b}} \quad (11)$$

The coefficient  $C_{m_{a,c}}$  is defined by the equation

$$M = C_{m_{a,c}} q \frac{S^2}{b} \quad (12)$$

where  $M$  is the total pitching moment.

**Induced drag.**—For any wing with a twist that is symmetrical about the wing center line, the induced-drag coefficient may be given by the equation

$$C_{D_i} = \frac{C_L^2}{\pi A u} + C_L \Delta c_i v + \Delta c_i^2 w \quad (13)$$

The factors  $u$ ,  $v$ , and  $w$  for wings with partial-span flaps, i. e., for the case of an abrupt twist, are given in figure 8.

The first term on the right-hand side of equation (13) is the usual induced-drag coefficient of an untwisted wing and the other two terms result from the aerodynamic wing twist introduced by deflecting the flaps. It can be seen from figure 8 that, for certain taper ratios, the  $v$  and the  $w$  factors are of opposite sign and their contributions counteract each other. In fact, under certain conditions, the sum of the last two terms may be slightly negative; and, as a result, the elliptical wing induced-drag coefficient may be approached. This tendency exists when the flaps are so placed and deflected that an elliptical loading is approximated.

## EXPERIMENTAL RESULTS

### APPARATUS AND TESTS

In order to provide a check on the reliability of the theoretical factors that have been presented, two tapered wings with partial-span flaps were tested. In addition, tests were made of three rectangular wings with full-span flaps to provide section data for use in calculating the characteristics of the tapered wings. The wings were made of aluminum alloy and had an area of 150 square inches.

A list of the tapered wings and the different flap lengths used is given in table I, together with the taper ratio, the aspect ratio, and the airfoil sections of the root and the construction tip (the extreme tip). The tips were rounded as shown in figure 1. The N. A. C. A. 23012 tapered wing had a moderate sweepback (line through quarter-chord points) but the N. A. C. A. 5-10-16 tapered wing had no sweepback. In the construction of the wings, straight-line elements were used between corresponding points of the root and the construction tip sections. For the N. A. C. A. 23012 wing, the chords of all sections along the span were in one plane; whereas, for the N. A. C. A. 5-10-16 wing, the highest points of the upper surface of each section were in one plane. The ordinates of the N. A. C. A. 5-10-16 wing are given in reference 4.

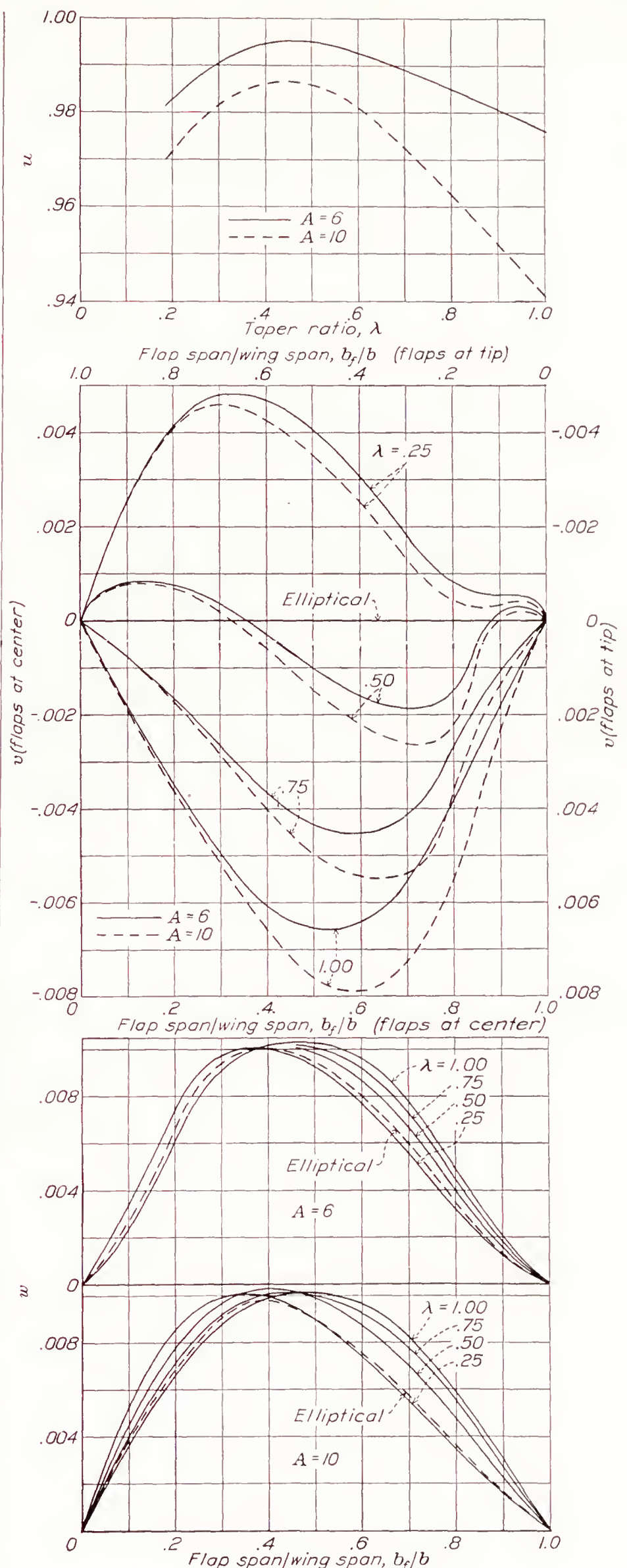


FIGURE 8.—Factors of induced drag,  $u$ ,  $v$ , and  $w$ .

$$C_{D_i} = \frac{C_L^2}{\pi A u} + C_L \Delta c_i v + \Delta c_i^2 w$$



The rectangular wings had N. A. C. A. 23009, 23012, and 23015 sections and were included to provide airfoil section characteristics to aid in calculating the characteristics of the tapered wings.

Plain  $0.2c$  flaps deflected downward  $20^\circ$  were built into all the wings and were made to simulate flaps pivoted about the midpoint of the thickness at  $0.8c$ . Fillets of small radii were used to join the flap to the wing and to seal the gap, as indicated at the top of figure 9.

All the wings were tested in the variable-density wind tunnel at a pressure of 20 atmospheres. The lift, the drag, and the pitching moment were measured at

$c_{m(a.c.)_0}$  are given about the aerodynamic-center position with the flap neutral.

The results of the tests of the tapered wings are presented in the usual manner in figures 12 to 17. In addition to the usual characteristics, the lift-curve peaks are given for two values of the effective Reynolds Number to indicate the scale effect on  $C_{L_{max}}$ . The Reynolds Number is based on the mean chord  $S/b$ . On the right side of the figures, effective profile-drag coefficients are given. This coefficient is the total drag coefficient with the induced-drag coefficient for elliptical span loading deducted, that is,  $C_{D_e} = C_D - C_L^2/\pi A$ . The values of  $C_{D_e}$  have been corrected to effective

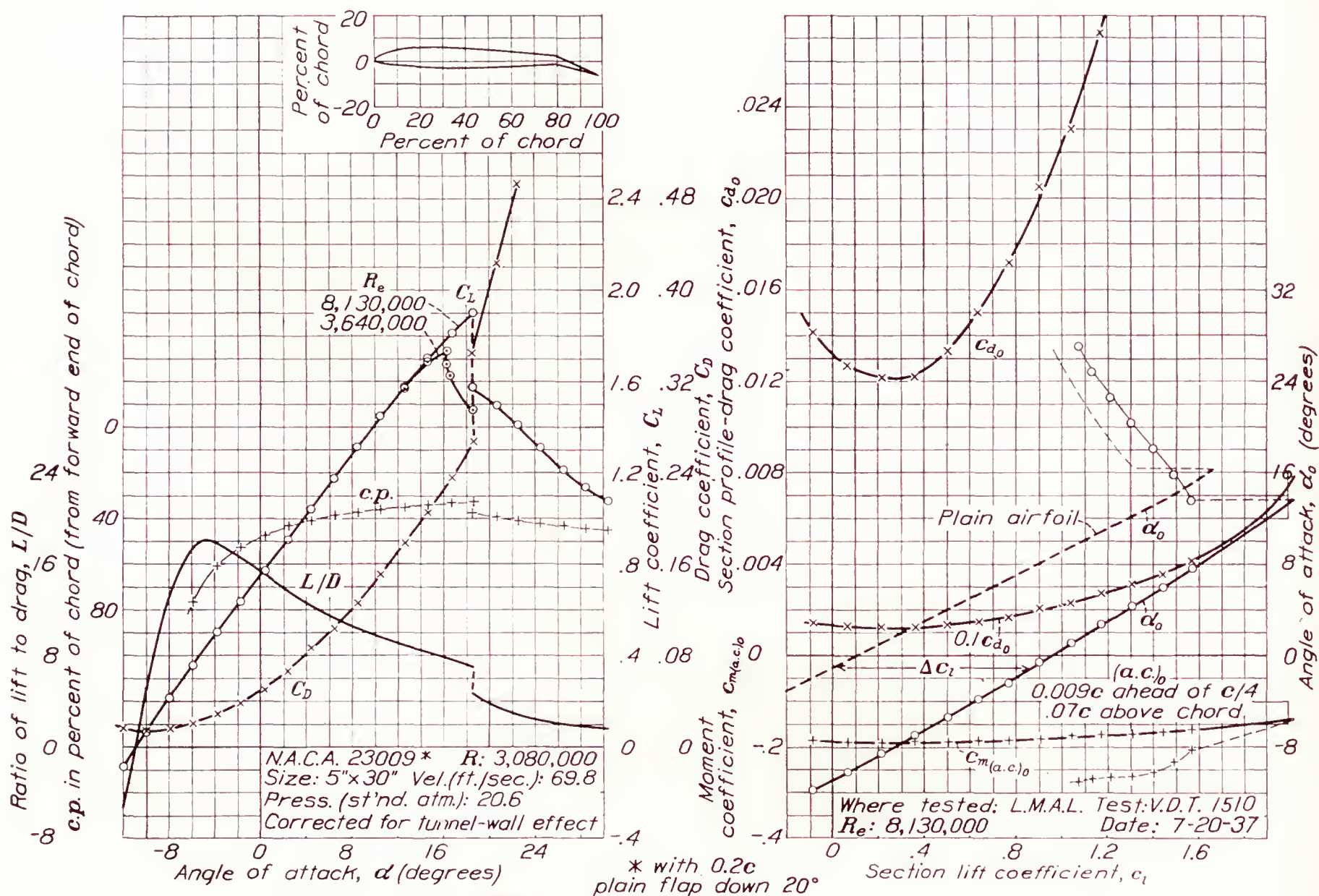


FIGURE 9.—The N. A. C. A. 23009 airfoil with  $0.2c$  plain flap down  $20^\circ$ .

the usual high Reynolds Number and, in addition, the maximum lift was measured at a lower Reynolds Number to indicate the scale effect on  $C_{L_{max}}$ . The method of making and correcting the tests and a description of the tunnel are given in reference 5.

The results of the tests are presented in the usual form as figures 9 to 17. The results of the tests of rectangular wings, plotted on the left side of figures 9 to 11, have been corrected to aspect ratio 6; whereas the results given on the right side have been corrected to airfoil section characteristics by the method explained in reference 6. The pitching-moment coefficients

Reynolds Number  $R_e$  by subtracting an increment (0.0011) to allow for the reduction in skin-friction drag when extrapolating from test to effective Reynolds Number (reference 6). The pitching-moment coefficients given are based on the mean chord  $S/b$  so that  $C_m = M/qS(S/b) = Mb/qS^2$ . The coefficients for each wing-and-flap combination are given about an axis through the aerodynamic center determined by the method given in the appendix of reference 4. The location of the aerodynamic center given in the upper part of the right side of the figures is measured from the quarter-chord point of the root chord and is in terms of  $S/b$ .



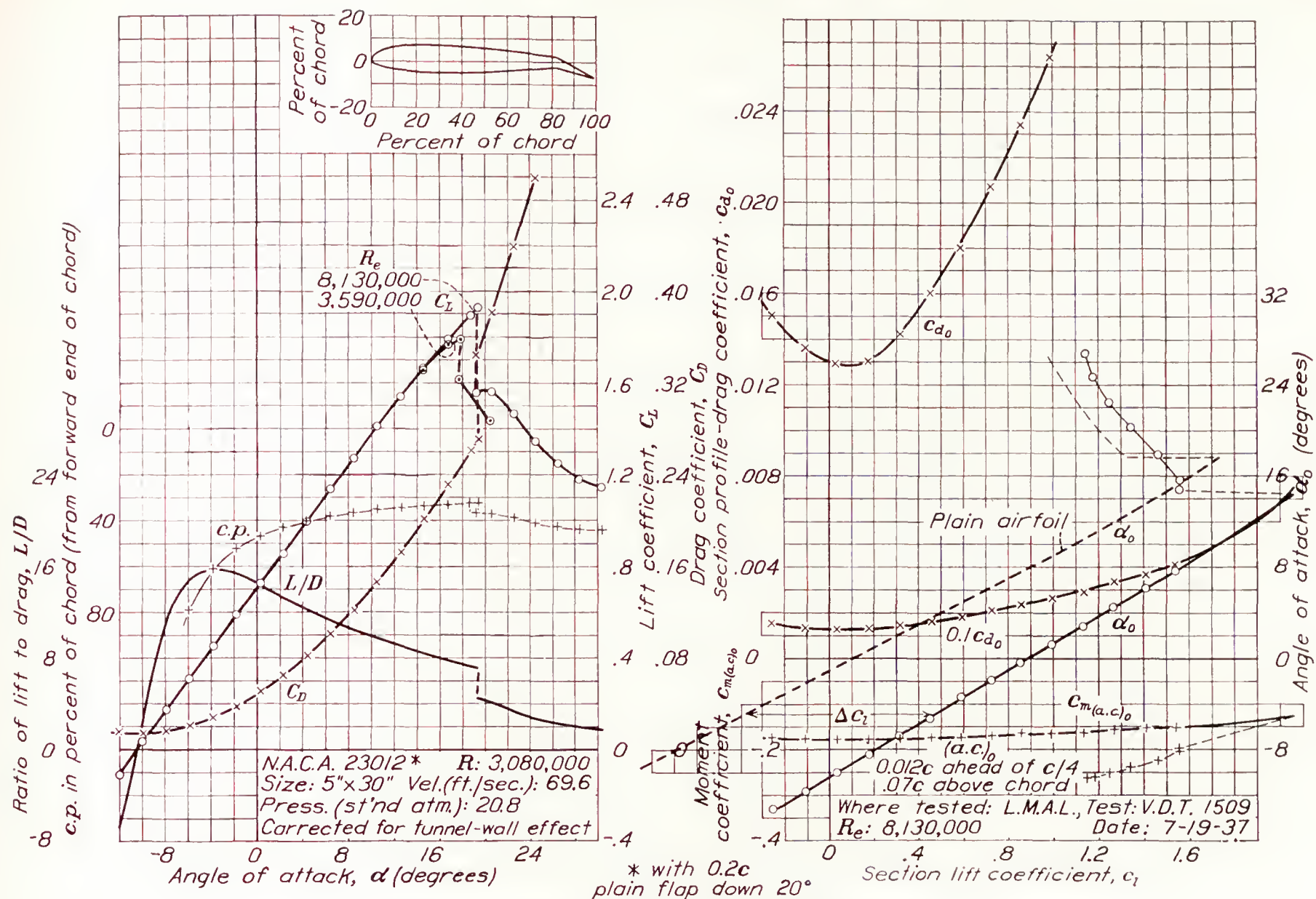


FIGURE 10.—The N. A. C. A. 23012 airfoil with 0.2c plain flap down 20°.

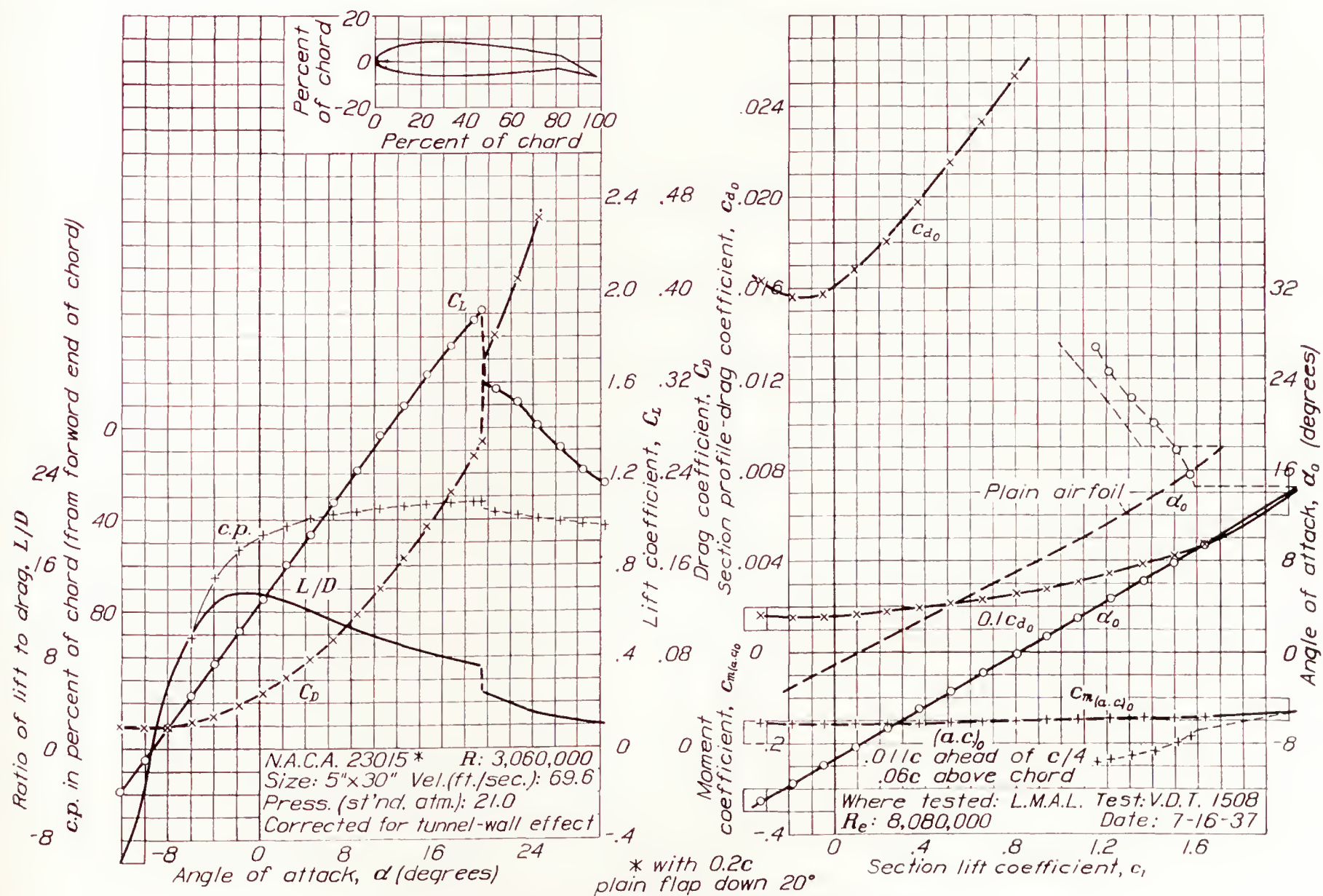


FIGURE 11.—The N. A. C. A. 23015 airfoil with 0.2c plain flap down 20°.



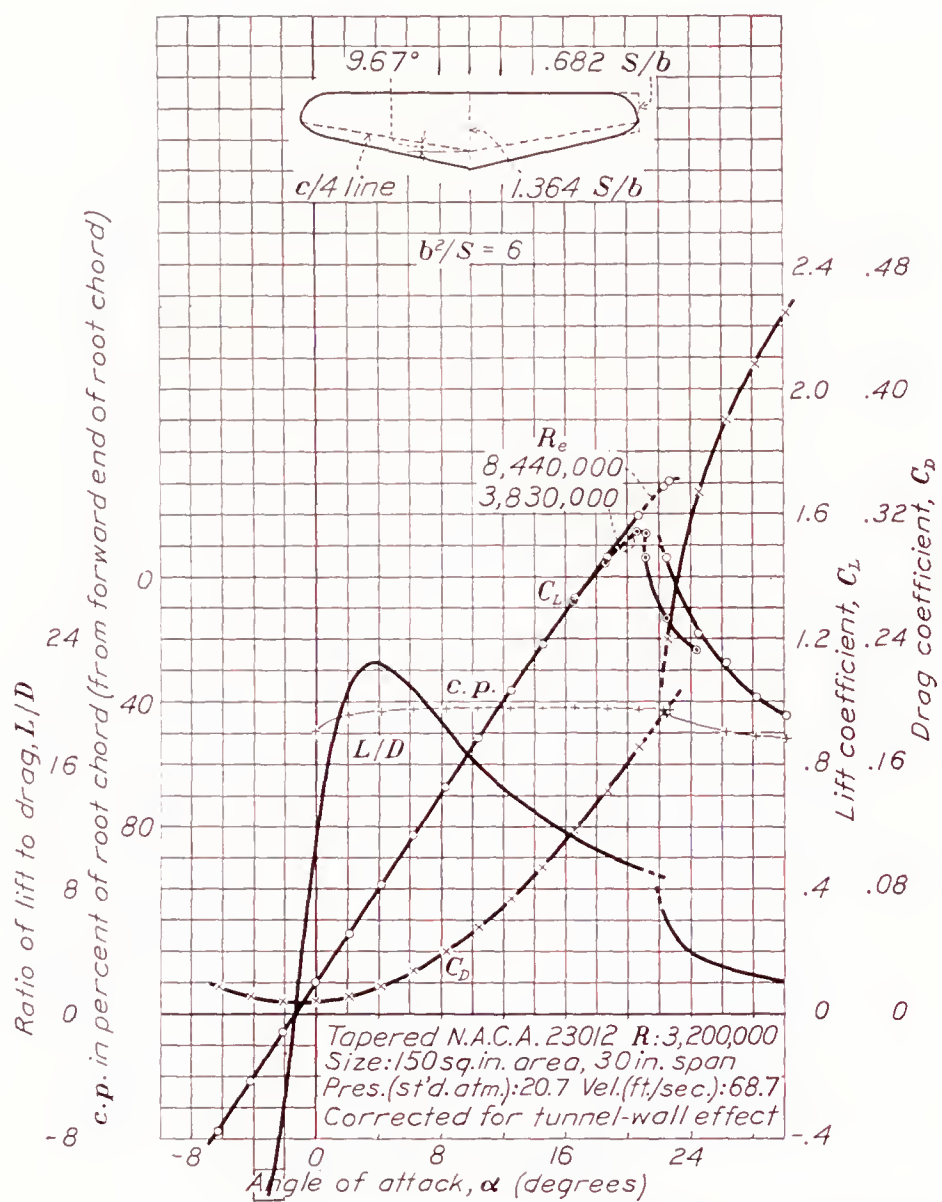


FIGURE 12.—The tapered N. A. C. A. 23012 airfoil.

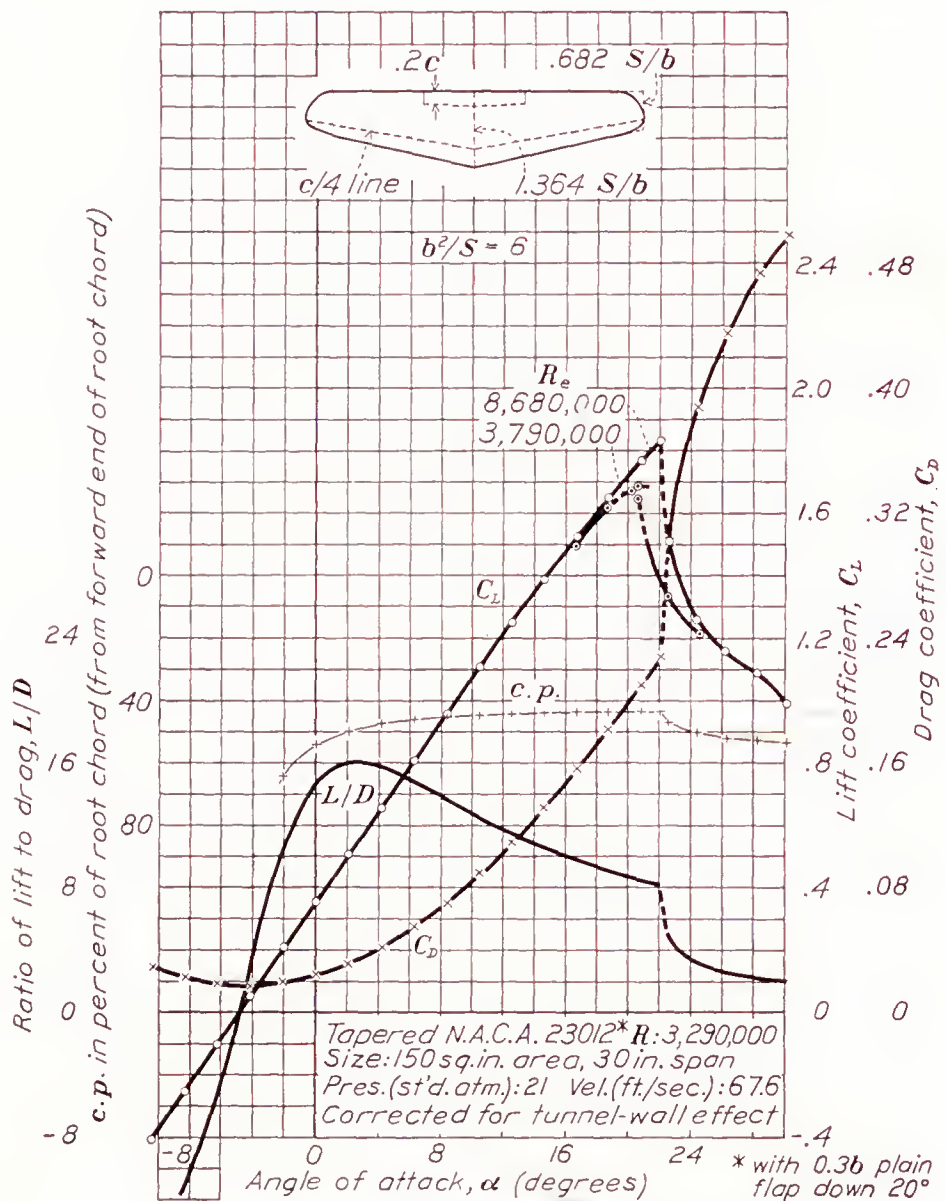


FIGURE 13.—The tapered N. A. C. A. 23012 airfoil with 0.36 plain flap down 20°.



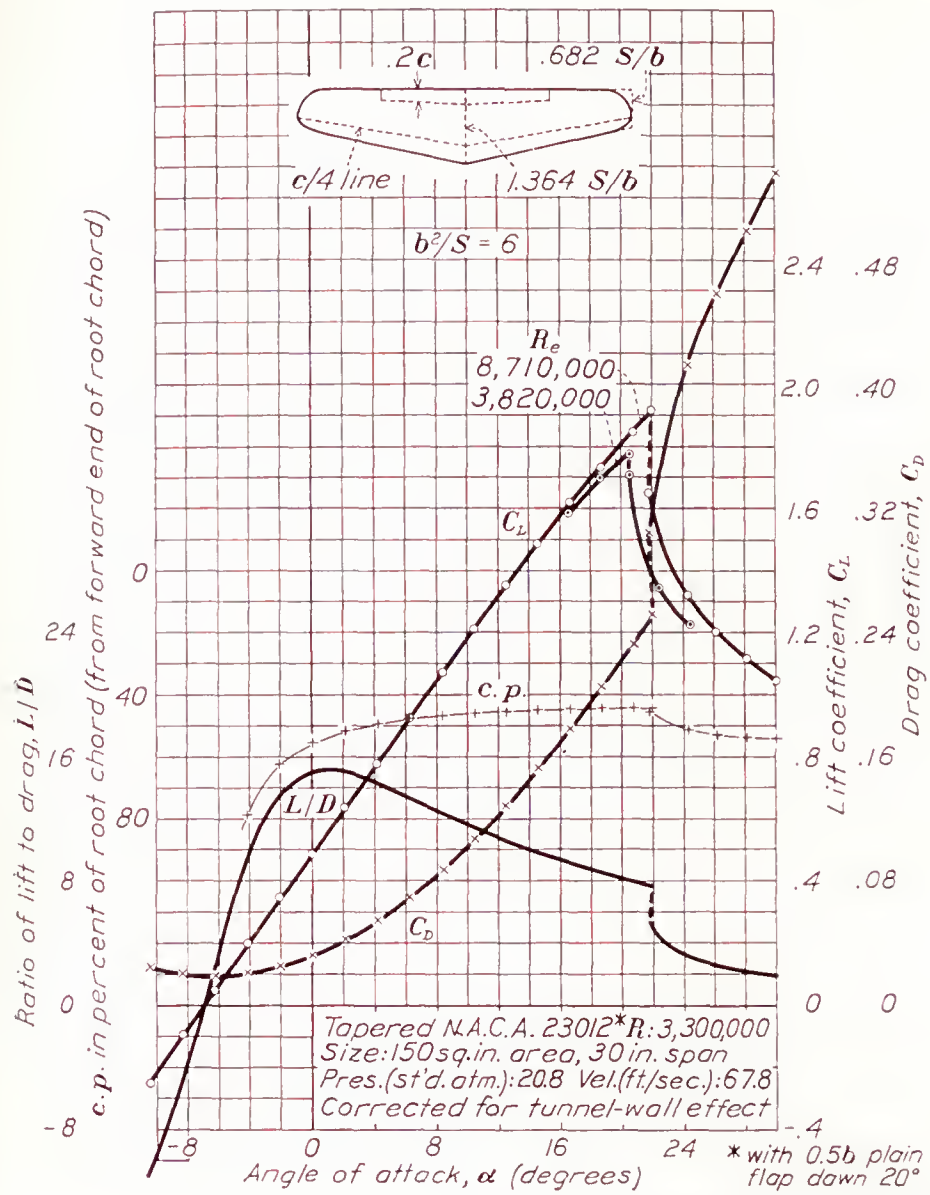


FIGURE 14.—The tapered N. A. C. A. 23012 airfoil with 0.5b plain flap down 20°.

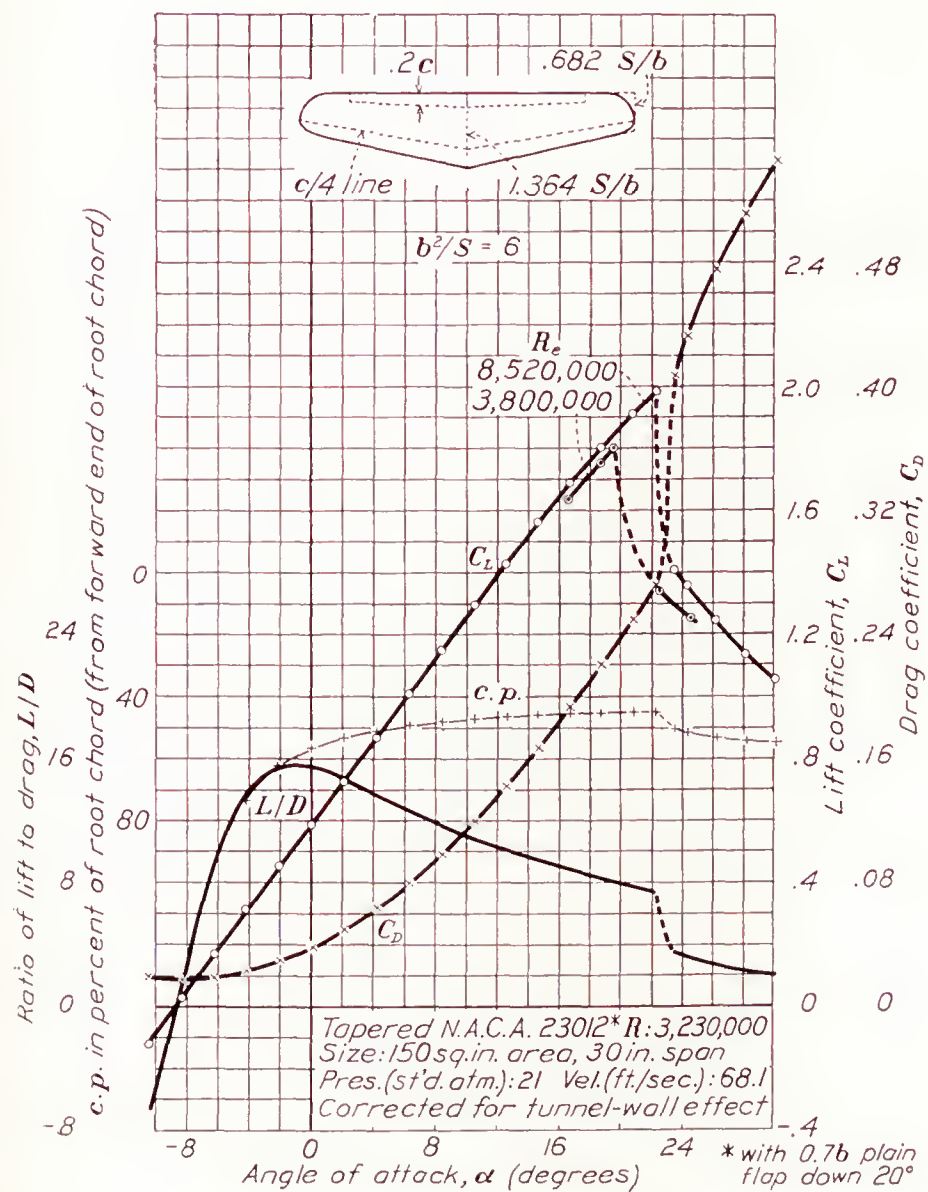


FIGURE 15.—The tapered N. A. C. A. 23012 airfoil with 0.7b plain flap down 20°.



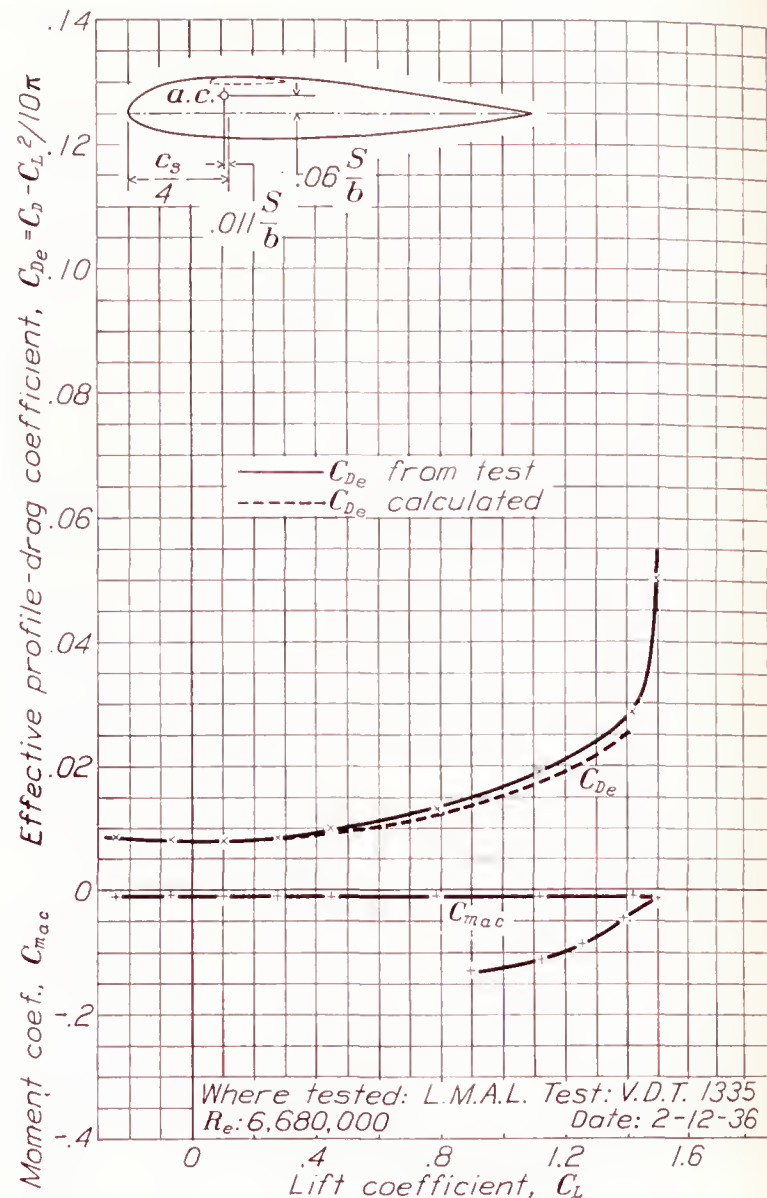
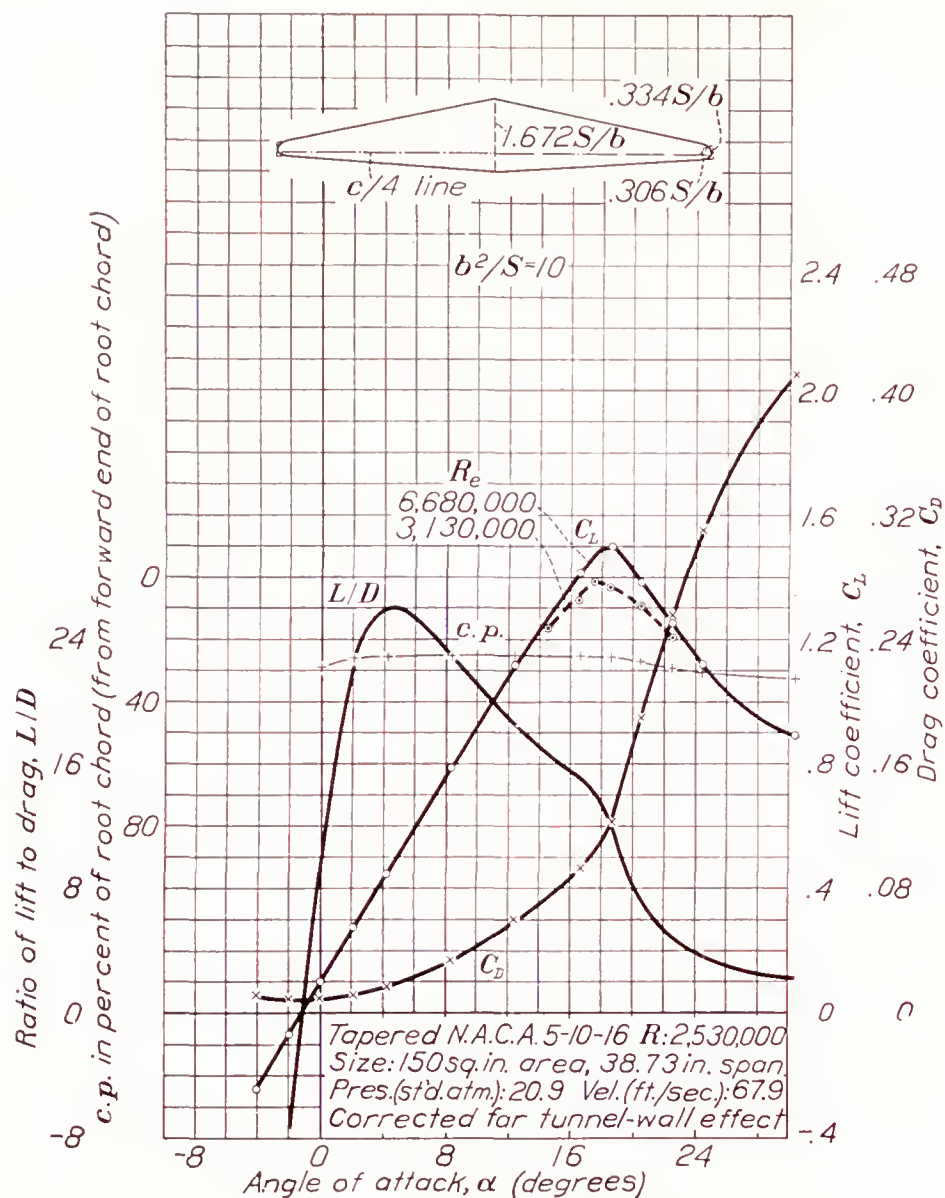


FIGURE 16.—The tapered N. A. C. A. 5-10-16 airfoil.

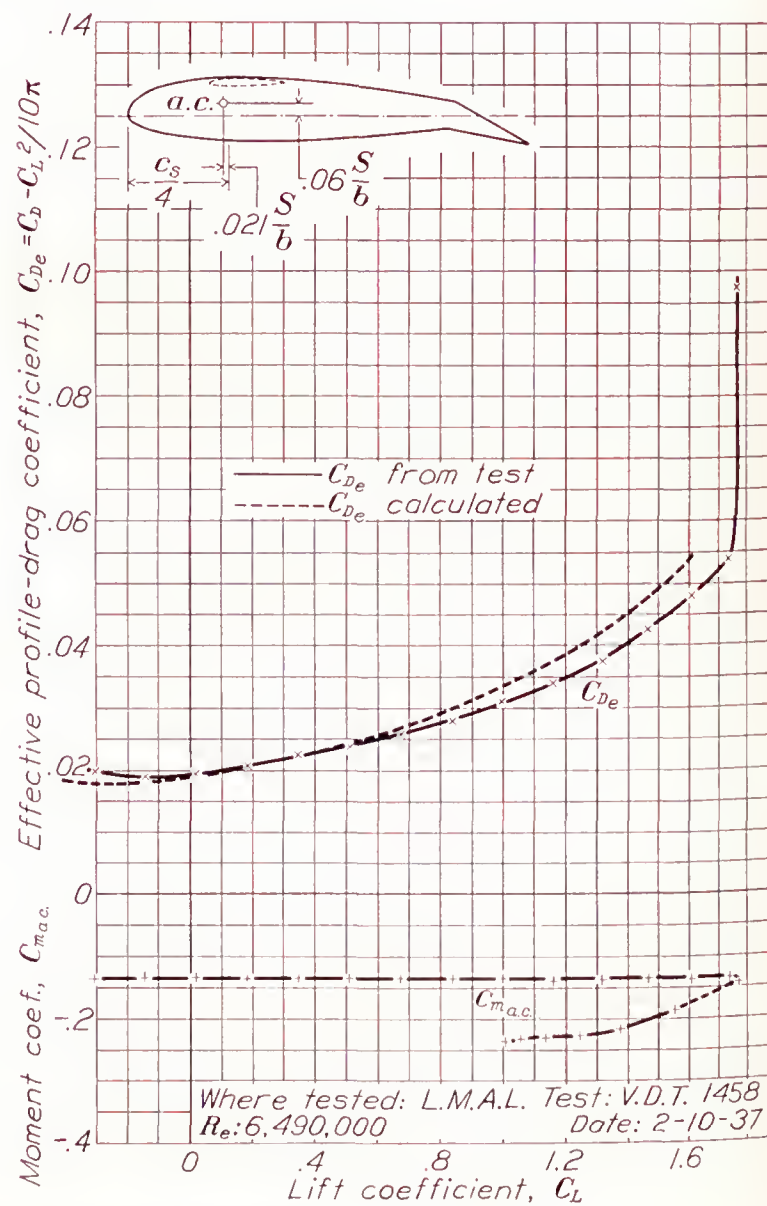
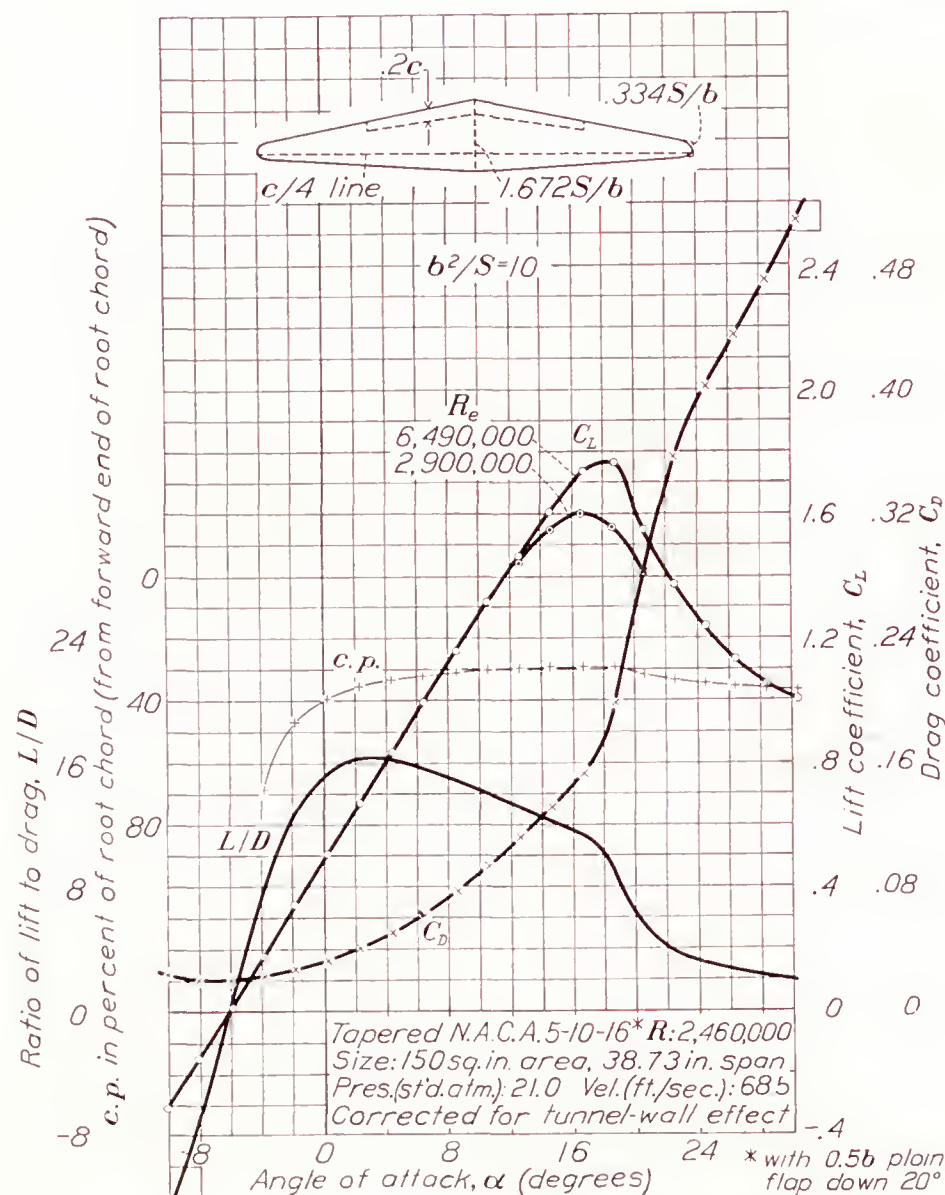


FIGURE 17.—The tapered N. A. C. A. 5-10-16 airfoil with 0.5b plain flap down 20°.



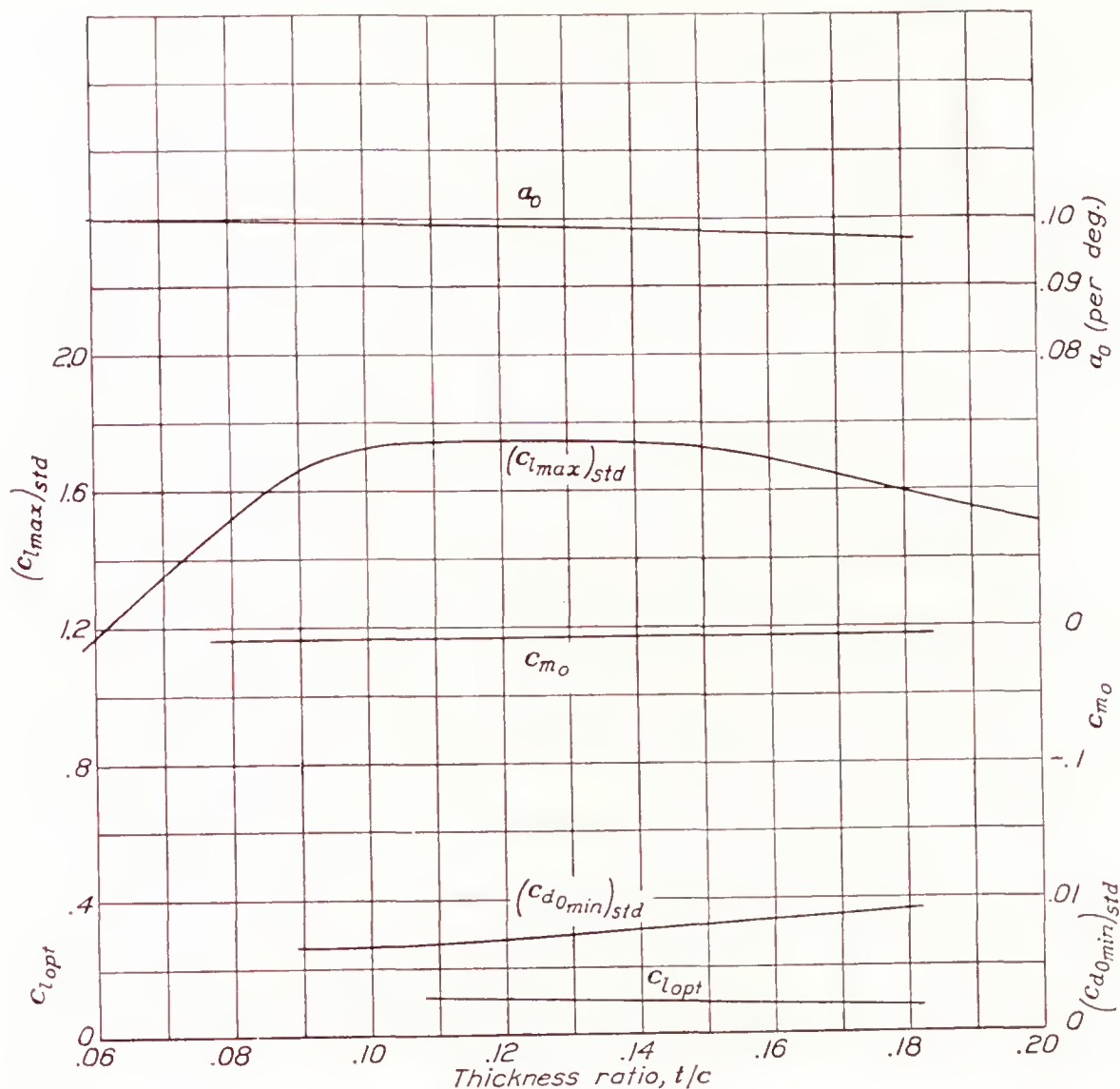


FIGURE 18.—Variation of section data with thickness. The N. A. C. A. 230 series airfoils; effective Reynolds Number, 8,200,000.

#### CALCULATED CHARACTERISTICS OF THE WINGS

The factors previously presented were applied to the calculation of the characteristics of the wings used in the tests and the results are summarized in table I. The calculations will be illustrated for the tapered N. A. C. A. 23012 wing with the  $0.5b$  flap.

**Angle of zero lift and lift-curve slope.**—The angle of zero lift by equation (2) is:

$$\alpha_{s(L=0)} = -1.2 - (6.07 \times 0.90) = -6.7^\circ$$

The value of  $\Delta c_l$  (0.90) was measured from figure 10 at approximately the average lift coefficient of the basic  $c_{l_b}$  distribution of the flapped portion of the wing. The average lift coefficient was estimated from column 15 of table II.

The lift-curve slope was calculated from equation (3), the value of  $f$  being taken from figure 3:

$$a = 0.999 \frac{0.091}{1 + \frac{57.3 \times 0.091}{\pi \times 6}} = 0.071$$

The value of  $\bar{a}_0$  (equation (4)), values of  $a_0$  and  $a_{0f}$  having been taken from figures 18 and 19, is

$$\bar{a}_0 = \frac{89.6}{150} \times 0.085 + \left(1 - \frac{89.6}{150}\right) \times 0.099 = 0.091$$

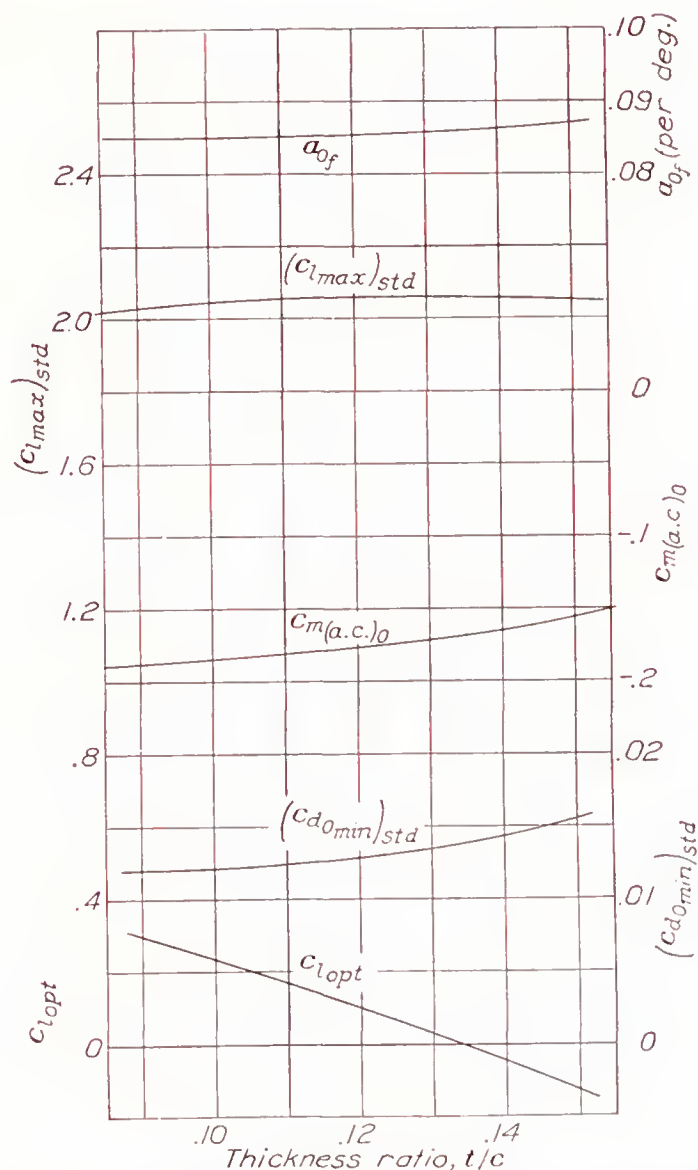


FIGURE 19.—Variation of section data with thickness. The N. A. C. A. 230 series airfoils with  $0.2c$  plain flap down  $20^\circ$ ; effective Reynolds Number, 8,200,000.



**Aerodynamic center and pitching moment.**—The  $x$  position was found directly from equation (6):

$$\frac{x_{a.c.}}{S/b} = HA \tan \Lambda = 0.214 \times 6 \times 0.1703 = 0.219$$

The appropriate values of  $\Lambda$  and  $H$  (fig. 5) were used and the aerodynamic centers of the wing sections were considered to be at the quarter-chord points.

The pitching-moment coefficient  $C_{m_s}$  due to the moments of the airfoil sections (equation (9)) was obtained, as shown in figure 20, from the area above the  $c_{m_{a.c.}} c^2$  curve. Figure 20 illustrates the general method that may be applied to any plan form and any distribution of  $c_{m_{a.c.}}$  across the span. The values of the necessary pitching-moment coefficients were taken from figures 18 and 19 and are for a value of  $c_l$  of zero, in which case  $c_{m_{a.c.}} = c_{m_{(a.c.)_0}}$ . If  $c_{m_{(a.c.)_0}}$  varies appreciably with  $c_l$ , it should be taken at the average value of  $c_l$  over the portion of the wing with flaps. In this example,  $C_{m_s}$  could also have been calculated from the values of  $E$  and  $E'$  given in figure 7 because the increment, as well as the initial value of the pitching-moment coefficient, was substantially constant across both the flapped and the unflapped parts of the span.

The pitching-moment coefficient due to the basic lift distribution is given by formula (7)

$$C_{m_{l_b}} = G \Delta c_l A \tan \Lambda = 0.029 \times 0.77 \times 6 \times 0.1703 = 0.023$$

The value of  $G$  was taken from figure 6 and the value of  $\Delta c_l$  was taken at an intermediate  $c_l$  ( $c_l = 1.0$ ) from figure 10 for the N. A. C. A. 23012 airfoil with flap. Although  $\Delta c_l$  varies with the  $c_l$  at which it is taken, the exact value used does not affect the value of  $C_{m_{l_b}}$  appreciably unless the sweepback is large. When the quarter-chord points do not lie on a straight line so that the angle of sweepback cannot be measured,  $C_{m_{l_b}}$  may be computed from formula (8). The total pitching-moment coefficient about the axis through the aerodynamic center is then

$$C_{m_{a.c.}} = C_{m_s} + C_{m_{l_b}} = -0.128 + 0.023 = -0.105$$

**Drag.**—The induced drag was calculated from formula (13) using values of  $u$ ,  $v$ , and  $w$  from figure 8 and a value of  $\Delta c_l$  at an intermediate value of  $c_l$  ( $c_l = 1.0$ ) for the N. A. C. A. 23012 airfoil with flap (fig. 10). Thus  $C_{D_i}$  for any value of  $C_L$  is

$$C_{D_i} = \frac{C_L^2}{\pi A \times 0.986} + (-0.0010)0.77 C_L + 0.0100(0.77)^2$$

Values of  $C_{D_i}$  were calculated for a series of values of  $C_L$ .

The profile-drag coefficient of the wings was calculated by an integration of the section profile drag along the semispan as given by

$$C_{D_0} = \frac{b}{S} \int_0^1 c_{d_0} c d \left( \frac{y}{b/2} \right)$$

This integration has been graphically performed as shown in figure 21. The value of  $c_{d_0}$  at any point will, of course, depend upon the airfoil section, the lift coefficient, and the Reynolds Number at that point. The calculations are illustrated in table II for a  $C_L$  of 0.8 and follow the method of reference 4.

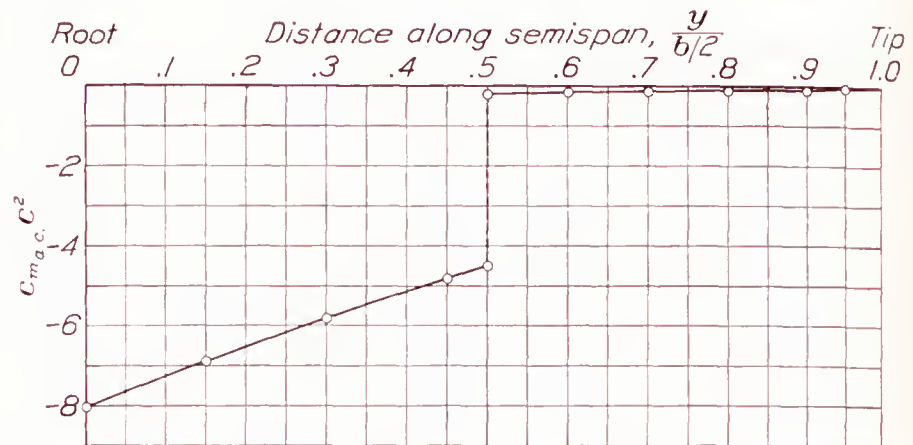


FIGURE 20.—Graphical determination of  $C_{m_s}$  for the N. A. C. A. 23012 airfoil with 0.5b plain flap.

$$C_{m_s} = \frac{b^2}{S^2} \int_0^1 c_{m_{a.c.}} c^2 d \left( \frac{y}{b/2} \right) = -0.128$$

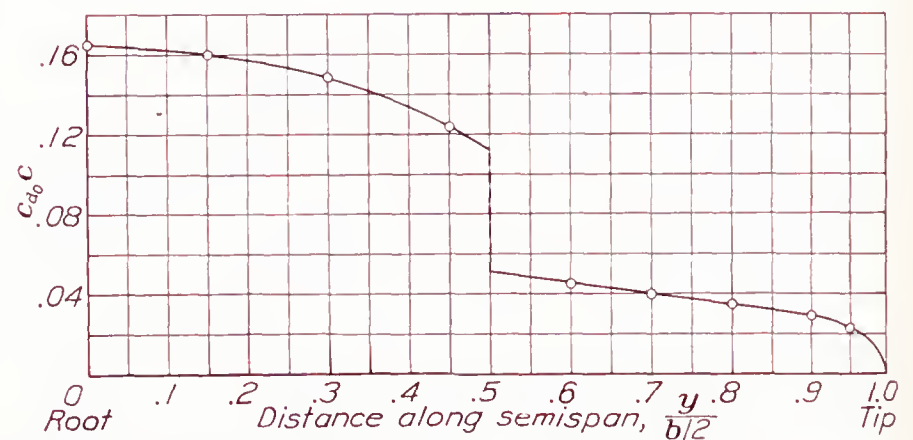


FIGURE 21.—Graphical determination of  $C_{D_0}$  for the N. A. C. A. 23012 tapered airfoil with 0.5b plain flap.

$$C_{D_0} = \frac{b}{S} \int_0^1 c_{d_0} c d \left( \frac{y}{b/2} \right) = 0.0184$$

Values of  $c_{d_0} c$  were calculated at intervals along the semispan using the known lift distributions. The values of  $(c_{l_{max}})_{std}$ ,  $(c_{d_{0min}})_{std}$ ,  $c_{l_{opv}}$ , and  $\Delta c_{l_{max}}$  that appear in the various columns of table II were obtained from figures 18, 19, and 22. Section data for other flap deflections may be found in references 6 and 7. The values of  $c_{d_{0min}}$  were extrapolated to the Reynolds Number of each point along the semispan by the method given in figure 23 of reference 4. Although the formula given in reference 4 was derived for sections with moderate camber, it should apply approximately to airfoils with flaps.

The  $c_l$  distribution for  $C_L = 0.8$  was obtained from the equation

$$c_l = C_L c_{l_{a1}} + c_{l_b}$$

where

$$c_{l_{a1}} = \frac{S}{cb} L_a \text{ and } c_{l_b} = \frac{\Delta c_l S}{cb} L_b$$



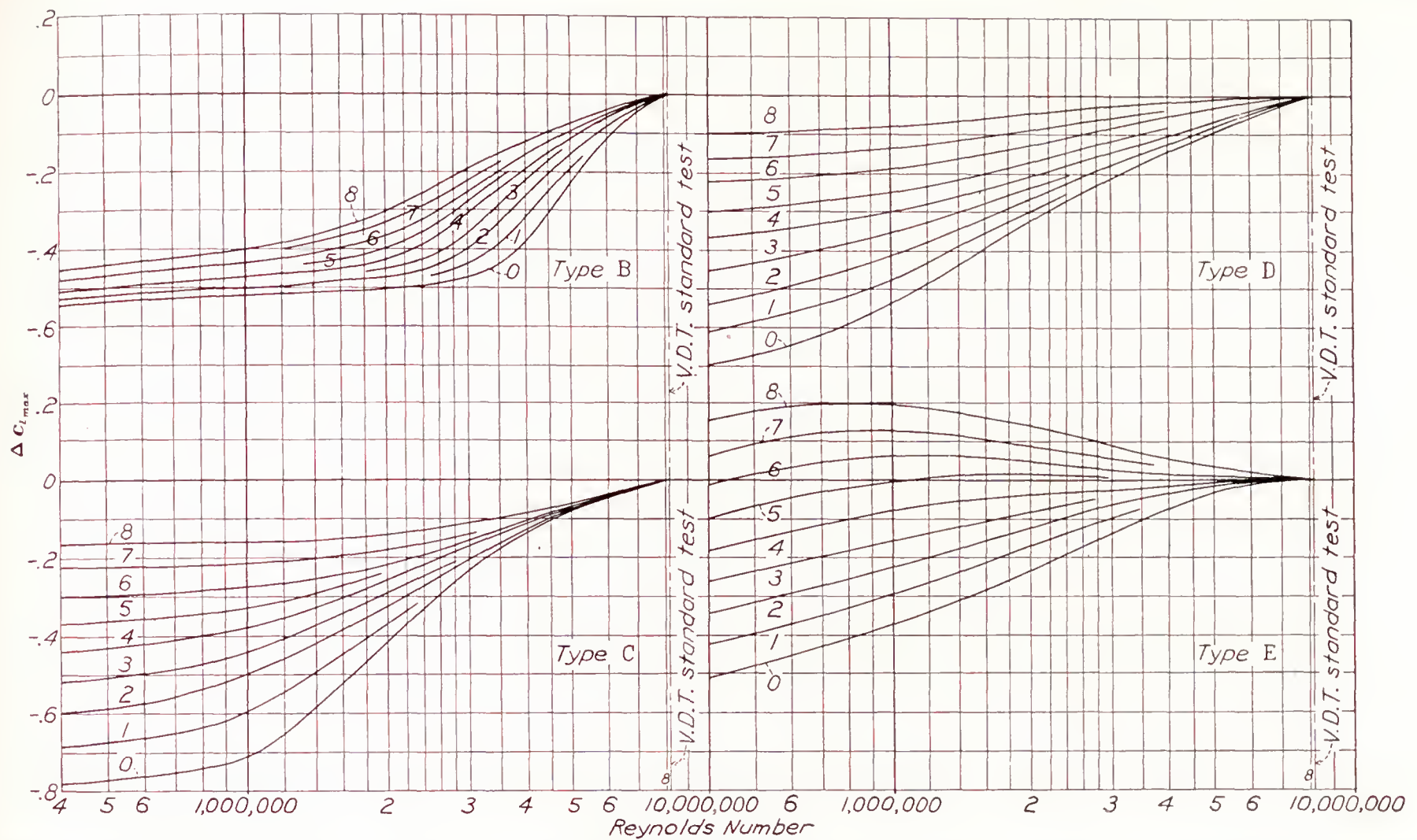


FIGURE 22.—Scale-effect corrections for  $c_{l_{max}}$ . In order to obtain the section maximum lift coefficient at the desired Reynolds Number, apply to the standard-test value the increment indicated by the curve that corresponds to the scale-effect designation (types B, C, D, or E) of the airfoil. (See reference 6, p. 32 and table II.)

The values of  $L_a$  and  $L_b$  at  $b_f/b=0.5$  were obtained from reference 2 by cross-plotting against  $b_f/b$ . The value of  $\Delta c_l$  at  $c_l=1.0$  for the flapped section was obtained from figure 10.

The profile-drag coefficient is given by the equation

$$c_{d0} = c_{d0_{min}} + \Delta c_{d0}$$

where  $\Delta c_{d0}$  depends on the quantity in column 19 of table II. Values of  $\Delta c_{d0}$  were obtained from figure 23 for the sections without flaps (data taken from reference 6) and from figure 24 for the N. A. C. A. 23012 section with flap.

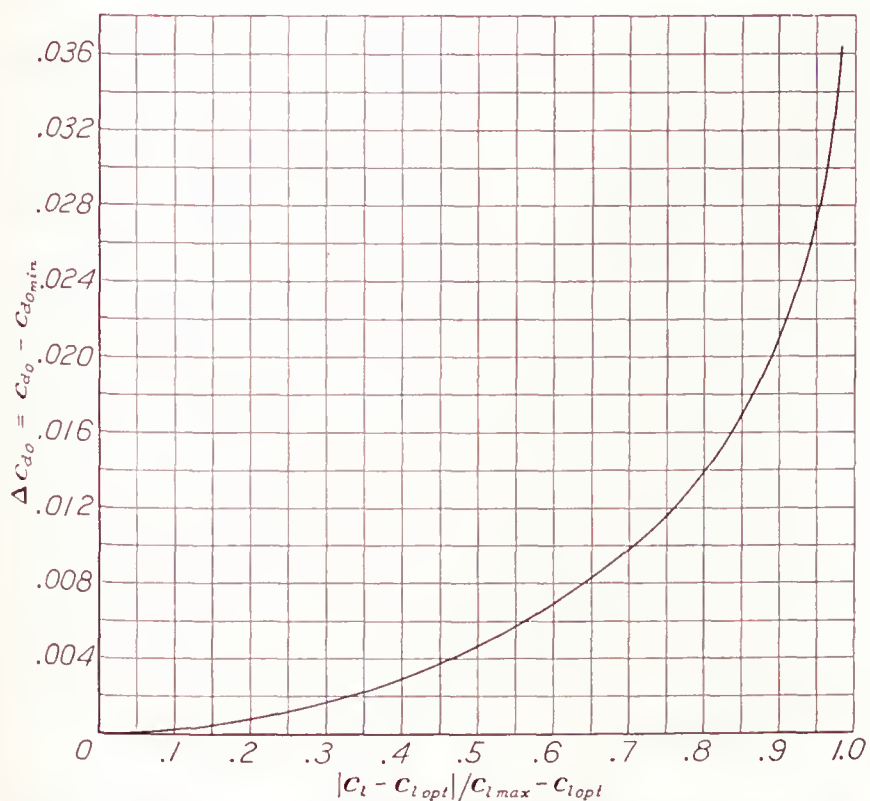


FIGURE 23.—Generalized variation of  $\Delta c_{d0}$  for airfoil sections with flaps neutral.

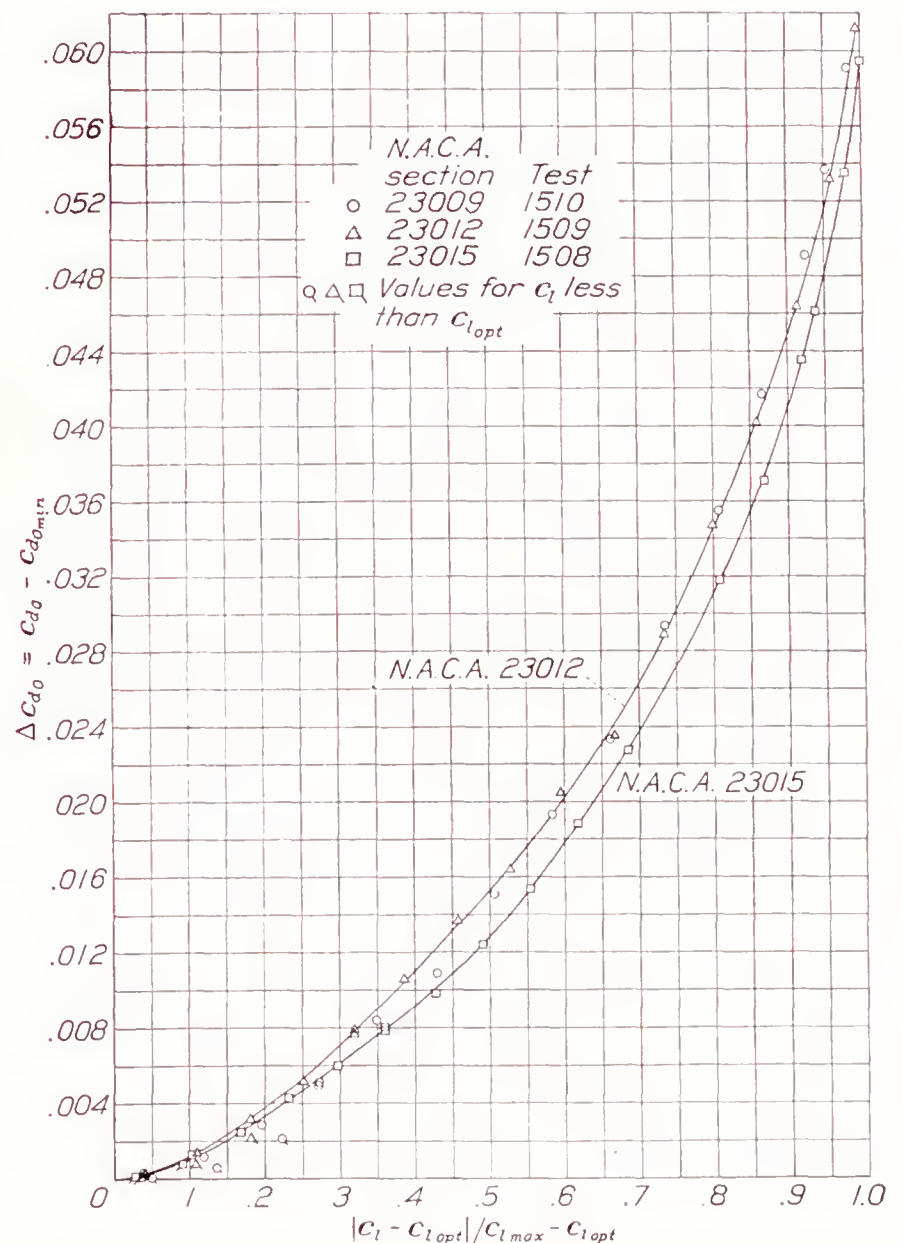


FIGURE 24.—Curves of  $\Delta c_{d0}$  for airfoil sections with 0.2c plain flaps down  $21^\circ$ .



The values of  $c_{d0}c$  given in column 22 of table II were plotted in figure 21 and extrapolated to the flap end. From the area under the curve,  $C_{D0}$  was found to be 0.0184. The process was repeated for other lift coefficients and for other wing-and-flap combinations and the results are plotted in figures 12 to 17 as effective profile-drag coefficients

$$C_{D_e} = C_{D0} + C_{D_i} - C_L^2/\pi A$$

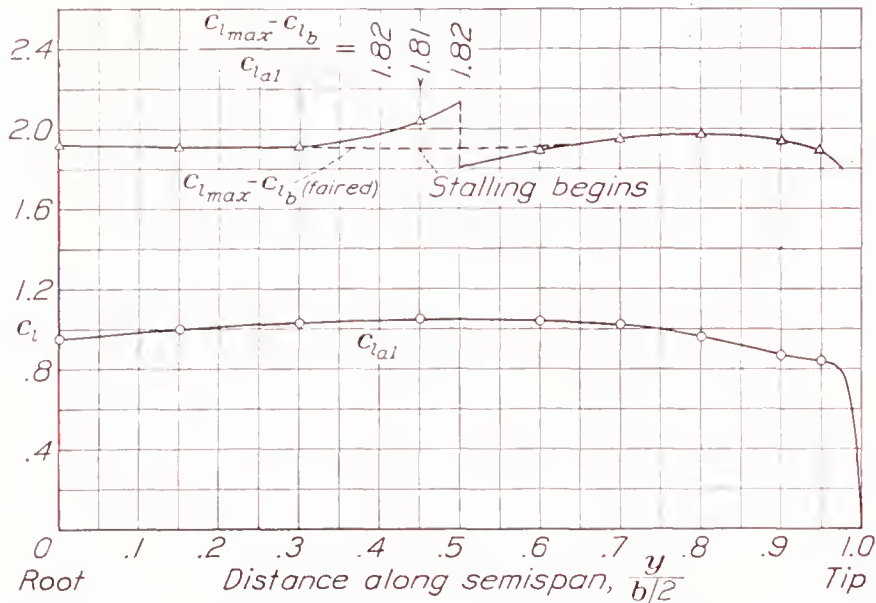


FIGURE 25.—Calculation of the  $C_L$  at which the N. A. C. A. 23012 airfoil with 0.5b plain flap begins to stall.

and the value of  $C_{L_{max}}$  as indicated on figure 25. The dashed curve faired through the flap end was used. The solid line, which passes through calculated values of  $c_{l_{max}} - c_{l_b}$ , would have indicated stalling at the plain section just outboard of the flap end at a low  $C_{L_{max}}$ . Observations of the action of tufts, however, indicate that stalling does not necessarily begin at this point. It appears to be preferable to fair  $c_{l_{max}} - c_{l_b}$  through the flap end, as shown. The calculated  $C_{L_{max}}$  value is then higher and in better agreement with the test value. Tuft observations of the wings with 0.3b and 0.7b flaps indicated that stalling began at a point other than the predicted point so that the method can be expected to give only a rough indication of  $C_{L_{max}}$ .

#### COMPARISON OF THE CALCULATED AND THE EXPERIMENTAL RESULTS

The calculated and the experimental results are compared in table I. The angles of zero lift and the lift-curve slopes are in good agreement. The  $x$  positions of the aerodynamic center are in fair agreement although the experimental aerodynamic-center positions move more and more ahead of the calculated position as the flap length is increased, probably owing to the forward movement of the position of the aerodynamic center

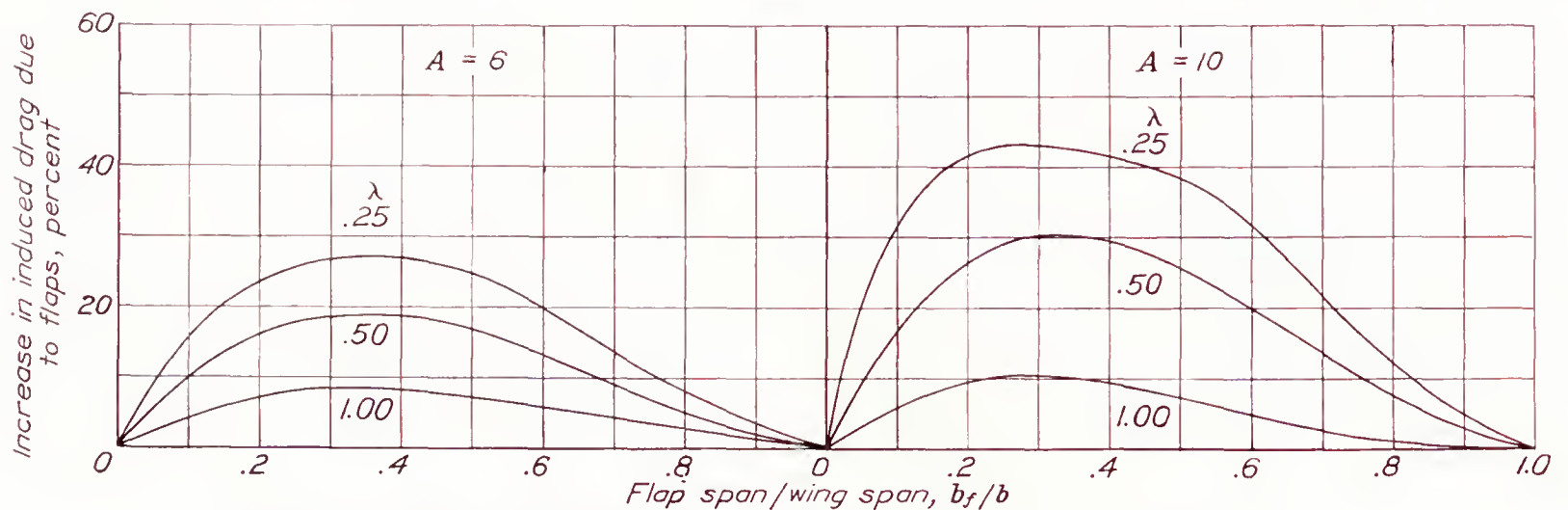


FIGURE 26.—Increase in induced drag due to the addition of flaps of various lengths.  $C_L$ , 1.0;  $\Delta c_l$ , 1.0.

**Maximum lift coefficient.**—The lift coefficients at which the wings should begin to stall were estimated by the method used in reference 1 except that, instead of plotting  $c_l$  for a series of values of  $C_L$ , the point at which a section lift coefficient reaches  $c_{l_{max}}$  ( $c_l$  curve becomes tangent to the  $c_{l_{max}}$  curve) was found more conveniently by first deducting  $c_{l_b}$  from  $c_{l_{max}}$  as in figure 25. (See column 23, table II.) The point at which the  $c_{l_{a1}}$  curve ( $c_{l_a}$  for  $C_L=1.0$ ) would become tangent if expanded to other lift coefficients then determines the point where stalling is predicted to start. This point is most easily found by calculating  $\frac{c_{l_{max}} - c_{l_b}}{c_{l_{a1}}}$  at several points along the semispan. The minimum value gives the location of the predicted stalling point

of the sections with small flap deflections. The pitching-moment coefficients are in good agreement except for the N. A. C. A. 5-10-16 wing with 0.5b flap.

The  $C_{D_e}$  curves given in figures 13 to 17 are in best agreement in the region of  $C_{D_{e_{min}}}$ . The divergence for higher and lower lift coefficients is more for these wings than for wings without flaps (reference 4).

Two values of  $C_{D_e}$  are listed in table I,  $C_{D_{e_{min}}}$  and  $C_{D_e}$  at  $C_L=0.7$ . It is interesting to note that, for the N. A. C. A. 23012 wing,  $C_{D_e}$  increases with flap length up to  $b_f/b=0.5$  but is then substantially the same at  $b_f/b=0.7$  as it is at 0.5. The reason for this variation is that the increase in profile drag with flap length is compensated by the reduction in induced drag beyond  $b_f/b=0.5$ . If plain flaps at a moderate angle are used



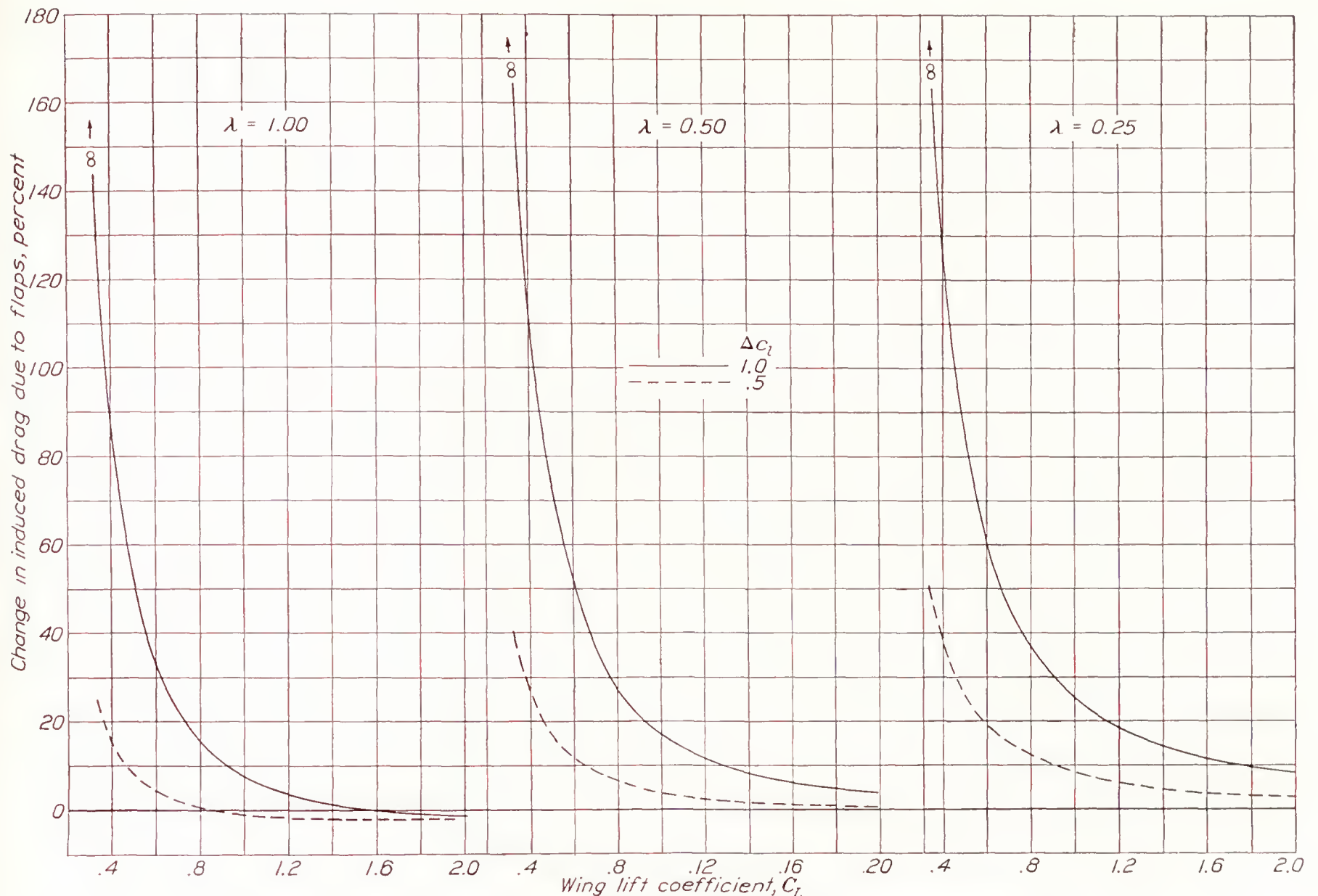


FIGURE 27.—Percentage change in induced drag relative to that for flaps neutral. 0.5b plain flap;  $A, 6$

$$\text{Percentage change given by } \frac{C_L \Delta c_l v + \Delta c_l^2 w}{C_L^2 / \pi A u} \times 100.$$

for take-off, as long a flap span as possible is therefore indicated to obtain the lowest drag. The decrease in induced drag with flap length beyond  $b_f/b$  equal to about 0.36 is illustrated in figure 26. The curves are given for various taper ratios, two values of  $A$ , and for  $C_L$  and  $\Delta c_l$  both equal to 1.0. A value of  $\Delta c_l = 1.0$  corresponds to an airfoil of moderate thickness with a 0.2c flap at an angle a little larger than  $20^\circ$ . The change of induced drag with lift coefficient is illustrated in figure 27 for a wing with half-span flap of aspect ratio 6 and for two values of  $\Delta c_l$ .

The calculated and the experimental  $C_{L_{opt}}$  values given in table I are in as good agreement as can be expected in view of the difficulty of determining  $c_{i_{opt}}$ . The agreement of the  $C_{L_{max}}$  values is fair.

#### CONCLUDING REMARKS

Although test results and the comparison with calculated results have been given only for the case of a plain flap deflected  $20^\circ$ , other test results were available for the N. A. C. A. 23012 wing with a split flap  $45^\circ$  down and with the same flap spans as those used herein. Comparison of the test and the calculated results for the split flap showed agreement similar to that obtained for the plain flap deflected  $20^\circ$ . It thus appears that fair estimates of the characteristics of tapered wings with partial-span flaps deflected various amounts can be obtained from the factors and the method given.

LANGLEY MEMORIAL AERONAUTICAL LABORATORY,  
NATIONAL ADVISORY COMMITTEE FOR AERONAUTICS,  
LANGLEY FIELD, VA., January 23, 1939.



## APPENDIX A

### SYMBOLS USED IN TEXT

$c_l$ , section lift coefficient.  
 $\Delta c_l$ , increment of section lift coefficient due to flap deflection.  
 $c_{l_b}$ , section basic lift coefficient ( $C_L=0$ ).  
 $c_{l_a}$ , section additional lift coefficient.  
 $c_{l_{a1}}$ , section additional lift coefficient for  $C_L=1.0$ .  
 $c_{d_0}$ , section profile-drag coefficient.  
 $\alpha_{s(L=0)}$ , wing angle of attack for zero lift, measured from the root chord.  
 $\alpha_{l_0_s}$ , angle of zero lift of root section.  
 $b$ , wing span.  
 $b_f$ , total flap span.  
 $S$ , area of wing.  
 $S_f$ , area of part of wing equipped with flaps.  
 $A$ , wing aspect ratio,  $b^2/S$ .  
 $\lambda$ , taper ratio,  $c_t/c_s$ .  
 $q$ , dynamic pressure.  
 $c$ , chord at any section along the span.  
 $c_t$ , tip chord (for rounded tips,  $c_t$  is the fictitious chord obtained by extending the leading and the trailing edges to the extreme tip).  
 $c_s$ , chord at root of wing or plane of symmetry.  
 $\Lambda$ , angle of sweepback measured between the lateral axis and a line through the aerodynamic centers (approximately the quarter-chord points) of the wing sections.  
 $\delta_f$ , flap angle.  
 $C_L$ , wing lift coefficient.  
 $C_D$ , wing drag coefficient.  
 $C_{D_0}$ , wing profile-drag coefficient.  
 $C_{D_e}$ , effective wing profile-drag coefficient.  
 $C_{D_i}$ , wing induced-drag coefficient.

$c_{m_{a.c.}}$ , section pitching-moment coefficient about section aerodynamic center.  
 $c_{m_{(1.c.)_0}}$ , section pitching-moment coefficient about aerodynamic-center position with flap neutral.  
 $c_{m_0}$ , section pitching-moment coefficient with flaps neutral.  
 $\Delta c_m$ , increase in section pitching-moment coefficient above  $c_{m_0}$  due to flap deflection.  
 $M$ , total wing pitching moment.  
 $M_{l_b}$ , wing pitching moment due to basic-lift forces.  
 $C_{m_{l_b}}$ , wing pitching-moment coefficient due to basic-lift forces.  
 $C_{m_s}$ , wing pitching-moment coefficient due to the pitching moments of the wing sections.  
 $C_{m_{a.c.}}$ , total wing pitching-moment coefficient about aerodynamic center.  
 $a$ , wing lift-curve slope.  
 $a_0$ , lift-curve slope of section without flap.  
 $a_{0f}$ , lift-curve slope of section with flap.  
 $x$ , moment arm measured from the quarter-chord point of the root chord and parallel to it (positive rearward).  
 $y$ , lateral distance.  
 $y_f$ , lateral distance to inboard end of flap.  
 $x_{a.c.}$ , coordinate of wing aerodynamic center.  
 $R_e$ , effective Reynolds Number.  
 $L_a$ , additional load parameter.  
 $L_b$ , basic load parameter.  
 $J$ , factor of angle of zero lift.  
 $H$ , factor of wing aerodynamic center.  
 $G$ , factor of basic-lift pitching moment.  
 $f$ , factor of wing lift-curve slope.  
 $E$  and  $E'$ , factors of section pitching moment.  
 $u, v, w$ , factors of induced drag.



## APPENDIX B

### AERODYNAMIC FACTORS IN TERMS OF THE FOURIER COEFFICIENTS

The various aerodynamic factors were obtained from a Fourier analysis in which the circulation  $\Gamma$  was expressed (see reference 2) by

$$\Gamma = \frac{c_s m_s V}{2} \sum A_n \sin n\theta$$

where

$c_s$  is the chord at plane of symmetry.

$m_s$ , slope of the section lift curve at the plane of symmetry, per radian.

$V$ , wind velocity.

$$\cos \theta = \frac{-y}{b/2}$$

If the Fourier coefficients of the plain wing at an angle of attack of one radian are denoted by  $A_n$  and if the Fourier coefficients for the same wings with a constant angle of attack extending over only the center of the span are denoted by  $a_n$ , the various aerodynamic factors (in terms of the Fourier coefficients) can be found from the following equations:

$$J = \frac{a_1}{A_1 m_0}$$

in which  $m_0$  is the slope of the lift curve at any section, per radian.

$$H = \frac{2}{\pi A_1} \left( \frac{A_1}{3} + \frac{A_3}{5} - \frac{A_5}{21} + \frac{A_7}{45} - \frac{A_9}{77} \cdot \cdot \cdot \right)$$

$$G = \frac{c_s A}{2b} \left[ \left( \frac{a_3}{5} - \frac{a_5}{21} + \frac{a_7}{45} + \cdot \cdot \cdot \right) - \frac{a_1}{A_1} \left( \frac{A_3}{5} - \frac{A_5}{21} + \frac{A_7}{45} + \cdot \cdot \cdot \right) \right]$$

$$u = \frac{1}{1 + \frac{1}{A_1^2} \sum_{3,5,7}^{\infty} n A_n^2}$$

$$v = \frac{c_s}{2b A_1} \sum_{3,5,7}^{\infty} n A_n \left( a_n - \frac{a_1}{A_1} A_n \right)$$

$$w = \frac{\pi A c_s^2}{16 b^2} \sum_{3,5,7}^{\infty} n \left( a_n - \frac{a_1}{A_1} A_n \right)^2$$

### REFERENCES

1. Anderson, Raymond F.: Determination of the Characteristics of Tapered Wings. T. R. No. 572, N. A. C. A., 1936.
2. Pearson, H. A.: Span Load Distribution for Tapered Wings with Partial-Span Flaps. T. R. No. 585, N. A. C. A., 1937.
3. Pearson, Henry A., and Jones, Robert T.: Theoretical Stability and Control Characteristics of Wings with Various Amounts of Taper and Twist. T. R. No. 635, N. A. C. A., 1938.
4. Anderson, Raymond F.: The Experimental and Calculated Characteristics of 22 Tapered Wings. T. R. No. 627, N. A. C. A., 1938.
5. Jacobs, Eastman N., and Abbott, Ira H.: The N. A. C. A. Variable-Density Wind Tunnel. T. R. No. 416, N. A. C. A., 1932.
6. Jacobs, Eastman N., and Sherman, Albert: Airfoil Section Characteristics as Affected by Variations of the Reynolds Number. T. R. No. 586, N. A. C. A., 1937.
7. Abbott, Ira H., and Greenberg, Harry: Tests in the Variable-Density Wind Tunnel of the N. A. C. A. 23012 Airfoil with Plain and Split Flaps. T. R. No. 661, N. A. C. A., 1939.



TABLE I  
COMPARISON OF CALCULATED AND EXPERIMENTAL CHARACTERISTICS  
[Wings with 0.2c plain flaps 20° down]

Wing	Flap length (frac- tion span)	$\lambda = c_t/c_s$	Aspect ratio	Root sec- tion, N. A. C. A.	Construc- tion tip section (extreme tip), N. A. C. A.	Sweep- back (deg.)	$\alpha_{\epsilon(L=0)}$ (deg.)		$\alpha$		$\frac{x_{a.c.}}{S/b}$ (1)	
							Experi- mental	Calcu- lated	Experi- mental	Calcu- lated	Experi- mental	Calcu- lated
Tapered N. A. C. A. 23012	$\left\{ \begin{array}{c} 0 \\ .3 \\ .5 \\ .7 \end{array} \right\}$	0.5	6	23012	23012	9.67	$\left\{ \begin{array}{c} -1.3 \\ -4.8 \\ -6.9 \\ -8.7 \end{array} \right\}$	$\left\{ \begin{array}{c} -1.2 \\ -4.6 \\ -6.7 \\ -8.6 \end{array} \right\}$	$\left\{ \begin{array}{c} 0.075 \\ .072 \\ .070 \\ .067 \end{array} \right\}$	$\left\{ \begin{array}{c} 0.076 \\ .073 \\ .071 \\ .069 \end{array} \right\}$	$\left\{ \begin{array}{c} 0.210 \\ .209 \\ .201 \\ .193 \end{array} \right\}$	$\left\{ \begin{array}{c} 0.219 \\ .219 \\ .219 \\ .219 \end{array} \right\}$
Tapered N. A. C. A. 5-10-16	$\left\{ \begin{array}{c} 0 \\ .5 \end{array} \right\}$	.2	10	23016	23009	0	$\left\{ \begin{array}{c} -1.2 \\ -6.2 \end{array} \right\}$	$\left\{ \begin{array}{c} -1.1 \\ -6.4 \end{array} \right\}$	$\left\{ \begin{array}{c} .083 \\ .079 \end{array} \right\}$	$\left\{ \begin{array}{c} .083 \\ .078 \end{array} \right\}$	$\left\{ \begin{array}{c} -.011 \\ -.021 \end{array} \right\}$	$\left\{ \begin{array}{c} 0 \\ 0 \end{array} \right\}$
Wing	$C_{m_{a.c.}}$		$C_{D_{0min}}$		$C_{L_{opt}}$		$C_{L_{max}}$		$C_{D_e}$ at $C_L=0.7$			
	Experi- mental	Calculated	Experi- mental	Calculated	Experi- mental	Calculated	Experi- mental	Calculated	Experi- mental	Calculated		
Tapered N. A. C. A. 23012	$\left\{ \begin{array}{c} -.014 \\ -.068 \\ -.106 \\ -.143 \end{array} \right\}$	$\left\{ \begin{array}{c} -.008 \\ -.068 \\ -.105 \\ -.142 \end{array} \right\}$	$\left\{ \begin{array}{c} 0.0076 \\ .0165 \\ .0175 \\ .0156 \end{array} \right\}$	$\left\{ \begin{array}{c} 0.0071 \\ .0155 \\ .0170 \\ .0158 \end{array} \right\}$	$\left\{ \begin{array}{c} 0.13 \\ .20 \\ .20 \\ .16 \end{array} \right\}$	$\left\{ \begin{array}{c} 0.09 \\ -.02 \\ .03 \\ .05 \end{array} \right\}$	$\left\{ \begin{array}{c} 1.71 \\ 1.83 \\ 1.91 \\ 1.98 \end{array} \right\}$	$\left\{ \begin{array}{c} 1.67 \\ 1.77 \\ 1.81 \\ 1.90 \end{array} \right\}$	$\left\{ \begin{array}{c} 0.0106 \\ .0182 \\ .0205 \\ .0203 \end{array} \right\}$	$\left\{ \begin{array}{c} 0.0100 \\ .0209 \\ .0226 \\ .0222 \end{array} \right\}$		
Tapered N. A. C. A. 5-10-16	$\left\{ \begin{array}{c} -.009 \\ -.136 \end{array} \right\}$	$\left\{ \begin{array}{c} -.007 \\ -.157 \end{array} \right\}$	$\left\{ \begin{array}{c} .0080 \\ .0190 \end{array} \right\}$	$\left\{ \begin{array}{c} .0081 \\ .0178 \end{array} \right\}$	$\left\{ \begin{array}{c} .03 \\ -.12 \end{array} \right\}$	$\left\{ \begin{array}{c} .10 \\ -.23 \end{array} \right\}$	$\left\{ \begin{array}{c} 1.50 \\ 1.77 \end{array} \right\}$	$\left\{ \begin{array}{c} 1.49 \\ 1.74 \end{array} \right\}$	$\left\{ \begin{array}{c} .0123 \\ .0262 \end{array} \right\}$	$\left\{ \begin{array}{c} .0113 \\ .0274 \end{array} \right\}$		

<sup>†</sup> Measured from the quarter-chord point of the root chord, positive toward the trailing edge.

TABLE II  
CALCULATION OF  $C_{D_0}$  FOR  $C_L=0.8$   
[N. A. C. A. 23012 tapered wing with 0.5b flap deflected downward 20°;  $R_e$  (based on  $S/b$ ) = 8,200,000]

1	2	3	4	5	6	7	8	9	10	11	12
Distance from center, fraction semispan, $\frac{y}{b/2}$	thickness chord $t/c$	Chord $c$ (in.)	Effective Reynolds Number $R_e$ (millions)	$(c_{l_{max}})_{std}$ at $R_e=8,200,000$	$\Delta c_{l_{max}}$ (fig. 22)	$c_{l_{max}}$ (5)+(6)	$(c_{d0min})_{std}$ at $R_e=8,200,000$	$c_{d0min}$	$c_{l_{opt}}$	$c_{l_{max}}-c_{l_{opt}}$	Load parameter $L_a$ (reference 2)
0.00	0.12	6.82	11.18	2.06	0.02	2.08	0.0128	0.0125	0.10	1.98	1.291
.15	.12	6.31	10.35	2.06	.02	2.08	.0128	.0126	.10	1.98	1.263
.30	.12	5.80	9.51	2.06	.01	2.07	.0128	.0127	.10	1.97	1.191
.45	.12	5.28	8.66	2.06	0	2.06	.0128	.0128	.10	1.96	1.107
.60	.12	4.77	7.82	1.75	-.01	1.74	.0071	.0072	.10	1.64	.995
.70	.12	4.43	7.26	1.75	-.02	1.73	.0071	.0072	.10	1.63	.908
.80	.12	4.09	6.71	1.75	-.03	1.72	.0071	.0072	.10	1.62	.789
.90	.12	3.50	5.74	1.75	-.06	1.69	.0071	.0074	.10	1.59	.607
.95	.12	2.66	4.36	1.75	-.10	1.65	.0071	.0076	.10	1.55	.447
1	13	14	15	16	17	18	19	20	21	22	23
$\frac{y}{b/2}$	$\frac{S}{cb} L_a = c_{l_{at}}$	Load parameter $L_b$ (reference 2)	$\frac{\Delta c_l S}{cb} L_b = c_{l_b}$	$C_L \times c_{l_{at}} = c_{l_a}$	$c_l$	$c_l - c_{l_{opt}}$	$\frac{ c_l - c_{l_{opt}} }{c_{l_{max}} - c_{l_{opt}}}$	$\Delta c_{d0}$	$c_d$ (9)+(20)	$c_{d0}c$	$c_{l_{max}} - c_{l_b}$
0.00	0.946	0.289	0.163	0.757	0.920	0.820	0.414	0.0117	0.0242	0.1650	1.92
.15	1.001	.276	.168	.801	.969	.869	.439	.0127	.0253	.1596	1.91
.30	1.027	.235	.156	.822	.978	.878	.446	.0129	.0256	.1485	1.91
.45	1.048	.030	.022	.838	.860	.760	.388	.0106	.0234	.1236	2.04
.60	1.043	-.190	-.153	.834	.681	.581	.354	.0023	.0095	.0453	1.89
.70	1.025	-.252	-.219	.820	.601	.501	.307	.0018	.0090	.0399	1.95
.80	.964	-.266	-.250	.771	.521	.421	.260	.0013	.0085	.0348	1.97
.90	.867	-.224	-.246	.694	.448	.348	.219	.0010	.0084	.0294	1.94
.95	.840	-.168	-.243	.672	.429	.329	.212	.0009	.0085	.0226	1.89



# REPORT No. 666

## AIRCRAFT RATE-OF-CLIMB INDICATORS

By DANIEL P. JOHNSON

### SUMMARY

*The theory of the rate-of-climb indicator is developed in a form adapted for application to the instrument in its present-day form. Compensations for altitude, temperature, and rate of change of temperature are discussed from the designer's standpoint on the basis of this theory. Certain dynamic effects, including instrument lag, and the use of the rate-of-climb indicator as a statoscope are also considered. Modern instruments are described. A laboratory test procedure is outlined and test results are given.*

### INTRODUCTION

Before rate-of-climb indicators were available, statoscopes were used by balloonists to detect departure from constant altitude. These instruments contained a closed chamber at atmospheric pressure. If the altitude changed, air would have to flow into or out of the chamber to equalize the pressure. This flow took place through a tube in which was trapped a small amount of liquid, so that the air passed in bubbles. The direction of motion of the bubbles showed whether the craft was rising or falling, and the frequency of occurrence showed the rate of change of altitude.

Later there was developed the balloon variometer, essentially a rate-of-climb indicator, in which the flow into the chamber took place through a capillary leak. The pressure difference across the leak, measured with a sensitive liquid manometer, provided a quantitative indication of the rate of climb. (See reference 1.) In some instruments, when it was desired to fly at constant altitude, the leak could be closed, whereupon the manometer would indicate the difference between the constant chamber pressure and the atmospheric pressure, thus providing a sensitive altimeter for use in holding the aircraft at a constant pressure altitude.

A U-tube manometer was usable as long as the rate-of-climb indicator was intended for use in the relatively steady balloon or dirigible, but the use of a liquid-type manometer presented serious difficulties in airplane maneuvers. On this account, a diaphragm cell was substituted for the manometer. For a fuller description of this type and earlier instruments, see reference

2. Considerable refinement was now possible in the instrument; the time lag has been decreased, and compensations for temperature effects and for change in sensitivity with altitude have recently been introduced, so that the indication corresponded reasonably well to the rate of climb in the standard atmosphere. Another recent improvement did away with the separate vacuum bottle that formed the closed chamber in service instruments and utilized the case of the indicator itself for this purpose. This change made possible a considerable saving in weight and increased the ease of installation.

Rate-of-climb indicators are now used both as indicators of level flight and as indicators of the rate of climb or descent. When the pilot is trying to maintain level flight, it is essential to know when the rate of climb is exactly zero and to have an immediate indication of small changes of altitude. Therefore, the instrument should have a zero point which does not shift under flight conditions and which may be conveniently adjusted to take care of secular changes. The time lag should be short enough to allow the instrument to respond to quick changes in altitude but not so short that the pointer becomes unsteady in gusty air.

A moderately accurate quantitative indication of the rate of climb or descent is desired in holding the airplane at an efficient climbing speed, in coming in for a landing, or in passenger service where there are restrictions on the rate of descent. The accuracy of present-day rate-of-climb indicators is quite adequate for these uses. The rate-of-climb indicator is the most important instrument on a glider, where it is essential to detect rising air currents promptly. It is a necessity on balloons and airships where altitude is controlled by valving lift gas and dropping ballast. In flight-testing aircraft there is desired a record and greater accuracy than is obtainable (even now) from rate-of-climb indicators and, accordingly, the rate of climb is usually computed from the indications of a barograph.

This paper was prepared with the cooperation and the financial support of the National Advisory Committee for Aeronautics.



## THEORETICAL DISCUSSION

The elements of a leak-type rate-of-climb indicator are shown in figure 1. The interior C of the instrument forms an insulated chamber, which is connected to the static pressure line through a leak B. The outlet A is also connected to the interior of a diaphragm cell D, which therefore serves to measure the differential pres-

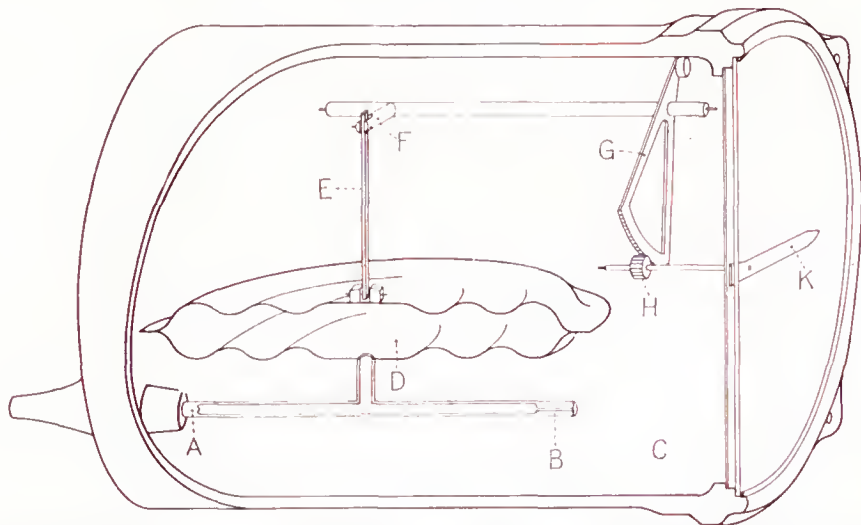


FIGURE 1.—Schematic diagram of a rate-of-climb indicator. A is the inlet from the static line; B, calibrated leak; C, chamber; D, diaphragm cell; E, link; F, crank; G, sector; H, pinion; and K, pointer.

sure across the leak. The displacement of the diaphragm is transmitted to the pointer by means of a suitable mechanical train, such as a link, bell crank, sector, and pinion.

## DEFINITION OF SYMBOLS

The symbols used in the discussion are defined below. Quantities used only once will be defined in the text.

$Z$ , pressure altitude in United States standard atmosphere.

$v = \frac{dZ}{dt}$ , rate of climb in the standard atmosphere.

$x$ , indication of instrument.

$V$ , volume of chamber C (fig. 1).

$t$ , time.

$\lambda$ , time constant.

$\lambda_{10} = 2.30\lambda$  = time lag.

$K$ , calibration coefficient.

$L$ , coefficient of rate of change of temperature.

$n$ , ratio of time constant to damping constant of instrument with leak removed.

$p, \rho, T$ , pressure, density, and absolute temperature of the free air.

$p_c, \rho_c, T_c$ , pressure, density, and absolute temperature of air in chamber.

$p_K, \rho_K, T_K$ , pressure, density, and absolute temperature of air at the leak.

$\mu$ , absolute viscosity of air (at leak).

$\alpha$ , leak coefficient.

$g$ , acceleration due to gravity.

$\Delta p = p_c - p$ , pressure drop across leak.

$m = \rho_c V$  = mass of air in chamber.

$R = \frac{p}{T\rho}$ , the gas constant for unit mass of air (3078 ft.<sup>2</sup>/sec.<sup>2</sup> ° C.).

$F$ , volume rate of flow of air outward through leak.

$a$ , rate of change in volume with respect to differential pressure.

$b$ , rate of change in volume with respect to atmospheric pressure.

$c$ , rate of change in volume with respect to instrument temperature.

$M = x/\Delta p$ , sensitivity of pressure gage.

## INITIAL ASSUMPTIONS

(a) The standard rate of climb will be based on the United States standard atmosphere (references 3 and 4), which was calculated from the La Place barometric equation:

$$dp = -\frac{gp}{RT}dZ \quad (1)$$

and, for altitudes below 35,000 feet, the following relation between altitude and temperature:

$$T = 288 - 0.0019812Z \quad (2)$$

By elimination of  $Z$  between these two equations and integration and substitution of the numerical values of the constants, there results for the standard atmosphere a relation between the pressure and temperature:

$$T/288 = (p/760)^{0.190} \quad (3)$$

(b) The relation between pressure drop across the leak and the flow  $F$  through it, may be put in the form

$$\Delta p = +\mu\alpha F \quad (4)$$

For the special case in which the leak is formed by a long capillary, equation (4) reduces to Poiseuille's law,

$$\Delta p = \frac{8l}{\pi r^4} \mu F \quad (5)$$

in which  $\alpha = \frac{8l}{\pi r^4}$ , where  $l$  is the length and  $r$  the radius of the capillary. The more general form is used since the leak need not be a capillary tube but may be much more complicated, perhaps involving separately or in combination, orifices or valves that are opened or closed by the mechanism of the device. The leak coefficient  $\alpha$  can be said to be dependent on the physical dimensions of the leak but subject to control by the designer to effect altitude and temperature compensation. The leak coefficient is a constant for the special case of laminar flow in a long capillary but may be a slowly varying function of the air density and rate of flow for other types of restrictions.

(c) Air is assumed to be a perfect gas so that for a unit mass

$$p = \rho RT \quad (6)$$

(d) In order to simplify the mathematical discussion, use will be made, wherever possible, of the fact that the difference between the pressures in the chamber, the leak, and in the free air, and the difference between temperature in the chamber and in the leak, are small with respect to the absolute values of those quantities,



so that the quantities  $\frac{\rho_c}{\rho_K}$ ,  $\frac{p_c}{p_K}$  and  $\frac{T_c}{T_K}$  may be set equal to unity without serious error.

(e) For convenience, the relation between the indication and the pressure drop across the leak is put in the form

$$M\Delta p = x \quad (7)$$

where  $M$  is the sensitivity of the pressure gage. The sensitivity is subject to control by the designer in order to obtain the desired calibration and to effect temperature and altitude compensation. This relation omits consideration of the effect of inertia and friction in the indicating mechanism. As far as these effects are subject to analysis, they may be introduced by substitution of a suitable differential equation for equation (7).

#### DEVELOPMENT OF THE GENERAL EQUATION

If the air pressure  $p$  is decreasing (ascent), there will be a flow of gas outward through the leak of the instrument at a rate given by the equation:

$$\begin{aligned} F &= -\frac{1}{\rho_K} \frac{dm}{dt} = -\frac{1}{\rho_K} \left[ \rho_c \frac{dV}{dt} + V \frac{d\rho_c}{dt} \right] \\ &= -\frac{\rho_c}{\rho_K} \left[ \frac{dV}{dt} + V \frac{1}{p_c} \frac{dp_c}{dt} - \frac{V}{T_c} \frac{dT_c}{dt} \right] \end{aligned} \quad (8)$$

Setting  $\frac{\rho_c}{\rho_K} = 1$  and substituting in equation (4), there is obtained

$$-\frac{\Delta p}{\mu \alpha V} = \frac{1}{p_c} \frac{dp_c}{dt} + \frac{1}{V} \frac{dV}{dt} - \frac{1}{T_c} \frac{dT_c}{dt} \quad (9)$$

The rate of change in volume is usually small and is incidental to the operation of the indicating means. It may be separated into three parts: due to changes in differential pressure  $\Delta p$ , to changes in atmospheric pressure  $p$ , and to changes in the instrument temperature  $T_c$ .

Therefore, one may set

$$\frac{dV}{dt} = a \frac{d\Delta p}{dt} + b \frac{dp}{dt} + c \frac{dT_c}{dt} \quad (10)$$

where the coefficients  $a$ ,  $b$ , and  $c$  are the rates of change of volume with respect to differential pressure, absolute pressure, and instrument temperature, respectively.

Now, since  $p_c = p + \Delta p$

$$\frac{1}{p_c} \frac{dp_c}{dt} = \frac{1}{p_c} \frac{dp}{dt} + \frac{1}{p_c} \frac{d\Delta p}{dt}$$

or, recalling that  $p_c$  is very nearly equal to  $p$ , there is obtained

$$\frac{1}{p_c} \frac{dp_c}{dt} = \frac{1}{p} \frac{dp}{dt} + \frac{1}{p} \frac{d\Delta p}{dt} \quad (11)$$

The rate of climb,  $v$ , may be introduced by the use of the barometric formula. From equation (1) it follows that

$$\frac{1}{p} \frac{dp}{dt} = -\frac{g}{RT} \frac{dZ}{dt} = -\frac{gv}{RT} \quad (12)$$

in which  $T$  is related to the free-air pressure,  $p$ , by

equation (3) for an instrument calibrated to the United States standard atmosphere.

The general equation for the leak-type of rate-of-climb indicator is now obtained by successive substitution into equation (9) from equations (10), (11), (12), and (7) and dividing by the coefficient of  $x$ :

$$\frac{\mu \alpha (V + ap)}{p} \frac{dx}{dt} + x = \frac{M \mu \alpha g (V + bp)}{RT} v + \mu \alpha M \left( \frac{V}{T_c} - c \right) \frac{dT_c}{dt} \quad (13)$$

#### INTERPRETATION OF THE GENERAL EQUATION

The general equation (13) may be rewritten in the form:

$$\lambda \frac{dx}{dt} + x = Kv + L \frac{dT_c}{dt} \quad (14)$$

in which

$$\lambda = \frac{\mu \alpha (V + ap)}{p} \quad (15a)$$

will be called the time constant,

$$K = \frac{M \mu \alpha g (V + bp)}{RT} \quad (15b)$$

the calibration coefficient, and

$$L = M \mu \alpha \left( \frac{V}{T_c} - c \right) \quad (15c)$$

the coefficient of the rate of change of temperature. The significance of these coefficients will now be discussed.

**Calibration coefficient—altitude and temperature compensation.**—If an instrument is subjected to a change of pressure at such a rate and under such conditions that the indication and the instrument temperature are constant, equation (14) will reduce to

$$x = Kv \quad (16)$$

It is desirable that an instrument be so constructed that the calibration coefficient  $K$  is, as nearly as possible, independent of altitude and of instrument temperature.

Of the various factors in the calibration coefficient  $K$ , the gas constant  $R$  and the acceleration of gravity  $g$  are constant; the viscosity  $\mu$  at the leak, and the temperature  $T$  of the free air, are variable but not subject to control by the designer and therefore must be compensated for; and the sensitivity  $M$  of the pressure gage, the leak coefficient  $\alpha$ , and the quantity  $(V + bp)$  are subject to control by the designer.

Of the uncontrolled variables, for which compensation must be made,  $\mu$  is nearly independent of the pressure and proportional to the absolute temperature  $T_c$  of the instrument. Compensation for its variation, known as temperature compensation, is obtained if the product of the three factors under the designer's control is maintained inversely proportional to the viscosity.

If, as is usually the case, it is desired that the instrument indicate the rate of change of altitude in the United States standard atmosphere, the temperature



$T$  is that given by equation (2) as a function of the standard altitude or by equation (3) as a function of the pressure. In order to obtain altitude compensation, that is, compensation for the variation of  $T$ , in the standard atmosphere, it is the problem of the designer to adjust the dependence on pressure of the three design factors under his control so that their product increases linearly with the altitude.

In the present-day instrument the volume  $V$  is generally constant, its variation being only that incidental to the operation of the mechanism; also  $b$  will be small, and therefore the quantity  $(V+bp)$  will change but slightly. Altitude and temperature compensation will therefore be obtained either by selection of the leak characteristic, or by the introduction of pressure-sensitive and temperature-sensitive auxiliary mechanisms that will produce the desired changes in the leak coefficient or in the pressure-gage sensitivity.

If an instrument is calibrated to indicate the rate of climb in the standard atmosphere, the true rate of climb may be obtained by multiplying the indication by the ratio of the existing free-air temperature to the temperature in the standard atmosphere at that pressure.

An instrument with constant  $\alpha$ ,  $M$ , and  $V$  could be graduated to read the true rate of climb in the existing atmosphere provided that the temperature at the leak be the same as the temperature of the free air. If the temperature at the leak were not the same as that of the free air, the ratio of the indication to the true rate of climb would be equal to  $T_K/T$ . (See reference 5.)

**Effect of rate of change of temperature.**—Since the instrument chamber does not have perfect thermal insulation, its temperature may change at a rate that will have a significant effect on the indication if it is exposed to surroundings at a greatly different temperature. Equation (14) may be written in the form:

$$\lambda \frac{dx}{dt} + x = K \left( v + \frac{L}{K} \frac{dT_c}{dt} \right) \quad (17)$$

where

$$\frac{L}{K} = \frac{R}{g} \frac{T}{T_c} \left( \frac{V - cT_c}{V + bp} \right)$$

In the foregoing ratio, the quantities  $\frac{T}{T_c}$  and  $\left( \frac{V - cT_c}{V + bp} \right)$  may be expected to have values not far from unity, and  $\frac{R}{g}$  has the constant value of 96.0 feet per degree centigrade. Therefore  $\frac{L}{K}$  will be of the order of 100 feet per degree centigrade.

The effect on the instrument of a change in temperature will be quite similar to that of a change in altitude. In particular, if the instrument temperature were rising at a rate of 1° C. per minute, the indication will be the same as though the altitude were increasing at a rate of about 100 feet per minute. Under extreme condi-

tions during an altitude flight, or after an airplane has been taken outdoors from a hangar, a temperature change at this rate might be obtained.

This effect may be decreased by improving the insulation of the chamber or be compensated by the introduction of an auxiliary mechanism that will shift the pointer of the indicator by an amount proportional to the rate of change of temperature.

**Time constant.**—If the instrument is subjected to a varying rate of climb, the indication will not follow the rate of climb exactly. If the rate of climb is constant and the initial indication is not equal to it, the indication will not immediately assume its final value but will

approach it slowly. If it is assumed that  $\frac{dT_c}{dt} = 0$  and

the calibration is such that  $K=1$ , the indication  $x$  is given by the solution of the general equation (14) in the form:

$$\lambda \frac{dx}{dt} + x = v \quad (18)$$

in which  $v$  is the imposed rate of climb.

For a constant value of  $v$ , the solution of this equation is the well-known expression for exponential decay

$$\frac{t}{\lambda} = \log_e \frac{x_0 - v}{x - v} \quad (19)$$

where  $x=x_0$  when the time  $t=0$ , and approaches the value of  $v$  as a limit, and where  $\lambda$  is the time constant. It may be seen that  $\lambda$  is the time required for the difference between the indication and its final constant value to decrease to  $1/e$  times the initial difference.

By reference to equation (15a) it will be seen that  $\lambda$  increases with increase of the viscosity of air (that is, with increasing instrument temperature) and increases with decreasing pressure (or increasing altitude). The time constant may be decreased by decreasing the volume  $V$  of the chamber, or by decreasing the leak coefficient  $\alpha$ . In order to keep the same value of the calibration coefficient  $K$ , a decrease in  $\alpha$  or  $V$  makes necessary an increase in  $M$ , the sensitivity of the pressure gage.

The rate of change of volume with respect to differential pressure (coefficient  $a$  in equations (10) and (15a)) may affect the time lag considerably. For example, in an instrument for which  $V=500$  cubic centimeters,  $p=20$  millimeters of water at an indication of 2,000 feet per minute; a change in volume of 1 cubic centimeter for this indication would double the time lag. An increase in the sensitivity of the pressure gage without changing the calibration or too great an increase in the value of the coefficient  $a$  will decrease the time lag.

Thus far there has been no consideration of the effect of inertia and friction in the indicating mechanism.



## DYNAMIC EFFECTS

These factors may be introduced by replacing equation (7) by a differential equation, such as

$$M\Delta p = l_2 \frac{d^2x}{dt^2} + l_1 \frac{dx}{dt} + x \quad (20)$$

where  $l_2$  and  $l_1$  are constants. In an actual installation, there may also be some external damping, as by a long line of small-bore tubing from the instrument to the static tube. Also the diaphragm cell of the pressure-measuring element may be vented to the outlet through a capillary leak. Consideration of the effect of any of these factors will lead to a general equation similar to equation (14) except that there will appear, in addition, terms containing second and higher derivatives of  $x$  with respect to time.

Draper and Schliestett (reference 6) have considered the problem in which the general equation involves the second derivative of  $x$  with respect to  $t$ .

Their equation,

$$\frac{\lambda}{n} \frac{d^2x}{dt^2} + \lambda \left( \frac{n+1}{n} \right) \frac{dx}{dt} + x = Kv \quad (21)$$

follows from a development similar to that used to obtain equation (14), neglecting the term involving the rate of change of temperature and substituting for equation (7) the differential equation

$$\frac{\lambda}{n} \frac{dx}{dt} + x = M\Delta p \quad (22)$$

It can be shown that the principal effect of the inclusion of second or higher derivatives in the general equation will be the addition to the solution of transient terms of rapid decay, the effect of which is important for a short time immediately after a change from one constant value of  $v$  to another, but may be neglected thereafter.

For example, consider an instrument for which  $K=1$ ,  $\lambda=4$  seconds, and  $n=5$ , which is subjected to an instantaneous change of rate of climb from an initial value of zero to a value  $v$  at time  $t=0$ . The solution of equation (18) for these conditions is:

$$v-x = ve^{-t/\lambda}$$

For the same initial conditions the solution of equation (21) is

$$v-x = \frac{5}{4}ve^{-t/\lambda} - \frac{1}{4}ve^{-5t/\lambda}$$

By the time  $t = \frac{\lambda}{2} = 2$  seconds the second term will be less than 3 percent of the first, and the two solutions will be, for practical purposes, equivalent except for a constant factor  $n/(n-1)$ .

Of course, the elasticity and the damping of the mechanism play an important part in the reaction of the instrument to such external disturbances as vibration. For instance, it is important that the design

be such that the resonance frequency of the indicator mechanism fall outside the frequency range of vibrations encountered in service.

## SENSITIVITY IN INDICATING LEVEL FLIGHT

For the purpose of determining the sensitivity of the instrument in indicating level flight, assume that the rate of climb is a sine function of the time, that is,

$$v = v_0 \sin \omega t \quad (23)$$

where  $2\pi/\omega$  is the period of the oscillation in rate of climb. Then equation (18) becomes

$$\lambda \frac{dx}{dt} + x = v_0 \sin \omega t$$

The steady state solution is of the form

$$x = \frac{v_0 \sin \omega t}{1 + \lambda^2 \omega^2} - \frac{\lambda \omega v_0 \cos \omega t}{1 + \lambda^2 \omega^2}$$

Two extreme cases may be noted.

(a) If  $\lambda\omega$  is very small, the solution reduces to

$$x = v_0 \sin \omega t$$

and the instrument is seen to indicate the rate of climb for moderately slow changes of altitude.

(b) If  $\lambda\omega$  is very large the solution becomes

$$x = \frac{-v_0 \cos \omega t}{\lambda \omega}$$

But the variation in altitude, as obtained by integrating equation (23), is

$$\Delta Z = -\frac{v_0}{\omega} \cos \omega t$$

and consequently

$$\lambda x = \Delta Z \quad (24)$$

Equation (24) shows that the response of the rate-of-climb indicator is proportional to the change of altitude for short-period variations in altitude. This fact makes the instrument a sensitive aid in maintaining level flight. Equation (24) is not only valid for short-period cyclic variations in altitude but is also approximately correct for any change in altitude, provided that the time required is less than the time constant  $\lambda$ .

A more exact analysis would take into account the manner in which the change of altitude occurred and the second-order lag effects discussed in the preceding section. For an instrument in which  $\lambda=4$  seconds and  $n=5$ , the indication for an instantaneous change of altitude is about two-thirds that calculated from equation (24) and is about 56 percent for an altitude change taking place at a constant rate in a time equal to the time constant. In experimental tests on typical instruments, the maximum indication after a rapid change of altitude was found to be about 70 percent of the indication calculated from equation (24).



The sensitivity of the rate-of-climb indicator to sudden changes of altitude may be illustrated by the following example. A rate-of-climb indicator whose time constant is 4 seconds is subjected to a sudden altitude change of 10 feet. By equation (24) the maximum indication would be

$$x = 10 \text{ ft.}/4 \text{ sec.} = 150 \text{ ft./min.}$$

If the correction be made for second-order dynamic effects, where  $n=5$ , this value will be reduced to  $x=100$  ft./min. for an instantaneous change or to  $x=84$  ft./min. for a change taking place in 4 seconds. Now, for a rate-of-climb indicator having a scale of 4,000 ft./min. per revolution of the pointer, the pointer motion for this 10-foot change of altitude would be  $9^\circ$  to  $7.5^\circ$  of arc. In a sensitive altimeter with 1,000 feet per pointer revolution, the pointer motion for a 10-foot change of elevation is  $3.6^\circ$  of arc. Thus the rate-of-climb indicator is ordinarily a little more than twice as sensitive to small, sudden changes of altitude as the sensitive altimeter.

The desirability of a sensitive indication of rapid changes in altitude, combined with the desirability of a short time lag, created a demand for an instrument having the smallest time constant feasible. When the time constant was reduced below 4 seconds, however, the instrument became unsteady in gusty air. The present value of the time constant in the neighborhood of 4 seconds is a compromise between quick response and steadiness.

#### EFFECT OF ADDITIONAL RESTRICTIONS

It is possible to modify the performance of the instrument somewhat by introducing additional obstructions to the flow of air in the instrument.

A restriction in the line leading to the diaphragm that damps pressure changes within the cell will avoid the unsteadiness associated with a short time lag. In the use of the instrument to indicate level flight, the effect of this damping is to increase the time interval between a sudden change in static pressure and the maximum indication of the instrument, although there will be no change in the time constant. The instrument will not respond to extremely quick changes of pressure, such as occur in gusty air, but the sensitivity of the instrument to pressure changes associated with the variations of the altitude of the aircraft as a whole will not be greatly affected. There will be a reduction of sensitivity of the instrument, when used as a rate-of-climb indicator, in the ratio  $\left(1 - \frac{1}{n}\right)$ .

A restriction in the static line, ahead of both the diaphragm connection and the leak, will not change the sensitivity of the instrument as an indicator of rate of climb but will increase the time lag and consequently decrease the sensitivity of the instrument as an indicator of level flight.

#### DESCRIPTION OF TYPICAL RATE-OF-CLIMB INDICATORS

Most rate-of-climb indicators in present-day use are similar in principle to that sketched in figure 1, for which the theory has been developed in previous sections. The mechanism is enclosed in a standard  $2\frac{3}{4}$ -inch dial case, of length from 4 to 6 inches. The weight of the instrument is about  $1\frac{1}{4}$  pounds. In common airplane rate-of-climb indicators, the pointer moves one-half revolution for a rate of climb of 2,000 feet per minute. The calibration extends from 2,000 to  $-3,000$  feet per minute, although most instruments will indicate rates of climb as great as  $\pm 4,000$  feet per minute. Instruments are equipped with a knob for resetting the pointer to zero.

The designs of the mechanisms by the various manufacturers differ chiefly in the methods by which the various compensations are obtained. For this reason the description of the various instruments will be limited largely to the means of obtaining the various compensations, together with an indication of significant departures from the typical design.

The rate-of-climb indicators used in airships, balloons, and gliders are similar to those used in airplanes except that a greater sensitivity and a smaller range are ordinarily desired.

**Kollsman.**—In the Kollsman rate-of-climb indicator, the correction for altitude and instrument temperature

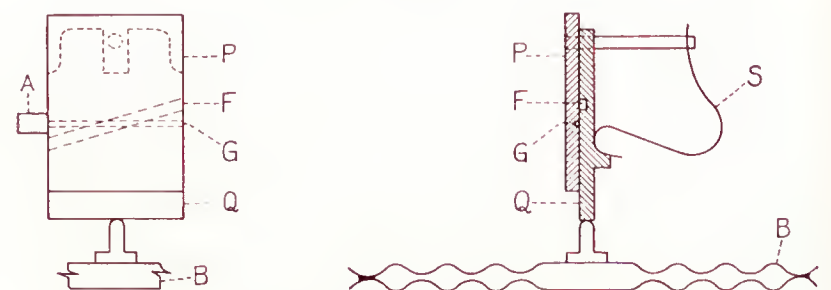


FIGURE 2.—Leak assembly of Kollsman rate-of-climb indicator. A is the inlet from the static line; B, diaphragm cell; F, groove in movable plate; G, groove in stationary plate; P, stationary plate; Q, movable plate; and S, spring.

is obtained by variation of the length of the capillary forming the leak. The leak (fig. 2) is formed by a groove G engraved on a fixed flat plate P upon which is laid another movable flat plate Q. A larger groove F is cut in the movable plate at an angle to the first and open to the chamber at both ends. Thus the groove G forms a small channel of capillary size that extends from the edge of the plate, where the connection to the static-pressure line A is made, to the point where the two grooves meet. The length of this channel may be varied by changing the position of the upper plate, which bears against a diaphragm cell B filled with air under pressure. By a proper choice of the pressure to which the cell is filled, it is possible to obtain simultaneous temperature and altitude compensation. If the instrument temperature decreases, the pressure in the auxiliary cell falls, the cell contracts, and the plate is moved so as to lengthen the capillary. This action increases the value of the leak coefficient  $\alpha$  (see equation (15b)) to compensate for the decrease of viscosity with decrease in temperature. If the altitude increases, the



pressure in the instrument falls, the cell expands, and the capillary shortens. The decrease of  $\alpha$  compensates for the decrease, with increasing altitude, of the factor  $T$  in the calibration coefficient  $K$ .

In one model, used by the air lines in transport service, the first quadrant of the scale represents a rate of climb of 500 feet per minute. At this point additional springs become effective so that the second quadrant of the scale is used for the range between 500 and 2,000 feet per minute. Thus, the pointer motion for small rates of climb is doubled and the instrument made more sensitive as an indication of level flight, without a decrease in the range of the instrument.

The mechanism is placed in a Dewar flask, closed in front by a metal face plate, backed with a one-half inch layer of cork. The thermal insulation is such that the temperature of the instrument changes at a very small rate, so that the effect of a changing temperature (see equation (14), last term, and equation (17)) is small enough to be neglected.

**Pioneer.**—The Pioneer rate-of-climb indicator has a leak unit of novel design. The leak is designed to have characteristics intermediate between that of an orifice and a capillary so that no separate mechanism to compensate for altitude is needed.

For a leak in which laminar flow obtains, as in a long capillary tube, the pressure drop at a given volume flow is nearly independent of the density. For an instrument using such a leak, the leak coefficient  $\alpha$  (equation (4)) would be constant and, if the other design factors of the calibration coefficients  $K$  (equation (15b)) are constant, the value of  $K$  would increase with decreasing values of  $T$ ; that is, with increasing altitude. On the other hand, if the leak were equivalent to an orifice the pressure drop at constant volume flow would be proportional to the density. For an instrument in which the leak is an orifice, the value of  $\alpha$  would be proportional to the density and  $K$  would decrease with decreasing density or increasing altitude. An instrument in which the leak is equivalent to a combination of orifice and capillary would have intermediate altitude characteristics. For this instrument, a combination is used for which the value of  $K$  is nearly constant between sea level and 30,000 feet.

A bimetallic element is used to compensate for changes in instrument temperature. In some models a means for compensating for rate of change of instrument temperature is also provided. Details of this feature have not been released.

#### LABORATORY TEST PROCEDURE AND TEST DATA

**Calibration at room temperature.**—The calibration at room temperature serves to show whether the instrument is properly calibrated, has a linear scale, and is properly compensated for altitude. A diagram of the apparatus used at the National Bureau of Standards is shown in figure 3. The instrument  $R$  is placed in a low-pressure chamber or bell jar  $C$  together with a calibrated sensitive altimeter  $A$  and means such as a

buzzer  $B$ , for providing sufficient vibration to eliminate the effect of friction in either instrument. The outlet of the test chamber is connected to a mercurial barometer  $M$  and to a needle valve  $V$  for controlling the flow of air. The needle valve is connected by means of a two-way stopcock  $T$  to a suction line  $S$  and to a line  $P$  supplying clean air under a pressure of an inch or two of mercury. The needle valve is set so as to pass air into or out of the chamber at such a rate that the indication of the rate-of-climb indicator is constant. The indication of the rate-of-climb indicator is compared with the standard rate of climb determined by timing with a stop watch the change in indication of the altimeter between two previously determined altitudes, say, 2,000 and 4,000 feet. The calibration of the altimeter may be checked independently with the aid of the mercury barometer.

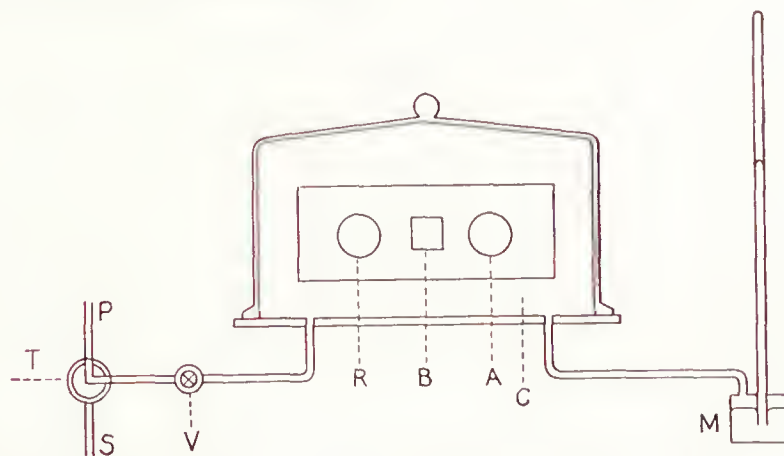


FIGURE 3.—Sketch of apparatus for making scale-error tests.  $A$  is the altimeter;  $B$ , buzzer;  $C$ , bell jar;  $M$ , mercury barometer;  $P$ , pressure line;  $R$ , rate-of-climb indicator;  $S$ , suction line;  $T$ , two-way stopcock; and  $V$ , needle valve.

Comparison of scale errors determined at altitudes near sea level with those determined at higher altitudes will provide a measure of the accuracy of the altitude compensation. The performance of five typical 1938 airplane instruments is shown in table I.

TABLE I.—SCALE ERRORS IN FEET PER MINUTE OF FIVE RATE-OF-CLIMB INDICATORS

[Scale errors are positive if indicated rate of climb or descent is greater than the standard rate. Changes in scale errors are positive if the indication is greater at the low temperature]

Interval (thous. of ft.)	Standard rate of climb (ft./min.)	Instruments				
		A	B	C	D	E
		Scale errors at 23° C.				
2 to 4.....	1,000	+5	-30	+35	+5	+30
2 to 4.....	2,000	+5	-15	+45	+35	+50
4 to 2.....	1,000	-15	-15	+20	-10	+20
4 to 2.....	2,000	-5	-35	+20	-15	+15
4 to 2.....	3,000	+25	-50	+40	-55	+40
15 to 17.....	2,000	+110	+70	+135	+125	+140
17 to 15.....	2,000	+100	+65	+105	+80	+105
28 to 30.....	2,000	+160	+90	+130	+140	+165
30 to 28.....	2,000	+145	+95	+120	+110	+155
Change in scale errors between 23° C. and -35° C. corrected for zero shift						
2 to 4.....	2,000	-10	-30	0	-10	+20
15 to 17.....	2,000	-70	-70	-30	-60	+15
28 to 30.....	2,000	-15	-15	+25	-20	+15
Zero shift between 23° C. and -35° C.						
		+30	-40	0	-20	-20



**Temperature test.**—The accuracy of the temperature compensation may be determined by comparison of the scale errors at room temperature with those obtained at a low temperature, say,  $-35^{\circ}\text{C}$ . Because of the effect of changing chamber temperature on the indication, considerable care must be taken to insure that the temperature of the instrument is constant during the test. For this reason, and because of the thermal insulation of the instrument chamber, the apparatus should be maintained at the test temperature for at least 2 hours. Air admitted to the bell jar should be carefully dried to prevent all possibility of condensation in the leak. It is better to dry the air by precooling to condense out moisture than by chemical means.

After temperature equilibrium has been established, the zero shift is observed, and the scale errors are determined by the same procedure as was used in the calibration test. The performance of typical 1938 airplane instruments with respect to temperature compensation is also shown in table I.

**Time lag.**—The time constant of a rate-of-climb indicator is usually calculated by means of equation (19) from observations made on the decay of the indication of the instrument. The instrument is first subjected to a certain rate of change of pressure which is then suddenly reduced to zero. The time required for the indication to fall from one definite value to another is observed. Although any pair of indications may be used, it has been found convenient to determine the time required for the indication to fall from 2,000 to 200 feet per minute, when the initial maximum indication is about 3,000 feet per minute and the final indication is zero. From equation (19) it is seen that this time of decay is given by

$$t = \lambda \log_e \left( \frac{2000-0}{200-0} \right) = 2.3\lambda$$

The time of decay between two indications whose ratio is 10:1 will be called the time lag  $\lambda_{10}$  and is seen to be 2.3 times the time constant  $\lambda$ .

A determination of the time lag will be based on timing the decay of the indication. Of more significance in the instrument is the decay of the differential pressure  $\Delta p$  across the leak. If the time constant of this decay is desired, there may be used an equation of the form of equation (19), except that the actual differential pressures are substituted for the indications.

In the development of equation (19), it was assumed that the calibration constant  $K$  was constant and of unit value. If the scale errors are such that the relation between indication and rate of climb is not substantially linear, the decay of indication will not be exponential and the time lag will have only an arbitrary significance. An error in zero setting may be allowed for by assigning to  $v$ , in equation (19), the value of the indication eventually reached when the rate of climb is zero.

In a determination of time lag a small error in zero setting will cause an error of the second order, provided the average of the time of decay in ascent and descent is taken. Thus, if the decay from positive rates of climb were being observed, and the zero setting were such that the instrument indicated  $+20$  feet per minute at zero rate of climb, the time of decay would be

$$t = \lambda \log_e \frac{2000-20}{200-20} = 2.41\lambda$$

For decay from negative rates of climb and the same zero setting,

$$t = \lambda \log_e \frac{-2000-20}{-200-20} = 2.22\lambda$$

The time of decay is about 5 percent high in one case and 4 percent low in the other, but the average is within  $\frac{1}{2}$  percent of the time obtained with the correct zero setting.

Three procedures for determining the time lag will be discussed. The first two give equivalent results and the third yields results not in agreement, for reasons which will be given.

(a) The instrument is set to zero and placed in the test apparatus, as described in the calibration test. Starting with a pressure in the bell jar lower than that of the atmosphere by an amount corresponding to a difference of, say, 2,000 feet, one admits air to the test chamber so that the pressure approaches that of the atmosphere at a rate corresponding to a constant indication between 2,500 and 3,000 feet per minute. When the pressure in the chamber is exactly equal to that of the atmosphere, the flow of air is stopped and the chamber opened to the atmosphere, as by disconnecting the tubing between the needle valve and the bell jar or by a valve with a large opening. The time required for the indication to fall from 2,000 to 200 feet per minute is measured with a stop watch. The observation is repeated except that the pressure is initially greater than the atmospheric pressure, and air is withdrawn from the chamber. The average of the two measured times is taken as  $\lambda_{10}$ .

(b) A small pressure is applied to the static pressure connection of the instrument. When the pressure is quickly released by opening the instrument to the atmosphere, the indication of rate of climb will rise to a maximum, then return to zero. The initial pressure is chosen of such magnitude (about 4 inches of water) that the maximum indication is between 2,500 and 3,000 feet per minute. The time of decay from 2,000 to 200 feet per minute is observed. The procedure is repeated, but with an initial suction, thus obtaining a rate of descent. The average of these two values for the time of decay is taken as the time lag  $\lambda_{10}$ . This method gives a result in good agreement with that obtained with the first method, provided that the maximum



indication in this method is approximately equal to the initial steady indication in the first method.

(e) With the instrument set to zero and placed in the test chamber, just as in method (a), the pressure in the chamber is made to change at such a rate that the indication of the instrument is constant at 2,500 feet per minute. At the desired pressure altitude the flow of air is cut off by closing a valve, the indication decays to zero, and the time of decay from 2,000 to 200 feet per minute is measured.

Tests show that method (c) yields a time of decay for both ascent and descent less than by either of the other two methods. The difference depends on the particular apparatus used and may be 20 percent or more. In method (c) the requirement of constant pressure in the test chamber is not satisfied during the timing interval but, because of temperature changes, the pressure is changing at a rate that introduces appreciable error. Suppose the time lag in ascent is being measured. While air is being withdrawn from the test chamber, the remaining air will be cooled slightly below the temperature of the surroundings. After the flow is stopped, the air in the test chamber will warm slowly, and consequently the pressure will increase. This condition is equivalent to a negative, instead of zero, rate of climb during the timing interval. When the time lag in descent is measured, the test chamber is warmed when air is being introduced; it cools slightly when the flow is stopped. Consequently, the pressure will decrease during the timing interval and the rate of climb will be positive. The equivalent rate of climb or descent due to these temperature adjustments may easily be of the order of 100 feet per minute or more.

Assume that an instrument tested by method (a) or (b) has an observed time of decay of 9.2 seconds. From equation (19) the time constant in seconds is

$$\lambda = 9.2 / \log_e \frac{2000 - 0}{200 - 0} = 4.0$$

Tested in descent by method (c) the same instrument would have a time of decay, in seconds, assuming a rate of climb during the timing interval of +100 feet per minute,

$$t = 4.0 \log_e \frac{-2000 - 100}{-200 - 100} = 7.8$$

For the test in ascent, the rate of climb would be -100 feet per minute during the timing interval, and the time of decay in seconds is

$$t = 4.0 \log_e \frac{2000 - (-100)}{200 - (-100)} = 7.8$$

The 15-percent discrepancy between 9.2 and 7.8 seconds is of the order observed in practice. It follows that method (e) may be used for comparative tests but, in order to obtain the time constant, it will be necessary to determine a correction factor for the particular testing apparatus and the type of instrument.

Typical present-day instruments have a time constant at sea level of the order of 4 seconds and a time lag  $\lambda_{10}$  as determined by method (a) or (b) of about 9 seconds. Equation (15a) indicates that the time constant varies inversely as the atmospheric pressure and therefore both it and the time lag increase with increasing altitude. If the other factors affecting the lag are constant, the values of the time constant and the time lag at 30,000 feet will be about 3.4 times that at sea level. In most instruments the ratio is somewhat less, because the lag is affected if the altitude compensation is made by control of the leak. The ratio of the time lag at 30,000 feet to that at sea level ranges from about 1.5 to 3.0 for a wide variety of instruments tested in the past 15 years, with the more recent types having a ratio between 1.5 and 2.0.

**Vibration test.**—The vibration test is designed to indicate the effect on the instrument of the vibration encountered in a service installation. It being out of the question to subject the instrument to all the possible modes of vibration that may be encountered, the practice has been to specify a standard vibration for the laboratory test. Accordingly, the instruments are subjected to a translational vibratory motion in a circular path one-thirty-second inch in diameter in a plane inclined 45° from the horizontal. The frequency range is 1,000 to 2,500 cycles per minute. The zero reading and the pointer oscillation are observed over the range of vibration frequencies. In addition, the instruments are vibrated for a 3-hour period at a constant frequency, usually at about 1,800 cycles per minute. The zero readings before and after the test are then compared.

The performance of a typical instrument under vibration is shown in the following table.

PERFORMANCE IN VIBRATION TEST

Frequency (c. p. m.)	Pointer oscillation (ft./min.)	Change of reading (ft./min.)
1,200	5	10
1,800	10	20
2,400	50	50
Change in zero after 3 hours' vibration, 10		

**Overpressure test.**—Certain airplane maneuvers, such as the power dive, will involve rates of descent, and occasionally rates of climb, far greater than the maximum indication of the instrument. The overpressure test will indicate whether the diaphragm or mechanism will be injured by the high differential pressures built up during such maneuvers. The instrument is subjected to a pressure change corresponding to a climb from sea level to 30,000 feet at a rate of 20,000 feet per minute, followed by a descent to sea level at a rate of 30,000 feet per minute. For a good modern instrument, the zero reading 1 minute after



the completion of this test will not differ from that before the test by more than 50 feet per minute; and, in 10 minutes, the zero reading will have returned almost to its original value.

**Leak test.**—It is necessary that the case of the rate-of-climb indicator be free from leaks since the case, vented to a static tube in the free air, is normally at a pressure differing from that in the cockpit of the airplane. In the test for case leaks, the static-pressure connection of the instrument is sealed off, and the pressure of the surroundings is reduced by 4 inches of water. A change in indication will be observed if the instrument leaks appreciably. Leaks are most likely to occur at the rim of the glass dial cover or at the packing of the shaft of the knob with which the zero setting is made.

#### INSTALLATION IN AIRCRAFT

In the usual airplane installation the case of the rate-of-climb indicator is connected to a static tube. The resistance to the flow of air should be kept low by providing a wide-bore line to the static tube. (See reference 7.) Although the lag due to the resistance of the tubing will not affect the response of the rate-of-climb indicator as seriously as that of the altimeter or air-speed indicator, it will somewhat reduce the response of the instrument when used as a level-flight indicator.

The static line should be leakproof. If an altimeter or an air-speed indicator is connected to the static line, a suction sufficient to cause an appreciable indication of the most sensitive instrument may be applied to the static tube and the holes sealed off. A change of indication after sealing will indicate a leak. If the rate-of-climb indicator is the only instrument in the static

line, a suction of, say, 4 inches of water may be applied and the static holes sealed. If the indication returns to zero after sealing, and the instrument indicates a descent when the holes are opened after an interval of 1 minute, the line may be regarded as leakproof.

Besides being leakproof the lines must be free of oil, dust, and water to avoid stoppage or entry to the instrument. A drain may be provided for the removal of water.

NATIONAL BUREAU OF STANDARDS,  
WASHINGTON, D. C., *January 6, 1939.*

#### REFERENCES

1. Bestelmeyer, A.: Zur Theorie des Ballonmanometers. *Phys. Zeitschr.*, vol. XI, 1910, S. 763-768.
2. Mears, Atherton H.: Statoscopes and Rate-of-Climb Indicators. Section II, part III of *Aeronautic Instruments*. Section II.—Altitude Instruments. T. R. No. 126, N. A. C. A., 1922, pp. 38-53.
3. Diehl, Walter S.: *Standard Atmosphere—Tables and Data* T. R. No. 218, N. A. C. A., 1925.
4. Brombacher, W. G.: *Altitude-Pressure Tables Based on the United States Standard Atmosphere*. T. R. No. 538, N. A. C. A., 1935.
5. Oppelt, W., and Wenk, F.: Theoretische Betrachtung des Luftdruckvariometers und Richtlinien für Entwurf und Prüfung. *Luftfahrtforschung*, Bd. 14, Lfg. 10, 20. Oct. 1937, S. 537-541.
6. Draper, C. S., and Schlietett, G. V. Dynamic Errors of the Rate-of-Climb Meter. *Jour. Aero. Sci.*, vol. 5, no. 11, Sept. 1938, pp. 426-430.
7. Wildhack, W. A.: Pressure Drop in Tubing in Aircraft Instrument Installations. T. N. No. 593, N. A. C. A., 1937.



# REPORT No. 667

## DETERMINATION OF THE PROFILE DRAG OF AN AIRPLANE WING IN FLIGHT AT HIGH REYNOLDS NUMBERS

By JOSEPH BICKNELL

### SUMMARY

*Flight tests were made to determine the profile-drag coefficients of a portion of the original wing surface of an all-metal airplane and of a portion of the wing made aerodynamically smooth and more nearly fair than the original section. The wing section was approximately the N. A. C. A. 2414.5. The tests were carried out over a range of airplane speeds giving a maximum Reynolds Number of 15,000,000. Tests were also carried out to locate the point of transition from laminar to turbulent boundary layer and to determine the velocity distribution along the upper surface of the wing.*

*The profile-drag coefficients of the original and of the smooth wing portions at a Reynolds Number of 15,000,000 were 0.0102 and 0.0068, respectively; i. e., the surface irregularities on the original wing increased the profile-drag coefficient 50 percent above that of the smooth wing.*

### INTRODUCTION

Only comparatively recently have profile-drag determinations in the upper range of flight Reynolds Numbers (10,000,000 to 30,000,000) been made, either in wind tunnels or in flight. Profile-drag coefficients up to a Reynolds Number of 13,000,000 have been determined in the 5- by 7-meter tunnel of the DVL (reference 1). In the variable-density tunnel of the N. A. C. A., similar measurements have been made up to an effective Reynolds Number of 8,000,000 (references 2 and 3). An extrapolation equation is suggested in reference 2 for extending the results to higher Reynolds Numbers.

In view of the simplicity of the momentum method of determining profile drag in flight (reference 4), a project was initiated to determine the profile drag of an airplane wing at as high Reynolds Numbers as possible. The project also included measurements to determine the point of transition from laminar to turbulent boundary layer on the upper surface of the wing and the distribution along the wing of the velocity just outside the boundary layer.

### APPARATUS AND METHODS

The flight tests were conducted on a Northrop attack airplane (A-17A), a low-wing single-engine monoplane. The tests were carried out on a panel of 5-foot 2-inch span located on the right wing. The inboard edge of this panel was at the juncture of the wing stub and the main wing panel, 5 feet 6 inches from the center line of the airplane. The propeller, 9 feet 9½ inches in diameter, was located 6 feet ahead of the wing leading edge. The test panel was sufficiently removed from the slipstream to avoid interference, especially in the high-speed condition in which the tests were made.

The panel was made smooth by filling the lap joints in the metal-wing covering and then cementing pieces of rubber sheeting to the wing surface in the spaces between the rows of rivets to build up the surface above the level of the rivet heads. The fairness of the wing was improved by cementing a layer of ½-inch-thick hard aluminum to the rubber. This metal was applied in several pieces, rolled to the contour of the wing. Finally, another layer of rubber was applied over the metal. This layer was continuous from the trailing edge around the leading edge and back to the trailing edge, where the two ends were sewed together. The surface of the rubber was sprayed with several coats of filler and was sanded and rubbed until it had a smooth, glossy finish (fig. 1).

On the lower surface of the smooth panel were three small, irremovable obstructions. These obstructions were downstream of the transition point, off to one side of the survey plane, and were faired. The drag and the interference due to these obstructions were estimated on the assumption of a drag coefficient of 1 based on their cross-sectional areas and a reasonable spreading of their wakes. Their estimated effect on the profile-drag coefficient was an increase of 0.0003. This amount has been subtracted from the profile-drag coefficients found by the momentum surveys.



The test panel of the smooth wing tapered in both chord and thickness ratio. The inner section was approximately the N. A. C. A. 2415.5 with a chord of 9.46 feet; the outer section was the N. A. C. A. 2413.5 with a chord of 8.20 feet. The profile in the plane of the wake surveys was approximately the N. A. C. A. 2414.5 section with a chord of 8.86 feet. Measured ordinates of this profile are given in table I, together with the computed ordinates of the N. A. C. A. 2414.5 section.

static tube is mounted so that it can turn about an axis nearly parallel to the wing chord line. (See fig. 1.) On the inboard end of this tube is fastened a short lever, the end of which is held in contact with a single-lobe plate cam by a spring. A ratchet wheel attached to the cam is advanced one tooth at a time by a click. The click is actuated by a bellows expanded hydraulically by the operation of a piston in the cockpit.

The dynamic and the static pressures of the free stream were obtained from a pitot-static tube mounted



FIGURE 1.—Finished smooth wing and survey apparatus.

The profile drag of the wing with the original surface was determined in the same plane as the smooth wing. The profile was approximately the N. A. C. A. 2414.5 section with a chord of 8.80 feet. Figure 2 shows a photograph of the original wing, and the details of the surface irregularities on this section are given in figure 3.

The profile drag was determined by the momentum method (reference 4). In these tests, the wake surveys were 8.4 percent of the chord behind the trailing edge of the wing. A traversing mechanism to measure, point by point, the total pressure and the static pressure in the wake was developed suitable for attachment to a metal wing. A tube supporting a pitot and a

on a boom near the wing tip. The static tube was calibrated against the static side of a suspended air-speed head.

Measurements to determine the boundary-layer transition point and the pressure distribution were made with three racks mounted on the upper surface, as shown in figure 4. Each rack had a static tube and a total-pressure tube. The static tube was made of 0.040-inch-diameter hypodermic tubing; the total-pressure tube was of the same size flattened at the mouth until its outside depth was 0.012 inch. The static tube was set about  $\frac{3}{16}$  inch from the wing surface; the total-pressure tube was in contact with the surface.



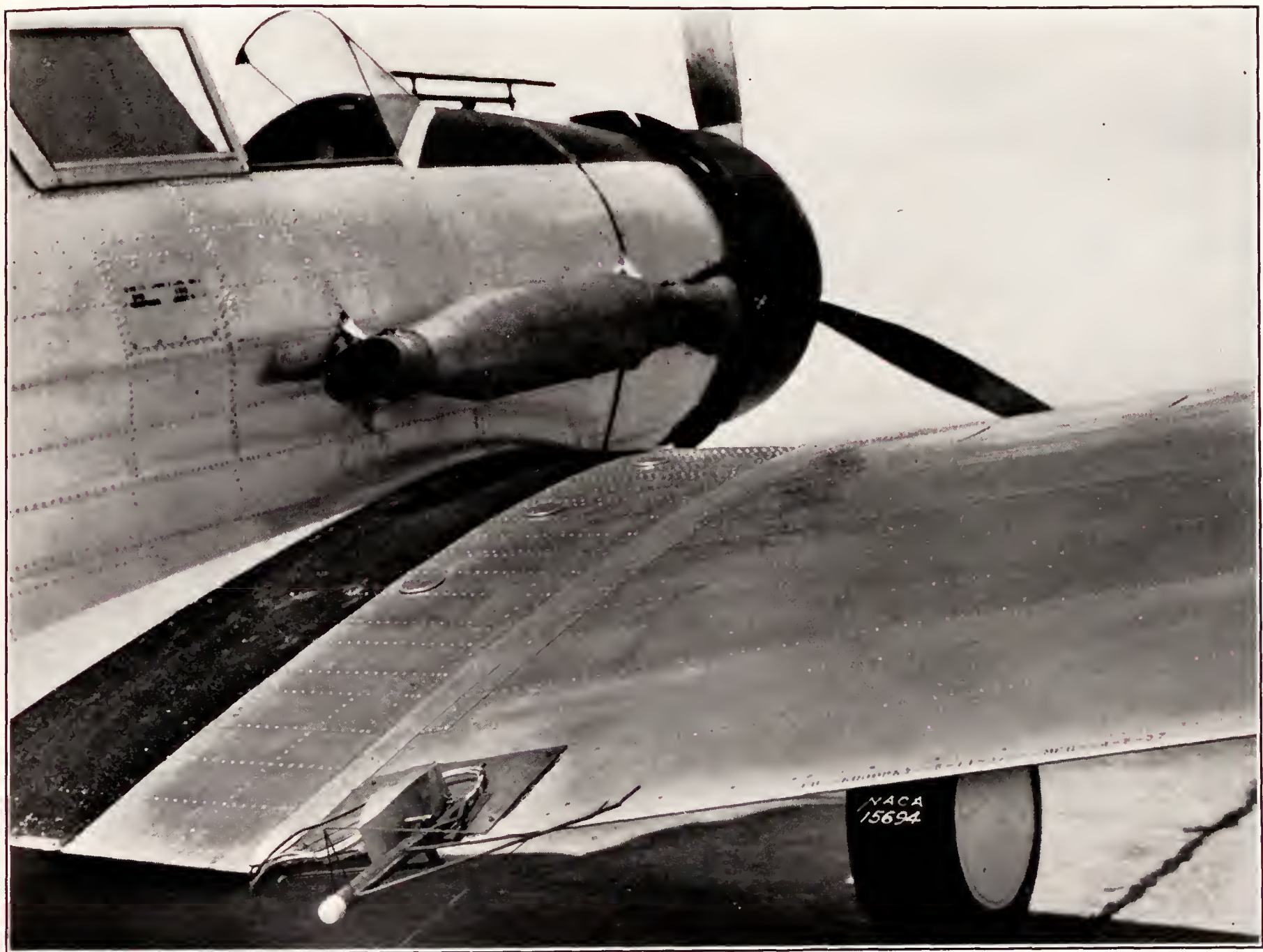




FIGURE 2.—Original wing.

- F*, Flush rivets,  $\frac{3}{32}$ -inch diameter  
*L*, Lap joint, facing backward  
*R*, Brazier-head rivets,  $\frac{3}{32}$ -inch diameter  
*r*, Brazier-head rivets,  $\frac{1}{16}$ -inch diameter  
*b*, Brazier-head rivets,  $\frac{3}{32}$ -inch diameter,  
not extending across wing but in survey plane  
*D*, Trailing edge of inspection door  
*D<sub>F</sub>*, Flush inspection door  
*P*, Perforation in wing flap  
*H*, Hinge   
*H<sub>F</sub>*, Flush hinge 

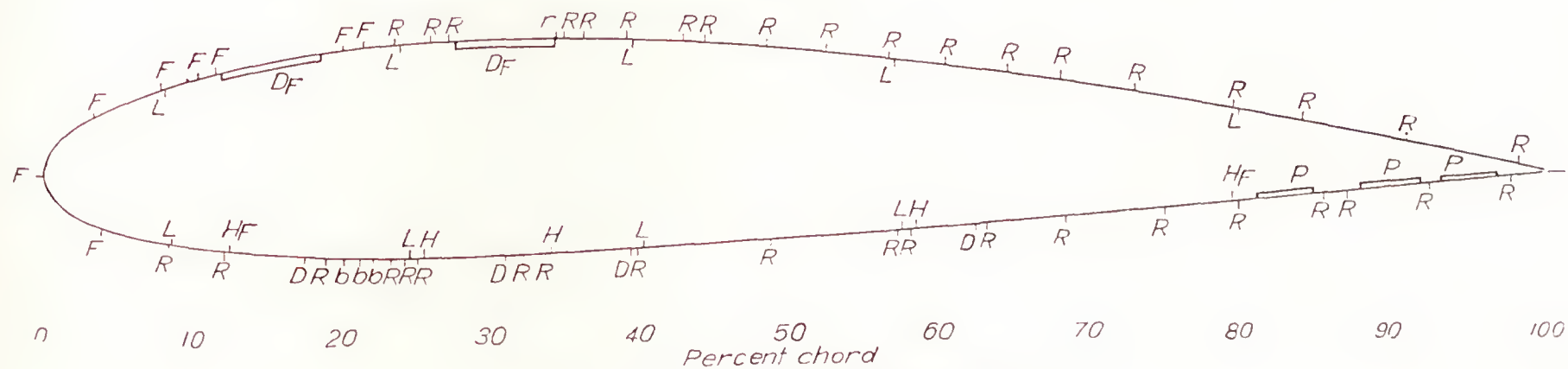


FIGURE 3.—Details of surface irregularities on original wing.



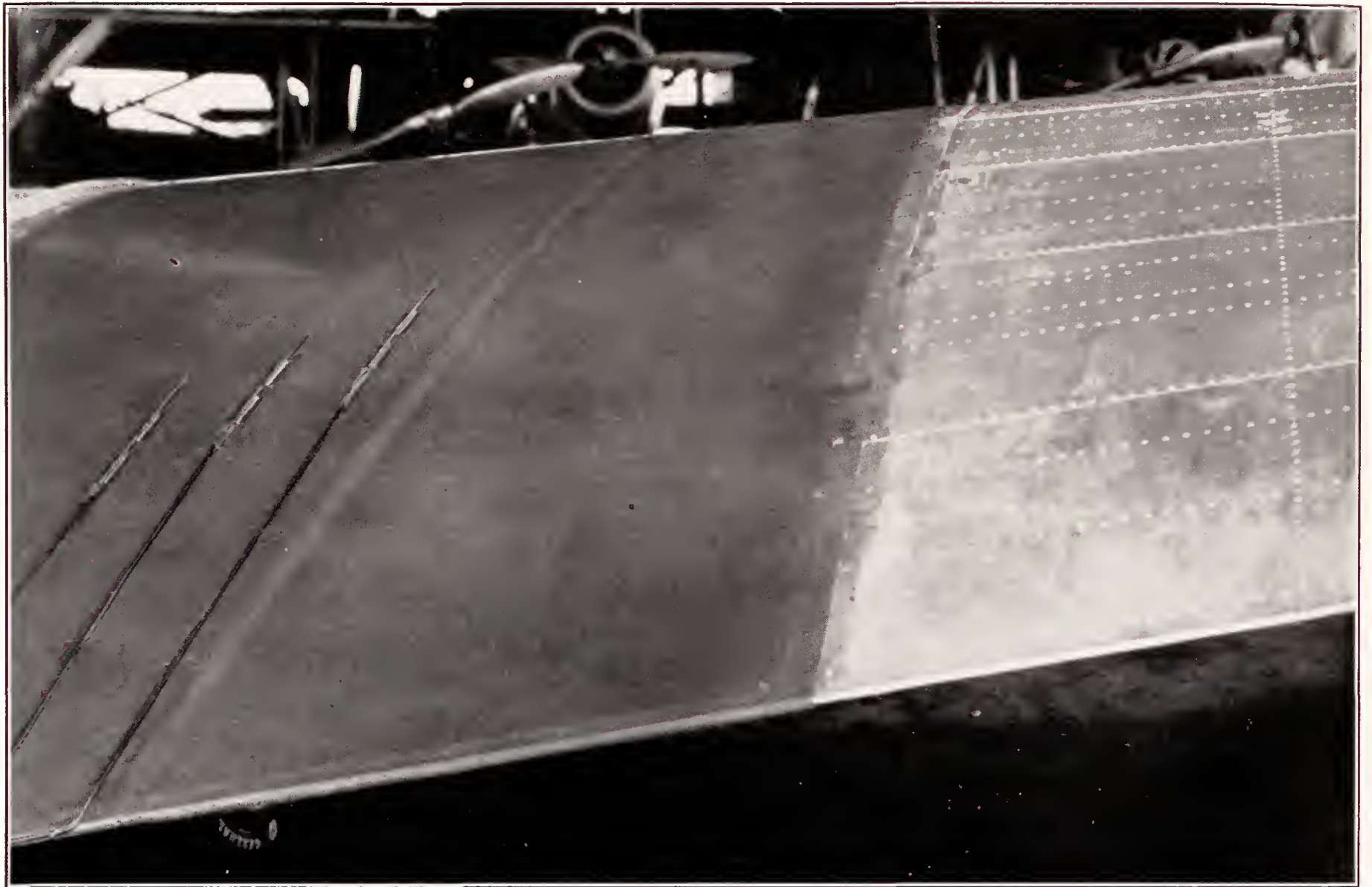


FIGURE 4.—Boundary-layer-tube racks mounted on wing.

The ratio of the dynamic pressure in the boundary layer close to the wing surface to the dynamic pressure just outside the boundary layer was computed and plotted against distance along the surface. The point where this curve shows an abnormal increase in the downstream direction was taken as the transition point from laminar to turbulent boundary layer.

#### RESULTS AND DISCUSSION

Wake surveys were made over the range of Reynolds Numbers from 11,000,000 to 15,000,000 (air-speed range 140 to 200 miles per hour indicated). The corresponding lift-coefficient range was 0.35 to 0.17. No attempt was made to vary the Reynolds Number  $R$  and the lift coefficient  $C_L$  independently, since the variation in profile-drag coefficient at constant lift coefficient over the Reynolds Number range that could be obtained in flight was of the same magnitude as that due to experimental errors. The air conditions for these tests ranged from a perfect smoothness to a roughness sufficient to cause small variations in the recorded air speed.

Measurements to determine the boundary-layer

transition point on the smooth wing were made at Reynolds Numbers of 11,000,000 and 14,000,000, corresponding to lift coefficients of 0.34 and 0.21, respectively.

Profile-drag coefficients were computed from the wake measurements by Jones' formula (reference 4)

$$c_{d_0} = 2 \int_W \sqrt{\frac{H_1 - p_1}{H_0 - p_0}} \left( 1 - \sqrt{\frac{H_1 - p_0}{H_0 - p_0}} \right) d\left(\frac{y}{c}\right)$$

where  $H$  is total pressure.

$p$ , static pressure.

$c$ , chord.

$W$ , wake.

$y$ , ordinate in survey plane normal to the free stream.

The subscript 0 refers to the free stream at infinity, and the subscript 1 refers to the measurement plane. As a check for possible errors that are a result of assuming the air incompressible, Jones' equation was redeveloped for compressible flow by introducing the equation of continuity and Bernoulli's equation for compressible flow. A complete derivation of the equation is given in the appendix. The final equation is

$$c_{d_0} = 2 \int_W \left\{ \sqrt{\frac{\rho_1}{\rho_0}} \frac{\sqrt{\frac{H_1 - p_1}{F_1} + \left[ (p_1 - p_0) + \frac{p_1}{2\gamma} \left( \frac{p_1 - p_0}{p_1} \right)^2 + \dots \right]}}}{\sqrt{\frac{H_0 - p_0}{F_0}}} \right\} \times \sqrt{\frac{H_1 - p_1}{H_0 - p_0}} \frac{F_0}{F_1} d\left(\frac{y}{c}\right)$$



where, in addition to the previously defined symbols,

$\rho$  is density.

$\gamma$ , ratio of specific heat at constant pressure to specific heat at constant volume.

$F$ , compressibility factor

$$\left[ 1 + \frac{1}{4}(U/V_c)^2 + \frac{1}{40}(U/V_c)^4 + \dots \right]$$

$V_c$ , speed of sound.

$U$ , velocity.

For the position of the survey head 8.4 percent of the chord from the trailing edge of the wing, the correction for compressibility at 200 miles per hour is one-tenth percent of the profile drag. Inasmuch as the static pressure in the wake is nearly equal to free-stream static

irregularities. The original wing had large circular perforations in the wing flap. This construction is not a normal one and undoubtedly accounted for some of the profile drag, although countersunk rivets had been used over the forward 23 percent of the upper surface and 8 percent of the lower surface to keep the drag of the original wing low. Over the range of lift coefficients tested, the profile-drag coefficient is constant within the experimental error and can be taken as  $c_{d0min}$ . The Reynolds Number range being small, variation of  $c_{d0}$  with Reynolds Number is expected to be very small. From reference 2, the variation of  $c_{d0}$  over the range of lift coefficients tested is also expected to be small.

It is also apparent that  $c_{d0}$  is independent of free-air roughness as no systematic variation was found for

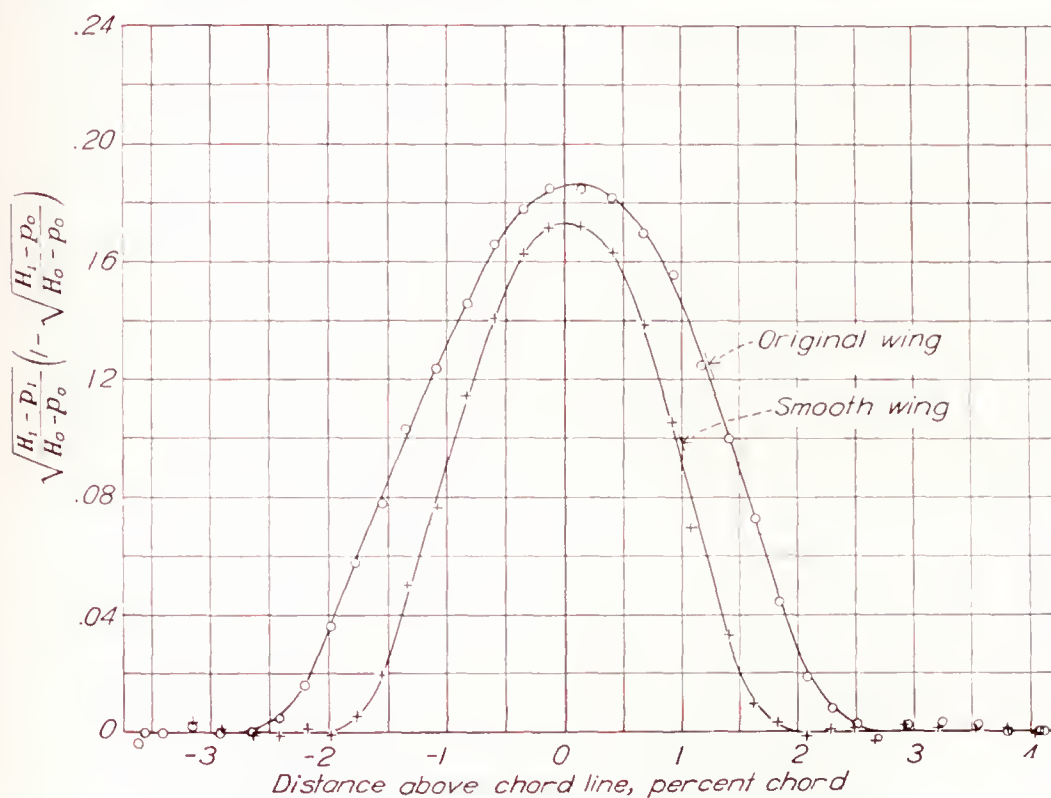


FIGURE 5.—Typical curves of momentum loss in wake.  $C_L$ , 0.23.

pressure, the density term is practically unity. The velocity in the wake being a large fraction of the stream velocity, the compressibility factors are approximately equal and cancel out. For the conditions tested, the correction applied to the profile-drag coefficient is negligible.

Typical curves of the momentum loss in the wake for the smooth and the original wing surfaces are given in figure 5. The position of the pitot tube was corrected to its effective center by the method given in reference 5.

The profile-drag coefficients for the smooth condition and the original condition of the wing of N. A. C. A. 2414.5 section are plotted against the lift coefficient of the complete airplane  $C_L$  in figure 6. A complete summary of the test conditions and results is given in table II.

The profile-drag coefficient of the smooth wing is 0.0068; of the original wing, 0.0102 for Reynolds Numbers from 12,000,000 to 15,000,000. Thus a profile-drag increase of 50 percent can be attributed to surface

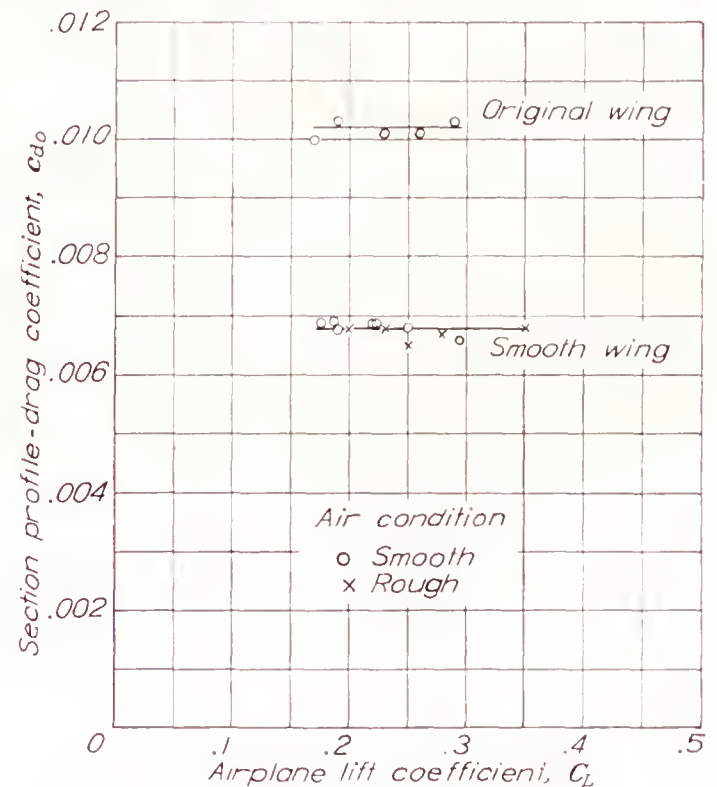


FIGURE 6.—Profile-drag coefficients for smooth and original N. A. C. A. 2414.5 sections.

different air conditions during the tests. This result has been pointed out by Jones (reference 6). Apparently the type of turbulence found in the atmosphere has no noticeable effect on the profile drag.

From drag data obtained in the variable-density tunnel for the N. A. C. A. 2400 series (reference 3), the interpolated  $c_{d0min}$  for the N. A. C. A. 2414.5 section at an effective Reynolds Number of 8,000,000 is 0.0067. If this value is extrapolated to 15,000,000 according to the formula (reference 2),

$$c_{d0min} = (c_{d0min})_{8 \times 10^6} \left( \frac{R}{8 \times 10^6} \right)^{-0.11}$$

a value of 0.0063 is obtained for  $c_{d0min}$ .

Profile-drag tests carried out in the 5- by 7-meter tunnel of the DVL on the N. A. C. A. 2409 and 2421 sections over a Reynolds Number range of 3,000,000 to 13,000,000 indicate a  $c_{d0min}$  value of 0.0065 for the N. A. C. A. 2414.5 section at a Reynolds Number of 15,000,000.



The  $c_{d_{0min}}$  value of 0.0068 for the smooth wing is probably slightly higher than it would have been for a true N. A. C. A. 2414.5 section in flight. This difference can be attributed to earlier transition, as pointed out in the discussion of the boundary-layer tests.

The results of the boundary-layer and the pressure-

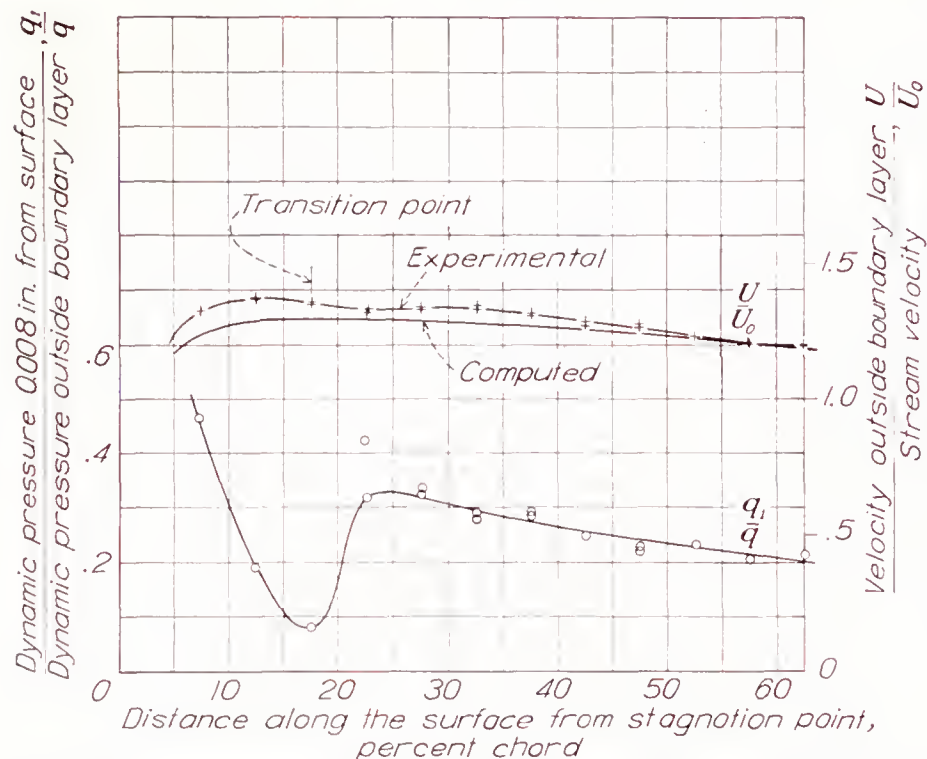


FIGURE 7.—Boundary-layer surveys on upper surface of smooth wing at  $C_L = 0.31$ . R, 11,100,000; N. A. C. A. 2414.5 section.

distribution surveys are shown in figures 7 and 8 as the velocity distribution along the surface and the ratio of the dynamic pressure  $q_1$  0.008 inch from the surface to the dynamic pressure  $q$  just outside the boundary layer.

From the  $q_1/q$  curve, the transition point for both flight conditions is 17.5 percent of the chord along the surface from the front stagnation point (14 percent of the chord along the chord line).

For  $C_L = 0.21$  (fig. 8), the curve of velocity distribution along the surface reaches a maximum at 14 percent of the chord along the surface. The negative velocity gradient (or positive pressure gradient) exerts thereafter an unstable influence on the laminar boundary layer. Transition to turbulent boundary layer with accompanying increase in skin friction follows soon after the velocity maximum. The tests at  $C_L = 0.34$  exhibit the same tendencies.

The dip in the experimental velocity distributions near the quarter-chord point is attributed to departures of the section tested from the true N. A. C. A. 2414.5 section. For comparison, the velocity distributions over the upper surface of a true N. A. C. A. 2414.5 section for the airplane lift coefficients corresponding to those of the boundary-layer tests have been plotted in figures 7 and 8. These distributions were obtained by interpolating between the pressure distributions for the N. A. C. A. 2400 series given in reference 7. Comparison of the experimental and the computed velocity distributions shows that the peak velocity of the computed distributions occurs farther downstream. The transition point would be expected to occur in the region

between 25 and 35 percent of the chord measured along the surface. The more forward position of the transition point observed in the tests could easily account for the difference in profile-drag coefficient found in these tests as compared with the DVL and the variable-density-tunnel tests.

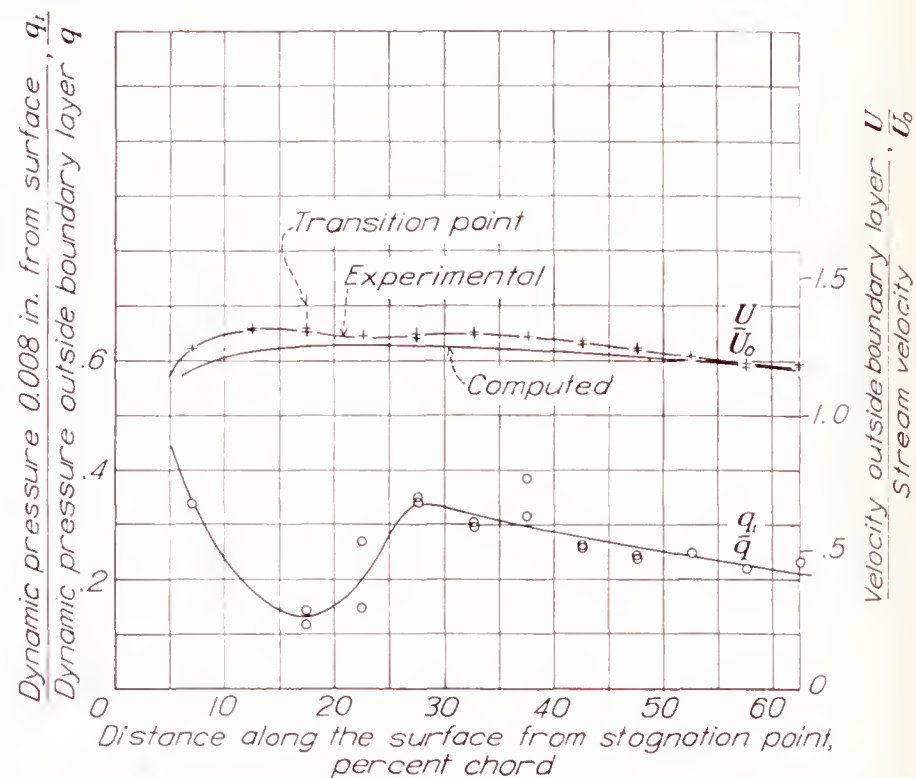


FIGURE 8.—Boundary-layer surveys on upper surface of smooth wing at  $C_L = 0.21$ . R, 14,000,000; N. A. C. A. 2414.5 section.

## CONCLUSIONS

Wake surveys made of a smooth wing of approximately N. A. C. A. 2414.5 section in flight at a Reynolds Number of 15,000,000 gave a minimum profile-drag coefficient of 0.0068. Surveys made of the original wing, which represents current metal construction, gave a profile-drag coefficient of 0.0102. Manufacturing irregularities in rivets, lap joints, access doors, and flap ventilating holes are thus responsible for a 50-percent increase in profile-drag coefficient, even though flush rivets were used over the forward 23 percent of the upper surface and 8 percent of the lower surface of the wing.

The boundary-layer surveys on the upper surface of the smooth wing showed that transition from laminar to turbulent boundary layer occurred at a position on the section tested more forward than would be expected on a true N. A. C. A. 2414.5 section. Differences in the transition-point location could easily account for the slight differences in the profile-drag coefficients of the N. A. C. A. 2414.5 section found in flight and in the DVL and the variable-density tunnels.

The boundary-layer surveys showed that transition occurred a short distance downstream from the point of minimum pressure.



## APPENDIX

### THE DERIVATION OF JONES' EQUATION FOR PROFILE DRAG IN A COMPRESSIBLE FLUID

Assume a two-dimensional body in a uniform stream (fig. 9). Assume that a plane is located far enough ahead of the body so that the static pressure is equal to the static pressure of the undistributed stream  $p_0$ . The velocity, the total pressure, and the density are given as  $U_0$ ,  $H_0$ , and  $\rho_0$ , respectively. Assume another plane far enough behind the body so that the static pressure is again the static pressure of the undisturbed stream,  $p_0$ . Over an elementary distance  $dy$ , normal to the undisturbed stream, the velocity, the total

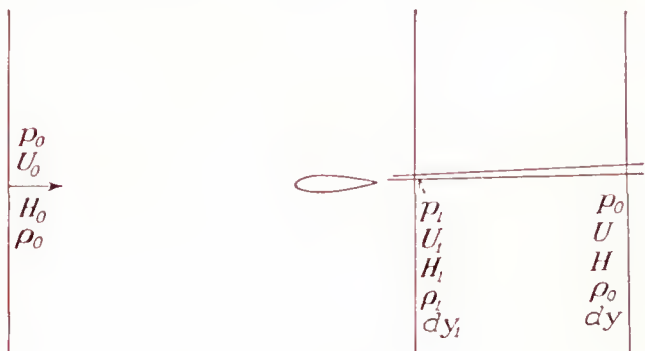


FIGURE 9.

pressure, and the density are given as  $U$ ,  $H$ , and  $\rho_0$ , respectively. The density here is equal to  $\rho_0$  since the static pressure is equal to  $p_0$ . Over an elementary distance  $dy_1$ , to be defined later, of the plane in which the wake surveys are made, the static pressure, the velocity, the total pressure, and the density are  $p_1$ ,  $U_1$ ,  $H_1$ , and  $\rho_1$ , respectively.

Since the static pressures at the forward and the rearward planes are equal, the profile drag per unit span can be equated to the integral of the difference in rate of momentum crossing these planes, namely,

$$D_0 = \int_W \rho_0 (U_0 - U) U dy$$

where the integral is taken only over the wake because there is no contribution outside the wake. Assume, as Jones does, that the wake can be considered as made up of "stream tubes" which do not mix as they pass from the measurement plane to the rearward plane and along each of which the total pressure is constant. Then, applying the equation of continuity along the stream tube, whose width is  $dy_1$  at the measurement plane and  $dy$  at the downstream plane,

$$\rho_0 U dy = \rho_1 U_1 dy_1$$

Substituting,

$$D_0 = \int_W (U_0 - U) \rho_1 U_1 dy_1$$

From Bernoulli's equation, in a compressible fluid,

$$H - p = \frac{\rho}{2} U^2 \left[ 1 + \frac{1}{4} \left( \frac{U}{V_c} \right)^2 + \frac{1}{40} \left( \frac{U}{V_c} \right)^4 + \dots \right]$$

where  $V_c$  is the local velocity of sound.

Let

$$F = \left[ 1 + \frac{1}{4} \left( \frac{U}{V_c} \right)^2 + \frac{1}{40} \left( \frac{U}{V_c} \right)^4 + \dots \right]$$

Then

$$U_0 = \sqrt{\frac{2}{\rho_0}} \sqrt{\frac{H_0 - p_0}{F_0}}$$

and

$$U_1 = \sqrt{\frac{2}{\rho_1}} \sqrt{\frac{H_1 - p_1}{F_1}}$$

Applying Bernoulli's equation for the compressible flow along a stream tube,

$$\frac{U^2}{2} + \frac{\gamma}{\gamma - 1} \frac{p_0}{\rho_0} = \frac{U_1^2}{2} + \frac{\gamma}{\gamma - 1} \frac{p_1}{\rho_1}$$

where  $\gamma$  is the ratio of the specific heat at constant pressure to the specific heat at constant volume, whence

$$U = \sqrt{\frac{2}{\rho_1} \frac{H_1 - p_1}{F_1} + \frac{2\gamma}{\gamma - 1} \left( \frac{p_1}{\rho_1} - \frac{p_0}{\rho_0} \right)}$$

Examine now the term

$$\frac{p_1}{\rho_1} - \frac{p_0}{\rho_0}$$

Assuming adiabatic changes of pressure and density,

$$\left( \frac{p_0}{\rho_0} \right)^{1/\gamma} = \left( \frac{p_1}{\rho_1} \right)^{1/\gamma}$$

whence, by substitution,

$$\frac{p_1}{\rho_1} - \frac{p_0}{\rho_0} = \frac{p_1}{\rho_1} \left[ 1 - \left( \frac{p_0}{p_1} \right)^{\frac{\gamma-1}{\gamma}} \right]$$

Now

$$\left( \frac{p_0}{p_1} \right)^{\frac{\gamma-1}{\gamma}} = \left( 1 + \frac{p_0 - p_1}{p_1} \right)^{\frac{\gamma-1}{\gamma}} = \left( 1 + \frac{p_0 - p_1}{p_1} \right)^{\frac{\gamma-1}{\gamma}}$$

and, expanding this expression by the binomial theorem,

$$\left( \frac{p_0}{p_1} \right)^{\frac{\gamma-1}{\gamma}} = 1 + \frac{\gamma-1}{\gamma} \frac{p_0 - p_1}{p_1} + \frac{\gamma-1}{\gamma} \frac{1}{2\gamma} \left( \frac{p_0 - p_1}{p_1} \right)^2 + \dots$$

Substituting

$$\frac{p_1}{\rho_1} - \frac{p_0}{\rho_0} = \frac{1}{\rho_1} \left[ \frac{\gamma-1}{\gamma} (p_1 - p_0) + \frac{\gamma-1}{2\gamma} \frac{p_1}{\gamma} \left( \frac{p_1 - p_0}{p_1} \right)^2 + \dots \right]$$



and, finally,

$$U = \sqrt{\frac{2}{\rho_1} \frac{H_1 - p_1}{F_1} + \frac{2}{\rho_1} \left[ (p_1 - p_0) + \frac{p_1}{2\gamma} \left( \frac{p_1 - p_0}{p_1} \right)^2 + \dots \right]}$$

Substituting the expressions for the velocities into the drag equation,

$$D_0 = \int_w \sqrt{\frac{2}{\rho_0} \frac{H_0 - p_0}{F_0}} - \sqrt{\frac{2}{\rho_1} \frac{H_1 - p_1}{F_1} + \frac{2}{\rho_1} \left[ (p_1 - p_0) + \frac{p_1}{2\gamma} \left( \frac{p_1 - p_0}{p_1} \right)^2 + \dots \right]} \times \rho_1 \sqrt{\frac{2}{\rho_1} \frac{H_1 - p_1}{F_1}} dy_1$$

Now

$$c_{d_0} = \frac{D_0}{c \frac{\rho_0}{2} U_0^2} = \frac{D_0 F_0}{c (H_0 - p_0)}$$

where  $c$  is the airfoil chord.

Finally

$$c_{d_0} = 2 \int_w \left\{ \sqrt{\frac{\rho_1}{\rho_0}} - \frac{\sqrt{\frac{H_1 - p_1}{F_1} + \left[ (p_1 - p_0) + \frac{p_1}{2\gamma} \left( \frac{p_1 - p_0}{p_1} \right)^2 + \dots \right]}}{\sqrt{\frac{H_0 - p_0}{F_0}}} \right\} \times \sqrt{\frac{H_1 - p_1}{H_0 - p_0} \frac{F_0}{F_1}} d\left(\frac{y}{c}\right)$$

If the velocities are so low that compressibility can be neglected,  $\rho_0 = \rho_1$ ;  $F_0 = F_1 = 1$ ; and  $\frac{p_1}{2\gamma} \left( \frac{p_1 - p_0}{p_1} \right)^2$  is negligible compared with  $p_1 - p_0$ . The drag equation reduces to the form given by Jones

$$c_{d_0} = 2 \int_w \sqrt{\frac{H_1 - p_1}{H_0 - p_0}} \left( 1 - \sqrt{\frac{H_1 - p_0}{H_0 - p_0}} \right) d\left(\frac{y}{c}\right)$$

#### REFERENCES

1. Doetsch, H.: Profilwiderstandsmessungen im grossen Windkanal der DVL. Luftfahrtforschung, Bd. 14, Lfg. 4/5, 20. April 1937, S. 173-178.
2. Jacobs, Eastman N., and Sherman, Albert: Airfoil Section Characteristics as Affected by Variations of the Reynolds Number. T. R. No. 586, N. A. C. A., 1937.
3. Jacobs, Eastman N., and Rhode, R. V.: Airfoil Section Characteristics as Applied to the Prediction of Air Forces and Their Distribution on Wings. T. R. No. 631, N. A. C. A., 1938.
4. The Cambridge University Aeronautics Laboratory: The Measurement of Profile Drag by the Pitot-Transverse Method. R. & M. No. 1688, British A. R. C., 1936.
5. Young, A. D., and Maas, J. N.: The Behaviour of a Pitot Tube in a Transverse Total-Pressure Gradient. R. & M. No. 1770, British A. R. C., 1937.
6. Jones, B. Melvill: Flight Experiments on the Boundary Layer. Jour. Aero. Sci., vol. 5, no. 3, Jan. 1938, pp. 81-94.
7. Garrick, I. E.: Determination of the Theoretical Pressure Distribution for Twenty Airfoils. T. R. No. 465, N. A. C. A., 1933.



TABLE I.—SECTION ORDINATES OF THE SMOOTH WING AND THE N. A. C. A. 2414.5 WING. CHORD, 8.86 FEET

[All values in percent chord]

Station	Smooth wing		N. A. C. A. 2414.5	
	Upper	Lower	Upper	Lower
0	0	0		0
1.25	2.45	-2.07	2.63	-1.98
2.5	3.42	-2.84	3.60	-2.75
5	4.75	-3.74	4.92	-3.69
7.5	5.72	-4.33	5.88	-4.30
10	6.43	-4.76	6.64	-4.70
15	7.57	-5.22	7.75	-5.20
20	8.34	-5.39	8.46	-5.42
25	8.83	-5.40	8.92	-5.45
30	9.10	-5.32	9.13	-5.37
40	8.98	-4.50	9.01	-5.01
50	8.32	-4.31	8.35	-4.45
60	7.34	-3.62	7.31	-3.71
70	5.96	-2.87	5.95	-2.90
80	4.25	-2.04	4.30	-2.04
90	2.32	-1.15	2.39	-1.11
95	1.28	-.70	1.31	-.65
100	.12	-.12	(.15)	(-.15)
100				0
L. E. Rad., 2.40 Slope of radius through end of chord: 2/20				

TABLE II.—SUMMARY OF PROFILE-DRAG TESTS

Wing lift coefficient, $C_L$	Reynolds Number, $R$ (millions)	Section profile-drag coefficient, $c_{d_0}$	Air condition
Smooth Wing			
0.35	10.9	0.0068	Rough.
.295	11.5	.0066	Smooth.
.28	11.7	.0067	Rough.
.25	12.4	.0065	Do.
.25	12.5	.0068	Smooth.
.23	13.0	.0068	Rough.
.22	13.5	.0069	Smooth.
.20	13.9	.0068	Rough.
.19	14.4	.0068	Smooth.
.225	13.1	.0069	Rough.
.185	14.1	.0039	Smooth.
.175	14.9	.0069	Do.
Original Wing			
0.29	11.9	0.0103	Smooth.
.26	12.4	.0101	Do.
.23	13.2	.0101	Do.
.19	14.6	.0103	Do.
.17	14.8	.0100	Do.







## REPORT No. 668

### WIND-TUNNEL INVESTIGATION OF N. A. C. A. 23012, 23021, AND 23030 AIRFOILS WITH VARIOUS SIZES OF SPLIT FLAP

By CARL J. WENZINGER and THOMAS A. HARRIS

#### SUMMARY

*An investigation has been made in the N. A. C. A. 7- by 10-foot wind tunnel of large-chord N. A. C. A. 23012, 23021, and 23030 airfoils with split flaps 10, 20, 30, and 40 percent of the wing chord to determine the section aerodynamic characteristics of the airfoils as affected by airfoil thickness, flap chord, and flap deflection. The complete section aerodynamic characteristics of all the combinations tested are given in the form of graphs of lift, drag, and pitching-moment coefficients, and certain applications to aerodynamic design are discussed.*

*The final maximum lift coefficients for the three airfoils tested with the  $0.20c_w$  flap were about equal. For the airfoils with the  $0.10c_w$  flap, the maximum lift coefficient decreased with airfoil thickness; for the airfoils with the  $0.30c_w$  or  $0.40c_w$  flaps, the maximum lift coefficient increased with airfoil thickness to a maximum value of 2.94. Within the range covered, the increment of maximum lift coefficient due to the split flaps was practically independent of Reynolds Number. The increase in minimum profile-drag coefficient with airfoil thickness was large, being about twice as great for the N. A. C. A. 23030 as for the 23012 plain airfoil.*

#### INTRODUCTION

The National Advisory Committee for Aeronautics is undertaking an extensive investigation of various high-lift arrangements to furnish information applicable to the design of wing combinations for the improvement of the safety and the performance of airplanes. Thus far, most of the tests have been made with wings having a thickness 12 percent of the wing chord and having the Clark Y or the N. A. C. A. 23012 profile. It appears very desirable at the present time, however, to extend the investigation to include wings having other thicknesses and also other airfoil profiles. The present report describes the results obtained from tests in the 7- by 10-foot wind tunnel of airfoils of various thicknesses equipped with high-lift devices.

The investigation was made of airfoils having thicknesses from 12 to 30 percent of the wing chord; these thicknesses are believed to cover the range likely to be met with in practice. Airfoil sections of the N. A. C. A.

230 series were used because they appear to be generally satisfactory for most purposes. The high-lift device investigated with the airfoils of various thicknesses was the simple split flap, which is used as a basis of comparison with other high-lift devices. Flaps ranging in chord from 10 to 40 percent of the wing chord were tested on each airfoil. These tests are expected to be followed at a later date with tests of slotted flaps on similar airfoils.

#### MODELS

##### PLAIN AIRFOILS

Three basic wings, or plain airfoils, were used in these tests; each had a chord of 3 feet and a span of 7 feet. The models were constructed of laminated wood and were built to the N. A. C. A. 23012, 23021, and 23030 profiles. The thickness of each of these airfoils is, respectively, 12, 21, and 30 percent of the wing chord,  $c_w$ . The ordinates for each of the three airfoils are listed in table I. The N. A. C. A. 23012 airfoil, which had been previously used for the investigation described in reference 1, was already available.

##### FLAPS

Four simple split flaps extending along the entire span were used with each model. The flap chords,  $c_f$ , were  $0.10c_w$ ,  $0.20c_w$ ,  $0.30c_w$ , and  $0.40c_w$  and were believed likely to cover the range of sizes that might be used in practice. (See figs. 1, 2, and 3.) The flaps were built of plywood braced at several points along the span and were arranged for setting at deflections from  $0^\circ$  to  $105^\circ$  down. The flap deflection,  $\delta_f$ , is measured between the lower surface of each airfoil and the flap, as shown in figures 1, 2, and 3.

#### TESTS

The models were mounted in the closed test section of the N. A. C. A. 7- by 10-foot wind tunnel so as to span the jet completely except for small clearances at each end. (See references 1 and 2.) The main airfoil was rigidly attached to the balance frame by torque tubes, which extended through the upper and the lower boundaries of the tunnel. The angle of attack of the model was set from outside the tunnel by rotating the torque tubes with a calibrated electric



drive. Approximately two-dimensional flow is obtained with this type of installation and the section characteristics of the model under test can be determined.

A dynamic pressure of 16.37 pounds per square foot was maintained for most of the tests, which corresponds to a velocity of 80 miles per hour under standard atmospheric conditions and to an average test Reynolds Number of about 2,190,000. Because of the

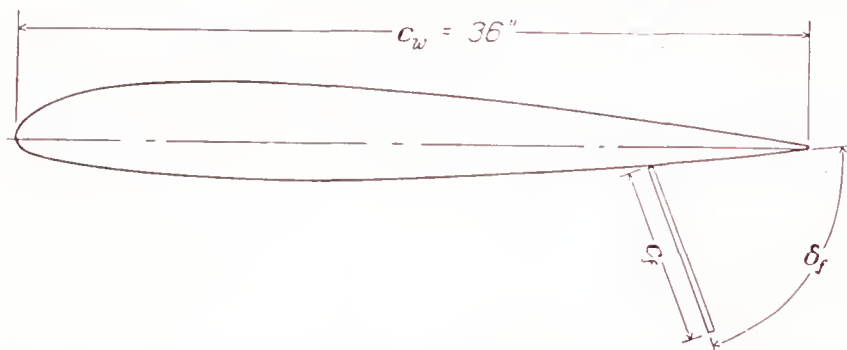


FIGURE 1.—Section of N. A. C. A. 23012 airfoil with split flaps.  $c_f = 0.10c_w, 0.20c_w, 0.30c_w, \text{ and } 0.40c_w$ .

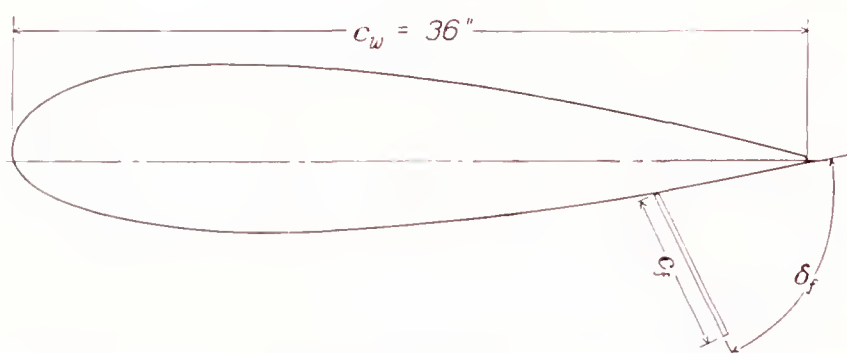


FIGURE 2.—Section of N. A. C. A. 23021 airfoil with split flaps.  $c_f = 0.10c_w, 0.20c_w, 0.30c_w, \text{ and } 0.40c_w$ .

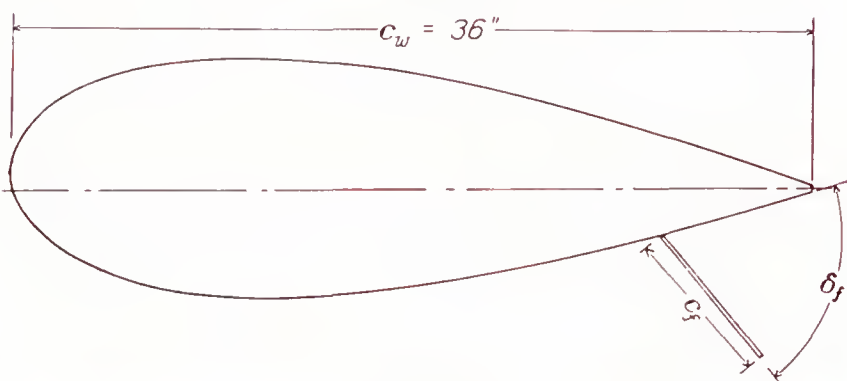


FIGURE 3.—Section of N. A. C. A. 23030 airfoil with split flaps.  $c_f = 0.10c_w, 0.20c_w, 0.30c_w, \text{ and } 0.40c_w$ .

turbulence in the wind tunnel, the effective Reynolds Number,  $R_e$ , was approximately 3,500,000. For all tests,  $R_e$  is based on the chord of the airfoil with the flap retracted and on a turbulence factor of 1.6 for the tunnel.

Each airfoil was tested by itself without the flap so that the characteristics of the plain airfoils could be determined. Each of the four split flaps was then tested on each of the three airfoils and deflected in  $10^\circ$  or  $15^\circ$  increments up to the deflection giving the highest value of the maximum lift coefficient.

An angle-of-attack range from  $-6^\circ$  to the angle of attack for maximum lift was covered in  $2^\circ$  increments for each test. Lift, drag, and pitching moment were measured at each angle of attack.

## RESULTS AND DISCUSSION

### COEFFICIENTS

All test results are given in standard section non-dimensional coefficient form for the airfoil and flap combinations corrected as explained in reference 1.

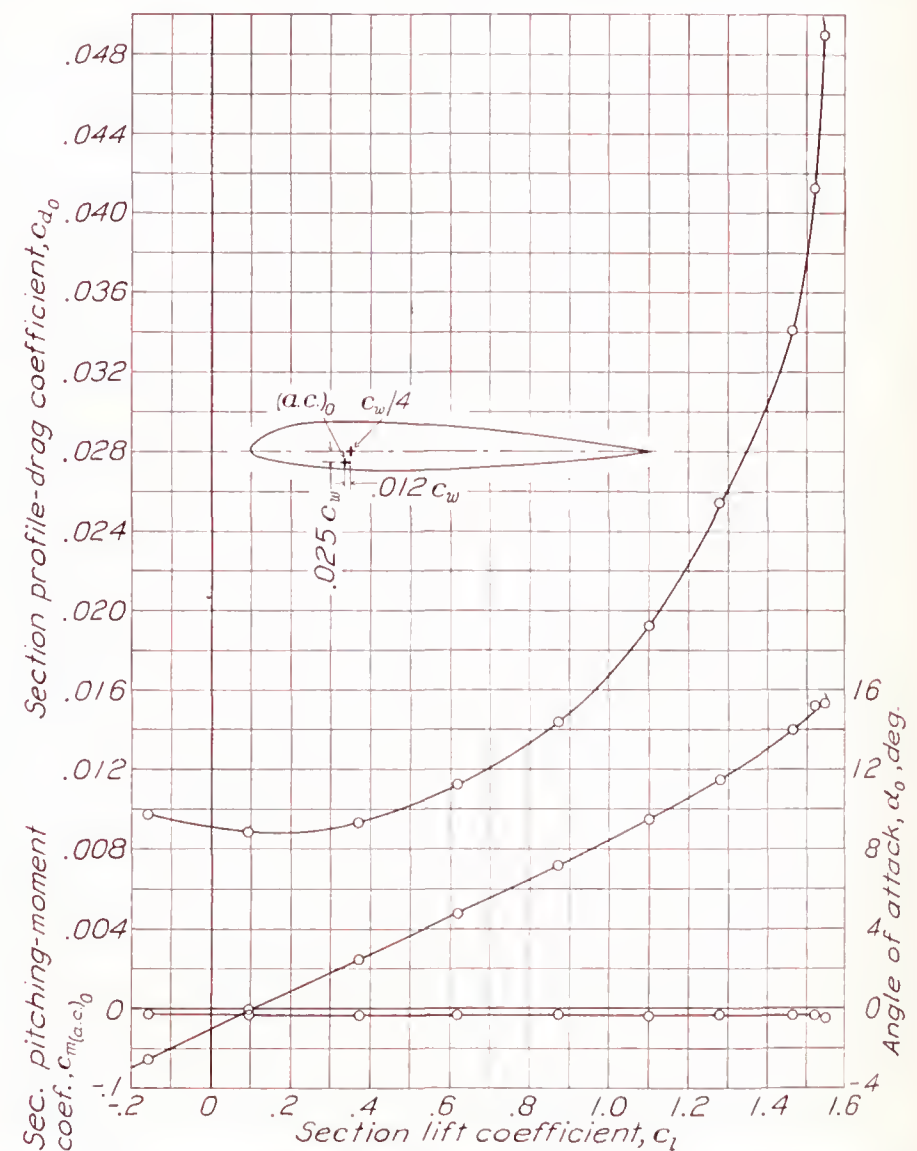


FIGURE 4.—Section aerodynamic characteristics of N. A. C. A. 23012 plain airfoil.

$c_l$ , section lift coefficient,  $l/qc_w$ .

$c_{d_0}$ , section profile-drag coefficient,  $d_0/qc_w$ .

$c_{m(a.c.)_0}$ , section pitching-moment coefficient about aerodynamic center of plain airfoil,  $m_{(a.c.)_0}/qc_w^2$ .

where

$l$  is section lift.

$d_0$ , section profile drag.

$m_{(a.c.)_0}$ , section pitching moment.

$q$ , dynamic pressure,  $1/2 \rho V^2$ .

$c_w$ , chord of basic airfoil with flap fully retracted.

and

$\alpha_0$  is angle of attack for infinite aspect ratio.

$\delta_f$ , flap deflection.



## PRECISION

The accuracy of the various measurements in the tests is believed to be within the following limits:

$\alpha_0$ -----	$\pm 0.1^\circ$	$c_{d0(c_l=1.0)}$ -----	$\pm 0.0006$
$c_{l_{max}}$ -----	$\pm 0.03$	$c_{d0(c_l=2.5)}$ -----	$\pm 0.002$
$c_{m(a.c.)_0}$ -----	$\pm 0.003$	$\delta_f$ -----	$\pm 0.2^\circ$
$c_{d0_{min}}$ -----	$\pm 0.0003$		

## SECTION AERODYNAMIC CHARACTERISTICS

**Plain airfoils.**—The section aerodynamic characteristics of the N. A. C. A. 23012 plain airfoil, as determined with the two-dimensional-flow installation, are shown

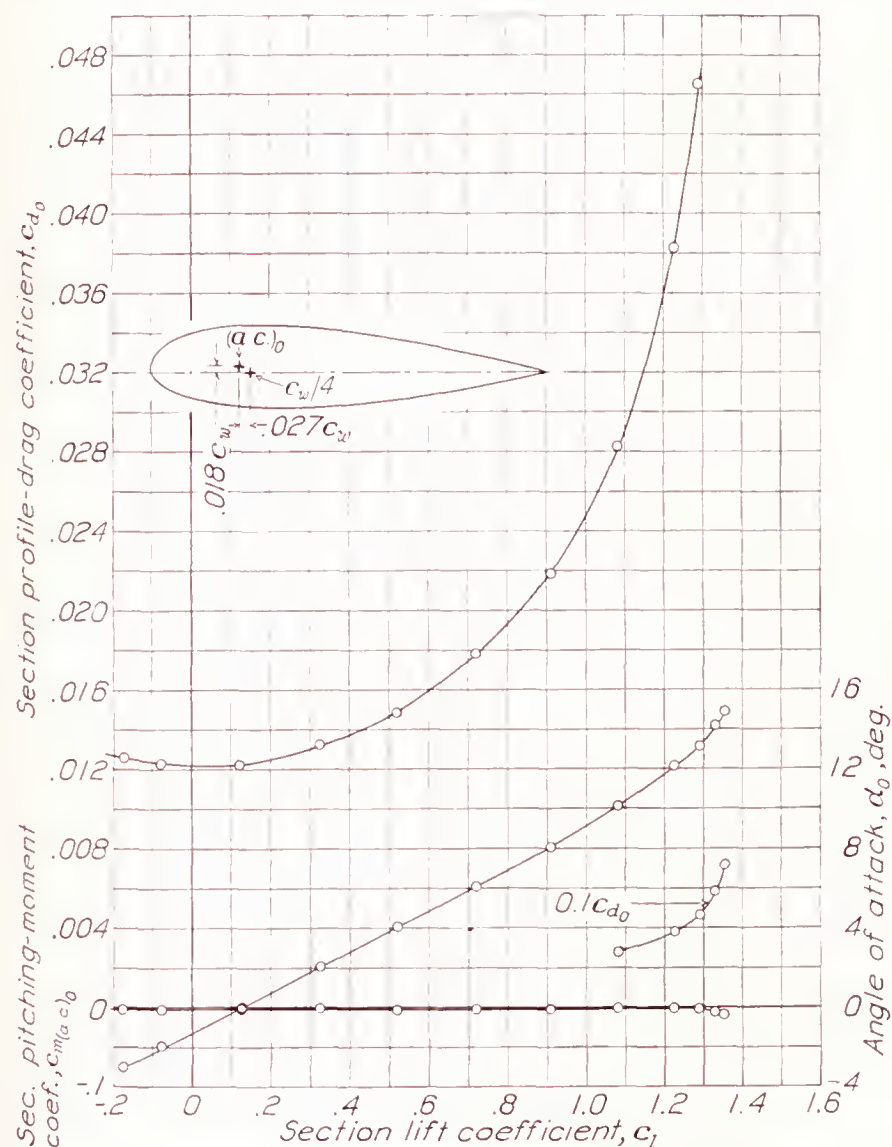


FIGURE 5.—Section aerodynamic characteristics of N. A. C. A. 23021 plain airfoil.

in figure 4. Similar results for the N. A. C. A. 23021 and the N. A. C. A. 23030 plain airfoils are given in figures 5 and 6, respectively. The data for the N. A. C. A. 23012 and 23021 airfoils are discussed in references 1 and 3, respectively, and therefore require no further discussion. The data for the N. A. C. A. 23030 airfoil, however, depart from the results of the thinner sections in several respects. The slope of the lift curve is only 0.068 as compared with about 0.105 for the N. A. C. A. 23012, although there is a marked increase in slope at angles of attack above  $2^\circ$ . The angle of attack for zero lift, however, is the same as for the N. A. C. A. 23012 and 23021 airfoils. The relatively flat-top lift curve given by the N. A. C. A. 23030 airfoil is probably typical of very thick airfoils. Its pitching-moment

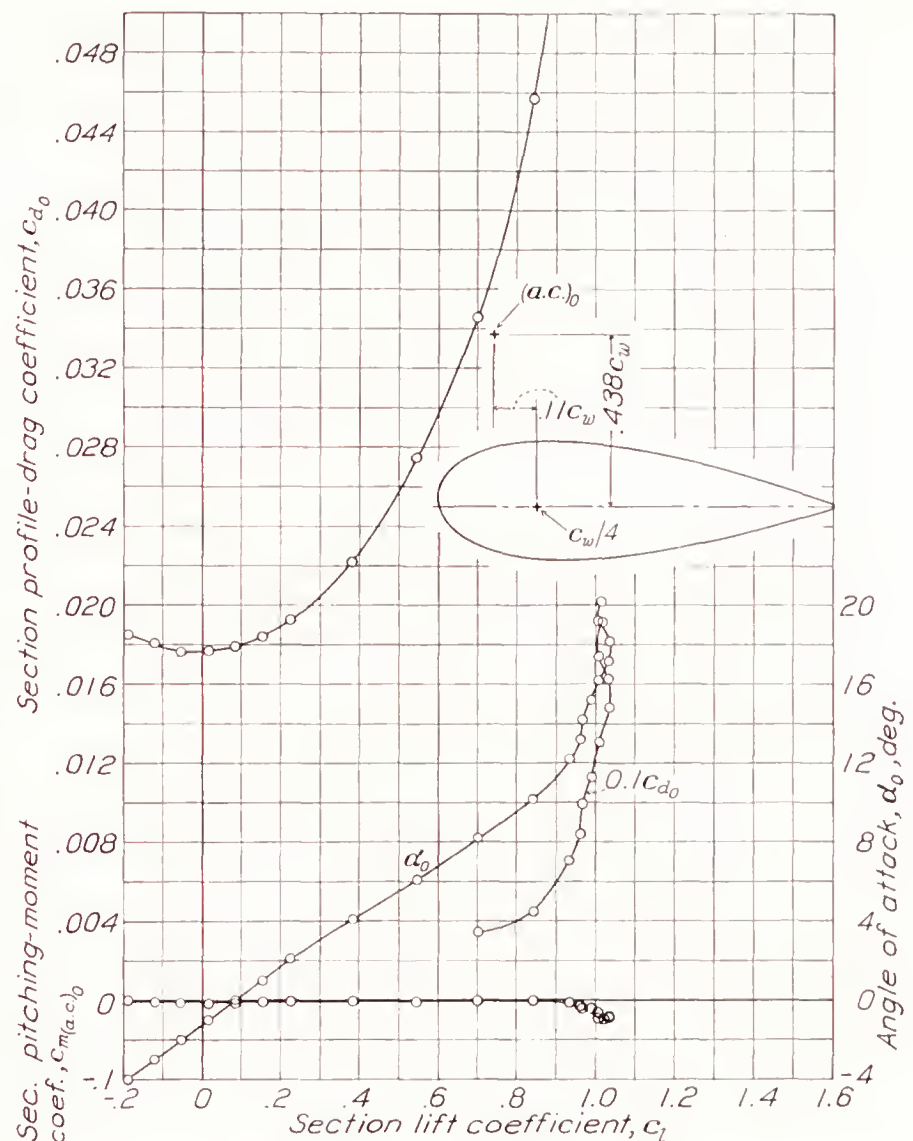


FIGURE 6.—Section aerodynamic characteristics of N. A. C. A. 23030 plain airfoil.

coefficient about the aerodynamic center is  $-0.002$  compared with  $-0.003$  for the N. A. C. A. 23021 and  $-0.009$  for the N. A. C. A. 23012. The most marked change is the position of the aerodynamic center of the plain airfoil; it is 11 percent of the chord ahead of the quarter-chord point of the wing and about 44 percent of the chord above the chord line.

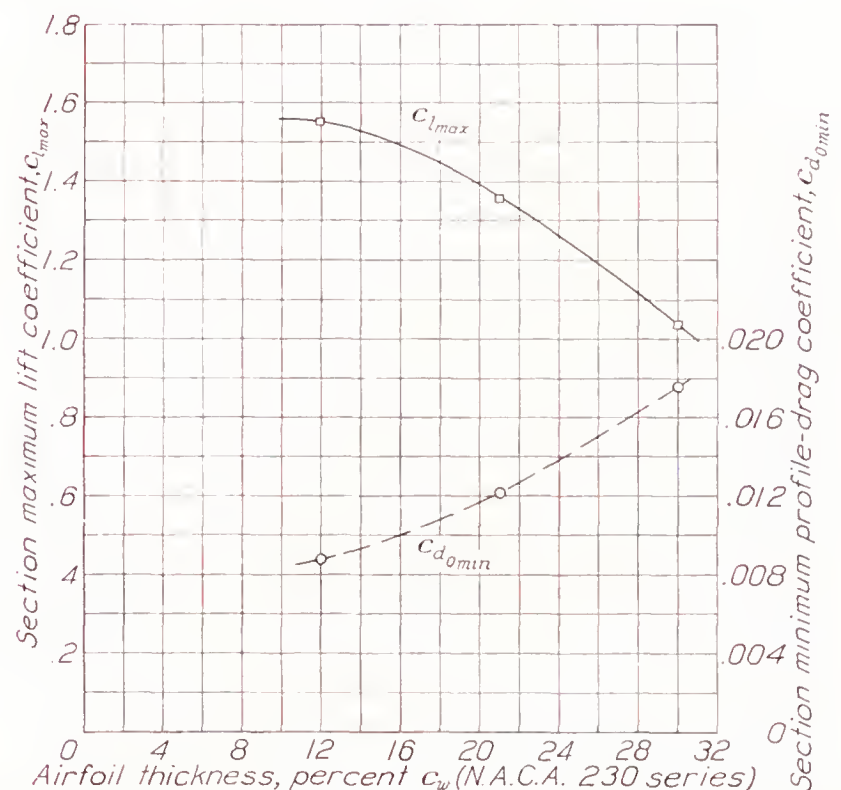


FIGURE 7.—Effect of thickness of plain airfoils on maximum lift and minimum drag.



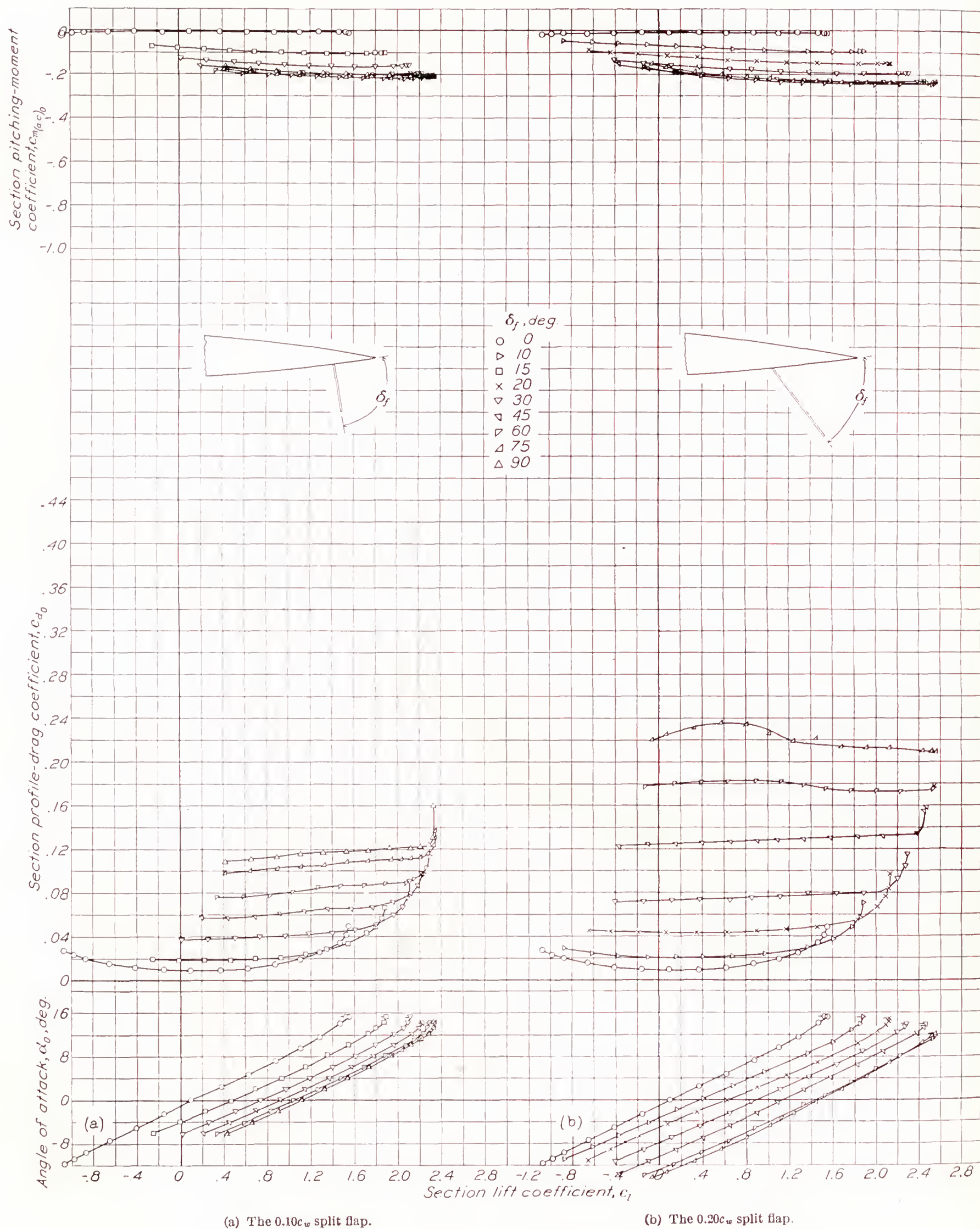


FIGURE 8.—Section aerodynamic characteristics of N. A. C. A. 23012 airfoil with various sizes of split flap.



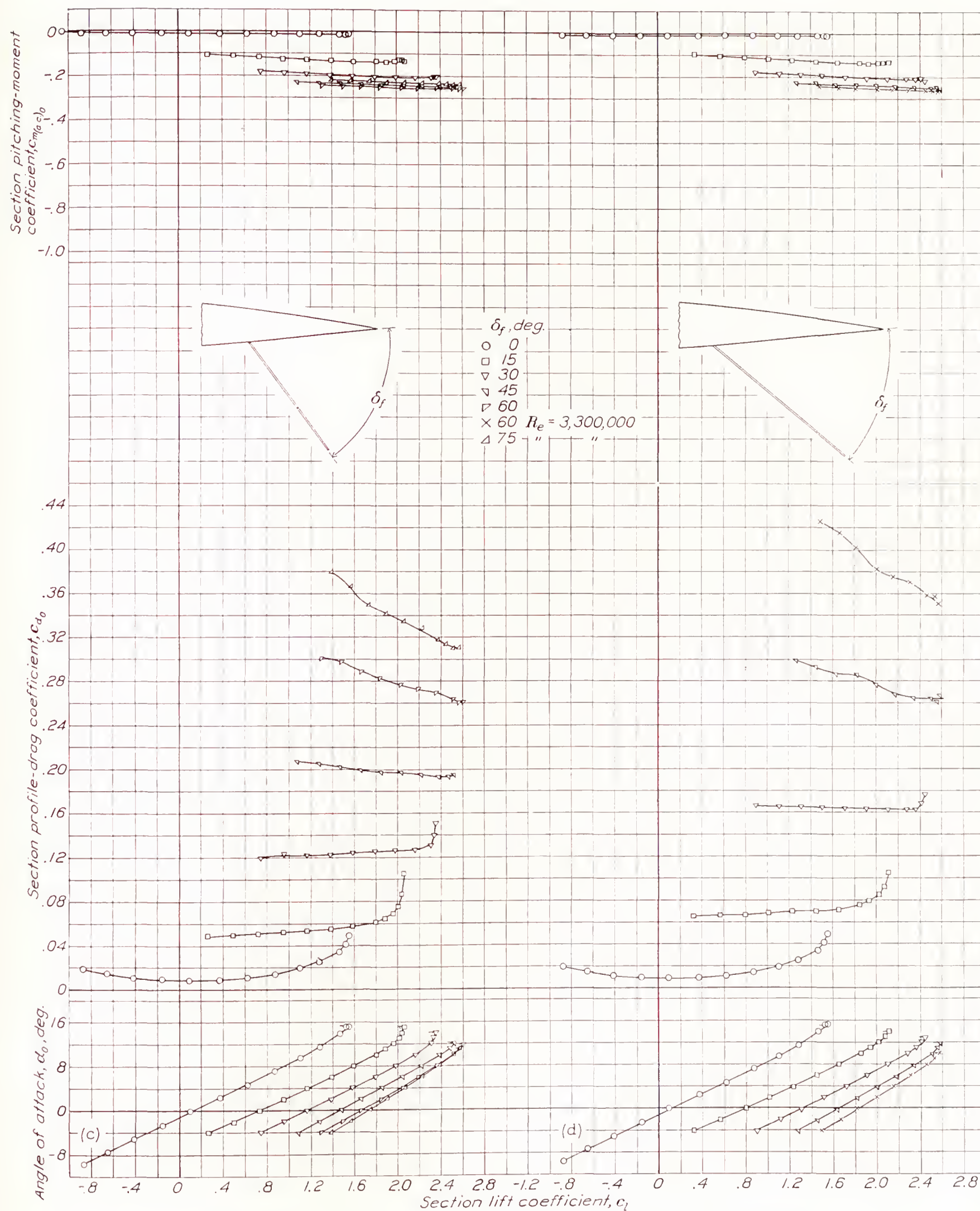


FIGURE 8.—Continued. Section aerodynamic characteristics of N. A. C. A. 23012 airfoil with various sizes of split flap.



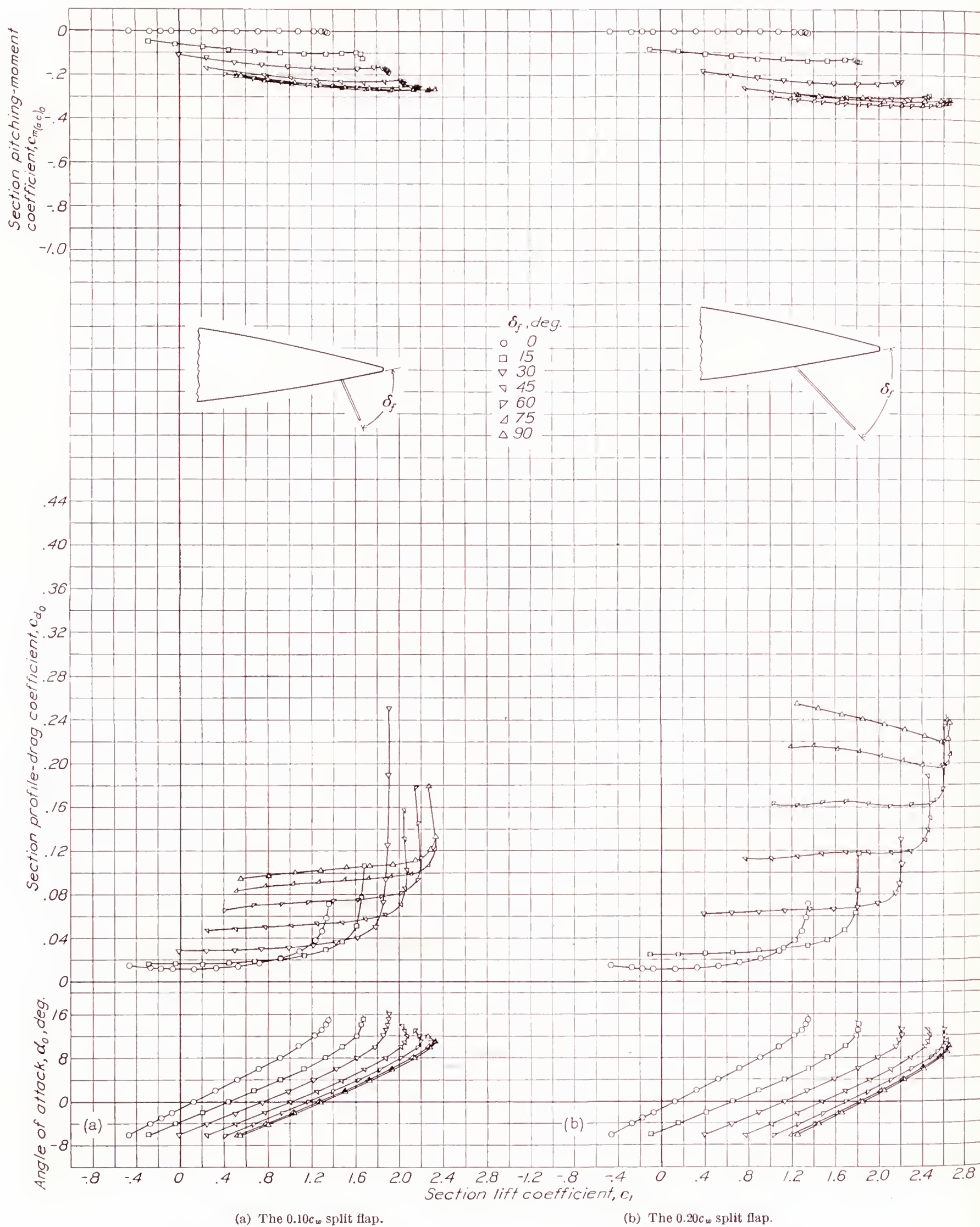


FIGURE 9.—Section aerodynamic characteristics of N. A. C. A. 23021 airfoil with various sizes of split flap.



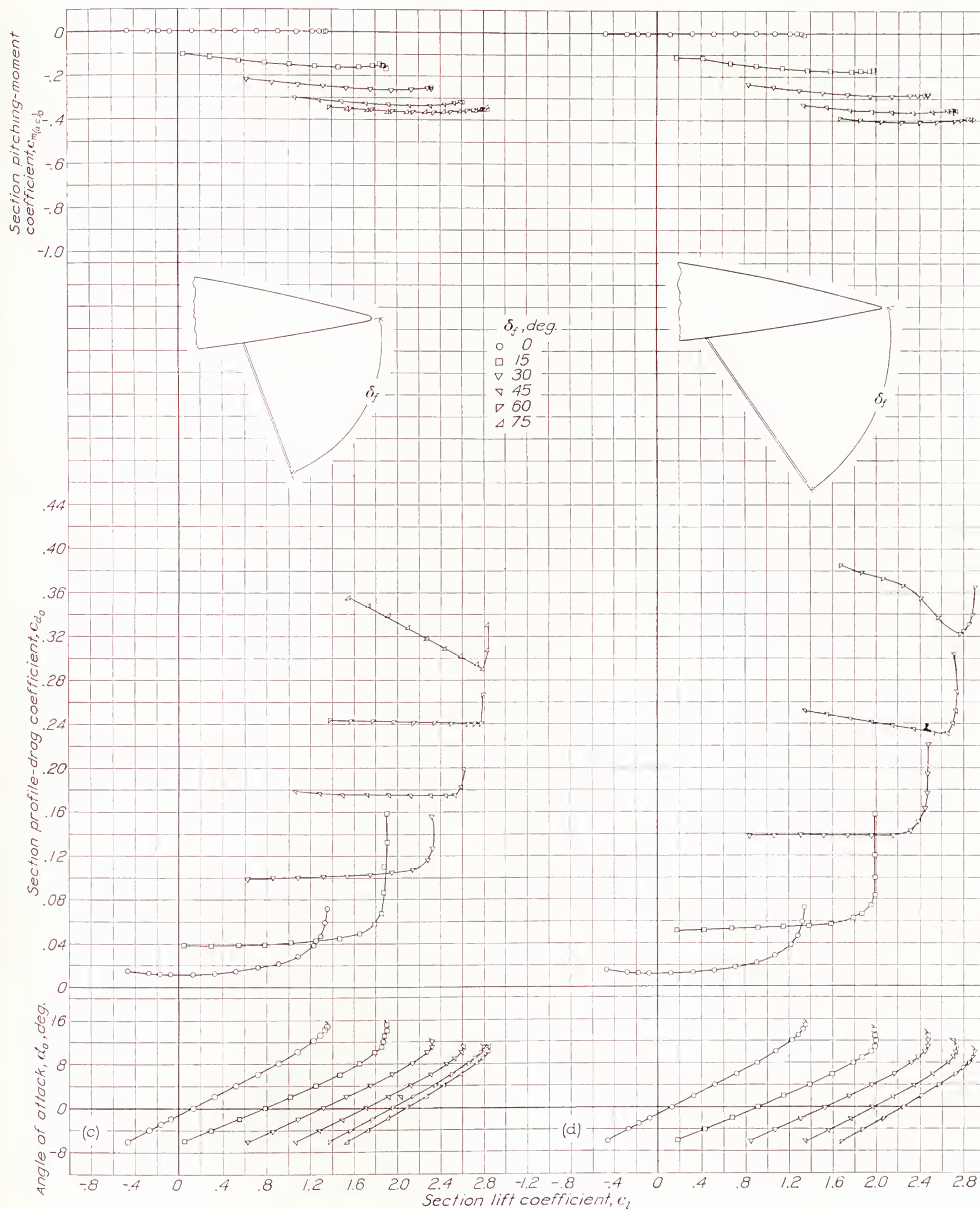


FIGURE 9.—Continued. Section aerodynamic characteristics of N. A. C. A. 23021 airfoil with various sizes of split flap.



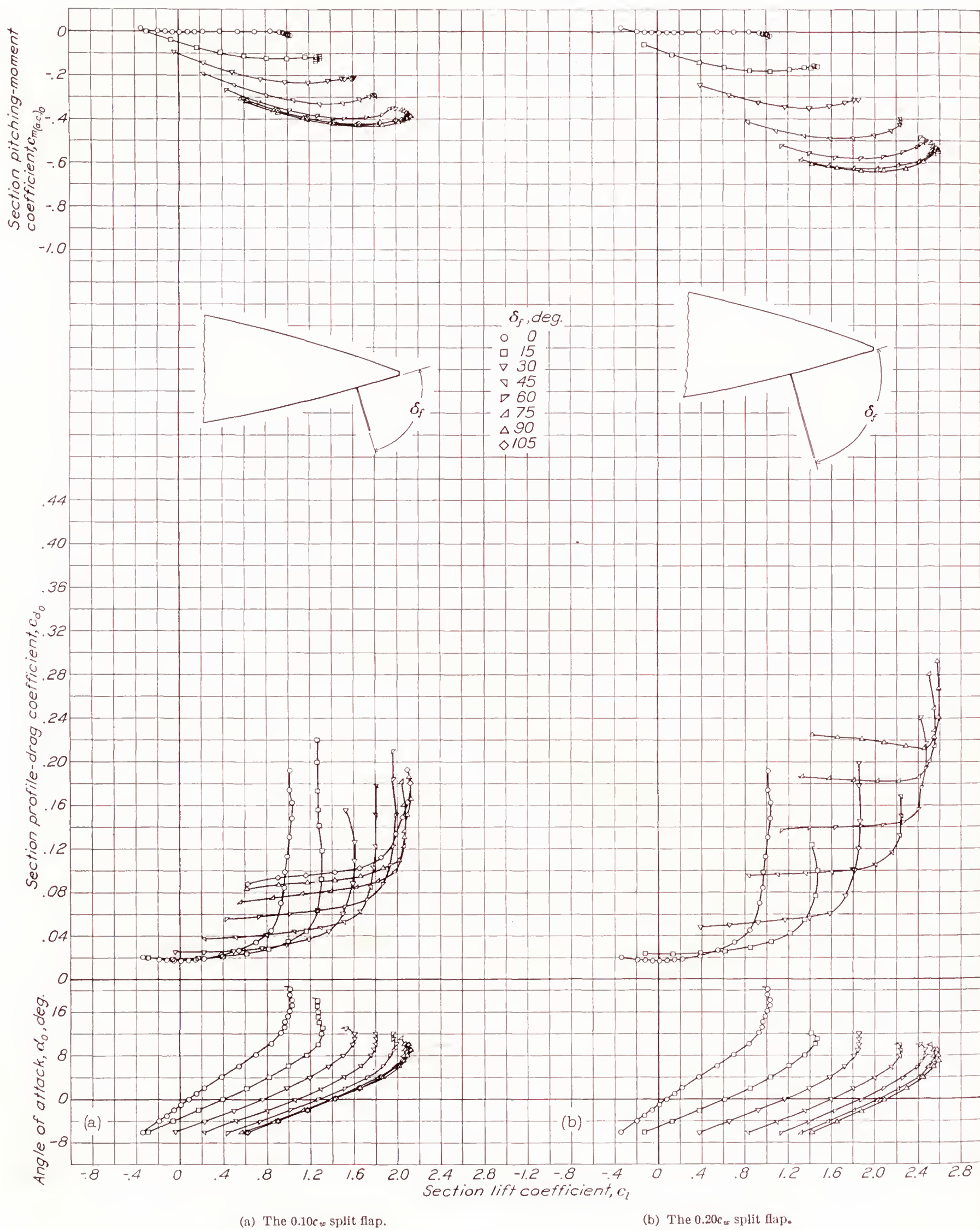


FIGURE 10.—Section aerodynamic characteristics of N. A. C. A. 23030 airfoil with various sizes of split flap.



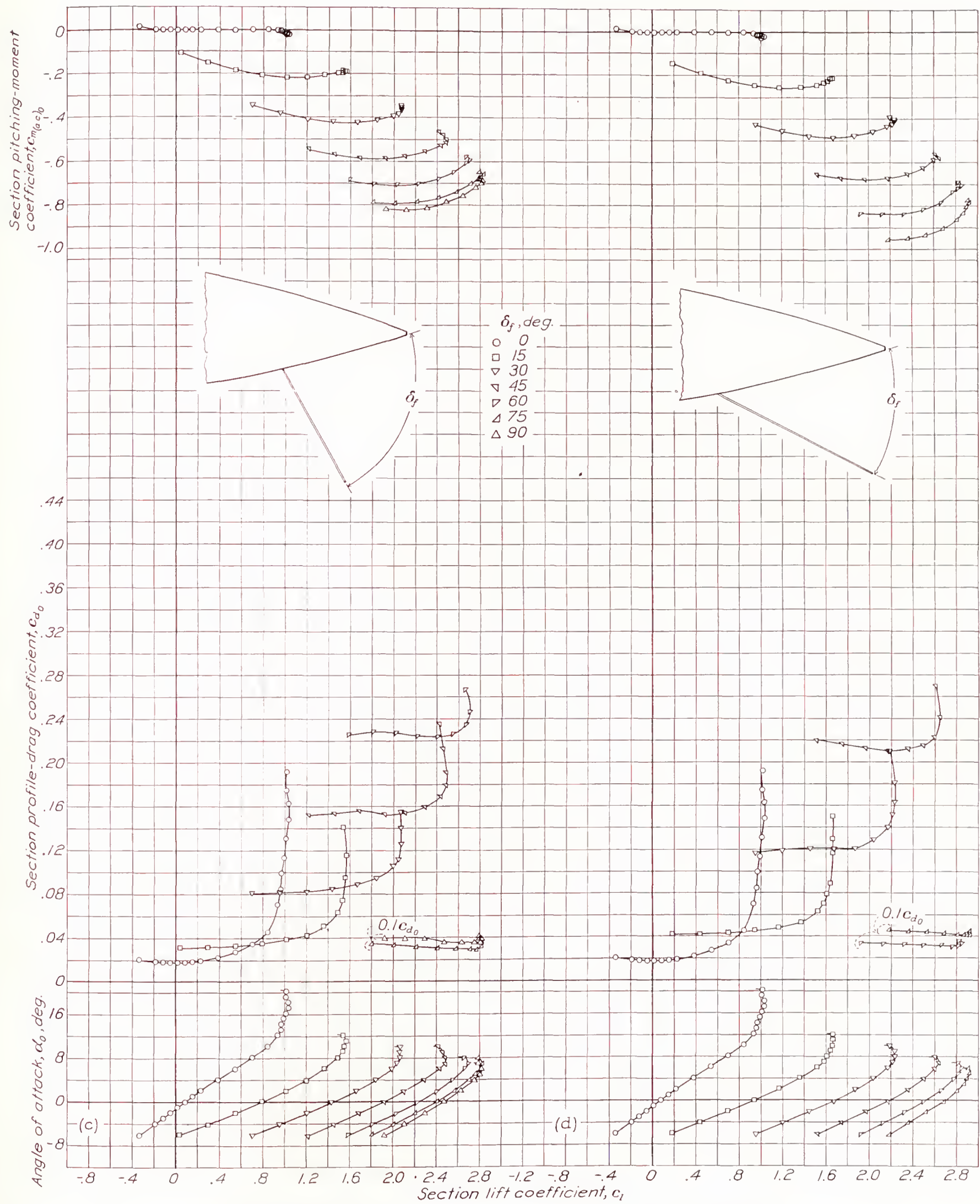


FIGURE 10.—Continued. Section aerodynamic characteristics of N. A. C. A. 23030 airfoil with various sizes of split flap.



The effects of a change in thickness of the plain airfoils on the minimum profile-drag coefficients and on the maximum lift coefficients are indicated in figure 7 for an effective Reynolds Number of 3,500,000. Although the minimum profile-drag coefficient increases rapidly with airfoil thickness and is nearly twice as great for the N. A. C. A. 23030 as for the N. A. C. A. 23012 airfoil (see fig. 7), it may be that structural considera-

**Airfoils with flaps.**—The section aerodynamic characteristics of the N. A. C. A. 23012 airfoil with the  $0.10c_w$ , the  $0.20c_w$ , the  $0.30c_w$ , and the  $0.40c_w$  split flaps are shown in figure 8. All these data were obtained at an effective Reynolds Number of 3,500,000, except as noted on the figure. The lift curves have about the same slopes as they did for the plain airfoils. The angle of attack for maximum lift decreases from

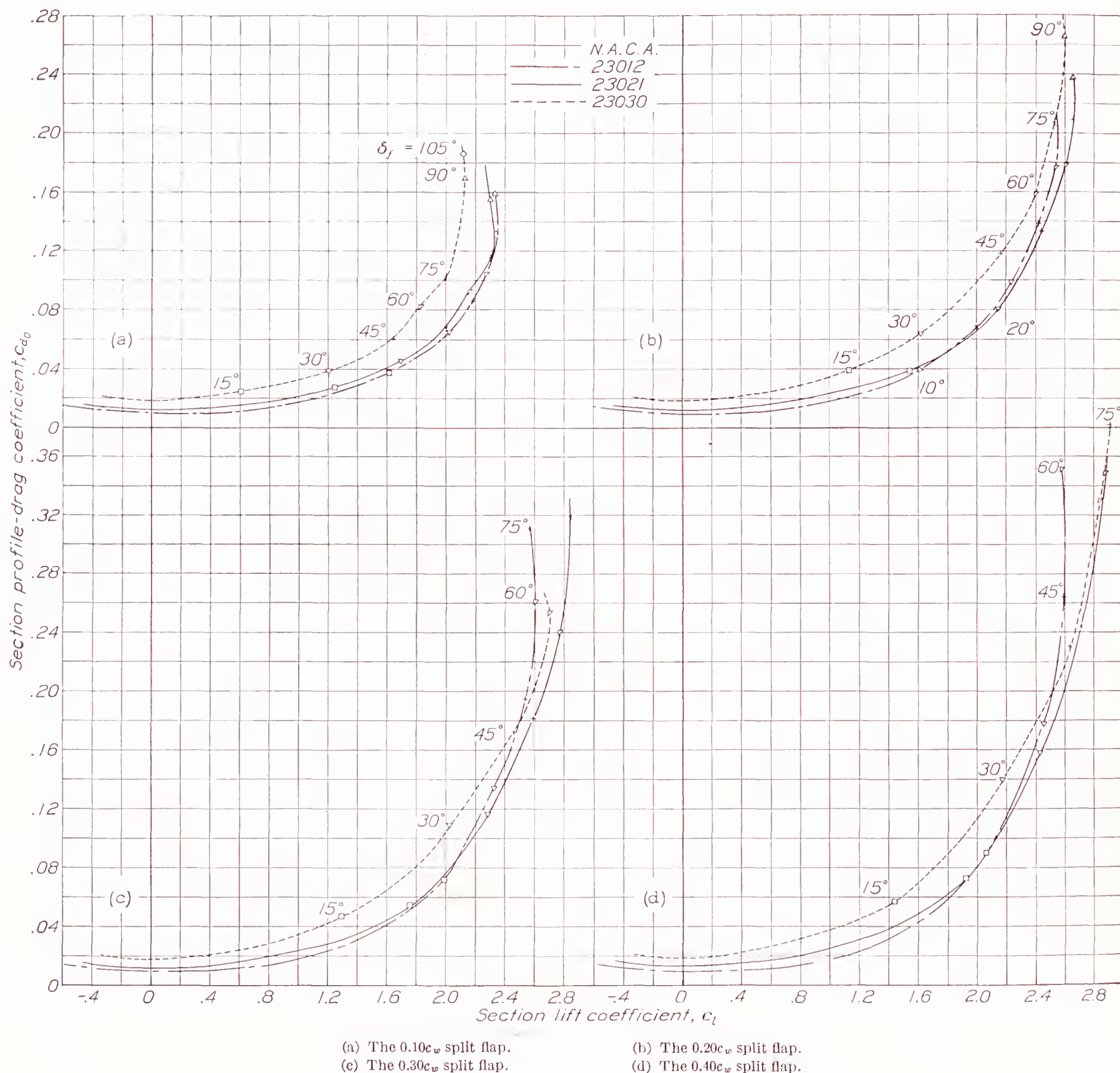


FIGURE 11.—Comparison of profile-drag coefficients for airfoils with split flaps.

tions will more than overbalance this drag increase in application to a given design. In other words, the probability should not be overlooked of actually obtaining desired characteristics with the thick sections because of the possibility of housing parts of the airplane entirely within the wing, which would be impossible with the thinner sections.

about  $15^\circ$  with the flap neutral to about  $14^\circ$  with the flap down  $30^\circ$ . With the flap down  $60^\circ$  or  $75^\circ$ , however, the angle of attack for maximum lift is only about  $10^\circ$  or  $12^\circ$ , a change of  $5^\circ$  or  $3^\circ$  from the plain airfoil. Changes of this magnitude in the angle of attack for maximum lift might have considerable effect on the manner in which a wing stalls for combinations with partial-span flaps.



Similar section aerodynamic data are given for the N. A. C. A. 23021 airfoil with flaps in figure 9 and for the N. A. C. A. 23030 airfoil with flaps in figure 10. The angle of attack for maximum lift with the thicker airfoils with the flap deflected decreases with increasing thickness and flap chord to values as low as  $5^\circ$ , a change of about  $10^\circ$  from the plain airfoil. It should also be noted that a considerable increase in the profile-drag coefficient is obtained with increase in the flap chord.

The pitching-moment coefficient about the aerodynamic center increases quite rapidly with flap chord, flap deflection, and airfoil thickness. The marked

lift coefficients less than 1.8; for lift coefficients greater than 1.8, it is lowest for the N. A. C. A. 23021 airfoil. The drag is lowest for the N. A. C. A. 23012 airfoil with the  $0.30c_w$  and the  $0.40c_w$  split flaps for lift coefficients less than about 2.1; for lift coefficients greater than 2.1, it is lowest for the N. A. C. A. 23021 airfoil. With the  $0.30c_w$  and the  $0.40c_w$  flaps, the drag is lower for the N. A. C. A. 23030 than for the N. A. C. A. 23012 airfoil for lift coefficients above 2.5.

A comparison of the parts of figure 11 shows the drag coefficients to be lowest for the smallest-chord flap suitable for a given lift coefficient for take-off.

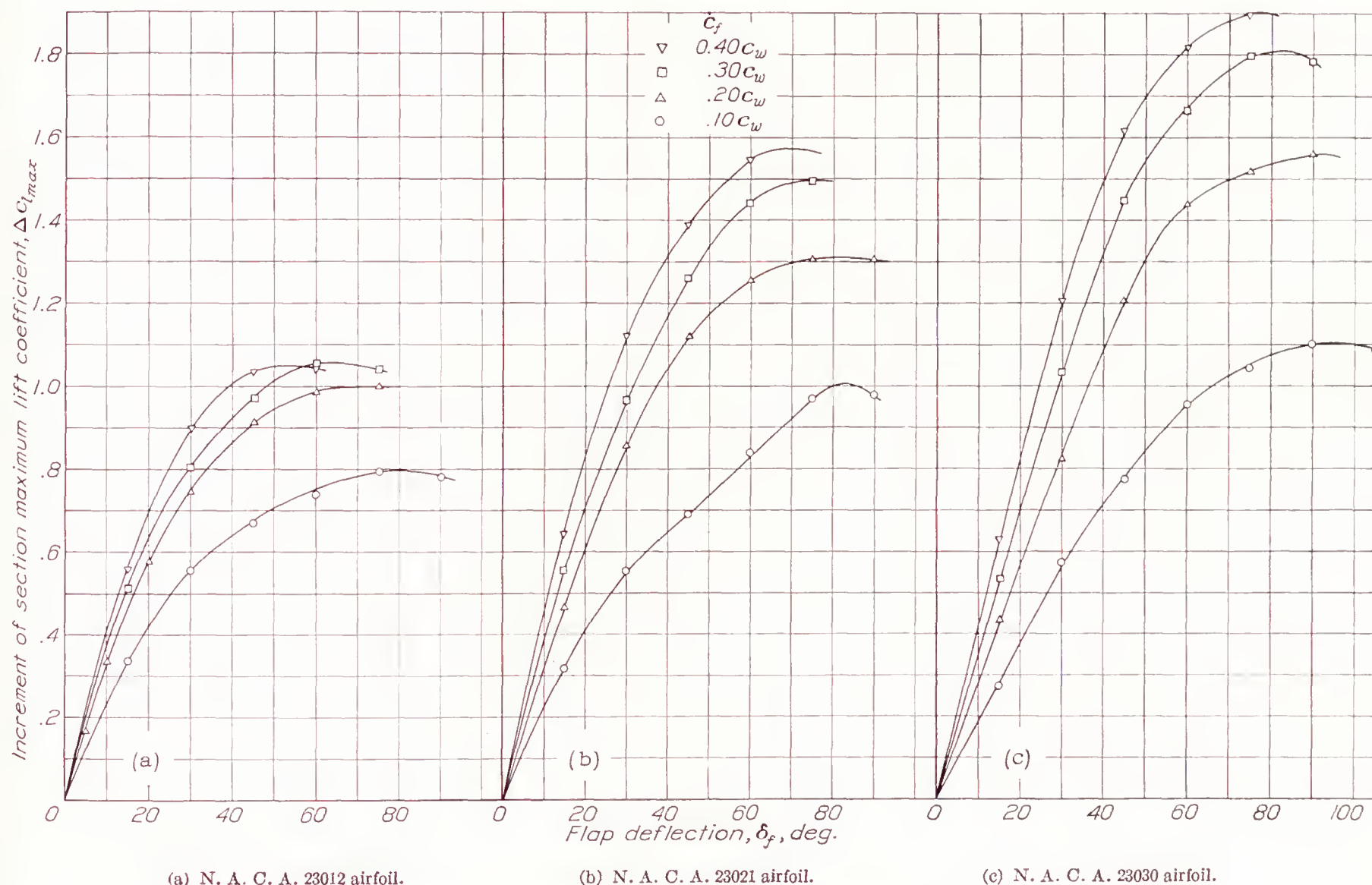


FIGURE 12.—Effect of split-flap deflection on increment of maximum lift coefficient for the various airfoils and flaps.

increase with airfoil thickness is probably caused by the fact that the aerodynamic center is unusually far above the chord line and ahead of the quarter-chord point for the thick airfoils.

#### COMPARISON OF AIRFOILS WITH FLAPS

**Effect on profile drag.**—The effect of the  $0.10c_w$  split flap on the profile drag of the three airfoils for various flap deflections is shown as envelope polar curves in figure 11 (a). Similar curves for the  $0.20c_w$ , the  $0.30c_w$ , and the  $0.40c_w$  flaps are given, respectively, in figures 11 (b), 11 (c), and 11 (d). With the  $0.10c_w$  flap, the drag is lowest throughout the complete lift range for the N. A. C. A. 23012 airfoil. The drag is lowest for the N. A. C. A. 23012 airfoil with the  $0.20c_w$  flaps for

All the combinations with the split flap have higher drag coefficients throughout the take-off range than do the combinations with slotted flaps, which were developed for the N. A. C. A. 23012 and 23021 airfoils and are reported in references 1 and 3.

**Effect on maximum lift.**—The effect of deflecting the split flaps on the increment of section maximum lift coefficient  $\Delta c_{l_{max}}$  is shown in figure 12, where  $\Delta c_{l_{max}}$  is plotted against  $\delta_f$  for all the combinations tested. The maximum  $\Delta c_{l_{max}}$  increases with airfoil thickness for all the flap chords. The flap deflection for maximum  $\Delta c_{l_{max}}$  decreases with increase in flap chord for any of the three airfoils. In figure 13, the maximum  $\Delta c_{l_{max}}$  is plotted for each flap against flap chord for the three



airfoils. The highest  $\Delta c_{l_{max}}$  for the N. A. C. A. 23012 airfoil was obtained with the  $0.30c_w$  flap, which was only slightly superior to the  $0.20c_w$  flap on this airfoil. The highest  $\Delta c_{l_{max}}$  for both the N. A. C. A. 23021 and the N. A. C. A. 23030 airfoils was obtained with the

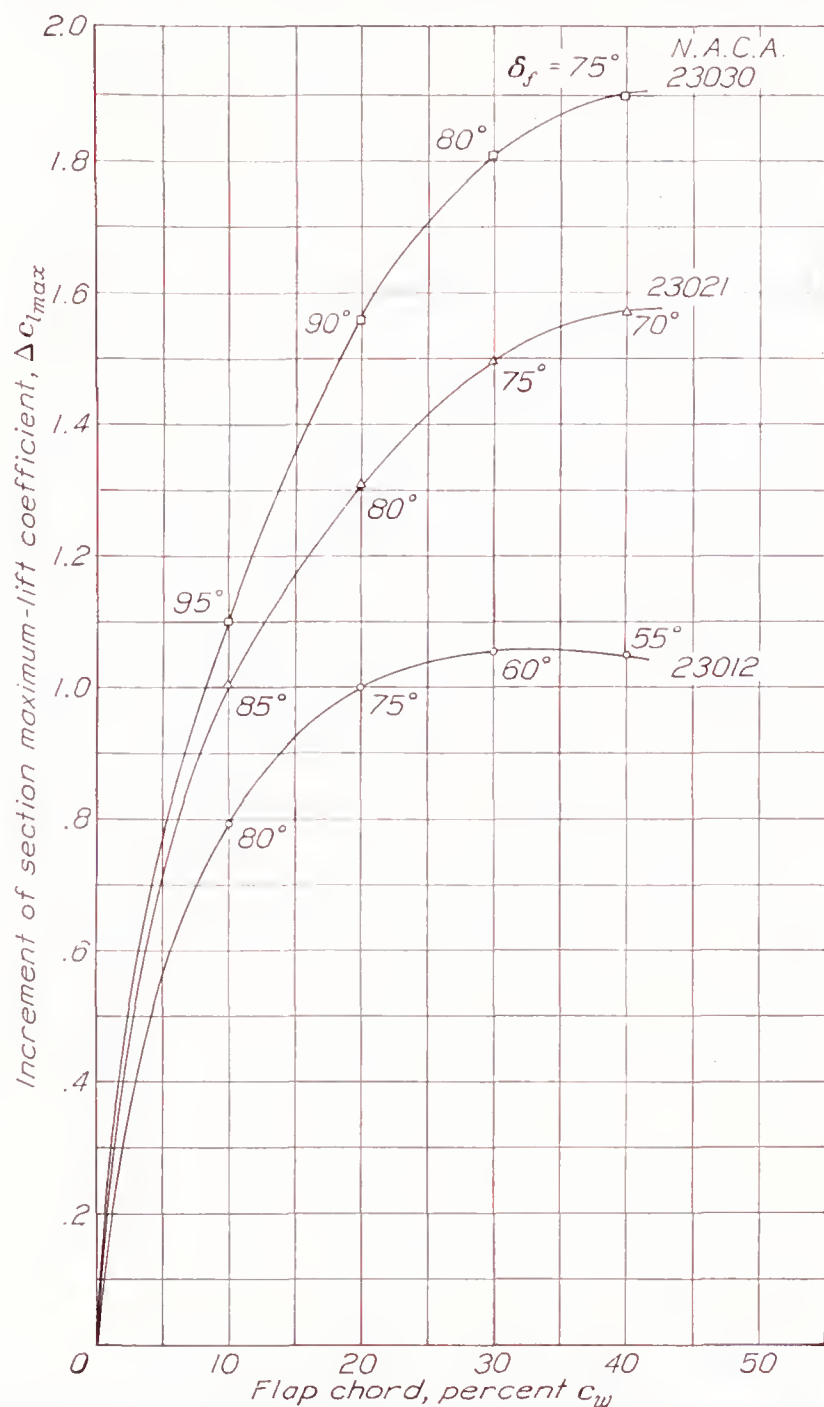


FIGURE 13.—Effect of chord of split flap on increment of maximum lift coefficient for three airfoil thicknesses.

$0.40c_w$  flap. The  $0.40c_w$  flap, however, gave little gain over the  $0.30c_w$  flap, and probably no gain would be obtained by the use of a flap chord greater than  $0.40c_w$  on the N. A. C. A. 23021 airfoil; for the N. A. C. A. 23030 airfoil, flaps of still larger chord might give a slight increase in  $\Delta c_{l_{max}}$ .

The increments of maximum lift coefficient increase quite markedly with airfoil thickness; the values of  $\Delta c_{l_{max}}$  vary from 1.05 for the N. A. C. A. 23012 to 1.9 for the N. A. C. A. 23030 airfoil. The final maximum lift coefficient, however, does not reflect this large difference in  $\Delta c_{l_{max}}$ , as is shown in figure 14, where  $c_{l_{max}}$  for the plain airfoils and for the airfoils with flaps is plotted against airfoil thickness. The large loss in lift with thickness for the plain airfoil very nearly balances the large gain in increment of maximum lift with thickness

for the airfoils with flaps. The final maximum lift coefficients for the N. A. C. A. 23012 and 23021 airfoils with the  $0.10c_w$  flap was 2.34, which is about 8 percent higher than it was for the N. A. C. A. 23030 airfoil. The maximum lift coefficient for the airfoils with the  $0.20c_w$  flap was 2.66 for the N. A. C. A. 23021 airfoil, which is about 4 percent higher than it was for the N. A. C. A. 23012 and 2 percent higher than it was for the N. A. C. A. 23030 airfoil. For the airfoils with the  $0.30c_w$  and the  $0.40c_w$  flaps, the maximum lift coefficient was 2.6 for the 23012 airfoil and increased about 11 percent with airfoil thickness for the 21-percent-thick airfoil. The maximum lift decreased slightly with thickness for the  $0.30c_w$  flap and increased slightly for the  $0.40c_w$  flap. The highest maximum lift coefficient, 2.94, was obtained with the  $0.40c_w$  flap on the N. A. C. A. 23030 airfoil. In spite of the loss in lift of the plain airfoils with thickness, if for structural reasons wing thicknesses are increased to as much as 30 percent, no loss in ultimate section maximum lift coefficient

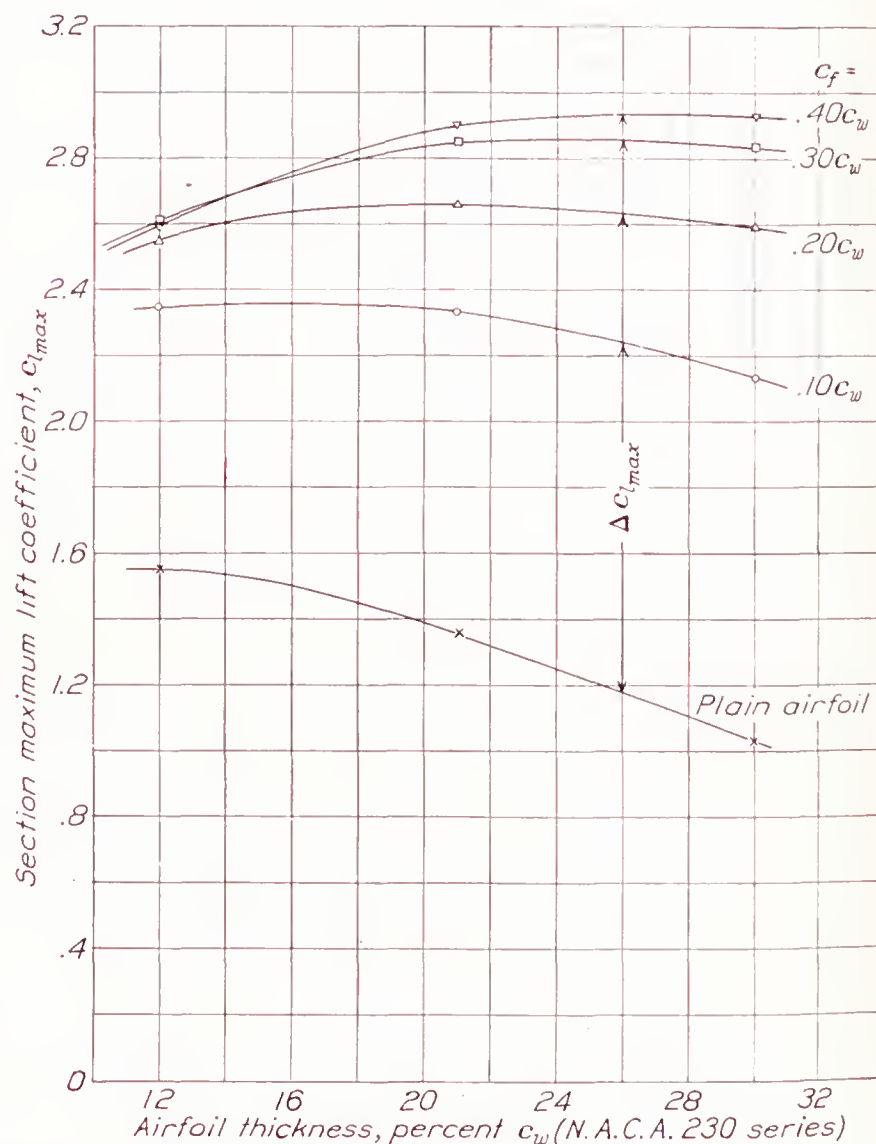


FIGURE 14.—Effect of airfoil thickness on maximum lift coefficient of N. A. C. A. 230 airfoils with and without split flaps.

will be encountered when split flaps with chords of  $0.20c_w$  or larger are used.

#### SCALE EFFECT

The scale effect on maximum lift coefficients for the plain airfoils and the airfoils with flaps, over the range available in the 7- by 10-foot wind tunnel, is shown in



figure 15, where  $c_{l_{max}}$  is plotted against the value of  $R_e$  of the tests. This figure shows a very definite scale effect on the maximum lift coefficient for the N. A. C. A. 23012 airfoil with or without flaps but shows practically none for the N. A. C. A. 23021 and 23030 airfoils with or without flaps. The increment of maximum lift coefficient is therefore practically independent of scale over the range that could be investigated.

#### APPLICATION OF OTHER AIRFOILS

The maximum lift coefficients for airfoils of the N. A. C. A. 430 and 630 series with split flaps may be computed with satisfactory accuracy by adding the

flap were about equal; for the airfoils with the  $0.10c_w$  flap, the maximum lift coefficient decreased with airfoil thickness; and for the airfoils with the  $0.30c_w$  and the  $0.40c_w$  flaps, the maximum lift coefficient increased with airfoil thickness.

Within the range covered, the increment of maximum lift coefficient due to the split flaps was practically independent of scale. The profile-drag coefficient increased quite rapidly with thickness for the plain airfoils and was about twice as large for the N. A. C. A. 23030 as for the 23012 airfoil.

LANGLEY MEMORIAL AERONAUTICAL LABORATORY,  
NATIONAL ADVISORY COMMITTEE FOR AERONAUTICS,  
LANGLEY FIELD, VA., March 10, 1939.

#### REFERENCES

1. Wenzinger, Carl J., and Harris, Thomas A.: Wind-Tunnel Investigation of an N. A. C. A. 23012 Airfoil with Various Arrangements of Slotted Flaps. T. R. No. 664, N. A. C. A., 1939.
2. Harris, Thomas A.: The 7 by 10 Foot Wind Tunnel of the National Advisory Committee for Aeronautics. T. R. No. 412, N. A. C. A., 1931.
3. Wenzinger, Carl J., and Harris, Thomas A.: Wind-Tunnel Investigation of an N. A. C. A. 23021 Airfoil with Various Arrangements of Slotted Flaps. T. R. No. 677, N. A. C. A., 1939.
4. Jacobs, Eastman N., Pinkerton, Robert M., and Greenberg, Harry: Tests of Related Forward-Camber Airfoils in the Variable-Density Wind Tunnel. T. R. No. 610, N. A. C. A., 1937.

TABLE I

#### ORDINATES FOR N. A. C. A. 230 AIRFOILS

[Stations and ordinates in percent of wing chord]

Station	23012		23021		23030	
	Upper surface	Lower surface	Upper surface	Lower surface	Upper surface	Lower surface
0		0		0	4.82	0
1.25	2.67	-1.23	4.87	-2.08	7.37	-2.63
2.5	3.61	-1.71	6.14	-3.14	8.90	-4.27
5	4.91	-2.26	7.93	-4.52	11.05	-6.54
7.5	5.80	-2.61	9.13	-5.55	12.57	-8.28
10	6.43	-2.92	10.03	-6.32	13.68	-9.65
15	7.19	-3.50	11.19	-7.51	15.20	-11.52
20	7.50	-3.97	11.80	-8.30	16.07	-12.61
25	7.60	-4.28	12.05	-8.76	16.46	-13.20
30	7.55	-4.46	12.06	-8.95	16.57	-13.46
40	7.14	-4.48	11.49	-8.83	15.89	-13.13
50	6.41	-4.17	10.40	-8.14	14.38	-12.11
60	5.47	-3.67	8.90	-7.07	12.34	-10.47
70	4.36	-3.00	7.09	-5.72	9.86	-8.42
80	3.08	-2.16	5.05	-4.13	7.03	-6.09
90	1.68	-1.23	2.76	-2.30	3.87	-3.40
95	.92	-.70	1.53	-1.30	2.15	-1.86
100	.13	-.13	.22	-.22	.32	-.32
L. E. radius	1.58		4.85		9.90	

Slope of radius through end of chord: 0.305

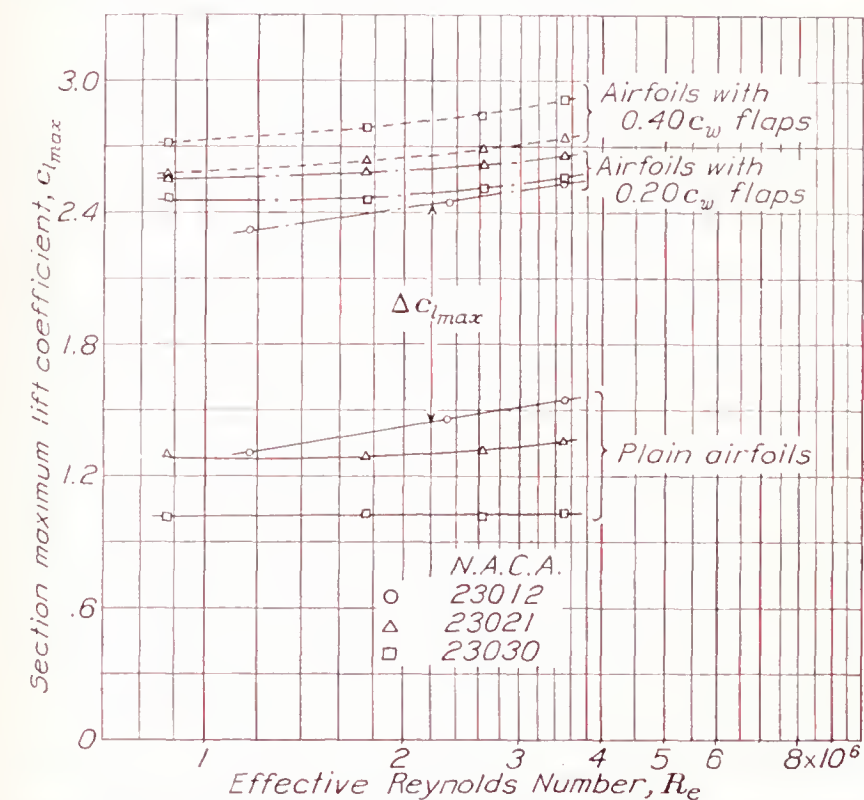


FIGURE 15.—Effect of scale on maximum lift coefficient of three airfoils with and without split flaps; 7- by 10-foot wind tunnel.

$\Delta c_{l_{max}}$  for the proper flap chord and airfoil thickness from the 230 series to the  $c_{l_{max}}$  of the plain airfoil under consideration. This procedure is justified for thicknesses from 9 to 21 percent, as indicated in reference 4. The same procedure would also probably be satisfactory for other airfoils with the position of maximum camber near the leading edge. It should be remembered in applying these data that they are section characteristics and that these maximum lift coefficients cannot be realized on a wing of finite span unless it is designed so that all sections reach maximum lift simultaneously.

#### CONCLUDING REMARKS

Aerodynamic data are made available for airfoils 12 to 30 percent thick with split flaps having chords 10 to 40 percent of the wing chord. The final maximum lift coefficients for the three airfoils tested with the  $0.20c_w$







## REPORT No. 669

# AIRFOIL SECTION DATA OBTAINED IN THE N. A. C. A. VARIABLE-DENSITY TUNNEL AS AFFECTED BY SUPPORT INTERFERENCE AND OTHER CORRECTIONS

By EASTMAN N. JACOBS and IRA H. ABBOTT

### SUMMARY

*The results of an investigation of the effect of support interference on airfoil drag data obtained in the variable-density tunnel are presented. As a result of the support interference, previously published airfoil data from the variable-density tunnel have shown too large drag coefficients and too large a rate of increase of drag coefficient with airfoil thickness. The practical effect of the corrections on the choice of the optimum section is briefly considered and corrected data for a selected list of airfoils are presented as a convenience to the designer. Methods of correcting published data for other airfoils are presented.*

### INTRODUCTION

Airfoil data obtained in the variable-density tunnel (reference 1) have been published (references 2 to 6) in forms that were considered at the time of publication to be most useful to the airplane designer. In the earlier publications (references 1 and 2), no corrections other than those for tunnel-wall effects and to infinite aspect ratio were applied to the data, and emphasis was placed on the pressing problem of obtaining good comparative data for judging the relative merits of airfoils rather than on obtaining absolute accuracy.

It was recognized that certain consistent errors were present in the data, but it was thought that the effect of these errors on the comparative value of the data was not of primary importance. Support-strut interference, for example, was considered to be a possible source of systematic error, but it was thought that this interference would not affect the order of merit of the airfoils tested except possibly in the case of very sensitive airfoils, which might also be similarly affected by the wing-strut intersections of biplanes common at the time. The turbulence of the air stream was thought not seriously to impair the comparative value of the data and, perhaps, even to be desirable, because the extensive turbulent boundary layers occurring on the models in the tunnel as a result of the turbulence would also be found in practice at high values of the Reynolds Number on conventional airfoils with the usual moderately rough surfaces. It was also considered that errors arising from failure of the conventional airfoil theory to predict section characteristics accurately from

the model tests would largely disappear when the data so derived were used to predict the characteristics of wings approximating the same plan form and aspect ratio as the models.

The absolute accuracy of the data was, however, improved from time to time by the investigation of consistent errors. An attempt to evaluate the effect of support interference on the measured drag coefficients was inconclusive (reference 4) and no corrections were applied. The data were further improved by the application of corrections for turbulence and for improvement of the approximations to section characteristics. The corrected coefficients were designated by lower-case symbols, such as  $c_{d_0}$ , as contrasted to the older  $C_{D_0}$ . One of the chief effects of these corrections was to reduce the profile-drag coefficients, particularly for the thicker airfoils.

As airfoil data at large values of the Reynolds Number became available from the N. A. C. A. full-scale tunnel (reference 7) and from foreign sources (references 8 to 13), even the corrected profile-drag coefficients obtained in the variable-density tunnel appeared to be too large. The discrepancy increased with airfoil thickness. The important practical effect is that the data from the variable-density tunnel apparently showed too large a variation of drag coefficient with airfoil thickness. Correct information regarding this variation may be of primary importance to the airplane designer in choosing the optimum airfoil sections for actual wings.

Further investigations of this subject were undertaken, one of the most important being an investigation of three symmetrical sections, N. A. C. A. 0009, 0012, and 0018, under conditions of low turbulence in the N. A. C. A. full-scale tunnel. Results from this investigation (references 14 and 15) indicate a smaller increase in drag with airfoil thickness than is indicated by the results from the N. A. C. A. variable-density tunnel. Furthermore, comparative tests were made in the two tunnels by applying strings to the surface of the N. A. C. A. 0012 airfoil to move the transition point to a predetermined position. These tests indicated that, for this airfoil, the discrepancies were too large to be ascribed to failure of the effective Reynolds Number concept to correct approximately for the drag as affected by transition.



Another correction, however, was suggested by the investigation in the full-scale tunnel. Differences between the results from force and momentum methods of measurement suggested the presence of increments of support-interference drag that increased with section thickness. Further tests, made with additional dummy supports, verified the presence of this type of support interference in the full-scale tunnel. Tests were therefore started in the variable-density tunnel to investigate any variation of support interference with airfoil thickness, in spite of the fact that previous investigations (see appendix of reference 4) had shown no definite corrections for two airfoils, the N. A. C. A. 0012 and 4412. Improvements of the balance of the variable-density tunnel were expected to enable greater accuracy than was obtainable from the previous balance arrangement. The results of this investigation indicate that marked increments of support-interference drag, easily measurable, are present in the drag results from the variable-density tunnel, the increment increasing with airfoil thickness.

The purpose of this report is to present the corrections for application to published results from the variable-density tunnel to give more reliable values of section profile-drag coefficient for airfoils of various thicknesses. The practical effect of the corrections on the choice of the optimum section is briefly considered. Comparison is made between some corrected drag data from the variable-density tunnel and from other sources to show the extent of the existing agreement. Corrected data for a selected list of airfoils are also presented as a convenience to the designer.

### METHOD

The standard method of testing in the variable-density tunnel, the model supports, and the method of determining the tare forces are described in reference 1. The usual tare tests determine the tare forces on the supports including the interference of the model on the supports. The conventional method of determining the balance-alinement correction by testing a symmetrical airfoil through positive and negative angles of attack determines the effects of balance and air-stream misalignment and any interference of the supports on the model that is equivalent to a change in air-flow direction.

The method selected for investigating the additional interference of the supports on the model was the same as that described in the appendix of reference 4. Tests were made of each airfoil supported by three different methods. Besides the method of using the usual support struts, tests were made with the models mounted on the usual supports with the addition of special supports and with the models mounted only on the special supports. The special supports consisted of three wires attached to the quarter-chord point of the model at each wing tip and of a sting and an angle-of-attack

strut so located as to be as free as possible from aerodynamic interference with the regular supports. The sting was symmetrical with respect to the airfoil and was attached near the trailing edge instead of to the lower surface, as usual.

The tares due to the special supports were determined from data obtained from the tests with the models on the regular supports with and without the special supports. These tares were then applied to the data obtained with the model on the special supports alone; the results were then compared with the data obtained in the customary manner to determine the unevaluated interference caused by the usual supports. This method does not eliminate balance deflections arising from sources other than aerodynamic forces on the model and the supports. A test was accordingly made with no model nor supports in the tunnel; the result showed that no such balance deflections were present.

The scope of the present investigation was limited to the study of the profile drag at low and moderate lift coefficients at the highest value of the test Reynolds Number ordinarily obtained (about 3,000,000). Tests were made of the N. A. C. A. 0012, 0018, 0025, 0030, and 0040 symmetrical airfoils to study the variation of support interference with airfoil thickness. The N. A. C. A. 43012, 43018, and 8318 airfoils were also tested to obtain an indication of the variation of support interference with camber.

## RESULTS AND DISCUSSION

### MINIMUM PROFILE-DRAG COEFFICIENTS

The effect of the support interference on the measured section minimum profile-drag coefficients is shown in figure 1. The increment of the minimum profile-drag coefficients caused by the support interference is plotted against airfoil thickness for the five symmetrical and the three cambered airfoils tested. The points for the five symmetrical airfoils lie on a fair curve passing through zero at zero airfoil thickness, the scatter of the points being small when consideration is taken of the difficulties involved in these tests. The points obtained for the N. A. C. A. 43012 and 43018 airfoils fall close to but on opposite sides of the curve for the symmetrical airfoils. The camber of these airfoils (4 percent) is about the upper limit of camber for the commonly used airfoils. The point obtained for the N. A. C. A. 8318 airfoil falls 0.0007 above the curve and would seem to indicate an increase in support interference for highly cambered airfoils. In this case, however, the point for the N. A. C. A. 43018 airfoil would be expected to fall between those for the N. A. C. A. 8318 and 0018 airfoils; whereas it falls slightly below that for the symmetrical airfoil. Inasmuch as each point was obtained from the results of three tests, two of which (those with the wire supports) were made with very large tare forces, the displacement of the point for the



N. A. C. A. 8318 airfoil from the fair curve is only of the order of the possible experimental error.

The shape of the curve of figure 1 suggests that the interference may be largely of the nature of a buoyancy effect, in which case the interference should be primarily a function of airfoil thickness; and other factors, such as camber, should ordinarily be minor variables. Accordingly, because the present tests fail to show significant variations with camber and because it is not considered practicable to make such tests for a large number of airfoils, the values obtained from the faired curve of figure 1 will ordinarily be used to correct the measured minimum profile-drag coefficients. These values are thought to represent the correction with sufficient accuracy for most applications of commonly

in the appendix (equation (1)), for the support interference and for the revised correction for the effective Reynolds Number. Corresponding values obtained from the support-interference tests are presented in the sixth column. The principal result is presented in the last column and represents the difference in minimum profile-drag coefficients between the data published in references 4 to 6 and those presented herein. Other published data may be corrected by the methods presented in the appendix.

TABLE I

## DATA ON CORRECTION OF MINIMUM DRAG OF SYMMETRICAL AIRFOILS

[Effective Reynolds Number, approximately 8,000,000]

N. A. C. A. airfoil	$C_{D_0}$ (reference 2)	$c_{d_0}$ (reference 5)	Support interference (fig. 1)	$c_{d_0}$ (corrected)	$c_{d_0}$ (from support-interference tests)	Correction increments <sup>a</sup>
0006	0.0065	0.0054	0.0005	0.0051	-----	0.0003
0009	.0074	.0064	.0007	.0058	-----	.0006
0012	.0083	.0069	.0010	.0060	0.0060	.0009
0015	.0093	.0077	.0013	.0064	-----	.0013
0018	.0108	.0088	.0016	.0071	.0073	.0017
0021	.0120	.0100	.0018	.0079	-----	.0021
0025	.0143	.0119	.0022	.0092	.0091	.0027

<sup>a</sup> Correction increments are sums of increments resulting from support-interference correction and change in method of correcting for effective Reynolds Number.  
<sup>b</sup> Reference 6.

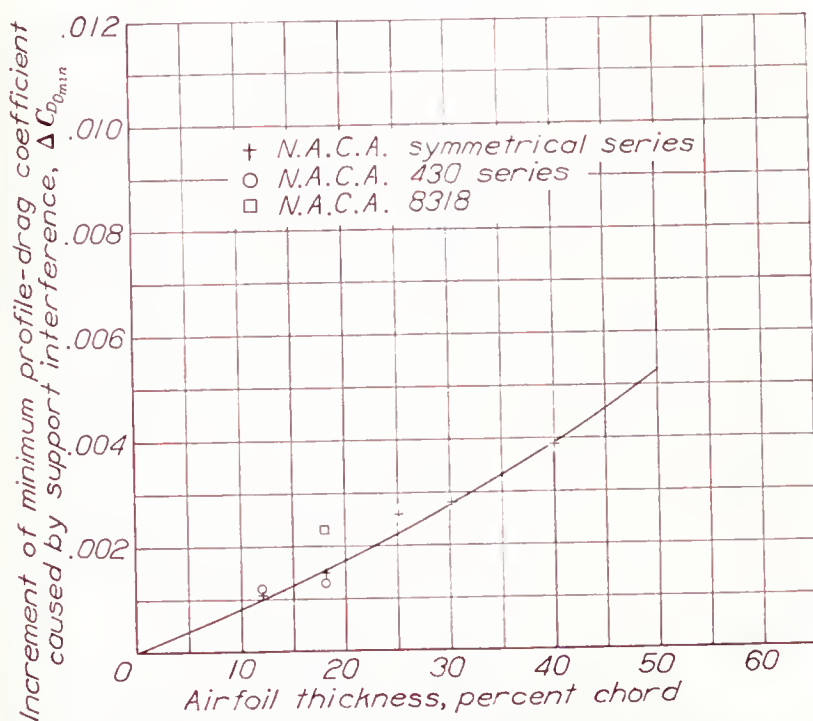


FIGURE 1.—Variation with airfoil thickness of the increment of minimum profile-drag coefficient caused by support interference for the N. A. C. A. variable-density tunnel.

used airfoils. The applicability of these values to data obtained at other values of the Reynolds Number is more doubtful, but such application appears to offer the best approximation possible at this time and, accordingly, will be made.

The corrected minimum profile-drag coefficients for the symmetrical airfoils from 9 to 25 percent thick are given in table I. The second column of this table gives the  $C_{D_0}$  values originally published in reference 2. The third column gives the  $c_{d_0}$  values taken from reference 5, except for the N. A. C. A. 0025. Some of these  $c_{d_0}$  values were obtained by correcting the  $C_{D_0}$  values for the drag increment (0.0011) to correct to the effective Reynolds Number and for the tip-drag increment (reference 4). The rest of the  $c_{d_0}$  values are from the results of more recent measurements similarly corrected. The fourth column gives the support-interference increments taken from the curve of figure 1. The finally corrected  $c_{d_0}$  values of the fifth column were obtained from the third column by correcting the data, according to the procedure suggested

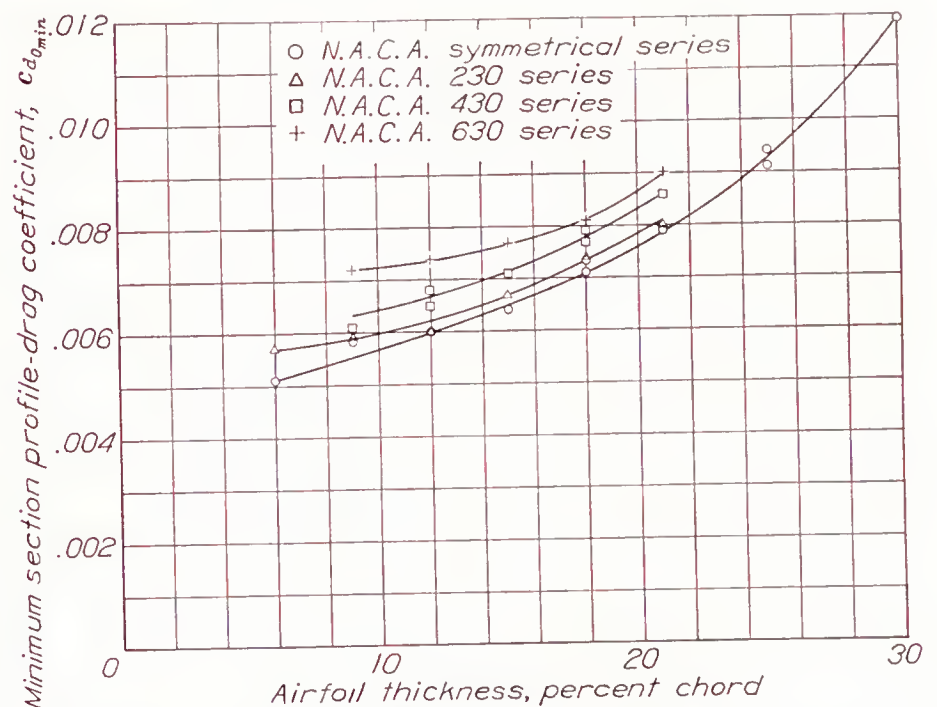


FIGURE 2.—Variation of minimum profile-drag coefficient with airfoil thickness. Effective Reynolds Number, 8,200,000.

The application of these corrections results in a greatly decreased variation of drag with airfoil thickness. This variation is shown for the N. A. C. A. symmetrical, 230, 430, and 630 series airfoils in figure 2, which may be considered a correction of figure 53 of reference 5. It is evident that the smaller increase in drag with section thickness will affect the choice of wing sections. The best simple criterion for the selection of wing sections being considered the speed-range index  $c_{l_{max}}/c_{d_{0min}}$ , figure 3 has been prepared from the corrected data of figure 2 to be used in connection with



figure 61 of reference 5 to study the effect of the correction on the thickness of the optimum section. The result of the comparison is shown in table II.

TABLE II  
EFFECT OF SUPPORT-INTERFERENCE CORRECTION  
ON OPTIMUM AIRFOIL THICKNESS

N. A. C. A. airfoils	Thickness of section for highest $c_{l_{max}}/c_{d_{0min}}$ (percent chord)	
	From reference 5	Corrected results (fig. 3)
Symmetrical series.....	11.5	12
230 series.....	9.5	10
430 series.....	10	10.5
230 series with 0.2c split flap.....	11	12.5

The change in optimum thickness is evidently small for airfoils without flaps. The losses associated with an airfoil that exceeds the optimum thickness, however,

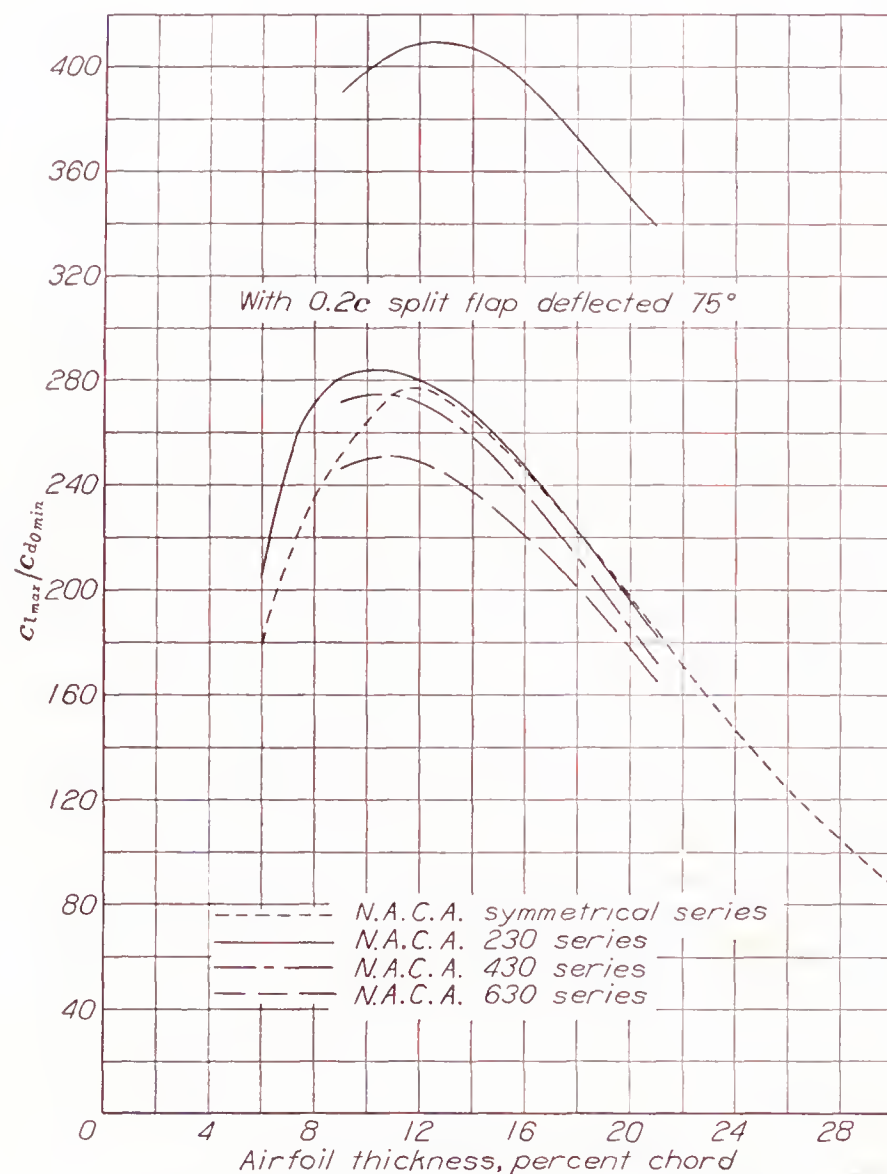


FIGURE 3.—Variation of  $c_{l_{max}}/c_{d_{0min}}$  with airfoil thickness.

become less marked so that a compromise airfoil will tend to be thicker by a greater amount than is indicated by table II. This conclusion is particularly significant when full advantage can be taken of the fact that the maximum-lift increment produced by a high-lift device may increase with section thickness. The upper curve

of figure 3 indicates that the optimum thickness for the 230 series may then increase to 12.5 or 13 percent and that the aerodynamic loss associated with thicker sections is considerably smaller than previously indicated.

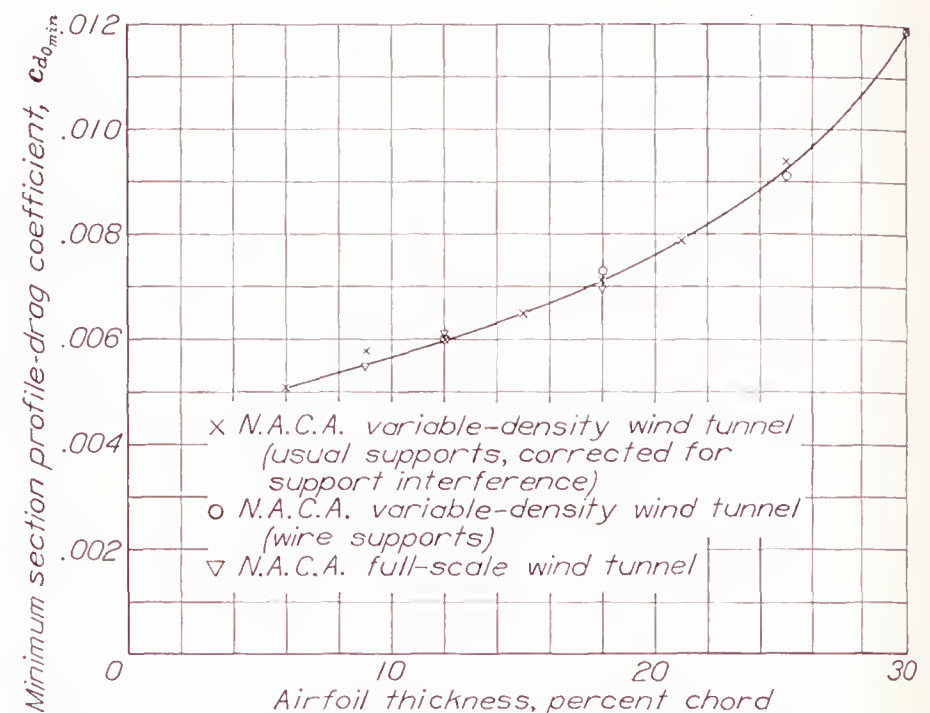


FIGURE 4.—Variation of minimum profile-drag coefficient with thickness for N. A. C. A. symmetrical airfoils. Effective Reynolds Number, 8,200,000.

Comparison of the corrected data from the variable-density tunnel with the available comparable data from other wind tunnels indicates a generally improved agreement. The close agreement obtained for the

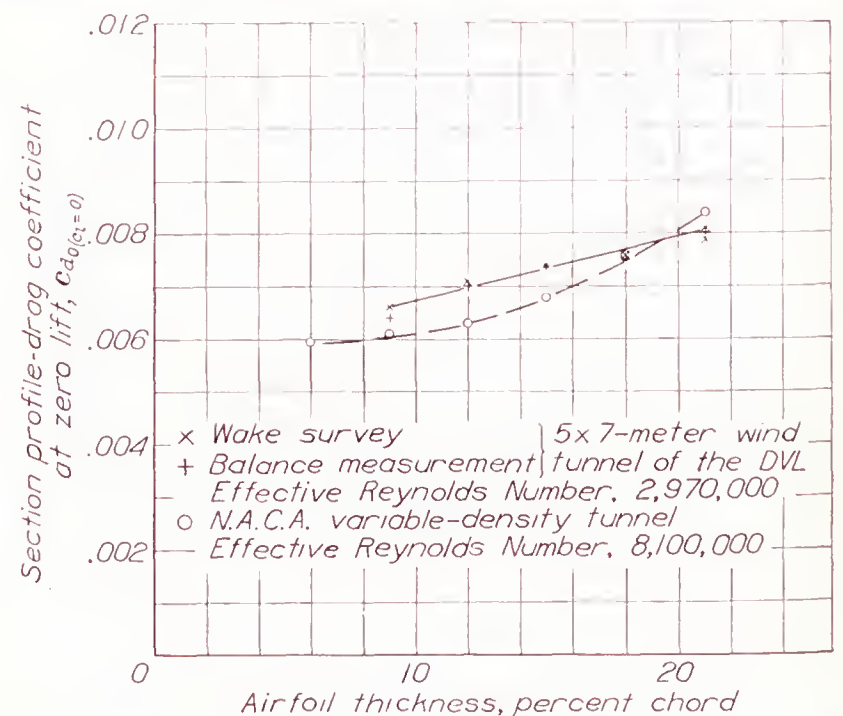


FIGURE 5.—Variation of profile-drag coefficient with thickness for N. A. C. A. 24 series airfoils.

N. A. C. A. 0009, 0012, and 0018 airfoils in the N. A. C. A. variable-density and full-scale tunnels (reference 14) is shown in figure 4.

Figure 5 shows a comparison between the profile-drag coefficients at zero lift for the N. A. C. A. 24 series airfoils as obtained in the variable-density tunnel and in the 5- by 7-meter tunnel of the DVL. The data were not obtained at the same value of the Reynolds Number, but the application of the correction to the



data from the variable-density tunnel has reduced the discrepancies.

Comparisons of minimum profile drag are made for the N. A. C. A. symmetrical series airfoils in figures 6 to 9; comparisons of profile-drag coefficients at zero lift are made for the N. A. C. A. 24 series airfoils in figure 10. In all cases, the data have been corrected to the proper effective Reynolds Number and for tip effects when necessary to make these data comparable with those from the variable-density tunnel. The agreement of the data for the N. A. C. A. 0009, 0012, and

0025 airfoil (fig. 9) is satisfactory. In the case of the N. A. C. A. 24 series airfoils (fig. 10), the chief discrepancy between the data from the variable-density tunnel and those from the 5- by 7-meter tunnel of the DVL (reference 11) is that the data from the DVL tunnel show a smaller rate of drag decrease with increasing Reynolds Number.

These discrepancies in the rate of decrease of the drag with increasing Reynolds Numbers as shown for the N. A. C. A. 0012 airfoil in figure 7 and for the N. A. C. A. 24 series airfoils in figure 10 are particularly important because, for large airplanes, the drag data must be extrapolated. The differences in the data are such as to cast some doubt on the applicability of the recommended extrapolation formula (reference 4), although no better formula can be suggested at this time. The need for additional data obtained at large Reynolds Numbers in tunnels of low turbulence is obvious.

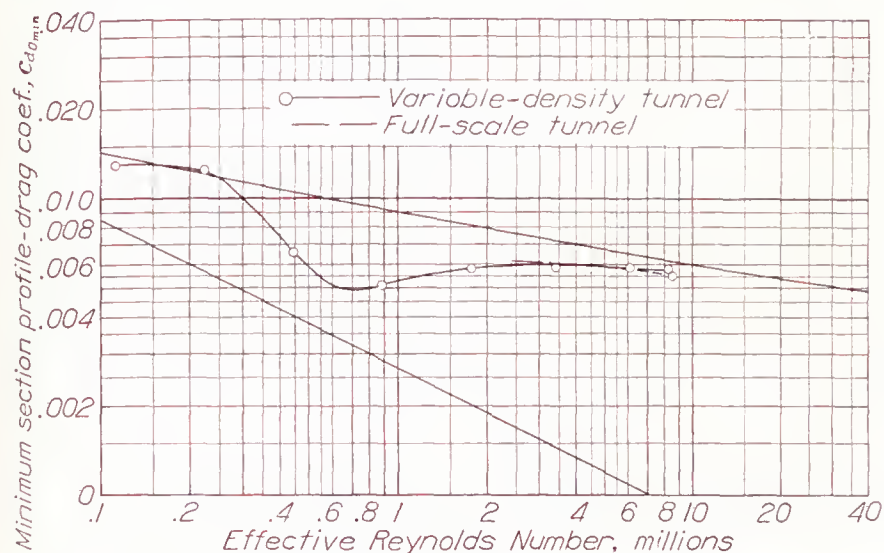


FIGURE 6.—Minimum profile-drag coefficients of N. A. C. A. 0009 airfoil as measured in the N. A. C. A. variable-density and full-scale tunnels.

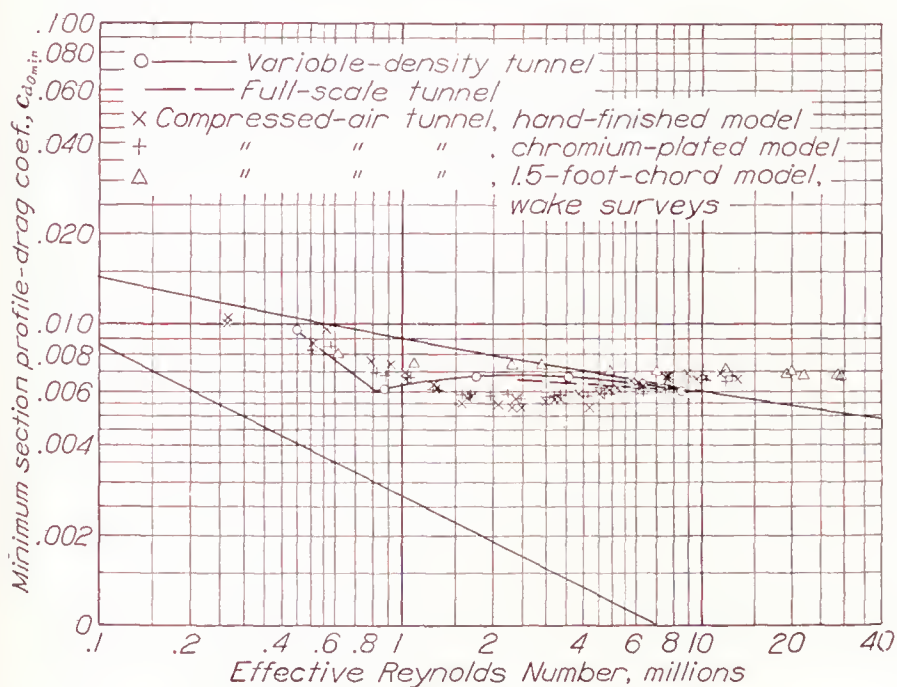


FIGURE 7.—Minimum profile-drag coefficients of the N. A. C. A. 0012 airfoil as measured in several wind tunnels.

0018 airfoils as obtained in the variable-density and the full-scale tunnels is seen to be generally satisfactory. The agreement of the data for the N. A. C. A. 0012 airfoil (fig. 7) as obtained in the variable-density tunnel and in the British compressed-air tunnel (references 12 and 13) cannot be considered satisfactory. In particular, the results from the compressed-air tunnel do not indicate a decrease of the minimum profile-drag coefficient with increasing Reynolds Numbers at the higher Reynolds Numbers. The agreement of the data obtained in the variable-density and the compressed-air tunnels (reference 12) for the N. A. C. A.

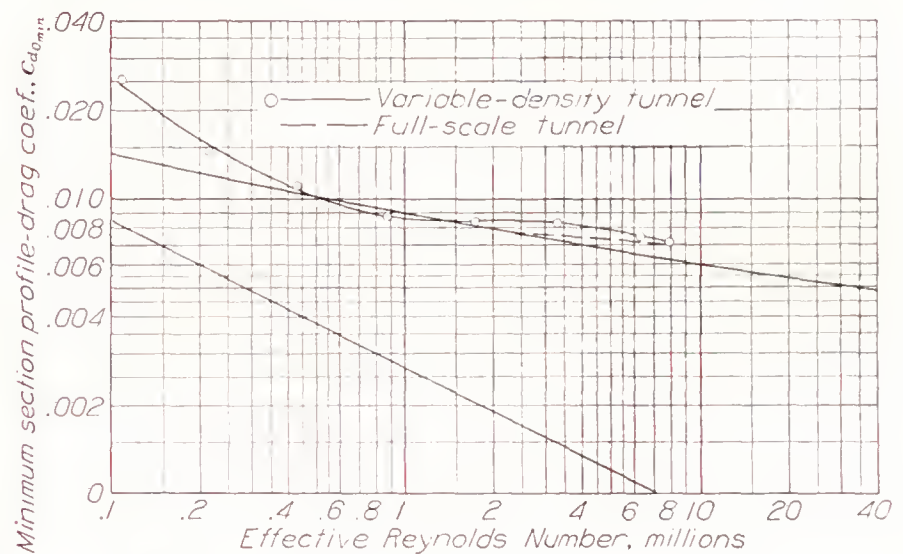


FIGURE 8.—Minimum profile-drag coefficients of the N. A. C. A. 0018 airfoil as measured in the N. A. C. A. variable-density and full-scale tunnels.

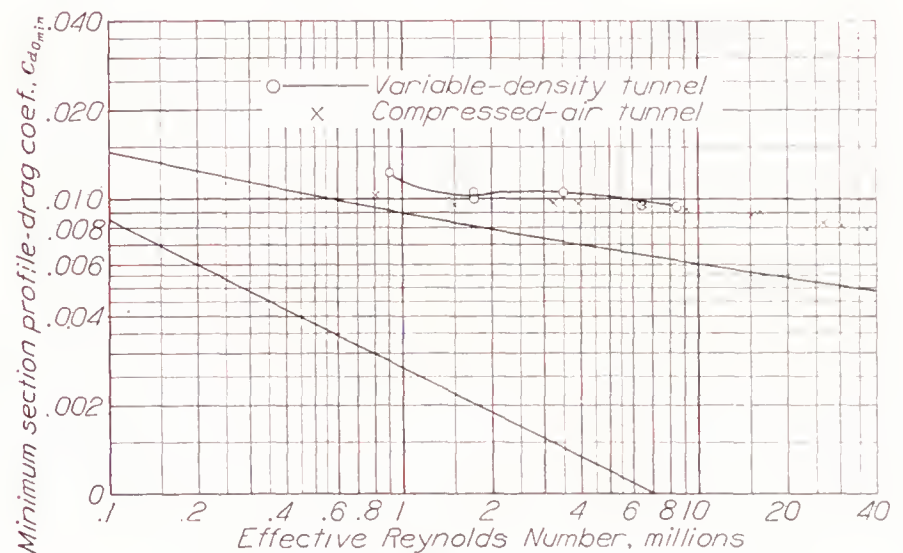


FIGURE 9.—Minimum profile-drag coefficients of the N. A. C. A. 0025 airfoil as measured in the N. A. C. A. variable-density tunnel and in the British compressed-air tunnel.

#### VARIATION OF SECTION PROFILE-DRAG COEFFICIENT WITH LIFT COEFFICIENT

Curves of section profile-drag coefficient plotted against section lift coefficient with the model mounted on the wire supports and on the usual supports are presented in figures 11 to 17 for seven of the airfoils tested. The data obtained with the models on the



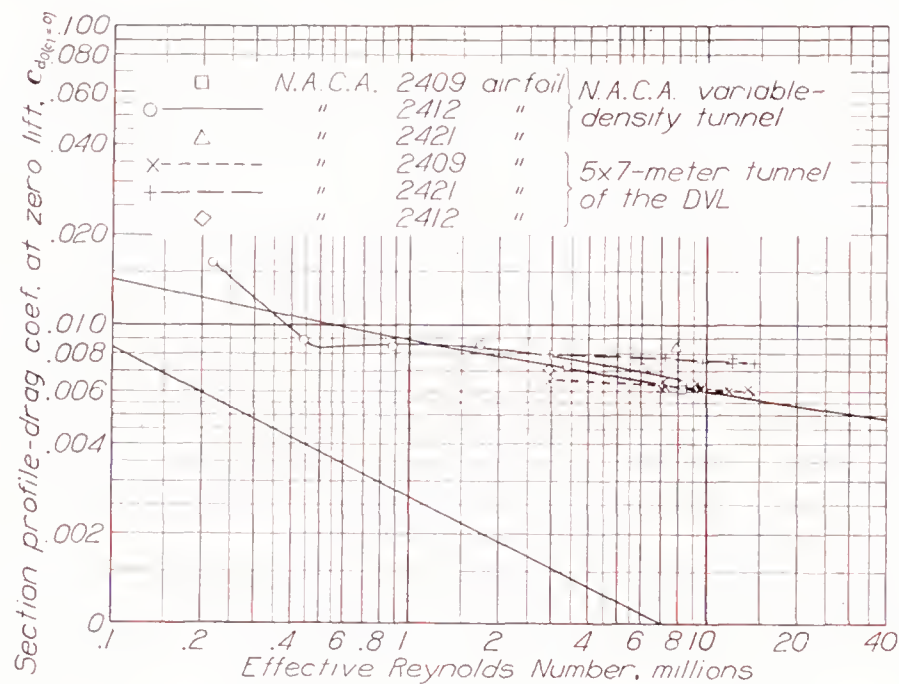


FIGURE 10.—Profile-drag coefficient of N. A. C. A. 24 series airfoils as measured at zero lift in the N. A. C. A. variable-density tunnel and in the 5- by 7-meter tunnel of the DVL.

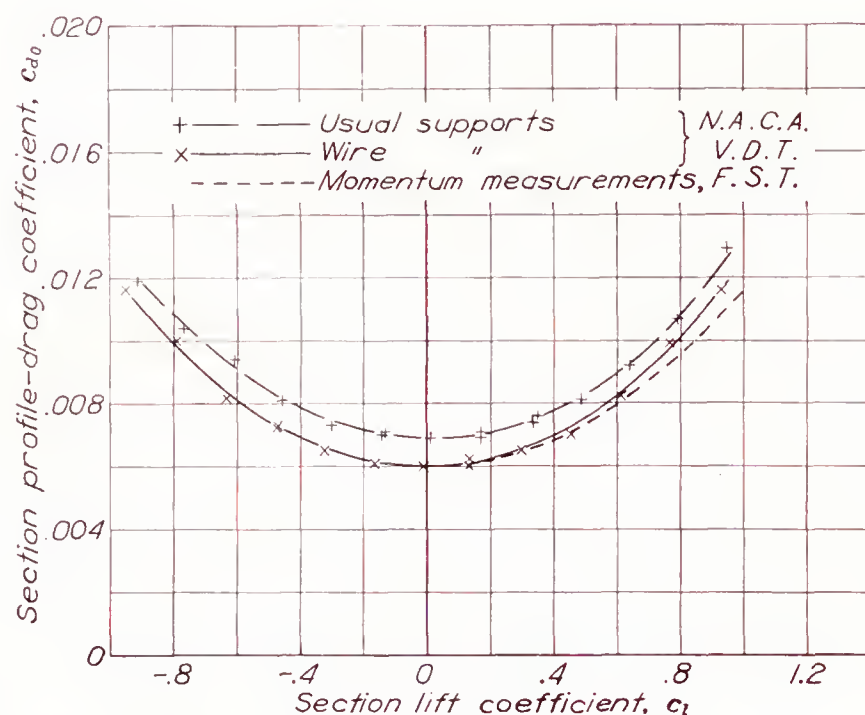


FIGURE 11.—Variation of profile-drag coefficient with lift coefficient. N. A. C. A. 0012 airfoil. Effective Reynolds Number, 8,200,000.

wire supports include all corrections and represent the best available approximation to the actual airfoil section characteristics. The two curves of each figure are comparable except for the presence of support interference in the data obtained with the model on the usual supports. The displacement between the two curves of each figure thus represents the support interference.

The data of figures 11 through 17 show a tendency for the support interference to decrease with increasing lift coefficients, this tendency being more marked for the cambered than for the symmetrical airfoils. This variation, however, is not consistent. The determination of the profile-drag coefficient at other than small lift coefficients from the support-interference tests was complicated by the fact that the air-stream direction at the airfoil was apparently dependent upon the support system used, necessitating the determination of the balance and the air-stream alinement from the tests of the

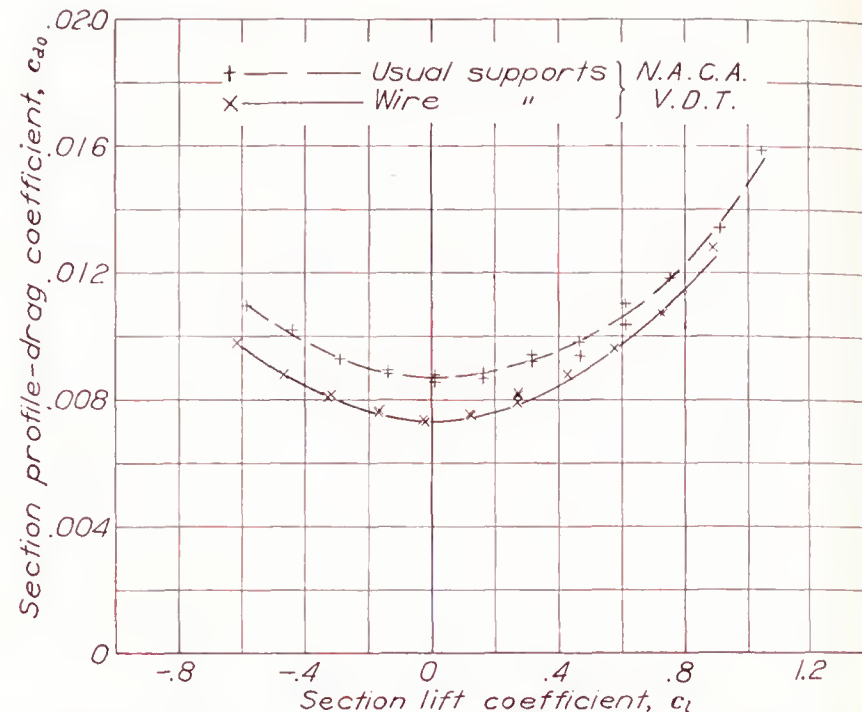


FIGURE 12.—Variation of profile-drag coefficient with lift coefficient. N. A. C. A. 0018 airfoil. Effective Reynolds Number, 8,200,000.

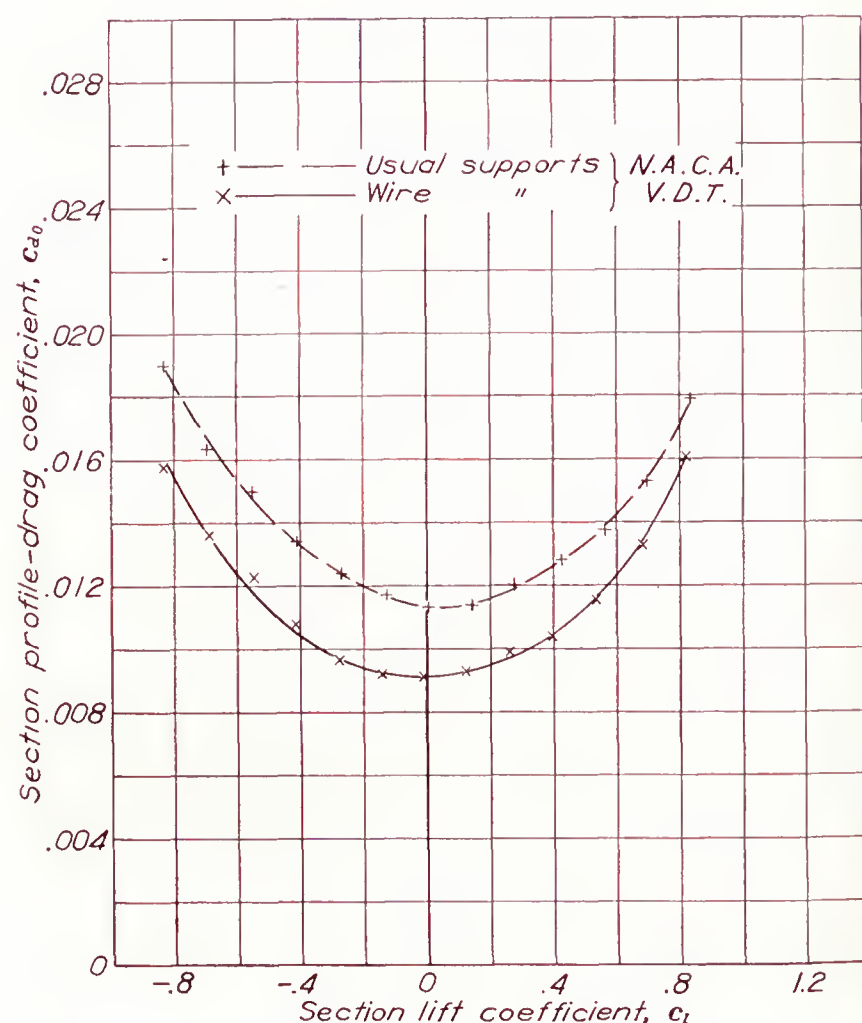


FIGURE 13.—Variation of profile-drag coefficient with lift coefficient. N. A. C. A. 0025 airfoil. Effective Reynolds Number, 8,200,000.

symmetrical airfoils. The data obtained were thought not to justify the application of a varying correction to the profile drag, and it was decided to apply the support-interference correction for the minimum profile-drag coefficient to all measured profile-drag coefficients.

The effect of applying this constant correction may be to indicate an optimum lift coefficient that is somewhat too high and to reduce the profile-drag coefficients at high positive lift coefficients more than is generally justified by these tests. Moreover, the effect of applying a proportional correction instead of a constant increment to the profile-drag coefficients to correct them



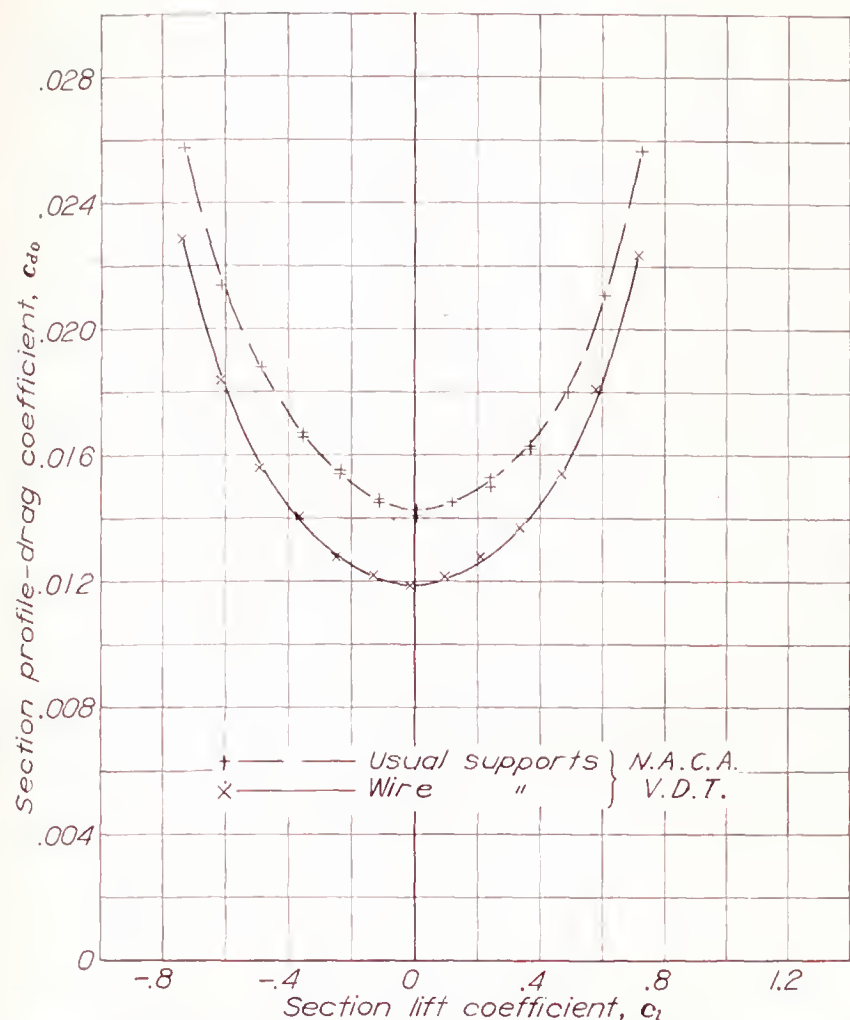


FIGURE 14.—Variation of profile-drag coefficient with lift coefficient. N. A. C. A. 0030 airfoil. Effective Reynolds Number, 8,200,000.

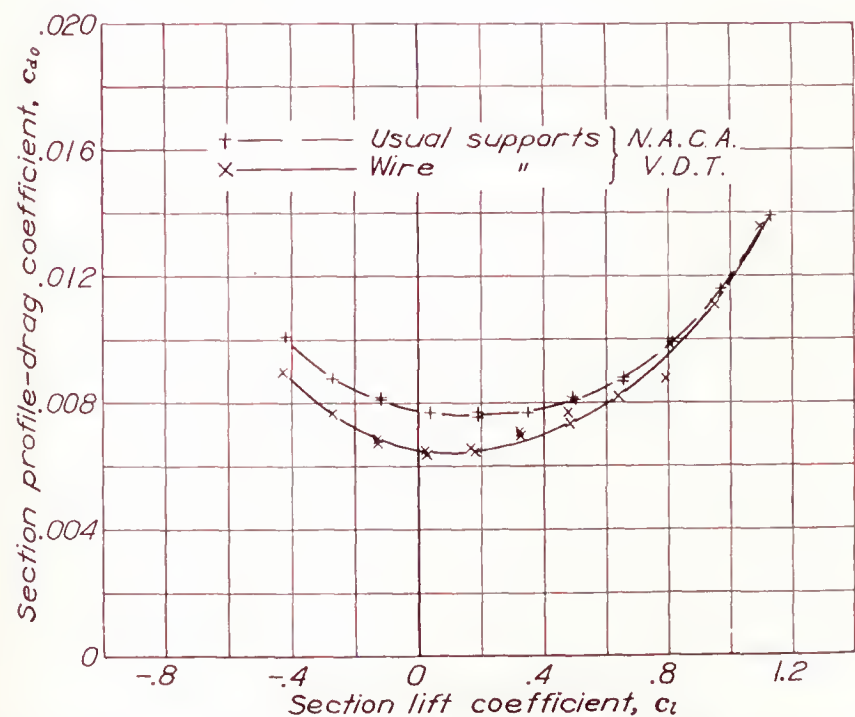


FIGURE 15.—Variation of profile-drag coefficient with lift coefficient. N. A. C. A. 43012 airfoil. Effective Reynolds Number, 8,200,000.

to the effective Reynolds Number is to reduce still further the profile-drag coefficients at large lift coefficients. Figure 11 shows a curve of profile-drag coefficients for the N. A. C. A. 0012 airfoil as obtained from wake surveys in the full-scale tunnel (reference 15) and

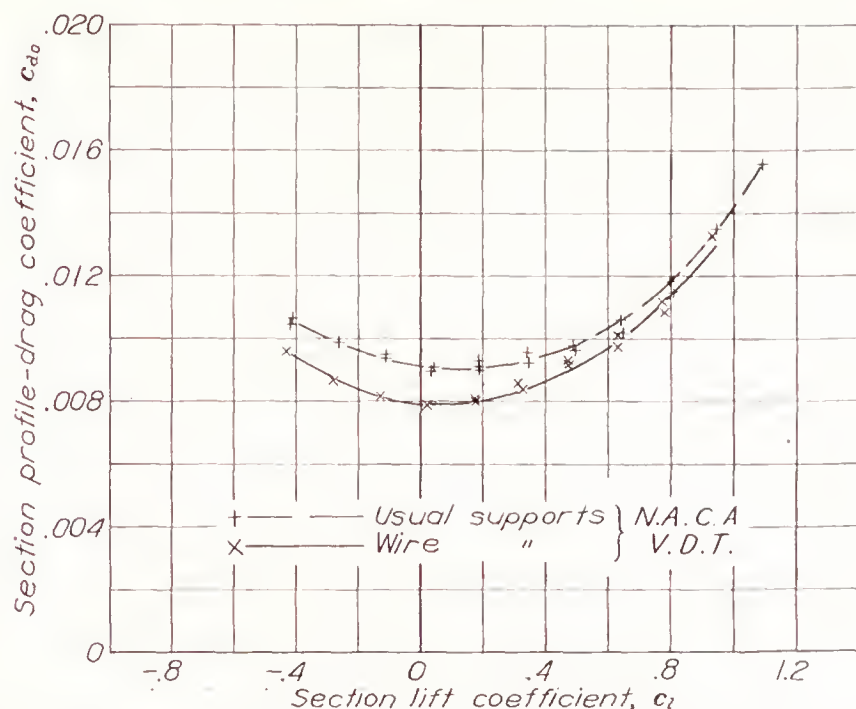


FIGURE 16.—Variation of profile-drag coefficient with lift coefficient. N. A. C. A. 43018 airfoil. Effective Reynolds Number, 8,200,000.

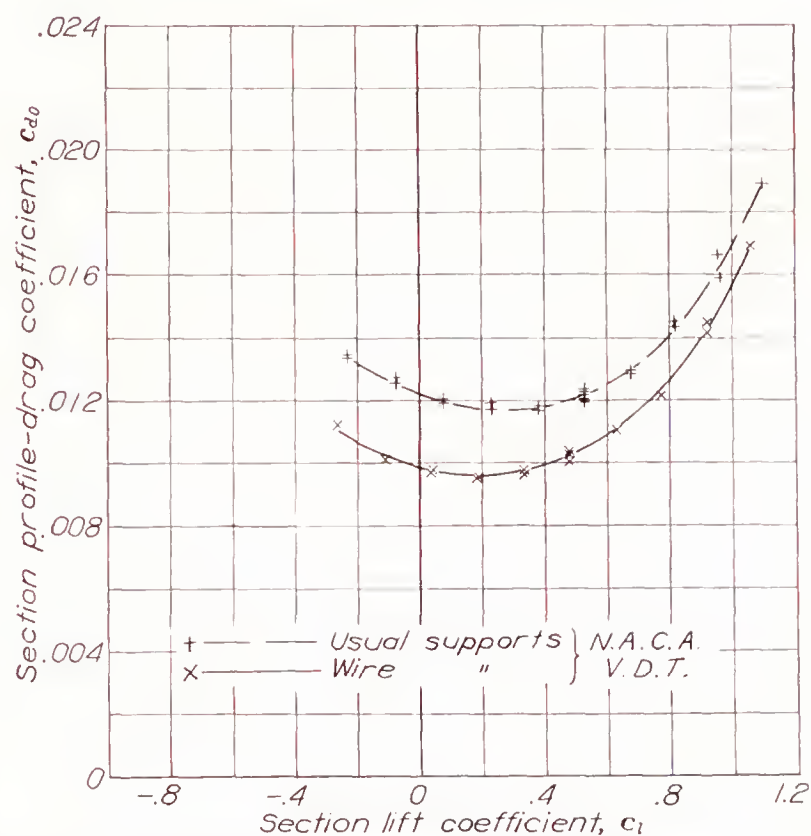


FIGURE 17.—Variation of profile-drag coefficient with lift coefficient. N. A. C. A. 8318 airfoil. Effective Reynolds Number, 8,200,000.

corrected to the effective Reynolds Number to be comparable with the variable-density-tunnel data. It will be seen that the profile-drag coefficients as obtained in the full-scale tunnel at the higher lift coefficients are lower than those obtained in the variable-density tunnel, indicating that the application of a constant support-interference correction probably does not result in too low profile-drag coefficients at moderate lift coefficients.



## DATA FOR COMMONLY USED AIRFOILS

As a convenience to designers, corrected data for a number of commonly used airfoils are presented in figures 18 to 59 and in table III. The left-hand side of each figure presents the data for rectangular airfoils corrected to an aspect ratio of 6 in free air but uncorrected for turbulence effects. The right-hand side of each figure presents the best approximation to the section characteristics, which are corrected as summarized in the appendix. These data supersede previous data published for these airfoils and are recommended for design use until more reliable data are available.

## CONCLUDING REMARKS

An investigation of the effect of support interference on airfoil drag data from the N. A. C. A. variable-density tunnel showed the presence in these data of large support-interference increments, increasing with

airfoil thickness. The effects of these increments were to make airfoil drag data from the variable-density tunnel appear high and to show too large a rate of drag increase with airfoil thickness. These increments have been evaluated and the corrected data are recommended for immediate use. A large amount of recent data, however, has suggested that these, or other corrections, to airfoil data obtained in the variable-density tunnel will not produce ultimately satisfactory results. It is planned, therefore, to obtain further airfoil section data under test conditions more favorable than those in the variable-density tunnel.

LANGLEY MEMORIAL AERONAUTICAL LABORATORY,  
NATIONAL ADVISORY COMMITTEE FOR AERONAUTICS,  
LANGLEY FIELD, VA., *February 13, 1939.*



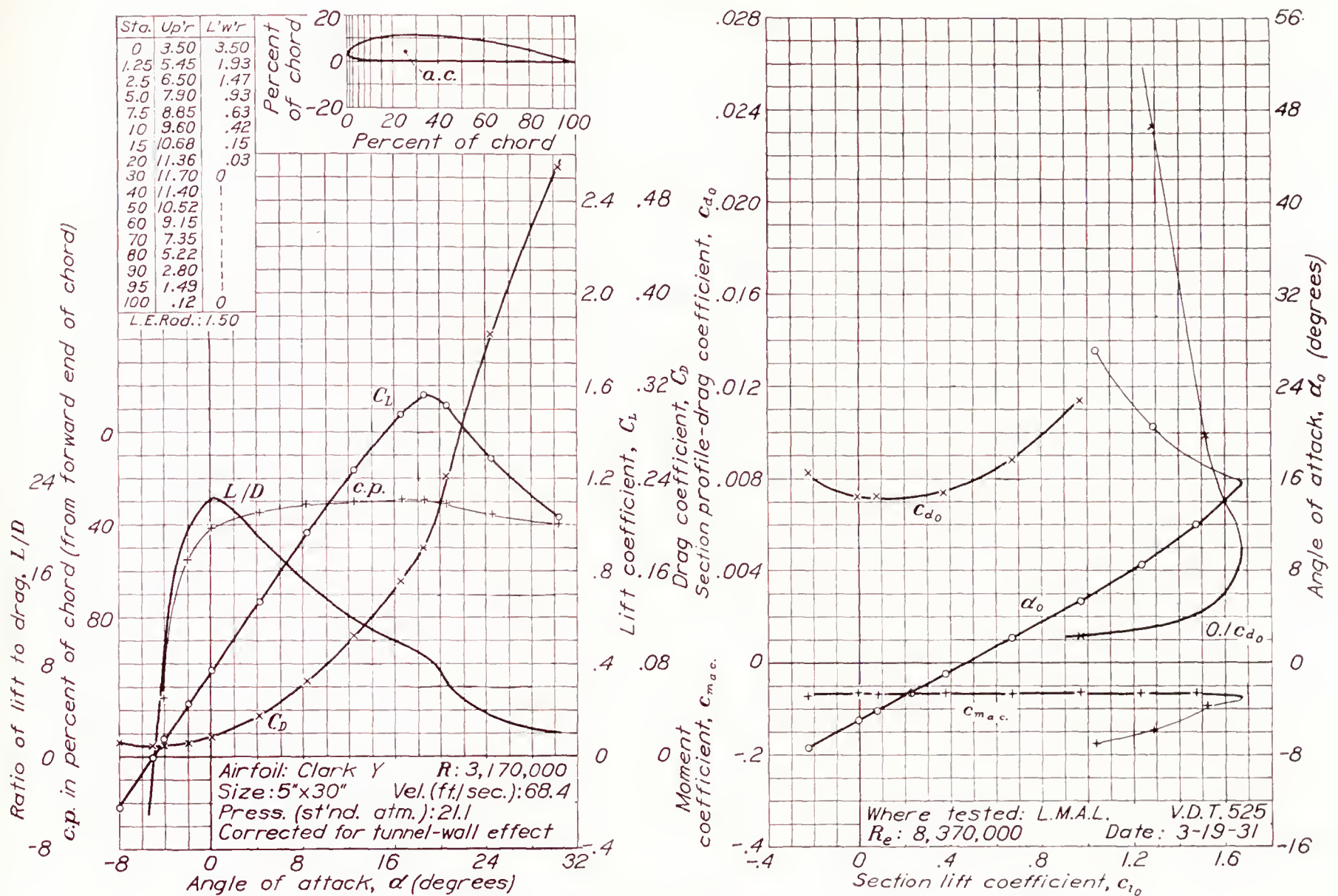


FIGURE 18.—Clark Y airfoil.

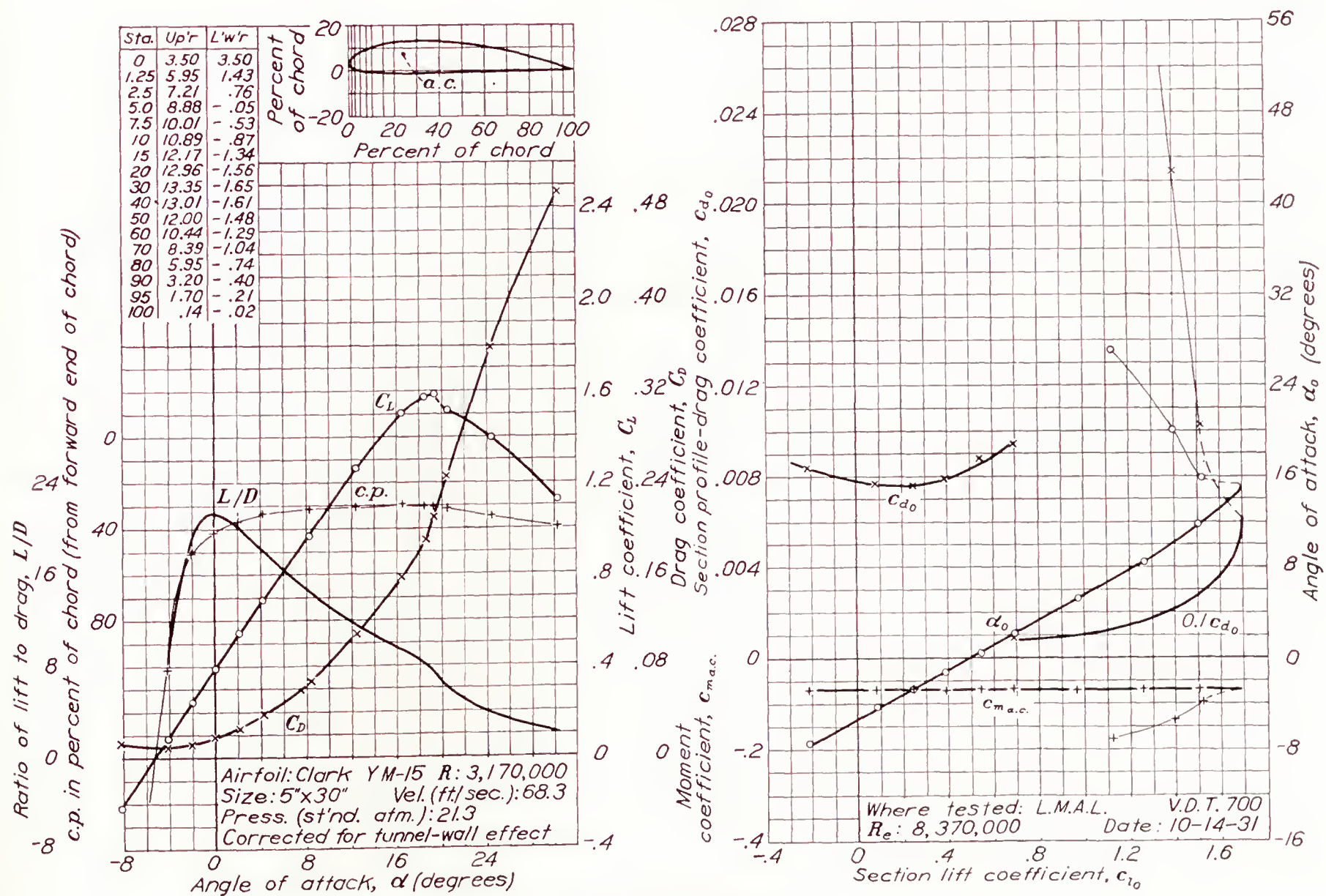


FIGURE 19.—Clark YM-15 airfoil.



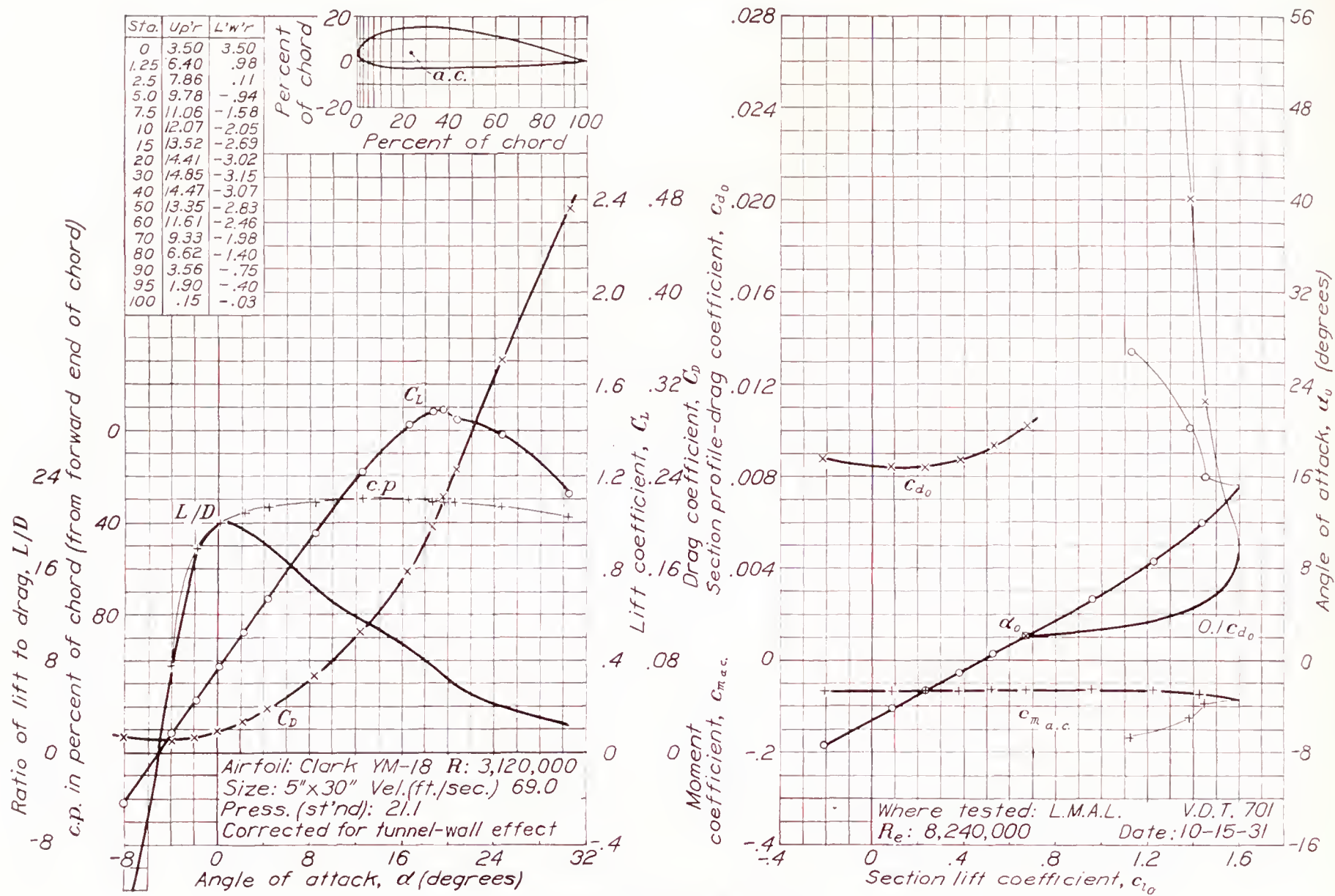


FIGURE 20.—Clark YM-18 airfoil.

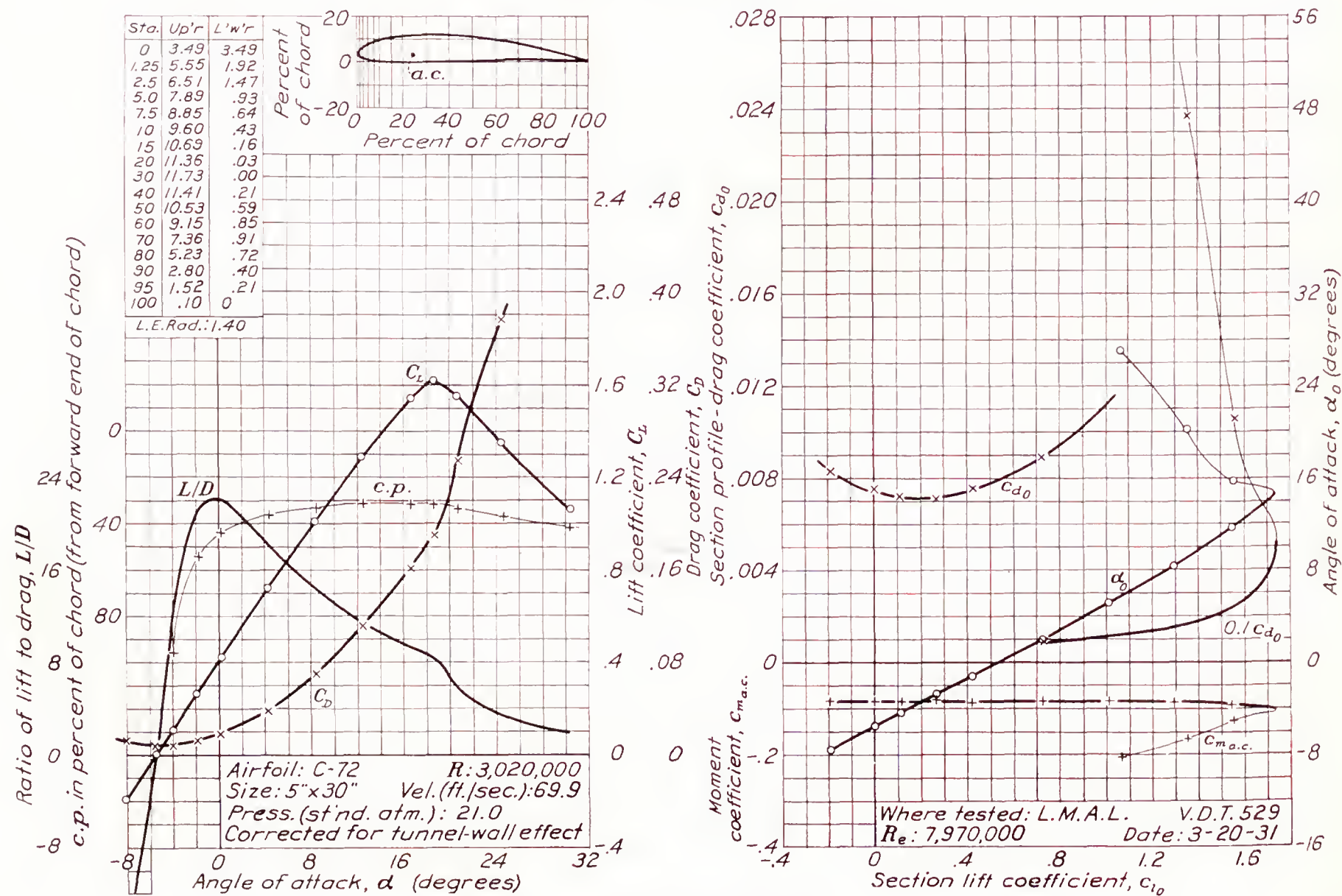


FIGURE 21.—Curtiss C-72 airfoil.



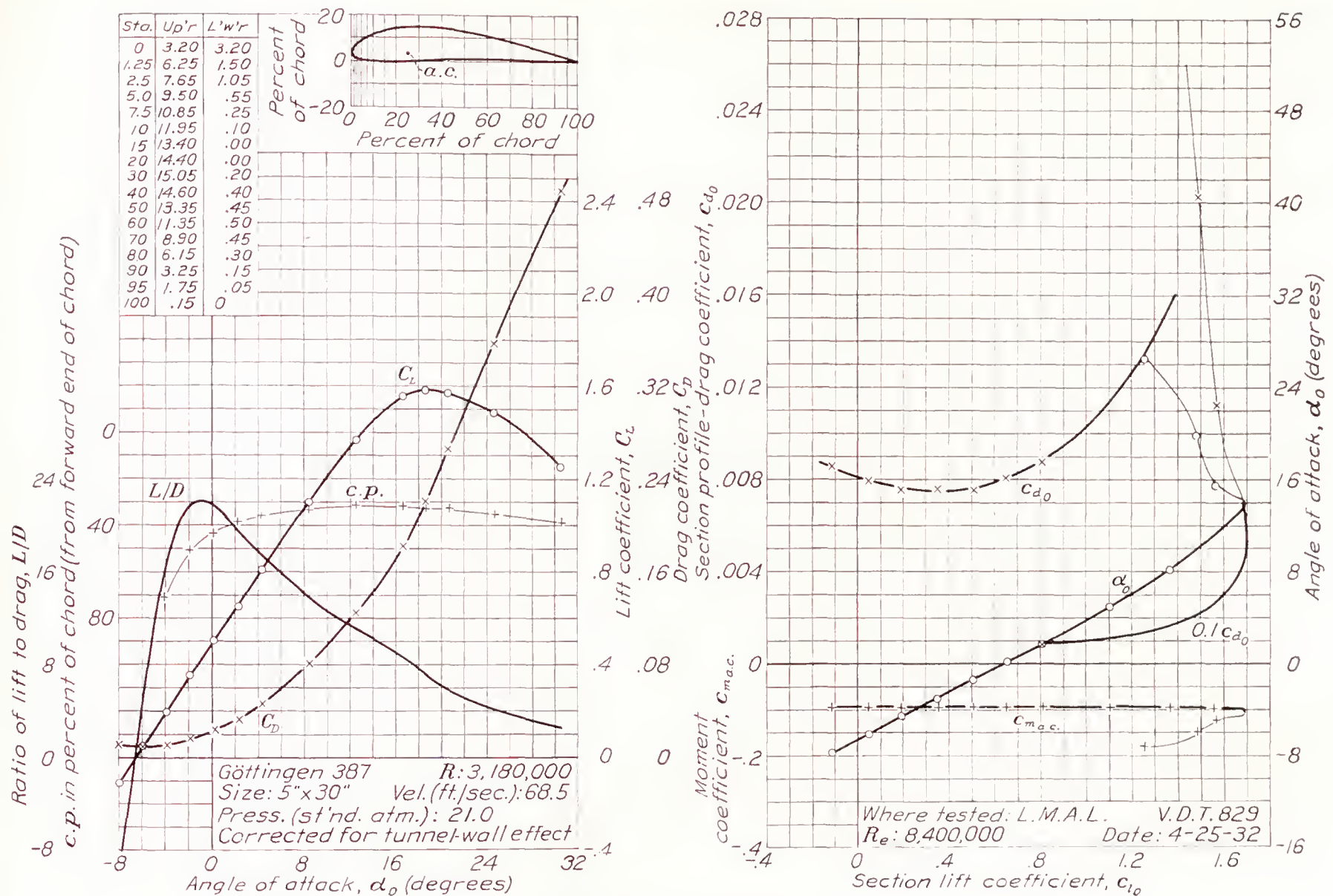


FIGURE 22.—Göttingen 387 airfoil.

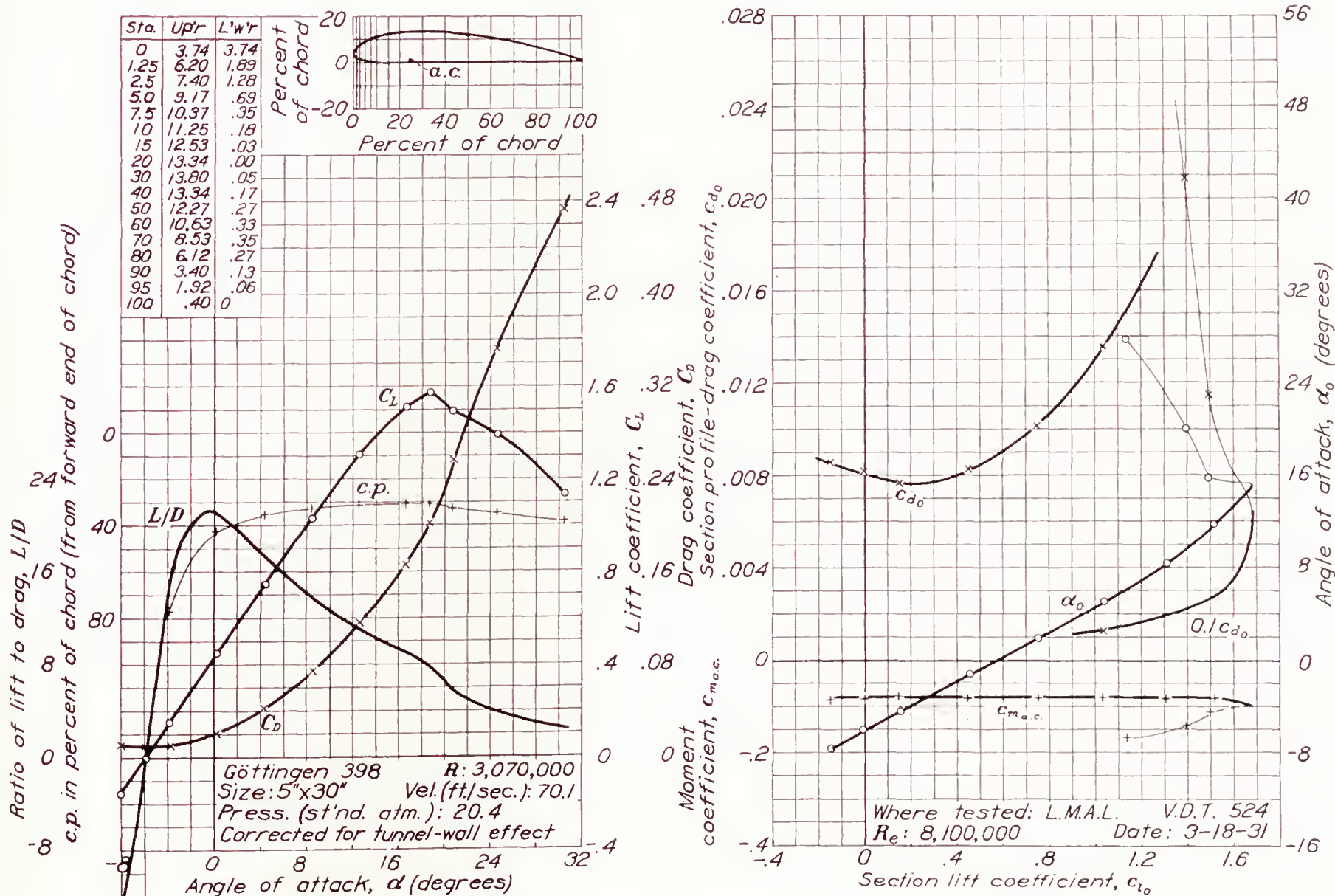


FIGURE 23.—Göttingen 398 airfoil.



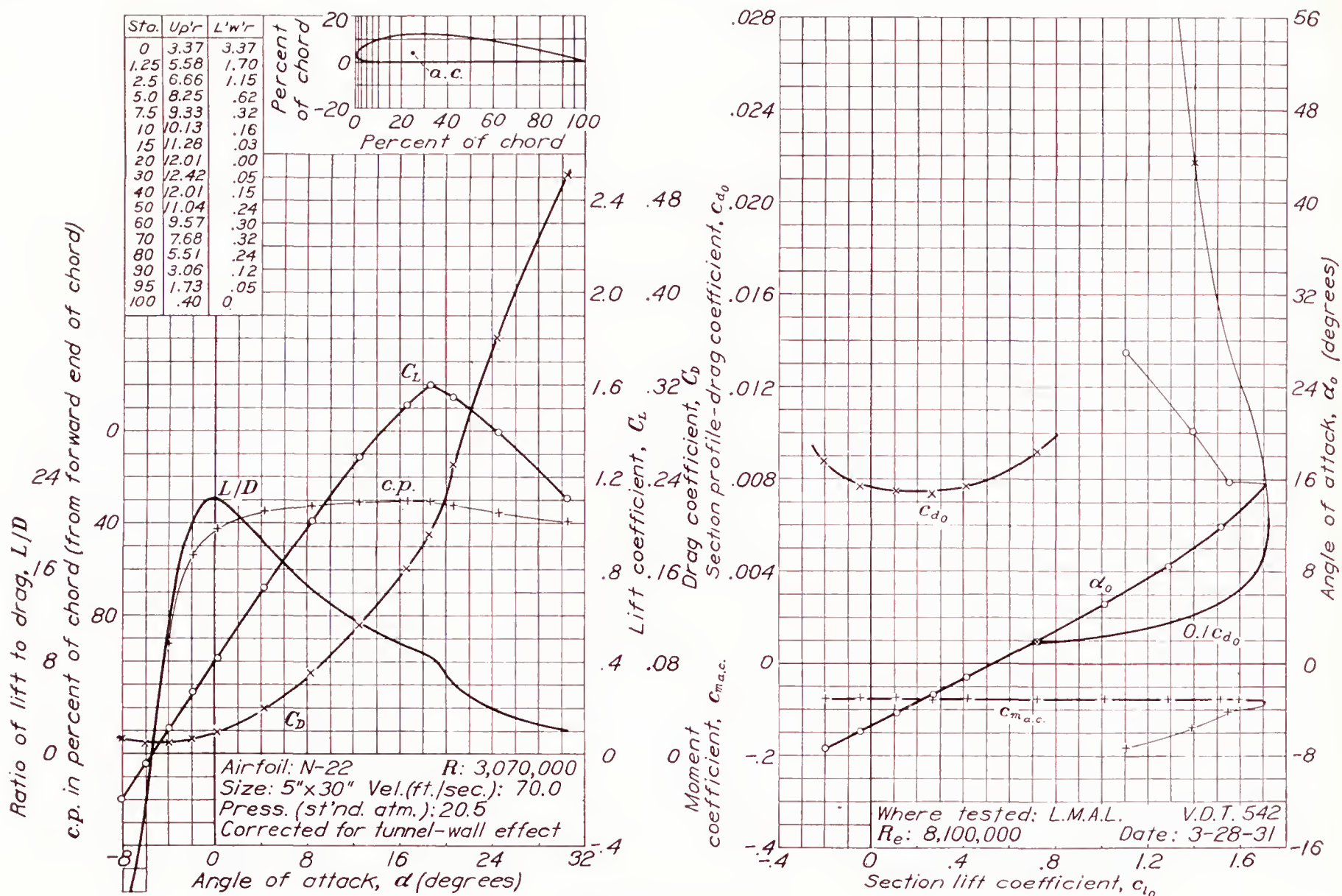


FIGURE 24.—N-22 airfoil.

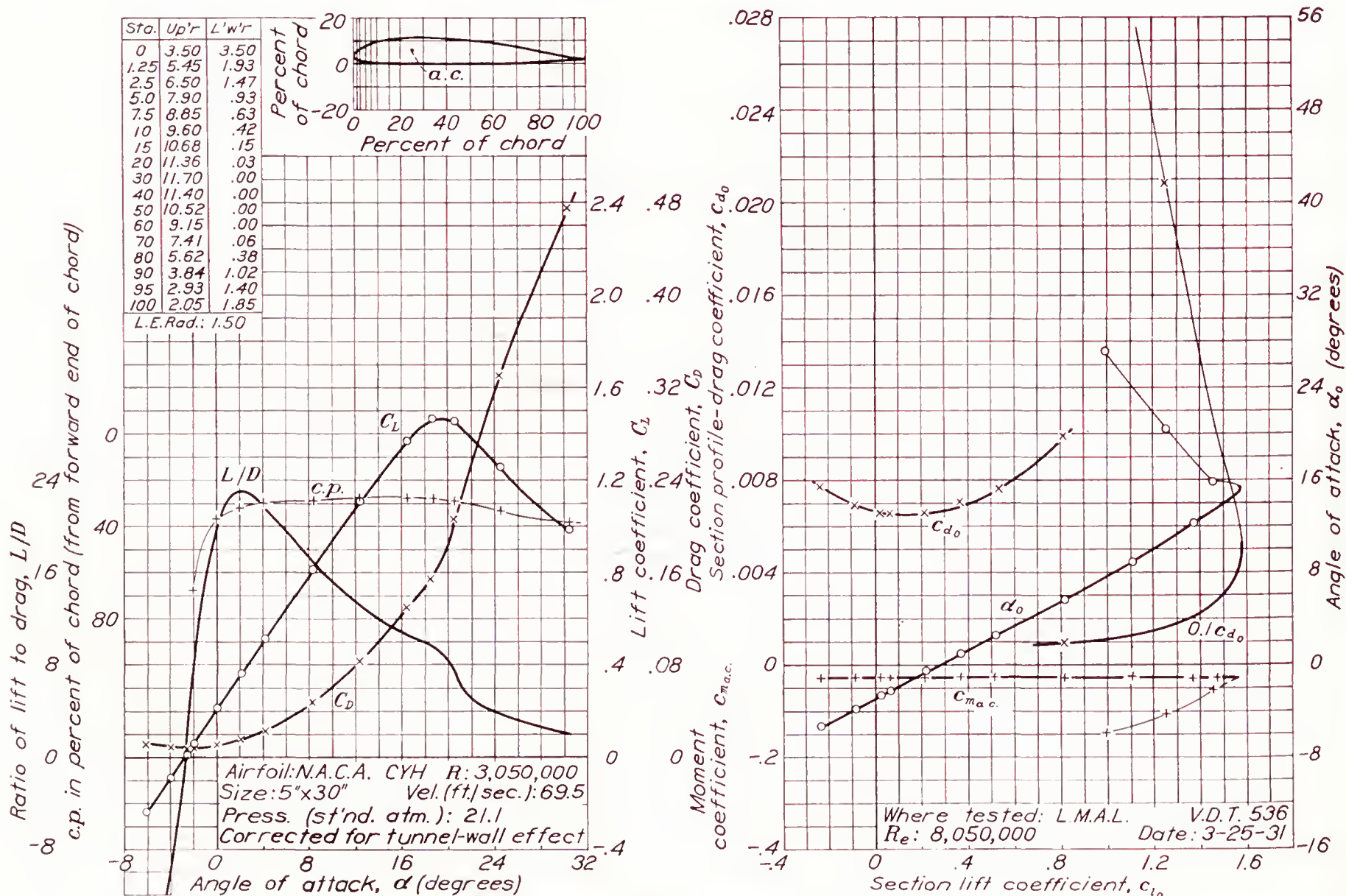


FIGURE 25.—N. A. C. A. CYH airfoil.



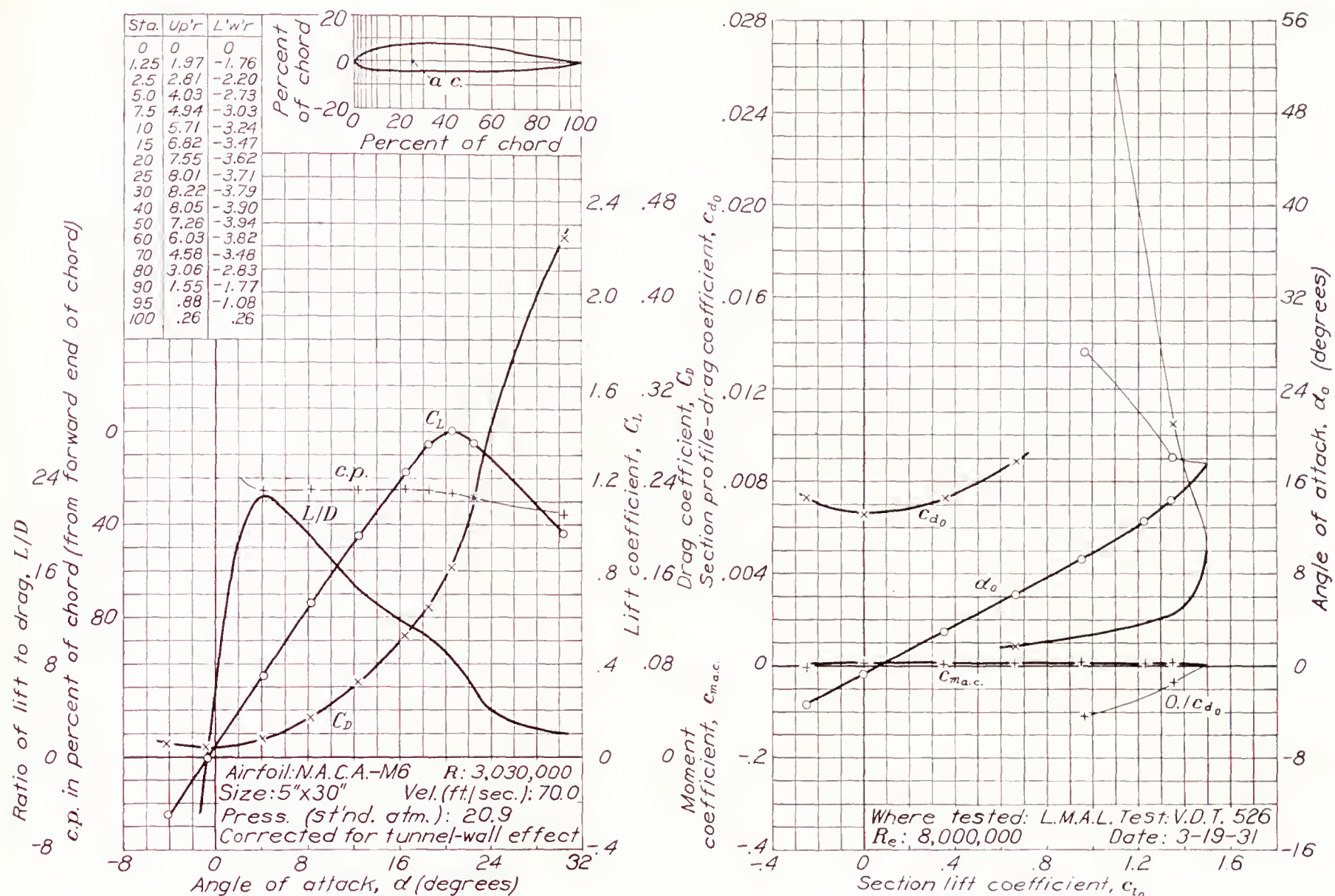


FIGURE 26.—N. A. C. A.-M6 airfoil.

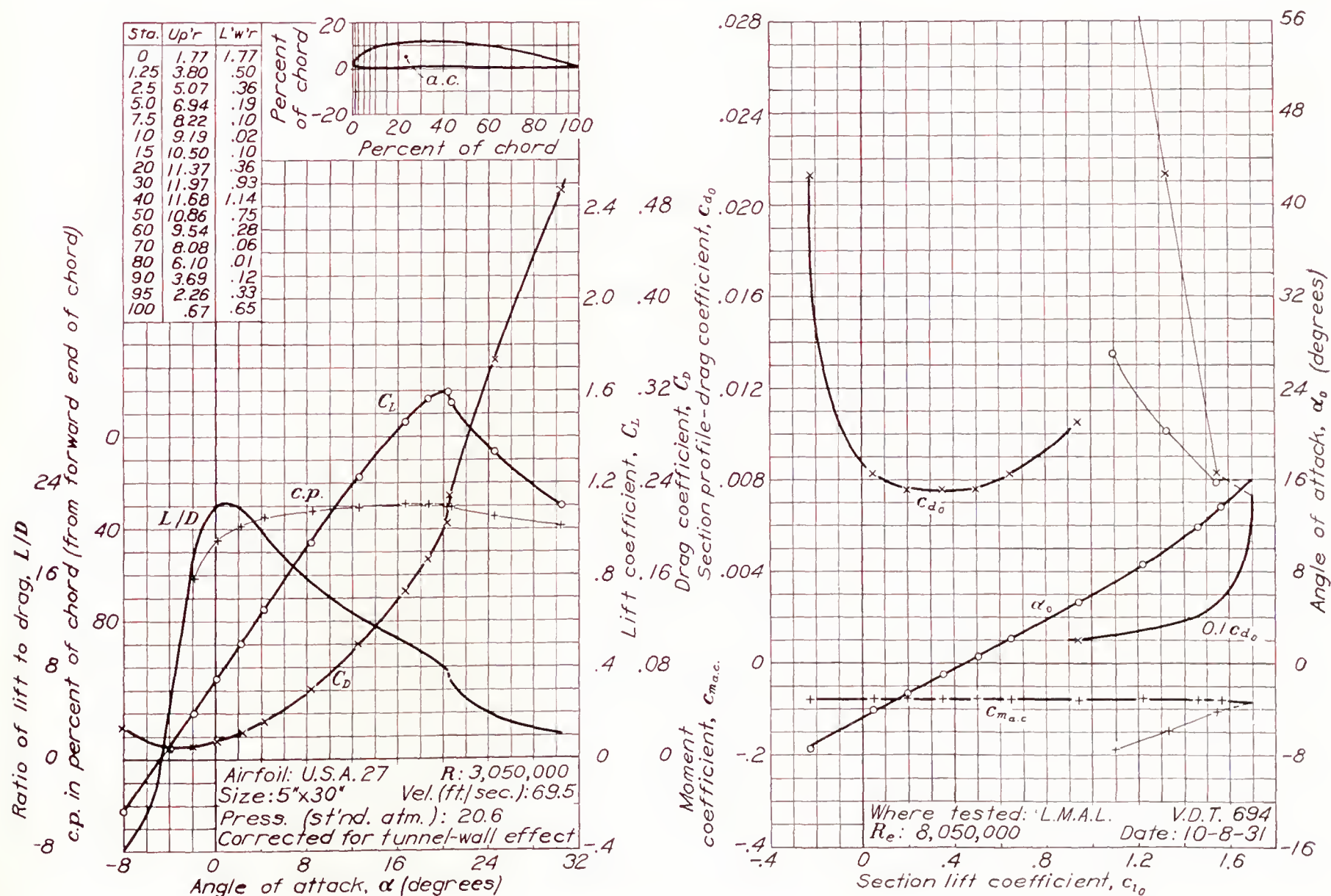


FIGURE 27.—U. S. A. 27 airfoil.



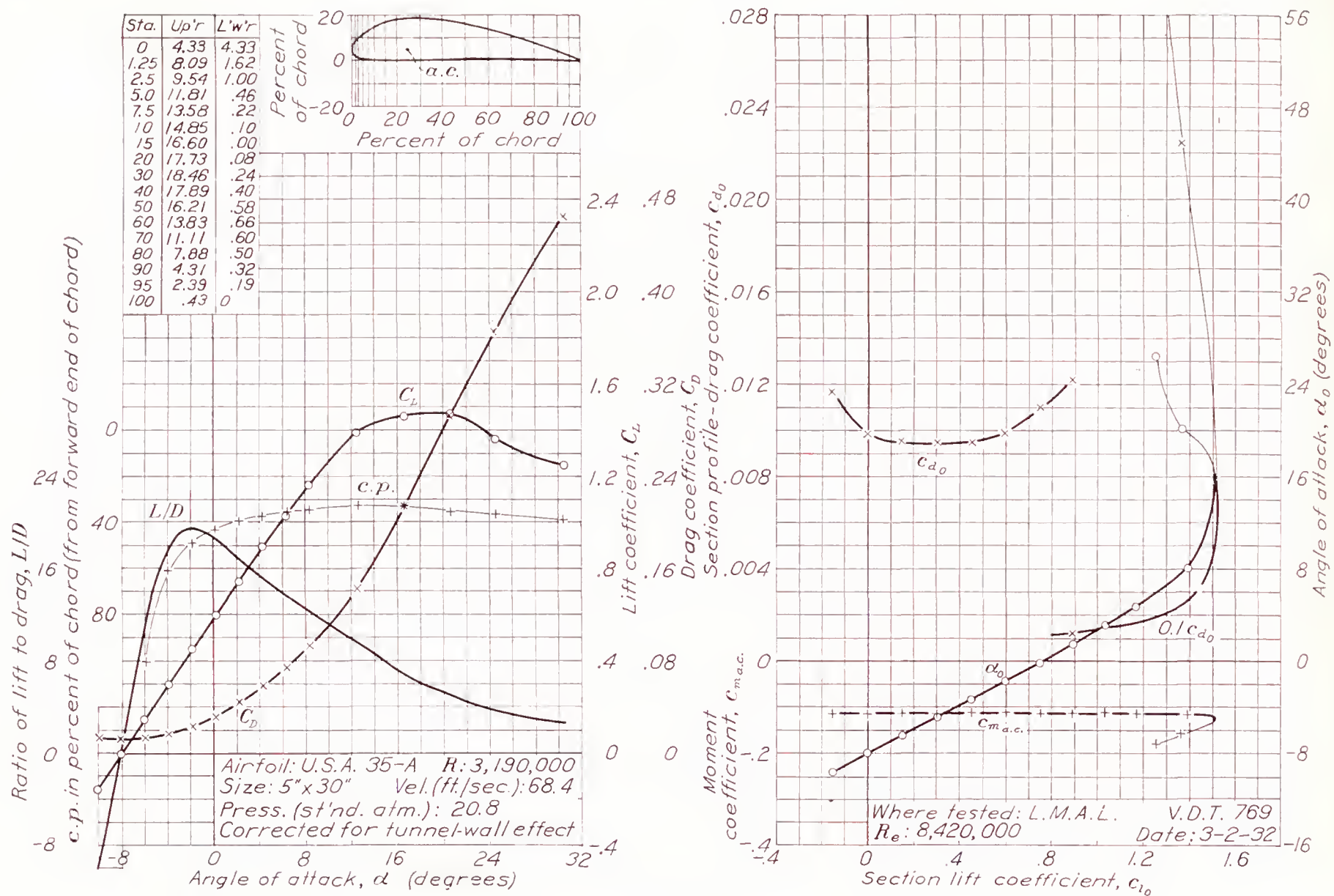


FIGURE 28.—U. S. A. 35-A airfoil.

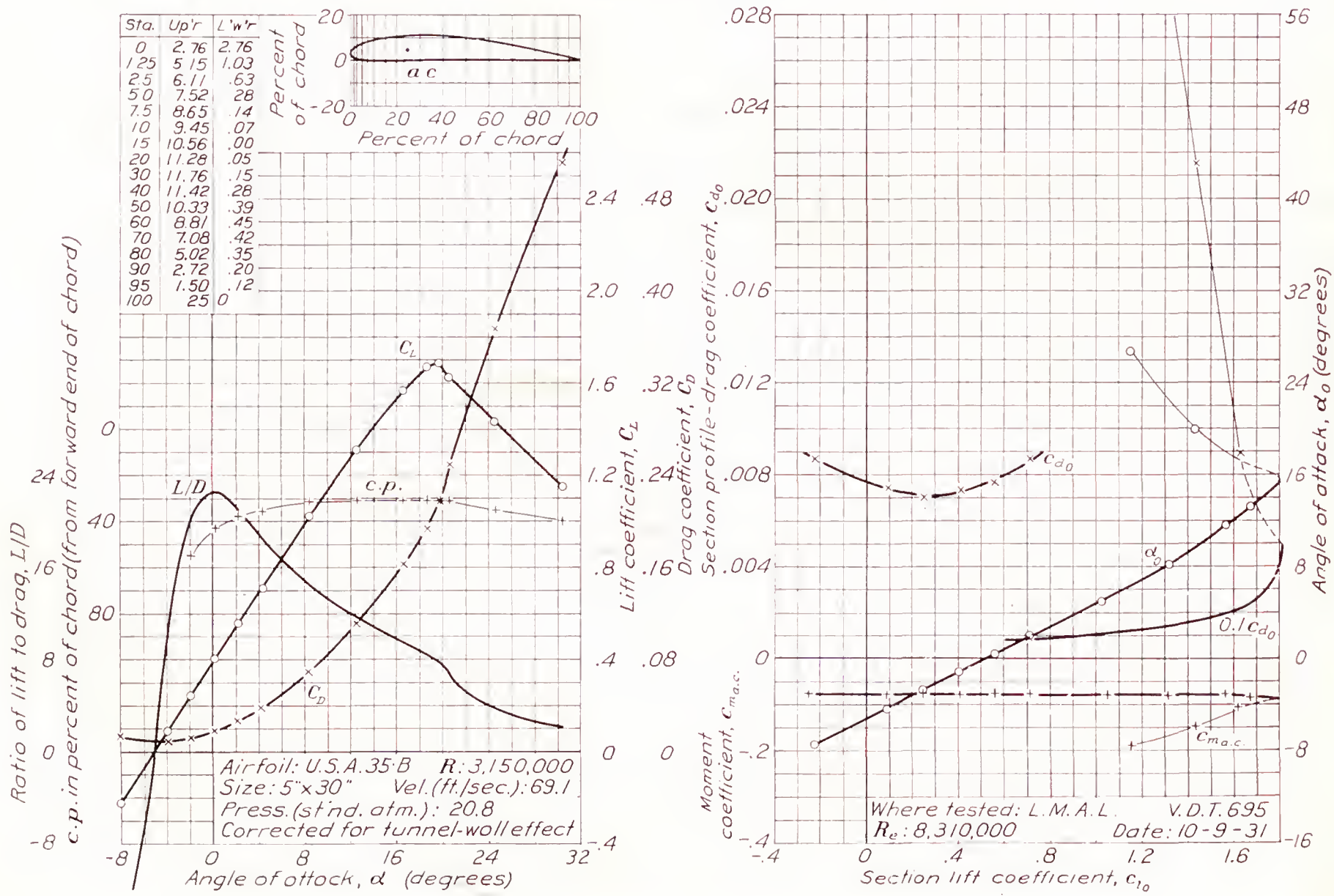


FIGURE 29.—U. S. A. 35-B airfoil.



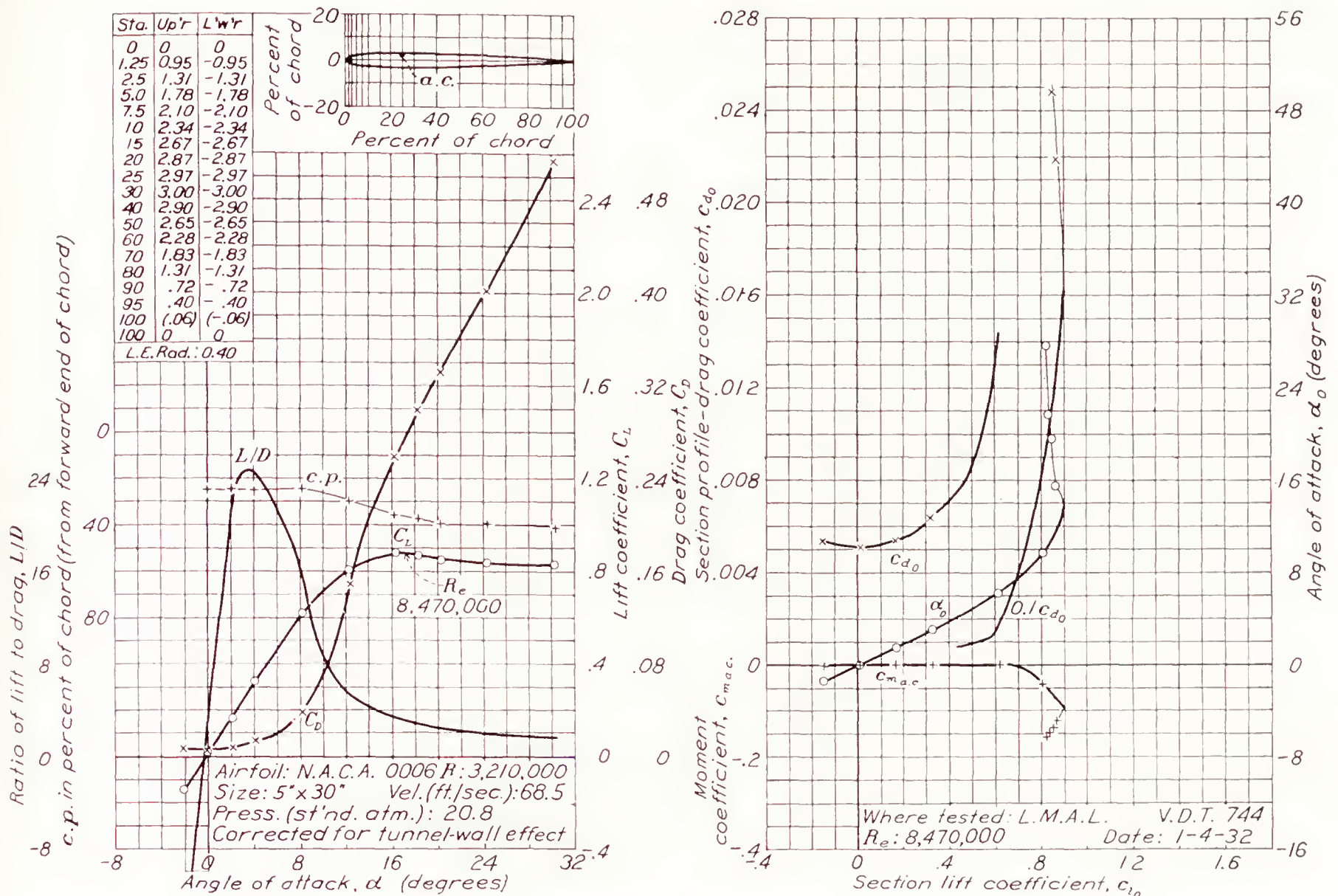


FIGURE 30.—N. A. C. A. 0006 airfoil.

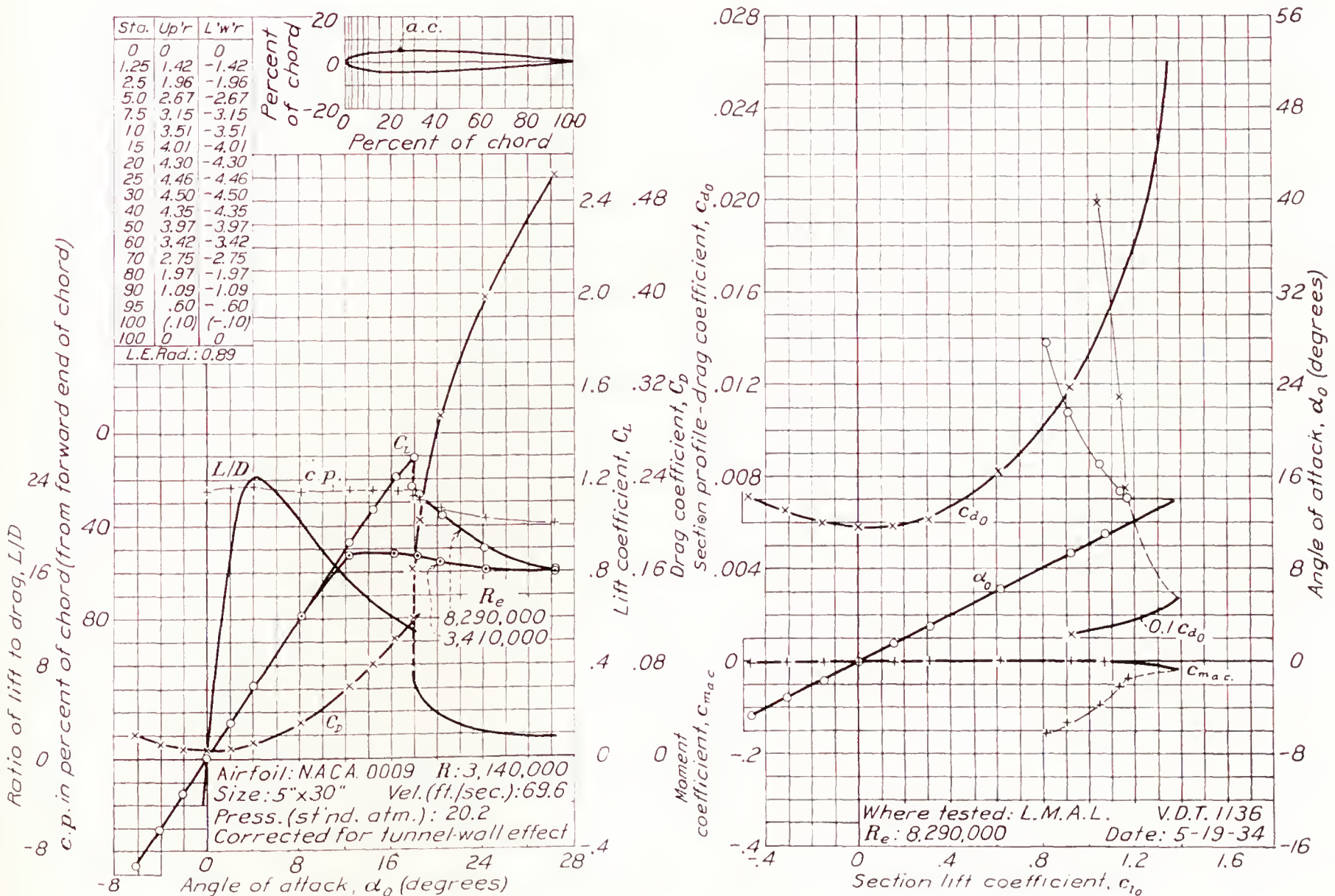


FIGURE 31.—N. A. C. A. 0009 airfoil.



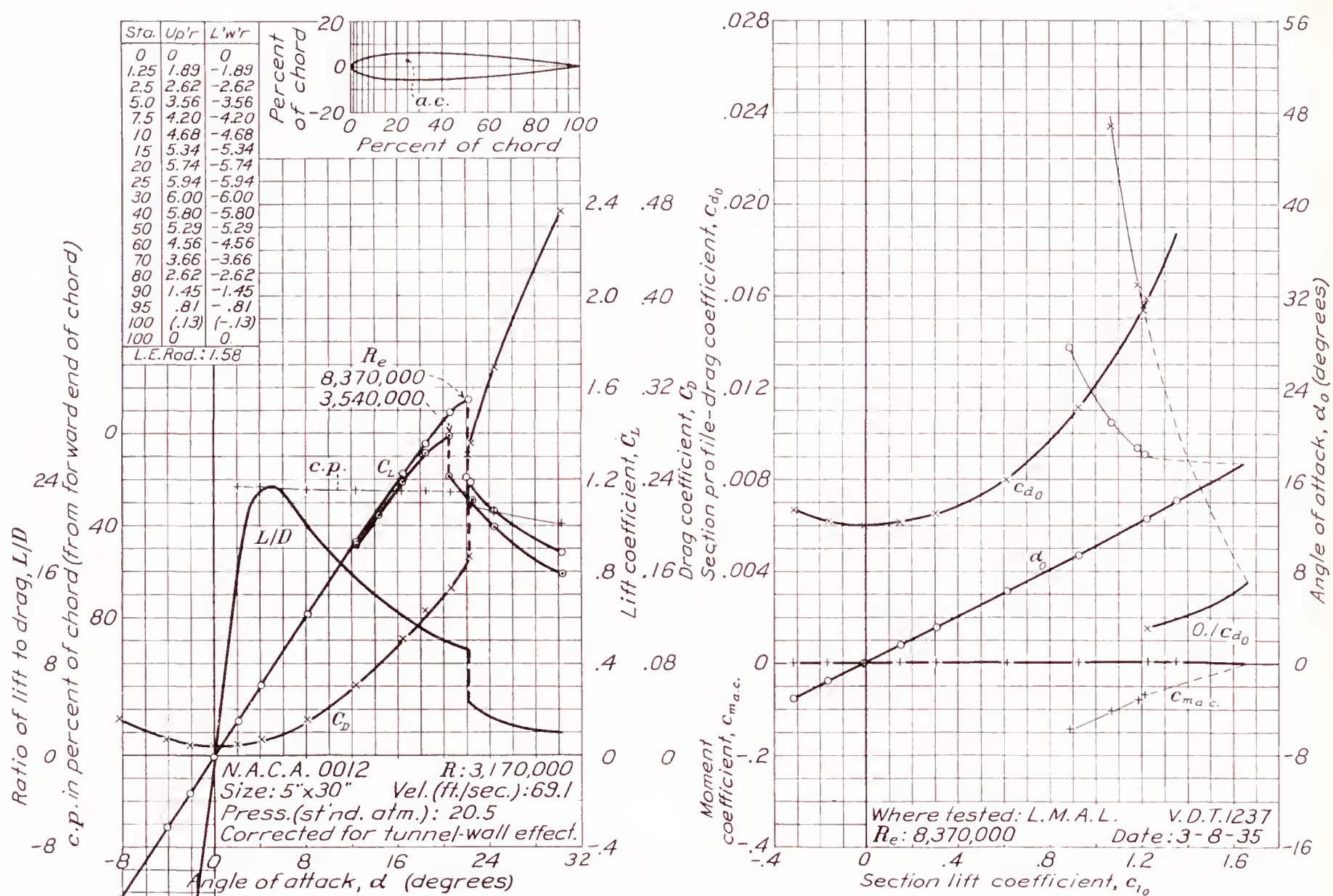


FIGURE 32.—N. A. C. A. 0012 airfoil.

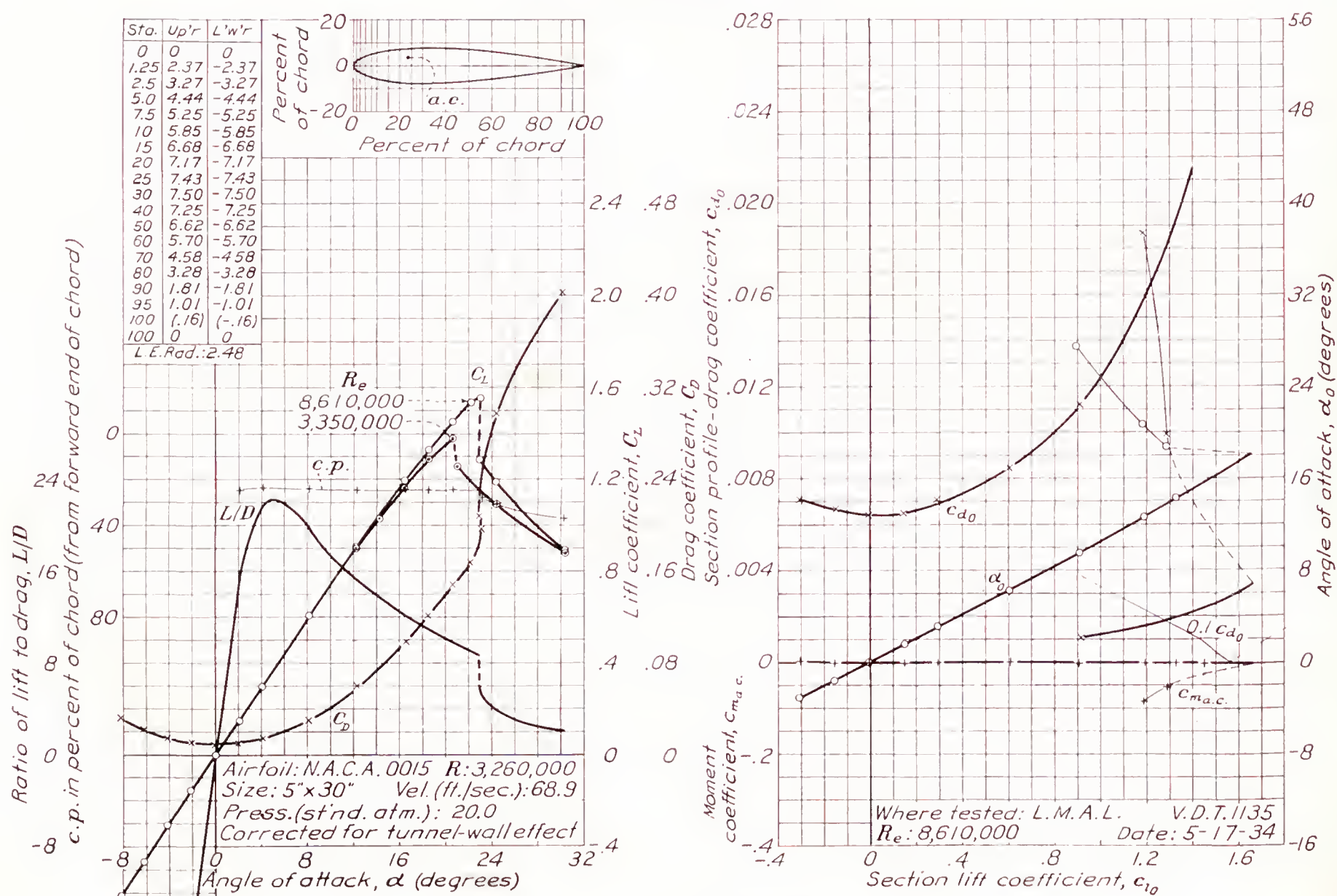


FIGURE 33.—N. A. C. A. 0015 airfoil.



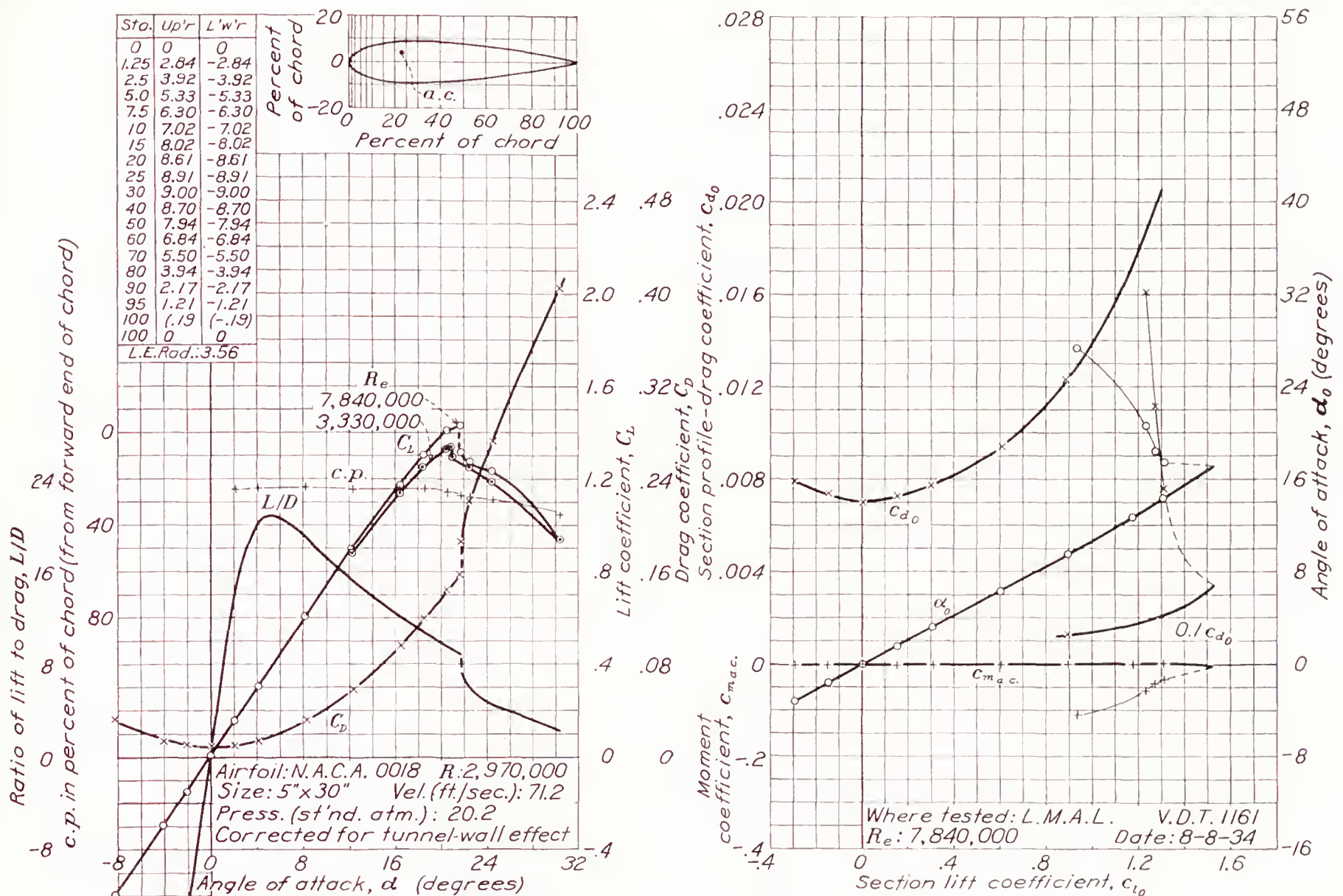


FIGURE 34.—N. A. C. A. 0018 airfoil.

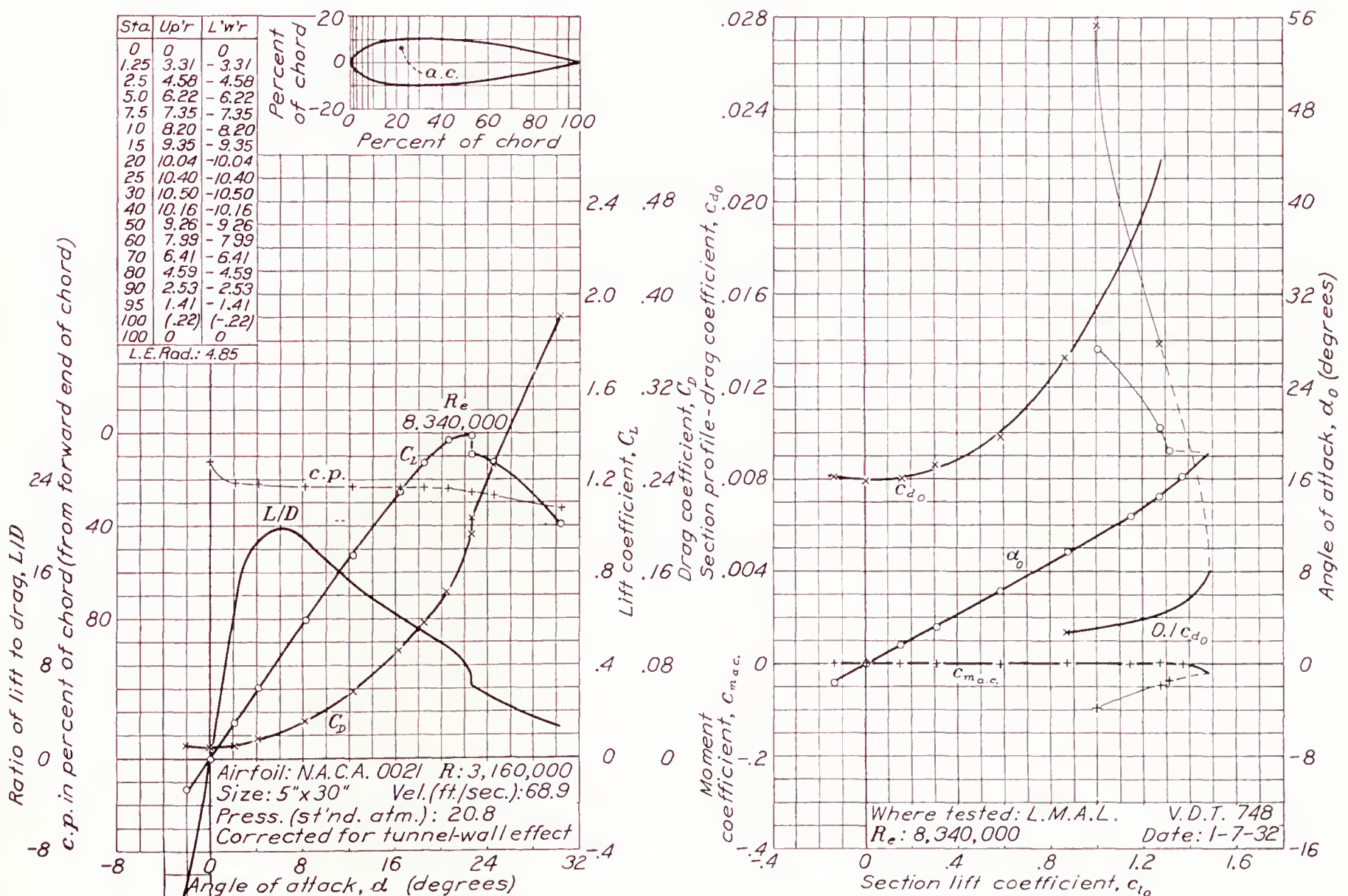


FIGURE 35.—N. A. C. A. 0021 airfoil.



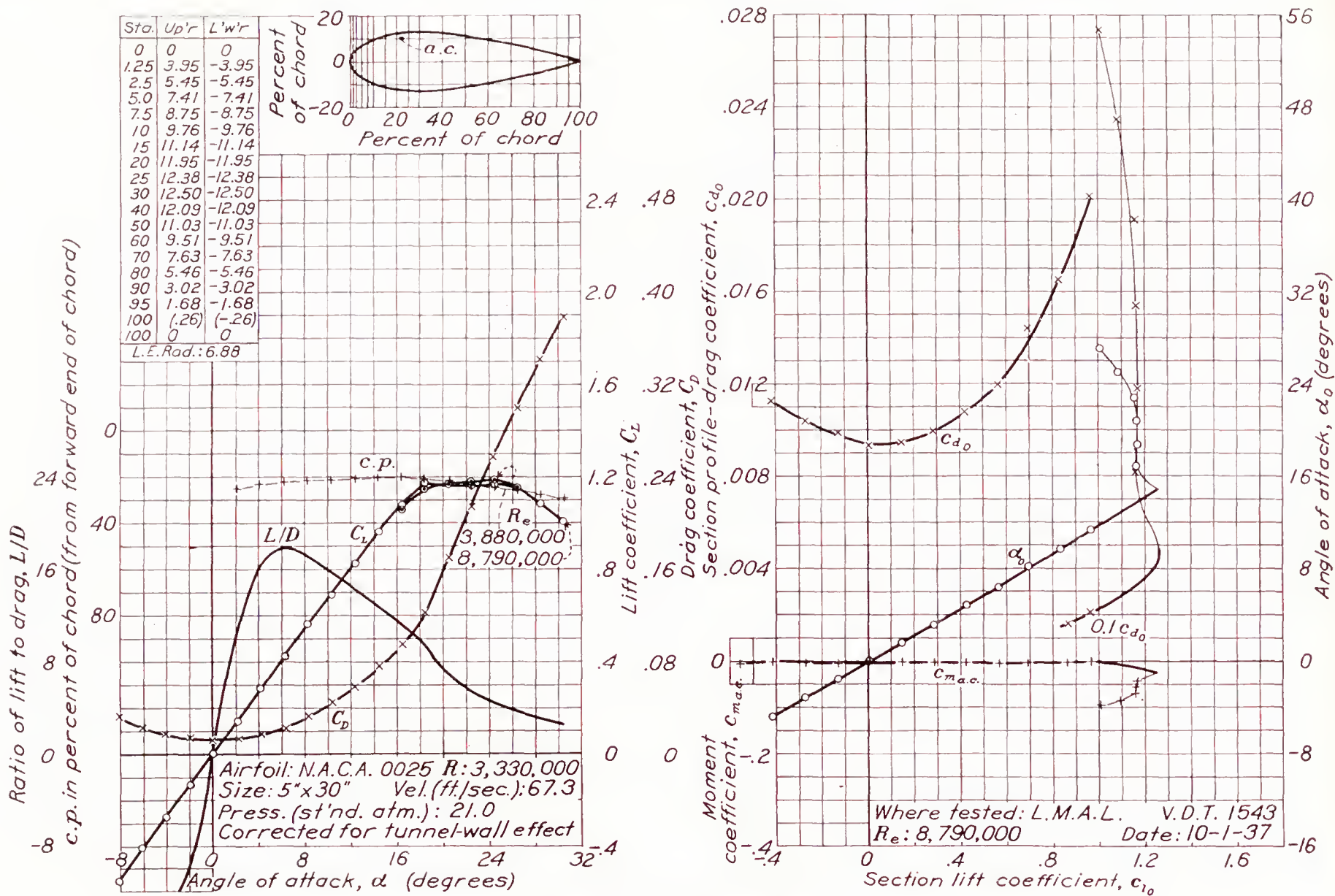


FIGURE 36.—N. A. C. A. 0025 airfoil.

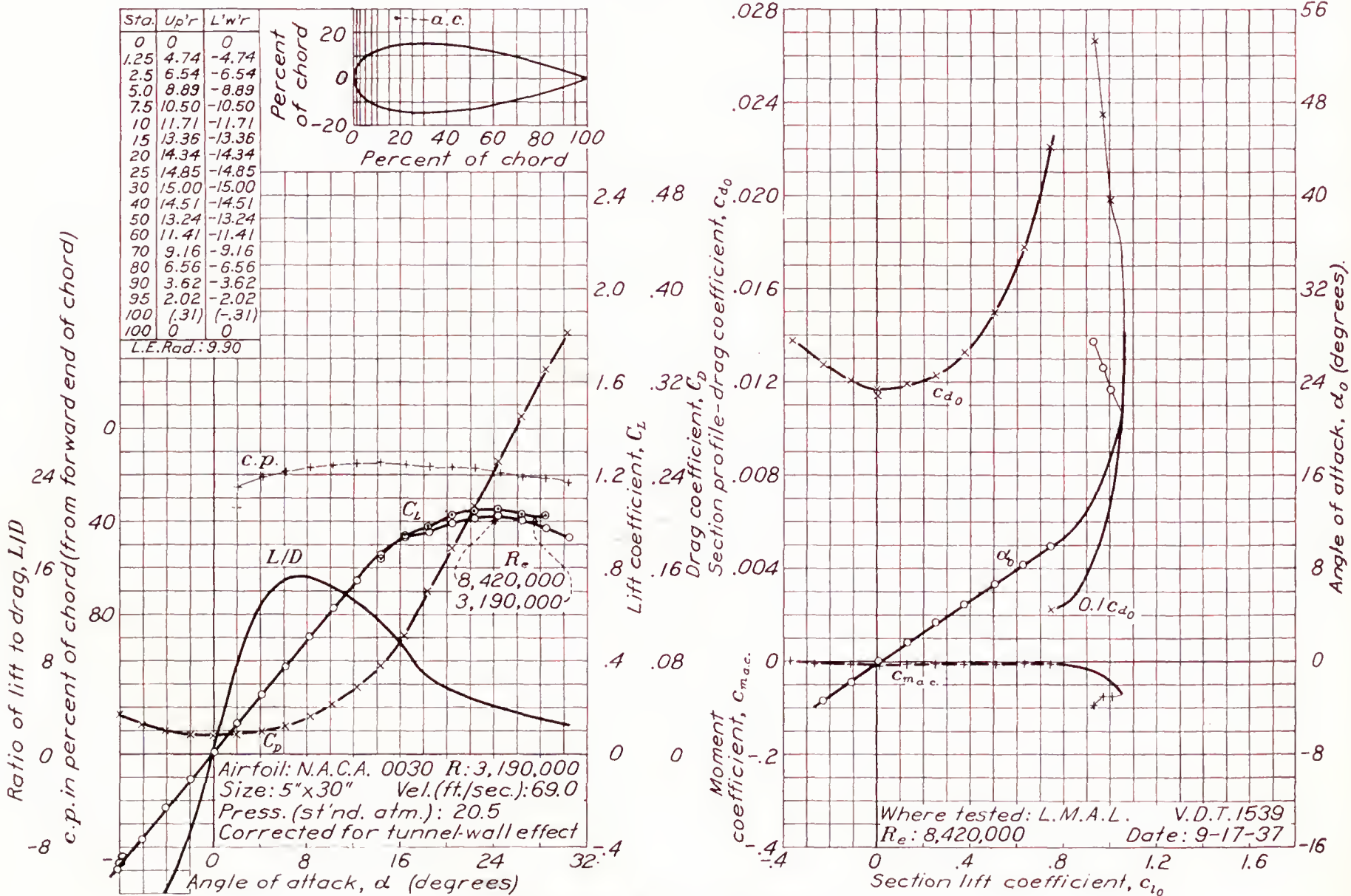


FIGURE 37.—N. A. C. A. 0030 airfoil.



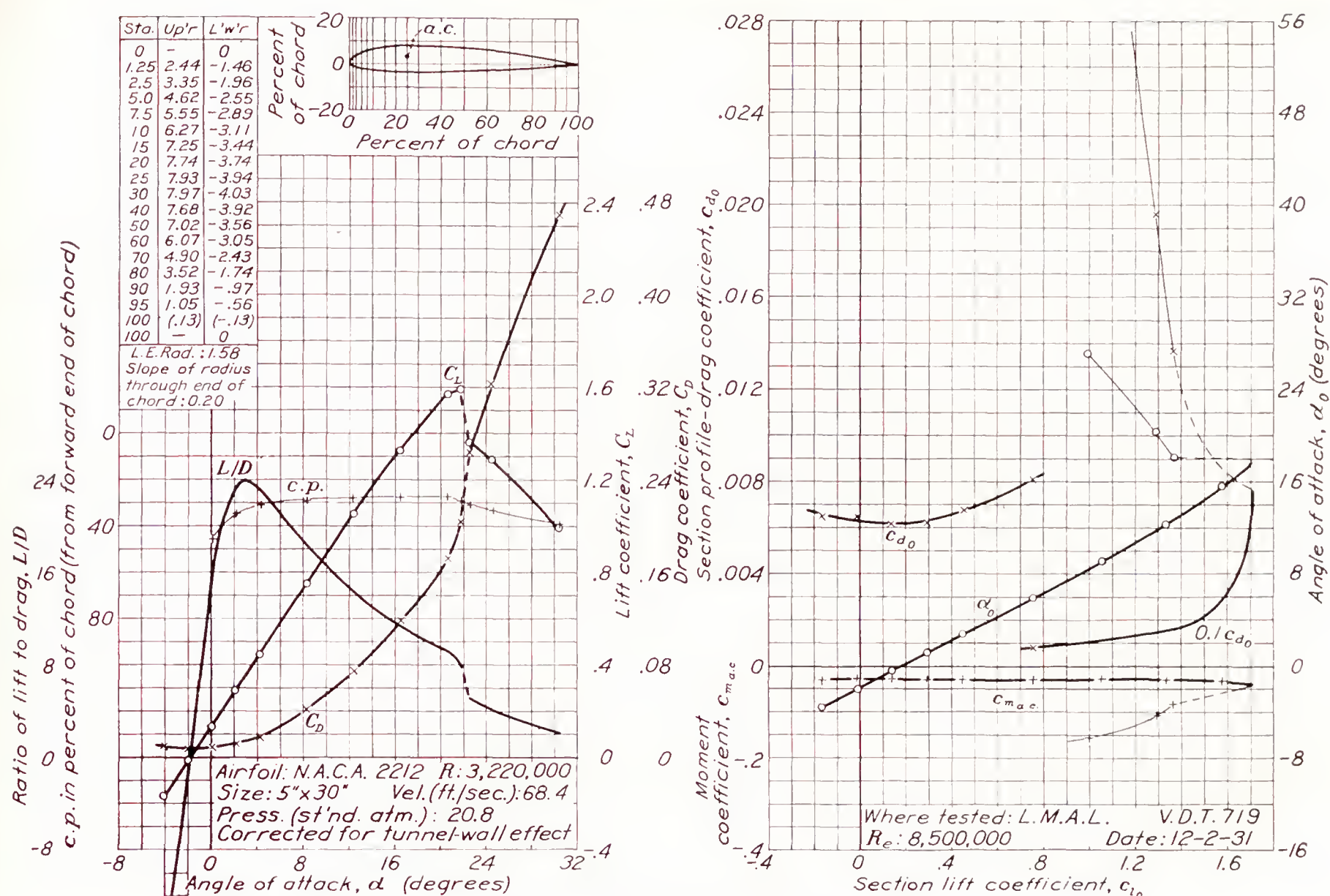


FIGURE 38.—N. A. C. A. 2212 airfoil.

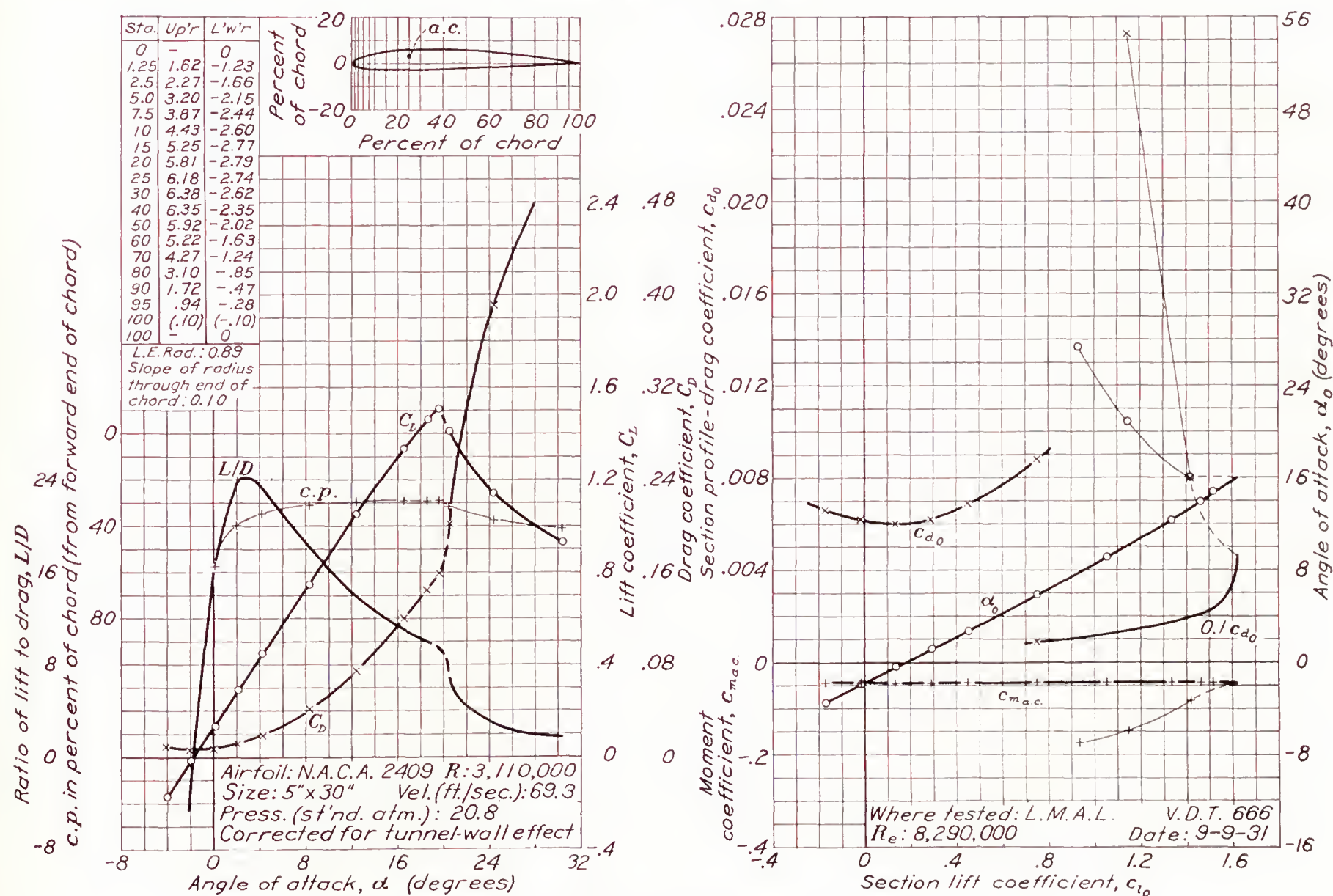


FIGURE 39.—N. A. C. A. 2409 airfoil.







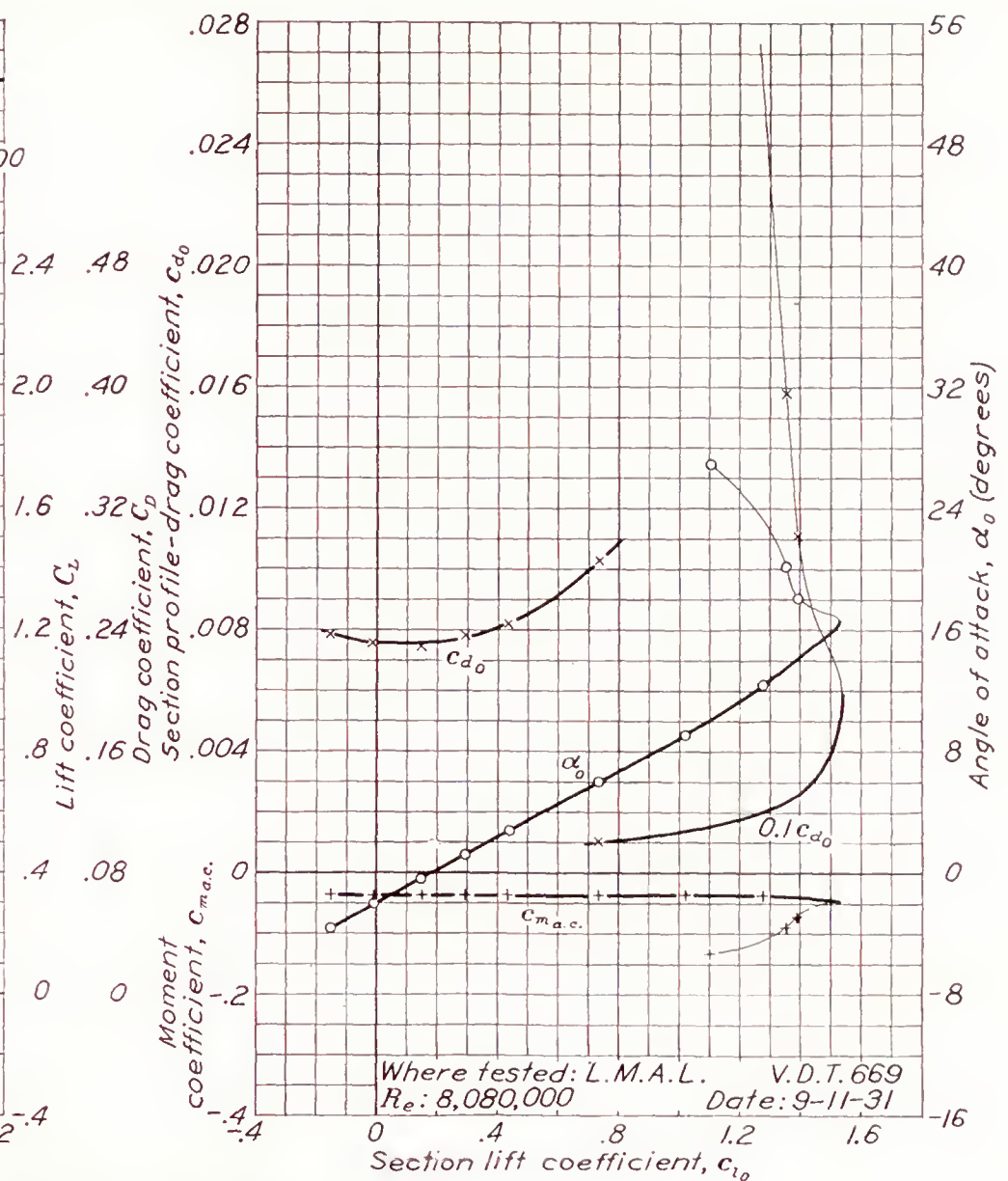
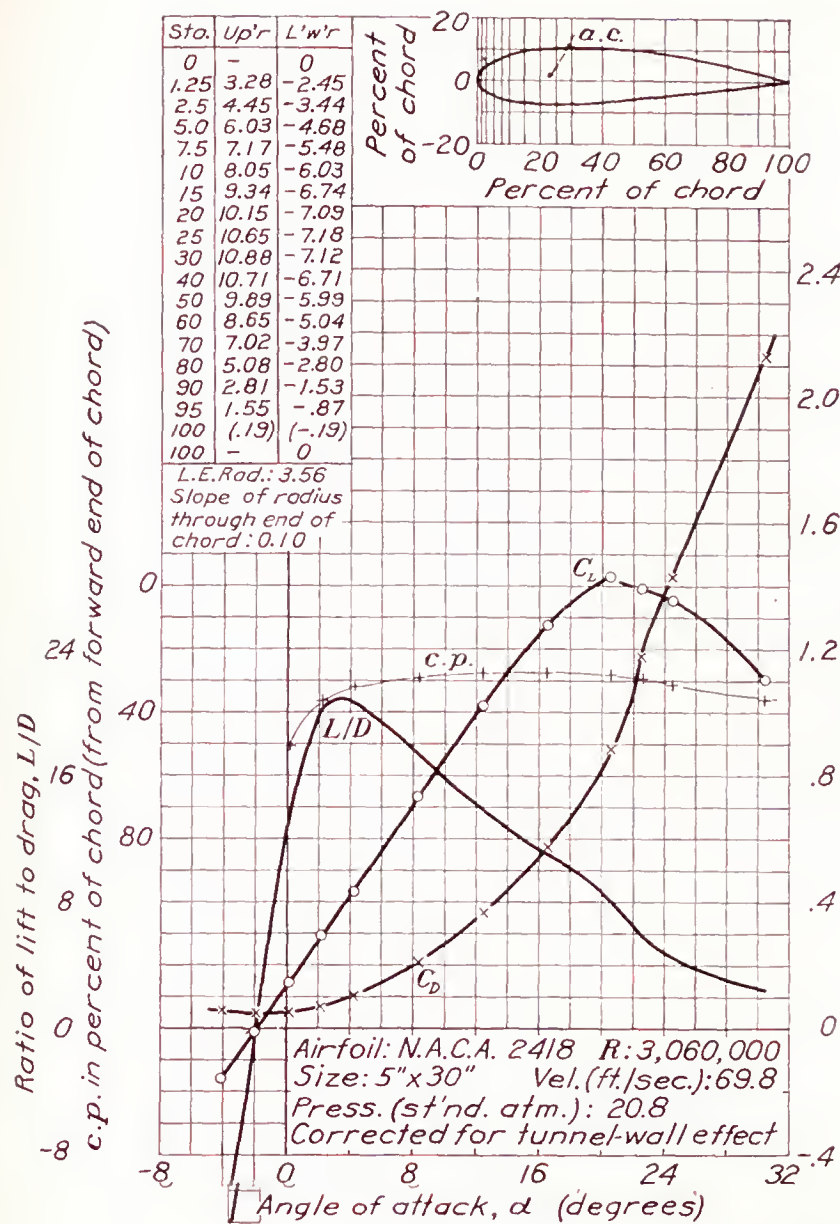


FIGURE 42.—N. A. C. A. 2418 airfoil.

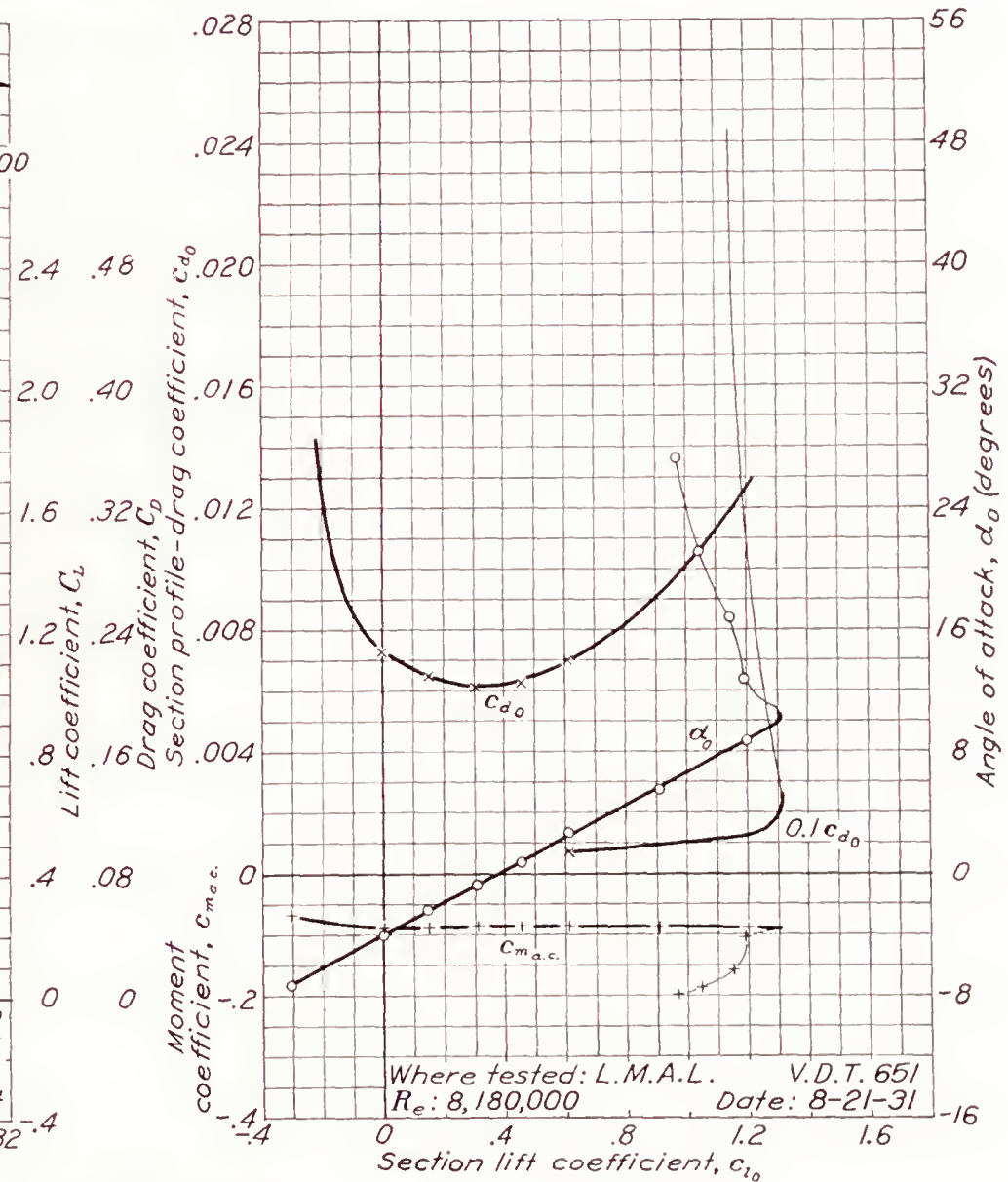
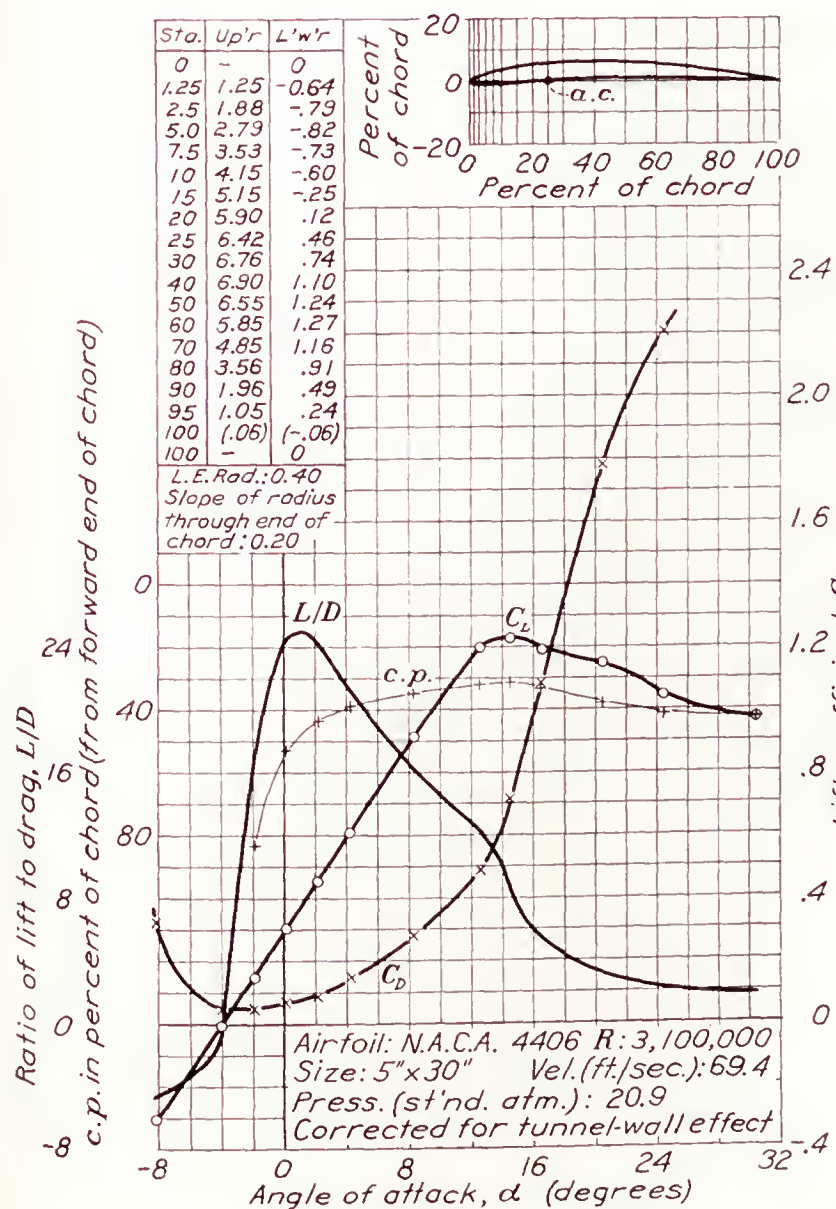


FIGURE 43.—N. A. C. A. 4406 airfoil.



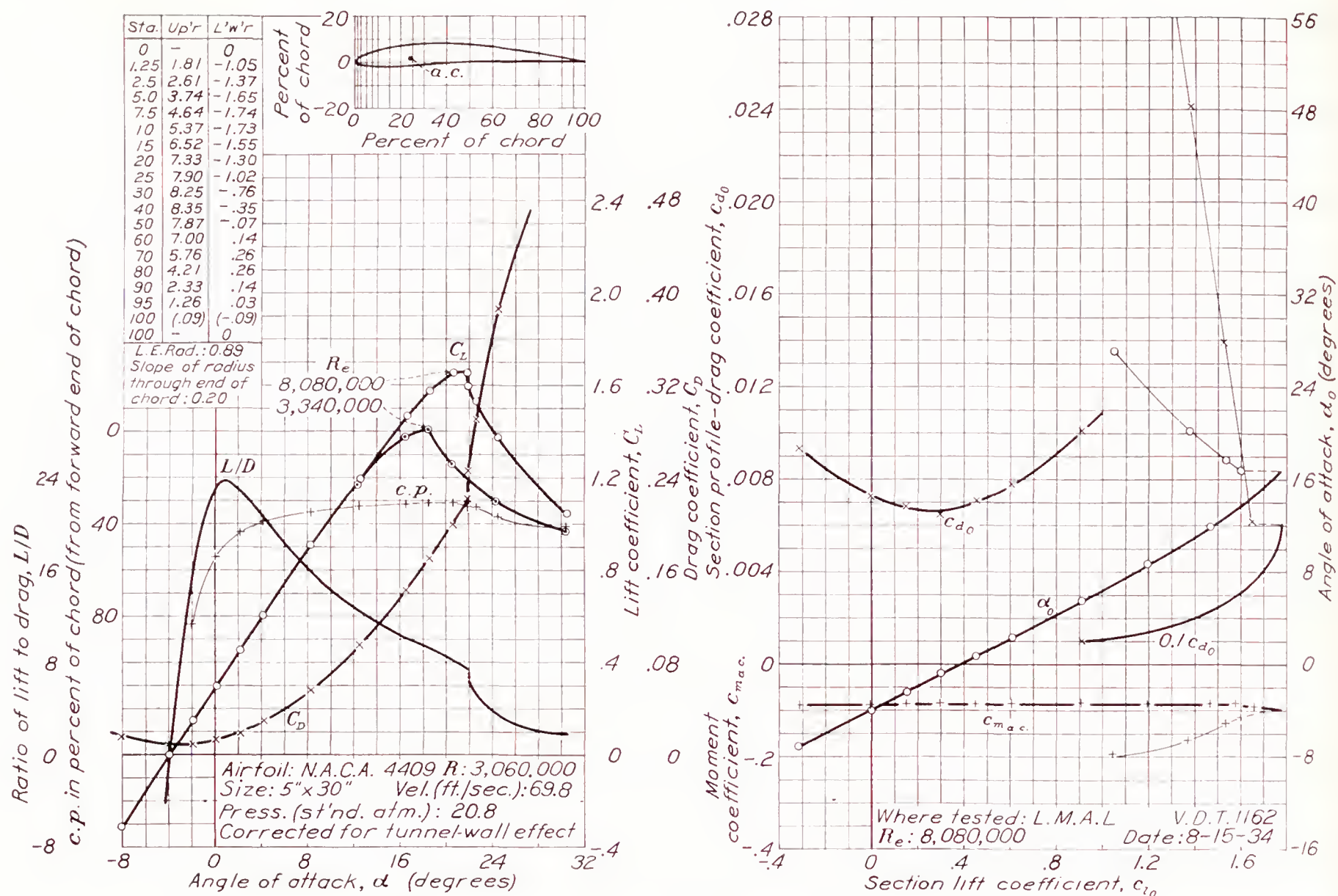


FIGURE 44.—N. A. C. A. 4409 airfoil.

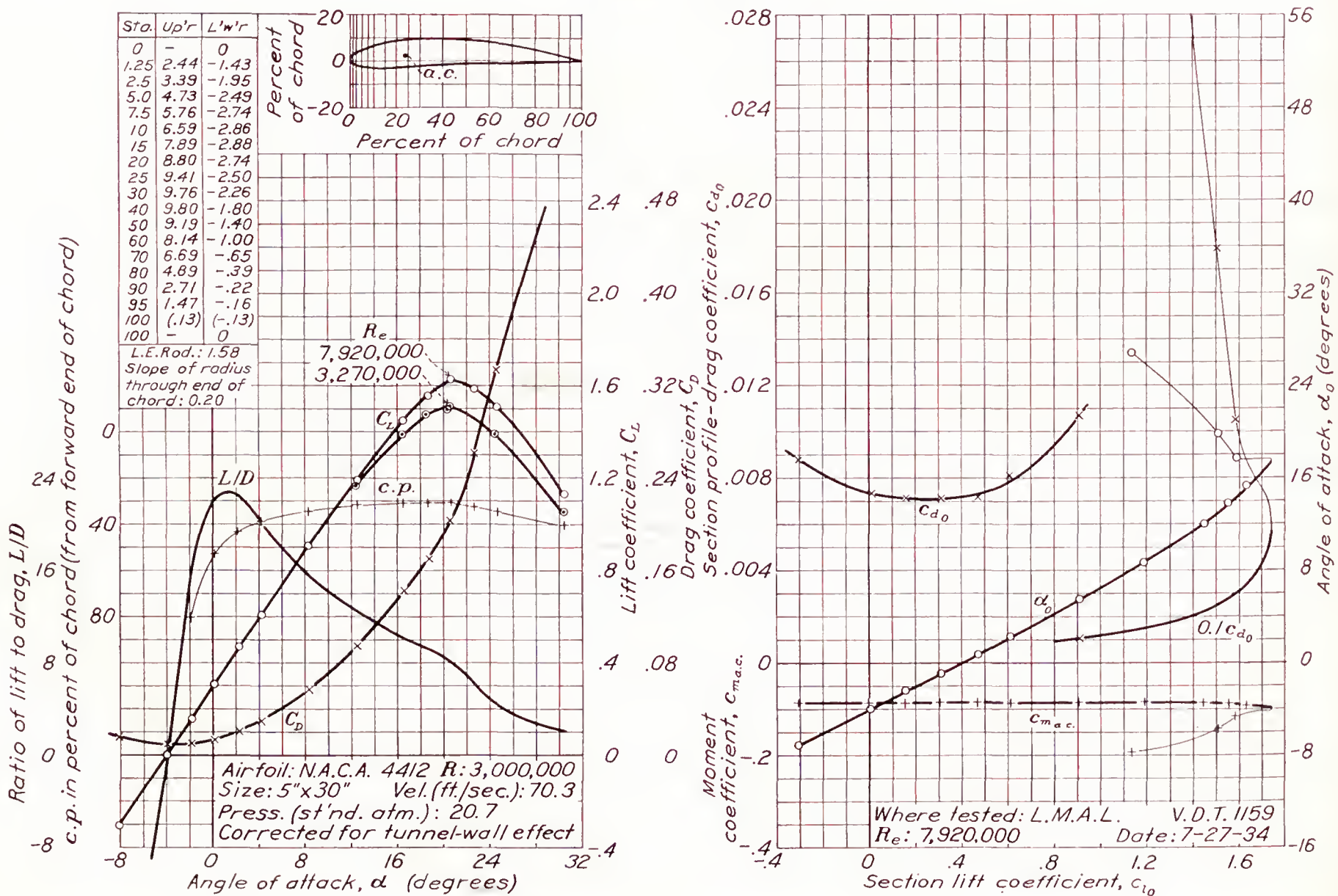


FIGURE 45.—N. A. C. A. 4412 airfoil.



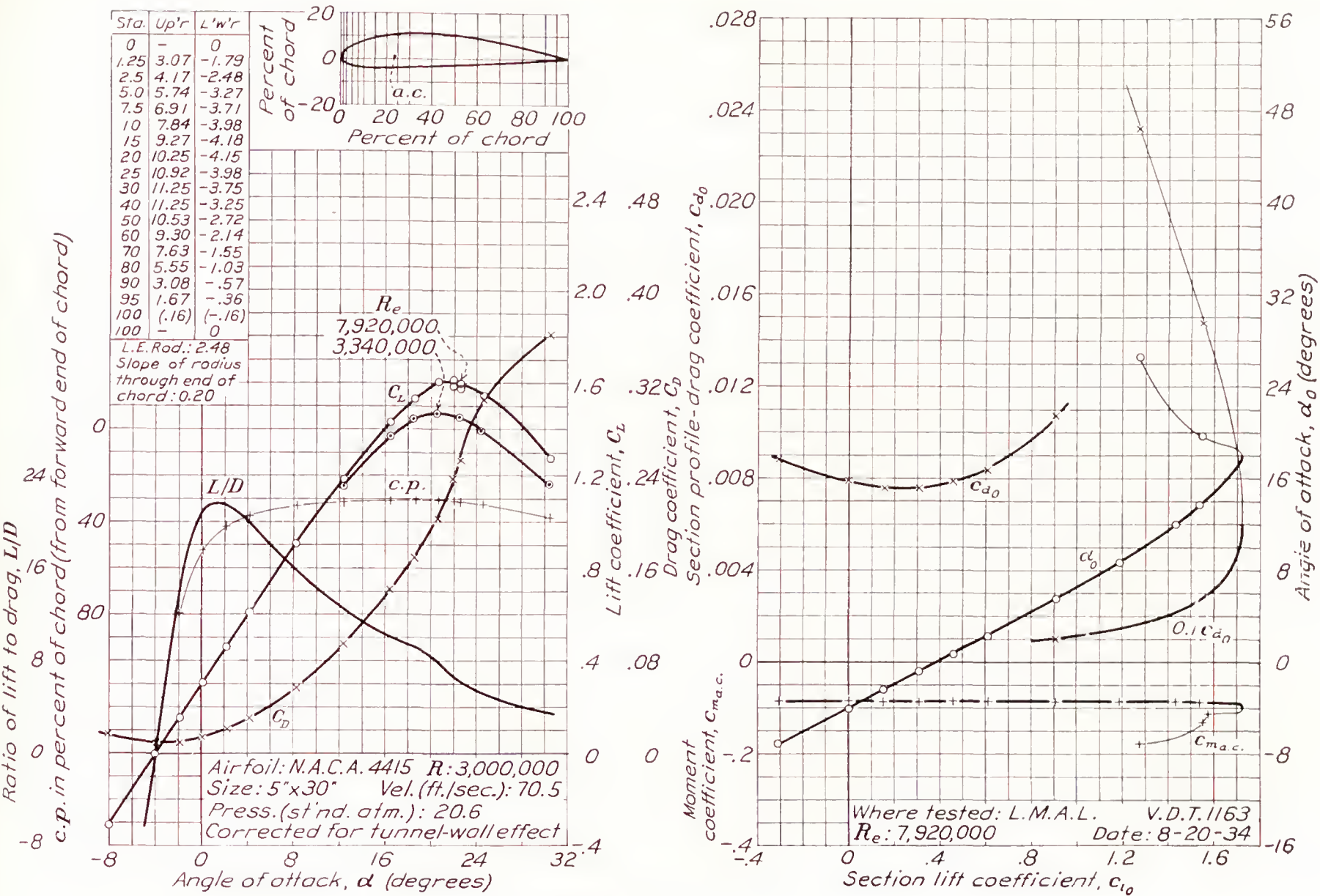


FIGURE 46.—N. A. C. A. 4415 airfoil.

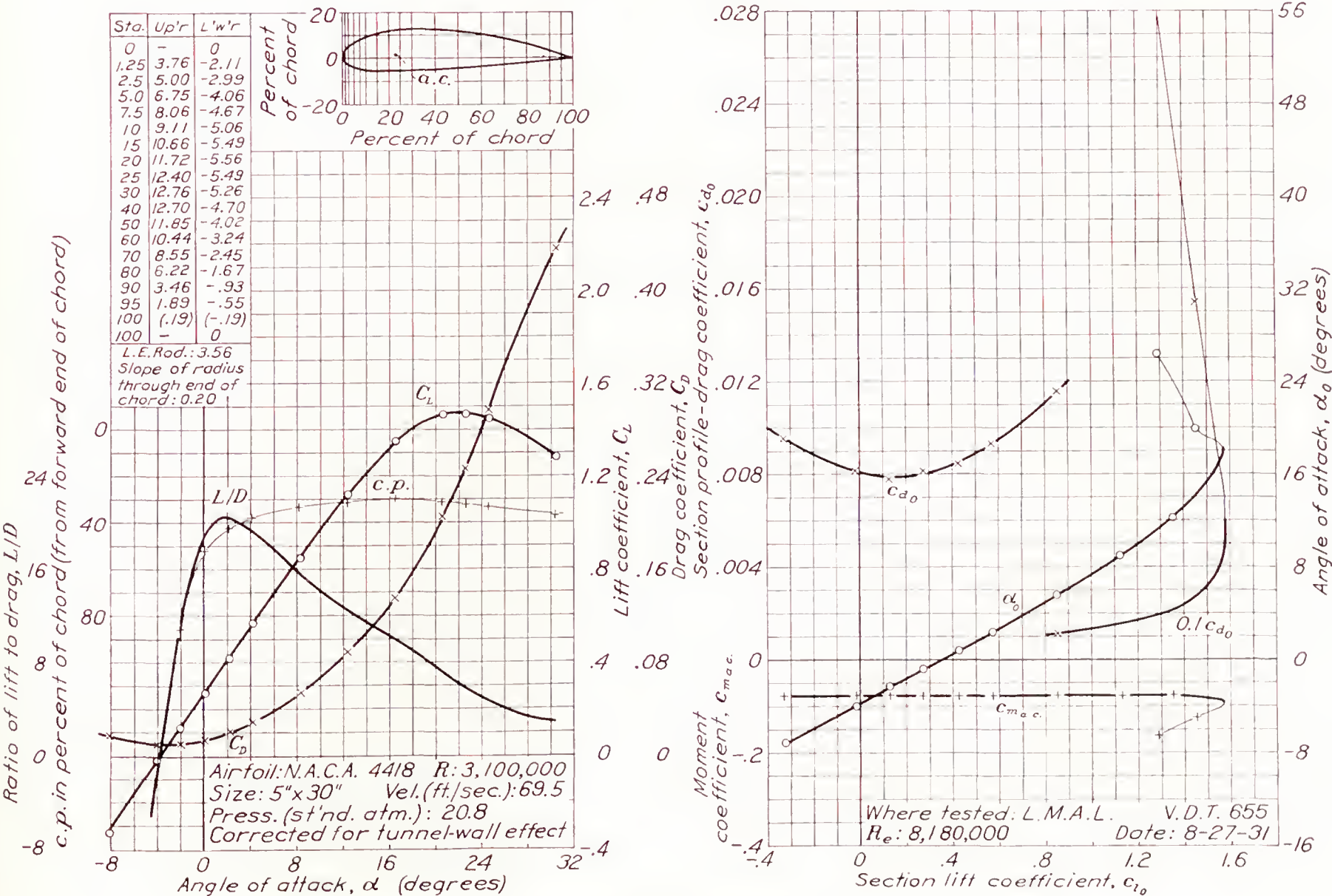


FIGURE 47.—N. A. C. A. 4418 airfoil.



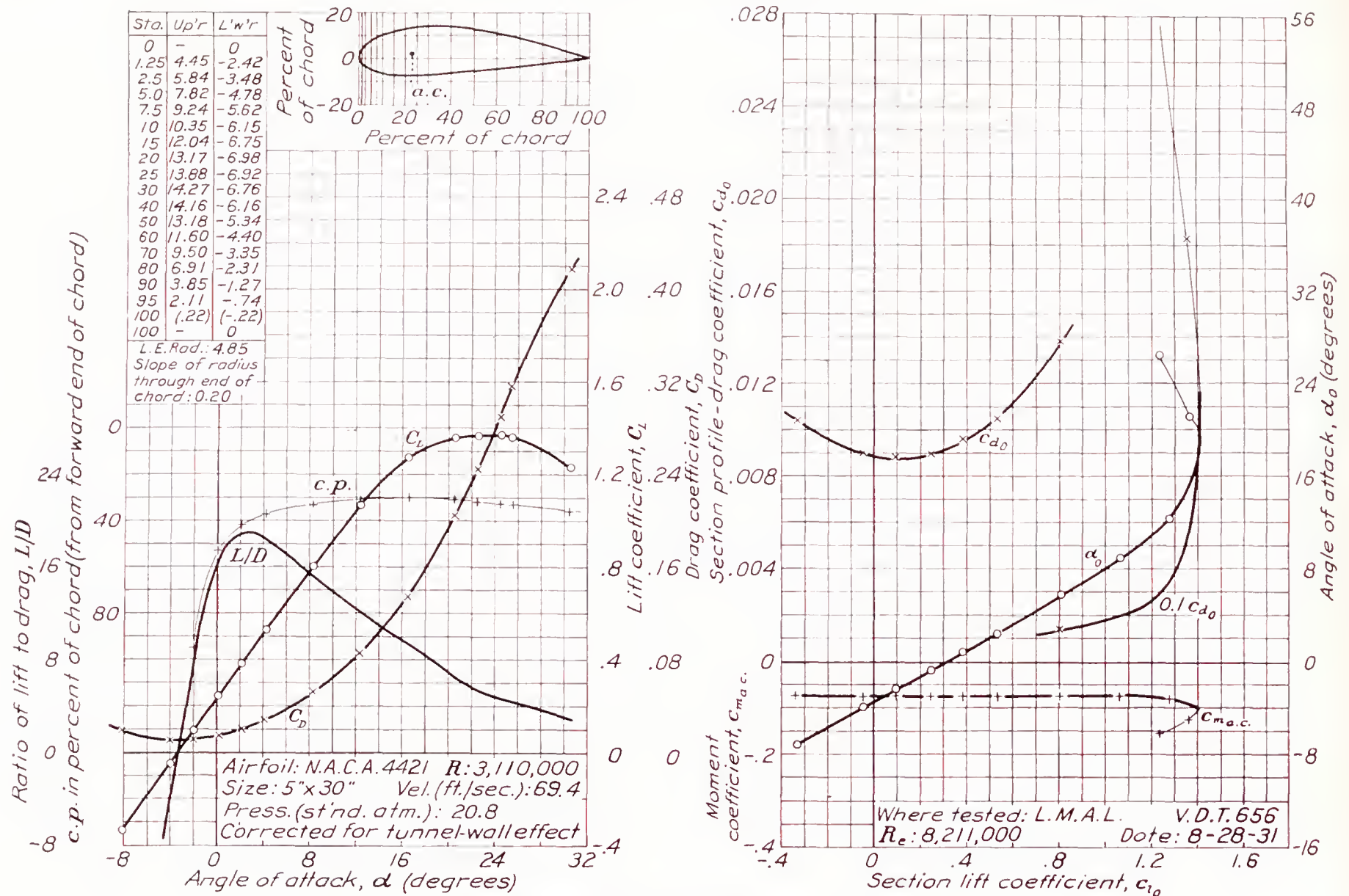


FIGURE 48.—N. A. C. A. 4421 airfoil.

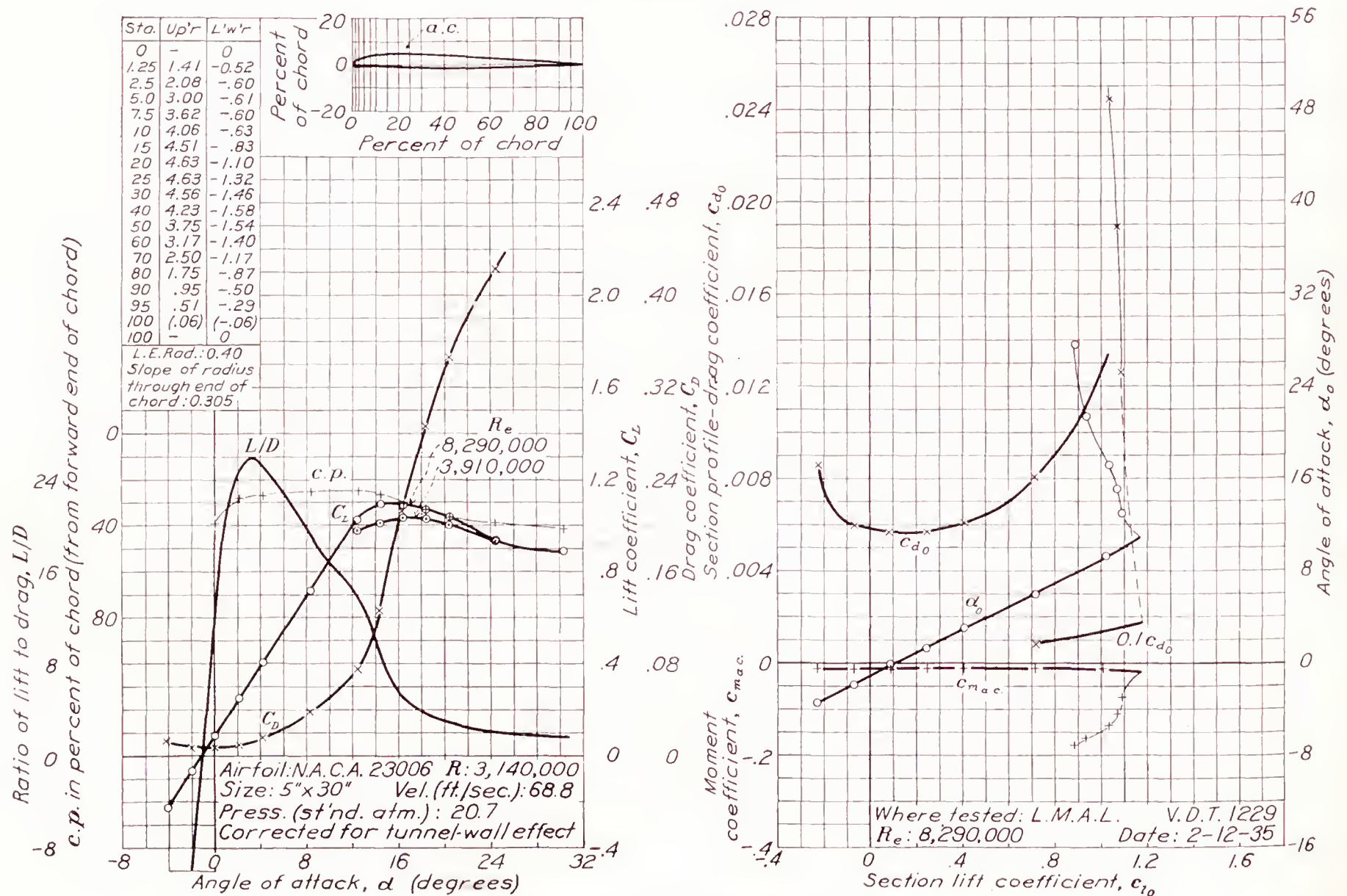


FIGURE 49.—N. A. C. A. 23006 airfoil.



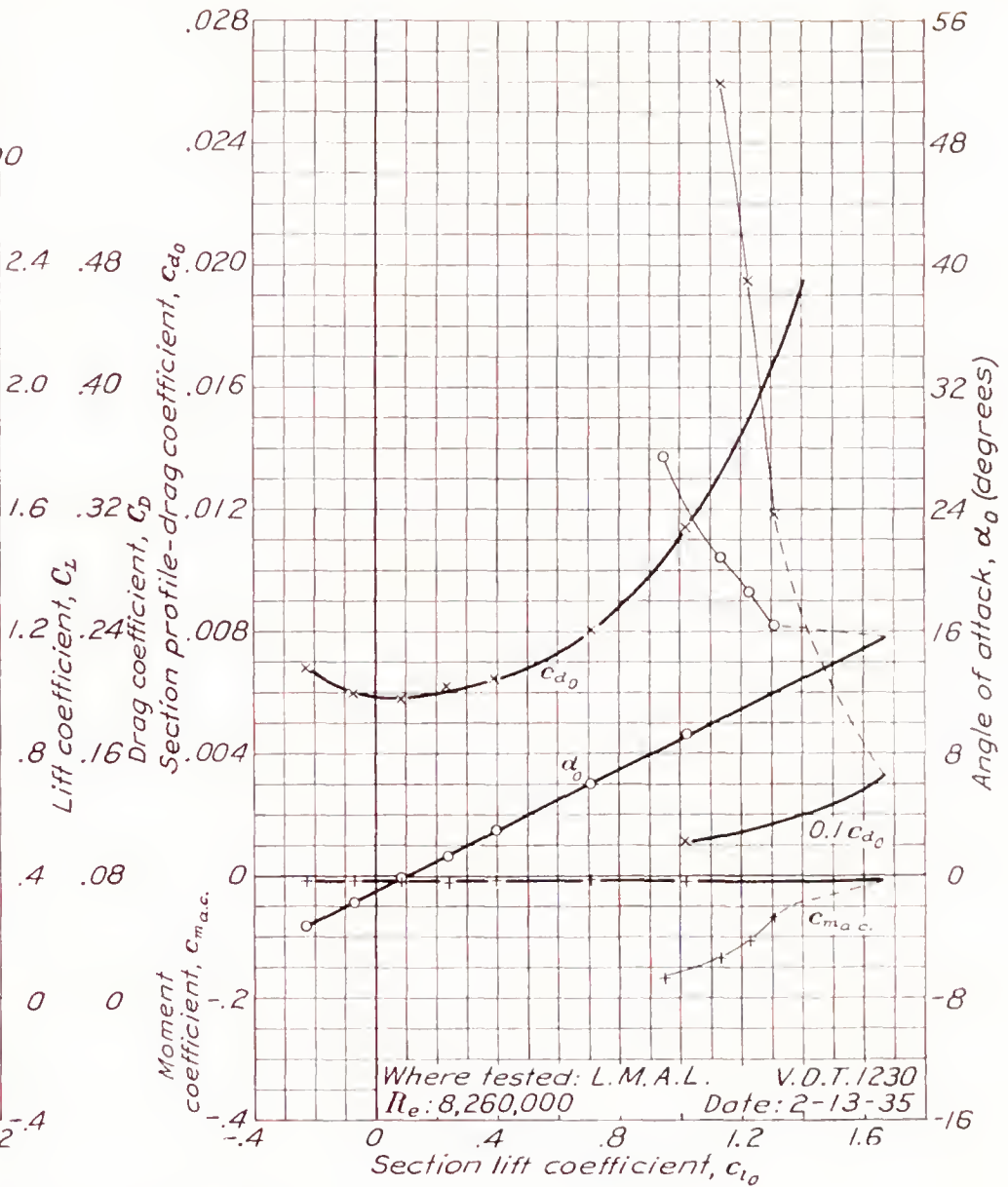
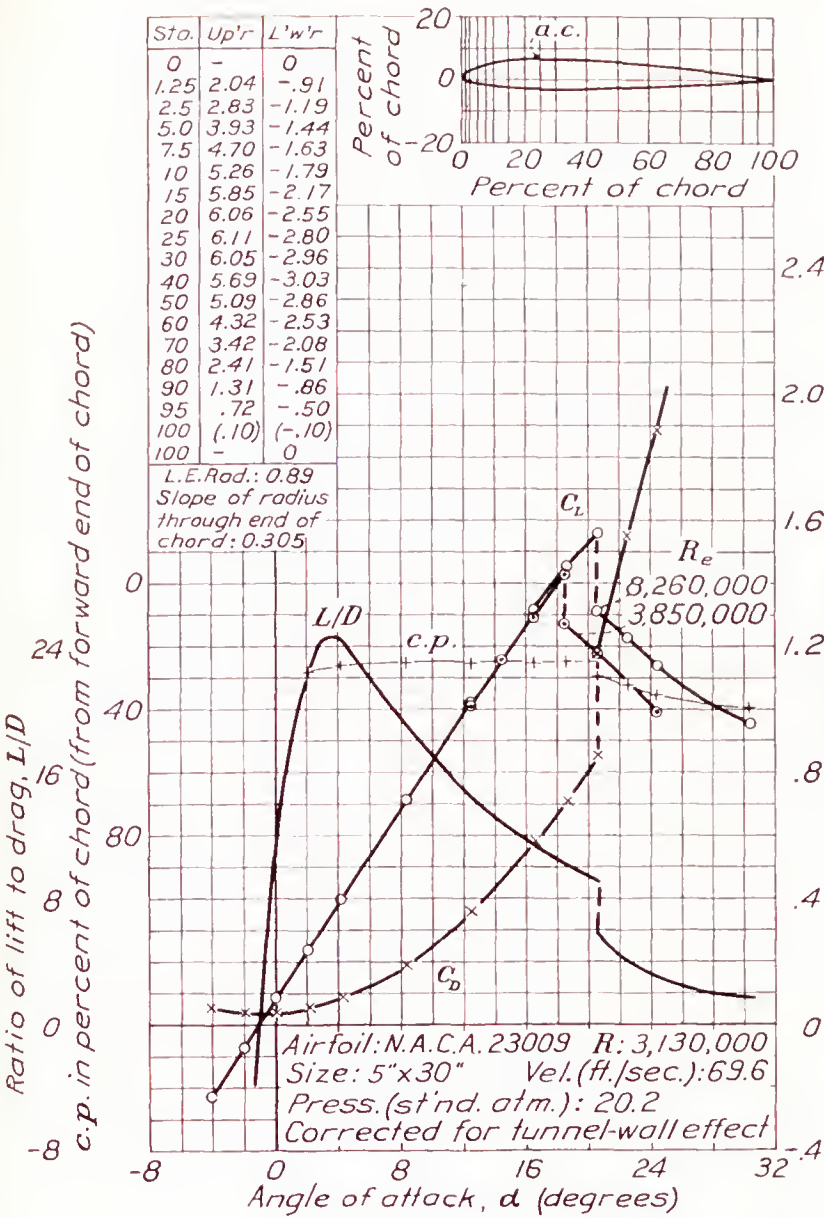


FIGURE 50.—N. A. C. A. 23009 airfoil.

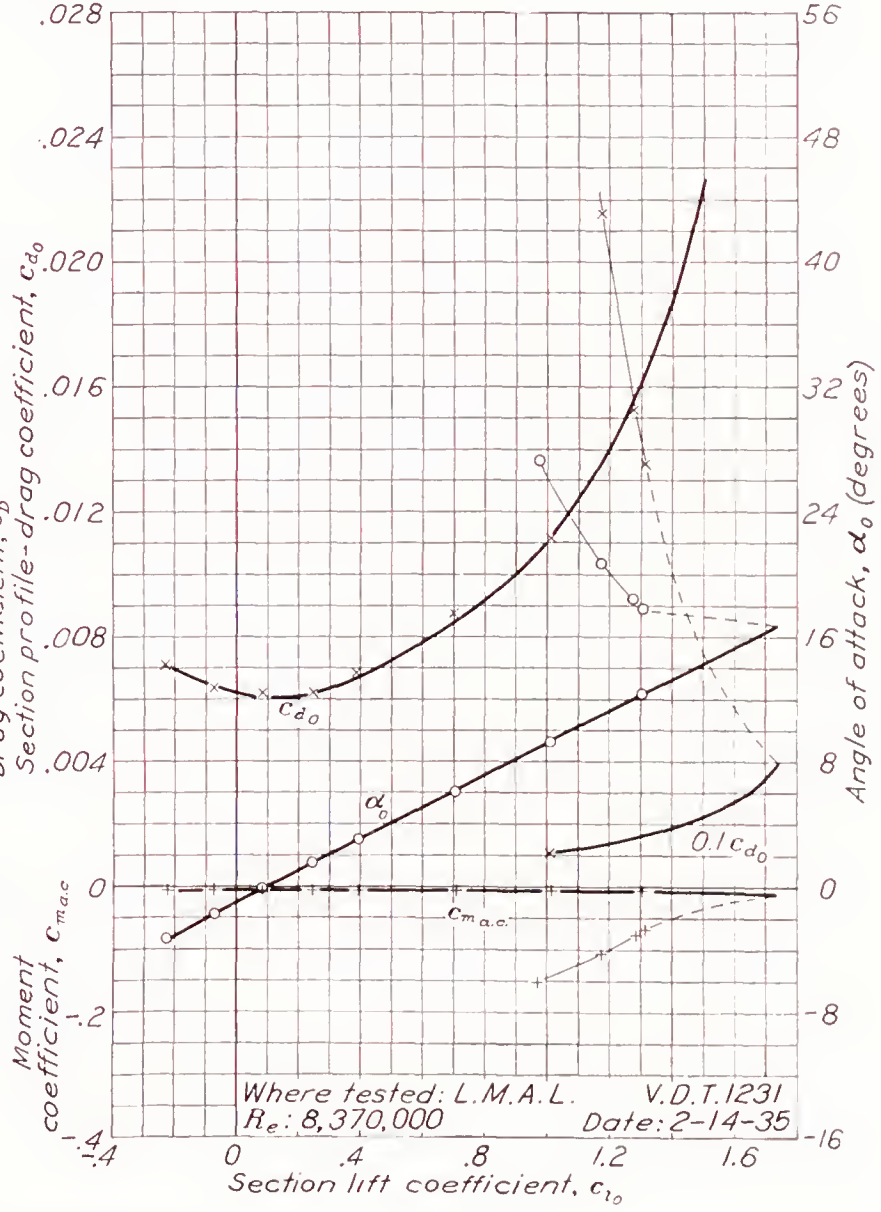
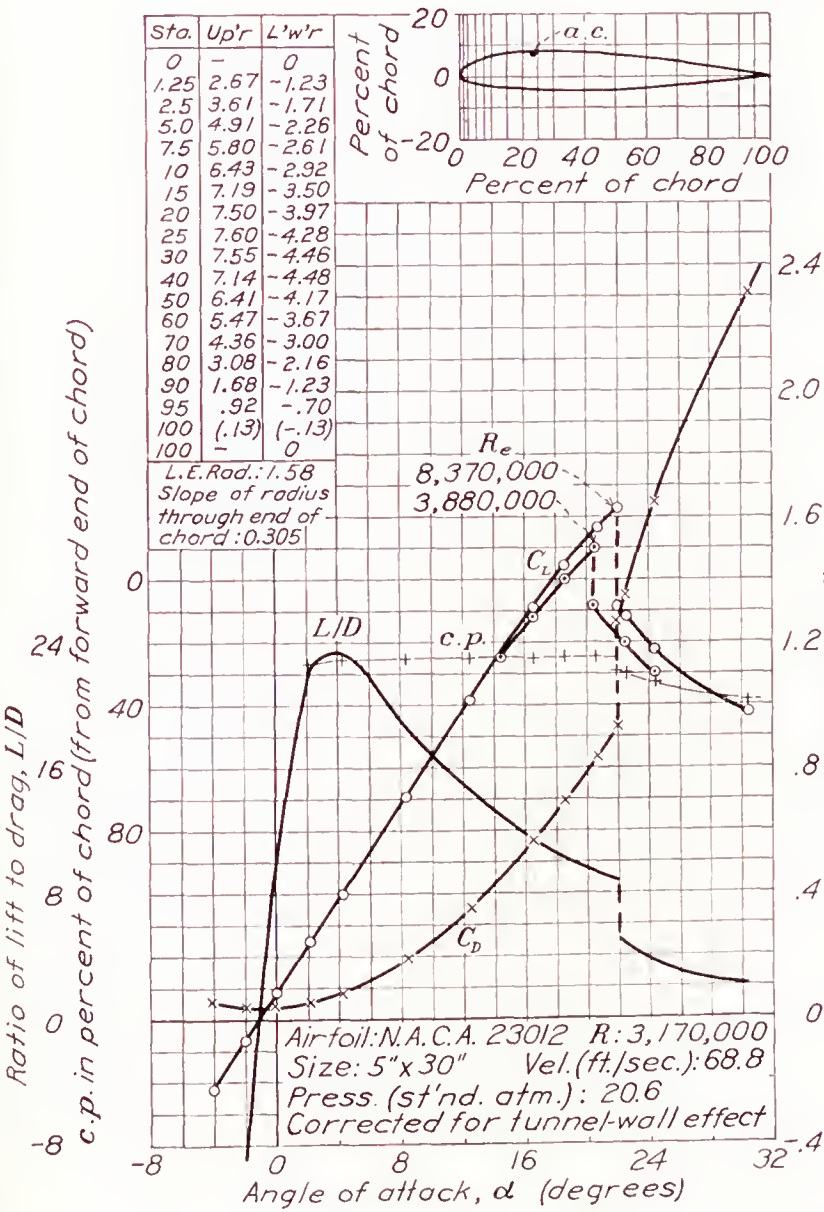


FIGURE 51.—N. A. C. A. 23012 airfoil.



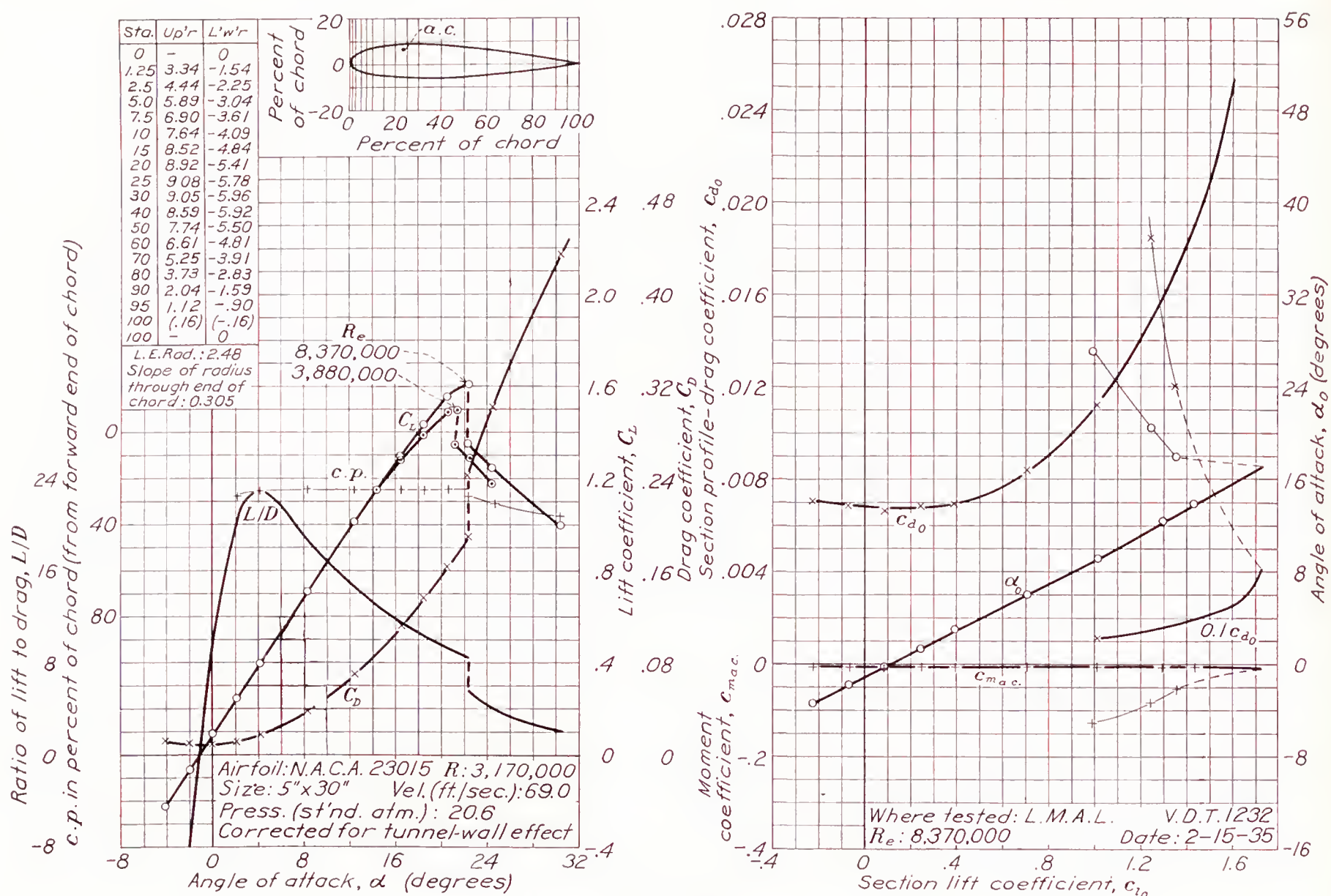


FIGURE 52.—N. A. C. A. 23015 airfoil.

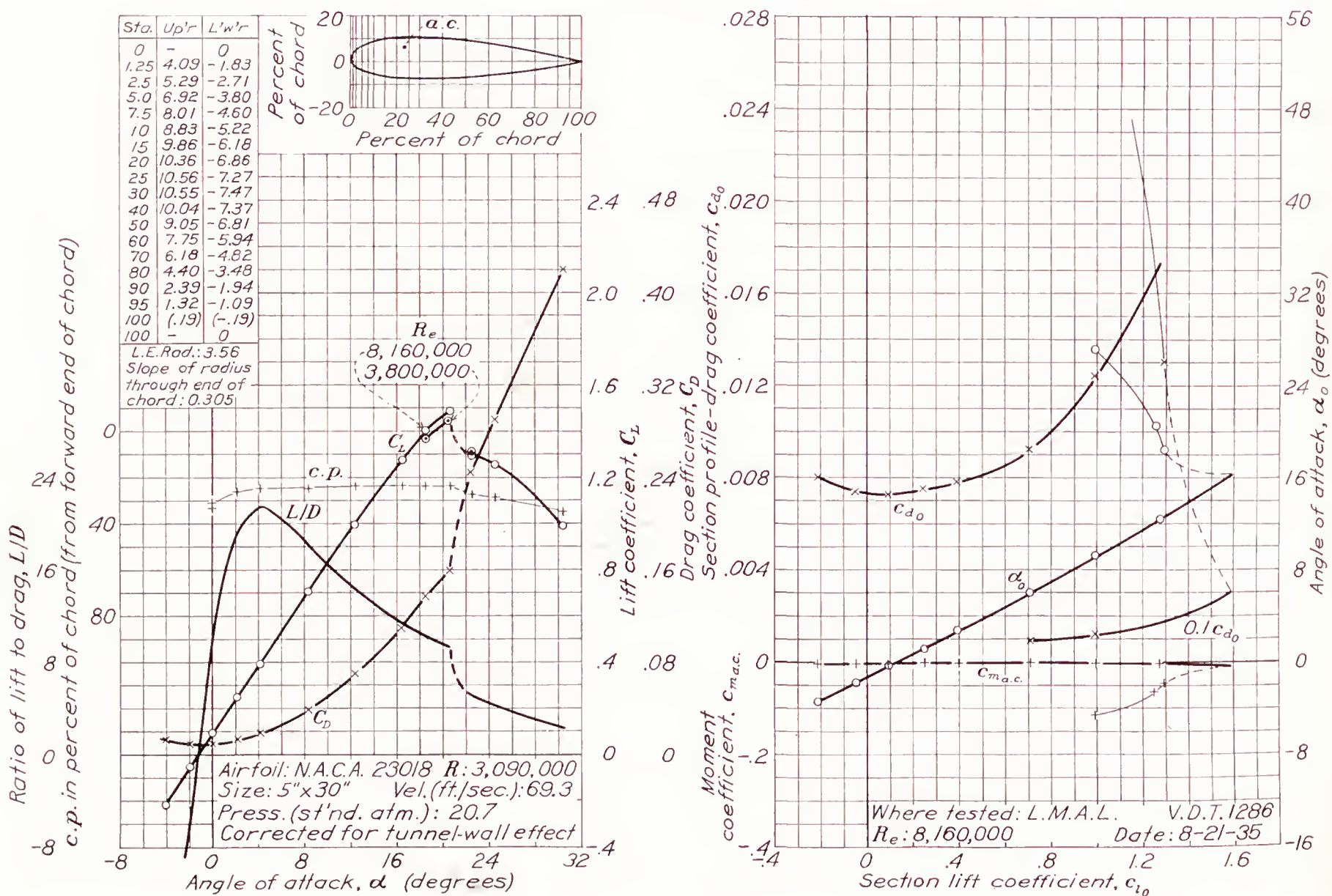


FIGURE 53.—N. A. C. A. 23018 airfoil.



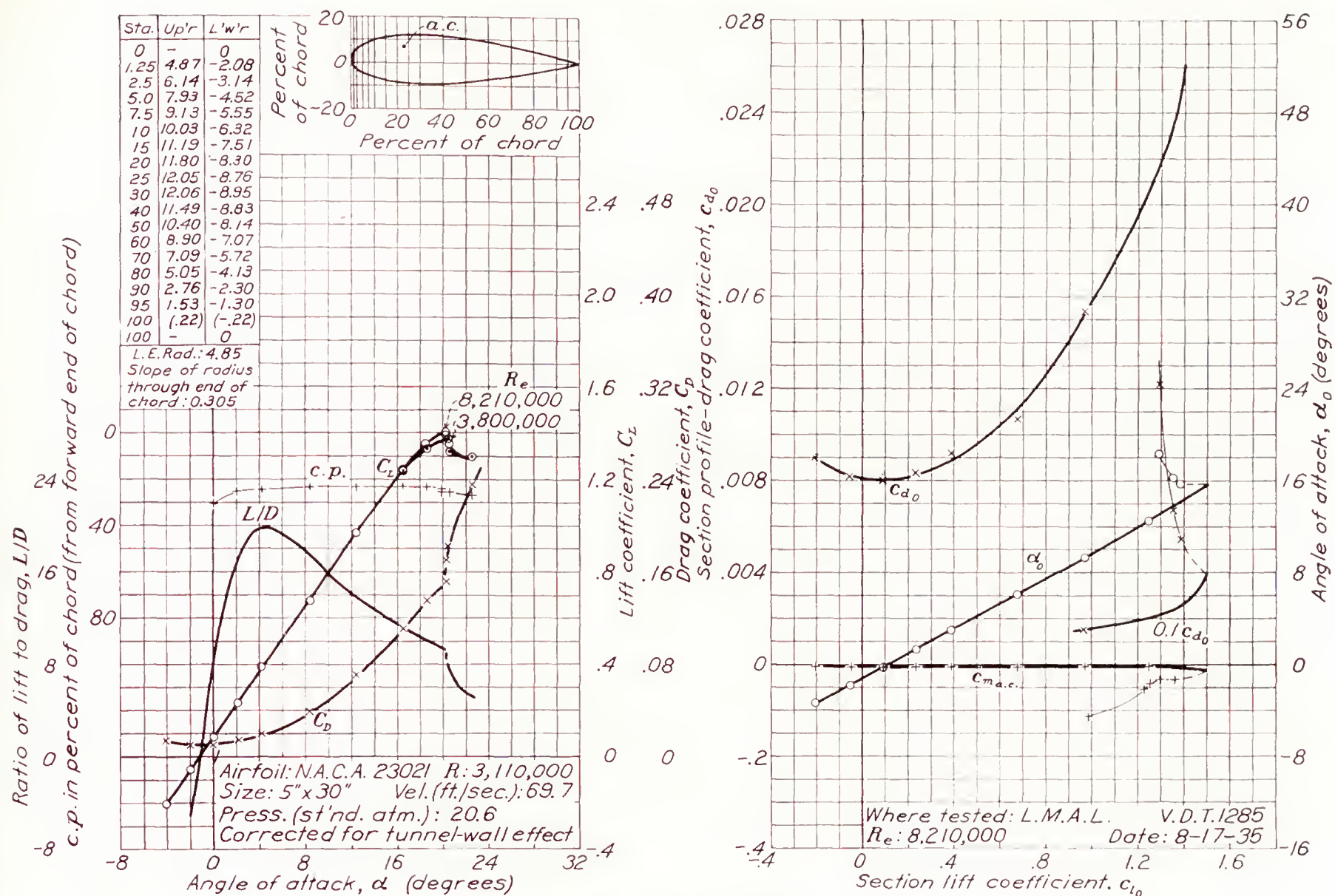


FIGURE 54.—N. A. C. A. 23021 airfoil.

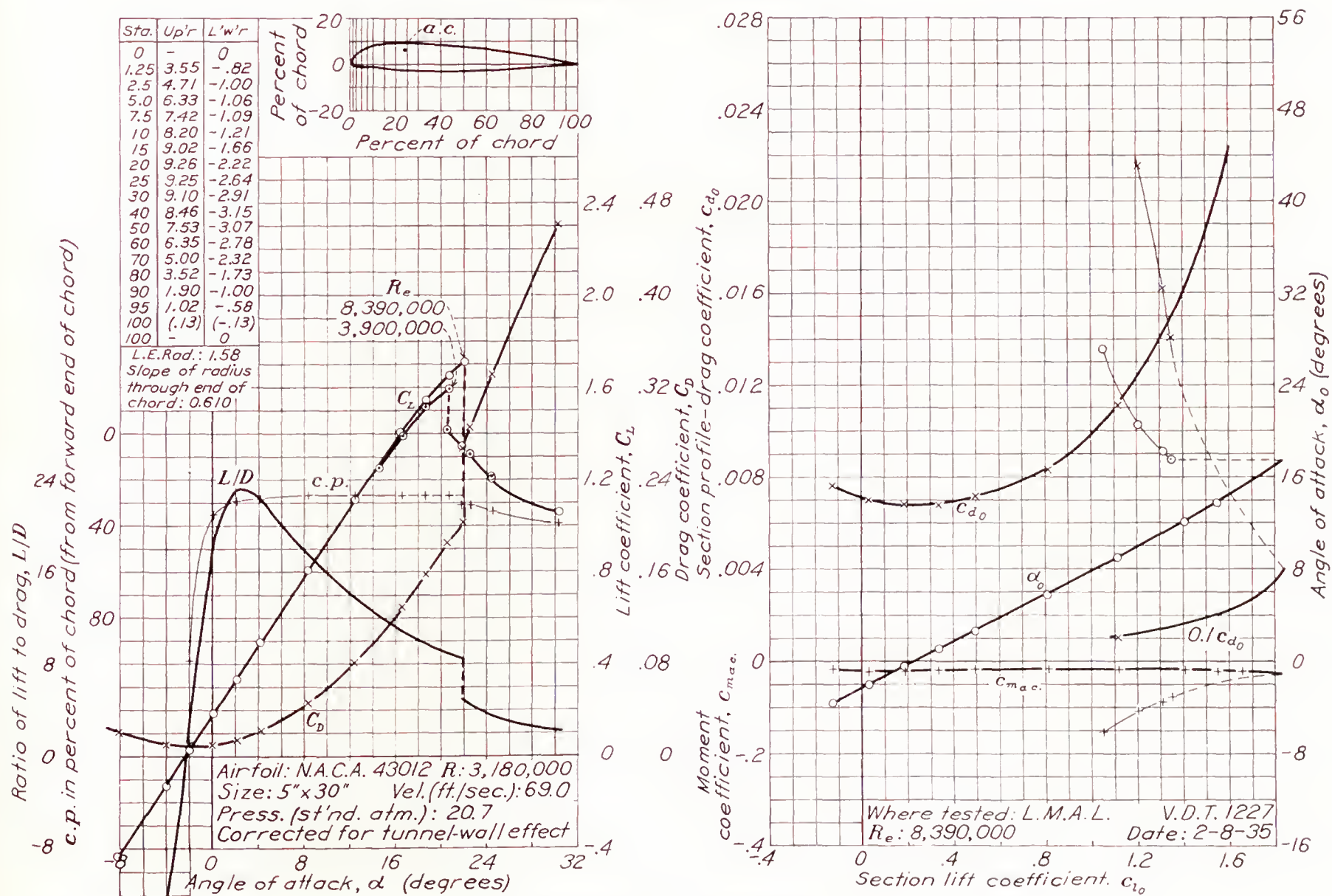


FIGURE 55.—N. A. C. A. 43012 airfoil.



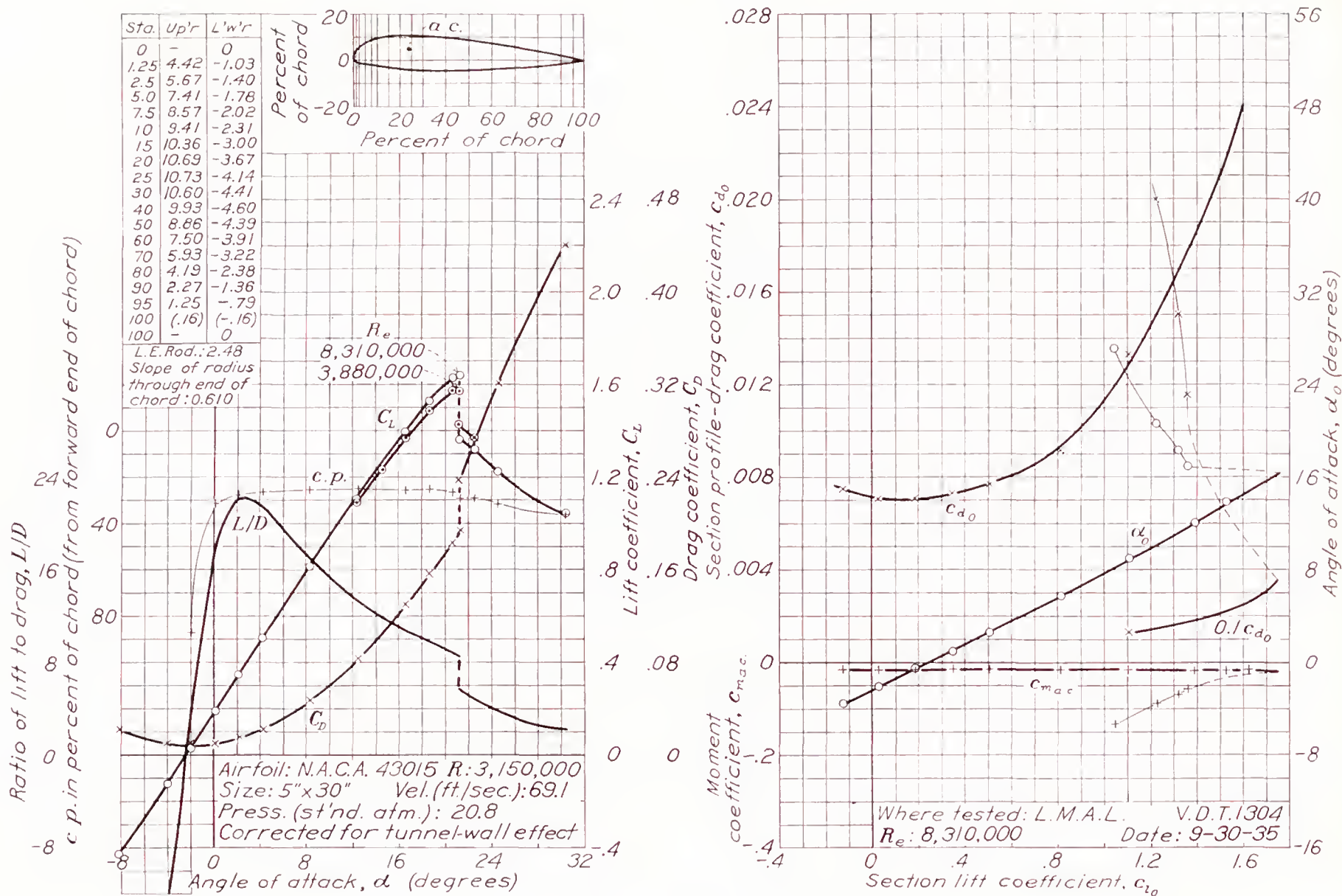


FIGURE 56.—N. A. C. A. 43015 airfoil.

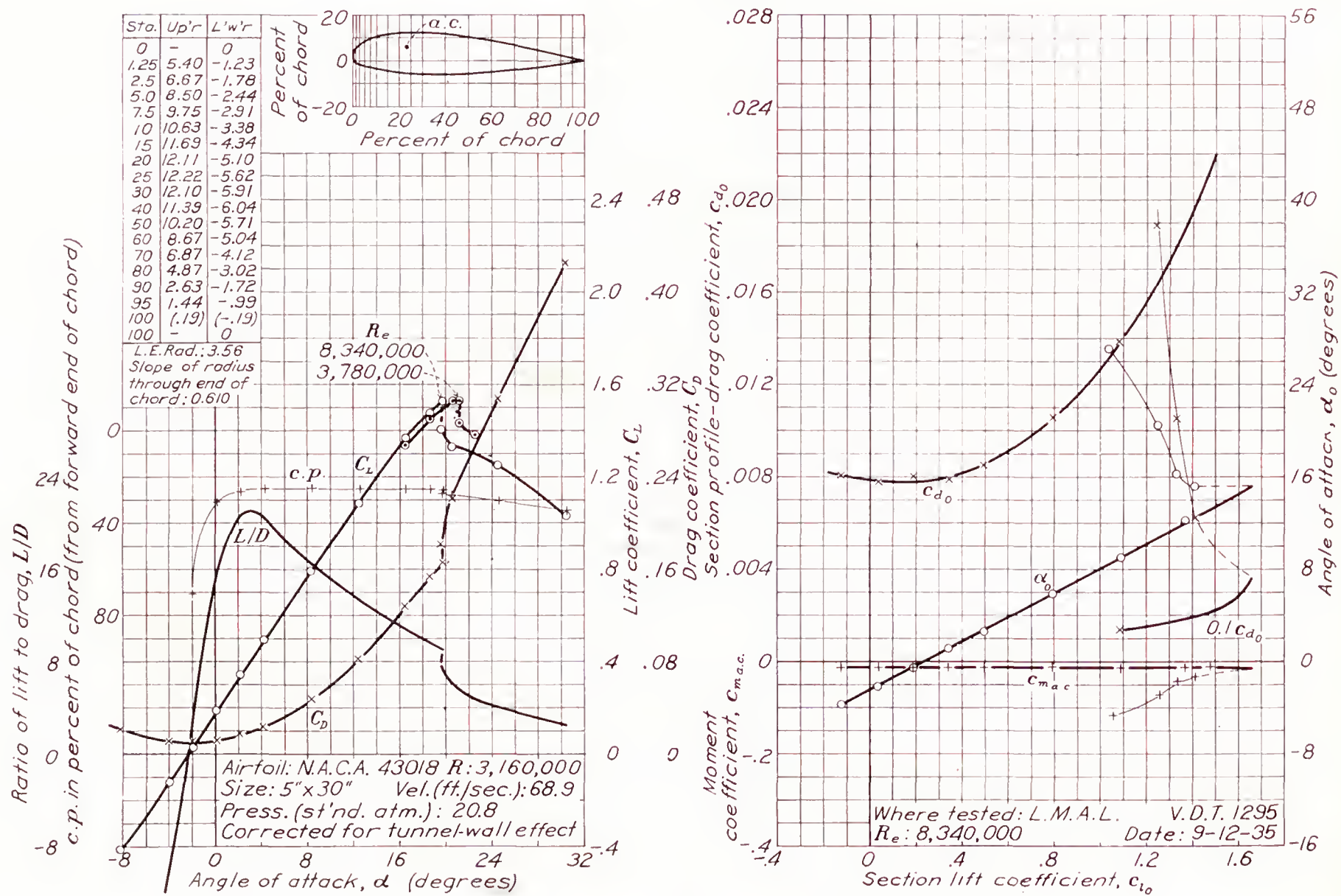


FIGURE 57.—N. A. C. A. 43018 airfoil.



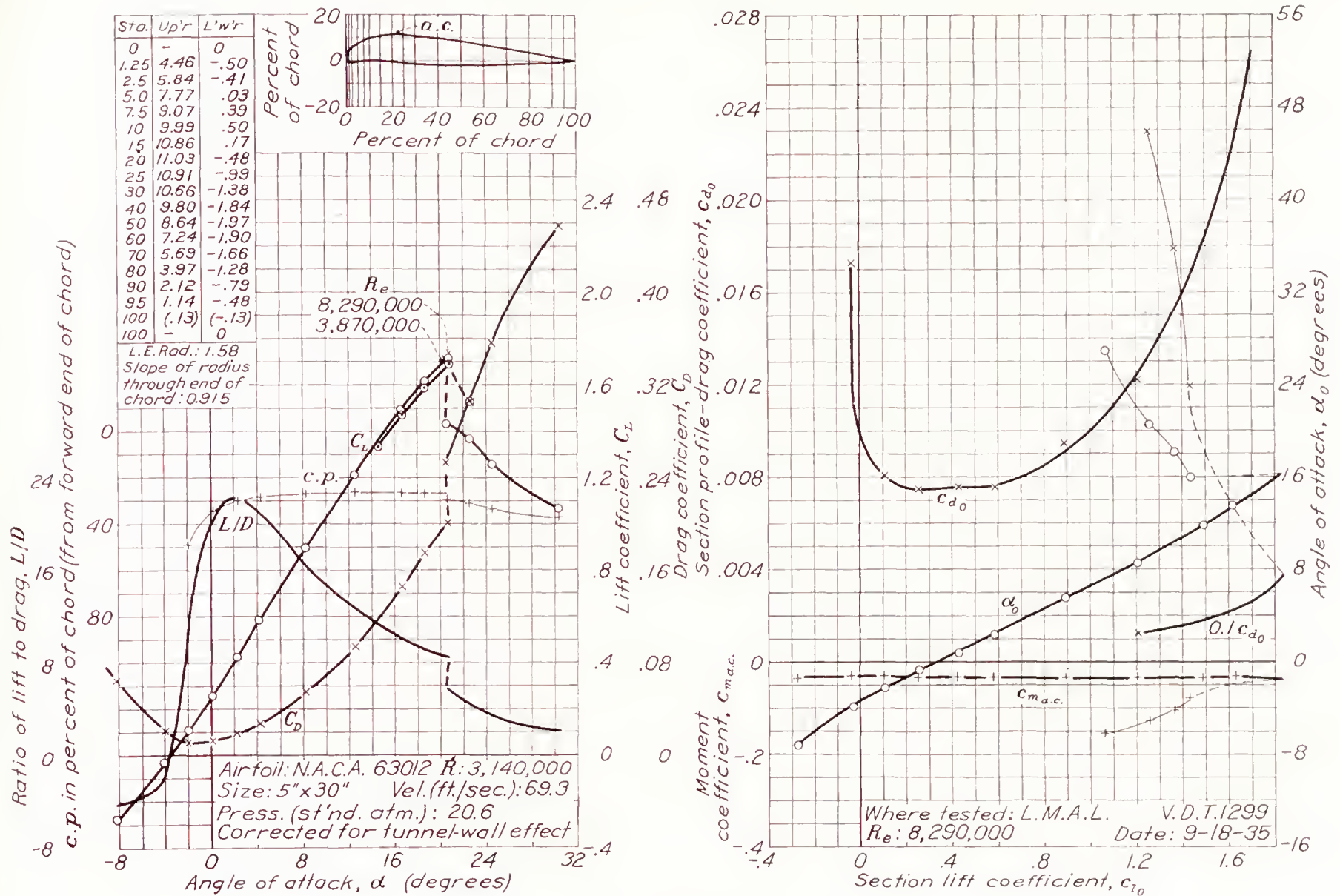


FIGURE 58.—N. A. C. A. 63012 airfoil.

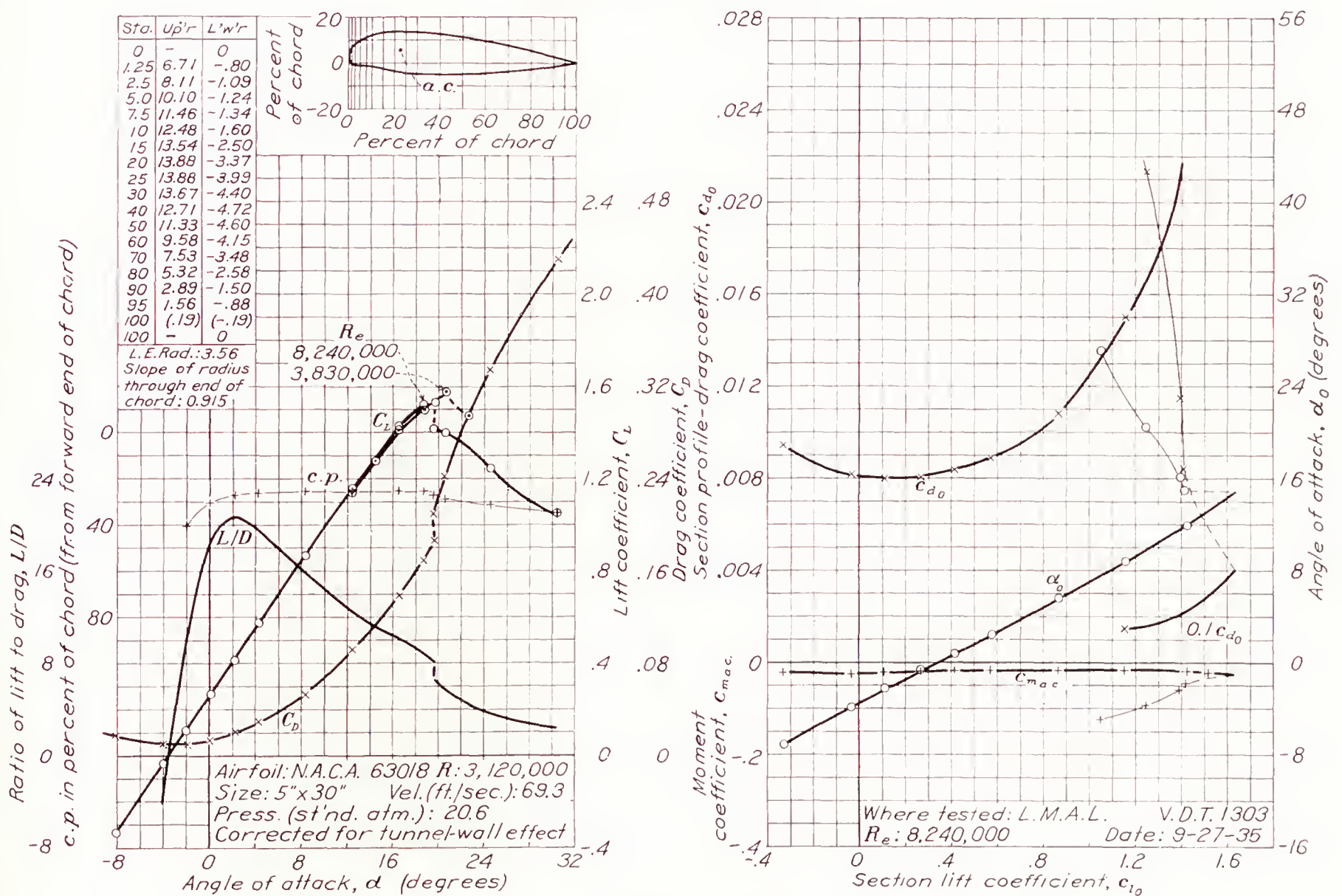


FIGURE 59.—N. A. C. A. 63018 airfoil.



## APPENDIX

### SUMMARY OF CORRECTIONS TO AIRFOIL DATA FROM THE N. A. C. A. VARIABLE-DENSITY TUNNEL

As a convenience to designers in correcting previously published data to be comparable with the data published in this report, a brief summary of the corrections now applied to airfoil section data is presented. These corrections apply to data obtained after January 1931 and most of them have been discussed in greater detail in reference 4. The corrections are presented in the order in which they are applied. Information is also given to aid in correcting previously published data.

**Corrections for tunnel-wall effects and to infinite aspect ratio.**—The formulas for correcting the data for tunnel-wall effects and to infinite aspect ratio are given in reference 1. Second-order effects not allowed for in these formulas have been investigated and found to be negligible for the usual tunnel tests. These corrections have been applied to all published data.

**Support-interference correction.**—The support-interference increment as obtained from figure 1 for the proper airfoil thickness is deducted from the drag or the profile-drag coefficients. A support-interference increment of the pitching-moment coefficient of 0.002 (see appendix of reference 4) is subtracted from the measured pitching moment. This second correction has already been applied to all published data.

**Corrections to section characteristics.**—The first-approximation section characteristics as obtained by correcting to infinite aspect ratio are unsatisfactory, first, because the airfoil theory does not represent with sufficient accuracy the flow about the tip portions of rectangular airfoils and, second, because the measured coefficients represent average values for all the sections along the span; whereas each section actually operates at a section lift coefficient that may differ markedly from the wing lift coefficient. The following corrections are therefore applied as a second approximation to the section characteristics.

$$\begin{aligned} c_{l_{max}} &= 1.07 C_{L_{max}} \\ a_0 &= 0.96 a_0' \\ \alpha_0 &= \alpha_0' + 0.39 C_L \text{ (deg.)} \end{aligned}$$

$$c_{d_0} = C_{D_0} + 0.0016 C_L^2 - \frac{1}{3}(t-6)0.0002(t \geq 6)$$

where  $t$  is the maximum thickness of the airfoil in percent of its chord and the primed values are those obtained from the first approximation. For some unusual cases, where the lift-curve peaks are very gradually rounding with little loss of lift beyond the stall, the maximum lift coefficients for the sections are increased by 4 percent instead of by 7 percent. The

curve of profile-drag coefficient against lift coefficient is modified at high lift coefficients (usually above about  $C_L=1$ ) owing to the change of  $c_{l_{max}}$  and the variation of  $c_{d_0}$  along the span, resulting in final values of  $c_{d_0}$  lower than those given by the formula in this range of lift coefficients (reference 4).

**Turbulence.**—The corrections for turbulence are made by use of the concept of an effective Reynolds Number. The scale effects that appear in the tunnel tend to correspond, in general, with those that would appear in flight at a higher Reynolds Number, which is therefore referred to as the "effective" Reynolds Number. The effective Reynolds Number is obtained by multiplying the test Reynolds Number by the turbulence factor, which is taken as 2.64 for the variable-density tunnel. This correction to the effective Reynolds Number necessitates a correction to the drag coefficient; this correction is applied by multiplying the profile-drag coefficient, after the foregoing corrections have been applied, by the ratio of the turbulent skin-friction coefficient of a flat plate at the effective Reynolds Number to that at the test Reynolds Number. This factor is taken as 0.85 for the usual test Reynolds Number of about 3,000,000. Because of the presence of induced velocities over the airfoil surface, this method is considered more justifiable than the method formerly used of subtracting a constant increment from the drag coefficients (see pp. 19–22, reference 4) but is obviously not applicable when large form drags are involved. For flapped airfoils, an approximate correction may be applied by subtracting the increments determined for the plain airfoil.

**Correction of previously published data.**—The important previously published airfoil data from the variable-density tunnel may be placed in five groups as regards the corrections needed to make the data comparable with those published herein. The five groups, and the corrections necessary, are as follows:

1. The data of group 1 are uncorrected except for those corrections described herein as having been applied to all published data. The other corrections should be applied in the order listed. These data are subject to a correction arising from a consistent error in measuring the dynamic pressure. If considered of sufficient importance, these data may be corrected by changing the coefficients to correspond to a reduction of measured dynamic pressure of 0.5 percent. (See appendix of reference 4.)

2. The data of group 2 are uncorrected except for those corrections described herein as having been applied to all published data. The other corrections should be applied in the order listed.



3. The data of group 3 are partly corrected. The corrections to section characteristics are satisfactory except for the maximum lift coefficient, which should be increased an additional 4 percent. A correction, no longer considered justifiable, has been applied to the aerodynamic-center position and may be removed by shifting the published positions back from the leading edge by  $0.005c$  and by doubling the vertical distance between the aerodynamic-center position and the chord line. The profile-drag coefficients may be corrected for the support interference and the revised correction to the effective Reynolds Number by the following formula:

$$c_{d0} = 0.85(c_{d0_{pub}} + 0.0011 - \Delta C_{D0_{min}}) \quad (1)$$

where  $\Delta C_{D0_{min}}$  is the proper support-interference increment obtained from figure 1.

4. The only correction needed for the data of group 4 is the correction to the profile-drag coefficients given in equation (1).

5. The data of group 5 need no corrections.

The data of the more important publications are classified in the following table

#### CLASSIFICATION OF PUBLISHED AIRFOIL DATA FROM THE N. A. C. A. VARIABLE-DENSITY WIND TUNNEL

Group	Published source	
	No. of N. A. C. A. Report	Figure or table
1	460	All material.
2	537	All figures.
3	586	Figures 2-24.
3	537	Table II.
3	586	All but figures 2-24.
4	610	All material.
4	628	Do.
5	631	Table I.

#### REFERENCES

1. Jacobs, Eastman N., and Abbott, Ira H.: The N. A. C. A. Variable-Density Wind Tunnel. T. R. No. 416, N. A. C. A., 1932.
2. Jacobs, Eastman N., Ward, Kenneth E., and Pinkerton, Robert M.: The Characteristics of 78 Related Airfoil

Sections from Tests in the Variable-Density Wind Tunnel. T. R. No. 460, N. A. C. A., 1933.

3. Jacobs, Eastman N., and Pinkerton, Robert M.: Tests in the Variable-Density Wind Tunnel of Related Airfoils Having the Maximum Camber Unusually Far Forward. T. R. No. 537, N. A. C. A., 1935.
4. Jacobs, Eastman N., and Sherman, Albert: Airfoil Section Characteristics as Affected by Variations of the Reynolds Number. T. R. No. 586, N. A. C. A., 1937.
5. Jacobs, Eastman N., Pinkerton, Robert M., and Greenberg, Harry: Tests of Related Forward-Camber Airfoils in the Variable-Density Wind Tunnel. T. R. No. 610, N. A. C. A., 1937.
6. Pinkerton, Robert M., and Greenberg, Harry: Aerodynamic Characteristics of a Large Number of Airfoils Tested in the Variable-Density Wind Tunnel. T. R. No. 628, N. A. C. A., 1938.
7. Jacobs, Eastman N., and Clay, William C.: Characteristics of the N. A. C. A. 23012 Airfoil from Tests in the Full-Scale and Variable-Density Tunnels. T. R. No. 530, N. A. C. A., 1935.
8. Relf, E. F., Jones, R., and Bell, A. H.: Tests of Six Aerofoil Sections at Various Reynolds Numbers in the Compressed Air Tunnel. R. & M. No. 1706, British A. R. C., 1936.
9. Williams, D. H., Brown, A. F., and Smyth, E.: Tests of Aerofoils R. A. F. 69 and R. A. F. 89, with and without Split Flaps, in the Compressed Air Tunnel. R. & M. No. 1717, British A. R. C., 1936.
10. Doetsch, H., and Kramer, M.: Systematic Airfoil Tests in the Large Wind Tunnel of the DVL. T. M. No. 852, N. A. C. A., 1938.
11. Doetsch, H.: Profilwiderstandsmessungen im grossen Windkanal der DVL. Luftfahrtforschung, Bd. 14, Hft. 4/5, 20. April 1937, S. 173-178.
12. Jones, R., and Williams, D. H.: The Profile Drag of Aerofoils at High Reynolds Numbers in the Compressed Air Tunnel. R. & M. No. 1804, British A. R. C., 1937.
13. Jones, R., and Williams, D. H.: The Effect of Surface Roughness on the Characteristics of the Aerofoils N. A. C. A. 0012 and R. A. F. 34. R. & M. No. 1708, British A. R. C., 1936.
14. Goett, Harry J., and Bullivant, W. Kenneth: Tests of N. A. C. A. 0009, 0012, 0018 Airfoils in the Full-Scale Tunnel. T. R. No. 647, N. A. C. A., 1938.
15. Goett, Harry J.: Experimental Investigation of the Momentum Method of Determining Profile Drag. T. R. No. 660, N. A. C. A., 1939.
16. Jacobs, Eastman N., and Rhode, R. V.: Airfoil Section Characteristics as Applied to the Prediction of Air Forces and Their Distribution on Wings. T. R. No. 631, N. A. C. A., 1938.



TABLE III  
AIRFOIL SECTION CHARACTERISTICS

Airfoil	N. A. C. A. reference (R=report, N=technical note)	Classification				Fundamental section characteristics										Derived and additional characteristics that may be used for structural design								
		Chord <sup>1</sup>	PD <sup>2</sup>	SE <sup>3</sup>	C <sub>L<sub>max</sub></sub> <sup>4</sup>	Effective Reynolds Number (millions) <sup>5</sup>	c <sub>l<sub>max</sub></sub>	α <sub>i0</sub> (deg.)	a <sub>0</sub> (per deg.)	c <sub>l<sub>opt</sub></sub>	c <sub>d0<sub>min</sub></sub>	c <sub>m a. c.</sub>	a. c. (per cent c. from c/4)		c <sub>l<sub>max</sub></sub> c <sub>d0<sub>min</sub></sub>	c. p. at c <sub>l<sub>max</sub></sub> (percent c)	Wing characteristics A=6; round tips		Thickness (percent c) at—			Camber (percent c)		
													Ahead	Above			m <sub>0</sub> (per radian)	C <sub>D<sub>min</sub></sub>	0.15c	0.65c	Maximum			
Clark Y	R 416	B	C 10	C 4	D	8.4	1.68	-5.0	0.092	0.12	0.0071	-0.059	1.1	4	237	29	4.07	0.0072	10.53	8.30	11.70	3.9		
Clark YM-15	N 412	C	D 10	D 4	C	8.4	1.70	-5.2	.094	.10	.0076	-.063	1.1	4	224	30	4.14	.0079	13.51	10.63	15.00	4.0		
Clark YM-18	N 412	C	E 10	E 4	C	8.2	1.60	-5.1	.091	.07	.0085	-.064	1.4	5	188	30	4.04	.0076	16.21	12.72	18.00	4.0		
Curtiss C-72	N 412	B	C 10	C 4	D	8.0	1.74	-5.6	.095	.23	.0071	-.034	1.0	3	245	30	4.18	.0075	10.53	7.39	11.73	4.0		
Göttingen 387	N 428	B	D 10	D 6	D	8.4	1.70	-6.6	.097	.30	.0076	-.093	.7	4	224	32	4.24	.0081	13.40	9.69	14.85	5.9		
Göttingen 393	N 412	B	D 10	D 5	D	8.1	1.68	-6.0	.094	.15	.0076	-.031	.4	1	221	31	4.14	.0079	12.50	9.27	13.75	4.9		
N-22	N 412	B	C 10	C 4	D	8.1	1.72	-5.4	.093	.17	.0075	-.075	.6	4	229	30	4.20	.0076	11.25	8.36	12.37	4.5		
N. A. C. A. CYH	N 412	B	C 11	C 3	D	8.1	1.58	-2.9	.095	.08	.0065	-.027	.7	6	243	28	4.18	.0066	10.53	8.50	11.70	3.1		
N. A. C. A. -M6	N 412	A	C 11	C 3	D	8.0	1.51	-1.8	.095	.03	.0066	.002	-4	0	229	26	4.18	.0066	10.29	9.00	12.01	2.4		
U. S. A. 27	N 412	B	C 10	C 6	B	8.1	1.71	-4.7	.094	.30	.0075	-.078	1.8	5	228	30	4.14	.0084	10.40	8.70	11.12	5.6		
U. S. A. 35-A	R 628	B	E 10	E 6	D	8.4	1.52	-8.0	.095	.38	.0094	-.111	.8	5	162	34	4.18	.0099	16.60	11.90	18.18	7.3		
U. S. A. 35-B	N 412	B	C 10	C 5	B	8.3	1.81	-5.2	.099	.35	.0071	-.076	.5	5	255	30	4.31	.0076	10.56	7.54	11.61	4.6		
N. A. C. A. 0006	R 460	A	A 10	A	D	8.5	.91	0	.098	0	.0051	0	.7	2	178	35	4.28	.0051	5.35	4.13	6.00	0		
N. A. C. A. 0009	R 586	A	B 10	B 0	A	8.3	1.39	0	.098	0	.0058	0	1.0	5	240	26	4.28	.0058	8.02	6.20	9.00	0		
N. A. C. A. 0012	R 583	A	C 10	C 0	A	8.4	1.66	0	.099	0	.0060	0	.6	3	277	26	4.32	.0060	10.69	8.27	12.00	0		
N. A. C. A. 0015	R 586	A	D 10	D 0	A	8.6	1.66	0	.097	0	.0064	0	1.2	4	259	25	4.24	.0064	13.36	10.33	15.00	0		
N. A. C. A. 0018	R 586	A	E 10	E 0	A	7.8	1.53	0	.096	0	.0070	0	1.7	4	219	25	4.20	.0070	16.04	12.40	18.00	0		
N. A. C. A. 0021	R 460	A	F 10	F 1	A	8.3	1.48	0	.093	0	.0080	0	3.0	6	185	24	4.11	.0080	18.71	14.46	21.00	0		
N. A. C. A. 0025		A		E 2	D	8.8	1.26	0	.085	0	.0094	0	2.7	5	134	25	3.82	.0094	22.27	17.22	25.00	0		
N. A. C. A. 0030		A			D	8.4	1.06	0	.074	0	.0117	-.005	6.9	26	91	19	3.48	.0117	26.72	20.66	30.00	0		
N. A. C. A. 2212	R 460	A	C 12	C 3	B	8.4	1.72	-1.8	.099	.12	.0062	-.029	.9	5	277	27	4.31	.0063	10.69	8.25	12.00	2		
N. A. C. A. 2409	R 460	A	B 10	B 2	B	8.1	1.62	-1.7	.099	.08	.0060	-.044	.7	4	270	28	4.31	.0061	8.02	6.50	9.00	2		
N. A. C. A. 2412	R 586	A	C 10	C 2	B	8.2	1.72	-2.0	.098	.14	.0061	-.043	.5	3	282	28	4.28	.0062	10.71	8.27	12.00	2		
N. A. C. A. 2415	R 460	A	D 10	D 2	C	8.0	1.66	-1.7	.097	.10	.0068	-.040	1.4	5	244	28	4.24	.0069	13.39	10.34	15.00	2		
N. A. C. A. 2418	R 460	A	E 10	E 2	C	8.0	1.53	-1.9	.094	.06	.0076	-.038	1.1	2	201	27	4.14	.0076	16.08	12.39	18.00	2		
N. A. C. A. 4403	R 460	A	A 10	A	D	8.1	1.32	-3.9	.100	.32	.0062	-.057	.4	0	213	32	4.34	.0071	5.40	4.16	6.00	4		
N. A. C. A. 4409	R 586	A	B 10	B 4	A	8.1	1.77	-3.9	.096	.26	.0066	-.088	.6	2	268	31	4.20	.0072	8.07	6.21	9.00	4		
N. A. C. A. 4412	R 586	A	C 10	C 4	D	7.9	1.74	-4.0	.098	.32	.0071	-.088	.8	2	245	31	4.28	.0073	10.77	8.28	12.00	4		
N. A. C. A. 4415	R 586	A	D 10	D 4	C	7.9	1.72	-4.0	.097	.22	.0076	-.085	1.0	1	226	31	4.24	.0079	13.45	10.34	15.00	4		
N. A. C. A. 4418	R 460	A	E 10	E 4	D	8.1	1.57	-3.7	.092	.13	.0079	-.078	1.4	1	199	31	4.07	.0081	16.15	12.40	18.00	4		
N. A. C. A. 4421	R 460	A	F 10	F 5	D	8.2	1.41	-3.4	.089	.08	.0088	-.071	1.9	2	160	32	3.96	.0089	18.79	14.48	21.00	4		
N. A. C. A. 23006	R 610	A	A 12	A	D	8.3	1.17	-1.2	.100	.15	.0057	-.012	1.0	8	205	26	4.34	.0058	5.34	4.13	6.00	1.8		
N. A. C. A. 23009	R 610	A	B 12	C 2	A	8.3	1.66	-1.1	.099	.08	.0059	-.009	.9	7	281	25	4.32	.0060	8.02	6.21	9.00	1.8		
N. A. C. A. 23012	R 610	A	C 12	D 2	A	8.4	1.74	-1.2	.100	.08	.0060	-.008	1.2	7	290	25	4.34	.0061	10.69	8.25	12.00	1.8		
N. A. C. A. 23015	R 610	A	D 12	D 2	A	8.4	1.73	-1.1	.098	.10	.0067	-.008	1.1	6	258	24	4.28	.0068	13.36	10.35	15.00	1.8		
N. A. C. A. 23018	R 610	A	E 12	E 2	B	8.2	1.58	-1.2	.097	.08	.0074	-.006	1.7	6	214	24	4.24	.0074	16.04	12.39	18.00	1.8		
N. A. C. A. 23021	R 610	A	F 12	E 2	B	8.2	1.50	-1.2	.092	.07	.0080	-.005	2.3	7	188	24	4.07	.0080	18.70	14.44	21.00	1.8		
N. A. C. A. 43012	R 610	A	C 12	D 4	A	8.4	1.84	-2.3	.100	.26	.0068	-.019	1.0	7	271	27	4.34	.0071	10.69	8.26	12.00	3.7		
N. A. C. A. 43015	R 610	A	D 12	D 4	A	8.3	1.76	-2.3	.101	.18	.0070	-.015	1.2	5	251	26	4.37	.0071	13.36	10.32	15.00	3.7		
N. A. C. A. 43018	R 610	A	E 12	E 4	C	8.3	1.63	-2.4	.096	.16	.0078	-.013	1.8	6	209	26	4.20	.0079	16.03	12.40	18.00	3.7		
N. A. C. A. 63012	R 610	A	C 12	D 6	A	8.3	1.84	-3.5	.100	.40	.0075	-.033	2.7	13	245	26	4.34	.0087	11.03	8.27	12.00	5.5		
N. A. C. A. 63018	R 610	A	E 12	E 7	A	8.2	1.63	-3.4	.097	.15	.0080	-.020	2.1	6	204	26	4.24	.0081	16.04	12.44	18.00	5.5		

<sup>1</sup> Type of chord. See reference 16.  
<sup>2</sup> Type of pressure distribution. See reference 16.  
<sup>3</sup> Type of scale effect on maximum lift. A signifies practically no scale effect. For other designations, see reference 4.  
<sup>4</sup> Type of lift-curve peak as shown in the sketches:



<sup>5</sup> Turbulence factor is 2.64.



## REPORT No. 670

# TENSILE ELASTIC PROPERTIES OF 18:8 CHROMIUM-NICKEL STEEL AS AFFECTED BY PLASTIC DEFORMATION

By D. J. McADAM, Jr. and R. W. MEES

### SUMMARY

*The relationship between stress and strain, and between stress and permanent set, for 18:8 alloy as affected by prior plastic deformation is discussed. Hysteresis and creep and their effects on the stress-strain and stress-set curves are also considered, as well as the influence of duration of the rest interval after cold work and the influence of plastic deformation on proof stresses, on the modulus of elasticity at zero stress ( $E_0$ ), and on the curvature of the stress-strain line. A constant ( $C_1$ ) is suggested to represent the variation of the modulus of elasticity with stress.*

*Curves of variation of proof stress with prior plastic deformation often have many oscillations between high and low values. Causes of the most abrupt of these oscillations are: Variation in the duration of the rest interval, and variation in the distribution of the experimental points throughout the range of extension. These oscillations probably are due in part to variations of internal stress. Variations in the rest interval generally have opposite effects on the slopes of the stress-set and the stress-strain curves. When  $E_0$ ,  $C_1$ , and the corresponding stress-set curve are known, a fairly good picture is available of the elastic strength. Slight prestretching, to the extent of a small fraction of 1 percent, generally causes considerable improvement in elastic strength. Whether most of the improvement is permanent can be established only by further experiment.*

*Comparison is made between values of  $E_0$  and  $C_1$  for 18:8 alloys and for other typical metals and alloys.*

### INTRODUCTION

This report deals with some phases of an investigation, which was sponsored by the National Advisory Committee for Aeronautics, of the elastic properties of high-strength aircraft metals. The tensile elastic properties of a widely used corrosion-resisting steel containing about 18 percent chromium and 8 percent nickel were investigated. In the annealed condition, this alloy is relatively soft. It can be strengthened by cold work but not (to an important extent) by heat

treatment. As its strength and elastic properties depend on the degree of cold work, the investigation considered the influence of cold work on these properties.

The elastic properties of a metal, as considered in this report, comprise the modulus of elasticity and the elastic strength. The elastic strength is generally expressed, for technical purposes, by one or more indices intended to represent the stress that causes the metal to reach, or even slightly to surpass, the boundary between elastic and inelastic deformation. This boundary was at one time considered to be definite and technically determinable. Below this boundary, the metal was assumed to behave in accordance with the mathematical theory of elasticity. The stress was assumed, in accordance with Hooke's law, to be proportional to the strain. On removal of stress the metal was assumed to return to the exact form that it had before the stress was applied. These properties were also assumed to be unchanged by subdivision or by variation of the size of the solid.

For some years, however, the meaning attached to the term "elastic strength" has been gradually changing. It has been found that the estimated proportional limit depends on the sensitivity of the method of measurement; the greater the sensitivity, the lower is the estimated proportional limit. Sayre (references 1 and 2) has shown, by an extremely sensitive method of measurement applied to ordinary steels and to some nonferrous metals, that the stress-strain line is probably curved throughout its entire length. Such curvature, moreover, is not necessarily due to a combination of elastic and plastic deformation. Mathematical studies of the probable variation of the attractive and repulsive forces with distance between the atoms of a space lattice seem to indicate that a curvilinear relationship between stress and strain is to be expected (reference 3). According to this view, Hooke's law is only an approximate representation of the stress-strain relationship within certain limits. A continuously curved stress-strain line obviously could not be utilized to find a definite boundary between elastic and inelastic deformation.



With development of knowledge of the microstructure of metals, it became evident that metals in general commercial use do not conform to another of the postulates of the mathematical theory of elasticity. These metals, which are made up of crystallites of varying orientation, are not unchanged by subdivision. Because of the varying orientation, the crystallites vary greatly in modulus of elasticity and elastic strength in any given direction in a polycrystalline body. In such a metal there could be no definite, technically determinable boundary between elastic and inelastic deformation. With increase in mean stress, the transition from elastic to plastic deformation is gradual.

It is conceivable, however, that a body could exhibit a curvilinear stress-strain relationship and a gradual transition from elastic to plastic deformation and yet be perfectly elastic below a certain stress. (By "perfect elasticity" is here meant the ability to resume at once its exact original form after removal of stress or after return, by any route, to the original stress.) The investigations of Hopkinson and Williams (reference 4) and Rowett (reference 5), however, have shown the existence of mechanical hysteresis at ranges of stress far below the elastic range. The investigations of Sayre (references 1 and 2) have confirmed these conclusions and have led to the view that hysteresis exists within any stress range. Such hysteresis, although it is generally called "elastic hysteresis," is evidence of imperfect elasticity, if perfect elasticity be defined as previously stated. According to the evidence, therefore, metals probably are not perfectly elastic at any stress.

Even the technically determined limits of elasticity are altered by slight surpassing of these limits (overstress). (See references 6 and 7.) Although the stress-strain relationship may be approximately linear before overstress, the relationship becomes curvilinear when the metal is retested immediately after release of the overstress. Rest of some overstressed metals at room temperature restores the stress-strain line to its original form. Restoration is hastened, however, by heating to 80°–100° C. (reference 7) or slightly higher. Among the metals that are thus restored to an approximately linear stress-strain relationship are the low-carbon steels. For some overstressed metals, however, complete restoration does not result from rest at room temperature or at 80°–100° C. but may result from heating at considerably higher temperatures.

As shown by Bauschinger (reference 6), overstress in tension causes immediate lowering of the elastic limit and yield point in compression, and vice versa. The stress-strain line is thus lowered more for stresses in the reverse direction than for stresses in the direction of the prior overstress. The elastic strength, in the direction opposite to the previous overstress, is not restored to its primitive value, even after rest or slight heating.

All these effects of overstress vary with the amount of the overstress (degree of prior plastic deformation). Study of the elastic properties of metals should therefore include study of the effects of slight overstress and of more severe cold work.

Even at stresses below the technically determined elastic limit, deformation may increase with time at constant load. A prevalent designation for such increase is "drift." After release of load, deformation generally continues for a time in the reverse direction to that of the loading. Such deformation is often termed "elastic after effect," although such a term is not generally appropriate. After fairly rapid increase or removal of load, a considerable part of the subsequent change of dimension may be due to "thermal creep." This effect is a purely elastic one caused by change of temperature. The phenomenon was first described and explained by Kelvin (reference 8). The importance of thermal creep has been emphasized more recently by Sayre (references 9, 10, and 11) and is discussed in more detail in a later section of this paper. The changes of dimensions under constant load or after removal of load, however, generally are not due entirely to thermal creep. They frequently consist almost entirely of a slower change of dimension, which may be discernible for hours, days, or even weeks. Both this slow creep and thermal creep proceed at rapidly decreasing rate. As the long-continued deformation after release of load is a type of inelastic action, such deformation is not appropriately termed "elastic" after effect.

There is evident need for clarification of the nomenclature for the elastic and the inelastic properties of metals. A general term is needed to designate any type of deformation occurring without increase of load. The word "creep," frequently used with this meaning, will be so used in this report. A fairly sharp distinction can be made between thermal creep and other types of creep. If there is a real difference in kind between the so-called drift and other types of slow deformation under constant load, however, the authors are not able to make such distinction in discussion of the data of this report.

The stress-strain line tends to be more curved for the 18:8 alloy steel than for carbon steels and ordinary alloy steels. The absence of a technically determinable proportional limit for this alloy, and for some other stainless steels, led to the specification of "proof stresses" as indices of elastic strength. A proof stress, as thus specified, must be endured without causing more than a designated amount of permanent deformation (permanent set) after release of the load. Such a test does not give a value for the elastic strength of a specimen but is merely intended to insure that the elastic strength is not below a certain limit. In the investigation of the elastic strength of metals, however, good use can be made of proof stresses determined



from stress-set curves; i. e., curves representing the influence of stress on permanent set (deformation remaining after release of load).

The investigation herewith reported has considered both the stress-set and the stress-strain relations. These two relations present complementary views of the elastic properties of a metal. The interrelationship between a stress-strain curve, hysteresis, creep, and permanent set, is discussed in part II. The method of obtaining correlated stress-set and stress-strain curves is illustrated and discussed in part III. The variations of the stress-set relationship and of the derived proof stresses with prior plastic extension, with the duration of the rest interval, and with the "extension spacing," are discussed in part IV. The variations of the stress-strain relationship with prior plastic extension, with duration of the rest interval, and with the extension spacing, as well as the variation of the modulus of elasticity with stress, are discussed in part V. Although this report is confined to results obtained with 18:8 chromium-nickel steel, results already obtained with other metals (to be discussed in a supplementary report) indicate that the conclusions are not limited (in qualitative application) to 18:8 alloy.

## I. MATERIALS, APPARATUS, AND METHODS

### MATERIALS AND SPECIMENS

The 18:8 corrosion-resistant alloy steels used in this investigation were of several compositions and had received various degrees of cold work. One of these steels, in two different degrees of hardness, is the same that was used in a previous investigation (results unpublished) for the Bureau of Aeronautics, Navy Department. The other steels were generously supplied by the Allegheny Ludlum Steel Corporation. They were some of the same materials that had been used by Dr. V. N. Krivobok of that company in investigating the effects of composition and cold work on some of the mechanical properties (reference 12). These steels were of four compositions, differing slightly in the proportions of chromium and nickel and in carbon content. They were supplied in three different degrees of hardness. Table I gives the compositions of all the materials and the mechanical properties of the materials as received.

In the serial designation given to each specimen, the first numeral represents the composition of the steel, and the numeral following the letter is the specimen number. The letter represents the degree of hardness; A represents annealed material, B represents half-hard material, and C represents hard material.

Only tension-test specimens were used in this investigation. The diameters of these specimens over their gage length and the corresponding bar diameters are given in table II. In order to obtain maximum accu-

racy in the determination of stresses, for the loading device used, the gage diameters were made as large as possible. In other respects, the specimens were according to the standard of the American Society for Testing Materials, for threaded specimens with 2-inch gage length. The ratio of gage length to diameter was not important in this investigation, because the investigation of elastic properties never required extension beyond the point of beginning local contraction.

### APPARATUS

A pendulum hydraulic testing machine of 50,000-pound capacity was used. (The accuracy of this machine is discussed later.) The specimens were held in grips with spherical seats. The extensometer used in some of the preliminary stress-strain measurements was a Ewing extensometer with 2:1 lever ratio. In later experiments, a Ewing extensometer with ratio 5:1 was used. The smallest scale division on this instrument corresponded to a change of length of 0.00008 inch, and readings could be estimated to about  $\pm 0.000008$  inch; this sensitivity corresponds to a strain sensitivity of  $\pm 4 \times 10^{-4}$  percent for the 2-inch gage length used. The Ewing extensometer measures the average of the extensions on two opposite sides of the specimen. In some of the later experiments, a pair of Tuckerman optical strain gages were used; these gages were attached to the opposite sides of the specimens. The smallest scale division on this extensometer corresponds to a change in length of 0.00004 inch. By means of a vernier on this instrument, it is possible to estimate changes of length to within about 0.000002 inch; this sensitivity corresponds to a strain sensitivity of  $1.0 \times 10^{-4}$  percent for the 2-inch gage length used.

### METHOD OF INVESTIGATION

The experiments consisted in determining the total strains at various stresses and the corresponding permanent extensions after release of load. The results thus obtained were used in plotting correlated stress-strain and stress-set curves. From the stress-set curves, proof stresses were obtained corresponding to permanent sets of 0.001, 0.003, 0.01, 0.03, and 0.10 percent. From the stress-strain curves, values were obtained for the modulus of elasticity.

As one object of the investigation was to determine the variation of elastic properties with plastic deformation, the previously mentioned correlated information was obtained with specimens that had received various degrees of cold work. Considerable information about the influence of prior plastic deformation could be obtained by comparing the results obtained with the annealed, the half-hard, and the hard steels. In order to investigate the effects of numerous smaller variations in prior plastic deformation, however, tests were not confined to specimens of the various steels as received.



By tension, specimens were extended by numerous short stages, and stress-strain and stress-set curves were obtained after each of these stages. With the same specimen, it was thus possible to obtain a sequence of curves representing the variation of elastic properties with plastic deformation.

#### ACCURACY OF DETERMINATION OF STRESS-SET CURVES

Permanent set was not measured at zero load, but at a load of 200 pounds. In order to determine the error in setting at this load, a series of extensometer readings were taken (with the same specimen) involving repeated increase of the load to a maximum (the selected

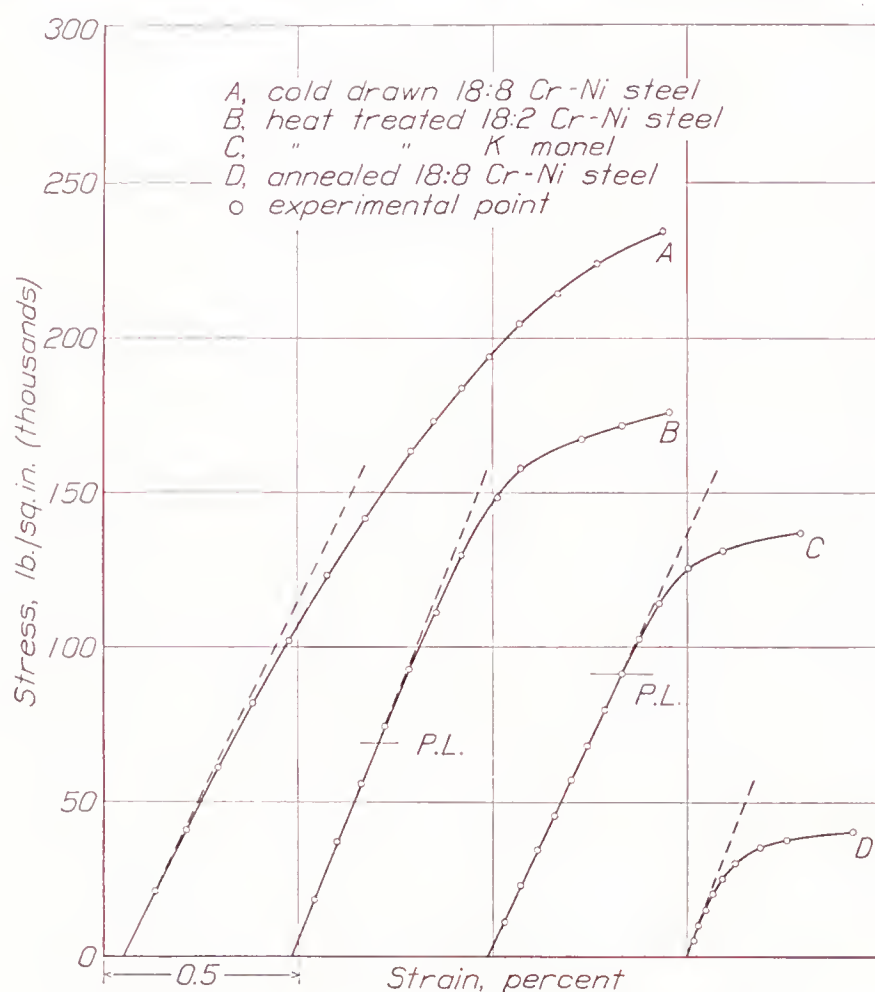


FIGURE 1.—Tensile stress-strain curves for four different metals.

value of this maximum being low enough to avoid permanent set) and reduction again to the minimum. The maximum difference between two successive readings at the minimum was equivalent to a load change of 6 pounds. This value corresponds to a stress error of 30 to 120 pounds per square inch, depending on the gage diameter of the specimen used. This stress error corresponds to a strain error of 0.0001 to 0.0004 percent, assuming a modulus of 30 million pounds per square inch. The effect of this error would be most important in determination of the lower part of a stress-set curve. As proof stresses in this report are based on permanent sets of 0.001, 0.003, 0.01, 0.03, and 0.10 percent, the corresponding maximum errors in these proof stresses would be 10 to 40 percent, 3 to 12 percent, 1 to 4 percent, 0.3 to 1.2 percent, and 0.1 to 0.4 percent, respectively.

When a stress-set curve was plotted, however, a number of determinations of permanent set were made and

the curve was faired through all these points. The probable error involved in determining proof stresses, therefore, would be somewhat less than those for single measurements. The percentage error in determining values for the lowest proof stress, 0.001 percent, evidently is rather large. The error, nevertheless, is insufficient to invalidate the results; as shown in a number of figures to be discussed later, variations of the 0.001-percent proof stress (with the various factors) are qualitatively similar to variations of the proof stresses corresponding to the higher values of permanent set.

## II. STRESS-STRAIN RELATIONSHIP, HYSTERESIS, AND CREEP

#### TYPICAL STRESS-STRAIN CURVES

Typical stress-strain curves, for annealed and for cold-drawn 18:8 steel, and for two alloys strengthened by heat treatment, are shown in figure 1. With the strain scale used in this figure, stress-strain lines B and C (representing the heat-treated alloys) appear straight, up to the indicated proportional limits. No proportional limit, however, can be found for either the cold-worked or the annealed 18:8 alloys. Even with this strain scale, it appears probable that the stress-strain lines for the 18:8 alloys are curved from the origin. With a more sensitive strain scale, the curvature would become prominent. For the heat-treated alloys, a more sensitive scale would cause the apparent proportional limits to be lower and less definite. Extremely sensitive strain measurements, such as those used by Sayre (references 1 and 2), probably would cause all the resultant stress-strain lines to be curved from the origin; all qualitative distinction between the curves for these four alloys would thus disappear.

#### GENERAL DESCRIPTION OF EXPERIMENTS ON HYSTERESIS AND CREEP

The stress-strain measurements indicated in figure 1 were made with gradually increasing load. If from some point on any of these curves the load had been gradually reduced to zero, the stress-strain relationship during this decrease would have followed a different curve. Even when the maximum stress is well below the technical elastic limit, the ascending and the descending curves generally do not coincide. The cycle of stress thus causes a hysteresis loop, which may or may not be closed at the bottom. The width of the loop and the degree of separation of the ascending and the descending curves at the bottom depend on the stress range, on the rate of loading, and on the number of previous cycles.

The interrelationship between stress, strain, and permanent set cannot be satisfactorily discussed without considering the influence of hysteresis and creep. In this report, some consideration will therefore be



given to hysteresis, its variation with cyclic repetition, and its relationship to positive and negative creep. Several series of hysteresis loops are shown in figures 2 and 3. In each of these series, the nominal stress range was between two constant tensile values; the lower value was only sufficient to facilitate reproducibility of strain measurement. With the stress range used for each specimen, considerable permanent set was obtained with the first cycles. The stresses were calculated by dividing the load by the cross-sectional area at the beginning of each cycle; this area was calculated from the original area by taking account of the prior plastic extension. The stresses so defined are termed "true stresses," to distinguish them from the nominal stresses based on the original cross-sectional area of the specimen.

In figure 2, the two rows of loops represent results of experiments with two specimens of one of the annealed 18:8 alloys. In order to avoid confusion, the origin of each loop has been shifted forward, by a constant abscissa interval, from the origin of the preceding loop. In each series, the experiments started with the material in its original condition. The number of each cycle in the series is given at the top. The cycle time, in minutes, is given at the top of each loop of the upper row and inside each loop of the lower row. The total plastic extension prior to each cycle is also given inside each loop. The time interval between cycles is indicated by the symbol at the beginning of each cycle. Each cycle, with one exception, was started immediately after the preceding cycle; one of the cycles was started a day after the preceding cycle. The abscissa scales for both rows are the same and are indicated at the bottom of the figure.

Because of the greater stress range in the cycles of the upper row, the plastic extension in the first few cycles was much greater in this row than in the lower row. Nevertheless, the permanent set per cycle evidently decreased more rapidly in the upper row than in the lower row. This difference in behavior doubtless is due to the much greater work-hardening obtained in the first few cycles of the upper row. Because of accidental overstressing, only 29 cycles could be obtained with the stress range represented by the lower row. A new specimen of the same material, therefore, was given 30 rapid cycles of the same stress range without observation of the strains, and the experiment was continued as represented in figure 3. The upper row of cycles in figure 2 will be discussed first. The lower row of figure 2 will then be discussed in connection with figure 3.

#### HYSTERESIS EXPERIMENTS WITH SPECIMEN 1A-5, FIGURE 2

The first four cycles in the upper row of figure 2 are represented by ordinary stress-strain curves. The first cycle, because of the relatively high stress applied to

this annealed material, caused an extension of 15 percent. The solid line represents the variation (with strain) of the nominal stress, that is, stress based on the original sectional area; the broken line represents the variation of the stress based on the actual cross section corresponding to the strain. Each of the other loops of the upper row is a plot of the true stress as previously defined.

Comparison of loops 1 to 4, with allowance for the fact that the abscissa scale is much more sensitive for loops 2, 3, and 4 than for loop 1, showed that each of these loops (both at the middle and at the bottom opening) is considerably narrower than the preceding loop. With continued cyclic repetition, however, the difference in form between any two adjacent loops gradually becomes smaller. In order to study these further variations, therefore, it is necessary to use a still more sensitive abscissa scale. This necessity suggests representation by stress-deviation curves. For loops 5 to 161, consequently, abscissas represent deviations, differences in strain from that corresponding to an assumed initial modulus line. The nearer this assumed modulus line is to tangency with the stress-strain curve at the origin, the more sensitive can the abscissa scale be made. With the assumption of an initial modulus of  $31 \times 10^6$  pounds per square inch, it has been possible to make the abscissa scale in figure 2 much more sensitive for loops 5 to 161 than for loops 2, 3, and 4.

During studies of the variations of the hysteresis loop with cyclic repetition, consideration may be given to the width of the loop at the middle, the width of the opening at the bottom, the deviation range of the loop, and the negative creep at the bottom. These deformation values, for the series of cycles represented by the upper row of figure 2, are listed in table III. This table contains information not only about the cycles represented in figure 2 but also about the other cycles not shown in the figure. For some of the cycles that are not represented in figure 2, stress-strain measurements were made; for other cycles, such as cycles 141 to 145, inclusive, no stress-strain measurements were made but the stress range was the same as for the measured cycles. The time for an unmeasured cycle, as shown in table III, was much less than for a measured cycle. The net plastic extension per cycle, consequently, was much less for the unmeasured than for the measured cycles.

With cyclic repetition, as shown in figure 2 and table III, the width of the loop at the middle and the width of the opening at the bottom, tend to decrease. The deviation range of the loop (abscissa range in fig. 2) also tends to decrease. This general trend of each of these values, however, is sometimes interrupted or masked by the effect of any marked variation of the cycle time or of the time interval between cycles. Each cycle represented in the upper row of figure 2 generally started immediately after the end of the pre-



ceding cycle. (The negative creep at the end of a cycle was viewed as part of that cycle.) After the 11 short cycles 141 to 154, however, there was a rest interval of 1 day. Loop 155, which immediately followed this rest interval, is much wider than loop 140. This widening effect, however, is only temporary; during several subsequent loops, the width rapidly decreases and the general trend is resumed.

The net permanent extension per cycle (width of the opening at the bottom of the loop) is the difference between the total positive and the total negative creep during the cycle. Most of the positive creep occurs at and near the top of the loop, and most of the negative creep occurs at and near the bottom. The bulging of the hysteresis loop in the first part of the descent from the top often gives qualitative evidence of positive creep. The amount of creep thus revealed, however, is somewhat less than the actual positive creep, because the descending stress-deviation line would curve rapidly to the left, if there were no positive creep. In the absence of direct measurement made during the cycle, the total positive or the total negative creep cannot be estimated for any of the cycles. Values for positive creep based on the bulging of the loop below the top, however, are listed in column 13 of table III. These values evidently have only qualitative significance.<sup>1</sup>

Positive creep during the first part of the descent from the top may have its counterpart in negative creep during the first part of the ascent from the bottom of the loop. In other words, if time is not given for negative creep at the bottom of a loop, the next loop may show evidence of negative creep during the first part of the ascent. This negative creep reduces the positive strain and thus increases the steepness of the first part of the ascent. Sometimes this negative creep is sufficient to cause actual deviation to the left in this part of the loop. In an investigation of stress-strain or stress-set relationship, therefore, care is necessary to eliminate or minimize the disturbing effect of negative creep, near the end of a cycle, on the form of the following stress-strain or stress-set curve. In the cycles represented in figure 2, and in most of the experiments represented in the following figures, the disturbing influence of negative creep was minimized by allowing a rest interval (indicated at the bottom of each cycle in fig. 2) before beginning the next cycle. Time was thus given for completion of important thermal creep and the most rapid part of the inelastic creep. As will be shown later, however, much longer time is necessary to eliminate entirely the influence of inelastic negative creep.

<sup>1</sup> The amount of positive creep during descent from the top depends on the time available for creep at and near the top of the ascent. It also depends on the rate of descent from the top. In the experiments represented in figs. 2 and 3, time was not given for completion of the fairly rapid creep at the top of the loop; after each reading, the cycle was immediately resumed. If even a few minutes had been allowed for creep at the top, the most rapid portion of the positive creep would have been completed. Forward creep during descent, therefore, would have been much less and probably would have had no discernible effect on the form of the loop.

In the series of cycles represented in the upper row of figure 2, and in the other measured cycles represented in table III, negative creep was determined 1 and 3 minutes after the end of the descent to the bottom of the loop. The positions after negative creep for 3 minutes are indicated in figure 2, and the amounts of creep during 1 and 3 minutes are listed in columns 11 and 12 of table III. That the rate of negative creep decreases rapidly with time is indicated by the fact that the creep during the first minute generally was greater than the additional creep during the next 2 minutes. In spite of the rapid decrease in rate, however, negative creep may sometimes be discernible for hours, days, or even weeks (reference 10).

#### HYSTERESIS EXPERIMENTS WITH SPECIMEN 1A-3, FIGURE 2

In the lower row of figure 2 the loops represent a series of 29 cycles obtained with another specimen of the same material but with a much smaller range of stress. Information about these cycles, and about the other cycles of the series, is given in table IV. The first four loops in the lower row represent variation of stress with strain; the other loops represent the variation of stress with deviation from an assumed initial modulus line. For some of the cycles not represented in figure 2, stress-strain measurements were made; for the others, stress-strain measurements were not made, but the stress range was the same as for the measured cycles. The unmeasured cycles were in two groups: cycles 14 to 19, inclusive, and cycles 22 to 27, inclusive. The time of an unmeasured cycle was much shorter than that of a measured cycle, and no time was allowed for negative creep between unmeasured cycles.

With cyclic repetition, the deviation range, the loop width, and the width of the opening at the bottom (net positive creep) tend to decrease. As in the upper row of loops, the decrease in these deformation values is greatest during the first cycles; with cyclic repetition, the rate of decrease tends to become gradually less, although this general trend is sometimes interrupted owing to changes in cycle time. In the lower row the loops are more irregular than in the upper row. Positive creep during descent from the top of the loop also is more prominent in the lower than in the upper row. This difference may be due to the fact that the stress range during the first cycle represented in the upper row was sufficient to carry the metal through the stage of most rapid work-hardening with deformation.

#### HYSTERESIS EXPERIMENTS WITH SPECIMEN 1A-4, FIGURE 3

Because of accidental overstress of specimen 1A-3, the series represented by the lower row of figure 2 and in table IV consisted of only 29 cycles. In order to study the effect of a larger number of cycles, with the same material and with the same stress range, another series was started with a new specimen, designated



1A-4. This series, consisting of 388 cycles, is represented by the hysteresis loops in figure 3; the corresponding numerical values are listed in table V. The first 30 cycles (not represented in fig. 3) were unmeasured cycles, intended merely to carry the specimen quickly through the stages that had already been studied by means of specimen 1A-3 (lower row of fig. 2). The total extension caused by the 30 initial rapid cycles applied to specimen 1A-4 unfortunately was not measured. This extension, however, doubtless was less than the extension caused by the 29 cycles, with much longer cycle time, applied to specimen 1A-3. Comparison of widths of loops in the two series indicates that the extension caused by the 30 rapid cycles applied to specimen 1A-4 was about 3.5 percent. Assuming a value of 3.5 percent, corresponding values for total permanent set at the end of the other cycles of the series have been estimated, and are listed in column 10 of table V.

For convenient arrangement of the symbols and legend in figure 3, it is assumed that the end of the measured negative creep is the end of the cycle. An interval of unmeasured creep is treated as an interval between cycles. The time allowed for negative creep at the end of a cycle, as indicated by the symbols and legend of figure 3, generally was either 2 or 3 minutes. When the total time for negative creep was 2 minutes, the amount of creep was measured at the end of the 2 minutes, and this time was assumed to be the end of the cycle; the next cycle was started immediately. When the total time for negative creep was 3 minutes, the amount of creep was measured at the end of 1 minute but not at the end of the 3 minutes. Although the next cycle was started at the end of the 3 minutes, the time interval between such cycles was assumed to be 2 minutes. Between cycles 80 and 81, the interval was 45 hours; between cycles 115 and 116, the interval was 3 days. In this series, as shown in table V, there were four groups of consecutive rapid cycles: cycles 48 to 78, inclusive; cycles 84 to 113, inclusive; cycles 119 to 273, inclusive; and cycles 276 to 375, inclusive.

Loop 31 of figure 3 is about as wide as loop 4 of the lower row of figure 2. The narrowing effect of the first four measured cycles applied to specimen 1A-3, therefore, was about equal to the effect of the first 30 rapid cycles applied to specimen 1A-4. That the relatively great width of loop 31 represents an unstable condition induced by the previous 30 rapid cycles is indicated by the greatly decreased width of loop 32. The effect on cycle 31 was as if some of the unpermitted creep of the first 30 cycles were transferred to cycle 31.

With cyclic repetition, the maximum width of the loop and the width of the opening at the bottom (net positive creep) gradually decrease. The positive creep during descent from the top of the loop, as indicated by the form of this part of the loop, also gradually

decreases. The decrease in these deformation values is rapid during the first few measured cycles but becomes slower with cyclic repetition. The general trend, however, is sometimes interrupted, owing to changes in cycle time or in the interval between cycles. The 31 rapid cycles following loop 47, for example, were followed by the slightly widened loop 79. This increased width, however, was only temporary; loop 80 is only about as wide as loop 47 and loop 81 is considerably narrower. That this difference in width between loops 80 and 81 probably is not due to the 2-day interval is indicated by the fact that rest between cycles generally causes the loop width to increase. The 3-day interval between cycles 115 and 116 caused loop 116 to be wider than loop 115. That loop 116 represents an unstable condition induced by the long prior rest interval is indicated by the fact that loops 117 and 118 are much narrower than loop 116 and are even narrower than loop 115. The 30 rapid cycles following loop 83 and without subsequent rest interval, and the 155 rapid cycles between loops 118 and 274, caused little change in the loop width.

After the 10 rapid cycles between loops 377 and 388, loop 388 is much wider (both at the middle and at the bottom opening) than loop 377. This increased width of loop 388, however, is due not to the preceding rapid cycles but to the great difference in cycle time. The greater time of cycle 388 gave opportunity for a much greater amount of positive creep. If additional cycles had been applied with the shorter cycle time generally used in this series, even the first of such cycles possibly would have given a loop no wider than loop 377; with further cyclic repetition, the loop width probably would have slowly decreased.

#### VARIATION OF CREEP WITH CYCLIC REPETITION

The negative creep at the bottom of the loop, as shown in tables III, IV, and V, decreased rapidly during the first few cycles, and changed little during further cyclic repetition. If negative creep at the end of each cycle had been measured for a much longer period, however, the results probably would show that cyclic repetition caused the negative creep to decrease at a generally decreasing rate (reference 13). Both net positive creep and negative creep, with repetition of cycles of constant stress range, probably approach zero. The width of the loop at the middle, however, probably does not approach zero but approaches a limiting value. With a completely closed loop, the form and the size probably would be independent of cycle time. The hysteresis represented by such a loop is sometimes termed "elastic hysteresis." A better name in frequent use is "statical hysteresis."

That the 388 cycles (applied to specimen 1A-4) have not caused the hysteresis to be entirely statical is demonstrated by the previously mentioned difference



between loops 377 and 388 of figure 3, and by the fact that these loops, unlike a loop representing statical hysteresis, are far from complete closure. Thousands, possibly millions, of cycles probably would have to be applied to this specimen to cause complete closure of the loop and to make the hysteresis entirely statical (reference 13). With much shorter cycle time (high cycle frequency), the number of cycles necessary to reach a condition of statical hysteresis would be still greater.

#### THERMAL CREEP

Negative creep frequently is called "elastic after effect." The probable reason for this name is that negative creep represents approach to the initial form and dimensions. One kind of negative creep, however, probably is due to plastic deformation of some parts of the microstructure, caused by internal stresses in the elastic portions of the microstructure. As a general name for the phenomenon, "elastic after effect" is therefore less suitable than "negative creep."

One kind of negative creep undoubtedly represents a truly elastic change of form due to the thermal influence of change of stress. Kelvin (reference 8) showed that elastic extension of a metal tends to cause slight lowering of temperature and that elastic compression (or removal of elastic tension) tends to cause slight elevation of temperature, provided that the temperature coefficient of expansion of the metal is positive. The opposite temperature changes occur if the coefficient of expansion is negative. After abrupt change of tensile or compressive stress, therefore, metal tends to absorb heat from its surroundings or to give up heat to its surroundings and thus tends to change in length until the difference in temperature between the metal and its surroundings disappears. This type of creep has been investigated by Sayre (references 9, 10, and 11) and by others and has been called "thermal creep."

As shown by Sayre, consideration should be given to the probable amount and duration of thermal creep after any abrupt change of stress. The total amount of thermal creep, which can be determined approximately by means of equations based on the mathematical investigation by Kelvin, depends on the temperature coefficients of expansion and of the modulus of elasticity as well as on the change of stress (reference 10). Consideration of these equations has led to the conclusion that, in the specimens of 18:8 alloy used in this investigation, the total thermal creep was 0.003 times the preceding abrupt elastic change of length. A value of about 0.0025 was obtained by Sayre for ordinary steel. For 18:8 alloy, however, the ratio would be somewhat greater, because the temperature coefficients of expansion and of the modulus of elasticity are greater for this alloy than for ordinary steel. Assuming that the ratio is 0.003 for 18:8 alloy, the total thermal creep

probably amounts to about 0.00001 percent per 1,000 pounds per square inch prior adiabatic change of stress.

The rate and the duration of thermal creep, because they depend on the rate of change of temperature of the metal, depend on the thermal conductivity of the metal, and on other factors affecting the rate of transfer of heat to and from the surroundings. With a relatively long wire, the rate of equalization of temperature depends almost entirely on the rate of radiation and convection and very little on the conduction of heat along the wire. Under such conditions, the duration of thermal creep, as stated by Sayre (reference 10), is nearly proportional to the diameter of the wire. With the relatively short, thick specimen used in the investigation, most of the heat transfer would be by conduction through the ends. Very little quantitative information is available about the duration of thermal creep under these conditions. Results mentioned by Farren and Taylor (reference 14) are somewhat contradictory. The impression gained from their paper, however, is that the thermal change (with the form of specimen used in this investigation) would generally be completed within about a minute. In order to minimize the effects of thermal creep, therefore, most of the readings of permanent set, described in the following sections, were made after a rest interval of at least 1 minute. The time needed for the rest interval obviously depends on the amount of the prior change of stress.

In a specimen under bending stress, change of stress causes opposite changes in temperature on opposite sides of the specimen. The resultant steep transverse temperature gradient thus causes the equalization to be much faster, and consequently causes the duration of thermal creep to be much shorter for bending than for tension or compression. For torsion, the amount of thermal creep is generally negligible because torsion causes practically no change in volume.

The stress range for the previously described loops of figures 2 and 3 was not great enough to cause important thermal creep. Even if the stress had been lowered rapidly from the maximum value of the cycle, the total negative thermal creep would have been less than 0.001 percent. The time required for the descent from the top to the bottom of each loop, moreover, was sufficient to allow completion of most of the thermal creep during the descent. The negative creep observed at the bottom of each loop was therefore almost entirely inelastic creep.

### III. STRESS-SET CURVES, STRESS-DEVIATION CURVES, AND PROOF STRESSES

Stress-strain (or stress-deviation) curves alone give incomplete information about the elastic properties of 18:8 alloy. This information needs to be supplemented



by study of the relationship between stress and resultant slight plastic deformation (permanent set). The method of obtaining correlated stress-set and stress-deviation curves is illustrated by the diagram at the right of the lower row of figure 3.

This diagram consists essentially of a series of hysteresis loops of gradually increasing range. Each experimental point in this diagram, with one exception, was obtained with merely enough delay to permit observation of the stress and the strain. The rate of variation of the load, however, was so slow that the influence of thermal creep probably was negligible. With the one exception mentioned, no time was allowed for negative creep at the bottom of a loop; the next loop was started immediately. (In most of the experiments to be described later, there was a time interval between any two loops.) The one exception in this series of loops is at the end of loop 4. After the immediate reading, represented by point E, there was a delay of 70 minutes before the beginning of loop 5. (Loop 5 has been shifted to the right as indicated by the scale at the bottom of the figure.) The rather large amount of negative creep during the 70-minute interval has shifted the beginning of loop 5 from E to F. As thermal creep was negligible, the negative creep from E to F was almost entirely inelastic.

The total permanent set after each loop is indicated by the abscissa of the corresponding point at the bottom of the loop. If the stress at the top of each loop is plotted against the total permanent set at the bottom of the loop, a curve is obtained representing the variation of permanent set with stress. Curves thus obtained are shown in the lower rows of figures 6, 8, 12, and 16 and in both rows of figure 20. They will be presented and discussed in part IV. In the obtaining of a stress-set curve, time was generally allowed for the most rapid part of the negative creep at the bottom of the loop. The amount of this creep generally increases with the previously applied stress.

The curve drawn through the tops of the series of gradually increasing loops in figure 3, is a stress-deviation curve. Such a curve, although it is obtained by a series of cycles, differs little in form and position from a stress-deviation curve obtained with continuous increase of load. From a series of gradually increasing loops, therefore, it is possible to obtain both a stress-set and a stress-deviation curve. Stress-deviation curves so obtained are shown in the upper rows of figures 6, 8, 12, and 16, discussed in part V.

Various proof stresses may be derived from a stress-set curve. By "proof stress" is meant the stress corresponding to an indicated value of permanent set. The values of permanent set utilized in establishing proof stresses in this report are 0.001, 0.003, 0.01, 0.03, and 0.10 percent. For any of these values of per-

manent set, the proof stress may be determined from a stress-set curve by estimating the ordinate at the corresponding abscissa. The steeper the slope of the stress-set curve, the higher are the corresponding proof stresses.

#### IV. THE INFLUENCE OF PRIOR PLASTIC DEFORMATION AND OF DURATION OF THE REST INTERVAL ON THE STRESS-SET CURVE AND ON THE DERIVED PROOF STRESSES

##### THE INFLUENCE OF PRIOR PLASTIC EXTENSION ON THE STRESS-SET CURVE AND ON THE DERIVED PROOF STRESSES, SPECIMEN 1B-1

In order to investigate the effect of prior plastic deformation on the stress-set curve and on the derived proof stresses, tension-test specimens of the various materials have been extended by numerous small stages to the point of beginning local contraction or even somewhat further. After each of these small stages a stress-set and generally a stress-deviation curve have been obtained. With a single specimen, therefore, it has frequently been possible to obtain a series of stress-set and stress-deviation curves. With the specimens of the less ductile materials, however, fewer of these curves could be obtained, and results from several specimens have sometimes been assembled in a single figure.

Attention will first be given to the stress-set curves in the lower row of figure 6 and to the derived diagram of figure 7. The results shown in these two figures were obtained with the same specimen of half-hard metal, 1B-1. This specimen was stretched in numerous short stages. Each of these stages consisted of a group of cycles of increasing range, similar to the previously described group shown at the right of figure 3. From each of these groups, a stress-set curve and a stress-deviation curve were obtained. Most of the stress-set curves are shown in the lower row of figure 6, and the corresponding stress-deviation curves are shown in the upper row.

In each of the cycles of a group, readings were taken without a rest interval. (In later experiments, with other specimens, readings in each cycle were taken after a rest interval, generally 1 minute.) The rate of increase or decrease of stress, however, was never faster than about 75,000 pounds per square inch per minute. For the smaller cycles of each group, the rate was only about 30,000 pounds per square inch per minute. In the last (largest) cycle of a group, in which the range of stress generally was considerably greater than any of the values indicated in the stress-set curves of figure 6, the plastic extension was relatively large. In this cycle, therefore, the reduction of stress from the maximum to the minimum was made very slowly; the time required for this reduction was 6 to 7 minutes. Between the last reading for each group of cycles and the first reading for the next group, there was a rest interval.



No time was given for negative creep before the readings, except before the initial reading for each group of cycles. Negative creep, however, would chiefly affect the positions of experimental points representing the effects of the higher stresses. The effect of allowance for negative creep on the form of the stress-set curve and on the proof stresses would probably be relatively small. Because of the slow rates of loading and unloading, moreover, the reproducibility of results probably was sufficiently good to permit a study of the influence of prior plastic extension and of the rest interval.

The rest interval between determinations of successive stress-set curves (or stress-deviation curves) varied from a few minutes to several days. The duration of the rest intervals is indicated, in figures 6 and 7 and in other diagrams, by various symbols, whose meaning is explained in the key of figure 7. In the experiments represented in figures 6 and 7, the rest interval generally was 2 to 6 minutes; a few of the intervals were much longer. The extensions indicated by the experimental points of figure 7 consisted entirely of groups of cycles like the group at the right of figure 3, with no extensions between these groups.

Comparison between the experimental points in figure 7 and the corresponding stress-set curves in figure 6 was facilitated by numbering consecutively the points in figure 7, and these numbers have been used to identify the corresponding curves of figure 6.

The initial stress-set curve, curve 1 of figure 6, shows permanent set at very low stress. With increase of stress, moreover, the permanent set increases very rapidly. The corresponding proof stresses, as indicated (for 0.001, 0.003, and 0.01 percent permanent set) by the short projecting lines at the left of figure 7, are low. The proof stresses for 0.10 percent permanent set cannot be obtained from any of the curves shown in this report but have been obtained from curves drawn with a less sensitive scale of abscissas. Curve 2 of figure 6 is much steeper than curve 1; the nearly vertical portion, moreover, is much greater in curve 2 than in curve 1. The slight plastic extension required to obtain curve 1 evidently has caused considerable improvement in elastic strength.

During several succeeding cycles, the improvement in elastic strength generally continues, as illustrated by curves 3, 4, and 5 of figure 6, and by the corresponding points in figure 7. With still more prior plastic extension, there is practically no further general improvement in the nominal proof stresses corresponding to permanent sets of 0.001 and 0.003 percent, and only slight improvement in the proof stress for 0.01 permanent set. The proof stresses corresponding to permanent sets of 0.03 percent and 0.10 percent, however, show continuous general improvement with increase in prior extension.

In the discussion of proof stress-deformation curves such as those of figure 7, chief attention will be given

to the curves representing the 0.001 percent and 0.003 percent proof stresses. In the consideration of elastic strength, more attention probably should be paid to these indices than to the 0.01, 0.03, and 0.10 percent proof stresses. The 0.01 percent proof stresses probably should be viewed as indices of resistance to yield rather than as indices of elastic strength.

The most conspicuous characteristic of the proof stress-deformation diagram (fig. 7) is the wide scatter of experimental points. This wide scatter cannot be attributed to experimental error but is due to the influence of several variables inseparably associated with investigation of the variation of proof stresses with plastic extension. In order to study the influence of plastic extension and of the associated variables on proof stresses, consecutive experimental points have been connected by straight lines. The graphs thus obtained, as will appear in the following discussion of this and other figures, should be viewed not as continuous "curves" of variation of proof stress with deformation but as a sequence of experimental points connected by straight lines. In the graphs so drawn in figure 7, there is tendency to zigzag oscillation between high and low values. A wide swing sometimes comprises several experimental points; for example, the swings between 20 and 23 and between 33 and 42. A few wide swings, however, are between adjacent points. An exceptionally high point tends to be followed immediately or shortly by an exceptionally low point, and vice versa. Examples of wide swing between adjacent points are 77-78, 102-103, 113-114.

These wide oscillations are superposed on a less abrupt wavelike oscillation of mean values. This wavelike oscillation is represented approximately by the broken curve for 0.001 percent proof stress in figure 7. Similar curves could be drawn for the 0.003 percent and the 0.01 percent proof stresses. Maxima and minima for all these curves would be at about the same abscissas. For the 0.001 percent proof stress, the highest wave crest is at prior plastic extension of about 0.4 percent. For the 0.003 percent proof stress, the wave crests are at about the same height at prior plastic extensions of 0.2 and 6 percent; with further extension, the heights of the wave crests evidently change very little. For the 0.01, 0.03, and 0.10 percent proof stress, the wave crests increase in height with increase in prior extension.

If the curves were drawn with ordinates representing true stress (stress based on the sectional area at the beginning of each stress-set determination), the curve for 0.001 percent proof stress would still have its highest maximum at about 0.4 percent prior extension but the maxima for the curves for other proof stresses would increase in height with increase in prior extension.

The oscillations in the proof stress-deformation curves of figure 7 correspond to variations in the stress-set curves. In the consideration of possible causes of



these variations, attention is attracted to the influence of the rest interval prior to the determination of each stress-set curve. This interval was 2 to 6 minutes for all the curves except three. For three curves, 98, 103, and 108, the prior rest interval ranged from about 80 minutes to 21 hours. These three curves are much less steep than the curves immediately preceding, and they correspond to exceptionally low points in figure 7. This fact suggests that the slope of the stress-set curve is greatly influenced by the prior rest interval.

In the literature, practically no reference has been made to the influence of the prior rest interval on the form of the stress-set curve. References 1, 5, 7, 9, 10, 11, 15, and 16 discuss the influence of rest interval on the form of the stress-strain curve. These references all report that overstress lowers (increases the rate of deviation of) the stress-strain curve. Before the overstress, the curve (for many metals) may have a long, nearly straight portion; after the overstress, the graph is curved from the origin. Rest after overstress, as generally reported (references 7, 15, and 16), tends to elevate the stress-strain curve in such a way as to restore the original nearly straight portion. With some metals, restoration of "elasticity" is complete after a rest interval at room temperature; with other metals, complete restoration requires a slight temporary elevation of temperature. On a stress-set curve, however, a rest interval evidently tends to have the opposite effect. With increase in the duration of rest, according to the evidence in figures 6 and 7, the stress-set curve becomes less steep. As some exceptionally low points in figure 7 were obtained after very short rest intervals, however, they must have been influenced by some factor other than the duration of the rest interval. This subject was further investigated, therefore, by additional experiments made with special attention to the influence of the rest interval.

THE INFLUENCE OF PRIOR PLASTIC EXTENSION AND OF DURATION OF THE REST INTERVAL ON THE STRESS-SET CURVE AND ON THE DERIVED PROOF STRESSES, SPECIMEN 1B-3

Another specimen of the same half-hard material was similarly extended by groups of cycles of application and removal of load. Results thus obtained are shown in figures 8 to 11. For these extensions, as for those represented in figures 6 and 7, there was a rest interval, but no extension interval, between successive groups of cycles.

In the determination of each stress-set curve (fig. 8) from a group of cycles, such as that shown at the right of the lower row of figure 3, the time schedule was different from that used in determining the stress-set curves of figure 6. Each reading of permanent set, represented by each experimental point in the lower row of figure 8, was obtained after a rest interval of 1 minute, after the stress had been reduced to the minimum value (about 1,500 pounds per square inch). The

time required for the reduction of stress from the maximum to the minimum value was about 1 minute for the smallest (first) cycle of a group, and 1½ to 2 minutes for the largest (last) cycle. The rest interval before reading probably was not enough for completion of negative creep induced by the large cycles. This creep, however, probably was small in comparison with the permanent set. Variations in form of the stress-set curves, therefore, can be attributed largely to the influence of prior plastic deformation and to varying duration of the rest interval.

A rest period intervened also between adjacent groups of cycles (adjacent stress-set curves). The duration of this rest interval is indicated approximately by the symbols in figures 8 and 9, which are explained by the key in figure 9. Further information about the influence of the rest interval was obtained by interspersing a number of intervals ranging from ½ hour to more than 48 hours among the much shorter intervals, 2 to 6 minutes.

The influence of duration of the rest interval is clearly shown by comparison of the stress-set curves in the lower row of figure 8 and by comparison of the heights of the corresponding experimental points in figure 9. Every relatively long prior rest interval resulted in a stress-set curve less steep than the curves immediately preceding and following. As some of the stress-set curves of this series are not shown in figure 8, the relative steepness of curves 8 to 27 of that figure can be deduced only from the relative heights of the corresponding experimental points in figure 9. As shown in figure 9, every experimental point representing a relatively long prior rest interval is lower in the diagram than the points immediately preceding and following. Of the exceptionally low points in figure 9, only one or two represent results obtained after a short rest interval, 2 to 6 minutes. The most conspicuous of these is 33, which appears to represent a recoil from the exceptionally high point 32.

The evidence appears conclusive, therefore, that the steepness of the tensile stress-set curve for this material tends to decrease with increase in the duration of the preceding rest period. In a consideration of the possible causes of this effect of the rest interval, attention is naturally directed to the effect of negative creep. A specimen in which negative creep had been permitted probably would exhibit more positive creep (permanent set) on reloading than would a specimen that had not been given opportunity for negative creep. In this connection, it is worthy of note that the effect of a 56-minute rest interval (curve 54) on the steepness of the stress-set curve was nearly as great as the effect of a longer interval. This fact appears to be consistent with the opinions of various investigators (reference 11) that the relationship between rate of creep and time is exponential.



The fact that the initial proof stresses are exceptionally low may not be attributable entirely to the long time that has been available for negative creep. To what extent these low initial values are attributable to prior negative creep or to other effects of a long rest period can be decided only after further investigation.

The wide zigzag oscillations so noticeable in figure 7 are again conspicuous in figure 9. Not all of the wide oscillations in this figure are attributable to differences in rest interval. The steep descent between 32 and 33, for example, evidently is due to some other cause. Differences in the rest interval evidently may be so interspersed as to intensify the oscillations and influence their spacing. A low point representing a long rest interval tends to be followed immediately by an abrupt rise to an exceptionally high point. This high point is followed by a descent, which is influenced considerably in steepness (of the straight connecting lines as drawn) by the position of the next point representing a long prior rest interval. This influence of the relative positions of the low points that represent long rest intervals is illustrated by the following examples. Between low points 19 and 24, which are relatively far apart, there is a steep rise and less steep descent. Between low points 31 and 37, which are still farther apart, there are two oscillations. Between low points 40 and 43, 43 and 46, 46 and 48, and 48 and 51, which are near together, there is a steep rise and an equally steep descent. Point 28 apparently is so placed that it shortens the rebound from point 27. The extension spacing of the interspersed points representing long rest intervals, evidently has much influence on the range of oscillation.

The initial stress-set curve of figure 8, like the initial curve of figure 6, is much less steep than the next succeeding curve. The form of curve 1 of figure 8 apparently indicates that permanent set is induced in this material by any stress, however small. Curve 2 shows that the elastic strength has been greatly improved because of the slight plastic extension in determining curve 1. Further plastic extension caused general further improvement of elastic strength, as shown by the stress-set curves of figure 8 and by the increase in height of the corresponding points in figure 9. This improvement continues at a generally decreasing rate until point 5 is reached. At this point begins the first important descent to a minimum. The position and height of this minimum is affected only slightly by point 7 representing a relatively long prior rest interval. The range of oscillation apparently tends to increase with prior plastic extension, at least to an extension of 12 to 18 percent. (A similar increase in range of oscillation with prior extension may be seen in fig. 7.)

The zigzag oscillations are superposed on a less abrupt wavelike curve. The curve for 0.001 percent proof stress, as in figure 7, reaches its first maximum at prior

extension of about 0.4 percent and its first minimum at an extension of about 2 or 3 percent. Even if the ordinates in figure 9 represented true stresses, the curve for 0.001 percent proof stress would show no continuous tendency to increase in height with increase in prior plastic extension beyond about 0.4 percent.

THE INFLUENCE OF PRIOR PLASTIC EXTENSION AND OF DURATION OF THE REST INTERVAL ON THE STRESS-SET CURVE AND ON THE DERIVED PROOF STRESSES. SPECIMEN 2A-1

In order to obtain further information about the influence of prior plastic extension and of duration of the rest interval on the stress-set curve and on the derived proof stresses, another series of experiments was made with a specimen of annealed material, 2A-1. Stress-set curves obtained in these experiments are shown in the lower row of figure 12, and the derived proof stresses are shown in figure 13. In these figures, ordinates represent "true stress," stress based on the sectional area at the beginning of determination of a stress-set curve.

In the previously described experiments, with specimens 1B-1 and 1B-3, extension was by a continuous series of stages, each comprising a group of cycles involved in the determination of a stress-set curve. In the experiments with specimen 2A-1, however, there were numerous pairs of adjacent short extensions separated by relatively long single extensions. Each pair of adjacent short extensions consisted of two adjacent groups of cycles involved in the determination of two stress-set curves. In each pair in figure 13, therefore, the experimental points are separated only by the extension involved in determining the first stress-set curve of the pair. As the first stress-set curve of each pair was obtained after a relatively long extension, the determination of this curve should be preceded by a relatively long rest interval. This rest interval, as shown in figure 13, was at least 20 minutes, often much longer. The second experimental point of a pair was obtained after a rest interval that varied from a few minutes to 20 minutes or more. From the relative positions of the experimental points of a pair, information may be obtained about the influence of duration of the rest interval.

In many instances, the stress-set curves of a pair were separated by a small intervening cycle (insufficient to cause important permanent extension but sufficient to influence the lower part of the following stress-set curve). The nominal maximum stress of this intervening cycle was 40,000 pounds per square inch. The second point of each pair with such an intervening cycle is indicated in figures 12 and 13 by a small diamond shaped symbol.

After the intervening cycle, the second stress-set curve of the pair was immediately determined. Although a rest interval of varying duration immediately preceded the intervening cycle, this cycle prevented the



rest interval from affecting the second stress-set curve of the pair.

With the annealed material used in these experiments, the range of oscillation in figure 13 does not attain the high values noted for half-hard material in figures 7 and 9. The range of oscillation, however, evidently tends to increase with the prior extension. The influence of duration of the rest interval on these oscillations is again conspicuous in figures 12 and 13. As shown in figure 12, stress-set curves obtained after relatively long rest intervals, generally are less steep than the curves immediately preceding and following. As shown in figure 13, the low point of each oscillation (with a few exceptions) represents a result obtained after a relatively long rest interval. Increase in duration of the rest interval, therefore, evidently tends to lower the stress-set curve and the derived proof stresses. The effect of increase in the rest interval appears to be large for the first hour; further increase in duration appears to have somewhat less effect.

The effect of the (previously described) small eye intervening between two consecutive stress-set curves is clearly revealed in figure 12. A stress-set curve immediately following such a cycle always extends vertically for a considerable distance, which evidently tends to increase with the prior plastic extension. In figure 13, all the corresponding points are at the tops of oscillations. Oscillation tops not occupied by such points are occupied by points obtained with short prior rest intervals; they are also the second points of pairs.

An intervening small eye, therefore, probably tends to accentuate the rebound from the low point of an oscillation, and a long rest interval tends to accentuate the recoil from the high point of an oscillation. There is need, however, for investigation of the effect of a rest interval after an intervening eye. Only part of the improvement in elastic properties caused by such a cycle may be permanent.

Although oscillations such as those shown in figure 13 are influenced by duration of the rest interval and by an intervening cycle, they probably are influenced by other factors, which are yet to be considered. The general impression gained from a study of figures 7, 9, and 13 is that an exceptionally low point, due to any cause, tends to be followed by an abrupt rise to an exceptionally high point. The spacing and the range of these oscillations evidently can be influenced by interspersing relatively long rest intervals among short rest intervals and also by interspersing other procedures that tend to influence the steepness of the stress-set curve.

The oscillations shown in figure 13 may be viewed as superposed on a less abrupt wavelike curve. For both the 0.001 percent and the 0.003 percent proof stresses, the first wave maximum probably is at a prior extension of 5 or 6 percent, and the first minimum is

at about 10 percent. These extensions are much greater for this annealed specimen than for the half-hard specimens represented in figures 7 and 9. For the 0.01, 0.03, and 0.10 percent proof stresses, the general trend (with prior extension) is continuously upward.

**THE INFLUENCE OF PRIOR PLASTIC EXTENSION AND OF DURATION OF THE REST INTERVAL ON THE STRESS-SET CURVE AND ON THE DERIVED PROOF STRESSES, SPECIMENS 2C-1, 3C-1, 4C-1, AND 5C-1**

The extension experiments previously described were made either with annealed material or with half-hard material that could be extended greatly before beginning to contract locally. The extension experiments now to be described were made with hard material, which could not be extended far before reaching maximum load condition. Results obtained with four specimens of hard material, differing slightly in composition, are shown in figures 16 and 17.

The initial stress-set curve for each specimen shows no vertical portion. Even the smallest stresses evidently caused permanent set. These curves, like the corresponding curves for annealed and half-hard metal, show no evidence of a real elastic limit of the metal as received. As shown by the increased steepness of curves 2, however, considerable improvement in elastic strength was caused by even the slight permanent extension made in determining curves 1. That most of this improvement is not due to the shortness of the rest interval between curves 1 and 2 will become evident in discussion of subsequent experiments in which the rest intervals between curves 1 and 2 were much longer.

With further plastic extension, as illustrated by the other curves of figure 16 and by the other experimental points in figure 17, the improvement in elastic strength continues more slowly. This improvement consists chiefly in elevation of the upper part of the stress-set curve, thus causing general continuing rise of the 0.03 percent and the 0.10 percent proof stress curves in figure 17. The curves for 0.001 and 0.003 percent proof stresses, however, reach maxima at extensions of 0.15 to 0.4 percent. Beyond this maximum in each curve, there are alternate descents and rises qualitatively similar to the oscillations shown in figures 7, 9, and 13.

Most of the rest intervals in these experiments were short, 2 to 6 minutes. A few results, however, were obtained with relatively long prior rest intervals. These occasional points evidently have much influence on the oscillations of the curves in figure 17. Such points, with a few exceptions, are low points of wide oscillations. Two of the exceptions are points 3 and 4 obtained with specimen 5C-1. Because these points are located on the abrupt rise due to the first slight plastic extensions, the depressing effect of the relatively long rest interval was not sufficient to interrupt the rise. Point 6 representing about the same rest



interval, however, is near the bottom of the recoil from the first rise. The relatively long rest interval here accentuates the recoil and gives an exceptionally low point.

Although the duration of the rest interval generally has considerable influence on the slope of the stress-set curve and on the derived proof stresses, the examples just cited (and others still to be discussed) seem to indicate that the oscillations of the proof stress-deformation curve are due in part to other factors.

**INFLUENCE OF PRIOR PLASTIC EXTENSION ON THE PROOF STRESS-DEFORMATION CURVES, SPECIMENS 2B-3, 2B-4, 3B-4, 2C-4, 5C-3, AND 5C-4**

It seemed desirable to investigate further the influence of duration of the rest interval and other factors, and especially to ascertain the form of the proof stress-deformation curve with the influence of variations in the rest interval eliminated or at least minimized. In the obtaining of the previously described proof stress-deformation curves, most of the rest intervals were short. When the proof stress-deformation curves now to be described were obtained, nearly all of the rest intervals were either medium (20 to 70 minutes) or long (17 or more hours). Typical stress-set curves thus obtained are shown in figure 20, and the corresponding proof stress-deformation curves are distributed among figures 21 to 24. With any one of the specimens represented in figure 20, nearly all of the rest intervals were of the same order. With specimens 2B-3, 3B-4, and 5C-3, nearly all of the intervals were of medium length, 30 to 70 minutes; a few intervals were about 1 day. With specimens 2B-4, 2C-4, and 5C-4, nearly all of the rest intervals were about 1 day; a few intervals were about 2 days.

The initial stress-set curve for each specimen represented in figure 20, like the initial stress-set curves obtained with previously described specimens, shows permanent set at all stresses. Comparison of curves 1 and 2 shows that even the slight plastic extension required for determining curves 1 caused considerable improvement in elastic strength. The fact that the rest intervals between curves 1 and 2 were relatively long appears to indicate that much of the improvement caused by this slight tensile extension is permanent. The permanence of the improvement, however, can be determined definitely only by additional experiments with much longer rest intervals.

**PROOF STRESS-DEFORMATION CURVES OBTAINED WITH REST INTERVALS OF A DAY OR MORE AT ROOM TEMPERATURE OR WITH REST INTERVALS OF 30 MINUTES IN BOILING WATER**

The results represented by the stress-set curves in figure 20 are typical of a number of results obtained with specimens of annealed, half-hard, and hard materials. From these stress-set curves are derived the proof stress-deformation curves of figures 21 to 29,

inclusive. The stress-set curves from which figures 25 to 29 are derived are not included in the report.

Extension of each of the specimens represented in figures 21 to 29 generally was by the previously described alternate long and short stages. The short stage consisted of a pair of adjacent groups of cycles involved in determination of a pair of adjacent stress-set curves. Each pair was separated by a relatively long extension interval from the pairs immediately preceding and following. The rest interval prior to the first stress-set curve of a pair was always at least 20 minutes, often much longer.

When the forms of the proof stress-deformation curves in figures 21 to 29 are studied, it is convenient to consider first the forms of the curves that are as free as possible from the influence of duration of the rest interval. With such curves as a basis of comparison, it should be possible to discern the modifying influence of the rest interval. For this reason, many of the diagrams of figures 21 to 29 were obtained with consistently long rest intervals, 18 hours or more. Such diagrams were obtained with specimens 2B-4 of figure 22, 2C-4 and 5C-4 of figure 24, and 4B-4 of figure 25.

Numerous experiments, by various investigators, have shown that restoration of "elasticity" after over-stress is greatly accelerated by even a short rest interval at the temperature of boiling water (reference 7). A rest interval of 30 minutes or less in boiling water was found to have as much effect as days of rest at room temperature. Most of the effects described in the literature, however, were obtained with carbon steels. The observed "restoration of elasticity," moreover, consisted in elevation of the stress-strain curve. Such experiments apparently give no assurance that treatment with boiling water would accelerate the effect of a rest interval on the stress-set curve of 18:8 alloy. Nevertheless, the effect of boiling water was tried, as a possible means of shortening the time required for obtaining a proof stress-deformation curve free from the influence of varying rest interval. Experiments were made with rest intervals of 30 minutes in boiling water interspersed with long rest intervals at room temperature. Proof stress-deformation curves, based on these experiments, were obtained with specimens 5B-3 of figure 25, 5B-4 of figure 26, and 3C-4 of figure 27.

The points obtained with a rest interval of 30 minutes in boiling water generally are no higher in the diagram than the points obtained with a rest interval of a day or more at room temperature. In each of the three diagrams, therefore, a single curve has been drawn to represent the results obtained with both of these rest conditions. A very different relationship is found when both medium and long rest intervals are at room temperature. As shown in the diagrams for specimens 3B-4 of figure 23, 4B-3 of figure 25, and 2C-3 of figure



27, points representing a rest interval of a day or more at room temperature are consistently below the points representing a rest interval of 20 to 70 minutes at room temperature. The changes occurring during the rest interval, therefore, evidently are much faster at 100° C. than at room temperature. The evidence indicates that a rest interval of 30 minutes in boiling water has practically the same effect as an interval of about 1 day at room temperature.

In the discussion of the form of the basic proof stress-deviation curve, attention will therefore be directed first to curves obtained either with rest intervals of 30 minutes in boiling water or entirely with long rest intervals at room temperature. Diagrams of this kind were obtained with seven specimens, 2B-4 of figure 22, 2C-4 and 5C-4 of figure 24, 4B-4 and 5B-3 of figure 25, 5B-4 of figure 26, and 3C-4 of figure 27. If some irregular oscillations between high and low values be disregarded, the results obtained with each of these specimens may be represented by a curve of about the same form. The first part of each curve, like the first part of the proof stress-deformation curves previously described, is a steep rise to a maximum, reached at a small prior plastic extension. Each curve then descends to a minimum, and again gradually ascends.

#### PROOF STRESS-DEFORMATION CURVES OBTAINED WITH MEDIUM REST INTERVAL (20-70 MINUTES)

Seven diagrams, distributed among figures 21, 23, 24, 25, 27, and 29, are based largely on experimental points obtained with medium rest intervals, 20 to 70 minutes. The six diagrams obtained with half-hard and hard material will be considered first. Each curve has the usual initial rise to a maximum, reached at a small prior extension, and the usual steep descent. The oscillations, however, are much more prominent in these curves than in the curves based entirely on long rest intervals. One of the oscillations generally involves a rebound from the first minimum to a second maximum at an extension of 1 to 2 percent. A few of the experimental points in these diagrams were obtained with a long rest interval (a day or more); each of these points generally is the first point of one of the previously described pairs, based on adjacent stress-set curves. The second point of a pair generally was obtained with a medium rest interval. Each point representing a long rest interval, with one exception, is at the bottom of an oscillation. The second point of such a pair, again with one exception, is much higher than the first, and sometimes is the high point of an oscillation. The interspersed points representing long rest intervals, therefore, generally tend to accentuate the oscillations between high and low values of proof stresses.

Even when both experimental points of a pair were obtained with medium rest intervals, the second point frequently is much higher than the first. Examples

of this relationship are points 5-6, 7-8, and 11-12, obtained with specimen 2B-3 of figure 21; points 4-5, obtained with specimen 5C-3 of figure 24; and points 11-12 obtained with specimen 4B-4 of figure 25. Frequently, also, the opposite relationship is found. A relatively low second point of a pair, however, generally is located somewhere in the recoil from the high point of an oscillation. Examples of such location in the recoil from a previous high point are pair 9-10 obtained with specimen 2B-3 of figure 21, pairs 7-8 and 11-12 obtained with specimen 3B-4 of figure 23, and pair 9-10 obtained with specimen 4C-3 of figure 27. When a pair of points follows a long single extension, the second point of the pair tends to be higher than the first. When the extension interval prior to a pair of points is rather short, the combined influence of variations in the rest interval and of the extension spacing of the preceding points may cause the second point of the pair to be no higher than the first. A short extension, when it is the first extension of a specimen or when it follows a long extension interval, evidently tends to increase the proof stresses.

The range of oscillation tends to be especially wide when alternate medium and long rest intervals occur within the extension range usually occupied by the first rapid rise and descent. An example of this is seen in the diagram for specimen 4B-3 of figure 25. The difference in rest interval between points 2-3 has caused premature and abrupt recoil from the first peak of the curve. This recoil is followed by an equally abrupt rebound, which causes point 5 to occupy an unusually high position, for a point representing a long rest interval. Another, less conspicuous, example of the influence of duration of the rest interval within this extension range, is found in the diagram for specimen 2C-3 of figure 27. These examples are additional illustrations of the previously mentioned fact that an exceptionally low point, however it may be caused, tends to be followed immediately or shortly by an exceptionally high point.

A curve drawn so as to follow approximately the first rise and descent, and then so as to follow the low points of oscillations in each of the six diagrams would be similar in form to the previously described basic curve obtained either with long rest intervals at room temperature or with rest intervals of 30 minutes in boiling water. The curve would first rise rapidly to a maximum, reached at small extension, would then descend rapidly, and again rise slowly to an extension of about 5 percent. The evidence appears to indicate that the basic curve for all these diagrams is of the same general form, but that the form may be obscured or masked by the influence of variations in the duration of the rest interval and in the extension spacing of the experimental points.



A diagram obtained with annealed specimen 5A-3 is shown in figure 29. In addition to the experimental points within the range of the first rapid rise and descent, there are four widely separated pairs of points. In three of these pairs, the first point represents a long rest interval. Every other point of the diagram, with one exception, represents a medium rest interval. The first point of each of the four pairs, whether it represents a long or medium rest interval, is lower than the second point. This fact tends to confirm the previously expressed view that the difference in height between the points of a pair depends not only on difference in the rest interval but also on the extension spacing. When a pair follows a relatively long single extension, the general tendency is for the second point of the pair to be higher than the first.

The range of oscillation obtained with annealed material tends to be smaller than the ranges obtained with half-hard or hard materials. The range evidently tends to increase with increase in the prior plastic deformation, whether the deformation is by tensile extension, by rolling, or by drawing.

A basic curve drawn to represent the points in this diagram would be of the wavelike form mentioned in connection with previously described diagrams. Because of the great range of extension, the curve would have several maxima and minima. The curve for 0.001 percent proof stress evidently would reach its first maximum at an extension of about 2 to 5 percent. All of the other basic curves, probably because of the great work-hardening rate for annealed material, evidently have a general upward tendency. The upward tendency is slight, however, for the curve representing 0.003 percent proof stress.

#### PROOF STRESS-DEFORMATION CURVES OBTAINED WITH INTERSPERSED LONG AND SHORT REST INTERVALS

Four diagrams, obtained with half-hard material, are based on experiments with both long and short rest intervals. These diagrams were obtained with specimens 2B-2 of figure 21, 3B-3 of figure 22, 4B-2 of figure 23, and 5B-2 of figure 26. The experimental points of each of these diagrams are arranged in pairs. The first point of each pair was obtained after a relatively long rest interval, 17 hours or more; the second point of each pair, with one exception, was obtained after a rest interval of 2 to 6 minutes. The exception is point 2 of 2B-2, which was obtained after a rest interval of 20 minutes.

Even with this wide difference in duration of the rest interval, the second point of a pair is not always higher than the first. In the diagram for specimen 2B-2 of figure 21, point 4 is no higher than point 3. These points, however, are at the bottom of the recoil from the first maximum. Every other second point of a

pair, in this diagram, is considerably higher than the first. The second points of pairs 5-6 and 9-10, owing to the great effect of the difference in rest interval, are much higher than the maximum of the initial rise.

In the diagram for specimen 3B-3 of figure 22, points 3 and 4 (belonging to the same pair) are at the same height. This pair, however, is at the crest of the initial rise. (The difference between points 1 and 2 is unusually small.) Every other second point of a pair is considerably higher than the first. The effect of the difference in rest interval is so great for pair 5-6, that point 6 is nearly as high as the initial maximum.

In the diagram for specimen 5B-2 of figure 26, every second point of a pair, with one exception, is higher than the first. The recoil from the initial maximum is so great that the first minimum is exceptionally low. The rebound from this minimum carries pair 5-6 to a considerably greater height than pair 3-4, and thus places point 6 at a second maximum.

In the diagram for specimen 4B-2 of figure 23, three of the second points of a pair are below the corresponding first points. The spacing, however, is such that point 3 is at the first maximum and point 4 is far down in the following descent. Point 7 is at the second maximum and point 8 is on the following descent. In this diagram, the extension spacing evidently is such as to overcome, in the instances mentioned, the effect of the difference in rest interval.

If curves were drawn in each of these four diagrams, so as to follow the initial rise and descent and then so as to follow the low points of the oscillations, the curves would be qualitatively similar to the previously described basic curves. In the diagram for specimen 4B-2, the extension spacing evidently is such that superposed oscillations are minimized, and a curve drawn in accordance with the experimental points would be similar in form to the basic curve.

In figures 28 and 29 are four diagrams obtained with four specimens of annealed material. In three of these diagrams, the first point of each pair generally was obtained after a long rest interval and the second point generally was obtained after a rest interval of 2 to 6 minutes. Almost invariably the second point of each pair is considerably higher than the first. A curve drawn so as to follow the initial rise and descent and then so as to follow the low points of the oscillations would have the previously described wavelike form. This curve, for each proof stress, would have a generally ascending course, passing through successively higher maxima, and minima. In this respect, the curves for 0.001 and 0.003 percent true proof stresses for annealed material differ from the corresponding curves for half-hard and hard materials. This difference probably is due to the much greater work-hardening rate for the annealed material.



## FACTORS INVOLVED IN THE FORM OF THE PROOF STRESS-DEFORMATION CURVE

In the previous discussion, it has been shown that the proof stress-deformation curve generally consists of abrupt oscillations superposed on a wavelike curve. It has also been shown that these oscillations are due in part to variations in the prior rest interval and in part to the extension spacing of the experimental points; also that an exceptionally low point tends to be followed immediately or shortly by an exceptionally high point, and vice versa.

The most probable cause of the wavelike form of the basic curve, of the influence of the extension spacing, and of the recoil and the rebound from high and low points, respectively, is variation of internal stress. Tensile internal stress tends to lower the proof stresses, especially the proof stresses corresponding to very small amounts of permanent set. Relief of internal stress by suitable tempering or annealing tends to elevate the proof stresses, especially the 0.001- to 0.003-percent proof stresses. Internal stress can also be relieved considerably by mechanical treatment. "Springing" (slight alternate bending) treatment tends to reduce internal stress in rolled or drawn rods. It has been suggested also that internal stress may be successfully relieved by slight prestretching by tension; some experiments have been made at the National Bureau of Standards to investigate the possibilities of this method. The use of mechanical methods of relief of internal stress would have certain advantages over the thermal method. One disadvantage of the thermal method is that the temperature necessary for relief of internal stress, as shown by investigation at the Bureau, tends to decrease the corrosion resistance of 18:8 alloy.

The suggested use of prestretching for relief of internal stress would imply that internal stress induced by severe rolling or drawing may be largely eliminated by slight tensile extension. The general impression has been that moderate tensile extension does not introduce important internal stress. Different views, however, have been expressed by a few investigators. Kuntze (references 16 and 17), after investigation with copper, concluded that tensile extension, up to 3 percent, increases internal stress in cold-rolled copper. Further information evidently is needed about the variation of internal stress with tensile extension.

The evidence presented as to the form of the proof stress-deformation curve for 18:8 alloy suggests that the form of the basic curve and also the superposed oscillations may be due largely to variations in internal stress. The variation of internal stress corresponding to the basic curve possibly is as follows: The first slight extension causes decrease of internal stress to a minimum, and thus causes a corresponding increase in proof stresses. Further extension, however, causes general increase of internal stress, with wavelike variations and with corresponding opposite variations in proof stresses.

These variations of internal stress probably are due to repeated increase of the internal stress to a limit, at which there is partial relief of internal stress by local flow in regions of highest tensile stress. Each relief of stress proceeds until a minimum is reached, at which the stress again begins to build up. Such variations of internal stress obviously would be influenced by the spacing of interspersed groups of cycles such as those used in determining stress-set curves. They would also be influenced by varying duration of the rest interval, because varying duration of the rest interval permits varying amounts of negative creep. The upper limit of internal stress, at which relief by local flow begins, evidently would increase with the increase in hardness due to plastic extension. This increase of internal stress would account for the increase in range of oscillation with increase in hardness.

The information obtained by means of the proof stress-deformation curves should be of practical application in the effort to obtain high elastic strength in cold-worked 18:8 alloy. In an attempt to relieve internal stress by slight tensile extension, especially in hard material, the amount of this extension probably should be slight and be carefully controlled. Additional evidence obviously is needed to establish the effects of slight plastic extension followed by a long rest interval on proof stresses and on positive and negative creep.

## V. THE STRESS-STRAIN RELATIONSHIP FOR 18:8 CHROMIUM-NICKEL STEEL

## STRESS-DEVIATION CURVES

An incomplete view of the elastic properties of a metal is obtained by considering only the relation between the stress and the deformation that remains after the stress has been released. Consideration should be given not only to the influence of stress on permanent set but also to the influence of stress on the accompanying total strain. In a structure or a machine, the greater part of the total strain is elastic strain. Part may be plastic strain. The plastic part of the total strain has been discussed in part IV. Attention will now be directed to the total strain and especially to the elastic component.

The incompleteness of the view obtained by considering only the stress-strain relationship is illustrated by the previously mentioned fact that the literature contains results of many investigations on the influence of a rest interval (after overstress) on the stress-strain curve but practically no information about the influence of a rest interval on the stress-set curves. The incompleteness of the view obtained by considering only the stress-set relationship will become apparent after consideration of the data now to be presented.

The relationship between a stress-set curve and the corresponding stress-strain curve has been illustrated and discussed in part III. In the determination of the



stress-set curves discussed in part IV, measurements were generally made of the corresponding total strains. The stress-strain relationship thus determined has been represented by stress-deviation curves. (The method of deriving a stress-deviation curve from a stress-strain curve has been described in pt. II.) Typical stress-deviation curves are shown in the upper rows of figures 6, 8, 12, and 16. Each stress-deviation curve is directly above the corresponding stress-set curve.

The deviations obtained directly from the measured strains are total deviations. These deviations are represented by the experimental points in the upper rows of figures 6, 8, 12, and 16, and each broken-line curve represents the variation of total deviation with stress. As total strain is the sum of the elastic strain and the corresponding permanent set, the stress-set curve directly below each stress-deviation curve can be used in making allowance for the permanent set, and in thus obtaining a curve representing more nearly the influence of stress on elastic strain. Each solid-line curve in the upper rows of figures 6, 8, 12, and 16 has been thus obtained from the corresponding broken-line curve, by deducting values of permanent set indicated by the stress-set curve immediately below.

The corrected stress-deviation curves of figures 6, 8, 12, and 16 will now be compared with the corresponding stress-set curves. It is of interest to observe whether the wide variations in the slope of the stress-set curve, variations that cause the wide oscillations in the proof stress-deformation curves (described in pt. IV), are accompanied by either similar or opposite variations in slope of the stress-deviation curve.

The initial stress-set curve, for each of the specimens tested (as shown in pt. IV), generally gives evidence of permanent set at even the lowest stresses, and the slope decreases rapidly with increase of stress. Stress-set curve 2 of each series generally shows great superiority, in these respects, over curve 1. The corresponding stress-deviation curves, however, show a quite different relationship. Uncorrected stress-deviation curve 1 in each of the four figures (figs. 6, 8, 12, and 16) differs little from curve 2 in initial slope, but the curvature is greater in curve 1 than in curve 2. Uncorrected stress-deviation curves 1 and 2 in each figure, therefore, differ much less than the corresponding stress-set curves.

The corrected stress-deviation curves 1 in these figures are initially steeper than curves 2. In this respect, therefore, the difference between stress-deviation curves 1 and 2 is opposite to the difference between the corresponding stress-set curves. The curvature, however, is greater in stress-deviation curve 1 than in stress-deviation curve 2.

It has also been shown in part IV that the stress-set curve varies greatly in steepness with prior plastic extension and that the steepness tends to oscillate

between high and low values. Also these oscillations are due in part to varying duration of the rest interval, and in part to the spacing of the stress-set curves throughout the total range of plastic extension. Comparison will now be made between these variations in steepness of the stress-set curve and the corresponding variations in steepness of the stress-deviation curve. In this comparison, consideration will be given first to some of the stress-set curves representing extremes of steepness.

In figure 6, stress-set curve 56 is much steeper and stress-set curve 57 is much less steep than the average, although each was obtained with a short rest interval. The corresponding stress-deviation curves, however, differ little in slope. Stress-set curve 77, which is steeper than the average, is followed by a curve that is much less steep than the average. The corresponding uncorrected stress-deviation curves, however, differ little in slope or curvature. Corrected stress-deviation curve 78, consequently, is much steeper than curve 77. The difference between the corrected stress-deviation curves, therefore, is opposite to the difference between the corresponding stress-set curves. The three stress-set curves 98, 103, and 108, obtained with relatively long rest intervals, are much less steep than the preceding curves. Uncorrected stress-deviation curves 98, 103, and 108, however, differ little in slope from the preceding curves. Corrected curves 98, 103, and 108, consequently, are steeper than the preceding curves. The evidence in figure 6 therefore suggests that variations in steepness of the stress-set curves, especially variations due to the duration of the rest interval, generally are accompanied by opposite variations in steepness of the elastic stress-deviation curve.

In figure 8, stress-set curves 31, 37, 40, 43, 46, 48, 51, and 54, obtained with relatively long rest intervals, are less steep than the curves immediately preceding. The corresponding corrected stress-deviation curves (with the exception of curves 31 and 54), however, are steeper than the curves immediately preceding.

As figure 12 was obtained with annealed material, the differences in steepness between the curves representing relatively long rest intervals and the curves immediately preceding, are generally less prominent than in figures 6 and 8 representing half-hard material. These differences in steepness generally tend to increase with the prior plastic extension. Inasmuch as consecutive curves corresponding to the larger prior extensions are few in figure 12, the evidence as to the comparative influence of duration of the rest interval on stress-set and stress-deviation curves is less conclusive in this figure than in figures 6 and 8. Four curves, nevertheless, will be used in comparison. Stress-set curves 7, 10, 13, and 19 are much less steep than the curves immediately preceding. Of the four corresponding corrected stress-deviation curves, curves 7 and 13 are slightly less steep than the preceding curves. Curves



10 and 19, however, are much steeper than the preceding curves, thus tending to confirm the evidence in figures 6 and 8: that the effect of duration of the rest interval on the corrected stress-deviation curve is opposite to the effect on the stress-set curve.

Figure 12 contains a number of pairs of stress-set curves that were obtained with an intervening small cycle in lieu of a rest interval (pt. IV). Consideration will now be given to the comparative effect of this small intervening cycle on the corresponding stress-set and stress-deviation curves. A stress-set curve following such a cycle, as shown in figure 12, invariably is steeper than either of the two adjacent curves. The influence of the small cycle on a stress-deviation curve can be determined by comparison of the curve with the following curve and not by comparison with the preceding curve, which has been influenced by the prior relatively long rest interval. The corrected stress-deviation curve following a small cycle evidently tends to be slightly steeper than the following curve. The effects of the small intervening cycle on both the stress-set and the corrected stress-deviation curve, therefore, were qualitatively the same. The effect of this small cycle (with no following rest interval), therefore, differed greatly from the effect of duration of the rest interval. This subject, however, needs further investigation, with introduction of a rest interval after the small cycle.

In figure 16, 6 stress-set curves were obtained with medium or long rest interval. Four of these stress-set curves, 8 of specimen 2C-1, 4 of specimen 3C-1, 5 of specimen 4C-1, and 6 of specimen 5C-1, are much less steep than the preceding curves. Of the corresponding corrected stress-deviation curves, curve 8 of specimen 2C-1 and curve 5 of specimen 4C-1 are slightly steeper than the preceding curves; the other two curves are about as steep as the preceding curves.

The evidence presented in figures 6, 8, 12, and 16 therefore indicates that conclusions as to the stress-strain curve cannot be drawn with certainty from the form of the stress-set curve. Neither can conclusions as to the stress-set curve be drawn from the form of the stress-strain curve. Duration of the rest interval, however, generally has opposite effects on the steepness of the stress-set and elastic stress-strain curves. Results obtained with other metals, to be included in a supplementary report, indicate that these conclusions are not limited in application to 18:8 chromium-nickel steel.

#### CURVES OF VARIATION OF THE MODULUS OF ELASTICITY WITH STRESS

A curved stress-strain relationship is much more clearly revealed and more readily studied by means of a stress-deviation curve than by means of a stress-strain curve. The stress-deviation curves of figures 6, 8, 12, and 16 all show prominent curvature. Curvature

is nearly as prominent in the corrected as in the uncorrected curves.

The fact that the slope of each curve decreases continuously from the origin evidently means that the modulus of elasticity decreases continuously with increase in stress. The modulus of elasticity at zero stress could be derived from the angle of slope of the tangent to the curve at the origin, allowance being made for the modulus of the assumed line from which the deviations are estimated. For any stress, the modulus could be derived similarly from the slope of the tangent to the stress-deviation curve at the corresponding point. It is generally more convenient, however, to derive the modulus from the slope of the secant drawn from the origin to the point (on the stress-deviation curve) corresponding to the given stress. This modulus, known as the "secant" modulus,<sup>2</sup> was used (in this investigation) to study the variation of the modulus with stress and with prior plastic extension.

Curves of variation of the modulus with stress have been derived from all the corrected stress-deviation curves and from a few of the uncorrected stress-deviation curves, of figures 8, 12, and 16, also from the ascending portions of many of the hysteresis loops of figures 2 and 3. The stress-modulus lines derived from the stress-deviation curves of figures 8, 12, and 16 are shown in figures 10, 14, and 18. Each stress-modulus line has been shifted to the right from the preceding line and has been given a separate abscissa scale. Abscissas, increasing from left to right, represent values of the secant modulus of elasticity. The scale of abscissas is indicated at the left of the upper row. Ordinates represent true stress, stress based on the cross section at the beginning of the determination of the curve.

The values for  $E_0$ , the modulus at zero stress, are merely extrapolated values, obtained by extending the stress-modulus line to zero ordinate. In figures 10 and 18, representing half-hard and hard material, respectively, nearly all the stress-modulus lines are straight, either throughout the entire represented extent or throughout all but the upper part of the extent. In figure 10, "corrected" line 1 is much less steep than any of the other corrected lines. Although this line is straight, the following two lines (and to a less extent line 4) are curved. With a few exceptions, all of the other lines of this figure are practically straight. In figure 18, lines 1 and nearly all the other lines are practically straight. In figure 14, representing annealed material, stress-modulus lines 1 to 12 are curved; the curvature decreases generally from line 1 to line 12. The other lines in this figure, with a few exceptions, are practically straight.

<sup>2</sup> It should be noted that this modulus differs from a frequently used "secant modulus," based on the variation of total strain with stress.



A linear relationship between stress and the secant modulus may be represented by the equation  $E=E_0-kS$ . In this equation,  $E$  represents the modulus at any stress  $S$ ;  $E_0$  represents the modulus at zero stress; and  $k$  represents the cotangent of the angle of slope of the stress-modulus line. (This equation evidently indicates that the corresponding stress-strain line is a parabola.) An equation of this form was found by Sayre (references 1 and 2) to represent the stress-modulus relationship for ordinary steels and for a number of nonferrous metals. Sayre's equation, however, represented the influence of stress on the tangent modulus. The tangent modulus obviously decreases more rapidly, with increase of stress, than the secant modulus. Values of  $k$  reported by Sayre for various metals, therefore, are not directly comparable with values obtained from the stress-modulus lines in figures 10, 14, and 18.

Bridgman (reference 18) found linear decrease in compressibility (linear increase in the volume modulus of elasticity) for many metals, with increase in hydrostatic compressive stress. As the constants published by Bridgman to represent this relationship are based on variation of the secant modulus, they are comparable with the values obtained from figures 10, 14, and 18.

Some years earlier, the authors of references 16 and 17 presented evidence of linear relationship between tensile stress and the "Dehnungszahl" ( $\alpha$ ), the reciprocal of the secant modulus of elasticity. As  $k$  is small, such a relationship evidently implies a nearly linear relationship between stress and the secant modulus throughout a considerable range of stress.

The constant  $k$  is a dimensionless index of the curvature of the stress-strain line. It is not entirely satisfactory, however, as an index of the influence of stress on the modulus of elasticity. For such an index, it appears desirable to use a constant that represents the fractional change of the modulus with stress although such a constant is not dimensionless. A suitable constant for this purpose may be obtained from the equation  $E=E_0(1-CS)$ . In this equation,  $E$ ,  $E_0$ , and  $S$  have the same significance as in the previous equation, and  $C$  is the new constant. This constant is equal to  $k/E_0$ , and is a small decimal fraction.

Stress-modulus lines for annealed steel 2A-1, obtained with prior extensions up to about 11 percent (compare figs. 14 and 15), are curved from the origin. A few of the lines obtained with harder material are similarly curved. For the curved lines, an equation representing the variation of the modulus with stress needs an additional term containing a second constant. Addition of such a term to each of the preceding two equations, gives the following equations:

$$E=E_0-k_1S-k_2S^2$$

and

$$E=E_0[1-C_1S(1+C_2S)] \text{ or } E=E_0(1-C_1S-C_1C_2S^2)$$

(Instead of using both constants in the third term on the right of each equation, a single constant could be used.)

For nearly all the corrected stress-modulus lines obtained with half-hard and hard material (figs. 10 and 18), and for most lines obtained with annealed material (fig. 14),  $C_2S$  is either zero or so small that it may be neglected. For curves 1 to 12 of figure 14 and for a few curves of figures 10 and 18,  $C_2S$  is not negligible. Values of  $C_1$  and  $C_2$  are indicated in figures 10, 14, and 18 by the numbers adjacent to the corrected stress-modulus lines. Values of  $C_1$  for the curved lines are based on the slopes of the tangents at the origin.

In figures 4 and 5 are stress-modulus lines obtained from the ascending portions of many of the hysteresis loops of figures 2 and 3. The stress-deviation lines in these hysteresis loops are based on total strain, because the loops could not be corrected for permanent set. As most of the plastic component for the ascending part of each curve is near the top, however, stress-modulus curves derived from the ascending curves of some of the hysteresis loops should give approximately correct values of  $E_0$  and  $C_1$ . Hysteresis loops suitable for such a purpose are loops obtained after so many cycles that the positive and negative creep per cycle is small.

All the hysteresis loops previously described (figs. 2 and 3) were obtained with annealed material. The loops in the upper row of figure 2 were obtained with a relatively large stress range, which caused about 15 percent plastic extension in the first loop. The derived stress-modulus lines, shown in the upper row of figure 4, are nearly straight. The loops in the lower row of figure 2 and in figure 3 were obtained with a much smaller stress range, which caused only about 3-percent plastic extension in the first loop. The derived stress-modulus lines, shown in the lower row of figure 4 and in figure 5, are curved. The great difference in plastic extension in the first loop probably is the cause of the great difference in curvature between the stress-modulus lines shown in the upper row of figure 4 and those shown in the lower row of figure 4 and in figure 5. This relationship between prior plastic extension and degree of curvature of the stress-modulus line is similar to that illustrated in figure 14. With increase in prior plastic extension, the curvature of this line (for annealed material) evidently tends to decrease, and the line generally is straight for extensions beyond about 10 percent.

Values of  $E_0$  and  $C_1$ , estimated from the stress-modulus lines in figures 4 and 5, are listed in tables III, IV, and V. Although these values were obtained from uncorrected stress-deviation curves, they generally fall within the range of values obtained from corrected stress-deviation curves for annealed material, as represented by the numbers adjacent to the solid-



line curves of figure 14. That values obtained from uncorrected stress-deviation lines generally differ little from values obtained from corrected lines is illustrated in figures 10, 14, and 18 by a few broken lines obtained from uncorrected stress-deviation curves of figures 6, 12, and 16. The broken lines in figures 10, 14, and 18 generally differ little, in position, slope, and curvature, from the corresponding solid lines. Under these conditions, values of  $E_0$  and  $C_1$  obtained with uncorrected stress-deviation lines evidently differ little from values obtained with corrected lines. The initial broken line for each of the steels represented in the three figures, however, differs considerably from the corresponding solid line. Values of  $E_0$  and  $C_1$ , obtained with initial uncorrected stress-modulus lines, therefore, may differ considerably from values obtained with corrected lines. Uncorrected lines generally give lower values of  $E_0$  and higher values of  $C_1$  than those obtained from corrected lines. The difference between values of  $C_1$  obtained from corrected and uncorrected lines is less than it would be if the stress-set curve and the corrected stress-strain curve were similar in form. As shown in figures 6, 12, and 16, the lower part of the stress-set line tends to be nearly straight, whereas the corrected stress-strain line generally is uniformly curved.

In table VI are listed the ranges of values for  $E_0$ ,  $k_1$ , and  $C_1$  obtained with the 18:8 alloy, for comparison with values similarly obtained with other metals. Three of these metals, an annealed steel containing 14 percent chromium and 2 percent nickel, a cold-drawn alloy containing about 13 percent chromium, 5 percent iron, and 82 percent nickel, and cold-drawn K-monel metal (heat-treatable), have been studied in connection with the general investigation of elastic properties of high-strength aircraft metals sponsored by the National Advisory Committee for Aeronautics. The curves upon which these values are based will be included in a supplementary report. Other values listed in the table were obtained from the previously mentioned data published by Sayre (references 1 and 2) and by Bridgman (reference 18). The values published by Sayre have been corrected to allow for the fact that his data represent the influence of stress on the tangent modulus.

The values of  $C_1$  for 18:8 alloy, given in table VI, range from 6 to 55. As illustrated by the curve for  $C_1$  in figure 30, to be discussed later, the upper limit of this range represents annealed, and the lower limit represents severely cold-worked metal. Even for severely cold-worked 18:8 alloy, the value of  $C_1$  is considerably higher than values obtained from Sayre's data, except the range listed for aluminum alloy. For the aluminum alloy, the upper limit of the listed range of  $C_1$  is about the same as the value for severely cold-worked 18:8 alloy. The values obtained with annealed 14:2 chromium-nickel steel, however, fall within the

range of values for 18:8 alloy. The ranges for cold-drawn Inconel and cold-drawn K-monel metal overlap the lower part of the range for 18:8 alloy.

The value for annealed 18:8 alloy is much higher than any other value listed in the table. This table, however, contains no value for an annealed pure metal or for any annealed single-phase alloy except 18:8 alloy. (The aluminum "hard-drawn and annealed" probably was merely heated for relief of internal stress.) Annealed pure metals and single-phase alloys generally give strongly curved stress-strain lines. This fact implies a high value of  $C_1$ . Some data published in reference 17 appear to indicate that  $C_1$  for annealed copper may be as high as about 360.

No quantitative information is available as to the influence of heat treatment on  $C_1$ . The steels used by Sayre were all of spring temper. It seems probable that higher values for  $C_1$  would be obtained with annealed steels than with quenched-and-tempered steels. It is worthy of note that his next highest range of  $C_1$  listed in table VI was obtained with an annealed steel. The influence of heat treatment on  $C_1$  evidently needs further investigation.

#### INFLUENCE OF PRIOR PLASTIC EXTENSION AND OF THE PRIOR REST INTERVAL ON $E_0$ AND $C_1$

For specimen 1B-3, the initial value of  $E_0$  (curve 1 of fig. 10) is about 32 million. As illustrated by curve 2, the slight plastic extension involved in the determination of curve 1 has decreased  $E_0$  from 32 to 25 million. Accompanying this decrease in  $E_0$  is a decrease in  $C_1$  from 43.9 to  $9.4 \times 10^{-7}$ . Similar though smaller differences exist between curves 1 and 2 obtained with specimens 2C-1, 3C-1, 4C-1, and 5C-1 of figure 18. (These differences for specimens 4C-1 and 5C-1 possibly are within the limits of experimental error.) These examples are not mentioned to imply that similar differences will be found between curves 1 and 2 obtained with every specimen. They are mentioned as illustrations of the fact that variations of  $E_0$ , with prior plastic extension and with duration of the rest interval generally are accompanied by similar variations of  $C_1$ . Numerous illustrations of this parallel variation of  $E_0$  and  $C_1$  may be found in figures 10, 14, and 18. The higher the modulus at zero stress, the less steep usually is the stress-modulus curve; that is, the higher is the index ( $C_1$ ) of variation of the modulus with stress. This relationship is clearly revealed in diagrams of a different type, now to be described.

In figures 11, 15, and 19 are shown curves derived from the stress-modulus curves of figures 10, 14, and 18. Abscissas in these curves represent prior plastic extension; ordinates represent values of  $E_0$  and  $C_1$  and of the secant modulus corresponding to an arbitrarily selected tensile stress, whose value is indicated by a subscript



number with the last three ciphers omitted. Attention will be directed first to the curves of variation of  $E_0$  and  $C_1$ .

Comparison of these two curves in each of the three figures shows that variations of  $E_0$  generally are accompanied by qualitatively similar variations of  $C_1$ . The most conspicuous example of this is the initial steep drop in the curves for  $E_0$  and  $C_1$  in figure 11. Qualitatively similar descent of both curves is found also in the diagrams of figure 19. An exception, however, is found in figure 15; the initial course of the curve for  $C_1$  in this figure is a steep rise instead of the usual initial steep descent. The initial value of  $C_1$  in figure 15 is lower than any of the values obtained with prior plastic extensions between zero and about 45 percent. This abnormally low initial value, however, possibly is not correct. The curve from which the low value was derived, curve 1 of figure 12, obviously is based on so few experimental points that its course is not well established. To a less extent, the same criticism applies to several of the curves following curve 1 of figure 12. There is considerable doubt, therefore, as to the reality of an initial increase of  $C_1$  with prior plastic extension. The doubt is accentuated by a study of figure 30, to be described later.

In figure 19, representing hard material, the initial trend of each curve, for both  $E_0$  and  $C_1$ , is downward. After the initial descent, the course of the curves gives no clear indication of a general trend for either  $E_0$  or  $C_1$ . The numerous irregularities probably are due to the influence of the variables previously discussed. For these materials, severely cold-worked prior to test,  $E_0$  and  $C_1$  evidently do not change much with further plastic extension. A broader view of the evidence, shown in figure 30 (to be discussed later), indicates that the general trend of  $C_1$ , with plastic extension, is downward at a gradually decreasing rate.

The curves for  $E_0$  and  $C_1$  in figures 11, 15, and 19 will now be compared with the corresponding curves of variation of proof stresses (figs. 9, 13, and 17). In this comparison, particular attention will be given to the influence of duration of the rest interval. It has been shown in part V that variation in the rest interval has opposite effects on the stress-deviation and stress-set curves. It is not surprising, therefore, to find that points representing relatively long rest intervals tend to be at the tops of oscillations in the curves of variation of  $E_0$  and  $C_1$ , whereas the corresponding points in the proof stress-deformation curves tend to be at the low points of oscillations. The range of oscillations, however, generally is much less in the curves of variation of  $E_0$  and  $C_1$  than in the curves of variation of proof stresses.

From corresponding values of  $E_0$  and  $C_1$ , the secant modulus may be calculated for any stress. The intermediate curves in figures 11, 15, and 19 represent the variations of the moduli corresponding to some arbi-

trarily selected stresses. In figures 11 and 13, these curves ( $E_{100}$ ) show the variations of the modulus corresponding to a tensile stress of 100,000 pounds per square inch. In figure 15, the intermediate curve ( $E_{50}$ ) shows the variation of the modulus corresponding to a stress of 50,000. Modulus values corresponding to stresses between zero and either 50,000 or 100,000 could readily be estimated from these diagrams by interpolation.

#### THE VARIATION OF $E_0$ AND $C_1$ WITH ULTIMATE TENSILE STRENGTH

The evidence presented in figures 11, 15, and 19 indicates that  $E_0$  and  $C_1$  generally decrease with increase in plastic extension, whether the experiments are made with annealed, half-hard, or hard material. The evidence suggests that  $E_0$  and  $C_1$ , for 18:8 alloy, generally tend to decrease with increase in the hardness due to cold work, whether the cold work is applied by rolling or by prestretching. It appeared possible, therefore, that values for  $E_0$  and  $C_1$  obtained with all the specimens tested could be combined in one diagram by use of some property that indicates, at least qualitatively, the amount of cold work applied either in rolling or prestretching. As the tensile strength generally is a good qualitative index of the amount of prior cold work, use has been made of this property in constructing a single diagram (fig. 30) to represent the variations of  $E_0$  and  $C_1$  with work-hardening.

Abseissas in figure 30 represent "true" tensile strength, based on the cross section at the beginning of the determination of each stress-modulus curve. (See p. 21.) The experimental points in this figure representing annealed, half-hard, and hard material are at the left, in the middle, and at the right, respectively.

The values for  $C_1$  will be considered first. Although there is considerable scatter of the experimental points representing values of  $C_1$ , the composite curve as drawn represents fairly well all of the experimental values except the initial values. With one exception, the points representing initial values are above the composite curve. This corresponds to the observation made in part II that, either because of some effect of the long prior rest interval or because of internal stress, the data based on the initial stress-set and stress-strain curves generally cannot readily be correlated with the data obtained after slight plastic extension. The inherent properties of the material apparently are best revealed by a second determination of stress-set and stress-deviation curves soon after the initial determinations made with the material as received.

With increase in tensile strength, as shown by the composite curve,  $C_1$  decreases. For annealed material the value evidently is many times the value for hard material, which means that the curvature of the stress-deviation line is much greater for annealed than for hard material. Although  $C_1$  generally tends to be less for hard than for half-hard material, the difference is slight.



The variation of  $E_0$  with increase in tensile strength is much more irregular than the variation of  $C_1$ . The general tendency is for  $E_0$  to decrease with increase in tensile strength. The effect on  $E_0$  of increase in tensile strength above about 150,000 pounds per square inch, however, is slight. The effect may be masked by other variables, such as differences in composition and microstructure. These variables evidently have more effect on  $E_0$  than on  $C_1$ .

Values of the modulus of elasticity corresponding to some arbitrarily selected tensile stresses have also been included in figure 30. Variation of these values with tensile strength is generally less than the variation of  $E_0$ .

### CONCLUSIONS

1. An incomplete view of the tensile elastic properties of 18:8 alloy is obtained by considering either the stress-strain or the stress-set relationship alone. Consideration should be given to both relationships.

2. In a study of the elastic properties, consideration should be given to the influence of hysteresis and of positive and negative creep.

3. Both the stress-set relationship and the stress-strain relationship are much influenced by duration of the rest interval. The influence of duration of the rest interval is due, in part at least, to the influence of negative creep.

4. Increase in the rest interval generally decreases the slope of the stress-set curve and thus decreases the proof stresses. Increase in the rest interval generally increases the slope of the "corrected" stress-strain curve.

5. Curves of variation of proof stresses with prior plastic extension often have many wide, abrupt oscillations superposed on a gradual wavelike mean curve. The wide oscillations generally are associated with varying duration of the rest interval and with variation in the extension spacing of the experimental points. The complexity of form of the proof-stress deformation curve possibly may be attributed in part to variation of internal stress with plastic extension.

6. With prior plastic extension, the proof stresses corresponding to small percentages of permanent set (0.001 to 0.003 percent) generally increase considerably to a maximum, reached at a small percentage of prior plastic extension, and then decrease to a minimum. Further extension causes irregular oscillations in the proof stresses.

7. From corresponding stress-strain and stress-set curves may be derived corrected stress-strain curves to represent approximately the variation of elastic strain with stress. From the corrected stress-strain curves may be derived curves of variation of the secant modulus (for these curves) with stress.

8. The stress-modulus line for annealed material that has received no prior plastic extension is strongly curved. With prior plastic extension, the curvature decreases and generally is negligible for extensions of

more than about 10 percent. For half-hard and hard materials, the stress-modulus lines generally are straight.

9. Straightness of the stress-modulus line indicates that the corresponding stress-strain lines are parabolas. The cotangent  $k_1$  of the angle of slope of the stress-modulus line is a dimensionless index of the degree of curvature of the stress-strain line. As an index of the fractional change of the secant modulus with stress, a suitable constant is  $C_1$ , which is equal to  $k_1/E_0$ . The modulus at zero stress  $E_0$  is obtained by extrapolating the stress-modulus line to zero stress.

10. When the stress-modulus line is curved from the origin,  $C_1$  may be based on the slope of the tangent at the origin, and a second constant  $C_2$  may be used to represent the curvature of the stress-modulus line. The second constant  $C_2$  is not generally necessary except for material that has been annealed and afterward has not been extended more than about 10 percent.

11. When  $E_0$ ,  $C_1$ , and the corresponding stress-set curve are known, as a function of the prior extension and the rest interval, a fairly good picture is available of the elastic strength.

12. With prior plastic extension, both  $E_0$  and  $C_1$  generally decrease. Variations in  $E_0$  generally are accompanied by similar variations in  $C_1$ .

13. In a practical estimation of the elastic strength of 18:8 alloy, the best procedure now available consists in determining the corrected stress-set and stress-deviation curves. From these may be estimated proof stresses and values of  $E_0$  and  $C_1$ . Much further information, however, may be obtained by determining (with the same specimen) a second stress-set curve and the corresponding stress-deviation curve and by deriving from these a second set of indices.

14. In specifications for elastic strength, possible use could be made of a specified lower limit for  $E_0$  and a specified upper limit for  $C_1$  to apply throughout a specified range of stress. Such a requirement, based on these indices, would have some advantages over the more arbitrary requirements now in use in some specifications. In addition to the suggested limitation of the form of the elastic stress-strain curve, specifications should include a proof-stress requirement for limitation of permanent set.

15. As indicated by conclusion 6, slight prestretching generally causes considerable improvement in elastic strength. Most of this improvement persists for at least a day. Whether most of the improvement is permanent can be determined only by further experiment. Slight prestretching, however, may prove to be of practical use as a means of improving the elastic strength of severely cold-worked material.

Although these conclusions apply specifically only to the tensile elastic properties of the bar material used in the investigation, it appears probable that they are applicable qualitatively to many other metals, in other shapes and sizes, and stressed in other ways. The



same methods of investigation, applied to several other alloys (previously mentioned), one of them a pearlitic alloy steel, show that these conclusions are applicable qualitatively to those alloys as well as to 18:8 alloy.

Now that some understanding has been obtained of the influence of plastic deformation and of accessory factors on the elastic strength of 18:8 alloy, it is desirable that an investigation be made of the superimposed influence of thermal treatment to reduce internal stress. Additional investigation of the various other factors, however, evidently is much needed.

NATIONAL BUREAU OF STANDARDS,  
WASHINGTON, D. C., *November 22, 1938.*

#### REFERENCES

1. Sayre, M. F.: Laws of Elastic Behavior in Metals. A. S. M. E. Trans., RP-56-7, vol. 56, No. 7, July 1934, pp. 555-558.
2. Sayre, M. F.: Elastic Properties and Their Relationship to Strength and to Strain Hardening. Trans. Amer. Soc. Metals, vol. 24, December 1936, pp. 932-942.
3. Dushman, S.: Cohesion and Atomic Structure. 4th Marburg Lecture. Proc. A. S. T. M., pt. 2, vol. 29, June 1929, pp. 7-64.
4. Hopkinson, B. H., and Williams, G. T.: The Elastic Hysteresis of Steel. Proc. Roy. Soc. (London), ser. A, vol. 87, 1912, pp. 502-511.
5. Rowett, F. E.: Elastic Hysteresis in Steel. Proc. Roy. Soc. (London), ser. A, vol. 89, March 2, 1914, pp. 528-543.
6. Bauschinger, J.: Mitteilungen aus den mechanischen Laboratorium der technischen Hochschule in München. Heft XIII, 1886.
7. Muir, J.: The Recovery of Iron from Overstrain. Phil. Trans. Roy. Soc., ser. A, vol. 193, 1900, pp. 1-46.
8. Kelvin, Lord: On the Thermo-elastic, Thermo-magnetic, and Pyroelectric Properties of Metals. Math. and Phys. Papers, vol. I, University Press, Cambridge, 1882, pp. 291-316.
9. Sayre, M. F.: Elastic After-Effect in Metals. Jour. Rheology, vol. 3, 1932, pp. 206-211.
10. Sayre, M. F.: Thermal Effects in Elastic and Plastic Deformation. Proc. A. S. T. M., vol. 32, pt. 2, 1932, pp. 584-592.
11. Sayre, M. F.: Plastic Behavior in the Light of Creep and Elastic Recovery Phenomena. A. S. M. E. Trans., RP-56-8, vol. 56, No. 7, July 1934, pp. 559-561.
12. Krivobok, V. N., and Lineoln, R. A.: Austenitic Stainless Alloys. Trans. Amer. Soc. Metals, vol. 25, September 1937, pp. 637-677.
13. Haigh, B. P.: Hysteresis in Relation to Cohesion and Fatigue. Trans. Faraday Soc., vol. 24, February 1928, pp. 125-137.
14. Farren, W. S., and Taylor, G. I.: The Heat Developed During Plastic Extension of Metals. Proc. Roy. Soc. (London), ser. A, vol. 107, 1925, pp. 422-451.
15. Galibourg, Jean: The Elastic Limit of Soft Steel Drawn into Wire. Comptes Rendus, vol. 194, May 9, 1932, pp. 1635-1637.
16. Kuntze, W.: Abhängigkeit der elastischen Dehnungszahl " $\alpha$ " des Kupfers von der Vorbehandlung. Zeitschr. für Metallkunde, Bd. 20, April 1928, S. 145-150.
17. Kuntze, W., Sachs, G., and Sieglerschmidt, H.: Elastizität, Statische Versuche und Dauerprüfung. Zeitschr. für Metallkunde, Bd. 20, February 1928, S. 64-68.
18. Bridgman, P. W.: The Physics of High Pressure. G. Bell and Sons, Ltd. (London), 1931.



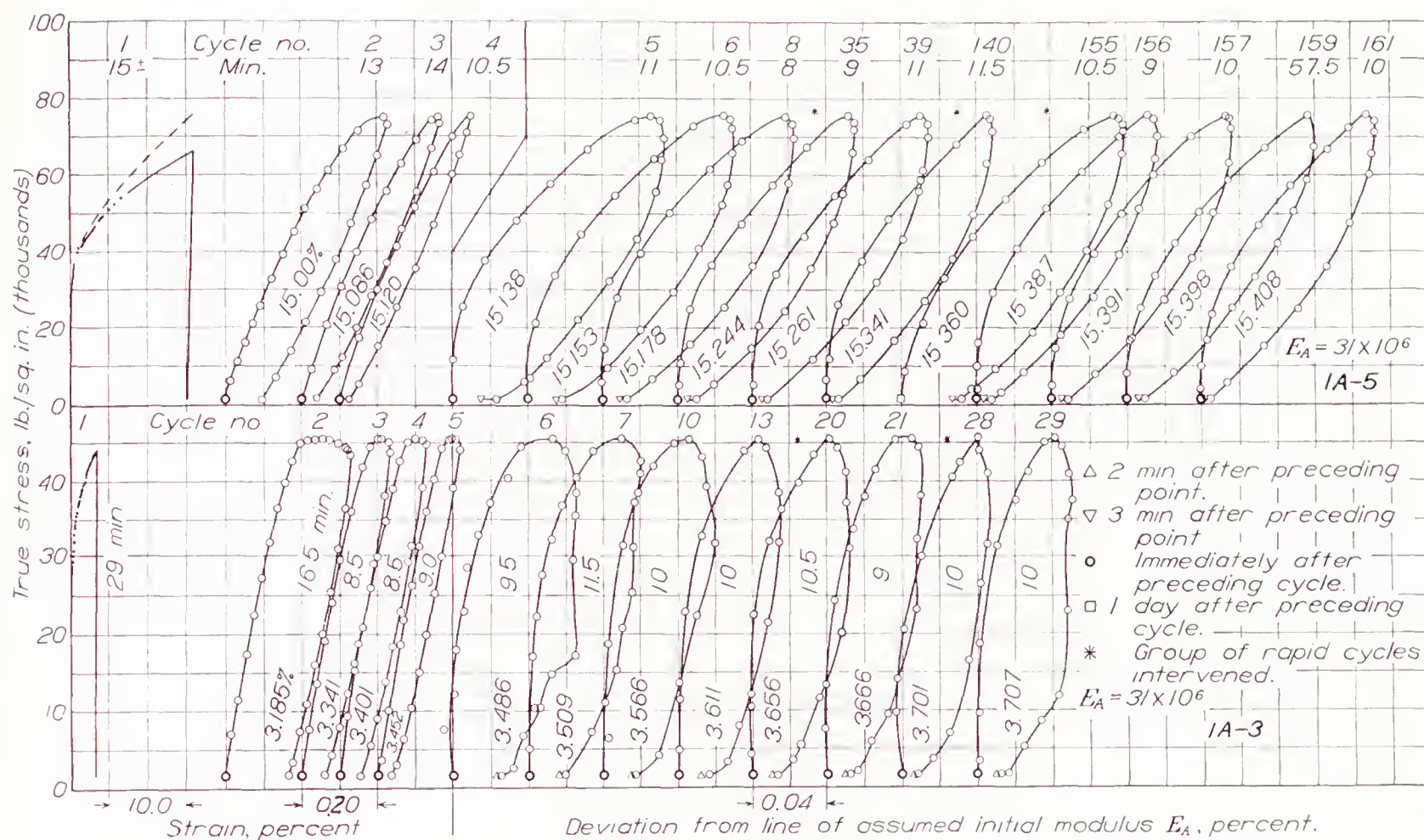


FIGURE 2.—Variation in form of hysteresis loops with cyclic repetition.

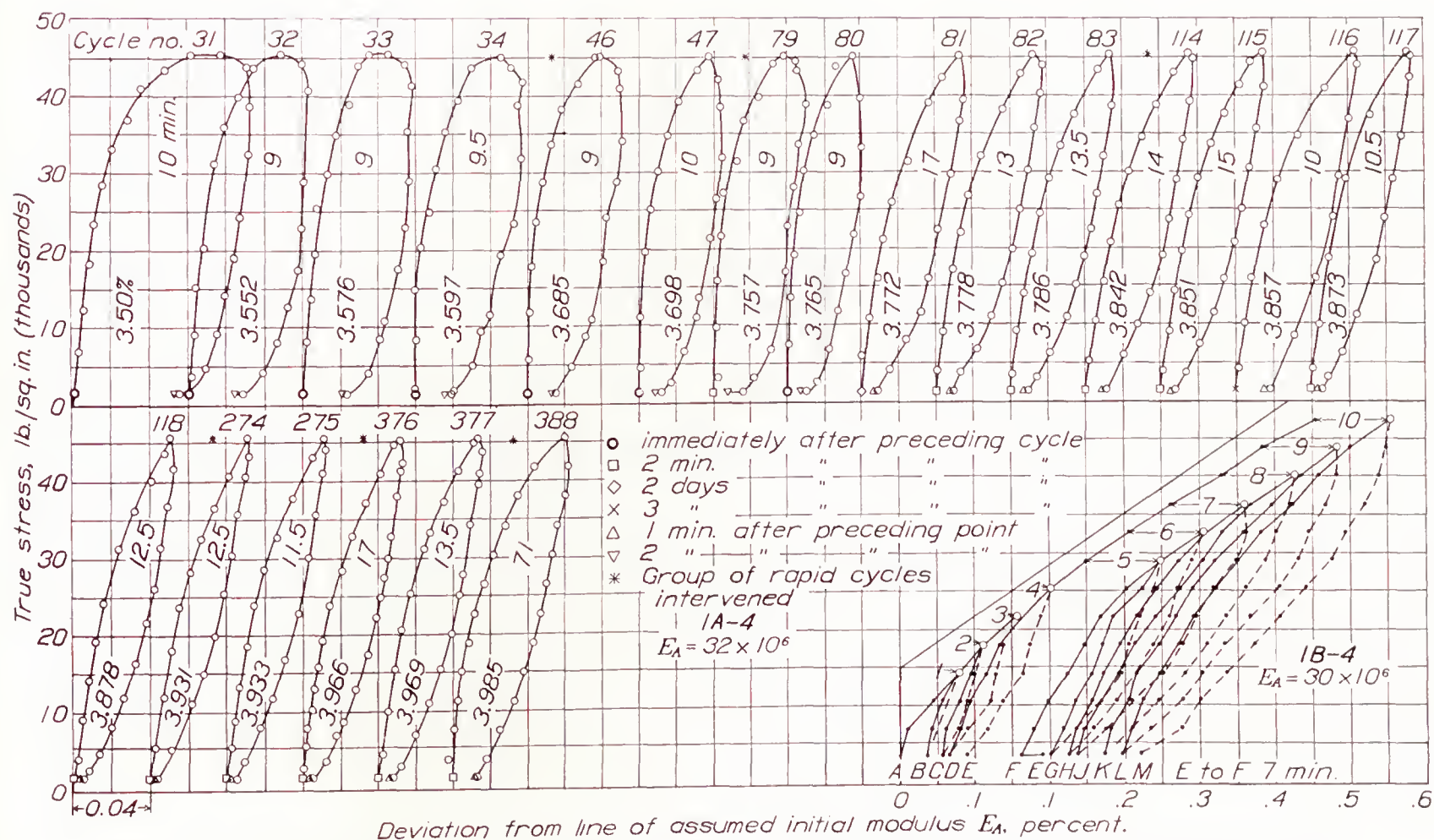


FIGURE 3.—Variation in form of hysteresis loops with cyclic repetition. Interrelationship between a stress-set and a stress-deviation curve.



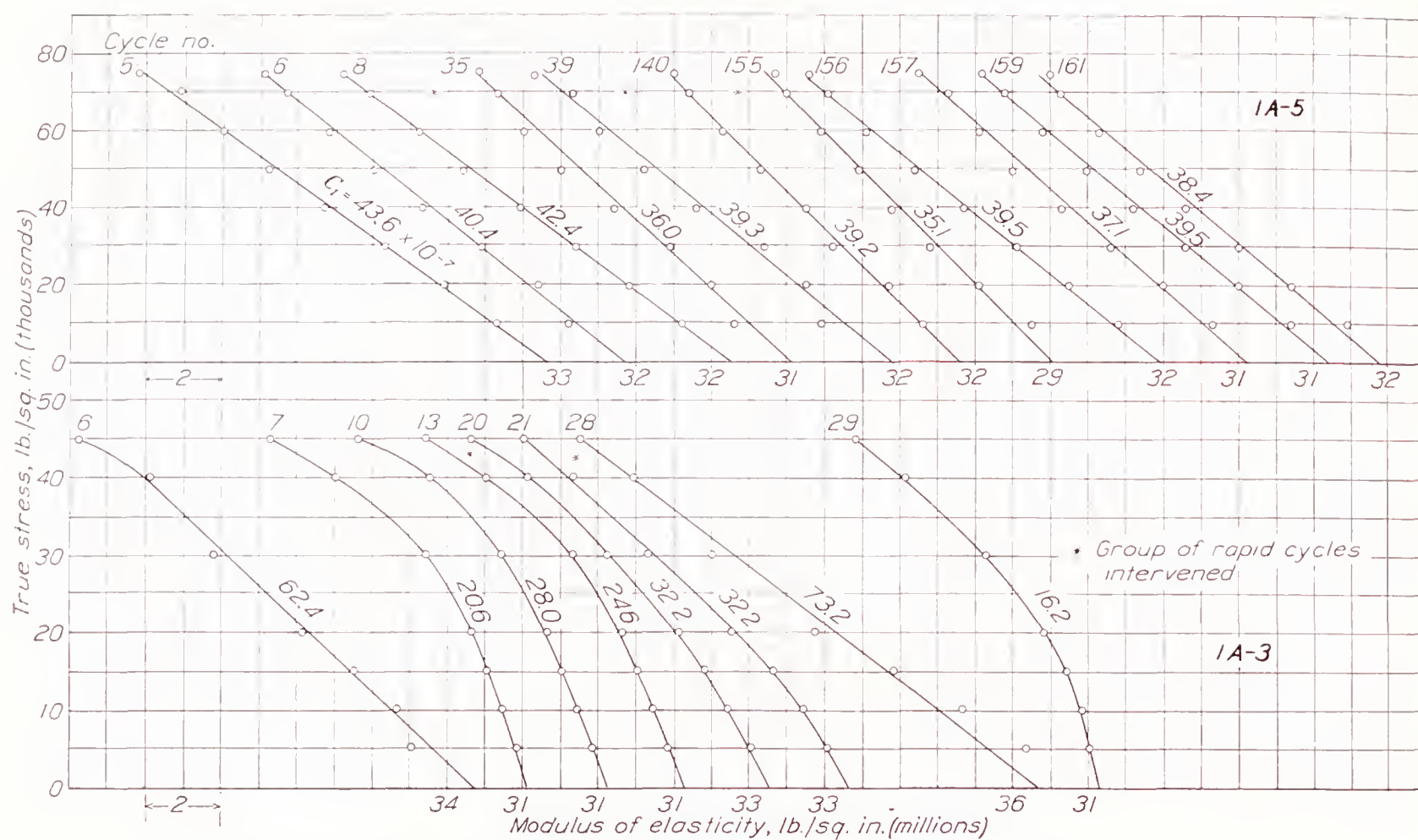


FIGURE 4.—Stress-modulus curves derived from the ascending portions of hysteresis loops of figure 2.

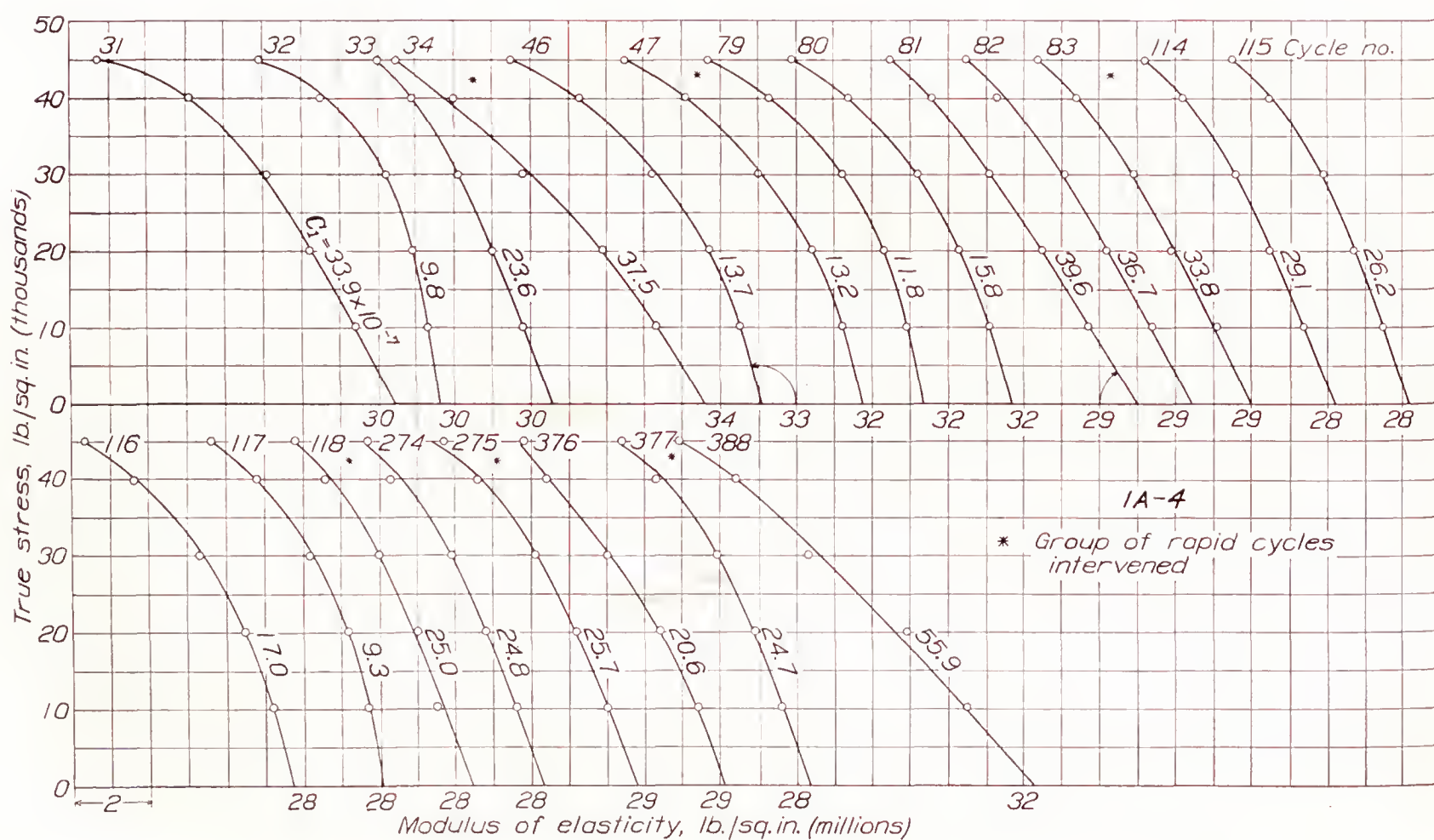


FIGURE 5.—Stress-modulus curves derived from the ascending portions of hysteresis loops of figure 3.



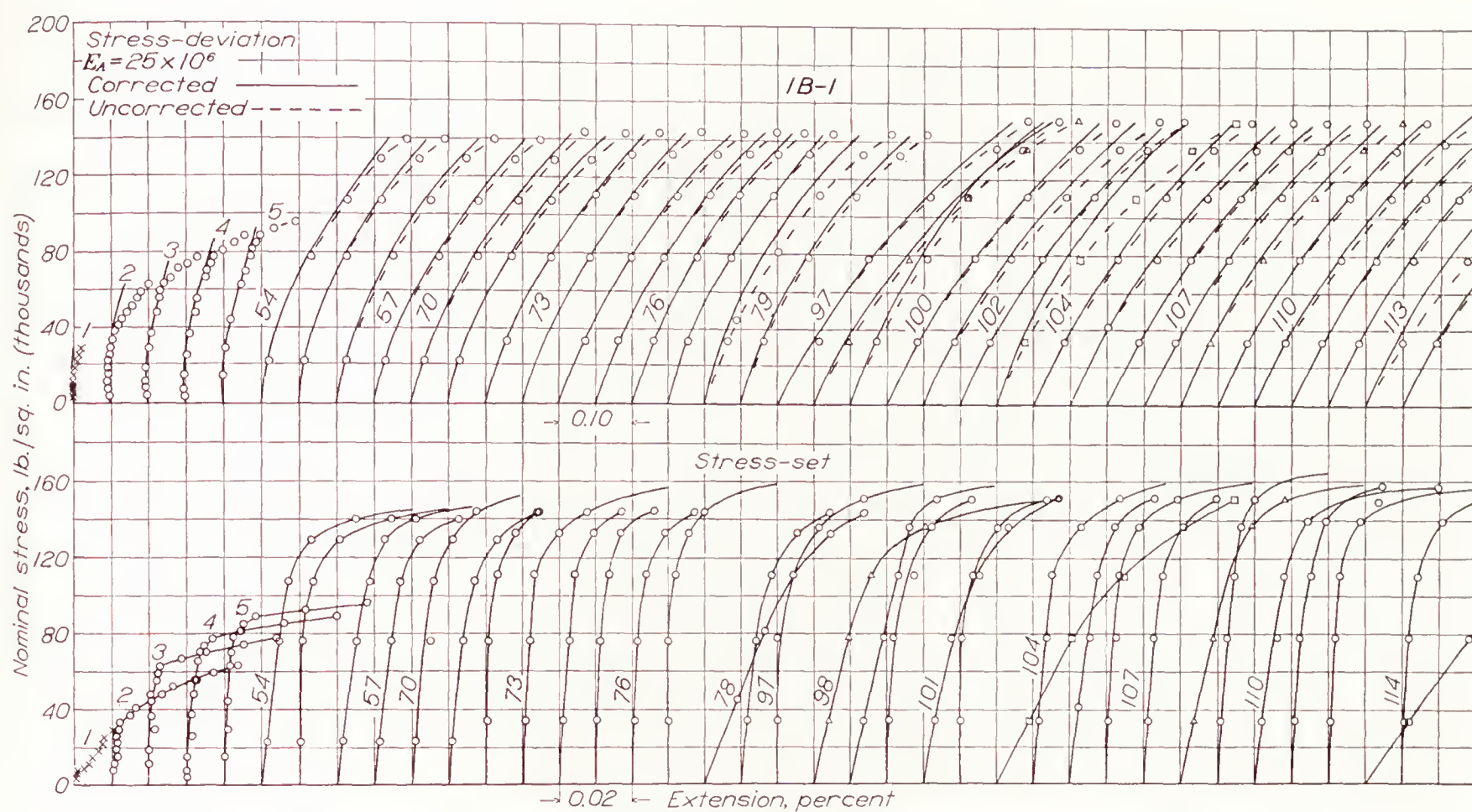


FIGURE 6.—Stress-set and stress-deviation curves obtained with a specimen of half-hard material (1B-1, table I).

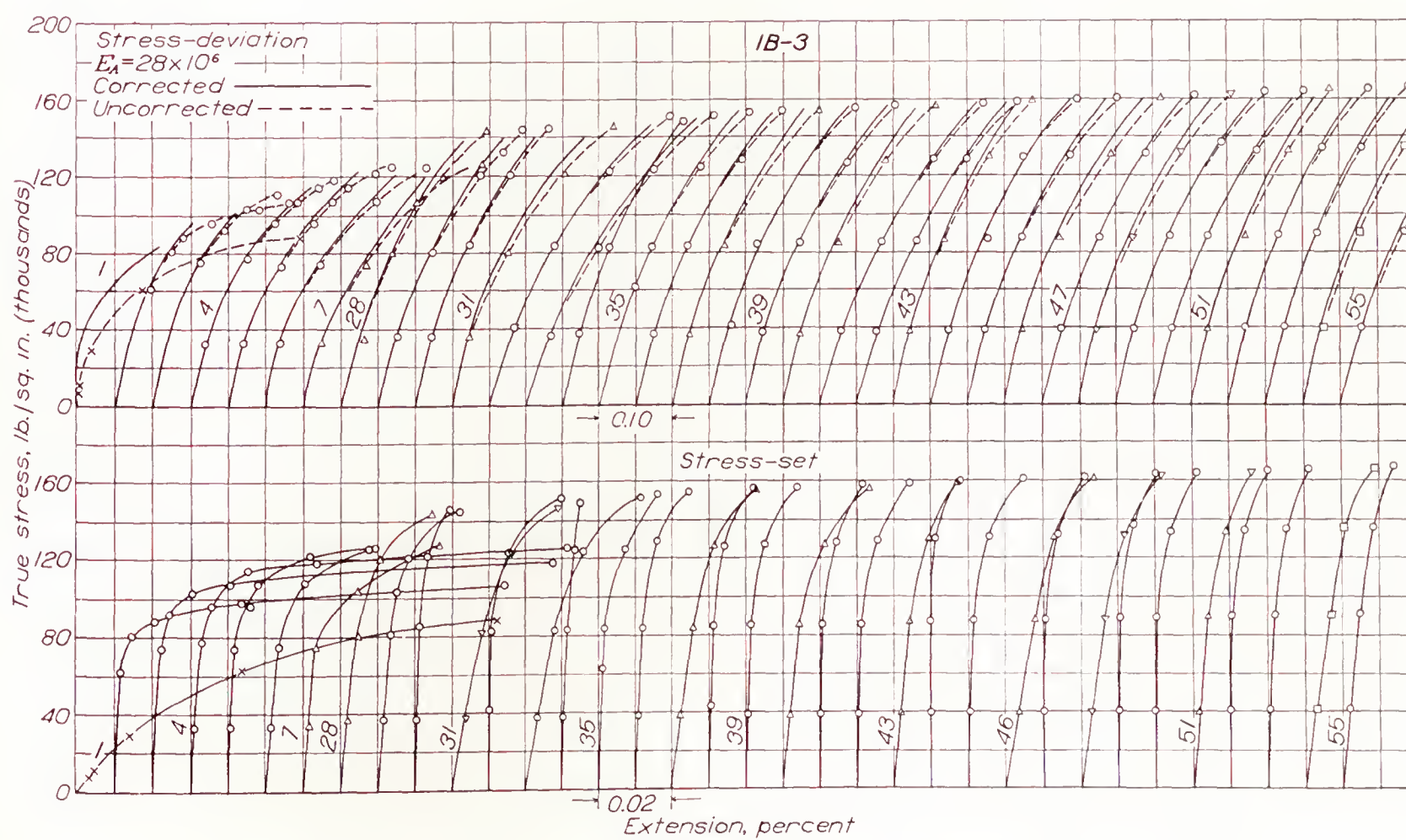


FIGURE 8.—Stress-set and stress-deviation curves obtained with a specimen of half-hard material (1B-3, table I).



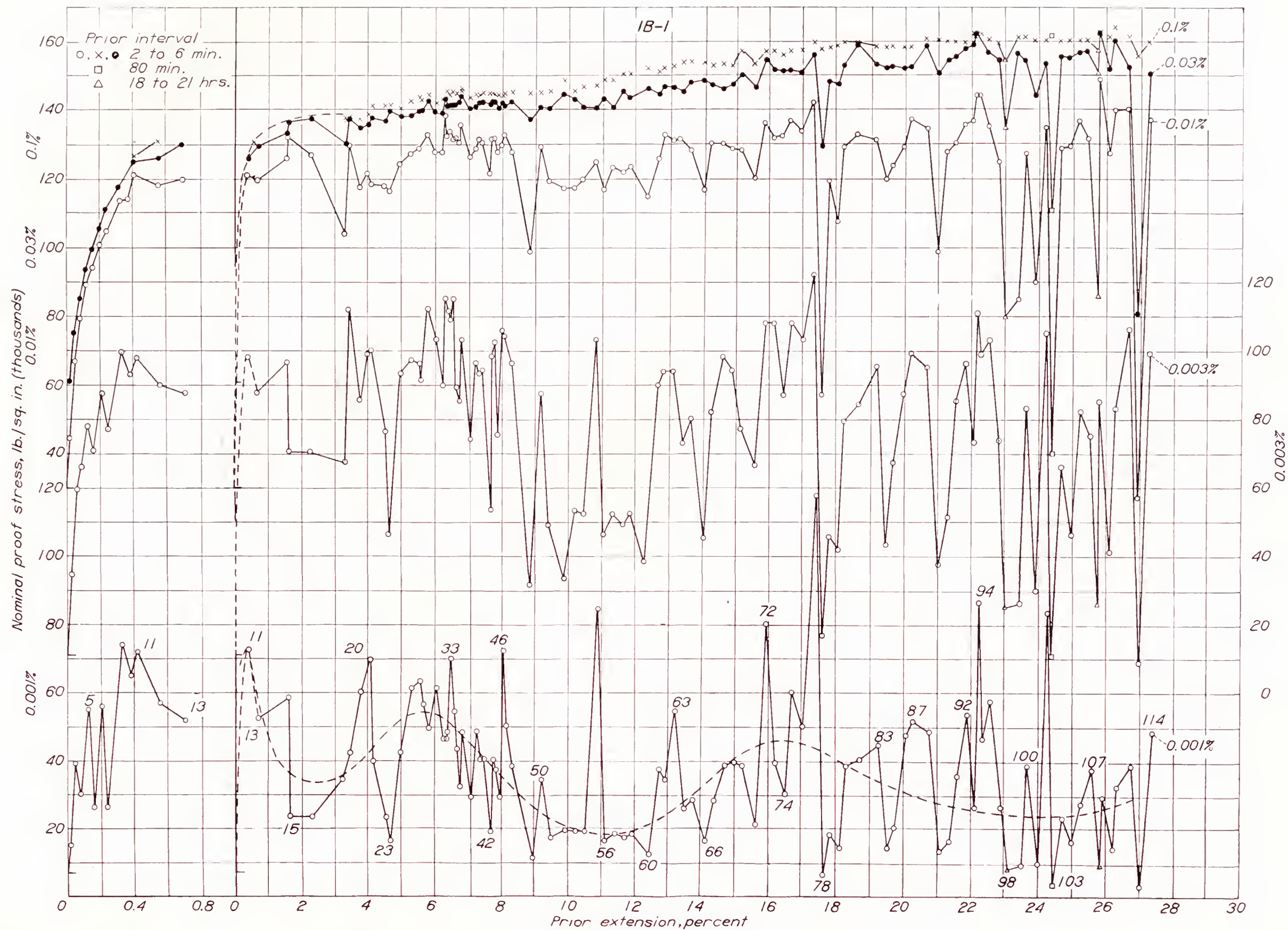


FIGURE 7.—Variation of proof stresses with prior plastic extension. Half-hard material (1B-1, table I).



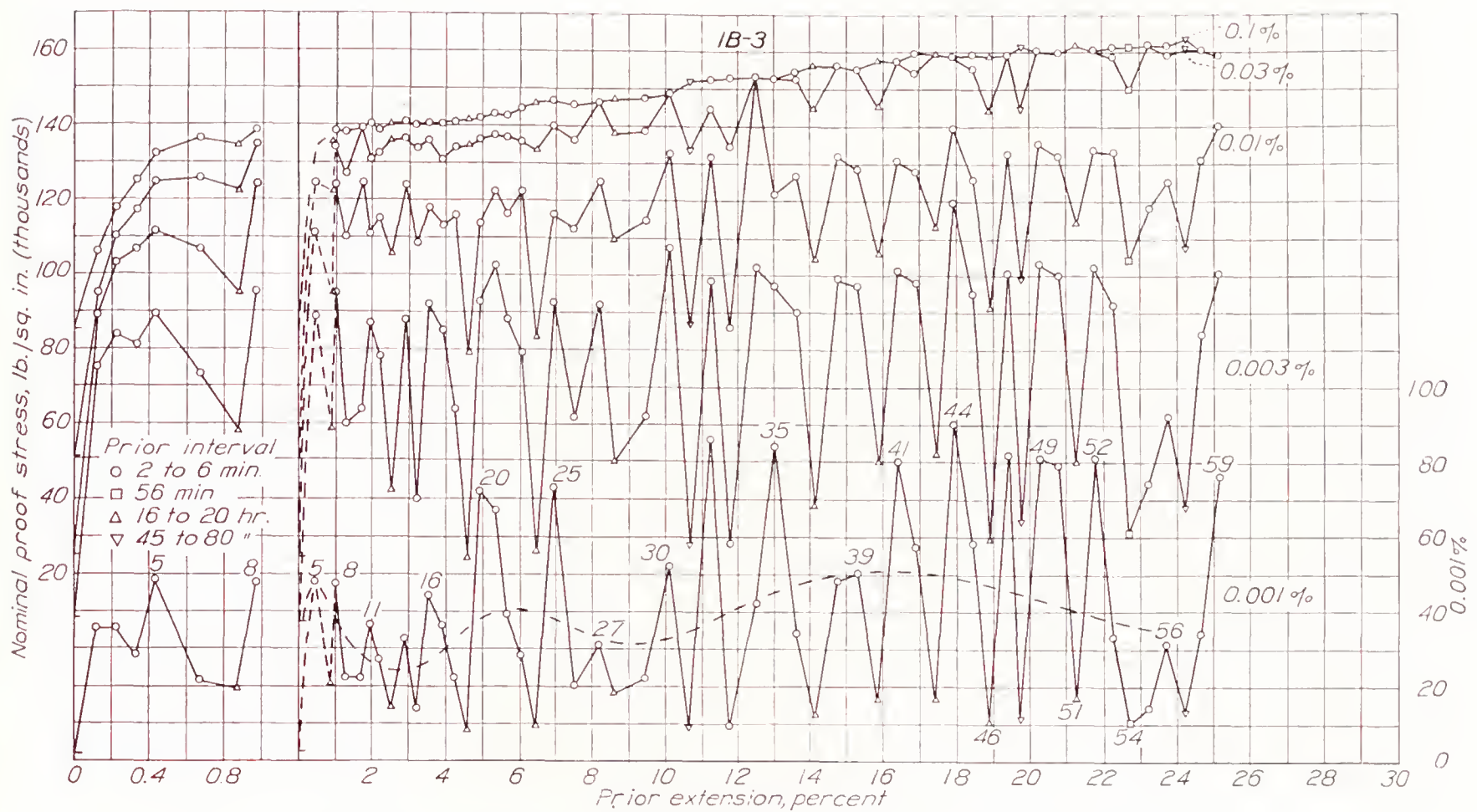


FIGURE 9.—Variation of proof stresses with plastic extension. Half-hard material (1B-3, table I).

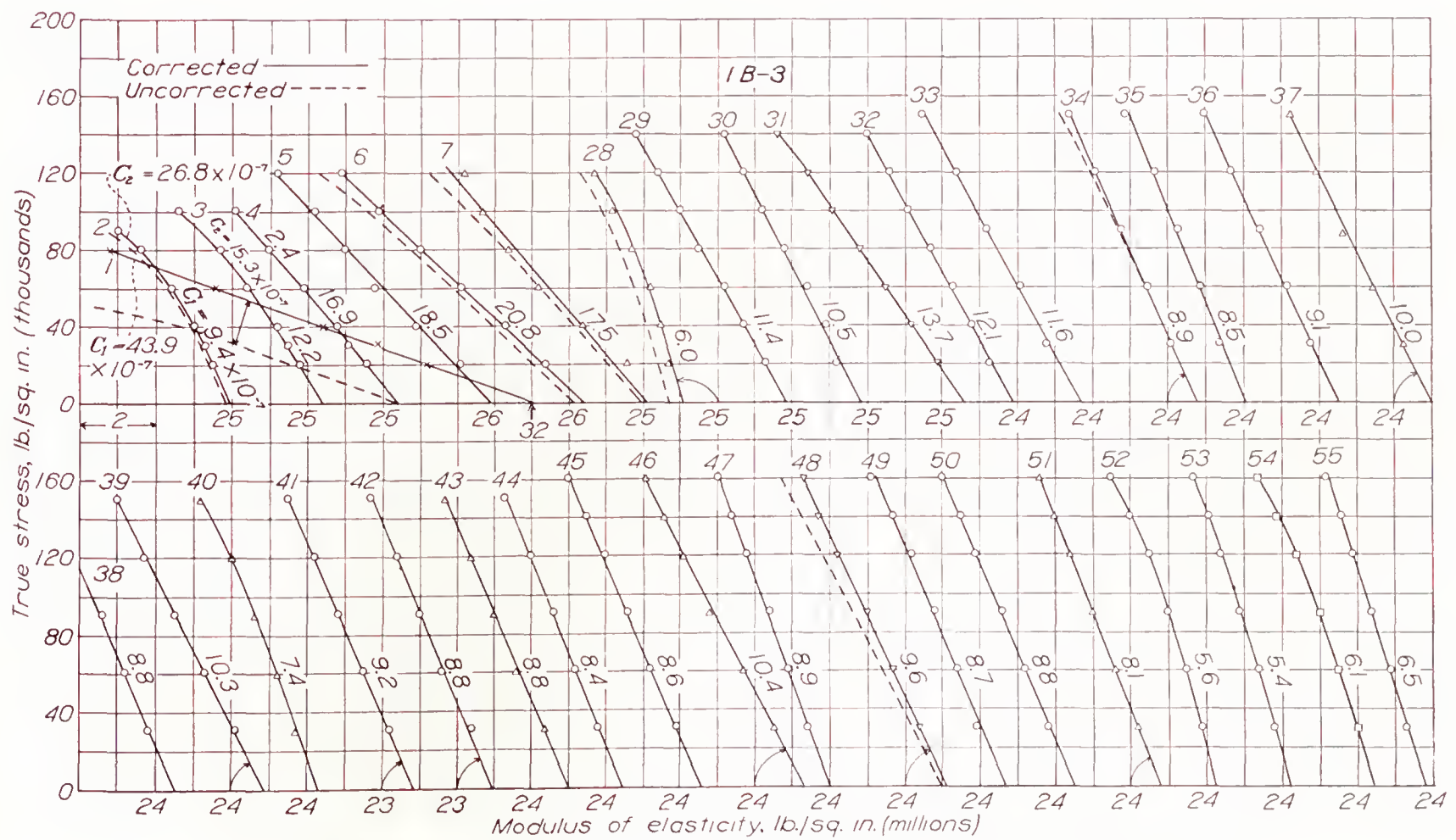


FIGURE 10.—Stress-modulus curves for half-hard material, derived from stress-deviation curves of figure 8.



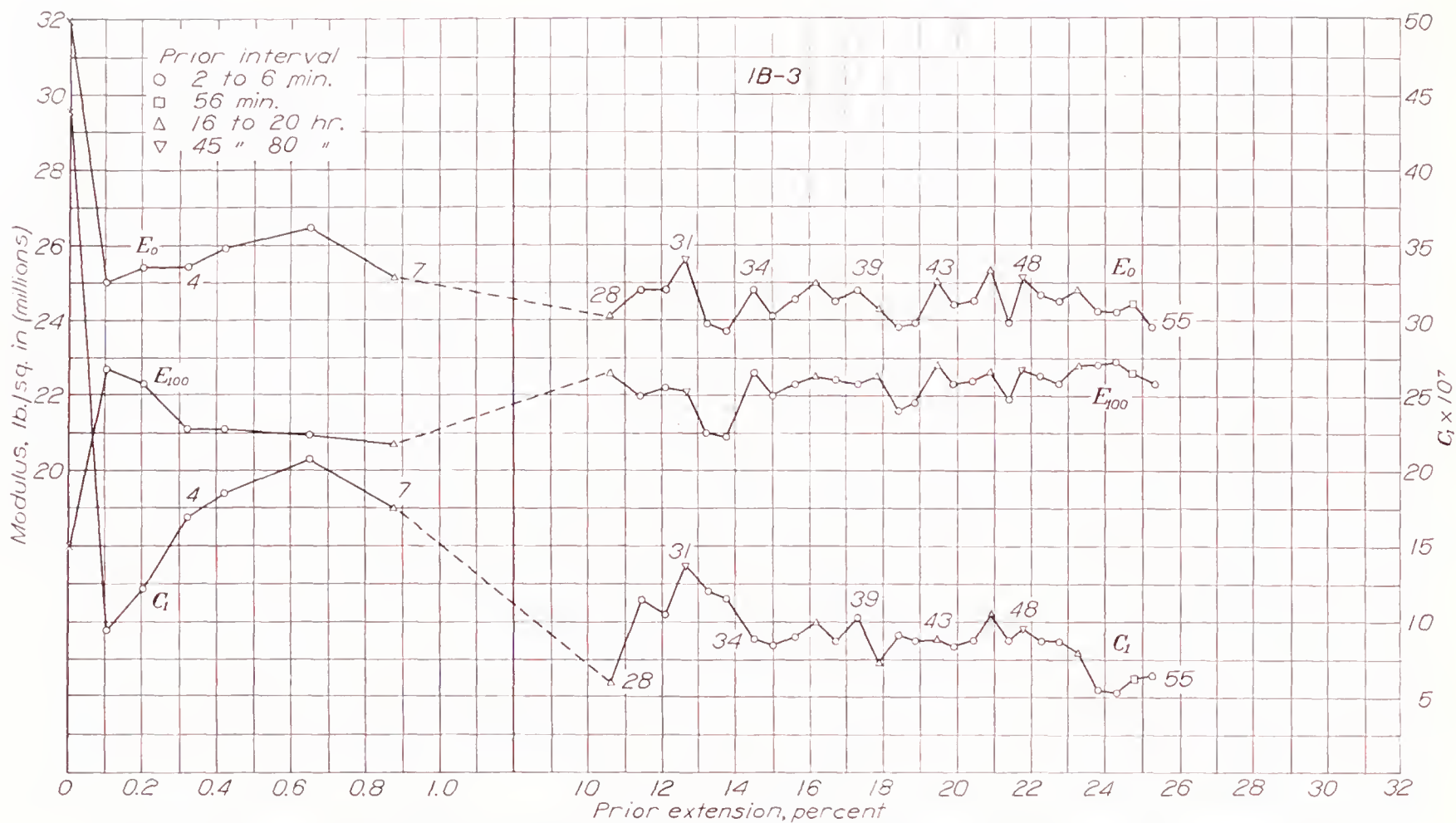
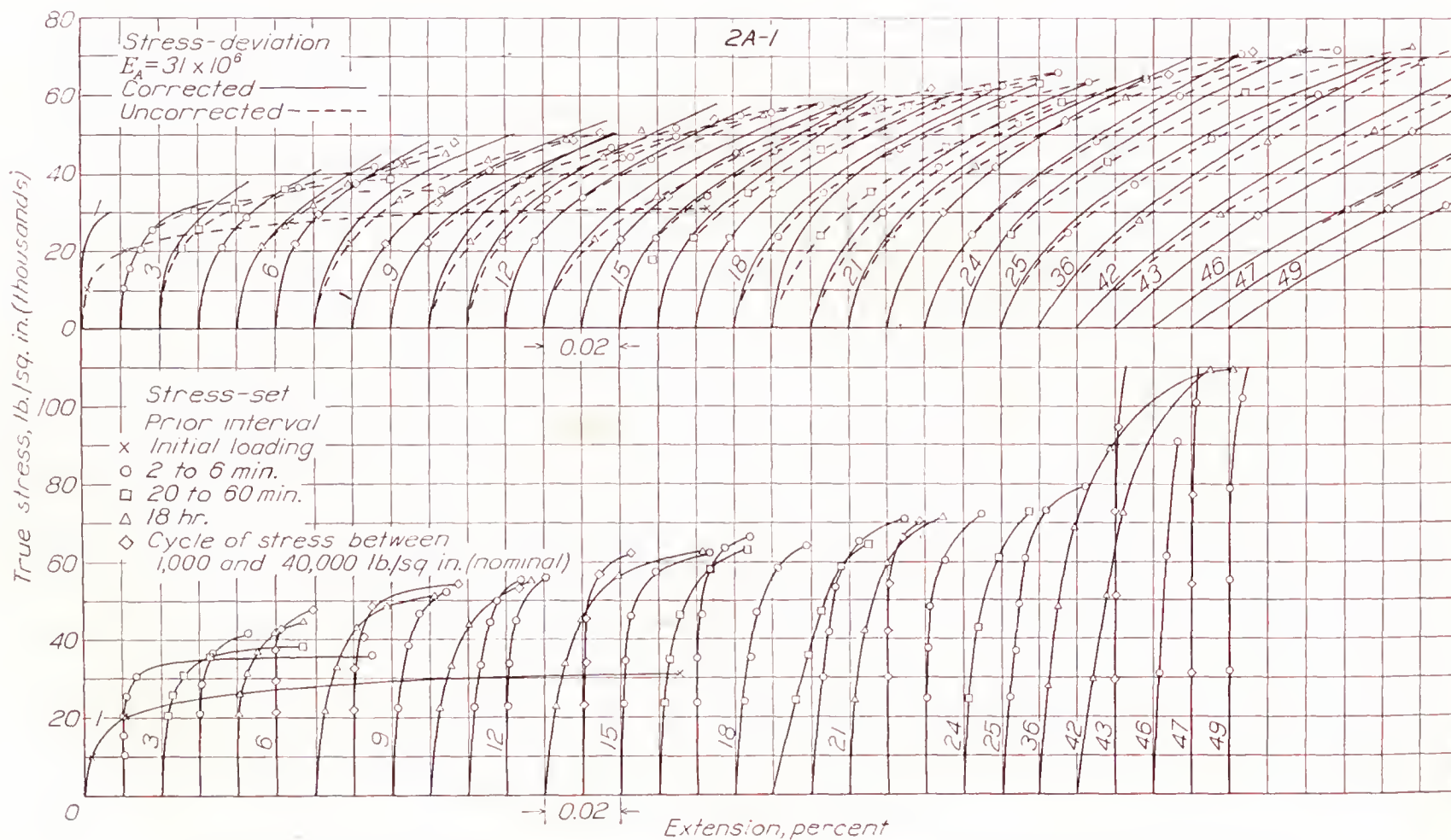
FIGURE 11.—Variation of the modulus of elasticity and of the index  $C_1$  with prior plastic extension. Half-hard material (1B-3, table I).

FIGURE 12.—Stress-set and stress-deviation curves obtained with a specimen of annealed material (2A-1, table I).



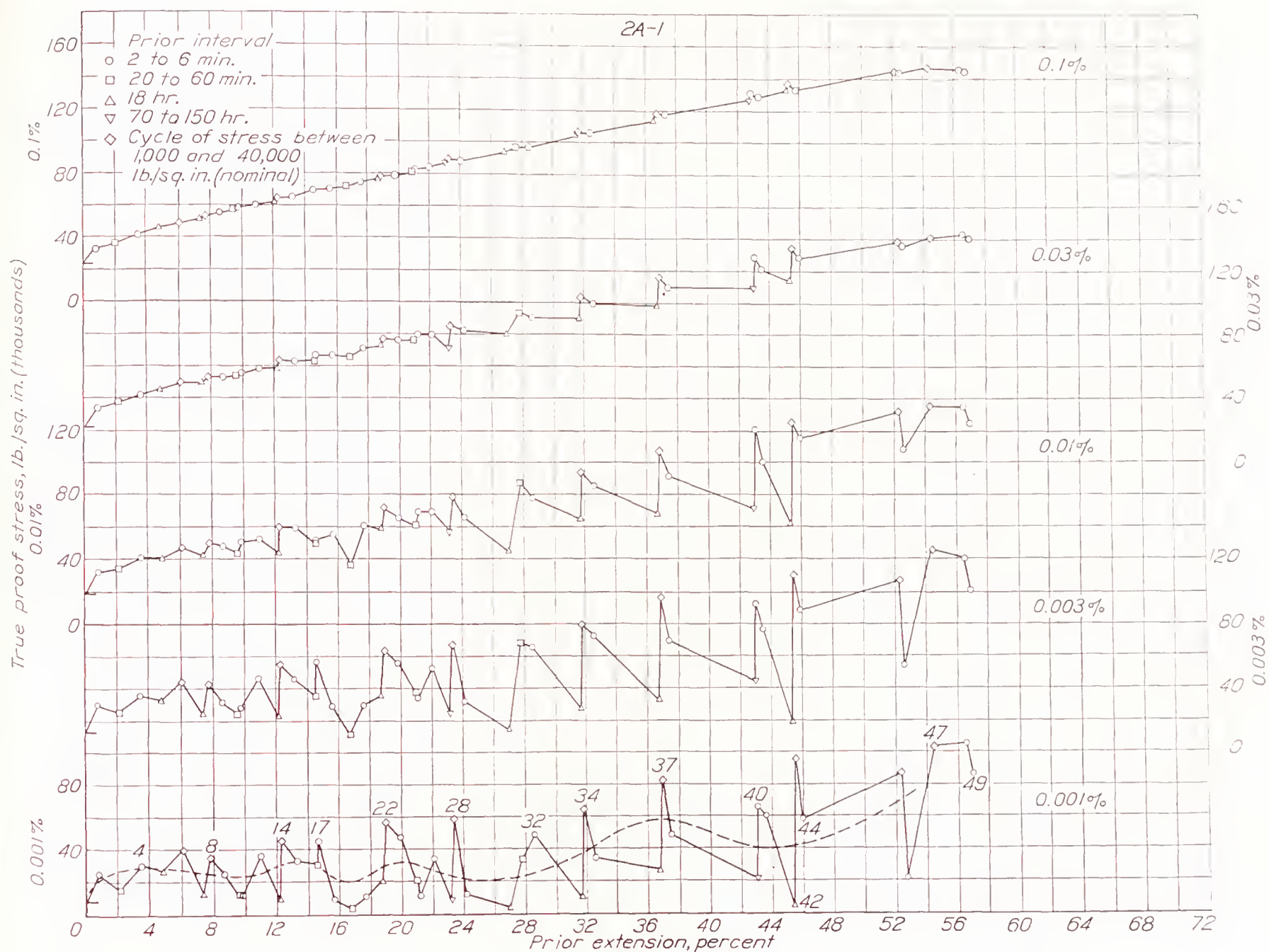


FIGURE 13.—Variation of proof stresses with prior plastic extension. Annealed material (2A-1, table I).

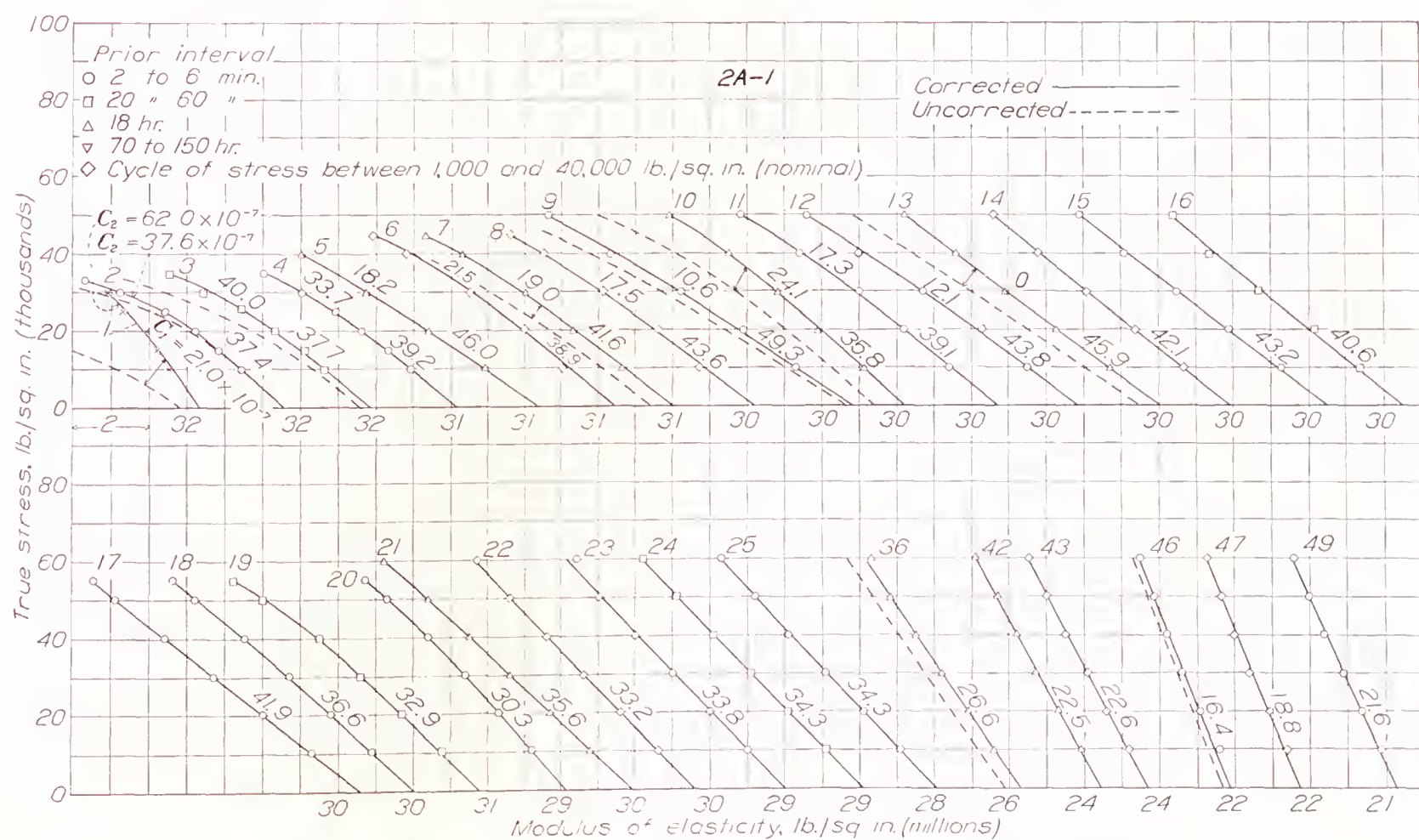


FIGURE 14.—Stress-modulus curves for annealed material, derived from stress-deviation curves of figure 12.



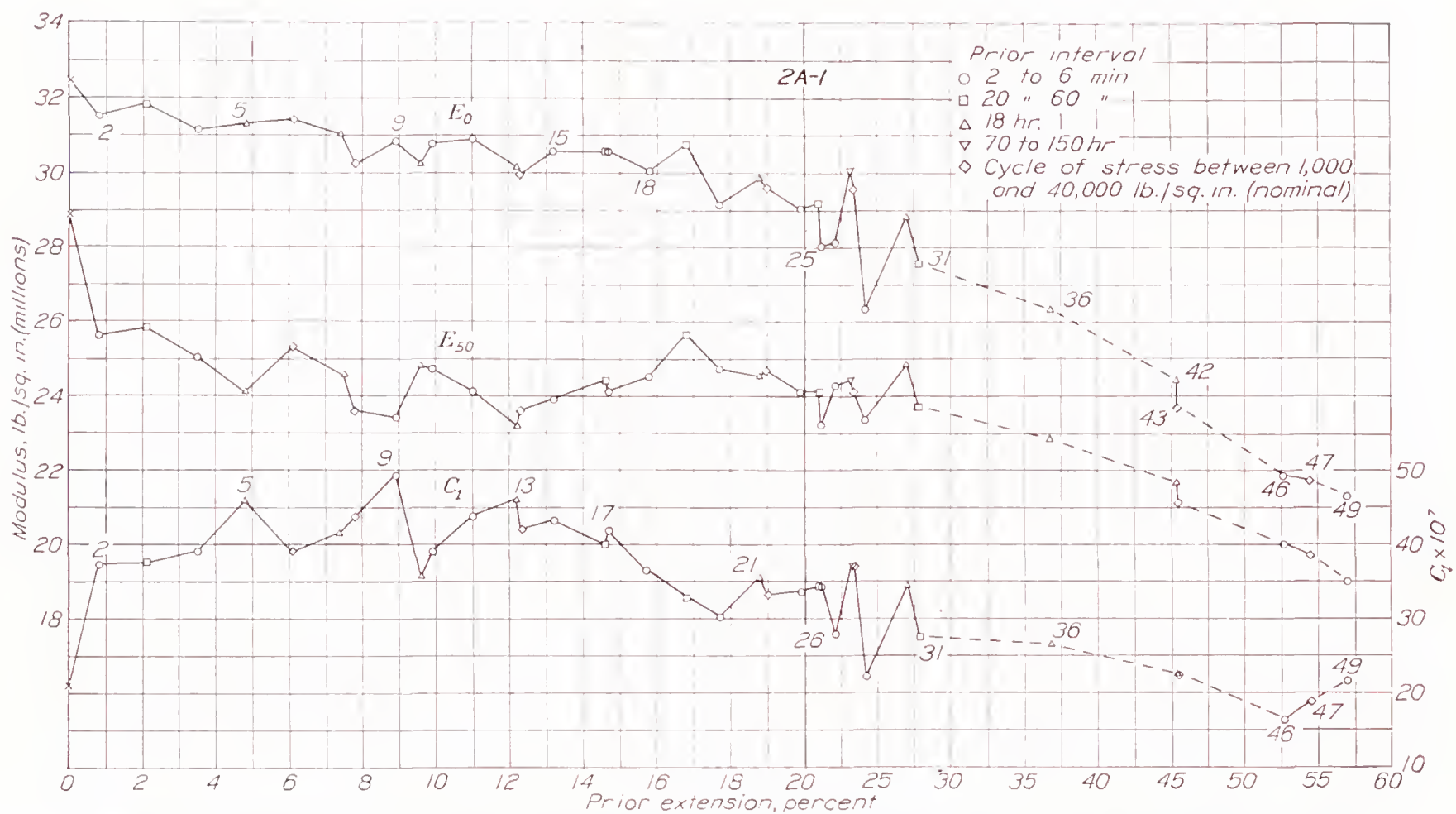


FIGURE 15.—Variation of the modulus of elasticity and of the index  $C_1$  with prior plastic extension. Annealed material (2A-1, table I).

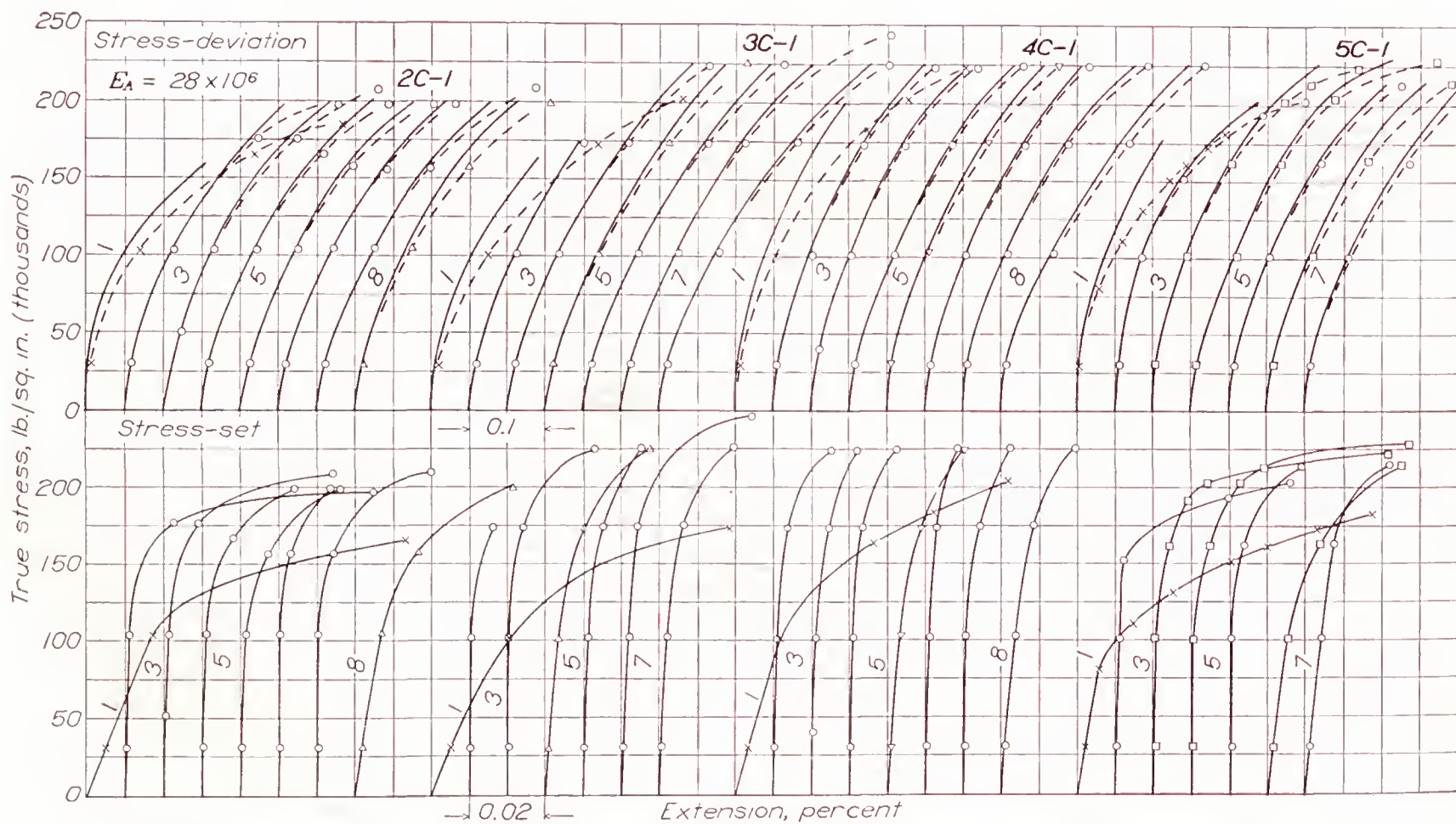


FIGURE 16.—Stress-set and stress-deviation curves obtained with four specimens of hard material (2C-1, 3C-1, 4C-1, 5C-1, table I).



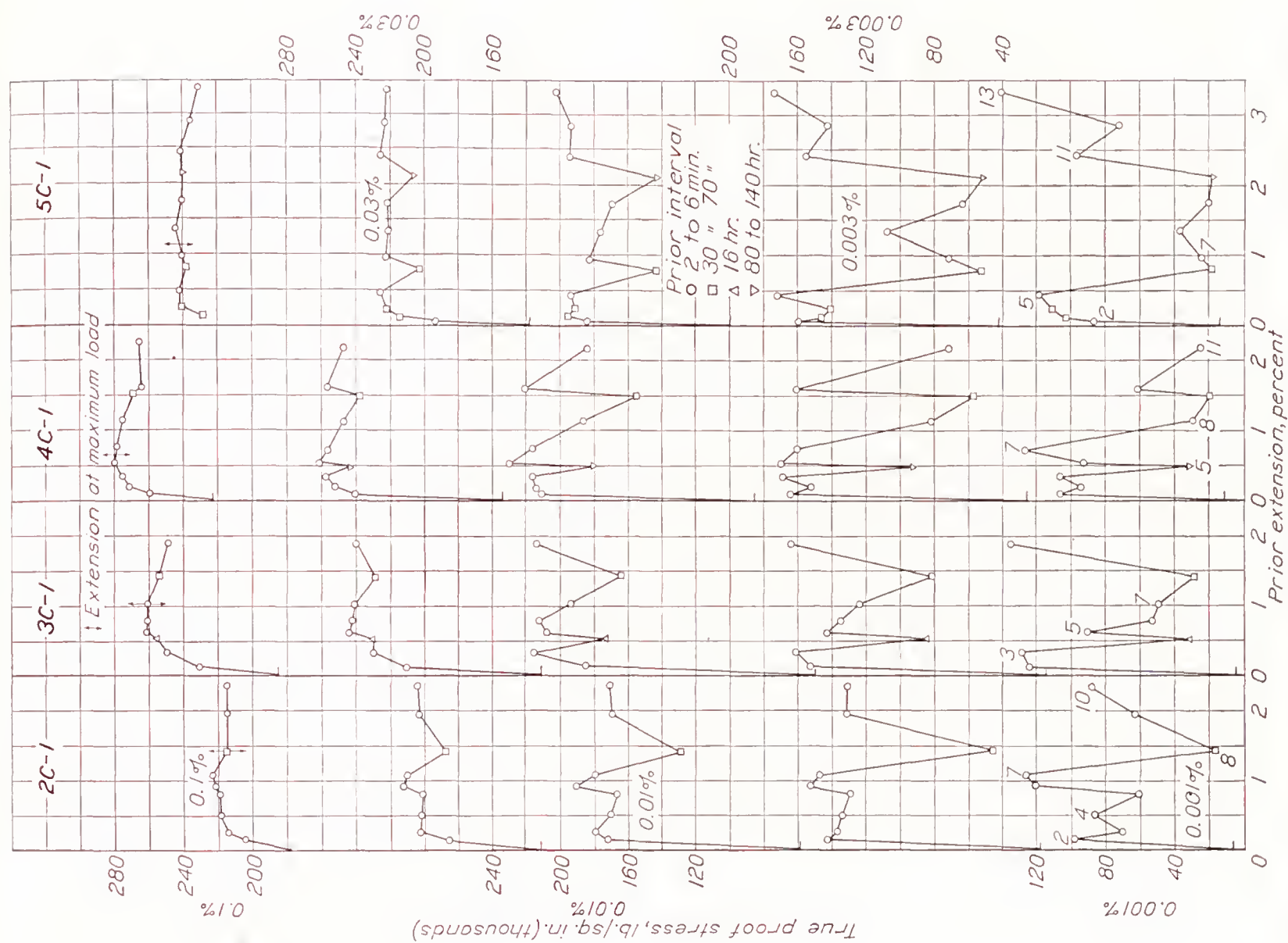


FIGURE 17.—Variation of proof stresses with prior plastic extension. Four specimens of hard material (2C-1, 3C-1, 4C-1, 5C-1, table I).

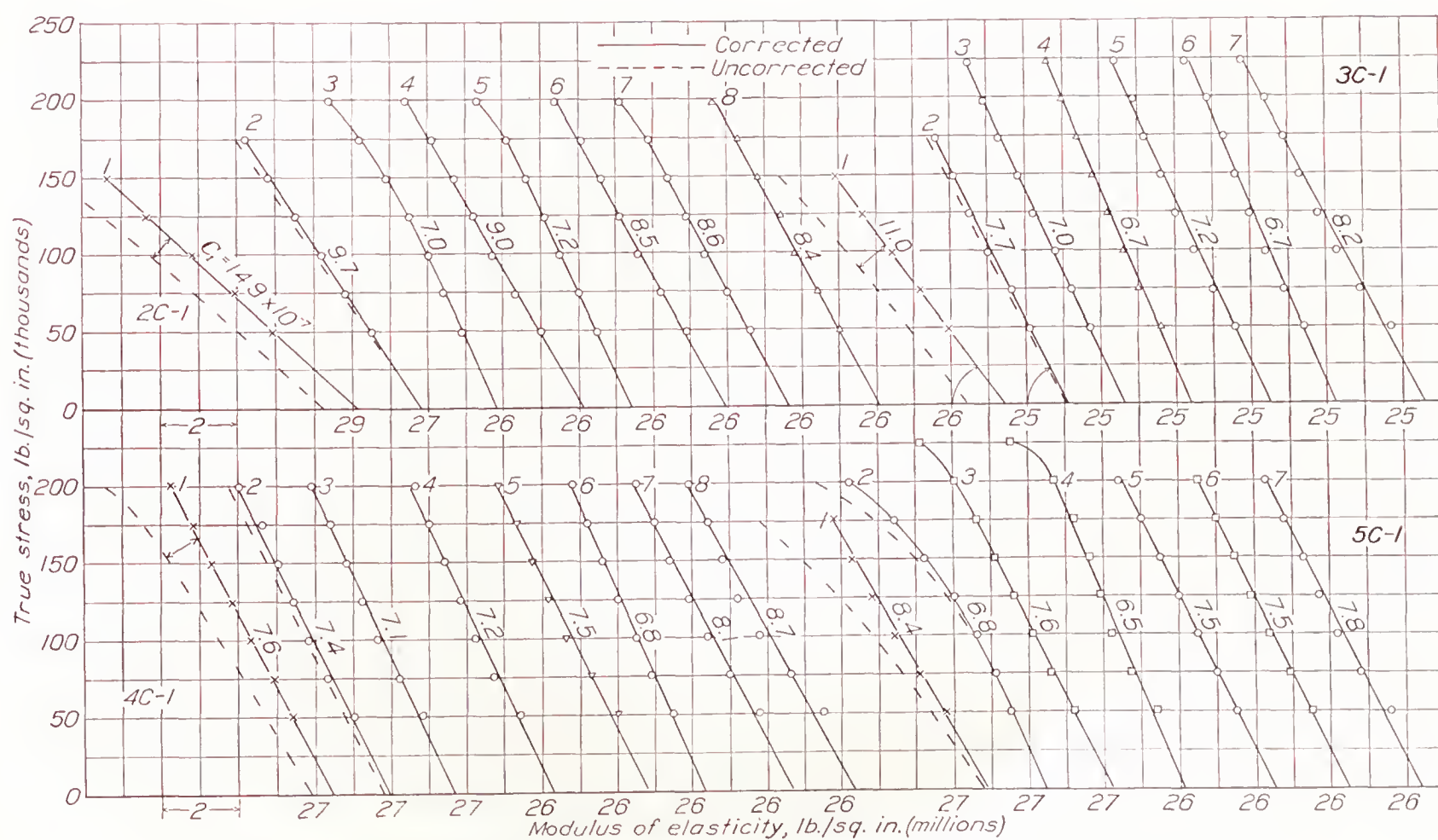


FIGURE 18.—Stress-modulus curves for hard material, derived from stress-deviation curves of figure 16.



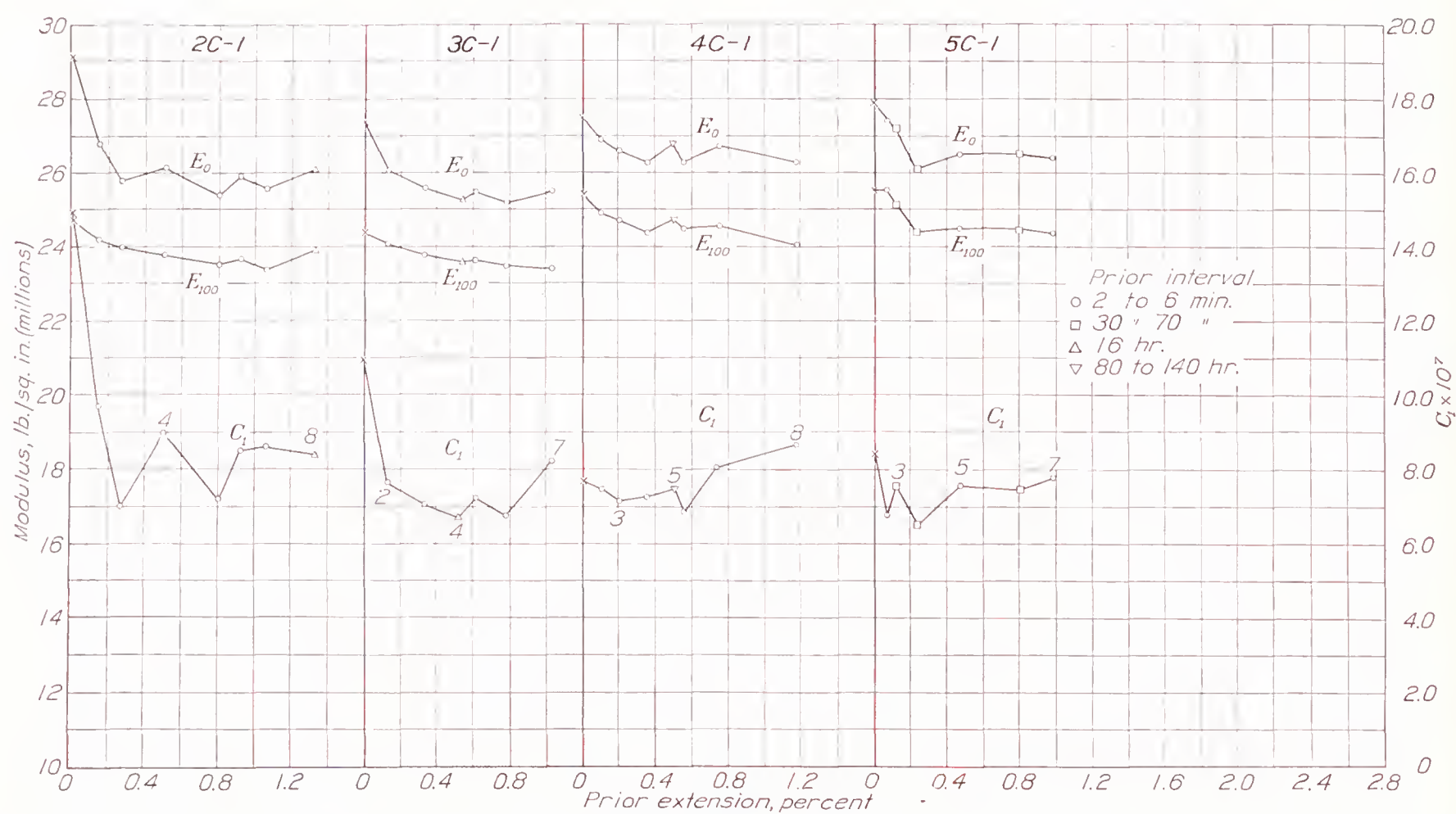


FIGURE 19.—Variation of the modulus of elasticity and of the index  $C_1$  with prior plastic extension. Four specimens of hard material (2C-1, 3C-1, 4C-1, 5C-1, table I).

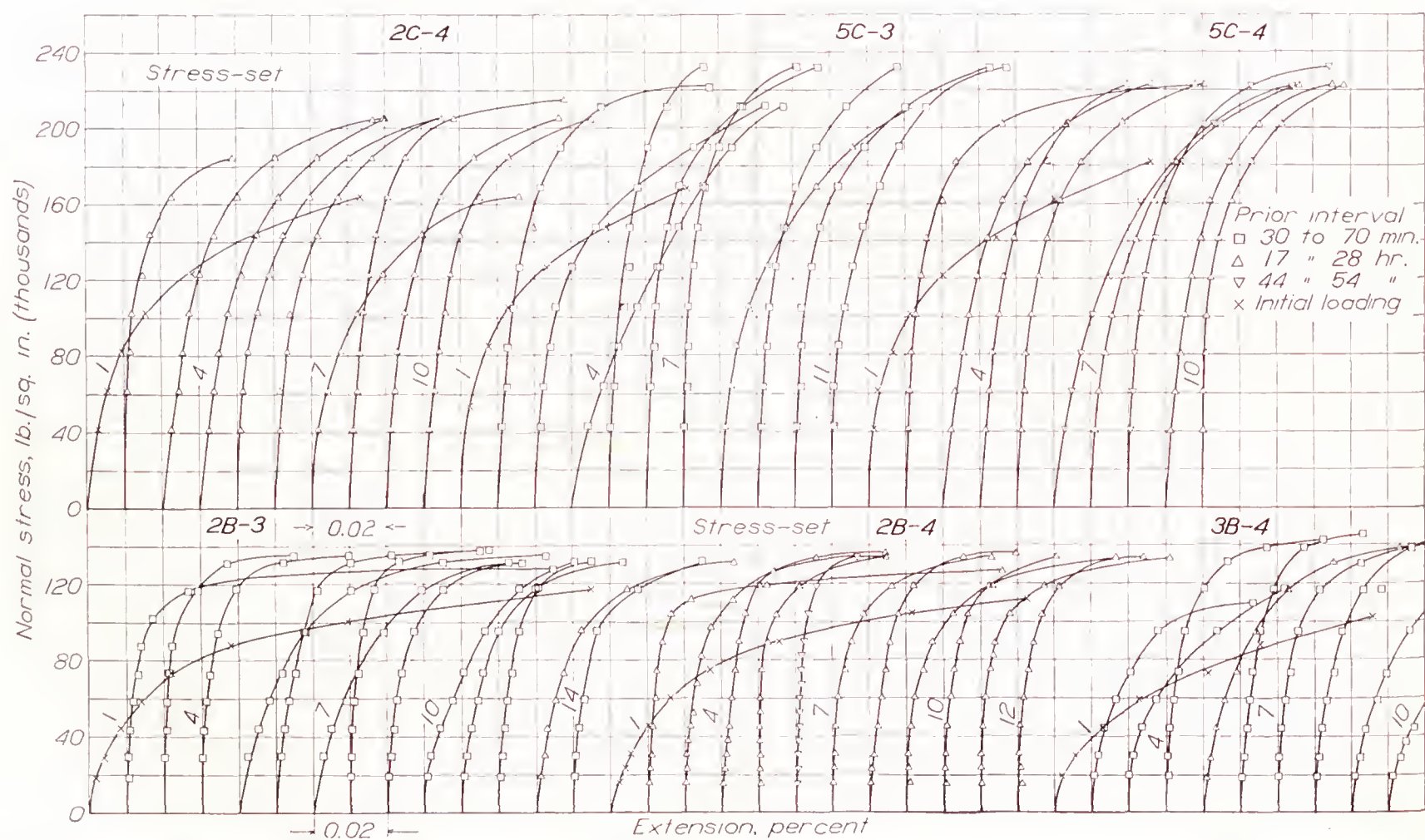


FIGURE 20.—Stress-set curves obtained with medium and long rest intervals. Three specimens each of half-hard and hard materials (2B-3, 2B-4, 3B-4, 2C-4, 5C-3, 5C-4, table I).



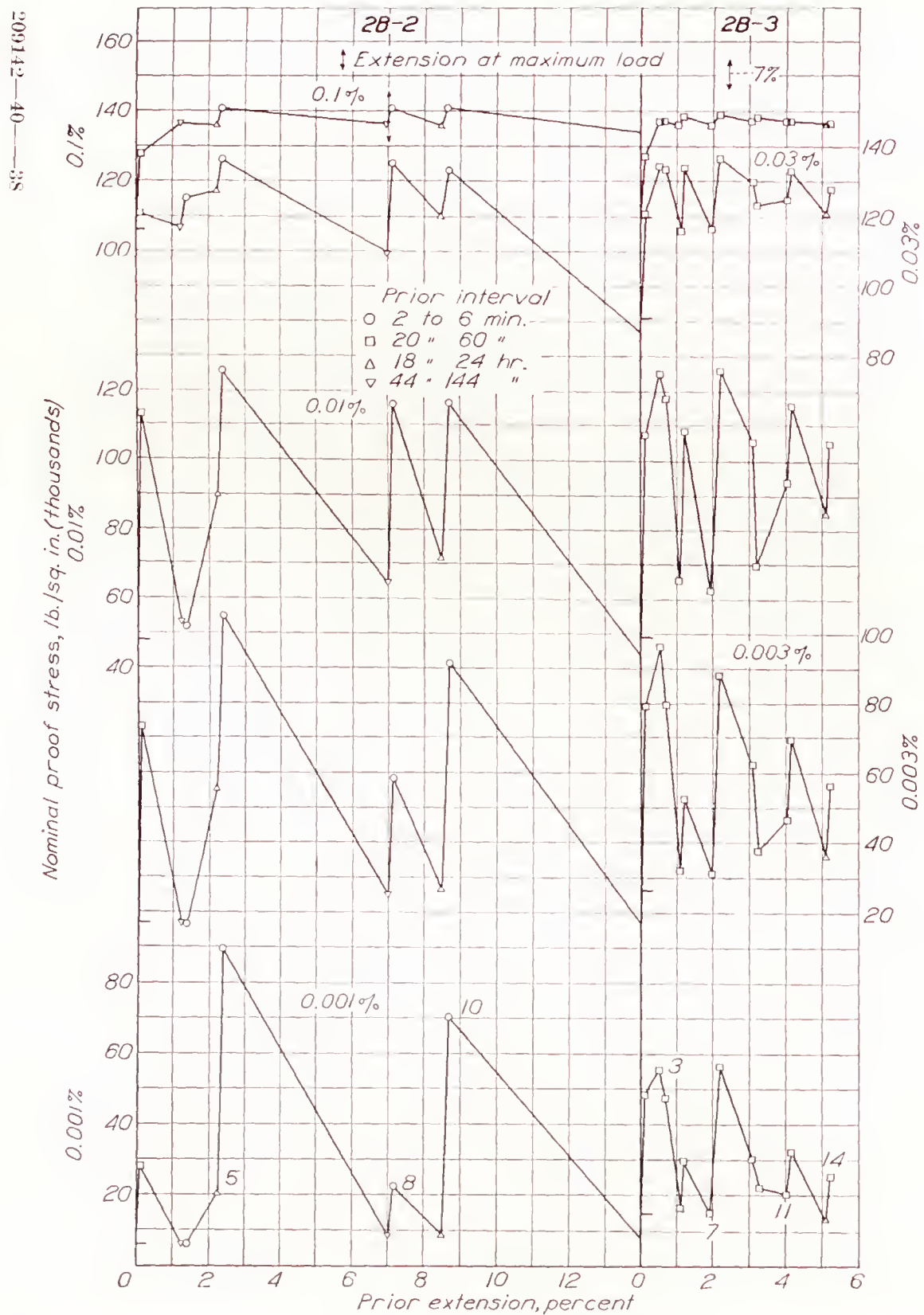


FIGURE 21.—Influence of duration of the rest interval on curves of variation of proof stress with plastic extension. Half-hard materials (2B-2, 2B-3, table I).

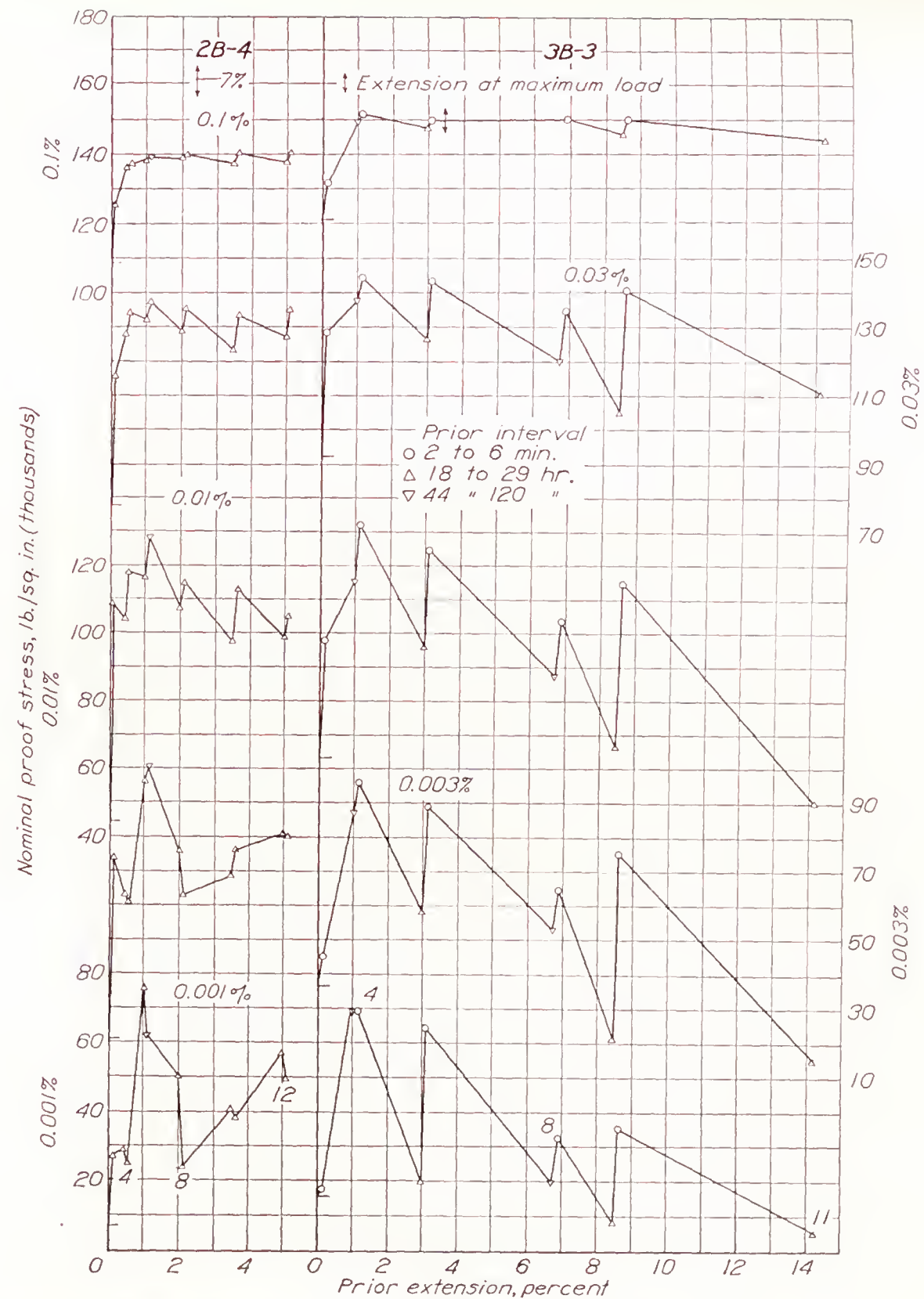


FIGURE 22.—Influence of duration of the rest interval on curves of variation of proof stress with plastic extension. Half-hard materials (2B-4, 3B-3, table I).



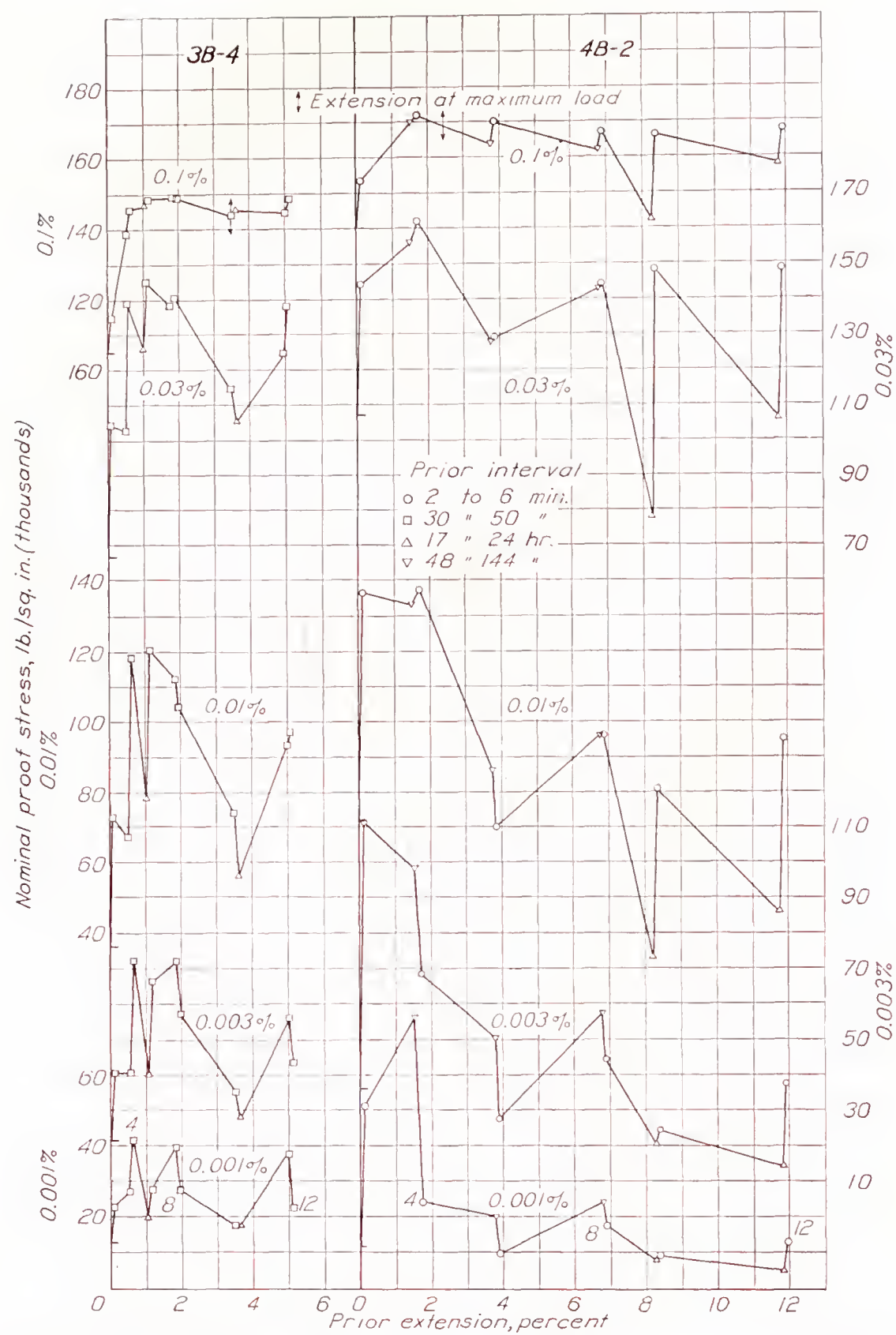


FIGURE 23.—Influence of duration of the rest interval on curves of variation of proof stress with plastic extension. Half-hard materials (3B-4, 4B-2, table I).

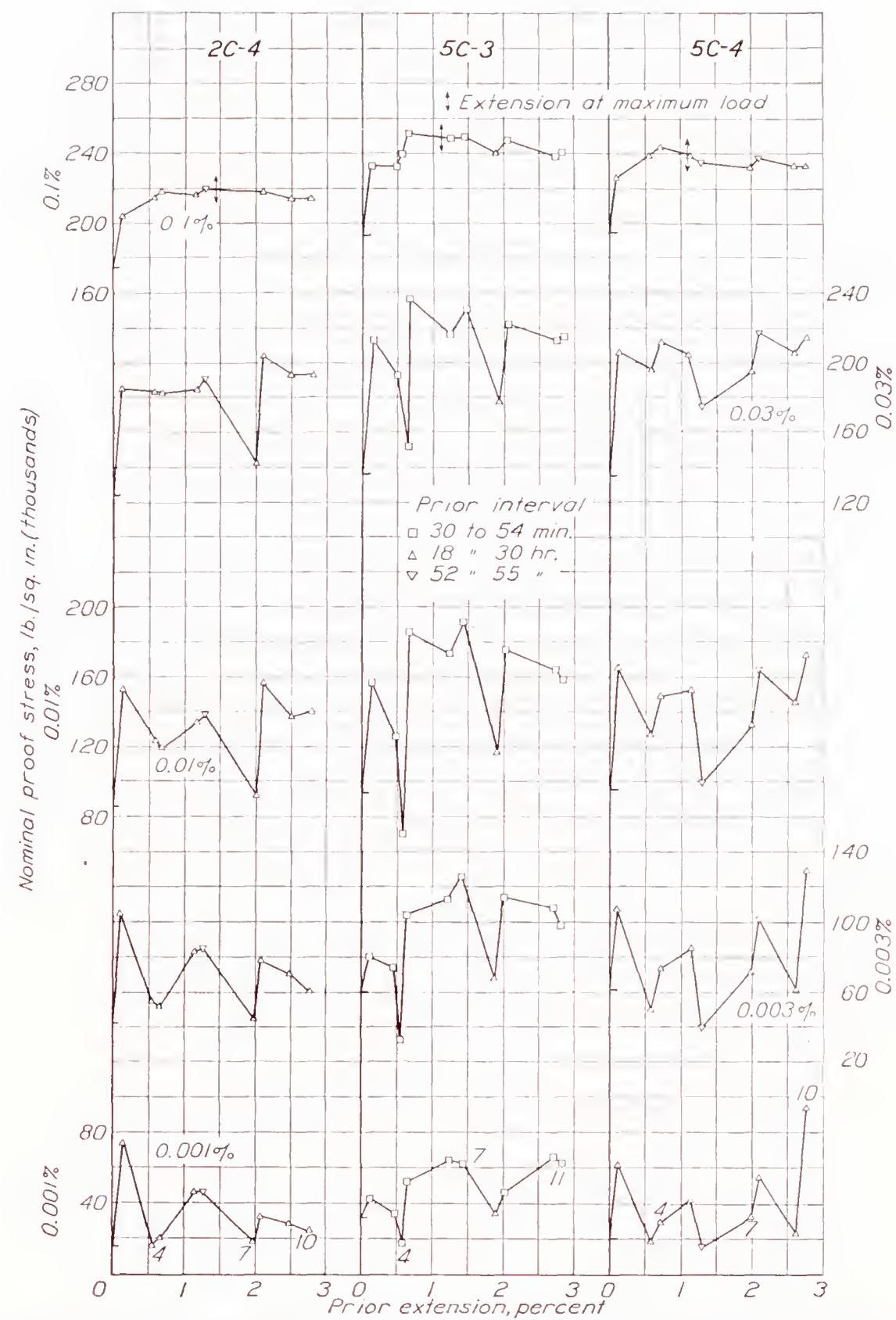


FIGURE 24.—Proof stress-deformation curves obtained entirely with either medium or long rest interval. Hard materials (2C-4, 5C-3, 5C-4, table I).



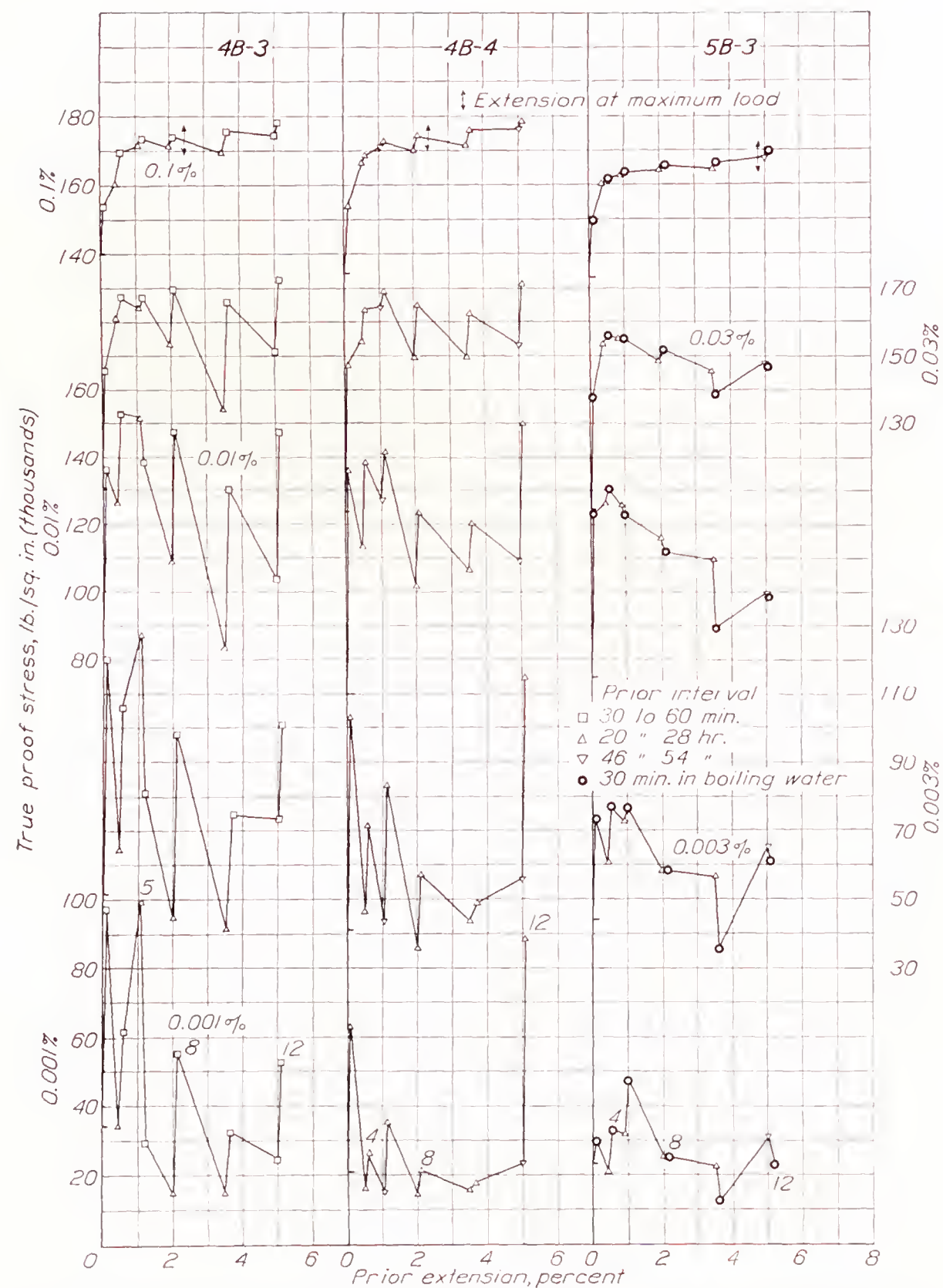


FIGURE 25.—Influence of medium and long rest intervals at room temperature and of 30 minutes at 100° C. on the proof stress-deformation curves. Half-hard materials (4B-3, 5B-4, 5B-3, table I).

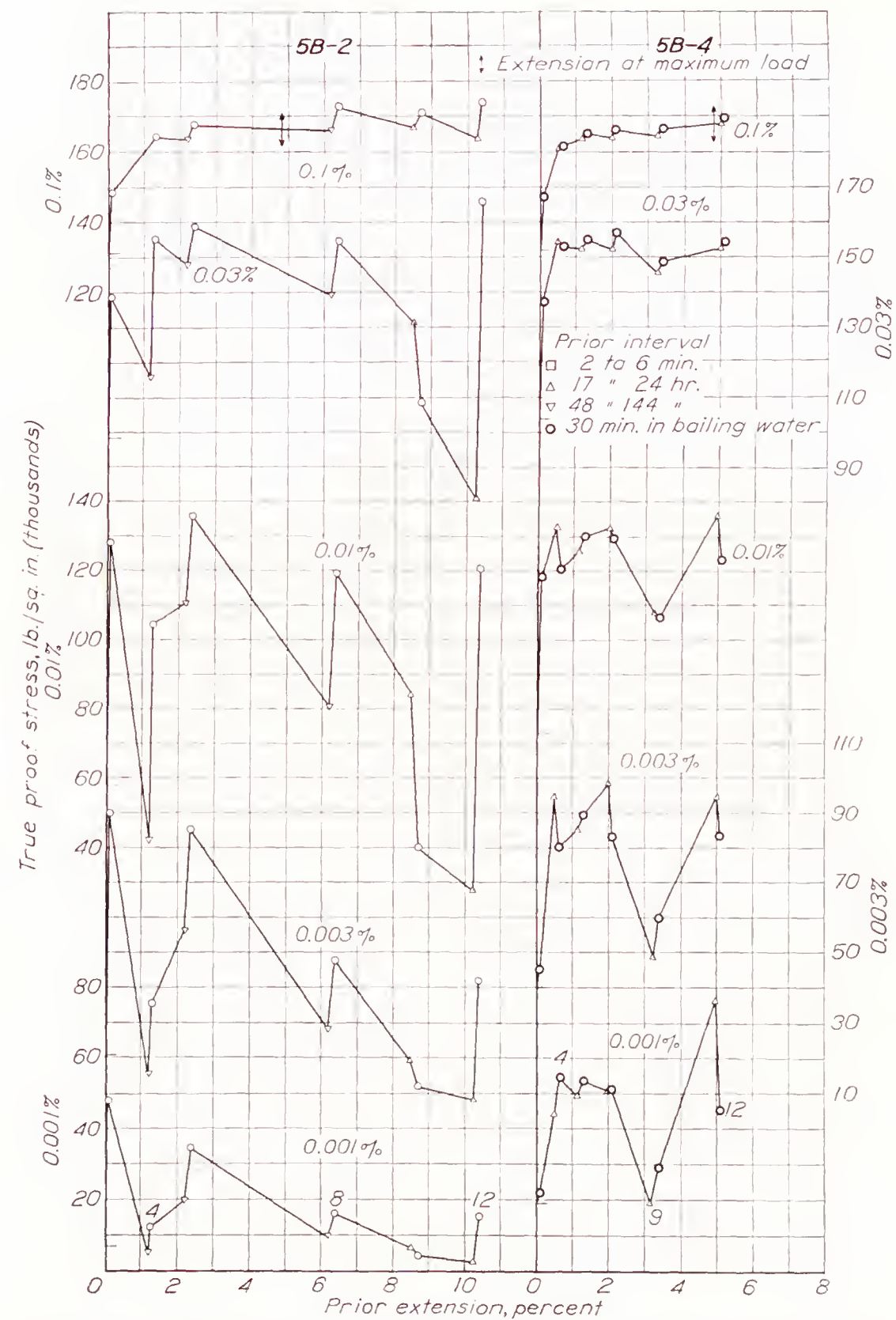


FIGURE 26.—Influence of short and long rest intervals at room temperature and of 30 minutes at 100° C. on the proof stress-deformation curves. Half-hard materials (5B-2, 5B-4, table I).



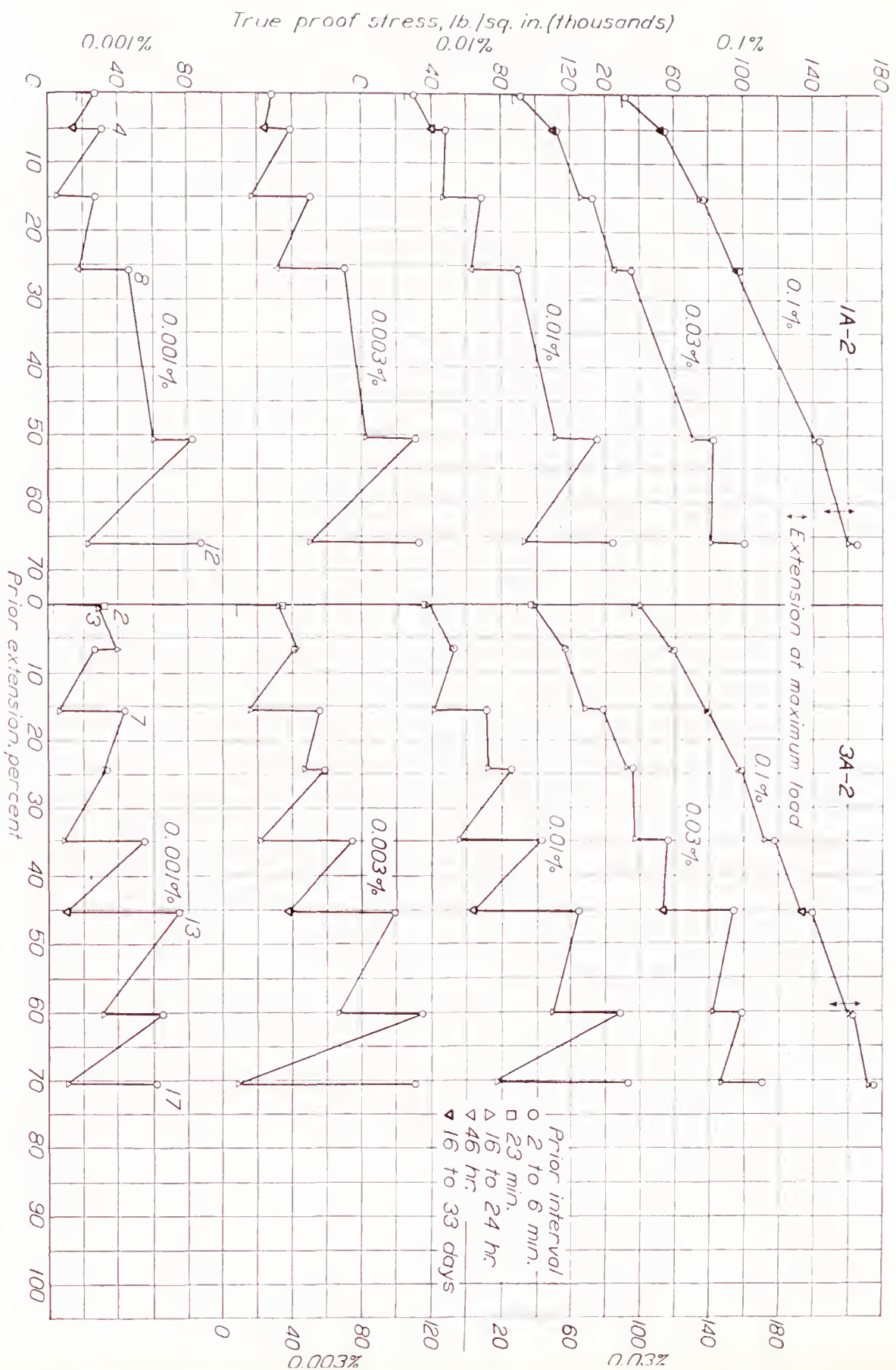


FIGURE 28.—Influence of short and long rest intervals on the proof stress-deformation curves. Annealed materials (1A-2, 3A-2, table I).

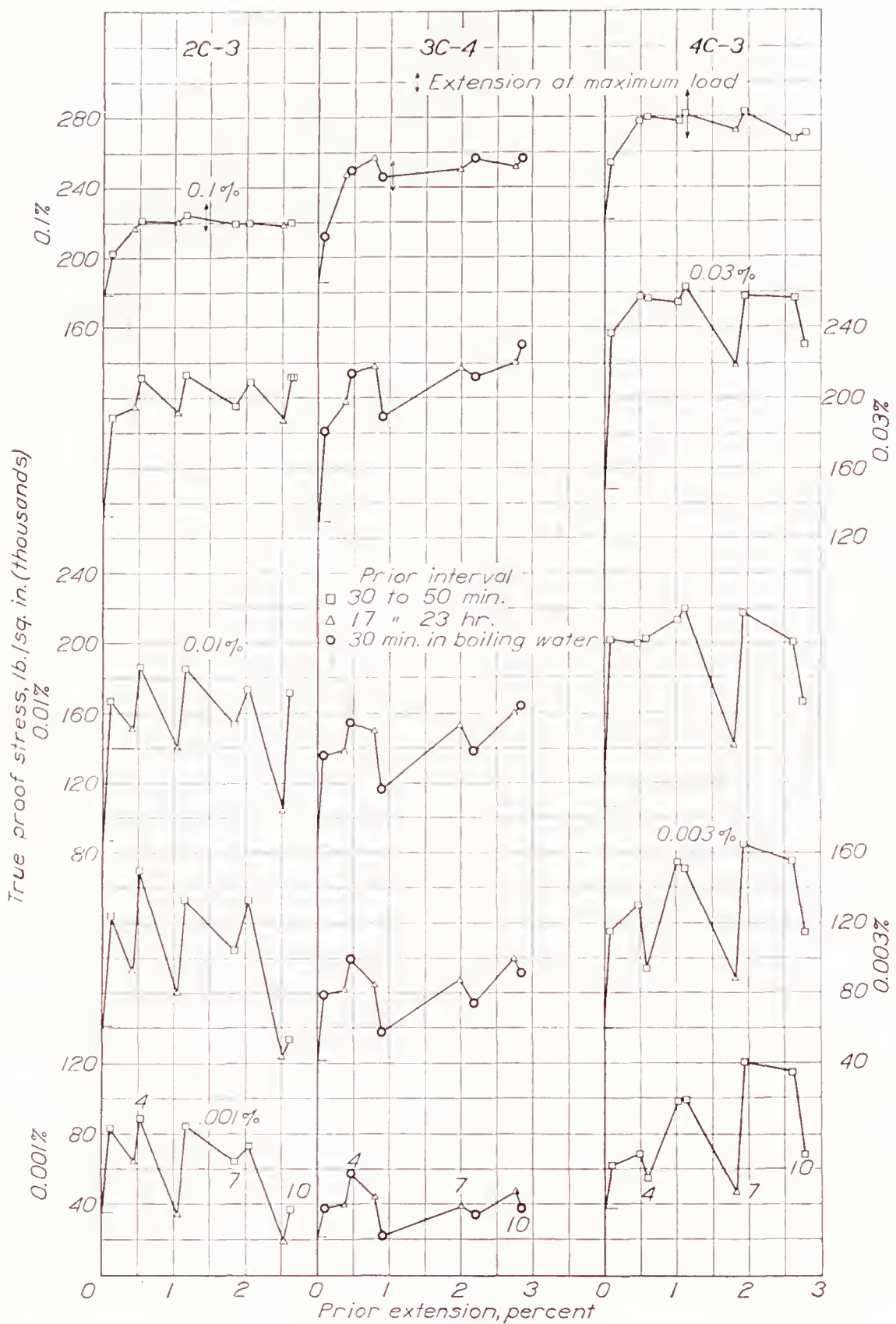


FIGURE 27.—Influence of medium and long rest intervals at room temperature and of 30 minutes at 100° C. on the proof stress-deformation curves. Hard materials (2C-3, 3C-4, 4C-3, table I).



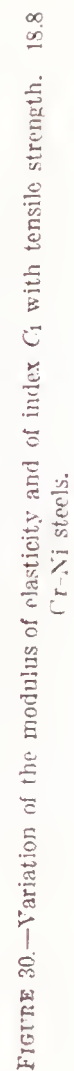




TABLE I.—CHEMICAL AND MECHANICAL PROPERTIES OF MATERIALS AS RECEIVED

Material <sup>a</sup>	Specimen	Condition	Chemical composition (percent)			Elongation in 2 inches (percent)		Reduction of area (percent)	Tensile strength (lb./sq. in.)	Initial proof stress (lb./sq. in.)					Initial proof ratio <sup>b</sup> (percent)				
			Cr	Ni	C	Maximum load	Total			0.10 percent	0.030 percent	0.010 percent	0.003 percent	0.001 percent	0.10 percent	0.030 percent	0.010 percent	0.003 percent	0.001 percent
1A	1A-2	Annealed	18.22	8.63	0.07	61.1	72.0	78.7	92,150	30,400	27,100	24,800	21,300	17,000	33.0	29.3	27.0	22.0	18.7
2A	2A-1	Annealed	18.7	9.5	.06	66.1	70.0	76.4	83,630	28,200	24,000	19,500	13,300	8,200	33.7	28.7	23.3	15.9	9.8
	2A-4									30,600	25,500	20,700	16,250	13,400	36.6	30.5	24.8	19.4	16.0
	Average									29,400	24,750	20,100	14,775	10,800	35.6	29.6	24.5	17.7	12.9
3A	3A-2	Annealed	18.4	8.9	0.7	58.7	66.3	74.8	90,630	35,800	28,900	22,200	8,200	2,500	39.6	31.9	24.3	9.1	2.8
	3A-3									35,050	30,200	25,100	19,400	15,000	38.7	33.3	27.7	21.4	16.5
	3A-4									35,250	30,800	25,700	21,000	16,200	38.0	34.0	28.4	23.2	17.9
	Average									35,370	29,970	24,330	16,200	11,230	39.0	33.0	26.8	17.8	12.3
4A	4A-2	Annealed	18.2	8.2	.11	56.2	66.0	71.7	98,630	40,500	35,300	29,000	22,000	9,000	41.1	35.8	29.4	22.3	9.1
	4A-3									41,900	36,000	30,500	25,950	21,800	42.5	36.5	30.9	26.3	22.1
	Average									41,200	35,650	29,750	23,970	15,400	41.8	36.1	30.2	24.3	15.6
5A	5A-2	Annealed	19.2	9.2	.11	54.1	66.0	74.7	91,360	36,600	30,400	25,800	20,000	12,500	40.0	33.2	28.2	21.9	13.7
	5A-3									36,600	31,100	25,500	21,200	15,500	40.1	34.0	27.9	23.2	17.0
	Average									36,600	30,750	25,650	20,600	14,000	40.05	33.6	28.1	22.5	15.4
1B	1B-1	Half hard	18.22	8.63	.07	24.2	28.5	78.7	150,630	85,200	50,900	29,300	10,780	6,850	56.4	33.8	19.5	7.1	4.5
	1B-3									89,900	61,300	39,100	22,000	13,800	59.7	40.7	25.9	15.1	9.2
	1B-5									89,800	62,300	42,300	26,500	16,200	59.6	41.3	28.1	17.6	10.7
	1B-6									89,400	61,000	41,700	25,100	16,500	59.3	40.4	27.7	16.7	10.9
	Average									88,580	58,880	35,370	18,580	11,200	59.0	39.1	23.4	12.3	7.4
2B	2B-2	Half hard	18.8	9.5	.06	7.03	18.5	61.1	143,130	106,500	76,400	48,500	17,000	6,000	74.4	52.7	33.9	11.9	4.2
	2B-3									110,000	81,300	49,200	26,500	14,500	76.8	56.8	34.4	17.8	10.1
	2B-4									108,500	77,500	44,030	21,000	7,000	75.7	54.9	31.1	14.7	4.9
	Average									108,330	78,400	47,730	21,500	9,170	75.6	54.8	33.4	15.1	6.4
3B	3B-2	Half hard	18.6	8.9	.07	3.46	16.3	61.6	153,860	120,900	93,500	63,200	34,800	18,700	78.6	60.8	41.1	22.6	12.1
	3B-3									121,000	92,300	63,500	36,500	15,500	78.7	60.0	41.3	23.7	10.1
	3B-4									105,800	66,500	38,100	21,300	12,000	68.8	43.2	24.8	13.8	7.8
	Average									115,900	84,100	54,930	30,870	15,400	75.3	54.7	35.7	20.1	10.1
4B	4B-2	Half hard	18.2	8.2	.11	2.42	14.3	55.1	173,690	139,300	107,000	72,500	36,600	11,500	80.1	61.8	41.7	20.4	6.6
	4B-3									140,000	109,500	77,400	51,500	34,000	80.6	63.0	45.7	29.7	19.6
	4B-4									136,400	104,200	70,000	41,000	21,000	78.5	60.0	40.3	23.6	12.1
	Average									138,530	106,900	73,300	42,830	22,170	79.8	61.5	42.6	24.7	12.8
5B	5B-2	Half hard	19.1	9.3	.12	4.80	15.8	56.8	164,830	131,200	98,000	58,000	21,000	7,000	79.6	59.5	35.2	12.7	4.2
	5B-3									132,800	104,300	75,000	44,000	24,000	80.6	63.3	45.5	26.7	14.6
	5B-4									132,200	104,000	73,000	40,000	19,000	80.2	63.1	44.3	24.3	11.5
	Average									132,100	102,100	68,670	35,000	16,670	80.1	61.9	41.6	21.2	10.1
2C	2C-1	Hard	18.8	9.4	.06	1.43	6.5	51.0	223,180	170,030	132,500	58,000	18,200	6,300	76.2	59.3	26.0	8.2	2.8
	2C-3									178,600	131,600	95,000	61,000	35,000	80.0	58.9	42.6	27.3	15.7
	2C-4									176,700	126,000	86,000	42,000	16,000	78.9	56.4	38.5	18.8	7.2
	Average									175,100	130,030	79,670	40,400	19,100	78.5	58.3	35.7	18.1	8.6
3C	3C-1	Hard	18.4	8.9	.07	1.03	5.5	52.9	259,380	184,700	131,000	55,000	15,000	5,000	71.3	50.5	19.3	5.8	1.9
	3C-4									186,000	130,200	80,000	43,000	22,000	71.6	50.2	32.7	16.7	8.5
	Average									185,350	130,600	67,500	29,000	13,500	71.45	50.35	26.0	11.2	5.2
4C	4C-1	Hard	18.3	8.1	.11	1.15	4.5	46.8	283,690	223,000	154,000	85,000	26,000	9,000	78.9	54.3	30.0	9.2	3.2
	4C-3									222,000	147,500	97,200	60,000	38,000	78.2	52.0	34.3	21.2	13.4
	Average									222,500	150,750	91,000	43,000	23,500	78.5	53.1	32.1	15.2	8.3
5C	5C-1	Hard	19.1	9.2	.14	1.12	5.75	55.3	246,830	138,000	100,000	42,000	14,000	-----	55.6	40.4	16.9	5.6	-----
	5C-3									192,800	136,000	94,300	60,000	32,000	77.7	54.9	38.1	24.2	12.9
	5C-4									194,200	135,500	95,000	62,500	20,800	78.4	54.7	38.4	25.2	8.4
	Average									193,500	136,500	96,430	54,830	22,270	78.05	55.1	39.0	22.1	9.0

<sup>a</sup> A represents annealed material; B represents half-hard material; C represents hard material. <sup>b</sup> Proof ratio is given as ratio of proof stress to tensile strength in percent.

TABLE II.—DIMENSIONS OF ROD MATERIAL AS RECEIVED AND OF TEST SPECIMENS

All specimens machined to standard 2-inch gage length. Fillets and reduced section machined with aid of templet designed for 0.505 inch gage diameter standard A. S. T. M. tensile specimen]

Material	Condition	Bar diameter <sup>1</sup> (inches)	Nominal gage diameter (inches)	Diameter of threaded ends (inches)
1A	Annealed	$\frac{5}{8}$	0.417	0.625
2A	do	$\frac{7}{8}$	.505	.750
3A	do	$\frac{7}{8}$	.505	.750
4A	do	$\frac{7}{8}$	.505	.750
5A	do	$\frac{7}{8}$	.505	.750
1B	Half hard	$\frac{5}{8}$	.417	.625
2B	do	$\frac{5}{8}$	.417	.625
3B	do	$\frac{5}{8}$	.417	.625
4B	do	$\frac{5}{8}$	.417	.625
5B	do	$\frac{5}{8}$	.417	.625
2C	Hard	$\frac{3}{8}$	.250	.375
3C	do	$\frac{3}{8}$	.250	.375
4C	do	$\frac{3}{8}$	.250	.375
5C	do	$\frac{3}{8}$	.250	.375

<sup>1</sup> As received.



TABLE III.—HYSTERESIS

SPECIMEN 1A-5

1	2	3	4	5	6	7	8	9	10	11	12	13	14	15
Cycle	True stress range (lb./sq. in.)	Total eyelet time (min.)	Time interval after preceding eyelet (hr.)	Strain range (percent)	Deviation range (percent)	Loop width (percent)	Permanent set due to eyelet (percent)		Total permanent set (percent)	Negative creep at bottom (percent)		Positive creep below top (percent)	Modulus $E_o$ (lb./sq. in.)	$C_1^a$ (sq. in./lb.)
							Before negative creep	Net		1 min.	3 min.			
1	1.4-75.5×10 <sup>3</sup>			15.3				15.00	15.00					
2	1.7-75.5	13.0	0	0.424		0.145	0.094	0.086	15.086	0.006	0.008			
3	1.7-75.5	14.0	0	.366		.092	.038	.034	15.120	.003	.004			
4	1.7-75.6	10.5	0	.349		.076	.022	.018	15.138	.002	.004			
5	1.7-75.6	11.0	0	.346	0.113	.074	.023	.015	15.153	.004	.008	0.008	32.6×10 <sup>6</sup>	43.6×10 <sup>-7</sup>
6	1.7-75.6	10.5	0	.345	.110	.069	.018	.015	15.168	.001	.003	.005	31.7	40.4
7	1.7-75.6	9.5	0	.338		.064	.013	.010	15.178	.002	.003			
8	1.7-75.6	8.0	0	.337	.103	.065	.013	.009	15.187	.003	.004	.005	32.5	42.2
9	1.7-50.8	10.0	0	.194		.025	.003	.000	15.187	.002	.003			
10-34	1.7-75.7	.6	0					.0023	15.244					
35	1.7-75.8	9.0	0	.329	.095	.055	.010	.005	15.249	.003	.005	.003	31.1	36.0
36	1.7-75.8	8.0	0	.330		.051	.008	.005	15.254	.002	.003			
37	1.7-75.8	8.5	0	.331		.054	.009	.003	15.257	.005	.006			
38	1.7-75.8	7.5	0	.330		.056	.009	.004	15.261	.003	.005			
39	1.7-75.8	11.0	0	.329	.095	.057	.008	.005	15.266	.002	.003	.005	31.8	39.3
40-139	1.7-75.9	.5	0					.0008	15.341					
140	1.7-75.9	12.0	0	.325	.089	.049	.006	.003	15.344	.002	.003	.003	31.6	39.2
141	1.7-75.9	12.0	0	.324		.049	.004	.002	15.346	.001	.002			
142	1.7-75.9	11.5	0	.325		.049	.006	.002	15.348	.003	.004			
143	1.7-75.9	12.0	0	.324		.050	.005	.002	15.350	.002	.003			
144-154	1.7-75.9	<sup>b</sup> (1.0)	24					<sup>b</sup> (.0009)	15.360					
155	1.7-75.9	10.0	24	.353	.119	.067	.032	.027	15.387	.004	.005	.005	29.1	35.1
156	1.7-75.9	9.0	0	.331	.097	.054	.008	.004	15.391	.002	.004	.005	31.95	39.5
157	1.7-75.9	10.0	0	.333	.096	.054	.009	.005	15.396	.003	.004	.003	31.25	37.1
158	1.7-75.9	9.5	0	.332		.052	.006	.002	15.398	.003	.004			
159	1.7-75.9	57.5	0	.335	.100	.055	.010	.006	15.404	.002	.004	.003	31.4	39.5
160	1.7-75.9	11.0	0	.330		.051	.007	.004	15.408	.002	.004			
161	1.7-76.0	10.0	0	.328	.092	.050	.005	.001	15.409	.003	.004	.004	31.8	38.4

<sup>a</sup> Values of  $C_1$  are given as fractional change of modulus per pound per square inch.

<sup>b</sup> Estimated value is indicated by parentheses.

TABLE IV.—HYSTERESIS

SPECIMEN 1A-3

1	2	3	4	5	6	7	8	9	10	11	12	13	14
Cycle	True stress range (lb./sq. in.)	Total eyelet time (min.)	Time interval after preceding eyelet (hr.)	Strain range (percent)	Deviation range (percent)	Loop width (percent)	Permanent set due to eyelet (percent)		Total permanent set (percent)	Negative creep at bottom (percent) 2 min.	Positive creep below top (percent)	Modulus $E_o$ (lb./sq. in.)	$C_1^a$ (sq. in./lb.)
							Before negative creep	Net					
1	1.4-45.5×10 <sup>3</sup>	29.0		3.36		3.20		3.185	3.185				
2	1.5-45.5	16.5	0	0.329		0.187	0.166	0.156	3.341	0.010			
3	1.5-45.5	8.5	0	.232		.092	.061	.060	3.401	.001			
4	1.5-45.5	8.5	0	.230		.083	.054	.051	3.452	.003			
5	1.5-45.6	9.0	0	.221	0.088	.084	.036	.034	3.486	.002	0.030		
6	1.5-45.6	9.5	0	.197	.066	.064	.025	.023	3.509	.002	.013	34.6×10 <sup>6</sup>	62.4×10 <sup>-7</sup>
7	1.5-45.6	11.5	0	.192	.060	.049	.019	.016	3.525	.003	.010	31.1	20.6
8	1.5-45.6	9.0	0	.198		.055	.025	.022	3.547	.003			
9	1.5-45.6	10.0	0	.193		.051	.021	.019	3.566	.002			
10	1.5-45.6	10.0	0	.188	.060	.050	.017	.015	3.581	.002	.014	31.2	28.0
11	1.5-45.6	11.0	0	.189		.045	.018	.016	3.596	.002			
12	1.5-45.6	11.0	0	.189		.047	.018	.015	3.611	.003			
13	1.5-45.6	10.0	0	.186	.054	.044	.016	.012	3.623	.004	.012	31.25	24.6
14-19	1.5-45.6	<sup>b</sup> 15.0	0					<sup>b</sup> .033	3.656				
20	1.5-45.6	10.5	0	.184	.050	.048	.013	.010	3.666	.003	.011	33.5	32.2
21	1.5-45.6	9.0	0	.182	.050	.045	.012	.009	3.675	.003	.004	33.55	32.2
22-27	1.5-45.6	<sup>b</sup> 15.0	0					<sup>b</sup> .026	3.701				
28	1.5-45.6	10.0	0	.183	.046	.038	.008	.006	3.707	.002	.005	36.6	73.2
29	1.5-45.6	10.0	0	.184	.049	.046	.012	.010	3.717	.002	.010	31.3	16.2

<sup>a</sup> Values of  $C_1$  are given as fractional change of modulus per pound per square inch.

<sup>b</sup> 6 eyelets.



TABLE V.—HYSTERESIS  
SPECIMEN 1A-4

1	2	3	4	5	6	7	8	9	10	11	12	13	14
Cycle	True stress range (lb./sq. in.)	Total cycle time (min.)	Time interval after preceding cycle (hr.:min.)	Strain range (percent)	Deviation range (percent)	Permanent set due to cycle (percent)		Total permanent set (percent)	Negative creep at bottom (percent)		Positive creep below top (percent)	Modulus $E_0$ (lb./sq. in.)	$C_1^a$ (sq. in./lb.)
						Before negative creep	Net		1 min.	2 min.			
1-30	1.5-45.5 $\times 10^3$	<sup>b</sup> (1.0)					<sup>b</sup> (3.50)	(3.50)					
31	1.5-45.6	10.0	0:0	0.224	0.093	0.055	0.052	3.552		0.003	0.015	30.4 $\times 10^6$	33.9 $\times 10^{-7}$
32	1.5-45.6	9.0	0:0	.194	.063	.028	.024	3.576		.004	.014	29.6	9.8
33	1.5-45.6	9.0	0:0	.189	.058	.023	.021	3.597		.002	.013	30.55	23.6
34	1.5-45.6	9.5	0:0	.184	.057	.019	.016	3.613		.003	.012	33.55	37.5
35-45	1.5-45.6	3.0	0:0					.0065					
46	1.5-45.7	9.0	0:0	.181	.051	.015	.013	3.698		.002	.012	32.0	13.7
47	1.5-45.7	10.0	0:0	.176	.045	.012	.009	3.707		.003	.007	31.7	13.2
48-78	1.5-45.7	.8	1:20					.0016					
79	1.5-45.7	9.0	0:0	.180	.050	.016	.008	3.765		.008	.012	31.3	11.8
80	1.5-45.7	9.0	0:0	.174	.040	.010	.007	3.772		.003	.004	31.65	15.8
81	1.5-45.7	17.0	45:0	.1925	.0598	.0085	.0064	3.778	0.0021		.007	29.95	39.6
82	1.5-45.7	13.0	0:02	.1909	.0574	.0094	.0072	3.786	.0022		.0036	29.4	36.7
83	1.5-45.7	13.5	0:02	.1915	.0552	.0095	.0069	3.793	.0026		.0022	29.0	33.8
84-113	1.5-45.7	.2	0:0					.0016					
114	1.5-45.7	14.0	0:02	.1934	.0580	.0109	.0088	3.851	.0021		.0027	28.2	29.1
115	1.5-45.7	15.0	0:02	.1932	.0555	.0081	.0066	3.857	.0015		.0004	28.2	26.2
116	1.5-45.7	10.0	72:0	.2025	.0654	.0189	.0159	3.873	.0030		.0016	27.7	17.0
117	1.5-45.7	10.5	0:02	.1899	.0540	.0065	.0046	3.878	.0019		.0025	28.1	9.3
118	1.5-45.7	12.5	0:02	.1882	.0525	.0059	.0036	3.881	.0023		.0025	28.4	25.0
119-273	1.5-45.7	.4	0:02				(.0003)	(3.931)					
274	1.5-45.8	12.5	0:02	.1888	.0513	.0039	.0023	3.933	.0016		.0013	28.3	24.8
275	1.5-45.8	11.5	0:02	.1892	.0522	.0053	.0026	3.936	.0027		.0012	28.8	25.7
276-375	1.5-45.8	(.4)	18:00				(.0003)	(3.966)					
376	1.5-45.8	17.0	0:02	.1883	.0530	.0057	.0033	3.969	.0024		.0030	29.1	20.6
377	1.5-45.8	13.5	0:02	.1905	.0560	.0083	.0061	3.975	.00.2		.0011	28.35	24.7
378-387	1.5-45.8	(1.0)	18:00				(.001)	3.985					
388	1.5-45.8	71.0	0:02	.1985	.0614	.0129	.0120	3.997	.0009		.0012	32.2	55.9

<sup>a</sup> Values of  $C_1$  are given as fractional change of modulus per pound per square inch.      <sup>b</sup> Estimated values are indicated by parenthesis.

TABLE VI.—VARIATION OF THE SECANT MODULUS OF ELASTICITY WITH STRESS  
[Values of  $E_0$  are given in million pounds per square inch.  $C_1=k_1/E_0$ ]

1	2	3	4	5	6
Material	Source	Modulus of elasticity, $E_0$	Type of modulus	$k_1$	$C_1$
18:8 Cr-Ni steel	This paper	21.0-32.0	Tension	15.6-172.0	6.0-55.0 $\times 10^{-7}$
Annealed 14:2 Cr-Ni steel		29.3-32.4	do	35.0- 77.0	10.4-24.6
Cold-drawn Inconel	To be reported	30.5-34.2	do	5.0- 25.3	1.6- 7.4
Cold-drawn K monel metal		24.2-25.6	do	13.3- 24.5	5.3- 9.8
Carbon steels	Sayre <sup>1</sup>	28.8-30.17	do	<sup>2</sup> 2.7- 4.6	<sup>2</sup> .90- 1.60
3½ percent nickel steel		28.95-29.2	do	<sup>2</sup> 2.6- 6.5	<sup>2</sup> .90- 2.23
Copper, cold-drawn		19.12	do	<sup>2</sup> 3.6	<sup>2</sup> 1.9
Brass, spring temper		14.3-15.5	do	<sup>2</sup> 2.8- 3.0	<sup>2</sup> 1.8- 2.0
Phosphor bronze, spring temper		14.70-15.58	do	<sup>2</sup> 3.2- 6.5	<sup>2</sup> 2.1- 4.4
17 SR/T aluminum-alloy wire	Bridgman <sup>3</sup>	10.28-10.29	do	<sup>2</sup> 3.7- 6.5	<sup>2</sup> 3.6- 6.4
Armco iron, annealed		19.14	Volume	10.1	5.3
99 percent nickel, drawn and annealed		26.05-26.24	do	14.7- 15.0	5.6- 5.7
Copper, cold-drawn		18.81-19.14	do	10.1- 10.2	5.3- 5.4
Aluminum, hard-drawn and annealed		10.32	do	3.9	3.8

<sup>1</sup> From references 1 and 2.      <sup>2</sup> Calculated from values given for tangent moduli.      <sup>3</sup> From reference 18.



## REPORT No. 671

### A THEORETICAL STUDY OF THE MOMENT ON A BODY IN A COMPRESSIBLE FLUID

By CARL KAPLAN

#### SUMMARY

The extension to a compressible fluid of Lagally's theorem on the moment on a body in an incompressible fluid and Poggi's method of treating the flow of compressible fluids are employed for the determination of the effect of compressibility on the moment on an arbitrary body. Only the case of the two-dimensional subsonic flow of an ideal compressible fluid is considered.

As examples of the application of the general theory, two well-known systems of profiles are treated; namely, the elliptic profile and the symmetrical Joukowski profiles with sharp trailing edges.

The effect of compressibility on the position of the center of pressure is also discussed. In order to determine this effect, it is necessary to calculate the additional circulation induced by the compressibility of the fluid for both the elliptic and the Joukowski profiles. For these two types of profile, the centers of pressure in the compressible and the incompressible fluids are found to coincide for a definite and fairly small angle of attack, which is essentially dependent on the thickness coefficients. For angles of attack less than this neutral angle, the center of pressure in the compressible fluid is farther from the nose and, for angles of attack greater than the neutral angle, nearer to the nose than the center of pressure in the incompressible fluid.

Several numerical examples of both the elliptic and the Joukowski profiles are given. The results show that, although the effect of compressibility on the moment and on the lift may be large, the effect on the center of pressure for conventional profiles is negligible. Thus, for a Joukowski profile, the maximum thickness of which is equal to 13 percent of the chord, the center of pressure moves toward the nose a distance equal to only 0.19 percent of the chord, where the angle of attack is  $6^\circ$  and  $v_0/c_0=0.70$ .

#### NOTATION

##### GENERAL SYMBOLS

$\xi, \eta$ , rectangular Cartesian coordinates in the plane of the obstacle.

$x, y$ , rectangular Cartesian coordinates in the plane of the circle.

$$\zeta = \xi + i\eta, z = x + iy$$

$r, \theta$ , polar coordinates in the plane of the circle.

$R$ , radius vector of a point far removed from the obstacle and also of a point far removed from the corresponding circle.

$r_0$ , radius of circle into which the profile is mapped.

$$\lambda = \frac{r_0}{r}$$

$v_r, v_\theta$ , components of the velocity in the radial and the circumferential directions in the  $z$  plane.

$v$ , magnitude of the velocity in the plane of the obstacle.

$c$ , magnitude of the local velocity of sound.

$\rho$ , density of the fluid.

$p$ , static pressure of the fluid.

$v_0, c_0, \rho_0, p_0$ , corresponding magnitudes in the undisturbed part of the fluid.

$\gamma$ , ratio of the specific heats ( $c_p/c_v$ ).

$\mu = \left(\frac{v_0}{c_0}\right)^2$ , square of the Mach number.

$\beta$ , angle of attack.

$\Gamma$ , circulation about the obstacle.

$$K = \frac{\Gamma}{2\pi r_0 v_0}$$

$L = \rho_0 v_0 \Gamma$ , lifting force on the obstacle.

$M$ , moment on the obstacle.

$c_c, c_i$ , centers of pressure, respectively, in the compressible and the incompressible fluids.

Subscripts  $c$  and  $i$  refer, respectively, to the compressible and the incompressible fluids.

$\Delta v_R, \Delta v_\delta$ , additional velocity components due to compressibility at a point  $P(R, \delta)$  far removed from the circle in the  $z$  plane.

$w$ , complex velocity potential of the fluid.

$\frac{dw}{d\zeta}$ , complex velocity in the plane of the obstacle.

$A_n, \bar{A}_n$ , complex and conjugate complex coefficients, respectively, in the power series development of  $\frac{dw}{d\zeta}$  (see equation (12)).



## SYMBOLS PERTAINING TO ELLIPTIC PROFILE

$c$ , semifocal distance.

$t$ , thickness ratio of ellipse (ratio of semi-minor and semimajor axes).

$$\sigma^2 = \frac{1-t}{1+t}, \text{ where } \sigma = \frac{c}{2r_0}.$$

$$\tanh \alpha = t$$

$M, N$ , functions of the thickness coefficient  $t$  only (see equation (24)).

## SYMBOLS PERTAINING TO JOUKOWSKI PROFILES

$\epsilon$ , thickness coefficient (see fig. 4).

$$h = \frac{\epsilon}{1+\epsilon}$$

$$k = \frac{1-\epsilon}{1+\epsilon} = 1-2h$$

$I, J$ , (see equation (26)).

$M, N$ , functions of the thickness coefficient  $\epsilon$  only (see equation (29)).

## DERIVATION OF THE FORMULA FOR THE MOMENT

Theodorsen's method (reference 1) of extending Lagally's formula for the force on a body in an incompressible fluid to a compressible fluid may be used to obtain the corresponding formula for the moment. The body is fixed in an infinite two-dimensional stream of a frictionless compressible fluid flowing uniformly in

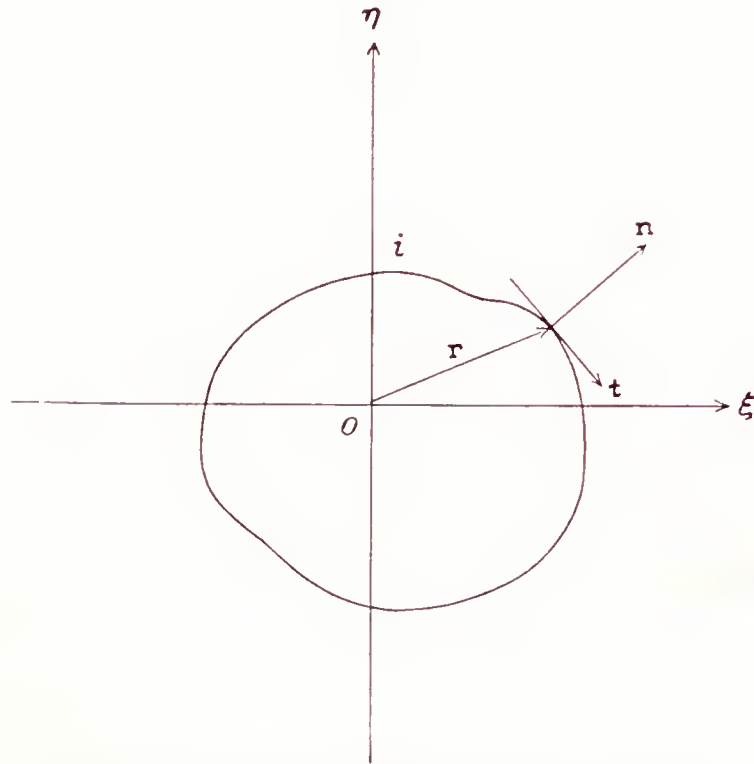


FIGURE 1.—Directions of tangent and normal on a contour.

the far field. Then the moment exerted on the body with respect to the origin of the coordinate system is given by (fig. 1)

$$M = - \int_i [\mathbf{r} \mathbf{n}] p \, ds \quad (1)$$

where the positive direction of the unit normal vector  $\mathbf{n}$  is taken from the boundary into the fluid,  $p$  is the pressure of the fluid,  $[\mathbf{r} \mathbf{n}]$  is the vector product of the radius vector  $\mathbf{r}$  and the unit normal vector  $\mathbf{n}$ , and  $ds$  is

the element of length along the profile taken positively in the direction of the unit tangent vector  $\mathbf{t}$ . With the directions of the unit tangent vector  $\mathbf{t}$  and the unit normal vector  $\mathbf{n}$  so chosen that they form a right-hand system, a positive value for the moment corresponds to a counterclockwise rotation.

According to one of the generalizations from Gauss' theorem, it may be shown that

$$\int_s \text{curl } p \mathbf{r} \, dS = \int_i [\mathbf{r} \mathbf{n}] p \, ds + \int_o [\mathbf{r} \mathbf{n}] p \, ds$$

where  $dS$  is the element of surface in a region  $S$  included between the obstacle  $i$  and an arbitrary curve  $o$  enclosing it.

Now

$$\text{curl } p \mathbf{r} = [\text{grad } p \mathbf{r}]$$

and, from the Euler equations of motion for steady flow (reference 1),

$$\text{grad } p = -1/2 \rho \text{ grad } v^2$$

Therefore

$$\text{curl } p \mathbf{r} = -1/2 \rho [\text{grad } v^2 \mathbf{r}]$$

Equation (1) then becomes

$$M = \int_o [\mathbf{r} \mathbf{n}] p \, ds + 1/2 \int_s \rho [\text{grad } v^2 \mathbf{r}] \, dS$$

Since the outer boundary is arbitrary, it may be chosen to be a large circle so that the vector product  $[\mathbf{r} \mathbf{n}] = 0$ . Hence

$$M = 1/2 \int_s \rho [\text{grad } v^2 \mathbf{r}] \, dS$$

But

$$\text{grad } v^2 = 2 (\mathbf{v} \text{ grad}) \mathbf{v} + 2 [\mathbf{v} \text{ curl } \mathbf{v}]$$

and

$$[(\mathbf{v} \text{ grad}) \mathbf{v} \mathbf{r}] = (\mathbf{v} \text{ grad}) [\mathbf{v} \mathbf{r}]$$

Therefore

$$M = \int_s \rho (\mathbf{v} \text{ grad}) [\mathbf{v} \mathbf{r}] \, dS + \int_s \rho \{ [\mathbf{v} \text{ curl } \mathbf{v}] \mathbf{r} \} \, dS \quad (2)$$

According to Gauss' theorem, if  $F$  denotes a scalar function, then

$$\int_s \text{div } \rho F \mathbf{v} \, dS = - \int_i \rho F (\mathbf{v} \mathbf{n}) \, ds - \int_o \rho F (\mathbf{v} \mathbf{n}) \, ds$$

But

$$\text{div } \rho F \mathbf{v} = F \text{ div } \rho \mathbf{v} + \rho (\mathbf{v} \text{ grad}) F$$

Hence

$$\begin{aligned} \int_s \rho (\mathbf{v} \text{ grad}) F \, dS &= - \int_s F \text{ div } \rho \mathbf{v} \, dS \\ &\quad - \int_i \rho F (\mathbf{v} \mathbf{n}) \, ds - \int_o \rho F (\mathbf{v} \mathbf{n}) \, ds \end{aligned}$$

From the manner in which  $F$  occurs in this formula, it is clear that the formula remains valid if  $F$  is replaced by a vector point function, say  $[\mathbf{v} \mathbf{r}]$ . That is,

$$\begin{aligned} \int_s \rho (\mathbf{v} \text{ grad}) [\mathbf{v} \mathbf{r}] \, dS &= \int_s [\mathbf{r} \mathbf{v}] \text{ div } \rho \mathbf{v} \, dS \\ &\quad + \int_i \rho [\mathbf{r} \mathbf{v}] (\mathbf{v} \mathbf{n}) \, ds + \int_o \rho [\mathbf{r} \mathbf{v}] (\mathbf{v} \mathbf{n}) \, ds \end{aligned}$$

Substituting from this equation into equation (2), it follows that

$$\begin{aligned} M &= \int_o \rho [\mathbf{r} \mathbf{v}] (\mathbf{v} \mathbf{n}) \, ds + \int_s [\mathbf{r} \mathbf{v}] \text{ div } \rho \mathbf{v} \, dS \\ &\quad - \int_s \rho \{ \mathbf{r} [\mathbf{v} \text{ curl } \mathbf{v}] \} \, dS \end{aligned} \quad (3)$$

where  $\int_i \rho [\mathbf{r} \mathbf{v}] (\mathbf{v} \mathbf{n}) \, ds = 0$  since  $(\mathbf{v} \mathbf{n}) = 0$  everywhere on the obstacle.<sup>1</sup>

In the problem considered herein, the compressible fluid is of uniform velocity  $v_0$  in the undisturbed stream

<sup>1</sup> This formula for the moment may be extended to three dimensions by letting  $\tau$  denote the region of flow between the body and a large sphere enclosing it;  $ds$  is then replaced by  $d\sigma$ , the element of surface on the outer sphere, and  $dS$  is replaced by  $d\tau$ , the element of volume in the region of flow  $\tau$ . Also, the moment now has three components and must be written as a vector, i. e.,  $\mathbf{M}$ .



and, furthermore, is assumed to be irrotational and free of sources in the region of flow  $S$ . The condition for irrotational motion is simply that  $\text{curl } \mathbf{v} = 0$ , and the absence of sources means that  $\text{div } \rho \mathbf{v} = 0$ . Therefore, equation (3) becomes

$$M = \int_0 \rho [\mathbf{r} \cdot \mathbf{v}] (\mathbf{v} \cdot \mathbf{n}) ds \quad (4)$$

where it is recalled that the outer boundary has been assumed to be a large circle of radius  $R$ . The vector product  $[\mathbf{r} \cdot \mathbf{v}]$  is then equal to  $Rv_\phi$  and the scalar product  $(\mathbf{v} \cdot \mathbf{n})$  is equal to  $-v_R$  since  $\mathbf{n} = -\mathbf{R}/R$ . Therefore

$$M = -R^2 \int_0^{2\pi} \rho v_R v_\phi d\phi \quad (5)$$

This simple expression for the moment about the origin, of the resultant force acting on the body, can be directly obtained by considering the rate at which angular momentum passes out of the region included between the outer circle and the body. Thus, the momentum per unit time passing normally through the element  $ds$  is  $\rho R v v_R d\phi$  and the arm is  $R \sin \mathbf{v} \cdot \mathbf{R}$ . The angular momentum is therefore  $\rho R^2 v \sin \mathbf{v} \cdot \mathbf{R} v_R d\phi$  or  $\rho R^2 v_R v_\phi d\phi$  and equation (5) follows.

### GENERAL DEVELOPMENTS

It may be well to emphasize at this point that the main problem of this paper lies in obtaining useful expansions for the velocity components  $v_R$  and  $v_\phi$  of a compressible fluid.

These expansions are obtained by making use of Poggi's conception of compressible flow. Thus the basic differential equation for the steady flow of a compressible fluid may be written as (reference 2)

$$\frac{\partial v_\xi}{\partial \xi} + \frac{\partial v_\eta}{\partial \eta} = \frac{1}{2c^2} \left( v_\xi \frac{\partial v^2}{\partial \xi} + v_\eta \frac{\partial v^2}{\partial \eta} \right)$$

The expression on the left-hand side is  $\text{div } \mathbf{v}$ , so that the expression on the right-hand side may be considered to represent a source distribution of a strength given by

$$\frac{1}{4\pi c^2} \left( v_\xi \frac{\partial v^2}{\partial \xi} + v_\eta \frac{\partial v^2}{\partial \eta} \right) d\xi d\eta$$

In the plane of the circle into which the profile of the obstacle is mapped by a suitable conformal transformation, the strength of the source distribution may be written as

$$\frac{1}{4\pi c^2} \left( v_r \frac{\partial v^2}{\partial \lambda} - \frac{v_\theta}{\lambda} \frac{\partial v^2}{\partial \theta} \right) \frac{r_0}{\lambda} d\lambda d\theta \quad (6)$$

where

$r, \theta$  are the polar coordinates of a point in the plane  $z(=x+iy)$  of the circle.

$\lambda = \frac{r_0}{r}$ , where  $r_0$  is the radius of the circle into which the profile is mapped.

$v_r = -\frac{\partial \phi}{\partial r}$ ,  $v_\theta = -\frac{1}{r} \frac{\partial \phi}{\partial \theta}$ , where  $\phi$  is the velocity potential of the flow.

$v$ , the magnitude of the velocity of the fluid in the plane of the profile.

$c$ , the magnitude of the local velocity of sound.

Poggi's method of approximating the flow of a perfect compressible fluid past an obstacle is based on the fact that the incompressible fluid is a good first approximation. A first approximation for the source distribution given by equation (6) is therefore obtained by substituting for  $v_r$ ,  $v_\theta$ , and  $v^2$  the values belonging to the incompressible fluid. It is further assumed that the Mach number  $v_0/c_0$  is small so that only terms involving the lowest order of  $v_0/c_0$  are to be considered. This assumption then limits the application of the analysis to stream velocities small in comparison with the velocity of sound. The disturbances to the main flow due to the presence of a body in the fluid may, however, be large.<sup>2</sup>

The density  $\rho$  and the pressure  $p$  of the fluid are then determined by the following equations (reference 2):

$$\left. \begin{aligned} \rho &= \rho_0 \left[ 1 + \frac{\gamma-1}{2} \mu \left( 1 - \frac{v^2}{v_0^2} \right) \right]^{\frac{1}{\gamma-1}} \\ &= \rho_0 \left[ 1 + 1/2 \mu \left( 1 - \frac{v_i^2}{v_0^2} \right) + \dots \right] \\ p &= \text{constant} - \frac{1}{2} \rho_0 v_c^2 - \frac{1}{4} \mu \rho_0 v_i^2 + \frac{1}{8} \mu \frac{\rho_0 v_i^4}{v_0^2} + \dots \end{aligned} \right\} \quad (7)$$

where the adiabatic equation of state has been adopted. Also,  $\mu = (v_0/c_0)^2$  and  $v_i$  and  $v_c$  are, respectively, the velocities in the incompressible and the compressible fluids.

It follows from equation (5), with the stipulation that only terms involving the square of the Mach number are to be retained, that:

$$\begin{aligned} M_c &= -\rho_0 v_0^2 R^2 \int_0^{2\pi} \left( \frac{v_R}{v_0} \frac{v_\phi}{v_0} \right)_c d\phi \\ &\quad - \frac{1}{2} \mu \rho_0 v_0^2 R^2 \int_0^{2\pi} \left( 1 - \frac{v_i^2}{v_0^2} \right) \left( \frac{v_R}{v_0} \frac{v_\phi}{v_0} \right)_i d\phi \end{aligned} \quad (8)$$

It is clear that the evaluation of the second integral presents no difficulties, for it involves only expressions of the well-known incompressible fluid-velocity components. The difficulty of the problem lies mainly in determining the velocity components  $v_R$  and  $v_\phi$  for a compressible fluid. Since the first integral is taken around a circle whose radius  $R$  may be infinite, it is obvious that the developments for  $v_R/v_0$  and  $v_\phi/v_0$  in the neighborhood of infinity need not go beyond the  $1/R^2$  terms.

In order to obtain the series for  $v_R/v_0$  and  $v_\phi/v_0$ , it is expedient to consider first the effect of a single source of unit strength situated at a point  $Q(r, \theta)$  in the plane of a circle. In the presence of a circular boundary of radius  $r_0$ , the velocity induced by a unit source at any

<sup>2</sup> In the approximation made by Glauert (reference 3),  $v_0$  is not small compared with  $c_0$  but the disturbances to the main flow  $v_0$  are assumed to be small.



point  $P(R, \delta)$  external to the boundary is given by (fig. 2):

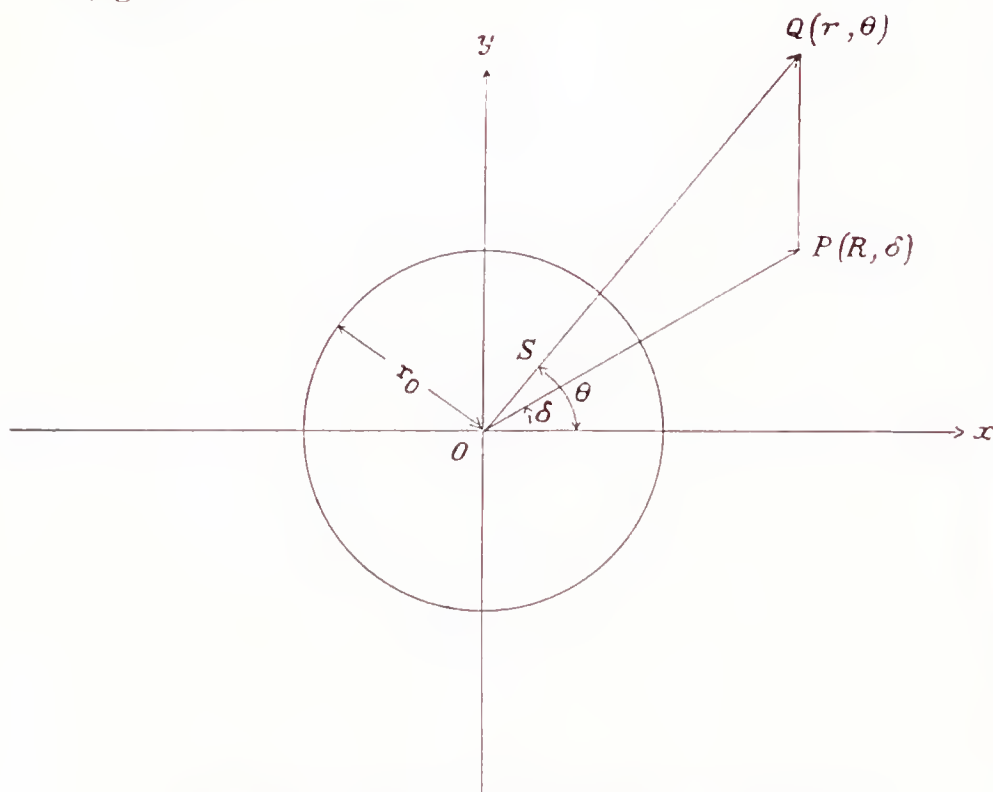


FIGURE 2.—Image of a simple source with regard to a circle.

$$\frac{dw}{dz} = -\left(\frac{1}{z_P - z_Q} + \frac{1}{z_P - z_S} - \frac{1}{z_P}\right) = -v_x + iv_y$$

where  $S$  is the point inverse to  $Q$  with respect to the circle;

$$z_P = Re^{i\delta}; \quad z_Q = re^{i\theta}; \quad \text{and} \quad z_S = \frac{r_0^2}{r}e^{i\theta}.$$

Then

$$v_x - iv_y = \frac{1}{Re^{i\delta} - re^{i\theta}} + \frac{1}{Re^{i\delta} - \frac{r_0^2}{r}e^{i\theta}} - \frac{1}{Re^{i\delta}}$$

or since

$$(-v_R + iv_\delta)e^{-i\delta} = -v_x + iv_y$$

for  $r_0 < r < R$

$$\begin{aligned} v_R &= \frac{1}{2R} \frac{1 - \frac{\lambda_P^2}{\lambda^2}}{1 - 2\frac{\lambda_P}{\lambda} \cos(\theta - \delta) + \frac{\lambda_P^2}{\lambda^2}} \\ &\quad + \frac{1}{2R} \frac{1 - \lambda_P^2 \lambda^2}{1 - 2\lambda_P \lambda \cos(\theta - \delta) + \lambda_P^2 \lambda^2} \\ v_\delta &= -\frac{1}{R} \frac{\frac{\lambda_P}{\lambda} \sin(\theta - \delta)}{1 - 2\frac{\lambda_P}{\lambda} \cos(\theta - \delta) + \frac{\lambda_P^2}{\lambda^2}} \\ &\quad - \frac{1}{R} \frac{\lambda_P \lambda \sin(\theta - \delta)}{1 - 2\lambda_P \lambda \cos(\theta - \delta) + \lambda_P^2 \lambda^2} \end{aligned}$$

and for  $R < r < \infty$

$$v_R = -\frac{1}{2R} \frac{1 - \frac{\lambda^2}{\lambda_P^2}}{1 - 2\frac{\lambda}{\lambda_P} \cos(\theta - \delta) + \frac{\lambda^2}{\lambda_P^2}}$$

$$\begin{aligned} &+ \frac{1}{2R} \frac{1 - \lambda_P^2 \lambda^2}{1 - 2\lambda_P \lambda \cos(\theta - \delta) + \lambda_P^2 \lambda^2} \\ v_\delta &= -\frac{1}{R} \frac{\frac{\lambda}{\lambda_P} \sin(\theta - \delta)}{1 - 2\frac{\lambda}{\lambda_P} \cos(\theta - \delta) + \frac{\lambda^2}{\lambda_P^2}} \\ &\quad - \frac{1}{R} \frac{\lambda_P \lambda \sin(\theta - \delta)}{1 - 2\lambda_P \lambda \cos(\theta - \delta) + \lambda_P^2 \lambda^2} \end{aligned}$$

where  $\lambda = r_0/r$  and  $\lambda_P = r_0/R$ .

Then, making use of the expansion

$$\frac{1 - q^2}{1 - 2q \cos(\theta - \delta) + q^2} = 1 + 2 \sum_{n=1}^{\infty} q^n \cos n(\theta - \delta)$$

it follows that the components of the velocity induced at any point  $P(R, \delta)$  by the source distribution given by equation (6) are:

$$\begin{aligned} \frac{\Delta v_R}{v_0} &= -\frac{\mu}{4\pi} \int_{\lambda_P}^1 \int_0^{2\pi} F \frac{\lambda_P}{\lambda} \left[ \frac{1}{2} + \sum_{n=1}^{\infty} \left( \frac{\lambda_P}{\lambda} \right)^n \cos n(\theta - \delta) \right] d\lambda d\theta \\ &\quad + \frac{\mu}{4\pi} \int_0^{\lambda_P} \int_0^{2\pi} F \frac{\lambda_P}{\lambda} \left[ \frac{1}{2} + \sum_{n=1}^{\infty} \left( \frac{\lambda}{\lambda_P} \right)^n \cos n(\theta - \delta) \right] d\lambda d\theta \\ &\quad - \frac{\mu}{4\pi} \int_0^1 \int_0^{2\pi} F \frac{\lambda_P}{\lambda} \left[ \frac{1}{2} + \sum_{n=1}^{\infty} (\lambda_P \lambda)^n \cos n(\theta - \delta) \right] d\lambda d\theta \quad (9) \end{aligned}$$

and

$$\begin{aligned} \frac{\Delta v_\delta}{v_0} &= \frac{\mu}{4\pi} \int_{\lambda_P}^1 \int_0^{2\pi} F \frac{\frac{\lambda_P^2}{\lambda^2} \sin(\theta - \delta)}{1 - 2\frac{\lambda_P}{\lambda} \cos(\theta - \delta) + \frac{\lambda_P^2}{\lambda^2}} d\lambda d\theta \\ &\quad + \frac{\mu}{4\pi} \int_0^{\lambda_P} \int_0^{2\pi} F \frac{\sin(\theta - \delta)}{1 - 2\frac{\lambda}{\lambda_P} \cos(\theta - \delta) + \frac{\lambda^2}{\lambda_P^2}} d\lambda d\theta \\ &\quad + \frac{\mu}{4\pi} \int_0^1 \int_0^{2\pi} F \frac{\lambda_P^2 \sin(\theta - \delta)}{1 - 2\lambda_P \lambda \cos(\theta - \delta) + \lambda_P^2 \lambda^2} d\lambda d\theta \quad (10) \end{aligned}$$

where

$$F = \left( \frac{v_r}{v_0} \frac{\partial \frac{v^2}{v_0^2}}{\partial \lambda} - \frac{v_\theta}{v_0} \frac{1}{\lambda} \frac{\partial \frac{v^2}{v_0^2}}{\partial \theta} \right)_i$$

The next step is to obtain the Fourier series expansion of the function  $F$  for an arbitrary profile. The profile is derived from a circle by means of the general conformal transformation

$$\zeta = z' + \frac{a_1}{z'} + \frac{a_2}{z'^2} + \dots$$

where the coefficients  $a_i$  are, in general, complex. In order to obtain the velocity of the fluid in the plane of the profile, it is first necessary to determine the velocity potential of the flow past a circle (fig. 3). Thus, sup-



pose that the undisturbed flow is of velocity  $v_0$  inclined at an angle  $\beta$  to the negative direction of the real axis and that the circulation is denoted by  $\Gamma$ . In terms of

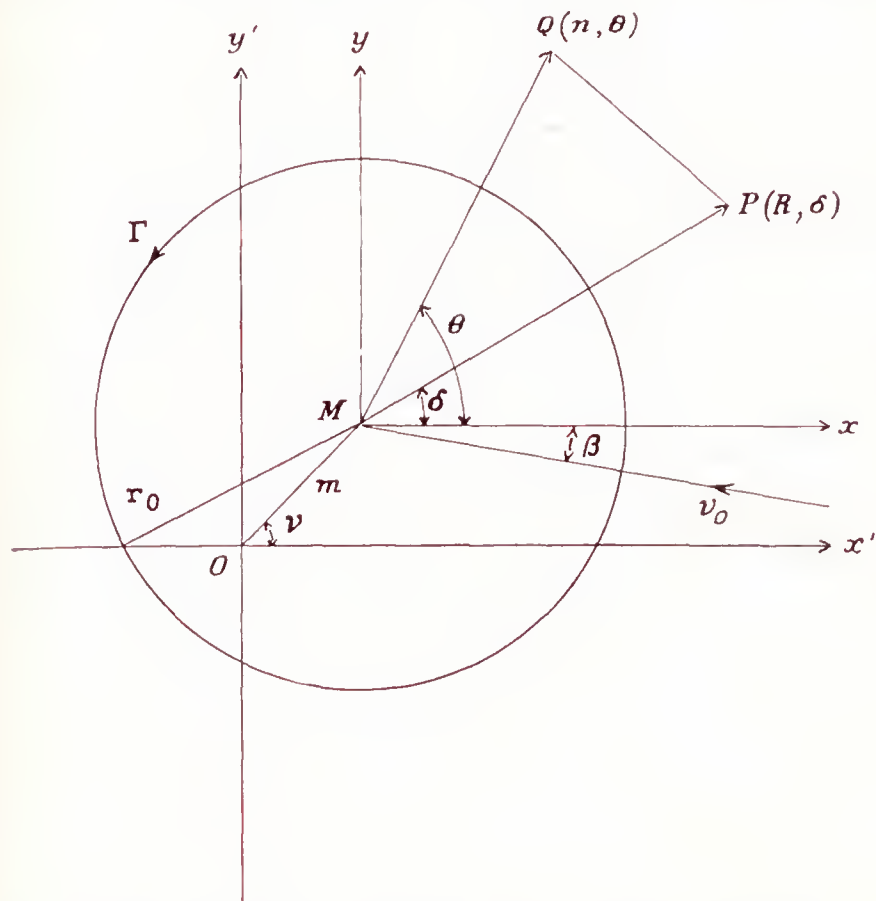


FIGURE 3.—Relation between  $z$  planes employed in general conformal transformation.

the complex coordinate  $z$ , with origin at the center of the circle, the potential function of the flow past the circle is:

$$w = v_0 \left( z e^{i\beta} + \frac{r_0^2}{z e^{i\beta}} \right) + \frac{i\Gamma}{2\pi} \log \frac{z e^{i\beta}}{r_0} \quad (11)$$

Also, the variables  $z$  and  $z'$  are connected by the equation

$$z' = z + me^{i\nu}$$

Therefore

$$\frac{dw}{d\zeta} = \frac{dw}{dz} \frac{dz}{dz'} \frac{dz'}{d\zeta} = \frac{v_0 e^{i\beta} - \frac{v_0 v_0^2 e^{-i\beta}}{z^2} + \frac{i\Gamma}{2\pi z}}{1 - \frac{a_1}{z'^2} - \frac{2a_2}{z'^3} - \dots}$$

Substituting for  $z'$  in terms of  $z$  and expanding in descending powers of  $z$ , this expression becomes:

$$\frac{1}{v_0} \frac{dw}{dz} = e^{i\beta} + \frac{i\Gamma}{2\pi v_0} \frac{1}{z} + (a_1 e^{i\beta} - r_0^2 e^{-i\beta}) \frac{1}{z^2} + \dots \quad (12)$$

It follows then, that:

$$\frac{1}{v_0} \frac{dw}{d\xi} = \sum_{n=0}^{\infty} \frac{A_n}{z^n}$$

where the  $A_n$ 's are, in general, complex.

In order to introduce the angle  $\theta - \delta$ , the general term of this series is multiplied by  $e^{-in\delta}/e^{-in\delta}$ .

Then

$$\frac{1}{v_0} \frac{dw}{d\zeta} = \sum_{k=0}^{\infty} \frac{A_k e^{-ik\delta}}{r^k e^{ik(\theta-\delta)}}$$

and

$$\frac{1}{v_0} \frac{dw}{d\zeta} = \sum_{j=0}^{\infty} \frac{\overline{A_j} e^{tj\delta}}{r^j e^{-tj(\theta-\delta)}}$$

Hence

$$\frac{v^2}{v_0^2} = \sum_{j=0}^{\infty} \sum_{k=0}^{\infty} \frac{A_k \bar{A}_j e^{i(j-k)\delta}}{r^{j+k}} e^{i(j-k)(\theta-\delta)}$$

The real and the imaginary parts of  $A_k \overline{A_j} e^{i(j-k)\delta}$  are, respectively:

$$\frac{A_k \overline{A_j} e^{i(j-k)\delta} + \overline{A_k} A_j e^{-i(j-k)\delta}}{2}$$

and

$$-i \frac{A_k \bar{A}_j e^{i(j-k)\delta} - \bar{A}_k A_j e^{-i(j-k)\delta}}{2}$$

Let

$$j-k=n$$

where  $n$  changes sign when  $j$  and  $k$  are interchanged and therefore takes values from  $-\infty$  to  $\infty$ .

Then

$$j+k=n+2k$$

and the expression for  $v^2/v_0^2$ , a real quantity, becomes:

$$\frac{v^2}{v_0^2} = \sum_{k=0}^{\infty} \sum_{n=-\infty}^{\infty} [A_{n,k} \cos n(\theta - \delta) + B_{n,k} \sin n(\theta - \delta)] \lambda^{n+2k} \quad (13)$$

where

$$A_{n,k} = \frac{A_k \bar{A}_{n+k} e^{in\delta} + \bar{A}_k A_{n+k} e^{-in\delta}}{2r_0^{n+2k}}$$

and

$$B_{n,k} = i \frac{A_k \bar{A}_{n+k} e^{in\delta} - \bar{A}_k A_{n+k} e^{-in\delta}}{2r_0^{n+2k}}$$

From the definition of  $n$ , it follows that:

$$A_{-n,k} = A_{n,k}$$

and

$$B_{-n,k} = -B_{n,k}$$

The terms of equation (13) can therefore be grouped in pairs, thus:

$$\begin{aligned} \frac{v^2}{v_0^2} = & \sum_{k=0}^{\infty} \lambda^{2k} A_{0,k} + 2 \sum_{n=1}^{\infty} \cos n(\theta - \delta) \sum_{k=0}^{\infty} A_{n,k} \lambda^{n+2k} \\ & + 2 \sum_{n=1}^{\infty} \sin n(\theta - \delta) \sum_{k=0}^{\infty} B_{n,k} \lambda^{n+2k} \end{aligned} \quad (14)$$

Also, from equation (11),

$$\left. \begin{aligned} \frac{v_r}{v_0} &= -(1 - \lambda^2) \cos (\theta - \delta) \cos (\delta + \beta) \\ &+ (1 - \lambda^2) \sin (\theta - \delta) \sin (\delta + \beta) \\ \frac{v_\theta}{v_0} &= (1 + \lambda^2) \cos (\theta - \delta) \sin (\delta + \beta) \\ &+ (1 + \lambda^2) \sin (\theta - \delta) \cos (\delta + \beta) + \lambda K \end{aligned} \right\} \quad (15)$$

and

where

$$K = \frac{\Gamma}{2\pi r_0 v_0}$$



Then, by means of equations (14) and (15), it becomes a simple matter to obtain the Fourier series for the function  $F$ . When the Fourier series for  $F$  is substituted into equations (9) and (10) and all terms containing powers of  $\lambda_P$  higher than the second are neglected, it follows, after some rather tedious but elementary integrations, that:

$$\begin{aligned} \frac{\Delta v_R}{v_0} = & -\frac{\mu}{2}\lambda_P[A_{1,0} \cos(\delta+\beta) - B_{1,0} \sin(\delta+\beta)] \\ & -\frac{\mu}{2}[A_{0,1} \cos(\delta+\beta) + KB_{1,0}]\lambda_P^2 \log \lambda_P \\ & -\mu\lambda_P^2\left[\frac{3}{8}A_{0,1} \cos(\delta+\beta) + \frac{1}{2}A_{2,0} \cos(\delta+\beta) \right. \\ & \left. -B_{2,0} \sin(\delta+\beta)\right] + \frac{\mu K}{4}\lambda_P^2 \sum_{n=1}^{\infty} \frac{2n+1}{n(n+1)} B_{1,n} \\ & + \frac{\mu}{2}\lambda_P^2 \cos(\delta+\beta) \sum_{n=1}^{\infty} \frac{n+1}{n(n+2)} A_{0,n+1} \\ & - \frac{\mu}{2}\lambda_P^2 \sum_{n=1}^{\infty} \frac{A_{2,n} \cos(\delta+\beta) - B_{2,n} \sin(\delta+\beta)}{n+1} \end{aligned} \quad (16)$$

and

$$\begin{aligned} \frac{\Delta v_\delta}{v_0} = & \frac{\mu}{2}\lambda_P[A_{1,0} \sin(\delta+\beta) - B_{1,0} \cos(\delta+\beta)] \\ & -\frac{\mu}{2}[A_{0,1} \sin(\delta+\beta) + KA_{1,0}]\lambda_P^2 \log \lambda_P \\ & + \mu\lambda_P^2\left[\frac{1}{8}A_{0,1} \sin(\delta+\beta) + \frac{3}{2}A_{2,0} \sin(\delta+\beta) + \frac{1}{2}KA_{1,0}\right] \\ & + \frac{\mu K}{4}\lambda_P^2 \sum_{n=1}^{\infty} \frac{2n+1}{n(n+1)} A_{1,n} \\ & + \frac{\mu}{2}\lambda_P^2 \sin(\delta+\beta) \sum_{n=1}^{\infty} \frac{n+1}{n(n+2)} A_{0,n+1} \\ & + \frac{\mu}{2}\lambda_P^2 \sum_{n=1}^{\infty} \frac{A_{2,n} \sin(\delta+\beta) + B_{2,n} \cos(\delta+\beta)}{n+1} \end{aligned} \quad (17)$$

Use has been made of the following definite integrals in obtaining  $\Delta v_\delta/v_0$ :

$$\int_0^{2\pi} \frac{\sin(\theta-\delta) \sin n(\theta-\delta) d\theta}{1-2h \cos(\theta-\delta) + h^2} = \begin{cases} 0 & \text{if } n=0 \\ \pi h^{n-1} & \text{if } n \geq 1 \end{cases}$$

$$\int_0^{2\pi} \frac{\sin(\theta-\delta) \cos n(\theta-\delta) d\theta}{1-2h \cos(\theta-\delta) + h^2} = 0$$

The velocity of the compressible fluid in the plane of the circle then has the following components:

$$\left. \begin{aligned} \left(\frac{v_R}{v_0}\right)_c &= -(1-\lambda_P^2) \cos(\delta+\beta) + \frac{\Delta v_R}{v_0} \\ \left(\frac{v_\delta}{v_0}\right)_c &= (1+\lambda_P^2) \sin(\delta+\beta) + \lambda_P K + \frac{\Delta v_\delta}{v_0} \end{aligned} \right\} \quad (18)$$

The calculation of the moment is facilitated by expressing the velocity of the compressible fluid in

complex form. Thus, as in the case of an incompressible fluid, a complex velocity is defined in the following way:

$$\frac{1}{v_0} \left(\frac{dw}{dz}\right)_c = \left(-\frac{v_R}{v_0} + i\frac{v_\delta}{v_0}\right) e^{-i\delta}$$

Then equation (8) for the moment assumes the Blasius form:

$$\begin{aligned} M_c = & -\frac{1}{2}\rho_0 v_0^2 R \cdot \text{P.} \oint \left(\frac{1}{v_0} \frac{dw}{dz}\right)_c^2 \frac{dz}{d\zeta} \zeta dz \\ & -\frac{1}{4}\mu\rho_0 v_0^2 R \cdot \text{P.} \oint \left(1 - \frac{v_i^2}{v_0^2}\right) \left(\frac{1}{v_0} \frac{dw}{dz}\right)_c^2 \frac{dz}{d\zeta} \zeta dz \end{aligned} \quad (19)$$

where the integrals are taken around a circle whose radius  $R$  approaches infinity.

Now, from equations (13), (16), (17), and (18), the expression for  $1/v_0 (dw/dz)_c$  may be written as:

$$\begin{aligned} \frac{1}{v_0} \left(\frac{dw}{dz}\right)_c = & e^{i\beta} + \frac{iKr_0}{z} - \frac{r_0^2 e^{-i\beta}}{z^2} + \frac{\mu}{4} \left[ (A_0 \bar{A}_1 e^{-i\beta} + \bar{A}_0 A_1 e^{i\beta}) \frac{1}{z} \right. \\ & + \frac{A_0 \bar{A}_1 e^{i\beta}}{R^2} z - \bar{A}_0 A_1 R^2 e^{i\beta} \frac{1}{z^3} \\ & + 2(A_1 \bar{A}_1 e^{-i\beta} - iKr_0 \bar{A}_0 A_1) \frac{1}{z^2} \log \frac{r_0}{R} + \frac{A_1 \bar{A}_1}{R^2} e^{i\beta} \\ & + \frac{1}{2} A_1 \bar{A}_1 e^{-i\beta} \frac{1}{z^2} + iKr_0 \frac{A_0 \bar{A}_1}{R^2} + iKr_0 \bar{A}_0 A_1 \frac{1}{z^2} \\ & + \frac{A_0 \bar{A}_2 e^{i\beta} z^2}{R^4} - 2\bar{A}_0 A_2 e^{-i\beta} \frac{R^2}{z^4} + 3\bar{A}_0 A_2 e^{i\beta} \frac{1}{z^2} \\ & + iK \frac{1}{z^2} \sum_{n=1}^{\infty} \frac{2n+1}{n(n+1)} \frac{\bar{A}_n A_{n+1}}{r_0^{2n-1}} \\ & \left. - \frac{2e^{-i\beta}}{z^2} \sum_{n=1}^{\infty} \frac{n+1}{n(n+2)} \frac{A_{n+1} \bar{A}_{n+1}}{r_0^{2n}} + \frac{2e^{i\beta}}{z^2} \sum_{n=1}^{\infty} \frac{1}{n+1} \frac{\bar{A}_n A_{n+2}}{r_0^{2n}} \right] \end{aligned}$$

Also, from equation (12) for  $\frac{1}{v_0} \frac{dw}{d\zeta}$ :

$$A_0 = e^{i\beta}, A_1 = iKr_0, A_2 = b^2 e^{i(\beta+2\gamma)} - r_0^2 e^{-i\beta}$$

where  $a_1 = b^2 e^{2i\gamma}$

Therefore

$$\begin{aligned} \frac{1}{v_0} \left(\frac{dw}{dz}\right)_c = & e^{i\beta} + \frac{iKr_0}{z} - \frac{r_0^2 e^{-i\beta}}{z^2} + \frac{\mu}{4} \left[ -\frac{iKr_0 e^{2i\beta}}{R^2} z \right. \\ & + \frac{4K^2 r_0^2 e^{-i\beta}}{z^2} \log \frac{r_0}{R} + \frac{2K^2 r_0^2}{R^2} e^{i\beta} + \frac{b^2 e^{i(\beta+2\gamma)} - r_0^2 e^{3i\beta}}{R^4} z^2 \\ & - \frac{iKr_0 R^2}{z^3} - \frac{K^2 r_0^2 e^{-i\beta}}{2z^2} - \frac{2R^2 b^2 e^{-i(\beta+2\gamma)} - r_0^2 e^{-3i\beta}}{z^4} \\ & + 3 \frac{b^2 e^{i(\beta+2\gamma)} - r_0^2 e^{-i\beta}}{z^2} + \frac{iK}{z^2} \sum_{n=1}^{\infty} \frac{2n+1}{n(n+1)} \frac{\bar{A}_n A_{n+1}}{r_0^{2n-1}} \\ & \left. - \frac{2e^{-i\beta}}{z^2} \sum_{n=1}^{\infty} \frac{n+1}{n(n+2)} \frac{A_{n+1} \bar{A}_{n+1}}{r_0^{2n}} + \frac{2e^{i\beta}}{z^2} \sum_{n=1}^{\infty} \frac{1}{n+1} \frac{\bar{A}_n A_{n+2}}{r_0^{2n}} \right] \end{aligned}$$



It may be noted that this expression is not an analytic function of  $z$ , since powers of  $R$  occur in some of the terms.

The first integral on the right-hand side of equation (19) for  $M_c$  then becomes:

$$\begin{aligned} & -\frac{1}{2}\rho_0 v_0^2 \text{R. P.} \oint \left( \frac{1}{v_0} \frac{dw}{dz} \right)_c^2 \frac{dz}{d\zeta} \zeta dz \\ & = -\frac{1}{2}\rho_0 v_0^2 \text{R. P.} \oint \left( \frac{1}{v_0} \frac{dw}{dz} \right)_c^2 \left( 1 + \frac{me^{i\nu}}{z} + \frac{2b^2 e^{2i\gamma}}{z^2} + \dots \right) z dz \\ & = 2\pi b^2 \rho_0 v_0^2 \sin 2(\beta + \gamma) + \rho_0 v_0 \Gamma m \cos(\beta + \nu) \\ & + \frac{\mu}{2} \left[ 3\pi b^2 \rho_0 v_0^2 \sin 2(\beta + \gamma) \right. \\ & + \frac{1}{2}\rho_0 v_0 \Gamma_i \text{R. P.} e^{i\beta} \sum_{n=1}^{\infty} \frac{2n+1}{n(n+1)} \frac{\bar{A}_n A_{n+1}}{r_0^{2n}} \\ & \left. - 2\pi \rho_0 v_0^2 \text{R. P.} i e^{2i\beta} \sum_{n=1}^{\infty} \frac{\bar{A}_n A_{n+2}}{(n+1)r_0^{2n}} \right] \end{aligned}$$

and the second integral:

$$\begin{aligned} & -\frac{1}{4}\mu \rho_0 v_0^2 \text{R. P.} \oint \left( 1 - \frac{v_i^2}{v_0^2} \right) \left( \frac{1}{v_0} \frac{dw}{dz} \right)_i^2 \frac{dz}{d\zeta} \zeta dz \\ & = \frac{\mu}{4} [2\pi b^2 \rho_0 v_0^2 \sin 2(\beta + \gamma) + \rho_0 v_0 \Gamma m \cos(\beta + \nu)] \end{aligned}$$

Therefore

$$\begin{aligned} M_c &= M_i \left( 1 + \frac{\mu}{2} \right) + \rho_0 v_0 \Delta \Gamma m \cos(\beta + \nu) \\ & + \frac{\mu}{2} \left[ -\frac{3}{2}\rho_0 v_0 \Gamma_i m \cos(\beta + \gamma) \right. \\ & + \frac{1}{2}\rho_0 v_0 \Gamma_i \text{R. P.} e^{i\beta} \sum_{n=1}^{\infty} \frac{2n+1}{n(n+1)} \frac{\bar{A}_n A_{n+1}}{r_0^{2n}} \\ & \left. - 2\pi \rho_0 v_0^2 \text{R. P.} i e^{2i\beta} \sum_{n=1}^{\infty} \frac{\bar{A}_n A_{n+2}}{(n+1)r_0^{2n}} \right] \quad (20) \end{aligned}$$

where  $M_i = 2\pi b^2 \rho_0 v_0^2 \sin 2(\beta + \gamma) + \rho_0 v_0 \Gamma_i m \cos(\beta + \nu)$  is the moment due to an incompressible fluid. The circulation  $\Gamma$  consists of the incompressible part  $\Gamma_i$  and the additional circulation  $\Delta \Gamma$  related to the additional flow.

Equation (20) for the moment  $M_c$  is applicable to arbitrary profiles, but it contains two infinite series that cannot, in general, be replaced by closed forms. In the case of a profile for which the conformal transformation to a circle contains a finite number of terms, the two infinite series may, however, sometimes be replaced by elementary functions. In the following, two such systems of profiles will be discussed, the elliptic and the Joukowski profiles.

#### THE ELLIPTIC PROFILE

It is well known that the Joukowski transformation

$$\zeta = z + \frac{c^2}{4z}$$

maps the circle of radius  $c/2$  with its center at the origin of the  $z$  plane into a line segment  $(-c, 0; c, 0)$  in the  $\zeta$  plane. Also, circles concentric with the base circle are transformed into a family of confocal ellipses with common foci at  $(-c, 0)$  and  $(c, 0)$ . If  $r_0 (> c/2)$  denotes the radius of one of these circles, then the semimajor and the semiminor axes of the ellipse into which it is transformed are, respectively,  $r_0 + c^2/4r_0$  and  $r_0 - c^2/4r_0$ . The thickness ratio  $t$  is then defined as

$$t = \frac{r_0 - \frac{c^2}{4r_0}}{r_0 + \frac{c^2}{4r_0}} = \frac{1 - \sigma^2}{1 + \sigma^2}$$

or

$$\sigma^2 = \frac{1-t}{1+t}$$

where

$$\sigma = \frac{c}{2r_0}$$

Now, for the case of the elliptic cylinder, equation (12) becomes:

$$\begin{aligned} \frac{1}{v_0} \frac{dw}{d\zeta} &= \frac{e^{i\beta} + \frac{i\Gamma_i}{2\pi v_0} \frac{1}{z} - \frac{r_0^2 e^{-i\beta}}{z^2}}{1 - \frac{c^2}{4z^2}} \\ &= \left( e^{i\beta} + \frac{i\Gamma_i}{2\pi v_0} \frac{1}{z} - \frac{r_0^2 e^{-i\beta}}{z^2} \right) \sum_{n=1}^{\infty} \left( \frac{c^2}{4z^2} \right)^n = \sum_{n=1}^{\infty} \frac{A_n}{z^n} \end{aligned}$$

or

$$A_0 = e^{i\beta}, \quad A_{2n+1} = iK_i r_0^{2n+1} \sigma^{2n}, \quad A_{2n} = e^{-i\beta} r_0^{2n} \sigma^{2n-2} (\sigma^2 e^{2i\beta} - 1)$$

where

$$K_i = \frac{\Gamma_i}{2\pi v_0 r_0}$$

Then

$$\begin{aligned} e^{i\beta} \sum_{n=1}^{\infty} \frac{2n+1}{n(n+1)} \frac{\bar{A}_n A_{n+1}}{r_0^{2n}} &= e^{i\beta} \sum_{n=1}^{\infty} \frac{4n+1}{2n(2n+1)} \frac{\bar{A}_{2n} A_{2n+1}}{r_0^{4n}} \\ &+ e^{i\beta} \sum_{n=0}^{\infty} \frac{4n+3}{(2n+1)(2n+2)} \frac{\bar{A}_{2n+1} A_{2n+2}}{r_0^{4n+2}} \\ &= iK_i r_0 (\sigma^2 - e^{2i\beta}) \sum_{n=1}^{\infty} \left( \frac{1}{2n} + \frac{1}{2n+1} \right) \sigma^{4n-2} \\ &+ iK_i r_0 (1 - \sigma^2 e^{2i\beta}) \sum_{n=0}^{\infty} \left( \frac{1}{2n+1} + \frac{1}{2n+2} \right) \sigma^{4n} \end{aligned}$$

and

$$\begin{aligned} \text{R. P.} e^{i\beta} \sum_{n=1}^{\infty} \frac{2n+1}{n(n+1)} \frac{\bar{A}_n A_{n+1}}{r_0^{2n}} \\ = K_i r_0 \sin 2\beta \left[ \sum_{n=1}^{\infty} \frac{\sigma^{4n-2}}{n} + \frac{1+\sigma^4}{2\sigma^4} \log \frac{1+\sigma^2}{1-\sigma^2} - \frac{1}{\sigma^2} \right] \end{aligned}$$

Similarly

$$\begin{aligned} i e^{2i\beta} \sum_{n=1}^{\infty} \frac{\bar{A}_n A_{n+2}}{(n+1)r_0^{2n}} &= i e^{2i\beta} \sum_{n=1}^{\infty} \frac{\bar{A}_{2n} A_{2n+2}}{(2n+1)r_0^{4n}} + i e^{2i\beta} \sum_{n=1}^{\infty} \frac{\bar{A}_{2n-1} A_{2n+1}}{2nr_0^{4n-2}} \\ &= i e^{2i\beta} r_0^2 (1 - 2\sigma^2 \cos 2\beta + \sigma^4) \sum_{n=1}^{\infty} \frac{\sigma^{4n-2}}{2n+1} + i e^{2i\beta} K_i^2 r_0^2 \sum_{n=1}^{\infty} \frac{\sigma^{4n-2}}{2n} \end{aligned}$$



and

$$R. P. i e^{2i\beta} \sum_{n=1}^{\infty} \frac{\bar{A}_n A_{n+2}}{(n+1)r_0^{2n}} \\ = -r_0^2 \sin 2\beta (1 - 2\sigma^2 \cos 2\beta + \sigma^4) \left( \frac{1}{2\sigma^4} \log \frac{1+\sigma^2}{1-\sigma^2} - \frac{1}{\sigma^2} \right) \\ - K_i^2 r_0^2 \sin 2\beta \sum_{n=1}^{\infty} \frac{\sigma^{4n-2}}{2n}$$

Therefore, since  $m=0$  and  $\nu=0$  for an elliptic profile, equation (20) becomes:

$$M_c = M_i \left\{ 1 + \frac{\mu}{2} + \frac{\mu}{2} (1 - 2\sigma^2 \cos 2\beta + \sigma^4) \left( \frac{1}{2\sigma^6} \log \frac{1+\sigma^2}{1-\sigma^2} - \frac{1}{\sigma^4} \right) \right. \\ \left. + \frac{\mu}{2} K_i^2 \left[ \frac{1+\sigma^4}{4\sigma^6} \log \frac{1+\sigma^2}{1-\sigma^2} - \frac{1}{2\sigma^4} - \frac{1}{\sigma^4} \log (1-\sigma^4) \right] \right\} \quad (21)$$

where  $M_i = \frac{\pi}{2} \rho_0 v_0^2 c^2 \sin 2\beta$ .

For thick profiles, or for small values of  $\sigma$ , this formula may be expressed as a power series in  $\sigma$ . Thus, by making use of the expansions

$$\log \frac{1+\sigma^2}{1-\sigma^2} = 2 \left( \sigma^2 + \frac{1}{3}\sigma^6 + \frac{1}{5}\sigma^{10} + \dots \right)$$

and

$$\log (1-\sigma^4) = - \left( \sigma^4 + \frac{1}{2}\sigma^8 + \frac{1}{3}\sigma^{12} + \dots \right)$$

it follows, from equation (21), that

$$M_c = M_i \left[ 1 + \frac{\mu}{2} + \frac{\mu}{2} (1 - 2\sigma^2 \cos 2\beta + \sigma^4) \left( \frac{1}{3} + \frac{1}{5}\sigma^4 + \frac{1}{7}\sigma^8 \right. \right. \\ \left. \left. + \dots \right) + \frac{\mu}{2} K_i^2 \left( \frac{5}{3} + \frac{23}{30}\sigma^4 + \frac{53}{105}\sigma^8 + \frac{95}{252}\sigma^{12} + \dots \right) \right]$$

It is seen from this equation that the value of  $\frac{M_c - M_i}{M_i}$  for the limiting case of a circle, for which  $t=1$  or  $\sigma=0$ , is:

$$\frac{M_c - M_i}{M_i} = \frac{\mu}{2} \frac{4 + 5K_i^2}{3}$$

On the other hand, equation (21) shows that, for the limiting case of a straight-line segment for which  $t=0$  or  $\sigma=1$  and the angle of attack  $\beta$  is finite,

$$\frac{M_c - M_i}{M_i} = \infty$$

It is to be noted that, although  $M_i$ , and therefore  $M_c$ , is zero when the angle of attack  $\beta$  is zero, the ratio  $\frac{M_c - M_i}{M_i}$  possesses the limiting value

$$\left( \frac{M_c - M_i}{M_i} \right)_{\beta=0} = \frac{\mu}{2} \left[ 1 + (1-\sigma^2)^2 \left( \frac{1}{2\sigma^6} \log \frac{1+\sigma^2}{1-\sigma^2} - \frac{1}{\sigma^4} \right) \right] \quad (22)$$

where  $K_i = 2 \sin \beta$ , according to the condition that the rear stagnation point occurs at the end of the major axis of the ellipse. For the two limiting cases of the circle and the straight-line segment, this ratio becomes, respectively:

$$\left( \frac{M_c - M_i}{M_i} \right)_{\beta=0} = \frac{4}{3} \frac{\mu}{2}$$

and

$$\left( \frac{M_c - M_i}{M_i} \right)_{\beta=0} = \frac{\mu}{2} \quad (23)$$

In appendix A, an independent derivation of equation (21), with  $K_i=0$ , is obtained by a direct integration of the pressures over the surface of an elliptic cylinder. It shows clearly the superiority of the present general method, in which all integrations are performed along a circle at infinity.

It is of interest to investigate the effect of compressibility on the center of pressure. If the rear stagnation point is supposed to be at the end of the major axis, it is immediately seen from the second of equations (18) that, for  $\delta=\pi$  and  $\lambda_P=1$ ,

$$\left( \frac{v_\delta}{v_0} \right)_{\delta=\pi} = -2 \sin \beta + K_i + \Delta K + \left( \frac{\Delta v_\delta}{v_0} \right)_{\delta=\pi} = 0$$

Since  $K_i = 2 \sin \beta$ , it follows that the additional circulation  $\Delta K$  is given by

$$\Delta K = - \left( \frac{\Delta v_\delta}{v_0} \right)_{\delta=\pi}$$

The problem of determining the additional circulation thus amounts to finding an expression for  $\Delta v_\delta/v_0$  at the stagnation point  $\delta=\pi$ . This calculation is given in appendix B and it is shown there that

$$\frac{\Delta \Gamma}{\Gamma_i} = \frac{\Delta K}{K_i} = \frac{\mu}{2} (M + N \sin^2 \beta) \quad (24)$$

where  $M$  and  $N$  are functions of the thickness coefficient  $t$  only. Table I presents values of  $M$  and  $N$  for various values of  $t$ .

TABLE I

$t$	$M$	$N$
0	1.00000	$\infty$
.1	1.09808	3.44779
.2	1.19225	2.48666
.3	1.28287	1.98162
.4	1.37929	1.63730
.5	1.45392	1.39813
.6	1.53503	1.20098
.7	1.61342	1.03754
.8	1.68916	.89794
.9	1.76185	.77605
1.0	1.83333	.66667

For the straight-line segment,  $\Delta \Gamma/\Gamma_i$  equals infinity if the value of  $\beta$  is other than zero but, for very thin profiles and vanishingly small angles of attack,

$$\frac{\Gamma_i + \Delta \Gamma}{\Gamma_i} = 1 + \frac{\mu}{2}$$

This result agrees with that given by Glauert (reference 3), namely:

$$\frac{\Gamma_i + \Delta \Gamma}{\Gamma_i} = \frac{1}{\sqrt{1-\mu}} = 1 + \frac{\mu}{2} + \dots$$

In reference 3, Glauert has also shown that the lifting force on a body in a compressible fluid is given by

$$L_c = \rho_0 v_0 \Gamma$$

or

$$L_c = L_i \left( 1 + \frac{\mu}{2} \right) \quad (25)$$



If  $c_c$  and  $c_i$  denote, respectively, the centers of pressure in the compressible and the incompressible fluids, then according to equations (23) and (25)

$$\frac{c_c}{c_i} = 1$$

That is, for a very thin profile and for vanishingly small angles of attack, the center of pressure is unaffected by the compressibility of the fluid. For the general elliptic profiles, it follows from equations (21) and (24) that

$$\frac{c_c}{c_i} = \frac{1 + \frac{\mu}{2} \left[ 1 + (1 - 2\sigma^2 \cos 2\beta + \sigma^4) \left( \frac{1}{2\sigma^6} \log \frac{1 + \sigma^2}{1 - \sigma^2} - \frac{1}{\sigma^4} \right) + 4 \sin^2 \beta \left[ \frac{1 + \sigma^4}{4\sigma^6} \log \frac{1 + \sigma^2}{1 - \sigma^2} - \frac{1}{2\sigma^4} - \frac{1}{\sigma^4} \log (1 - \sigma^4) \right] \right]}{1 + \frac{\mu}{2} (M + N \sin^2 \beta)}$$

It may be shown from this expression that, for any given ellipse, there exists an angle of attack  $\beta$ , independent of the stream velocity  $v_0$ , to the first order of  $\mu$ , for which the ratio  $c_c/c_i$  equals unity. Furthermore, if the angle of attack is  $\begin{cases} \text{greater} \\ \text{less} \end{cases}$  than this neutral value of  $\beta$ , then  $c_c/c_i$  is  $\begin{cases} \text{greater} \\ \text{less} \end{cases}$  than unity and the center of pressure  $c_c$  in the compressible fluid is  $\begin{cases} \text{farther from} \\ \text{nearer to} \end{cases}$  the origin than the center of pressure  $c_i$  in the incompressible fluid. Table II presents the neutral values of  $\beta$  for the entire range of ellipses including the straight-line profile and the circle.

TABLE II

$t$	$\cos 2\beta$	$\beta_{\text{neutral}}$	
		Degrees	Minutes
0	1.00000	0	0
.1	.98302	5	17
.2	.96199	7	56
.3	.94116	9	53
.4	.92173	11	25
.5	.90348	12	40
.6	.88687	13	46
.7	.87148	14	42
.8	.85965	15	22
.9	.84474	16	11
1.0	.83333	16	47

As a numerical example, consider an elliptic cylinder with a thickness coefficient  $t = \frac{1}{2}$  and with  $v_0/c_0 = \frac{1}{2}$ . In this case, the neutral angle of attack  $\beta$  is given by  $\cos 2\beta = 0.90348$ , or  $\beta = 12^\circ 40'$ . If the angle of attack is increased to  $15^\circ$ , say, then

$$\frac{M_c}{M_i} = 1.20776, \quad \frac{L_c}{L_i} = 1.19345$$

and

$$\frac{c_c}{c_i} = 1.012$$

Now

$$c_i = \frac{a}{2}(1 - t)$$

Therefore

$$\frac{c_c - c_i}{2a} = 0.0015$$

or the motion of the center of pressure away from the origin is 0.15 percent of the chord. Again, if the angle of attack is vanishingly small, then  $\cos \beta \cong 1$  and  $\sin \beta \cong \beta$ , and

$$\frac{M_c}{M_i} = 1.14486, \quad \frac{L_c}{L_i} = 1.18174$$

Then

$$\frac{c_c - c_i}{2a} = -0.0039$$

or the motion of the center of pressure toward the origin is 0.39 percent of the chord. In general, when the angle of attack  $\beta$  is vanishingly small, the center of pressure  $c_c$  in the compressible fluid is nearer to the origin than the center of pressure  $c_i$  in the incompressible fluid. Table III gives values for  $\left( \frac{c_c - c_i}{2a} \right)_{\beta=0}$  for various values of  $t$  and for the critical values of  $\mu$ .<sup>3</sup>

TABLE III

$t$	$\mu_{\text{crit}}$	$\left( \frac{c_c}{c_i} \right)_{\beta=0}$	$\left( \frac{c_c - c_i}{2a} \right)_{\beta=0}$
0	1.00000	1.00000	0
.1	.73445	.97960	-.00459
.2	.57608	.96988	-.00602
.3	.46677	.96459	-.00620
.4	.39514	.96155	-.00577
.5	.33293	.96038	-.00495
.6	.28944	.95971	-.00403
.7	.25120	.96003	-.00300
.8	.22212	.96037	-.00198
.9	.19714	.96118	-.00097
1.0	.17640	.96204	0

### THE SYMMETRICAL JOUKOWSKI PROFILE

The Joukowski profiles are derived by means of the conformal transformation

$$\zeta = z' + \frac{a^2}{z'}$$

which maps the circle of radius  $a$  with its center at the origin of the  $z'$  plane into a line segment  $(-2a, 0; 2a, 0)$  in the  $\zeta$  plane. Any other circle of radius  $r_0 (> a)$  with its center lying on the real axis at a distance  $a\epsilon$  from  $O$  (see fig. 4) and touching the base circle at  $(-a, 0)$  is mapped into a symmetrical Joukowski profile with a sharp trailing edge. The variables  $z$  and  $z'$  are connected by the equation

$$z' = \epsilon a + z$$

The circulation  $\Gamma_i$  is chosen in accordance with the Kutta-Joukowski hypothesis that the rear stagnation point of the flow occurs at the point  $A$  of the circle. In

<sup>3</sup> The critical value of  $\mu$  is defined as that value of  $\mu$  at which the maximum velocity of the fluid at the surface of the obstacle just attains the local velocity of sound. A list of such values of  $\mu$  for a set of elliptic cylinders with the angle of attack equal to zero is given in table IV of reference 4.







(22) of reference 2 by evaluating  $\Delta v_\delta/v_c$  for  $\delta=\pi$  and is written as follows (see appendix D):

$$\frac{\Delta\Gamma}{\Gamma_i} = -\frac{1}{2\sin\beta}\left(\frac{\Delta v_\delta}{v_0}\right)_{\delta=\pi} = \frac{\mu}{2}(M+N\sin^2\beta) \quad (29)$$

where  $M$  and  $N$  depend only on the thickness coefficient  $\epsilon$  of the profile. Table IV lists values of  $M$  and  $N$  for several values of  $\epsilon$ .

TABLE IV

$\epsilon$	$M$	$N$
0	1.00000	$\infty$
.03	1.03242	3.76210
.05	1.05496	3.73331
.10	1.11153	2.88585
.20	1.21659	2.17368
.30	1.32617	1.80592
.40	1.40925	1.56348
.50	1.49044	1.38092

It is interesting to note that  $M=1$  for a straight-line profile but that  $N$  is infinite on account of a term containing  $\log \epsilon$ . For very thin profiles and vanishingly small angles of attack, however,

$$\frac{\Gamma_i + \Delta\Gamma}{\Gamma_i} = 1 + \frac{\mu}{2} \quad (30)$$

This result agrees with Glauert's well-known formula (see section on the elliptic cylinder)

$$\frac{\Gamma_i + \Delta\Gamma}{\Gamma_i} = \frac{1}{\sqrt{1-\mu}} = 1 + \frac{\mu}{2} + \dots$$

It follows from equations (26) and (27) that, for an infinitely thin profile with an angle of attack so small that  $\sin\beta \cong \beta$  and  $\cos\beta \cong 1$ ,

$$\frac{M_c}{M_i} = 1 + \frac{\mu}{2} \quad (31)$$

With  $L_c = \rho_0 v_0 (\Gamma_i + \Delta\Gamma)$  and  $L_i = \rho_0 v_0 \Gamma_i$ , it therefore follows from equations (30) and (31) that

$$\frac{M_c}{L_c} = \frac{M_i}{L_i}$$

or

$\frac{c_c}{c_i} = 1$  (as in the case of the ellipse). In general, according to equations (26) and (29),

$$\frac{c_c}{c_i} = \frac{1 + \frac{\mu}{2} \left[ 1 + \frac{\epsilon(1+\epsilon)}{1+\epsilon(1+\epsilon)} \left( -\frac{3}{2} + M + N \sin^2\beta \right) + \frac{(1+\epsilon)^2}{1+\epsilon(1+\epsilon)} (I+J) \right]}{1 + \frac{\mu}{2} (M + N \sin^2\beta)} \quad (32)$$

Again, as in the case of elliptic cylinders, a neutral value for  $\beta$  is obtained when the centers of pressure in the compressible and the incompressible fluids coincide. It may be shown by means of numerical examples that, when the angle of attack is less than the neutral value of  $\beta$ , the center of pressure  $c_c$  in the compressible fluid moves from its position  $c_i$  in the incompressible fluid toward the origin and that, when the angle of attack is greater than the neutral value of  $\beta$ , the center of pressure  $c_c$  moves toward the nose of the profile.

In order to gain some idea as to the order of magnitude of the movement of the center of pressure due to compressibility, consider the case of a thin profile, say  $\epsilon=0.05$ . Then equation (32) becomes

$$\frac{c_c}{c_i} = \frac{1 + \frac{\mu}{2} (7.00142 - 5.95991 \cos 2\beta)}{1 + \frac{\mu}{2} (2.92162 - 1.86666 \cos 2\beta)}$$

Letting  $c_c$  and  $c_i$  coincide, i. e.,  $c_c/c_i=1$ , yields

$$\cos 2\beta = 0.99671$$

or a neutral angle

$$\beta = 2^\circ 20'$$

If the angle of attack is taken to be  $0^\circ$ , then

$$\frac{c_c}{c_i} = \frac{1 + 0.52075 \mu}{1 + 0.52748 \mu}$$

which shows that  $c_c$  is nearer the origin than  $c_i$ . It is seen that the movement of the center of pressure is very small. Thus, even for a large value of  $v_0/c_0$ , say 0.70, the center of pressure moves only about 0.07 percent of the chord toward the origin.

Again, if the angle of attack is increased to  $4^\circ$ ,

$$\frac{c_c}{c_i} = \frac{1 + 0.54975 \mu}{1 + 0.53656 \mu}$$

which shows that  $c_c$  is nearer the nose of the profile than  $c_i$ . The center of pressure in this case, with  $v_0/c_0=0.70$ , moves about 0.13 percent of the chord toward the nose.

This numerical example indicates that, although the effect of compressibility on the lift and the moment of a thin airfoil may be large, namely

$$\frac{L_c - L_i}{L_i} = 0.25517, \quad \frac{M_c - M_i}{M_i} = 0.25847$$

for

$$\beta = 0^\circ, \quad \frac{v_0}{c_0} = 0.70$$

and

$$\frac{L_c - L_i}{L_i} = 0.26938, \quad \frac{M_c - M_i}{M_i} = 0.26291$$

for

$$\beta = 4^\circ, \quad \frac{v_0}{c_0} = 0.70$$

the effect on the center of pressure may be considered negligible.

As an example of a thicker airfoil, let  $\epsilon=0.10$ . The thickness of Joukowski airfoils is proportional to  $\epsilon$  and a value of  $\epsilon$  of 0.10 gives a maximum thickness of about 0.13 times the chord, a value rarely exceeded in practice. For this case, equation (32) becomes:



$$\frac{c_c}{c_i} = \frac{1 + \frac{\mu}{2}(5.43168 - 4.34449 \cos 2\beta)}{1 + \frac{\mu}{2}(2.55446 - 1.44293 \cos 2\beta)}$$

Putting  $c_c/c_i=1$  yields

$$\cos 2\beta = 0.99161$$

or a neutral angle

$$\beta = 3^\circ 42'$$

If the angle of attack is taken to be  $0^\circ$  and  $v_0/c_0=0.70$ , then

$$\frac{c_c}{c_i} = \frac{1.26636}{1.27232} = 0.99531$$

or the center of pressure is displaced toward the origin a distance equal to 0.12 percent of the chord.

If the angle of attack is increased to  $6^\circ$  with  $v_0/c_0=0.70$ , then

$$\frac{c_c}{c_i} = \frac{1.28962}{1.28005} = 1.00748$$

or the center of pressure is displaced toward the nose of the airfoil a distance equal to 0.19 percent of the chord.

#### CONCLUDING REMARKS

It has been shown that, for a thin airfoil and for small angles of attack, the moment is given by equation (31):

$$M_c = M_i \left( 1 + \frac{\mu}{2} \right)$$

This result is, however, limited to small values of  $\mu$ . On the other hand, Glauert (reference 3) has shown that the lift on an airfoil in a compressible fluid is given by

$$L_c = \frac{L_i}{\sqrt{1-\mu}} = L_i \left( 1 + \frac{\mu}{2} + \dots \right)$$

The validity of this formula depends on the assumption that the velocity at the surface of the airfoil does not differ appreciably from the undisturbed velocity  $v_0$ , although the velocity in the undisturbed stream may be large. This assumption means that the airfoil must be thin and the angle of attack small. The similarity of the two preceding formulas, insofar as the first power of  $\mu$  is concerned, strongly suggests that the expression for the moment on a thin airfoil at small angles of attack and for large stream velocities is given by:

$$M_c = \frac{M_i}{\sqrt{1-\mu}} \quad (33)$$

This result is indeed implied in Glauert's work, where it is stated that the lift distribution along the chord remains unaltered but that the strength of each elementary vortex is increased by the factor  $(1-\mu)^{-\frac{1}{2}}$ .

In view of this discussion, it would appear that a more accurate expression for the moment  $M_c$  may be

obtained by introducing the factor  $(1-\mu)^{-\frac{1}{2}}$  into equation (20). Thus, equation (20) is replaced by

$$\begin{aligned} M_c = & \frac{1}{\sqrt{1-\mu}} \left\{ M_i + \rho_0 v_0 \Delta \Gamma m \cos (\beta + \sigma) \right. \\ & + \frac{\mu}{2} \left[ -\frac{3}{2} \rho_0 v_0 \Gamma_i m \cos (\beta + \sigma) \right. \\ & + \frac{1}{2} \rho_0 v_0 \Gamma_i \text{ R. P. } e^{i\beta} \sum_{n=1}^{\infty} \frac{2n+1}{n(n+1)} \frac{\bar{A}_n A_{n+1}}{r_0^{2n}} \\ & \left. \left. - 2\pi \rho_0 v_0^2 \text{ R. P. } i e^{2i\beta} \sum_{n=1}^{\infty} \frac{\bar{A}_n A_{n+2}}{(n+1)r_0^{2n}} \right] \right\} \quad (34) \end{aligned}$$

This formula differs from equation (20) in that it is valid for large stream velocities and differs from equation (33) in that it estimates the effect of large disturbances to the main flow  $v_0$  because of the presence of an obstacle.

As an example, consider the case of symmetrical Joukowski airfoils with sharp trailing edges. Equation (26) is then replaced by

$$\begin{aligned} M_c = & \frac{M_i}{\sqrt{1-\mu}} \left\{ 1 + \frac{\epsilon(1+\epsilon)}{1+\epsilon(1+\epsilon)} \frac{\Delta \Gamma}{\Gamma_i} \right. \\ & \left. + \frac{\mu}{2} \left[ -\frac{3}{2} \frac{\epsilon(1+\epsilon)}{1+\epsilon(1+\epsilon)} + \frac{(1+\epsilon)^2}{1+\epsilon(1+\epsilon)} (I+J) \right] \right\} \quad (35) \end{aligned}$$

In an analogous manner, the formula for the lift becomes

$$L_c = \frac{L_i}{\sqrt{1-\mu}} \left[ 1 + \frac{\mu}{2} (-1 + M + N \sin^2 \beta) \right] \quad (36)$$

As a numerical example, consider an airfoil for which  $\epsilon=0.10$ . For this case

$$M = 1.11153$$

$$N = 2.88585$$

$$\frac{\Delta \Gamma}{\Gamma_i} = \frac{\mu}{2} (1.11153 + 2.88585 \sin^2 \beta)$$

and

$$(1+\epsilon)^2 (I+J) = 4.80317 - 4.66366 \cos 2\beta$$

Table V gives the values of  $\frac{2}{\mu} \frac{\Delta \Gamma}{\Gamma_i}$  and of  $(1+\epsilon)^2 (I+J)$  for several angles of attack.

TABLE V

$\beta$ (deg.)	$\frac{2}{\mu} \frac{\Delta \Gamma}{\Gamma_i}$	$(1+\epsilon)^2 (I+J)$
0	1.11153	0.13951
2	1.11505	.15089
4	1.12557	.18489
6	1.14306	.24141
8	1.16743	.32018
10	1.19855	.42078

Table VI lists the values of the ratios  $M_c/M_i$  and  $L_c/L_i$  as given by equations (35) and (36), respectively, for various values of  $v_0/c_0$ . The last column gives the values of  $M_c/M_i$  (or  $L_c/L_i$ ) calculated from equation (33).



TABLE VI

$\frac{v_0}{c_0}$ $\beta$ (deg.)	$\frac{M_c}{M_i}$						$\frac{L_c}{L_i}$						$\frac{1}{\sqrt{1-\mu}}$
	0	2	4	6	8	10	0	2	4	6	8	10	
0	1.00000	1.00000	1.00000	1.00000	1.00000	1.00000	1.00000	1.00000	1.00000	1.00000	1.00000	1.00000	1.00000
.40	1.09871	1.09964	1.10240	1.10700	1.11340	1.12165	1.10084	1.10114	1.10206	1.10359	1.10572	1.10843	1.09110
.50	1.16732	1.16885	1.17342	1.18102	1.19168	1.20513	1.17083	1.17134	1.17286	1.17538	1.17890	1.18339	1.15473
.60	1.26962	1.27200	1.27913	1.29098	1.30749	1.32857	1.27509	1.27589	1.27825	1.28219	1.28767	1.29467	1.25000
.70	1.43005	1.43383	1.44469	1.46276	1.48794	1.52008	1.43854	1.43975	1.44336	1.44936	1.45772	1.46840	1.40028
.75	1.54896	1.55347	1.56693	1.58933	1.62053	1.66038	1.55932	1.56081	1.56529	1.57272	1.58308	1.59632	1.51189
.80	1.71317	1.71982	1.73571	1.76379	1.80293	1.85291	1.72615	1.72803	1.73364	1.74297	1.75596	1.77256	1.66667
.85	1.95812	1.96538	1.98710	2.02321	2.07353	2.13779	1.97480	1.97722	1.98443	1.99643	2.01314	2.03448	1.89832

Figures 5 and 6 show graphs based on table VI with  $M_c/M_i$  and  $L_c/L_i$ , respectively, as ordinates and the Mach number  $v_0/c_0$  as the abscissa. The dashed curves represent the Glauert approximation

$$\frac{M_c}{M_i} = \frac{L_c}{L_i} = \frac{1}{\sqrt{1-\mu}}$$

It is seen from an examination of the table and the curves that, below the neutral angle of attack (in this case  $3^\circ 42'$ ), the Glauert approximation is better for the moment than for the lift but that, above this angle, the approximation is better for the lift than for the mo-

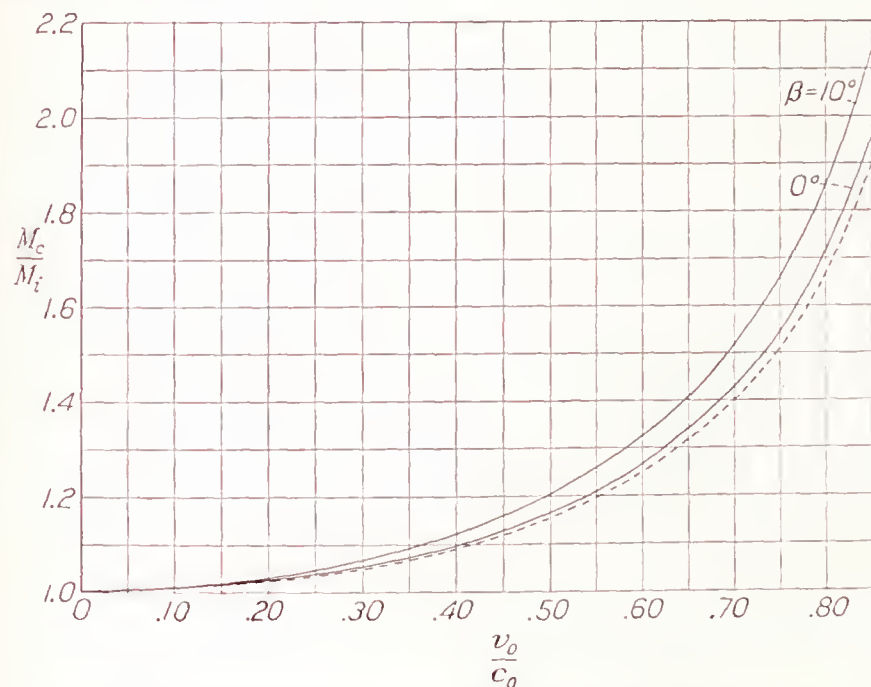


FIGURE 5.—The variation of the ratio  $M_c/M_i$  with the Mach number  $v_0/c_0$ .

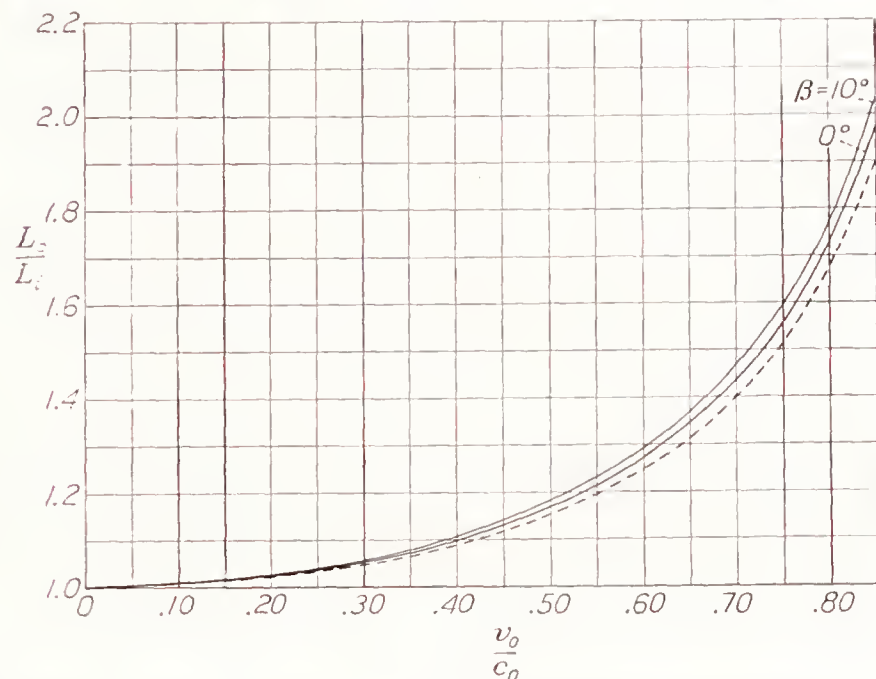


FIGURE 6.—The variation of the ratio  $L_c/L_i$  with the Mach number  $v_0/c_0$ .

ment. In any case, it appears that, at least for thin airfoils and for small angles of attack, the Glauert approximation for both the moment and the lift is sufficiently good. It then follows that the effect of compressibility on the center of pressure is negligible.

LANGLEY MEMORIAL AERONAUTICAL LABORATORY,  
NATIONAL ADVISORY COMMITTEE FOR AERONAUTICS,  
LANGLEY FIELD, VA., March 24, 1939.



## APPENDIX A

### EFFECT OF COMPRESSIBILITY ON THE COUPLE ABOUT AN ELLIPTIC CYLINDER

The moment on a body due to the fluid motion is, according to equation (1), given by

$$M = - \int_i [\mathbf{r} \mathbf{n}] p \, ds$$

where the positive direction of the normal vector  $\mathbf{n}$  is taken from the body into the fluid. The components of the vectors  $\mathbf{r}$  and  $\mathbf{n}$  are, respectively,  $(x, y)$  and  $(\cos \mathbf{n}x, \cos \mathbf{n}y)$ .

Therefore

$$[\mathbf{r} \mathbf{n}] = x \cos \mathbf{n}y - y \cos \mathbf{n}x$$

From figure 1, it is seen that

$$dx = ds \cos \mathbf{n}y \text{ and } dy = -ds \cos \mathbf{n}x$$

Hence

$$M = - \oint p(x \, dx + y \, dy) = - \frac{1}{2} \oint p \, dr^2$$

Now, the equations of transformation from Cartesian to elliptic coordinates are:

$$x = c \cosh \xi \cos \eta, \quad y = c \sinh \xi \sin \eta$$

or

$$z = c \cosh (\xi + i\eta)$$

where  $\xi$  takes on all values from zero to infinity and  $\eta$  takes on all values from 0 to  $2\pi$ . Then  $\xi = \text{constant}$  and  $\eta = \text{constant}$  represent confocal ellipses and hyperbolas, respectively, the distance between the foci being  $2c$ .

For any given ellipse  $\xi = \alpha$ , say,

$$x = c \cosh \alpha \cos \eta, \quad y = c \sinh \alpha \sin \eta$$

or

$$r^2 = c^2 (\cosh^2 \alpha \cos^2 \eta + \sinh^2 \alpha \sin^2 \eta)$$

Then

$$dr^2 = -c^2 \sin 2\eta \, d\eta$$

Therefore

$$M = - \frac{1}{2} c^2 \int_0^{2\pi} p \sin 2\eta \, d\eta$$

Now, according to equation (7), the pressure  $p$  in a compressible fluid is given by

$$p = \text{constant} \left[ \frac{1}{2} \rho_0 v_c^2 - \frac{1}{4} \mu \rho_0 v_i^2 + \frac{1}{8} \mu \frac{\rho_0 v_i^4}{v_0^2} + \dots \right]$$

so that

$$M_c = \frac{1}{4} \rho_0 c^2 \int_0^{2\pi} v_c^2 \sin 2\eta \, d\eta + \frac{1}{8} \mu \rho_0 c^2 \int_0^{2\pi} v_i^2 \sin 2\eta \, d\eta - \frac{1}{16} \mu \frac{\rho_0 c^2}{v_0^2} \int_0^{2\pi} v_i^4 \sin 2\eta \, d\eta$$

The last two integrals in this expression are easily obtained since they involve a knowledge only of the

velocity  $v_i$  in the incompressible fluid. Thus, suppose the elliptic cylinder to be in a flow of velocity  $v_0$  inclined at an angle  $\beta$  to the negative direction of the real axis and the circulation to be taken as zero. Then, if  $r_0$  is the radius of the circle into which the ellipse  $\xi = \alpha$  is mapped by the Joukowski transformation,

$$z = z' + \frac{c^2}{4z'}$$

and the complex potential of the flow past the circle is

$$w = v_0 \left( z' e^{i\beta} + \frac{r_0^2}{z' e^{i\beta}} \right)$$

it follows that the complex velocity is given by

$$\frac{1}{v_0} \frac{dw}{dz} = \frac{e^{i\beta} - \frac{r_0^2}{z'^2 e^{i\beta}}}{1 - \frac{c^2}{4z'^2}}$$

On the surface of the cylinder,  $z' = r_0 e^{i\theta}$ . Therefore,

$$\frac{1}{v_0} \frac{dw}{dz} = \frac{e^{i\beta} - e^{-i(2\theta+\beta)}}{1 - \frac{c^2}{4r_0^2} e^{-2i\theta}}$$

and

$$\frac{v_i^2}{v_0^2} = 2 \frac{1 - \cos 2(\theta + \beta)}{1 - 2\sigma^2 \cos 2\theta + \sigma^4}$$

where

$$\sigma = \frac{c}{2r_0}$$

Now, from the Joukowski transformation,

$$z' = \frac{z + \sqrt{z^2 - c^2}}{2}$$

where the positive sign of the radical has been chosen in order that the regions at infinity of the  $z$  and  $z'$  planes shall coincide.

Then if  $(x, y)$  is replaced by the elliptic coordinates  $(\xi, \eta)$ , i. e.,  $z = c \cosh (\xi + i\eta)$ , it follows that:

$$z' = \frac{c}{2} e^{\xi + i\eta}$$

or, on the surface of the cylinder,

$$r_0 e^{i\theta} = \frac{c}{2} e^{\alpha e^{i\eta}}$$

Therefore

$$\sigma = e^{-\alpha} \text{ and } \theta = \eta$$

and

$$\frac{v_i^2}{v_0^2} = 2 \frac{1 - \cos 2(\eta + \beta)}{1 - 2e^{-2\alpha} \cos 2\eta + e^{-4\alpha}} = \frac{e^{2\alpha} [1 - \cos 2(\eta + \beta)]}{\cosh 2\alpha - \cos 2\eta}$$



With this expression for  $v_i^2/v_0^2$ , it is very easy to calculate the last two integrals in the expression for  $M_c$ .

Thus

$$\begin{aligned} & \frac{1}{8}\mu\rho_0c^2\int_0^{2\pi}v_i^2\sin 2\eta d\eta \\ &= \frac{1}{8}\mu\rho_0v_0^2c^2e^{2\alpha}\int_0^{2\pi}\frac{1-\cos 2(\eta+\beta)}{\cosh 2\alpha-\cos 2\eta}\sin 2\eta d\eta \end{aligned}$$

Now

$$\int_0^{2\pi}\frac{\sin 2n\eta d\eta}{\cosh 2\alpha-\cos 2\eta}=0$$

and

$$\int_0^{2\pi}\frac{\cos 2n\eta d\eta}{\cosh 2\alpha-\cos 2\eta}=2\pi e^{-2n\alpha}\operatorname{csch} 2\alpha$$

Therefore

$$\frac{1}{8}\mu\rho_0c^2\int_0^{2\pi}v_i^2\sin 2\eta d\eta=\frac{1}{4}\mu\pi\rho_0v_0^2c^2\sin 2\beta$$

Similarly,

$$\int_0^{2\pi}\frac{\sin 2n\eta d\eta}{(\cosh 2\alpha-\cos 2\eta)^2}=0$$

and

$$\int_0^{2\pi}\frac{\cos 2n\eta d\eta}{(\cosh 2\alpha-\cos 2\eta)^2}=2\pi e^{-2n\alpha}\operatorname{csch}^2 2\alpha (\coth 2\alpha+n)$$

Hence,

$$\begin{aligned} & -\frac{1}{16}\frac{\mu\rho_0c^2}{v_0^2}\int_0^{2\pi}v_i^4\sin 2\eta d\eta \\ &= -\frac{1}{16}\mu\rho_0v_0^2c^2e^{4\alpha}\int_0^{2\pi}\frac{[1-\cos 2(\eta+\beta)]^2}{(\cosh 2\alpha-\cos 2\eta)^2}\sin 2\eta d\eta \\ &= \frac{1}{2}\mu\pi\rho_0v_0^2c^2\frac{e^{2\alpha}-\cos 2\beta}{e^{-2\alpha}-e^{2\alpha}}\sin 2\beta \end{aligned}$$

The sum of the two integrals becomes simply

$$-\frac{1}{4}\mu\pi\rho_0v_0^2c^2\frac{\cosh 2\alpha-\cos 2\beta}{\sinh 2\alpha}\sin 2\beta$$

It is much more difficult to calculate the first integral in the expression for  $M_c$ , for it is necessary in this case to know the velocity  $v_c$  at the surface of the elliptic cylinder in a compressible fluid. For this purpose, it is convenient to make use of equation (13) of reference 2. This equation, when applied to the case of an elliptic profile, becomes

$$\begin{aligned} \frac{\Delta v}{v_0} &= \frac{\mu}{2}\left\{\frac{\cos 2\beta-\sigma^2}{\sigma^2}\sin (\eta+\beta)\right. \\ &+ \sum_{n=1}^{\infty}(2n+1)\sin [(2n+1)\eta+\beta]\int_0^1\lambda^{2n+1}a_{2n}d\lambda \\ &- \sum_{n=1}^{\infty}(2n+1)\sin [(2n+1)\eta-\beta]\int_0^1\lambda^{2n-1}a_{2n+2}d\lambda \\ &+ 4\sin \beta\sum_{n=1}^{\infty}n\cos 2n\eta\int_0^1\lambda^{2n-1}a_{2n}d\lambda \\ &- \sin 2\beta\sum_{n=1}^{\infty}\sigma^{2n-2}\cos [(2n+1)\eta+\beta] \\ &+ \sin 2\beta\sum_{n=1}^{\infty}\sigma^{2n-2}\cos [(2n-1)\eta-\beta] \\ &\left.+ 2\sin \beta\sin 2\beta\sum_{n=1}^{\infty}\sigma^{2n-2}\sin 2n\eta\right\} \end{aligned}$$

where  $\lambda=r_0/r$ ,  $\sigma=c/2r_0$ , and the  $a_{2n}$ 's are the coefficients of the cosine terms in the Fourier development of  $v_i^2/v_0^2$  in the region of flow. For the elliptic cylinder

$$\begin{aligned} \frac{v_i^2}{v_0^2} &= \frac{1-2\lambda^2\cos 2(\theta+\beta)+\lambda^4}{1-2\sigma^2\lambda^2\cos 2\theta+\sigma^4\lambda^4} \\ &= \frac{1}{2}a_0+\sum_{n=1}^{\infty}(a_{2n}\cos 2n\theta+b_{2n}\sin 2n\theta) \end{aligned}$$

so that

$$\begin{aligned} a_0 &= 2\frac{1+\lambda^4(1-2\sigma^2\cos 2\beta)}{1-\sigma^4\lambda^4} \\ a_{2n} &= 2\frac{\sigma^2(1+\lambda^4)-(1+\sigma^4\lambda^4)\cos 2\beta}{\sigma^2(1-\sigma^4\lambda^4)}(\sigma\lambda)^{2n} \\ b_{2n} &= \frac{2}{\sigma^2}(\sigma\lambda)^{2n}\sin 2\beta \end{aligned}$$

Now, it is recalled that  $\Delta v/v_0$  refers to the plane of the circle into which the elliptic profile is mapped by the Joukowski transformation. Therefore

$$\frac{v_c^2}{v_0^2}=\frac{1}{1-2\sigma^2\cos 2\eta+\sigma^4}\left[2\sin (\eta+\beta)+\frac{\Delta v}{v_0}\right]$$

or

$$\frac{v_c^2}{v_0^2}\sin 2\eta=\frac{\sin 2\eta}{1-2\sigma^2\cos 2\eta+\sigma^4}\left[2\sin (\eta+\beta)+\frac{\Delta v}{v_0}\right]$$

But

$$\frac{\sin 2\eta}{1-2\sigma^2\cos 2\eta+\sigma^4}=\sum_{n=1}^{\infty}\sigma^{2n-2}\sin 2n\eta$$

Therefore, the first integral in the expression for  $M_c$  becomes

$$\begin{aligned} \frac{1}{4}\rho_0v_0^2c^2\int_0^{2\pi}\frac{v_c^2}{v_0^2}\sin 2\eta d\eta &= \frac{1}{2}\pi\rho_0v_0^2c^2\sin 2\beta\left\{1+\frac{\mu}{2}\left[\frac{\cos 2\beta-\sigma^2}{\sigma^2}\right.\right. \\ &+ 2\frac{1-\sigma^2\cos 2\beta}{1-\sigma^4}+\sum_{n=1}^{\infty}(2n-1)\sigma^{2n-2}\int_0^1\lambda^{2n-1}a_{2n-2}d\lambda \\ &\left.\left.-\sum_{n=1}^{\infty}(2n+1)\sigma^{2n-2}\int_0^1\lambda^{2n-1}a_{2n+2}d\lambda\right]\right\} \end{aligned}$$

The last two integrals in this expression may be written as

$$\begin{aligned} & 2\sum_{n=1}^{\infty}n\sigma^{2n-2}\int_0^1\lambda^{2n-1}(a_{2n-2}-a_{2n+2})d\lambda \\ & - \sum_{n=1}^{\infty}\sigma^{2n-2}\int_0^1\lambda^{2n-1}(a_{2n-2}+a_{2n+2})d\lambda \\ &= 2\sum_{n=1}^{\infty}n\sigma^{4n-6}\int_0^1[\sigma^2(1+\lambda^4)-(1+\sigma^4\lambda^4)\cos 2\beta]\lambda^{4n-2}d\lambda^2 \\ & - \sum_{n=1}^{\infty}\sigma^{4n-6}\int_0^1\frac{\sigma^2(1+\lambda^4)-(1+\sigma^4\lambda^4)\cos 2\beta}{1-\sigma^4\lambda^4}(1+\sigma^4\lambda^4)\lambda^{4n-2}d\lambda^2 \\ &= 2\int_0^1\frac{\sigma^2(1+\lambda^4)-(1+\sigma^4\lambda^4)\cos 2\beta}{\sigma^2(1-\sigma^4\lambda^4)^2}d\lambda^2 \\ & - \int_0^1\frac{\sigma^2(1+\lambda^4)-(1+\sigma^4\lambda^4)\cos 2\beta}{\sigma^2(1-\sigma^4\lambda^4)^2}(1+\sigma^4\lambda^4)d\lambda^2 \\ &= \int_0^1\frac{\sigma^2(1+\lambda^4)-(1+\sigma^4\lambda^4)\cos 2\beta}{\sigma^2(1-\sigma^4\lambda^4)}d\lambda^2=-\frac{1-\sigma^2\cos 2\beta}{\sigma^4} \\ & + \frac{1-2\sigma^2\cos 2\beta+\sigma^4}{2\sigma^6}\log\frac{1+\sigma^2}{1-\sigma^2} \end{aligned}$$



Therefore

$$\frac{1}{4}\rho_0 v_0^2 c^2 \int_0^{2\pi} \frac{v_c^2}{v_0^2} \sin 2\eta d\eta = \frac{\pi}{2}\rho_0 v_0^2 c^2 \sin 2\beta \left\{ 1 + \frac{\mu}{2} \left[ \frac{\cos 2\beta - \sigma^2}{\sigma^2} + 2 \frac{1 - \sigma^2 \cos 2\beta}{1 - \sigma^4} - \frac{1 - \sigma^2 \cos 2\beta}{\sigma^4} + \frac{1 - 2\sigma^2 \cos 2\beta + \sigma^4}{2\sigma^6} \log \frac{1 + \sigma^2}{1 - \sigma^2} \right] \right\}$$

Finally

$$M_c = M_i \left\{ 1 + \frac{\mu}{2} \left[ \frac{\cos 2\beta - \sigma^2}{\sigma^2} + 2 \frac{1 - \sigma^2 \cos 2\beta}{1 - \sigma^4} - \frac{1 - \sigma^2 \cos 2\beta}{\sigma^4} + \frac{1 - 2\sigma^2 \cos 2\beta + \sigma^4}{2\sigma^6} \log \frac{1 + \sigma^2}{1 - \sigma^2} \right] - \frac{\mu}{2} \frac{\cosh 2\alpha - \cos 2\beta}{\sinh 2\alpha} \right\}$$

where

$$M_i = \frac{\pi}{2} \rho_0 v_0^2 c^2 \sin 2\beta$$

Replacing  $e^{-2\alpha}$  by  $\sigma^2$ :

$$M_c = M_i \left[ 1 + \frac{\mu}{2} + \frac{\mu}{2} (1 - 2\sigma^2 \cos 2\beta + \sigma^4) \left( \frac{1}{2\sigma^6} \log \frac{1 + \sigma^2}{1 - \sigma^2} - \frac{1}{\sigma^4} \right) \right]$$

This expression agrees with equation (21) when the circulation is taken to be zero.

## APPENDIX B

### THE CALCULATION OF $\Delta v_\delta/v_0$ FOR AN ELLIPTIC CYLINDER AT $\delta = \pi$

Equation (13) of reference 2 gives an expression for  $\Delta v_\delta/v_0$  independent of the shape of the obstacle. In order to evaluate  $\Delta v_\delta/v_0$ , it is necessary to know the Fourier development of  $v_i^2/v_0^2$ . For an elliptic cylinder, with the circulation chosen so that the rear stagnation point occurs at the end of the major axis, it may be easily shown by means of the Joukowski transformation and the complex velocity potential of the flow about a circular cylinder that:

$$\frac{v_i^2}{v_0^2} = \frac{(1 + 2\lambda \cos \theta + \lambda^2)[1 - 2\lambda \cos(\theta + 2\beta) + \lambda^2]}{1 - 2\sigma^2 \lambda^2 \cos 2\theta + \sigma^4 \lambda^4} = \frac{1}{2} a_0 + \sum_{n=1}^{\infty} (a_n \cos n\theta + b_n \sin n\theta)$$

where

$\lambda = r_0/r$ ,  $\sigma = c/2r_0$ ,  $\beta$  is the angle of attack, and  $r$ ,  $\theta$  are the polar coordinates of a point in the region of flow.

The Fourier series for  $v_i^2/v_0^2$  is obtained by making use of the expansion

$$\frac{1}{1 - 2\sigma^2 \lambda^2 \cos 2\theta + \sigma^4 \lambda^4} = \frac{1}{1 - \sigma^4 \lambda^4} \left[ 1 + 2 \sum_{n=1}^{\infty} (\sigma^2 \lambda^2)^n \cos 2n\theta \right]$$

and it may be shown without difficulty that

$$\begin{aligned} a_0 &= \frac{2(1 + \lambda^2)^2}{1 - \sigma^4 \lambda^4} - \frac{4\lambda^2 \cos 2\beta}{1 - \sigma^2 \lambda^2} \\ a_{2n} &= 2 \left[ \frac{(1 + \lambda^2)^2}{1 - \sigma^4 \lambda^4} - \frac{1 + \sigma^2 \lambda^2}{\sigma^2(1 - \sigma^2 \lambda^2)} \cos 2\beta \right] (\sigma \lambda)^{2n} \\ a_{2n+1} &= \frac{4\lambda(1 + \lambda^2) \sin^2 \beta}{1 - \sigma^2 \lambda^2} (\sigma \lambda)^{2n} \\ b_{2n} &= 2\lambda^2 (\sigma \lambda)^{2n-2} \sin 2\beta \\ b_{2n+1} &= \frac{2\lambda(1 + \lambda^2) \sin 2\beta}{1 + \sigma^2 \lambda^2} (\sigma \lambda)^{2n} \end{aligned}$$

Equation (13) of reference 2 may then be written as

$$\begin{aligned} \left( \frac{\Delta v_\delta}{v_0} \right)_{\delta=\pi} &= \frac{\mu}{2} \left[ \sin \beta + \cos \beta \sum_{n=1}^{\infty} (2n+1) \int_0^1 \lambda^{2n+1} b_{2n} d\lambda \right. \\ &\quad - 2 \cos \beta \sum_{n=0}^{\infty} (n+1) \int_0^1 \lambda^{2(n+1)} b_{2n+1} d\lambda \\ &\quad - \cos \beta \sum_{n=0}^{\infty} (2n+1) \int_0^1 \lambda^{2n-1} b_{2n+2} d\lambda \\ &\quad + 2 \cos \beta \sum_{n=0}^{\infty} (n+1) \int_0^1 \lambda^{2n} b_{2n+3} d\lambda - \sin \beta \int_0^1 \lambda a_0 d\lambda \\ &\quad - \sin \beta \sum_{n=1}^{\infty} (2n+1) \int_0^1 \lambda^{2n+1} a_{2n} d\lambda \\ &\quad + 2 \sin \beta \sum_{n=0}^{\infty} (n+1) \int_0^1 \lambda^{2(n+1)} a_{2n+1} d\lambda \\ &\quad - \sin \beta \sum_{n=0}^{\infty} (2n+1) \int_0^1 \lambda^{2n-1} a_{2n+2} d\lambda \\ &\quad + 2 \sin \beta \sum_{n=0}^{\infty} (n+1) \int_0^1 \lambda^{2n} a_{2n+3} d\lambda \\ &\quad + 4 \sin \beta \sum_{n=0}^{\infty} (n+1) \int_0^1 \lambda^{2n+1} a_{2n+2} d\lambda \\ &\quad \left. - 2 \sin \beta \sum_{n=0}^{\infty} (2n+1) \int_0^1 \lambda^{2n} a_{2n+1} d\lambda \right] \end{aligned}$$

If the expressions for  $a_n$  and  $b_n$  are inserted and the integrations performed, it follows after considerable but straightforward labor that

$$\begin{aligned} \left( \frac{\Delta v_\delta}{v_0} \right)_{\delta=\pi} &= \frac{\mu}{2} \left\{ \sin \beta - \frac{1}{\sigma^2} \sin 3\beta + \frac{1}{\sigma^3} [(1 + \sigma)^2 \log(1 + \sigma) \right. \\ &\quad - (1 - \sigma)^2 \log(1 - \sigma)] (\sin \beta + \sin 3\beta) \\ &\quad - \frac{1}{\sigma^4} [(1 + \sigma^2)^2 \log(1 + \sigma^2) - (1 - \sigma^2)^2 \log(1 - \sigma^2)] \sin \beta \\ &\quad \left. + \frac{8 \log(1 - \sigma^4)}{\sigma^2} \sin^3 \beta - \frac{12}{\sigma^2} \sin \beta \log(1 + \sigma^2) \right\} \end{aligned}$$



The additional circulation  $\Delta K$  is given by

$$\Delta K = -\left(\frac{\Delta v_\delta}{v_0}\right)_{\delta=\pi}$$

(See section on the elliptic profile.)

Therefore, with  $K_i = 2 \sin \beta$ , it follows that

$$\frac{\Delta \Gamma}{\Gamma_i} = \frac{\Delta K}{K_i} = \frac{\mu}{2}(M + N \sin^2 \beta)$$

where

$$\begin{aligned} M &= \frac{3-\sigma^2}{2\sigma^2} + \frac{2}{\sigma^2} \log(1+\sigma^2) \\ &\quad + \frac{1+6\sigma^2+\sigma^4}{4\sigma^4} \log \frac{1+\sigma^2}{1-\sigma^2} - \frac{1+\sigma^2}{\sigma^3} \log \frac{1+\sigma}{1-\sigma} \\ N &= \frac{1+\sigma^2}{\sigma^3} \log \frac{1+\sigma}{1-\sigma} - \frac{2}{\sigma^2} [1 + \log(1+\sigma^2)] \end{aligned}$$

It is interesting to note that, for the limiting case of a circular cylinder  $\sigma=0$ , the foregoing equation yields

$$\left(\frac{\Delta \Gamma}{\Gamma_i}\right)_{circle} = \frac{\mu}{2} \left(\frac{11}{6} + \frac{2}{3} \sin^2 \beta\right)$$

and compares with Poggi's result (reference 5)

$$\left(\frac{\Delta \Gamma}{\Gamma_i}\right)_{circle} = \frac{11}{12} \mu$$

For the straight-line profile  $\sigma=1$ , it is seen that  $M=1$  and  $N=\infty$ . For an infinitely thin profile and a vanishingly small angle of attack, however,

$$\left(\frac{\Delta \Gamma}{\Gamma_i}\right)_{line} = \frac{1}{2} \mu$$

and compares with Glauert's formula (reference 3):

$$\frac{\Delta \Gamma}{\Gamma_i} = -1 + \frac{1}{\sqrt{1-\mu}} = \frac{1}{2} \mu + \dots$$

## APPENDIX C

### EVALUATION OF $I$

$$\begin{aligned} \sum_{n=1}^{\infty} \frac{2n+1}{n(n+1)} \frac{\bar{A}_n A_{n+1}}{r_0^{2n+1}} &= \sum_{n=1}^{\infty} \frac{\bar{A}_n A_{n+1}}{n r_0^{2n+1}} + \sum_{n=2}^{\infty} \frac{\bar{A}_{n-1} A_n}{n r_0^{2n-1}} \\ &= \frac{3}{2} \frac{\bar{A}_1 A_2}{r_0^3} + \frac{5}{6} \frac{\bar{A}_2 A_3}{r_0^5} + \frac{a^4}{r_0^4 k^5} (1-2k \cos 2\beta + k^2) \sum_{n=3}^{\infty} \frac{k^{2n}}{n} \\ &\quad + \frac{a^4}{r_0^4 k^7} (1-2k \cos 2\beta + k^2) \sum_{n=4}^{\infty} \frac{k^{2n}}{n} \end{aligned}$$

Since

$$-\sum_{n=1}^{\infty} \frac{k^{2n}}{n} = \log(1-k^2), \quad A_1 = 2ir_0 \sin \beta, \quad A_2 = a^2 e^{i\beta} - r_0^2 e^{-i\beta}$$

and  $A_3 = a^2 r_0 (k e^{i\beta} - e^{-i\beta})$ , it follows that

$$\begin{aligned} \sum_{n=1}^{\infty} \frac{2n+1}{n(n+1)} \frac{\bar{A}_n A_{n+1}}{r_0^{2n+1}} &= -\frac{a^4}{r_0^4} \frac{1+k^2}{k^7} (1-2k \cos 2\beta + k^2) \log(1-k^2) \\ &\quad - \frac{a^4}{r_0^4 k^5} (1-2k \cos 2\beta + k^2) \left(1 + \frac{3}{2} k^2 + \frac{5}{6} k^4\right) \\ &\quad - 3i \sin \beta \left(\frac{a^2}{r_0^2} e^{i\beta} - e^{-i\beta}\right) \\ &\quad + \frac{5}{6} \frac{a^2}{r_0^2} \left(\frac{a^2}{r_0^2} e^{-i\beta} - e^{i\beta}\right) (k e^{i\beta} - e^{-i\beta}) \end{aligned}$$

Therefore

$$\begin{aligned} I &= \text{R. P. } i \frac{1-e^{2i\beta}}{2 \sin 2\beta} \sum_{n=1}^{\infty} \frac{2n+1}{n(n+1)} \frac{\bar{A}_n A_{n+1}}{r_0^{2n+1}} \\ &= -\frac{a^4}{r_0^4} \frac{1+k^2}{2k^7} (1-2k \cos 2\beta + k^2) \log(1-k^2) \\ &\quad - \frac{a^4}{2r_0^4 k^5} (1-2k \cos 2\beta + k^2) \left(1 + \frac{3}{2} k^2 + \frac{5}{6} k^4\right) \\ &\quad + \frac{a^2}{6r_0^2} (9+5k) (1-\cos 2\beta) + \frac{5}{12} \frac{a^2}{r_0^2} (1-k) \left(1 - \frac{a^2}{r_0^2}\right) \end{aligned}$$

Now

$$\frac{a}{r_0} = \frac{1}{1+\epsilon} \quad \text{and} \quad k = \frac{1-\epsilon}{1+\epsilon}$$

Therefore

$$\epsilon = \frac{1-k}{1+k} \quad \text{and} \quad \frac{a}{r_0} = \frac{1+k}{2}$$

Hence

$$\begin{aligned} (1+\epsilon)^2 I &= \frac{(1+k)^2}{8k^5} (1-2k \cos 2\beta + k^2) \left[ \frac{1+k^2}{k^2} \log \frac{1}{1-k^2} \right. \\ &\quad \left. - \left(1 + \frac{3}{2} k^2 + \frac{5}{6} k^4\right) \right] + \frac{1}{6} (9+5k) (1-\cos 2\beta) \\ &\quad + \frac{5}{48} (3+k) (1-k)^2 \end{aligned}$$

For small values of  $k$ , or thick airfoils,

$$\begin{aligned} (1+\epsilon)^2 I &= (1+k)^2 (1-2k \cos 2\beta + k^2) \left( \frac{7}{96} k + \frac{9}{160} k^3 \right. \\ &\quad \left. + \frac{11}{240} k^5 + \dots \right) + \frac{1}{6} (9+5k) (1-\cos 2\beta) \\ &\quad + \frac{5}{48} (3+k) (1-k)^2 \end{aligned}$$

### EVALUATION OF $J$

$$\begin{aligned} \sum_{n=1}^{\infty} \frac{\bar{A}_n A_{n+2}}{(n+1)r_0^{2n+2}} &= \frac{\bar{A}_1 A_3}{2r_0^4} + \frac{\bar{A}_3 A_4}{3r_0^6} + \sum_{n=4}^{\infty} \frac{\bar{A}_{n-1} A_{n+1}}{n r_0^{2n}} \\ &= \frac{a^4 (1-2k \cos 2\beta + k^2)}{r_0^4 k^6} \sum_{n=4}^{\infty} \frac{k^{2n}}{n} - i \frac{a^2}{r_0^2} \sin \beta (k e^{i\beta} - e^{-i\beta}) \\ &\quad + \frac{1}{3} \frac{a^2 k}{r_0^2} (k e^{i\beta} - e^{-i\beta}) \left( \frac{a^2}{r_0^2} e^{-i\beta} - e^{i\beta} \right) \\ &= -\frac{a^4 (1-2k \cos 2\beta + k^2)}{r_0^4 k^6} \log(1-k^2) \\ &\quad - \frac{a^4 (1-2k \cos 2\beta + k^2)}{r_0^4 k^4} \left(1 + \frac{k^2}{2} + \frac{k^4}{3}\right) - i \frac{a^2}{r_0^2} \sin \beta (k e^{i\beta} - e^{-i\beta}) \\ &\quad + \frac{1}{3} \frac{a^2 k}{r_0^2} (k e^{i\beta} - e^{-i\beta}) \left( \frac{a^2}{r_0^2} e^{-i\beta} - e^{i\beta} \right) \end{aligned}$$



Therefore

$$\begin{aligned} J &= -\text{R. P.} \frac{ie^{2i\beta}}{\sin 2\beta} \sum_{n=1}^{\infty} \frac{\bar{A}_n A_{n+2}}{(n+1)r_0^{2n+2}} \\ &= -\frac{a^4(1-2k \cos 2\beta + k^2)}{r_0^4 k^6} \log(1-k^2) \\ &\quad - \frac{a^4(1-2k \cos 2\beta + k^2)}{r_0^4 k^4} \left(1 + \frac{k^2}{2} + \frac{k^4}{3}\right) \\ &\quad + \frac{a^2}{6r_0^2} (3+2k)(1-2k \cos 2\beta + k^2) \\ &\quad + \frac{a^2 k}{2r_0^2} (1-k) + \frac{1}{3} \frac{a^2 k^2}{r_0^2} \left(\frac{a^2}{r_0^2} - k\right) \end{aligned}$$

and

$$\begin{aligned} (1+\epsilon)^2 J &= \frac{(1+k)^2}{4k^4} (1-2k \cos 2\beta + k^2) \left[ \frac{1}{k^2} \log \frac{1}{1-k^2} \right. \\ &\quad \left. - \left(1 + \frac{k^2}{2} + \frac{k^4}{3}\right) \right] + \frac{1}{6} (3+2k)(1-2k \cos 2\beta + k^2) \\ &\quad + \frac{1}{2} k(1-k) + \frac{1}{12} k^2(1-k)^2 \end{aligned}$$

For small values of  $k$ , or thick airfoils,

$$\begin{aligned} (1+\epsilon)^2 J &= (1+k)^2 (1-2k \cos 2\beta + k^2) \left( \frac{1}{16} k^2 \right. \\ &\quad \left. + \frac{1}{20} k^4 + \frac{1}{24} k^6 + \dots \right) + \frac{1}{6} (3+2k)(1-2k \cos 2\beta + k^2) \\ &\quad + \frac{1}{2} k(1-k) + \frac{1}{12} k^2(1-k)^2 \end{aligned}$$

## APPENDIX D

### EVALUATION OF $(\Delta v_\delta/v_0)_{\delta=\pi}$ FOR THE CASE OF A JOUKOWSKI PROFILE

According to equation (22) of reference 2,  $(\Delta v_\delta/v_0)_{\delta=\pi}$  takes the following form:

$$\begin{aligned} \left(\frac{\Delta v_\delta}{v_0}\right)_{\delta=\pi} &= \frac{\mu}{2} \sin \beta \left\{ -\frac{1}{2} + \frac{h}{k^2} \left( h + 2k + 2kh^2 - \frac{5}{6} h^3 \right) \right. \\ &\quad \left. + \frac{(h+k)^2}{k^3} \left( -3 - 3kh + \frac{3}{2} k - h^2 k^2 + \frac{5}{6} kh^2 \right) \right. \\ &\quad \left. + \frac{2h^2(1-k)^2}{k^5} \left[ 1 - \frac{1}{2} k^2 + \frac{1-k^2}{k^2} \log(1-k^2) \right] \right. \\ &\quad \left. + \frac{8h(1-h)^3(2-3h)}{k^5} \left[ kh^2 - \frac{1-h}{2} \right. \right. \\ &\quad \left. \left. + (1-h)^2 + 2h(1-h) \log(1+k) \right] \right. \\ &\quad \left. + \frac{4h^2(1-h)^4}{k^6} [\log(1-k) + 4h^2 \log(1+k) - k^2] \right\} \\ &\quad + \frac{\mu}{2} \sin^3 \beta \left\{ \frac{4(h+k)^2}{k^3} \left( 1 + hk + \frac{1}{3} h^2 k^2 \right) \right. \\ &\quad \left. + \frac{4h^2}{k^2} \left[ -1 + \frac{k}{2} - \frac{1}{3} hk + \frac{2}{k^2} + \frac{2(1-k^2)}{k^4} \log(1-k^2) \right] \right. \\ &\quad \left. + \frac{8(1-h)^3}{k^3} \left[ kh^2 - \frac{1-h}{2} + (1-h)^2 + 2h(1-h) \log(1+k) \right] \right. \\ &\quad \left. + \frac{4(1-h)^4}{k^5} [\log(1-k) + 4h^2 \log(1+k) - k^2] \right\} \end{aligned}$$

where

$$h = \frac{\epsilon}{1+\epsilon} \text{ and } k = \frac{1-\epsilon}{1+\epsilon}$$

When this expression for  $(\Delta v_\delta/v_0)_{\delta=\pi}$  was obtained, a slight error was found in equations (19) of reference 2. The expressions for  $a_1 - \bar{a}_1$  and  $b_1 - \bar{b}_1$  should be as follows:

$$\begin{aligned} a_1 - \bar{a}_1 &= \frac{2\lambda \cos 2\beta}{k^2} \left[ h(h+2k) + 2h^3 k \lambda^2 \right] \\ &\quad - \frac{2h^2 \lambda}{k} \frac{1 + \lambda^2(1-2k \cos 2\beta)}{1 - k^2 \lambda^2} \end{aligned}$$

and

$$b_1 - \bar{b}_1 = -\frac{2\lambda \sin 2\beta}{k^2} \left[ h(h+2k) + 2kh^3 \lambda^2 \right]$$

It is to be noted in the expression for  $(\Delta v_\delta/v_0)_{\delta=\pi}$  that most of the terms contain powers of  $k$  in the denominator. It appears at first, then, that the coefficients of  $\sin \beta$  and  $\sin^3 \beta$  may become infinite for  $k=0$ . This apparent difficulty disappears, however, when  $(\Delta v_\delta/v_0)_{\delta=\pi}$  is expressed as a power series in  $k$ . It is then found that the terms involving reciprocal powers of  $k$  cancel and the following expression results:

$$\begin{aligned} \left(\frac{\Delta v_\delta}{v_0}\right)_{\delta=\pi} &= \frac{\mu}{2} \sin \beta \left( -\frac{689}{192} + \frac{309}{160} k - \frac{289}{672} k^2 + \frac{7}{32} k^3 - \frac{191}{640} k^4 + \dots \right) \\ &\quad + \frac{\mu}{2} \sin^3 \beta \left( -\frac{41}{24} - \frac{689}{240} k - \frac{13}{24} k^2 - \frac{1373}{1680} k^3 - \frac{163}{560} k^4 - \dots \right) \end{aligned}$$

### REFERENCES

1. Theodorsen, Theodore: The Reaction on a Body in a Compressible Fluid. Jour. Aero. Sci., vol. 4, no. 6, April 1937, pp. 239-240.
2. Kaplan, Carl: Compressible Flow about Symmetrical Joukowski Profiles. T. R. No. 621, N. A. C. A., 1938.
3. Glauert, H.: The Effect of Compressibility on the Lift of an Aerofoil. R. & M. No. 1135, British A. R. C., 1928.
4. Kaplan, Carl: Two-Dimensional Subsonic Compressible Flow past Elliptic Cylinders. T. R. No. 624, N. A. C. A., 1938.
5. Poggi, Lorenzo: Campo di velocità in una corrente piana di fluido compressibile. L'Aerotecnica, vol. XII, fasc. 12, Dec. 1932, pp. 1579-1593.



## REPORT No. 672

# FREE-SPINNING WIND-TUNNEL TESTS OF A LOW-WING MONOPLANE WITH SYSTEMATIC CHANGES IN WINGS AND TAILS

## IV. EFFECT OF CENTER-OF-GRAVITY LOCATION

By OSCAR SEIDMAN and A. I. NEIHOUSE

### SUMMARY

*Eight wings and three tails, covering a wide range of aerodynamic characteristics, were independently ballasted so as to be interchangeable with no change in mass distribution. For each of the 24 resulting wing-tail combinations, observations were made of the steady spin for four control settings and of recoveries for five control manipulations. The results are presented in the form of charts comparing the spin characteristics. The tests are part of a general investigation being made in the N. A. C. A. free-spinning tunnel to determine the effects of systematic changes in wing and tail arrangement upon the steady-spin and the recovery characteristics of a conventional low-wing monoplane for various load distributions.*

*The present tests are a continuation of the investigation, the entire series of tests performed for the basic loading being repeated with the center of gravity 10 percent forward and 10 percent back of the normal location at 25 percent of the mean chord. The results are compared with those for the basic loading condition.*

*For all tail and wing arrangements, there was a definite effect of center-of-gravity location, the forward location giving steeper spins and faster recoveries and the rearward location giving flatter spins and slower recoveries than the basic center-of-gravity location. The spin coefficient  $\Omega b/2V$  increased as the center of gravity was moved forward and decreased as the center of gravity was moved back. In general, there was a tendency for the rate of descent to increase and for the sideslip to become more outward as the center of gravity was moved forward. The wing of N. A. C. A. 6718 section, however, generally gave more inward sideslip for the forward center-of-gravity location than for the rearward location. The importance of center-of-gravity location, wing arrangement, and control manipulations increased as the effectiveness of the tail unit decreased.*

### INTRODUCTION

The N. A. C. A. has undertaken a systematic investigation in the free-spinning wind tunnel to determine

the effect of independent variations in dimensional and mass characteristics on the spin characteristics of airplanes (reference 1).

The results of tests of each of eight wings and three tails on a low-wing monoplane model for a basic loading condition, representative of an average of values for 21 American airplanes for which the moments of inertia were available, have been reported in reference 1. Results with weight distributed chiefly along the fuselage and with weight distributed chiefly along the wings are presented in references 2 and 3, respectively. The present paper deals with the effect of center-of-gravity position. In addition to the tests for the basic loading condition with the center of gravity at 25 percent of the mean wing chord, tests were made with the center of gravity at 15 and at 35 percent of the mean wing chord. The range of center-of-gravity locations thus covered is not likely to be greatly exceeded.

The major wing variables include tip shape, airfoil section, plan form, and flaps. The Army standard tapered wing, also included in the test program, combines changes in plan form and thickness. The three tail arrangements range from a combination utilizing full-length rudder and raised stabilizer on a deep fuselage, designed to be extremely efficient in providing yawing moment for recovery, to a more nearly conventional type with the rudder completely above a shallow fuselage and almost completely shielded by the horizontal surfaces.

### APPARATUS AND METHODS

A general description of model construction and testing technique in the N. A. C. A. free-spinning tunnel is given in reference 4. The models are constructed of balsa, reinforced with spruce and bamboo. In order to reduce the weight, the fuselage and the wings are hollowed out, the external contours being maintained by silk tissue paper on reinforcing ribs. The desired load distribution is attained by suitable location of lead weights.



Figures 1 to 5 show special structural features of the model used in the present investigation. The wing and the tail units are independently removable and interchangeable to permit testing any combination. The exchange of units can be made without any change in mass distribution. The mass distribution can also be changed without changing the wing or the tail arrangement. A clockwork delay-action mechanism is installed to actuate the controls for recovery.

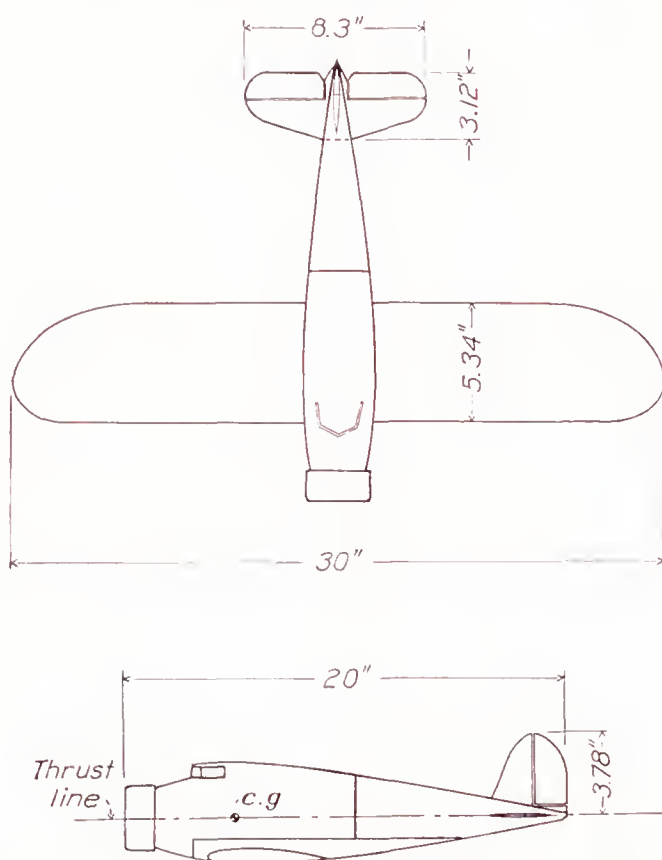


FIGURE 1.—Low-wing monoplane model with detachable tail and wing.

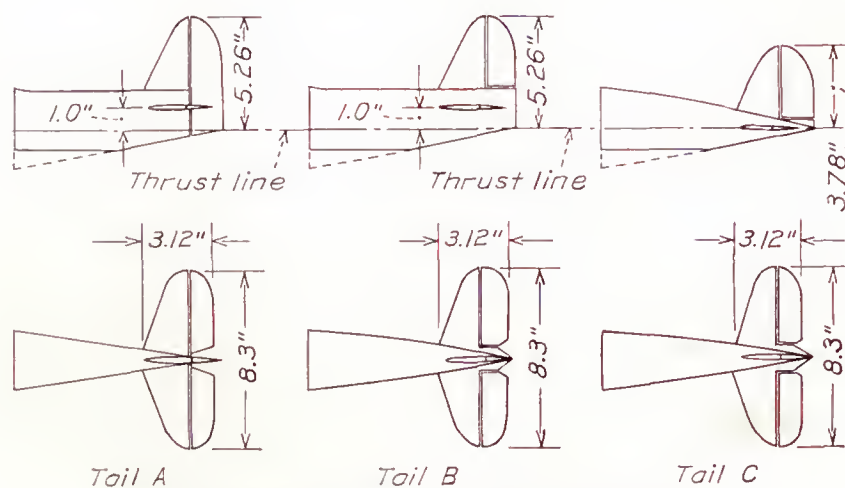
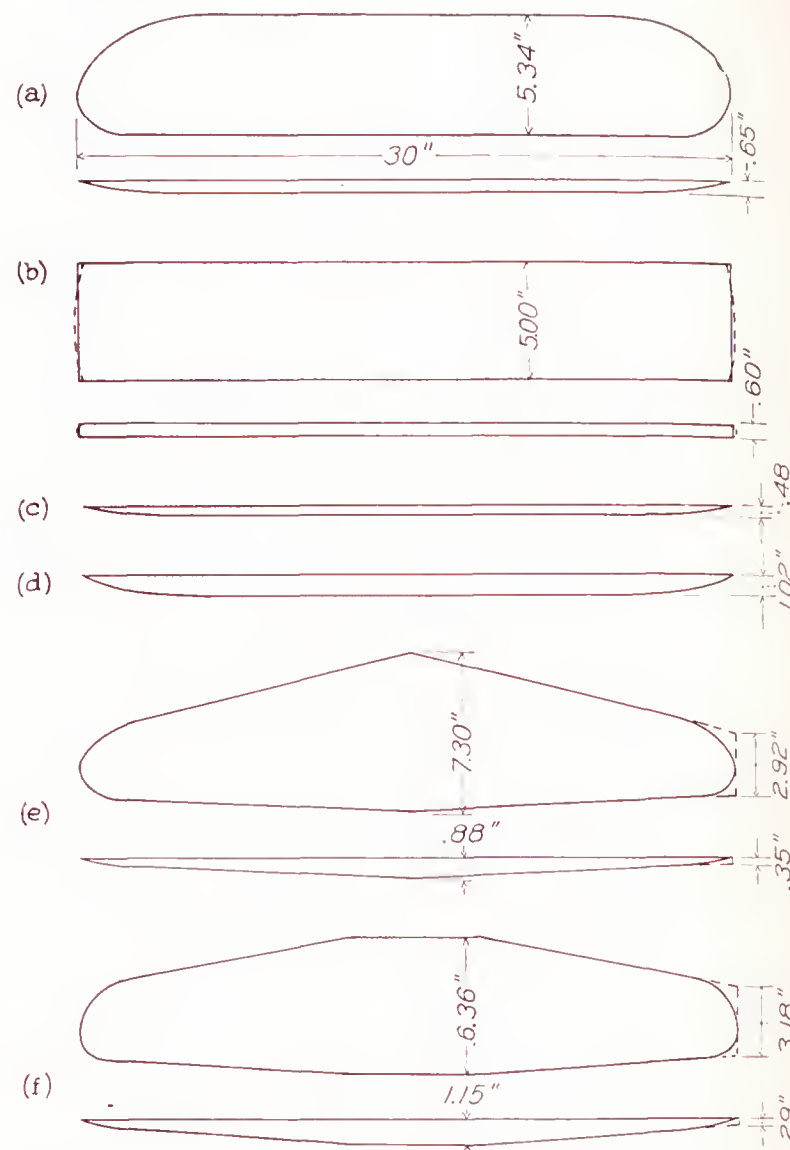


FIGURE 3.—Tails used on low-wing monoplane.

The model was not scaled from any particular airplane but was designed to be a representative low-wing cabin monoplane with a cowled radial engine and with landing gear retracted. Dimensional characteristics of the model and of the eight wings and the three tails are given on the line drawings of figures 1, 2, and 3. For convenience in making comparisons, the model may be



- (a) Wing 1—23012 rectangular with Army tips; wing 2—23012 with 20 percent full span split flaps at 60°.  
 (b) Wing 3—23012 rectangular with rectangular tips; wing 4—23012 rectangular with faired tips.  
 (c) Wing 5—0009 rectangular with Army tips (plan same as wing 1).  
 (d) Wing 6—G718 rectangular with Army tips (plan same as wing 1).  
 (e) Wing 7—23012 5:2 taper with Army tips.  
 (f) Wing 8—23018-09 standard Army wing. (2:1 taper, square center, Army tips.)

FIGURE 2.—Wings used on low-wing monoplane. N. A. C. A. wing sections.

considered a  $\frac{1}{15}$ -scale model of either a fighter or a four-place cabin airplane, tested at an altitude of 6,000 feet. The full-scale characteristics for the present loadings and for tail C would be:

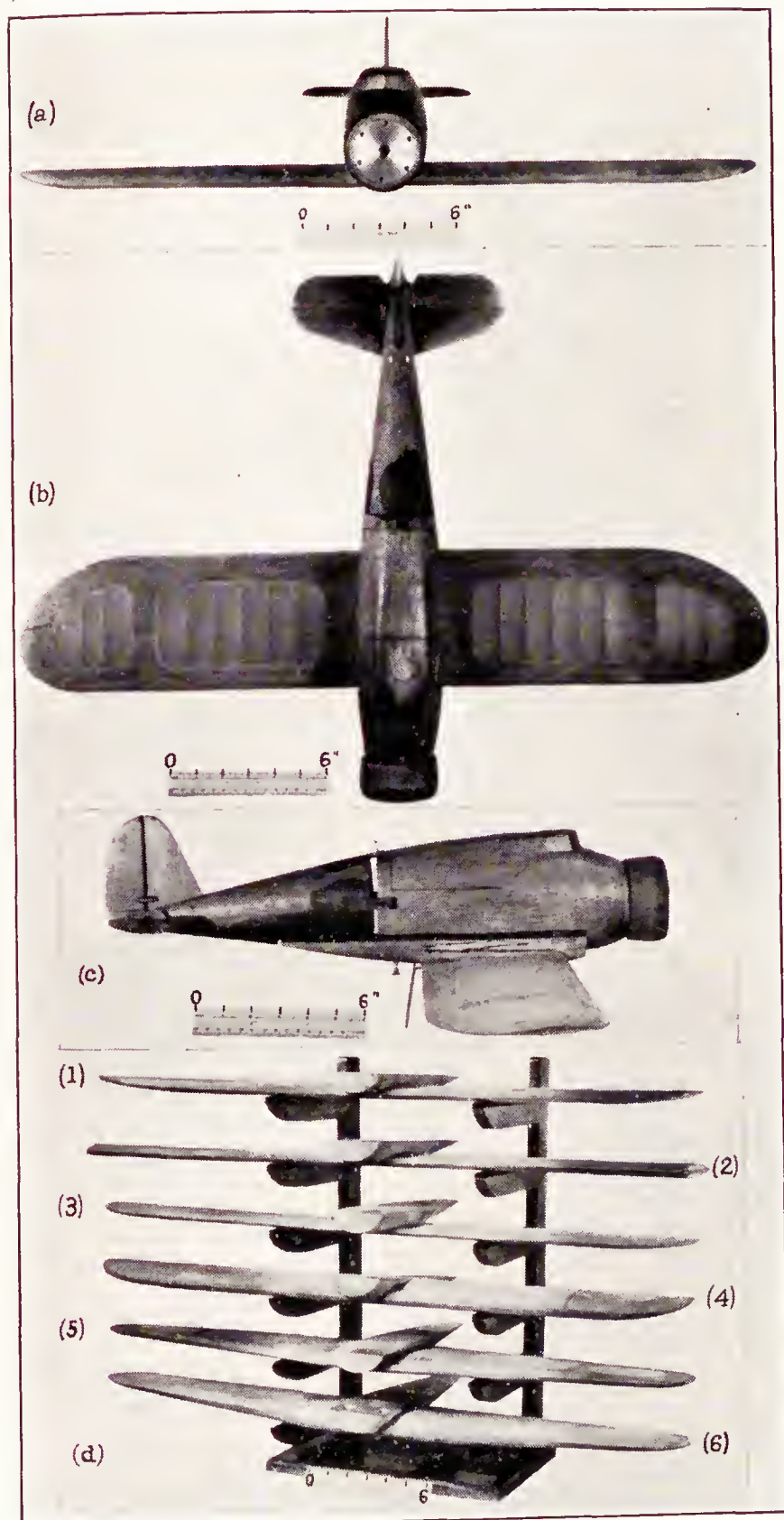
Weight ( $W$ )	4,720 lb.
Mean wing chord ( $c=S/b$ )	75 in.
Span ( $b$ )	37.5 ft.
Wing area ( $S$ )	234.4 sq. ft.
Aspect ratio	6
Distance from quarter-chord point to elevator hinge	16.6 ft.
Distance from quarter-chord point to rudder hinge	16.9 ft.
Fin area	6.8 sq. ft.
Rudder area	6.9 sq. ft.
Stabilizer area	19.8 sq. ft.
Elevator area	12.9 sq. ft.
Control travel	Rudder: $\pm 30^\circ$ Elevator: 30° up 20° down



Principal moments of inertia for the three center-of-gravity locations:

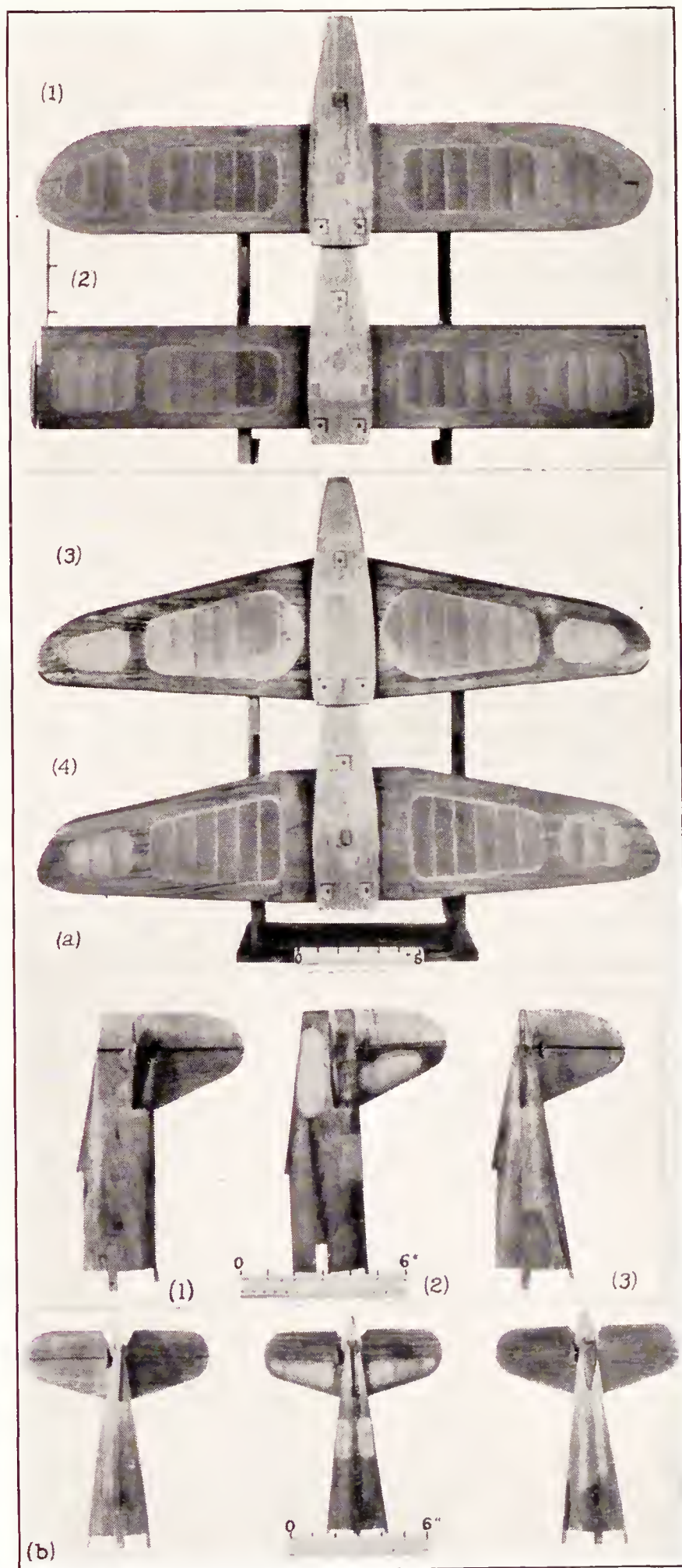
$$\begin{array}{ll} A = mk_x^2 & \text{-----} 2,760 \text{ slug-feet}^2 \\ B = mk_y^2 & \text{-----} 3,970 \text{ slug-feet}^2 \\ C = mk_z^2 & \text{-----} 6,150 \text{ slug-feet}^2 \end{array}$$

where  $A$ ,  $B$ , and  $C$  are moments of inertia about and  $k_x$ ,  $k_y$ , and  $k_z$  are the radii of gyration about the  $X$ ,  $Y$ , and  $Z$  axes, respectively.



(a) Front view.  
(b) Plan view.  
(c) Side view, showing detachable parts.  
(d) Low-wing monoplane wings: (1) Wings 1 and 2; (2) wings 3 and 4; (3) wing 5; (4) wing 6; (5) wing 7; (6) wing 8.

FIGURE 4.—Low-wing monoplane model.



(a) (1) Rectangular wing with Army tips; (2) rectangular wing with interchangeable rectangular and faired tips; (3) 5:2 tapered wing with Army tips; (4) 2:1 Army standard tapered wing with square center.  
(b) (1) Tail A, deep fuselage and long rudder; (2) tail B, deep fuselage and short rudder; (3) tail C, shallow fuselage and short rudder.

FIGURE 5.—Interchangeable wings and tails of low-wing monoplane model.



The nondimensional mass-distribution parameters for the different center-of-gravity locations are:

	Center-of-gravity location		
	Forward	Normal	Rearward
Relative density of airplane to air, $\mu = \frac{W}{g\rho S b}$	7	7	7
Pitching-moment inertia parameter, $\frac{W b^2}{g(C-A)}$	61	61	61
Rolling-moment and yawing-moment inertia parameter, $\frac{C-B}{C-A}$	0.64	0.64	0.64
$\frac{b}{k_x}$	8.7	8.7	8.7
$\frac{x}{c}$	0.15	0.25	0.35
$\frac{z}{c}$	0	0	0

where

- $\rho$  is the air density.
- $b$ , span of wing.
- $S$ , area of wing.
- $x$ , distance of the center of gravity back of the leading edge of the mean chord.
- $z$ , distance of the center of gravity below the thrust line.
- $c$ , mean wing chord.

Figures 1 and 4 show the model with the basic wing (wing 1) and tail C installed. This wing is of N. A. C. A. 23012 section with rectangular plan form and Army tips. (The tip contour is derived as described in reference 5.) In common with the other wings, it has an area of 150 square inches, a span of 30 inches, and no dihedral, twist, or sweepback.

The seven remaining wings (figs. 2 and 5) have varied dimensional characteristics as follows:

Wing 2: N. A. C. A. 23012 section, rectangular with Army tips, 20-percent-chord split flaps deflected 60°.

Wing 3: N. A. C. A. 23012 section, rectangular with rectangular tips.

Wing 4: N. A. C. A. 23012 section, rectangular with faired tips.

Wing 5: N. A. C. A. 0009 section, rectangular with Army tips.

Wing 6: N. A. C. A. 6718 section, rectangular with Army tips.

Wing 7: N. A. C. A. 23012 section, 5:2 taper with Army tips.

Wing 8: N. A. C. A. 23018-09 section, Army standard plan form (square center section, 2:1 taper in both plan form and thickness, and Army tips).

Each wing is mounted on the model at an angle of incidence equal to the angle of zero lift for the particular section. The stabilizer is set at zero incidence for each tail. There is no fin offset.

The three tails designated A, B, and C are shown in figures 3 and 5. Tail C, representing a conventional shallow fuselage with rudder completely above the tail cone, has the following dimensional characteristics:

Vertical tail area: 6 percent wing area (3 percent rudder and 3 percent fin).

Fuselage side area, back of leading edge of stabilizer: 2 percent wing area.

Vertical tail length (from wing quarter-chord point to rudder hinge axis): 45 percent wing span (2.70c).

Horizontal tail area: 14 percent wing area (5.5 percent elevator and 8.5 percent stabilizer).

Horizontal tail length (from wing quarter-chord point to elevator hinge axis): 44 percent wing span (2.64c).

Tail B was derived from tail C by increasing the fuselage depth, raising the stabilizer and the elevators, and installing approximately the original fin and rudder atop the deepened fuselage. For tail B, the vertical areas are:

Vertical tail area: 6 percent wing area.

Fuselage side area back of leading edge of stabilizer: 5.5 percent wing area.

Tail A is similar to tail B except for full-length rudder construction and slightly increased elevator cut-out. For tail A, the vertical areas are:

Vertical tail area: 8 percent wing area (5 percent rudder and 3 percent fin).

Fuselage side area back of leading edge of stabilizer: 3.4 percent wing area.

#### TESTS AND RESULTS

For each wing and tail combination with each center-of-gravity location, spin tests were made for four control settings:

- (a) Rudder 30° with the spin; elevators neutral.
- (b) Rudder 30° with the spin; elevators 20° down.
- (c) Rudder 30° with the spin; elevators 30° up.
- (d) Rudder neutral; elevators neutral.

Recovery from (a) and (b) was attempted by reversal of the rudder, from (c) by complete reversal of both controls and also by neutralizing both controls, and from (d) by moving the rudder full against the spin and the elevators full down.

The angle of attack  $\alpha$ , the angle of sideslip  $\beta$ , the rate of descent  $V$ , the spin coefficient  $\Omega b/2V$ , and turns for recovery are plotted in 12 charts (figs. 6 to 17), grouped so as to permit ready comparison of the effects of center-of-gravity location, tip shape, plan form, section, flaps, and Army standard wing.

The data on these charts are believed to represent the true model values within the following limits (see reference 4):

$\alpha$	$\pm 3^\circ$
$\beta$	$\pm 1\frac{1}{2}^\circ$
Turns for recovery	$\pm \frac{1}{4}$ turn
$\Omega b/2V$	$\pm 3$ percent
$V$	$\pm 2$ percent

For certain isolated spins in which it was difficult to control the model in the tunnel owing to high air speed or to wandering or oscillatory motion, the foregoing limits may be exceeded.

Some of the results originally presented for the basic loading (reference 1) have been revised in the present figures as a result of additional data from check spins.



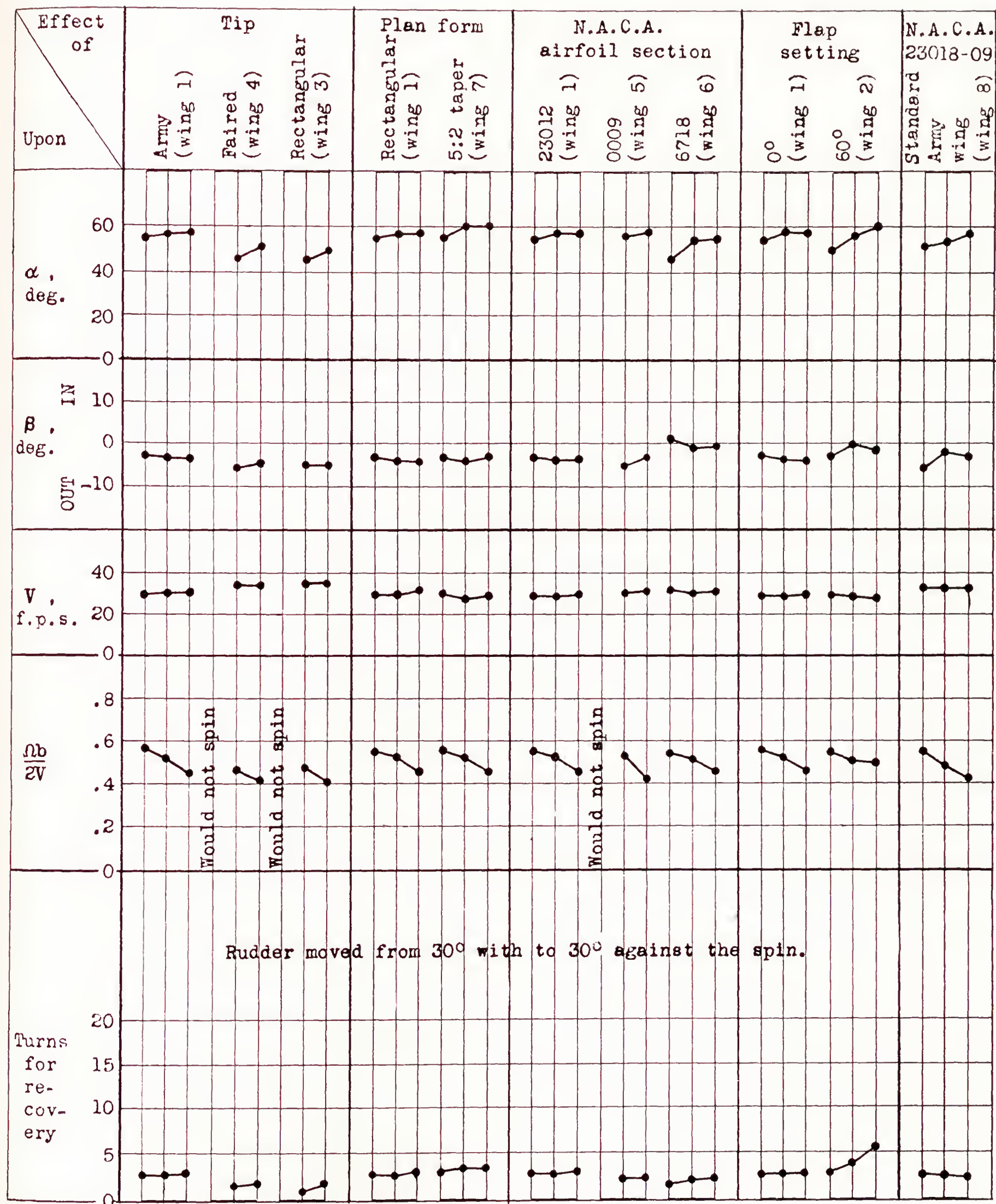


FIGURE 6.—The effect of various wings on the spin characteristics. (Wing has rectangular plan form, Army tips, N. A. C. A. 23012 section, except as noted.) Center-of-gravity location at 15, 25, and 35 percent mean chord, plotted left to right; tail A; rudder 30° with; elevators 0°.



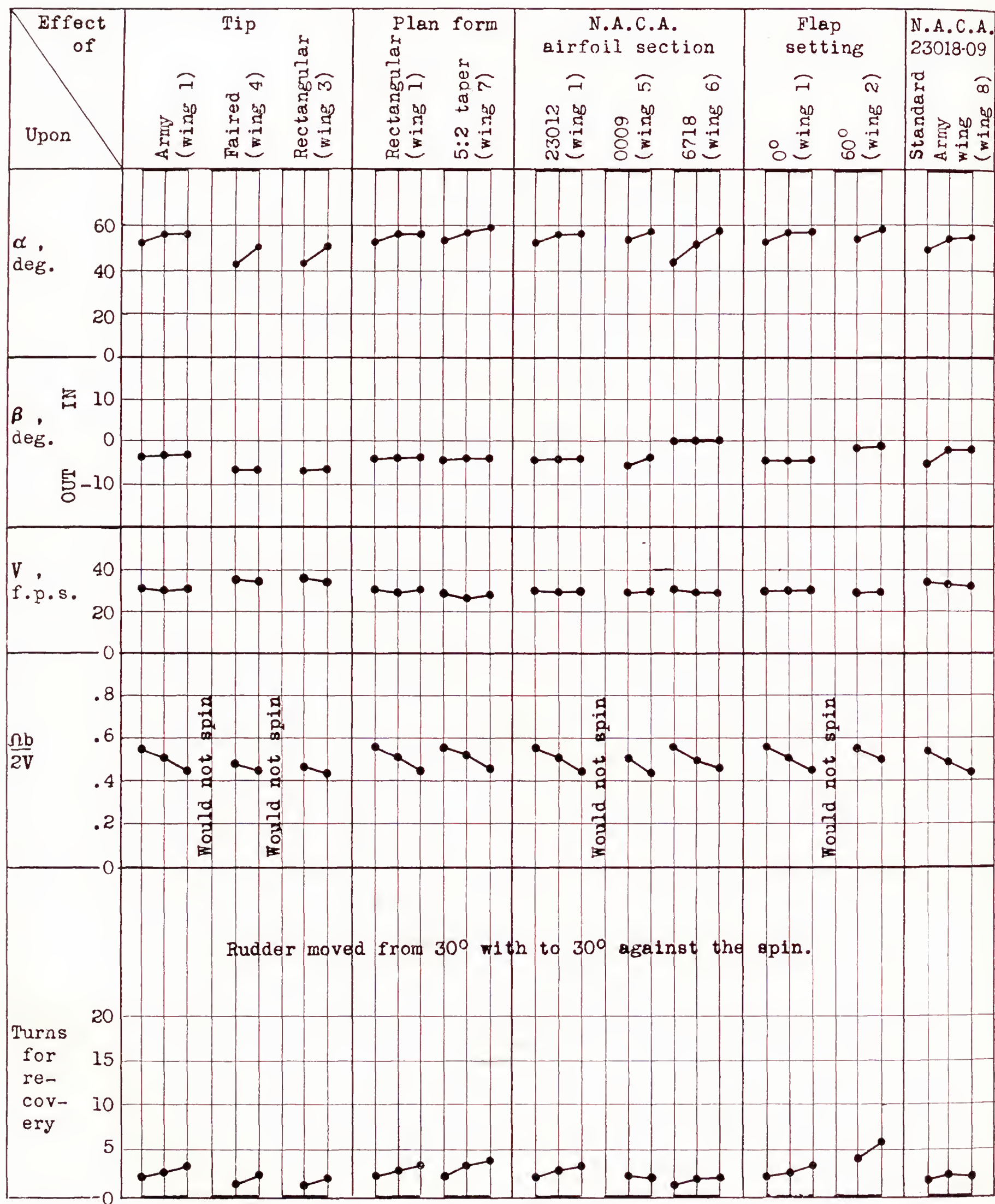


FIGURE 7.—The effect of various wings on the spin characteristics. (Wing has rectangular plan form, Army tips, N. A. C. A. 23012 section, except as noted.) Center-of-gravity location at 15, 25, and 35 percent mean chord, plotted left to right; tail A; rudder 30° with; elevators 20° down.



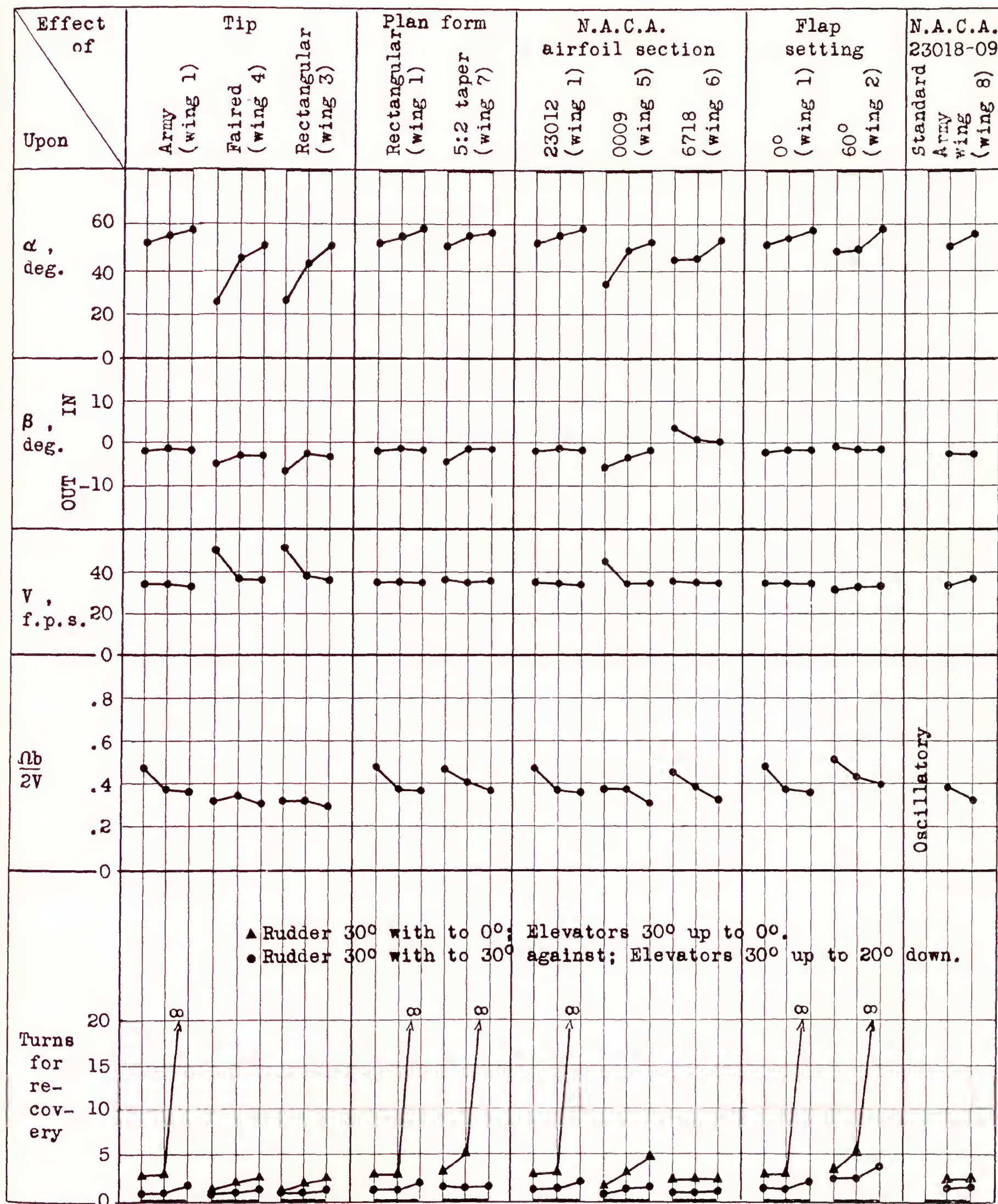


FIGURE 8.—The effect of various wings on the spin characteristics. (Wing has rectangular plan form, Army tips, N. A. C. A. 23012 section, except as noted.) Center-of-gravity location at 15, 25, and 35 percent mean chord, plotted left to right; tail A; rudder 30° with; elevators 30° up.



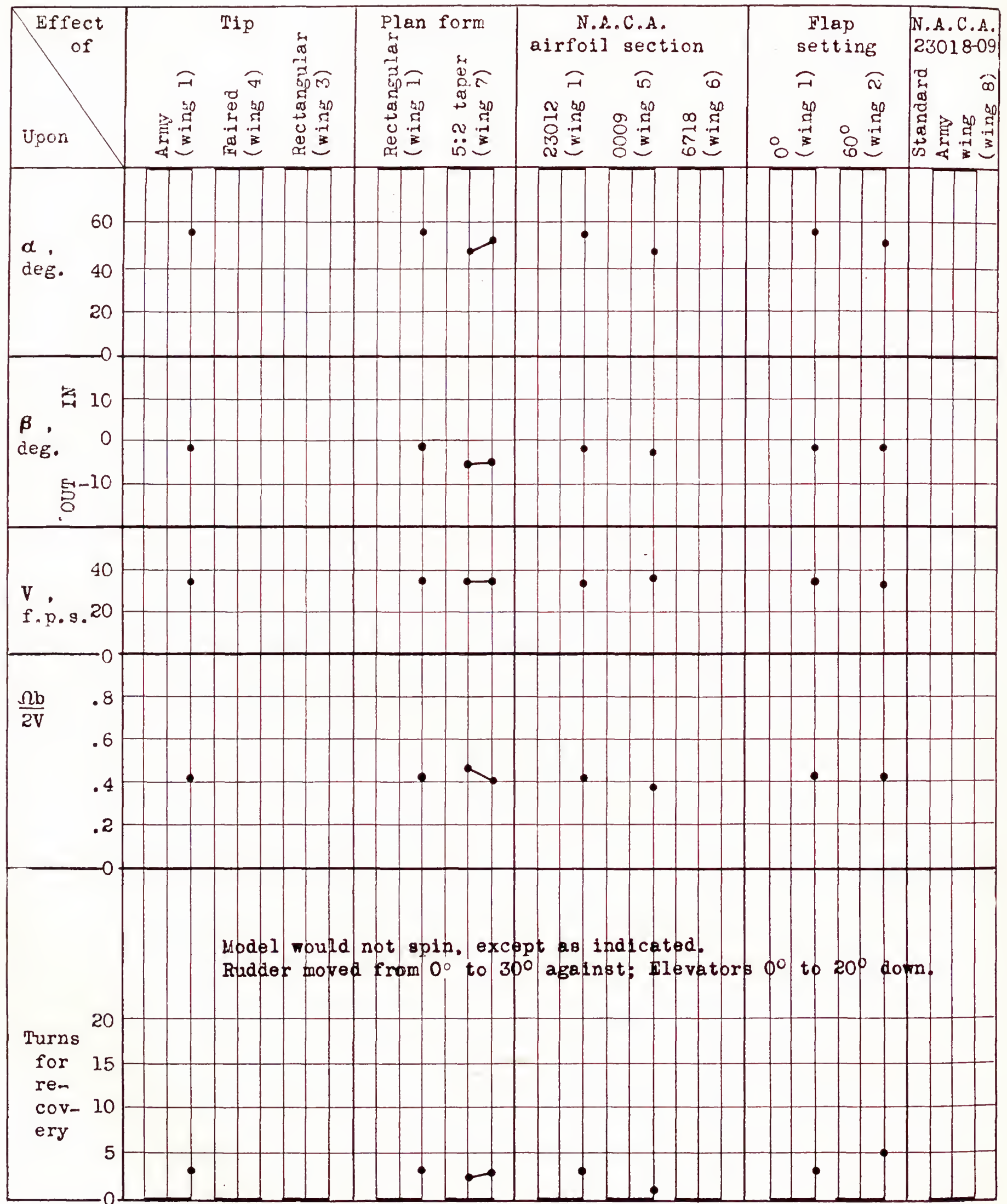


FIGURE 9.—The effect of various wings on the spin characteristics. (Wing has rectangular plan form, Army tips, N. A. C. A. 23012 section, except as noted.) Center-of-gravity location at 15, 25, and 35 percent mean chord, plotted left to right; tail A; rudder 0°; elevators 0°.



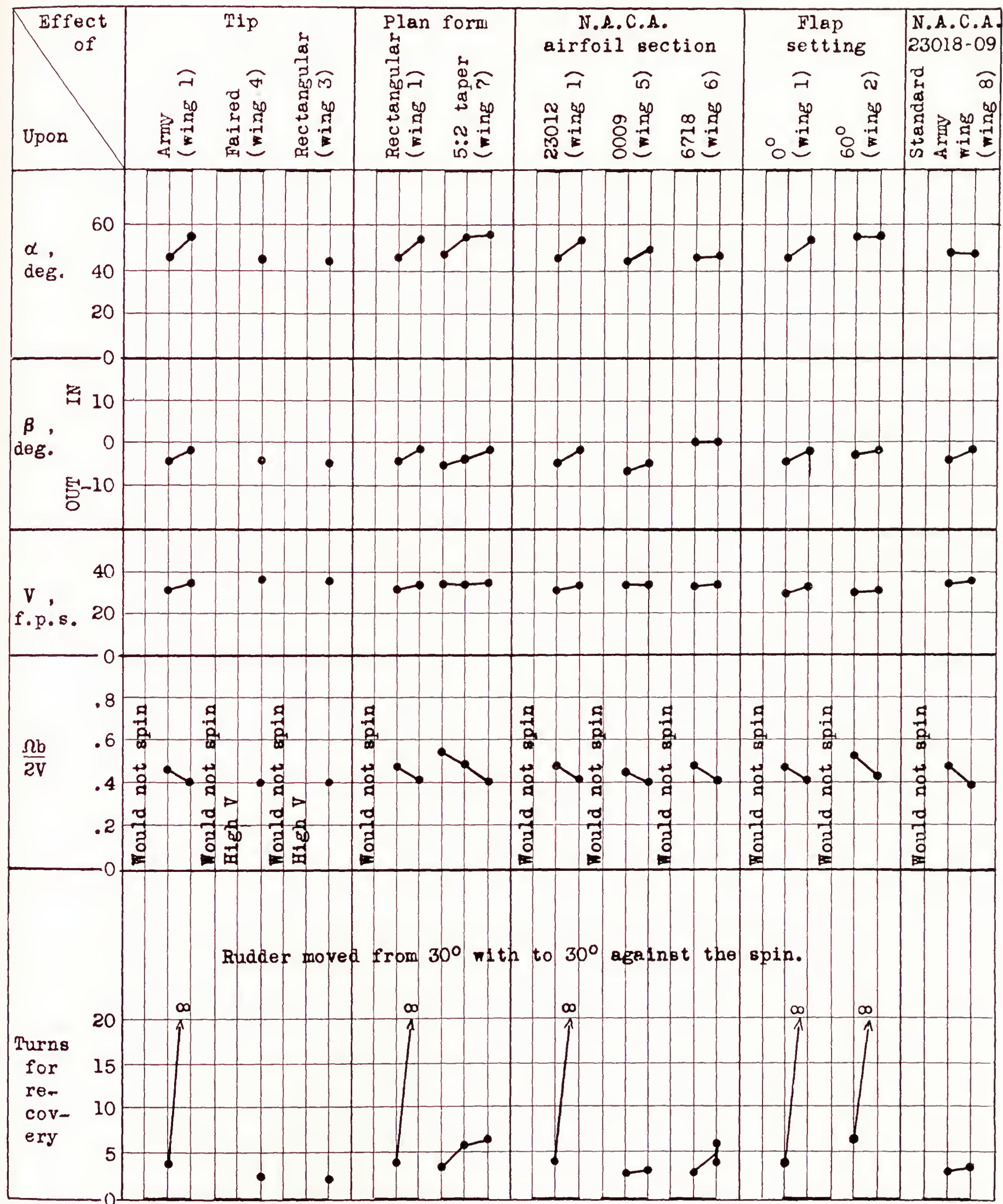


FIGURE 10.—The effect of various wings on the spin characteristics. (Wing has rectangular plan form, Army tips, N. A. C. A. 23012 section, except as noted.) Center-of-gravity location at 15, 25, and 35 percent mean chord, plotted left to right; tail B; rudder 30° with; elevators 0°.



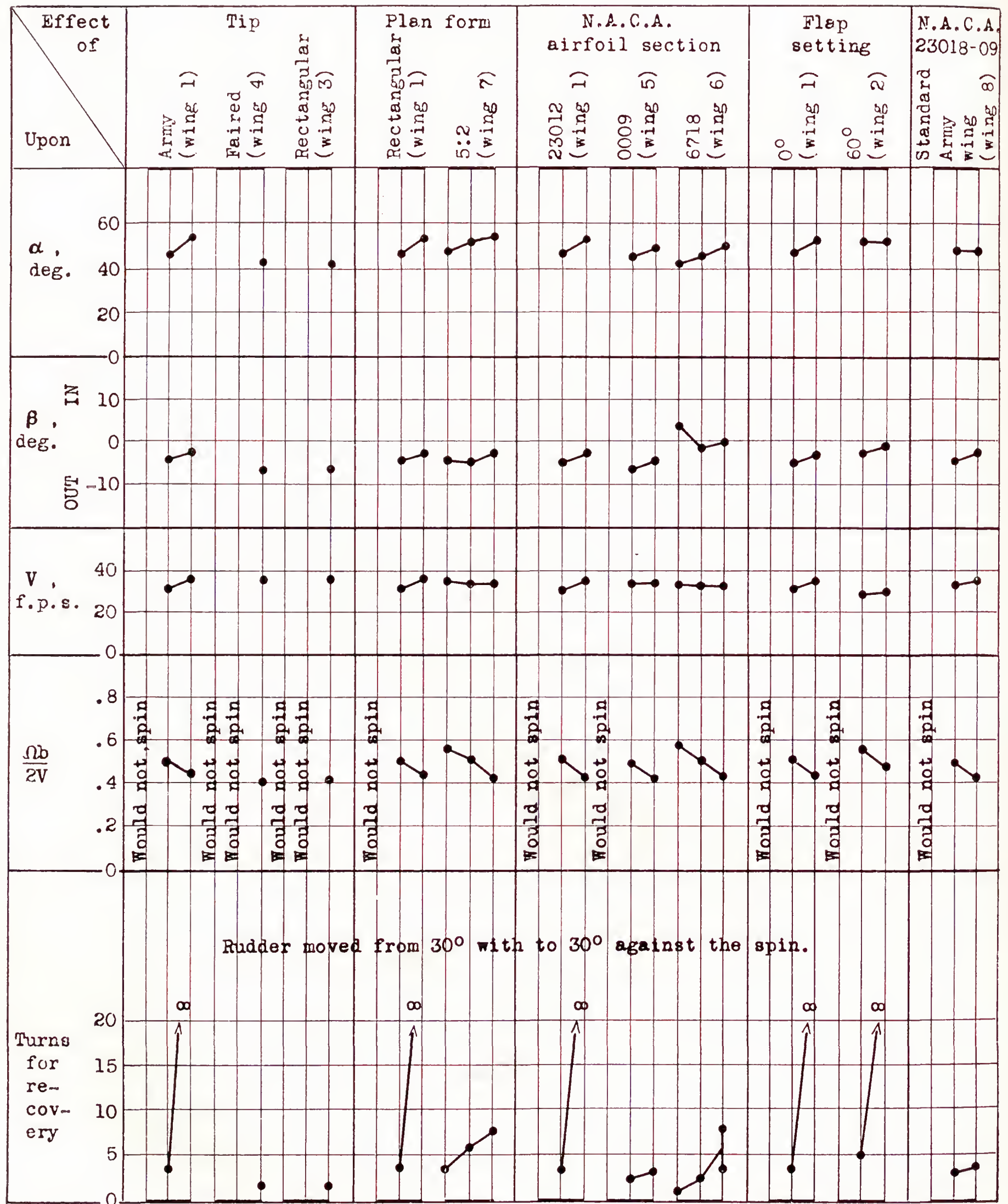


FIGURE 11.—The effect of various wings on the spin characteristics. (Wing has rectangular plan form, Army tips, N. A. C. A. 23012 section, except as noted.) Center-of-gravity location at 15, 25, and 35 percent mean chord, plotted left to right; tail B; rudder 30° with; elevators 20° down.



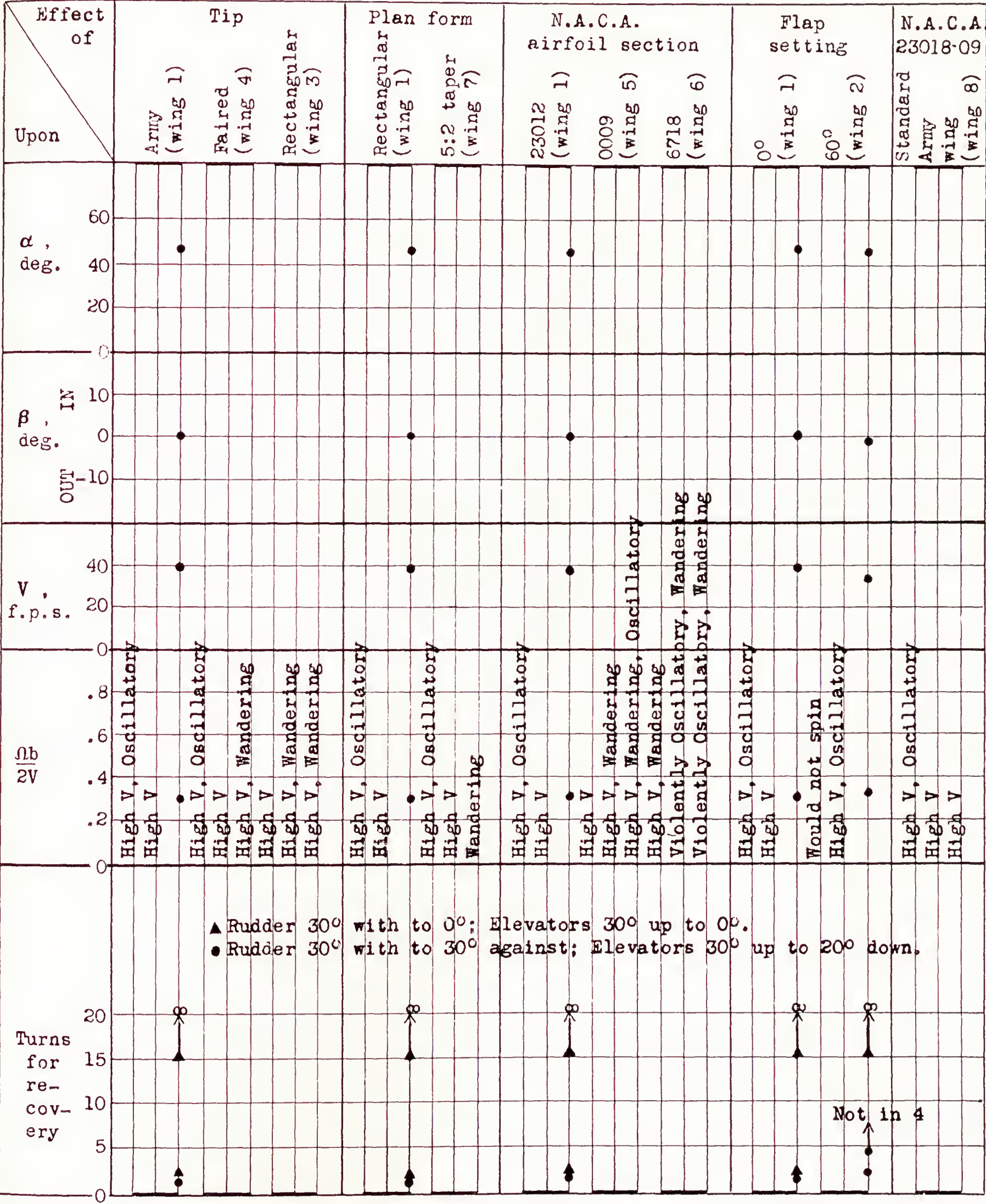


FIGURE 12.—The effect of various wings on the spin characteristics. (Wing has rectangular plan form, Army tips, N. A. C. A. 23012 section, except as noted.) Center-of-gravity location at 15, 25, and 35 percent mean chord, plotted left to right; tail B; rudder 30° with; elevators 30° up.



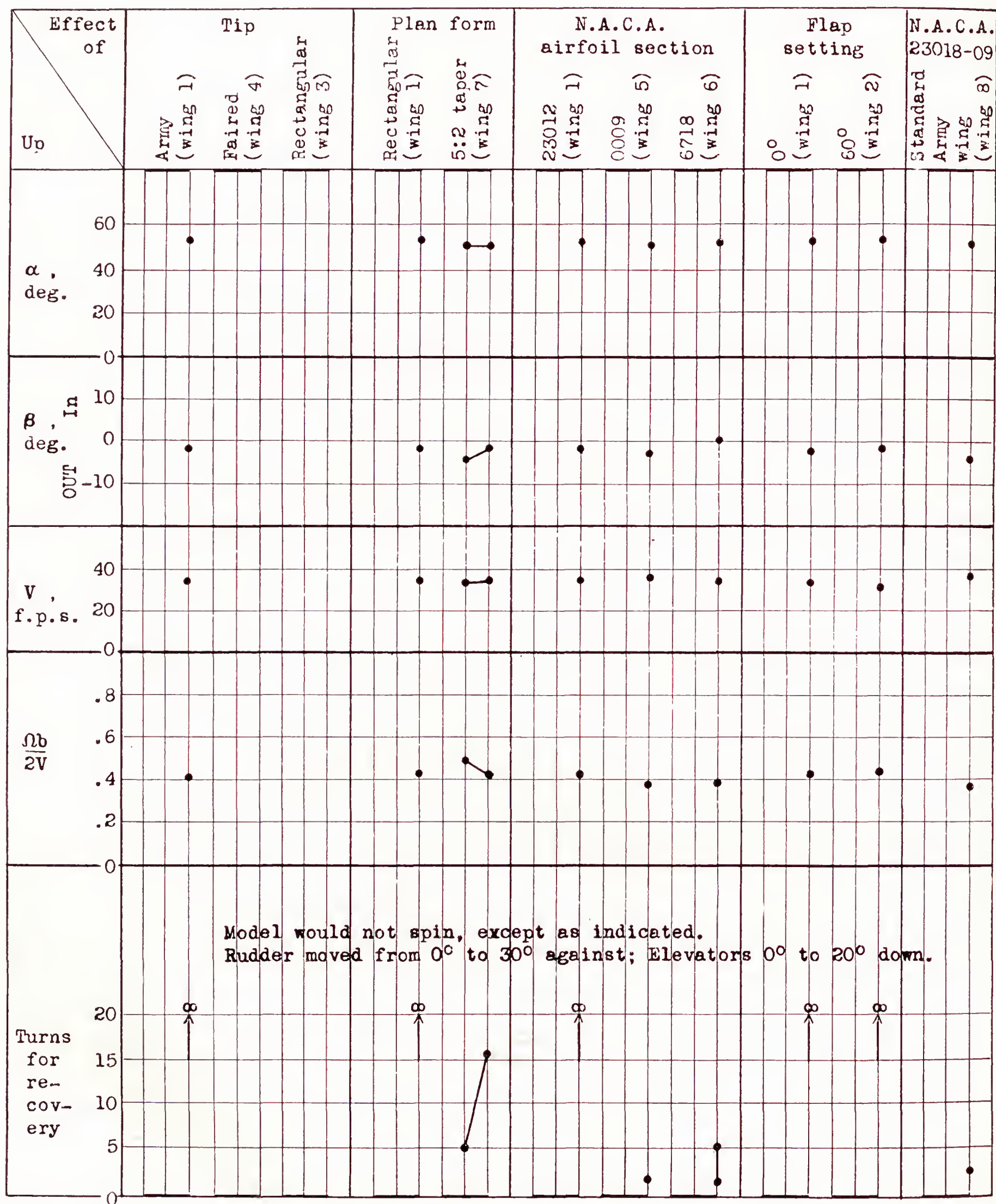


FIGURE 13.—The effect of various wings on the spin characteristics. (Wing has rectangular plan form, Army tips, N. A. C. A. 23012 section, except as noted.) Center-of-gravity location at 15, 25, and 35 percent mean chord, plotted left to right; tail B; rudder 0°; elevators 0°.



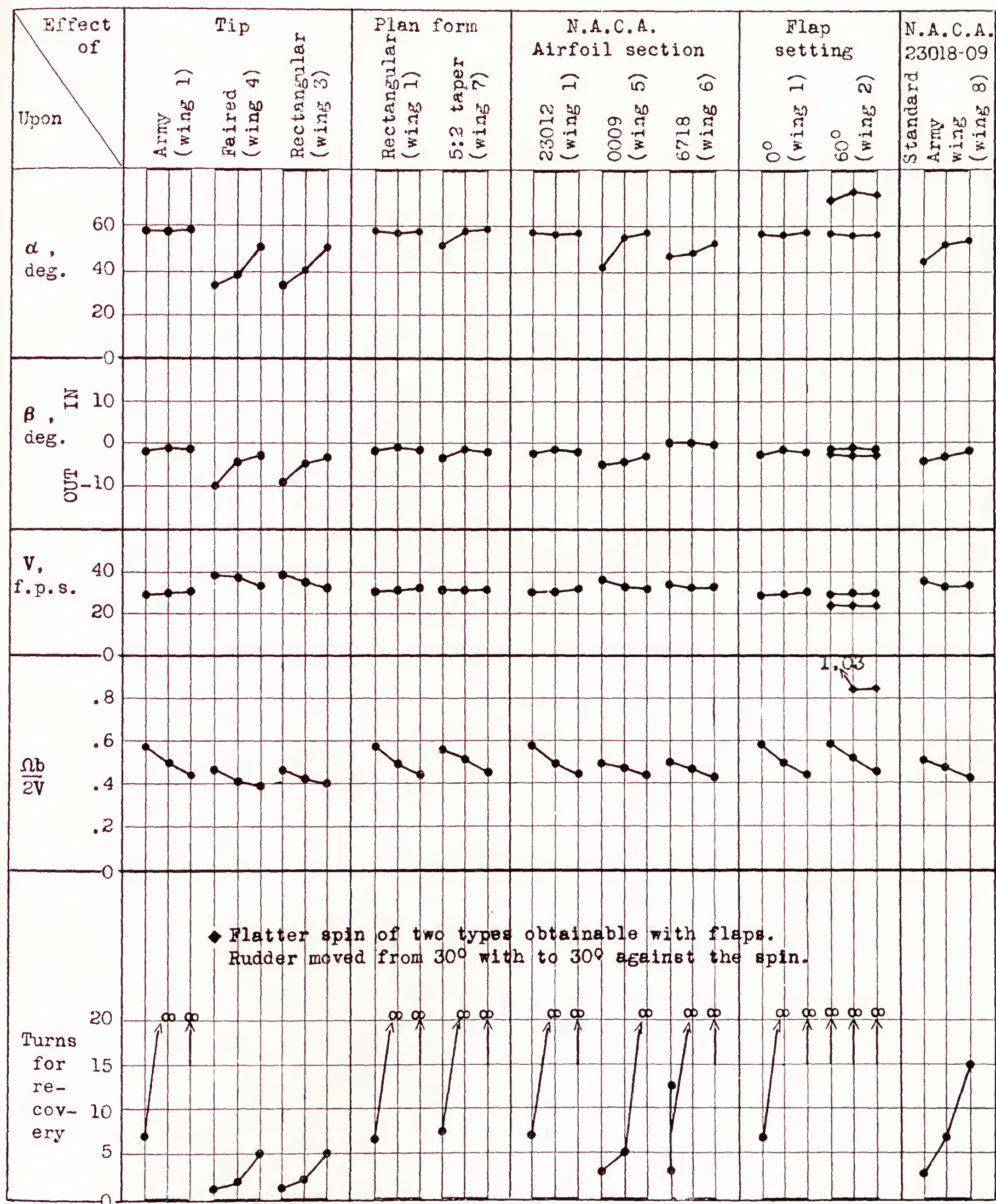


FIGURE 14.—The effect of various wings on the spin characteristics. (Wing has rectangular plan form, Army tips, N. A. C. A. 23012 section, except as noted.) Center-of-gravity location at 15, 25, and 35 percent mean chord, plotted left to right; tail C; rudder 30° with; elevators 0°.



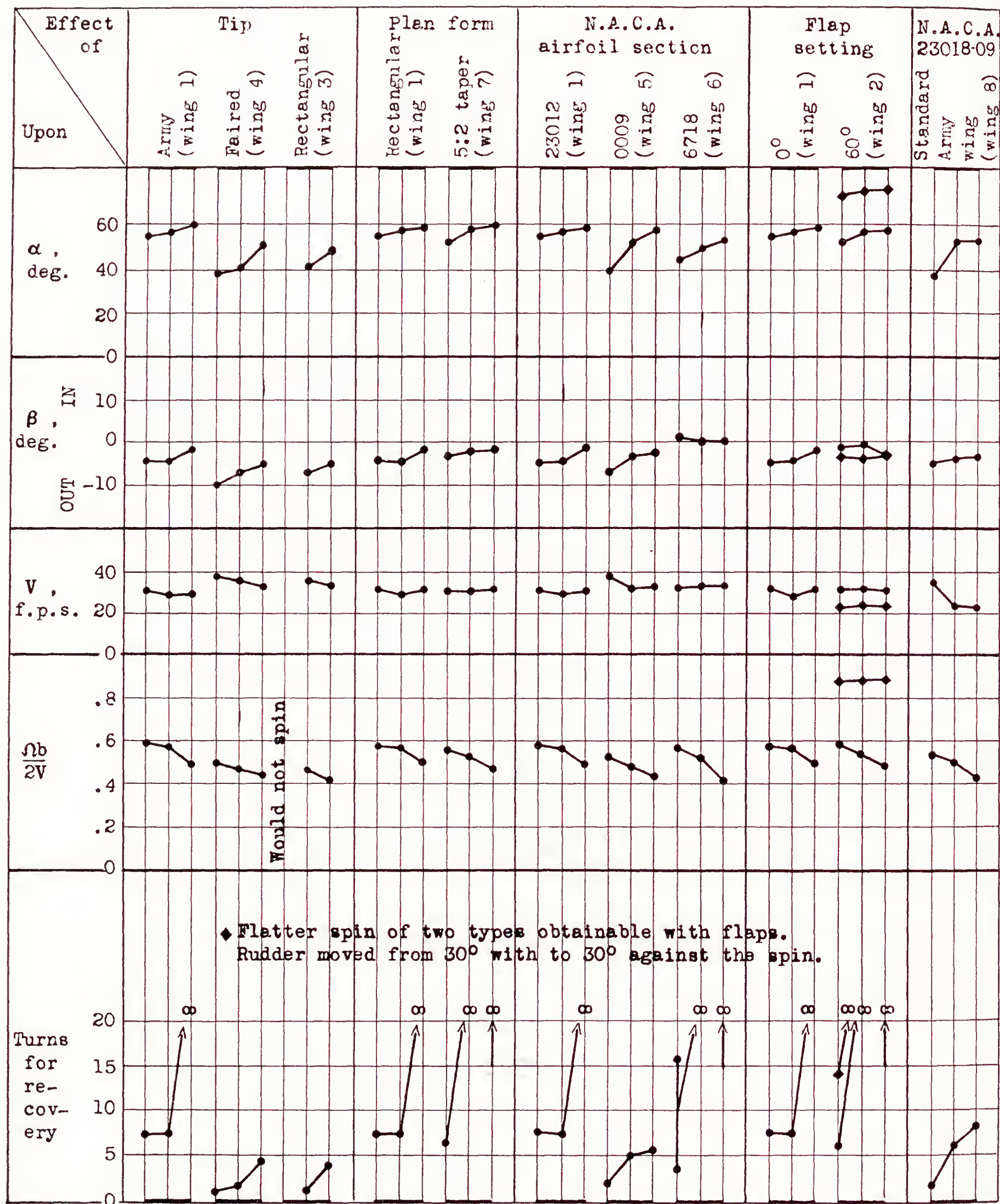


FIGURE 15.—The effect of various wings on the spin characteristics. (Wing has rectangular plan form, Army tips, N. A. C. A. 23012 section, except as noted.)  
Centre-of-gravity location at 15, 25, and 35 percent mean chord, plotted left to right; tail C; rudder 30° with; elevators 20° down.



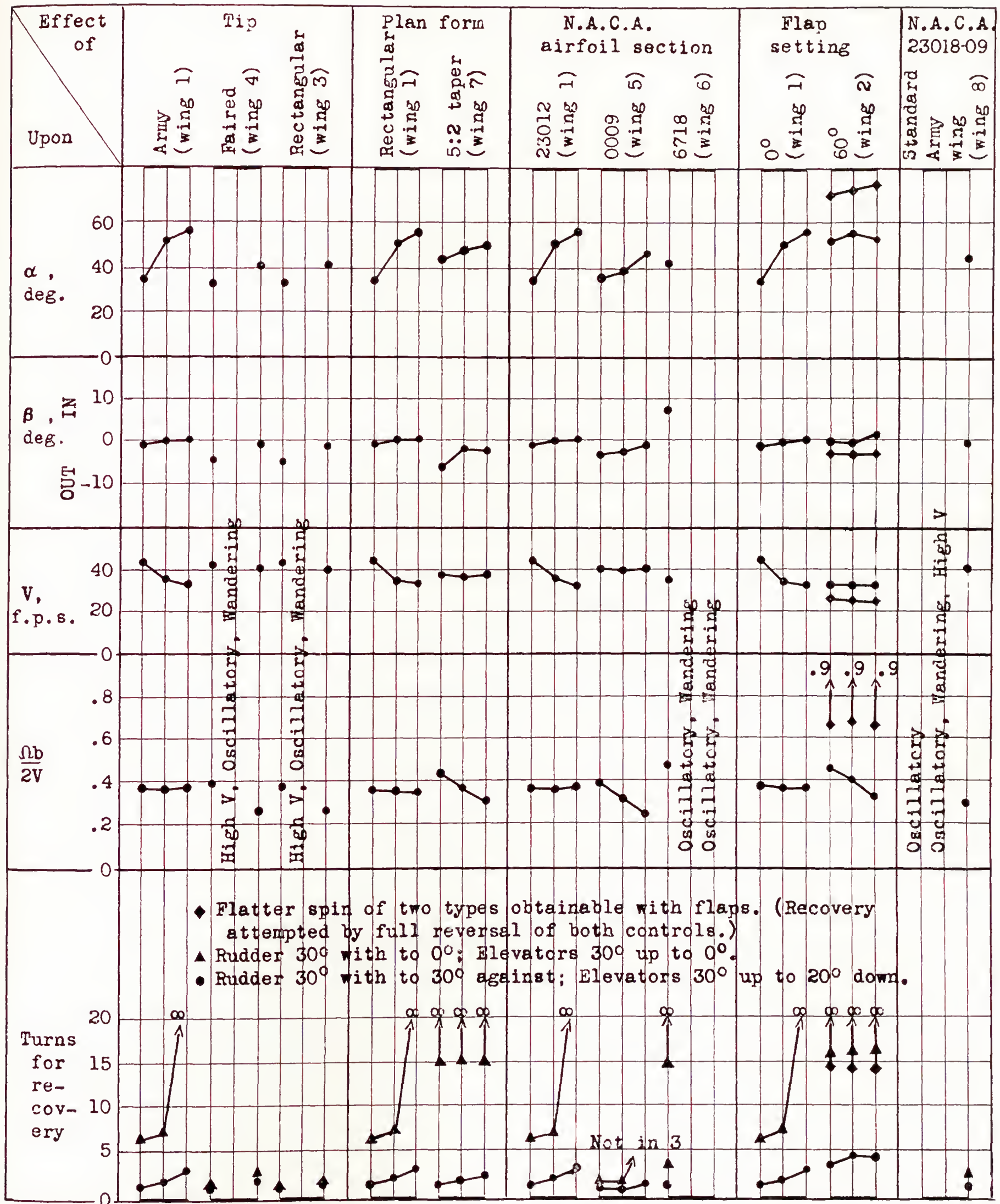


FIGURE 16.—The effect of various wings on the spin characteristics. (Wing has rectangular plan form, Army tips, N. A. C. A. 23012 section, except as noted.) Center-of-gravity location at 15, 25, and 35 percent mean chord, plotted left to right; tail C; rudder 30° with; elevators 30° up.



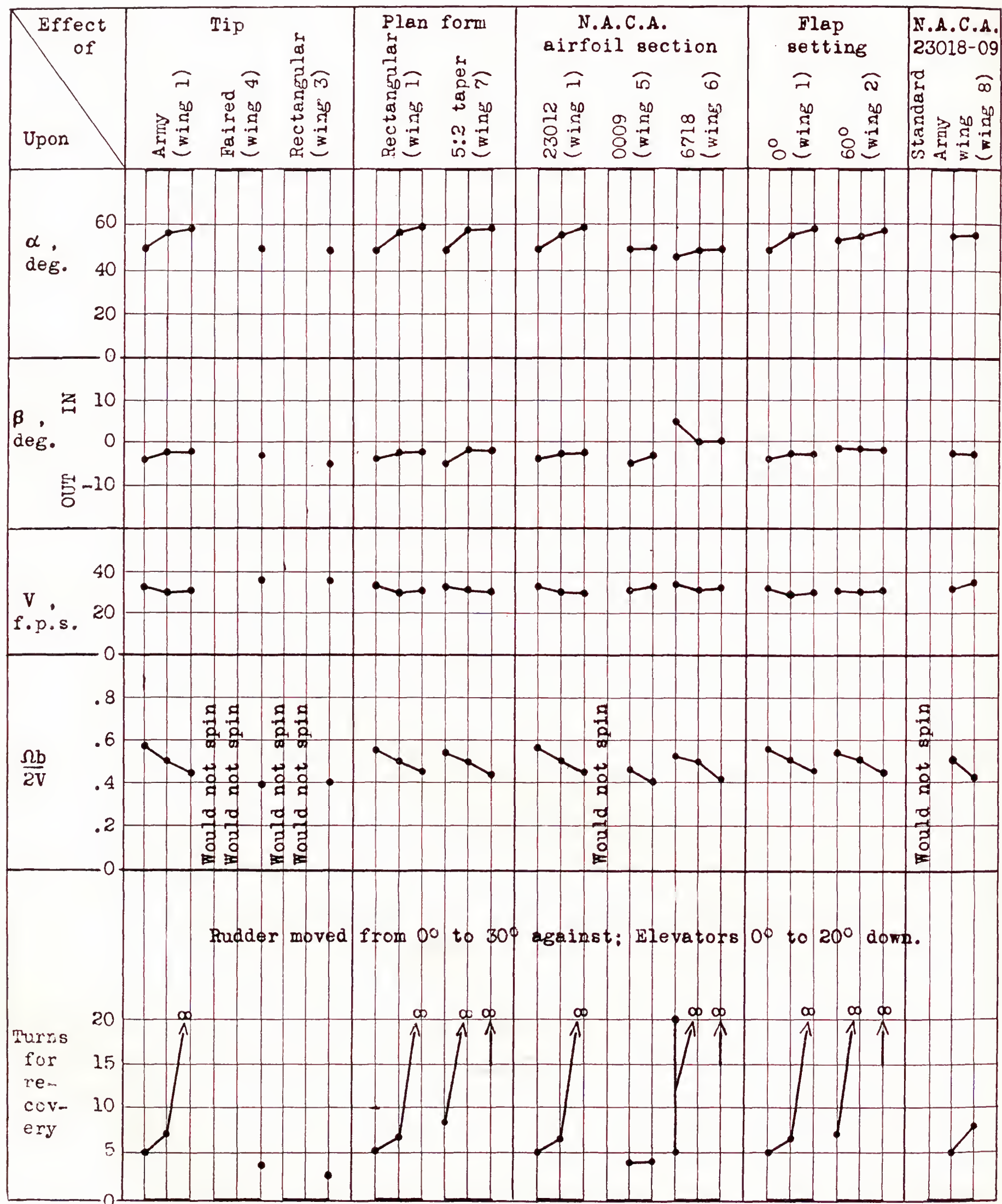


FIGURE 17.—The effect of various wings on the spin characteristics. (Wing has rectangular plan form, Army tips, N. A. C. A. 23012 section, except as noted.) Center-of-gravity location at 15, 25, and 35 percent mean chord, plotted left to right; tail C; rudder 0°; elevators 0°.



## DISCUSSION

As noted in references 4 and 6, variations have been observed between model spin-test results and corresponding full-scale spin-test results for a given airplane, probably because of the difference of the Reynolds Number between the tests.

Some remarks on the spin parameters given in figures 6 to 17 appear desirable before proceeding with the discussion of the results. The number of turns for recovery is, of course, the basic parameter and probably the only one of interest from the viewpoint of the pilot. The other parameters, the angle of attack, the angle of sideslip, the rate of descent, and the coefficient  $\Omega b/2V$ , define the steady spin prior to the recovery attempt. The steady-spin parameters and their correlation with the number of turns for recovery are of considerable importance from research considerations and, consequently, are treated at length in the following discussion.

**Tests with tail A (figs. 6 to 9).**—Figures 6, 7, and 8 give results for rudder with the spin for different elevator settings. With elevators neutral or down, recoveries were attempted by rudder reversal alone. With elevators up, recoveries were attempted by simultaneous reversal of both controls and by simultaneously neutralizing both controls. Figure 9 gives results for spins with controls neutral, recovery being effected by moving the rudder to full against the spin and the elevators to full down.

The figures indicate that moving the center of gravity from the rearward to the forward location tended to improve the recovery characteristics. The effect was most noticeable for rudder reversal with elevators down and for both controls neutralized. The greatest improvements were obtained for the conditions that had previously given the worst recoveries, the effect of wing variables becoming less important as the center of gravity was moved forward.

As regards the steady-spin parameters, moving the center of gravity forward decreased the angle of attack for all wings at all elevator settings. For wings 3, 4, and 5, this effect was very pronounced when the elevators were up. When the elevators were set at neutral or down, the nose-down tendency apparently increased sufficiently with these wings to put the model out of the autorotation range so that no spins could be obtained. The wing with flaps deflected (wing 2) also gave no spin when the elevators were down and the center of gravity was forward. Outward sideslip generally increased as the center of gravity moved forward, particularly when the elevators were up. The wing of N. A. C. A. 6718 section (wing 6), which normally gave the least outward sideslip, tended to spin with inward sideslip for the forward center-of-gravity location. The rate of vertical descent  $V$  generally changed very little with center-of-gravity location. Large decreases in angle of attack, however, such as for wings 3, 4, and 5, are accompanied by a considerably increased rate of

descent. The spin coefficient  $\Omega b/2V$  increased generally for the steeper spins with the center of gravity forward. When the change in center-of-gravity location considerably increased  $V$ , however, the value of  $\Omega b/2V$  did not increase.

The effect of difference in tip shape between the rectangular tips and the rounded Army tips was pronounced, the rectangular tips giving the steepest spins, the most outward sideslip, and the fastest recoveries. The difference in results for the rectangular and the faired tips was slight, as might be expected from the small differences in tip shape. Conditions were most critical when the center of gravity was forward with elevators neutral or down. For these cases, the model passed from the nonspinning to the spinning regime as the wing tips were rounded. As the tips were rounded, the sideslip became less outward. This decrease of outward sideslip is in agreement with results from the spin balance (reference 7), which show that the wing with rounded tips, because of its greater autorotative tendency, will require less outward sideslip to produce the rolling moment needed for spinning equilibrium than does the wing with rectangular tips. It is probable that the change in yawing moment due to the decrease in the outward sideslip accounts for the obtaining of a spin with the rounded tips for control settings for which the model would not spin with the rectangular tips when the center of gravity was forward.

The vertical velocity  $V$  decreased as the tips became rounded. This decrease appears reasonable because the larger angles of attack give larger drag coefficients. As the drag must balance the fixed weight of the model, the vertical velocity must decrease when the drag coefficient increases. The spin coefficient  $\Omega b/2V$  generally increased when the tips were rounded.

Tapering a wing causes a reduction of the chord at the tip and a concentration of the area at the center. On this basis, tapering is somewhat similar to rounding the wing tip and might therefore be expected to have a similar effect. Results on the spin balance indicate such a tendency (reference 7). Results of the present investigation indicate that, as regards recovery characteristics, the wing of 5:2 taper is generally, but not always, slightly worse than the wing with rounded tips.

The tested sections embodied variations in both thickness and camber. These variables had no consistent effect on the recovery or the steady-spin characteristics except for the sideslip angle  $\beta$ . There was a tendency for the sideslip to increase algebraically (become more inward) as the camber (and thickness) increased. This result is in agreement with the results from the spin balance (reference 8). Moving the center of gravity forward increased the outward sideslip for the wing of N. A. C. A. 0009 section, had little effect for the wing of N. A. C. A. 23012 section, and tended to make the sideslip more inward for the wing of N. A. C. A.



6718 section. The wing of N. A. C. A. 23012 section consistently gave the flattest spins and the poorest recoveries. Wings 5 and 6 gave similar recoveries but, with the center of gravity forward, the wing of N. A. C. A. 0009 section (wing 5) would not spin with the elevators neutral or down.

Recoveries with flaps deflected were generally slower than for the plain wing. The effect of center-of-gravity location was much more pronounced when the flaps were deflected. The wing with flaps, like the wing of N. A. C. A. 6718 section, gave less outward sideslip than the basic wing (wing 1). This effect was predicted in reference 9 on the basis of tests made on the spin balance. In this reference, it was also predicted that split flaps would probably have an adverse effect on the recovery characteristics.

The Army standard wing, which is of 2:1 taper, would appear to belong between the rectangular wing with rounded tips and the 5:2 tapered wing according to the plan-form dimensions. The results indicate, however, that the Army standard wing is somewhat better than the rectangular wing with rounded tips (wing 1). The difference probably is a result of the effect of the taper in thickness.

The effect of control setting on the spin characteristics is given by a comparison of figures 6 to 9. Recoveries by rudder reversal with the elevators neutral or down were very similar except when the flaps were deflected and the center of gravity was forward. For these conditions, the model would not spin when the elevators were down. Simultaneous reversal of both controls from elevator-up spins gave the most rapid recoveries. Experience in the spin tunnel indicates that rudder reversal with elevators held up generally will give recoveries similar to those obtained by simultaneous reversal of both controls. Elevator setting had little effect upon the angle of attack of the steady spin. The elevator-up spins, however, were slightly steeper and had higher rates of descent, less outward sideslip, and lower values of  $\Omega b/2V$  than the elevator-down spins. When the center of gravity was forward, several wings that gave spins with the elevators up would not spin when the elevators were set down. For these wings, the effect of center-of-gravity movement was more pronounced than for the remaining wings. With these wings, the pitching moment due to setting the elevators down added to the pitching moment due to moving the center of gravity forward was sufficient to prevent spinning equilibrium.

The results with tail A indicated that, in general, the fastest recoveries were associated with the steepest spins which, in turn, were associated with the highest rates of descent. This indication is in agreement with the general belief that a flat spin (high  $\alpha$ ) will usually lead to a slow recovery. For a given center-of-gravity location, the steepest spins were associated with the lowest values of  $\Omega b/2V$ . When the center of gravity

was moved forward, however, the values of  $\Omega b/2V$  increased, although the recoveries became faster. There seemed to be no consistent relationship between turns for recovery and sideslip angle  $\beta$ .

**Tests with tail B (figs. 10 to 13).**—As previously noted, tail B differs from tail A primarily in that the rudder area was reduced from 5 to 3 percent of the wing area by making the portion of the rudder behind the fuselage the fixed fin area. The results of the tests with the reduced rudder area are given in figures 10 to 13, corresponding to figures 6 to 9 for tail A.

A comparison between the two groups of figures shows that tail B gave consistently steeper spins than tail A for all center-of-gravity locations and elevator settings when the rudder was with the spin, probably because of the increase in the fixed vertical surface. In some instances, spins could not be obtained with tail B for conditions that gave spins with tail A. For all conditions where tail B gave spins, however, the recoveries were slower than with tail A. The comparison shows the importance of unshielded rudder area for effecting satisfactory recoveries from fully developed spins. With the rudder neutral, the two tails generally gave very similar spins, although in two instances spins were obtained with tail B under conditions for which none were obtained with tail A, the differences probably being the result of the slightly greater elevator cut-out of tail A with a corresponding smaller rudder-shielding effect.

The general nature of the effects of center-of-gravity location, wing arrangement, and control setting for tail B was very similar to that for tail A. The magnitudes of the effects were much greater, however, to the extent of being critical as regards the recovery characteristics. With the basic wing, for example, with flaps either up or down and the elevators neutral or down, the model passed from a nonspinning to a nonrecovery regime with tail B as the center of gravity was shifted from the forward to the rearward location. With tail A, the model would spin with these same wing arrangements and elevator settings for all center-of-gravity locations tested, and recoveries were reasonably rapid even for the rearward location. The critical effects of center-of-gravity location, such as those discussed, probably account for some of the large differences between pilots' experiences with certain airplanes.

**Tests with tail C (figs. 14 to 17).**—When tail C (the fin and rudder of tail B atop a shallow fuselage) was installed on the model, the spins when the rudder was with the spin were very similar to those with tail A. The decreased rudder area with the spin apparently tended to balance the effect of decreased fin area. The lack of rudder control, however, generally led to very much poorer recovery characteristics with tail C. Use of improper control manipulation for recovery, such as moving the elevators down before reversing the rudder or not completely reversing the rudder, was especially



detrimental to recovery results, even for the rectangular wing with rectangular tips when the center of gravity was back. The effect of center-of-gravity location became increasingly important with this tail and the effect of the lack of both fin and rudder area below the horizontal surfaces was very apparent. With this tail arrangement, deflecting the flaps tended to give two types of spins, one very flat and one more normal.

The effects of center-of-gravity location, wing arrangement, and control-setting variations gave trends similar to those for tails A and B, but the inferiority of this tail was most apparent. Improper control manipulation gave poor recovery characteristics for all except the best combination of loading and wing arrangements.

With tail C, the poorest arrangement from spinning considerations, the model was especially critical to variations in center-of-gravity location, wing arrangement, or control manipulation; and the trends obtained with tails A and B were even more apparent with tail C. A comparison of the three tail arrangements indicates that, as the design of the tail approaches that of tail A with sufficient fin and rudder area below the horizontal surfaces, variations in center-of-gravity location, wing arrangement, and control manipulation become less important; but that, if the design simulates that of tail C, the need of exercising care in selection of wing design, the deviation from normal center-of-gravity location, and the control movements in a spin become matters of great importance.

### CONCLUSIONS

By analysis of the data presented, the following conclusions may be obtained:

Effects of center-of-gravity location:

1. In nearly every case, moving the center of gravity forward steepens the spin, increases  $\Omega b/2V$ , and improves recovery; whereas moving the center of gravity back flattens the spin, decreases  $\Omega b/2V$ , and retards recovery.

2. Forward movement of the center-of-gravity position tends to produce more outward sideslip, except for the wing of N. A. C. A. 6718 section for which the reverse is true.

Effects of wings:

1. *Tip shape*.—Rectangular and faired tips give the steepest spins and the most rapid recoveries. The Army tip consistently gives flatter spins and slower recoveries.

2. *Plan form*.—The wing of 5:2 taper generally gives slower recoveries than the rectangular wing.

3. *Section*.—The N. A. C. A. 23012 section consistently exhibits the poorest recovery characteristics. The N. A. C. A. 0009 section gives the most outward sideslip; whereas the N. A. C. A. 6718 section gives inward sideslip.

4. *Flaps*.—Flaps generally retard recovery. There is little effect for tails A and B, however, when the center of gravity is forward.

5. *Army standard wing*.—The Army standard wing gives more satisfactory recovery characteristics than the basic rectangular wing.

Effects of control setting:

1. In some instances, recoveries from spins with elevators down are somewhat more rapid than from spins with elevators neutral but, in general, there is little difference.

2. Holding the elevators up results in the steepest spins from which, by reversal of both controls, the most rapid recoveries are obtained.

Effects of tail arrangement:

1. The tail with deepened fuselage, raised stabilizer and elevators, and full-length rudder gives the most satisfactory recoveries, although the tail with deepened fuselage, raised stabilizer and elevators, and short rudder gives the steepest spins.

2. The more nearly conventional tail (short rudder atop a shallow fuselage) gives the slowest recoveries.

3. The importance of the other variables increases as the effectiveness of the tail unit decreases.

Relationships between spin characteristics:

1. For a given tail arrangement, steep spins are usually associated with high rates of descent and rapid recoveries; for a given center-of-gravity location, steep spins are associated with low  $\Omega b/2V$ .

2. For any center-of-gravity position, there is no consistent relationship between the sideslip of the steady spin and the turns required for recovery.

LANGLEY MEMORIAL AERONAUTICAL LABORATORY,  
NATIONAL ADVISORY COMMITTEE FOR AERONAUTICS,  
LANGLEY FIELD, VA., March 28, 1939.

### REFERENCES

1. Seidman, Oscar, and Neihouse, A. I.: Free-Spinning Wind-Tunnel Tests of a Low-Wing Monoplane with Systematic Changes in Wings and Tails. I. Basic Loading Conditions. T. N. No. 608, N. A. C. A., 1937.
2. Seidman, Oscar, and Neihouse, A. I.: Free-Spinning Wind-Tunnel Tests of a Low-Wing Monoplane with Systematic Changes in Wings and Tails. II. Mass Distributed Along the Fuselage. T. N. No. 630, N. A. C. A., 1937.
3. Seidman, Oscar, and Neihouse, A. I.: Free-Spinning Wind-Tunnel Tests of a Low-Wing Monoplane with Systematic Changes in Wings and Tails. III. Mass Distributed Along the Wings. T. N. No. 664, N. A. C. A., 1938.
4. Zimmerman, C. H.: Preliminary Tests in the N. A. C. A. Free-Spinning Wind Tunnel. T. R. No. 557, N. A. C. A., 1936.
5. Shortal, Joseph A.: Effect of Tip Shape and Dihedral on Lateral-Stability Characteristics. T. R. No. 548, N. A. C. A., 1935.



- |   |   |
|---|---|
| <p>6. Bamber, M. J., and House, R. O.: Spinning Characteristics of the XN2Y-1 Airplane Obtained from the Spinning Balance and Compared with Results from the Spinning Tunnel and from Flight Tests. T. R. No. 607, N. A. C. A., 1937.</p> <p>7. Bamber, M. J., and House, R. O.: Spinning Characteristics of Wings. III—A Rectangular and a Tapered Clark Y Monoplane Wing with Rounded Tips. T. N. No. 612, N. A. C. A., 1937.</p> | <p>8. Bamber, M. J., and House, R. O.: Spinning Characteristics of Wings. V—N. A. C. A. 0009, 23018, and 6718 Monoplane Wings. T. N. No. 633, N. A. C. A., 1938.</p> <p>9. Bamber, M. J.: Aerodynamic Effects of a Split Flap on the Spinning Characteristics of a Monoplane Model. T. N. No. 515, N. A. C. A., 1934.</p> |
|---|---|



## REPORT No. 673

### EXPERIMENTAL VERIFICATION OF THE THEORY OF OSCILLATING AIRFOILS

By ABE SILVERSTEIN and UPSHUR T. JOYNER

#### SUMMARY

*Measurements have been made of the lift on an airfoil in pitching oscillation with a continuous-recording, instantaneous-force balance. The experimental values for the phase difference between the angle of attack and the lift are shown to be in close agreement with the theory.*

#### INTRODUCTION

The theory for the lift of infinite-span airfoils oscillating in pitch with small amplitude in a uniform stream of perfect fluid has been exhaustively studied and now provides a basis for the aerodynamic analysis of the flutter problem. Wagner's theory (reference 1) for calculating the lift on an airfoil in nonuniform motion has been followed by those of Küssner (reference 2), Glauert (reference 3), and Theodorsen (reference 4); Garrick has indicated (reference 5) that the several theories are in agreement. Jones has given certain approximations (reference 6) to account for the effect of finite span.

At the suggestion of Theodorsen, tests have been made to obtain experimental data for a direct comparison of the measured lift on an oscillating airfoil with that predicted by the theory. The accuracy of the theory has been essentially substantiated in a less direct manner by the agreement of experimental and theoretically predicted flutter phenomena.

In a comparison of an oscillating airfoil with one in uniform motion, the theory indicates that the principal effect of the oscillation is to change the angle of attack at which a given lift occurs; for example, zero lift on an oscillating symmetrical airfoil does not occur at zero angle of attack. The phase difference between the lift and the angle of attack depends on the location of the axis along the airfoil chord and on a nondimensional parameter describing the wave length of the oscillating vortex sheet in the airfoil wake. For an infinite frequency of oscillation and a forward location of the axis, the lift would lead the angular displacement by  $180^\circ$ . At finite frequencies, the countervorticity of the oscil-

lating vortex sheet produces, in general, a lag that opposes the inertia effect causing the leading force. At low frequencies, the lag predominates; and, at zero frequency (steady motion), the lag again disappears.

It was planned to verify the theory by measurements of the phase difference between the lift and the angle of attack for an airfoil in rotational oscillation at various frequencies and air speeds. For these measurements, an instantaneous-force balance was designed with which the lift and the angle of attack of an oscillating airfoil could be continuously recorded. The measurements were made in a 2- by 3-foot tunnel on a symmetrical airfoil of about 5-inch chord and 18 percent thickness. The axis of rotation was located at the quarter-chord point of the airfoil. Measurements were taken for values of frequencies and air speeds that covered the useful flutter range.

#### SYMBOLS

- $\alpha$ , angle of attack ( $\alpha = \alpha_0 \sin pt$ ).
- $\alpha_0$ , amplitude of oscillation.
- $b$ , half chord of airfoil.
- $v$ , air speed at infinity.
- $p$ ,  $2\pi$  times the frequency of oscillations.
- $k$ , reduced frequency ( $pb/v$ ); wave length in vortex sheet is  $2\pi b/k$ .
- $a$ , coordinate of axis of oscillation. (See reference 4.)
- $L$ , lift force on airfoil.
- $t$ , time.
- $F$  and  $G$ , circulation functions. (See reference 4.)
- $\delta$ , phase difference between angle of attack and lift for oscillating airfoil. Positive values indicate a leading force.
- $\theta$ , phase difference due to natural frequency of recording instrument.
- $n$ , damping constant of airfoil and balance.
- $r$ ,  $2\pi$  times natural frequency of vibration of airfoil and balance.
- $A$ , aspect ratio.



## PHASE RELATIONS FOR OSCILLATING AIRFOILS

Following the method of Theodorsen (reference 4), the lift on an airfoil oscillating in pitch, in a uniform stream of perfect fluid, with one degree of freedom about an axis parallel to the span is given (reference 5) as

$$L = \rho b^2 (v \pi \alpha_0 p \cos pt + \pi b a \alpha_0 p^2 \sin pt) \\ + 2\pi \rho v b F \left[ v \alpha_0 \sin pt + b \left( \frac{1}{2} - a \right) \alpha_0 p \cos pt \right] \\ + 2\pi \rho v b G \left[ v \alpha_0 \cos pt - b \left( \frac{1}{2} - a \right) \alpha_0 p \sin pt \right] \quad (1)$$

Regrouping terms and substituting  $k = pb/v$  and  $a = -\frac{1}{2}$  (axis at quarter-chord line), the expression becomes

$$L = \pi \rho b \alpha_0 v^2 (k + 2kF + 2G) \cos pt \\ + \pi \rho b \alpha_0 v^2 \left( -\frac{1}{2}k^2 + 2F - 2kG \right) \sin pt \quad (2)$$

or

$$L = A_0 \sin pt + B_0 \cos pt \quad (3)$$

in which

$$\left. \begin{aligned} A_0 &= \pi \rho b \alpha_0 v^2 \left( -\frac{1}{2}k^2 + 2F - 2kG \right) \\ B_0 &= \pi \rho b \alpha_0 v^2 (k + 2kF + 2G) \end{aligned} \right\} \quad (4)$$

Expression (3) may be readily rewritten as

$$L = C_0 \sin (pt + \delta) \quad (5)$$

in which

$$\delta = \tan^{-1} (B_0/A_0) \quad (6)$$

and

$$C_0 = \sqrt{A_0^2 + B_0^2} \quad (7)$$

The angle  $\delta$  is the phase difference due to the oscillation, and  $C_0$  is a measure of the slope of the lift curve for the oscillating wing. It will be noted from equations (4) and (6) that the value of the phase angle  $\delta$  is a function of  $k$ ,  $F$ , and  $G$ . The term  $k$  is a fundamental parameter that links together the frequency of the wing oscillation and the air speed. It may be noted that  $2\pi/k$  is the distance between successive waves in the vortex sheet in terms of the half-chord length  $b$  as a reference length. The functions  $F$  and  $G$  determine the circulation so as to satisfy the Kutta condition for the oscillating airfoil, and their values are given as functions of  $1/k$  for the case of an infinite-span airfoil in reference 4. For finite aspect ratio, reference 6 gives certain approximate corrections employing "effective" values of  $F$  and  $G$ .

## APPARATUS AND TEST METHOD

The tests were conducted in the  $\frac{1}{15}$ -scale model of the N. A. C. A. full-scale wind tunnel, which is described in reference 7. The test section was modified to a 2- by 3-foot rectangle with sides but without top or bottom. The side walls served as end plates for the airfoil that spanned the 3-foot width of the jet. Surveys across the tunnel air stream showed variations of  $\pm 2$  percent in the dynamic pressure and  $\pm 0.6^\circ$  in the

air-stream direction, the effects of which were not considered important enough to warrant correction.

A diagram and a photograph of the apparatus used are shown in figures 1 and 2, respectively. The airfoil F (fig. 1) was an 18-percent-thick symmetrical section with a chord of  $5\frac{3}{16}$  inches and a span of  $36\frac{3}{4}$  inches. It was of hollow construction with 0.016-inch sheet-aluminum covering and weighed only 0.66 pound. The counterweight I, the end plates C, the mounting shafts, and the self-aligning ball bearings B brought the total weight of the oscillating assembly up to 1.52 pounds. The airfoil projected through the sides of the test section L, and separate end plates C were attached that rotated with the airfoil to prevent air leakage through the walls due to the airfoil pressures. This arrangement was used to achieve an effective aspect ratio approaching that for an infinite-span airfoil. The axis of oscillation, i. e., the axis of the mounting shafts, was located at the quarter-chord point of the airfoil.

The instantaneous force balance was designed to measure the force on one end of the airfoil by measuring the deflection of a stiff spring P to which the airfoil was attached. The attachment was made by means of a self-aligning ball bearing, which provided freedom for the wing to rotate about its axis and for the spring to deflect without restraint. In order to record the deflection of the spring, two styluses were arranged to rotate the mirrors J and N and thereby displace light beams that were focused on a sensitized film. The spring deflections in both the lift and the drag directions were recorded by mirrors J and N. (This paper is confined to a discussion of the lift forces only.) In order to obtain a continuous record, the recording film was attached to a circular drum rotated by a synchronous motor H at a constant film speed of 39 inches per second. The balance was calibrated by means of loads applied at the center of the airfoil.

The design of the spring P was dictated by the consideration that accurate measurements of the phase difference by means of a spring require the natural frequency of the vibrating system to be considerably higher than the impressed frequency. The angle of lag  $\theta$  of the recorded force behind the impressed force in terms of the natural frequency of the vibrating system  $r$  is given (reference 8) as

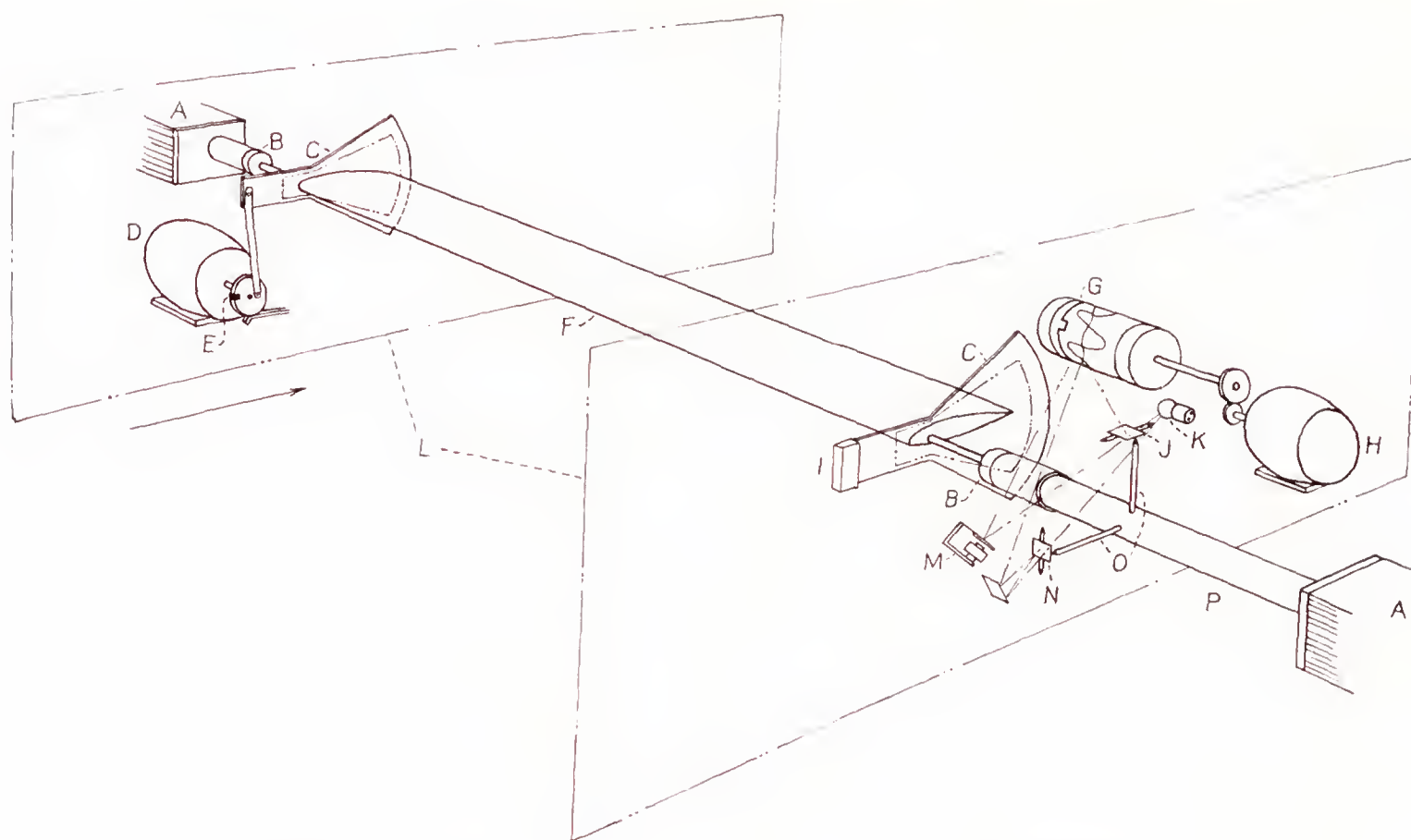
$$\theta = \tan^{-1} \frac{2pn}{r^2 - p^2}$$

in which  $n$ , the damping coefficient, is obtained from a measurement of the decrease in amplitude of successive vibrations. That is,

$$A_2 = A_1 e^{-nt}$$

in which  $A_1$  and  $A_2$  are the amplitudes of successive vibrations occurring in the period  $t$ . The values of the constants  $n$  and  $r/2\pi$  for the wing and the balance are





- |                                  |                               |
|----------------------------------|-------------------------------|
| A, supports.                     | I, counterweight.             |
| B, self-aligning ball bearings   | J, lift mirror.               |
| C, end plates on airfoil.        | K, light.                     |
| D, direct-current driving motor. | L, sides of wind tunnel.      |
| E, timing-unit contacts.         | M, timing unit.               |
| F, airfoil.                      | N, drag mirror.               |
| G, film drum and record.         | O, stylus.                    |
| H, synchronous-motor film drive. | P, tubular cantilever spring. |

FIGURE 1.—Airfoil and continuously recording balance used in the oscillating-airfoil tests.

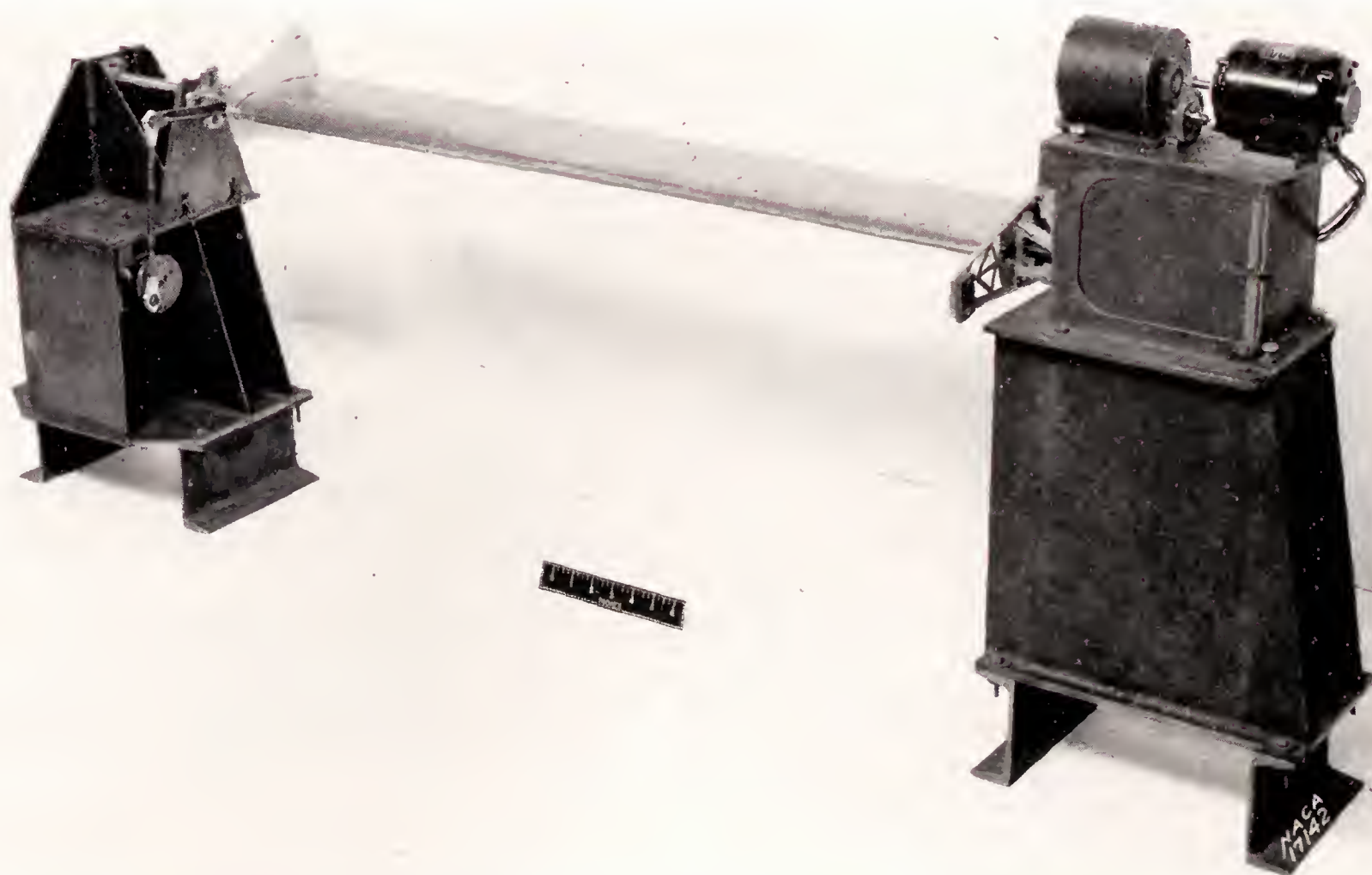


FIGURE 2.—Airfoil and balance installation used to measure the forces on an oscillating airfoil.



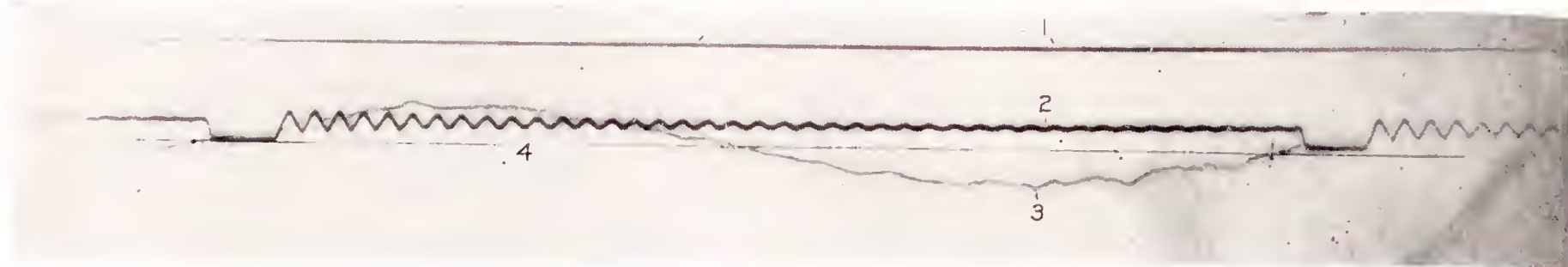


FIGURE 3.—Typical photographic record obtained with oscillating-airfoil balance.

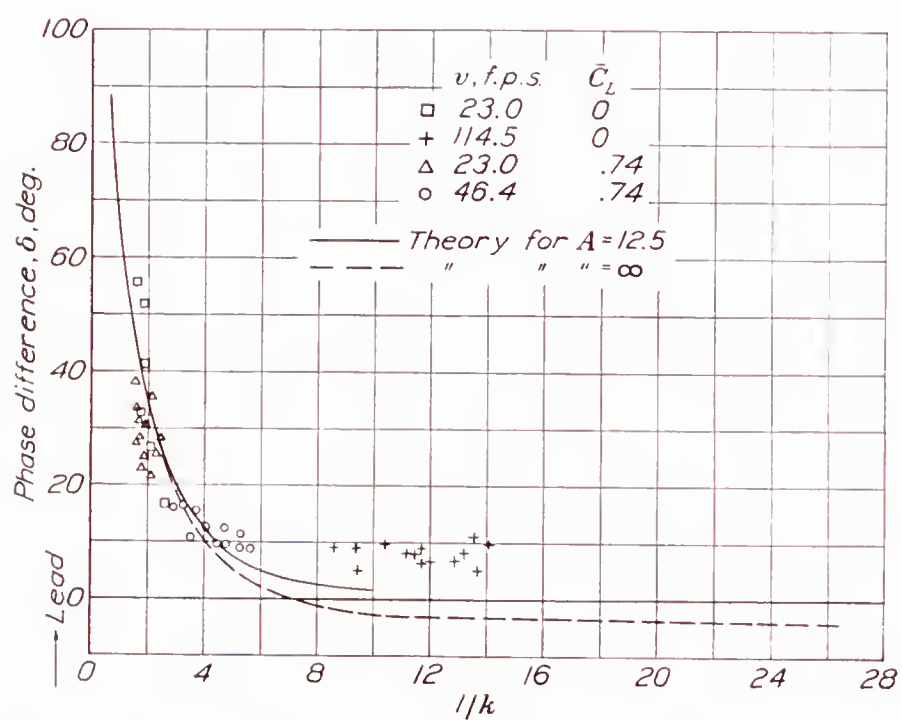
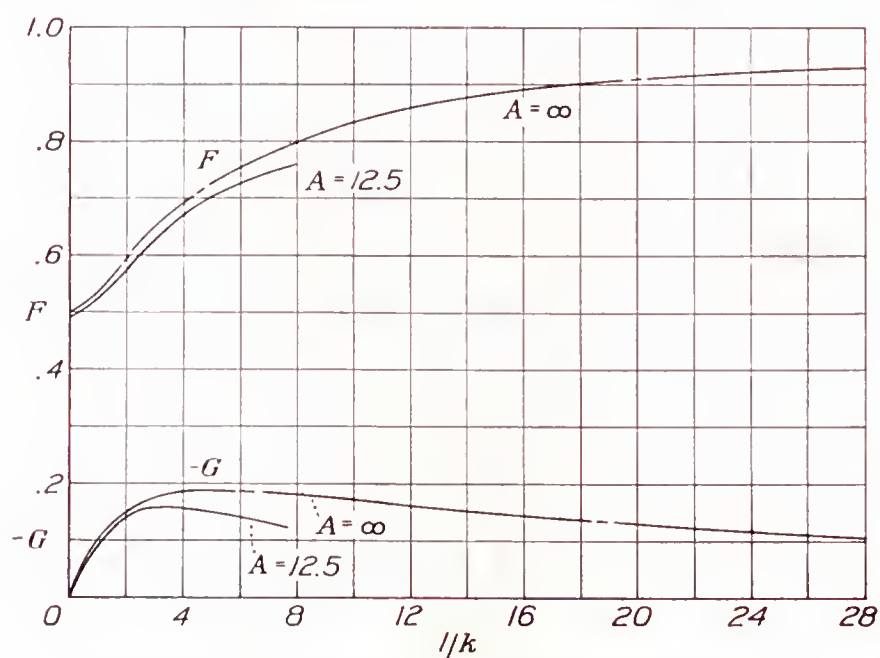
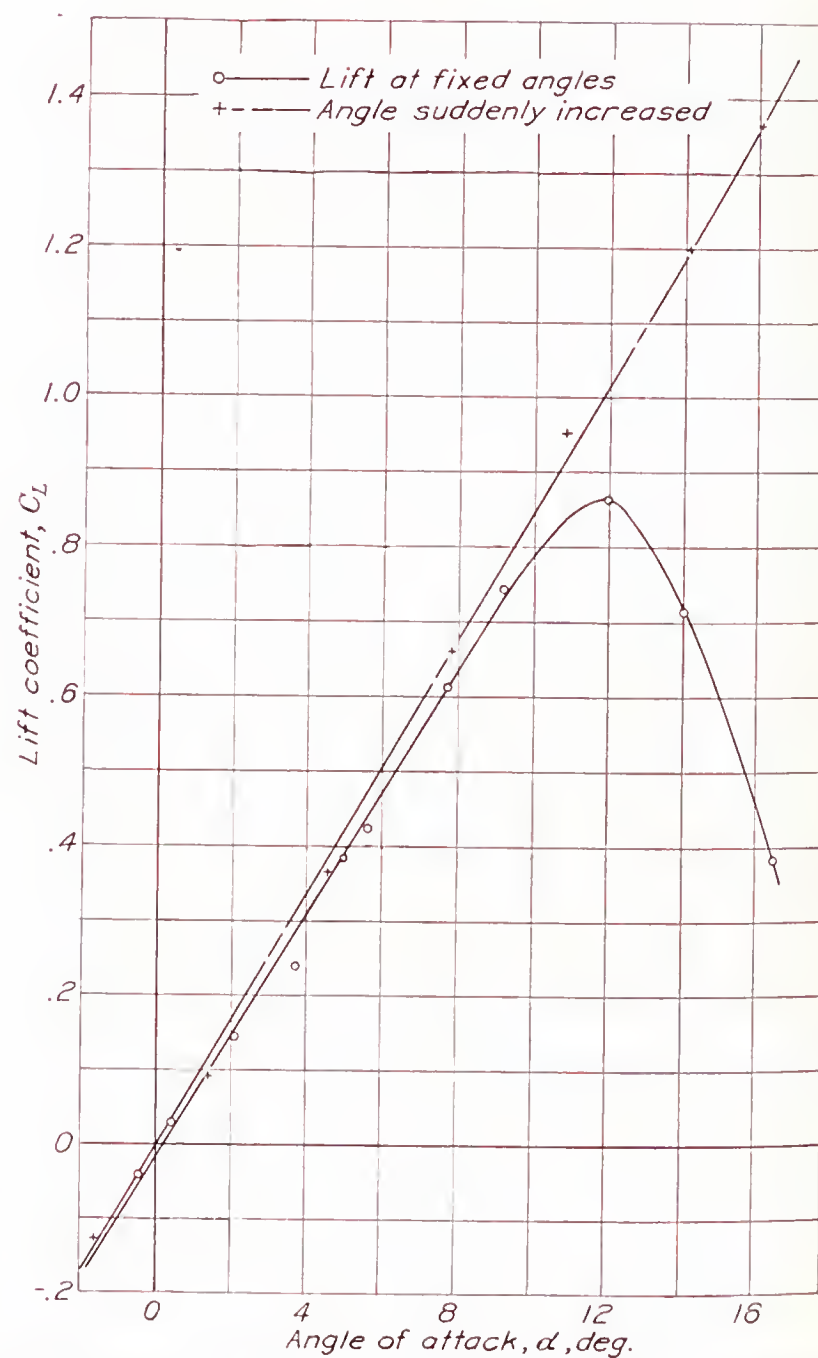
FIGURE 4.—Comparison of experimental and theoretical values of the phase difference  $\delta$  for various values of the parameter  $1/k$ .FIGURE 6.—Theoretical values of circulation functions  $F$  and  $G$ .

FIGURE 5.—Lift curves for the airfoil tested in steady motion at fixed angles and for a test in which the angle of attack was suddenly increased.



14.8 and 53.5, respectively. The value of  $r/2\pi$  for the spring P is 280 cycles per second. Since all the tests with the balance were made at oscillation frequencies lower than 17 cycles per second, the maximum phase error was  $1.8^\circ$ , which is of the same magnitude as the experimental errors.

It was necessary to balance dynamically the oscillating mass about the axis of rotation. For this purpose, a weight I was placed ahead of the axis of rotation to provide static and dynamic balance within the accuracy of the balance measurements.

The wing was oscillated in approximately sinusoidal motion about its axis by the direct-current motor D, which was controllable so that any desired frequency could be obtained. The wing was oscillated at the end opposite to the one at which the forces were measured. A time history of the angular position of the airfoil was recorded on the same film that was used to record the forces. This record was obtained by means of a rotating contact E attached to the driving motor. Once each revolution, this contact energized an electromagnet M, which deflected a mirror and moved a light beam on the film G. The lag of the timing system was measured by an oscillograph and found to be 0.0014 second.

A typical record of the measurements taken photographically with the oscillating-airfoil balance is shown in figure 3. Line 1 (fig. 3) is a stationary reference line; line 2 is the record of the timing element; and line 3 is the trace of the deflection of spring P and therefore is a record of the lift on the airfoil. The oscillations occurring in the timing line 2 are of no interest.

If, for example, oscillation about the angle of zero lift is assumed, the intersection of the lift line 3 with the zero line 4 determines the point of zero lift. By static calibration, the angular position of the airfoil corresponding to this point on the record is readily determined. A small correction is applied to take into account the lag in the timing unit. The phase angle is then directly obtained as the difference between the angular position of the curves for zero lift and zero angle.

### RESULTS AND DISCUSSION

The measured phase difference  $\delta$  for various values of the parameter  $1/k$  are shown in figure 4. It will be noted in some cases that the same value of  $1/k$  was obtained with several values of  $p$  and  $v$ .

Before the theoretical values of  $\delta$  could be computed, it was necessary to determine the effective aspect ratio of the airfoil for the test conditions. This value was derived from the value of the lift-curve slope determined by means of static lift observations at numerous angles of attack (fig. 5). The effective aspect ratio is 12.5,

which may be compared with the geometric value of 7.07. The leakage around the end plates of the airfoil prevented the realization of a higher value of the effective aspect ratio. For comparison, the lift curve is given (fig. 5) for the case in which the angle of attack of the airfoil is suddenly increased. The slope of the curve is about the same; the stalling of the moving airfoil at the higher angles of attack, however, does not occur.

The values of  $F$  and  $G$  corresponding to the effective aspect ratio were obtained from reference 6 and are shown in figure 6 against  $1/k$ . Values for an infinite-span airfoil from reference 4 are also shown. The theoretical values of  $\delta$  computed by equation (6) with values of  $F$  and  $G$  from figure 6 are shown with the experimental results in figure 4. Consideration was given to changing the inertia terms in equation (6) to take into account the decreased virtual volume due to the finite span of the airfoil. Calculations indicate this effect to be inappreciable.

The experimental and the theoretical values for the finite-span airfoil show phase differences of no more than about  $5^\circ$ . The corrections applied to the infinite-aspect-ratio theory to take the finite span into account are in the direction of improving the agreement between the theory and experiments.

It is noted that, at low frequencies of oscillation (large values of  $1/k$ , fig. 4), a lead that is consistently larger than expected appears. The study of the cause of this discrepancy will be left for a future investigation.

LANGLEY MEMORIAL AERONAUTICAL LABORATORY,  
NATIONAL ADVISORY COMMITTEE FOR AERONAUTICS,  
LANGLEY FIELD, VA., April 24, 1939.

### REFERENCES

1. Wagner, Herbert: Über die Entstehung des Dynamischen Auftriebes von Tragflügeln. Z. f. a. M. M., Bd. 5, Heft 1, Feb. 1925, S. 17-35.
2. Küssner, Hans Georg: Schwingungen von Flugzeugflügeln. Jahrb. 1929, DVL, S. 313-334.
3. Glauert, H.: The Force and Moment on an Oscillating Aerofoil. R. & M. No. 1242, British A. R. C., 1929.
4. Theodorsen, Theodore: General Theory of Aerodynamic Instability and the Mechanism of Flutter. T. R. No. 496, N. A. C. A., 1935.
5. Garrick, I. E.: Propulsion of a Flapping and Oscillating Airfoil. T. R. No. 567, N. A. C. A., 1936.
6. Jones, Robert T.: The Unsteady Lift of a Finite Wing. T. N. No. 682, N. A. C. A., 1939.
7. Theodorsen, Theodore, and Silverstein, Abe: Experimental Verification of the Theory of Wind-Tunnel Boundary Interference. T. R. No. 478, N. A. C. A., 1934.
8. Timoshenko, S.: Vibration Problems in Engineering. D. Van Nostrand Co., Inc., 1928, pp. 24-27.







## REPORT No. 674

### COOLING ON THE FRONT OF AN AIR-COOLED ENGINE CYLINDER IN A CONVENTIONAL ENGINE COWLING

By M. J. BREVOORT and U. T. JOYNER

#### SUMMARY

*Measurements were made of the cooling on the fronts of model cylinders in a conventional cowling for cooling in both the ground and the cruising conditions. The mechanisms of front and rear cooling are essentially different. Cooling on the rear baffled part of the cylinders continually increases with increasing fin width.*

*For the front of the cylinder, an optimum fin width was found to exist beyond which an increase in width reduced the heat transfer.*

*The heat-transfer coefficient on the front of the cylinders was larger on the side of the cylinder facing the propeller swirl than on the opposite side. This effect became more pronounced as the fin width was increased. These results are introductory to the study of front cooling and show the general effect of the several test parameters.*

#### INTRODUCTION

Most of the information available regarding cooling on the front of a cylinder of a radial air-cooled engine has been obtained from wind-tunnel tests on an un-baffled section of a cylinder. The nature of the air flow within the front of a conventional N. A. C. A. cowling was shown in reference 1 to be very different from the steady flow obtained in a free air stream; it is therefore probable that the cooling will be very different for the two conditions. There is every reason to believe that front cooling will not show the same dependence on fin spacing and fin width for the peculiar air-flow conditions found in the front of a cowling as for the baffled part of the cylinder.

The advisability of baffling the entire cylinder and resorting to blower cooling should not be admitted until front cooling in a conventional cowling has been exhaustively studied. The details of the mechanism by which front cooling is accomplished and the power expended for this cooling will be discussed in this report.

In reference 2 it was shown that an engine nacelle of 52-inch diameter in an air stream of 100 miles per hour had 32 pounds drag with a hemispherical nose, 42 pounds drag with a flat plate in the nose, and 45 pounds with the nose open. The tests for all three arrangements were made with the skirt closed, which gave no air for cooling. It is thus seen that, at 100 miles per

hour, about 13 pounds more drag can be expected with an open nose than with a streamline nose. All these values were reduced when a nacelle having a better afterbody was tested. The best value for the difference between a good conventional nose and a streamline nose now appears to be only one-fifth of the value of 13 pounds given in reference 2.

It was shown in reference 3 that the order of the cost of cooling the rear of the cylinders is 1 to 1½ percent of the engine power for a representative engine. Inasmuch as the power cost of cooling the front of the cylinders is independent of the power of the engine enclosed in the cowling, this front cooling power will amount to only about 1 percent of the power of a 2,000-horsepower engine at 300 miles per hour. Thus, the total power required for cooling would amount to not more than 2½ percent of the brake horsepower of a large engine. If the wing has a thickness comparable with the engine diameter, the form drag will disappear almost entirely and the power cost of the engine installation will be close to the power cost of cooling.

It was further found (reference 2) that the cooling of the front of the cylinders compared quite favorably with the cooling of the rear baffled part of the cylinders in spite of the fact that no directed air velocity could be measured over the front of the cylinders. Hot-wire measurements showed about 70 percent as much cooling in the front of the engine as in the free air stream. The open nose, which contributes about 3 pounds drag at 100 miles per hour, therefore gives very satisfactory front cooling. Since this drag increases proportionally with the dynamic pressure and since the cylinder finning must be adequate to give satisfactory cooling of the engine at the climbing speed, it is obvious that, at the cruising speed, much more power is required and more cooling is realized than is necessary on the front of the cylinders.

On the ground and to a lesser extent in the take-off, almost no positive pressure exists in the front of an open-nose cowling. The factors affecting the pressure in the front of the cowling are explained in reference 1 for the ground condition. It was shown that, when the hub and the propeller shank had no blade section, the pressure developed by the blade sections near the outer edge of the cowling opening was largely lost by



the hub section. By the use of propellers with blade sections close to the hub or by the use of spinners, a pressure was maintained over the front of the engine. The most practicable arrangement was a fixed disk set behind the propeller, which left an annular opening between the inner edge of the cowling and the outer edge of the disk with sufficient open area to allow the entry of the air without an appreciable energy loss. This annular opening must be behind a working section of the propeller and, for the case of ground cooling, large-diameter openings are preferable. The forward or backward position of the disk had a marked effect on the pressure developed.

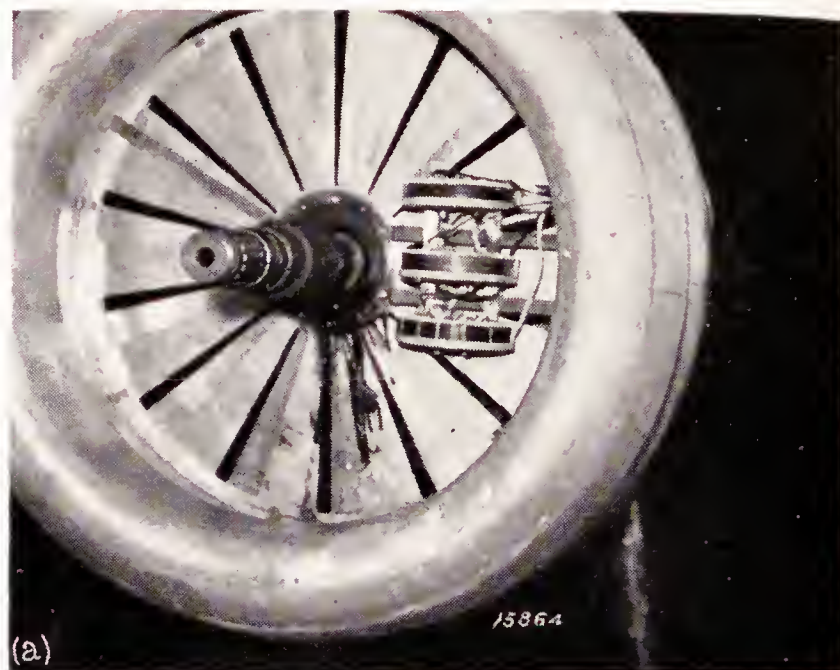
An effect on the pressure developed, resulting from a change with air speed of the configuration of flow around the cowling, was found on nose 7 and spinner 10 (reference 4). In the particular arrangement reported in reference 4, the air flow around the cowling changed with the speed in such a manner as to give a high  $\Delta p/q$  in the take-off condition and a relatively low  $\Delta p/q$  at a high speed. It is probable that a spinner, adjustable forward and backward, employed behind the propeller might be a practicable means of controlling the front pressures and the front cooling. It is further shown in reference 1 that, when the airplane is on the ground, a swirl exists in the front of the engine; this swirl depends upon the propeller speed, the diameter of the cowling, and the engine conductivity.

The mechanism of rear cooling and the means of obtaining the maximum cooling at the rear have been described in references 2, 5, 6, and 7. These reports show the power for cooling and how this power can be most usefully employed by the choice of optimum baffle shape and baffle length for the fin spacing used. They also point out how much the cooling can be improved by decreasing the fin spacing.

The present report gives the results of a study to determine the cooling in the front of an engine cowling for the ground and the cruising conditions at various locations within the cowling with and without a spinner; several fin spacings and fin widths were used. A knowledge of the distribution of cooling ability within the cowling is also required and this knowledge is obtained from the same measurements used to determine the effect of fin dimensions on cooling and the effect of operating conditions on cooling.

#### APPARATUS AND METHODS

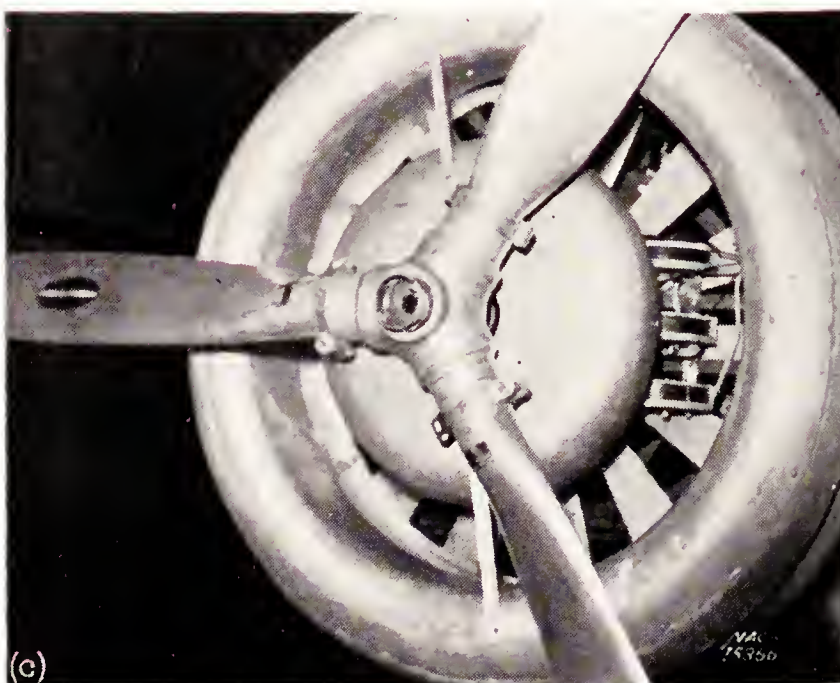
All the tests were made in the nose of a full-scale cowling-nacelle combination in the N. A. C. A. 20-foot tunnel. The diameter of the opening in the front of the cowling was 35 inches. The engine was represented by a baffle plate of variable opening (fig. 1 (a) and (b)) to simulate engine conductivities ranging from 0 to 0.116.



(a) Test cylinders in place; engine conductivity, 0.037.



(b) Test cylinders and wooden cylinders in place; engine conductivity, 0.116.



(c) Test cylinders, 24-inch round-edge disk, and propeller in place; engine conductivity, 0.116.

FIGURE 1.—General views of test set-up.



Propeller E was used for all the tests. It has Navy plan form 3790; the hub sections are shown in figure 1 (c).

Eight half cylinders, similar to the one shown in figure 2, were made of brass to the dimensions given in table I. The diameter at the base of the fins was 5.81 inches and the thickness of the wall was  $\frac{1}{8}$  inch for all

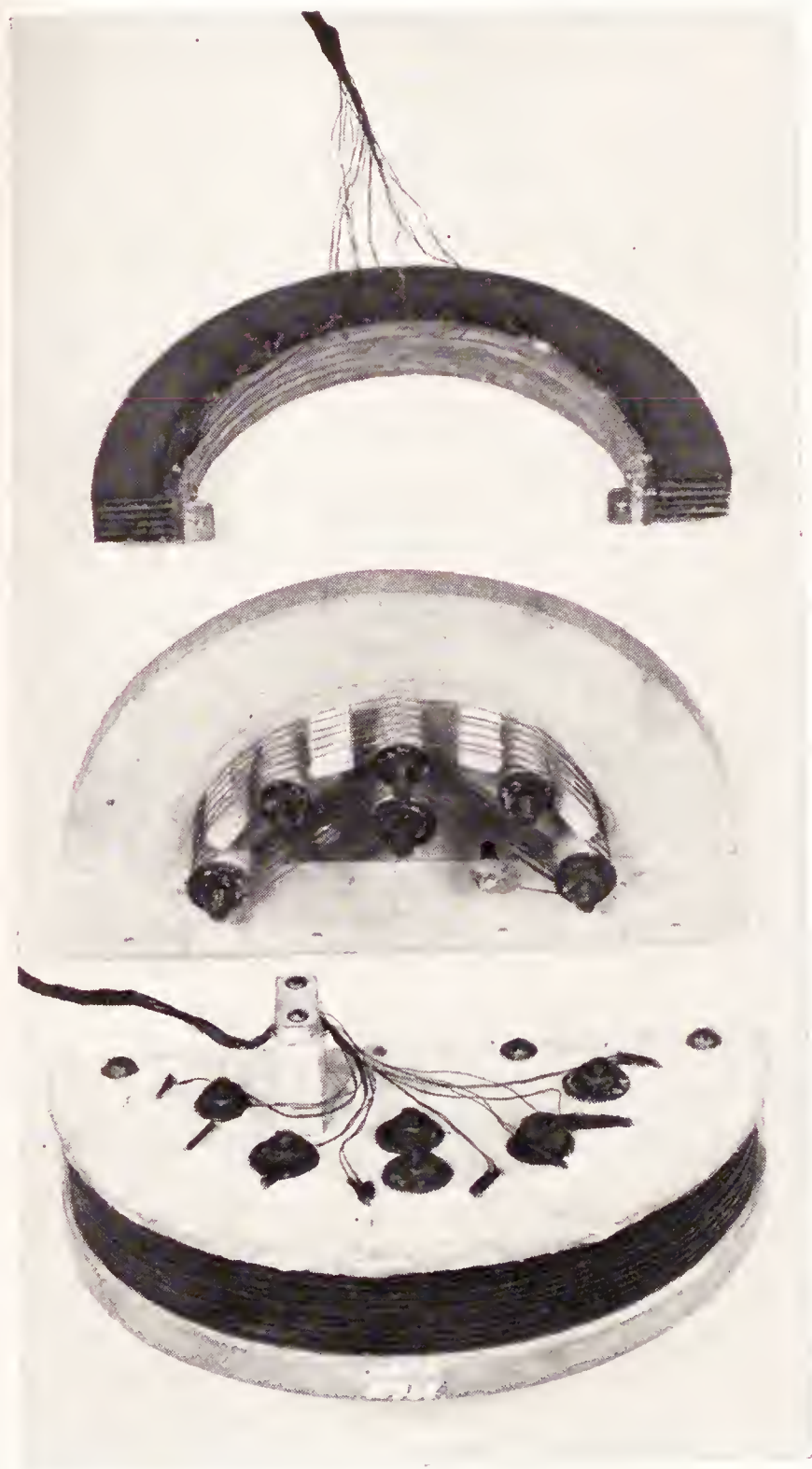


FIGURE 2.—Detailed view of test cylinder.

cylinders. The length of each cylinder was approximately 1 inch and the inside diameter was 5.56 inches. The fin thicknesses desired in these cylinders were estimated, from the values given in reference 7, for the optimum thickness for the maximum cooling of the baffled part of a cylinder. No information being available regarding optimum thickness for maximum cooling of a cylinder in an open cowling, the use of these values is permissible because the fin thickness is not a very critical quantity.

TABLE I  
CYLINDERS TESTED

Cylinder	Fin width (in.)	Fin spacing (in.)	Fin thickness (in.)	Number of fins on cylinder	Length of cylinder (in.)	Area $9.18 \times \text{length}$ (sq. in.)
I	0.5	0.031	0.012	23	1.083	9.88
II	.5	.062	.016	12	.980	8.95
III	.5	.125	.021	7	1.062	9.68
IV	1.0	.031	.016	21	1.045	9.53
V	1.0	.062	.025	12	1.110	10.12
VI	1.0	.125	.033	6	.955	8.72
VII	2.0	.062	.031	11	1.050	9.57
VIII	2.0	.125	.040	6	1.020	9.30

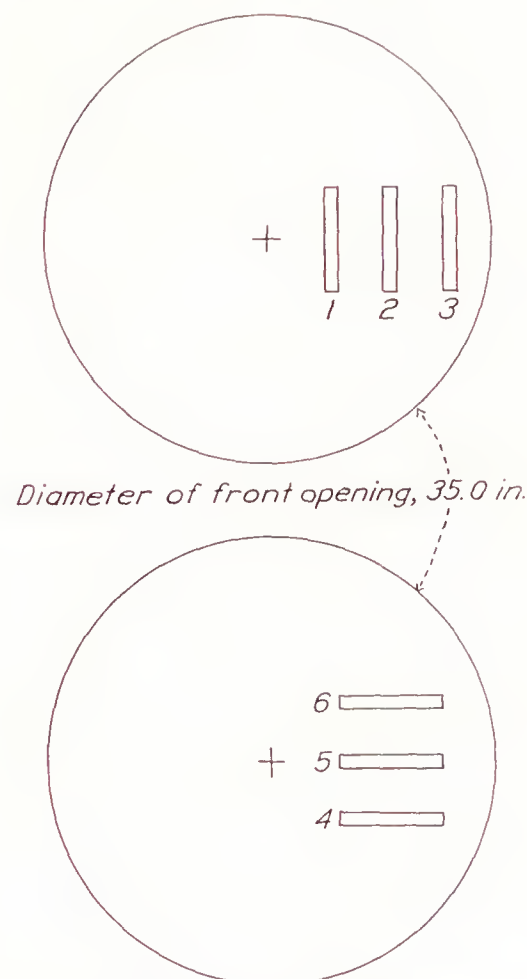


FIGURE 3.—Positions in which cylinders were tested.

Eight thermocouples were sunk into the middle of the cylinder wall at equal intervals around the circumference and welded to the cylinder. The temperature of the cylinder wall was determined by measuring the thermocouple electromotive force with a potentiometer. By this method, temperatures could be measured with an accuracy of about  $\pm 0.3^\circ \text{F}$ .

Each test cylinder was mounted on a heating unit (fig. 2) to form a complete test unit, also shown in figure 2. All tests were made with three of these test units mounted on a bracket. (See fig. 1 (a).) The three heating units were made from the same kind of wire and had the same resistance. Current was passed through the three heating units in series so that equal quantities of heat were generated in the three test units. About 275 watts were dissipated in each unit.

The six positions in which the cylinders were tested are shown in figure 3; the cylinders mounted in these positions are shown in figure 1 (b) and (a).

In order to reproduce as closely as possible the actual conditions of air flow over the front of an engine, two



wooden cylinders 4 inches in diameter were mounted as shown in figure 1 (b) for most of the tests with the cylinders in positions 1, 2, and 3.

A round-edge disk (fig. 1 (c)) 24 inches in diameter was designed according to the information given in reference 1 so that its size would be optimum for an engine conductivity of 0.100.

The values of  $\Delta p/q$  obtained in the cruising condition were 2.2, 1.8, 1.6, and 1.4 for conductivities of 0, 0.037, 0.078, and 0.116, respectively.

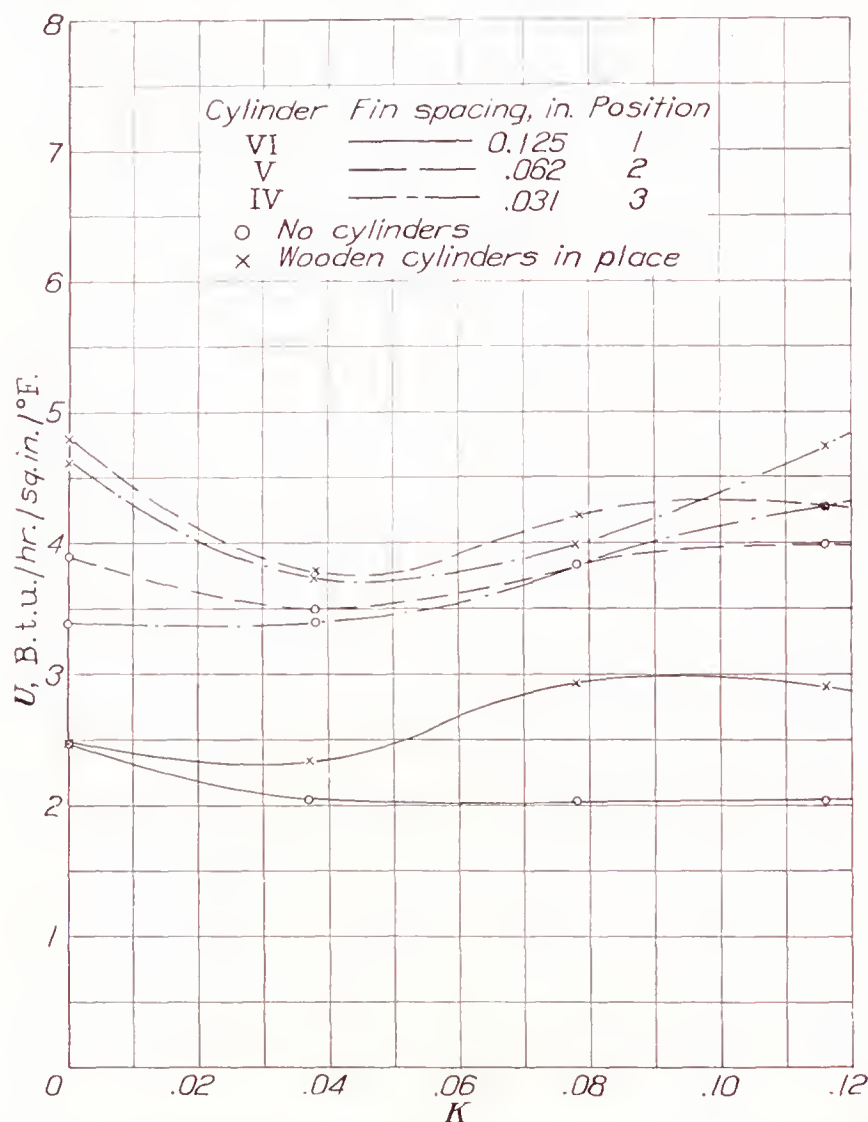


FIGURE 4.—Variation of average heat-transfer coefficient with engine conductivity for three cylinders, with and without wooden cylinders in place. Ground run.

#### METHOD OF CALCULATING OVER-ALL HEAT-TRANSFER COEFFICIENT

The average cylinder-wall temperature was obtained by taking the arithmetic mean temperature of the eight thermocouples in the cylinder wall. This mean temperature, together with the cylinder-base area and the heat input per hour, makes it possible to calculate  $U$  as follows:

$$U = \frac{0.75H}{A(t_m - t_a)} \quad (1)$$

where

$U$  is the over-all heat-transfer coefficient, B. t. u. per hour per square inch wall area per °F.

$H$ , heat input per hour, B. t. u. per hour.

$A$ , cylinder-wall area, square inches.

$t_m$ , mean temperature of the cylinder wall, °F.

$t_a$ , free-air temperature, °F.

The factor (0.75) in the numerator of equation (1) was introduced to take into account the heat lost through the asbestos end plates and base. This factor was determined as a good average value from experiments with one of the test units. In the experiments made to determine these values, the temperature and the quantity of the air heated by the fins were measured separately from that of the air heated by the asbestos, and the heat given to each was determined.

#### GROUND COOLING

The results of the ground tests are presented in figures 4 to 10. These figures show the variation of the average over-all heat-transfer coefficient  $U$  with engine conductivity  $K$  for the particular conditions tested.

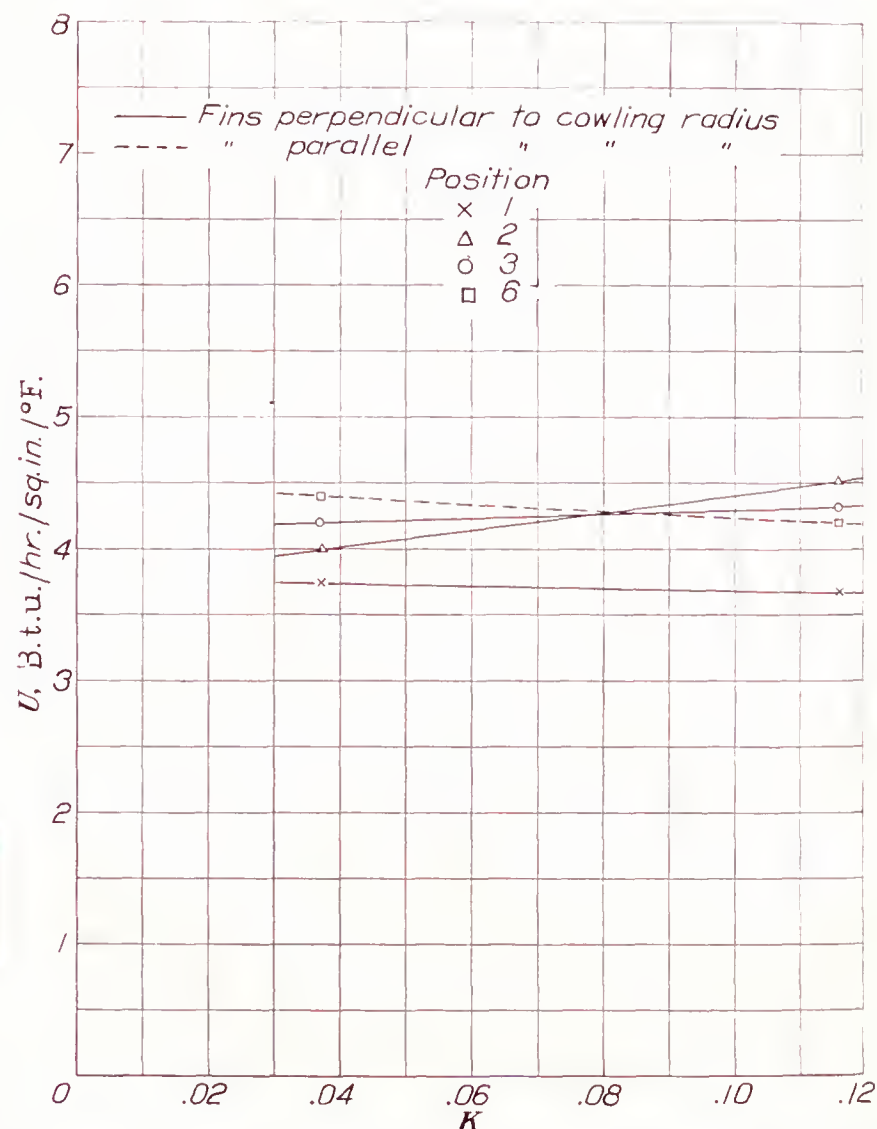
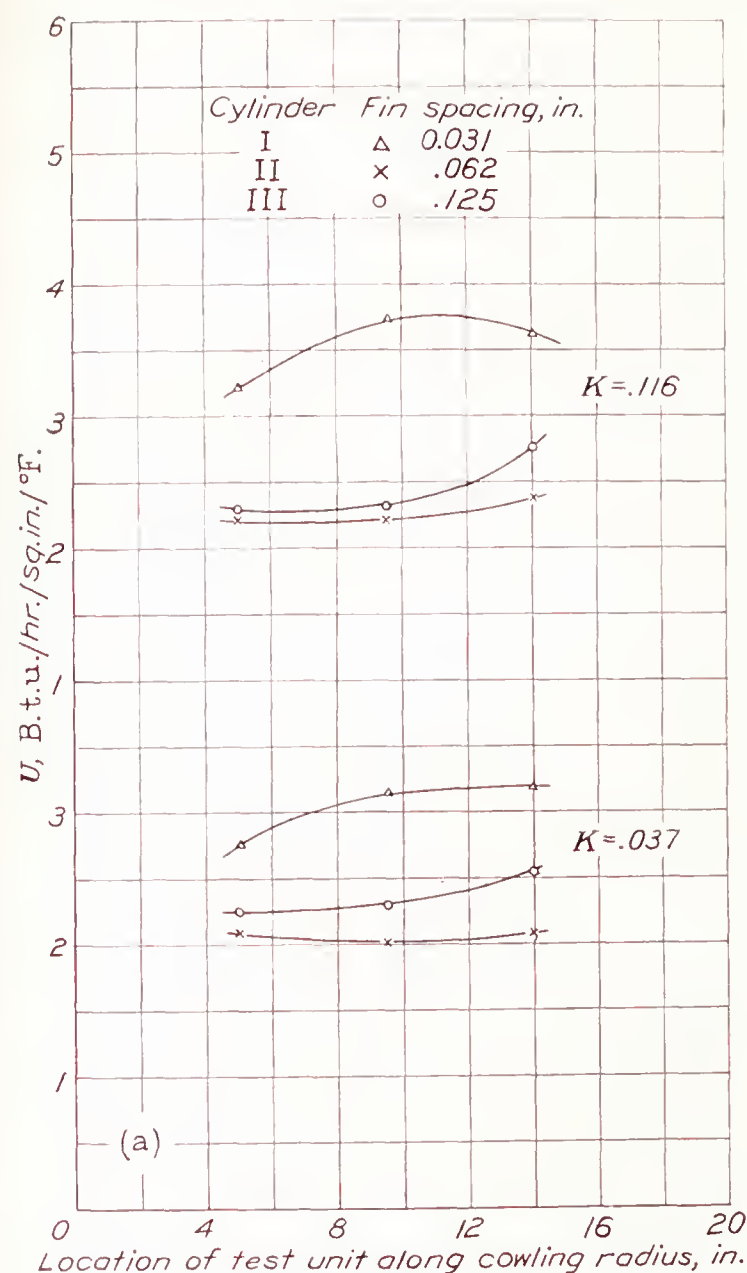


FIGURE 5.—Variation of average heat-transfer coefficient with engine conductivity for cylinder V in four test positions. Ground run.

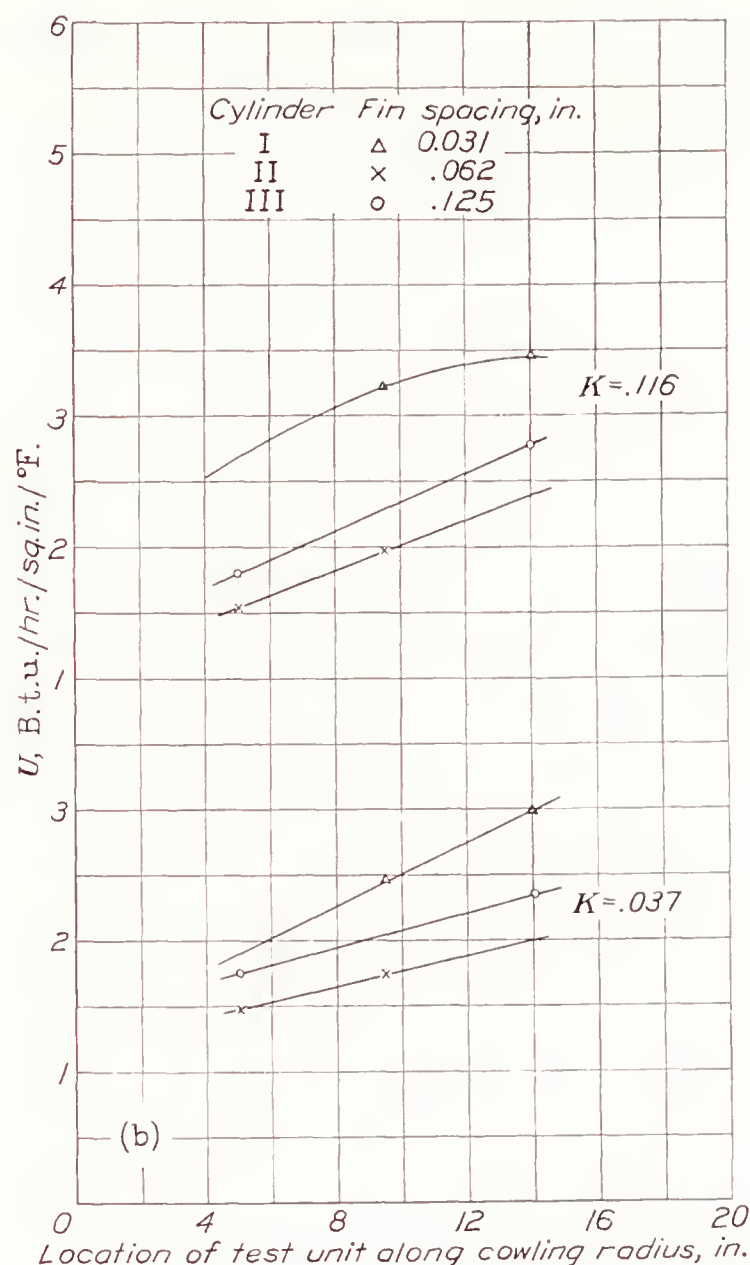
Most of the ground-cooling tests were made with the propeller operating at 985 r. p. m. In a few of the tests, from which the values shown in figures 6 (a), 6 (b), and 7 were calculated, the propeller was operated at 900 r. p. m. All such tests were made at zero air speed.

The effect of the addition of the two wooden cylinders (fig. 1 (b)) on the cooling of the test cylinders (fig. 4) is to increase the cooling somewhat in all cases tested, the increase in cooling being about the same for each cylinder.





(a) No disk.



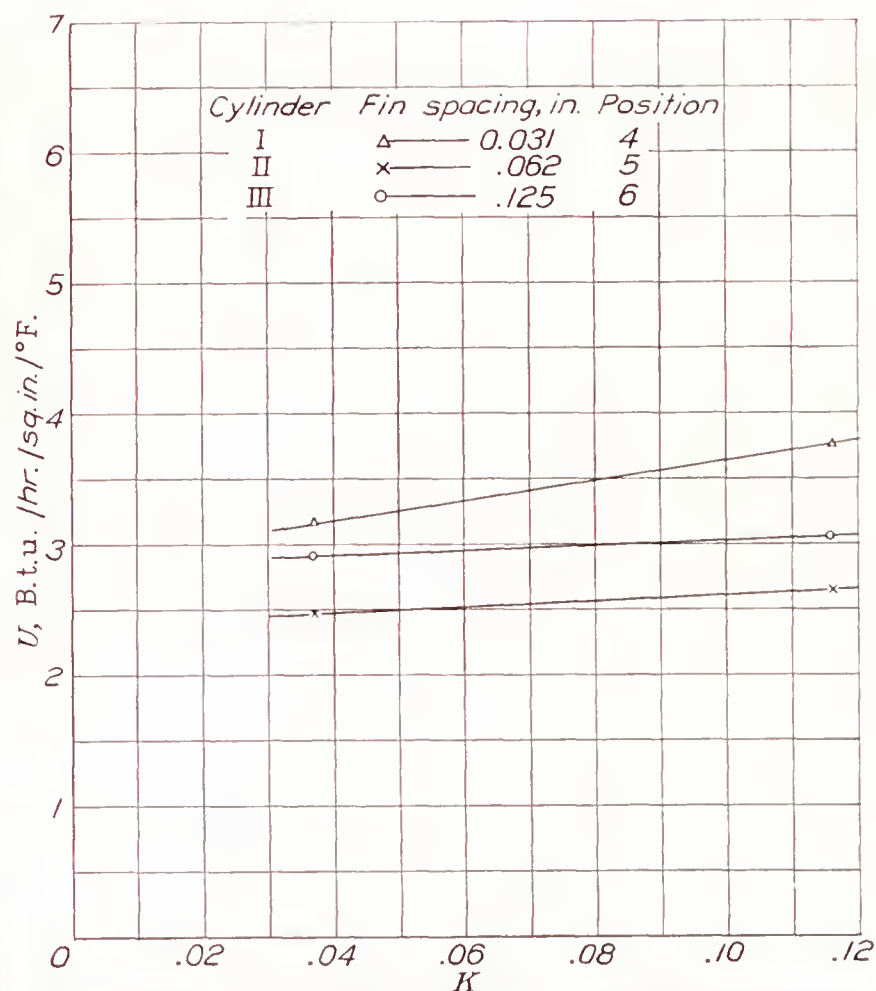
(b) 24-inch round-edge disk.

FIGURE 6.—Variation of average heat-transfer coefficient with location along the cowling radius for three cylinders having  $\frac{1}{2}$ -inch fin width tested in positions 1, 2, and 3. Ground run.

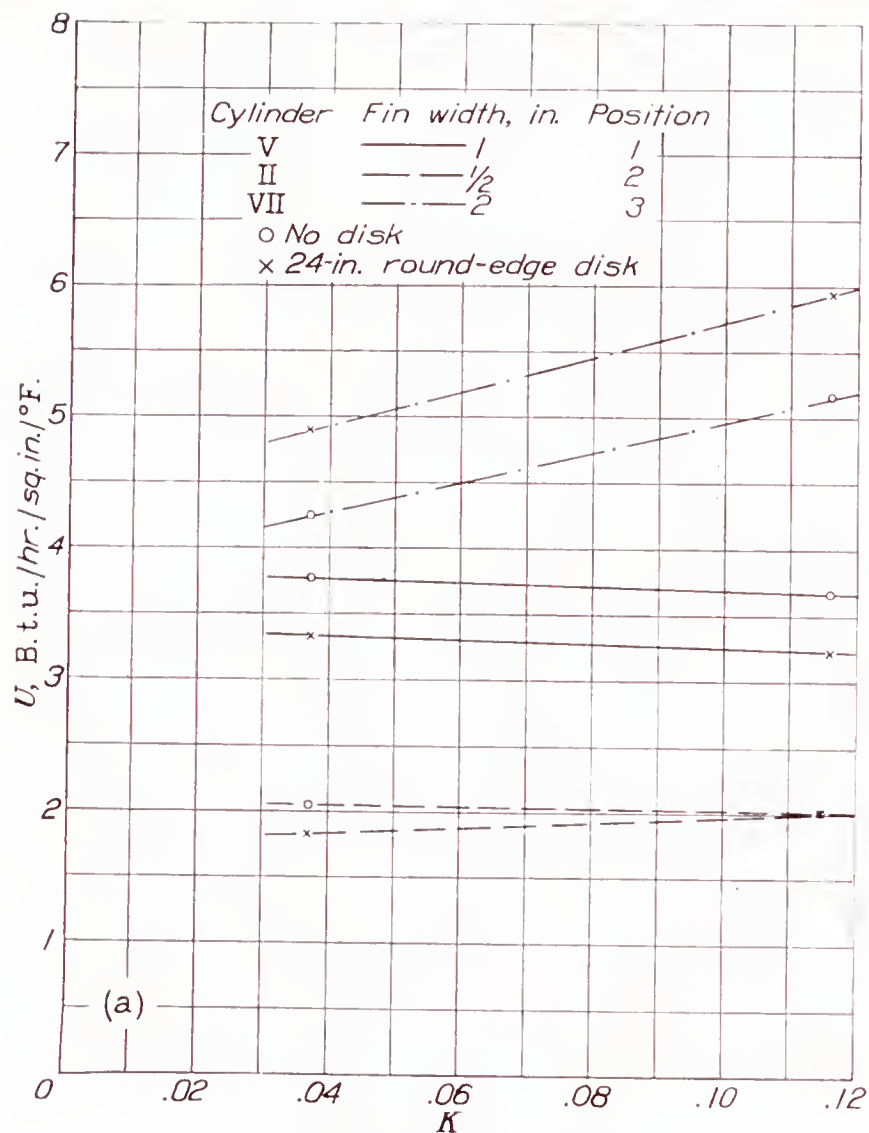
The variation in cooling along the front of a cylinder barrel from base to head (figs. 5 and 6 (a)) is shown to be small in an open-front cowling for the ground-cooling condition. Cooling on the cylinder head, which corresponds roughly to cooling in positions 4, 5, and 6, is of the same order as cooling on the barrel in the open-front cowling. This relation may be seen by comparing figures 6 (a) and 7 and also by examining figure 5. From the results shown by these figures, it can be said that the position of the test cylinder in the cowling and its orientation with respect to the propeller swirl are not so important as fin spacing and width in determining front cooling for the ground condition.

The effect of adding the round-edge disk in front of the cowling (fig. 1 (c)) varies from a slight increase to a 20-percent decrease in cooling. This variation can be seen by referring to figures 8 and 9 and by comparing figures 6 (a) and 6 (b).

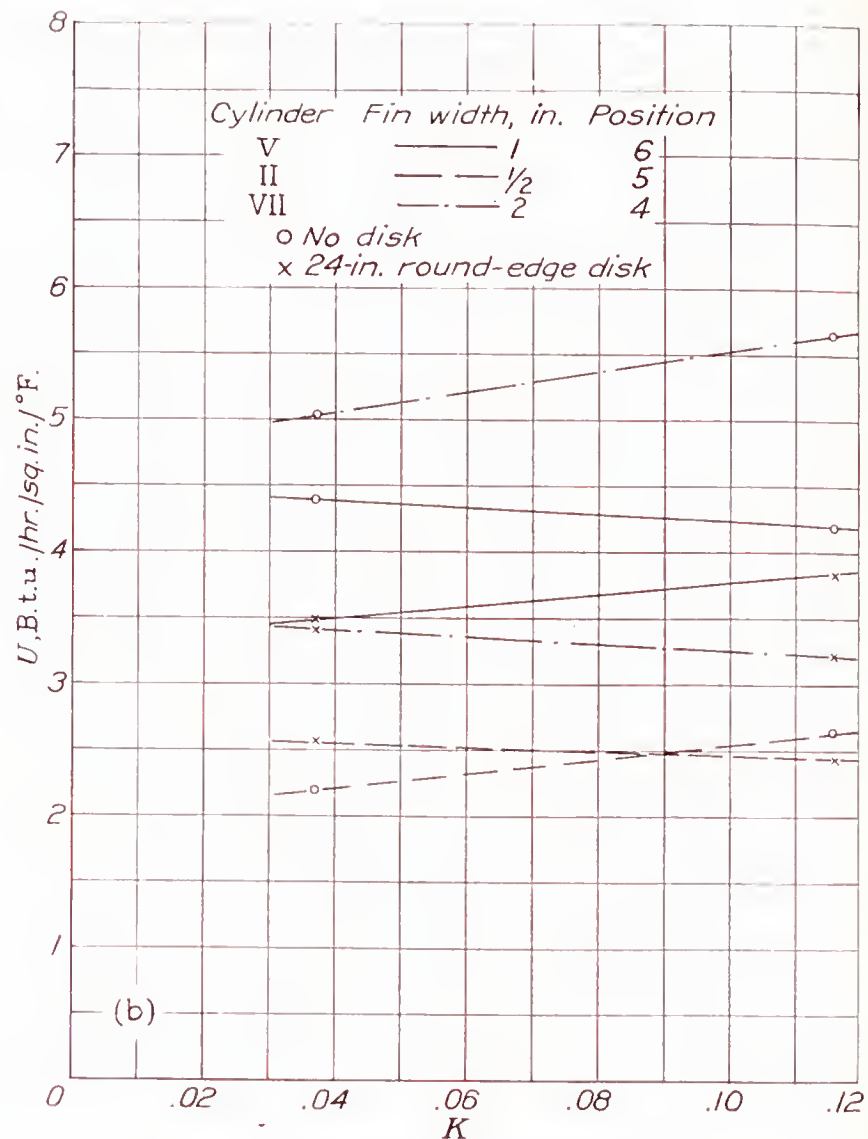
In position 3, the test cylinder is exposed to the air flow coming through the slot between the disk and the cowling, and the cooling is as good as or slightly better than the cooling in an open-nose cowling. (Cf. figs. 6 (a) and 6 (b) and see figs. 8 (a) and 9 (a).)

FIGURE 7.—Variation of average heat-transfer coefficient with engine conductivity for three cylinders having  $\frac{1}{2}$ -inch fin width tested in positions 4, 5, and 6. Ground run.

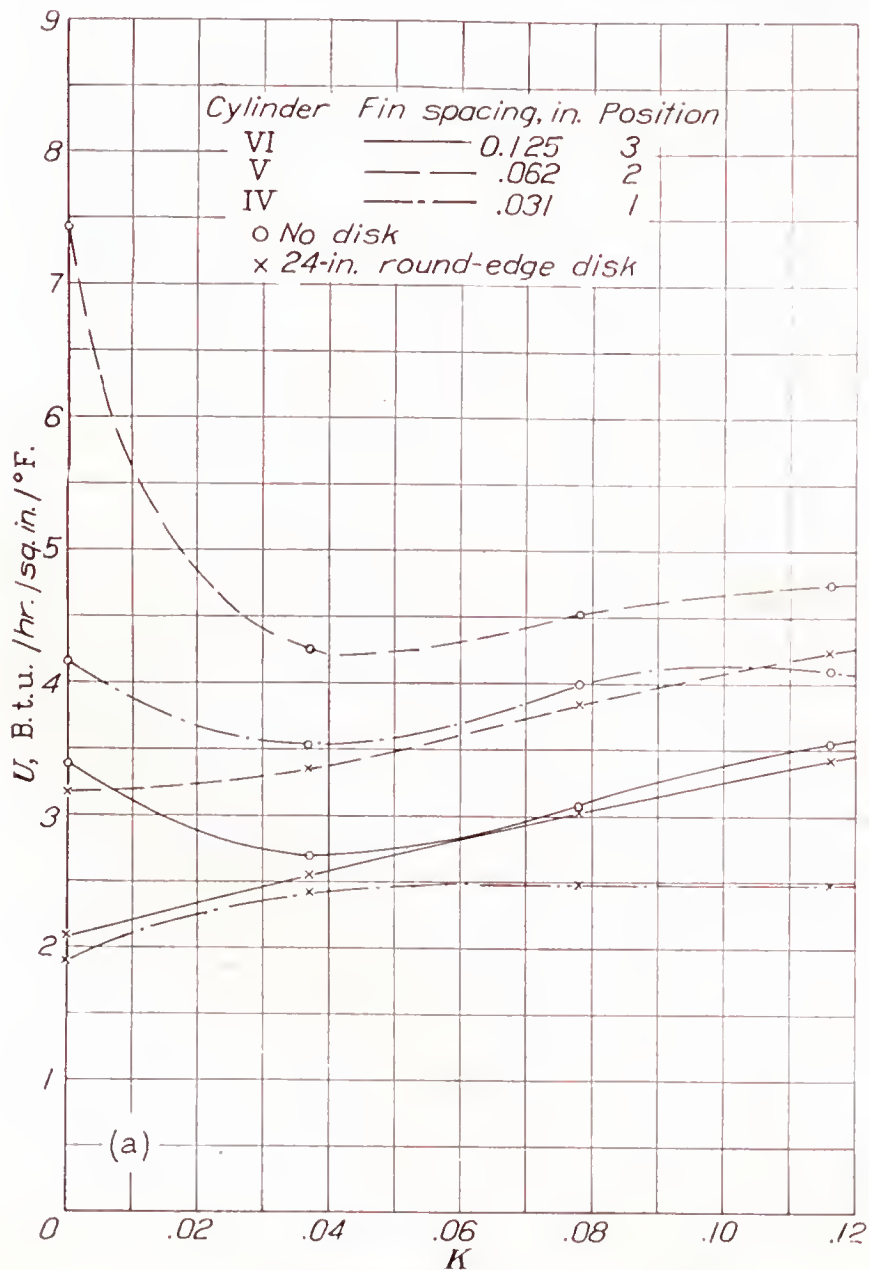




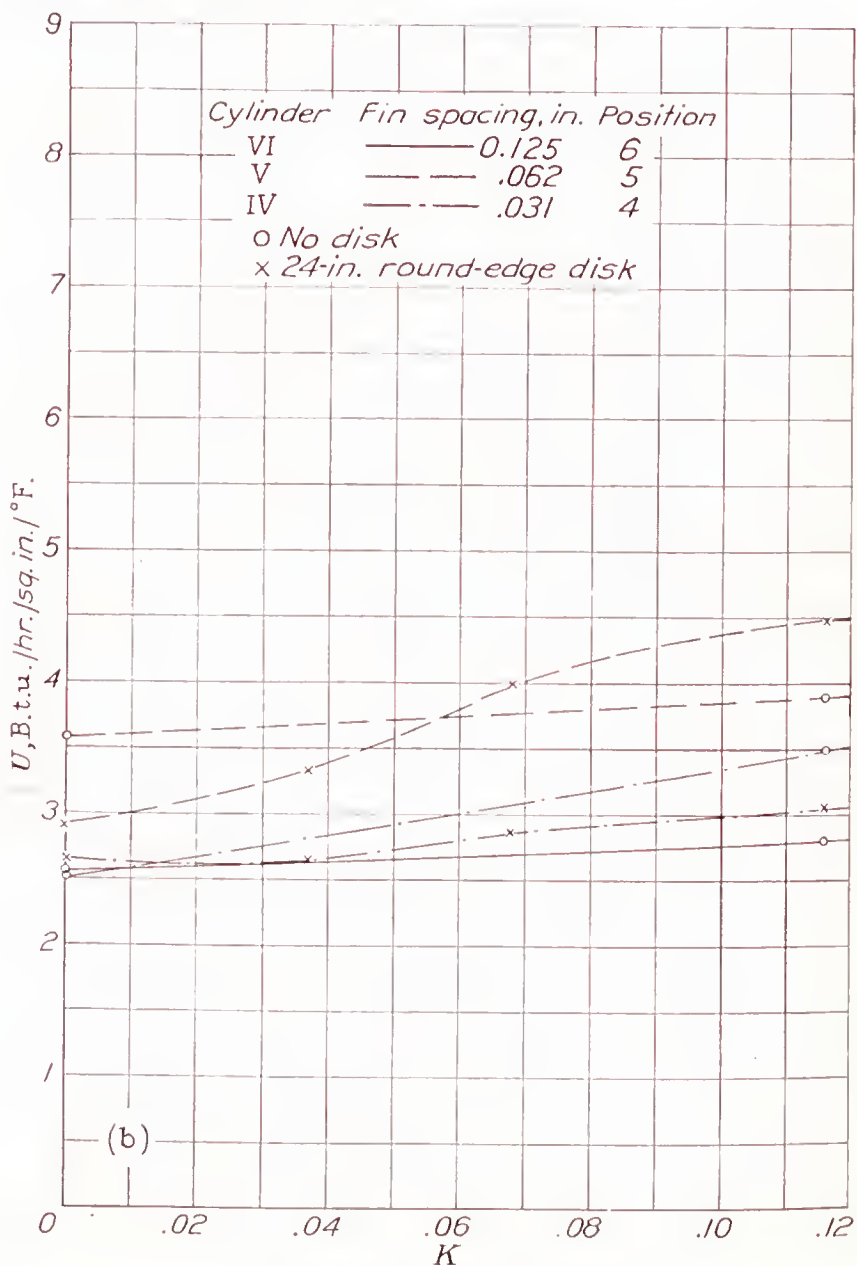
(a) Tested in positions 1, 2, and 3.



(b) Tested in positions 4, 5, and 6.

FIGURE 8.—Variation of average heat-transfer coefficient with engine conductivity for three cylinders having  $\frac{1}{16}$ -inch fin spacing tested with and without disk in nose. Ground run.

(a) Tested in positions 1, 2, and 3.



(b) Tested in positions 4, 5, and 6.

FIGURE 9.—Variation of average heat-transfer coefficient with engine conductivity for three cylinders having 1-inch fin width tested with and without disk in nose. Ground run.



It thus appears that the addition of a disk, if desirable for increasing the pressure available for cooling the baffled part of the cylinder, would not reduce the barrel cooling by more than 20 percent and would slightly increase the cooling on the head.

The effect of fin width is shown in figure 10 for the three fin spacings used. Obviously, there should be an optimum fin width, and it is interesting to note that this optimum is reached within the practicable range. This optimum width undoubtedly depends upon the operating condition. The undesirability of extremely wide fins on the front of a cylinder is clearly demonstrated.

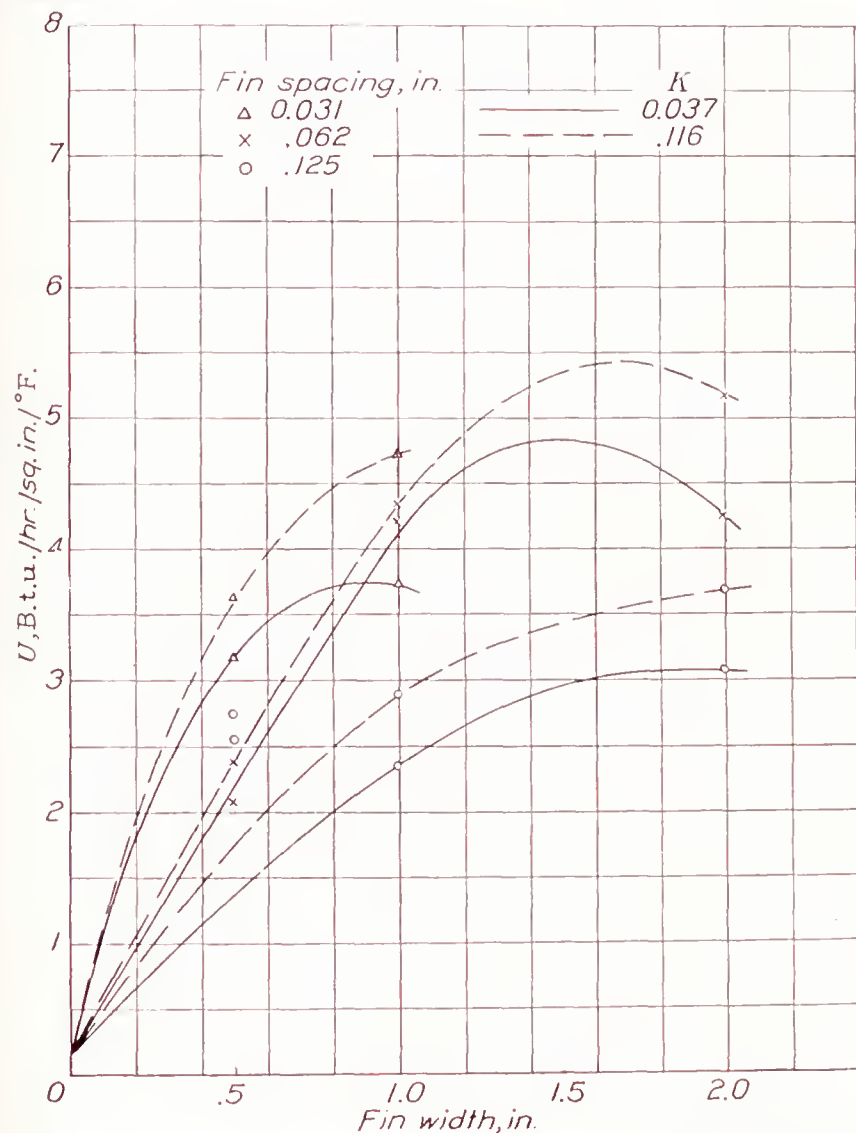


FIGURE 10.—Variation of average heat-transfer coefficient with fin width for three fin spacings at two engine conductivities. All tests in position 3 with wooden cylinders in place. Ground run.

The results from ground-cooling tests indicate that any noticeable change in cooling with changing engine conductivity is in the direction of a slight increase in front cooling with increasing conductivity. Since the supply of heat was insufficient to raise the temperature of the air in the cowling more than a negligible amount, the improvement must be due to increased air flow between the fins. This improvement may, however, be caused by a change in type of flow rather than directly by the flow through the engine. This point needs further study on a set-up better adapted to the investigation.

#### COOLING IN THE CRUISING CONDITION

All the cooling tests made in the cruising condition were conducted at the same value of  $P_c$ , where

$$P_c = \frac{P}{qSV}$$

and  $P$  is the power supplied to the propeller shaft.  
 $q$ , dynamic pressure.  
 $S$ , propeller disk area.  
 $V$ , air velocity.

In the cruising condition the propeller is run at various speeds, depending on the air speed; consequently, the swirl induced in the front of the cowling by the propeller varies with the air speed. The tests made at speeds of 40 and 75 miles per hour had propeller speeds of 500 and 895 r. p. m., respectively. These speeds were lower than the propeller speed of 985 r. p. m. at which the ground-cooling tests were made. The tests at 100 miles per hour were made with a propeller speed of 1,145 r. p. m.

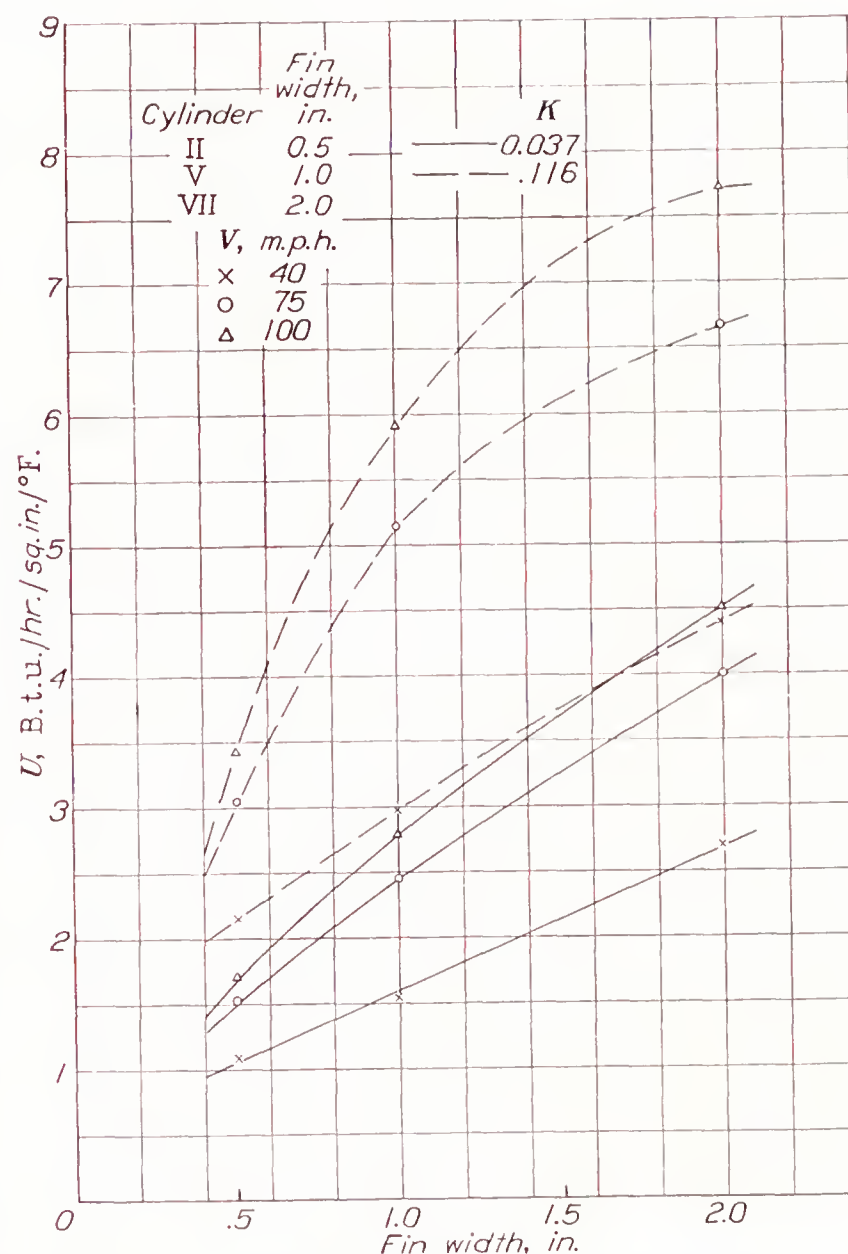
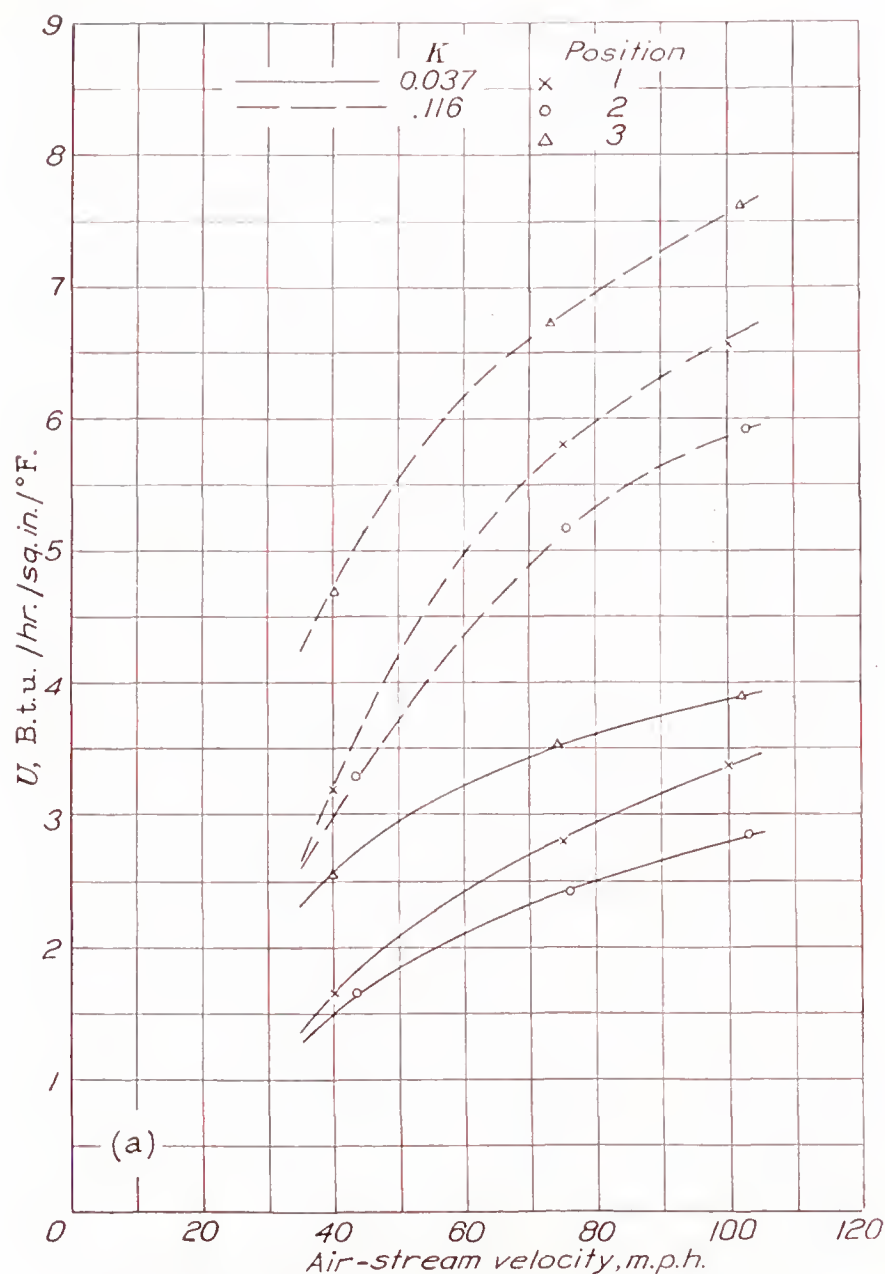


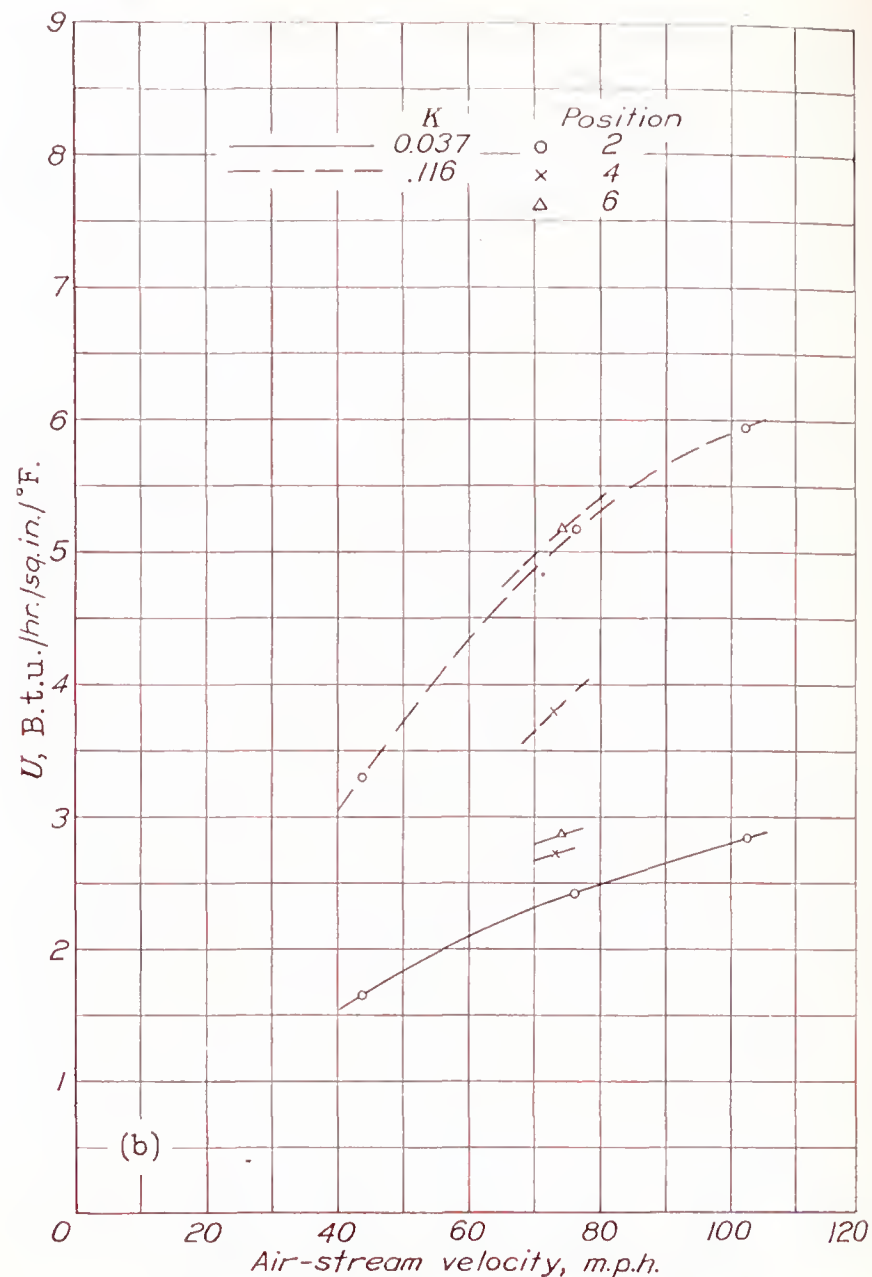
FIGURE 11.—Variation of average heat-transfer coefficient with fin width for three cylinders having  $\frac{1}{16}$ -inch fin spacing, for two engine conductivities and three air-stream velocities. All tests in position 2 with wooden cylinders in place. Cruising condition.

The value of the heat-transfer coefficient increases with increasing values of engine conductivity, air speed, and fin width up to a certain optimum width, for all the cylinders tested. All these effects can be seen in figure 11.





(a) Tested in positions 1, 2, and 3 with wooden cylinders in place.



(b) Tested in positions 2, 4, and 6. No wooden cylinders.

FIGURE 12.—Variation of average heat-transfer coefficient with air-stream velocity for cylinder V for two engine conductivities. Cruising condition.

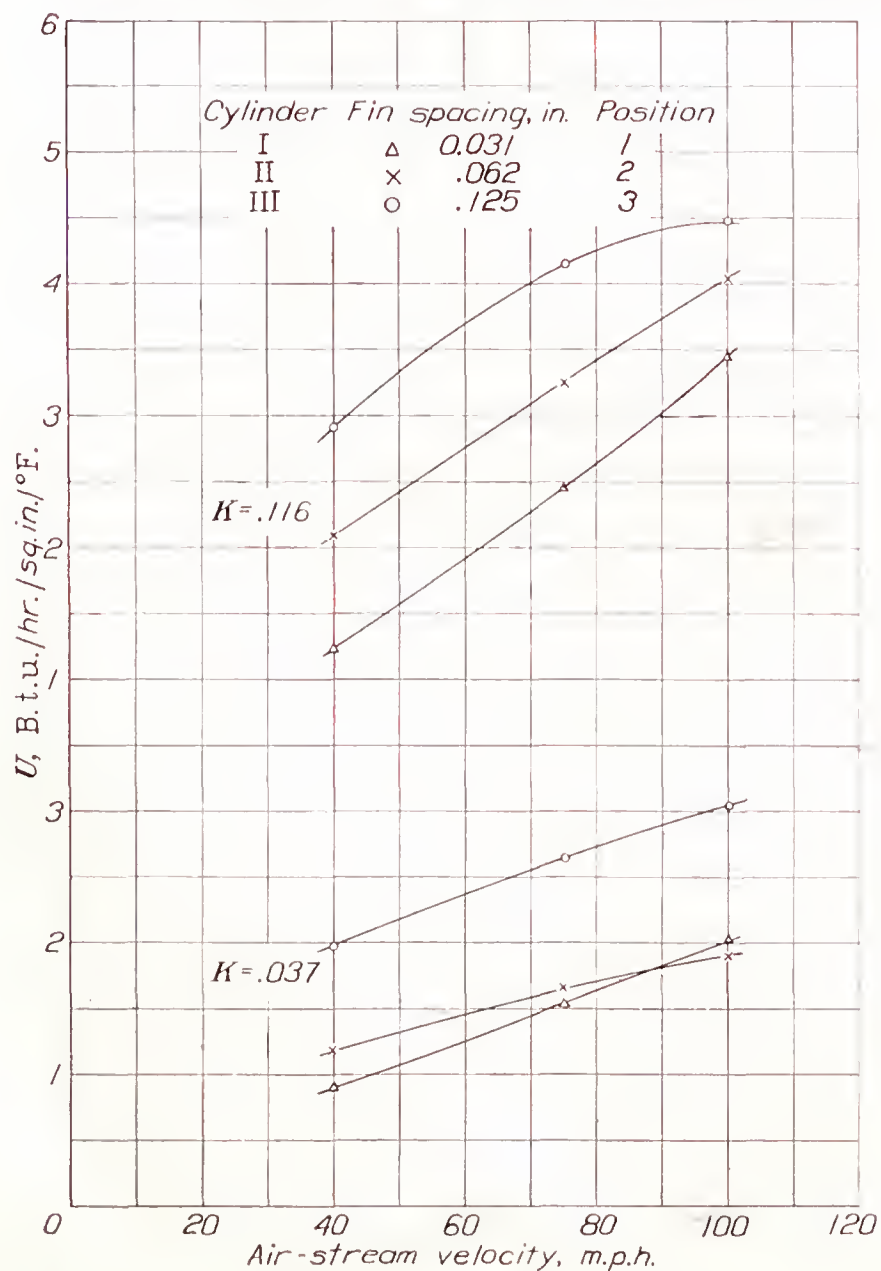
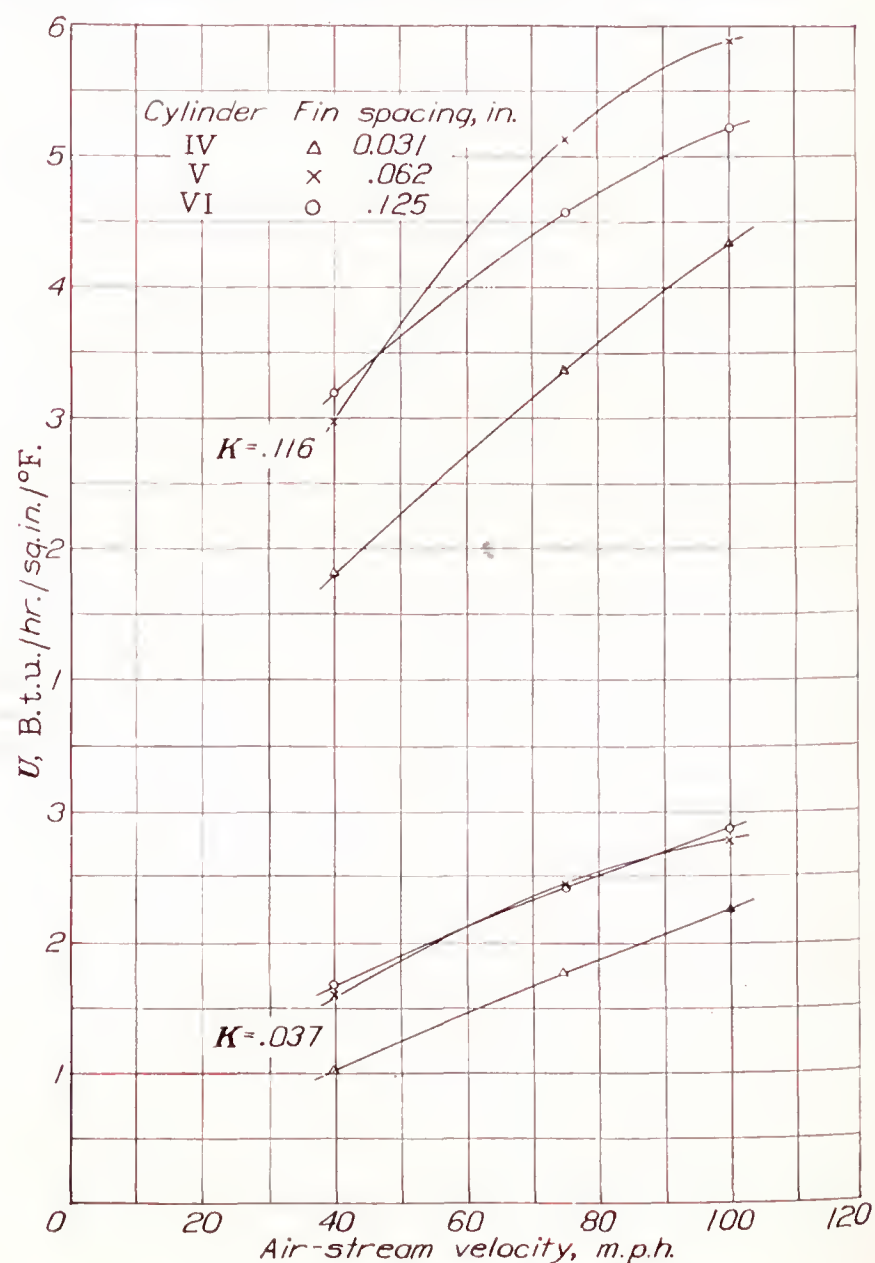
FIGURE 13.—Variation of average heat-transfer coefficient with air-stream velocity for three cylinders having  $\frac{1}{2}$ -inch fin width in positions 1, 2, and 3 for two engine conductivities. Wooden cylinders in place. Cruising condition.

FIGURE 14.—Variation of average heat-transfer coefficient with air-stream velocity for three cylinders having 1-inch fin width in position 2 for two engine conductivities. Wooden cylinders in place. Cruising condition.



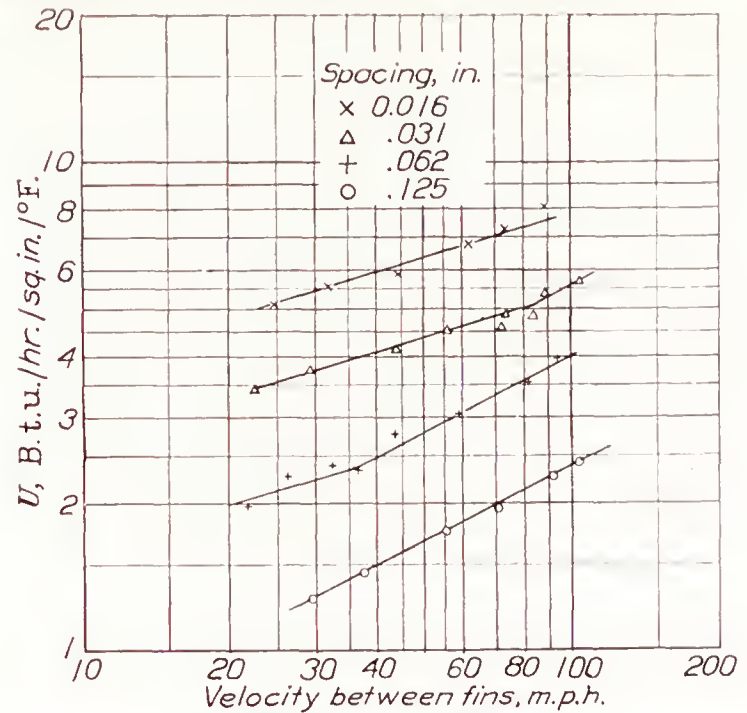
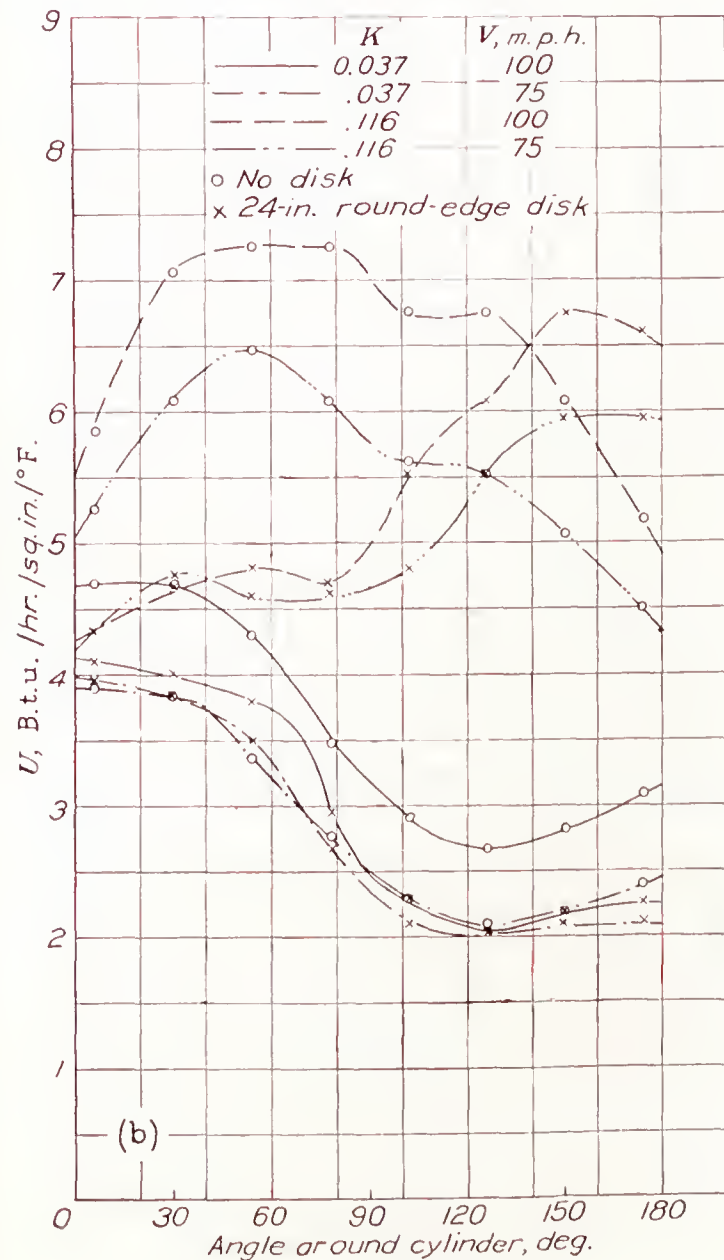
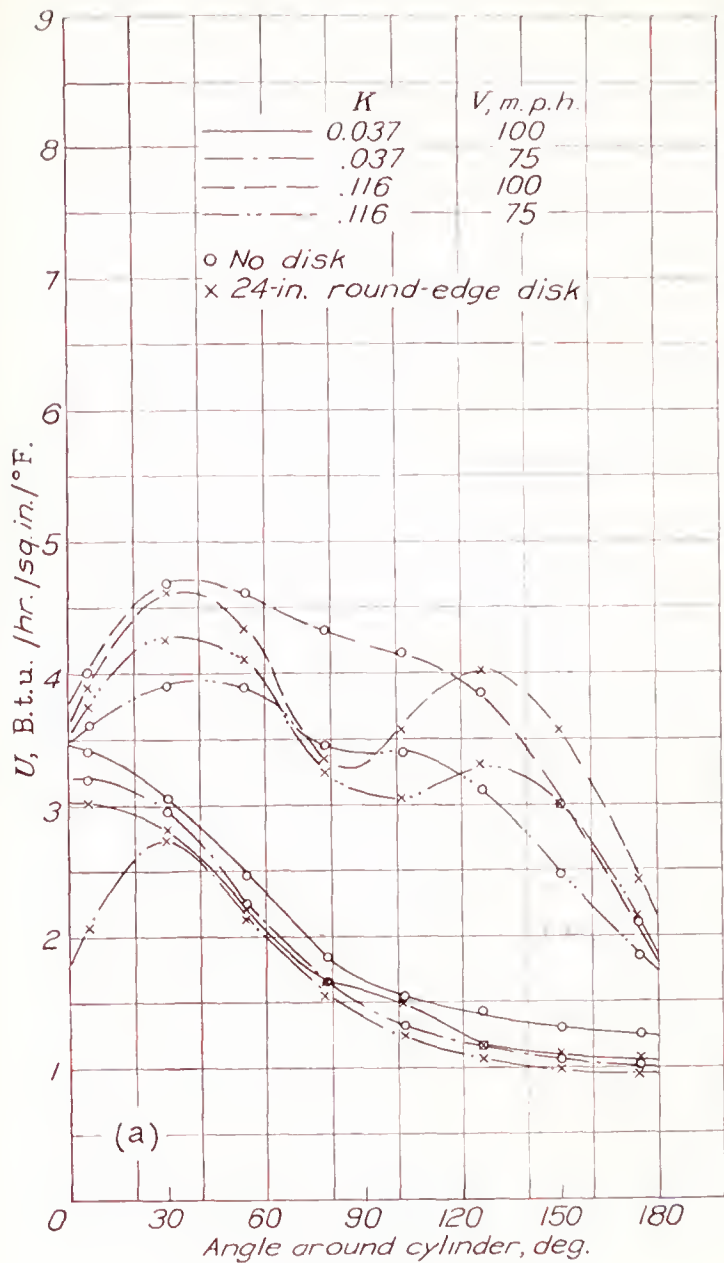


FIGURE 15.—Variation of average heat-transfer coefficient with velocity between the fins on the baffled part of the cylinder.

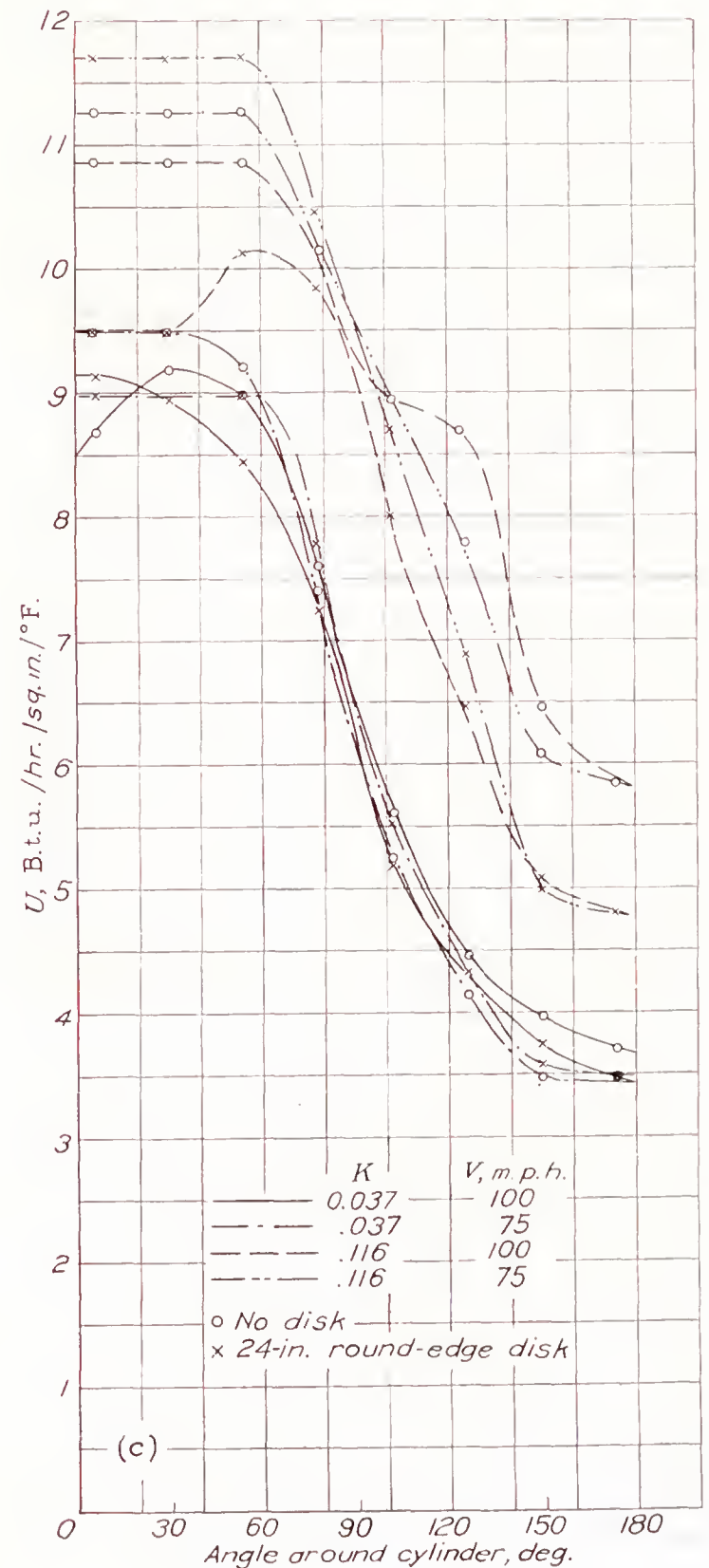


FIGURE 16.—Variation of local heat-transfer coefficient with angle around cylinder for three cylinders having  $\frac{1}{16}$ -inch fin spacing at two engine conductivities and two air-stream velocities, with and without disk in nose. Wooden cylinders in place. Cruising condition.



The variation in cooling with change in air-stream velocity is shown in figures 12, 13, and 14. When these figures are compared with figure 15, which shows heat-transfer coefficients for the rear baffled part of a cylinder as reported in reference 7, it is seen that the cooling on the front of a cylinder compares quite favorably with the cooling on the rear baffled part for the cruising condition.

Figure 16 shows the variation of cooling around a cylinder barrel for cylinders II, V, and VII when the zero angle is on the side of the cylinder facing the propeller swirl. The results show considerably more cooling on the side facing the propeller swirl than on the

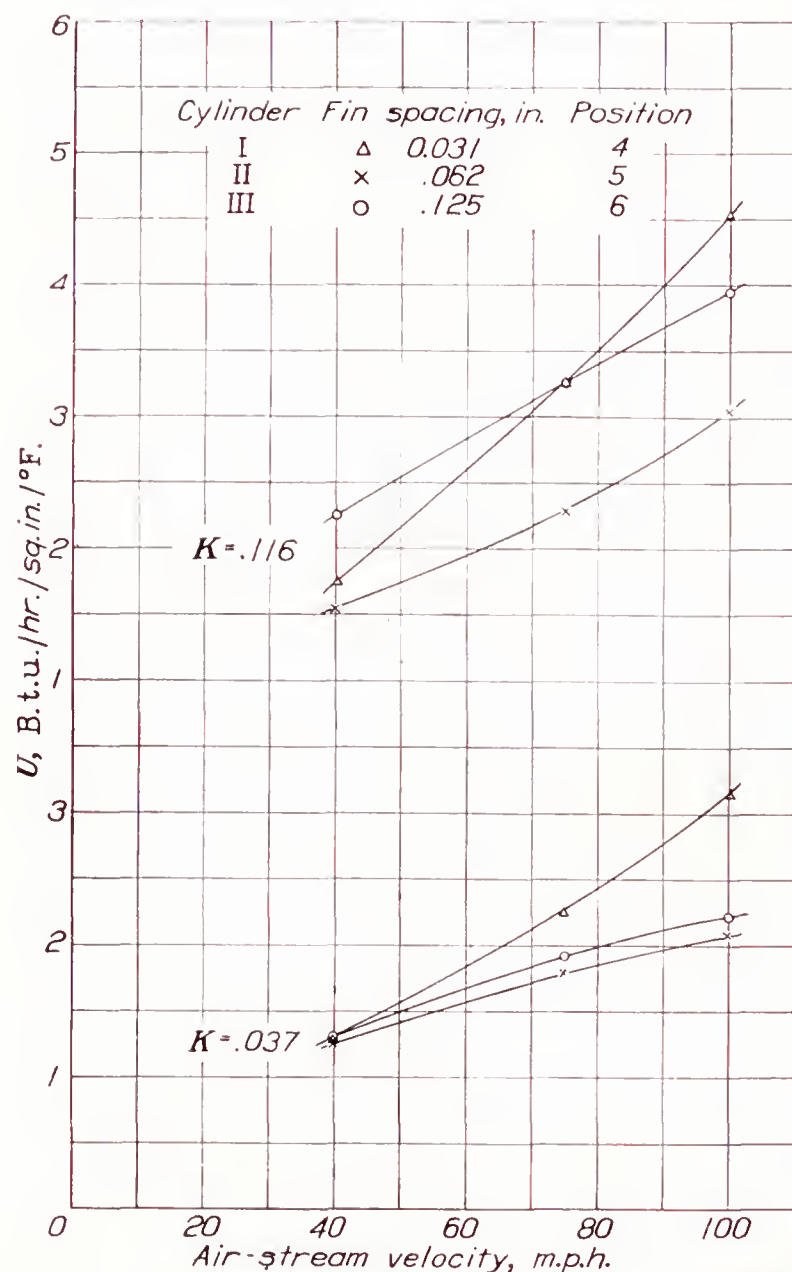


FIGURE 17.—Variation of average heat-transfer coefficient with air-stream velocity for three cylinders having  $\frac{1}{2}$ -inch fin width in positions 4, 5, and 6, with two engine conductivities. Cruising condition.

other side of the cylinder. The large effect of the engine conductivity on cooling is also apparent.

The large variation in cooling around a cylinder, especially with wide fins, suggests that either an unsymmetrical baffle could be fitted to even out the temperature distribution or the exhaust valve could be located in the region of good cooling to take advantage of the unequal temperature distribution.

Cooling of cylinders in positions 4, 5, and 6 shows about the same general dependence on air-stream velocity as has already been noted for the other positions. (See fig. 17.)

## DISCUSSION

The data presented in figure 6 are rather unexpected; i. e., a spacing of 0.062 inch gave a lower heat-transfer coefficient in the ground condition than either a smaller or a larger spacing with the fins of  $\frac{1}{2}$ -inch width. In order to check this apparently anomalous behavior, three cylinders were placed in a duct where the air

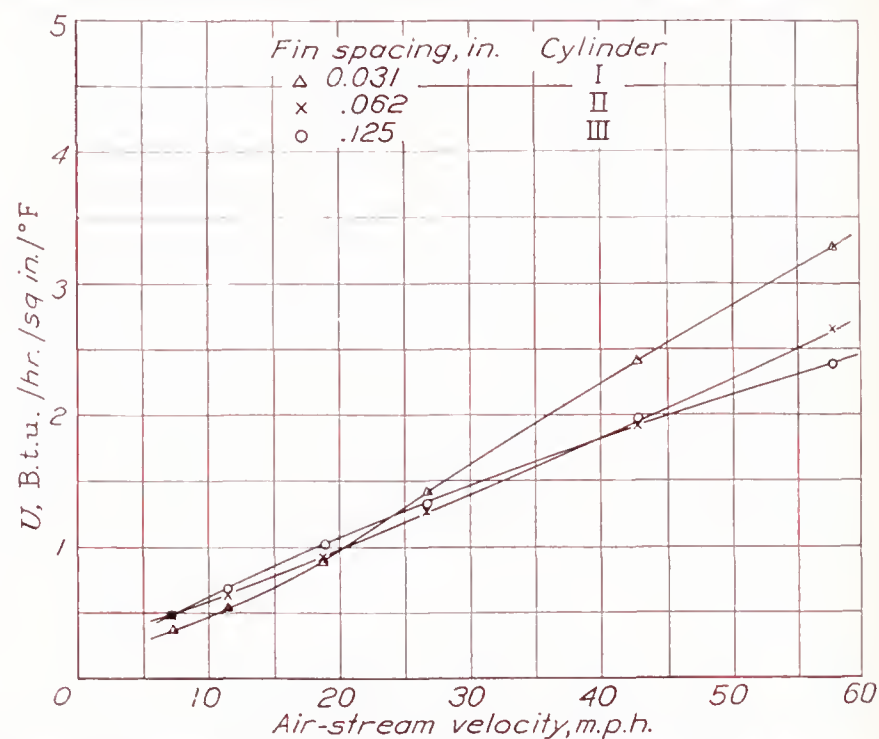


FIGURE 18.—Variation of average heat-transfer coefficient with air-stream velocity for three cylinders having  $\frac{1}{2}$ -inch fin width. Duct tests.

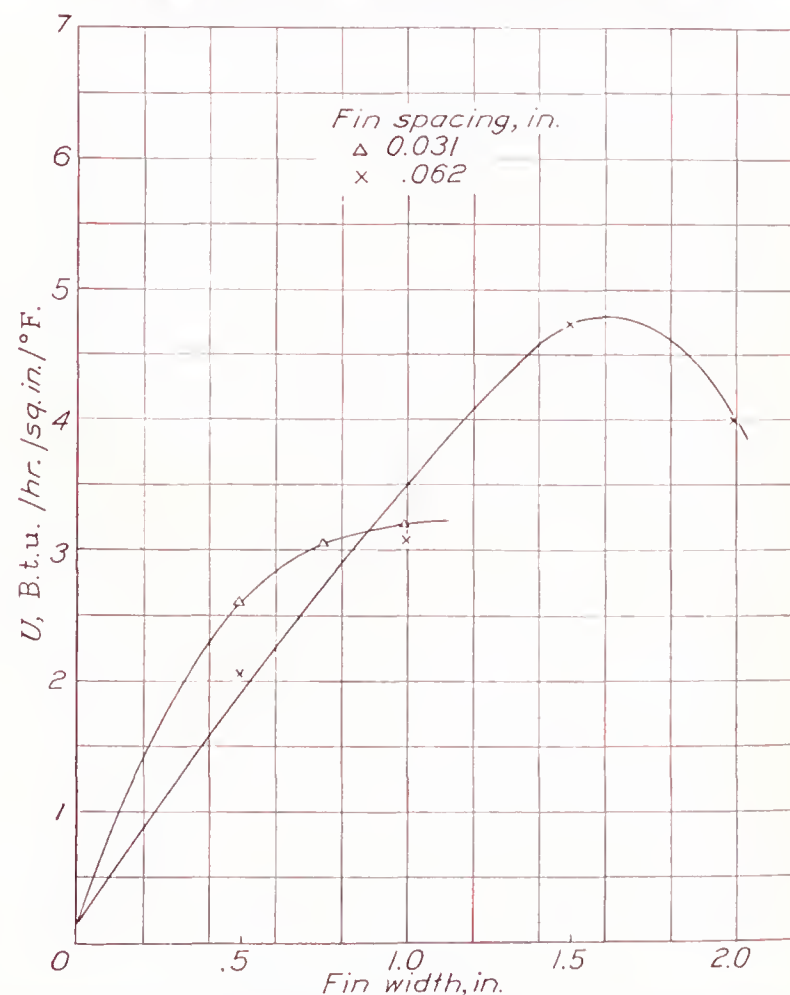


FIGURE 19.—Variation of average heat-transfer coefficient with fin width for two fin spacings at an air-stream velocity of 40 miles per hour. Duct tests.

velocity could be varied. The results of this series of tests are presented in figure 18. The small spacings gave a higher coefficient in the high-speed range, and the larger spacings gave a higher coefficient in the low-speed range. Thus, all the curves must cross. Tests run only within certain speed ranges (see fig. 18) will obviously give some surprising results.



Figure 10 also presents both interesting and important results, inasmuch as some of the curves indicate an optimum fin width. Although the curves were drawn through the test points in quite an obvious manner, additional points would have been more convincing.

In order to investigate this matter further, several of the model cylinders were tested in a duct. Cylinder VII was cut down to 1½-inch fin width, and cylinder IV was cut down to ¾-inch fin width. These tests (fig. 19) show maximum heat transfer at the same fin widths as the tunnel tests.

Although the duct tests did not exactly reproduce conditions in the front of a cowl, the tests do show that an un baffled cylinder under certain conditions does have an optimum fin width that falls within the practicable range.

This very important result must be due to the fact that the air flow penetrates to only a limited depth between the fins, as can be seen from figure 18, which shows that the 0.031-inch spacing is too small for its width at low air speeds. Consequently, the air-flow penetration between the fins is restricted and the cooling is poorer than with larger spacings, which allow the air to penetrate deeper. At high air speeds, however, there is sufficient dynamic pressure to cause the air to penetrate all the way to the cylinder wall, even with the 0.031-inch spacing. Full advantage is thus taken of the large fin area associated with narrow spacing, and the fine spacing cools better than either of the coarser spacings.

From the foregoing discussion, it is apparent that an optimum fin width must exist for each combination of fin spacing and air speed. The optimum width is probably the width that allows the air flow to penetrate just to the cylinder wall. For smaller fin widths, the cooling area is reduced. For larger fin widths, the depth of penetration of the air flow is no greater, so that the inner part of the wider fin serves merely as a resistance to heat flow along the fins. The cylinder wall therefore operates at a correspondingly higher temperature while dissipating the same quantity of heat, and the over-all heat-transfer coefficient is lower than with optimum fin width.

The flow on the side of the cylinder facing the propeller swirl or the air stream probably penetrates well to the cylinder wall even in the cylinder with wide fins but undoubtedly leaks out rather rapidly. This probability accounts for the large variation in cooling around the cylinder, which is shown in figure 16(c). Figures 20(a) and 20(b) show a similar variation in cooling around the cylinder for the ground condition. Figure 20(c) shows that a cylinder in position 5 has the best cooling on the side toward the outside of the cowl.

The variation of the heat-transfer coefficient with spacing at various air speeds can probably be explained by the nature of the flow. It appears that the small spacings at low air speeds have too much resistance to

air flow to allow the cooling air to penetrate to the cylinder wall. This idea is substantiated by the results in figures 10, 13, and 14, where it can be seen that small spacings are relatively better on narrow fin widths.

The position of the test cylinder in the front of an open cowl or the orientation of the fins to the propeller swirl has little effect on the cooling of the cylinder. When a disk is added to the front of the cowl, the cooling is somewhat reduced except over parts of the cylinder barrel and head that are exposed to the air stream coming through the slot, where little effect is noticed. The orientation of the fins remains relatively unimportant.

The nature of the air flow that cools the front of cylinders is complex. (See reference 1.) It is composed of at least three types of flow: First, the swirl in the front of the cowl, which is caused by the rotating propeller; second, the fore-and-aft pulsating flow, which is caused by the alternate passage of the propeller blades with the associated regions of high pressure behind them and the open spaces between blades that permit air to escape back through the propeller disk; and third, the straight flow through the cowl, which is caused by high pressure in the front of the cowl as a result of high air speed or propeller speed. The straight type of flow is greatly influenced by engine conductivity.

The results presented herein indicate that the heat-transfer coefficient for the ground-cooling condition is roughly the same as for cruising conditions at 60 to 80 miles per hour. Since front cooling in the cruising condition is about the same with or without a propeller operating in front of the engine (see reference 2), it appears that the third type of flow, namely, straight flow through the cowl, controls the configuration of flow and the cooling in the front of the cowl for the cruising condition.

For the ground-cooling condition, there is very little flow straight through the cowl; the first two types of flow, namely, swirl and pulsating flow, must account for the good heat-transfer coefficient obtained. The effect of engine conductivity on cooling is nevertheless important because a large conductivity permits the cooling air to be frequently changed, thus preventing a condition in which air remains in the cowl long enough to warm up by continual contact with the hot cylinders and thus impair the cooling.

The results of all the tests show that the cooling on the front compares favorably with that on the rear baffled part of the cylinder. This same result was noted in reference 2. The further fact that this front cooling is obtained relatively more cheaply than baffled cooling makes the desirability of using a closed-nose cowl questionable. If fin design is not improved and blower cooling is resorted to as the only alternative, a considerable increase in the cost of cooling will be necessary to give the same cooling; the power increase



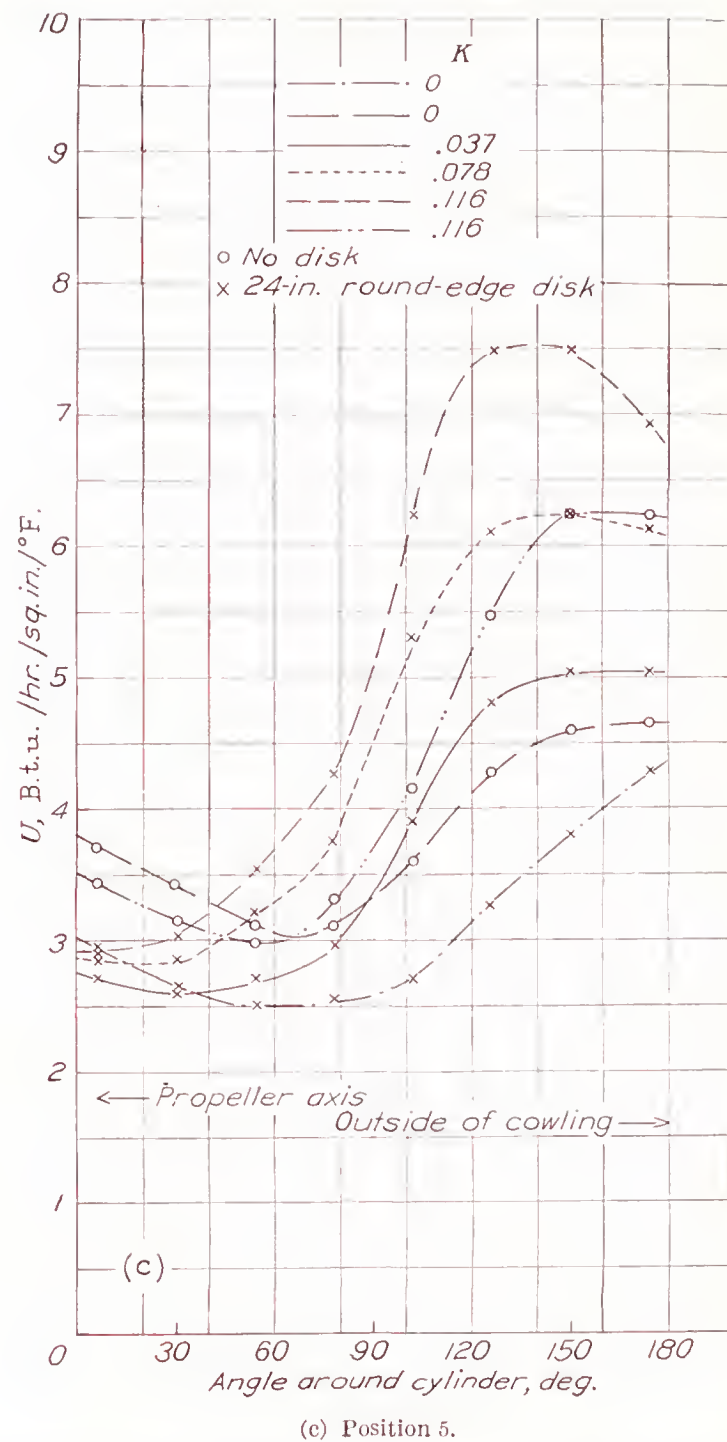
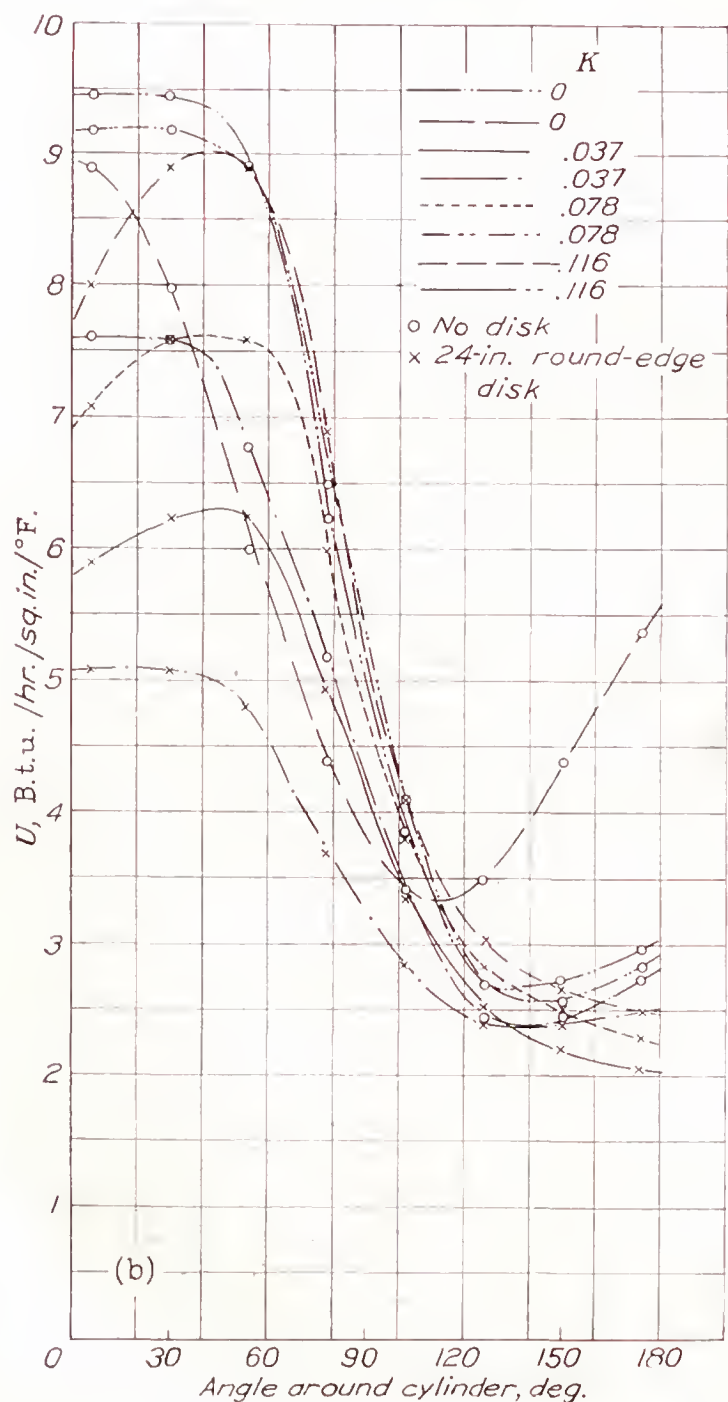
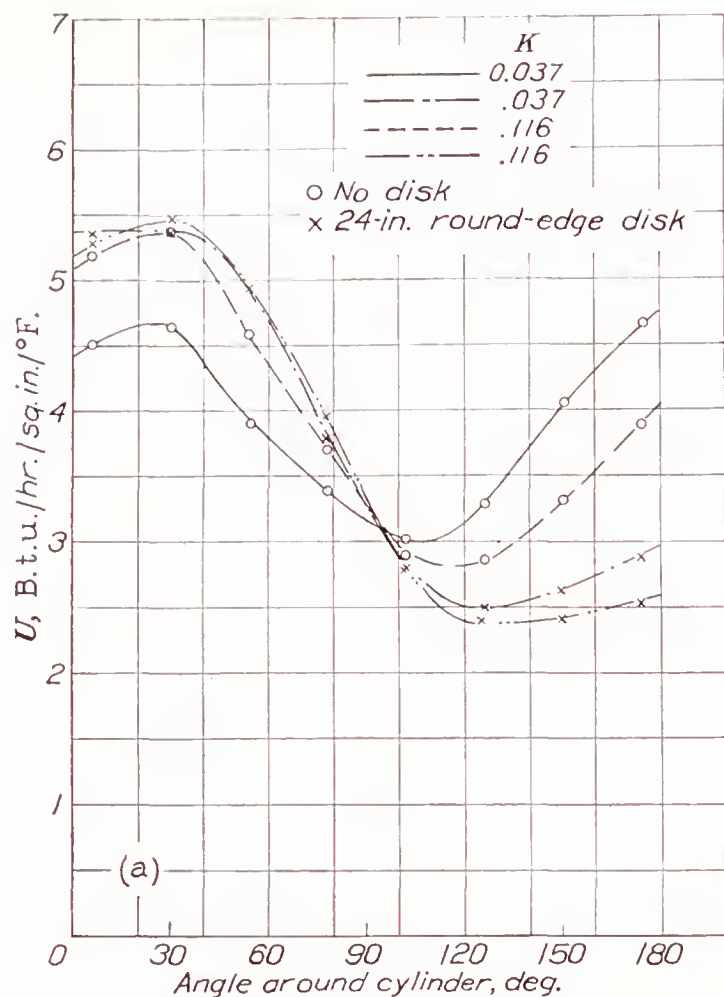


FIGURE 20.—Variation of local heat-transfer coefficient with angle around cylinder for cylinder V with  $\frac{1}{16}$ -inch fin spacing and 1-inch fin width for several engine conductivities, with and without disk in nose. Wooden cylinders. Ground condition.

will be roughly proportional to the fifth power of the cooling.

Although the results presented in this report are believed to be representative of the quantitative values of the heat-transfer coefficient to be realized on an actual engine, their chief value lies in the fact that they indicate the comparative importance of various cooling parameters and also the manner in which the variation of each individual parameter affects the cooling of a cylinder.

The results herein presented serve to introduce the problem of front cooling and to give a preliminary answer. The problem should be further studied with a set-up where actual engine cylinders in a cowling can be tested under operating conditions simulating ground, climb, and cruising conditions. In this manner, the relative cooling of the front and the rear of the cylinder, as well as the effect of fin dimensions, fin arrangement, and baffle arrangement on cooling, can be determined. This information is especially important because recent



cooling determinations (results unpublished) show that the power cost for this cooling is lower by far than the power cost of any other arrangement, in addition to the advantage of the extreme simplicity of the cooling system.

#### CONCLUSIONS

The cooling in the front of a cowling was:

1. Not greatly dependent on the position or the orientation of the cylinder within the cowling for usual engine conductivities.
2. Improved by an increase in engine conductivity in the cruising condition.
3. A function of the propeller speed, improving as the speed increased.
4. A function of fin width, the optimum fin width falling within the usable range.
5. Improved by narrower spacing to the point where the air-flow resistance was too high.
6. Increased by an increase in air speed.
7. Slightly decreased by the use of a stationary disk behind the propeller.

LANGLEY MEMORIAL AERONAUTICAL LABORATORY,  
NATIONAL ADVISORY COMMITTEE FOR AERONAUTICS,  
LANGLEY FIELD, VA., *April 5, 1939.*

#### REFERENCES

1. Stickle, George W., and Joyner, Upshur T.: The Pressure Available for Ground Cooling in Front of the Cowling of Air-Cooled Airplane Engines. T. N. No. 673, N. A. C. A., 1938.
2. Theodorsen, Theodore, Brevoort, M. J., and Stickle, George W.: Full-Scale Tests of N. A. C. A. Cowlings. T. R. No. 592, N. A. C. A., 1937.
3. Brevoort, M. J., Stickle, George W., and Ellerbrock, Herman H., Jr.: Cooling Tests of a Single-Row Radial Engine with Several N. A. C. A. Cowlings. T. R. No. 596, N. A. C. A., 1937.
4. Theodorsen, Theodore, Brevoort, M. J., and Stickle, George W.: Cooling of Airplane Engines at Low Air Speeds. T. R. No. 593, N. A. C. A., 1937.
5. Brevoort, Maurice J.: Energy Loss, Velocity Distribution, and Temperature Distribution for a Baffled Cylinder Model. T. N. No. 620, N. A. C. A., 1937.
6. Brevoort, Maurice J.: The Effect of Air-Passage Length on the Optimum Fin Spacing for Maximum Cooling. T. N. No. 649, N. A. C. A., 1938.
7. Brevoort, M. J.: Principles Involved in the Cooling of a Finned and Baffled Cylinder. T. N. No. 655, N. A. C. A., 1938.







## REPORT No. 675

### EFFECTS OF ELEVATOR NOSE SHAPE, GAP, BALANCE, AND TABS ON THE AERODYNAMIC CHARACTERISTICS OF A HORIZONTAL TAIL SURFACE

By HARRY J. GOETT and J. P. REEDER

#### SUMMARY

*Results are presented showing the effects of gap, elevator nose shape, balance, cut-out, and tabs on the aerodynamic characteristics of a horizontal tail surface tested in the N. A. C. A. full-scale tunnel.*

*The presence of a gap caused an 18 percent reduction in the variation of normal force with elevator deflection but the size of the gap (between  $0.005\bar{c}$  and  $0.010\bar{c}$ ) was an unimportant factor. At small elevator deflections, the effectiveness of aerodynamic balance of the elevator in reducing hinge moments was much lower with the tapered nose than with the blunt nose. The tapered nose, however, maintained its effectiveness to much greater deflections and gave a greater maximum normal-force increment than did the blunt nose. With the blunt nose, the hinge moments were reduced 30 and 40 percent with 10- and 20-percent balances, respectively. This reduction is fairly uniform up to the stall of the elevator. The decrease in normal force and hinge moment caused by a cut-out was proportional to the area removed. The variation in tab effectiveness with a change in tab span was found to be approximately proportional to the area-moment of the tab about the elevator hinge line. A comparison of the various experimental aerodynamic characteristics with those computed from Glauert's thin-airfoil theory for hinged flaps is also given.*

#### INTRODUCTION

The tail-surface investigation being carried on in the N. A. C. A. full-scale wind tunnel includes the determination of isolated tail-surface characteristics and the variation in these characteristics caused by wing, fuselage, and slipstream interference. The subject report deals with certain factors influencing the characteristics of the isolated tail surface.

Examination of existing data shows a lack of information in regard to the effect of elevator nose shape and gap upon tail-surface characteristics, particularly with reference to aerodynamic balance of the elevator. Data are also lacking concerning the effects of elevator cut-out and of trailing-edge tabs on large-chord flaps. The importance of some of these variables is indicated in references 1 and 2. The tests reported herein were therefore carried out to determine the effects of these

factors on a tail surface of representative design. In the analysis, the differences between the experimental results and those obtained from the thin-airfoil theory have been indicated so that the conclusions may be readily generalized.

#### SYMBOLS

The symbols used in the report are defined as follows:

$A$ , aspect ratio.

$R$ , Reynolds Number.

$C_N$ , normal-force coefficient ( $C_L \cos \alpha + C_D \sin \alpha$ ).

$C_C$ , chord-force coefficient ( $C_D \cos \alpha - C_L \sin \alpha$ ).

$H_e$ , elevator hinge moment.

$C_{h_e}$ , elevator hinge-moment coefficient  $-\frac{H_e}{q \bar{c}_e^2 b_e}$ .

$\Delta C_{h_e}$ , change in  $C_{h_e}$  with  $\delta_t$ .

$\alpha$ , angle of attack of the tail, deg.

$\delta_e$ , elevator angle (downward deflection positive).

$\delta_t$ , tab angle (downward deflection positive).

$S$ , area.

$b$ , span.

$c$ , chord.

$\bar{c}$ , average chord.

$\bar{c}_e^2$ , mean square of elevator chords.

$a_0$ , slope of section lift or normal-force curve (per deg.).

$a_1$ , slope of lift or normal-force curve, elevator fixed (per deg.).

Subscripts:

$e$ , elevator.

$b$ , balance.

$t$ , tab.

Symbols with no subscripts refer to the entire horizontal tail surface.

#### APPARATUS

The tests were conducted in the full-scale wind tunnel described in reference 3. The tail surface is shown mounted in the tunnel jet in figure 1.

The dimensions of the tail surface are given in figure 2. The taper ratio was 2:1 and the locus of the 0.55 $\bar{c}$  stations (the hinge line) was perpendicular to the line of symmetry. The  $S_e/S$  ratio was 0.41 and the aspect ratio was 4.7. The cut-out area was equal to 3 percent of the tail area.



Removable elevator-nose and stabilizer-tail blocks (see fig. 3) were provided so that the elevator balance, the nose shape, and the gap could be varied. Provision was made for minimum, 10-percent, and 20-percent



FIGURE 1.—Tail surface mounted in the full-scale tunnel

balances with the balance distributed along the span of the elevator in proportion to the local chord. With the minimum-balance nose, 4 percent of the elevator area projected forward of the hinge line but, since this overhang was less than the section thickness at the hinge

Provision was made on all the arrangements for  $\frac{9}{64}$ -inch and  $\frac{3}{32}$ -inch gaps, equal to  $0.005\bar{c}$  and  $0.010\bar{c}$ . Zero gap was obtained for the minimum balance by sealing the gap.

The trailing-edge tab, equal to 18 percent of the elevator area, was divided into inboard, middle, and outboard sections of approximately equal areas that could be individually deflected.

The device for the measurement of the elevator hinge moment was housed in the center section of the tail and consisted of a calibrated torsion rod to which the hinge moment was transmitted. The deflection of this rod caused the rotation of a self-synchronous motor in the tail, which in turn controlled a similar motor in the scale house where the deflection was measured.

### TESTS

Preliminary tests were made to determine the tare, the blocking, and the tunnel corrections according to the procedure outlined in reference 4.

Lift, drag, and hinge moments were measured on the following tail arrangements for elevator deflections from  $0^\circ$  to  $30^\circ$  and for angles of attack from  $-12^\circ$  to  $20^\circ$ .

- (1) Minimum balance, zero gap (no hinge moments measured).
- (2) Minimum balance,  $0.005\bar{c}$  and  $0.010\bar{c}$  gaps.
- (3) Minimum balance,  $0.005\bar{c}$  gap, cut-out covered.

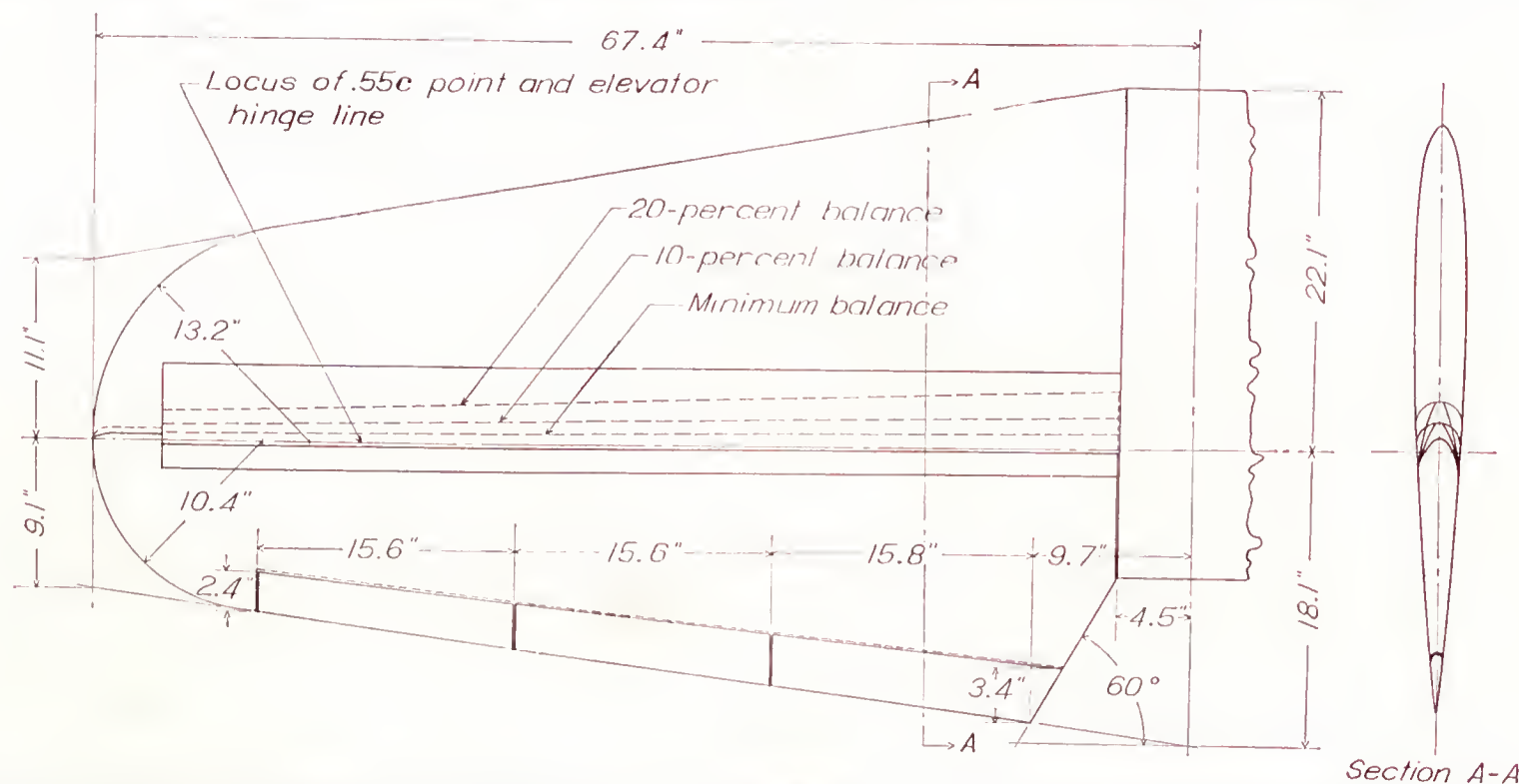


FIGURE 2.—Horizontal tail surface. Total area, 27 sq. ft.; stabilizer area, 15.9 sq. ft.; elevator area, 11.1 sq. ft.; taper ratio, 2:1; aspect ratio, 4.7; airfoil section, N. A. C. A. 0009.

line, this arrangement was used for comparison with zero-balance results computed from thin-airfoil theory. The blunt and the tapered nose shapes are shown in figure 3. The blunt nose was formed by making the leading-edge radius equal to one-half the section thickness. Only one nose shape was provided for the minimum balance; it has been used for comparison with both the blunt and the tapered noses of the 10- and the 20-percent balances.

- (4) Minimum balance,  $0.005\bar{c}$  gap, tab deflections from  $0^\circ$  to  $-30^\circ$ , with:

- (a) Full-span tabs.
- (b) Inboard and middle tabs.
- (c) Inboard tabs.
- (d) Middle tabs.
- (e) Outboard tabs.

- (5) 10-percent balance, tapered nose,  $0.005\bar{c}$  and  $0.010\bar{c}$  gaps.



(6) 10-percent balance, blunt nose,  $0.005\bar{c}$  and  $0.010\bar{c}$  gaps.

(7) 20-percent balance, tapered nose,  $0.005\bar{c}$  and  $0.010\bar{c}$  gaps.

(8) 20-percent balance, blunt nose,  $0.005\bar{c}$  and  $0.010\bar{c}$  gaps.

All the foregoing tests were conducted at a tunnel air speed of 65 miles per hour corresponding to a Reynolds Number of 1,460,000 based on the average chord. Further tests between speeds of 25 and 80 miles per hour were made to determine the scale effect on elevator hinge moments.

## RESULTS AND DISCUSSION

### NORMAL-FORCE CHARACTERISTICS

The variation of normal-force coefficient and chord-force coefficient with angle of attack for various arrangements of elevator balance, nose shape, and gap and for elevator deflections from  $0^\circ$  to  $30^\circ$  is given in figures 4 to 9. The  $C_C$  curves for the  $0.010\bar{c}$  gap arrangements are omitted because they are the same as those for the  $0.005\bar{c}$  gap except in the region of the stall.

The slope of the normal-force coefficient,  $dC_N/d\alpha$ , for an N. A. C. A. 0009 airfoil of 4.7 aspect ratio and 2:1 taper, as computed from the aspect-ratio correction formula (see the appendix), is 0.069. This value is to be compared with the experimental slope of 0.063 obtained for the zero-gap condition (fig. 4), which was reduced to 0.060 when a gap was introduced (fig. 5). It will be noted that, for elevator deflections up to  $10^\circ$ , the deflections, the nose shape, and the gap size had a negligible effect on the slope, causing not more than a  $\pm 0.002$  variation from the average value of 0.060; at a  $\delta_e$  of  $20^\circ$ , the average slope decreased to about 0.056. Tests with the elevator cut-out covered showed no change in slope when the coefficients were based on the increased area.

The effect of the gap appears on the  $C_N$  curves mainly as a shift in the angle of zero lift for elevator deflections other than zero. This shift causes a decrease in the  $dC_N/d\delta_e$  slope for the arrangements with gap, which will be noted in figure 10 (a). The zero-gap arrangement has a slope of 0.043 (up to  $\delta_e$  of  $15^\circ$ ), which is decreased to approximately 0.032 when a gap is introduced. These slopes are, respectively, 93 percent and 75 percent of the corresponding slopes computed from thin-airfoil theory. (See equation (1), appendix.) The difference in slope between the  $0.005\bar{c}$  and the

$0.010\bar{c}$  arrangements is small at angles below the stall. For some nose shapes, the larger gap causes an earlier stall. (See  $\delta_e = 20^\circ$  and  $30^\circ$ , fig. 8.)

The addition of aerodynamic balance increases the  $dC_N/d\delta_e$  slope (figs. 10 (b) and (c)). The tapered nose gives a slightly lower slope at small elevator deflections than do the blunt noses, probably because of the more marked shielding effect of the stabilizer. The tapered

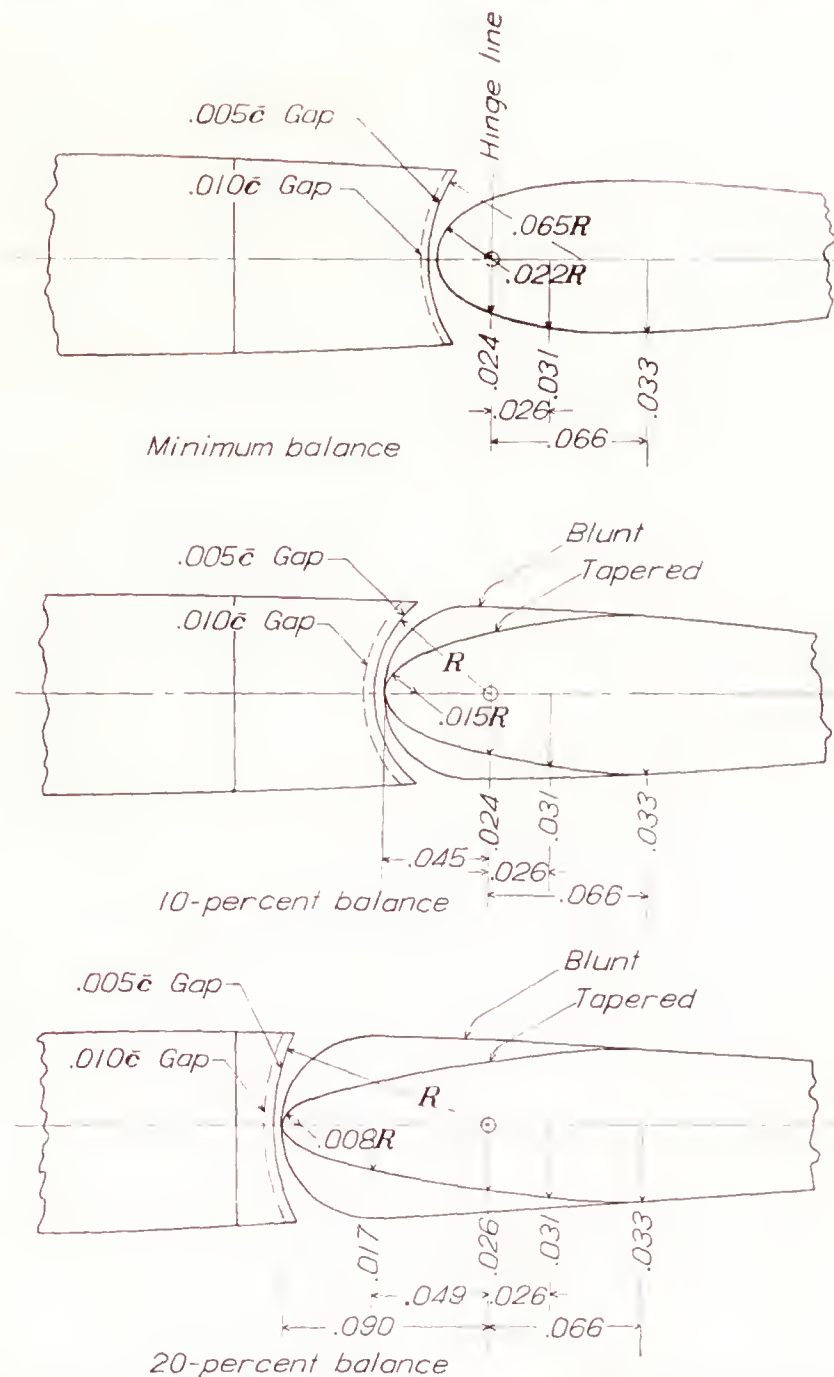


FIGURE 3.—Elevator-nose and stabilizer-tail blocks of the horizontal-tail surface. Nose ordinates given in fractions of local chord.

nose, however, permits the maintenance of elevator effectiveness to much larger deflections and gives a greater maximum increment of normal-force coefficient. For instance, the 20-percent-balance blunt nose gives a maximum increment of only 0.75, as compared with a value of 1.05 obtainable with the tapered nose of equal balance.



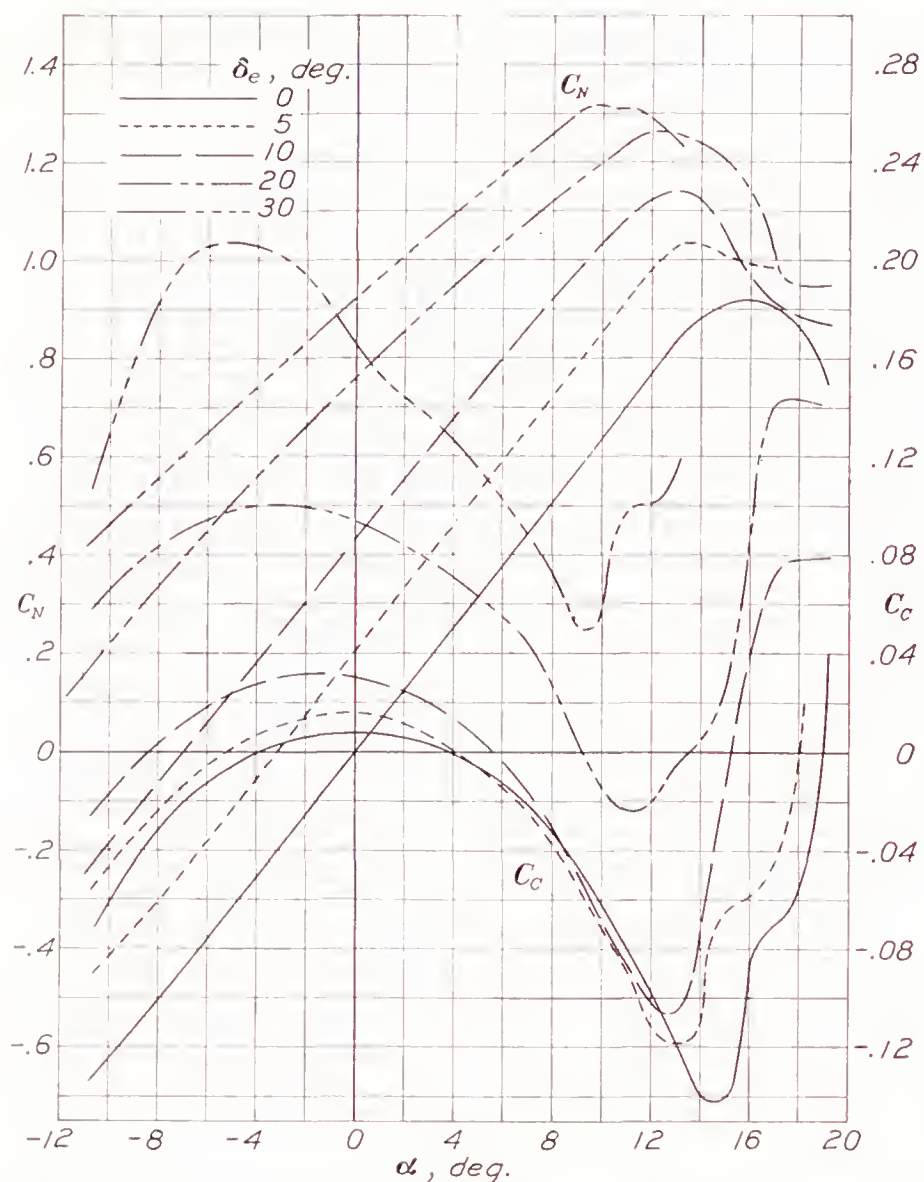


FIGURE 4.—Variation of  $C_N$  and  $C_c$  with  $\alpha$  at various elevator deflections for minimum balance, zero gap.

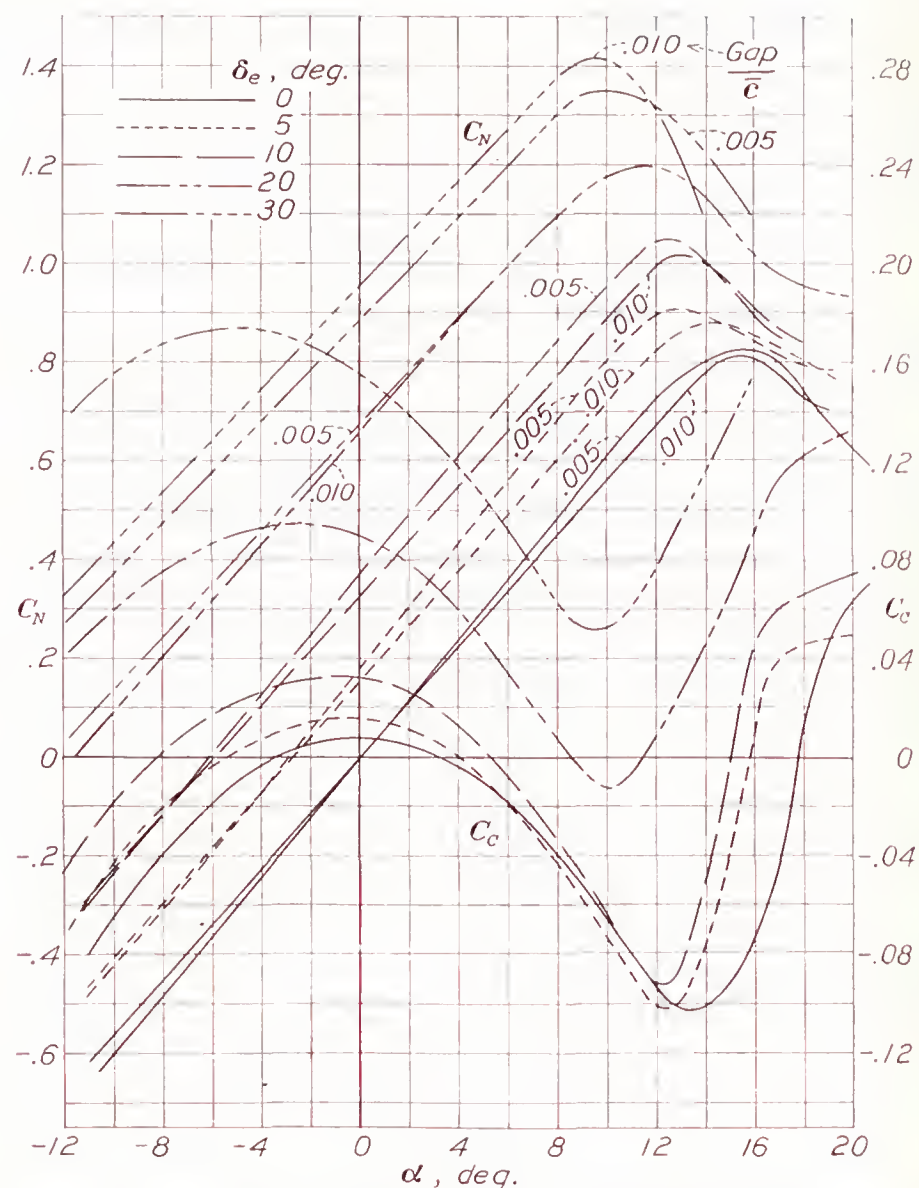


FIGURE 6.—Variation of  $C_N$  and  $C_c$  with  $\alpha$  at various elevator deflections for 10-percent balance, tapered nose, 0.005 $\bar{c}$  and 0.010 $\bar{c}$  gap.

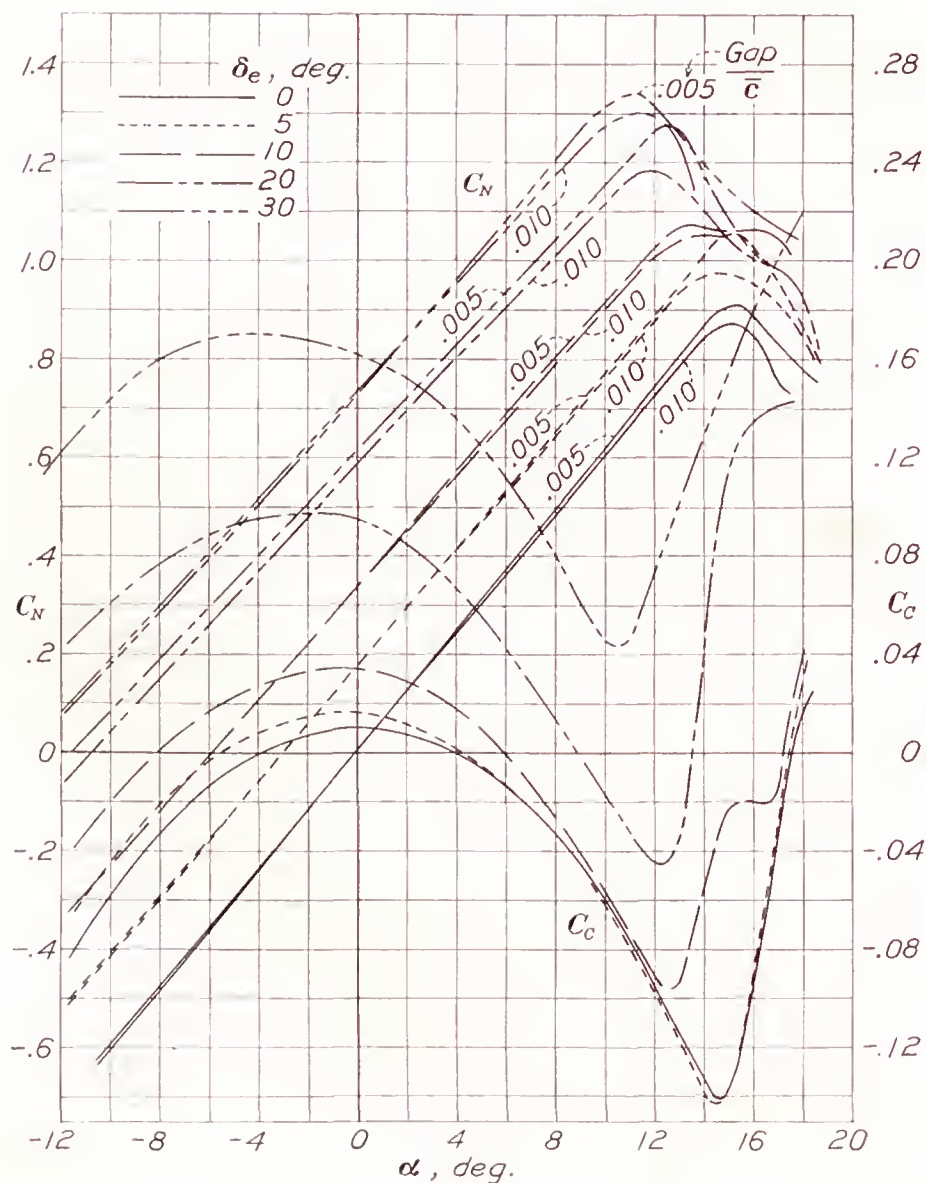


FIGURE 5.—Variation of  $C_N$  and  $C_c$  with  $\alpha$  at various elevator deflections for minimum balance, 0.005 $\bar{c}$  and 0.010 $\bar{c}$  gap.

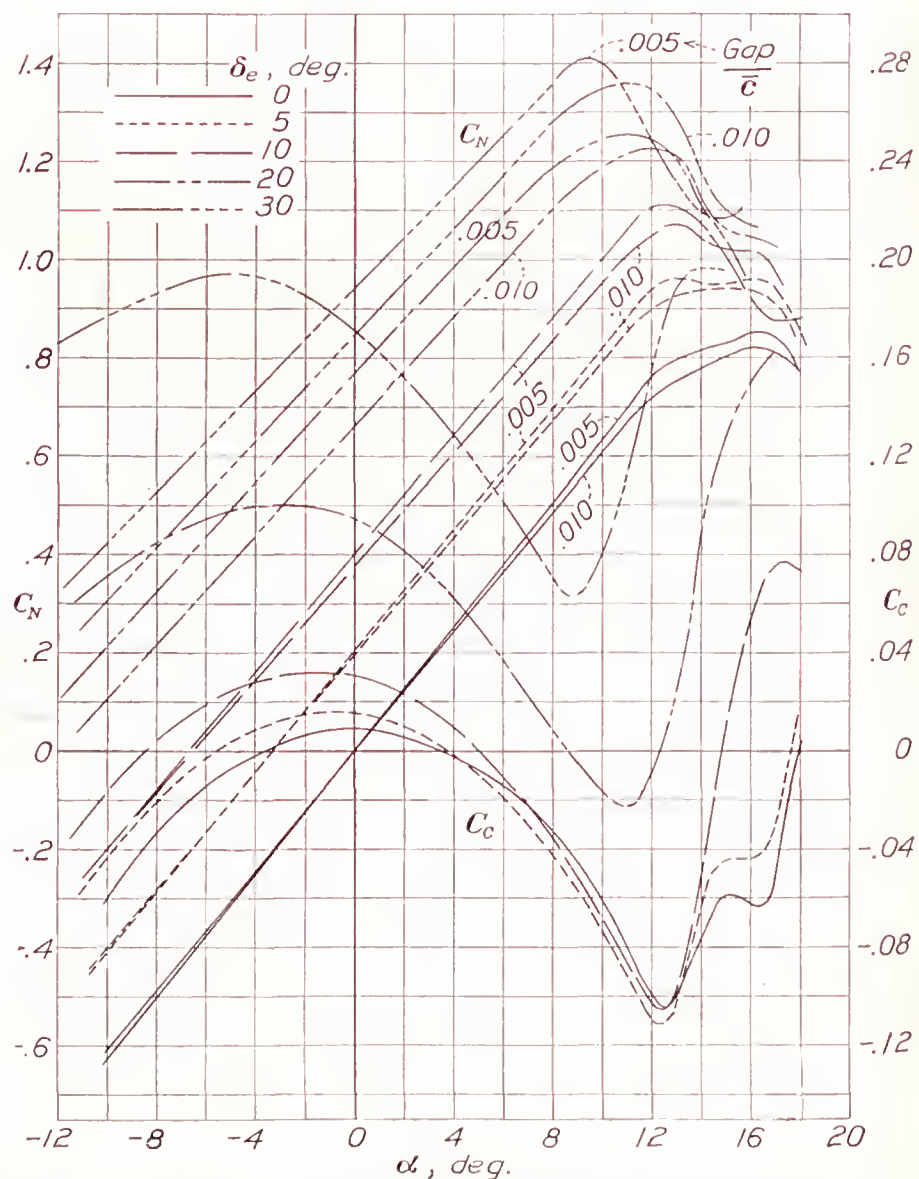


FIGURE 7.—Variation of  $C_N$  and  $C_c$  with  $\alpha$  at various elevator deflections for 10-percent balance, blunt nose, 0.005 $\bar{c}$  and 0.010 $\bar{c}$  gap.



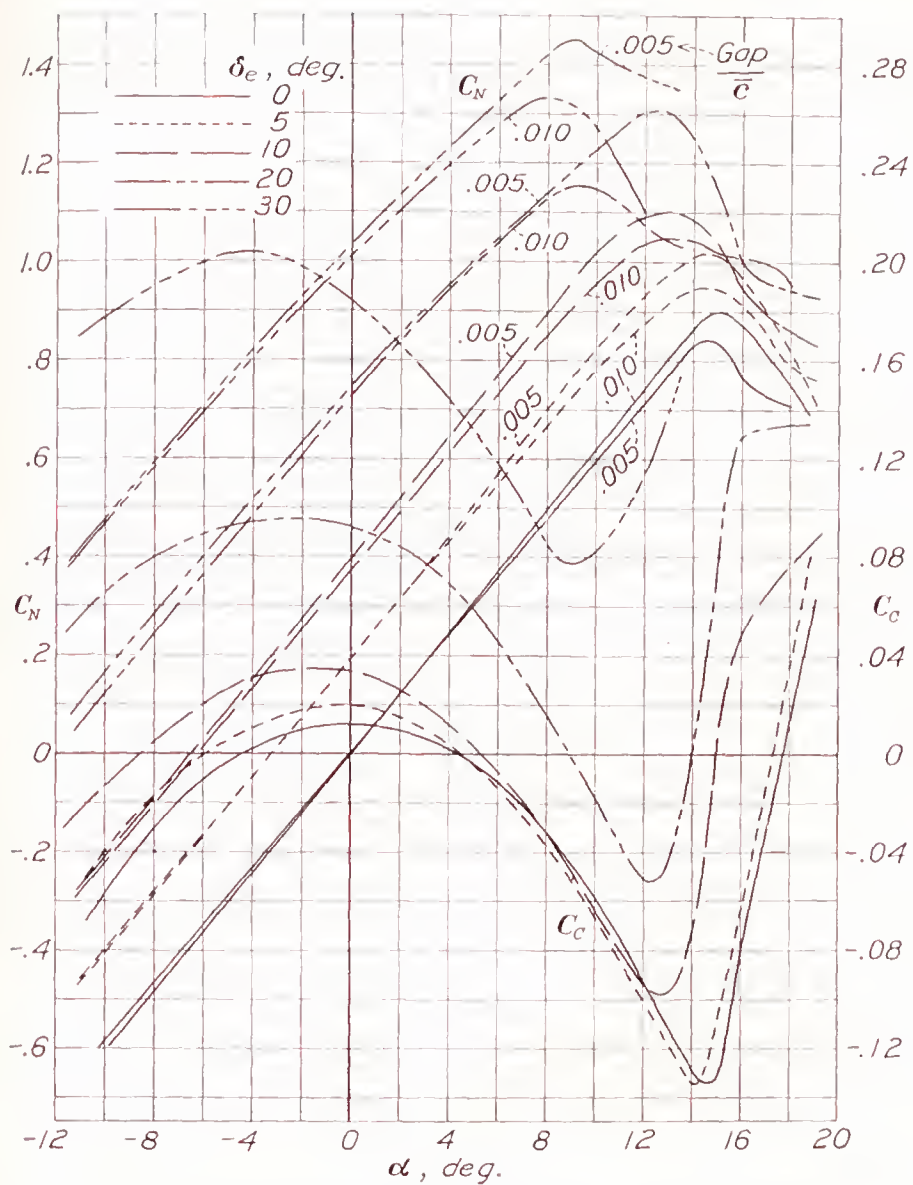


FIGURE 8.—Variation of  $C_N$  and  $C_c$  with  $\alpha$  at various elevator deflections for 20 percent balance, tapered nose, 0.005 $\bar{c}$  and 0.010 $\bar{c}$  gap.

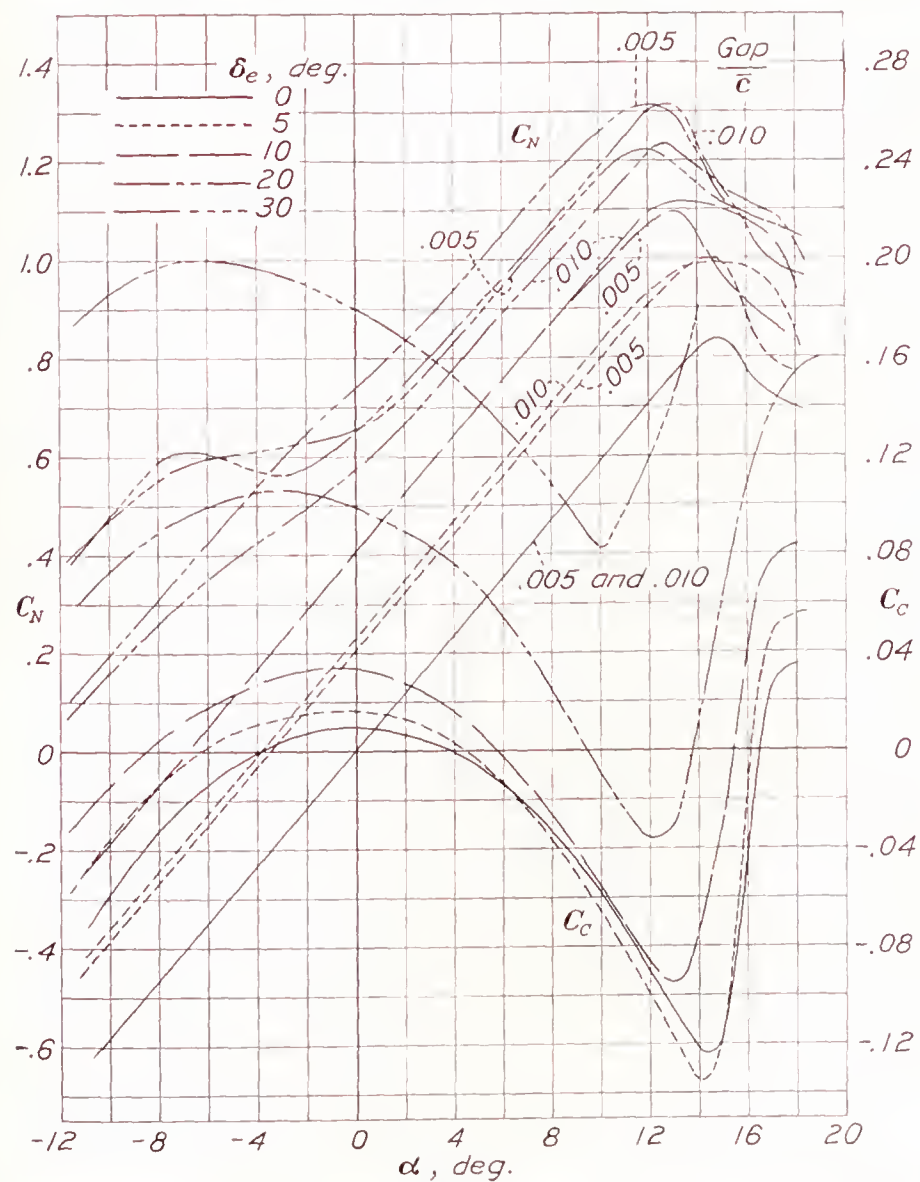


FIGURE 9.—Variation of  $C_N$  and  $C_c$  with  $\alpha$  at various elevator deflections for 20 percent balance, blunt nose, 0.005 $\bar{c}$  and 0.010 $\bar{c}$  gap.

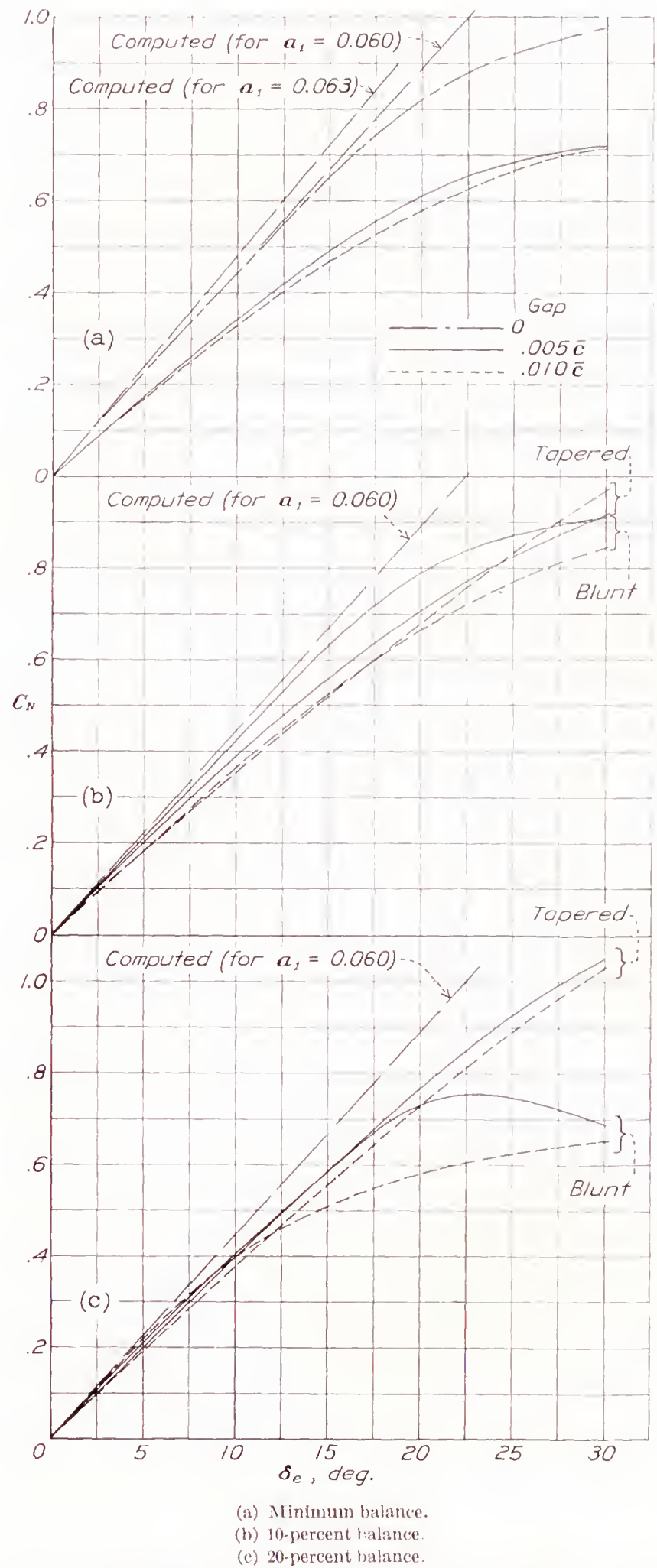


FIGURE 10.—Effect of gap and nose shape on variation of  $C_N$  with  $\delta_e$ .  $\alpha = 0^\circ$



The results shown in figure 10 are for an angle of attack of zero, but they are characteristic of the results obtained within an angle-of-attack range of  $\pm 8^\circ$ .

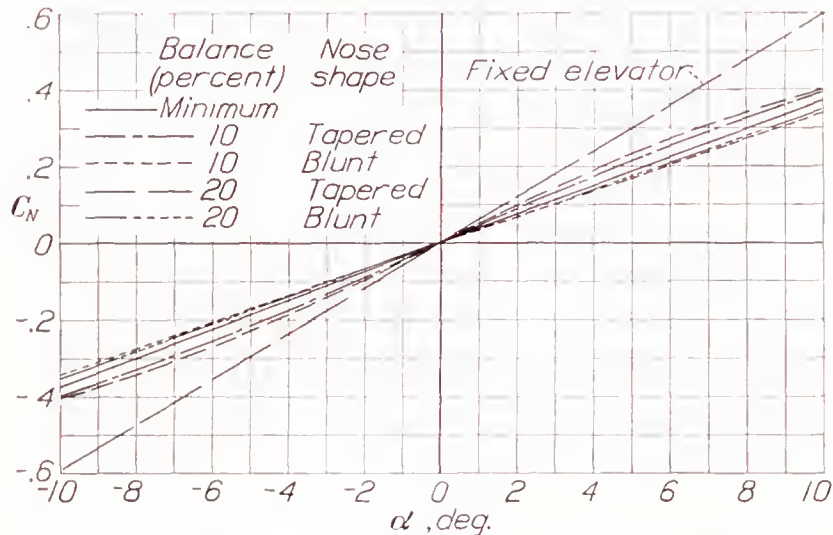


FIGURE 11.—Variation of  $C_N$  with  $\alpha$ . Elevator free;  $0.005\bar{c}$  gap.

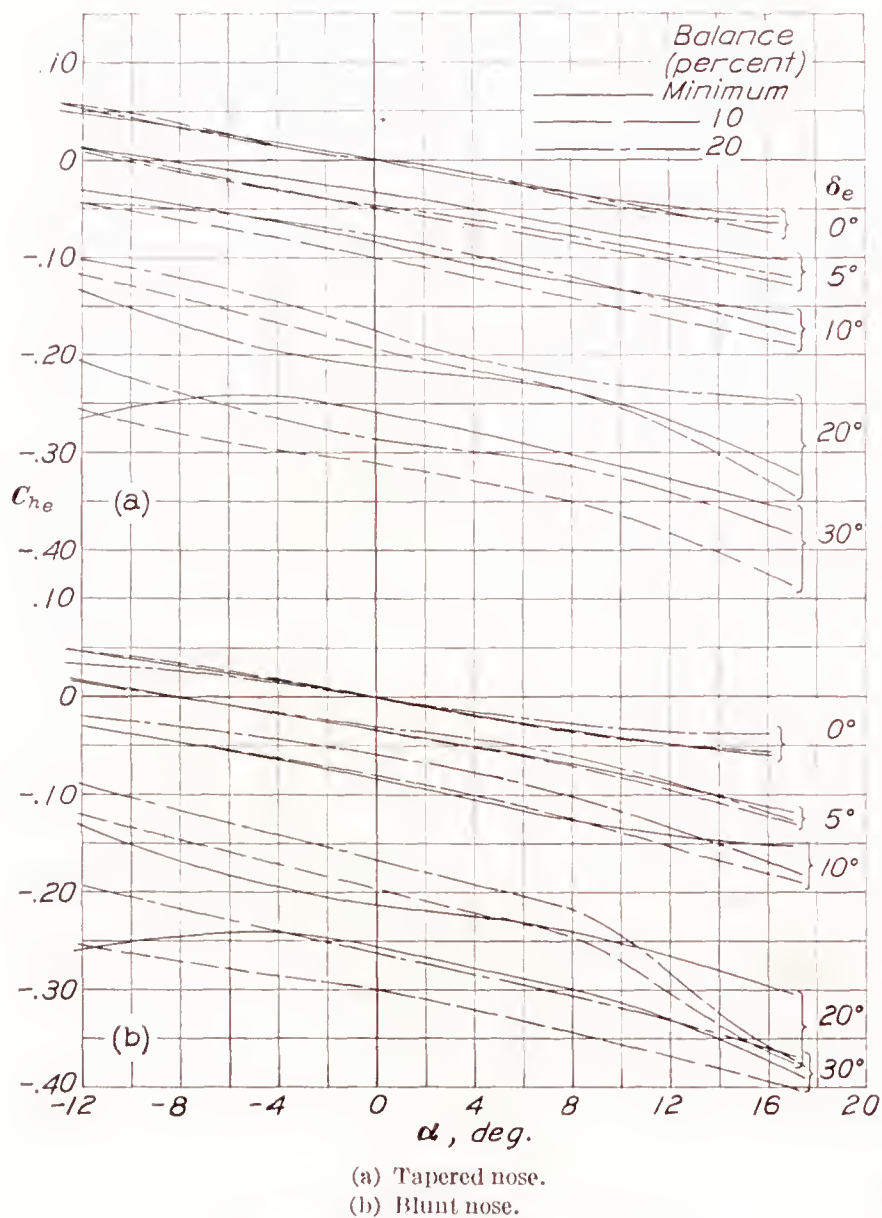


FIGURE 12.—Variation of  $C_h$  with  $\alpha$ .  
(a) Tapered nose.  
(b) Blunt nose.

The elevator-free lift-curve slopes for all the tail arrangements with the  $0.005\bar{c}$  gap are shown in figure 11. The experimental slope for the minimum balance is 0.037; the slope computed from thin-airfoil theory is

0.035. (See equation (2) in appendix.) An investigation of a number of other unbalanced tails, for which data are given in reference 2, shows that this close correspondence between the experimental and the

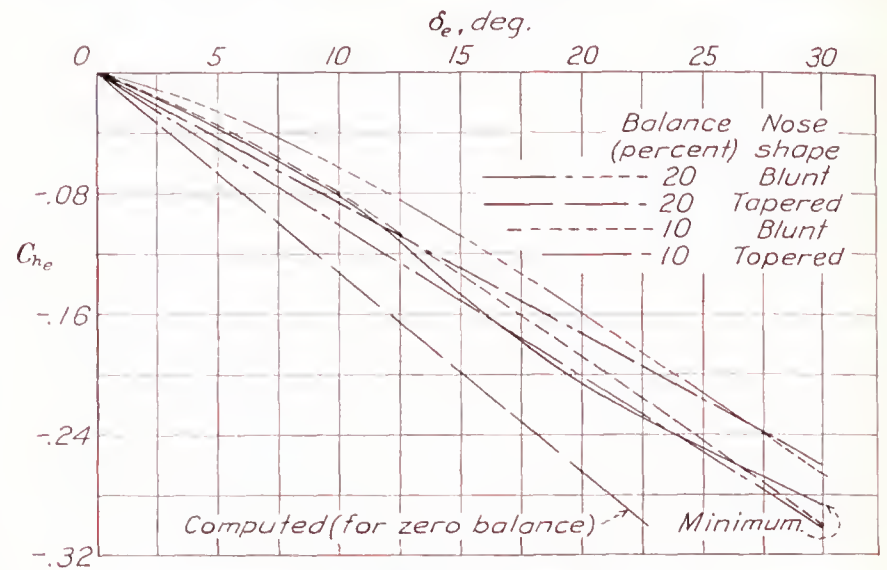


FIGURE 13.—Variation of  $C_h$  with  $\delta_e$ .  $\alpha = 0^\circ$ .

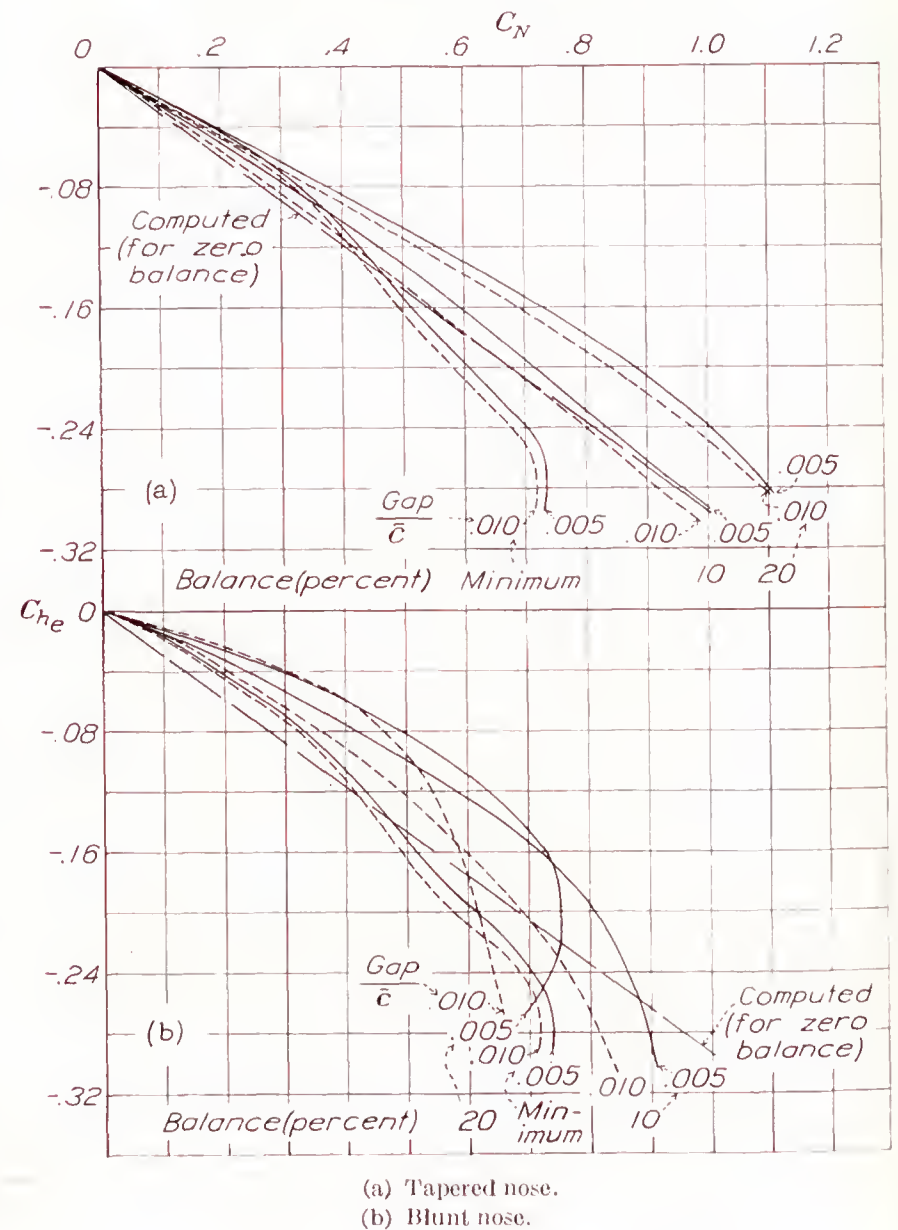


FIGURE 14.—Variation of  $C_h$  with  $C_N$ .  $\alpha = 0^\circ$ .  
(a) Tapered nose.  
(b) Blunt nose.

computed slopes is not general. Experimental slopes computed from the results in reference 2 varied from 15 percent to 40 percent in excess of the computed slope.



## HINGE-MOMENT CHARACTERISTICS

The variation of hinge-moment coefficient with angle of attack for the various tail arrangements is shown in figure 12. These curves are applicable to both the 0.005 $\bar{c}$  and the 0.010 $\bar{c}$  gap arrangements because the size of these gaps caused negligible variations. The  $dC_{h_e}/d\alpha$  slope computed from thin-airfoil theory is

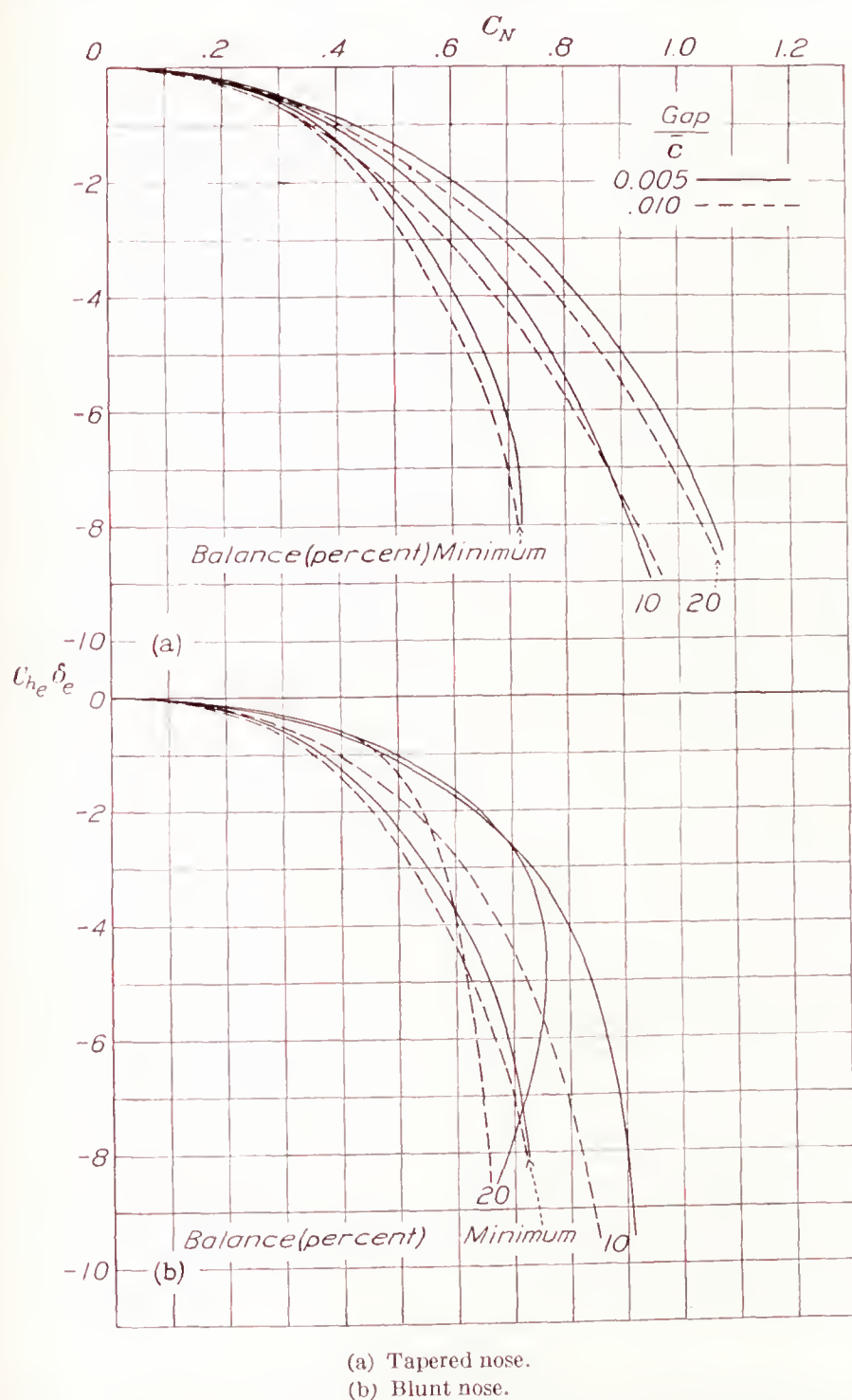


FIGURE 15.—Variation of stick-force criterion  $C_{h_e} \delta_e$  with  $C_N$  for various tab arrangements.  $\alpha=0^\circ$ .

−0.0073, which compares with an average experimental value of −0.0045. There appears to be no systematic variation of slope with nose shape, balance, or elevator deflection, these factors causing a spread of no more than  $\pm 0.0005$  from the average value.

A cross plot of elevator hinge-moment coefficient against elevator deflection is given in figure 13 for each of the balance and nose-shape arrangements. These curves are for an angle of attack of  $0^\circ$  but are characteristic of the values obtained over a range of angles

from  $\pm 8^\circ$ . It will be noted that  $dC_{h_e}/d\delta_e$  varies from 0.55 to 0.75 of the value computed from thin-airfoil theory for an unbalanced elevator. The effect of the cut-out on this slope is proportional to the area removed; the scale effect between speeds of 25 and 80 miles per hour (Reynolds Number equal to 560,000 to

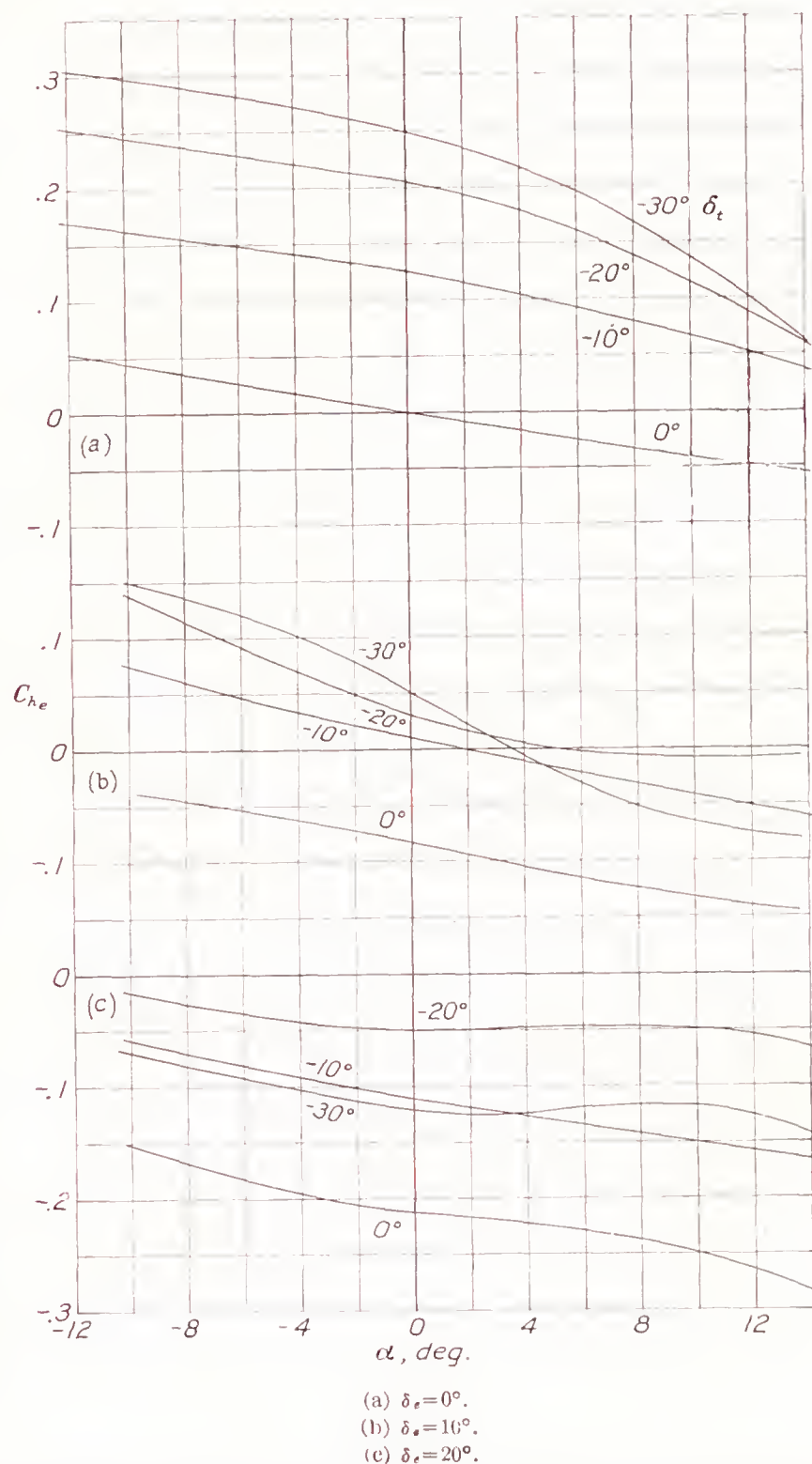


FIGURE 16.—Variation of  $C_{h_e}$  with  $\alpha$  for various deflections of the full-span tab.

1,800,000 based on the average chord) was found to be negligible.

A criterion of balance effectiveness is the reduction produced in  $C_{h_e}$  for a given  $C_N$ . Figure 14 shows this characteristic. A uniform reduction in  $C_{h_e}$  up to the point at which the elevator stalls is obtained with the blunt-nose balances; the balancing effect of the tapered noses, however, varies markedly with elevator deflection but remains effective to much higher values of  $C_N$



than for the blunt noses. Table I summarizes the balancing effect of the various balances and nose shapes. The relatively close agreement of the experimental

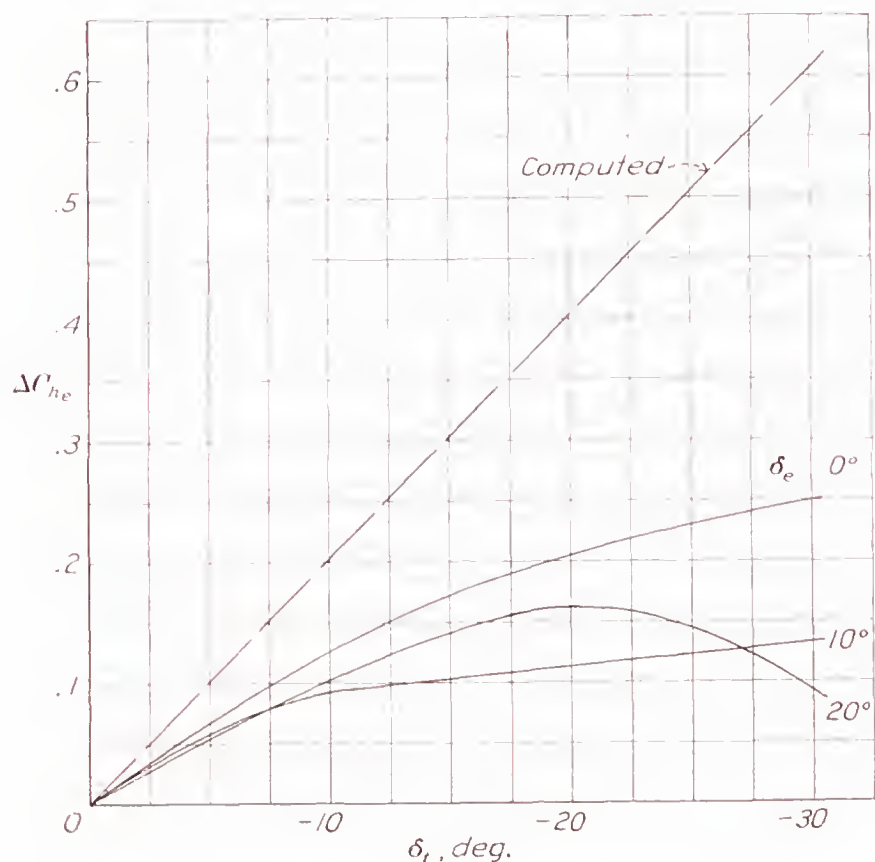


FIGURE 17.—Variation of  $\Delta C_{h_e}$  with  $\delta_t$  for full-span tab.  $\alpha=0^\circ$ .

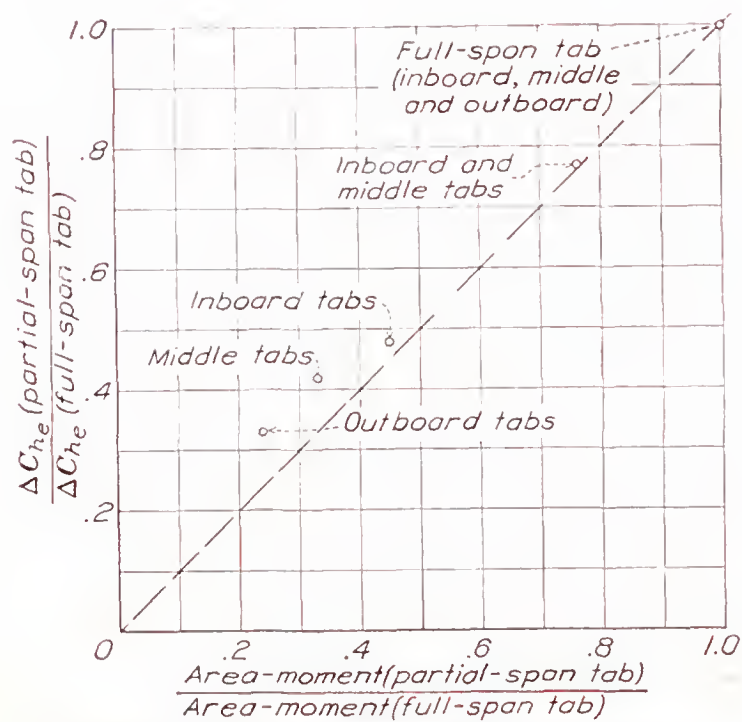
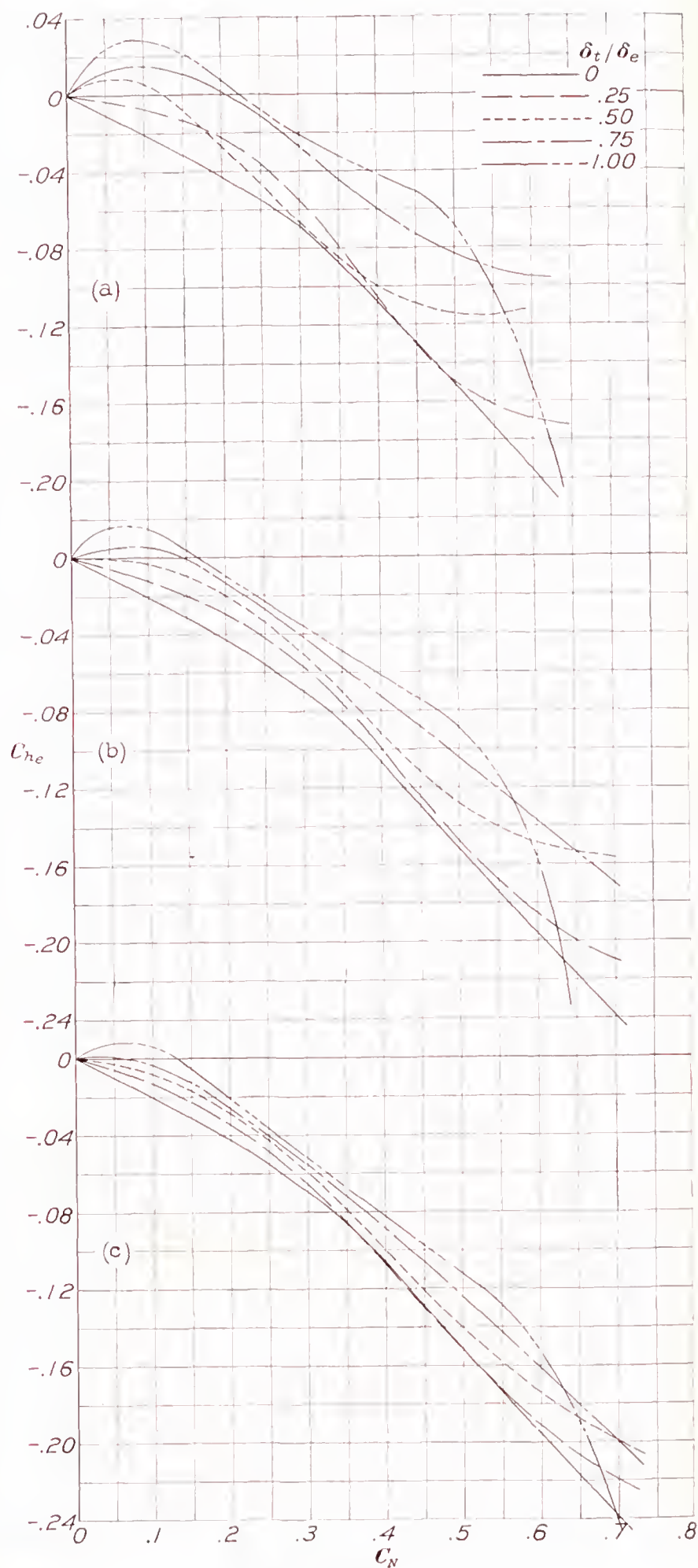


FIGURE 18.—Variation of tab effectiveness with tab span.

$dC_N/dC_{h_e}$  slope compared with that computed by thin-airfoil theory is due to the fact that a decrease in  $dC_N/d\delta_e$  caused by the gap is compensated by a corresponding decrease in  $dC_{h_e}/d\delta_e$ .



(a) Full-span tab.  
(b) Inboard and middle tabs.  
(c) Inboard tab.

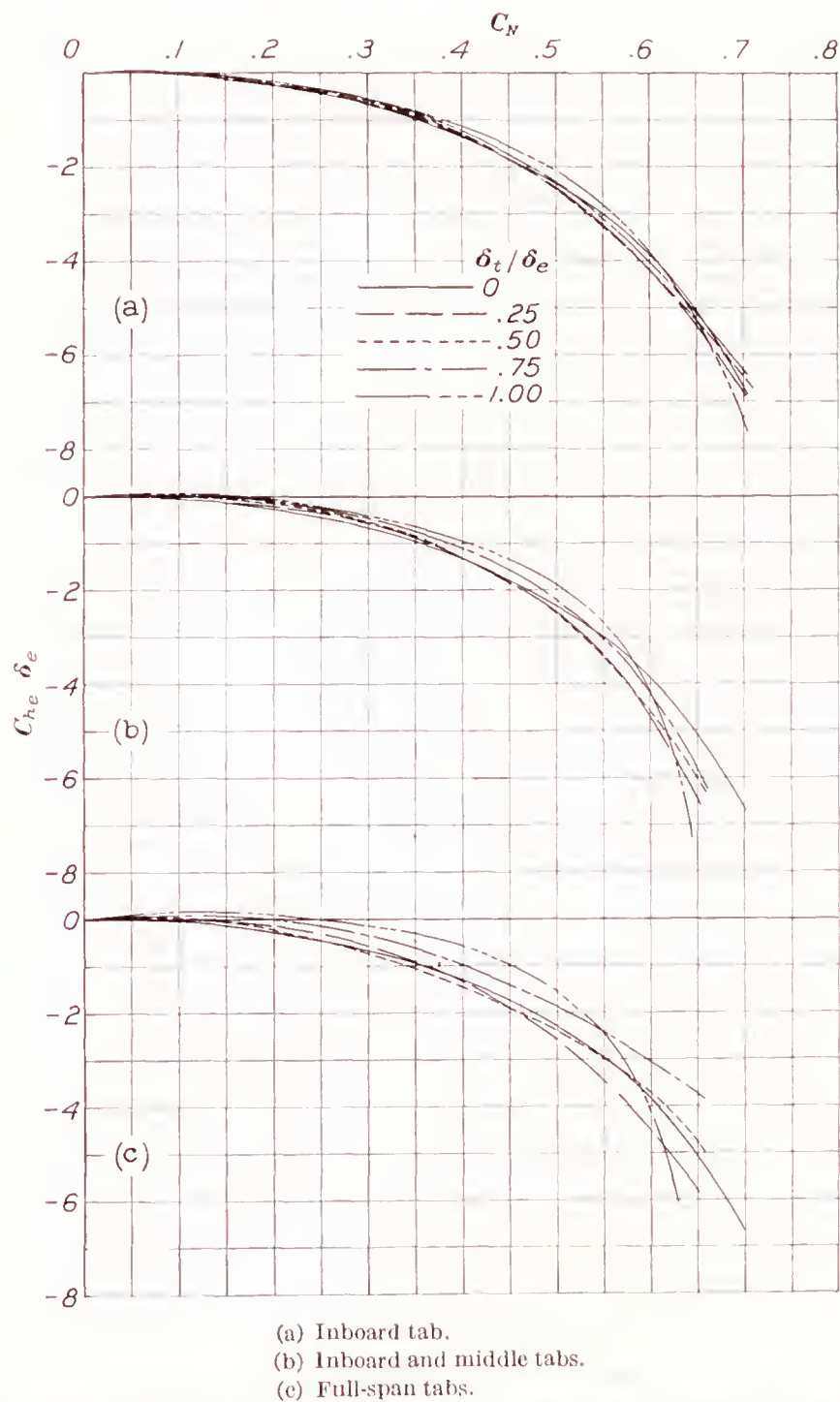
FIGURE 19.—Variation of  $C_{h_e}$  with  $C_N$  for various tab span and  $\delta_t/\delta_e$  ratios.  $\alpha=0^\circ$



TABLE I

REDUCTION IN  $C_{h_e}$  PRODUCED BY VARIOUS BALANCE AND NOSE-SHAPE ARRANGEMENTS; 0.005 $\bar{c}$  GAP

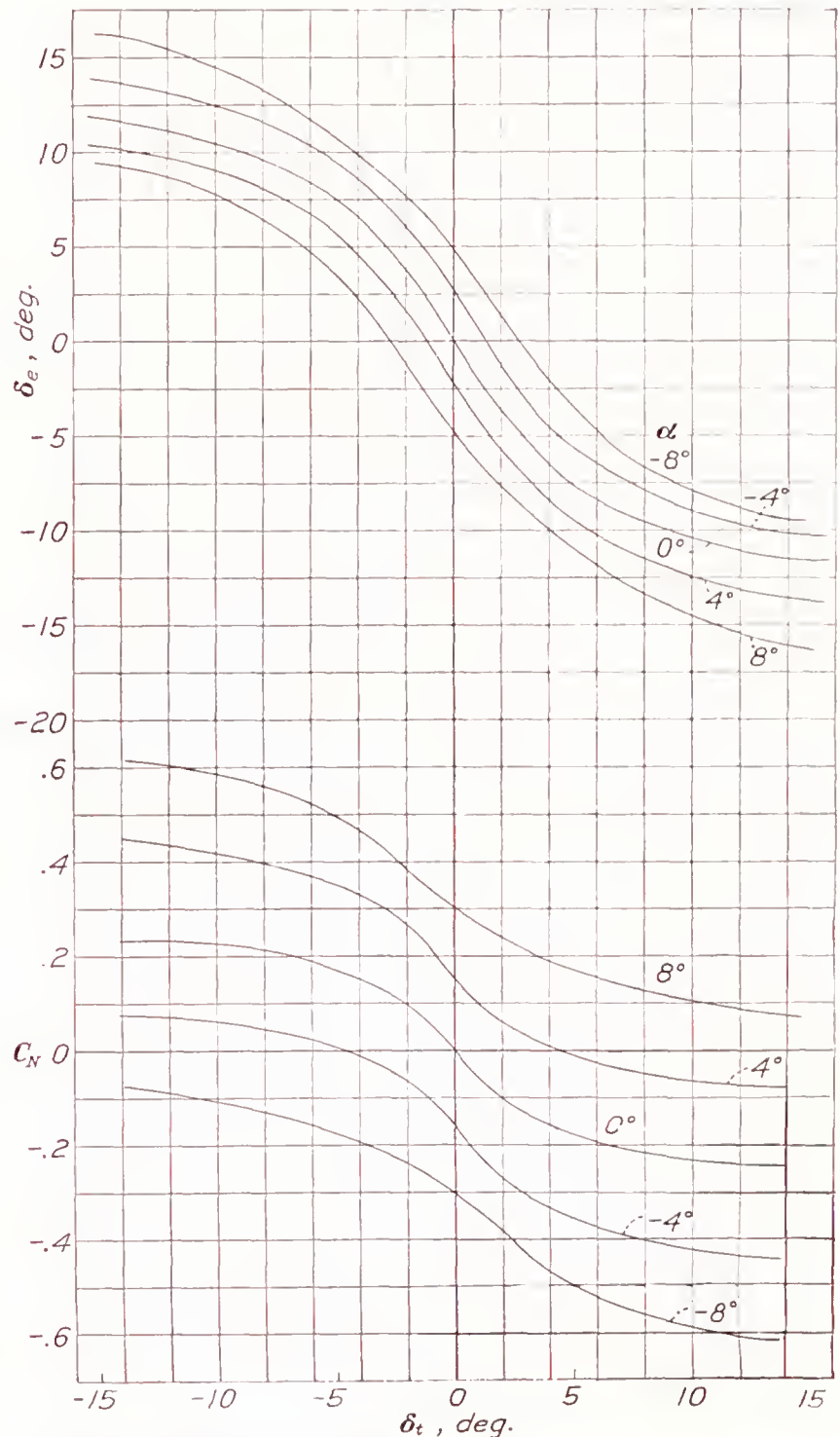
Balance (percent)	Nose shape	Percentage reduction in $C_{h_e}$ (compared with minimum balance) for a given $C_N$
10	(Blunt)	30
	(Tapered)	0-20
20	(Blunt)	40
	(Tapered)	0-40

FIGURE 20.—Variation of stick-force criterion,  $C_{h_e} \delta_e$  with  $C_N$  for various tab arrangements,  $\alpha=0^\circ$ .

Another criterion of balance effectiveness is the variation of  $C_{h_e} \delta_e$  with  $C_N$ . This criterion takes into account the possible reduction in  $C_N$  for a given elevator deflection that may be caused by the balancing device (necessitating a change in the mechanical advantage of the control system). The development of this criterion

is given in detail in reference 5. Figure 15 shows a comparison on this basis of the various arrangements.

It should be noted that all the hinge-moment results presented herein are for either 0.005 $\bar{c}$  or 0.010 $\bar{c}$  gap. Further tests appear desirable to obtain comparative results for arrangements with the gap sealed.

FIGURE 21.—Variation of  $\delta_e$  and  $C_N$  with  $\delta_t$ . Minimum-balance elevator.

## TAB CHARACTERISTICS

The variation in elevator hinge-moment coefficient with angle of attack for various full-span tab and elevator deflections is shown in figure 16. These results are for minimum balance. There is a wide variation in tab effectiveness with  $\delta_e$ , the effectiveness being greatest at small elevator deflections. Figure 17, which is a cross plot of  $\Delta C_{h_e}$  against  $\delta_t$  (for  $\alpha=0^\circ$ ), shows that the tab effectiveness (for  $\delta_e=0^\circ$ ) decreases with  $\delta_t$  to about 50 percent of the computed value at  $\delta_t=-30^\circ$ . For elevator deflections of  $10^\circ$  and  $20^\circ$ ,



a larger variation from the computed values is observed and the effectiveness decreases still further at positive angles of attack. (See fig. 16.)

The relative effectiveness of partial-span tabs compared with full-span tabs is shown in figure 18. The change in hinge moment produced by a given tab

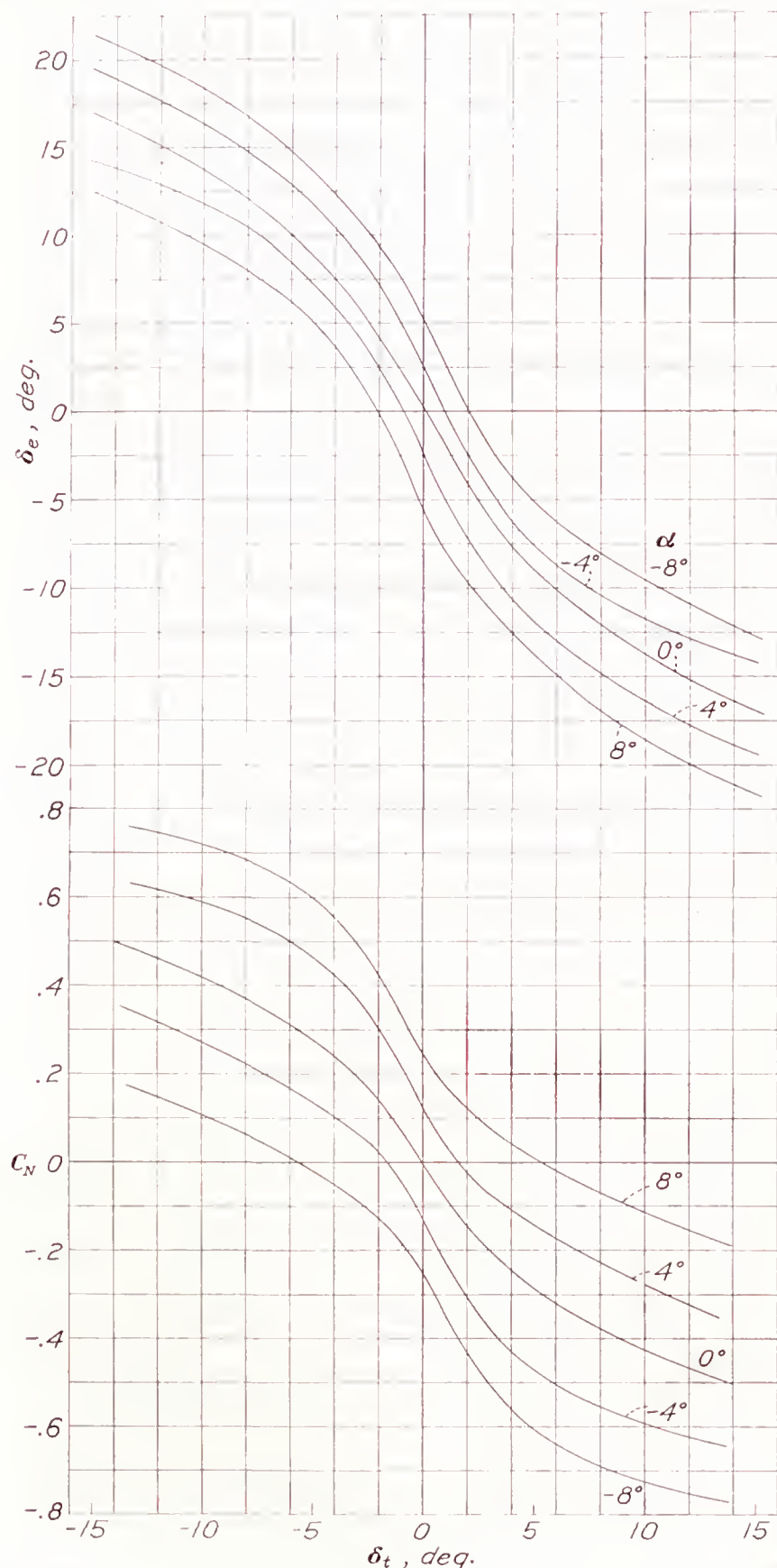


FIGURE 22.—Variation of  $\delta_e$  and  $C_N$  with  $\delta_t$ . 20-percent-balance; blunt-nose elevator.

deflection is approximately proportional to the area-moment of the tabs about the hinge line. Partial-span tab characteristics may thus be deduced by assuming the variation in  $\Delta C_{h_e}$  for a given tab deflection to be proportional to the ratio of the area-moment of the partial-span tab to that of the full-span tab. In this manner, partial-span tab characteristics similar to those given for the full-span tabs in figure 16 can be obtained.

Figure 19 shows the balancing effect of full-span, inboard and middle, and inboard tabs for various  $\delta_t/\delta_e$  ratios. If the tendency of tabs to overbalance at small elevator deflections is overcome (for example, by delaying the tab deflection until the elevator has been slightly deflected), the tab becomes a very effective balancing device. It also appears that still more desirable balancing characteristics can be obtained by the use of balance tabs in combination with a tapered-nose aerodynamic balance, which remains effective at large elevator deflections where the tab effectiveness falls off.

Figure 20 shows the variation of the stick-force criterion  $C_{h_e}\delta_e$  with  $C_N$  for various tab arrangements.

The rapid decrease in tab effectiveness at the larger tab and elevator deflections limits the use of tabs as a servocontrol device. This effect is shown in figure 21, which indicates the variation in elevator deflection  $\delta_e$  and normal-force coefficient  $C_N$  with tab deflection  $\delta_t$ . On an unbalanced elevator, the maximum change in  $\delta_e$  of  $\pm 12^\circ$  (measured from the free-floating position with  $\delta_t$  equal to  $0^\circ$ ) is obtainable with the full-span tab and corresponds to a  $\Delta C_N$  of  $\pm 0.30$ . These characteristics can be considerably improved, as shown in figure 22, if tabs are used on an elevator with aerodynamic balance. With the 20-percent blunt-nose balance, a  $\delta_e$  of about  $\pm 17^\circ$  and a  $\Delta C_N$  of  $\pm 0.50$  are obtained.

## CONCLUSIONS

1. The experimental variation of normal force with angle of attack ( $dC_N/d\alpha$ ) for the various tail arrangements was from 10 to 15 percent less than that computed from the aspect-ratio correction formula.

2. The presence of a gap caused a marked decrease in the value of the variation of normal force with elevator deflection ( $dC_N/d\delta_e$ ) but the size of the gap was unimportant (between  $0.005\bar{c}$  and  $0.010\bar{c}$ ) at angles below the stall. With some nose shapes, however, the larger gap caused an earlier stall.

3. The effect of aerodynamic balance varied greatly with nose shape. Tapered noses produced little balance at small elevator deflections but maintained the elevator effectiveness at much larger elevator deflections than did the blunt noses.

4. The decrease in normal force and hinge moment caused by the cut-out was proportional to the area removed.

5. The effectiveness of the tabs with change in span was approximately proportional to their area-moments about the elevator hinge line.

LANGLEY MEMORIAL AERONAUTICAL LABORATORY,  
NATIONAL ADVISORY COMMITTEE FOR AERONAUTICS,  
LANGLEY FIELD, VA., April 27, 1939.



## APPENDIX

The computation of the characteristics of the tail surface, based on the thin-airfoil theory developed in reference 6, is used throughout the report as a basis for comparison. An outline of the computation follows.

The main characteristics of a flapped airfoil may be computed from the equations:

$$\begin{aligned} C_L &= a_1(\alpha + \lambda_1\delta_e + \lambda_2\delta_t) \\ C_{h_e} &= -u C_L - v_{11}\delta_e + v_{12}\delta_t \end{aligned}$$

where  $\lambda_1$ ,  $\lambda_2$ ,  $u$ ,  $v_{11}$ , and  $v_{12}$  are constants dependent upon the flap-chord ratios  $E_1$  and  $E_2$ ; their values have been determined by the thin-airfoil theory (reference 6). The lift-curve slope  $a_1$  is dependent upon aspect ratio and plan form.

The tail surface tested was designed so that the area ratios of the elevator and the tab corresponded approximately to their chord ratios over the span. The pertinent data and the necessary constants for the computation of the lift and the hinge-moment characteristics about the elevator hinge line are:

For elevator:

$$\begin{aligned} \frac{E_e}{E} &= 0.41. \\ \lambda_1 &= 0.753. \\ u &= 0.121. \\ v_{11} &= 0.0078. \end{aligned}$$

For tab:

$$\begin{aligned} \frac{E_t}{E} &= 0.08. \\ \lambda_2 &= 0.357. \\ v_{12} &= 0.0175. \end{aligned}$$

The characteristics that can be determined (using the measured value of  $a_1 = 0.060$  except as noted) are:

$$\begin{aligned} \left(\frac{dC_L}{d\delta_e}\right)_\alpha &= \lambda_1 a_1 = 0.045 \\ &= 0.047 \text{ (for } a_1 = 0.063) \end{aligned} \quad (1)$$

The elevator-free lift-curve slope is obtained by setting  $C_{h_e} = 0$ . Then

$$\left(\frac{dC_L}{d\alpha}\right)_{C_{h_e}=0} = \frac{a_1}{1 + a_1\left(\frac{\lambda_1 u}{v_{11}}\right)} = 0.035 \quad (2)$$

$$\left(\frac{dC_{h_e}}{d\alpha}\right)_{\delta_e} = -u a_1 = -0.0073 \quad (3)$$

$$\left(\frac{dC_{h_e}}{d\delta_e}\right)_\alpha = -u\left(\frac{dC_L}{d\delta_e}\right)_\alpha - v_{11} = -0.0133 \quad (4)$$

$$\left(\frac{dC_{h_e}}{dC_L}\right)_\alpha = \frac{\left(\frac{dC_{h_e}}{d\delta_e}\right)_\alpha}{\left(\frac{dC_L}{d\delta_e}\right)_\alpha} = -0.295 \quad (5)$$

$$\left(\frac{dC_{h_e}}{d\delta_t}\right)_\alpha = -u\lambda_2 a_1 - v_{12} = -0.020 \quad (6)$$

The slope of the section lift curve for an N. A. C. A. 0009 section is 0.095, as determined from the data given in reference 4. By means of the aspect-ratio correction formula given in reference 7,

$$a_1 = f \frac{a_0}{1 + \frac{57.3a_0}{\pi A}} \quad (7)$$

(where  $f=1$  for the plan form and the shape of the tail surface tested) a slope of 0.069 is determined for a tail surface of aspect ratio 4.7 and 2:1 taper.

## REFERENCES

1. Bradfield, F. B.: A Collection of Wind Tunnel Data on the Balancing of Controls. R. & M. No. 1420, British A. R. C., 1932.
2. Silverstein, Abe, and Katzoff, S.: Aerodynamic Characteristics of Horizontal Tail Surfaces. T. R. (to be published) N. A. C. A.
3. DeFrance, Smith J.: The N. A. C. A. Full-Scale Wind Tunnel. T. R. No. 459, N. A. C. A., 1933.
4. Goett, Harry J., and Bullivant, W. Kenneth: Tests of N. A. C. A. 0009, 0012, and 0018 Airfoils in the Full-Scale Tunnel. T. R. No. 647, N. A. C. A., 1938.
5. Harris, Thomas A.: Reduction of Hinge Moments of Airplane Control Surfaces by Tabs. T. R. No. 528, N. A. C. A., 1935.
6. Perring, W. G. A.: The Theoretical Relationships for an Aerofoil with a Multiply Hinged Flap System. R. & M. No. 1171, British A. R. C., 1928.
7. Anderson, Raymond F.: Determination of the Characteristics of Tapered Wings. T. R. No. 572, N. A. C. A., 1936.







## REPORT No. 676

### SURFACE HEAT-TRANSFER COEFFICIENTS OF FINNED CYLINDERS

By HERMAN H. ELLERBROCK, Jr. and ARNOLD E. BIERMANN

#### SUMMARY

*An investigation to determine and correlate the experimental surface heat-transfer coefficients of finned cylinders with different air-stream cooling arrangements was conducted at the Langley Memorial Aeronautical Laboratory from 1932 to 1938. The investigation covered the determination of the effect of fin width, fin space, fin thickness, and cylinder diameter on the heat transfer. Wind-tunnel tests were made in the free air stream with and without baffles and also with various devices for creating a turbulent air stream. Tests were also made with blower cooling.*

*A variation of the initial turbulence of the tunnel air stream was found to have little effect on the heat transfer. Correlation of the surface heat-transfer coefficients was found possible by plotting a factor involving the heat-transfer coefficients, the fin space, and the conductivity of the cooling air against a factor involving the velocity, the density, and the viscosity of the cooling air and the fin space, the fin width, and the cylinder diameter.*

#### INTRODUCTION

The large number of variables that affect the heat transfer from finned cylinders and the complexity of their relationships makes it difficult to determine optimum fin designs from experimental data alone. Investigations at this laboratory (reference 1) have shown that the heat transfer can be calculated from an equation involving the fin dimensions, the surface heat-transfer coefficient  $q$ , and the thermal conductivity of the metal. The value of  $q$  depends on the fin design, the air-stream characteristics, and the method of cooling. The air-stream characteristics include the weight velocity, the conductivity, the viscosity, and the intensity and the scale of the turbulence of the cooling air. No satisfactory method of calculating the heat-transfer coefficient  $q$  has been found and its value must therefore be experimentally determined.

In previous experiments, the value of  $q$  was first established for cylinders having fins of various dimensions tested in a wind tunnel without cylinder baffles (reference 1). These tests were undertaken before baffles were generally used around the cylinders of

radial air-cooled engines. Tests were later made to determine  $q$  with several types of baffle. (See reference 2.) These tests were made prior to the introduction of the pressure-baffled engine and were made in the wind tunnel with the air stream passing around and through the baffles. At this time, an investigation was also made to determine the advantages of the completely jacketed finned cylinder in which the cooling air is forced through the jacket by means of a blower as compared with the pressure-baffled engine.

The surface heat-transfer coefficients and the pressure differences across the cylinders were determined with blower cooling for a number of cylinders having different fin designs (reference 3). Further tests in a wind tunnel (reference 4) were made on cylinders with fins more closely spaced than those tested in references 1, 2, and 3 in order to determine the coefficients with blower cooling and with and without baffles. In addition, tests were made to determine the pressure differences for a variation of air flow across a large number of jacketed cylinders and cylinders with baffles and also to determine the air flow between the fins (references 5, 6, and 7).

The investigation has been extended to obtain additional data on the effect of the fin dimensions on  $q$ . Cylinders of three different diameters have been tested to determine the effect of diameter on the pressure drop and the heat-transfer coefficient. Several copper cylinders with different fin widths and spacings and one aluminum-alloy cylinder were tested primarily to substantiate the effect of thermal conductivity in the heat-transfer equation previously mentioned. Data are also presented in this report showing the effect of turbulence on  $q$  over a range of turbulence intensities.

The object of this report is to present the recent information that has been obtained on the heat-transfer coefficient  $q$  and, in addition, to show that all available data on  $q$  can be correlated for each air-flow arrangement in terms of functions defining a single curve and involving the fin dimensions, the cylinder diameter, and the air-stream characteristics. This information should permit the calculation of the best fin proportions for the conditions of air flow that are of general interest.



The present report includes tests on 58 cylinders with fins having widths from 0.37 inch to 3 inches, mean spaces from 0.010 inch to 0.50 inch, and mean thicknesses from 0.026 inch to 0.27 inch. The results of some of the tests have already been published. The variation in cylinder diameter was from 3.66 to 6.34 inches.

The tests were conducted at the Langley Memorial Aeronautical Laboratory from 1932 to 1938.

## APPARATUS

### TEST CYLINDERS

A description of the cylinders tested and the air-flow arrangements used is given in table I.

TABLE I.—Cylinders tested

Cylinder	Fin space (in.)	Fin width (in.)	Fin thickness (in.)	Cylinder diameter at fin root (in.)	Material	Fin shape	Air-flow arrangement <sup>1</sup>
1	0.330	1.47	0.270	4.66	Steel	Tapered.	1, 4.
2	.270	1.47	.230				1, 4.
3	.220	1.32	.180				1, 4.
4	.170	1.32	.130				1, 4.
5	.140	1.22	.110				1, 4.
6	.150	1.22	.090				1.
7	.185	1.22	.065				1.
8	.100	1.22	.100				1, 4.
9	.075	.97	.075				1.
10	.210	1.22	.040				1.
11	.131	1.22	.035				1, 3.
12	.102	1.22	.035				1, 3.
13	.077	1.22	.035				1, 2, 3.
14	.048	1.22	.035				1, 2, 3.
15	.022	1.22	.035				1, 2, 3.
16	.210	.97	.040				1.
17	.110	.97	.040				1.
18	.101	.97	.035				1, 2, 3.
19	.077	.97	.035				1, 2, 3.
20	.048	.97	.035				1, 2, 3.
21	.022	.97	.035				1, 2, 3.
22	.210	.67	.040				1.
23	.110	.67	.040				1.
24	.101	.67	.035				1, 2, 3.
25	.077	.67	.035				1, 2, 3.
26	.048	.67	.035				1, 2, 3.
27	.022	.67	.035				1, 2, 3.
28	.210	.37	.040	3.66	Copper	Rectangular.	1.
29	.110	.37	.040				1.
30	.060	.37	.040				1, 4.
31	.101	.37	.035				1, 2, 3.
32	.077	.37	.035				1, 2, 3.
33	.048	.37	.035				1, 2, 3.
34	.022	.37	.035				1, 2, 3.
35	.080	3.00	.035				3.
36	.055	3.00	.035				3.
37	.028	3.00	.035				3.
38	.035	.37	.035	6.34	Steel	Rectangular.	3.
39	.124	.50	.026				3.
40	.120	.52	.030				3.
42	.500	1.50					
43	.375	1.50					
44	.250	1.50					
45	.125	1.50					
46	.031	1.50					
47	.500	.75					
48	.250	.75					
49	.125	.75		4.66	Steel	Rectangular.	
50	.062	.75					
51	.031	.75					
52	.500	.375					
53	.250	.375					
54	.125	.375					
55	.062	.375					
56	.031	.375					
57	.010	.67	.035				
58	.200	.85	.050	4.66	Aluminum alloy	Rectangular.	
59	.200	1.66	.050				
60	Smooth cylinder—no fins.						1, 4.

<sup>1</sup> Numbers indicate:

- 1, cylinder in free air stream, no baffles.
- 2, cylinder in free air stream, with baffles.
- 3, cylinder enclosed in jacket, blower supplying the air.
- 4, cylinder in free air stream with axis 45° to air stream.

The fin section in figure 1 shows the significance of  $w$ , fin width;  $s$ , fin space;  $s_b$ , fin space at the fin root; and  $t$ , fin thickness. The test cylinders were electri-

cally heated and were tested with guard rings, as described in reference 1. The assembled over-all length of the test section and the guard rings was, in every case, approximately 10 inches. For convenience in referring to the finned cylinders, a nomenclature giving the fin space, the fin width, and the fin thickness has been devised. For example, the designation 0.101-0.67-0.035 represents a finned cylinder having an average fin space of 0.101 inch, a fin width

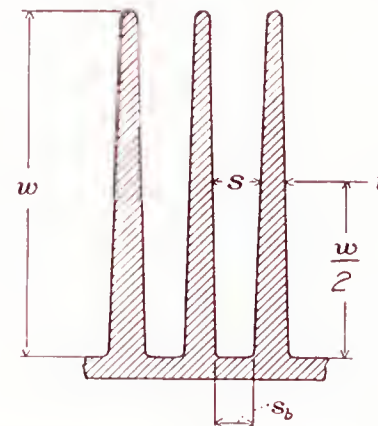


FIGURE 1.—Section showing significance of  $w$ ,  $s$ ,  $s_b$ , and  $t$ .

of 0.67 inch, and an average fin thickness of 0.035 inch. The designations corresponding to the cylinders in table I can be obtained by combining the values given in columns 2, 3, and 4.

### BAFFLES AND JACKETS

The type of baffle used for the tests of the cylinder with baffles in the free air stream is shown in figure 2 (a).

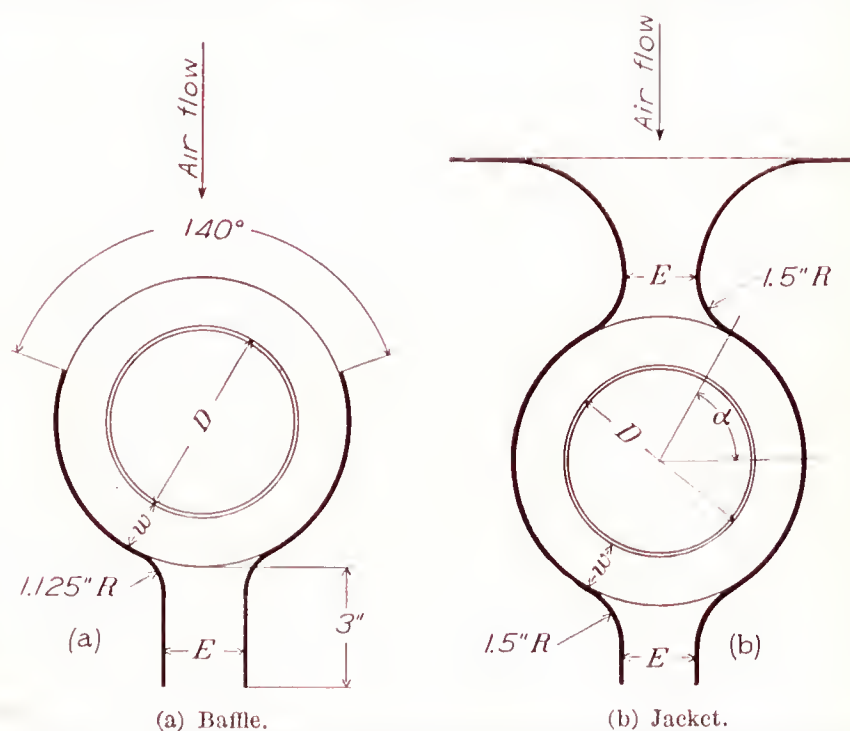


FIGURE 2.—Type of baffle and jacket used in tunnel and blower-cooling tests.

The ratio of the area of the exit to the area between the fins was approximately 2.

The apparatus used in the blower-cooling tests is described in references 3 and 5. The jacket used in these tests is shown in figure 2 (b). The ratio of the entrance or the exit area of the jacket to the flow area between the fins was approximately 1.6 for all of the cylinders except the copper cylinders, for which the ratio varied from 1.0 to 1.7.



## TESTS

The tests covered in this report are listed in table I. In addition to the blower-cooling tests, this work included wind-tunnel tests with baffles, without baffles, and with the cylinder axis at  $45^\circ$  with respect to the air stream. The methods of testing have been described in references 1 to 5.

The tests to determine the effect of turbulence on the heat-transfer coefficient were made in the wind tunnel with the 0.077–0.37–0.035 steel cylinder with baffles starting  $90^\circ$  from the front of the cylinder ( $180^\circ$  opening) and with various devices for creating different amounts of turbulence. Tests with small-scale turbulence were made for the following four conditions:

- (1) With honeycomb.
- (2) With screen.
- (3) Without honeycomb or screen.
- (4) With honeycomb and screen.

The honeycomb was constructed of 0.35-inch-diameter tubes of 3-inch length. The screen was of  $\frac{1}{2}$ -inch mesh with wires of 0.092-inch diameter and was similar to a screen previously tested at the National Bureau of Standards for its turbulence-creating properties (reference 8). In the tests of reference 8, the screen was found to produce a very turbulent flow when placed 141 wire diameters ahead of the point of measurement. In the present tests, an indication of the intensity of turbulence was obtained for the foregoing conditions by the conventional sphere method. The turbulence factors were determined with a sphere 4 inches in diameter by the method described in reference 9. The four conditions of turbulence gave the following turbulence factors, which indicate the range covered:

With honeycomb	1.41
Without honeycomb or screen	1.89
With screen	2.96
With honeycomb and screen	3.21

A large value of the turbulence factor indicates a high degree of turbulence.

A larger scale turbulence was produced by placing a drum of 9-inch diameter various distances between 0.3 inch and 13 inches ahead of the test cylinder. These tests were made with the axis of the drum both perpendicular and parallel to the cylinder axis.

Tests previously reported (reference 10) showed high rates of heat flow when the fin-plane/air-stream angle was between  $30^\circ$  and  $60^\circ$ . Evidence shows that the front portions of cylinders placed within an N. A. C. A. cowl are cooled by a flow consisting mainly of large swirls incident upon the fins at various angles. It is very likely that, in the tests with an N. A. C. A. cowl, the flow phenomena between fins may be similar to that with different fin-plane/air-stream angles. In order to obtain more complete data on this subject, the range of the previous tests on fin-plane/air-stream angle has been extended to determine the effect of fin

dimensions on the heat transfer of cylinders having a fin-plane/air-stream angle of  $45^\circ$ .

The heat lost from air-cooled engine cylinders by direct radiation is generally considered negligible as compared with the heat lost by convection. Some consideration has been given, however, to the merits of black-enamel surfaces for improving the heat transfer. Wind-tunnel tests were made to determine the effect of different thicknesses of black enamel and of oiled surfaces on the surface heat-transfer coefficient of a cylinder without fins. The use of a surface without fins avoided any effect of change of space between fins caused by the enamel or oil thickness. The enamel was a black baking japan applied by spraying and was baked for 1 hour at  $400^\circ$  F.

With blower cooling, measurements were made of the heat transfer, the weight of air used, and the pressure drop; with the other three air-flow arrangements, only heat-transfer measurements were obtained for a range of tunnel air speeds.

## SYMBOLS

- $c_p$ , specific heat of fluid at constant pressure, B. t. u. per pound per  $^\circ$ F.
- $d$ , diameter of pipe, inches.
- $d_e$ , equivalent diameter of duct  $[4ws/2(w+s)]$ , inches.
- $D$ , cylinder diameter at fin root, inches.
- $g$ , acceleration of gravity, feet per second per second.
- $k_m$ , thermal conductivity of metal, B. t. u. per square inch through 1 inch per hour per  $^\circ$ F.
- $k_a$ , thermal conductivity of air, B. t. u. per square inch through 1 inch per second per  $^\circ$ F.
- $l$ , equivalent length for straight tube ( $\phi R_a$ ), feet.
- $q$ , surface heat-transfer coefficient, B. t. u. per square inch total surface area per hour per  $^\circ$ F. temperature difference between surface and inlet cooling air.
- $q_{av}$ , surface heat-transfer coefficient, B. t. u. per square inch total surface area per hour per  $^\circ$ F. temperature difference between surface and average cooling air.
- $R_a$ , average radius from center of cylinder to finned surface  $\left(\frac{R_b}{12} + \frac{w}{2 \times 12}\right)$ , feet.
- $R_b$ , radius from center of cylinder to fin root ( $D/2$ ), inches.
- $s$ , average space between adjacent fin surfaces, inches.
- $s_b$ , space between adjacent fin surfaces at fin root, inches.
- $t$ , thickness of fins, inches.
- $U$ , over-all heat-transfer coefficient, B. t. u. per square inch base area per  $^\circ$ F. temperature difference between cylinder wall and cooling air per hour.



$V$ , velocity of air in tunnel throat in air-flow arrangements 1, 2, and 4 or average velocity between fins in air-flow arrangement 3, feet per second. (See table I.)

$w$ , fin width, inches.

$W$ , quantity of air flowing, pounds per second.

$\rho_1 g$ , specific weight of air in front of jacket in air-flow arrangement 3 or specific weight of air in tunnel throat in front of cylinder in air-flow arrangements 1, 2, and 4, pounds per cubic foot.

$\rho_2 g$ , specific weight of air in rear of jacket in cooling method 3, pounds per cubic foot.

$\rho_{av} g$ , average specific weight of air  $\frac{\rho_1 g + \rho_2 g}{2}$ , pounds per cubic foot.

$\rho_0 g$ , specific weight of air at 29.92 inches Hg and 80° F. (0.0734 lb./cu. ft.), pounds per cubic foot.

$\varphi$ , equivalent angle of curvature ( $\alpha + \pi/2$ ), radians.

$\alpha$ , (See fig. 2(b)), radians.

$\mu$ , absolute viscosity of air, pounds per second per foot.

$\Delta p_1$ , pressure difference across cylinder, inches of water.

$\Delta p_2$ , pressure difference caused by loss of velocity head from exit of skirt of baffle or jacket, inches of water.

$\Delta p_{total}$ , total pressure difference across set-up ( $\Delta p_1 + \Delta p_2$ ), inches of water.

### COMPUTATIONS

The surface heat-transfer coefficient  $q$  was obtained by dividing the heat input per hour by the product of the total cooling-surface area and the difference between the average temperature of the cooling surface and the entering-air temperature. A complete description of the methods used in calculating the results has been presented in references 1, 3, 4, and 5. The viscosity and the conductivity of the air were based on an average of the cylinder and the mean air temperatures for air-flow arrangement 3 and on an average of the cylinder and the tunnel-throat temperatures for air-flow arrangements 1, 2, and 4. The temperature of the outlet air was calculated from the heat input to the cylinder, the quantity of air flowing over the cylinder, and the temperature of the inlet air. All tunnel air speeds and pressure differences have been corrected to a specific weight of air of 0.0734 pound per cubic foot.

In studies of the heat transfer from pipes, it is customary to base the average heat-transfer coefficient  $q_{av}$  on the difference between the average surface and the average fluid temperatures. In the application of finned-surface heat-transfer data to engine cylinders and to the calculation of optimum fin constructions to meet various conditions of weight and pressure drop, it

has been found advantageous to base  $q$  on the difference between the entering inlet-air temperature and the average surface temperature. When the over-all heat-transfer coefficient  $U$  is calculated from  $q_{av}$ , it is necessary to determine the temperature rise of the air. This temperature rise, in turn, depends upon the value of the  $U$  that is being determined. For optimum fin calculations with limiting pressure differences, it is readily seen that the use of  $q_{av}$  complicates the problem. If the effect of flow-path length on  $q$ , based on inlet-air temperature, is known, the calculations of the heat transfer can be made in a simple manner. In the present investigation, the effect of flow-path length on  $q$  based on inlet-air temperature has been determined over a range of lengths that is large as compared with the range found on aircraft-engine cylinders.

An additional advantage in using  $q$  or  $U$  based on the inlet-air temperature is that the over-all heat-transfer coefficient  $U$  is proportional to the rate of heat transfer, which is a function of the power developed. Thus an increase of  $U$  is also an indication as to how much the power can be increased. The proportionality of the over-all heat-transfer coefficient to the rate of heat transfer does not hold for  $U$  based on the average air temperature. The heat-transfer coefficients in the present report for the blower-cooling set-up have been calculated; both the difference between the average surface and the average air temperatures and the difference between the average surface and the inlet-air temperature were used. The heat-transfer coefficients based on the former temperature difference were calculated to determine whether factors used to correlate pipe data would be applicable to finned-cylinder data. For the other air-flow arrangements, only the inlet-air temperature difference was used.

### SURFACE HEAT-TRANSFER COEFFICIENTS

The over-all heat-transfer coefficient  $U$  of finned cylinders can be calculated from the following equation, which was derived in reference 1:

$$U = \frac{q}{s+t} \left[ \frac{2}{a} \left( 1 + \frac{w}{2R_b} \right) \tanh aw' + s_b \right] \quad (1)$$

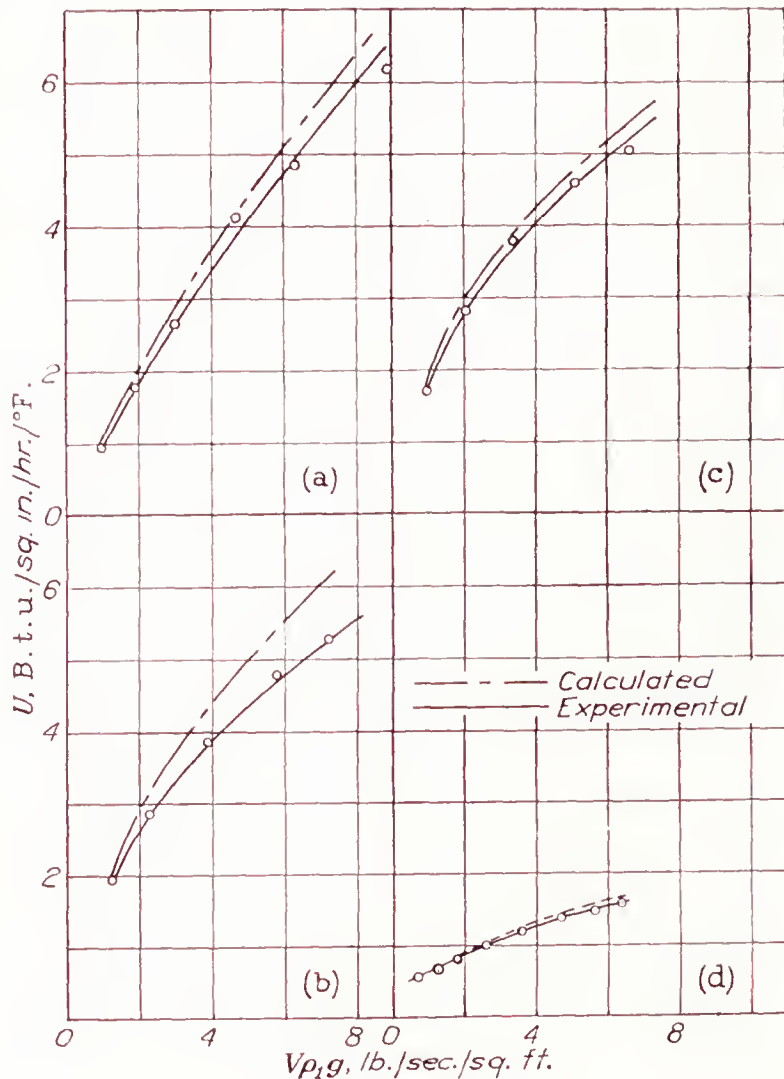
where  $a = \sqrt{2q/k_m t}$  and  $w' = w + t/2$ . Equation (1) has been experimentally verified for a large number of steel cylinders having a thermal conductivity  $k_m$  of 2.17 B. t. u. per square inch through 1 inch per hour per °F.

In the present investigation, further verification has been made of this equation for pure copper, in which  $k_m$  was taken as 18.04, and for aluminum Y alloy, in which  $k_m$  was taken as 7.66. When aluminum or aluminum alloy is hereinafter mentioned, aluminum Y alloy is meant. The results of these tests are shown in figure 3 for three copper cylinders having different fin designs and for one aluminum-alloy cylinder. These cylinders were tested with blower cooling. The values of  $U$  calculated from equation (1) conform reasonably well with the experimental values of  $U$ .



In equation (1), variables  $k_m$  and  $q$  depend upon experimental tests. Sufficiently accurate data are generally available for the values of  $k_m$ . The various possible factors that could affect the surface heat-transfer coefficient  $q$  of finned cylinders may be enumerated as follows:

1. Characteristics of surface.
2. Intensity and scale of turbulence.
3. Fin and cylinder dimensions: space, width, thickness, and diameter.
4. The weight velocity, the conductivity, and the viscosity of the cooling air.



	$s$ (in.)	$w$ (in.)	$t$ (in.)	Set-up	Material
(a)-----	0.028	3	0.035	Blower cooling-----	Copper.
(b)-----	.055	3	.035	do-----	Do.
(c)-----	.08	3	.035	do-----	Do.
(d)-----	.20	1.66	.050	do-----	Aluminum.

FIGURE 3.—Comparison of calculated and experimental values of  $U$  for metals of high thermal conductivity.

The effect of each of these factors will now be considered.

#### EFFECT OF SURFACE CHARACTERISTICS

The results of the tests on the smooth-enameled cylinder are shown in figure 4 for wind-tunnel tests at a constant air speed of 52 miles per hour. These tests show a slight improvement in  $q$  with enamel thicknesses up to 0.002 inch; beyond this thickness, the heat transfer decreases and, with thicknesses greater than 0.005 inch, it becomes less than it is without enamel. The highest heat transfer is presumably obtained with

just sufficient enamel to produce a smooth, black surface; any further increase in thickness results in a lowered heat transfer caused by decreased thermal conductivity.

In the tests to determine the effect of an oil film on the heat transfer, the effect of the air stream and the heated cylinder surface was continuously to decrease the oil-film thickness; and it was difficult to arrive at a satisfactory conclusion from these tests. The oil film had no measurable effect on the heat transfer obtained during these tests.

#### EFFECT OF TURBULENCE

The results of the tests with different devices for creating turbulence are shown in figure 5. A single curve adequately represents the data for design purposes. A maximum deviation of the test points of

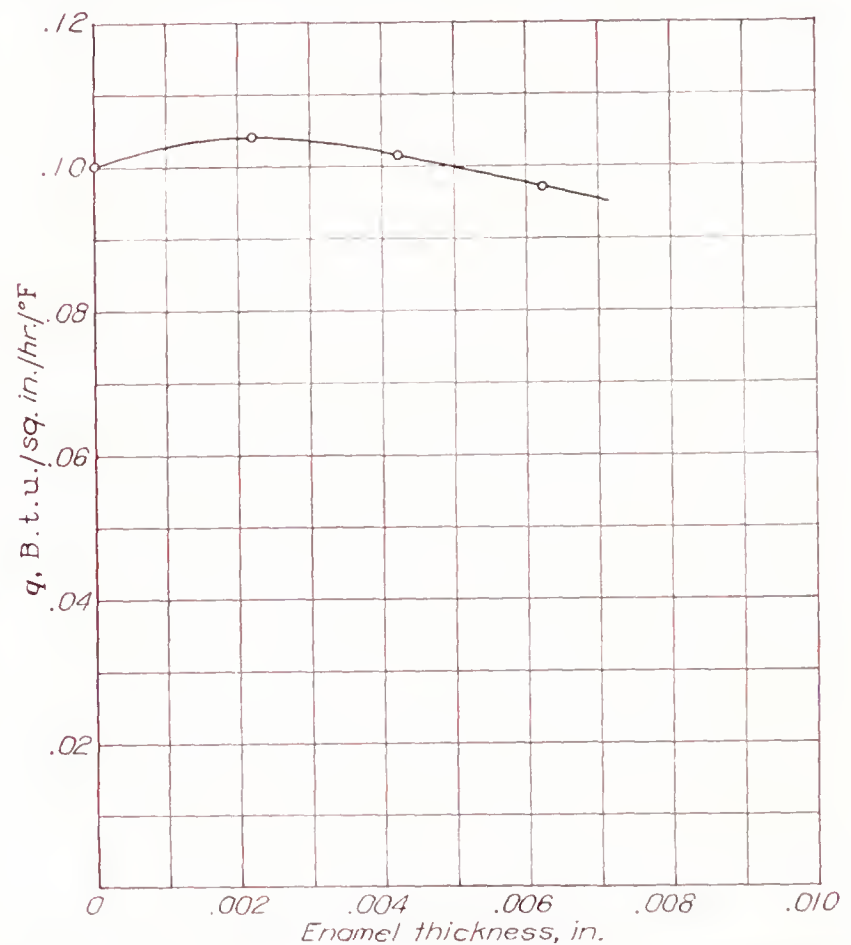


FIGURE 4.—Effect of enamel on surface heat-transfer coefficient  $q$  of a smooth cylinder.

approximately 10 percent is caused by placing the 9-inch drum parallel and at distances between 0.3 inch and 13 inches from the test cylinder. The drum in this position caused a blocking effect in addition to the air swirl, and the condition is therefore outside the range of useful design. If the test points for this condition are disregarded, much less deviation is obtained and the conclusion may be drawn that the scale and the intensity of turbulence in the tunnel air stream for the range covered in these tests have an inappreciable effect on the heat transfer.

Although the turbulence impressed upon the air stream had little effect on the heat transfer, another flow condition produced between the fins when the fin-plane/air-stream angle lies between  $30^\circ$  and  $60^\circ$  has resulted in high rates of heat transfer (reference 10).



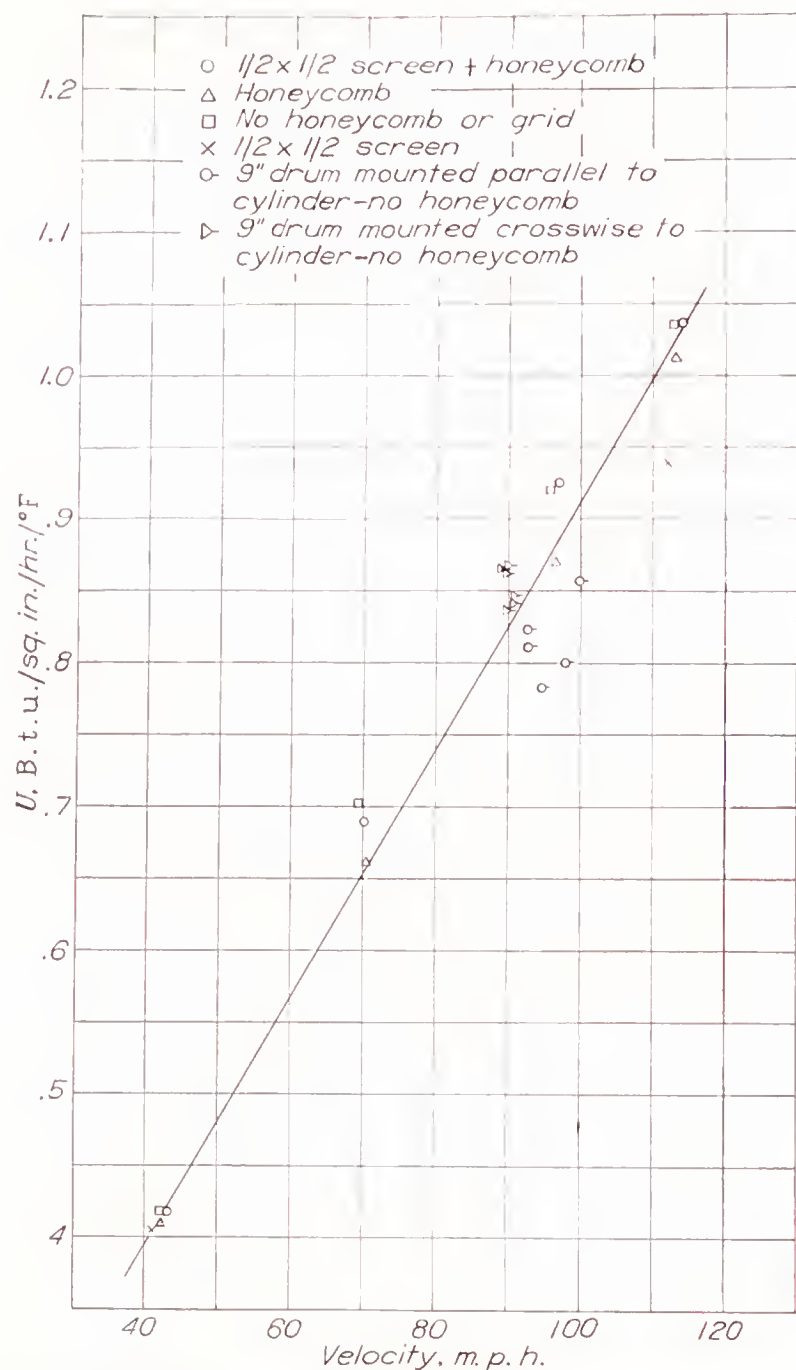


FIGURE 5.—Effect of turbulence devices on the over-all heat-transfer coefficient  $U$  of the 0.077-0.37-0.035 cylinder with 90° baffles.

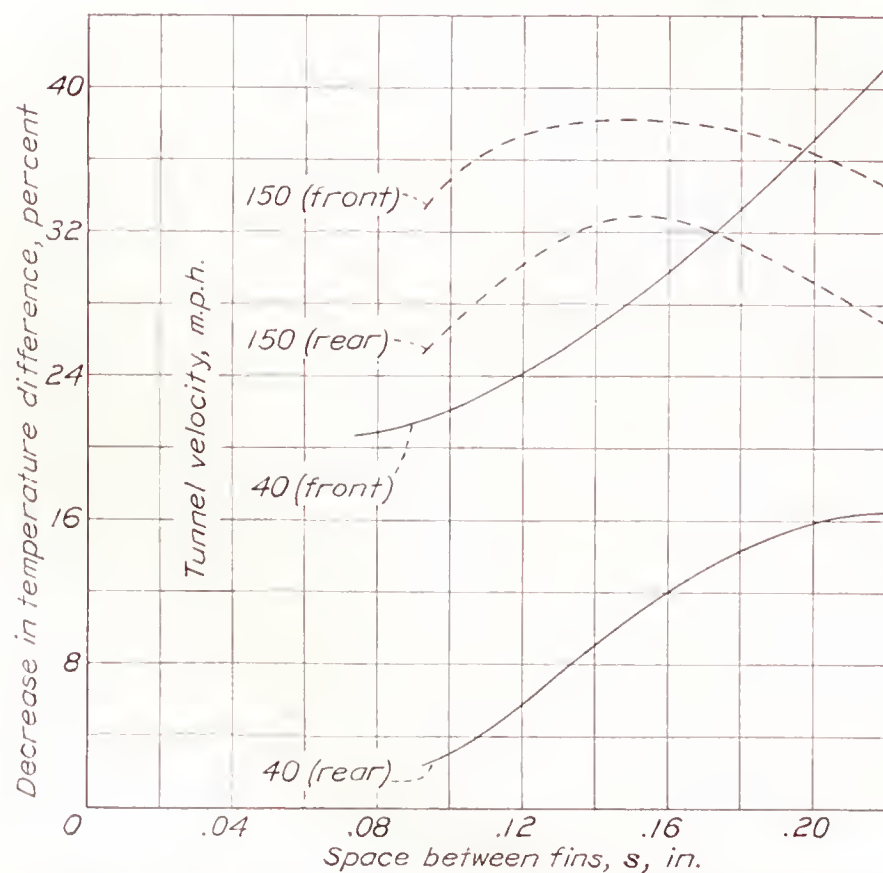


FIGURE 6.—Percentage decrease in temperature difference of cylinders with a fin-plane/air-stream angle of 45° as compared with the same cylinders at a fin-plane/air-stream angle of 0°.

Although the nature of the flow between the fins for this condition is not definitely known, lampblack-kerosene pictures of the flow over the fin surfaces indicate that, when the air stream strikes the fins at an oblique angle, vortices formed between the fins move around the cylinder with the general flow. Additional information on the result of this condition is given in figure 6. This figure shows the percentage improvement in cooling obtained with the 45° fin-plane/air-stream angle as compared with the parallel-flow condition for the front and the rear locations on the cylinder for a range of fin spacing. In general, the improvement becomes less with closely spaced fins.

#### EFFECT OF CYLINDER DIAMETER

The data on  $q$  for the 0.124-0.50-0.026 cylinder of 3.66-inch diameter and the 0.12-0.52-0.03 cylinder of

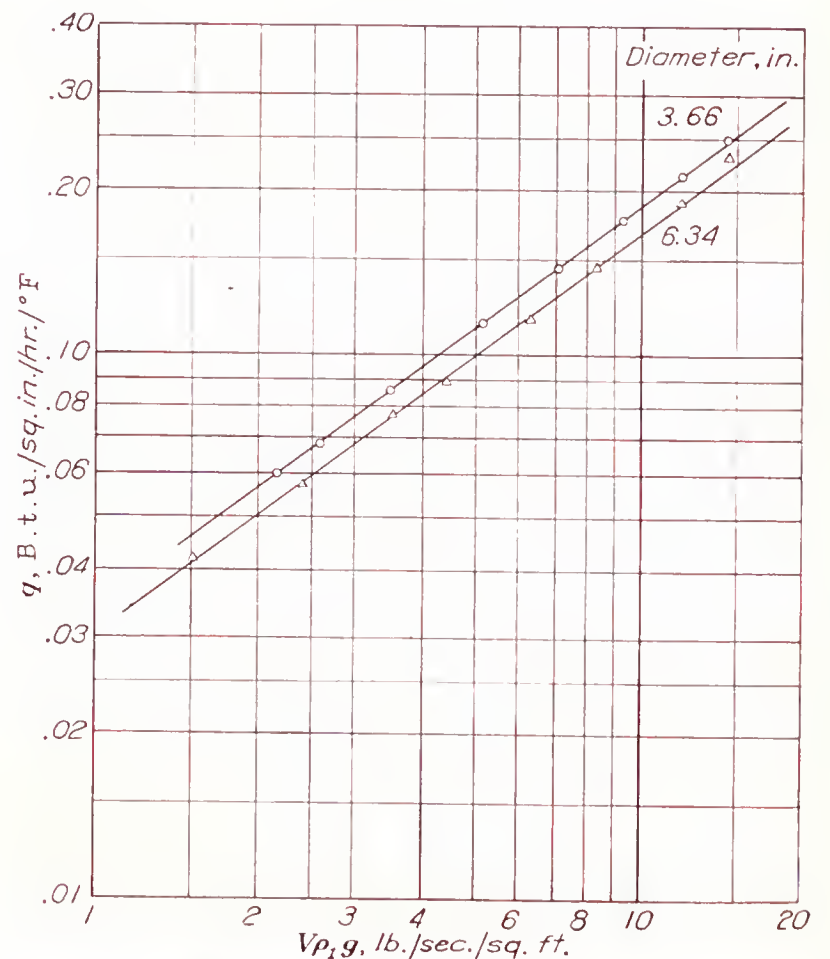


FIGURE 7.—Surface heat-transfer coefficients  $q$  for two cylinder diameters.

6.34-inch diameter are plotted in figure 7 to show the effect of cylinder diameter. For the range of data obtained, the relation between  $q$  and  $D$  can be conveniently expressed by

$$q \propto \frac{1}{D^{0.25}}$$

Empirical functions determined from tests with coiled pipes show that  $q$  varies as an inverse function of the radius of curvature of the coils (reference 11, p. 179). Little information is available to indicate more completely the relationship between the cylinder diameter and  $q$ .



CORRELATION OF VARIABLES AFFECTING  $q$ 

In the mechanism of heat transfer by convection in pipes, the velocity gradient across the stream does not follow any simple relation but apparently involves two zones: the film layer and the turbulent core. Three methods of attack have been used to predict the heat transfer, namely:

1. By mathematical analysis.
2. By analogy between results from heat transfer and friction.
3. By dimensional analysis.

With turbulent flow, the application of mathematical analysis has met with little success. Analogies between heat transfer and friction hold only for simple cases, such as for straight pipes. The use of dimensional analysis has been the most successful method of attack, the constants in the equations being experimentally determined. For the conditions of viscous flow, mathematical analysis has been used with greater success; here again the experimental results are checked only by applying empirical corrections to the theory.

The heat transfer of straight pipes and ducts has been correlated by means of various dimensionless factors. McAdams (reference 11, pp. 203-210) has recorrelated a greater part of the available data on straight pipes in the viscous region according to a theoretical equation that assumes a parabolic velocity distribution and an absence of free convection currents. This equation can be approximately represented, for values of  $Wc_p/k_a l$  greater than 10, by the equation

$$\frac{q_{av}d}{k_a} = 1.65 \left( \frac{Wc_p}{k_a l} \right)^{1/3} \quad (2)$$

By the substitution of the weight velocity and the area for  $W$ , equation (2) can be rearranged as follows:

$$\frac{q_{av}d}{k_a} = 1.5 \left( \frac{V\rho_1 g d c_p}{k_a} \times \frac{d}{l} \right)^{1/3} \quad (3)$$

For air, the Prandtl number,  $c_p \mu / k_a$ , is approximately 1, and substitution in equation (3) gives the Nusselt number as a function of the Reynolds Number and the  $d/l$  ratio of the pipe

$$\frac{q_{av}d}{k_a} = 1.5 \left( \frac{V\rho_1 g d}{\mu} \times \frac{d}{l} \right)^{1/3} \quad (4)$$

The designation of the symbols are as previously given but the dimensions are so chosen as to make both sides of equations (2), (3), and (4) dimensionless.

Colburn (reference 12) has pointed out that McAdams' correlations show that data on heating fall above the theoretical curve and that data on cooling fall about equally above and below the theoretical equation. Colburn attributed the discrepancy be-

tween the theory and the data to free convection effects and to velocity distributions different from that assumed in deriving the equation. Accordingly, Colburn amplified equation (2) to include these effects by introducing a factor  $\Phi$ , which involves the Grashof number and the ratio of the viscosity of the fluid, based on an arithmetic mean temperature of the fluid to the viscosity of the fluid based on an average fluid-film temperature. Equation (2) has been found, however, to apply with a fair degree of accuracy when the Grashof number and the ratio of the viscosities are approximately 1.

For the turbulent region, the Nusselt number has been found to be a function of the Reynolds Number and the Prandtl number; and, as the value of the Prandtl number is approximately 1 for air, it can be eliminated from the equations with little error.

In previous investigations, the heat-transfer data of rectangular ducts have been correlated in a manner similar to that of pipes by using an "equivalent" diameter equal to four times the area of the duct divided by the perimeter. Practically no data are available on the effect of curvature in ducts other than pipes. In tests on coiled pipes, the Nusselt number was found to be a function of the ratio of the radius of the pipe to the radius of curvature in addition to the factors already mentioned.

The correlation of heat-transfer data for finned cylinders is made more difficult than the correlation for pipes because of the complicated shape of finned cylinders and the fact that the boundary-layer velocity gradient between the fins from the front to the rear probably changes. The flow passages between the fins of finned cylinders can be considered as curved ducts, especially when baffles or a jacket is used. It is possible that the variables—heat-transfer coefficient, cylinder and fin dimensions, and air-stream characteristics—can be correlated by means of one or more of the dimensionless factors considered in the foregoing paragraphs. Owing to the difficulty of applying mathematics to this problem, recourse was had to the experimental results with blower cooling to determine empirical relationships for correlating the data.

Colburn (reference 12) found that, in the turbulent region, data on pipes could be correlated if the viscosity was based on the film temperature of the fluid, a mean of the average surface and the average fluid temperatures; whereas, in the viscous region, it made no difference whether the fluid or the film temperature was used. In the following correlation of heat-transfer data, the viscosity and the conductivity of the cooling air for both the turbulent and the viscous flow regions were based on the film temperature of the fluid.



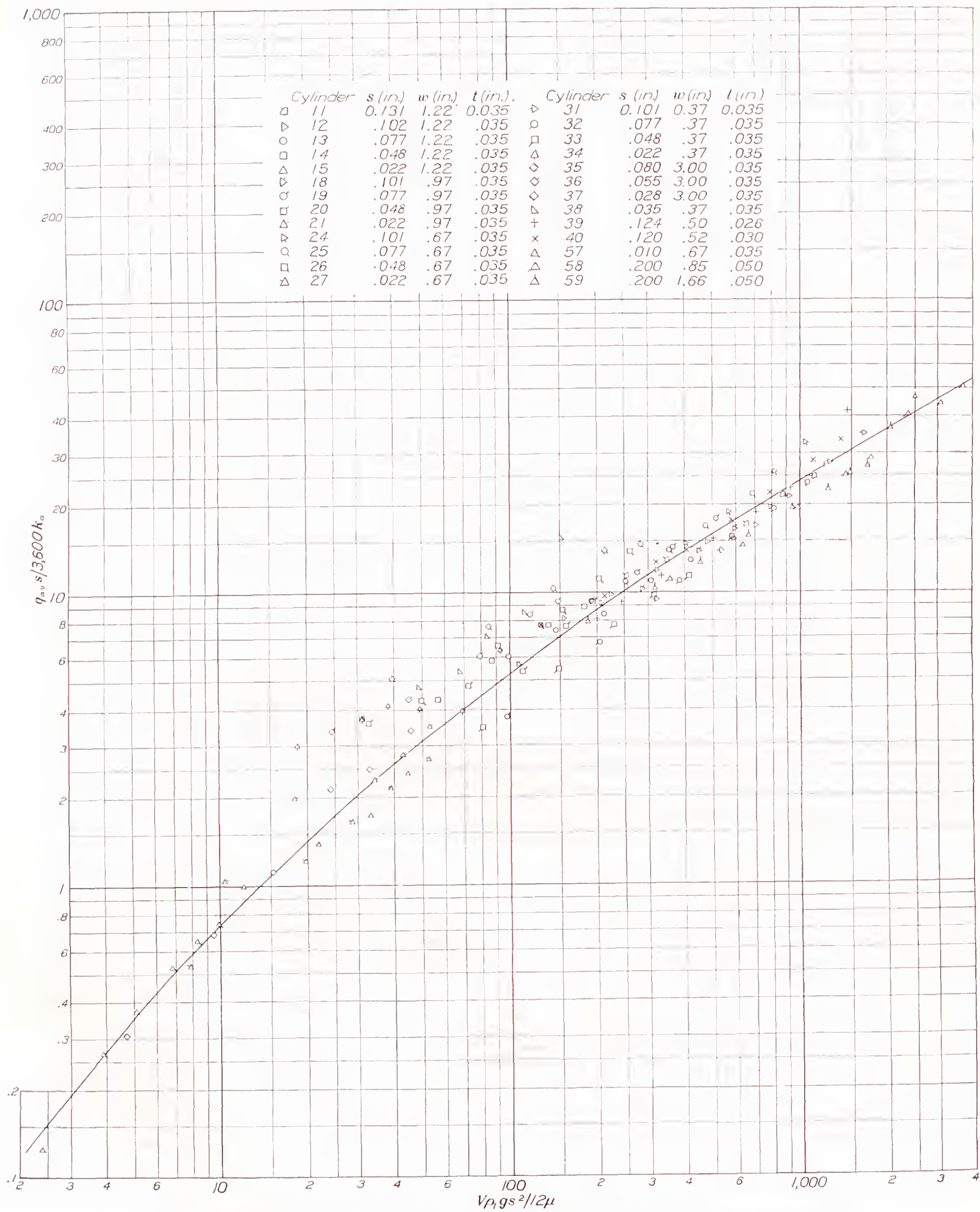
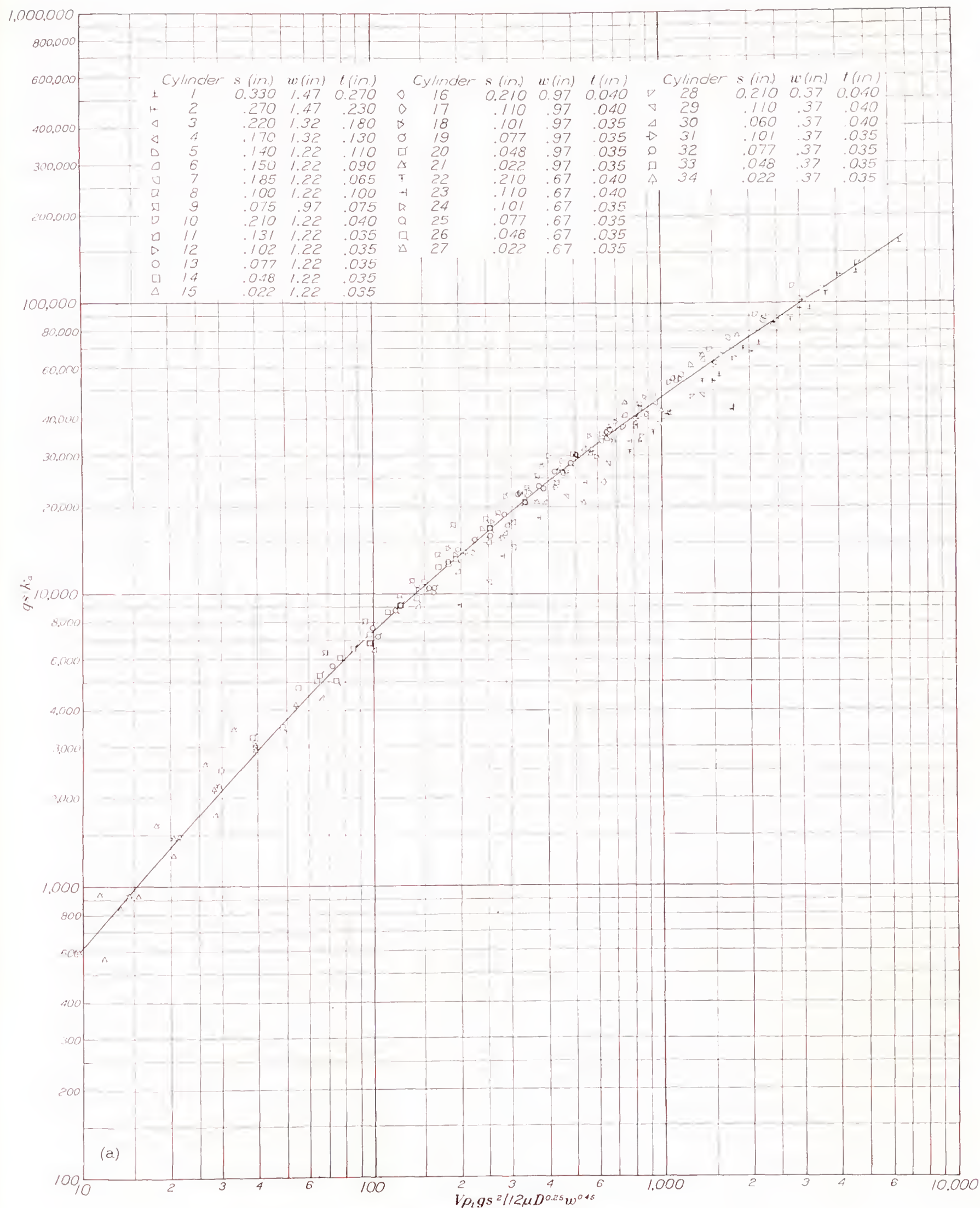


FIGURE 8.—Relation between factors involving  $q_{av}$ , fin dimensions, and air-stream characteristics for blower cooling.

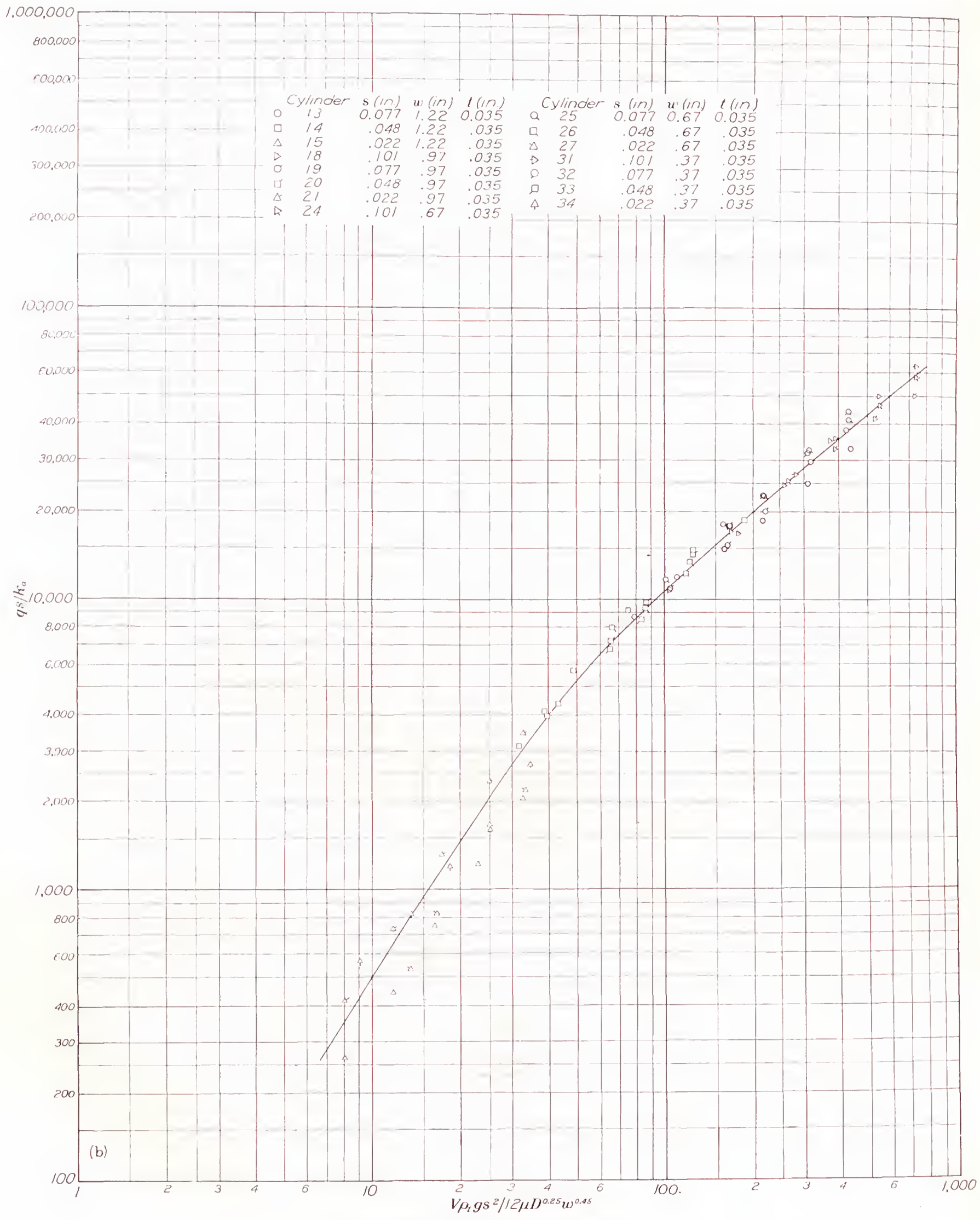




(a) Cylinder in free air stream, no baffles.

FIGURE 9.—Relation between factors involving  $q$ , fin dimensions, cylinder diameter, and air-stream characteristics.

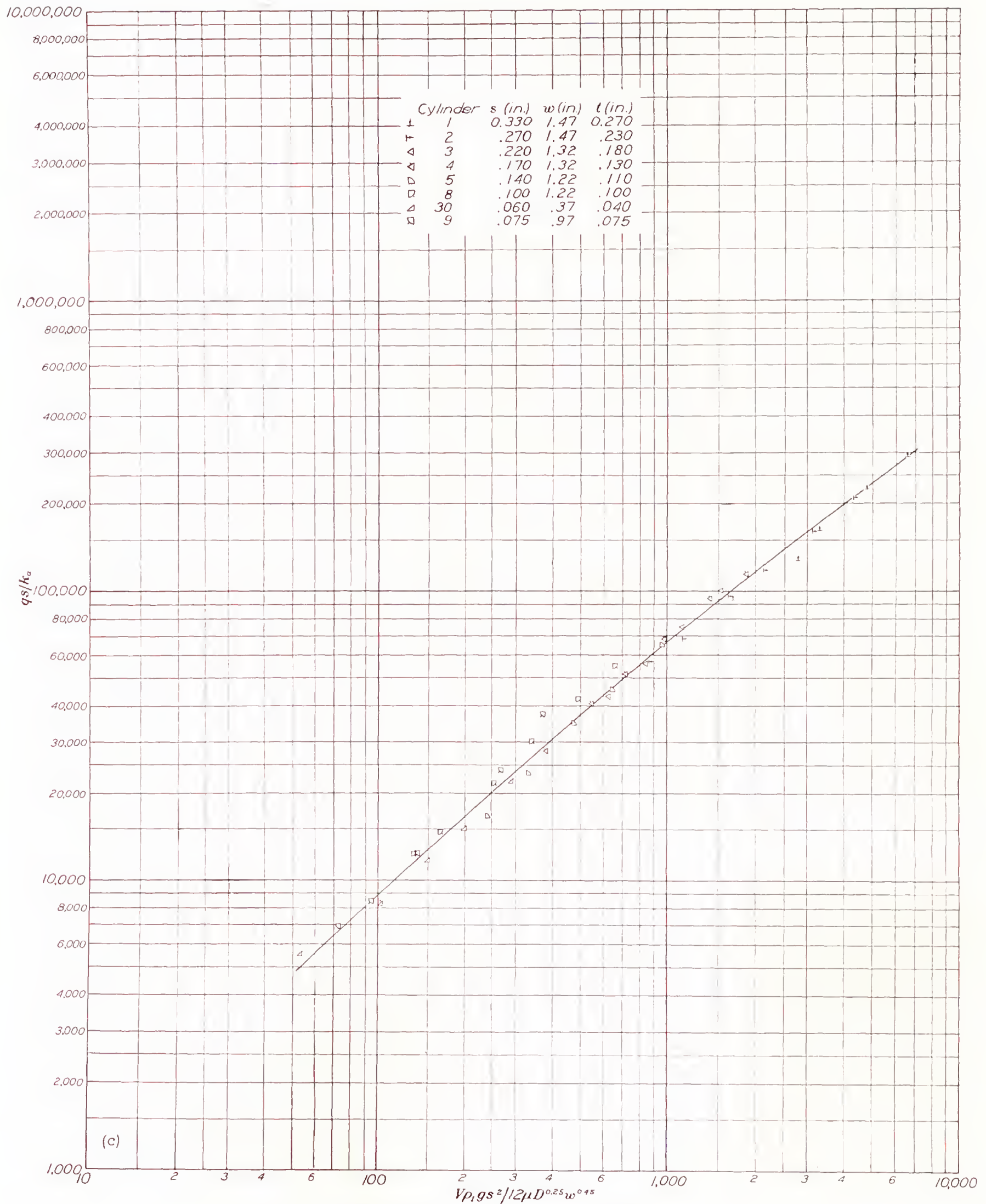




(b) Cylinder in free air stream, 140° baffles.

FIGURE 9—Continued.—Relation between factors involving  $q$ , fin dimensions, cylinder diameter, and air-stream characteristics.

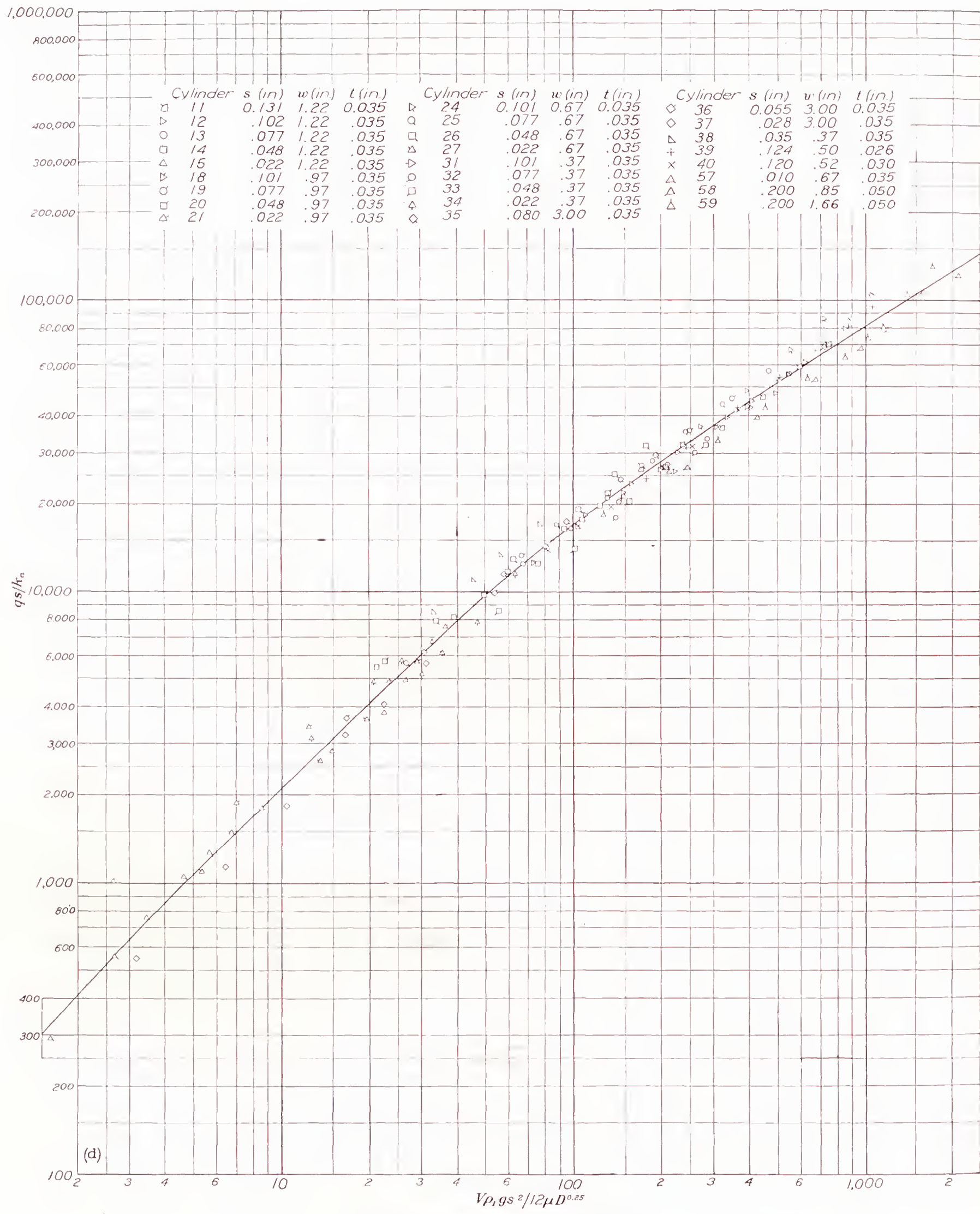




(c) Cylinder in free air stream, cylinder axis 45° to air stream.

FIGURE 9—Continued.—Relation between factors involving  $q$ , fin dimensions, cylinder diameter, and air-stream characteristics.





(d)

(d) Cylinder enclosed in jacket, blower cooling.

FIGURE 9—Continued.—Relation between factors involving  $q$ , fin dimensions, cylinder diameter, and air-stream characteristics.



In the correlation of the data of the present tests, the heat-transfer coefficients were based on the difference between the average surface temperature and the average fluid temperature. The correct temperature difference to use in calculating heat-transfer coefficients depends upon the temperature distributions of the surface and the fluid along the duct length. In cases where the surface temperatures remain approximately constant throughout the length of the duct, the correct average temperature difference is the logarithmic mean average. In cases where the surface temperatures rise linearly with that of the fluid, as is practically always true for air-cooled finned cylinders, the difference between the average surface and the average fluid temperatures should be used.

In the present investigation, little success toward correlating the data was had by plotting Nusselt number against Reynolds Number as is done in the heat-transfer tests of pipes in the turbulent region or by plotting the results in which the factors in equation (4) were used. The equivalent diameter and the length of passage were used in these calculations. The calculations showed that the Grashof number and the ratio of viscosities mentioned previously were practically 1, so that the factor  $\Phi$  was considered not to enter into the correlation.

After several trials, it was found that the best correlation of the data could be obtained by plotting as follows:

$$\frac{q_{av}s}{3600k_a} = f\left(\frac{V\rho_1gs}{12\mu}s\right) \quad (5)$$

where  $q_{av}s/3600k_a$  is a Nusselt number and  $V\rho_1gs/12\mu$  is a Reynolds Number. The replacement of  $s$  by  $d_e$ , the equivalent diameter of the passage, resulted in a satisfactory correlation but with a greater dispersion of the test points than when  $s$  was used. Figure 8 shows the results of the tests with blower cooling plotted according to equation (5). Efforts to correlate the data by inserting  $w$ ,  $D$ , or  $l$  in the right-hand side of equation (5) to make this factor dimensionless were unsatisfactory.

Figure 9 shows the variation of  $q$  with fin and cylinder dimensions and air-stream characteristics for four different air-flow arrangements. The functions given for each arrangement are purely empirical and hold for the range of conditions tested. It was found that, for the cylinders with and without baffles and for the cylinders tested at  $45^\circ$  fin-plane/air-stream angle,

$$\frac{qs}{k_a} = f'\left(\frac{V\rho_1gs^2}{12\mu D^{0.25}w^{0.45}}\right) \quad (6)$$

and, for the blower-cooling arrangement,

$$\frac{qs}{k_a} = f''\left(\frac{V\rho_1gs^2}{12\mu D^{0.25}}\right) \quad (7)$$

The curves of figure 9 represent the data well enough for all practical purposes.

## PRESSURE DIFFERENCES WITH BLOWER COOLING

### EFFECT OF FIN SPACE AND WIDTH

The weight velocity required between fins to obtain the desired values of  $q$  often requires much higher pressure differences than are available. For this reason, the pressure drop across finned cylinders is of considerable interest.

The pressure differences across cylinders enclosed in jackets similar to the one shown in figure 2 (b) have been determined for a large number of cylinders in addition to those tested in this investigation (reference 5). Paired curves of all these data are plotted in figure 10. The effect of the fin width on the pressure difference for the range of widths covered between 0.37 inch and 1.5 inches was negligible.

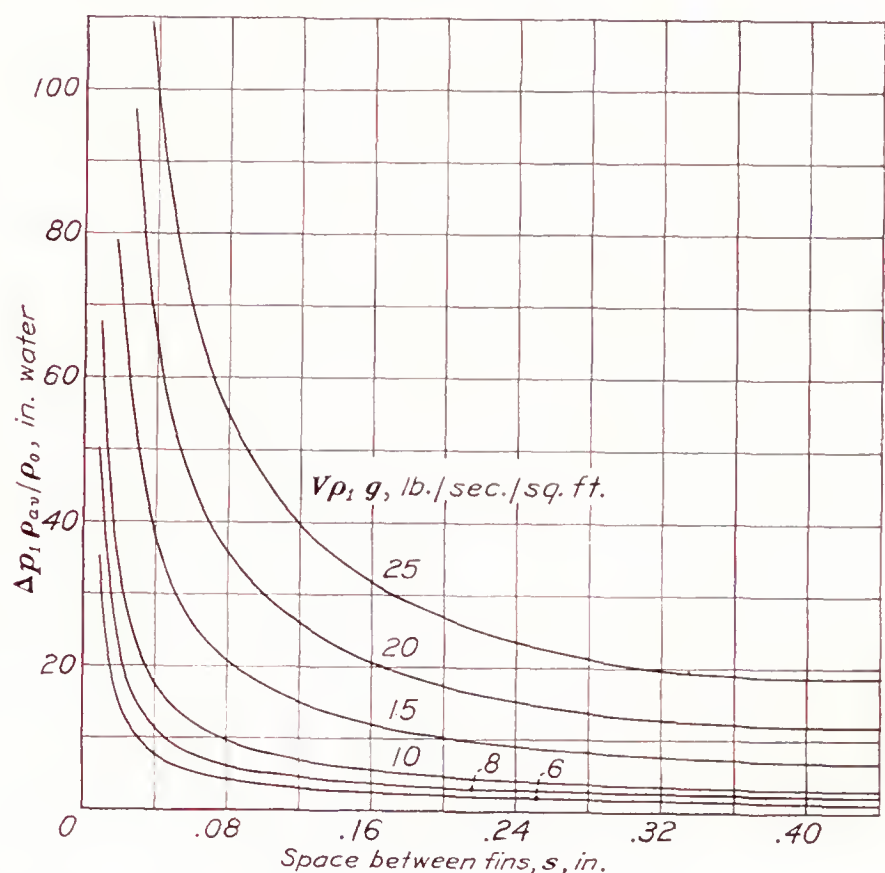


FIGURE 10.—Effect of fin space on pressure difference across finned cylinders at several weight velocities of the cooling air. Fin widths from 0.37 to 1.5 inches. Blower cooling.

Since the foregoing results were published, additional measurements of pressure drop have been made on a cylinder having a fin width of 3 inches and fin spaces of 0.028, 0.055, and 0.08 inch. These data show a higher pressure drop for the same fin spacing than was obtained with the narrower fin widths. Previous tests (reference 5) have shown that the pressure difference is directly proportional to the length  $l$  of the flow path. The data obtained with the 3-inch fins are plotted in figure 11 in terms of  $\Delta p_1/l$  together with curves obtained by cross-plotting figure 10 for the same values of fin space as were used in the cylinders with wide fins. The length  $l$  of the flow path for the cylinders of figure 10 was taken as an average value corresponding to an average fin width of 0.935 inch. The data for the 3-inch fins were in good agreement with the curves cross-plotted from figure 10 for all but the smallest value of  $s$ . From these data it may be concluded that, for the useful range of



fin spacing, the pressure drop is proportional to the length of the flow path. The pressure difference is affected by the fin width in direct proportion to the effect of the width on the length of the flow path.

#### EFFECT OF CYLINDER DIAMETER

The values of  $\Delta p_1/l$  for the cylinders of diameters 3.66 and 6.34 inches are also plotted in figure 11 for comparison with the data from the 4.66-inch-diameter cylinder. With the exception of the data for the small-diameter cylinder at the low weight velocities, the pressure drop across the cylinders again varies as the length of the flow path and is affected by the cylinder diameter in direct proportion to the effect of the diameter on the length of the flow path.

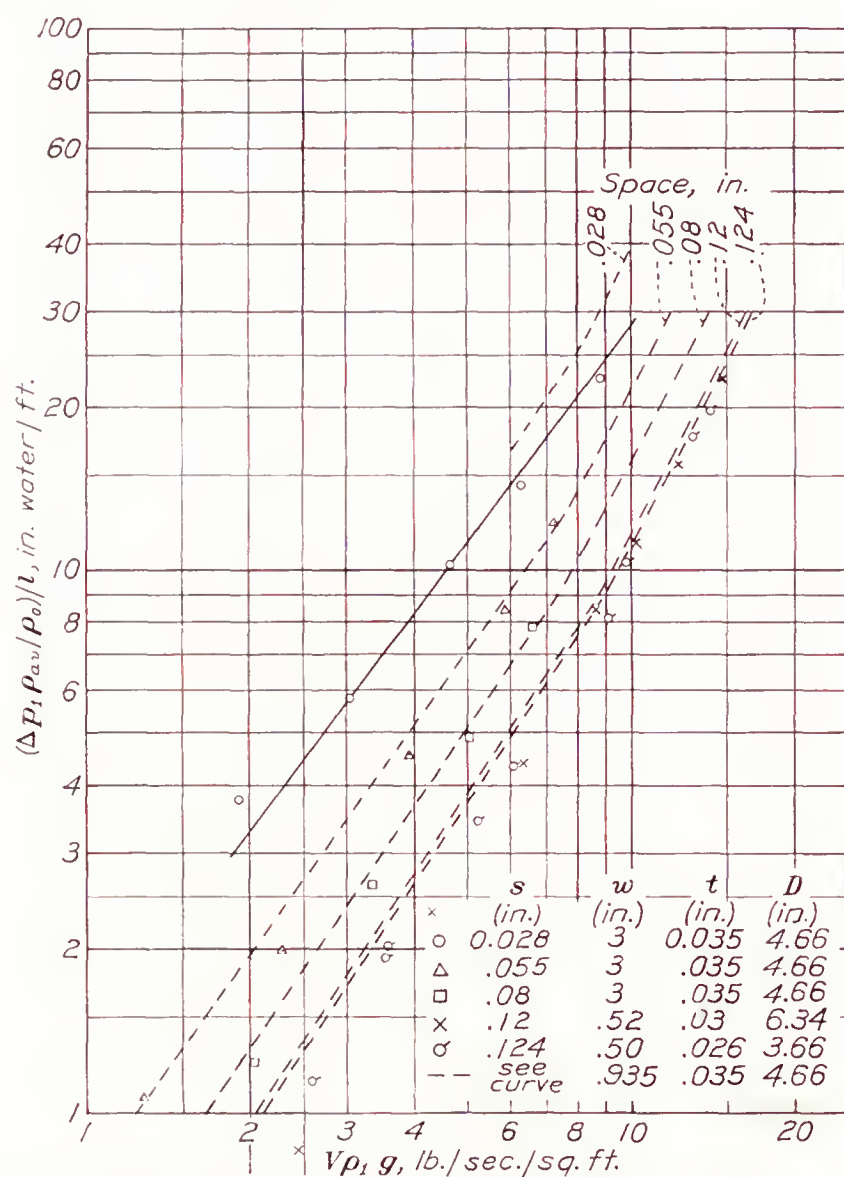


FIGURE 11.—Effect of weight velocity of cooling air on the pressure difference per foot length of path  $l$  for cylinders of different fin widths and diameters.

#### CONCLUSIONS

1. The surface heat-transfer coefficients of finned cylinders can be correlated for any one air-flow arrangement by plotting a factor involving the surface heat-transfer coefficients, the fin space, and the conductivity of the cooling air against a factor involving the velocity,

the density, and the viscosity of the cooling air and the fin space, the fin width, and the cylinder diameter.

2. A variation of the initial turbulence in the tunnel air stream for the range covered in the present tests had very little effect on the surface heat-transfer coefficient.

3. The improvement in heat transfer obtained with a fin-plane/air-stream angle of  $45^\circ$  as compared with one of  $0^\circ$  is appreciably affected by the value of the space between fins.

4. The pressure difference across a finned cylinder is affected by the fin width, the cylinder diameter, and the front baffle opening in direct proportion to the effect that these three dimensions have on the length of path  $l$  as defined in the report.

LANGLEY MEMORIAL AERONAUTICAL LABORATORY,  
NATIONAL ADVISORY COMMITTEE FOR AERONAUTICS,  
LANGLEY FIELD, VA., April 27, 1939.

#### REFERENCES

1. Biermann, Arnold E., and Pinkel, Benjamin: Heat Transfer from Finned Metal Cylinders in an Air Stream. T. R. No. 488, N. A. C. A., 1934.
2. Schey, Oscar W., and Rollin, Vern G.: The Effect of Baffles on the Temperature Distribution and Heat-Transfer Coefficients of Finned Cylinders. T. R. No. 511, N. A. C. A., 1934.
3. Schey, Oscar W., and Ellerbrock, Herman H., Jr.: Blower Cooling of Finned Cylinders. T. R. No. 587, N. A. C. A., 1937.
4. Biermann, Arnold E.: Heat Transfer from Cylinders Having Closely Spaced Fins. T. N. No. 602, N. A. C. A., 1937.
5. Rollin, Vern G., and Ellerbrock, Herman H., Jr.: Pressure Drop across Finned Cylinders Enclosed in a Jacket. T. N. No. 621, N. A. C. A., 1937.
6. Brevoort, Maurice J.: Energy Loss, Velocity Distribution, and Temperature Distribution for a Baffled Cylinder Model. T. N. No. 620, N. A. C. A., 1937.
7. Brevoort, M. J., and Rollin, Vern G.: Air Flow around Finned Cylinders. T. R. No. 555, N. A. C. A., 1936.
8. Schubauer, G. B.: A Turbulence Indicator Utilizing the Diffusion of Heat. T. R. No. 524, N. A. C. A., 1935.
9. Platt, Robert C.: Turbulence Factors of N. A. C. A. Wind Tunnels as Determined by Sphere Tests. T. R. No. 558, N. A. C. A., 1936.
10. Schey, Oscar W., and Biermann, Arnold E.: Heat Dissipation from a Finned Cylinder at Different Fin-Plane/Air-Stream Angles. T. N. No. 429, N. A. C. A., 1932.
11. McAdams, William H.: Heat Transmission. McGraw-Hill Book Co., Inc., 1933.
12. Colburn, Allan P.: A Method of Correlating Forced Convection Heat Transfer Data and a Comparison with Fluid Friction. Trans. Am. Inst. Chem. Eng., vol. XXIX, 1933, pp. 174-210.



## REPORT No. 677

# WIND-TUNNEL INVESTIGATION OF AN N. A. C. A. 23021 AIRFOIL WITH VARIOUS ARRANGEMENTS OF SLOTTED FLAPS

By CARL J. WENZINGER and THOMAS A. HARRIS

### SUMMARY

*An investigation has been made in the N. A. C. A. 7- by 10-foot wind tunnel of a large-chord N. A. C. A. 23021 airfoil with several arrangements of 25.66-percent-chord slotted flaps to determine the section aerodynamic characteristics as affected by slot shape, flap shape, flap location, and flap deflection. The flap positions for maximum lift, the polars for arrangements considered favorable for take-off and climb, and the complete section aerodynamic characteristics for selected optimum arrangements were determined. A discussion is given of the relative merits of the various arrangements for certain selected criteria. A comparison is made of a slotted flap on the N. A. C. A. 23021 airfoil with a corresponding slotted flap previously developed for the N. A. C. A. 23012 airfoil.*

*The best slotted-flap arrangement on the N. A. C. A. 23021 airfoil gave the same maximum lift coefficient as the best slotted flap on the N. A. C. A. 23012 airfoil. The drag coefficients were higher with the N. A. C. A. 23021 airfoil, but the pitching-moment coefficients were about equal for comparable arrangements.*

### INTRODUCTION

The National Advisory Committee for Aeronautics is undertaking an extensive investigation of various wing-flap combinations to furnish information applicable to the aerodynamic design of high-lift devices for improving the safety and the performance of airplanes. A high-lift device capable of producing high lift with variable drag for landing and high lift with low drag for take-off and initial climb is believed to be desirable. Other desirable aerodynamic features are: no increase in drag with the flap neutral; small change in pitching moment with flap deflection; low forces required to operate the flap; and freedom from possible hazard due to icing.

A very promising arrangement of a simple slotted flap developed for the N. A. C. A. 23012 airfoil is reported in reference 1. Further improvement, from a consideration of high lift coefficients and low drag at high and intermediate lift coefficients, was obtained by the addi-

tion of an auxiliary slotted flap to the main flap (reference 2). Another type of slotted flap, aerodynamically superior but structurally more complicated, is the venetian-blind flap reported in reference 3. All these flap arrangements were tested on the N. A. C. A. 23012 airfoil.

In the present report, the results are given of the tests of a relatively thick airfoil, the N. A. C. A. 23021, with several arrangements of 25.66-percent-chord slotted flaps. This investigation included two flap shapes, each of which was tested with several slot shapes.

### MODELS

#### PLAIN AIRFOIL

The basic wing, or the plain airfoil, used in these tests was built to the N. A. C. A. 23021 profile and has a chord of 3 feet and a span of 7 feet; the ordinates for the section are given in table I. The model was built with solid laminated mahogany nose and trailing-edge pieces and solid mahogany ribs. The portion between the nose and the trailing edge was covered with tempered wallboard. The trailing-edge section of this model was easily removable so that the model could be quickly altered for tests of different flap arrangements.

#### SLOTTED FLAPS

The slotted flaps and the slot shapes were built of solid laminated mahogany. The slot shapes were bolted to the main airfoil in place of the solid trailing edge. The flaps were mounted on special hinges that permitted considerable latitude in the location of the flaps with respect to the main airfoil.

**Flaps.**—Two flap shapes were tested. Flap 1 (fig. 1 and table I), corresponding to flap 1 of reference 1, has a small nose radius and was designed to give only a small break in the airfoil lower surface when undeflected. It also lends itself to use with a door to seal the break in the lower surface of the airfoil with the flap undeflected.

Flap 2 corresponds to flap 2 of reference 1, which gave the lowest drag at high and intermediate lift coefficients on the N. A. C. A. 23012 airfoil. This flap is shown in figure 2 and its ordinates are given in table I. This flap shape was obtained by combining the nose of



an N. A. C. A. 6330 airfoil with the trailing-edge portion of the main wing. It was designed to give low drag at intermediate and high lift coefficients.

**Slot shapes.**—Slot shape a, which was used in combination with both flaps, is shown in figures 1 (a) and 2 (a). This slot shape was designed to give a minimum break in the lower surface of the wing and, consequently, to have the smallest effect on the drag with the flap neutral. Slot shape b is similar to slot shape h of reference 1, which gave the lowest drag at intermediate

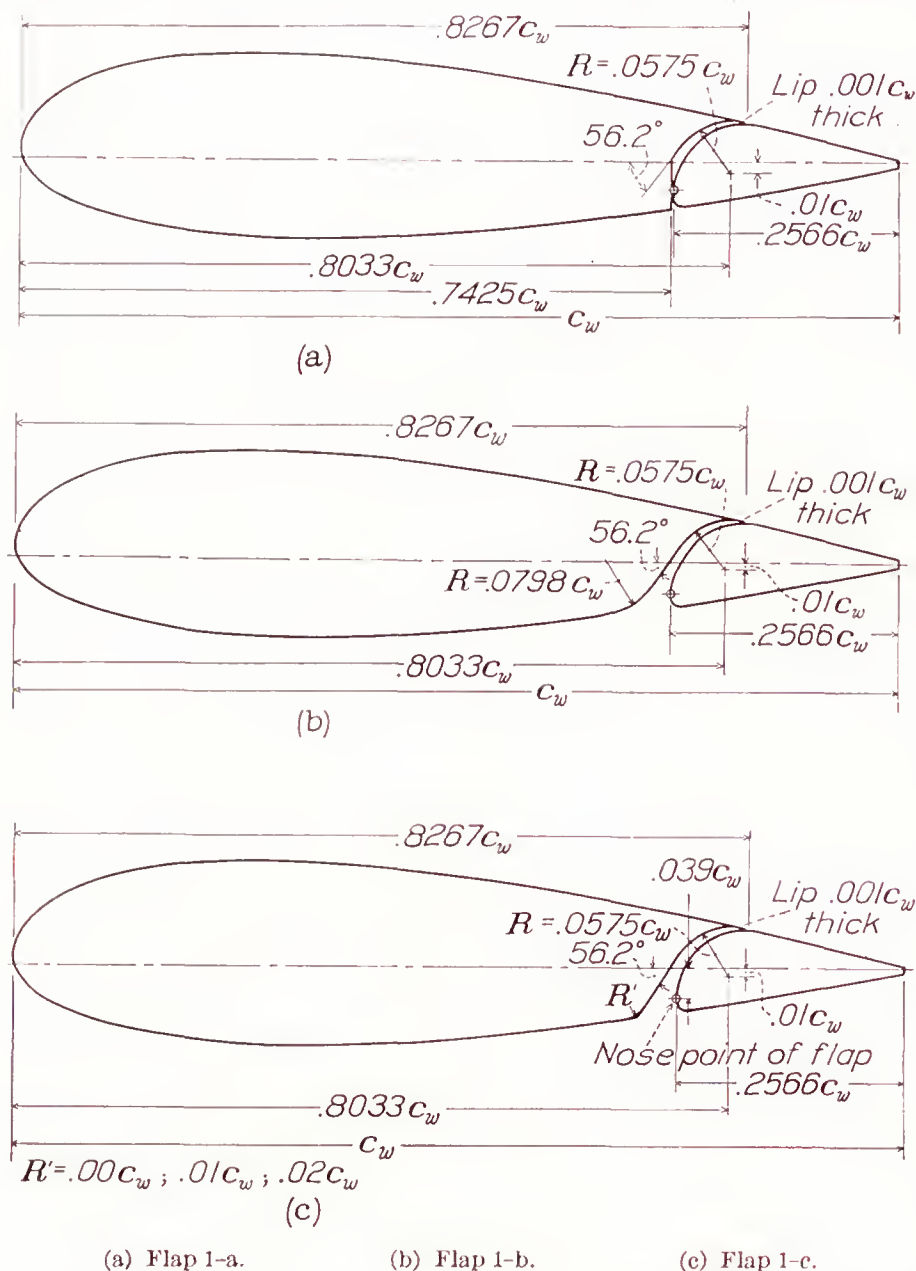


FIGURE 1.—Sections of N. A. C. A. 23021 airfoil with arrangements of slotted flap 1.

and high lift coefficients for take-off. This slot shape was also used in combination with both flaps and is shown in figures 1 (b) and 2 (b). Slot shape c was especially designed so that a door could be used to close the break in the lower surface of the wing with the flap neutral. This slot shape was used only in combination with flap 1 and was similar to shape b except for the entry radius. Slot shape c<sub>0</sub> has a sharp entry, and shapes c<sub>1</sub> and c<sub>2</sub> have entry radii 1 and 2 percent of the wing chord, respectively. All the slots were designed to be sealed by the slot lip at the exit on the upper surface of the wing with the flaps neutral.

The models were made to a tolerance of  $\pm 0.015$  inch.

## TESTS

The models were mounted in the closed test section of the N. A. C. A. 7- by 10-foot wind tunnel so that they completely spanned the jet except for small clearances at each end. (See references 1 and 4.) The main airfoil was rigidly attached to the balance frame by torque tubes, which extended through the upper and the lower boundaries of the tunnel. The angle of attack of the model was set from outside the tunnel by rotating the torque tubes with a calibrated drive. Approximately two-dimensional flow is obtained with this type of installation and the section characteristics of the model under test can be determined.

A dynamic pressure of 16.37 pounds per square foot was maintained for most of the tests, corresponding to a velocity of 80 miles per hour under standard atmospheric

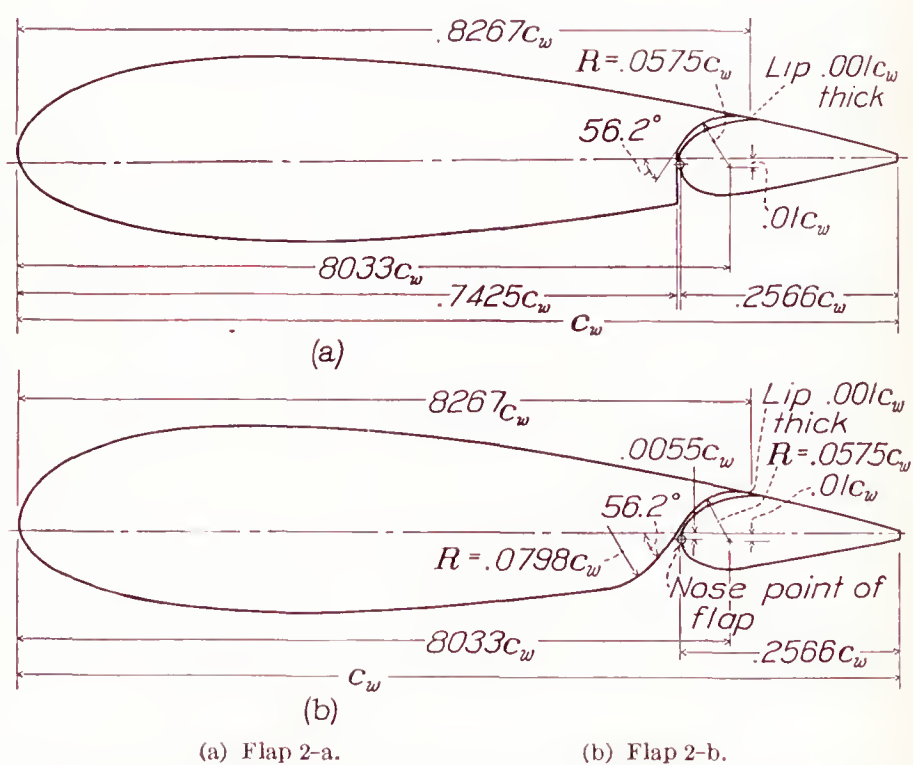


FIGURE 2.—Sections of N. A. C. A. 23021 airfoil with arrangements of slotted flap 2.

conditions and to an average test Reynolds Number of about 2,190,000. Because of the turbulence in the wind tunnel, the effective Reynolds Number  $R_e$  (reference 5) was approximately 3,500,000. For all tests,  $R_e$  is based on the chord of the airfoil with the flap retracted and on a turbulence factor of 1.6 for the tunnel.

**Plain airfoil.**—Tests were first made of the plain airfoil over the complete angle-of-attack range from  $-6^\circ$  to the stall. In addition to this test, scale-effect tests were made of maximum lift coefficient over the range available in the 7- by 10-foot wind tunnel.

**Slotted flaps.**—With each slotted-flap arrangement, tests were made to determine the effect on minimum drag of the breaks in the wing lower surface at the slot entrance with the flap retracted. Tests were also made to determine the effect of the flap hinges with the flaps in their retracted positions. The tests of slotted flaps 1-a, 1-b, 2-a, and 2-b consisted in surveys of flap



position and deflection to determine the optimum path of the flap from a consideration of low drag throughout the complete lift range and of the highest maximum lift for each flap deflection. Tests were made of slotted flaps 1-c<sub>0</sub>, 1-c<sub>1</sub>, and 1-c<sub>2</sub> along the optimum path as determined for slotted flap 1-b. Data were obtained for all tests throughout the angle-of-attack range from -6° to the stall at 10° increments of flap deflection from 0° to 60°. No data were obtained above the stall because of the unsteady conditions of the model. Lift, drag, and pitching moments were measured for all positions of the flap over the complete angle-of-attack range tested.

Scale-effect tests of maximum lift were also made of slotted flap 2-b at the optimum position for maximum lift with the 50° flap deflection.

### RESULTS AND DISCUSSION COEFFICIENTS

All test results are given in standard section non-dimensional coefficient form corrected as explained in reference 1.

$c_l$ , section lift coefficient ( $l/qc_w$ ).

$c_{d0}$ , section profile-drag coefficient ( $d_0/qc_w$ ).

$c_{m(a.c.)_0}$ , section pitching-moment coefficient about aerodynamic center of plain airfoil ( $m_{(a.c.)_0}/qc_w^2$ ).

where

$l$  is section lift.

$d_0$ , section profile drag.

$m_{(a.c.)_0}$ , section pitching moment.

$q$ , dynamic pressure ( $1/2 \rho V^2$ ).

$c_w$ , chord of basic airfoil with the flap fully retracted.

and

$\alpha_0$  is angle of attack for infinite aspect ratio.

$\delta_f$ , flap deflection.

### PRECISION

The accuracy of the various measurements in the tests is believed to be within the following limits:

$\alpha_0$ -----	$\pm 0.1^\circ$
$c_{l_{max}}$ -----	$\pm 0.03$
$c_{m(a.c.)_0}$ -----	$\pm 0.003$
$c_{d0_{min}}$ -----	$\pm 0.0003$
$c_{d0(c_l=1.0)}$ -----	$\pm 0.0006$
$c_{d0(c_l=2.5)}$ -----	$\pm 0.002$
$\delta_f$ -----	$\pm 0.2^\circ$
Flap position -----	$\pm 0.001c_w$

No corrections for flap-hinge fittings have been applied to the data because no effect could be measured with the flaps neutral. No attempt was made to determine the effect of the hinges with the flaps deflected because their effect was believed to be small and because of the great number of tests required. It is believed that the relative merits of the various flaps

are not appreciably affected because the same hinge fittings were used with all the airfoil-flap combinations.

### PLAIN AIRFOIL

**Aerodynamic characteristics.**—The complete section aerodynamic characteristics of the plain N. A. C. A. 23021 airfoil are given in figure 3. Comparison with previously published data obtained from tests of a finite-span model and corrected to infinite aspect ratio

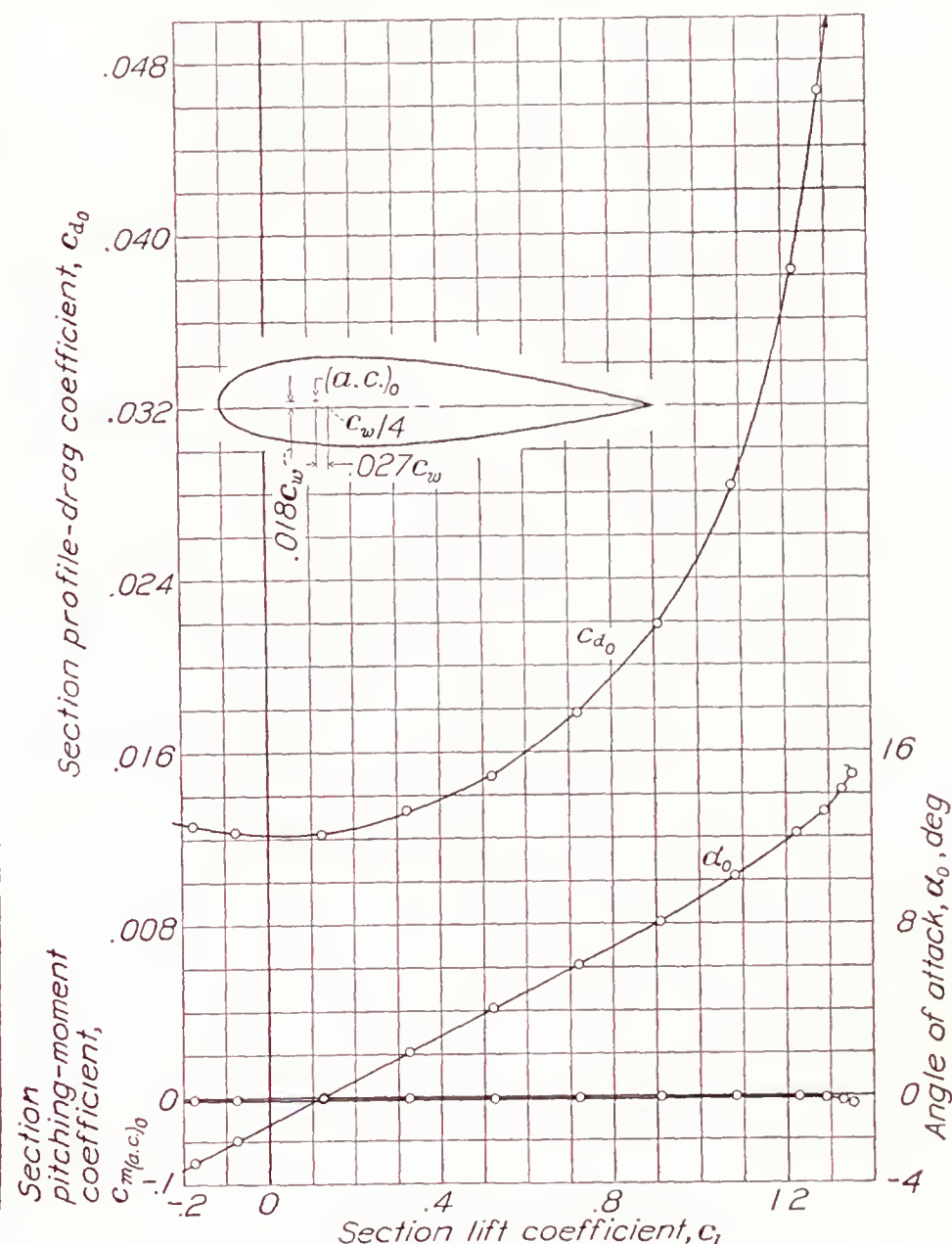


FIGURE 3.—Section aerodynamic characteristics of N. A. C. A. 23021 plain airfoil.

(reference 5) shows insignificant differences in the results. The slope of the lift curve and the values of the minimum drag coefficient are slightly higher for the present tests than for some of the results at a considerably higher Reynolds Number given in reference 5. The pitching-moment coefficient and the vertical location of the aerodynamic center above the chord line are slightly lower. The chordwise location of the aerodynamic center is the same for both sets of data. These differences are about the same as those observed between the results of previous two- and three-dimensional-flow tests of the N. A. C. A. 23012 airfoil (reference 1). The data for the N. A. C. A. 23021 airfoil given herein are directly comparable with the data for the N. A. C. A. 23012 (references 1, 2, and 3). When comparisons with other airfoils are made, it should be remembered



that no correction for tunnel effect has been applied to these data except for the lift, as explained in reference 1.

**Effect on profile drag of breaks in surface of airfoil at slot entrance.**—The effects of the breaks in the lower surface of the airfoil with the flaps undeflected are shown in figure 4. No measurable effect was evident from the breaks caused by the thickness of the slot lip in the upper surface of the airfoil. The increment of profile-drag coefficient,  $\Delta c_{d_0}$ , was smallest for slotted flap 1-a;  $\Delta c_{d_0}$  varied from 0.0002 at zero lift to 0.0006 at a lift coefficient of 1.0. Slotted flap 2-a had a constant increment of profile-drag coefficient of 0.0006

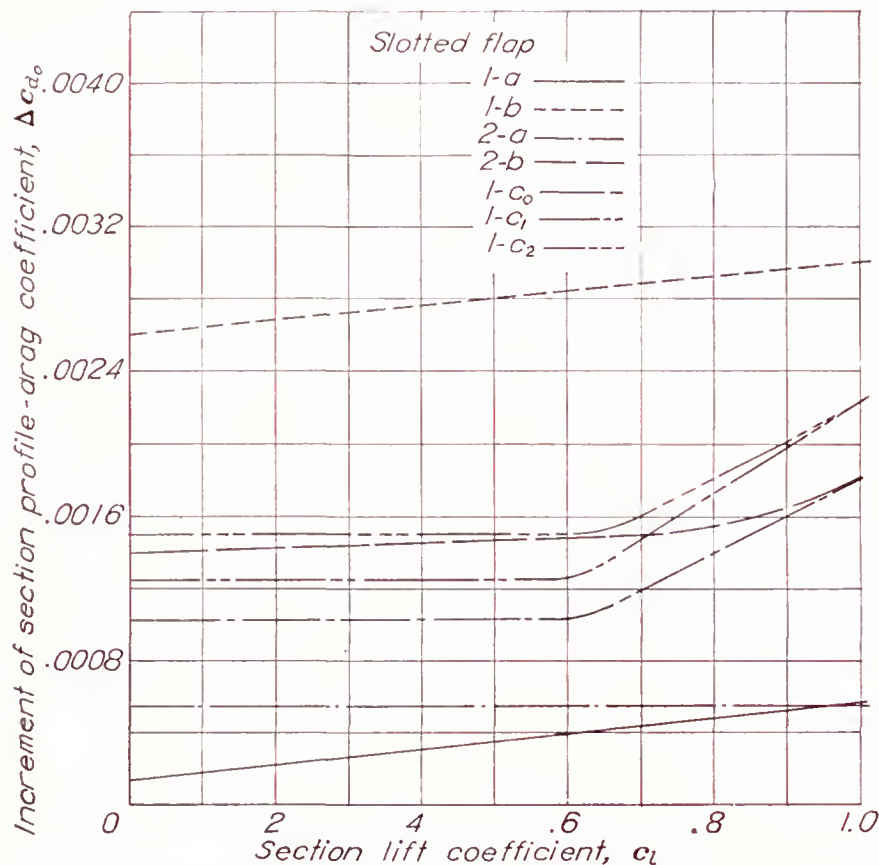


FIGURE 4.—Effect of slot openings in lower surface of airfoil on profile-drag coefficient.  $\delta_f, 0^\circ$ .

for all lift coefficients from zero lift to a lift coefficient of 1.0. Slotted flaps 1- $c_0$  and 1- $c_1$  gave approximately constant increments of profile-drag coefficient of about 0.0010 and 0.0012, respectively, up to a lift coefficient of 0.6, beyond which the increments increased to 0.0018 and 0.0022 at a lift coefficient of 1.0. Slotted flaps 1- $c_2$  and 2-b gave about the same increment of profile-drag coefficient, 0.0014 to 0.0015, for lift coefficients less than 0.6, beyond which the increments increased to 0.0022 and 0.0018, respectively, at a lift coefficient of 1.0. Slotted flap 1-b was inferior to all other arrangements, the increment of profile-drag coefficient increasing nearly linearly from 0.0026 at zero lift to 0.0030 at a lift coefficient of 1.0.

It is probable that a door could be fitted to any of the arrangements in such a manner as to seal the break in the airfoil lower surface without measurably increasing the profile-drag coefficient of the wing with the flap neutral over that of the plain wing.

#### SLOTTED-FLAP ARRANGEMENT

**Determination of optimum arrangements for maximum lift.**—The data presented in this section are the results of the maximum-lift investigation of the various flap-and-slot combinations in which the flap, at a given deflection, was located at points over a considerable area with respect to the main airfoil. The data are presented as contours of the position of the nose point of the flap for a given lift coefficient. The nose point of the flap is defined as the point of tangency of a line drawn perpendicular to the airfoil chord and tangent to the leading-edge arc of the flap when neutral, as shown in figures 1 and 2.

The complete maximum-lift data for slotted flaps 1-a, 1-b, 2-a, and 2-b deflected  $10^\circ$ ,  $20^\circ$ ,  $30^\circ$ ,  $40^\circ$ ,  $50^\circ$ , and  $60^\circ$  are given in figures 5 to 8, respectively. An inspection of these figures shows that the contours are not closed with all combinations for flap deflections less than  $30^\circ$ . The position for maximum lift coefficient is not very critical and only a sufficient number of positions were taken to cover any practical path along which the flap is likely to be operated. Furthermore, it is probable that the optimum flap position for these deflections will be chosen from a consideration of drag and ease of mechanical operation.

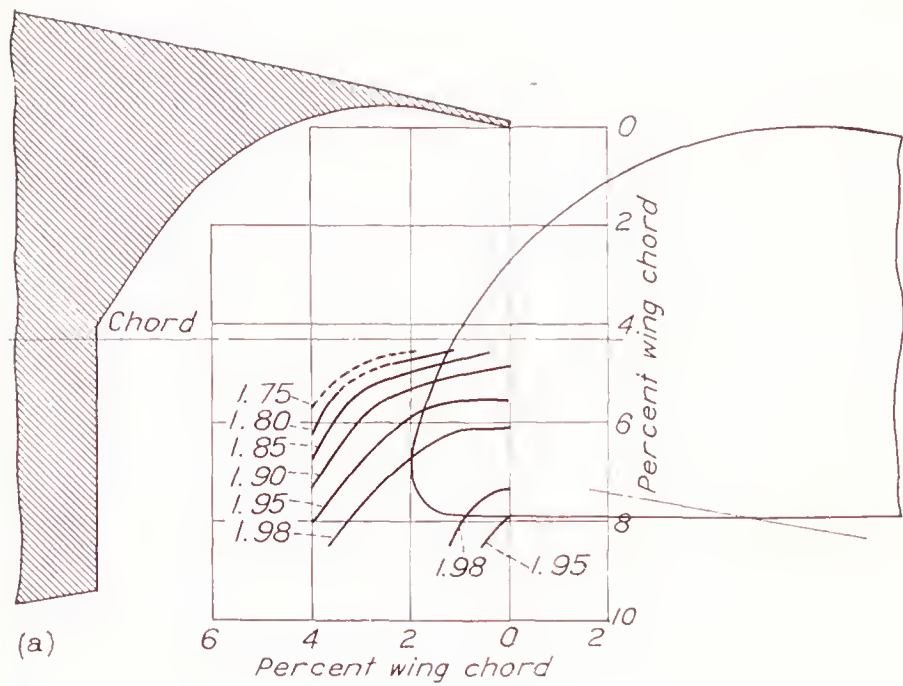
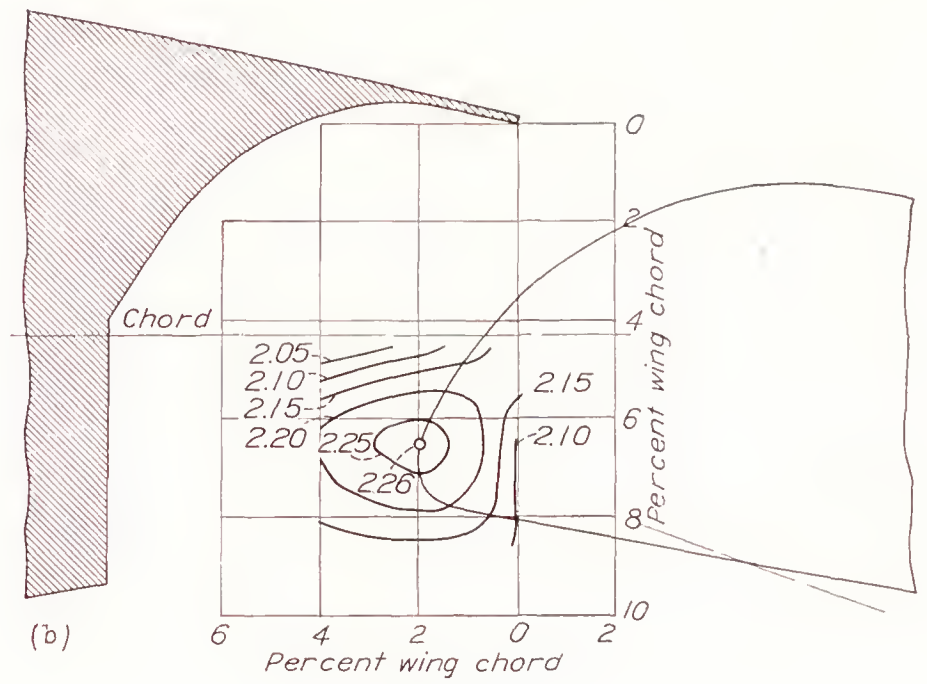
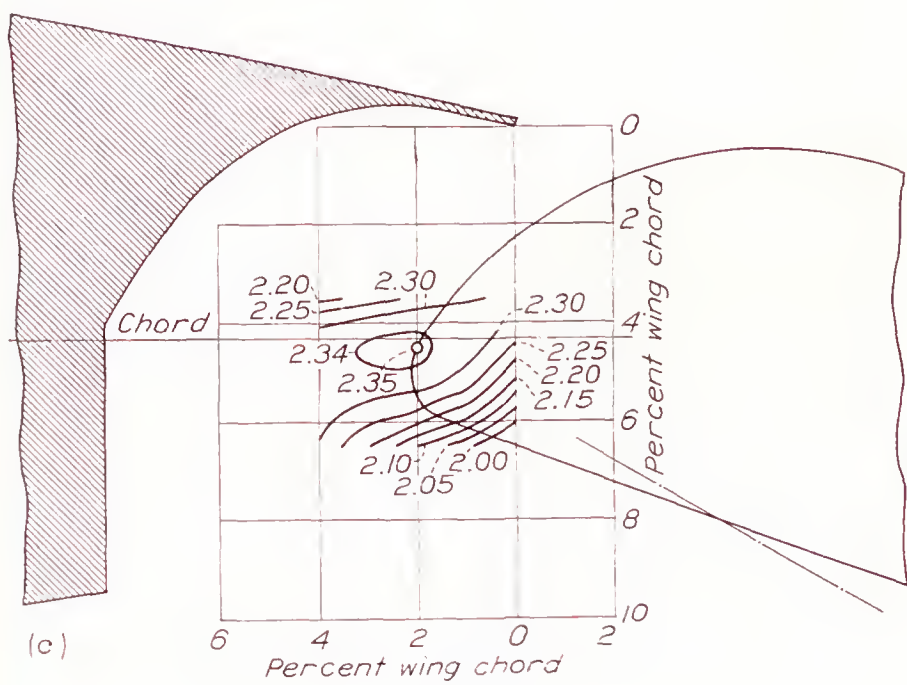
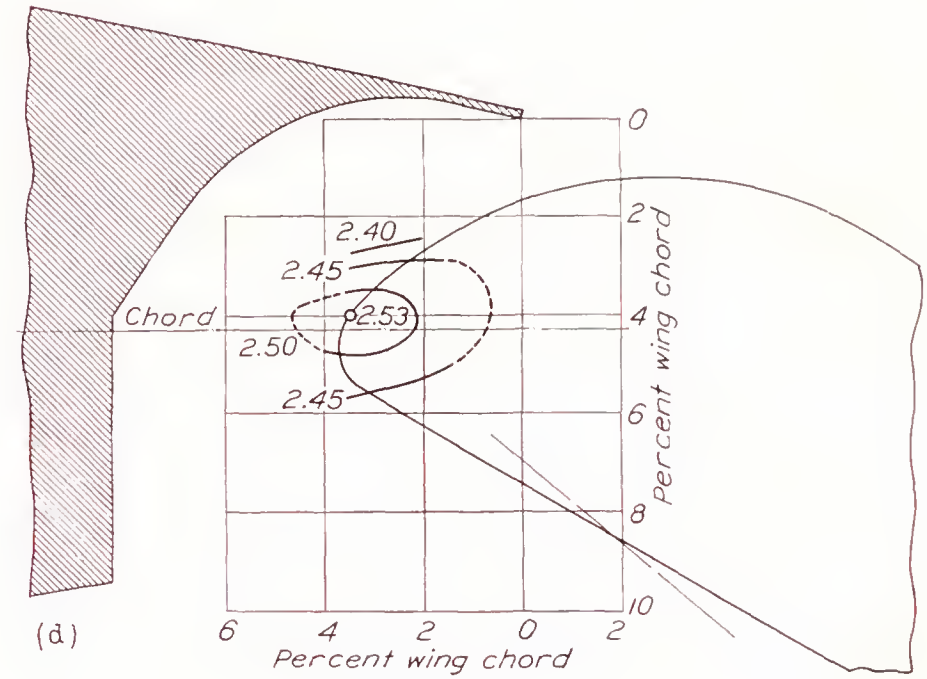
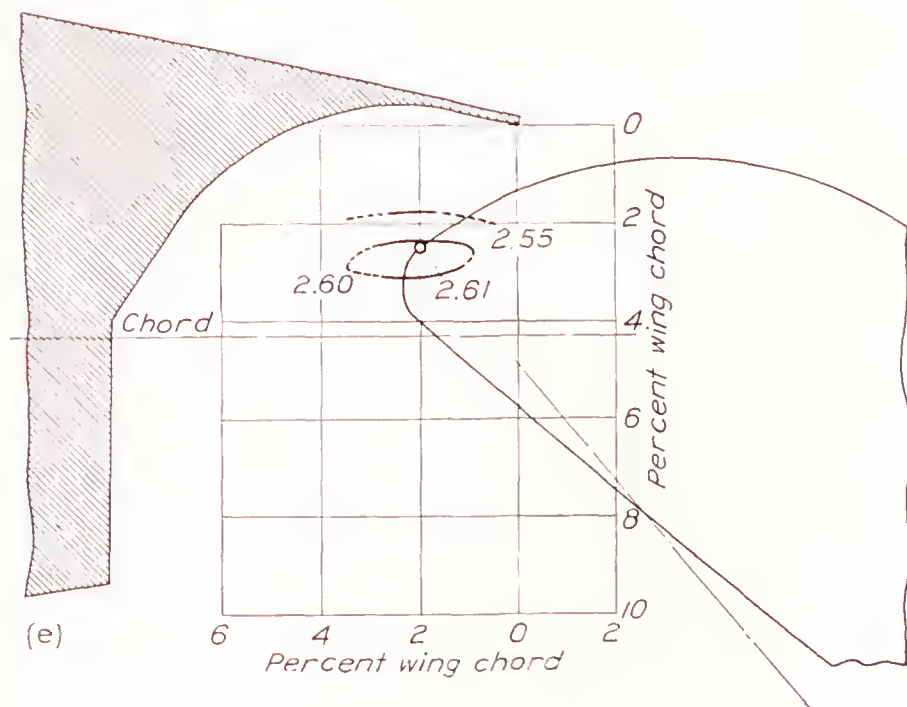
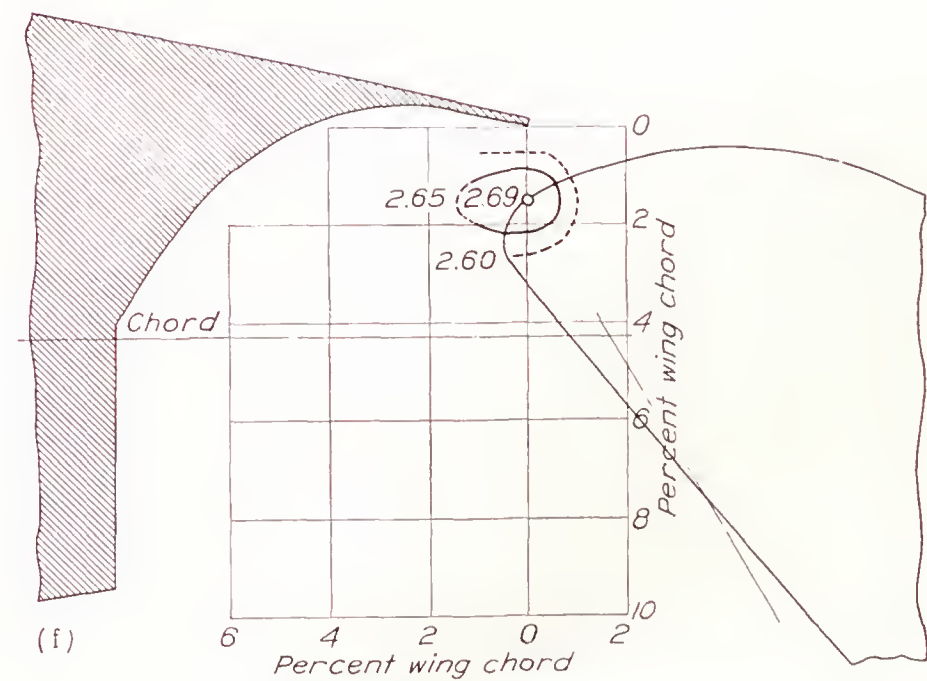
The position of the flaps for maximum lift coefficient becomes much more critical for flap deflections from  $40^\circ$  to  $60^\circ$ . The maximum lift coefficient was obtained for slotted flaps 1-a and 1-b with the flap deflected  $60^\circ$  and the nose point 1.5 percent of the wing chord directly below the slot lip. With slotted flaps 2-a and 2-b, the maximum lift coefficient at  $50^\circ$  flap deflection was obtained with the flap nose point about 2.5 percent of the wing chord directly below the slot lip.

From these contours, it should be possible for the designer to choose the best path for the flap to follow from a consideration of maximum lift coefficient alone. If, from structural considerations, it is not possible to use the best aerodynamic path, the loss caused by using a compromise path can be immediately evaluated. Complete section aerodynamic characteristics of selected optimum arrangements for each flap deflection are given in a later section of this report.

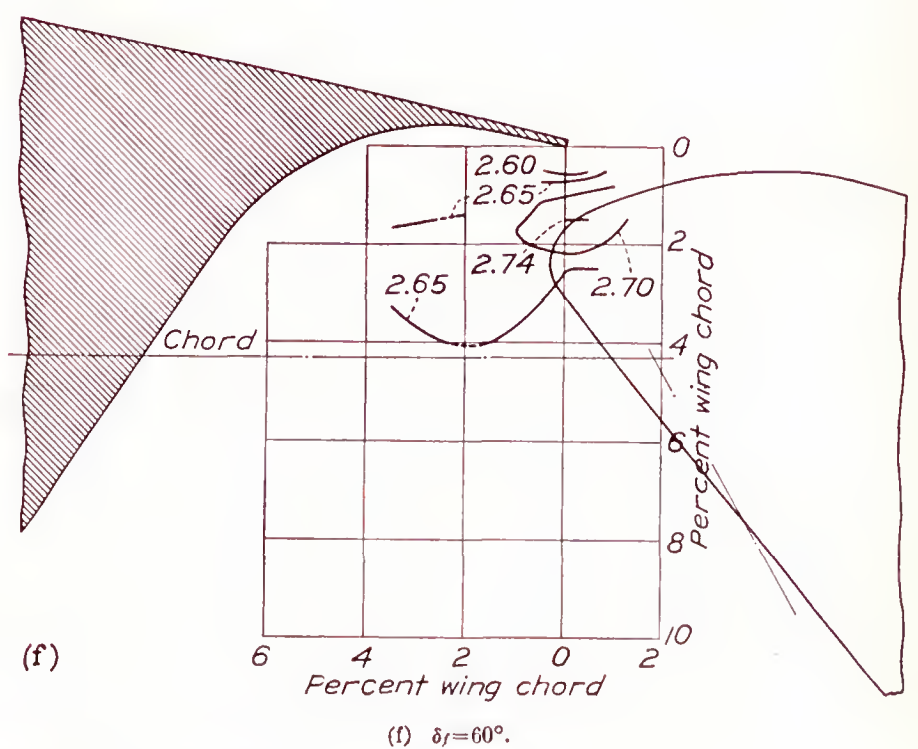
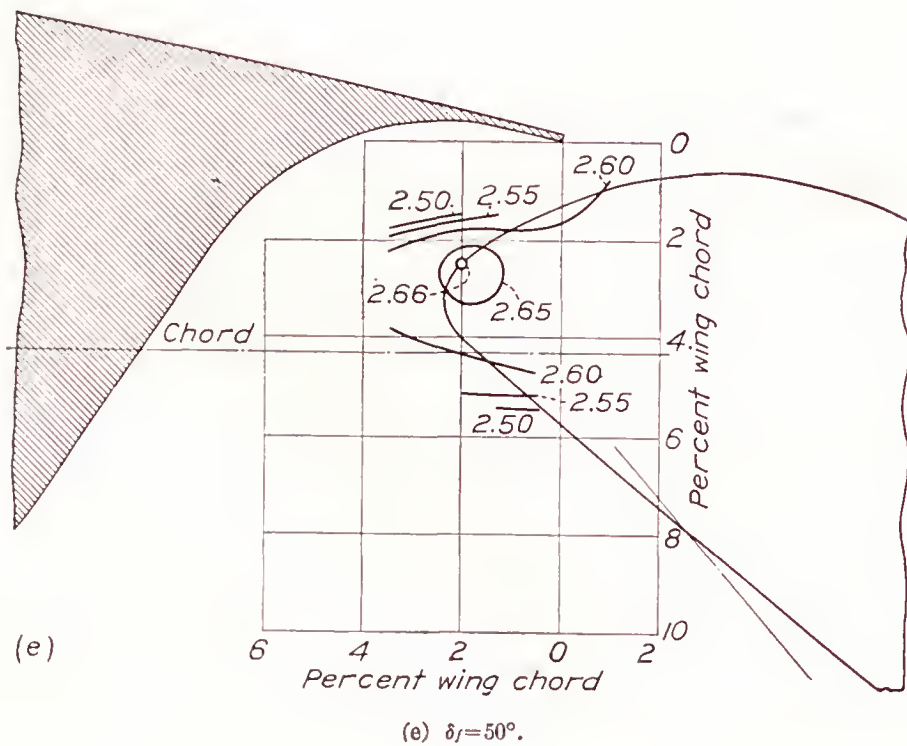
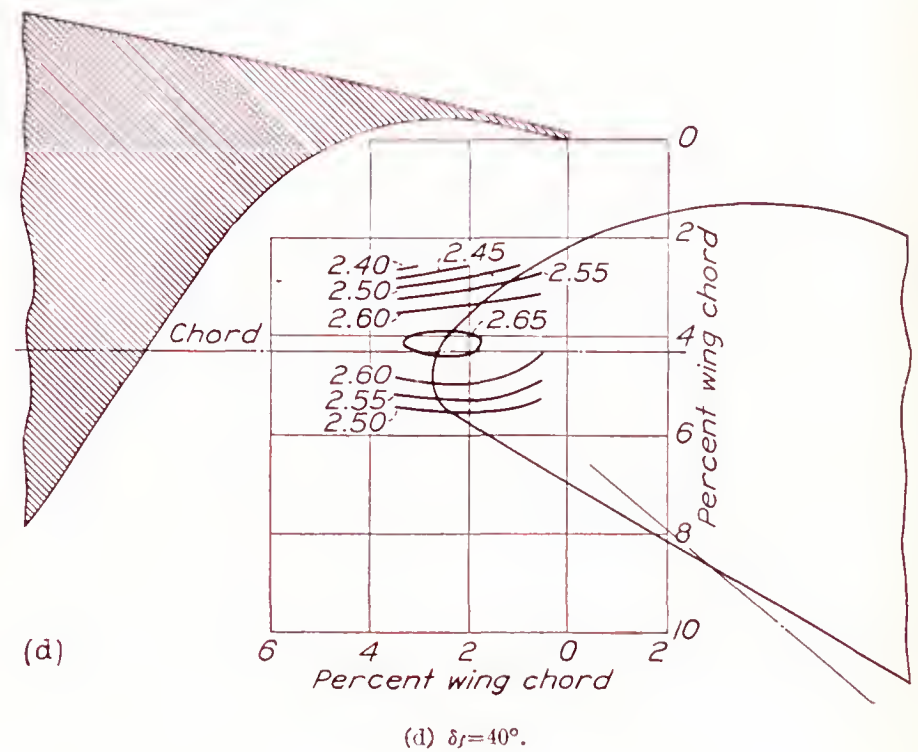
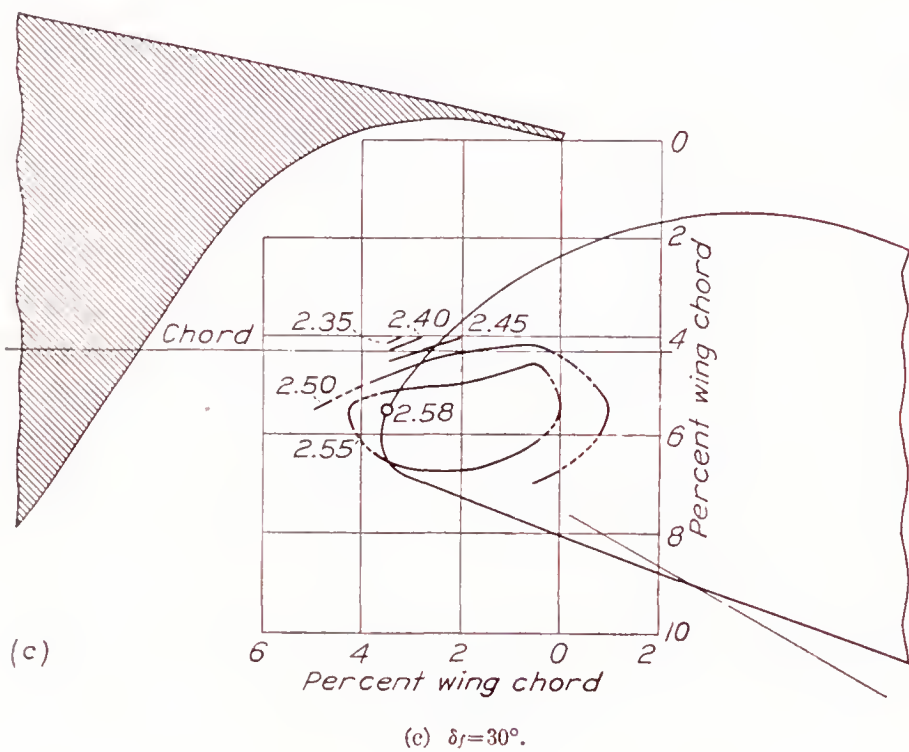
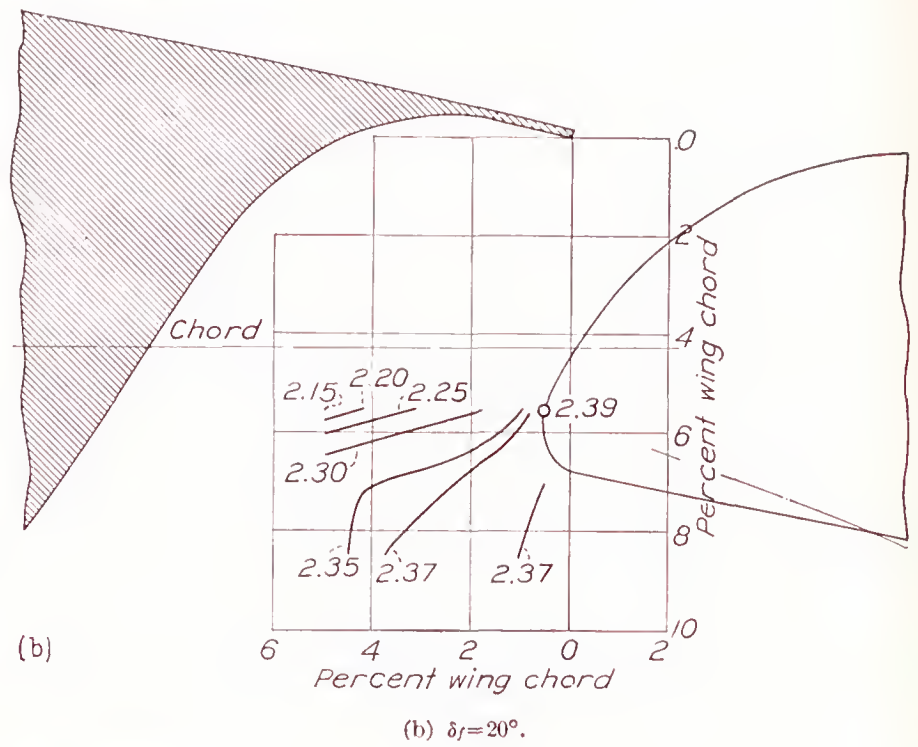
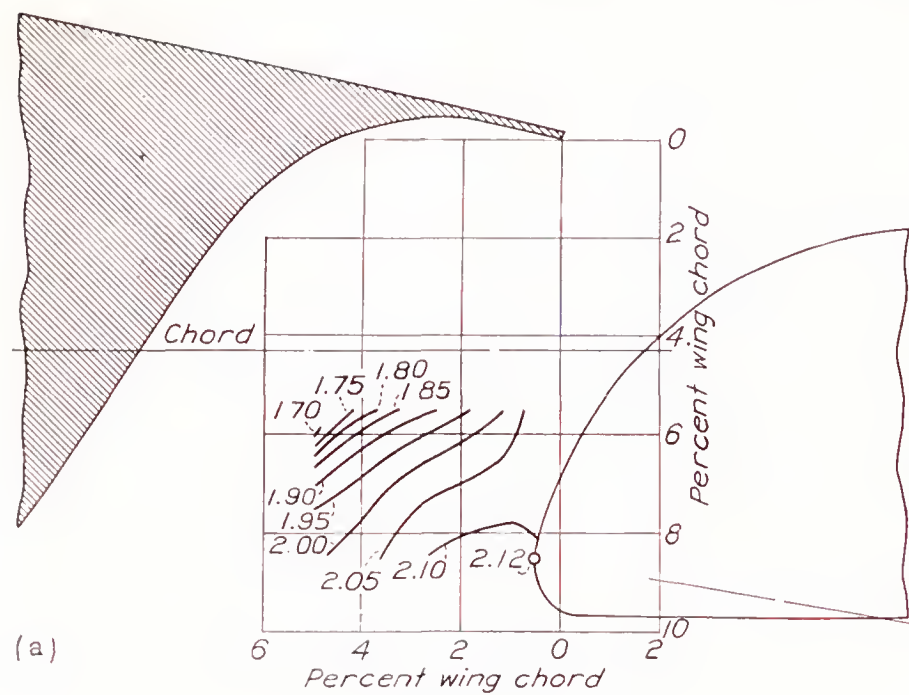
**Determination of optimum arrangements for profile drag.**—Optimum positions of the several flaps for the conditions of low drag for take-off and initial climb to clear an obstacle were determined. The sole criterion for a given lift coefficient is the drag coefficient.

The most important single factor in unassisted take-off distance is the value of the lift coefficient for take-off because the higher the lift coefficient, the lower the take-off speed and, other conditions being equal, the shorter the distance required to clear a given obstacle.

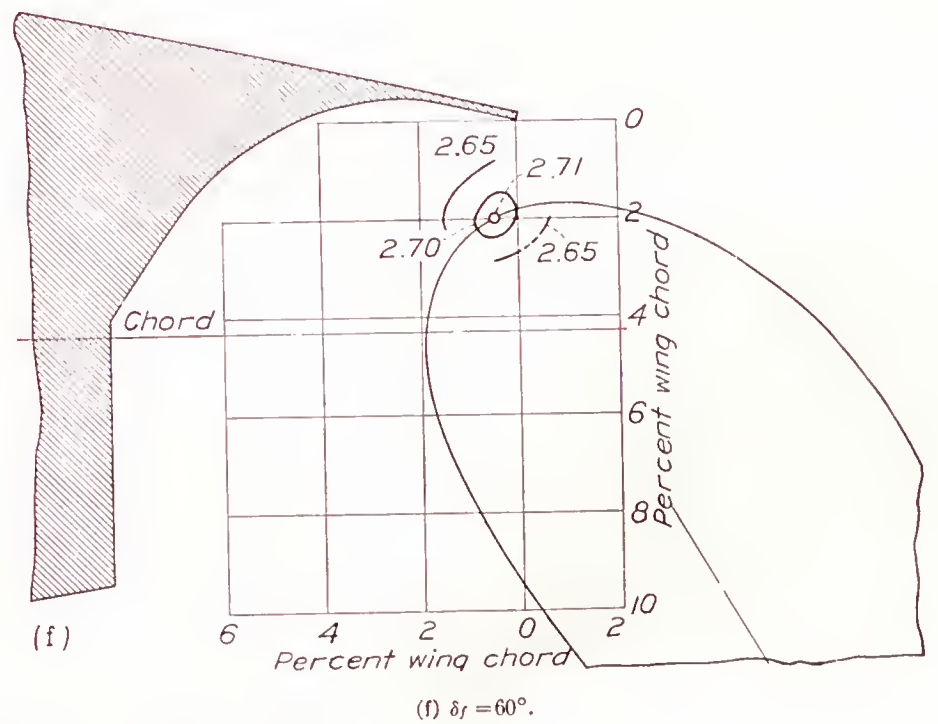
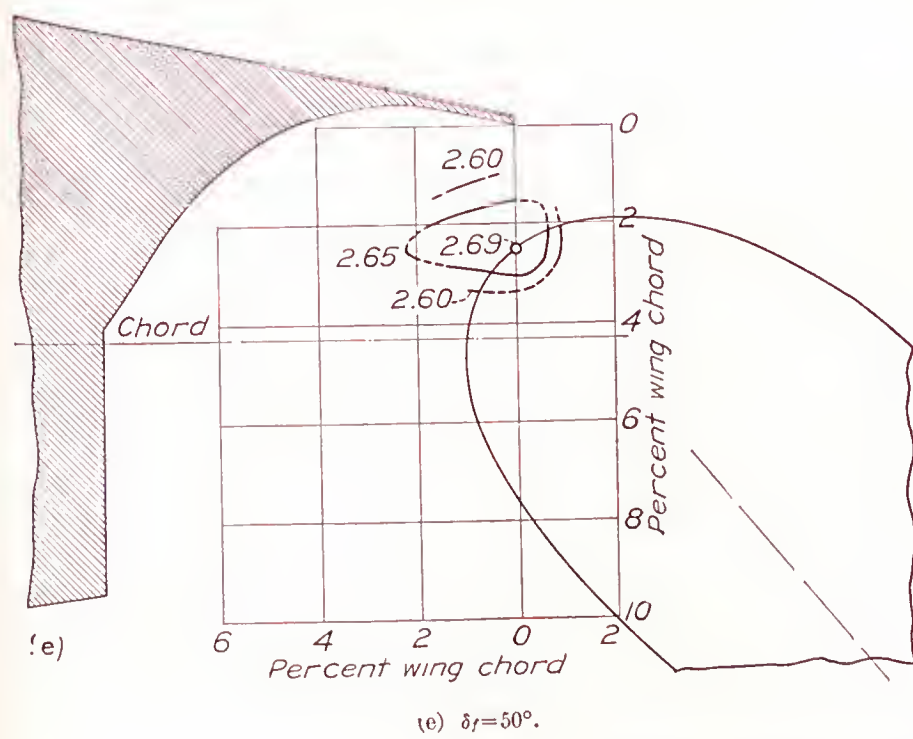
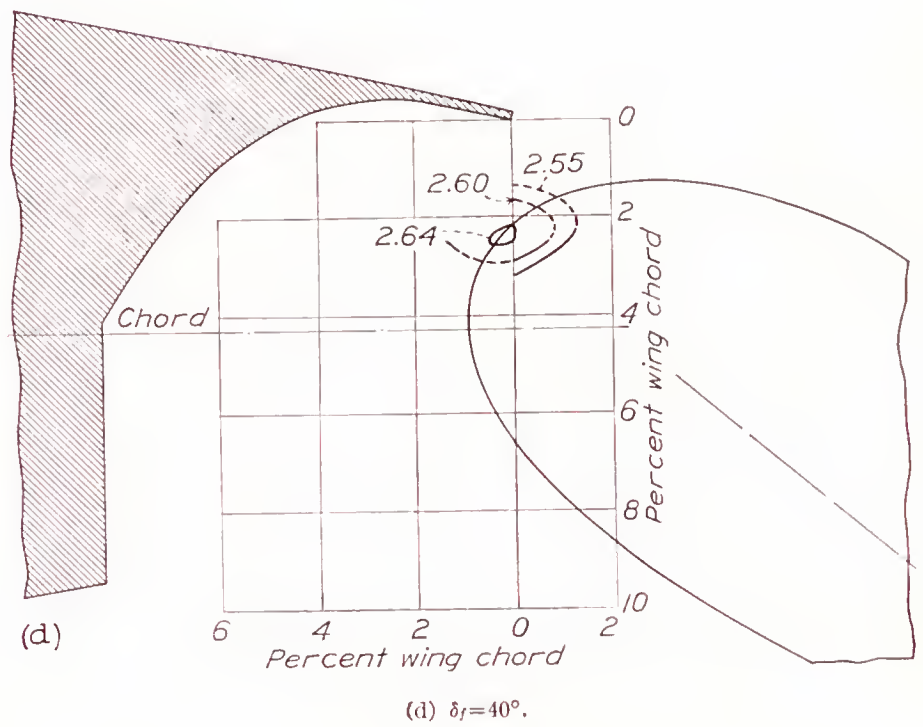
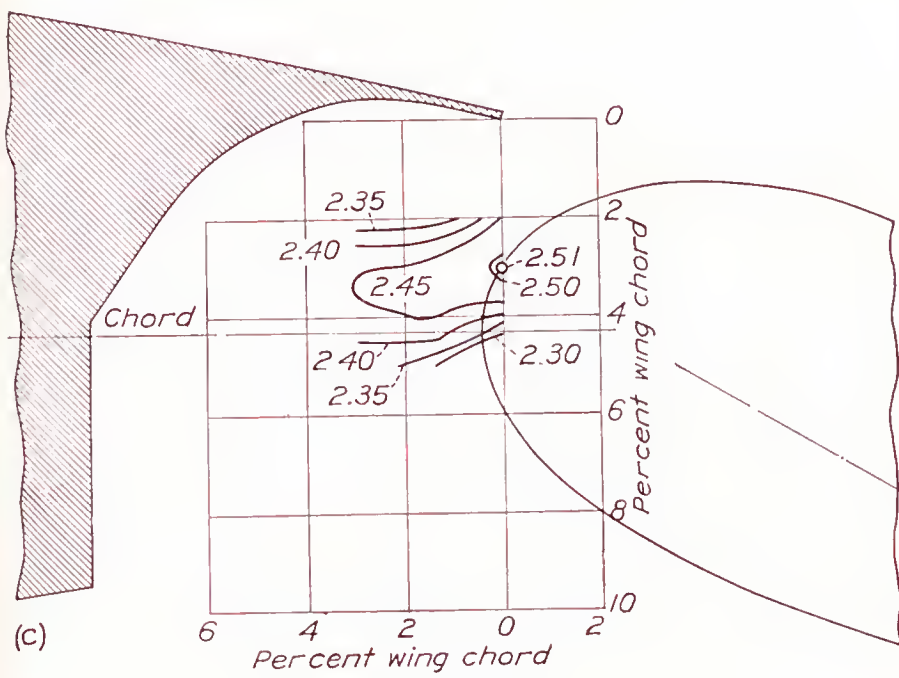
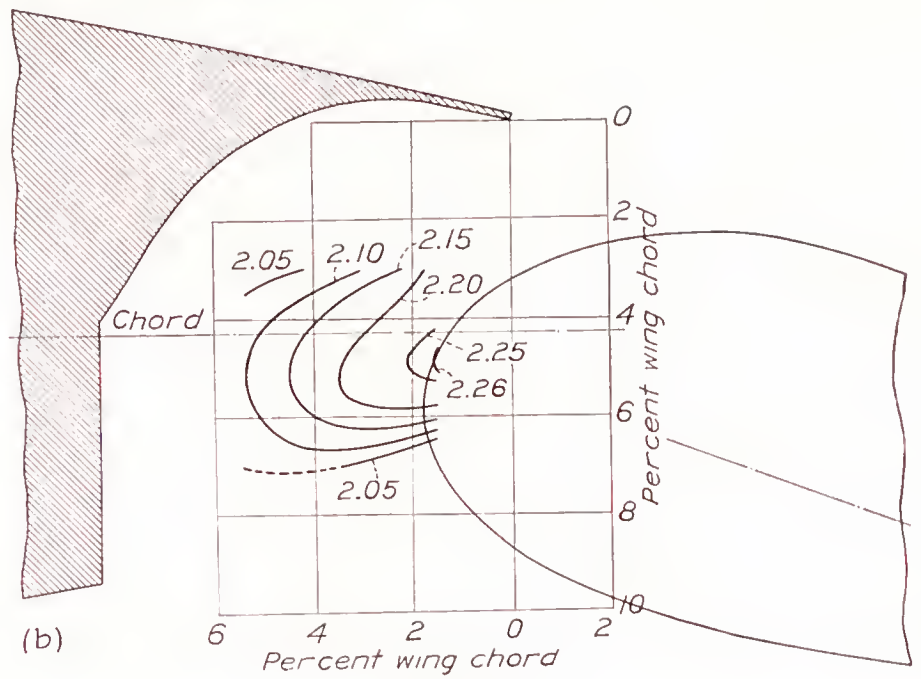
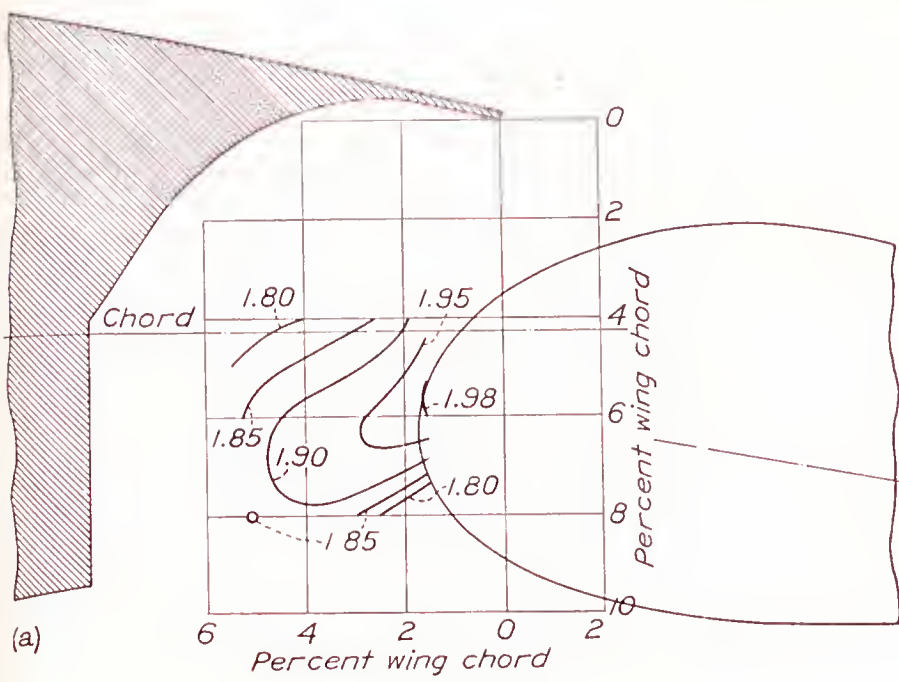


(a)  $\delta_f = 10^\circ$ (b)  $\delta_f = 20^\circ$ (c)  $\delta_f = 30^\circ$ (d)  $\delta_f = 40^\circ$ (e)  $\delta_f = 50^\circ$ (f)  $\delta_f = 60^\circ$ FIGURE 5.—Contours of flap location for  $c_{l_{max}}$ . Slotted flap 1-a.

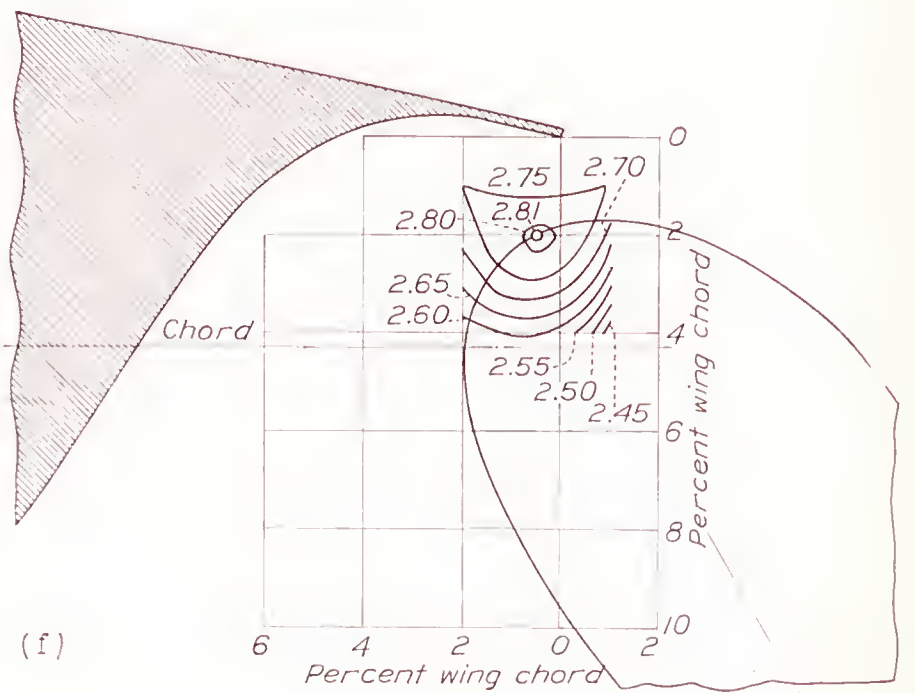
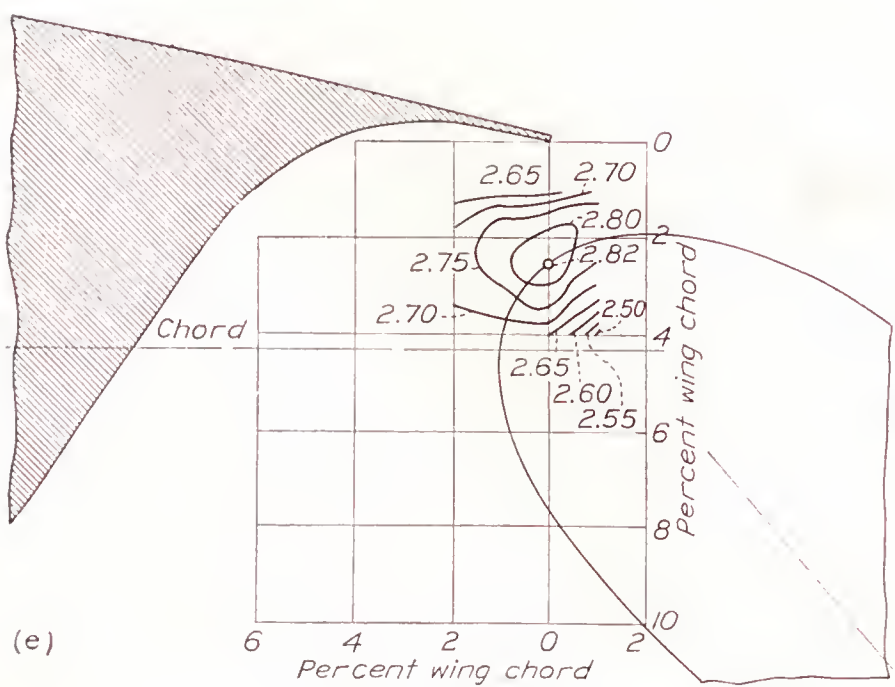
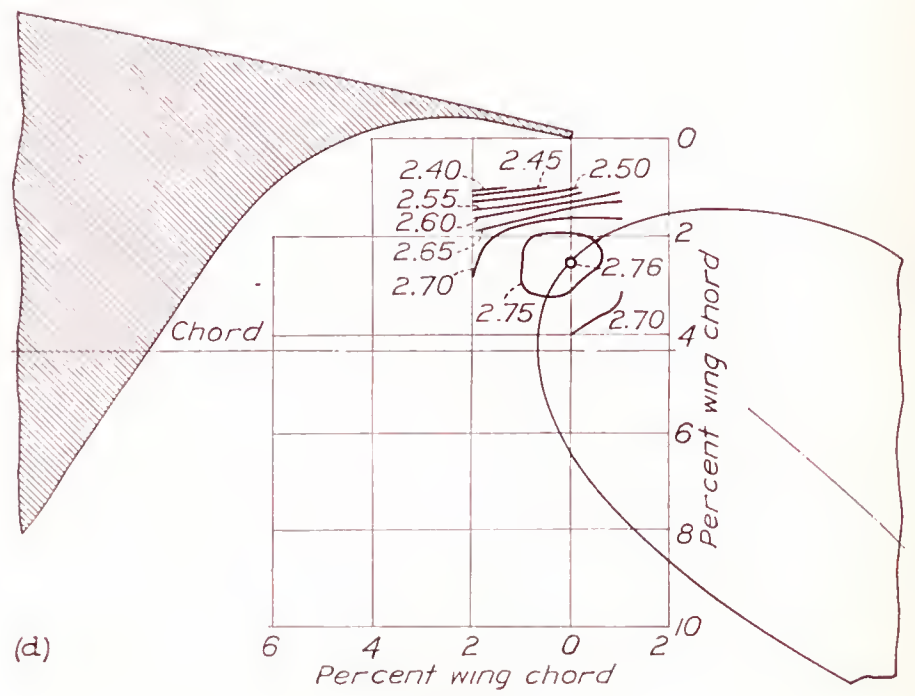
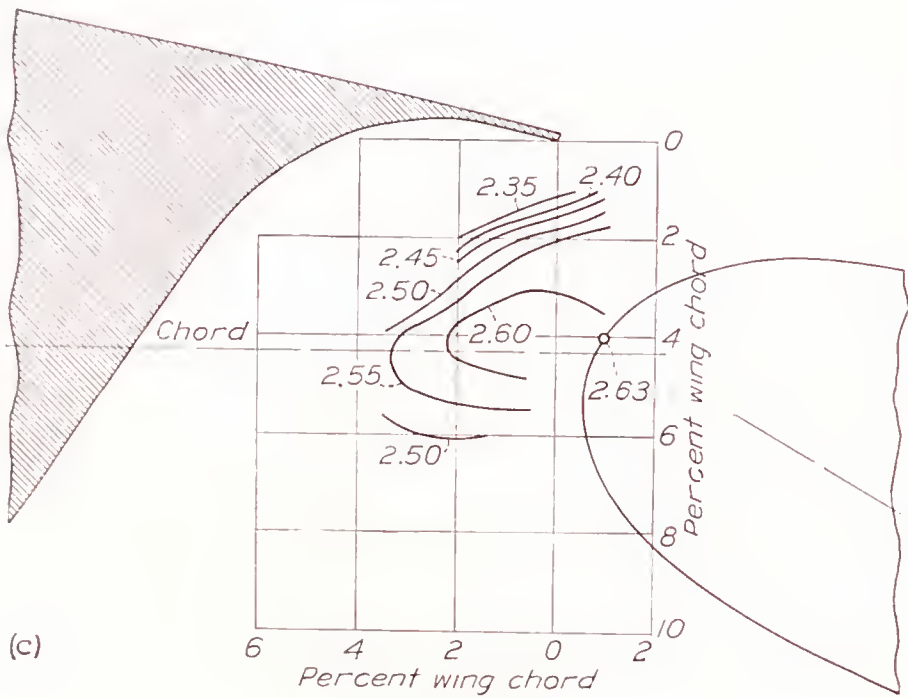
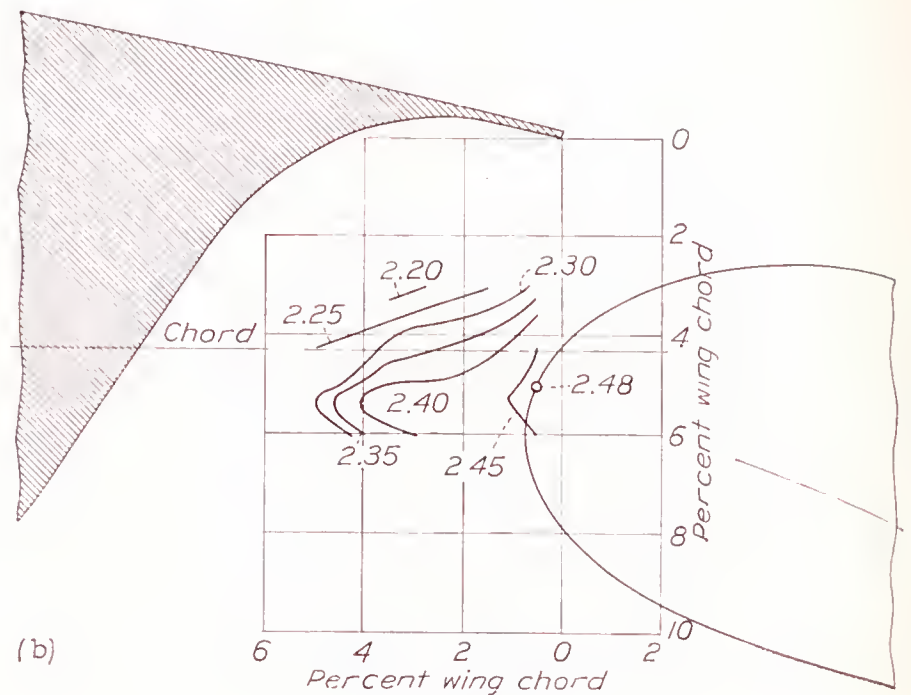
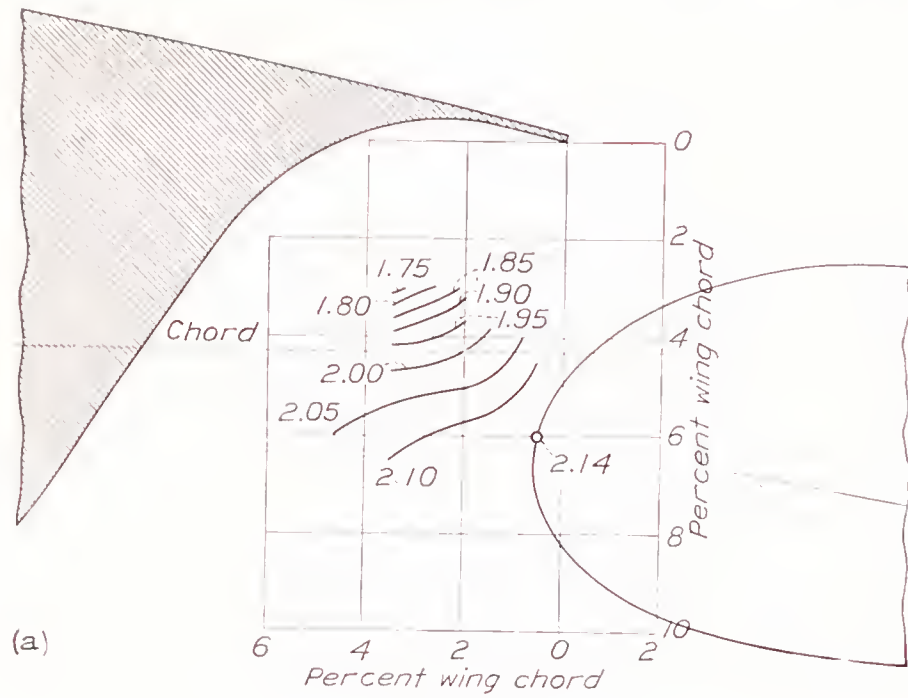


FIGURE 6.—Contours of flap location for  $c_{l_{max}}$ . Slotted flap 1-b.



FIGURE 7.—Contours of flap location for  $c_{l_{max}}$ . Slotted flap 2-a.



FIGURE 8.—Contours of flap location for  $c_{l,max}$ . Slotted flap 2-b.



The limiting conditions are the power available to overcome the drag at the higher lift coefficients and the excess available lift required from considerations of safety. The data are given, therefore, as contours of the nose position of the flap for constant drag coefficients at certain selected lift coefficients,  $c_l=1.0$ , 1.5, 2.0, and 2.5, and for flap deflections that cover the range for which the drag coefficient is decreased by deflecting the flap.

The complete drag data for slotted flaps 1-a, 1-b,

Section aerodynamic characteristics of selected optimum arrangements.—The complete section aerodynamic characteristics of selected optimum arrangements of slotted flaps 1-a, 1-b, 2-a, and 2-b are given in figures 13 to 16, respectively. The optimum arrangements were chosen from a consideration of low drag coefficients at the specified lift coefficients for flap deflections from  $10^\circ$  to  $30^\circ$  and from a consideration of maximum lift coefficient alone for flap deflections from  $40^\circ$  to  $60^\circ$ . In addition to the optimum arrangements,

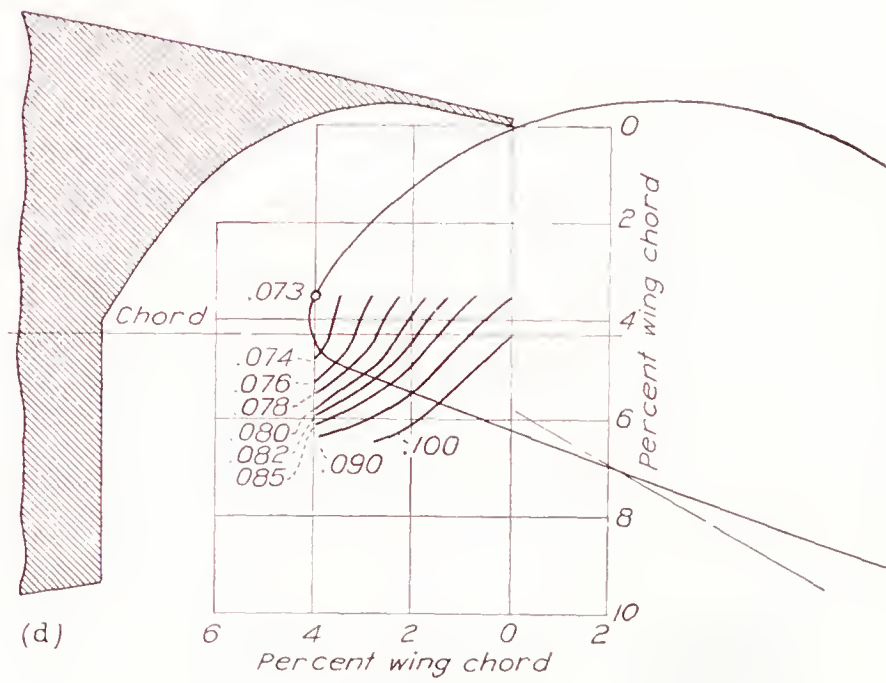
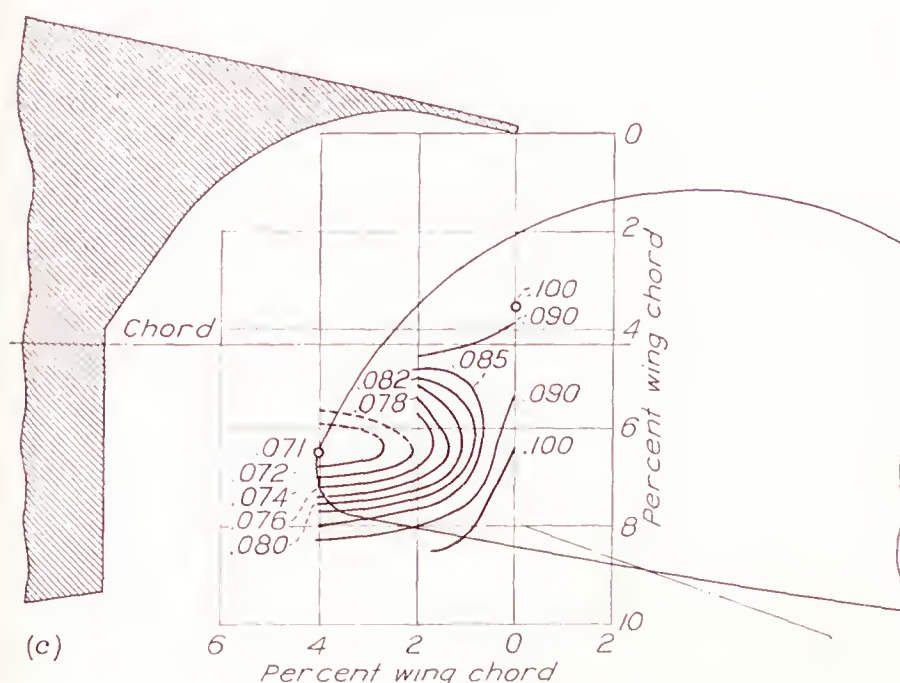
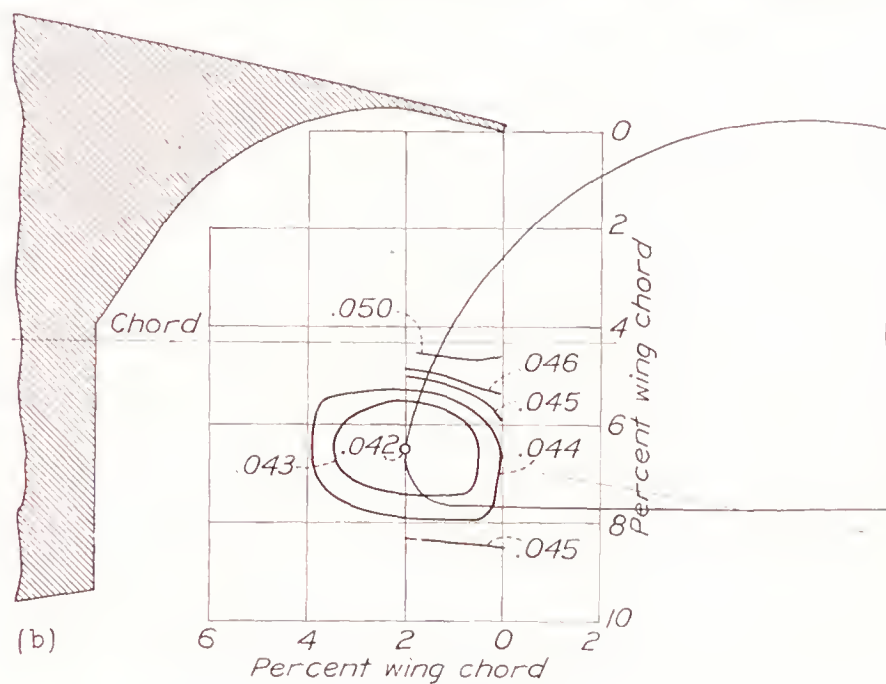
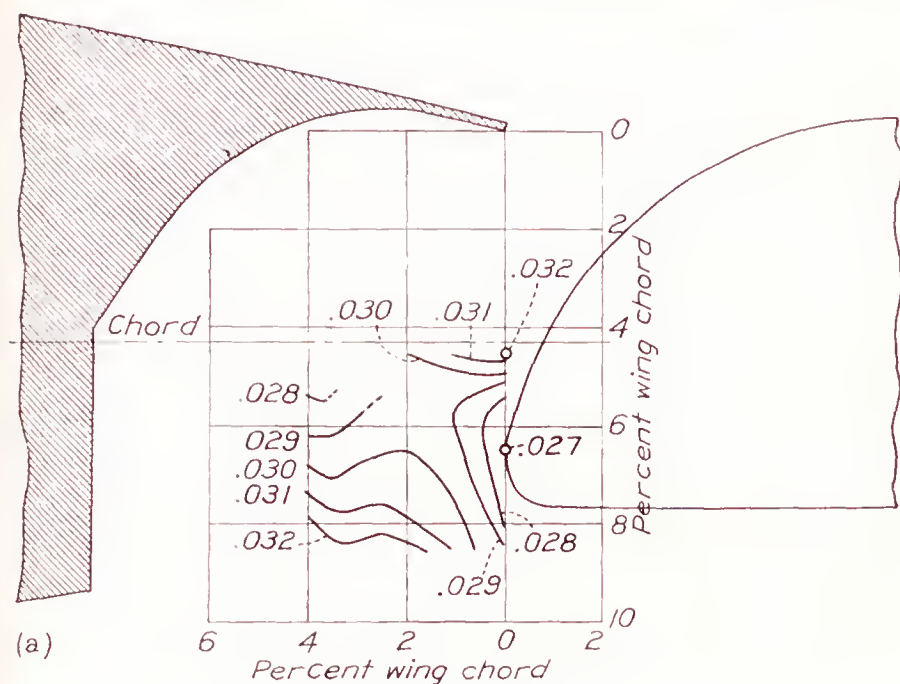
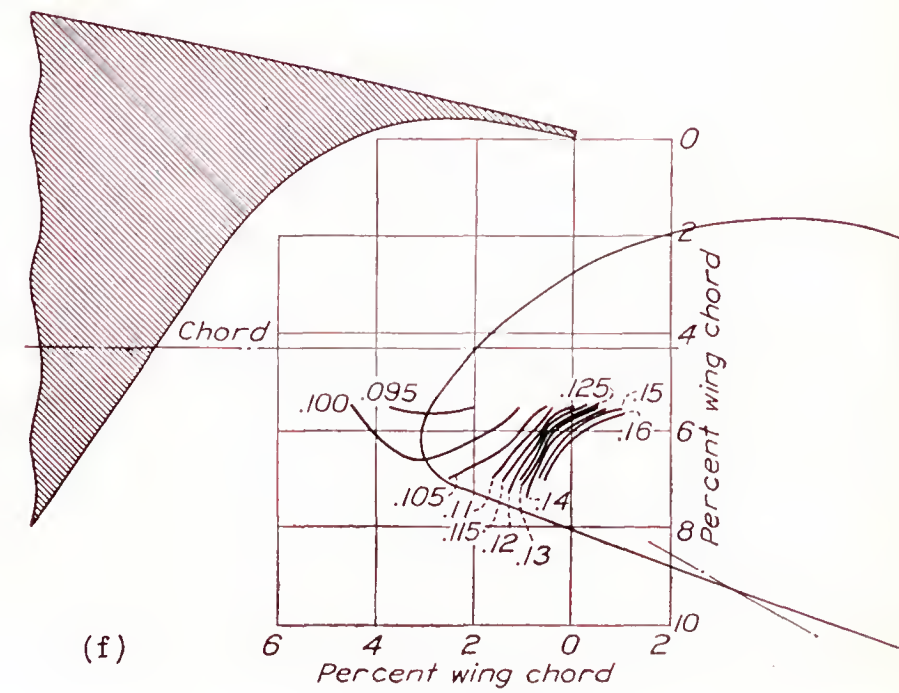
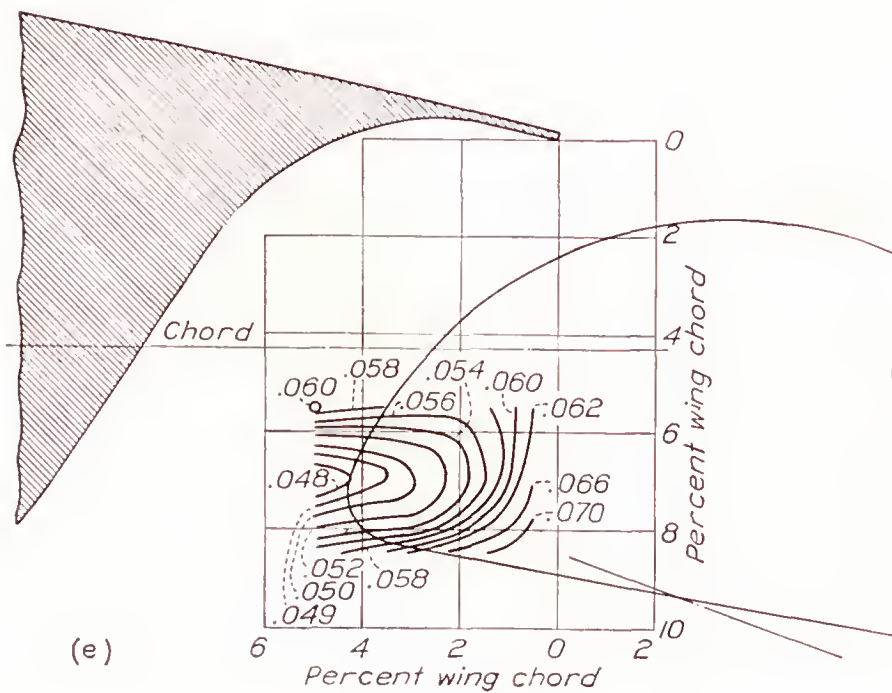
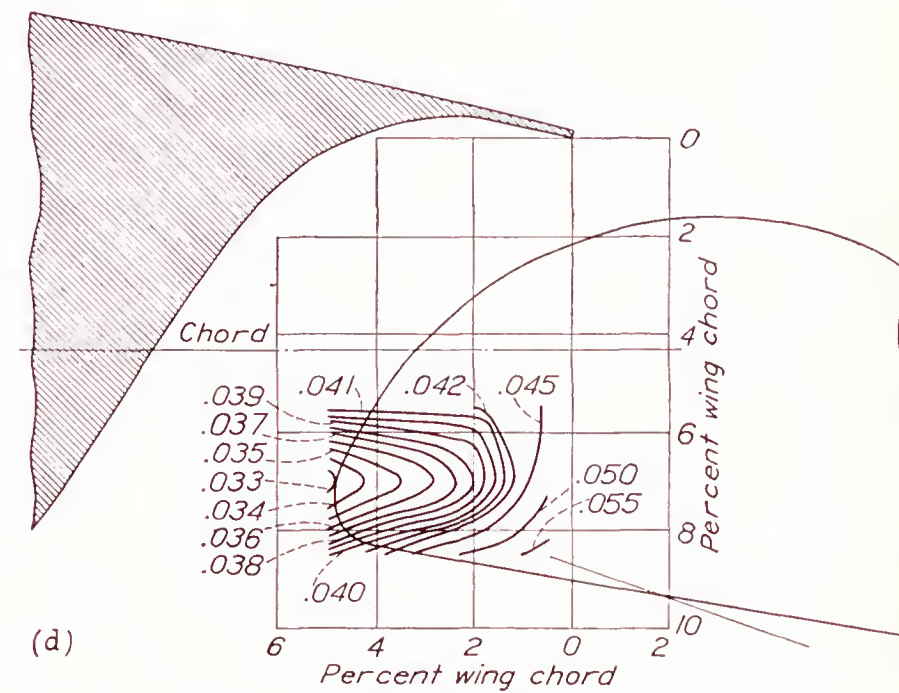
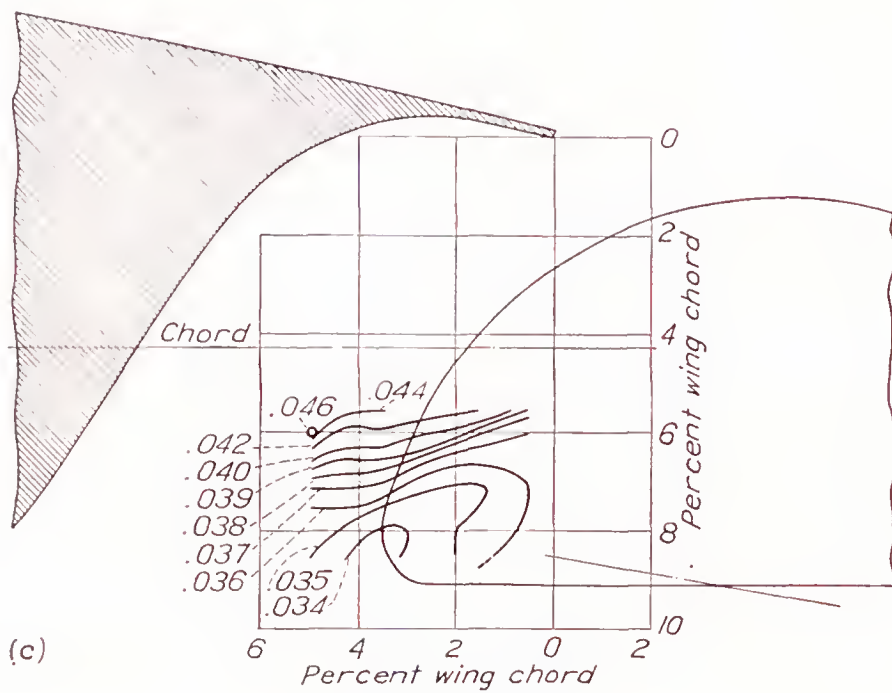
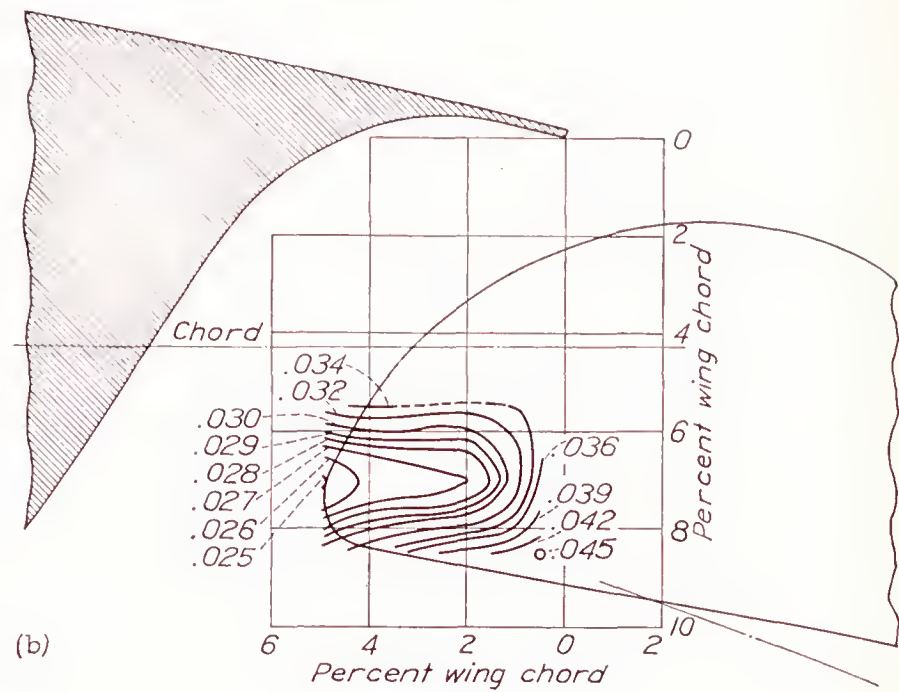
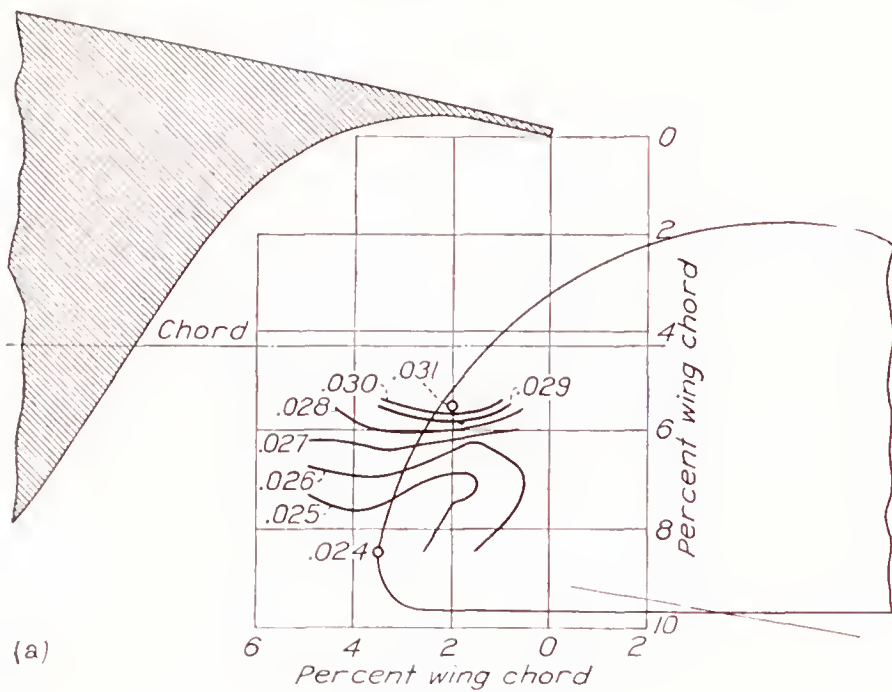


FIGURE 9.—Contours of flap location for  $c_{d_0}$ . Slotted flap 1-a.

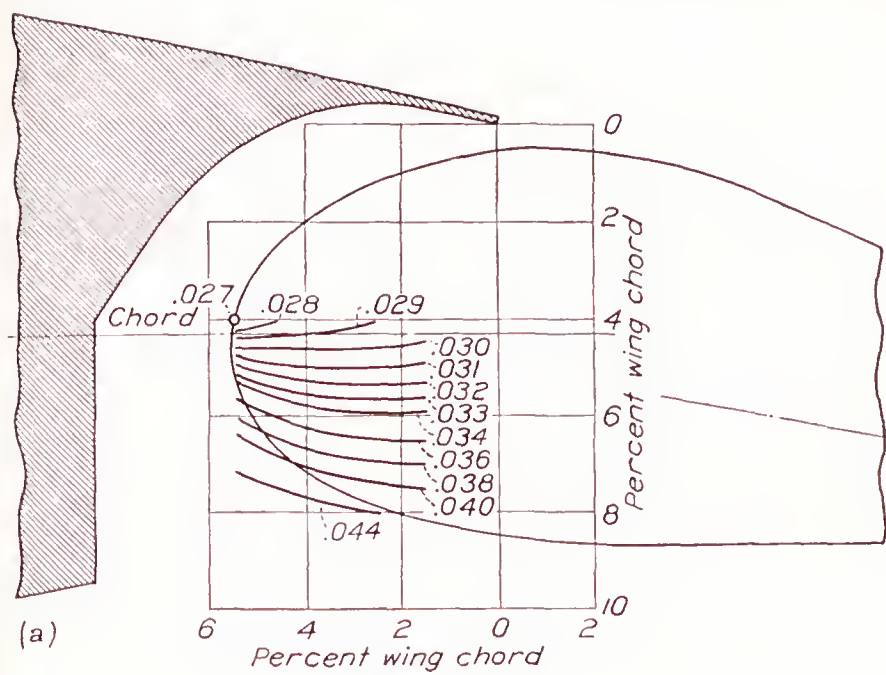
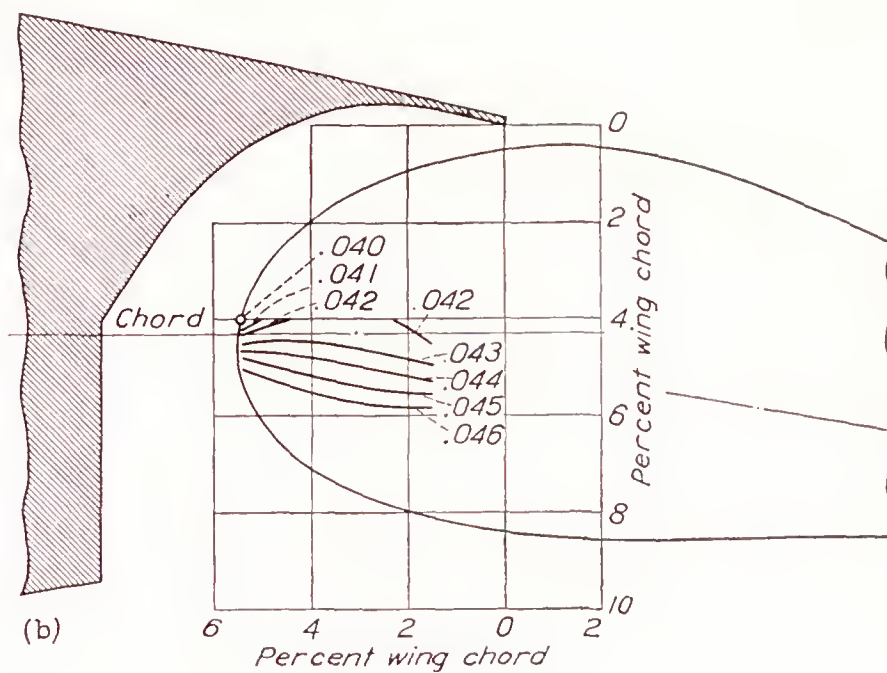
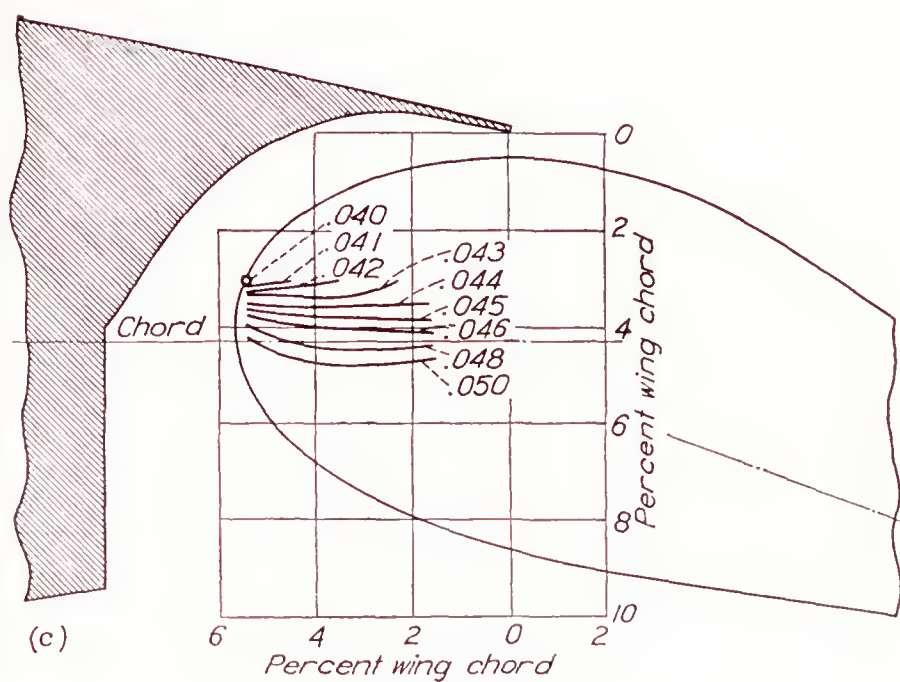
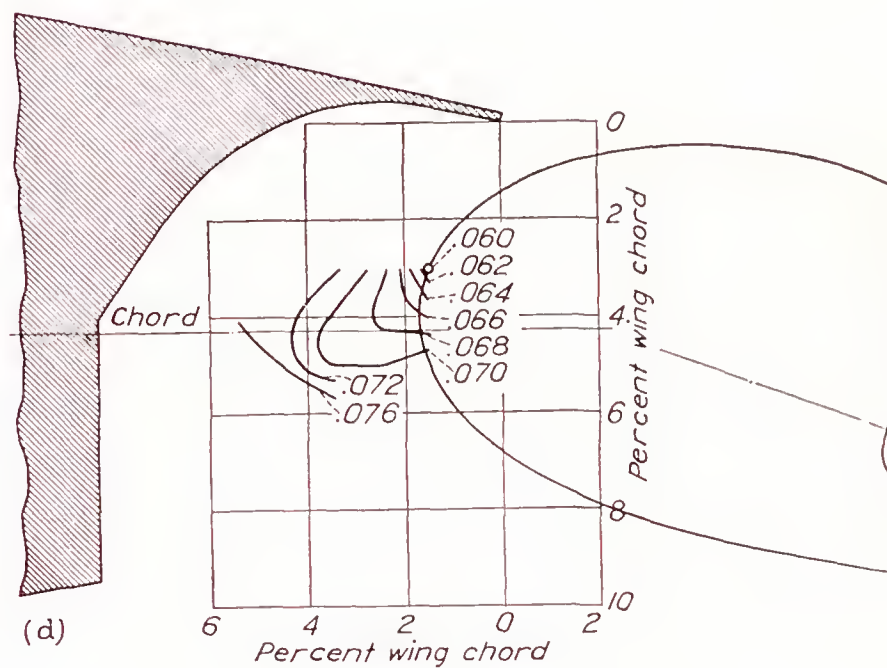
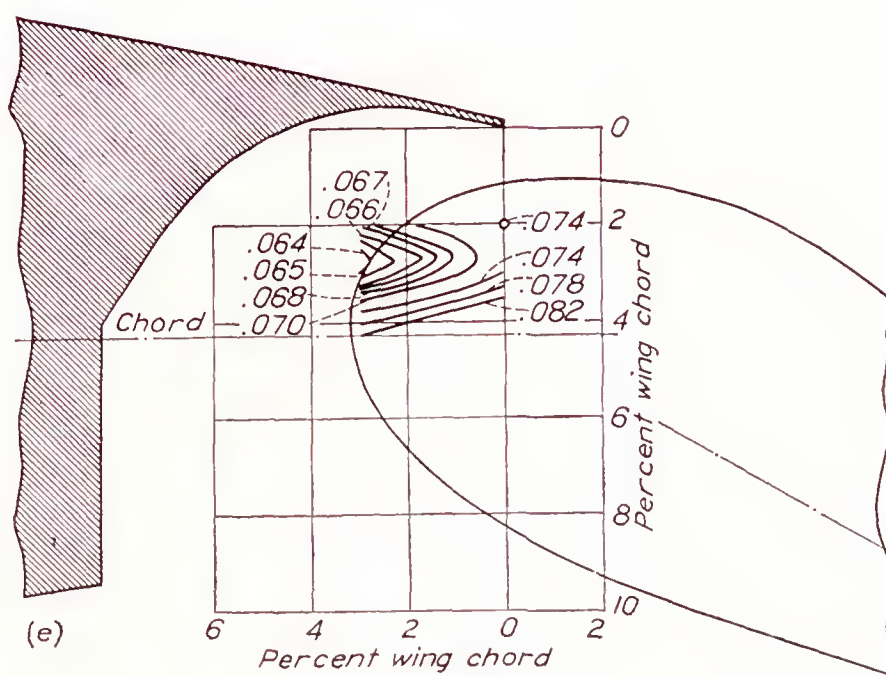
2-a, and 2-b are given in figures 9 to 12, respectively. Where the minimum drag coefficients were approximately the same for a given lift coefficient at two flap settings, both sets of data are given. From these data, optimum paths for the nose points of the several flaps may be chosen from a consideration of drag coefficients at the various lift coefficients. If it is structurally impossible to follow the optimum path, the additional drag coefficient caused by the deviation will be available. Insufficient data were obtained to close all the contours, but most of the practicable arrangements are believed to be within the range covered.

data are also given for certain arrangements that appear structurally simpler. A table included in each figure shows the nose position of the flap for the various deflections and the points are plotted on the diagrams. The selected optimum path referred to hereinafter is shown by the broken line through the points and is a compromise between aerodynamic and structural considerations. The aerodynamic characteristics shown in these figures are typical; complete data for other positions of the various flaps at the several flap deflections are available upon request.

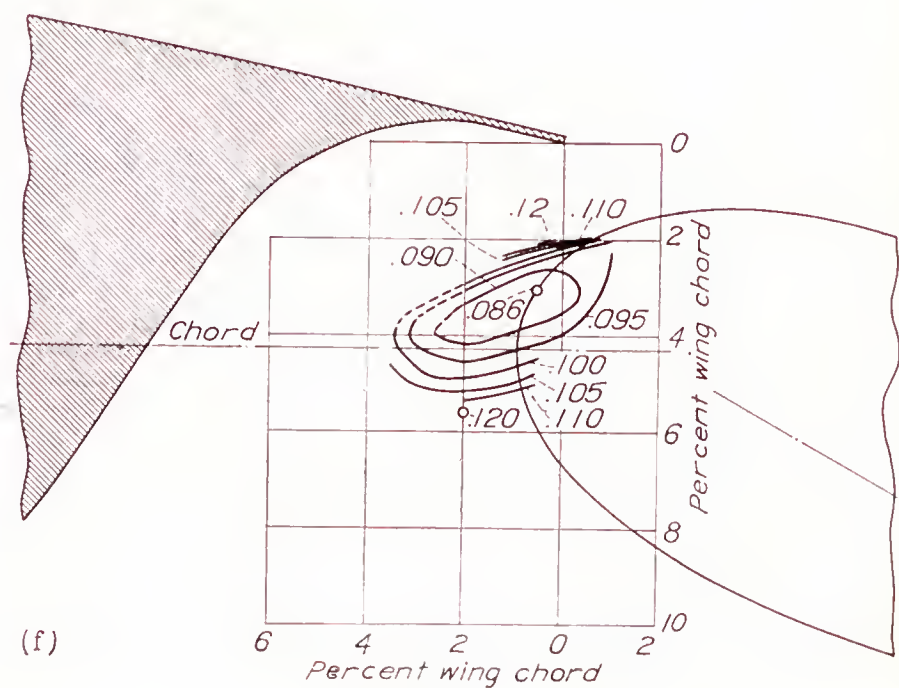
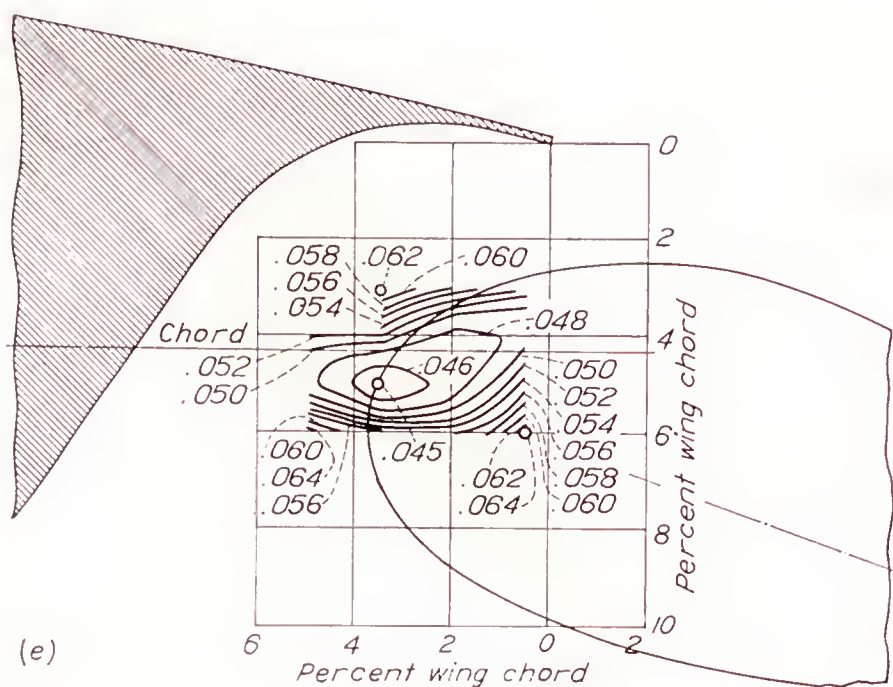
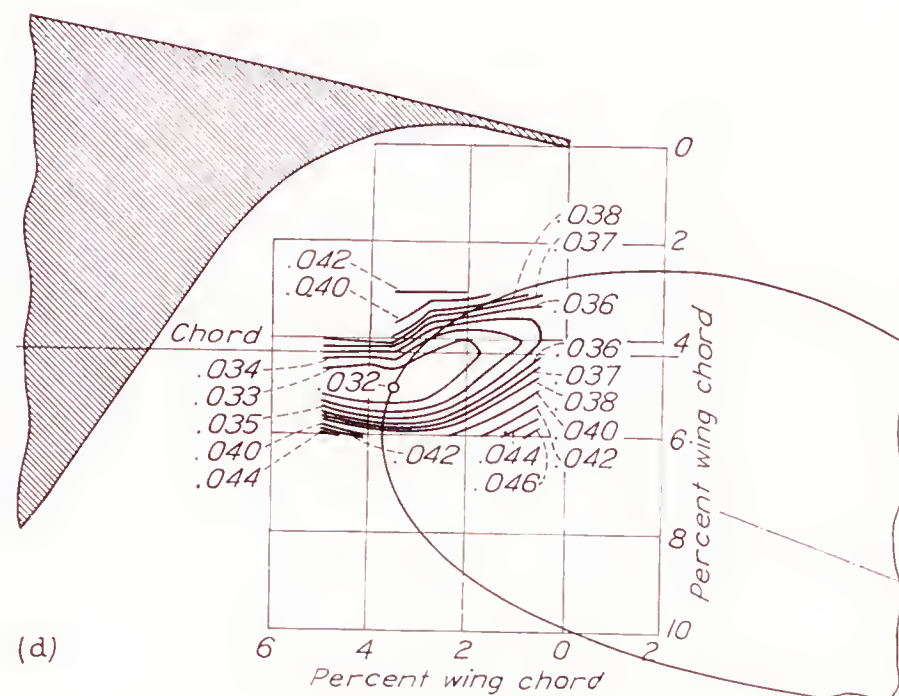
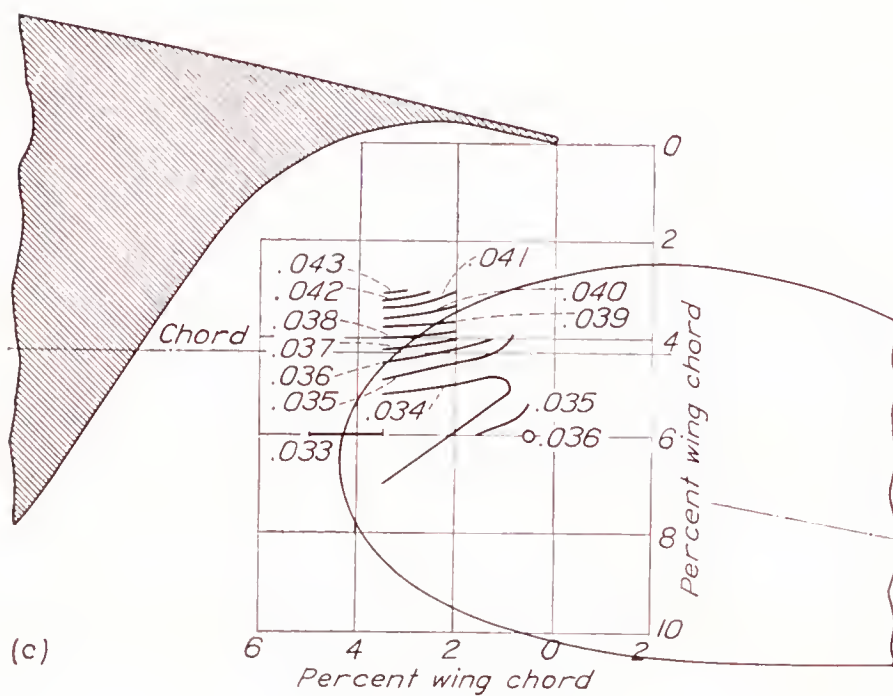
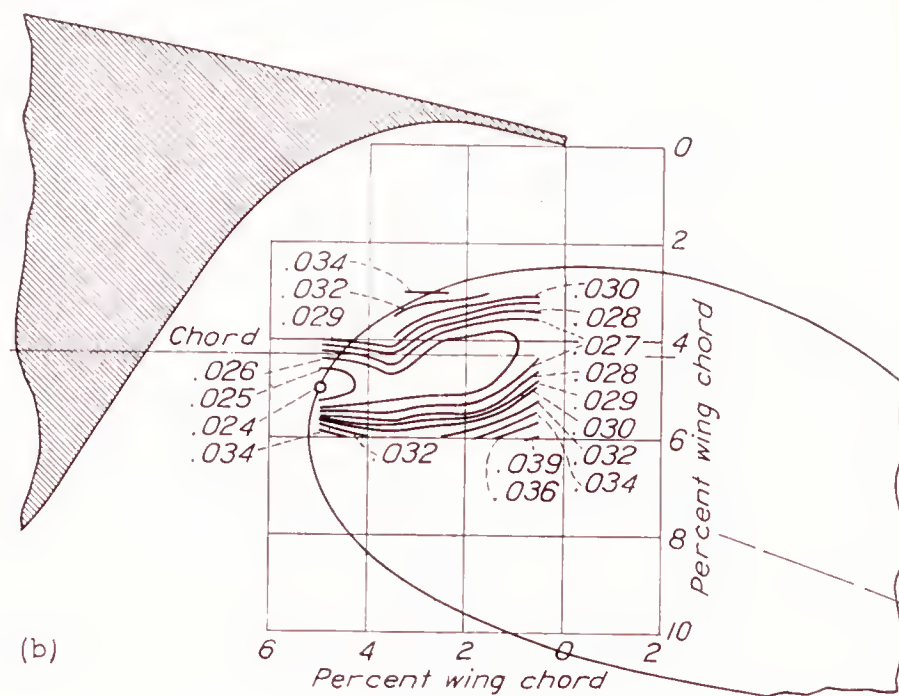
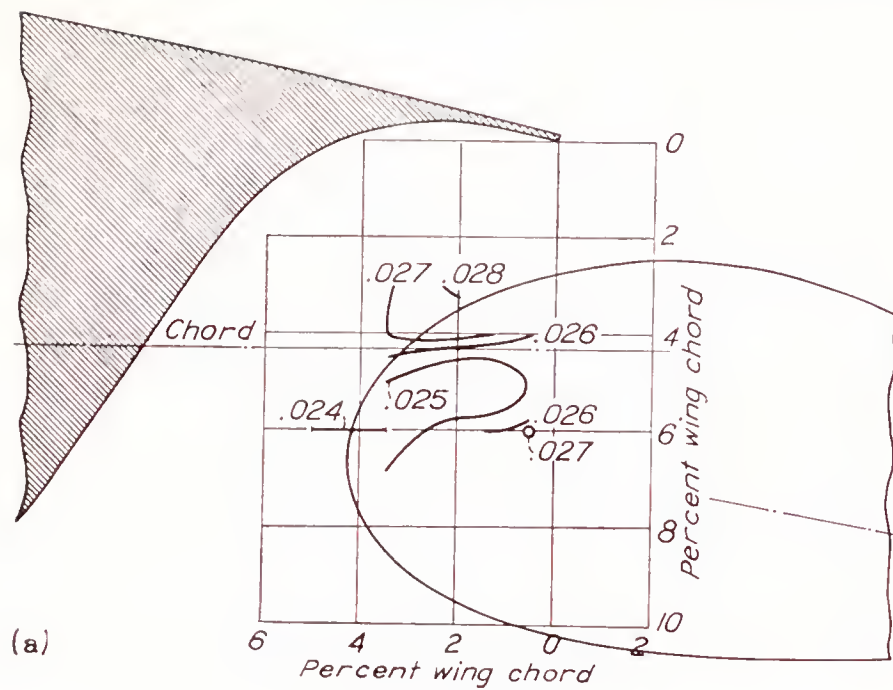


FIGURE 10.—Contours of flap location for  $c_{d_0}$ . Slotted flap 1-b.



(a)  $c_l=1.0$ ;  $\delta_f=10^\circ$ (b)  $c_l=1.5$ ;  $\delta_f=10^\circ$ (c)  $c_l=1.5$ ;  $\delta_f=20^\circ$ (d)  $c_l=2.0$ ;  $\delta_f=20^\circ$ (e)  $c_l=2.0$ ;  $\delta_f=30^\circ$ FIGURE 11.—Contours of flap location for  $c_{d0}$ . Slotted flap 2-a.



FIGURE 12—Contours of flap location for  $c_{l_f}$ . Slotted flap 2-b.



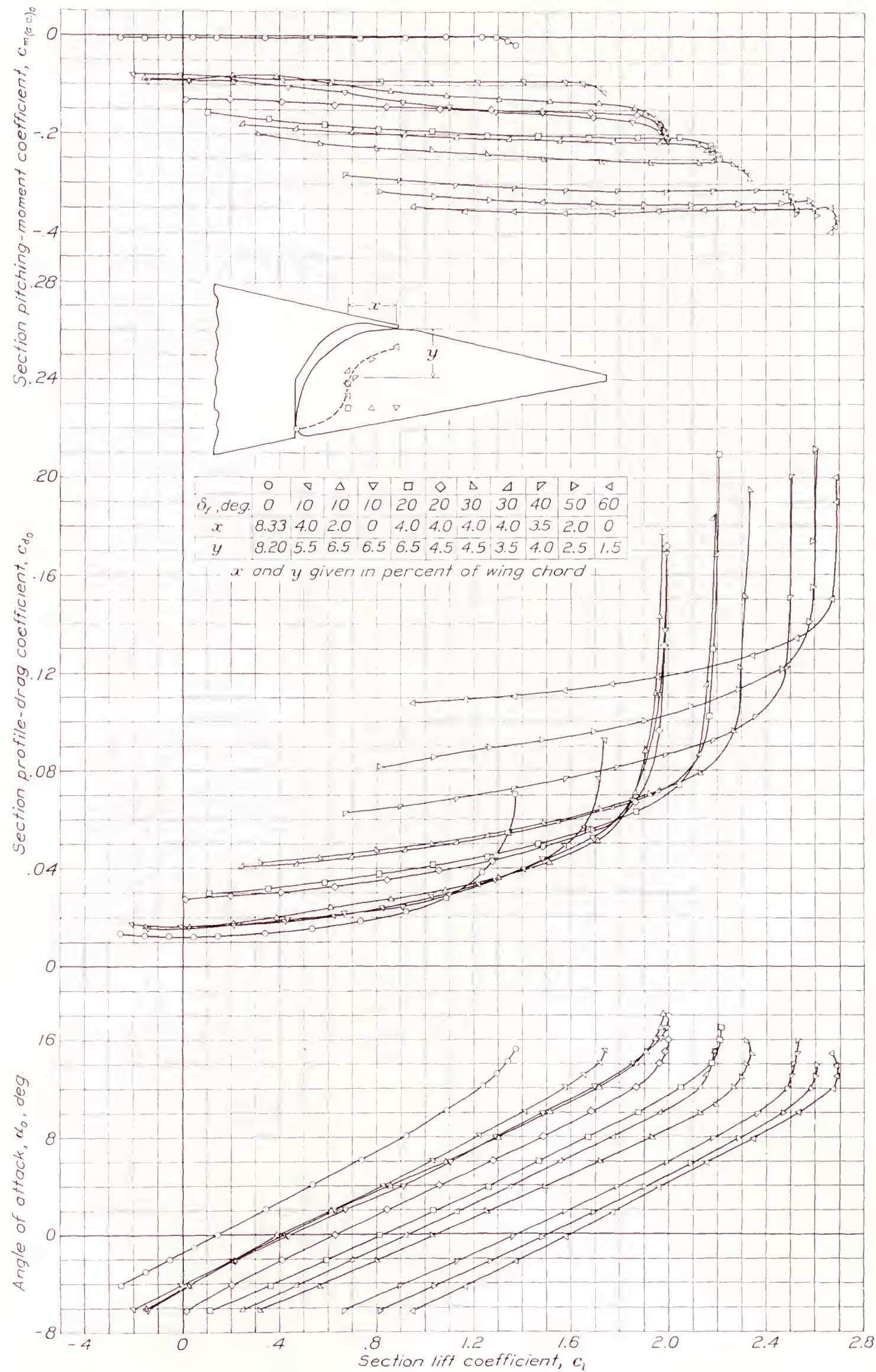


FIGURE 13.—Section aerodynamic characteristics of N. A. C. A. 23021 airfoil with slotted flap 1-a.



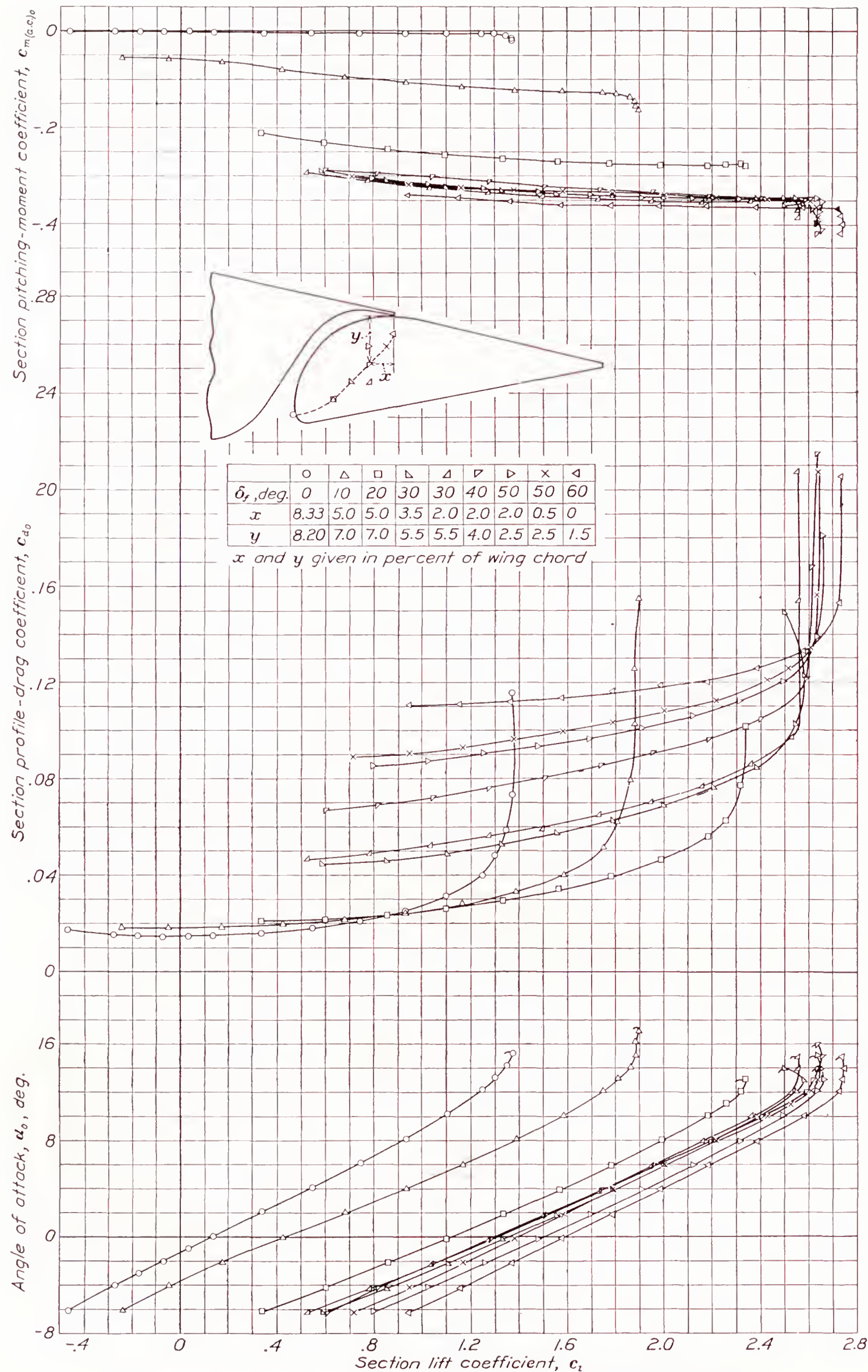


FIGURE 14.—Section aerodynamic characteristics of N. A. C. A. 23021 airfoil with slotted flap 1-b.



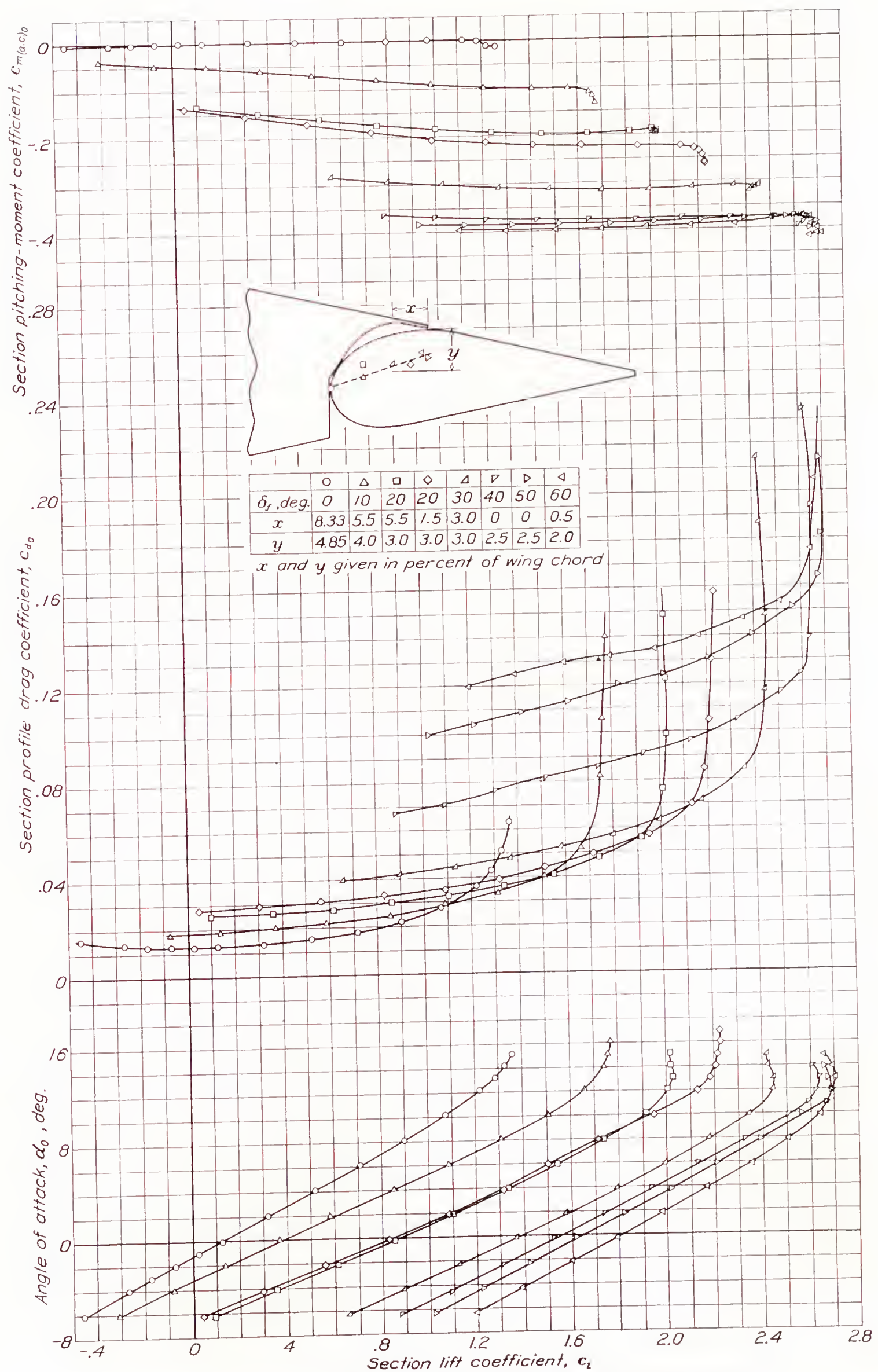


FIGURE 15.—Section aerodynamic characteristics of N. A. C. A. 23021 airfoil with slotted flap 2-a.



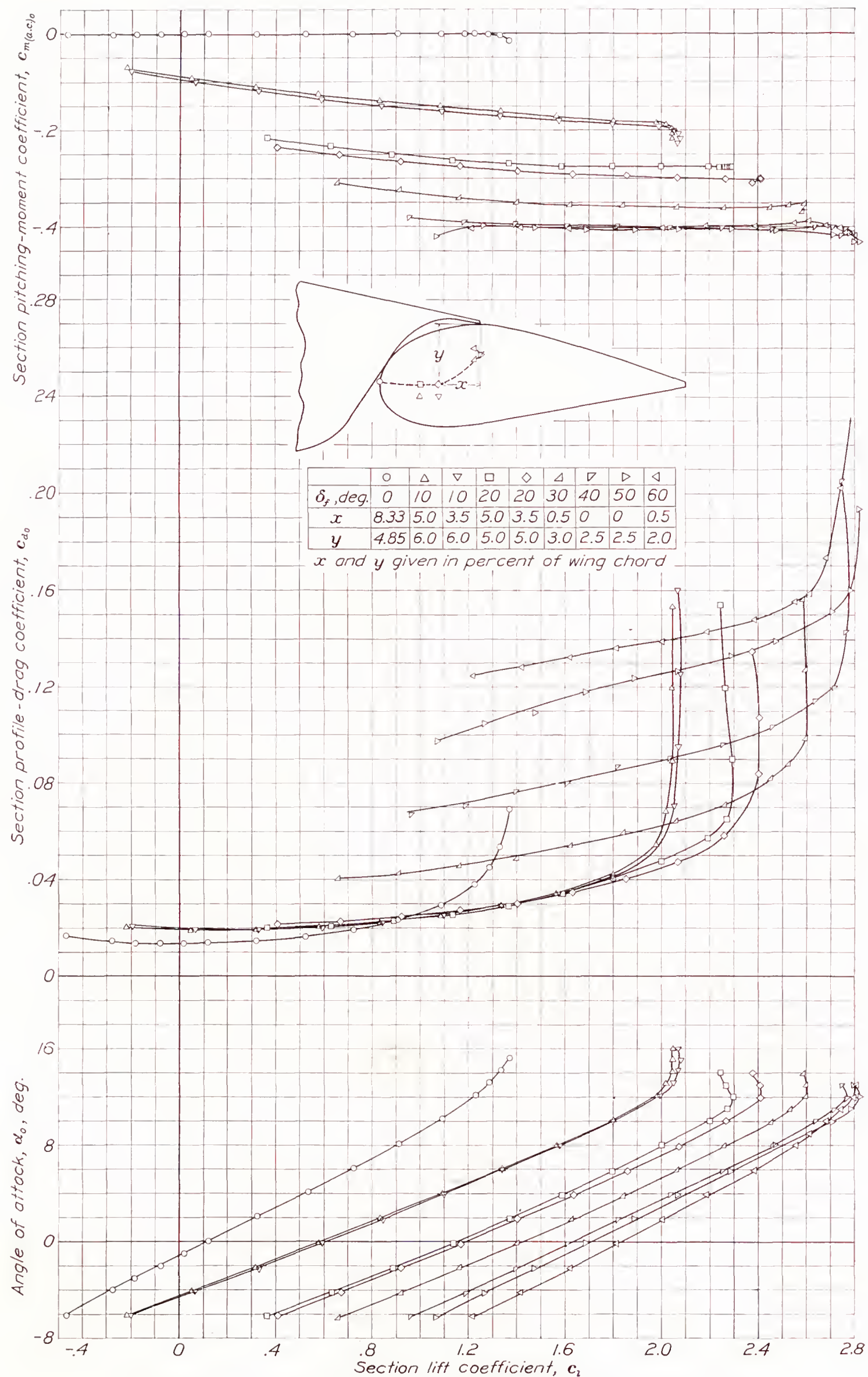


FIGURE 16.—Section aerodynamic characteristics of N. A. C. A. 23021 airfoil with slotted flap 2-b.



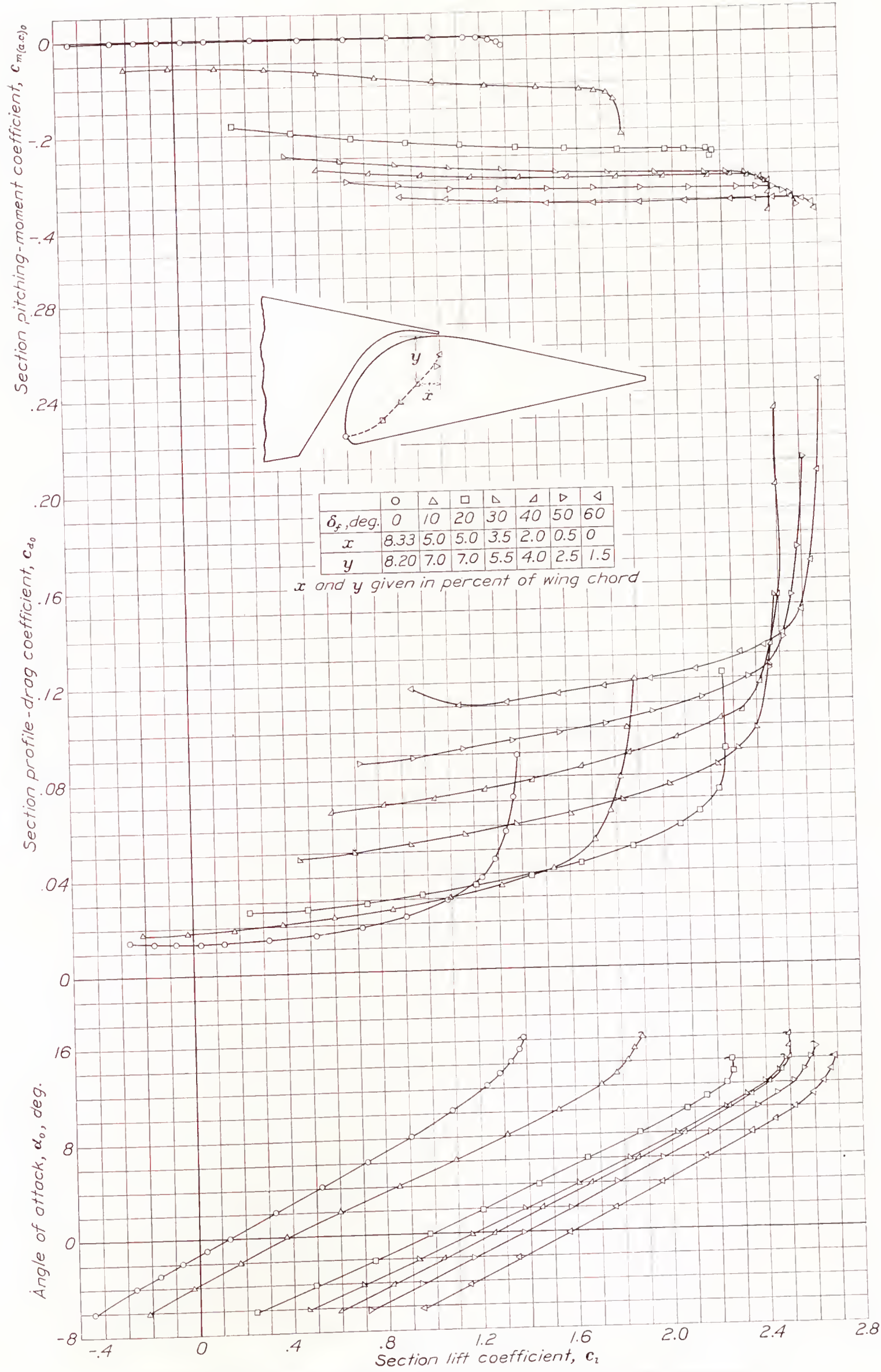
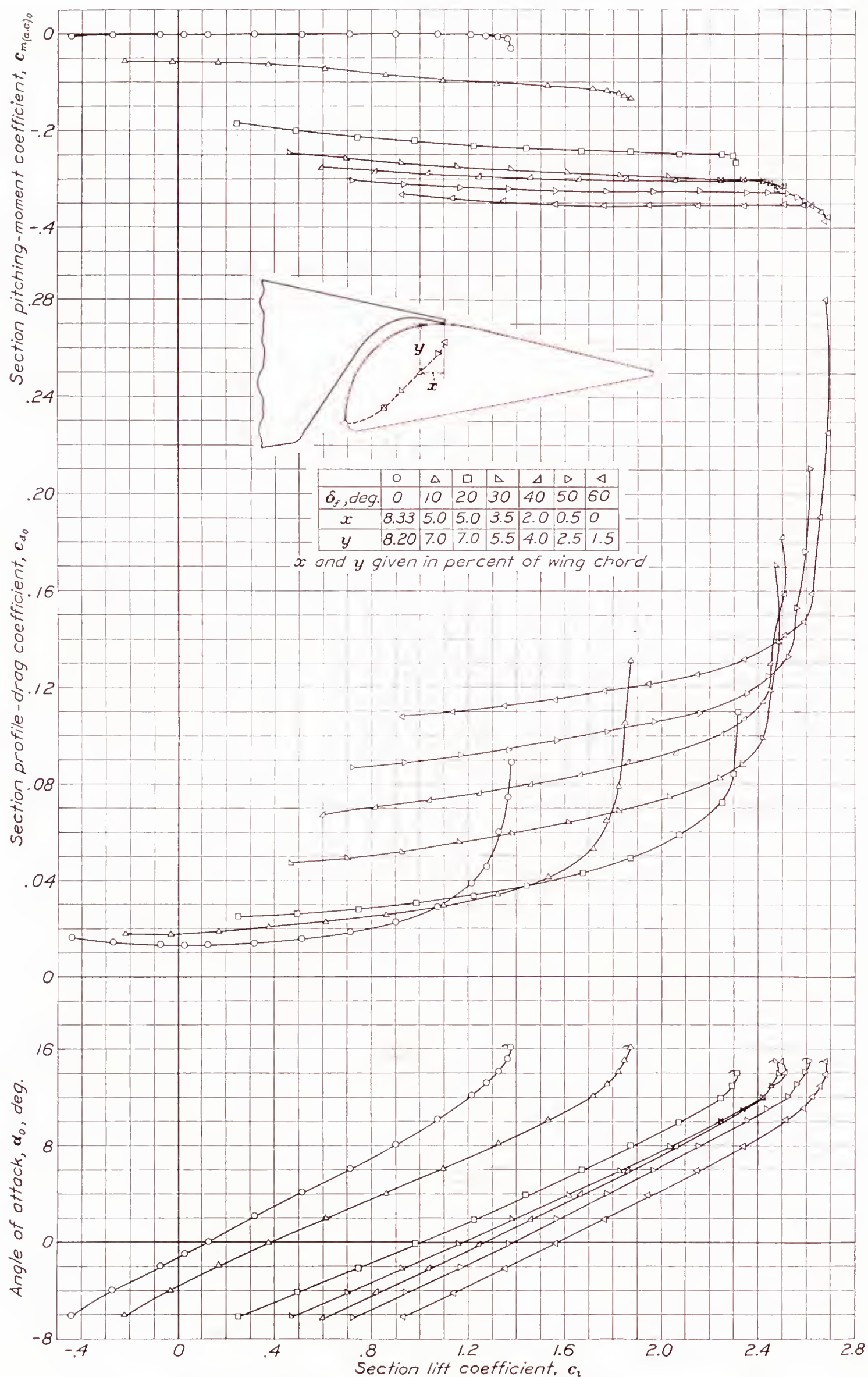
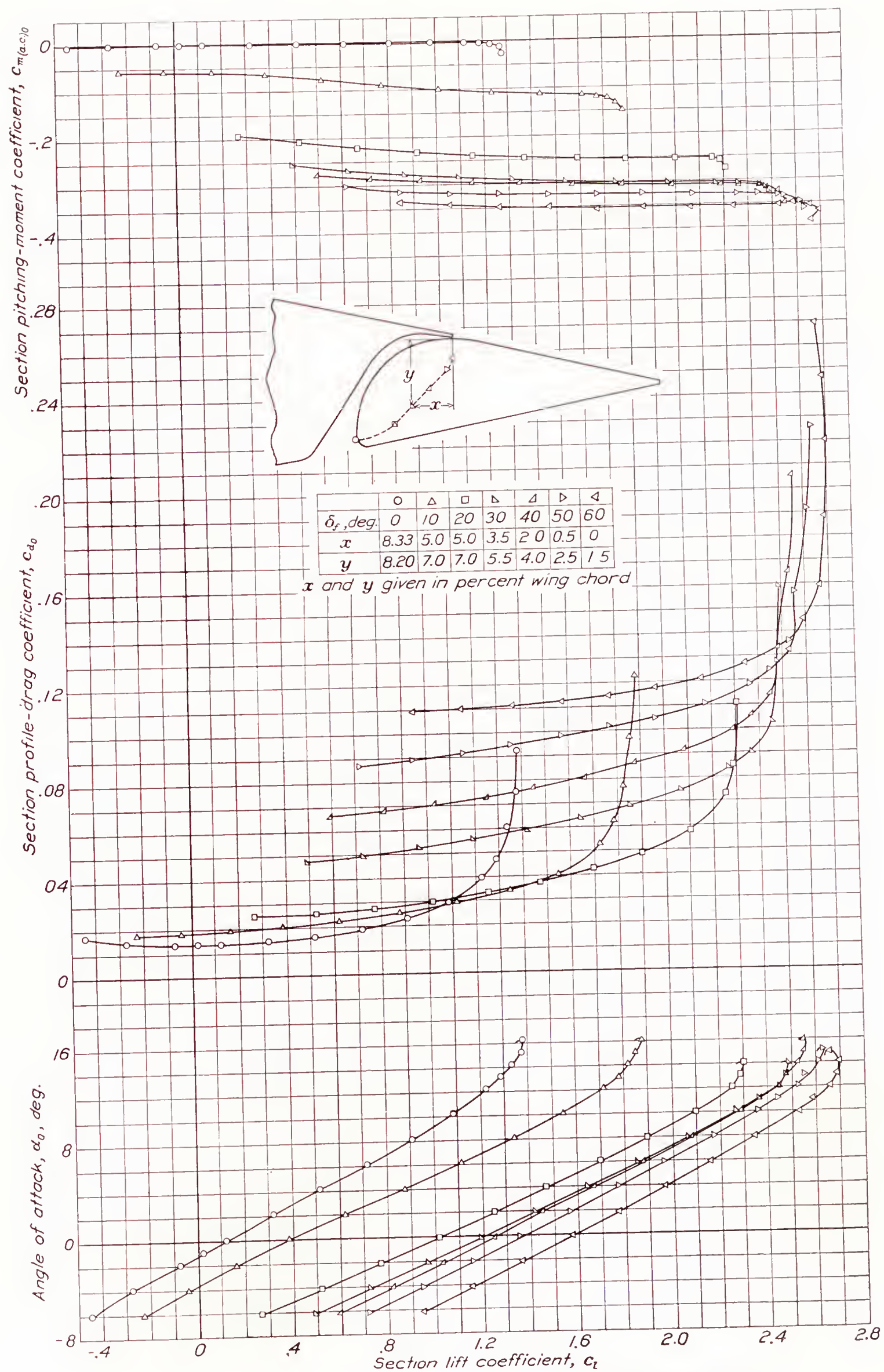


FIGURE 17.—Section aerodynamic characteristics of N. A. C. A. 23021 airfoil with slotted flap 1-c<sub>0</sub>.



FIGURE 18.—Section aerodynamic characteristics of N. A. C. A. 23021 airfoil with slotted flap 1-c<sub>1</sub>.



FIGURE 19.—Section aerodynamic characteristics of N. A. C. A. 23021 airfoil with slotted flap 1-c<sub>2</sub>.



The complete section aerodynamic characteristics on slotted flaps 1-c<sub>0</sub>, 1-c<sub>1</sub>, and 1-c<sub>2</sub> are given in figures 17 to 19, respectively. These data are all that were obtained for these slotted flaps. The path of the flap nose used for all three arrangements was the same as for slotted flap 1-b.

**Comparison of selected optimum arrangements.**—In order to compare the drags of the various flap arrangements, envelope polars are given in figure 20 for the slotted-flap arrangements of figures 13 to 16. This figure shows slotted flap 2-b to be superior for take-off at any lift coefficient from 1.0 up to the maximum lift coefficient. Slotted flap 1-b is only slightly inferior to slotted flap 2-b over the same lift range. Slotted flaps 1-a and 2-a are both inferior to 1-b throughout the lift range from lift coefficients of 1.0 to that for maximum lift, flap 2-a being slightly superior to flap 1-a. A comparison of slotted flaps 1-b, 1-c<sub>0</sub>, 1-c<sub>1</sub>, and 1-c<sub>2</sub> for the take-off condition is given in figure 21 as envelope polars. Slotted flap 1-b, which has an 8-percent radius at the slot entry, is superior to the others. The slot entry with the sharp edge (slotted flap 1-c<sub>0</sub>) appears to be the least desirable although there is little difference among the three.

For lift coefficients less than 1.0, the plain wing has lower drag coefficients than any of the arrangements with the flaps deflected; therefore, if a door were used to seal the break in the lower surface of the wing at the slot entrance, all the slotted-flap arrangements would be of equal merit for lift coefficients less than 1.0. The use of a door would probably be more complicated with slotted flaps 1-b and 2-b than with 1-c<sub>0</sub>, 1-c<sub>1</sub>, or 1-c<sub>2</sub>; because of structural considerations, no definite conclusion can therefore be drawn as to which slotted flap would be superior. From a purely aerodynamic consideration, however, slotted flap 2-b is superior for conditions of take-off and initial climb to clear a given obstacle.

A comparison of slotted flaps 1-a, 1-b, 2-a, and 2-b as lift-increasing devices is shown in figure 22 where the increments of maximum lift coefficient  $\Delta c_{l_{max}}$  are plotted against flap deflection when the flap is moved along the optimum path previously mentioned. Slotted flap 2-b is superior as a lift-increasing device, and the maximum increase in  $\Delta c_{l_{max}}$  is obtained with a flap deflection of 50° with only a slight loss at a flap deflection of 60°. The other slotted-flap arrangements are all somewhat inferior to 2-b, the maximum lift coefficient being from 3 percent less for slotted flap 1-b to about 4 percent less for slotted flaps 1-a and 2-a.

The change in slot-entry radius had a negligible effect on the maximum increments of maximum lift coefficient as shown in figure 23, where  $\Delta c_{l_{max}}$  is plotted against flap deflection for slotted flaps 1-b, 1-c<sub>0</sub>, 1-c<sub>1</sub>, and 1-c<sub>2</sub>, all flaps being deflected along the optimum path selected for flap 1-b.

The scale effect for the range available in the 7- by

10-foot wind tunnel is shown in figure 24, where the  $c_{l_{max}}$  for the plain airfoil and the  $c_{l_{max}}$  for slotted flap 2-b at the optimum deflection ( $\delta_f=50^\circ$ ) are plotted against effective Reynolds Number. A comparison of the two curves shows a slight increase in  $\Delta c_{l_{max}}$  with an increase in scale but it is probable that, if the increment were considered to be independent of scale in applying the results at higher values of the Reynolds Number, the result would be conservative. It should be remembered, however, that the maximum lifts presented in this report are section, or infinite-aspect-ratio, characteristics and will not be realized on a finite-aspect-ratio wing except for one with an elliptic lift distribution.

A further comparison of the various slotted-flap arrangements is given in the following table:

Slotted flap	$c_{l_{max}}$	$\frac{c_{l_{max}}}{c_{d_{0_{min}}}}$	$\frac{c_{l_{max}}}{c_{d_{0_{(c_l=0.2)}}}}$	$\frac{c_{l_{max}}}{c_{d_{0_{(c_l=0.4)}}}}$	$\frac{c_{l_{max}}}{c_{d_{0_{(c_l=0.6)}}}}$	$(l/d)(0.9c_{l_{max}})$	$c_{m_{max}}$
None	1.35	111	108	98	85	32.4	-0.003
1-a	2.69	218	212	191	164	18.6	-.260
1-b	2.74	185	180	165	146	19.1	-.365
2-a	2.71	212	207	190	164	16.1	-.395
2-b	2.82	207	203	185	161	16.3	-.405
1-c <sub>0</sub>	2.69	204	199	182	158	18.2	-.355
1-c <sub>1</sub>	2.69	200	196	179	155	17.8	-.355
1-c <sub>2</sub>	2.69	197	192	176	154	18.5	-.355

The maximum efficiency for a given landing speed will be obtained with the airfoil that gives the highest ratio of maximum lift coefficient to the drag coefficient for cruising. A comparison on this basis of the several slotted-flap arrangements shows slotted flap 1-a to be superior to any of the other arrangements for the conditions assumed. When the cruising speed is obtained at a lift coefficient of 0.6, flap 2-a is equally as good as 1-a, and 2-b is only slightly inferior to either. If a door were used to close the break in the lower surface of the wing when the flaps are neutral, the speed-range ratio ( $c_{l_{max}}/c_{d_{0_{min}}}$ ) would be highest for slotted flap 2-b because it has the highest maximum lift coefficient. The optimum slotted flap from consideration of speed-range ratio will, therefore, depend upon whether a door is used to close the break in the lower surface of the wing with the flap neutral.

The ratio of lift to drag at  $0.9c_{l_{max}}$ ,  $(l/d)(0.9c_{l_{max}})$ , is a criterion of the maximum gliding angle; the lower the ratio, the steeper the angle of glide. The ratios tabulated in the table were obtained by dividing  $0.9c_{l_{max}}$  with the respective flaps deflected 60°, by the drag coefficient at  $0.9c_{l_{max}}$ . Slotted flaps 2-a and 2-b will give the steepest gliding angle on this basis.

In order to control the glide-path angle, it is desirable to have available not only a low ratio of  $l/d$  at a high lift coefficient but also a high ratio of  $l/d$ . Slotted flap 2-b is superior in this respect, for the maximum lift is practically the same for flap deflections from 40° to 60° but the profile-drag coefficient for  $\delta_f=40^\circ$  is only about one-half of its value for  $\delta_f=60^\circ$ . (See fig. 20.)



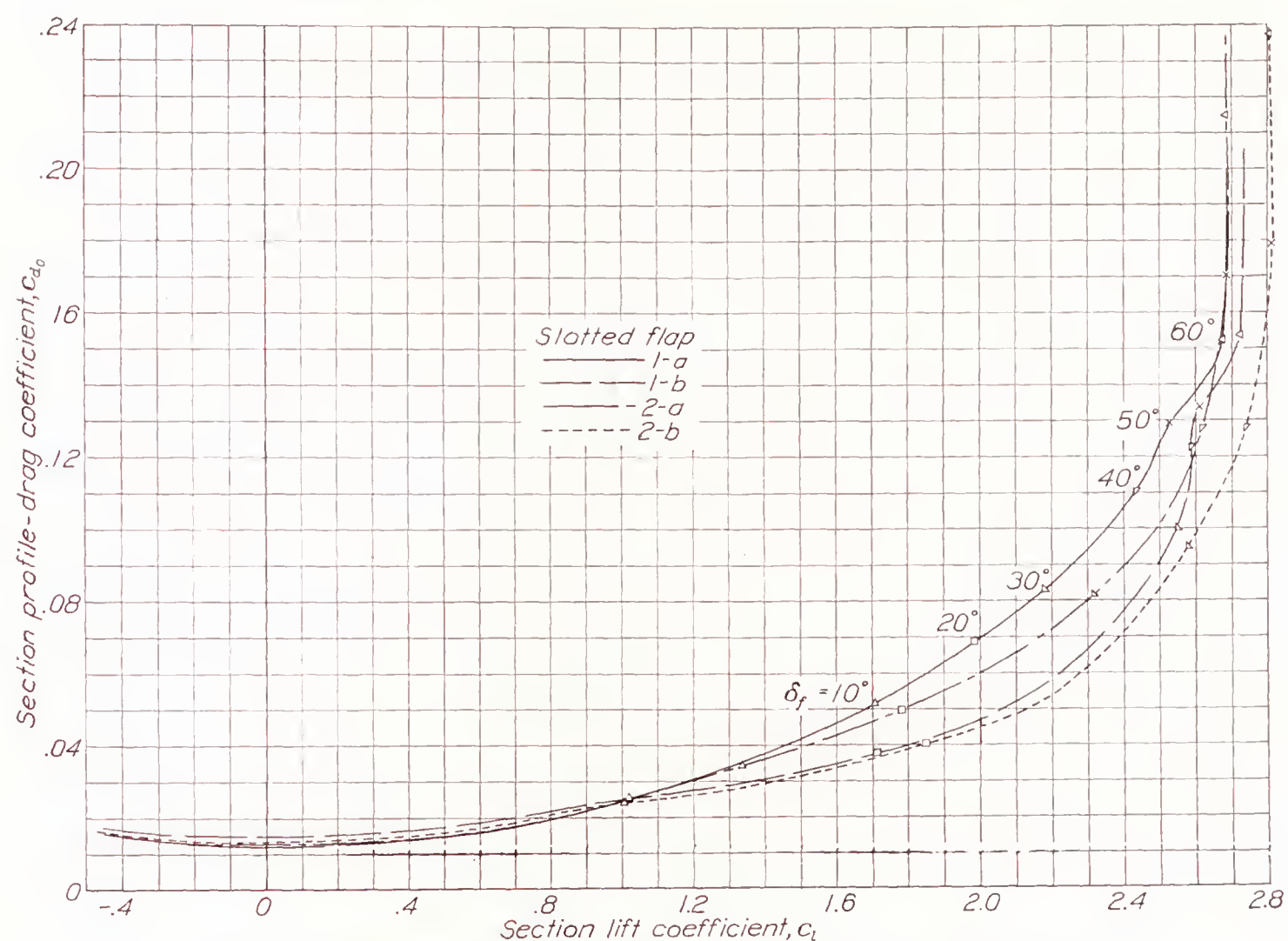


FIGURE 20.—Comparison of profile-drag coefficients for slotted flaps 1-a, 1-b, 2-a, and 2-b.

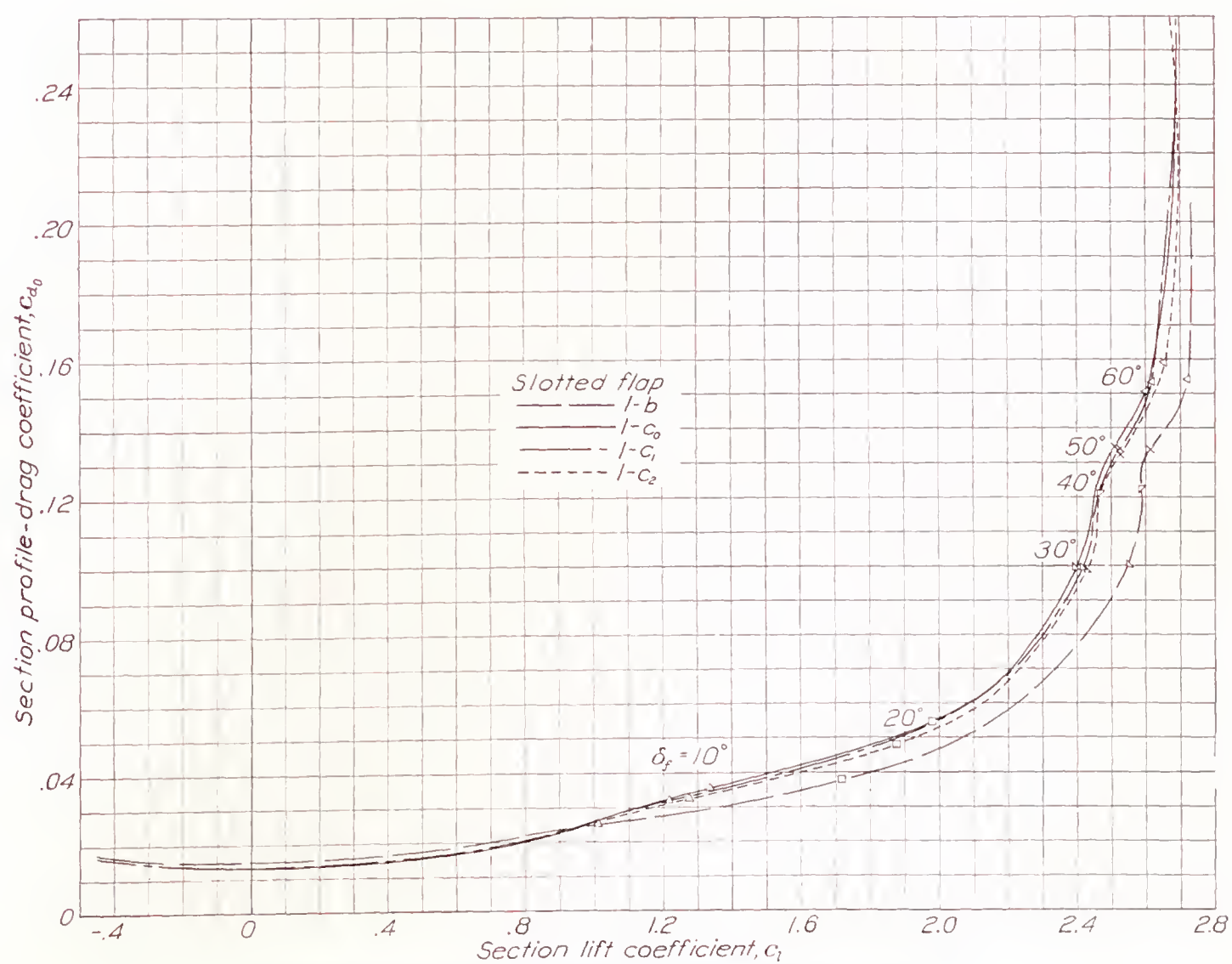


FIGURE 21.—Effect of slot-entry radius on profile-drag coefficient of airfoil.



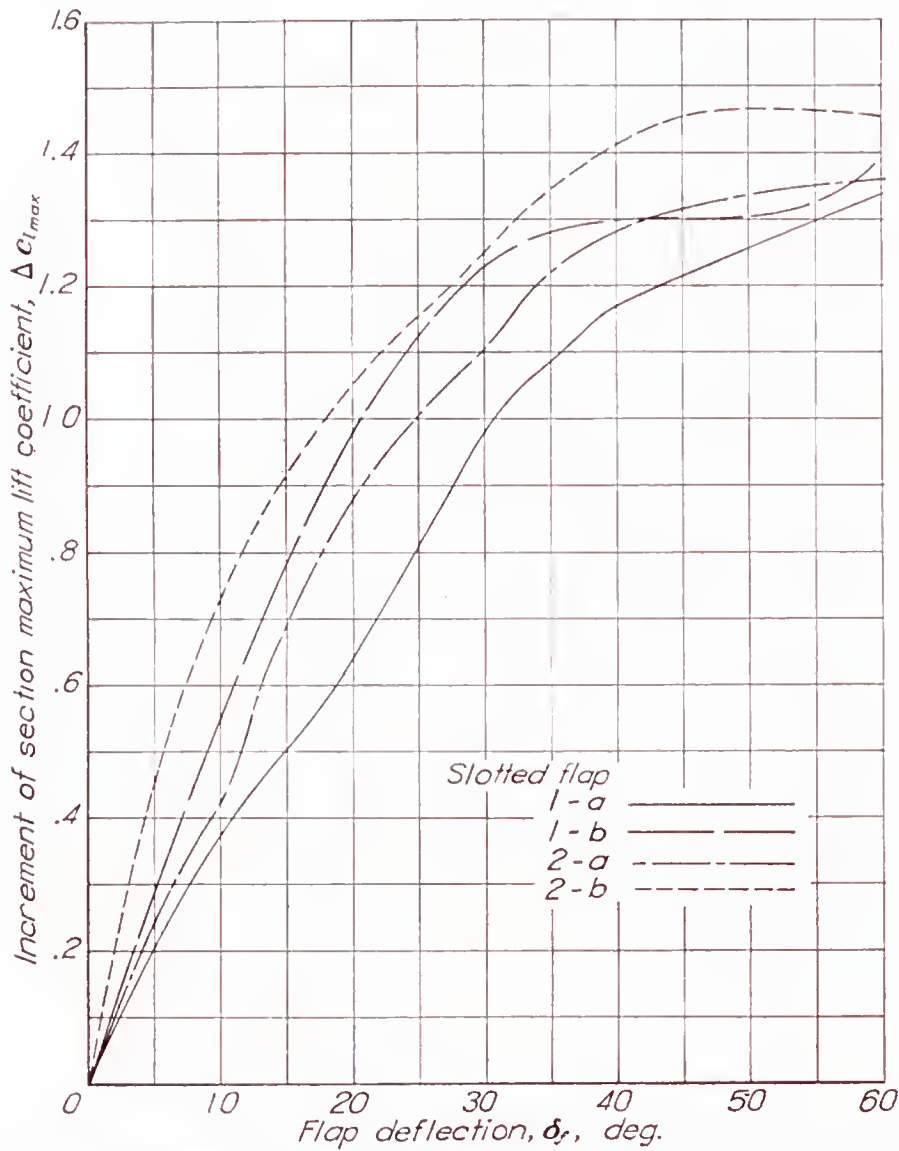


FIGURE 22.—Comparison of increments of maximum lift coefficient for slotted flaps 1-a, 1-b, 2-a, and 2-b when moved and deflected along the selected optimum paths.

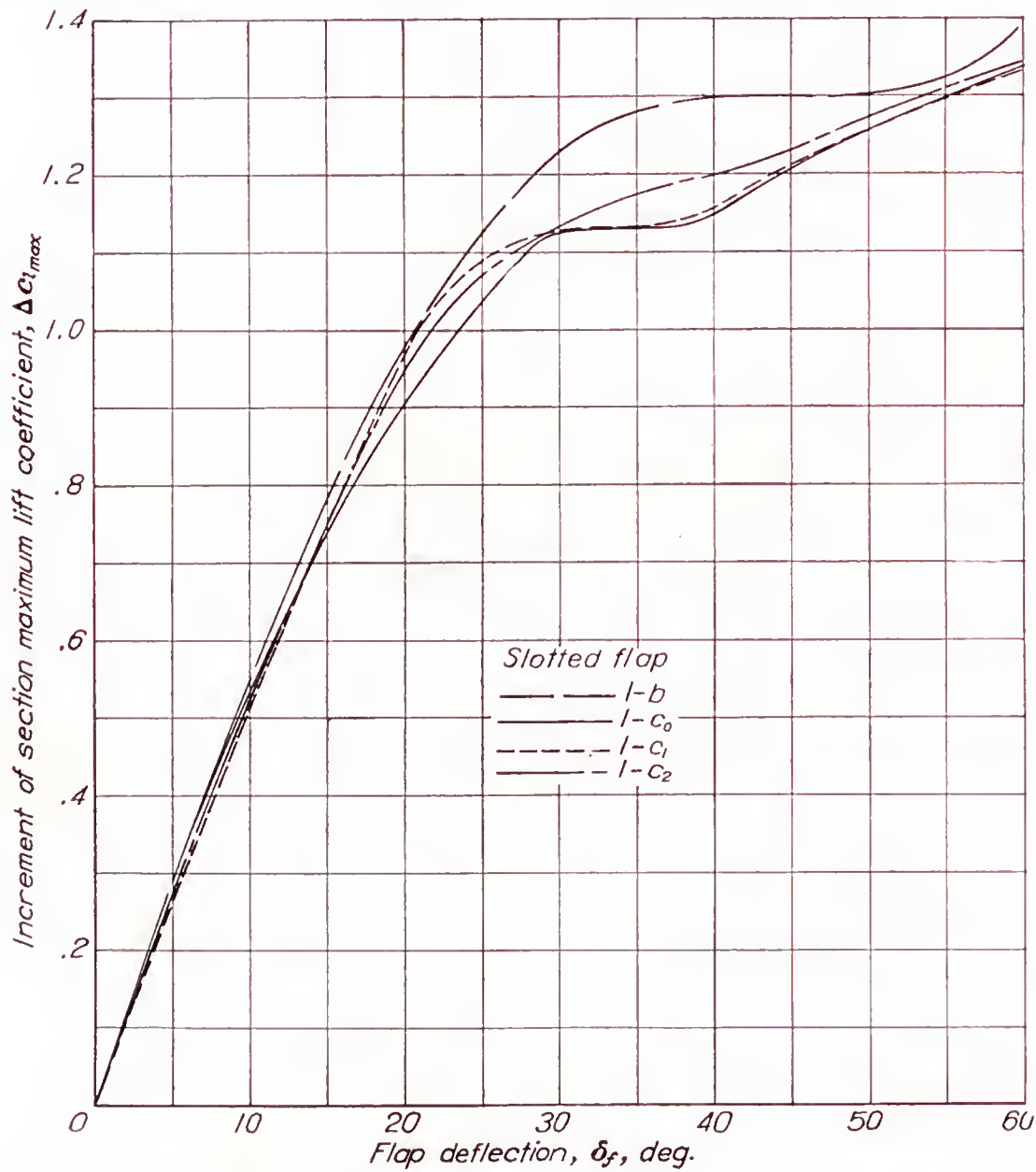


FIGURE 23.—Effect of slot-entry radius on increment of maximum lift coefficient of airfoil when the flaps are moved and deflected along the selected optimum path for flap 1-b.



Reference to figure 16 also shows that, beyond this range of flap deflections, there is practically no change in the pitching-moment coefficient and only about a  $1^\circ$  shift in the angle of attack at a lift coefficient of 2.6 with a  $20^\circ$  change in flap deflection from  $60^\circ$  to  $40^\circ$ .

The tabulated maximum pitching-moment coefficient  $c_{m_{max}}$  is the maximum obtained in the useful-flight range. Slotted flaps 2-a and 2-b have the highest, and nearly equal, values of  $c_{m_{max}}$ , these values being 6 percent higher than any of those for arrangements of flap 1. The pitching-moment coefficients obtained with the slotted flaps on the N. A. C. A. 23021 airfoil are about the same as those obtained for corresponding flap arrangements on the N. A. C. A. 23012 airfoil reported in reference 1.

**Comparison with slotted flap on N. A. C. A. 23012 airfoil.**—The envelope polars for slotted flap 2-b on the N. A. C. A. 23021 airfoil and for the corresponding slotted flap 2-h on the N. A. C. A. 23012 airfoil (reference 1) are plotted in figure 25 for comparison. The two curves are quite similar, with the curve for the N. A. C. A. 23021 airfoil consistently showing a somewhat higher drag coefficient for all lift coefficients throughout the normal-flight range. The maximum lift for either arrangement is the same. The final selection of airfoil thickness will probably be a compromise between aerodynamic and structural requirements.

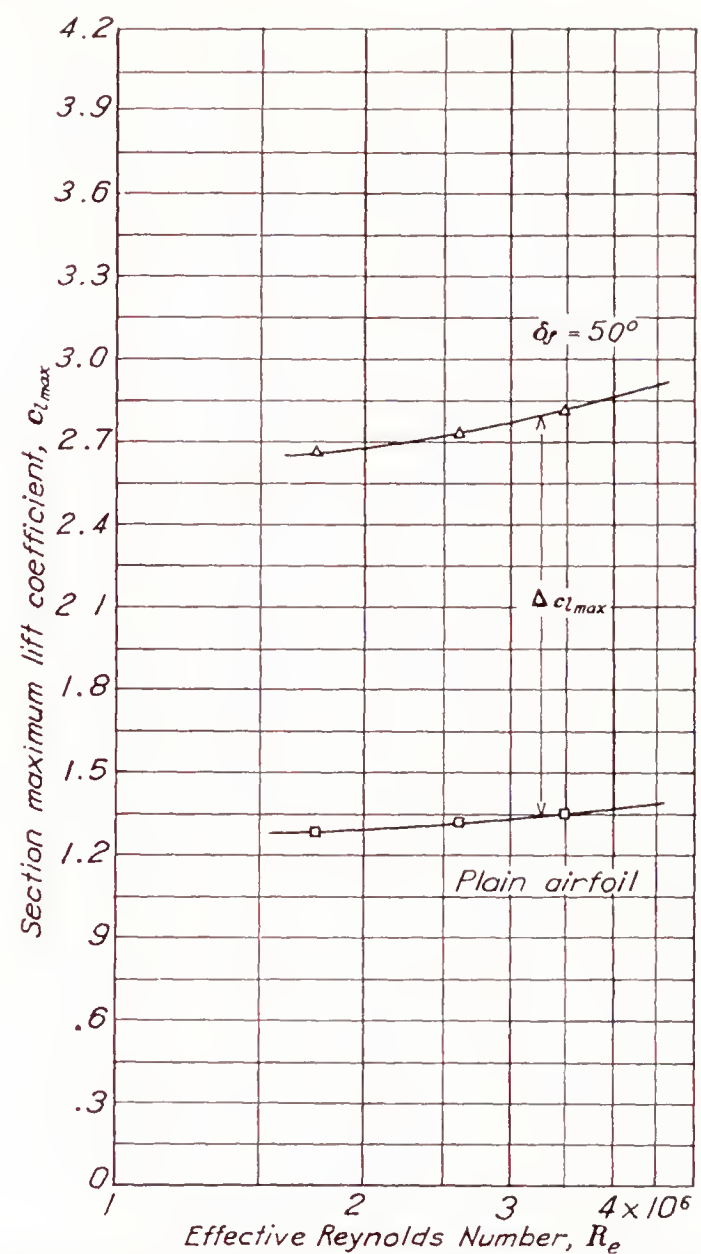


FIGURE 24.—Scale effect on maximum lift coefficient of N. A. C. A. 23021 airfoil with slotted flap 2-b at optimum location.

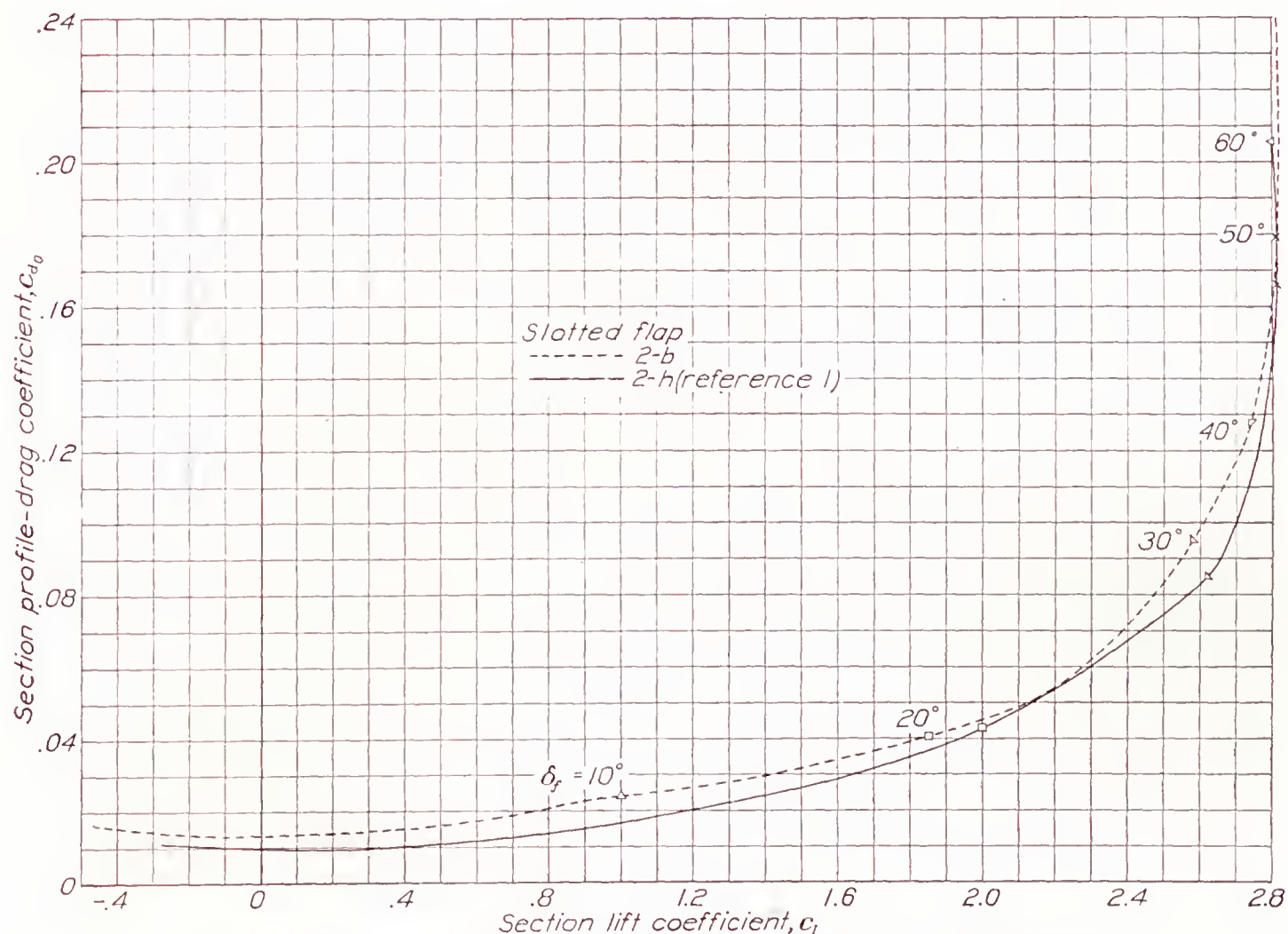


FIGURE 25.—Comparison of slotted flaps on N. A. C. A. 23012 and N. A. C. A. 23021 airfoils.



CONCLUDING REMARKS

If a door were used to close the break in the lower surface of the wing with the flaps neutral, slotted flap 2-b would be superior to any of the flaps tested on the basis of maximum lift coefficient, speed-range ratio, control of the angle of glide, and low drag for take-off and initial climb. Of the other combinations without a door, slotted flap 1-a gave the highest speed-range ratio, but slotted flap 2-b is still superior in other respects. The pitching-moment coefficients were about the same for the slotted flap on the N. A. C. A. 23021 airfoil as for the corresponding arrangements on the N. A. C. A. 23012 airfoil. The final selection of the optimum slotted flap will probably be a compromise in which structural considerations will be the deciding factor.

LANGLEY MEMORIAL AERONAUTICAL LABORATORY,  
NATIONAL ADVISORY COMMITTEE FOR AERONAUTICS,  
LANGLEY FIELD, VA., *February 24, 1939.*

REFERENCES

1. Wenzinger, Carl J., and Harris, Thomas A.: Wind-Tunnel Investigation of an N. A. C. A. 23012 Airfoil with Various Arrangements of Slotted Flaps. T. R. No. 664, N. A. C. A., 1939.

2. Wenzinger, Carl J., and Gauvain, William E.: Wind-Tunnel Investigation of an N. A. C. A. 23012 Airfoil with a Slotted Flap and Three Types of Auxiliary Flap. T. R. No. 679, N. A. C. A., 1939.

3. Wenzinger, Carl J., and Harris, Thomas A.: Preliminary Wind-Tunnel Investigation of an N. A. C. A. 23012 Airfoil with Various Arrangements of Venetian-Blind Flaps. T. R. (to be published), N. A. C. A., 1940.

4. Harris, Thomas A.: The 7 by 10 Foot Wind Tunnel of the National Advisory Committee for Aeronautics. T. R. No. 412, N. A. C. A., 1931.

5. Jacobs, Eastman N., and Sherman, Albert: Airfoil Section Characteristics as Affected by Variations of the Reynolds Number. T. R. No. 586, N. A. C. A., 1940.

TABLE I  
ORDINATES FOR AIRFOIL AND FLAP SHAPES

[Stations and ordinates in percent of wing chord]

N. A. C. A. 23021 airfoil			Flap 1			Flap 2		
Station	Upper surface	Lower surface	Station	Upper surface	Lower surface	Station	Upper surface	Lower surface
0		0	0		-3.90	0	-0.55	-0.55
1.25	4.87	-2.08	.32	-1.68	-4.63	.32	.59	-1.81
2.5	6.14	-3.14	.64	-1.85	-4.82	.64	1.08	-2.30
5	7.93	-4.52	1.28	.34	-4.87	1.28	1.89	-2.88
7.5	9.13	-5.55	1.93	1.28	-4.75	1.93	2.44	-3.28
10	10.03	-6.32	2.57	1.95	-4.64	2.57	2.88	-3.53
15	11.19	-7.51	5.14	3.60	-4.23	5.14	3.96	-3.91
20	11.80	-8.30	7.70	4.28	-3.79	7.70	4.26	-3.79
25	12.05	-8.76	10.27	3.99	-3.34	10.27	3.99	-3.34
30	12.06	-8.95	12.83	3.42	-2.84	12.83	3.42	-2.84
40	11.49	-8.83	15.40	2.83	-2.36	15.40	2.83	-2.36
50	10.40	-8.14	17.96	2.21	-1.86	17.96	2.21	-1.86
60	8.90	-7.07	20.53	1.56	-1.35	20.53	1.56	-1.35
70	7.09	-5.72	23.10	.90	-.81	23.10	.90	-.81
80	5.05	-4.13	25.66	.22	-.22	25.66	.22	-.22
90	2.76	-2.30						
95	1.53	-1.30						
100	.22	-.22						
			Center of L. E. arc			Center of L. E. arc		
			1.00	-3.90		2.89	-0.55	
			L. E. radius: 1.00			L. E. radius: 2.89		
L. E. radius: 4.85. Slope of radius through end of chord: 0.305								



## REPORT No. 678

# INTERFERENCE OF TAIL SURFACES AND WING AND FUSELAGE FROM TESTS OF 17 COMBINATIONS IN THE N. A. C. A. VARIABLE-DENSITY TUNNEL

By ALBERT SHERMAN

### SUMMARY

*An investigation of the interference associated with tail surfaces added to wing-fuselage combinations was included in the interference program in progress in the N. A. C. A. variable-density tunnel. The results indicate that, in aerodynamically clean combinations, the increment of the high-speed drag can be estimated from section characteristics within useful limits of accuracy. The interference appears mainly as effects on the downwash angle and as losses in the tail effectiveness and varies with the geometry of the combination. An interference burble, which markedly increases the glide-path angle and the stability in pitch before the actual stall, may be considered a means of obtaining satisfactory stalling characteristics for a complete combination.*

### INTRODUCTION

The investigation that the Committee has been conducting in the variable-density wind tunnel of the aerodynamic interference between the wing and the fuselage (references 1 to 6) has been extended to include the interference associated with the tail surfaces. Comparable data at large scale are thus made available on the aerodynamic interference between the component parts of related complete combinations.

Representative wing-fuselage combinations were tested, to which had been added two different types of tail surface: conventionally arranged tail surfaces of semi-elliptical plan form and rectangular horizontal tail surfaces with elliptical end plates. The tests were restricted to the conditions of zero elevator deflection and zero yaw, and the effects of the interference on the drag, the downwash angle, and the tail effectiveness were mainly considered. Effects of the following variables were studied: wing position, angle of wing setting, form of tail surface, and form of wing-root juncture. A comparison of calculated and experimental data on the downwash angle at the tail is also included.

### MODELS AND TESTS

The wing employed is the tapered wing described in reference 1; it is a duralumin model having an area of 150 square inches, aspect ratio 6, taper ratio 2, and the N. A. C. A. 0018 section at the root and the N. A.

C. A. 0009 section at the tip. It was combined with the fuselage in the standard longitudinal position,

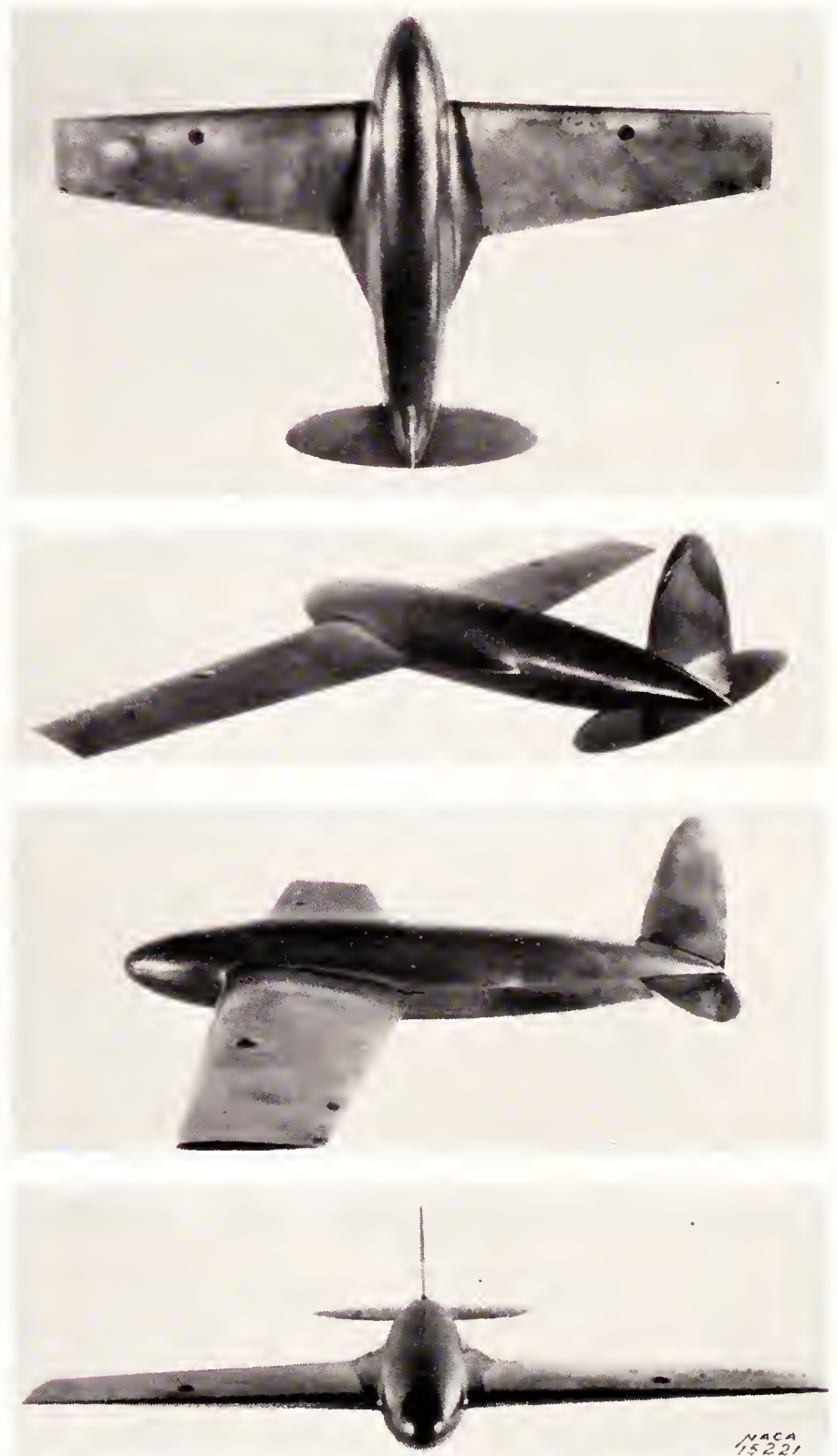


FIGURE 1.—Combination 314 showing elliptical tail surfaces.

$d/c=0$ . The fuselage is the round fuselage described in reference 1; it is an airship form having a length of



20.156 inches and a fineness ratio of 5.86. The tapered fillets (reference 1) were carefully constructed of plaster

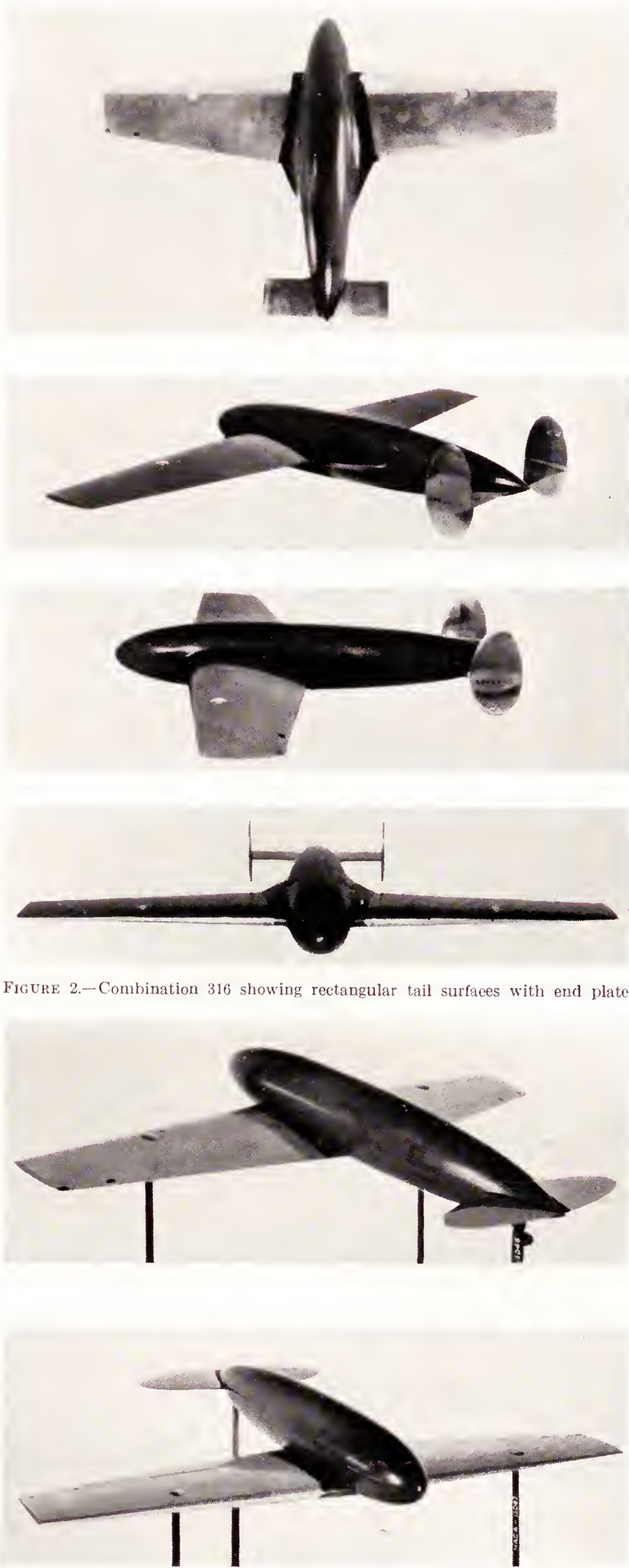
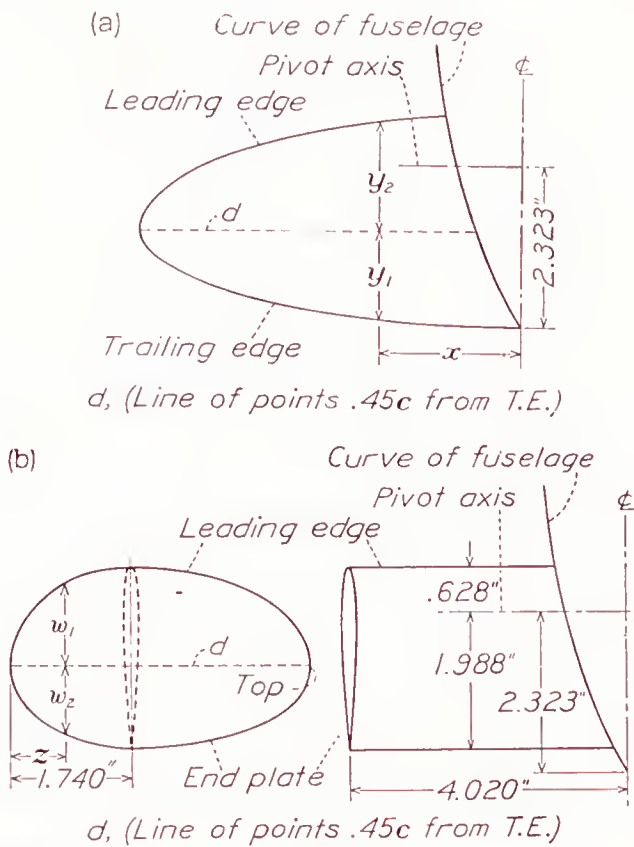


FIGURE 2.—Combination 316 showing rectangular tail surfaces with end plates.

FIGURE 3 —Combination 329 showing unfilleted juncture.

tion (reference 5). Figures 1, 2, and 3 are photographs of interesting combinations and show the proportions of the tail surfaces and their location on the fuselage axis.

The details of the tail surfaces are given in figure 4. For the elliptical tail surfaces, the vertical surface is identical with each of the horizontal surfaces. The tail with end plates has approximately the same total wetted area as the elliptical horizontal and vertical tail surfaces, but its calculated total-lift-curve slope was predicted from the theory of reference 7 to be 84



	$x$ (in.)	$y_1$ (in.)	$y_2$ (in.)
(a) Elliptical tail surface: Fin area: 11.46 sq. in.; 0.076 of wing area. Area horizontal surfaces (including 4.08 sq. in. in fuselage): 27.00 sq. in.; 0.18 of wing area.	0	1.403	-----
	1.0	1.381	-----
	2.0	1.308	1.598
	3.0	1.177	1.439
	4.0	.965	1.179
	5.0	.588	.718
	5.51	0	0
	$z$	$w_1$	$w_2$
(b) Tail surface with end plate: Fin (end plates) area: 17.88 sq. in.; 0.119 of wing area. Area horizontal surfaces (including 3.70 sq. in. in fuselage): 21.02 sq. in.; 0.14 of wing area.	0	0	0
	.240	.728	.596
	1.240	1.378	1.126
	2.240	1.412	1.154
	3.240	1.178	.964
	4.240	.416	.340
	4.352	0	0

FIGURE 4.—Details of the tail surfaces—N. A. C. A. 0009 sections.

percent as large. Only very small fillets were used at the tail surfaces (see figs. 1 and 2) because filleting was believed unnecessary for the junctures employed. The test results do not indicate that larger fillets would be an improvement. Table V contains the descriptions of the combinations (314 to 330) that make up this investigation.

The combinations were tested in the variable-density wind tunnel (reference 8) at a test Reynolds Number of approximately 3,100,000, corresponding to an effective Reynolds Number of 8,200,000 for  $C_{L_{max}}$ . (See reference 1.) In addition, values of the maximum lift coefficient were obtained at a reduced speed correspond-

of paris and were given the polished lacquer finish now standard for the wing-fuselage-interference investiga-



ing to an effective Reynolds Number of 3,700,000. The testing procedure and the test precision were about the same as for an airfoil (reference 8). The three-component balance of the variable-density wind tunnel restricted the study of the vertical tail surfaces to the zero-yaw condition.

based on the projected wing area of 150 square inches and on the mean chord of 5 inches. The methods for analysis of the test data and for presentation of the test results are explained in reference 1.

Tables I and II, taken from reference 1, contain the aerodynamic characteristics of the wing and of the

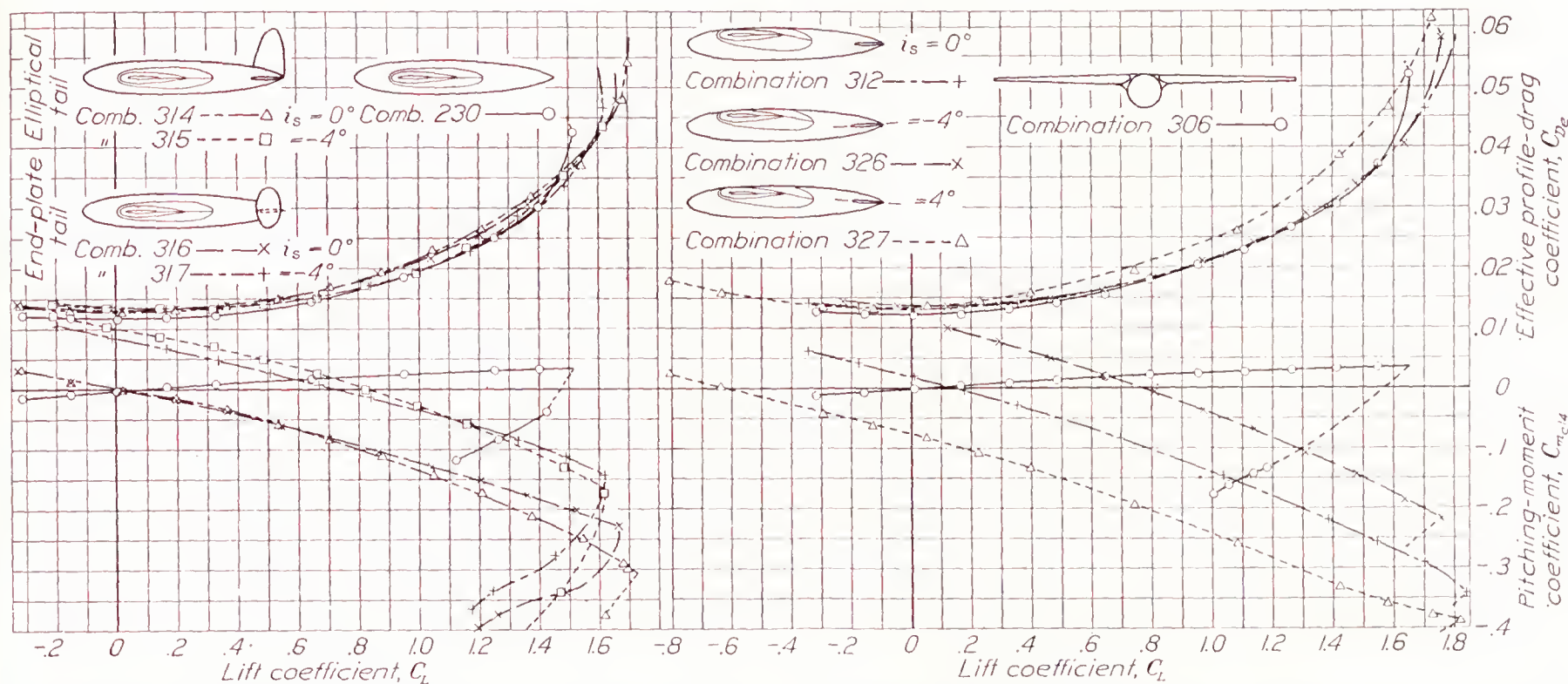


FIGURE 5.—Characteristics of midwing combinations with various tail surfaces. Tapered N. A. C. A. 0018-09 airfoil and round fuselage;  $k/c=0$ ;  $i_w=0^\circ$ .

FIGURE 6.—Effects of tail setting on the characteristics of high-wing combinations. Tapered N. A. C. A. 0018-09 airfoil and round fuselage;  $k/c=0.22$ ;  $i_w=0^\circ$ .

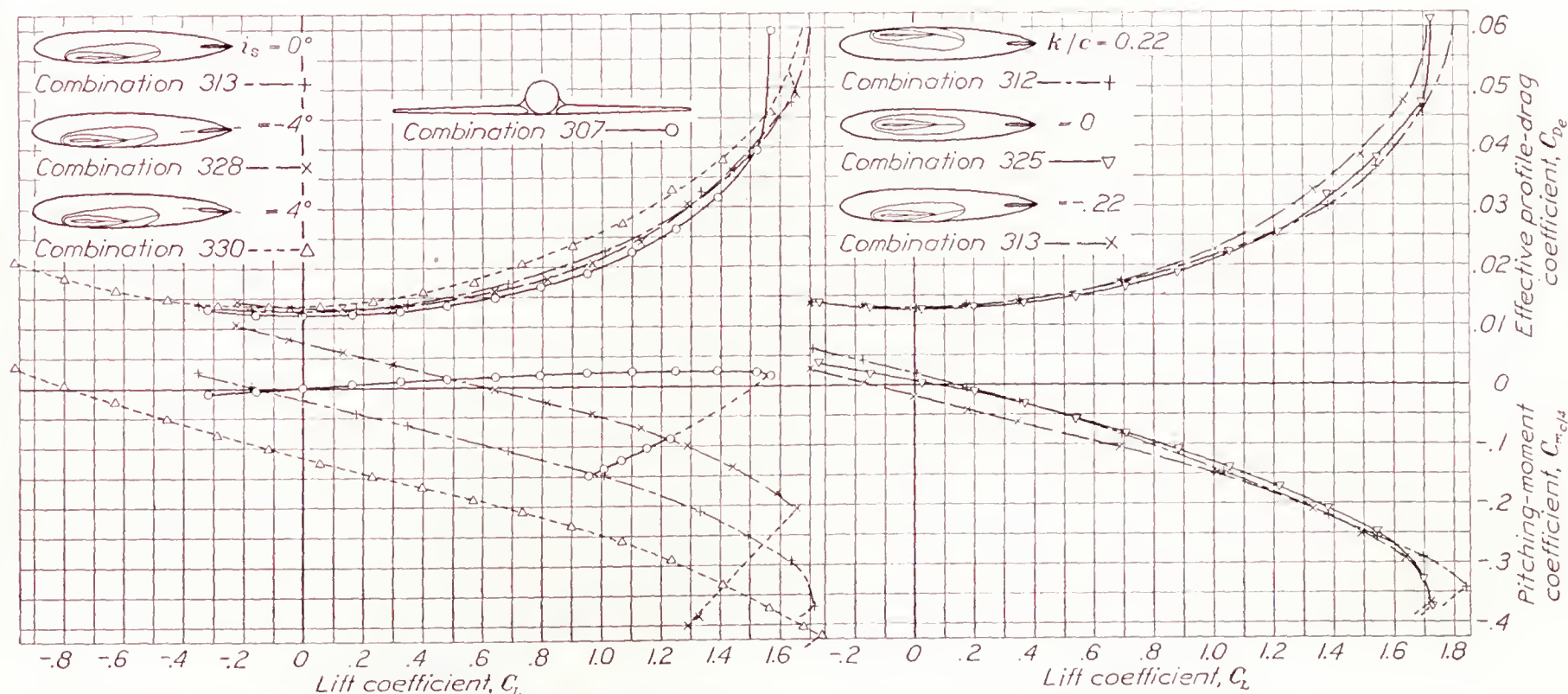


FIGURE 7.—Effects of tail setting on the characteristics of low-wing combinations. Tapered N. A. C. A. 0018-09 airfoil and round fuselage;  $k/c=-0.22$ ;  $i_w=0^\circ$ .

FIGURE 8.—Effects of wing vertical position. Tapered N. A. C. A. 0018-09 airfoil and round fuselage;  $i_w=0^\circ$ ;  $i_s=0^\circ$ .

## RESULTS

The test results are given in tables I, II, III, IIIa, and V supplemented by figures 5 to 10. Data from previous reports are included for comparison. Additional derived data on tail interference and downwash angle at the tail are presented in the text of the discussion and in figure 11. The aerodynamic characteristics are given as standard nondimensional coefficients

fuselage, respectively. Table III, continued from reference 6, presents the sums of the *fuselage* characteristics and interferences ( $\Delta C_L$ ,  $\Delta C_{De}$ ,  $\Delta C_{m_c/4}$ ) for the different combinations at various angles of attack. Table IIIa, continued from reference 6, presents the sums of the characteristics and interferences of the *tail surfaces*. The characteristics of the combinations themselves can be determined by adding the corresponding items in tables I, III, and IIIa.



Table IV of reference 1, which presents the data for disconnected combinations (combinations for which the forces on the components are measured separately), is omitted herein as it is in references 2 to 6 because no further tests of this nature were performed. The table numbers are maintained as in reference 1, however, to preserve the continuity of the published test results of the interference investigation.

Table V, continued from reference 6, contains the principal geometric and aerodynamic characteristics of the combinations. The values  $d/c$  and  $k/c$  represent the longitudinal and the vertical displacements, respectively, of the wing quarter-chord axis measured (in mean chord lengths) positive ahead of and above the quarter-length point of the fuselage axis. The value

tions with tail surfaces, however, the lift at an arbitrary angle of trim, i. e., where  $C_{m_{cl/4}}=0$ , is given instead.

$n_0$ ,

aerodynamic-center position, indicating approximately the location of the aerodynamic center ahead of the wing quarter-chord axis as a fraction of the mean wing chord. Numerically,  $n_0$  equals  $dC_{m_{cl/4}}/dC_L$  at zero lift. For the combinations with tail surfaces, however,  $n_0$  is given instead for the arbitrary trim condition, i. e., at  $C_{m_{cl/4}}=0$ .

$C_{m_0}$ ,

pitching moment at zero lift.

$C_{L_{ib}}$ ,

lift coefficient at the interference burble, i. e., the value of the lift coefficient beyond which

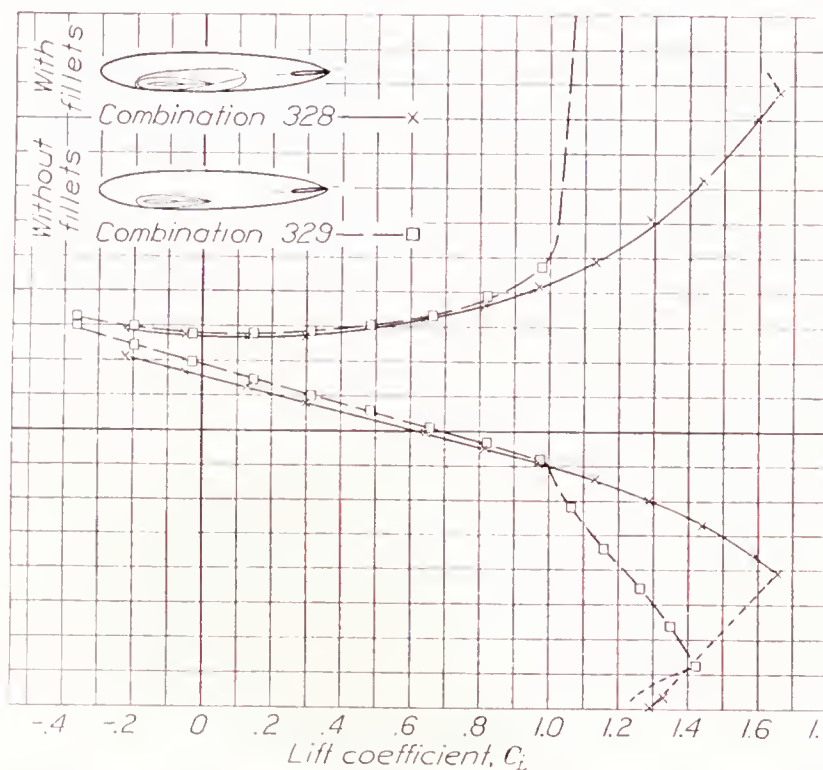


FIGURE 9.—Effects of fillets on the characteristics of low-wing combinations. Tapered N. A. C. A. 0018-09 airfoil and round fuselage;  $k/c=-0.22$ ;  $i_w=0^\circ$ ;  $i_s=-4^\circ$ .

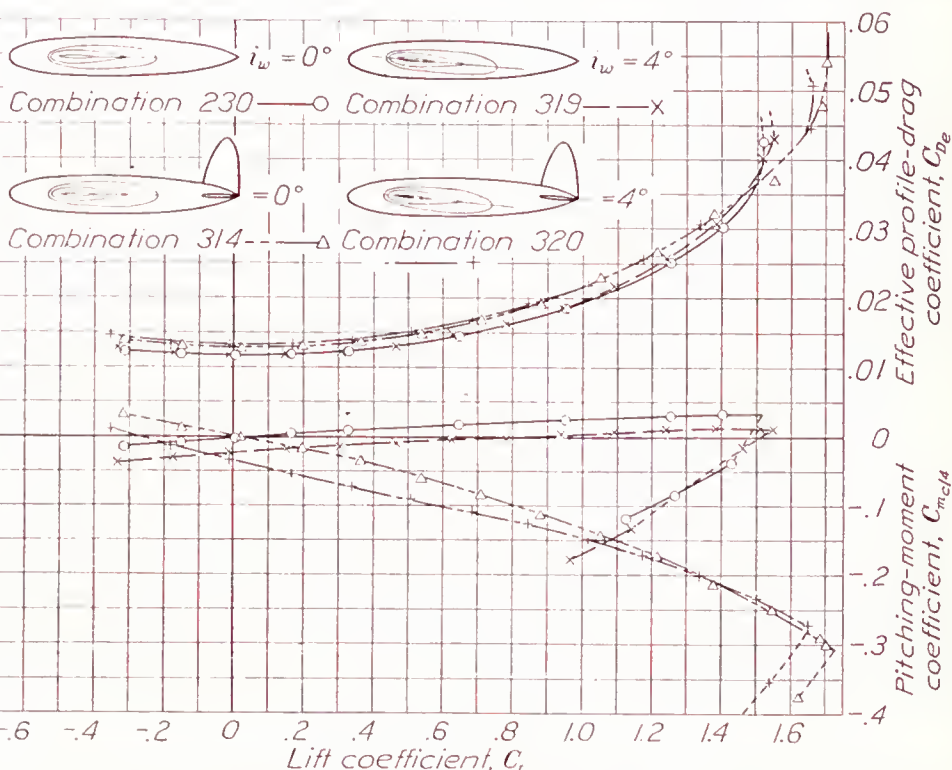


FIGURE 10.—Effects of wing setting on the characteristics of midwing combinations. Tapered N. A. C. A. 0018-09 airfoil and round fuselage;  $k/c=0$ ;  $i_s=0^\circ$ .

$i_w$  is the angle of wing setting with respect to the fuselage axis and  $i_s$  is the setting of the tail surfaces relative to the wing.

The last nine columns of table V present the following important aerodynamic characteristics:

- $a$ , lift-curve slope (in degree measure) as determined in the range of low lift coefficients for an effective aspect ratio of 6.86. This value of the aspect ratio differs from the actual value for the models because the lift results are not otherwise corrected for tunnel-wall interference.
- $e$ , Oswald's airplane, or span, efficiency factor. (See reference 1.)
- $C_{D_{e_{min}}}$ , minimum effective profile-drag coefficient  $\left(C_D - \frac{C_L^2}{\pi A}\right)_{min}$  corresponding to the test Reynolds Number.
- $C_{L_{opt}}$ , optimum lift coefficient, i. e., the lift coefficient corresponding to  $C_{D_{e_{min}}}$ . For the combina-

the air flow has a tendency to break away as indicated by an abnormal drag increase.

$C_{L_{max}}$ ,

maximum lift coefficient given for two different values of the effective Reynolds Number. (See reference 1.) The turbulence factor employed in this report to obtain the effective  $R$  from the test  $R$  is 2.64.

As in reference 2, the values of the effective Reynolds Number differ somewhat from those given in reference 1 because of a later determination of the turbulence factor for the tunnel. The values of the effective Reynolds Number given in reference 1 can be corrected by multiplying by 1.1.

The data thus presented for the combinations with tail surfaces are directly applicable to design purposes only at the attitude for trim, that is, when the pitching moment about the center of gravity is zero. At other attitudes, the conditions of the tests cannot be reproduced in steady flight. The most important interference effects for tail surfaces, however, should be satisfactorily indicated over the range of lift coefficients by these results.



## DISCUSSION

## LIFT

The horizontal tail surfaces at constant setting add to the lifting area of a combination and should therefore increase the lift-curve slope. For the combinations tested, the gain in lift-curve slope amounted, within the limits of the test accuracy, practically to the value that would be calculated from the lift expected of the tail operating alone as a wing, the downwash and the wake interferences being neglected. The observed increases in the maximum lift (table V) naturally cannot be considered real as they were obtained with undeflected elevators and highly unbalanced pitching moments. The effect on the maximum lift of the interference of tail surfaces with elevators deflected is outside the scope of this investigation.

## DRAG

The experimental increments of the minimum drag coefficients of the combinations due to the semielliptical tail surfaces at  $0^\circ$  setting (0.00035 to 0.00055 per surface) agree within the test accuracy with a value estimated from section characteristics and the wetted area (0.00045 per surface). This agreement shows that no large resultant interference effect of the tail surfaces could have been present. The horizontal tail surfaces set  $\pm 4^\circ$  show larger contributions to the minimum drag than those set  $0^\circ$ , but the differences are generally too small to be important. (See table V.)

Over the range of low to moderate lift coefficients, the variation in the drag increment also was unimportant for two of the tail settings investigated ( $0^\circ$  and  $-4^\circ$ ) and, moreover, was often favorable (figs. 5, 6, and 7). For a tail setting of  $4^\circ$ , however, this variation was appreciable and adverse.

From the foregoing considerations it can be concluded that, with regard to the high-speed or cruising drag, cleanly constructed tail surfaces within the normal range of tail settings may be satisfactorily allowed for in design by simple calculations based on section characteristics and the wetted area, neglecting interferences. Incidentally, the data indicate how low a drag should be expected from cleaning up the conventional airplane design. The value of 0.0135 ( $R=3 \times 10^6$ ) for the effective profile-drag coefficient for combinations 314 and 315 (fig. 5) at a  $C_L$  of about 0.3 represents the drag obtainable for a small airplane. In view of the turbulence present in the air stream of the variable-density wind tunnel and the unevaluated part of the support-strut interference, this value is believed to be conservative. Extrapolation of the drag values given in this report to higher Reynolds Numbers can be made by the methods described in reference 9.

## PITCHING MOMENT

The horizontal tail surfaces are employed to provide stability in pitch. They form what is essentially an

airfoil operating under the influence of an interfering body, the wing-fuselage combination. The most important interferences at the tail may be separated into two effects: that on the flow direction, or the downwash; and that on the flow velocity, or the wake.

**Downwash and wake.**—When the wing-fuselage combination is lifting, the downflow components induced by the vortex pattern in the air stream reduce the effective angle of attack at the tail by an amount referred to as the “downwash angle”  $\epsilon$ .

The evaluation of  $\epsilon$  is necessary in stability calculations. A method exists for the prediction of the

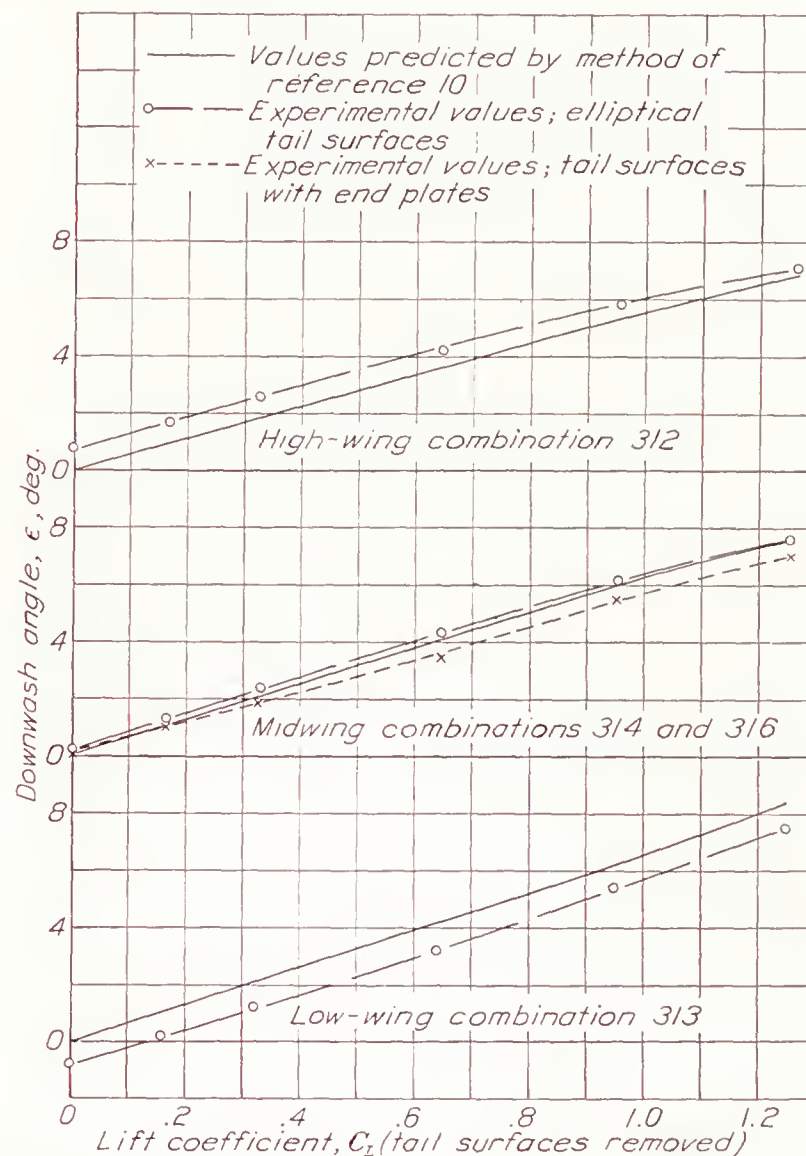


FIGURE 11.—Comparison of experimental and predicted values of the downwash angle at the tail.  $A=6.86$ .

downwash angle at the tail associated with any type of wing (reference 10), but the amount that  $\epsilon$  is modified by the interference in a wing-fuselage combination remains to be found. Figure 11 gives a comparison of values of the average downwash angle over the tail span as calculated by the method of reference 10 and as derived from the experimental results for the elliptical tail surfaces on the high-wing, the midwing, and the low-wing combinations. Experimental values of  $\epsilon$  for the tail with end plates on the midwing combination are included. The method employed to obtain the experimental values was as follows: At each specified angle of attack, the rate of change of pitching moment with the angle of attack of the tail was determined from the pitching moments for tail settings of



$-4^\circ$ ,  $0^\circ$ , and  $4^\circ$ . Next, the change produced in the pitching moment by adding the tail surfaces was divided by the rate just derived to give the effective angle of attack of the tail. The experimental value of the downwash angle  $\epsilon$ , then, was the difference between the geometric angle of attack of the tail and its effective angle of attack. This procedure avoided the complications of the wake interference and the tail effectiveness.

It can be seen from figure 11 that, for the elliptical tail on the symmetrical midwing combination, the agreement between the predicted and the experimental downwash angles is good over the range of low to moderate lift coefficients. Apparently, the interference of the fuselage and the junctures was negligible. For the high-wing and the low-wing combinations, the agreement is poor. The discrepancy, however, is practically constant, therefore of little importance in stability calculations, and is of opposite sign for the high-wing and the low-wing combinations. Apparently, at zero lift the tail surfaces have already an initial effective angle of attack of approximately  $0.8^\circ$  for the low-wing and  $-0.8^\circ$  for the high-wing combinations. (See pitching-moment curves of figs. 6, 7, and 8.) The geometrical asymmetry, then, produces an initial deviation in the flow at the tail impossible to derive from a theory that considers only the wing. A comparison of figures 7 and 9 shows that most of this interference is chargeable to the fillets. The same effect can be produced, however, by other sources of asymmetry, such as wing setting. (Cf. curves of pitching moment in fig. 10, and also  $C_{m_0}$  for combinations 314 and 322 in table V.)

Figure 5 shows that, for zero tail setting and at low to moderate lift coefficients, the tail surfaces with end plates produce as large a change in the pitching moment as the elliptical tail surfaces, indicating that they should have as high a slope of the total-lift curve. The slope for the end-plate tail, however, has been calculated to be only 84 percent of that for the elliptical tail. This calculation appears corroborated, moreover, by the change in the pitching moment at zero lift developed by the end-plate tail, corresponding to a change from  $0^\circ$  to  $-4^\circ$  in tail setting, which was also about 84 percent of the change produced by the elliptical tail (fig. 5). The apparent inconsistency may be explained by the experimental, and unexpected, circumstance that the average downwash angle affecting the end-plate tail was slightly less than that affecting the elliptical tail and balanced its lower lift-curve slope. (See fig. 11. Refer also to pitching-moment curves in fig. 5.) No explanation for this difference in downwash is offered. Further investigation of tail surfaces of dif-

ferent geometric characteristics may provide a better understanding of the nature of such interference phenomena.

**Stability at the stall.**—The problem of obtaining satisfactory stalling characteristics is commanding attention in connection with the refined present-day monoplanes. An essential feature of a satisfactory stall is that it give ample warning, associated preferably with rapidly increasing stability in pitch. Figure 9 presents the aerodynamic characteristics for a low-wing unfilleted combination of moderate aspect ratio (see fig. 3) that employs a common method of achieving such a stall, an interference burble (see reference 1); the burble occurred at a lift coefficient of about 1.0, which is above the climbing range, and resulted in a loss of downwash at the tail. As the angle of attack was increased, the lift continued to increase slowly to the maximum but the diving moment and the drag rose precipitously, insuring a steeper glide path, an appreciable increase in stability in pitch, and thus a warning of the approaching stall. It is understood from flight results that some tail buffeting may occur simultaneously; this buffeting is an unmistakable warning that cannot be overlooked. The interference burble can be delayed to a higher lift coefficient, if so desired, and the cost in maximum lift and minimum drag can be reduced by small fillets. The use of the interference burble is therefore not necessarily a makeshift solution in the design of airplanes for acceptable stalling characteristics.

**Tail factor.**—The tail factor,  $\eta_t$ , may be defined as the ratio of experimental to calculated changes in the pitching moment due to the horizontal tail surfaces. The calculated changes may be derived from the geometric and the aerodynamic characteristics of the tail surfaces with due allowance for the downwash angle and the flow velocity at the tail as affected by the wake. Ordinarily, the factor is derived from the experimental and the calculated changes in the pitching moment of the combination produced by different settings of the tail surfaces for a given angle of attack of the wing. This procedure avoids the complications involved with the downwash angle at the tail. Such a derivation results, however, in a factor corresponding to a *varying angle of tail setting* rather than one for a *varying angle of attack of the combination* as a whole. The interferences associated with various tail-surface settings might possibly differ, and hence the factor as ordinarily obtained would not strictly apply to stability calculations for which the tail changes angle together with the combination. As will be shown later, however, the variation in tail factor over a moderate range of angles of tail setting is generally unimportant for combinations such as reported herein.



If the tail factor is derived as described, it will differ from unity by an amount proportional to the *unevaluated* interference. Reference 10 contains methods of obtaining the interference behind the wing. The interference with a fuselage present remains to be investigated. The following table presents a comparison of tail factors for various combinations with allowance made for the interference of the wing alone in accordance with the methods of reference 10.

COMPARISON OF TAIL FACTORS FOR DIFFERENT WING-FUSELAGE COMBINATIONS

Combination	$k/c$	$i_w$ (deg.)	$i_s$ (deg.)	Tail factor, $\eta_t$ (averaged for $i_s=0^\circ$ to $\pm 4^\circ$ )			$\Delta\left(\frac{dC_{m_{c/4}}}{dC_L}\right)$ due to tail surfaces		
				$\alpha=0^\circ$	$\alpha=4^\circ$	$\alpha=12^\circ$	$\alpha=0^\circ$	$\alpha=4^\circ$	$\alpha=12^\circ$
Elliptical tail surfaces									
314-----	0	0	0	}0.90	0.91	0.91	{-0.128 -.127	-0.157 -.146	-0.202 -.196
315-----	0	0	-4						
327-----	.22	0	4	}.79	.82	.90	-.164	-.198	-.221
312 <sup>1</sup> -----	.22	0	0						
326-----	.22	0	-4	}.81	.82	.90	-.167	-.180	-.213
330-----	-.22	0	4						
313 <sup>1</sup> -----	-.22	0	0	{.81 .79	.81 .79	.90 .84	-.160	-.151	-.158
328-----	-.22	0	-4						
Tail surfaces with end plates									
316-----	0	0	0	}0.92	0.89	0.89	{-0.132 -.143	-0.160 -.150	-0.164 -.157
317-----	0	0	-4						

<sup>1</sup> From reference 6.

Notice that  $\eta_t$  is practically constant for the symmetrical midwing combinations over the range of angles of attack investigated. For the high-wing and the low-wing combinations, the factor shows greater amounts of unevaluated interference at low angles of attack than for the midwing combination. Most of the difference is believed to result from the asymmetry introduced by the fillets. (Notice in fig. 9 the reduction of slope in the pitching-moment curve associated with the fillets.) It appears, therefore, that a knowledge of the interference behind a wing alone is insufficient for calculating the effectiveness of tail surfaces in combinations. Until further research more fully evaluates the interference at the tail of combinations, estimates based upon test results, such as in this report, must be relied upon in stability calculations.

The values of  $\eta_t$  given are obviously averages for the two tail settings employed in each derivation. For any combination chosen, at a specified angle of attack, the downwash angle and the wake interference may be assumed unchanged for various tail settings. Under such conditions, a variation in the change produced in the slope of the pitching-moment curve by adding tail surfaces  $\Delta\left(\frac{dC_{m_{c/4}}}{dC_L}\right)$  is a direct indication of a variation in the tail factor. From the columns of  $\Delta\left(\frac{dC_{m_{c/4}}}{dC_L}\right)$  in the preceding table, it can be concluded that the tail setting did not, in general, greatly affect the tail factor

at the lower lift coefficients within the range investigated and within the accuracy of the data. It appears, therefore, that a factor derived from a small range of tail settings is reasonably applicable to horizontal tail surfaces that change angle together with the combination as a whole. Check calculations with the data using factors so derived corroborated this conclusion by correctly predicting the curves of pitching moment produced by the tail surfaces.

The factors of the tail with end plates in the symmetrical midwing combination are practically the same as those of the elliptical tail. (Cf. also values of  $\Delta\left(\frac{dC_{m_{c/4}}}{dC_L}\right)$ .) This agreement indicates that the unevaluated interference is not intimately connected with the geometry of the tail surfaces themselves.

## CONCLUSIONS

The results of the present tests show that:

1. The increment of the drag in the high-speed range caused by adding tail surfaces in the normal range of tail settings to clean combinations can be estimated within useful limits of accuracy from the section characteristics and the wetted area, the interference being neglected.
2. The interference of the fuselage in symmetrical midwing combinations on the downwash angle behind the wing is small.
3. The effect of asymmetry in the combination is to introduce a corresponding initial deviation in the air stream at the tail.
4. The effective downwash angle at the tail may vary somewhat with the geometry of the tail surfaces under consideration.
5. An interference burble for a combination of wing, fuselage, and tail surfaces may be considered a satisfactory means of producing acceptable stalling characteristics.
6. For combinations such as were investigated, large fillets at the tail-surface junctures are unnecessary.
7. Knowledge of the interference behind the wing alone is not sufficient for evaluating the effectiveness of tail surfaces added to wing-fuselage combinations.

LANGLEY MEMORIAL AERONAUTICAL LABORATORY,  
NATIONAL ADVISORY COMMITTEE FOR AERONAUTICS,  
LANGLEY FIELD, VA., November 5, 1938.

## REFERENCES

1. Jacobs, Eastman N., and Ward, Kenneth E.: Interference of Wing and Fuselage from Tests of 209 Combinations in the N. A. C. A. Variable-Density Tunnel. T. R. No. 540, N. A. C. A., 1935.
2. Sherman, Albert: Interference of Wing and Fuselage from Tests of 28 Combinations in the N. A. C. A. Variable-Density Tunnel. T. R. No. 575, N. A. C. A., 1936.



3. Sherman, Albert: Interference of Wing and Fuselage from Tests of 30 Combinations in the N. A. C. A. Variable-Density Tunnel. Combinations with Triangular and Elliptical Fuselages. T. R. (to be published), N. A. C. A., 1940.

4. Sherman, Albert: Interference of Wing and Fuselage from Tests of 18 Combinations in the N. A. C. A. Variable-Density Tunnel. Combinations with Split Flaps. T. N. No. 640, N. A. C. A., 1938.

5. Sherman, Albert: Interference of Wing and Fuselage from Tests of 17 Combinations in the N. A. C. A. Variable-Density Tunnel. Combinations with Special Junctures. T. N. No. 641, N. A. C. A., 1938.

6. Sherman, Albert: Interference of Wing and Fuselage from Tests of Eight Combinations in the N. A. C. A. Variable-

Density Tunnel. Combinations with Tapered Fillets and Straight-Side Junctures. T. N. No. 642, N. A. C. A., 1938.

7. von Kármán, Th., and Burgers, J. M.: Single Wing with Shields at Ends. Vol. II, div. E, sec. 19 of Aerodynamic Theory, W. F. Durand, ed., Julius Springer (Berlin), 1935, pp. 211-212.

8. Jacobs, Eastman N., and Abbott, Ira H.: The N. A. C. A. Variable-Density Wind Tunnel. T. R. No. 416, N. A. C. A., 1932.

9. Jacobs, Eastman N., and Sherman, Albert: Airfoil Section Characteristics as Affected by Variations of the Reynolds Number. T. R. No. 586, N. A. C. A., 1937.

10. Silverstein, Abe, and Katzoff, S.: Design Charts for Predicting Downwash Angles and Wake Characteristics behind Plain and Flapped Wings. T. R. No. 648, N. A. C. A., 1939.

TABLE I  
AIRFOIL CHARACTERISTICS

Airfoil	$C_L$	$C_{D_e}$	$C_{m_{c/4}}$	$C_L$	$C_{D_e}$	$C_{m_{c/4}}$	$C_L$	$C_{D_e}$	$C_{m_{c/4}}$
	$\alpha=0^\circ$			$\alpha=4^\circ$			$\alpha=12^\circ$		
Tapered N. A. C. A. 0018-09.....	0.000	0.0093	0.000	0.305	0.0099	0.006	0.910	0.0146	0.013

TABLE II  
FUSELAGE CHARACTERISTICS

Fusel- lage	En- gine	$C_L$	$C_D$	$C_{m_P}^1$	$C_L$	$C_D$	$C_{m_P}^1$	$C_L$	$C_D$	$C_{m_P}^1$	$C_L$	$C_D$	$C_{m_P}^1$	$C_L$	$C_D$	$C_{m_P}^1$
		$\alpha=0^\circ$			$\alpha=4^\circ$			$\alpha=8^\circ$			$\alpha=12^\circ$			$\alpha=16^\circ$		
Round	None	0.000	0.0041	0.000	0.001	0.0042	0.016	0.005	0.0049	0.028	0.011	0.0062	0.035	0.019	0.0085	0.038

<sup>1</sup> Pitching-moment coefficient about the quarter-chord point of the fuselage.

TABLE III

LIFT AND INTERFERENCE, DRAG AND INTERFERENCE, AND PITCHING MOMENT AND INTERFERENCE OF FUSELAGE IN WING-FUSELAGE COMBINATIONS

Com- bina- tion	$\Delta C_L$	$\Delta C_{D_e}$	$\Delta C_{m_{c/4}}$	$\Delta C_L$	$\Delta C_{D_e}$	$\Delta C_{m_{c/4}}$	$\Delta C_L$	$\Delta C_{D_e}$	$\Delta C_{m_{c/4}}$
	$\alpha=0^\circ$			$\alpha=4^\circ$			$\alpha=12^\circ$		
230	0.003	0.0024	-0.003	0.023	0.0024	0.003	0.042	0.0049	0.012
319	-.016	.0024	-.023	-.001	.0025	-.019	.030	.0040	-.009
321	-.020	.0028	-.022	-.004	.0027	-.016	.019	.0035	-.002
306	.008	.0029	-.001	.019	.0033	.003	.044	.0059	.012
307	-.008	.0029	.001	.013	.0028	.005	.037	.0044	.011
308	-.017	.0025	.009	-.011	.0027	.017	-.004	.0052	.032
309	.017	.0025	-.009	.036	.0027	-.004	.046	.0047	.006
187	.009	.0031	-.008	.026	.0036	-.001	.029	.0069	.010

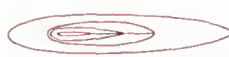
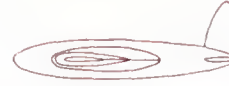
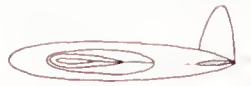














TABLE IIIa

LIFT AND INTERFERENCE, DRAG AND INTERFERENCE, AND PITCHING MOMENT AND INTERFERENCE OF TAIL SURFACES IN COMBINATIONS

Com- bina- tion	$\Delta C_L$	$\Delta C_{D_e}$	$\Delta C_{m_{c/4}}$	$\Delta C_L$	$\Delta C_{D_e}$	$\Delta C_{m_{c/4}}$	$\Delta C_L$	$\Delta C_{D_e}$	$\Delta C_{m_{c/4}}$
	$\alpha=0^\circ$			$\alpha=4^\circ$			$\alpha=12^\circ$		
310	0.005	0.0011	0.009	0.030	0.0012	-0.050	0.097	0.0025	-0.190
311	-.005	.0011	-.009	.022	.0015	-.062	.078	.0041	-.166
312	-.003	.0007	.020	.027	.0008	-.037	.083	.0015	-.172
313	.003	.0007	-.020	.027	.0014	-.073	.061	.0038	-.171
314	.015	.0011	.003	.033	.0015	-.043	.097	.0046	-.167
315	-.035	.0018	.107	-.007	.0010	.063	.046	.0006	-.052
316	.015	.0014	.003	.037	.0017	-.046	.091	.0031	-.152
317	-.019	.0019	.088	.009	.0013	.040	.054	.0010	-.058
318									
320	.003	.0015	-.010	.033	.0015	-.059	.075	.0033	-.151
322	.006	.0012	-.016	.031	.0016	-.067	.074	.0041	-.164
323	-.037	.0021	.091	-.017	.0017	.035	.022	.0027	-.058
324	.004	.0014	-.008	.029	.0015	-.060	.076	.0028	-.161
325	.019	.0010	.006	.039	.0013	-.042	.099	.0036	-.164
326	-.056	.0015	.125	-.032	.0008	.068	.016	.0007	-.061
327	.042	.0015	-.082	.071	.0027	-.142	.128	.0058	-.283
328	-.042	.0015	.082	-.021	.0009	.029	.020	.0019	-.069
329	-.038	.0015	.107	-.017	.0008	.045	.038	.0021	-.065
330	.056	.0015	-.125	.075	.0033	-.178	.118	.0084	-.281



TABLE V  
PRINCIPAL AERODYNAMIC CHARACTERISTICS OF THE COMBINATIONS









Diagrams representing combinations	Combination	Remarks	Longitudinal position d/c	Vertical position k/c	Angle of wing setting $i_w$ (deg.)	Lift-curve slope (per deg.) $\frac{a}{A=6.86}$	Span efficiency factor $e$	$C_{D_{e_{min}}}$	$C_{L_{opt}}$	Aero-dynamic-center-position $x_0$	$C_{m_0}$	Lift coefficient at interference burble $^1 C_{L_{ib}}$	$^2 C_{L_{max}}$	
													Effective $R=8.2 \times 10^6$	Effective $R=3.7 \times 10^6$
Tapered N. A. C. A. 0018-09 airfoil with round fuselage														
		Wing alone				0.077	0.90	0.0093	0.00	0.020	0.000	A1.4	a1.48	a1.23
	230	(From reference 2.) Tapered fillets. (Plaster finish.)	0	0	0	.080	3.85	.0117	.00	.026	.000	A1.5	a1.52	a1.27
	314	Tapered fillets. Vertical and horizontal tail surfaces. $i_s=0^\circ$ .	0	0	0	.086	5.85	.0128	6.02	7-1.100	.002	A1.7	a1.73	a1.47
	315	$i_s=-4^\circ$ ; otherwise same as combination 314.	0	0	0	.087	5.90	.0133	6.82	7-1.156	.102	A1.6	a1.62	a1.31
	316	Tapered fillets. Tail surfaces with end plates. $i_s=0^\circ$ .	0	0	0	.086	4.85	.0132	6.02	7-1.098	.001	A1.6	a1.67	a1.40
	317	$i_s=-4^\circ$ ; otherwise same as combination 316.	0	0	0	.087	5.90	.0134	6.75	7-1.122	.086	A1.6	a1.62	a1.33
	318	Washed-out fillets. Vertical and horizontal tail surfaces. $i_s=0^\circ$ .	0	0	4	.086	5.85	.0142	6-1.33	7-1.129	-.044	A1.4	a1.42	a1.38
	319	Symmetrical tapered fillets.	0	0	4	.080	4.85	.0117	.02	.027	-.021	A1.5	a1.55	a1.25
	320	Same as combination 319 but with vertical and horizontal tail surfaces. $i_s=0^\circ$ .	0	0	4	.087	5.85	.0132	6-1.29	7-1.115	-.033	A1.6	a1.66	a1.36
	321		0	0	4	.080	4.85	.0120	.02	.034	-.021	A1.5	a1.50	a1.22
	322	Vertical and horizontal tail surfaces. $i_s=0^\circ$ .	0	0	4	.087	4.85	.0133	6-1.32	7-1.116	-.039	A1.6	a1.67	a1.35
	323	$i_s=-4^\circ$ ; otherwise same as combination 322.	0	0	4	.086	5.85	.0138	6.51	7-1.110	.062	A1.6	a1.60	a1.31
	324	Tail surfaces with end plates. $i_s=0^\circ$ .	0	0	4	.086	4.85	.0135	6-1.28	7-1.114	-.032	A1.6	a1.65	a1.34
	325	Tapered fillets. Horizontal tail surfaces. $i_s=0^\circ$ .	0	0	0	.086	4.85	.0127	6.06	7-1.087	.005	A1.7	a1.72	a1.41
	306	(From reference 6.) Tapered fillets.	0	.22	0	.080	.85	.0122	-.02	.032	-.001	A1.6	a1.65	a1.36
	312	(From reference 6.) Tapered fillets. Horizontal tail surfaces. $i_s=0^\circ$ .	0	.22	0	.087	5.85	.0129	6.14	7-1.133	.019	A1.8	a1.84	a1.50
	326	$i_s=-4^\circ$ ; otherwise same as combination 312.	0	.22	0	.085	4.85	.0137	6.77	7-1.166	.116	A1.7	a1.76	a1.46
	327	$i_s=4^\circ$ ; otherwise same as combination 312.	0	.22	0	.086	4.80	.0133	6-1.61	7-1.125	-.077	A1.8	a1.81	a1.50
	308	(From reference 6.) Straight-side junctures.	0	.22	0	.078	5.85	.0118	-.03	.041	.010	A1.5	a1.58	a1.27
	310	(From reference 6.) Straight-side junctures. Horizontal tail surfaces. $i_s=0^\circ$ .	0	.22	0	.086	5.85	.0128	6.13	7-1.127	.016	A1.7	a1.75	a1.46

See footnotes at end of table.

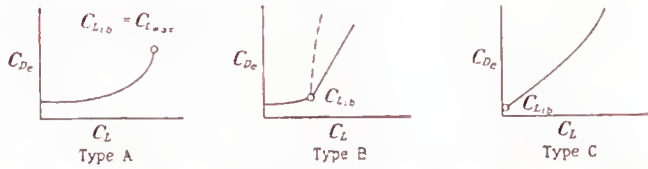


TABLE V—Continued

PRINCIPAL AERODYNAMIC CHARACTERISTICS OF THE COMBINATIONS—Continued

Diagrams representing combinations	Combina- tion	Remarks	Longi- tudi- nal posi- tion d/c	Verti- cal posi- tion k/c	Angle of wing set- ting $i_w$ (deg.)	Lift- curve slope (per deg.) $a$ $A=6.86$	Span effi- ciency factor $e$	$C_{D_{e_{min}}}$	$C_{L_{opt}}$	Aero- dy- namie- center position $n_0$	$C_{m_0}$	Lift coeffi- cient at inter- ference burbles $C_{L_{ib}}^1$	$^2 C_{L_{max}}$	
													Effec- tive $R=$ $8.2 \times$ $10^6$	Effec- tive $R=$ $3.7 \times$ $10^6$
Tapered N. A. C. A. .0018-09 airfoil with round fuselage														
	307	(From reference 6.) Ta- pered fillets.	0	-.22	0	.081	4.85	.0122	.02	.030	.001	A1.5	e1.57	a1.26
	313	(From reference 6.) Ta- pered fillets. Horizontal tail surfaces. $i_s=0^\circ$ .	0	-.22	0	.087	5.85	.0129	<sup>6</sup> -.15	<sup>7</sup> -.127	-.019	A1.7	e1.72	a1.37
	328	$i_s=-4^\circ$ ; otherwise same as combination 313.	0	-.22	0	.086	4.85	.0133	<sup>6</sup> .61	<sup>7</sup> -.125	.077	A1.6	e1.66	a1.30
	187	(From reference 1).....	0	-.22	0	.079	.85	.0124	-.02	.039	-.008	B.9	e1.33	a1.14
	329	Horizontal tail surfaces. $i_s=-4^\circ$ .	0	-.22	0	.085	5.90	.0139	<sup>6</sup> .69	<sup>7</sup> -.137	.095	B1.0	e1.42	a1.23
	330	$i_s=4^\circ$ ; otherwise same as combination 313.	0	-.22	0	.086	5.80	.0137	<sup>6</sup> -.77	<sup>7</sup> -.166	-.115	A1.6	e1.74	a1.38
	309	(From reference 6.) Straight-side junctures.	0	-.22	0	.079	4.85	.0118	.03	.041	-.010	A1.5	e1.50	a1.23
	311	(From reference 6.) Straight-side junctures. Horizontal tail surfaces. $i_s=0^\circ$ .	0	-.22	0	.086	5.85	.0128	<sup>6</sup> -.13	<sup>7</sup> -.125	-.016	A1.6	e1.66	a1.40

<sup>1</sup> Letters refer to types of drag curves associated with the interference burble as follows:



<sup>2</sup> Letters refer to condition at maximum lift as follows: <sup>a</sup>, reasonably steady at  $C_{L_{max}}$ ; <sup>b</sup>, small loss of lift beyond  $C_{L_{max}}$ ; <sup>c</sup>, large loss of lift beyond  $C_{L_{max}}$  and uncertain value of  $C_{L_{max}}$ .

<sup>3</sup> Poor agreement in high-speed range.

<sup>4</sup> Poor agreement over whole range.

<sup>5</sup> Poor agreement in high-lift range.

<sup>6</sup>  $C_L$  at  $C_{m_{c/4}}=0$  for combinations with tail surfaces.

<sup>7</sup>  $n_0=dC_{m_{c/4}}/dC_L$  at  $C_{m_{c/4}}=0$  for combinations with tail surfaces.



## REPORT No. 679

# WIND-TUNNEL INVESTIGATION OF AN N. A. C. A. 23012 AIRFOIL WITH A SLOTTED FLAP AND THREE TYPES OF AUXILIARY FLAP

By CARL J. WENZINGER and WILLIAM E. GAUVAIN

### SUMMARY

An investigation was made in the N. A. C. A. 7- by 10-foot wind tunnel to determine the aerodynamic section characteristics of an N. A. C. A. 23012 airfoil with a single main slotted flap equipped successively with auxiliary flaps of the plain, split, and slotted types. A test installation was used in which an airfoil of 7-foot span was mounted vertically between the upper and the lower sides of the closed test section so that two-dimensional flow was approximated.

On the basis of maximum lift coefficient, low drag at moderate and high lift coefficients, and high drag at high lift coefficients, the optimum combination of the arrangements was found to be the double slotted flap. All the auxiliary flaps tested, however, increased the magnitudes of the pitching moments over those of the main slotted flap alone.

### INTRODUCTION

Many different types of high-lift device have been investigated by the N. A. C. A. in an extensive program of research for increasing safety in flight. Some of these devices are located at the leading edge of the wing and others at the trailing edge. One of the most promising of the devices is a recently developed arrangement of slotted trailing-edge flap. This slotted flap (reference 1) is capable of giving high maximum lift coefficients, low drag at moderate and high lift coefficients, and high drag at high lift coefficients. This flap therefore appears well suited for improving take-off and landing characteristics.

Results of a few preliminary tests of a slotted flap with a small split flap mounted on it (reported also in reference 1) indicate that such an arrangement has considerable promise as a high-lift device. As a further development in enlarging the possibilities of the slotted flap, the investigation has been extended to include multiple flaps. The present report gives the results of an investigation of an airfoil with a medium-size main slotted flap combined with each of three different types of smaller auxiliary flap: split, plain, and slotted. Each combination of the auxiliary flaps was tested at a series of deflections for several deflections of the main flap. Measurements of lift, drag,

and pitching moments were made in the 7- by 10-foot wind tunnel.

### APPARATUS AND TESTS

#### MODELS

The basic model, or plain airfoil, was built to the N. A. C. A. 23012 profile and has a chord of 3 feet and a span of 7 feet. The solid nosepiece was made of laminated mahogany, the ribs and the slot form were of pine, and the intermediate section was covered with tempered waterproofed wallboard. All the flaps were made of wood.

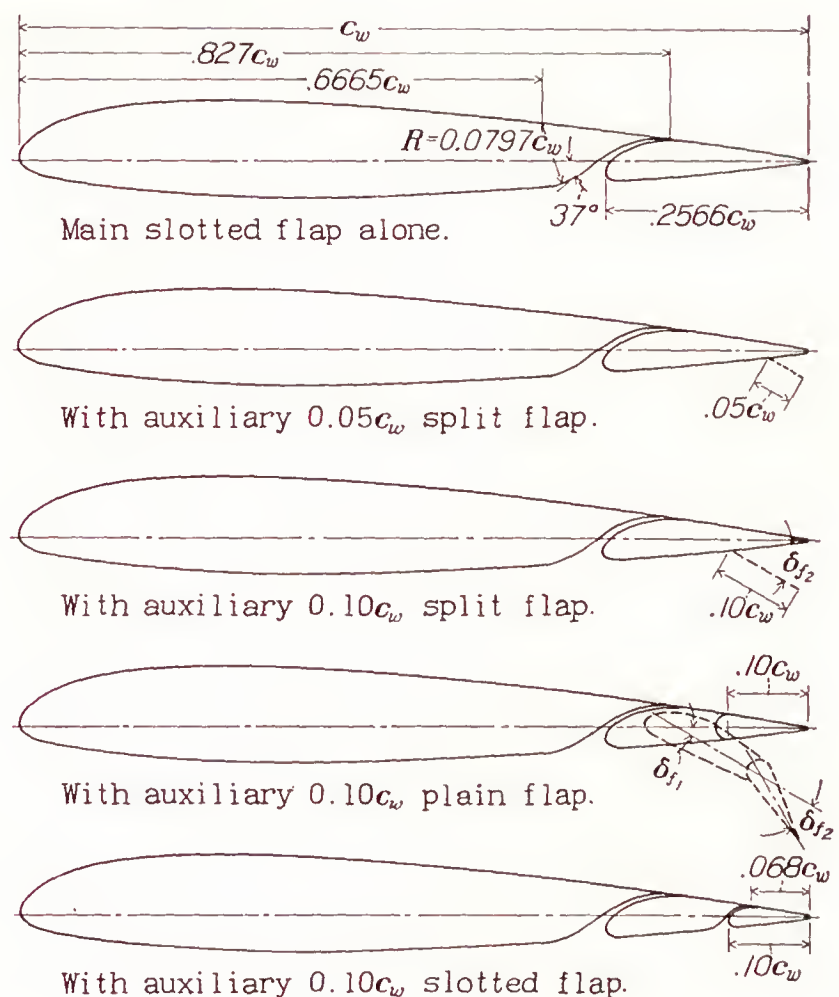
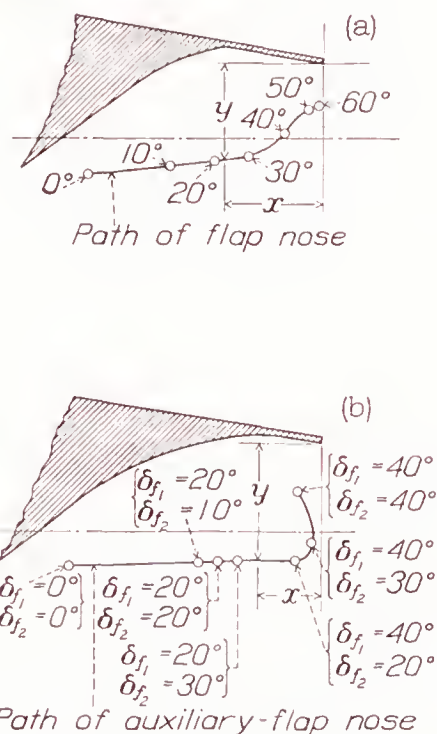


FIGURE 1.—Section view of the N. A. C. A. 23012 airfoil with the main slotted flap and the auxiliary flaps.

The main slotted flap has a chord 25.66 percent of the wing chord  $c_w$ ; this flap together with its slot shape (fig. 1) is the same as the arrangement designated 2-h in reference 1. The flap was mounted on the airfoil with three fittings along the span that permitted setting the flap at the optimum location for each deflection.



The ordinates for this flap and the slot shape are given in table I, and the optimum path of the nose of the flap for various deflections (from reference 1) is given in figure 2 (a). The nose point of the flap is defined as the point of tangency of a line drawn normal to the airfoil chord and tangent to the leading-edge arc of the flap when neutral.



(a) Path of the main slotted flap for various deflections on the N. A. C. A. 23012 airfoil.

Path of flap nose for various flap deflections. Distances measured from lower edge of lip in percent airfoil chord, $c_w$		
$\delta_{f1}$ (deg.)	$x$	$y$
0	8.36	3.91
10	5.41	3.63
20	3.83	3.45
30	2.63	3.37
40	1.35	2.43
50	.50	1.63
60	.12	1.48

(b) Path of the auxiliary 0.10 $c_w$  slotted flap for various deflections on the main slotted flap.

Path of flap nose for various flap deflections. Distances measured from lower edge of lip in percent airfoil chord, $c_w$			
$\delta_{f1}$ (deg.)	$\delta_{f2}$ (deg.)	$x$	$y$
0	0	3.22	1.58
20	10	1.55	1.52
20	20	1.32	1.50
20	30	1.06	1.50
40	20	.32	1.50
40	30	.06	1.27
40	40	.25	.59

FIGURE 2.—Optimum locations of the slotted flaps.

Two widths of split flap were tested: one has a chord 0.05 $c_w$  and the other a chord 0.10 $c_w$  (fig. 1). Each of these flaps was fastened to the lower surface of the main slotted flap by screws and blocks cut to different angles

for the various flap deflections. The flap hinge axes were set in from the trailing edge of the main flap an amount equal to the chord of the split flaps.

The plain flap has a chord 0.10 $c_w$  and is formed from a portion of the main slotted flap, as shown in figure 1. This flap is arranged for locking at various angles, both up and down, with respect to the main flap. The gap between the plain-flap nose and the main slotted flap was sealed with a light grease for all tests to prevent leakage of air through the gap.

The auxiliary slotted flap (fig. 1) has a chord 0.10 $c_w$ ; the shapes of both the flap and the slot are similar to those of the main slotted flap. The ordinates for the auxiliary slotted flap and the slot shape are also given in table I. This flap was mounted on the main slotted flap by special fittings that allowed the small flap to be located at any point over a considerable area with respect to the main flap. This arrangement makes it possible to determine the optimum locations of the small slotted flap for the various deflections investigated. (See fig. 2(b).)

#### TEST INSTALLATION

The model was mounted in the closed test section of the 7- by 10-foot wind tunnel so as to span the jet completely except for small clearances at each end. (See references 1 and 2.) The main airfoil was rigidly attached to the balance frame by torque tubes, which extended through the upper and the lower sides of the tunnel. The angle of attack of the model was set from outside the tunnel by rotating the torque tubes with a calibrated drive. Approximately two-dimensional flow is obtained with this type of installation and the section characteristics of the model under test can be determined. (See reference 1.)

#### TESTS

All the tests were made at a dynamic pressure of 16.37 pounds per square foot, corresponding to an air speed of about 80 miles per hour at standard sea-level conditions. The average test Reynolds Number, based on the airfoil chord, was 2,190,000. This test Reynolds Number, when converted to an effective Reynolds Number that takes account of the turbulence in the air stream, is 3,500,000. (Effective Reynolds Number=average test Reynolds Number $\times$ turbulence factor; turbulence factor for the tunnel is 1.6.)

Tests were made of the airfoil with the main slotted flap first neutral and then deflected various amounts along the optimum flap path shown in figure 2 (a). Each of the two auxiliary split flaps was next tested with deflections of 15°, 30°, 45°, and 60° for various deflections of the main slotted flap. Similar tests were then made of the auxiliary plain flap in combination with the main slotted flap.



The auxiliary slotted flap was deflected  $10^\circ$ ,  $20^\circ$ ,  $30^\circ$ ,  $40^\circ$ , and  $50^\circ$  with the main slotted flap set neutral, and surveys were made to determine the optimum auxiliary-flap positions and deflections for maximum lift and steep angles of climb. Surveys were also made to determine whether these positions changed with deflection of the main slotted flap, but no surveys were made to determine whether the optimum path of the main slotted flap changed with deflection of the auxiliary flap. The optimum path finally chosen for the auxiliary slotted flap is shown in figure 2 (b).

A sufficient number of angles of attack at each of the various deflections were investigated to determine envelope polars over the complete lift range from zero to maximum lift. Lift, drag, and pitching moments were measured for all positions of the flaps over the angle-of-attack range tested. No flap hinge moments or flap loads were obtained.

## RESULTS AND DISCUSSION

### COEFFICIENTS

All test results are given in standard section non-dimensional coefficient form as follows:

$c_l$ , section lift coefficient ( $l/qc_w$ ).

$c_{d0}$ , section profile-drag coefficient ( $d_0/qc_w$ ).

$c_{m(a.c.)_0}$ , section pitching-moment coefficient about aerodynamic center of plain airfoil ( $m_{(a.c.)_0}/qc_w^2$ ).

where

$l$  is section lift.

$d_0$ , section profile drag.

$m_{(a.c.)_0}$ , section pitching moment.

$q$ , dynamic pressure ( $1/2\rho V^2$ ).

$c_w$ , chord of basic airfoil with flap fully retracted.

and

$\delta_{f_1}$  is the setting of main slotted flap with respect to airfoil, degrees.

$\delta_{f_2}$ , setting of auxiliary flap with respect to main flap, degrees.

$\alpha_0$ , angle of attack for infinite aspect ratio.

### PRECISION

From repeat tests, the accidental experimental errors in the results presented herein are believed to lie within the following limits:

$\alpha_0$ -----	$\pm 0.25^\circ$
$c_{l_{max}}$ -----	$\pm 0.03$
$c_{m(a.c.)_0}$ -----	$\pm 0.003$
$c_{d0(c_l=0)}$ -----	$\pm 0.0003$
$c_{d0(c_l=1.0)}$ -----	$\pm 0.0006$
$c_{d0(c_l=2.5)}$ -----	$\pm 0.002$

Main-flap angle, $\delta_{f_1}$ -----	$\pm 0.3^\circ$
Main-flap position-----	$\pm 0.002c_w$
Auxiliary-flap angle, $\delta_{f_2}$ -----	$\pm 0.2^\circ$
Auxiliary-flap position-----	$\pm 0.001c_w$

The lift and the drag have been corrected for tunnel-wall effects, as explained in reference 1.

With certain arrangements of the main slotted flap with the auxiliary flap deflected, it was possible to obtain two sets of data, both of which are shown on the curves of section aerodynamic characteristics. Because of the innumerable possible combinations, the optimum nose path determined in reference 1 for the main flap was used. The slot opening for a main-flap deflection of approximately  $30^\circ$  in combination with some settings of the auxiliary flap seems to be critical since most of the double readings occurred with this arrangement. Undoubtedly, a more stable combination could have been found by adjusting the gap of the main flap but this procedure would have required more time than was available for these tests.

The profile-drag coefficient  $c_{d0}$  of the airfoil-flap combinations has not been corrected for the effects of the various flap-hinge fittings. From previous tests of the airfoil with the main slotted flap (reference 1), it was found that the drag of the fittings did not exceed 0.001. The main-flap fittings used in the present tests were smaller than those mentioned and, as the auxiliary-flap fittings of the present model were small, it was estimated that their drag would not exceed 0.001.

### SECTION AERODYNAMIC CHARACTERISTICS

**Main slotted flap.**—The section aerodynamic characteristics of the airfoil with only the main slotted flap are included as a basis for comparison (fig. 3). The present data agree well with those given in reference 1, the chief difference being that the maximum lift is about 3 percent lower for the model used in these tests. This difference may be attributed to the use of an entirely different model and to slight differences in the accuracy of the flap setting.

It should be noted that the drag coefficients given for all the arrangements with the flap neutral include the drag due to the breaks in the wing surface for the slot. If this drag increase is considered to be too great, it can be eliminated by the use of a door to close the openings for the flap-neutral condition. (See table II.)

**Airfoil with main slotted flap and auxiliary split flaps.**—Section aerodynamic characteristics of the airfoil with the slotted flap combined with the  $0.05c_w$  split flap are given in figures 4 to 8; similar data for the airfoil with the slotted flap and the  $0.10c_w$  split flap are given in figures 9 to 13. Envelope polar curves for these arrangement are plotted in figures 14 and 15.



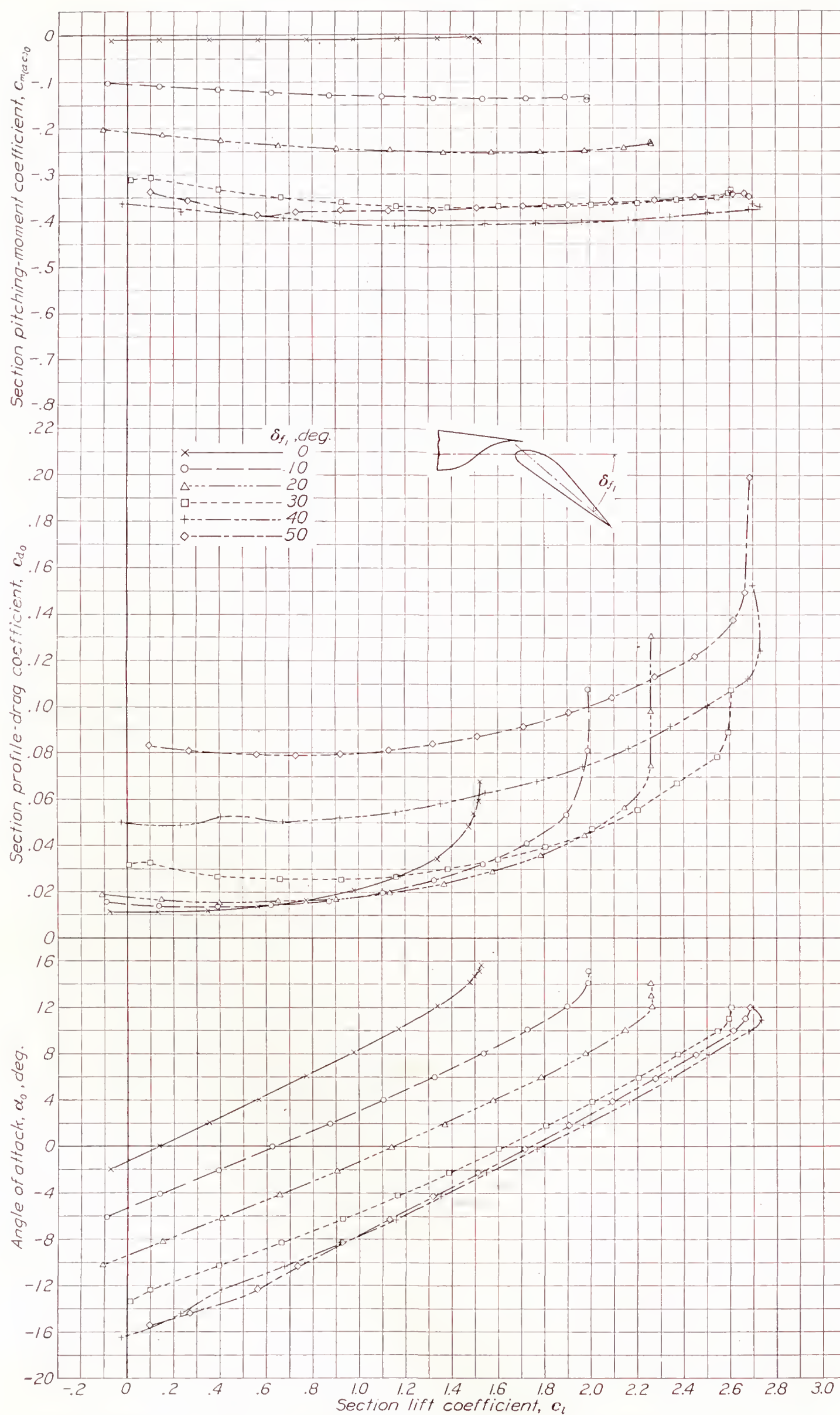


FIGURE 3.—Section characteristics of the N. A. C. A. 23012 airfoil with the main slotted flap deflected various amounts.



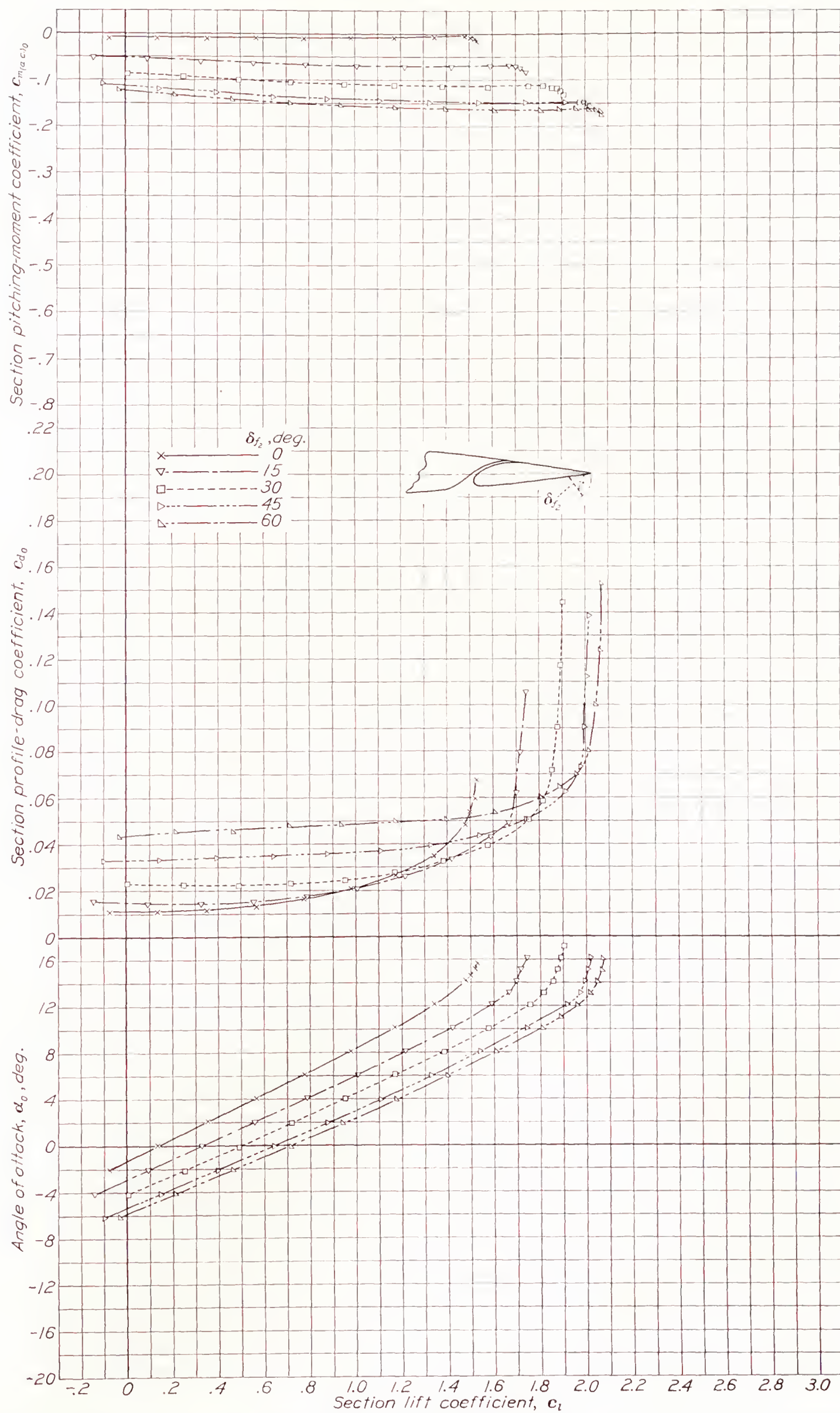


FIGURE 4.—Section characteristics of the N. A. C. A. 23012 airfoil with the main slotted flap deflected 0° and the auxiliary 0.05 $c_w$  split flap deflected various amounts.



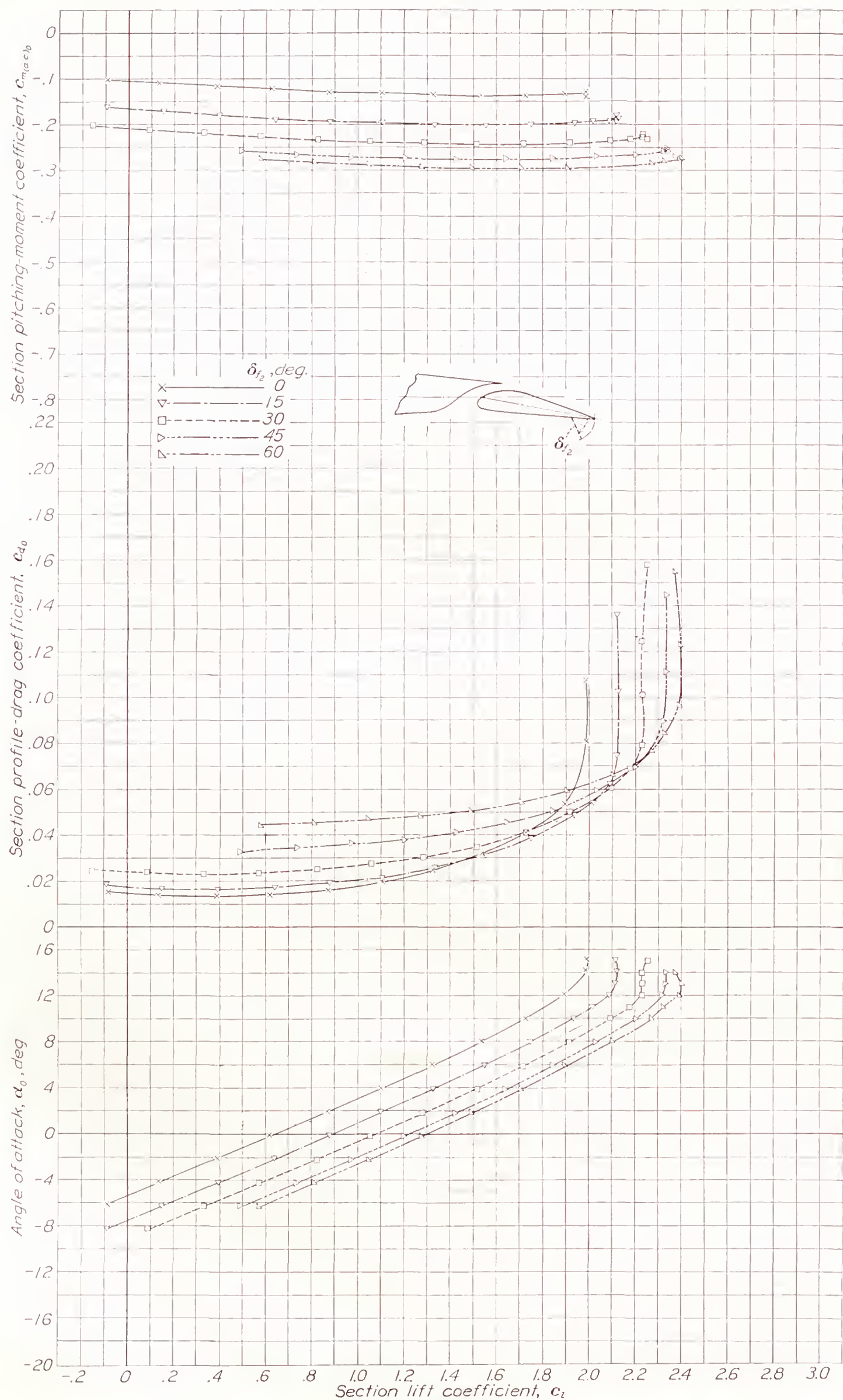


FIGURE 5.—Section characteristics of the N. A. C. A. 23012 airfoil with the main slotted flap deflected  $10^\circ$  and the auxiliary  $0.05c$  split flap deflected various amounts.



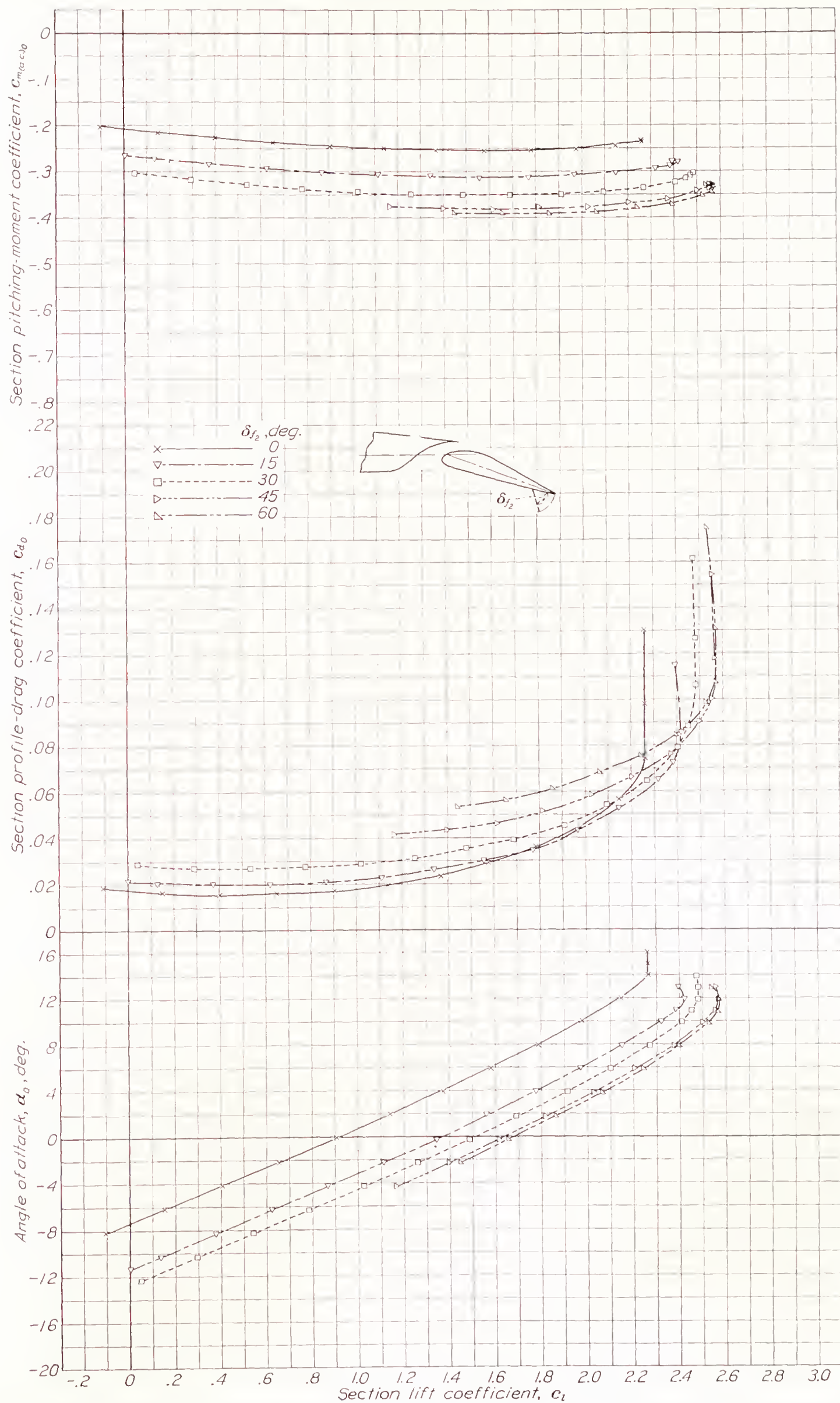


FIGURE 6.—Section characteristics of the N. A. C. A. 23012 airfoil with the main slotted flap deflected  $20^\circ$  and the auxiliary  $0.05c_w$  split flap deflected various amounts.



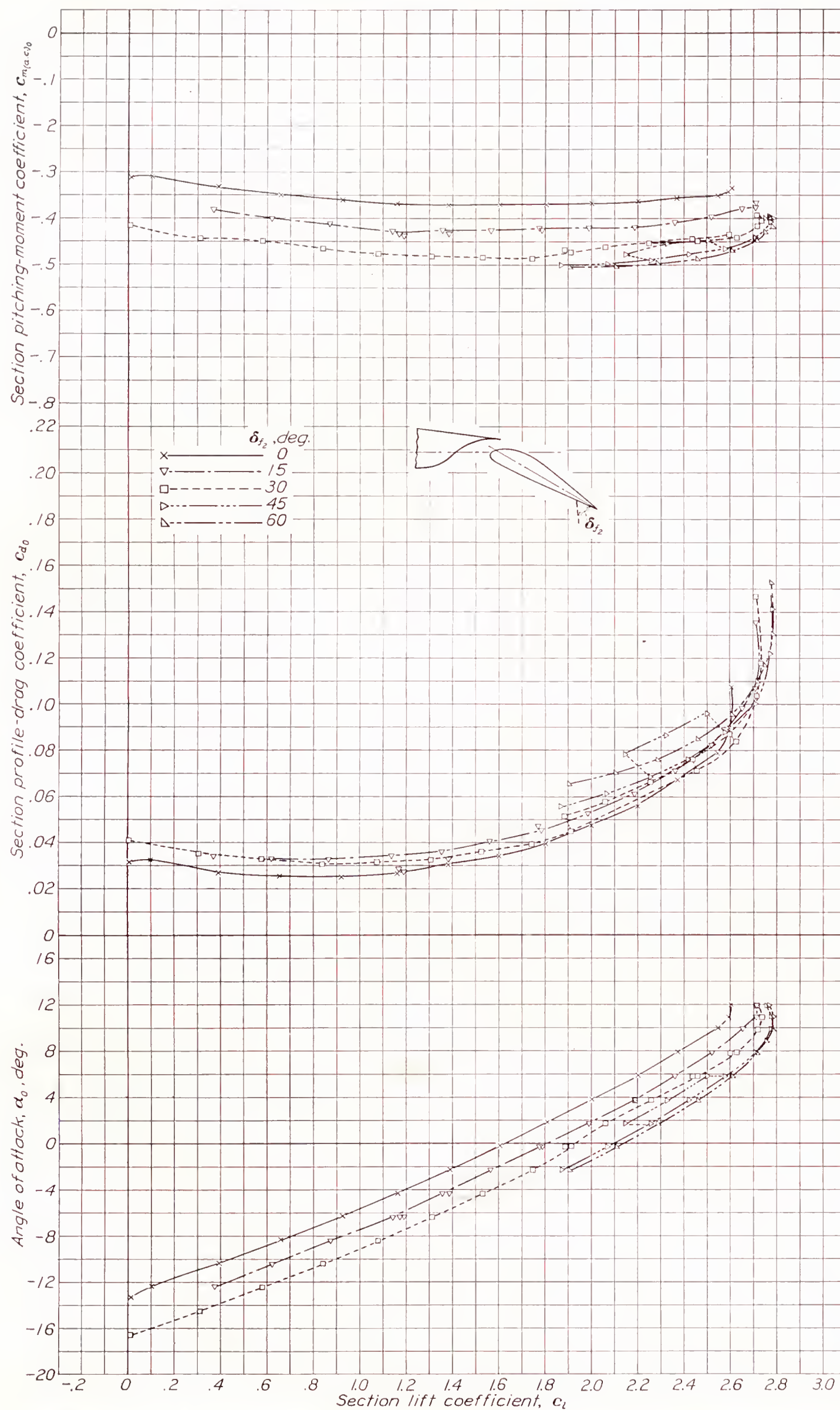
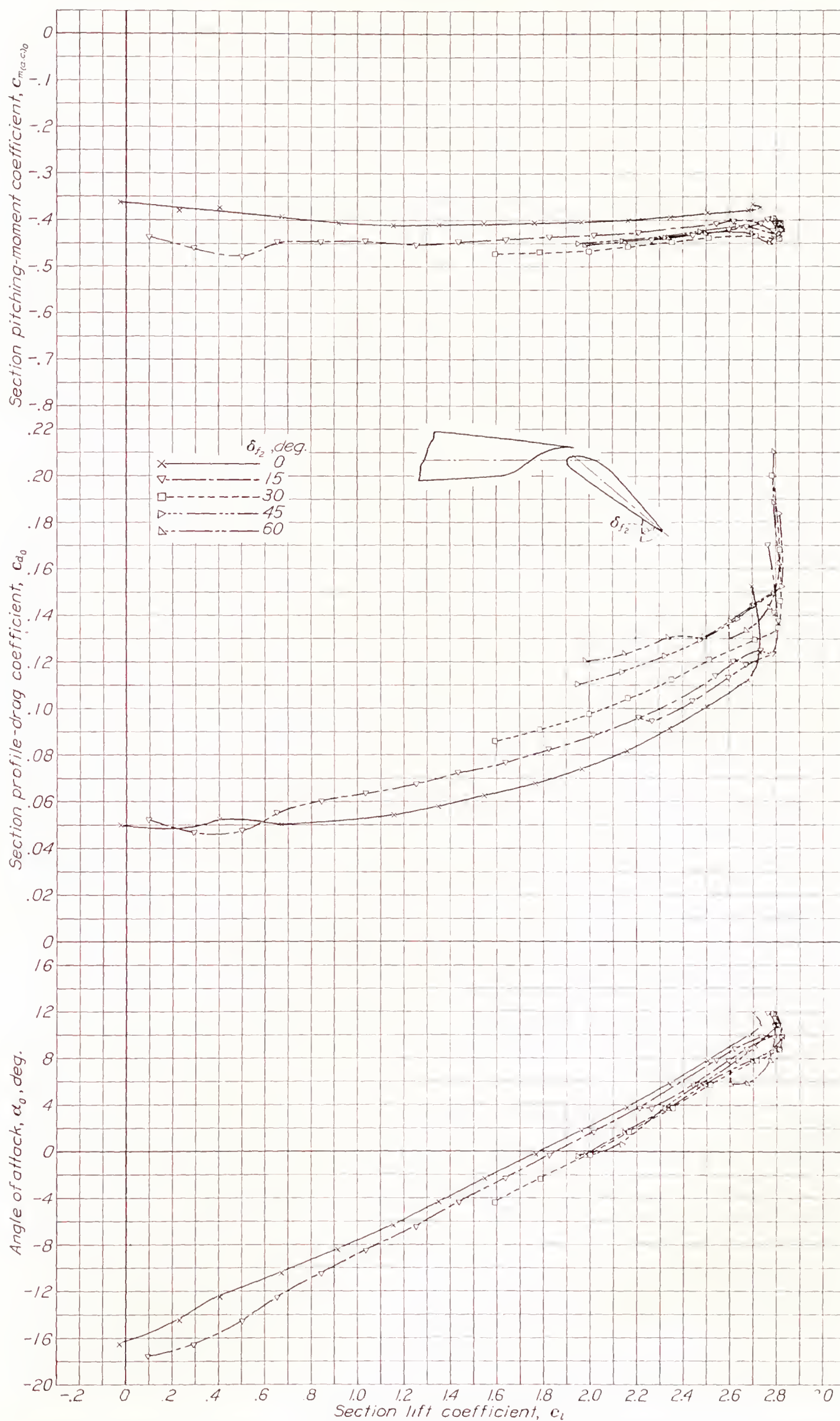


FIGURE 7.—Section characteristics of the N. A. C. A. 23012 airfoil with the main slotted flap deflected 30° and the auxiliary 0.05 $c_{\text{ch}}$  split flap deflected various amounts.



FIGURE 8.—Section characteristics of the N. A. C. A. 23012 airfoil with the main slotted flap deflected  $40^\circ$  and the auxiliary  $0.05c_w$  split flap deflected various amounts.



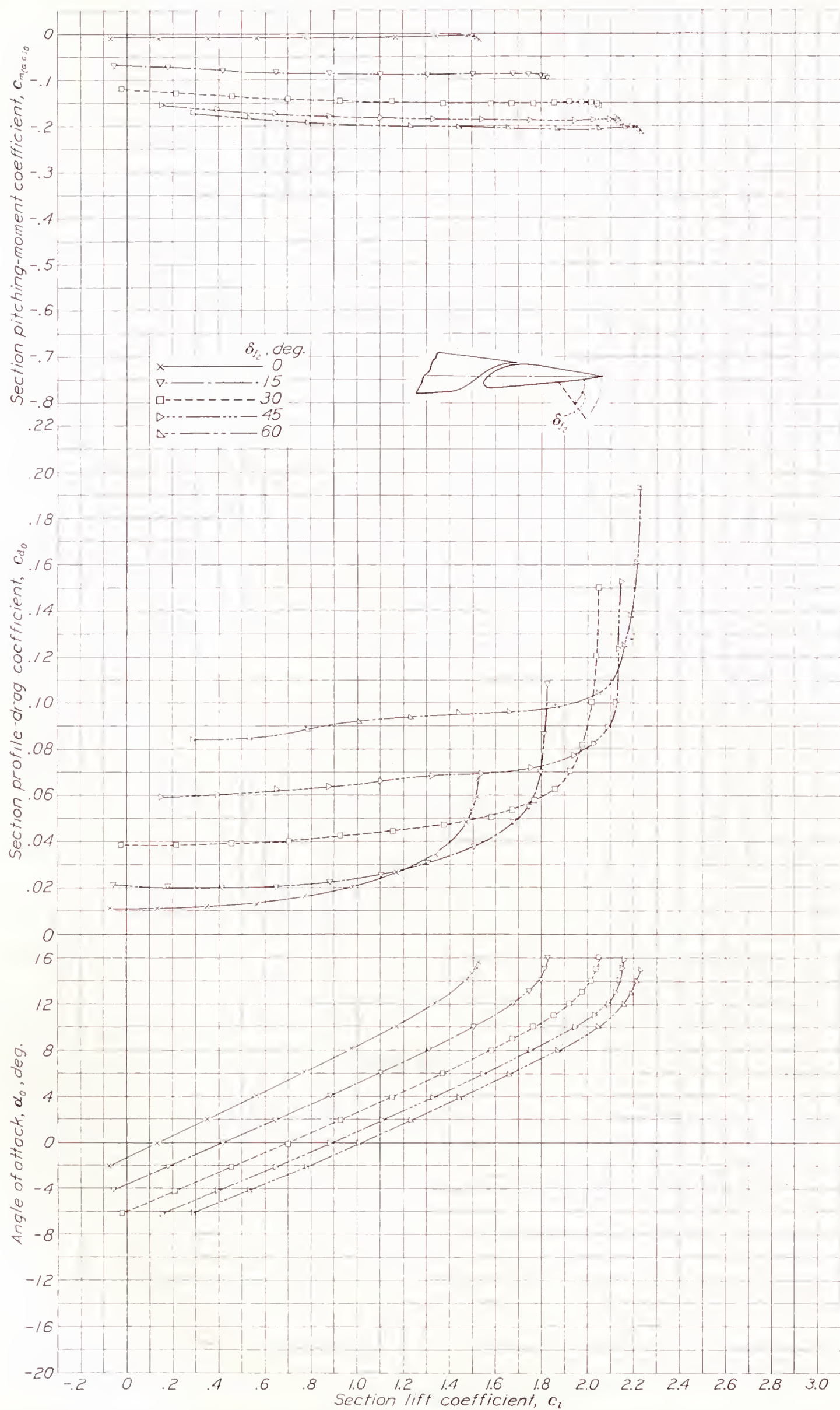


FIGURE 9.—Section characteristics of the N. A. C. A. 23012 airfoil with the main slotted flap deflected  $0^\circ$  and the auxiliary  $0.10c_w$  split flap deflected various amounts.



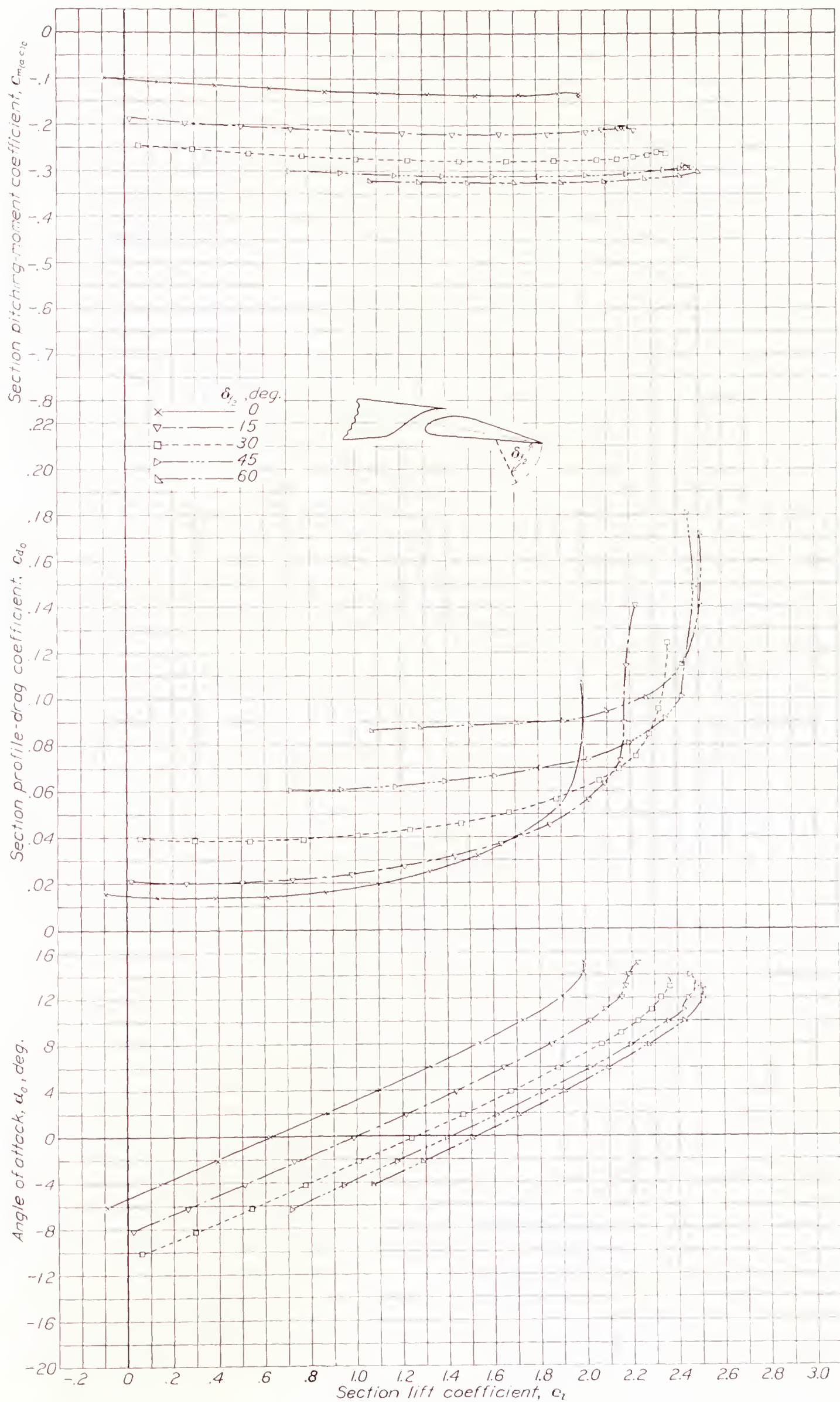


FIGURE 10.—Section characteristics of the N. A. C. A. 23012 airfoil with the main slotted flap deflected  $10^\circ$  and the auxiliary  $0.10c_w$  split flap deflected various amounts.



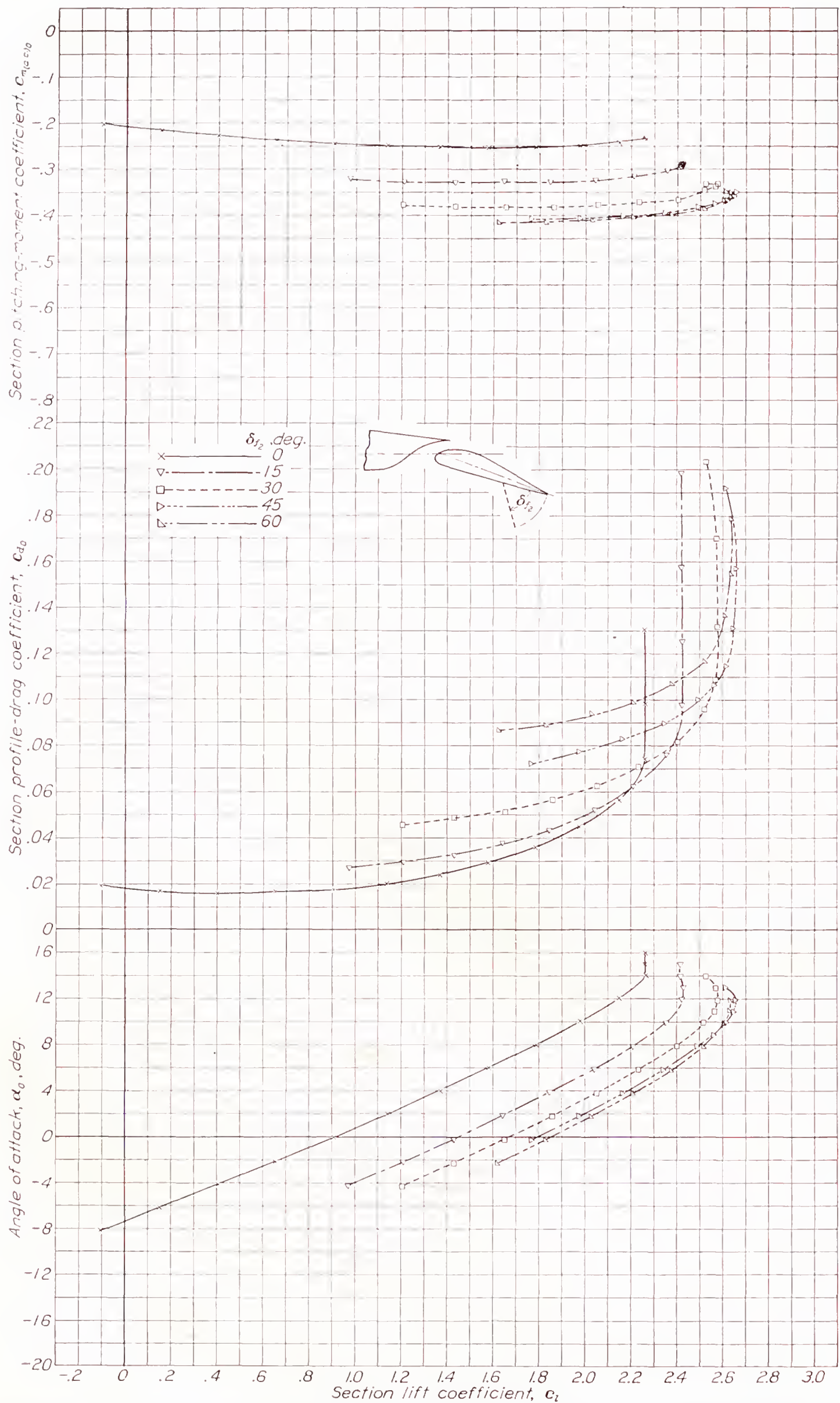
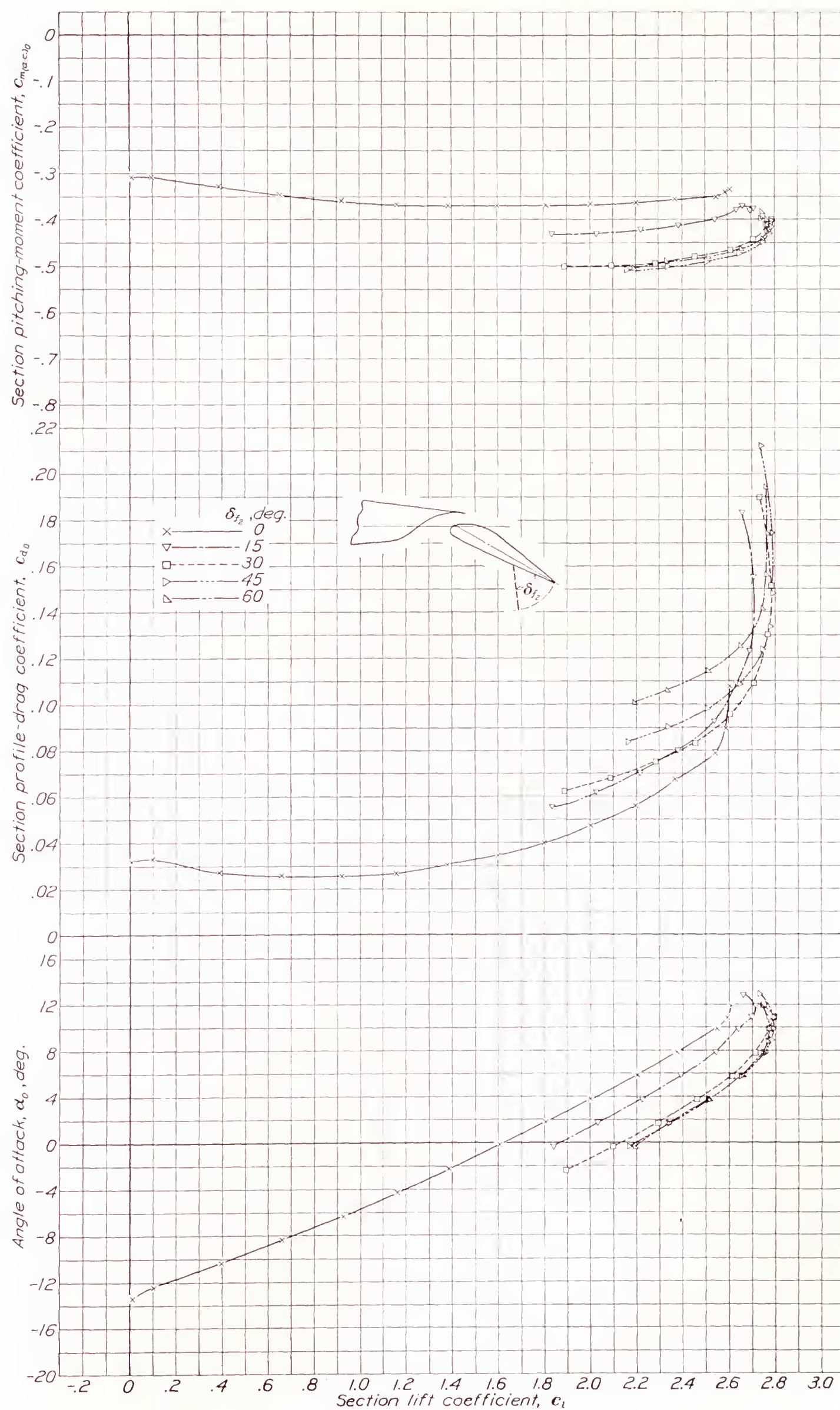


FIGURE 11.—Section characteristics of the N. A. C. A. 23012 airfoil with the main slotted flap deflected 20° and the auxiliary 0.10  $c_w$  split flap deflected various amounts



FIGURE 12—Section characteristics of the N. A. C. A. 23012 airfoil with the main slotted flap deflected 30° and the auxiliary 0.10c<sub>s</sub> split flap deflected various amounts



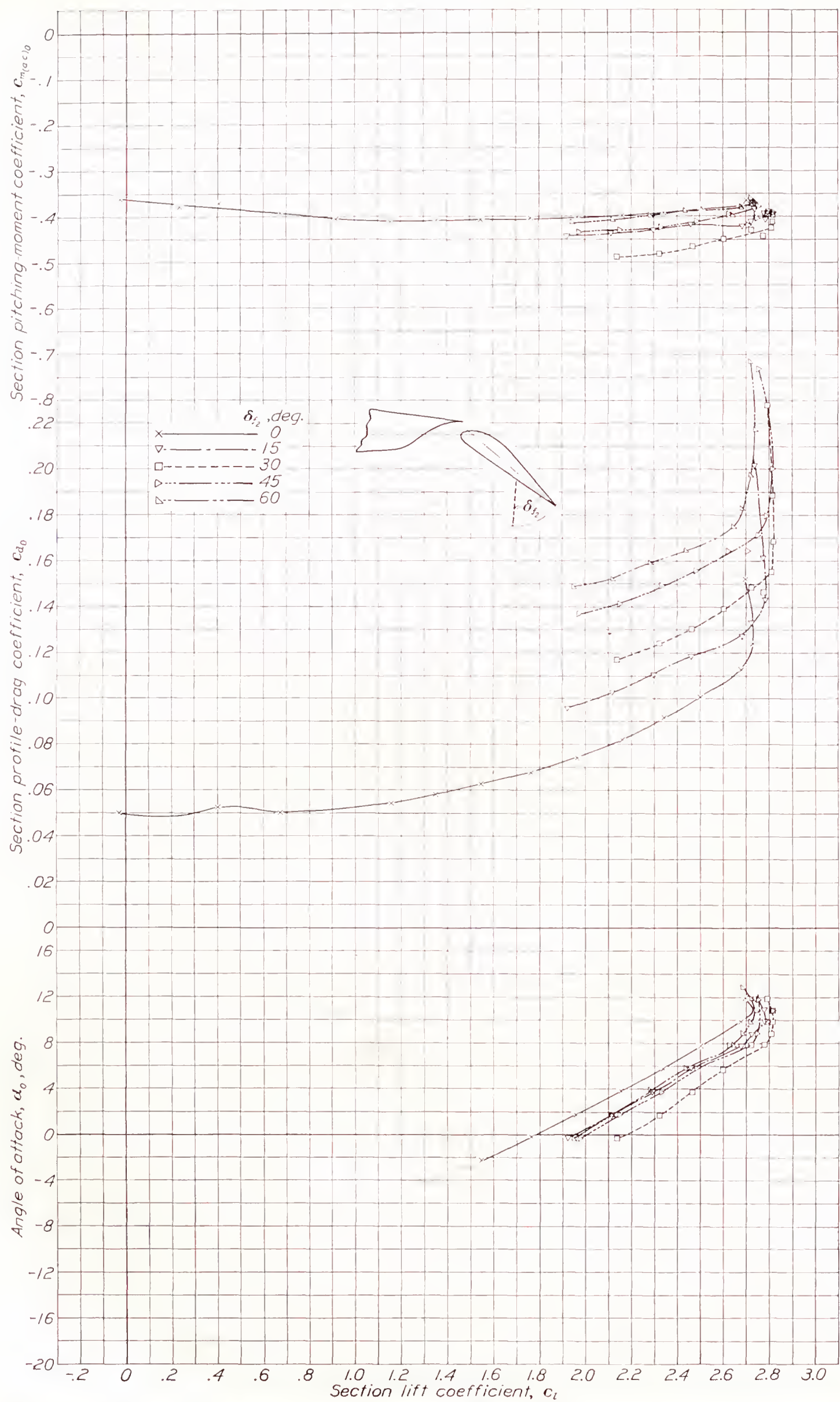
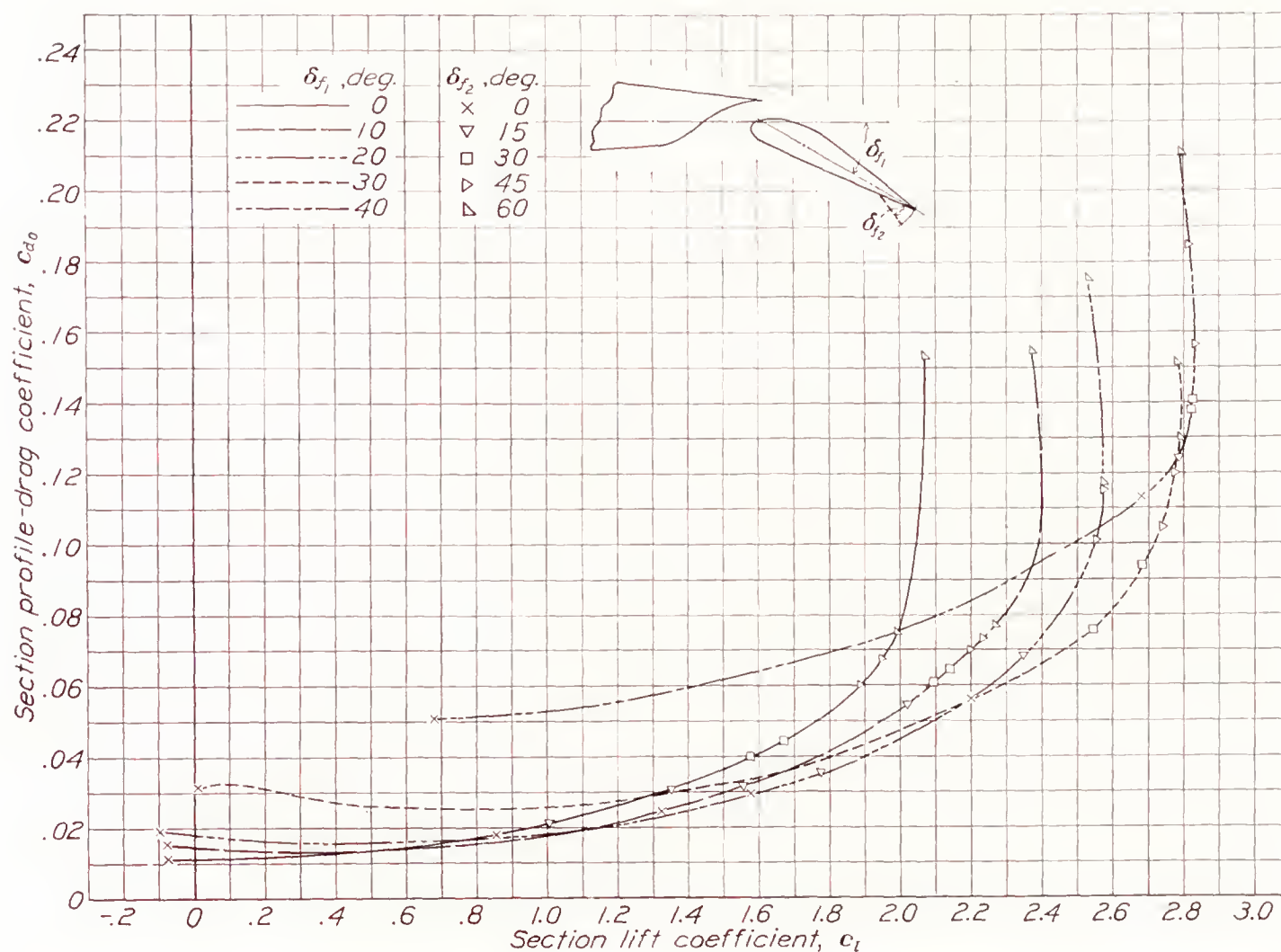
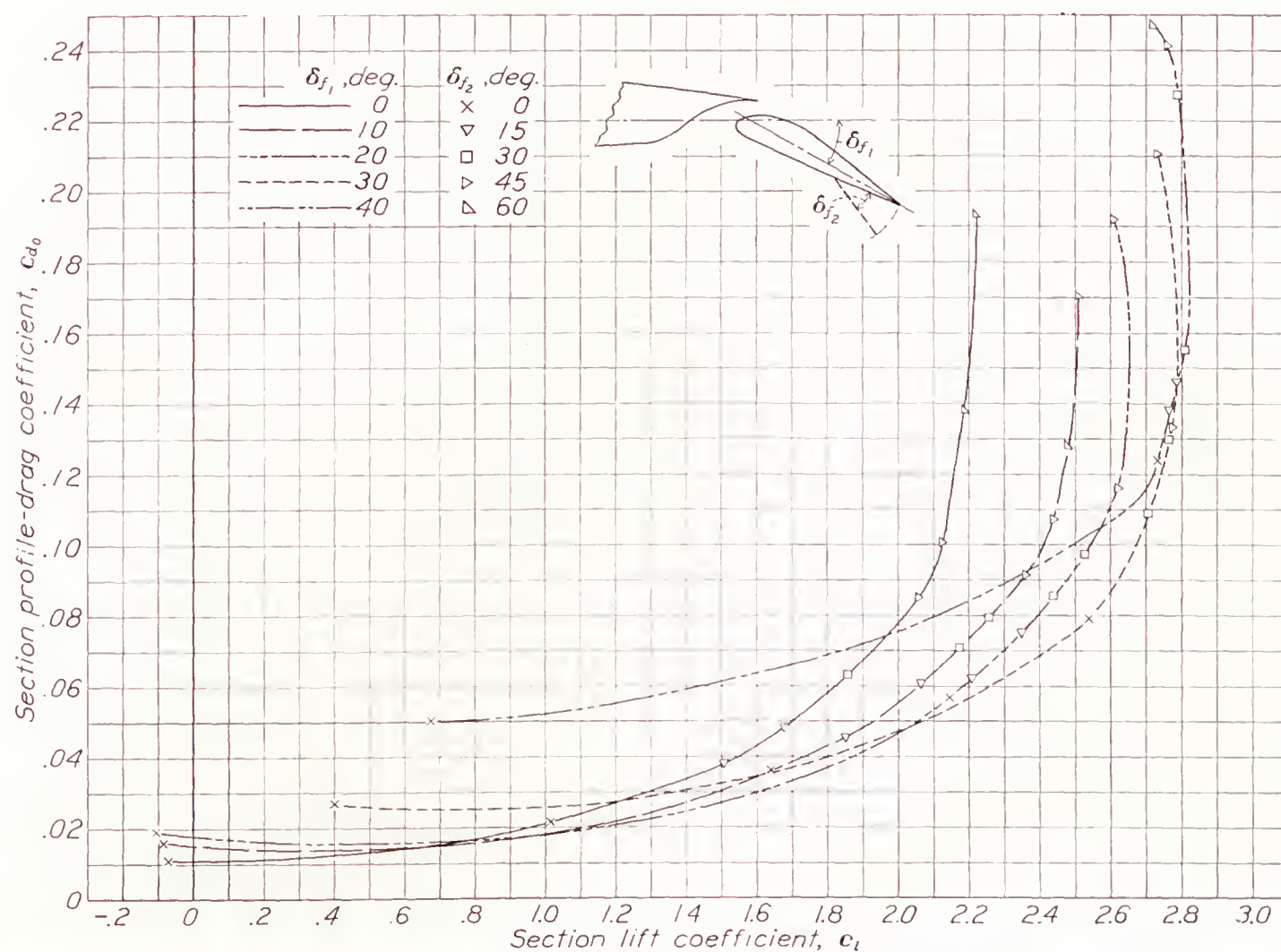


FIGURE 13.—Section characteristics of the N. A. C. A. 23012 airfoil with the main slotted flap deflected  $40^\circ$  and the auxiliary  $0.10c_w$  split flap deflected various amounts.



FIGURE 14.—Envelope polar curves for the N. A. C. A. 23012 airfoil with the main slotted flap and the auxiliary 0.05 $c_w$  split flap.FIGURE 15.—Envelope polar curves for the N. A. C. A. 23012 airfoil with the main slotted flap and the auxiliary 0.10 $c_w$  split flap.



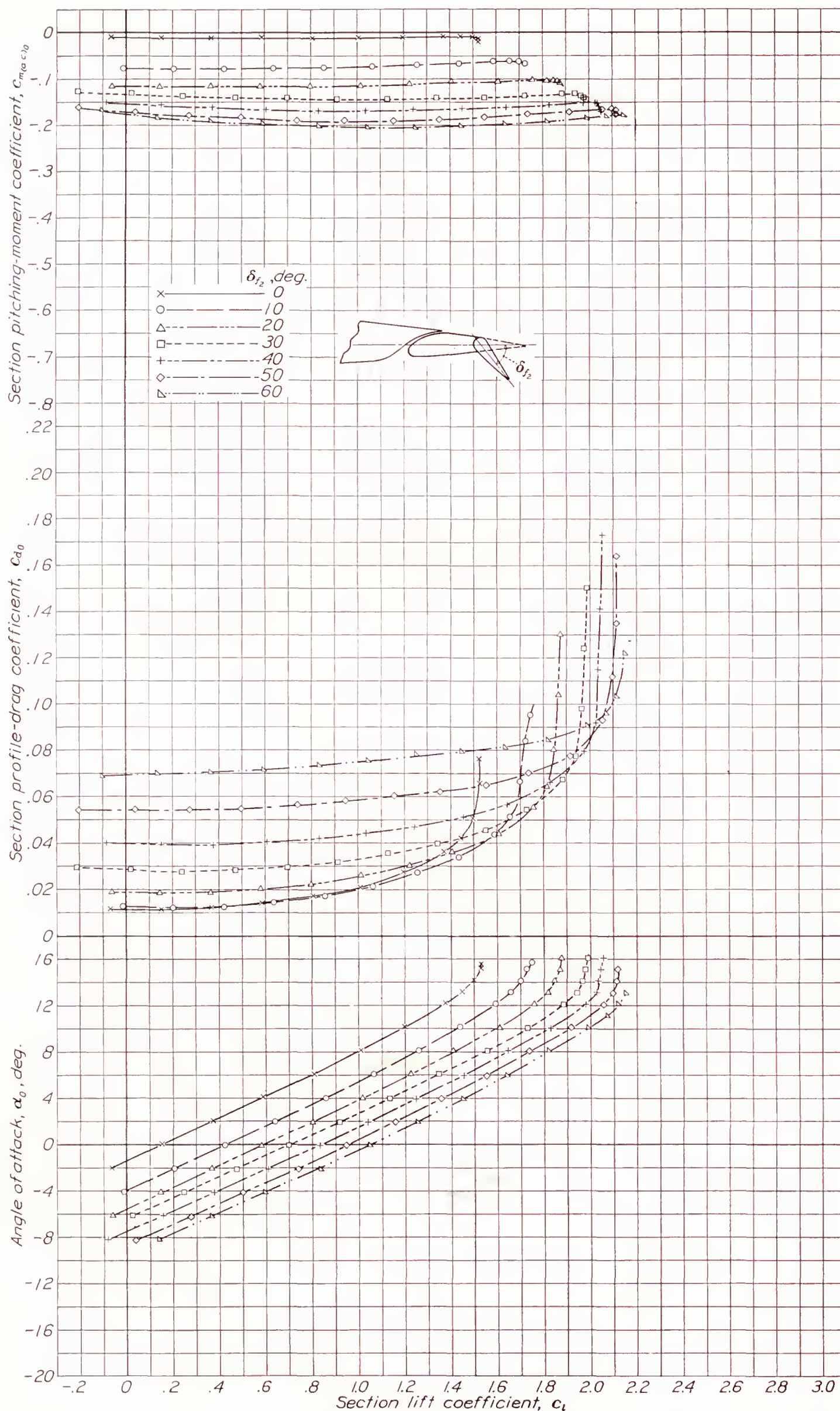


FIGURE 16.—Section characteristics of the N. A. C. A. 23012 airfoil with the main slotted flap deflected  $0^\circ$  and the auxiliary  $0.10c_w$  plain flap deflected various amounts



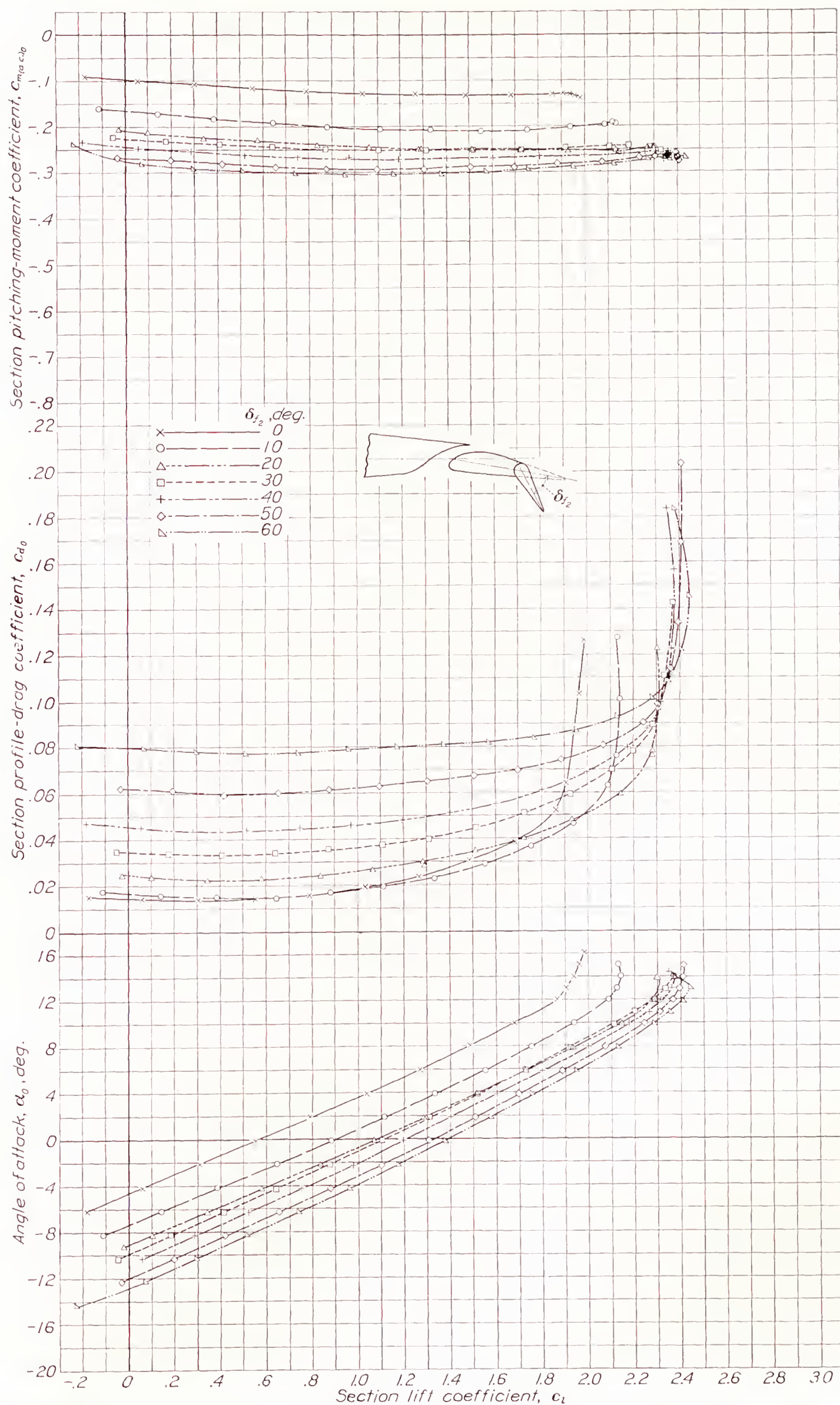


FIGURE 17.—Section characteristics of the N. A. C. A. 23012 airfoil with the main slotted flap deflected  $10^\circ$  and the auxiliary  $0.10c_w$  plain flap deflected various amounts.



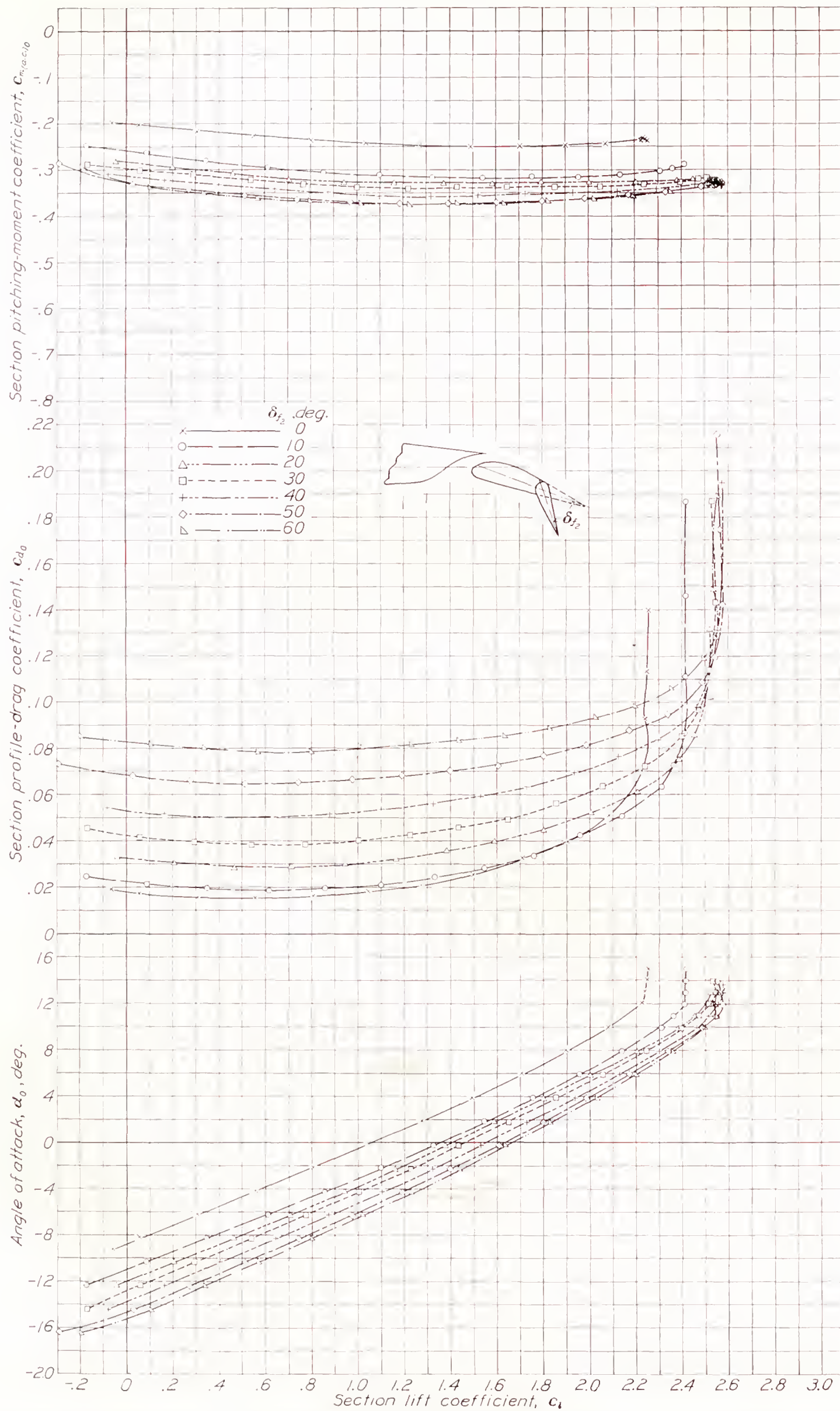


FIGURE 18.—Section characteristics of the N. A. C. A. 23012 airfoil with the main slotted flap deflected  $20^\circ$  and the auxiliary  $0.10c_w$  plain flap deflected various amounts.



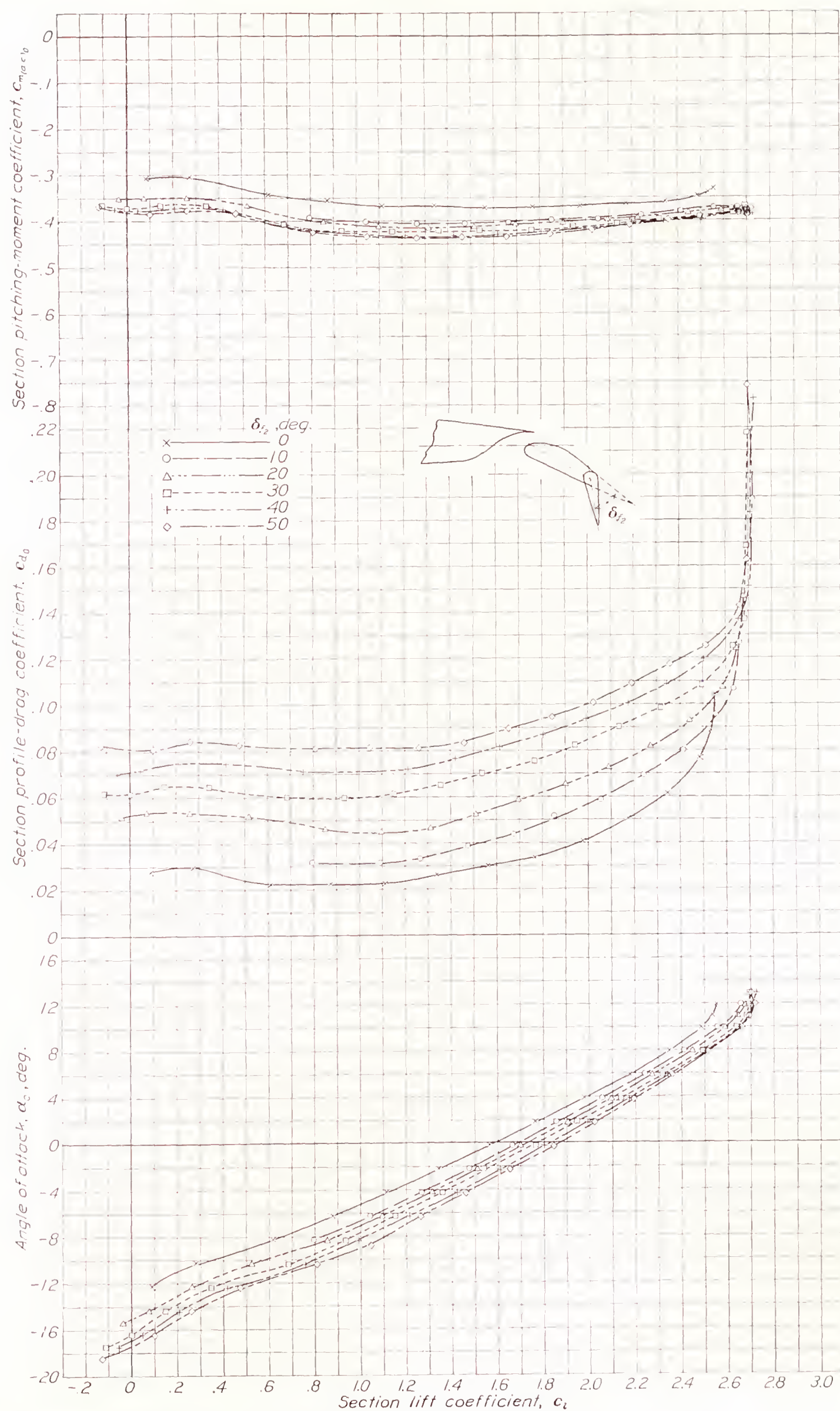


FIGURE 19.—Section characteristics of the N. A. C. A. 23012 airfoil with the main slotted flap deflected 30° and the auxiliary 0.10 $c_w$  plain flap deflected various amounts.



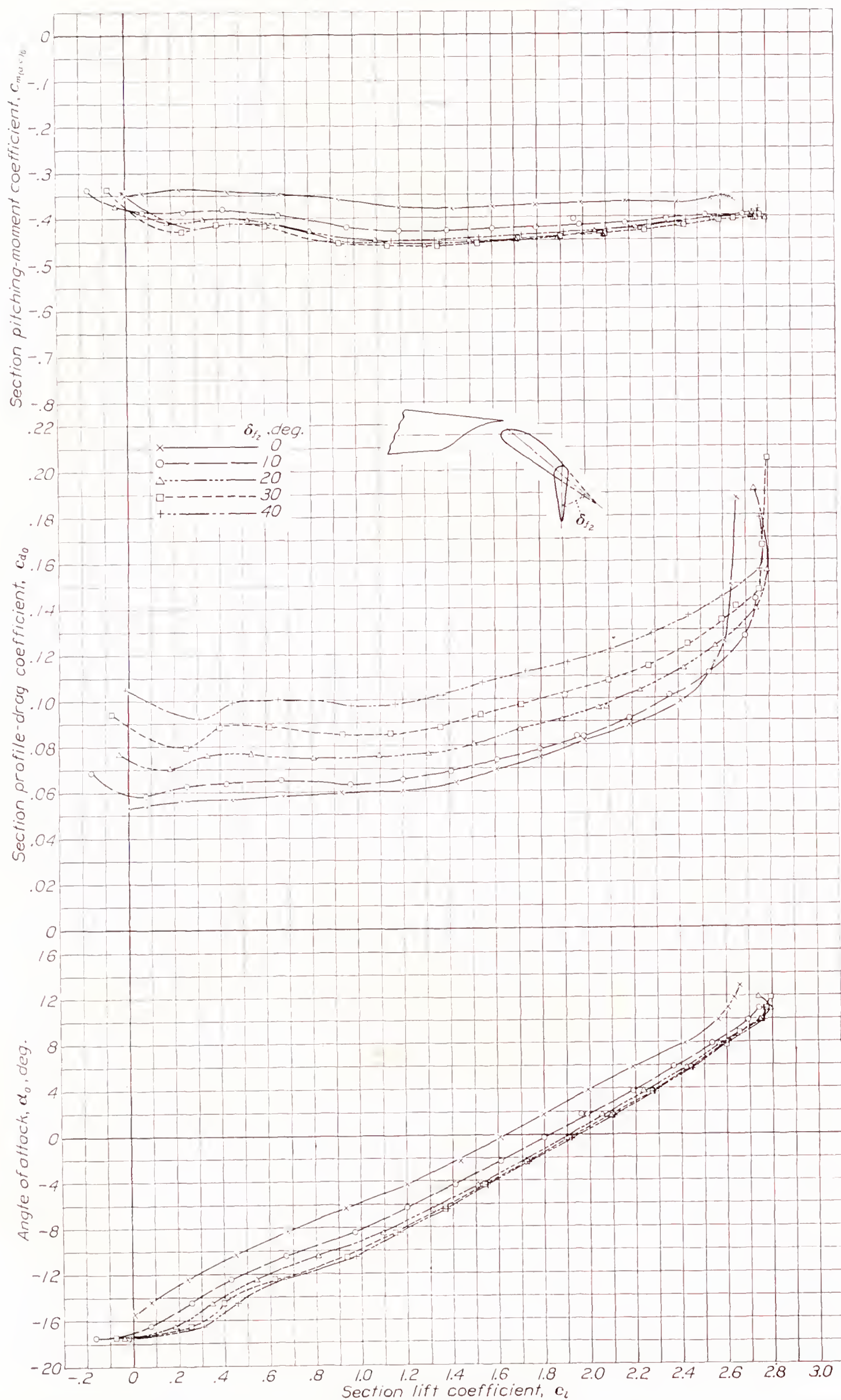


FIGURE 20.—Section characteristics of the N. A. C. A. 23012 airfoil with the main slotted flap deflected 40° and the auxiliary 0.10  $c_u$  plain flap deflected various amounts.



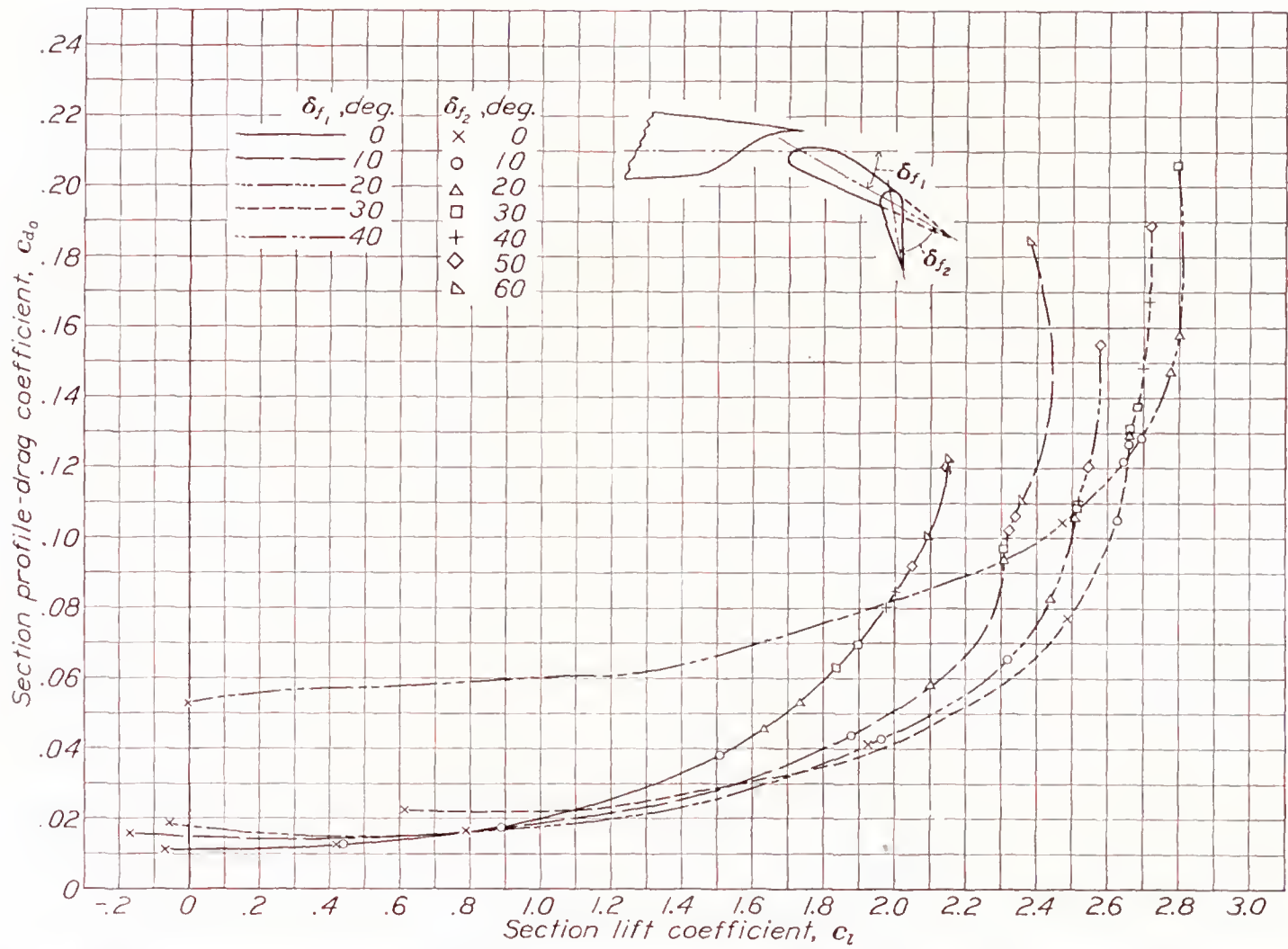


FIGURE 21.—Envelope polar curves for the N. A. C. A. 23012 airfoil with the main slotted flap and the auxiliary 0.10 $c_w$  plain flap.

Optimum path of auxiliary-flap nose for various flap deflections. Distances measured from lower edge of lip in percent of airfoil chord $c_w$		
$\delta_{f_2}$ (deg.)	$x$	$y$
0	3.22	1.58
10	.55	2.77
20	.32	2.50
30	.06	1.27
40	.25	.59
50	.42	.47

Optimum path of flap nose for figure 22.

Optimum path of auxiliary-flap nose for various flap deflections. Distances measured from lower edge of lip in percent of airfoil chord $c_w$		
$\delta_{f_2}$ (deg.)	$x$	$y$
0	3.22	1.58
10	1.55	1.52
20	1.32	1.50
30	1.06	1.50
40	.75	.59
50	.42	.47

Optimum path of flap nose for figure 23.

Optimum path of auxiliary-flap nose for various flap deflections. Distances measured from lower edge of lip in percent of airfoil chord $c_w$		
$\delta_{f_2}$ (deg.)	$x$	$y$
0	3.22	1.58
10	.55	1.77
20	.32	1.50
30	.06	1.27
40	.25	.59

Optimum path of flap nose for figure 24.



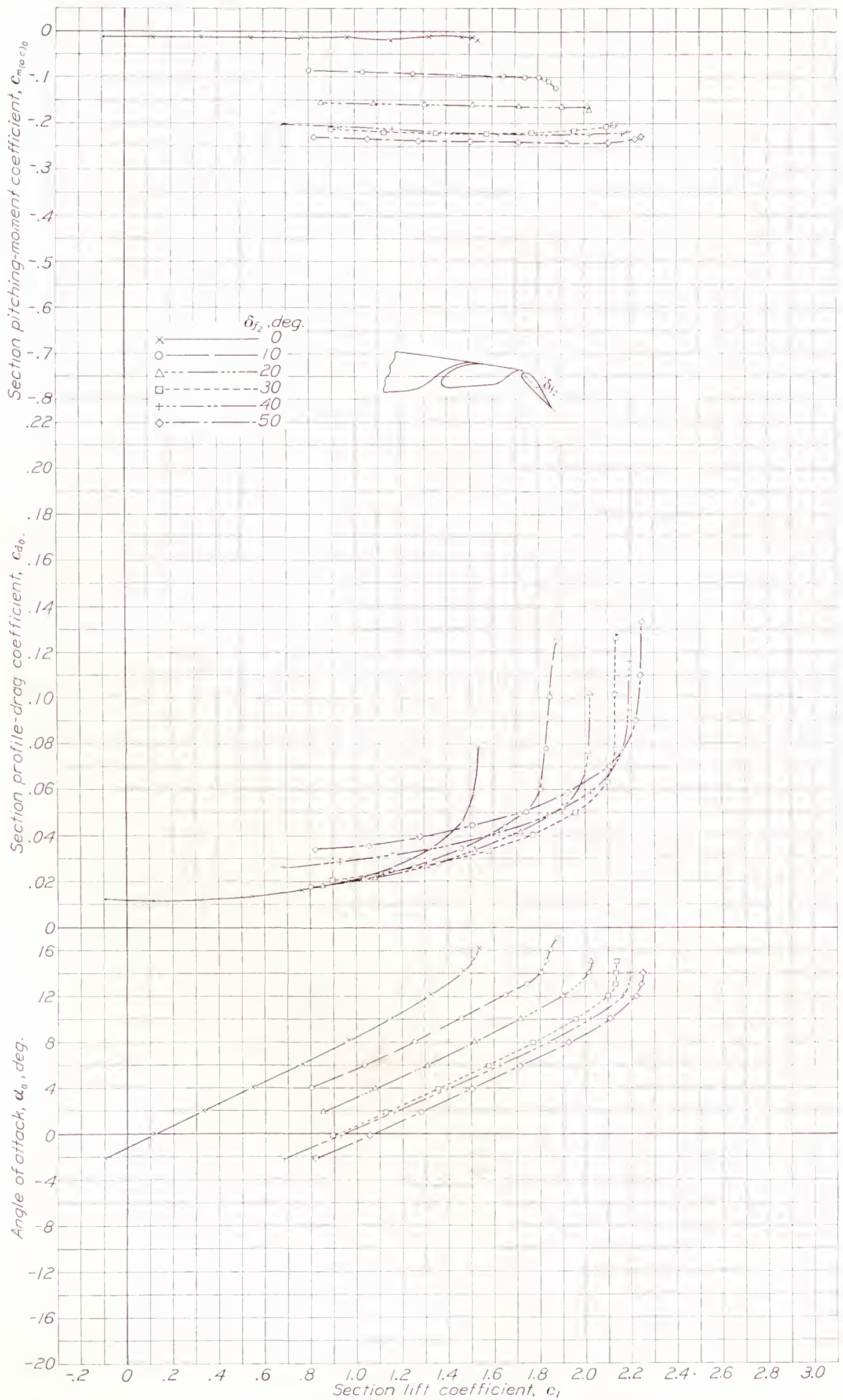
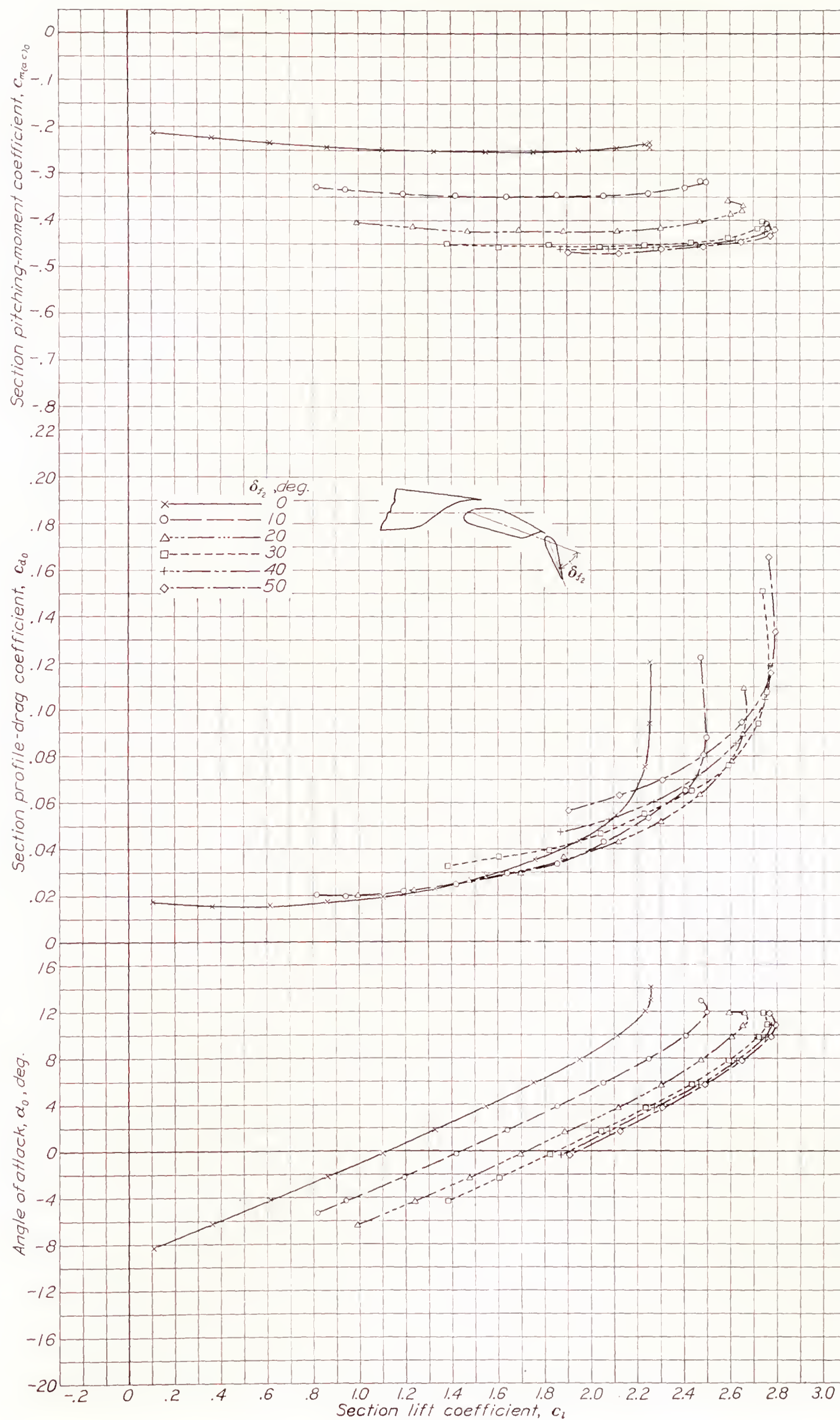


FIGURE 22.—Section characteristics of the N. A. C. A. 23012 airfoil with the main slotted flap deflected  $0^\circ$  and the auxiliary  $0.10c_w$  slotted flap deflected various amounts.



FIGURE 23.—Section characteristics of the N. A. C. A. 23012 airfoil with the main slotted flap deflected 20° and the auxiliary 0.10 $c_w$  slotted flap deflected various amounts.



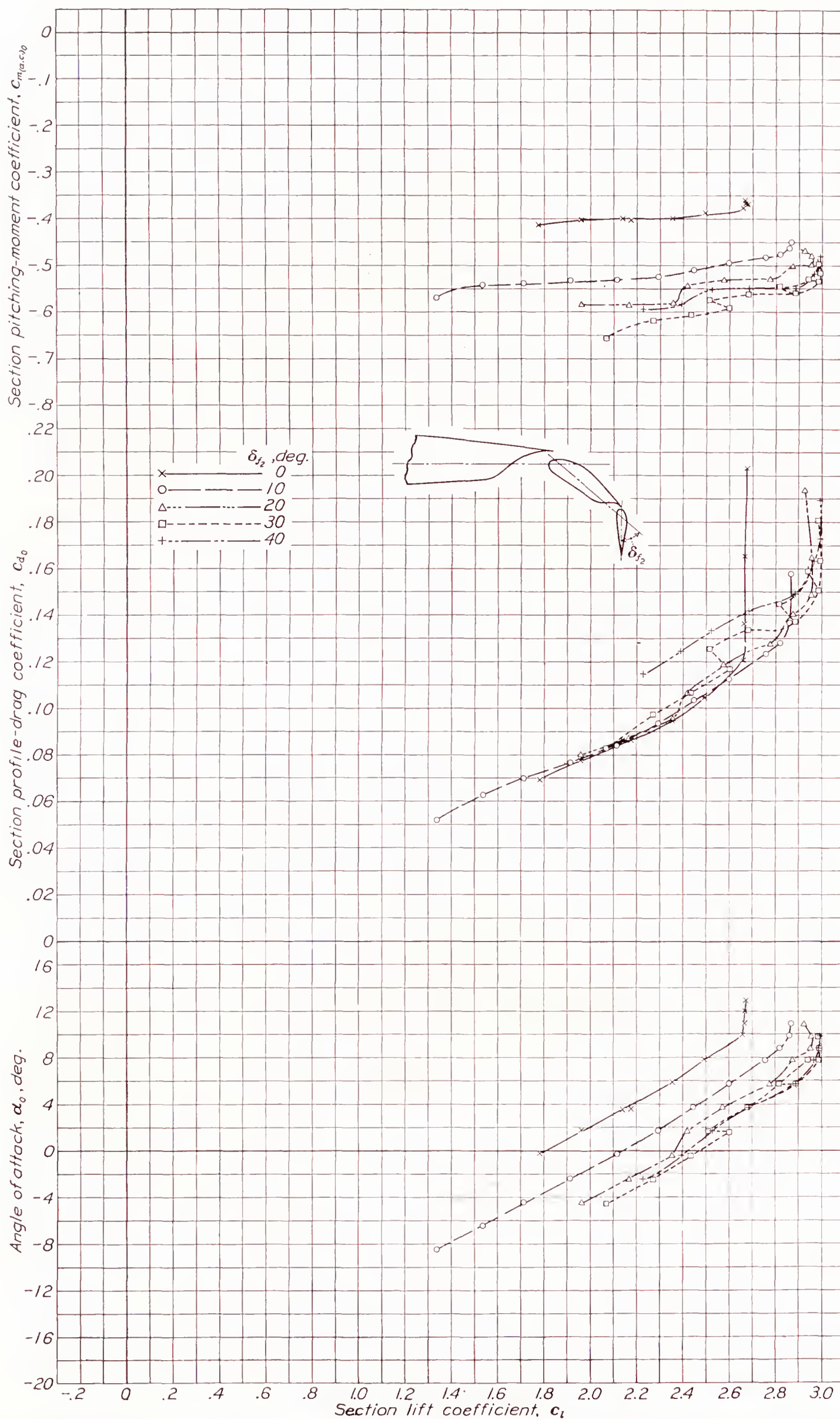


FIGURE 24 —Section characteristics of the N. A. C. A. 23012 airfoil with the main slotted flap deflected  $40^\circ$  and the auxiliary  $0.10c_w$  slotted flap deflected various amounts.



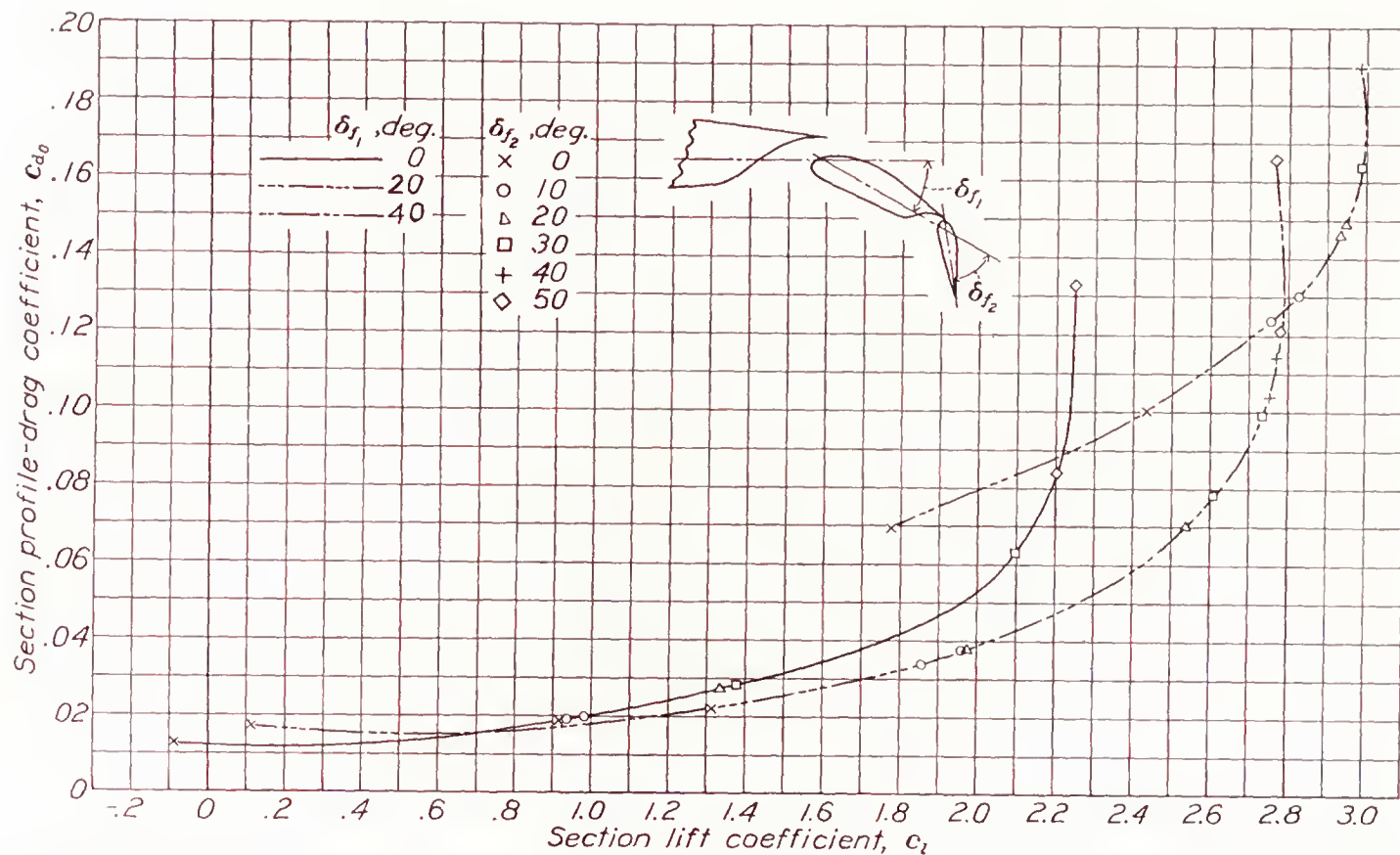
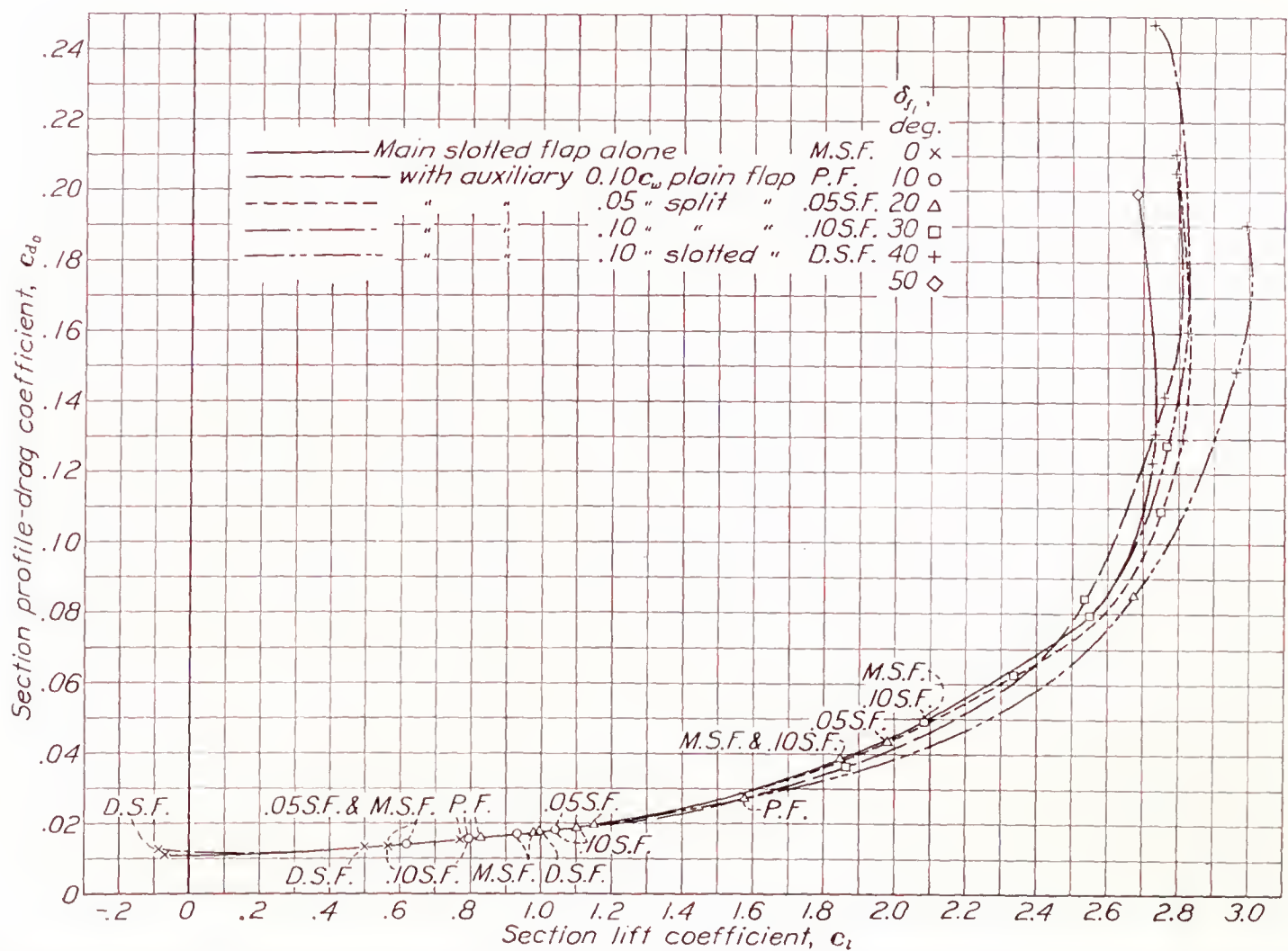
FIGURE 25.—Envelope polar curves for the N. A. C. A. 23012 airfoil with the main slotted flap and the auxiliary 0.10 $c_w$  slotted flap.

FIGURE 26.—Envelope of envelope polar curves for the N. A. C. A. 23012 airfoil with the main slotted flap and various auxiliary flaps.



The envelope polar curves provide a convenient method for the comparison of the lift and the drag characteristics at various deflections of the combination of main and auxiliary flaps. Each envelope curve shows, for the combination being considered, the lowest drag obtainable at a given lift coefficient for a fixed deflection of the main flap. Figure 14 indicates that the  $0.05c_w$  split flap will improve the effect of the main slotted flap alone for fixed main-flap deflections of  $10^\circ$ ,  $20^\circ$ ,  $30^\circ$ , and  $40^\circ$  when the split flap is deflected to give lift coefficients higher than 1.3, 1.6, 2.2, and 2.7. Similarly, figure 15 indicates that, for fixed main-flap deflections of  $10^\circ$ ,  $20^\circ$ ,  $30^\circ$ , and  $40^\circ$ , a beneficial effect will be obtained from the  $0.10c_w$  split flap when it is deflected beyond the corresponding lift coefficients of 1.7, 2.2, 2.6, and 2.75.

**Airfoil with main slotted flap and auxiliary plain flap.**—Section aerodynamic characteristics of the airfoil with the main slotted flap combined with the  $0.10c_w$  plain flap are given in figures 16 to 20, and envelope polar curves for the combination are plotted in figure 21. As for the combination of the slotted flap with the split flaps, some benefit is obtained. For fixed main-flap deflections of  $10^\circ$ ,  $20^\circ$ ,  $30^\circ$ , and  $40^\circ$ , figure 21 indicates that a beneficial effect will be obtained from the  $0.10c_w$  plain flap when it is deflected at lift coefficients beyond 0.8, 1.95, 2.5, and 2.5, respectively.

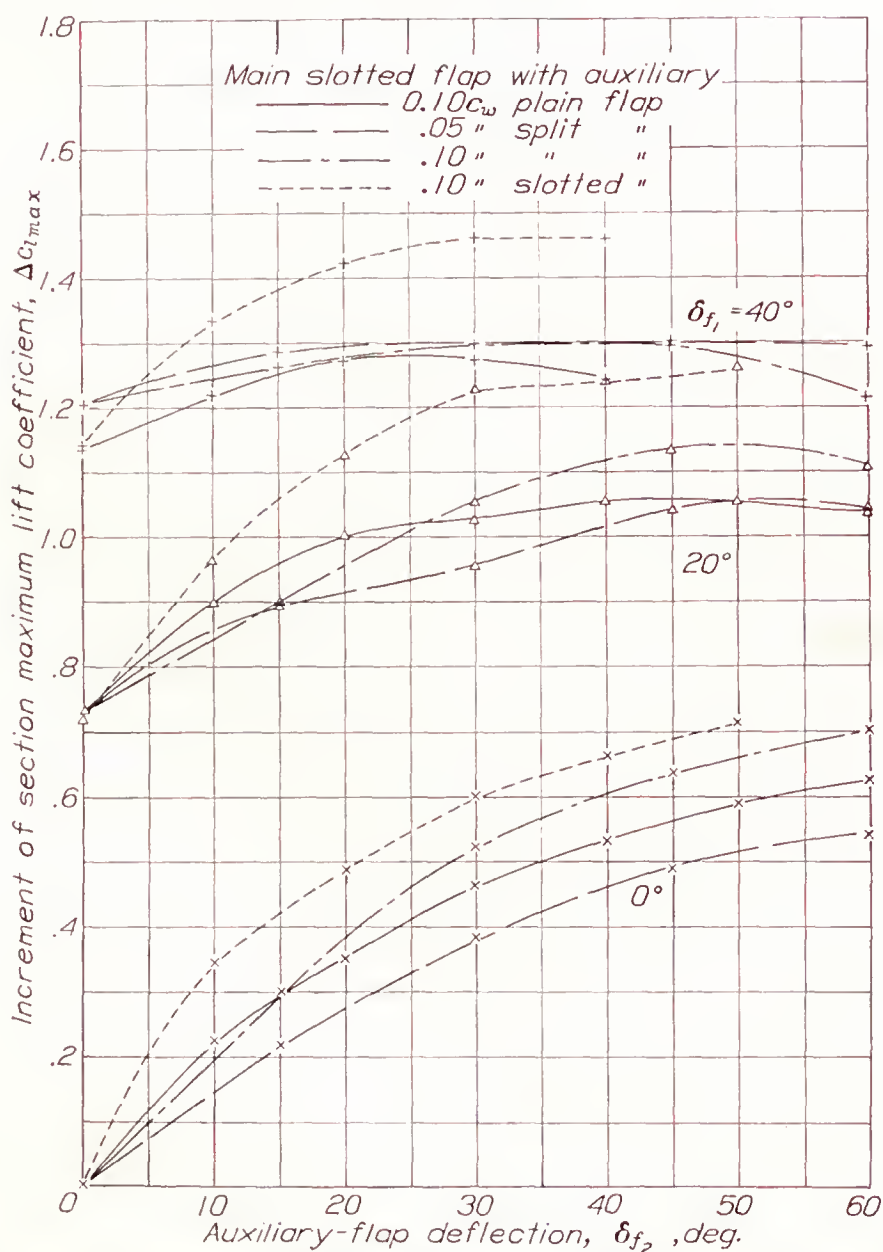


FIGURE 27.—Effect on section maximum-lift increment of various flap arrangements on the N. A. C. A. 23012 airfoil.

**Airfoil with main slotted flap and auxiliary slotted flap.**—Section aerodynamic characteristics of the airfoil with the main slotted flap combined with the auxiliary  $0.10c_w$  slotted flap are given in figures 22, 23, and 24; and envelope polar curves for the combination are plotted in figure 25. As previously mentioned, some preliminary tests were made to determine the optimum path of the auxiliary slotted flap for given deflections of the main flap; the optimum paths chosen are shown in figures 22, 23, and 24. A beneficial effect will be obtained from the auxiliary slotted flap for fixed main-flap deflections of  $20^\circ$  and  $40^\circ$  when the auxiliary flap is deflected at lift coefficients beyond 1.35 and 2.45.

#### COMPARISON OF THE FLAP ARRANGEMENTS TESTED

An envelope of each of the series of envelope polar curves given in figures 14, 15, 21, and 25 has been plotted for each flap arrangement in figure 26. This figure shows that, from lift coefficients of 1.1 up to the stall, the lift and the drag characteristics of the airfoil with the main slotted flap can be improved by the addition of an auxiliary flap of the split or slotted type. The auxiliary plain flap offers an improvement over only two portions of the lift range, between  $c_l=1.1$  and 2.45 and from 2.73 to the stall. The superiority of the main slotted flap with the auxiliary slotted flap for high lift with low drag, which is very important for take-off and steep angles of climb, is immediately evident. High lift with high drag for landing purposes could be obtained by deflecting the slotted flaps to angles greater than  $40^\circ$ .

The various flap arrangements tested are also compared in table II. A comparison is made of the profile-drag coefficients at several different lift coefficients with the corresponding pitching moments and flap deflections; in the last two columns are given the ratio of lift to drag at maximum lift (an indication of the steepest gliding angle available), and the ratio of maximum lift to the drag at a lift coefficient of 0.2 (criterion of the speed range). The main slotted flap with the auxiliary slotted flap also shows up favorably in these comparisons, except as regards the pitching moments. For nearly all conditions, this combination has the highest pitching moments of the arrangements tested and this characteristic must be given consideration in applications to design.

The effect of the various flap arrangements in increasing the maximum lift of the airfoil is shown in figure 27 where values of the maximum-lift increment  $\Delta c_{l_{max}}$  are plotted against deflections of the auxiliary flaps for given deflections of the main slotted flap. The superiority of the main slotted flap with the auxiliary slotted flap is immediately evident. It will be noted that, with the main slotted flap deflected  $40^\circ$  (its setting for  $c_{l_{max}}$ ) and the auxiliary slotted flap deflected  $30^\circ$  or  $40^\circ$ , an increase of 1.46 in the maximum lift coefficient is possible. This increase almost



doubles the maximum lift of the airfoil with flaps neutral, and still further increases might be expected with larger flaps and thicker airfoil sections. Further investigation along these lines is planned.

### CONCLUSIONS

1. The optimum arrangement of the main and the auxiliary flap combinations tested is the main slotted flap with the auxiliary slotted flap, which has more favorable characteristics than the single main slotted flap on the basis of maximum lift coefficient, low drag at moderate and high lift coefficients, and high drag at high lift coefficients.

2. The auxiliary split flap or the auxiliary plain flap combined with the main slotted flap slightly improves the aerodynamic characteristics of the wing and flap combination at high lift coefficients.

3. All auxiliary flaps tested in combination with the wing and the main flap increase the magnitudes of the pitching moments over those of the wing and the main slotted flap alone.

LANGLEY MEMORIAL AERONAUTICAL LABORATORY,  
NATIONAL ADVISORY COMMITTEE FOR AERONAUTICS,  
LANGLEY FIELD, VA., *October 31, 1938.*

### REFERENCES

1. Wenzinger, Carl J., and Harris, Thomas A.: Wind-Tunnel Investigation of an N. A. C. A. 23012 Airfoil with Various Arrangements of Slotted Flaps. T. R. No. 664, N. A. C. A., 1939.
2. Harris, Thomas A.: The 7 by 10 Foot Wind Tunnel of the National Advisory Committee for Aeronautics. T. R. No. 412, N. A. C. A., 1931.

TABLE I

#### ORDINATES FOR FLAP AND SLOT SHAPES

[Stations and ordinates in percent of airfoil chord]

Main slotted flap		
Station	Upper surface	Lower surface
0	-1.29	-1.29
.40	-.32	-2.05
.72	.04	-2.21
1.36	.61	-2.36
2.00	1.04	-2.41
2.64	1.40	-2.41
3.92	1.94	-----
5.20	2.30	-----
5.66	-----	-2.16
6.48	2.53	-----
7.76	2.63	-----
9.03	2.58	-----
10.31	2.46	-----
15.66	1.68	-1.23
20.66	.92	-.70
25.66	.13	-.13
Center of leading-edge arc: 0.91    -1.29		
Leading-edge radius: 0.91.		

Contour of main slot	
Station	Ordinate
72.32	-1.02
74.57	.67
76.32	1.76
77.82	2.30
79.32	2.65
80.82	2.82
82.70	2.64
Center of arc: 66.65    4.67	
Radius of arc: 7.97.	

Auxiliary slotted flap		
Station	Upper surface	Lower surface
0	-0.43	-0.43
.25	.06	-.84
.50	.31	-.92
.75	.49	-.98
1	.63	-1.00
1.50	.85	-1.02
2	.99	-1.00
2.50	1.08	-.96
3	1.12	-----
3.50	1.12	-----
4	1.06	-----
Center of leading-edge arc: 0.43    -0.43		
Leading-edge radius: 0.43.		

Contour of auxiliary slot	
Station	Ordinate
89.50	-0.86
89	-.48
90	.28
90.50	.66
91	.90
91.50	1.05
92	1.17
92.50	1.22
93	1.15
93.23	1.13
Center of arc: 89.59    1.52	
Radius of arc: 3.05.	

TABLE II

#### COMPARISON OF FLAP ARRANGEMENTS TESTED

$C_l$	$C_{d_0}$	$C_m(a.e.)_0$	$\delta f_1$ (deg.)	$\delta f_2$ (deg.)	$L/D$ at $C_{l_{max}}$	$\frac{C_{l_{max}}}{C_{d_0}(C_l=0.2)}$	
PLAIN N. A. C. A. 23012 AIRFOIL							
0 1.0 1.5 <sup>2</sup> 1.55	<sup>1</sup> 0.0088 .017 .037 .049	-0.010 -.010 -.010 -.015	----- ----- ----- -----	----- ----- ----- -----	31.62	176.2	
MAIN SLOTTED FLAP ALONE							
0 1.0 1.5 2.0 2.5 <sup>2</sup> 2.73	<sup>1</sup> 0.0110 .018 .027 .045 .076 .13	-0.110 -.130 -.246 -.253 -.265 -.352 -.370	0 10 20 20 20 30 40	----- ----- ----- ----- ----- ----- -----			21.00
WITH AUXILIARY 0.05 $c_u$ SPLIT FLAP							
0 1.0 1.5 2.0 2.5 <sup>2</sup> 2.83	<sup>1</sup> 0.0110 .018 .027 .045 .073 .16	-0.010 -.130 -.253 -.306 -.448 -.420	0 10 20 20 30 40	0 0 0 15 30 45	17.69	246.1	
WITH AUXILIARY 0.10 $c_u$ SPLIT FLAP							
0 1.0 1.5 2.0 2.5 <sup>2</sup> 2.82	<sup>1</sup> 0.0110 .018 .027 .046 .076 .17	-0.010 -.130 -.245 -.253 -.247 -.353 -.425	0 10 20 20 20 30 40	0 0 0 0 0 0 30			16.59
WITH AUXILIARY 0.10 $c_u$ PLAIN FLAP							
0 1.0 1.5 2.0 2.5 <sup>2</sup> 2.80	<sup>1</sup> 0.0114 .018 .026 .042 .079 .16	-0.015 -.240 -.250 -.367 -.345 -.402	0 20 20 30 30 40	0 0 0 0 0 20	17.50	243.5	
WITH AUXILIARY 0.10 $c_u$ SLOTTED FLAP							
0 1.0 1.5 2.0 2.5 <sup>2</sup> 3.00	<sup>1</sup> 0.0118 .018 .026 .039 .066 .17	-0.020 -.245 -.348 -.424 -.400 -.520	0 20 20 20 20 40	0 0 10 20 20 30			17.34

<sup>1</sup> Minimum drag.

<sup>2</sup> Maximum lift.







## REPORT No. 680

# THE EFFECT OF NACELLE-PROPELLER DIAMETER RATIO ON BODY INTERFERENCE AND ON PROPELLER AND COOLING CHARACTERISTICS

By JAMES G. McHUGH and ELDRIDGE H. DERRING

### SUMMARY

*An investigation was conducted in the N. A. C. A. 20-foot tunnel to determine the slipstream drag, the body interference, and the cooling characteristics of nacelle-propeller combinations with different ratios of nacelle diameter to propeller diameter. Four combinations of geometrically similar propellers and nacelles, mounted on standard wing supports, were tested with values of the ratio of nacelle diameter to propeller diameter of 0.25, 0.33, and 0.44.*

*The results show that (1) the effect of variation in the ratio of nacelle diameter to propeller diameter on propulsive efficiency is not important until the nacelle becomes approximately one-third of the propeller diameter but, beyond that point, the propulsive efficiency decreases rapidly with further increase in relative body size; (2) the net efficiency of a nacelle-propeller combination decreases rapidly with increasing values of the ratio of nacelle diameter to propeller diameter; (3) the presence of a spinner over the propeller hub increases the propulsive efficiency by an amount varying from  $1\frac{1}{2}$  to 4 percent; and (4) the maximum pressure drop available with adjustable cowling flaps is about 20 percent greater than the maximum pressure drop available with an adjustable-length cowling skirt.*

### INTRODUCTION

Considerable information has recently been made available concerning the propulsive and the cooling characteristics of a full-scale air-cooled radial-engine nacelle-propeller combination having a ratio of the nacelle diameter to the propeller diameter of approximately 0.43. Very little information is available concerning the effects of variation of that ratio on the slipstream drag, the body interference, and the efficiencies of a propeller-nacelle combination or on the cooling-air-flow characteristics of a nacelle-propeller combination.

Most present-day estimates of the variation in propulsive efficiency with the ratio of nacelle diameter to propeller diameter are based on the results reported in references 1 and 2. Those investigations were conducted with an uncowed radial engine and low-pitch propellers, and the results are not applicable to present practice. Only a few isolated tests are available for

determining the effect of variation in the ratio of nacelle diameter to propeller diameter on the cooling-air-flow characteristics.

In order to supply additional information on this subject, the N. A. C. A. has instituted an investigation of wing-nacelle-propeller interference and cooling characteristics. The investigation includes: (a) determinations of the drag and of the propeller and cooling characteristics of four combinations of geometrically similar model propellers and nacelles having values of the ratio of nacelle diameter to propeller diameter of 0.25, 0.33, and 0.44; and (b) determinations of the lift, the drag, and the propeller and cooling characteristics of the same combinations of propellers and nacelles operating in conjunction with a 5- by 15-foot N. A. C. A. 23018 airfoil. This report presents the results of part (a); part (b) is reported in reference 3.

The present report gives the results obtained from tests of geometrically similar 3-blade propellers of diameter  $D$  of 36 and 48 inches (3 and 4 feet) operating in conjunction with geometrically similar nacelles of diameter  $d$  of 12 and 16 inches, making possible the  $d/D$  ratios of 0.25, 0.33, and 0.44. Results obtained from other tests in which free-propeller conditions were approached are also presented. The effects of a variation in the ratio of nacelle diameter to propeller diameter on the propeller characteristics and on the slipstream drag as well as the effects of nacelle interference on propeller power and thrust are shown. Also included are the results of determinations of the cooling characteristics of all the combinations tested in addition to comparisons, on one nacelle, of adjustable cowling flaps with an adjustable-length cowling skirt as a means of controlled cooling.

### APPARATUS AND METHODS

The N. A. C. A. 20-foot wind tunnel in which these tests were conducted is described in reference 4. The tests were conducted at air speeds from 20 to 80 miles per hour.

Two geometrically similar sheet-aluminum nacelles, 12 and 16 inches in diameter (fig. 1), with nose 7 of reference 5 were used in the investigation.



The engine was simulated by fine-mesh wire screens, the resistance of which had been adjusted to give the desired conductivity. The conductivity was determined from measurements of the quantity of air flow through the cowling and of the pressure drop across the

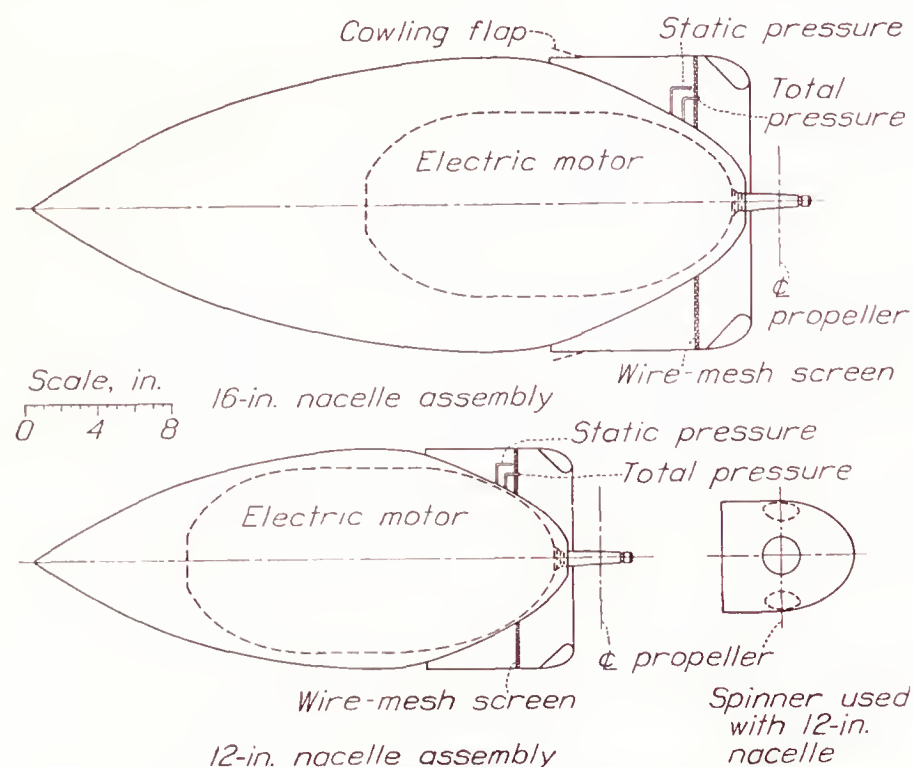


FIGURE 1.—Spinner and nacelle models used in propeller-nacelle investigation.

screens that simulated the engine. From these measurements, the conductivity  $K$  (reference 5) was found to be 0.085 for the 16-inch nacelle and 0.072 for the 12-inch nacelle.

For certain of the tests, the cowling-exit area of the 16-inch nacelle was varied both by adjusting the cowling flaps (fig. 1) and by reducing the length of the cowling skirt.

Two 3-blade propellers, 36 and 48 inches in diameter, having Clark Y sections and geometrically similar to propeller 6101 (reference 5) except for variable- instead of controllable-pitch hubs, were used in the investigation. The pitch of both propellers could be adjusted by turning the blades in the hub. For these tests, the blades were set at  $15^\circ$ ,  $20^\circ$ ,  $25^\circ$ ,  $30^\circ$ ,  $35^\circ$ , and  $40^\circ$  at 0.75 of the tip radius. Characteristic curves of blade width, blade thickness, and pitch distribution are given in figure 2.

The spinner shown in figure 1 was tested in conjunction with the 48-inch propeller and the 12-inch nacelle.

The propellers were driven by a water-cooled alternating-current induction motor, which developed 25 horsepower at 3,600 r. p. m. Current was supplied to the motor by a variable-frequency alternator and speed control was obtained by varying the frequency. The power output of the motor was obtained from a calibration involving motor torque, revolution speed, and active current.

The test set-ups were mounted in the air stream on the standard airfoil supports (reference 6) and all thrust and

drag forces were measured by automatic recording balances on the test-chamber floor.

For that portion of the test program in which it was desired to obtain free-propeller characteristics, the propeller was driven through a 3-foot extension shaft. The motor with its extension shaft was supported between the standard airfoil supports as shown in figure 3. The complete assembly was shielded from the air stream by a metal fairing that was supported from the fixed shields around the airfoil supports (fig. 4). The characteristics of the propeller alone when operating in the presence of the nacelles were obtained by attaching the nacelles to the extension-shaft fairing behind the propeller.

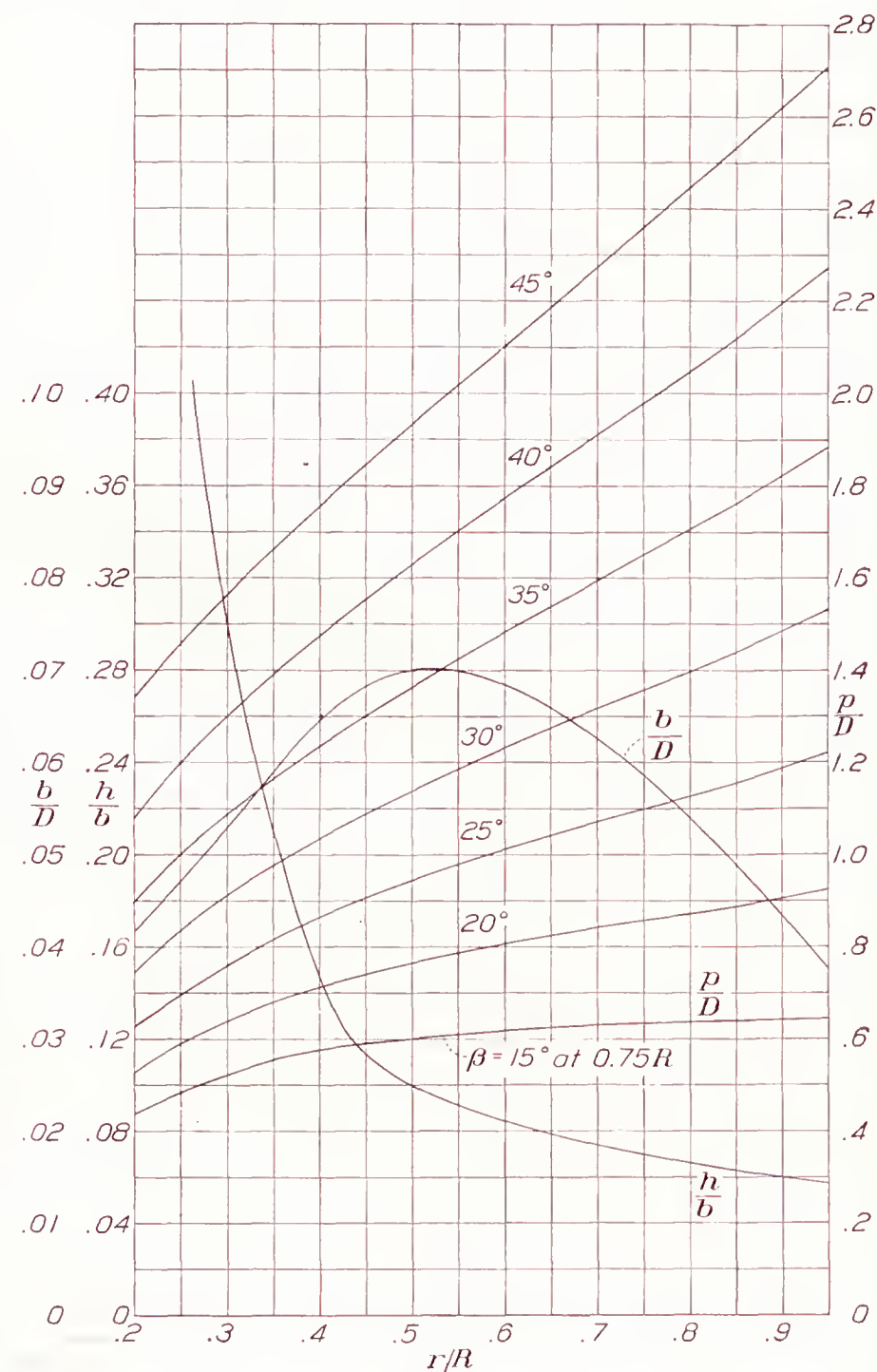


FIGURE 2.—Blade-form curves for propellers tested.  $D$ , diameter;  $R$ , radius to the tip;  $r$ , station radius;  $b$ , section chord;  $h$ , section thickness;  $p$ , geometric pitch;  $\beta$ , blade angle.

The extension shaft was not used for the tests of the nacelle-propeller units. The motor was built into the nacelle and was supported between the airfoil supports as shown in figure 3. At the beginning of this part of the test program, the supporting strut (which will subsequently be called strut 1) was large and made a bad intersection with the nacelle, thereby causing separation





The 12-inch nacelle.



The propeller alone.



The 12-inch nacelle with spinner.



The propeller in the presence of the 12-inch nacelle.



The 16-inch nacelle.



The propeller in the presence of the 16-inch nacelle.

FIGURE 3.—Nacelle arrangements tested.

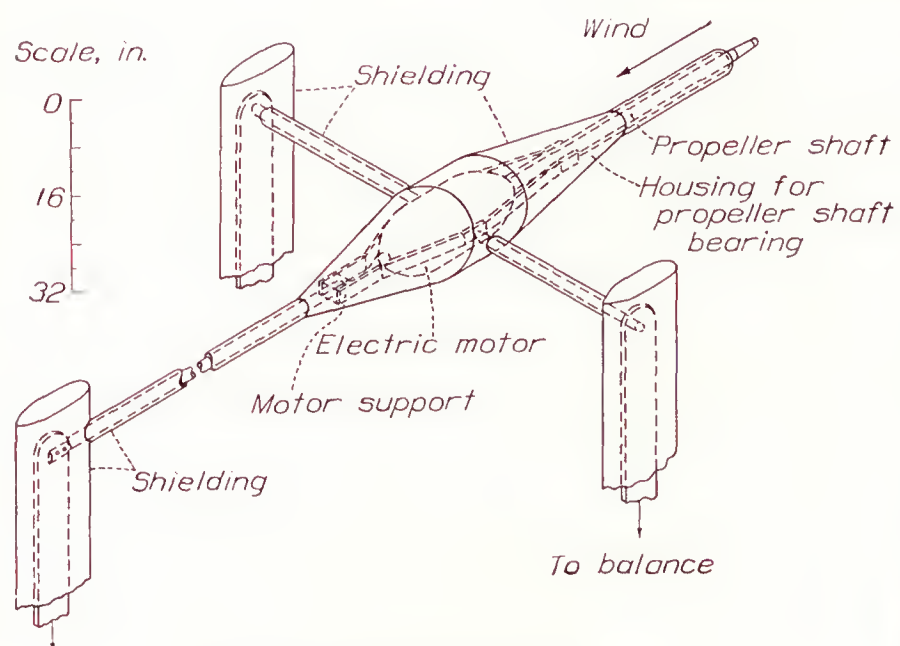


FIGURE 4.—Set-up for tests of free propeller.

of the air flow over all that portion of the nacelle behind the strut and producing unreasonably high values of the nacelle drag. Strut 1 was later replaced with a much

smaller strut (subsequently called strut 3), which was well filleted at its juncture with the nacelle and which gave no indication of causing separation of the air flow over the nacelle.

With each nacelle and cowling arrangement, a test was made with the propeller removed. Readings of the drag and of the pressure drop through the cowling were taken at various air speeds from 20 to 80 miles per hour. The propeller was then installed on the motor shaft, and tests were made with the propeller operating. During these tests, the propeller revolution speed was held constant and the air speed was varied until the maximum air speed available was reached; the air speed was then held constant and the propeller revolution speed was varied to cover the rest of the propeller operating range. Simultaneous readings of power, thrust, revolution speed, air speed, and pressure drop through the engine were taken at frequent intervals.



The tare drag of the supports was determined by attaching to the nacelle a single dummy strut, geometrically similar to the ones that supported the nacelle. Drag tests were made with and without the dummy strut in place. The tare drag was then determined on the assumption that the increase in drag due to the presence of the dummy strut was one-half of the total strut and interference drag. The tare drag with the propeller operating was not determined.

The nacelle arrangements tested are shown in figure 3.

The various combinations on which measurements of propeller characteristics were obtained are listed in the following table.

	Propeller diameter (in.)	Nacelle diameter (in.)	Cowling-flap angle (deg.)	Blade angle at 0.75R (deg.)					
				15	20	25	30	35	40
Motor and supports shielded.	36	No nacelle	-----	15	20	25	30	35	40
	36	12	0	15	20	25	30	35	40
	36	16	0	15	20	25	30	35	40
	48	No nacelle	-----	15	20	25	30	35	40
	48	12	0	15	20	25	30	35	40
	48	16	0	15	20	25	30	35	40
Motor and nacelle supported by strut 1.	36	16	0	15	20	25	30	35	40
	48	16	0	15	20	25	30	35	40
	48	16	5	15	20	25	-----	-----	-----
	48	16	10	15	20	25	-----	-----	-----
	48	16	15	15	20	25	-----	-----	-----
	48	16	20	15	20	25	-----	-----	-----
Motor and nacelle supported by strut 3.	36	12	0	15	20	25	30	35	40
	48	12	0	15	20	25	30	35	40
	48	12	0	15	20	25	30	35	40
	48	12	0	15	20	25	30	35	40
	48	12	0	15	20	25	30	35	40
	48	12	0	15	20	25	30	35	40

<sup>a</sup> With spinner.

In order to determine the relative drag and the cooling-air-flow characteristics of the nacelle when the cowling-exit area was varied, additional tests with propeller removed were made of the 16-inch nacelle. The tests were made with the cowling flaps (fig. 1) set at different angles and with a series of cowlings with different skirt lengths.

#### SYMBOLS AND COEFFICIENTS

The symbols and coefficients used in the report are defined as follows:

- $q$ , dynamic pressure of air ( $\frac{1}{2}\rho V^2$ ).
- $\rho$ , mass density of air.
- $V$ , velocity of air stream.
- $n$ , propeller revolution speed.
- $Q$ , aerodynamic torque of propeller.
- $D_n$ , drag of cowling-nacelle unit with propeller removed.
- $\Delta D$ , change in body drag due to propeller slipstream.
- $R$ , net force on thrust balance.
- $T$ , thrust of propeller operating in presence of body (tension in crankshaft).
- $T_f$ , propeller thrust in free air (no body).
- $\Delta T$ , change in propeller thrust due to influence of body ( $T - T_f$ ).

$d$ , diameter of body behind propeller.

$D$ , diameter of propeller.

$d/D$ , ratio of nacelle diameter to propeller diameter.

$P$ , power supplied to propeller ( $2\pi Qn$ ).

$\beta$ , propeller blade angle at 0.75 radius.

$C_{D_n}$ , nacelle drag coefficient  $\left[ \frac{D_n}{q(\pi d^2/4)} \right]$ .

$T_c$ , propulsive thrust-loading coefficient  $\left( \frac{T - \Delta D}{\rho V^2 D^2} \right)$ .

$T_{ca}$ , apparent propeller thrust-loading coefficient ( $T/\rho V^2 D^2$ ).

$T_{cf}$ , free-propeller thrust-loading coefficient ( $T_f/\rho V^2 D^2$ ).

$T_{c\Delta D}$ , slipstream-drag coefficient ( $\Delta D/\rho V^2 D^2$ ).

$\Delta T_c$ , body-interference thrust coefficient ( $\Delta T/\rho V^2 D^2$ ).

$C_T$ , propulsive thrust coefficient  $\left( \frac{T - \Delta D}{\rho n^2 D^4} \right)$ .

$C_{Ta}$ , apparent propeller thrust coefficient ( $T/\rho n^2 D^4$ ).

$C_{Tf}$ , free-propeller thrust coefficient ( $T_f/\rho n^2 D^4$ ).

$C_{T0}$ , net thrust coefficient  $\left( \frac{T - \Delta D - D_n}{\rho n^2 D^4} \right)$ .

$C_P$ , power coefficient ( $P/\rho n^3 D^5$ ).

$\eta_a$ , apparent propeller efficiency ( $TV/P$ ).

$\eta_f$ , free-propeller efficiency ( $T_f V/P$ ).

$\eta$ , propulsive efficiency  $\left[ \frac{(T - \Delta D)V}{P} \right]$ .

$\eta_0$ , net efficiency  $\left[ \frac{(T - \Delta D - D_n)V}{P} \right]$ .

$\eta_{max}$ , envelope propulsive efficiency from  $C_s$  design chart.

$V/nD$ , advance-diameter ratio of propeller.

$C_s$ , speed-power coefficient ( $\sqrt[5]{\rho V^5/Pn^2}$ ).

$P_c$ , power disk-loading coefficient ( $4P/\pi D^2 q V$ ).

$K$ , conductivity of the engine (reference 5).

$\Delta p$ , pressure drop across engine.

$\sqrt{\Delta p/\rho n^2 D^2}$ , cooling-air-flow coefficient.

$F_1, F_2, F_3$ , body-interference factors.

#### RESULTS AND DISCUSSION

A study was made of the effects of variation in the value of the ratio  $d/D$  on the characteristics of a series of nacelle-propeller combinations, and the results are presented. First presented are the propeller characteristics obtained at various values of the ratio  $d/D$  and an analysis of the values to determine the magnitude of the mutual interferences that exist between the propeller and the nacelle. The cooling characteristics at the same values of  $d/D$  and, in addition, the results of incidental tests to determine the effect of various types of control of cowling-exit area on cooling-air flow are then presented.



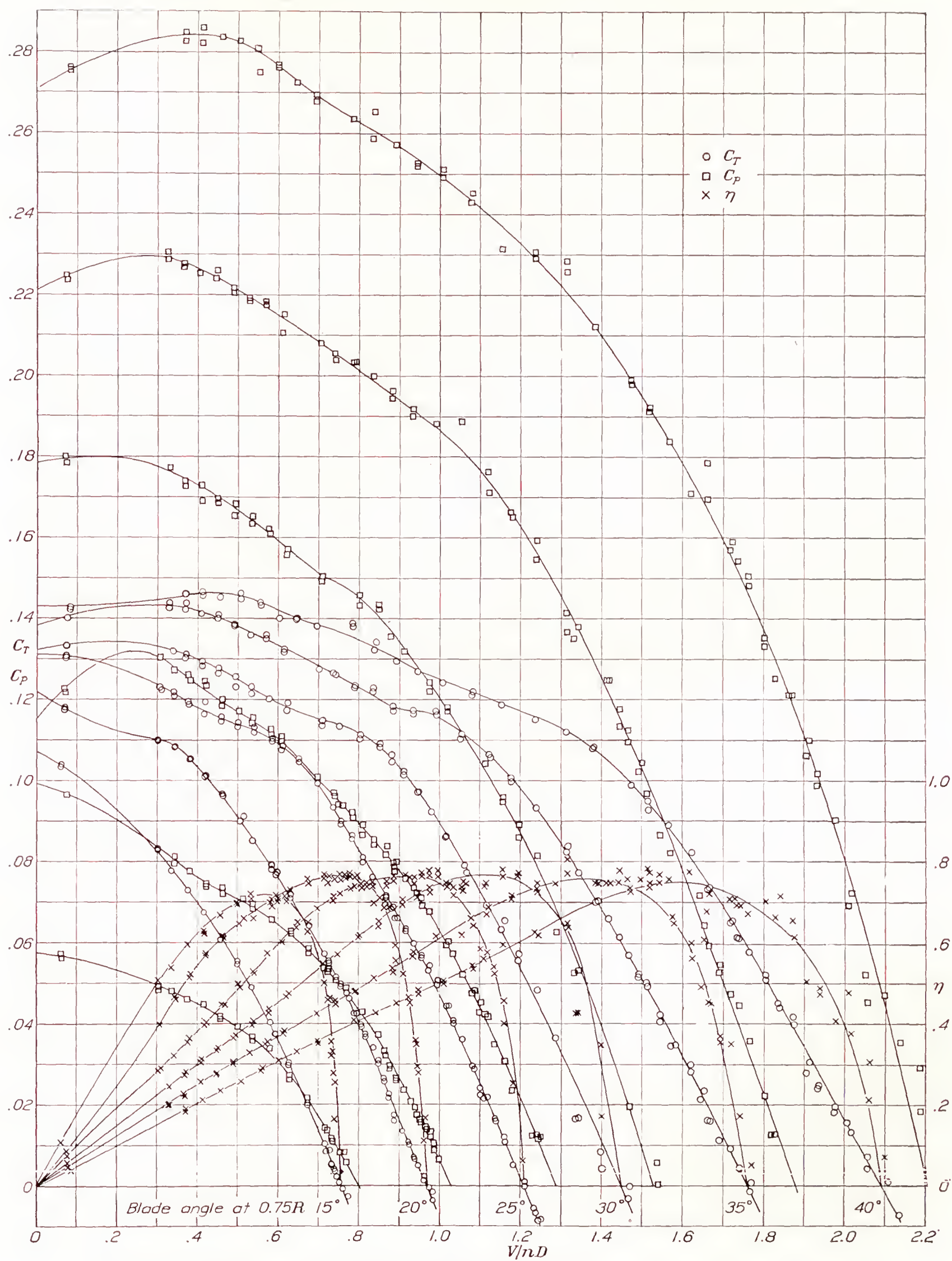


FIGURE 5.—Typical propeller-test results for six blade angles; 36-inch propeller operating in conjunction with 16-inch nacelle.



## PROPELLER CHARACTERISTICS AND INTERFERENCE EFFECTS

All propeller data were reduced to the standard non-dimensional coefficients and were plotted as functions of  $V/nD$ . Representative test results are plotted in figure 5 to show the variation of the test points.

In figure 6 a comparison is made of the results of tests with two different supports for the motor nacelle. It is to be noted that a much higher value of propulsive efficiency was obtained when strut 1 was used to support the nacelle than when the nacelle was supported by

fact that misleading results may be obtained from tests of propellers in conjunction with bodies of such form as to allow the critical flow condition encountered with strut 1 to occur. The ensuing analyses of propeller characteristics in this report are based on test results obtained when the nacelle was supported by strut 3. With this supporting arrangement, any discrepancy in the results due to the effect of strut interference is believed to be quite small.

In order to show the over-all effects of variation in

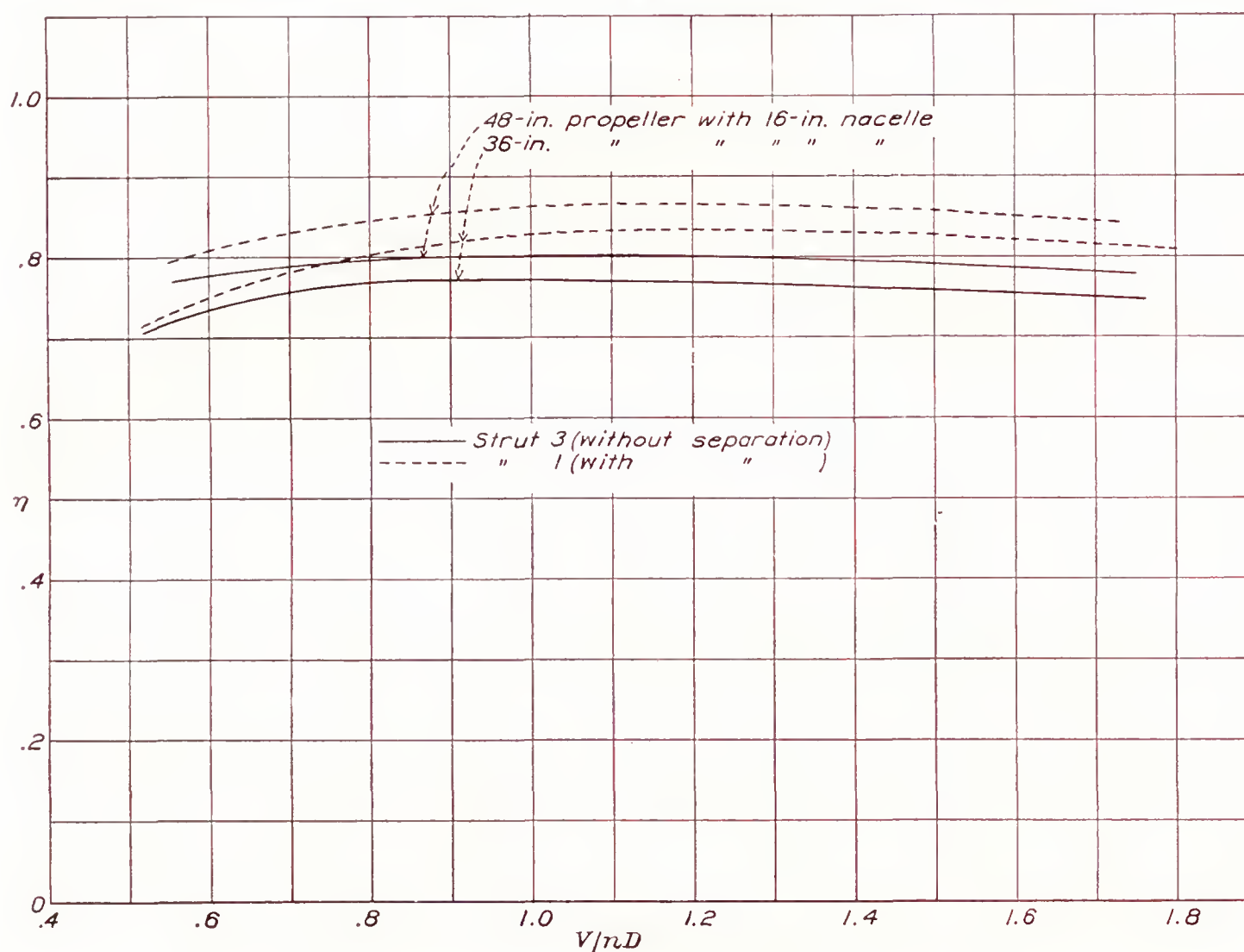


FIGURE 6.—Effect of strut interference on envelope curves of propulsive efficiency.

strut 3. The cause of this difference in propulsive efficiency was determined from a study of the air flow over the nacelle by attaching streamers to its surface and studying their actions in the air stream with and without the propeller operating. When the nacelle was supported by strut 1 with the propeller removed, the air flow separated over all that portion of the nacelle back of the strut intersection but, with the propeller operating, the effect of the slipstream was to shift the separation point downstream by several inches. The slipstream thus caused an effective reduction in nacelle drag and a high value of propulsive efficiency was therefore obtained. A similar study of the flow when the nacelle was supported by strut 3 revealed that the separation point was near the tail and was apparently uninfluenced by the propeller slipstream.

As a result of this study, it is desired to stress the

$d/D$  on the efficiencies of the nacelle-propeller combinations, the envelope curves of apparent, propulsive, and net efficiency for the various arrangements tested are given as a function of  $V/nD$  in figure 7 and as a function of  $C_s$  in figure 8. Attention is called to the fact that the results given for values of  $d/D$  of 0.10 and 0.13 in figures 7 and 8 were obtained from tests with no nacelle behind the propeller. In those cases, the value of  $d/D$  is the ratio of the diameter of the extension-shaft fairing to the propeller diameter.

The increase in both propulsive and net efficiency that can be obtained through the use of a spinner is also shown in figures 7 and 8. At the value of  $d/D$  of 0.25, at which tests were made with a spinner over the propeller hub, the gain obtained varied from about 1 percent in the take-off range to about 4 percent in the high-speed range.



Figure 9 summarizes the results given in figures 7 and 8 and illustrates quite clearly the variation at both constant  $V/nD$  and constant  $C_s$  of the various efficiencies rapid decrease in net efficiency with increasing values of  $d/D$ . The divergence of the two sets of curves from each other is explained on the premise that, although

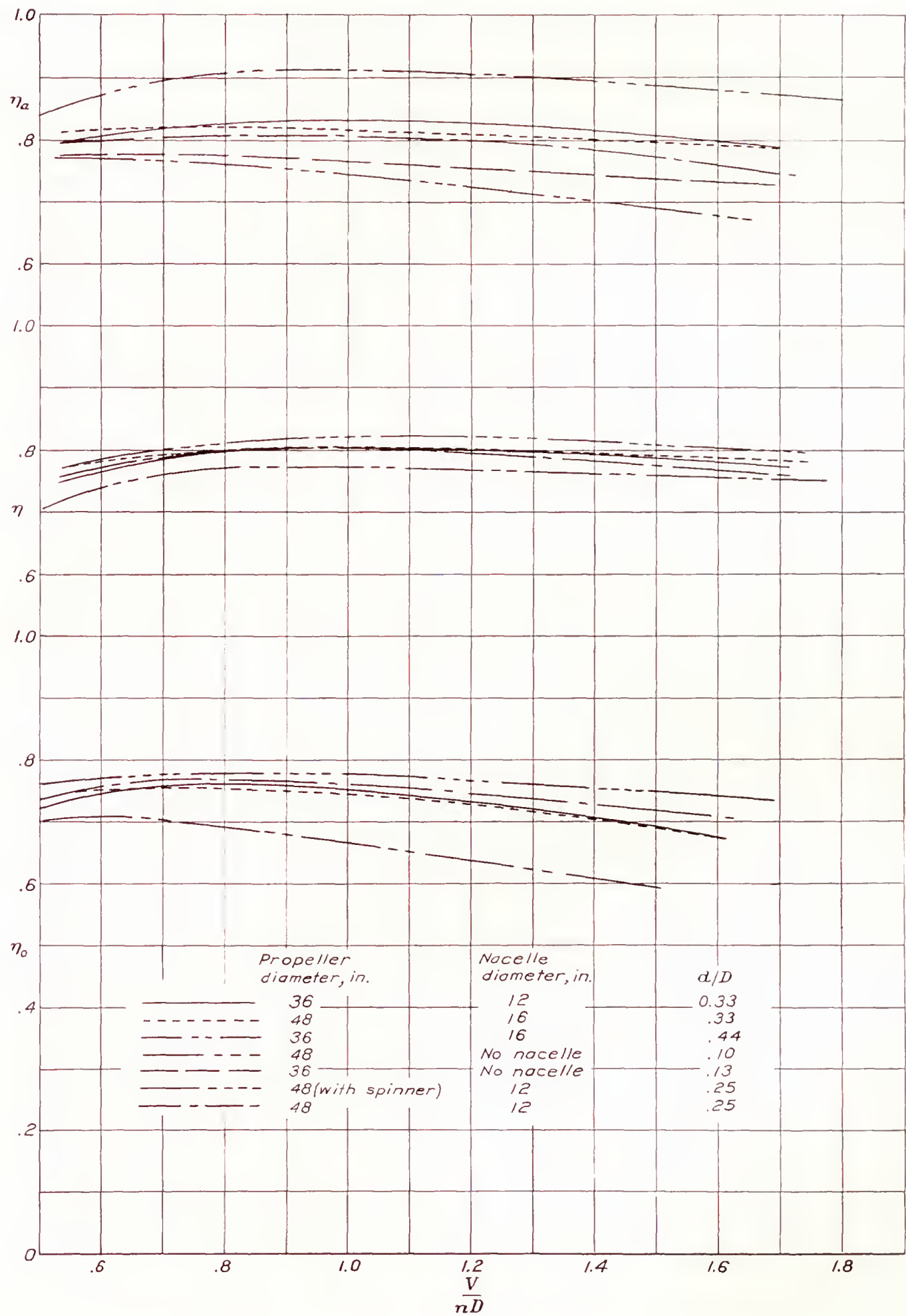


FIGURE 7.—The variation of apparent, propulsive, and net efficiency envelopes with  $V/nD$ .

with relative body size. The chosen values of  $V/nD$  and  $C_s$  roughly correspond to the take-off and cruising conditions of a representative transport airplane. There is a rapid increase in apparent efficiency and a the increase in body size causes an increase in apparent thrust owing to the greater reaction created between body and propeller, the net thrust of the combination has been reduced owing to the increase in body drag.



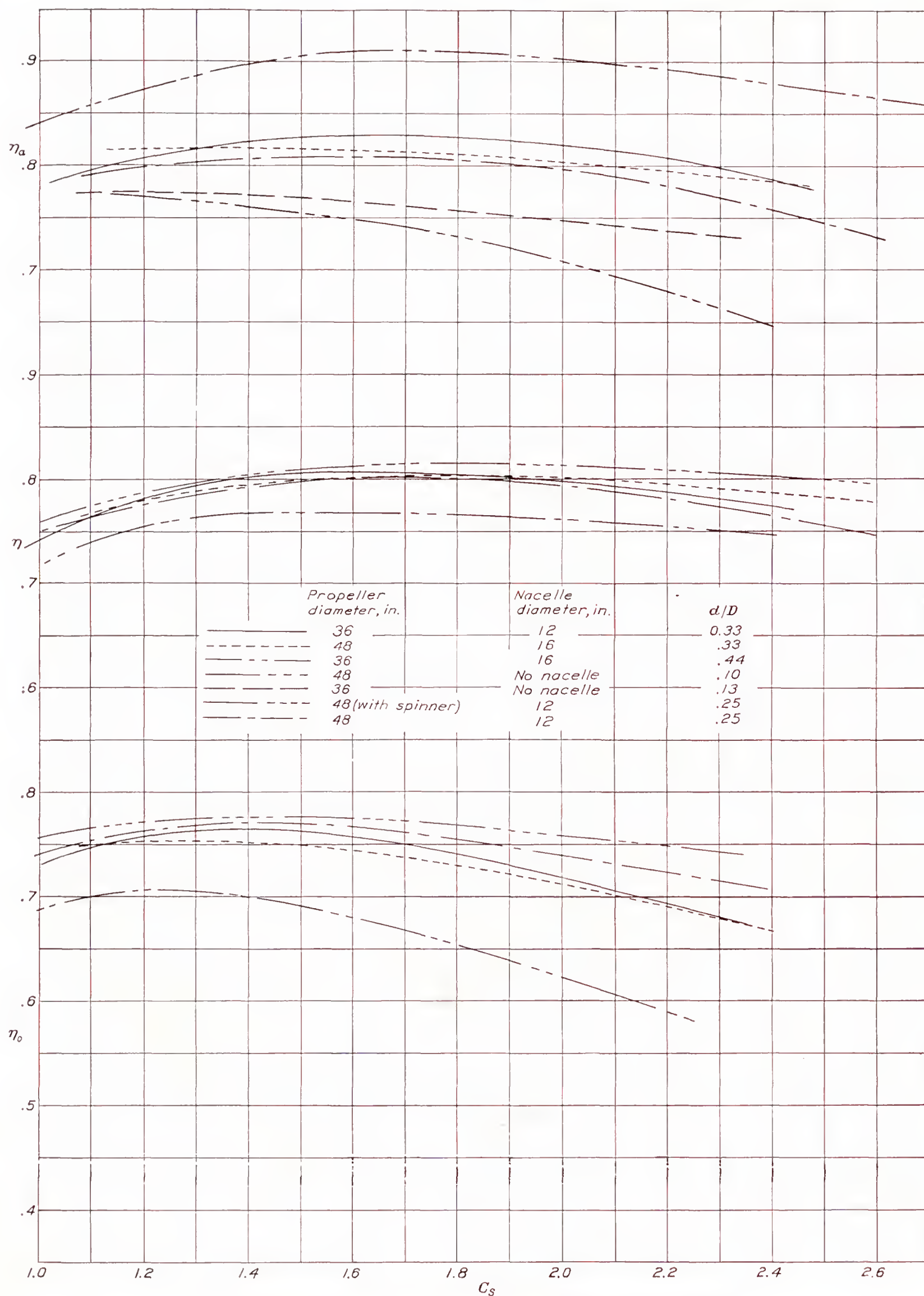
FIGURE 8.—The variation of apparent, propulsive, and net efficiency envelopes with  $C_s$ .



Figure 10 is presented to show the effect of the  $d/D$  ratio on the parameters that influence the selection of a propeller. The ideal efficiency of a propeller is directly dependent on power disk loading. The effect of change in value of  $d/D$  is, in turn, to alter the power disk loading. The use of the power disk-loading coefficient  $P_c$  as the independent variable in figure 10 is therefore very convenient in that it allows comparisons of the other important design coefficients at a constant value of power disk loading. The other coefficients shown in figure 10 were obtained from design charts of the type shown in figure 11 and from similar charts in which  $1/\sqrt{P_c}$  was the independent variable. Figure 10 is of extreme interest because it shows in concise form, for all the combinations tested with strut 3, the following important information:  $C_s$  at  $V/nD$  for  $\eta_{max}$ ;  $V/nD$  for  $\eta_{max}$ ; and the values of  $\eta_{max}$  and  $\beta$  that are usually obtained from the conventional  $C_s$  design charts. At the same time it permits their comparison at a constant value of power disk loading.

The values of  $\eta_{max}$  obtained at  $d/D=0.33$  are nearly the same as those obtained at  $d/D=0.25$ . The difference is of the order of one-half of 1 percent and may be within the experimental error of the results. At the lower ratio, however, there may be a loss in propulsive efficiency owing to the fact that a relatively small body does not tend to make inoperative the inefficient hub and root sections of the propeller and therefore a larger portion of the power is wasted than if the propeller were operating in front of a larger body.

The propulsive efficiency obtained at  $d/D=0.44$  is of the order of 4 or 5 percent lower than that obtained at either of the other ratios. Inspection of the results given in figure 10 and of the envelope curves of propulsive efficiency given in figures 7 and 8 indicates that, for practical installations, the effect of  $d/D$  on propulsive efficiency is relatively unimportant at values of  $d/D$  less than 0.33. At higher values of  $d/D$ ,  $\eta$  decreases rapidly with increasing values of  $d/D$ . This result is in agreement with the result anticipated from extrapolation of previous test results.

The differences in propulsive efficiency that have been discussed thus far are attributed to the fact that the presence of a body behind an operating propeller has two opposing effects. The presence of the body alters the air-flow pattern through the propeller and changes its power and thrust disk loadings to different values from those which obtained when no body is present. As shown in figure 12, the propeller thrust (crankshaft tension) and power absorbed by a propeller of given diameter operating at a given velocity, revolution speed, and blade angle are not the same when the propeller operates in the presence of a body as they are when the propeller operates in a free air stream. This effect is herein referred to as a "body-interference" effect. The presence of the body in the slipstream

has an additional effect owing to the fact that it is subjected to an increment of drag over and above the drag that would obtain if the propeller were not operating. This drag increment is commonly referred to as the "slipstream" drag.

The magnitudes of the body interference effects were evaluated by determining, at conditions of equal average power disk loading, the difference between the

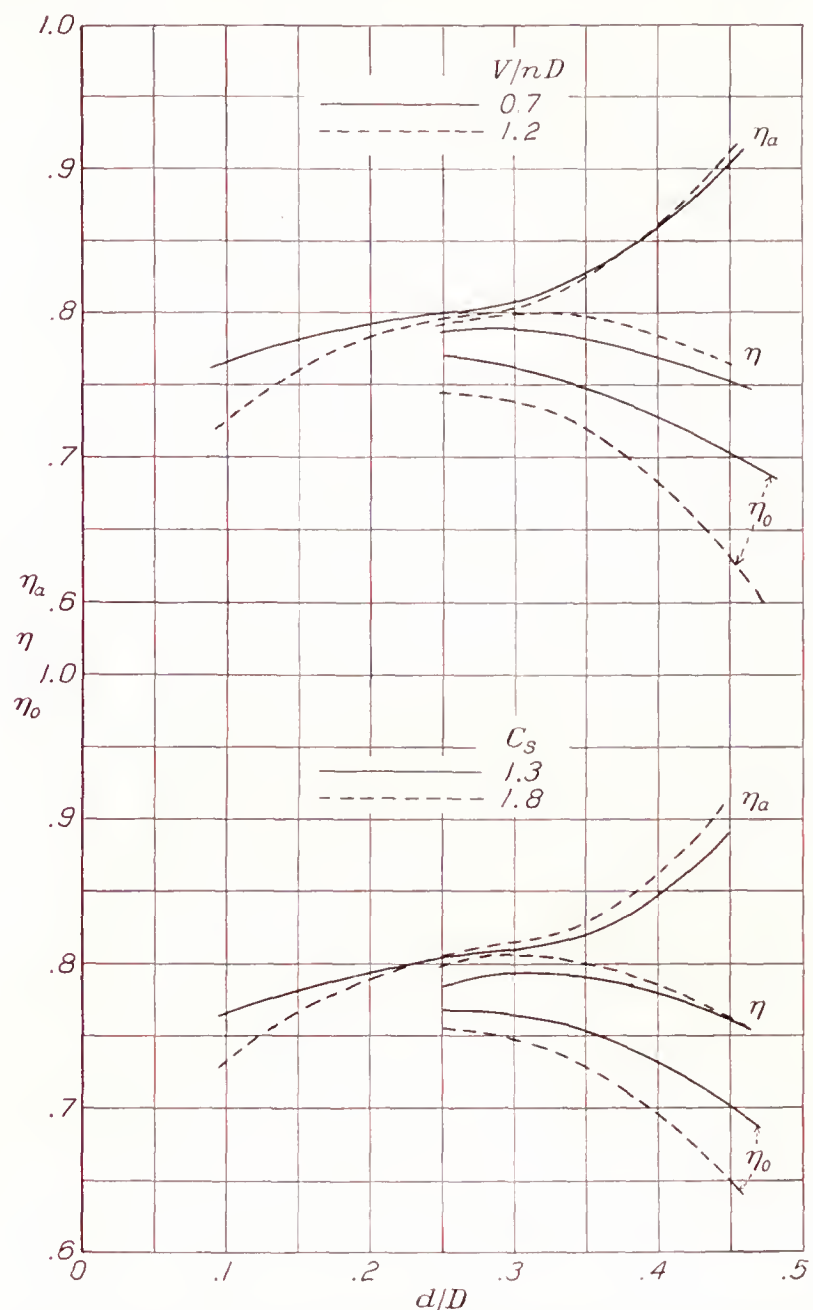


FIGURE 9.—The variation of apparent, propulsive, and net efficiency envelopes with  $d/D$ .

thrust-loading coefficient  $T_{c_f}$  of the propeller in free air and the thrust-loading coefficient of the propeller subjected to body interference  $T_{c_a}$ . In coefficient form, the interference thrust can be expressed as follows:

$$\Delta T_c = T_{c_a} - T_{c_f}$$

Figure 13 shows the variation of the body-interference thrust coefficient  $\Delta T_c$  with the free-propeller thrust-loading coefficient  $T_{c_f}$  for all values of  $d/D$  and blade-angle setting at which tests were conducted. It is to be noted that, although the results for any one value of blade-angle setting follow a straight line throughout the important operating range of the propeller, the values obtained from the various blade angles depart slightly from a mean line. Insufficient data were avail-



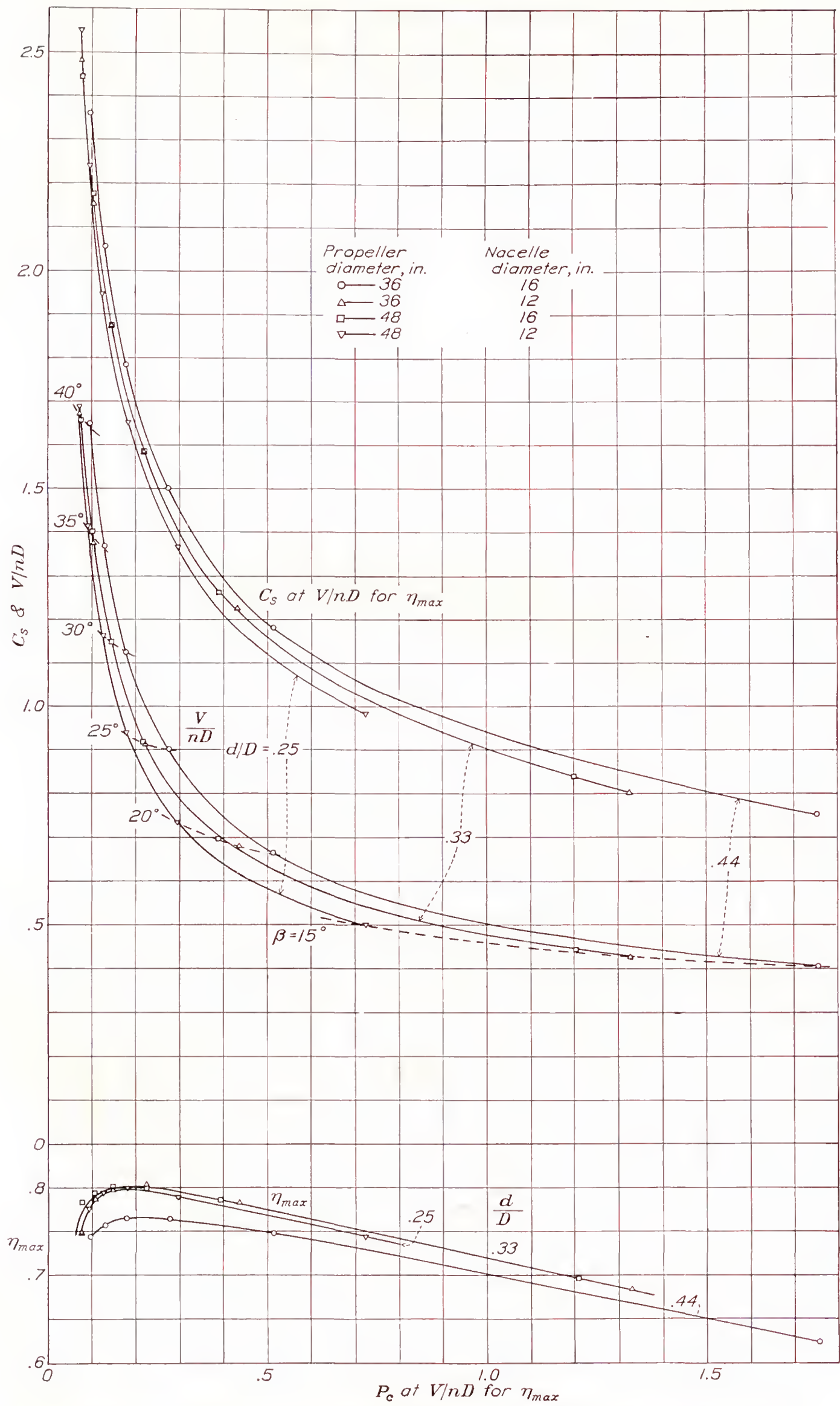


FIGURE 10.—The variation of propeller design parameters with  $P_e$  at  $V/nD$  for  $\eta_{max}$  for various values of  $d/D$ .



able to determine the secondary effects that may have caused this departure; the representation of the variation of  $\Delta T_c$  with  $T_{c_f}$  by a single straight line for all blade angles was therefore considered to be justified.

The method used to evaluate the slipstream drag was basically similar to that used to determine the body-interference effects. The slipstream drag is the differ-

tion, there can be but one value of the power coefficient at a given value of  $V/nD$ .

The variation of slipstream-drag coefficient  $T_{c_{\Delta D}}$  determined by the method previously outlined with the apparent propeller thrust-loading coefficient is shown for the various propeller-nacelle combinations in figure 14. There is considerable dispersion of the plotted points but, by the same reasoning used in the

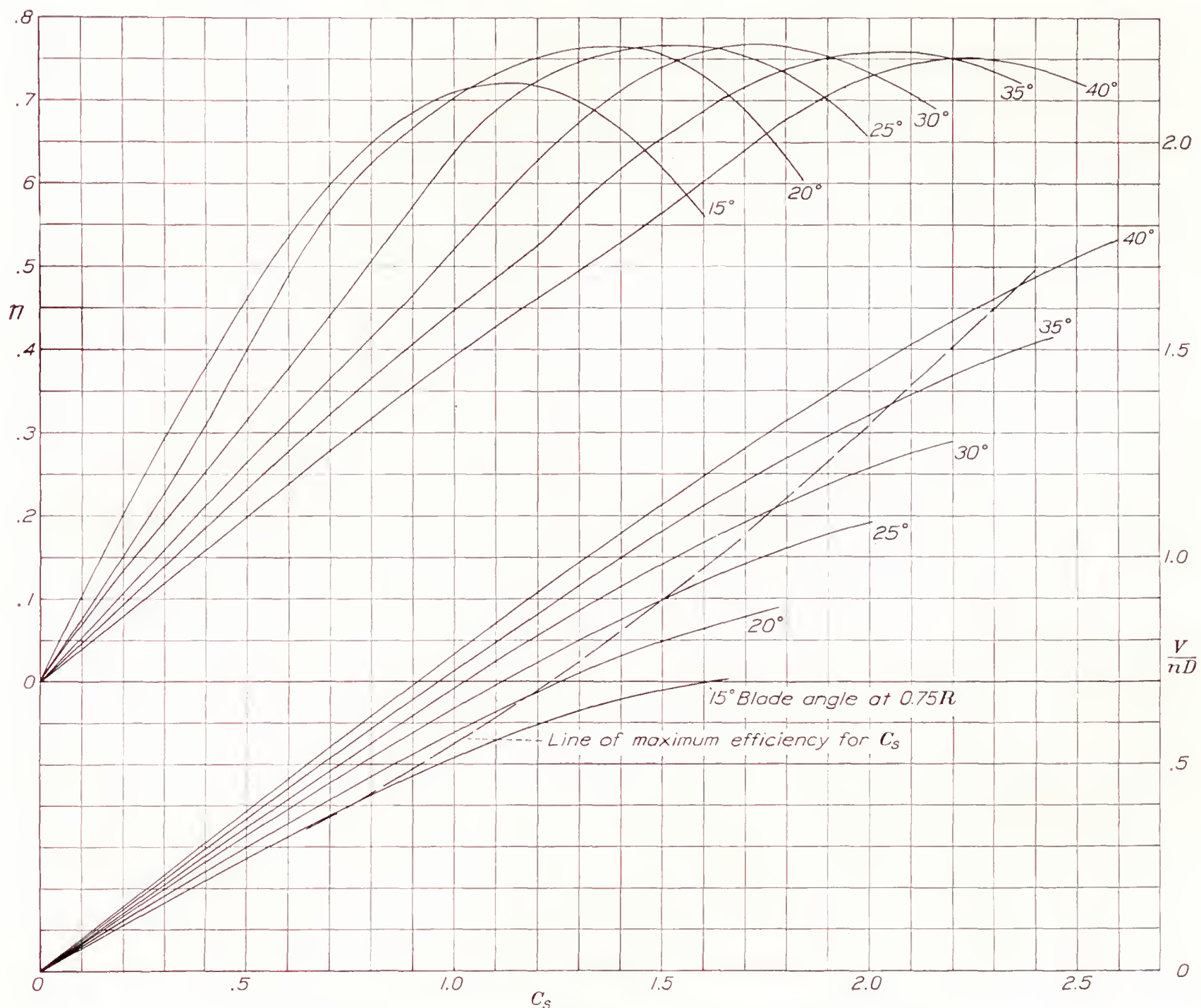


FIGURE 11.—Representative design chart; 36-inch propeller and 16-inch nacelle.

ence between the propeller thrust  $T$  and the propulsive thrust ( $T - \Delta D$ ) and, in coefficient form, can be defined as follows:

$$T_{c_{\Delta D}} = \frac{\Delta D}{\rho V^2 D^2} = \frac{T}{\rho V^2 D^2} - \frac{T - \Delta D}{\rho V^2 D^2}$$

It can be readily determined by taking the difference, at equal values of  $V/nD$ , between the apparent thrust-loading coefficient of the propeller operating in the presence of the nacelle and the propulsive thrust-loading coefficient of the propeller-nacelle combination. Such a comparison is made at equal values of the power loading because, for a given propeller-nacelle combina-

case of figure 13, the representation of the variation of  $T_{c_{\Delta D}}$  with  $T_{c_a}$  by a single straight line was considered to be justified.

Inspection of figures 13 and 14 reveals that the values of  $\Delta T_c$  and  $T_{c_{\Delta D}}$  can be expressed as follows:

$$\Delta T_c = F_1 + F_2 T_{c_f} \quad (1)$$

and

$$T_{c_{\Delta D}} = F_3 T_{c_a} \quad (2)$$

In the following analysis, it will be shown that the propulsive thrust of a propeller-nacelle combination can be expressed in terms of the free-propeller thrust and the factors  $F_1$ ,  $F_2$ , and  $F_3$ .



By definition, the propulsive thrust-loading coefficient is

$$T_c = \frac{T - \Delta D}{\rho V^2 D^2}$$

Evaluating  $T_c$  in terms of  $T_{cf}$  and the interference factors gives

$$T_c = \frac{T - \Delta D}{\rho V^2 D^2} = \frac{T_f + \Delta T - \Delta D}{\rho V^2 D^2} \quad (3)$$

Substituting values from equations (1) and (2)

$$T_c = \frac{T_f}{\rho V^2 D^2} + \left( F_1 + F_2 \frac{T_f}{\rho V^2 D^2} \right) - F_3 \frac{T}{\rho V^2 D^2} \quad (4)$$

Since

$$T = T_f + \Delta T$$

then

$$T_c = \frac{T_f}{\rho V^2 D^2} + \left( F_1 + F_2 \frac{T_f}{\rho V^2 D^2} \right) - F_3 \left[ \frac{T_f}{\rho V^2 D^2} + \left( F_1 + F_2 \frac{T_f}{\rho V^2 D^2} \right) \right] \quad (5)$$

Expanding and simplifying

$$T_c = \frac{T_f}{\rho V^2 D^2} (1 + F_2 - F_3 - F_2 F_3) + (F_1 - F_1 F_3) \quad (6)$$

Let

$$A = (1 + F_2 - F_3 - F_2 F_3) \quad (7)$$

$$B = (F_1 - F_1 F_3) \quad (8)$$

Then

$$T_c = AT_{cf} + B \quad (9)$$

Values of  $F_1$ ,  $F_2$ , and  $F_3$  obtained from figures 13 and 14 together with computed values of  $A$  and  $B$  are given as a function of  $d/D$  in figure 15. The values probably possess no great degree of accuracy and may be considerably different for geometrically different bodies and propellers. They are of value, however, in that they show the relative importance of the various interference factors and may therefore be useful in analyzing other test data. If other data are not available, the factors shown in figure 15 may be used to estimate the thrust characteristics at a given value of the ratio  $d/D$  when the characteristics at some other value of  $d/D$  are known.

For example, let the subscript  $x$  indicate coefficients and factors that apply to the  $d/D$  ratio for which no test data are available and let the subscript  $k$  indicate corresponding coefficients and factors that apply to the ratio for which test data are available. It can then be said that

$$T_{cx} = A_x T_{cf} + B_x \quad (10)$$

and

$$T_{ck} = A_k T_{cf} + B_k \quad (11)$$

Equating both equations to  $T_{cf}$  and solving for  $T_{cx}$ ,

$$T_{cx} = \frac{A_x}{A_k} [T_{ck} - B_k] + B_x \quad (12)$$

If  $T_{cf}$  is known,  $T_{cx}$  may be estimated by the relation given in equation (10).

It should be borne in mind that the relations developed in this analysis hold only when the various thrust coefficients involved are all taken at equal values of  $P_c$ .

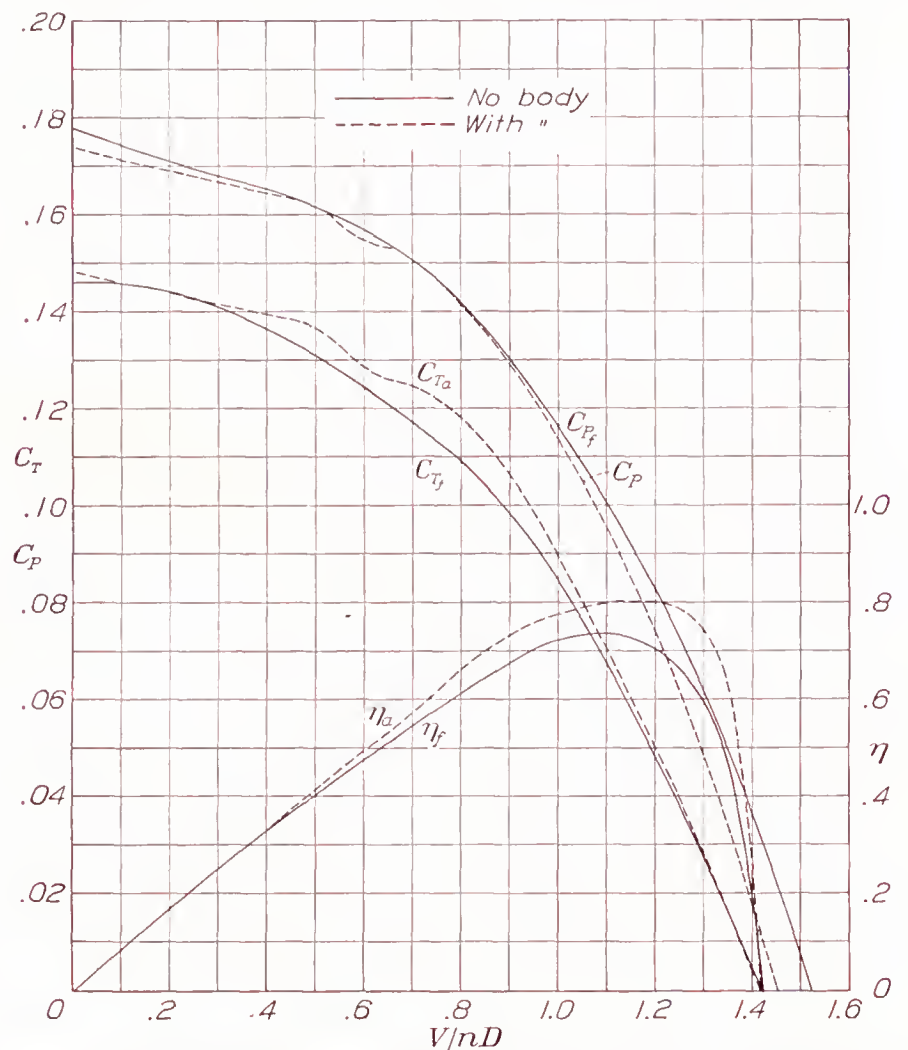


FIGURE 12.—Comparison of characteristics of 48-inch propeller in free air with characteristics of the same propeller operating in presence of 16-inch nacelle. Blade angle, 30°.

#### COOLING CHARACTERISTICS

For the presentation of the cooling characteristics, the nondimensional cooling-air flow coefficient  $\sqrt{\Delta p / \rho n^2 D^2}$  has been introduced. The values obtained from all pressure-drop measurements with the propeller operating were converted to this coefficient and plotted as a function of  $V/nD$ . Such a method of presenting the results is of advantage because it allows the results of measurements of pressure drop both with the propeller removed and with the propeller operating to be presented on the same chart. The measurements with the propeller removed can be presented as a function of  $V/nD$  in terms of  $\sqrt{\Delta p / \rho n^2 D^2}$  because on such a chart the slope of any straight line through the origin is

$$\frac{\sqrt{\Delta p / \rho n^2 D^2}}{V/nD} = \frac{1}{\sqrt{2}} \sqrt{\frac{\Delta p}{q}} \quad (13)$$



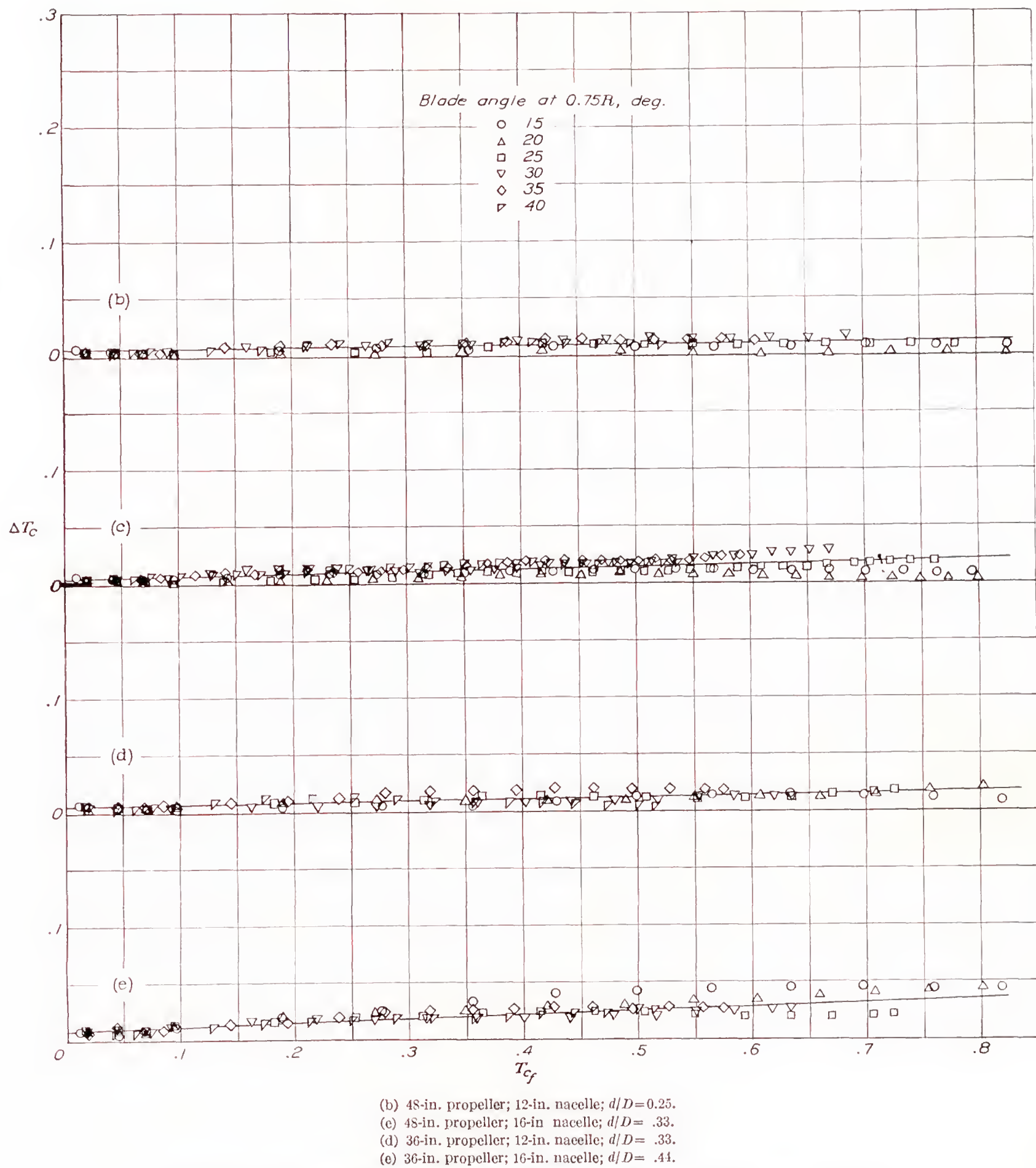


FIGURE 13.—The variation of interference-thrust coefficients with free-propeller thrust-loading coefficients.



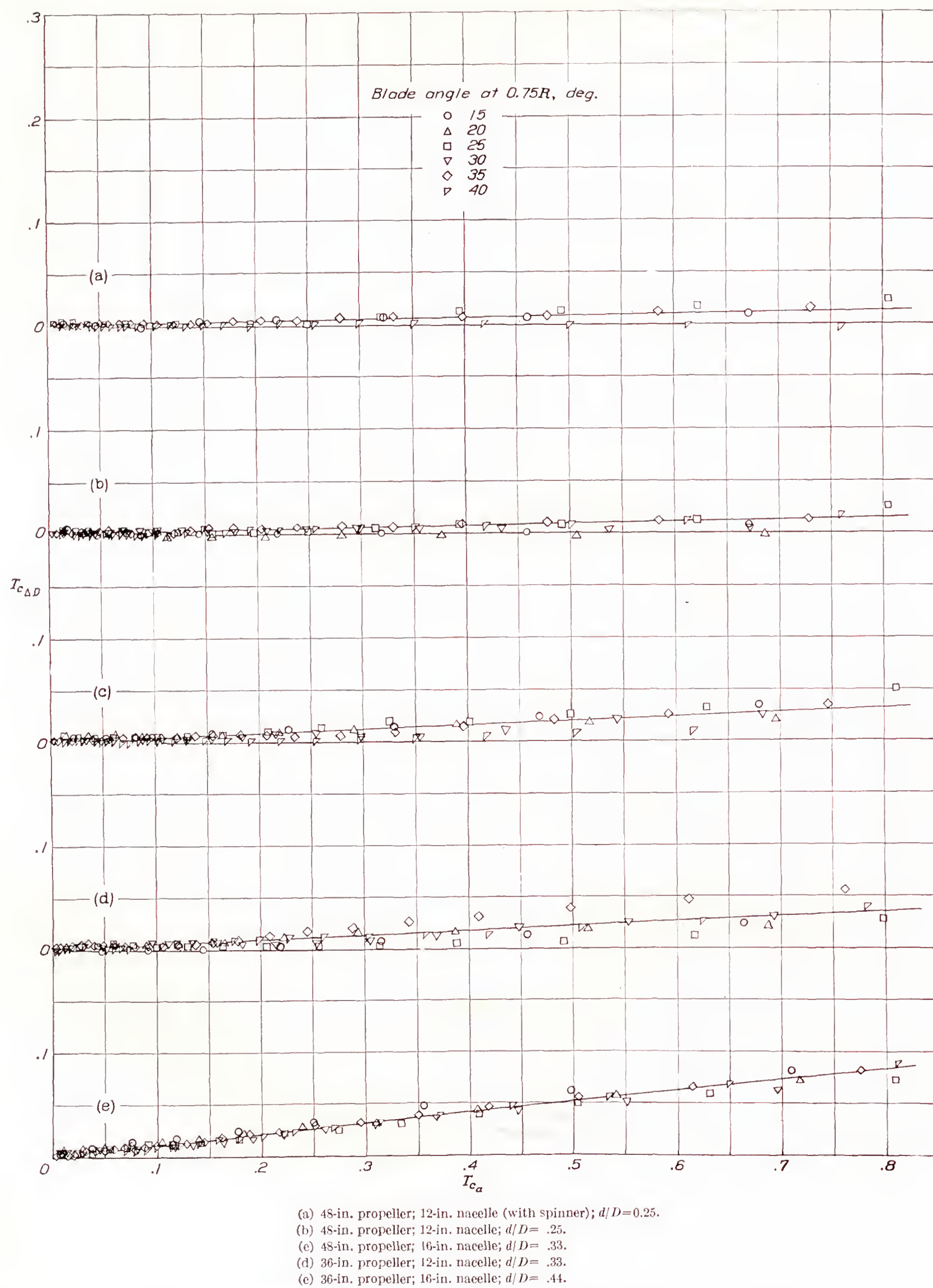


FIGURE 14.—The variation of slipstream-drag coefficients with apparent propeller thrust-loading coefficients.



Except for a slight variation with Reynolds Number, the value of  $\Delta p/q$  obtained with the propeller removed is essentially constant. By the substitution in equation (13) of the value of  $\Delta p/q$  obtained from tests with the propeller removed, an expression giving the pressure drop under that condition is obtained and a straight line satisfying this expression can be drawn on the plot of  $\sqrt{\Delta p/\rho V^2 D^2}$  against  $V/nD$ . Such a line represents, for the case under consideration, the pressure available without the effect of the propeller. From the results presented on such a chart, the pressure drop available can be determined, when  $\rho$ ,  $V$ ,  $n$ , and  $D$  are known, from equation (13) and the quantity

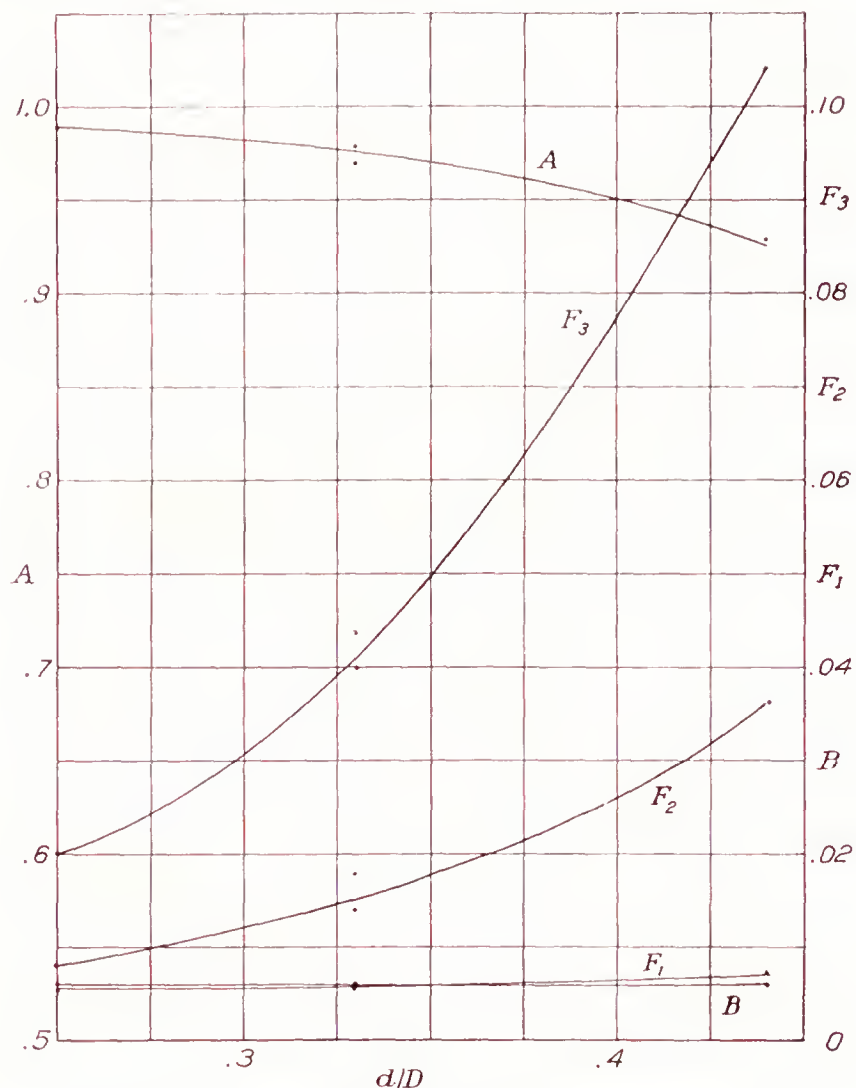


FIGURE 15.—The variation of body interference factors with  $d/D$ .

of air flow can be determined from the relation shown in equation (2) of reference 5.

The effect of variation in  $d/D$  on the cooling-air-flow coefficient is given in figure 16. The trend of the results is in agreement with that indicated by previous investigations. At high values of  $V/nD$ , i. e., high velocities, the effect of the propeller was practically the same for all blade-angle settings and, for all cases, the propeller decreased the pressure drop below the corresponding values obtained with the propeller removed. At low values of  $V/nD$ , the effect of the propeller was largely dependent on blade-angle setting and tended to increase the pressure drop, except in the extreme case shown in figure 16 (c), where the nacelle diameter was only 25 percent of the propeller diameter. In this case, the propeller showed a slightly favorable effect at high blade-angle settings but, at blade-angle settings below

25°, the propeller actually caused a reversal of flow at low values of  $V/nD$ .

It was believed that the poor cooling characteristics obtained from tests of the propeller-nacelle combination giving a value of  $d/D$  of 0.25 might be due to the fact that, at this value of the ratio, the hub was so large relative to the entrance at the front of the cowling that it was creating an adverse pressure gradient and thus causing the air to flow away from the entrance. An additional series of tests was therefore conducted on the same arrangement but with the propeller hub covered by the spinner shown in figure 1. Comparison of the results obtained with the spinner with those obtained without the spinner (fig. 16) reveals that, with the propeller operating, the spinner caused no appreciable change in the pressure-drop coefficients. This result was contrary to expectation and may be partly explained by the comparison of the pressure-drop coefficients obtained with the propeller removed and with and without the spinner in place. Further reference to figure 16 shows that the pressure drop obtained with the spinner in place was about 20 percent less than that obtained when the spinner was removed. It therefore appears that the spinner had two effects, one of which compensated for the other. It restricted the cowling entrance and caused large total-pressure entrance losses, but it improved the air flow over the hub enough to compensate for the adverse effects of restricting the entrance.

The results of tests, with the propeller operating, to determine the effect on cooling characteristics of varying the exit area by cowling flaps are presented in figure 17. For all values of  $V/nD$ , the cooling coefficient increases linearly with the cowling-exit area until the exit area becomes about 10 percent of the nacelle cross-sectional area. At larger values of the exit opening, the slope of the cooling-coefficient curves decreases rapidly until, at an exit area of about 20 percent of the cross-sectional area of the nacelle, it appears that there is but little to be gained through further increase in exit area.

The relative merits of adjustable cowling flaps and an adjustable-length cowling skirt as a means of controlling the pressure drop across the engine are compared, on the basis of test results obtained with the propeller removed, in figures 18 and 19. From figure 18, which compares the effectiveness of the two methods, it is seen that both are of about equal merit for exit areas up to about 10 percent of the engine cross-sectional area. For larger exit areas, the greater effectiveness of adjustable cowling flaps becomes increasingly important; when the exit area is 25 percent of the cross-sectional area, the cowling flaps give a value of  $\Delta p/q$  of 1.22 as compared with the value of 0.83 obtained with the adjustable-length skirt. It is of further interest to note from figure 18 that the maximum pressure attainable with cowling flaps is apparently much higher than can be obtained with an adjustable-length skirt.



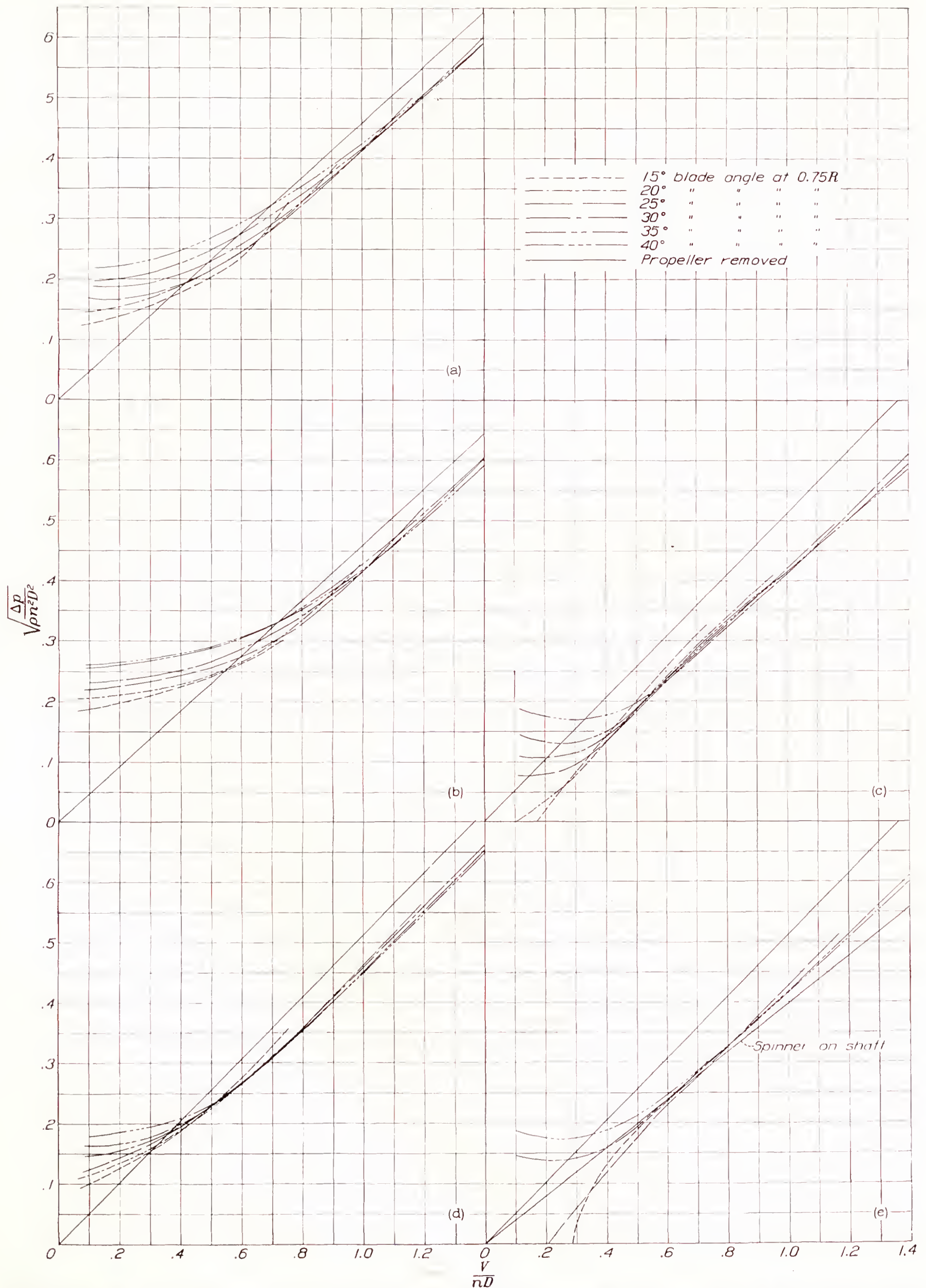


FIGURE 16—The variation of  $\sqrt{\Delta p / \rho n^2 D^2}$  with  $V/nD$  for the various nacelle-propeller combinations tested. Cowling-flap angle,  $0^\circ$ ; the 16-in. nacelle;  $K$ , 0.085; the 12-in. nacelle;  $K$ , 0.072. (See page 743 for sublegends.)



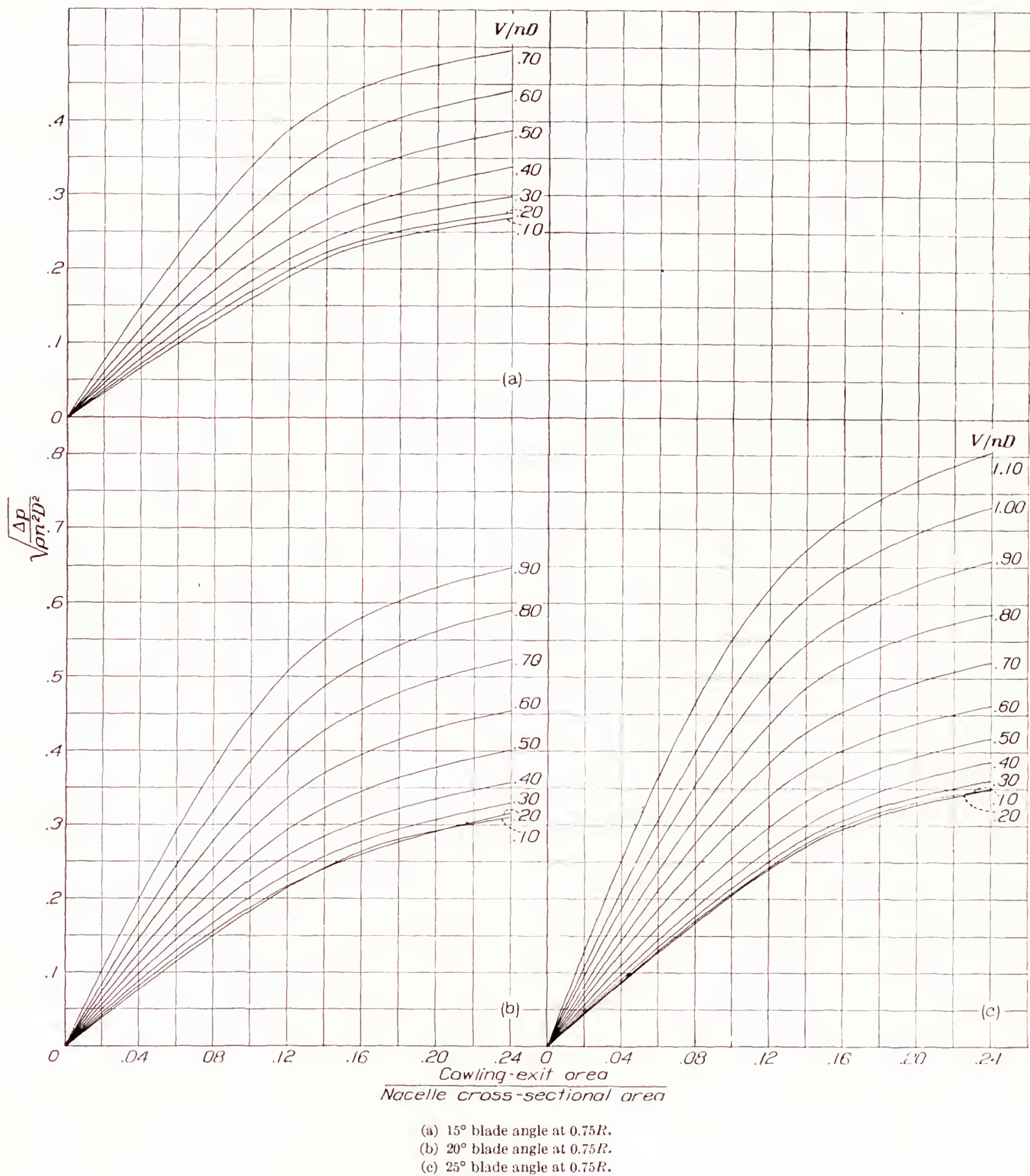


FIGURE 17.—The variation of  $\sqrt{\Delta p / \rho n^2 D^2}$  with ratio of cowling exit area to nacelle cross-sectional area. Exit area varied by cowling flaps. The 48-in. diameter propeller; the 16-in. diameter nacelle;  $K$ , 0.085.

FIGURE 16. Sublegends.

(a) 48-in. propeller; 16-in. nacelle;  $d/D = 0.33$ .  
 (b) 36-in. propeller; 16-in. nacelle;  $d/D = .44$ .

(c) 48-in. propeller; 12-in. nacelle;  $d/D = 0.25$ .  
 (d) 36-in. propeller; 12-in. nacelle;  $d/D = .33$ .

(e) 48-in. propeller (with spinner); 12 in. nacelle;  $d/D = 0.25$ .



From the results shown in figure 18, it may appear that cowling flaps are greatly superior to the adjustable-length cowling skirt. Comparisons in figure 19 of the variation of drag with pressure drop obtained with the two systems indicate, however, that cowling flaps are slightly inferior from considerations of drag. It is to be noted that, up to a value of  $\Delta p/q$  of 0.65, the drag coefficient obtained with the variable-length skirt is

ference to show the variation of propulsive thrust with variations in that ratio.

With the arrangements tested, the effect of variation in the ratio of nacelle diameter to propeller diameter on propulsive efficiency was unimportant until the nacelle became approximately one-third of the propeller diameter but, beyond that point, the propulsive efficiency decreased rapidly with further increase in relative

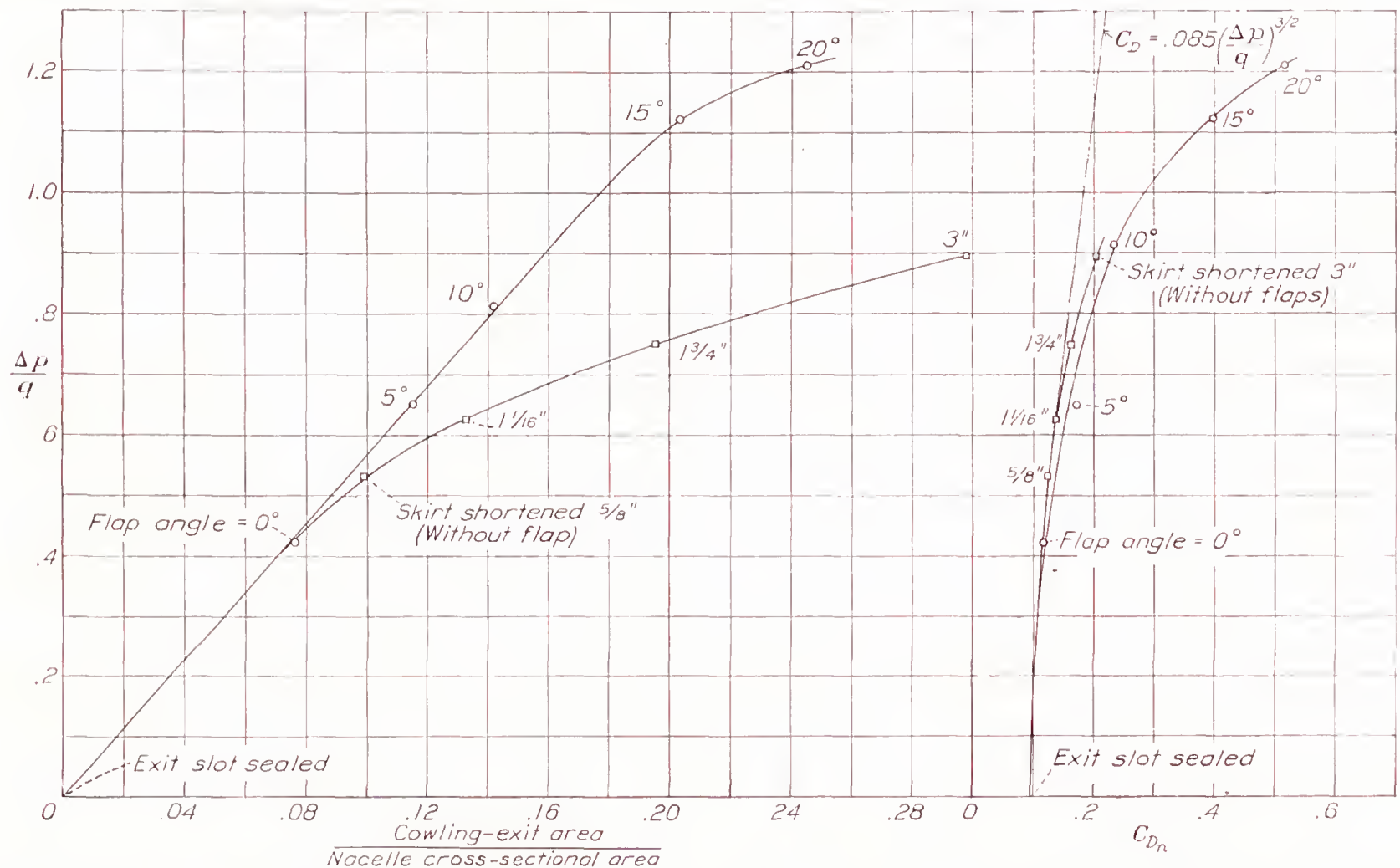


FIGURE 18.—The variation of  $\Delta p/q$  with ratio of cowling-exit area to nacelle cross-sectional area. Comparison of effect of varying exit area by cowling flaps with effect of varying exit area by reduction in cowling-skirt length. The 16-inch nacelle;  $K$ , 0.085.

FIGURE 19.—The variation of  $\Delta p/q$  with  $C_{D_n}$ . Comparison of effect of varying exit area by cowling flaps with effect of varying exit area by reduction in cowling-skirt length. The 16-inch nacelle;  $K$ , 0.085.

the same as the theoretical cooling drag for 100 percent pump efficiency (reference 7); whereas the values of drag coefficient obtained with the cowling flaps begin to depart from the theoretical curve at a value of  $\Delta p/q$  of 0.35.

In general, the difference in drag created by the two methods is negligible in the range of values of  $\Delta p/q$  that prevail under high-speed flight conditions and is relatively small in the take-off and climbing range.

#### CONCLUDING REMARKS

These results indicate the manner in which the efficiency of a nacelle-propeller combination is dependent on the ratio of the nacelle diameter to the propeller diameter. An empirical relation has been developed from measurements of slipstream drag and body inter-

body size. The highest value of net efficiency was obtained at the lowest value of the ratio of nacelle diameter to propeller diameter at which tests were made and the value decreased with increasing value of that ratio.

Tests of one nacelle-propeller combination having a ratio of nacelle diameter to propeller diameter of 0.25 showed that the presence of a spinner over the propeller hub increased the propulsive efficiency by an amount varying from 1½ to 4 percent.

Drag and cooling-air-flow measurements showed that, for a given volume of cooling-air flow, the drag of a conventional N. A. C. A. radial air-cooled engine cowling is slightly lower when fitted with an adjustable-length cowling skirt than when fitted with adjustable cowling flaps but showed that the maximum pressure



drop available with adjustable cowling flaps is about 20 percent greater than the maximum pressure available with an adjustable-length skirt.

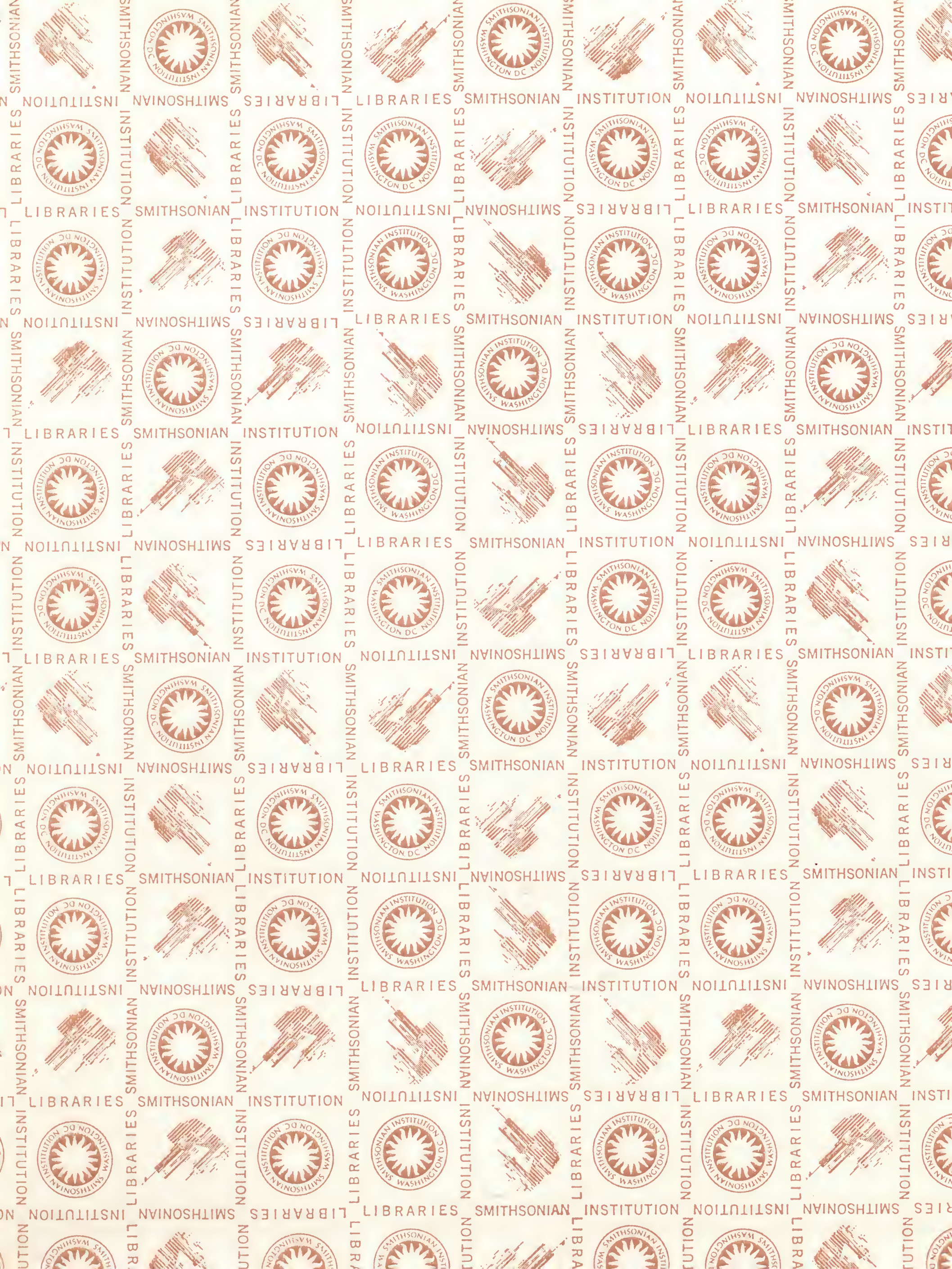
LANGLEY MEMORIAL AERONAUTICAL LABORATORY,  
NATIONAL ADVISORY COMMITTEE FOR AERONAUTICS,  
LANGLEY FIELD, VA., *April 17, 1939.*

#### REFERENCES

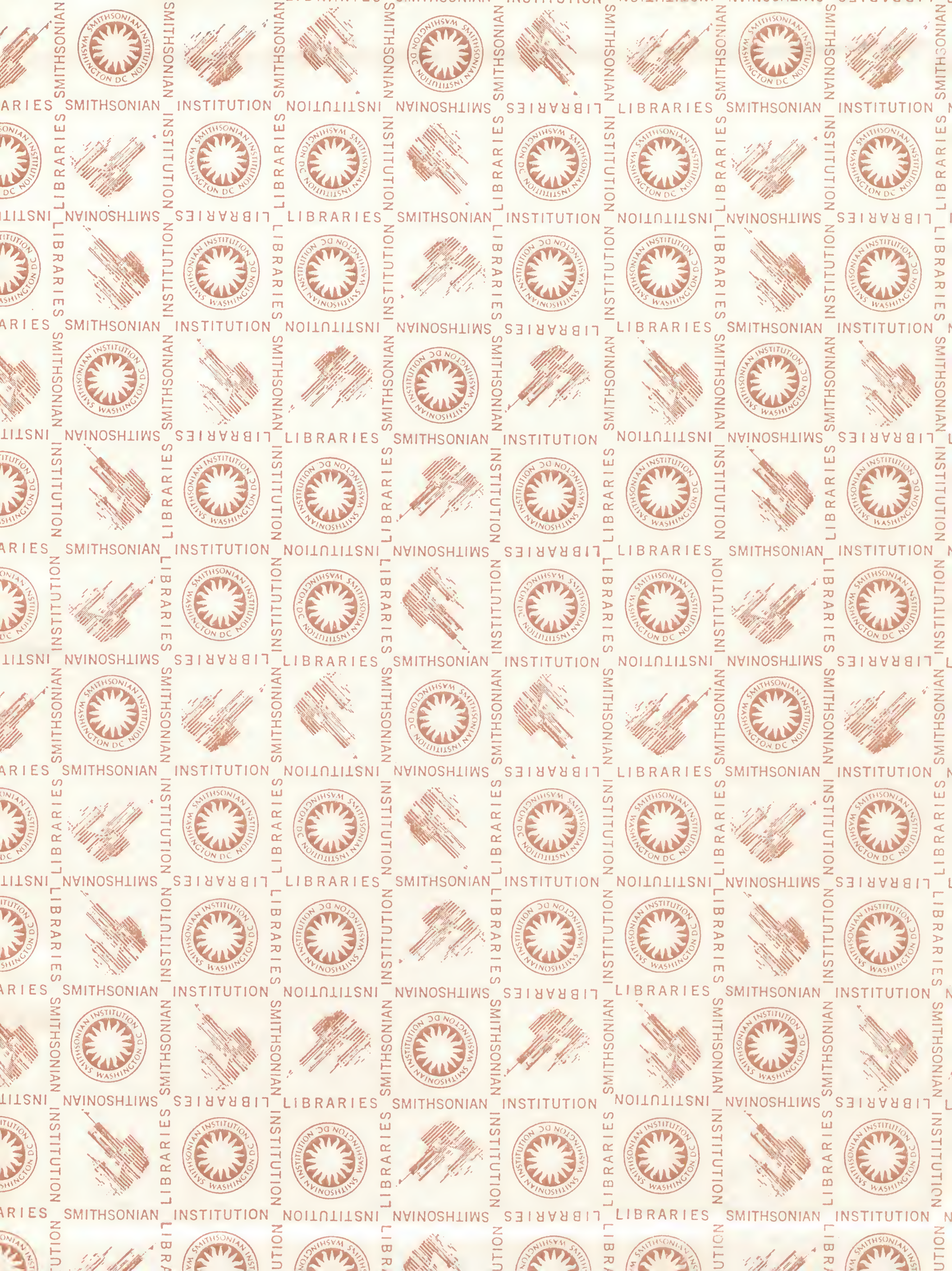
1. Weick, Fred E.: The Effect of Reduction Gearing on Propeller-Body Interference as Shown by Full Scale Wind Tunnel Tests. T. R. No. 338, N. A. C. A., 1930.
2. Weick, Fred E.: Full-Scale Wind Tunnel Tests with a Series of Propellers of Different Diameters on a Single Fuselage. T. R. No. 339, N. A. C. A., 1930.
3. McHugh, James G.: Tests of Several Model Nacelle-Propeller Arrangements in Front of a Wing. T. R. (to be published), N. A. C. A., 1940.
4. Weick, Fred E., and Wood, Donald H.: The Twenty-Foot Propeller Research Tunnel of the National Advisory Committee for Aeronautics. T. R. No. 300, N. A. C. A., 1928.
5. Theodorsen, Theodore, Brevoort, M. J., and Stickle, George W.: Full-Scale Tests of N. A. C. A. Cowlings. T. R. No. 592, N. A. C. A., 1937.
6. Wood, Donald H.: Tests of Large Airfoils in the Propeller Research Tunnel, Including Two with Corrugated Surfaces. T. R. No. 336, N. A. C. A., 1929.
7. Wood, Donald H.: Design of Cowlings for Air-Cooled Aircraft Engines. S. A. E. Jour., vol. 41, no. 6, Dec. 1937. pp. 581-595.













SMITHSONIAN LIBRARIES



3 9088 01800 8623